The Role of Triplet States in Light-Induced Reactions: Spectroscopic Insights into Energy and Light Conversion Pathways

Dissertation zur Erlangung des Grades eines

Doktor rerum naturalium (Dr. rer. nat.)

am Fachbereich Chemie, Pharmazie, Geografie und Geowissenschaften

der Johannes Gutenberg-Universität Mainz

im Promotionsfach Chemie

vorgelegt von

Till Jakob Balthasar Zähringer

geb. in Freiburg im Breisgau.

Mainz, Juni 2025

JOHANNES GUTENBERG UNIVERSITÄT MAINZ

JG|U

Diese elektronische Version der Dissertation ist unter der Lizenz
Namensnennung – Keine Bearbeitungen (CC BY-ND 4.0) veröffentlicht.

Dekanin: Prof. Dr. Eva Rentschler

Erstgutachter: [redacted]

Zweitgutachter: [redacted]

Eigenständigkeitserklärung

Hiermit erkläre ich, Till Jakob Balthasar Zähringer,

dass ich die vorliegende Arbeit mit dem Titel:

„The Role of Triplet States in Light-Induced Reactions: Spectroscopic Insights into Energy and Light Conversion Pathways“

selbstständig verfasst und keine anderen als die angegebenen Quellen und Hilfsmittel (dazu zählen auch KI-basierte Anwendungen oder Werkzeuge*) benutzt habe. Sämtliche wörtlichen oder sinngemäßen Übernahmen und Zitate sind kenntlich gemacht und nachgewiesen (dies gilt auch für Texte, die durch generative KI, wie Chat GPT erzeugt wurden). Ich versichere, dass ich keine Hilfsmittel verwendet habe, deren Nutzung die Prüferin oder der Prüfer explizit ausgeschlossen hat. Im Anhang „Nutzung KI-Tools“ habe ich die verwendeten KI-Tools dokumentiert. Mit Abgabe der vorliegenden Leistung übernehme ich die Verantwortung für das eingereichte Gesamtprodukt. Ich verantworte damit auch jegliche KI-generierten Inhalte, die ich in meine Arbeit übernommen habe. Die Richtigkeit übernommener (KI-generierter) Aussagen und Inhalte habe ich nach bestem Wissen und Gewissen geprüft. Mir ist bekannt, dass ein Verstoß gegen die genannten Punkte prüfungsrechtliche Konsequenzen hat und insbesondere dazu führen kann, dass die Promotionsleistung als mit „nicht bestanden“ bewertet wird. Die Einschreibung kann für bis zu zwei Jahre widerrufen werden, wenn Studierende zweimal oder häufiger bei Prüfungsleistungen täuschen (§ 69 Abs. 4 und 5 HochSchG).

_____

Ort, Datum und Unterschrift

Danksagung

Zuallererst möchte ich meinem Doktorvater, Prof. [redacted], danken. Seine hervorragende Betreuung, wertschätzende Führung und stete Ermutigung haben mich in meiner wissenschaftlichen Arbeit, aber auch ganz persönlich unterstützt und geprägt. Darüber hinaus hat er meinen Werdegang als Wissenschaftler mit Weitsicht begleitet und gefördert und mir dadurch eine Grundlage für meine Zukunft in der Wissenschaft geschaffen. Dafür bin ich ihm besonders dankbar.

Ein besonderer Dank gilt auch meinem Zweitgutachter, Prof. [redacted], für die Annahme des Gutachtens.

Ein ebenso großer Dank gilt meinen Kolleginnen und Kollegen [redacted] und [redacted] Durch ihre Offenheit, Hilfsbereitschaft und den stets respektvollen Umgang miteinander haben sie eine Arbeitsatmosphäre geschaffen, in der produktives und kreatives Arbeiten möglich war. Der Austausch mit ihnen – sowohl über wissenschaftliche Fragen als auch über persönliche Herausforderungen – war für mich von unschätzbarem Wert.

Außerdem möchte ich allen Studierenden danken, die Teil des Arbeitskreises Kerzig waren oder sind – für die bereichernde gemeinsame Zeit, den kollegialen Austausch und die vielen schönen Momente. Ein besonderer Dank gilt dabei [redacted] und [redacted], deren Bachelorarbeiten ich betreuen durfte. Ihre tatkräftige Unterstützung war eine wertvolle Hilfe für meine eigene Forschung.

Meiner Familie danke ich für die emotionale Unterstützung, die vielen Gespräche und das Vertrauen, das sie mir auf meinem Weg zur Promotion entgegengebracht haben. Ganz besonders danke ich meiner Partnerin [redacted], die mit ihrer Liebe, Geduld und Zuversicht in jeder Phase dieser Arbeit an meiner Seite stand.

Nicht zuletzt danke ich meinen Freunden [redacted] und [redacted] Mit ihnen hatte ich außerhalb der Arbeit viele unvergessliche Erlebnisse, die mir geholfen haben, die Höhen und Tiefen der Promotion zu meistern.

1 Abstract

Triplet–triplet energy transfer-driven photoreactions offer distinct advantages over those induced by excited singlet states, including longer excited state lifetimes and lower excitation energies. These features make triplet–triplet energy transfer (TTET) highly attractive for applications in catalysis, light harvesting, and energy conversion. However, the mechanistic understanding of many triplet-driven photoreactions remains limited due to the non-emissive nature of most organic chromophore triplet states and the complexity of photochemical pathways. This thesis addresses these challenges by using advanced spectroscopic techniques to resolve TTET mechanisms across a broad range of systems, organized in three thematic parts: mechanistic studies, photoisomerization, and photon upconversion. The first part focuses on the direct observation of interactions between energy donors (photosensitizers) and acceptors, aiming at understanding the initial step of energy transfer. In the first project, TTET is demonstrated between chromophores embedded within DNA helices. The observed strong distance dependence and low efficiency of long-range TTET, possibly via a tunneling mechanism, in this system support the hypothesis that DNA has evolved as a photoprotective scaffold. This work offers rare spectroscopic insights into DNA-mediated energy transfer and contributes to the topic of photosensitized DNA damage. Subsequent projects shift the focus toward TTET-driven photocatalysis. A polyazahelicene was found to operate dually as a photoredox catalyst and as a triplet sensitizer for *E*→*Z* alkene isomerization. In two other synthetically valuable reactions, TTET was identified as the reaction pathway in reactions previously not achievable by energy transfer photocatalysis. This conclusion was primarily drawn by excluding competing pathways and identifying key intermediate species. In the second part, the focus is on the triplet-sensitized isomerization of olefins, an emerging strategy for stereodivergent synthesis and energy storage systems. In particular, the *E*→*Z* isomerization of alkenylboronates – valuable intermediates in organic synthesis due to their versatility and the traceless nature of the boron group – was spectroscopically investigated. Mapping triplet state energies and lifetimes provided a detailed picture of the isomerization dynamics. Mechanistic insights translated into practical reaction improvements. This concept was extended to fluorinated *β*-borylacrylates. Their selective isomerization was harnessed as a key step in a multistep synthesis route toward biologically relevant targets. Further, this chapter explores norbornadiene–quadricyclane photoswitches, promising candidates for molecular solar thermal energy storage (MOST). The inherent limitation of direct excitation, stemming from its poor absorption of visible light and low photoisomerization quantum yield, was overcome using TTET. A set of aryl-substituted norbornadienes was evaluated in combination with both metal-based and organic sensitizers. The quantum yield of norbornadiene-to-quadricyclane conversion approached unity under optimized conditions. The best system had a hitherto unreported solar-to-chemical energy storage efficiency of 5.8%. In a follow-up study, norbornadiene derivatives extended with acetylene were investigated, expanding the understanding of structure–property relationships and clarifying design criteria for future generations of energy-storing photoswitches. The final part addresses photon upconversion via

triplet–triplet annihilation (TTA–UC), a method for generating a high-energy photon from a singlet-excited state by combining two lower energy triplet states. A novel BODIPY-derived sensitizer with excellent photostability was introduced and used in a green-to-blue upconversion system. The singlet-excited state of the annihilator was exploited in photocatalytic applications for challenging substrate reductions that would otherwise not be achieved under green light irradiation. The following projects pursued the design of annihilators capable of upconversion into the UVB (280–315 nm) and UVC (<280 nm) regions, where conventional light sources are inefficient or unsustainable. A biphenyl-based annihilator was synthesized and shown to produce UVB emission (S_1 = 4.04 eV) for the first time under blue light excitation. Following this, a benzene-based annihilator was developed that further pushed emission energies (S_1 = 4.15 eV), with most photons emitted in the UVB range. This annihilator was applied in a UC–FRET scheme to activate inert aliphatic carbonyls. Such substrates typically require harsh conditions, demonstrating the practical potential of these systems. A maximum emission (S_1 = 4.33 eV) approaching the UVB/UVC boundary (~280 nm), was achieved with another benzene-derived annihilator, thus setting a new benchmark for TTA–UC systems. Key to this success was the identification of a high-triplet-energy sensitizer capable of efficient TTET to the annihilator. Limitations for visible-to-UV TTA-UC were evaluated, laying the groundwork for future improvements. Lastly, recent advances in visible-to-UV photon upconversion were reviewed and summarized, highlighting applications in photocatalysis, bond activation, and photopolymerization. This comprehensive review provides a practical framework for developing upconversion-driven photoreactions.

Overall, this thesis demonstrates how mechanistic insight – gained through state-of-the-art spectroscopic techniques – can guide the design of efficient energy donors and acceptors, improve reaction conditions, and enable practical applications. The findings advance both fundamental understanding and development in TTET-driven catalysis, solar energy storage, and photon upconversion.

Kurzzusammenfassung

Photochemische Prozesse, die über Triplett–Triplett-Energietransfer (TTET) verlaufen zeichnen sich gegenüber solchen im angeregten Singulett-Zustand durch längere Lebensdauern und geringere Energien angeregter Zustände aus. Diese Eigenschaften machen TTET besonders attraktiv für Anwendungen in der Katalyse, der Lichtnutzung und der molekularen Energieumwandlung. Dennoch ist das mechanistische Verständnis vieler Triplett-getriebener Reaktionen bislang begrenzt – nicht zuletzt, weil organische Triplett-Zustände häufig nicht emittieren und photochemische Reaktionsverläufe komplex sind. Ziel dieser Arbeit ist es, mithilfe moderner spektroskopischer Methoden TTET-Mechanismen aufzuklären, gegliedert in drei thematische Kapitel: mechanistische Studien, Triplett-sensibilisierte Isomerisierungen und Aufwärtskonversion von Photonen. Im ersten Teil wird der initiale Energietransfer zwischen Sensibilisatoren und Akzeptoren untersucht. Unter anderem konnte TTET zwischen DNA-gebundenen Chromophoren nachgewiesen werden. Dabei zeigte sich, dass der Energietransfer stark von der Entfernung abhängt und über längere Distanzen nur sehr ineffizient abläuft, vermutlich über einen Tunnelmechanismus. Das spricht dafür, dass DNA einen natürlichen Schutzmechanismus gegenüber Triplett-induzieren Schäden entwickelt hat. Gleichzeitig liefert die Arbeit wertvolle Einblicke in photochemische Prozesse innerhalb von DNA. Ein weiteres Projekt widmet sich der TTET-Photokatalyse. Hier konnte gezeigt werden, dass ein Polyazahelicen sowohl als Photoredox-Katalysator als auch als Triplett-Sensibilisator für *E*→*Z*-Isomerisierungen fungiert. Bei zwei weiteren synthetisch wertvollen Reaktionen, bei denen ein solcher Mechanismus bislang nicht erfolgreich umgesetzt wurde, konnte TTET als Reaktionsweg identifiziert werden. Dies gelang vor allem durch den Ausschluss alternativer Reaktionspfade und die Identifizierung zentraler Zwischenprodukte. Ein Schwerpunkt im zweiten Teil liegt in der Triplett-sensibilisierten Isomerisierung von Olefinen, die für die stereodivergente Synthese und Energiespeicherung zunehmend an Bedeutung gewinnt. Insbesondere die *E*→*Z*-Isomerisierung von Alkenylboronaten – wertvolle Zwischenprodukte in der organischen Synthese aufgrund ihrer Vielseitigkeit und der rückstandslos entfernbaren Borgruppe – wurde umfassend spektroskopisch charakterisiert. Die Bestimmung der Energien und Lebensdauern der Triplett-Zustände ermöglichte eine detaillierte Darstellung der Reaktionsdynamik, wodurch die Reaktionsbedingungen gezielt optimiert werden konnten. Dieses Konzept wurde auf fluorierte *β*-Borylacrylate ausgeweitet. Die selektive Isomerisierung wurde als entscheidender Schritt in einer mehrstufigen Syntheseroute zu biologisch relevanten Verbindungen genutzt. Darüber hinaus wurden Norbornadien–Quadrizyklan-Photoschalter untersucht, die als molekulare Speicher für Solarenergie dienen können (*Molecular Solar Thermal Energy Storage*, MOST). Die inhärenten Limitierungen der direkten Anregung, aufgrund geringer Absorption im sichtbaren Bereich und niedriger Quantenausbeuten, konnten durch TTET überwunden werden. Die vielversprechendste Kombination aus Sensibilisator und Norbornadien-Derivat erreichte eine bisher nicht berichtete solare Energieumwandlungseffizienz von 5,8 %. In Folgestudien wurden mit Acetylen erweiterte Norbornadiene analysiert, wodurch für zukünftige Entwicklungen wertvolle Rückschlüsse über Struktur–Eigenschafts-Beziehungen gezogen werden. Der dritte Teil befasst sich mit der Aufwärtskonversion von Photonen durch

Triplett–Triplett-Annihilierung (TTA–UC), einem Mechanismus, bei dem die Energien zweier Triplett-Zustände verwendet werden, um einen einzigen energiereichen angeregten Singulett-Zustand zu erzeugen. Zunächst wurde ein BODIPY-basierter und hervorragend photostabiler Sensibilisator entwickelt, der in dem TTA–UC System die Umwandlung von grünem zu blauem Licht und damit photokatalytische Reduktionen ermöglicht hat, die sonst nicht zugänglich wären. In weiteren Projekten wurde gezielt die Entwicklung neuer Annihilatoren verfolgt, die eine Aufwärtskonversion über UVB (280–315 nm) bis in den UVC-Bereich (<280 nm) ermöglichen. In diesen Spektralbereichen sind konventionelle Lichtquellen ineffizient oder nicht praktikabel. Ein biphenylbasierter Annihilator wurde synthetisiert und konnte erstmals in einem TTA–UC System unter Anregung mit blauem Licht UVB-Emission (S_1 = 4,04 eV) erzeugen. Anschließend wurde ein Benzol-Annihilator mit erhöhter Singulett-Energie von S_1 = 4,15 eV entwickelt, wobei der Großteil der emittierten Photonen im UVB-Bereich lag. Dieser Annihilator wurde in einem UC–FRET-System eingesetzt, um inerte aliphatische Carbonylverbindungen zu aktivieren. Diese Substrate reagieren üblicherweise nur unter harschen Reaktionsbedingungen. Damit konnte das praktische Potential dieser Systeme eindrucksvoll demonstriert werden. Mit einem anderen benzolbasierten Annihilator wurde eine maximale Emission (S_1 = 4,33 eV) nahe der Grenze zwischen UVB und UVC (~280 nm) erreicht und damit ein neuer Maßstab für TTA–UC-Systeme gesetzt. Entscheidend für diesen Erfolg war die Identifikation eines Sensibilisators mit besonders hoher Triplett-Energie, der einen effizienten TTET zum Annihilator ermöglichte. Abseits der Erfolge wurden zentrale Limitierungen identifiziert, welche die Grundlage für gezielte Weiterentwicklungen zukünftiger Systeme bilden. Abschließend wird der aktuelle Forschungsstand zur sichtbar-zu-UV-TTA–UC zusammengefasst – mit besonderem Fokus auf Anwendungen in der Photokatalyse, Bindungsaktivierung und Photopolymerisation. Diese umfassende Darstellung dient als praxisnahe Orientierungshilfe zur Entwicklung photochemischer Reaktionen, die auf der Aufwärtskonversion basieren.

Insgesamt zeigt diese Dissertation, wie mechanistische Einblicke – gewonnen durch moderne spektroskopische Methoden – die Entwicklung effizienter photochemischer Systeme ermöglichen. Die Ergebnisse tragen sowohl zum grundlegenden Verständnis als auch zur praktischen Umsetzung Triplett-getriebener Prozesse in Katalyse, Energiespeicherung und Lichtumwandlung bei.

2 Projects

This thesis is based on the following projects that have been published or accepted as scientific manuscripts in peer-reviewed journals.

[A] **"Direct Observation of Triplet–triplet Energy Transfer in DNA Between Energy Donor and Acceptor C-Nucleotides"**, S. Häcker†, T. J. B. Zähringer†, H.-A. Wagenknecht*, C. Kerzig*, *JACS Au*, **2025**, DOI: 10.1021/jacsau.5c00364.
† Equal contribution, ordered alphabetically.

[B] "**Mechanistic investigations of polyaza[7]helicene in photoredox and energy transfer catalysis**" J. Rocker†, T. J. B. Zähringer†, M. Schmitz, T. Opatz, C. Kerzig*, *Beilstein J. Org. Chem.* **2024**, *20*, 1236–1245.
† Equal contribution, ordered alphabetically.

[C] **"Arylthianthrenium Salts for Triplet Energy Transfer Catalysis"**, Y. Cai, T. K. Roy, T. J. B. Zähringer, B. Lansbergen, C. Kerzig*, T. Ritter*, *J. Am. Chem. Soc.* **2024**, *146*, 30474–30482.

[D] **"Vinylcyclopropane [3+2] Cycloaddition with Acetylenic Sulfones Based on Visible Light Photocatalysis"**, A. Luque, J. Groß, T. J. B. Zähringer, C. Kerzig, T. Opatz*, *Chem. Eur. J.* **2022**, *28*, e202104329.

[E] "**Direct Observation of Triplet States in the Isomerization of Alkenylboronates by Energy Transfer Catalysis**", T. J. B. Zähringer†, M. Wienhold†, R. Gilmour*, C. Kerzig*, *J. Am. Chem. Soc.* **2023**, *145*, 21576–21586.
† Equal contribution.

[F] "**Geometric Isomerisation of Bifunctional Alkenyl Fluoride Linchpins: Stereodivergence in Amide and Polyene Bioisostere Synthesis**", M. Wienhold, B. Kweon, C. McLaughlin, M. Schmitz, T. J. B. Zähringer, C. G. Daniliuc, C. Kerzig*, R. Gilmour*, *Angew. Chem. Int. Ed.* **2023**, *135*, e202304150.

[G] "**Triplet-Sensitized Switching of High-Energy-Density Norbornadienes for Molecular Solar Thermal Energy Storage with Visible Light**", T. J. B. Zähringer*, N. Perez Lopez, R. Schulte, M. Schmitz, H. Ihmels, C. Kerzig*, *Angew. Chem. Int. Ed.* **2025**, *64*, e202414733.

[H] "**Extension of the π-system of monoaryl-substituted norbornadienes with acetylene bridges: influence on the photochemical conversion and storage of light energy**", R. Schulte, D. Schade, T. Paululat, T. J. B. Zähringer, C. Kerzig, H. Ihmels*, *Beilstein J. Org. Chem.* **2024**, *20*, 3061–3068.

[I] "**A new green-to-blue upconversion system with efficient photoredox catalytic properties**", J. Castellanos-Soriano, T. J. B. Zähringer, J. C. Herrera-Luna, M. C. Jiménez, C. Kerzig*, R. Pérez-Ruiz*, *Phys. Chem. Chem. Phys.* **2023**, *25*, 12041–12049.

[J] *"***Purely organic Vis-to-UV upconversion with an excited annihilator singlet beyond 4 eV**", T. J. B. Zähringer, M.-S. Bertrams, C. Kerzig*, *J. Mater. Chem. C* **2022**,*10*, 4568–4573.

[K] "**Blue-to-UVB Upconversion, Solvent Sensitization and Challenging Bond Activation Enabled by a Benzene-Based Annihilator**", T. J. B. Zähringer, J. A. Moghtader, M. Bertrams, B. Roy, M. Uji, N. Yanai, C. Kerzig*, *Angew. Chem. Int. Ed.* **2023**, *62*, e202215340.

[L] "**Pushing the limit of triplet–triplet annihilation photon upconversion towards the UVC range**", T. J. B. Zähringer, C. Heusel, M. Schmitz, F. Glorius, C. Kerzig*, *Chem. Commun*, **2025**, *accepted*, DOI: 10.1039/D5CC01834J.

[M] "**Visible-to-UV Photon Upconversion: Recent Progress in New Materials and Applications**", M. Uji†, T. J. B. Zähringer†, C. Kerzig*, N. Yanai*, *Angew. Chem. Int. Ed.* **2023**, *62*, e202301506.
† Equal contribution.

The results of these projects are presented in Chapter 5-7. Each Chapter begins with the necessary theoretical background and a concise overview of the relevant literature. A short introduction and summary of the respective project precedes the corresponding published manuscript.

The following manuscripts were published by the author, which are not part of the thesis:

[N] "**Metal-Free Twofold Electrochemical C−H Amination of Activated Arenes: Application to Medicinally Relevant Precursor Synthesis**", L. J. Wesenberg, E. Diehl, T. J. B. Zähringer, C. Dörr, D. Schollmeyer, A. Shimizu, J. Yoshida, U. A. Hellmich, S. R. Waldvogel*, *Chem. Eur. J.* **2020**, *26*, 17574–17580.

[O] "**Enhanced hybrid photocatalytic dry reforming using a phosphated Ni-CeO2 nanorod heterostructure**", A. Tavasoli, A. Gouda, T. J. B. Zähringer, Y. F. Li, H. Quaid, C. J. Viasus Perez, R. Song, M. Sain, G. Ozin*, *Nat. Commun.* **2023**, *14*, 1435.

Table of Contents

1 Abstract 5

2 Projects 9

3 Introduction 13

3.1 Spin States and Their Roles in Molecular Photochemistry 15

3.2 Molecular Electronic State Transitions 16

3.3 Triplet Photosensitizers 19

3.4 Energy Transfer 23

4 Outline of Projects 29

5 Spectroscopic Insights into Triplet Energy Transfer Pathways 32

5.1 Triplet–Triplet Energy Transfer in DNA Between Energy Donor and Acceptor C-Nucleotides 33

5.2 Triplet Energy Transfer Catalysis 45

6 Triplet Energy Transfer-Catalyzed Photoisomerization Reactions 79

6.1 Mechanistic Studies of the Photoisomerization of Alkenylboronates Using Thioxanthone as Photosensitizer 81

6.2 Photoswitching of Norbornadienes for Solar Energy Storage Applications 105

7 Photon Upconversion via Triplet–Triplet Annihilation 129

7.1 A New Green-to-Blue Upconversion System with Efficient Photoredox Catalytic Properties 133

7.2 Design of Novel UVB Annihilators 145

7.3 Visible-to-UV Photon Upconversion: Recent Progress in New Materials and Applications 171

8 Conclusion and Outlook 195

9 References 199

10 Appendix 211

10.1 Use of AI tools 211

10.2 Supporting Information for Project [A] 212

10.3 Supporting Information for Project [B] 246

10.4 Supporting Information for Project [C] 262

10.5 Supporting Information for Project [D] 461

10.6 Supporting Information for Project [E] 544

10.7 Supporting Information for Project [F] 589
10.8 Supporting Information for Project [G] 736
10.9 Supporting Information for Project [H] 782
10.10 Electronic Supplementary for Project [I] 818
10.11 Electronic Supplementary for Project [J] 877
10.12 Supporting Information for Project [K] 904
10.13 Electronic Supplementary for Project [L] 933
11 Curriculum Vitae 948

3 Introduction

This Chapter provides the theoretical foundation necessary to understand the relevance and significance of triplet–triplet energy transfer, thereby laying the groundwork for the research presented in Projects **[A]** through **[M]**.

It has long been known that sunlight can alter the properties of certain materials – examples include the bleaching of dyes, the stimulation of plant growth, and even photochromism.[1] However, it was not until the 19th century that chemists began to recognize the potential of light-driven transformations, at a time when the understanding of molecular structure was still in its infancy. Early photochemical reactions often took weeks or even months to complete, as sunlight – virtually the only available light source – was used in its unfocused form. Notable historical examples include the photodimerization of styrenes, observed by Bertram and Kürsten,[2] and the photoisomerization of olefins, described by Perkin.[3] These were primarily macroscopic observations, such as changes in melting point, and lacked a mechanistic understanding at the molecular level, which had not yet been developed. The modern model based on quantized electronic energy states was still unknown. Nevertheless, as early as the beginning of the 20th century, Giacomo Ciamician recognized the immense energy potential of sunlight, envisioning it as the only truly sustainable energy source for modern society: “On the arid lands there will spring up industrial colonies without smoke and without smokestacks; forests of glass tubes will extend over the plains and glass buildings will rise everywhere; inside of these will take place the photochemical processes that hitherto have been the guarded secret of the plants[…]”.[4]

Despite these promises, the efficient use of light in chemical processes still presents significant challenges, primarily due to the intermittency of the reactive species formed upon light absorption: Under ambient conditions, essentially all molecules reside in their electronic ground state. Upon absorbing a photon – providing energy in its most concentrated form – a molecule may be promoted to an electronically excited state. These excited states unlock reaction pathways that are otherwise thermally inaccessible. However, their high energy also makes them inherently unstable. The key challenge is to intercept and exploit these intermediate states before they relax back to the ground state, releasing their energy as heat. Capturing this brief window of reactivity remains a central pursuit in modern photochemistry. This fundamental challenge – the competition between productive reactivity and non-productive recombination – also plays a pivotal role in the optimization of devices such as LEDs and photovoltaic cells.[5,6] In molecular photochemistry, particular attention has turned to triplet-excited states for driving photochemical transformations.[7–11] For most photoactive compounds, the triplet-excited state is not only the lowest-energy excited state and thus thermodynamically preferred but also exhibits

significantly longer lifetimes due to the spin-forbidden nature of the transition back to the ground state. This extended lifetime grants triplet states a distinct reactivity compared to their singlet states.[12]

Exploiting the triplet state of a chromophore allows for activation of a substrate through, for example, energy or electron transfer processes, after which the substrate proceeds along a desired reaction pathway. Importantly, the chromophore (in this context referred to as a photosensitizer) itself is typically regenerated during the reaction, and the photon acts as a traceless reagent. As a result, these photocatalytic processes are often regarded as sustainable and resource-efficient.[13]

Triplet energy transfer catalysis has recently attracted considerable attention across a broad range of photoreactions, including triplet–triplet annihilation photon upconversion (TTA–UC),[14,15] synthetic pathways such as photoswitching,[11,16] deracemization,[10,17] cycloaddition,[18,19] selective homolytic bond cleavages,[20,21] and biological applications such as singlet oxygen generation,[22] among others.

For example, TTA–UC enables the combination of the energy of two low-energy photons into a single higher-energy photon, thereby permitting photochemical reactions that would otherwise be inaccessible at the initial excitation energy.[14] Another prominent application is the triplet-sensitized formation of metastable isomers. Here, the accumulation of a metastable configuration from a thermodynamically stable isomer can be exploited to store energy or access otherwise challenging molecular architectures for synthetic purposes.[11,16]

Although analytical techniques and the general understanding of photophysical processes have advanced markedly since the early reports by Bertram, Kürsten, and Perkin, mechanistic insights into many modern triplet-mediated transformations still rely heavily on indirect evidence. This challenge arises because many chromophores have non-emissive triplet states, requiring transient absorption spectroscopy for their detection.[23] This is even more critical in complex systems, such as biological environments, where the behavior observed in simpler solution-phase systems cannot be directly extrapolated.

The limitation of relying solely on indirect measurements is that an incomplete mechanistic understanding often leads to suboptimal reaction conditions or even false conclusions.[24–26] In contrast, a detailed spectroscopic investigation of triplet energy transfer between an energy donor and an acceptor can uncover straightforward strategies for improving photochemical processes – leading to faster reaction rates, broader substrate scope, lower photon energy requirements, and more straightforward catalyst design.[27]

In this thesis, triplet energy transfer plays a central role across all research projects. All projects are cataloged into (i) Chapter 5 “Spectroscopic Insights into Triplet Energy Transfer Pathways” (project **[A]** to **[D]**) (ii) Chapter 6 “Triplet Energy Transfer–Catalyzed Photoisomerization Reactions” (project **[E]** to **[H]**), (iii) and Chapter 7 “Photon Upconversion via Triplet–Triplet Annihilation” (project **[I]** to **[M]**). Nevertheless, a unifying aspect of all projects is the identification and characterization of intermediate triplet states through spectroscopic techniques, supported by irradiation experiments or quantum mechanical calculations.

3.1 Spin States and Their Roles in Molecular Photochemistry

Considering a closed-shell molecule, the Pauli exclusion principle for fermions requires that each molecular orbital is occupied by not more than two electrons with opposite spin orientations.[28] As a result, the total spin quantum number S of a fully occupied orbital is always zero. This configuration is typical for molecules under standard conditions and is referred to as the singlet ground state with the singlet wave function.[29]

During light absorption an electron may be removed from one of its ground state orbitals and added to another molecular orbital resulting in an electronically excited state. Considering the scenario of an electron excitation from a fully-occupied orbital (φ_a) to a former empty orbital (φ_b) – resulting in two half-occupied orbitals – the Pauli exclusion principle no longer requires opposite spins. The total spin can then be S = 0 (singlet state, opposite spins) or S = 1 (triplet state, parallel spins) for the same orbital configuration. The triplet state wave function (with a multiplicity, M = 3) has three possible spin orientations: M_S = –1, 0, 1 that are degenerate in the absence of an external magnetic field.[28,29]

The combined spin and orbital wave function for the electron pair must be antisymmetric. As the spin state is antisymmetric for S = 0 and symmetric for S = 1, the corresponding orbital wave functions must be symmetric and antisymmetric, respectively. For the two electrons, the spatial part of the possible singlet (ψ_S) and triplet (ψ_T) wavefunctions are thus expressed as:[28,30]

$$\psi_S = \frac{1}{\sqrt{2}}[\varphi_a(1)\varphi_b(2) + \varphi_a(2)\varphi_b(1)] \quad (1)$$

$$\psi_T = \frac{1}{\sqrt{2}}[\varphi_a(1)\varphi_b(2) - \varphi_a(2)\varphi_b(1)] \quad (2)$$

The energetic difference between singlet and triplet state depends on the exchange integral of the wave function, which is lower for the antisymmetric wave function of the triplet (cf. Hund's rule). The excited state with the lowest energy of a closed-shell singlet ground state molecule is thus almost always a triplet state, although recently some expetions from this rule have been reported.[31,32] Since the lowest excited state often serves as the reactive species in bimolecular reactions, the prevalence of triplet states in this role underscores their central importance in light-driven chemical transformations.[7]

3.2 Molecular Electronic State Transitions

In the simplest scenario a photon is absorbed by a molecule inducing an electronic state transition from a lower energy orbital to a higher energy orbital. During excitation it is assumed that the nuclear geometry is unaffected (Born-Oppenheimer approximation).[28] The final state is typically an electronically and vibrationally excited state that may undergo several vibrational relaxations and radiative and non-radiative electronic transitions summarized in a Jablonski diagram (Figure 1).

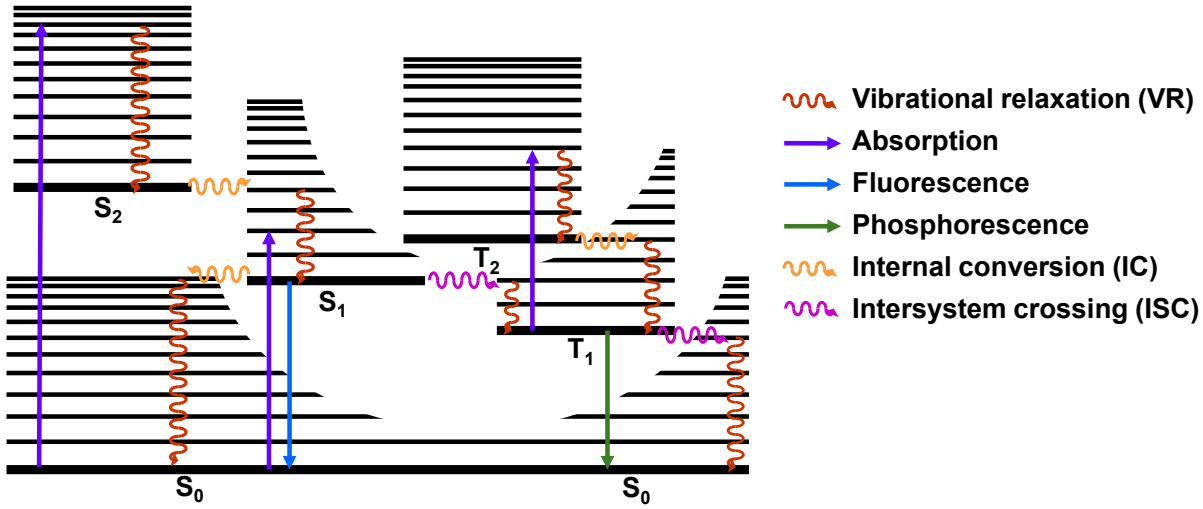

Figure 1: Jablonski-like energy diagram of relevant electronic state transitions of a prototypical singlet ground state molecule.[29,33]

The Jablonski diagram is a simplified representation of a molecule's energy potential, where thick lines correspond to the vibrational ground state of an electronic state, while the thin lines above represent their vibrationally excited states. After electronic excitation, molecules often populate vibrationally excited states, which rapidly lose excess vibrational energy through vibrational relaxation (VR). This occurs via intermolecular collisions (e.g with solvent molecules) or intramolecular redistribution among other vibrational modes. In solution, VR typically occurs with a rate constant of approximately 10^{13} s^{-1}.[29,33]

Non-radiative deactivation pathways include internal conversion (IC) and intersystem crossing (ISC) with typical rate constants of 10^{11}–10^{9} s^{-1} and 10^{13}–10^{3} s^{-1}, respectively. Both processes involve isoenergetic transitions between electronic states, with IC occurring between states of the same spin multiplicity (e.g., $S_2 \rightarrow S_1$), while ISC involves a transition between states of different multiplicities (e.g., $S_1 \rightarrow T_1$).[29,30,33,34]

Excitation does not necessarily have to take place from the ground state. For instance, the triplet state can absorb a second photon yielding a higher triplet-excited state. The absorption characteristics of the triplet state usually differ from the ground state. This is the foundation of pump-probe technique, where an ensemble of molecules is excited by a strong light pulse, while a second light pulse (or intense cw

detection light) is used to record the absorption features of the excited state with respect to the ground state.[23,29]

Radiative transitions, in contrast, involve the emission of a photon. Fluorescence in general corresponds to the emission from an excited state back to the ground state (e.g. $S_1 \rightarrow S_0$) without a change in spin multiplicity, whereas phosphorescence occurs when an excited state transitions to the ground state associated with a change of multiplicity (e.g. $T_1 \rightarrow S_0$). The decay rate constant for fluorescence is on the order of 10^{10}–10^{7} s^{-1}, while the decay rate constant for phosphorescence can take values between 10^{6}–10^{0} s^{-1}.[33,35]

In a strictly non-relativistic framework with neglected spin-orbit coupling, electronic transitions between states of different spin multiplicities (e.g. phosphorescence and intersystem crossing) are formally forbidden due to the orthogonality of spin wavefunctions. This is known as the spin selection rule, which states that transitions between singlet and triplet states should have a transition probability of zero.[12,28]

In real systems, however, these transitions occur. Electrons in orbitals with non-zero angular momentum have a magnetic dipole momentum that interacts with the magnetic moment of the spin through spin-orbit coupling (SOC). The spin and orbital angular momentum are no longer “precise” quantum numbers, allowing ISC and phosphorescence to occur. Typically, these spin forbidden transitions occur on significantly longer timescales compared to spin allowed ones. However, under certain conditions, their decay rate constants can surpass those of formally allowed transitions. In the following, the mechanisms that enhance ISC enabling it to compete with – or even surpass – other deactivation pathways such as IC and fluorescence will be discussed.[34–36]

Intersystem crossing

ISC is a non-radiative transition pathway that changes the multiplicity of the excited state. The magnitude of SOC directly influences the ISC rate by inducing partial spin mixing. The ISC rate constant k_{ISC} between an initial singlet state ψ_S and a final triplet state ψ_T can be approximated under the condition that the coupling between the states is weak compared to their adiabatic energy difference:[36]

$$k_{ISC} \propto \left|\langle \psi_S | \hat{H}_{SOC} | \psi_T \rangle\right|^2 |\langle \nu_S | \nu_T \rangle|^2 \delta(E_S - E_T) \quad (3)$$

Where $\hat{H}_{SOC}$ is the spin-orbit operator, ν_S and ν_T denote vibrational states of the initial and final wavefunctions with vibrational state energy of E_S and E_T, respectively. This expression highlights two key contributions to ISC. (i) the electronic SOC contribution, governed by the spin-orbit interaction between the singlet and triplet states; (ii) the vibronic coupling contribution, expressed by the overlap of vibrational states between the two electronic states.[36]

Spin-orbit coupling is particularly sensitive to the atomic number Z of the atoms involved, scaling approximately as Z^4. This heavy-atom effect explains why ISC rates tend to be significantly higher in molecules containing heavy elements. However, this approximation fails when the involved singlet and

triplet states are energetically close, or the transition involves a significant change in orbital angular momentum.

El-Sayed's rule provides a qualitative understanding of ISC efficiency based on the conservation of total angular momentum. For efficient ISC, a change in spin must be accompanied by a corresponding change in orbital angular momentum. As a consequence, ISC between states of the same orbital character (e.g. $^1(\pi, \pi^*) \rightarrow ^3(\pi, \pi^*)$) is typically much slower than ISC involving a change in orbital type (e.g. $^1(\pi, \pi^*) \rightarrow ^3(n, \pi^*)$). This explains why ISC rates are generally higher for molecules with $n \rightarrow \pi^*$ transitions compared to purely $\pi \rightarrow \pi^*$ transitions, as the former involves a greater change in orbital character, facilitating spin-orbit coupling.[37,38]

As of now, only purely electronic coupling was considered. The vibronic coupling term in the ISC rate expression accounts for the overlap between vibrational states of the singlet and triplet manifolds. In the weak coupling regime, the transition probability follows an exponential dependence on the adiabatic energy difference, a relationship known as the energy gap law.[39] However, this rule applies strictly only when the two states are nested, meaning they have similar molecular geometries. In contrast, under strong coupling conditions, where the two states exhibit significant differences in their potential energy surfaces along a nuclear coordinate, the ISC rate may increase with a larger energy gap.[40] This occurs because greater nuclear displacement enhances non-adiabatic coupling, leading to stronger mixing between electronic states. The equation provided above accounts for direct spin-orbit coupling, which assumes that electronic and vibrational degrees of freedom remain decoupled, which is a good assumption for rigid molecules.

However, this assumption breaks down in highly flexible molecules where nuclear and electronic motions are strongly coupled and where there is a high density of excited states. In such systems, spin-vibronic coupling must be considered, as it involves coupled electronic, spin, and nuclear dynamics. When vibrational and electronic motions become intertwined, the ISC rate is no longer determined solely by direct SOC effects but also by vibronic contributions that modulate spin-orbit interactions.[36,41,42]

Molecules that undergo rapid intersystem crossing (ISC) to the triplet manifold can be harnessed to transfer triplet energy to potential energy acceptors such as substrates in photocatalysis. Such molecules, known as triplet sensitizers, play a central role in triplet state photochemistry due to their ability to efficiently populate the triplet state. Their high ISC rates typically result from one or more of the mechanisms discussed previously. The following chapter will introduce key examples of triplet sensitizers, with a focus on how their molecular structures and electronic properties influence both triplet state energies and ISC efficiency.

3.3 Triplet Photosensitizers

The primary function of a triplet photosensitizer is to efficiently absorb (visible and UV) light and generate triplet states that can sensitize substrates incapable of directly reaching the triplet state or doing so with very low efficiency. A good photosensitizer typically has a long triplet-excited state lifetime sufficient to drive bimolecular reactions and a small energy gap between the singlet-excited and the triplet-excited state, so that energy loss during the population of the triplet state is minimal.[43,44] The energy gap between the singlet- and triplet-excited state (ΔE_{ST}) is given as twice the exchange integral (cf. Eq. (1) and (2)). The exchange integral can be minimized by deplanarization or by minimizing HOMO/LUMO interactions.[45] This can be achieved by ensuring orthogonality between the involved orbitals (e.g., *n*- and *π*-orbitals in heteroarenes such as ketones) or by employing charge-transfer (CT) molecules, where donor and acceptor moieties are spatially separated.[46] Herein, key classes, which exhibit these properties, will be explored, including ketones, metal complexes, and thermally activated delayed fluorescence (TADF) emitters.

Ketones

In traditional triplet state-related photochemistry, which dominated much of the 20th century, UV-absorbing ketones such as benzophenone, acetophenone, acetone, and thioxanthone have been the primary focus.[47–49] Following El-Sayed's rule, these compounds exhibit, after photon absorption, high ISC rates from the lowest singlet-excited state to an almost isoenergetic triplet state with a different orbital character.[37] For thioxanthone (TX), this process involves a transition from $^1(\pi,\pi^*)\rightarrow{}^3(n,\pi^*)$, followed by IC to the lowest triplet state, $^3(n,\pi^*)\rightarrow{}^3(\pi,\pi^*)$ (Figure 2).[50]

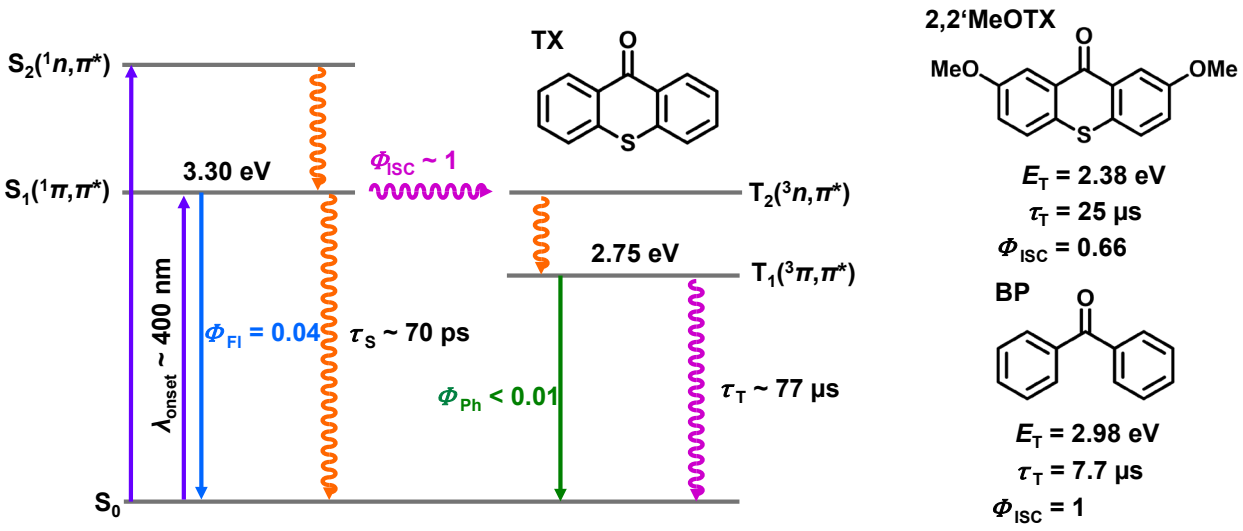

Figure 2: Schematic energy diagram of thioxanthone in acetonitrile and relevant photophysical properties of common ketone photosensitizers.[43,44,51–53] Electronic transitions are color-coded as in Figure 1. For simplicity, vibrational relaxation is not explicitly shown.

In acetonitrile, a common solvent for thioxanthone, ISC is particularly efficient, with a quantitative ISC rate, a triplet lifetime of 77 µs,[51] and a triplet state energy of 2.75 eV.[51] In more polar or protic solvents, the electronic state $^3(n,\pi^*)$ is destabilized, resulting in much slower ISC.[52] The triplet energy of thioxanthone can be adjusted through substitution; for example, double methoxy substitutions at positions 2 and 2' (2,2'MeOTX) lower the triplet energy to 2.38 eV (Figure 2).[43] In contrast, benzophenone (BP) has a higher triplet energy of 2.98 eV, but its triplet lifetime is shorter than that of thioxanthone (Figure 2).[51] This is because, after ISC to the triplet state, the singlet state can be repopulated via back ISC.[53] Since deactivation from the S_1 state occurs much more rapidly, the overall triplet lifetime decreases. This process, generally coined as "thermally activated delayed fluorescence" (TADF), not only affects triplet state lifetimes but also defines an important class of triplet photosensitizers (*vide infra*).

Transition metal complexes

Transition metal complexes initially gained significant attention for their role in dye-sensitized solar cells,[54,55] biomarkers, oxygen sensors[56], photoredox catalysis[57,58] and OLED device fabrication.[59,60] In the latter light emission arises from electron-hole recombination, which form excitons in either singlet or triplet spin states. Due to spin statistics and the threefold degeneracy of triplet states, 75% of the generated excitons are triplets, while only 25% are singlets. In purely organic compounds, triplet states are typically non-emissive, leading to energy loss and reduced emission efficiency.[12] However, the presence of a heavy metal center in transition metal complexes induces strong SOC, facilitating efficient ISC and enabling phosphorescence. High phosphorescence quantum yield allows these complexes to utilize triplet excitons effectively, making them highly attractive for OLED applications where efficient light emission is crucial.[60]

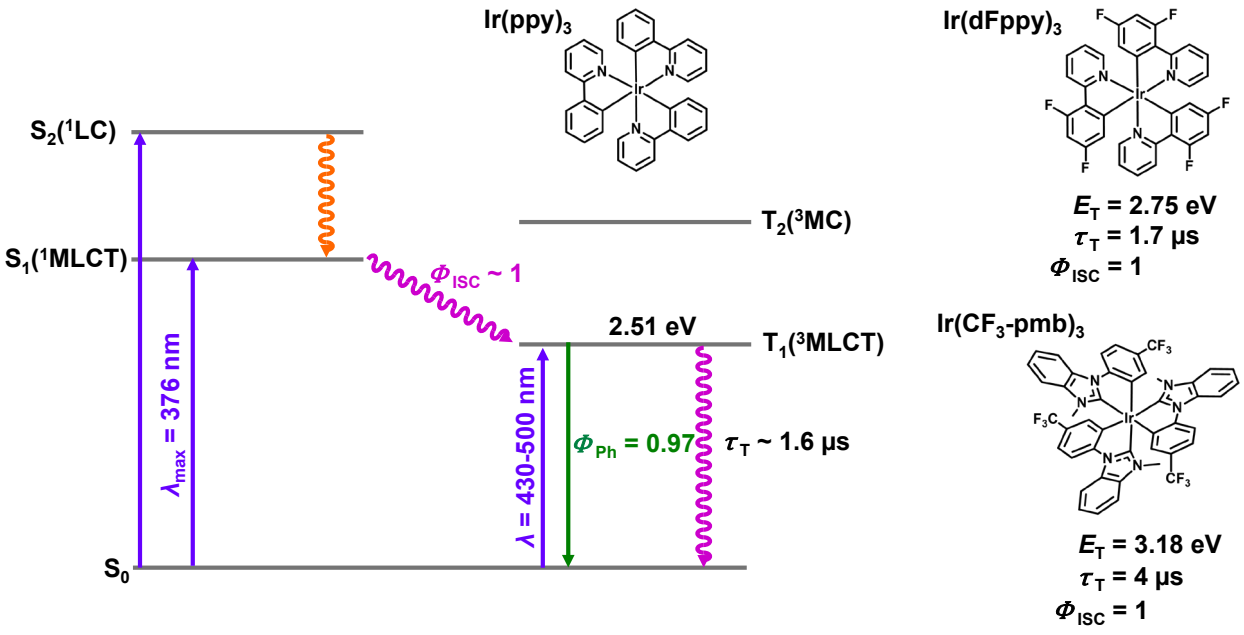

Figure 3: Schematic energy diagram of $Ir(ppy)_3$ in toluene and relevant photophysical properties of other Ir metal complexes.[9,59,61] Electronic transitions are color-coded as in Figure 1, for simplicity, vibrational relaxation is not explicitly shown.

Iridium complexes, particularly the neutral tris(2-phenylpyridine)iridium ($Ir(ppy)_3$) (Figure 3), exemplify these properties, achieving quantitative ISC quantum yields.[59] The first absorption maximum of $Ir(ppy)_3$ is at 376 nm, corresponding to a $d \rightarrow \pi^*$ transition characteristic of metal-to-ligand charge transfer (^{1}MLCT), followed by rapid and nearly quantitative ISC to the ^{3}MLCT state. Additionally, owing to strong SOC, absorption between 430 nm and 500 nm yields direct excitation into ^{3}MLCT states.[59] This avoids energy losses accompanied by ISC from the singlet state to the triplet state. The triplet state of $Ir(ppy)_3$, with an energy of 2.51 eV, is highly reducing (-1.7 V vs. SCE), making it well-suited for photoredox catalysis, but also finds applications in energy transfer catalysis.[57,62] Although its triplet lifetime (1.6 µs) is shorter than that of purely organic triplet photosensitizers, it remains sufficient for bimolecular reactions.[59] Incorporating electron-withdrawing substituents, such as fluorine, into the ligand framework raises the emission and triplet state energies by significantly stabilizing the HOMO while having minimal influence on the LUMO.[9] For example, tris(3,5-difluoro-2-(2-pyridinyl)phenyl)iridium ($Ir(dFppy)_3$) exhibits a triplet state energy of 2.75 eV, demonstrating tunable photophysical properties for advanced photocatalytic and optoelectronic applications (Figure 3).[8] Notably, the Ir metal complex $Ir(CF_3\text{-pmb})_3$ achieves an exceptionally high triplet state energy of 3.18 eV, due to the strong ligand field of the carbene ligand, greatly surpassing the typical ~2.8 eV[7,63] limit observed for most triplet photosensitizers (Figure 3).[61,64]

Thermally activated delayed fluorescence (TADF) emitters

In recent years, thermally activated delayed fluorescence (TADF) emitters have gained significant attention in the development of novel OLED systems.[46,65–67] Rather than emitting from the triplet state the triplet excitons are harvested through reverse intersystem crossing (rISC) back to the singlet state.

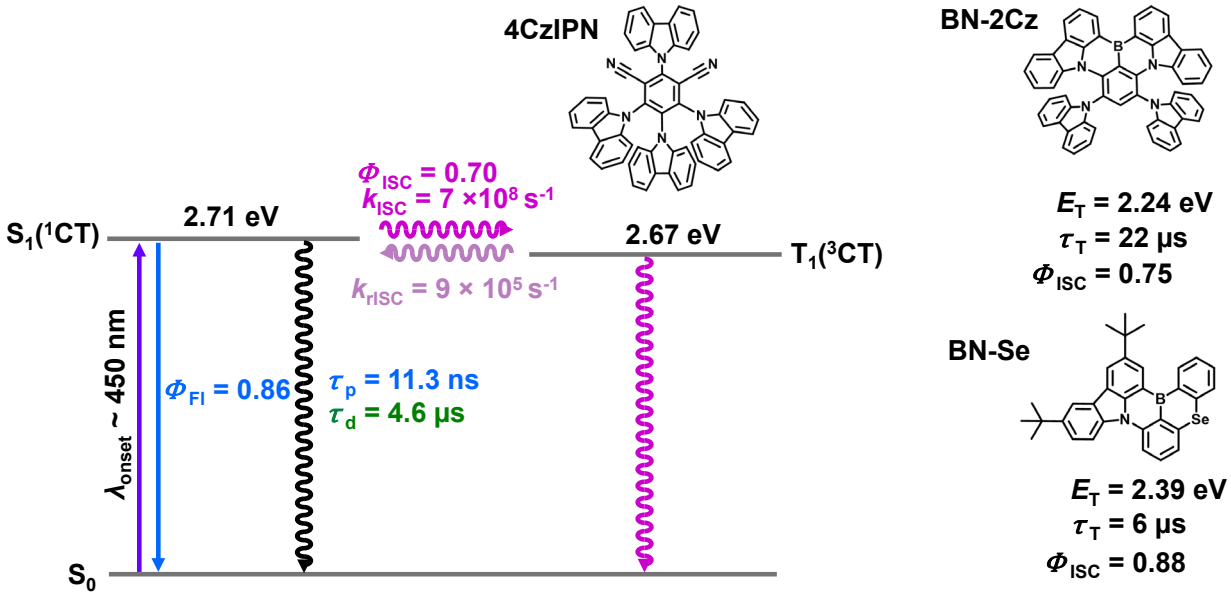

Figure 4: Schematic energy diagram of 4CzIPN in toluene and relevant photophysical properties of 4CzIPN, BN-2Cz and BN-Se.[68–70] Electronic transitions are color-coded as in Figure 1, for simplicity, vibrational relaxation is not explicitly shown.

This process is effective only when the energy difference between the triplet and singlet excited states is small – typically within the range of thermally accessible energy (< 0.2 eV). A well-known TADF emitter, 2,4,5,6-tetrakis(9H-carbazol-9-yl)isoindoline-1,3-dione (4CzIPN), consists of donor-acceptor units that enable efficient charge transfer (Figure 4).[71,72] In this molecule, the carbazole (Cz) groups act as the electron donors, while the isophthalonitrile (IPN) core serves as the electron acceptor. Due to the strong charge-transfer character of the transition between the highest occupied molecular orbital (HOMO), primarily localized on the donor units, and the lowest unoccupied molecular orbital (LUMO), mainly distributed on the acceptor unit, the exchange interactions and the singlet-triplet energy gap are substantially small. However, the mechanism behind the fast (reverse) intersystem crossing is more complex, as multiple factors contribute to its efficiency. A purely CT-based description cannot fully account for the ISC rate, given the minimal spatial overlap between the electronic states. Instead, the coupling between singlet and triplet states is explained by second-order interactions with locally excited (LE) states, which are promoted through vibronic coupling.[30,68] The small energy gap further enhances ISC as stated by the energy gap law. Although these compounds were initially developed for the conversion of triplet states to singlet states, their high ISC rates in both directions, along with a minimal singlet-triplet energy gap and long triplet lifetimes, make these purely organic chromophores well-suited for photocatalytic applications.[73] The compounds BN-2Cz and BN-Se with boron/nitrogen (B/N)-based polycyclic frameworks have been optimized for triplet energy transfer processes exhibiting high ISC quantum yields (>0.75) and long triplet lifetimes (>6 µs) (Figure 4).[69,70,74]

Boron-dipyrromethenes (BODIPYs)

Boron-dipyrromethenes (BODIPYs) are a class of organoboron compounds initially recognized for their high fluorescence quantum yields and exceptional photostability, making them valuable for applications such as light-harvesting antennas,[75] fluorescent probes,[76] and photodynamic therapy.[77] Modifications to the parent structure, 4,4-difluoro-4-bora-3a,4a-diaza-s-indacene (BODIPY) (Figure 5), can significantly enhance intersystem crossing (ISC) rates. The ease of synthetic functionalization further establishes BODIPYs as a promising organic alternative to metal-based photosensitizers.[78] Various chemical modifications that enhance spin-orbit coupling (SOC) and consequently ISC rates include: (i) halogenation (e.g. BODIPY-I_2, Figure 5), exploiting the heavy-atom effect,[79,80] (ii) BODIPY dyads incorporating electron-donating moieties on the electron-accepting BODIPY, which promote a charge-transfer (CT) excited state (e.g. BODIPY-$Ph(OMe)_3$, Figure 5),[81,82] and (iii) BODIPY dimers, which gain high ISC rates through small a singlet-triplet energy gap (ΔE_{ST}) via singlet exciton coupling and the involvement of CT intermediate states in triplet state population (e.g. BODIPY-3-BODIPY, Figure 5).[83]

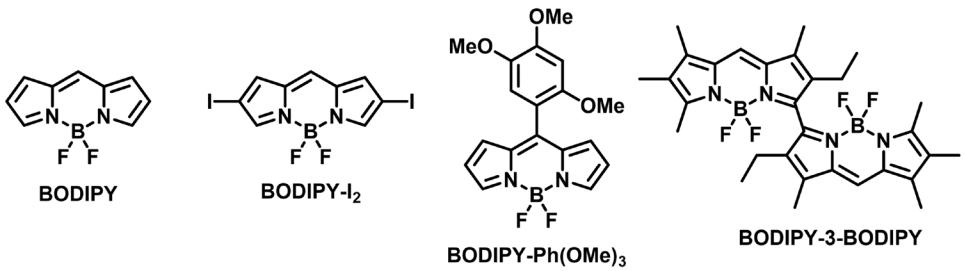

Figure 5: Molecular structures of selected boron-dipyrromethenes for triplet energy transfer catalysis.

Selecting an appropriate photosensitizer for a given reaction is far from straightforward. Excited states store considerable energy and can interact with substrates through various pathways beyond simple energy transfer (*vide infra*). For instance, excited ketones can abstract hydrogen atoms from substrates,[47,48] while metal complexes often have high excited state redox potentials that favor electron transfer processes.[84,85] Additionally, the triplet energy of the photosensitizer must be carefully chosen: it must be high enough to sensitize the desired substrate, yet not so high that it inadvertently activates other species in the system, potentially leading to side reactions or reversal of the target transformation.[11]

With few exceptions, the triplet energies of common photosensitizers rarely exceed ~2.8 eV. Small carbonyl compounds like acetone (3.44 eV) and acetophenone (3.21 eV) offer higher triplet energies but absorb only weakly in the UVB range, making them unsuitable for most practical applications beyond mechanistic or spectroscopic investigations of triplet states.[8] It is only in recent years that organometallic photosensitizers have been developed that combine triplet energies exceeding 3 eV with efficient UVA absorption, although their synthesis continues to be complex.[61,86,87] While this represents a significant advance – especially since both sunlight and commercial UVA LEDs can readily supply such energies – utilizing visible light, where the solar spectrum is most dominant,[88] imposes an upper limit of ~3.1 eV. This sets a practical boundary for usable excitation energy in triplet energy transfer one-photon chemistry.[7]

3.4 Energy Transfer

In addition to the intrinsic deactivation pathways discussed earlier, excited state deactivation can also proceed via bimolecular quenching mechanisms. These involve intermolecular interactions where an excited molecule (denoted as the donor, D) transfers energy or electrons to a ground state molecule (denoted as the acceptor, A). Such quenching processes can occur through energy transfer, electron transfer, or hydrogen atom transfer, each governed by distinct mechanisms. Electron and hydrogen atom transfer do not play a significant role in the context of this work and the reader is referred to the literature for a detailed description of the processes.[12,29,51,89]

Energy transfer quenching occurs when an excited donor molecule transfers its energy to an acceptor thereby returning to the ground state.

$$D^* + A \rightarrow D + A^* \quad (4)$$

This process can be classified into radiative and nonradiative mechanisms. In radiative energy transfer (trivial energy transfer), the donor emits a photon, which is subsequently absorbed by the acceptor. Since no direct molecular interaction occurs between the donor and acceptor, the donor's lifetime remains unaffected. However, the emission spectrum may appear distorted due to reabsorption effects. Strictly speaking, this is not a bimolecular quenching mechanism but rather an energy relay through space.[29]

Coulombic mechanism:

Also known as Förster resonance energy transfer (FRET), this mechanism relies on long-range dipole-dipole interactions (typically less than 10 nm) between the donor and acceptor and does not require physical contact. The rate constant of energy transfer is best described as a function of the donor's and acceptor's photophysical properties:

$$k_{\mathrm{FRET}}(r_{\mathrm{AD}}) = 8.8 \cdot 10^{-25} \frac{K^2 \cdot \phi_{\mathrm{D}}}{n^4 \cdot r_{\mathrm{AD}}^6 \cdot \tau_{\mathrm{D}}} \cdot J_{\mathrm{F}} \quad (5)$$

where K^2 is the orientation factor (with K^2 = 2/3 for random orientation), ϕ_{D} is the emission quantum yield of the excited donor, r_{AD} is the donor-acceptor distance in Å, and J_{F} is the Förster spectral overlap integral describing the overlap between donor emission and acceptor absorption spectra in cm^{-1}, n is the refractive index, τ_{D} is the donor lifetime in s.[12]

The same selection rules for the electronic dipole transition apply for the donor and the acceptor. Thus, owing to the spin conservation rule, energy transfer between molecules of the same multiplicity (e.g. singlet-singlet energy transfer) is the most observed form of coulombic energy transfer. However, triplet-singlet energy transfer can occur if the donor exhibits a long-lived triplet state with sufficient spectral overlap and a high phosphorescence quantum yield.[90] The distance dependence decreases with the sixth power, which is why dipole-dipole coulombic energy transfer can occur over large distances up to 10 nm. This can result in energy transfer rate constants that exceed the diffusion limit of the solvent.[12]

Exchange mechanism:

The exchange mechanism, also known as the Dexter-type mechanism, is based on short-range electron exchange between the donor and acceptor. This process is best described as a simultaneous two-electron exchange transfer: One electron of the donor from the former LUMO is transferred to the LUMO of the acceptor, while simultaneously one electron from the former HOMO of the acceptor is transferred to the HOMO of the acceptor. Although no net charge is transported, its kinetics can be described by Marcus theory.[12,91] The rate constant follows an exponential dependence:

$$k_{\mathrm{Dex}}(r_{\mathrm{AD}}) = H \cdot J_{\mathrm{D}} \cdot \exp\left(-\beta \cdot \frac{r_{\mathrm{AD}}}{2}\right) \quad (6)$$

where *H* represents the electronic coupling term, J_D is the Dexter spectral overlap integral between the donor's emission and the acceptor's absorption spectrum, β is the attenuation factor describing the decay of electronic wavefunction overlap, and r_{AD} is the donor-acceptor distance. In a simplified model, β can be considered as the sum of the attenuation factors for both electron and hole transfer.[12,92] In analogy to Marcus theory[91], the rate constant drops exponentially with increasing distance r_{AD}. The Dexter spectral overlap integral is normalized over the absorption and emission spectrum of acceptor and donor. Hence, unlike FRET, it is not dependent on the oscillator strength of the donor.[12]

Dexter energy transfer is only efficient when the donor and acceptor are in close proximity, typically requiring direct molecular contact, reflected in the exponential distance dependence. This interaction leads to the formation of an encounter complex, which must obey spin conservation rules. As a result, triplet–triplet energy transfer (TTET) becomes feasible, provided that the total spin of the donor-acceptor system remains unchanged. The ability to populate triplet states that are otherwise inaccessible via direct excitation makes Dexter energy transfer a powerful tool in photochemistry.[12,29]

In solution, the rate constant for Dexter energy transfer is constrained by the diffusion limit (k_{diff}) of the solvent, assuming that each molecular collision leads to successful energy transfer. This condition is typically met when the triplet energy of the donor is higher than that of the acceptor, allowing for efficient energy transfer. However, when the energy gap between the donor and acceptor approaches the thermal energy available at ambient conditions, the efficiency for separation of a thermally equilibrated encounter complex follows Boltzmann's distribution law.[93]

$$\frac{n_{A*}}{n_{D*}} = \exp\left(-\frac{\Delta E}{RT}\right) \tag{7}$$

As the process becomes increasingly endergonic, the rate constant decreases exponentially. This expression was first derived by Sandros:[94]

$$k_{Dex} = \frac{k_{diff}}{1 + \exp\left(-\frac{\Delta E}{RT}\right)} \tag{8}$$

However, slightly uphill energy transfer is still feasible even if the energy transfer rate constant is several magnitudes below diffusion for many systems. If the substrate concentration is high and the triplet photosensitizer has a long lifetime, even highly unfavored energy transfer processes can proceed with near-unity quantum yields.[63]

Since Sandros' initial work, numerous energy transfer systems have been studied that exhibit significant deviations from the expected behavior. One key deviation arises usually when the molecular geometry of the relaxed triplet-excited acceptor differs substantially from its ground state geometry. In this case the vertical energy difference (no change to the ground state geometry) is much greater than the adiabatic energy difference (from singlet ground state geometry to the energy-relaxed triplet geometry). This

observation has been termed non-vertical energy transfer, and is best described by the “hot band” model (Figure 6).[95] In this model thermally accessible vibrational states in the ground state acceptor that closely resemble the relaxed triplet state geometry are populated and effectively decrease the energy gap.[96] Thus, the vertical excitation energy is in general higher than the experimentally observed triplet energy. To account for such effects, Balzani extended the original model, formulating a more universally applicable expression for energy transfer dynamics.[97] The greater the structural distortion between these states, the more pronounced is the deviation from classical Sandros behavior. This phenomenon is commonly observed in triplet energy transfer-driven isomerization of alkenes, where the triplet-excited state, capable of free rotation around the former double bond, adopts a highly distorted relaxed geometry. (see Chapter 6).

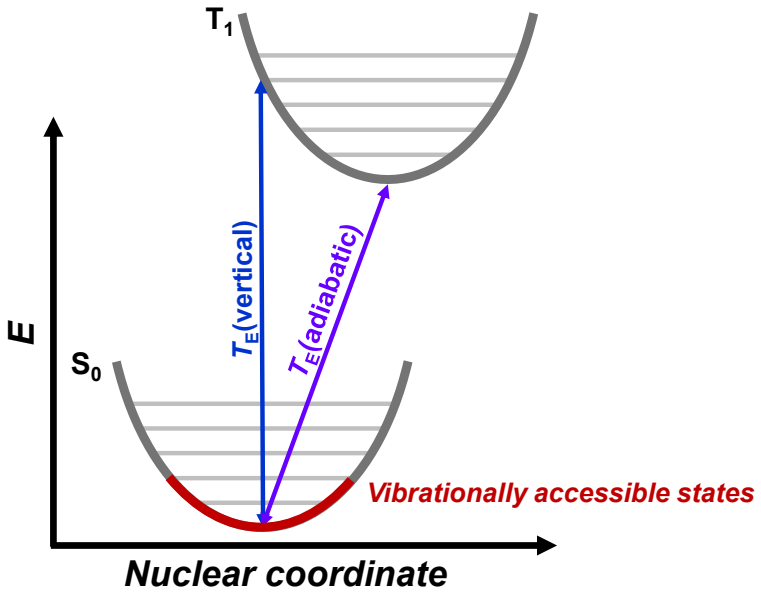

Figure 6: Schematic energy diagram depicting the “hot-band model”. Thermally available vibrational states with a similar nuclear configuration as the triplet excited state are populated thereby effectively reducing the required energy for sensitization.[96]

Bridge- and solvent-mediated triplet energy transfer

In the exchange mechanism, both energy and electron transfer exhibit an exponential decrease in efficiency with increasing distance between the donor and acceptor due to the diminishing overlap of their molecular orbitals (see equation (6)). In a quantum mechanical sense this is described by the probability of an electron or hole tunneling through the effective barrier height (ΔE_{eff}) imposed between the donor and acceptor, which in vacuum corresponds to the ionization energy and electron affinity, respectively.[98]

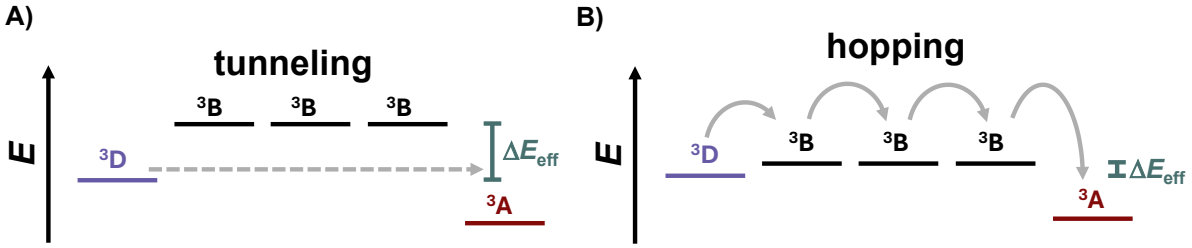

Figure 7: Energy diagram of tunneling (A)) and hopping (B)) mechanism for TTET in a system comprising an energy donor (D) bridging units (B) and an energy acceptor (A).

In practice, the triplet energy donor and acceptor are generally not separated in vacuum but by solvent molecules (through-space) or bridging units (through-bond). The medium between the donor and acceptor then influences the probability of charge or energy tunneling by effectively lowering ΔE_{eff} (Figure 7A).[99,100] If ΔE_{eff} between donor and bridging units is similar or lower than the thermally available energy, energy hopping can occur, where the bridging unit occupies real intermediate excited states (Figure 7B). The hopping mechanism is usually several orders of magnitude faster than the tunneling mechanism.[101,102]

However, in many systems where the donor and acceptor are held at a fixed separation, the experimentally observed distance dependence of exchange-type energy transfer is often shallower than predicted by this simple tunneling model. This deviation is explained by the superexchange mechanism, in which coupling with intermediate bridge orbitals facilitates charge or energy transfer.[99,100,103] Since Dexter-type energy transfer can be described by a simultaneous electron and hole transfer process, the attenuation factor is approximated as the sum of the attenuation factor for electron and hole transfer in that system.[12,92] However, this assumption breaks down when virtual intermediate states or charge-separated states participate in the energy transfer pathway. In these cases, the attenuation factor is reduced and approaches the values typical for hole or electron transfer.[104,105]

Triplet–triplet annihilation

Triplet–triplet annihilation (TTA) is a special case of triplet–triplet energy transfer in which both interacting chromophores exist in an excited triplet state. Depending on whether the participating species are identical or different, TTA can be classified as homo-TTA (between identical molecules) or hetero-TTA (between different molecules).[106–108] In this work, only homo-TTA is considered, and it will be referred to as TTA throughout. The process begins with the formation of a triplet pair encounter complex, where two triplet-excited molecules come into close proximity. At this stage, the triplet states can no longer be treated as independent entities. In the strong exchange coupling regime, where each individual triplet state has three possible spin orientations (see Chapter 3.1), their interaction leads to 3 × 3 = 9 possible spin combinations, forming the eigenstates of the encounter complex (Figure 8). These nine eigenstates are distributed as follows:[109–111] One spin-0 (singlet) state, three spin-1 (triplet) states, and five spin-2 (quintet) states.

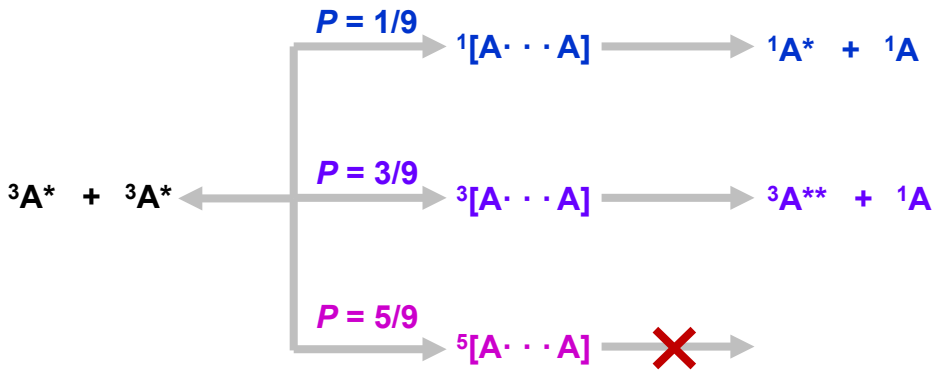

Figure 8: Formation and dissociation possibilities of triplet pair encounter complexes in the strong coupling regime. The probability (*P*) is given for each multiplicity.

Following their formation, triplet pair complexes can either dissociate back into individual triplet states or undergo energy redistribution. In the latter case, the combined excited state energy ($2 \times E_T$) is transferred onto a single molecule, while the other returns to the ground state, typically a singlet state (Figure 8). The spin multiplicity of the resulting molecular states, however, must match the spin configuration of the original triplet pair. It follows:

- Spin-0 (singlet) complex: Results in one singlet-excited molecule and one ground state molecule. This is the productive pathway exploited in photon upconversion applications.
- Spin-1 (triplet) complex: Yields one higher excited triplet state, which typically relaxes to the lowest triplet state, and one ground state molecule. This pathway is considered unproductive, as it ultimately leads to deactivation of one triplet state.
- Spin-2 (quintet) complex: In theory, this would result in a quintet-excited molecule; however, quintet states are thermodynamically inaccessible in nearly all relevant TTA systems. As a result, these complexes dissociate back into two separate triplet states, effectively making this pathway thermodynamically closed.

Thus, in practical TTA systems, only the spin-0 complex contributes to a productive formation of singlet-excited states, while spin-1 and spin-2 complexes either lead to triplet deactivation or reversion to the original triplet states. This mechanism is exploited in photon upconversion processes where two lower energy photons are essentially fused into one of higher energy (see Chapter 7).[15,112–114]

4 Outline of Projects

Triplet states, absent in conventional thermal “two-electron” chemistry, are relatively long-lived, energetically excited open-shell intermediates that exhibit distinct and often complex reactivity patterns. Understanding the mechanistic pathways of these states in triplet–triplet energy transfer (TTET) is crucial for the effective design and optimization of photochemical reactions.

The objective of this thesis is to characterize TTET processes using spectroscopic methods and apply the findings to improve reaction design. This work investigates these mechanisms through both indirect and direct approaches, with a focus on nanosecond transient absorption (TA) spectroscopy. Each chapter addresses specific challenges in photochemistry, but all emphasize the essential role of triplet states in photochemical reactions. While the projects span a variety of systems and applications, they share a common goal: to understand and control TTET processes – either by uncovering their fundamental mechanisms or by using spectroscopic insights to optimize sensitizers, acceptors, and reaction conditions.

The thesis is structured into three main chapters. Chapter 5 “Spectroscopic Insights into Triplet Energy Transfer Pathways” focuses on characterizing TTET processes. Chapter 6 “Triplet Energy Transfer-Catalyzed Photoisomerization Reactions” and Chapter 7 “Photon Upconversion via Triplet–Triplet Annihilation” both build on similar spectroscopic insights, directly applying them to energy and light conversion processes. Achieving optimal efficiency and functionality in these processes requires careful design and comprehensive photochemical characterization.

Spectroscopic Insights into Triplet Energy Transfer Pathways

The projects **[A]** to **[D]** deal with the elucidation of mechanistic pathways in distance-dependent energy transfer and photocatalytic reactions. The aim of these studies was to deepen the understanding of the photo-induced TTET (or in some cases electron transfer) reaction of the excited donor with the acceptor.

In Project **[A]**, triplet energy migration between C-nucleotides of a triplet energy donor and an energy acceptor incorporated into DNA at varying distances is investigated. Human DNA is susceptible to photodamage induced by solar UV light exposure.[115,116] While electron transfer processes in DNA are extensively characterized, TTET remains comparatively less understood despite its role in DNA degradation.[102,117–119] In this work, TTET was directly monitored using TA spectroscopy, revealing that a tunneling mechanism via nucleobase triplet states is likely part of the energy transfer pathway.

Projects **[B]** through **[D]** examine mechanistic features of photocatalytic processes, applying similar methodologies across distinct chemical transformations. Project **[B]** centers on a polyazahelicene chromophore, which belongs to a compound class not traditionally regarded as photocatalysts or photosensitizers despite their notable ISC quantum yields.[120–122] Their excited state reactivity was ambiguous,[123] inspiring this study to distinguish between singlet- and triplet-excited state reactivity and to develop reaction design strategies that harness both. In project **[C]**, the interactions between the

photosensitizer thioxanthone[51] and arylthianthrenium salts were explored – synthetically useful compounds previously used in photoredox chemistry but not yet evaluated in energy transfer pathways.[124–126] By identifying transient signatures of intermediate species,[127] the proposed mechanism was confirmed. Lastly in project **[D]**, TTET from Iridium complexes to a vinylcyclopropane is investigated, a substrate commonly employed in the construction of complex tetracycles.[128] An energy transfer-induced [3 + 2] cycloaddition with acetylenes was proposed, though the energetic mismatch initially rendered this implausible.

Triplet Energy Transfer-Catalyzed Photoisomerization Reactions

Projects **[E]** through **[H]** investigate triplet-sensitized photoisomerization of olefins. Specifically, projects **[E]** and **[F]** focus on the triplet energy transfer pathways involving alkenylboronates. These chromophores exhibit high selectivity in photocatalytic *E*→*Z* isomerization reactions and offer excellent post-functionalization opportunities owing to the pinacol boronic ester group.[11,129] The goal of these studies was to explicitly validate the mechanistic aspects of the postulated triplet-sensitized isomerization. In order to achieve this, the triplet states of these alkenes were, for the first time, directly monitored and their triplet state energies were characterized. These detailed mechanistic insights were then exploited for the optimization of the *E*→*Z* isomerization reactions.[130] Furthermore, this concept was extended to fluorinated alkenylboronates, chemically stable motifs that act as effective amide isosteres, making them particularly appealing for biological applications.[131,132] Clarifying these mechanistic details aimed at facilitating the integration of triplet-sensitized isomerization reactions into synthetically valuable reaction sequences.

Projects **[G]** and **[H]** similarly investigate the triplet-sensitized isomerization of norbornadiene derivatives into quadricyclanes. This reversible transformation is noteworthy for its capability to store solar energy through the formation of strained bonds upon excitation and later to release this energy as heat – a concept known as molecular solar thermal energy storage (MOST).[133] As direct excitation methods present significant drawbacks, a triplet-sensitization approach could potentially overcome these limitations. Yet, recent studies have largely neglected this method.[16,134,135] Hence, aryl-substituted norbornadienes[136,137] were investigated using an analogous methodology as employed in projects **[E]** and **[F]**. The triplet–triplet energy transfer step and the transient triplet states of these photoswitches were characterized through detailed spectroscopic analyses. These findings facilitated the optimization of reaction conditions for novel triplet-sensitized MOST systems, including the effective integration of a multistate photoswitch into a visible light-driven system demonstrating unprecedented solar conversion efficiency. Furthermore, aryl-substituted norbornadienes featuring acetylene bridging units were studied revealing their photochemical properties, which are relevant for both direct excitation and sensitization. The so obtained insights significantly enhance the understanding of norbornadiene-based photoswitches, despite reduced functionality compared to their parent compounds without acetylene bridges.

Photon Upconversion via Triplet–Triplet Annihilation

Projects **[I]** through **[M]** focus on photon upconversion through triplet–triplet annihilation (TTA–UC), a process that enables the combination of two lower-energy photons into one of higher energy.[14] This two-photon mechanism offers compelling advantages across a range of applications, particularly in contexts where conventional one-photon approaches fall short (e.g. due to filter effects or as a result of UV-induced photodamage).

In project **[I]**, a novel BODIPY-inspired photosensitizer was developed. Coupled with a suitable annihilator, this fully organic system enabled efficient green-to-blue upconversion, characterized by good photostability. The system was thus further applied to green light-driven photoredox catalysis of synthetically challenging transformations. Mechanistic clarity was achieved through TA spectroscopy, which allowed for the direct observation of key transient intermediates.

Projects **[J]**, **[K]**, and **[L]** address the challenge of generating UVB light from visible-light excitation – a particularly attractive target given the inefficiency of conventional light sources at these wavelengths. At the beginning of this thesis, no TTA–UC system had been demonstrated to emit beyond the UVB threshold (315 nm).[138] These projects introduced three unprecedented annihilators based on benzene and biphenyl frameworks, offering emission properties previously unattained. In all three projects an initial annihilator design was assessed by DFT calculations of the triplet state energies. Further, the TTA–UC mechanism was carefully investigated by TA spectroscopy. Substitution with TIPS-ethynyl groups of the annihilator scaffolds proved to be essential in tuning the photophysical properties of the biphenyl and benzene annihilators.[139] Project **[J]** employed biphenyl-based annihilators that were combined with an organic TADF and an Ir-based photosensitizer. Project **[K]** extended these principles to a benzene-based annihilator bearing two TIPS-ethynyl groups. When paired with an organic sensitizer, the system yielded upconverted UVB emission with good quantum yields taking the extremely high photon energy into account. The annihilator's singlet-excited state was subsequently leveraged in a singlet energy transfer reaction with inert carbonyl compounds. This complex UC–FRET process was validated through a combination of advanced spectroscopic and irradiation experiments. A related monosubstituted derivative, notable for its exceptional emission energy approaching the UVC region, was also investigated. Although a compatible sensitizer was not initially available, the chromophore's potential was clear. In project **[L]**, this was addressed by pairing the potential annihilator with an UVA absorbing Ir sensitizer[61] having an exceptionally high triplet energy. TTET was successfully achieved, resulting in UVC-range upconverted emission and extending the current boundaries of high-energy TTA–UC. The project also highlighted the present challenges in advancing photon upconversion in the UVC regime.

Finally, project **[M]** presents a review of recent advances in vis-to-UV TTA–UC. It surveys developments in chromophore design, integration into solid media, and applications across photocatalysis, bond activation, and photopolymerization. Four fundamentally different mechanisms – based on energy or electron transfer – are identified. A dedicated section summarizes the novel UVB annihilators introduced in this thesis, offering a roadmap for implementing TTA–UC in advanced photochemical applications.

5 Spectroscopic Insights into Triplet Energy Transfer Pathways

Photochemical reactions are inherently distinct from traditional polar or two-electron chemistry, as they involve high-energy open-shell intermediates and either energy or single-electron transfer mechanisms.[12] To unravel such complex pathways, researchers often rely on indirect characterization techniques – such as cyclic voltammetry and steady-state UV-vis or emission spectroscopy – that are accessible in most laboratories.[140] While valuable for supporting proposed mechanisms, these methods cannot provide direct evidence of transient species that are often involved as intermediates in the photoreactions.[141]

The growing need for mechanistic insight into photochemical reaction pathways has driven interest in more definitive techniques, particularly from synthetic and spectroscopic photochemistry communities.[24,25] One such powerful tool is time-resolved transient absorption (TA) spectroscopy. TA spectroscopy enables the observation of short-lived intermediates that are invisible to emission-based methods.[23,27,142] In a typical TA experiment, a pulsed laser excites a significant fraction of the substrate (often the photosensitizer) in solution, while a broadband white probe light monitors the formation and decay of intermediates following excitation and bimolecular quenching.

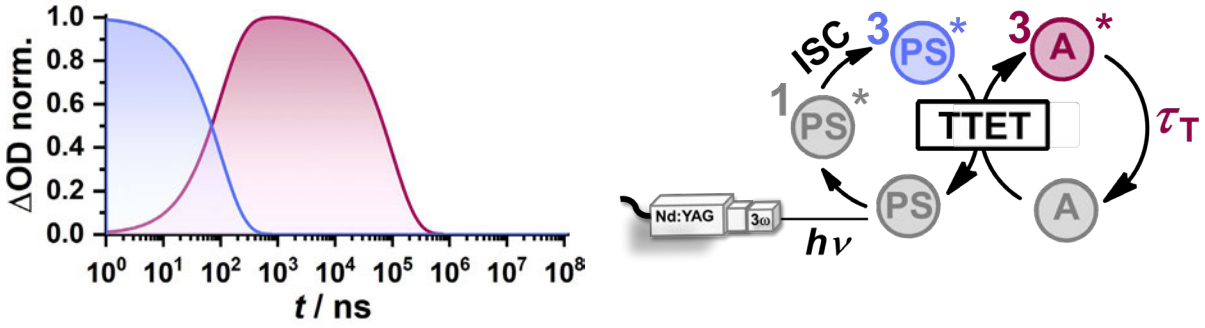

Figure 9: Typical kinetic TA signals tracking TTET between a photosensitizer (PS) and an energy acceptor (A) after laser pulse excitation. In the selected example, TTET occurs with a time constant of 100 ns, while the acceptor triplet decays with τ_T = 100 µs.

In bimolecular photoreactions, relevant timescales range from nanoseconds to milliseconds. The TA signatures of energy transfer and electron transfer pathways are intrinsically different: electron transfer typically generates long-lived open-shell species such as radical cations or anions with millisecond lifetimes, whereas TTET results in transient triplet states with nano- to microsecond lifetimes.[51,141] Figure 9 illustrates a representative laser flash photolysis (LFP) experiment, in which a photosensitizer (PS) is excited by a laser pulse and after ISC yields the triplet state, followed by TTET to an energy acceptor (A). The intensity of the TA signals of PS and A are monitored at a given wavelength over time on a semi-logarithmic scale. In the absence of secondary processes, TTET typically results in a clean return of the absorption bands to the baseline, without leaving any persistent spectral features.

This chapter summarizes four projects – **[A]**, **[B]**, **[C]**, and **[D]** – that collectively address a central question of this thesis – the operative mechanism of the photochemical reactions under investigation.

In project **[A]** triplet energy transfer was directly observed between an energy donor and acceptor that had been integrated into DNA double strands at different separation distances. The study revealed that TTET is mediated by a tunneling mechanism with possible involvement of the triplet states of the intervening nucleobases. Yet, long-range TTET is effectively suppressed when hopping is not viable, which likely evolved as a light protection mechanism by DNA.[116,143]

Projects **[B]**, **[C]**, and **[D]** focus on the characterization of the triplet energy transfer in photocatalytic reactions. In Project **[B]**, the mode of action of a polyazahelicene was explored. It was found to function both as a highly reducing photocatalyst in its singlet-excited state and as an effective triplet photosensitizer in photoisomerization reactions. In project **[C]** the photo-cleavage of thianthrenium salts using thioxanthone as photosensitizer was investigated. While the cleavage of such salts is generally attributed to photo-induced electron transfer in the literature,[125,126,144] this study reveals that fragmentation instead follows triplet sensitization by thioxanthone. Finally, in project **[D]** the mechanism of a [3 + 2] cycloaddition between a vinylcyclopropane and acetylenic sulfones initiated by Ir-based photocatalysts was examined. Spectroscopic investigations and DFT calculations pointed to an energy transfer pathway as the key step in the visible light-driven reaction.

5.1 Triplet–Triplet Energy Transfer in DNA Between Energy Donor and Acceptor C-Nucleotides

Solar UV light can damage DNA and potentially cause skin cancer.[115,116] While DNA usually protects itself by ultrafast decay of excited states through charge recombination, some excited singlet states still initiate photochemical reactions such as cyclobutane pyrimidine dimer (CPD) formation.[145,146] In addition to this singlet photochemistry, triplet states also contribute to DNA damage, including oxidation and cross-linking.[147] It is well-described how the nucleobases participate in electron transfer processes as bridging units that substantially extend the electron transfer distance by lowering the effective energy barrier height.[117,119] In the same regard triplet energy can migrate across a DNA double helix leading to CPD as well.[102,148] However, it remains unclear how TTET in DNA leads to damage due to challenges in targeting triplet states at defined sites.[149] Understanding these mechanisms is key to unravel UV-induced pathways to skin cancer. Recent studies have employed photosensitizers to generate triplet states in DNA, measuring CPD damage as a function of the distance from the photosensitizer.[102,148] While indirect methods suggest triplet–triplet energy transfer, their shallow distance dependence and reliance on emission-based techniques leave the mechanism ambiguous.[150,151] In project **[A]**, an energy donor and acceptor were embedded in DNA helices with different separations. This study provides the first direct spectroscopic evidence of exchange-type triplet energy transfer through DNA, clarifying previous findings

and extending the current understanding of DNA photosensitization. The findings support a tunneling mechanism in which energy transfer is mediated by intervening thymine bases, which possess the lowest triplet energy among the nucleobases. Nevertheless, the study concludes that DNA is generally an inefficient conduit for triplet energy transfer when hopping pathways are unavailable. This limited conductivity serves as a natural photoprotective mechanism, aligning with the phototoxicity threshold of 2.8 eV proposed by Miranda et *al.*[143]

Summary:

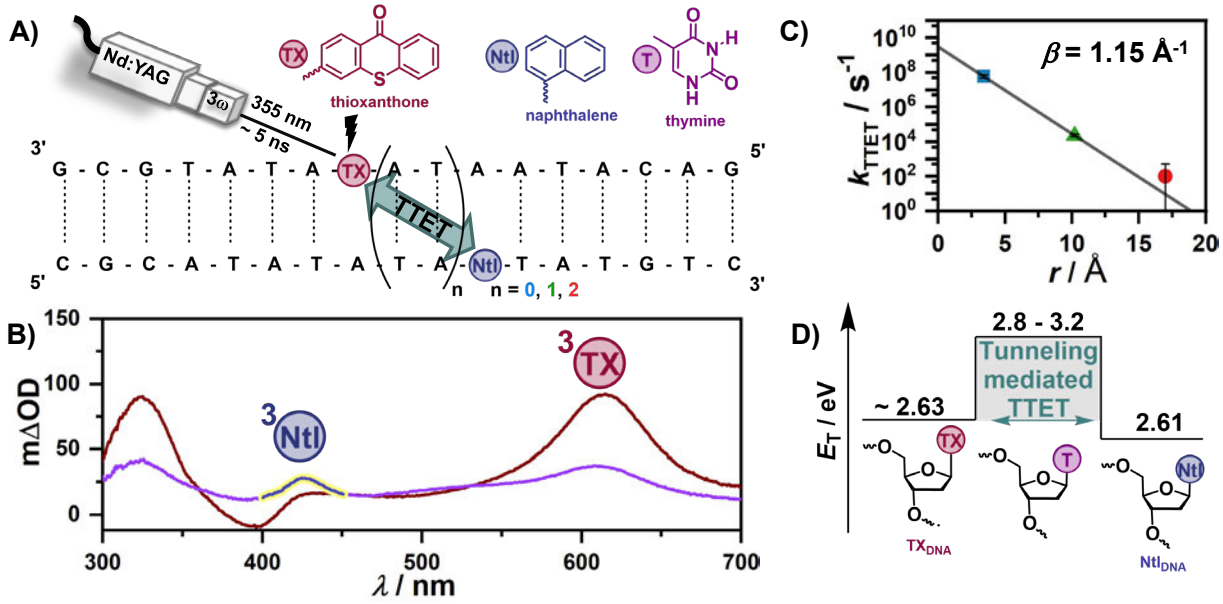

Figure 10: Overview of the results for the direct observation of TTET between C-nucleosides of thioxanthone (TX_{DNA}) and naphthalene (Ntl_{DNA}) in DNA. A) Sequences of DNA double strands modified with TX_{DNA} and Ntl_{DNA}. B) TA spectra of the DNA sample n = 0 (purple) after 355 nm pulsed laser excitation, and reference sample lacking Ntl_{DNA} (red). C) Experimentally-observed TTET rates from $^3TX_{DNA}$ to Ntl_{DNA} plotted against the distance. D) Schematic energy diagram with postulated tunneling mechanism facilitated by the thymine triplet state.

In project **[A]**, the distance dependence of TTET between C-nucleosides of thioxanthone (TX, donor) and naphthalene (Ntl, acceptor) embedded in DNA was directly observed and characterized. To investigate this, three DNA constructs were prepared, each with a different donor–acceptor separation, along with three reference samples lacking the naphthalene moiety (Figure 10A). Laser flash photolysis using 355 nm pulses was employed to selectively excite the thioxanthone chromophore in the DNA strands (TX_{DNA}). Upon excitation of reference samples without Ntl_{DNA}, the triplet state of TX was consistently formed, exhibiting clear spectral features in the TA spectrum (Figure 10B). In contrast, when Ntl_{DNA} was present in the n = 0 sample, the TX_{DNA} signal was quenched, as confirmed by the corresponding TA spectrum. The small energy gap between $^3TX_{DNA}$ (~2.63 eV) and $^3Ntl_{DNA}$ (2.61 eV) allowed for the establishment of an equilibrium between the triplet states in the DNA sample with directly adjacent donor and acceptor groups. The rate of triplet energy transfer was found to strongly depend on the spatial separation between TX_{DNA} and Ntl_{DNA}. For the shortest separation (adjacent positioning, n = 0), a rapid transfer rate of (k_{TTET} = (58.8 ± 11.7) 10^6 s^{-1} was measured. In contrast, increasing the separation to four

intervening A–T base pairs effectively suppressed any detectable energy transfer. From these measurements, an attenuation factor of 1.15 $Å^{-1}$ was extracted (Figure 10C), consistent with a tunneling-based mechanism in which the energy barrier is imposed by the intervening thymine (Figure 10A for structure) nucleobases (Figure 10D). These results underscore that DNA is a poor conductor of triplet energy. Although π-stacking lowers the triplet energy of nucleobases, it remains high enough to limit long-range energy transfer from UVA-absorbing triplet donors and effectively blocks sensitization by visible light-absorbing dyes, which typically have triplet energies below 2.7 eV.

Project **[A]** was published as a research article:

"Direct Observation of Triplet-Triplet Energy Transfer in DNA Between Energy Donor and Acceptor C-Nucleotides"

Reprinted with permission from S. Häcker, T. J. B. Zähringer, H.-A. Wagenknecht, C. Kerzig, *JACS Au*, **2025**, *ASAP*. DOI: https://doi.org/10.1021/jacsau.5c00364 Copyright 2025 American Chemical Society.

The reference is attached in the following pages and can be cited corresponding to ref.[A]. The supporting information can be found in Chapter 10.2.

Author contributions: C. Kerzig and H.-A. Wagenknecht ideated the Project and provided general guidance. S. Häcker synthesized and characterized the DNA samples. T. J. B. Zähringer performed the spectroscopic analysis. The manuscript was written by all authors.

JACS Au
AN OPEN ACCESS JOURNAL OF THE AMERICAN CHEMICAL SOCIETY

Open Access
This article is licensed under CC-BY 4.0

pubs.acs.org/jacsau
Article

Direct Observation of Triplet−Triplet Energy Transfer in DNA between Energy Donor and Acceptor C-Nucleotides

Sebastian Häcker,[§] Till J. B. Zähringer,[§] Hans-Achim Wagenknecht,* and Christoph Kerzig*

Cite This: https://doi.org/10.1021/jacsau.5c00364
Read Online

ACCESS | Metrics & More | Article Recommendations | Supporting Information

ABSTRACT: Investigating the migration of excited-state energy in DNA is crucial for a deep understanding of protection mechanisms and light-induced DNA damage. While numerous reports focused on single electron transfer and Förster-type energy transfer in DNA, studies on the Dexter-type triplet−triplet energy transfer are scarce, in particular, those with direct detection of photoexcited triplet states. Herein, we present direct measurements of the distance-dependent triplet−triplet energy transfer rates through DNA by using transient absorption spectroscopy. This was achieved through the synthetic incorporation of thioxanthone as an energy donor and naphthalene as an energy acceptor into a DNA double strand at defined positions. The energy transfer rates strongly depend on the number of A-T base pairs (up to four) separating the energy donor from the energy acceptor. We observed a fast energy transfer rate with a time constant of 17 ns for the DNA sample in which the donor and acceptor are directly adjacent in the DNA. By analyzing two additional donor−acceptor distances, a steep exponential distance dependence with an attenuation factor of 1.15 $Å^{-1}$ could be obtained. Our results demonstrate that DNA acts as a poor conductor of triplet energy when energy donors with triplet energies below 2.7 eV are used, complementing more indirect studies on sensitized DNA damage.

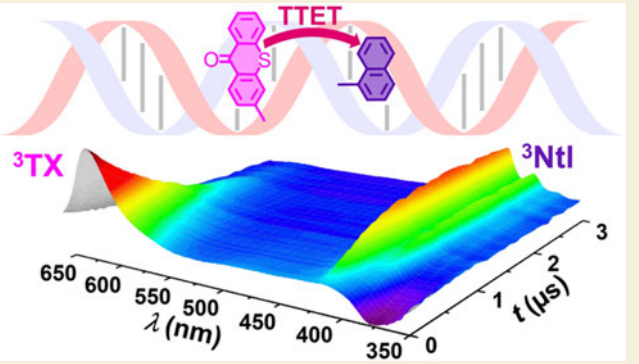

KEYWORDS: *DNA, energy transfer, oligonucleotides, photochemistry, time-resolved spectroscopy*

Downloaded via UNIV MAINZ on June 16, 2025 at 16:12:58 (UTC).
See https://pubs.acs.org/sharingguidelines for options on how to legitimately share published articles.

INTRODUCTION

Solar ultraviolet (UV) light can be a threat to DNA, leading to light-induced DNA damage which, in the worst case, can lead to skin cancer.[1−3] Nonetheless, in most cases, the excited states in DNA decay extremely fast (<1 ps) into charge-separated states. These return to their ground state through charge recombination, a property of DNA that protects it from light-induced damage.[4−6] However, excited singlet states can also lead to photochemical reactions. For example, cyclobutane pyrimidine dimers (CPDs) are the most common DNA damage and are formed by singlet photochemistry on ultrafast time scale and in a nearly barrierless reaction at the site of excitation.[7−9] In addition to the well-studied singlet photochemistry in DNA, it has been shown that excited triplet states also play an important role in the formation of DNA damage such as one-electron oxidation, cross-linking or CPDs.[10−15] Singlet energy transfer typically occurs via dipole−dipole interactions, known as Förster Resonance Energy Transfer (FRET),[16] from an excited donor to an acceptor. In contrast, triplet−triplet energy transfer (TTET) proceeds predominantly through the exchange mechanism (Dexter-type),[17] which shares mechanistic similarities with electron transfer.[18] Dexter energy transfer requires orbital overlap and, therefore, close proximity between the donor and acceptor. The range of triplet energy transfer can be significantly extended by introducing bridging units that enable through-bond energy transfer,[19] a phenomenon extensively studied in molecular systems.[20,21] In certain cases, triplet-to-singlet energy transfer via dipole−dipole interactions has also been observed,[22] or both mechanisms may operate in tandem.[23] Depending on the thermodynamic barriers introduced by the bridging units, energy transfer may occur sequentially through intermediate states via a hopping mechanism, provided these states are energetically accessible, or through tunneling. The mechanism by which triplet energy transfer in DNA leads to DNA damage is not yet fully understood, primarily because it is challenging to excite and localize triplet states in DNA at defined positions. Yet understanding the different photochemical mechanisms leading to DNA damage is crucial for elucidating the different pathways to skin cancer.

Received: March 31, 2025
Revised: May 19, 2025
Accepted: May 20, 2025

© XXXX The Authors. Published by American Chemical Society

In recent studies, triplet states of DNA bases have been made accessible by photosensitizers, which were selectively incorporated into the DNA as C-nucleosides. By indirect detection methods, we observed distance-dependent energy transfer in the DNA leading to CPD damage.[24−26] Localized triplet states of DNA bases have been spectroscopically observed,[27−29] and emission-based measurements involving DNA-intercalated metal complexes as energy donors suggest the occurrence of triplet−triplet energy transfer.[30,31] However, the observed shallow distance dependence of energy migration deviates from the predictions of the exchange mechanism,[30,31] instead aligning more closely with long-range Förster transfer[32,33] or a combination of both mechanisms.[30] This highlights the limitations of relying on indirect, emission-based techniques, which can introduce ambiguity regarding the underlying mechanism, particularly in complex systems like DNA.[34] Another study led by Brun and Harriman used intercalated acridine orange as energy donor tracking energy transfer to a palladium complex by transient absorption methods.[35] However, a definitive conclusion is challenging, as dipole−dipole interactions occurred simultaneously, and the lack of covalent bonding between the energy donor and acceptor further complicated the interpretation of the results. To the best of our knowledge, we provide the first direct evidence of an exchange-type triplet energy transfer through DNA, demonstrated using transient absorption spectroscopy. Our study thus complements prior experimental and theoretical studies on triplet states and photosensitization in DNA.[36−43]

RESULTS AND DISCUSSION

Design of the Study

We selected thioxanthone (TX) as the triplet energy donor and naphthalene (Ntl) as the triplet energy acceptor. This extensively studied donor−acceptor pair has well-established triplet−triplet absorption spectra (see Scheme 1) and energy transfer kinetics, making it a textbook example for triplet−triplet energy transfer.[44] Moreover, the long triplet state lifetimes of both the donor and acceptor chromophore (>10 μs),[45] which is typical for organic chromophores, facilitate the detection of slower quenching processes anticipated at greater donor−acceptor distances. The triplet state energy of thioxanthone is reported at 2.75 eV[46] giving the required thermodynamic driving force for the energy transfer to naphthalene (2.63 eV).[45] Notably, this energy should be insufficient to directly sensitize the DNA bases by triplet−triplet energy transfer,[40,47] in alignment with our prior study monitoring CPD damage with a thioxanthone C-nucleoside as the sensitizer.[26] These characteristics make the TTET donor−acceptor pair an ideal candidate for studying triplet energy migration in DNA in a direct fashion. In this study, the triplet energy donor thioxanthone and the triplet energy acceptor naphthalene were integrated into complementary DNA strands, both as C-nucleosides at specific distances using phosphoramidite chemistry. We investigate three DNA double strands abbreviated as **TX-Ntl-*n***, along with three reference DNA samples labeled **TX-*n*** (where n = 0, 1, 2), corresponding to the number of two alternating A-T base pairs separating the TX and Ntl C-nucleosides (see Scheme 1). The reference samples were synthesized under identical conditions, however, at the position of the Ntl C-nucleoside, the initial base (thymine) is reinstalled. This allows us to directly assess the presence and absence of the energy acceptor on the photochemistry of the TX C-nucleoside.

Scheme 1. Top: Structure of Energy Donor (TX) and Acceptor (Ntl) Containing C-Nucleosides and Color-Coded Reference Triplet−Triplet Absorption Spectra Obtained for the Isolated Chromophores in Acetonitrile upon 355 nm Laser Excitation[a]

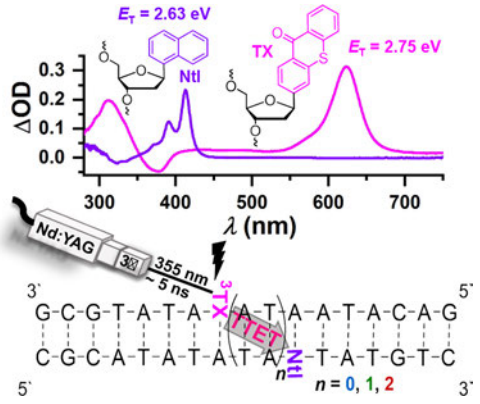

[a]Bottom: Schematic representation of the DNA double strands **TX-Ntl-*n*** used to analyze the distance dependence of the TTET kinetics in DNA double strands.

Synthesis

The synthesis of the corresponding thioxanthone C-nucleoside as a DNA building block for our study was reported previously by one of our groups. The naphthalene C-nucleoside **4** was obtained by a similar synthetic approach.[26] Briefly, the first and key step is a Heck reaction. The TBDMS-protected glycal **1** for this reaction was obtained from TBDMS-protected thymidine by elimination of thymine, while 1-bromonaphthalene was available from a commercial supplier.[48] In this case the catalyst $Pd_2(dba)_3$ with the ligand Q-Phos proved to be most effective with a combined yield of 79% of singly and doubly TBDMS-protected product **2**. The TBDMS group in the 2'-position shields the down face of the glycal **1**. As a result, the Heck reaction occurs stereoselectively to the desired and natural-like β-anomer **2**. The further reactions are deprotection of the TBDMS groups of **2**, stereoselective reduction of the carbonyl group at the 3′-position of **3** and conversion of **4** in two steps to the desired phosphoramidite **6** were carried out following our previously established procedures (Scheme 2).[26]

The DNA double strands **TX-Ntl-0**, **TX-Ntl-1** and **TX-Ntl-2** were prepared using the TX- and Ntl-containing phosphoramidites as DNA building blocks. Both phosphoramidites were characterized by ^{1}H and ^{31}P NMR spectroscopy as well as HR ESI-MS (Figures S27−S29). The resulting DNA single strands were synthesized via automated oligonucleotide solid-phase synthesis and purified by RP-HPLC through fractional collection. Fractions containing the desired DNA strand, determined by MALDI-TOF-MS, were combined, and the purity was confirmed again using analytical RP-HPLC (Figures S32−S34). The complementary DNA single strands modified either with TX or Ntl were annealed to double strands by heating to 90 °C for 10 min and slow cooling to room temperature. As control DNA samples, double strands were prepared without the triplet energy acceptor naphthalene (Figure 1, top). Furthermore, a reference DNA sample containing only Ntl (**Ntl-Control**) was prepared (i.e., without

https://doi.org/10.1021/jacsau.5c00364
JACS Au XXXX, XXX, XXX−XXX

Scheme 2. Synthesis of Naphthalene C-Nucleoside 4 and Phosphoramidite 6 as DNA Building Block

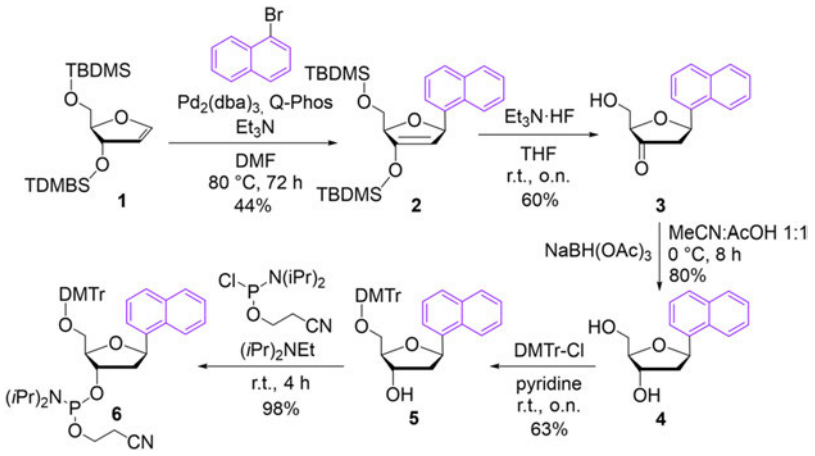

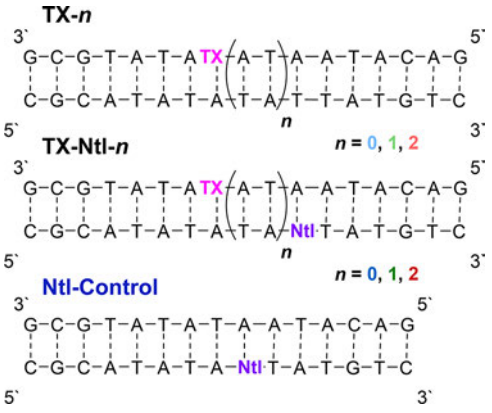

Figure 1. Top: Sequences of DNA double strands **TX-*n*** modified with TX and **TX-Ntl-*n*** modified with both TX and Ntl. Bottom: color-coded UV−vis absorption spectra of 90 μM DNA double strands **TX-*n***, **TX-Ntl-*n*** and **Ntl-Control** (dark blue) in aqueous buffer solution (250 mM NaCl, 10 mM Na−P_i buffer, pH 7.0) and of 80 μM thioxanthone (pink) or 200 μM naphthalene (purple) in MeCN.

TX; see Figure 1 for its structure). The unmodified DNA single strands for the latter double strands were purchased.

Optical Spectroscopy

The UV−vis absorption spectra of all DNA double strands show ∼ 20 nm red shifts of the long-wavelength absorption band of thioxanthone to 397 nm compared to the absorption spectrum of thioxanthone in acetonitrile with a maximum at 378 nm (Figure 1, bottom). The observed red shift can be explained by the more polar DNA environment, assuming that the TX chromophore is intercalated in the DNA base stack. This leads to a stabilization of the S_1 (π-π*) state.[49] As a result, a relatively high concentration (90 μM, based on double-strand DNA) of the samples was required to ensure efficient excitation at our laser wavelength 355 nm and sensitive TA detection accordingly. As is evident from the reference spectra of naphthalene in MeCN and the DNA double strand **Ntl-Control** (see Figure 1), both the naphthalene chromophore and the conventional DNA bases do not absorb at 355 nm, ensuring selective laser excitation of TX (see Section S4.2 for further control experiments).

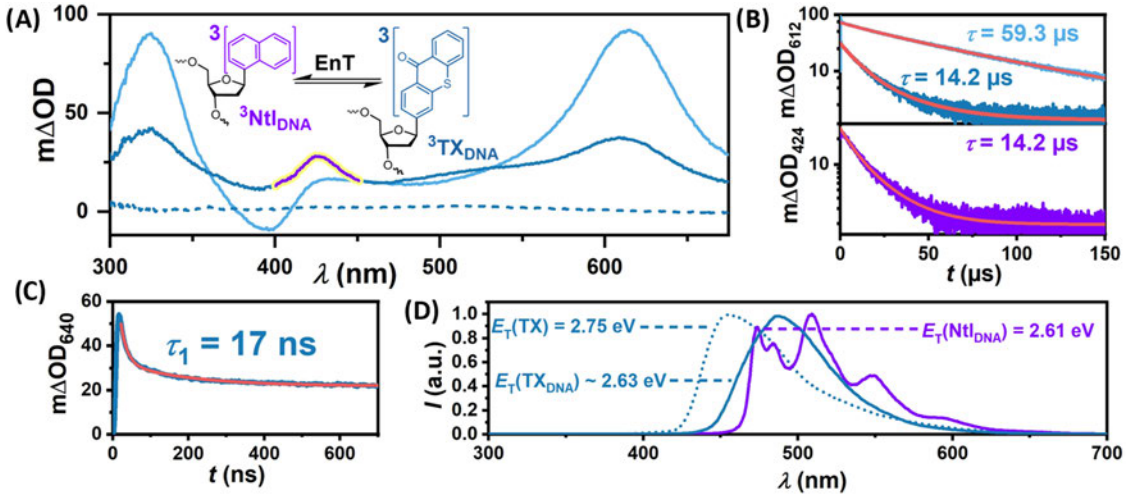

Figure 2. Mechanistic studies of **TX-Ntl-0** (dark blue) and **TX-0** (light blue) with 355 nm laser pulses. (A) Transient absorption spectra recorded 100 ns after excitation. The triplet−triplet absorption band of Ntl_{DNA} is highlighted in purple. (B) and (C) Time-resolved measurements at different detection wavelengths and time scales. (D) Time-gated 77 K emission of TX in MeCN (dotted line) and **TX-Ntl-0** in aqueous buffer (250 mM NaCl, 10 mM Na−P_i buffer, pH 7.0) integrated 10 ms − 100 ms (blue) and 4.0 to 4.3 s (purple) after laser excitation.

https://doi.org/10.1021/jacsau.5c00364
JACS Au XXXX, XXX, XXX−XXX

Transient absorption spectroscopy employing a pulsed 355 nm laser (~20 mJ, ~5 ns pulse duration) was used to excite the DNA double strands in deaerated aqueous solution containing 250 mM NaCl and 10 mM Na−P_i buffer (buffer pH 7: 6.1 mM sodium phosphate monobasic and 3.9 mM sodium phosphate dibasic). The first sample we investigated was **TX-Ntl-0**, in which TX and Ntl are adjacent without any base pairs in between, together with the reference DNA double strand **TX-0**. We first analyzed the TA spectrum of **TX-0**. Immediately following excitation (100 ns), two absorption bands appeared at 320 and 612 nm, along with a ground-state bleach (GSB) observed at ~ 400 nm (Figure 2A).

These bands are associated with a TX-localized triplet state of the C-nucleotide of TX ($^3TX_{DNA}$),[46] which is rapidly generated via intersystem crossing from the singlet-excited state.[50] Compared to the triplet absorption spectrum of TX in MeCN (Figure S1A), the bands exhibit slight shifts, a phenomenon previously noted for TX in protic solvents and attributed to substitution at position 2.[51] We obtain a triplet state lifetime of 59.3 μs for **TX-0** (Figure 2B, top panel), within the lifetime range of unquenched ^{3}TX and its derivatives in aprotic and protic solvents.[52−54] We conclude that the triplet-excited state of the C-nucleotide of TX is not quenched by the DNA bases in line with prior investigations, where CPD as a result of triplet−triplet energy transfer was only observed for triplet energy donors with higher triplet energies (>2.80 eV).[26] Exciting the DNA **TX-Ntl-0** yielded an additional absorption band centered at 424 nm alongside the triplet absorption spectrum of TX directly after excitation (a 100 ns delay time was used to ensure the absence of stray light and fluorescence). This absorption band could be attributed to the Ntl-localized triplet state of the C-nucleotide ($^3Ntl_{DNA}$). Compared to the triplet absorption spectrum of Ntl in MeCN (Figure S1A), the fine structure is lost due to broadening and the spectrum is shifted to longer wavelengths. However, these observations can be traced back to the solvent influence on the Ntl triplet[55] and to the conversion of Ntl to the 2′-deoxyribofuranoside at the α-position.[56] In line with our observations, Kiefhaber et al. reported a similar transient absorption spectrum for ^{3}Ntl, with a peak at 420 nm, when they investigated the TTET dynamics between TX and Ntl connected by a peptide bridge.[57] We found that both transient species concurrently decay with a lifetime of 14.2 μs (Figure 2B). Assigning the species with the ~420 nm absorption band to $^3Ntl_{DNA}$ raises the question of why both $^3Ntl_{DNA}$ and $^3TX_{DNA}$ appear to form after excitation (100 ns delay) and decay with essentially identical lifetimes. This is particularly puzzling given that (i) we have ruled out the direct excitation of Ntl_{DNA} and (ii) the proposed energy transfer mechanism suggests that $^3Ntl_{DNA}$ should be generated during the quenching of $^3TX_{DNA}$. Indeed, the C-nucleotides of TX and Ntl in the **TX-Ntl-0** DNA are in close proximity (3.4 Å based on regular stacking distance),[58] which is within the typical distance required for efficient Dexter-type energy transfer (<1 nm). Consequently, we expect the energy transfer to occur nearly instantaneously (<100 ns). However, detection in that range is challenging due to the strong fluorescence signal from TX (see also Section S4.4), which causes detector saturation. For this reason, a detection wavelength of 640 nm was chosen for $^3TX_{DNA}$ (Figure 2C), where the TX singlet state does not emit anymore. Time-resolved measurements show indeed a more complex kinetic scenario, and a biexponential fit resulted in a lifetime of 17 ns for the faster component, superimposed by the longer lifetime (compare Figure 2B). The seemingly incomplete quenching of $^3TX_{DNA}$ prompted us to conduct time-gated 77 K emission spectroscopy. Interestingly, we observed two emission signals at different time intervals, which can be attributed to the phosphorescence of $^3TX_{DNA}$ followed by that of $^3Ntl_{DNA}$ (Figure 2D). Compared to the phosphorescence of TX in MeCN, the emission from the thioxanthone C-nucleoside is significantly red-shifted (~40 nm), indicating a decrease in triplet state energy. Similar environment effects on triplet-related properties in DNA were predicted and observed before.[26,59,60]

We propose that the lower triplet state energy of TX_{DNA} reduces the energy gap to $^3Ntl_{DNA}$, which enables back energy transfer (bTTET) at room temperature reaching an equilibrated state.[61−63] At 77 K bTTET becomes negligibly slow as is evident from time-gated emission spectra shown in Figure S11. Based on all these observations, we estimate the triplet state energy of Ntl_{DNA} to be 2.61 eV. Determining the triplet energy of TX_{DNA} is more challenging due to its broad phosphorescence spectrum. However, using the relative distribution of triplet states between Ntl_{DNA} and TX_{DNA} at 77 K and in the equilibrated state at room temperature, we estimate its energy to be approximately 2.63 eV (see Section S4.7 of the SI for details). These energy estimations support the assumption that TX has a lower triplet state energy than the DNA bases, consistent with the absence of characteristic transient absorption bands from the nucleotides.[40] Emission quenching of singlet-excited TX_{DNA} seems to be a minor process and occurs on a shorter time scale than the observed initial $^3TX_{DNA}$ decay and $^3Ntl_{DNA}$ formation (Section S4.4), ruling out significant contributions of Förster-like energy transfer processes. To summarize the results obtained for DNA **TX-Ntl-0**, after the formation of $^3TX_{DNA}$ we unequivocally observe rapid triplet−triplet energy transfer to Ntl_{DNA} with $k_{TTET} = (58.8 \pm 11.7) \times 10^6\ s^{-1}$ (see SI for calculation of k_{TTET}), reaching an equilibrated state[64] of $^3TX_{DNA}$ and $^3Ntl_{DNA}$ owing to the almost isoenergetic triplet states. These triplet states decay on a much longer time scale (k_{TTET}, $k_{bTTET} \gg k_{TX}$, k_{Ntl}). Interestingly such an energy transfer equilibrium has also been described by Kiefhaber et al. for the same donor−acceptor pair in a peptide environment.[57]

Next, we examined the DNA double strand **TX-Ntl-1**, with two A-T base pairs separating the TX and Ntl C-nucleotides, in conjunction with the reference DNA **TX-1**. The TA spectra recorded 100 ns after 355 nm laser excitation are almost identical for these DNA samples (Figure 3A).

Yet, time-resolved measurements of $^3TX_{DNA}$ at 612 nm, where it can be monitored in isolation, reveal a faster deactivation in the presence of Ntl_{DNA} (**TX-Ntl-1**) in comparison to its absence (**TX-1**). This observation suggests $^3TX_{DNA}$ quenching by Ntl_{DNA} (Figure 3B). Indeed, we observe the formation of the $^3Ntl_{DNA}$ band at longer delay times (inset of Figures 3A, and S9). Comparative kinetic measurements at 424 nm show the slow formation of $^3Ntl_{DNA}$ in **TX-Ntl-1** (Figure 3C). This signal rise cannot be observed for **TX-1**, which again shows a lifetime being typical for unquenched ^{3}TX. For this rather slow quenching process, we ruled out the possibility of inter-DNA energy transfer (from TX of one DNA double strand to Ntl in another DNA double strand, compare results with **TX-Ntl-2** presented below) and attribute this to intra-DNA triplet energy migration from $^3TX_{DNA}$ to Ntl_{DNA} (in the same DNA double strand). Moreover, $^3TX_{DNA}$ was only moderately quenched by dissolved oxygen in the air-saturated

https://doi.org/10.1021/jacsau.5c00364
JACS Au XXXX, XXX, XXX−XXX

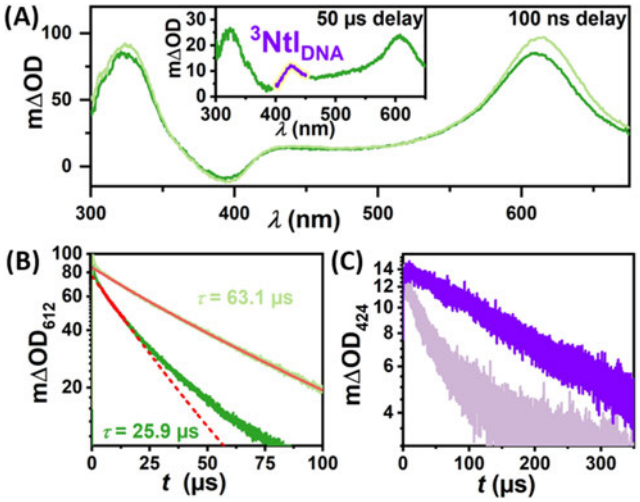

Figure 3. Mechanistic studies of **TX-Ntl-1** (dark green) and **TX-1** (light green) with 355 nm laser pulses. (A) TA spectra recorded 100 ns after excitation. Inset: TA spectrum of **TX-Ntl-1** recorded 50 μs after excitation. The triplet−triplet absorption band of Ntl_{DNA} is highlighted in purple. (B) Kinetic TA measurements at 612 nm. (C) Kinetic TA measurements of **TX-Ntl-1** (purple) and **TX-1** (light purple) at 424 nm.

solution of **TX-0**, underscoring the protective geometry of the DNA backbone. To determine the energy transfer constant, the decay trace of $^3TX_{DNA}$ at 612 nm was fitted monoexponentially until the energy transfer efficiency η_{EnT} reaches ∼ 30% and back energy transfer has to play a minor role, making the reasonable assumption that TTET is faster than bTTET. Using the unquenched (τ = 63.1 μs) and quenched lifetime of $^3TX_{DNA}$ (τ = 25.9 μs) we calculate an energy transfer rate constant of $k_{TTET} = (22.7 \pm 4.0) \times 10^3\ s^{-1}$. In contrast to **TX-Ntl-0** the (back) energy transfer constant in **TX-Ntl-1** is several orders of magnitude slower due to the larger separation of the C-nucleotides in the DNA (10.2 Å), and on the same order as the triplet decay constants of TX_{DNA} and Ntl_{DNA} ($k_{TTET} > k_{bTTET} \sim k_{TX}, k_{Ntl}$). As a result, an equilibrium-like state is reached on a much slower time scale (Figure S9C).

Lastly, the DNA double strands **TX-Ntl-2** and **TX-2** were examined. Virtually identical TA spectra are observed after excitation (Figure 4A). However, in contrast to the pair with the shorter donor−acceptor distance investigated in Figure 3, kinetic traces of $^3TX_{DNA}$ yield essentially identical lifetimes, taking experimental errors into account. Only a minor lifetime

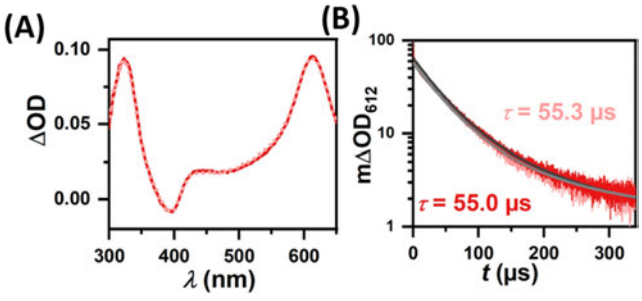

Figure 4. Mechanistic studies of **TX-Ntl-2** (dark red) and **TX-2** (light red) with 355 nm laser pulses. (A) TA spectra recorded 100 ns after excitation. (B) Kinetic TA measurements at 612 nm.

decrease from 55.3 ± 0.8 to 55.0 ± 0.9 μs is observed with the introduction of the Ntl C-nucleotide into the DNA double strand (Figure 4B). The high photostability of the DNA samples allowed us to perform several independent sets of measurements, supporting the reliability of the obtained lifetimes (see Section S4.7). Based on this, we calculated an energy transfer constant of (100 ± 400) s^{-1}. However, we would like to note that the deviation is higher than the calculated energy transfer constant and should be seen as an upper limit while $k_{TTET} = 0\ s^{-1}$ sets the lower limit. In any case, at this donor−acceptor distance with four A-T base pairs in-between the donor and the acceptor (17 Å), TTET becomes negligibly small. Given that $^3TX_{DNA}$ is virtually not quenched by Ntl in **TX-Ntl-2** on this long time scale which would enable efficient diffusion of large DNA fragments, we can also exclude the possibility of inter-DNA energy transfer as a competing pathway alongside the primary intra-DNA energy migration. In a somewhat related system with a methoxyxanthone C-nucleoside as light absorber, the CPD yields are very similar for double stands with zero or four separating A-T base pairs.[65] The completely different behavior observed in this study with a drastically more pronounced distance dependence already indicates a Dexter-like instead of a FRET-like energy migration mechanism.

During our experimental work, we observed a secondary process in all TX-containing DNA samples following 355 nm laser excitation, likely associated with the neighboring DNA bases. However, this process is unrelated to the primary focus of this study on triplet energy migration and does not affect the results. A detailed description, along with several control experiments, is provided in the Supporting Information (Section S4.3).

Distance-Dependence of Triplet−Triplet Energy Transfer

The above-mentioned triplet−triplet energy transfer rates in the three DNA samples with varying donor−acceptor separation were plotted against the respective donor−acceptor distance on a semilogarithmic scale (Figure 5). The distance dependence of electron transfer (ET) and TTET, both governed by exchange-type mechanisms between a donor and an acceptor, is empirically described by the exponential rate equation $k_{DA} = k_0 \cdot \exp(-\beta \cdot r_{DA})$.[20,21,66,67] Where β is the attenuation factor and it is fundamentally determined by the effective barrier height, ΔE_{eff}, which inversely correlates with the probability of electron tunneling.[68,69] In the so-called superexchange mechanism, coupling between donor and acceptor is facilitated by orbitals of bridging units, which greatly surpasses the two-electron exchange integral in magnitude.[70,71] In a simplified model proposed by Closs et al.,[72] the attenuation factor for ET is approximately half that of TTET, which can be conceptualized as the simultaneous exchange of two electrons broadly supported by *ab initio* and semiempirical calculations.[73] However, this assumption does not hold true, when intermediate virtual donor−acceptor CT or bridge-localized excited states are involved in the energy transfer pathways.[19] In such a scenario, the β value can be lower than the sum of the superexchange constants of electron and hole transfer (see Section S5 for further explanations).[71,74]

In environments with high barrier heights (ΔE_{eff} > 1 eV), such as vacuum or certain solvents, β values typically range from 1.5 to 5 $Å^{-1}$.[74,75] Molecular bridging significantly enhances the exchange mechanism between donor and acceptor attributed to a reduced ΔE_{eff} and low lying virtual

https://doi.org/10.1021/jacsau.5c00364
JACS Au XXXX, XXX, XXX−XXX

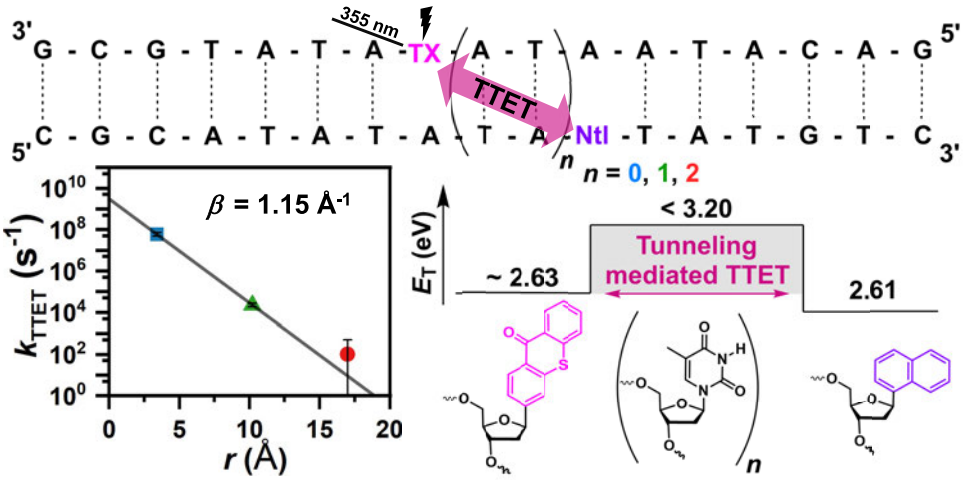

n	$\tau(^3TX_{DNA})$ (μs)	$\tau_{ref}(^3TX_{DNA})$ (μs)	k_{TTET} (s^{-1})
0	(17 ± 3.4) × 10^{-3}	59.3 ± 3.3	(58.8 ± 11.7) × 10^6 (■)
1	25.9 ± 2.6	63.1 ± 4.7	(22.7 ± 4.0) × 10^3 (▲)
2	55.0 ± 1.0	55.3 ± 1.0	(0.1 ± 0.4) × 10^3 (●)

Figure 5. Sequences of DNA double strands **TX-Ntl-*n***, experimentally observed distance dependence of triplet−triplet energy transfer from $^3TX_{DNA}$ to Ntl_{DNA}, schematic energy diagram of triplet−triplet energy transfer with plausible tunneling mechanism via the thymine triplet state. The table displays the quenched (τ for **TX-Ntl-*n***) and unquenched (τ_{ref} for **TX-*n***) TX triplet lifetimes and the resulting TTET rate constants. See Table S1 for details.

bridge states that mediate electronic coupling. For instance, TTET between Ru and Os complexes employing aromatic spacers such as phenyleneethynylene[76,77] and phenylene[78] units are typically associated with attenuation factors <1 $Å^{-1}$. If the effective barrier height approaches the available thermal energy, TTET and ET can occur via a hopping mechanism with real intermediate states, significantly extending the transfer range and reducing β to values as low as <0.1 $Å^{-1}$.[79,80]

The DNA double helix presents a distinctive structure with arrays of π-stacked nucleobases separated by 3.4 Å. This configuration favors charge and energy transfer along the bases (through-space) rather than along the sugar−phosphate backbone (through-bond).[81] Tunneling and hopping mechanisms for charge transfer, particularly hole transfer, have been extensively studied in DNA systems.[81−90] In contrast, research on TTET within DNA remains limited and is usually based on indirect detection methods.[24,26,30,35] The handful of studies on this topic are further complicated by the combined effects of Förster- and Dexter-type energy transfer between intercalated donor and acceptor molecules.[30,35] These interactions obscure a clear understanding of the underlying mechanisms leading to vastly different β values and contradicting interpretations.[31]

Among the free nucleotides thymidine has the lowest triplet state energy (E_T = 3.2 eV).[40,91,92] In recent studies, led by one of our groups, the distance dependence of triplet−triplet energy transfer in DNA using high triplet energy donors was thoroughly investigated by detecting the formation of T−T dimers. When sensitizers with E_T > 3.0 eV where employed, a shallow distance dependence (0.13−0.37 $Å^{-1}$) suggested that a hopping mechanism was operative.[24,26] The triplet energies of the free nucleotides (≥3.2 eV) cannot support such a hopping mechanism, however stabilizing effects in DNA can significantly lower triplet state energies.[93] For instance, an average triplet state energy of 2.8 eV has been inferred for thymine in supercoiled circular DNA.[47] Accurately determining triplet state energies of nucleobases within the DNA stack is challenging, as they are influenced by distinct local environments. Recently, the triplet state energy of thymine in poly-A-T sequences − most relevant to our system − has been calculated at 3.0 eV using a free energy perturbation method that accounts for DNA effects.[94]

Applying the above-mentioned fit function, we obtain an attenuation factor of 1.15 $Å^{-1}$, which is considerably higher than values reported in previous studies of long-range TTET in DNA using triplet sensitizers with E_T > 3.0 eV[24,26] and more resembling reports of insulating bridging units in other molecular systems.[68,95] Hence, a hopping mechanism involving intermediate states of DNA bases[26,34,39] is unlikely, which is consistent with the absence of triplet state signals from DNA bases in the transient absorption spectra.[40] Considering the effective barrier height between the triplet donor (~2.63 eV) and the bridge (calculated at 3.0 eV for poly-A-T sequences) the attenuation factor supports a concerted TTET exchange mechanism, however, the involvement of virtual bridge or CT states cannot be excluded completely (see Section S5 for details).[94] Based on these findings, we propose that a tunneling mechanism facilitates intra-DNA energy transfer in **TX-Ntl-1** and most likely in **TX-Ntl-2** as well.[70,76,77,96] The most plausible scenario involves a through-space mediated exchange interaction across the A-T pairs (Figure 5).

CONCLUSIONS

In this study, we have demonstrated that the DNA structure supports triplet energy transfer between thioxanthone (donor) and naphthalene (acceptor), which proceeds via a tunneling mechanism when a direct donor−acceptor orbital overlap is not feasible. Both chromophores were placed as artificial C-nucleotides at defined places in the DNA sequences. Through transient absorption spectroscopy, we provide direct evidence for triplet−triplet energy transfer and determined energy transfer rates for three specific donor−acceptor separations: directly adjacent (3.4 Å), separated by two (10.2 Å) and by

https://doi.org/10.1021/jacsau.5c00364
JACS Au XXXX, XXX, XXX−XXX

four alternating A-T base pairs (17 Å). From these measurements, we calculated an attenuation factor of 1.15 $Å^{-1}$, consistent with related DNA electron transfer studies. Notably, the energy transfer rate observed in the DNA double strand with longest separation between donor and acceptor shows that energy migration becomes negligible at a donor−acceptor separation of four base pairs (17 Å) comparable to molecular donor−acceptor systems with insulating bridging units.[68,95] This highlights DNA as a relatively poor conductor of triplet energy when hopping is thermodynamically unfeasible. While the triplet state energy of nucleobases is reduced due to π-stacking in DNA, it remains sufficiently high to suppress long-ranged energy migration by UVA-absorbing triplet donors and is likely entirely impractical when using visible light-absorbing sensitizers, whose triplet energies are usually well below 2.7 eV.[45,97] This serves as an effective protective mechanism for DNA against sunlight-driven sensitization. These findings align with the conclusions of Miranda et al., who established an alert limit for phototoxicity in chemicals at an $E_T \sim 2.8$ eV.[47]

■ ASSOCIATED CONTENT

Data Availability Statement

All experimental data have been provided in the main text and the SI. The data sets shown in the main paper be found under https://doi.org/10.25358/openscience-12363.

Supporting Information

The Supporting Information is available free of charge at https://pubs.acs.org/doi/10.1021/jacsau.5c00364.

Materials and methods, experimental details, characterization data, additional steady-state and time-resolved spectroscopic results, raw data sets, and control experiments (PDF)

■ AUTHOR INFORMATION

Corresponding Authors

Hans-Achim Wagenknecht − *Institute of Organic Chemistry, Karlsruhe Institute of Technology (KIT), Karlsruhe 76131, Germany*; orcid.org/0000-0003-4849-2887; Email: wagenknecht@kit.de

Christoph Kerzig − *Department of Chemistry, Johannes Gutenberg University Mainz, Mainz 55128, Germany*; orcid.org/0000-0002-1026-1146; Email: ckerzig@uni-mainz.de

Authors

Sebastian Häcker − *Institute of Organic Chemistry, Karlsruhe Institute of Technology (KIT), Karlsruhe 76131, Germany*

Till J. B. Zähringer − *Department of Chemistry, Johannes Gutenberg University Mainz, Mainz 55128, Germany*

Complete contact information is available at: https://pubs.acs.org/10.1021/jacsau.5c00364

Author Contributions

[§]S.H. and T.J.B.Z. contributed equally to this paper, names ordered alphabetically.

Notes

The authors declare no competing financial interest.

■ ACKNOWLEDGMENTS

We acknowledge generous financial support from the JGU Mainz the KIT and the German Research Foundation (DFG, grant number KE 2313/7-1). T.J.B.Z. is grateful to the German Federal Environmental Foundation (DBU) for a PhD fellowship (grant number 20022/028).

■ REFERENCES

(1) Pfeifer, G. P.; Besaratinia, A. UV Wavelength-Dependent DNA Damage and Human Non-Melanoma and Melanoma Skin Cancer. *Photochem. Photobiol. Sci.* **2012**, *11* (1), 90−97.

(2) Cadet, J.; Douki, T. Formation of UV-Induced DNA Damage Contributing to Skin Cancer Development. *Photochem. Photobiol. Sci.* **2018**, *17* (12), 1816−1841.

(3) Taylor, J. S. Unraveling the Molecular Pathway from Sunlight to Skin Cancer. *Acc. Chem. Res.* **1994**, *27* (3), 76−82.

(4) Crespo-Hernández, C. E.; Cohen, B.; Hare, P. M.; Kohler, B. Ultrafast Excited-State Dynamics in Nucleic Acids. *Chem. Rev.* **2004**, *104* (4), 1977−2020.

(5) Middleton, C. T.; De La Harpe, K.; Su, C.; Law, Y. K.; Crespo-Hernández, C. E.; Kohler, B. DNA Excited-State Dynamics: From Single Bases to the Double Helix. *Annu. Rev. Phys. Chem.* **2009**, *60* (1), 217−239.

(6) Kohler, B. Nonradiative Decay Mechanisms in DNA Model Systems. *J. Phys. Chem. Lett.* **2010**, *1* (13), 2047−2053.

(7) Heil, K.; Pearson, D.; Carell, T. Chemical Investigation of Light Induced DNA Bipyrimidine Damage and Repair. *Chem. Soc. Rev.* **2011**, *40* (8), 4271−4278.

(8) Cadet, J.; Grand, A.; Douki, T. Solar UV Radiation-Induced DNA Bipyrimidine Photoproducts: Formation and Mechanistic Insights. In *Photoinduced Phenomena in Nucleic Acids II*; Barbatti, M.; Borin, A. C.; Ullrich, S., Eds. Topics in Current Chemistry; Springer International Publishing: Cham, 2014; Vol. *356*, pp 249−275 DOI: 10.1007/128_2014_553.

(9) Schreier, W. J.; Schrader, T. E.; Koller, F. O.; Gilch, P.; Crespo-Hernández, C. E.; Swaminathan, V. N.; Carell, T.; Zinth, W.; Kohler, B. Thymine Dimerization in DNA Is an Ultrafast Photoreaction. *Science* **2007**, *315* (5812), 625−629.

(10) Cadet, J.; Douki, T.; Ravanat, J.-L.; Di Mascio, P. Sensitized Formation of Oxidatively Generated Damage to Cellular DNA by UVA Radiation. *Photochem. Photobiol. Sci.* **2009**, *8* (7), 903−911.

(11) Epe, B. DNA Damage Spectra Induced by Photosensitization. *Photochem. Photobiol. Sci.* **2012**, *11* (1), 98−106.

(12) Cuquerella, M. C.; Lhiaubet-Vallet, V.; Cadet, J.; Miranda, M. A. Benzophenone Photosensitized DNA Damage. *Acc. Chem. Res.* **2012**, *45* (9), 1558−1570.

(13) Aparici-Espert, I.; Garcia-Lainez, G.; Andreu, I.; Miranda, M. A.; Lhiaubet-Vallet, V. Oxidatively Generated Lesions as Internal Photosensitizers for Pyrimidine Dimerization in DNA. *ACS Chem. Biol.* **2018**, *13* (3), 542−547.

(14) Francés-Monerris, A.; Hognon, C.; Miranda, M. A.; Lhiaubet-Vallet, V.; Monari, A. Triplet Photosensitization Mechanism of Thymine by an Oxidized Nucleobase: From a Dimeric Model to DNA Environment. *Phys. Chem. Chem. Phys.* **2018**, *20* (40), 25666−25675.

(15) Wagenknecht, H.-A. Remote Photodamaging of DNA by Photoinduced Energy Transport. *ChemBioChem* **2022**, *23* (2), No. e202100265.

(16) Förster, Th. Mechanisms of Energy Transfer. In *Comprehensive Biochemistry*; Elsevier, 1967; Vol. *22*, pp 61−80 DOI: 10.1016/B978-1-4831-9712-8.50010-2.

(17) Dexter, D. L. A Theory of Sensitized Luminescence in Solids. *J. Chem. Phys.* **1953**, *21* (5), 836−850.

(18) Hsu, C.-P. The Electronic Couplings in Electron Transfer and Excitation Energy Transfer. *Acc. Chem. Res.* **2009**, *42* (4), 509−518.

(19) Skourtis, S. S.; Liu, C.; Antoniou, P.; Virshup, A. M.; Beratan, D. N. Dexter Energy Transfer Pathways. *Proc. Natl. Acad. Sci. U.S.A.* **2016**, *113* (29), 8115−8120.

(20) Wenger, O. S. Photoinduced Electron and Energy Transfer in Phenylene Oligomers. *Chem. Soc. Rev.* **2011**, *40* (7), 3538.
(21) Albinsson, B.; Mårtensson, J. Excitation Energy Transfer in Donor−Bridge−Acceptor Systems. *Phys. Chem. Chem. Phys.* **2010**, *12* (27), 7338.
(22) Galley, W. C.; Stryer, L. Triplet-Singlet Energy Transfer in Proteins. *Biochemistry* **1969**, *8* (5), 1831−1838.
(23) Cravcenco, A.; Ye, C.; Gräfenstein, J.; Börjesson, K. Interplay between Förster and Dexter Energy Transfer Rates in Isomeric Donor−Bridge−Acceptor Systems. *J. Phys. Chem. A* **2020**, *124* (36), 7219−7227.
(24) Antusch, L.; Gaß, N.; Wagenknecht, H.-A. Elucidation of the Dexter-Type Energy Transfer in DNA by Thymine−Thymine Dimer Formation Using Photosensitizers as Artificial Nucleosides. *Angew. Chem., Int. Ed.* **2017**, *56* (5), 1385−1389.
(25) Gaß, N.; Wagenknecht, H.-A. Synthesis of Benzophenone Nucleosides and Their Photocatalytic Evaluation for [2 + 2] Cycloaddition in Aqueous Media. *Eur. J. Org. Chem.* **2015**, *2015* (30), 6661−6668.
(26) Häcker, S.; Schrödter, M.; Kuhlmann, A.; Wagenknecht, H.-A. Probing of DNA Photochemistry with C-Nucleosides of Xanthones and Triphenylene as Photosensitizers To Study the Formation of Cyclobutane Pyrimidine Dimers. *JACS Au* **2023**, *3* (7), 1843−1850.
(27) Wang, X.; Martínez-Fernández, L.; Zhang, Y.; Wu, P.; Kohler, B.; Improta, R.; Chen, J. Ultrafast Formation of a Delocalized Triplet-Excited State in an Epigenetically Modified DNA Duplex under Direct UV Excitation. *J. Am. Chem. Soc.* **2024**, *146* (3), 1839−1848.
(28) Eisinger, J.; Shulman, R. G. Excited Electronic States of DNA. *Science* **1968**, *161* (3848), 1311−1319.
(29) Lamola, A. A.; Guéron, M.; Yamane, T.; Eisinger, J.; Shulman, R. G. Triplet State of DNA. *J. Chem. Phys.* **1967**, *47* (7), 2210−2217.
(30) Hurley, D. J.; Tor, Y. Donor/Acceptor Interactions in Systematically Modified Ru^{II} − Os^{II} Oligonucleotides. *J. Am. Chem. Soc.* **2002**, *124* (44), 13231−13241.
(31) Holmlin, R. E.; Tong, R. T.; Barton, J. K. Long-Range Triplet Energy Transfer between Metallointercalators Tethered to DNA: Importance of Intercalation, Stacking, and Distance. *J. Am. Chem. Soc.* **1998**, *120* (37), 9724−9725.
(32) Lakowicz, J. R.; Piszczek, G.; Kang, J. S. On the Possibility of Long-Wavelength Long-Lifetime High-Quantum-Yield Luminophores. *Anal. Biochem.* **2001**, *288* (1), 62−75.
(33) Kang, J. S.; Piszczek, G.; Lakowicz, J. R. Enhanced Emission Induced by FRET from a Long-Lifetime, Low Quantum Yield Donor to a Long-Wavelength, High Quantum Yield Acceptor. *J. Fluoresc.* **2002**, *12* (1), 97−103.
(34) Giese, B. Long-Distance Charge Transport in DNA: The Hopping Mechanism. *Acc. Chem. Res.* **2000**, *33* (9), 631−636.
(35) Brun, A. M.; Harriman, A. Energy- and Electron-Transfer Processes Involving Palladium Porphyrins Bound to DNA. *J. Am. Chem. Soc.* **1994**, *116* (23), 10383−10393.
(36) Zhang, X.; Hu, H.; Liu, W.; Wang, Y.; Liu, J.; Wu, P. Selective Heavy Atom Effect Forming Photosensitizing Hot Spots in Double-Stranded DNA Matrix. *J. Phys. Chem. Lett.* **2021**, *12* (38), 9205−9212.
(37) Jin, P.; Wang, J.-N.; Wang, X.; Jia, M.; Pan, H.; Mei, Y.; Chen, J. Tracking the Early Stage of Triplet-Induced Photodamage in a DNA Dimer and Oligomer Containing 5-Methylcytosine. *J. Phys. Chem. B* **2023**, *127* (31), 6878−6886.
(38) Lu, C.; Gutierrez-Bayona, N. E.; Taylor, J.-S. The Effect of Flanking Bases on Direct and Triplet Sensitized Cyclobutane Pyrimidine Dimer Formation in DNA Depends on the Dipyrimidine, Wavelength and the Photosensitizer. *Nucleic Acids Res.* **2021**, *49* (8), 4266−4280.
(39) Blancafort, L.; Voityuk, A. A. Thermally Induced Hopping Model for Long-Range Triplet Excitation Energy Transfer in DNA. *Phys. Chem. Chem. Phys.* **2018**, *20* (7), 4997−5000.
(40) Gut, I. G.; Wood, P. D.; Redmond, R. W. Interaction of Triplet Photosensitizers with Nucleotides and DNA in Aqueous Solution at Room Temperature. *J. Am. Chem. Soc.* **1996**, *118* (10), 2366−2373.
(41) Nakatani, K.; Yoshida, T.; Saito, I. Photochemistry of Benzophenone Immobilized in a Major Groove of DNA: Formation of Thermally Reversible Interstrand Cross-Link. *J. Am. Chem. Soc.* **2002**, *124* (10), 2118−2119.
(42) Vendrell-Criado, V.; Rodríguez-Muñiz, G. M.; Cuquerella, M. C.; Lhiaubet-Vallet, V.; Miranda, M. A. Photosensitization of DNA by 5-Methyl-2-Pyrimidone Deoxyribonucleoside: (6 - 4) Photoproduct as a Possible Trojan Horse. *Angew. Chem., Int. Ed.* **2013**, *52* (25), 6476−6479.
(43) Curutchet, C.; Voityuk, A. A. Triplet−Triplet Energy Transfer in DNA: A Process That Occurs on the Nanosecond Timescale. *Angew. Chem., Int. Ed.* **2011**, *50* (8), 1820−1822.
(44) Klán, P.; Wirz, J. *Photochemistry of Organic Compounds: From Concepts to Practice*; Wiley: Chichester, West Sussex, U.K, 2009.
(45) Montalti, M.; Credi, A.; Prodi, L.; Gandolfi, M. T. *Handbook of Photochemistry*; CRC Press, 2006 DOI: 10.1201/9781420015195.
(46) Zähringer, T. J. B.; Wienhold, M.; Gilmour, R.; Kerzig, C. Direct Observation of Triplet States in the Isomerization of Alkenylboronates by Energy Transfer Catalysis. *J. Am. Chem. Soc.* **2023**, *145* (39), 21576−21586.
(47) Bosca, F.; Lhiaubet-Vallet, V.; Cuquerella, M. C.; Castell, J. V.; Miranda, M. A. The Triplet Energy of Thymine in DNA. *J. Am. Chem. Soc.* **2006**, *128* (19), 6318−6319.
(48) Cameron, M. A.; Cush, S. B.; Hammer, R. P. Facile Preparation of Protected Furanoid Glycals from Thymidine. *J. Org. Chem.* **1997**, *62* (26), 9065−9069.
(49) Dalton, J. C.; Montgomery, F. C. Solvent Effects on Thioxanthone Fluorescence. *J. Am. Chem. Soc.* **1974**, *96* (19), 6230−6232.
(50) Ley, C.; Morlet-Savary, F.; Jacques, P.; Fouassier, J. P. Solvent Dependence of the Intersystem Crossing Kinetics of Thioxanthone. *Chem. Phys.* **2000**, *255* (2−3), 335−346.
(51) Ferreira, G. C.; Schmitt, C. C.; Neumann, M. G. Dependence of the Thioxanthone Triplet-Triplet Absorption Spectrum with Solvent Polarity and Aromatic Ring Substitution. *J. Braz. Chem. Soc.* **2006**, *17* (5), 905−909.
(52) Yip, R. W.; Szabo, A. G.; Tolg, P. K. Triplet State of Ketones in Solutions. Quenching Rate Studies of Thioxanthenone Triplets by Flash Absorption. *J. Am. Chem. Soc.* **1973**, *95* (13), 4471−4472.
(53) Amirzadeh, G.; Schnabel, W. On the Photoinitiation of Free Radical Polymerization-Laser Flash Photolysis Investigations on Thioxanthone Derivatives. *Makromol. Chem.* **1981**, *182* (10), 2821−2835.
(54) Balta, D. K.; Temel, G.; Aydin, M.; Arsu, N. Thioxanthone Based Water-Soluble Photoinitiators for Acrylamide Photopolymerization. *Eur. Polym. J.* **2010**, *46* (6), 1374−1379.
(55) Grabner, G.; Rechthaler, K.; Mayer, B.; Köhler, G.; Rotkiewicz, K. Solvent Influences on the Photophysics of Naphthalene: Fluorescence and Triplet State Properties in Aqueous Solutions and in Cyclodextrin Complexes. *J. Phys. Chem. A* **2000**, *104* (7), 1365−1376.
(56) Takemura, T.; Hara, K.; Baba, H. Observation and Interpretation of Triplet-Triplet Absorption Spectra of Substituted Naphthalenes. *Bull. Chem. Soc. Jpn.* **1971**, *44* (4), 977−984.
(57) Bieri, O.; Wirz, J.; Hellrung, B.; Schutkowski, M.; Drewello, M.; Kiefhaber, T. The Speed Limit for Protein Folding Measured by Triplet−Triplet Energy Transfer. *Proc. Natl. Acad. Sci. U.S.A.* **1999**, *96* (17), 9597−9601.
(58) Watson, J. D.; Crick, F. H. C. The Structure of DNA. *Cold Spring Harbor Symp. Quant. Biol.* **1953**, *18* (0), 123−131.
(59) Nogueira, J. J.; Oppel, M.; González, L. Enhancing Intersystem Crossing in Phenotiazinium Dyes by Intercalation into DNA. *Angew. Chem., Int. Ed.* **2015**, *54* (14), 4375−4378.
(60) Curutchet, C.; Voityuk, A. A. Environment Effects on Triplet−Triplet Energy Transfer in DNA. *Chem. Phys. Lett.* **2011**, *512* (1−3), 118−122.
(61) Zähringer, T. J. B.; Moghtader, J. A.; Bertrams, M.; Roy, B.; Uji, M.; Yanai, N.; Kerzig, C. Blue-to-UVB Upconversion, Solvent Sensitization and Challenging Bond Activation Enabled by a

Benzene-Based Annihilator. *Angew. Chem., Int. Ed.* **2023**, *62* (8), No. e202215340.
(62) Strieth-Kalthoff, F.; Henkel, C.; Teders, M.; Kahnt, A.; Knolle, W.; Gómez-Suárez, A.; Dirian, K.; Alex, W.; Bergander, K.; Daniliuc, C. G.; Abel, B.; Guldi, D. M.; Glorius, F. Discovery of Unforeseen Energy-Transfer-Based Transformations Using a Combined Screening Approach. *Chem* **2019**, *5* (8), 2183−2194.
(63) Mongin, C.; Moroz, P.; Zamkov, M.; Castellano, F. N. Thermally Activated Delayed Photoluminescence from Pyrenyl-Functionalized CdSe Quantum Dots. *Nat. Chem.* **2018**, *10* (2), 225−230.
(64) Yarnell, J. E.; Wells, K. A.; Palmer, J. R.; Breaux, J. M.; Castellano, F. N. Excited-State Triplet Equilibria in a Series of Re(I)-Naphthalimide Bichromophores. *J. Phys. Chem. B* **2019**, *123* (35), 7611−7627.
(65) Kuhlmann, A.; Bihr, L.; Wagenknecht, H.-A. How Far Does Energy Migrate in DNA and Cause Damage? Evidence for Long-Range Photodamage to DNA. *Angew. Chem., Int. Ed.* **2020**, *59* (40), 17378−17382.
(66) Ricks, A. B.; Brown, K. E.; Wenninger, M.; Karlen, S. D.; Berlin, Y. A.; Co, D. T.; Wasielewski, M. R. Exponential Distance Dependence of Photoinitiated Stepwise Electron Transfer in Donor−Bridge−Acceptor Molecules: Implications for Wirelike Behavior. *J. Am. Chem. Soc.* **2012**, *134* (10), 4581−4588.
(67) Lewis, F. D.; Wu, T.; Zhang, Y.; Letsinger, R. L.; Greenfield, S. R.; Wasielewski, M. R. Distance-Dependent Electron Transfer in DNA Hairpins. *Science* **1997**, *277* (5326), 673−676.
(68) Andréasson, J.; Kajanus, J.; Mårtensson, J.; Albinsson, B. Triplet Energy Transfer in Porphyrin Dimers: Comparison between π- and σ-Chromophore Bridged Systems. *J. Am. Chem. Soc.* **2000**, *122* (40), 9844−9845.
(69) Jensen, K. K.; Van Berlekom, S. B.; Kajanus, J.; Mårtensson, J.; Albinsson, B. Mediated Energy Transfer in Covalently Linked Porphyrin Dimers. *J. Phys. Chem. A* **1997**, *101* (12), 2218−2220.
(70) Albinsson, B.; Martensson, J. Long-Range Electron and Excitation Energy Transfer in Donor−Bridge−Acceptor Systems. *J. Photochem. Photobiol., C* **2008**, *9* (3), 138−155.
(71) Lai, R.; Liu, Y.; Luo, X.; Chen, L.; Han, Y.; Lv, M.; Liang, G.; Chen, J.; Zhang, C.; Di, D.; Scholes, G. D.; Castellano, F. N.; Wu, K. Shallow Distance-Dependent Triplet Energy Migration Mediated by Endothermic Charge-Transfer. *Nat. Commun.* **2021**, *12* (1), No. 1532.
(72) Closs, G. L.; Piotrowiak, Piotr.; MacInnis, J. M.; Fleming, G. R. Determination of Long-Distance Intramolecular Triplet Energy-Transfer Rates. Quantitative Comparison with Electron Transfer. *J. Am. Chem. Soc.* **1988**, *110* (8), 2652−2653.
(73) Clayton, A. H. A.; Scholes, G. D.; Ghiggino, K. P.; Paddon-Row, M. N. Through-Bond and Through-Space Coupling in Photoinduced Electron and Energy Transfer: An *Ab Initio* and Semiempirical Study. *J. Phys. Chem. A* **1996**, *100* (26), 10912−10918.
(74) Curutchet, C.; Voityuk, A. A. Distance Dependence of Triplet Energy Transfer in Water and Organic Solvents: A QM/MD Study. *J. Phys. Chem. C* **2012**, *116* (42), 22179−22185.
(75) Gray, H. B.; Winkler, J. R. Long-Range Electron Transfer. *Proc. Natl. Acad. Sci. U.S.A.* **2005**, *102* (10), 3534−3539.
(76) Eng, M. P.; Ljungdahl, T.; Mårtensson, J.; Albinsson, B. Triplet Excitation Energy Transfer in Porphyrin-Based Donor−Bridge−Acceptor Systems with Conjugated Bridges of Varying Length: An Experimental and DFT Study. *J. Phys. Chem. B* **2006**, *110* (13), 6483−6491.
(77) Harriman, A.; Khatyr, A.; Ziessel, R.; Benniston, A. C. An Unusually Shallow Distance-Dependence for Triplet-Energy Transfer. *Angew. Chem., Int. Ed.* **2000**, *39* (23), 4287−4290.
(78) Welter, S.; Salluce, N.; Belser, P.; Groeneveld, M.; De Cola, L. Photoinduced Electronic Energy Transfer in Modular, Conjugated, Dinuclear Ru(II)/Os(II) Complexes. *Coord. Chem. Rev.* **2005**, *249* (13−14), 1360−1371.
(79) Huang, Z.; Xu, Z.; Huang, T.; Gray, V.; Moth-Poulsen, K.; Lian, T.; Tang, M. L. Evolution from Tunneling to Hopping Mediated Triplet Energy Transfer from Quantum Dots to Molecules. *J. Am. Chem. Soc.* **2020**, *142* (41), 17581−17588.
(80) Welter, S.; Lafolet, F.; Cecchetto, E.; Vergeer, F.; De Cola, L. Energy Transfer by a Hopping Mechanism in Dinuclear Ir^{III}/Ru^{II} Complexes: A Molecular Wire? *ChemPhysChem* **2005**, *6* (11), 2417−2427.
(81) Murphy, C. J.; Arkin, M. R.; Jenkins, Y.; Ghatlia, N. D.; Bossmann, S. H.; Turro, N. J.; Barton, J. K. Long-Range Photoinduced Electron Transfer Through a DNA Helix. *Science* **1993**, *262* (5136), 1025−1029.
(82) Wagenknecht, H.-A. Reductive Electron Transfer and Transport of Excess Electrons in DNA. *Angew. Chem., Int. Ed.* **2003**, *42* (22), 2454−2460.
(83) Wagenknecht, H.-A. Electron Transfer Processes in DNA: Mechanisms, Biological Relevance and Applications in DNA Analytics. *Nat. Prod. Rep.* **2006**, *23* (6), 973.
(84) Murphy, C. J.; Arkin, M. R.; Ghatlia, N. D.; Bossmann, S.; Turro, N. J.; Barton, J. K. Fast Photoinduced Electron Transfer through DNA Intercalation. *Proc. Natl. Acad. Sci. U.S.A.* **1994**, *91* (12), 5315−5319.
(85) Giese, B.; Spichty, M. Long Distance Charge Transport through DNA: Quantification and Extension of the Hopping Model. *ChemPhysChem* **2000**, *1* (4), 195−198.
(86) Kelley, S. O.; Barton, J. K. Electron Transfer Between Bases in Double Helical DNA. *Science* **1999**, *283* (5400), 375−381.
(87) Siriwong, K.; Voityuk, A. A. Electron Transfer in DNA. *WIREs Comput. Mol. Sci.* **2012**, *2* (5), 780−794.
(88) Kawai, K.; Majima, T. Hole Transfer Kinetics of DNA. *Acc. Chem. Res.* **2013**, *46* (11), 2616−2625.
(89) Senthilkumar, K.; Grozema, F. C.; Guerra, C. F.; Bickelhaupt, F. M.; Lewis, F. D.; Berlin, Y. A.; Ratner, M. A.; Siebbeles, L. D. A. Absolute Rates of Hole Transfer in DNA. *J. Am. Chem. Soc.* **2005**, *127* (42), 14894−14903.
(90) Takada, T.; Kawai, K.; Fujitsuka, M.; Majima, T. Direct Observation of Hole Transfer through Double-Helical DNA over 100 Å. *Proc. Natl. Acad. Sci. U.S.A.* **2004**, *101* (39), 14002−14006.
(91) Wood, P. D.; Redmond, R. W. Triplet State Interactions between Nucleic Acid Bases in Solution at Room Temperature: Intermolecular Energy and Electron Transfer. *J. Am. Chem. Soc.* **1996**, *118* (18), 4256−4263.
(92) Nguyen, M. T.; Zhang, R.; Nam, P.-C.; Ceulemans, A. Singlet−Triplet Energy Gaps of Gas-Phase RNA and DNA Bases. A Quantum Chemical Study. *J. Phys. Chem. A* **2004**, *108* (31), 6554−6561.
(93) Allahkaram, L.; Monari, A.; Dumont, E. The Behavior of Triplet Thymine in a Model B-DNA Strand. Energetics and Spin Density Localization Revealed by Ab Initio Molecular Dynamics Simulations† *. *Photochem. Photobiol.* **2022**, *98* (3), 633−639.
(94) García-Messeguer, R.; Navarrete-Miguel, M.; Martí, S.; Tuñón, I.; Roca-Sanjuán, D. DNA Triplet Energies by Free Energy Perturbation Theory. *J. Chem. Theory Comput.* **2025**, *21* (3), 1353−1359.
(95) Keller, R. A. Intramolecular Energy Transfer between Triplet States of Weakly Interacting Chromophores. II. Compounds in Which the Chromophores Are Perpendicular to Each Other. *J. Am. Chem. Soc.* **1968**, *90* (8), 1940−1944.
(96) Tan, Z.; Kote, R.; Samaniego, W. N.; Weininger, S. J.; McGimpsey, W. G. Intramolecular Singlet−Singlet and Triplet−Triplet Energy Transfer in Adamantyl-Linked Trichromophores. *J. Phys. Chem. A* **1999**, *103* (38), 7612−7620.
(97) Dutta, S.; Erchinger, J. E.; Strieth-Kalthoff, F.; Kleinmans, R.; Glorius, F. Energy Transfer Photocatalysis: Exciting Modes of Reactivity. *Chem. Soc. Rev.* **2024**, *53* (3), 1068−1089.

https://doi.org/10.1021/jacsau.5c00364
JACS Au XXXX, XXX, XXX−XXX

5.2 Triplet Energy Transfer Catalysis

Molecular photocatalysis has experienced a remarkable surge of interest in recent years.[27,57,152,153] This growth is largely driven by the fact that photocatalytic processes are generally considered more sustainable and resource-efficient than conventional chemical methods.[13,154,155] Despite this, most of the research has concentrated on photoredox catalysis, whereas TTET remains comparatively underexplored. Only recently has TTET gained broader interest, as it enables unique synthetic transformations that are inaccessible via photoinduced ET mechanisms.[7,8,63] Interestingly, many photocatalysts used in photoredox catalysis also serve as efficient triplet photosensitizers.[72,156,157] A prominent example is $Ir(ppy)_3$, whose triplet state can participate in both reductive quenching and energy transfer processes.[59,62,158] This dual functionality raises a fundamental mechanistic question: how can one distinguish whether a reaction proceeds via energy or electron transfer, especially when both pathways are plausible.[141] Distinguishing between these mechanistic routes is crucial not only for understanding reactivity but also for guiding the rational design of photocatalysts and reaction conditions. This is the central question in projects **[B]** to **[D]**. Although these studies were motivated by distinct photocatalytic transformations involving structurally diverse molecular classes (*vide infra*), the mechanistic investigations followed a common strategy. In each study, the reaction pathways were explored through a combined approach involving multiple complementary experimental techniques, supported by computational analysis. Among these methods, transient absorption spectroscopy emerged as the most central and decisive tool for elucidating the underlying mechanisms. As described below, the projects **[B]** to **[D]** exemplify the powerful synergy that arises when synthetic and spectroscopic photochemistry communities collaborate, highlighting how interdisciplinary efforts can advance the field of photochemistry and yield a better understanding of photochemical processes in general.

Mechanistic investigations of polyaza[7]helicene in photoredox and energy transfer catalysis

Project **[B]** investigated a polyazahelicene, which represents a relatively new class of molecular scaffolds that have only recently attracted attention in photochemistry.[120,159–161] To date, only a limited number of studies have explored their use as photocatalysts.[123,162,163] Nevertheless, this chromophore class holds promise as a purely organic alternative to more commonly employed transition metal photocatalysts (see Chapter 3.3 for details).[123] In a previous study, the singlet-excited state of a polyazahelicene (2.99 eV) was harnessed in a three-component sulfonylation/arylation reaction (3CR).[123] It was proposed that the highly reducing singlet-excited state initiates the reaction by reducing cyanopyridine, and is subsequently regenerated via an electron transfer from *p*-toluenesulfinate to the oxidized photocatalyst. While this mechanism was supported by emission-based quenching experiments and measurements of the redox potentials, direct evidence for the involvement of radical ionic intermediates remained elusive.

This raises a particularly intriguing question about the reaction pathway, given that polyazahelicenes often exhibit notable ISC rates.[121,122,164] Yet, they have not been broadly regarded as triplet photosensitizers so

far albeit great photorobustness and recyclability.[123] Since the triplet state of such a purely organic chromophore is typically non-emissive, it cannot be detected in steady-state emission spectroscopy. In light of this, the reactivity of the newly developed photocatalyst, polyaza[7]helicene (referred to as Aza), was investigated in project **[B]** with a focus on both its singlet and triplet excited states. While the proposed mechanism of the 3CR was confirmed through direct spectroscopic evidence, the formation of a triplet state following excitation of Aza was also observed. This triplet state was subsequently utilized in triplet-sensitized isomerization reactions, underscoring the dual role of Aza as both a photocatalyst and a triplet photosensitizer.

Summary:

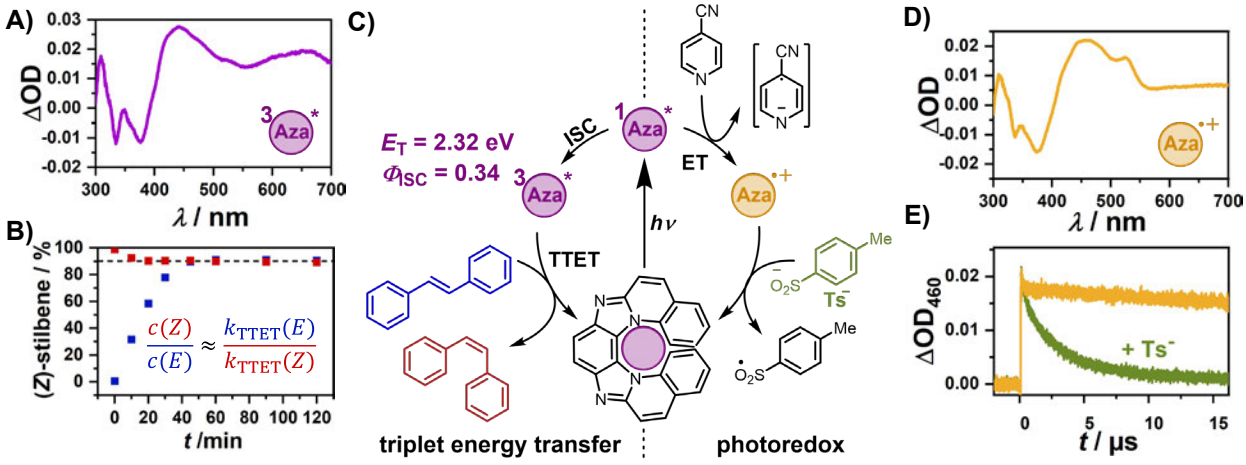

Figure 11: Overview of project **[B]**. A) TA spectrum of ^{3}Aza. B) Irradiation experiments of (*E*)-stilbene (blue) and (*Z*)-stilbene (red) with 2 mol % Aza under 427 nm LED light irradiation. C) Mechanism of the 3CR with Aza as the reducing photocatalyst and *E*→*Z* isomerization of stilbene with Aza as the triplet photosensitizer. D) TA spectrum of the radical cation of Aza. E) Kinetic TA traces of the radical cation of Aza in the absence (yellow) and presence of Ts^-.

In project **[B]** the three-component sulfonylation/arylation reaction[123] was investigated with 355 nm laser pulses (Figure 11C, right mechanism). It was postulated that the singlet-excited Aza reduces cyanopyridine followed by an oxidation of *p*-toluenesulfinate regenerating the photocatalyst. LFP experiments using 355 nm laser pulses of the chromophore showed that a non-negligible amount of triplet states are formed with a quantum yield of 0.34, which already demonstrated the need for a full elucidation of the reaction sequence (Figure 11A). Time-resolved measurements revealed that the radical cation of the photocatalyst was essentially only generated from the singlet-excited state in the presence of cyanopyridine, while the triplet state of the photocatalyst was insufficiently populated owing to rapid quenching of the singlet-excited state. Although the radical anion of cyanopyridine could not be detected, the formation of the transient radical cation of Aza was confirmed (Figure 11D). By focusing the laser pulse on a smaller spot, the photocatalyst was ionized in a consecutive two-photon-absorption process.[165–167] The ability to generate this intermediate species was exploited to identify the second reaction step, where the oxidized photocatalyst is regenerated by *p*-toluenesulfinate (Ts^-). The TA signal of the radical cation of Aza was quenched in the presence of Ts^- (Figure 11E).

The high ISC quantum yield of 0.34 made this chromophore interesting for applications as a triplet photosensitizer. 77 K phosphorescence measurements revealed a triplet state energy of 2.32 eV, which is between the triplet states of (*E*)-stilbene (2.13 eV) and (*Z*)-stilbene (2.36 eV) (see Chapter 6 for details on stilbene *E*→*Z* photoisomerization).[51] In this context, Aza was considered a perfect photosensitizer to selectively sensitize the *E*-isomer effectively, accumulating the *Z*-isomer (Figure 11C, left mechanism). Quenching experiments revealed a ratio of 9:1 for the energy transfer rate constants to the *E*- and *Z*-isomer of stilbene. This was corroborated by irradiation experiments with a 427 nm LED that revealed a photostationary state of 9:1 of *E*:*Z* as well (Figure 11B). Additionally, a remarkable turnover number of 4440 was observed for the compound Aza and a photostability over other triplet photosensitizers such as $[Ru(bpy)_3]^{2+}$ was demonstrated. Further, Aza was utilized as a triplet photosensitizer in a cyclization reaction of cinnamyl chloride. In conclusion, the versatility of Aza as a photoredox catalyst and triplet photosensitizer was demonstrated in this study, potentially paving the way for a broader use of polyazahelicenes in molecular photochemistry.

Project **[B]** was published as a research article:

"**Mechanistic investigations of polyaza[7]helicene in photoredox and energy transfer catalysis**"

Reproduced from Reference: J. Rocker, T. J. B. Zähringer, M. Schmitz, T. Opatz, C. Kerzig, *Beilstein J. Org. Chem.* **2024**, *20*, 1236–1245. With permission from Beilstein-Institut.

The article is Open Access and licensed under CC BY-NC 4.0 (https://creativecommons.org/licenses/by/4.0/). It can be cited corresponding to ref.[B]. The reference is attached in the following pages and the supporting information can be found in Chapter 10.3.

Author contributions: C. Kerzig ideated the Project and provided general guidance. J. Rocker performed the synthesis and irradiation experiments under the supervision of T. Opatz. T. J. B. Zähringer performed spectroscopic measurements. M. Schmitz performed the DFT calculations and determined the ISC quantum yield.

BEILSTEIN JOURNAL OF ORGANIC CHEMISTRY

Mechanistic investigations of polyaza[7]helicene in photoredox and energy transfer catalysis

Johannes Rocker[§], Till J. B. Zähringer[§], Matthias Schmitz, Till Opatz and Christoph Kerzig[*]

Full Research Paper

Open Access

Address:
Department of Chemistry Johannes Gutenberg University, Duesbergweg 10–14, 55128 Mainz, Germany

Email:
Christoph Kerzig[*] - ckerzig@uni-mainz.de

* Corresponding author
§ Equal contributors ordered alphabetically.

Keywords:
energy transfer; laser spectroscopy; organocatalyst; photoredox; time-resolved spectroscopy

Beilstein J. Org. Chem. **2024,** *20,* 1236–1245.
https://doi.org/10.3762/bjoc.20.106

Received: 16 February 2024
Accepted: 16 May 2024
Published: 28 May 2024

This article is part of the thematic issue "Harnessing light energy with molecules".

Guest Editor: H. A. Wegner

© 2024 Rocker et al.; licensee Beilstein-Institut.
License and terms: see end of document.

Abstract

Organic photocatalysts frequently possess dual singlet and triplet photoreactivity and a thorough photochemical characterization is essential for efficient light-driven applications. In this article, the mode of action of a polyazahelicene catalyst (Aza-H) was investigated using laser flash photolysis (LFP). The study revealed that the chromophore can function as a singlet-state photoredox catalyst in the sulfonylation/arylation of styrenes and as a triplet sensitizer in energy transfer catalysis. The singlet lifetime is sufficiently long to exploit the exceptional excited state reduction potential for the activation of 4-cyanopyridine. Photoinduced electron transfer generating the radical cation was directly observed confirming the previously proposed mechanism of a three-component reaction. Several steps of the photoredox cycle were investigated separately, providing deep insights into the complex mechanism. The triplet-excited Aza-H, which was studied with quantitative LFP, is formed with a quantum yield of 0.34. The pronounced triplet formation was exploited for the isomerization reaction of (*E*)-stilbene to the *Z*-isomer and the cyclization of cinnamyl chloride. Catalyst degradation mainly occurs through the long-lived Aza-H triplet (28 µs), but the photostability is greatly increased when the triplet efficiently reacts in a catalytic cycle such that turnover numbers exceeding 4400 are achievable with this organocatalyst.

Introduction

The emergence of photoredox chemistry in recent years was pioneered by the introduction of photocatalysts (PC) based on metals such as Ru and Ir [1-6]. However, due to the high cost and limited availability of precious metals, organic photocatalysts have become a focal point of academic and industrial research [7-15]. Most of the established organic catalysts (acridinium salts [16-19], cyanoarenes [8,20-22], quinones [23,24], etc.) [10,25] are cationic and electron-deficient and tend to act as

excited state oxidants in a reductive quenching cycle. Only recently, more reducing catalyst classes have been investigated, including second-generation cyanoarenes [8], arylamines [26], phenothiazines, phenazines and phenoxazines [9,27,28], which can act as excited state reductants comparable to precious metal-based photoredox catalysts. Singlet-excited organic chromophores often have short lifetimes, limiting their use in collision-based electron/energy transfer reactions unless high substrate concentrations are used [29,30]. In contrast, triplet states populated via intersystem crossing (ISC) have much longer lifetimes and can efficiently react at lower substrate concentrations [30]. Prominent examples include: (i) carbonyl compounds such as benzophenone [31,32] and thioxanthone [33-35], (ii) TADF emitters with small singlet-triplet energy splitting [8,36], (iii) substitution with heavy atoms such as sulphur [37] and halides [38] for fast ISC, or a combination of the above-mentioned methods [39]. However, the longer lifetime of the triplet state usually comes at the expense of a lower energetic driving force. Helicenes in particular show an increased ISC rate compared to planar molecules, which is attributed to an enhanced spin-orbit coupling that is sensitive to their degree of non-planarity [40], where the helical structure allows for mixing between the singlet and triplet π,π*-states [41,42]. In addition, the insertion of heteroatoms such as nitrogen further enhances ISC due to a spin-orbit coupling between n,π*-states and π,π*-states [40], as stated by El Sayed's rule [43]. However, helicenes have not been broadly considered as potential photocatalysts or sensitizers or their applications were unsuccessful [44]. Recently, one of our groups exploited the highly reducing polyaza[7]helicene (Aza-H, see Scheme 1 for its structure) for sulfonylation/arylation three-component reactions (3-CRs) and it has been shown that substituting the helicene core with functional groups is a viable approach to fine-tune the photochemical properties [45,46], as has been demonstrated for other organic and metal-based chromophores.

Our study focused on investigating the reaction mechanism of the recently reported sulfonylation/arylation [45,46] reaction using laser flash photolysis (LFP). LFP is a powerful spectroscopic tool in photocatalysis that allows us not only to distinguish between energy and electron transfer but also to detect transient triplet states and radicals, yielding clear-cut evidence for the proposed reaction mechanism [47-57]. We found that quenching of the singlet-excited Aza-H by 4-cyanopyridine is the main pathway for the 3-CR, while the triplet state of our catalyst, which is formed with a quantum yield as high as 0.34, is essentially non-reactive under our conditions. Cyanopyridine- and sulfinate-derived radicals are produced in equal concentrations in the catalytic cycle, suggesting that radical coupling is indeed the final reaction step to give the stable sulfonylation/arylation product. The triplet of Aza-H with its relatively high formation quantum yield and an energy of 2.32 eV can be used for isomerizing photoswitches like stilbene and for the cyclization of cinnamyl chloride. Our goal was not only to clarify the reaction pathway but also to provide a clear method for distinguishing between singlet and triplet reactivity of the Aza-H photocatalyst through spectroscopic measurements. The careful characterization of the versatile Aza-H photochemistry might contribute to the development of a new class of photoactive catalysts that can compete with traditional metal complexes and well-known organic chromophores (as listed above).

Results and Discussion

A thorough understanding of the operation principles of a photocatalyst is essential for the development of improved catalysts and efficient photoreactions. To this end, the photochemical properties of photocatalysts such as metal complexes and organic chromophores and their roles in catalytic cycles have been extensively studied leading to numerous findings and novel reaction pathways [55,58-61]. Lately, polyazahelicenes have gained some attention by synthetic groups [62-66]. However, this chromophore class is underexplored concerning its photochemical reactivity. The main reaction class catalyzed by excited-state polyazahelicene Aza-H so far is the redox-neutral addition of sulfinates and cyanopyridines, under elimination of cyanide, to styrenes in a three-component reaction. The proposed mechanism was derived from the redox potentials of Aza-H and the substrates and initial steady-state fluorescence quenching experiments (Scheme 1, left), but detailed mechanistic insights and direct evidence of the transient radical ions could not be obtained yet [45].

Figure 1A illustrates the absorption and emission spectra of Aza-H in MeCN/H_2O (9:1). The low reduction potential of singlet-excited Aza-H ($PC^{\bullet+}/PC^*$ = –1.87 V vs SCE) led us to propose that the singlet-excited photocatalyst is oxidized by 4-cyanopyridine (4CP) ($4CP/4CP^{\bullet-}$ = −1.81 V vs SCE) as the first step in this multicomponent reaction (Scheme 1, left). The oxidized photocatalyst ($PC^{\bullet+}/PC$ = +1.12 V vs SCE) is then regenerated by an electron transfer from sodium *p*-toluenesulfinate (TsNa) ($Ts^{\bullet}/Ts^{-}$ = +0.70 V vs SCE) closing the photocatalytic cycle [45]. Unlike other prominent photocatalysts, little to nothing is known about the reactivity, the photophysical properties or the radical ions of polyazahelicenes. The moderate fluorescence quantum yield of 48% (in MeCN) [46] implies that a non-emissive triplet-excited state (at room temperature) could also be generated via intersystem crossing, potentially initiating electron transfer reaction sequences. 77 K emission measurements were thus carried out and they showed short-lived fluorescence and long-lived emission (phosphorescence) that was assigned to the triplet state of Aza-H with an energy of 2.32 eV (Figure 1A). Quantum mechanical computations of the Aza-H

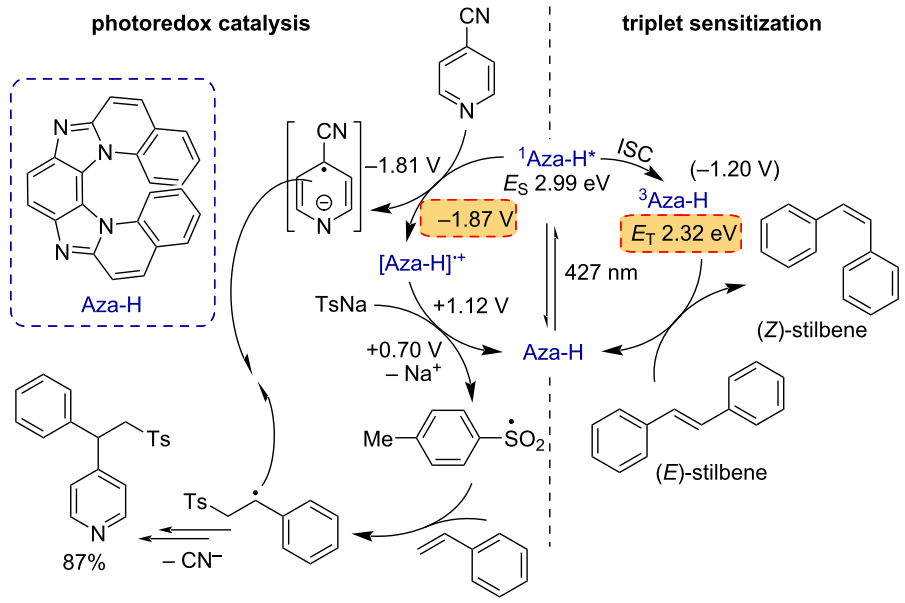

Scheme 1: Left: Reaction mechanism of the 3-CR with Aza-H as the photocatalyst. Potentials are given vs SCE. Right: Isomerization of stilbene using Aza-H as triplet sensitizer.

triplet state yielded a triplet energy of 2.17 eV (adiabatic), which is in good agreement with the experimental value (see Supporting Information File 1 for further information). Consequently, triplet reactivity cannot be excluded, given that photoinduced electron transfer reactions with excited singlet states or singlet radical pairs frequently suffer from low cage escape quantum yields [67,68].

Aza-H exhibits a relatively long singlet lifetime of 9.6 ns (see Figure 4E), which is sufficient for diffusion-controlled energy or electron transfer at moderate substrate concentrations. Transient absorption (TA) spectra of an Ar-saturated Aza-H solution were recorded with an LFP setup using 355 nm pulses (20 mJ) of ≈5 ns duration (see Supporting Information File 1 for experimental details). A delay of 250 ns was used between excitation and detection, which is sufficiently long to avoid the detection of the singlet-excited state (Figure 1B, black). Two broad TA bands peaking at 441 nm and 640 nm were observed that we assign to ^{3}Aza-H. However, on longer time scales the shape of the spectrum changes significantly (Figure S4, Supporting Information File 1) indicating that more than one absorbing species is generated. Measurements on an air-saturated solution under otherwise identical conditions gave a completely different spectrum (Figure 1B, red) and we assume that the triplet state of Aza-H is almost fully quenched by oxygen at the selected delay, which is supported by additional kinetic measurements (see below). The second transient species is identified as the ionization product resulting from a consecutive two-photon absorption at the selected high laser intensity [69,70], yielding the corresponding long-lived radical cation with second-order decay that is typical for oxidized/reduced species, and a solvated electron as by-product. The latter is in equilibrium with the dimeric solvent radical anion in MeCN, it weakly absorbs in our detection window and this species is rather short-lived compared to the triplet as well as the radical cation [71]. The oscillator strengths for the electronic transitions of ^{3}Aza-H (purple) and the radical cation Aza-H$^{\bullet+}$ (red) were computed using TD-DFT (see Supporting Information File 1 for details). These computational results, which are included in Figure 1B, align well with the experimentally observed absorption bands in the visible region, supporting our assignment.

The observed behavior of the Aza-H transient species in Ar-saturated/air-saturated solution is also reflected in the kinetic traces at 440 nm and 640 nm (Figure 1B, inset). Following the decay of the transient triplet species (^{3}Aza-H), essentially the same signal is reached irrespective of the presence of oxygen or argon in the solution. The contribution of the radical cation to the TA signal at 640 nm is only minor, which allows us to estimate a triplet lifetime of ≈28 µs at this detection wavelength. Based on our observations, an isolated triplet spectrum can be obtained from the spectral difference between the black and the red spectrum in Figure 1B, as shown in the purple spectrum displayed in Figure 1B (compare to Figure 3B, where the generated radical cation is fully quenched by TsNa).

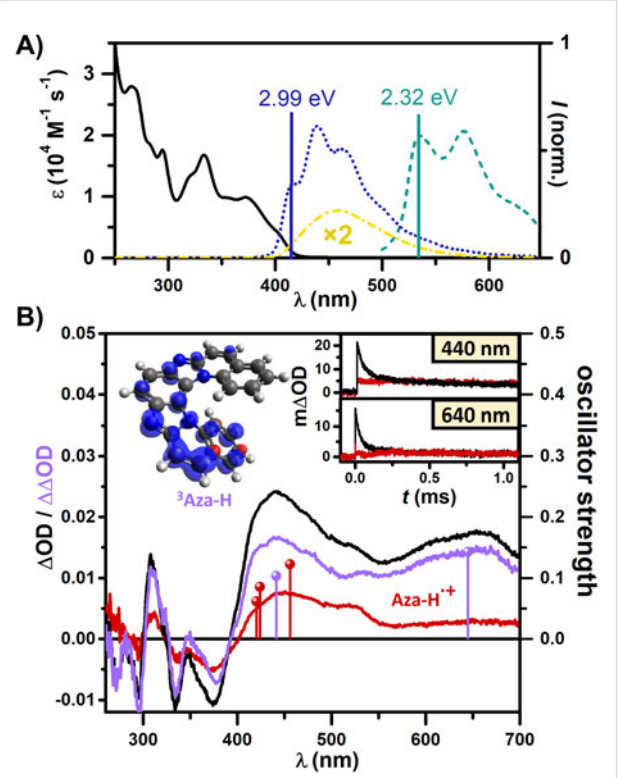

Figure 1: A) Room-temperature absorption (black) and emission (yellow) spectra of Aza-H recorded in MeCN/H_2O (9:1), and fluorescence (blue) and phosphorescence (green) spectra measured at 77 K in MeOH/EtOH (4:1). B) Transient absorption spectra of 25 μM (initial ground-state absorbance at the laser wavelength, 0.2) Aza-H in Ar-saturated (black) and air-saturated (red) MeCN/H_2O (9:1) recorded after 250 ns and the difference spectrum of both (purple) upon excitation with 355 nm laser pulses. Spin density of ^{3}Aza-H and the predicted electronic transitions in the visible region (transitions with oscillator strengths f below 0.05 are not shown) of ^{3}Aza-H (purple) and Aza-H$^{\bullet+}$ (red). Inset: Kinetic measurements at 440 nm and 640 nm.

Since all substrate compounds in the 3-CR mixture (4CP, TsNa and α-methylstyrene) cause fluorescence quenching, albeit to different degrees (see Supporting Information File 1), we recorded post-quenching TA spectra with Aza-H and the different substrates. Adding 200 mM 4CP to a deoxygenated solution of Aza-H quenches the fluorescence almost completely (η > 93%). The post-quenching TA spectrum (250 ns delay) strongly correlates with what we identified as the radical cation, Aza-H$^{\bullet+}$, which is in perfect agreement with our proposed photoinduced electron transfer step, while no triplet-excited Aza-H is observed (Figure 2A, blue spectrum). Since the direct ionization of Aza-H also contributes to this spectrum, we recorded a spectrum of only Aza-H in air-saturated solution (red spectrum) and used it to separate the signal that only stems from the oxidative quenching step (green spectrum). This correction likely overestimates the contribution of the two-photon process to the radical cation signal in the presence of 4CP, considering that quenching competes with ionization already during the laser pulse. Kinetic measurements of the radical cation species show multiexponential decay, probably due to recombination of the radical cation and radical anion (Figure 2A, inset). Despite the reported absorption maximum for 4CP$^{\bullet-}$ at 398 nm [72], we were unable to detect this species, as emphasized by Figure S5 and the discussion in Supporting Information File 1. Similarly, our attempts to identify 4CP$^{\bullet-}$ in an analogous experiment that employed Ir(ppy)$_3$ as a well-characterized reference photoreductant were also unsuccessful [73,74], probably due to an overall small extinction coefficient of the radical anion (Figure S6 in Supporting Information File 1 and the corresponding discussion). To investigate the triplet reactivity of Aza-H, a lower concentration of 4CP (5 mM) was used, quenching the singlet excited photocatalyst only partially (η ≈ 25%) and allowing triplet-excited Aza-H to be generated (Figure 2B). Kinetic traces of the triplet state show minor quenching upon the addition of 4CP (Figure 2B, inset), while the initial triplet signal is reduced as expected. However, considering the rather long triplet lifetime (in comparison to the singlet-excited state lifetime), the quenching rate constant is roughly four orders of magnitude lower than singlet quenching ($k_q \approx 10^5$ M^{-1} s^{-1}). This is in good agreement with the reported high triplet energy of 4CP [75] at 3.08 eV compared to 2.32 eV of ^{3}Aza-H and the lower reduction potential provided by the Aza-H triplet (−1.20 V vs SCE).

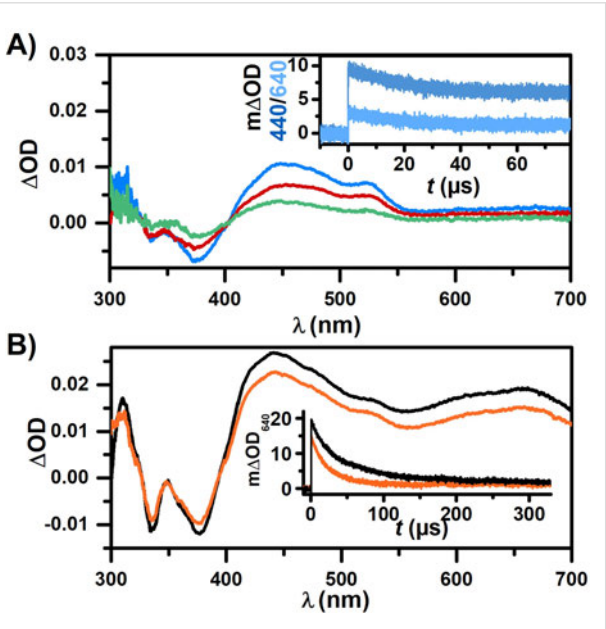

Figure 2: Mechanistic LFP experiments of 25 μM Aza-H with 4CP in MeCN/H_2O (9:1) after 355 nm laser pulses. A) TA spectra recorded after 250 ns of solely Aza-H in air-saturated solution (red), in Ar-saturated solution with 200 mM 4CP (blue) and the difference spectrum of both (green). Inset: Kinetic traces of Aza-H with 200 mM 4CP at 440 nm and 640 nm. B) TA spectra recorded after 250 ns of Aza-H in Ar-saturated solution in the absence (black) and presence (orange) of 5 mM 4CP. Inset: Kinetic traces at 640 nm.

Hence, we concluded that triplet quenching by 4CP plays a negligible role at typical substrate concentrations (>100 mM) used for lab-scale irradiation experiments. Following the proposed mechanism, the catalyst is then regenerated by an electron transfer from TsNa. However, we also observed minor fluorescence quenching of the photocatalysts by TsNa (see Figure S8, Supporting Information File 1), which prompted us to conduct additional LFP experiments to eliminate this as the primary reaction pathway (Figure 3A). Unlike quenching by 4CP, the addition of TsNa only shows signals that we assigned to the triplet spectrum of Aza-H in Figure 1B. Although the singlet-excited photocatalyst is quenched by TsNa, indicated by the reduced triplet formation of Aza-H, our conclusion is that this quenching is unproductive as no new photoproducts are observed. Interestingly, in contrast to all previous measurements, no signal of the Aza-H radical cation generated through two-photon absorption is detected. This can be easily rationalized as the radical cation is most likely rapidly quenched by TsNa (compare the proposed reaction mechanism regenerating the oxidized catalyst). That reasoning is consistent with kinetic traces at 440 nm that show the isolated decay of triplet Aza-H when TsNa is present, while the longer-lived signatures of Aza-H$^{\bullet+}$ are only visible in the absence of TsNa (Figure 3A, inset). In order to analyse the thermal electron transfer, we prepared an aerated solution of Aza-H with a lower concentration of TsNa (200 µM). We presumed this would enable us to exclusively monitor Aza-H$^{\bullet+}$ quenching by TsNa, since any triplet Aza-H would be deactivated by oxygen (see above). The ionization efficiency of Aza-H exhibits a quadratic dependence on the laser intensity. Consequently, focussing the laser on a narrow excitation spot on the sample ensured a significant generation of Aza-H$^{\bullet+}$ while minimizing the concentration of triplet-excited Aza-H. Initially, the same amount of radical cation is detected after the addition of TsNa, but the Aza-H$^{\bullet+}$ signal at 460 nm decays much faster and reaches the baseline after only 10 µs (Figure 3B). Kinetic measurements yielded a rate constant as high as ≈10^9 M^{-1} s^{-1} for the reaction between Aza-H$^{\bullet+}$ and TsNa (Figure 3B, inset), which implies that potential side reactions cannot compete. The TA spectra clearly reach baseline level after Aza-H$^{\bullet+}$ quenching by TsNa, indicating that the catalyst is regenerated (ground-state bleach recovery below 400 nm in Figure 3A and 3B) by that reaction, which is in line with the proposed thermal electron transfer. However, both the sulfonyl radical and 4CP$^{\bullet-}$ do not absorb in our detection window, hampering further kinetic and mechanistic investigations. Nevertheless, both radicals must be formed as quenching by-products based on our spectroscopic studies, either in the photoinduced or in the subsequent and rapid thermal electron transfer. For stoichiometry reasons, these radicals are formed in equal concentrations in the catalytic cycle and, therefore, the proposed radical recombination to yield the final product (with intervening addition of the sulfonyl radical to excess styrene, see Scheme 1) can be regarded as most-likely reaction pathway. Furthermore, we carried out pK value determinations for the protonation of Aza-H, both in its ground state and in the excited singlet state (see Figure S10 in Supporting Information File 1 and the corresponding section for details). Based on our studies in aqueous ethanol, Aza-H is a weak photobase but protonation is seen to be unimportant in neutral and alkaline solutions. However, these studies might be important for explaining reactivity changes when Aza-H is employed in photoreactions requiring or releasing Brønsted acids. During the 3-CR experiment, we observed a decomposition of the catalyst that occurred faster than in the absence of any additives (see studies on inherent photostability presented below). Our observations also revealed that while the styrene does not significantly quench the singlet state of Aza-H, it quenches the triplet state, suggesting that the formation of triplet-excited styrene via energy transfer is feasible (see Figure S7, Supporting Information File 1) [76]. A reaction course plot in the absence of 4CP and TsNa revealed rapid decomposition of the photocatalyst, presumably in a [2 + 2]-photocycloaddition with the styrene component as observed in mass spectrometry (see Figure S17 and Figure S18 in Supporting Information File 1 for details).

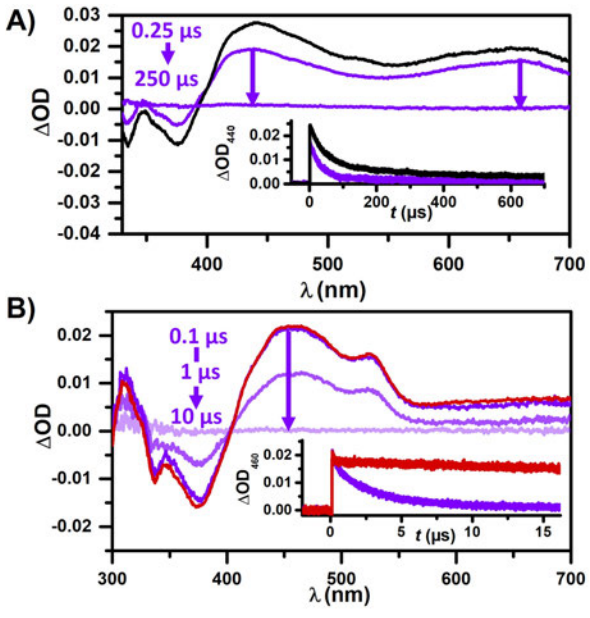

Figure 3: Mechanistic investigations of Aza-H with TsNa by LFP studies. A) Transient absorption measurements of 25 µM Aza-H in the absence of TsNa recorded after 0.25 µs (black) and presence of 50 mM TsNa recorded after 0.25 µs and 250 µs (purple) in deaerated MeCN/H_2O (9:1). Inset: Kinetic measurements at 440 nm. B) TA spectra of the radical cation of Aza-H (aerated MeCN/H_2O (9:1) solution) in the absence of TsNa recorded after 0.1 µs (red) and in the presence of TsNa after 0.1 µs, 1 µs and 10 µs (purple). Inset: Kinetic traces at 460 nm.

Consequently, the degradation of Aza-H is more efficient at the end of the reaction when incomplete deactivation of the excited singlet state leads to the (more efficient) formation of the triplet state. The occurrence of triplet reactivity of the catalyst as an undesirable side reaction highlights the importance of investigating the triplet state properties and this also initiated our search for a productive use of ^{3}Aza-H. The moderate fluorescence quantum yield of 0.48 indicates that pronounced triplet state formation might take place. Quantitative LFP measurements were performed to determine the ISC quantum yield, Φ_{ISC}, using the well-studied photosensitizer $[Ru(bpy)_3]Cl_2$ (Rubpy) as reference for actinometry [78-80]. This approach involved employing identical excitation conditions at 355 nm (Figure 4A) and monitoring the GSB of Rubpy with a literature-reported difference extinction coefficient, $\Delta\varepsilon_{455}$(Rubpy*) = −10100 M^{-1} cm^{-1} [37,79], following excitation (Figure 4B). 0.3 mM methyl viologen (MV^{2+}) were added to Aza-H to quantitatively quench the triplet-excited photocatalyst in an electron transfer reaction yielding Aza-$H^{\bullet+}$ and $MV^{\bullet+}$, which are clearly observed in the TA spectrum (Figure 4D). For the Φ_{ISC} determination described below, we assume a cage escape quantum yield of 100%, which is reasonable for the photoinduced electron transfer between a heavy atom-free sensitizer-quencher pair in the triplet manifold [67,68,81]. Quenching of the short-lived singlet excited Aza-H at our low quencher concentration was excluded by lifetime-based quenching experiments (Figure 4E). By observing the kinetic traces at the isosbestic point of Aza-$H^{\bullet+}$ (395 nm), we were able to exclusively track the formation of $MV^{\bullet+}$ (Figure 4C). To rule out the formation of any other products apart from Aza-$H^{\bullet+}$, we utilized a reference spectrum of $MV^{\bullet+}$ obtained through spectroelectrochemistry [77]. The difference spectrum depicted in Figure 4D closely resembles the Aza-H radical cation spectrum already obtained through photoionization and singlet state quenching (see above), substantiating the reliability of our procedure. Taking the literature-known extinction coefficient of the methyl viologen radical cation $\Delta\varepsilon_{395}(MV^{\bullet+}) \approx 39000$ M^{-1} cm^{-1} [82] to calculate its concentration and the initial Aza-H excited-state concentration obtained through Rubpy* actinometry allows us to determine the ISC quantum yield. This procedure was conducted at two excitation intensities: 7.0 mJ and 11.8 mJ (see Supporting Information File 1 for details) yielding an ISC quantum yield of 0.34. The mild excitation energies also ensured that the formation of directly ionized Aza-H was negligible for the evaluation of the ISC quantum yield.

With a promising ISC quantum yield of 0.34 and a triplet energy of approximately 2.32 eV, the triplet-triplet energy transfer (TTET) to (*E*)-stilbene (E_T = 2.13 eV) [76] should be feasible, while an energy transfer to (*Z*)-stilbene (E_T = 2.36 eV) [76] is energetically uphill and therefore much slower. Triplet quenching experiments of Aza-H with increasing (*Z*)-stilbene and (*E*)-stilbene concentrations were performed (Figure 5A and B). We obtained quenching efficiencies and rate constants that are in line with our measured triplet energy of Aza-H.

Irradiating a 50 mM solution of either (*E*)-stilbene or (*Z*)-stilbene and Aza-H (2 mol %) in MeCN (Figure S19, Supporting

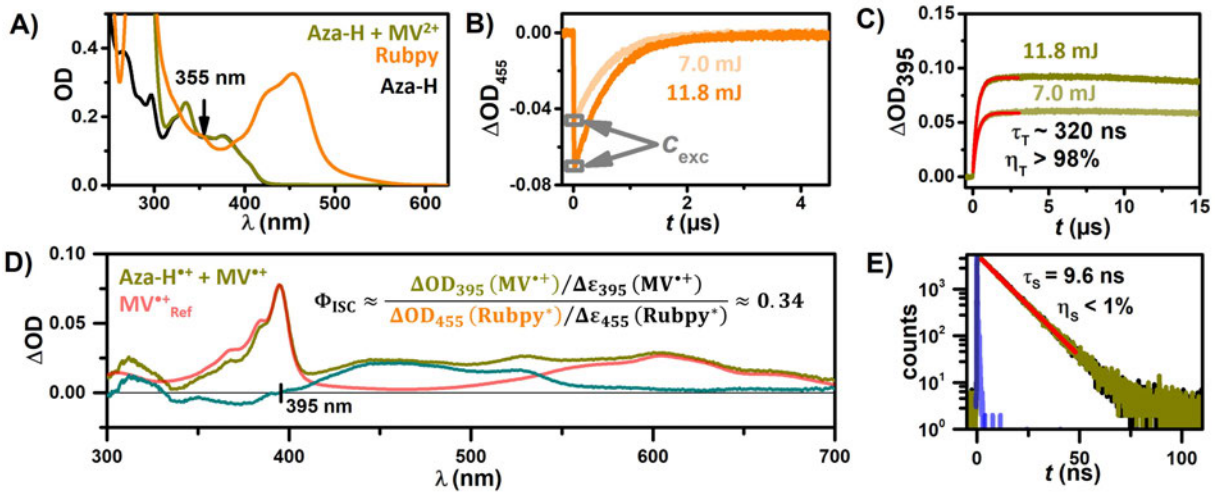

Figure 4: Data sets employed for the calculation Φ_{ISC} of Aza-H based on the ground state bleach of Rubpy as the actinometry reference signal following excitation by 355 nm laser pulses with energies of 7.0 mJ and 11.8 mJ. Aza-H and MV^{2+} were prepared in deaerated MeCN and Rubpy in deaerated H_2O. A) Absorption spectra of Rubpy, Aza-H, and Aza-H with 0.3 mM MV^{2+}. B) and C) Transient absorption measurements of Rubpy at 455 nm and Aza-H with MV^{2+} at 395 nm. D) Absorption spectrum of $MV^{\bullet+}$ obtained from Ref [77], transient absorption spectrum of Aza-H with 0.3 mM MV^{2+} and the difference spectrum of both spectra (cyan). E) Emission lifetime of Aza-H in the presence (dark yellow) and absence (black) of 0.3 mM MV^{2+}.

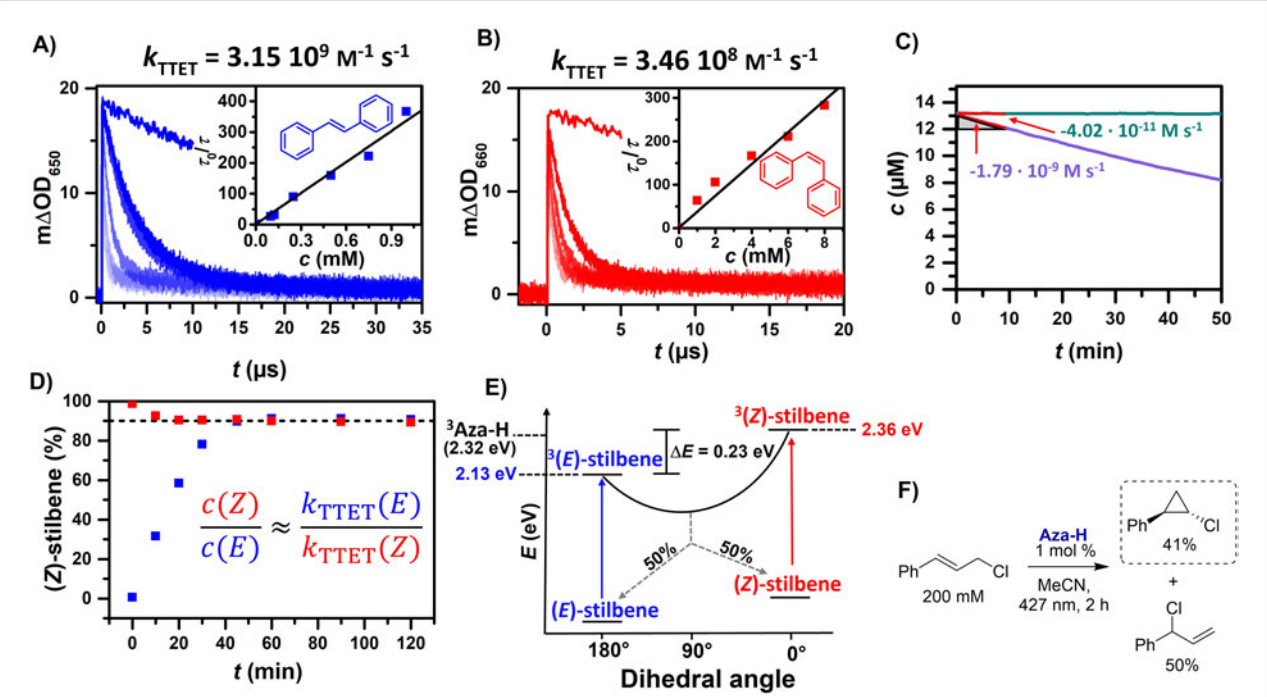

Figure 5: Stilbene isomerization and additional energy transfer experiments. A) and B) Triplet quenching experiments of Aza-H with increasing (*E*)-stilbene and (*Z*)-stilbene concentrations. Insets: Corresponding Stern–Volmer plots. C) Photostability measurements of Aza-H in deaerated MeCN in the absence (purple) and presence of 10 mM (*E*)-stilbene (green). A 390 nm LED from Kessil set to 50% intensity (distance 6 cm) was used as the excitation light source. D) Irradiation experiments of (*E*)-stilbene (blue) and (*Z*)-stilbene (red) with 2 mol % Aza-H employing a 427 nm LED as light source. E) Schematic energy diagram of triplet sensitized *E*/*Z* isomerization of stilbene. F) Reaction scheme of the cyclization of cinnamyl chloride using Aza-H as the triplet sensitizer. See Supporting Information File 1 for details.

Information File 1) reaches an equilibrium at an *Z*/*E*-ratio of 91:9 (Figure 5D). Moreover, the *Z*/*E*-ratio is perfectly reflected by the ratio of the triplet energy transfer rates, which is in line with reported similar efficiencies for the formation of both isomers starting from the perpendicular triplet state (Figure 5E) [35,83].

In contrast to styrene substrates, mass spectrometry shows no addition products of catalyst and stilbene. Hence, the photocatalyst is not consumed by side reactions. Photostability measurements have also demonstrated that the inclusion of a triplet quencher like stilbene significantly enhances the longevity of the Aza-H chromophores, outperforming other well-known organic and metal-based photocatalysts such as 4CzIPN, riboflavin and $[Ru(bpy)_3](PF_6)_2$ (Figure 5C and Supporting Information File 1). A remarkable turnover number of 4440 was achieved when 1 M stilbene was used (see Supporting Information File 1 for more information). Furthermore, the photocatalyst was utilized in a photosensitized cyclization reaction of cinnamyl chloride [84]. This photoreaction was originally established by Xu et al., but its success was limited to costly Ir-based photocatalysts. Lifetime-based quenching experiments of ^{3}Aza-H with increasing cinnamyl chloride concentration revealed an energy transfer rate of 10^6 M^{-1} s^{-1} (Figure S9, Supporting Information File 1). Although this rate is four orders of magnitude slower than the diffusion limit in MeCN, the long triplet lifetime ensures a quenching efficiency of 85% when a concentration of 200 mM cinnamyl chloride is used. Exposed to 427 nm irradiation with 1 mol % Aza-H 41% of the chlorocyclopropane and 50% of the branched allylic chloride was produced, which can be recycled to the cinnamyl chloride as demonstrated recently [84].

Conclusion

The experiments presented in this paper have demonstrated the wealth of information accessible by laser spectroscopic studies with a novel polyazahelicene photocatalyst. Its excited singlet state is the key species in a three-component sulfonylation/arylation reaction, whereas the unexplored triplet state is responsible for the decomposition of the photocatalyst. Photoinduced radical cation formation and thermal regeneration could be unambiguously observed, providing deep mechanistic insights into the underlying reaction mechanism. On the other hand, the relatively high triplet formation quantum yield of Aza-H along with its triplet energy on the order of 2.3 eV permit efficient and metal-free reactions via energy transfer catalysis, as shown for the photosensitized isomerization of stilbene and cinnamyl chloride. We believe that our findings pave the way for a

broader usage of the inherently chiral polyazahelicene photocatalyst class, both in photoredox and energy transfer catalysis.

Supporting Information

Supporting Information File 1

General information, detailed experimental procedures, additional spectroscopic data, quantum-mechanical calculations, photostability and photoisomerization experiments.
[https://www.beilstein-journals.org/bjoc/content/supplementary/1860-5397-20-106-S1.pdf]

Funding

We acknowledge generous financial support from the JGU Mainz and the German Federal Environmental Foundation (DBU, Ph.D. fellowship to T.J.B.Z., grant number 20022/028). M.S. is grateful to the Chemical Industry Funds for a Kekulé fellowship.

ORCID® iDs

Johannes Rocker - https://orcid.org/0000-0001-8334-3807
Till J. B. Zähringer - https://orcid.org/0000-0001-9285-3980
Matthias Schmitz - https://orcid.org/0000-0003-0246-3036
Till Opatz - https://orcid.org/0000-0002-3266-4050
Christoph Kerzig - https://orcid.org/0000-0002-1026-1146

Data Availability Statement

All experimental data sets supporting the findings of this study are available in the main article and/or the supporting information. The data sets shown in the main paper and DFT output files are accessible via the JGU library and the homepage of the corresponding author.

References

1. Twilton, J.; Le, C.; Zhang, P.; Shaw, M. H.; Evans, R. W.; MacMillan, D. W. C. *Nat. Rev. Chem.* **2017,** *1,* 0052. doi:10.1038/s41570-017-0052
2. Prier, C. K.; Rankic, D. A.; MacMillan, D. W. C. *Chem. Rev.* **2013,** *113,* 5322–5363. doi:10.1021/cr300503r
3. Staveness, D.; Bosque, I.; Stephenson, C. R. J. *Acc. Chem. Res.* **2016,** *49,* 2295–2306. doi:10.1021/acs.accounts.6b00270
4. Koike, T.; Akita, M. *Inorg. Chem. Front.* **2014,** *1,* 562–576. doi:10.1039/c4qi00053f
5. Teegardin, K.; Day, J. I.; Chan, J.; Weaver, J. *Org. Process Res. Dev.* **2016,** *20,* 1156–1163. doi:10.1021/acs.oprd.6b00101
6. Meyer, F.; Halasyamani, P. S.; Masson, G. *ACS Org. Inorg. Au* **2023,** *3,* 1–3. doi:10.1021/acsorginorgau.2c00062
7. Liu, Q.; Huo, C.; Fu, Y.; Du, Z. *Org. Biomol. Chem.* **2022,** *20,* 6721–6740. doi:10.1039/d2ob00807f
8. Speckmeier, E.; Fischer, T. G.; Zeitler, K. *J. Am. Chem. Soc.* **2018,** *140,* 15353–15365. doi:10.1021/jacs.8b08933
9. Corbin, D. A.; Lim, C.-H.; Miyake, G. M. *Aldrichimica Acta* **2019,** *52,* 7–21.
10. Romero, N. A.; Nicewicz, D. A. *Chem. Rev.* **2016,** *116,* 10075–10166. doi:10.1021/acs.chemrev.6b00057
11. Crisenza, G. E. M.; Melchiorre, P. *Nat. Commun.* **2020,** *11,* 803. doi:10.1038/s41467-019-13887-8
12. Pfund, B.; Hutskalova, V.; Sparr, C.; Wenger, O. S. *Chem. Sci.* **2023,** *14,* 11180–11191. doi:10.1039/d3sc02768f
13. Singh, S.; Tripathi, K. N.; Singh, R. P. *Org. Biomol. Chem.* **2022,** *20,* 5716–5720. doi:10.1039/d2ob00943a
14. Neumann, M.; Füldner, S.; König, B.; Zeitler, K. *Angew. Chem., Int. Ed.* **2011,** *50,* 951–954. doi:10.1002/anie.201002992
15. Majek, M.; Jacobi von Wangelin, A. *Acc. Chem. Res.* **2016,** *49,* 2316–2327. doi:10.1021/acs.accounts.6b00293
16. Fukuzumi, S.; Kotani, H.; Ohkubo, K.; Ogo, S.; Tkachenko, N. V.; Lemmetyinen, H. *J. Am. Chem. Soc.* **2004,** *126,* 1600–1601. doi:10.1021/ja038656q
17. Fischer, C.; Kerzig, C.; Zilate, B.; Wenger, O. S.; Sparr, C. *ACS Catal.* **2020,** *10,* 210–215. doi:10.1021/acscatal.9b03606
18. MacKenzie, I. A.; Wang, L.; Onuska, N. P. R.; Williams, O. F.; Begam, K.; Moran, A. M.; Dunietz, B. D.; Nicewicz, D. A. *Nature* **2020,** *580,* 76–80. doi:10.1038/s41586-020-2131-1
19. Sau, S. C.; Schmitz, M.; Burdenski, C.; Baumert, M.; Antoni, P. W.; Kerzig, C.; Hansmann, M. M. *J. Am. Chem. Soc.* **2024,** *146,* 3416–3426. doi:10.1021/jacs.3c12766
20. Nakamura, M.; Dohno, R.; Majima, T. *Chem. Commun.* **1997,** 1291–1292. doi:10.1039/a702230a
21. Jonas, M.; Blechert, S.; Steckhan, E. *J. Org. Chem.* **2001,** *66,* 6896–6904. doi:10.1021/jo010144b
22. Hintz, S.; Mattay, J.; van Eldik, R.; Fu, W.-F. *Eur. J. Org. Chem.* **1998,** 1583–1596. doi:10.1002/(sici)1099-0690(199808)1998:8<1583::aid-ejoc1583>3.0.co;2-r
23. Cavedon, C.; Sletten, E. T.; Madani, A.; Niemeyer, O.; Seeberger, P. H.; Pieber, B. *Org. Lett.* **2021,** *23,* 514–518. doi:10.1021/acs.orglett.0c04026
24. Ohkubo, K.; Fujimoto, A.; Fukuzumi, S. *J. Am. Chem. Soc.* **2013,** *135,* 5368–5371. doi:10.1021/ja402303k
25. Fukuzumi, S.; Ohkubo, K. *Org. Biomol. Chem.* **2014,** *12,* 6059–6071. doi:10.1039/c4ob00843j
26. Noto, N.; Saito, S. *ACS Catal.* **2022,** *12,* 15400–15415. doi:10.1021/acscatal.2c05034
27. Lee, Y.; Kwon, M. S. *Eur. J. Org. Chem.* **2020,** 6028–6043. doi:10.1002/ejoc.202000720
28. Du, Y.; Pearson, R. M.; Lim, C.-H.; Sartor, S. M.; Ryan, M. D.; Yang, H.; Damrauer, N. H.; Miyake, G. M. *Chem. – Eur. J.* **2017,** *23,* 10962–10968. doi:10.1002/chem.201702926
29. Joshi-Pangu, A.; Lévesque, F.; Roth, H. G.; Oliver, S. F.; Campeau, L.-C.; Nicewicz, D.; DiRocco, D. A. *J. Org. Chem.* **2016,** *81,* 7244–7249. doi:10.1021/acs.joc.6b01240
30. Glaser, F.; Kerzig, C.; Wenger, O. S. *Angew. Chem., Int. Ed.* **2020,** *59,* 10266–10284. doi:10.1002/anie.201915762
31. Dewanji, A.; Krach, P. E.; Rueping, M. *Angew. Chem., Int. Ed.* **2019,** *58,* 3566–3570. doi:10.1002/anie.201901327
32. Strieth-Kalthoff, F.; James, M. J.; Teders, M.; Pitzer, L.; Glorius, F. *Chem. Soc. Rev.* **2018,** *47,* 7190–7202. doi:10.1039/c8cs00054a
33. Nikitas, N. F.; Gkizis, P. L.; Kokotos, C. G. *Org. Biomol. Chem.* **2021,** *19,* 5237–5253. doi:10.1039/d1ob00221j
34. Alonso, R.; Bach, T. *Angew. Chem.* **2014,** *126,* 4457–4460. doi:10.1002/ange.201310997

35. Zähringer, T. J. B.; Wienhold, M.; Gilmour, R.; Kerzig, C. *J. Am. Chem. Soc.* **2023,** *145,* 21576–21586. doi:10.1021/jacs.3c07678
36. Bryden, M. A.; Zysman-Colman, E. *Chem. Soc. Rev.* **2021,** *50,* 7587–7680. doi:10.1039/d1cs00198a
37. Bertrams, M.-S.; Kerzig, C. *Chem. Commun.* **2021,** *57,* 6752–6755. doi:10.1039/d1cc01947c
38. Chen, K.; Dong, Y.; Zhao, X.; Imran, M.; Tang, G.; Zhao, J.; Liu, Q. *Front. Chem. (Lausanne, Switz.)* **2019,** *7,* 821. doi:10.3389/fchem.2019.00821
39. Manna, M. K.; Shokri, S.; Wiederrecht, G. P.; Gosztola, D. J.; Ayitou, A. J.-L. *Chem. Commun.* **2018,** *54,* 5809–5818. doi:10.1039/c8cc01553h
40. Schmidt, K.; Brovelli, S.; Coropceanu, V.; Beljonne, D.; Cornil, J.; Bazzini, C.; Caronna, T.; Tubino, R.; Meinardi, F.; Shuai, Z.; Brédas, J.-L. *J. Phys. Chem. A* **2007,** *111,* 10490–10499. doi:10.1021/jp075248q
41. Weigang, O. E., Jr.; Turner, J. A.; Trouard, P. A. *J. Chem. Phys.* **1966,** *45,* 1126–1134. doi:10.1063/1.1727727
42. Sapir, M.; Donckt, E. V. *Chem. Phys. Lett.* **1975,** *36,* 108–110. doi:10.1016/0009-2614(75)85698-3
43. El-Sayed, M. A. *J. Chem. Phys.* **1963,** *38,* 2834–2838. doi:10.1063/1.1733610
44. Görner, H.; Stammel, C.; Mattay, J. *J. Photochem. Photobiol., A* **1999,** *120,* 171–179. doi:10.1016/s1010-6030(98)00423-7
45. Rocker, J.; Opatz, T. *ACS Org. Inorg. Au* **2022,** *2,* 415–421. doi:10.1021/acsorginorgau.2c00022
46. Rocker, J.; Dresel, J. A.; Krieger, L. A.; Eckhardt, P.; Ortuño, A. M.; Kitzmann, W. R.; Clever, G. H.; Heinze, K.; Opatz, T. *Chem. – Eur. J.* **2023,** *29,* e202301244. doi:10.1002/chem.202301244
47. Zhang, Y.; Lee, T. S.; Favale, J. M.; Leary, D. C.; Petersen, J. L.; Scholes, G. D.; Castellano, F. N.; Milsmann, C. *Nat. Chem.* **2020,** *12,* 345–352. doi:10.1038/s41557-020-0430-7
48. Talbott, E. D.; Burnett, N. L.; Swierk, J. R. *Chem. Phys. Rev.* **2023,** *4,* 031312. doi:10.1063/5.0156850
49. Buzzetti, L.; Crisenza, G. E. M.; Melchiorre, P. *Angew. Chem., Int. Ed.* **2019,** *58,* 3730–3747. doi:10.1002/anie.201809984
50. Kutta, R. J.; Großkopf, J.; van Staalduinen, N.; Seitz, A.; Pracht, P.; Breitenlechner, S.; Bannwarth, C.; Nuernberger, P.; Bach, T. *J. Am. Chem. Soc.* **2023,** *145,* 2354–2363. doi:10.1021/jacs.2c11265
51. Glaser, F.; Kerzig, C.; Wenger, O. S. *Chem. Sci.* **2021,** *12,* 9922–9933. doi:10.1039/d1sc02085d
52. De Kreijger, S.; Gillard, M.; Elias, B.; Troian-Gautier, L. *ChemCatChem* **2024,** *16,* e202301100. doi:10.1002/cctc.202301100
53. Pitre, S. P.; McTiernan, C. D.; Scaiano, J. C. *Acc. Chem. Res.* **2016,** *49,* 1320–1330. doi:10.1021/acs.accounts.6b00012
54. Kamogawa, K.; Kato, Y.; Tamaki, Y.; Noguchi, T.; Nozaki, K.; Nakagawa, T.; Ishitani, O. *Chem. Sci.* **2024,** *15,* 2074–2088. doi:10.1039/d3sc06059d
55. Kandoth, N.; Pérez Hernández, J.; Palomares, E.; Lloret-Fillol, J. *Sustainable Energy Fuels* **2021,** *5,* 638–665. doi:10.1039/d0se01454k
56. Tian, L.; Till, N. A.; Kudisch, B.; MacMillan, D. W. C.; Scholes, G. D. *J. Am. Chem. Soc.* **2020,** *142,* 4555–4559. doi:10.1021/jacs.9b12835
57. Li, P.; Deetz, A. M.; Hu, J.; Meyer, G. J.; Hu, K. *J. Am. Chem. Soc.* **2022,** *144,* 17604–17610. doi:10.1021/jacs.2c07107
58. Ruccolo, S.; Qin, Y.; Schnedermann, C.; Nocera, D. G. *J. Am. Chem. Soc.* **2018,** *140,* 14926–14937. doi:10.1021/jacs.8b09109
59. Stevenson, B. G.; Spielvogel, E. H.; Loiaconi, E. A.; Wambua, V. M.; Nakhamiyayev, R. V.; Swierk, J. R. *J. Am. Chem. Soc.* **2021,** *143,* 8878–8885. doi:10.1021/jacs.1c03693
60. Coles, M. S.; Quach, G.; Beves, J. E.; Moore, E. G. *Angew. Chem., Int. Ed.* **2020,** *59,* 9522–9526. doi:10.1002/anie.201916359
61. Dutta, S.; Erchinger, J. E.; Strieth-Kalthoff, F.; Kleinmans, R.; Glorius, F. *Chem. Soc. Rev.* **2024,** *53,* 1068–1089. doi:10.1039/d3cs00190c
62. Otani, T.; Tsuyuki, A.; Iwachi, T.; Someya, S.; Tateno, K.; Kawai, H.; Saito, T.; Kanyiva, K. S.; Shibata, T. *Angew. Chem., Int. Ed.* **2017,** *56,* 3906–3910. doi:10.1002/anie.201700507
63. Otani, T.; Sasayama, T.; Iwashimizu, C.; Kanyiva, K. S.; Kawai, H.; Shibata, T. *Chem. Commun.* **2020,** *56,* 4484–4487. doi:10.1039/d0cc01194k
64. Otani, T.; Sasayama, T.; Horiuchi, M.; Okauchi, S.; Kawai, H.; Kitahara, M.; Imai, Y.; Shibata, T. *Helv. Chim. Acta* **2021,** *104,* e2100016. doi:10.1002/hlca.202100016
65. Yu, Z.; Shi, G.; Wang, K.-P.; Xu, L.-Z.; Chen, S.; Hu, Z.-Q. *Tetrahedron* **2023,** *130,* 133178. doi:10.1016/j.tet.2022.133178
66. Kise, K.; Ooi, S.; Saito, H.; Yorimitsu, H.; Osuka, A.; Tanaka, T. *Angew. Chem., Int. Ed.* **2022,** *61,* e202301100. doi:10.1002/anie.202112589
67. Kavarnos, G. J.; Turro, N. J. *Chem. Rev.* **1986,** *86,* 401–449. doi:10.1021/cr00072a005
68. Neumann, S.; Wenger, O. S.; Kerzig, C. *Chem. – Eur. J.* **2021,** *27,* 4115–4123. doi:10.1002/chem.202004638
69. Bohne, C.; Abuin, E. B.; Scaiano, J. C. *J. Am. Chem. Soc.* **1990,** *112,* 4226–4231. doi:10.1021/ja00167a018
70. Kerzig, C.; Goez, M. *Phys. Chem. Chem. Phys.* **2015,** *17,* 13829–13836. doi:10.1039/c5cp01711d
71. Grills, D. C.; Lymar, S. V. *J. Phys. Chem. B* **2022,** *126,* 262–269. doi:10.1021/acs.jpcb.1c08946
72. Kalyanaraman, V.; Rao, C. N. R.; George, M. V. *J. Chem. Soc. B* **1971,** 2406. doi:10.1039/j29710002406
73. Lipp, B.; Kammer, L. M.; Kücükdisli, M.; Luque, A.; Kühlborn, J.; Pusch, S.; Matulevičiūtė, G.; Schollmeyer, D.; Šačkus, A.; Opatz, T. *Chem. – Eur. J.* **2019,** *25,* 8965–8969. doi:10.1002/chem.201901175
74. Zhao, H.; Simpson, P. V.; Barlow, A.; Moxey, G. J.; Morshedi, M.; Roy, N.; Philip, R.; Zhang, C.; Cifuentes, M. P.; Humphrey, M. G. *Chem. – Eur. J.* **2015,** *21,* 11843–11854. doi:10.1002/chem.201500951
75. Motten, A. G.; Kwiram, A. L. *J. Chem. Phys.* **1981,** *75,* 2608–2615. doi:10.1063/1.442414
76. Montalti, M.; Credi, A.; Prodi, L.; Gandolfi, M. T. *Handbook of Photochemistry,* 3rd ed.; CRC Press: Boca Raton, FL, USA, 2006. doi:10.1201/9781420015195
77. Skaisgirski, M.; Larsen, C. B.; Kerzig, C.; Wenger, O. S. *Eur. J. Inorg. Chem.* **2019,** 4256–4262. doi:10.1002/ejic.201900453
78. Ripak, A.; De Kreijger, S.; Elias, B.; Troian-Gautier, L. *STAR Protoc.* **2023,** *4,* 102312. doi:10.1016/j.xpro.2023.102312
79. Müller, P.; Brettel, K. *Photochem. Photobiol. Sci.* **2012,** *11,* 632–636. doi:10.1039/c2pp05333k
80. Kerzig, C.; Goez, M. *Phys. Chem. Chem. Phys.* **2014,** *16,* 25342–25349. doi:10.1039/c4cp04156a
81. Olmsted, J.; Meyer, T. J. *J. Phys. Chem.* **1987,** *91,* 1649–1655. doi:10.1021/j100290a071
82. Tran, T.-T.; Ha-Thi, M.-H.; Pino, T.; Quaranta, A.; Lefumeux, C.; Leibl, W.; Aukauloo, A. *J. Phys. Chem. Lett.* **2018,** *9,* 1086–1091. doi:10.1021/acs.jpclett.8b00169

83. Kuramochi, H.; Tsutsumi, T.; Saita, K.; Wei, Z.; Osawa, M.; Kumar, P.; Liu, L.; Takeuchi, S.; Taketsugu, T.; Tahara, T. *Nat. Chem.* **2024,** *16,* 22–27. doi:10.1038/s41557-023-01397-6
84. Xu, B.; Troian-Gautier, L.; Dykstra, R.; Martin, R. T.; Gutierrez, O.; Tambar, U. K. *J. Am. Chem. Soc.* **2020,** *142,* 6206–6215. doi:10.1021/jacs.0c00147

License and Terms

This is an open access article licensed under the terms of the Beilstein-Institut Open Access License Agreement (https://www.beilstein-journals.org/bjoc/terms), which is identical to the Creative Commons Attribution 4.0 International License (https://creativecommons.org/licenses/by/4.0). The reuse of material under this license requires that the author(s), source and license are credited. Third-party material in this article could be subject to other licenses (typically indicated in the credit line), and in this case, users are required to obtain permission from the license holder to reuse the material.

The definitive version of this article is the electronic one which can be found at:
https://doi.org/10.3762/bjoc.20.106

Arylthianthrenium salts for triplet energy transfer catalysis

Project **[C]** investigated the triplet-sensitized homolytic cleavage of arylthianthrenium salts as a novel strategy to enable synthetically valuable transformations. These salts have gained prominence in the photoredox community as versatile aryl (pseudo)halide surrogates, owing to the high reactivity of their polarized C–X bonds in the ground state.[125,126,168] These substrates are readily reduced by photocatalysts, forming an unstable intermediate that fragments into neutral thianthrene and a highly reactive aryl radical. This aryl radical can then be harnessed in a wide range of C–C and C–X (X = N, O, S, P, halogen) bond-forming reactions.[124,144,169–172] The use of photoredox and transition metal catalysis with thianthrenium salts for C–C and C–heteroatom coupling is now well established. Alternatively, direct excitation of aryl (pseudo)halides typically induces homolytic cleavage to generate two radical species, potentially enabling novel reactivity pathways. However, such excitation generally requires harsh UVC light.[173]

In contrast, triplet sensitization of aryl halides requires less photon energy for activation by using a suitable sensitizer. However, this strategy is generally not viable, as the triplet energies of simple aryl halides exceed those of commonly available triplet photosensitizers.[7,8] In contrast, arylthianthrenium salts (ArTTs) contain both a positively charged, strongly electron-accepting sulfur atom and a neutral, electron-donating sulfur atom. This electronic configuration was hypothesized to result in a lower triplet energy compared to aryl halides.[144] Based on this rationale, it was proposed in project **[C]** that arylthianthrenium salts could be triplet-sensitized by photosensitizers such as thioxanthone (TX), leading to fragmentation into the persistent thianthrenium radical cation and a highly reactive aryl radical – species that could enable distinct reaction pathways. This mechanistic hypothesis was confirmed through spectroscopic studies that provided direct evidence for the formation of the thianthrenium radical cation, a species not accessible via electron transfer, thereby establishing TTET as the operative mechanism with much higher inherent quantum yields compared to direct excitation. Additionally, the triplet energies of the arylthianthrenium salts were experimentally determined and found to be lower by about 0.5 eV than those of comparable aryl bromides,[174] consistent with the proposed sensitization pathway. These mechanistic insights paved the way for 1,2-arylfunctionalization reactions of ethylene – a transformation that remained inaccessible using other activation strategies or aryl (pseudo)halides under visible light conditions.[175]

Summary:

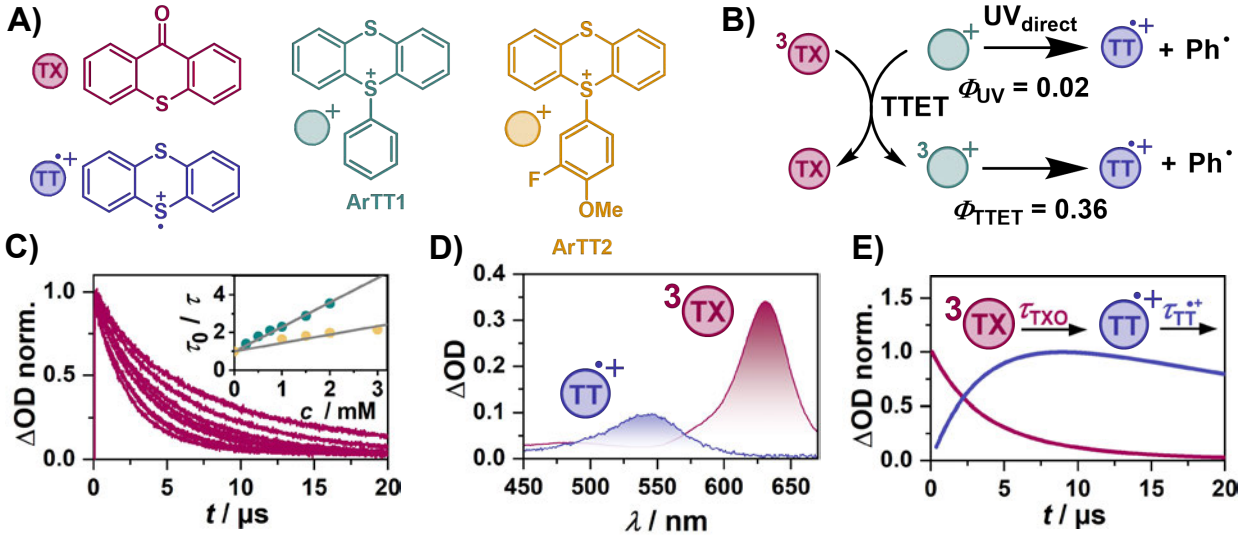

Figure 12: Overview of project **[C]**. A) Molecular structures of TX, ArTT1, ArTT2, and the thianthrenium radical cation ($TT^{\bullet+}$). B) Mechanism of triplet-sensitized homolytic cleavage of ArTT1 and comparison of direct (Φ_{UV}) and sensitized bond homolysis quantum yields (Φ_{TTET}). C) Triplet quenching experiments of ^{3}TX with ArTT2. Inset: Stern–Volmer analyses of ^{3}TX with ArTT1 and ArTT2 as quencher (color-coded). D) TA spectra of triplet-excited TX (red) and the thianthrenium radical cation (blue). E) Kinetic TA trace of the formation and decay of the thianthrenium radical cation.

In project **[C]**, ArTTs acted as energy acceptors in a triplet energy transfer catalytic reaction, enabling synthetically valuable arylethylation reactions of amines and alcohols. In the proposed mechanism (Figure 12B) the arylthianthrenium salt (ArTT1) is triplet-sensitized and fragments into the persistent thianthrenium radical cation ($TT^{\bullet+}$) and the highly reactive aryl radical after homolytic cleavage (see Figure 12A for molecular structures). The aryl radical is intercepted by ethylene to form a reactive homobenzyl radical that recombines with $TT^{\bullet+}$ to yield an alkylthianthrenium salt. In a separate reaction the thianthrenium moiety can then be replaced by a nucleophile. The reaction conditions were optimized using a prototypical substrate (ArTT2), with TX identified as the most effective triplet photosensitizer (see Figure 12A for molecular structures). The proposed mechanism – featuring a triplet energy transfer step from TX to the ArTTs – was investigated spectroscopically using ArTT1 and ArTT2. Stern–Volmer analyses yielded triplet energy transfer rate constants that aligned with both the calculated and experimentally determined triplet energies of ArTT1 and ArTT2 (Figure 12C). Upon energy transfer, homolytic cleavage of the ArTTs should yield the persistent $TT^{\bullet+}$, which exhibits a characteristic absorption band at 543 nm in the visible region.[127] Following 355 nm laser pulse excitation and complete deactivation of ^{3}TX in the presence of ArTT1 the TA spectrum closely resembles the steady-state absorption spectrum of $TT^{\bullet+}$ (Figure 12D). A lifetime analysis revealed its immediate formation after quenching of the TX triplet state – supporting a triplet-mediated pathway (Figure 12E). Control experiments excluded TX-derived photoproducts resulting from electron or hydrogen atom transfer. Quantitative laser studies enabled a direct comparison of the quantum efficiency of $TT^{\bullet+}$ formation via UV excitation versus triplet sensitization (Figure 12B). The results demonstrated that

the energy transfer pathway was inherently more efficient, with up to an 18-fold quantum yield increase in radical cation generation using TX sensitization. Building on these mechanistic insights, a substrate scope was established using ArTTs with comparable triplet energies that could be effectively sensitized by TX. The straightforward installation of nucleophiles at the thianthrenium position enabled broad functional group tolerance and diversification.

Project **[C]** was published as a research article:

"**Arylthianthrenium Salts for Triplet Energy Transfer Catalysis**"

Reprinted with permission from Y. Cai, T. K. Roy, T. J. B. Zähringer, B. Lansbergen, C. Kerzig, T. Ritter, *J. Am. Chem. Soc.* **2024**, *146*, 30474–30482. Copyright 2024 American Chemical Society.

The reference is attached in the following pages and can be cited corresponding to ref.[C]. The supporting information can be found in Chapter 10.4.

Author contributions: T. Ritter ideated the project. Y. Cai and T. K. Roy performed the sensitizer screening and developed the reaction and substrate scope under the supervision of T. Ritter. T. J. B. Zähringer performed mechanistic investigations of the triplet energy transfer step under the guidance of C. Kerzig. B. Lansbergen performed computational studies. The manuscript was written by Y. Cai, T. J. B. Zähringer, C. Kerzig and T. Ritter.

JACS
JOURNAL OF THE AMERICAN CHEMICAL SOCIETY
pubs.acs.org/JACS

Open Access
This article is licensed under CC-BY 4.0

Article

Arylthianthrenium Salts for Triplet Energy Transfer Catalysis

Yuan Cai, Triptesh Kumar Roy, Till J. B. Zähringer, Beatrice Lansbergen, Christoph Kerzig,* and Tobias Ritter*

Cite This: J. Am. Chem. Soc. 2024, 146, 30474−30482

Read Online

ACCESS | Metrics & More | Article Recommendations | Supporting Information

ABSTRACT: Sigma bond cleavage through electronically excited states allows synthetically useful transformations with two radical species. Direct excitation of simple aryl halides to form both aryl and halogen radicals necessitates UV-C light, so undesired side reactions are often observed and specific equipment is required. Moreover, only aryl halides with extended π systems and comparatively low triplet energy are applicable to synthetically useful energy transfer catalysis. Here we show the conceptual advantages of arylthianthrenium salts (ArTTs) for energy transfer catalysis with high energy efficiency compared to conventional aryl (pseudo)halides and their utility in arylation reactions of ethylene. The fundamental advance is enabled by the low triplet energy of ArTTs that may originate in large part from the electronic interplay between the distinct sulfur atoms in the tricyclic thianthrene scaffold, which is not accessible in either simple (pseudo)halides or other conventional sulfonium salts.

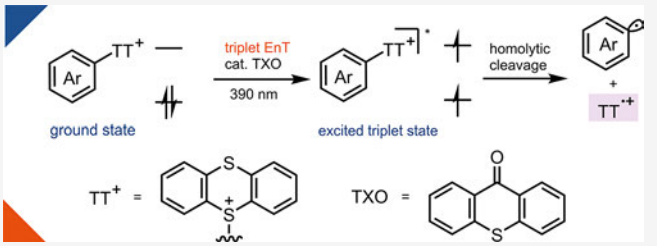

INTRODUCTION

Aryl (pseudo)halides are versatile electrophiles in organic synthesis owing to the broad reactivity of their polar C−X bond in ground state (Figure 1a).[1,2] Electronically excited aryl halides can undergo homolysis of the C−X bond to form two synthetically useful radical species, a reactivity that is usually unattainable from the ground state on account of the large bond dissociation energy (BDE) of the C−X bonds, for example around 84 kcal·mol^{-1} for aryl bromides.[3] Yet, aryl halides typically do not absorb in the visible spectrum, so UV light, often in the UV−C spectrum (<280 nm), is required for their excitation, which delivers over 102 kcal·mol^{-1} of energy, capable of cleaving many organic bonds, including C−C (~83 kcal·mol^{-1}) and C−H bonds (~100 kcal·mol^{-1}) (Figure 1b).[4] Visible light (380−800 nm) provides photons with less than 75 kcal·mol^{-1} energy, which allows most organic covalent bonds to remain intact. Additionally, visible light is safer, more accessible, and does not require special equipment, such as quartz glassware. However, simple aryl (pseudo)halides must typically be excited through direct excitation to a singlet state with UV-C light. Electronic excitation through triplet energy transfer (EnT) processes from an excited sensitizer are promising but have not been applied to simple aryl halides with visible light.[5−8] Because triplet energy (E_T) and spin multiplicity are transferred via concurrent electron exchange between an excited photosensitizer donor and the substrate acceptor, the excited high-energy singlet state of the substrate is circumvented. Nevertheless, sensitization of simple aryl halides requires higher triplet energy than is obtainable from photosensitizers with visible light absorption, which generally exhibit triplet energies of less than 66 kcal·mol^{-1}.[6−8] Only special aryl halides with an appropriate electronic structure have a sufficiently low triplet energy for successful excitation, for example, through extended π systems.[9] Aryl halides with highly conjugated or fused aryl systems, such as biphenyl and naphthyl halides, have low enough triplet energies (60−64 kcal·mol^{-1})[9] and can be used in energy transfer catalysis with visible light.[10,11] For simple aryl halides, high energy photons (less than 280 nm) from UV light and quartz glassware must be used.[10] High-power LEDs with high electricity-to-light conversion efficiencies are only available with wavelengths starting from about 365 nm.[12] Other synthetically useful, colorless molecules with a triplet energy of less than 66 kcal·mol^{-1} include, for example, styrene-derived substrates,[6−8] disulfides,[13] benzophenone-based oxime carbonates,[14] fused arenes,[15] α-keto esters,[16] N−N pyridinium ylides,[17] and naphthyl ketones.[18] Aryldiazonium and−iodonium compounds primarily function as electron acceptors rather than energy acceptors as a result of their high reduction potentials that can be rationalized, in part, by their positive charge, which favors capturing an electron instead of accepting energy from an excited photosensitizer.[19] Although both single electron transfer (SET) and EnT can generate synthetically useful aryl radicals from aryl (pseudo)halides, SET produces negatively charged (pseudo)halides after mesolytic cleavage,

Received: August 14, 2024
Revised: October 14, 2024
Accepted: October 15, 2024
Published: October 28, 2024

Downloaded via UNIV MAINZ on June 16, 2025 at 16:07:06 (UTC).
See https://pubs.acs.org/sharingguidelines for options on how to legitimately share published articles.

© 2024 The Authors. Published by American Chemical Society

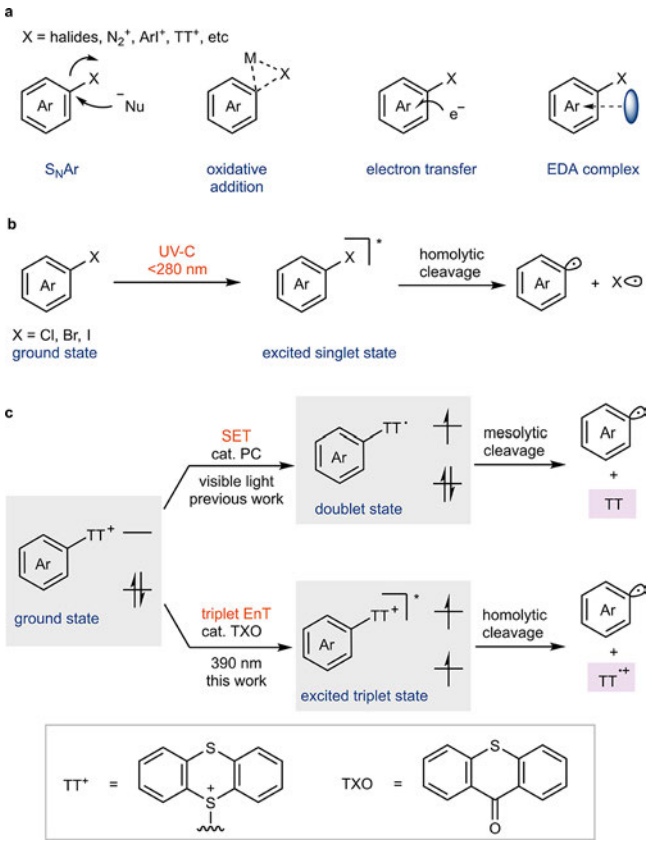

Figure 1. Reactivity of aryl electrophiles in ground and excited states. (a) Fundamental reactivity for aryl electrophiles in the ground state. Ar, aryl group; Nu, nucleophile; M, transition metal; X, (pseudo)halide; EDA, electron donor–acceptor. (b) Homolytic cleavage of C–X bonds in aryl halides from excited singlet state obtained under UV-C radiation. UV-C, Ultraviolet C. (c) Mesolytic cleavage of ArTTs through SET and homolytic cleavage of ArTTs through triplet EnT with 390 nm light. SET, single electron transfer; EnT, energy transfer; TXO, thioxanthone.

whereas EnT generates neutral (pseudo)halogen radicals after homolytic cleavage, and thereby provides a conceptually different reactivity mode that can be exploited for distinct reaction chemistry beyond what is possible with SET chemistry.[20] So far, a general platform for visible light-induced homolysis of the C–X bond in aryl electrophiles is lacking, both in terms of direct excitation and triplet energy transfer, and synthetically useful transformations based on excited aryl electrophiles still rely on the use of harmful UV light.[4,21] ArTTs have been shown to participate in various mechanisms, for example, transition metal catalysis,[22] photoredox catalysis,[23] direct excitation with 254 nm light,[21] and charge transfer processes.[24] Herein, we analyze the electronic structure of arylthianthrenium salts, describe their differences to aryl halides and other aryl-based positively charged pseudohalides, such as aryldiazonium salts, and show that arylthianthrenium salts undergo productive energy transfer to enable chemistry (Figure 1c).[25]

Manipulation of HOMO/LUMO energy states and triplet energy with electron donor and acceptor substituents to obtain bipolar molecules has been widely employed in the development of phosphorescent organic light-emitting diodes (PhOLEDs) and organic photocatalysts.[26] A priori, triplet energies cannot be derived from HOMO–LUMO gaps, yet, it is acknowledged that triplet energies are correlated with the degree of conjugation in molecules,[6,9] and so are HOMO–LUMO gaps. Arylthianthrenium salts[22] possess a positively charged, therefore strongly electron-accepting, sulfur atom, and a neutral, electron-donating sulfur atom, the combination of which may result in a lower HOMO–LUMO gap and in a lower triplet energy. We speculate that the lower triplet energy of ArTTs may be determined by the dipolar structure of the thianthrenium substituent itself, and not primarily influenced by the arene, and should therefore render ArTTs with varying aryls promising candidates for energy transfer catalysis with visible light. Furthermore, cationic ArTTs are less likely to engage in SET with commonly used photosensitizers when compared to other aryl-based cations such as phenyl diazonium (−0.1 V vs SCE) and −iodonium salts (−0.8 V vs SCE) due to their more negative reduction potential (−1.5 V vs SCE).[23] Energy transfer to arylthianthrenium salts would result in an excited triplet state and the formation of aryl radicals and the persistent thianthrenium radical cation ($TT^{\bullet+}$) upon homolysis, which is distinct from single electron transfer (SET) and electron donor–acceptor (EDA) complex pathways that form neutral thianthrene after mesolytic cleavage. The conceptually different reactivity mode of EnT offers distinct opportunities for reaction chemistry beyond what SET or EDA complex pathways have enabled, and may result in significantly higher quantum yields and thereby energy efficiency. As a proof of concept, we demonstrate the 1,2-arylfunctionalization reactions of ethylene,[27] a transformation currently inaccessible with other activation modes and other aryl (pseudo)halides with visible light.[28]

RESULTS AND DISCUSSION

Reaction Development. To probe our hypothesis that ArTTs could act as energy acceptor and undergo homolytic C–S bond cleavage, we exposed arylthianthrenium salt **1** to 390 nm LED irradiation in the presence of various photocatalysts under 1 atm of ethylene gas. Efficiency of the reaction correlated with the triplet energy of the photosensitizer and not with the reduction potentials of the excited state (Figure 2a), which points toward an EnT process as opposed to an SET process. By employing the commonly used thioxanthone (TXO) photosensitizer, with a triplet energy of 65.5 kcal·mol^{-1},[31] the desired arylethyl thianthrenium salt **2** was formed in 82% yield within 2 min at −78 °C. No reactivity was observed under the optimized conditions in the absence of TXO, even with an extended reaction time of 30 min or with substrates having extended conjugation (Scheme S1), which shows that direct excitation of the arylthianthrenium slats is less efficient than energy transfer from an excited sensitizer. At 25 °C, the solubility of ethylene in acetone is significantly lower than at −78 °C, which leads to the formation of hydrodefunctionalized byproducts via hydrogen abstraction by aryl radicals. Longer reaction time results in lower yield, presumably due to unproductive energy transfer to the product alkyl thianthrenium salt. The catalyst loading can be as low as 1.0 mol %, which is uncommon when utilizing TXO as a photocatalyst because of the occurrence of undesired hydrogen atom abstraction with excited TXO.[32] The low catalyst loading can be attributed to either the absence of a proper hydridic hydrogen atom in the reaction or efficient energy transfer facilitated by significant overlap between excited TXO and thianthrenium salts (vide infra). Other photosensitizers with triplet energies below 62.8 kcal·mol^{-1} all exhibit less than 2%

https://doi.org/10.1021/jacs.4c11099
J. Am. Chem. Soc. 2024, 146, 30474−30482

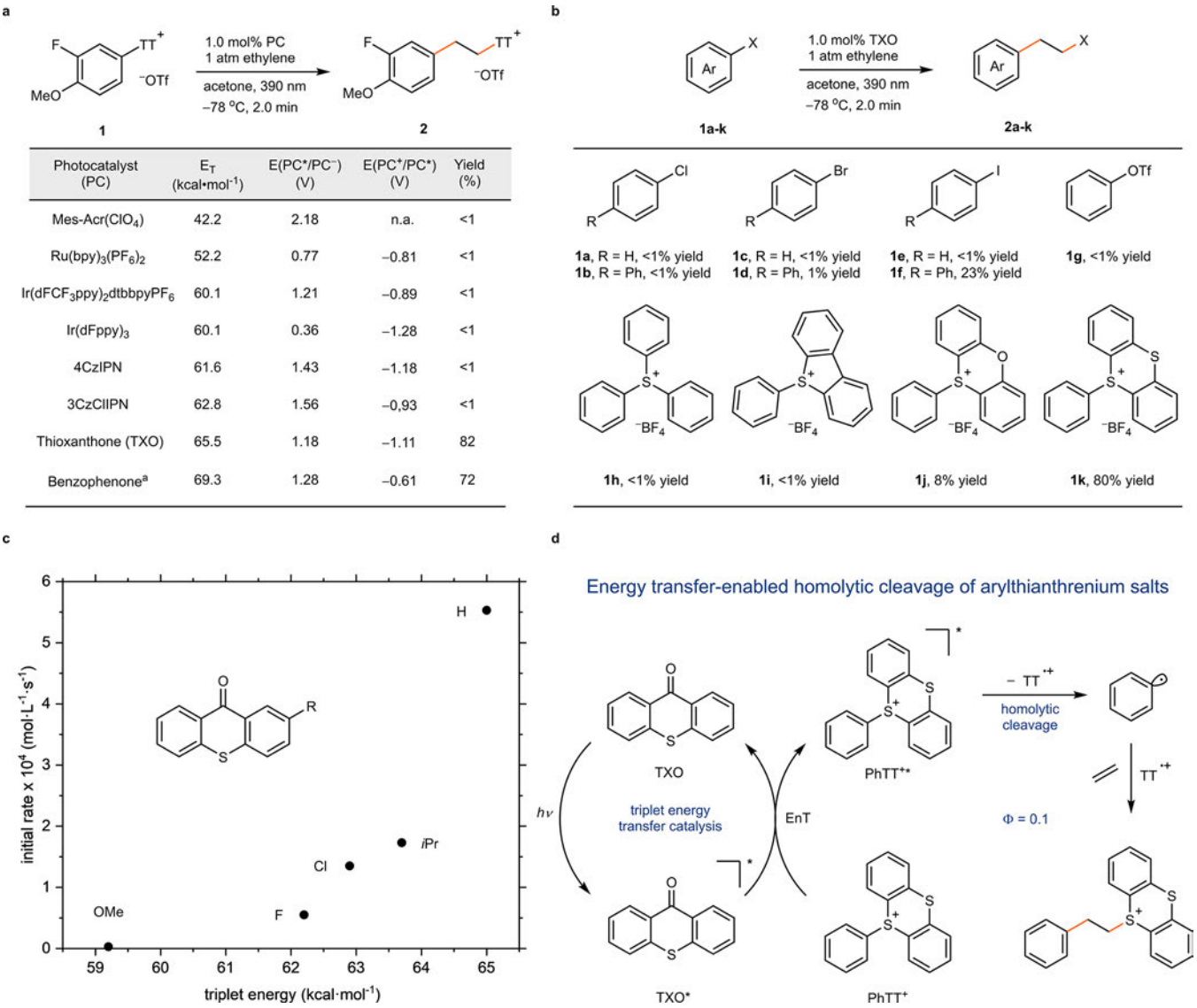

Photocatalyst (PC)	E_T (kcal·mol^{-1})	E(PC*/PC$^-$) (V)	E(PC$^+$/PC*) (V)	Yield (%)
Mes-Acr(ClO_4)	42.2	2.18	n.a.	<1
Ru(bpy)$_3$(PF_6)$_2$	52.2	0.77	−0.81	<1
Ir(dFCF$_3$ppy)$_2$dtbbpyPF_6	60.1	1.21	−0.89	<1
Ir(dFppy)$_3$	60.1	0.36	−1.28	<1
4CzIPN	61.6	1.43	−1.18	<1
3CzClIPN	62.8	1.56	−0,93	<1
Thioxanthone (TXO)	65.5	1.18	−1.11	82
Benzophenone[a]	69.3	1.28	−0.61	72

Figure 2. Development and application of arylthianthrenium salts for triplet energy transfer catalysis. (a) Evaluation of different photocatalysts in the 1,2-arylfunctionalization reactions of ethylene with arylthianthrenium salt **1**. Triplet energies (E_T) and reduction potentials (E vs SCE) were taken from refs 29 and 30. [a]20 mol % catalyst loading, 20 min. OTf, triflate; Mes-Acr, 9-mesityl-10-methylacridinium ion; bpy, 2,2′-bipyridyl; ppy, 2-phenylpyridyl; 4CzIPN, 2,4,5,6-tetrakis(9*H*-carbazol-9-yl)isophthalonitrile; 3CzClIPN, 2,4,6-tris(9*H*-carbazol-9-yl)-5-chloroisophthalonitrile; n.a., not available. (b) Evaluation of different aryl (pseudo)halides with thioxanthone as photosensitizer. (c) Correlation between reaction rates and triplet energies of different 2-substituted TXO photosensitizers. Triplet energies are calculated values (Table S13). (d) Proposed mechanism.

conversion. Benzophenone, a photosensitizer with a higher triplet energy of 69.3 kcal·mol^{-1},[29] requires a catalyst loading of 20 mol % and a prolonged reaction time of 20 min to afford a similar yield, likely due to the low absorption coefficient at 390 nm. Phenyl chloride (**1a**), bromide (**1c**), iodide (**1e**), and triflate (**1g**) do not show reactivity under the same conditions (Figure 2b), likely owing to their high triplet energy (∼82 kcal·mol^{-1}),[9] which renders the triplet state energetically inaccessible with visible light sensitization. Although biphenyl halides (**1b**, **1d**, **1f**) have an energetically reachable triplet energy of around 63 kcal·mol^{-1},[9] they do not participate in an efficient reaction, possibly on account of prohibitively high BDEs of the C−X bonds,[33] or less efficient energy transfer owing to lower overlap with the excited sensitizer compared to thianthrenium salts (vide infra). Other phenyl sulfonium salts, like triphenylsulfonium (**1h**)[34] and 5-phenyldibenzothiophenium salts (**1i**),[35] show negligible reactivity even with a reaction time of 30 min (Scheme S2), possibly as a result of the instability of the diphenyl sulfide− or dibenzothiophene radical cation,[36] the high triplet energy of **1h**, insufficient overlap, or a combination of these factors. Although the phenoxathiin radical cation is also persistent,[36] reaction of its corresponding salt (**1j**) is less efficient than with arylthianthreniums.

Mechanistic Investigations. Diaryl ketones are often employed as triplet photosensitizers rather than photoredox catalysts, primarily owing to their high triplet energy, notable efficiencies in intersystem crossing (typically $\Phi_{ISC} > 0.90$), and long-lived triplet excited states of approximately 50 μs.[29] Use of several 2-substituted TXOs with different triplet energy and reduction potentials illustrates a positive correlation between triplet state energy and reaction rates, which is consistent with the involvement of an EnT pathway (Figure 2c). The absence of a positive correlation between reaction rates and redox

https://doi.org/10.1021/jacs.4c11099
J. Am. Chem. Soc. 2024, 146, 30474−30482

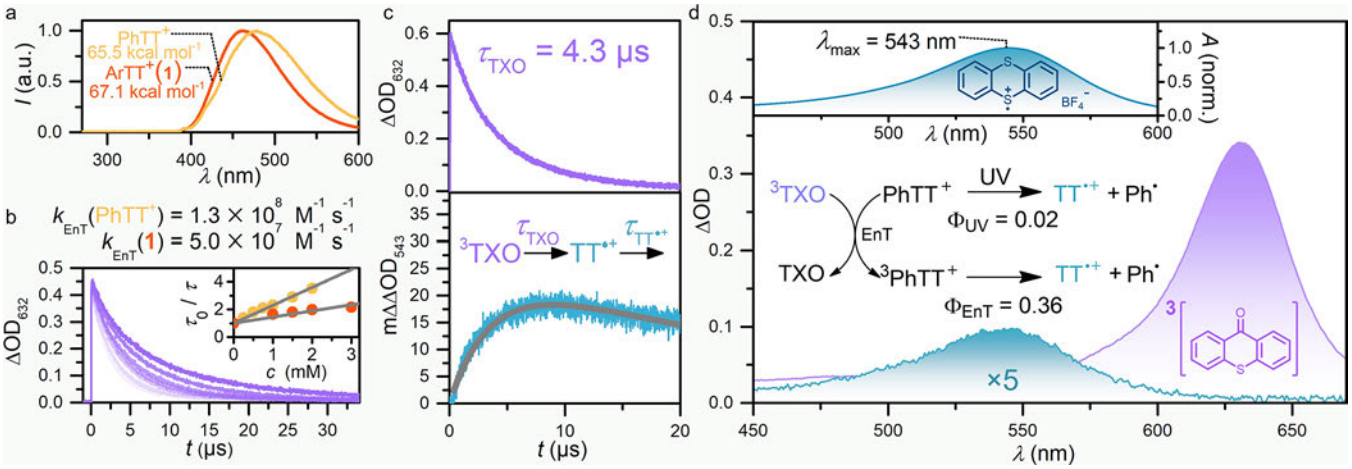

Figure 3. Mechanistic studies through photophysical analysis. (a) Phosphorescence measurements of $PhTT^+$ and **1** at 77 K. (b) Stern–Volmer analysis of ^{3}TXO quenching by $PhTT^+$ and **1**. (c) Kinetic traces of ^{3}TXO quenching (top) and isolated $TT^{\bullet+}$ formation and decay (bottom). (d) Transient absorption spectra of 50 μM TXO and 1 mM $PhTT^+$ after 50 ns (purple) and 50 μs (cyan) and comparison of direct and sensitized bond homolysis. Inset: absorption spectrum of thianthrenium radical cation (as tetrafluoroborate).

potentials of TXOs in both ground and excited states renders an SET pathway less likely (Figure S8). Furthermore, electronically excited TXO (−1.11 V vs SCE) and benzophenone (−0.61 V vs SCE)[29] exhibit insufficient reduction potentials for single electron reduction of ArTTs (∼ − 1.5 V vs SCE).[23] The lack of an observable interaction between ArTTs and TXO in the ground state, as observed from UV–vis studies, renders the formation of an electron donor–acceptor (EDA) complex unlikely (Figure S4).[24] Triplet quenchers, such as anthracene and cyclooctatetraene, decelerate or even inhibit the reaction, which is also consistent with an EnT pathway (Table S10). A quantum yield value of Φ = 0.1 is below 1 and consistent with a pathway that does not proceed via a chain mechanism. The observed positive but relatively small Hammett ρ value of 1.8 (Figure S10) aligns with the reduction of positive charge on the aromatic ring in the transition state. The bond dissociation energy (BDE) of the exocyclic C–S bond in $PhTT^+$ has been computed to be only at 64.2 kcal·mol^{-1}, slightly lower than its triplet state energy (65.5 kcal·mol^{-1}), which implies the prospect for synthetically useful homolytic cleavage following sensitization.

To obtain further mechanistic insights, we carried out detailed laser flash photolysis experiments. The 77 K phosphorescence spectra obtained upon pulsed excitation for $PhTT^+$ and $ArTT^+$ (**1**) give experimental triplet energies (Figure 3a) that are in agreement with computed E_T values (see below) and comparable to that of ^{3}TXO. In line with an almost isoenergetic ($PhTT^+$) and a slightly thermodynamically uphill ($ArTT^+$, **1**) EnT process, we measured quenching rate constants that are slower than the diffusion limit by about 2 orders of magnitude (Figure 3b). Such a fast energy transfer rate is consistent with the estimated and expected time scales for highly efficient energy transfer reactions and does not indicate a chain reaction mechanism (see Supporting Information page S57). Transient absorption studies revealed that upon ^{3}TXO quenching a single intermediate (Figure 3c) with a characteristic spectrum in the visible range is formed, which we could unambiguously assign to $TT^{\bullet+}$ (Figure 3d).[37] TXO-derived products that would result from a photoinduced SET can be excluded,[38] substantiating the anticipated EnT process followed by homolytic bond cleavage. In contrast, SET is the primary quenching mechanism with $Ir(dFppy)_3$ (Figure S1). Quantitative laser experiments with the excitation wavelength 355 nm allowed us to compare the quantum efficiency of $TT^{\bullet+}$ and aryl radical (that do not absorb in our detection range) generation upon direct UV excitation and sensitization at 20 °C. Based on our results, the EnT approach is inherently more efficient by as much as a factor of 18, highlighting another advantage of the strategy presented herein. These mechanistic studies explain the impressively short reaction times and considerable overall quantum yield observed at lower temperatures. We believe that highly efficient photocatalytic reaction protocols as presented herein are required for the development of photoreactions on a larger scale and industrially scalable photoreactions.

Based on our collective experimental findings, we propose an operative mechanism as shown in Figure 2d, in which electronically excited TXO sensitizes ArTTs through energy transfer to yield triplet-excited ArTTs that undergoes rapid homolysis of the labile C–S bond to produce an aryl radical and persistent $TT^{\bullet+}$. The aryl radical adds to ethylene to form a highly reactive primary homobenzyl radical. At low conversion, when the concentration of the persistent TT radical cation is low, the transient aryl and alkyl radicals may preferentially undergo side reactions, such as hydrodefunctionalization and dimerization, the products of which have been observed under the optimized reaction conditions. As the reaction progresses, the persistent $TT^{\bullet+}$ can accumulate and eventually recombine with the alkyl radical to form the desired product. Because $TT^{\bullet+}$ is persistent, as opposed to radicals derived from other aryl (pseudo)halides, productive radical recombination is not challenged by side reactions resulting from $TT^{\bullet+}$, as could be expected from other radicals, such as hydrogen atom abstraction from chlorine and bromine radicals,[39] and decomposition of diphenyl sulfide-[34] or iodobenzene radical cations.[40] The observation of crossover products in a radical scrambling experiment (Figure S9) using two different salts, Ar^1TT^+ and Ar^2TFT^+, indicates that radicals escape from the solvent cage prior to the C–S bond formation process.

Computational Study of Ground and Triplet States of Aryl (Pseudo)halides. Density functional theory (DFT) calculations were conducted to elucidate the conceptual difference between ArTTs and other aryl (pseudo)halides in

https://doi.org/10.1021/jacs.4c11099
J. Am. Chem. Soc. 2024, 146, 30474–30482

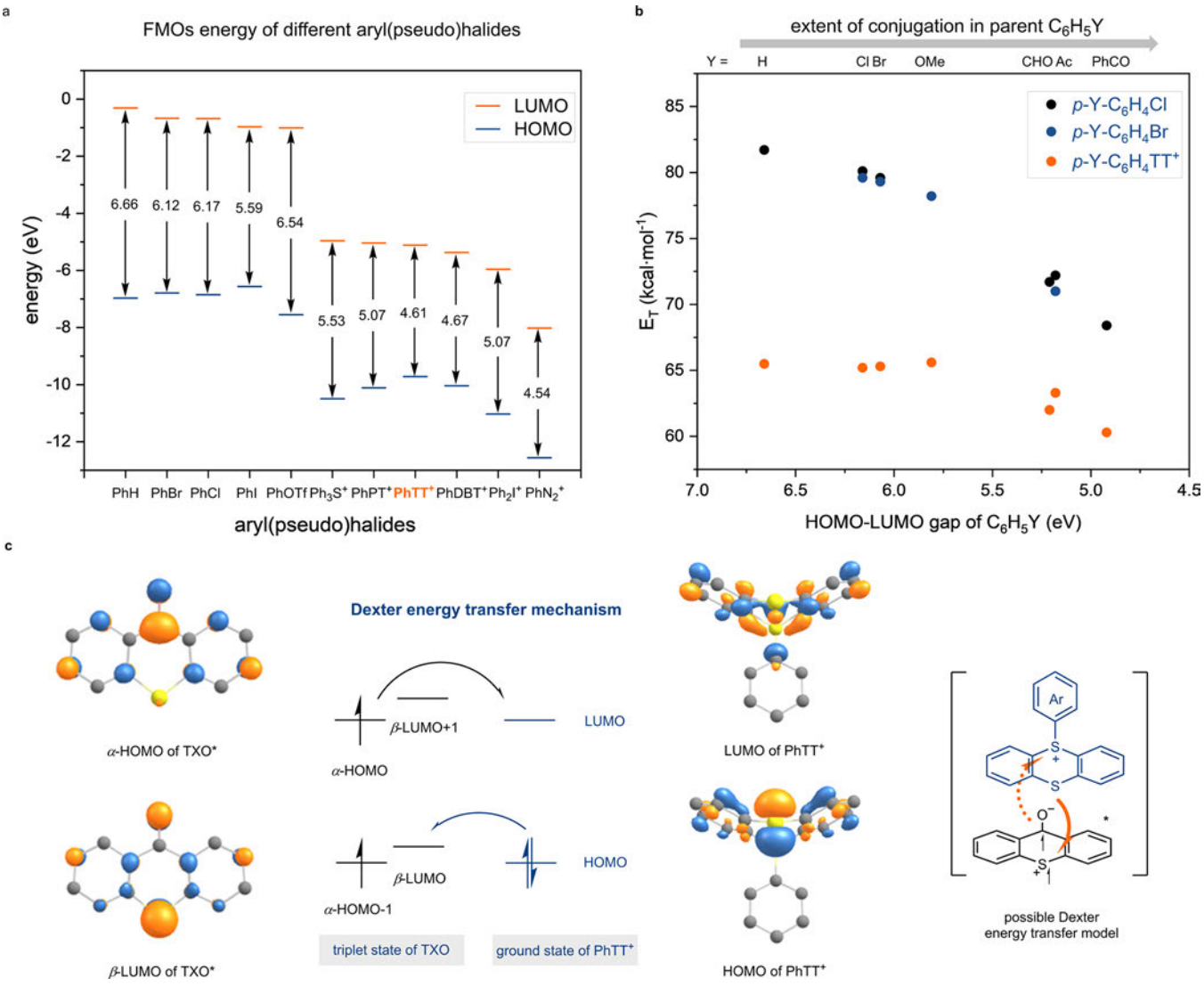

Figure 4. Computational study of aryl (pseudo)halides and Dexter energy transfer mechanism. (a) Comparison of frontier molecular orbitals energy of different aryl (pseudo)halides. FMOs, frontier molecular orbitals; Ph, phenyl; OTf, triflate; Ph_3S^+, triphenylsulfonium; $PhPT^+$, 10-phenylphenoxathiinium; $PhDBT^+$, 5-phenyldibenzothiophenium; Ph_2I^+, diphenyl iodonium salt; PhN_2^+, phenyl diazonium salt. (b) Relationship between triplet energy of aryl (pseudo)halides *p*-Y-C_6H_4X and conjugation extent of their parent C_6H_5Y. Triplet energies for *p*-Y-C_6H_4Cl and *p*-Y-C_6H_4Br were taken from ref 9. Ac, acetyl group; E_T, triplet energy; X, (pseudo)halide; Y, substituent. (c) Dexter energy transfer mechanism and possible Dexter energy transfer model.

energy transfer chemistry. Although the bent geometry of the thianthrenium framework limits extensive conjugation potential,[22] the calculation results predict that $PhTT^+$ exhibits a narrower HOMO−LUMO gap in comparison to phenyl halides and other structurally similar phenyl sulfonium salts (Figure 4a). As for other positively charged aryl-substituted salts, the LUMO of $PhTT^+$ is significantly lower than for neutral aryl halides, yet its HOMO is comparatively high when compared to the other cations, possibly a result of the electron-rich neutral sulfur atom, which leads to a smaller HOMO−LUMO gap. $PhTT^+$ is computed to have a triplet energy of 65.5 kcal·mol^{-1} that is in agreement with the experimental value, significantly lower than that of corresponding phenyl halides (~82 kcal·mol^{-1})[9] and triphenyl sulfonium salt (~75 kcal·mol^{-1}).[34] While phenyl diazonium and -iodonium salts also possess low triplet energies of 61.8 kcal·mol^{-1} (Table S14) and 64.3 kcal·mol^{-1}, respectively,[40−42] their lower LUMO energy levels likely result in higher electron affinity and faster electron transfer than for ArTTs.[19] DFT calculations also indicate that the frontier molecular orbitals of phenyl halides are mainly located within the aromatic π system, while the TT framework contributes significantly to the frontier molecular orbitals of ArTTs (Table S14). Likewise, the triplet state energies of ArTTs appear to be governed by the TT substituent, which remains similar between 60−66 kcal·mol^{-1}, largely independent of the aryl substituent (Figure 4b). In contrast, the triplet energy of aryl halides is significantly influenced by substituents, and exhibits a stronger correlation with the HOMO−LUMO gaps of their parent arenes.

The reaction is rapid and reaches full conversion within 2 min at a catalyst loading of just 1.0 mol % and a reaction temperature of −78 °C. We propose that the geometry of the electronic overlap between excited TXO and ArTTs plays an important role: In a Dexter energy transfer process, simultaneous exchange of electrons between excited photosensitizer and substrate result in energy transfer (Figure 4c).[43]

https://doi.org/10.1021/jacs.4c11099
J. Am. Chem. Soc. 2024, 146, 30474−30482

Table 1. Substrate Scope in Arylation Reactions of Ethylene[a]

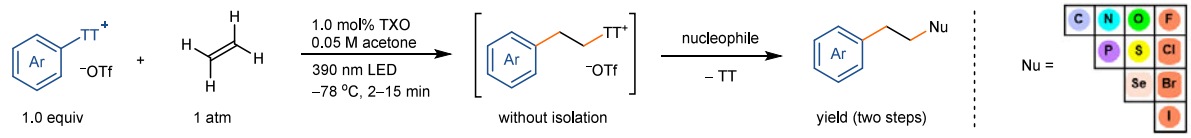

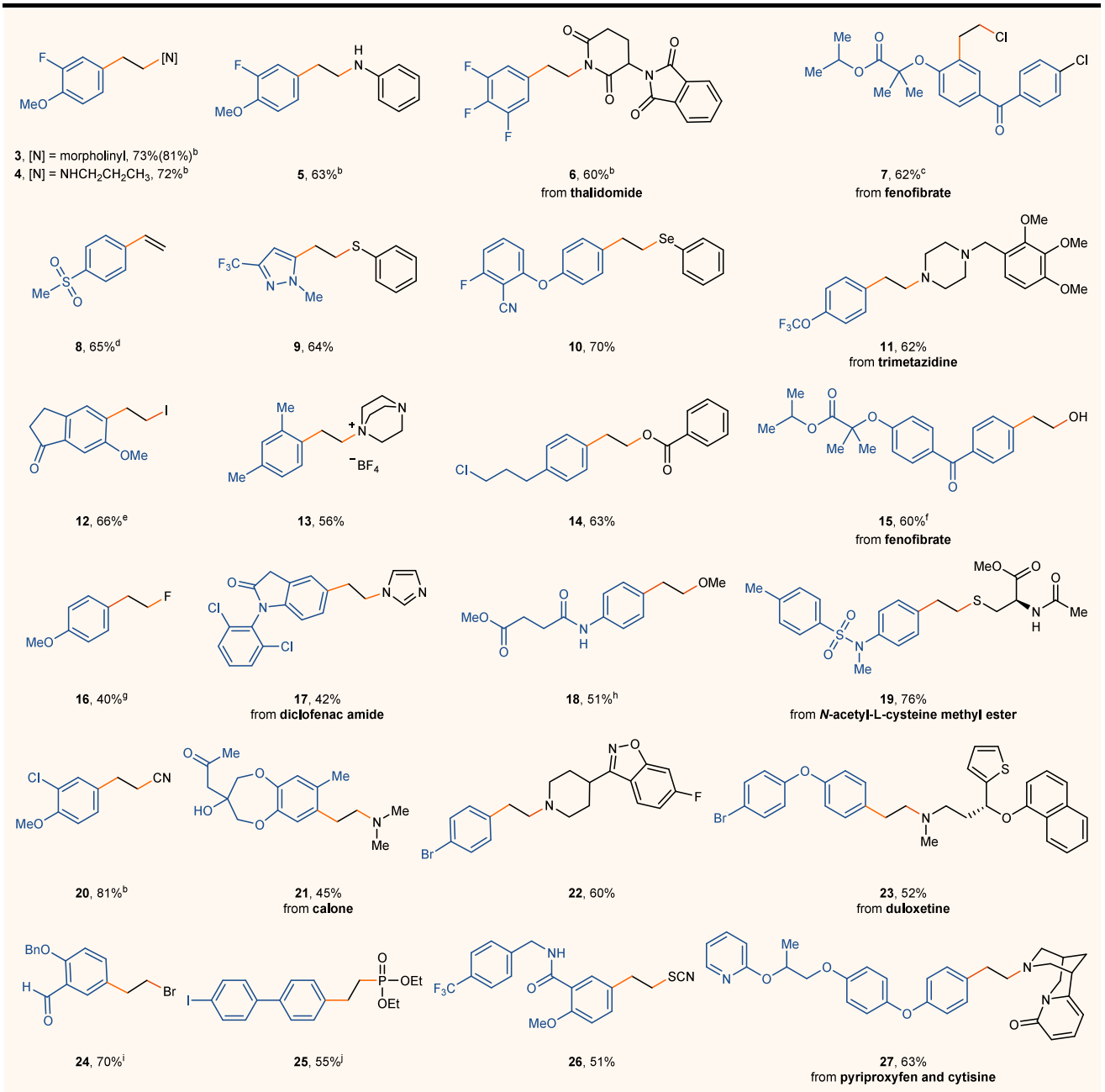

[a]Reaction conditions: arylthianthrenium salt (0.20 mmol), ethylene (1 atm), and TXO in acetone (c = 0.50 mM, 4.0 mL, 2.0 μmol, 1.0 mol %) at −78 °C under 40 W 390 nm LED for 2−15 min. Subsequently, base and nucleophile were added, and the reaction mixture was stirred for 12 h. Refer to the Supporting Information for experimental details for each substrate. [b]Tetrabutylammonium bromide (TBAB, 77 mg, 0.24 mmol, 1.2 equiv) was added in the first step and allowed to react at −94 °C for 10 min. [c]Tetrabutylammonium chloride (TBACl) was used. [d]DBU was used. [e]KI was used. [f]Water was used at 55 °C. [g]Triethylamine trihydrofluoride was used at 55 °C. [h]Anhydrous methanol was used as solvent in the second step at 55 °C. [i]NaBr was used.

The frontier molecular orbitals (α-HOMO and β-LUMO) of the excited TXO are predominantly situated on the carbon of the carbonyl group and the sulfur atom, respectively, while those of the ground state $PhTT^+$ are primarily located on the neutral and positively charged sulfur atoms, respectively. Given the analogous tricyclic fused ring system of TXO and thianthrenium, the spatial alignment of the frontier molecular orbitals of excited TXO and ground state $PhTT^+$ coincides. In

https://doi.org/10.1021/jacs.4c11099
J. Am. Chem. Soc. 2024, 146, 30474−30482

view of the significant impact of orbital interactions on energy transfer rates,[43] the interplay between thianthrenium and TXO may result in rapid energy transfer. Such a hypothesis would also provide additional insight into why arylthianthreniums react more favorably, even than those special aryl pseudohalides (Figure 2b) with appropriate triplet energy, and why other well-established photosensitizers such as benzophenone are significantly less efficient. Such fortuitous energy transfer, based on the thianthrenium structure, is yet another example of how thianthrene-chemistry can elicit desired chemical reactivity beyond what is currently possible with conventional (pseudo)halides.

Substrate Scope. ArTTs with different substituents display comparable triplet energy between 60−65 kcal·mol^{-1}, lower than the triplet energy of TXO, which suggests a broad theoretical scope of aryl electrophiles for productive and chemoselective sensitization. As shown in Table 1, a variety of ArTTs bearing ortho-, meta-, and para-substituted aryls, and electron-rich, -neutral, and -poor aryls, as well as mono-, di-, and trisubstituted aryls, are tolerated. In our prior research utilizing aryl halides as energy acceptors, only substrates featuring highly conjugated biphenyl and naphthyl frameworks are effective with visible light, and 280 nm UV-C light is necessary when employing simple aryl halides.[10] Here, no such limitation was observed and 390 nm light could be used for all examples. Various functional groups, heteroaromatic compounds, and complex molecules are well-tolerated. Given the higher triplet energy of aryl halides compared to ArTTs, halides (**7**, **22**, **25**) remain untouched and can be potentially utilized in subsequent transformations. The large functional group tolerance may also be explained by a chemoselective Dexter energy transfer that is fastest between the TXO photosensitizer and the thianthrenium group based on their structural and electronic similarity, and leave other functional groups, potentially sensitive to energy transfer and hydrogen atom transfer, untouched. The main side products include hydrodefunctionalization, which can be reduced by further decreasing the reaction temperature to −94 °C, thereby increasing the solubility of ethylene, and the Minisci byproduct, which can be minimized by carefully controlling the reaction time or suppressed by adding a bromide nucleophile to capture the alkyl thianthrenium salt (Scheme S5).

The resulting primary arylethyl thianthrenium salts serve as effective alkyl electrophiles for subsequent transformations.[44,45] By employing amines as nucleophiles in the same pot, a useful yet otherwise challenging three-component aminoarylation reaction involving aryl electrophiles, alkenes, and amines was achieved (Table 1).[46] In previous studies with different approaches, aminoarylation of alkenes showed a wide range of alkenes, yet the scope of amines was limited to azide and nitriles.[47−49] In our study, both the scope of amines and the tolerance toward functional groups are extensive. A wide range of amines, including cyclic and acyclic, primary, secondary, and tertiary, along with aliphatic and aromatic amines, all demonstrate excellent compatibility. A variety of valuable β-arylethylamines are synthesized, which are privileged pharmacophores found in a range of biologically active natural products and pharmaceuticals, particularly in molecules that act on the central nervous system.[47,48] Oxygen-, sulfur-, and chloride-based nucleophiles allow for the direct synthesis of β-arylethyl ethers, thioethers, and chlorides, all of which are found in various pharmaceuticals and bioactive molecules. Nucleophiles based on carbon, phosphine, other halides, and selenium are all compatible, which demonstrates the versatile ability of neutral thianthrene to function as excellent leaving group. Chloride and bromide can be successfully added at the beginning of the reaction, whereas other nucleophiles such as iodide, aliphatic amine, carboxylate, and thiophenolate cannot, likely a consequence of their competitive reaction with the thianthrenium radical cation (Scheme S4). The wide variety of aromatic components and nucleophiles allows for fragment coupling through a $-CH_2CH_2-$ linker (**27**). Nucleophiles with high basicity, such as fluoride, and carbon nucleophiles like cyanide, malonates or acetylides, resulted in low yield (<40%) because of competing elimination reactions, a side reactivity also observed with other nucleophiles except halides (Cl, Br, I), sulfur, and selenium-based ones. The elimination side reaction can be mitigated by converting alkylthianthrenium salts to alkyl bromides in situ before adding the nucleophile, as uncharged alkyl bromides are less prone to elimination. When a non-nucleophilic base, such as DBU was employed, elimination was observed exclusively, and vinylated arene (**8**) was obtained. Various alkenes beyond ethylene, such as α-olefins, styrenes, and Michael acceptors, have been tested successfully. However, the secondary or tertiary alkyl thianthrenium salts formed by the addition of ArTTs to substituted alkenes are not stable toward elimination. To retain synthetic utility, reactions with substituted olefins must be conducted in the presence of bromide to in situ displace the thianthrene leaving group to afford the corresponding alkyl bromides, which can be further functionalized (Table S1).

CONCLUSIONS

We have demonstrated the conceptual advantage of ArTTs to enable visible light-mediated triplet energy transfer catalysis. Our study highlights the pivotal role of the two sulfur atoms in reducing the HOMO−LUMO gap and triplet energy of ArTTs. In view of the small influence of the aryl group, various ArTTs exhibit similar triplet energy. The large structural and electronic overlap between the excited TXO and thianthrenium framework facilitates rapid visible light-driven energy transfer with much higher inherent quantum yields compared to direct UV excitation.[50] By employing ArTTs as energy acceptors, we have presented synthetically valuable arylethylation reactions of amines, alcohols and other nucleophiles. Further exploration of thianthrenium salts as acceptor for triplet energy transfer catalysis may unveil additional useful reaction chemistry.

ASSOCIATED CONTENT

Supporting Information

The Supporting Information is available free of charge at https://pubs.acs.org/doi/10.1021/jacs.4c11099.

Experimental procedures, spectroscopic data, and NMR spectra of all products (PDF)

AUTHOR INFORMATION

Corresponding Authors

Christoph Kerzig − *Department of Chemistry, Johannes Gutenberg University Mainz, 55128 Mainz, Germany;* orcid.org/0000-0002-1026-1146; Email: ckerzig@uni-mainz.de

Tobias Ritter − *Max-Planck-Institut für Kohlenforschung, 45470 Mülheim an der Ruhr, Germany; Institute of Organic*

Chemistry, RWTH Aachen University, 52074 Aachen, Germany; orcid.org/0000-0002-6957-450X; Email: ritter@kofo.mpg.de

Authors

Yuan Cai − *Max-Planck-Institut für Kohlenforschung, 45470 Mülheim an der Ruhr, Germany;* orcid.org/0000-0003-0026-4930

Triptesh Kumar Roy − *Max-Planck-Institut für Kohlenforschung, 45470 Mülheim an der Ruhr, Germany; Institute of Organic Chemistry, RWTH Aachen University, 52074 Aachen, Germany*

Till J. B. Zähringer − *Department of Chemistry, Johannes Gutenberg University Mainz, 55128 Mainz, Germany;* orcid.org/0000-0001-9285-3980

Beatrice Lansbergen − *Max-Planck-Institut für Kohlenforschung, 45470 Mülheim an der Ruhr, Germany*

Complete contact information is available at: https://pubs.acs.org/10.1021/jacs.4c11099

Funding

Open access funded by Max Planck Society.

Notes

The authors declare the following competing financial interest(s): T.R. may benefit from thianthrenium-related sales.

■ ACKNOWLEDGMENTS

We thank the MPI für Kohlenforschung for funding. Y.C. acknowledges the Alexander von Humboldt Foundation for a Humboldt Research Fellowship. We thank F. Kohler and D. Kampen for mass spectrometry analysis, G. Breitenbruch and C. Heidgen for HPLC separation, and R. Petzold for transient absorption spectroscopy sample preparation. We thank Dr. J. Mateos-Lopez, Dr. E. de Pedro Beato, Dr. J. Kim, and Dr. Q. Cheng for helpful discussions.

■ REFERENCES

(1) Ackermann, L. *Modern Arylation Methods*; Wiley-VCH: Weinheim, Germany, 2009.
(2) Terrier, F. *Modern Nucleophilic Aromatic Substitution*; Wiley-VCH: Weinheim, Germany, 2013.
(3) Grimshaw, J.; de Silva, A. P. Photochemistry and photocyclization of aryl halides. *Chem. Soc. Rev.* **1981**, *10*, 181−203.
(4) Liu, W.; Li, J.; Huang, C.-H.; Li, C.-J. Aromatic Chemistry in the Excited State: Facilitating Metal-Free Substitutions and Cross-Couplings. *Angew. Chem., Int. Ed.* **2020**, *59*, 1786−1796.
(5) (a) Skubi, K. L.; Blum, T. R.; Yoon, T. P. Dual catalysis strategies in photochemical synthesis. *Chem. Rev.* **2016**, *116*, 10035−10074. (b) Großkopf, J.; Kratz, T.; Rigotti, T.; Bach, T. Enantioselective Photochemical ReactionsEnabled by Triplet Energy Transfer. *Chem. Rev.* **2022**, *122*, 1626−1653.
(6) (a) Strieth-Kalthoff, F.; James, M. J.; Teders, M.; Pitzer, L.; Glorius, F. Energy transfer catalysis mediated by visible light: principles, applications, directions. *Chem. Soc. Rev.* **2018**, *47*, 7190−7202. (b) Dutta, S.; Erchinger, J. E.; Strieth-Kalthoff, F.; Kleinmans, R.; Glorius, F. Energy transfer photocatalysis: exciting modes of reactivity. *Chem. Soc. Rev.* **2024**, *53*, 1068−1089.
(7) (a) Zhou, Q.-Q.; Zou, Y.-Q.; Lu, L.-Q.; Xiao, W.-J. Visible-light-induced organic photochemical reactions through energy-transfer pathways. *Angew. Chem., Int. Ed.* **2019**, *58*, 1586−1604. (b) Zou, Y.-Q.; Duan, S.-W.; Meng, X.-G.; Hu, X.-Q.; Gao, S.; Chen, J.-R.; Xiao, W.-J. Visible light induced intermolecular [2 + 2]-cycloaddition reactions of 3-ylideneoxindoles through energy transferpathway. *Tetrahedron* **2012**, *68*, 6914−6919.
(8) Strieth-Kalthoff, F.; Glorius, F. Triplet energy transfer photocatalysis: unlocking the next level. *Chem* **2020**, *6*, 1888−1903.
(9) Montalti, M.; Credi, A.; Prodi, L.; Gandolfi, M. T. *Handbook of Photochemistry*, 3rd ed.; CRC Press: Boca Raton, FL, 2006.
(10) Zhang, L.; Israel, E. M.; Yan, J.; Ritter, T. Copper-mediated etherification via aryl radicals generated from triplet states. *Nat. Synth.* **2022**, *1*, 376−381.
(11) Zhang, Y.; Xu, J.; Guo, H. Light-Induced Intramolecular Iodine-Atom Transfer Radical Addition of Alkyne: An Approach from Aryl Iodide to Alkenyl Iodide. *Org. Lett.* **2019**, *21*, 9133−9137.
(12) Hirayama, H.; Fujikawa, S.; Kamata, N. Recent progress in AlGaN-based deep-UV LEDs. *Electron. Commun. Jpn.* **2015**, *98*, 1−8.
(13) Teders, M.; Henkel, C.; Anhäuser, L.; Strieth-Kalthoff, F.; Gómez-Suárez, A.; Kleinmans, R.; Kahnt, A.; Rentmeister, A.; Guldi, D.; Glorius, F. The energy-transfer-enabled biocompatible disulfide−ene reaction. *Nat. Chem.* **2018**, *10*, 981−988.
(14) Patra, T.; Das, M.; Daniliuc, C. G.; Glorius, F. Metal-free, photosensitized oxyimination of unactivated alkenes with bifunctional oxime carbonates. *Nat. Catal.* **2021**, *4*, 54−61.
(15) Ma, J.; Chen, S.; Bellotti, P.; Guo, R.; Schäfer, F.; Heusler, A.; Zhang, X.; Daniliuc, C.; Brown, M. K.; Houk, K. N.; Glorius, F. Photochemical Intermolecular Dearomative Cycloaddition of Bicyclic Azaarenes with Alkenes. *Science* **2021**, *371*, 1338−1345.
(16) Zheng, J.; Dong, X.; Yoon, T. P. Divergent photocatalytic reactions of α-ketoesters under triplet sensitization and photoredox conditions. *Org. Lett.* **2020**, *22*, 6520−6525.
(17) Lee, W.; Koo, Y.; Jung, H.; Chang, S.; Hong, S. Energy-transfer-induced [3 + 2] cycloadditions of N−N pyridinium ylides. *Nat. Chem.* **2023**, *15*, 1091−1099.
(18) Guo, R.; Chang, Y.-C.; Herter, L.; Salome, C.; Braley, S. E.; Fessard, T. C.; Brown, M. K. Strain-Release [$2\pi + 2\sigma$] Cycloadditions for the Synthesis of Bicyclo[2.1.1]hexanes Initiated by Energy Transfer. *J. Am. Chem. Soc.* **2022**, *144*, 7988−7994.
(19) Kvasovs, N.; Gevorgyan, V. Contemporary methods for generation of aryl radicals. *Chem. Soc. Rev.* **2021**, *50*, 2244−2259.
(20) Huang, H.-M.; Bellotti, P.; Ma, J.; Dalton, T.; Glorius, F. Bifunctional reagents in organic synthesis. *Nat. Rev. Chem.* **2021**, *5*, 301−321.
(21) Zhao, Y.; Yu, C.; Liang, W.; Patureau, F. W. Photochemical (Hetero-)Arylation of Aryl Sulfonium Salts. *Org. Lett.* **2021**, *23*, 6232−6236.
(22) Berger, F.; Plutschack, M. B.; Riegger, J.; Yu, W.; Speicher, S.; Ho, M.; Frank, N.; Ritter, T. Site-selective and versatile aromatic C−H functionalization by thianthrenation. *Nature* **2019**, *567*, 223−228.
(23) Li, J.; Chen, J.; Sang, R.; Ham, W.-S.; Plutschack, M. B.; Berger, F.; Chabbra, S.; Schnegg, A.; Genicot, C.; Ritter, T. Photoredox catalysis with aryl sulfonium salts enables site-selective late-stage fluorination. *Nat. Chem.* **2020**, *12*, 56−62.
(24) Dewanji, A.; van Dalsen, L.; Rossi-Ashton, J. A.; Gasson, E.; Crisenza, G. E. M.; Procter, D. J. A general arene C−H functionalization strategy via electron donor−acceptor complex photoactivation. *Nat. Chem.* **2023**, *15*, 43−52.
(25) (a) Cai, Y.; Roy, T. K.; Zähringer, T. J. B.; Lansbergen, B.; Kerzig, C.; Ritter, T. Arylthianthrenium salts for triplet energy transfer catalysis. *ChemRxiv* **2024**, DOI: 10.26434/chemrxiv-2024-gq4gf. During the preparation of this article, a report on the synthesis of 1,2-arylheteroaryl ethanes using aryldibenzothiophenium salts appeared. See: (b) Liu, T.; Li, T.; Tea, Z. Y.; Wang, C.; Shen, T.; Lei, Z.; Chen, X.; Zhang, W.; Wu, J. Modular assembly of arenes, ethylene and heteroarenes for the synthesis of 1,2-arylheteroaryl ethanes. *Nat. Chem.* **2024**, *16*, 1705.
(26) (a) Tao, Y. T.; Yang, C. L.; Qin, J. G. Organic host materials for phosphorescent organic light-emitting diodes. *Chem. Soc. Rev.* **2011**, *40*, 2943−2970. (b) Speckmeier, E.; Fischer, T. G.; Zeitler, K. A toolbox approach to construct broadly applicable metal-free catalysts for photoredox chemistry: deliberate tuning of redox potentials and importance of halogens in donor-acceptor cyanoarenes. *J. Am. Chem. Soc.* **2018**, *140*, 15353−15365.

(27) (a) Saini, V.; Stokes, B. J.; Sigman, M. S. Transition-metal-catalyzed laboratory scale carbon−carbon bond-forming reactions of ethylene. *Angew. Chem., Int. Ed.* **2013**, *52*, 11206−11220. (b) Yu, X.-Y.; Chen, J.-R.; Xiao, W.-J. Visible Light-Driven Radical-Mediated C−C Bond Cleavage/Functionalization in Organic Synthesis. *Chem. Rev.* **2021**, *121*, 506−561.
(28) Pan, H.; Ge, H.; He, R.; Huang, W.; Wang, L.; Wei, Y.; Sa, R.; Wang, Y.-J.; Yuan, R. Photo-induced chloride atom transfer radical addition and aminocarbonylation reactions. *Asian J. Org. Chem.* **2019**, *8*, 1513−1518.
(29) Romero, N. A.; Nicewicz, D. A. Organic photoredox catalysis. *Chem. Rev.* **2016**, *116*, 10075−10166.
(30) Teegardin, K.; Day, J. I.; Chan, J.; Weaver, J. Advances in photocatalysis: a microreview of visible-light-mediated ruthenium- and iridium-catalyzed organic transformations. *Org. Process Res. Dev.* **2016**, *20*, 1156−1163. (b) Speckmeier, E.; Fischer, T. G.; Zeitler, K. A Toolbox Approach to Construct Broadly Applicable Metal-Free Catalysts for Photoredox Chemistry: Deliberate Tuning of Redox Potentials and Importance of Halogens in Donor−Acceptor Cyanoarenes. *J. Am. Chem. Soc.* **2018**, *140*, 15353−15365.
(31) Elliott, L. D.; Kayal, S.; George, M. W.; Booker-Milburn, K. Rational design of triplet sensitizers for the transfer of excited state photochemistry from UV to visible. *J. Am. Chem. Soc.* **2020**, *142*, 14947−14956.
(32) Nikitas, N. F.; Gkizis, P. L.; Kokotos, C. G. Thioxanthone: a powerful photocatalyst for organic reactions. *Org. Biomol. Chem.* **2021**, *19*, 5237−5253.
(33) Luo, Y.-R. *Handbook of Bond Dissociation Energies in Organic Compounds*; CRC Press: Boca Raton, FL, 2003.
(34) Dektar, J. L.; Hacker, N. P. Photochemistry of triarylsulfonium salts. *J. Am. Chem. Soc.* **1990**, *112*, 6004−6015.
(35) Aukland, M. H.; Šiauciulis, M.; West, A.; Perry, G. J. P.; Procter, D. J. Metal-free photoredox-catalysed formal C−H/C−H coupling of arenes enabled by interrupted Pummerer activation. *Nat. Catal.* **2020**, *3*, 163−169.
(36) Wu, J.; Wang, Z.; Chen, X.-Y.; Wu, Y.; Wang, D.; Peng, Q.; Wang, P. Para-selective borylation of monosubstituted benzenes using a transient mediator. *Sci. China: Chem.* **2020**, *63*, 336−340.
(37) de Sorgo, M.; Wasserman, B.; Szwarc, M. Aggregation of Salts of Thianthrene Radical Cations. *J. Phys. Chem.* **1972**, *76*, 3468−3471.
(38) Zähringer, T. J. B.; Wienhold, M.; Gilmour, R.; Kerzig, C. Direct Observation of Triplet States in the Isomerization of Alkenyl boronates by Energy Transfer Catalysis. *J. Am. Chem. Soc.* **2023**, *145*, 21576−21586.
(39) Cao, H.; Tang, X.; Tang, H.; Yuan, Y.; Wu, J. Photoinduced intermolecular hydrogen atom transfer reactions in organic synthesis. *Chem. Catal.* **2021**, *1*, 523−598.
(40) Devoe, R. J.; Sahyun, M. R. V.; Serpone, N.; Sharma, D. K. Transient intermediates in the photolysis of iodonium cations. *Can. J. Chem.* **1987**, *65*, 2342−2349.
(41) Milanesi, S.; Fagnoni, M.; Albini, A. (Sensitized) Photolysis of Diazonium Salts as a Mild General Method for the Generation of Aryl Cations. Chemoselectivity of the Singlet and Triplet 4-Substituted Phenyl Cations. *J. Org. Chem.* **2005**, *70*, 603−610.
(42) Dektar, J. L.; Hacker, N. P. Photochemistry of Diaryliodonium Salts. *J. Org. Chem.* **1990**, *55*, 639−647.
(43) Arias-Rotondo, D. M.; McCusker, J. K. The photophysics of photoredox catalysis: a roadmap for catalyst design. *Chem. Soc. Rev.* **2016**, *45*, 5803−5820.
(44) Paul, S.; Filippini, D.; Silvi, M. Polarity transduction enables the formal electronically mismatched radical addition to alkenes. *J. Am. Chem. Soc.* **2023**, *145*, 2773−2778.
(45) Holst, D. E.; Dorval, C.; Winter, C. K.; Guzei, I. A.; Wickens, Z. K. Regiospecific Alkene Aminofunctionalization via an Electrogenerated Dielectrophile. *J. Am. Chem. Soc.* **2023**, *145*, 8299−8307.
(46) Kwon, Y.; Wang, Q. Recent advances in 1,2-amino(hetero)-arylation of alkenes. *Chem.—Asian J.* **2022**, *17*, No. e202200215.
(47) Bunescu, A.; Abdelhamid, Y.; Gaunt, M. J. Multicomponent alkene azido-arylation by anion-mediated dual catalysis. *Nature* **2021**, *598*, 597−603.
(48) Cai, Y.; Chatterjee, S.; Ritter, T. Photoinduced copper-catalyzed late-stage azidoarylation of alkenes via arylthianthrenium salts. *J. Am. Chem. Soc.* **2023**, *145*, 13542−13548.
(49) Prasad Hari, D.; Hering, T.; König, B. The photoredox-catalyzed Meerwein addition reaction: intermolecular amino-arylation of alkenes. *Angew. Chem., Int. Ed.* **2014**, *53*, 725−728.
(50) Goti, G.; Manal, K.; Sivaguru, J.; Dell'amico, L. The impact of UV light on synthetic photochemistry and photocatalysis. *Nat. Chem.* **2024**, *16*, 684−692.

https://doi.org/10.1021/jacs.4c11099
J. Am. Chem. Soc. 2024, 146, 30474−30482

Vinylcyclopropane [3+2] cycloaddition with acetylenic sulfones based on visible light photocatalysis

Lastly, project **[D]** focused on the triplet energy transfer step in a [3 + 2] cycloaddition between a vinylcyclopropane (VCP) and acetylenic sulfones, leading to the formation of complex tetracyclic scaffolds.[176] These highly functionalized structures, featuring contiguous stereocenters, are commonly found in natural products and exhibit a wide range of biological activities.[177,178] To access such frameworks, activated VCPs are typically required as three-carbon synthons in [3 + 2] cycloadditions.[179] For non-activated VCPs, the most established strategy employed Rh-catalyzed reactions.[128,180] Other approaches involved electron transfer processes, while energy transfer strategies had remained largely unexplored.[181–183] In this context, the project aimed to develop a novel visible light-induced TTET method for the intermolecular [3 + 2] cycloaddition of non-activated VCPs, with the goal of opening new synthetic pathways and expanding the repertoire of methods for constructing complex molecular architectures. The reaction mechanism was investigated through a combination of control experiments, DFT calculations, and TA spectroscopy. Although the VCP displayed a relatively high triplet energy – seemingly inaccessible by most Ir photosensitizers, even in the case of uphill energy transfer (see Chapter 3.4) – the mechanistic studies allowed electron transfer pathways to be ruled out. The results instead supported the conclusion that the release of ring strain upon sensitization of the VCP likely facilitates the energy transfer step, enabling the reaction to proceed despite the unfavorable triplet energy alignment. Finally, a broad substrate scope of the alkynyl sulfones with bearing electron-neutral, electron-rich, and electron withdrawing aromatic rings was found to be applicable in this TTET-driven cycloaddition reaction.

Summary:

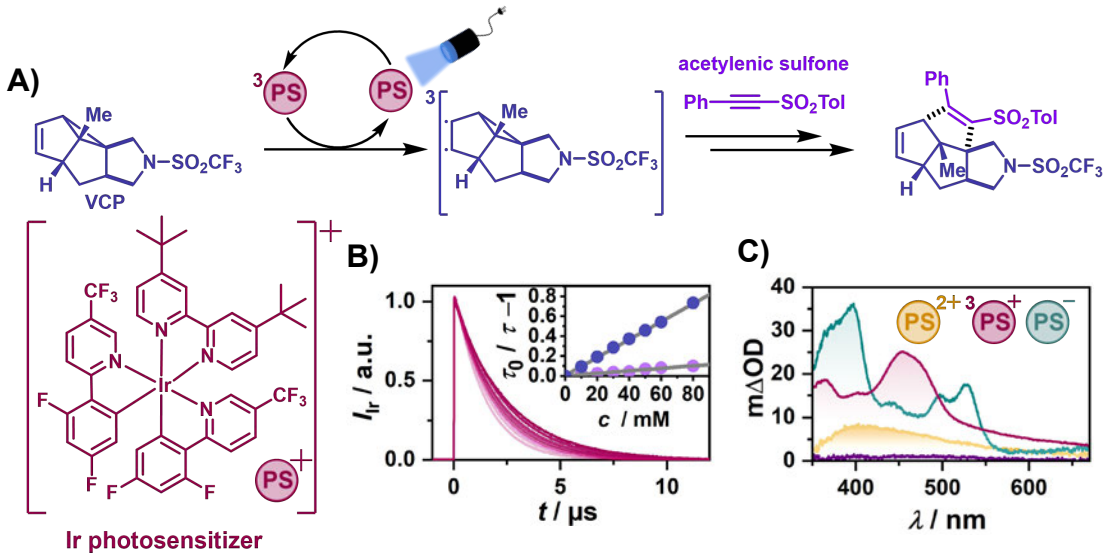

Figure 13: Overview of project **[D]**. A) Proposed energy transfer step for the triplet-sensitized [3 + 2] photocycloaddition. B) Luminescence quenching of PS in the presence of VCP. Inset: Stern–Volmer analyses of PS with VCP (blue) and acetylenic sulfone (purple) as quencher. C) TA spectra of triplet-excited PS, the reduced and oxidized species of PS. The baseline TA spectrum (purple) was recorded in the presence of the substrates following complete deactivation of PS.

In this project, the triplet-sensitized [3 + 2] photocycloaddition between a vinylcyclopropane (VCP) and acetylenic sulfones using a scope of Ir photosensitizers was investigated. Both the VCP and the acetylenic sulfones were synthesized via two-step procedures. Reaction conditions were optimized using the VCP and the acetylenic sulfone (1-methyl-4-((phenylethynyl)sulfonyl)benzene) as displayed in Figure 13A, including a screen of various commonly used photocatalysts. A mechanistic pathway was proposed involving TTET from Ir-based photosensitizers to the VCP. This energy transfer generates a triplet biradical intermediate, which subsequently reacts with the acetylenic sulfones in a [3 + 2] cycloaddition, yielding complex tetracyclic products (Figure 13A). To support this mechanism, control experiments were conducted, including Stern–Volmer analyses with both substrates (Figure 13B) using the Ir complex in Figure 13A as photosensitizer. Quenching by VCP was found to proceed significantly faster than by the acetylenic sulfone. Although the quenching efficiencies were several orders of magnitude below the diffusion limit in methanol, the TTET process was still considered efficient at the employed VCP concentrations. DFT calculations support the proposed mechanism. Although they predict a higher adiabatic triplet energy for the VCP relative to the Ir-based photosensitizers, the release of ring strain upon sensitization may provide a sufficient driving force to enable energy transfer assuming that the process occurs on a timescale comparable to molecular collisions and TTET from the excited Ir complex. TA spectroscopy with 355 nm laser excitation was used to analyze the products of the quenching process. Following complete quenching of the Ir complex by VCP (and additional acetylenic sulfone), only baseline signals were observed in the TA spectra. This absence of signal ruled out photoinduced electron transfer mechanisms, which would otherwise produce distinct signatures of oxidized or reduced Ir species.[184] Reference spectra were recorded by combining the Ir complex with appropriate electron donors and acceptors (Figure 13C).[185] The data suggested that the triplet biradical formed from VCP has a short lifetime and undergoes rapid reaction with the acetylenic sulfone, likely outpacing its formation via TTET. Thus, this intermediate could not be detected under the conditions used in the LFP setup. Similar results were obtained when (1-cyclopropylvinyl)benzene was used as the quencher, further supporting the proposed mechanistic model.

Project **[D]** was published as a research article:

"**Vinylcyclopropane [3+2] Cycloaddition with Acetylenic Sulfones Based on Visible Light Photocatalysis**"

Reproduced from Reference: A. Luque, J. Groß, T. J. B. Zähringer, C. Kerzig, T. Opatz, *Chem. Eur. J.* **2022**, *28*, e202104329.

The article is Open Access and licensed under CC BY-NC 4.0 (https://creativecommons.org/licenses/by/4.0/). It can be cited corresponding to ref.[D]. The reference is attached in the following pages and the supporting information can be found in Chapter 10.5.

Author contributions: T. Opatz conceived the project. A. Luque developed the reaction and substrate scope and performed the sensitizer screening under guidance of T. Opatz. J. Groß performed quantum mechanical calculations. T. J. B. Zähringer performed mechanistic investigations of the triplet energy transfer step under the guidance of C. Kerzig. The manuscript was written by A. Luque, T. J. B. Zähringer, C. Kerzig and T. Opatz.

Check for updates

Chemistry–A European Journal
Research Article
doi.org/10.1002/chem.202104329
Chemistry Europe
European Chemical Societies Publishing

www.chemeurj.org

Vinylcyclopropane [3+2] Cycloaddition with Acetylenic Sulfones Based on Visible Light Photocatalysis**

Adriana Luque,[a] Jonathan Groß,[a] Till J. B. Zähringer,[a] Christoph Kerzig,[a] and Till Opatz*[a]

Abstract: The first intermolecular visible light [3+2] cycloaddition reaction performed on a *meta* photocycloadduct employing acetylenic sulfones is described. The developed methodology exploits the advantages of combining UV and visible-light in a two-step sequence that provides a photogenerated cyclopropane which, through a strain-release process, generates a new cyclopentane ring while significantly increasing the molecular complexity. Mechanistic studies and DFT calculations indicate an energy transfer pathway for the visible light-driven reaction step. This strategy could be extended to simpler vinylcyclopropanes.

Introduction

Functionalized five-membered carbocyclic rings containing contiguous stereocenters are found in a wide array of natural products with diverse biological activities.[1] Therefore, simple and efficient methods to access highly substituted cyclopentanes and cyclopentenes within a polycyclic framework are particularly desirable in current organic and medicinal chemistry research.[2] One major general strategy to access them involves [3+2] cycloadditions, a powerful method that in a single step allows the formation of two new σ bonds and vicinal quaternary centers.[3] Vinylcyclopropanes (VCPs) represent an important class of reactive cyclopropane that can participate in this cycloaddition as three-carbon synthons, especially if they bear electron-withdrawing groups on the cyclopropane ring.[4] However, the use of non-activated VCP as a competent intermolecular cycloaddition partner is still limited. In particular, the use of Rh catalysts[5] is the most developed strategy for cycloadditions of non-activated VCPs and finding other catalyst systems and protocols that can exploit a wider range of VCP reactivity patterns remains a challenge. The merging of visible-light photocatalysis with the [3+2] cycloaddition involving VCPs already proved useful in strain-releasing fragmentation reactions in the assembly of larger-ring systems, but mainly used activated cyclopropanes as the substrates. Most reported examples are based on electron transfer (ET) photoredox processes,[6] while transformations proceeding through energy transfer (EnT) are underdeveloped.[7] The broad substrate scope, often relatively independent of the electronic nature, makes the energy transfer process attractive for a wide set of applications.

Considering the lack of examples of intermolecular transition metal-catalyzed visible light [3+2] cycloadditions involving nonactivated VCPs through EnT, we studied the scope of the same UV-driven strain-promoted/visible light strain-releasing sequence employed in our previous work on cyclopropyl ketones[8] by using *meta* photocycloadduct bearing a vinylcyclopropane substructure as substrates in a visible light-mediated intermolecular [3+2] cycloaddition (Scheme 1). This strategy which has gradually gained attention from the synthetic community,[9] uses the inherent ring-strain of the photogenerated intermediate as a thermodynamic driving force for the subsequent ring expansion. In other words, the first UV light induced transformation provides a complex fused ring skeleton that is otherwise difficult to obtain.[10] This *meta* photocycloadduct is prone to undergo an irreversible ring-opening due to the intrinsic strain of the three-membered ring.[11] This feature will be exploited in the second, visible light-induced transformation by reacting with an alkyne in a [3+2] cycloaddition reaction resulting in the formation of a new complex tetracycle.[12]

In general, non-activated alkynes display low reactivity in this type of cycloadditions, initial experiments using the *meta* photocycloadduct **4** and simple alkynes with different catalytic systems showed no reactions. After much optimization, we found the use of acetylenic sulfones to be an attractive

Scheme 1. UV and visible light activation sequence.

[a] A. Luque, J. Groß, T. J. B. Zähringer, Prof. Dr. C. Kerzig, Prof. Dr. T. Opatz
Johannes Gutenberg University
Department of Chemistry
Duesbergweg 10–14, 55128 Mainz (Germany)
E-mail: opatz@uni-mainz.de

[**] A previous version of this manuscript has been deposited on a preprint server (https://doi.org/10.26434/chemrxiv-2021-k7k1w).

Supporting information for this article is available on the WWW under https://doi.org/10.1002/chem.202104329

© 2022 The Authors. Chemistry - A European Journal published by Wiley-VCH GmbH. This is an open access article under the terms of the Creative Commons Attribution Non-Commercial NoDerivs License, which permits use and distribution in any medium, provided the original work is properly cited, the use is non-commercial and no modifications or adaptations are made.

© 2022 The Authors. Chemistry - A European Journal published by Wiley-VCH GmbH

alternative. The sulfonyl group lowers the LUMO energy of the adjacent π-bond increasing their reactivity as dienophiles while providing the means for controlling the regiochemistry of the cycloaddition.[13] Furthermore, the sulfonyl group can be removed by different methods making the acetylenic sulfones useful reagents for a variety of cycloadditions.[14]

Results and Discussion

Our test of the new design started with the photo-induced intramolecular arene-olefin *meta*-cycloaddition of the *N*-allyl-1,1,1-trifluoro-*N*-(2-methylbenzyl)methanesulfonamide (**3**) which was synthesized in two steps: a reductive amination of 2-methyl-benzaldehyde (**1**) with allylamine, followed by the reaction with trifluoromethanesulfonic anhydride. The irradiation of **3** in anhydrous cyclohexane furnished two isomeric *meta*-photocycloadducts in 72% yield (ratio: 9:1), with the linear isomer **4** being favored over the angular isomer **5** (Scheme 2).

The acetylenic sulfones **6** as reaction partners were prepared in a two-step synthesis. The first step is the preparation of the intermediates β-iodovinyl sulfones using either the cerium(IV) ammonium nitrate (CAN) mediated reaction of aryl sulfinates and sodium iodide with alkynes[15] or the iodine-promoted reaction of the same substrates using water as solvent.[16] The second step was the dehydroiodination of the β-iodovinyl sulfones with potassium carbonate under reflux to afford the corresponding acetylenic sulfones in relatively good yields (see the Supporting Information).[15]

Reaction optimization

The screening of various photocatalysts for the [3+2] photocycloaddition with visible light was performed on *meta* photocycloadduct **4** and the acetylenic sulfone **6a** as the coupling partners (Supporting Information, Table S1). The desired product **7a** was obtained in appreciable yields (53% and 63%, respectively) when employing $[Ir(ppy)_2(dtbbpy)]PF_6$ (**PC I**, 2.5 mol%) and phenanthrene (**PC VI**, 100 mol%). In further optimization studies (Supporting Information, Tables S2, S3 and S4), the yield of **7a** could be increased to 85% when employing **PC I** with concomitant reduction of the catalyst loading to 2 mol% when using 2 equivalents of **6a**. Moreover, the cycloaddition proceeded with higher yields in polar solvents and at higher concentrations (0.15 M in CH_3OH).

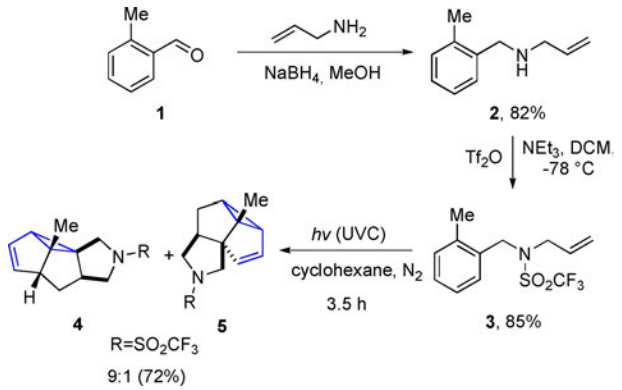

Scheme 2. Preparation of the *meta* photocycloadduct **4**.

Substrate scope

Having optimized the reaction conditions, the scope of the synthesized alkynyl sulfones **6** (Scheme 3) was explored next. Substrates bearing electron-neutral, electron-rich, and electron-withdrawing aromatic rings were found to be suitable substrates. Alkyl groups on the sulfone moiety also provided the desired product in moderate to good yields (**7i** and **7j**). However, aromatic groups at the triple bond were required for

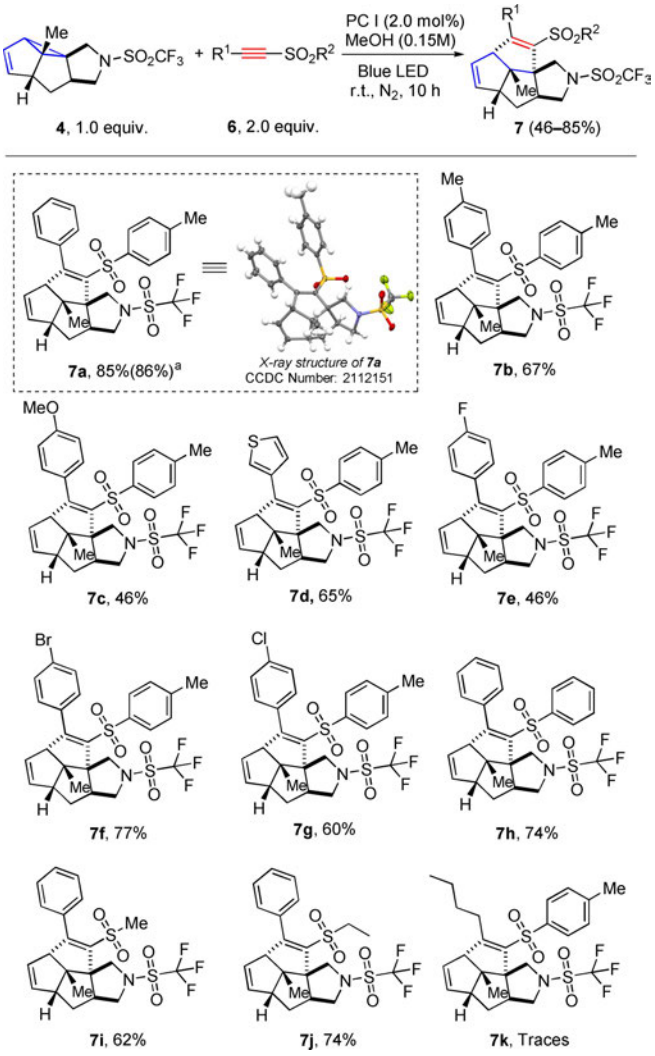

Scheme 3. Substrate scope of the formal [3+2] cycloaddition. All yields are those of isolated products.[a] **PC III** and Blue LED 440 nm was used (see Supporting Information for details).

© 2022 The Authors. Chemistry - A European Journal published by Wiley-VCH GmbH

15213765, 2022, 18, Downloaded from https://chemistry-europe.onlinelibrary.wiley.com/doi/10.1002/chem.202104329 by Universitatsbibliothek Mainz, Wiley Online Library on [16/06/2025]. See the Terms and Conditions (https://onlinelibrary.wiley.com/terms-and-conditions) on Wiley Online Library for rules of use; OA articles are governed by the applicable Creative Commons License

the reaction to proceed successfully; substrate **6k** featuring a butyl-substituted alkynyl sulfone gave no reaction.

At this point, the essential factors governing the catalyst reactivity used in this reaction were investigated by analyzing the results of the screening (Table 1). To distinguish the two possible mechanisms, ET or EnT, the redox potentials, and the calculated triplet energy of the *meta* photocycloadduct **4** were compared with those of the catalysts (Supporting Information, Table S7).

Table 1. Evaluation of photocatalysts in the [3+2] cycloaddition.

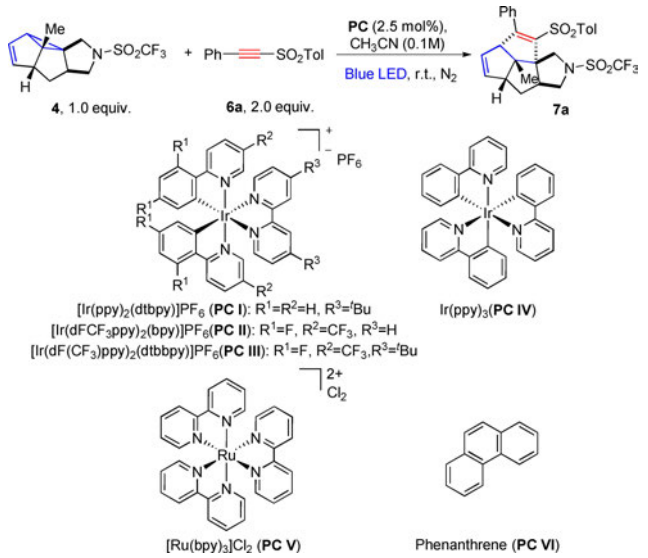

Entry	PC	$E_{1/2}(M^*/M^+)/E_{1/2}(M^*/M^-)$ (V vs. SCE)	E_T (kcal/mol)[a]	Yield (%)[b]
1	VI[c]	−2.10/+1.27	61.9	63
2	III	−0.89/+1.21	60.1	49
3	II	−1.00/+1.32	60.0	51
4	IV	−1.73/+0.31	55.2	49
5	I	−0.96/+0.66	49.2	53
6	V	−0.81/+0.77	46.0	traces

[a] 1 kcal mol^{-1} = 4.184 kJ mol^{-1}. [b] isolated yields. [c] 100 mol% of catalyst loading and UV/vis CFL bulb was used.

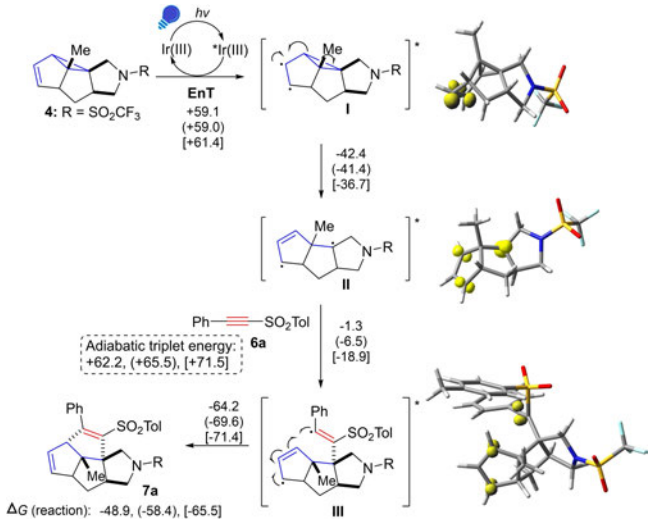

Scheme 4. Mechanistic proposal for the [3+2] photocycloaddition. The reported adiabatic energy differences obtained with different functionals are given in kcal mol^{-1} (no bracket: (U)B3LYP, parentheses: (U)CAM-B3LYP, square bracket: (U)M06-2X). The spin densities (yellow, isovalue = 0.04) were plotted for the triplet intermediates **I**–**III**.

In the cyclic voltammograms of **4** (Supporting Information, Figure S7), oxidation and reduction features were observed with half-peak potentials of +1.96 V vs. SCE and −1.65/−1.34 V vs. SCE, respectively. Analyzing the reducing power of the catalyst **PC IV** (entry 4)[17] and **PC VI** (entry 1)[18] after excitation with that of **4** reveals that an oxidative quenching is feasible. However, the reduction potentials of the *meta* photocycloadduct are not sufficient to be reduced by the photoexcited states of the catalyst **PC V** (entry 6)[19] or the other iridium catalysts (entries 2–3, 5).[20] Likewise, reductive quenching could be ruled out based on the oxidation potentials of all the catalysts. On the other hand, there is no clear correlation between the triplet energies of the catalysts or photosensitizers and the reaction yield, making a Dexter energy transfer (sensitization)[21] also difficult. The Gibbs free energy of each reaction intermediate was predicted using density functional theory (DFT) as it has already be done in the literature for related reactions (Scheme 4).[22] While the reaction follows an overall exergonic pathway, releasing 48.9 kcal mol^{-1} of energy, the computed adiabatic triplet energy of **4** (59.1 kcal mol^{-1}) is considerably higher than those of **PC I** and **PC IV** (entries 4 and 5) but is low enough for the rest of iridium catalysts and **PC VI**. Although there is no compelling evidence for an energy transfer process based on these results, the direct excitation of the VCP moiety by UV irradiation of **4** also gives rise to **7a** in 27% yield (see the Supporting Information).[23]

Mechanistic studies

Several control experiments were performed to gain insight into the reaction mechanism. First, radical trapping using (2,2,6,6-tetramethylpiperidin-1-yl)oxyl (TEMPO) completely inhibits the reaction, indicating it may proceed through a radical pathway. To determine whether the reaction involves an efficient[24] radical chain mechanism, we performed a light on-off experiment showing no product formation in the dark phases (Figure 1). Initial intensity-based Stern-Volmer quenching experiments on **PC I** indicated that the phosphorescence of the catalyst could be quenched by **4**, suggesting an electron or energy transfer from the excited triplet state of the catalyst (see the Supporting Information). To get more reliable kinetic results, we turned to lifetime-based Stern–Volmer studies using laser flash photolysis (LFP). We selected **PC III** (the Ir catalyst with the highest triplet energy), which efficiently catalyzed our initial test reaction under optimized conditions (86% yield of **7a**) indicating the very same reaction mechanism as with **PC I**. Furthermore, **PC III** is well-suited for mechanistic investigations by LFP as it is known to possess clearly observable spectroscopic signatures in all states that might occur during photocatalytic cycles.[25] Linear Stern-Volmer plots were obtained clearly demonstrating that quenching by the *meta* photo-

© 2022 The Authors. Chemistry - A European Journal published by Wiley-VCH GmbH

15213765, 2022, 18, Downloaded from https://chemistry-europe.onlinelibrary.wiley.com/doi/10.1002/chem.202104329 by Universitatsbibliothek Mainz, Wiley Online Library on [16/06/2025]. See the Terms and Conditions (https://onlinelibrary.wiley.com/terms-and-conditions) on Wiley Online Library for rules of use; OA articles are governed by the applicable Creative Commons License

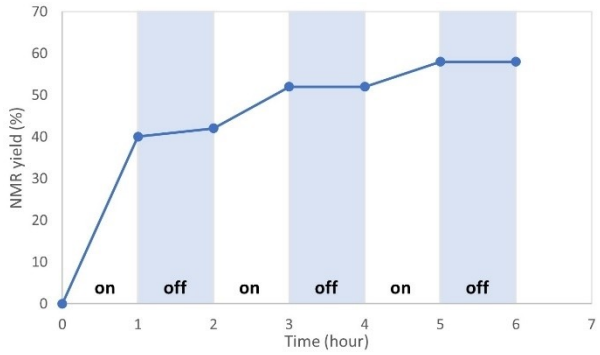

Figure 1. Visible light irradiation on/off experiment.

cycloadduct **4** is much faster than with the acetylenic sulfone **6a** (Figure 2, top). Despite the high triplet energy of **PC III** (Table 1), the quenching rate constant for the reaction between the excited catalyst and **4** ($4\times10^6\ M^{-1}s^{-1}$) is slower than the diffusion limit by almost 4 orders of magnitude. However, under typical conditions used for lab-scale photocatalysis with substrate concentrations on the order of 0.1 M, quenching can be quite efficient.

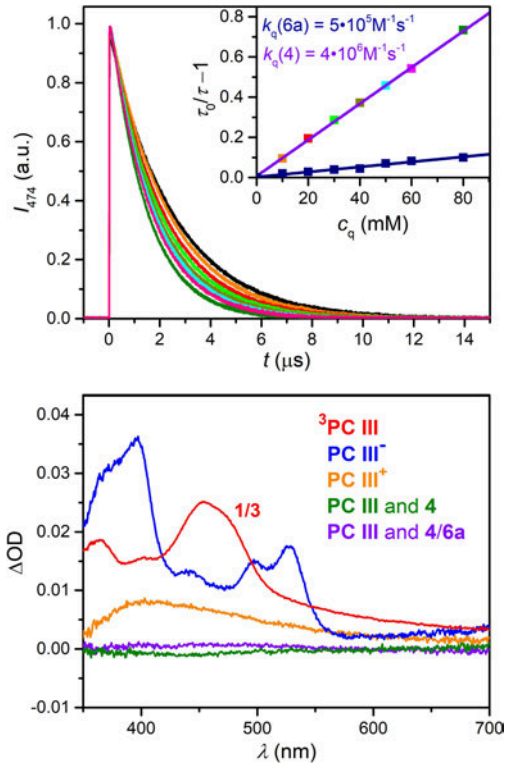

Figure 2. Mechanistic studies upon excitation with 355 nm laser pulses. Top: emission decay kinetics of excited **PC III** (32 µM) in the presence of varying concentrations of **4** in Ar-saturated MeCN. Inset: Stern-Volmer plots of **PC III** and **4** (purple fit, the colored symbols correspond to the same quencher concentration as in the main plot), and **PC III** combined with **6a** (dark blue). Bottom: transient absorption spectra of the triplet-excited state (^{3}**PC III**), the reduced species (**PC III**$^-$), the oxidized species (**PC III**$^+$), as well as in the presence of **4** and **4**/**6a** (80 mM) in Ar-saturated MeCN obtained by LFP. Apart from the triplet spectrum, all spectra have been recorded after the photoluminescence decay of **PC III** (see Supporting Information for details).

Next, we tried to directly identify the quenching product(s) by measuring transient absorption (TA) spectra with our LFP setup[26] upon selective excitation of **PC III**. Reference spectra (Figure 2, bottom; see Supporting Information for details) of the photocatalyst triplet, its one-electron-oxidized as well as its reduced species were recorded in the reaction medium (MeCN) prior to experiments with the substrates of this study. TA spectra with quencher (**4** and/or **6a**) concentrations ensuring about 50% ^{3}**PC III** quenching were measured. These spectra did not show any noticeable TA signals (green and purple spectra in Figure 2), but intense photocatalyst-derived bands in the transient spectra are expected for both oxidative and reductive quenching pathways, based on our reference measurements. Hence, our TA experiments summarized in Figure 2 (bottom) allow us to exclude quenching via ET.[27]

Accordingly, we propose a catalytic cycle as shown in Scheme 4 with an energy transfer as initial photochemical activation step. First, **PC I** (or **PC III**) acts as a sensitizer, transferring energy from its ^{3}MLCT state to the vinylcyclopropane moiety in **4**, generating the triplet state of the latter, which undergoes a rearrangement followed by a radical addition of the acetylenic sulfone to generate the intermediate **III**. A subsequent ring-closure reaction affords the final tetracycle **7**. The occurrence of radical intermediate **III** is supported by the finding that aromatic substituents at R^1 are required for the reaction to proceed. The absence of new signals in the TA spectra right after significant energy transfer quenching can be explained as follows: The catalyst triplet signals completely return to the baseline for EnT mechanisms and the substrate-derived intermediates **II** and **III** (compare, Scheme 4) are expected to absorb very weakly (and predominantly in the UV region), owing to the lack of π-conjugation and adjacent functional groups. The light absorbing properties of the triplet diradical intermediates **II** and **III** were predicted by means of time-dependent DFT. For the excitation of **II** and **III**, an energy of at least 3.67 eV (oscillator strength $f=0.0002$) and 2.71 eV ($f=0.0093$) is required for the first excited state. Local absorption maxima were predicted to be at 239 nm and 282 nm, respectively (see Supporting Information). Moreover, the exact factors governing the lifetimes of diradicals are not fully understood[28] and these species might be too short-lived for their efficient detection. Ring-opening of intermediate **I** in its triplet state is most likely faster by orders of magnitudes than for the well-known (doublet) alkyl cyclopropane radical clock (ring-opening rate constant, $1.3\times10^8\ s^{-1}$),[29] considering the accelerating effects of substituents and/or fused rings at the cyclopropane moiety.[30] We speculate that strain release and the associated substantial energy gain could potentially occur on a similar timescale as molecular collision and the actual Dexter energy transfer from the excited iridium complex. Such a concerted reaction mechanism (without the presence of intermediate **I**) could explain the observed quenching and energy transfer product when **PC I** is used, for which the generation of intermediate **I** via conventional mechanisms would be endergonic by about 10 kcal mol^{-1} (9.9 kcal mol^{-1}).

© 2022 The Authors. Chemistry - A European Journal published by Wiley-VCH GmbH

15213765, 2022, 18, Downloaded from https://chemistry-europe.onlinelibrary.wiley.com/doi/10.1002/chem.202104329 by Universitatsbibliothek Mainz, Wiley Online Library on [16/06/2025]. See the Terms and Conditions (https://onlinelibrary.wiley.com/terms-and-conditions) on Wiley Online Library for rules of use; OA articles are governed by the applicable Creative Commons License

This is clearly beyond the current limit for uphill energy transfer reactions,[31] rendering this stepwise pathway highly unlikely. Similar counter-thermodynamic reactions are well-established in the PCET community for concerted proton-coupled electron transfer reactions, but they seem underexplored for energy transfer catalysis. Moreover, concerted ring-opening to yield the low-energy triplet intermediate **II** would block back-EnT reaction channels, which frequently reduce the overall performance of uphill energy transfer reactions.

The mechanistic alternative of an EnT from the PC to the alkynylsulfone appears less likely as the triplet energy of the latter is higher (62.2 kcal mol^{-1}), no gain from a follow-up reaction such as the ring-opening of the VCP can occur and the reaction of the triplet alkynylsulfone to the VCP should occur at the distal carbon of the C=C double bond, which contradicts the observed regiochemistry. To further corroborate that only the vinylcyclopropane substructure of **4** is involved in the mechanism of this reaction, experiments with different substrates were performed. LFP experiments with photocatalyst **PC III** and (1-cyclopropylvinyl)benzene (**8**) as quencher gave a quenching rate constant of 5×10^8 M^{-1} s^{-1} (see Supporting Information), i.e. about two orders of magnitude faster than obtained with substrate **4** (Figure 2). We again excluded electron transfer quenching pathways by transient absorption measurements and the observed higher rate constant is consistent with the expectations for a Dexter-type energy transfer, given that the in silico triplet energy of **8** (49.3 kcal mol^{-1}) is lower than that of **4**. The preparative [3+2] cycloaddition with **8** and the *meta* photocycloadduct **11** (used as an inseparable mixture of isomers without further purification) yielded the expected products in 46 and 39% yield, respectively (Scheme 5). The procedure is thus likely applicable to other VCP-type products of intra- or intermolecular photocycloadditions and permits the construction of complex skeletons in only two consecutive photochemical transformations. Two further commercial and naturally ocurring VCPs, ethyl *trans*-chrysanthemate and (1*S*,3*R*)-*cis*-4-carene, could also successfully be reacted, albeit only in moderate yields, see the Supporting Information.

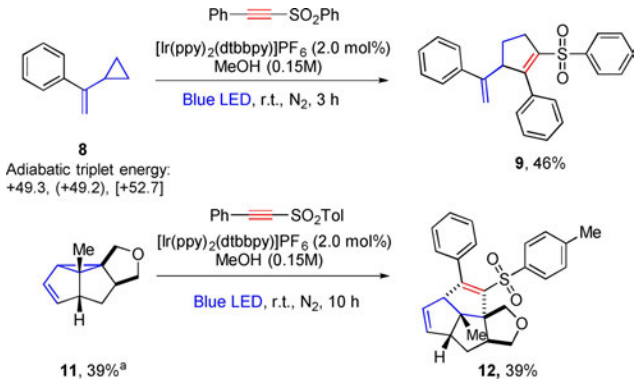

Scheme 5. Alternative substrates in the [3+2] photocycloaddition under standard conditions. The predicted energy differences are given in kcal mol^{-1} (no bracket: (U)B3LYP, parentheses: (U)CAM-B3LYP, square bracket: (U)M06-2X). [a] Inseparable mixture.

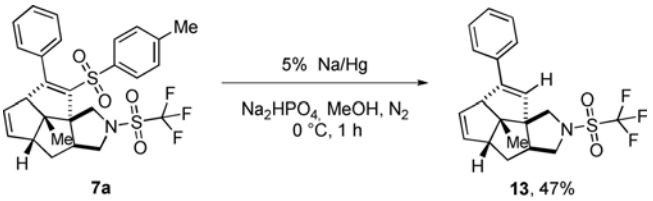

Scheme 6. Selective desulfonylation of tetracycle **7a**.

To extend the synthetic utility of the method, tetracyle **7a** was exemplarily subjected to a selective reductive desulfonylation, producing a styrene moiety suitable for further follow-up reactions (Scheme 6).

Conclusions

A visible light-mediated [3+2] cycloaddition of *meta*-photocycloadducts and acetylenic sulfones has been developed. Catalytic amounts of iridium complexes act as triplet sensitizers as indicated by DFT calculations and time-resolved optical spectroscopy, which allowed us to exclude photoinduced electron transfer reactions. The methodology highlights the power of a consecutive UV/visible light activation sequence involving the generation of a strained intermediate and subsequent catalytic strain release.

Crystallographic data

Deposition number 2112151 (for **7a**) contain the supplementary crystallographic data for this paper. These data are provided free of charge by the joint Cambridge Crystallographic Data Centre and Fachinformationszentrum Karlsruhe Access Structures service.

Acknowledgements

Financial support of the DFG (grants Op90/12-1 and Ke2313/3-1) is gratefully acknowledged. The authors also thank Leander Geske (Mainz) for assistance with preparative HPLC, Luca Großmann (Mainz) for assistance with cyclic voltammetry, Dr. Dieter Schollmeyer (Mainz) for crystallography, Dr. Johannes C. Liermann (Mainz) for NMR spectroscopy and Dr. Christopher Kampf (Mainz) for mass spectrometry. The authors gratefully acknowledge the computing time granted on the supercomputer Mogon at Johannes Gutenberg-University Mainz (hpc.uni-mainz.de). C.K. is grateful to the Chemical Industry Funds for a Liebig fellowship. Open Access funding enabled and organized by Projekt DEAL.

© 2022 The Authors. Chemistry - A European Journal published by Wiley-VCH GmbH

15213765, 2022, 18, Downloaded from https://chemistry-europe.onlinelibrary.wiley.com/doi/10.1002/chem.202104329 by Universitatsbibliothek Mainz, Wiley Online Library on [16/06/2025]. See the Terms and Conditions (https://onlinelibrary.wiley.com/terms-and-conditions) on Wiley Online Library for rules of use; OA articles are governed by the applicable Creative Commons License

Conflict of Interest

The authors declare no conflict of interest.

Data Availability Statement

The data that support the findings of this study are available in the supplementary material of this article.

Keywords: cycloaddition · density functional theory calculations · photochemistry · ring strain · strain release · vinylcyclopropane

[1] a) S. Aoki, Y. Watanabe, M. Sanagawa, A. Setiawan, N. Kotoku, M. Kobayashi, *J. Am. Chem. Soc.* **2006**, *128*, 3148–3149; b) C. M. Hasler, G. Acs, P. M. Blumberg, *Cancer Res.* **1992**, *52*, 202–208; c) C. Kiewert, V. Kumar, O. Hildmann, M. Rueda, J. Hartmann, R. S. Naik, J. Klein, *Brain Res.* **2007**, *1128*, 70–78; d) M. Kubo, C. Okada, J. M. Huang, K. Harada, H. Hioki, Y. Fukuyama, *Org. Lett.* **2009**, *11*, 5190–5193; e) S. M. Ogbourne, A. Suhrbier, B. Jones, S. J. Cozzi, G. M. Boyle, M. Morris, D. McAlpine, J. Johns, T. M. Scott, K. P. Sutherland, J. M. Gardner, T. T. Le, A. Lenarczyk, J. H. Aylward, P. G. Parsons, *Cancer Res.* **2004**, *64*, 2833–2839.
[2] a) M. Lautens, W. Klute, W. Tam, *Chem. Rev.* **1996**, *96*, 49–92; b) X. P. Zeng, Z. Y. Cao, Y. H. Wang, F. Zhou, J. Zhou, *Chem. Rev.* **2016**, *116*, 7330–7396.
[3] Z. Wang, J. Liu, Beilstein, *J. Org. Chem.* **2020**, *16*, 3015–3031.
[4] J. Wang, S. A. Blaszczyk, X. Li, W. Tang, *Chem. Rev.* **2021**, *121*, 110–139.
[5] a) L. Jiao, S. Ye, Z.-X. Yu, *J. Am. Chem. Soc.* **2008**, *130*, 7178–7179; b) P. Liu, P. H. Cheong, Z. X. Yu, P. A. Wender, K. N. Houk, *Angew. Chem. Int. Ed.* **2008**, *47*, 3939–3941; *Angew. Chem.* **2008**, *120*, 4003–4005; c) P. Liu, L. E. Sirois, P. H. Cheong, Z. X. Yu, I. V. Hartung, H. Rieck, P. A. Wender, K. N. Houk, *J. Am. Chem. Soc.* **2010**, *132*, 10127–10135; d) S. C. Wang, D. J. Tantillo, *J. Organomet. Chem.* **2006**, *691*, 4386–4392; e) Z. X. Yu, P. H. Cheong, P. Liu, C. Y. Legault, P. A. Wender, K. N. Houk, *J. Am. Chem. Soc.* **2008**, *130*, 2378–2379; f) Z.-X. Yu, P. A. Wender, K. N. Houk, *J. Am. Chem. Soc.* **2004**, *126*, 9154–9155.
[6] a) X. Gu, X. Li, Y. Qu, Q. Yang, P. Li, Y. Yao, *Chem. Eur. J.* **2013**, *19*, 11878–11882; b) B. S. Karki, L. Devi, A. Pokhriyal, R. Kant, N. Rastogi, *Chem. Asian J.* **2019**, *14*, 4793–4797; c) Z. Lu, M. Shen, T. P. Yoon, *J. Am. Chem. Soc.* **2011**, *133*, 1162–1164; d) S. Maity, M. Zhu, R. S. Shinabery, N. Zheng, *Angew. Chem. Int. Ed. Engl.* **2012**, *51*, 222–226; *Angew. Chem.* **2012**, *124*, 226–230; e) Y. Q. Zou, L. Q. Lu, L. Fu, N. J. Chang, J. Rong, J. R. Chen, W. J. Xiao, *Angew. Chem. Int. Ed. Engl.* **2011**, *50*, 7171–7175; *Angew. Chem.* **2011**, *58*, 1586–1604.
[7] D. F. Chen, C. H. Chrisman, G. M. Miyake, *ACS Catal.* **2020**, *10*, 2609–2614.
[8] J. Paternoga, J. Kühlborn, N. O. Rossdam, T. Opatz, *J. Org. Chem.* **2021**, *86*, 3232–3248.
[9] A. Luque, J. Paternoga, T. Opatz, *Chem. Eur. J.* **2021**, *27*, 4500–4516.
[10] a) D. C. Blakemore, A. Gilbert, *Tetrahedron Lett.* **1994**, *35*, 5267–5270; b) X.-C. Guo, Q.-Y. Chen, *J. Fluorine Chem.* **1999**, *97*, 149–156.
[11] a) R. D. Bach, O. Dmitrenko, *J. Am. Chem. Soc.* **2004**, *126*, 4444–4452; b) M. A. Cavitt, L. H. Phun, S. France, *Chem. Soc. Rev.* **2014**, *43*, 804–818; c) M. S. Gordon, *J. Am. Chem. Soc.* **1980**, *102*, 7419–7422.
[12] If not stated otherwise, products were always obtained as racemic mixtures.
[13] A. Gavezzotti in *The Chemistry of Sulphones and Sulphoxides* (Eds.: S., Patai, Z., Rappoport, C. J. M., Stirling), Wiley, New York, **1988**, p. 1–32.
[14] a) T. G. Back, *Tetrahedron* **2001**, *57*, 5263–5301; b) T. G. Back, K. N. Clary, D. Gao, *Chem. Rev.* **2010**, *110*, 4498–4553.
[15] V. Nair, A. Augustine, T. D. Suja, *Synthesis* **2002**, *2002*, 2259–2265.
[16] Y. Sun, A. Abdukader, D. Lu, H. Zhang, C. Liu, *Green Chem.* **2017**, *19*, 1255–1258.
[17] a) M. S. Lowry, J. I. Goldsmith, J. D. Slinker, R. Rohl, R. A. Pascal, G. G. Malliaras, S. Bernhard, *Chem. Mater.* **2005**, *17*, 5712–5719; b) J. D. Slinker, A. A. Gorodetsky, M. S. Lowry, J. Wang, S. Parker, R. Rohl, S. Bernhard, G. G. Malliaras, *J. Am. Chem. Soc.* **2004**, *126*, 2763–2767.
[18] a) G. J. Hoijtink, **1958**, *77*, 555–558; b) F. Wilkinson, A. Farmilo, *J. Chem. Soc. Faraday Trans. 2* **1984**, *80*, 1117–1124.
[19] a) C. R. Bock, J. A. Connor, A. R. Gutierrez, T. J. Meyer, D. G. Whitten, B. P. Sullivan, J. K. Nagle, *J. Am. Chem. Soc.* **1979**, *101*, 4815–4824; b) C. K. Prier, D. A. Rankic, D. W. C. MacMillan, *Chem. Rev.* **2013**, *113*, 5322–5363.
[20] T. Koike, M. Akita, *Inorg. Chem. Front.* **2014**, *1*, 562–576.
[21] F. Strieth-Kalthoff, M. J. James, M. Teders, L. Pitzer, F. Glorius, *Chem. Soc. Rev.* **2018**, *47*, 7190–7202.
[22] a) T. R. Blum, Z. D. Miller, D. M. Bates, I. A. Guzei, T. P. Yoon, *Science* **2016**, *354*, 1391–1395; b) M. J. James, J. L. Schwarz, F. Strieth-Kalthoff, B. Wibbeling, F. Glorius, *J. Am. Chem. Soc.* **2018**, *140*, 8624–8628; c) J. Zhao, J. L. Brosmer, Q. Tang, Z. Yang, K. N. Houk, P. L. Diaconescu, O. Kwon, *J. Am. Chem. Soc.* **2017**, *139*, 9807–9810.
[23] For an intramolecular cycloaddition of this general type, see: C. S. Penkett, J. A. Woolford, I. J. Day, M. P. Coles, *J. Am. Chem. Soc.* **2010**, *132*, 4–5.
[24] M. A. Cismesia, T. P. Yoon, *Chem. Sci.* **2015**, *6*, 5426–5434.
[25] a) Y. Qin, R. Sun, N. P. Gianoulis, D. G. Nocera, *J. Am. Chem. Soc.* **2021**, *143*, 2005–2015; b) B. Xu, L. Troian-Gautier, R. Dykstra, R. T. Martin, O. Gutierrez, U. K. Tambar, *J. Am. Chem. Soc.* **2020**, *142*, 6206–6215.
[26] a) M. S. Bertrams, C. Kerzig, *Chem. Commun.* **2021**, *57*, 6752–6755; b) T. J. B. Zähringer, M. S. Bertrams, C. Kerzig, *J. Mater. Chem. C.* **2022**. https://doi.org/10.1039/D1TC04782E
[27] F. M. Hormann, C. Kerzig, T. S. Chung, A. Bauer, O. S. Wenger, T. Bach, *Angew. Chem. Int. Ed.* **2020**, *59*, 9659–9668; *Angew. Chem.* **2020**, *132*, 9746–9755.
[28] L. J. Johnston, J. C. Scaiano, *Chem. Rev.* **1989**, *89*, 521–547.
[29] D. Griller, K. U. Ingold, *Acc. Chem. Res.* **1980**, *13*, 317–323.
[30] M. Newcomb, P. H. Toy, *Acc. Chem. Res.* **2000**, *33*, 449–455.
[31] F. Strieth-Kalthoff, C. Henkel, M. Teders, A. Kahnt, W. Knolle, A. Gómez-Suárez, K. Dirian, W. Alex, K. Bergander, C. G. Daniliuc, B. Abel, D. M. Guldi, F. Glorius, *Chem* **2019**, *5*, 2183–2194.

Manuscript received: December 3, 2021
Accepted manuscript online: February 8, 2022
Version of record online: March 4, 2022

© 2022 The Authors. Chemistry - A European Journal published by Wiley-VCH GmbH

15213765, 2022, 18, Downloaded from https://chemistry-europe.onlinelibrary.wiley.com/doi/10.1002/chem.202104329 by Universitätsbibliothek Mainz, Wiley Online Library on [16/06/2025]. See the Terms and Conditions (https://onlinelibrary.wiley.com/terms-and-conditions) on Wiley Online Library for rules of use; OA articles are governed by the applicable Creative Commons License

6 Triplet Energy Transfer-Catalyzed Photoisomerization Reactions

Photoswitches are a class of molecules that undergo reversible structural changes upon exposure to light, enabling them to switch between two or more (meta)stable isomeric states. This unique photochemical behavior makes them valuable in a wide range of applications, from electronics and molecular solar energy storage systems, optical data storage, stereodivergent synthesis to drug delivery.[186–193]

The principle of photoswitching involves (light-induced) transitions between ground state isomers with different electronic and geometric properties. Typically, a thermodynamically stable isomer absorbs a photon, leading to an excited-state configuration that can either relax back to the original state or transition to a metastable isomer. The efficiency of this process is characterized by the photoisomerization quantum yield, which determines the fraction of molecules undergoing conversion. The metastable isomers typically exhibit distinct absorption spectra compared to the thermodynamically stable one. Under continuous irradiation, when the formation and depletion rates of all isomers become equal, a photostationary state (PSS) is established. The composition of the PSS is governed by the molar absorption coefficients of each isomer at the excitation wavelength and their respective photoisomerization quantum yields (Figure 14B).[194]

A prominent class of photoswitches are alkenes, where photoisomerization occurs around a single double bond, leading to two distinct ground state isomers: *E* and *Z*, with dihedral angles of 180° and 0°, respectively.[194] The *E*-isomer is typically the thermodynamically more stable configuration and readily prepared by employing strong acids,[195] halogens,[196] and metal hydrides.[197] The contra-thermodynamic direction, however, presents a challenge that cannot be overcome through conventional thermal methods. In this context, light provides a unique means of perturbing the thermal equilibrium by promoting molecules to electronically excited states.[11]

The *E*→*Z* photoisomerization of alkenes has been extensively investigated, resulting in a well-established mechanistic understanding. Upon photoexcitation, an electron is promoted from a bonding (π) orbital to an antibonding (π*) orbital, effectively lowering the bond order and permitting rotation around the previously rigid double bond. As a result, the excited state features a significantly altered energy landscape that arises from electronic or steric repulsion, with a local minimum corresponding to a highly distorted geometry – typically with a dihedral angle near 90°. From this twisted conformation, the molecule undergoes internal conversion back to the ground state. Once on the ground-state surface, relaxation proceeds along one of two pathways, ultimately yielding either the *E*- or *Z*-isomer. This process is illustrated for the well-known photoswitch stilbene in Figure 14A. Both *E*- and *Z*-isomer of stilbene absorb in the UV range, but with different molar extinction coefficients, allowing the PSS to be effectively tuned by selecting the excitation wavelength (Figure 14C). However, achieving complete conversion is practically

impossible, as re-excitation and reverse isomerization inevitably occur, preventing full depletion of either isomer.[194,198–200]

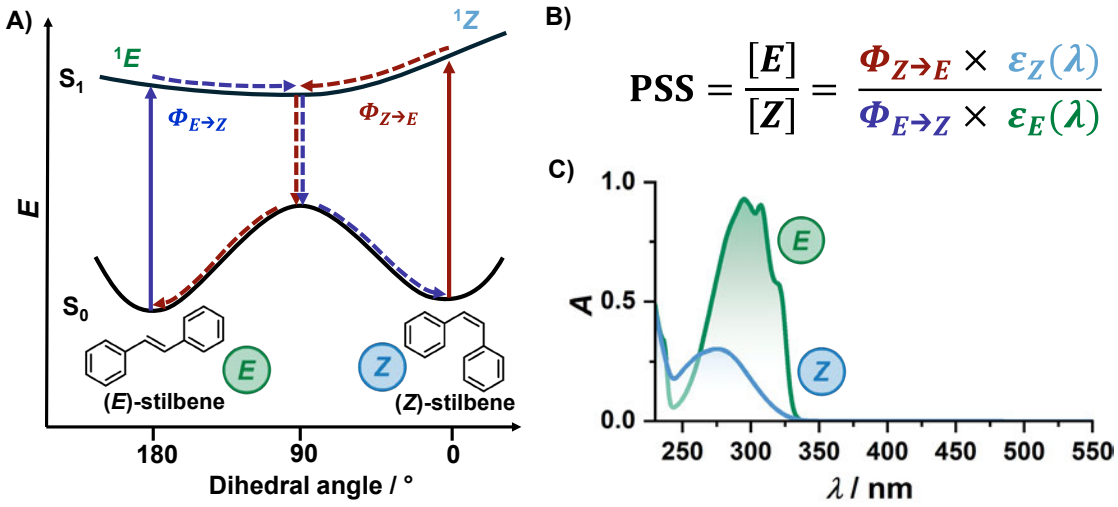

Figure 14: A) Schematic potential energy curves of ground state and first singlet- and triplet-excited state of stilbene. B) Equation of the PSS for simple alkenes. C) Relative absorption of the *E*- and *Z*-isomers plotted against the wavelength.[194,198,201]

The triplet state requires less energy to access than the singlet-excited state, yet direct excitation into the triplet manifold does not occur due to its spin-forbidden nature.[51] To circumvent this limitation, triplet photosensitizers are commonly employed to facilitate population of the triplet state via energy transfer.[200] As for stilbene, similar to the singlet-excited state, the triplet state potential energy surface exhibits a minimum at a 90° dihedral angle between the substituents (Figure 15A).[202] At this geometry, a conical intersection with the ground state enables efficient ISC, promoting relaxation to the either *E* or *Z* ground state configuration. For that reason, most alkenes have triplet state lifetimes of a few nanoseconds.[203,204] In systems utilizing triplet sensitization, the PSS is no longer dictated by the molar extinction coefficients of the *E*- and *Z*-isomers. Instead, it is governed by the triplet state energy of the *E*- and *Z*-isomers and the employed sensitizers and the energy transfer rates (k_{TTET} × [Q]) to each isomer (Figure 15A).[29]

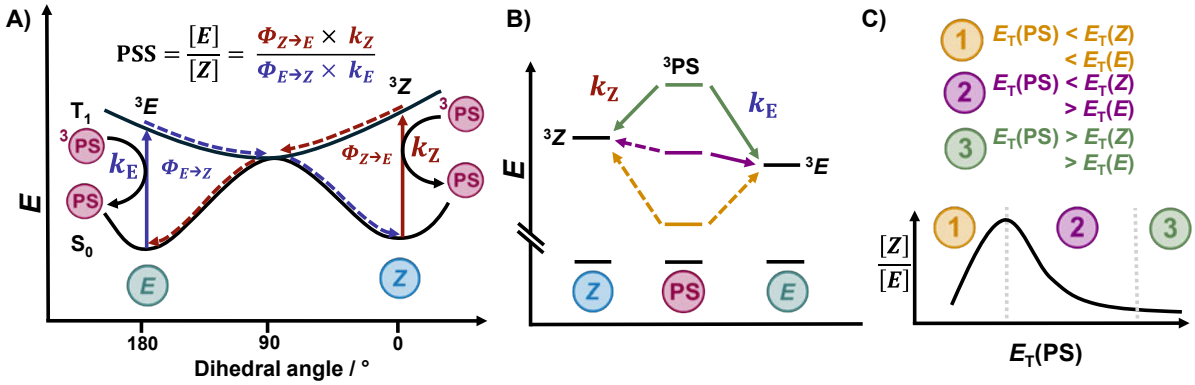

Figure 15: A) Schematic potential energy curves of the ground state and first triplet-excited state of stilbene. B) Energy diagram of (*E*)- and (*Z*)-stilbene and triplet photosensitizers with different triplet state energies. C) Schematic *E*/*Z* ratio of stilbene plotted against the triplet energy of the photosensitizer.

(*E*)-stilbene has a triplet state energy of 2.13 eV, whereas (*Z*)-stilbene has a higher triplet energy at 2.36 eV owing to 1,3-allylic strain.[51] If the triplet energy of the photosensitizer is significantly greater than that of both isomers, TTET occurs at diffusion-controlled rates, and the resulting PSS closely reflects the ratio of the photoisomerization quantum yields (Figure 15B and C). As the triplet energy of the photosensitizer is gradually reduced, the thermodynamic driving force for TTET to the *Z*-isomer diminishes, while TTET to the *E*-isomer remains diffusion-controlled. This shift leads to a selectivity bias toward the *Z*-isomer in the PSS (Figure 15C).[29,200] If the triplet energy of the photosensitizer drops further – below the triplet energy of the *E*-isomer – one might expect a slower reaction rate. However, experimental results show an increase in the fraction of the *Z*-isomer in the PSS albeit very slow reaction times.[29] This counterintuitive phenomenon is attributed to non-vertical energy transfer, which is discussed in Chapter 3.4.[202] Upon further lowering of the sensitizer's triplet state energy, the reaction eventually comes to a complete halt.

This chapter presents projects **[E]**, **[F]**, **[G]**, and **[H]**, all centered on isomerization reactions driven by triplet energy transfer. Projects **[E]** and **[F]** examine the triplet-sensitized isomerization of alkenylboronates using thioxanthone as a photosensitizer. In project **[E]**, the triplet state of a prototypical alkenylboronate is, for the first time, unambiguously confirmed using TA spectroscopy, leading to the development of optimized reaction conditions of the photoisomerization reaction. Project **[F]** extends this concept to fluorinated alkenylboronates and integrates the isomerization process into synthetically useful transformations. Projects **[G]** and **[H]** explore the triplet-sensitized switching of norbornadiene derivatives for molecular solar thermal energy storage (MOST). In project **[G]**, TTET to aryl-substituted norbornadienes using transition metal complexes and organic photosensitizers is thoroughly characterized by TA spectroscopy, providing insights that enabled the development of MOST systems with unmatched efficiencies. Project **[H]** builds on this by introducing acetylene-bridges between the norbornadiene derivatives and evaluating their potential in TTET-driven energy storage applications. In summary, the discoveries presented in this chapter not only enhance the mechanistic understanding of triplet-sensitized isomerization reactions but also leverage these insights to improve reaction conditions.

6.1 Mechanistic Studies of the Photoisomerization of Alkenylboronates Using Thioxanthone as Photosensitizer

Mechanistic studies on triplet-sensitized alkene isomerization have long been a cornerstone of classical photochemistry.[1,11,194,200] Pioneering work by Hammond and co-workers,[200–202,205,206] followed by contributions from Tokumaru[207–212] and Lewis,[213–215] laid the foundation for understanding the triplet-sensitized isomerization of simple (typically styrenyl-like) alkenes using various hydrocarbon photosensitizers. These thorough investigations provided deep mechanistic insight into the behavior of such substrates. However, they primarily focused on simple, symmetric, and nonpolar alkenes but do not

explore synthetic applications. In contrast, nature offers numerous examples of *E*/*Z* isomerization involving complex polyenes.[216,217] A quintessential case is the mammalian visual cycle, which is initiated by the photoinduced isomerization of 11-*cis*-retinal to all-*trans*-retinal and concludes with the regeneration of rhodopsin – processes facilitated by highly specialized isomerase enzymes.[218]

In recent years, organic photochemists have revived triplet-sensitized isomerization as a powerful and selective strategy in synthetic chemistry.[7,11,18,63,219] This renewed interest has enabled the stereo-controlled construction of complex polyene architectures, highlighting the potential of this method as a versatile tool for modern stereochemical synthesis.[129,220]

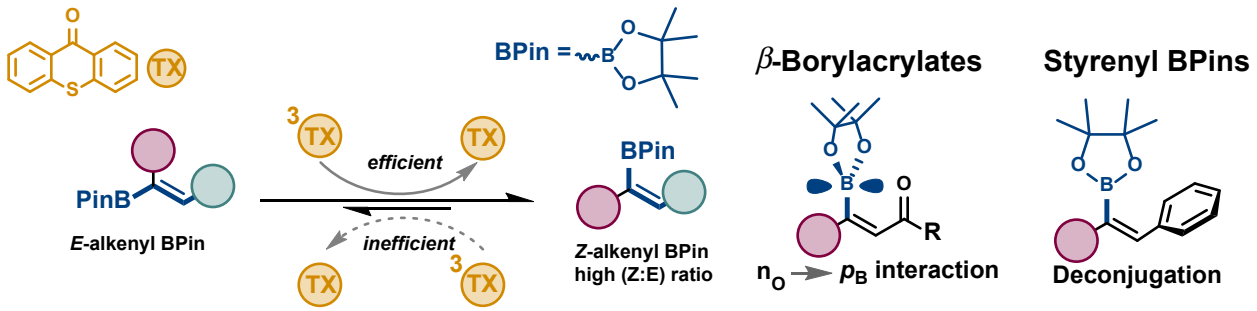

Figure 16: Postulated mechanism of the triplet-sensitized isomerization reaction of BPin alkenes using thioxanthone as sensitizer and postulated destabilization effects raising the *Z*-isomer's triplet energy.

For alkenes to be effectively exploited in such applications, two key requirements must be met: (i) a sufficient triplet energy gap between the isomers to allow for selective photosensitization, and (ii) the presence of substituents that facilitate downstream functionalization. In this context, the boronic acid pinacol ester (BPin) has emerged as particularly promising linchpins in alkene building blocks (Figure 16).[129,130,221,222] Their utility stems from their inherent stability, ease of installation, and broad versatility in subsequent transformations: the BPin moiety can be readily and tracelessly removed during post-functionalization, enhancing the synthetic utility of these compounds over inert alkenes such as stilbene.[223] Further, when combined with a suitable photosensitizer, BPin-containing alkenes selectively yield the *Z*-isomer. For *β*-borylacrylates the selectivity is attributed to Lewis-type $n_o \rightarrow p_B$ interactions in the bifurcated *Z*-isomer, which induce a 90° rotation of the C(sp²)–B bond.[129] In styrenylboronates the BPin group induces an out-of-plane rotation of the phenyl group leading to deconjugation.[130] These geometric distortions raise the triplet energy of the *Z*-isomer, favoring its formation. Although the proposed mechanisms are chemically intuitive, direct experimental evidence for TTET remained elusive. This limitation was partly due to the use of thioxanthone (and similar ketones) as photosensitizer.[11,129] Its non-emissive triplet state makes direct observation of energy transfer challenging and complicates mechanistic investigations. Notably, the triplet state of thioxanthone was initially employed as a photoinitiator in type II photopolymerization reactions.[47,224,225] In this function, triplet-excited thioxanthone participates in a hydrogen abstraction or photoinduced electron transfer reactions. To clarify these mechanistic ambiguities the photoisomerization reaction of alkenylboronates using thioxanthone as a triplet photosensitizer was systematically investigated in project **[E]**.

Summary:

In project **[E]**, two prototypical alkenylboronates and two well-characterized cinnamoyl chromophores were studied employing a combined approach of transient absorption spectroscopy, irradiation experiments, and DFT calculations. Both *E*- and *Z*-isomers of all four alkenes were examined through quenching and irradiation studies in the presence of thioxanthone. The findings for the *E*- and *Z*-isomer of the styrenyl boron species (structures shown in Figure 17A) provided the most detailed insights into the reaction mechanism and were therefore the primary focus of this study.

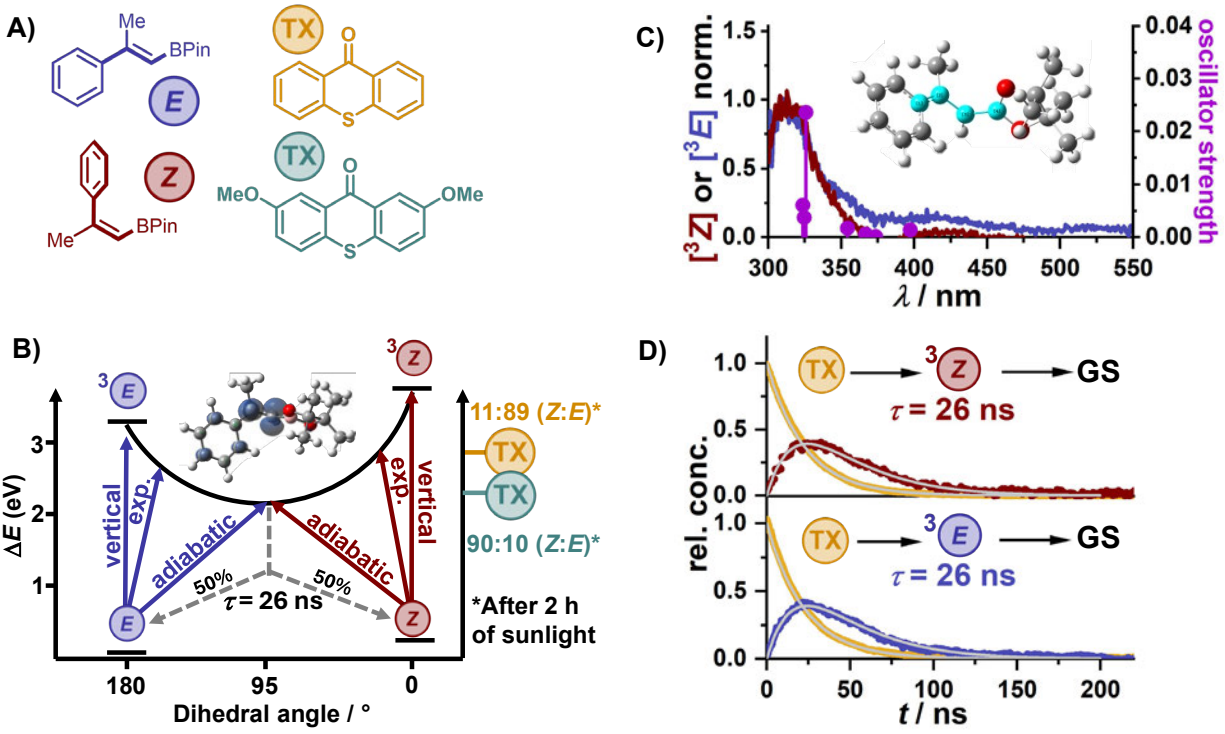

Figure 17: Mechanistic investigations of the triplet-sensitized isomerization of alkenes. A) Molecular structure of the investigated alkenylboronate isomers, TX and MeOTX. B) Schematic energy diagram of the triplet sensitization of the *E*- and *Z*-isomer of the styrenyl boron species. C) TA spectrum of the relaxed triplet geometry of alkenylboronate. D) Kinetic TA traces of triplet state of the *E*- and *Z*-isomer.

The results confirmed that TTET is the operative mechanism, while electron and hydrogen transfer pathways do not play any role. The quenching rate ratios accurately reflected the PSS, indicating a 50:50 distribution to the *E*- and *Z*-isomers in the geometry-relaxed triplet state (Figure 17B).

Subsequently, the quenching products and their excited-state dynamics were investigated. Due to the (ultra)short lifetimes of most triplet-excited alkenes, TA spectra were recorded during energy transfer at high quencher concentrations to accumulate high concentrations of quencher-derived intermediates. For the styrenyl boron species, a novel UV absorption band superimposed with the thioxanthone triplet state was observed for both isomers and assigned to the transient triplet state. The difference spectra of the *E*- and *Z*-isomer were nearly identical, a finding further supported by TD-DFT calculations of the oscillator strength of the adiabatic triplet state (Figure 17C). These results suggest that excitation of either isomer

leads to the same geometry-relaxed triplet intermediate. Time-resolved measurements enabled the determination of the triplet state lifetime, which was found to be 26 ns for both isomers (Figure 17D). The triplet energies of the *E*- and *Z*-isomers were then investigated. While DFT calculations yielded significant discrepancies between the adiabatic (relaxed) and vertical triplet energies, neither matched experimental observations: the adiabatic energies failed to account for the observed selectivity, while the vertical energies were too high to be accessed by thioxanthone sensitization (Figure 17B). To resolve this, Stern–Volmer experiments were conducted using a series of homologous iridium complexes, allowing for the experimental determination of triplet energies. Using a modified Sandros equation, these values were estimated and then used to guide the design of an optimized photosensitizer. A thioxanthone-derived triplet sensitizer with a matching triplet energy was applied to the *E*→*Z* photoisomerization reaction, achieving both high selectivity and efficiency (Figure 17B). As a result, the reaction protocol was refined through spectroscopic optimization. The costly iridium photosensitizer was successfully replaced by an inexpensive, commercially available organic photosensitizer. Additionally, the original 24-hour LED irradiation was replaced with two hours of sunlight, significantly enhancing sustainable aspects of the reaction.

Project **[E]** was published as a research article:

"**Direct Observation of Triplet States in the Isomerization of Alkenylboronates by Energy Transfer Catalysis**"

Reprinted with permission from: T. J. B. Zähringer, M. Wienhold, R. Gilmour, C. Kerzig, *J. Am. Chem. Soc.* **2023**, *145*, 21576–21586. Copyright 2023 American Chemical Society.

The reference is attached in the following pages and can be cited corresponding to ref.[E]. The supporting information can be found in Chapter 10.6.

Author contributions: C. Kerzig and R. Gilmour conceived the Project. M. Wienhold synthesized the alkenylboronates and performed LED irradiation experiments. C. Kerzig performed the DFT calculations. T. J. B. Zähringer performed the spectroscopic measurements and sunlight irradiation experiments. The manuscript was written by R. Gilmour, C. Kerzig and T. J. B. Zähringer.

JACS
JOURNAL OF THE AMERICAN CHEMICAL SOCIETY
pubs.acs.org/JACS
Article

Direct Observation of Triplet States in the Isomerization of Alkenylboronates by Energy Transfer Catalysis

Till J. B. Zähringer,[‖] Max Wienhold,[‖] Ryan Gilmour,[*] and Christoph Kerzig[*]

Cite This: J. Am. Chem. Soc. 2023, 145, 21576−21586
Read Online

ACCESS | Metrics & More | Article Recommendations | Supporting Information

ABSTRACT: Alkenylboronates are versatile building blocks for stereocontrolled synthesis owing to the traceless nature of the boron group that can be leveraged to achieve highly selective geometric isomerization. Using thioxanthone as an inexpensive photocatalyst, the photoisomerization of these species continues to provide an expansive platform for stereodivergent synthesis, particularly in the construction of bioactive polyenes. Although mechanistic investigations are consistent with light-driven energy transfer, direct experimental evidence remains conspicuously absent. Herein, we report a rigorous mechanistic investigation using two widely used alkenylboronates alongside relevant reference compounds. Through the combination of irradiation experiments, transient absorption spectroscopic studies, kinetic modeling, and DFT calculations with all isomers of the model compounds, it has been possible to unequivocally detect and characterize the perpendicular triplet generated by energy transfer. Our results serve not only as a blueprint for mechanistic studies that are challenging with organic sensitizers, but these guidelines delineated have also enabled the development of more sustainable reaction conditions: for the first time, efficient organocatalytic isomerization under sunlight irradiation has become feasible.

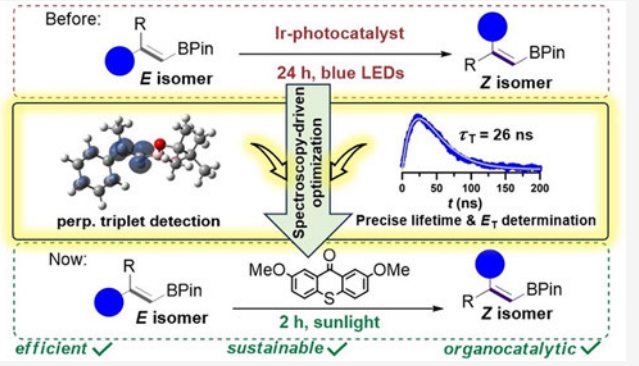

Downloaded via UNIV MAINZ on June 16, 2025 at 16:03:23 (UTC).
See https://pubs.acs.org/sharingguidelines for options on how to legitimately share published articles.

INTRODUCTION

Thioxanthone (TX) has a venerable history in the vibrant arena of energy transfer catalysis[1−4] but despite its popularity, delineating the mechanistic nuances of reactions mediated by this popular organocatalyst is complicated by its nonemissive triplet state.[5−8] In contrast to many photoactive metal complexes,[9−11] invoking TX room-temperature emission quenching in support of triplet energy transfer is inappropriate, and thus, unifying catalysis data with detailed photophysical investigations would be highly enabling for future reaction design. Of the multitude of photochemical processes mediated by thioxanthone with hydrogen abstraction, electron transfer or energy transfer events being mechanistic key steps,[3,12−17] this low molecular weight catalyst has proven to be highly adept in facilitating the geometric $E \rightarrow Z$ isomerization of a plenum of activated alkenes.[18−23] Furthermore, the deracemization of chiral alkenes catalyzed by chiral TX derivatives has also recently been reported.[24] Representative deployments include the isomerization of β-boryl acrylates,[25−27] elaborately substituted fumarates,[28,29] and photocatalytic cascade reactions to generate well-defined drug discovery vectors.[30,31] These transformations are assumed to occur by selective energy transfer from excited state thioxanthone (TX*) to the starting *E*-isomer: upon excitation, a transient triplet state intermediate is generated that can be processed to either the substrate or product isomers, thereby accumulating the *Z*-isomer in the reaction mixture (an energy diagram explaining this mechanism for our specific substrate is presented in the Results and Discussion section). Selectivity biases can be introduced to these processes by strategically leveraging an array of stabilizing[25,26,28,32] or destabilizing interactions[30,31,33−36] to shorten the π-system in the product. This leads to a photostationary state (PSS) composition that, if effective, heavily favors the energetically higher-lying *Z*-alkene (Figure 1). However, this seemingly simple mechanistic picture is frequently complicated by additional electron transfer reactions, typically producing substrate radical cations of the *Z*-isomer,[37−41] depending on the sensitizer and the electronic properties of the olefinic substrate.

Despite the success of this catalyst in light-enabled processes, the direct observation of triplet states generated in TX-mediated isomerization reactions remains conspicuously absent.[10,33−36,42] To address this gap in the geometric isomerization literature, analyses of the photosensitization of

Received: July 18, 2023
Published: September 20, 2023

ACS Publications
© 2023 The Authors. Published by American Chemical Society

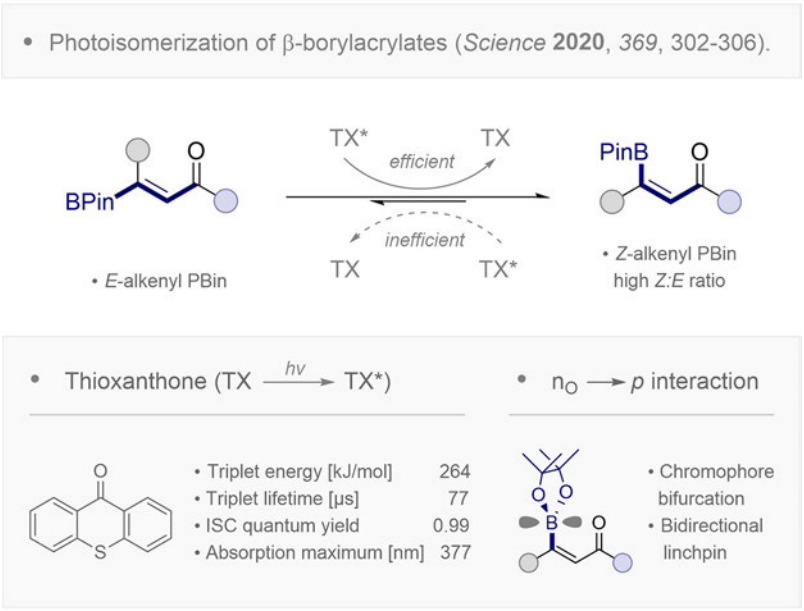

Figure 1. Geometric $E \rightarrow Z$ isomerization of β-boryl acrylates and a summary of the photophysical properties of thioxanthone (TX).

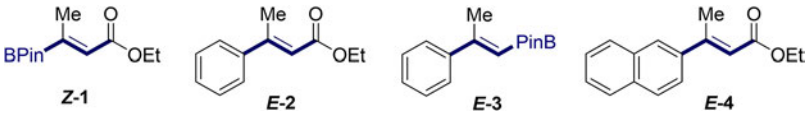

Figure 2. Alkenyl boron substrates and reference compounds investigated in this study.

alkenylboronates have been conducted,[10,27,43,44] but clear evidence for the existence of their triplet states could not be obtained.

The particular substrate class under investigation was selected due to its impact in synthetic and medicinal chemistry[45]: This is a direct consequence of the traceless nature of the boron moiety and the growing interest in organoboron motifs in (photo)catalysis in a broader sense.[46−48] To investigate the triplet states formed in the geometric isomerization of alkenyl boron species enabled by thioxanthone, two vinyl boron substrates (*Z*-**1** and *E*-**3**; see Figure 4 for explanations on the stereochemical assignment) were studied in detail and compared to the well-investigated cinnamoyl chromophores[1,49] (*E*-**2** and *E*-**4**, Figure 2). Our approach relying on transient absorption (TA)-based key methods[50−59] allowed us to unambiguously identify perpendicular triplet states of alkenyl boron species and to experimentally determine hitherto unknown properties such as triplet energies and lifetimes. As will be demonstrated, this understanding has provided a straightforward, mechanism-guided optimization of reaction conditions for the isomerization of these geometrically programmable alkene blocks.

RESULTS AND DISCUSSION

There has been a long-standing interest in investigating triplet alkenes and photoisomerization reactions, dating back to the pioneering studies of Hammond and Saltiel in the 1960s.[60−62] The synergy between experiment and theory has been recurrent in the prediction, study, and rationalization of isomerizations involving simple alkenes such as stilbene derivatives.[63] Owing to the negligibly small triplet formation quantum yield of most olefins and the (ultra)short lifetimes of their triplet states, indirect approaches have been developed for triplet lifetime estimations.[49] The advent of laser flash photolysis (LFP) has enabled the development of time-resolved quenching sequences to monitor the dynamics of short-lived triplet alkenes indirectly.[64−66] In some cases, the direct observation of aromatic olefin triplets with nanosecond triplet lifetimes was successful using a triplet sensitizer and highly optimized experimental conditions.[67,68] However, such sophisticated analyses of photochemical intermediates are under-represented in contemporary photocatalysis. In principle, LFP is a well-established method, but it is not available in most organic chemistry laboratories.[69] This is unfortunate given the potential such approaches hold in resolving mechanistic ambiguities and rendering the process more efficient and sustainable through a better understanding of the key factors that determine the efficiency of photocatalytic reactions.[50,53,55,70−77]

Contemporary studies in the photocatalysis field are frequently accompanied by emission-based quenching experiments, which can be carried out without specific knowledge of advanced spectroscopic techniques. The nonemissive nature of ^{3}TX and related purely organic triplet states[78−81] at room temperature unavoidably militates for more sophisticated absorption-based techniques such as LFP. Before conducting detailed mechanistic studies, we therefore summarized TX's absorption and emission properties using steady-state and time-resolved methods (see Supporting Information, Chapter S6, for details). The ground-state absorption (along with the DFT-predicted absorption maximum) and emission spectra of TX are illustrated in Figure 3: although weak fluorescence is detected, its reported lifetime of 70 ps[82] is far too short for efficient energy or electron transfer reactions based on collision under our conditions (see discussion on quenching efficiencies below and Figures S21 and S28). Singlet-excited TX is known

https://doi.org/10.1021/jacs.3c07678
J. Am. Chem. Soc. 2023, 145, 21576−21586

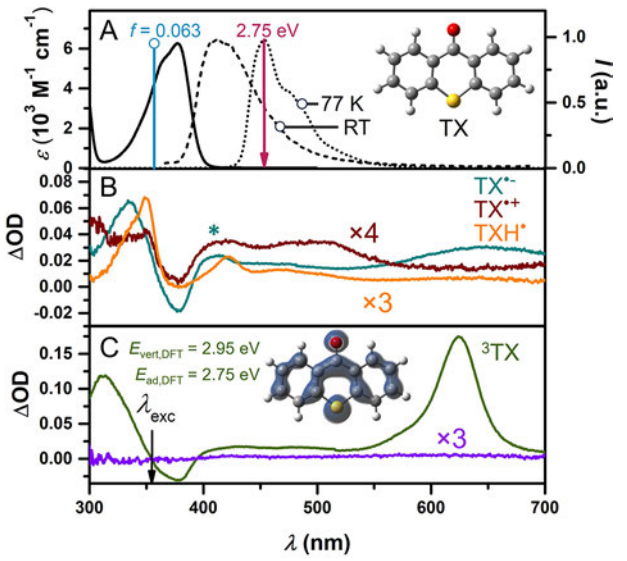

Figure 3. (A) Calibrated absorption spectrum of TX (solid line), fluorescence (dashed line) at room temperature (RT) in MeCN, and phosphorescence at 77 K (dotted line) in MeTHF, along with the DFT-calculated (B3LYP/6-311+G(d,p) level of theory) TX structure and the predicted intense electronic transition in the visible/UVA region (all other transitions have oscillator strengths f below 0.001 and are not shown). (B) TA spectra of the radical anion (cyan), radical cation (brown), and ketyl radical (orange) recorded in Ar-saturated MeCN after 355 nm laser pulse excitation (see the Supporting Information for details). The cyan asterisk marks the absorption band of the DABCO radical cation[87] as a byproduct of the TX radical anion. (C) TA spectrum of triplet-excited TX in Ar-saturated MeCN recorded 50 ns after excitation with 355 nm laser pulses and DFT-calculated TX triplet structure with spin densities and predicted vertical (vert) and adiabatic (ad) triplet energies. TA spectra recorded immediately after quenching of triplet-excited TX with all E/Z-alkenes used in this study showed no traces of TX-derived intermediates after ^{3}TX decay (see the purple spectrum for an example).

to rapidly populate a long-lived triplet state with a lifetime of 77 μs.[83] Yet, phosphorescence is only detected at low temperatures (77 K), making emission-based mechanistic studies practically impossible to perform. The detection and characterization of such nonemissive excited states and their quenching products can be achieved by TA spectroscopy. Therefore, the TA spectrum of ^{3}TX, which is characterized by two prominent peaks at 315 and 625 nm as well as a ground-state bleach at 380 nm was measured (Figure 3C). Our setup (Supporting Information, Chapter S1) allows photoreactions to be monitored with extremely high sensitivity, as is evident from the very high signal-to-noise ratio resembling that of ground-state UV/vis spectra.

Electron transfer (ET) and hydrogen atom transfer (HAT) reactions are usually accompanied by clearly detectable absorption characteristics of the TX-derived quenching products such as the radical anion TX$^{\bullet-}$,[84] the radical cation TX$^{\bullet+}$,[85] as well as the ketyl radical TXH$^{\bullet}$.[86] We collated the TA spectra of these transient species (Figure 3B) by employing appropriate quenchers for ET and HAT processes (see Supporting Information, Section S6, for details). In contrast to these ET or HAT quenching studies with long-lived photoproducts, the deactivation of ^{3}TX by triplet−triplet energy transfer (TTET) with olefinic substrates (compare Figure 2) yields ground-state TX and baseline levels in the postquenching TA spectra (Figure 3C, see discussion below). Typically, all TX-derived doublet species are characterized by a maximum absorption at ∼350 nm, a minimum or even a ground-state bleach at 380 nm, and broad absorption features in the visible region (400−700 nm). The latter signatures of the different doublet species are easily distinguishable and, most importantly, they allow a clear differentiation from triplet-excited TX, which highlights the attractiveness of TA spectroscopy for mechanistic studies of TX-initiated photoreactions. We believe that this "fact sheet" of all pertinent TX properties in one graph (Figure 3) will greatly facilitate spectroscopic investigations for scientists who are entering the field of mechanistic studies in photocatalysis.

Having established the spectroscopic properties of TX and its derived photochemical intermediates, we then conducted photoisomerization experiments upon selective TX excitation at 402 nm (see Section S1 of the Supporting Information for details) with both E- and Z-isomers of all substrates under study (Figure 4). As expected, the same composition is

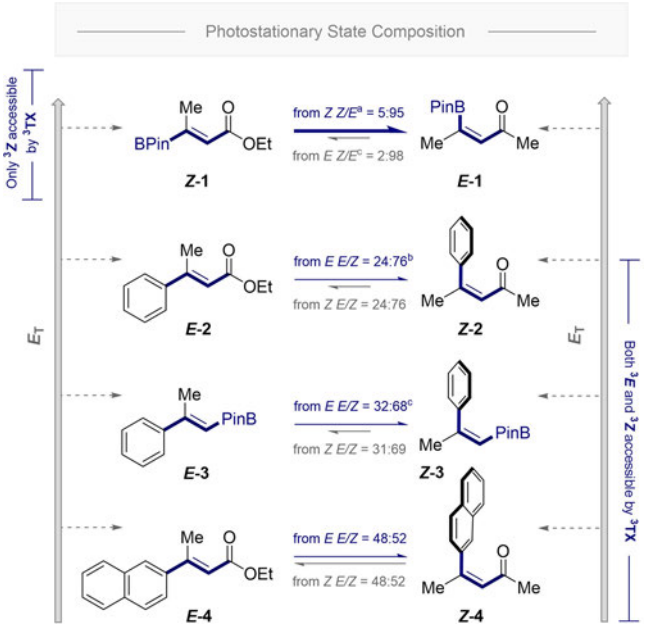

Figure 4. Photocatalysis experiments with the alkenyl boron substrates of interest and reference compounds. Conditions: all reactions were run on a 0.3 mmol scale using 5 mol % of thioxanthone as the catalyst and irradiated for 1 h at 402 nm. (a) Stereochemical assignment follows the IUPAC nomenclature and reflects the priority C > B > H. E/Z ratios were determined by ^{1}H NMR integration. (b) Ratio after 24 h of irradiation, E/Z = 24:76. (c) Ratio after 24 h of irradiation, E/Z = 31:69.

essentially reached starting from either isomer after 24 h of photoirradiation. The vinyl boron substrate **1** reaches a PSS composition that strongly favors E-**1** (∼20:1). In sharp contrast, almost equal isomer concentrations are found for the naphthyl derivative **4** (48:52). Compounds **2** and **3** reach PSSs that are biased toward the corresponding E-isomers (with 24:76 and 31:69, respectively). The existence of a PSS that is accessible from both sides is in line with a triplet energy transfer equilibrium for all substrates. Selected experiments with only 1 h of photoirradiation gave identical results, implying high photoisomerization quantum yields considering

https://doi.org/10.1021/jacs.3c07678
J. Am. Chem. Soc. 2023, 145, 21576−21586

Table 1. Key Properties of the *E*- and *Z*-Alkene Isomers and Their Triplet States

entry	E_T/eV[a]	ΔE_T/eV[a]	dihedral angle of perp. triplet[b]	τ_T/ ns[c]	λ_{max} (T_1)/nm[d]	k_{TTET} /10^9 M^{-1} s^{-1}[e]		E/Z[f]
E-**1**	3.76	+0.31	90° (1.70)	N.A.	N.A.	0.019	(30.7)	98:2 (49)
Z-**1**	3.45					0.583		95:5 (19)
E-**2**	3.25	−0.37	97° (1.58)	<15	321	6.76	(0.38)	24:76 (0.32)
Z-**2**	3.62					2.60		24:76 (0.32)
E-**3**	3.31	−0.42	95° (1.59)	26	317	7.02	(0.46)	32:68 (0.47)
Z-**3**	3.73					3.25		31:69 (0.45)
E-**4**	2.87	−0.17	97° (1.53)	<15	382	11.8	(0.85)	48:52 (0.92)
Z-**4**	3.04					10.0		48:52 (0.92)

[a]Vertical triplet energies estimated by DFT at the B3LYP/6-311+G(d,p) level of theory. [b]Spin densities at the former alkene moiety shown in brackets. [c]Experimentally determined triplet lifetime. [d]Experimentally determined triplet absorption maximum. [e]TTET rates obtained by Stern−Volmer experiments using TX as the energy donor with k_Z divided by k_E shown in brackets. [f]E/Z ratios after irradiation with TX are taken from Figure 4.

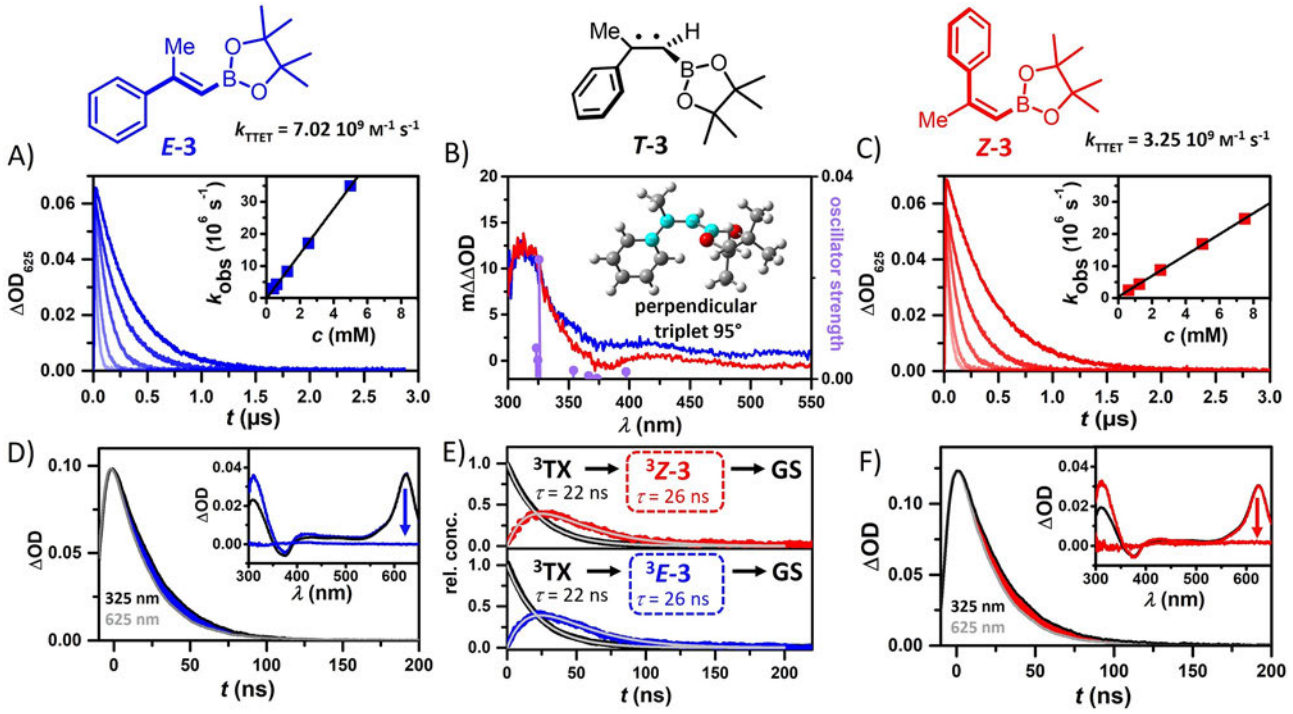

Figure 5. Mechanistic investigations of the excited triplet state *T*-**3** of *E*-**3** (blue) and *Z*-**3** (red) by transient absorption spectroscopy with 355 nm laser pulses (pulse width of ∼5 ns). If not stated otherwise, a solution of 50 μM TX with either 7.5 mM *E*-**3** or 16 mM *Z*-**3** in Ar-saturated MeCN was used for all experiments. (A and C) Triplet quenching experiments of TX with different concentrations of *E*-**3** and *Z*-**3**; insets: the corresponding Stern−Volmer plot. (B) Double difference TA spectra of *E*-**3** and *Z*-**3** after ^{3}TX sensitization obtained from the inset in either (D) or (F) and oscillator strengths of the transitions computed for *T*-**3** by TD-DFT methods. For reliable separation, the spectra were scaled at 625 nm, where *T*-**3** does not absorb. (D and F) Kinetic measurements of TX with *E*-**3** or *Z*-**3** at 325 and 625 nm; insets: TA spectra of TX in the absence of a quencher (black) (delay: 1 μs, integration time: 20 ns) and in combination with *E*-**3** (recorded after 30 or 200 ns, integration time: 20 ns) or *Z*-**3** (recorded after 30 or 200 ns, integration time: 20 ns). (E) Kinetic traces at 625 nm (black) compared to the difference of the kinetic traces (325 and 625 nm) with global fit analyses. The data sets from (D and F) were used. See the text and Supporting Information (Chapter S6) for details.

the moderate optical output power (less than 5 W) of the employed LEDs.

These observations can be rationalized by inspection of the different triplet energies of the isomers. The twisted geometry of the product isomers leads to bifurcation of the previously conjugated system, and this raises the triplet state energy; energy transfer is thus favored by the energetically more accessible isomer. Based on the isomerization results using the TX photosensitizer, whose triplet energy equates to 265 kJ/mol (corresponding to 2.75 eV and a phosphorescence maximum at ∼450 nm in MeTHF as displayed in Figure 3A), it is reasonable to conclude that only the *Z*-isomer of **1** is readily accessible by ^{3}TX, thereby almost quantitatively converting this substrate to *E*-**1** upon irradiation. When the triplet energies of *E*/*Z* alkenes decrease as larger conjugated systems are installed, this phenomenon becomes less noticeable, reaching a point where the energy transfer steps to both isomers have nearly identical efficiencies, which is exemplified by isomers *E*-**4** and *Z*-**4**. DFT calculations of the readily accessible vertical triplet energies[10,88,89] for all *E*- and *Z*-isomers corroborate these observations with about 0.2−0.4 eV higher triplet energies for the enriched isomers in the PSSs (Table 1): this provides further evidence of an energy transfer-driven isomerization (a more extended discussion on computed and experimental triplet energies is given below). In contrast to the nonrelaxed vertical triplets, the energy-

https://doi.org/10.1021/jacs.3c07678
J. Am. Chem. Soc. 2023, 145, 21576−21586

optimized triplet states for all alkenes adopt a perpendicular configuration (hereafter referred to as *T*) with the substituents related through dihedral angles very close to 90°. Spin density calculations clearly show that the two unpaired electrons in the optimized triplet structures are mainly localized on the alkene carbon atoms, with some delocalization over the phenyl and naphthyl rings in substrates **2**, **3**, and **4** (Table 1 and Supporting Information, Chapter S3). Starting from these perpendicular triplet structures, ISC and relaxation back to the respective ground state occur, resulting in either *Z*- or *E*-isomer formation.

Isomerization was then studied by LFP with 5 ns laser pulses at 355 nm. This wavelength was selected because TX absorbs strongly, while most substrate isomers are completely transparent (Supporting Information, Figures S8−S11). Triplet quenching experiments of TX with the *E*/*Z* alkenes yielded quenching rate constants that are displayed in Figure 5A/C and Table 1 (see the Supporting Information for all raw data sets). Strikingly, the ratios of the energy transfer rates k_Z/k_E are in very good agreement with the *E*/*Z* ratios that are reached in the PSSs. These findings imply that starting from the perpendicular triplets ***T***, both ground-state isomers are formed with equal efficiency.[60] Pronounced deviations from the approximate 50:50 splitting (which applies particularly well to **3**; compare the last two columns in Table 1) have been frequently reported for larger or sterically demanding molecules,[42,63,90] underscoring the importance of combining irradiation experiments and kinetic investigations.

Having fully characterized the quenching kinetics, we further investigated potential quenching products with a focus on the dynamics of the alkene triplet states. While we conducted mechanistic studies on at least one isomer of each alkene, only the findings for *E*-**3** and *Z*-**3** are displayed in Figure 5. Corresponding measurements for the remaining alkenes can be found in the Supporting Information. Generally, only baseline spectra were observed following complete ^{3}TX quenching. Two crucial conclusions were drawn from these observations: (i) The main reaction mechanism cannot involve electron transfer or hydrogen atom transfer steps since no long-lived species are detectable on a microsecond time scale (compare TX-derived photoproducts in Figure 3B). (ii) If triplet−triplet energy transfer is the primary reaction pathway, the triplet-excited alkenes either do not absorb in our spectral range or have lifetimes that are shorter than that of the quenched TX triplet. For the following mechanistic studies, the concentrations of both isomers were adjusted such that essentially identical quenching efficiencies and ^{3}TX lifetimes result. This allowed us to compare the results directly. It was assumed that the lifetime of triplet-excited *T*-**3** is on the order of a few nanoseconds[1,2] and thus increased quencher concentrations accordingly such that product triplet formation and decay likely occur on similar time scales. TA spectra were recorded during ^{3}TX sensitization (30 ns after excitation), and they strongly resemble the triplet−triplet absorption spectrum of TX itself (Figure 5D/F, insets). This is expected since triplet-excited olefins usually have much smaller molar absorption coefficients compared to those of TX. To identify deviations from ^{3}TX, an independently recorded reference TA spectrum of only ^{3}TX was normalized to the observed absorption level at 625 nm, where the triplet-excited alkenes are not expected to absorb owing to their rather short conjugated systems. When these spectra are superimposed, a slightly increased absorption in the UV region clearly becomes noticeable. After subtracting these TA spectra (with and without the alkenylboronate), a double difference spectrum is obtained that we assign to the short-lived quenching product, the perpendicular triplet state *T*-**3**. Notably, both double difference spectra acquired from *E*-**3** and *Z*-**3** match almost perfectly with an absorption maximum at ∼320 nm, yielding clear-cut evidence that the identical perpendicular triplet state *T*-**3** is generated by the sensitization of both isomers (Figure 5B). The estimated oscillator strengths for the computed transitions of *T*-**3** are shown in Figure 5B and further substantiate our assignment.

The kinetic behavior of *T*-**3** was investigated at 325 nm, where both *T*-**3** and ^{3}TX absorb, and compared to the kinetic traces at 625 nm, where ^{3}TX can be observed in isolation (Figure 5D/F). To enable a better comparison, the postpulse amplitudes at both wavelengths were normalized. Evidently, another absorbing species with much weaker signals than observed for ^{3}TX is detectable at 325 nm, seemingly delayed to the ^{3}TX absorption (highlighted in blue for *E*-**3** and in red for *Z*-**3**). The double difference kinetic traces of these measurements are given in Figure 5E. These difference curves and the corresponding ^{3}TX traces were simulated and simultaneously fitted with conventional A $\overset{k1}{\rightarrow}$ B $\overset{k2}{\rightarrow}$ C kinetics[91,92] (Figure 5E) with k_1 being dynamic ^{3}TX quenching to give *T*-**3** (1/22 ns) and k_2 being the *T*-**3** decay ($1/\tau_T$). This analysis gave a *T*-**3** lifetime τ_T of 26 ns under our conditions, regardless of whether the *E* or *Z* isomer was used. The triplet state lifetime should be virtually independent of the quencher concentration and thus a similar analysis was performed with half the alkene concentration. We obtained the very same *T*-**3** lifetime (Supporting Information, Figure S22) and negative control experiments in the absence of *E*/*Z*-**3** (Supporting Information, Figure S26), which we regard as validation of the applicability of our method. The rather short lifetime of triplet states is commonly observed for small alkene molecules and rationalized by the accelerated ISC rates at the perpendicular configuration.[93] Similar measurements were performed with the other *E*/*Z* alkenes. In the case of compound **1**, no absorbing species was detected during or after sensitization other than ^{3}TX (Figure S23). This is, however, expected, as the *T*-**1** state is likely hard to detect as a result of weak absorption signals in the absence of phenyl/naphthyl rings in the detection range and a probably even shorter lifetime. For the *E*/*Z* isomers of the cinnamoyl chromophore **2**, an analogous analysis of the TA spectra showed a maximum at ∼320 nm. A reliable lifetime analysis was impossible with our nanosecond setup but our results allow us to estimate an upper limit of 15 ns (Figure S24), which is in line with previous investigations of unsubstituted cinnamate (10.3 ns, estimated using steady-state kinetics and quenching product analysis).[49] Similar results were obtained for the naphthyl-substituted alkene **4** showing a triplet absorption maximum at 382 nm but a short lifetime (<15 ns, Figure S25). It is postulated that with increasing substituent mass, the lifetime increases due to several factors such as inhibiting oscillation at the perpendicular configuration or conjugative delocalization of the radical termini.[49,93] However, we do not observe this trend for the cinnamoyl derivatives, indicating that the substituent effects are more complex and need further clarification.

Whereas the relative vertical triplet energies are useful for explaining trends in a qualitative manner, their actual values are far too high to explain the efficient sensitization observed with TX (compare with Table 1). In contrast, the so-called adiabatic

https://doi.org/10.1021/jacs.3c07678
J. Am. Chem. Soc. 2023, 145, 21576−21586

triplet energies, which correspond to the respective energy difference between the E/Z ground state and energy-optimized triplet $\boldsymbol{T}$, can be regarded as the lower limit. These calculated adiabatic triplet energies lie at 2.0 to 2.3 eV for the four alkenes under investigation and would thus predict a completely unselective sensitization process with TX. Using the same DFT method, we could perfectly reproduce the experimental triplet energy of TX with the adiabatic energy value (compare Figure 3). As in our case, such simple DFT methods gave triplet energies in good to excellent agreement with experimentally observed values[41,94,95] and they might be most useful for systems with small structural changes between the singlet ground state and the energy-optimized triplet.

In order to account for the disparity between the calculated parameters, thermodynamic predictions, and spectroscopic results, it is necessary to consider the geometric changes of the olefinic quencher (and the excited sensitizer) upon excitation (deactivation). The phenomenon referred to as "nonvertical" energy transfer, which falls between the purely vertical and the adiabatic scenario, is particularly evident for the highly distorted excited state geometries observed in several studied alkenes.[96,97] Hence, with straightforward calculations, it is essentially unpredictable for a novel substrate class whether the calculated vertical or the adiabatic triplet energy is closer to the experimental value. This debate, and the usefulness of experimental triplet energies for optimizing reaction conditions, prompted us to measure these quantities for *E*-**3** and *Z*-**3**. Triplet energy determinations at room temperature should result in more reliable results than phosphorescence measurements in frozen matrices (77 K), where structural changes cannot occur on the time scale of the actual energy transfer.[98] We, therefore, selected a series of structurally related Ir complexes with well-known triplet energies (Supporting Information, Section S5.2) as energy donors and measured the energy transfer rate constants with both olefin isomers in MeCN at 293 K (Figure 6A). Selected control experiments again allowed us to exclude electron transfer quenching. These sensitizers have the advantage that their triplet quenching studies can be carried out by monitoring time-resolved emission, which is faster and more sensitive than TA-based techniques.

The rate constants so obtained were plotted against the known sensitizer triplet energies and fitted with a thermal activation model for endothermic energy transfer (Figure 6; Supporting Information, Section S5.2).[68,96,98,99] With the reasonable assumption of similar diffusion rates for both isomers, we obtained not only the triplet energy difference (0.14 eV) but also absolute values for the experimental triplet energies of both isomers: 2.78 and 2.92 eV for *E*-**3** and *Z*-**3**, respectively. Interestingly, the experimental triplet energies are halfway between the computed vertical and adiabatic triplet energies, which is displayed in Figure 7 along with the additional theoretical and experimental results obtained for **3**. This simple estimation of experimental values from the average of vertical and adiabatic triplet energies might be useful as an initial guess to select proper sensitizers for isomerizations of related alkenylboronates without time-consuming experiments.

Inspection of the quenching kinetics measured for TX and its commercially available MeOTX derivative (see Figure 8 for the structure) reveals a discrepancy: The triplet energy transfer rates are much faster than those measured with iridium complexes possessing isoenergetic triplet states (Figure 6A). Furthermore, energy transfer with TX is clearly faster (up to

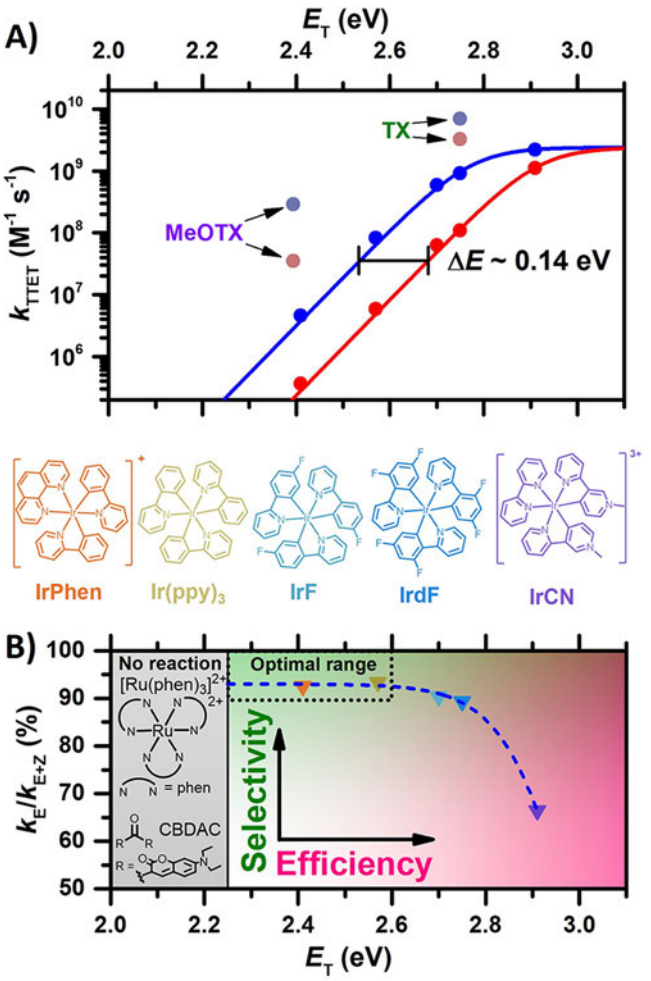

Figure 6. (A) Triplet energy transfer rates of two TX-based and various Ir-based sensitizers to *E*-**3** (blue) and *Z*-**3** (red) plotted against their triplet energies with the thermal bond activation model fitted to the experimental data. (B) Graph displaying the selectivity and efficiency of the photoisomerization of *E*-**3** driven by Ir-based sensitizers. The energy transfer rates to *E*-**3** (k_E) divided by the sum of both rates (k_{E+Z}) are plotted against the sensitizer triplet energy. This quotient is defined as the selectivity parameter. The blue dashed line is a spline fit to guide the eye and has no mechanistic implications. See the text for details.

7.0×10^9 M^{-1} s^{-1}) than the diffusion limit determined for the iridium complex**3** pairs (~2.5×10^9 M^{-1} s^{-1}). We speculate that two effects are responsible for these seemingly unusual observations. First, diffusion of the small organic dyes must be much faster compared to the larger iridium complexes. It is worth mentioning that the classical "diffusion limit" found in textbooks is based on the assumption of identical molecular radii of both reaction partners, which certainly does not hold true in the metal complex-driven sensitization. Second, the orbital overlap required for a Dexter energy transfer is likely facilitated by TX derivatives. In this case, both SOMOs of the triplets can interact with the substrate, whereas for the metal complexes with metal-to-ligand charge transfer states, only the upper SOMO (i.e., the former ligand-localized LUMO) can efficiently overlap with acceptor orbitals in an exchange mechanism. However, regardless of whether TX (Table 1) or Ir(ppy)$_3$ (Supporting Information, Table S2) is used as the sensitizer, the PSS composition for **3** can be predicted with the energy transfer rate constants in a very reliable manner. This

https://doi.org/10.1021/jacs.3c07678
J. Am. Chem. Soc. 2023, 145, 21576−21586

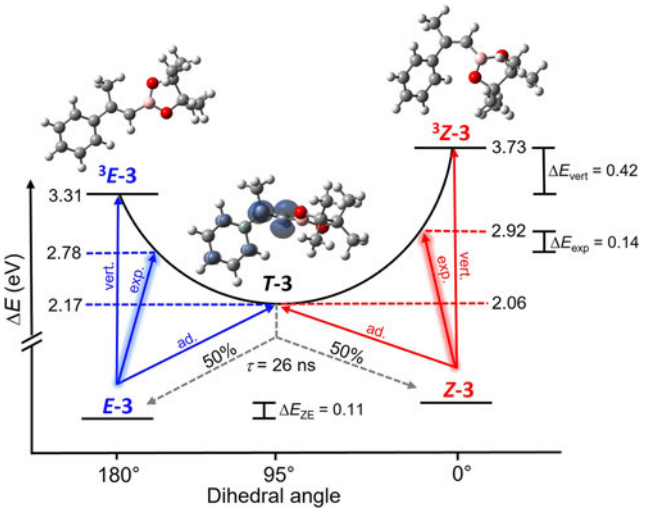

Figure 7. Relative energies of the ground states and triplet states of *E*-**3** and **Z**-**3** together with DFT-computed spin densities of the perpendicular triplet state *T*-**3**, pertinent structures, and key experimental findings.

encouraged us to plot the calculated sensitization selectivities for all of the iridium complexes under study (Figure 6B). An optimal range of the sensitizer triplet energy between 2.25 and 2.60 eV for selective isomerization can be identified. Upon increasing the sensitizer's triplet energy beyond 2.6 eV, isomerization in both directions becomes thermodynamically feasible and the selectivity bias decreases,[60] yielding more than 10% of the undesired starting material in the PSS (blue dashed line in Figure 6B). Sensitizers with triplet energies lower than 2.25 eV do not catalyze the isomerization of **3**, as our control experiments with $[Ru(phen)_3]^{2+}$ (2.19 eV)[100,101] and with a ketocoumarin (~2.20 eV)[49,102] have established. The PSS composition is essentially determined by two factors: (i) the triplet decay ratio to the *E*/*Z* ground state, which is an inherent property of the respective olefinic substrate, and (ii) the relative rates of *E*/*Z* sensitization depending on the relative triplet energies of the isomers and the employed sensitizer. Since the experimental triplet energy differences of *E*/*Z* isomers are typically on the order of 0.2 eV[1] (0.14 eV in our case), exclusive sensitization of only one isomer is frequently not feasible. Thus, quantitative conversion is only viable for very few substrates,[21] and herein, an upper limit of 94% *Z*-isomer is reached (Figure 6).

It seems natural to assume that the quenching efficiencies and overall reaction quantum yields drop significantly at the lower limit of the optimal energy range. Using the natural triplet lifetime in combination with the quenching rate constant and the actual substrate concentration (60 mM in the case of **3**, see the Supporting Information), quenching efficiencies for the sensitizer triplet can be calculated with easy-to-use kinetic equations.[56] At this substrate concentration, quenching efficiencies exceeding 50% for a typical organic sensitizer with a 25 μs lifetime can already be achieved with a TTET rate constant as low as $\sim 7 \times 10^5$ M^{-1} s^{-1}. For an iridium complex with a 1 μs lifetime this half-quenching rate constant amounts to $\sim 2 \times 10^7$ M^{-1} s^{-1} under otherwise identical conditions. These kinetic simulations (see the Supporting Information for details and kinetic plots) demonstrate that the triplet energy transfer rate constants may be orders of magnitude slower than the diffusion limit while maintaining high reaction efficiencies.

Based on all these experiments and kinetics as well as efficiency considerations, we identified the thioxanthone derivative MeOTX[23] as an ideal candidate for a metal-free isomerization of the test substrate **3**. So far, $Ir(ppy)_3$ (1 mol%) and typically 24 h of intense blue irradiation were required for obtaining the desired *Z*-isomer in ≥90% yield (see the

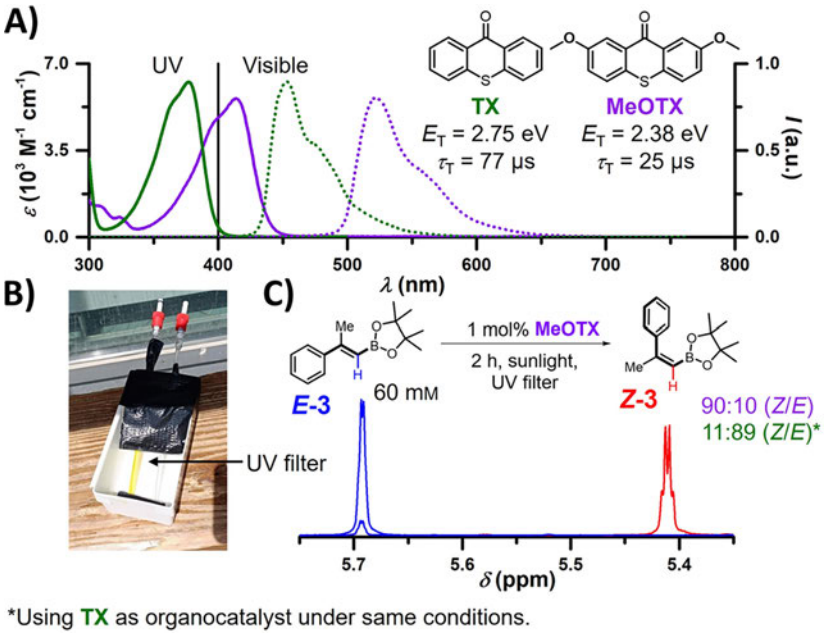

Figure 8. (A) Absorption (solid) in MeCN and 77 K emission (dotted) in MeTHF spectra of TX and MeOTX. (B) Typical setup for solar-driven isomerization experiments of *E*-**3**. A UV filter was used to suppress potential UV-induced side reactions. (C) Reaction scheme and conditions of photoisomerization in Ar-saturated CD_3CN and NMR spectra that display the olefinic H signals of *E*-**3** (blue) and *Z*-**3** (red) taken before and after irradiation with MeOTX.

https://doi.org/10.1021/jacs.3c07678
J. Am. Chem. Soc. 2023, 145, 21576−21586

Supporting Information and ref 27). MeOTX is sold for about 50 € per mmol, which makes MeOTX cheaper than $Ir(ppy)_3$ by a factor of ~20. In contrast to TX, MeOTX readily absorbs visible light and with its triplet properties and quenching rate constants (Figures 6A and 8A), we predict a quenching efficiency exceeding 99% in the presence of 60 mM *E*-**3** and a *Z*/*E* ratio of 89:11 in the PSS. To test this predicted efficiency and to exploit the improved absorption properties of the catalyst, we conducted the experiments using sunlight instead of artificial light sources driven by electricity.[103] For this, the solutions were prepared in Teflon-sealed NMR tubes with CD_3CN as the solvent, allowing for straightforward reaction control by NMR spectroscopy (Figure 8B). To prevent direct excitation of the isomers, a UV filter was employed. As a control experiment, we performed a sunlight-driven isomerization experiment using conventional TX (see the Supporting Information for experimental details). Gratifyingly, after only 2 h of exposure to sunlight, a PSS with 90% of the desired *Z*-**3** was observed using 1 mol% of MeOTX (Figure 8C; 85:15 after 1 h). In contrast, the experiment with conventional TX reached a ratio of 11:89 (8:92 after 1 h), which significantly deviates from the PSS observed after violet LED excitation (68:32), indicating that the sunlight-driven reaction is much slower in this case. Thus, guided by mechanistic studies, an efficient and selective protocol has been developed under milder and more sustainable reaction conditions.

CONCLUSIONS

This study demonstrates the wealth of information that can be distilled through detailed mechanistic studies on the sensitized geometric isomerization of alkenylboronates (Figure 7). Direct evidence for the formation of the corresponding perpendicular triplet was obtained for the first time, which can be generated from both ground state isomers and decays back to them with equal probability. Key properties that are relevant for both spectroscopists and synthetic chemists were determined experimentally, and this has led to guidelines for reaction design and post facto rationalization. Practitioners of photocatalysis can benefit from triplet lifetime data in the context of developing synthetically valuable processes, such as trapping or cycloaddition events.[10,104] Moreover, the experimental triplet energies (which cannot be calculated in a straightforward manner) of both isomers enable the proper selection of effective sensitizers (Figure 8). Importantly, these novel data sets hold great promise in gleaning a better understanding of triplet biradicals, whose properties require clarification.[105,106] Furthermore, a careful comparison of kinetic results for photoactive Ir complexes and TX-based photosensitizers with essentially identical triplet energies revealed an unexpected discrepancy, which we were able to trace back to differences in their diffusion coefficients and the orbital overlap with the energy acceptor. Based on these findings, it is reasonable to conclude that while the literature-reported triplet energy of a sensitizer is certainly a good initial guess, it is insufficient for the selection of the ideal sensitizer. The impact of this combined kinetic and mechanistic approach has been demonstrated in rendering the isomerization of alkenylboronates efficient by using only sunlight irradiation, and it is envisioned that this attractive approach can be translated to other photocatalysis settings.

ASSOCIATED CONTENT

Data Availability Statement

All experimental and computational data have been provided in the main text and the Supporting Information. The data sets shown in the main paper and DFT output files can be found under http://doi.org/10.25358/openscience-9554.

Supporting Information

The Supporting Information is available free of charge at https://pubs.acs.org/doi/10.1021/jacs.3c07678.

Experimental details, synthetic protocols and characterization data, additional spectroscopic results as well as raw data sets, and quantum-mechanical calculations (PDF)

AUTHOR INFORMATION

Corresponding Authors

Ryan Gilmour − *Organisch-Chemisches Institut, Westfälische Wilhelms-Universität Münster, 48149 Münster, Germany; Cells in Motion (CiM) Interfaculty Center, 48149 Münster, Germany;* orcid.org/0000-0002-3153-6065; Email: ryan.gilmour@uni-muenster.de

Christoph Kerzig − *Department of Chemistry, Johannes Gutenberg University Mainz, 55128 Mainz, Germany;* orcid.org/0000-0002-1026-1146; Email: ckerzig@uni-mainz.de

Authors

Till J. B. Zähringer − *Department of Chemistry, Johannes Gutenberg University Mainz, 55128 Mainz, Germany*

Max Wienhold − *Organisch-Chemisches Institut, Westfälische Wilhelms-Universität Münster, 48149 Münster, Germany*

Complete contact information is available at: https://pubs.acs.org/10.1021/jacs.3c07678

Author Contributions

‖T.J.B.Z. and M.W. contributed equally to this paper.

Notes

The authors declare no competing financial interest.

ACKNOWLEDGMENTS

We acknowledge generous financial support from the JGU Mainz, the WWU Münster, the German Research Foundation (DFG, grant numbers KE 2313/3-1 and KE 2313/7-1), and the German Federal Environmental Foundation (DBU, PhD fellowship to T.J.B.Z., grant number 20022/028). We thank Prof. Johannes Wahl for allowing us to use his glovebox for sample preparation and David J. Pauly as well as Philipp Reichert for the preparation of Ir-based sensitizers.

REFERENCES

(1) Montalti, M.; Credi, A.; Prodi, L.; Gandolfi, M. T. *Handbook of Photochemistry*, 3rd ed.; CRC/Taylor & Francis: Boca Raton, 2006.

(2) Großkopf, J.; Kratz, T.; Rigotti, T.; Bach, T. Enantioselective Photochemical Reactions Enabled by Triplet Energy Transfer. *Chem. Rev.* **2022**, *122* (2), 1626−1653.

(3) Nikitas, N. F.; Gkizis, P. L.; Kokotos, C. G. Thioxanthone: A Powerful Photocatalyst for Organic Reactions. *Org. Biomol. Chem.* **2021**, *19* (24), 5237−5253.

(4) Strieth-Kalthoff, F.; Glorius, F. Triplet Energy Transfer Photocatalysis: Unlocking the Next Level. *Chem.* **2020**, *6* (8), 1888−1903.

(5) Li, X.; Kutta, R. J.; Jandl, C.; Bauer, A.; Nuernberger, P.; Bach, T. Photochemically Induced Ring Opening of Spirocyclopropyl Oxindoles: Evidence for a Triplet 1,3-Diradical Intermediate and Deracemization by a Chiral Sensitizer. *Angew. Chem., Int. Ed.* **2020**, *59* (48), 21640−21647.
(6) Ahuja, S.; Jockusch, S.; Ugrinov, A.; Sivaguru, J. Energy Transfer Catalysis by Visible Light: Atrop- and Regio-Selective Intermolecular [2 + 2]-Photocycloaddition of Maleimide with Alkenes. *Eur. J. Org. Chem.* **2020**, *2020* (10), 1478−1481.
(7) Mundt, R.; Villnow, T.; Ziegenbein, C. T.; Gilch, P.; Marian, C.; Rai-Constapel, V. Thioxanthone in Apolar Solvents: Ultrafast Internal Conversion Precedes Fast Intersystem Crossing. *Phys. Chem. Chem. Phys.* **2016**, *18* (9), 6637−6647.
(8) Angulo, G.; Grilj, J.; Vauthey, E.; Serrano-Andrés, L.; Rubio-Pons, Ò.; Jacques, P. Ultrafast Decay of the Excited Singlet States of Thioxanthone by Internal Conversion and Intersystem Crossing. *ChemPhysChem* **2010**, *11* (2), 480−488.
(9) Singh, K.; Staig, S. J.; Weaver, J. D. Facile Synthesis of *Z* -Alkenes via Uphill Catalysis. *J. Am. Chem. Soc.* **2014**, *136* (14), 5275−5278.
(10) Liu, Y.; Ni, D.; Stevenson, B. G.; Tripathy, V.; Braley, S. E.; Raghavachari, K.; Swierk, J. R.; Brown, M. K. Photosensitized [2 + 2]-Cycloadditions of Alkenylboronates and Alkenes. *Angew. Chem., Int. Ed.* **2022**, *61* (25), No. e202200725.
(11) Arias-Rotondo, D. M.; McCusker, J. K. The Photophysics of Photoredox Catalysis: A Roadmap for Catalyst Design. *Chem. Soc. Rev.* **2016**, *45* (21), 5803−5820.
(12) Kolb, D.; Morgenstern, M.; König, B. Decarbonylation of Benzaldehydes by Dual Photoorgano-Cobalt Catalysis. *Chem. Commun.* **2023**, *59*, 8592.
(13) Oddy, M. J.; Kusza, D. A.; Petersen, W. F. Visible-Light Mediated Metal-Free 6π-Photocyclization of *N* -Acrylamides: Thioxanthone Triplet Energy Transfer Enables the Synthesis of 3,4-Dihydroquinolin-2-Ones. *Org. Lett.* **2021**, *23* (22), 8963−8967.
(14) Grover, J.; Prakash, G.; Teja, C.; Lahiri, G. K.; Maiti, D. Metal-Free Photoinduced Hydrogen Atom Transfer Assisted C(Sp^3)−H Thioarylation. *Green Chem.* **2023**, *25* (9), 3431−3436.
(15) Chen, Y.-C.; Liu, T.-Y.; Li, Y.-H. Photoreactivity Study of Photoinitiated Free Radical Polymerization Using Type II Photoinitiator Containing Thioxanthone Initiator as a Hydrogen Acceptor and Various Amine-Type Co-Initiators as Hydrogen Donors. *J. Coat. Technol. Res.* **2021**, *18* (1), 99−106.
(16) Christmann, J.; Allonas, X.; Ley, C.; Croutxé-Barghorn, C. The Role of Ketyl Radicals in Free Radical Photopolymerization: New Experimental and Theoretical Insights. *Polym. Chem.* **2019**, *10* (9), 1099−1109.
(17) Liashuk, O. S.; Grygorenko, O. O.; Volovenko, Y. M.; Waser, J. Photochemical [2 + 2] Cycloaddition of Alkynyl Boronates. *Chem. − Eur. J.* **2023**, No. e202301650.
(18) Metternich, J.; Gilmour, R. Photocatalytic E → Z Isomerization of Alkenes. *Synlett* **2016**, *27* (18), 2541−2552.
(19) Pearson, C. M.; Snaddon, T. N. Alkene Photo-Isomerization Inspired by Vision. *ACS Cent. Sci.* **2017**, *3* (9), 922−924.
(20) Molloy, J. J.; Morack, T.; Gilmour, R. Positional and Geometrical Isomerisation of Alkenes: The Pinnacle of Atom Economy. *Angew. Chem., Int. Ed.* **2019**, *58* (39), 13654−13664.
(21) Neveselý, T.; Wienhold, M.; Molloy, J. J.; Gilmour, R. Advances in the *E* → *Z* Isomerization of Alkenes Using Small Molecule Photocatalysts. *Chem. Rev.* **2022**, *122* (2), 2650−2694.
(22) Corpas, J.; Mauleón, P.; Gómez Arrayás, R.; Carretero, J. C. *E*/*Z* Photoisomerization of Olefins as an Emergent Strategy for the Control of Stereodivergence in Catalysis. *Adv. Synth. Catal.* **2022**, *364* (8), 1348−1370.
(23) Elliott, L. D.; Kayal, S.; George, M. W.; Booker-Milburn, K. Rational Design of Triplet Sensitizers for the Transfer of Excited State Photochemistry from UV to Visible. *J. Am. Chem. Soc.* **2020**, *142* (35), 14947−14956.
(24) Kratz, T.; Steinbach, P.; Breitenlechner, S.; Storch, G.; Bannwarth, C.; Bach, T. Photochemical Deracemization of Chiral Alkenes via Triplet Energy Transfer. *J. Am. Chem. Soc.* **2022**, *144* (23), 10133−10138.
(25) Molloy, J. J.; Schäfer, M.; Wienhold, M.; Morack, T.; Daniliuc, C. G.; Gilmour, R. Boron-Enabled Geometric Isomerization of Alkenes via Selective Energy-Transfer Catalysis. *Science* **2020**, *369* (6501), 302−306.
(26) Wienhold, M.; Molloy, J. J.; Daniliuc, C. G.; Gilmour, R. Coumarins by Direct Annulation: B-Borylacrylates as Ambiphilic C_3 -Synthons. *Angew. Chem., Int. Ed.* **2021**, *60* (2), 685−689.
(27) Molloy, J. J.; Metternich, J. B.; Daniliuc, C. G.; Watson, A. J. B.; Gilmour, R. Contra-Thermodynamic, Photocatalytic *E* → *Z* Isomerization of Styrenyl Boron Species: Vectors to Facilitate Exploration of Two-Dimensional Chemical Space. *Angew. Chem., Int. Ed.* **2018**, *57* (12), 3168−3172.
(28) Neveselý, T.; Molloy, J. J.; McLaughlin, C.; Brüss, L.; Daniliuc, C. G.; Gilmour, R. Leveraging the Nπ* Interaction in Alkene Isomerization by Selective Energy Transfer Catalysis. *Angew. Chem., Int. Ed.* **2022**, *61* (2), No. e202113600.
(29) Kerzig, C.; Wenger, O. S. Reactivity Control of a Photocatalytic System by Changing the Light Intensity. *Chem. Sci.* **2019**, *10* (48), 11023−11029.
(30) Neveselý, T.; Daniliuc, C. G.; Gilmour, R. Sequential Energy Transfer Catalysis: A Cascade Synthesis of Angularly-Fused Dihydrocoumarins. *Org. Lett.* **2019**, *21* (23), 9724−9728.
(31) Poplata, S.; Tröster, A.; Zou, Y.-Q.; Bach, T. Recent Advances in the Synthesis of Cyclobutanes by Olefin [2 + 2] Photocycloaddition Reactions. *Chem. Rev.* **2016**, *116* (17), 9748−9815.
(32) Hostmann, T.; Neveselý, T.; Gilmour, R. Illuminating *Anti* -Hydrozirconation: Controlled Geometric Isomerization of an Organometallic Species. *Chem. Sci.* **2021**, *12* (31), 10643−10648.
(33) Onneken, C.; Bussmann, K.; Gilmour, R. Inverting External Asymmetric Induction via Selective Energy Transfer Catalysis: A Strategy to B-Chiral Phosphonate Antipodes. *Angew. Chem., Int. Ed.* **2020**, *59* (1), 330−334.
(34) Faßbender, S. I.; Molloy, J. J.; Mück-Lichtenfeld, C.; Gilmour, R. Geometric *E* → *Z* Isomerisation of Alkenyl Silanes by Selective Energy Transfer Catalysis: Stereodivergent Synthesis of Triarylethylenes via a Formal *Anti* -Metallometallation. *Angew. Chem.* **2019**, *131* (51), 18792−18799.
(35) Metternich, J. B.; Artiukhin, D. G.; Holland, M. C.; Von Bremen-Kühne, M.; Neugebauer, J.; Gilmour, R. Photocatalytic *E* → *Z* Isomerization of Polarized Alkenes Inspired by the Visual Cycle: Mechanistic Dichotomy and Origin of Selectivity. *J. Org. Chem.* **2017**, *82* (19), 9955−9977.
(36) Metternich, J. B.; Gilmour, R. A Bio-Inspired, Catalytic *E* → *Z* Isomerization of Activated Olefins. *J. Am. Chem. Soc.* **2015**, *137* (35), 11254−11257.
(37) Glaser, F.; Wenger, O. S. Sensitizer-Controlled Photochemical Reactivity *via* Upconversion of Red Light. *Chem. Sci.* **2022**, *14* (1), 149−161.
(38) Kuriyama, Y.; Arai, T.; Sakuragi, H.; Tokumaru, K. Effects of Sensitizer Spin Multiplicity on Electron-Transfer Initiated Isomerization of *Cis* -Stilbene. *Chem. Lett.* **1988**, *17* (7), 1193−1196.
(39) Lewis, F. D.; Bedell, A. M.; Dykstra, R. E.; Elbert, J. E.; Gould, I. R.; Farid, S. Photochemical Generation, Isomerization, and Oxygenation of Stilbene Cation Radicals. *J. Am. Chem. Soc.* **1990**, *112* (22), 8055−8064.
(40) Goez, M.; Eckert, G. Photoinduced Electron Transfer Reactions of Aryl Olefins. 2. Cis−Trans Isomerization and Cycloadduct Formation in Anethole−Fumaronitrile Systems in Polar Solvents. *J. Am. Chem. Soc.* **1996**, *118* (1), 140−154.
(41) Fischer, C.; Kerzig, C.; Zilate, B.; Wenger, O. S.; Sparr, C. Modulation of Acridinium Organophotoredox Catalysts Guided by Photophysical Studies. *ACS Catal.* **2020**, *10* (1), 210−215.
(42) Wienhold, M.; Kweon, B.; McLaughlin, C.; Schmitz, M.; Zähringer, T. J. B.; Daniliuc, C. G.; Kerzig, C.; Gilmour, R. Geometric Isomerisation of Bifunctional Alkenyl Fluoride Linchpins: Stereodivergence in Amide and Polyene Bioisostere Synthesis. *Angew. Chem., Int. Ed.* **2023**, *62*, No. e202304150.

(43) Brégent, T.; Bouillon, J.; Poisson, T. Photocatalyzed $E \rightarrow Z$ Contra-thermodynamic Isomerization of Vinyl Boronates with Binaphthol. *Chem. – Eur. J.* **2021**, *27* (56), 13966–13970.
(44) Corpas, J.; Gomez-Mendoza, M.; Ramírez-Cárdenas, J.; De La Peña O'Shea, V. A.; Mauleón, P.; Gómez Arrayás, R.; Carretero, J. C. One-Metal/Two-Ligand for Dual Activation Tandem Catalysis: Photoinduced Cu-Catalyzed Anti-Hydroboration of Alkynes. *J. Am. Chem. Soc.* **2022**, *144* (28), 13006–13017.
(45) Brown, D. G.; Boström, J. Analysis of Past and Present Synthetic Methodologies on Medicinal Chemistry: Where Have All the New Reactions Gone?: Miniperspective. *J. Med. Chem.* **2016**, *59* (10), 4443–4458.
(46) Marotta, A.; Adams, C. E.; Molloy, J. J. The Impact of Boron Hybridisation on Photocatalytic Processes. *Angew. Chem., Int. Ed.* **2022**, *61* (38), No. e202207067.
(47) Pang, Y.; Chen, S.; Han, J.; Zhu, C.; Zhao, C.; Xie, J. Dimeric Manganese-Catalyzed Hydroalkenylation of Alkynes with a Versatile Silicon-Based Directing Group. *Angew. Chem., Int. Ed.* **2023**, *62*, No. e202306922.
(48) Keita, H.; Meek, S. J. Synthesis of Quaternary and Tertiary Carbon-Substituted Arenes by Lewis Base Promoted Site-Selective Coupling with Allylic Nucleophiles. *Angew. Chem., Int. Ed.* **2023**, *62*, No. e202306277.
(49) Herkstroeter, W. G.; Farid, S. Photodimerization — Relevant Triplet State Parameters of Methyl Cinnamate, Diethyl 1,4-Phenylenediacrylate and Methyl 1-Naphthylacrylate. *J. Photochem.* **1986**, *35* (1), 71–85.
(50) Tian, L.; Till, N. A.; Kudisch, B.; MacMillan, D. W. C.; Scholes, G. D. Transient Absorption Spectroscopy Offers Mechanistic Insights for an Iridium/Nickel-Catalyzed C–O Coupling. *J. Am. Chem. Soc.* **2020**, *142* (10), 4555–4559.
(51) Buzzetti, L.; Crisenza, G. E. M.; Melchiorre, P. Mechanistic Studies in Photocatalysis. *Angew. Chem., Int. Ed.* **2019**, *58* (12), 3730–3747.
(52) Wang, C.; Malinoski, A. Perspective: Mechanistic Investigations of Photocatalytic Processes with Time-Resolved Optical Spectroscopy. *J. Chem. Phys.* **2022**, *157* (16), 160901.
(53) Zeman, C. J.; Kim, S.; Zhang, F.; Schanze, K. S. Direct Observation of the Reduction of Aryl Halides by a Photoexcited Perylene Diimide Radical Anion. *J. Am. Chem. Soc.* **2020**, *142* (5), 2204–2207.
(54) Strieth-Kalthoff, F.; Henkel, C.; Teders, M.; Kahnt, A.; Knolle, W.; Gómez-Suárez, A.; Dirian, K.; Alex, W.; Bergander, K.; Daniliuc, C. G.; Abel, B.; Guldi, D. M.; Glorius, F. Discovery of Unforeseen Energy-Transfer-Based Transformations Using a Combined Screening Approach. *Chem* **2019**, *5* (8), 2183–2194.
(55) Ripak, A.; De Kreijger, S.; Sampaio, R. N.; Vincent, C. A.; Cauët, É.; Jabin, I.; Tambar, U. K.; Elias, B.; Troian-Gautier, L. Photosensitized Activation of Diazonium Derivatives for C–B Bond Formation. *Chem. Catal.* **2023**, *3* (2), No. 100490.
(56) Glaser, F.; Kerzig, C.; Wenger, O. S. Multi-Photon Excitation in Photoredox Catalysis: Concepts, Applications. *Methods. Angew. Chem. Int. Ed.* **2020**, *59* (26), 10266–10284.
(57) Zähringer, T. J. B.; Moghtader, J. A.; Bertrams, M. S.; Roy, B.; Uji, M.; Yanai, N.; Kerzig, C. Blue-to-UVB Upconversion, Solvent Sensitization and Challenging Bond Activation Enabled by a Benzene-Based Annihilator. *Angew. Chem., Int. Ed. Engl.* **2023**, *62* (8), No. e202215340.
(58) Mims, D.; Herpich, J.; Lukzen, N. N.; Steiner, U. E.; Lambert, C. Readout of Spin Quantum Beats in a Charge-Separated Radical Pair by Pump-Push Spectroscopy. *Science* **2021**, *374* (6574), 1470–1474.
(59) Han, G.; Li, G.; Huang, J.; Han, C.; Turro, C.; Sun, Y. Two-Photon-Absorbing Ruthenium Complexes Enable near Infrared Light-Driven Photocatalysis. *Nat. Commun.* **2022**, *13* (1), 2288.
(60) Hammond, G. S.; Saltiel, Jack; Lamola, A. A.; Turro, N. J.; Bradshaw, J. S.; Cowan, D. O.; Counsell, R. C.; Vogt, Volker; Dalton, Christopher Mechanisms of Photochemical Reactions in Solution. XXII. [1] Photochemical *Cis-Trans* Isomerization. *J. Am. Chem. Soc.* **1964**, *86* (16), 3197–3217.
(61) Unett, D. J.; Caldwell, R. A. The Triplet State of Alkenes: Structure, Dynamics Energetics and Chemistry. *Res. Chem. Intermed.* **1995**, *21* (7), 665–709.
(62) Hammond, G. S.; Saltiel, Jack Photosensitized *Cis-Trans* Isomerization of the Stilbenes. *J. Am. Chem. Soc.* **1962**, *84* (24), 4983–4984.
(63) Arai, Tatsuo; Tokumaru, Katsumi Photochemical One-Way Adiabatic Isomerization of Aromatic Olefins. *Chem. Rev.* **1993**, *93* (1), 23–39.
(64) Caldwell, R. A.; Pac, C. An Olefin Triplet Lifetime Measurement by Electron Transfer Interception. *Chem. Phys. Lett.* **1979**, *64* (2), 303–306.
(65) Caldwell, R. A.; Cao, C. V. Structural Effects on Twisted Olefin Triplet Lifetimes Styrene Derivatives. *J. Am. Chem. Soc.* **1982**, *104* (23), 6174–6180.
(66) Caldwell, R. A.; Singh, M. Lifetimes of Conjugated Diene Triplets. *J. Am. Chem. Soc.* **1982**, *104* (22), 6121–6122.
(67) Bonneau, R. Cis—Trans Isomerization of Styrenes via the Triplet Pathway: The Perpendicular Triplet State Observed by Laser Flash Photolysis. *J. Photochem.* **1979**, *10* (6), 439–449.
(68) Goerner, H. Triplet States of Phenylethylenes in Solution. Energies, Lifetimes, and Absorption Spectra of 1,1-Diphenyl-, Triphenyl-, and Tetraphenylethylene Triplets. *J. Phys. Chem.* **1982**, *86* (11), 2028–2035.
(69) Scaiano, J. C. A Beginners Guide to Understanding the Mechanisms of Photochemical Reactions: Things You Should Know If Light Is One of Your Reagents. *Chem. Soc. Rev.* 2023, DOI: 10.1039/D3CS00453H.
(70) Coles, M. S.; Quach, G.; Beves, J. E.; Moore, E. G. A Photophysical Study of Sensitization-Initiated Electron Transfer: Insights into the Mechanism of Photoredox Activity. *Angew. Chem., Int. Ed.* **2020**, *59* (24), 9522–9526.
(71) Neumann, S.; Wenger, O. S.; Kerzig, C. Controlling Spin-Correlated Radical Pairs with Donor–Acceptor Dyads: A New Concept to Generate Reduced Metal Complexes for More Efficient Photocatalysis. *Chem. – Eur. J.* **2021**, *27*, 4115–4123.
(72) Ting, S. I.; Garakyaraghi, S.; Taliaferro, C. M.; Shields, B. J.; Scholes, G. D.; Castellano, F. N.; Doyle, A. G. ^{3} d-d Excited States of Ni(II) Complexes Relevant to Photoredox Catalysis: Spectroscopic Identification and Mechanistic Implications. *J. Am. Chem. Soc.* **2020**, *142* (12), 5800–5810.
(73) Romero, N. A.; Nicewicz, D. A. Mechanistic Insight into the Photoredox Catalysis of Anti-Markovnikov Alkene Hydrofunctionalization Reactions. *J. Am. Chem. Soc.* **2014**, *136* (49), 17024–17035.
(74) Budzák, Š.; Jovaišaitė, J.; Huang, C. Y.; Baronas, P.; Tulaitė, K.; Juršėnas, S.; Jacquemin, D.; Hecht, S. Mechanistic Insights into the Photoisomerization of *N,N′* -Disubstituted Indigos. *Chemistry* **2022**, *28* (26), No. e202200496.
(75) Noël, T.; Zysman-Colman, E. The Promise and Pitfalls of Photocatalysis for Organic Synthesis. *Chem. Catal.* **2022**, *2* (3), 468–476.
(76) Bhattacherjee, A.; Sneha, M.; Lewis-Borrell, L.; Tau, O.; Clark, I. P.; Orr-Ewing, A. J. Picosecond to Millisecond Tracking of a Photocatalytic Decarboxylation Reaction Provides Direct Mechanistic Insights. *Nat. Commun.* **2019**, *10* (1), 5152.
(77) Sittel, S.; Sell, A. C.; Hofmann, K.; Wiedemann, C.; Nau, J. P.; Kerzig, C.; Manolikakes, G.; Heinze, K. Visible-Light Induced Fixation of SO_2 into Organic Molecules with Polypyridine Chromium(III) Complexes. *ChemCatChem* **2023**, *15* (6), No. e202201562.
(78) Bortolato, T.; Cuadros, S.; Simionato, G.; Dell'Amico, L. The Advent and Development of Organophotoredox Catalysis. *Chem. Commun.* **2022**, *58* (9), 1263–1283.
(79) Speckmeier, E.; Fischer, T. G.; Zeitler, K. A Toolbox Approach To Construct Broadly Applicable Metal-Free Catalysts for Photoredox Chemistry: Deliberate Tuning of Redox Potentials and

Importance of Halogens in Donor−Acceptor Cyanoarenes. *J. Am. Chem. Soc.* **2018**, *140* (45), 15353−15365.
(80) Bryden, M. A.; Millward, F.; Matulaitis, T.; Chen, D.; Villa, M.; Fermi, A.; Cetin, S.; Ceroni, P.; Zysman-Colman, E. Moving Beyond Cyanoarene Thermally Activated Delayed Fluorescence Compounds as Photocatalysts: An Assessment of the Performance of a Pyrimidyl Sulfone Photocatalyst in Comparison to 4CzIPN. *J. Org. Chem.* **2023**, *88* (10), 6364−6373.
(81) Romero, N. A.; Nicewicz, D. A. Organic Photoredox Catalysis. *Chem. Rev.* **2016**, *116* (17), 10075−10166.
(82) Burget, D.; Jacques, P. Dramatic Solvent Effects on Thioxanthone Fluorescence Lifetime. *J. Lumin.* **1992**, *54* (3), 177−181.
(83) Allonas, X.; Ley, C.; Bibaut, C.; Jacques, P.; Fouassier, J. P. Investigation of the Triplet Quantum Yield of Thioxanthone by Time-Resolved Thermal Lens Spectroscopy: Solvent and Population Lens Effects. *Chem. Phys. Lett.* **2000**, *322* (6), 483−490.
(84) Yates, S. F.; Schuster, G. B. Photoreduction of Triplet Thioxanthone by Amines: Charge Transfer Generates Radicals That Initiate Polymerization of Olefins. *J. Org. Chem.* **1984**, *49* (18), 3349−3356.
(85) Rodrigues, M. R.; Neumann, M. G. Mechanistic Study of Tetrahydrofuran Polymerization Photoinitiated by a Sulfonium Salt/Thioxanthone System. *Macromol. Chem. Phys.* **2001**, *202* (13), 2776−2782.
(86) Allen, N. S.; Catalina, F.; Green, P. N.; Green, W. A. Photochemistry of Thioxanthones—IV. Spectroscopic and Flash Photolysis Study on Novel n-Propoxy and Methyl, n-Propoxy Derivatives. *Eur. Polym. J.* **1986**, *22* (10), 793−799.
(87) Halpern, A. M.; Forsyth, D. A.; Nosowitz, M. Flash Photolysis of Saturated Amines in Acetonitrile Solution at 248 Nm: Formation of Radical Cations. *J. Phys. Chem.* **1986**, *90* (12), 2677−2679.
(88) Luque, A.; Groß, J.; Zähringer, T. J. B.; Kerzig, C.; Opatz, T. Vinylcyclopropane [3 + 2] Cycloaddition with Acetylenic Sulfones Based on Visible Light Photocatalysis. *Chem.—Eur. J.* **2022**, *28* (18), No. e202104329.
(89) Fang, C.; Oruganti, B.; Durbeej, B. How Method-Dependent Are Calculated Differences between Vertical, Adiabatic, and 0−0 Excitation Energies? *J. Phys. Chem. A* **2014**, *118* (23), 4157−4171.
(90) Snyder, J. J.; Tise, F. P.; Davis, R. D.; Kropp, P. J. Photochemistry of Alkenes. 7. E.Dblarw. Z Isomerization of Alkenes Sensitized with Benzene and Derivatives. *J. Org. Chem.* **1981**, *46* (18), 3609−3611.
(91) Wang, C.; Reichenauer, F.; Kitzmann, W. R.; Kerzig, C.; Heinze, K.; Resch-Genger, U. Efficient Triplet-Triplet Annihilation Upconversion Sensitized by a Chromium(III) Complex via an Underexplored Energy Transfer Mechanism. *Angew. Chem., Int. Ed.* **2022**, *61* (27), No. e202202238.
(92) Kerzig, C.; Goez, M. Highly Efficient Green-Light Ionization of an Aryl Radical Anion: Key Step in a Catalytic Cycle of Electron Formation. *Phys. Chem. Chem. Phys.* **2014**, *16* (46), 25342−25349.
(93) Caldwell, R. A. Intersystem Crossing in Organic Photochemical Intermediates. *Pure Appl. Chem.* **1984**, *56* (9), 1167−1177.
(94) Gray, V.; Dreos, A.; Erhart, P.; Albinsson, B.; Moth-Poulsen, K.; Abrahamsson, M. Loss Channels in Triplet−Triplet Annihilation Photon Upconversion: Importance of Annihilator Singlet and Triplet Surface Shapes. *Phys. Chem. Chem. Phys.* **2017**, *19* (17), 10931−10939.
(95) Harada, N.; Sasaki, Y.; Hosoyamada, M.; Kimizuka, N.; Yanai, N. Discovery of Key TIPS-Naphthalene for Efficient Visible-to-UV Photon Upconversion under Sunlight and Room Light**. *Angew. Chem., Int. Ed.* **2021**, *60* (1), 142−147.
(96) Herkstroeter, W. G.; Hammond, G. S. Mechanisms of Photochemical Reactions in Solution. XXXIX. [1] Study of Energy Transfer by Kinetic Spectrophotometry. *J. Am. Chem. Soc.* **1966**, *88* (21), 4769−4777.
(97) Balzani, V.; Bolletta, F.; Scandola, F. Vertical and "Nonvertical" Energy Transfer Processes. A General Classical Treatment. *J. Am. Chem. Soc.* **1980**, *102* (7), 2152−2163.
(98) Edhborg, F.; Olesund, A.; Albinsson, B. Best Practice in Determining Key Photophysical Parameters in Triplet−Triplet Annihilation Photon Upconversion. *Photochem. Photobiol. Sci.* **2022**, *21* (7), 1143−1158.
(99) Sandros, K.; Haglid, F.; Ryhage, R.; Ryhage, R.; Stevens, R. Transfer of Triplet State Energy in Fluid Solutions. III. Reversible Energy Transfer. *Acta Chem. Scand.* **1964**, *18*, 2355−2374.
(100) Vlcek, A. A.; Dodsworth, E. S.; Pietro, W. J.; Lever, A. B. P. Excited State Redox Potentials of Ruthenium Diimine Complexes; Correlations with Ground State Redox Potentials and Ligand Parameters. *Inorg. Chem.* **1995**, *34* (7), 1906−1913.
(101) Juris, A.; Balzani, V.; Barigelletti, F.; Campagna, S.; Belser, P.; Von Zelewsky, A. Ru(II) Polypyridine Complexes: Photophysics, Photochemistry, Eletrochemistry, and Chemiluminescence. *Coord. Chem. Rev.* **1988**, *84*, 85−277.
(102) Uji, M.; Harada, N.; Kimizuka, N.; Saigo, M.; Miyata, K.; Onda, K.; Yanai, N. Heavy Metal-Free Visible-to-UV Photon Upconversion with over 20% Efficiency Sensitized by a Ketocoumarin Derivative. *J. Mater. Chem. C* **2022**, *10* (12), 4558−4562.
(103) Cambié, D.; Dobbelaar, J.; Riente, P.; Vanderspikken, J.; Shen, C.; Seeberger, P. H.; Gilmore, K.; Debije, M. G.; Noël, T. Energy-Efficient Solar Photochemistry with Luminescent Solar Concentrator Based Photomicroreactors. *Angew. Chem., Int. Ed.* **2019**, *58* (40), 14374−14378.
(104) Hörmann, F. M.; Kerzig, C.; Chung, T. S.; Bauer, A.; Wenger, O. S.; Bach, T. Triplet Energy Transfer from Ruthenium Complexes to Chiral Eniminium Ions: Enantioselective Synthesis of Cyclobutanecarbaldehydes by [2 + 2] Photocycloaddition. *Angew. Chem., Int. Ed.* **2020**, *59* (24), 9659−9668.
(105) Johnston, L. J.; Scaiano, J. C. Time-Resolved Studies of Biradical Reactions in Solution. *Chem. Rev.* **1989**, *89* (3), 521−547.
(106) Abe, M. Diradicals. *Chem. Rev.* **2013**, *113* (9), 7011−7088.

Geometric isomerization of bifunctional alkenyl fluoride linchpins: stereodivergence in amide and polyene bioisostere synthesis

The amide functional group plays a central role in the architecture of biomolecules, including numerous clinically approved pharmaceuticals.[226] Fluoroalkenes have emerged as highly effective amide bond isosteres, closely mimicking the electronic profile of the amide linkage while offering enhanced metabolic stability at enzymatically labile sites.[227] As with natural amides, the stereochemistry of alkenyl fluorides can govern the biological activity of the molecule.[228] Typically, the *Z*-isomer is thermodynamically favored and therefore readily accessible.[229] While several sophisticated catalytic strategies have been developed to control the stereoselective synthesis of these motifs, there remains a lack of simple and general methods for *Z*→*E* isomerization.[230] This issue was addressed in the second project **[F]**, applying a similar approach as in project **[E]** to fluorinated alkenylboronates.

Summary:

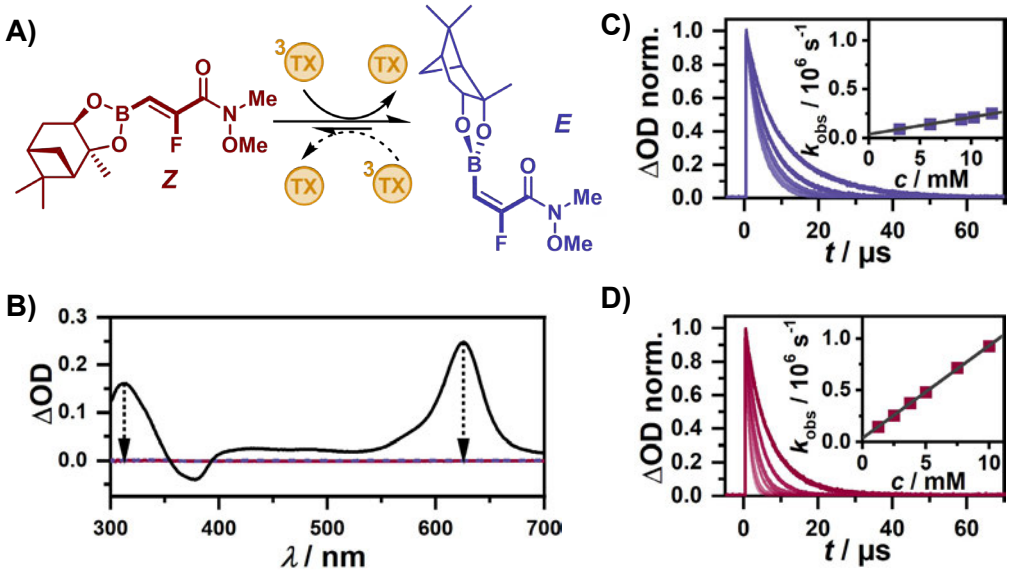

Figure 18: Mechanistic studies of the fluorinated Weinreb amide isomers *Z* and *E* using TA spectroscopy. A) Postulated mechanism with TX as triplet photosensitizer. B) TA spectra recorded before (black) and after complete quenching of TX with *Z* and *E*. The arrows indicate the return to the base line level C) and D) Color-coded Stern–Volmer analyses of TX with *E* (blue) and *Z* (red) as quencher.

The second project **[F]** focused on the *Z*→*E* photoisomerization of fluorinated *β*-borylacrylates, designed as amide-analogous structural motifs. The Weinreb amide derivative Z was subjected to irradiation in the presence of a range of organic triplet photosensitizers (Figure 18A). Among these, thioxanthone delivered the highest isomerization efficiency and selectivity. TA measurements confirmed TTET from thioxanthone to the alkene based on the absence of TX-derived photoproducts of hydrogen atom or electron transfer (Figure 18B). Moreover, the TTET rates correlated well with the *Z*/*E* ratios observed in the irradiation experiments (Figure 18C and D). These findings were consistent with the relative triplet state energies of the *Z*- and *E*-isomers as calculated by DFT.

A substrate scope study, including various substitution patterns at the amide moiety and the introduction of a *β*-methyl group (resulting in a tetrasubstituted alkene), demonstrated the broad applicability and robustness of the methodology. X-ray crystallography further validated the proposed 90° rotation of the C(sp²)–B bond and bifurcation of the alkene, which leads to $n_o \rightarrow p_B$ stabilization effects. The synthetic utility of the reaction was showcased through its seamless integration into the synthesis of fluorinated retinoid analogues, highlighting its potential in complex molecule construction.

Project **[F]** was published as a research article:

"**Geometric Isomerisation of Bifunctional Alkenyl Fluoride Linchpins: Stereodivergence in Amide and Polyene Bioisostere Synthesis**"

Reproduced from Reference: M. Wienhold, B. Kweon, C. McLaughlin, M. Schmitz, T. J. B. Zähringer, C. G. Daniliuc, C. Kerzig, R. Gilmour, *Angew. Chem. Int. Ed.* **2023**, *135*, e202304150.

The article is Open Access and licensed under CC BY-NC 4.0 (https://creativecommons.org/licenses/by/4.0/) and can be cited corresponding to ref.[F]. The reference is attached in the following pages and the supporting information can be found in Chapter 10.7.

Author Contributions: R. Gilmour conceived the Project and provided overall guidance. M. Wienhold, B. Kweon, and C. McLaughlin conducted the synthesis of the fluorinated alkenes, performed the irradiation experiments, and explored the substrate scope. C. G. Daniliuc carried out the X-ray crystallographic analyses. M. Schmitz was responsible for the DFT calculations under the supervision of C. Kerzig. Transient absorption measurements were performed by T. J. B. Zähringer under the supervision of C. Kerzig.

Check for updates

How to cite: *Angew. Chem. Int. Ed.* **2023**, *62*, e202304150
doi.org/10.1002/anie.202304150

Fluorine Chemistry | Hot Paper

Geometric Isomerisation of Bifunctional Alkenyl Fluoride Linchpins: Stereodivergence in Amide and Polyene Bioisostere Synthesis

Max Wienhold, Byeongseok Kweon, Calum McLaughlin, Matthias Schmitz, Till J. B. Zähringer, Constantin G. Daniliuc, Christoph Kerzig, and Ryan Gilmour**

Dedicated to Professor Erick M. Carreira on the occasion of his 60th birthday

Abstract: Amide groups are pervasive across the chemical space continuum, where their structural and pharmacological importance, juxtaposed with the hydrolytic vulnerabilities, continues to fuel bioisostere development. Alkenyl fluorides have a venerable history as effective mimics (Ψ[CF=CH]) owing to the planarity of the motif and intrinsic polarity of the C(sp^2)–F bond. However, emulating the *s-cis* to the *s-trans* isomerisation of a peptide bond with fluoro-alkene surrogates remains challenging, and current synthetic solutions only enable access to a single configuration. Through the design of an ambiphilic linchpin based on a fluorinated β-borylacrylate, it has been possible to leverage energy transfer catalysis to affect this unprecedented isomerisation process: this provides geometrically-programmable building blocks that can be functionalised at either terminus. Irradiation at $\lambda_{max} = 402$ nm with inexpensive thioxanthone as a photocatalyst enables rapid, effective isomerisation of tri- and tetra-substituted species (up to *E*/*Z* 98:2 in 1 h), providing a stereodivergent platform for small molecule amide and polyene isostere discovery. Application of the methodology in target synthesis and initial laser spectroscopic studies are disclosed together with crystallographic analyses of representative products.

Introduction

The evolutionary success of amides in the bioactive natural product repertoire has galvanised interest in emulating this venerable structural motif through bioisostere design.[1] In contemporary drug discovery, this strategy enables the pharmacological advantages of leveraging peptide bonds to be reconciled with their metabolic susceptibilities in vivo.[2] Whilst effective mimesis requires the electronic and structural footprint of the parent motif to be recreated, amides present an additional stereochemical challenge on account of *s-cis* to *s-trans* isomerisation.[3] This conspicuous feature of the amide bond is particularly relevant when biological function is encoded by configuration.[4] Alkenyl fluorides Ψ[CF=CH] have proven to be highly effective amide bond isosteres, where the polar nature of the C(sp^2)–F bond enables the steric and electronic signature of the native motif to be simulated (Figure 1A).[5] This ability to concurrently regulate configuration and protect enzymatically vulnerable sites[6] has been expertly leveraged to enhance the hydrolytic stability of HDAC inhibitors[7] and to increase plasma and microsomal stability in peptide mimetics such as Tyr^1-Ψ[(Z)CF=CH]–Gly^2 Leu-enkephalin (Figure 1B).[8] In the realm of kinase inhibitor design, installation of the *E*-fluoro-enone motif in 5-fluoroenoneresorcynolide has been advantageous in safeguarding the structural integrity of the API.[9]

A compelling example of the importance of alkenyl fluoride configuration on biological activity is illustrated by comparing the respective IC_{50} values of factor Xa inhibitors.[10] A seemingly subtle inversion of alkene geometry, from the *Z*- to *E*-isomer, results in a 60-fold enhancement, thereby demonstrating the value of sterodivergence platforms in enhancing bioactivity.

This strategic importance of mono-fluoro olefins in functional small molecule discovery continues to provide a powerful impetus for selective reaction development. Olefination strategies[11–14] have been key facilitators in enabling alkenyl fluorides to be validated as amide bond isosteres, but achieving satisfactory levels of stereocontrol continue to limit application. Whilst most methods favor formation of the (often lower-energy) *Z*-isomer,[15] strategies to enable the stereoselective preparation of the corresponding *E*-isomer are rare[16] and often suffer from scope limitations. These stoichiometric approaches have been complemented by advances in alkene cross metathesis[17–19] and selective defluoroborylation,[20] thereby allowing stereoselectivity to be regulated at the catalyst level. However, to the best of our knowledge, strategies to enable the simple *Z*→*E* isomer-

[*] M. Wienhold, B. Kweon, Dr. C. McLaughlin, Dr. C. G. Daniliuc, Prof. Dr. R. Gilmour
Organisch Chemisches Institut, Westfälische Wilhelms-Universität Münster
Corrensstraße 36, 48149 Münster (Germany)
E-mail: ryan.gilmour@uni-muenster.de
M. Schmitz, T. J. B. Zähringer, Prof. Dr. C. Kerzig
Department of Chemistry, Johannes Gutenberg University Mainz
Duesbergweg 10–14, 55128 Mainz (Germany)
E-mail: ckerzig@uni-mainz.de

© 2023 The Authors. Angewandte Chemie International Edition published by Wiley-VCH GmbH. This is an open access article under the terms of the Creative Commons Attribution License, which permits use, distribution and reproduction in any medium, provided the original work is properly cited.

© 2023 The Authors. Angewandte Chemie International Edition published by Wiley-VCH GmbH

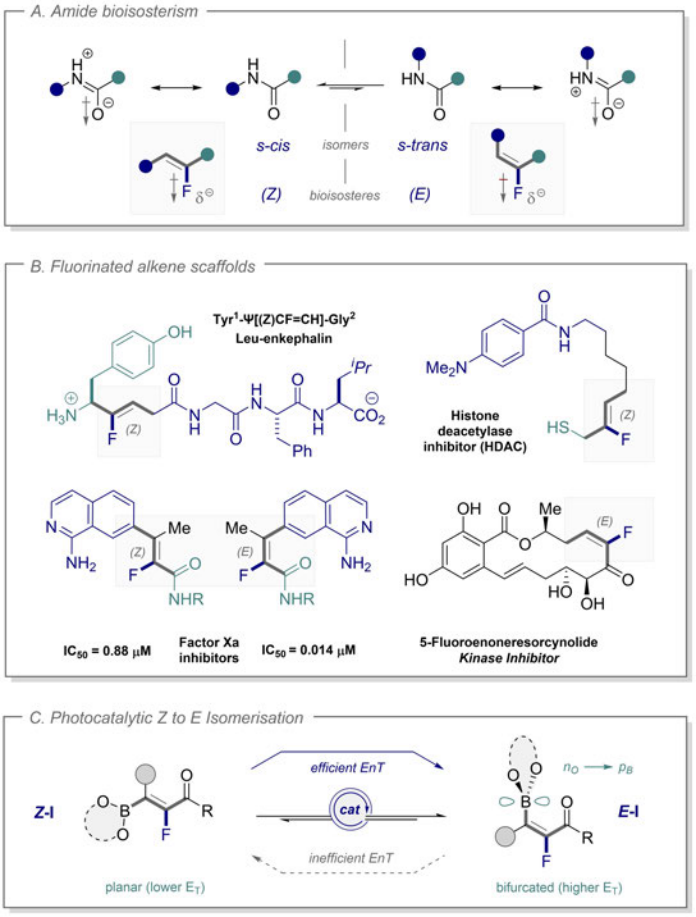

Figure 1. Alkenyl fluorides as amide bond bioisosteres and selected bioactive small molecules containing this structural motif.

isation of alkenyl fluorides are conspicuous in their absence (Figure 1C). Not only would this platform emulate the behavior of the native scaffold, but it would also mitigate the lengthy synthesis campaigns required to access both isomers independently.[5,21]

It was therefore envisaged that fluorinated β-boryl acrylates, such as ***Z*-I**, would be appealing starting materials from which to develop an operationally simple isomerisation protocol based on selective energy transfer catalysis.[22–24] Identification of an appropriate small molecule sensitizer would then allow selective excitation of the *Z*-isomer and accumulation of the desired *E*-configured product. In the starting *Z*-isomer, the planar chromophore includes the vacant *p*-orbital of the boron substituent, whereas Lewis-type $n_O \rightarrow p_B$ interactions bifurcates the chromophore in the product *E*-isomer. This results in 90° rotation of the C(sp^2)–B bond raises the triplet energy of the product and provides a foundation for directionality. In addition to their well-defined photophysical properties, these ambiphilic linchpins lend themselves to bidirectional, post-isomerisation functionalisation through stereospecific cross coupling and carbonyl modification chemistry. Furthermore, by extending the tri-substituted series to tetra-substitution,[25] analogs might be generated that would be suitable as both tertiary amides and as alkene surrogates for fluoro-mimetic development.[26]

Results and Discussion

Despite the efficiency of isomerisation in non-fluorinated systems,[22,23] we were acutely aware that fluorine incorporation would present a significant challenge in the working blueprint: structurally related aryl boronic esters and acids bearing halogen substituents in the *ortho*-position are susceptible to a range of decomposition pathways.[27] Consequently, the robust pinanediol boronic ester was selected for further exploration. To validate the working hypothesis, the conversion of ***Z*-1** to ***E*-1** was investigated using a range of simple organic photosensitizers with varying triplet energies (Table 1). Whilst initial attempts to affect isomerisation with 9-fluorenone ($\lambda = 402$ nm) proved to be unsuccessful ($E:Z = 8:92$, Table 1, entry 1), catalysts with higher triplet energies proved to be more effective. Isomerisation with Michler's ketone ($\lambda = 365$ nm) led to an enhanced selectivity ($E:Z = 54:46$, entry 2) albeit at the expense of the yield. Extending the trend further to catalysts with higher triplet energies, such as thioxanthone and benzophenone, enabled the desired product to be obtained with good

© 2023 The Authors. Angewandte Chemie International Edition published by Wiley-VCH GmbH

15213773, 2023, 27, Downloaded from https://onlinelibrary.wiley.com/doi/10.1002/anie.202304150 by Universitätsbibliothek Mainz, Wiley Online Library on [16/06/2025]. See the Terms and Conditions (https://onlinelibrary.wiley.com/terms-and-conditions) on Wiley Online Library for rules of use; OA articles are governed by the applicable Creative Commons License

Table 1: Reaction optimisation of the energy transfer-enabled isomerisation.[a]

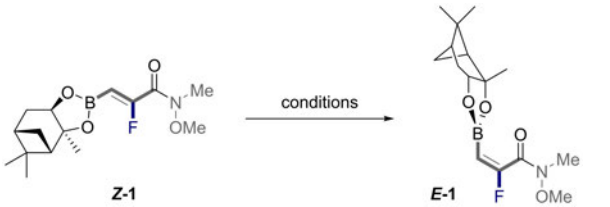

entry	catalyst	wavelength λ [nm]	E_T [kJ mol^{-1}]	yield [%][b]	E/Z[c]
1	9-fluorenone	402	223	98	8:92
2	Michler's Ketone	365	255	27	54:46
3	thioxanthone	402	265	87	91:9
4	benzophenone	365	289	90	94:6
5[d]	benzophenone	365	289	60	60:40
6[d]	thioxanthone	402	265	86 (53)	95:5
7[d]	thioxanthone	/	265	>98	<1:99
8[d]	/	402	/	>98	<1:99

[a] Reactions were conducted in MeCN under irradiation for 16 h. [b] Determined by ^{1}H NMR using 1,3,5-trimethoxybenzene as the internal standard; isolated yield reported in parenthesis. [c] Determmined from the crude reaction mixture. [d] Reaction time 1 h.

yields and selectivities ($E:Z$ = 91:9 and = 94:6, entries 3 and 4) after 16 h. Although reactions with benzophenone required extended reaction times (entry 4 versus 5), it was possible to reach high levels of selectivity after only 1 h with thioxanthone (entry 6, E/Z 95:5). Moreover, control reactions in the absence of light and photocatalysts support the postulated energy transfer paradigm (entries 7 and 8).

The presence of the fluorine atom allowed the conversion of ***Z-1*** (−93.64 ppm) to ***E-1*** (−84.52 ppm) to be conveniently monitored by time course ^{19}F NMR spectroscopy. As is evident from Figure 2, the isomerisation proceeds smoothly and the photostationary composition is reached after 60 minutes.

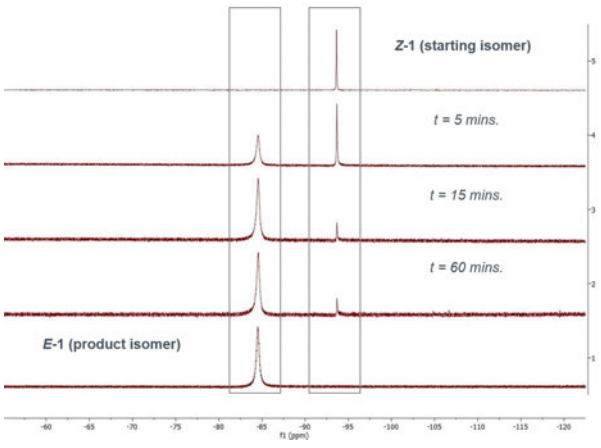

Figure 2. Time course study of the photochemical isomerisation. From top to bottom: [5] Starting material ***Z-1***, [4] Reaction mixture after 5 min irradiation time, [3] Reaction mixture after 15 min irradiation time, [2] Reaction mixture after 60 min irradiation time, [1] Isolated product ***E-1***.

To establish the scope and limitations of the photocatalytic isomerisation of alkenyl fluorides, the impact of modifying the carbonyl substituent was explored (Figure 3).

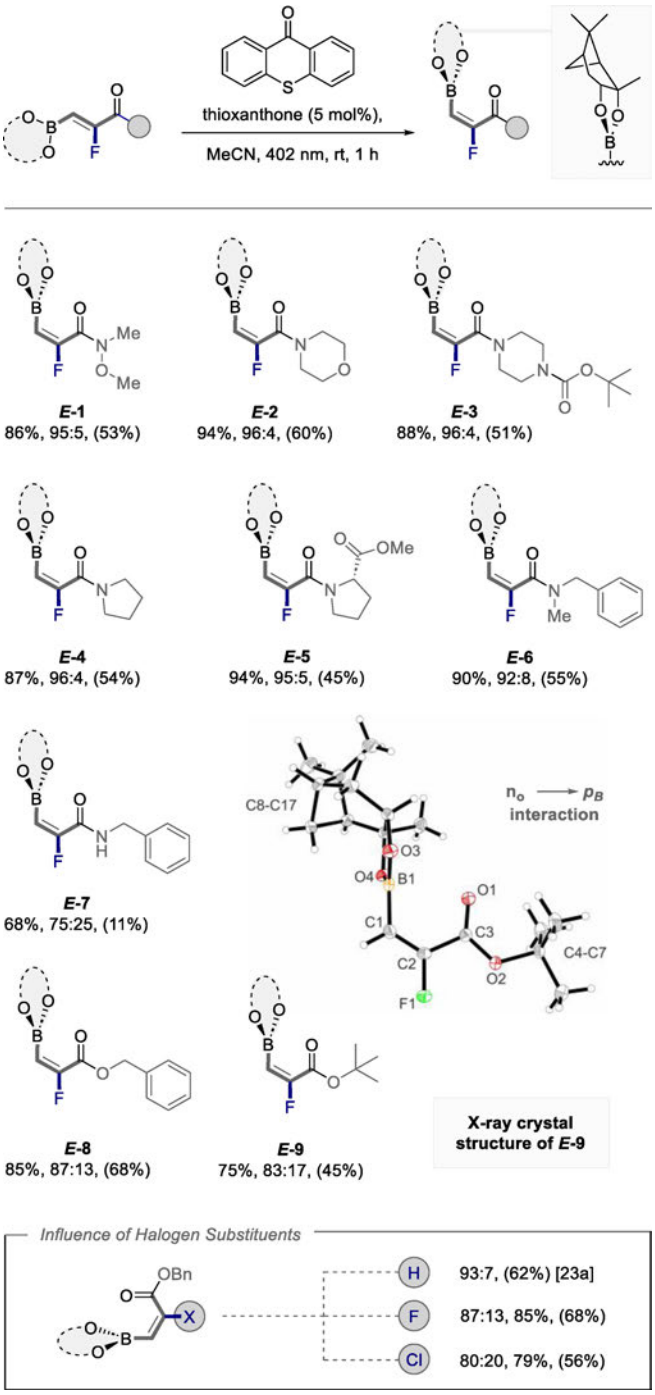

Figure 3. Scope and limitations of the energy transfer-enabled isomerisation and X-ray crystal structure analysis illustrating the origin of selectivity. Thermal ellipsoids are shown at 50% probability. Isolated yields given in parenthesis. $E:Z$ ratios determined by ^{1}H NMR spectroscopy of the crude reaction mixture. Isolated yield of major isomer.

© 2023 The Authors. Angewandte Chemie International Edition published by Wiley-VCH GmbH

15213773, 2023, 27, Downloaded from https://onlinelibrary.wiley.com/doi/10.1002/anie.202304150 by Universitätsbibliothek Mainz, Wiley Online Library on [16/06/2025]. See the Terms and Conditions (https://onlinelibrary.wiley.com/terms-and-conditions) on Wiley Online Library for rules of use; OA articles are governed by the applicable Creative Commons License

Replacing the Weinreb amide (***E*-1**, *E*/*Z* 95:5) by cyclic secondary amides was found to have little effect on the reaction outcome. This enabled morpholine ***E*-2** and piperidine ***E*-3** to be prepared with high levels of *E*-selectivity (*E*/*Z* 96:4). The ring size also proved to be inconsequential, with the pyrolidine (***E*-4**) and proline (***E*-5**) derivatives being generated with *E*/*Z* selectivities of 96:4 and 95:5, respectively.

Acyclic amides were also found to be compatible with the reaction conditions (***E*-6**, *E*:*Z* 92:8) but it is interesting to note that the isomerisation of secondary amides, such as ***E*-7**, occurred with a reduction in selectivity (*E*:*Z* 75:25). Extension of the scope to esters was also possible as is illustrated by the benzyl and *tert*-butyl derivatives ***E*-8** and ***E*-9**, respectively.

Gratifyingly it was possible to isolate a crystal of ***E*-9** that was suitable for X-ray crystallographic analysis.[28] This revealed a 90° rotation of the C(sp^2)–B bond to allow for a stabilising interaction between the oxygen of the carbonyl group and the empty *p*-orbital of the boron substituent (please see Figure 4, bottom and the Supporting Information).

Bifurcation of the chromophore raises the triplet energy, thereby providing a structural foundation to rationalise selective energy transfer. This triplet energy change was confirmed by kinetic measurements and DFT calculations (see mechanistic studies for Weinreb amide **1** presented below). It is pertinent to note that the B–O distance between the boron and the carbonyl oxygen in compounds ***E*-9** and ***Z*-14** is almost identical (B1–O1: 2.646 Å for ***E*-9** and B1–O3: 2.657 Å for ***Z*-14**, respectively), and the boron coordination geometry remains trigonal planar.

To investigate the impact of the halogen substituent on the efficiency of the energy transfer process, a comparative analysis of the H, F, Cl series based on compound ***E*-8** was conducted (Figure 3, bottom). Under the standard reaction conditions, the photostationary state composition of the non-halogenated species was highest (*Z*:*E* = 93:7), and systematic decreases in selectivity were observed in the order H > F > Cl. This experimental observation is in line with the impact of *para*-substituents on the triplet energies of *trans*-stilbenes, which follow the order H ≥ F > Cl > Br > I.[29]

To further expand the method to tetrasubstituted alkenes, a series of β-Me derivatives were exposed to the standard isomerisation conditions (Figure 4). Gratifyingly, it was possible to isolate ***Z*-10** in 70 % yield with high levels of stereoselectivity (*Z*:*E* 93:7). Moreover, replacing the Weinreb amide by an ester functionality did not impede the reaction, and allowed ***Z*-11** to be generated with a *Z*/*E*-ratio of 98:2. The reaction conditions were also found to be compatible with pinacol boronic esters such as the Weinreb amide ***Z*-12** and tertiary amide ***Z*-13** (up to *Z*:*E* = 94:6).

Crystal structure analysis of the substrate and product isomers ***E*-14**[28] and ***Z*-14**[28] provided an additional insight to support the proposed origin of selectivity. In the starting *E*-isomer, the chromophore is fully conjugated with the boron *p*-orbital aligned with the enone π-system. Upon isomerisation, the C(sp^2)–B bond is no longer in conjugation but

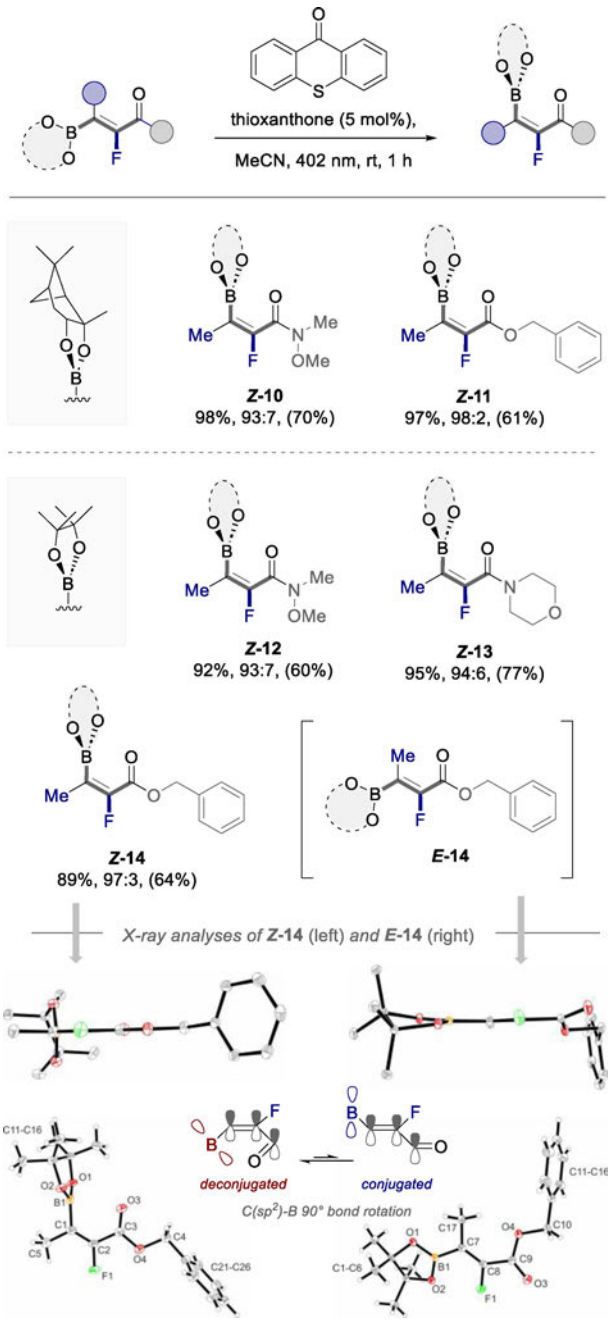

Figure 4. Scope and limitations of the energy transfer-catalysed isomerisation of tetra-substituted alkenes and crystal structure analysis to rationalise the origin of selectivity. Thermal ellipsoids are shown at 50% probability. Isolated yields given in parenthesis. *E*:*Z* ratios determined by ^{1}H NMR spectroscopy of the crude reaction mixture. Please note that the IUPAC descriptors (*E* and *Z*) are inverted relative to Figure 3 on account of the higher priority of the methyl group versus B (In Figure 4, C > B; In Figure 3 B > H).

lies orthogonal to the π-orbitals. The bifurcation of the chromophore is compensated by a stabilising $n_O \rightarrow p_B$ interaction, which prevents re-excitation and allows the two alkene isomers to be photochemically distinguished.

To demonstrate the synthetic utility of the isomerisation in synthesis, the stereocontrolled construction of retinoid-

© 2023 The Authors. Angewandte Chemie International Edition published by Wiley-VCH GmbH

15213773, 2023, 27, Downloaded from https://onlinelibrary.wiley.com/doi/10.1002/anie.202304150 by Universitätsbibliothek Mainz, Wiley Online Library on [16/06/2025]. See the Terms and Conditions (https://onlinelibrary.wiley.com/terms-and-conditions) on Wiley Online Library for rules of use; OA articles are governed by the applicable Creative Commons License

like fluorinated polyenes was conducted (Scheme 1).[30] To that end, aryl bromide **15** was prepared in two steps from commercial 2-bromophenol, and subjected to a stereospecific cross-coupling with ***Z*-10** to yield Weinreb amide **16** in 74 % yield. The configuration of the fluoroalkene was unequivocally established by single crystal X-ray diffraction.[28] This simple sequence illustrates the value of the C(sp^2)-substituent as a traceless chromophore extension. Following the successful installation of the first fluorinated alkene unit in a *Z*-selective fashion, subsequent reduction of the Weinreb amide was conducted to generate aldehyde **17**. Utilising the elegant boron-Wittig reaction developed by Morken and co-workers,[31] boronic ester **18** was synthesised in 68 % yield. Subsequent bromodeboronation provided access to the intermediate vinyl bromide **19** in preparation for subsequent coupling events. From this common precursor, a second stereospecific coupling reaction with ***E*-20** was performed to generate triene **21**, which is an analogue of the potential type 2 diabetes treatment CS018.[32] To further illustrate the modularity of this approach to fluorinated polyenes, bromine **19** was unified with ***E*-9** to yield the difluorinated triene **22** in 78 % yield.

Finally, the photoisomerisation was investigated by laser flash photolysis (LFP, see Supporting Information for details). Mechanistic studies with thioxanthone (TX) as the catalyst cannot be performed via straightforward emission quenching experiments owing to the non-emissive nature of its photoactive triplet state. Therefore, the sensitised isomerisation by TX of ***E*-1** and ***Z*-1** was studied by LFP with 355 nm laser pulses (Figure 5A) ensuring selective TX excitation. The triplet state of TX is characterised by two main absorption peaks at 315 nm and 625 nm that are

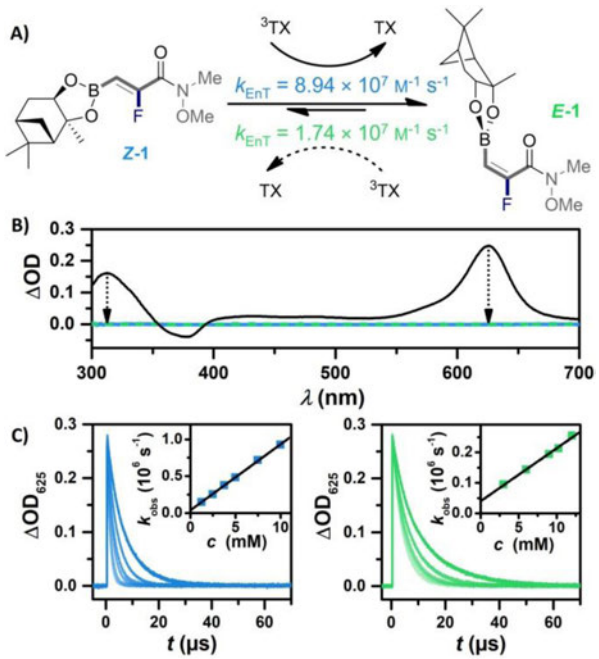

Figure 5. Sensitised isomerisation of ***E*-1** and ***Z*-1** studied by LFP with 355 nm laser pulses in deaerated MeCN. A) Structures and triplet-triplet energy transfer rates using TX as sensitiser. B) TA spectra of 50 μM TX (black, recorded 1 μs after excitation) in the absence of quencher and with 10 mM ***E*-1** (green, recorded 40 μs after excitation) or ***Z*-1** (blue, recorded 11 μs after excitation). C) Quenching experiments of ^{3}TX with varying concentrations of ***Z*-1** (left) and ***E*-1** (right). Inset: Corresponding Stern–Volmer analysis.

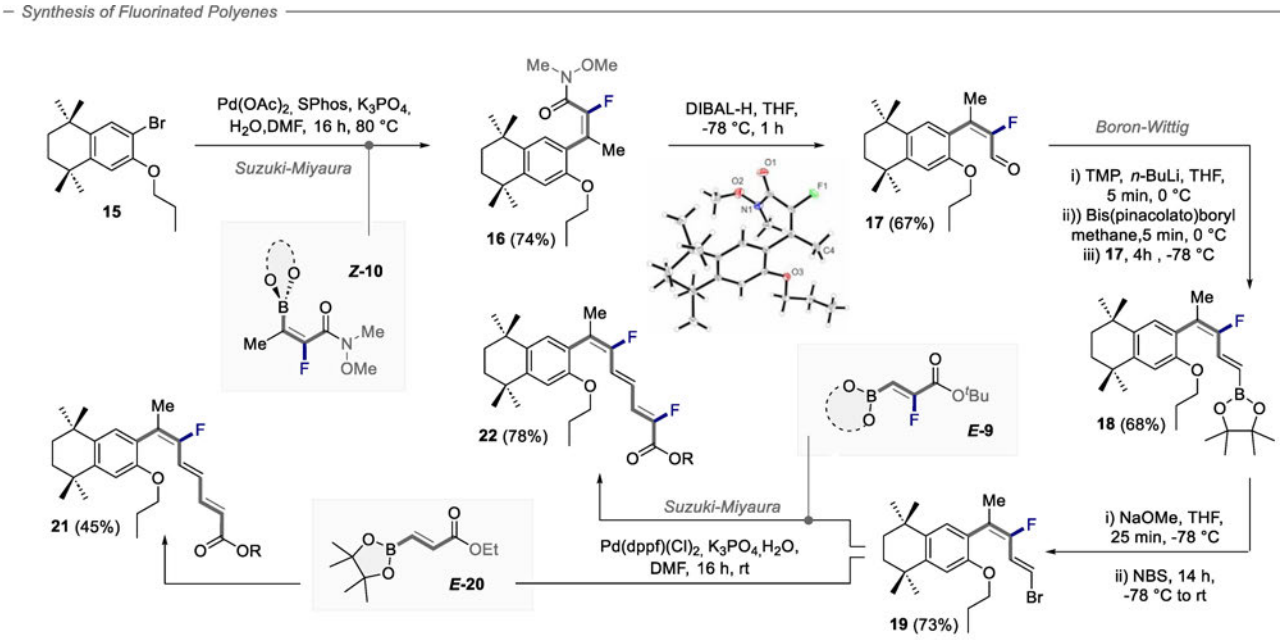

Scheme 1. Application of the photocatalytic isomerisation of alkenyl fluorides in the stereocontrolled syntheses of fluorinated retinoids **21** and **22**. Crystal structure of compound **16**. Thermal ellipsoids are shown at 50 % probability.

© 2023 The Authors. Angewandte Chemie International Edition published by Wiley-VCH GmbH

15213773, 2023, 27, Downloaded from https://onlinelibrary.wiley.com/doi/10.1002/anie.202304150 by Universitätsbibliothek Mainz, Wiley Online Library on [16/06/2025]. See the Terms and Conditions (https://onlinelibrary.wiley.com/terms-and-conditions) on Wiley Online Library for rules of use; OA articles are governed by the applicable Creative Commons License

observable in the transient absorption (TA) spectrum with a natural lifetime of ≈73 μs (Figure 5B) under these conditions. In the presence of either isomer, the triplet state is quenched and only baseline level is observed following ^{3}TX deactivation. Electron transfer (ET) or hydrogen atom transfer (HAT) reactions with the participation of TX or similar derivatives would unavoidably result in pronounced TX-derived signals in the TA spectra,[33] which is not the case. Taking the quenching efficiencies exceeding 70 %, and the high sensitivity of the employed apparatus into account, the baseline-like spectra are in excellent agreement with triplet-triplet energy transfer (EnT) as being the only reaction pathway in the isomerisation reaction of ***E*-1** and ***Z*-1**:[34] the very short lifetime of the acceptor triplet obtained is also typical behavior of triplet-excited olefins. Stern–Volmer experiments were then conducted with varying concentrations of both isomers, and revealed a faster EnT rate for ***Z*-1** (8.94×10^7 M^{-1}s^{-1}) than for ***E*-1** (1.74×10^7 M^{-1}s^{-1}) by as much as a factor of five. These results indicate an increased triplet state energy of ***E*-1**, which is in line with the chromophore shortening to enable the $n_o\rightarrow p_B$ interaction. Moreover, ***Z*-1** is converted to the perpendicular triplet more rapidly than the corresponding *E* isomer (Figure 1), which results in a photostationary state enriched with ***E*-1**. These spectroscopic findings are not only in line with the experimentally observed composition of the photocatalytic mixture after lab-scale photoirradiation, but they also follow the triplet energy trend calculated using DFT methods (see Supporting Information).

Conclusion

In conclusion, an operationally simple geometric isomerisation of alkenyl fluorides has been enabled by selective energy transfer catalysis using inexpensive thioxanthone (up to *E*/*Z* 98:2 in 1 h). Aided by X-ray structural analysis, the selectivity of the process can be rationalised by chromophore bifurcation in the product: this is a consequence of a stabilising $n_o\rightarrow p_B$ interaction that requires 90° rotation of the C(sp^2)–B bond. This enabling process eliminates the current reliance on lengthy, independent synthesis campaigns to compare the biological effects of monofluoro alkene geometry in amide and polyene biomimetics. The transformation has been validated in bidirectional synthesis campaigns using an ambiphilic linchpin, and showcased in the stereocontrolled syntheses of fluorinated retinoid analogues. It is envisaged that this platform will contribute to the growing arsenal of enabling technologies to facilitate catalyst-based stereodivergent synthesis.[35]

Acknowledgements

We acknowledge generous financial support from the WWU Münster, the JGU Mainz, the Alexander von Humboldt Foundation (fellowship to C.M.), the German Federal Environmental Foundation (DBU, grant number 20022/028) and the European Union Horizon 2020 research and innovation programme under the Marie Skłodowska-Curie grant agreement No 956324 (PhotoReAct) (fellowship to B.K.). Open Access funding enabled and organized by Projekt DEAL.

Conflict of Interest

The authors declare no conflict of interest.

Data Availability Statement

The data that support the findings of this study are available in the Supporting Information of this article.

Keywords: Bioisosteres · Catalysis · Fluorine · Isomerisation · Polyenes

[1] S. Kumari, A. V. Carmona, A. K. Tiwari, P. C. Trippier, *J. Med. Chem.* **2020**, *63*, 12290–12358.
[2] S. Lepri, M. Ceccarelli, N. Milani, G. Cruciani, *Proc. Natl. Acad. Sci. USA* **2017**, *114*, E3178–E3187.
[3] a) R. J. Abraham, S. L. R. Ellison, P. Schonholzer, W. A. Thomas, *Tetrahedron* **1986**, *42*, 2101–2110; b) G. Fischer, *Chem. Soc. Rev.* **2000**, *29*, 119–127.
[4] For studies describing the influence of amide orientation on biological activity see: a) A. Niida, K. Tomita, M. Mizumoto, H. Tanigaki, T. Terada, S. Oishi, A. Otaka, K. I. Inui, N. Fujii, *Org. Lett.* **2006**, *8*, 613–616; b) X. J. Wang, B. Xu, A. B. Mullins, F. K. Neiler, F. A. Etzkorn, *J. Am. Chem. Soc.* **2004**, *126*, 15533–15542; c) M. Marraud, V. Dupont, V. Grand, S. Zerkout, A. Lecoq, G. Boussard, J. Vidal, A. Collet, A. Aubry, *Biopolymers* **1993**, *33*, 1135–1148.
[5] a) T. Allemendinger, E. Felder, E. Hungerbuehler in *ACS Symposium Series 456* (Ed.: J. T. Welch), American Chemical Society, Washington, **1991**, pp. 186–195; b) P. A. Bartlett, A. Otake, *J. Org. Chem.* **1995**, *60*, 3107–3111; c) "Fluorinated Moieties for Replacement of Amide and Peptide Bonds": T. Taguchi, H. Yanai in *Fluorine in Medicinal Chemistry and Chemical Biology* (Ed.: I. Ojima), Wiley, Hoboken, **2009**; d) S. Couve-Bonnaire, D. Cahard, X. Pannecoucke, *Org. Biol. Chem.* **2007**, *5*, 1151–1157; e) N. A. Meanwell, *J. Med. Chem.* **2011**, *54*, 2529–2591; f) G. Landelle, M. Bergeron, M.-O. Turcotte-Savard, J.-F. Paquin, *Chem. Soc. Rev.* **2011**, *40*, 2867–2908; g) M. Drouin, J.-D. Hamel, J.-F. Paquin, *Synthesis* **2018**, *50*, 881–995.
[6] a) D. O'Hagan, *Chem. Soc. Rev.* **2008**, *37*, 308–319; b) L. E. Zimmer, C. Sparr, R. Gilmour, *Angew. Chem.* **2011**, *123*, 12062.
[7] S. Osada, S. Sano, M. Ueyama, Y. Chuman, H. Kodama, K. Sakaguchi, *Bioorg. Med. Chem.* **2010**, *18*, 605–611.
[8] R. A. Altman, K. K. Sharma, L. G. Rajewski, P. C. Toren, M. J. Baltezor, M. Pal, S. N. Karad, *ACS Chem. Neurosci.* **2018**, *9*, 1735–1742.
[9] a) R. Jogireddy, S. Barluenga, N. Winssinger, *ChemMedChem* **2010**, *5*, 670–673; b) H. Du, T. Matsushima, M. Spyvee, M. Goto, H. Shirota, F. Gusovsky, K. Chiba, M. Kotake, N. Yoneda, Y. Eguchi, L. DiPietro, J.-C. Harmange, S. Gilbert, X.-Y. Li, H. Davis, Y. Jiang, Z. Zhang, R. Pelletier, N. Wong, H. Sakurai, H. Yang, H. Ito-Igarashi, A. Kimura, Y. Kuboi, Y. Mizui, I. Tanaka, M. Ikemori-Kawada, Y. Kawakami, A.

© 2023 The Authors. Angewandte Chemie International Edition published by Wiley-VCH GmbH

15213773, 2023, 27, Downloaded from https://onlinelibrary.wiley.com/doi/10.1002/anie.202304150 by Universitätsbibliothek Mainz, Wiley Online Library on [16/06/2025]. See the Terms and Conditions (https://onlinelibrary.wiley.com/terms-and-conditions) on Wiley Online Library for rules of use; OA articles are governed by the applicable Creative Commons License

Inoue, T. Kawai, Y. Kishi, Y. Wang, *Bioorg. Med. Chem. Lett.* **2009**, *19*, 6196–6199.
[10] Y. Song, L. Clizbe, C. Bhakta, W. Teng, W. Li, P. Wong, B. Huang, U. Sinha, G. Park, A. Reed, R. M. Scarborough, B. Y. Zhu, *Bioorg. Med. Chem. Lett.* **2002**, *12*, 2043–2046.
[11] a) M. Kajjout, M. Smietana, J. Leroy, C. Rolando, *Tetrahedron Lett.* **2013**, *54*, 1658–1660; b) G. Hirai, E. Nishizawa, D. Kakumoto, M. Morita, M. Okada, D. Hashizume, S. Nagashima, M. Sodeoka, *Chem. Lett.* **2015**, *44*, 1389–1391.
[12] a) A. K. Ghosh, B. Zajc, *Org. Lett.* **2006**, *8*, 1553–1556; b) B. Zajc, S. Kake, *Org. Lett.* **2006**, *8*, 4457–4460; c) E. Pfund, C. Lebargy, J. Rouden, T. Lequeux, *J. Org. Chem.* **2007**, *72*, 7871–787; d) A. K. Ghosh, S. Banerjee, S. Sinha, S. B. Kang, B. Zajc, *J. Org. Chem.* **2009**, *74*, 3689–3697; e) M. He, A. K. Ghosh, B. Zajc, *Synlett* **2008**, 999–1004; f) C. Calata, E. Pfund, T. Lequeux, *Tetrahedron Lett.* **2011**, *67*, 1398–1405.
[13] a) J. T. Welch, R. W. Herbert, *J. Org. Chem.* **1990**, *55*, 4782–4784; b) L. G. Boros, B. De Corte, R. H. Gimi, J. T. Welch, Y. Wu, R. E. Handschumacher, *Tetrahedron Lett.* **1994**, *35*, 6033–6036.
[14] M.-H. Yang, S. S. Matikonda, R. A. Altman, *Org. Lett.* **2013**, *15*, 3894–3897.
[15] For selected reviews, see: a) H. Yanai, T. Taguchi, *Eur. J. Org. Chem.* **2011**, 5939–5954; b) M. Drouin, J.-D. Hamel, J.-F. Paquin, *Synthesis* **2018**, *50*, 881–955.
[16] For selected examples, see a) H. Machleidt, R. Wessendorf, *Justus Liebigs Ann. Chem.* **1964**, *674*, 1–10; b) G. E. Moghadam, J. Seyden-Penne, *Bull. Soc. Chim. Fr.* **1985**, 448–454; c) Y. Yamaki, A. Shigenaga, J. Li, Y. Shimohigashi, A. Otaka, *J. Org. Chem.* **2009**, *74*, 3278–3285.
[17] S. Fustero, A. Simón-Fuentes, P. Barrio, G. Haufe, *Chem. Rev.* **2015**, *115*, 871–930.
[18] A. Nouaille, X. Pannecoucke, T. Poisson, S. Couve-Bonnaire, *Adv. Synth. Catal.* **2021**, *363*, 2140–2147.
[19] Q. Liu, Y. Mu, T. Koengeter, R. R. Schrock, A. H. Hoveyda, *Nat. Chem.* **2022**, *14*, 463–473.
[20] H. Sakaguchi, Y. Uetake, M. Ohashi, T. Niwa, S. Ogoshi, T. Hosoya, *J. Am. Chem. Soc.* **2017**, *139*, 12855–12862.
[21] G. Dutheuil, C. Paturel, X. Lei, S. Couve-Bonnaire, X. Pannecouke, *J. Org. Chem.* **2006**, *71*, 4316–4319.
[22] For reviews on photocatalytic geometric alkene isomerisation, see a) T. Neveselý, M. Wienhold, J. J. Molloy, R. Gilmour, *Chem. Rev.* **2022**, *122*, 2650–2694; b) A. Marotta, C. E. Adams, J. J. Molloy, *Angew. Chem. Int. Ed.* **2022**, *61*, e202207067; c) J. J. Molloy, T. Morack, R. Gilmour, *Angew. Chem. Int. Ed.* **2019**, *58*, 13654–13664; d) J. B. Metternich, R. Gilmour, *Synlett* **2016**, *27*, 2541–2552.
[23] a) J. J. Molloy, M. Schäfer, M. Wienhold, T. Morack, C. G. Daniliuc, R. Gilmour, *Science* **2020**, *369*, 302–306; b) M. Wienhold, J. J. Molloy, C. G. Daniliuc, R. Gilmour, *Angew. Chem. Int. Ed.* **2021**, *60*, 685–689.
[24] For an application in dual activation tandem catalysis, see: J. Corpas, M. Gomez-Mendoza, J. Ramírez-Cárdenas, V. A. de la Peña O'Shea, P. Mauleón, R. Gómez Arrayás, J. C. Carretero, *J. Am. Chem. Soc.* **2022**, *144*, 13006–13017.
[25] A. A. Berger, J.-S. Völler, N. Budisa, B. Koksch, *Acc. Chem. Res.* **2017**, *50*, 2093–2103.
[26] T. Neveselý, J. J. Molloy, C. McLaughlin, L. Brüss, C. G. Daniliuc, R. Gilmour, *Angew. Chem. Int. Ed.* **2022**, *61*, e202113600.
[27] a) D. G. Hall, *Structure, Properties, and Preparation Of Boronic Acid Derivatives. Overview of Their Reactions and Applications*, Wiley-VCH, Weinheim, **2005**; b) T. Kinzel, Y. Zhang, S. L. Buchwald, *J. Am. Chem. Soc.* **2010**, *132*, 14073–14075; c) P. A. Cox, M. Reid, A. G. Leach, A. D. Campbell, E. J. King, G. C. Lloyd-Jones, *J. Am. Chem. Soc.* **2017**, *139*, 13156–13165.
[28] Deposition Numbers 2249213 (for ***E*-9**), 2249215 (for ***E*-14**), 2249214 (for ***Z*-14**), and 2250334 (for ***Z*-16**) contains the supplementary crystallographic data for this paper. These data are provided free of charge by the joint Cambridge Crystallographic Data Centre and Fachinformationszentrum Karlsruhe Access Structures service.
[29] H. Görner, *J. Phys. Chem.* **1989**, *93*, 1826–1832.
[30] B. H. Lipshutz, G. C. Clososki, W. Chrisman, D. W. Chung, D. B. Ball, J. Howell, *Org. Lett.* **2005**, *7*, 4561–4564.
[31] J. R. Coombs, L. Zhang, J. P. Morken, *Org. Lett.* **2015**, *17*, 1708–1711.
[32] a) T. Deng, S. Shan, Z. Bin Li, Z. W. Wu, C. Z. Liao, B. Ko, X. P. Lu, J. Cheng, Z. Q. Ning, *Biol. Pharm. Bull.* **2005**, *28*, 1192–1196; b) S. S. Canan Koch, L. J. Dardashti, J. J. Hebert, S. K. White, G. E. Croston, K. S. Flatten, R. A. Heyman, A. M. Nadzan, *J. Med. Chem.* **1996**, *39*, 3229–3234.
[33] a) S. F. Yates, G. B. Schuster, *J. Org. Chem.* **1984**, *49*, 3349–3356; b) M. R. Rodrigues, M. G. Neumann, *Macromol. Chem. Phys.* **2001**, *202*, 2776–2782.
[34] a) A. Luque, J. Groß, T. J. B. Zähringer, C. Kerzig, T. Opatz, *Chem. Eur. J.* **2022**, *28*, e20210432; b) Y. Liu, D. Ni, B. G. Stevenson, V. Tripathy, S. E. Braley, K. Raghavachari, J. R. Swierk, M. K. Brown, *Angew. Chem. Int. Ed.* **2022**, *61*, e202200725.
[35] S. Krautwald, E. M. Carreira, *J. Am. Chem. Soc.* **2017**, *139*, 5627–5639.

Manuscript received: March 22, 2023
Accepted manuscript online: May 5, 2023
Version of record online: May 24, 2023

© 2023 The Authors. Angewandte Chemie International Edition published by Wiley-VCH GmbH

15213773, 2023, 27, Downloaded from https://onlinelibrary.wiley.com/doi/10.1002/anie.202304150 by Universitätsbibliothek Mainz, Wiley Online Library on [16/06/2025]. See the Terms and Conditions (https://onlinelibrary.wiley.com/terms-and-conditions) on Wiley Online Library for rules of use; OA articles are governed by the applicable Creative Commons License

6.2 Photoswitching of Norbornadienes for Solar Energy Storage Applications

Solar energy is set to play an inevitable role in meeting the growing energy demands of modern society.[231] However, one of the key challenges in transitioning from fossil fuels to sustainable alternatives lies in the intermittent nature of solar power generation.[232] In traditional oil- and coal-based power generation, energy is stored in chemical bonds and released on demand through combustion. To emulate this principle, considerable effort have been directed toward storing solar energy in the form of chemical fuels, such as hydrogen from water splitting or synthetic hydrocarbons derived from CO_2.[233,234] While hydrogen and synthetic hydrocarbon fuels offer high energy densities and can be efficiently stored, their production often suffers from low solar-to-fuel conversion efficiencies or relies on expensive, tailor-made catalysts.[235,236] In contrast, concentrated sunlight can be directly used to heat or melt materials, thereby storing energy in the form of thermal energy. However, this approach is significantly limited by heat dissipation over time and is therefore only suitable for short-term energy storage.[237]

Against this backdrop, molecular photoswitches have emerged as promising candidates for solar energy storage.[186,187,238,239] This approach is based on the photoinduced formation of a metastable isomer upon exposure to sunlight (Figure 19A). The metastable species, being higher in energy, can later revert to its original form while releasing the stored energy as heat. Such a system ,referred to as molecular solar thermal energy storage (MOST) system, constitutes a closed and fully reversible energy storage cycle. Its scalability and simplicity make it particularly attractive for applications such as household heating – where solar energy can be captured on sunny, warm days without requiring insulation and released as thermal energy months later during cold, dark periods (Figure 19B).[133]

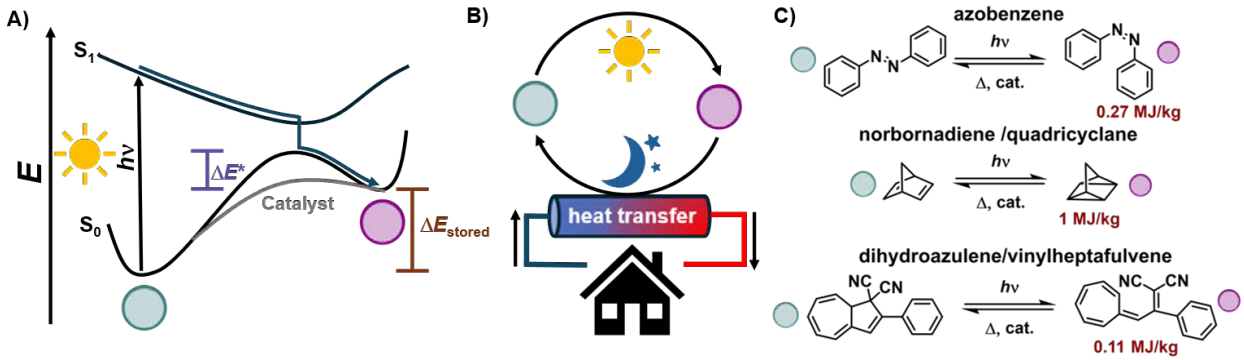

Figure 19: A) Schematic energy diagram illustrating the sunlight-driven transition from the thermodynamically stable configuration to the metastable isomer. B) Overview of the MOST concept. C) Representative examples of photoswitch scaffolds used in prominent MOST systems.

For photoswitches to be viable in practical applications, the isomer pair must store a sufficient amount of energy to be competitive. As outlined in Chapter 6, the *E*→*Z* isomerization of alkenes such as stilbene, while conceptually attractive, typically provides an energy difference between the thermodynamically stable and metastable isomers that is too small for effective solar energy storage.[198] To overcome this

limitation, strategies have been developed to introduce chemical bond strain into the metastable isomer, thereby increasing its energy content. In this context, a variety of organic and organometallic chromophores have been investigated as promising candidates for MOST systems. The photoswitchable systems that have been considered for MOST are azobenzenes (*cis–trans* isomerization),[239–242] norbornadiene/quadricyclane derivatives,[208,243–246] spiropyran/merocyanine systems,[242,247] diarylethenes (*cis–trans* isomerization),[191,248] anthracenes/dimers,[249] dihydroazulene/vinylheptafulvene pairs,[250,251] and fulvalene–tetracarbonyl diruthenium complexes (Figure 19C for prominent examples).[252] Essentially all studies concern direct excitation of the photoswitch into the singlet-excited state from where isomerization into the metastable isomer occurs. In order to be viable, the following criteria for a MOST system were first derived by Bren and Yoshida:[134,253]

- Strong absorption in the visible spectral range,
- Energy storage capacity exceeding 300 kJ/kg,
- Long-term stability of the stored energy in the photoisomer,
- High quantum yield for the forward (photoinduced) isomerization and efficient energy release through thermal or catalytic back-conversion,
- Availability of inexpensive and robust chromophores with sufficient chemical stability.

Although each MOST system presents unique advantages and limitations, none has yet met all the key criteria to a degree that makes them truly competitive. The norbornadiene/quadricyclane (NB/QC) pair stands out as one of the most promising and extensively studied photoswitch mainly due to the high energy storage density. Upon photoexcitation, norbornadiene (NB) undergoes an intramolecular [2 + 2] cycloaddition to form the highly strained quadricyclane isomer (Figure 19C). The quadricyclane stores ~ 1 MJ/kg,[254] coupled with a long half-life of the metastable state, which makes it highly attractive.[255] Yet, both isomers only weakly absorb in the UVB. The singlet-excited state of NB is characterized by an ultrashort lifetime < 1 ps,[256] requiring an excitation energy of ~ 5 eV,[257] and a relatively low isomerization quantum yield of 0.03–0.05.[258,259] Due to its exclusive absorption in the UVB, where solar irradiance is minimal, the unsubstituted NB is largely impractical for MOST applications.

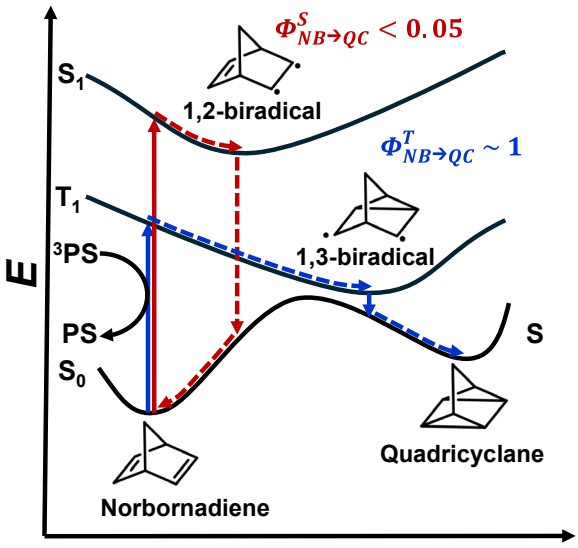

Figure 20: Schematic energy diagram of direct and triplet-sensitized isomerization of norbornadiene to quadricyclane.[260]

In contrast, the triplet state lies significantly lower in energy (~ 2.7 eV),[261] with a typical lifetime for olefines of 6.2 ns[261] and an isomerization quantum yield approaching unity.[260] The stark difference in isomerization efficiency between the singlet and triplet states can be attributed to their respective relaxed geometries. The triplet-excited state favors a 1,3-biradical geometry that closely resembles the quadricyclane structure, whereas the singlet-excited state adopts a 1,2-biradical configuration, more similar to that of NB (Figure 20).[260,262,263] Despite this inherent advantage of triplet–triplet energy transfer over direct photoexcitation, it remains relatively underexplored in current literature.[186,187,244] Most recent studies have focused instead on red-shifting the absorption spectrum to better match solar irradiance and enhancing the isomerization quantum yield. In this vein, NB derivatives have been engineered with push–pull conjugation systems and increased steric hindrance.[244] Notably, Moth-Poulsen and co-workers have systematically investigated various substitution patterns on the NB scaffold, identifying cyano acceptor groups and ethynyl-substituted aromatic donors as the most effective modifications.[264] These tailored photoswitches have already been evaluated in pilot-scale studies at the kilogram level.[244,265] While such modifications significantly improve solar absorption and moderately enhance the isomerization quantum yield, they also tend to reduce the overall energy storage density and often shorten the half-life of the metastable quadricyclane isomer.[266,267] This trade-off can be partially mitigated by incorporating multiple NB (or other photoswitches) units onto a single chromophore scaffold.[136,268,269] However, such complex molecular designs requiring multi-step synthesis are difficult to produce in a cost-effective and sustainable manner. These considerations highlight the intrinsic challenge of MOST system development: improving one parameter often compromises another.

In this context, triplet-sensitized isomerization of norbornadiene remains relatively underexplored. While it has been investigated to some extent – often alongside early studies on triplet-sensitized isomerization of other classic photoswitches – these efforts have primarily focused on mechanistic elucidation rather than practical application.[134,208,261,270,271]

Early studies focused primarily on NB either in its unsubstituted form or bearing cyano, alkyl, ester, and small acene substituents.[134,271,272] Various triplet sensitizers have been employed, including acridones,[273] ketones,[134,270] metal complexes,[86,254,274,274,275] and nanoparticles.[276] More recently, NB has been covalently linked to organic photosensitizers for applications in energy storage and phosphorescence switching, however, these complex and costly synthetic pathways are impractical for large-scale use.[277,278] Although triplet-mediated isomerization offers a significantly higher quantum yield than direct excitation, many systems suffer from rapid degradation due to the high reactivity of NB in its triplet state.[208,270] As the triplet state is lower in energy, isomerization would require less energy input (or less energetic photons) to accomplish the same metastable configuration. However, even neglecting energy losses a high triplet energy sensitizer (> 2.7 eV) is required that will only utilize a limited portion of the visible solar spectrum. While substitution of NB can reduce its triplet energy, inconsistent results have hindered conversion efficiency.[272]

In this context, project **[G]** investigated a series of aryl-substituted norbornadienes through triplet-sensitization studies and detailed spectroscopic analysis. Two naphthyl-substituted norbornadienes[137] were chosen because of the characteristic absorption features of the naphthyl triplet state in the UVA/visible range (Figure 21A).[51] Additionally, a multistate photoswitch comprising three NB units on a benzene core was studied. This compound is of particular interest for MOST applications, as it exhibits the highest reported energy storage density among NB-based systems.[136] However, investigating this photoswitch poses a challenge due to the coexistence of up to four isomeric forms. To aid interpretation, a reference compound bearing a single NB unit (PhNB) was studied alongside the multistate photoswitch. Furthermore, in project **[H]** monoaryl-substituted NBs were modified with acetylene linkers to extend the π-system. The impact of this extension on isomerization behavior and energy storage performance by direct excitation or triplet-sensitization was systematically examined.

As the main goal of this part of the thesis, novel MOST systems utilizing a triplet sensitization approach have been identified, which, under optimal conditions, can achieve an overall quantum yield approaching 1. As a consequence, each absorbed photon triggers a single NB to QC isomerization event. The TTET step was extensively investigated, including the multistate photoswitch, by employing a sophisticated combination of spectroscopic analysis and quantum mechanical calculations. The solar spectral match was significantly broadened without compromising the energy storage density. Multiple conversion cycles further demonstrated the viability of this underexplored sensitization approach. While modifications involving acetylene bridges proved to be less effective, they provided valuable insights for the design of future photoswitch systems. These findings are expected to pave the way for the development of TTET-driven MOST applications and advance a broader understanding of triplet state reactivity.

Summary:

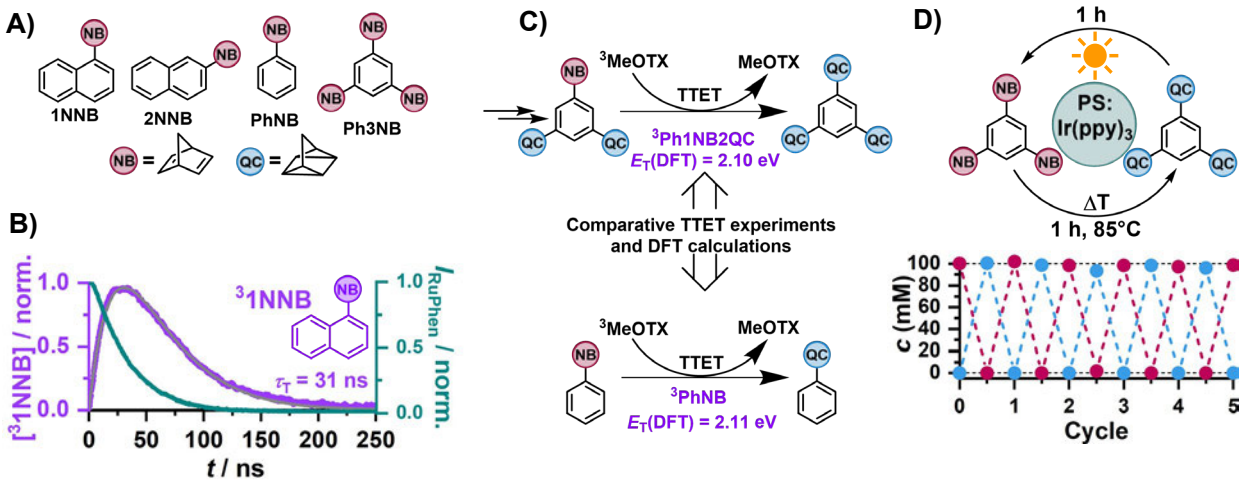

Figure 21: A) Molecular structures of investigated norbornadienes. B) Kinetic traces of RuPhen ($[Ru(phen)_3]^{2+}$) emission and TA signal of triplet-excited 1NNB. C) Spectroscopic and quantum mechanical studies of the multistate norbornadiene Ph3NB in comparison to the reference compound PhNB. D) Multiple conversion cycles of Ph3NB under sunlight irradiation.

At the outset of these studies, the photoconversion properties of NB derivatives (Figure 21A for structures) under direct excitation were evaluated. As expected for small organic chromophores, excitation required UV light, and re-excitation of the resulting quadricyclanes led to incomplete back-conversion yields.[136,137,279] This limitation prompted the hypothesis that triplet sensitization of norbornadienes could not only improve spectral overlap with sunlight but also enable more efficient conversion. Indeed, detailed spectroscopic analyses unequivocally confirmed TTET as the operative pathway. A similar approach as in project **[E]** was applied to detect the short-lived triplet state of 1NNB. Employing $[Ru(phen)_3]^{2+}$ (RuPhen) as a triplet photosensitizer and using high concentrations of 1NNB enabled the reliable detection of the transient triplet state (Figure 21B). Irradiation experiments resulted in complete conversion, and isomerization quantum yields of unity were determined for both 1NNB and Ph3NB, highlighting the effectiveness of triplet sensitization compared to direct excitation.

The triplet energies of the NB derivatives were determined through a combination of DFT calculations and Stern–Volmer quenching experiments. As for the multistate Ph3NB during conversion, four different isomers can be present, complicating the spectroscopic description of each isomer dramatically. Hence, PhNB was used as a reference structure for the last and most important conversion step of Ph3NB (Figure 21C). The results support that the triplet state energy of the NB bearing isomers is roughly identical and only the last conversion to the (full) quadricyclane increases the triplet state energy substantially.

This approach facilitated the identification of both organic and metal-based photosensitizers absorbing in the blue and green spectral regions – where solar irradiance is most intense. Multiple conversion cycles of Ph3NB with $Ir(ppy)_3$ as the photosensitizer under sunlight irradiation (1 h) demonstrated efficient photoswitching and excellent system robustness (Figure 21D). As a result, the absorption onset of these

triplet-sensitized MOST systems was red-shifted by approximately 200 nm. This spectral expansion led to a marked improvement in solar energy conversion, with the efficiency of the multistate Ph3NB–$Ir(ppy)_3$ system increasing from 0.5% to 5.8% – the highest reported to date.

Project **[G]** was published as a research article:

"**Triplet-Sensitized Switching of High-Energy-Density Norbornadienes for Molecular Solar Thermal Energy Storage with Visible Light**"

Reprinted from Reference: T. J. B. Zähringer, N. Perez Lopez, R. Schulte, M. Schmitz, H. Ihmels, C. Kerzig, *Angew. Chem. Int. Ed.* **2025**, *64*, e202414733.

The article is Open Access and licensed under CC BY-NC 4.0 (https://creativecommons.org/licenses/by/4.0/). It can be cited corresponding to ref.[G]. The reference is attached in the following pages and the supporting information can be found in Chapter 10.8.

Author contributions: T. J. B. Zähringer and C. Kerzig conceived and designed the Project. R. Schulte conducted the synthesis of the norbornadiene derivatives under the supervision of H. Ihmels. Spectroscopic measurements and irradiation experiments were carried out by T. J. B. Zähringer and N. Perez Lopez. M. Schmitz performed the DFT calculations.

Check for updates

How to cite: *Angew. Chem. Int. Ed.* **2025**, *64*, e202414733
doi.org/10.1002/anie.202414733

Solar Energy Storage **Hot Paper**

Triplet-Sensitized Switching of High-Energy-Density Norbornadienes for Molecular Solar Thermal Energy Storage with Visible Light

Till J. B. Zähringer, Nico Perez Lopez, Robin Schulte, Matthias Schmitz, Heiko Ihmels, and Christoph Kerzig**

Abstract: Norbornadiene-based photoswitches have emerged as promising candidates for harnessing and storing solar energy, holding great promise as a viable solution to meet the growing energy demands. Despite their potential, the effectiveness of their direct photochemical conversion into the resulting quadricyclanes has room for improvement owing to (i) moderate quantum yields, (ii) poor overlap with the solar spectrum and (iii) photochemical back reactions. Herein, we present an approach to enhance the performance of such molecular solar thermal energy storage (MOST) systems through the triplet-sensitized conversion of aryl-substituted norbornadienes. Our study combines deep spectroscopic analyses, irradiation experiments, and quantum mechanical calculations to elucidate the energy transfer mechanism and inherent advantages of the resulting MOST systems. We demonstrate remarkable quantum yields using readily available sensitizers under both LED and solar light irradiation, significantly surpassing those achieved through direct excitation with photons of higher energy. In contrast to the conventional approach, light-induced back reactions of the high-energy products do not play any role, allowing quantitative switching within minutes. These results not only underscore the potential of triplet-sensitized MOST systems to leverage the high energy storage capabilities of multistate photoswitches but they might also stimulate the broader usage of sensitization strategies in photochemical energy conversion.

Introduction

The unpredictability and non-continuity of solar energy reaching the Earth's surface cannot yet be compensated by reliable energy storage systems. Promising methods of conserving solar energy are achieved by initially converting it to electrical energy and storing it as mechanical, electrochemical, or chemical energy.[1] In this context, so-called molecular solar thermal energy storage (MOST) systems that directly capture solar energy and release thermal energy on demand attracted much interest.[2–6] MOST systems are based on molecular photoswitches[7–9] that upon excitation store energy through reversible chemical bond formation or isomerization processes. Among them, norbornadiene-, azobenzene-, and dihydroazulene-based structures are the most extensively studied systems.[6,10,11] Already more than 30 years ago, Yoshida and Bren' et al. defined essential criteria that must be met by molecular systems for efficiently storing solar energy.[12,13] Briefly,

(1) absorptivity in the visible spectral range,
(2) energy storage capabilities above 300 kJ/kg,
(3) prolonged conservation of the stored energy by the photoisomer,
(4) high quantum yield of the photochemical forward isomerization and a high efficiency of the backward reaction upon thermal or catalytic initiation,
(5) readily available and cheap chromophores with sufficient stability.

The photoinduced [2+2] cycloaddition of norbornadiene (NB) has long been recognized as a promising reaction for energy storage applications.[12,14] This is due to its high energy storage capability (~1000 kJ/kg)[15] and the sufficient half-life[16] of the photoisomer quadricyclane (QC). Direct excitation of NB is, however, not practical due to the poor solar spectral overlap (Figure S28) and the low conversion quantum yield ($\Phi_{NB\rightarrow QC} = 0.03–0.05$).[17,18] With these challenges in mind, novel NB structures exhibiting pull-push conjugation at one NB double bond, steric hindrance as well as multistate photoswitches were developed.[13,19–23] These modifications successfully improve key properties such as solar spectral match, energy storage density and/or thermal half-life. Nonetheless, it is important to note that improvements in one characteristic often entail a compromise with other attributes.[19] In stark contrast to direct excitation forming the high energy S_1 state, isomerization reactions are frequently feasible from the lower-lying T_1 triplet state (Figure 1A).[12,24–27] Direct excitation to the triplet state is

[*] T. J. B. Zähringer, N. Perez Lopez, M. Schmitz, Prof. Dr. C. Kerzig
Department of Chemistry
Johannes Gutenberg University Mainz
Duesbergweg 10–14, 55128 Mainz, Germany
E-mail: tizaehri@uni-mainz.de
ckerzig@uni-mainz.de
R. Schulte, Prof. Dr. H. Ihmels
Department of Chemistry-Biology, and Center of Micro- and Nanochemistry and (Bio)Technology (Cμ)
University of Siegen
Adolf-Reichwein-Str. 2, 57068 Siegen, Germany

© 2024 The Authors. Angewandte Chemie International Edition published by Wiley-VCH GmbH. This is an open access article under the terms of the Creative Commons Attribution License, which permits use, distribution and reproduction in any medium, provided the original work is properly cited.

© 2024 The Authors. Angewandte Chemie International Edition published by Wiley-VCH GmbH

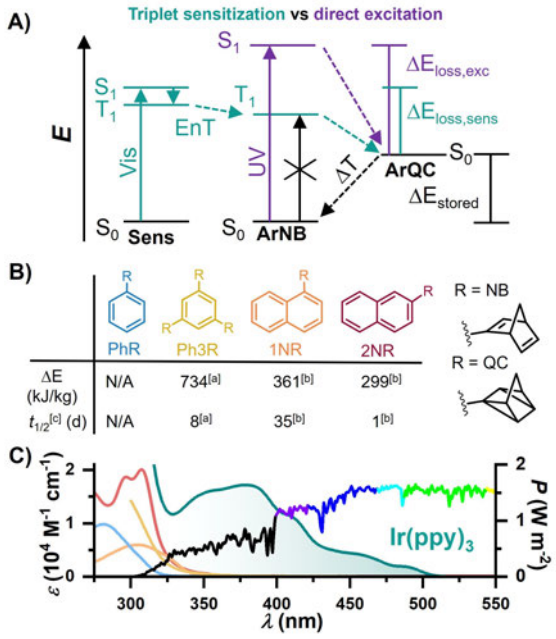

Figure 1. A) Energy diagram of the isomerization of aryl-substituted norbornadienes (ArNB) to the respective quadricyclane (ArQC) following direct excitation in comparison to triplet sensitization. B) Molecular structures of aryl-substituted norbornadiene photoswitches. [a] Taken from Ref [43] [b] Taken from Ref [44], along with key properties. [c] Reaction enthalpy for cycloreversion and thermal half-life of the ArQC calculated at 25 °C. C) Color-coded absorption spectra of the norbornadienes and a prototypical sensitizer (green line, see below for its structure and properties) overlaid by the terrestrial solar irradiation spectrum.[45]

spin-forbidden and not observed for NB and a triplet sensitizer is thus required. The triplet state energy of NB, reported to be on the order of 2.7 eV,[28] is better accessible with light of the solar spectrum compared to the singlet-excited state. As a further benefit, the sensitization approach not only minimizes energy losses in the isomerization process but also permits inherently higher quantum efficiencies, because the isomerization of unsubstituted NB via the triplet-excited state is intrinsically favored ($\Phi_{NB\rightarrow QC} \sim 1$). This is due to the nature of the geometrically relaxed triplet state (as a 1,3 diradical) resembling closely the QC structure.[28,29] Yet, two problems arise with the sensitization-driven conversion of NB: (i) Sensitizing the triplet state (2.7 eV, 459 nm), requires high-energy sensitizers that, owing to energy loss, absorb only a small fraction of the sunlight reaching Earth. In this context, ketones,[12] acridones,[30] Cu(I)-complexes,[31,32] transition-metal doped TiO_2,[33] Rh-[34] and Ir-complexes[35,36] sensitizers and covalently bond sensitizer-norbonadiene structures[37,38] have been explored. Fast degradation of these sensitizers and/or costly synthesis renders them impractical for repeated large-scale applications. (ii) NB is a highly reactive species in the triplet state and quickly degrades, reacting with the sensitizer itself making it unsuitable for multiple conversion cycles.[39,40] To address these issues, norbornadienes bearing functional groups were investigated. While the triplet energy of these derivatives was essentially reduced, the interconversion efficiency to QC is negatively affected such that quantum yields well below 20 % resulted, and even cycloreversion to the NB isomer was observed.[41,42]

All these findings highlight the complexities encountered in the development of new photoswitches for energy storage. The process is far from straightforward due to the diverse effects of structural modifications on the relevant MOST criteria. A profound understanding of the underlying mechanisms is crucial to overcome these hurdles, potentially paving the way for significant advancements in the field.[14,46] Recently, one of our groups introduced mono-, bis- and tris-norbornadienyl substituted arenes that can be readily synthesized by a Suzuki–Miyaura coupling reaction.[43,44] Exceptional energy storage densities (up to 734 kJ/kg) are achieved nearing those of unsubstituted NB as a result of the low molecular weight.[47] However, direct excitation by solar irradiation is inefficient because excitation is only accomplished by the marginal UV fraction (<350 nm) (Figure 1C). The combination of π-extension lowering the excited-state energies and the absence of donor as well as acceptor groups potentially avoids photoinduced electron transfer. Hence, we speculated that these promising multi-chromophoric photoswitches[48] could serve as a basis for exploring the potential of triplet energy transfer-driven MOST systems. In this work, four aryl-norbornadiene derivatives (Figure 1B) were selected that not only are highly promising regarding MOST applications but also enable us to clarify key photophysical properties focusing on triplet-excited states. Through deep kinetic and mechanistic analyses, substantiated by quantum mechanical calculations and visible light driven conversion cycles, we gained substantial insights into the sensitized MOST systems. As we will show, these systems can be driven using visible photons close to the maximum of the terrestrial solar spectrum (~440–550 nm) with quantum yields approaching unity. Combined with the high energy density and the long half-life of the ArQC isomers (compare, Figure 1B), the MOST systems presented herein satisfy essentially all aspects that are crucial for MOST applications.

Results and Discussion

Selection of Photoswitch–Sensitizer Pairs and Initial Energy Transfer Studies

Among the aryl-substituted norbornadienes (Figure 1B), Ph3NB is especially appealing due to its superior physical properties, the possibility of accessing multiple states, and increased energy density achieved by incorporating several energy storage units in one molecule.[48] Nevertheless, spectroscopic investigations of multistate photoswitches are challenging, which is why PhNB, bearing a single NB moiety, serves as a reference compound in these studies. The isomer pair 1NNB/1NQC is notable for its 35-day half-life, which is highly advantageous for MOST applications.[44] Furthermore, the distinctive absorption features of the naphthalene scaffold facilitate mechanistic investigations in

© 2024 The Authors. Angewandte Chemie International Edition published by Wiley-VCH GmbH

15213773, 2025, 2, Downloaded from https://onlinelibrary.wiley.com/doi/10.1002/anie.202414733 by Universitatsbibliothek Mainz, Wiley Online Library on [16/06/2025]. See the Terms and Conditions (https://onlinelibrary.wiley.com/terms-and-conditions) on Wiley Online Library for rules of use; OA articles are governed by the applicable Creative Commons License

ground-state UV/Vis and transient absorption spectra. Although its structural isomer, 2NNB, may not possess equally appealing characteristics, examining it in conjunction with 1NNB may offer valuable understanding of how small structural changes affect the performance of photoswitches. Thus, our investigations employed both naphthalene derivatives that were initially combined with the well-studied triplet sensitizer $[Ru(phen)_3](PF_6)_2$ (RuPhen). The following experiments were conducted with 1NNB and 2NNB, for clarity only the results for 1NNB are displayed in the main manuscript (see Chapter S8.1). Initial Stern–Volmer experiments in MeCN revealed that excited RuPhen (unquenched lifetime, ~500 ns)[49] is effectively quenched by the norbornadienes suggesting that triplet-triplet energy transfer (EnT) is feasible (Figure 2A). However, studying triplet-excited states of organic chromophores via sensitization, especially those with (ultra)short lifetimes like the 6.2 ns[28] observed for unsubstituted norbornadiene, can be challenging because triplet formation and decay occur on similar time scales. Laser flash photolysis (LFP) with optical detection is a well-suited method in this scenario, enabling the direct examination of such transient, non-emissive triplet states that are otherwise difficult to probe.[46,50–52] Pulsed laser excitation at 532 nm allowed us to selectively excite RuPhen and to study quenching products by transient absorption (TA) spectroscopy. High concentrations of 1NNB (55 mM) were employed to accumulate ^{3}1NNB in large amounts facilitating precise and reliable measurements. After complete sensitizer quenching (pink spectrum in Figure 2B), only the baseline level of RuPhen was detected. This allows us to exclude long-lived photoproducts typically generated by electron transfer or irreversible side reactions, which is also consistent with the anticipated short triplet lifetime. A TA spectrum recorded during the quenching process initially resembles the triplet-triplet absorption spectrum of RuPhen (Figure 2B).[53] Closer inspection, however, revealed decisive differences. A reference ^{3}RuPhen spectrum recorded under similar conditions was appropriately scaled to match in the region >600 nm, where we do not expect ^{3}1NNB to absorb. Subtracting this TA spectrum allows us to delineate what is presumed to be the triplet absorption spectrum of 1NNB, characterized by absorption bands at 460 nm, 382 nm and a shoulder at 365 nm. Comparing this absorption spectrum to unsubstituted naphthalene we find similar absorption bands around 400 nm (Figure S23). The additional broad absorption between 400 and 500 nm is also predicted by TD-DFT calculations (Figure S2). The TA spectrum of ^{3}RuPhen exhibits an isosbestic point at 496 nm, which lays the grounds for the isolated monitoring of the formation and deactivation of ^{3}1NNB (Figure 2C). Fitting this measurement with conventional A (^{3}RuPhen) → B (^{3}1NNB) → C (photoproduct) kinetics a lifetime of 31 ns is obtained for ^{3}1NNB.[50] This is indeed much shorter than reported for the naphthalene triplet (~15 µs),[54] indicating a much more efficient chemical deactivation pathway. Additional experiments with 2NNB yielded an even shorter lifetime (<15 ns). Interestingly, Takamuku et al. reported significantly longer triplet lifetimes for similar norbornadienyl-naphthalene derivatives that included an extra carboxylate group.[42] However, these derivatives performed poorly, attributed to low conversion yields, and even cycloreversion was observed. Microsecond lifetimes and degradation issues were recently observed for donor-acceptor substituted norbornadienes in related sensitization laser experiments.[46] Hence, it seems natural to assume that short triplet lifetimes, as observed for two aryl-substituted norbornadienes (1NNB and 2NNB), are beneficial for sensitized MOST applications.

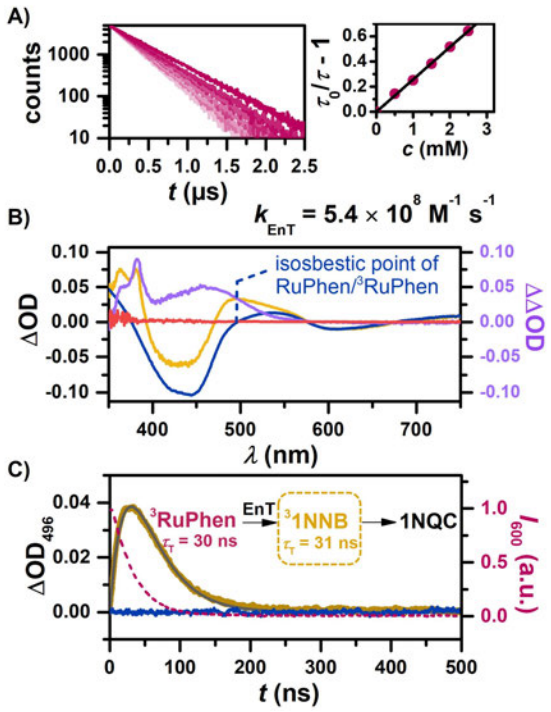

Figure 2. Mechanistic investigations of the triplet state of 1NNB by laser flash photolysis using 532 nm laser pulses. A) Kinetic emission of RuPhen with increasing 1NNB concentration and corresponding Stern–Volmer analysis. B) TA spectra of a solution of 100 µM RuPhen in the absence (dark blue) and presence of 55 mM 1NNB in deaerated MeCN recorded 30 ns (orange) and 1 µs (pink) after excitation (integration time, 20 ns). The reference spectrum of ^{3}RuPhen was scaled to match in the region >600 nm in order to determine the respective difference spectrum (purple). C) Kinetic TA traces of both solutions at the isosbestic point of RuPhen (496 nm) and kinetic emission of RuPhen in the presence of 1NNB (dotted purple line). The triplet lifetime of 1NNB was determined by a kinetic analysis[50] (gray line).

Characterizing the Triplet-Sensitized Conversion to Quadricyclane

To confirm the expected energy transfer-induced switching, we investigated the lab-scale transformation of 1NNB to 1NQC. A solution of 1NNB with RuPhen in Ar-saturated MeCN was monitored by steady-state absorption measurements during 525 nm LED irradiation (Figure 3A). The system reached a photostationary state within 20 minutes under our conditions. Larger-scale NMR irradiation experi-

© 2024 The Authors. Angewandte Chemie International Edition published by Wiley-VCH GmbH

15213773, 2025, 2, Downloaded from https://onlinelibrary.wiley.com/doi/10.1002/anie.202414733 by Universitatsbibliothek Mainz, Wiley Online Library on [16/06/2025]. See the Terms and Conditions (https://onlinelibrary.wiley.com/terms-and-conditions) on Wiley Online Library for rules of use; OA articles are governed by the applicable Creative Commons License

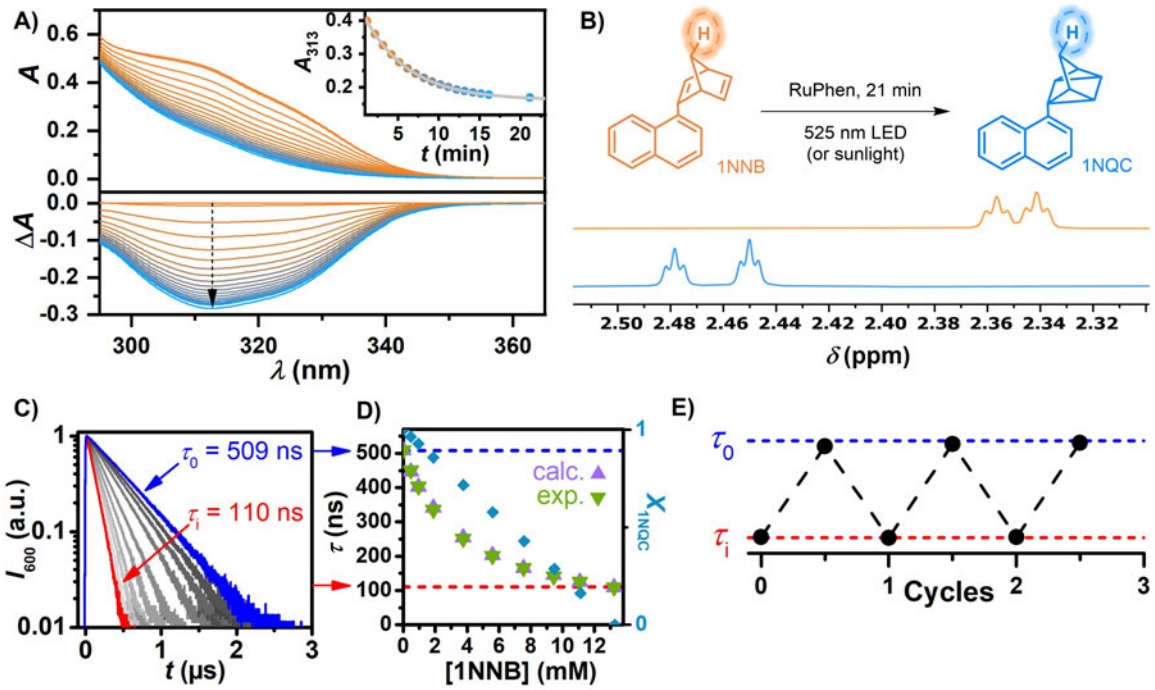

Figure 3. Quantification of the photoswitch state using NMR, UV/Vis absorption and room-temperature phosphorescence lifetime measurements. A) Steady-state UV/Vis measurements of 0.1 mM 1NNB and 100 μM RuPhen in Ar-saturated MeCN, irradiated with a 525 nm LED. The absorption spectra are corrected by the absorption of RuPhen, which was used as baseline. Inset: Absorption at 313 nm plotted against irradiation time, fitted using an exponential decay function. B) NMR spectra displaying characteristic signals of 1NNB and 1NQC measured before and after 525 nm LED irradiation of a solution with 170 μM RuPhen and 30 mM 1NNB in Ar-saturated CD_3CN. C) Kinetic emission of 250 μM RuPhen and a total quencher concentration of 13.2 mM with varying ratios of 1NNB and 1NQC in Ar-saturated MeCN upon 532 nm laser excitation. D) Experimental and calculated RuPhen lifetime plotted against the residual 1NNB concentration, and corresponding fraction of 1NQC. E) RuPhen lifetime monitored at 600 nm after laser excitation of 22.5 mM 1NNB and 250 μM RuPhen in Ar-saturated MeCN during repeated irradiation (7 min, 525 nm LED) and heating (21 h, 65 °C) cycles.

ments with a RuPhen loading as low as 0.6 % indeed revealed that full conversion is achieved (Figure 3B). Even under solar irradiation 1NNB rapidly converts to 1NQC (Figure S41). In contrast, direct excitation in the absence of a sensitizer leads to inefficient and incomplete conversion (25 % 1NQC) as the absorption of the corresponding photoisomer is usually not negligible causing undesired photoreversion (Figure S41).[6,43] Upon direct 315 nm excitation of a strongly diluted 1NNB solution (20 μM) up to 80 % of the desired 1NQC could be obtained in the photostationary state.[55] Hence, the sensitization approach not only improved the overlap with the solar spectrum by about 200 nm but also allows rapid and complete conversion of larger amounts of 1NNB.

At different conversion stages of 1NNB to 1NQC kinetic laser measurements indicate a progressive increase of the sensitizer's emission lifetime (Figure 3C). At full conversion (100 % 1NQC) RuPhen maintains its inherent unquenched triplet lifetime, which is unaffected by 1NQC despite relatively high concentrations. This seems reasonable since the conversion of the double bonds to the quadricyclane unit renders the compound structurally similar to alkyl-substituted naphthalene effectively changing the triplet energy. Complementary DFT calculations of the lowest excited triplet states of 1NNB and 1NQC reveal significant spin density on the double bonds of the NB moiety while contributions of the quadricyclane unit are negligible (SI, Chapter S3). Assuming that the triplet energy is similar to that of naphthalene (~2.6 eV) the energy transfer rate constant with the sensitizer RuPhen (2.19 eV) is expected to be negligibly low,[56] which is in line with our observations. Rearrangement of the Stern–Volmer equation (Chapter S1) led us to derive a method to monitor the progress of the conversion of 1NNB to 1NQC simply based on the readily accessible RuPhen emission. Lifetime measurements of RuPhen were carried out with varying ratios of 1NNB and 1NQC (Figure 3D). We observed that the measured lifetime perfectly correlates with the calculated lifetime (i.e., calculated based on the 1NNB concentration and the EnT rate constant). This confirms the validity of this strategy, which has clear advantages over NMR- and UV/Vis-based techniques as it is fast and it does not rely on strongly diluted solutions. This simple method can be easily adopted in most laboratories to efficiently obtain information of the photoisomerization progress and does not require sophisticated laboratory setups.[40] Conversion cycles of 1NNB were monitored by this simplistic approach (Figure 3E).

© 2024 The Authors. Angewandte Chemie International Edition published by Wiley-VCH GmbH

15213773, 2025, 2, Downloaded from https://onlinelibrary.wiley.com/doi/10.1002/anie.202414733 by Universitatsbibliothek Mainz, Wiley Online Library on [16/06/2025]. See the Terms and Conditions (https://onlinelibrary.wiley.com/terms-and-conditions) on Wiley Online Library for rules of use; OA articles are governed by the applicable Creative Commons License

Switching Quantum Yield and Triplet Energy Determinations

The efficiency of the light-driven part of MOST systems is fundamentally determined by the overall quantum yield Φ expressed as follows in our sensitized system:

$$\Phi = \Phi_{ISC} \times \Phi_{EnT} \times \Phi_{NB\rightarrow QC} \quad (1)$$

Under operational conditions, the intersystem crossing quantum yield (Φ_{ISC}) of RuPhen[57] and the triplet energy transfer quantum yield (Φ_{EnT}) approach unity, as demonstrated by kinetic simulations (SI; Figure S14). The quantum yield for the intrinsic transformation of triplet-excited NB to QC ($\Phi_{NB\rightarrow QC}$) is a pivotal metric. This quantity was obtained for 1NNB through relative chemical actinometry by using $Ir(ppy)_3$ as the sensitizer for both switching 1NNB and catalyzing a well-established reference reaction (SI, Chapter S5).[58] The findings indicated that the isomerization quantum yield for 1NNB is very close to unity within the experimental error (1.01 ± 0.06), paving the way for solar energy conversion systems with ideal efficiencies. Having established the highly efficient sensitized conversion of an aryl-norbornadiene to the corresponding quadricyclane, we conducted a more detailed series of experiments. These experiments focus on the triplet state energies of our chromophores to identify the most suitable sensitizer.[50,59] In this context, a series of metal complex sensitizers with known triplet energies was employed in quenching studies with the energy acceptors 1NNB, 2NNB and PhNB (Figure 4).

Essentially diffusion-controlled energy transfer rate constants were observed with the high-energy sensitizers (triplet energy >2.7 eV). These rate constants decrease as expected with the sensitizer's triplet energy. Although the energy transfer rate decreases by two orders of magnitude when $[Os(phen)_3]^{2+}$ is used, high concentrations of 1NNB and 2NNB, which would be required for larger-scale applications, could ensure substantial energy transfer efficiencies (Figure S14). Given that $[Os(phen)_3]^{2+}$ absorbs light across the entire visible spectrum, significant solar harvesting efficiencies can in principle be realized with this sensitizer–photoswitch couple. Based on the results displayed in Figure 4, we estimate a triplet energy of 2.39 eV for 1NNB, 2.41 eV for 2NNB and 2.56 eV for PhNB (see Chapter S4.1). Given that such deep spectroscopic insights are tricky to obtain with all intermediates of the multistate switch Ph3NB, DFT calculations were carried out to estimate the adiabatic triplet energies of all isomers as well as the benchmark core structures benzene (PhH) and naphthalene (NH) (see Table 1 and Supporting Information Chapter S3). While the calculations likely underestimate the triplet energies due to the large structural changes after vertical excitation, a pattern is observed. The naphthyl-quadricyclanes possess triplet state energies ~0.5 eV higher compared with their corresponding norbornadienes, aligning them closely with the benchmark structure NH. Spin density analyses underscore significant contributions from the double bonds in the norbornadiene moieties, whereas the corresponding quadricyclanes closely resemble naphthalene triplets, as detailed in Chapter S3. This notable triplet energy difference between the photoisomers corroborates the observed selective quenching of ^{3}RuPhen with 1NNB. Additional mechanistic investigations were conducted using the high triplet energy sensitizer thioxanthone TX (2.75 eV), in combination with 1NNB. We observed that the conversion of 1NNB to 1NQC is incomplete and the triplet lifetime of TX is still substantially quenched. These observations let us conclude that reactivation of 1NQC is in principle feasible (Chapter S8.3), further underscoring the importance of mechanistic studies and triplet energy determinations.

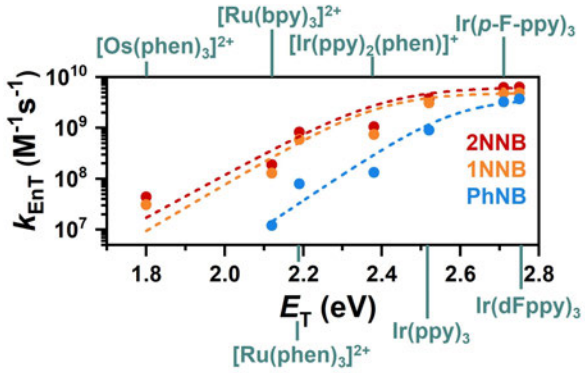

Figure 4. Rate constants of triplet energy transfer between excited metal sensitizers and norbornadienes plotted against the triplet energies of the energy donors with a thermal bond activation model fitted to the experimental data. The energy transfer rates in MeCN were determined by Stern–Volmer analyses. A fit function related to the Sandros equation was selected. For details see SI, Chapter S4.1.

Table 1: Triplet energies computed by DFT of arenes, aryl-substituted norbornadienes and corresponding quadricyclane isomers (B3LYP/6-311+G(d,p) level of theory).

Compound	E_T[a]/eV
PhH	3.83[b]
PhNB	2.11
PhQC	0.90[c]
Ph3NB	2.08
Ph2NB1QC	2.10
Ph1NB2QC	2.10
Ph3QC	4.20
NH	2.69[d]
1NNB	1.97
1NQC	2.51
2NNB	1.99
2NQC	2.64

[a] Adiabatic triplet state energies. [b] Experimental triplet energy of benzene, 3.9 eV.[60] [c] Bond cleavage during optimization (one bond within the QC moiety). [d] Experimental triplet energy of naphthalene, 2.63 eV.[54]

© 2024 The Authors. Angewandte Chemie International Edition published by Wiley-VCH GmbH

15213773, 2025, 2, Downloaded from https://onlinelibrary.wiley.com/doi/10.1002/anie.202414733 by Universitatsbibliothek Mainz, Wiley Online Library on [16/06/2025]. See the Terms and Conditions (https://onlinelibrary.wiley.com/terms-and-conditions) on Wiley Online Library for rules of use; OA articles are governed by the applicable Creative Commons License

Mechanistic Studies with the Multistate Photoswitch

The calculated triplet energies of the benzene derivatives Ph3NB, Ph2NB1QC, Ph1NB2QC and PhNB are virtually identical. In accordance with this result, we find that the spin density in the triplet excited state of each NB-containing isomer of the multistate switch is mostly located on only one NB moiety (Figure 5), which is expected for meta-substituted benzene derivatives.

Analyzing the conversion of Ph3NB to Ph3QC by spectroscopic methods is somewhat cumbersome involving three separate isomerization reactions. While the first photoisomerization step can be monitored spectroscopically when stopping the Ph3NB sensitization at very low conversion, the second and third steps require tedious isolation of the isomers Ph2NB1QC and Ph1NB2QC. The last conversion of Ph1NB2QC to Ph3QC, however, is key for optimal performance and typically the hardest to achieve by direct excitation.[43] The calculated triplet energy of PhNB is very similar to that of Ph1NB2QC and this allows us to assume that when disregarding steric effects the photophysical properties of both compounds are comparable. These detailed investigations enabled us to identify 2,7-dimethoxy-thioxanthone (MeOTX) as an appropriate sensitizer for the conversion of the multistate Ph3NB, along with monosubstituted PhNB as reference compound. The UV/Vis absorption spectrum of MeOTX is red-shifted by about 40 nm compared to TX such that MeOTX readily absorbs blue light ($\varepsilon_{440nm} = 580\ M^{-1}\ cm^{-1}$) and exhibits a triplet state energy of 2.38 eV[50] with a lifetime of ~15 µs in toluene (Figure 6).[61]

Although triplet energy transfer from MeOTX to Ph3NB and PhNB (experimental triplet energy, 2.56 eV) is seemingly thermodynamically uphill, efficient isomerization remains feasible for three reasons: (i) Even at EnT rate constants significantly below the diffusion limit, the energy transfer efficiency can approach high values due to the much longer triplet lifetime of MeOTX compared to the employed metal sensitizers (Figure S14). (ii) The short triplet lifetime of the norbornadienes ensures conversion to quadricyclane before undesired back energy transfer to the sensitizer can occur, which usually limits uphill energy transfer. (iii) Thioxanthone-derived sensitizers are reported to have lower reorganization energies compared to Ir-based sensitizers. This ultimately results in faster sensitization even when the triplet energies of the sensitizers are comparable.[62] LFP quenching studies with ^{3}MeOTX revealed efficient and comparable energy transfer rate constants to the chromophores PhNB and Ph3NB (Figure 5). These experiments substantiate the conclusions drawn from quantum mechanical calculations. NMR-scale experiments confirm that MeOTX quantitatively converts Ph3NB to Ph3QC under 440 nm LED irradiation (Figure S39). Based on our findings on all norbornadiene derivatives analyzed in this study, we conclude that the conversion of each norbornadiene unit (which cannot be distinguished by ^{1}H NMR spectroscopy;

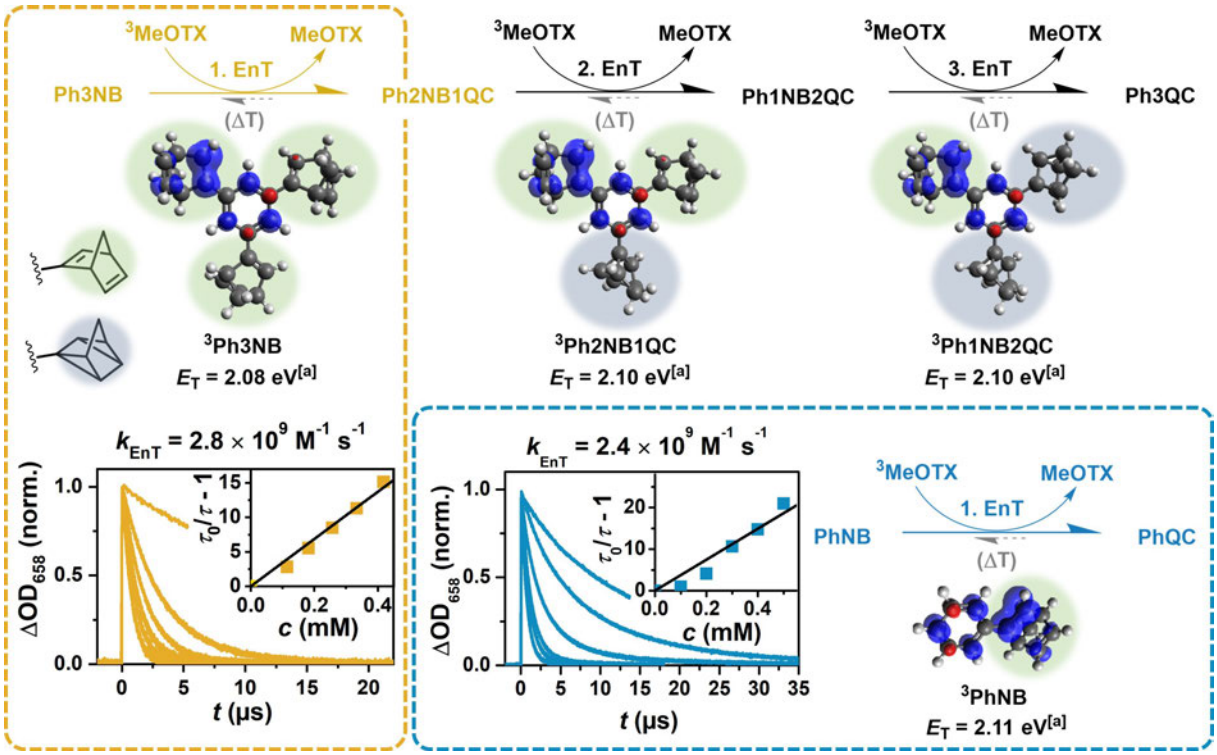

Figure 5. Reaction scheme of the cyclization of Ph3NB (top) and PhNB (bottom right) to the corresponding quadricyclane isomer using MeOTX as sensitizer (see Figure 6 for its structure). Comparative Stern–Volmer quenching experiments for the respective (first) energy transfer step are shown. The spin densities of the triplet-excited starting compounds (Ph3NB and PhNB) and the intermediates Ph2NB1QC and Ph1NB2QC are displayed below each energy transfer step (B3LYP/6-311+G(d,p) level of theory). [a] Computed by DFT (see Table 1).

© 2024 The Authors. Angewandte Chemie International Edition published by Wiley-VCH GmbH

15213773, 2025, 2, Downloaded from https://onlinelibrary.wiley.com/doi/10.1002/anie.202414733 by Universitatsbibliothek Mainz, Wiley Online Library on [16/06/2025]. See the Terms and Conditions (https://onlinelibrary.wiley.com/terms-and-conditions) on Wiley Online Library for rules of use; OA articles are governed by the applicable Creative Commons License

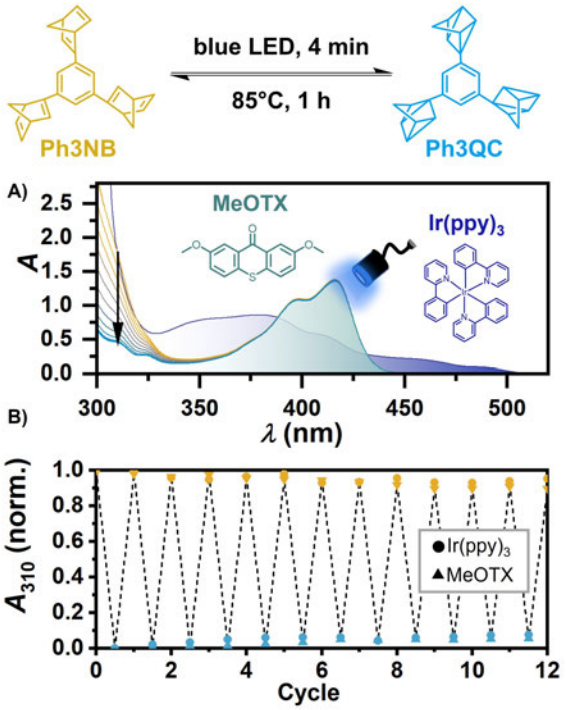

Figure 6. A) Photometric monitoring of the isomerization of Ph3NB to Ph3QC. A solution of 400 μM Ph3NB with 245 μM MeOTX as sensitizer in deaerated toluene was used. A 440 nm LED served as the light source. Absorption spectra were recorded with intervals of 20 s. Complementary experiments with $Ir(ppy)_3$ can be found in the Supporting Information (Figure S29). For clarity only the starting absorption spectrum of 300 μM Ph3NB with 50 μM $Ir(ppy)_3$ is displayed. B) Normalized absorption at 310 nm of the reversible conversion between Ph3NB and Ph3QC by sequential irradiation (440 nm, 4 min) and thermal treatment (85 °C, 1 h) for a total of 12 cycles using $Ir(ppy)_3$ or MeOTX as photosensitizer.

see SI, Chapter S6, for details) can be considered as equally efficient and light-driven back reactions are regarded to be unimportant owing to the high triplet energy of Ph3QC. A remarkable inherent quantum efficiency for the conversion of Ph3NB ($\Phi_{NB\rightarrow QC}$) approaching 100 % was determined by relative actinometry (SI, Chapter S6). Given that, under operational conditions (compare equation 1), nearly every absorbed photon converts one norbornadiene unit, the maximum efficiency has already been reached. To the best of our knowledge, this highly efficient visible light-driven MOST system with its high energy storage capabilities and its long thermal stability of the photoisomer (compare Figure 1) is unprecedented, combining beneficial properties of four essential MOST criteria as discussed in the introduction.

Photostability and Multiple Solar-Driven Conversion Cycles

The photostability is another factor determining the practicability of a MOST system. To estimate the stability, several irradiation/thermal treatment cycles using a 440 nm LED were performed with a solution containing MeOTX and Ph3NB, and monitored by steady-state absorption (Figure 6A). Over 12 conversion cycles the degradation is marginal (Figure 6B) and mainly a result of unquenched sensitizer decomposition typical for organic chromophores (Figure S31). Using $Ir(ppy)_3$ as sensitizer not only enables the harvesting of photons up to 523 nm but also reduced the decomposition to ~1 % per cycle, which compares favorably with the stability of a strongly related multiswitch arylnorbornadiene investigated upon 315 nm excitation.[43] To demonstrate the applicability of the $Ir(ppy)_3$–Ph3NB MOST system at high norbornadiene concentrations, we tested a solution with 100 mM Ph3NB and 0.59 mol % $Ir(ppy)_3$. This solution underwent five cycles of irradiation and thermal treatment using visible sunlight, deliberately avoiding direct UV excitation of Ph3NB (Figure 7). Even at elevated concentrations, the degradation remained minimal. We attribute the comparatively high photostability of the sensitized MOST system to the absence of electron transfer processes that are typically observed when highly functionalized compounds are used as quenchers.[63,64]

For the promising $Ir(ppy)_3$–Ph3NB MOST system with the specified concentrations, we calculated a maximum energy storage efficiency of 5.8 %. This compares very favorably to the efficiency of 0.53 % for direct solar excitation of Ph3NB (SI, Chapter S7) and to that of most systems so far analyzed with this efficiency parameter.[3,65–68]

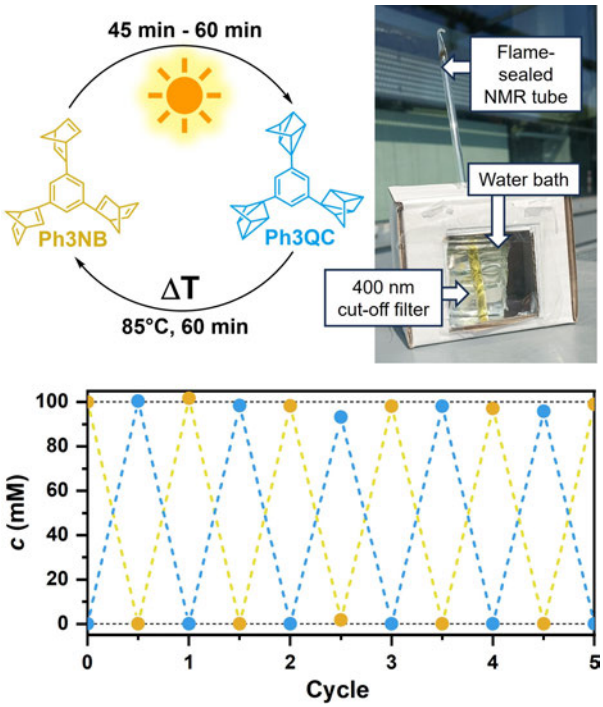

Figure 7. Experimental setup of the solar-driven conversion cycles of a solution of 100 mM Ph3NB with 590 μM $Ir(ppy)_3$ (0.59 mol %) and 26.9 mM bibenzyl (standard) in Ar-saturated deuterated toluene. The concentrations of Ph3NB and Ph3QC are given for each cycle.

© 2024 The Authors. Angewandte Chemie International Edition published by Wiley-VCH GmbH

15213773, 2025, 2, Downloaded from https://onlinelibrary.wiley.com/doi/10.1002/anie.202414733 by Universitatsbibliothek Mainz, Wiley Online Library on [16/06/2025]. See the Terms and Conditions (https://onlinelibrary.wiley.com/terms-and-conditions) on Wiley Online Library for rules of use; OA articles are governed by the applicable Creative Commons License

Conclusion

As has emerged from this work, the combination of photostable sensitizers with aryl-norbornadiene switches as energy acceptors is a highly promising field for obtaining MOST systems with outstanding properties. Through the combination of quenching studies, detailed LFP experiments, quantitative irradiation experiments and quantum mechanical calculations we could unambiguously show that (i) aryl-substituted norbornadienes inherently have low triplet energies paving the way for 200 nm red-shifts of the photoaction spectrum compared to direct UV excitation, (ii) the resulting triplets rapidly deactivate to give the desired quadricyclanes with quantum yields very close to 100 % and (iii) quantitative unidirectional switching via sensitization is feasible. The wealth of information from this study adds to inherently unique properties of recently discovered aryl-norbornadienes such as superior energy densities of the photoisomers and sufficiently long conservation times. Based on our promising results, our study might stimulate the broader application of sensitization strategies in MOST systems. In summary, our results not only deepen the understanding of triplet-sensitized photoisomerization processes and the critical parameters influencing MOST applications but also introduce a visible light-driven MOST system that combines outstanding energy conversion and storage efficiencies with promising robustness for the first time.

Supporting Information

The Supporting Information contains synthetic and experimental procedures, spectroscopic data, detailed mechanistic investigations including quantum yield determinations, kinetic simulations and Stern–Volmer plots, as well as quantum chemical calculations. The authors have cited additional references within the Supporting Information.[69–80]

Acknowledgements

We acknowledge generous financial support from the JGU Mainz, SusInnoScience, the German Research Foundation (DFG, grant number KE 2313/3-1) and the German Federal Environmental Foundation (DBU, Ph.D. fellowship to T.J.B.Z., grant number 20022/028). M.S. is grateful to the Chemical Industry Funds for a Kekulé fellowship. R.S. is grateful to the House of Young Talents (University of Siegen) and the Stiftung Nagelschneider for PhD fellowships. Open Access funding enabled and organized by Projekt DEAL.

Conflict of Interest

The authors declare no conflict of interest.

Data Availability Statement

The data that support the findings of this study are available in the main article and/or the supplementary material. The data sets shown in the main paper and DFT output files are accessible via the JGU library and the homepage of the corresponding author.

Keywords: Energy Transfer · MOST · Solar Energy Conversion · Sustainable Chemistry · Time-Resolved Spectroscopy

[1] A. G. Olabi, C. Onumaegbu, T. Wilberforce, M. Ramadan, M. A. Abdelkareem, A. H. Al-Alami, *Energy* **2021**, *214*, 118987.
[2] K. Moth-Poulsen, D. Ćoso, K. Börjesson, N. Vinokurov, S. K. Meier, A. Majumdar, K. P. C. Vollhardt, R. A. Segalman, *Energy Environ. Sci.* **2012**, *5*, 8534.
[3] Z. Wang, H. Hölzel, K. Moth-Poulsen, *Chem. Soc. Rev.* **2022**, *51*, 7313–7326.
[4] J. Usuba, G. G. D. Han, *Trends Chem.* **2023**, *5*, 577–580.
[5] L. Dong, Y. Feng, L. Wang, W. Feng, *Chem. Soc. Rev.* **2018**, *47*, 7339–7368.
[6] Z. Wang, P. Erhart, T. Li, Z.-Y. Zhang, D. Sampedro, Z. Hu, H. A. Wegner, O. Brummel, J. Libuda, M. B. Nielsen, K. Moth-Poulsen, *Joule* **2021**, *5*, 3116–3136.
[7] J. Isokuortti, K. Kuntze, M. Virkki, Z. Ahmed, E. Vuorimaa-Laukkanen, M. A. Filatov, A. Turshatov, T. Laaksonen, A. Priimagi, N. A. Durandin, *Chem. Sci.* **2021**, *12*, 7504–7509.
[8] T. Saßmannshausen, A. Kunz, N. Oberhof, F. Schneider, C. Slavov, A. Dreuw, J. Wachtveitl, H. A. Wegner, *Angew. Chem. Int. Ed.* **2024**, *63*, e202314112.
[9] U. Pischel, J. Andréasson, D. Gust, V. F. Pais, *ChemPhysChem* **2013**, *14*, 28–46.
[10] A. Gimenez-Gomez, L. Magson, B. Peñin, N. Sanosa, J. Soilán, R. Losantos, D. Sampedro, *Photochem* **2022**, *2*, 694–716.
[11] C. Sun, C. Wang, R. Boulatov, *ChemPhotoChem* **2019**, *3*, 268–283.
[12] V. A. Bren', A. D. Dubonosov, V. I. Minkin, V. A. Chernoivanov, *Russ. Chem. Rev.* **1991**, *60*, 451–469.
[13] Z. Yoshida, *J. Photochem.* **1985**, *29*, 27–40.
[14] K. D. Borne, J. C. Cooper, M. N. R. Ashfold, J. Bachmann, S. Bhattacharyya, R. Boll, M. Bonanomi, M. Bosch, C. Callegari, M. Centurion, M. Coreno, B. F. E. Curchod, M. B. Danailov, A. Demidovich, M. Di Fraia, B. Erk, D. Faccialà, R. Feifel, R. J. G. Forbes, C. S. Hansen, D. M. P. Holland, R. A. Ingle, R. Lindh, L. Ma, H. G. McGhee, S. B. Muvva, J. P. F. Nunes, A. Odate, S. Pathak, O. Plekan, K. C. Prince, P. Rebernik, A. Rouzée, A. Rudenko, A. Simoncig, R. J. Squibb, A. S. Venkatachalam, C. Vozzi, P. M. Weber, A. Kirrander, D. Rolles, *Nat. Chem.* **2024**, *16*, 499–505.
[15] D. P. Schwendiman, C. Kutal, *J. Am. Chem. Soc.* **1977**, *99*, 5677–5682.
[16] G. S. Hammond, N. J. Turro, A. Fischer, *J. Am. Chem. Soc.* **1961**, *83*, 4674–4675.
[17] B. C. Roquitte, *J. Am. Chem. Soc.* **1963**, *85*, 3700–3700.
[18] N. Ivanoff, F. Lahmani, J. F. Delouis, J. L. Le Gouill, *J. Photochem.* **1974**, *2*, 199–220.
[19] K. Jorner, A. Dreos, R. Emanuelsson, O. El Bakouri, I. Fdez. Galván, K. Börjesson, F. Feixas, R. Lindh, B. Zietz, K. Moth-Poulsen, H. Ottosson, *J. Mater. Chem. A* **2017**, *5*, 12369–12378.
[20] V. Gray, A. Lennartson, P. Ratanalert, K. Börjesson, K. Moth-Poulsen, *Chem. Commun.* **2014**, *50*, 5330–5332.
[21] R. R. Weber, C. N. Stindt, A. M. J. Van Der Harten, B. L. Feringa, *Chem. Eur. J.* **2024**, e202400482.

© 2024 The Authors. Angewandte Chemie International Edition published by Wiley-VCH GmbH

15213773, 2025, 2, Downloaded from https://onlinelibrary.wiley.com/doi/10.1002/anie.202414733 by Universitatsbibliothek Mainz, Wiley Online Library on [16/06/2025]. See the Terms and Conditions (https://onlinelibrary.wiley.com/terms-and-conditions) on Wiley Online Library for rules of use; OA articles are governed by the applicable Creative Commons License

[22] A. S. Aslam, L. M. Muhammad, A. E. Hillers-Bendtsen, K. V. Mikkelsen, K. Moth-Poulsen, *Chem. Eur. J.* **2024**, e202401430.
[23] M. Jevric, A. U. Petersen, M. Mansø, S. Kumar Singh, Z. Wang, A. Dreos, C. Sumby, M. B. Nielsen, K. Börjesson, P. Erhart, K. Moth-Poulsen, *Chem. Eur. J.* **2018**, *24*, 12767–12772.
[24] T. Neveselý, M. Wienhold, J. J. Molloy, R. Gilmour, *Chem. Rev.* **2022**, *122*, 2650–2694.
[25] Z. Wang, L. Fernandez, A. S. Aslam, M. Shamsabadi, L. M. Muhammad, K. Moth-Poulsen, *Responsive Mater.* **2023**, *1*, e20230012.
[26] J. Gemen, J. R. Church, T.-P. Ruoko, N. Durandin, M. J. Białek, M. Weißenfels, M. Feller, M. Kazes, M. Odaybat, V. A. Borin, R. Kalepu, Y. Diskin-Posner, D. Oron, M. J. Fuchter, A. Priimagi, I. Schapiro, R. Klajn, *Science* **2023**, *381*, 1357–1363.
[27] K. Kuntze, J. Isokuortti, J. J. Van Der Wal, T. Laaksonen, S. Crespi, N. A. Durandin, A. Priimagi, *Chem. Sci.* **2024**, *15*, 11684–11698.
[28] A. M. Helms, Richard A. Caldwell, *J. Am. Chem. Soc.* **1995**, *117*, 358–361.
[29] N. J. Turro, W. R. Cherry, M. F. Mirbach, M. J. Mirbach, *J. Am. Chem. Soc.* **1977**, *99*, 7388–7390.
[30] A. H. A. Tinnemans, B. Den Ouden, A. Mackor, H. J. T. Bos, *Recl. Trav. Chim. Pays-Bas* **1985**, *104*, 109–116.
[31] F. Franceschi, M. Guardigli, E. Solari, C. Floriani, A. Chiesi-Villa, C. Rizzoli, *Inorg. Chem.* **1997**, *36*, 4099–4107.
[32] C. Kutal, D. P. Schwendiman, P. Grutsch, *Sol. Energy* **1977**, *19*, 651–655.
[33] L. Pan, J.-J. Zou, X. Zhang, L. Wang, *Ind. Eng. Chem. Res.* **2010**, *49*, 8526–8531.
[34] G. W. Sluggett, N. J. Turro, H. D. Roth, *J. Phys. Chem. A* **1997**, *101*, 8834–8838.
[35] L. Schmid, F. Glaser, R. Schaer, O. S. Wenger, *J. Am. Chem. Soc.* **2022**, *144*, 963–976.
[36] P. A. Grutsch, Charles. Kutal, *J. Am. Chem. Soc.* **1986**, *108*, 3108–3110.
[37] F.-Y. Meng, I.-H. Chen, J.-Y. Shen, K.-H. Chang, T.-C. Chou, Y.-A. Chen, Y.-T. Chen, C.-L. Chen, P.-T. Chou, *Nat. Commun.* **2022**, *13*, 797.
[38] M. Upadhyay, R. Deka, D. Ray, *J. Phys. Chem. Lett.* **2024**, 3191–3196.
[39] A. A. Gorman, R. L. Leyland, *Tetrahedron Lett.* **1972**, *13*, 5345–5348.
[40] O. Brummel, F. Waidhas, U. Bauer, Y. Wu, S. Bochmann, H.-P. Steinrück, C. Papp, J. Bachmann, J. Libuda, *J. Phys. Chem. Lett.* **2017**, *8*, 2819–2825.
[41] Hideo. Ikezawa, Charles. Kutal, Katsutoshi. Yasufuku, Hiroshi. Yamazaki, *J. Am. Chem. Soc.* **1986**, *108*, 1589–1594.
[42] K. Nakabayashi, H. Nishino, S. Toki, S. Takamuku, *Int. J. Radiat. Appl. Instrum. Part C Radiat. Phys. Chem.* **1989**, *34*, 809–815.
[43] R. Schulte, S. Afflerbach, T. Paululat, H. Ihmels, *Angew. Chem. Int. Ed.* **2023**, *62*, e202309544.
[44] R. Schulte, S. Afflerbach, H. Ihmels, *Eur. J. Org. Chem.* **2023**, *26*, e202201398.
[45] "The American Society for Testing and Materials (ASTM) G-173, 'Reference Air Mass 1.5 Spectra,'" can be found under https://www.nrel.gov/grid/solar-resource/spectra.html, **2003**.
[46] W. Alex, P. Lorenz, C. Henkel, T. Clark, A. Hirsch, D. M. Guldi, *J. Am. Chem. Soc.* **2022**, *144*, 153–162.
[47] K. Maruyama, K. Terada, Y. Naruta, Y. Yamamoto, *Chem. Lett.* **1980**, *9*, 1259–1262.
[48] R. J. Salthouse, K. Moth-Poulsen, *J. Mater. Chem. A* **2024**, *12*, 3180–3208.
[49] A. Juris, V. Balzani, F. Barigelletti, S. Campagna, P. Belser, A. Von Zelewsky, *Coord. Chem. Rev.* **1988**, *84*, 85–277.
[50] T. J. B. Zähringer, M. Wienhold, R. Gilmour, C. Kerzig, *J. Am. Chem. Soc.* **2023**, *145*, 21576–21586.
[51] J. C. Scaiano, *Chem. Soc. Rev.* **2023**, *52*, 6330–6343.
[52] J. Rocker, T. J. B. Zähringer, M. Schmitz, T. Opatz, C. Kerzig, *Beilstein J. Org. Chem.* **2024**, *20*, 1236–1245.
[53] A. C. Sell, J. C. Wetzel, M. Schmitz, A. W. Maijenburg, G. Woltersdorf, R. Naumann, C. Kerzig, *Dalton Trans.* **2022**, *51*, 10799–10808.
[54] M. Montalti, A. Credi, L. Prodi, M. T. Gandolfi, *Handbook of Photochemistry*, CRC Press, **2006**.
[55] R. Schulte, H. Ihmels, *Beilstein J. Org. Chem.* **2022**, *18*, 368–373.
[56] F. Strieth-Kalthoff, C. Henkel, M. Teders, A. Kahnt, W. Knolle, A. Gómez-Suárez, K. Dirian, W. Alex, K. Bergander, C. G. Daniliuc, B. Abel, D. M. Guldi, F. Glorius, *Chem* **2019**, *5*, 2183–2194.
[57] J. N. Demas, D. G. Taylor, *Inorg. Chem.* **1979**, *18*, 3177–3179.
[58] Y. Shindo, K. Horie, I. Mita, *J. Photochem.* **1984**, *26*, 185–192.
[59] F. Edhborg, A. Olesund, B. Albinsson, *Photochem. Photobiol. Sci.* **2022**, *21*, 1143–1158.
[60] J. P. Doering, *J. Chem. Phys.* **1969**, *51*, 2866–2870.
[61] L. D. Elliott, S. Kayal, M. W. George, K. Booker-Milburn, *J. Am. Chem. Soc.* **2020**, *142*, 14947–14956.
[62] A. Solé-Daura, F. Maseras, *Chem. Sci.* **2024**, *15*, 13650–13658.
[63] W. Schwarz, K. M. Dangel, J. Bargon, G. Jones, *J. Am. Chem. Soc.* **1982**, *104*, 5686–5689.
[64] Q. Hong Wu, B. Wen Zhang, Y. Fu Ming, Y. Cao, *J. Photochem. Photobiol. Chem.* **1991**, *61*, 53–63.
[65] Z. Wang, A. Roffey, R. Losantos, A. Lennartson, M. Jevric, A. U. Petersen, M. Quant, A. Dreos, X. Wen, D. Sampedro, K. Börjesson, K. Moth-Poulsen, *Energy Environ. Sci.* **2019**, *12*, 187–193.
[66] Z. Wang, H. Hölzel, L. Fernandez, A. S. Aslam, P. Baronas, J. Orrego-Hernández, S. Ghasemi, M. Campoy-Quiles, K. Moth-Poulsen, *Joule* **2024**, S2542435124002885.
[67] Z. Wang, J. Udmark, K. Börjesson, R. Rodrigues, A. Roffey, M. Abrahamsson, M. B. Nielsen, K. Moth-Poulsen, *ChemSusChem* **2017**, *10*, 3049–3055.
[68] W. Sun, Z. Shangguan, X. Zhang, T. Dang, Z. Zhang, T. Li, *ChemSusChem* **2023**, *16*, e202300582.
[69] T. J. B. Zähringer, M.-S. Bertrams, C. Kerzig, *J. Mater. Chem. C* **2022**, *10*, 4568–4573.
[70] E. C. Constable, P. R. Raithby, D. N. Smit, *Polyhedron* **1989**, *8*, 367–369.
[71] M. S. Lowry, W. R. Hudson, R. A. Pascal, S. Bernhard, *J. Am. Chem. Soc.* **2004**, *126*, 14129–14135.
[72] O. Baumgärtel, G. Szeimies, *Chem. Ber.* **1983**, *116*, 2180–2204.
[73] F. Neese, *WIREs Comput. Mol. Sci.* **2012**, *2*, 73–78.
[74] M. D. Hanwell, D. E. Curtis, D. C. Lonie, T. Vandermeersch, E. Zurek, G. R. Hutchison, *J. Cheminformatics* **2012**, *4*, 17.
[75] A. A. Vlcek, E. S. Dodsworth, W. J. Pietro, A. B. P. Lever, *Inorg. Chem.* **1995**, *34*, 1906–1913.
[76] Y. Wei, Y. Li, Z. Li, X. Xu, X. Cao, X. Zhou, C. Yang, *Inorg. Chem.* **2021**, *60*, 19001–19008.
[77] V. Balzani, F. Bolletta, F. Scandola, *J. Am. Chem. Soc.* **1980**, *102*, 2152–2163.
[78] I. Antol, *J. Comput. Chem.* **2013**, *34*, 1439–1445.
[79] K. Raghavachari, R. C. Haddon, H. D. Roth, *J. Am. Chem. Soc.* **1983**, *105*, 3110–3114.
[80] T. Hofbeck, H. Yersin, *Inorg. Chem.* **2010**, *49*, 9290–9299.

Manuscript received: August 3, 2024
Accepted manuscript online: September 9, 2024
Version of record online: November 2, 2024

© 2024 The Authors. Angewandte Chemie International Edition published by Wiley-VCH GmbH

15213773, 2025, 2, Downloaded from https://onlinelibrary.wiley.com/doi/10.1002/anie.202414733 by Universitatsbibliothek Mainz, Wiley Online Library on [16/06/2025]. See the Terms and Conditions (https://onlinelibrary.wiley.com/terms-and-conditions) on Wiley Online Library for rules of use; OA articles are governed by the applicable Creative Commons License

Summary:

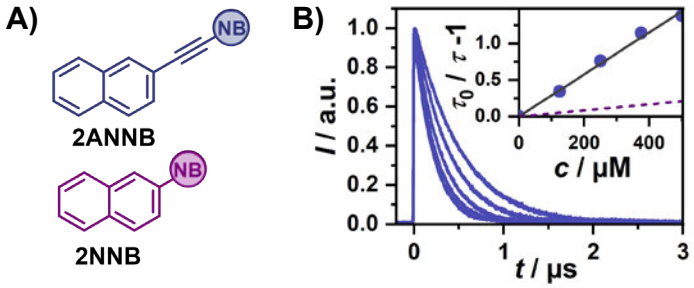

Figure 22: A) Molecular structure of acetylene-extended aryl-norbornadiene 2ANNB and reference compound 2NNB (without acetylene linker). B) Stern–Volmer experiment of the $^3[Os(phen)_3]^{2+}$ quenching by 2ANNB. The dotted line corresponds to the quenching rate constant with 2NNB as quencher.

In project **[H]**, further red-shifting of the norbornadienes was achieved by extending their π-conjugation through the incorporation of acetylene linkers. A Stern–Volmer analysis comparing the modified norbornadiene 2ANNB (Figure 22A) with its parent compound 2NNB (lacking the acetylene linker) using $[Os(phen)_3]^{2+}$ revealed a significantly increased TTET rate constant (Figure 22B). This finding indicates a lowered triplet energy in 2ANNB, consistent with its red-shifted ground state absorption spectrum. The results demonstrate that $[Os(phen)_3]^{2+}$ is a suitable triplet photosensitizer capable of absorbing across the entire visible range. In this case, direct excitation of the extended systems proved even less effective than triplet sensitization due to substantial photodegradation. However, the incorporation of acetylene linkers also led to a reduced half-life of the metastable quadricyclane, rendering these structural modifications less suitable for MOST applications. Nonetheless, they provide valuable insights into future design strategies of norbornadienes tailored for either direct excitation or triplet sensitization.

Project **[H]** was published as a research article:

"Extension of the π-system of monoaryl-substituted norbornadienes with acetylene bridges: influence on the photochemical conversion and storage of light energy"

Reproduced from Reference: R. Schulte, D. Schade, T. Paululat, T. J. B. Zähringer, C. Kerzig, H. Ihmels, *Beilstein J. Org. Chem.* **2024**, *20*, 3061–3068. With permission from Beilstein-Institut.

The article is licensed under CC BY-NC 4.0 (https://creativecommons.org/licenses/by/4.0/) and was reproduced from ref.[H]. The reference is attached in the following pages and the supporting information can be found in Chapter 10.9.

Author contributions: H. Ihmels ideated the study. R. Schulte and D. Schade synthesized the substrates and performed irradiation experiments. T. Paululat assisted with time-resolved NMR irradiation experiments. T. J. B. Zähringer performed energy transfer studies under the guidance of C. Kerzig.

BEILSTEIN JOURNAL OF ORGANIC CHEMISTRY

Extension of the π-system of monoaryl-substituted norbornadienes with acetylene bridges: influence on the photochemical conversion and storage of light energy

Robin Schulte[1], Dustin Schade[1], Thomas Paululat[1], Till J. B. Zähringer[2], Christoph Kerzig[2] and Heiko Ihmels[*1]

Full Research Paper

Open Access

Address:
[1]Department of Chemistry-Biology, Center of Micro- and Nanochemistry and (Bio-)Technology (Cμ), University of Siegen, Adolf-Reichwein-Str. 2, 57068 Siegen, Germany and [2]Department of Chemistry, Johannes Gutenberg University Mainz, Duesbergweg 10–14, 55128 Mainz, Germany

Email:
Heiko Ihmels[*] - ihmels@chemie.uni-siegen.de

* Corresponding author

Keywords:
light energy conversion; photochemistry; photochromism; quadricyclanes; Sonogashira–Hagihara coupling

Beilstein J. Org. Chem. **2024,** *20,* 3061–3068.
https://doi.org/10.3762/bjoc.20.254

Received: 23 August 2024
Accepted: 06 November 2024
Published: 21 November 2024

This article is part of the thematic issue "Harnessing light energy with molecules".

Guest Editor: H. A. Wegner

© 2024 Schulte et al.; licensee Beilstein-Institut.
License and terms: see end of document.

Abstract

The photochromic norbornadiene/quadricyclane pair is a promising system for molecular solar thermal (MOST) energy storage, with which solar energy may be converted, stored, and released as heat in one integral molecular system. Herein, we present the synthesis of mono-, bis-, and tris-norbornadiene derivatives with alkynylbenzene and alkynylnaphthalene core units, along with studies of their photochemical properties. The target compounds were synthesized by Sonogashira–Hagihara coupling reactions of 2-bromonorbornadiene and the corresponding arylacetylenes. The norbornadienes showed absorption maxima in the range of 310–345 nm and long-wavelength zero onsets of up to 420 nm. The photoisomerization quantum yields were as high as 59% per photoisomerization event and the resulting quadricyclanes showed half-lives of up to 8 h at room temperature. Furthermore, the norbornadienes were transformed quantitatively into their quadricyclane photoproducts by irradiation with green light (520 nm) in the presence of a photosensitizer.

Introduction

The application of sustainable energy storage and supply has become a very important issue both from an economic and ecological point of view. In particular, the global energy demand is continuously expanding because of the increasing population, the development of new, energy-intensive technologies and overconsumption of energy [1,2]. In this context, windpower plants and solar photovoltaic systems have become increasingly important contributions to the overall available energy, al-

though both technologies still pose some problems regarding the storage of the converted energy [3-8]. This drawback may be solved with the progress in battery technology, however, the use of high-performance batteries still requires some problematic materials, which are difficult to access, hardly recyclable, or which may harm the environment [9]. Thus, in the present situation, the efficient and flexible conversion and storage of energy requires the variable combination of different, complementary storage systems, and as a consequence, the development of alternative methods for energy storage is still an important task to contribute to the mix of storage systems. One promising approach towards storage of solar energy is represented by the molecular solar thermal (MOST) energy storage systems, which have the ability to convert and store (sun)light energy in reversible photochemical reactions. Specifically, this approach is based on photoactive compounds that are converted into photoisomers with higher energy upon absorption of light. In turn, this reaction is reversible, thus allowing to release the stored chemical energy as heat in a specifically triggered back reaction [7,8,10-13]. For a practicable MOST system, some key parameters have to be ensured, such as absorption in the range of the solar spectrum, a high quantum yield of the photoreaction, long half-lives of the photoproducts, and a high energy storage density [7,8,12-14]. In this context, several different MOST systems have been explored, including, for example, anthracenes [15], azobenzenes [16-19], dihydroazulenes [20,21], or azaborines [22,23]. However, the most prominent feasible MOST system is the [2 + 2] photocycloaddition–cycloreversion cycle between norbornadiene (**1a**) and quadricyclane (**2a**), which has several advantageous properties (Scheme 1) [8,14,24]. In particular, this system shows a high energy storage capacity of up to 1 MJ/kg, and the energy can be conveniently released in form of heat by controlled photolysis, thermolysis, or catalysis [8,14]. However, the parent norbornadiene (**1a**) only absorbs ultraviolet light, which is of limited availability in sunlight. Furthermore, the photoisomerization quantum yield is very low and therefore not suitable for an application [7,8,14]. One promising way to overcome these disadvantages is the introduction of a donor–acceptor system at the norbornadiene double bonds, which has resulted in the development of new generations of modified norbornadiene derivatives with diverse variations of donor and acceptor substituents [25-32]. However, such a modification often leads to higher molar masses and thus to lower energy densities [7,25,33]. Consequently, further fine tuning of the substituents is necessary to accomplish a reasonable balance between the MOST parameters. Hence, to increase the energy density and to induce a decent red shift of the absorption, two, three or even more norbornadiene units may be combined in one integral molecule by attachment to a shared, linking arene unit, such as realized in bis- and tris-norbornadienes **1b–f** (Figure 1) [7,12,30,34,35]. In this particular case, derivatives with only one substituent at the norbornadiene double bond exhibited favorable storage properties because of a lower molecular weight, however, their absorption still lies in the UV range [30]. Therefore, we aimed at further modification of the core structure of bis-and tris-

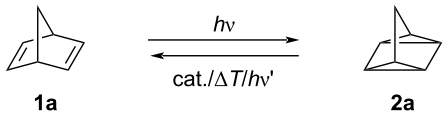

Scheme 1: Photoinduced [2 + 2]-cycloaddition–cycloreversion cycle of norbornadiene (**1a**) and quadricyclane (**2a**).

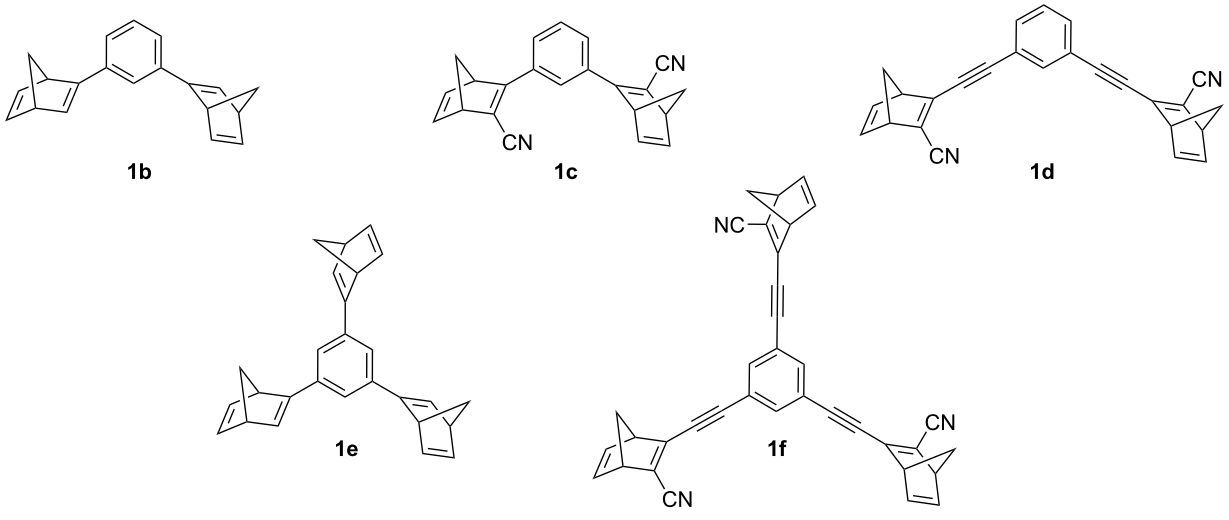

Figure 1: Representative bis- and tris-norbornadienyl-substituted benzene derivatives.

norbornadienes, which may lead to a more pronounced red shift of the absorption while maintaining the high energy density. As this has been shown in other cases already [34], we anticipated that the integration of an acetylene bridge between the arene core and the norbornadiene units in compounds **1h**–**n** may induce these effects. Herein, we present the synthesis of these target molecules and our studies of their photochemical and physicochemical properties with a focus on energy conversion and storage.

Results and Discussion

The norbornadiene derivatives **1h**–**l**,**n** were synthesized by Sonogashira–Hagihara coupling reaction of 2-bromonorbornadiene (**1g**) [36] with the corresponding arylacetylenes **3a**–**g** (Scheme 2). As an exception, 1,4-bis-norbornadienylnaphthalene (**1m**) could not be obtained by this route because the product could not be separated from the complex product mixture. The monosubstituted derivatives **1h** and **1i** were isolated in good yields (60–68%), whereas the bis- and tris-substituted derivatives **1j**–**l**,**n** were only obtained in low yields (26–40%). The latter were more difficult to isolate because by-products interfered with the chromatographic separation; however, these yields are similar to the ones reported for resembling norbornadienes [34,37]. The novel compounds **1h**–**l**,**n** were identified and fully characterized by NMR spectroscopy (^{1}H, ^{13}C, COSY, HSQC, HMBC), melting point, and elemental analysis. All products showed the characteristic ^{1}H NMR spectroscopic signals of norbornadienes, in particular two signals at ca. 2.10 ppm and 2.20 ppm (7-CH_2) and two broad singlets between 3 and 4 ppm (bridgehead 1- and 4-CH). In addition, typical ^{13}C NMR shifts of the aryl-substituted acetylenes at ca. 85 ppm and 95 ppm were observed. The norbornadienes **1h**–**l**,**n** exhibit very good solubility in organic solvents, like ethyl acetate, chloroform, or benzene, whereas they have poor solubility in cyclohexane, acetonitrile, or ethanol. In polar protic solvents, like methanol or water, they are insoluble.

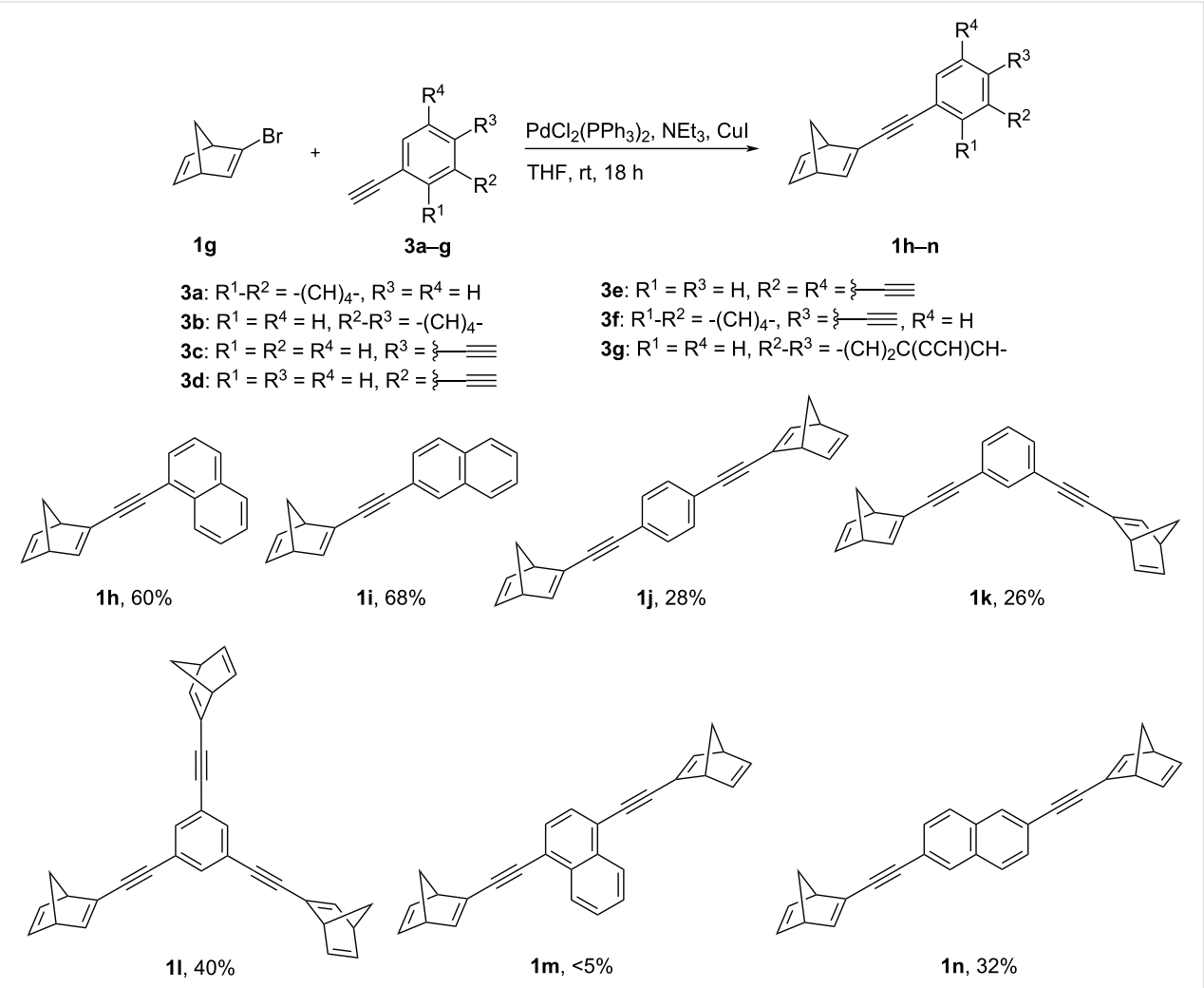

Scheme 2: Synthesis of alkynyl-arene-linked norbornadienes **1h–n** by Sonogashira–Hagihara coupling reactions.

The absorption spectra of compounds **1h–l**,**n** were recorded in different solvents (Table 1, cf., Supporting Information File 1, Figure S1). In general, the employed solvents had only a marginal influence on the absorption properties of each compound. With slight variations caused by the different substitution patterns, the compounds **1h–l**,**n** showed the characteristic long-wavelength bands with maxima between 310 nm (**1k**) and 345 nm (**1n**) and low-energy zero onsets from 345 nm (**1k**) to 420 nm (**1n**). Hence, the red shift of the absorption bands correlates with the size of the respective π-system of the derivatives, and is, thus, more pronounced for the naphthalene-bridged compounds. Likewise, the increased size of the conjugated π-system also led to a red shift of the absorption bands in comparison with the ones of the corresponding norbornadiene derivatives without acetylene bridges (**1b**,**e**) [29,30]. Accordingly, a slightly more pronounced red shift (20 nm) has been reported for derivatives **1d** and **1f** which carry an additional electron-acceptor in the 3-position of the norbornadiene unit [33,34].

The photoisomerization of the norbornadiene derivatives **1h–l**,**n** (Scheme 3) was investigated photometrically in cyclohexane (20 μM, Figure 2), because the norbornadienes and the corresponding quadricyclanes are sufficiently soluble in this solvent and because it allows direct comparison with literature data [30,34]. As a general trend, the long-wavelength absorption maximum of each substrate decreased for all derivatives during the photoreaction, whereas the blue-shifted maximum of the photoproduct was formed. In addition, isosbestic points were observed for the derivatives **1h** (A), **1i** (B), **1k** (D), and **1l** (E). The irradiations of the derivatives **1h**, **1i**, **1k**, and **1l** were

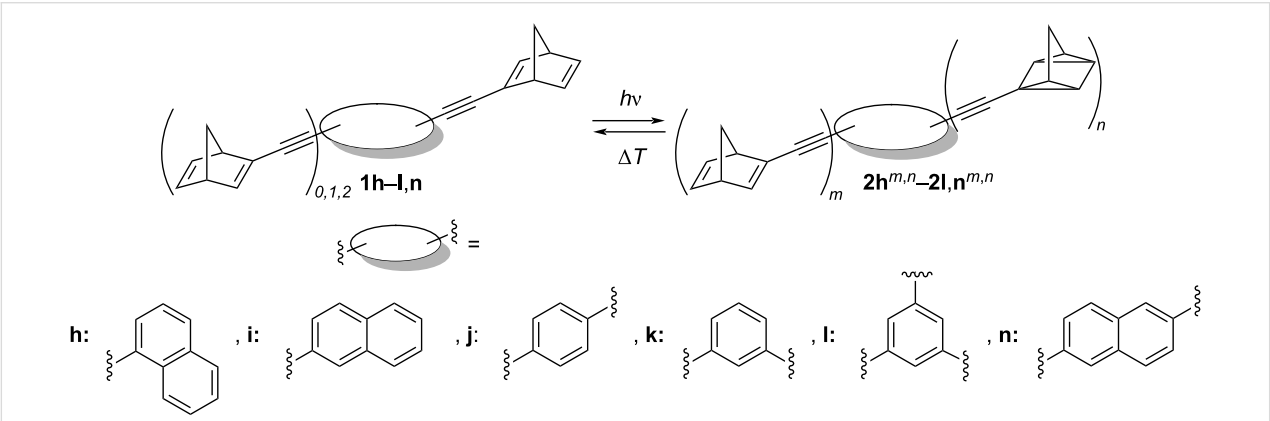

Scheme 3: Photoisomerization of norbornadiene derivatives **1h–l**,**n** (20 μM) to quadricyclanes **2h–l**,**n** in cyclohexane**,** *m* = number of norbornadienylethynyl units, *n* = number of quadricyclylethynyl units.

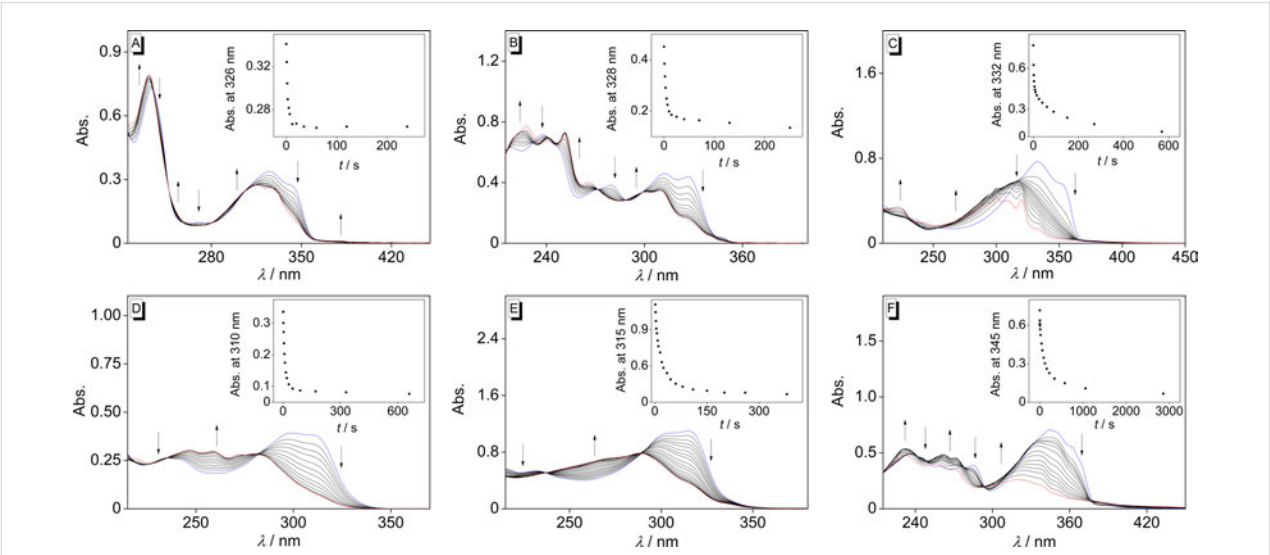

Figure 2: Photometric monitoring of the irradiation of **1h** (A), **1i** (B), **1j** (C), **1k** (D), **1l** (E), and **1n** (F); λ_{ex} = 315 nm (**1h**, **1i**, **1k**, and **1l**) or 340 nm (**1j**, **1n**). Insets: plot of absorption at long-wavelength maximum versus irradiation time *t*.

stopped once no more changes of the absorbance spectra were observed. In the case of compounds **1j** and **1n**, the endpoint of the photoreaction could not be identified, as a steady decrease of the whole absorption spectra during irradiation indicated secondary decomposition reactions.

We previously reported triplet energy transfer between ^{3}[Ru(phen)$_3$](PF$_6$)$_2$ and the corresponding arylnorbornadienes without an acetylene bridge, such as **1o**, leading to efficient and quantitative conversion to the quadricylanes (Scheme 4) [38]. Hence, we assumed that triplet-sensitized isomerization of the mono-, bis-, and tris-norbornadiene derivatives with an alkynylbenzene and alkynylnaphthalene core is also feasible. Quenching experiments of [Ru(phen)$_3$](PF$_6$)$_2$ (triplet energy E_T = 2.19 eV [39]) with **1i** in acetonitrile yielded a triplet energy transfer rate of $k_{EnT} = 5.8 \times 10^9$ M^{-1} s^{-1} indicating very efficient deactivation of the triplet sensitizer (Figure S4 in Supporting Information File 1). This rate is approximately an order of magnitude faster compared with the corresponding naphthylnorbornadiene **1o** without the acetylene bridge, which has a reported triplet energy of 2.41 eV (for details, see Supporting Information File 1, chapter S7). These results suggest that the triplet energy of **1i** is significantly lower than 2.4 eV and even triplet sensitizers with lower triplet energies than that of [Ru(phen)$_3$](PF$_6$)$_2$ could be employed for this reaction, which might even allow red light-driven switching.

In addition to these kinetic studies, the photoisomerization reactions of **1i** and **1l** (20 µM) were investigated in the presence of [Ru(phen)$_3$](PF$_6$)$_2$ (20 µM) at λ_{ex} = 520 nm in acetonitrile (Scheme 4). This solvent was required because of the solubility of the sensitizer. Under these conditions, both derivatives **1i** and **1l** showed the same development of absorption spectra during irradiation as upon direct irradiation, although the reaction times were significantly higher, most likely because of the much weaker molar absorption coefficient of [Ru(phen)$_3$](PF$_6$)$_2$ at 520 nm (≈900 M^{-1} cm^{-1}), and the fact that the photosensitization process is bimolecular (Figure 3). Indeed, the quenching

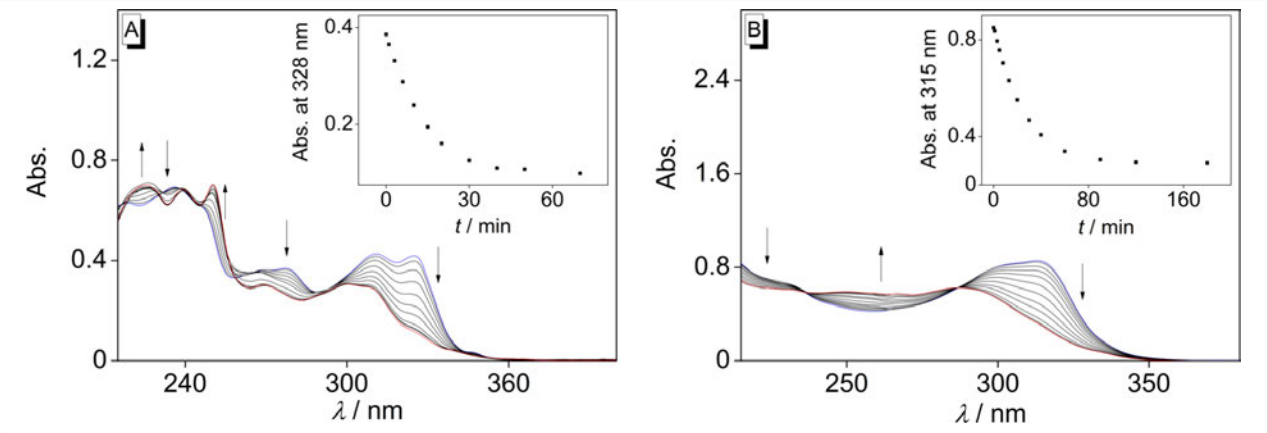

Figure 3: Photometric monitoring of the irradiation of **1i** (A) and **1l** (B) in the presence of [Ru(phen)$_3$](PF$_6$)$_2$; λ_{ex} = 520 nm. For clarity, the absorption of the sensitizer has been deducted. Insets: plot of absorption at long-wavelength maximum versus irradiation time *t* [38].

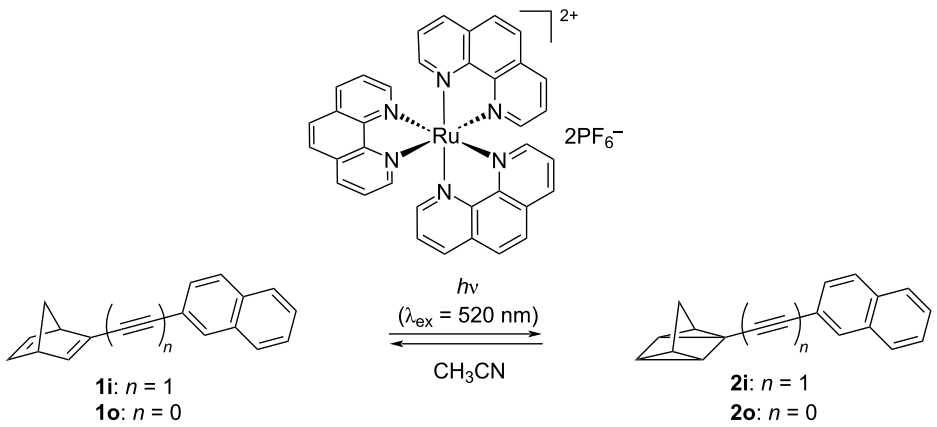

Scheme 4: Triplet-sensitized photoisomerization of norbornadiene **1o** to quadricyclane **2o**.

efficiency of triplet-excited $[Ru(phen)_3](PF_6)_2$ by **1i** was calculated to be as low as 5% under the highly diluted conditions required for the experiments in Figure 3.

In order to gain structural information about the photoproducts, the photoisomerization reactions were also examined by ^{1}H NMR spectroscopy. Initially, all derivatives showed the isomerization reactions to the corresponding quadricyclane derivatives, as identified by the characteristic ^{1}H NMR signal pattern of the quadricyclane fragment with five multiplets at around 1.6 ppm, 1.7 ppm, 1.8 ppm, 2.1 ppm, and 2.2 ppm. However, after relatively short irradiation times of only 30 min, additional signals were detected in the spectrum, which could not be assigned to distinct by-products or secondary products. Unfortunately, the NMR signals of the by-products overlapped with the ones of the norbornadiene and the quadricyclane signals, so that the quantitative analysis of the photostationary state was not possible with NMR spectroscopy. These observations are surprising, since the 3-acceptor-substituted derivatives and the ones without acetylene linkers have been reported to be converted quantitatively into their corresponding quadricyclanes [24,29,30,34].

As the photometric analysis of the photosensitized reaction of **1i** and **1l** pointed to a relatively clean and robust reaction, the irradiation of **1i** in the presence of $[Ru(phen)_3](PF_6)_2$ at λ_{ex} = 520 nm was additionally monitored by in situ NMR spectroscopy [40] (Figure S41 in Supporting Information File 1). With this experiment, it was shown unambiguously that **1i** was quantitatively converted into the corresponding quadricyclane **2i** in the presence of the triplet sensitizer, as clearly indicated by the exclusive formation of the NMR signals of the photoproduct **2a** at 1.60–1.63 ppm, 1.69–1.71 ppm, 1.82–1.85 ppm, 2.07–2.11 ppm, and 2.21–2.25 ppm. Thus, it is possible to convert this monosubstituted norbornadiene efficiently into the corresponding quadricyclane with visible light, and thus also by sunlight. Unfortunately, the derivatives **1h** and **1j–l**,**n** could not be investigated in the presence of the photosensitizer because these substrates have no sufficient solubility in acetonitrile.

To assess the efficiency of the photoreactions, photoisomerization quantum yields were determined in cyclohexane by actinometry (λ_{ex} = 310 nm or 340 nm) [41,42]. The quantum yields varied from only 1% per conversion event, i.e. per norbornadiene unit, for the naphthyl-substituted derivative **1n** to 59% for the *m*-phenyl-linked derivative **1k** (Table 1). In general, the derivatives **1h–l**,**n** showed significantly lower quantum yields than the 3-cyano-substituted derivatives **1d** and **1f** and the analogues **1c** and **1e** without an alkyne linker [29,30,34]. As the only exception, the *m*-substituted derivative **1k** has a higher quantum yield than its analog **1b**, which is, however, still lower than the one of the cyano-substituted norbornadiene **1c** [30,34]. In addition, substitution at the 2- and 2,6-position of the naphthalene unit resulted in low quantum yields, whereas the attachment of the norbornadiene at the 1- or 1,4-position led to significantly higher quantum yields, which is in accordance with previous observations with naphthyl-substituted derivatives [29,30]. Apparently, there is no obvious correlation between the quantum yields of the photoreactions and substitution pattern of the norbornadiene in this series, except for a rough trend that naphthyl-linked derivatives, in particular the ones substituted in the 2-position, have lower quantum yields than the phenyl-linked ones. This lack of correlation may indicate that several different factors and processes contribute to different extent to the course of the photoreaction, for example, steric hindrance and resulting torsion angles between the arene unit and norbornadiene, deactivation of the excited state by intersystem crossing (ISC), internal conversion (IC), or quenching by structural relaxation, etc.

Finally, the half-life, $t_{1/2}$, of the quadricyclane derivatives **2h–l**,**n** was determined by kinetic analysis of the thermally in-

Table 1: Photochemical and physicochemical parameters of the norbornadiene–quadricyclane interconversion of **1h–l**,**n** in cyclohexane.

	λ_{max} [nm][a]	λ_{onset} [nm][b]	λ_{onset} [nm][c]	Φ [%][d]	$\Delta G^{\neq}$ [kJ mol^{-1}][e]	$t_{1/2}$ [h][f]
1h	326	386	366	31 (31)	97	3.6
1i	328	352	357	6 (6)	96	3.0
1j	332	400	392	10 (5)	97	3.1
1k	310	345	336	59 (30)	99	7.8
1l	315	345	355	16 (8)	99	7.6
1n	345	420	412	1 (0.5)	n.d.[g]	n.d.[g]

[a]Long-wavelength absorption maximum of norbornadiene. [b]Zero-onset of norbornadiene absorption (at ε = 10 L mol^{-1} cm^{-1}). [c]Long-wavelength absorption of quadricyclane (at ε = 10 L mol^{-1} cm^{-1}). [d]Quantum yield of photoisomerization per photoconversion event, absolute value in brackets, determined by actinometry. [e]Activation enthalpy of thermally induced cycloreversion of the quadricyclane; determined from Eyring equation. [f]Half-life of the quadricyclane at 20 °C, determined from Eyring equation. [g]Not determined.

duced cycloreversion to the corresponding norbornadiene derivatives **1h–l**,**n** at 60 °C. From these data, the rate constants of the cycloreversion reactions were generated according to first-order kinetics and used to calculate the enthalpy and entropy of activation with the Eyring equation (Table 1, cf. Supporting Information File 1, equation S5). The analyses revealed half-lives of the quadricyclanes from 3.0 h to 7.8 h, which are essentially in the same range as the ones of analogues with an acceptor-substituent in the 3-position of the norbornadiene [34]. Notably, the quadricyclane derivatives with sterically more demanding substituents in the 2-position of the norbornadiene unit, such as **1e**, showed longer half-lives. Therefore, compounds **1h–l**,**n** have significanty lower half-lives than the corresponding analogues without an alkyne linker [29,30].

Conclusion

In summary, a small series of mono-, bis-, and tris-norbornadiene derivatives with alkynylbenzene and alkynylnaphthalene core units was made available in reasonable yields by Sonogashira–Hagihara coupling reactions and the potential of these compounds for MOST applications was assessed. In particular, the compounds showed red-shifted absorption of up to 420 nm. Upon direct irradiation, the norbornadienes are converted into the corresponding quadricyclanes, which have short half-lives of only a few hours. The photoisomerization quantum yields were, with one exception, relatively low, as compared with the ones of other, structurally resembling norbornadiene derivatives [30,34]. Moreover, upon prolonged reaction time, significant amounts of unidentified by-products formed. Nevertheless, it was shown exemplarily that the photoisomerization can be performed under milder conditions and upon excitation with visible light in the presence of $[Ru(phen)_3](PF_6)_2$ as a photosensitizer. Under these conditions, the derivatives **1i** and **1l** were converted quantitatively into quadricyclanes by irradiation with green light. Thus, it was shown with the latter results that the photosensitization with suitable triplet sensitizers enables mild conversion of visible light in chemical energy in quantitative photoreactions of norbornadienes, even in cases that are rather problematic under direct irradiation.

The original target design, starting from the promising class of solely hydrocarbon-based, monoaryl-substituted norbornadienes, aimed primarily at the optimization of the absorption properties without adversely affecting the other advantageous MOST properties. However, although the integration of alkyne-linker units into otherwise unsubstituted arene-linked mono-, bis-, and tris-norbornadienes resulted in the anticipated red shift of the absorption, this slight advantage was established to the disadvantage of other relevant MOST properties, especially photostability. From these results, it may be concluded that the sole addition of alkyne units to optimize MOST materials should be handled carefully because in some cases, like the one reported herein, it may result in an unfavorable tradeoff between the distinct MOST properties. After all, it still remains a challenge to design MOST materials with well-balanced advantageous properties. Based on the results presented herein, it may be proposed that the optimization of monoaryl-substituted norbornadienes along these lines should focus more on the factors that lead to improved stability, energy storage capacity and back reaction of the quadricyclane, and not primarily on the implementation of red-shifted absorption into the visible range. Specifically, the latter can easily be addressed in a more efficient way by the application of a suitable photosensitizer, as shown exemplarily in this work.

Supporting Information

Supporting Information File 1

Experimental section and complete set of NMR spectra.
[https://www.beilstein-journals.org/bjoc/content/supplementary/1860-5397-20-254-S1.pdf]

Funding

Financial support was provided by the University of Siegen. R.S. is grateful to the House of Young Talents (University of Siegen) and the Stiftung Nagelschneider for the Ph.D. fellowships. T.J.B.Z. thanks the Deutsche Bundesstiftung Umwelt (DBU) for a Ph.D. fellowship.

ORCID® iDs

Christoph Kerzig - https://orcid.org/0000-0002-1026-1146
Heiko Ihmels - https://orcid.org/0000-0003-0969-0426

Data Availability Statement

All data that supports the findings of this study is available in the published article and/or the supporting information of this article.

References

1. Ramanauske, N.; Balezentis, T.; Streimikiene, D. *Technol. Forecast. Soc. Change* **2023,** *193,* 122628. doi:10.1016/j.techfore.2023.122628
2. Lam, D. *Popul. Environ.* **2023,** *45,* 10. doi:10.1007/s11111-023-00422-7
3. Duarah, P.; Haldar, D.; Patel, A. K.; Dong, C.-D.; Singhania, R. R.; Purkait, M. K. *Bioresour. Technol.* **2022,** *348,* 126791. doi:10.1016/j.biortech.2022.126791
4. Copley, J. *Compet. Change* **2023,** *27,* 429–448. doi:10.1177/10245294221120986
5. Breeze, P. A. Solar Power. *Power generation technologies,* 3rd ed.; Newnes: Amsterdam, Netherlands, 2019; pp 293–321. doi:10.1016/b978-0-08-102631-1.00013-4

6. Milanić, O. Š.; Pratt, J. A. *Introduction to energy and sustainability;* Wiley-VCH: Weinheim, Germany, 2021; pp 51–469.
7. Wang, Z.; Hölzel, H.; Moth-Poulsen, K. *Chem. Soc. Rev.* **2022,** *51,* 7313–7326. doi:10.1039/d1cs00890k
8. Orrego-Hernández, J.; Dreos, A.; Moth-Poulsen, K. *Acc. Chem. Res.* **2020,** *53,* 1478–1487. doi:10.1021/acs.accounts.0c00235
9. Iloeje, C. O.; Xavier, A. S.; Graziano, D.; Atkins, J.; Sun, K.; Cresko, J.; Supekar, S. D. *iScience* **2022,** *25,* 104830. doi:10.1016/j.isci.2022.104830
10. Wang, Z.; Erhart, P.; Li, T.; Zhang, Z.-Y.; Sampedro, D.; Hu, Z.; Wegner, H. A.; Brummel, O.; Libuda, J.; Nielsen, M. B.; Moth-Poulsen, K. *Joule* **2021,** *5,* 3116–3136. doi:10.1016/j.joule.2021.11.001
11. Dong, L.; Feng, Y.; Wang, L.; Feng, W. *Chem. Soc. Rev.* **2018,** *47,* 7339–7368. doi:10.1039/c8cs00470f
12. Salthouse, R. J.; Moth-Poulsen, K. *J. Mater. Chem. A* **2024,** *12,* 3180–3208. doi:10.1039/d3ta05972c
13. Yoshida, Z.-i. *J. Photochem.* **1985,** *29,* 27–40. doi:10.1016/0047-2670(85)87059-3
14. Bren', V. A.; Dubonosov, A. D.; Minkin, V. I.; Chernoivanov, V. A. *Russ. Chem. Rev.* **1991,** *60,* 451–469. doi:10.1070/rc1991v060n05abeh001088
15. Jones, G., II; Reinhardt, T. E.; Bergmark, W. R. *Sol. Energy* **1978,** *20,* 241–248. doi:10.1016/0038-092x(78)90103-2
16. Kolpak, A. M.; Grossman, J. C. *Nano Lett.* **2011,** *11,* 3156–3162. doi:10.1021/nl201357n
17. Taoda, H.; Hayakawa, K.; Kawase, K.; Yamakita, H. *J. Chem. Eng. Jpn.* **1987,** *20,* 265–270. doi:10.1252/jcej.20.265
18. Wang, Z.; Losantos, R.; Sampedro, D.; Morikawa, M.-a.; Börjesson, K.; Kimizuka, N.; Moth-Poulsen, K. *J. Mater. Chem. A* **2019,** *7,* 15042–15047. doi:10.1039/c9ta04905c
19. Lennartson, A.; Roffey, A.; Moth-Poulsen, K. *Tetrahedron Lett.* **2015,** *56,* 1457–1465. doi:10.1016/j.tetlet.2015.01.187
20. Arpa, E. M.; Durbeej, B. *Chem.: Methods* **2023,** *3,* e202200060. doi:10.1002/cmtd.202200060
21. Skov, A. B.; Petersen, J. F.; Elm, J.; Frandsen, B. N.; Santella, M.; Kilde, M. D.; Kjaergaard, H. G.; Mikkelsen, K. V.; Nielsen, M. B. *ChemPhotoChem* **2017,** *1,* 206–212. doi:10.1002/cptc.201600046
22. Brough, S. A.; Lamm, A. N.; Liu, S.-Y.; Bettinger, H. F. *Angew. Chem., Int. Ed.* **2012,** *51,* 10880–10883. doi:10.1002/anie.201203546
23. Edel, K.; Yang, X.; Ishibashi, J. S. A.; Lamm, A. N.; Maichle-Mössmer, C.; Giustra, Z. X.; Liu, S.-Y.; Bettinger, H. F. *Angew. Chem., Int. Ed.* **2018,** *57,* 5296–5300. doi:10.1002/anie.201712683
24. Kuisma, M. J.; Lundin, A. M.; Moth-Poulsen, K.; Hyldgaard, P.; Erhart, P. *J. Phys. Chem. C* **2016,** *120,* 3635–3645. doi:10.1021/acs.jpcc.5b11489
25. Gray, V.; Lennartson, A.; Ratanalert, P.; Börjesson, K.; Moth-Poulsen, K. *Chem. Commun.* **2014,** *50,* 5330–5332. doi:10.1039/c3cc47517d
26. Jevric, M.; Petersen, A. U.; Mansø, M.; Kumar Singh, S.; Wang, Z.; Dreos, A.; Sumby, C.; Nielsen, M. B.; Börjesson, K.; Erhart, P.; Moth-Poulsen, K. *Chem. – Eur. J.* **2018,** *24,* 12767–12772. doi:10.1002/chem.201802932
27. Wang, Z.; Roffey, A.; Losantos, R.; Lennartson, A.; Jevric, M.; Petersen, A. U.; Quant, M.; Dreos, A.; Wen, X.; Sampedro, D.; Börjesson, K.; Moth-Poulsen, K. *Energy Environ. Sci.* **2019,** *12,* 187–193. doi:10.1039/c8ee01011k
28. Schulte, R.; Ihmels, H. *Beilstein J. Org. Chem.* **2022,** *18,* 368–373. doi:10.3762/bjoc.18.41
29. Schulte, R.; Afflerbach, S.; Ihmels, H. *Eur. J. Org. Chem.* **2023,** *26,* e202201398. doi:10.1002/ejoc.202201398
30. Schulte, R.; Afflerbach, S.; Paululat, T.; Ihmels, H. *Angew. Chem., Int. Ed.* **2023,** *62,* e202309544. doi:10.1002/anie.202309544
31. Aslam, A. S.; Muhammad, L. M.; Erbs Hillers-Bendtsen, A.; Mikkelsen, K. V.; Moth-Poulsen, K. *Chem. – Eur. J.* **2024,** *30,* e202401430. doi:10.1002/chem.202401430
32. Weber, R. R.; Stindt, C. N.; van der Harten, A.-L. M. J.; Feringa, B. L. *Chem. – Eur. J.* **2024,** *30,* e202401512. doi:10.1002/chem.202401512
33. Quant, M.; Lennartson, A.; Dreos, A.; Kuisma, M.; Erhart, P.; Börjesson, K.; Moth-Poulsen, K. *Chem. – Eur. J.* **2016,** *22,* 13265–13274. doi:10.1002/chem.201602530
34. Mansø, M.; Petersen, A. U.; Wang, Z.; Erhart, P.; Nielsen, M. B.; Moth-Poulsen, K. *Nat. Commun.* **2018,** *9,* 1945. doi:10.1038/s41467-018-04230-8
35. Kilde, M. D.; Mansø, M.; Ree, N.; Petersen, A. U.; Moth-Poulsen, K.; Mikkelsen, K. V.; Nielsen, M. B. *Org. Biomol. Chem.* **2019,** *17,* 7735–7746. doi:10.1039/c9ob01545k
36. Tranmer, G. K.; Yip, C.; Handerson, S.; Jordan, R. W.; Tam, W. *Can. J. Chem.* **2000,** *78,* 527–535. doi:10.1139/v00-047
37. Mansø, M.; Tebikachew, B. E.; Moth-Poulsen, K.; Nielsen, M. B. *Org. Biomol. Chem.* **2018,** *16,* 5585–5590. doi:10.1039/c8ob01470a
38. Zähringer, T. J. B.; Perez Lopez, N.; Schulte, R.; Schmitz, M.; Ihmels, H.; Kerzig, C. *Angew. Chem., Int. Ed.* **2024,** e202414733. doi:10.1002/anie.202414733
39. Vlcek, A. A.; Dodsworth, E. S.; Pietro, W. J.; Lever, A. B. P. *Inorg. Chem.* **1995,** *34,* 1906–1913. doi:10.1021/ic00111a043
40. Paululat, T.; Rabe, M.; Berdnikova, D. V. *J. Magn. Reson.* **2021,** *327,* 106990. doi:10.1016/j.jmr.2021.106990
41. Stranius, K.; Börjesson, K. *Sci. Rep.* **2017,** *7,* 41145. doi:10.1038/srep41145
42. Hatchard, C. G.; Parker, C. A. *Proc. R. Soc. London, Ser. A* **1956,** *235,* 518–536. doi:10.1098/rspa.1956.0102

License and Terms

This is an open access article licensed under the terms of the Beilstein-Institut Open Access License Agreement (https://www.beilstein-journals.org/bjoc/terms), which is identical to the Creative Commons Attribution 4.0 International License (https://creativecommons.org/licenses/by/4.0). The reuse of material under this license requires that the author(s), source and license are credited. Third-party material in this article could be subject to other licenses (typically indicated in the credit line), and in this case, users are required to obtain permission from the license holder to reuse the material.

The definitive version of this article is the electronic one which can be found at:
https://doi.org/10.3762/bjoc.20.254

7 Photon Upconversion via Triplet–Triplet Annihilation

Photon upconversion (UC) in general describes a process where the energy of multiple photons is combined into one photon of higher energy. Multiple mechanisms have been described so far that follow this process. Among them are simultaneous two-photon-absorption (TPA),[280] second harmonic generation (SHG),[281] upconversion nanoparticles (UCNPs),[282] and triplet–triplet annihilation upconversion (TTA–UC).[14] Yet, TTA–UC is the only mechanism that can operate using non-coherent and mild excitation light sources (e.g. sunlight) making it an attractive alternative for generating higher-energy photons in certain applications compared to conventional one-photon photochemistry.[283]

TTA–UC usually requires a photosensitizer and a triplet energy acceptor that can undergo triplet–triplet annihilation (annihilator). A schematic energy diagram of the mechanism is displayed in Figure 23A. First, the photosensitizer (PS) absorbs a photon yielding the triplet-excited state after intersystem crossing (^{3}PS*). In some cases, the sensitizer can be directly promoted into the triplet state.[284] Next, triplet energy transfer to the annihilator (A) follows. Two triplet-excited annihilators (^{3}A*) can then undergo triplet–triplet annihilation to form one singlet-excited state (^{1}A*) (see Chapter 3.4 for details).[14,29,285] The singlet-excited annihilator can finally emit a photon. A basic feature of TTA–UC is that the incident photon energy used to excite the sensitizer is lower than the energy of the photon emitted by the annihilator from the singlet-excited state, commonly referred to as the anti-Stokes shift.

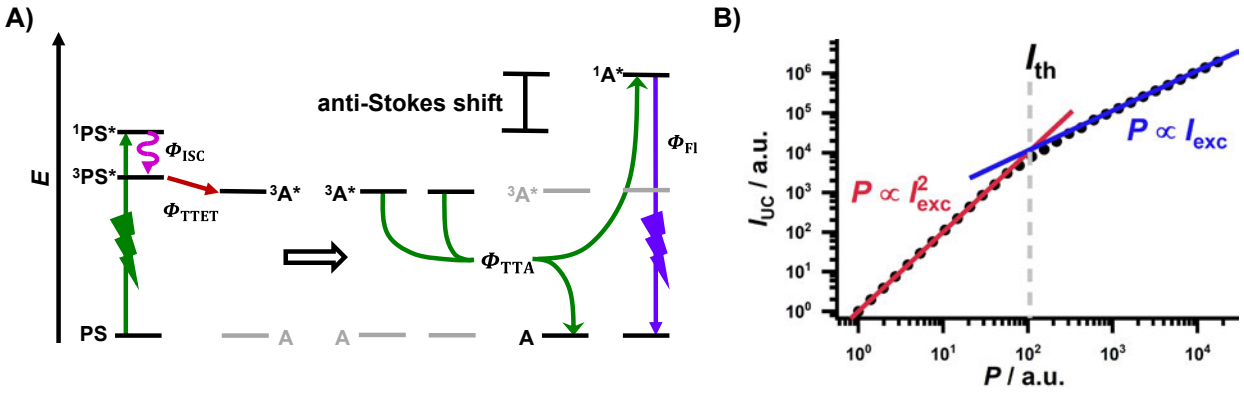

Figure 23: A) Schematic energy diagram of TTA–UC mechanism (see text for details). B) UC emission intensity plotted against the excitation power for a typical TTA–UC system on a double logarithmic scale. The quadratic (red) and linear (blue) regimes are fitted with linear functions.

The efficiency of this process is most commonly reported as the upconversion quantum yield Φ_{UC}, which is essentially the number of photons that are absorbed by the sensitizer compared to the number of photons emitted by the annihilator. The upconversion quantum yield can be factorized into the quantum yield of each individual step during TTA–UC:

$$\Phi_{UC} = \Phi_{ISC} \times \Phi_{TTET} \times \Phi_{TTA} \times \Phi_{Fl} \times f \quad (9)$$

Where Φ_{ISC} is the intersystem crossing quantum yield, Φ_{TTET} is the triplet–triplet energy transfer quantum yield, Φ_{TTA} is triplet–triplet annihilation quantum yield, Φ_{Fl} is the fluorescence quantum yield of the annihilator and f is the spin-statistical probability of forming a singlet-excited state after TTA. Since two photons are required in the process, the theoretical limit of Φ_{UC} is defined at 0.5. Φ_{ISC} and Φ_{Fl} are intrinsic properties of the sensitizer and annihilator, while Φ_{TTET} and Φ_{TTA} depend on the concentration of the species. They can all approach unity in theory.

The spin-statistical factor f describes the ratio of generated singlet-excited molecules to the formation of triplet pair encounter complexes of the annihilator. If each triplet encounter pair were formed with equal probability, a spin-statistical limit of 1/9 would apply (compare Figure 8).[111] However, since the quintet channel is thermodynamically inaccessible for nearly all organic chromophores and the triplet channel effectively deactivates one triplet state while allowing the other to undergo TTA again, f is recalculated with a limit of 2/5.[110] In real systems, the spin factor is affected by various factors, including the chemical structure and energetics of the annihilator. For example, bulky substituents can influence molecular orientation during the formation of the triplet encounter pair, thereby impacting inter-triplet exchange coupling.[110,286,287] Additionally, the energy levels of higher excited states play a crucial role in determining f. If a higher-lying triplet state is energetically close to 2 × T_1, it can either enhance non-radiative decay, thereby decreasing f, or promote reverse intersystem crossing to the singlet from the triplet manifold, which increases f.[109,288,289] The triplet channel may also be suppressed if the energy of T_2 is higher than 2 x T_1.[290]

A fundamental property of TTA–UC is the threshold intensity (I_{th}), which defines the excitation intensity at which the system reaches its optimal efficiency (Figure 23B). In the low excitation intensity regime, the TTA pathway is inefficient, and most triplet-excited annihilators undergo natural decay to the ground state. Here, the upconverted emission (I_{UC}) follows a quadratic dependence on the excitation intensity (I_{exc}). At high excitation intensities, TTA is the dominant decay pathway, while the fraction of natural triplet decay is negligible. In this regime, I_{UC} exhibits a linear relationship with I_{exc}. The system slowly transitions from quadratic to linear behavior, as the incident light intensity increases from low to high.

To determine I_{th}, I_{UC} is plotted against I_{exc} on a double-logarithmic scale. Two linear fits – one for the low-intensity (quadratic) regime and another for the high-intensity (linear) regime – are used to identify I_{th} as the intersection of these two fits (Figure 23B). At this threshold, exactly half of the triplet states decay via the TTA pathway, while the other half undergoes natural decay.

The general requirements for annihilators are:

- High fluorescence quantum yield
- 2 × T_1 > S_1 (but large ΔE_{ST} required for anti-Stokes shift)
- Long triplet lifetime
- High spin statistical factor f

Common annihilators are typically derived from heteroarenes[289,291] diketopyrrolopyrroles,[292,293] phenylenes,[86,294,295] acenes,[138,139,296,297] pyrenes, and rylenes[109,290,298] (Figure 24). These compounds are usually functionalized with alkyl, aryl, nitrile,[299] alkylsilyl groups,[139,286] and heteroarenes[299] which serve multiple purposes, primarily tuning the excited singlet and triplet state energies[45] and preventing excimer formation.[286,299,300]

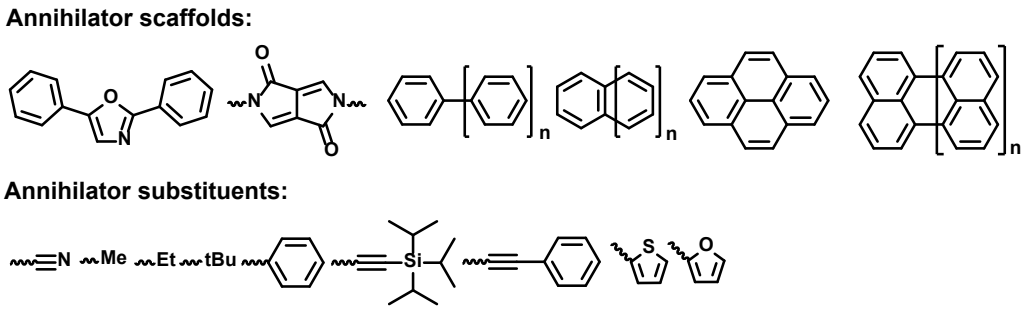

Figure 24: Molecular structure of common annihilator scaffolds and typical substituents.

Key criteria for sensitizers include:

- A high absorption coefficient within the incident light range while maintaining a low absorption coefficient in the annihilator's emission range.
- High ISC quantum yield
- Long triplet lifetime
- Small ΔE_{ST}

Common sensitizers can be classified into five categories: (i) ketones, (ii) thermally activated delayed fluorescence (TADF) emitters, (iii) metal complexes, (iv) hybrid organic/inorganic nanoparticles, and (v) BODIPYs. The underlying mechanisms that enable a high ISC quantum yield and a small singlet-triplet energy gap in these molecules are discussed in Chapter 3.3. Ketones such as biacetyl and 3,3′-carbonylbis(7-diethylaminocoumarin) (CBDAC) are cost-effective to produce but generally suffer from poor stability.[291,301] TADF emitters have gained significant attention in the TTA–UC community due to their small singlet-triplet energy gap and high ISC rates as purely organic chromophores. Representative examples include B,N-heteroarene-based compounds[69,74,302] and cyanoarene-based donor-acceptor chromophores,[289,294] such as 4CzIPN, BN-2Cz, and BN-Se (see Figure 3 for molecular structures). Metal complexes typically feature Ir,[139,291] Ru,[303] Os,[284,304] Pd,[283,305] or Pt as the central metal, coordinated with ligands such as porphyrins, phenylpyridyl, and bipyridyl derivatives. In contrast, hybrid nanoparticles are generally composed of semiconductors like PbS,[306–308] ZnSe,[138] $CuInS_2$,[309] $CsPbBr_3$,[310] and InP.[311,312] These materials exhibit short-lived excited states, requiring the coordination of triplet acceptors at their outer surface to facilitate triplet energy transfer. BODIPYs have frequently been considered as triplet sensitizers for their large molar absorption coefficient, high photostability, and ease of synthetic modification.[313,314]

The first report of UC emission dates back to 1962 when Parker and Hatchard observed the delayed emission of naphthalene sensitized by phenanthrene.[315] They proposed a triplet–triplet quenching mechanism that, for the first time, described a species carrying the combined energy of two triplet states. In the following years research focused on different combinations of organic aromatic compounds for TTA–UC.[316–318] However, its attraction beyond fundamental scientific research stayed limited likely due to the absence of suitable sensitizers. TTA–UC was rediscovered in the 21st century, with the introduction of photoactive metal complexes as triplet sensitizers.[319] Baluschev et al. demonstrated its potential and advantages over other two-photon processes, particularly its ability to operate with non-coherent light and low excitation intensities.[283,320] They employed a TTA–UC system consisting of a palladium porphyrin sensitizer and diphenylanthracene annihilator, using sunlight as the excitation source. Since then, TTA–UC has advanced in various areas, including mechanistic studies,[109,110] efficiency improvements,[289] and the development of numerous applications[113]. These applications can be classified into four categories: (i) synthetic applications that utilize the high singlet state energy of the annihilator in photoredox or energy transfer catalysis;[112,296,304] (ii) polymer curing (e.g., in 3D printing);[321] (iii) soft tissue bioimaging and photodynamic therapy (biological/medical applications);[322] and (iv) harnessing sub-bandgap photons for solar cells and photovoltaic applications.[323] A key advantage of TTA–UC in nearly all these applications is its deeper penetration depth compared to one-photon photochemistry. This property is particularly beneficial when aiming to trigger a sub-surface reaction in a material with a uniform reaction rate. In conventional photochemistry, high-energy photons are rapidly attenuated at the surface, leading to a concentrated reaction zone near the surface and an uneven distribution of reaction rates throughout the material. In contrast, with TTA–UC, the excitation light can penetrate deeper before generating higher-energy photons in situ, enabling a more uniform and selective reaction profile.

This chapter presents projects **[I]**, **[J]**, **[K]**, **[L]**, and **[M]**, all of which are centered around the process of TTA–UC. Project **[I]** explored a novel BODIPY-based triplet sensitizer that was combined with 2,5,8,11-tetra-*tert*-butylperylene as the annihilator in a purely organic green-to-blue TTA–UC system. The excited singlet state of the annihilator generated by the UC scheme was further exploited for substrate activation and subsequent synthetic applications. Projects **[J]** through **[L]** focused on the identification of new UV annihilators. In project **[J]**, a biphenyl-based annihilator is introduced – capable of blue-to-UVB TTA–UC – with a singlet excited-state energy for the first time exceeding 4 eV. Project **[K]** reported the discovery of a benzene-based annihilator with even higher emission energy for blue-to-UVB TTA–UC, suitable for activating otherwise inert UVB-absorbing substrates. Finally, project **[L]** presents a TTA–UC strategy employing another benzene-based annihilator in combination with a high triplet energy sensitizer, enabling the upconversion of UVA light reaching in the UVC range. The discoveries of project **[J]**, **[K]**, and **[L]** have expanded the range of TTA–UC starting at the UVA/UVB border of 315 nm to covering the complete UVB spectrum and reaching into UVC. Not only was the limit of TTA–UC considerably pushed but it was also demonstrated that the highly energetic singlet states could be utilized in a subsequent activation of inert substrates. Project **[M]** provides a review of recent advances in visible-to-UV TTA–UC, cataloging all reported sensitizer–annihilator pairs by their excited-state energies. It covered strategies to enhance efficiency and lower excitation thresholds, highlighted key systems with large anti-Stokes shifts, and

included a dedicated section on Blue-to-UVB TTA–UC based on this thesis. The review also outlined chemical applications of UV annihilators and discussed developments in upconversion films.

Collectively, projects **[I]** to **[M]** significantly advanced the field of TTA–UC through the development of new sensitizer and annihilator structures. They broadened both the spectral range and practical applications of TTA–UC, demonstrating its potential not just as an alternative light source but as a mild and effective tool for direct substrate activation. These findings offer valuable insights for both the TTA–UC community and synthetic organic chemists.

7.1 A New Green-to-Blue Upconversion System with Efficient Photoredox Catalytic Properties

For synthetic applications, a key advantage of TTA–UC is that higher energy levels or redox potentials can be achieved that are not limited by the energy of the incident photons. This enables the use of well-established sensitizers in combination with suitable annihilators that would otherwise be ineffective in initiating the reaction.[112] Additionally, the lower energy of the incident photons enables more selective substrate activation, whereas higher-energy photons increase the substrate scope being limited owing to unintended absorption and possible side reactions. Two examples that make use of the high singlet-excited state energy are: (i) The photodimerization of anthracene: $[Ru(dmb)_3]^{2+}$ acts as sensitizer and the annihilator anthracene acts as the substrate, undergoing a [4 + 4] cycloaddition with another ground state annihilator from the singlet-excited state.[303] (ii) A dehalogenation reaction of aryl bromides was achieved with a sensitizer-annihilator combination of biacetyl and PPO irradiated with a 430 nm pulsed laser (15 mJ).[324] However, a major drawback of TTA–UC for photoredox catalysis is the stability issue associated with the process, as well as the complex and costly production of precious metal complexes frequently employed.[112,296,303] In light of these challenges, BODIPY-based triplet sensitizers have gained attention as promising alternatives due to their superior photostability, cost-effective production, and ease of functionalization, making them attractive candidates for TTA–UC applications.[325]

In project **[I]**, a metal-free upconversion system that enables challenging reductions under green light excitation was developed. A tailor-made BODIPY-like triplet sensitizer combined triplet formation, high photostability, and effective energy transfer, generating a strongly reducing singlet-excited state annihilator (~2 V). The use of durable green light sources made this approach broadly accessible for selective photoredox catalysis. This work broadens the scope of BODIPY sensitizers and advances the use of TTA–UC in driving photoredox reactions.

Summary:

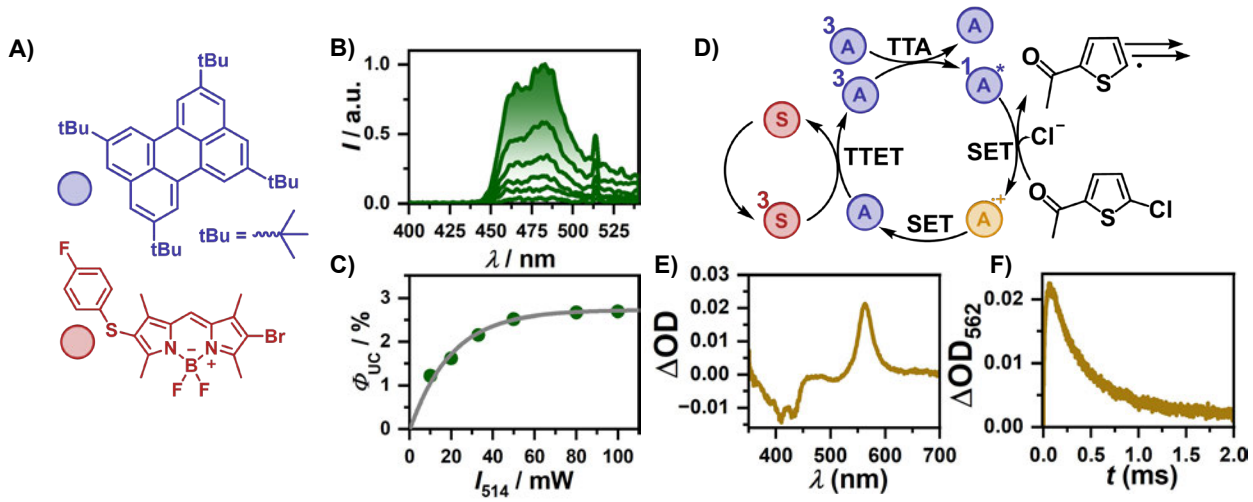

Figure 25: Spectroscopic investigation of the green-to-blue UC system. A) Molecular structures of TBPe and BODIPY-Br. B) UC emission after 514 nm cw laser excitation. C) UC quantum yield plotted against the cw laser intensity. D) Mechanism of TTA–UC enabled oxidation of 2-acetyl-5-chlorothiophene. E) TA spectrum of TBPe radical cation F) Kinetic TA traces of TBPe radical cation.

A novel asymmetric BODIPY triplet sensitizer is introduced, 6-bromo-2-(4-fluorophenyl)thio-1,3,5,7-tetramethyl4,4-difluoro-4-bora-3a,4a-diaza-s-indacene (BODIPY-Br), for TTA–UC with subsequent photoredox applications (Figure 25A). The parent BODIPY was modified with a 4-fluorophenyl sulfide group on one side of the chromophore and a bromine atom on the opposite side resulted in an asymmetric structure with strong absorption in the green region, moderate ISC rates, and a long-lived triplet state. The ISC quantum yield was determined to be 0.16 through relative laser flash photolysis (LFP) actinometry using $[Os(phen)_3](PF_6)_2$ as the reference system. 2,5,8,11-Tetra-*tert*-butylperylene (TBPe) was identified as a suitable annihilator based on 77 K phosphorescence measurements (Figure 25A). The sensitizer-annihilator pair was thoroughly examined using LFP with 532 nm laser pulses, providing clear evidence of the TTA–UC mechanism. The upconversion quantum yield was determined to be 2.7% under continuous-wave (cw) laser excitation at 514 nm (Figure 25B and C). This UC system was successfully applied to catalyze challenging reduction reactions under green-light excitation (Figure 25D). Upon the addition of 2-acetyl-5-chlorothiophene as a substrate, the oxidized species of TBPe, formed via electron transfer, was spectroscopically detected, confirming the photoredox activity of the system (Figure 25E and F).

Project **[I]** was published as a research article:

"**A new green-to-blue upconversion system with efficient photoredox catalytic properties**"

Reproduced from Reference: J. Castellanos-Soriano, T. J. B. Zähringer, J. C. Herrera-Luna, M. C. Jiménez, C. Kerzig, R. Pérez-Ruiz, *Phys. Chem. Chem. Phys.* **2023**, *25*, 12041–12049. With permission from the PCCP Owner Societies.

The article is Open Access (licensed under CC BY-NC 3.0 https://creativecommons.org/licenses/by/3.0/) and was reproduced from ref.[I]. The reference is attached in the following pages and the supporting information can be found in Chapter 10.10.

Author contributions: R. Pérez-Ruiz conceived the Project. J. Castellanos-Soriano J. C. Herrera-Luna and M. C. Jiménez carried out the synthesis, electrochemical characterization and irradiation experiments. T. J. B. Zähringer performed spectroscopy measurements under the guidance of C. Kerzig. The manuscript was written by J. Castellanos-Soriano, T. J. B. Zähringer, R. Pérez-Ruiz and C. Kerzig.

PCCP

PAPER

View Article Online
View Journal | View Issue

Check for updates

Cite this: *Phys. Chem. Chem. Phys.*, 2023, **25**, 12041

A new green-to-blue upconversion system with efficient photoredox catalytic properties†

Jorge Castellanos-Soriano, [a] Till J. B. Zähringer, [b] Jorge C. Herrera-Luna, [a] M. Consuelo Jiménez, [a] Christoph Kerzig *[b] and Raúl Pérez-Ruiz *[a]

Received 21st February 2023,
Accepted 4th April 2023

DOI: 10.1039/d3cp00811h

rsc.li/pccp

The design and development of new triplet–triplet annihilation upconversion (TTA-UC) systems combining triplet sensitizers with acceptor compounds have attracted considerable interest. In this vein, sensitizers made from purely organic dyes rather than transition-metal complexes appear to be more convenient from an environmental point of view. BODIPYs are a very well-known class of dyes with applications in a widespread range of scientific areas. Owing to the versatility of BODIPYs, we present herein a new asymmetric BODIPY with excellent photophysical properties to be used as an appropriate sensitizer in a bimolecular TTA-UC system. Detailed spectroscopic measurements demonstrated the ability of this new design to sensitize TTA-UC by combination with a suitable acceptor such as 2,5,8,11-tetra-*tert*-butylperylene (**TBPe**), allowing a successful conversion of green to blue light. The singlet-excited **TBPe** so obtained is capable of activating aryl chlorides reductively which initiated the functionalization of *N*-methylpyrrole (Meerwein-type arylation) and formation of both substituted triarylethylenes (Mizoroki–Heck reaction) and heteroarene phosphonates (photo-Arbuzov reaction). Product yields reveal that our TTA-UC system behaved as a highly efficient photocatalytic entity.

Open Access Article. Published on 05 April 2023. Downloaded on 6/16/2025 5:07:55 PM.
This article is licensed under a Creative Commons Attribution-NonCommercial 3.0 Unported Licence.

Introduction

Photon upconversion based on triplet–triplet annihilation (TTA-UC) has attracted considerable interest in the last decade due to its applicability to a broad range of scientific areas such as anticounterfeiting,[1] solar fuels,[2,3] photovoltaics,[4–7] biophotonics,[8–12] and more recently in photoredox catalysis.[13–15] The motivation for employing this phenomenon is mainly due to two reasons: (i) the development of numerous TTA-UC systems (from hybrid organic/inorganic to purely organic materials) that provide lots of chances for their applications,[16] and (ii) the high efficiency at low excitation intensities with non-coherent light[17,18] in comparison with other UC systems based on two-photon absorption.[19]

Typical TTA-UC implies the association of multistep photochemical events (Fig. 1A). After absorption of low energy photons ($h\nu_1$), the triplet excited state (T_1) of the sensitizer (or a donor) is produced by intersystem crossing (ISC) from the singlet excited state (S_1). Subsequently, triplets of the annihilator (or an acceptor) are populated through triplet–triplet energy transfer (TTEnT) from the triplets of the sensitizer (the Dexter mechanism). When two annihilator molecules at their triplet states are able to collide during their lifetimes, a higher singlet energy level is formed by means of triplet–triplet annihilation (TTA) and delayed upconverted fluorescence ($h\nu_2$) is consequently generated. The emission energy of the new photon is greater than the energy of the initially absorbed photon, making this procedure one of the most attractive wavelength conversion technologies.

Based on the literature data, Pd and Pt porphyrins as sensitizers[20] coupled with organic emitters like rubrene,[21] perylene[22] and diphenylanthracene[23] are found to be the most common TTA-UC systems. The triplet formation of the sensitizers occurs efficiently *via* spin–orbital interactions promoted by the heavy atoms (noble metals such as Pd and Pt), permitting the UC luminescence of the system. Investigations regarding other sensitizers such as semiconductor nanocrystals,[24] quantum dots,[25] perovskites,[26] lanthanide complexes,[27] complexes with more earth-abundant metals,[28,29] molecules showing TADF (thermally activated delayed fluorescence),[30] and electron donor–acceptor dyads[31] have also been reported. Most of these systems require expensive and complex sensitizers, presenting somehow several drawbacks including low photostability, structural instability, and a limited usable range of solvent conditions. Therefore, the employment of more readily available and organic sensitizers with high extinction coefficients in the appropriate absorption region, high photostability, and

[a] *Departamento de Química, Universitat Politècnica de Valencia, Camino de Vera S/N, 46022, Valencia, Spain. E-mail: raupreru@upv.es*
[b] *Department of Chemistry, Johannes Gutenberg University Mainz, Duesbergweg 10-14, 55128, Mainz, Germany. E-mail: ckerzig@uni-mainz.de*

† Electronic supplementary information (ESI) available. CCDC 2236113 and 2236116. For ESI and crystallographic data in CIF or other electronic format see DOI: https://doi.org/10.1039/d3cp00811h

Open Access Article. Published on 05 April 2023. Downloaded on 6/16/2025 5:07:55 PM.
This article is licensed under a Creative Commons Attribution-NonCommercial 3.0 Unported Licence.

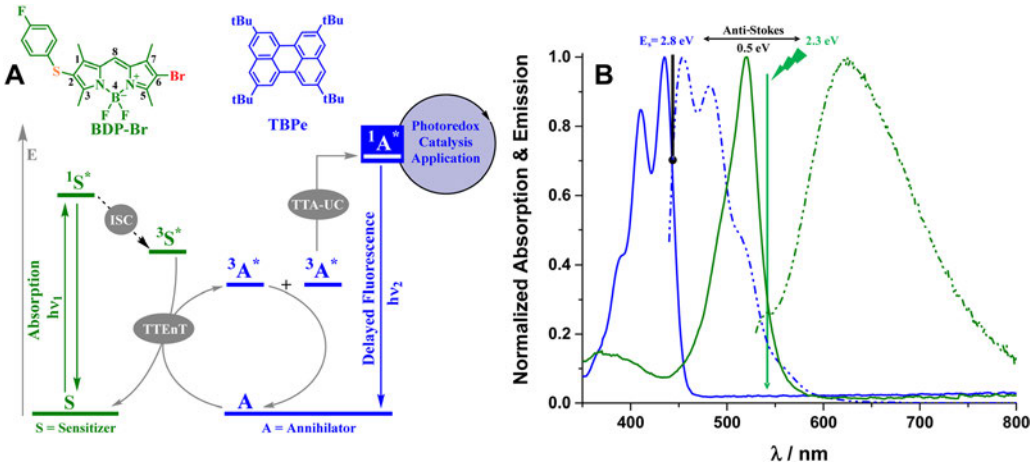

Fig. 1 (A): Schematic representation of the corresponding photophysical events associated with the TTA-UC phenomenon enabled by the **BDP-Br** (sensitizer) and **TBPe** (annihilator) pair and its implementation in photoredox catalysis. (B): Normalized absorption (solid line) and emission (dashed dotted line) spectra of **BDP-Br** (green) and **TBPe** (blue) in 8 μM aerated acetonitrile/dimethylacetamide (4/1 v/v) solution.

insensitivity to solvent environments appears to be more desirable.

In this context, boron dipyrromethene (BODIPY) derivatives fulfill the abovementioned criteria and the addition of halogen substituents (the so-called internal heavy-atom effect)[32] directly onto the chromophore, not to the peripheral moieties, provides a direct effect on the ISC quantum yield and the population of triplets substantially enhances.[33–35] Thus, the number of reports on the photosensitization of TTA-UC using BODIPY-based donors has increased over the last few years.[36,37] Encouraged by this continuous evolution and on the basis of the viable and straightforward functionalization of the BODIPY framework, it would be of great interest to construct new BODIPY dyes with special properties to be used as suitable sensitizers in a bimolecular TTA-UC system.

As a matter of fact, we have herein prepared an asymmetric BODIPY (6-bromo-2-(4-fluorophenyl)thio-1,3,5,7-tetramethyl-4,4-difluoro-4-bora-3*a*,4*a*-diaza-*s*-indacene, **BDP-Br**, Fig. 1A) in which the presence of heteroatoms such as sulfur atoms plus one bromine is expected to not only alter the energy level of the triplet state but also shift the UV-Vis absorption band to the green region. This molecular design permits a lower energetic light input ($\lambda_{exc} > 530$ nm) and milder reaction conditions, while avoiding iodine atoms that frequently result in rather photolabile dyes. The ability to successfully sensitize TTA-UC in solution has been demonstrated through spectroscopic methods, employing an adequate acceptor such as 2,5,8,11-tetra-*tert*-butylperylene (**TBPe**).

Moreover, the generation of highly energetic species by this phenomenon (Fig. 1B) seems useful for the application of photoredox catalysis *via* upconversion. Hence, the activation of an aryl chloride with a high-energy demanding bond using this novel TTA-UC couple has led to different chemical transformations such as *N*-methylpyrrole functionalization, the production of a triarylethylene compound and the formation of a new C–P bond. These three overall redox-neutral reactions have been investigated based on product analysis and spectroscopic measurements, supporting the relationship between the photophysical (ISC, TTEnT, and TTA) and photochemical (SET, radical trapping, and C–C or C–P couplings) events.

Results and discussion

Synthesis of BDP-Br

As stated above, one of the main goals in this study was to synthesize a new BODIPY-like sensitizer to be involved in a bimolecular system for TTA-UC purposes. Interestingly, this new entity possesses an asymmetric structure with a 4-fluorophenyl sulfide group attached to one side of the chromophore whereas a bromine atom was attached to the opposite side of the chromophore. This disposition conferred a particular electronic density with the occurrence of strong absorption of visible light, an efficient ISC, and a long-lived triplet state.

Based on the reported data on sulfenylation of pyrroles catalyzed by copper,[38] the addition of 4-fluorothiophenol to the starting material 3,5-dimethylpyrrole-2-carboxaldehyde was first carried out, obtaining a 50% yield of the corresponding product **A** (Fig. 2). The next step was crucial in the construction of an asymmetrical structure and the condensation of compound **A** with 2,4-dimethylpyrrole led to the formation of intermediate dipyrromethane **B** with 68% yield. Now, the treatment of **B** with a base such as triethylamine followed by boron trifluoride diethyl etherate[39] yielded 66% of the BODIPY derivative **BDP** (2-(4-fluorophenyl)thio-1,3,5,7-tetramethyl-4,4-difluoro-4-bora-3*a*,4*a*-diaza-*s*-indacene, Fig. 2) whose structure was confirmed by X-ray analysis. The last step consisted of the addition of a bromine atom to **BDP** by NBS (*N*-bromosuccinimide) treatment and the target compound **BDP-Br** was quantitatively obtained. The location of bromine at position 6 was successfully supported by X-ray analysis (Fig. 2). It should be noted that structural determination by single-crystal X-ray diffraction revealed not only that both BODIPY species crystallise in the triclinic space group $P\bar{1}$ but also the planarity of the

This journal is © the Owner Societies 2023

Open Access Article. Published on 05 April 2023. Downloaded on 6/16/2025 5:07:55 PM.
This article is licensed under a Creative Commons Attribution-NonCommercial 3.0 Unported Licence.

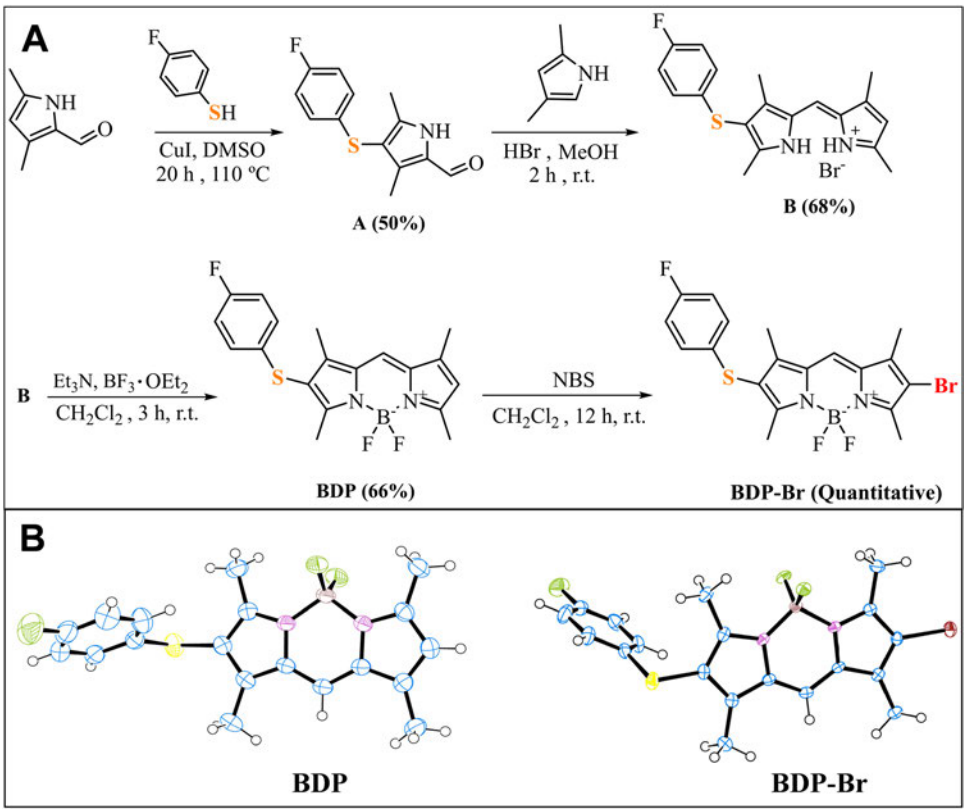

Fig. 2 (A): Synthetic route for the formation of **BDP-Br**. For more details on the synthetic procedures, see the ESI.† (B): ORTEP pictures of the X-ray structures of **BDP** and **BDP-Br**.

BODIPY core was confirmed which was extended through the bromine group in the case of **BDP-Br**. Thus, the design of **BDP-Br** could have a high impact on the ISC quantum yield. On the one hand, the presence of the 4-fluorophenyl sulfide group would give rise to a weakly emissive twisted intramolecular charge-transfer excited state (TICT)[40] between the sulfur's lone electron pair and an excited electron-deficient BODIPY moiety. On the other hand, chromophore structures bearing heavy atoms such as Br would affect directly the triplet state lifetime of the molecule and would stabilize the ISC process.[41] Therefore, **BDP-Br** appears to be the ideal choice to be applied to both TTA-UC and photoredox catalysis.

General photophysical and photochemical properties of BDP-Br

Regarding optical characterization, we investigated the photophysical properties of **BDP-Br**, which include absorption/emission bands, molar absorption coefficients, Stokes shifts, fluorescence quantum yields, emission rate constants, singlet energies and lifetimes in different solvents (Table 1). The absorption spectra of **BDP-Br** in all solvents presented an absorption band ($\lambda_{max.abs}$) in the green region (517–527 nm), being only weakly dependent on the solvent polarity (see Fig. S5 in the ESI†). It displayed molar extinction coefficients (ε), Stokes shifts ($\Delta\bar{\nu}$) and fluorescence lifetimes in the same order of magnitude as found for similar BODIPYs.[40] Interestingly, lower absolute fluorescence quantum yields (Φ_F) were obtained in more polar solvents, suggesting that the intersystem crossing efficiency from the lowest singlet excited state to the triplet would be enhanced by the internal heavy-atom effect or the formation of a TICT state. Besides, the phosphorescence spectrum of **BDP-Br** in the ethanol matrix at 77 K was recorded at λ_{max} of 780 nm (Fig. S6 in the ESI†), and was in accordance with those of halogen-substituted BODIPYs previously reported.[42] Furthermore, the lowest triplet energy (E_T) of **BDP-Br** was estimated to be 1.68 eV, which was found to be larger than that of **TBPe** (1.53 eV)[15] and makes energy transfer possible from the T_1 of **BDP-Br** to the T_1 of **TBPe**.

Table 1 Photophysical properties of **BDP-Br**

Solvent	$\lambda_{max.abs}$ [a]	$\lambda_{max.em}$ [a]	ε [b]	$\Delta\bar{\nu}$ [c]	E_S [d]	Φ_F [e]	τ_F [f]	k_F [g]
MeOH	517	612	44 600	3003	2.30	0.05	2.1	2.4×10^7
ACN	520	614	29 500	2944	2.18	0.05	2.0	2.0×10^7
DMSO	522	630	25 070	3284	2.25	0.04	2.5	1.6×10^7
DMA	525	625	66 670	3048	2.21	0.04	2.2	1.8×10^7
DCM	525	609	26 700	2628	2.27	0.10	2.3	4.3×10^7
Hexane	527	587	25 070	1939	2.28	0.30	3.5	8.5×10^7
ACN/DMA (4 : 1)	524	625	36 600	3084	2.26	0.04	2.5	1.6×10^7

[a] Maximum absorption/emission peak (in nm). [b] Molar extinction coefficient (in M^{-1} cm^{-1}). [c] Stokes shifts (in cm^{-1}). [d] Singlet energy (in eV). [e] Absolute fluorescence quantum yield. [f] Singlet lifetime (in ns). [g] Fluorescence rate constant (in s^{-1}). MeOH: methanol; DMSO: dimethylsulfoxide; DCM: dichloromethane; DMA: *N*,*N*-dimethylacetamide; ACN: acetonitrile.

Open Access Article. Published on 05 April 2023. Downloaded on 6/16/2025 5:07:55 PM.
This article is licensed under a Creative Commons Attribution-NonCommercial 3.0 Unported Licence.

To investigate the inherent photostability of the novel sensitizer, comparative stability measurements under monochromatic green light excitation with the widely used reference compound $[Ru(bpy)_3](PF_6)_2$ were carried out.[43] These semi-quantitative studies (Fig. S10, ESI†) revealed the outstanding photostability of **BDP-Br** – its photodegradation quantum yield is lower than that of the (already quite stable) $[Ru(bpy)_3]^{2+}$ by about two orders of magnitude.

ISC quantum yield of BDP-Br

One of the key parameters to determine the TTA-UC efficiency is the ISC quantum yield (Φ_{ISC}) of the sensitizer. This value is regularly estimated by singlet oxygen measurements in an indirect fashion, whereas a direct method can yield more reliable results. In this context, the Φ_{ISC} of **BDP-Br** was determined using laser flash photolysis actinometry[44,45] with the well-defined Φ_{ISC} of $[Os(phen)_3](PF_6)_2$ as the reference system. Briefly, this method is based on identical excitation conditions at a laser wavelength of 532 nm (Fig. 3A), adding a known concentration of **TBPe** (10 mM) to the sensitizers. Then, the triplet energy transfer efficiency η_{TTEnT} is compared after excitation (Fig. 3B and C) and the generation of the triplet-excited perylene[46] is detected using transient absorption spectroscopy (*vide infra* for more detailed TTEnT measurements with the **BDP-Br–TBPe** pair). Since we are using the same acceptor, the relative concentration of the generated ^{3}**TBPe*** is given by the ratio of $\frac{\Delta OD}{\Delta OD_{Ref}}$ at a selected wavelength (Fig. 3D). Considering the widely accepted $\Phi_{ISC,Ref}$ value for $[Os(phen)_3](PF_6)_2$ as 1, a Φ_{ISC} of 0.16 for **BDP-Br** was estimated (see eqn (1) and the ESI† for more experimental details). Based on the literature data that unsubstituted BODIPY shows negligible ISC,[47] herein it clearly appears that ISC is substantially accelerated for **BDP-Br**, allowing us to employ this BODIPY derivative as the sensitizer for triplet energy transfer-driven chemistry. The overall higher fluorescence quantum yield and a longer singlet lifetime of **BDP** compared to those of **BDP-Br** allow us to attribute the increased ISC quantum yield mainly to the heavy atom effect of the bromine atom rather than the fluorophenyl sulfide moiety (see Table 1 and Table S1, ESI†). The favorable absorption properties of **BDP-Br** with only one dominant absorption band in the green region and weak absorptivity in the blue region (*vide supra*) together with its high photostability make it a suitable candidate for a green-to-blue upconversion system.

BDP-Br and TBPe pair for TTA-UC

Considering the triplet state energy of **BDP-Br** as 1.68 eV, **TBPe** was selected as the suitable annihilator owing to its rather low triplet state energy of 1.53 eV[15] and high singlet-excited state energy of 2.81 eV, while the *tert*-butyl groups suppress unwanted excimer formation.[46] Given that ultrafast photoprocesses cannot be expected for our bimolecular UC system in the diluted solution,[48–50] we believed that laser flash photolysis (LFP) experiments in the ns–μs timescale range was the appropriate choice to further investigate the TTA-UC system (Fig. 4). Thus, a pronounced ground state bleach and a broad absorption band centered at around 640 nm and 450 nm were observed right after the laser pulse (λ_{exc} = 532 nm and ~10 ns pulse duration) (Fig. 4A). All signals decay to baseline with a natural lifetime of ~100 μs (Fig. 4B) and we assigned them to the triplet-excited **BDP-Br**. Stern–Volmer experiments were performed using **TBPe** as the quencher, yielding a TTEnT rate constant of 4.1×10^9 M^{-1} s^{-1} in line with the reported triplet energies (Fig. 4B). With the addition of **TBPe**, new absorption bands are detected in the TA spectrum (red) after **BDP-Br** has been fully quenched and the kinetic traces in Fig. 4A (inset) clearly demonstrate that quenching and photoproduct formation occur with identical rates. The new transient species shows absorption peaks at 484 nm and 453 nm which can be safely ascribed to the triplet state of **TBPe** (Fig. 4A, red spectrum).[46]

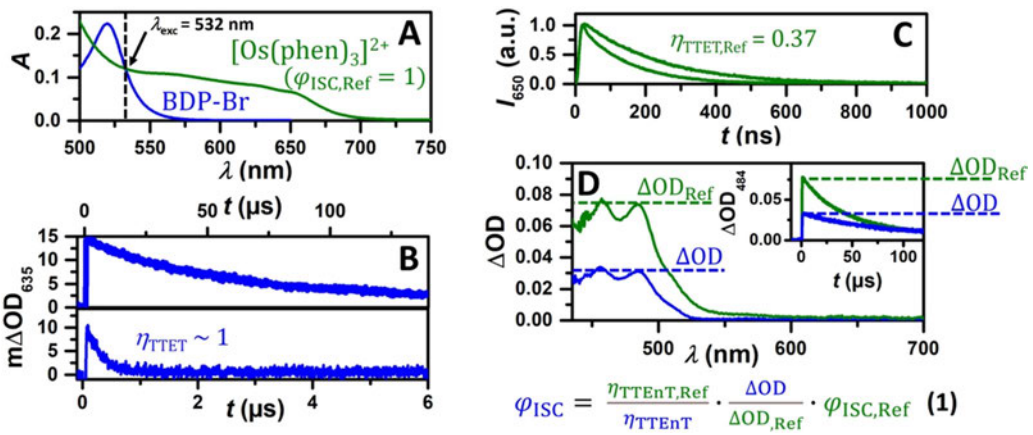

Fig. 3 Data sets used for the ISC quantum yield determination of **BDP-Br**. (A): Absorption spectra of deaerated 7 μM **BDP-Br** and deaerated 76 μM $[Os(phen)_3](PF_6)_2$ in ACN. (B): Kinetic traces of ^{3}**BDP-Br** in the absence (upper panel) and presence (lower panel) of 10 mM **TBPe**. (C): Kinetic measurements of the $[Os(phen)_3](PF_6)_2$ phosphorescence in the absence and presence of **TBPe**. (D): Transient absorption spectra of **BDP-Br** and $[Os(phen)_3](PF_6)_2$ with 10 mM **TBPe** recorded 1 μs after excitation with 532 nm laser pulses. Laser pulses of constant energy (12 mJ) were used in this series of experiments. Inset: kinetic measurements at 484 nm.

This journal is © the Owner Societies 2023

Open Access Article. Published on 05 April 2023. Downloaded on 6/16/2025 5:07:55 PM.
This article is licensed under a Creative Commons Attribution-NonCommercial 3.0 Unported Licence.

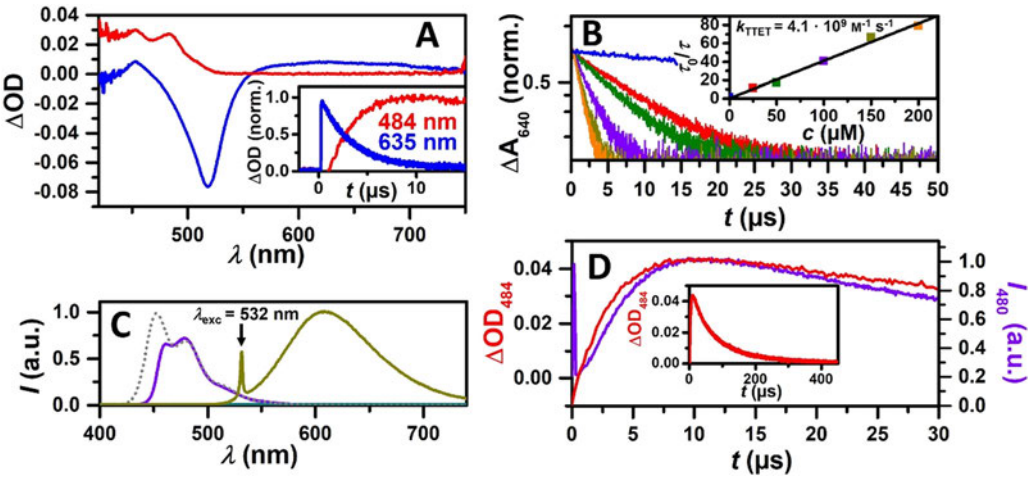

Fig. 4 Mechanistic LFP experiments using 532 nm laser pulses. If not stated otherwise, a solution of 9 μM **BDP-Br** and 100 μM **TBPe** in deaerated ACN was used. (A) TA spectra of **BDP-Br** in the presence (red) and absence (blue) of **TBPe** recorded after 2 μs (blue) or 30 μs (red). Inset: corresponding kinetic traces. (B) **BDP-Br** triplet quenching experiments with increasing **TBPe** concentrations. Inset: the corresponding Stern–Volmer plot. (C) Time-gated emission spectra of **TBPe** (green, integration time: 2–200 μs), **BDP-Br** (dark yellow, integration time: 0–100 ns) and **BDP-Br** *with* **TBPe** (purple, integration time: 2–200 μs). For comparison, an emission spectrum of a strongly diluted (1 μM) **TBPe** solution (dotted grey line) after direct excitation using 355 nm laser pulses is shown. (D) Kinetic traces of ^{3}**TBPe** at 484 nm and UC emission at 480 nm. Inset: the kinetic trace of ^{3}**TBPe** on a longer timescale.

Having established the TTEnT step, we then turned to the annihilation process. Individually, the sensitizer only shows fluorescence peaking at ~610 nm while no emission is detected from the annihilator after pulsed 532 nm excitation (Fig. 4C). When combined, however, emission signals with a spectral upshift respective to the excitation wavelength with maxima at 480 nm and 461 nm are detected. The detection time window (2–200 μs after excitation) allowed us to exclude the prompt emission of **TBPe** and **BDP-Br** such that delayed fluorescence expected for TTA-UC can be selectively observed. A spectrum containing the prompt emission of **TBPe** in a highly diluted solution is shown in Fig. 4C for comparison. It should be noted that inner filter effects in the absorption–emission overlap region become apparent at concentrations >10 μM (Fig. S11, ESI†). Kinetic traces of both the ^{3}**TBPe** absorption at 484 nm and the ^{1}**TBPe*** emission concurrently reach a maximum at ~11 μs (Fig. 4D). The faster increase and decrease of the UC emission compared to the triplet concentration is in line with the bimolecular nature of the annihilation process and provides further evidence for TTA-UC.[51]

In addition to the time-resolved studies that provided deep insights into the novel TTA-UC system, we investigated the UC efficiency using a 514 nm cw laser for excitation (Fig. 5). The UC emission peaking at 484 nm gradually enhanced with increasing laser intensity (10–100 mW). A spectral upshift of 0.40 eV was observed when the singlet-excited state energy of **TBPe** and the excitation wavelength (almost perfectly corresponding to the **BDP-Br** absorption maximum) were considered. To determine the UC quantum yield, Φ_{UC}, $[(Ru(bpy)_3](PF_6)_2$ was used as the reference system (see the ESI† for details of the method).[52] As depicted in the inset of Fig. 5, the Φ_{UC} for our metal-free system (with a theoretical limit of 50%) was found to reach a maximum of 2.7%. Despite the fact that this value was lower

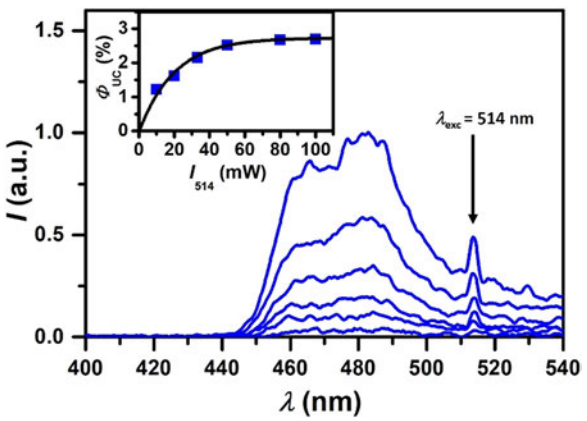

Fig. 5 Photon upconversion studies of 28 μM **BDP-Br** and 100 μM **TBPe** in deaerated ACN using a 514 nm cw laser for excitation. Main plot: UC Emission spectra with increasing laser intensity. Inset: the external UC quantum yield plotted against the laser intensity. See the text and ESI† for details.

than others from quantum-yield-optimized systems, the performance of the current TTA-UC system to act as the photocatalyst to drive challenging photoredox reactions appeared to be sufficient since well-known bimolecular systems that show Φ_{UC} well below 1% were able to trigger photochemical transformations such as reductive pollutant degradation.[53] Furthermore, the moderate quantum yield is likely compensated by the very high sensitizer and annihilator photostability (*vide supra*).

Application of the BDP-Br/TBPe system to photoredox catalysis

Several biphotonic excitation strategies in photoredox catalysis have been developed over the last few years in order to address critical bond activations or electron transfers under mild

Open Access Article. Published on 05 April 2023. Downloaded on 6/16/2025 5:07:55 PM.
This article is licensed under a Creative Commons Attribution-NonCommercial 3.0 Unported Licence.

conditions and using lower-energy visible light. Reactions such as two-photon absorption (TPA)[54] and consecutive photo-induced electron transfer (conPET)[55] can be carried out using a single photocatalyst. In the case of TTA-UC, a bimolecular system governs the catalytic cycle by the energy input of two photons where the primary photosensitizer transfers the absorbed energy to the co-catalyst (annihilator). Although the application of this technology to chemical transformations has been recently reviewed,[13] there is still plenty of room concerning the employment of improved systems. Therefore, in view of the outstanding TTA-UC properties of the **BDP-Br/TBPe** system, this couple was embedded as the photocatalyst into different challenging intermolecular coupling reactions.

To this end, we first explored the feasibility of activating 2-acetyl-5-chlorothiophene as the model reagent with visible light employing the **BDP-Br/TBPe** system. Quenching experiments were carried out by means of transient absorption spectroscopy (TAS) under conditions that are similar to those of the photocatalytic studies (Fig. 6A). Clearly, the delayed fluorescence intensity of **TBPe** gradually decreased in the presence of increasing amounts of the quencher. Indeed, the Stern–Volmer analysis of delayed emission quenching (Fig. 6A inset) revealed a K_{SV} of 117 M^{-1}; taking into account this value and the **TBPe** singlet lifetime (τ_F = 5 ns in ACN/DMA 4/1 v/v, see the ESI† for details), the fluorescence quenching rate constant, $k_q(S_1)$, was found to be 2.3 × 10^{10} M^{-1} s^{-1}, indicating that the target compound quenches the delayed ^{1}**TBPe*** with a diffusion-controlled rate. A very similar Stern–Volmer constant (K_{SV} = 135 M^{-1}) was obtained for ^{1}**TBPe*** quenching by 2-acetyl-5-chlorothiophene upon the direct excitation of **TBPe** (λ_{exc} = 405 nm) in neat ACN, supporting the UC-driven activation mechanism.

To further demonstrate the interaction between TTA-generated ^{1}**TBPe*** and 2-acetyl-5-chlorothiophene through an initial electron transfer step and to identify possible transient intermediates, additional time-resolved studies were performed (Fig. 6B). Hence, irradiation of the **BDP-Br/TBPe** system (λ_{exc} = 532 nm) in the presence of 2-acetyl-5-chlorothiophene was carried out. Interestingly, a new absorption band at *ca.* 560 nm was clearly observed which was safely ascribed to the **TBPe** radical cation (**TBPe**$^{\bullet+}$) based on the literature data.[56] From the temporal profile at 560 nm (Fig. 6C), a lifetime on the order of 400 μs was estimated for this intermediate.

In addition, thermodynamic analysis for ET processes strongly supported these data. The free energy change (ΔG_{ET} in kcal mol^{-1}) associated with the ET process was estimated by the application of the Weller equation.[57] The oxidation potential (E°(**TBPe**$^{\bullet+}$/**TBPe**)) of **TBPe** (Fig. 6D) and its singlet and triplet energy (E^*(S_1 or T_1), for details see the ESI†) were experimentally obtained. Their corresponding values are 0.88 V *vs.* SCE, 64.6 and 34.6 kcal mol^{-1}, respectively. The resulting excited-state oxidation potential for the **TBPe**'s S_1 state is as high as −1.93 V *vs.* SCE, which should permit challenging photocatalytic reductions *via* TTA-UC.

Considering the reduction potential of the model reagent 2-acetyl-5-chlorothiophene (−1.66 V *vs.* SCE),[58] the ΔG_{ET} (S_1) and ΔG_{ET} (T_1) values were estimated as −6.0 kcal mol^{-1} and +23.9 kcal mol^{-1}, respectively. Therefore, the activation of 2-acetyl-5-chlorothiophene by delayed ^{1}**TBPe*** would be an exergonic process, whereas the mechanism from ^{3}**TBPe*** is

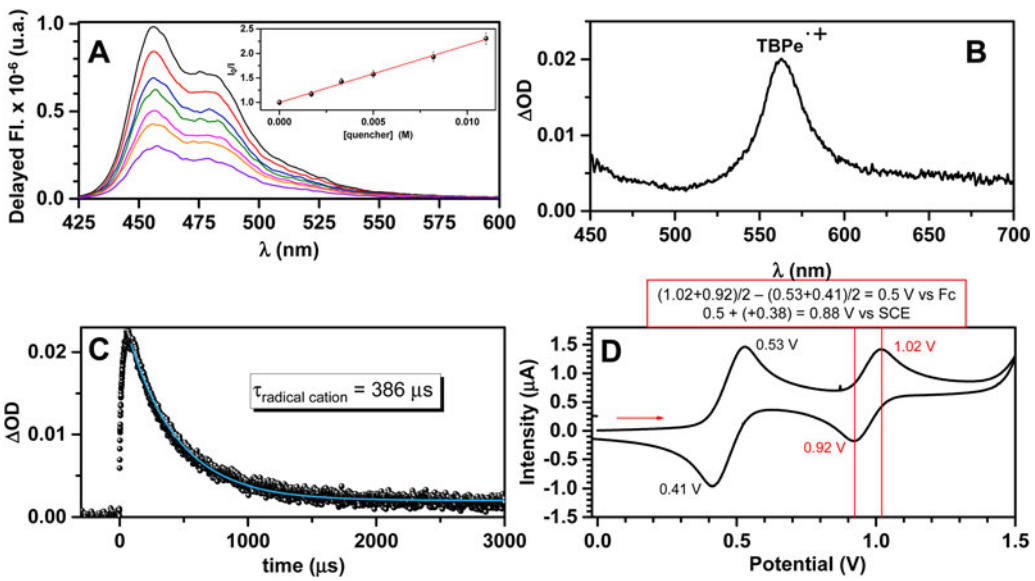

Fig. 6 Activation of the model reagent by delayed fluorescence ^{1}**TBPe***. (A): Delayed fluorescence spectra of a mixture of **BDP-Br** (0.1 mM) and **TBPe** (1 mM) in anaerobic ACN/DMA (4/1 v/v) solution recorded 2 μs after the laser pulse (λ_{exc} = 532 nm) in the presence of increasing amounts of 2-acetyl-5-chlorothiophene (up to 11 mM); inset: the Stern–Volmer plot to obtain k_q (S_1); experimental errors were lower than 5% of the obtained values. (B): TAS measurements (λ_{exc} = 532 nm) of **BDP-Br** (0.1 mM) and **TBPe** (1 mM) in the anaerobic ACN solution in the presence of 10 mM of 2-acetyl-5-chlorothiophene recorded 140 μs after the laser pulse. (C): Temporal profile of the **TBPe** radical cation monitored at 560 nm. The blue line is the fit function used to estimate the lifetime. (D): Cyclic voltammogram for an ACN solution of **TBPe** (0.1 mM).

This journal is © the Owner Societies 2023

Open Access Article. Published on 05 April 2023. Downloaded on 6/16/2025 5:07:55 PM.
This article is licensed under a Creative Commons Attribution-NonCommercial 3.0 Unported Licence.

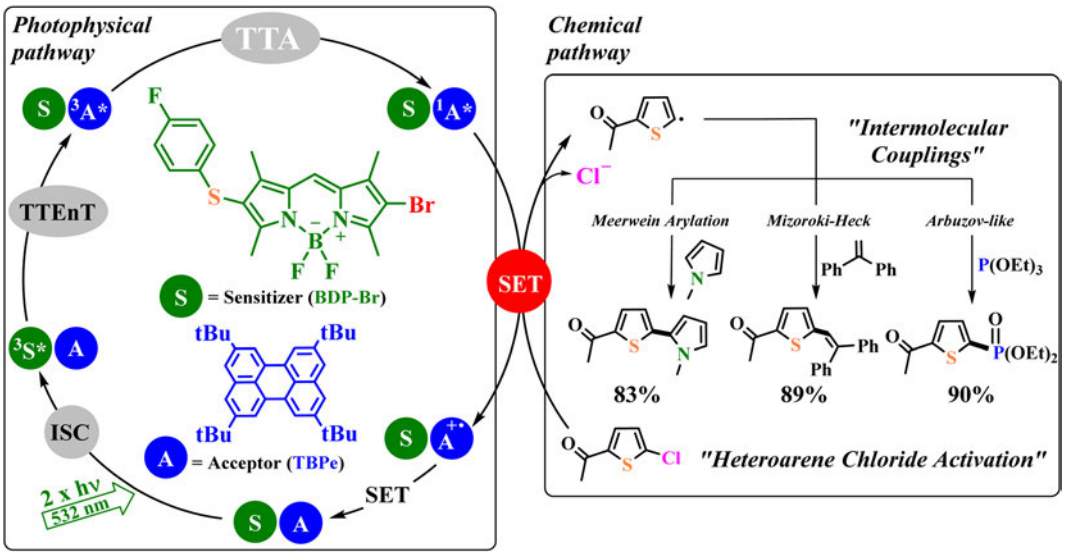

Fig. 7 Mechanism of TTA-UC enabled by the **BDP-Br**(S)/**TBPe**(A) pair and its adaptation to photoredox catalysis through a SET-initiated reductive activation of an aryl chloride. Involvement of sequential processes ISC, TTEnT, TTA and SET as key steps. ISC = intersystem crossing; TTEnT = triplet–triplet energy transfer; TTA = triplet–triplet annihilation; SET = single-electron transfer.

thermodynamically unfeasible. Same calculations were indeed performed for **BDP-Br** with the question whether this species could act as an activator. Considering the experimental data of **BDP-Br** (E_{ox} = + 1.23 V *vs.* SCE, $E(S_1)$ = 52.1 kcal mol^{-1} and $E(T_1)$ = 38.7 kcal mol^{-1}, see the ESI† for details), both ΔG_{ET} (S_1) and ΔG_{ET} (T_1) were estimated as positive values (+13.8 kcal mol^{-1} and +27.2 kcal mol^{-1}, respectively), ruling out any ET from the excited **BDP-Br**.

These results allowed us to conclude that the activation of 2-acetyl-5-chlorothiophene was successfully powered using the TTA-UC system through a SET process (Fig. 7). Thus, the conversion of low energy light (2.3 eV) into the higher energy delayed **^{1}TBPe*** (2.8 eV) allowed the one-electron injection, giving rise to the formation of the unstable radical anion of the model compound which rapidly released chloride to afford the corresponding heteroarene radical. This reactive species could be now trapped by adequate nucleophiles to produce complex compounds (Fig. 7). Therefore, we investigated the application of this cascade of processes (TTA-UC + SET + intermolecular coupling) to different important reactions such as the Meerwein arylation or the Mizoroki–Heck reaction in order to functionalize the thiophene ring by C–C coupling and the Arbuzov-like reaction to construct the corresponding thiophene phosphonate.

The photocatalyzed Meerwein arylation is a classic reaction in which aryl diazonium salts were employed as aryl radical precursors.[59] However, most of these species are not neither commercially available nor stable in the presence of air, being their employment sometimes detrimental. In this context, aryl halides were used as alternative electrophilic reagents in such reactions. Recently, a TTA-UC system based on the diiodo-BOPHY-like derivative as the sensitizer and 9,10-diphenylanthracene as the annihilator photocatalyzed the coupling reaction between our model compound (2-acetyl-5-chlorothiophene) and *N*-methylpyrrole, yielding 62% of the final biaryl product.[60] The instability of the sensitizer under the irradiation conditions (λ_{exc} = 450 nm) could be an important factor for the incomplete conversion of the starting material or the lack of more product formation. Thus, we focused our attention on the same reaction utilizing **BDP-Br**/**TBPe** as the TTA-UC photocatalytic system. Optimal conditions (see Table S2 for the optimization of the model reaction in the ESI†) involved catalytic amounts of **BDP-Br** (2% mol) and **TBPe** (10% mol), with pulsed laser irradiation in the green region at 532 nm in ACN/DMA (4/1 v/v) solution for 4 hours under anaerobic conditions. The result was markedly improved to that previously obtained with an 83% yield of the final product. It is worth mentioning that the ACN/DMA mixture as a solvent was found to be ideal not only for enhancing the selectivity of the process but also for favoring the complete dissolution of **TBPe**.

At the same shape, TTA-UC technology was very recently applied to the photocatalyzed Mizoroki–Heck reaction to obtain substituted triarylethylenes using aryl halides (especially bromides) as aryl radical precursors.[61] With the optimizing conditions stated above, our model compound was subjected to green-light photolysis (λ_{exc} = 532 nm) in the presence of diphenylethylene as the trapping agent and catalytic amounts of the **BDP-Br**/**TBPe** system (for detailed information on the reaction conditions, see the ESI†). Full conversion of the starting material was observed after 4 hours of irradiation and an excellent 89% yield of the final product was obtained. This finding notably improved the previous example (*i.e.*, 49%)[61] despite the lower-energy light input and the shortened irradiation time, confirming the efficiency of the photocatalytic activity of the TTA-UC couple.

Biphotonic-based methods for the C–P bond formation of (hetero)aryl halides with trialkyl phosphite *via* the visible-light-induced photo-Arbuzov reaction have been barely explored.[58,62]

Open Access Article. Published on 05 April 2023. Downloaded on 6/16/2025 5:07:55 PM.
This article is licensed under a Creative Commons Attribution-NonCommercial 3.0 Unported Licence.

In particular, these studies followed a consecutive photoinduced electron transfer (ConPET) mechanism using organic dyes as photocatalysts together with a sacrificial agent as the base. As far as we are aware, the photo-Arbuzov reaction catalyzed using a TTA-UC system has not been attempted yet and we were interested whether this protocol could be a powerful strategy to forge new C(sp^2)–P bonds under mild conditions. The phosphorylation of the model compound, 2-acetyl-5-chlorothiophene, was thus carried out in the presence of **BDP-Br/TBPe** as the TTA-UC photocatalytic system under the optimal conditions (for detailed information on the reaction conditions, see the ESI†). Interestingly, the targeted product was obtained with an excellent 90% yield, which was comparable to the previously reported value (91%)[58] in spite of the absence of sacrificial agents.

Conclusions

In summary, we have developed a purely organic upconversion system that efficiently catalyzes challenging reductions under green-light excitation conditions. Our tailor-made BODIPY sensitizer shows efficient triplet formation and energy transfer to the selected annihilator, while possessing outstanding photostability properties compared to the most famous photoactive metal complex as the reference. The excited annihilator singlet obtained *via* upconversion is a strong photoreductant providing about 2 V of reductive power. Given the low price and durability of green light sources such as frequency-doubled Nd:YAG lasers (which are also the key components of most commercial laser pointers) and green diode-based lamps compared to blue lasers and diodes, our approach should be within reach for most photochemical laboratories to activate substrates in a selective fashion under metal-free conditions.

Author contributions

All authors discussed the results and reviewed the manuscript.

Conflicts of interest

There are no conflicts of interest.

Acknowledgements

We thank the Generalitat Valenciana (project CIDEGENT/2018/044), the Spanish Government (project PID2019-105391GB-C22 funded by MCIN/AEI/10.13039/501100011033), the German Federal Environmental Foundation (DBU, PhD fellowship to T. J. B. Z., grant number 20022/028) and the German Research Foundation (DFG, grant number KE 2313/3-1) for financial support. We also thank Prof. Julia Pérez-Prieto for spectroscopic facilities.

References

1 A. L. Hagstrom, H.-L. Lee, M.-S. Lee, H.-S. Choe, J. Jung, B.-G. Park, W.-S. Han, J.-S. Ko, J.-H. Kim and J. H. Kim, *ACS Appl. Mater. Interfaces*, 2018, **10**, 8985–8992.
2 M. Barawi, F. Fresno, R. Pérez-Ruiz and V. A. de la Peña O'Shea, *ACS Appl. Energy Mater.*, 2019, **2**, 207–211.
3 V. Gray, D. Dzebo, M. Abrahamsson, B. Albinsson and K. Moth-Poulsen, *Phys. Chem. Chem. Phys.*, 2014, **16**, 10345–10352.
4 T. F. Schulze and T. W. Schmidt, *Energy Environ. Sci.*, 2015, **8**, 103–125.
5 L. Frazer, J. K. Gallaher and T. W. Schmidt, *ACS Energy Lett.*, 2017, **2**, 1346–1354.
6 T. Dilbeck and K. Hanson, *J. Phys. Chem. Lett.*, 2018, **9**, 5810–5821.
7 Y. Zhou, C. Ruchlin, A. J. Robb and K. Hanson, *ACS Energy Lett.*, 2019, **4**, 1458–1463.
8 H.-L. Lee, J. H. Park, H.-S. Choe, M.-S. Lee, J.-M. Park, N. Harada, Y. Sasaki, N. Yanai, N. Kimizuka, J. Zhu, S. H. Bhang and J.-H. Kim, *ACS Appl. Mater. Interfaces*, 2019, **11**, 26571–26580.
9 Q. Liu, M. Xu, T. Yang, B. Tian, X. Zhang and F. Li, *ACS Appl. Mater. Interfaces*, 2018, **10**, 9883–9888.
10 S. H. C. Askes, M. S. Meijer, T. Bouwens, I. Landman and S. Bonnet, *Molecules*, 2016, **21**, 1460.
11 Q. Liu, T. Yang, W. Feng and F. Li, *J. Am. Chem. Soc.*, 2012, **134**, 5390–5397.
12 C. Wohnhaas, A. Turshatov, V. Mailänder, S. Lorenz, S. Baluschev, T. Miteva and K. Landfester, *Macromol. Biosci.*, 2011, **11**, 772–778.
13 R. Pérez-Ruiz, *Top. Curr. Chem.*, 2022, **380**(23), 1–12.
14 F. Glaser, C. Kerzig and O. S. Wenger, *Angew. Chem., Int. Ed.*, 2020, **59**, 10266–10284.
15 B. D. Ravetz, A. B. Pun, E. M. Churchill, D. N. Congreve, T. Rovis and L. M. Campos, *Nature*, 2019, **565**, 343–346.
16 S. Wen, J. Zhou, P. J. Schuck, Y. D. Suh, T. W. Schmidt and D. Jin, *Nat. Photonics*, 2019, **13**, 828–838.
17 M. Wu, T.-A. Lin, J. O. Tiepelt, V. Bulović and M. A. Baldo, *Nano Lett.*, 2021, **21**, 1011–1016.
18 E. Radiunas, S. Raišys, S. Juršėnas, A. Jozeliūnaitė, T. Javorskis, U. Šinkevičiūtė, E. Orentas and K. Kazlauskas, *J. Mater. Chem. C*, 2020, **8**, 5525–5534.
19 J. Zhou, Q. Liu, W. Feng, Y. Sun and F. Li, *Chem. Rev.*, 2015, **115**, 395–465.
20 J. Zhao, W. Wu, J. Sun and S. Guo, *Chem. Soc. Rev.*, 2013, **42**, 5323–5351.
21 Y. Y. Cheng, T. Khoury, R. G. C. R. Clady, M. J. Y. Tayebjee, N. J. Ekins-Daukes, M. J. Crossley and T. W. Schmidt, *Phys. Chem. Chem. Phys.*, 2010, **12**, 66–71.
22 S. Hoseinkhani, R. Tubino, F. Meinardi and A. Monguzzi, *Phys. Chem. Chem. Phys.*, 2015, **17**, 4020–4024.
23 D. Dzebo, K. Moth-Poulsen and B. Albinsson, *Photochem. Photobiol. Sci.*, 2017, **16**, 1327–1334.
24 R. Weiss, Z. A. VanOrman, C. M. Sullivan and L. Nienhaus, *ACS Mater. Au*, 2022, **2**, 641–654.

This journal is © the Owner Societies 2023

Open Access Article. Published on 05 April 2023. Downloaded on 6/16/2025 5:07:55 PM.
This article is licensed under a Creative Commons Attribution-NonCommercial 3.0 Unported Licence.

25 Z. A. VanOrman, C. R. Conti, G. F. Strouse and L. Nienhaus, *Chem. Mater.*, 2021, **33**, 452–458.
26 Z. A. VanOrman, H. K. Drozdick, S. Wieghold and L. Nienhaus, *J. Mater. Chem. C*, 2021, **9**, 2685–2694.
27 N. Kiseleva, P. Nazari, C. Dee, D. Busko, B. S. Richards, M. Seitz, I. A. Howard and A. Turshatov, *J. Phys. Chem. Lett.*, 2020, **11**, 2477–2481.
28 M. Yang, S. Sheykhi, Y. Zhang, C. Milsmann and F. N. Castellano, *Chem. Sci.*, 2021, **12**, 9069–9077.
29 C. Wang, F. Reichenauer, W. R. Kitzmann, C. Kerzig, K. Heinze and U. Resch-Genger, *Angew. Chem., Int. Ed.*, 2022, **61**, e202202238(3 of 8).
30 W. Chen, F. Song, S. Tang, G. Hong, Y. Wu and X. Peng, *Chem. Commun.*, 2019, **55**, 4375–4378.
31 Y. Hou, J. Liu, N. Zhang and J. Zhao, *J. Phys. Chem. A*, 2020, **124**, 9360–9374.
32 P. Yuster and S. I. Weissman, *J. Chem. Phys.*, 1949, **17**, 1182.
33 T. Yogo, Y. Urano, Y. Ishitsuka, F. Maniwa and T. Nagano, *J. Am. Chem. Soc.*, 2005, **127**, 12162–12163.
34 X. Xiao, W. Tian, M. Imran, H. Cao and J. Zhao, *Chem. Soc. Rev.*, 2021, **50**, 9686–9714.
35 J. M. Lee, J.-M. Park, J. Ho Yoon, J.-H. Kim and J. P. Kim, *ChemPhotoChem*, 2023, e202200326.
36 K. Chen, Y. Dong, X. Zhao, M. Imran, G. Tang, J. Zhao and Q. Liu, *Front. Chem.*, 2019, **7**, 821.
37 N. A. Bumagina, E. V. Antina, A. A. Ksenofontov, L. A. Antina, A. A. Kalyagin and M. B. Berezin, *Coord. Chem. Rev.*, 2022, **469**, 214684.
38 D. Alves, R. G. Lara, M. E. Contreira, C. S. Radatz, L. F. B. Duarte and G. Perin, *Tetrahedron Lett.*, 2012, **53**(26), 3364–3368.
39 E. V. Antina, M. B. Berezin, N. A. Dudina, S. L. Burkova and A. Y. Nikonovab, *Russ. J. Inorg. Chem.*, 2014, **59**(10), 1427–1434.
40 E. Palao, T. Slanina and P. Klán, *Chem. Commun.*, 2016, **52**, 11951–11954.
41 K. N. Solov'ev and E. A. Borisevich, *Phys.-Usp.*, 2005, **48**, 231–253.
42 X.-F. Zhang, X. Yang, K. Niu and H. Geng, *J. Photochem. Photobiol., A*, 2014, **285**, 16–20.
43 J. B. Bilger, C. Kerzig, C. B. Larsen and O. S. Wenger, *J. Am. Chem. Soc.*, 2021, **143**, 1651–1663.
44 M.-S. Bertrams and C. Kerzig, *Chem. Commun.*, 2021, **57**, 6752–6755.
45 P. Müller and K. Brettel, *Photochem. Photobiol. Sci.*, 2012, **11**, 632–636.
46 C. Ye, V. Gray, K. Kushwaha, S. K. Singh, P. Erhart and K. Börjesson, *Phys. Chem. Chem. Phys.*, 2020, **22**, 1715–1720.
47 A. Schmitt, B. Hinkeldey, M. Wild and G. Jung, *J. Fluoresc.*, 2009, **19**, 755–758.
48 C. Wang, M. Sun, H. Wang and G. Zhao, *J. Phys. Chem. Lett.*, 2023, **14**, 164–169.
49 C. Wang, L. Ma, S. Wang and G. Zhao, *J. Phys. Chem. Lett.*, 2021, **12**, 12129–12134.
50 C. Wang, Y. Liu, X. Feng, C. Zhou, Y. Liu, X. Yu and G. Zhao, *Angew. Chem., Int. Ed.*, 2019, **59**, 11642–11646.
51 Y. Murakami and K. Kamada, *Phys. Chem. Chem. Phys.*, 2021, **23**, 18268–18282.
52 K. Suzuki, A. Kobayashi, S. Kaneko, K. Takehira, T. Yoshihara, H. Ishida, Y. Shiina, S. Oishic and S. Tobita, *Phys. Chem. Chem. Phys.*, 2009, **11**, 9850–9860.
53 B. Pfund, D. M. Steffen, M. R. Schreier, M.-S. Bertrams, C. Ye, K. Börjesson, O. S. Wenger and C. Kerzig, *J. Am. Chem. Soc.*, 2020, **142**, 10468–10476.
54 C. Kerzig, X. Guo and O. S. Wenger, *J. Am. Chem. Soc.*, 2019, **141**, 2122–2127.
55 I. Ghosh, T. Ghosh, J. I. Bardagi and B. König, *Science*, 2014, **346**, 725–728.
56 C. A. Steren, H. van Willigen, L. BiczoÂk, N. Gupta and H. Linschitz, *J. Phys. Chem.*, 1996, **100**, 8920–8926.
57 ΔG_{ET} (kcal mol^{-1}) = 23.06 x (E_{ox} – E_{RED}) – E^*(S_1 or T_1): A. Weller, *Z. Phys. Chem.*, 1982, **133**, 93–98.
58 J. C. Herrera-Luna, D. Díaz Díaz, M. C. Jiménez and R. Pérez-Ruiz, *ACS Appl. Mater. Interfaces*, 2021, **13**, 48784–48794.
59 D. Prasad Hari and B. König, *Angew. Chem., Int. Ed.*, 2013, **52**, 4734–4743.
60 C. G. López-Calixto, M. Liras, V. A. de la Peña O'Shea and R. Pérez-Ruiz, *Appl. Catal., B*, 2018, **237**, 18–23.
61 F. Garnes-Portolés, R. Greco, J. Oliver-Meseguer, J. Castellanos-Soriano, M. C. Jiménez, M. López- Haro, J. C. Hernández-Garrido, M. Boronat, R. Pérez-Ruiz and A. Leyva-Pérez, *Nat. Catal.*, 2021, **4**, 293–303.
62 R. S. Shaikh, S. J. S. Düsel and B. König, *ACS Catal.*, 2016, **6**, 8410–8414.

7.2 Design of Novel UVB Annihilators

In contrast to other developments in TTA–UC, the field of Vis-to-UV has been significantly less explored. The first documented example of TTA–UC from the visible to the UV was reported in 2006 by Castellano et al., who utilized $Ir(ppy)_3$ as a sensitizer and 3,8-di-*tert*-butylpyrene (3,8-DBP) as an annihilator. In recent years, a few UV annihilator structures have been developed.[158] Notable examples include 5-diphenyloxazole (PPO),[291] 1,4-bis((triisopropylsilyl)ethynyl)-naphthalene (1,4-TIPS-Nph),[139,289,301] 2,7-di-*tert*-butylpyrene (2,7-DBP),[326] *p*-quaterphenyl (QP),[294] *p*-terphenyl (TP),[294] and 1,5-naphthalenedisulfonate (1,5-NDS) (Figure 26).[296] Among the reported systems, 1,4-TIPS-Nph stands out due to its exceptionally low threshold intensity, which is attributed to its long triplet lifetime (2.2 ms).[139] Albinsson et al. demonstrated its full potential in combination with the TADF sensitizer 4CzBN, achieving an upconversion quantum yield of 0.17. They attributed this efficiency to a high spin factor of 0.54, surpassing the commonly predicted limit of 0.4.[289]

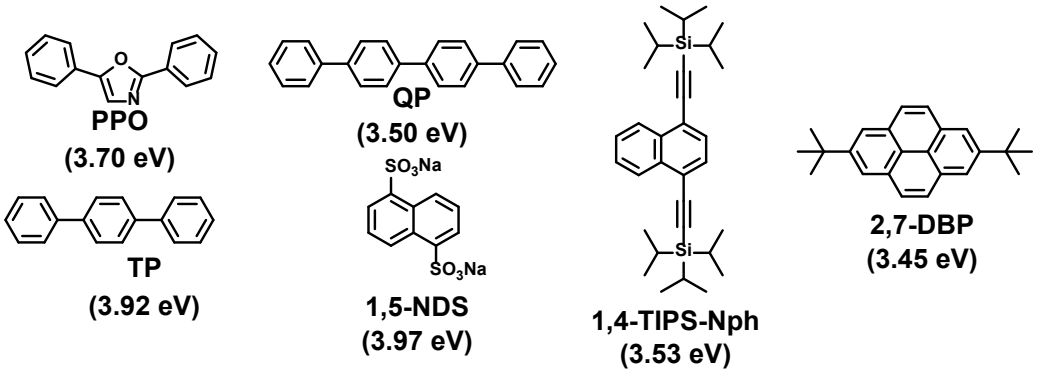

Figure 26: Molecular structure of selected UV annihilators with singlet-excited state energies in brackets.

While some Vis-to-UV TTA–UC systems have been successfully implemented in various applications, they all generate photon energies (or singlet-excited state energies) within the UVA range.[327] This range is already accessible via commercially available high-efficiency LEDs, and the solar spectrum provides a non-negligible contribution in the UVA region.[88,328]

To this day, virtually all photoreactions requiring UVB and UVC irradiation still rely on conventional light sources such as mercury, excimer, and xenon arc lamps.[329–331] These sources suffer from short operational lifetimes and poor electricity-to-light conversion efficiencies. Notably, mercury lamps remain widely in use despite their toxicity and significant environmental concerns, with the World Health Organization (WHO) ranking mercury among the top 10 chemicals of major public health concern.[332] The lack of sustainable alternatives is particularly striking, given the increasing importance of UVB-driven processes, such as wastewater treatment and the disinfection of viral pathogens like SARS-CoV-2.[333–335] In principle, TTA–UC could offer a mild and energy-efficient approach to generating UVB (4.43–3.94 eV, 280–315 nm) or UVC (>4.43 eV, <280 nm) photons by pooling the energy of two visible photons (<3.1 eV; >400 nm). Indeed, TTA–UC presents several additional key advantages over conventional one-photon UV chemistry: (i) It eliminates the need for specialized UVB-transparent glassware. (ii) The singlet-excited

state of the annihilator can be generated directly at the site of the target substrate, minimizing optical losses associated with external excitation. (iii) Using visible light as the excitation source significantly improves penetration depth, as UV light is strongly attenuated in many media.[336] Yet, at the outset of these projects, virtually no reports had documented TTA–UC surpassing the UVA/UVB boundary at 315 nm.

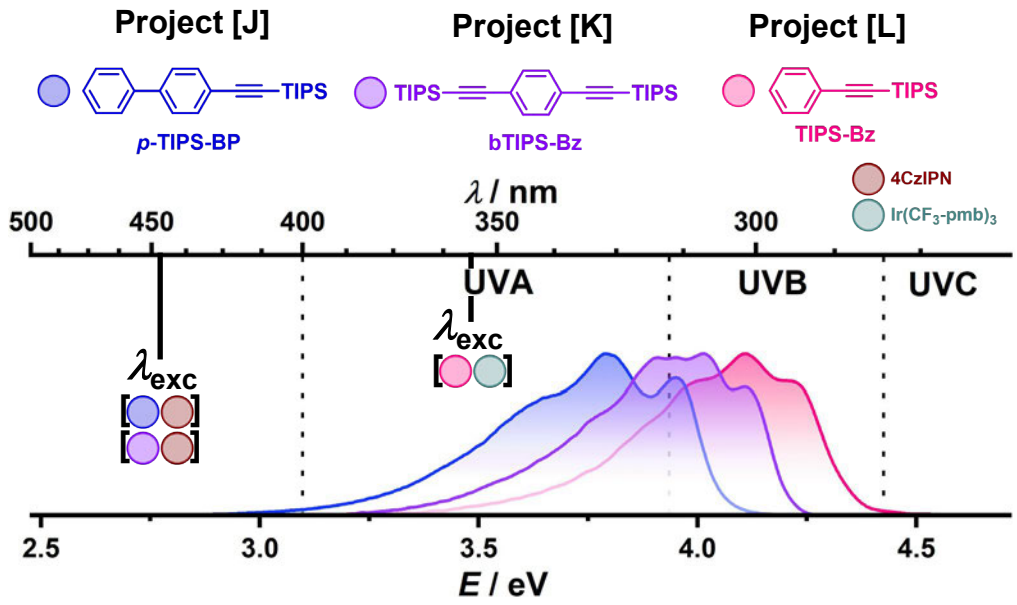

Figure 27: Overview of UVB annihilator projects **[J]**, **[K]** and **[L]**. Molecular structure and emission spectra of the UVB annihilators. For molecular structures of 4CzIPN and Ir(CF_3-pmb)$_3$ see Figure 4 and Figure 3.

When project **[J]** was initiated, the highest recorded singlet state energy among known annihilators was 1,5-NDS, which exhibited a value of 3.97 eV, just below the 4 eV threshold.[296] This benchmark was surpassed with the discovery of *p*-TIPS-BP, which demonstrated a singlet state energy of 4.04 eV when paired with the purely organic sensitizer 4CzIPN (Figure 27). This combination enabled clear UVB emission in a blue light-driven TTA–UC system.

Building on this success, benzene was explored in project **[K]** as a potential annihilator scaffold (Figure 27). The *para*-substituted TIPS-ethynyl derivative of benzene (bTIPS-Bz) was coupled with 4CzIPN in a blue-light-driven UC system, achieving a singlet state energy of 4.15 eV. This not only resulted in significant UVB emission but also enabled a subsequent Förster resonance energy transfer (FRET)-mediated bond activation mechanism, demonstrating the applicability of TTA–UC for photochemical transformations. In the same project, the monosubstituted benzene derivative (TIPS-Bz) was considered as a potential annihilator. However, its triplet energy (calculated at 3.06 eV) was too high to be efficiently sensitized in a blue light-driven UC system.

In a follow-up study (project **[L]**), TIPS-Bz was instead paired with the high-triplet-energy sensitizer Ir(CF_3-pmb)$_3$ (3.18 eV), which successfully sensitized the annihilator (Figure 27). This resulted in UC emission peaking at 300 nm, further extending the limits of TTA–UC and advancing towards the UVC region.

Projects **[J]**, **[K]**, and **[L]** extended the reach of TTA–UC from the UVA/UVB border (315 nm) into the full UVB and even UVC range. These studies not only pushed the energetic limits of TTA–UC but also showed that the resulting high-energy singlet states can drive reactions with otherwise inert substrates. The use of TIPS-ethynyl groups proved key in enhancing annihilator performance, offering a valuable blueprint for designing future high-energy annihilators.

Summary:

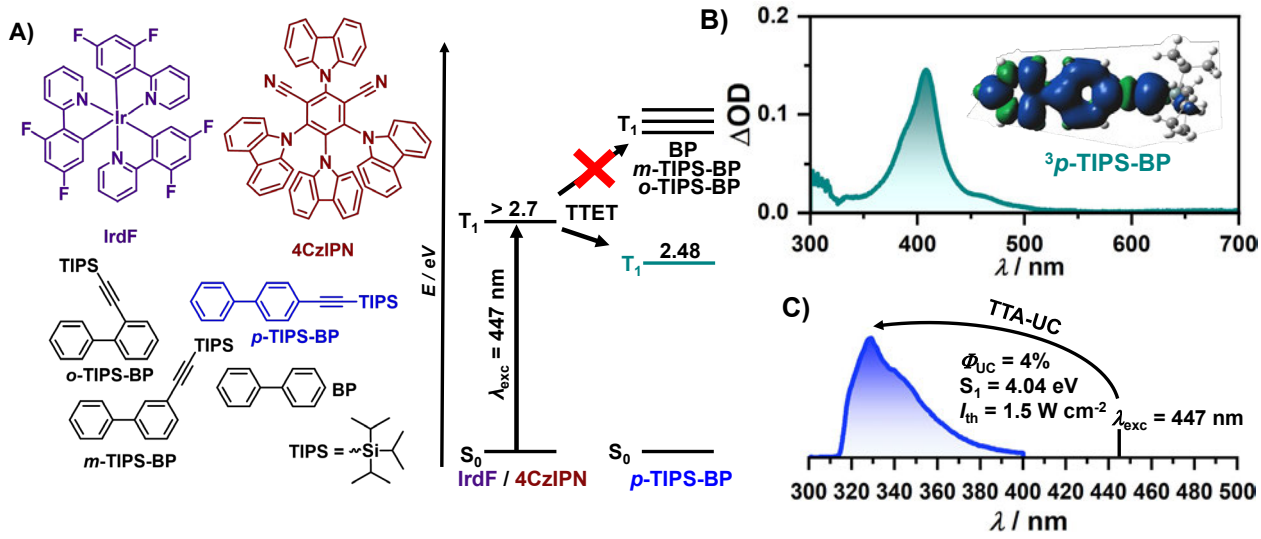

Figure 28: Mechanistic investigations of the *p*-TIPS-BP UC schemes with 355 nm laser pulses. A) Molecular structures of annihilators and sensitizers and schematic energy diagram of TTET. B) TA spectrum of and calculated spin density of ^{3}*p*-TIPS-BP. C) Emission of the *p*-TIPS-BP–4CzIPN UC scheme emission after cw laser excitation at 447 nm.

In project **[J]**, biphenyl was explored as a potential UV annihilator in a TTA–UC system driven by blue light. However, with a triplet state energy of 2.84 eV and a singlet state energy of 4.33 eV, biphenyl was unsuitable for blue-light-driven upconversion.[51] To address this, TIPS-ethynyl substitution was proposed to lower the triplet state energy, as observed in similar structures (Figure 28A).

DFT calculations of *ortho*-, *meta*-, and *para*-substituted biphenyl revealed that the *para*-isomer exhibited the lowest triplet energy at 2.48 eV (Figure 28A).The *para*-substituted biphenyl (*p*-TIPS-BP) was then synthesized according to the Sonogashira coupling reaction. A complete photophysical characterization of this compound revealed beneficial properties for TTA–UC: a higher fluorescence quantum yield (by a factor of three) and a shorter singlet state lifetime compared to the parent molecule biphenyl.

The singlet state energy was determined to be 4.04 eV, the highest reported for a TTA–UC system at the time. *p*-TIPS-BP was then studied using LFP with a 355 nm pulsed laser in combination with the sensitizers 4CzIPN and IrdF (Figure 28A for the structures) with triplet state energies of 2.72 eV and 2.75 eV, respectively. In both cases, TTET was confirmed as the exclusive pathway between the sensitizers and *p*-TIPS-BP. The triplet energy transfer constants were determined at k_{TTET} = 1.4 × 10^8 M^{-1} s^{-1} and k_{TTET} = 11.4 × 10^8 M^{-1} s^{-1} using 4CzIPN and IrdF as sensitizers, respectively. After TTET, the transient

triplet state of *p*-TIPS-BP was detected (Figure 28B), followed by delayed fluorescence of *p*-TIPS-BP. Spectroscopic evidence confirmed the bimolecular nature of TTA, fully validating the TTA–UC process.

The efficiency of the two UC systems was then characterized using a 447 nm cw laser. While the TTET rate constant was higher for the *p*-TIPS-BP–IrdF system, the UC quantum yield (up to 4%) and threshold intensity (1.5 W cm^{-2}) were superior in the purely organic *p*-TIPS-BP–4CzIPN combination (Figure 28C). High concentrations of *p*-TIPS-BP facilitated near-complete deactivation of 4CzIPN, whereas the strong UV absorption of IrdF introduced filter effects that negatively impacted the UC performance.

Project **[J]** was published as a research article:

"Purely organic Vis-to-UV upconversion with an excited annihilator singlet beyond 4 eV"

Reproduced from Reference: T. J. B. Zähringer, M.-S. Bertrams, C. Kerzig, *J. Mater. Chem. C* **2022**,*10*, 4568–4573. with permission from the Royal Society of Chemistry.

The article can be cited corresponding to ref.[J]. The reference is attached in the following pages and the supporting information can be found in Chapter 10.11.

Author contributions: The Project was conceptualized by C. Kerzig. Synthesis and spectroscopic characterization were performed by T. J. B. Zähringer. M.-S. Bertrams performed TCSPC measurements. C. Kerzig performed DFT calculations. The manuscript was written by C. Kerzig and T. J. B. Zähringer.

Journal of Materials Chemistry C

ROYAL SOCIETY OF CHEMISTRY

COMMUNICATION

View Article Online
View Journal | View Issue

Published on 04 November 2021. Downloaded by Johannes Gutenberg Universitaet Mainz on 4/15/2025 8:10:27 PM.

Check for updates

Cite this: *J. Mater. Chem. C*, 2022, **10**, 4568

Received 6th October 2021,
Accepted 3rd November 2021

DOI: 10.1039/d1tc04782e

rsc.li/materials-c

Purely organic Vis-to-UV upconversion with an excited annihilator singlet beyond 4 eV†

Till J. B. Zähringer, Maria-Sophie Bertrams and Christoph Kerzig *

The conversion of visible light into high-energy UV photons *via* sensitized triplet–triplet annihilation (TTA-UC) could pave the way for several energy-demanding applications. However, only a handful of annihilator chromophores for Vis-to-UV upconversion are known and the current limit for the excited-state energy of the UV emitter in TTA-UC schemes is below 4 eV, *i.e.*, in the spectral region (>310 nm) where the sun still provides a considerable photon flux. Herein, we present a novel biphenyl-based annihilator with a highly fluorescent singlet state at 4.04 eV. This annihilator can be combined with a widely-used TADF sensitizer to yield an efficient blue-light (2.77 eV) driven upconversion system with unprecedented properties.

Several photochemical processes such as water splitting,[1–3] waste-water treatment[4] and the photocatalytic activation of inert molecules[5–7] require more energy than a single visible photon[5,8–13] can provide. In principle, highly energetic UV light could be exploited for all these applications, but the efficient and mercury-free generation of UV light below 320 nm by artificial light sources is challenging[14,15] and the solar spectrum sharply drops in that region. Hence, converting two visible photons into UV light or high-lying excited states with energies exceeding 4 eV, which corresponds to UVB photons with wavelengths shorter than 310 nm, would most likely enable several applications under mild reaction conditions.[1]

The sTTA mechanism is highly attractive for converting visible[16,17] or even NIR[18,19] photons into radiation of higher energy at non-coherent low photon fluxes.[20–23] Vis-to-UV upconversion *via* sTTA was initially observed by Castellano in 2009.[24] This field is experiencing a revival as a result of recent upconversion-driven applications for challenging chemical transformations in the greater context of photocatalysis.[1,4,7,25]

Department of Chemistry, Johannes Gutenberg University Mainz, Duesbergweg 10–14, Mainz 55128, Germany. E-mail: ckerzig@uni-mainz.de

† Electronic supplementary information (ESI) available: Experimental details, photophysical properties, additional upconversion and control experiments as well as quantum-mechanical calculations. See DOI: 10.1039/d1tc04782e

So far, only five different types of UV annihilators have been identified: PPO,[24,26,27] terphenyl,[28] quarterphenyl,[28] pyrene[29–32] and naphthalene[3,4,33–36] (and their derivatives).[2,36] The energies of these excited annihilator singlets (S_1) produced through sTTA with visible (blue or violet) light as energy input have typical values on the order of 3.6 eV. This corresponds to photons with ~350 nm, where the sun still provides a noticeable light intensity. Naphthalene derivatives with bulky (*t*Bu) or ionic (sulfonate) groups are the current record holders with S_1 energies slightly below 4 eV.[3,4,36,37]

Chemical modification[38] of known UC-inactive chromophores might bring about new UV annihilators, whose S_1 energies surpass the 4 eV holy grail of Vis-to-UV upconversion. We speculated that biphenyl is a promising starting point and selected so-called TIPS or TIPS-ethynyl (triisopropylsilylethynyl) substituents, because such silicon-containing groups have proven very successful for improving the performance and the energetics of several UC systems.[34,35,39,40] Given that the triplet energy of unmodified biphenyl is as high as 2.84 eV,[37] its sensitization in a UC scheme with blue light (*e.g.* 447 nm; 2.77 eV) would not even be feasible for an idealized system lacking energy loss. Guided by DFT calculations (see ESI† Section S3 for details), we substituted biphenyl with one TIPS group in the *para* position (see Fig. 1 for its structure). The resulting ***p*-TIPS-BP** has (i) a triplet accessible with blue-light absorbing sensitizers, (ii) undergoes efficient TTA, and (iii) is suitable for blue-to-UV upconversion with a highly emissive S_1 state at 4.04 eV, as we will show by detailed steady-state and time-resolved spectroscopic techniques.

Fig. 1 contains the absorption and luminescence spectra of ***p*-TIPS-BP** and the prominent carbazoyl dicyanobenzene-based TADF emitter **4CzIPN**, together with the pertinent thermodynamic and photophysical data. Since its discovery by Adachi in 2012,[41] **4CzIPN** has been successfully employed as photosensitizer in upconversion schemes[28,31,42] and as catalyst in several photoreactions.[43] Its unique properties, including intense blue-light absorptivity (λ_{max} = 435 nm), a high triplet formation yield (about 70% under our conditions, see ESI† for details), a

This journal is © The Royal Society of Chemistry 2022

Published on 04 November 2021. Downloaded by Johannes Gutenberg Universitaet Mainz on 4/15/2025 8:10:27 PM.

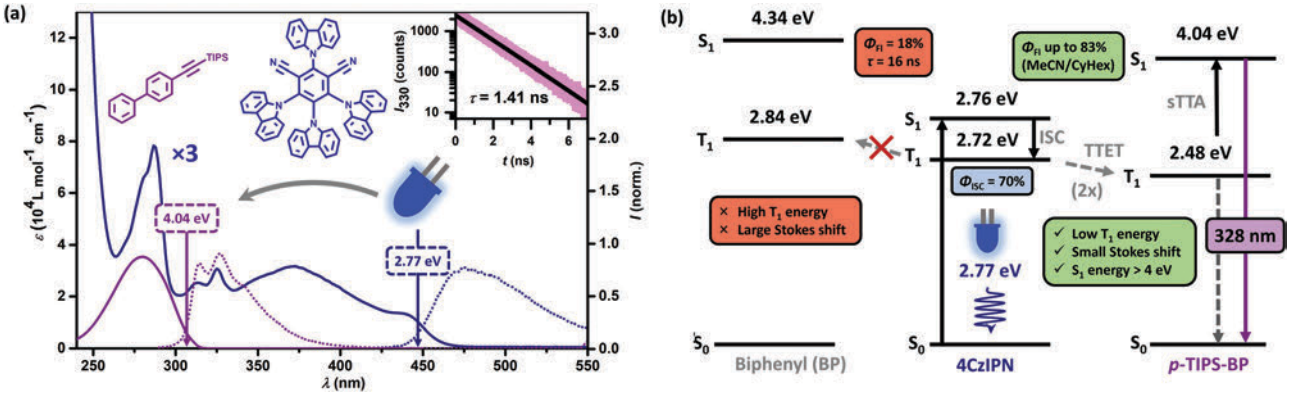

Fig. 1 (a) UV-Vis absorption and normalized emission spectra of sensitizer (**4CzIPN**, blue) and annihilator (***p*-TIPS-BP**, purple) in cyclohexane with the upconversion excitation wavelength (447 nm) and the annihilator's S_1 energy being highlighted, as well as the fluorescence lifetime of ***p*-TIPS-BP** (inset). (b) Energy diagram visualizing the pertinent properties of the upconversion scheme presented herein. For details, see text and ESI.†

high-lying (2.72 eV) triplet state, and a long room-temperature triplet lifetime (see below) make **4CzIPN** an ideal sensitizer for our study. Among the three isomers of TIPS biphenyl, which have been prepared by Sonogashira coupling reactions starting from commercial bromo derivatives (ESI,† Section S2.1), ***p*-TIPS-BP** clearly has outstanding properties. TIPS substitution in *para* position reduces the S_1 energy of biphenyl by merely 7%, whereas the triplet energy is lowered by 13%. Moreover, the unusually large Stokes shift of biphenyl is reduced to about 50% for ***p*-TIPS-BP** (ESI,† Fig. S8). These combined factors pave the way for efficient sensitization of ***p*-TIPS-BP** and for obtaining large anti-Stokes shifts of the resulting UC schemes. In addition, ***p*-TIPS-BP** is more highly emissive than biphenyl by at least a factor of three (depending on the solvent, see Table S3, ESI†) and, in line with the Strickler–Berg equation,[15,44,45] its emission lifetime is reduced drastically (Fig. 1a, inset). The short lifetime of the annihilator's emission, which peaks at 314 and 327 nm, is beneficial for suppressing side reactions such as FRET[23] or excimer formation.[46,47] The *ortho* and *meta* TIPS biphenyl isomers did not show all these favorable properties (ESI,† Section S7), likely due to sterics (*ortho* isomer) and the less pronounced electronic and mesomeric effects compared to *para* substitution. In the following paragraphs, we will present and compare the results obtained for ***p*-TIPS-BP** combined with either **4CzIPN** or the widely-used tris-cyclometalated iridium complex with difluorophenylpyridine ligands *fac*-Ir(4′,6′-dF-ppy)$_3$, hereafter abbreviated as **IrdF**. We anticipate that the comparative investigation of two sensitizer-annihilator couples should provide deeper insights than a single UC system could. For solubility reasons and the pronounced excited-state stabilization of **4CzIPN** in polar solvents (see ESI† Section S4 for details),[48] however, we were forced to use different solvents for both upconversion systems. We selected cyclohexane for the **4CzIPN**–***p*-TIPS-BP** couple, while the **IrdF**–***p*-TIPS-BP** combo was studied in MeCN. The UV-Vis absorption and emission spectra of ***p*-TIPS-BP** are largely solvent-independent, as measurements in cyclohexane, THF and MeCN revealed (ESI,† Section S9).

Laser flash photolysis (LFP) studies using a frequency-tripled Nd:YAG laser (355 nm, ~5 ns pulse duration) for selective excitation of both sensitizers were carried out to analyze the triplet quenching kinetics. Triplet lifetimes of **IrdF** (unquenched lifetime, 2.0 μs) in the presence of various ***p*-TIPS-BP** concentrations were monitored by time-resolved emission experiments (Fig. 2b). For experimental reasons, transient absorption studies (Fig. 2a) provided a better sensitivity to measure the lifetime of **4CzIPN's** charge-transfer triplet state (unquenched lifetime, 7.9 μs). This is due to detector saturation during emission measurements with our LFP setup, resulting from intense prompt fluorescence[49] signals of the

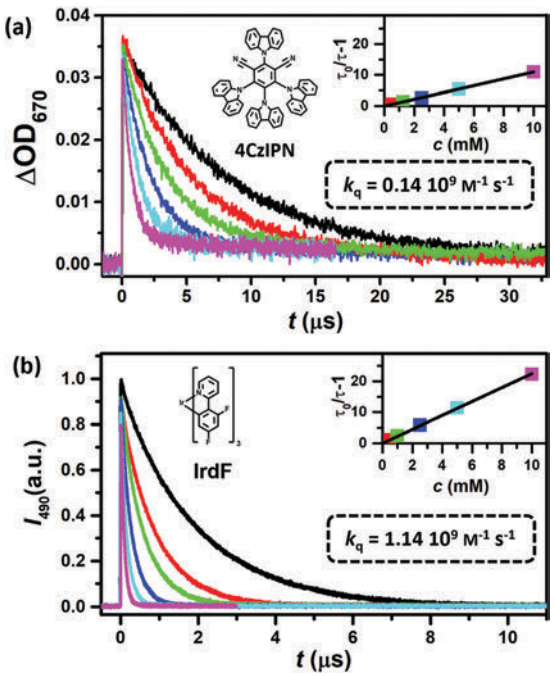

Fig. 2 Triplet quenching kinetics upon sensitizer excitation with 355 nm laser pulses. (a) Transient absorption data for **4CzIPN** (20 μM) in the absence and presence of ***p*-TIPS-BP** in Ar-saturated cyclohexane (main plot). (b) Emission decay kinetics of excited **IrdF** (38.5 μM) in the presence of several ***p*-TIPS-BP** concentrations in Ar-saturated MeCN. The quencher concentrations in the corresponding Stern–Volmer plots (insets) are shown with the same color codes as in the main plots.

Published on 04 November 2021. Downloaded by Johannes Gutenberg Universitaet Mainz on 4/15/2025 8:10:27 PM.

TADF emitter. Lifetime-based Stern–Volmer analyses (Fig. 2, insets) yielded quenching rate constants of 1.1×10^9 M^{-1} s^{-1} and 1.4×10^8 M^{-1} s^{-1} for **IrdF** and **4CzIPN**, respectively. Quasi-quantitative triplet quenching (>90%) is thus feasible at rather low ***p*-TIPS-BP** concentrations (~10 mM) for both systems.

The higher quenching rate constant obtained for ^{3}**IrdF** (2.75 eV) compared to that for ^{3}**4CzIPN** (2.72 eV) might indicate that a triplet–triplet energy transfer (TTET) is the underlying mechanism. However, steric considerations and spin density distributions of the inherently different sensitizers might affect the orbital overlap and the rate constant of a Dexter-type energy transfer accordingly. Additional LFP studies with transient absorption detection were carried out to monitor the quenching product directly (Fig. 3). The addition of ***p*-TIPS-BP** results in a new absorbing species in the transient absorption spectra (purple spectra in Fig. 3a and b). This species is generated with the very same rate constant as the decay of the respective sensitizer triplet (compare, red and blue kinetic traces in Fig. 3), and it shows an intense absorption band with a solvent-independent absorption maximum at ~408 nm. The absence of sensitizer-related absorption bands in the spectra recorded right after the quenching process as well as the observed solvent-independence rule out electron transfer quenching. We regard our LFP studies as direct evidence for the formation of ^{3}***p*-TIPS-BP** *via* TTET in both cases. This assignment is collaborated by TD-DFT calculations on ^{3}***p*-TIPS-BP** (ESI,† Fig. S4). Our calculations predict an intense absorption band peaking at ~420 nm, which is in very good agreement with the experimental findings. The transient absorption signals of ^{3}***p*-TIPS-BP** are quite long-lived and they completely return to baseline on a 200 μs timescale (ESI,† Fig. S11). These results are also in line with the triplet character of the initial quenching product, and they indicate the absence of detrimental side reactions.

Next, we turned to the TTA step of the upconversion mechanism under study. Three solutions containing the sensitizer (**4CzIPN**), the annihilator, or both were investigated by time-gated emission spectroscopy upon 355 nm laser excitation (Fig. 4). A detection window with a delay of 7 μs (relative to the laser pulse) was used to avoid scattering light and intense signals of the unquenched **4CzIPN** emission; the integration occurred over a period long enough for the complete deactivation of all triplet states. A solution containing both the sensitizer *and* the annihilator is required to detect delayed UV emission of singlet-excited ***p*-TIPS-BP** (^{1}***p*-TIPS-BP***), as is demonstrated by the results summarized in the main plot of Fig. 4.[50] Even more direct evidence for the sTTA mechanism is shown in the inset of Fig. 4, which compares kinetic traces monitoring either ^{3}***p*-TIPS-BP** (through the transient absorption at 408 nm) or ^{1}***p*-TIPS-BP*** (*via* its emission at 328 nm). The concentrations of both species reach their maxima with similar kinetics (after about 2 μs following the laser pulse) and at longer timescales, the ^{1}***p*-TIPS-BP*** concentration decays more rapidly than that of ^{3}***p*-TIPS-BP**. All these results are in perfect accordance with ^{3}***p*-TIPS-BP** being the origin of the delayed/upconverted ^{1}***p*-TIPS-BP*** emission as well as with the bimolecular nature of the annihilation process.[51] The observed sensitizer emission in the green delayed emission spectrum (Fig. 4) must originate from back TTET[4,52–54] from ^{3}***p*-TIPS-BP** to **4CzIPN** since the direct **4CzIPN** emission has decayed completely before the beginning of the selected detection window. This can be rationalized by the low triplet energy differences. Similar results were obtained for the **IrdF**-containing UC system

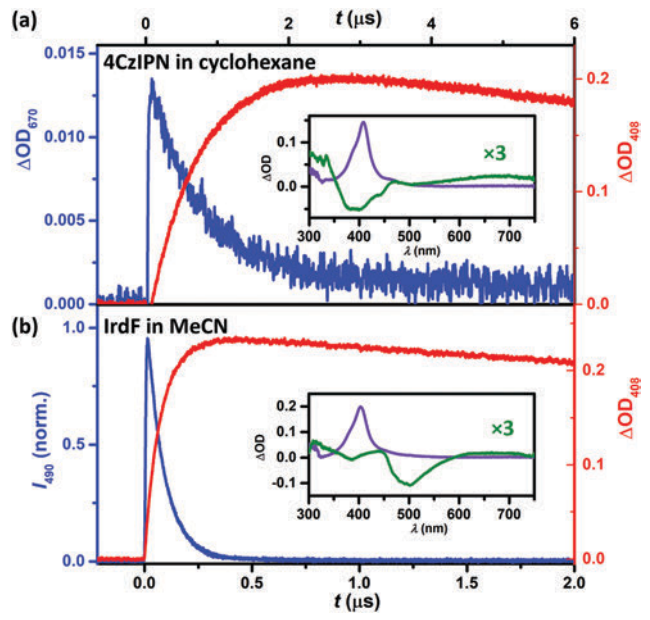

Fig. 3 Identification of the ***p*-TIPS-BP** triplet by LFP studies (355 nm excitation). (a) Transient absorption traces monitored at 670 nm (quenching, blue) and 408 nm (product formation, red) upon excitation of **4CzIPN** (20 μM) and ***p*-TIPS-BP** (10 mM) in Ar-saturated cyclohexane, with transient absorption spectra of the initial triplet (green) and the quenching product (purple) shown in the inset. (b) Similar data sets as in (a) but with **IrdF** (38 μM in MeCN) as the sensitizer and with emission detection of its triplet decay monitored at 490 nm.

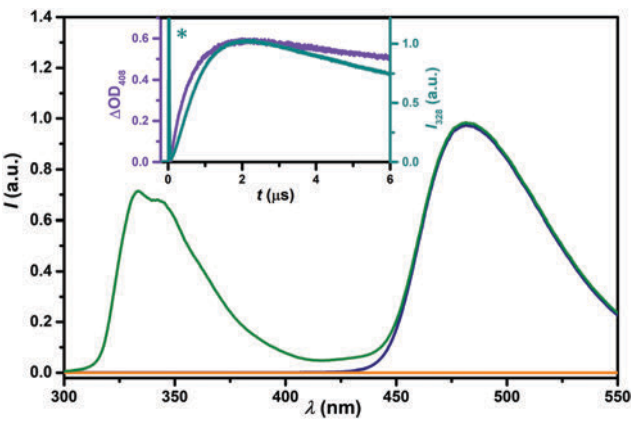

Fig. 4 LFP experiments in Ar-saturated cyclohexane solutions containing 20 μM **4CzIPN** and/or 10 mM ***p*-TIPS-BP** after excitation with 355 nm laser pulses. Main plot: normalized time-gated (delay, 7 μs; integration over 300 μs) emission spectra of the complete upconversion system (green), only **4CzIPN** (blue), and only ***p*-TIPS-BP** (orange). Inset: time-resolved emission (328 nm) and transient absorption (408 nm) traces upon excitation of the UC system. The asterisk marks laser stray light.

This journal is © The Royal Society of Chemistry 2022

Published on 04 November 2021. Downloaded by Johannes Gutenberg Universitaet Mainz on 4/15/2025 8:10:27 PM.

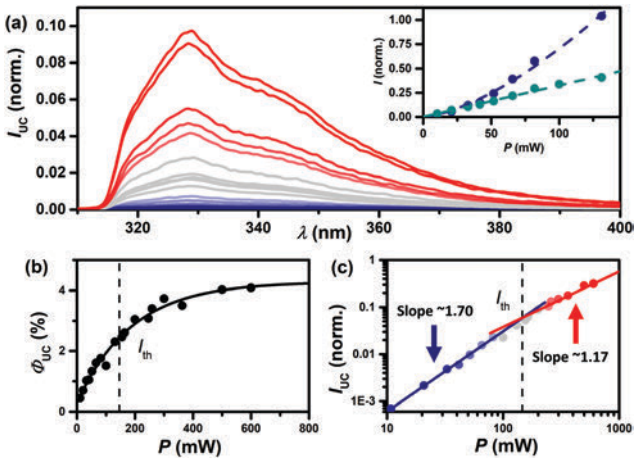

Fig. 5 Photon upconversion studies with deoxygenated solutions containing 44 μM **4CzIPN** and 10 mM ***p*-TIPS-BP** in cyclohexane : toluene (9 : 1) using a cw laser for excitation at 447 nm (OD_{447} = 0.2). (a) Main plot: power-dependent spectra of the normalized upconverted emission. Inset: quadratic power dependence of upconverted emission (blue) and linear power dependence of normalized sensitizer photoluminescence (green). (b) External quantum yield Φ_{UC} plotted against the laser power. (c) Normalized UC emission plotted against the laser power on a double-logarithmic scale. The pseudo-threshold intensity I_{th}[60] was determined by the point of intersection. See text and ESI† for details and further explanations.

(ESI,† Fig. S12). In addition to the time-gated emission spectra of Fig. 4, we performed kinetic experiments and found an excellent correlation between the ^{3}***p*-TIPS-BP** lifetime and the elongated sensitizer emission lifetime (ESI,† Fig. S16).[4,52] These results strongly support the above-mentioned back TTET.

Finally, we had a look at the upconverted emission upon continuous wave (cw) excitation and at its power dependence. Higher sensitizer concentrations than used for the LFP experiments were selected for these measurements to improve the TTA-UC performance.[55] However, in the case of the **4CzIPN–*p*-TIPS-BP** system, we had to add 10% v/v of toluene as co-solvent for solubility reasons (ESI,† Section S4). The resulting optical densities at the excitation wavelength 447 nm were between 0.1 and 0.2. The annihilator concentrations were chosen such that the TTET efficiencies exceeded 90%.

Fig. 5 collates the blue-to-UV upconversion results obtained for our purely organic system (similar data sets with the Ir sensitizer are shown in the ESI,† Fig. S13). Intense UV emission[50] from ^{1}***p*-TIPS-BP***** with a non-linear power dependence is clearly observable upon 447 nm excitation (Fig. 5a, the output power must be multiplied by 10 cm^{-2} for its conversion to power density). Taking the long-wavelength absorption maximum of **4CzIPN** (435 nm) and the maximum of the upconverted emission (328 nm),[23] we obtained an anti-Stokes shift of 0.93 eV. A frequently used more optimistic definition of the anti-Stokes shift with the excitation wavelength (447 nm) and the high-energy emission peak in the absence of inner filter effects (314 nm) gave a value as high as 1.17 eV, which is among the highest anti-Stokes shifts for TTA-UC systems reported to date.[39,40,56–59]

The complete UC power dependence is displayed in Fig. 5b and c and it has been recorded relative to the unquenched sensitizer emission as quantum yield reference (see ESI† for details). The maximum UC quantum yield for the **4CzIPN–*p*-TIPS-BP** pair amounts to 4.0% (with a theoretical maximum of 50%), which is relatively high considering that most Vis-to-UV UC systems are highly inefficient.[2] Comparative investigations on the UC power dependence with the **IrdF–*p*-TIPS-BP** system (ESI,† Fig. S13) gave significantly lower UC quantum yields. We speculate that pronounced filter effects resulting from the intense UV absorption of the Ir complex are the main reason for this efficiency difference (ESI,† Fig. S7). The so-called threshold excitation intensity I_{th} for the **4CzIPN–*p*-TIPS-BP** system was estimated from the crossing point of the (almost) quadratic[60] and (almost) linear fitting lines in Fig. 5c. With I_{th} equalling 147 mW (corresponding to ~1.5 W cm^{-2}), this value is far above solar irradiation power densities. However, additional UC experiments with a conventional blue LED (440 nm) gave intense UV emission signals (ESI,† Fig. S14). These results are clear evidence for the applicability of our novel UV light generator under typical lab conditions without the need for advanced laser setups and associated safety issues. The UV upconversion signal slowly decays over one hour of intense photoirradiation with our 447 nm laser (ESI,† Fig. S6). Control experiments on **4CzIPN** alone revealed that the (slow) sensitizer decomposition is one main reason for the observed upconversion signal decrease over time. This indicates acceptable stability of our novel UV annihilator under UC conditions.

Compared to the only other system in which blue light is converted to UV photons below 345 nm,[4] the quantum yield of the **4CzIPN–*p*-TIPS-BP** upconversion couple investigated herein is higher by about two orders of magnitude. All other prior studies with annihilator singlets approaching 4 eV[3,36] had to rely on violet excitation light (405 nm), which reduces the achievable anti-Stokes shift drastically. The recently developed blue-to-UV UC system by Yanai and co-workers[34] shows an impressive quantum yield exceeding 10% and a surprisingly low threshold intensity of about 1 mW cm^{-2}, but the annihilator's S_1 energy is 0.5 eV lower than observed for our novel system. This comparison demonstrates the challenge of developing UC systems that possess all desired properties simultaneously. TIPS-ethynyl groups significantly improve the annihilator properties of anthracene,[39] naphthalene,[34,35] and biphenyl (this work), and it seems that these groups not only increase the fluorescence quantum yield but also the spin statistical factor f by allowing the productive conversion of the encounter complexes during the TTA step. However, additional studies are required to understand and fully exploit the potential of these unique functional groups.

Conclusions

In summary, we have demonstrated that biphenyl can be converted into a novel UV-emissive annihilator by a simple chemical modification. The energy of the emissive state of the resulting compound ***p*-TIPS-BP** compares favourably to those of the limited number of known UV annihilators. The novel

Published on 04 November 2021. Downloaded by Johannes Gutenberg Universitaet Mainz on 4/15/2025 8:10:27 PM.

biphenyl combined with **4CzIPN** as an energy-matched TADF sensitizer provides the very first Vis-to-UV upconversion system with an emissive state beyond 4 eV. Furthermore, it possesses the highest anti-Stokes shift observed so far upon blue light excitation of an upconversion system. We anticipate that our novel upconversion-driven access to highly energetic UV light could not only stimulate the quest for novel UV-emissive annihilators but also lay the grounds for challenging chemical applications in the greater context of photocatalysis and wastewater treatment. Thermodynamically, much higher-lying emissive states, whose emission spectra peak in the UVB region (280 nm to 315 nm), would be accessible when using violet or UVA light instead of blue input photons as in our case. The identification of unexplored annihilator chromophores would be required for this breakthrough, and we hope our study could trigger this development.

Conflicts of interest

There are no conflicts to declare.

Acknowledgements

We acknowledge generous financial support from the JGU Mainz, SusInnoScience and the German Research Foundation (DFG, grant number KE 2313/3-1). C. K. is grateful to the Chemical Industry Funds for a Liebig fellowship. We thank Dr Christopher Kampf for recording mass spectra.

Notes and references

1 Y. Du, X. Ai, Z. Li, T. Sun, Y. Huang, X. Zeng, X. Chen, F. Rao and F. Wang, *Adv. Photonics Res.*, 2021, **2**, 2000213.
2 V. Gray, in *Photochemistry*, ed. A. Albini and S. Protti, Royal Society of Chemistry, Cambridge, 2019, vol. 47, pp. 404–420.
3 Y. Murakami, A. Motooka, R. Enomoto, K. Niimi, A. Kaiho and N. Kiyoyanagi, *Phys. Chem. Chem. Phys.*, 2020, **22**, 27134–27143.
4 B. Pfund, D. M. Steffen, M. R. Schreier, M.-S. Bertrams, C. Ye, K. Börjesson, O. S. Wenger and C. Kerzig, *J. Am. Chem. Soc.*, 2020, **142**, 10468–10476.
5 F. Glaser, C. Kerzig and O. S. Wenger, *Angew. Chem., Int. Ed.*, 2020, **59**, 10266–10284.
6 I. Ghosh, T. Ghosh, J. I. Bardagi and B. König, *Science*, 2014, **346**, 725–728.
7 M. Majek, U. Faltermeier, B. Dick, R. Pérez-Ruiz and A. Jacobi von Wangelin, *Chem. – Eur. J.*, 2015, **21**, 15496–15501.
8 B. D. Ravetz, A. B. Pun, E. M. Churchill, D. N. Congreve, T. Rovis and L. M. Campos, *Nature*, 2019, **565**, 343–346.
9 L. Marzo, S. K. Pagire, O. Reiser and B. König, *Angew. Chem., Int. Ed.*, 2018, **57**, 10034–10072.
10 C. K. Prier, D. A. Rankic and D. W. C. MacMillan, *Chem. Rev.*, 2013, **113**, 5322–5363.
11 J. M. R. Narayanam and C. R. J. Stephenson, *Chem. Soc. Rev.*, 2011, **40**, 102–113.
12 T. R. Blum, Z. D. Miller, D. M. Bates, I. A. Guzei and T. P. Yoon, *Science*, 2016, **354**, 1391–1395.
13 J. Castellanos-Soriano, J. C. Herrera-Luna, D. Díaz Díaz, M. C. Jiménez and R. Pérez-Ruiz, *Org. Chem. Front.*, 2020, **7**, 1709–1716.
14 S. Horikoshi, D. Yamamoto, K. Hagiwara, A. Tsuchida, I. Matsumoto, Y. Nishiura, Y. Kiyoshima and N. Serpone, *Photochem. Photobiol. Sci.*, 2019, **18**, 328–335.
15 M.-S. Bertrams and C. Kerzig, *Chem. Commun.*, 2021, **57**, 6752–6755.
16 T. N. Singh-Rachford and F. N. Castellano, *Coord. Chem. Rev.*, 2010, **254**, 2560–2573.
17 J. Zhao, S. Ji and H. Guo, *RSC Adv.*, 2011, **1**, 937–950.
18 P. Bharmoria, H. Bildirir and K. Moth-Poulsen, *Chem. Soc. Rev.*, 2020, **49**, 6529–6554.
19 Y. Sasaki, S. Amemori, N. Yanai and N. Kimizuka, *Bull. Chem. Soc. Jpn.*, 2021, **94**, 1760–1768.
20 A. Monguzzi, R. Tubino, S. Hoseinkhani, M. Campione and F. Meinardi, *Phys. Chem. Chem. Phys.*, 2012, **14**, 4322–4332.
21 V. Gray, D. Dzebo, M. Abrahamsson, B. Albinsson and K. Moth-Poulsen, *Phys. Chem. Chem. Phys.*, 2014, **16**, 10345–10352.
22 W. Sun, A. Ronchi, T. Zhao, J. Han, A. Monguzzi and P. Duan, *J. Mater. Chem. C*, 2021, **9**, 14201–14208.
23 Y. Zhou, F. N. Castellano, T. W. Schmidt and K. Hanson, *ACS Energy Lett.*, 2020, **5**, 2322–2326.
24 T. N. Singh-Rachford and F. N. Castellano, *J. Phys. Chem. A*, 2009, **113**, 5912–5917.
25 M. Barawi, F. Fresno, R. Pérez-Ruiz and V. A. de la Peña O'Shea, *ACS Appl. Energy Mater.*, 2019, **2**, 207–211.
26 S. He, X. Luo, X. Liu, Y. Li and K. Wu, *J. Phys. Chem. Lett.*, 2019, **10**, 5036–5040.
27 V. Gray, P. Xia, Z. Huang, E. Moses, A. Fast, D. A. Fishman, V. I. Vullev, M. Abrahamsson, K. Moth-Poulsen and M. Lee Tang, *Chem. Sci.*, 2017, **8**, 5488–5496.
28 N. Yanai, M. Kozue, S. Amemori, R. Kabe, C. Adachi and N. Kimizuka, *J. Mater. Chem. C*, 2016, **4**, 6447–6451.
29 F. Glaser, C. Kerzig and O. S. Wenger, *Chem. Sci.*, 2021, **12**, 9922–9933.
30 W. Zhao and F. N. Castellano, *J. Phys. Chem. A*, 2006, **110**, 11440–11445.
31 Q. Chen, Y. Liu, X. Guo, J. Peng, S. Garakyaraghi, C. M. Papa, F. N. Castellano, D. Zhao and Y. Ma, *J. Phys. Chem. A*, 2018, **122**, 6673–6682.
32 P. Duan, N. Yanai and N. Kimizuka, *Chem. Commun.*, 2014, **50**, 13111–13113.
33 Z. A. VanOrman and L. Nienhaus, *Matter*, 2021, **4**, 2625–2626.
34 N. Harada, Y. Sasaki, M. Hosoyamada, N. Kimizuka and N. Yanai, *Angew. Chem., Int. Ed.*, 2021, **60**, 142–147.
35 Y. Wei, K. Pan, Y. Li, X. Cao, X. Zhou and C. Yang, *preprint*, DOI: 10.33774/chemrxiv-2021-mq00r-v2.
36 L. Hou, A. Olesund, S. Thurakkal, X. Zhang and B. Albinsson, *Adv. Funct. Mater.*, 2021, 2106198.
37 M. Montalti, A. Credi, L. Prodi and M. T. Gandolfi, *Handbook of photochemistry*, CRC/Taylor & Francis, Boca Raton, 3rd edn, 2006.

 This journal is © The Royal Society of Chemistry 2022

Published on 04 November 2021. Downloaded by Johannes Gutenberg Universitaet Mainz on 4/15/2025 8:10:27 PM.

38 X. Wang, R. Tom, X. Liu, D. N. Congreve and N. Marom, *J. Mater. Chem. C*, 2020, **8**, 10816–10824.
39 N. Nishimura, V. Gray, J. R. Allardice, Z. Zhang, A. Pershin, D. Beljonne and A. Rao, *ACS Mater. Lett.*, 2019, **1**, 660–664.
40 R. Haruki, Y. Sasaki, K. Masutani, N. Yanai and N. Kimizuka, *Chem. Commun.*, 2020, **56**, 7017–7020.
41 H. Uoyama, K. Goushi, K. Shizu, H. Nomura and C. Adachi, *Nature*, 2012, **492**, 234–238.
42 H.-L. Lee, M.-S. Lee, H. Park, W.-S. Han and J.-H. Kim, *Korean J. Chem. Eng.*, 2019, **36**, 1791–1798.
43 M. A. Bryden and E. Zysman-Colman, *Chem. Soc. Rev.*, 2021, **50**, 7587–7680.
44 S. J. Strickler and R. A. Berg, *J. Chem. Phys.*, 1962, **37**, 814–822.
45 J. Mohanty and W. M. Nau, *Photochem. Photobiol. Sci.*, 2004, **3**, 1026–1031.
46 C. Ye, V. Gray, J. Mårtensson and K. Börjesson, *J. Am. Chem. Soc.*, 2019, **141**, 9578–9584.
47 T. N. Singh-Rachford, R. R. Islangulov and F. N. Castellano, *J. Phys. Chem. A*, 2008, **112**, 3906–3910.
48 D. Jespersen, B. Keen, J. I. Day, A. Singh, J. Briles, D. Mullins and J. D. Weaver, *Org. Process Res. Dev.*, 2019, **23**, 1087–1095.
49 Y. Olivier, B. Yurash, L. Muccioli, G. D'Avino, O. Mikhnenko, J. C. Sancho-García, C. Adachi, T.-Q. Nguyen and D. Beljonne, *Phys. Rev. Mater.*, 2017, **1**, 075602.
50 Owing to the higher annihilator concentration there is a filter effect at the high-energy edge of the *p*-TIPS-BP emission compared to the spectrum shown in Fig. 1, which has been recorded for a strongly diluted solution.
51 Y. Murakami and K. Kamada, *Phys. Chem. Chem. Phys.*, 2021, **23**, 18268–18282.
52 D. Meroni, A. Monguzzi and F. Meinardi, *J. Chem. Phys.*, 2020, **153**, 114302.
53 J. Perego, J. Pedrini, C. X. Bezuidenhout, P. E. Sozzani, F. Meinardi, S. Bracco, A. Comotti and A. Monguzzi, *Adv. Mater.*, 2019, **31**, 1903309.
54 J. Isokuortti, S. R. Allu, A. Efimov, E. Vuorimaa-Laukkanen, N. V. Tkachenko, S. A. Vinogradov, T. Laaksonen and N. A. Durandin, *J. Phys. Chem. Lett.*, 2020, **11**, 318–324.
55 A. Haefele, J. Blumhoff, R. S. Khnayzer and F. N. Castellano, *J. Phys. Chem. Lett.*, 2012, **3**, 299–303.
56 Y. Wei, Y. Li, M. Zheng, X. Zhou, Y. Zou and C. Yang, *Adv. Opt. Mater.*, 2020, **8**, 1902157.
57 Y. Wei, M. Zheng, L. Chen, X. Zhou and S. Liu, *Dalton Trans.*, 2019, **48**, 11763–11771.
58 C. Fan, L. Wei, T. Niu, M. Rao, G. Cheng, J. J. Chruma, W. Wu and C. Yang, *J. Am. Chem. Soc.*, 2019, **141**, 15070–15077.
59 J. B. Bilger, C. Kerzig, C. B. Larsen and O. S. Wenger, *J. Am. Chem. Soc.*, 2021, **143**, 1651–1663.
60 A perfectly quadratic behaviour cannot be observed, not even under low-power LED conditions. This is most likely due to back TTET complicating the kinetics. We regard I_{th} as a pseudo-threshold intensity in our case, which might still be useful to characterize our upconversion system.

Summary:

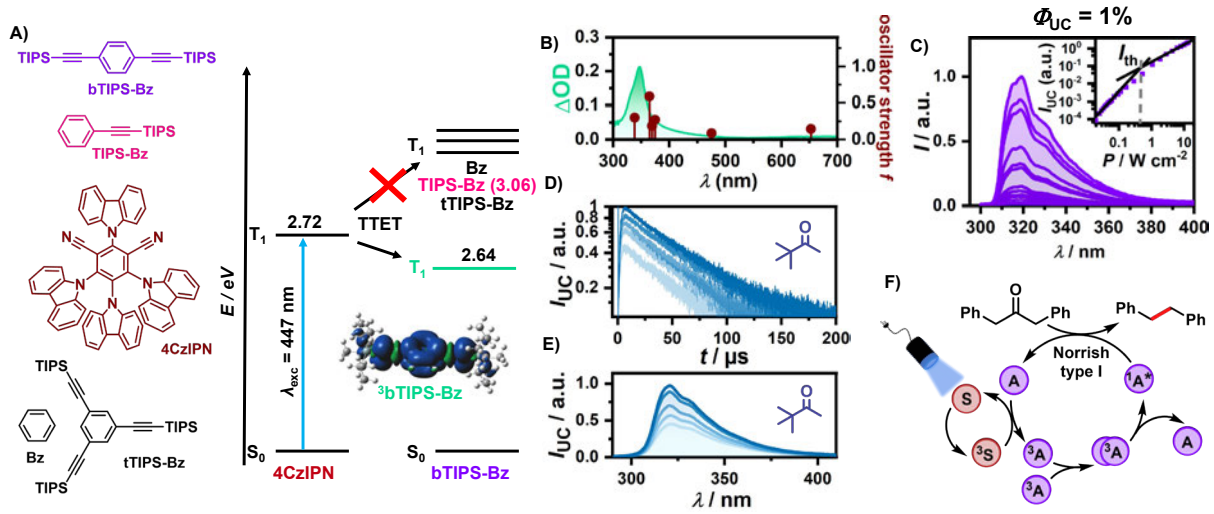

Figure 29: Mechanistic investigations of the bTIPS-Bz–4CzIPN UC system and subsequent substrate activation. A) Molecular structures of investigated chromophores and schematic energy diagram of the TTET step. B) TA spectrum and calculated oscillator strength of bTIPS-Bz. C) UC emission under 447 nm cw laser excitation. Inset: UC emission plotted against the laser intensity. D) Kinetic traces of the UC emission with increasing pinacolone concentration. E) Spectral UC emission with increasing pinacolone concentration. F) Mechanism of the UC–FRET sequence using the substrate dibenzyl ketone.

Project **[K]** investigated a benzene-based chromophore as a potential UVB annihilator. While benzene exhibits superior emission properties in the UVB range, its triplet energy of 3.9 eV is inaccessible to any known triplet sensitizers. Drawing on insights from the biphenyl-based annihilator and previous studies, the substitution of benzene with TIPS-ethynyl groups was explored. DFT calculations guided the evaluation of various substitution patterns, revealing that *para*-disubstitution (bTIPS-Bz) resulted in the lowest calculated triplet state energy of 2.57 eV (Figure 29A). Consequently, bTIPS-Bz was synthesized using the Sonogashira coupling reaction. The monosubstituted derivative (TIPS-Bz) was also considered; however, its calculated triplet energy of 3.06 eV was too high for sensitization in a blue-light-driven TTA–UC system, which corresponds to photon energies of approximately 2.7 eV. Phosphorescence measurements at 77 K confirmed a triplet energy of 2.64 eV for bTIPS-Bz, supporting the significant triplet state energy reduction predicted by DFT. Additionally, the singlet state energy was determined to be 4.15 eV, with an emission maximum at 308 nm and over 50% of its emitted photons in the UVB range. The fluorescence quantum yield increased from 0.07 to 0.48, while the fluorescence lifetime was reduced from 30 ns to 3.2 ns relative to unsubstituted benzene. The TTET and TTA steps of this UC system were thoroughly characterized using laser flash photolysis with 355 nm laser pulse excitation. The triplet state of bTIPS-Bz was detected by TA spectroscopy and corroborated by the computed oscillator strength (Figure 29B). Following excitation, an emission maximum at 318 nm was observed after the deactivation of 4CzIPN and was conclusively attributed to the triplet–triplet annihilation of ^{3}bTIPS-Bz. An upconversion quantum yield of 1% and a threshold intensity of 471 mW cm^{-2} were determined using a 447 nm continuous wave laser for this annihilator-sensitizer system (Figure 29C). The UC system exhibited stable

UC emission over 60 minutes of continuous exposure to 445 nm cw laser light, demonstrating its potential for efficient activation of UVB-absorbing substrates.

It was hypothesized that the high singlet-excited state energy of bTIPS-Bz could be utilized for FRET activation of inert compounds. To investigate this UC–FRET process, mechanistic LFP experiments were conducted using two carbonyl compounds, acetone and pinacolone, as FRET acceptors. As the concentrations of acetone and pinacolone in the UC solution increased, the amplitude of the kinetic traces of the UC emission decreased, whereas the kinetic traces of ^{3}TIPS-Bz remained largely unaffected (Figure 29D). This indicates that the TTA–UC mechanism is not disrupted by the presence of carbonyls until the singlet-excited state of bTIPS-Bz is reached. Notably, the UC emission spectrum uniformly decreased upon the introduction of carbonyls, suggesting that energy transfer occurs via FRET rather than a simple emission-reabsorption mechanism, which would selectively reduce the emission only at wavelengths where the carbonyls absorb (Figure 29E).

To further support the UC–FRET sequence (Figure 29F for mechanism), NMR-scale irradiation experiments were performed using blue (440 nm) LEDs. The UC system was irradiated in the presence of pinacolone and dibenzyl ketone, both of which undergo Norrish type I fragmentation upon excitation to their singlet-excited states. The formation of stable fragmentation products, isobutylene and bibenzyl, was confirmed by NMR spectroscopy. In contrast, no product formation was observed unless both the sensitizer and the annihilator were present, providing strong evidence that the UC–FRET process successfully facilitated substrate activation.

Project **[K]** was published as a research article:

“**Blue-to-UVB Upconversion, Solvent Sensitization and Challenging Bond Activation Enabled by a Benzene-Based Annihilator**”

Reproduced from reference: T. J. B. Zähringer, J. A. Moghtader, M. Bertrams, B. Roy, M. Uji, N. Yanai, C. Kerzig, *Angew. Chem. Int. Ed.* **2023**, *62*, e202215340.

The article is Open Access and licensed under CC BY-NC 4.0 (https://creativecommons.org/licenses/by/4.0/). It was reproduced from ref.[K]. The reference is attached in the following pages and the supporting information can be found in Chapter 10.12.

Author contributions: The Project was conceptualized by C. Kerzig. Synthesis, spectroscopic characterization and irradiation experiments were performed by T. J. B. Zähringer and J. A. Moghtader. B. Roy and M. Uji performed the measurements for the UC quantum yield and the threshold intensity, supervised by N. Yanai. The manuscript was written by C. Kerzig and T. J. B. Zähringer.

Check for updates

Photochemistry Very Important Paper

How to cite: *Angew. Chem. Int. Ed.* **2023**, *62*, e202215340
International Edition: doi.org/10.1002/anie.202215340
German Edition: doi.org/10.1002/ange.202215340

Blue-to-UVB Upconversion, Solvent Sensitization and Challenging Bond Activation Enabled by a Benzene-Based Annihilator

Till J. B. Zähringer, Julian A. Moghtader, Maria-Sophie Bertrams, Bibhisan Roy, Masanori Uji, Nobuhiro Yanai, and Christoph Kerzig**

Abstract: Several energy-demanding photoreactions require harsh UV light from inefficient light sources. The conversion of low-energy visible light to high-energy singlet states via triplet-triplet annihilation upconversion (TTA-UC) could offer a solution for driving such reactions under mild conditions. We present the first annihilator with an emission maximum in the UVB region that, combined with an organic sensitizer, is suitable for blue-to-UVB upconversion. The annihilator singlet was successfully employed as an energy donor in subsequent FRET activations of aliphatic carbonyls. This hitherto unreported UC-FRET reaction sequence was directly monitored using laser spectroscopy and applied to mechanistic irradiation experiments demonstrating the feasibility of Norrish chemistry. Our results provide clear evidence for a novel blue light-driven substrate or solvent activation strategy, which is important in the context of developing more sustainable light-to-chemical energy conversion systems.

Introduction

Highly energetic photons with wavelengths in the UVB region (280–315 nm) are unavoidably required to initiate numerous useful photochemical reactions[1,2] and to detoxify many pollutants photochemically.[3,4] However, two main drawbacks render the broad usage of UVB-driven reactions somewhat cumbersome. Firstly, UVB light is practically not contained in the solar spectrum and the generation of UVB photons typically requires mercury lamps,[5] excimer-based lamps,[6] or the high-energy tail of xenon arc lamps[4]—all of them suffer from rather short lifespans well below 2000 h and electricity-to-UVB conversion efficiencies close to zero. Secondly, conventional glassware used in chemical laboratories has a low UVB transparency, which is why more expensive quartz glass is required for conventional UVB photochemistry.

In principle, the energy of two visible photons efficiently generated by long-lived LEDs can be pooled to achieve similar reactivities as obtained by direct UVB excitation. Among all known photon pooling or two-photon mechanisms,[7–11] upconversion via sensitized triplet-triplet annihilation (TTA-UC) provides the most attractive alternative to direct high-energy one-photon excitation, because TTA-UC can be employed to convert two low-energy photons at moderate photon fluxes into one highly energetic singlet-excited state.[12–23] The latter can either emit one photon of higher energy or directly activate a compound being inert under one-photon conditions at the given excitation wavelength. This strategy has already been exploited for a variety of selective photoreactions upon excitation with inexpensive diode-based continuous wave (cw) light sources,[24] including isomerizations,[25–27] dehalogenations,[28–30] cycloadditions,[31,32] C–C coupling[24,33,34] and cyclization[30] reactions as well as polymerizations.[30,35–37] While all these UC-driven reactions are elegant, in particular when red/NIR photons with high penetration depth are used,[30,38–40] they can likely be initiated by LEDs in a direct manner. Efficient high-power LEDs are available with numerous visible and some UVA (315–400 nm) peak wavelengths, but efficient ready-to-use LEDs with UVB emission do not exist for technical reasons.[41] Consequently, it is highly desirable to develop visible light-driven UC systems that are capable of producing UVB photons to potentially replace harmful and inefficient light sources.

The first visible light-driven TTA-UC system with pronounced UV emission was reported in 2009.[42] The interest in this methodology recently received a boost by some applications under remarkably mild conditions and pioneering observations such as the blue-light driven photocatalytic activation of aryl bromides,[43] water splitting,[44,45] the quantitative decomposition of a typical water pollutant,[28] and the development of systems with very high quantum yields for UVA generation.[46–48] Nevertheless, only a few basic structures for UV annihilators have been identified until now (biphenyl,[49–51] PPO and strongly related

[*] T. J. B. Zähringer, J. A. Moghtader, M.-S. Bertrams, Prof. Dr. C. Kerzig
Department of Chemistry, Johannes Gutenberg University Mainz
Duesbergweg 10–14, 55128 Mainz (Germany)
E-mail: ckerzig@uni-mainz.de

Dr. B. Roy, M. Uji, Prof. Dr. N. Yanai
Department of Applied Chemistry, Graduate School of Engineering, Center for Molecular Systems (CMS), Kyushu University
744 Moto-oka, Nishi-ku, Fukuoka 819-0395 (Japan)
E-mail: yanai@mail.cstm.kyushu-u.ac.jp

© 2022 The Authors. Angewandte Chemie International Edition published by Wiley-VCH GmbH. This is an open access article under the terms of the Creative Commons Attribution Non-Commercial License, which permits use, distribution and reproduction in any medium, provided the original work is properly cited and is not used for commercial purposes.

© 2022 The Authors. Angewandte Chemie International Edition published by Wiley-VCH GmbH

heterocycles,[42,48,52–54] terphenyl,[54,55] quarterphenyl,[55] pyrene[34,56–58] as well as naphthalene[28,37,46,51,54,59–61]) and all these annihilators mainly show UVA and violet emission with either a negligible fraction of emitted UVB[62] photons or no UVB emission at all. The identification of an annihilator with dominant UVB emission and the concomitant high excited singlet state energy well beyond 4 eV could expand the toolbox of photochemists drastically, given that Vis-to-UV upconversion holds great promise for energy-demanding photochemical applications.[63,64] Herein, we present the first compound that deserves the label UVB annihilator: Its emission peaks in the UVB region at 309 nm, about half of the photons emitted via fluorescence lie in the UVB range (Figure 1) and, in combination with a suitable blue light-absorbing sensitizer, blue-to-UV upconversion can be observed with diode-based light sources. The resulting upconversion system was characterized by in-depth mechanistic studies using several spectroscopic techniques and employed for an underexplored upconversion-Förster resonance energy transfer (UC-FRET)[65,66] reaction sequence. As we will show by meaningful proof-of-concept experiments, this novel strategy can not only be exploited for solvent excitation—a typical approach in synthetic UVB photochemistry[1,2,6,67]—but also for high-energy carbonyl photochemistry.[68,69]

Results and Discussion

Chemical intuition suggests that reducing the conjugated π-system from biphenyl to benzene would increase the annihilator's singlet-excited state energy and shift its peak emission from the UVA into the high-energy UVB region. However, the triplet of unsubstituted benzene at 3.9 eV[70] is inaccessible in blue light-driven upconversion schemes as the input photon energy is on the order of 2.7 eV in this case. Modifications on the annihilator scaffolds with the protection group TIPS-ethynyl (triisopropylsilylethynyl) have shown to lower the triplet energy substantially while maintaining relatively high energies of the upconverted emission.[46,50,71–74] Hence, we speculated that benzene would follow a similar trend although previous calculations predicted a very pronounced HOMO–LUMO gap decrease.[75] Our DFT calculations of several benzene derivatives with different TIPS-ethynyl substitution patterns provided initial information about the triplet energies (Figure 2B, see Section S3 of the Supporting Information for details). While the calculated triplet energies of single-substituted **TIPS-Bz** (3.06 eV) and symmetrical threefold substituted **tTIPS-Bz** (2.97 eV) still exceed our input energy limit, the twofold substitution (**bTIPS-Bz**), however, yielded a rather low triplet energy of 2.57 eV. For that reason, we synthesized **bTIPS-Bz** (and reference compounds) via a Sonogashira coupling reaction (see Supporting Information for details, Section S2). The absorption and normalized emission spectra are shown in Figure 2C. As expected, the two TIPS-ethynyl substituents on benzene cause a red-shift of the absorption and emission peaks (compare Figure S5). Gratifyingly, the emission spectrum of **bTIPS-Bz** peaks in the UVB, about half of all emitted photons are in the UVB range, and its singlet-excited state energy is as high as 4.15 eV, corresponding to a photon energy of 299 nm. Owing to the superincrease of the molar absorptivity (Figure S5), the fluorescence rate constant of **bTIPS-Bz** is increased drastically compared to that of benzene.[76–78] In direct consequence, (i) the fluorescence lifetime in solution (Figure S14) is shortened from 30 ns (benzene) to 3.2 ns (**bTIPS-Bz**) and (ii) the fluorescence quantum yield reaches an attractive value of $\Phi_{Fl}=0.48$ for **bTIPS-Bz**, compared to $\Phi_{Fl}=0.07$ for benzene.[79,80] From 77 K phosphorescence measurements, we obtained a triplet energy of 2.64 eV for **bTIPS-Bz** (Figure S17), which is in very good agreement

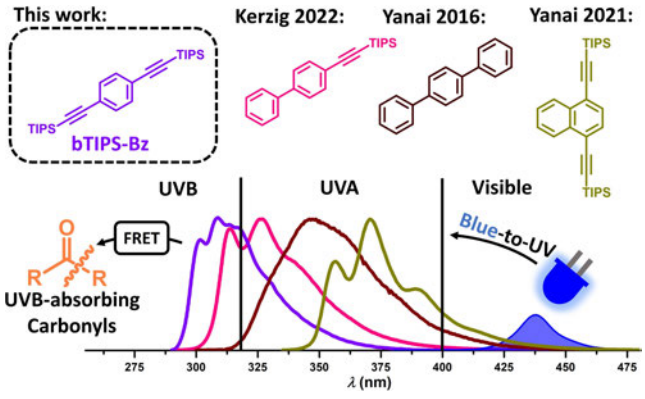

Figure 1. Structures and emission spectra of recently used annihilators for blue-to-UV upconversion. This work: Novel benzene-based annihilator (**bTIPS-Bz**) suitable for blue-to-UVB upconversion that has been successfully employed as an energy donor in a subsequent FRET activation of UVB-absorbing carbonyls.

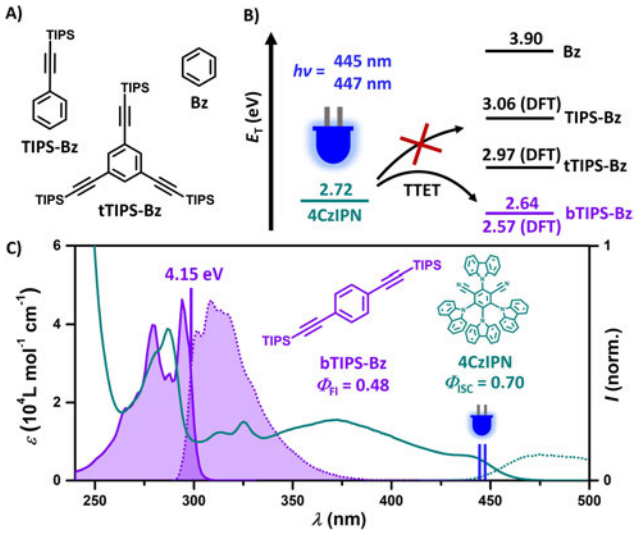

Figure 2. A) Structures of **TIPS-Bz**, **tTIPS-Bz** and **Bz**. B) Energy diagram visualizing the lowest triplet-excited state energies of **4CzIPN**, unsubstituted benzene, and TIPS-ethinyl substituted benzenes. C) Structures, absorption (solid line), and normalized emission (dotted line) spectra of **bTIPS-Bz** and **4CzIPN** in cyclohexane. The excitation wavelengths (445 nm and 447 nm) used for upconversion measurements are indicated by blue vertical lines.

© 2022 The Authors. Angewandte Chemie International Edition published by Wiley-VCH GmbH

15213773, 2023, 8, Downloaded from https://onlinelibrary.wiley.com/doi/10.1002/anie.202215340 by Universitatsbibliothek Mainz, Wiley Online Library on [15/04/2025]. See the Terms and Conditions (https://onlinelibrary.wiley.com/terms-and-conditions) on Wiley Online Library for rules of use; OA articles are governed by the applicable Creative Commons License

with that estimated by DFT calculations. Given that isoenergetic and even slightly uphill sensitization is feasible,[31,81–83] TTA-UC with **bTIPS-Bz** as annihilator is clearly within reach using blue photons.

For this study, we have chosen the well-known carbazoyl dicyanobenzene-based TADF emitter **4CzIPN** (Figure 2B and C) as the triplet sensitizer. In addition to OLED applications,[84] **4CzIPN** has been successfully employed in energy transfer catalysis[85,86] and TTA-UC schemes.[50,55,87] Its high triplet energy (2.72 eV in cyclohexane), high triplet formation yield (about 70 %)[88] and strong absorptivity in the blue make it ideal for our blue light-driven upconversion system.[50] For solubility reasons, toluene was used as co-solvent (10 vol. %), which does not negatively affect the pertinent properties of our photoactive compounds (see ref. [50] and Figures S6/S14). The combined key properties of both **4CzIPN** and **bTIPS-Bz** are summarized in Figures 2B and C. Transient absorption (TA) and emission spectroscopy using laser flash photolysis (LFP) were performed with a 355 nm laser (≈5 ns pulse duration) to investigate the upconversion system in detail. The initial energy transfer from ^{3}**4CzIPN** to **bTIPS-Bz** proceeds with a quenching rate constant of $k_{TTET} = 6.2 \times 10^7\ M^{-1} s^{-1}$ (Figure 3A), which is not only in line with the rather small triplet energy difference between ^{3}**bTIPS-Bz** and ^{3}**4CzIPN** but also sufficiently rapid for efficient quenching (>85 %) of ^{3}**4CzIPN** at moderate concentrations (>9 mM). In contrast, no quenching of the other TIPS-ethynyl substituted benzenes—**TIPS-Bz** and **tTIPS-Bz**—was observed, highlighting the unique photochemical properties of **bTIPS-Bz**. Further TA measurements were carried out to monitor the quenching product. The ^{3}**4CzIPN** quenching by **bTIPS-Bz** gave rise to a TA spectrum with a pronounced absorption band peaking at 348 nm (purple spectrum in Figure 3B) that completely returns to baseline (Figure S18) with wavelength-independent kinetics and a much longer lifetime (≈120 μs) compared to ^{3}**4CzIPN** alone (7.9 μs, see Figure S12 and corresponding discussion for further explanations). TD-DFT calculations on ^{3}**bTIPS-Bz** predict an intense absorption peak at 360 nm matching our experiments well (see calculated transitions in Figure 3B and Section S3 of the Supporting Information for details). We, therefore, assign the spectrum displayed in Figure 3B (purple) to ^{3}**bTIPS-Bz** generated through triplet-triplet energy transfer TTET.

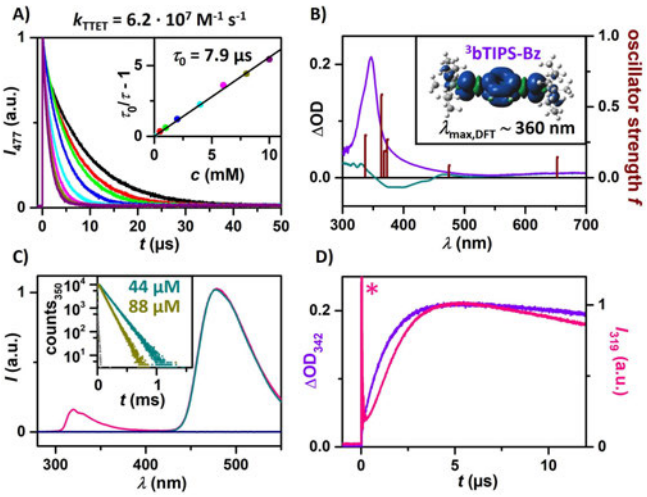

Figure 3. Mechanistic LFP experiments with 355 nm laser pulses of ≈5 ns duration. If not stated otherwise 20 μM **4CzIPN** and 10 mM **bTIPS-Bz** in Ar-saturated cyclohexane:toluene (9:1) were used. A) Luminescence quenching experiments of **4CzIPN** (detection wavelength, 477 nm) at different annihilator concentrations. Inset: corresponding Stern–Volmer plot. B) Transient absorption spectra of only **4CzIPN** (cyan) recorded 1 μs after the laser pulse and combined with **bTIPS-Bz** after 6 μs (purple) and oscillator strength of ^{3}**bTIPS-Bz** computed by TD-DFT. Inset: Computed spin density of the triplet state of **bTIPS-Bz** with $\lambda_{max,DFT}$ of the predicted main absorption bands. C) Normalized time-gated (delay, 6 μs; integration over 500 μs) emission spectra of the complete upconversion system (pink), only **4CzIPN** (cyan), and only **bTIPS-Bz** (dark blue). Inset: Time-resolved upconversion emission plotted logarithmically at different sensitizer concentrations under pulsed excitation at 445 nm. D) Time-resolved emission (319 nm) and transient absorption (342 nm) traces upon excitation of the UC system. The asterisk marks laser stray light.

Having established sensitized annihilator triplet formation, we next examined the TTA step. Three solutions containing either **bTIPS-Bz**, **4CzIPN**, or both in combination were prepared and investigated using time-gated emission spectroscopy. The detection window after 355 nm excitation was selected such that direct sensitizer and annihilator emission can be excluded. Out of the three solutions, only that with **4CzIPN** *and* **bTIPS-Bz** shows the expected singlet emission in the UV (Figure 3C) providing evidence for delayed annihilator emission, which has to be a result of TTA. The similar triplet energies imply the possibility of back-energy transfer in the triplet manifold. Kinetic emission traces monitoring delayed ^{1}**bTIPS-Bz*** emission at 350 nm with increasing sensitizer concentration confirm a back-TTET (Figure 3C, inset), as indicated by the delayed emission lifetime decrease.[28,89,90] Moreover, we observed that the triplet lifetime of ^{3}**bTIPS-Bz** correlates with the weak elongated **4CzIPN** emission from back-TTET (Figure S13), and we attribute the remaining spectral emission of **4CzIPN** in Figure 3C to this energy transfer equilibrium.[50,89]

More direct evidence for the UV emission originating from TTA-UC is given in Figure 3D. Kinetic traces simultaneously monitoring ^{3}**bTIPS-Bz** (absorption at 342 nm) and ^{1}**bTIPS-Bz*** (emission at 319 nm) show that both reach a maximum at $t = 6$ μs. Owing to the bimolecular nature of the annihilation process, the rise and fall of the singlet emission intensity are in a quadratic relation to the triplet concentration [^{3}**bTIPS-Bz**], resulting in the characteristic behavior displayed in Figure 3D.[91] We then characterized the efficiency of this novel blue-to-UVB TTA-UC scheme with two blue diode-based cw lasers at either 447 nm or 445 nm (see Supporting Information for detailed descriptions of both setups). We found that a sensitizer concentration of 44 μM gave a good compromise between the overall quantum yield and the threshold intensity I_{th}. Although higher sensitizer concentrations are regarded to be beneficial for lowering I_{th},[92] i.e., for achieving high quantum yields at low light intensities, we found a higher I_{th} at 88 μM (see

© 2022 The Authors. Angewandte Chemie International Edition published by Wiley-VCH GmbH

15213773, 2023, 8, Downloaded from https://onlinelibrary.wiley.com/doi/10.1002/anie.202215340 by Universitatsbibliothek Mainz, Wiley Online Library on [15/04/2025]. See the Terms and Conditions (https://onlinelibrary.wiley.com/terms-and-conditions) on Wiley Online Library for rules of use; OA articles are governed by the applicable Creative Commons License

Figure S7). This observation is most likely a result of back-TTET with sensitizer ground state molecules as an additional deactivation pathway of the annihilator triplet.

The main plot in Figure 4A collates the upconverted emission with increasing laser intensity (10–800 mW) peaking at 318 nm with intense emission in the UVB region. The higher annihilator concentration causes filter effects of the annihilator emission in its absorption-emission overlap region (compare spectra in Figures 2C and 4A), thereby shifting the apparent emission maximum. However, the absorption of the ^{1}**bTIPS-Bz***-emitted photons by additives in solution could occur below 310 nm—it would simply compete with annihilator self-absorption. Using the observed UC emission maximum in combination with the absorption maximum of **4CzIPN** (435 nm), the anti-Stokes shift amounts to 1.04 eV.[16] A frequently employed but less conservative anti-Stokes shift determination would yield a value as high as 1.24 eV, taking the excitation wavelength (447 nm) and the **bTIPS-Bz** emission peak in the absence of inner filter effects (309 nm). Regardless of the actual method, the anti-Stokes shift of our system is among the largest reported so far for visible light-driven UC schemes.[72,82,93–100]

Figures 4B and C focus on power-dependent UC measurements. The achievable upconversion quantum yields Φ_{UC} at the highest laser intensities amount to values close to 1 % (with a theoretical maximum of 50 %) using both 447 nm and 445 nm excitation. A rather low I_{th} of 471 mW cm^{-2} was determined (using the 445 nm setup with higher beam quality), enabling decent UC efficiencies already with commercially available blue LEDs (Figure S15). Moreover, irradiating the UC system at the threshold intensity shows only minor degradation over one hour (Figure 4A, inset). Higher sensitizer concentrations (88 μM) seem to be beneficial for the photostability of this system. A more systematic understanding of the factors governing efficient upconversion into the UV region seems to be required, considering the typically poor performance parameters of most known Vis-to-UV UC systems.[49,101] The most straightforward future strategies for developing Vis-to-UVB UC systems with higher overall quantum yields are to increase the anninilator emission quantum yield (48%) by up to a factor of two and to avoid back-TTET with sensitizers possessing higher tripler energies that could also result in UC systems operating at lower annihilator concentrations (i.e., with less pronounced filter effects). Nevertheless, the promising efficiency and long-term stability led us to speculate that our unprecedented UC system with pronounced UVB emission could perhaps drive energy-demanding reactions that usually require high-energy UVB light sources, either with the singlet-excited annihilator as reacting key species or via an emission-reabsorption sequence.[102]

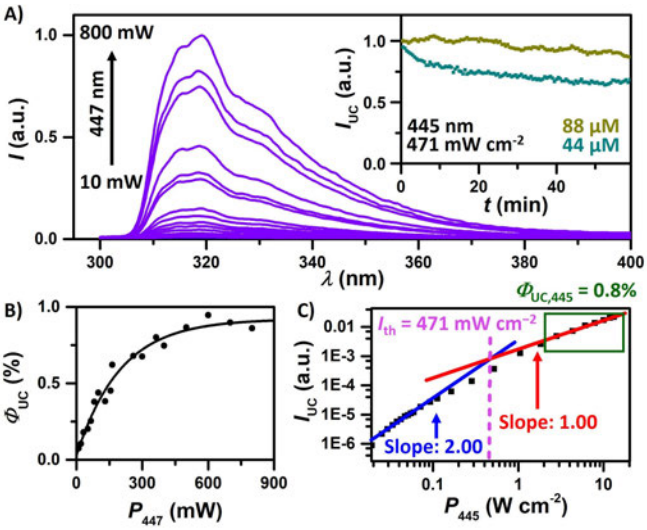

Figure 4. Photon upconversion studies with deoxygenated solutions containing 44 or 88 μM **4CzIPN** and 10 mM **bTIPS-Bz** in cyclohexane: toluene (9:1) using a cw laser for excitation at 447 nm or 445 nm. A) Power-dependent spectra of the normalized upconverted emission. Inset: Photostability measurement at different sensitizer concentrations at a cw laser power of 471 mW cm^{-2}. B) External upconversion quantum yield, Φ_{UC}, plotted against the laser power (with 44 μM **4CzIPN**). C) Normalized UC emission plotted against the laser power on a double-logarithmic scale (with 44 μM **4CzIPN**). The threshold intensity I_{th} was determined from the crossing point. See Supporting Information for details.

We proposed that the high singlet-excited state energy of **bTIPS-Bz** could be exploited for a subsequent FRET activation of relatively inert substances (Figure 5A) with a rich UV photochemistry. UC-FRET reaction sequences have been suggested with less energetic excited states of the energy acceptor that would be accessible with efficient LEDs,[65,66,103] but in our high-energy case, such an alternative does not exist. For our study, we chose pinacolone (**PC**) and acetone (**AC**)—both absorb only below 320 nm and thus usually require harmful UVB light sources for excitation. Figure 5B visualizes the spectral overlap between the **bTIPS-Bz** emission and the absorption of the carbonyl compounds. Although the molar absorption coefficients of such aliphatic carbonyls are rather low due to the symmetry-forbidden nature of the nπ* transitions, the pronounced spectral overlap suggests that non-radiative energy transfer via the FRET mechanism is still feasible, whose efficiency linearly depends on the spectral overlap integrals.[104] NMR-scale and mechanistic LFP experiments were conducted to monitor the UC-FRET sequence. Figure 5E shows kinetic traces of the **bTIPS-Bz** emission at 318 nm with increasing **PC** and **AC** concentrations. While the formation and decay rates of the singlet emission signals are essentially unaffected by the addition of the carbonyl compound, the overall emission intensity is reduced drastically. This contrasts strongly with time-resolved measurements of the **bTIPS-Bz** triplet state where no change with the addition of **PC** or **AC** (neither in concentration nor in lifetime) is observed (Figure S8). Thus, the initial amount of ^{1}**bTIPS-Bz*** produced via annihilation has to be unaffected by the addition of the carbonyls and we conclude that the attenuated UC emission signal must originate from direct excited-singlet state quenching[43] (most likely via FRET) or reabsorption effects. An estimation of the latter, i.e., reabsorbed photons by the carbonyls through radiative energy transfer, revealed that non-radiative excited state quenching is the main pathway at

© 2022 The Authors. Angewandte Chemie International Edition published by Wiley-VCH GmbH

15213773, 2023, 8, Downloaded from https://onlinelibrary.wiley.com/doi/10.1002/anie.202215340 by Universitatsbibliothek Mainz, Wiley Online Library on [15/04/2025]. See the Terms and Conditions (https://onlinelibrary.wiley.com/terms-and-conditions) on Wiley Online Library for rules of use; OA articles are governed by the applicable Creative Commons License

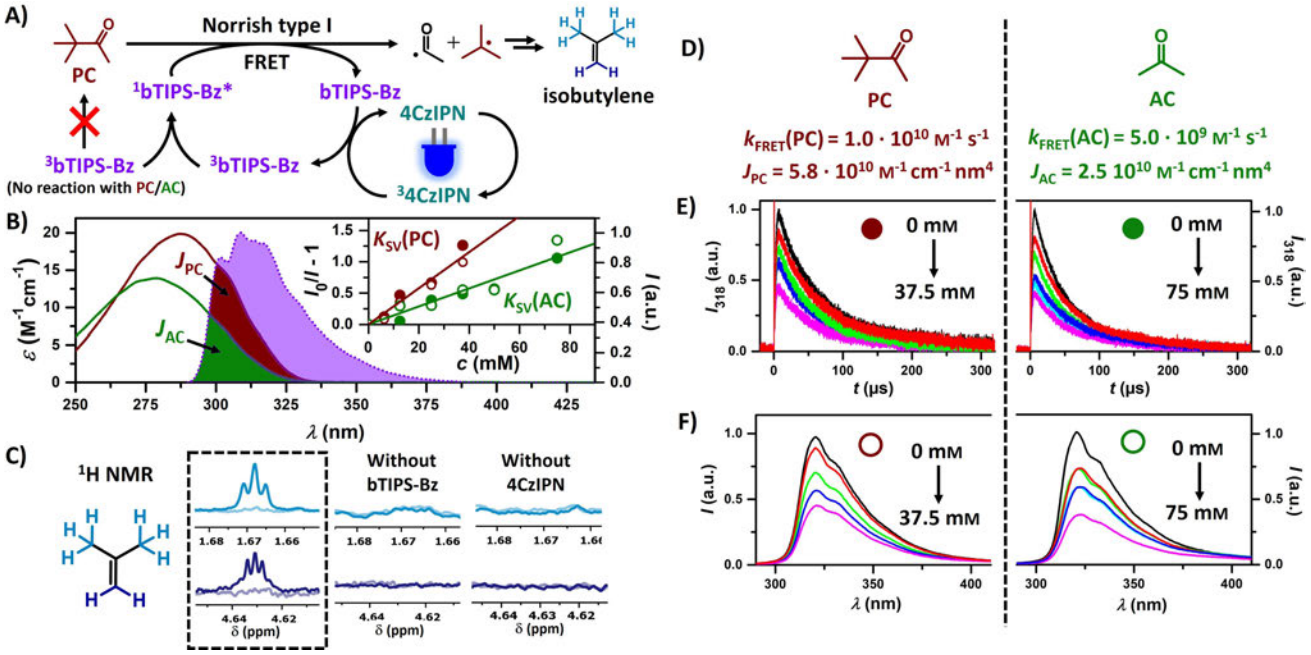

Figure 5. A) Upconversion mechanism and subsequent FRET sensitization of pinacolone resulting in a Norrish type I reaction and formation of isobutylene. B) Absorption spectra (solid line) of pinacolone (dark red), acetone (green), and normalized emission (dotted line) of **bTIPS-Bz** in cyclohexane with the spectral overlap being highlighted. Inset: Stern–Volmer plot corresponding to quenching of upconverted **bTIPS-Bz** emission by the carbonyl compounds. C) NMR scale experiment of 100 μM **4CzIPN**, 10 mM **bTIPS-Bz**, and 100 mM pinacolone in Ar-saturated cyclohexane: toluene (9:1) with control experiments before and after 30 min irradiation at 447 nm with 1.1 W. Shown are the ^{1}H NMR signals of isobutylene as a stable product of the UC-FRET-driven Norrish reaction. D) Comparison of FRET efficiencies between pinacolone and acetone. E) and F) Mechanistic LFP experiments with 355 nm laser pulses of ≈10 ns duration of 20 μM **4CzIPN** and 10 mM **bTIPS-Bz** in Ar-saturated cyclohexane: toluene (9:1) with different concentrations of pinacolone and acetone used for the Stern–Volmer plots in the inset of panel B). E) Time-resolved emission at 318 nm. F) Normalized time-gated (delay, 6 μs; integration over 500 μs) emission spectra.

our detection wavelength used in Figure 5E (see Supporting Information Section S6). Further time-gated spectra of the UV emission yielded a very similar decrease in intensity (Figure 5F). Moreover, the signal intensity in the region above 330 nm (where the carbonyls do not absorb) is almost equally reduced compared to the emission peak (318 nm) (Figure S9). All these findings are in perfect accordance with a FRET process between **^{1}bTIPS-Bz*** and the carbonyls being the main quenching mechanism of the upconverted emission. Similar quenching experiments were also performed with a cw laser (447 nm) to demonstrate the feasibility of this energy transfer sequence with a non-pulsed visible light source (Figure S10). Next, we investigated the energy transfer efficiency in detail. In principle FRET is still feasible at larger molecular distances (up to 100 nm), meaning that the energy transfer rate can exceed the classical diffusion limit for collision-induced quenching. As a result of the low molar absorption coefficients of the carbonyls, we pre-calculated rather small Förster distances of 0.7 nm and 0.8 nm for **AC** and **PC** (Section S1.8 of the Supporting Information), suggesting that the quenching constant will be close to or slightly higher than the diffusion-controlled rate constant in cyclohexane ($k_{diff} = 6.7 \times 10^9\ M^{-1} s^{-1}$).[105] The **^{1}bTIPS-Bz*** emission intensity from either kinetic measurements (filled circle, raw data from Figure 5E) or time-gated spectra (open circle, raw data from Figure 5F) are plotted against the carbonyl concentration in a Stern–Volmer graph (Figure 5B, inset). Conventional Stern–Volmer analyses gave quenching constants k_{FRET} of $5.0 \times 10^9\ M^{-1} s^{-1}$ for **AC** and $1.0 \times 10^{10}\ M^{-1} s^{-1}$ for **PC**, respectively (Figure 5D). Direct fluorescence lifetime quenching experiments upon UVB excitation of **bTIPS-Bz** with different acetone concentrations gave a similar result ($k_{FRET} = 6.4 \times 10^9\ M^{-1} s^{-1}$, see Figure S11 and corresponding discussion in the Supporting Information). The ratios of the energy transfer rate constants and the corresponding spectral overlap integrals J_{PC} and J_{AC} are practically identical, providing further evidence for the novel blue-to-UVB UC-FRET reaction sequence. Efficient photoredox reactions between the high-energy annihilator singlet and the carbonyl compounds or the sensitizer itself can be excluded as we could not detect any signatures of radical ions (Figures S8 and S18 in the Supporting Information).

The diverse photochemistry of carbonyl compounds is well described in the literature.[1,2,67–69] Acetone almost quantitatively produces a highly energetic triplet state (triplet energy, ≈3.5 eV) upon direct excitation, which explains its dual use as solvent and sensitizer in conventional UVB photoreactions. Monitoring the acetone triplet produced via UC-FRET by spectroscopic methods is very challenging owing to its rather slow formation and the relatively high concentrations of potential triplet energy acceptors in our system. However, pinacolone undergoes efficient Norrish type I fragmentation generating a more

© 2022 The Authors. Angewandte Chemie International Edition published by Wiley-VCH GmbH

15213773, 2023, 8, Downloaded from https://onlinelibrary.wiley.com/doi/10.1002/anie.202215340 by Universitatsbibliothek Mainz, Wiley Online Library on [15/04/2025]. See the Terms and Conditions (https://onlinelibrary.wiley.com/terms-and-conditions) on Wiley Online Library for rules of use; OA articles are governed by the applicable Creative Commons License

stabilized carbon-centered radical (Figure 5A)[106] compared to that formed by acetone. This isobutyl radical is hard to track spectroscopically, but isobutylene as its stable disproportionation product[107] (Figure 5A) is sufficiently soluble in our mixture and possesses a characteristic ^{1}H NMR spectrum.[108] We, therefore, performed several NMR-scale irradiation experiments with **PC**. Irradiating the whole UC system together with 100 mM **PC** using our cw laser (447 nm) for 30 min resulted in the formation of new peaks in the NMR spectrum that unambiguously correspond to isobutylene (Figure 5C, see Section S8.2 for details). Control experiments with either annihilator or sensitizer missing did not show any evidence for product generation. To demonstrate that this high-energy Norrish chemistry is also viable with commercial blue LEDs, the same irradiation experiment was carried out with two blue LEDs (440 nm). Similar amounts of isobutylene were detected (Figure S29), confirming the promising performance parameters and the potential of our UC system for future lab-scale applications without UVB lamps.

Finally, we turned to the substrate dibenzyl ketone, which is known to undergo efficient Norrish fragmentation under UV photolysis ($\lambda < 325$ nm) and subsequent C–C bond formation of the resulting radicals.[69] The coupling product dibenzyl has been observed clearly employing our UC-FRET strategy with blue LEDs (Figures S31–S33). This coupling reaction under mercury-free and very mild conditions highlights that more synthetically useful photoreactions are generally feasible employing our new approach.

Conclusion

In summary, we have demonstrated that UVB emitters can be incorporated in blue light-driven upconversion schemes. Reaching the UVB region with blue input photons for the first time is certainly beyond a pushing-the-limits study because this technology enables unreported substrate and solvent activation strategies that cannot be carried out with efficient and sustainable light sources in a direct manner. Our mechanistic investigations provide unambiguous evidence for a hitherto unreported blue-to-UVB UC-FRET sequence expanding the applicability of upconversion for driving challenging chemical reactions. These key findings pave the way for exploiting the full potential of this attractive two-photon mechanism in light-driven bond activation. The incorporation of such high-energy upconversion systems in solid or gel-like environments for large-scale applications might represent the next challenge and even LED-driven UVA-to-UVC upconversion systems, which have the potential to replace mercury lamps completely, seem to be within reach based on our results. The latter would require further efforts in developing both novel annihilators and energy-matched sensitizers that are highly photostable. For that, a deeper understanding of TTA[73,109–112] is required, and regarding sensitizer development, the upconversion community will strongly benefit from the recent progress in Dexter energy transfer catalysis.[49,113–116]

Acknowledgements

We acknowledge generous financial support from the JGU Mainz, SusInnoScience, the German Research Foundation (DFG, grant number KE 2313/3-1), the German Federal Environmental Foundation (DBU, PhD fellowship to T.J.B.Z., grant number 20022/028), the Murata Science Foundation, Research Foundation for Opto-Science and Technology and JSPS KAKENHI (JP20H02713, JP22K19051, JP22F21031). C.K. is grateful to the Chemical Industry Funds for a Liebig fellowship. B.R. acknowledges JSPS for a fellowship to conduct research in Japan (P21031). We thank Johannes Rocker for recording mass spectra and Prof. Till Opatz for allowing us to use his equipment. Open Access funding enabled and organized by Projekt DEAL.

Conflict of Interest

The authors declare no conflict of interest.

Data Availability Statement

The data that support the findings of this study are available in the Supporting Information of this article. The raw data sets presented in the main manuscript can be found under http://doi.org/10.25358/openscience-8436.

Keywords: Energy Transfer · Photochemistry · Sustainable Chemistry · Time-Resolved Spectroscopy · Upconversion

[1] P. Klán, J. Wirz, *Photochemistry of Organic Compounds: From Concepts to Practice*, Wiley, Chichester, **2009**.
[2] N. Hoffmann, *Chem. Rev.* **2008**, *108*, 1052–1103.
[3] G. S. Pozan, A. Kambur, *Appl. Catal. B* **2013**, *129*, 409–415.
[4] N. Zhang, G. Liu, H. Liu, Y. Wang, Z. He, G. Wang, *J. Hazard. Mater.* **2011**, *192*, 411–418.
[5] O. Shvydkiv, S. Gallagher, K. Nolan, M. Oelgemöller, *Org. Lett.* **2010**, *12*, 5170–5173.
[6] A. G. Griesbeck, N. Maptue, S. Bondock, M. Oelgemöller, *Photochem. Photobiol. Sci.* **2003**, *2*, 450–451.
[7] F. Glaser, C. Kerzig, O. S. Wenger, *Angew. Chem. Int. Ed.* **2020**, *59*, 10266–10284; *Angew. Chem.* **2020**, *132*, 10350–10370.
[8] J. Castellanos-Soriano, J. C. Herrera-Luna, D. Díaz Díaz, M. C. Jiménez, R. Pérez-Ruiz, *Org. Chem. Front.* **2020**, *7*, 1709–1716.
[9] Y. Kobayashi, J. Abe, *Chem. Soc. Rev.* **2022**, *51*, 2397–2415.
[10] I. Ghosh, L. Marzo, A. Das, R. Shaikh, B. König, *Acc. Chem. Res.* **2016**, *49*, 1566–1577.
[11] M. Cybularczyk-Cecotka, J. Szczepanik, M. Giedyk, *Nat. Catal.* **2020**, *3*, 872–886.
[12] V. Gray, D. Dzebo, M. Abrahamsson, B. Albinsson, K. Moth-Poulsen, *Phys. Chem. Chem. Phys.* **2014**, *16*, 10345–10352.
[13] J. Zhao, S. Ji, H. Guo, *RSC Adv.* **2011**, *1*, 937–950.
[14] T. N. Singh-Rachford, F. N. Castellano, *Coord. Chem. Rev.* **2010**, *254*, 2560–2573.
[15] T. F. Schulze, T. W. Schmidt, *Energy Environ. Sci.* **2015**, *8*, 103–125.
[16] Y. Zhou, F. N. Castellano, T. W. Schmidt, K. Hanson, *ACS Energy Lett.* **2020**, *5*, 2322–2326.

© 2022 The Authors. Angewandte Chemie International Edition published by Wiley-VCH GmbH

15213773, 2023, 8, Downloaded from https://onlinelibrary.wiley.com/doi/10.1002/anie.202215340 by Universitatsbibliothek Mainz, Wiley Online Library on [15/04/2025]. See the Terms and Conditions (https://onlinelibrary.wiley.com/terms-and-conditions) on Wiley Online Library for rules of use; OA articles are governed by the applicable Creative Commons License

[17] Z. Xu, Z. Huang, T. Jin, T. Lian, M. L. Tang, *Acc. Chem. Res.* **2021**, *54*, 70–80.
[18] J. Pedrini, A. Monguzzi, *J. Photonics Energy* **2017**, *8*, 022005.
[19] L. Zeng, L. Huang, J. Han, G. Han, *Acc. Chem. Res.* **2022**, *55*, 2604–2615.
[20] T. Lin, C. F. Perkinson, M. A. Baldo, *Adv. Mater.* **2020**, *32*, 1908175.
[21] H. Liu, X. Yan, L. Shen, Z. Tang, S. Liu, X. Li, *Mater. Horiz.* **2019**, *6*, 990–995.
[22] S. Baluschev, T. Miteva, V. Yakutkin, G. Nelles, A. Yasuda, G. Wegner, *Phys. Rev. Lett.* **2006**, *97*, 143903.
[23] F. Edhborg, A. Olesund, B. Albinsson, *Photochem. Photobiol. Sci.* **2022**, *21*, 1143–1158.
[24] R. Pérez-Ruiz, *Top. Curr. Chem.* **2022**, *380*, 23.
[25] J. B. Bilger, C. Kerzig, C. B. Larsen, O. S. Wenger, *J. Am. Chem. Soc.* **2021**, *143*, 1651–1663.
[26] Y. Wei, H. Xian, X. Lv, F. Ni, X. Cao, C. Yang, *Mater. Horiz.* **2021**, *8*, 606–611.
[27] A. Tokunaga, L. M. Uriarte, K. Mutoh, E. Fron, J. Hofkens, M. Sliwa, J. Abe, *J. Am. Chem. Soc.* **2019**, *141*, 17744–17753.
[28] B. Pfund, D. M. Steffen, M. R. Schreier, M.-S. Bertrams, C. Ye, K. Börjesson, O. S. Wenger, C. Kerzig, *J. Am. Chem. Soc.* **2020**, *142*, 10468–10476.
[29] C. Kerzig, O. S. Wenger, *Chem. Sci.* **2018**, *9*, 6670–6678.
[30] B. D. Ravetz, A. B. Pun, E. M. Churchill, D. N. Congreve, T. Rovis, L. M. Campos, *Nature* **2019**, *565*, 343–346.
[31] C. Wang, F. Reichenauer, W. R. Kitzmann, C. Kerzig, K. Heinze, U. Resch-Genger, *Angew. Chem. Int. Ed.* **2022**, *61*, e202202238; *Angew. Chem.* **2022**, *134*, e202202238.
[32] R. R. Islangulov, F. N. Castellano, *Angew. Chem. Int. Ed.* **2006**, *45*, 5957–5959; *Angew. Chem.* **2006**, *118*, 6103–6105.
[33] C. G. López-Calixto, M. Liras, V. A. de la Peña O'Shea, R. Pérez-Ruiz, *Appl. Catal. B* **2018**, *237*, 18–23.
[34] F. Glaser, C. Kerzig, O. S. Wenger, *Chem. Sci.* **2021**, *12*, 9922–9933.
[35] N. Awwad, A. T. Bui, E. O. Danilov, F. N. Castellano, *Chem* **2020**, *6*, 3071–3085.
[36] A. Caron, G. Noirbent, D. Gigmes, F. Dumur, J. Lalevée, *Macromol. Rapid Commun.* **2021**, *42*, 2100047.
[37] Y. Wei, K. Pan, X. Cao, Y. Li, X. Zhou, C. Yang, *CCS Chem.* **2022**, *4*, 3852–3863.
[38] B. D. Ravetz, N. E. S. Tay, C. L. Joe, M. Sezen-Edmonds, M. A. Schmidt, Y. Tan, J. M. Janey, M. D. Eastgate, T. Rovis, *ACS Cent. Sci.* **2020**, *6*, 2053–2059.
[39] L. Huang, W. Wu, Y. Li, K. Huang, L. Zeng, W. Lin, G. Han, *J. Am. Chem. Soc.* **2020**, *142*, 18460–18470.
[40] P. Bharmoria, H. Bildirir, K. Moth-Poulsen, *Chem. Soc. Rev.* **2020**, *49*, 6529–6554.
[41] H. Hirayama, S. Fujikawa, N. Kamata, *Electron. Commun. Jpn.* **2015**, *98*, 1–8.
[42] T. N. Singh-Rachford, F. N. Castellano, *J. Phys. Chem. A* **2009**, *113*, 5912–5917.
[43] M. Majek, U. Faltermeier, B. Dick, R. Pérez-Ruiz, A. Jacobi von Wangelin, *Chem. Eur. J.* **2015**, *21*, 15496–15501.
[44] A. Monguzzi, A. Oertel, D. Braga, A. Riedinger, D. K. Kim, P. N. Knüsel, A. Bianchi, M. Mauri, R. Simonutti, D. J. Norris, F. Meinardi, *ACS Appl. Mater. Interfaces* **2017**, *9*, 40180–40186.
[45] M. Barawi, F. Fresno, R. Pérez-Ruiz, V. A. de la Peña O'Shea, *ACS Appl. Energy Mater.* **2019**, *2*, 207–211.
[46] N. Harada, Y. Sasaki, M. Hosoyamada, N. Kimizuka, N. Yanai, *Angew. Chem. Int. Ed.* **2021**, *60*, 142–147; *Angew. Chem.* **2021**, *133*, 144–149.
[47] M. Uji, N. Harada, N. Kimizuka, M. Saigo, K. Miyata, K. Onda, N. Yanai, *J. Mater. Chem. C* **2022**, *10*, 4558–4562.
[48] A. Olesund, J. Johnsson, F. Edhborg, S. Ghasemi, K. Moth-Poulsen, B. Albinsson, *J. Am. Chem. Soc.* **2022**, *144*, 3706–3716.
[49] L. Schmid, F. Glaser, R. Schaer, O. S. Wenger, *J. Am. Chem. Soc.* **2022**, *144*, 963–976.
[50] T. J. B. Zähringer, M.-S. Bertrams, C. Kerzig, *J. Mater. Chem. C* **2022**, *10*, 4568–4573.
[51] X. Lin, Z. Chen, Y. Han, C. Nie, P. Xia, S. He, J. Li, K. Wu, *ACS Energy Lett.* **2022**, *7*, 914–919.
[52] S. He, X. Luo, X. Liu, Y. Li, K. Wu, *J. Phys. Chem. Lett.* **2019**, *10*, 5036–5040.
[53] V. Gray, P. Xia, Z. Huang, E. Moses, A. Fast, D. A. Fishman, V. I. Vullev, M. Abrahamsson, K. Moth-Poulsen, M. Lee Tang, *Chem. Sci.* **2017**, *8*, 5488–5496.
[54] L. Hou, A. Olesund, S. Thurakkal, X. Zhang, B. Albinsson, *Adv. Funct. Mater.* **2021**, *31*, 2106198.
[55] N. Yanai, M. Kozue, S. Amemori, R. Kabe, C. Adachi, N. Kimizuka, *J. Mater. Chem. C* **2016**, *4*, 6447–6451.
[56] W. Zhao, F. N. Castellano, *J. Phys. Chem. A* **2006**, *110*, 11440–11445.
[57] Q. Chen, Y. Liu, X. Guo, J. Peng, S. Garakyaraghi, C. M. Papa, F. N. Castellano, D. Zhao, Y. Ma, *J. Phys. Chem. A* **2018**, *122*, 6673–6682.
[58] P. Duan, N. Yanai, N. Kimizuka, *Chem. Commun.* **2014**, *50*, 13111–13113.
[59] Y. Murakami, A. Motooka, R. Enomoto, K. Niimi, A. Kaiho, N. Kiyoyanagi, *Phys. Chem. Chem. Phys.* **2020**, *22*, 27134–27143.
[60] Z. A. VanOrman, L. Nienhaus, *Matter* **2021**, *4*, 2625–2626.
[61] J. A. Kübler, B. Pfund, O. S. Wenger, *JACS Au* **2022**, *2*, 2367–2380.
[62] The only known Vis-to-UV upconversion system with pronounced UVB emission (ref. [49]) requires violet excitation light (405 nm) and operates with quantum yields and threshold intensities that are unattractive for lab-scale applications.
[63] B. S. Richards, D. Hudry, D. Busko, A. Turshatov, I. A. Howard, *Chem. Rev.* **2021**, *121*, 9165–9195.
[64] Y. Du, X. Ai, Z. Li, T. Sun, Y. Huang, X. Zeng, X. Chen, F. Rao, F. Wang, *Adv. Photonics Res.* **2021**, *2*, 2000213.
[65] S. H. C. Askes, M. Kloz, G. Bruylants, J. T. M. Kennis, S. Bonnet, *Phys. Chem. Chem. Phys.* **2015**, *17*, 27380–27390.
[66] W. Wang, Q. Liu, C. Zhan, A. Barhoumi, T. Yang, R. G. Wylie, P. A. Armstrong, D. S. Kohane, *Nano Lett.* **2015**, *15*, 6332–6338.
[67] C. Michelin, N. Hoffmann, *ACS Catal.* **2018**, *8*, 12046–12055.
[68] A. Albini, *Photochem. Photobiol. Sci.* **2021**, *20*, 161–181.
[69] J. C. Scaiano, K. G. Stamplecoskie, G. L. Hallett-Tapley, *Chem. Commun.* **2012**, *48*, 4798–4808.
[70] J. P. Doering, *J. Chem. Phys.* **1969**, *51*, 2866–2870.
[71] P. Bharmoria, F. Edhborg, H. Bildirir, Y. Sasaki, S. Ghasemi, A. Mårtensson, N. Yanai, N. Kimizuka, B. Albinsson, K. Börjesson, K. Moth-Poulsen, *J. Mater. Chem. A* **2022**, *10*, 21279–21290.
[72] N. Nishimura, V. Gray, J. R. Allardice, Z. Zhang, A. Pershin, D. Beljonne, A. Rao, *ACS Mater. Lett.* **2019**, *1*, 660–664.
[73] K. J. Fallon, E. M. Churchill, S. N. Sanders, J. Shee, J. L. Weber, R. Meir, S. Jockusch, D. R. Reichman, M. Y. Sfeir, D. N. Congreve, L. M. Campos, *J. Am. Chem. Soc.* **2020**, *142*, 19917–19925.
[74] A. Maliakal, K. Raghavachari, H. Katz, E. Chandross, T. Siegrist, *Chem. Mater.* **2004**, *16*, 4980–4986.
[75] G. Malloci, G. Cappellini, G. Mulas, A. Mattoni, *Thin Solid Films* **2013**, *543*, 32–34.
[76] S. J. Strickler, R. A. Berg, *J. Chem. Phys.* **1962**, *37*, 814–822.
[77] J. Mohanty, W. M. Nau, *Photochem. Photobiol. Sci.* **2004**, *3*, 1026.

© 2022 The Authors. Angewandte Chemie International Edition published by Wiley-VCH GmbH

15213773, 2023, 8, Downloaded from https://onlinelibrary.wiley.com/doi/10.1002/anie.202215340 by Universitatsbibliothek Mainz, Wiley Online Library on [15/04/2025]. See the Terms and Conditions (https://onlinelibrary.wiley.com/terms-and-conditions) on Wiley Online Library for rules of use; OA articles are governed by the applicable Creative Commons License

[78] M.-S. Bertrams, C. Kerzig, *Chem. Commun.* **2021**, *57*, 6752–6755.
[79] M. Luria, M. Ofran, G. Stein, *J. Phys. Chem.* **1974**, *78*, 1904–1909.
[80] W. R. Dawson, M. W. Windsor, *J. Phys. Chem.* **1968**, *72*, 3251–3260.
[81] S. He, Y. Han, J. Guo, K. Wu, *J. Phys. Chem. Lett.* **2022**, *13*, 1713–1718.
[82] J. Isokuortti, S. R. Allu, A. Efimov, E. Vuorimaa-Laukkanen, N. V. Tkachenko, S. A. Vinogradov, T. Laaksonen, N. A. Durandin, *J. Phys. Chem. Lett.* **2020**, *11*, 318–324.
[83] F. Strieth-Kalthoff, C. Henkel, M. Teders, A. Kahnt, W. Knolle, A. Gómez-Suárez, K. Dirian, W. Alex, K. Bergander, C. G. Daniliuc, B. Abel, D. M. Guldi, F. Glorius, *Chem* **2019**, *5*, 2183–2194.
[84] H. Uoyama, K. Goushi, K. Shizu, H. Nomura, C. Adachi, *Nature* **2012**, *492*, 234–238.
[85] M. A. Bryden, F. Millward, T. Matulaitis, D. Chen, M. Villa, A. Fermi, S. Cetin, P. Ceroni, E. Zysman-Colman, *J. Org. Chem.* **2022**, https://doi.org/10.1021/acs.joc.2c01137.
[86] M. A. Bryden, E. Zysman-Colman, *Chem. Soc. Rev.* **2021**, *50*, 7587–7680.
[87] T. C. Wu, D. N. Congreve, M. A. Baldo, *Appl. Phys. Lett.* **2015**, *107*, 031103.
[88] R. Ishimatsu, S. Matsunami, K. Shizu, C. Adachi, K. Nakano, T. Imato, *J. Phys. Chem. A* **2013**, *117*, 5607–5612.
[89] D. Meroni, A. Monguzzi, F. Meinardi, *J. Chem. Phys.* **2020**, *153*, 114302.
[90] J. Perego, J. Pedrini, C. X. Bezuidenhout, P. E. Sozzani, F. Meinardi, S. Bracco, A. Comotti, A. Monguzzi, *Adv. Mater.* **2019**, *31*, 1903309.
[91] Y. Murakami, K. Kamada, *Phys. Chem. Chem. Phys.* **2021**, *23*, 18268–18282.
[92] A. Haefele, J. Blumhoff, R. S. Khnayzer, F. N. Castellano, *J. Phys. Chem. Lett.* **2012**, *3*, 299–303.
[93] Z. A. VanOrman, C. R. Conti, G. F. Strouse, L. Nienhaus, *Chem. Mater.* **2021**, *33*, 452–458.
[94] C. J. Imperiale, P. B. Green, M. Hasham, M. W. B. Wilson, *Chem. Sci.* **2021**, *12*, 14111–14120.
[95] W. Yin, T. Yu, J. Chen, R. Hu, G. Yang, Y. Zeng, Y. Li, *ACS Appl. Mater. Interfaces* **2021**, *13*, 57481–57488.
[96] R. Haruki, Y. Sasaki, K. Masutani, N. Yanai, N. Kimizuka, *Chem. Commun.* **2020**, *56*, 7017–7020.
[97] C. Fan, L. Wei, T. Niu, M. Rao, G. Cheng, J. J. Chruma, W. Wu, C. Yang, *J. Am. Chem. Soc.* **2019**, *141*, 15070–15077.
[98] Y. Wei, Y. Li, M. Zheng, X. Zhou, Y. Zou, C. Yang, *Adv. Opt. Mater.* **2020**, *8*, 1902157.
[99] Y. Wei, M. Zheng, L. Chen, X. Zhou, S. Liu, *Dalton Trans.* **2019**, *48*, 11763–11771.
[100] L. Huang, Y. Zhao, H. Zhang, K. Huang, J. Yang, G. Han, *Angew. Chem. Int. Ed.* **2017**, *56*, 14400–14404; *Angew. Chem.* **2017**, *129*, 14592–14596.
[101] V. Gray in *Photochemistry* (Eds.: A. Albini, S. Protti), Royal Society of Chemistry, Cambridge, **2019**, pp. 404–420.
[102] S. H. C. Askes, A. Bahreman, S. Bonnet, *Angew. Chem. Int. Ed.* **2014**, *53*, 1029–1033; *Angew. Chem.* **2014**, *126*, 1047–1051.
[103] M. S. Meijer, V. S. Talens, M. F. Hilbers, R. E. Kieltyka, A. M. Brouwer, M. M. Natile, S. Bonnet, *Langmuir* **2019**, *35*, 12079–12090.
[104] Th. Förster, *Ann. Phys.* **1948**, *437*, 55–75.
[105] M. Montalti, A. Credi, L. Prodi, M. T. Gandolfi, *Handbook of Photochemistry*, CRC/Taylor & Francis, Boca Raton, **2006**.
[106] M. C. Jiménez, P. Leal, M. A. Miranda, R. Tormos, *J. Chem. Soc. Chem. Commun.* **1995**, 2009–2010.
[107] D. H. Slater, S. S. Collier, J. G. Calvert, *J. Am. Chem. Soc.* **1968**, *90*, 268–273.
[108] S. J. Peters, T. M. Blood, M. E. Kassabaum, *Eur. J. Org. Chem.* **2009**, 6104–6108.
[109] V. Gray, A. Dreos, P. Erhart, B. Albinsson, K. Moth-Poulsen, M. Abrahamsson, *Phys. Chem. Chem. Phys.* **2017**, *19*, 10931–10939.
[110] C. Ye, V. Gray, J. Mårtensson, K. Börjesson, *J. Am. Chem. Soc.* **2019**, *141*, 9578–9584.
[111] D. G. Bossanyi, Y. Sasaki, S. Wang, D. Chekulaev, N. Kimizuka, N. Yanai, J. Clark, *JACS Au* **2021**, *1*, 2188–2201.
[112] L. Vaghi, F. Rizzo, J. Pedrini, A. Mauri, F. Meinardi, U. Cosentino, C. Greco, A. Monguzzi, A. Papagni, *Photochem. Photobiol. Sci.* **2022**, *21*, 913–921.
[113] Y. Zhang, Y. Niu, Y. Guo, J. Wang, Y. Zhang, S. Liu, X. Shen, *Angew. Chem. Int. Ed.* **2022**, *61*, e202212201; *Angew. Chem.* **2022**, *134*, e202212201.
[114] M. R. Schreier, X. Guo, B. Pfund, Y. Okamoto, T. R. Ward, C. Kerzig, O. S. Wenger, *Acc. Chem. Res.* **2022**, *55*, 1290–1300.
[115] E. A. Martynova, V. A. Voloshkin, S. G. Guillet, F. Bru, M. Beliš, K. Van Hecke, C. S. J. Cazin, S. P. Nolan, *Chem. Sci.* **2022**, *13*, 6852–6857.
[116] T. O. Paulisch, L. A. Mai, F. Strieth-Kalthoff, M. J. James, C. Henkel, D. M. Guldi, F. Glorius, *Angew. Chem. Int. Ed.* **2022**, *61*, e202112695; *Angew. Chem.* **2022**, *134*, e202112695.

Manuscript received: October 18, 2022
Accepted manuscript online: November 18, 2022
Version of record online: January 16, 2023

© 2022 The Authors. Angewandte Chemie International Edition published by Wiley-VCH GmbH

15213773, 2023, 8, Downloaded from https://onlinelibrary.wiley.com/doi/10.1002/anie.202215340 by Universitatsbibliothek Mainz, Wiley Online Library on [15/04/2025]. See the Terms and Conditions (https://onlinelibrary.wiley.com/terms-and-conditions) on Wiley Online Library for rules of use; OA articles are governed by the applicable Creative Commons License

Summary:

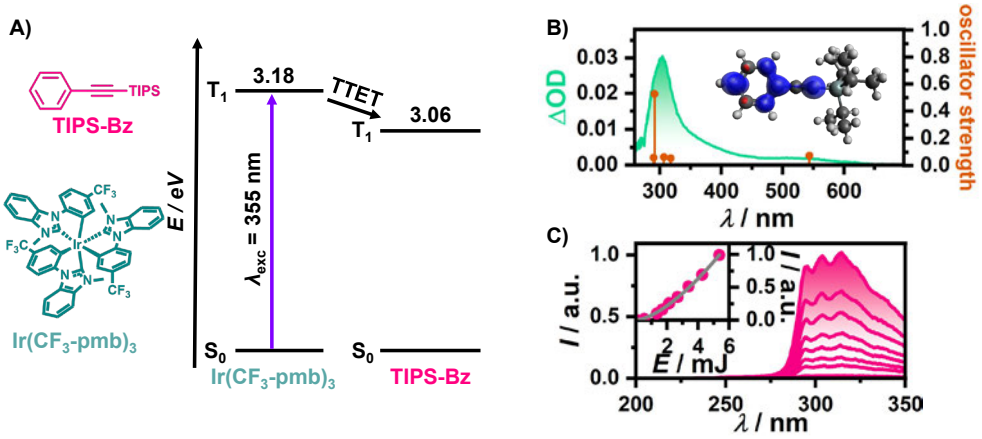

Figure 30: Mechanistic investigations of the TIPS-Bz–Ir(CF_3-pmb)$_3$ UC scheme with 355 nm laser pulses. A) Molecular structures of TIPS-Bz and Ir(CF_3-pmb)$_3$ and schematic energy diagram of TTET. B) TA spectrum and calculated oscillator strength of ^{3}TIPS-Bz. C) Time-gated TIPS-Bz emission after triplet energy transfer with increasing laser pulse energy. Inset: Emission intensity plotted against the laser pulse energy.

In project **[L]**, TIPS-Bz was investigated as a UV annihilator in combination with the iridium complex Ir(CF_3-pmb)$_3$ (Figure 30A). For the first time, upconverted emission approaching the UVC range was observed, accompanied by a record-breaking singlet state energy of 4.33 eV for TIPS-Bz. DFT calculations estimated the triplet state energy of TIPS-Bz at 3.06 eV, making TTET from Ir(CF_3-pmb)$_3$ (E_T = 3.18 eV) feasible. The key photophysical properties relevant to TTA–UC were determined for both the annihilator and the sensitizer.

TTET was confirmed through LFP. After complete deactivation of Ir(CF_3-pmb)$_3$, the TA absorption of ^{3}TIPS-Bz was recorded and further corroborated by TD-DFT calculations of the oscillator strength (Figure 30B). Excitation of the annihilator–sensitizer pair with 355 nm laser pulses resulted in a concurrent formation and decay of the annihilator triplet and sensitizer triplet, respectively.

The bimolecular nature of TTA was demonstrated by the non-linear increase in upconverted emission with respect to laser pulse energy (Figure 30C). However, no upconverted emission was detected under steady-state 370 nm LED irradiation, which was attributed to strong reabsorption by Ir(CF_3-pmb)$_3$ in the emission range of TIPS-Bz. To mitigate this issue, TIPS-Bz was further modified by introducing a para-positioned *tert*-butyl group, intended to lower the triplet state energy and enable sensitization with lower-energy sensitizers. However, DFT calculations revealed an insufficient reduction in triplet state energy (3.02 eV), and the TTET rate decreased compared to the parent molecule, likely due to the steric hindrance introduced by the bulky *tert*-butyl group. Lastly, two major hurdles were identified: (i) achieving a larger singlet-triplet energy gap approaching the theoretical limit of 2 × E_{T1} ~ E_{S1}, which is crucial for visible-to-UVC TTA–UC, and (ii) developing a sensitizer that exhibits strong absorption in the visible/UVA range while minimizing absorption in the UVB/UVC region.

Project **[L]** was published as a research article:

“**Pushing the Limit of Triplet-Triplet Annihilation Photon Upconversion Towards the UVC Range**”

Reproduced from Reference: T. J. B. Zähringer, C. Heusel, M. Schmitz, F. Glorius and C. Kerzig, *accepted*. with permission from the Royal Society of Chemistry.

The article is Open Access and licensed under CC BY-NC 3.0 (https://creativecommons.org/licenses/by/3.0/). It and can be cited corresponding to ref.[L]. The reference is attached in the following pages and the supporting information can be found in Chapter 10.13.

Author contributions: C. Kerzig conceived the Project and provided general guidance. C. Heusel prepared the sensitizer under the guidance of F. Glorius. T. J. B. Zähringer carried out the synthesis and general spectroscopic measurements of the annihilators. M. Schmitz performed DFT calculations of the annihilators. T. J. B. Zähringer wrote the initial draft of the manuscript.

ChemComm

COMMUNICATION

View Article Online
View Journal

Check for updates

Cite this: DOI: 10.1039/d5cc01834j

Received 1st April 2025,
Accepted 15th May 2025

DOI: 10.1039/d5cc01834j

rsc.li/chemcomm

Open Access Article. Published on 22 May 2025. Downloaded on 6/16/2025 5:15:04 PM.
This article is licensed under a Creative Commons Attribution 3.0 Unported Licence.

Pushing the limit of triplet–triplet annihilation photon upconversion towards the UVC range†

Till J. B. Zähringer,[a] Corinna Heusel,[b] Matthias Schmitz,[a] Frank Glorius[b] and Christoph Kerzig*[a]

Triplet–triplet annihilation photon upconversion (TTA-UC) provides a milder alternative to traditional UVB/UVC photochemistry. However, suitable sensitizer-annihilator pairs are scarce, in particular in the high-energy UV regime. Herein, we present a benzene-based annihilator that, paired with a suitable sensitizer, generates upconverted emission approaching the UVC region for the first time.

Combining the energy of two photons into a single photon of higher energy offers significant advantages over traditional direct excitation. Using longer-wavelength incident light enhances penetration depth,[1,2] which is relevant for biomedical applications, and enables the utilization of sub-bandgap photons in photovoltaics[3,4] or photoelectrochemical cells[5] thereby improving solar efficiency.[6] Among the mechanisms for photon energy fusion,[7,8] triplet–triplet annihilation upconversion (TTA-UC)[9,10] stands out as the most promising, because it operates effectively under non-coherent and low-intensity excitation as that provided by commercial LEDs[11] or even sunlight.[12,13] The first reported TTA-UC system employed anthracene as an annihilator, producing violet emission.[14] Since then, the field has advanced considerably in converting lower-energy near-infrared (NIR)[12,15–17] or red light into higher energy visible light. In contrast, progress in visible-to-UV TTA-UC[10,13,18–20]—particularly below the UVA range (<315 nm)[10,21–23]—has been much slower. This lag is notable because it does not align with the practical needs of light sources for photochemical reactions:[24,25] modern visible/UVA LEDs (>370 nm)[26] are already highly efficient, and many photochemical reactions[27] can readily utilize sunlight, which contains a non-negligible proportion of UVA.[28] However, in the UVB (280–315 nm) and UVC (<280 nm) range, both are most inadequate. To this day, highly inefficient and hazardous UVB sources, such as mercury[29] and excimer lamps,[30] remain the commonly used options, underscoring the urgent need for TTA-UC as an alternative for generating light in this spectral region. The slow progress in UVB TTA-UC can be attributed to several challenges. A key obstacle is the limited availability of UV annihilator structures. To date only benzene,[11] naphthalene,[23,31] and biphenyl[21,22] derivatives have been identified as being capable of approaching the UVB range while no structures are reported for the UVC range (Fig. 1). This absence is likely due to the inherently large singlet–triplet energy gap required for Vis-to-UVC TTA-UC and the limited understanding of how to precisely modulate these energy gaps in such molecules.[32] The best results for UV annihilators have been achieved by modifying the annihilator scaffold with so-called TIPS-ethynyl ((triisopropylsilyl)ethynyl) groups that greatly reduced the triplet energy compared to the parent molecule.[11,13,21,33] Recently, we reported a novel benzene-based annihilator substituted with two

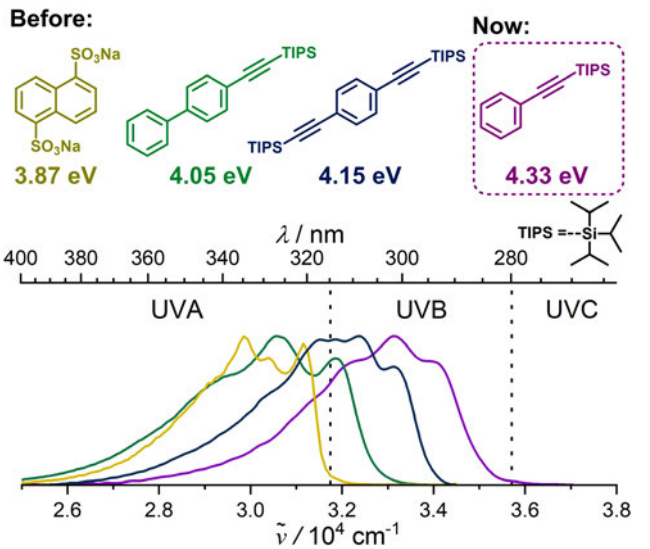

Fig. 1 Structures and emission spectra of high-energy UV annihilators in comparison to the novel UV annihilator **TIPS-Bz**.

[a] Department of Chemistry, Johannes Gutenberg University Mainz, Duesbergweg 10–14, 55128, Mainz, Germany. E-mail: ckerzig@uni-mainz.de
[b] Organisch-Chemisches Institut, University of Münster, Corrensstraße 36, 48149, Münster, Germany

† Electronic supplementary information (ESI) available. See DOI: https://doi.org/10.1039/d5cc01834j

Open Access Article. Published on 22 May 2025. Downloaded on 6/16/2025 5:15:04 PM.
This article is licensed under a Creative Commons Attribution 3.0 Unported Licence.

TIPS-ethynyl groups in *para*-position. That annihilator was capable of blue-to-UVB TTA-UC, achieving the highest UC emission energy recorded to date (Fig. 1).[11] In contrast, the monosubstituted benzene derivative (**TIPS-Bz**) could not be utilized in such a blue-light-driven UC system, as its triplet state energy (E_T) was estimated at 3.06 eV by DFT calculations and it is thus too high for sensitization. However, the high-energy emission of **TIPS-Bz** (Fig. 1) suggested its potential as a candidate for UVB/UVC photon upconversion when paired with an appropriate sensitizer. Yet, discovering suitable sensitizers for **TIPS-Bz** presents another significant challenge. This is because to enable sensitization of **TIPS-Bz** ($E_T > 3.0$ eV) by violet/UVA light (<400 nm, >3.1 eV) energy losses must be minimized. In general sensitizers employed for TTA-UC exhibit small triplet–singlet energy splitting, such as B,N-heteroarene based[34,35] and cyanoarene[11,18] based donor–acceptor chromophores or metal complexes capable of direct triplet-state excitation.[36] The triplet state energy of these sensitizers typically does not exceed ~2.8 eV,[37,38] which is insufficient to effectively sensitize potential UVB/C annihilators. In contrast, the metal complex [Ir(CF_3-pmb)$_3$] (see Fig. 2A for its structure) demonstrates an exceptional triplet state energy of 3.18 eV.[39,40] The high triplet state energy was exploited by one of our groups in a challenging De Mayo-type ring expansion reaction that is not feasible with commercial high triplet state Ir sensitizers.[39] We now report a novel sensitizer-annihilator pair based on **TIPS-Bz** as annihilator and the high triplet energy sensitizer [Ir(CF_3-pmb)$_3$] (**Ir**). A record-breaking upconverted UVB emission approaching the UVC range was achieved, with an unprecedented excited singlet state energy of 4.33 eV (Fig. 1). Mechanistic investigations are provided that highlight the advantages and challenges of this UC system. This study thus represents another breakthrough in the field of UV photon upconversion, advancing the practical limits of TTA-UC and paving the way for future developments.

The synthesis of the annihilator triisopropyl(ethynyl)-benzene and (**TIPS-Bz**) and *fac*-[Ir(CF_3-pmb)$_3$] (**Ir**) followed literature reports.[11,39] The room-temperature absorption and emission spectra of **TIPS-Bz** and **Ir** are shown in Fig. 2B. **TIPS-Bz** has an excited singlet state energy of 4.33 eV, a low extinction coefficient of the long-wavelength absorption band with a maximum at 280 nm ($\varepsilon_{280} < 1000$ M^{-1} cm^{-1}), a fluorescence quantum yield of 0.19 ± 0.02 and a fluorescence lifetime of 19.9 ns, in line with the Strickler–Berg relationship.[41] A direct comparison of **TIPS-Bz** with benzene and other benzene-derived annihilators is provided in Chapter S4 (ESI†). Generally, the substitution of benzene with TIPS-ethynyl increases the fluorescence quantum yield, reduces the excited-state singlet lifetime, and induces a red shift in both the absorption and emission spectra, a trend that has been observed for naphthalene as well.[33] We estimate a decreased triplet state energy of 3.06 eV from DFT calculations compared to the parent benzene molecule (3.9 eV).[42] **Ir** readily absorbs UVA light and can be selectively excited with 355 nm laser pulses. The triplet–triplet absorption spectrum is presented in Fig. 2C, and time-resolved measurements indicate a triplet state lifetime of 4 μs (Fig. 2D), which is sufficient to enable efficient bimolecular quenching. The high triplet state energy of 3.18 eV[39] makes

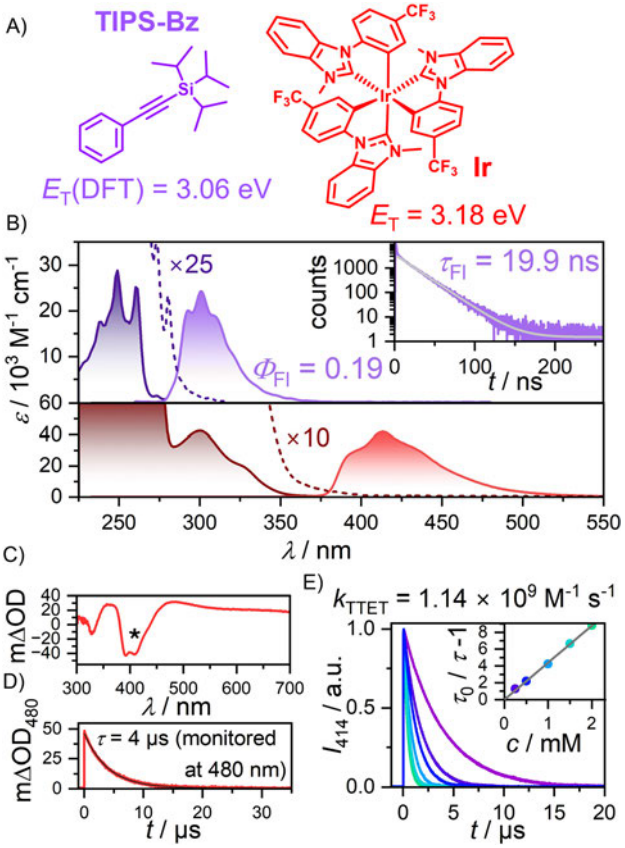

Fig. 2 (A) Molecular structures of **Ir** and **TIPS-Bz**. (B) Absorption and emission spectra of **TIPS-Bz** in cyclohexane (inset: fluorescence lifetime) and of **Ir** in benzene. (C) Transient absorption (TA) spectrum of **Ir** 100 ns after excitation with 355 nm laser pulses in benzene. The asterisk marks the emission of **Ir** (D) Kinetic TA trace of **Ir** in benzene. (E) Quenching studies of 25 μM **Ir** with different concentrations of **TIPS-Bz** in benzene. Inset: Stern–Volmer analysis.

triplet–triplet energy transfer (TTET) to **TIPS-Bz** (3.06 eV) thermodynamically feasible, qualifying **Ir** as a potential sensitizer for the upconversion system under study. Indeed, the phosphorescence of **Ir** in Ar-saturated benzene is quenched upon addition of increasing **TIPS-Bz** concentrations (Fig. 2E). A Stern–Volmer analysis yielded a quenching rate constant of 1.14 × 10^9 M^{-1} s^{-1} (Fig. 2E, inset). To investigate the TTET process, a transient absorption (TA) spectrum of a solution containing **TIPS-Bz** and **Ir** was recorded after the initial deactivation of the sensitizer triplet. The relatively low sensitizer concentration minimizes filter effects at wavelengths $\lambda < 320$ nm. After quenching a TA band with a maximum at 304 nm is observed, which is attributed to the triplet–triplet absorption of ^{3}**TIPS-Bz** (Fig. 3A). This assignment is supported by TD-DFT calculations, which predict a maximum oscillator strength at 291 nm. Time-resolved measurements show the simultaneous formation of ^{3}**TIPS-Bz** as the luminescence of **Ir** is quenched (Fig. 3B). Under the selected conditions a triplet lifetime of 34 μs is measured for **TIPS-Bz** (Fig. S1, ESI†). After complete deactivation of ^{3}**TIPS-Bz** only baseline level is detected (Fig. S3, ESI†). This gives us unequivocal proof of triplet–triplet energy transfer between the sensitizer and

 This journal is © The Royal Society of Chemistry 2025

Open Access Article. Published on 22 May 2025. Downloaded on 6/16/2025 5:15:04 PM.
This article is licensed under a Creative Commons Attribution 3.0 Unported Licence.

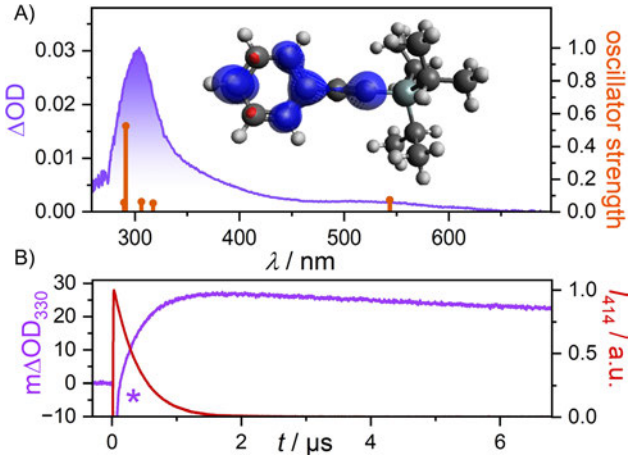

Fig. 3 TA measurements of **Ir** and **TIPS-Bz** in Ar-saturated benzene with 355 nm laser pulses (A) TA spectrum of **Ir** (6.25 μM) and 1 mM **TIPS-Bz** recorded 4 μs after excitation shown together with the oscillator strength calculated by TD-DFT (B3LYP/6-311+G(d,p) level of theory). (B) Kinetic measurements of **Ir** (25 μM) emission and transient absorption of **TIPS-Bz** (2 mM).

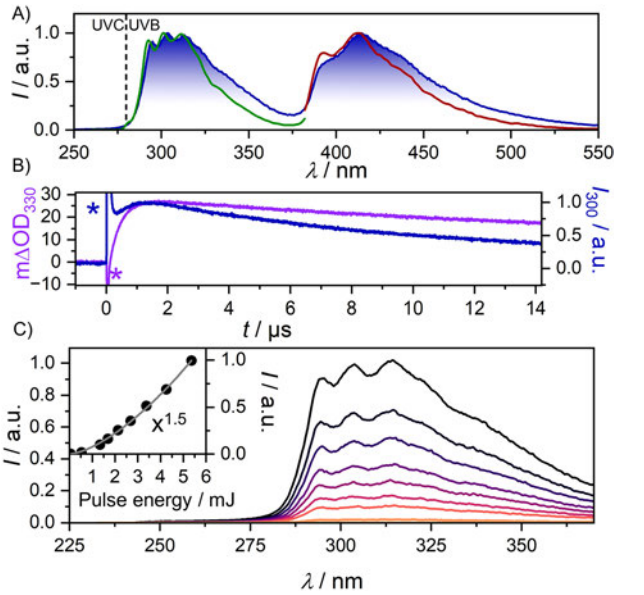

Fig. 4 Mechanistic investigations of 25 μM **Ir** and 2 mM **TIPS-Bz** in Ar-saturated benzene. (A) Time-gated emission spectrum after 355 nm laser pulse excitation (blue, 4–204 μs) and after 280 nm excitation (green and red, normalized to the maximum in the UV and visible region). (B) Kinetic traces of the ^{1}**TIPS-Bz*** emission and transient absorption of ^{3}**TIPS-Bz**. (C) Excitation-intensity dependent delayed emission spectra. Inset: Emission maximum plotted against laser pulse intensity with a pulse duration of ~5 ns. See text for details.

TIPS-Bz. With the TTET step established, we investigated the triplet–triplet annihilation (TTA) process of **TIPS-Bz**. For this study, a solution containing 25 μM **Ir** and 2 mM **TIPS-Bz** was selected, ensuring 95% deactivation of the excited sensitizer, a critical factor for efficient triplet–triplet annihilation.[9] Reabsorption by **TIPS-Bz** does not play a significant factor since the lowest electronic transition (*e.g.* in the range of 280–320 nm) exhibits weak absorption presumably as it is symmetry forbidden.[43] This is advantageous for upconversion since reabsorption typically leads to a reduced upconversion quantum yield.[18] Time-gated emission spectra were recorded throughout the complete deactivation of ^{3}**TIPS-Bz** (integration window: 4–204 μs after laser pulse excitation, Fig. 4A, blue spectrum). A signal in the UVB range is detected, which resembles the fluorescence spectrum of **TIPS-Bz** in diluted solution (Fig. 2B). Differences between these two spectra likely stems from inner filter effects of **Ir** owing to the large molar absorption coefficient ε of **Ir** in that range. Directly exciting the solution containing the UC system at 280 nm yields a practically identical emission spectrum in the UV (Fig. 4A, green spectrum). Further control experiments do not suggest the formation of excimers (Fig. S2, ESI†).[33] Additionally, we detect post-quenching emission of **Ir** (compare to direct excitation at 280 nm, red spectrum). We assume that this emission stems from back-TTET and singlet energy transfer from ^{1}**TIPS-Bz*** to **Ir**.[11] Time-resolved transient absorption (TA) measurements of ^{3}**TIPS-Bz** and the emission of ^{1}**TIPS-Bz*** are shown in Fig. 4B. While strong artifacts are observed immediately after laser pulse excitation likely due to remaining stray light, the signals of both species concurrently reach a maximum, while the ^{1}**TIPS-Bz*** emission decays faster than ^{3}**TIPS-Bz**.[9] Time-gated emission spectra were recorded with increasing laser pulse excitation intensities (Fig. 4C). Integration over the UC emission spectrum revealed a nonlinear dependence on the laser power, consistent with the bimolecular nature of the TTA process. Altogether, these findings provide clear evidence that the observed UVB emission originates from TTA-UC. Unfortunately, steady-state UC emission could not be detected with a 370 nm LED as light source. This absence is presumably due to the absorption characteristics of **Ir**, whose ε is two orders of magnitude lower at 370 nm than in the UVB region. Consequently, achieving sufficient concentrations of ^{3}**TIPS-Bz** for TTA under mild 370 nm LED excitation necessitates a high concentration of **Ir**, which in turn enhances reabsorption losses. Ideally, the sensitizer should have an absorption minimum in the spectral region of UC emission.[13,44] This highlights one of the major challenges of upconversion in the UVB/C range, where most photoactive compounds have large extinction coefficients ($\varepsilon_{UVB/C} > 10^3$ M^{-1} cm^{-1}), which makes this a practically unavoidable loss channel in diffusion based UC in solution. Hence, under our UC conditions, considering the excitation and excited singlet state energy, the anti-Stokes shift (0.83 eV) remains below typical values of related systems.[10] To address this challenge, **TIPS-Bz** was further modified by introducing a *tert*-butyl group at the *para*-position (**4tBu-TIPS-Bz**). This modification was intended to lower the triplet energy, potentially allowing sensitization by a broader range of sensitizers. However, the calculated triplet energy of 3.02 eV remains too high to provide significant benefits. While the UC system **4tBu-TIPS-Bz-Ir** remains functional under 355 nm laser pulse excitation, its energy transfer constant and photostability are notably lower than those of **TIPS-Bz**, making it a less favorable system overall (see Chapter S5 for details, ESI†).

This study demonstrates that a benzene annihilator functionalized with a TIPS-ethynyl group can be integrated into a TTA-UC

Open Access Article. Published on 22 May 2025. Downloaded on 6/16/2025 5:15:04 PM.
This article is licensed under a Creative Commons Attribution 3.0 Unported Licence.

system, achieving emission near the UVC range. This was realized using the high-triplet-energy sensitizer *fac*-[Ir(CF_3-pmb)$_3$], which efficiently sensitizes the high-lying triplet state of **TIPS-Bz**. A thorough investigation of the TTA-UC mechanism provided unequivocal evidence of the process, pushing the feasibility of TTA-UC into higher-energy regions. However, these findings also highlight critical challenges for UVC upconversion. Future efforts towards Vis-to-UVC photon upconversion should prioritize increasing the singlet–triplet gap of the annihilator by appropriate functionalization, bringing it closer to the theoretical thermodynamic limit for TTA (*i.e.* $2 \times E_{T1} \sim E_{S1}$).[32,45] This will effectively enable sensitization with sensitizers having lower triplet energies. Additionally, the development of an optimally matched sensitizer remains crucial—one that balances high absorption in the UVA/purple spectral range with minimal absorptivity in the UVB/C region to reduce losses.[46]

This work was supported by the German Research Foundation (DFG, grant number KE 2313/3-1 and GL 349/7-2 within priority program SPP 2102) and the German Federal Environmental Foundation (DBU, grant number 20022/028).

Data availability

All experimental data have been provided in the main text and the ESI.† The data sets shown in the main paper can be found under **https://doi.org/10.25358/openscience-12308**.

Conflicts of interest

The authors declare no conflict of interest.

Notes and references

1 M. R. Hamblin, *Dalton Trans.*, 2018, **47**, 8571–8580.
2 Q. Zhou, B. M. Wirtz, T. H. Schloemer, M. C. Burroughs, M. Hu, P. Narayanan, J. Lyu, A. O. Gallegos, C. Layton, D. J. Mai and D. N. Congreve, *Adv. Mater.*, 2023, **35**, 2301563.
3 Y. Shang, S. Hao, C. Yang and G. Chen, *Nanomaterials*, 2015, **5**, 1782–1809.
4 D. Beery, T. W. Schmidt and K. Hanson, *ACS Appl. Mater. Interfaces*, 2021, **13**, 32601–32605.
5 M. Barawi, F. Fresno, R. Pérez-Ruiz and V. A. De La Peña O'Shea, *ACS Appl. Energy Mater.*, 2019, **2**, 207–211.
6 T. Trupke, M. A. Green and P. Würfel, *J. Appl. Phys.*, 2002, **92**, 4117–4122.
7 M. Haase and H. Schäfer, *Angew. Chem., Int. Ed.*, 2011, **50**, 5808–5829.
8 M. Pawlicki, H. A. Collins, R. G. Denning and H. L. Anderson, *Angew. Chem., Int. Ed.*, 2009, **48**, 3244–3266.
9 Y. Murakami and K. Kamada, *Phys. Chem. Chem. Phys.*, 2021, **23**, 18268–18282.
10 M. Uji, T. J. B. Zähringer, C. Kerzig and N. Yanai, *Angew. Chem., Int. Ed.*, 2023, **62**, e202301506.
11 T. J. B. Zähringer, J. A. Moghtader, M. Bertrams, B. Roy, M. Uji, N. Yanai and C. Kerzig, *Angew. Chem., Int. Ed.*, 2023, **62**, e202215340.
12 W. Liang, C. Nie, J. Du, Y. Han, G. Zhao, F. Yang, G. Liang and K. Wu, *Nat. Photonics*, 2023, **17**, 346–353.
13 N. Harada, Y. Sasaki, M. Hosoyamada, N. Kimizuka and N. Yanai, *Angew. Chem., Int. Ed.*, 2021, **60**, 142–147.
14 C. A. Parker and C. G. Hatchard, *Proc. R. Soc. Lond. Ser. Math. Phys. Sci.*, 1962, **269**, 574–584.
15 Z. Huang, D. E. Simpson, M. Mahboub, X. Li and M. L. Tang, *Chem. Sci.*, 2016, **7**, 4101–4104.
16 T. N. Singh-Rachford, A. Nayak, M. L. Muro-Small, S. Goeb, M. J. Therien and F. N. Castellano, *J. Am. Chem. Soc.*, 2010, **132**, 14203–14211.
17 T. N. Singh-Rachford and F. N. Castellano, *Coord. Chem. Rev.*, 2010, **254**, 2560–2573.
18 A. Olesund, J. Johnsson, F. Edhborg, S. Ghasemi, K. Moth-Poulsen and B. Albinsson, *J. Am. Chem. Soc.*, 2022, **144**, 3706–3716.
19 H.-L. Lee, M.-S. Lee, H. Park, W.-S. Han and J.-H. Kim, *Korean J. Chem. Eng.*, 2019, **36**, 1791–1798.
20 Y. Murakami, A. Motooka, R. Enomoto, K. Niimi, A. Kaiho and N. Kiyoyanagi, *Phys. Chem. Chem. Phys.*, 2020, **22**, 27134–27143.
21 T. J. B. Zähringer, M.-S. Bertrams and C. Kerzig, *J. Mater. Chem. C*, 2022, **10**, 4568–4573.
22 L. Schmid, F. Glaser, R. Schaer and O. S. Wenger, *J. Am. Chem. Soc.*, 2022, **144**, 963–976.
23 X. Lin, Z. Chen, Y. Han, C. Nie, P. Xia, S. He, J. Li and K. Wu, *ACS Energy Lett.*, 2022, **7**, 914–919.
24 B. Lehmann, *Photochem. Photobiol.*, 2005, **81**, 1246–1251.
25 N. Zhang, G. Liu, H. Liu, Y. Wang, Z. He and G. Wang, *J. Hazard. Mater.*, 2011, **192**, 411–418.
26 H. Hirayama, S. Fujikawa and N. Kamata, *Electron. Commun. Jpn.*, 2015, **98**, 1–8.
27 T. J. B. Zähringer, M. Wienhold, R. Gilmour and C. Kerzig, *J. Am. Chem. Soc.*, 2023, **145**, 21576–21586.
28 Reference Air Mass 1.5 Spectra, **https://www.nrel.gov/grid/solar-resource/spectra.html**, (accessed March 24, 2025).
29 T. Chang, S. You, B. Yu and H. Kong, *J. Hazard. Mater.*, 2007, **141**, 784–792.
30 A. G. Griesbeck, N. Maptue, S. Bondock and M. Oelgemöller, *Photochem. Photobiol. Sci.*, 2003, **2**, 450–451.
31 B. Pfund, D. M. Steffen, M. R. Schreier, M.-S. Bertrams, C. Ye, K. Börjesson, O. S. Wenger and C. Kerzig, *J. Am. Chem. Soc.*, 2020, **142**, 10468–10476.
32 W. Zeng, C. Zhong, H. Bronstein and F. Plasser, *Angew. Chem., Int. Ed.*, 2025, e202502485.
33 A. Olesund, S. Ghasemi, K. Moth-Poulsen and B. Albinsson, *J. Am. Chem. Soc.*, 2023, **145**, 22168–22175.
34 J. Li, M. Zhang, L. Zeng, L. Huang and X. Wang, *Angew. Chem., Int. Ed.*, 2023, **62**, e202303093.
35 X. Cao, K. Pan, J. Miao, X. Lv, Z. Huang, F. Ni, X. Yin, Y. Wei and C. Yang, *J. Am. Chem. Soc.*, 2022, **144**, 22976–22984.
36 Y. Sasaki, S. Amemori, H. Kouno, N. Yanai and N. Kimizuka, *J. Mater. Chem. C*, 2017, **5**, 5063–5067.
37 F. Strieth-Kalthoff, M. J. James, M. Teders, L. Pitzer and F. Glorius, *Chem. Soc. Rev.*, 2018, **47**, 7190–7202.
38 S. Dutta, J. E. Erchinger, F. Strieth-Kalthoff, R. Kleinmans and F. Glorius, *Chem. Soc. Rev.*, 2024, **53**, 1068–1089.
39 T. O. Paulisch, L. A. Mai, F. Strieth-Kalthoff, M. J. James, C. Henkel, D. M. Guldi and F. Glorius, *Angew. Chem., Int. Ed.*, 2022, **61**, e202112695.
40 K. Tsuchiya, S. Yagai, A. Kitamura, T. Karatsu, K. Endo, J. Mizukami, S. Akiyama and M. Yabe, *Eur. J. Inorg. Chem.*, 2010, 926–933.
41 M.-S. Bertrams and C. Kerzig, *Chem. Commun.*, 2021, **57**, 6752–6755.
42 J. P. Doering, *J. Chem. Phys.*, 1969, **51**, 2866–2870.
43 J. N. Murrell and J. A. Pople, *Proc. Phys. Soc. Sect. A*, 1956, **69**, 245–252.
44 A. Monguzzi, J. Mezyk, F. Scotognella, R. Tubino and F. Meinardi, *Phys. Rev. B*, 2008, **78**, 195112.
45 L. Naimovičius and A. B. Pun, *Trends Chem.*, 2025, S2589597425000425.
46 Y. Zhou, F. N. Castellano, T. W. Schmidt and K. Hanson, *ACS Energy Lett.*, 2020, **5**, 2322–2326.

 This journal is © The Royal Society of Chemistry 2025

7.3 Visible-to-UV Photon Upconversion: Recent Progress in New Materials and Applications

Many studies employing visible-to-UV TTA–UC primarily emphasize the application, often without examining how the systems actually interact with the components central to the intended functionality. Frequently, no mechanistic rationale is offered, or only speculative distinctions are made between energy and electron transfer processes involving the excited annihilator.[337] However, a deeper mechanistic understanding would greatly support the rational design and optimization of visible-to-UV TTA–UC systems for targeted applications. The review article produced in project **[M]** addressed this gap by presenting a detailed overview of the diverse chemical applications of UV annihilators driven by upconversion, systematically categorized by application type and underlying reaction mechanism. It also analyzed the advantages and limitations of various energy and electron transfer pathways, providing valuable guidance for researchers who aim to apply these mechanisms in conventional UV photochemistry. Further, the review article summarizes the most recent advances in visible-to-UV photon upconversion reported in the literature. A perspective of future work is given which focuses on improving material stability, extending excitation wavelengths, and integrating with nanotechnology and optics to broaden real-world use. In addition, a dedicated section on blue-to-UVB TTA–UC, which contextualizes the results in Chapter 7.2 of this thesis, was included.

Summary:

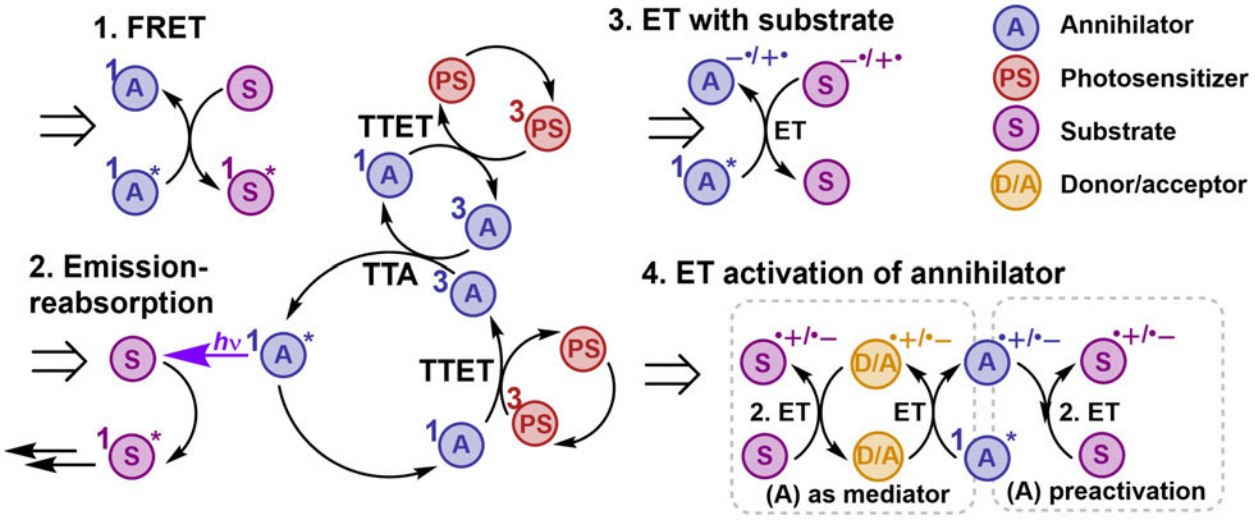

Figure 31: Schematic overview of possible reaction mechanisms initiated by visible-to-UV TTA–UC. The singlet-excited annihilator can act as an energy donor in non-radiative (Pathway 1) or radiative (Pathway 2) energy transfer processes. Alternatively, it can engage in electron transfer directly with the substrate (Pathway 3), or indirectly by forming a radical ion through prior electron exchange with a donor or acceptor before reacting with the substrate (Pathway 4). See main text for details.

Project **[M]** reviewed recent advancements in visible-to-UV photon upconversion in a comprehensive article. The review systematically cataloged all reported annihilator–sensitizer pairs employed in visible-to-

UV TTA–UC, classifying them by their singlet- and triplet-excited state energies. It examined molecular design strategies aimed at optimizing upconversion quantum yields while reducing excitation threshold intensities. Notable examples were highlighted for their large anti-Stokes shifts, low excitation thresholds, and overall high efficiencies. The review also addressed recent developments in implementing Vis-to-UV TTA–UC in solid-state films. A dedicated chapter further summarized progress in blue-to-UVB TTA–UC, based on results from this thesis. For a detailed overview, the reader is referred to Chapter 7.2.

In addition, the article presented a thorough survey of the diverse chemical applications of UV annihilators powered by upconversion, categorized by application type and underlying reaction mechanism. Overall, four pathways were identified that are initiated by visible-to-UV TTA–UC (Figure 31). These mechanisms fall into two main categories: energy transfer and electron transfer. Energy transfer may occur either via FRET, a non-radiative process (Pathway 1), or through reabsorption of emitted light by a substrate (Pathway 2), often located in a separate reaction vessel. When the substrate is present in the same upconversion solution, it is possible to distinguish between radiative and non-radiative FRET using spectral quenching of the upconverted emission, as established in project **[C]**. In the simplest case, UC-initiated electron transfer takes place directly between the singlet-excited annihilator and the substrate, leading to the desired photochemical reaction (Pathway 3). Alternatively, the singlet-excited annihilator can first undergo electron transfer with an additional electron donor or acceptor, forming radical ions, which then react with the substrate (Pathway 4). Although this mechanism may initially appear more complex than direct electron transfer between the singlet-excited annihilator and the substrate, it offers a key advantage: the radical ions formed have significantly longer lifetimes than the short-lived singlet state, allowing sufficient time for bimolecular quenching to occur. However, this benefit often comes at the cost of a reduced thermodynamic driving force. The article discusses the advantages and limitations of these upconversion-based energy and electron transfer pathways, offering valuable insights for researchers aiming to integrate such mechanisms into conventional UV-driven photochemical processes.

Project **[M]** was published as a review article:

"**Visible-to-UV Photon Upconversion: Recent Progress in New Materials and Applications**"

Reproduced from Reference: M. Uji, T. J. B. Zähringer, C. Kerzig, N. Yanai, *Angew. Chem. Int. Ed.* **2023**, *62*, e202301506.

The article is licensed under CC BY-NC 4.0 (https://creativecommons.org/licenses/by/4.0/) and can be cited corresponding to ref.[M]. The reference is attached in the following pages.

Author contributions: N. Yanai and M. Uji reviewed the literature and contributed to the writing of "2. Figure-of-merits of TTA-UC"," 3.1. Sensitizer and Annihilator Chromophores", "3.2. Vis-to-UV TTA-UC in Bulk Solution", "3.3 Large UC Spectral Shift", and "3.5. Vis-to-UV TTA-UC in Films", C. Kerzig and T. J. B. Zähringer reviewed the literature and wrote chapters "3.4 Vis-to-UVB TTA-UC Systems" and "4. Chemical Applications of Vis-to-UV TTA-UC".

Check for updates

How to cite: *Angew. Chem. Int. Ed.* **2023,** *62,* e202301506
doi.org/10.1002/anie.202301506

Photochemistry

Visible-to-UV Photon Upconversion: Recent Progress in New Materials and Applications

Masanori Uji[+], Till J. B. Zähringer[+], Christoph Kerzig, and Nobuhiro Yanai**

Angewandte International Edition Chemie

© 2023 Wiley-VCH GmbH

Abstract: Ultraviolet (UV, $\lambda < 400$ nm) light is essential for various photochemical reactions, but its intensity in the solar spectrum is very low, and light sources that artificially generate high-energy UV light are inefficient and environmentally unfriendly. A solution to this problem is photon upconversion (UC) from visible (vis, $\lambda > 400$ nm) light to UV light. Among several mechanisms, UC based on triplet-triplet annihilation (TTA-UC) in particular has made remarkable progress in recent years. The development of new chromophores has enabled highly efficient conversion of low-intensity visible light into UV light. In this review, we summarize the recent development of visible-to-UV TTA-UC, from the development of chromophores and their production into films to their application in various photochemical processes such as catalysis, bond activation and polymerization. Finally, challenges and opportunities in future material development and applications will be discussed.

1. Introduction

Ultraviolet (UV) light ($\lambda < 400$ nm) plays a pivotal role in wastewater treatment, sterilization, and applications in numerous photochemical reactions such as solar hydrogen production and artificial photosynthesis.[1–7] However, since the proportion of UV light in the sunlight spectrum in our living environment is as low as only 5 %,[8] a great deal of effort has been devoted to effective UV light generation. Artificial generation of UVB light using mercury,[9] excimer-based lamps,[10] or the high-energy tail of xenon arc lamps[2] is currently inefficient and environmentally unfriendly and their energy consumption is high.

As an alternative route, photon upconversion (UC) from visible (vis, $\lambda > 400$ nm) light to UV light has recently received widespread attention. There are a few mechanisms of vis-to-UV UC: second harmonic generation (SHG),[11–13] two-photon absorption (TPA),[14–16] multi-step excitation of lanthanides,[17–19] and triplet-triplet annihilation (TTA).[4–7,20–53] Among these mechanisms, TTA-based upconversion (TTA-UC) is particularly promising because of its ability to achieve high UC quantum yields at low excitation light intensities such as solar irradiance.

TTA-UC usually consists of two chromophores, a triplet sensitizer and an annihilator (Figure 1a). In the typical mechanism of TTA-UC, a sensitizer molecule is first photoexcited to the excited singlet state ($S_{1,S}$), followed by intersystem crossing (ISC) from $S_{1,S}$ to the excited triplet state ($T_{1,S}$). Triplet energy transfer (TET) from sensitizer to annihilator occurs, producing an excited triplet annihilator ($T_{1,A}$). TTA between two annihilator triplets $T_{1,A}$ results in the formation of one annihilator excited singlet state ($S_{1,A}$) and one ground state ($S_{0,A}$). Finally, the annihilator in the $S_{1,A}$ state returns to the ground state and shows delayed fluorescence, which has higher energy than the excitation light.

Since Castellano et al. reported the first vis-to-UV TTA-UC system in 2006,[20] numerous combinations of sensitizers and annihilators have been developed. Especially in the last few years, the discovery of superior chromophores has significantly increased the efficiency of vis-to-UV TTA-UC, allowing the use of weak visible light. Furthermore, initial high-energy annihilators with emission spectra approaching 300 nm have been developed. This has made it possible to apply vis-to-UV TTA-UC to various photochemical reactions. In this article, we will first briefly describe the parameters to be evaluated for TTA-UC, and then summarize the energy levels of the chromophores and TTA-UC performances reported so far. In addition, examples of applications to photoredox catalysis, bond activation, and photopolymerization reactions will be presented, along with mechanistic considerations and discussions.

2. Figure-of-Merits of TTA-UC

2.1. Upconversion Efficiency

UC efficiency is one of the most important parameters for characterizing the TTA-UC process. The TTA-UC efficiency (η_{UC}, theoretical maximum: 100 %) can be expressed as the product of the efficiency of each process as shown in the following equation,[54,55]

$$\eta_{UC} = f\Phi_{ISC}\Phi_{TET}\Phi_{TTA}\Phi_{F} \quad (1)$$

where f is the singlet production probability by TTA, Φ_{ISC}, Φ_{TET}, Φ_{TTA}, and Φ_{F} are the quantum yields of ISC, TET, TTA, and annihilator fluorescence, respectively. Since TTA-UC includes a bimolecular process and two photons are required to produce one higher energy photon, the theoretical maximum of the UC quantum yield (Φ_{UC}) is 50 %. It is common practice to normalize the maximum value to 100 % by using the UC efficiency η_{UC} obtained by doubling the UC quantum yield Φ_{UC}. The various definitions of the UC efficiency are nicely summarized in a recent review.[55]

[*] M. Uji,[+] N. Yanai
Department of Applied Chemistry, Graduate School of Engineering, Kyushu University
744 Moto-oka, Nishi-ku, Fukuoka 819-0395 (Japan)
E-mail: yanai@mail.cstm.kyushu-u.ac.jp
T. J. B. Zähringer,[+] C. Kerzig
Department of Chemistry, Johannes Gutenberg University Mainz
Duesbergweg 10–14, 55128 Mainz (Germany)
E-mail: ckerzig@uni-mainz.de
N. Yanai
FOREST, JST
4-1-8 Honcho, Kawaguchi, Saitama 332-0012 (Japan)
[+] These authors contributed equally to this work.

© 2023 Wiley-VCH GmbH

15213773, 2023, 25, Downloaded from https://onlinelibrary.wiley.com/doi/10.1002/anie.202301506 by Universitätsbibliothek Mainz, Wiley Online Library on [15/04/2025]. See the Terms and Conditions (https://onlinelibrary.wiley.com/terms-and-conditions) on Wiley Online Library for rules of use; OA articles are governed by the applicable Creative Commons License

2.2. Threshold Excitation Intensity

Another important parameter in evaluating TTA-UC is the threshold excitation light intensity (I_{th}) (Figure 1b).[56–58] The time evolution of the exciton populations, excited sensitizer triplet (T_S), annihilator triplet (T_A), and annihilator singlet (S_A), can be described as follows,

$$\partial T_S/\partial t = \alpha I_{exc} - k_S^T T_S - k_{tr} T_S \quad (2)$$

$$\partial T_A/\partial t = k_{tr} T_S - k_A^T T_A - \gamma_{TT} T_A^2 \quad (3)$$

$$\partial S_A/\partial t = 0.5 f \gamma_{TT} T_A^2 - k_A^S S_A \quad (4)$$

where α is the sensitizer's absorption coefficient at the excitation wavelength, I_{exc} is the excitation light intensity, k_S^T, k_A^T, k_A^S are the rate constants for the deactivation of sensitizer triplet, annihilator triplet, and annihilator singlet, respectively, k_{tr} is the rate constant for the TET from sensitizer to annihilator, and γ_{TT} is the second-order rate constant for TTA. In the low excitation intensity region, the TTA channel is negligibly small relative to the triplet spontaneous decay, so the annihilator mostly returns to the ground state ($S_{0,A}$) before TTA. Therefore, it can be approximated as $k_A^T T_A \gg \gamma_{TT} T_A^2$, and S_A can be written as

$$S_A = 0.5 f \frac{\gamma_{TT}}{k_A^S} \left[\frac{k_{tr}/k_A^T}{k_S^T + k_{tr}} \right]^2 (\alpha I_{exc})^2 \propto \boldsymbol{I_{exc}^2} \quad (5)$$

where the UC emission intensity shows a quadratic dependence on the excitation light intensity. On the other hand, in the high excitation intensity region, it can be approximated as $k_A^T T_A \ll \gamma_{TT} T_A^2$, and S_A can be written as

$$S_A = 0.5 f \frac{1}{k_A^S} \left[\frac{k_{tr}}{k_S^T + k_{tr}} \right] \alpha I_{exc} \propto \boldsymbol{I_{exc}} \quad (6)$$

where the excitation intensity dependence of UC emission intensity turned to be linear. By increasing the excitation intensity, the slope of the double logarithmic plot of UC emission intensity versus excitation light intensity changes from quadratic to linear, and I_{th}, the intersection of each line, can be expressed by equating equations (5) and (6),

$$I_{th} = (\alpha \gamma_{TT})^{-1} \left[\frac{k_{tr}}{k_S^T + k_{tr}} \right]^{-1} (k_A^T)^2 = (\alpha \Phi_{TET} \gamma_{TT})^{-1} \tau_T^{-2} \quad (7)$$

where τ_T is the lifetime of annihilator triplet excited state. The I_{th} is used as a guide for the excitation light intensity required

Masanori Uji received his B.Eng. (2021) and M.Eng. (2023) in chemistry at Kyushu university. Currently, he is a Ph.D. candidate working under the supervision of Nobuhiro Yanai. His research focuses on photon upconversion from visible to UV light via triplet-triplet annihilation and its applications.

Till Zähringer received his B.Sc. (2019) and M.Sc. (2021) in chemistry at the Johannes Gutenberg University Mainz. During his master studies, he completed a six-month research internship under the guidance of G. A. Ozin at the University of Toronto in Canada. Currently, he is a Ph.D. candidate working under the supervision of Christoph Kerzig, where he is focusing on UV light generation by triplet-triplet annihilation upconversion and its application to sustainable processes. His doctoral research is funded through a fellowship from the German Federal Environmental Foundation (DBU).

Christoph Kerzig studied chemistry at the University of Halle (Germany), where he obtained his Ph.D. under the supervision of Martin Goez in 2017. He then joined the group of Oliver S. Wenger at the University of Basel (Switzerland) with a Leopoldina postdoctoral fellowship. During his research stay in Basel, he was also a visiting scientist in Gothenburg (Sweden), working on upconversion with Karl Börjesson. He started his independent career in 2020 at the Johannes Gutenberg University Mainz as a tenure track Assistant Professor and Liebig fellow. His research focuses on mechanistic photochemistry, optical spectroscopy, and multiphoton chemistry. He recently received the ADUC award of the German Chemical Society.

Nobuhiro Yanai is an Associate Professor in the Department of Applied Chemistry at Kyushu University, Japan. He earned his Ph.D. from Kyoto University in 2011 under Prof. Susumu Kitagawa and Prof. Takashi Uemura on guest properties in metal-organic frameworks. He was a postdoctoral fellow with Prof. Steve Granick at the University of Illinois at Urbana-Champaign, where he experienced colloid and soft matter sciences. He joined Kyushu University in 2012, and currently leads a group that creates photofunctional materials for photon upconversion, dynamic nuclear polarization, and quantum sensing. He has received several awards including The Wiley Young Researcher Award, The Asian and Oceanian Photochemistry Association Prize for Young Scientists, and Award for Young Chemists, Chemical Society of Japan.

© 2023 Wiley-VCH GmbH

15213773, 2023, 25, Downloaded from https://onlinelibrary.wiley.com/doi/10.1002/anie.202301506 by Universitätsbibliothek Mainz, Wiley Online Library on [15/04/2025]. See the Terms and Conditions (https://onlinelibrary.wiley.com/terms-and-conditions) on Wiley Online Library for rules of use; OA articles are governed by the applicable Creative Commons License

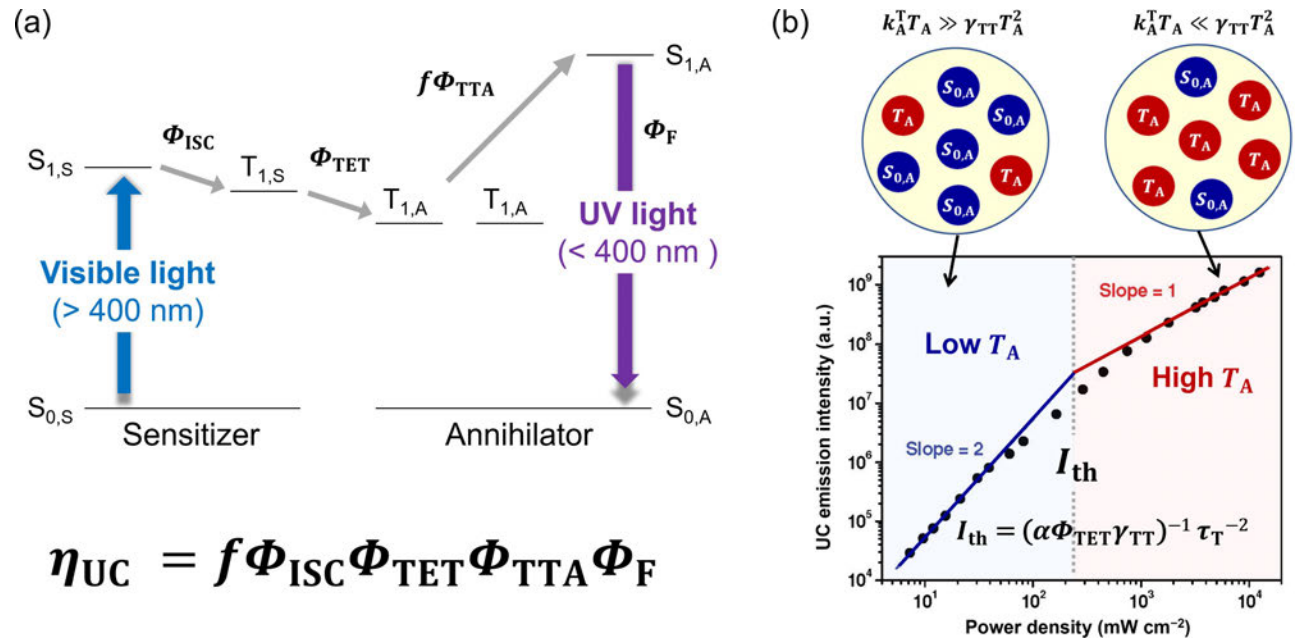

Figure 1. (a) Energy diagram of vis-to-UV TTA-UC together with parameters related to TTA-UC efficiency η_{UC}.[54,55] (b) Determination of threshold excitation intensity I_{th} and its related parameters.[56–58]

to optimize the TTA-UC system. A threshold intensity lower than the excitation light intensity used in each application is desirable. To obtain a low I_{th}, it is important that the sensitizer absorptivity at an excitation wavelength is high, the sensitizer/emitter pair has high TET efficiency, and the emitter triplet has high diffusivity and long lifetime.

3. Reported Examples of Vis-to-UV TTA-UC

3.1. Sensitizer and Annihilator Chromophores

To date, vis-to-UV TTA-UC has been reported using various sensitizer-annihilator combinations in organic solvents,[4,6,7,20,22,23,25,27–35,38–50,53] water,[5,29,37] and films.[21,26,27,51,52] Table 1 summarizes these reported examples with their TTA-UC efficiency η_{UC} and threshold excitation light intensity I_{th}.

To achieve vis-to-UV TTA-UC with high η_{UC}, low I_{th}, and large spectral upshift, the following conditions are desired for the sensitizer,

(1) Large absorption coefficients in the visible region
(2) Small absorption coefficients in the UV region
(3) High ISC efficiency (Φ_{ISC})
(4) Small S_1-T_1 energy gap (ΔE_{ST})
(5) Long excited triplet lifetime

Metal complexes[5,6,20,23,24,26,29,36,37,39,44,47,52] and semiconductor nanocrystals[30,32,34,40,41,43,45] have been adopted as triplet sensitizers because the heavy metals (Cd, Cs, Ir, Pb, Ru, and Zn) enhance the spin-orbit interaction, resulting in efficient ISC. On the other hand, several sensitizers that do not contain heavy metals have also been reported.[4,7,21,22,25,27,28,31,33,35,38,42,46,48–51,53] For example, it is widely known that chromophores with carbonyl groups exhibit high ISC efficiency even without heavy metals thanks to the large spin-orbit interaction caused by the distinct change in orbital symmetry during the transition from the singlet to the triplet state.[22,48,59–63] Furthermore, organic molecules with a small S_1-T_1 energy gap (ΔE_{ST}) that exhibit thermally activated delayed fluorescence (TADF) also show high ISC efficiency despite the absence of heavy metals.[7,27,28,31,33,35,42,46,49,50] In addition, the semiconductor nanocrystals and TADF compounds have the advantage that the small ΔE_{ST} reduces the energy loss in the ISC process and provides a large UC spectral shift. The sensitizer should have less absorption in the UV region in terms of not quenching the UC emission in the UV region. This is difficult for semiconductor nanocrystals and common TADF molecules, but has been achieved for Ir-coumarin complexes[23,24,39,52] and multi-resonance TADF molecules.[42,49] Sensitizer molecules employed so far are shown in Figure 2, together with their Φ_{ISC}, absorption onset in the visible region ($S_{1,onset}$) and triplet energy levels.[5,20,22,23,29,38,39,42,44,46–49,59,64–79] The Φ_{ISC} of 4CzPN was estimated as 1-Φ_{PF}[78] according to the literature,[46] where Φ_{PF} is the fluorescence quantum yield of the prompt component.

The requirements for annihilators are as follows,

(1) High fluorescence quantum yield in the UV region
(2) $S_{1,A}$ lower than twice the $T_{1,A}$ energy
(3) $T_{1,A}$ energy lower than $T_{1,S}$ energy (and excitation energy)
(4) Large S_1-T_1 energy gap (ΔE_{ST})
(5) Long excited triplet lifetime
(6) Large f value

© 2023 Wiley-VCH GmbH

15213773, 2023, 25, Downloaded from https://onlinelibrary.wiley.com/doi/10.1002/anie.202301506 by Universitätsbibliothek Mainz, Wiley Online Library on [15/04/2025]. See the Terms and Conditions (https://onlinelibrary.wiley.com/terms-and-conditions) on Wiley Online Library for rules of use; OA articles are governed by the applicable Creative Commons License

Table 1: Summary of vis-to-UV TTA-UC systems reported to date. The theoretical maximum of TTA-UC efficiency η_{UC} is normalized to be 100%.

Sensitizer	Annihilator	Environment	Excitation wavelength (nm)	UC emission wavelength (nm)	η_{UC} (%)	I_{th} (mW cm^{-2})	Reference
$Ir(ppy)_3$	Pyrene	Organic solvent	450	~390	···	···	[20]
$Ir(ppy)_3$	3,8-DBP	Organic solvent	450	~390	···	···	[20]
2MeOTX	PPO	PMMA film	410	364	···	···	[21]
Biacetyl	PPO	Organic solvent	442	360	1.16 ± 0.04	···	[22]
$Ir(C6)_2(acac)$	2,7-DBP	Organic solvent	445	376	2.0	4.58	[23]
$Ir(C6)_2(acac)$	2,7-DBP	Gel in DMF	445	~395	···	28	[24]
Biacetyl	PPO	Organic solvent	430	370	0.24	···	[25]
Ir(ppy-DBP)	2,7-DBP	Polyurethane Film	450	378	2.6	···	[26]
4CzIPN	*p*-Quarterphenyl (QP)	Organic solvent	445	353	3.9	7.7×10^2	[28]
4CzIPN	*p*-Terphenyl (TP)	Organic solvent	445	343	2.8	$\sim1.7\times10^3$	[28]
4CzPN	2,7-DBP	Organic solvent	450	378	4.4	···	[27]
4CzPN-DBP	2,7-DBP	Organic solvent	450	378	3.7	···	[27]
4CzPN-DBP	2,7-DBP	Polyurethane Film	450	388	···	···	[27]
CdS/ZnS/1NCA	PPO	Organic solvent	405	355	5.2 ± 0.5	···	[30]
$[Ru(bpy)_3]^{2+}$	$PyCO_2^-$	water	488	382	···	···	[29]
4CzPN-DBP	2,7-DBP	Organic solvent	450	376	1.7	···	[31]
$CsPbX_3$/1NCA	PPO	Organic solvent	445	363	>4	4.7×10^3	[34]
4CzIPN	Pyrene	Organic solvent	445	394	1.3	$>2.0\times10^3$	[33]
$CsPbBr_3$/1NCA	PPO	Organic solvent	443	355	10.2	1.9×10^3	[32]
Biacetyl	PPO	Organic solvent	445	370	···	···	[4]
$Ir(ppy)_3$	P_{66614}PPOS	Ionic liquid	445	378	0.44	61	[36]
FIrpic–Dec	*p*-Terphenyl (cationic)	water	445	390	0.1	$>4.0\times10^3$	[37]
IrFsppy	1,5-NDS	water	447	335	7.0×10^{-2}	···	[5]
$Ir(C6)_2(acac)$	1,4-TIPS-Nph	Organic solvent	445	372	20.5	2.3	[39]
4CzIPN	R/S-TP	Organic solvent	445	385	7.9	75	[35]
BuCIA	2,6-DTBN	Organic solvent	405	322	8.2	1.3×10^3	[38]
$Ir(ppy)_3$	2,7-DBP	Organic solvent	447	376	9.6	···	[6]
CdS/3PCA	PPO	Organic solvent	405	363	20.8	9.5×10^2	[40]
4CzIPN	*p*-TIPS-BP	Organic solvent	447	328	8.0	$\sim1.5\times10^3$	[50]
$CsPbBr_3$/PPOS	1,4-TIPS-Nph	Organic solvent	515	375	1.4×10^{-2}	1.6×10^3	[41]
CBDAC	1,4-TIPS-Nph	Organic solvent	445	373	20.3	38.0	[48]
BN-2Cz	1,4-TIPS-Nph	Organic solvent	517	375	8.6	2.1×10^2	[49]
BN-2Cz-*t*Bu	1,4-TIPS-Nph	Organic solvent	517	375	4.0	9.2	[49]
ZnSe/ZnS/BCA	2,6-DTBN	Organic solvent	405	337	6.2 ± 0.2	2.4×10^3	[45]

© 2023 Wiley-VCH GmbH

15213773, 2023, 25, Downloaded from https://onlinelibrary.wiley.com/doi/10.1002/anie.202301506 by Universitatsbibliothek Mainz, Wiley Online Library on [15/04/2025]. See the Terms and Conditions (https://onlinelibrary.wiley.com/terms-and-conditions) on Wiley Online Library for rules of use; OA articles are governed by the applicable Creative Commons License

Sensitizer	Annihilator	Environment	Excitation wavelength (nm)	UC emission wavelength (nm)	η_{UC} (%)	I_{th} (mW cm^{-2})	Reference
$CsPbBr_3$-PTA	PPO	Organic solvent	473	355	4.5 ± 0.5	2.2×10^3	[43]
$CsPbBr_3$-PTA	PPO	Organic solvent	443	355	12.2 ± 0.8	1.6×10^3	[43]
4CzBN	1,4-TIPS-Nph	Organic solvent	405	373	26.2	2.2×10^2	[46]
[Zn(*m*-L)$_2$]	1,4-TMS-Nph	Organic solvent	447	371	1.5	···	[44]
4CzIPN	bTIPS-Bz	Organic solvent	445, 447	319	~2	4.7×10^2	[7]
Ir(tmd)	2,7-DBP	Organic solvent	447	376	6.4	1.2×10^2	[47]
Ir(ppy)$_3$, Ir(ppy)$_2$, Ir(tmd), CBDAC, 4CzIPN	Pyrene, DBP, 1,4-TIPS-Nph, PPO	micelles in water	447	375-395	···	···	[47]
BN-Se	1,4-TIPS-Nph	Organic solvent	464	374	21.4	···	[42]
BN-Se	1,4-TIPS-Nph	Organic solvent	464	374	16.5	1.3	[42]
BN-Se	1-NTA	Organic solvent	464	345	7.1	···	[42]
CBDAC	PPO	Neat film	440	390-393	8.6	13.8-17.0	[51]
Ir(C6)$_2$(acac)	1,4-TIPS-Nph	Porous film	445	372	27.6	20.4	[52]
Ir(C6)$_2$(acac)	1,4-TIPS-Nph	Porous film with microlens array	445	372	···	< 0.6	[52]
Biacetyl	PPO	Monomer	532	380	···	···	[53]

As an annihilator, it should have a relatively small conjugated structure to the extent that it emits in the UV region, a rigid conjugated structure to show a long triplet lifetime, a large f value, and a pronounced overlap between HOMO and LUMO for large ΔE_{ST}. Annihilator molecules employed so far are shown in Figure 3, together with their singlet and triplet energy levels estimated by reported experimental values.[5,7,23,39,40,42,44,46,49,50,66,67,80–83] As an exception, the triplet energy levels of *p*-TIPS-BP[50] were determined by DFT calculations. Also, the triplet energy level of 1,4-TMS-Nph[44] was anticipated to correspond to that of 1,4-TIPS-Nph[39] with a similar structure.

3.2. Vis-to-UV TTA-UC in Bulk Solution

The first clear demonstration of vis-to-UV TTA-UC was reported in 2006 by Castellano et al. using Ir(ppy)$_3$ (ppy = 2-phenylpyridine) as sensitizer and pyrene or 3,8-di-*tert*-butylpyrene (3,8-DBP) as annihilator (Figure 4a).[20] The modification of pyrene with the bulky *tert*-butyl group avoids excimer formation at long wavelengths, and the excitation of the mixed solution of Ir(ppy)$_3$ and 3,8-DBP by 450 nm pulsed laser resulted in the upconverted emission with significant portion in the UV range (Figure 4b). In 2009, the same group demonstrated the first example of heavy metal-free vis-to-UV TTA-UC using 2,3-butanedione (biacetyl) as a sensitizer and 2,5-diphenyloxazole (PPO) as an annihilator (Figure 4c).[22] A mixed biacetyl/PPO benzene solution was irradiated with a 442 nm continuous laser at 0.389 W cm^{-2}, and singlet emission from PPO was obtained at λ_{em} = 360 nm with a maximum η_{UC} of 1.16 % ±0.04 % (Figure 4d). Subsequently, over the period through 2019, a variety of sensitizer/annihilator combinations were developed toward high η_{UC} and low I_{th}, but it remained difficult to develop systems that can balance them out.[4,20–34] The highest η_{UC} of 10.2 % before 2020 was reported by Wu et al. using perovskite nanocrystals as the sensitizer and PPO as the annihilator.[32] However, I_{th} was about 1.9 W cm^{-2}, which is much higher than the solar irradiance of a few mW cm^{-2} (Figure 4e–g). It was difficult to reduce I_{th} because increasing the concentration of semiconductor nanocrystals to enhance the visible absorbance leads to the severe reabsorption of upconverted UV emission.

In 2020, Yanai et al. developed a novel annihilator, 1,4-bis((triisopropylsilyl)ethynyl)-naphthalene (1,4-TIPS-Nph), which made a breakthrough in boosting the performance of vis-to-UV TTA-UC (Figure 5a).[39] Prior to this work, Yanai, Kimizuka et. al. reported a low I_{th} by using an excellent sensitizer, Ir(C6)$_2$(acac) (C6 = coumarin 6, acac = acetylacetone) with strong visible absorption and weak UV absorption (Figure 5a).[23,24] The weak UV absorption suppresses the reabsorption of upconverted UV emission and the singlet back energy transfer from annihilator to sensitizer. However, the TTA-UC efficiency η_{UC} was limited to 2.0 % because the employed 2,7-di-tert-butylpyrene (2,7-DBP)

© 2023 Wiley-VCH GmbH

15213773, 2023, 25, Downloaded from https://onlinelibrary.wiley.com/doi/10.1002/anie.202301506 by Universitatsbibliothek Mainz, Wiley Online Library on [15/04/2025]. See the Terms and Conditions (https://onlinelibrary.wiley.com/terms-and-conditions) on Wiley Online Library for rules of use; OA articles are governed by the applicable Creative Commons License

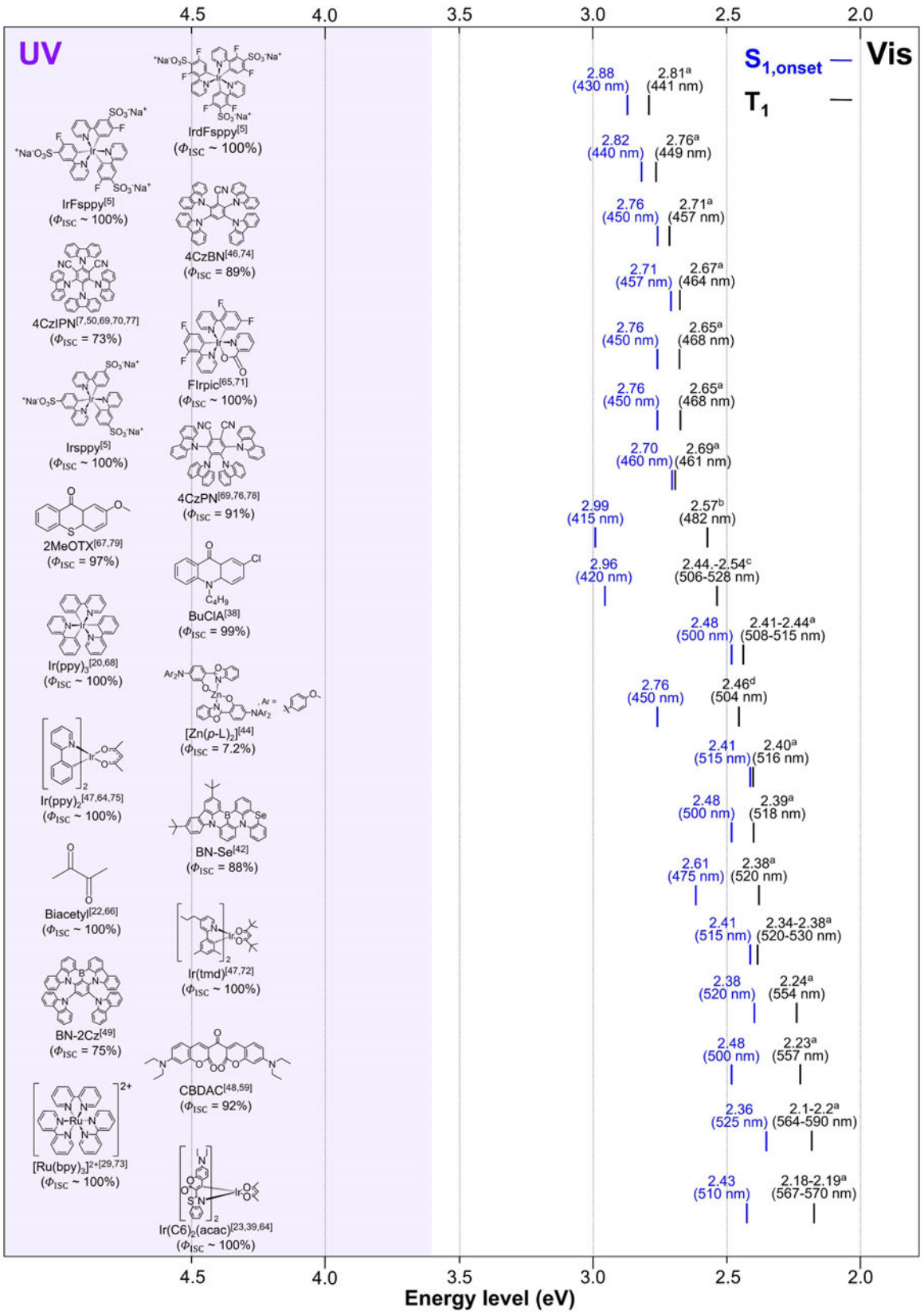

Figure 2. Energy levels of the absorption onset in the visible region ($S_{1,onset}$), triplet excited states and Φ_{ISC} of sensitizers for vis-to-UV TTA-UC. [a] Determined from the phosphorescence wavelength. [b] Determined by measuring the equilibration between the triplet-triplet (T-T) absorptions of reference and 2MeOTX in pulse photolysis experiments. [c] Estimated by DFT calculations (B3LYP/6-31G++(d,p)). (d) Estimated by TD-DFT (PBE1PBE/def2SV(P), PCM(CH_2Cl_2).

© 2023 Wiley-VCH GmbH

15213773, 2023, 25, Downloaded from https://onlinelibrary.wiley.com/doi/10.1002/anie.202301506 by Universitatsbibliothek Mainz, Wiley Online Library on [15/04/2025]. See the Terms and Conditions (https://onlinelibrary.wiley.com/terms-and-conditions) on Wiley Online Library for rules of use; OA articles are governed by the applicable Creative Commons License

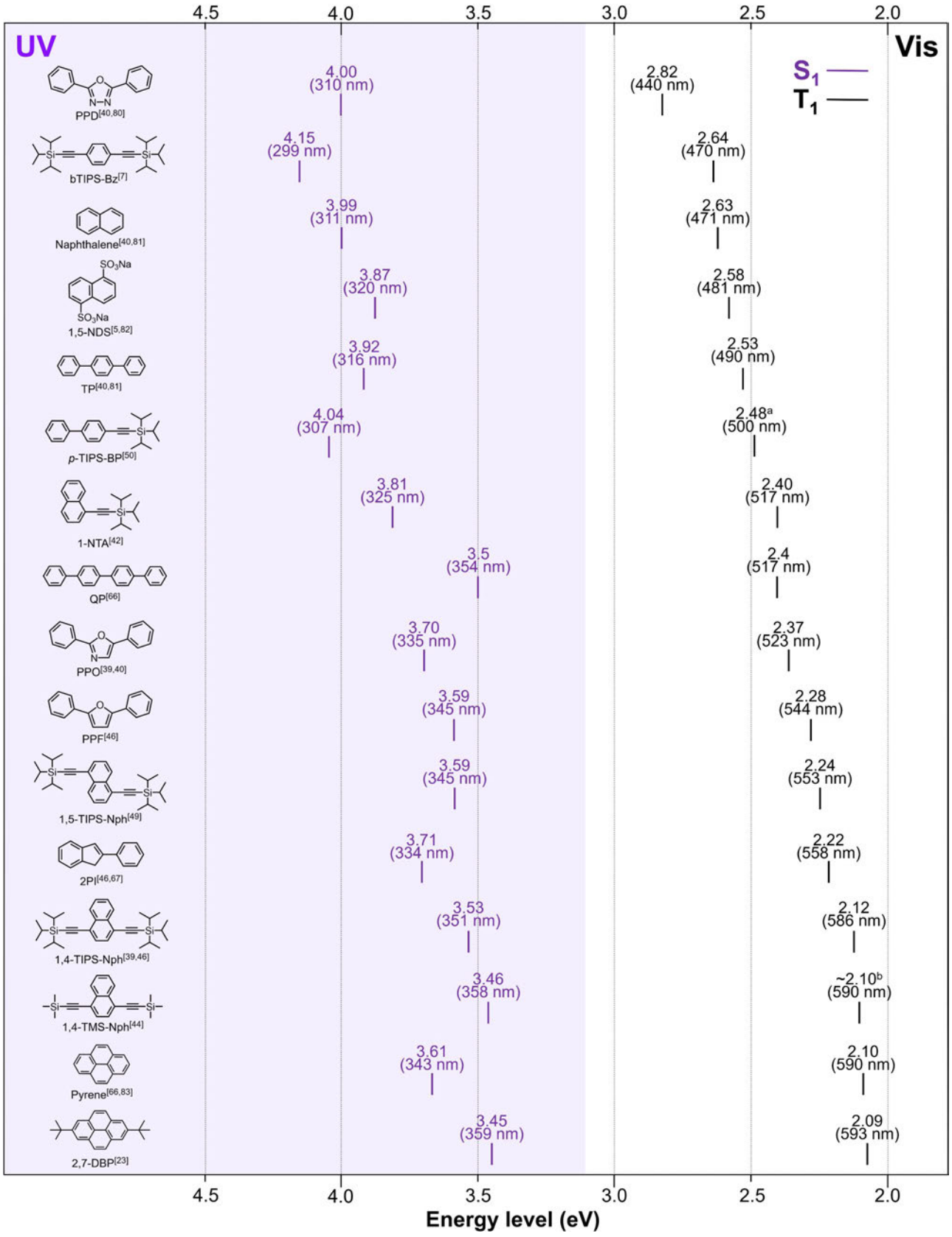

Figure 3. Energy levels of singlet and triplet excited states of annihilators for vis-to-UV TTA-UC estimated by reported experimental values. The S_1 states are determined from the intersection of normalized absorption and fluorescence spectra. [a] Estimated by DFT calculations (B3LYP/6-311 + G(d,p)). [b] Anticipated to correspond to the triplet energy level of 1,4-TIPS-Nph with a similar structure.

© 2023 Wiley-VCH GmbH

15213773, 2023, 25, Downloaded from https://onlinelibrary.wiley.com/doi/10.1002/anie.202301506 by Universitätsbibliothek Mainz, Wiley Online Library on [15/04/2025]. See the Terms and Conditions (https://onlinelibrary.wiley.com/terms-and-conditions) on Wiley Online Library for rules of use; OA articles are governed by the applicable Creative Commons License

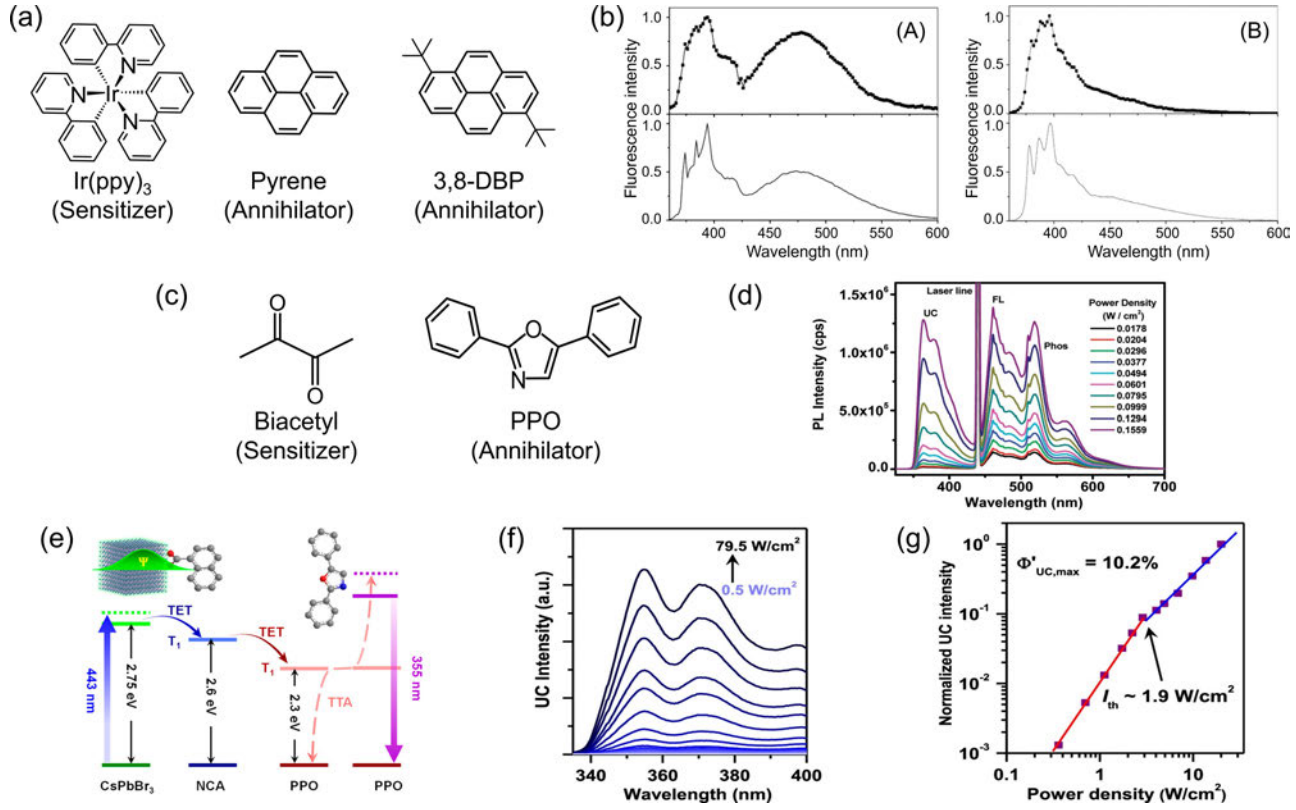

Figure 4. (a) Molecular structures of $Ir(ppy)_3$ (sensitizer), pyrene (annihilator) and 3,8-DBP (annihilator). (b) UC emission of (A) $Ir(ppy)_3$/Pyrene and (B) $Ir(ppy)_3$/3,8-DBP in deaerated CH_2Cl_2. (c) Molecular structures of biacetyl (sensitizer) and PPO (annihilator). (d) UC emission of biacetyl/PPO in deaerated benzene. (e) Energy level diagram of $CsPbBr_3$-NCA (sensitizer) and PPO (annihilator). (f) UC emission spectra of the $CsPbBr_3$-NCA/PPO with varying excitation power densities. (g) Integrated UC emission intensities as a function of the excitation power density. (b) Reproduced and modified with permission.[20] Copyright 2006, American Chemical Society; (d) Reproduced and slightly modified with permission.[22] Copyright 2009, American Chemical Society; (e–g) Reproduced with permission.[32] Copyright 2019, American Chemical Society.

forms excimer at high concentration, and the triplet energy level of PPO is too high to be sensitized by $Ir(C6)_2(acac)$. Therefore, novel annihilators have been required to develop systems that exhibit high UC efficiency and low I_{th}. On the other hand, 1,4-TIPS-Nph has a low enough triplet energy ($T_1 \approx 2.1$ eV) to be sensitized by $Ir(C6)_2(acac)$, thanks to the effective conjugation through the TIPS-ethynyl groups. By irradiating a mixed THF solution of 1,4-TIPS-Nph/$Ir(C6)_2$-(acac) with a 445 nm cw laser, a prominent UC emission from 1,4-TIPS-Nph was observed in the UV region ($\lambda_{em} =$ 372 nm, Figure 5b). The TTA-UC efficiency η_{UC} reached 20.5 %, updating the maximum TTA-UC efficiency of the previously reported vis-to-UV TTA system by more than two times (Figure 5c). In addition, the obtained I_{th} of 1.1 mW cm^{-2} with 300 μM of the sensitizer was lower than the solar irradiance of 1.4 mW cm^{-2} for the wavelength range of 445 ± 5 nm (Figure 5d). The production of upconverted UV light with weak light sources such as solar simulator and room LED was also demonstrated (Figure 5e).

The discovery of 1,4-TIPS-Nph in 2020 led to several reports of systems exceeding 20 % TTA-UC efficiency.[42,46,48,52] In 2022, Yanai et al. reported the first heavy metal-free vis-to-UV TTA-UC efficiency with over 20 % UC efficiency using a ketocoumarin derivative (CBDAC) as a heavy metal-free sensitizer (Figure 6a),[48] more than doubling the previous highest value of 8.2 %.[38] It is widely known that chromophores with carbonyl groups such as benzophenone exhibit high ISC efficiency Φ_{ISC} due to their large spin-orbit interaction even without heavy metals based on the El-sayed rule.[22,60] Ketocoumarins have also been used in TTA-UC in the visible range as heavy metal-free triplet sensitizers with these characteristics.[62] Among ketocoumarin derivatives, CBDAC exhibits a large absorption coefficient in the visible region and a small absorption coefficient in the UV region similar to $Ir(C6)_2$-(acac), and has been reported to exhibit a Φ_{ISC} as high as 92 % in benzene.[59,61–63] A UC emission maximum was observed at $\lambda_{em} = 373$ nm by irradiating a deaerated toluene solution of CBDAC and 1,4-TIPS-Nph with a 445 nm laser (Figure 6b). The obtained η_{UC} was 20.3 %, which is comparable to the η_{UC} with $Ir(C6)_2(acac)$ (Figure 6c).

In the same year, Albinsson et al. achieved a higher η_{UC} of 26.2 % using 4CzBN, a heavy metal-free TADF sensitizer showing high Φ_{ISC} of 89 % in toluene (Figure 6d).[46] This value is the highest value of the current heavy metal-free vis-to-UV TTA-UC. Since the UC spectral shape and peak intensity are affected by a secondary inner filter effect at the high energy end of the spectrum caused by the overlap of UC emission and sample absorption,[55] they corrected for this reabsorption effect and estimate the generated UC

© 2023 Wiley-VCH GmbH

15213773, 2023, 25, Downloaded from https://onlinelibrary.wiley.com/doi/10.1002/anie.202301506 by Universitätsbibliothek Mainz, Wiley Online Library on [15/04/2025]. See the Terms and Conditions (https://onlinelibrary.wiley.com/terms-and-conditions) on Wiley Online Library for rules of use; OA articles are governed by the applicable Creative Commons License

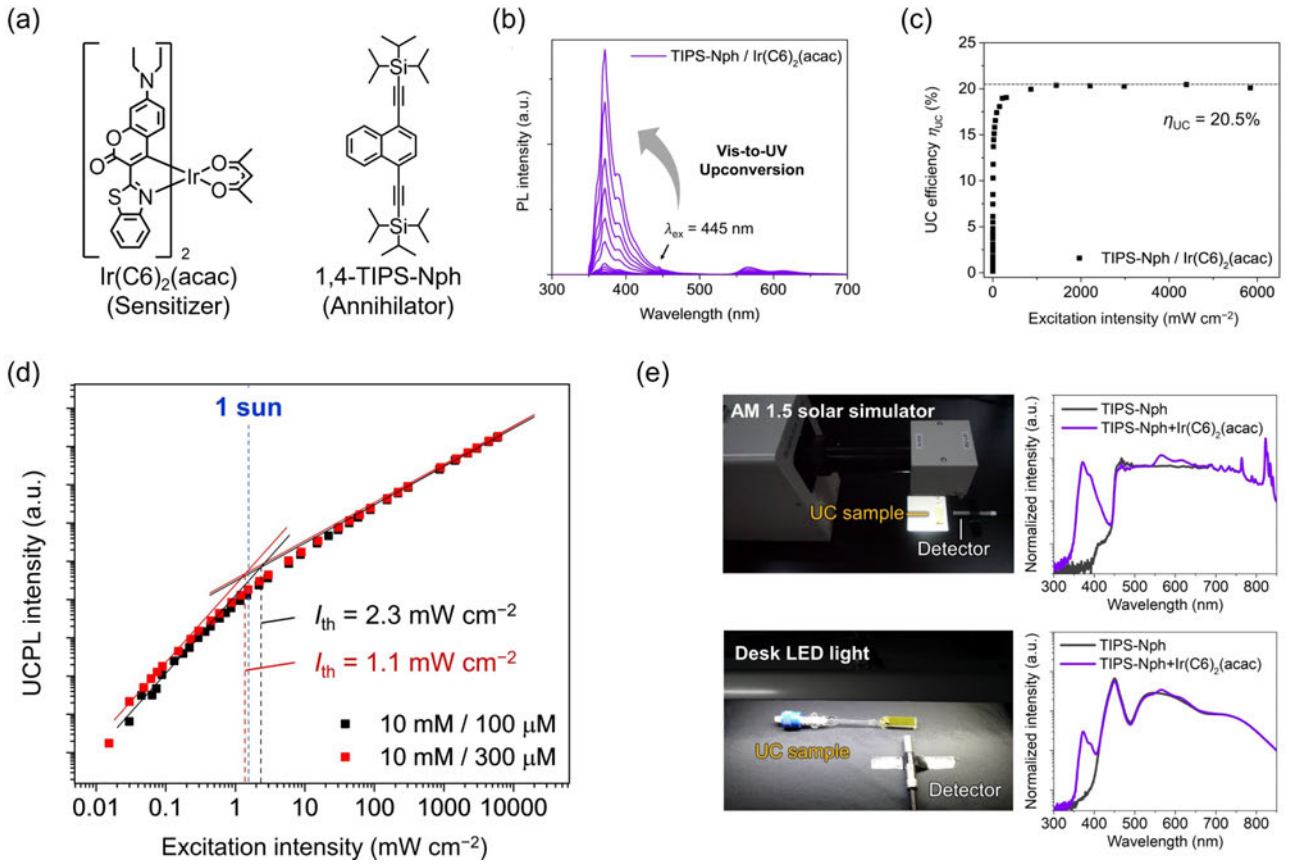

Figure 5. (a) Molecular structures of $Ir(C6)_2(acac)$ (sensitizer) and 1,4-TIPS-Nph (annihilator). (b) UC emission spectra of the $Ir(C6)_2(acac)$ and 1,4-TIPS-Nph in deaerated THF at various excitation light intensities from 0.030 mW cm^{-2} to 5.8 W cm^{-2} (λ_{ex} = 445 nm). (c) η_{UC} of $Ir(C6)_2(acac)$ and 1,4-TIPS-Nph in deaerated THF at various excitation light intensities of the 445 nm laser. (d) Excitation intensity dependence of UC emission intensity. Blue line indicates the intensity of sunlight (1.4 mW cm^{-2} for 445 ± 5 nm). (e) UC emission spectra of the $Ir(C6)_2(acac)$ and 1,4-TIPS-Nph under AM 1.5 solar simulator or desk LED light. (a–e) Reproduced with permission.[39] Copyright 2020, Wiley-VCH GmbH.

quantum yield ($\Phi_{UC,g}$, 50 % theoretical limit) (Figure 6e). The reabsorption correction gave a $\eta_{UC,g}$ of 33.6 %, which corresponds to $2\Phi_{UC,g}$ (Figure 6f). Interestingly, this reabsorption correction unveils the significantly high f value of 54 % for 1,4-TIPS-Nph, confirming the promising potential 1,4-TIPS-Nph as the TTA-UC UV emitter.

In addition, Yang et al. also achieved a high η_{UC} of 21.4 % by using multi-resonance TADF (MR-TADF) molecule as a sensitizer.[42] Common TADF molecules have a highly twisted structure of electron donor and acceptor groups, which causes large vibrational coupling and vibrational relaxation.[84] On the other hand, MR-TADF molecules, originally proposed by Hatakeyama et al.,[85] consist of a boron/nitrogen (B/N)-based polycyclic framework and can achieve small Stokes shifts and extremely sharp absorption/emission due to the conflicting resonance effects of B and N atoms. Yang et al. developed a novel MR-TADF sensitizer denoted as BN-Se (Figure 6g), in which a Se atom is embedded in the 4,4′-diazaboroline (N/B/N) framework to achieve a high Φ_{ISC} of 88 % in toluene due to the heavy atom effect. Similar to the concept of $Ir(C6)_2(acac)$, BN-Se exhibits a large absorption coefficient in the visible region and a small absorption coefficient in the UV region. When combined with 1,4-TIPS-Nph, these characteristics of BN-Se resulted in a high TTA-UC efficiency of more than 20 % (Figure 6h). Under conditions with higher sensitizer concentrations, although the η_{UC} was reduced to 16.5 % due to a slight triplet back energy transfer from the annihilator to the sensitizer and reabsorption of UC emission, a significantly low I_{th} of 1.3 mW cm^{-2}, comparable to solar irradiance, was obtained (Figure 6i). The reported examples of vis-to-UV TTA-UC systems are summarized in Table 1, and yearly η_{UC} improvement is plotted in Figure 7a. For about 14 years since 2006, it had been difficult to achieve a high TTA-UC efficiency, but the discovery of the key 1,4-TIPS-Nph in 2020 made it possible to realize a vis-to-UV TTA-UC system with η_{UC} exceeding 20 % (Figure 7a).[39,42,46,48,52] In addition, it became clear that the use of appropriate sensitizers with large absorption coefficients in the visible region and small absorption coefficients in the UV region is crucial to achieve both η_{UC} above 20 % and low I_{th} equivalent to solar irradiance (< 10 mW cm^{-2}) (Figure 7b).[39]

3.3. Large UC Spectral Shift

Thanks to the development of new annihilators with low T_1, vis-to-UV TTA-UC systems with larger UC spectral shift

© 2023 Wiley-VCH GmbH

15213773, 2023, 25, Downloaded from https://onlinelibrary.wiley.com/doi/10.1002/anie.202301506 by Universitätsbibliothek Mainz, Wiley Online Library on [15/04/2025]. See the Terms and Conditions (https://onlinelibrary.wiley.com/terms-and-conditions) on Wiley Online Library for rules of use; OA articles are governed by the applicable Creative Commons License

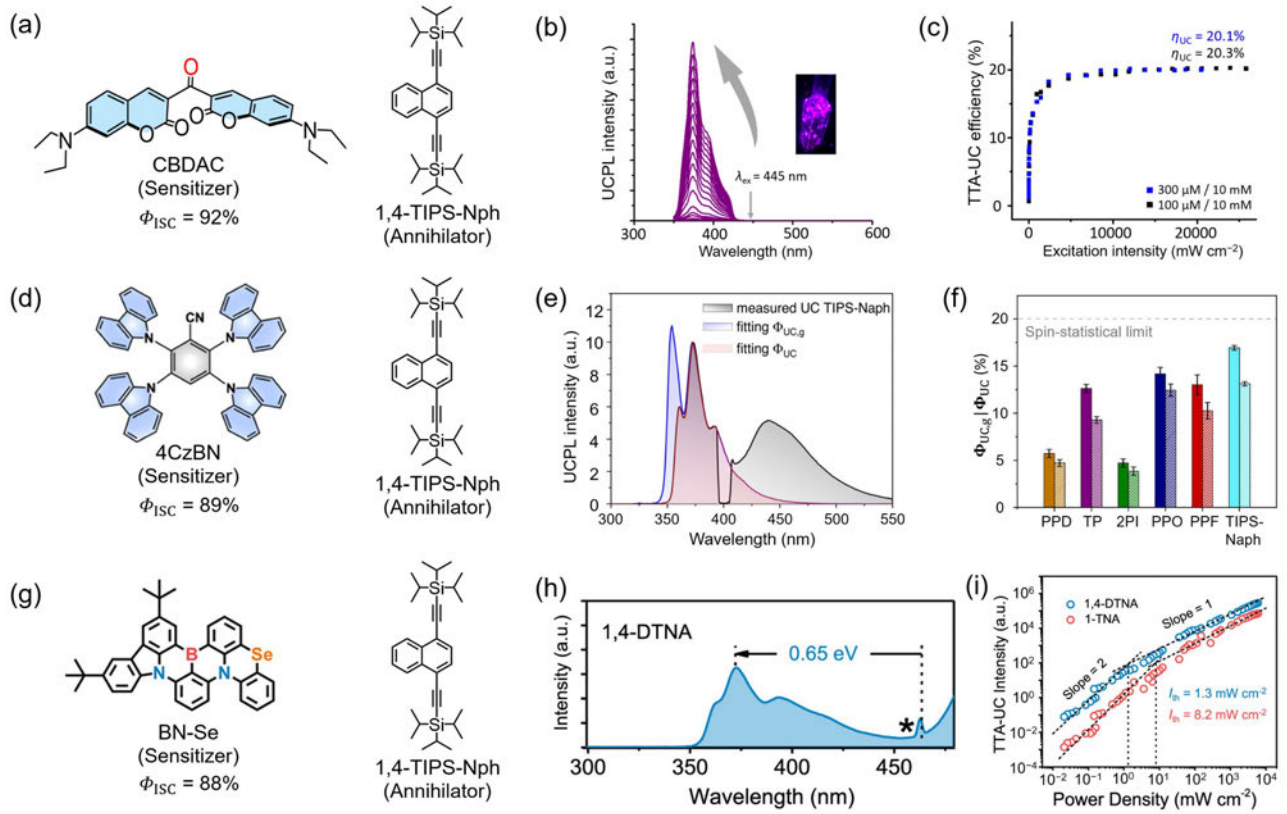

Figure 6. (a) Molecular structures of CBDAC (sensitizer) and 1,4-TIPS-Nph (annihilator). (b) UC emission spectra of the CBDAC/1,4-TIPS-Nph in deaerated toluene at various excitation light intensities from 1.3 mW cm^{-2} to 25.8 W cm^{-2} (λ_{ex} = 445 nm). (c) η_{UC} of CBDAC/1,4-TIPS-Nph in deaerated toluene at various excitation light intensities of the 445 nm laser. (d) Molecular structures of 4CzBN (sensitizer) and 1,4-TIPS-Nph (annihilator). (e) UC emission spectra of the 4CzBN/1,4-TIPS-Nph in deaerated toluene (λ_{ex} = 405 nm). (f) Internal (solid) and external (striped) UC quantum yields for each annihilator when paired with 4CzBN. Standard deviations based on the results of three independent samples are indicated by black error bars. (g) Molecular structures of BN-Se (sensitizer) and 1,4-TIPS-Nph (annihilator). (h) UC emission spectrum of the BN-Se/1,4-TIPS-Nph in deaerated toluene (λ_{ex} = 464 nm). (i) Excitation light intensity dependence of UC emission intensity of the BN-Se/1,4-TIPS-Nph. (a–c) Reproduced with permission.[48] Copyright 2022, The Royal Society of Chemistry; (d–f) Reproduced and modified with permission.[46] Copyright 2022, American Chemical Society; (g–i) Reproduced and modified with permission.[42] Copyright 2022, American Chemical Society.

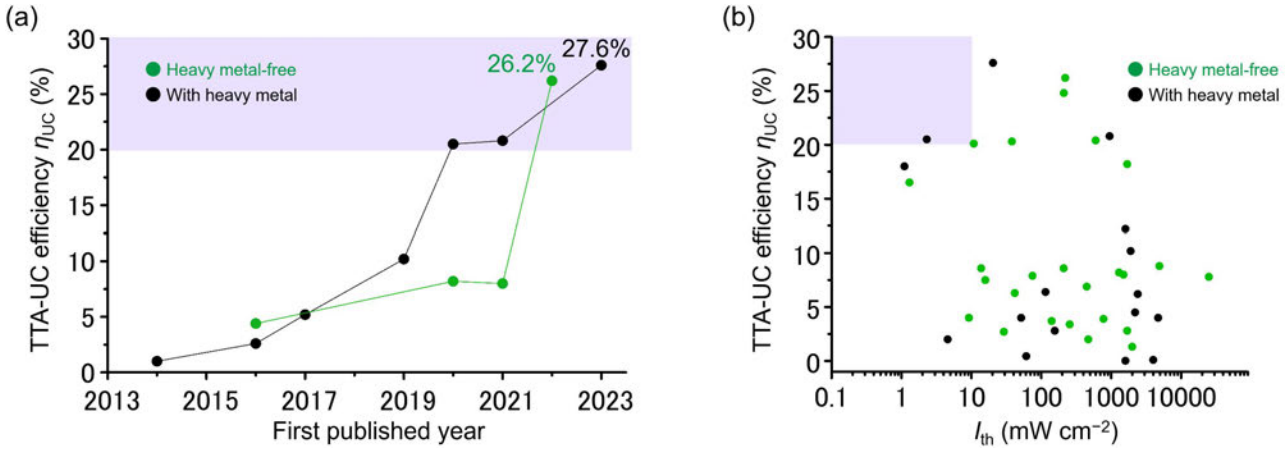

Figure 7. (a) Record η_{UC} value of vis-to-UV TTA-UC to date. (b) Summary of η_{UC} against I_{th} reported to date.

have been achieved.[41–43,49] Yanai et al. demonstrated a green-to-UV TTA-UC system using perovskite nanocrystals (PNCs) as a sensitizer (Figure 8a, b).[41] The energy loss due to the ISC from S_1 to T_1 of common sensitizer molecules makes it difficult to realize TTA-UC with large UC spectral shifts from wavelengths above 500 nm to the UV region. To

© 2023 Wiley-VCH GmbH

15213773, 2023, 25, Downloaded from https://onlinelibrary.wiley.com/doi/10.1002/anie.202301506 by Universitatsbibliothek Mainz, Wiley Online Library on [15/04/2025]. See the Terms and Conditions (https://onlinelibrary.wiley.com/terms-and-conditions) on Wiley Online Library for rules of use; OA articles are governed by the applicable Creative Commons License

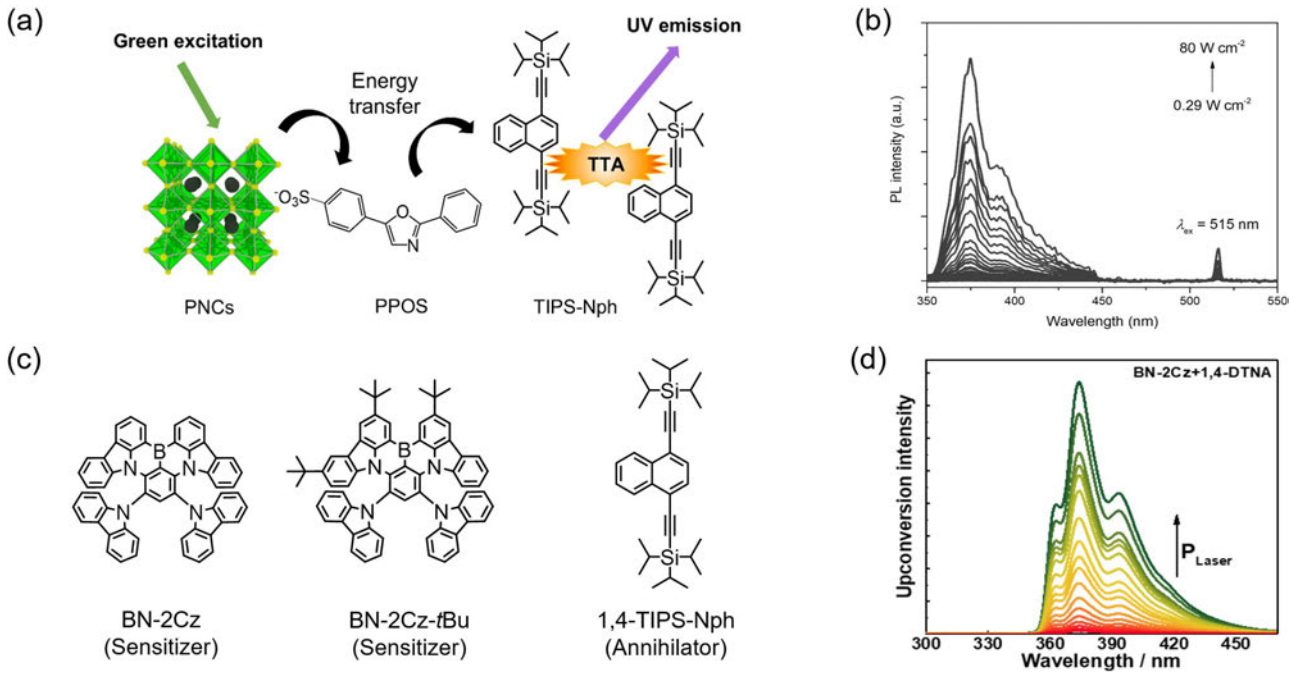

Figure 8. (a) Molecular structures of PNCs (sensitizer), PPOS (transmitter), and 1,4-TIPS-Nph (annihilator). (b) UC emission spectra of PNCs/PPOS/1,4-TIPS-Nph at different excitation light intensity in deaerated toluene from 0.29 W cm^{-2} to 80 W cm^{-2} (λ_{ex} = 445 nm). (c) Molecular structures of BN-2Cz, BN-2Cz-*t*Bu (sensitizer) and 1,4-TIPS-Nph (annihilator). (d) UC emission spectra of BN-2Cz/1,4-TIPS-Nph at different excitation light intensity in deaerated toluene (λ_{ex} = 517 nm). (a, b) Reproduced with permission.[41] Copyright 2021, The Royal Society of Chemistry; (d) Reproduced with permission.[49] Copyright 2022, Chinese Chemical Society.

circumvent this energy loss, inorganic semiconductor nanocrystals with small ΔE_{ST}, such as quantum dots and PNCs, have recently been employed as next-generation triplet sensitizers.[30,32,34,40,41,43,45] The same group has reported the first example of TTA-UC sensitized by PNCs.[86] Subsequently, various vis-to-UV TTA-UC systems using PNCs as sensitizers were reported, but the examples have been limited to excitation by blue light with wavelengths below 500 nm.[32,34] This is due to the lack of suitable transmitters that can receive triplet energy from green light-absorbing PNCs with small energy loss and annihilators with lower triplet energy level. They found that ionic transmitter (2-phenyloxazol-5-yl)benzenesulfonate (PPOS)[36] can bind to PNC surface and receive triplet energy from green light-absorbing PNC. The combination of PNC-PPOS with 1,4-TIPS-Nph formed an energy cascade suitable for TTA-UC from green to UV (Figure 8a). Under excitation by a 515 nm laser, a deaerated toluene solution of PNCs, P_{66614}PPOS and 1,4-TIPS-Nph showed an UC emission at 375 nm with a large UC spectral shift of 0.90 eV (Figure 8b).

Yang et al. have reported green-to-UV TTA-UC by using MR-TADF sensitizers BN-2Cz and BN-2Cz-*t*Bu (Figure 8c).[49] The small energy loss ΔE_{ST} in the ISC process of the MR-TADF sensitizers is beneficial to enlarge the UC spectral shift. By combining the MR-TADF sensitizer with the annihilator with low triplet energy level, 1,4-TIPS-Nph, green-to-UV TTA-UC with a large energy gain of 0.91 eV and a high η_{UC} of 8.6 % was achieved (Figure 8d).

3.4. Vis-to-UVB TTA-UC Systems

The high photon energy (4.43–3.94 eV) of UVB light (280–315 nm) has been used in traditional photochemistry for activating solvents or highly inert compounds.[87] Since then, it has become a crucial part in many other applications such as pollutant degradation[2,3] and disinfection,[88] which have become essential tasks in our modern life. Yet, with the direct usage of UVB photons, two problems arise: (i) the solar spectrum drops sharply in the UVB region, and LEDs cannot readily produce UVB photons in an efficient and sustainable manner (Figure 9 upper graph). Conventional UVB sources such as mercury lamps,[9] excimer-based lamps,[10] or the high-energy tail of xenon arc lamps[2] have relatively short lifetimes and efficiencies in converting electricity into UVB radiation that approach zero. (ii) Traditional laboratory glassware is non-transparent for UVB irradiation; hence more expensive quartz glass is necessarily required. TTA-UC could offer a solution to generating UVB emission by pooling the energy of two visible photons in a mild and potentially more efficient way. However, most known UV annihilators emit within the UVA range (315–400 nm, see Table 1 and Figure 3) as illustrated with the popular annihilators 1,4-TIPS-Nph and PPO (lower part of Figure 9), which is insufficient for most of the above-mentioned applications.

To this day, the emission spectra of only a few annihilators approach or exceed the UVB/UVA border, which corresponds to excited-state singlet energies of the annihilators on the order of 4 eV. In 2020 Wenger and

© 2023 Wiley-VCH GmbH

15213773, 2023, 25, Downloaded from https://onlinelibrary.wiley.com/doi/10.1002/anie.202301506 by Universitätsbibliothek Mainz, Wiley Online Library on [15/04/2025]. See the Terms and Conditions (https://onlinelibrary.wiley.com/terms-and-conditions) on Wiley Online Library for rules of use; OA articles are governed by the applicable Creative Commons License

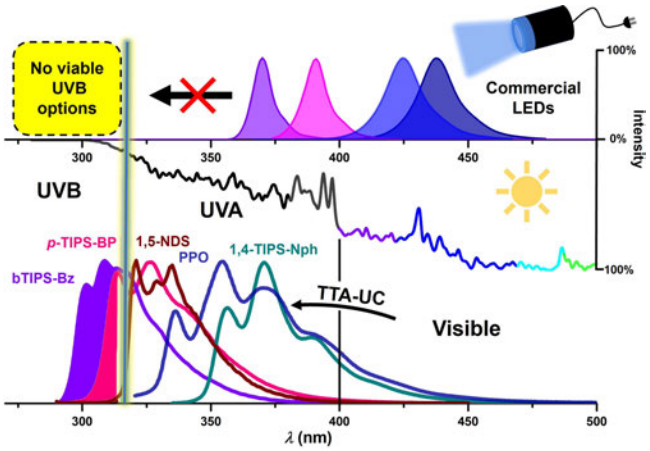

Figure 9. Upper graph: Emission spectra of typical commercially available LEDs and the solar irradiance. Lower graph: Emission spectra of prominent UVA annihilators and the novel UVB annihilators *p*-TIPS-BP and bTIPS-Bz recorded in strongly diluted solutions.

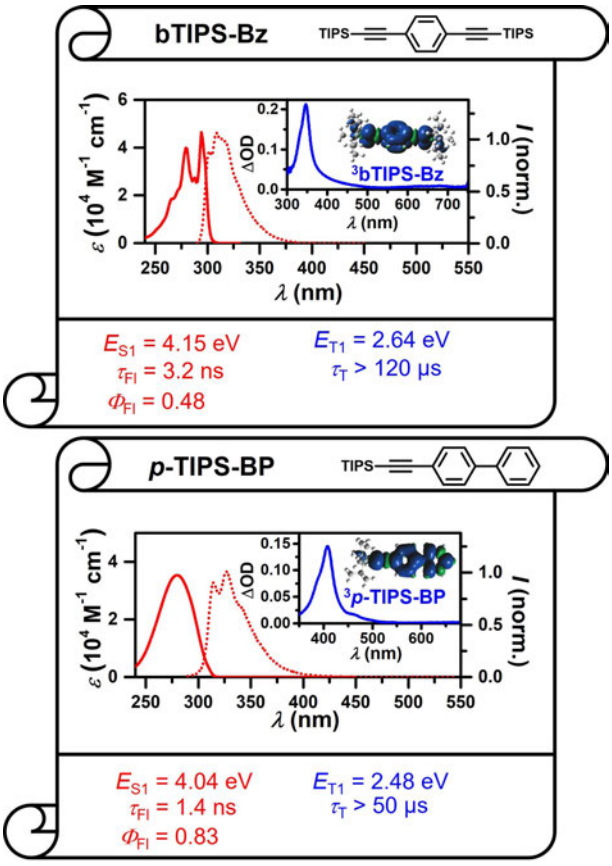

Figure 10. "Fact sheets" of the UVB annihilators bTIPS-Bz and *p*-TIPS-BP, including ground state and triplet-triplet absorption spectra, emission spectra, excited-state energies and lifetimes as well as the fluorescence quantum yields.

Kerzig introduced a water-soluble naphthalene annihilator with two sulfonate groups (1,5-NDS) with a singlet energy of 3.9 eV and an emission maximum at 321 nm nearing the UVB/UVA border (315 nm).[5] The annihilator properties of 1,5-NDS were already observed in 2014, but the identification of a suitable sensitizer was challenging owing to the inherent difficulties of UC in water.[5,82] A different naphthalene-derived annihilator (2,6-di-*tert*-butylnaphthalene) was used by Murakami et al. in combination with an acridone triplet sensitizer yielding quite intense upconverted emission down to the <330 nm region.[38] Following this, a novel UC system comprising ZnSe/ZnS core/shell QDs with carboxylated biphenyl as triplet mediator and the very same naphthalene annihilator was developed by Wu et al..[45] In 2022, Albinsson et al. combined the TADF emitter 4CzBN with a high triplet energy (2.7 eV) with several annihilators. Among them, PPD derived from PPO (see Figure 3 for the structures) was identified as a novel annihilator compound with a singlet energy as high as 3.99 eV, which resulted in a vis-to-UV UC scheme showing minor UVB emission.[46] In the same year, Zähringer, Bertrams and Kerzig reported on a biphenyl-based annihilator with a singlet-excited state energy of 4.04 eV, providing evident emission in the UVB.[50] A single substitution in the *para* position with a TIPS-ethynyl group was sufficient to decrease its triplet energy, which allowed blue light-driven (447 nm) vis-to-UV upconversion. The prototypal TADF emitter 4CzIPN was employed making it a purely organic UC system with promising UC quantum efficiencies of ~8%. The main photophysical properties of the annihilator are summarized in Figure 10. Very recently, Yanai and Kerzig introduced a novel benzene-derived annihilator that is pushing the limits of vis-to-UV upconversion. Strong UVB emission with an exceptional singlet-excited energy of 4.15 eV was observed (Figures 9 and 10).[7] Not only was UC achievable with blue light (spectral shift of 1.13 eV) but the high singlet state energy was also exploited in subsequent bond activations of inert substances (see chapter 4 for details) demonstrating the usefulness of TTA-UC in the context of high-energy chemistry. Once again, the favorable properties originate from the TIPS-ethynyl groups lowering the triplet energy of benzene to 2.64 eV, while maintaining a very high singlet energy. Although some effort has been put into understanding the role of substituents on the annihilator scaffold, it is still not fully understood why TIPS-ethynyl is so beneficial.[7,50] A deeper understanding of the influence of such alkylsilyl-substituents and their optimization could accelerate the development of even better annihilators. Ideally, the annihilator molecule should be as small as possible to allow for fast diffusion (i.e. by using short alkyl groups connected to the silicon atom), while maintaining sufficient steric bulkiness to prevent excimer formation.[89,90] Alterations on the alkyl chain seemingly do not affect the electronic properties, as a comparison of naphthalenes with TMS[44] and TIPS[39] groups (compare, Figure 3) and comparative DFT calculations on benzene derivatives[7] indicate. The quantum efficiency of the only blue-to-UVB UC system (bTIPS-Bz and 4CzIPN) was rather moderate with 2%, which is most likely due to unproductive back-TET to the sensitizer ground state. In principle, this could be greatly improved by using sensitizers with higher triplet energies. However, the lack thereof becomes noticeable when triplet

© 2023 Wiley-VCH GmbH

15213773, 2023, 25, Downloaded from https://onlinelibrary.wiley.com/doi/10.1002/anie.202301506 by Universitätsbibliothek Mainz, Wiley Online Library on [15/04/2025]. See the Terms and Conditions (https://onlinelibrary.wiley.com/terms-and-conditions) on Wiley Online Library for rules of use; OA articles are governed by the applicable Creative Commons License

sensitizers above 2.7 eV are required that still absorb in the visible region.[91] With that prerequisite, the group of Wenger developed a novel sensitizer with a triplet energy as high as 2.99 eV that readily absorbs violet light (405 nm).[92] Its potential was demonstrated in combination with 4,4′-di-*tert*-butyl-biphenyl as the annihilator showing deep UVB emission and an exceptional singlet energy of 4.25 eV. The overall UC quantum yield was likely too low to be employed in any kind of chemical reaction or application. However, these promising results will certainly stimulate further interest in the development of novel organic and metal-based sensitizers for TTA-UC.

Moreover, the excited state reduction and oxidation potentials of the singlet-excited annihilators are much underexplored, and further studies might expand the scope of UC-driven electron transfer chemistry substantially (see chapter 4 for electron transfer applications). So far, mainly PPO as UVA annihilator has been used as an electron donor or acceptor in such photoredox reactions.[25,93] It seems natural to assume that higher photoredox reactivities, which are estimated from excited-state oxidation or reduction potentials, are within reach when UVB annihilators with concomitantly higher excited-state energies are employed. The photoredox activity of the basic annihilator structure under study can also be tuned in either direction by altering the substitution pattern. For instance, unsubstituted naphthalene has an excited-state oxidation potential of −2.3 V vs SCE.[66] A modification with electron-donating groups as for naproxen (NPX) increases that potential substantially to −2.7 V vs SCE[5] (see chapter 4 for further details). The high singlet-excited state energies of benzene- and biphenyl-derived annihilators imply high excited-state reduction/oxidation potentials, which could be exploited in challenging photoredox chemistry in an elegant manner. We believe that the recent progress of UC systems with very high annihilator singlet-state energies will trigger the development of optimized systems for various energy-demanding applications.

3.5. Vis-to-UV TTA-UC in Films

For practical applications of vis-to-UV TTA-UC, it is important to develop not only solution systems but also film systems. In 2016, Ma et al. reported TTA-UC films composed of Ir(ppy-DBP) and 2,7-DBP.[26] As matrix, polyurethane was employed due to its favorable mechanical and optical properties as well as its suitable processability.[94] In general, diffusion is restricted in film systems, which greatly inhibits the energy transfer from sensitizer to annihilator and the TTA process compared to solution systems.[94–97] To overcome this issue, they designed a bichromophoric sensitizer by conjugating an organic annihilator and an Ir complex to generate long-lived triplet excitons via intramolecular energy transfer (intra-TET) (Figure 11a). In such bichromophoric scaffolds, not only a triplet lifetime expressed by a reversible intra-TET,[98–106] but the triplet energy levels of a donor and acceptor can also be independently tuned. They found that the sensitization capability in films is highly sensitive to the linker joining the Ir complex and the acceptor group, and that bichromophoric sensitizer with shorter donor-acceptor spacers give more favorable TTA results. UC emission derived from 2,7-DBP in the UV region with a η_{UC} of 2.6 % was obtained by excitation with a 450 nm Xe lamp (Figure 11b, c).

Murakami et al. have reported a vis-to-UV TTA-UC film composed of CBDAC as the sensitizer and PPO as the annihilator (Figure 11d).[51] The control of the temperature gradient on the surface enables formation of a bicomponent polycrystalline organic film from a melt of a sensitizer/annihilator blend (Figure 11e). By irradiating the UC film with a laser light at 440 nm, an UC emission peaked at 390–393 nm was observed with a η_{UC} of 8.6 % and high photostability of more than 100 hours under atmospheric conditions. In addition, a low I_{th} corresponding to about 0.3 sun was obtained under broadband light generated by a solar simulator (AM1.5 spectrum with a 413 nm long-pass filter) (Figure 11f).

Recently, Yanai et al. developed a porous film impregnation method where an upconverting low-volatile solution is introduced into a porous film.[52] Impregnating a porous film with a sponge structure with UC solution is a very simple and general method, and highly transparent films are easily formed. They sandwiched a sponge-structured porous film impregnated with hexyl benzoate containing the UC chromophores 1,4-TIPS-Nph and $Ir(C6)_2(acac)$ between quartz substrates and sealed it in a glove box (Figure 11g). The resulting UC film with high transparency maintained good performance of bulk solution and exhibited the highest η_{UC} of 27.6 % in film systems (Figure 11h, i). The higher η_{UC} of the film than that of bulk solution in hexyl benzoate (16.7 %) is reasonable, considering the less reabsorption in the thinner sample geometry. The η_{UC} value of the film approaches the previously-reported generated UC efficiency $\eta_{UC,g}$ of 33.6 % which was calculated by reabsorption correction of the experimental value (26.2 %).[46] Taking advantage of the fact that the film created by the porous film impregnation method can be combined with any substrate, they have succeeded in utilizing even weaker light by combining it with a microlens array (MLA) (Figure 11j). Polymer lens arrays and microcavities have been used to reduce the excitation light intensity required to obtain UC.[107–110] When the obtained UC film was combined with the MLA, the UC film's I_{th} value became too low to determined and should be lower than 0.60 mW cm^{-2} (0.43 sun) (Figure 11k). Solutions showing vis-to-UV TTA-UC, which have been studied extensively, are not easy to combine with MLAs. The porous film impregnation method can easily produce a UC film while maintaining the high TTA-UC efficiency of the solution and can be combined with MLAs to utilize the light of subsolar intensity.

4. Chemical Applications of Vis-to-UV TTA-UC

The large amount of energy stored in a singlet-excited state of a UV annihilator enables various chemical applications driven by UC. Not only are the reaction conditions

© 2023 Wiley-VCH GmbH

15213773, 2023, 25, Downloaded from https://onlinelibrary.wiley.com/doi/10.1002/anie.202301506 by Universitätsbibliothek Mainz, Wiley Online Library on [15/04/2025]. See the Terms and Conditions (https://onlinelibrary.wiley.com/terms-and-conditions) on Wiley Online Library for rules of use; OA articles are governed by the applicable Creative Commons License

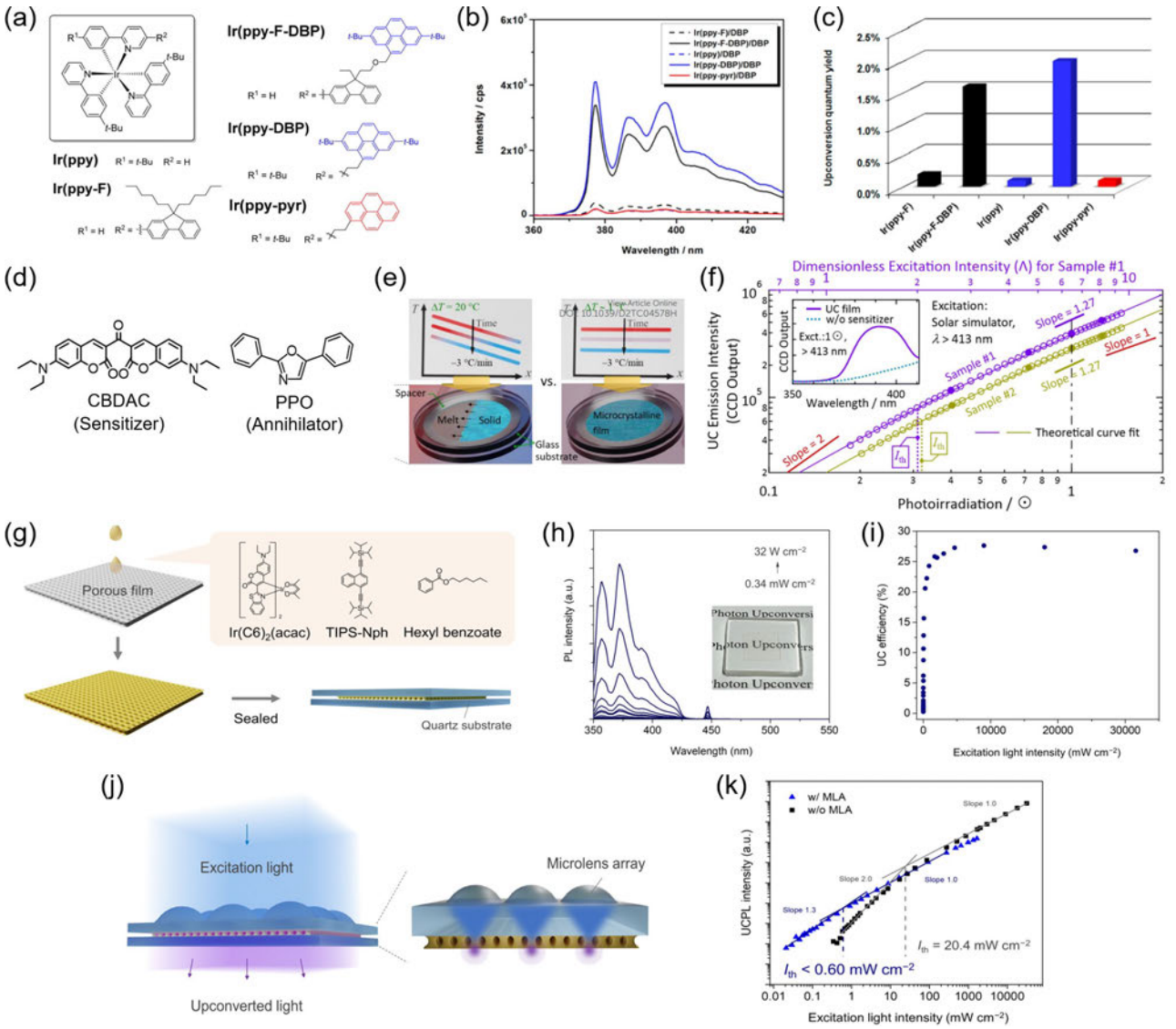

Figure 11. (a) Molecular structures of Ir^{III} complexes (sensitizer). (b) UC emission spectra and (c) UC efficiency of 2,7-DBP mixed with different sensitizers in deaerated toluene ($\lambda_{ex}=450$ nm). (d) Molecular structures of CBDAC (sensitizer) and PPO (annihilator). (e) Schematic illustration of CBDAC/PPO neat film formation under a controlled temperature gradient. (f) Dependence of the UC emission intensity on the irradiance (in unit of sun, ⊙) of simulated sunlight, which passed through a $\lambda > 413$ nm long-pass filter placed above the sample. (g) Schematic illustration of porous film impregnation method using $Ir(C6)_2(acac)$/1,4-TIPS-Nph, and hexyl benzoate as a solvent. (h) UC emission spectra of the film at various excitation light intensities from 0.34 mW cm^{-2} to 32 W cm^{-2} ($\lambda_{ex}=445$ nm). Inset is a photograph of the film sealed between quartz substrates. (i) UC efficiencies of the porous film containing $Ir(C6)_2(acac)$/1,4-TIPS-Nph solution in different excitation light intensities ($\lambda_{ex}=445$ nm). (j) Schematic illustration of integrating a porous film with a microlens array (MLA). (k) UCPL intensities at 372 nm of the film integrated with a microlens array (w/MLA, blue triangle) and without a microlens array (w/o MLA, black square) at different excitation intensities ($\lambda_{ex}=445$ nm). (a–c) Reproduced and modified with permission.[26] Copyright 2016, American Chemical Society; (e, f) Reproduced with permission.[51] Copyright 2023, The Royal Society of Chemistry; (g–k) Reproduced and slightly modified under CC BY-NC-ND 4.0 license.[52]

inherently milder compared to direct UV excitation, but the TTA-UC approach also offers additional advantages.[111,112] First, affordable visible-light sources[113] excite the UC system more selectively than UV light sources could excite a target molecule in a complex mixture of an application-related system. Second, visible photons driving the UC mechanism penetrate deeper into the sample than UV photons used for conventional (i.e. direct) photochemical mechanisms. Third, the two-photon nature of TTA-UC allows precise spatial control such that the excited annihilator singlets are produced exactly where they are required while operating with non-coherent low-power light sources. The following two examples relying on visible light from focused cw light sources demonstrate this behavior. Vis-to-UV TTA-UC was very recently exploited for (i) three-dimensional nanolithography based on two-photon acrylate polymerization with the famous PPO annihilator[53] and (ii) to release the bright fluorescence probe fluorescein from a non-emissive *o*-nitrobenzyl cage. Selective uncaging oc-

© 2023 Wiley-VCH GmbH

15213773, 2023, 25, Downloaded from https://onlinelibrary.wiley.com/doi/10.1002/anie.202301506 by Universitätsbibliothek Mainz, Wiley Online Library on [15/04/2025]. See the Terms and Conditions (https://onlinelibrary.wiley.com/terms-and-conditions) on Wiley Online Library for rules of use; OA articles are governed by the applicable Creative Commons License

curred almost one centimeter below the sample surface using a PPO-containing UC micelle.[47]

These beneficial properties of vis-to-UV UC systems have already been used for several chemical applications, which we categorize into three types: (I) photocatalysis, (II) bond activation, and (III) photopolymerization[49,53,114] (e.g. for 3D printing)[115] or photoligation[49] reactions. Both small molecule activation via photoredox[5,25,116] or energy transfer[6,7] catalysis and photocatalytic hydrogen generation[4,117] fall into category (I). We use the term bond activation (II) in a broader sense, including the decomposition of persistent pollutants,[5,118] photo-switching[119–121] and photo-uncaging.[47] Key advantages of vis-to-UV TTA-UC and application examples are summarized in Figure 12.

Some of the above-mentioned applications were carried out with DPA[119,121] or related anthracene-based[114–118,120] annihilators that emit at the blue edge of the visible spectrum. However, we included these examples as we are confident that even more versatile applications within these categories will result in the near future, owing to the recent UV annihilator development summarized herein. In this chapter, we will highlight selected application examples and discuss mechanistic possibilities for the UC-related key steps.

Many studies employing vis-to-UV TTA-UC focus on the feasibility of novel applications without analyzing how the UC systems interact with the molecules, substrates, catalysts or materials that are important for the new function or application. There is often no mechanistic guess or merely a (sometimes) speculative differentiation between energy (EnT) or electron transfer (ET) interactions with the excited annihilator.[93] However, a deeper mechanistic understanding would strongly facilitate the optimization of vis-to-UV UC systems for a given application. Rather than extensively presenting examples for the applications summarized in Figure 12, we describe and compare the different mechanistic scenarios (Figure 13), which are more diverse than the simplified EnT or ET pathways. For that, we selected studies that are either characterized by a rather obvious mechanism or supported by detailed mechanistic and spectroscopic investigations. The term *substrate* (S), which is common in

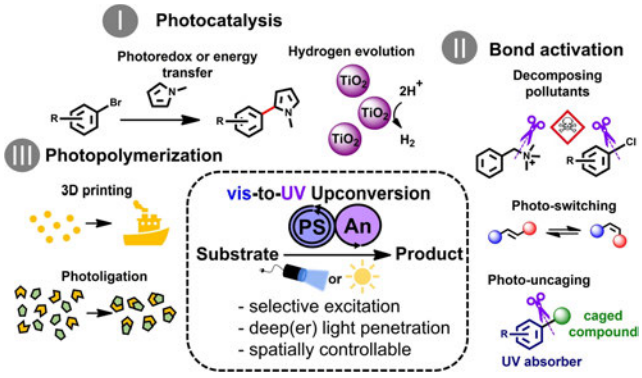

Figure 12. Schematic illustration of various applications that are initiated by vis-to-UV upconversion and key advantages of this methodology.

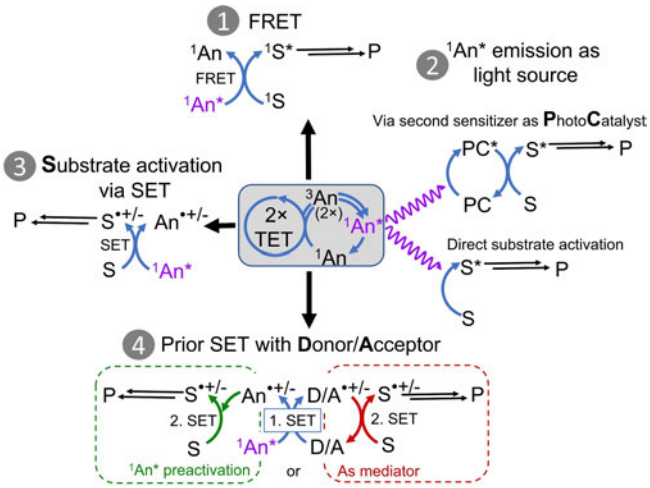

Figure 13. Possible reaction mechanisms triggered by vis-to-UV TTA-UC. The annihilator singlet serves as an energy donor in energy transfer processes (radiative and non-radiative) or it participates in electron transfer of a substrate (S) to yield a product (P). See text for details and abbreviations.

photocatalysis, is used throughout Figure 13, but we stress that, depending on the application, it has to be replaced by e.g. monomer, pollutant, photoswitch or photocage.

Pathways (1) and (2) can be classified as EnT, whereas mechanisms (3) and (4) operate through a single-electron transfer (SET) starting from the singlet-excited annihilator ^{1}An*. EnT between ^{1}An* and a suitable energy acceptor can in principle occur through a non-radiative Förster resonance energy transfer (FRET, pathway (1)) or via a radiative emission-reabsorption sequence (mechanism (2) in Figure 13).[7,122,123] Depending on the application, the energy acceptor is either the substrate itself[7] or a secondary absorber acting as a catalyst[4,121] or photoinitiator. In a solution containing ^{1}An* *and* the energy acceptor at rather high concentrations, pathways (1) and (2) are equally feasible, but most prior studies do not solve this mechanistic ambiguity. A straightforward selection method is provided by Stern–Volmer quenching studies of the spectral UC emission, as recently described by Yanai, Kerzig et al.[7] For a pure FRET (1), the whole ^{1}An* emission spectrum is quenched with Stern–Volmer-like kinetics, while under conditions with mechanism (2) being dominant, the ^{1}An* emission in the region of the substrate absorption is reabsorbed only.

To optimize mechanism (2), in which vis-to-UV UC is employed as light source, the overall UC efficiency needs to be as high as possible. Furthermore, the "substrate" or photocatalyst should absorb most of the UC photons. This condition usually requires a pronounced spectral overlap in combination with a high substrate concentration or a long optical pathlength for this reabsorption step of the radiative EnT (compare, Beer–Lambert law). In contrast, for the UC-FRET reaction sequence to be efficient, a high ^{1}An* generation yield through TTA-UC is essential but the annihilator emission quantum yield does not necessarily need to be high. A precondition for the non-radiative

© 2023 Wiley-VCH GmbH

15213773, 2023, 25, Downloaded from https://onlinelibrary.wiley.com/doi/10.1002/anie.202301506 by Universitätsbibliothek Mainz, Wiley Online Library on [15/04/2025]. See the Terms and Conditions (https://onlinelibrary.wiley.com/terms-and-conditions) on Wiley Online Library for rules of use; OA articles are governed by the applicable Creative Commons License

mechanism (2) is again the spectral overlap between ^{1}An* emission and "substrate" absorption. However, even a moderate overlap is sufficient for highly efficient FRET under application-related conditions.

Although it is our impression that mechanism (2) is operating in most reported EnT-based vis-to-UV UC systems where ^{1}An* and the substrate are sufficiently close (typical FRET distances are below 100 nm), it was not until very recently that unambiguous mechanistic evidence was provided for the UC-FRET sequence.[7] Employing the recently developed UVB annihilator bTIPS-Bz combined with the TADF sensitizer 4CzIPN, Yanai, Kerzig et al. demonstrated FRET activation of three carbonyl compounds via upconversion (Figure 14a–c). Mechanistically, triplet quenching by the carbonyls was ruled out and time-resolved as well spectral (to exclude mechanism (2)) UC measurements provided deep insights into the system (Figure 14c). Moreover, the carbonyl activation rate constants perfectly correlate with the respective spectral overlap, which is in line with a FRET mechanism (Figure 14b). For a complete and detailed description of this rather complex mechanistic investigation we refer to ref.[7]. The vis-to-UV UC-FRET reaction sequence was employed for NMR-scale Norrish reactions such as the dibenzyl formation shown in Figure 14a. Given the high energy of the UVB annihilator well beyond 4 eV, that visible-light driven system has the potential for numerous photocatalytic applications that would otherwise require UV light below 350 nm. A drawback of this one-pot approach containing the UC system and the substrate in the very same solution is the possibility of undesired EnT reactions that might reduce the overall reaction quantum yield drastically. Another FRET event between the singlet-excited carbonyl and the sensitizer in its ground state is in principle feasible, and, more importantly, a TET (Dexter mechanism) between the carbonyl triplet produced after intersystem crossing and the annihilator ground state. Both back-EnT processes compete with the α-cleavage yielding the photoproduct. Hence, this UC-FRET activation sequence can be recommended for substrates that rapidly or irreversibly react to the final product (i.e. faster than collision-based energy transfer).

The mechanistic question is greatly simplified when the UC system and the secondary absorber are not in the same phase. In this case, only radiative energy transfer can take place owing to spatial separation and the long distance between ^{1}An* and the secondary absorber. By the same token, detrimental back-EnT processes cannot occur, but the efficiency of the vis-to-UV UC system that drives the application has to be high as indicated above. In recent examples, that spatial separation is either realized by using a solid secondary absorber in combination with a liquid UC system,[4] or with two separated solutions.[49,119–121] An example for the former case with the UC system exclusively operating through mechanism (2) is illustrated in Figure 14d. In a seminal proof-of-concept study, vis-to-UV UC-driven hydrogen evolution is presented with a photoelectrochemical cell relying on TiO_2 as a photoanode.[4] The annihilator emission (PPO) is reabsorbed by TiO_2, which is essentially inactive under the blue-light conditions employed to excite

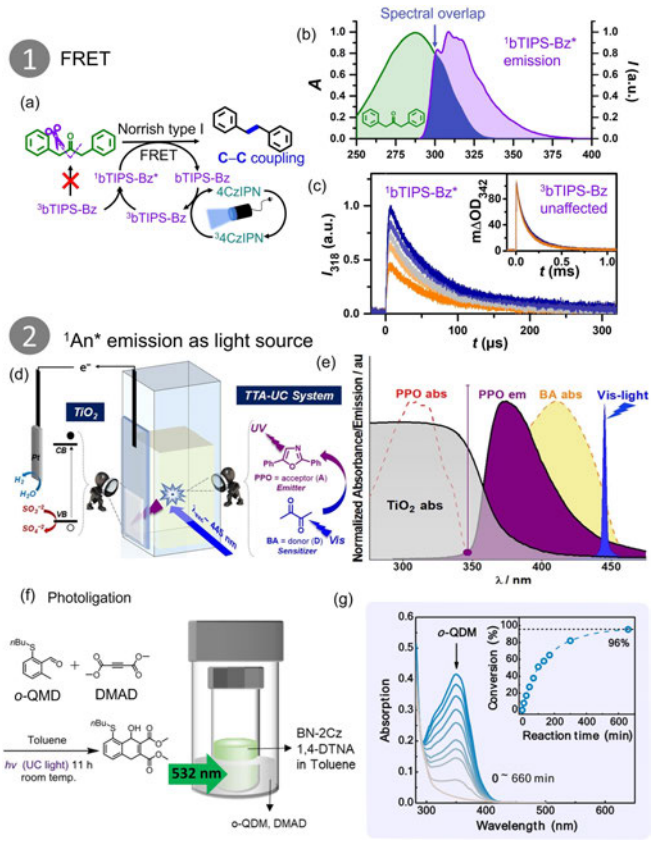

Figure 14. Selected application examples for radiative and non-radiative (FRET) energy transfer processes after vis-to-UV TTA-UC. (a) Upconversion mechanism of bTIPS-Bz and 4CzIPN and subsequent FRET to 1,3-diphenylacetone resulting in a Norrish type I reaction and C–C coupling. (b) Absorption spectrum of 1,3-diphenylacetone and emission spectrum of bTIPS-Bz with highlighted spectral overlap. (c) Kinetic traces of the UC emission with increasing concentration of an energy acceptor. Inset: Corresponding kinetic measurements of the triplet-excited state of bTIPS-Bz. (d) Schematic illustration of the TTA-UC-driven photoelectrochemical (PEC) cell with a TiO_2 photoanode. (e) Normalized UC emission and normalized absorption spectra of PPO, biacetyl, and TiO_2. (f) Photoligation with upconverted light employing the 1,4-TIPS-Nph annihilator and spatially separated UC and reaction solutions. (g) Conversion of the photocaged diene (o-quinodimethane thioether, o-QDM) during UC-driven photoligation observed via its near UV absorption decrease. (d–e) Reproduced with permission.[4] Copyright 2019, American Chemical Society. (f–g) Reproduced and slightly modified with permission.[49] Copyright 2022, Chinese Chemical Society.

the sensitizer biacetyl (BA) (Figure 14e). The generated holes in the valence band after charge separation are captured by the sacrificial donor sulfite and the produced hot electrons migrate to a Pt electrode finally producing H_2. Semiconductors such as TiO_2 in combination with lanthanide UC have already been used for the degradation of pollutants via reactive oxygen species.[124,125] Furthermore, water splitting catalysts are reported to be wavelength-dependent with higher efficiencies in the high-energy UV range than in the visible or near-UV.[126] These observations indicate that semiconductors indirectly excited by vis-to-UV UC have an enormous potential for further chemical

© 2023 Wiley-VCH GmbH

15213773, 2023, 25, Downloaded from https://onlinelibrary.wiley.com/doi/10.1002/anie.202301506 by Universitätsbibliothek Mainz, Wiley Online Library on [15/04/2025]. See the Terms and Conditions (https://onlinelibrary.wiley.com/terms-and-conditions) on Wiley Online Library for rules of use; OA articles are governed by the applicable Creative Commons License

applications. A similar kind of physical separation between rare but highly desirable solid vis-to-UV UC systems and solutions will likely play a key role in future applications, which will predominantly operate via mechanism (2).

Another example exploiting mechanism (2) with spatial separation is displayed in the lower part of Figure 14. In 2022, Cao, Yang et al.[49] performed a ligation with a mixture of a photocaged diene[127] and an acetylene in a UV-induced Diels–Alder reaction, using green light and the UC system presented in Figure 8d. The authors clearly used ^{1}An* as light source for the *o*-QDM excitation with separated vessels (see Figure 14f–g for details). Photoligation is frequently used for connecting two polymer chains or for the post-functionalization of polymers,[128] which is why we added this technique to category III in Figure 12.

The main advantage of spatial separation with the two-chamber approach[49,119–121] is the individual optimization of both the UC system and the application-related reaction solution, for example with regard to the solvent choice, which represents a critical parameter for practically all TTA-UC pairs. However, in particular for the UV region below 350 nm, vis-to-UV systems with higher TTA-UC efficiencies and lower threshold intensities are required for broader applications of this methodology.

Finally, we turn to the SET-based pathways displayed in mechanisms (3) and (4) of Figures 13 and 15. In the most straightforward scenario (3), direct "substrate" activation is initiated by an SET event with ^{1}An* produced through TTA-UC as reaction partner. This mechanism was clearly observed for several applications in the context of photoredox catalysis and for the degradation of model pollutants in water. Most of these studies focussed on reductive substrate activations,[5,6,25,118] but there is a very recent study led by Glaser and Wenger dealing with oxidative photocatalysis,[116] albeit with DCA (9,10-dicyanoanthracene) as non-UV annihilator. Alternatively, a prior SET reaction between ^{1}An* and an electron donor[6] or acceptor[116] to yield a radical ion that finally reacts with the substrate is possible, which is summarized in mechanism (4) of Figure 13. Employing an aromatic amine (DMA, see Figure 15c) as electron donor and a pyrene annihilator sensitized by Ir(ppy)$_3$, Wenger et al.[6] observed *^{1}An* preactivation* via *SET* to yield a long-lived and highly reducing (−2.1 V vs. SCE) pyrene radical anion. This strategy was exploited for photocatalytic dehalogenations, pinacol couplings and detosylation reactions under blue light excitation with a cw laser (447 nm) or an LED (440 nm) as light source. Direct evidence for the pyrene radical anion and its mechanistic key role was obtained through laser flash photolysis. Another study from the same group focused on a UC system producing ^{1}DCA* (corresponding to ^{1}An*) in the presence of naphthalene as electron acceptor. The resulting naphthalene radical cation in its function as redox *mediator* then activates different substrates oxidatively.[116] These conceptually different approaches summarized in mechanism (4) of Figure 13 result in an intrinsic advantage over mechanism (3): the radical ions are longer lived than ^{1}An* by at least three orders of magnitude, allowing ample time for bimolecular reactions with potential substrates.

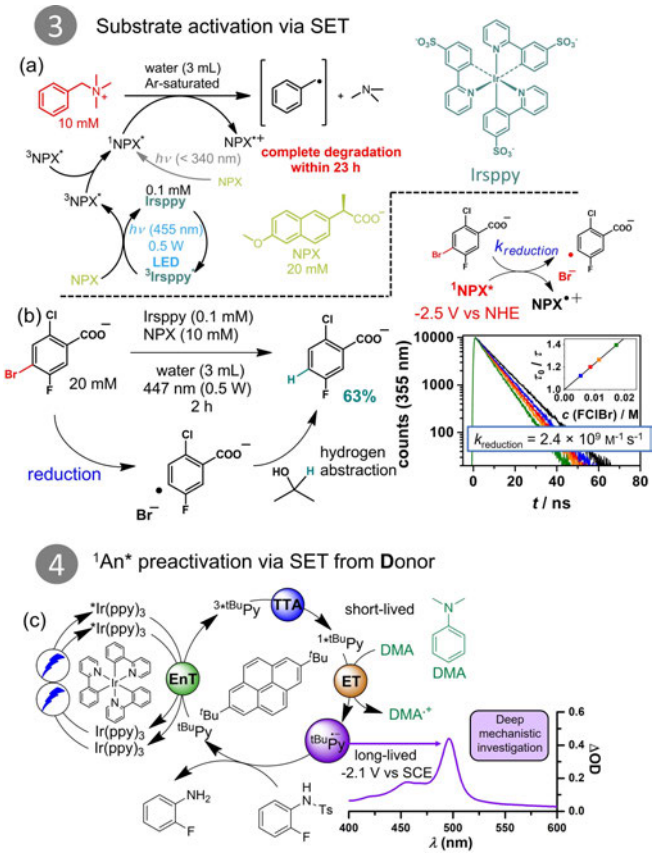

Figure 15. Vis-to-UV TTA-UC as driving force in photoredox reactions. (a) Direct activation of a quaternary ammonium compound via SET from the annihilator singlet in water (annihilator: naproxen (NPX) and sensitizer: Irsppy). (b) Left: Reaction scheme and conditions showing the dehalogenation of 4-bromo-2-chloro-5-fluoro-benzoate initiated by the UC system shown in (a). Right: Corresponding Stern–Volmer fluorescence quenching experiments. (a–b) Reproduced and modified with permission.[5] Copyright 2020, American Chemical Society. (c) Singlet-excited pyrene is generated by UC and (pre)activated by an electron donor. The resulting pyrene radical anion triggers several reactions and the mechanism was thoroughly investigated. Reproduced and slightly modified with permission.[6] Copyright 2021, The Royal Society of Chemistry.

This kinetic advantage comes at a price: The additional exergonic SET step (compare, mechanisms (3) and (4)) is usually accompanied by a lower thermodynamic reactivity of the activating species in terms of the achievable redox potential for substrate activation. However, the increased complexity of mechanism (4) allows a more precise redox potential fine tuning, which might improve the selectivity for sensitive substrates. Both SET-based mechanisms (3 and 4) rely on exactly one photoinduced electron transfer with a photoexcited singlet state. These reaction steps suffer from inherently low yields owing to spin-allowed, fast and unproductive recombination of singlet radical pairs in the so-called solvent cage.[129,130] The selection of proper additional donors or acceptors with inherently high cage-escape yields such as DMA or naphthalene could positively affect overall quantum yields of TTA-UC-driven applications.

© 2023 Wiley-VCH GmbH

15213773, 2023, 25, Downloaded from https://onlinelibrary.wiley.com/doi/10.1002/anie.202301506 by Universitätsbibliothek Mainz, Wiley Online Library on [15/04/2025]. See the Terms and Conditions (https://onlinelibrary.wiley.com/terms-and-conditions) on Wiley Online Library for rules of use; OA articles are governed by the applicable Creative Commons License

The selected example for mechanism (3) is less complicated from the mechanistic point of view, but it has been realized in a challenging environment for TTA-UC systems —neat water.[29] Tri-anionic Irsppy (see Figure 15a for its structure) belongs to a series of tailor-made iridium complexes for photochemical applications in water.[131] In 2020, Wenger, Kerzig et al. successfully combined the sensitizer Irsppy with the drug molecule naproxen (NPX) as aqueous annihilator, which is an extremely strong reductant in its ^{1}An* state. Its excited-state oxidation potential has been estimated with −2.5 V vs. NHE, corresponding to about −2.7 V vs. SCE. The resulting vis-to-UV UC system has been used for the challenging decomposition of a persistent benzyltrialkylammonium compound (Figure 15a)[5] as model pollutant for alkyldimethylbenzylammonium chloride (ADBAC), and it initiated a carbon-bromine bond cleavage in a photocatalytic hydrodehalogenation (Figure 15b). Highly reducing dimethylketyl radicals produced upon hydrogen abstraction by the aryl radical close the catalytic cycle such that the annihilator is practically not consumed in this reaction. In-cage recombination is regarded to be a minor problem for these two examples, which is due to the dissociative nature of the photoinduced SET interfering with unproductive recombination.

Red- or even NIR-light driven UC systems received considerable attention in recent years, both from a fundamental and an application-related point of view.[132–135] However, the annihilators that can be incorporated in these systems are not sufficiently reactive in their singlet-excited states for most applications presented in this chapter. To express this situation in numbers, these excited annihilators (^{1}An*) store well below 3 eV of energy (corresponding to 413 nm) and provide less than 2 V of reductive or oxidative power. This comparison with low-energy TTA-UC systems nicely demonstrates that vis-to-UV UC is indeed required for energy-demanding applications. Pushing the current limits regarding efficiencies and EnT or ET reactivities will therefore expand the current application scope of UC-driven reactions significantly, and we hope that this chapter will support this development.

5. Conclusions

This Review summarizes recent significant developments in vis-to-UV TTA-UC. First, we summarized the energy levels and performance parameters of the sensitizer/annihilator chromophores reported so far and discussed the molecular design to obtain high UC efficiency η_{UC} and low threshold excitation intensity I_{th}. At present, the maximum UC efficiency η_{UC} is 27.6 % shown by the film system using Ir(C6)$_2$(acac) and 1,4-TIPS-Nph as sensitizer and annihilator, respectively, and there is still room for further development considering that higher values have been obtained for TTA-UC in the visible region.[136,137] The introduction of modern strategies such as higher T_2 energies than twice of T_1, reverse intersystem crossing (RISC) from higher triplet levels T_n to S_1, and orientation control between chromophores, are expected to further improve the UC efficiency.[138–140]

Sensitizers and annihilators that enable large UC spectral shifts were also introduced. TADF molecules and semiconductor nanocrystals with small ΔE_{ST} are useful as sensitizers, and in combination with recently developed relatively large ΔE_{ST} annihilators, wavelength conversion such as green-to-UV and blue-to-UVB has recently become possible. For solar hydrogen production, it is desirable to convert as much visible light as possible into UV light, and it is expected to develop annihilators that can utilize excitation light with wavelengths longer than the current limit of green light around 500 nm. On the other hand, for decomposition of toxic substances in water and cleavage/formation of high-energy chemical bonds, generation of UVC light (λ = 200–280 nm) in addition to UVB light (λ = 280–315 nm) is a major challenge. Here, in addition to blue or violet light, UVA light (λ = 315–400 nm) may be used as excitation light.

We have also described the material design to achieve excellent vis-to-UV TTA-UC performance even in the film state, and furthermore, to efficiently induce TTA-UC even at sub-solar light intensities. The development of more efficient and stable film materials for use in diverse real-world applications is still needed in the future. Optimization of matrices and processes to successfully convert chromophores into films and integration with optics and plasmonics to further enhance the performance of the resulting films will become even more important. In addition, UC material deployments through nanoengineering will be necessary to expand the range of applications.[141]

The versatile applications of the new vis-to-UV TTA-UC chromophores and materials that have been developed so far for photochemical reactions were also presented, which we categorize into photocatalysis, bond activation and photopolymerization. TTA-UC has the potential to generate UV light with much higher efficiency and lower energy consumption than conventional artificial UV light sources. Furthermore, since the excitation light is long-wavelength, TTA-UC can generate high-energy UVB light inside a container with low UVB light transmission, such as common laboratory glassware, and many new nonhazardous applications will be proposed to take full advantage of this feature.

Considering the energy gap law, TTA-UC on the high-energy side targeting UV light has a good potential to achieve extremely high UC efficiency at low excitation intensity due to its high fluorescence efficiency and long triplet lifetime. We believe that the future of TTA-UC as an ultraviolet light source is ultrabright.

Acknowledgements

This work was partly supported by JSPS KAKENHI (JP20H02713, JP22K19051), the JST-FOREST Program (JPMJFR201Y), The Murata Science Foundation, Research Foundation for Opto-Science and Technology, the German Research Foundation (DFG, grant number KE 2313/3-1), the German Federal Environmental Foundation (DBU, grant number 20022/028), and Kyushu University Platform

© 2023 Wiley-VCH GmbH

15213773, 2023, 25, Downloaded from https://onlinelibrary.wiley.com/doi/10.1002/anie.202301506 by Universitätsbibliothek Mainz, Wiley Online Library on [15/04/2025]. See the Terms and Conditions (https://onlinelibrary.wiley.com/terms-and-conditions) on Wiley Online Library for rules of use; OA articles are governed by the applicable Creative Commons License

of Inter-/Transdisciplinary Energy Research (Q-PIT) through its "Module-Research Program".

Conflict of Interest

The authors declare no conflict of interest.

Keywords: Energy Transfer · Photochemistry · Photon Upconversion · Sustainable Chemistry · Triplet-Triplet Annihilation

[1] N. Hoffmann, *Chem. Rev.* **2008**, *108*, 1052–1103.
[2] N. Zhang, G. Liu, H. Liu, Y. Wang, Z. He, G. Wang, *J. Hazard. Mater.* **2011**, *192*, 411–418.
[3] G. S. Pozan, A. Kambur, *Appl. Catal. B* **2013**, *129*, 409–415.
[4] M. Barawi, F. Fresno, R. Pérez-Ruiz, V. A. de la Peña O'Shea, *ACS Appl. Energy Mater.* **2019**, *2*, 207–211.
[5] B. Pfund, D. M. Steffen, M. R. Schreier, M.-S. Bertrams, C. Ye, K. Börjesson, O. S. Wenger, C. Kerzig, *J. Am. Chem. Soc.* **2020**, *142*, 10468–10476.
[6] F. Glaser, C. Kerzig, O. S. Wenger, *Chem. Sci.* **2021**, *12*, 9922–9933.
[7] T. J. B. Zähringer, J. A. Moghtader, M.-S. Bertrams, B. Roy, M. Uji, N. Yanai, C. Kerzig, *Angew. Chem. Int. Ed.* **2023**, *62*, e202215340; *Angew. Chem.* **2023**, *135*, e202215340.
[8] Reference Air Mass 1.5 Spectra (ASTM G-173-03). https://www.nrel.gov/grid/solar-resource/spectra-am1.5.html (accessed Jan. 10, 2023).
[9] O. Shvydkiv, S. Gallagher, K. Nolan, M. Oelgemöller, *Org. Lett.* **2010**, *12*, 5170–5173.
[10] A. G. Griesbeck, N. Maptue, S. Bondock, M. Oelgemöller, *Photochem. Photobiol. Sci.* **2003**, *2*, 450–451.
[11] H. Zhang, G. Wang, L. Guo, A. Geng, Y. Bo, D. Cui, Z. Xu, R. Li, Y. Zhu, X. Wang, C. Chen, *Appl. Phys. B* **2008**, *93*, 323–326.
[12] G. Yang, *Mol. Syst. Des. Eng.* **2020**, *5*, 985–995.
[13] C. T. Chen, G. L. Wang, X. Y. Wang, Z. Y. Xu, *Appl. Phys. B* **2009**, *97*, 9–25.
[14] B. Zou, R. Liu, F. Wang, A. Pan, L. Cao, Z. L. Wang, *J. Phys. Chem. B* **2006**, *110*, 12865–12873.
[15] C. F. Zhang, Z. W. Dong, G. J. You, S. X. Qian, H. Deng, H. Gao, L. P. Yang, Y. Li, *Appl. Phys. Lett.* **2005**, *87*, 051920.
[16] E. V. Chelnokov, N. Bityurin, I. Ozerov, W. Marine, *Appl. Phys. Lett.* **2006**, *89*, 171119.
[17] Y. Du, Y. Wang, Z. Deng, X. Chen, X. Yang, T. Sun, X. Zhang, G. Zhu, S. F. Yu, F. Wang, *Adv. Opt. Mater.* **2020**, *8*, 1900968.
[18] E. L. Cates, A. P. Wilkinson, J. H. Kim, *J. Lumin.* **2015**, *160*, 202–209.
[19] E. L. Cates, M. Cho, J. H. Kim, *Environ. Sci. Technol.* **2011**, *45*, 3680–3686.
[20] W. Zhao, F. N. Castellano, *J. Phys. Chem. A* **2006**, *110*, 11440–11445.
[21] P. B. Merkel, J. P. Dinnocenzo, *J. Lumin.* **2009**, *129*, 303–306.
[22] T. N. Singh-Rachford, F. N. Castellano, *J. Phys. Chem. A* **2009**, *113*, 5912–5917.
[23] P. Duan, N. Yanai, N. Kimizuka, *Chem. Commun.* **2014**, *50*, 13111–13113.
[24] P. Duan, N. Yanai, H. Nagatomi, N. Kimizuka, *J. Am. Chem. Soc.* **2015**, *137*, 1887–1894.
[25] M. Majek, U. Faltermeier, B. Dick, R. Pérez-Ruiz, A. Jacobi von Wangelin, *Chem. Eur. J.* **2015**, *21*, 15496–15501.
[26] X. Jiang, X. Guo, J. Peng, D. Zhao, Y. Ma, *ACS Appl. Mater. Interfaces* **2016**, *8*, 11441–11449.
[27] J. Peng, X. Guo, X. Jiang, D. Zhao, Y. Ma, *Chem. Sci.* **2016**, *7*, 1233–1237.
[28] N. Yanai, M. Kozue, S. Amemori, R. Kabe, C. Adachi, N. Kimizuka, *J. Mater. Chem. C* **2016**, *4*, 6447–6451.
[29] K. A. El Roz, F. N. Castellano, *Chem. Commun.* **2017**, *53*, 11705–11708.
[30] V. Gray, P. Xia, Z. Huang, E. Moses, A. Fast, D. A. Fishman, V. I. Vullev, M. Abrahamsson, K. Moth-Poulsen, M. Lee Tang, *Chem. Sci.* **2017**, *8*, 5488–5496.
[31] Q. Chen, Y. Liu, X. Guo, J. Peng, S. Garakyaraghi, C. M. Papa, F. N. Castellano, D. Zhao, Y. Ma, *J. Phys. Chem. A* **2018**, *122*, 6673–6682.
[32] S. He, X. Luo, X. Liu, Y. Li, K. Wu, *J. Phys. Chem. Lett.* **2019**, *10*, 5036–5040.
[33] H.-L. Lee, M.-S. Lee, H. Park, W.-S. Han, J.-H. Kim, *Korean J. Chem. Eng.* **2019**, *36*, 1791–1798.
[34] K. Okumura, N. Yanai, N. Kimizuka, *Chem. Lett.* **2019**, *48*, 1347–1350.
[35] D. Han, X. Yang, J. Han, J. Zhou, T. Jiao, P. Duan, *Nat. Commun.* **2020**, *11*, 5659.
[36] S. Hisamitsu, J. Miyano, K. Okumura, J. K.-H. Hui, N. Yanai, N. Kimizuka, *ChemistryOpen* **2020**, *9*, 14–17.
[37] Y. Kawashima, H. Kouno, K. Orihashi, K. Nishimura, N. Yanai, N. Kimizuka, *Mol. Syst. Des. Eng.* **2020**, *5*, 792–796.
[38] Y. Murakami, A. Motooka, R. Enomoto, K. Niimi, A. Kaiho, N. Kiyoyanagi, *Phys. Chem. Chem. Phys.* **2020**, *22*, 27134–27143.
[39] N. Harada, Y. Sasaki, M. Hosoyamada, N. Kimizuka, N. Yanai, *Angew. Chem. Int. Ed.* **2021**, *60*, 142–147; *Angew. Chem.* **2021**, *133*, 144–149.
[40] L. Hou, A. Olesund, S. Thurakkal, X. Zhang, B. Albinsson, *Adv. Funct. Mater.* **2021**, *31*, 2106198.
[41] M. Koharagi, N. Harada, K. Okumura, J. Miyano, S. Hisamitsu, N. Kimizuka, N. Yanai, *Nanoscale* **2021**, *13*, 19890–19893.
[42] X. Cao, K. Pan, J. Miao, X. Lv, Z. Huang, F. Ni, X. Yin, Y. Wei, C. Yang, *J. Am. Chem. Soc.* **2022**, *144*, 22976–22984.
[43] S. He, Y. Han, J. Guo, K. Wu, *J. Phys. Chem. Lett.* **2022**, *13*, 1713–1718.
[44] J. A. Kübler, B. Pfund, O. S. Wenger, *JACS Au* **2022**, *2*, 2367–2380.
[45] X. Lin, Z. Chen, Y. Han, C. Nie, P. Xia, S. He, J. Li, K. Wu, *ACS Energy Lett.* **2022**, *7*, 914–919.
[46] A. Olesund, J. Johnsson, F. Edhborg, S. Ghasemi, K. Moth-Poulsen, B. Albinsson, *J. Am. Chem. Soc.* **2022**, *144*, 3706–3716.
[47] Q. Zhou, B. M. Wirtz, T. H. Schloemer, M. C. Burroughs, M. Hu, P. Narayanan, J. Lyu, A. O. Gallegos, C. Layton, D. J. Mai, D. N. Congreve, *ChemRxiv.* **2022**, https://doi.org/10.26434/chemrxiv-2022-8ppfr.
[48] M. Uji, N. Harada, N. Kimizuka, M. Saigo, K. Miyata, K. Onda, N. Yanai, *J. Mater. Chem. C* **2022**, *10*, 4558–4562.
[49] Y. Wei, K. Pan, X. Cao, Y. Li, X. Zhou, C. Yang, *CCS Chem.* **2022**, *4*, 3852–3863.
[50] T. J. B. Zähringer, M.-S. Bertrams, C. Kerzig, *J. Mater. Chem. C* **2022**, *10*, 4568–4573.
[51] R. Enomoto, Y. Murakami, *J. Mater. Chem. C* **2023**, *11*, 1678–1683.
[52] N. Harada, M. Uji, B. Singh, N. Kimizuka, N. Yanai, *J. Mater. Chem. C* **2023**, DOI: 10.1039/D3TC00236E https://doi.org/10.26434/chemrxiv-2023-jplm7.
[53] Z. Luo, D. Wang, K. Li, D. Zhong, L. Xue, Z. Gan, C. Xie, *J. Phys. Chem. Lett.* **2023**, *14*, 709–715.
[54] A. Monguzzi, R. Tubino, S. Hoseinkhani, M. Campione, F. Meinardi, *Phys. Chem. Chem. Phys.* **2012**, *14*, 4322–4332.

© 2023 Wiley-VCH GmbH

15213773, 2023, 25, Downloaded from https://onlinelibrary.wiley.com/doi/10.1002/anie.202301506 by Universitätsbibliothek Mainz, Wiley Online Library on [15/04/2025]. See the Terms and Conditions (https://onlinelibrary.wiley.com/terms-and-conditions) on Wiley Online Library for rules of use; OA articles are governed by the applicable Creative Commons License

[55] Y. Zhou, F. N. Castellano, T. W. Schmidt, K. Hanson, *ACS Energy Lett.* **2020**, *5*, 2322–2326.
[56] A. Monguzzi, J. Mezyk, F. Scotognella, R. Tubino, F. Meinardi, *Phys. Rev. B* **2008**, *78*, 195112.
[57] Y. Y. Cheng, T. Khoury, R. G. Clady, M. J. Tayebjee, N. J. Ekins-Daukes, M. J. Crossley, T. W. Schmidt, *Phys. Chem. Chem. Phys.* **2010**, *12*, 66–71.
[58] A. Haefele, J. Blumhoff, R. S. Khnayzer, F. N. Castellano, *J. Phys. Chem. Lett.* **2012**, *3*, 299–303.
[59] D. P. Specht, P. A. Martic, S. Farid, *Tetrahedron* **1982**, *38*, 1203–1211.
[60] S. Aloïse, C. Ruckebusch, L. Blanchet, J. Réhault, G. Buntinx, J. P. Huvenne, *J. Phys. Chem. A* **2008**, *112*, 224–231.
[61] J. B. Borak, D. E. Falvey, *Photochem. Photobiol. Sci.* **2010**, *9*, 854–860.
[62] D. Huang, J. Sun, L. Ma, C. Zhang, J. Zhao, *Photochem. Photobiol. Sci.* **2013**, *12*, 872–882.
[63] R. Dong, K. K. Chen, P. Wang, N. Zhang, S. Guo, Z. M. Zhang, T. B. Lu, *Dyes Pigm.* **2019**, *166*, 84–91.
[64] S. Lamansky, P. Djurovich, D. Murphy, F. Abdel-Razzaq, H. E. Lee, C. Adachi, P. E. Burrows, S. R. Forrest, M. E. Thompson, *J. Am. Chem. Soc.* **2001**, *123*, 4304–4312.
[65] R. J. Holmes, S. R. Forrest, Y.-J. Tung, R. C. Kwong, J. J. Brown, S. Garon, M. E. Thompson, *Appl. Phys. Lett.* **2003**, *82*, 2422–2424.
[66] M. Montalti, A. Credi, L. Prodi, M. T. Gandolfi, *Handbook of photochemistry*, CRC/Taylor & Francis, Boca Raton, **2006**.
[67] P. B. Merkel, J. P. Dinnocenzo, *J. Photochem. Photobiol. A* **2008**, *193*, 110–121.
[68] T. Sajoto, P. I. Djurovich, A. B. Tamayo, J. Oxgaard, W. A. Goddard, M. E. Thompson, *J. Am. Chem. Soc.* **2009**, *131*, 9813–9822.
[69] H. Uoyama, K. Goushi, K. Shizu, H. Nomura, C. Adachi, *Nature* **2012**, *492*, 234–238.
[70] R. Ishimatsu, S. Matsunami, K. Shizu, C. Adachi, K. Nakano, T. Imato, *J. Phys. Chem. A* **2013**, *117*, 5607–5612.
[71] E. Baranoff, B. F. E. Curchod, *Dalton Trans.* **2015**, *44*, 8318–8329.
[72] K.-H. Kim, E. S. Ahn, J.-S. Huh, Y.-H. Kim, J.-J. Kim, *Chem. Mater.* **2016**, *28*, 7505–7510.
[73] K. Xu, J. Zhao, E. G. Moore, *Photochem. Photobiol. Sci.* **2016**, *15*, 995–1005.
[74] D. Zhang, M. Cai, Y. Zhang, D. Zhang, L. Duan, *Mater. Horiz.* **2016**, *3*, 145–151.
[75] N. Okamura, K. Ishiguro, T. Maeda, S. Yagi, *Chem. Lett.* **2017**, *46*, 1086–1089.
[76] C. Wang, C. Deng, D. Wang, Q. Zhang, *J. Phys. Chem. C* **2018**, *122*, 7816–7823.
[77] H. Noda, X. K. Chen, H. Nakanotani, T. Hosokai, M. Miyajima, N. Notsuka, Y. Kashima, J. L. Brédas, C. Adachi, *Nat. Mater.* **2019**, *18*, 1084–1090.
[78] T. Serevičius, R. Skaisgiris, J. Dodonova, K. Kazlauskas, S. Juršėnas, S. Tumkevičius, *Phys. Chem. Chem. Phys.* **2020**, *22*, 265–272.
[79] J. Gao, Y. Zhao, X. You, Y. Geng, G. Shan, Z. Su, Y. Gao, *J. Mater. Chem. C* **2022**, *10*, 5425–5432.
[80] C. Rulliere, P. C. Roberge, *Chem. Phys. Lett.* **1983**, *97*, 247–252.
[81] A. P. Marchetti, D. R. Kearns, *J. Am. Chem. Soc.* **1967**, *89*, 768–777.
[82] C. Kerzig, M. Goez, *Phys. Chem. Chem. Phys.* **2014**, *16*, 25342–25349.
[83] A. Picchiotti, A. Nenov, A. Giussani, V. I. Prokhorenko, R. J. D. Miller, S. Mukamel, M. Garavelli, *J. Phys. Chem. Lett.* **2019**, *10*, 3481–3487.
[84] J.-M. Teng, Y.-F. Wang, C.-F. Chen, *J. Mater. Chem. C* **2020**, *8*, 11340–11353.
[85] T. Hatakeyama, K. Shiren, K. Nakajima, S. Nomura, S. Nakatsuka, K. Kinoshita, J. Ni, Y. Ono, T. Ikuta, *Adv. Mater.* **2016**, *28*, 2777–2781.
[86] K. Mase, K. Okumura, N. Yanai, N. Kimizuka, *Chem. Commun.* **2017**, *53*, 8261–8264.
[87] P. Klán, J. Wirz, *Photochemistry of Organic Compounds: From Concepts to Practice*, Wiley, Chichester, West Sussex, U.K, **2009**.
[88] F. Chiappa, B. Frascella, G. P. Vigezzi, M. Moro, L. Diamanti, L. Gentile, P. Lago, N. Clementi, C. Signorelli, N. Mancini, A. Odone, *J. Hosp. Infect.* **2021**, *114*, 63–78.
[89] C. Ye, V. Gray, J. Mårtensson, K. Börjesson, *J. Am. Chem. Soc.* **2019**, *141*, 9578–9584.
[90] C. Ye, V. Gray, K. Kushwaha, S. Kumar Singh, P. Erhart, K. Börjesson, *Phys. Chem. Chem. Phys.* **2020**, *22*, 1715–1720.
[91] F. Strieth-Kalthoff, M. J. James, M. Teders, L. Pitzer, F. Glorius, *Chem. Soc. Rev.* **2018**, *47*, 7190–7202.
[92] L. Schmid, F. Glaser, R. Schaer, O. S. Wenger, *J. Am. Chem. Soc.* **2022**, *144*, 963–976.
[93] R. Pérez-Ruiz, *Top. Curr. Chem.* **2022**, *380*, 23.
[94] J.-H. Kim, F. Deng, F. N. Castellano, J.-H. Kim, *Chem. Mater.* **2012**, *24*, 2250–2252.
[95] S. H. Lee, J. R. Lott, Y. C. Simon, C. Weder, *J. Mater. Chem. C* **2013**, *1*, 5142–5148.
[96] A. Monguzzi, F. Bianchi, A. Bianchi, M. Mauri, R. Simonutti, R. Ruffo, R. Tubino, F. Meinardi, *Adv. Energy Mater.* **2013**, *3*, 680–686.
[97] F. Marsico, A. Turshatov, R. Peköz, Y. Avlasevich, M. Wagner, K. Weber, D. Donadio, K. Landfester, S. Baluschev, F. R. Wurm, *J. Am. Chem. Soc.* **2014**, *136*, 11057–11064.
[98] W. E. Ford, M. A. J. Rodgers, *J. Phys. Chem.* **1992**, *96*, 2917–2920.
[99] M. Hissler, A. Harriman, A. Khatyr, R. Ziessel, *Chem. Eur. J.* **1999**, *5*, 3366–3381.
[100] R. Passalacqua, F. Loiseau, S. Campagna, Y. Q. Fang, G. S. Hanan, *Angew. Chem. Int. Ed.* **2003**, *42*, 1608–1611; *Angew. Chem.* **2003**, *115*, 1646–1649.
[101] X.-Y. Wang, A. D. Guerzo, R. H. Schmehl, *J. Photochem. Photobiol. C* **2004**, *5*, 55–77.
[102] N. D. McClenaghan, Y. Leydet, B. Maubert, M. T. Indelli, S. Campagna, *Coord. Chem. Rev.* **2005**, *249*, 1336–1350.
[103] A. Lavie-Cambot, C. Lincheneau, M. Cantuel, Y. Leydet, N. D. McClenaghan, *Chem. Soc. Rev.* **2010**, *39*, 506–515.
[104] G. Ragazzon, P. Verwilst, S. A. Denisov, A. Credi, G. Jonusauskas, N. D. McClenaghan, *Chem. Commun.* **2013**, *49*, 9110–9112.
[105] S. A. Denisov, Y. Cudré, P. Verwilst, G. Jonusauskas, M. Marín-Suárez, J. F. Fernández-Sánchez, E. Baranoff, N. D. McClenaghan, *Inorg. Chem.* **2014**, *53*, 2677–2682.
[106] F. N. Castellano, *Acc. Chem. Res.* **2015**, *48*, 828–839.
[107] L. Liang, D. B. L. Teh, N. D. Dinh, W. Chen, Q. Chen, Y. Wu, S. Chowdhury, A. Yamanaka, T. C. Sum, C. H. Chen, N. V. Thakor, A. H. All, X. Liu, *Nat. Commun.* **2019**, *10*, 1391.
[108] Q. Liu, H. Liu, D. Li, W. Qiao, G. Chen, H. Ågren, *Nanoscale* **2019**, *11*, 14070–14078.
[109] D. Polak, R. Jayaprakash, T. P. Lyons, L. Á. Martínez-Martínez, A. Leventis, K. J. Fallon, H. Coulthard, D. G. Bossanyi, K. Georgiou, A. J. Petty II, J. Anthony, H. Bronstein, J. Yuen-Zhou, A. I. Tartakovskii, J. Clark, A. J. Musser, *Chem. Sci.* **2020**, *11*, 343–354.
[110] M. Wu, T. A. Lin, J. O. Tiepelt, V. Bulović, M. A. Baldo, *Nano Lett.* **2021**, *21*, 1011–1016.
[111] J. Castellanos-Soriano, J. C. Herrera-Luna, D. D. Díaz, M. C. Jiménez, R. Pérez-Ruiz, *Org. Chem. Front.* **2020**, *7*, 1709–1716.

© 2023 Wiley-VCH GmbH

15213773, 2023, 25, Downloaded from https://onlinelibrary.wiley.com/doi/10.1002/anie.202301506 by Universitätsbibliothek Mainz, Wiley Online Library on [15/04/2025]. See the Terms and Conditions (https://onlinelibrary.wiley.com/terms-and-conditions) on Wiley Online Library for rules of use; OA articles are governed by the applicable Creative Commons License

[112] F. Glaser, C. Kerzig, O. S. Wenger, *Angew. Chem. Int. Ed.* **2020**, *59*, 10266–10284; *Angew. Chem.* **2020**, *132*, 10350–10370.
[113] Y. Du, X. Ai, Z. Li, T. Sun, Y. Huang, X. Zeng, X. Chen, F. Rao, F. Wang, *Adv. Photonics Res.* **2021**, *2*, 2000213.
[114] A. Caron, G. Noirbent, D. Gigmes, F. Dumur, J. Lalevée, *Macromol. Rapid Commun.* **2021**, *42*, 2100047.
[115] S. N. Sanders, T. H. Schloemer, M. K. Gangishetty, D. Anderson, M. Seitz, A. O. Gallegos, R. C. Stokes, D. N. Congreve, *Nature* **2022**, *604*, 474–478.
[116] F. Glaser, O. S. Wenger, *Chem. Sci.* **2023**, *14*, 149–161.
[117] T. Yu, Y. Liu, Y. Zeng, J. Chen, G. Yang, Y. Li, *Chem. Eur. J.* **2019**, *25*, 16270–16276.
[118] C. Kerzig, O. S. Wenger, *Chem. Sci.* **2018**, *9*, 6670–6678.
[119] W. Larsson, M. Morimoto, M. Irie, J. Andréasson, B. Albinsson, *Chem. Eur. J.* **2023**, *29*, e202203651.
[120] Y. Wei, H. Xian, X. Lv, F. Ni, X. Cao, C. Yang, *Mater. Horiz.* **2021**, *8*, 606–611.
[121] J. B. Bilger, C. Kerzig, C. B. Larsen, O. S. Wenger, *J. Am. Chem. Soc.* **2021**, *143*, 1651–1663.
[122] S. H. C. Askes, M. Kloz, G. Bruylants, J. T. M. Kennis, S. Bonnet, *Phys. Chem. Chem. Phys.* **2015**, *17*, 27380–27390.
[123] S. H. C. Askes, A. Bahreman, S. Bonnet, *Angew. Chem. Int. Ed.* **2014**, *53*, 1029–1033; *Angew. Chem.* **2014**, *126*, 1047–1051.
[124] B. S. Richards, D. Hudry, D. Busko, A. Turshatov, I. A. Howard, *Chem. Rev.* **2021**, *121*, 9165–9195.
[125] S. P. Sahu, S. L. Cates, H.-I. Kim, J.-H. Kim, E. L. Cates, *Environ. Sci. Technol.* **2018**, *52*, 2973–2980.
[126] T. Takata, J. Jiang, Y. Sakata, M. Nakabayashi, N. Shibata, V. Nandal, K. Seki, T. Hisatomi, K. Domen, *Nature* **2020**, *581*, 411–414.
[127] F. Feist, L. L. Rodrigues, S. L. Walden, T. W. Krappitz, T. R. Dargaville, T. Weil, A. S. Goldmann, J. P. Blinco, C. Barner-Kowollik, *J. Am. Chem. Soc.* **2020**, *142*, 7744–7748.
[128] J. T. Offenloch, M. Gernhardt, J. P. Blinco, H. Frisch, H. Mutlu, C. Barner-Kowollik, *Chem. Eur. J.* **2019**, *25*, 3700–3709.
[129] S. Neumann, O. S. Wenger, C. Kerzig, *Chem. Eur. J.* **2021**, *27*, 4115–4123.
[130] G. J. Kavarnos, N. J. Turro, *Chem. Rev.* **1986**, *86*, 401–449.
[131] M. R. Schreier, X. Guo, B. Pfund, Y. Okamoto, T. R. Ward, C. Kerzig, O. S. Wenger, *Acc. Chem. Res.* **2022**, *55*, 1290–1300.
[132] L. Zeng, L. Huang, J. Han, G. Han, *Acc. Chem. Res.* **2022**, *55*, 2604–2615.
[133] P. Bharmoria, H. Bildirir, K. Moth-Poulsen, *Chem. Soc. Rev.* **2020**, *49*, 6529–6554.
[134] A. Tokunaga, L. M. Uriarte, K. Mutoh, E. Fron, J. Hofkens, M. Sliwa, J. Abe, *J. Am. Chem. Soc.* **2019**, *141*, 17744–17753.
[135] B. D. Ravetz, A. B. Pun, E. M. Churchill, D. N. Congreve, T. Rovis, L. M. Campos, *Nature* **2019**, *565*, 343–346.
[136] M. Yang, S. Sheykhi, Y. Zhang, C. Milsmann, F. N. Castellano, *Chem. Sci.* **2021**, *12*, 9069–9077.
[137] A. Ronchi, A. Monguzzi, *Chem. Phys. Rev.* **2022**, *3*, 041301.
[138] R. Ieuji, K. Goushi, C. Adachi, *Nat. Commun.* **2019**, *10*, 5283.
[139] D. G. Bossanyi, Y. Sasaki, S. Wang, D. Chekulaev, N. Kimizuka, N. Yanai, J. Clark, *JACS Au* **2021**, *1*, 2188–2201.
[140] L. Vaghi, F. Rizzo, J. Pedrini, A. Mauri, F. Meinardi, U. Cosentino, C. Greco, A. Monguzzi, A. Papagni, *Photochem. Photobiol. Sci.* **2022**, *21*, 913–921.
[141] T. Schloemer, P. Narayanan, Q. Zhou, E. Belliveau, M. Seitz, D. N. Congreve, *ACS Nano* **2023**, *17*, 3259–3288.

Manuscript received: January 31, 2023
Accepted manuscript online: March 7, 2023
Version of record online: April 5, 2023

© 2023 Wiley-VCH GmbH

15213773, 2023, 25, Downloaded from https://onlinelibrary.wiley.com/doi/10.1002/anie.202301506 by Universitätsbibliothek Mainz, Wiley Online Library on [15/04/2025]. See the Terms and Conditions (https://onlinelibrary.wiley.com/terms-and-conditions) on Wiley Online Library for rules of use; OA articles are governed by the applicable Creative Commons License

8 Conclusion and Outlook

This thesis presents a detailed investigation into the photochemistry of molecular triplet states, with a particular focus on TTET between sensitizers and acceptors. While covering diverse systems and applications, all projects aim to understand and control TTET processes – either by elucidating their mechanisms or optimizing sensitizers, acceptors, and reaction conditions.

To explore these mechanisms, a range of complementary techniques was employed. Among them, nanosecond TA spectroscopy served as the central analytical tool throughout the work, enabling the direct observation of non-emissive triplet states and transient intermediates. TA spectroscopy not only revealed the presence and behavior of triplet-excited species but also allowed exclusion of alternative pathways such as electron or hydrogen atom transfer based on their specific spectral signatures. Stern–Volmer quenching alongside steady-state absorption and emission spectroscopy provided valuable indirect insights into excited-state properties, particularly triplet energy levels. These experimental results were complemented by density functional theory (DFT) calculations, which provided theoretical estimates of triplet energies, spin densities, and oscillator strengths.

In project **[A]**, TTET within DNA constructs containing a thioxanthone donor and naphthalene acceptor at varying distances was directly observed by using TA spectroscopy. The derived TTET attenuation factor indicated a tunneling mechanism, likely mediated by the thymine triplet state. The steep distance dependence suggested that DNA nucleobases have high triplet energies, effectively serving as barriers to long-range energy transfer and potentially protecting DNA from photoinduced triplet sensitization by solar radiation. These findings significantly contribute to the understanding of DNA photodamage induced by localized triplet states.[143] Projects **[B]**, **[C]**, and **[D]** focused on synthetic photocatalytic systems, where TA spectroscopy again proved to be essential for tracking excited states, reactive intermediates, and product formation. Notably, project **[B]** demonstrated the versatility of a polyazahelicene chromophore functioning in both photoredox and TTET catalysis. Project **[C]** succeeded in detecting the thianthrenium radical cation formed via TTET to arylthianthrenium salts, allowing quantitative comparison of direct excitation and sensitized pathways. By identifying transient signatures of the thianthrenium radical cation, the study validated TTET from thioxanthone, excluding an electron transfer mechanism and enabling novel synthetic applications through energy transfer catalysis. Project **[D]** explored TTET with a vinylcyclopropane substrate, although a triplet energy mismatch seemed to hinder efficient transfer. Through detailed mechanistic work, a non-classical energy transfer mechanism involving strain release was proposed – an effect not accounted for by conventional Dexter-type energy transfer kinetics.

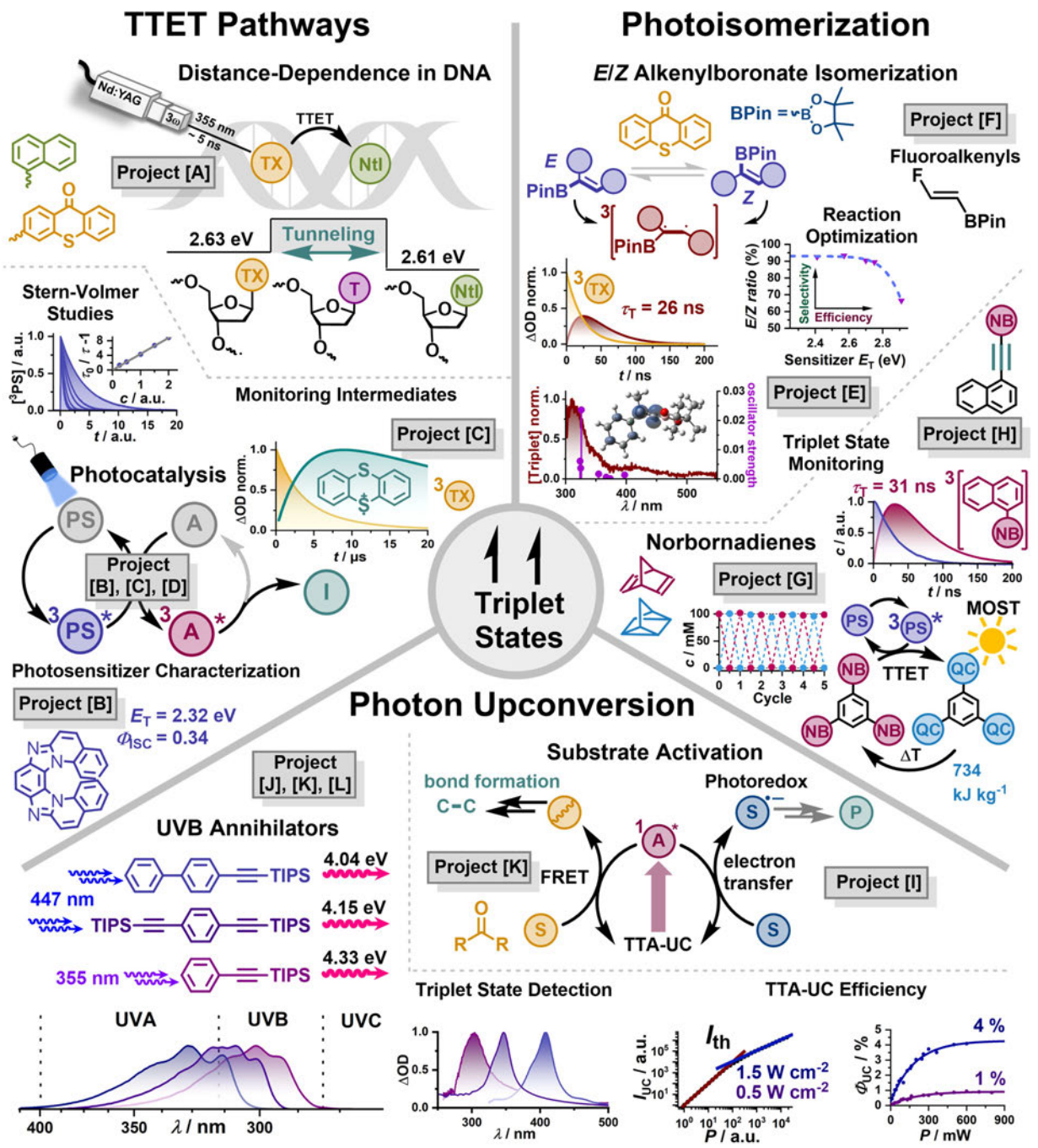

Figure 32: Overview of the research projects presented in this thesis.

Together, these projects on TTET pathways deepen our mechanistic understanding in both biological and synthetic contexts, demonstrating how detailed spectroscopic investigation can reveal subtle energy transfer pathways and guide the rational design of photocatalytic systems with improved performance. This foundational knowledge opens new avenues for innovation in triplet-sensitized photochemistry.

Projects **[E]** through **[H]** focused on triplet state isomerization reactions where identification and characterization of triplet states directly guided the optimization of reaction conditions. In project **[E]**, the triplet states of alkenylboronates were observed for the first time, and their characterization enabled the

replacement of costly iridium catalysts and prolonged LED irradiation with a commercially available organic sensitizer and brief sunlight exposure – conditions unattainable through conventional optimization approaches. This strategy was extended in project **[F]** to fluorinated *β*-borylacrylates, robust amide isosteres prevalent in biochemistry, demonstrating the versatility and practicality of triplet-sensitized isomerization protocols.

Project **[G]** investigated the triplet sensitization of aryl-norbornadiene photoswitches to generate metastable aryl-quadricyclanes, pivotal to molecular solar thermal (MOST) energy storage systems. By integrating a multistate photoswitch into a solar-driven, triplet-sensitized MOST setup, a tenfold increase in solar conversion efficiency was achieved compared to direct excitation. This enhancement was attributed to the nearly unity quantum yield of norbornadiene-to-quadricyclane conversion under optimized triplet-sensitized conditions, which is unachievable by direct excitation. Moreover, the use of a visible-light-absorbing sensitizer extended solar spectral overlap (from ~320 nm to ~520 nm). A millimolar-scale irradiation experiment confirmed the system's high photostability. These findings challenge prevailing assumptions in the MOST community and lay the grounds for pilot studies with increased photoswitch quantities. A follow-up study (project **[H]**) on acetylene-bridged aryl-norbornadienes, though not enhancing MOST performance, provided valuable insights for future photoswitch design.

Projects **[I]** through **[M]** focus on photon upconversion via triplet–triplet annihilation (TTA–UC). A combined computational and spectroscopic approach guided the rational design of novel upconversion systems. Project **[I]** successfully introduced a novel BODIPY-like triplet sensitizer into a green-to-blue TTA–UC scheme applied to demanding photoredox reactions. Projects **[J]**, **[K]**, and **[L]** expanded the TTA–UC operational range by developing UVB-emitting annihilators, significantly extending beyond the prior UVA border toward the UVC spectrum. These achievements address the challenging generation of UVB light, which remains inefficient with conventional light sources. Detailed characterization revealed how variations in annihilator scaffolds and TIPS-ethynyl functionalization modulate upconversion performance, informing the future design of high-efficiency annihilators. These systems generate high-energy singlet states with emission in the UVB range, enabling challenging photochemical transformations under visible light. This was exemplified in project **[K]**, where activation of inert UVB-absorbing carbonyl compounds facilitated C–C bond formation. However, these studies also highlight inherent limitations of solution-based TTA–UC, notably increased reabsorption losses at higher emission energies. Transitioning to thin-film architectures may mitigate these losses and improve efficiency. This prospect is, among others, discussed in project **[M]**, a review article that summarizes current developments and applications of visible-to-UV TTA–UC systems in photocatalysis, bond activation, and photopolymerization. As a comprehensive overview it serves as a valuable guide for photochemists seeking appropriate upconversion strategies to drive reactions under milder conditions.

Together, these projects underscore the benefit and richness of mechanistic insight accessible through state-of-the-art spectroscopic techniques and the power of interdisciplinary collaboration. Historically, triplet state chemistry research focused largely on mechanistic and photophysical aspects,[194,202–204,338] but this thesis exemplifies how mechanistic spectroscopic studies can result in practical photochemical

applications under highly attractive reaction conditions. By bridging previously isolated research communities, this work highlights the profound synergy that arises when synthetic and spectroscopic chemists collaborate – advancing knowledge and enabling progress. This thesis illustrates the unique potential of triplet states exemplified by their incorporation into energy conversion and challenging synthetic transformations. Moreover, these advances in visible-to-UV photon upconversion, enabled by clever molecular design strategies, significantly broaden the accessible wavelength range to the UVB/UVC boundary (280 nm).

Looking forward, further popularization and integration of advanced spectroscopic methods will accelerate the discovery of efficient photocatalytic processes that complement the remarkable advances already seen in photoredox catalysis.[23–25,57,141,152] Continued exploration and application of triplet energy transfer mechanisms hold promise for developing sustainable, energy-efficient photochemical technologies with broad scientific and industrial impact. The thorough spectroscopic characterizations and results in this thesis will hopefully contribute to this development for light and energy conversion processes.

9 References

[A] S. Häcker, T. J. B. Zähringer, H.-A. Wagenknecht, C. Kerzig, *JACS Au*, **2025**, DOI: 10.1021/jacsau.5c00364.

[B] J. Rocker, T. J. B. Zähringer, M. Schmitz, T. Opatz, C. Kerzig, *Beilstein J. Org. Chem*. **2024**, *20*, 1236–1245.

[C] Y. Cai, T. K. Roy, T. J. B. Zähringer, B. Lansbergen, C. Kerzig, T. Ritter, *J. Am. Chem. Soc.* **2024**, *146*, 30474–30482.

[D] A. Luque, J. Groß, T. J. B. Zähringer, C. Kerzig, T. Opatz, *Chem. Eur. J.* **2022**, *28*, e202104329.

[E] T. J. B. Zähringer, M. Wienhold, R. Gilmour, C. Kerzig, *J. Am. Chem. Soc.* **2023**, *145*, 21576–21586.

[F] M. Wienhold, B. Kweon, C. McLaughlin, M. Schmitz, T. J. B. Zähringer, C. G. Daniliuc, C. Kerzig, R. Gilmour, *Angew. Chem. Int. Ed.* **2023**, *135*, e202304150.

[G] T. J. B. Zähringer, N. Perez Lopez, R. Schulte, M. Schmitz, H. Ihmels, C. Kerzig, *Angew. Chem. Int. Ed.* **2025**, *64*, e202414733.

[H] R. Schulte, D. Schade, T. Paululat, T. J. B. Zähringer, C. Kerzig, H. Ihmels, *Beilstein J. Org. Chem.* **2024**, *20*, 3061–3068.

[I] J. Castellanos-Soriano, T. J. B. Zähringer, J. C. Herrera-Luna, M. C. Jiménez, C. Kerzig, R. Pérez-Ruiz, *Phys. Chem. Chem. Phys.* **2023**, *25*, 12041–12049.

[J] T. J. B. Zähringer, M.-S. Bertrams, C. Kerzig, *J. Mater. Chem. C* **2022**,*10*, 4568–4573.

[K] T. J. B. Zähringer, J. A. Moghtader, M. Bertrams, B. Roy, M. Uji, N. Yanai, C. Kerzig, *Angew. Chem. Int. Ed.* **2023**, *62*, e202215340.

[L] T. J. B. Zähringer, C. Heusel, M. Schmitz, F. Glorius, C. Kerzig, *Chem. Commun,* **2025**, DOI: 10.1039/D5CC01834J.

[M] M. Uji, T. J. B. Zähringer, C. Kerzig, N. Yanai, *Angew. Chem. Int. Ed.* **2023**, *62*, e202301506.

[1] H. D. Roth, *Angew. Chem. Int. Ed. Engl.* **1989**, *28*, 1193–1207.

[2] J. Bertram, R. Kürsten, *J. Prakt. Chem.* **1895**, *51*, 316–325.

[3] W. H. Perkin, *J. Chem. Soc., Trans.* **1881**, *39*, 409–452.

[4] G. Ciamician, *Science* **1912**, *36*, 385–394.

[5] R. K. Willardson, E. R. Weber, G. Mueller, *Semiconductors and Semimetals: Electroluminescence I*, Elsevier, Burlington, **1999**.

[6] A. Polman, M. Knight, E. C. Garnett, B. Ehrler, W. C. Sinke, *Science* **2016**, *352*, aad4424.

[7] S. Dutta, J. E. Erchinger, F. Strieth-Kalthoff, R. Kleinmans, F. Glorius, *Chem. Soc. Rev.* **2024**, *53*, 1068–1089.

[8] F. Strieth-Kalthoff, F. Glorius, *Chem* **2020**, *6*, 1888–1903.

[9] F. Strieth-Kalthoff, M. J. James, M. Teders, L. Pitzer, F. Glorius, *Chem. Soc. Rev.* **2018**, *47*, 7190–7202.

[10] J. Großkopf, T. Kratz, T. Rigotti, T. Bach, *Chem. Rev.* **2022**, *122*, 1626–1653.

[11] T. Neveselý, M. Wienhold, J. J. Molloy, R. Gilmour, *Chem. Rev.* **2022**, *122*, 2650–2694.

[12] V. Balzani, P. Ceroni, A. Juris, *Photochemistry and Photophysics: Concepts, Research, Applications*, Wiley-VCH, Weinheim, Germany, **2014**.

[13] G. E. M. Crisenza, P. Melchiorre, *Nat. Commun.* **2020**, *11*, 803.

[14] T. N. Singh-Rachford, F. N. Castellano, *Coord. Chem. Rev.* **2010**, *254*, 2560–2573.

[15] V. Gray, D. Dzebo, M. Abrahamsson, B. Albinsson, K. Moth-Poulsen, *Phys. Chem. Chem. Phys.* **2014**, *16*, 10345–10352.

[16] K. Kuntze, J. Isokuortti, J. J. Van Der Wal, T. Laaksonen, S. Crespi, N. A. Durandin, A. Priimagi, *Chem. Sci.* **2024**, *15*, 11684–11698.

[17] P.-Z. Wang, W.-J. Xiao, J.-R. Chen, *Nat. Rev. Chem.* **2022**, *7*, 35–50.

[18] S. Poplata, A. Tröster, Y.-Q. Zou, T. Bach, *Chem. Rev.* **2016**, *116*, 9748–9815.

[19] M. J. James, J. L. Schwarz, F. Strieth-Kalthoff, B. Wibbeling, F. Glorius, *J. Am. Chem. Soc.* **2018**, *140*, 8624–8628.

[20] J. E. Erchinger, R. Hoogesteger, R. Laskar, S. Dutta, C. Hümpel, D. Rana, C. G. Daniliuc, F. Glorius, *J. Am. Chem. Soc.* **2023**, *145*, 2364–2374.

[21] D. S. Lee, V. K. Soni, E. J. Cho, *Acc. Chem. Res.* **2022**, *55*, 2526–2541.

[22] R. Schmidt, *Photochem. Photobiol.* **2007**, *82*, 1161–1177.

[23] J. C. Scaiano, *Chem. Soc. Rev.* **2023**, *52*, 6330–6343.

[24] M. Villa, A. Fermi, F. Calogero, A. Gualandi, P. Franchi, M. Lucarini, B. Ventura, P. G. Cozzi, P. Ceroni, *Angew. Chem. Int. Ed.* **2025**, e202420009.

[25] M. Marchini, G. Bergamini, P. G. Cozzi, P. Ceroni, V. Balzani, *Angew. Chem. Int. Ed.* **2017**, *56*, 12820–12821.

[26] J. A. Moghtader, M. Bertrams, D. Schollmeyer, C. Kerzig, *Angew. Chem. Int. Ed.* **2025**, e202509203.

[27] S. B. Beil, S. Bonnet, C. Casadevall, R. J. Detz, F. Eisenreich, S. D. Glover, C. Kerzig, L. Næsborg, S. Pullen, G. Storch, N. Wei, C. Zeymer, *JACS Au* **2024**, *4*, 2746–2766.

[28] P. W. Atkins, J. de Paula, R. S. Friedman, *Physical Chemistry: Quanta, Matter, and Change*, Oxford University Press, Oxford, **2014**.

[29] H. G. O. Becker, Ed. , *Einführung in Die Photochemie*, Thieme, Stuttgart, **1983**.

[30] M. K. Etherington, J. Gibson, H. F. Higginbotham, T. J. Penfold, A. P. Monkman, *Nat. Commun.* **2016**, *7*, 13680.

[31] N. Aizawa, Y.-J. Pu, Y. Harabuchi, A. Nihonyanagi, R. Ibuka, H. Inuzuka, B. Dhara, Y. Koyama, K. Nakayama, S. Maeda, F. Araoka, D. Miyajima, *Nature* **2022**, *609*, 502–506.

[32] R. Pollice, P. Friederich, C. Lavigne, G. D. P. Gomes, A. Aspuru-Guzik, *Matter* **2021**, *4*, 1654–1682.

[33] J. R. Lakowicz, *Principles of Fluorescence Spectroscopy*, Springer, New York, NY, **2010**.

[34] C. M. Marian, *Annu. Rev. Phys. Chem.* **2021**, *72*, 617–640.

[35] G. Baryshnikov, B. Minaev, H. Ågren, *Chem. Rev.* **2017**, *117*, 6500–6537.

[36] T. J. Penfold, E. Gindensperger, C. Daniel, C. M. Marian, *Chem. Rev.* **2018**, *118*, 6975–7025.

[37] S. K. Lower, M. A. El-Sayed, *Chem. Rev.* **1966**, *66*, 199–241.

[38] M. A. El-Sayed, *J. Chem. Phys.* **1963**, *38*, 2834–2838.

[39] R. Englman, J. Jortner, *Mol. Phys.* **1970**, *18*, 145–164.

[40] M. Etinski, C. M. Marian, *Phys. Chem. Chem. Phys.* **2010**, *12*, 15665.

[41] J. Tatchen, N. Gilka, C. M. Marian, *Phys. Chem. Chem. Phys.* **2007**, *9*, 5209.

[42] M. Etinski, V. Rai-Constapel, C. M. Marian, *J. Chem. Phys.* **2014**, *140*, 114104.

[43] L. D. Elliott, S. Kayal, M. W. George, K. Booker-Milburn, *J. Am. Chem. Soc.* **2020**, *142*, 14947–14956.

[44] J. Zhao, W. Wu, J. Sun, S. Guo, *Chem. Soc. Rev.* **2013**, *42*, 5323.

[45] W. Zeng, C. Zhong, H. Bronstein, F. Plasser, *Angew. Chem. Int. Ed.* **2025**, e202502485.

[46] X.-K. Chen, D. Kim, J.-L. Brédas, *Acc. Chem. Res.* **2018**, *51*, 2215–2224.

[47] G. Amirzadeh, W. Schnabel, *Makromol. Chem.* **1981**, *182*, 2821–2835.

[48] C. Walling, M. J. Gibian, *J. Am. Chem. Soc.* **1965**, *87*, 3361–3364.

[49] W. M. Moore, G. S. Hammond, R. P. Foss, *J. Am. Chem. Soc.* **1961**, *83*, 2789–2794.

[50] C. Ley, F. Morlet-Savary, P. Jacques, J. P. Fouassier, *Chem. Phys.* **2000**, *255*, 335–346.

[51] M. Montalti, A. Credi, L. Prodi, M. T. Gandolfi, *Handbook of Photochemistry*, CRC Press, **2006**.

[52] D. Burget, P. Jacques, *J. Lumin.* **1992**, *54*, 177–181.

[53] M. W. Wolf, K. D. Legg, R. E. Brown, L. A. Singer, J. H. Parks, *J. Am. Chem. Soc.* **1975**, *97*, 4490–4497.

[54] B. O'Regan, M. Grätzel, *Nature* **1991**, *353*, 737–740.

[55] Z. Xu, B. Hu, J. Howe, *J. Appl. Phys.* **2008**, *103*, 043909.

[56] P. I. Djurovich, D. Murphy, M. E. Thompson, B. Hernandez, R. Gao, P. L. Hunt, M. Selke, *Dalton Trans.* **2007**, 3763.

[57] C. K. Prier, D. A. Rankic, D. W. C. MacMillan, *Chem. Rev.* **2013**, *113*, 5322–5363.

[58] F. Glaser, O. S. Wenger, *Coord. Chem. Rev.* **2020**, *405*, 213129.

[59] T. Hofbeck, H. Yersin, *Inorg. Chem.* **2010**, *49*, 9290–9299.

[60] H. Yersin, *Highly Efficient OLEDs with Phosphorescent Materials*, Wiley-VCH, Weinheim, **2008**.

[61] T. O. Paulisch, L. A. Mai, F. Strieth-Kalthoff, M. J. James, C. Henkel, D. M. Guldi, F. Glorius, *Angew. Chem. Int. Ed.* **2022**, *61*, e202112695.

[62] A. McNally, C. K. Prier, D. W. C. MacMillan, *Science* **2011**, *334*, 1114–1117.

[63] F. Strieth-Kalthoff, C. Henkel, M. Teders, A. Kahnt, W. Knolle, A. Gómez-Suárez, K. Dirian, W. Alex, K. Bergander, C. G. Daniliuc, B. Abel, D. M. Guldi, F. Glorius, *Chem* **2019**, *5*, 2183–2194.

[64] K. Tsuchiya, S. Yagai, A. Kitamura, T. Karatsu, K. Endo, J. Mizukami, S. Akiyama, M. Yabe, *Eur. J. Inorg. Chem.* **2010**, *2010*, 926–933.

[65] J.-M. Teng, Y.-F. Wang, C.-F. Chen, *J. Mater. Chem. C* **2020**, *8*, 11340–11353.

[66] Y. Tao, K. Yuan, T. Chen, P. Xu, H. Li, R. Chen, C. Zheng, L. Zhang, W. Huang, *Adv. Mater.* **2014**, *26*, 7931–7958.

[67] K. Goushi, K. Yoshida, K. Sato, C. Adachi, *Nat. Photon.* **2012**, *6*, 253–258.

[68] H. Noda, X.-K. Chen, H. Nakanotani, T. Hosokai, M. Miyajima, N. Notsuka, Y. Kashima, J.-L. Brédas, C. Adachi, *Nat. Mater.* **2019**, *18*, 1084–1090.

[69] Y. Shi, H. Gou, H. Wu, S. Wan, K. Wang, J. Yu, X. Zhang, C. Ye, *J. Phys. Chem. Lett.* **2024**, *15*, 4647–4654.

[70] Y. Wei, K. Pan, X. Cao, Y. Li, X. Zhou, C. Yang, *CCS Chem* **2022**, *4*, 3852–3863.

[71] H. Uoyama, K. Goushi, K. Shizu, H. Nomura, C. Adachi, *Nature* **2012**, *492*, 234–238.

[72] T.-Y. Shang, L.-H. Lu, Z. Cao, Y. Liu, W.-M. He, B. Yu, *Chem. Commun.* **2019**, *55*, 5408–5419.

[73] M. A. Bryden, E. Zysman-Colman, *Chem. Soc. Rev.* **2021**, *50*, 7587–7680.

[74] X. Cao, K. Pan, J. Miao, X. Lv, Z. Huang, F. Ni, X. Yin, Y. Wei, C. Yang, *J. Am. Chem. Soc.* **2022**, *144*, 22976–22984.

[75] M. E. El-Khouly, S. Fukuzumi, F. D'Souza, *ChemPhysChem* **2014**, *15*, 30–47.

[76] L.-Y. Niu, H. Li, L. Feng, Y.-S. Guan, Y.-Z. Chen, C.-F. Duan, L.-Z. Wu, Y.-F. Guan, C.-H. Tung, Q.-Z. Yang, *Anal. Chim. Acta* **2013**, *775*, 93–99.

[77] A. Kamkaew, S. H. Lim, H. B. Lee, L. V. Kiew, L. Y. Chung, K. Burgess, *Chem. Soc. Rev.* **2013**, *42*, 77–88.

[78] E. Bassan, A. Gualandi, P. G. Cozzi, P. Ceroni, *Chem. Sci.* **2021**, *12*, 6607–6628.

[79] T. Slanina, P. Shrestha, E. Palao, D. Kand, J. A. Peterson, A. S. Dutton, N. Rubinstein, R. Weinstain, A. H. Winter, P. Klán, *J. Am. Chem. Soc.* **2017**, *139*, 15168–15175.

[80] T. Yogo, Y. Urano, Y. Ishitsuka, F. Maniwa, T. Nagano, *J. Am. Chem. Soc.* **2005**, *127*, 12162–12163.

[81] M. A. Filatov, S. Karuthedath, P. M. Polestshuk, H. Savoie, K. J. Flanagan, C. Sy, E. Sitte, M. Telitchko, F. Laquai, R. W. Boyle, M. O. Senge, *J. Am. Chem. Soc.* **2017**, *139*, 6282–6285.

[82] W. Hu, X.-F. Zhang, X. Lu, S. Lan, D. Tian, T. Li, L. Wang, S. Zhao, M. Feng, J. Zhang, *J. Lumin.* **2018**, *194*, 185–192.

[83] C. Schäfer, R. Ringström, J. Hanrieder, M. Rahm, B. Albinsson, K. Börjesson, *Nat. Commun.* **2024**, *15*, 8705.

[84] F. Monti, A. Baschieri, L. Sambri, N. Armaroli, *Acc. Chem. Res.* **2021**, *54*, 1492–1505.

[85] R. Bevernaegie, S. A. M. Wehlin, B. Elias, L. Troian-Gautier, *ChemPhotoChem* **2021**, *5*, 217–234.

[86] L. Schmid, F. Glaser, R. Schaer, O. S. Wenger, *J. Am. Chem. Soc.* **2022**, *144*, 963–976.

[87] L. M. Cañada, J. Kölling, Z. Wen, J. I.-C. Wu, T. S. Teets, *Inorg. Chem.* **2021**, *60*, 6391–6402.

[88] "The American Society for Testing and Materials (ASTM) G-173, 'Reference Air Mass 1.5 Spectra,'" can be found under https://www.nrel.gov/grid/solar-resource/spectra.html, **2003**.

[89] G. J. Kavarnos, in *Photoinduced Electron Transfer I* (Ed.: J. Mattay), Springer Berlin Heidelberg, Berlin, Heidelberg, **1990**, pp. 21–58.

[90] A. Cravcenco, C. Ye, J. Gräfenstein, K. Börjesson, *J. Phys. Chem. A* **2020**, *124*, 7219–7227.

[91] R. A. Marcus, *J. Chem. Phys.* **1956**, *24*, 966–978.

[92] A. H. A. Clayton, G. D. Scholes, K. P. Ghiggino, M. N. Paddon-Row, *J. Phys. Chem.* **1996**, *100*, 10912–10918.

[93] P. Klán, J. Wirz, *Photochemistry of Organic Compounds: From Concepts to Practice*, Wiley, Chichester, West Sussex, U.K, **2009**.

[94] H. L. J. Bäckström, K. Sandros, J.-E. Lindgren, E. Varde, G. Westin, *Acta Chem. Scand.* **1960**, *14*, 48–62.

[95] W. Huang, Z. Dong, *Chem* **2024**, *10*, 3270–3272.

[96] M. V. Popescu, R. S. Paton, *Chem* **2024**, *10*, 3428–3443.

[97] V. Balzani, F. Bolletta, F. Scandola, *J. Am. Chem. Soc.* **1980**, *102*, 2152–2163.

[98] H. B. Gray, J. R. Winkler, *Proc. Natl. Acad. Sci. U.S.A.* **2005**, *102*, 3534–3539.

[99] B. Albinsson, J. Mårtensson, *Phys. Chem. Chem. Phys.* **2010**, *12*, 7338.

[100] O. S. Wenger, *Chem. Soc. Rev.* **2011**, *40*, 3538.

[101] Z. Huang, Z. Xu, T. Huang, V. Gray, K. Moth-Poulsen, T. Lian, M. L. Tang, *J. Am. Chem. Soc.* **2020**, *142*, 17581–17588.

[102] S. Häcker, M. Schrödter, A. Kuhlmann, H.-A. Wagenknecht, *JACS Au* **2023**, *3*, 1843–1850.

[103] C. Curutchet, A. A. Voityuk, *J. Phys. Chem. C* **2012**, *116*, 22179–22185.

[104] S. S. Skourtis, C. Liu, P. Antoniou, A. M. Virshup, D. N. Beratan, *Proc. Natl. Acad. Sci. U.S.A.* **2016**, *113*, 8115–8120.

[105] R. Lai, Y. Liu, X. Luo, L. Chen, Y. Han, M. Lv, G. Liang, J. Chen, C. Zhang, D. Di, G. D. Scholes, F. N. Castellano, K. Wu, *Nat. Commun.* **2021**, *12*, 1532.

[106] B. Nickel, G. Roden, *Chem. Phys.* **1982**, *66*, 365–376.

[107] B. Nickel, *Chem. Phys. Lett.* **1979**, *68*, 17–20.

[108] T. W. Schmidt, F. N. Castellano, *J. Phys. Chem. Lett.* **2014**, *5*, 4062–4072.

[109] L. Naimovičius, E. Radiunas, M. Dapkevičius, P. Bharmoria, K. Moth-Poulsen, K. Kazlauskas, *J. Mater. Chem. C* **2023**, *11*, 14826–14832.

[110] D. G. Bossanyi, Y. Sasaki, S. Wang, D. Chekulaev, N. Kimizuka, N. Yanai, J. Clark, *JACS Au* **2021**, *1*, 2188–2201.

[111] K. Itoh, *Pure Appl. Chem.* **1978**, *50*, 1251–1259.

[112] F. Glaser, C. Kerzig, O. S. Wenger, *Angew. Chem. Int. Ed.* **2020**, *59*, 10266–10284.

[113] L. Zeng, L. Huang, J. Han, G. Han, *Acc. Chem. Res.* **2022**, *55*, 2604–2615.

[114] T. Schloemer, P. Narayanan, Q. Zhou, E. Belliveau, M. Seitz, D. N. Congreve, *ACS Nano* **2023**, *17*, 3259–3288.

[115] G. P. Pfeifer, A. Besaratinia, *Photochem. Photobiol. Sci.* **2012**, *11*, 90–97.

[116] J. Cadet, T. Douki, *Photochem Photobiol Sci* **2018**, *17*, 1816–1841.

[117] H.-A. Wagenknecht, *Angew. Chem. Int. Ed.* **2003**, *42*, 2454–2460.

[118] K. Kawai, T. Majima, *Acc. Chem. Res.* **2013**, *46*, 2616–2625.

[119] S. O. Kelley, J. K. Barton, *Science* **1999**, *283*, 375–381.

[120] T. Otani, T. Sasayama, M. Horiuchi, S. Okauchi, H. Kawai, M. Kitahara, Y. Imai, T. Shibata, *Helv. Chim. Acta* **2021**, *104*, e2100016.

[121] O. E. Weigang, J. A. Turner, P. A. Trouard, *J. Chem. Phys.* **1966**, *45*, 1126–1134.

[122] M. Sapir, E. V. Donckt, *Chem. Phys. Lett.* **1975**, *36*, 108–110.

[123] J. Rocker, T. Opatz, *ACS Org. Inorg. Au* **2022**, *2*, 415–421.

[124] Y. Cai, S. Chatterjee, T. Ritter, *J. Am. Chem. Soc.* **2023**, *145*, 13542–13548.

[125] R. I. Patel, B. Saxena, A. Sharma, *J. Org. Chem.* **2025**, acs.joc.5c00194.

[126] H. Meng, M.-S. Liu, W. Shu, *Chem. Sci.* **2022**, *13*, 13690–13707.

[127] X. Chen, X. Kuang, Y. Wu, J. Zhou, P. Wang, *Chin. J. Chem.* **2023**, *41*, 1979–1986.

[128] L. Jiao, S. Ye, Z.-X. Yu, *J. Am. Chem. Soc.* **2008**, *130*, 7178–7179.

[129] J. J. Molloy, M. Schäfer, M. Wienhold, T. Morack, C. G. Daniliuc, R. Gilmour, *Science* **2020**, *369*, 302–306.

[130] J. J. Molloy, J. B. Metternich, C. G. Daniliuc, A. J. B. Watson, R. Gilmour, *Angew. Chem. Int. Ed.* **2018**, *57*, 3168–3172.

[131] G. Fischer, *Chem. Soc. Rev.* **2000**, *29*, 119–127.

[132] R. J. Abraham, S. L. R. Ellison, P. Schonholzer, W. A. Thomas, *Tetrahedron* **1986**, *42*, 2101–2110.

[133] Z. Wang, H. Hölzel, K. Moth-Poulsen, *Chem. Soc. Rev.* **2022**, *51*, 7313–7326.

[134] V. A. Bren', A. D. Dubonosov, V. I. Minkin, V. A. Chernoivanov, *Russ. Chem. Rev.* **1991**, *60*, 451–469.

[135] K. Moth-Poulsen, D. Ćoso, K. Börjesson, N. Vinokurov, S. K. Meier, A. Majumdar, K. P. C. Vollhardt, R. A. Segalman, *Energy Environ. Sci.* **2012**, *5*, 8534.

[136] R. Schulte, S. Afflerbach, T. Paululat, H. Ihmels, *Angew. Chem. Int. Ed.* **2023**, *62*, e202309544.

[137] R. Schulte, H. Ihmels, *Beilstein J. Org. Chem.* **2022**, *18*, 368–373.

[138] X. Lin, Z. Chen, Y. Han, C. Nie, P. Xia, S. He, J. Li, K. Wu, *ACS Energy Lett.* **2022**, *7*, 914–919.

[139] N. Harada, Y. Sasaki, M. Hosoyamada, N. Kimizuka, N. Yanai, *Angew. Chem. Int. Ed.* **2021**, *60*, 142–147.

[140] J. L. Tyler, D. Trauner, F. Glorius, *Chem. Soc. Rev.* **2025**, *54*, 3272–3292.

[141] L. Buzzetti, G. E. M. Crisenza, P. Melchiorre, *Angew. Chem. Int. Ed.* **2019**, *58*, 3730–3747.

[142] S. De Kreijger, M. Gillard, B. Elias, L. Troian-Gautier, *ChemCatChem* **2023**, e202301100.

[143] F. Bosca, V. Lhiaubet-Vallet, M. C. Cuquerella, J. V. Castell, M. A. Miranda, *J. Am. Chem. Soc.* **2006**, *128*, 6318–6319.

[144] F. Berger, M. B. Plutschack, J. Riegger, W. Yu, S. Speicher, M. Ho, N. Frank, T. Ritter, *Nature* **2019**, *567*, 223–228.

[145] J. S. Taylor, *Acc. Chem. Res.* **1994**, *27*, 76–82.

[146] B. Kohler, *J. Phys. Chem. Lett.* **2010**, *1*, 2047–2053.

[147] K. Nakatani, T. Yoshida, I. Saito, *J. Am. Chem. Soc.* **2002**, *124*, 2118–2119.

[148] L. Antusch, N. Gaß, H. Wagenknecht, *Angew. Chem. Int. Ed.* **2017**, *56*, 1385–1389.

[149] A. M. Brun, A. Harriman, *J. Am. Chem. Soc.* **1994**, *116*, 10383–10393.

[150] D. J. Hurley, Y. Tor, *J. Am. Chem. Soc.* **2002**, *124*, 13231–13241.

[151] R. E. Holmlin, R. T. Tong, J. K. Barton, *J. Am. Chem. Soc.* **1998**, *120*, 9724–9725.

[152] N. A. Romero, D. A. Nicewicz, *Chem. Rev.* **2016**, *116*, 10075–10166.

[153] J. Twilton, C. Le, P. Zhang, M. H. Shaw, R. W. Evans, D. W. C. MacMillan, *Nat. Rev. Chem.* **2017**, *1*, 0052.

[154] A. Albini, M. Fagnoni, *Green Chem.* **2004**, *6*, 1.

[155] L. Marzo, S. K. Pagire, O. Reiser, B. König, *Angew. Chem. Int. Ed.* **2018**, *57*, 10034–10072.

[156] L. Schmid, C. Kerzig, A. Prescimone, O. S. Wenger, *JACS Au* **2021**, *1*, 819–832.

[157] P. Rana, N. Singh, P. Majumdar, S. Prakash Singh, *Coord. Chem. Rev.* **2022**, *470*, 214698.

[158] W. Zhao, F. N. Castellano, *J. Phys. Chem. A* **2006**, *110*, 11440–11445.

[159] T. Otani, T. Sasayama, C. Iwashimizu, K. S. Kanyiva, H. Kawai, T. Shibata, *Chem. Commun.* **2020**, *56*, 4484–4487.

[160] T. Otani, A. Tsuyuki, T. Iwachi, S. Someya, K. Tateno, H. Kawai, T. Saito, K. S. Kanyiva, T. Shibata, *Angew. Chem. Int. Ed.* **2017**, *56*, 3906–3910.

[161] K. Kise, S. Ooi, H. Saito, H. Yorimitsu, A. Osuka, T. Tanaka, *Angew. Chem. Int. Ed.* **2022**, *61*, e202112589.

[162] J. Rocker, J. A. Dresel, L. A. Krieger, P. Eckhardt, A. M. Ortuño, W. R. Kitzmann, G. H. Clever, K. Heinze, T. Opatz, *Chem. Eur. J.* **2023**, *29*, e202301244.

[163] H. Görner, C. Stammel, J. Mattay, *J. Photochem. Photobiol. A: Chem.* **1999**, *120*, 171–179.

[164] K. Schmidt, S. Brovelli, V. Coropceanu, D. Beljonne, J. Cornil, C. Bazzini, T. Caronna, R. Tubino, F. Meinardi, Z. Shuai, J.-L. Brédas, *J. Phys. Chem. A* **2007**, *111*, 10490–10499.

[165] M. Goez, C. Kerzig, *Angew. Chem. Int. Ed.* **2012**, *51*, 12606–12608.

[166] C. Kerzig, M. Goez, *Phys. Chem. Chem. Phys.* **2014**, *16*, 25342–25349.

[167] S. C. Wallace, M. Grätzel, J. K. Thomas, *Chem. Phys. Lett.* **1973**, *23*, 359–362.

[168] S. Timmann, Z. Feng, M. Alcarazo, *Chem. Eur. J.* **2024**, *30*, e202402768.

[169] P. S. Engl, A. P. Häring, F. Berger, G. Berger, A. Pérez-Bitrián, T. Ritter, *J. Am. Chem. Soc.* **2019**, *141*, 13346–13351.

[170] F. Juliá, J. Yan, F. Paulus, T. Ritter, *J. Am. Chem. Soc.* **2021**, *143*, 12992–12998.

[171] E. M. Alvarez, Z. Bai, S. Pandit, N. Frank, L. Torkowski, T. Ritter, *Nat. Synth.* **2023**, *2*, 548–556.

[172] M.-S. Liu, H.-W. Du, W. Shu, *Chem. Sci.* **2022**, *13*, 1003–1008.

[173] Y. Zhao, C. Yu, W. Liang, F. W. Patureau, *Org. Lett.* **2021**, *23*, 6232–6236.

[174] J. Grimshaw, A. P. De Silva, *Chem. Soc. Rev.* **1981**, *10*, 181.

[175] H. Pan, H. Ge, R. He, W. Huang, L. Wang, Y. Wei, R. Sa, Y. Wang, R. Yuan, *Asian J. Org. Chem.* **2019**, *8*, 1513–1518.

[176] J. Paternoga, J. Kühlborn, N. O. Rossdam, T. Opatz, *J. Org. Chem.* **2021**, *86*, 3232–3248.

[177] S. M. Ogbourne, A. Suhrbier, B. Jones, S.-J. Cozzi, G. M. Boyle, M. Morris, D. McAlpine, J. Johns, T. M. Scott, K. P. Sutherland, J. M. Gardner, T. T. T. Le, A. Lenarczyk, J. H. Aylward, P. G. Parsons, *Cancer Research* **2004**, *64*, 2833–2839.

[178] M. Kubo, C. Okada, J.-M. Huang, K. Harada, H. Hioki, Y. Fukuyama, *Org. Lett.* **2009**, *11*, 5190–5193.

[179] J. Wang, S. A. Blaszczyk, X. Li, W. Tang, *Chem. Rev.* **2021**, *121*, 110–139.

[180] P. Liu, L. E. Sirois, P. H.-Y. Cheong, Z.-X. Yu, I. V. Hartung, H. Rieck, P. A. Wender, K. N. Houk, *J. Am. Chem. Soc.* **2010**, *132*, 10127–10135.

[181] S. Maity, M. Zhu, R. S. Shinabery, N. Zheng, *Angew. Chem. Int. Ed.* **2012**, *51*, 222–226.

[182] Y. Zou, L. Lu, L. Fu, N. Chang, J. Rong, J. Chen, W. Xiao, *Angew. Chem. Int. Ed.* **2011**, *50*, 7171–7175.

[183] D.-F. Chen, C. H. Chrisman, G. M. Miyake, *ACS Catal.* **2020**, *10*, 2609–2614.

[184] J. P. Phelan, S. B. Lang, J. S. Compton, C. B. Kelly, R. Dykstra, O. Gutierrez, G. A. Molander, *J. Am. Chem. Soc.* **2018**, *140*, 8037–8047.

[185] C.-J. Wallentin, J. D. Nguyen, P. Finkbeiner, C. R. J. Stephenson, *J. Am. Chem. Soc.* **2012**, *134*, 8875–8884.

[186] A. Gimenez-Gomez, L. Magson, B. Peñin, N. Sanosa, J. Soilán, R. Losantos, D. Sampedro, *Photochem* **2022**, *2*, 694–716.

[187] C. Sun, C. Wang, R. Boulatov, *ChemPhotoChem* **2019**, *3*, 268–283.

[188] M. Russew, S. Hecht, *Adv. Mater.* **2010**, *22*, 3348–3360.

[189] J. Usuba, G. G. D. Han, *Trends Chem.* **2023**, *5*, 577–580.

[190] M. Irie, M. Morimoto, in *Photochemistry* (Eds.: A. Albini, S. Protti), Royal Society Of Chemistry, Cambridge, **2019**, pp. 457–497.

[191] M. Irie, T. Fukaminato, K. Matsuda, S. Kobatake, *Chem. Rev.* **2014**, *114*, 12174–12277.

[192] J. Andréasson, U. Pischel, *Isr. J. Chem* **2013**, *53*, 236–246.

[193] U. Pischel, J. Andréasson, D. Gust, V. F. Pais, *ChemPhysChem* **2013**, *14*, 28–46.

[194] D. J. Unett, R. A. Caldwell, *Res. Chem. Intermed.* **1995**, *21*, 665–709.

[195] J. S. Meek, *J. Chem. Educ.* **1975**, *52*, 541.

[196] C. Liebermann, *Ber. Dtsch. Chem. Ges.* **1890**, *23*, 512–516.

[197] J. Yu, M. J. Gaunt, J. B. Spencer, *J. Org. Chem.* **2002**, *67*, 4627–4629.

[198] D. H. Waldeck, *Chem. Rev.* **1991**, *91*, 415–436.

[199] H. Kuramochi, T. Tsutsumi, K. Saita, Z. Wei, M. Osawa, P. Kumar, L. Liu, S. Takeuchi, T. Taketsugu, T. Tahara, *Nat. Chem.* **2024**, *16*, 22–27.

[200] Jack. Saltiel, G. S. Hammond, *J. Am. Chem. Soc.* **1963**, *85*, 2515–2516.

[201] D. Valentine, G. S. Hammond, *J. Am. Chem. Soc.* **1972**, *94*, 3449–3454.

[202] G. S. Hammond, Jack. Saltiel, A. A. Lamola, N. J. Turro, J. S. Bradshaw, D. O. Cowan, R. C. Counsell, Volker. Vogt, Christopher. Dalton, *J. Am. Chem. Soc.* **1964**, *86*, 3197–3217.

[203] R. A. Caldwell, C. V. Cao, *J. Am. Chem. Soc.* **1982**, *104*, 6174–6180.

[204] R. A. Caldwell, C. Pac, *Chem. Phys. Lett.* **1979**, *64*, 303–306.

[205] W. G. Herkstroeter, G. S. Hammond, *J. Am. Chem. Soc.* **1966**, *88*, 4769–4777.

[206] G. S. Hammond, Peter. Wyatt, C. D. DeBoer, N. J. Turro, *J. Am. Chem. Soc.* **1964**, *86*, 2532–2533.

[207] I. Anger, M. Sundahl, O. Wennerstroem, K. Sandros, T. Arai, K. Tokumaru, *J. Phys. Chem.* **1992**, *96*, 7027–7032.

[208] T. Arai, T. Wakabayashi, H. Sakuragi, K. Tokumaru, *Chem. Lett.* **1985**, *14*, 279–282.

[209] T. Arai, T. Oguchi, T. Wakabayashi, M. Tsuchiya, Y. Nishimura, S. Oishi, H. Sakuragi, K. Tokumaru, *BCSJ* **1987**, *60*, 2937–2943.

[210] T. Arai, T. Karatsu, H. Misawa, Y. Kuriyama, H. Okamoto, T. Hiresaki, H. Furuuchi, H. Zeng, H. Sakuragi, K. Tokumaru, *Pure Appl. Chem.* **1988**, *60*, 989–998.

[211] T. Arai, T. Iwasaki, K. Tokumaru, *Chem. Lett.* **1993**, *22*, 691–694.

[212] Tatsuo. Arai, Katsumi. Tokumaru, *Chem. Rev.* **1993**, *93*, 23–39.

[213] F. D. Lewis, Peter. Teng, Eric. Weitz, *J. Am. Chem. Soc.* **1986**, *108*, 2818–2826.

[214] F. D. Lewis, J. D. Oxman, *J. Am. Chem. Soc.* **1981**, *103*, 7345–7347.

[215] P. P. Teng, E. Weitz, F. D. Lewis, *J. Am. Chem. Soc.* **1982**, *104*, 5518–5519.

[216] L. Zechmeister, *Chem. Rev.* **1944**, *34*, 267–344.

[217] C. Dugave, L. Demange, *Chem. Rev.* **2003**, *103*, 2475–2532.

[218] G. Wald, *Science* **1968**, *162*, 230–239.

[219] R. Alonso, T. Bach, *Angew. Chem. Int. Ed.* **2014**, *53*, 4368–4371.

[220] S. Kahremany, C. L. Sander, G. P. Tochtrop, A. Kubas, K. Palczewski, *Org. Biomol. Chem.* **2019**, *17*, 8125–8139.

[221] H. Fang, A. García-Eguizábal, Y. J. Hsueh, C. G. Daniliuc, I. Funes-Ardoiz, J. J. Molloy, *Angew. Chem. Int. Ed.* **2025**, *64*, e202418651.

[222] B. Kweon, L. Blank, J. Soika, A. Messara, C. G. Daniliuc, R. Gilmour, *Angew. Chem. Int. Ed.* **2024**, *63*, e202404233.

[223] D. G. Hall, Ed. , *Boronic Acids: Preparation and Applications in Organic Synthesis and Medicine*, Wiley, **2005**.

[224] D. K. Balta, G. Temel, M. Aydin, N. Arsu, *Eur. Polym. J.* **2010**, *46*, 1374–1379.

[225] N. F. Nikitas, P. L. Gkizis, C. G. Kokotos, *Org. Biomol. Chem.* **2021**, *19*, 5237–5253.

[226] V. R. Pattabiraman, J. W. Bode, *Nature* **2011**, *480*, 471–479.

[227] S. Kumari, A. V. Carmona, A. K. Tiwari, P. C. Trippier, *J. Med. Chem.* **2020**, *63*, 12290–12358.

[228] Y. Song, L. Clizbe, C. Bhakta, W. Teng, W. Li, P. Wong, B. Huang, U. Sinha, G. Park, A. Reed, R. M. Scarborough, B.-Y. Zhu, *Bioorg. Med. Chem. Lett.* **2002**, *12*, 2043–2046.

[229] H. Yanai, T. Taguchi, *Eur. J. Org. Chem.* **2011**, *2011*, 5939–5954.

[230] S. Fustero, A. Simón-Fuentes, P. Barrio, G. Haufe, *Chem. Rev.* **2015**, *115*, 871–930.

[231] N. Kannan, D. Vakeesan, *Renew. Sustain. Energy Rev.* **2016**, *62*, 1092–1105.

[232] A. Evans, V. Strezov, T. J. Evans, *Renew. Sustain. Energy Rev.* **2012**, *16*, 4141–4147.

[233] D. Gust, T. A. Moore, A. L. Moore, *Acc. Chem. Res.* **2009**, *42*, 1890–1898.

[234] J. H. Montoya, L. C. Seitz, P. Chakthranont, A. Vojvodic, T. F. Jaramillo, J. K. Nørskov, *Nat. Mater.* **2017**, *16*, 70–81.

[235] R. J. Detz, J. N. H. Reek, B. C. C. Van Der Zwaan, *Energy Environ. Sci.* **2018**, *11*, 1653–1669.

[236] P. D. Tran, L. H. Wong, J. Barber, J. S. C. Loo, *Energy Environ. Sci.* **2012**, *5*, 5902.

[237] G. Alva, L. Liu, X. Huang, G. Fang, *Renew. Sustain. Energy Rev.* **2017**, *68*, 693–706.

[238] F. Hemauer, H. Steinrück, C. Papp, *ChemPhysChem* **2024**, *25*, e202300806.

[239] L. Dong, Y. Feng, L. Wang, W. Feng, *Chem. Soc. Rev.* **2018**, *47*, 7339–7368.

[240] H. M. D. Bandara, S. C. Burdette, *Chem. Soc. Rev.* **2012**, *41*, 1809–1825.

[241] J. Isokuortti, K. Kuntze, M. Virkki, Z. Ahmed, E. Vuorimaa-Laukkanen, M. A. Filatov, A. Turshatov, T. Laaksonen, A. Priimagi, N. A. Durandin, *Chem. Sci.* **2021**, *12*, 7504–7509.

[242] T. Saßmannshausen, A. Kunz, N. Oberhof, F. Schneider, C. Slavov, A. Dreuw, J. Wachtveitl, H. A. Wegner, *Angew. Chem. Int. Ed.* **2024**, *63*, e202314112.

[243] M. Rosi, A. Sgamellotti, F. Franceschi, C. Floriani, *Inorg. Chem.* **1999**, *38*, 1520–1522.

[244] J. Orrego-Hernández, A. Dreos, K. Moth-Poulsen, *Acc. Chem. Res.* **2020**, *53*, 1478–1487.

[245] W. Alex, P. Lorenz, C. Henkel, T. Clark, A. Hirsch, D. M. Guldi, *J. Am. Chem. Soc.* **2022**, *144*, 153–162.

[246] A. Dreos, Z. Wang, J. Udmark, A. Ström, P. Erhart, K. Börjesson, M. B. Nielsen, K. Moth-Poulsen, *Adv. Energy Mater.* **2018**, *8*, 1703401.

[247] G. Berkovic, V. Krongauz, V. Weiss, *Chem. Rev.* **2000**, *100*, 1741–1754.

[248] L. Hou, W. Larsson, S. Hecht, J. Andréasson, B. Albinsson, *J. Mater. Chem. C* **2022**, *10*, 15833–15842.

[249] H. Bouas-Laurent, J.-P. Desvergne, A. Castellan, R. Lapouyade, *Chem. Soc. Rev.* **2000**, *29*, 43–55.

[250] S. L. Broman, M. B. Nielsen, *Phys. Chem. Chem. Phys.* **2014**, *16*, 21172–21182.

[251] Z. Wang, J. Udmark, K. Börjesson, R. Rodrigues, A. Roffey, M. Abrahamsson, M. B. Nielsen, K. Moth-Poulsen, *ChemSusChem* **2017**, *10*, 3049–3055.

[252] H. Nakai, K. Isobe, *Coord. Chem. Rev.* **2010**, *254*, 2652–2662.

[253] Z. Yoshida, *J. Photochem.* **1985**, *29*, 27–40.

[254] D. P. Schwendiman, C. Kutal, *J. Am. Chem. Soc.* **1977**, *99*, 5677–5682.

[255] G. S. Hammond, N. J. Turro, A. Fischer, *J. Am. Chem. Soc.* **1961**, *83*, 4674–4675.

[256] F. J. Hernández, J. M. Cox, J. Li, R. Crespo-Otero, S. A. Lopez, *J. Org. Chem.* **2023**, *88*, 5311–5320.

[257] J. C. Cooper, D. M. P. Holland, R. A. Ingle, M. Bonanomi, D. Faccialà, N. De Oliveira, A. R. Abid, J. Bachmann, S. Bhattacharyya, K. Borne, M. Bosch, M. Centurion, K. Chen, R. J. G. Forbes, H. V. S. Lam, A. Odate, A. Rudenko, A. S. Venkatachalam, C. Vozzi, E. Wang, P. M. Weber, M. N. R. Ashfold, A. Kirrander, D. Rolles, *J. Chem. Phys.* **2024**, *160*, 064305.

[258] B. C. Roquitte, *J. Am. Chem. Soc.* **1963**, *85*, 3700–3700.

[259] N. Ivanoff, F. Lahmani, J. F. Delouis, J. L. Le Gouill, *Journal of Photochemistry* **1974**, *2*, 199–220.

[260] N. J. Turro, W. R. Cherry, M. F. Mirbach, M. J. Mirbach, *J. Am. Chem. Soc.* **1977**, *99*, 7388–7390.

[261] A. M. Helms, Richard. A. Caldwell, *J. Am. Chem. Soc.* **1995**, *117*, 358–361.

[262] S. Kita, K. Fukui, *Bull. Chem. Soc. Jpn.* **1969**, *42*, 66–70.

[263] L. Salem, C. Rowland, *Angew. Chem. Int. Ed. Engl.* **1972**, *11*, 92–111.

[264] M. Quant, A. Lennartson, A. Dreos, M. Kuisma, P. Erhart, K. Börjesson, K. Moth-Poulsen, *Chem. Eur. J.* **2016**, *22*, 13265–13274.

[265] Z. Wang, A. Roffey, R. Losantos, A. Lennartson, M. Jevric, A. U. Petersen, M. Quant, A. Dreos, X. Wen, D. Sampedro, K. Börjesson, K. Moth-Poulsen, *Energy Environ. Sci.* **2019**, *12*, 187–193.

[266] K. Jorner, A. Dreos, R. Emanuelsson, O. El Bakouri, I. Fdez. Galván, K. Börjesson, F. Feixas, R. Lindh, B. Zietz, K. Moth-Poulsen, H. Ottosson, *J. Mater. Chem. A* **2017**, *5*, 12369–12378.

[267] K. Börjesson, A. Lennartson, K. Moth-Poulsen, *ACS Sustainable Chem. Eng.* **2013**, *1*, 585–590.

[268] A. Vlasceanu, M. Koerstz, A. B. Skov, K. V. Mikkelsen, M. B. Nielsen, *Angew. Chem. Int. Ed.* **2018**, *57*, 6069–6072.

[269] A. Kunz, H. A. Wegner, *ChemSystemsChem* **2021**, *3*, e2000035.

[270] A. A. Gorman, R. L. Leyland, *Tetrahedron Lett.* **1972**, *13*, 5345–5348.

[271] Hideo. Ikezawa, Charles. Kutal, Katsutoshi. Yasufuku, Hiroshi. Yamazaki, *J. Am. Chem. Soc.* **1986**, *108*, 1589–1594.

[272] K. Nakabayashi, H. Nishino, S. Toki, S. Takamuku, *International Journal of Radiation Applications and Instrumentation. Part C. Radiation Physics and Chemistry* **1989**, *34*, 809–815.

[273] A. H. A. Tinnemans, B. Den Ouden, A. Mackor, H. J. T. Bos, *Recl. Trav. Chim. Pays-Bas* **1985**, *104*, 109–116.

[274] C. Kutal, D. P. Schwendiman, P. Grutsch, *Solar Energy* **1977**, *19*, 651–655.

[275] G. W. Sluggett, N. J. Turro, H. D. Roth, *J. Phys. Chem. A* **1997**, *101*, 8834–8838.

[276] L. Pan, J.-J. Zou, X. Zhang, L. Wang, *Ind. Eng. Chem. Res.* **2010**, *49*, 8526–8531.

[277] F.-Y. Meng, I.-H. Chen, J.-Y. Shen, K.-H. Chang, T.-C. Chou, Y.-A. Chen, Y.-T. Chen, C.-L. Chen, P.-T. Chou, *Nat. Commun.* **2022**, *13*, 797.

[278] M. Upadhyay, R. Deka, D. Ray, *J. Phys. Chem. Lett.* **2024**, 3191–3196.

[279] R. Schulte, S. Afflerbach, H. Ihmels, *Eur. J. Org. Chem.* **2023**, *26*, e202201398.

[280] M. Pawlicki, H. A. Collins, R. G. Denning, H. L. Anderson, *Angew. Chem. Int. Ed.* **2009**, *48*, 3244–3266.

[281] D. A. Kleinman, *Phys. Rev.* **1962**, *128*, 1761–1775.

[282] M. Haase, H. Schäfer, *Angew. Chem. Int. Ed.* **2011**, *50*, 5808–5829.

[283] S. Baluschev, T. Miteva, V. Yakutkin, G. Nelles, A. Yasuda, G. Wegner, *Phys. Rev. Lett.* **2006**, *97*, 143903.

[284] Y. Sasaki, S. Amemori, H. Kouno, N. Yanai, N. Kimizuka, *J. Mater. Chem. C* **2017**, *5*, 5063–5067.

[285] Y. Murakami, K. Kamada, *Phys. Chem. Chem. Phys.* **2021**, *23*, 18268–18282.

[286] A. Olesund, S. Ghasemi, K. Moth-Poulsen, B. Albinsson, *J. Am. Chem. Soc.* **2023**, *145*, 22168–22175.

[287] E. Radiunas, L. Naimovičius, S. Raišys, A. Jozeliūnaitė, E. Orentas, K. Kazlauskas, *J. Mater. Chem. C* **2022**, *10*, 6314–6322.

[288] L. Vaghi, F. Rizzo, J. Pedrini, A. Mauri, F. Meinardi, U. Cosentino, C. Greco, A. Monguzzi, A. Papagni, *Photochem. Photobiol. Sci.* **2022**, *21*, 913–921.

[289] A. Olesund, J. Johnsson, F. Edhborg, S. Ghasemi, K. Moth-Poulsen, B. Albinsson, *J. Am. Chem. Soc.* **2022**, *144*, 3706–3716.

[290] S. Hoseinkhani, R. Tubino, F. Meinardi, A. Monguzzi, *Phys. Chem. Chem. Phys.* **2015**, *17*, 4020–4024.

[291] T. N. Singh-Rachford, F. N. Castellano, *J. Phys. Chem. A* **2009**, *113*, 5912–5917.

[292] A. B. Pun, L. M. Campos, D. N. Congreve, *J. Am. Chem. Soc.* **2019**, *141*, 3777–3781.

[293] F. Qi, H.-J. Feng, Y. Peng, L.-H. Jiang, L. Zeng, L. Huang, *ACS Appl. Mater. Interfaces* **2024**, *16*, 7512–7521.

[294] N. Yanai, M. Kozue, S. Amemori, R. Kabe, C. Adachi, N. Kimizuka, *J. Mater. Chem. C* **2016**, *4*, 6447–6451.

[295] T. J. B. Zähringer, M.-S. Bertrams, C. Kerzig, *J. Mater. Chem. C* **2022**, *10*, 4568–4573.

[296] B. Pfund, D. M. Steffen, M. R. Schreier, M.-S. Bertrams, C. Ye, K. Börjesson, O. S. Wenger, C. Kerzig, *J. Am. Chem. Soc.* **2020**, *142*, 10468–10476.

[297] Y. Murakami, A. Motooka, R. Enomoto, K. Niimi, A. Kaiho, N. Kiyoyanagi, *Phys. Chem. Chem. Phys.* **2020**, *22*, 27134–27143.

[298] Q. Zhou, M. Zhou, Y. Wei, X. Zhou, S. Liu, S. Zhang, B. Zhang, *Phys. Chem. Chem. Phys.* **2017**, *19*, 1516–1525.

[299] K. J. Fallon, E. M. Churchill, S. N. Sanders, J. Shee, J. L. Weber, R. Meir, S. Jockusch, D. R. Reichman, M. Y. Sfeir, D. N. Congreve, L. M. Campos, *J. Am. Chem. Soc.* **2020**, *142*, 19917–19925.

[300] C. Ye, V. Gray, K. Kushwaha, S. Kumar Singh, P. Erhart, K. Börjesson, *Phys. Chem. Chem. Phys.* **2020**, *22*, 1715–1720.

[301] M. Uji, N. Harada, N. Kimizuka, M. Saigo, K. Miyata, K. Onda, N. Yanai, *J. Mater. Chem. C* **2022**, *10*, 4558–4562.

[302] J. Li, M. Zhang, L. Zeng, L. Huang, X. Wang, *Angew. Chem. Int. Ed.* **2023**, *62*, e202303093.

[303] R. R. Islangulov, F. N. Castellano, *Angew. Chem. Int. Ed.* **2006**, *45*, 5957–5959.

[304] F. Glaser, O. S. Wenger, *Chem. Sci.* **2023**, *14*, 149–161.

[305] T. N. Singh-Rachford, F. N. Castellano, *J. Phys. Chem. A* **2008**, *112*, 3550–3556.

[306] Z. Huang, Z. Xu, M. Mahboub, Z. Liang, P. Jaimes, P. Xia, K. R. Graham, M. L. Tang, T. Lian, *J. Am. Chem. Soc.* **2019**, *141*, 9769–9772.

[307] C. J. Imperiale, P. B. Green, M. Hasham, M. W. B. Wilson, *Chem. Sci.* **2021**, *12*, 14111–14120.

[308] T. A. Welsch, M. F. Doty, *ACS Appl. Opt. Mater.* **2024**, acsaom.4c00340.

[309] Y. Han, S. He, X. Luo, Y. Li, Z. Chen, W. Kang, X. Wang, K. Wu, *J. Am. Chem. Soc.* **2019**, *141*, 13033–13037.

[310] Y. Han, X. Luo, R. Lai, Y. Li, G. Liang, K. Wu, *J. Phys. Chem. Lett.* **2019**, *10*, 1457–1463.

[311] R. Lai, Y. Sang, Y. Zhao, K. Wu, *J. Am. Chem. Soc.* **2020**, *142*, 19825–19829.

[312] K. Chen, Q. Luan, T. Liu, B. Albinsson, L. Hou, *Responsive Materials* **2024**, e20240030.

[313] Z. Wang, J. Zhao, *Org. Lett.* **2017**, *19*, 4492–4495.

[314] W. Wu, X. Cui, J. Zhao, *Chem. Commun.* **2013**, *49*, 9009.

[315] C. A. Parker, C. G. Hatchard, *Proc. R. Soc. Lond. A* **1962**, *269*, 574–584.

[316] C. A. Parker, C. G. Hatchard, T. A. Joyce, *Nature* **1965**, *205*, 1282–1284.

[317] C. A. Parker, in *Advances in Photochemistry* (Eds.: W.A. Noyes, G.S. Hammond, J.N. Pitts), Wiley, **1964**, pp. 305–383.

[318] C. A. Parker, T. A. Joyce, *Chem. Commun. (London)* **1968**, 749.

[319] J. L. Charlton, R. Dabestani, J. Saltiel, *J. Am. Chem. Soc.* **1983**, *105*, 3473–3476.

[320] P. E. Keivanidis, S. Baluschev, T. Miteva, G. Nelles, U. Scherf, A. Yasuda, G. Wegner, *Adv. Mater.* **2003**, *15*, 2095–2098.

[321] S. N. Sanders, T. H. Schloemer, M. K. Gangishetty, D. Anderson, M. Seitz, A. O. Gallegos, R. C. Stokes, D. N. Congreve, *Nature* **2022**, *604*, 474–478.

[322] Q. Dou, L. Jiang, D. Kai, C. Owh, X. J. Loh, *Drug Discov. Today* **2017**, *22*, 1400–1411.

[323] J.-H. Kim, J.-H. Kim, *J. Am. Chem. Soc.* **2012**, *134*, 17478–17481.

[324] M. Majek, U. Faltermeier, B. Dick, R. Pérez-Ruiz, A. Jacobi von Wangelin, *Chem. Eur. J.* **2015**, *21*, 15496–15501.

[325] C. G. López-Calixto, M. Liras, V. A. De La Peña O'Shea, R. Pérez-Ruiz, *Appl. Catal. B: Environ.* **2018**, *237*, 18–23.

[326] H.-L. Lee, M.-S. Lee, H. Park, W.-S. Han, J.-H. Kim, *Korean J. Chem. Eng.* **2019**, *36*, 1791–1798.

[327] M. Barawi, F. Fresno, R. Pérez-Ruiz, V. A. De La Peña O'Shea, *ACS Appl. Energy Mater.* **2019**, *2*, 207–211.

[328] H. Hirayama, S. Fujikawa, N. Kamata, *Electron. Commun. Jpn.* **2015**, *98*, 1–8.

[329] B. Lehmann, *Photochem. Photobiol.* **2005**, *81*, 1246–1251.

[330] N. Zhang, G. Liu, H. Liu, Y. Wang, Z. He, G. Wang, *J. Hazard. Mater.* **2011**, *192*, 411–418.

[331] A. G. Griesbeck, N. Maptue, S. Bondock, M. Oelgemöller, *Photochem. Photobiol. Sci.* **2003**, *2*, 450–451.

[332] *Exposure to Mercury: Preventing Disease Through Healthy Environments*, World Health Organization, Geneva, **2021**.

[333] G. S. Pozan, A. Kambur, *Appl. Catal. B: Environ.* **2013**, *129*, 409–415.

[334] R. Salgado, V. J. Pereira, G. Carvalho, R. Soeiro, V. Gaffney, C. Almeida, V. V. Cardoso, E. Ferreira, M. J. Benoliel, T. A. Ternes, A. Oehmen, M. A. M. Reis, J. P. Noronha, *J. Hazard. Mater.* **2013**, *244–245*, 516–527.

[335] F. Nicastro, G. Sironi, E. Antonello, A. Bianco, M. Biasin, J. R. Brucato, I. Ermolli, G. Pareschi, M. Salvati, P. Tozzi, D. Trabattoni, M. Clerici, *Sci. Rep.* **2021**, *11*, 14805.

[336] L. Finlayson, I. R. M. Barnard, L. McMillan, S. H. Ibbotson, C. T. A. Brown, E. Eadie, K. Wood, *Photochem. Photobiol.* **2022**, *98*, 974–981.

[337] R. Pérez-Ruiz, *Top. Curr. Chem.* **2022**, *380*, 23.

[338] G. S. Hammond, Jack. Saltiel, *J. Am. Chem. Soc.* **1963**, *85*, 2516–2517.

10 Appendix

10.1 Use of AI tools

AI TOOL	USED FOR	WHY	WHEN
CHATGPT	Rewriting of text drafts	Correct grammar and improve overall readability	Throughout the entire thesis

10.2 Supporting Information for Project [A]

Supporting Information for

Direct Observation of Triplet–Triplet Energy Transfer in DNA between Energy Donor and Acceptor C-Nucleotides

Sebastian Häcker [a§], Till J. B. Zähringer [b§], Hans-Achim Wagenknecht [a]*, and Christoph Kerzig [b]*

[a] *Institute of Organic Chemistry, Karlsruhe Institute of Technology (KIT), 76131 Karlsruhe, Germany*
[b] *Department of Chemistry, Johannes Gutenberg University Mainz, Duesbergweg 10-14, 55128 Mainz, Germany*

* Email: wagenknecht@kit.de
* Email: ckerzig@uni-mainz.de
§ S.H. and T.J.B.Z. contributed equally to this paper, names ordered alphabetically.

Table of Contents

1. General information ... 2
2. DNA synthesis and purification ... 4
3. Synthesis ... 5
4. Additional spectroscopic measurements ... 8
   4.1 Triplet-triplet energy transfer of ^{3}TX to Ntl in MeCN ... 8
   4.2 Measurements with DNA control samples ... 9
   4.3 Characterization of photoproduct X ... 9
   4.4 Fluorescence lifetime measurements ... 13
   4.5 Triplet quenching by oxygen ... 14
   4.6 TA spectra of **TX-1** and **TX-Ntl-1** ... 15
   4.7 Kinetic TA traces of **TX-Ntl-2** and **TX-2** ... 15
   4.8 77 K emission spectra of **TX-Ntl-0** and triplet energy of TX_{DNA} ... 16
5. Further discussion of the energy transfer mechanism ... 17
6. Images of ^{1}H, ^{13}C and ^{31}P NMR spectra and of MS analyses ... 18
7. DNA analyses and melting temperatures ... 28
8. Images of MS and HPLC analyses of the DNA ... 30
9. References ... 32

1. General information

Materials

Unless specifically mentioned, all chemicals used for synthesis or optical spectroscopy were commercially obtained and used as received. The solvents and compounds for optical spectroscopy, together with manufacturer and purity, are as follows: acetonitrile, 99.9%, Fisher Scientific; thioxanthone, 97%, Sigma-Aldrich (purified by recrystallization from toluene/EtOAc prior to use); naphthalene, 97%, Alfa Aesar; deoxyadenosine, >99%, Thermo Scientific; thymidine >99%, Thermo Scientific; NaP_i buffer pH 7: Sodium phosphate monobasic, >98%, Sigma-Aldrich; Sodium phosphate dibasic, >98.5%, Riedel-de Haën; doubly distilled H_2O (Merck Milli-Q Direct 8); ultrapure Millipore MilliQ water with a specific resistance of 18.2 MΩ cm.

Argon from Nippon Gases (5.0) was used for removing dissolved oxygen before all experiments related to optical spectroscopy.

Unmodified oligonucleotides were purchased from Metabion.

NMR spectroscopy

^{1}H NMR (400 MHz), ^{13}C NMR (101 MHz), and ^{31}P NMR (162 MHz) spectra were measured on a Bruker Avance 400. The chemical shifts in the ^{1}H and ^{13}C NMR spectra are reported in parts per million (ppm) relative to tetramethylsilane as an internal standard. The chemical shifts in the ^{31}P NMR spectra are also reported in ppm relative to the deuterated solvent. The coupling constant (*J*) is given in Hertz (Hz), and the multiplicity of signals are reported as follows: s (singlet), d (doublet), t (triplet), m (multiplet), dt (doublet of triplets), td (triplet of doublets), dd (doublet of doublets), tt (triplet of triplets) and ddd (doublet of doublet of doublets).

Mass Spectrometry

Mass spectrometry was performed on a Finnigan MAT 95 with FAB and EI as ionization methods. ESI mass spectrometry was performed on a Thermo Fisher Scientific Q Exactive (Orbitrap). Oligonucleotides were identified by MALDI mass spectrometry using an AXIMA Confidence spectrometer from Shimadzu. The matrix contained 3-hydroxypicolinic acid (in MeCN/ doubly distilled H_2O 1:1) and diammonium hydrogen citrate (0.44 M in doubly distilled H_2O) in a 9:1 ratio.

HPLC

A Thermo Scientific Dionex Ultimate 3000 HPLC system, equipped with an autosampler, pump module, column oven, multi-diode array detector, fluorescence detector and fraction collector, was used for the semi-preparative purification of oligonucleotides as well as for their analytical characterization. A Supercosil LC 318 column (25 cm x 10 mm, 5 µm) from VDS Optilab was used for the semi-preparative purification. A VDSpher OptiBio Pur 300 S18-SE from VDS Optilab was used for the analytical determination of the oligonucleotides.

Melting temperatures

Melting temperatures of DNA double strands (2.5 µM DNA, 250 mM NaCl, 10 mM Na-P_i buffer, 10-90 °C, 0.5 °C/min, step width 0.5 °C) were recorded with a Cary 3500 Multicell UV-Vis spectrometer.

Steady-state measurements

Absorption spectra were recorded with a Perkin Elmer LAMBDA 365 UV-Vis spectrophotometer. All spectra were recorded at room temperature (295 ± 3 K) using 10 mm quartz glass cuvettes.

Laser flash photolysis (LFP)

The LP980KS setup from Edinburgh Instruments equipped with an Nd:YAG laser from Quantel (Q-smart 450) was employed for transient absorption and emission spectroscopy. The frequency-tripled (355 nm) output served as the excitation source. The laser pulse duration was ~5 ns and the pulse frequency was 10 Hz. The typical pulse energy used for transient absorption and emission studies was ~20 mJ. A constant laser pulse energy was used within a series of experiments, which was ensured by power measurements before, after and in-between the experiments. The laser power was measured using a pyroelectric detector with attenuator (QE25LP-S-MB-QED-D0) from Gentec-eo combined with the integra software. Detection of transient absorption spectra occurred on an iCCD camera from Andor. Kinetic traces at selected wavelengths were recorded using a photomultiplier tube. The spectroscopic experiments were performed at 293 K using a cuvette holder that allows temperature control. If not stated otherwise the TA spectra were integrated over 100 ns. Longpass filters (385 nm or 400 nm, both from Newport) were used for transient absorption measurements with detection wavelengths exceeding 600 nm to exclude contributions from second-order signals.

77 K Phosphorescence measurements

77 K measurements were carried out with the LP980KS setup. The standard cuvette holder was replaced by a dewar that holds a 4 mm glass tube surrounded by liquid nitrogen.

Time-correlated single photon counting (TCSPC)

The *mini*-τ setup from Edinburgh Instruments (time-correlated single photon counting (TCSPC) technique) equipped with a pulsed laser (EPL-375, excitation at 371.1 nm, pulse width 58.3 ps) was employed for fluorescence lifetime measurements of the DNA double strands at 293 K. Stray light was removed with band pass filters and neutral density filters were used to avoid oversaturation of the detector.

Excited state lifetime determination and TTET rate constants

If not stated otherwise, a biexponential fit function was used to determine the weighted average lifetime of the fluorescence and transient triplet-excited states. The kinetic transient absorption spectra of **TX-Ntl-n** and **TX-n** (n = 0, 1, 2) where fitted after 4 µs after laser pulse excitation in order to exclude the secondary process (see Section S4.3 for details).

Triplet energy transfer rates, k_{TTET}, within the DNA double strands between TX and Ntl were determined by the following equation. Where τ_{obs} is the measured lifetime of the DNA double strand (**TX-Ntl-n**, n = 0, 1, 2) and τ_{ref} is the reference triplet state lifetime of TX in the absence of Ntl (**TX-n**, n = 0, 1, 2),

$$k_{\mathrm{TTET}} = \frac{1}{\tau_{\mathrm{obs}}} - \frac{1}{\tau_{\mathrm{ref}}} = k_{\mathrm{obs}} - k_{\mathrm{ref}} \quad (1)$$

Table S1: Triplet state decay constants k_{ref} of **TX-n** (n= 0, 1, 2), triplet state decay constants k_{obs} of **TX-Ntl-n** (n= 0, 1, 2) and calculated TTET rate constants k_{TTET}.

Sample	k_{ref} (s^{-1})	k_{obs} (s^{-1})	k_{TTET} (s^{-1})
TX-Ntl-0	$(16.9 \pm 0.9) \times 10^3$	$(58.8 \pm 11.7) \times 10^6$ [a]	$(58.8 \pm 11.7) \times 10^6$
TX-Ntl-1	$(15.9 \pm 1.1) \times 10^3$	$(38.6 \pm 3.9) \times 10^3$ [b]	$(22.7 \pm 4.0) \times 10^3$
TX-Ntl-2	$(18.1 \pm 0.3) \times 10^3$	$(18.2 \pm 0.3) \times 10^3$	$(0.1 \pm 0.4) \times 10^3$

[a] Rate determined from the faster component of the biexponential fit function in Figure 2C (main text). Estimated relative error 20%. [b] Rate obtained by fitting the curve in the 4-14 µs range monoexponentially shown in Figure 3B (main text). Estimated relative error 10%.

2. DNA synthesis and purification

Reagents and controlled-pore glass (CPG) (1 µmol) were purchased from ABI and GlenResearch. Oligonucleotide synthesis was carried out under an argon atmosphere using an H-6 DNA/RNA synthesizer from K&A Laborgeräte. The coupling protocol was modified for the incorporation of thioxanthone- and naphthalene-phosphoramidites (Table S2). The modified oligonucleotides were synthesized as trityl-on oligonucleotides and pre-purified using Glen-Pak DNA Purification Cartidges before purification by semi-preparative HPLC with the following conditions: mobile phase A = NH_4OAc buffer (50 mM, pH 7), mobile phase B = acetonitrile, flow rate 2.5 mL/min, UV/Vis detection at 260, 280 and 310/385 nm. After purification, the oligonucleotides were lyophilized, and their concentrations were determined by absorbance at 260 nm using a Nanodrop ND-1000 spectrophotometer. Analytical characterization of purified oligonucleotides was performed via RP-HPLC under the following conditions: mobile phase A = NH_4OAc buffer (50 mM, pH 7), mobile phase B = acetonitrile (gradient: 1-45% B), flow rate = 1.0 mL/min, UV/Vis detection at 260, 280 and 310/385 nm.

Table S2: Coupling protocol of thioxanthone- and naphthalene-phosphoramidite.

	Time [0.1 s]	Source	Mixed	Destin	S.Col.Ptr.	Lag time [s]	Branch
				BRANCH			
1	4	TET		COL	ON		
2	6	AMD	TET	COL			
3					ON		
4						99	
5						99	
6						99	
7						99	
8						99	
9						99	
10						99	
11						99	
12	6	AMD	TET	COL	ON		
13					ON		
14						99	
15						99	
16						99	
17						99	
18						99	
19						99	
20						99	
21						99	
22	4	TET		COL	ON		
23					ON		
24	20	ACN		M_W			
25	20	GAS		M_W			

3. Synthesis

Synthesis of **2**

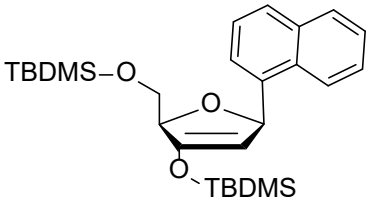

2a

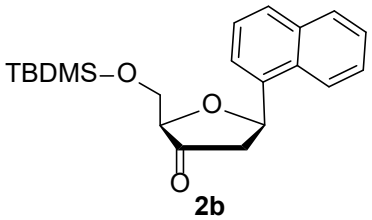

2b

In an argon-flushed flask 1-bromonaphthalene (1.00 eq.), Glykal **1** (1.00 eq.) and triethylamine (2.15 eq.) were dissolved in dimethylformamide, stirred at room temperature for 10 min and degassed using freeze-pump-thaw method. Subsequently $Pd_2(dba)_3$ (0.05 eq.) and Q-Phos (0.20 eq.) were added and the reaction mixture was stirred at 80 °C for 72 h. The solvent was removed under reduced pressure and the crude product was purified by column chromatography (SiO_2, gradient cyclohexane/EtOAc 10:1 → 3:1) to obtain **2a** (44%) and **2b** (35%) as a colorless solid.

2a:

^{1}H NMR (400 MHz, $CDCl_3$) δ 8.15 – 8.10 (m, 1H), 7.88 – 7.84 (m, 1H), 7.81 – 7.74 (m, 2H), 7.54 – 7.42 (m, 3H), 6.53 (dd, *J* = 3.8, 1.6 Hz, 1H), 5.03 (t, *J* = 1.8 Hz, 1H), 4.69 (tt, *J* = 4.3, 2.2 Hz, 1H), 3.91 (dd, *J* = 11.2, 2.3 Hz, 1H), 3.76 (dd, *J* = 11.2, 4.6 Hz, 1H), 0.96 (s, 9H), 0.83 (s, 9H), 0.23 (d, *J* = 17.4 Hz, 6H), –0.07 (d, *J* = 3.8 Hz, 6H).

^{13}C NMR (101 MHz, $CDCl_3$) δ 151.30, 138.87, 133.70, 131.19, 128.75, 127.91, 126.03, 125.73, 125.45, 124.19, 123.45, 101.34, 84.37, 80.93, 64.73, 27.07, 26.12, 25.73, 18.64, 18.22, –4.69, –4.73, –5.26, –5.31.

HR-MS (ESI, $[M+H]^+$) m/z: found: 471.2744; calc.: 471.2745.

2b:

^{1}H NMR (400 MHz, $CDCl_3$) δ 8.04 – 7.99 (m, 1H), 7.94 – 7.87 (m, 2H), 7.83 (d, *J* = 8.2 Hz, 1H), 7.56 – 7.47 (m, 3H), 5.89 (dd, *J* = 11.2, 5.7 Hz, 1H), 4.16 (t, *J* = 2.6 Hz, 1H), 4.10 – 4.01 (m, 2H), 3.04 (dd, *J* = 17.7, 5.7 Hz, 1H), 2.55 (dd, *J* = 17.7, 11.2 Hz, 1H), 0.88 (s, 9H), 0.12 (s, 3H), 0.08 (s, 3H).

^{13}C NMR (101 MHz, $CDCl_3$) δ 129.12, 128.64, 126.47, 125.97, 125.82, 125.77, 123.28, 123.03, 120.47, 119.58, 110.71, 82.94, 75.10, 62.68, 45.92, 25.97, –5.24, –5.47.

HR-MS (ESI, $[M+H]^+$) m/z: found: 357.1879; calc.: 357.1880.

Synthesis of 3

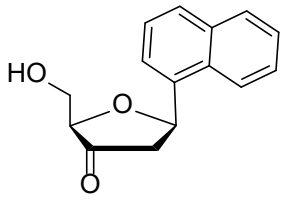

3

In an argon-flushed flask **2** (1.00 eq.) was dissolved in dry THF. The mixture was cooled down to 0 °C, $Et_3N{\cdot}3HF$ (8.00 eq.) was added and stirred at room temperature overnight. The solvent was removed under reduced pressure and the crude product was purified by column chromatography (SiO_2, gradient CH_2Cl_2 → CH_2Cl_2/MeOH 10:1) to obtain **3** as a colorless solid (60%).

^{1}H NMR (400 MHz, $CDCl_3$) δ 8.03 – 7.97 (m, 1H), 7.91 – 7.83 (m, 2H), 7.75 (d, *J* = 7.1 Hz, 1H), 7.58 – 7.49 (m, 3H), 5.90 (dd, *J* = 11.1, 5.7 Hz, 1H), 4.17 (t, *J* = 3.5 Hz, 1H), 4.05 – 3.97 (m, 2H), 3.11 – 3.03 (m, 1H), 2.71 – 2.61 (m, 1H).

^{13}C NMR (101 MHz, $CDCl_3$) δ 213.93, 135.31, 133.88, 130.66, 129.13, 129.07, 126.64, 126.03, 125.61, 123.09, 122.79, 82.43, 75.08, 61.65, 44.79.

HR-MS (ESI, $[M+H]^+$) m/z: found: 243.1015; calc.: 243.1016.

Synthesis of 4

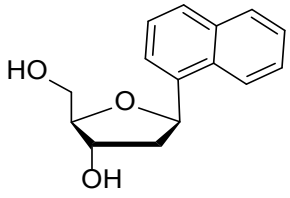

4

In an argon-flushed flask **3** (1.00 eq) was dissolved in AcOH/MeCN (1:3) and sodium triacetoxyborohydride (8.00 eq) was added at 0 °C. The reaction mixture was stirred at room temperature for 40 min and quenched afterwards with the same volume EtOH/H_2O (1:1). The solvent was removed under reduced pressure and the crude product was purified by column chromatography (SiO_2, gradient CH_2Cl_2→ CH_2Cl_2/MeOH 10:1) to obtain **4** as a colorless solid in a yield of 80%.

^{1}H NMR (400 MHz, $CDCl_3$) δ 8.09 – 8.01 (m, 1H), 7.87 (dd, *J* = 7.9, 1.7 Hz, 1H), 7.79 (d, *J* = 8.2 Hz, 1H), 7.65 (dt, *J* = 7.3, 1.1 Hz, 1H), 7.56 – 7.45 (m, 3H), 5.90 (dd, *J* = 10.1, 5.7 Hz, 1H), 4.50 (dt, *J* = 6.1, 2.7 Hz, 1H), 4.13 (td, *J* = 4.5, 3.4 Hz, 1H), 3.95 – 3.79 (m, 2H), 2.51 (ddd, *J* = 13.3, 5.8, 2.3 Hz, 1H), 2.15 (ddd, *J* = 13.3, 10.1, 6.5 Hz, 1H).

^{13}C NMR (101 MHz, $CDCl_3$) δ 137.08, 133.83, 130.81, 128.94, 128.26, 126.27, 125.81, 125.62, 123.48, 122.02, 87.03, 73.93, 63.60, 43.30.

HR-MS (ESI, $[M]^+$) m/z: found: 244.1094; calc.: 244.1094.

Synthesis of 5

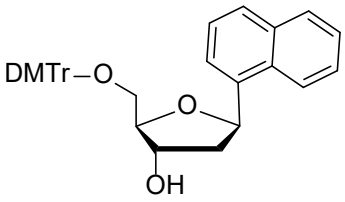

5

In an argon-flushed flask **4** (1.00 eq.) was dissolved in dry pyridine. 4,4`-Dimethoxytriphenylmethylchlorid (1.50 eq.) was gradually added to the reaction mixture and stirred at room temperature overnight. The solvent was removed under reduced pressure and the crude product was purified by column chromatography (SiO_2, gradient CH_2Cl_2→ CH_2Cl_2/acetone 20:1) to obtain **5** as a colorless solid in a yield of 63%.

^{1}H NMR (400 MHz, $CDCl_3$) δ 7.99 – 7.91 (m, 1H), 7.80 – 7.75 (m, 1H), 7.71 – 7.52 (m, 2H), 7.47 – 7.27 (m, 4H), 7.23 – 7.12 (m, 5H), 7.10 – 7.04 (m, 3H), 6.73 (d, *J* = 8.9 Hz, 4H), 5.79 (dt, *J* = 9.5, 6.4 Hz, 1H), 4.39 (ddd, *J* = 7.4, 5.3, 2.9 Hz, 1H), 4.08 – 3.98 (m, 1H), 3.77 (ddd, *J* = 31.1, 11.4, 4.3 Hz, 2H), 2.48 – 2.33 (m, 1H), 2.13 – 1.98 (m, 1H).

^{13}C NMR (101 MHz, $CDCl_3$) δ 158.78, 139.60, 130.27, 129.28, 128.93, 128.48, 128.36, 128.24, 128.00, 127.91, 127.23, 126.25, 126.09, 125.79, 125.62, 123.48, 122.01, 113.32, 87.03, 73.95, 63.61, 55.40, 43.33.

HR-MS (EI, $[M]^+$) m/z: found: 546.2399; calc.: 546.2401..

Synthesis of 6

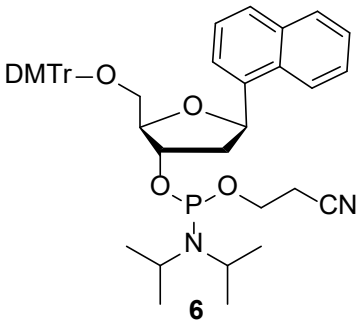

6

In an argon-flushed flask **5** (1.00 eq.) was dissolved in abs. CH_2Cl_2. N,N-Diisopropylethylamine (3.50 eq) was added to the reaction mixture at room temperature. Subsequently, 2-Cyanoethyl N,N-diisopropylchlorophosphoramidite (1.50 eq.) was added and the mixture stirred for 3 h. The crude product was purified by column chromatography (SiO_2, CH_2Cl_2/acetone 50:1 + 0,1% Et_3N) to obtain **6** as a colorless solid in a yield of 98%.

^{1}H NMR (400 MHz, $CDCl_3$) δ 8.12 – 8.05 (m, 1H), 7.91 – 7.84 (m, 1H), 7.83 – 7.74 (m, 2H), 7.53 – 7.42 (m, 5H), 7.39 (ddd, *J* = 8.8, 4.3, 1.9 Hz, 4H), 7.31 – 7.27 (m, 1H), 7.25 – 7.17 (m, 2H), 6.85 – 6.77 (m, 4H), 5.88 (dt, *J* = 10.3, 5.3 Hz, 1H), 4.64 – 4.53 (m, 1H), 4.35 – 4.29 (m, 1H), 3.92 – 3.80 (m, 1H), 3.80 – 3.77 (m, 6H), 3.77 – 3.54 (m, 3H), 3.46 – 3.31 (m, 2H), 2.72 – 2.52 (m, 2H), 2.52 – 2.44 (m, 1H), 2.21 – 2.08 (m, 1H), 1.30 – 1.15 (m, 9H), 1.10 (d, *J* = 6.8 Hz, 3H).

^{31}P NMR (162 MHz, $CDCl_3$) δ 148.4, 147.9.

HR-MS (ESI, $[M+H]^+$) m/z: found: 747.3550; calc.: 747.3558.

4. Additional spectroscopic measurements

4.1 Triplet-triplet energy transfer of ^{3}TX to Ntl in MeCN

To serve as a reference for the DNA samples, we characterized a solution of TX both in the presence and absence of 1 mM Ntl in deaerated acetonitrile (MeCN) using transient absorption spectroscopy. It is important to note that the triplet state lifetime of both TX and Ntl is significantly influenced by excitation intensity and excited state concentration, which can lead to self-quenching and annihilation.[1–3] Upon excitation, TX nearly quantitatively and instantaneously forms the triplet state, exhibiting characteristic maxima at 320 nm and 625 nm, along with a ground-state bleach (GSB) at 380 nm in the transient absorption spectrum (Figure S1A, red spectrum) with a measured lifetime of 23.0 µs (Figure S1B).[4] In the presence of 1 mM Ntl (Figure S1C, purple spectrum), ^{3}TX is quantitatively (>99%) quenched (τ_{obs} = 19 ns) according to excited state quenching dynamics,[5] and ^{3}Ntl is formed with a maximum at 410 nm (Figure S1A). The triplet state lifetime of Ntl was measured to be 15.0 µs (Figure S1B) under our conditions. The triplet energy of TX is 2.75 eV,[4] which is 0.12 eV higher than that of Ntl (2.63 eV);[5] this thermodynamic driving force is sufficient for an approximately diffusion-controlled (k_{TTET} ~ 10^{10} M^{-1} s^{-1}) energy transfer rate constant in line with reported energy transfer rate constants for this donor-acceptor system.[6,7]

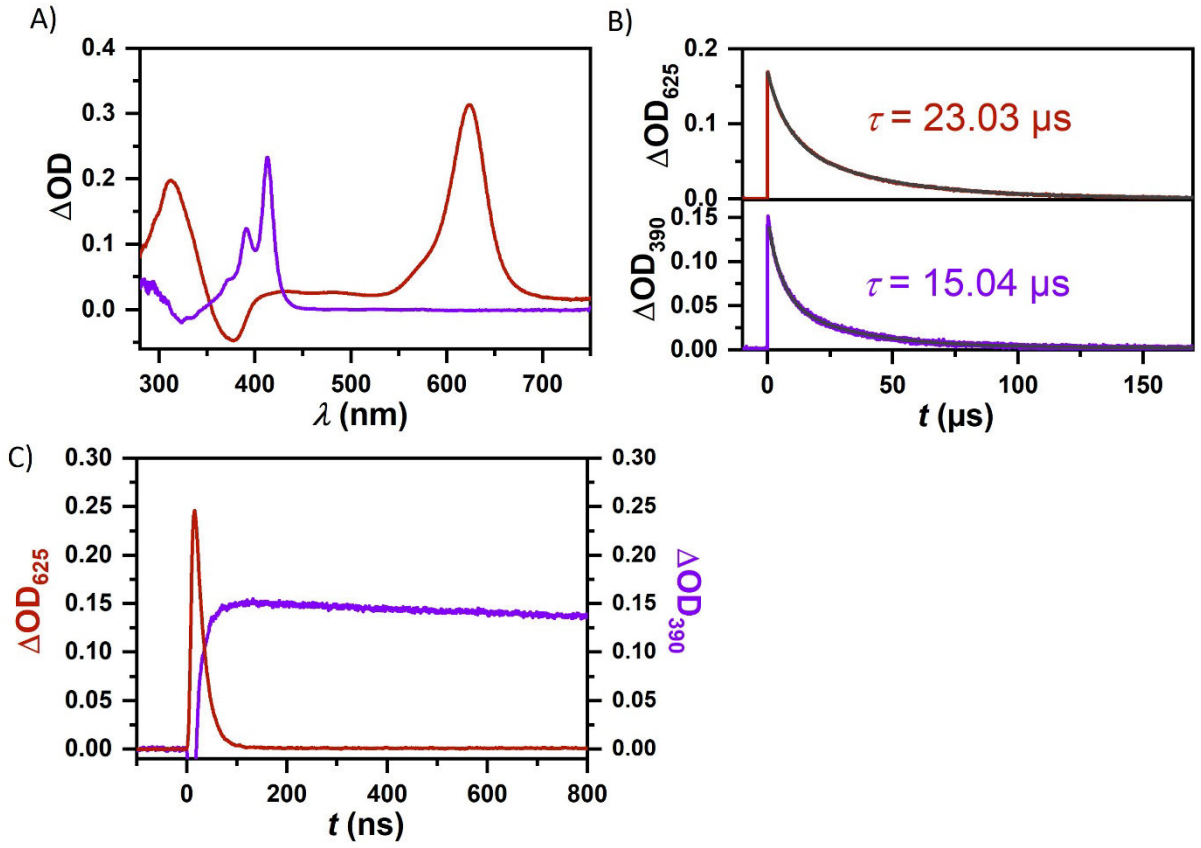

Figure S1: Transient absorption spectra of 20 µM TX in the absence (red) and in the presence of 1 mM Ntl (purple) in deaerated MeCN excited by 355 nm laser pulses of ~5 ns duration (20 mJ per pulse). A) TA spectra recorded 600 ns after excitation. B) Top panel: Time-resolved absorption of ^{3}TX (in the absence of Ntl). Bottom panel: Time-resolved absorption of ^{3}Ntl. C) Simultaneous deactivation of ^{3}TX (625 nm, red) and formation of ^{3}Ntl (390 nm, purple) on a nanosecond timescale.

4.2 Measurements with DNA control samples

To exclude direct excitation of the DNA double strands, two control samples were investigated by LFP with 355 nm laser pulses. The sample **Control** lacked both TX and Ntl, whereas the **Ntl-Control** contained only Ntl, with TX replaced by the initial thymine base (Figure S2A). TA spectra of the control samples in deaerated aqueous solution (250 mM NaCl, 10 mM Na-P_i-buffer) recorded 100 ns after the initial laser pulse did not show the formation of any transient species (Figure S2B and S2C).

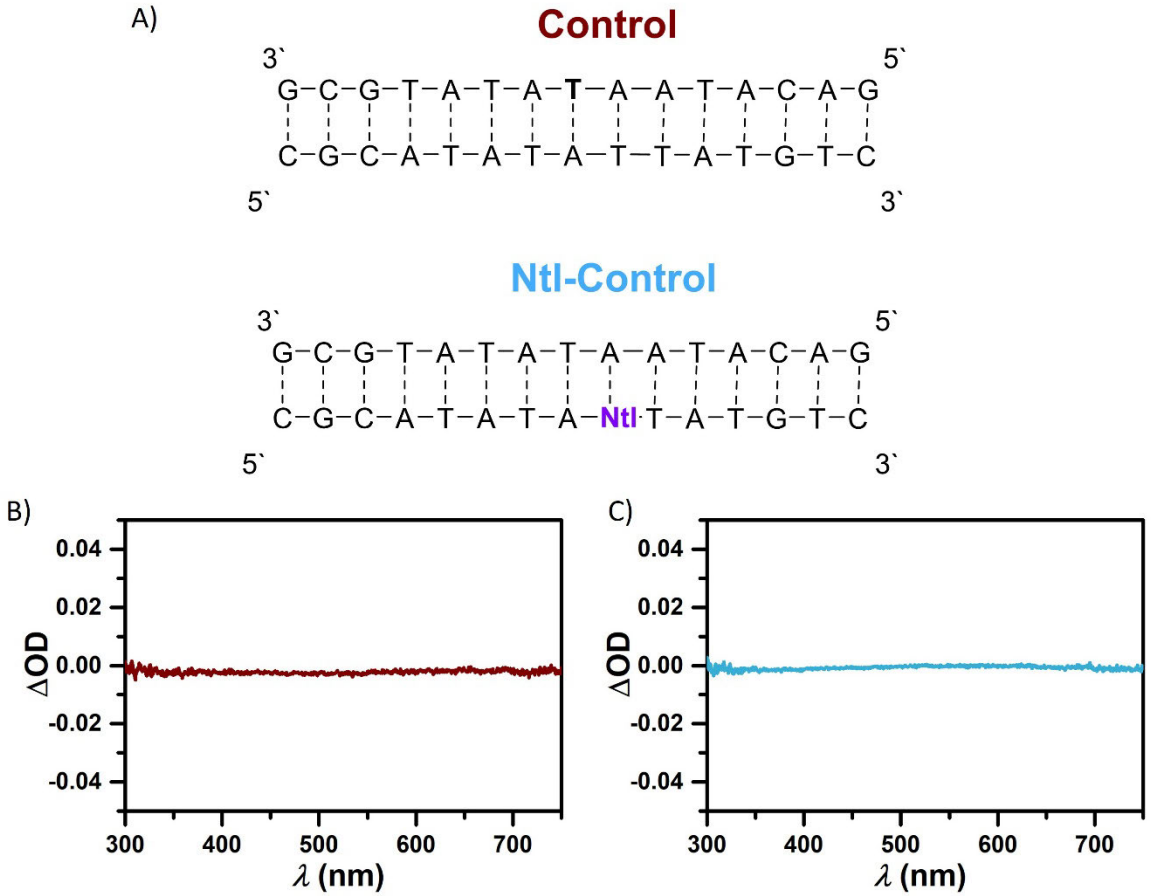

Figure S2: A) Structures of control DNA double strand samples. TA spectra of B) **Control** and C) **Ntl-Control** recorded in deaerated aqueous solution (250 mM NaCl, 10 mM Na-Pi-buffer) 100 ns after 355 nm laser pulses.

4.3 Characterization of photoproduct X

Apart from the triplet energy transfer between TX and Ntl, a secondary independent process was identified. This phenomenon was noted for all DNA samples containing TX and is for example shown for **TX-2** (Figure S3), although essentially identical observations were made for the other TX-containing samples.

Directly after excitation with 355 nm laser pulses an additional transient species was observed, exhibiting a broad absorption peak centered at 610 nm (Figure S3A), with a much faster decay than that of the TX triplet state (Figure S3B, top panel). Furthermore, this decay is accompanied by the formation of another transient species at 525 nm referred to as photoproduct X (Figure S3A and Figure S3B, bottom panel). The decay of X at 525 nm is superimposed by ^{3}TX, and our results indicate that it does not significantly absorb at 612 nm (Figure S3C). However, when compared to the kinetic traces at 612 nm we observe a similar lifetime to ^{3}TX of the photoproduct indicating that the process is reversible. We note that this process was not only observed in all samples but is also independent of the presence or absence of Ntl in the counter strand, albeit to different degrees (Figure S3D).

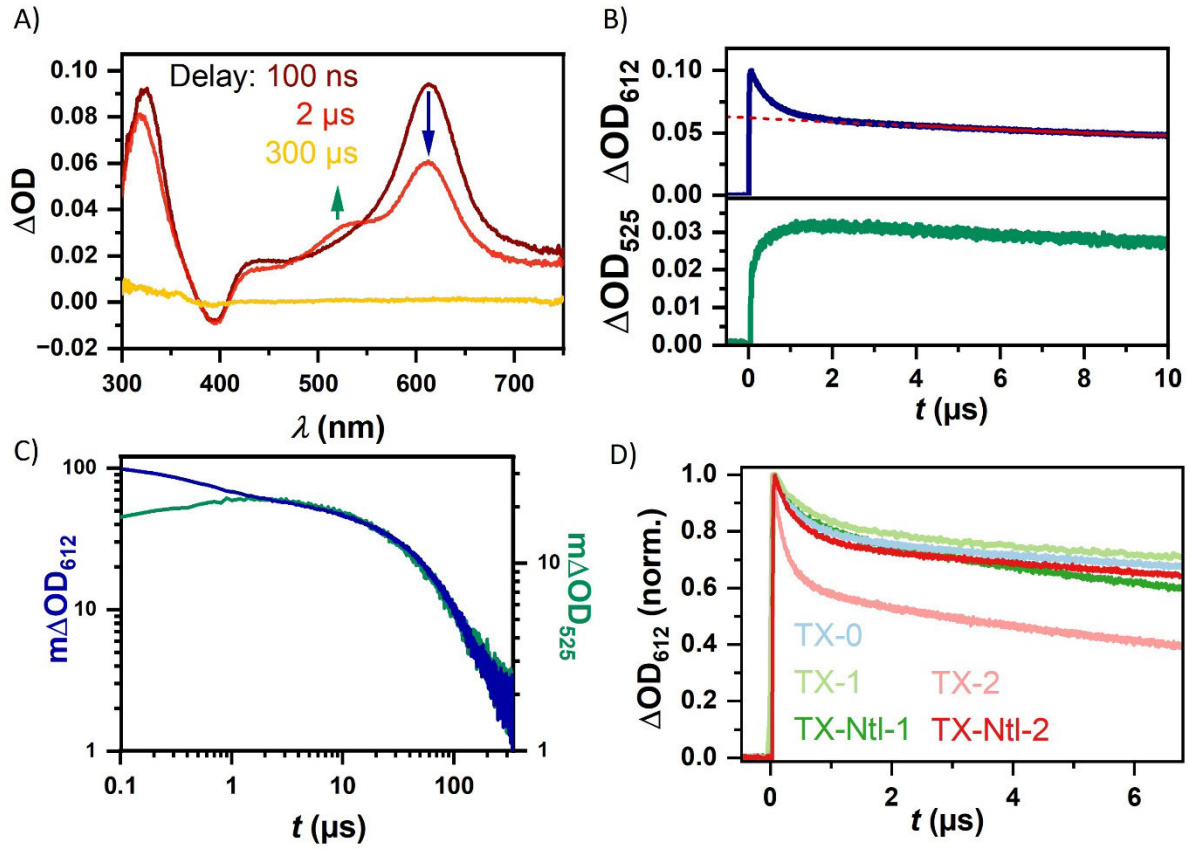

Figure S3: TA spectra of **TX-2** in deaerated aqueous solution (250 mM NaCl, 10 mM Na-P_i buffer). A) Spectra recorded 100 ns, 2 µs and 300 µs after excitation. B) Kinetic measurements at 612 nm (top panel, with monoexponential fit function of the ^{3}TX decay (red line), fitted 4 µs after excitation and extrapolated to the pre-fitting region) and at 525 nm (bottom panel). C) Kinetic measurements at 612 nm and at 525 nm for a comparison of the signals of the unexpected species on a double-logarithmic scale. D) Normalized kinetic traces at 612 nm of several DNA samples.

In contrast, only baseline levels are detected in the absence of TX following 355 nm laser pulses (see Section S4.2). To explore the novel species further the single-stranded DNA containing TX (**ssTX-0**) was examined. Exciting this sample at 355 nm produced results similar to those observed previously. Although the triplet state lifetime of TX is shorter in the single-stranded sample, we still see the formation of the secondary process (Figure S4). Based on these measurements, we conclude that the signals do not stem from denatured double-stranded DNA or interstrand crosslinking following the hydrogen abstraction reaction but instead originate from the strand containing the TX C-nucleotide.

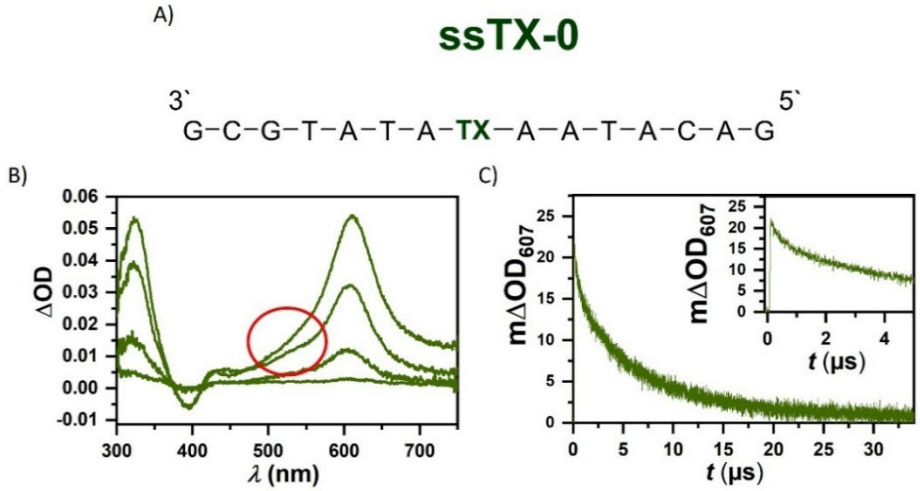

Figure S4: A) Structure of single strand sample **ssTX-0**. B) TA spectra of 90 µM single strand sample in deaerated aqueous solution (250 mM NaCl, 10 mM Na-P_i buffer) recorded 100 ns, 1 µs, 5 µs and 25 µs after 355 nm excitation. The red circle indicates the photoproduct. C) Kinetic measurements at 607 nm. Inset: Post-pulse signals (0-5 µs) on enlarged scale.

It was hypothesized that the secondary process could be a result of a two-photon absorption process, given that photoionization was observed for several chromophores in polar media upon 355 nm ns-laser excitation.[8–10] Hence, we studied the laser excitation intensity dependence of the sample **TX-2** by TA spectroscopy at different time delays and laser intensities ranging from 2.7 mJ to 58 mJ (Figure S5A and B). Selected wavelengths were plotted against the laser intensity (Figure S5C). However, the formation of X at 525 nm (2 µs delay), the broad signal at 612 nm (100 ns delay) and the transient absorption of ^{3}TX at 612 nm (2 µs delay) do not show quadratic behavior, which would be indicative of a two-photon process. The difference transient absorption spectrum of **TX-2** recorded at 100 ns and 2 µs (adjusted for the decay of ^{3}TX) is shown in Figure S5D. The negative signal at 525 nm corresponds to the photoproduct X. The difference spectrum shows two maxima at 320 nm and 612 nm as well as a minimum at 380 nm.

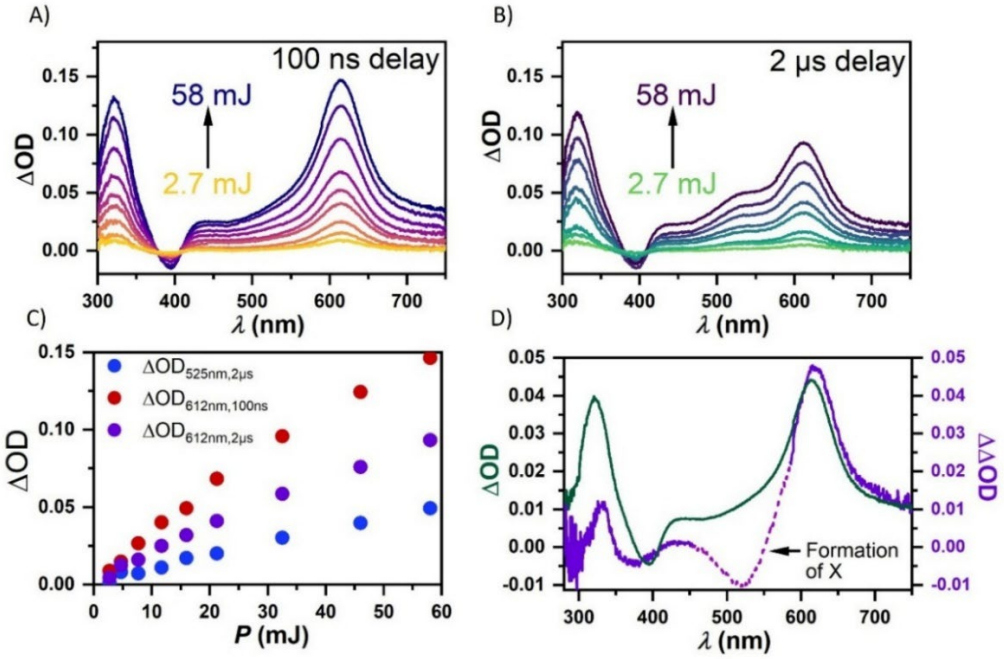

Figure S5: Laser intensity dependent measurements of **TX-2** with excitation energies ranging from 2.7 mJ to 58 mJ. A) TA spectra recorded A) 100 ns and B) 2 µs after excitation. C) Transient absorption signals at selected wavelengths plotted against the laser intensity. D) TA spectrum recorded after 100 ns (green) and difference TA spectrum of 100 ns delay and 2 µs delay (purple), adjusted for the decay of ^{3}TX (compare Figure S3B), the formation of photoproduct X is highlighted by dashed lines.

The close similarity between the difference spectrum in Figure S5D and the TA spectrum of $^3TX_{DNA}$ itself led us to investigate the influence of nearby nucleotides on TX. An Ar-saturated solution of TX in a 4:1 (v/v) mixture of H_2O and MeCN was prepared and examined with and without 100 mM thymidine or deoxyadenosine (Figure S6). The steady-state absorption spectrum of TX was already altered by the addition of 100 mM deoxyadenosine, a change that cannot be explained by the absorption of deoxyadenosine itself (λ_{onset} < 325 nm, Figure S6A). The absorption maximum at 386 nm is slightly red-shifted and its intensity is reduced, while the absorption below 350 nm is increased.

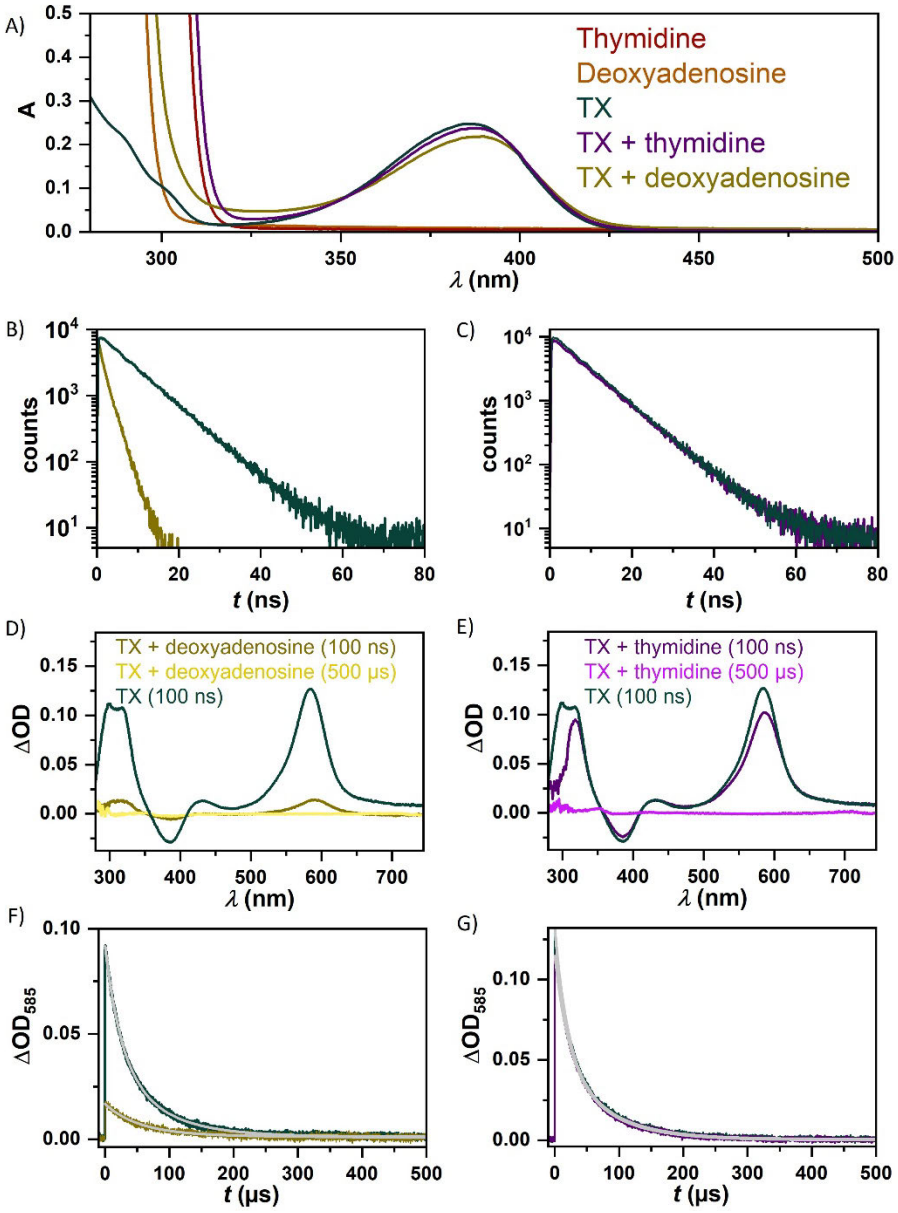

Figure S6: Quenching experiments of 5 µM TX (dark green) with 100 mM of the nucleotides thymidine (violet) and deoxyadenosine (dark yellow) in Ar-saturated H_2O/MeCN (v/v 4:1). A) Absorption spectra of the compounds. B) Time-resolved emission of TX in the presence and absence of deoxyadenosine (same color code as in A). C) Time-resolved emission of TX in the presence and absence of thymidine. D) TA Spectra of TX in the absence (delay: 100 ns) and presence of deoxyadenosine (delay: 100 ns and 500 µs). D) TA Spectra of TX in the absence (delay: 100 ns) and presence of thymidine (delay: 100 ns and 500 µs). F) Time-resolved transient absorption at 585 nm in the presence and absence of deoxyadenosine. G) Time-resolved transient absorption at 585 nm in the presence and absence of thymidine.

This effect was not observed to the same extent when thymidine was added, suggesting that the ribose moiety is not responsible for the change. Fluorescence quenching of TX was only observed with the addition of deoxyadenosine (Figure S6B and C). A reduction in triplet state formation of TX in the presence of deoxyadenosine was noted, likely due to singlet state quenching (Figure S6D). Under the

same conditions, nearly identical triplet absorption spectra of TX were observed with or without thymidine (Figure S6E). These findings appear contradictory, as the excited singlet state of adenosine (> 4 eV)[11] should not be accessible via energy transfer from singlet-excited TX (3.3 eV)[12]. Electron or hydrogen atom transfer reactions can also be excluded (or they are non-productive), as no thioxanthone-derived photoproducts were detected after excitation (Figure S6D and S6E). We propose the formation of a five-membered electron donor-acceptor ring between the carbonyl moiety of thioxanthone and the adenine moiety, as has been suggested for acetone quenching by adenine.[13] The partial protonation of the carbonyl group could explain the red shift in the ground-state absorption and the acceleration of excited singlet state deactivation.[14] An emission shift due to singlet-exciplex formation could not be observed with the addition of adenosine.[15]

Based on these control experiments, it is reasonable to conclude that the adenosine nucleotide adjacent to the thioxanthone C-nucleotide (twice) in the DNA structures may influence the excited state properties of thioxanthone, as observed in Figure S3. However, we note that this interaction between thioxanthone and adenosine occurs consistently across all samples with almost identical kinetics. Therefore, as a result of all control and reference experiments carried out by us, our primary investigation of triplet-triplet energy transfer between $^3TX_{DNA}$ and Ntl_{DNA} is not negatively affected by this interaction.

4.4 Fluorescence lifetime measurements

The fluorescence lifetime of the samples **TX-Ntl-0**, **TX-0**, **TX-Ntl-1**, **TX-1**, **TX-Ntl-2** and **TX-2** were measured by TCSPC using a pulsed laser at 371.1 nm (Figure S7). Using a biexponential fit function we determined τ_1, τ_2 and the amplitude weighted average lifetime τ_{avg} as displayed in Table S3.

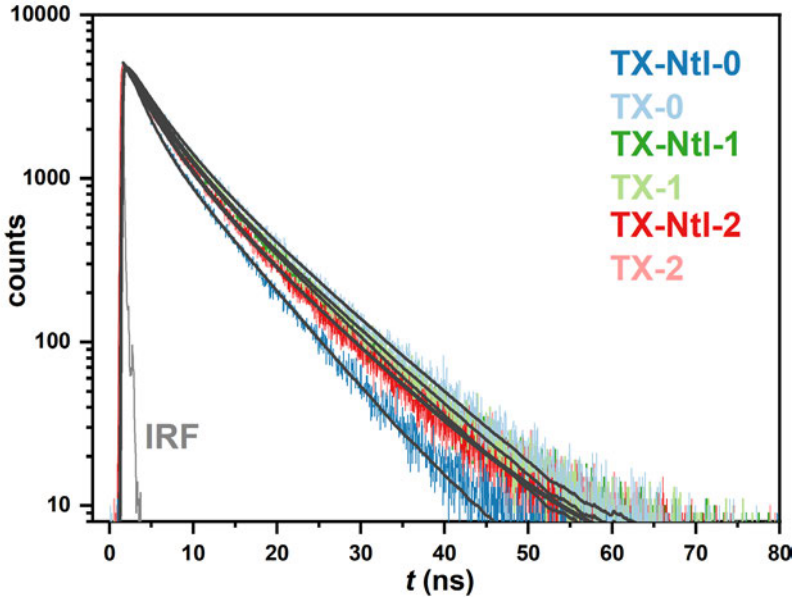

Figure S7: Time-resolved fluorescence measurements of **TX-Ntl-0**, **TX-0**, **TX-Ntl-1**, **TX-1**, **TX-Ntl-2** and **TX-2** in deaerated aqueous solution (250 mM NaCl, 10 mM Na-Pi buffer) upon pulsed laser excitation (371.1 nm) fitted with a biexponential decay function. Lifetimes are given in Table S3. Detection occurred between 425 and 475 nm using a suitable optical filter.

In comparison to the fluorescence lifetime of TX in organic solvents like acetonitrile (MeCN), which is 70 ps, the fluorescence lifetime of TX incorporated into double-stranded DNA samples is over two orders of magnitude longer but comparable to the lifetimes that we obtained in H_2O/MeCN (Figure S6B). This extended lifetime is anticipated when polar protic solvents are utilized. For instance, in methanol (MeOH), the lifetime of TX increases to 2.55 ns, and in a mixture of acetonitrile and water (v/v 3:2), it reaches 4.9 ns.[14,16]

Table S3: Fluorescence lifetimes (τ_1, τ_2, τ_{avg}) of DNA samples **TX-Ntl-0**, **TX-0**, **TX-Ntl-1**, **TX-1**, **TX-Ntl-2** and **TX-2** determined using a biexponential decay function following TCSPC measurements with a pulsed laser at 371.1 nm.

Sample	τ_1 (ns)	τ_2 (ns)	τ_{avg} (ns)
TX-Ntl-0	2.07	7.22	4.31
TX-0	3.66	9.53	6.40
TX-Ntl-1	2.82	8.58	5.66
TX-1	3.33	9.21	5.92
TX-Ntl-2	3.50	9.19	5.59
TX-2	3.35	9.35	5.52

4.5 Triplet quenching by oxygen

In an air-saturated solution, the lifetime of ^{3}TX (**TX-0**) decreases from 59.3 µs to 29.9 µs due to the presence of oxygen, which acts as a triplet state quencher (Figure S8). Taking the high ionic strength into account, the O_2 solubility (c = 0.29 mM in neat water at 20°C)[5] is lower by ~10 % (i.e., 0.261 mM).[17] We estimate a quenching rate constant of ~ $6.4 \cdot 10^7$ M^{-1} s^{-1}, using the observed lifetimes and the above-mentioned oxygen concentration. This is roughly two orders of magnitude lower than diffusion-based quenching in water. We propose that the DNA backbone provides significant shielding to the C-nucleotides of TX and Ntl, effectively preventing inter-DNA energy transfer, which would be highly inefficient at the 90 µM concentration of the DNA samples and could not account for the observed energy transfer rate in **TX-Ntl-1**.

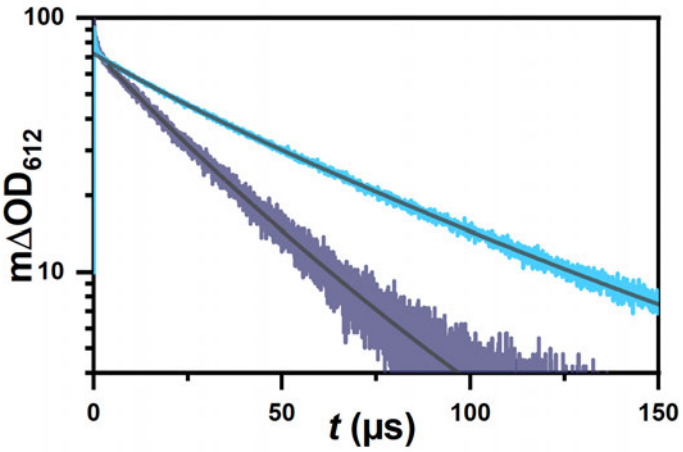

Figure S8: Time-resolved TA traces of **TX-0** in Ar-saturated (blue) and air-saturated (violet) aqueous solution (250 mM NaCl, 10 mM Na-P_i buffer).

4.6 TA spectra of **TX-1** and **TX-Ntl-1**

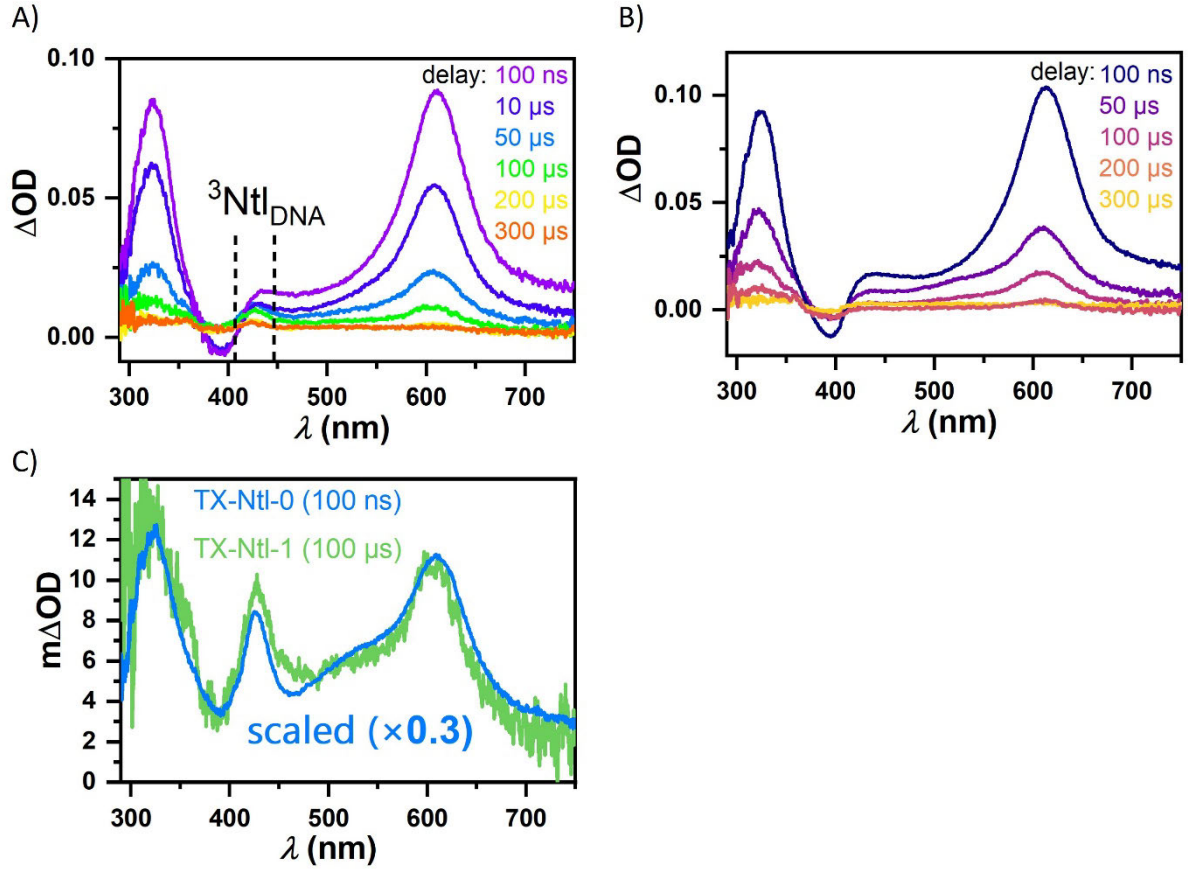

Figure S9: TA spectra of A) **TX-Ntl-1** and B) **TX-1** in deaerated aqueous solution (250 mM NaCl, 10 mM Na-P$_i$ buffer) recorded after different time delays. C) Direct comparison of TA spectra of **TX-Ntl-0** recorded after 100 ns (scaled) and of **TX-Ntl-1** after 100 µs.

4.7 Kinetic TA traces of **TX-Ntl-2** and **TX-2**

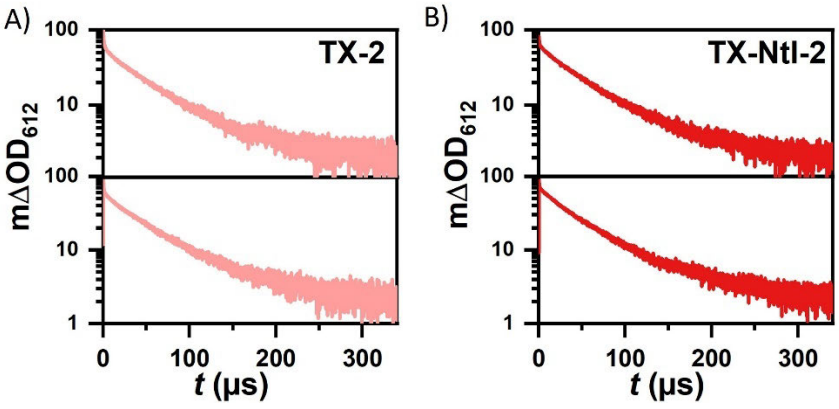

Figure S10: Kinetic TA traces of **TX-2** (A)) and **TX-Ntl-2** (B)) in deaerated aqueous solution (250 mM NaCl, 10 mM Na-P$_i$ buffer), recorded independently. Top panel: initial measurement; Bottom panel: measured after ~ 24 h. Each measurement comprises 40 individual measurements.

Two independent sets of TX$_{DNA}$ lifetime measurements for **TX-2** and **TX-Ntl-2** were conducted on separate days. The consistency between these measurements underscores the high photostability of the DNA samples, supporting the reliability of the obtained lifetimes. Final values were calculated by averaging the results from both sets.

4.8 77 K emission spectra of **TX-Ntl-0** and triplet energy of TX_{DNA}

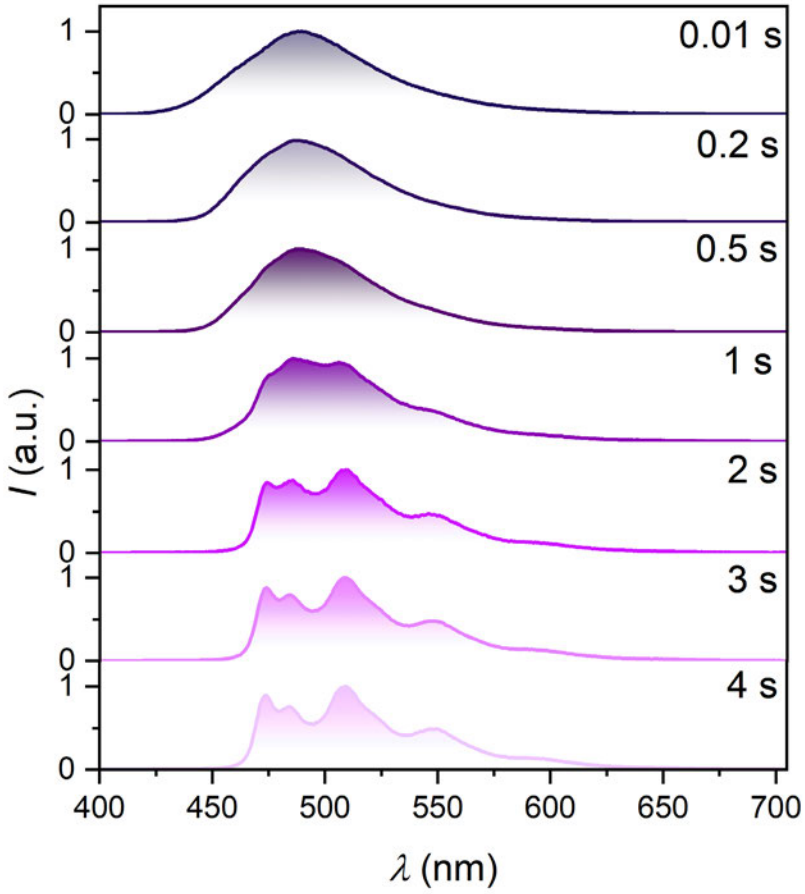

Figure S11: Time-gated 77 K emission spectra of **TX-Ntl-0** in frozen water (250 mM NaCl, 10 mM Na-Pi buffer) after 355 nm laser pulse excitation. Time delays to the excitation were set between 0.01 and 4 s. The integration window ranged from 100 ms to 300 ms.

The difference in triplet energy between $^3TX_{DNA}$ and $^3Ntl_{DNA}$ was estimated on the basis of room temperature (293 K) TA spectra and 77 K emission spectra of **TX-Ntl-0** according to the Boltzmann distribution expressed below:[18–20]

$$\ln\left(\frac{n_2}{n_1}\right) = -\frac{1}{T}\cdot\frac{\Delta E}{R} \qquad (2)$$

Where $\frac{n_2}{n_1}$ is the ratio between $^3TX_{DNA}$ and $^3Ntl_{DNA}$ in the equilibrated state, T is the temperature, R is the gas constant, and ΔE is the energy difference. The ratio $\frac{n_2}{n_1}$ was estimated at 293 K based on the reduction of the triplet absorption maximum of TX_{DNA} at 612 nm (Figure 2A, main paper) to be 0.61 (i.e., in the TTET equilibrium), assuming that $^3TX_{DNA}$ is not deactivated by alternative loss channels. The phosphorescence spectra of $^3TX_{DNA}$ and $^3Ntl_{DNA}$ at 77 K are almost entirely superimposed making it difficult to determine an exact ratio. However, assuming that the phosphorescence quantum yield is similar for both emitters and that only $^3TX_{DNA}$ emits at 450 nm, we estimated a ratio of $\frac{n_2}{n_1} = 0.05$ as an upper limit. Using these ratios, we obtained an energy difference of $\Delta E \sim 0.02$ eV. Given that the triplet state energy of $^3Ntl_{DNA}$ was determined at 2.61 eV from the fine-structured phosphorescence spectrum, we estimated the triplet state energy of $^3TX_{DNA}$ at ~ 2.63 eV.

5. Further discussion of the energy transfer mechanism

Bridge-mediated triplet-triplet energy transfer can occur through various coupling mechanisms possibly involving virtual intermediate states.[21–23] The assumption that the TTET attenuation factor is the sum of the individual electron and hole contributions no longer holds when electron and hole transfer do not occur concertedly forming intermediate charge transfer (CT) states or bridge-localized excited states.[22–25] Instead, the attenuation factor is more likely governed by the rate-limiting initial transfer step, i.e. either electron or hole transfer reaching a virtual CT state, followed by a rapid complementary electron/hole transfer.[23]

These virtual states are essentially undetectable using conventional spectroscopic techniques. Nonetheless, as with standard electron (or hole) transfer, by semi-classical theory the attenuation factor can be related to the effective barrier height, with the transfer rate being proportional to the electronic coupling matrix element.[21] This prediction was shown to be in good agreement with experimental values. [26]

$$\Delta E_{\text{eff}} = \left(\frac{\hbar}{8m_e}\right)\beta^2 = \left(0.952\ \text{eV Å}^2\right)\beta^2 \qquad (3)$$

If virtual CT states dominate the Dexter pathway, the theoretically determined barrier height would be expected to approximate the experimental value. With the attenuation factor determined in our study (1.15 $Å^{-1}$), we calculate an effective barrier height of 1.26 eV using equation (3). Given that this barrier height is defined by the energy gap between the donor (~2.63 eV for TX_{DNA}) and the bridge (thymine), this value would exceed the triplet energy of even free thymine.[27] In fact, literature reports place the triplet energy of thymine in poly A-T sequences at 3.0 eV, which would suggest a much weaker distance dependence than observed.[28] This discrepancy indicates that bridge-mediated coupling and virtual CT states play a negligible role in the TTET pathway in our study, and it rather suggests a concerted transfer mechanism.[22,23,29]

6. Images of ^{1}H, ^{13}C and ^{31}P NMR spectra and of MS analyses

Compound 2a

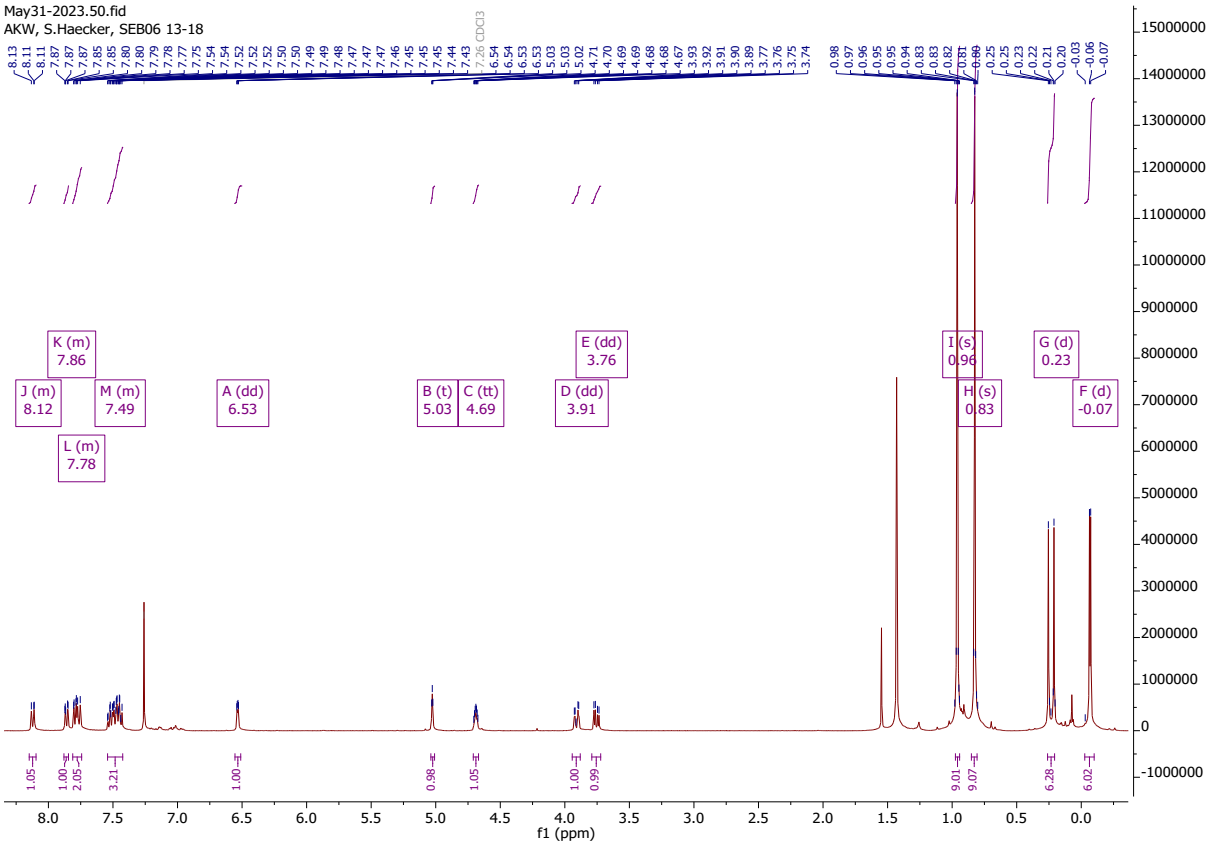

Figure S12: ^{1}H NMR (400 MHz, $CDCl_3$) of **2a**.

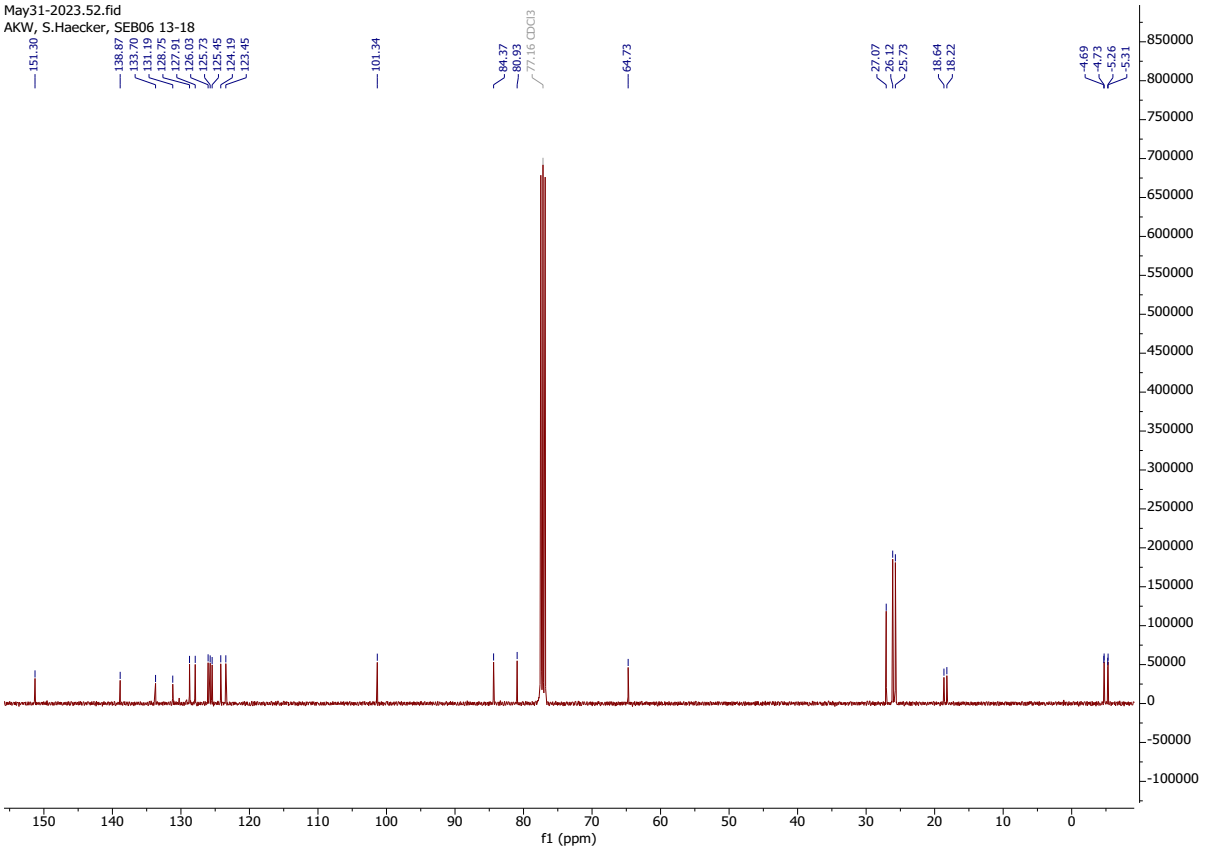

Figure S13: ^{13}C NMR (101 MHz, $CDCl_3$) of **2a**.

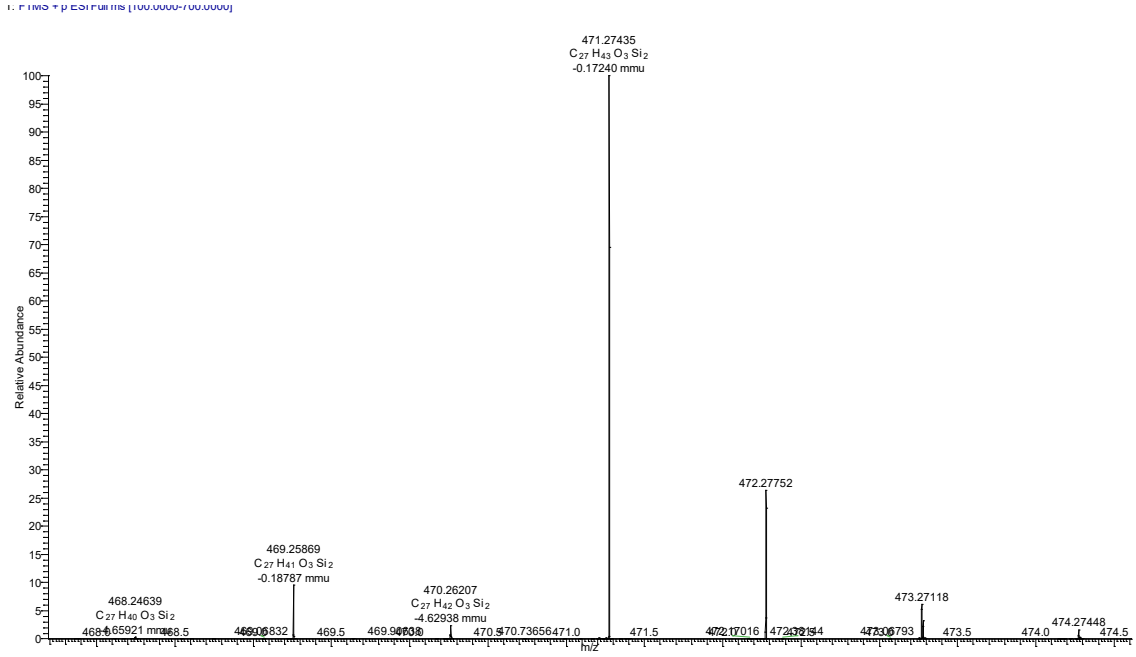

Figure S14: HR ESI-MS analysis of **2a**.

Compound 2b

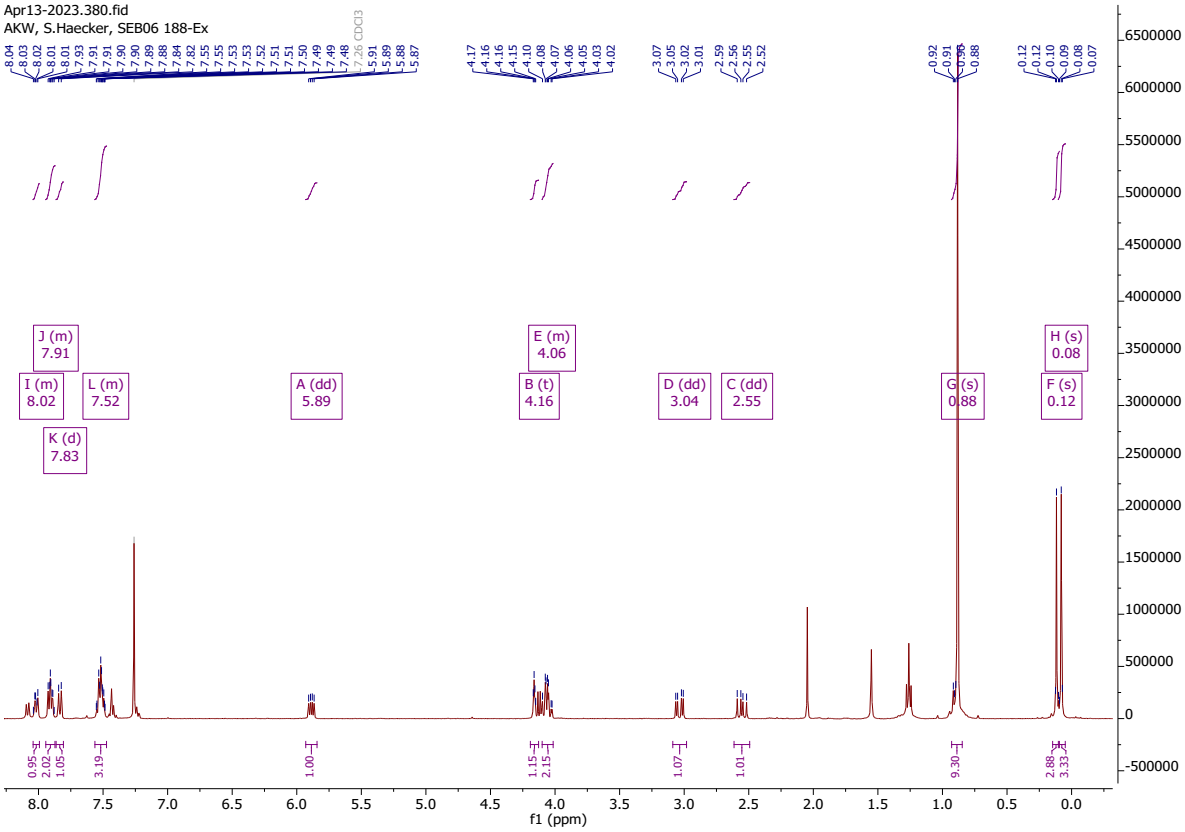

Figure S15: ^{1}H NMR (400 MHz, $CDCl_3$) of **2b**.

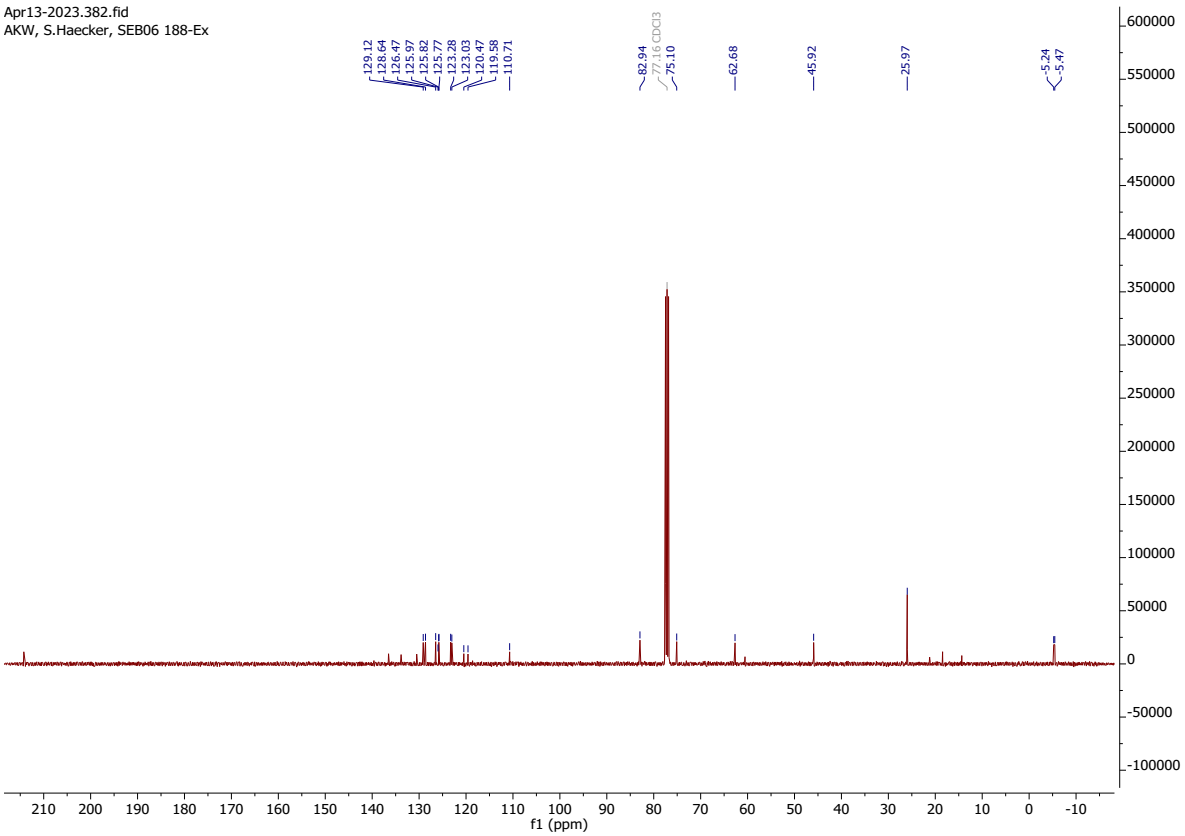

Figure S16: ^{13}C NMR (101 MHz, $CDCl_3$) of **2b**.

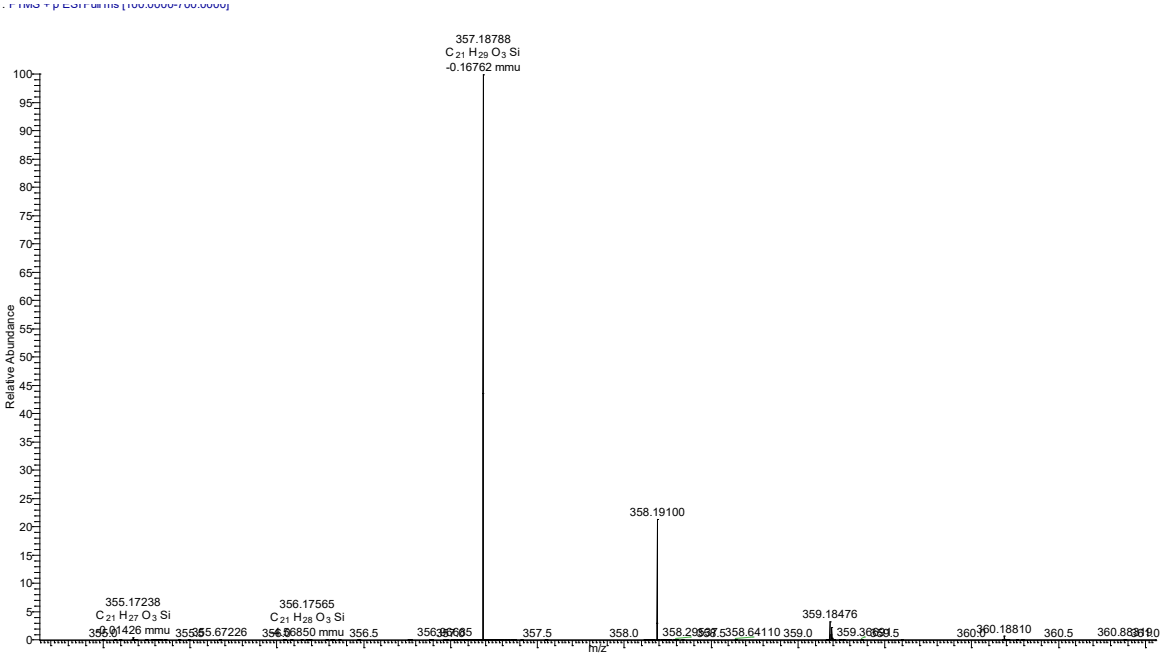

Figure S17: HR ESI-MS analysis of **2b**.

Compound 3

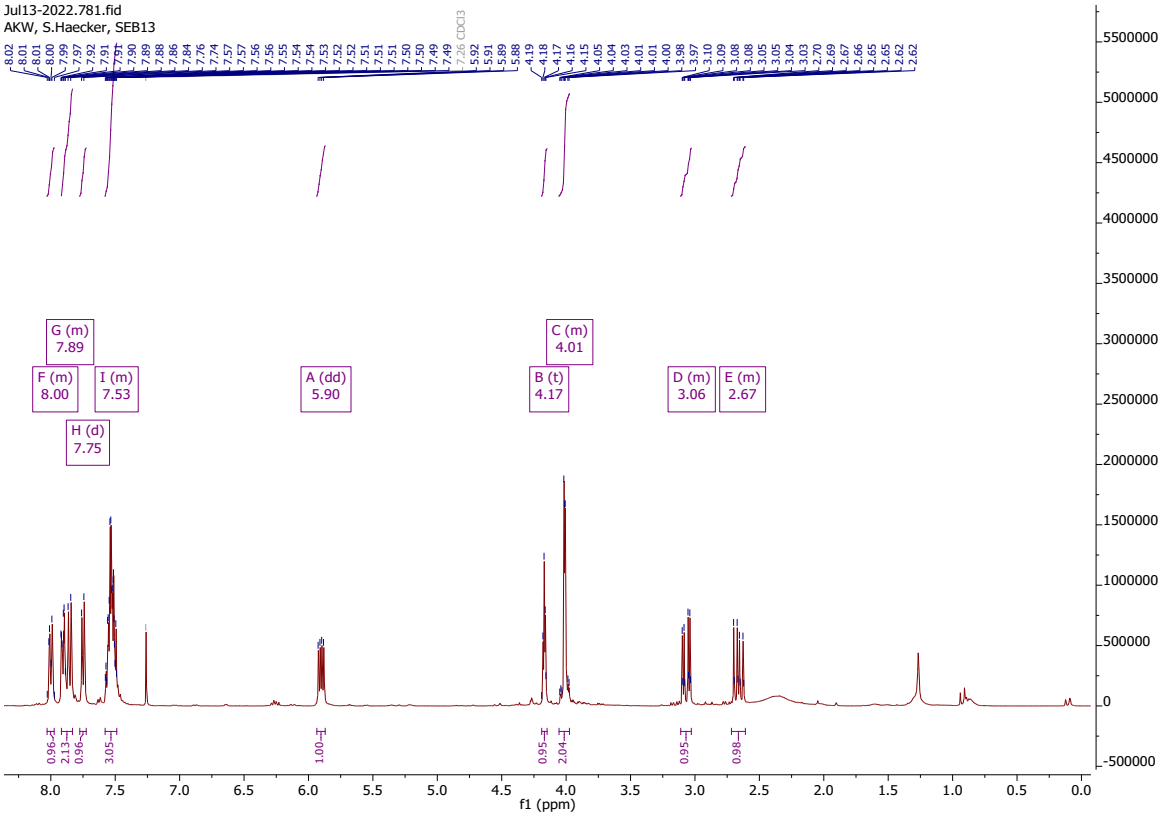

Figure S18: ^{1}H NMR (400 MHz, $CDCl_3$) of **3**.

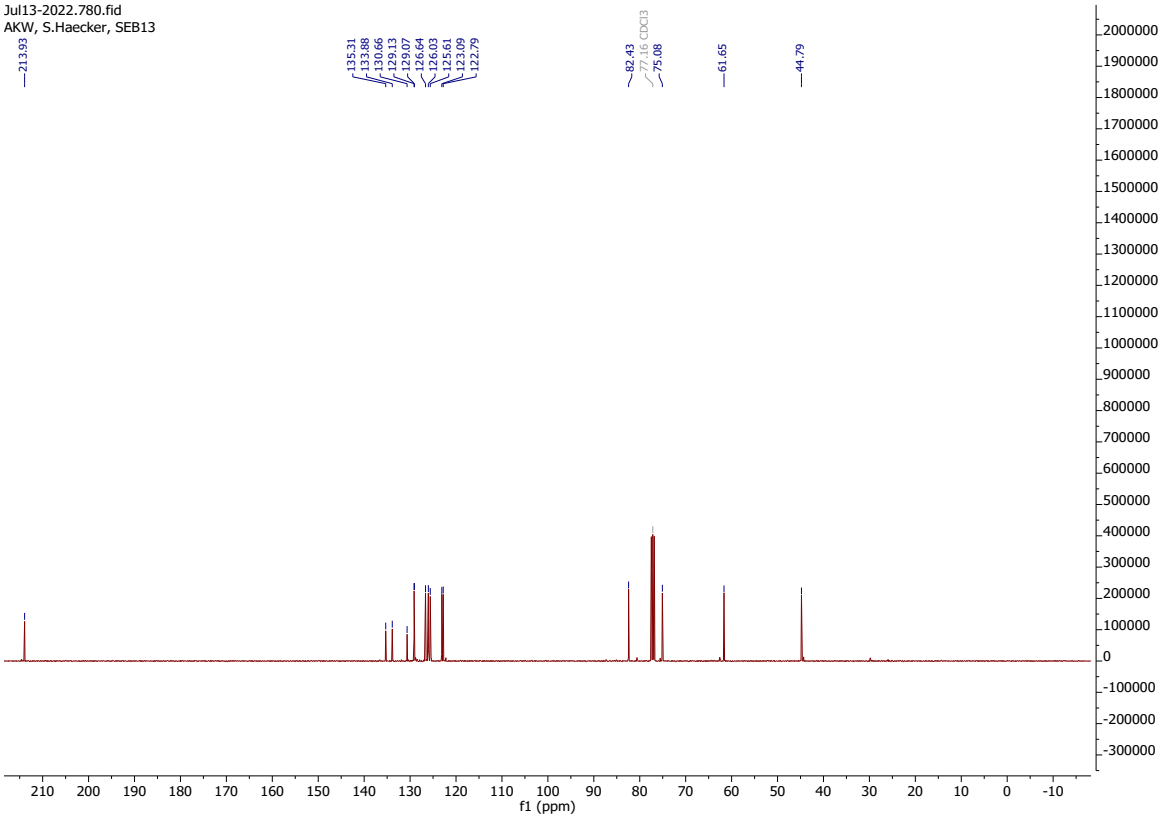

Figure S19: ^{13}C NMR (101 MHz, $CDCl_3$) of **3**.

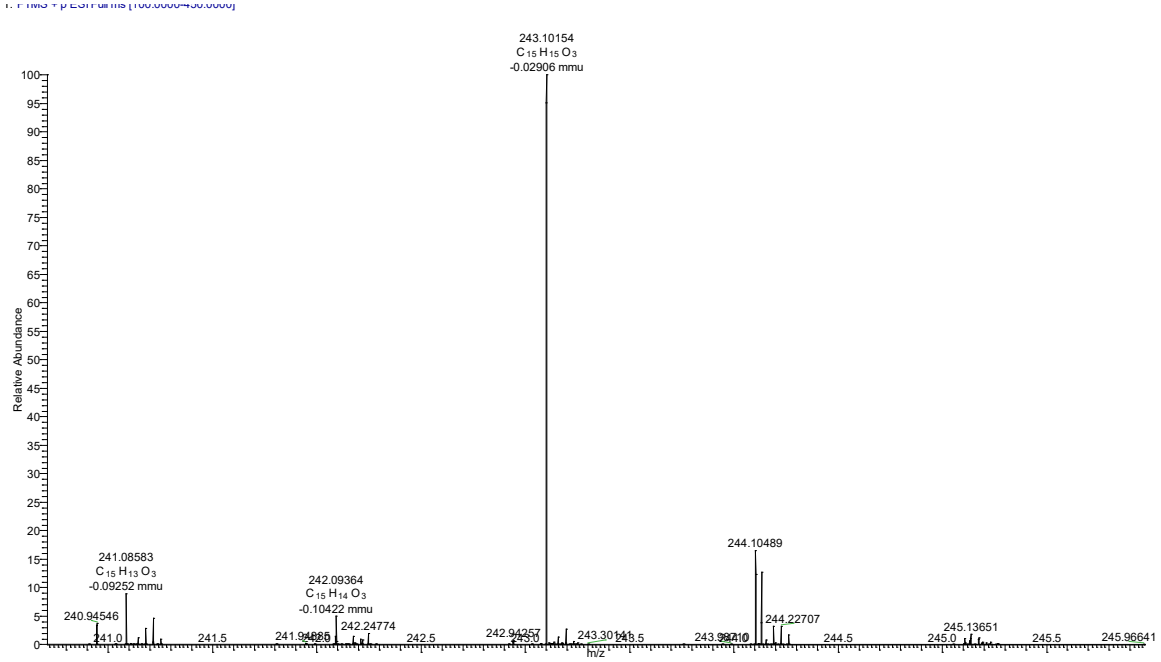

Figure S20: HR ESI-MS analysis of **3**.

Compound 4

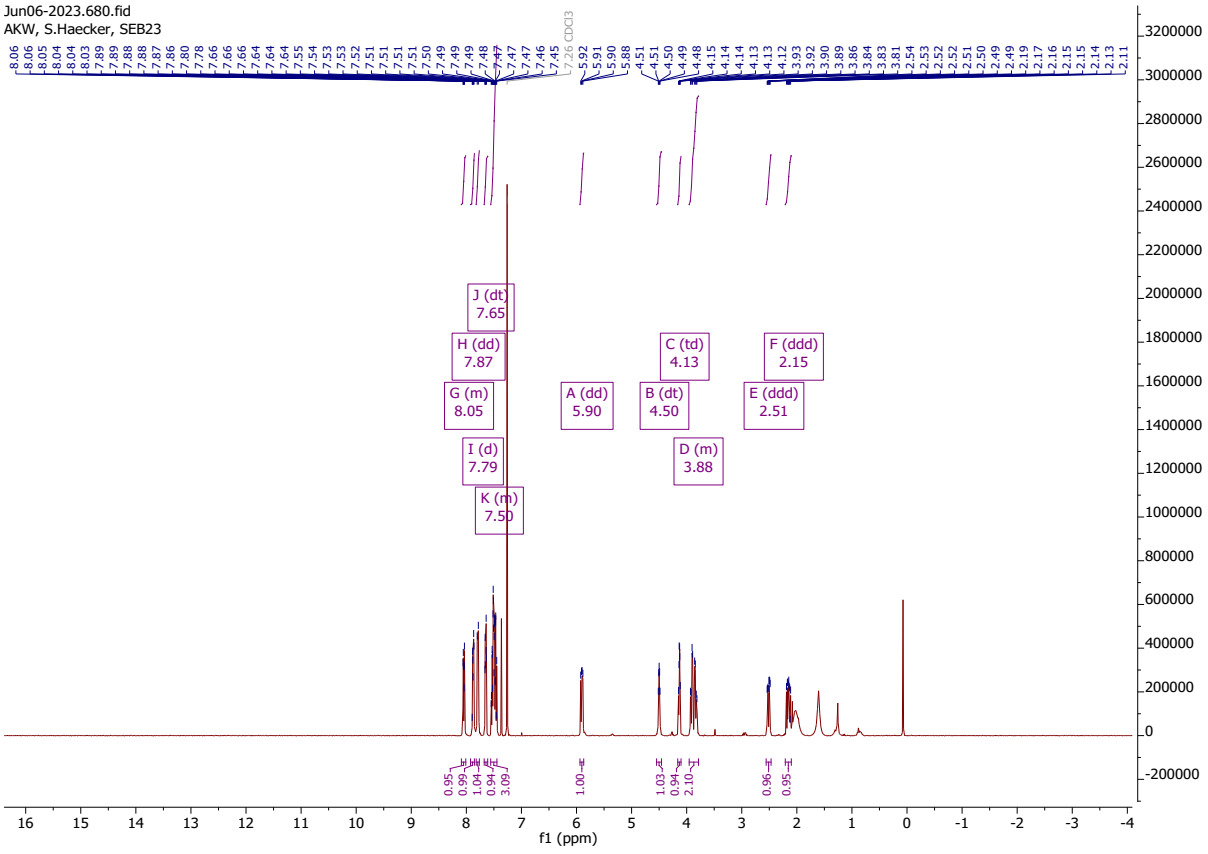

Figure S21: ^{1}H NMR (400 MHz, $CDCl_3$) of **4**.

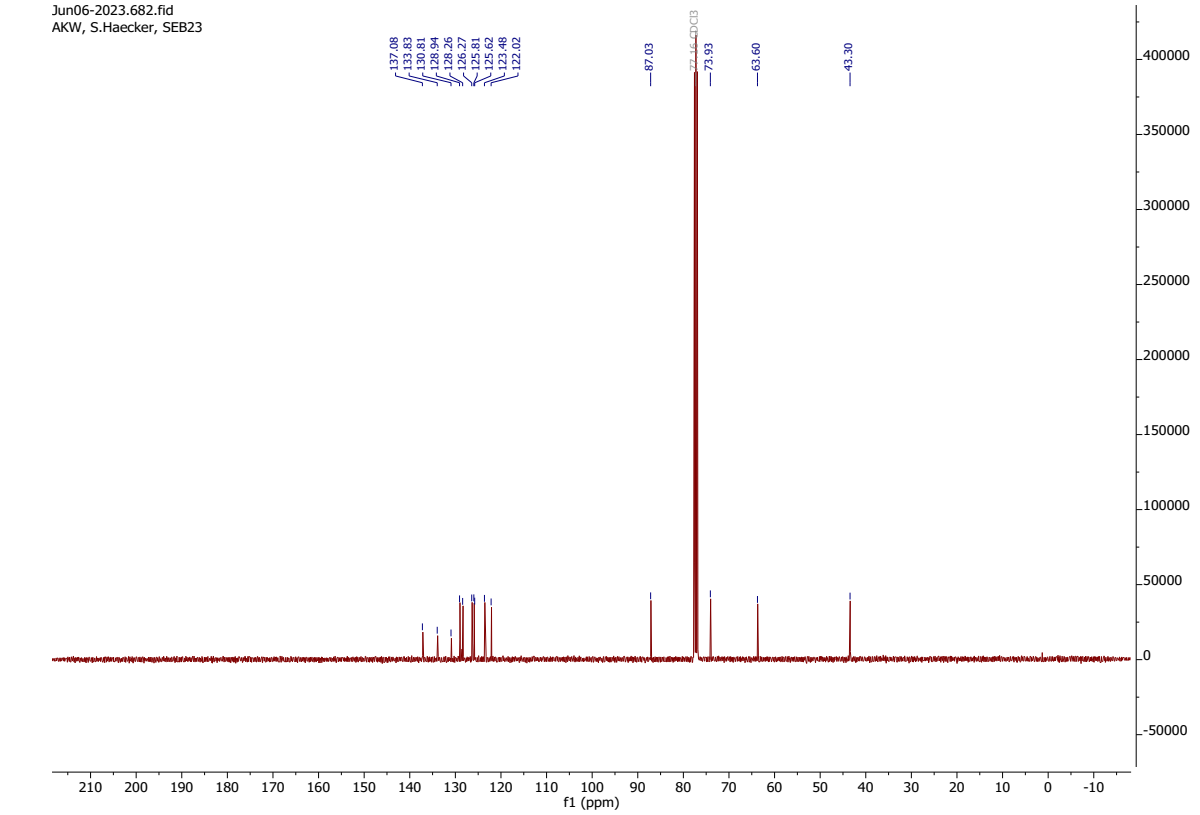

Figure S22: ^{13}C NMR (101 MHz, $CDCl_3$) of **4**.

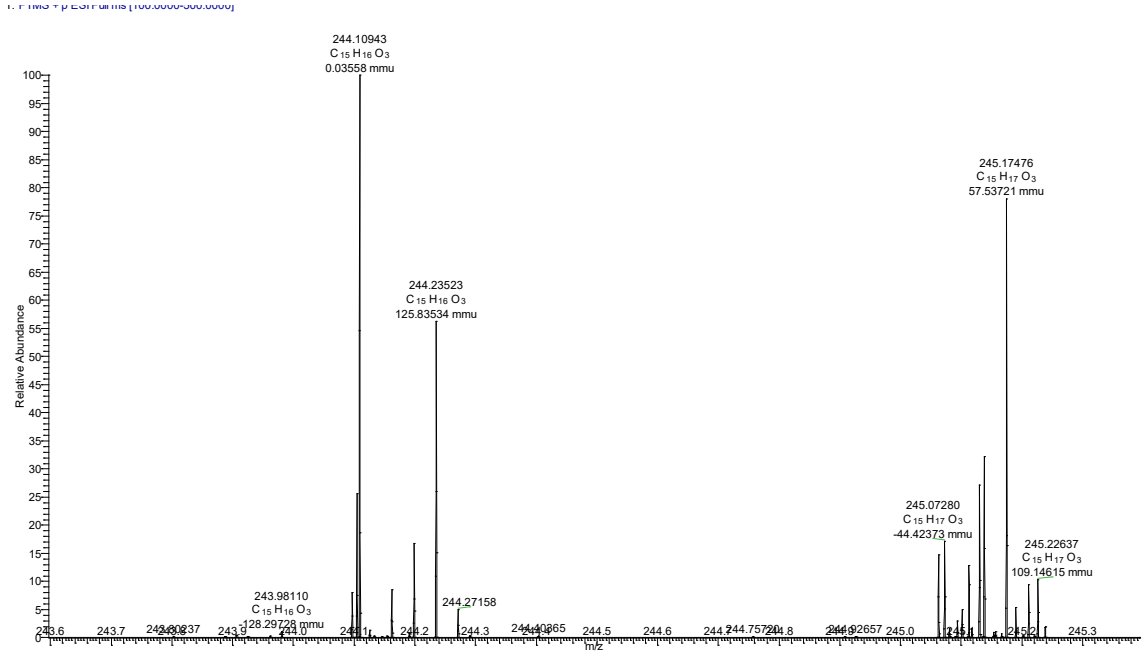

Figure S23: HR ESI-MS analysis of **4**.

Compound 5

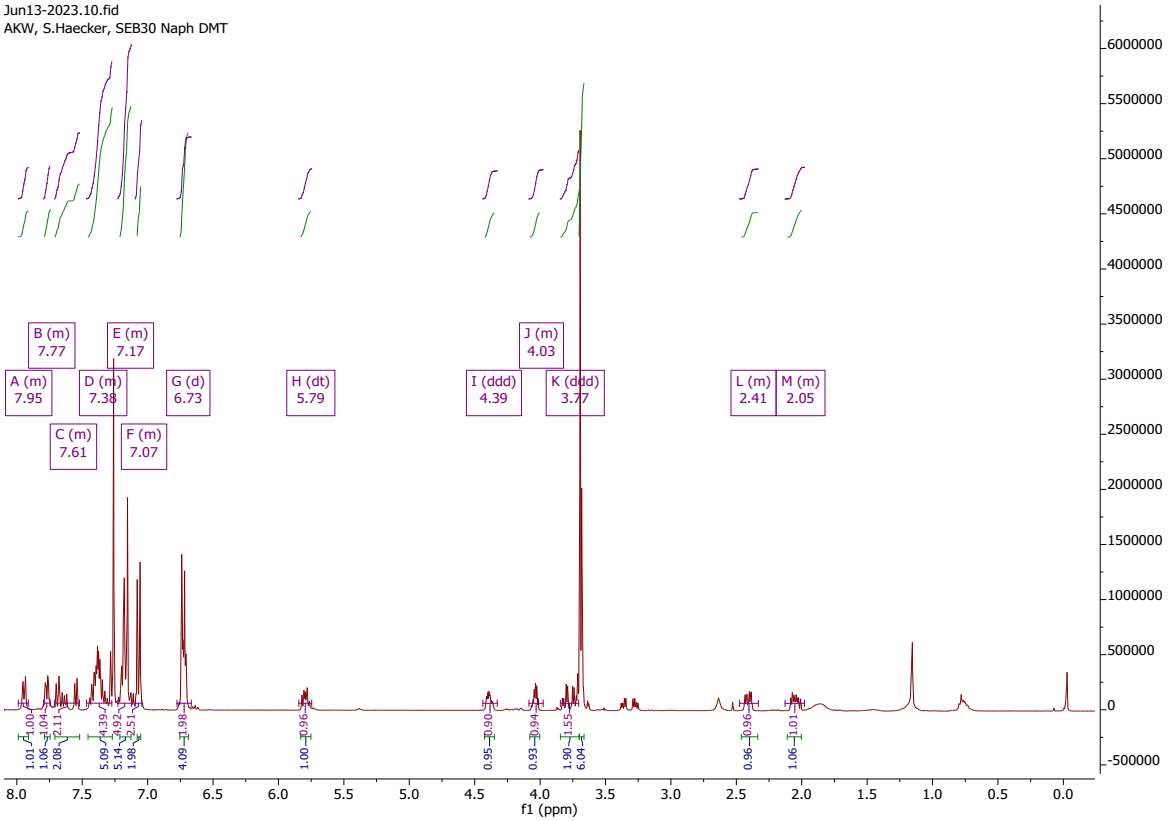

Figure S24: ^{1}H NMR (400 MHz, $CDCl_3$) of **5**.

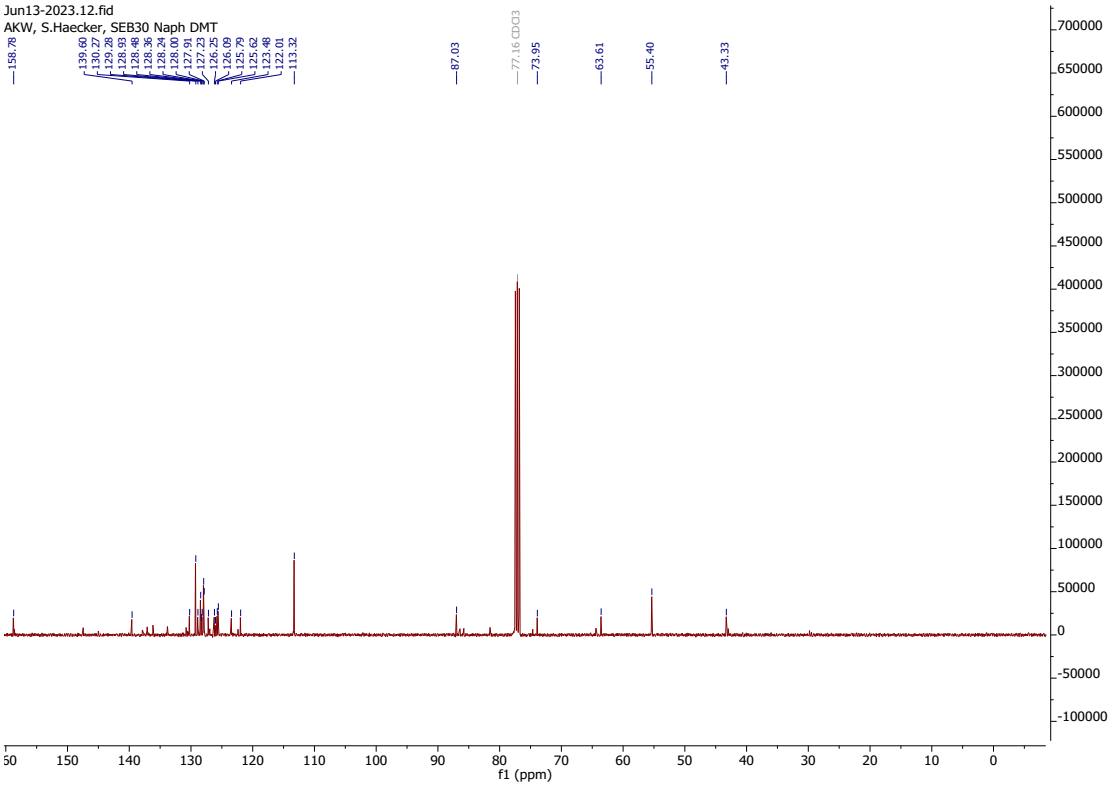

Figure S25: ^{13}C NMR (101 MHz, $CDCl_3$) of **5**.

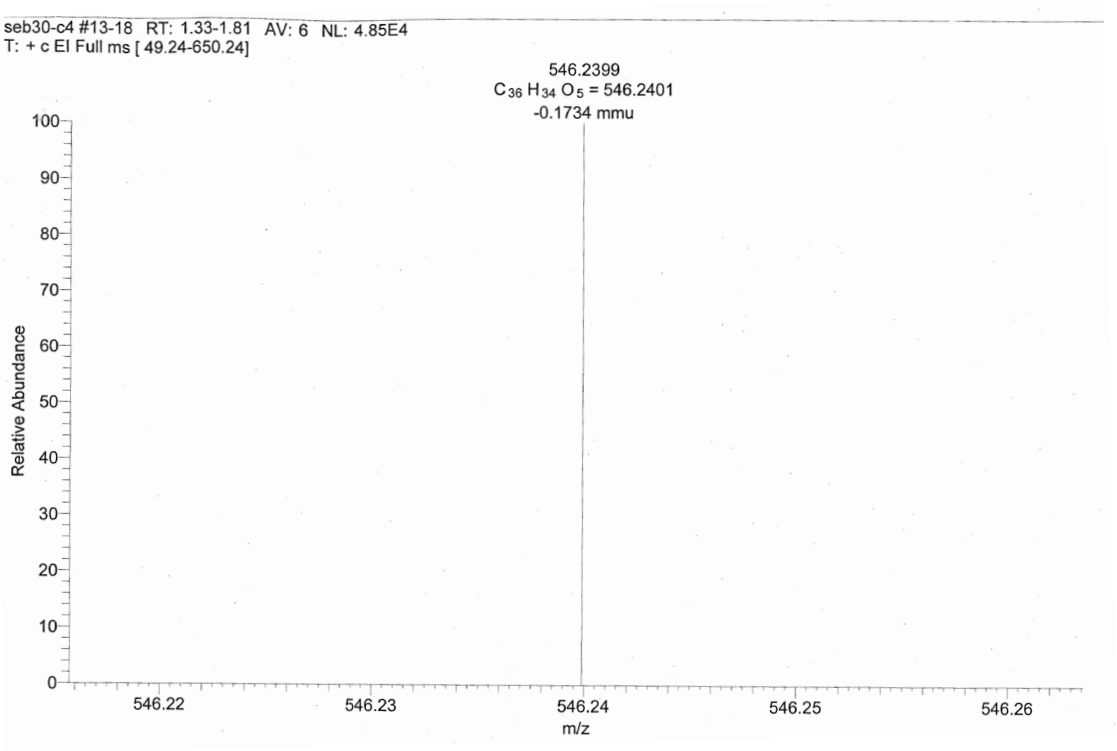

Figure S26: HR-EI-MS analysis of **5**.

Compound 6

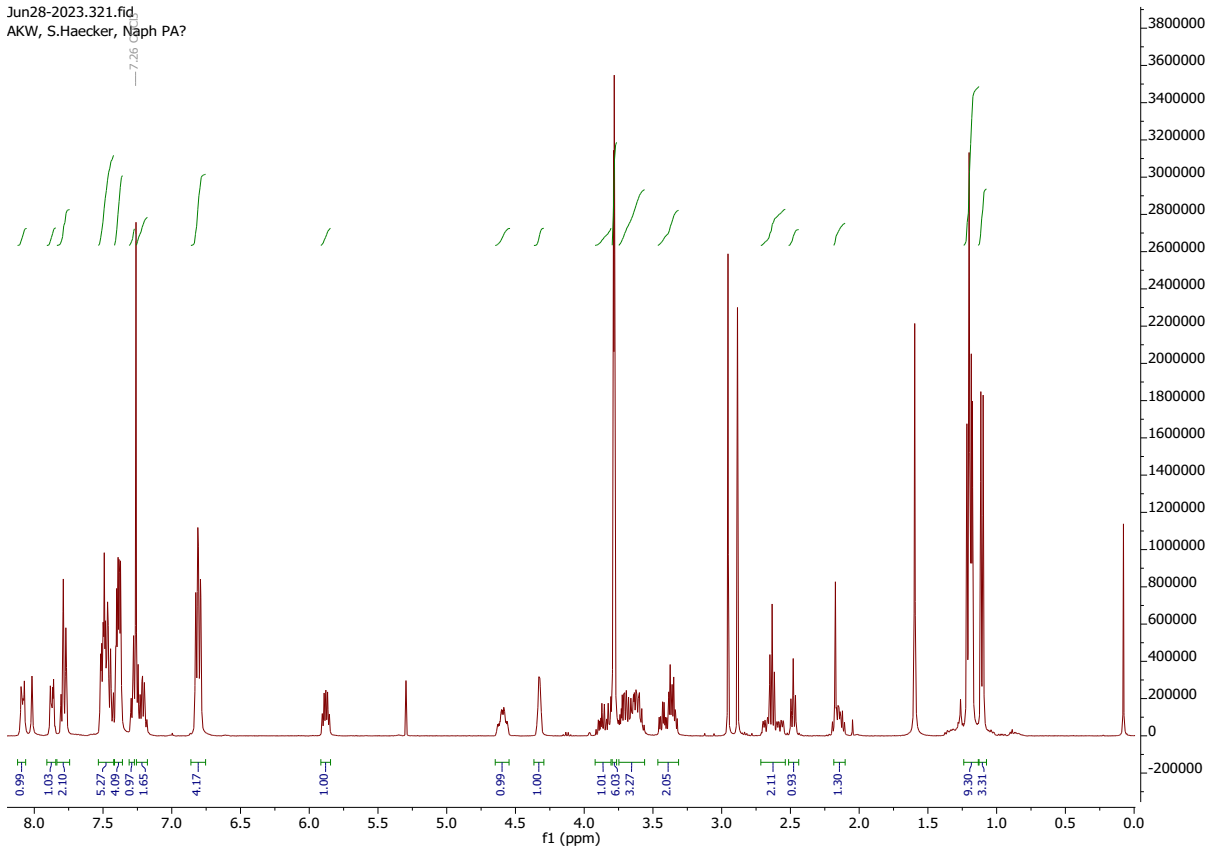

Figure S27: ^{1}H NMR (400 MHz, $CDCl_3$) of **6**.

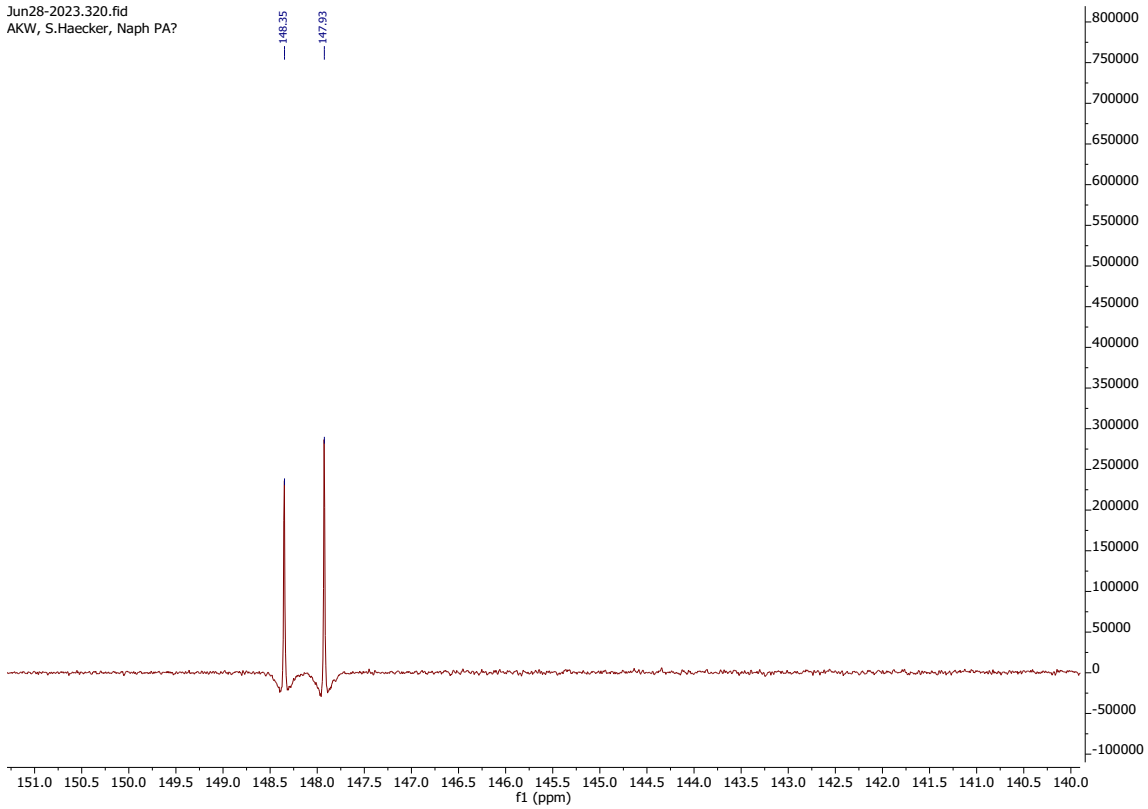

Figure S28: ^{31}P NMR (162 MHz, $CDCl_3$) of **6**.

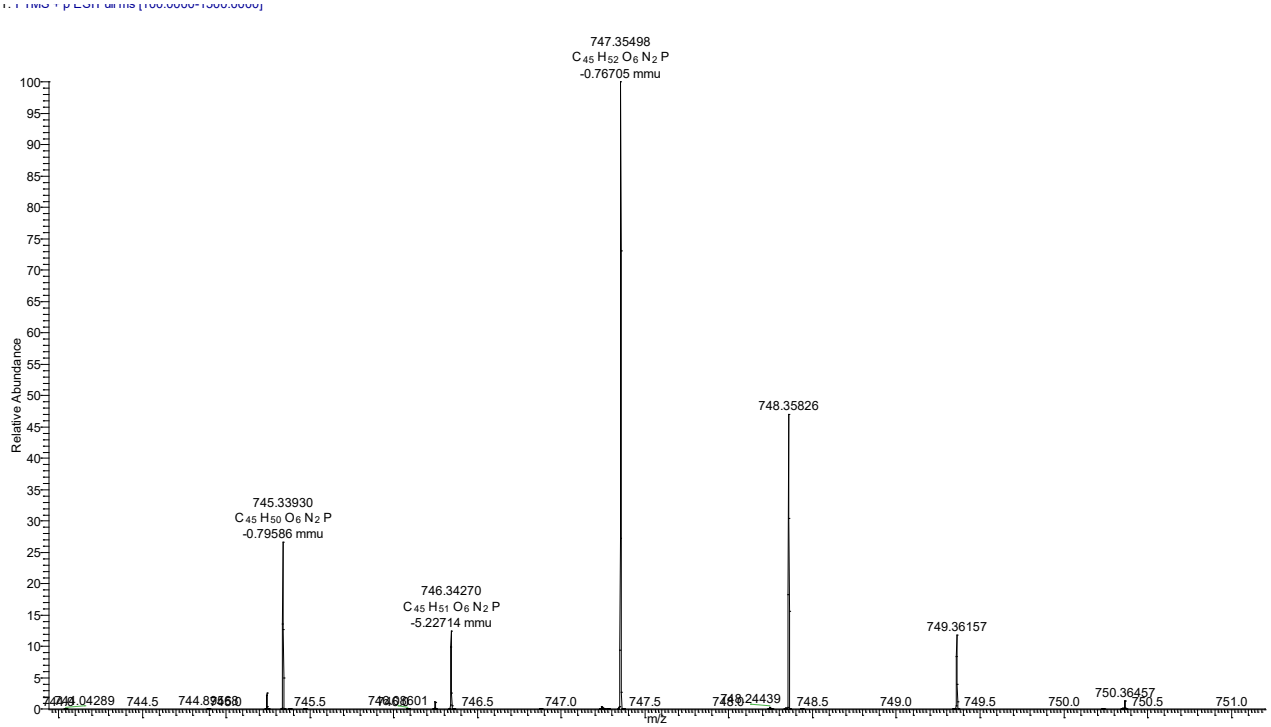

Figure S29: HR ESI-MS analysis of **6**.

7. DNA analyses and melting temperatures

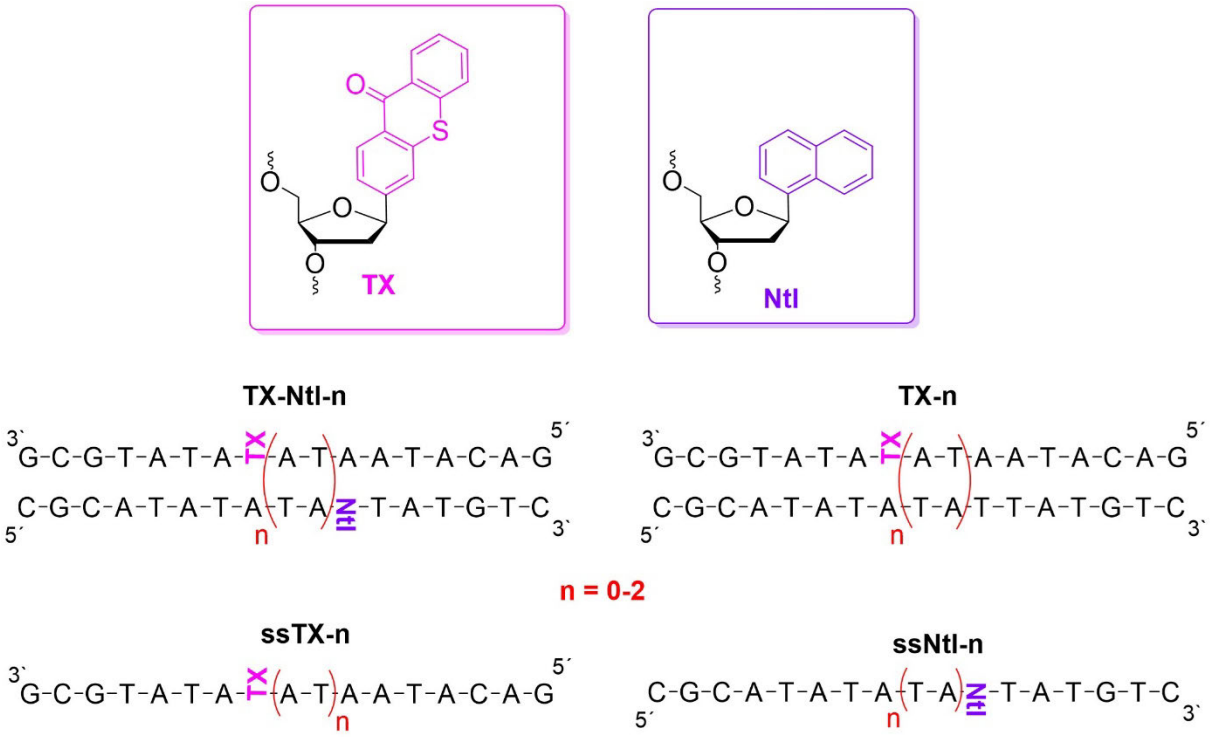

Figure S30: Overview of Thioxanthone (**TX**)- and Naphthalene (**Ntl**)-modified single-stranded oligonucleotides (**ssTX-n** and **ssNtl-n**), as well as the hybridized DNA double-strands (**TX-Ntl-n** and **TX-n**).

The extinction coefficients ε_{260} of the single strand oligonucleotides (**ssTX-n** and **ssNtl-n**) were determined using the following equation in $M^{-1} \cdot cm^{-1}$:

$$\varepsilon_{260} = \varepsilon_{260}X + (nA^* \varepsilon_A(15400) + nT^* \varepsilon_T(8800) + nG^* \varepsilon_G(11700) + nC^* \varepsilon_C(7300))^* 0.9 \quad (4)$$

Table S4: Extinction coefficient and MS (MALDI-TOF) data of the synthesized TX- and Ntl- modified single strands **ssTX/Ntl-n**.

ssTX/Ntl-n	ε_{260} nm [$M^{-1} \cdot cm^{-1}$]	Mass calcd. [Da]	Mass found [Da]
ssTX-0	189850	4684	4683
ssTX-1	211630	5301	5298
ssTX-2	233410	5918	5920
ssNtl-0	139610	4542	4542
ssNtl-1	161390	5159	5161
ssNtl-2	183170	5776	5776

Table S5 Melting temperatures of the annealed DNA: **TX-n** and **TX-Ntl-n**.

DNA	Melting temperature [°C]
TX-0	52°C
TX-Ntl-0	48°C
TX-1	54°C
TX-Ntl-1	46°C
TX-2	56°c
TX-Ntl-2	50°C

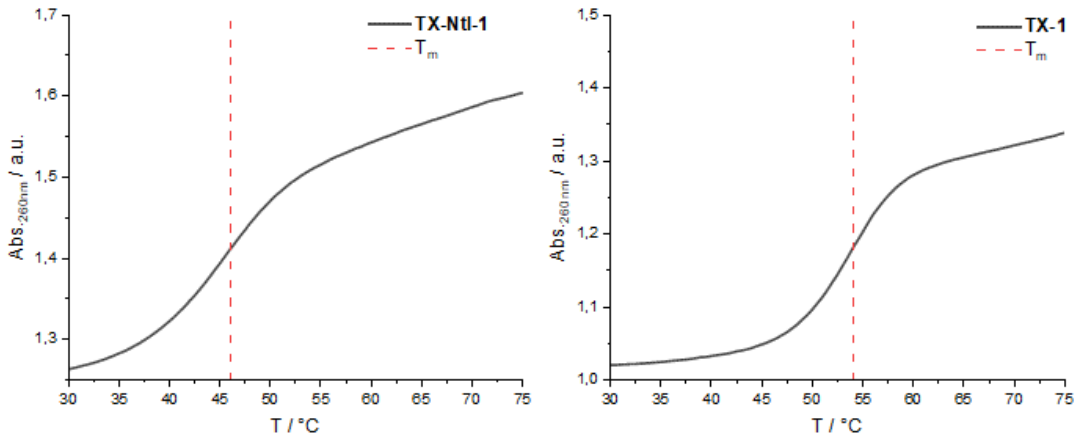

Figure S31: Exemplary melting curve at 260 nm for **TX-1** (right) and **TX-Ntl-1** (left).

8. Images of MS and HPLC analyses of the DNA

The **ssTX-n** oligonucleotides have been previously described and published in the literature.[30]

ssNtl-0:

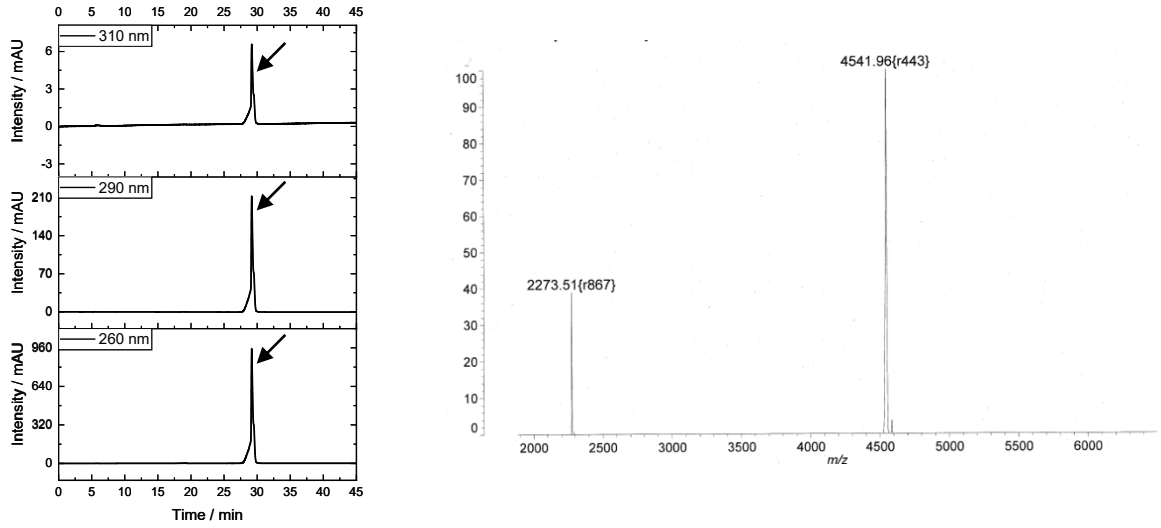

Figure S32: Left: HPLC analysis (260 nm, 290 nm and 310 nm) of **ssNtl-0**. Right: MALDI-TOF-MS analysis of **ssNtl-0**.

ssNtl-1:

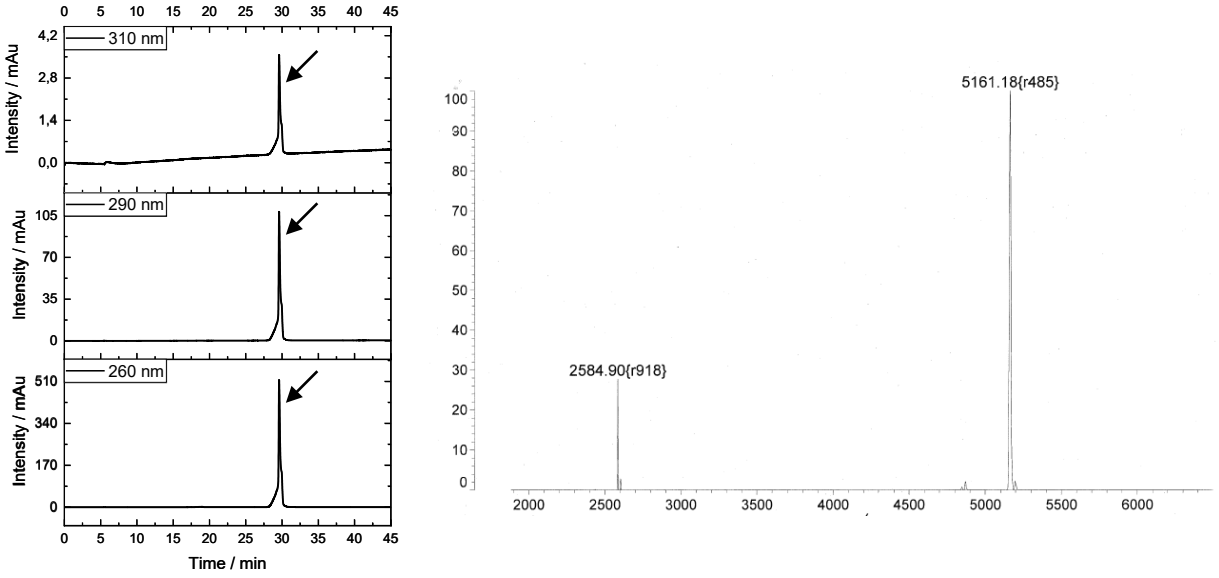

Figure S33: Left: HPLC analysis (260 nm, 290 nm and 310 nm) of **ssNtl-1**. Right: MALDI-TOF-MS analysis of **ssNtl-1**.

ssNtl-2:

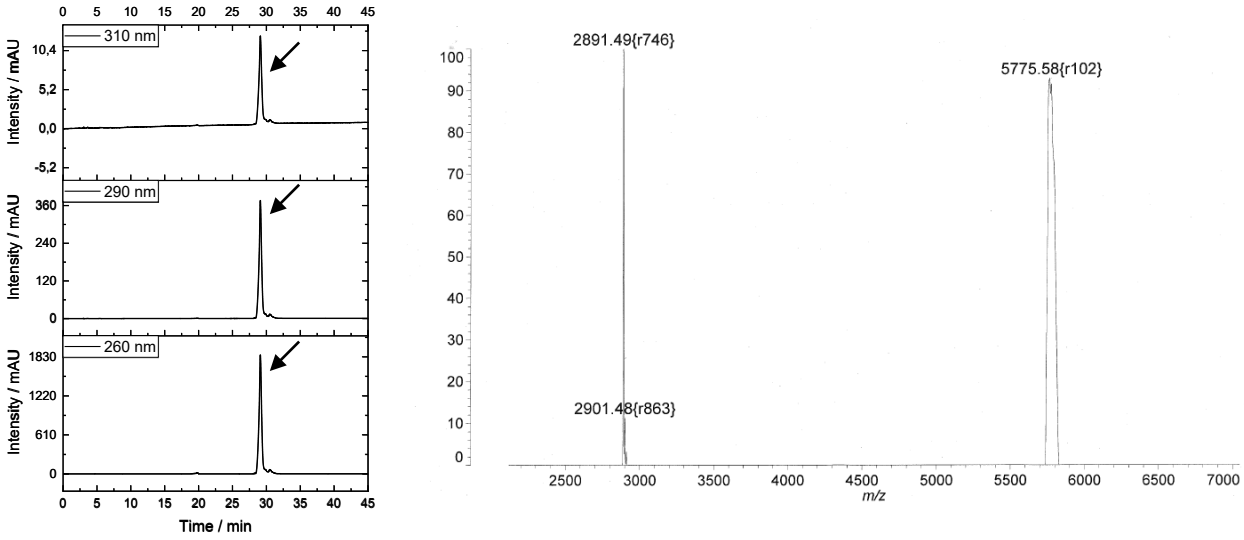

Figure S34: Left: HPLC analysis (260 nm, 290 nm and 310 nm) of **ssNtl-2**. Right: MALDI-TOF-MS analysis of **ssNtl-2**.

9. References

(1) DeBoer, C. D.; Schlessinger, R. H. Rate of the Self-Quenching Reaction for Thioxanthone Triplets. *J. Am. Chem. Soc.* **1972**, *94* (2), 655–656. https://doi.org/10.1021/ja00757a067.

(2) Gudem, M.; Kowalewski, M. Triplet-triplet Annihilation Dynamics of Naphthalene. *Chem. – Eur. J.* **2022**, *28* (40), e202200781. https://doi.org/10.1002/chem.202200781.

(3) Tfibel, F.; Lindqvist, L. Excited Singlet Yield in T-T Annihilation, a Comparative Study of Naphthalene and Anthracene in Solution. *Chem. Phys.* **1975**, *10* (2–3), 471–478. https://doi.org/10.1016/0301-0104(75)87059-5.

(4) Zähringer, T. J. B.; Wienhold, M.; Gilmour, R.; Kerzig, C. Direct Observation of Triplet States in the Isomerization of Alkenylboronates by Energy Transfer Catalysis. *J. Am. Chem. Soc.* **2023**, *145* (39), 21576–21586. https://doi.org/10.1021/jacs.3c07678.

(5) Montalti, M.; Credi, A.; Prodi, L.; Gandolfi, M. T. *Handbook of Photochemistry*, 0 ed.; CRC Press, 2006. https://doi.org/10.1201/9781420015195.

(6) Bieri, O.; Wirz, J.; Hellrung, B.; Schutkowski, M.; Drewello, M.; Kiefhaber, T. The Speed Limit for Protein Folding Measured by Triplet–Triplet Energy Transfer. *Proc. Natl. Acad. Sci.* **1999**, *96* (17), 9597–9601. https://doi.org/10.1073/pnas.96.17.9597.

(7) Klán, P.; Wirz, J. *Photochemistry of Organic Compounds: From Concepts to Practice*; Wiley: Chichester, West Sussex, U.K, 2009.

(8) Kerzig, C.; Goez, M. Generating Hydrated Electrons through Photoredox Catalysis with 9-Anthrolate. *Phys. Chem. Chem. Phys.* **2015**, *17* (21), 13829–13836. https://doi.org/10.1039/C5CP01711D.

(9) Wallace, S. C.; Grätzel, M.; Thomas, J. K. Laser Photoionization of Aromatic Hydrocarbons in Micellar Solution. *Chem. Phys. Lett.* **1973**, *23* (3), 359–362. https://doi.org/10.1016/0009-2614(73)85097-3.

(10) Dhenadhayalan, N.; Selvaraju, C. Role of Photoionization on the Dynamics and Mechanism of Photoinduced Electron Transfer Reaction of Coumarin 307 in Micelles. *J. Phys. Chem. B* **2012**, *116* (16), 4908–4920. https://doi.org/10.1021/jp301412c.

(11) Guéron, M.; Eisinger, J.; Shulman, R. G. Excited States of Nucleotides and Singlet Energy Transfer in Polynucleotides. *J. Chem. Phys.* **1967**, *47* (10), 4077–4091. https://doi.org/10.1063/1.1701580.

(12) Allen, N. S. *Photopolymerisation and Photoimaging Science and Technology*; Springer Netherlands: Dordrecht, 1989. https://doi.org/10.1007/978-94-009-1127-7.

(13) Li, H.; Yao, S.; Zuo, Z.; Wang, W.; Zhang, J.; Lin, N. Characterization of the Reactive Intermediates in Laser Flash Photolysis of Adenine, Adenosine and dAMP Using Acetone as Photosensitizer. *J. Photochem. Photobiol. B* **1995**, *28* (1), 65–70. https://doi.org/10.1016/1011-1344(94)07095-6.

(14) Krystkowiak, E.; Maciejewski, A.; Kubicki, J. Spectral and Photophysical Properties of Thioxanthone in Protic and Aprotic Solvents: The Role of Hydrogen Bonds in S_1 -Thioxanthone Deactivation. *ChemPhysChem* **2006**, *7* (3), 597–606. https://doi.org/10.1002/cphc.200500375.

(15) Dossot, M.; Allonas, X.; Jacques, P. Singlet Exciplexes between a Thioxanthone Derivative and Substituted Aromatic Quenchers: Role of the Resonance Integral. *Chem. – Eur. J.* **2005**, *11* (6), 1763–1770. https://doi.org/10.1002/chem.200400269.

(16) Burget, D.; Jacques, P. Dramatic Solvent Effects on Thioxanthone Fluorescence Lifetime. *J. Lumin.* **1992**, *54* (3), 177–181. https://doi.org/10.1016/0022-2313(92)90006-U.

(17) MacArthur, C. G. Solubility of Oxygen in Salt Solutions and the Hydrates of These Salts. *J. Phys. Chem.* **1916**, *20* (6), 495–502. https://doi.org/10.1021/j150168a003.

(18) Geitenbeek, R. G.; Prins, P. T.; Albrecht, W.; Van Blaaderen, A.; Weckhuysen, B. M.; Meijerink, A. $NaYF_4:Er^{3+}$,Yb^{3+} /SiO_2 Core/Shell Upconverting Nanocrystals for Luminescence Thermometry up to 900 K. *J. Phys. Chem. C* **2017**, *121* (6), 3503–3510. https://doi.org/10.1021/acs.jpcc.6b10279.

(19) Back, M.; Ueda, J.; Brik, M. G.; Tanabe, S. Pushing the Limit of Boltzmann Distribution in Cr^{3+} -Doped $CaHfO_3$ for Cryogenic Thermometry. *ACS Appl. Mater. Interfaces* **2020**, *12* (34), 38325–38332. https://doi.org/10.1021/acsami.0c08965.

(20) Yarnell, J. E.; Wells, K. A.; Palmer, J. R.; Breaux, J. M.; Castellano, F. N. Excited-State Triplet Equilibria in a Series of Re(I)-Naphthalimide Bichromophores. *J. Phys. Chem. B* **2019**, *123* (35), 7611–7627. https://doi.org/10.1021/acs.jpcb.9b05688.
(21) Gray, H. B.; Winkler, J. R. Long-Range Electron Transfer. *Proc. Natl. Acad. Sci.* **2005**, *102* (10), 3534–3539. https://doi.org/10.1073/pnas.0408029102.
(22) Skourtis, S. S.; Liu, C.; Antoniou, P.; Virshup, A. M.; Beratan, D. N. Dexter Energy Transfer Pathways. *Proc. Natl. Acad. Sci.* **2016**, *113* (29), 8115–8120. https://doi.org/10.1073/pnas.1517189113.
(23) Lai, R.; Liu, Y.; Luo, X.; Chen, L.; Han, Y.; Lv, M.; Liang, G.; Chen, J.; Zhang, C.; Di, D.; Scholes, G. D.; Castellano, F. N.; Wu, K. Shallow Distance-Dependent Triplet Energy Migration Mediated by Endothermic Charge-Transfer. *Nat. Commun.* **2021**, *12* (1), 1532. https://doi.org/10.1038/s41467-021-21561-1.
(24) Closs, G. L.; Johnson, M. D.; Miller, J. R.; Piotrowiak, P. A Connection between Intramolecular Long-Range Electron, Hole, and Triplet Energy Transfers. *J. Am. Chem. Soc.* **1989**, *111* (10), 3751–3753. https://doi.org/10.1021/ja00192a044.
(25) Curutchet, C.; Voityuk, A. A. Distance Dependence of Triplet Energy Transfer in Water and Organic Solvents: A QM/MD Study. *J. Phys. Chem. C* **2012**, *116* (42), 22179–22185. https://doi.org/10.1021/jp306280y.
(26) Wenger, O. S. Photoinduced Electron and Energy Transfer in Phenylene Oligomers. *Chem. Soc. Rev.* **2011**, *40* (7), 3538. https://doi.org/10.1039/c1cs15044h.
(27) Wood, P. D.; Redmond, R. W. Triplet State Interactions between Nucleic Acid Bases in Solution at Room Temperature: Intermolecular Energy and Electron Transfer. *J. Am. Chem. Soc.* **1996**, *118* (18), 4256–4263. https://doi.org/10.1021/ja954340+.
(28) García-Messeguer, R.; Navarrete-Miguel, M.; Martí, S.; Tuñón, I.; Roca-Sanjuán, D. DNA Triplet Energies by Free Energy Perturbation Theory. *J. Chem. Theory Comput.* **2025**, *21* (3), 1353–1359. https://doi.org/10.1021/acs.jctc.4c01583.
(29) Luo, X.; Han, Y.; Chen, Z.; Li, Y.; Liang, G.; Liu, X.; Ding, T.; Nie, C.; Wang, M.; Castellano, F. N.; Wu, K. Mechanisms of Triplet Energy Transfer across the Inorganic Nanocrystal/Organic Molecule Interface. *Nat. Commun.* **2020**, *11* (1), 28. https://doi.org/10.1038/s41467-019-13951-3.
(30) Häcker, S.; Schrödter, M.; Kuhlmann, A.; Wagenknecht, H.-A. Probing of DNA Photochemistry with C-Nucleosides of Xanthones and Triphenylene as Photosensitizers To Study the Formation of Cyclobutane Pyrimidine Dimers. *JACS Au* **2023**, *3* (7), 1843–1850. https://doi.org/10.1021/jacsau.3c00167.

10.3 Supporting Information for Project [B]

BEILSTEIN JOURNAL OF ORGANIC CHEMISTRY

Supporting Information

for

Mechanistic investigations of polyaza[7]helicene in photoredox and energy transfer catalysis

Johannes Rocker, Till J. B. Zähringer, Matthias Schmitz, Till Opatz and Christoph Kerzig

Beilstein J. Org. Chem. **2024,** *20,* 1236–1245. doi:10.3762/bjoc.20.106

General information, detailed experimental procedures, additional spectroscopic data, quantum-mechanical calculations, photostability and photoisomerization experiments

License and Terms: This is a supporting information file under the terms of the Creative Commons Attribution License (https://creativecommons.org/licenses/by/4.0). Please note that the reuse, redistribution and reproduction in particular requires that the author(s) and source are credited and that individual graphics may be subject to special legal provisions.
The license is subject to the *Beilstein Journal of Organic Chemistry* terms and conditions: (https://www.beilstein-journals.org/bjoc/terms)

Contents

I. General information S1
II. Quantum-mechanical computations S4
III. Additional mechanistic and kinetic data S5
IV. Photostability measurements S10
V. Additional information for the isomerization of stilbene and cinnamyl chloride S13
VI. References S14

I. General information

Solvents, reagents and reaction setup

All solvents and reagents were obtained from commercial suppliers and used without further purification unless otherwise stated (4-cyanopyridine, 98%, Sigma-Aldrich; riboflavin, >99%, Sigma-Aldrich; (*Z*)-stilbene, 95%, Thermo Scientific; (*E*)-stilbene, 98%, TCI; MeCN, >99%, VWR Chemicals; $[Ru(bpy)_3]Cl_2$, 99.95%, Sigma-Aldrich; cinnamyl chloride, 95%, Thermo Scientific; *fac*-$Ir(ppy)_3$, 99%, Sigma-Aldrich; *N*,*N*′-dimethyl-4,4′-bipyridinium dichloride (methyl viologen), 98%, Sigma-Aldrich; ammonium hexafluorophosphate, 98%, abcr; sodium *p*-toluenesulfinate (TsNa), 95%, Sigma-Aldrich; α-methylstyrene, >99%, Sigma-Aldrich).

α-Methylstyrene was passed through basic Al_2O_3 to remove the stabilizer. 4-Cyanopyridine was sublimed before use. The azahelicene catalyst (Aza-H) was prepared in two steps according to the previously described procedure [1]. The photocatalyst 4CzIPN was synthesized analogous to the method described in Ref [2]. The hexafluorophosphate salts of $[Ru(bpy)_3]Cl_2$ and *N*,*N*′-dimethyl-4,4′-bipyridinium dichloride have been prepared via precipitation from water upon addition of ammonium hexafluorophosphate and thorough washing with water.

Unless mentioned otherwise, argon from Nippon Gases (5.0) was used for removing dissolved oxygen before all experiments related to optical spectroscopy. Aqueous solutions were prepared using ultrapure Millipor Milli-Q water with a specific resistance of 18.2 MΩ cm.

Mass spectra and HPLC

Reversed phase-HPLC measurements and reaction controls were performed on a 1260-series HPLC-system (Agilent) equipped with an integrated diode array detector and coupled with a single quadrupole LC/MSD with ESI source. A C18-column (Ascentis Express C18, 3 cm × 2.1 mm × 2.7 µm) and a flow rate of 0.7 mL/min with a gradient of 10–90% MeCN/H_2O + 0.1% during 10 min were used for routine analysis.
High-resolution mass spectra were recorded on a 6545 QTOF-LC/MS (Agilent).

Gas chromatography

Gas chromatography was performed on an 8890 GC (Agilent) with split-detection on a 5977 single quadrupole MSD and an FID using helium as carrier gas. The stationary phase used was a HP 5MS UI GC column (Agilent, 30 m × 0.25 mm, film thickness 0.25 µm) and the temperature program as follows: injector temp. 250 °C, transfer line temp. 250 °C, MS source temp. 230 °C, quadrupole temp. 150 °C oven temperature 2 min @ 40 °C → 50 °C/min to 320 °C → 7.4 min @ 320 °C.

Steady-state measurements

UV–vis absorption spectra were recorded on a Thermo Scientific Evolution 201 UV-Visible Spectrophotometer and a Perkin Elmer LAMBDA 365 UV-Vis spectrophotometer at room temperature (295 ± 3 K) in 10 mm quartz cuvettes.

Fluorescence spectra were recorded on an FP-8300 spectrofluorometer (JASCO) and Perkin Elmer FL-6500 spectrometer in 10 mm quartz cuvettes.

Time-resolved photostability measurements were recorded with the Perkin Elmer FL-6500 spectrometer.

Photochemical setup

Photoreaction were performed by irradiation with a 40 W LED PR160L-427nm (Kessil, average intensity of PR160 series 352 mW/cm^2, measured from 1 cm distance)[a] set to full intensity. The reactions were held close to room temperature via a small fan. The reaction mixtures were set up in soda-lime glass 12 mL screw cap tubes or in 20 mL borosilicate reaction tubes and were placed in 5–7 cm distance from the light source. The absorption of the glass should be negligible at the wavelength range used.

Photostability measurements were performed by irradiating the solution in a custom-made Schlenk-cuvette with a 40 W LED PR160L-390 nm from Kessil.

NMR spectroscopy

NMR spectra were recorded on a Bruker Avance-III HD spectrometer (^{1}H NMR: 300 MHz, ^{13}C NMR: 75.5 MHz). Chemical shifts are referenced to residual solvent signals ($CDCl_3$: ^{1}H 7.26 ppm, ^{13}C 77.16 ppm) and reported in parts per million (ppm) relative to tetramethylsilane (TMS).

Laser flash photolysis

The LP980KS setup from Edinburgh Instruments equipped with an Nd:YAG laser from Litron (Nano LG 300-10) was employed for transient absorption and time-resolved emission spectroscopy. The frequency-tripled output with a wavelength of 355 nm served as the excitation source. The laser pulse duration was ≈5 ns and the pulse frequency was 10 Hz. The typical pulse energy used for transient absorption and emission studies was 20 mJ. A beam expander was used to increase the spatial overlap between laser pulse and probe lamp. A beam compressor was used to increase the laser intensity/area. Detection of transient absorption spectra occurred on an iCCD camera from Andor. Kinetic traces at

[a] As stated by the manufacturer.

selected wavelengths were recorded using a photomultiplier tube. The laser power was measured using a pyroelectric detector with attenuator (QE25LP-S-MB-QED-D0) from Gentec-EO combined with the integra software. The spectroscopic experiments were performed at 293 K using a cuvette holder that allows temperature control. If not stated otherwise the TA spectra were integrated over 100 ns.

77 K measurements were carried out with the LFP setup. The cuvette holder was replaced by a dewar that positions a 4 mm glass tubes within the laser beam. The singlet state and triplet state energy of Aza-H were determined at the position of the first (i.e. high-energy) emission shoulder or maximum.

Fluorescence lifetime measurements

The *mini-*τ setup from Edinburgh Instruments (time-correlated single photon counting (TCSPC) technique) equipped with a pulsed LED (EPLED-375, excitation at ≈371 nm) was employed for fluorescence lifetime measurements of Aza-H at 293 K. Stray light was removed with an integrated band-pass filter from 525 nm to 575 nm.

Preparation of deoxygenated solutions for photostability measurements

Unless noted otherwise, the solutions for photostability experiments were deoxygenated in custom-made Schlenk-cuvettes [2] by three freeze-pump-thaw cycles using argon as an inert gas, liquid N_2 for cooling, and Schlenk line vacuum (down to 0.2 mbar).

II. Quantum-mechanical computations

DFT calculations were performed with the program Orca 5.0.4[3]. The functional B3LYP and the basis set 6-311+G(d,p) were used. After each geometry optimization, vibrational frequencies were calculated. In each case, no imaginary vibration frequencies were obtained, indicating convergence on minimum structures. Additional single-point calculations were carried out with Mulliken population analyses to obtain the frontier orbitals of the singlet ground state. The geometry optimization of the triplet state was performed starting from the energy-minimized singlet ground state geometry as initial guess. The triplet state energy (adiabatic) was determined by subtracting the energy of the optimized triplet state from the energy of the optimized singlet ground state. To determine electronic excitation energies and oscillator strengths of the lowest 30 transitions, TD-DFT calculations were performed with previously geometry-optimized structures at the same level of theory. For clarity, only the transitions with an oscillator strength above 0.05 are displayed in the main part (see Figure 1B). Transitions below 400 nm, where the ground-state absorption of Aza-H influences the TA spectra, were also excluded. Additional single-point calculations were carried out to obtain the spin densities of the optimized triplet or doublet states based on Mulliken population analysis. The structures, spin densities (iso value: 0.005) and frontier orbitals were displayed using the software Avogadro1.2.0.[4] The color code for the atoms in the ball and stick representation is as follows: carbon (black), hydrogen (white), nitrogen (bue). In the depiction of spin densities, blue-colored surfaces denote positive spin densities, whereas red-colored surfaces denote negative spin densities (as in Figure 1B of the main paper). The different signs of the wave function in the depiction of the frontier orbitals are also indicated by the colors blue and red.

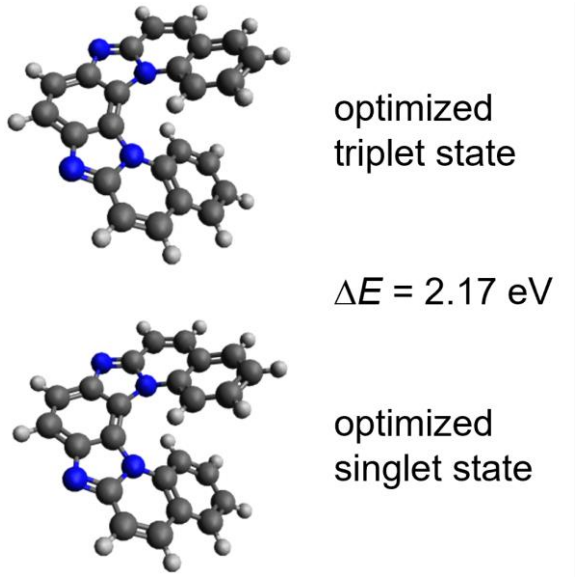

Figure S1: Left: Optimized structures of the Aza-H singlet ground state and the lowest-energy triplet state of Aza-H at B3LYP/6-311+G(d,p) level of theory, along with the respective energy difference.

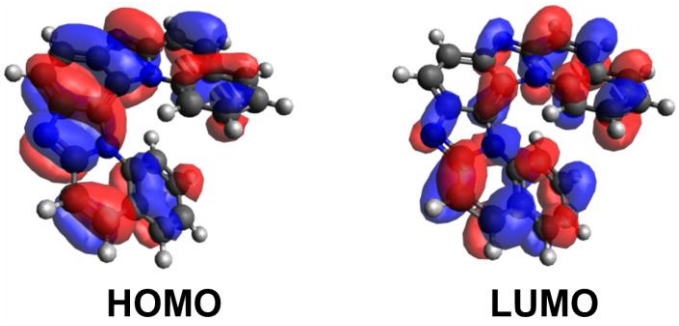

Figure S2: Frontier orbitals of the Aza-H singlet ground state.

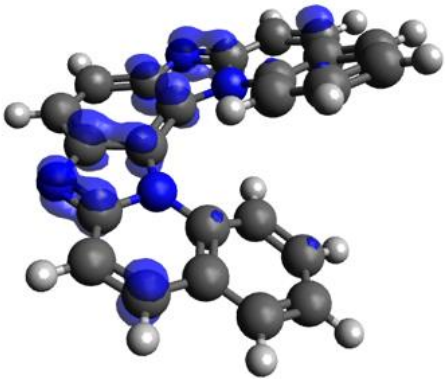

Figure S3: Structure and spin density of geometry-optimized Aza-H$^{\bullet+}$ (charge: +1, multiplicity: 2).

III. Additional mechanistic and kinetic data

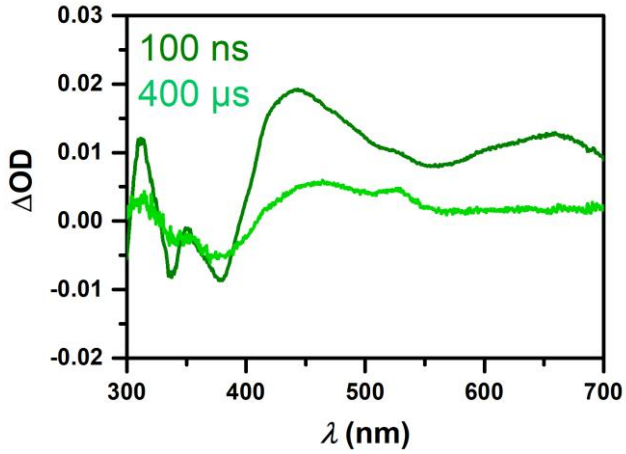

Figure S4: TA spectra of 25 µM Aza-H in Ar-saturated MeCN/H_2O (9:1) recorded 100 ns and 400 µs after 355 nm laser pulses.

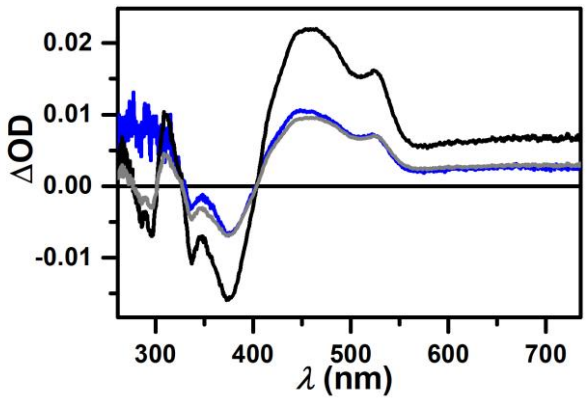

Figure S5: TA spectra in MeCN/H_2O (9:1) recorded 250 ns after 355 nm laser pulses. 25 µM Aza-H in aerated solution (black), 25 µM Aza-H with 200 mM 4CP in Ar-saturated solution (blue). The spectrum of Aza-H was obtained using optics that increase the laser intensity/area by a factor of 4, thereby resulting in higher ionization yields of Aza-H and a spectrum of higher quality accordingly. The spectrum of solely Aza-H has been scaled to fully match the spectrum with 200 mM 4CP (gray).

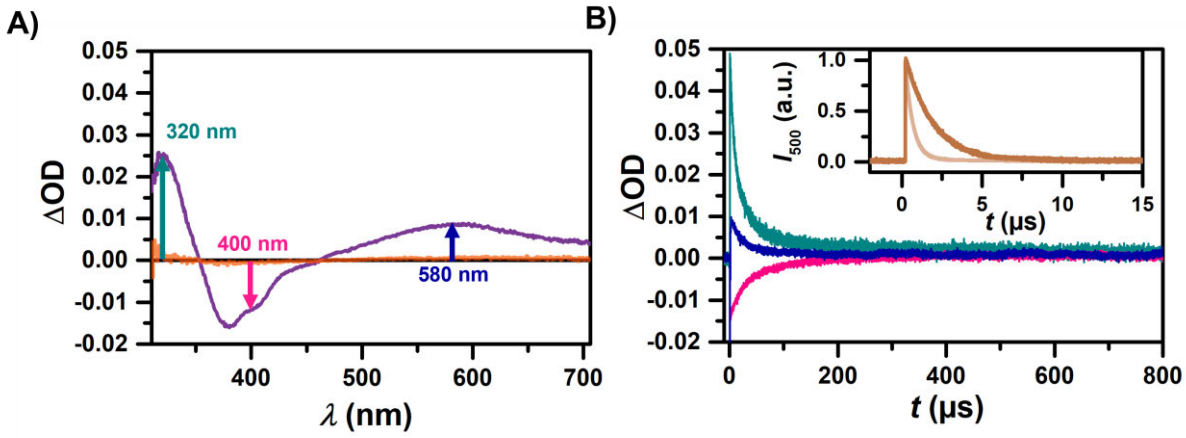

Figure S6: Mechanistic investigations of a solution with 10 µM $Ir(ppy)_3$ and 32.2 mM 4CP in deaerated MeCN with 355 nm laser pulses. A) TA spectra recorded 10 µs (purple) and 200 µs (orange) after excitation. B) Kinetic traces at 320 nm (dark green), 400 nm (pink) and 580 nm (dark blue). Inset: Kinetic emission of $Ir(ppy)_3$ in the absence and presence of 4CP.

It has been reported that, similar to Aza-H, the excited state of $Ir(ppy)_3$ can initiate the reduction of 4CP[5,6], resulting in the formation of the one-electron oxidized $Ir(ppy)_3$ and the radical anion of 4CP. LFP was used to investigate a solution containing 10 µM $Ir(ppy)_3$ and 32.2 mM 4CP in MeCN, with the aim of identifying the radical anion of 4CP. With the addition of 4CP, the phosphorescence of $Ir(ppy)_3$ is substantially quenched (Figure S6B, inset). A TA spectrum was recorded 10 µs after excitation ensuring that $Ir(ppy)_3$* is fully quenched (Figure S6A). In comparison to the literature spectrum of $Ir(ppy)_3^{\bullet+}$ [7], no detectable absorbing species is observed at the reported absorption maximum of 398 nm for $4CP^{\bullet-}$ [8]. Time-resolved measurements were conducted at 320 nm, 400 nm, and 580 nm, revealing similar decay kinetics. Following the decay of $Ir(ppy)_3^{\bullet+}$, a TA spectrum was obtained 200 µs after excitation, which showed only a baseline level (Figure S6A). Based on these results, we conclude that the 4CP radical anion exhibits weak absorption and is not detectable when reduced by either Aza-H or $Ir(ppy)_3$ using our LFP setup.

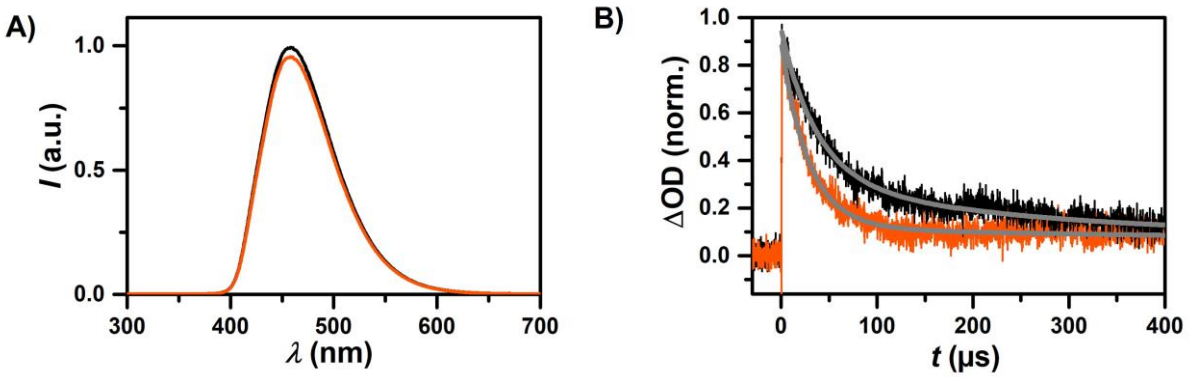

Figure S7: Quenching experiments of Aza-H with 355 nm laser pulses in the absence (black) and presence (orange) of 100 mM α-methylstyrene in deaerated MeCN/H_2O (9:1). A) Emission spectra recorded 10 ns after excitation. B) Kinetic measurements at 650 nm with corresponding triplet lifetimes.

The kinetic measurements at 650 nm were fitted with a biexponential decay function. The fit yielded two lifetimes of which the shorter is assigned to the triplet state of Aza-H. A triplet lifetime reduction from 36.2 µs to 28.6 µs is obtained by the addition α-methylstyrene. The lifetimes are slightly longer than the isolated lifetime of ^{3}Aza-H (≈28 µs, see main paper for details) due to the superimposed and non-monoexponential decay of the radical cation.

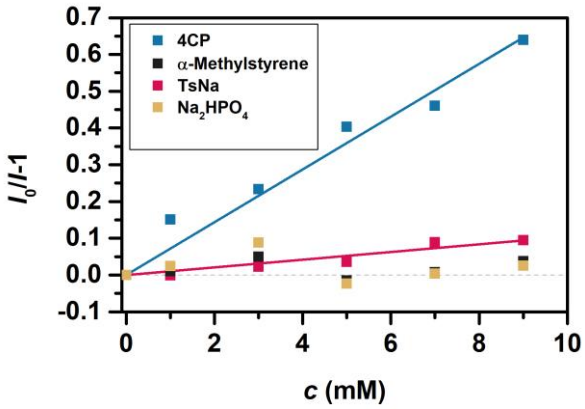

Figure S8: Stern–Volmer plots of the fluorescence quenching of Aza-H by components/additives of the 3-CR. 4CP quenches the fluorescence (K_{SV} = 71.8 M^{-1}) efficiently. TsNa shows weaker quenching (K_{SV} = 10.5 M^{-1}) and the addition of α-methylstyrene and Na_2HPO_4 shows no or only minor quenching of the singlet state.[1]

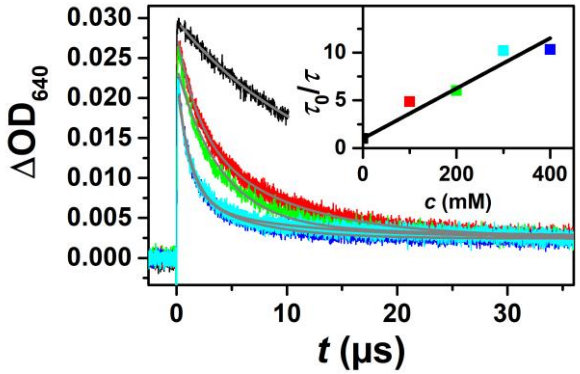

Figure S9: Triplet quenching experiments of Aza-H upon 355 nm excitation in Ar-saturated MeCN solution with increasing cinnamyl chloride concentration. Inset: corresponding Stern–Volmer plot using the lifetime of the short-lived species from the respective biexponential fit.

Moreover, the involvement of protonated states of the catalyst was investigated. Since the structure of Aza-H contains two (benz)imidazole moieties, the pK_a of the first protonation step was expected to be in a similar range (imidazole 7.05, benzimidazole 5.55) [9] for the ground state. In excited state Aza-H the protonation may occur at a different pH. The ground state and excited state pK_a values of Aza-H were determined from absorption and fluorescence spectra respectively measured at different pH values in aqueous EtOH (10%, $c = 10^{-5}$ M) (Figure S10). The absorption values at the wavelengths 230 nm and 355 nm were plotted against the pH. As two protonation sites are available in Aza-H the presence of two pK_a values was expected and is visible as two steps in the absorption plots (Figure S11). The data were fitted with [Eq. (1)], which describes the equilibrium of two interdependent pK_a values [7].

$$A_{\mathrm{total}} = \frac{A_{\mathrm{A_2}} + A_{\mathrm{A_2H}_m} 10^{m(\mathrm{p}K_2 - \mathrm{pH})} + A_{\mathrm{A_2H}_{n+m}} 10^{n\cdot \mathrm{p}K_1 + m\cdot \mathrm{p}K_2 - (n+m)\mathrm{pH}}}{1 + 10^{m(\mathrm{p}K_2 - \mathrm{pH})} + 10^{n\cdot \mathrm{p}K_1 + m\cdot \mathrm{p}K_2 - (n+m)\mathrm{pH}}}$$

[Eq. (1)]

Prior to analysis, the fluorescence spectra were corrected with the factor $A_{280\mathrm{nm},7.825} \cdot A_{280\mathrm{nm,pH}}^{-1}$ to account for the pH dependence of the absorbance at the excitation wavelength (280 nm). The emission intensities at the wavelengths 460 nm and 540 nm were plotted against the pH and fitted with (Eq. 1), substituting the absorbance for the fluorescence intensity, yielding pK_1 and pK_2 of the excited state Aza-H*****. The ground state pK_a values calculated from the absorbance data at 230 nm and 355 nm are in agreement within the range of the standard error, while the excited state values obtained from the fluorescence intensities at 460 nm and 540 nm differ by 0.31 for pK_1 and 0.40 for pK_2, taking their errors into account. Nevertheless, a shift in acidity of about two orders of magnitude for pK_1 and about two and a half orders of magnitude for pK_2 can be observed upon excitation of Aza-H, with the excited Aza-H* being much more readily protonated.

The acidity of the catalyst in the ground state is higher (pK_a = 3.70) than for benzimidazole and imidazole, while a protonation of the excited state is already observed under slightly acidic conditions (pH < 6) in the solvent system used. However, the addition of a base (Na_2HPO_4) to the conducted 3-CR, resulting in an increased pH, and the low water content of 10% make the contribution of protonated forms of the catalyst unlikely. As was shown previously [1] the addition of an acid in a similar reaction does not deactivate the catalyst, making it a reasonable assumption that the protonated form also exhibits catalytic activity.

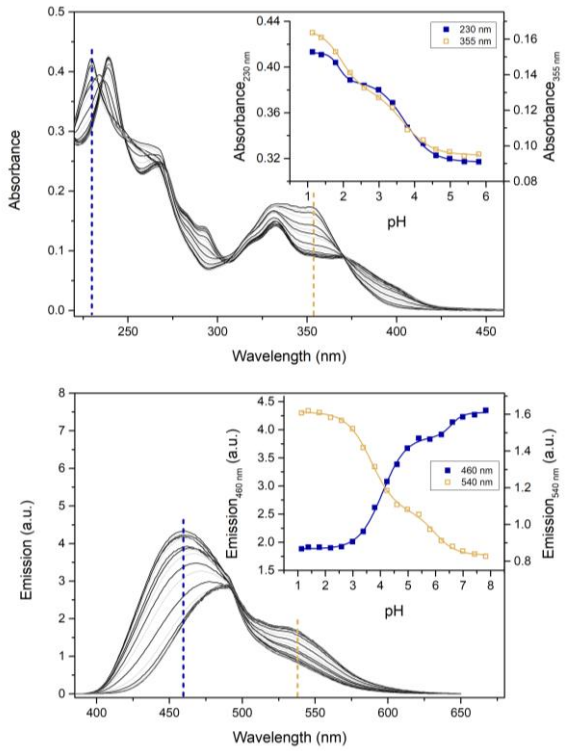

Figure S10: pH dependent absorbance and emission of Aza-H. Insets: Plot of absorption and emission against pH at specific wavelengths and curve fits with (Eq. 1).

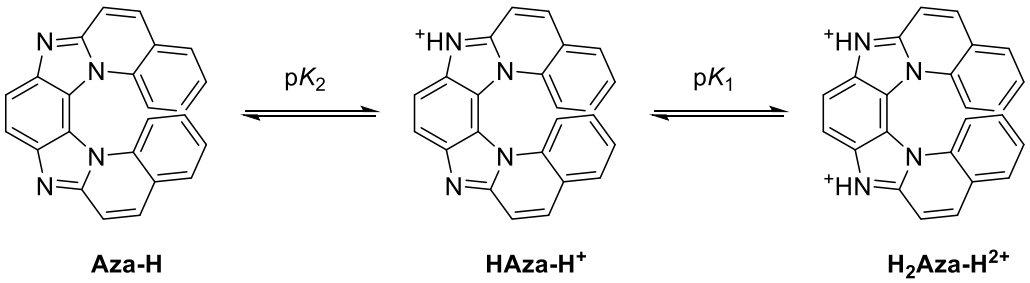

Figure S11: Molecular structures of Aza-H and first and second protonation step of Aza-H.

Table 1: pK_a values of Aza-H in ground and exited state.

	pK_1	pK_2
Ground State		
230 nm	1.87±0.05	3.73±0.04
355 nm	1.93±0.07	3.67±0.11
Excited State		
460 nm	4.07±0.03	6.57±0.09
540 nm	3.67±0.06	5.99±0.09

IV. Photostability measurements

The photostability of Aza-H was compared to riboflavin, $[Ru(bpy)_3](PF_6)_2$ and 4CzIPN. A 390 nm LED from Kessil was selected as the excitation light source, since all four chromophores readily absorb at this wavelength. The optical density of all four photocatalysts was standardized to 0.1 at 390 nm. Emission spectra were taken before and after the photostability measurement to detect any emissive species generated during the experiment. However, no new emissive species were detected, allowing us to relate the emission intensity to the concentration. The relative degradation was estimated by fitting a linear function to the first 10 minutes (2 minutes for riboflavin due to fast decomposition) of the experiment.

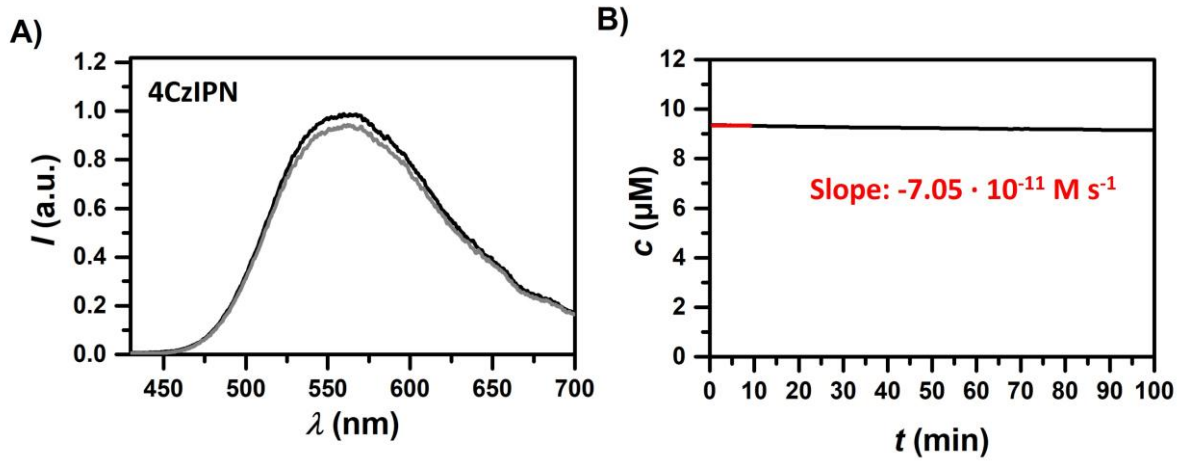

Figure S12: Photostability measurement of 9.3 µM 4CzIPN in deaerated MeCN. A 390 nm LED from Kessil set to 50% intensity (distance 6 cm) was used as the excitation light source. A) Emission spectrum recorded before (black) and after (gray) the measurement. B) Concentration (derived from the emission intensity recorded at 550 nm) of 4CzIPN plotted against the irradiation time. The first 10 min were used to determine the slope.

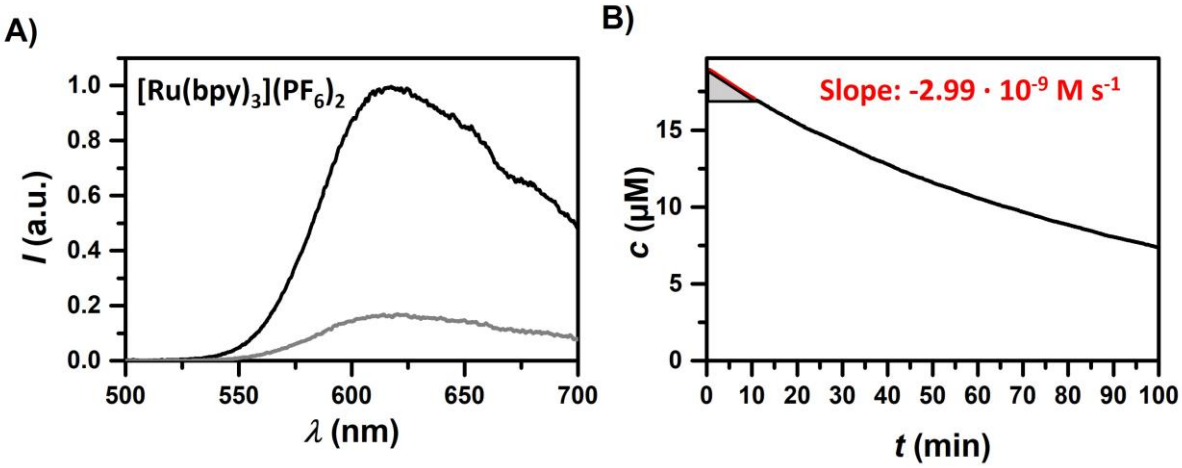

Figure S13: Photostability measurement of 19.0 µM $[Ru(bpy)_3](PF_6)_2$ in deaerated MeCN. A 390 nm LED from Kessil set to 50% intensity (distance 6 cm) was used as the excitation light source. A) Emission spectrum recorded before (black) and after (gray) the measurement. B) Concentration (derived from the emission intensity recorded at 600 nm) of $[Ru(bpy)_3](PF_6)_2$ plotted against the irradiation time. The first 10 min were used to determine the slope.

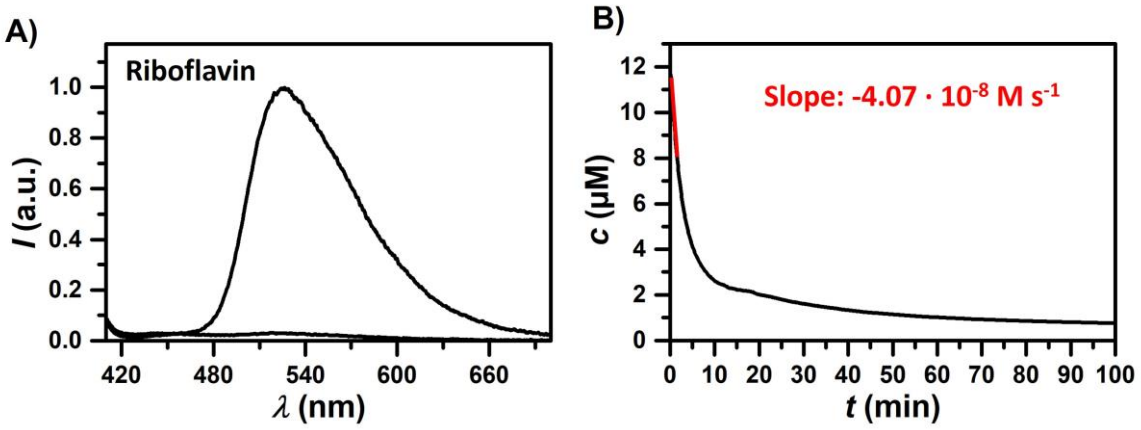

Figure S14: Photostability measurement of 11.2 µM riboflavin in deaerated H_2O. A 390 nm LED from Kessil set to 50% intensity (distance 6 cm) was used as the excitation light source. A) Emission spectrum recorded before (black) and after (gray) the measurement. B) Concentration of riboflavin plotted against the irradiation time. The first 2 min were used to determine the slope.

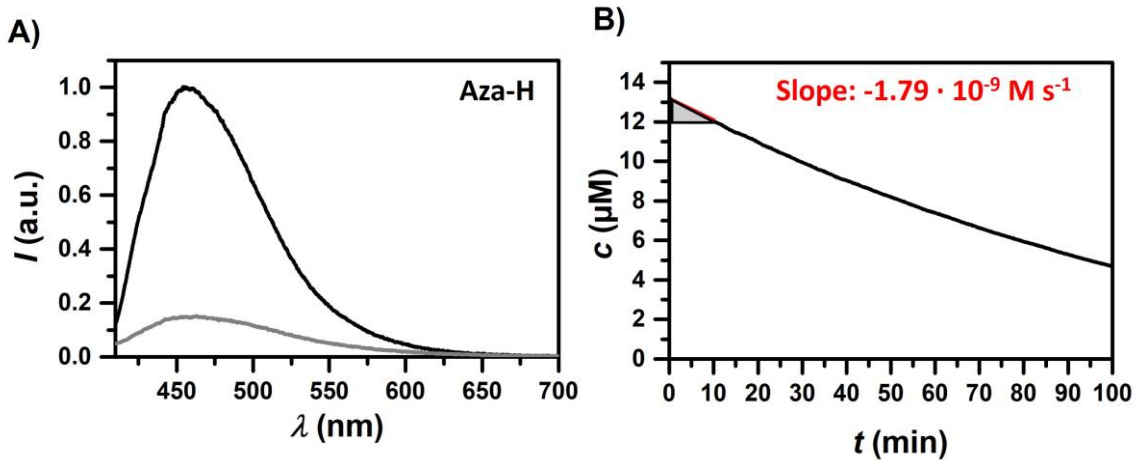

Figure S15: Photostability measurement of 13.2 µM Aza-H in deaerated MeCN. A 390 nm LED from Kessil set to 50% intensity (distance 6 cm) was used as the excitation light source. A) Emission spectrum recorded before (black) and after (gray) the measurement. B) Concentration (derived from the emission intensity recorded at 455 nm) of Aza-H plotted against the irradiation time. The first 10 min were used to determine the slope.

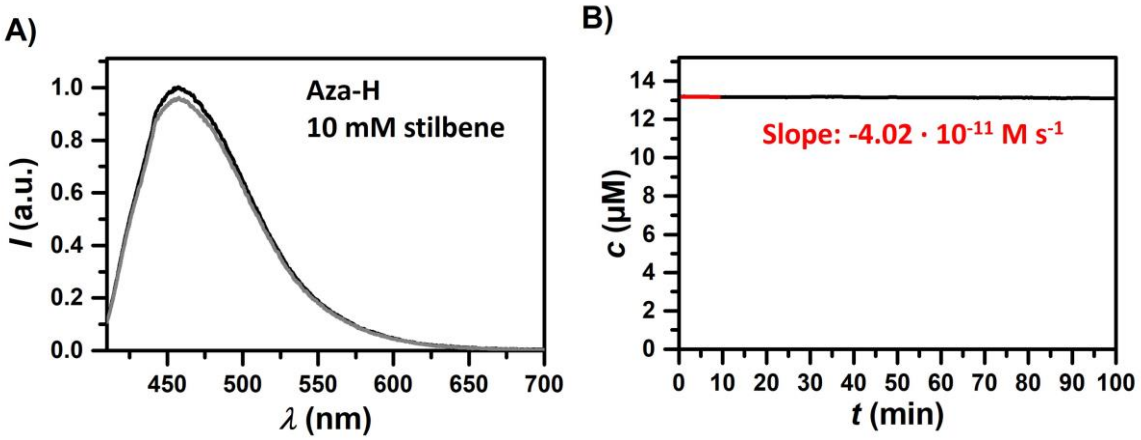

Figure S16: Photostability measurement of 13.2 µM Aza-H and 10 mM (*E*)-stilbene in deaerated MeCN. A 390 nm LED from Kessil set to 50% intensity (distance 6 cm) was used as the excitation light source. A) Emission spectrum recorded before (black) and after (gray) the measurement. B) Concentration (derived from the emission intensity recorded at 455 nm) of Aza-H plotted against the irradiation time. The first 10 min were used to determine the slope.

The addition of 10 mM (*E*)-Stilbene ensures that the triplet-excited Aza-H is rapidly quenched. We observe that the inherent photostability of Aza-H increases by a factor of 44. Hence, we attribute the comparatively fast decomposition of (unquenched) Aza-H to the long-lived triplet state.

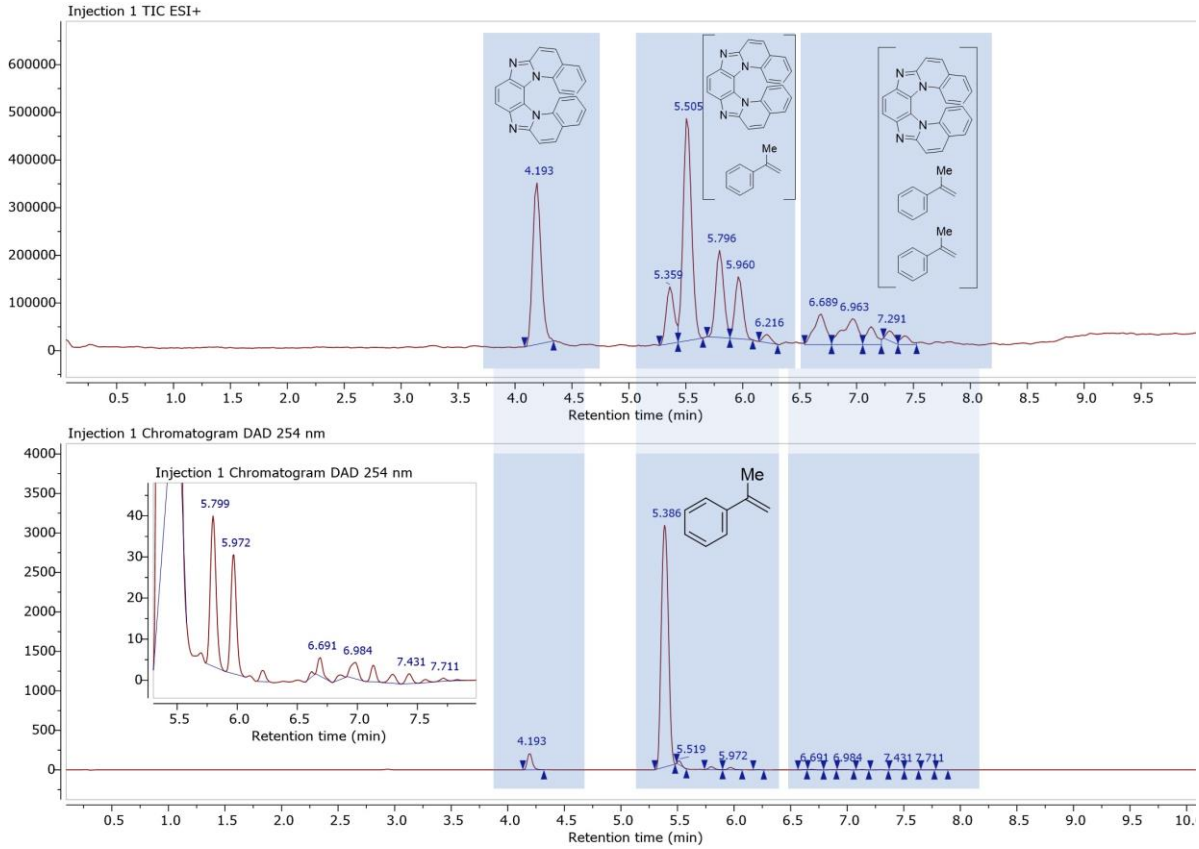

Figure S17: Total ion count and UV-absorption traces from LC-MS measurements of irradiated solution of Aza-H and α-methylstyrene. Five peaks are found which correlate to mono-addition of the styrene and ten peaks correlate to double-addition of the styrene to Aza-H.

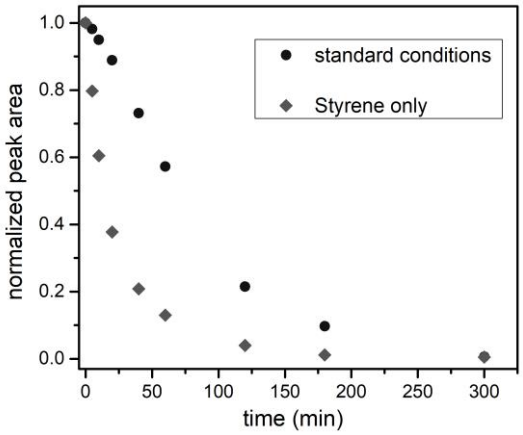

Figure S18: Reaction course plots of the normalized peak area of Aza-H under standard conditions and with styrene only. Standard conditions: To the 12 mL tube equipped with a magnetic stir bar cyanopyridine (0.15 mmol, 1.0 equiv), sodium sulfinate (0.1 mmol, 2.0 equiv), $Na_2HPO_4 \cdot H_2O$ (0.3 mmol, 53.4 mg, 2.0 equiv) and azahelicene catalyst 9 (7.5 µmol, 2.7 mg, 0.05 equiv) were added and sealed with a septum. The vial was then evacuated and flushed with nitrogen three times. Styrene (0.3 mmol, 2.0 equiv) and freshly degassed acetonitrile/H_2O (9:1, 8 mL) were added via syringe [1].

V. Additional information for the isomerization of stilbene and cinnamyl chloride

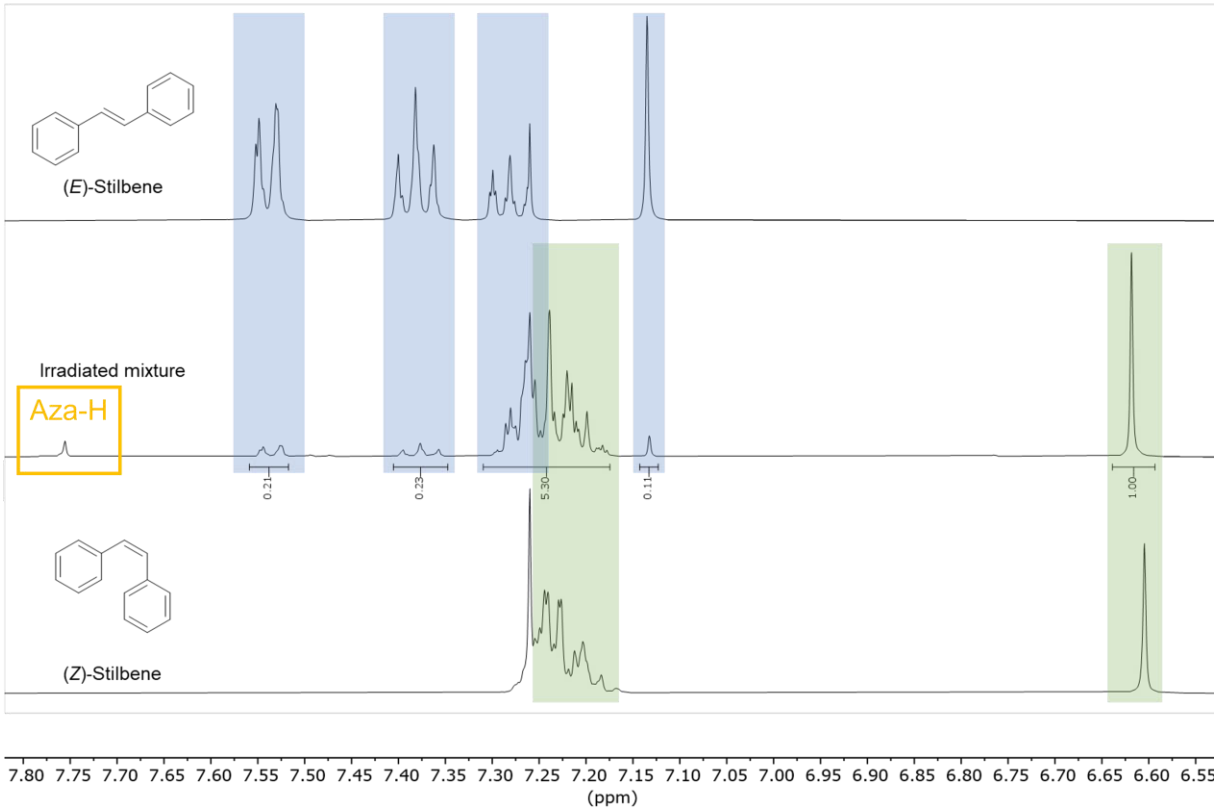

Figure S19: Sample NMR spectra of (*E*)-stilbene (top), the irradiated mixture (1 h, 427 nm) with Aza-H (middle) and (*Z*)-stilbene (bottom). Conditions: (*E*)-Stilbene 50 mM + Aza-H 1 mM in degassed MeCN.

The chemical shifts of the ethylene protons of the irradiated mixture agree with the control measurements of the commercially obtained isomers (7.13 ppm for (*E*)-stilbene and 6.61 ppm for (*Z*)-stilbene). The ratio of E/Z was determined by the signal intensity of (*E*)-stilbene at 7.13 ppm and (*Z*)-stilbene at 6.61 ppm. The signal at 7.75 ppm is assigned to the photocatalyst Aza-H. GC analysis confirmed the *E*/*Z*-ratios obtained from the NMR spectra and revealed no side product formation after the reaction. For the reaction course plot (main article Figure 5D), samples were taken from an irradiated mixture of stilbene (single isomer, 50 mM) and Aza-H (1 mM) in MeCN after times *t* and subjected to GC analysis. Integration of the FID trace was used to determine the *E*/*Z*-ratios.

For the TON experiments, a MeCN solution containing Aza-H (0.1 mM, 0.07 mol %) and nearly saturated with (*E*)-stilbene (0.14 M) was irradiated for 14 h (427 nm). GC analysis gave an *E*/*Z*-ratio of 17:83 corresponding to a TON of 1160. An even higher TON was achieved, when a suspension of (*E*)-stilbene ("1 M") and Aza-H (0.1 mM, 0.01 mol %) in MeCN was irradiated. After 100 h, an *E*/*Z*-ratio of 56:44 corresponding to a TON of 4400 was observed. The generated liquid *Z*-isomer is more soluble in the solvent MeCN and remains in solution, allowing more *E*-isomer to dissolve and isomerize.

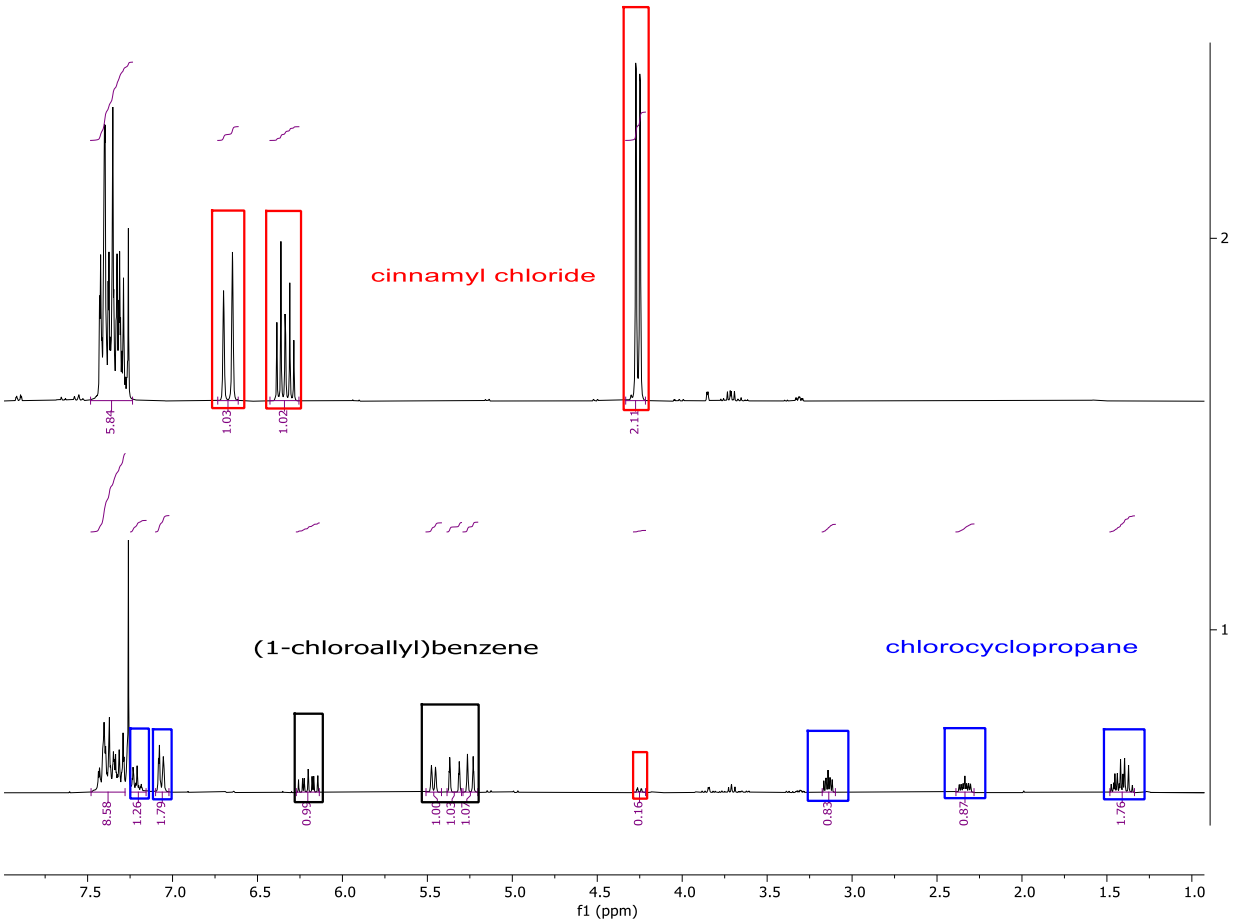

Figure 20: NMR spectra of the cinnamyl chloride cyclization reaction before and after irradiation in $CDCl_3$. The solution of cinnamyl chloride (0.2 M) and Aza-H (2 mM) in MeCN was irradiated for 2 h (427 nm).

The NMR peaks of the chlorocyclopropane and the (1-chloroallyl)benzene are in accordance with the literature[10]. The yield of the chlorocyclopropane and (1-chloroallyl)benzene were determined by the relative ratios of the isolated signals. (3.17–3.12 ppm for the chlorocyclopropane (2H), 5.48 ppm for (1-chloroallyl)benzene (2H) and 4.25 ppm for cinnamyl chloride (2H)). No side products were observed by NMR or GC.

VI. References

(1) Rocker, J.; Opatz, T. *ACS Org. Inorg. Au* **2022**, *2*, 415–421. doi:10.1021/acsorginorgau.2c00022

(2) Zähringer, T. J. B.; Bertrams, M.-S.; Kerzig, C. *J. Mater. Chem. C* **2022**, *10*, 4568–4573. doi:10.1039/D1TC04782E

(3) Neese, F. *WIREs Comput. Mol. Sci.* **2012**, *2*, 73–78. doi:10.1002/wcms.81

(4) Hanwell, M. D.; Curtis, D. E.; Lonie, D. C.; Vandermeersch, T.; Zurek, E.; Hutchison, G. R. *J. Cheminformatics* **2012**, *4*, 17. doi:10.1186/1758-2946-4-17

(5) Vorob'ev, Y. *Chem. Heterocycl. Compd.* **2019**, *55*, 90–92

(6) Lipp, B.; Kammer, L. M.; Kücükdisli, M.; Luque, A.; Kühlborn, J.; Pusch, S.; Matulevičiūtė, G.; Schollmeyer, D.; Šačkus, A.; Opatz, T. *Chem. Eur. J.* **2019**, *25*, 8965–8969. doi:10.1002/chem.201901175

(7) Zhao, H.; Simpson, P. V.; Barlow, A.; Moxey, G. J.; Morshedi, M.; Roy, N.; Philip, R.; Zhang, C.; Cifuentes, M. P.; Humphrey, M. G. *Chem. Eur. J.* **2015**, *21*, 11843–11854. doi:10.1002/chem.201500951

(8) Kalyanaraman, V.; Rao, C. N. R.; George, M. V. *J. Chem. Soc. B Phys. Org.* **1971**, 2406. doi:10.1039/j29710002406

(9) Walba, H.; Isensee, R. W. *J. Org. Chem.* **1961**, *26*, 2789–2791. doi:10.1021/jo01066a039

(10) Xu, B.; Troian-Gautier, L.; Dykstra, R.; Martin, R. T.; Gutierrez, O.; Tambar, U. K. *J. Am. Chem. Soc.* **2020**, *142*, 6206–6215. doi:10.1021/jacs.0c00147

10.4 Supporting Information for Project [C]

SUPPORTING INFORMATION

Arylthianthrenium Salts for Triplet Energy Transfer Catalysis

Yuan Cai[1], Triptesh Kumar Roy[1,2], Till J. B. Zähringer[3], Beatrice Lansbergen[1], Christoph Kerzig[3,*], and Tobias Ritter[1,2,*]

[1]Max-Planck-Institut für Kohlenforschung, Kaiser-Wilhelm-Platz 1, 45470 Mülheim an der Ruhr, Germany.

[2]Institute of Organic Chemistry, RWTH Aachen University, Landoltweg 1, 52074 Aachen, Germany

[3]Department of Chemistry, Johannes Gutenberg University Mainz, 55128 Mainz, Germany.

*ckerzig@uni-mainz.de

*ritter@kofo.mpg.de.

TABLE OF CONTENTS

TABLE OF CONTENTS 1

MATERIALS AND METHODS 6

EXPERIMENTAL DATA 8

Scope of arylthianthrenium salts and nucleophiles 8

General procedure 8

Arylethylamine **3** 9

Arylethylamine **4** 11

Arylethylamine **5** 11

Thalidomide-derived arylethylamine **6** 13

Fenofibrate-derived arylethyl chloride **7** 14

Vinyl arene **8** 15

Arylethyl thioether **9** 16

Arylethyl selenoether **10** 17

Trimetazidine-derived arylethylamine **11** 18

Arylethyl iodide **12** 19

Arylethylammonium salt **13** 20

Arylethyl benzoate **14** 21

Fenofibrate-derived 2-arylethanol **15** 22

Arylethyl fluoride **16** 23

Diclofenac amide-derived arylethylamine **17** 24

Arylethyl methyl ether **18** 25

Cysteine-derived arylethyl thioether **19** 26

Arylpropionitrile **20** 27

Calone-derived arylethylamine **21** 28

Arylethylamine **22** 29

Duloxetine-derived arylethylamine **23** 30

Arylethyl bromide **24** 31

Arylethyl phosphonate **25** 32

Arylethyl thiocyanate **26** 33

Pyriproxyfen- and cytisine-derived arylethylamine **27** 34

Scope of alkenes 35

Arylethyl bromide **28** 36

Arylethyl bromide **29** 36

Arylethyl bromide **30** 37

Arylethyl bromide **31** 38

Arylethyl bromide **32** 39
Arylethyl bromide **33** 40
Arylethyl bromide **34** 41
Arylethyl bromide **35** 42
Arylethyl bromide **36** 43

Condition optimization 44

Mechanistic studies 54

Transient absorption spectroscopy and related spectroscopic studies 54
Analysis of energy transfer rate and expected timescales 57
UV-vis absorption spectrum of reaction mixtures 58
Cyclic voltammograms 59
Relationship between reaction rates and triplet energy or redox potentials 60
Quantum yield measurement 64
Reaction in the presence of triplet quencher 66
Radical scrambling experiment 67
Hammett plot 68

DFT CALCULATIONS 70

Methods 70

Comparison with reported data 70

Visualization of frontier molecular orbitals and triplet energy of arylpseudohalides 73

HOMO/LUMO energy of arylpseudohalides 77

Visualization of frontier molecular orbitals of TXO 78

Bond dissociation energy of thianthrenium salts 79

Cartesian coordinates of the optimized species 80

SPECTROSCOPIC DATA 115

^{1}H NMR of arylethylamine **3** 115

^{13}C NMR of arylethylamine **3** 116

^{19}F NMR of arylethylamine **3** 117

^{1}H NMR of arylethylamine **4** 118

^{13}C NMR of arylethylamine **4** 119

^{19}F NMR of arylethylamine **4** 120

^{1}H NMR of arylethylamine **5** 121

^{13}C NMR of arylethylamine **5** 122

^{19}F NMR of arylethylamine **5** 123

^{1}H NMR of thalidomide-derived arylethylamine **6** 124

^{13}C NMR of thalidomide-derived arylethylamine **6** 125

^{19}F NMR of thalidomide-derived arylethylamine **6** 126

^{1}H NMR of fenofibrate-derived arylethyl chloride **7** 127

^{13}C NMR of fenofibrate-derived arylethyl chloride **7** 128

^{1}H NMR of vinyl arene **8** 129

^{13}C NMR of vinyl arene **8** 130

^{1}H NMR of arylethyl thioether **9** 131

^{13}C NMR of arylethyl thioether **9** 132

^{19}F NMR of arylethyl thioether **9** 133

^{1}H NMR of arylethyl selenoether **10** 134

^{13}C NMR of arylethyl selenoether **10** 135

^{19}F NMR of arylethyl selenoether **10** 136

^{1}H NMR of trimetazidine-derived arylethylamine **11** 137

^{13}C NMR of trimetazidine-derived arylethylamine **11** 138

^{19}F NMR of trimetazidine-derived arylethylamine **11** 139

^{1}H NMR of arylethyl iodide **12** 140

^{13}C NMR of arylethyl iodide **12** 141

^{1}H NMR of arylethylammonium salt **13** 142

^{13}C NMR of arylethylammonium salt **13** 143

^{19}F NMR of arylethylammonium salt **13** 144

^{1}H NMR of arylethyl benzoate **14** 145

^{13}C NMR of arylethyl benzoate **14** 146

^{1}H NMR of fenofibrate-derived 2-arylethanol **15** 147

^{13}C NMR of fenofibrate-derived 2-arylethanol **15** 148

^{1}H NMR of arylethyl fluoride **16** 149

^{13}C NMR of arylethyl fluoride **16** 150

^{19}F NMR of arylethyl fluoride **16** 151

^{1}H NMR of diclofenac amide-derived arylethylamine **17** 152

^{13}C NMR of diclofenac amide-derived arylethylamine **17** 153

^{1}H NMR of arylethyl methyl ether **18** 154

^{13}C NMR of arylethyl methyl ether **18** 155

^{1}H NMR of cysteine-derived arylethyl thioether **19** 156

^{13}C NMR of cysteine-derived arylethyl thioether **19** 157

^{1}H NMR of arylpropionitrile **20** 158

^{13}C NMR of arylpropionitrile **20** 159

^{1}H NMR of calone-derived arylethylamine **21** 160

^{13}C NMR of calone-derived arylethylamine **21** 161

^{1}H NMR of arylethylamine **22** 162

^{13}C NMR of arylethylamine **22** 163

^{19}F NMR of arylethylamine **22** 164

^{1}H NMR of duloxetine-derived arylethylamine **23** 165

^{13}C NMR of duloxetine-derived arylethylamine **23** 166

^{1}H NMR of arylethyl bromide **24** 167

^{13}C NMR of arylethyl bromide **24** 168

^{1}H NMR of arylethyl phosphonate **25** 169

^{13}C NMR of arylethyl phosphonate **25** 170

^{31}P NMR of arylethyl phosphonate **25** 171

^{1}H NMR of arylethyl thiocyanate **26** 172

^{13}C NMR of arylethyl thiocyanate **26** 173

^{19}F NMR of arylethyl thiocyanate **26** 174

^{1}H NMR of pyriproxyfen- and cytisine-derived arylethylamine **27** 175

^{13}C NMR of pyriproxyfen- and cytisine-derived arylethylamine **27** 176

^{1}H NMR of arylethyl bromide **28** 177

^{13}C NMR of arylethyl bromide **28** 178

^{1}H NMR of arylethyl bromide **29** 179

^{13}C NMR of arylethyl bromide **29**.....180

^{1}H NMR of arylethyl bromide **30**.....181

^{13}C NMR of arylethyl bromide **30**.....182

^{1}H NMR of arylethyl bromide **31**.....183

^{13}C NMR of arylethyl bromide **31**.....184

^{1}H NMR of arylethyl bromide **32**.....185

^{13}C NMR of arylethyl bromide **32**.....186

^{31}P NMR of arylethyl bromide **32**.....187

^{1}H NMR of arylethyl bromide **33**.....188

^{13}C NMR of arylethyl bromide **33**.....189

^{1}H NMR of arylethyl bromide **34**.....190

^{13}C NMR of arylethyl bromide **34**.....191

^{1}H NMR of arylethyl bromide **35**.....192

^{13}C NMR of arylethyl bromide **35**.....193

^{1}H NMR of arylethyl bromide **36**.....194

^{13}C NMR of arylethyl bromide **36**.....195

REFERENCES.....196

MATERIALS AND METHODS

All air- and moisture-insensitive reactions were carried out under ambient atmosphere and monitored by thin-layer chromatography (TLC). Concentration under reduced pressure was performed by rotary evaporation at 25–40 °C at an appropriate pressure. Purified compounds were further dried under high vacuum (0.010–0.005 mbar). Yields refer to purified and spectroscopically pure compounds. All air- and moisture-sensitive manipulations were performed using oven-dried glassware (120 °C for a minimum of 12 hours) and standard Schlenk techniques under an atmosphere of argon.

Solvents

Anhydrous MeCN was obtained from *Phoenix Solvent Drying Systems*. Anhydrous acetone was dried by storage over MgSO4. All deuterated solvents were purchased from *Euriso-Top*.

Chromatography

Thin layer chromatography (TLC) was performed using EMD TLC plates pre-coated with 250 μm thickness silica gel 60 F254 plates and visualized by fluorescence quenching under 254 nm UV light or permanganate stain. Flash chromatography was performed using silica gel (40–63 μm particle size) purchased from Geduran®.

Spectroscopy and Instruments

NMR spectra were recorded on a *Bruker Ascend* TM 500 spectrometer operating at 500 MHz, 471 MHz and 126 MHz, for ^{1}H, ^{19}F, and ^{13}C acquisitions, respectively. Chemical shifts are reported in ppm with the solvent residual peak as the internal standard. For ^{1}H NMR: $CDCl_3$, 7.26; CD_3CN, 1.96; For ^{13}C NMR: $CDCl_3$, 77.16; CD_3CN, 1.32.[1] ^{19}F NMR spectra were referenced using a unified chemical shift scale based on the ^{1}H resonance of tetramethylsilane (1% v/v solution in the respective solvent). Data is reported as follows: s = singlet, d = doublet, t = triplet, q = quartet, quin = quintet, sext = sextet, sept = septet, m = multiplet, bs = broad singlet; coupling constants in Hz. The LP980KS setup from Edinburgh Instruments equipped with an Nd:YAG laser from Quantel (Q-Smart 450) was employed for transient absorption and time-resolved emission spectroscopy. The frequency-tripled output with a wavelength of 355 nm served as the excitation source. The laser pulse duration was ~5 ns and the pulse frequency was 10 Hz. The pulse energy used for transient absorption and emission studies was 10-30 mJ. Detection of transient absorption spectra occurred on an iCCD camera from Andor. Kinetic traces were recorded using a photomultiplier tube. The transient absorption experiments were performed at 293 K. If not stated otherwise the TA spectra were integrated over 100 ns. 77 K emission measurements were carried out with the LP980KS setup. The standard cuvette holder was replaced by a dewar that holds a 4 mm glass tube surrounded by liquid nitrogen. A 1:1 mixture of EtOH and MeOH was used as the solvent. The phosphorescence spectra in Fig. 3b (main paper) were integrated over 10 ms.

Triplet-triplet energy transfer rate constants

Triplet-triplet energy transfer rate constants using TXO as a sensitizer were determined through Stern-Volmer analyses. Unless otherwise specified, low laser intensities were employed to avoid self-quenching effects of TXO. The lifetimes were obtained by fitting the transient absorption data sets with a monoexponential decay function.

Starting materials

All substrates were used as received from commercial suppliers. Arylthianthrenium salts[2] and 2-substituted thioxanthones[3] were prepared according to published procedures. Chemicals were purchased from *Sigma-Aldrich*, *TCI*, or *Alfa Aesar*.

EXPERIMENTAL DATA

Scope of arylthianthrenium salts and nucleophiles

General procedure

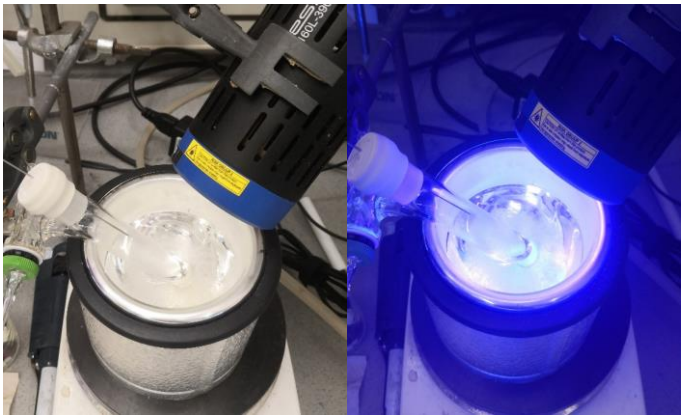

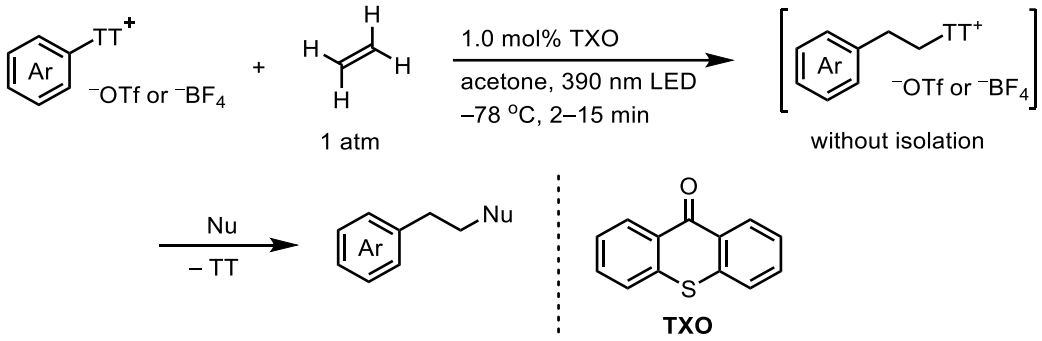

To a 5-mL Schlenk tube containing a Teflon-coated magnetic stirring bar were added arylthianthrenium salt (0.200 mmol, 1.00 equiv) and thioxanthone (TXO) in acetone (c = 0.50 mM, 4.0 mL, 2.0 μmol, 1.0 mol%). The tube was sealed with a rubber septum and immersed in a dry ice/acetone bath at −78°C. A balloon filled with ethylene gas was connected to a long needle, which was inserted to the tube through the rubber septum. Roughly 100 ml of ethylene gas was bubbled through the solution over a time period of approximately 5 minutes, and excess gas was released through the side arm, all while avoiding exposure to light. The valve of the side arm was closed, and the needle was withdrawn from the solution but remained in the headspace of the vessel. The reaction mixture was then subjected to irradiation by one Kessil PR160-390 nm LED with 100% intensity (40 W, ~6 cm away) for a period of ranging from 2 to 15 minutes, all while maintaining the bath temperature at −78°C. The progress of the reaction was monitored at 2, 5, 10, and 15 min by ^{1}H NMR spectroscopy. The complete conversion of arylthianthrenium salt was confirmed by comparing the ^{1}H NMR spectrum of the crude reaction mixture with that of pure arylthianthrenium salt, with particular attention to the disappearance of the characteristic doublet peak at around 8.6 ppm, typically occurring within 5 minutes. Then, nucleophile (0.24 mmol, 1.2 equiv) and base (0.40 mmol, 2.0 equiv) were added. The resulting mixture was stirred for 12 h without exposure to light. During this period, the reaction temperature was gradually allowed to rise to 23 ºC. In certain cases, heating and solvent changes were required as part of the process.

Subsequently, silica gel (5–10 mL) was added, and the reaction mixture was concentrated to dryness under reduced pressure. The resulting residue was purified by chromatography on silica gel to afford the desired product.

Notes:

1. Exercise caution when handling the high-pressure ethylene gas cylinder during balloon filling.
2. The purity of ArTTs is crucial for achieving high yield, as colored impurities may quench the excited photosensitizer.
3. Ensure a clear dry ice/acetone bath, as a turbid solution can diminish irradiation efficiency.
4. A clear reaction solution is also crucial for irradiation efficiency. Reactivity comparisons between **1** with $^{-}$OTf and $^{-}BF_4$ counterions didn't show obvious difference, given their comparable solubility in acetone at –78°C. However, during substrate scope investigations, it was observed that $^{-}BF_4$ counterions occasionally led to lower solubility compared to $^{-}$OTf, resulting in reduced yields. In such cases, extending the reaction time, diluting the solution, or employing acetonitrile as a solvent or cosolvent may enhance the yields. Further details on these observations have been outlined in the detailed procedure for each substrate.
5. Eliminate HCl when using amine/HCl salts as starting materials, as chloride can act as a competitive nucleophile.
6. To enhance light exposure, it is recommended to incline the tube slightly, ensuring a more effective irradiation by maximizing the surface area exposed to light.

Arylethylamine 3

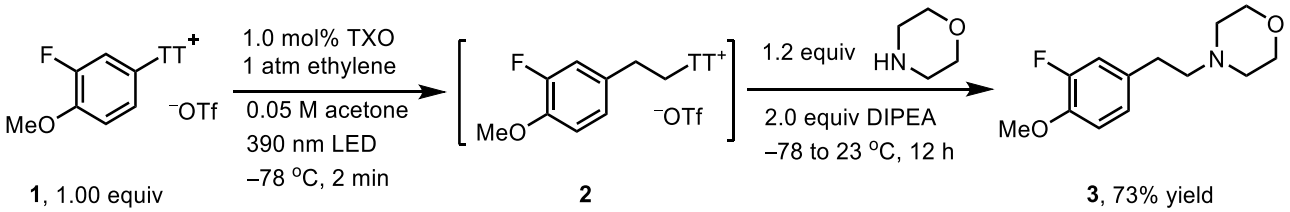

1, 1.00 equiv **2** **3**, 73% yield

To a 5-mL Schlenk tube containing a Teflon-coated magnetic stirring bar were added arylthianthrenium salt **1** (98.0 mg, 0.200 mmol, 1.00 equiv) and thioxanthone in acetone (c = 0.50 mM, 4.0 mL, 2.0 μmol, 1.0 mol%). The tube was sealed with a rubber septum and immersed in a dry ice/acetone bath at –78°C. A balloon filled with ethylene gas was connected to a long needle, which was inserted to the tube through the rubber septum. Roughly 100 ml of ethylene gas was bubbled through the solution over a time period of approximately 5 minutes, and excess gas was released through the side arm, all while avoiding exposure to light. The valve of the side arm was closed, and the needle was withdrawn from the solution but remained in the headspace of the vessel. The reaction mixture was then subjected to irradiation by one Kessil PR160-390 nm LED with 100% intensity (40 W, ~6 cm away) for 2 minutes, all while maintaining the bath temperature at –78°C. Then, morpholine (21 μL, 21 mg, 0.24 mmol, 1.2 equiv) and DIPEA (70 μL, 52 mg, 0.40 mmol, 2.0 equiv) were added. The resulting mixture was stirred for 12 h without exposure to light. During this period, the reaction

temperature was gradually allowed to rise to 23 ºC. Subsequently, silica gel (5–10 mL) was added, and the reaction mixture was concentrated to dryness under reduced pressure. The resulting residue was purified by chromatography on silica gel (EtOAc/Et_3N = 100:1) to afford **3** as a colorless liquid in 73% yield (34.9 mg).

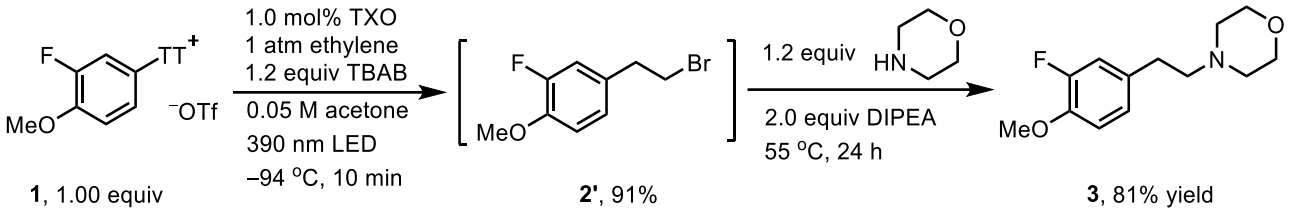

To a 5-mL Schlenk tube containing a Teflon-coated magnetic stirring bar were added arylthianthrenium salt **1** (98.0 mg, 0.200 mmol, 1.00 equiv), tetrabutylammonium bormide (TBAB, 77 mg, 0.24 mmol, 1.2 equiv), and thioxanthone in acetone (c = 0.50 mM, 4.0 mL, 2.0 μmol, 1.0 mol%). The tube was sealed with a rubber septum and immersed in a liquid nitrogen/acetone bath at –94°C. A balloon filled with ethylene gas was connected to a long needle, which was inserted to the tube through the rubber septum. Roughly 100 ml of ethylene gas was bubbled through the solution over a time period of approximately 5 minutes, and excess gas was released through the side arm, all while avoiding exposure to light. The valve of the side arm was closed, and the needle was withdrawn from the solution but remained in the headspace of the vessel. The reaction mixture was then subjected to irradiation by one Kessil PR160-390 nm LED with 100% intensity (40 W, ~6 cm away) for 10 minutes, all while maintaining the bath temperature at –94°C. Then, morpholine (21 μL, 21 mg, 0.24 mmol, 1.2 equiv) and DIPEA (70 μL, 52 mg, 0.40 mmol, 2.0 equiv) were added. The resulting mixture was stirred at 55 ºC for 24 h without exposure to light. Subsequently, silica gel (5–10 mL) was added, and the reaction mixture was concentrated to dryness under reduced pressure. The resulting residue was purified by chromatography on silica gel (EtOAc/Et_3N = 100:1) to afford **3** as a colorless liquid in 81% yield (38.7 mg).

R_f = 0.20 (EtOAc/Et_3N = 100:1).

NMR Spectroscopy:

^{1}H NMR (500 MHz, $CDCl_3$, 23 ºC, δ): 6.96 (dd, *J* = 12.3, 1.8 Hz, 1H), 6.93 – 6.86 (m, 2H), 3.87 (s, 3H), 3.75 (t, *J* = 4.6 Hz, 4H), 2.74 (dd, *J* = 9.8, 6.3 Hz, 2H), 2.60 – 2.54 (m, 2H), 2.52 (t, *J* = 4.5 Hz, 4H).

^{13}C NMR (125 MHz, $CDCl_3$, 23 ºC, δ): 152.2 (d, *J* = 245.5 Hz), 145.9 (d, *J* = 10.7 Hz), 133.2 (d, *J* = 6.0 Hz), 124.1 (d, *J* = 3.5 Hz), 116.3 (d, *J* = 18.0 Hz), 113.5 (d, *J* = 2.3 Hz), 67.0, 60.6, 56.3, 53.7, 32.3.

^{19}F NMR (471 MHz, $CDCl_3$, 23 ºC, δ): –135.55 (dd, *J* = 12.2, 7.7 Hz).

HRMS-ESIpos (m/z) calc'd for $C_{13}H_{19}FNO_2$ $[M+H]^+$, 240.1394; found, 240.1394; deviation: –0.1 ppm.

Arylethylamine 4

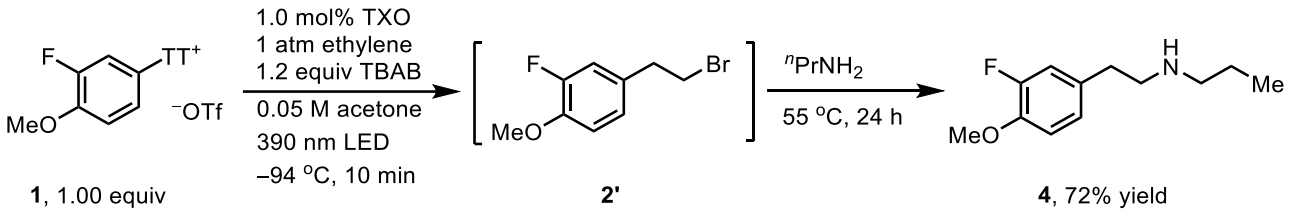

To a 5-mL Schlenk tube containing a Teflon-coated magnetic stirring bar were added arylthianthrenium salt **1** (98.0 mg, 0.200 mmol, 1.00 equiv), tetrabutylammonium bormide (TBAB, 77 mg, 0.24 mmol, 1.2 equiv), and thioxanthone in acetone (c = 0.50 mM, 4.0 mL, 2.0 μmol, 1.0 mol%). The tube was sealed with a rubber septum and immersed in a liquid nitrogen/acetone bath at –94°C. A balloon filled with ethylene gas was connected to a long needle, which was inserted to the tube through the rubber septum. Roughly 100 ml of ethylene gas was bubbled through the solution over a time period of approximately 5 minutes, and excess gas was released through the side arm, all while avoiding exposure to light. The valve of the side arm was closed, and the needle was withdrawn from the solution but remained in the headspace of the vessel. The reaction mixture was then subjected to irradiation by one Kessil PR160-390 nm LED with 100% intensity (40 W, ~6 cm away) for 10 minutes, all while maintaining the bath temperature at –94°C. Then, propylamine (0.5 mL) was added and the resulting mixture was stirred at 55 ºC for 24 h without exposure to light. Subsequently, silica gel (5–10 mL) was added, and the reaction mixture was concentrated to dryness under reduced pressure. The resulting residue was purified by chromatography on silica gel (EtOAc/Et_3N = 100:1) to afford **4** as a colorless liquid in 72% yield (30.4 mg).

R_f = 0.20 (EtOAc/Et_3N = 100:1).

NMR Spectroscopy:

^{1}H NMR (500 MHz, $CDCl_3$, 23 ºC, δ): 7.03 – 6.84 (m, 3H), 3.88 (s, 3H), 2.85 (td, *J* = 7.1, 1.0 Hz, 2H), 2.75 (t, *J* = 7.3 Hz, 2H), 2.66 – 2.53 (m, 2H), 1.63 – 1.39 (m, 2H), 0.91 (t, *J* = 7.4 Hz, 3H).

^{13}C NMR (125 MHz, $CDCl_3$, 23 ºC, δ): 152.3 (d, *J* = 245.4 Hz), 145.9 (d, *J* = 10.7 Hz), 133.3, 124.2 (d, *J* = 3.4 Hz), 116.3 (d, *J* = 17.9 Hz), 113.5 (d, *J* = 2.2 Hz), 56.4, 51.8, 51.0, 35.5, 23.2, 11.8.

^{19}F NMR (471 MHz, $CDCl_3$, 23 ºC, δ): –135.55.

HRMS-ESIpos (m/z) calc'd for $C_{12}H_{19}FNO$ $[M+H]^+$, 212.1445 found, 212.1448 deviation: –1.3 ppm.

Arylethylamine 5

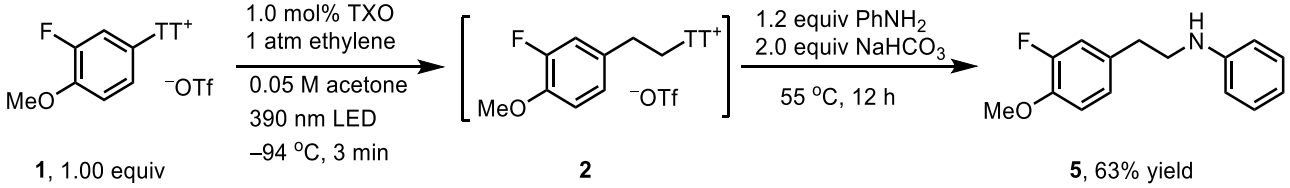

To a 5-mL Schlenk tube containing a Teflon-coated magnetic stirring bar were added arylthianthrenium salt **1** (98.0 mg, 0.200 mmol, 1.00 equiv) and thioxanthone in acetone (c = 0.50 mM, 4.0 mL, 2.0 μmol, 1.0 mol%). The tube was sealed with a rubber septum and immersed in a liquid nitrogen/acetone bath at −94°C. A balloon filled with ethylene gas was connected to a long needle, which was inserted to the tube through the rubber septum. Roughly 100 ml of ethylene gas was bubbled through the solution over a time period of approximately 5 minutes, and excess gas was released through the side arm, all while avoiding exposure to light. The valve of the side arm was closed, and the needle was withdrawn from the solution but remained in the headspace of the vessel. The reaction mixture was then subjected to irradiation by one Kessil PR160-390 nm LED with 100% intensity (40 W, ~6 cm away) for 3 minutes, all while maintaining the bath temperature at −94°C. Then, aniline (23 μL, 23 mg, 0.24 mmol, 1.2 equiv) and $NaHCO_3$ (34 mg, 0.40 mmol, 2.0 equiv) were added. The resulting mixture was stirred at 55 ºC for 12 h without exposure to light. Subsequently, silica gel (5−10 mL) was added, and the reaction mixture was concentrated to dryness under reduced pressure. The resulting residue was purified by chromatography on silica gel (hexanes/EtOAc = 10:1) to afford **5** as a colorless liquid in 63% yield (30.9 mg).

R_f = 0.22 (hexanes/EtOAc = 10:1).

NMR Spectroscopy:

^{1}H NMR (500 MHz, $CDCl_3$, 23 ºC, δ): 7.21 (dd, *J* = 8.6, 7.3 Hz, 2H), 7.02 – 6.89 (m, 4H), 6.75 (t, *J* = 7.3 Hz, 1H), 6.64 (d, *J* = 7.5 Hz, 1H), 3.91 (s, 4H), 3.40 (t, *J* = 7.0 Hz, 2H), 2.88 (t, *J* = 7.0 Hz, 2H).

^{13}C NMR (125 MHz, $CDCl_3$, 23 ºC, δ): 152.4 (d, *J* = 246.0 Hz), 147.9, 146.2 (d, *J* = 10.7 Hz), 132.4 (d, *J* = 6.0 Hz), 129.3, 124.3 (d, *J* = 3.4 Hz), 117.6, 116.4 (d, *J* = 17.9 Hz), 113.6 (d, *J* = 2.3 Hz), 113.0, 56.4, 45.0, 34.6.

^{19}F NMR (471 MHz, $CDCl_3$, 23 ºC, δ): −135.16 (dd, *J* = 12.1, 6.7 Hz).

HRMS-EI (m/z) calc'd for $C_{15}H_{16}FNO$ $[M]^+$, 245.1210; found, 245.1211; deviation: −0.3 ppm.

Thalidomide-derived arylethylamine 6

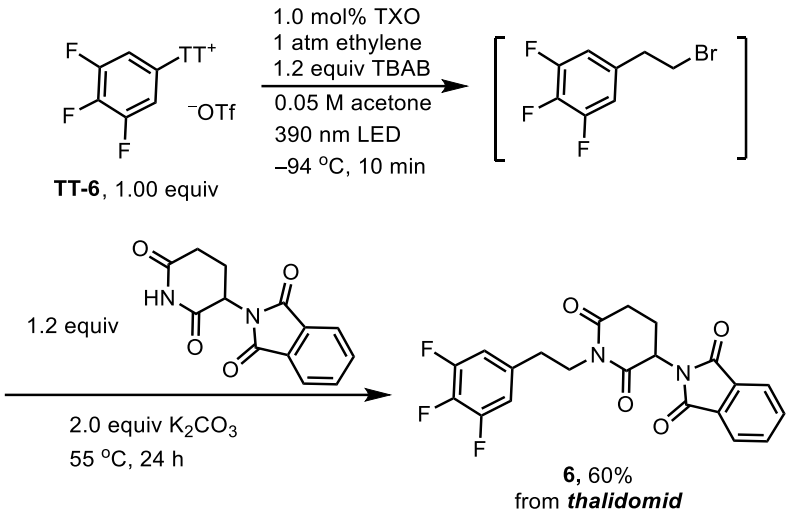

To a 5-mL Schlenk tube containing a Teflon-coated magnetic stirring bar were added **TT-6** (99.2 mg, 0.200 mmol, 1.00 equiv), tetrabutylammonium bormide (TBAB, 77 mg, 0.24 mmol, 1.2 equiv), and thioxanthone in acetone (c = 0.50 mM, 4.0 mL, 2.0 μmol, 1.0 mol%). The tube was sealed with a rubber septum and immersed in a liquid nitrogen/acetone bath at –94°C. A balloon filled with ethylene gas was connected to a long needle, which was inserted to the tube through the rubber septum. Roughly 100 ml of ethylene gas was bubbled through the solution over a time period of approximately 5 minutes, and excess gas was released through the side arm, all while avoiding exposure to light. The valve of the side arm was closed, and the needle was withdrawn from the solution but remained in the headspace of the vessel. The reaction mixture was then subjected to irradiation by one Kessil PR160-390 nm LED with 100% intensity (40 W, ~6 cm away) for 10 minutes, all while maintaining the bath temperature at –94°C. Then, thalidomide (62 mg, 0.24 mmol, 1.2 equiv) and K_2CO_3 (55 mg, 0.40 mmol, 2.0 equiv) were added. The resulting mixture was stirred at 55 ºC for 24 h without exposure to light. Subsequently, silica gel (5–10 mL) was added, and the reaction mixture was concentrated to dryness under reduced pressure. The resulting residue was purified by chromatography on silica gel (hexanes/EtOAc = 3:1) to afford **6** as a colorless liquid in 60% yield (49.9 mg).

R*f* = 0.18 (hexanes/EtOAc = 3:1).

NMR Spectroscopy:

^{1}H NMR (500 MHz, $CDCl_3$, 23 ºC, δ): 7.91 (dd, *J* = 5.5, 3.1 Hz, 2H), 7.80 (dd, *J* = 5.5, 3.1 Hz, 2H), 6.91 (dd, *J* = 8.1, 6.4 Hz, 2H), 5.13 – 4.94 (m, 1H), 4.10 – 4.01 (m, 1H), 4.02 – 3.92 (m, 1H), 2.96 (dd, *J* = 13.0, 2.8 Hz, 1H), 2.85 – 2.68 (m, 4H), 2.25 – 2.08 (m, 1H).

^{13}C NMR (125 MHz, $CDCl_3$, 23 ºC, δ): 170.6, 168.5, 167.4, 151.1 (ddd, *J* = 249.7, 9.8, 3.8 Hz), 138.6 (dt, *J* = 249.8, 15.4 Hz), 134.5, 131.7, 123.8, 113.0 (dd, *J* = 16.0, 4.9 Hz), 50.1, 41.1, 33.2, 31.8, 22.0.

^{19}F NMR (471 MHz, $CDCl_3$, 23 ºC, δ): –134.78 (dd, *J* = 20.7, 8.3 Hz, 2F), –163.55 (tt, *J* = 20.7, 6.5 Hz, 1F).

HRMS-ESIpos (m/z) calc'd for $C_{21}H_{15}F_3N_2O_4$ $[M+H]^+$, 417.1057; found, 417.1058; deviation: –0.4 ppm.

Fenofibrate-derived arylethyl chloride 7

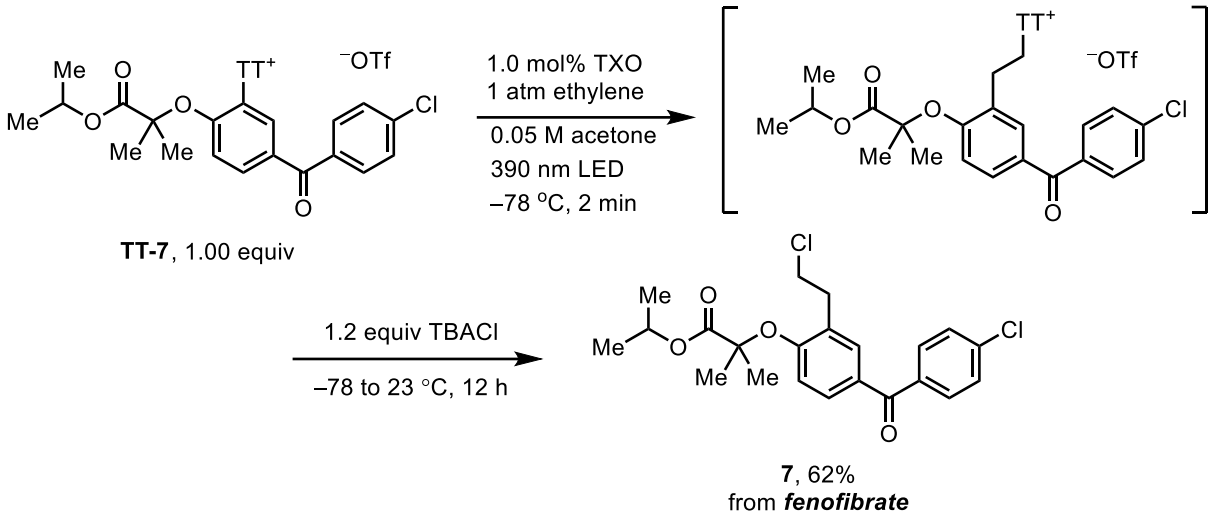

To a 5-mL Schlenk tube containing a Teflon-coated magnetic stirring bar were added **TT-7** (145 mg, 0.200 mmol, 1.00 equiv) and thioxanthone in acetone (c = 0.50 mM, 4.0 mL, 2.0 μmol, 1.0 mol%). The tube was sealed with a rubber septum and immersed in a dry ice/acetone bath at –78°C. A balloon filled with ethylene gas was connected to a long needle, which was inserted to the tube through the rubber septum. Roughly 100 ml of ethylene gas was bubbled through the solution over a time period of approximately 5 minutes, and excess gas was released through the side arm, all while avoiding exposure to light. The valve of the side arm was closed, and the needle was withdrawn from the solution but remained in the headspace of the vessel. The reaction mixture was then subjected to irradiation by one Kessil PR160-390 nm LED with 100% intensity (40 W, ~6 cm away) for 2 minutes, all while maintaining the bath temperature at –78°C. Then, tetrabutylammonium chloride (TBACl, 67 mg, 0.24 mmol, 1.2 equiv) was added. The resulting mixture was stirred for 12 h without exposure to light. During this period, the reaction temperature was gradually allowed to rise to 23 ºC. Subsequently, silica gel (5–10 mL) was added, and the reaction mixture was concentrated to dryness under reduced pressure. The resulting residue was purified by chromatography on silica gel (hexanes/EtOAc = 10:1) first and further purified by HPLC [YMC Pack Triart C18 (30×150 mm: 5 μm), 77.5:22.5 MeOH/H_2O (v/v), flow rate = 42.5 mL/min, 35 ºC] to afford **7** as a colorless liquid in 62% yield (52.4 mg).

$\mathbf{R_f}$ = 0.28 (hexanes/EtOAc = 10:1).

NMR Spectroscopy:

^{1}H NMR (500 MHz, $CDCl_3$, 23 ºC, δ): 7.72 (d, *J* = 8.5 Hz, 2H), 7.70 (d, *J* = 2.2 Hz, 1H), 7.63 (dd, *J* = 8.6, 2.3 Hz, 1H), 7.47 (d, *J* = 8.5 Hz, 2H), 6.71 (d, *J* = 8.6 Hz, 1H), 5.07 (hept, *J* = 6.3 Hz, 1H), 3.79 (t, *J* = 7.1 Hz, 2H), 3.15 (t, *J* = 7.1 Hz, 2H), 1.72 (s, 6H), 1.18 (d, *J* = 6.2 Hz, 6H).

^{13}C NMR (125 MHz, $CDCl_3$, 23 ºC, δ): 194.2, 172.8, 157.9, 138.4, 136.4, 133.5, 131.2, 130.5, 129.8,

128.5, 128.0, 113.8, 79.6, 69.4, 43.4, 34.5, 25.6, 21.5.

HRMS-ESIpos (m/z) calc'd for $C_{22}H_{24}O_4Cl_2Na$ $[M+Na]^+$, 445.0944; found, 445.0941; deviation: +0.7 ppm.

Vinyl arene 8

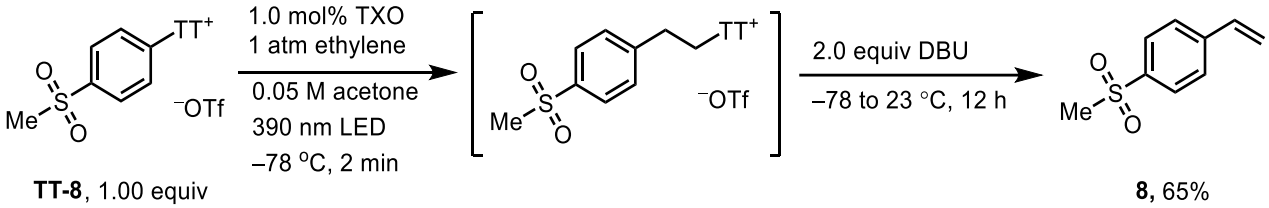

To a 5-mL Schlenk tube containing a Teflon-coated magnetic stirring bar were added **TT-8** (104 mg, 0.200 mmol, 1.00 equiv) and thioxanthone in acetone (c = 0.50 mM, 4.0 mL, 2.0 μmol, 1.0 mol%). The tube was sealed with a rubber septum and immersed in a dry ice/acetone bath at –78°C. A balloon filled with ethylene gas was connected to a long needle, which was inserted to the tube through the rubber septum. Roughly 100 ml of ethylene gas was bubbled through the solution over a time period of approximately 5 minutes, and excess gas was released through the side arm, all while avoiding exposure to light. The valve of the side arm was closed, and the needle was withdrawn from the solution but remained in the headspace of the vessel. The reaction mixture was then subjected to irradiation by one Kessil PR160-390 nm LED with 100% intensity (40 W, ~6 cm away) for 2 minutes, all while maintaining the bath temperature at –78°C. Then, 1,8-diazabicyclo[5.4.]undec-7-ene (DBU, 60 μL, 61 mg, 0.40 mmol, 2.0 equiv) was added. The resulting mixture was stirred for 12 h without exposure to light. During this period, the reaction temperature was gradually allowed to rise to 23 ºC. Subsequently, silica gel (5–10 mL) was added, and the reaction mixture was concentrated to dryness under reduced pressure. The resulting residue was purified by chromatography on silica gel (hexanes/EtOAc = 20:1) to afford **8** as a colorless liquid in 65% yield (23.5 mg).

R_f = 0.30 (hexanes/EtOAc = 20:1).

NMR Spectroscopy:

^{1}H NMR (500 MHz, $CDCl_3$, 23 ºC, δ): 7.91 (d, *J* = 8.4 Hz, 2H), 7.60 (d, *J* = 8.5 Hz, 2H), 6.79 (dd, *J* = 17.6, 10.9 Hz, 1H), 5.93 (d, *J* = 17.6 Hz, 1H), 5.49 (d, *J* = 10.9 Hz, 1H), 3.07 (s, 3H).

^{13}C NMR (125 MHz, $CDCl_3$, 23 ºC, δ): 142.9, 139.3, 135.2, 127.7, 127.0, 118.0, 44.6.

HRMS-EI (m/z) calc'd for $C_9H_{10}SO_2$ $[M]^+$, 182.0396; found, 182.0399; deviation: –1.6 ppm.

Arylethyl thioether 9

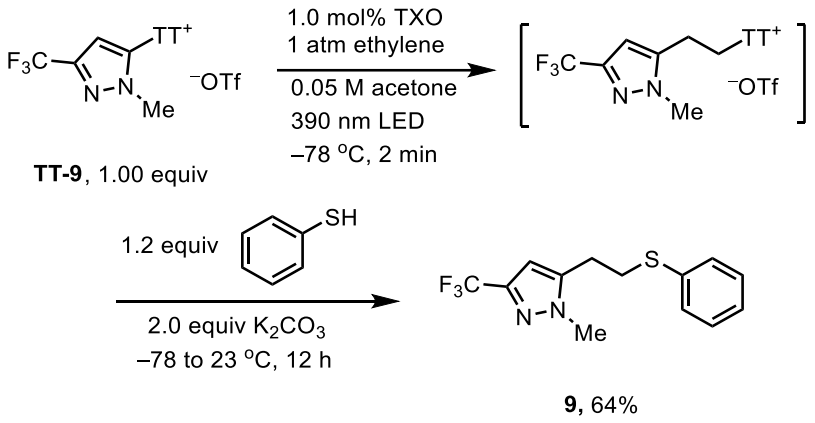

To a 5-mL Schlenk tube containing a Teflon-coated magnetic stirring bar were added **TT-9** (103 mg, 0.200 mmol, 1.00 equiv) and thioxanthone in acetone (c = 0.50 mM, 4.0 mL, 2.0 μmol, 1.0 mol%). The tube was sealed with a rubber septum and immersed in a dry ice/acetone bath at –78°C. A balloon filled with ethylene gas was connected to a long needle, which was inserted to the tube through the rubber septum. Roughly 100 ml of ethylene gas was bubbled through the solution over a time period of approximately 5 minutes, and excess gas was released through the side arm, all while avoiding exposure to light. The valve of the side arm was closed, and the needle was withdrawn from the solution but remained in the headspace of the vessel. The reaction mixture was then subjected to irradiation by one Kessil PR160-390 nm LED with 100% intensity (40 W, ~6 cm away) for 2 minutes, all while maintaining the bath temperature at –78°C. Then, thiophenol (24 μL, 26 mg, 0.24 mmol, 1.2 equiv) and K_2CO_3 (55 mg, 0.40 mmol, 2.0 equiv) were added. The resulting mixture was stirred for 12 h without exposure to light. During this period, the reaction temperature was gradually allowed to rise to 23 ºC. Subsequently, silica gel (5–10 mL) was added, and the reaction mixture was concentrated to dryness under reduced pressure. The resulting residue was purified by chromatography on silica gel (hexanes/EtOAc = 5:1) to afford **9** as a colorless liquid in 64% yield (36.5 mg).

R_f = 0.30 (hexanes/EtOAc = 5:1).

NMR Spectroscopy:

^{1}H NMR (500 MHz, $CDCl_3$, 23 ºC, δ): 7.42 – 7.36 (m, 2H), 7.37 – 7.31 (m, 2H), 7.30 – 7.23 (m, 1H), 6.37 (s, 1H), 3.79 (s, 3H), 3.29 – 3.11 (m, 2H), 2.95 (t, *J* = 7.5 Hz, 2H).

^{13}C NMR (125 MHz, $CDCl_3$, 23 ºC, δ): 142.4, 141.3 (q, *J* = 38.1 Hz), 134.9, 130.1, 129.2, 126.9, 121.3 (q, *J* = 268.3 Hz), 103.2 (q, *J* = 2.3 Hz), 36.8, 32.6, 25.8.

^{19}F NMR (471 MHz, $CDCl_3$, 23 ºC, δ): –62.07.

HRMS-ESIpos (m/z) calc'd for $C_{13}H_{13}F_3N_2NaS$ $[M+Na]^+$, 309.0644; found, 309.0643; deviation: +0.2 ppm.

Arylethyl selenoether 10

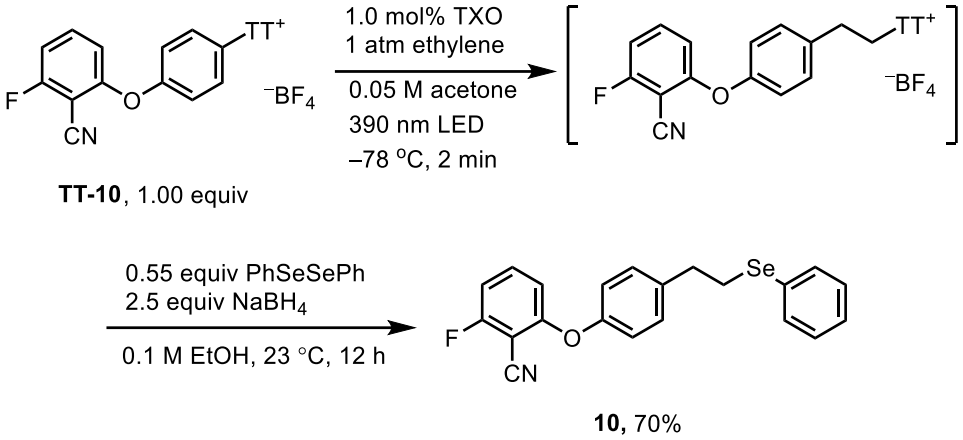

To a 5-mL Schlenk tube containing a Teflon-coated magnetic stirring bar were added **TT-10** (103 mg, 0.200 mmol, 1.00 equiv) and thioxanthone in acetone (c = 0.50 mM, 4.0 mL, 2.0 μmol, 1.0 mol%). The tube was sealed with a rubber septum and immersed in a dry ice/acetone bath at −78°C. A balloon filled with ethylene gas was connected to a long needle, which was inserted to the tube through the rubber septum. Roughly 100 ml of ethylene gas was bubbled through the solution over a time period of approximately 5 minutes, and excess gas was released through the side arm, all while avoiding exposure to light. The valve of the side arm was closed, and the needle was withdrawn from the solution but remained in the headspace of the vessel. The reaction mixture was then subjected to irradiation by one Kessil PR160-390 nm LED with 100% intensity (40 W, ~6 cm away) for 2 minutes, all while maintaining the bath temperature at −78°C. Then, the solvent was removed and the crude alkyl thianthrenium salt was directly used for the next step. To another 5-mL Schlenk tube containing a Teflon-coated magnetic stirring bar were added diphenyl diselenide (34 mg, 0.11 mmol, 0.55 equiv) and EtOH (2 mL, c = 0.1 M). Sodium borohydride (19 mg, 0.5 mmol, 2.5 equiv) was added in three portions at 0 °C. The reaction was warmed to room temperature and stirred for 1 h. The resulting mixture was added to the crude alkyl thianthrenium salt and stirred for 12 h. The resulting solution was diluted with ethyl acetate (10 mL), washed by water (10 mL) and brine (10 mL), dried over Na_2SO_4, and concentrated under reduced pressure. The resulting residue was purified by chromatography on silica gel (hexanes/EtOAc = 10:1) to afford **10** as a colorless liquid in 70% yield (55.3 mg).

R_f = 0.14 (hexanes/EtOAc = 10:1).

NMR Spectroscopy:

^{1}H NMR (500 MHz, $CDCl_3$, 23 °C, δ): 7.53 (dd, *J* = 7.6, 1.9 Hz, 2H), 7.43 (td, *J* = 8.5, 6.4 Hz, 1H), 7.34 – 7.26 (m, 3H), 7.28 – 7.22 (m, 2H), 7.05 (d, *J* = 8.5 Hz, 2H), 6.89 (t, *J* = 8.3 Hz, 1H), 6.60 (d, *J* = 8.6 Hz, 1H), 3.26 – 3.14 (m, 2H), 3.04 (t, *J* = 7.8 Hz, 2H).

^{13}C NMR (125 MHz, $CDCl_3$, 23 °C, δ): 164.1 (d, *J* = 259.4 Hz), 161.2 (d, *J* = 4.1 Hz), 152.9, 138.5, 134.8 (d, *J* = 10.1 Hz), 132.7, 130.2, 130.0, 129.2, 127.0, 120.5, 111.6 (d, *J* = 3.2 Hz), 111.2, 109.5 (d, *J* = 19.3 Hz), 93.5 (d, *J* = 18.2 Hz), 35.9, 28.7.

^{19}F NMR (471 MHz, $CDCl_3$, 23 ºC, δ): –104.68 – –104.96 (m).

HRMS-EI (m/z) calc'd for $C_{21}H_{16}FNOSe$ $[M]^+$, 397.0376; found, 397.0381; deviation: –1.3 ppm.

Trimetazidine-derived arylethylamine 11

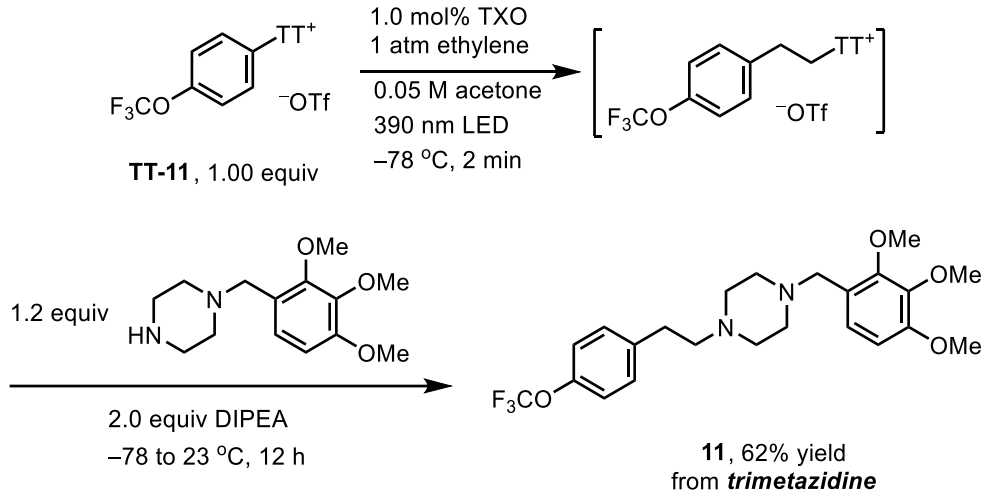

To a 5-mL Schlenk tube containing a Teflon-coated magnetic stirring bar were added **TT-11** (105 mg, 0.200 mmol, 1.00 equiv) and thioxanthone in acetone (c = 0.50 mM, 4.0 mL, 2.0 μmol, 1.0 mol%). The tube was sealed with a rubber septum and immersed in a dry ice/acetone bath at –78°C. A balloon filled with ethylene gas was connected to a long needle, which was inserted to the tube through the rubber septum. Roughly 100 ml of ethylene gas was bubbled through the solution over a time period of approximately 5 minutes, and excess gas was released through the side arm, all while avoiding exposure to light. The valve of the side arm was closed, and the needle was withdrawn from the solution but remained in the headspace of the vessel. The reaction mixture was then subjected to irradiation by one Kessil PR160-390 nm LED with 100% intensity (40 W, ~6 cm away) for 2 minutes, all while maintaining the bath temperature at –78°C. Then, trimetazidine (64 mg, 0.24 mmol, 1.2 equiv) and DIPEA (70 μL, 52 mg, 0.40 mmol, 2.0 equiv) were added. The resulting mixture was stirred for 12 h without exposure to light. During this period, the reaction temperature was gradually allowed to rise to 23 ºC. Subsequently, silica gel (5–10 mL) was added, and the reaction mixture was concentrated to dryness under reduced pressure. The resulting residue was purified by chromatography on silica gel ($EtOAc/Et_3N$ = 100:1) to afford **11** as a colorless liquid in 62% yield (56.4 mg).

R_f = 0.30 ($EtOAc/Et_3N$ = 100:1).

NMR Spectroscopy:

^{1}H NMR (500 MHz, $CDCl_3$, 23 ºC, δ): 7.13 (d, *J* = 8.6 Hz, 2H), 7.07 – 7.00 (m, 2H), 6.91 (d, *J* = 8.5 Hz, 1H), 6.55 (d, *J* = 8.5 Hz, 1H), 3.81 (s, 3H), 3.79 (s, 3H), 3.77 (s, 3H), 3.43 (s, 2H), 2.77 – 2.68 (m, 2H), 2.56 – 2.49 (m, 2H), 2.48 (s, 8H).

^{13}C NMR (125 MHz, $CDCl_3$, 23 ºC, δ): 152.9, 152.7, 147.5, 142.3, 139.2, 129.9, 125.2, 123.9, 120.9, 120.5 (d, *J* = 256.4 Hz), 106.9, 61.2, 60.8, 60.3, 56.5, 56.0, 53.3, 52.8, 33.0.

^{19}F NMR (471 MHz, $CDCl_3$, 23 ºC, δ): –57.94.

HRMS-ESIpos (m/z) calc'd for $C_{23}H_{30}F_3N_2O_4$ $[M+H]^+$, 455.2152; found, 455.2154; deviation: –0.5 ppm.

Arylethyl iodide 12

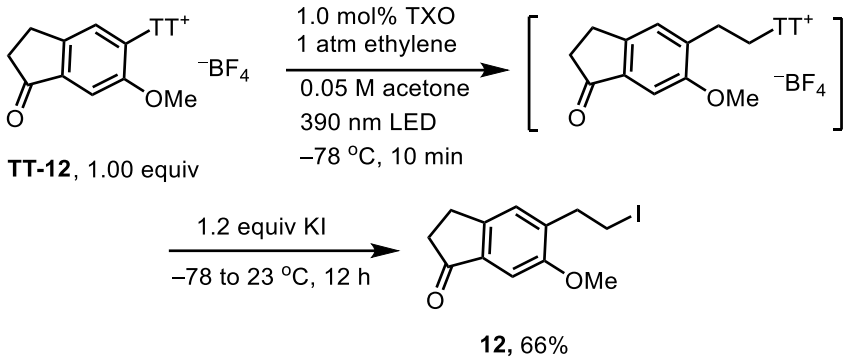

To a 5-mL Schlenk tube containing a Teflon-coated magnetic stirring bar were added **TT-12** (92.4 mg, 0.200 mmol, 1.00 equiv) and thioxanthone in acetone (c = 0.50 mM, 4.0 mL, 2.0 μmol, 1.0 mol%). The tube was sealed with a rubber septum and immersed in a dry ice/acetone bath at –78°C. A balloon filled with ethylene gas was connected to a long needle, which was inserted to the tube through the rubber septum. Roughly 100 ml of ethylene gas was bubbled through the solution over a time period of approximately 5 minutes, and excess gas was released through the side arm, all while avoiding exposure to light. The valve of the side arm was closed, and the needle was withdrawn from the solution but remained in the headspace of the vessel. The reaction mixture was then subjected to irradiation by one Kessil PR160-390 nm LED with 100% intensity (40 W, ~6 cm away) for 10 minutes, all while maintaining the bath temperature at –78°C. Then, potassium iodide (40 mg, 0.24 mmol, 1.2 equiv) was added. The resulting mixture was stirred for 12 h without exposure to light. During this period, the reaction temperature was gradually allowed to rise to 23 ºC. Subsequently, silica gel (5–10 mL) was added, and the reaction mixture was concentrated to dryness under reduced pressure. The resulting residue was purified by chromatography on silica gel (hexanes/EtOAc = 10:1) first and further purified by HPLC (YMC Triart C18 (30×150 mm: 5 μm), 60:40 to 90:10 MeCN/H_2O (v/v), flow rate = 20.0 mL/min, 35 ºC) to afford **12** as a colorless solid in 66% yield (41.6 mg).

R_f = 0.20 (hexanes/EtOAc = 10:1).

NMR Spectroscopy:

^{1}H NMR (500 MHz, $CDCl_3$, 23 ºC, δ): 7.55 (s, 1H), 6.90 (s, 1H), 3.94 (s, 3H), 3.37 (t, *J* = 7.6 Hz, 2H), 3.21 (t, *J* = 7.6 Hz, 2H), 3.14 – 3.05 (m, 2H), 2.74 – 2.62 (m, 2H).

^{13}C NMR (125 MHz, $CDCl_3$, 23 ºC, δ): 205.3, 163.1, 157.3, 130.0, 129.4, 125.2, 107.3, 55.8, 36.4, 35.2, 25.9, 4.3.

HRMS-ESIpos (m/z) calc'd for $C_{12}H_{13}INaO2$ $[M+Na]^+$, 338.9852; found, 338.9854; deviation: –0.4 ppm.

Arylethylammonium salt 13

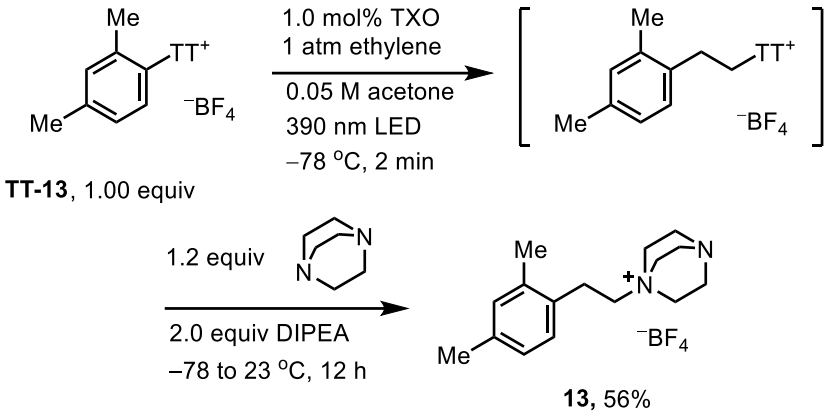

To a 5-mL Schlenk tube containing a Teflon-coated magnetic stirring bar were added **TT-13** (81.4 mg, 0.200 mmol, 1.00 equiv) and thioxanthone in acetone (c = 0.50 mM, 4.0 mL, 2.0 μmol, 1.0 mol%). The tube was sealed with a rubber septum and immersed in a dry ice/acetone bath at –78°C. A balloon filled with ethylene gas was connected to a long needle, which was inserted to the tube through the rubber septum. Roughly 100 ml of ethylene gas was bubbled through the solution over a time period of approximately 5 minutes, and excess gas was released through the side arm, all while avoiding exposure to light. The valve of the side arm was closed, and the needle was withdrawn from the solution but remained in the headspace of the vessel. The reaction mixture was then subjected to irradiation by one Kessil PR160-390 nm LED with 100% intensity (40 W, ~6 cm away) for 2 minutes, all while maintaining the bath temperature at –78°C. Then, 1,4-diazabicyclo(2.2.2)octane (DABCO, 27 mg, 0.24 mmol, 1.2 equiv) and DIPEA (70 μL, 52 mg, 0.40 mmol, 2.0 equiv) were added. The resulting mixture was stirred for 12 h without exposure to light. During this period, the reaction temperature was gradually allowed to rise to 23 ºC. Subsequently, silica gel (5–10 mL) was added, and the reaction mixture was concentrated to dryness under reduced pressure. The resulting residue was purified by chromatography on silica gel (DCM/MeOH = 10:1) to afford **13** as a colorless solid in 56% yield (37.1 mg).

R_f = 0.26 (DCM/MeOH = 10:1).

NMR Spectroscopy:

^{1}H NMR (500 MHz, CD_3CN, 23 ºC, δ): 7.12 (d, *J* = 7.7 Hz, 1H), 7.07 (s, 1H), 7.03 (d, *J* = 7.6 Hz, 1H), 3.34 (t, *J* = 7.5 Hz, 6H), 3.30 – 3.22 (m, 2H), 3.17 (t, *J* = 7.5 Hz, 8H), 3.06 – 2.97 (m, 2H), 2.32 (s, 3H), 2.30 (s, 3H).

^{13}C NMR (125 MHz, CD_3CN, 23 ºC, δ): 137.2, 136.3, 131.3, 130.8, 129.5, 127.1, 63.8, 52.2, 44.8, 24.7, 20.0, 18.2.

^{19}F NMR (471 MHz, CD_3CN, 23 ºC, δ): –152.41, –152.46.

HRMS-ESIpos (m/z) calc'd for $C_{16}H_{25}N_2$ $[M–BF_4]^+$, 245.2012; found, 245.2013; deviation: –0.4 ppm.

Arylethyl benzoate 14

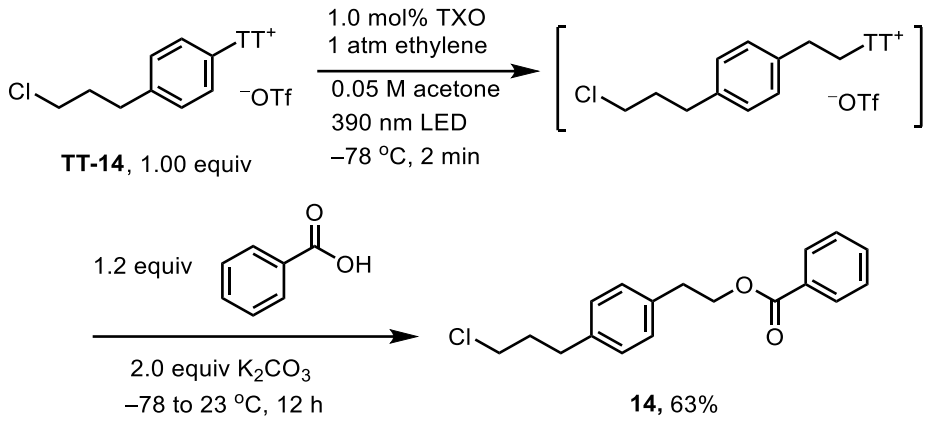

To a 5-mL Schlenk tube containing a Teflon-coated magnetic stirring bar were added **TT-14** (107 mg, 0.200 mmol, 1.00 equiv) and thioxanthone in acetone (c = 0.50 mM, 4.0 mL, 2.0 μmol, 1.0 mol%). The tube was sealed with a rubber septum and immersed in a dry ice/acetone bath at –78°C. A balloon filled with ethylene gas was connected to a long needle, which was inserted to the tube through the rubber septum. Roughly 100 ml of ethylene gas was bubbled through the solution over a time period of approximately 5 minutes, and excess gas was released through the side arm, all while avoiding exposure to light. The valve of the side arm was closed, and the needle was withdrawn from the solution but remained in the headspace of the vessel. The reaction mixture was then subjected to irradiation by one Kessil PR160-390 nm LED with 100% intensity (40 W, ~6 cm away) for 2 minutes, all while maintaining the bath temperature at –78°C. Then, benzoic acid (29 mg, 0.24 mmol, 1.2 equiv) and K_2CO_3 (55 mg, 0.40 mmol, 2.0 equiv) were added. The resulting mixture was stirred for 12 h without exposure to light. During this period, the reaction temperature was gradually allowed to rise to 23 ºC. Subsequently, silica gel (5–10 mL) was added, and the reaction mixture was concentrated to dryness under reduced pressure. The resulting residue was purified by chromatography on silica gel (hexanes/EtOAc = 20:1) to afford **14** as a colorless liquid in 63% yield (38.1 mg).

R_f = 0.27 (hexanes/EtOAc = 20:1).

NMR Spectroscopy:

^{1}H NMR (500 MHz, $CDCl_3$, 23 ºC, δ): 8.08 – 8.03 (m, 2H), 7.63 – 7.55 (m, 1H), 7.47 (t, *J* = 7.8 Hz, 2H), 7.25 (d, *J* = 8.1 Hz, 2H), 7.19 (d, *J* = 8.0 Hz, 2H), 4.55 (t, *J* = 7.0 Hz, 2H), 3.55 (t, *J* = 6.5 Hz, 2H), 3.09 (t, *J* = 7.0 Hz, 2H), 2.79 (t, *J* = 7.4 Hz, 2H), 2.18 – 2.03 (m, 2H).

^{13}C NMR (125 MHz, $CDCl_3$, 23 ºC, δ): 166.5, 139.0, 135.7, 132.9, 130.3, 129.6, 129.1, 128.7, 128.4, 65.5, 44.2, 34.8, 34.0, 32.4.

HRMS-ESIpos (m/z) calc'd for $C_{18}H_{19}ClNaO_2$ $[M+Na]^+$, 325.0966; found, 325.0966; deviation: +0.0 ppm.

Fenofibrate-derived 2-arylethanol 15

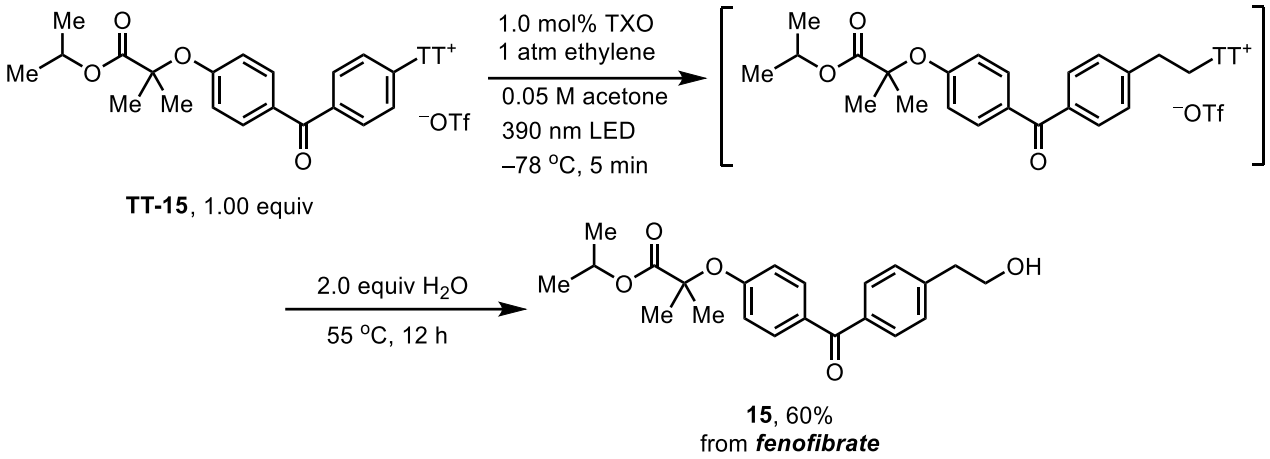

To a 5-mL Schlenk tube containing a Teflon-coated magnetic stirring bar were added arylthianthrenium salt **1** (138 mg, 0.200 mmol, 1.00 equiv) and thioxanthone in acetone (c = 0.50 mM, 4.0 mL, 2.0 μmol, 1.0 mol%). The tube was sealed with a rubber septum and immersed in a dry ice/acetone bath at –78°C. A balloon filled with ethylene gas was connected to a long needle, which was inserted to the tube through the rubber septum. Roughly 100 ml of ethylene gas was bubbled through the solution over a time period of approximately 5 minutes, and excess gas was released through the side arm, all while avoiding exposure to light. The valve of the side arm was closed, and the needle was withdrawn from the solution but remained in the headspace of the vessel. The reaction mixture was then subjected to irradiation by one Kessil PR160-390 nm LED with 100% intensity (40 W, ~6 cm away) for 5 minutes, all while maintaining the bath temperature at –78°C. Then, water (7.2 μL, 7.2 mg, 0.40 mmol, 2.0 equiv) was added. The resulting mixture was stirred at 55 ºC for 12 h without exposure to light. Subsequently, silica gel (5–10 mL) was added, and the reaction mixture was concentrated to dryness under reduced pressure. The resulting residue was purified by chromatography on silica gel (hexanes/EtOAc = 2:1) to afford **15** as a colorless liquid in 60% yield (44.3 mg).

R_f = 0.20 (hexanes/EtOAc = 2:1).

NMR Spectroscopy:

^{1}H NMR (500 MHz, $CDCl_3$, 23 ºC, δ): 7.77 (d, *J* = 8.9 Hz, 2H), 7.73 (d, *J* = 8.2 Hz, 2H), 7.35 (d, *J* = 8.1 Hz, 2H), 6.88 (d, *J* = 8.8 Hz, 2H), 5.10 (hept, *J* = 6.3 Hz, 1H), 3.93 (t, *J* = 6.6 Hz, 2H), 2.97 (t, *J* = 6.5 Hz, 2H), 1.22 (d, *J* = 6.3 Hz, 6H).

^{13}C NMR (125 MHz, $CDCl_3$, 23 ºC, δ): 195.3, 173.2, 159.5, 143.3, 136.4, 132.0, 130.7, 130.1, 128.9, 117.2, 79.4, 69.3, 63.3, 39.2, 25.4, 21.5.

HRMS-ESIpos (m/z) calc'd for $C_{22}H_{26}NaO_5$ $[M+Na]^+$, 393.1672; found, 393.1674; deviation: –0.5 ppm.

Arylethyl fluoride 16

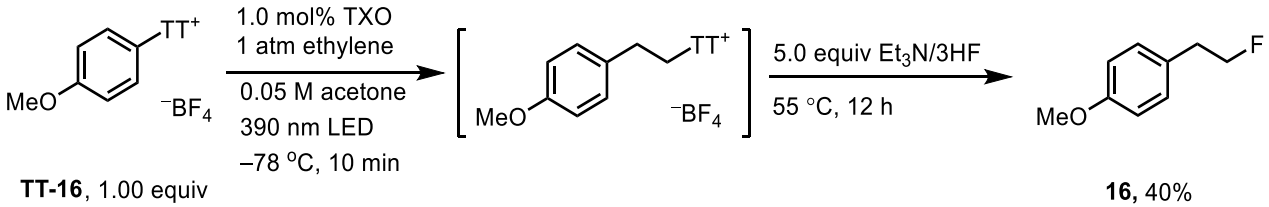

TT-16, 1.00 equiv

16, 40%

To a 5-mL Schlenk tube containing a Teflon-coated magnetic stirring bar were added **TT-16** (81.8 mg, 0.200 mmol, 1.00 equiv) and thioxanthone in acetone (c = 0.50 mM, 4.0 mL, 2.0 μmol, 1.0 mol%). The tube was sealed with a rubber septum and immersed in a dry ice/acetone bath at –78°C. A balloon filled with ethylene gas was connected to a long needle, which was inserted to the tube through the rubber septum. Roughly 100 ml of ethylene gas was bubbled through the solution over a time period of approximately 5 minutes, and excess gas was released through the side arm, all while avoiding exposure to light. The valve of the side arm was closed, and the needle was withdrawn from the solution but remained in the headspace of the vessel. The reaction mixture was then subjected to irradiation by one Kessil PR160-390 nm LED with 100% intensity (40 W, ~6 cm away) for 10 minutes, all while maintaining the bath temperature at –78°C. Then, triethylamine trihydrofluoride (163 μL, 161 mg, 1.0 mmol, 5.0 equiv) was added. The resulting mixture was stirred at 55 ºC for 12 h without exposure to light. Subsequently, silica gel (5–10 mL) was added, and the reaction mixture was concentrated to dryness under reduced pressure. The resulting residue was purified by chromatography on silica gel (hexanes/EtOAc = 20:1) to afford **16** as a colorless liquid in 40% yield (12.2 mg).

R_f = 0.26 (hexanes/EtOAc = 20:1).

NMR Spectroscopy:

^{1}H NMR (500 MHz, $CDCl_3$, 23 ºC, δ): 7.18 (d, *J* = 8.6 Hz, 2H), 6.89 (d, *J* = 8.6 Hz, 2H), 4.62 (dt, *J* = 47.1, 6.7 Hz, 2H), 3.82 (s, 3H), 2.99 (dt, *J* = 22.8, 6.7 Hz, 2H).

^{13}C NMR (125 MHz, $CDCl_3$, 23 ºC, δ): 158.4, 129.9, 129.1 (d, *J* = 7.0 Hz), 114.0, 84.3 (d, *J* = 168.7 Hz), 55.3, 36.1 (d, *J* = 20.3 Hz).

^{19}F NMR (471 MHz, $CDCl_3$, 23 ºC, δ): –214.91 – –215.32 (m).

HRMS-EI (m/z) calc'd for $C_9H_{11}FO$ $[M]^+$, 154.0788; found, 154.0790; deviation: –0.8 ppm.

Diclofenac amide-derived arylethylamine 17

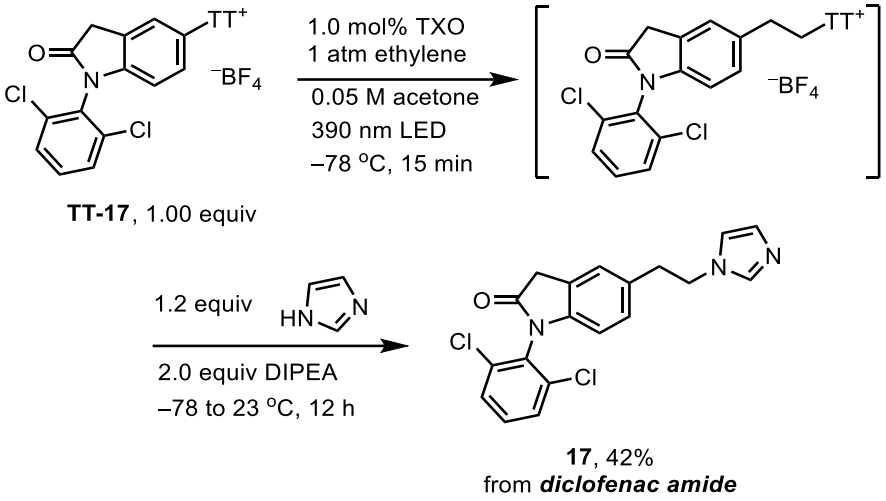

To a 5-mL Schlenk tube containing a Teflon-coated magnetic stirring bar were added **TT-17** (116 mg, 0.200 mmol, 1.00 equiv) and thioxanthone in acetone (c = 0.50 mM, 4.0 mL, 2.0 μmol, 1.0 mol%). The tube was sealed with a rubber septum and immersed in a dry ice/acetone bath at −78°C. A balloon filled with ethylene gas was connected to a long needle, which was inserted to the tube through the rubber septum. Roughly 100 ml of ethylene gas was bubbled through the solution over a time period of approximately 5 minutes, and excess gas was released through the side arm, all while avoiding exposure to light. The valve of the side arm was closed, and the needle was withdrawn from the solution but remained in the headspace of the vessel. The reaction mixture was then subjected to irradiation by one Kessil PR160-390 nm LED with 100% intensity (40 W, ~6 cm away) for 15 minutes, all while maintaining the bath temperature at −78°C. Then, imidazole (16 mg, 0.24 mmol, 1.2 equiv) and DIPEA (70 μL, 52 mg, 0.40 mmol, 2.0 equiv) were added. The resulting mixture was stirred for 12 h without exposure to light. During this period, the reaction temperature was gradually allowed to rise to 23 ºC. Subsequently, silica gel (5−10 mL) was added, and the reaction mixture was concentrated to dryness under reduced pressure. The resulting residue was purified by chromatography on silica gel (EtOAc/MeOH = 20:1) first and further purified by HPLC (Eclipse Plus C18 (21.2×150 mm: 5 μm), 60:40 to 85:15 MeOH/NH_4HCO_3 (aq.) (v/v), flow rate = 20.0 mL/min, 35 ºC) to afford **17** as a colorless liquid in 42% yield (31.3 mg).

$\mathbf{R}_f$ = 0.35 (EtOAc/MeOH = 20:1).

NMR Spectroscopy:

^{1}H NMR (500 MHz, $CDCl_3$, 23 ºC, δ): 7.52 (d, *J* = 8.1 Hz, 2H), 7.46 – 7.31 (m, 2H), 7.07 (d, *J* = 8.6 Hz, 2H), 6.89 (s, 1H), 6.90 (d, *J* = 9.0 Hz, 1H), 6.34 (d, *J* = 8.0 Hz, 1H), 4.19 (t, *J* = 7.1 Hz, 2H), 3.75 (s, 2H), 3.06 (t, *J* = 7.1 Hz, 2H).

^{13}C NMR (125 MHz, $CDCl_3$, 23 ºC, δ): 173.4, 142.3, 137.1, 135.4, 132.2, 130.8, 130.4, 129.3, 129.0, 128.1, 125.2, 124.8, 118.8, 109.3, 48.7, 37.5, 35.7.

HRMS-ESIpos (m/z) calc'd for $C_{19}H_{16}Cl_2N_3O$ $[M+H]^+$, 372.0665; found, 372.0664; deviation: +0.2 ppm.

Arylethyl methyl ether 18

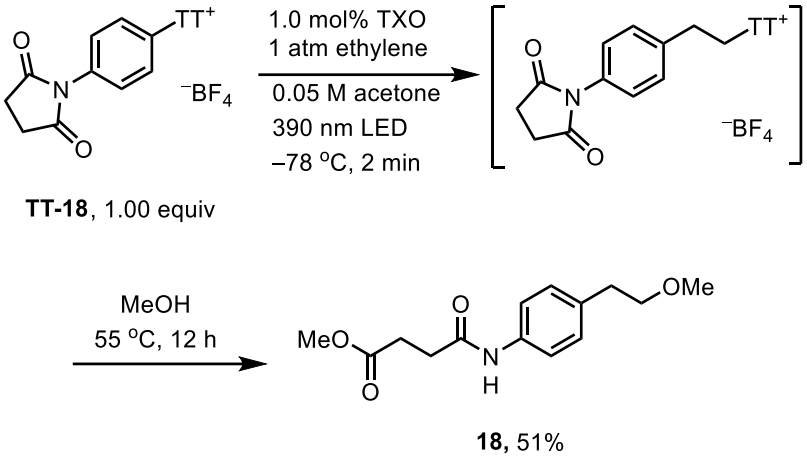

To a 5-mL Schlenk tube containing a Teflon-coated magnetic stirring bar were added **TT-18** (95.2 mg, 0.200 mmol, 1.00 equiv), thioxanthone in acetone (c = 0.50 mM, 4.0 mL, 2.0 μmol, 1.0 mol%), and acetonitrile (2 mL). The tube was sealed with a rubber septum and immersed in a dry ice/acetone bath at −78°C. A balloon filled with ethylene gas was connected to a long needle, which was inserted to the tube through the rubber septum. Roughly 100 ml of ethylene gas was bubbled through the solution over a time period of approximately 5 minutes, and excess gas was released through the side arm, all while avoiding exposure to light. The valve of the side arm was closed, and the needle was withdrawn from the solution but remained in the headspace of the vessel. The reaction mixture was then subjected to irradiation by one Kessil PR160-390 nm LED with 100% intensity (40 W, ~6 cm away) for 2 minutes, all while maintaining the bath temperature at −78°C. Then, the solvent was removed and anhydrous methanol (1 mL) was added. The resulting mixture was stirred at 55 ºC for 12 h without exposure to light. Subsequently, the reaction mixture was cooled to room temperature and diluted with ethyl acetate (10 mL). Silica gel (5–10 mL) was added, and the reaction mixture was concentrated to dryness under reduced pressure. The resulting residue was purified by chromatography on silica gel (hexanes/EtOAc = 1:1) to afford **18** as a colorless liquid in 51% yield (27.0 mg).

$\mathbf{R_f}$ = 0.23 (hexanes/EtOAc = 1:1).

NMR Spectroscopy:

^{1}H NMR (500 MHz, $CDCl_3$, 23 ºC, δ): 7.58 (s, 1H), 7.44 (d, *J* = 8.1 Hz, 2H), 7.18 (d, *J* = 8.1 Hz, 2H), 3.73 (s, 3H), 3.59 (t, *J* = 7.1 Hz, 2H), 3.36 (s, 3H), 2.86 (t, *J* = 7.0 Hz, 2H), 2.77 (t, *J* = 6.6 Hz, 2H), 2.67 (t, *J* = 6.6 Hz, 2H).

^{13}C NMR (125 MHz, $CDCl_3$, 23 ºC, δ): 173.6, 169.6, 136.0, 135.0, 129.3, 119.9, 73.6, 58.7, 52.0, 35.6, 32.1, 29.3.

HRMS-EI (m/z) calc'd for $C_{14}H_{19}NO_4$ $[M]^+$, 265.1309; found, 265.1311; deviation: −1.1 ppm.

Cysteine-derived arylethyl thioether 19

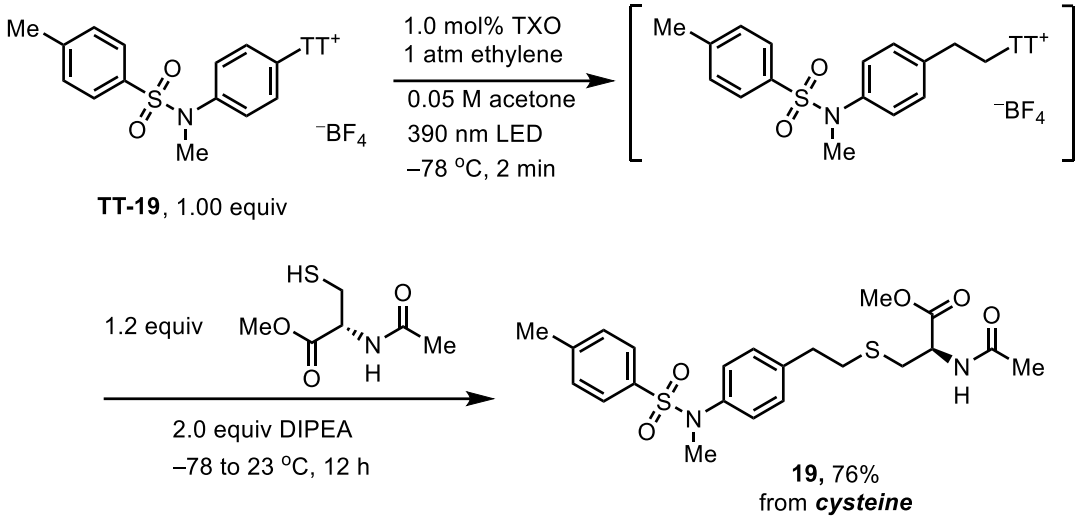

To a 5-mL Schlenk tube containing a Teflon-coated magnetic stirring bar were added **TT-19** (97.2 mg, 0.200 mmol, 1.00 equiv) and thioxanthone in acetone (c = 0.50 mM, 4.0 mL, 2.0 μmol, 1.0 mol%). The tube was sealed with a rubber septum and immersed in a dry ice/acetone bath at –78°C. A balloon filled with ethylene gas was connected to a long needle, which was inserted to the tube through the rubber septum. Roughly 100 ml of ethylene gas was bubbled through the solution over a time period of approximately 5 minutes, and excess gas was released through the side arm, all while avoiding exposure to light. The valve of the side arm was closed, and the needle was withdrawn from the solution but remained in the headspace of the vessel. The reaction mixture was then subjected to irradiation by one Kessil PR160-390 nm LED with 100% intensity (40 W, ~6 cm away) for 2 minutes, all while maintaining the bath temperature at –78°C. Then, *N*-acetyl-L-cysteine methyl ester (45 mg, 0.24 mmol, 1.2 equiv) and DIPEA (70 μL, 52 mg, 0.40 mmol, 2.0 equiv) were added. The resulting mixture was stirred for 12 h without exposure to light. During this period, the reaction temperature was gradually allowed to rise to 23 ºC. Subsequently, silica gel (5–10 mL) was added, and the reaction mixture was concentrated to dryness under reduced pressure. The resulting residue was purified by chromatography on silica gel (hexanes/EtOAc = 1:3) to afford **19** as a colorless liquid in 76% yield (70.2 mg).

R_f = 0.16 (hexanes/EtOAc = 1:3).

NMR Spectroscopy:

^{1}H NMR (500 MHz, $CDCl_3$, 23 ºC, δ): 7.42 (d, *J* = 7.9 Hz, 2H), 7.25 (d, *J* = 8.0 Hz, 2H), 7.11 (d, *J* = 8.1 Hz, 2H), 7.01 (d, *J* = 8.3 Hz, 2H), 6.42 (d, *J* = 7.6 Hz, 1H), 4.81 (dt, *J* = 7.6, 5.2 Hz, 1H), 3.76 (s, 3H), 3.13 (s, 3H), 3.02 (dd, *J* = 13.8, 5.2 Hz, 1H), 2.95 (dd, *J* = 13.9, 5.4 Hz, 1H), 2.84 (dd, *J* = 9.0, 6.3 Hz, 2H), 2.76 (dd, *J* = 8.1, 5.6 Hz, 2H), 2.42 (s, 3H), 2.04 (s, 3H).

^{13}C NMR (125 MHz, $CDCl_3$, 23 ºC, δ): 171.3, 169.9, 143.6, 139.9, 139.2, 133.5, 129.4, 128.9, 127.9, 126.7, 52.7, 51.9, 38.1, 35.6, 34.2, 33.8, 23.1, 21.6.

HRMS-ESIpos (m/z) calc'd for $C_{22}H_{28}N_2NaO_5S_2$ $[M+Na]^+$, 487.1332; found, 487.1335; deviation: –0.7 ppm.

Arylpropionitrile 20

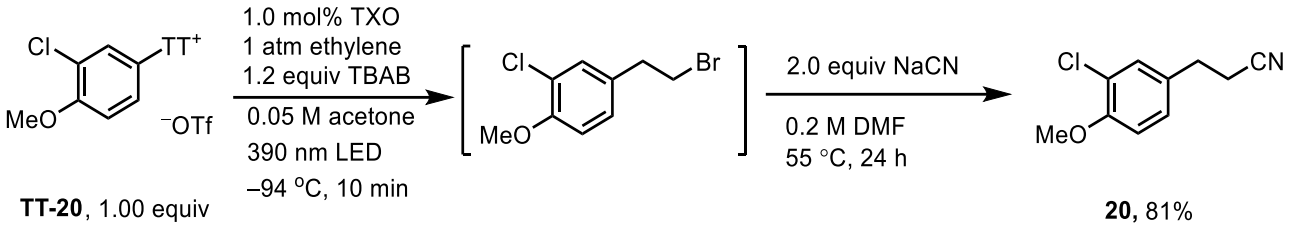

To a 5-mL Schlenk tube containing a Teflon-coated magnetic stirring bar were added **TT-20** (101 mg, 0.200 mmol, 1.00 equiv), tetrabutylammonium bormide (TBAB, 77 mg, 0.24 mmol, 1.2 equiv), and thioxanthone in acetone (c = 0.50 mM, 4.0 mL, 2.0 μmol, 1.0 mol%). The tube was sealed with a rubber septum and immersed in a liquid nitrogen/acetone bath at −94 °C. A balloon filled with ethylene gas was connected to a long needle, which was inserted to the tube through the rubber septum. Roughly 100 ml of ethylene gas was bubbled through the solution over a time period of approximately 5 minutes, and excess gas was released through the side arm, all while avoiding exposure to light. The valve of the side arm was closed, and the needle was withdrawn from the solution but remained in the headspace of the vessel. The reaction mixture was then subjected to irradiation by one Kessil PR160-390 nm LED with 100% intensity (40 W, ~6 cm away) for 10 minutes, all while maintaining the bath temperature at −94°C. Then, the solvent was removed, and NaCN (20 mg, 0.40 mmol, 2.0 equiv) and DMF (1 mL) were added. The resulting mixture was stirred at 55 ºC for 24 h without exposure to light. The resulting solution was diluted with ethyl acetate (20 mL), washed by brine (3 × 10 mL), dried over Na_2SO_4, and concentrated under reduced pressure. The resulting residue was purified by chromatography on silica gel (hexanes/EtOAc = 5:1) to afford **20** as a colorless liquid in 81% yield (31.8 mg).

R_f = 0.20 (hexanes/EtOAc = 5:1).

NMR Spectroscopy:

^{1}H NMR (500 MHz, $CDCl_3$, 23 ºC, δ): 7.26 (d, *J* = 2.2 Hz, 1H), 7.13 (dd, *J* = 8.4, 2.2 Hz, 1H), 6.92 (d, *J* = 8.4 Hz, 1H), 3.91 (s, 3H), 2.90 (t, *J* = 7.3 Hz, 2H), 2.61 (t, *J* = 7.4 Hz, 2H).

^{13}C NMR (125 MHz, $CDCl_3$, 23 ºC, δ): 154.2, 131.1, 130.0, 127.7, 122.7, 118.9, 112.4, 56.2, 30.5, 19.5.

HRMS-EI (m/z) calc'd for $C_{10}H_{10}ClNO$ $[M]^+$, 195.0445; found, 195.0448; deviation: −1.3 ppm.

Calone-derived arylethylamine 21

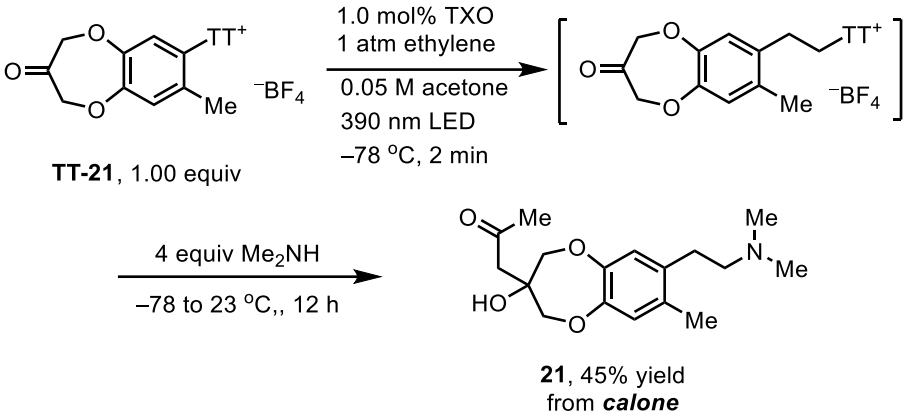

To a 5-mL Schlenk tube containing a Teflon-coated magnetic stirring bar were added **TT-21** (95.8 mg, 0.200 mmol, 1.00 equiv) and thioxanthone in acetone (c = 0.50 mM, 4.0 mL, 2.0 μmol, 1.0 mol%). The tube was sealed with a rubber septum and immersed in a dry ice/acetone bath at –78°C. A balloon filled with ethylene gas was connected to a long needle, which was inserted to the tube through the rubber septum. Roughly 100 ml of ethylene gas was bubbled through the solution over a time period of approximately 5 minutes, and excess gas was released through the side arm, all while avoiding exposure to light. The valve of the side arm was closed, and the needle was withdrawn from the solution but remained in the headspace of the vessel. The reaction mixture was then subjected to irradiation by one Kessil PR160-390 nm LED with 100% intensity (40 W, ~6 cm away) for 2 minutes, all while maintaining the bath temperature at –78°C. Then, dimethylamine in THF (c = 2 M, 0.4 mL, 0.8 mmol, 4 equiv) was added. The resulting mixture was stirred for 12 h without exposure to light. During this period, the reaction temperature was gradually allowed to rise to 23 ºC. Subsequently, silica gel (5–10 mL) was added, and the reaction mixture was concentrated to dryness under reduced pressure. The resulting residue was purified by chromatography on silica gel (hexanes/EtOAc = 2:1) first and further purified by HPLC (YMC Pack Pro C18 (30×150 mm: 5 μm), 55:45 to 90:10 MeOH/ 20 mM NH_4HCO_3 (aq.) (v/v), flow rate = 42 mL/min, 35 ºC) to afford **21** as a colorless liquid in 45% yield (27.7 mg).

R_f = 0.27 (hexanes/EtOAc = 2:1).

NMR Spectroscopy:

^{1}H NMR (500 MHz, $CDCl_3$, 23 ºC, δ): 6.78 (s, 1H), 6.76 (s, 1H), 4.06 (dd, *J* = 12.1, 1.3 Hz, 2H), 3.99 (dd, *J* = 12.1, 0.9 Hz, 2H), 2.89 (s, 2H), 2.72 – 2.64 (m, 2H), 2.48 – 2.42 (m, 2H), 2.32 (s, 6H), 2.28 (s, 3H), 2.23 (s, 3H).

^{13}C NMR (125 MHz, $CDCl_3$, 23 ºC, δ): 209.9, 148.2, 148.2, 133.8, 131.4, 122.5, 121.5, 77.2, 77.2, 73.4, 60.2, 46.2, 45.4, 31.8, 30.8, 18.5.

HRMS-ESIpos (m/z) calc'd for $C_{17}H_{26}NO_4$ $[M+H]^+$, 308.1856; found, 308.1857; deviation: –0.3 ppm.

Arylethylamine 22

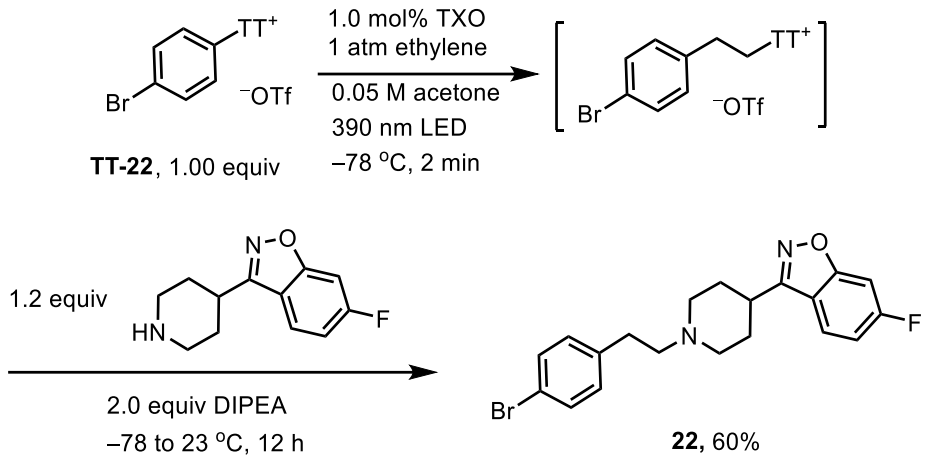

To a 5-mL Schlenk tube containing a Teflon-coated magnetic stirring bar were added **TT-22** (104 mg, 0.200 mmol, 1.00 equiv) and thioxanthone in acetone (c = 0.50 mM, 4.0 mL, 2.0 μmol, 1.0 mol%). The tube was sealed with a rubber septum and immersed in a dry ice/acetone bath at –78°C. A balloon filled with ethylene gas was connected to a long needle, which was inserted to the tube through the rubber septum. Roughly 100 ml of ethylene gas was bubbled through the solution over a time period of approximately 5 minutes, and excess gas was released through the side arm, all while avoiding exposure to light. The valve of the side arm was closed, and the needle was withdrawn from the solution but remained in the headspace of the vessel. The reaction mixture was then subjected to irradiation by one Kessil PR160-390 nm LED with 100% intensity (40 W, ~6 cm away) for 2 minutes, all while maintaining the bath temperature at –78°C. Then, 6-fluoro-3-(4-piperidinyl)-1,2-benzisoxazole (53 mg, 0.24 mmol, 1.2 equiv) and DIPEA (70 μL, 52 mg, 0.40 mmol, 2.0 equiv) were added. The resulting mixture was stirred for 12 h without exposure to light. During this period, the reaction temperature was gradually allowed to rise to 23 ºC. Subsequently, silica gel (5–10 mL) was added, and the reaction mixture was concentrated to dryness under reduced pressure. The resulting residue was purified by chromatography on silica gel (hexanes/EtOAc = 1:1) to afford **22** as a colorless liquid in 60% yield (48.1 mg).

R_f = 0.21 (hexanes/EtOAc = 1:1).

NMR Spectroscopy:

^{1}H NMR (500 MHz, $CDCl_3$, 23 ºC, δ): 7.73 (dd, *J* = 9.0, 5.1 Hz, 1H), 7.47 – 7.39 (m, 2H), 7.26 (d, *J* = 8.5 Hz, 1H), 7.13 (d, *J* = 7.8 Hz, 2H), 7.08 (t, *J* = 9.0 Hz, 1H), 3.15 (d, *J* = 11.9 Hz, 3H), 2.83 (t, *J* = 7.9 Hz, 2H), 2.66 (t, *J* = 8.1 Hz, 2H), 2.36 – 2.21 (m, 2H), 2.12 (d, *J* = 8.1 Hz, 4H).

^{13}C NMR (125 MHz, $CDCl_3$, 23 ºC, δ): 164.1 (d, *J* = 250.8 Hz), 163.9 (d, *J* = 13.7 Hz), 161.0, 131.5, 130.5, 122.6 (d, *J* = 11.1 Hz), 119.9, 117.3, 112.5, 112.3, 97.5 (d, *J* = 26.8 Hz), 60.4, 53.5, 34.5, 33.1, 30.5.

^{19}F NMR (471 MHz, $CDCl_3$, 23 ºC, δ): –109.59.

HRMS-ESIpos (m/z) calc'd for $C_{20}H_{21}FBrN_2O$ $[M+H]^+$, 403.0816; found, 403.0819; deviation: –0.7 ppm.

Duloxetine-derived arylethylamine 23

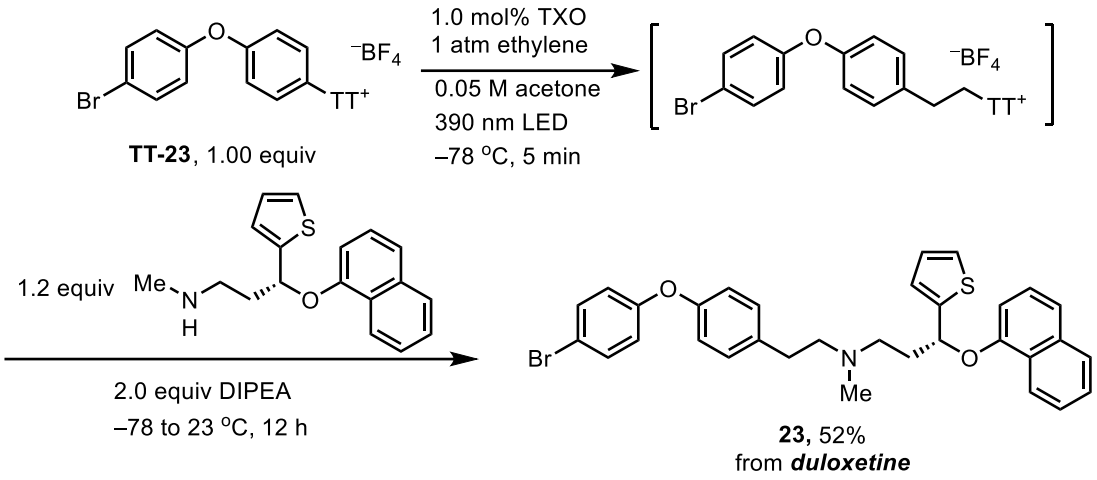

To a 5-mL Schlenk tube containing a Teflon-coated magnetic stirring bar were added **TT-23** (110 mg, 0.200 mmol, 1.00 equiv) and thioxanthone in acetone (c = 0.50 mM, 4.0 mL, 2.0 μmol, 1.0 mol%). The tube was sealed with a rubber septum and immersed in a dry ice/acetone bath at –78°C. A balloon filled with ethylene gas was connected to a long needle, which was inserted to the tube through the rubber septum. Roughly 100 ml of ethylene gas was bubbled through the solution over a time period of approximately 5 minutes, and excess gas was released through the side arm, all while avoiding exposure to light. The valve of the side arm was closed, and the needle was withdrawn from the solution but remained in the headspace of the vessel. The reaction mixture was then subjected to irradiation by one Kessil PR160-390 nm LED with 100% intensity (40 W, ~6 cm away) for 5 minutes, all while maintaining the bath temperature at –78°C. Then, duloxetine (71 mg, 0.24 mmol, 1.2 equiv) and DIPEA (70 μL, 52 mg, 0.40 mmol, 2.0 equiv) were added. The resulting mixture was stirred for 12 h without exposure to light. During this period, the reaction temperature was gradually allowed to rise to 23 ºC. Subsequently, silica gel (5–10 mL) was added, and the reaction mixture was concentrated to dryness under reduced pressure. The resulting residue was purified by chromatography on silica gel (hexanes/EtOAc/Et_3N = 75:25:1) to afford **23** as a colorless solid in 52% yield (59.2 mg).

R_f = 0.21 (hexanes/EtOAc/Et_3N = 75:25:1).

NMR Spectroscopy:

^{1}H NMR (500 MHz, $CDCl_3$, 23 ºC, δ): 8.50 – 8.34 (m, 1H), 7.93 – 7.78 (m, 1H), 7.54 – 7.48 (m, 2H), 7.41 (d, *J* = 8.0 Hz, 3H), 7.32 – 7.24 (m, 1H), 7.24 (d, *J* = 4.9 Hz, 1H), 7.13 (d, *J* = 6.0 Hz, 2H), 7.04 – 7.00 (m, 1H), 6.98 – 6.93 (m, 1H), 6.94 – 6.89 (m, 2H), 6.89 – 6.82 (m, 3H), 5.75 (t, *J* = 6.0 Hz, 1H), 2.72 (h, *J* = 6.1 Hz, 3H), 2.64 (t, *J* = 7.2 Hz, 3H), 2.46 (dt, *J* = 13.4, 6.7 Hz, 1H), 2.36 (d, *J* = 2.5 Hz, 3H), 2.22 (dt, *J* = 14.2, 6.9 Hz, 1H).

^{13}C NMR (125 MHz, $CDCl_3$, 23 ºC, δ): 156.9, 154.7, 153.5, 145.4, 136.1, 134.6, 132.6, 130.1, 127.5,

126.5, 126.3, 126.2, 125.8, 125.2, 124.7, 124.6, 122.2, 120.5, 120.1, 119.1, 115.3, 107.1, 74.5, 59.5, 53.6, 42.2, 36.7, 33.1.

HRMS-ESIpos (m/z) calc'd for $C_{32}H_{31}BrSNO_2$ $[M+H]^+$, 572.1254; found, 572.1262; deviation: –1.41 ppm.

Arylethyl bromide 24

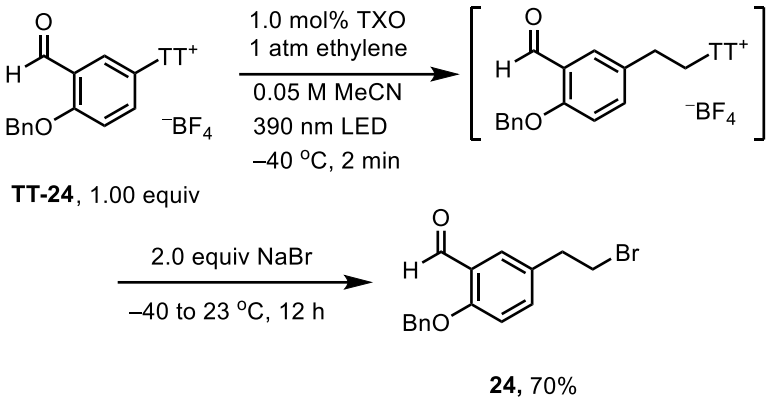

To a 5-mL Schlenk tube containing a Teflon-coated magnetic stirring bar were added **TT-24** (102 mg, 0.200 mmol, 1.00 equiv) and thioxanthone in MeCN (c = 0.50 mM, 4.0 mL, 2.0 μmol, 1.0 mol%). The tube was sealed with a rubber septum and immersed in a dry ice/MeCN bath at around –40°C. A balloon filled with ethylene gas was connected to a long needle, which was inserted to the tube through the rubber septum. Roughly 100 ml of ethylene gas was bubbled through the solution over a time period of approximately 5 minutes, and excess gas was released through the side arm, all while avoiding exposure to light. The valve of the side arm was closed, and the needle was withdrawn from the solution but remained in the headspace of the vessel. The reaction mixture was then subjected to irradiation by one Kessil PR160-390 nm LED with 100% intensity (40 W, ~6 cm away) for 2 minutes, all while maintaining the bath temperature at –40°C. Then, sodium bromide (42 mg, 0.40 mmol, 2.0 equiv) was added. The resulting mixture was stirred for 12 h without exposure to light. During this period, the reaction temperature was gradually allowed to rise to 23 ºC. Subsequently, silica gel (5–10 mL) was added, and the reaction mixture was concentrated to dryness under reduced pressure. The resulting residue was purified by chromatography on silica gel (hexanes/EtOAc = 3:1) first and further purified by HPLC (YMC Pro C18 (30×150 mm: 5 μm), 60:40 to 90:10 MeCN/H_2O (v/v), flow rate = 20.0 mL/min, 35 ºC) to afford **24** as a colorless liquid in 70% yield (44.6 mg).

R_f = 0.18 (hexanes/EtOAc = 3:1).

NMR Spectroscopy:

^{1}H NMR (500 MHz, $CDCl_3$, 23 ºC, δ): 10.56 (s, 1H), 7.73 (d, *J* = 2.4 Hz, 1H), 7.51 – 7.33 (m, 6H), 7.04 (d, *J* = 8.5 Hz, 1H), 5.21 (s, 2H), 3.57 (t, *J* = 7.3 Hz, 2H), 3.16 (t, *J* = 7.3 Hz, 2H).

^{13}C NMR (125 MHz, $CDCl_3$, 23 ºC, δ): 189.6, 160.1, 136.3, 136.0, 131.6, 128.8, 128.3, 128.2, 127.3, 125.1, 113.3, 70.6, 38.1, 32.9.

HRMS-ESIpos (m/z) calc'd for $C_{16}H_{15}BrNaO_2$ $[M+Na]^+$, 341.0148; found, 341.0149; deviation: –0.4 ppm.

Arylethyl phosphonate 25

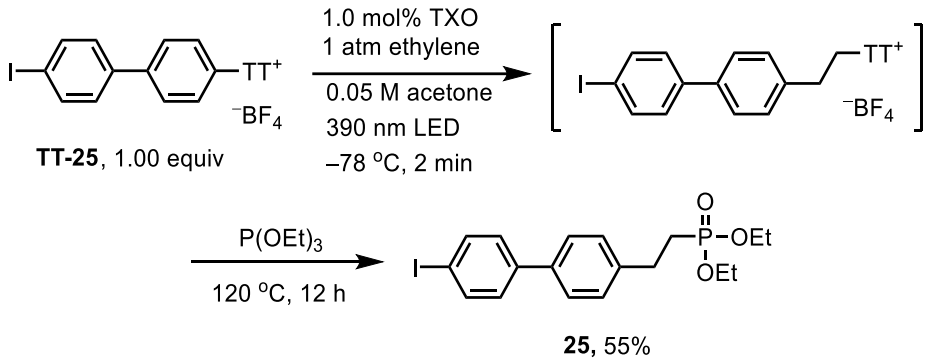

25, 55%

To a 5-mL Schlenk tube containing a Teflon-coated magnetic stirring bar were added **TT-25** (116 mg, 0.200 mmol, 1.00 equiv), thioxanthone in acetone (c = 0.50 mM, 4.0 mL, 2.0 μmol, 1.0 mol%), and MeCN (2 mL). The tube was sealed with a rubber septum and immersed in a dry ice/acetone bath at –78°C. A balloon filled with ethylene gas was connected to a long needle, which was inserted to the tube through the rubber septum. Roughly 100 ml of ethylene gas was bubbled through the solution over a time period of approximately 5 minutes, and excess gas was released through the side arm, all while avoiding exposure to light. The valve of the side arm was closed, and the needle was withdrawn from the solution but remained in the headspace of the vessel. The reaction mixture was then subjected to irradiation by one Kessil PR160-390 nm LED with 100% intensity (40 W, ~6 cm away) for 2 minutes, all while maintaining the bath temperature at –78°C. Then, the solvent was removed and triethyl phosphite (0.25 mL) was added. The resulting mixture was stirred at 120 ºC for 12 h without exposure to light. Subsequently, the reaction mixture was cooled down to room temperature and diluted with ethyl acetate (10 mL). Silica gel (5–10 mL) was added, and the reaction mixture was concentrated to dryness under reduced pressure. The resulting residue was purified by chromatography on silica gel (DCM/EtOAc = 1:1) first and further purified by HPLC (YMC Pack Pro C18 (30×150 mm: 5 μm), 80:20 to 95:5 MeOH/H_2O (v/v), flow rate = 42 mL/min, 35 ºC) to afford **25** as a colorless solid in 55% yield (48.9 mg).

$\mathbf{R}_f$ = 0.20 (DCM/EtOAc = 1:1).

NMR Spectroscopy:

^{1}H NMR (500 MHz, $CDCl_3$, 23 ºC, δ): 7.77 (d, *J* = 8.4 Hz, 2H), 7.51 (d, *J* = 8.1 Hz, 2H), 7.33 (d, *J* = 8.4 Hz, 2H), 7.30 (d, *J* = 8.1 Hz, 2H), 4.25 – 4.00 (m, 4H), 3.13 – 2.90 (m, 2H), 2.26 – 2.02 (m, 2H), 1.35 (t, *J* = 7.1 Hz, 6H).

^{13}C NMR (125 MHz, $CDCl_3$, 23 ºC, δ): 140.6 (d, *J* = 17.3 Hz), 140.4, 138.2, 137.8, 128.8, 128.6, 127.0, 92.9, 61.6 (d, *J* = 6.5 Hz), 28.3 (d, *J* = 4.3 Hz), 27.6 (d, *J* = 139.5 Hz), 16.5 (d, *J* = 6.0 Hz).

^{31}P NMR (203 MHz, $CDCl_3$, 23 ºC, δ): 30.6.

HRMS-EI (m/z) calc'd for $C_{18}H_{22}IPO_3$ $[M]^+$, 444.0346; found, 444.0347; deviation: –0.3 ppm.

Arylethyl thiocyanate 26

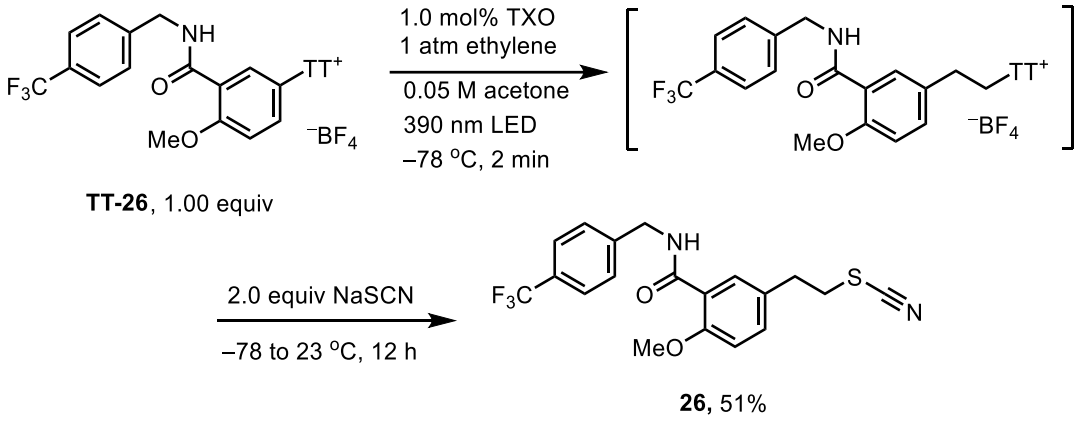

To a 5-mL Schlenk tube containing a Teflon-coated magnetic stirring bar were added **TT-26** (122 mg, 0.200 mmol, 1.00 equiv) and thioxanthone in acetone (c = 0.50 mM, 4.0 mL, 2.0 μmol, 1.0 mol%). The tube was sealed with a rubber septum and immersed in a dry ice/acetone bath at –78°C. A balloon filled with ethylene gas was connected to a long needle, which was inserted to the tube through the rubber septum. Roughly 100 ml of ethylene gas was bubbled through the solution over a time period of approximately 5 minutes, and excess gas was released through the side arm, all while avoiding exposure to light. The valve of the side arm was closed, and the needle was withdrawn from the solution but remained in the headspace of the vessel. The reaction mixture was then subjected to irradiation by one Kessil PR160-390 nm LED with 100% intensity (40 W, ~6 cm away) for 2 minutes, all while maintaining the bath temperature at –78°C. Then, sodium thiocyanate (32 mg, 0.40 mmol, 2.0 equiv) was added. The resulting mixture was stirred for 12 h without exposure to light. During this period, the reaction temperature was gradually allowed to rise to 23 ºC. Subsequently, silica gel (5–10 mL) was added, and the reaction mixture was concentrated to dryness under reduced pressure. The resulting residue was purified by chromatography on silica gel (hexanes/EtOAc = 2:1) to afford **26** as a colorless liquid in 51% yield (40.1 mg).

R_f = 0.19 (hexanes/EtOAc = 2:1).

NMR Spectroscopy:

^{1}H NMR (500 MHz, $CDCl_3$, 23 ºC, δ): 8.34 (t, *J* = 5.9 Hz, 1H), 8.12 (d, *J* = 2.5 Hz, 1H), 7.61 (d, *J* = 8.1 Hz, 2H), 7.49 (d, *J* = 8.0 Hz, 2H), 7.37 (dd, *J* = 8.4, 2.5 Hz, 1H), 7.00 (d, *J* = 8.4 Hz, 1H), 4.75 (d, *J* = 5.9 Hz, 2H), 3.98 (s, 3H), 3.23 – 3.16 (m, 2H), 3.17 – 3.10 (m, 2H).

^{13}C NMR (125 MHz, $CDCl_3$, 23 ºC, δ): 165.2, 156.8, 142.9, 133.6, 132.3, 130.6, 129.5 (q, *J* = 32.3 Hz), 127.7, 125.6 (q, *J* = 3.7 Hz), 124.2 (d, *J* = 271.8 Hz), 121.3, 111.9, 111.8, 56.2, 43.3, 35.1, 35.0.

^{19}F NMR (471 MHz, $CDCl_3$, 23 ºC, δ): –62.45.

HRMS-ESIpos (m/z) calc'd for $C_{19}H_{18}F_3SN_2O_2$ $[M+H]^+$, 395.1036; found, 395.1037; deviation: –0.3 ppm.

Pyriproxyfen- and cytisine-derived arylethylamine 27

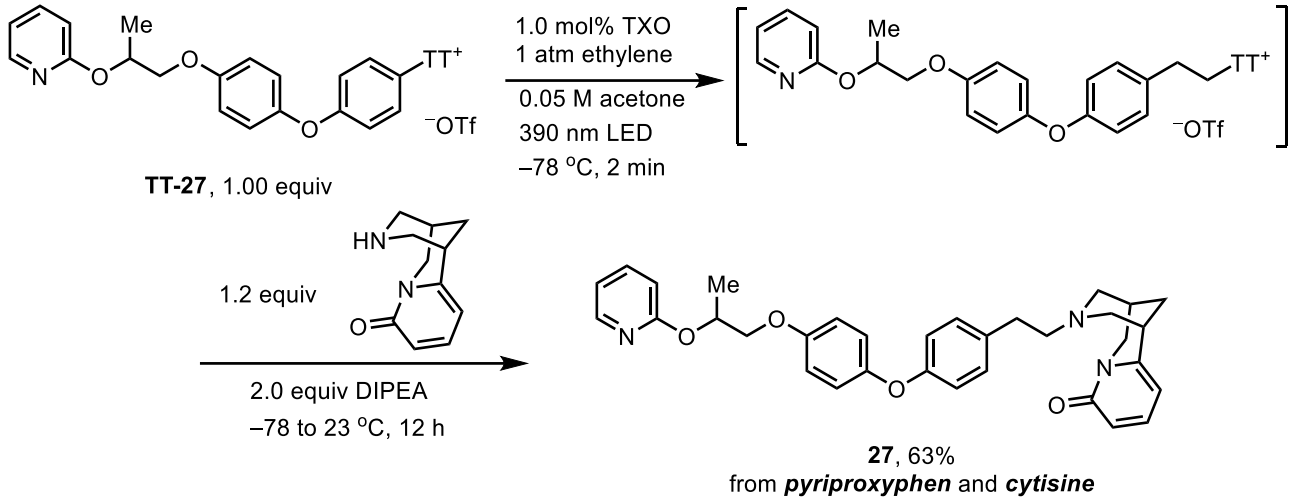

To a 5-mL Schlenk tube containing a Teflon-coated magnetic stirring bar were added **TT-27** (137 mg, 0.200 mmol, 1.00 equiv) and thioxanthone in acetone (c = 0.50 mM, 4.0 mL, 2.0 μmol, 1.0 mol%). The tube was sealed with a rubber septum and immersed in a dry ice/acetone bath at −78°C. A balloon filled with ethylene gas was connected to a long needle, which was inserted to the tube through the rubber septum. Roughly 100 ml of ethylene gas was bubbled through the solution over a time period of approximately 5 minutes, and excess gas was released through the side arm, all while avoiding exposure to light. The valve of the side arm was closed, and the needle was withdrawn from the solution but remained in the headspace of the vessel. The reaction mixture was then subjected to irradiation by one Kessil PR160-390 nm LED with 100% intensity (40 W, ~6 cm away) for 2 minutes, all while maintaining the bath temperature at −78°C. Then, cytisine (46 mg, 0.24 mmol, 1.2 equiv) and DIPEA (70 μL, 52 mg, 0.40 mmol, 2.0 equiv) were added. The resulting mixture was stirred for 12 h without exposure to light. During this period, the reaction temperature was gradually allowed to rise to 23 ºC. Subsequently, silica gel (5−10 mL) was added, and the reaction mixture was concentrated to dryness under reduced pressure. The resulting residue was purified by chromatography on silica gel (pure EtOAc) to afford **27** as a colorless solid in 63% yield (67.6 mg).

R*f* = 0.20 (pure EtOAc).

NMR Spectroscopy:

^{1}H NMR (500 MHz, CD_3CN, 23 ºC, δ): 8.16 (ddd, *J* = 5.0, 2.1, 0.8 Hz, 1H), 7.66 (ddd, *J* = 8.4, 7.1, 2.0 Hz, 1H), 7.30 (dd, *J* = 9.0, 6.9 Hz, 1H), 6.98 – 6.89 (m, 7H), 6.74 (d, *J* = 8.3 Hz, 1H), 6.70 (d, *J* = 8.6 Hz, 2H), 6.25 (dd, *J* = 9.0, 1.3 Hz, 1H), 6.07 (dd, *J* = 6.9, 1.4 Hz, 1H), 5.63 – 5.52 (m, 1H), 4.18 (dd, *J* = 10.3, 6.0 Hz, 1H), 4.12 (dd, *J* = 10.3, 4.1 Hz, 1H), 3.83 (d, *J* = 15.3 Hz, 1H), 3.77 (ddd, *J* = 15.4, 6.4, 1.0 Hz, 1H), 2.97 (d, *J* = 27.4 Hz, 1H), 2.56 (d, *J* = 6.8 Hz, 1H), 2.44 (d, *J* = 23.7 Hz, 1H), 2.33 (t, *J* = 13.0 Hz, 1H), 1.88 – 1.80 (m, 1H), 1.79 – 1.74 (m, 1H), 1.42 (d, *J* = 6.4 Hz, 3H).

^{13}C NMR (125 MHz, CD_3CN, 23 ºC, δ): 163.2, 163.1, 156.1, 155.0, 152.5, 150.7, 146.9, 139.1, 139.0, 135.3, 129.9, 120.4, 116.9, 115.7, 115.6, 111.2, 104.6, 71.0, 69.3, 60.2, 59.9, 59.2, 49.9, 35.3, 31.5,

28.0, 25.4, 16.0.

HRMS-ESIpos (m/z) calc'd for $C_{33}H_{36}N_3O_4$ $[M+H]^+$, 538.2700; found, 538.2702; deviation: –0.3 ppm.

Scope of alkenes

We have tested various alkenes beyond ethylene, including α-olefins, styrenes, and Michael acceptors (Table S1). All of these substrates exhibit desired reactivity. The yield is lower than with ethylene itself, likely due to competitive elimination of the secondary or tertiary alkyl thianthrenium salts formed by the addition of ArTTs to substituted alkenes. However, substituted alkenes can be utilized in the presence of bromide nucleophiles to afford alkyl bromides in 53–81% yields. Unactivated monosubstituted alkenes, such as propene, can be applied and potentially used to synthesize drug-related amphetamine candidates via amination. 1,1- and 1,2-Disubstituted alkenes like 2-methylpentene, 2-methylacrylate, and fumarate also work well, providing secondary and tertiary alkyl bromides that otherwise difficult to synthesize from other methods. Styrene and Michael acceptors, such as acrylonitrile, acrylamide, vinyl sulfone, and vinyl phosphonate, also perform well, yielding activated alkyl bromides suitable for further transformations.

Table S1 Substrate scope of alkenes

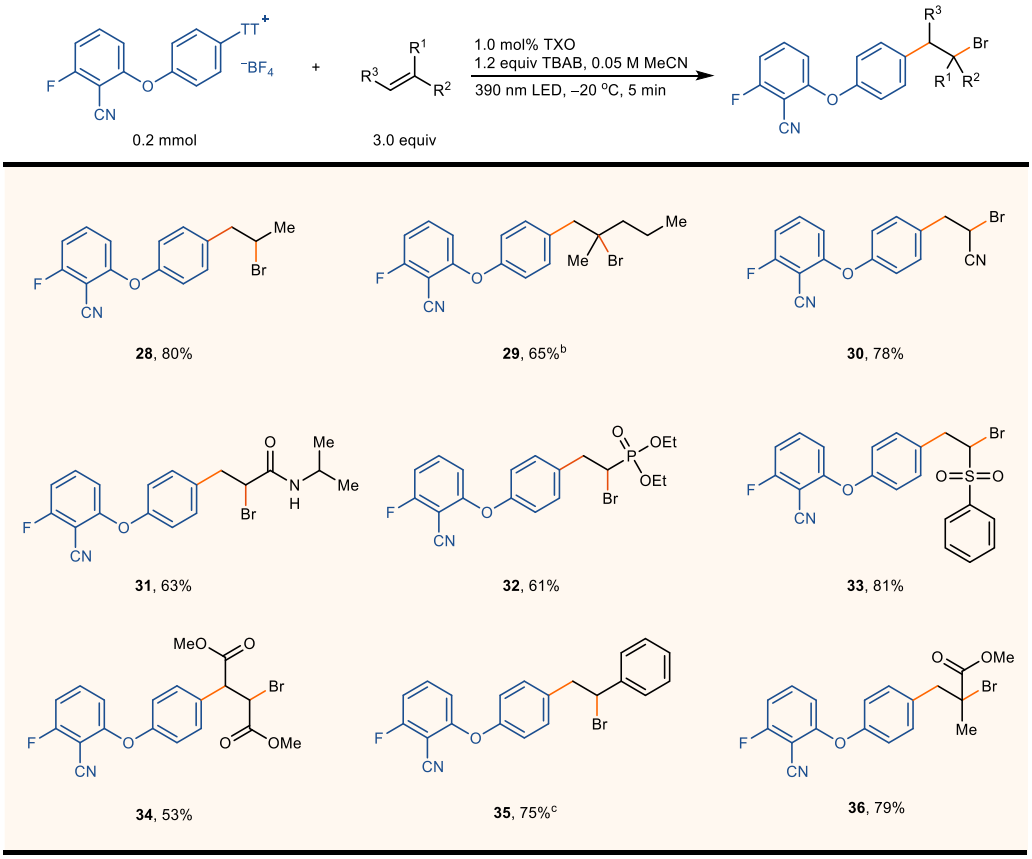

[a]Reaction conditions: arylthianthrenium salt (0.20 mmol), alkenes (0.60 mmol, 3.0 equiv), TBAB (77 mg, 0.24 mmol, 1.2 equiv), and TXO in MeCN (c = 0.50 mM, 4.0 mL, 2.0 μmol, 1.0 mol%) at –20 °C under 40 W 390 nm LED for 5 min. [b]10 equiv alkene used. [c]15 min.

Arylethyl bromide 28

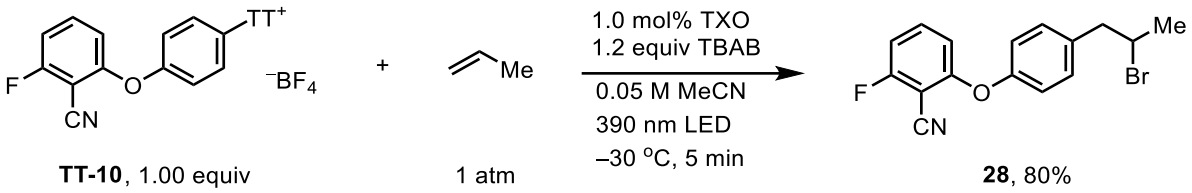

TT-10, 1.00 equiv 1 atm **28**, 80%

To a 5-mL Schlenk tube containing a Teflon-coated magnetic stirring bar were added **TT-10** (103 mg, 0.200 mmol, 1.00 equiv), tetrabutylammonium bormide (TBAB, 77 mg, 0.24 mmol, 1.2 equiv), and thioxanthone in acetonitrile (c = 0.50 mM, 4.0 mL, 2.0 μmol, 1.0 mol%). The tube was sealed with a rubber septum and immersed in a methanol/water (40/60) dry ice bath at –30°C. A balloon filled with propylene gas was connected to a long needle, which was inserted to the tube through the rubber septum. Roughly 100 ml of propylene gas was bubbled through the solution over a time period of approximately 5 minutes, and excess gas was released through the side arm, all while avoiding exposure to light. The valve of the side arm was closed, and the needle was withdrawn from the solution but remained in the headspace of the vessel. The reaction mixture was then subjected to irradiation by one Kessil PR160-390 nm LED with 100% intensity (40 W, ~6 cm away) for 5 minutes, all while maintaining the bath temperature at –30°C. Then, the reaction temperature was allowed to rise to 23 ºC. Silica gel (5–10 mL) was added, and the reaction mixture was concentrated to dryness under reduced pressure. The resulting residue was purified by chromatography on silica gel (hexanes/EtOAc = 10:1) to afford **28** as a colorless liquid in 80% yield (53.4 mg).

$\mathbf{R_f}$ = 0.21 (hexanes/EtOAc = 10:1).

NMR Spectroscopy:

^{1}H NMR (500 MHz, $CDCl_3$, 23 ºC, δ): 7.45 (td, *J* = 8.5, 6.4 Hz, 1H), 7.29 (d, *J* = 8.5 Hz, 2H), 7.08 (d, *J* = 8.5 Hz, 2H), 6.90 (td, *J* = 8.4, 0.8 Hz, 1H), 6.64 (dt, *J* = 8.7, 0.9 Hz, 1H), 4.32 (h, *J* = 6.7 Hz, 1H), 3.22 (dd, *J* = 14.2, 7.5 Hz, 1H), 3.13 (dd, *J* = 14.2, 6.6 Hz, 1H), 1.75 (d, *J* = 6.7 Hz, 3H).

^{13}C NMR (125 MHz, $CDCl_3$, 23 ºC, δ): 164.1 (d, *J* = 259.7 Hz), 161.1 (d, *J* = 4.1 Hz), 153.3, 136.0, 134.9 (d, *J* = 10.2 Hz), 131.0, 120.3, 111.8 (d, *J* = 3.5 Hz), 111.1, 109.6 (d, *J* = 19.5 Hz), 93.6 (d, *J* = 18.0 Hz), 50.3, 46.6, 25.8.

HRMS-ESIpos (m/z) calc'd for $C_{16}H_{13}FBrNONa$ $[M+Na]^+$, 356.0057; found, 356.0055; deviation: +0.6 ppm.

Arylethyl bromide 29

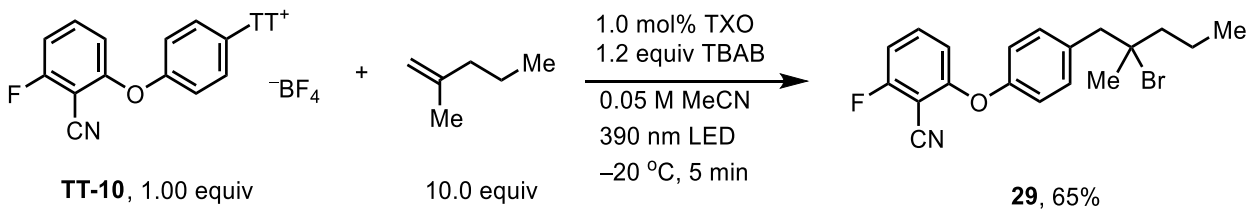

TT-10, 1.00 equiv 10.0 equiv **29**, 65%

To a 5-mL Schlenk tube containing a Teflon-coated magnetic stirring bar were added **TT-10** (103 mg, 0.200

mmol, 1.00 equiv), tetrabutylammonium bormide (TBAB, 77 mg, 0.24 mmol, 1.2 equiv), and thioxanthone in acetonitrile (c = 0.50 mM, 4.0 mL, 2.0 μmol, 1.0 mol%). The tube was sealed with a rubber septum and immersed in a methanol/water (30/70) dry ice bath at –20°C. A balloon filled with argon gas was connected to a long needle, which was inserted to the tube through the rubber septum. Roughly 100 ml of argon gas was bubbled through the solution over a time period of approximately 5 minutes, and excess gas was released through the side arm, all while avoiding exposure to light. The valve of the side arm was closed, and the needle was withdrawn from the solution but remained in the headspace of the vessel. 2-Methyl-1-pentene (246 μL, 168 mg, 2.00 mmol, 10.0 equiv) was added and the reaction mixture was then subjected to irradiation by one Kessil PR160-390 nm LED with 100% intensity (40 W, ~6 cm away) for 5 minutes, all while maintaining the bath temperature at –20°C. Then, the reaction temperature was allowed to rise to 23 ºC. Silica gel (5–10 mL) was added, and the reaction mixture was concentrated to dryness under reduced pressure. The resulting residue was purified by chromatography on silica gel (hexanes/EtOAc = 10:1) to afford **29** as a colorless liquid in 65% yield (48.8 mg).

R*f* = 0.30 (hexanes/EtOAc = 10:1).

NMR Spectroscopy:

^{1}H NMR (300 MHz, $CDCl_3$, 23 ºC, δ): 7.53 – 7.40 (m, 1H), 7.35 (d, *J* = 8.5 Hz, 2H), 7.07 (d, *J* = 8.6 Hz, 2H), 6.96 – 6.85 (m, 1H), 6.66 (d, *J* = 8.6 Hz, 1H), 3.27 (d, *J* = 14.0 Hz, 1H), 3.16 (d, *J* = 14.0 Hz, 1H), 1.97 – 1.57 (m, 4H), 1.72 (s, 3H), 1.00 (t, *J* = 7.0 Hz, 3H).

^{13}C NMR (75 MHz, $CDCl_3$, 23 ºC, δ): 164.0 (d, J = 259.5 Hz), 161.0 (d, J = 4.1 Hz), 153.3, 134.8 (d, J = 10.4 Hz), 134.5, 132.6, 119.7, 111.8 (d, J = 3.5 Hz), 111.1, 109.6 (d, J = 19.5 Hz), 93.6 (d, J = 17.9 Hz), 71.8, 50.6, 47.3, 31.0, 19.3, 14.0.

HRMS-ESIpos (m/z) calc'd for $C_{19}H_{19}FBrNONa$ $[M+Na]^+$, 398.0526; found, 398.0524; deviation: +0.6 ppm.

Arylethyl bromide 30

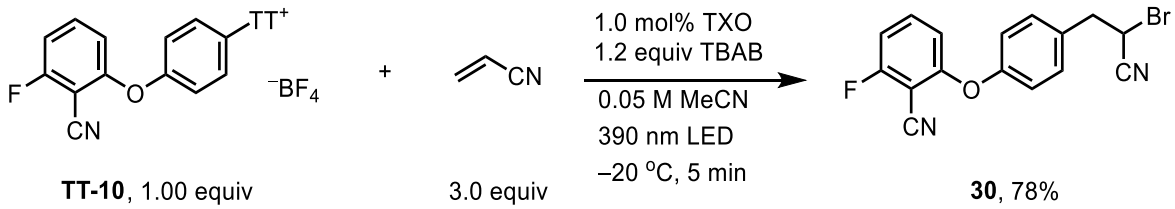

TT-10, 1.00 equiv 3.0 equiv **30**, 78%

To a 5-mL Schlenk tube containing a Teflon-coated magnetic stirring bar were added **TT-10** (103 mg, 0.200 mmol, 1.00 equiv), tetrabutylammonium bormide (TBAB, 77 mg, 0.24 mmol, 1.2 equiv), and thioxanthone in acetonitrile (c = 0.50 mM, 4.0 mL, 2.0 μmol, 1.0 mol%). The tube was sealed with a rubber septum and immersed in a methanol/water (30/70) dry ice bath at –20°C. A balloon filled with argon gas was connected to a long needle, which was inserted to the tube through the rubber septum. Roughly 100 ml of argon gas was bubbled through the solution over a time period of approximately 5 minutes, and excess gas was released through the side arm, all while avoiding exposure to light. The valve of the side arm was closed, and the

needle was withdrawn from the solution but remained in the headspace of the vessel. Acrylonitrile (40 μL, 32 mg, 0.60 mmol, 3.0 equiv) was added and the reaction mixture was then subjected to irradiation by one Kessil PR160-390 nm LED with 100% intensity (40 W, ~6 cm away) for 5 minutes, all while maintaining the bath temperature at –20°C. Then, the reaction temperature was allowed to rise to 23 ºC. Silica gel (5–10 mL) was added, and the reaction mixture was concentrated to dryness under reduced pressure. The resulting residue was purified by chromatography on silica gel (hexanes/EtOAc = 5:1) to afford **30** as a colorless liquid in 78% yield (53.8 mg).

R*f* = 0.20 (hexanes/EtOAc = 5:1).

NMR Spectroscopy:

^{1}H NMR (300 MHz, $CDCl_3$, 23 ºC, δ): 7.48 (td, *J* = 8.5, 6.4 Hz, 1H), 7.39 (d, *J* = 8.6 Hz, 2H), 7.13 (d, *J* = 8.6 Hz, 2H), 6.94 (td, *J* = 8.4, 0.8 Hz, 1H), 6.67 (dd, *J* = 8.5, 0.8 Hz, 1H), 4.48 (t, *J* = 7.3 Hz, 1H), 3.42 (d, *J* = 7.3 Hz, 2H).

^{13}C NMR (75 MHz, $CDCl_3$, 23 ºC, δ): 164.0 (d, *J* = 259.8 Hz), 160.4 (d, *J* = 4.0 Hz), 154.5, 134.9 (d, *J* = 10.3 Hz), 131.8, 131.3, 120.6, 116.7, 112.1 (d, *J* = 3.5 Hz), 110.9, 110.0 (d, *J* = 19.5 Hz), 93.9 (d, *J* = 18.2 Hz), 41.7, 27.1.

HRMS-ESIpos (m/z) calc'd for $C_{16}H_{10}FBrN_2ONa$ $[M+Na]^+$, 366.9853; found, 366.9852; deviation: +0.1 ppm.

Arylethyl bromide 31

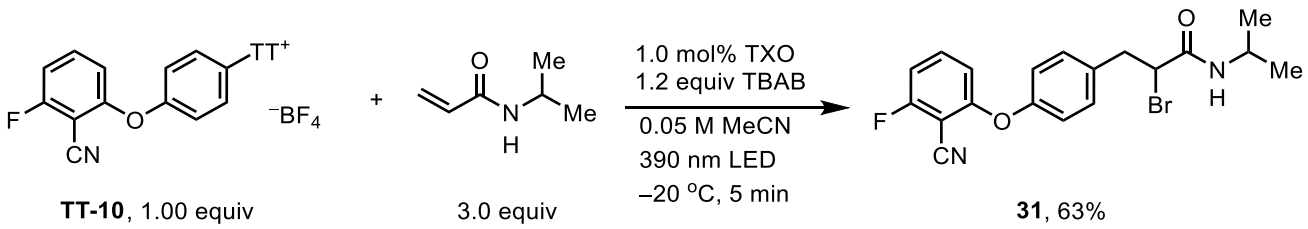

TT-10, 1.00 equiv 3.0 equiv **31**, 63%

To a 5-mL Schlenk tube containing a Teflon-coated magnetic stirring bar were added **TT-10** (103 mg, 0.200 mmol, 1.00 equiv), *N*-Isopropylacrylamide (68 mg, 0.60 mmol, 3.0 equiv), tetrabutylammonium bormide (TBAB, 77 mg, 0.24 mmol, 1.2 equiv), and thioxanthone in acetonitrile (c = 0.50 mM, 4.0 mL, 2.0 μmol, 1.0 mol%). The tube was sealed with a rubber septum and immersed in a methanol/water (30/70) dry ice bath at –20°C. A balloon filled with argon gas was connected to a long needle, which was inserted to the tube through the rubber septum. Roughly 100 ml of argon gas was bubbled through the solution over a time period of approximately 5 minutes, and excess gas was released through the side arm, all while avoiding exposure to light. The valve of the side arm was closed, and the needle was withdrawn from the solution but remained in the headspace of the vessel. The reaction mixture was then subjected to irradiation by one Kessil PR160-390 nm LED with 100% intensity (40 W, ~6 cm away) for 5 minutes, all while maintaining the bath temperature at –20°C. Then, the reaction temperature was allowed to rise to 23 ºC. Silica gel (5–10 mL) was added, and the reaction mixture was concentrated to dryness under reduced pressure. The resulting residue was purified by chromatography on silica gel (hexanes/EtOAc = 3:1) to afford **31** as a colorless solid in 63%

yield (51.0 mg).

R_f = 0.30 (hexanes/EtOAc = 2:1).

NMR Spectroscopy:

^{1}H NMR (500 MHz, $CDCl_3$, 23 ºC, δ): 7.48 – 7.39 (m, 1H), 7.31 (d, *J* = 8.5 Hz, 2H), 7.05 (d, *J* = 8.5 Hz, 2H), 6.90 (t, *J* = 8.4 Hz, 1H), 6.61 (d, *J* = 8.5 Hz, 1H), 6.13 (d, *J* = 7.9 Hz, 1H), 4.46 (t, *J* = 6.5 Hz, 1H), 4.10 – 3.99 (m, 1H), 3.53 (dd, *J* = 14.4, 5.8 Hz, 1H), 3.33 (dd, *J* = 14.3, 7.2 Hz, 1H), 1.14 (d, *J* = 6.6 Hz, 6H).

^{13}C NMR (125 MHz, $CDCl_3$, 23 ºC, δ): 166.7, 164.1 (d, *J* = 259.4 Hz), 161.0 (d, *J* = 4.1 Hz), 153.6, 134.9 (d, *J* = 10.2 Hz), 134.5, 131.4, 120.2, 111.9 (d, *J* = 3.5 Hz), 111.1, 109.7 (d, *J* = 19.4 Hz), 93.6 (d, *J* = 18.3 Hz), 51.4, 42.3, 40.8, 22.4, 22.3.

HRMS-ESIpos (m/z) calc'd for $C_{19}H_{18}FBrN_2O_2Na$ $[M+Na]^+$, 427.0428; found, 427.0427; deviation: +0.3 ppm.

Arylethyl bromide 32

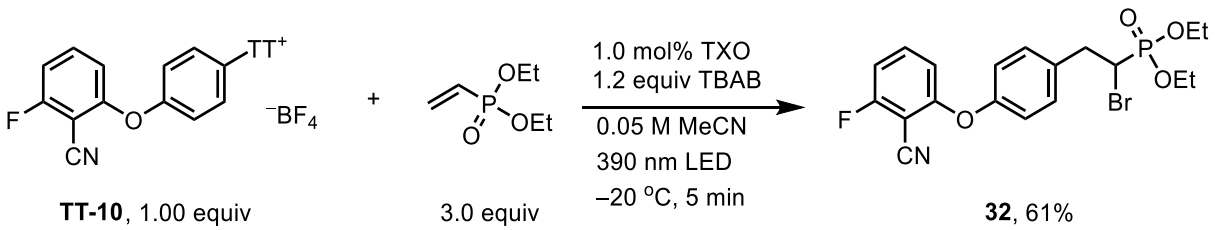

TT-10, 1.00 equiv 3.0 equiv **32**, 61%

To a 5-mL Schlenk tube containing a Teflon-coated magnetic stirring bar were added **TT-10** (103 mg, 0.200 mmol, 1.00 equiv), tetrabutylammonium bormide (TBAB, 77 mg, 0.24 mmol, 1.2 equiv), and thioxanthone in acetonitrile (c = 0.50 mM, 4.0 mL, 2.0 μmol, 1.0 mol%). The tube was sealed with a rubber septum and immersed in a methanol/water (30/70) dry ice bath at −20°C. A balloon filled with argon gas was connected to a long needle, which was inserted to the tube through the rubber septum. Roughly 100 ml of argon gas was bubbled through the solution over a time period of approximately 5 minutes, and excess gas was released through the side arm, all while avoiding exposure to light. The valve of the side arm was closed, and the needle was withdrawn from the solution but remained in the headspace of the vessel. Diethyl vinylphosphonate (93 μL, 99 mg, 0.60 mmol, 3.0 equiv) was added and the reaction mixture was then subjected to irradiation by one Kessil PR160-390 nm LED with 100% intensity (40 W, ~6 cm away) for 5 minutes, all while maintaining the bath temperature at −20°C. Then, the reaction temperature was allowed to rise to 23 ºC. Silica gel (5–10 mL) was added, and the reaction mixture was concentrated to dryness under reduced pressure. The resulting residue was purified by chromatography on silica gel (hexanes/EtOAc = 1:2) to afford **32** as a colorless liquid in 61% yield (55.6 mg).

R_f = 0.30 (hexanes/EtOAc = 1:2).

NMR Spectroscopy:

^{1}H NMR (300 MHz, $CDCl_3$, 23 ºC, δ): 7.43 (td, *J* = 8.5, 6.4 Hz, 1H), 7.30 (d, *J* = 8.5 Hz, 2H), 7.06 (d, *J* = 8.5 Hz, 2H), 6.88 (td, *J* = 8.4, 0.8 Hz, 1H), 6.61 (d, *J* = 8.6 Hz, 1H), 4.37 – 4.16 (m, 4H), 3.97 (ddd, *J* = 11.3, 9.9, 3.4 Hz, 1H), 3.59 (ddd, *J* = 14.9, 7.2, 3.4 Hz, 1H), 3.10 (ddd, *J* = 14.9, 11.3, 8.3 Hz, 1H), 1.37 (t, *J* = 7.0 Hz, 6H).

^{13}C NMR (75 MHz, $CDCl_3$, 23 ºC, δ): 163.9 (d, *J* = 259.4 Hz), 160.8 (d, *J* = 4.1 Hz), 153.4, 134.8 (d, *J* = 10.3 Hz), 134.6, 130.9, 120.2, 111.7 (d, *J* = 3.5 Hz), 111.0, 109.6 (d, *J* = 19.5 Hz), 93.5 (d, *J* = 18.1 Hz), 64.0 (d, *J* = 7.1 Hz), 63.5 (d, *J* = 6.9 Hz), 42.4 (d, *J* = 155.7 Hz), 37.9, 16.4 (d, *J* = 2.4 Hz), 16.3 (d, *J* = 2.4 Hz).

^{31}P NMR (122 MHz, $CDCl_3$, 23 ºC, δ): 19.27.

HRMS-ESIpos (m/z) calc'd for $C_{19}H_{20}FBrNPO_4Na$ $[M+Na]^+$, 478.0190; found, 478.0191; deviation: –0.2 ppm.

Arylethyl bromide 33

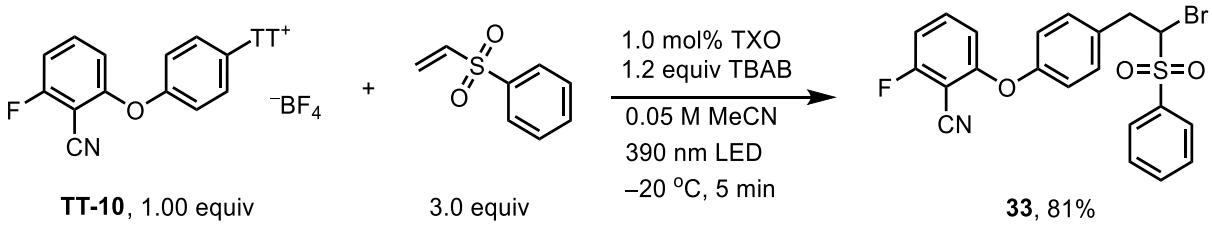

TT-10, 1.00 equiv 3.0 equiv **33**, 81%

To a 5-mL Schlenk tube containing a Teflon-coated magnetic stirring bar were added **TT-10** (103 mg, 0.200 mmol, 1.00 equiv), tetrabutylammonium bormide (TBAB, 77 mg, 0.24 mmol, 1.2 equiv), phenyl vinyl sulfone (102 mg, 0.60 mmol, 3.0 equiv), and thioxanthone in acetonitrile (c = 0.50 mM, 4.0 mL, 2.0 μmol, 1.0 mol%). The tube was sealed with a rubber septum and immersed in a methanol/water (30/70) dry ice bath at –20°C. A balloon filled with argon gas was connected to a long needle, which was inserted to the tube through the rubber septum. Roughly 100 ml of argon gas was bubbled through the solution over a time period of approximately 5 minutes, and excess gas was released through the side arm, all while avoiding exposure to light. The valve of the side arm was closed, and the needle was withdrawn from the solution but remained in the headspace of the vessel. The reaction mixture was then subjected to irradiation by one Kessil PR160-390 nm LED with 100% intensity (40 W, ~6 cm away) for 5 minutes, all while maintaining the bath temperature at –20°C. Then, the reaction temperature was allowed to rise to 23 ºC. Silica gel (5–10 mL) was added, and the reaction mixture was concentrated to dryness under reduced pressure. The resulting residue was purified by chromatography on silica gel (hexanes/acetone = 4:1) to afford **33** as a colorless solid in 81% yield (74.5 mg).

R_f = 0.20 (hexanes/acetone = 4:1).

NMR Spectroscopy:

^{1}H NMR (500 MHz, $CDCl_3$, 23 ºC, δ): 8.04 (d, *J* = 7.0 Hz, 2H), 7.76 (t, *J* = 7.5 Hz, 1H), 7.64 (t, *J* = 7.9 Hz, 2H), 7.45 (td, *J* = 8.5, 6.4 Hz, 1H), 7.30 (d, *J* = 8.6 Hz, 2H), 7.07 (d, *J* = 8.5 Hz, 2H), 6.91 (t, *J* = 8.4 Hz, 1H), 6.62 (d, *J* = 8.6 Hz, 1H), 4.88 (dd, *J* = 11.4, 2.7 Hz, 1H), 3.95 (dd, *J* = 14.6, 2.7 Hz, 1H), 3.13

(dd, *J* = 14.6, 11.4 Hz, 1H).

^{13}C NMR (125 MHz, $CDCl_3$, 23 ºC, δ): 164.0 (d, *J* = 259.8 Hz), 160.7 (d, *J* = 4.1 Hz), 153.9, 135.1, 135.0 (d, *J* = 10.2 Hz), 134.8, 132.6, 131.3, 130.1, 129.3, 120.5, 112.0 (d, *J* = 3.5 Hz), 111.1, 109.9 (d, *J* = 19.6 Hz), 93.8 (d, *J* = 18.0 Hz), 66.2, 36.8.

HRMS-ESIpos (m/z) calc'd for $C_{21}H_{15}FBrNO_3SNa$ $[M+Na]^+$, 481.9832; found, 481.9830; deviation: +0.6 ppm.

Arylethyl bromide 34

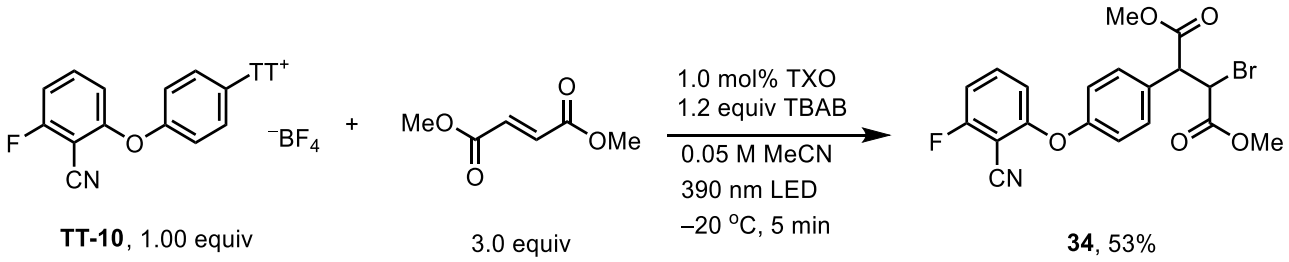

TT-10, 1.00 equiv 3.0 equiv **34**, 53%

To a 5-mL Schlenk tube containing a Teflon-coated magnetic stirring bar were added **TT-10** (103 mg, 0.200 mmol, 1.00 equiv), tetrabutylammonium bormide (TBAB, 77 mg, 0.24 mmol, 1.2 equiv), dimethyl fumarate (86 mg, 0.60 mmol, 3.0 equiv), and thioxanthone in acetonitrile (c = 0.50 mM, 4.0 mL, 2.0 μmol, 1.0 mol%). The tube was sealed with a rubber septum and immersed in a methanol/water (30/70) dry ice bath at –20°C. A balloon filled with argon gas was connected to a long needle, which was inserted to the tube through the rubber septum. Roughly 100 ml of argon gas was bubbled through the solution over a time period of approximately 5 minutes, and excess gas was released through the side arm, all while avoiding exposure to light. The valve of the side arm was closed, and the needle was withdrawn from the solution but remained in the headspace of the vessel. The reaction mixture was then subjected to irradiation by one Kessil PR160-390 nm LED with 100% intensity (40 W, ~6 cm away) for 5 minutes, all while maintaining the bath temperature at –20°C. Then, the reaction temperature was allowed to rise to 23 ºC. Silica gel (5–10 mL) was added, and the reaction mixture was concentrated to dryness under reduced pressure. The resulting residue was purified by chromatography on silica gel (hexanes/EtOAc = 5:1) to afford **34** as a colorless solid in 53% yield (46.2 mg).

R_f = 0.20 (hexanes/EtOAc = 5:1).

NMR Spectroscopy:

Major isomer

^{1}H NMR (500 MHz, $CDCl_3$, 23 ºC, δ): 7.51 – 7.44 (m, 1H), 7.44 (d, *J* = 8.5 Hz, 2H), 7.07 (d, *J* = 8.6 Hz, 2H), 6.94 (td, *J* = 8.4, 0.8 Hz, 1H), 6.65 (d, *J* = 8.5 Hz, 1H), 4.84 (d, *J* = 11.6 Hz, 1H), 4.35 (d, *J* = 11.6 Hz, 1H), 3.79 (s, 3H), 3.61 (s, 3H).

^{13}C NMR (125 MHz, $CDCl_3$, 23 ºC, δ): 170.6, 168.0, 164.1 (d, *J* = 260.0 Hz), 160.2 (d, *J* = 4.0 Hz), 155.0, 134.9 (d, *J* = 10.2 Hz), 131.3, 130.3, 120.4, 112.5 (d, *J* = 3.5 Hz), 110.9, 110.3 (d, *J* = 19.6 Hz), 94.2 (d, *J* = 17.8 Hz), 55.4, 53.1, 52.8, 43.9.

HRMS-ESIpos (m/z) calc'd for $C_{19}H_{15}FBrNO_5Na$ $[M+Na]^+$, 458.0010; found, 458.0007; deviation: +0.7 ppm.

Arylethyl bromide 35

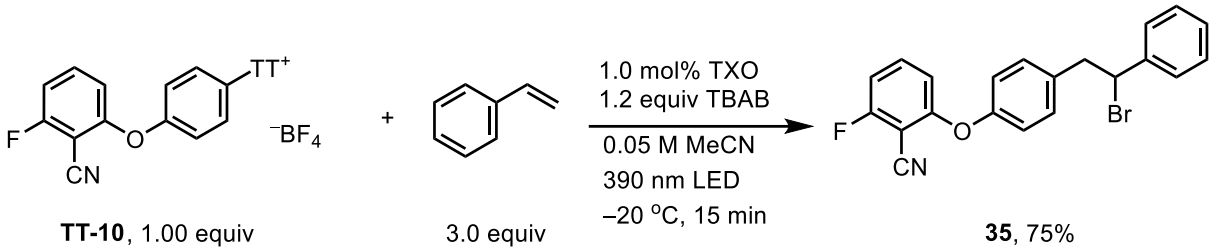

TT-10, 1.00 equiv 3.0 equiv **35**, 75%

To a 5-mL Schlenk tube containing a Teflon-coated magnetic stirring bar were added **TT-10** (103 mg, 0.200 mmol, 1.00 equiv), tetrabutylammonium bormide (TBAB, 77 mg, 0.24 mmol, 1.2 equiv), and thioxanthone in acetonitrile (c = 0.50 mM, 4.0 mL, 2.0 μmol, 1.0 mol%). The tube was sealed with a rubber septum and immersed in a methanol/water (30/70) dry ice bath at −20°C. A balloon filled with argon gas was connected to a long needle, which was inserted to the tube through the rubber septum. Roughly 100 ml of argon gas was bubbled through the solution over a time period of approximately 5 minutes, and excess gas was released through the side arm, all while avoiding exposure to light. The valve of the side arm was closed, and the needle was withdrawn from the solution but remained in the headspace of the vessel. Styrene (69 μL, 62 mg, 0.60 mmol, 3.0 equiv) was added and the reaction mixture was then subjected to irradiation by one Kessil PR160-390 nm LED with 100% intensity (40 W, ~6 cm away) for 15 minutes, all while maintaining the bath temperature at −20°C. Then, the reaction temperature was allowed to rise to 23 ºC. Silica gel (5–10 mL) was added, and the reaction mixture was concentrated to dryness under reduced pressure. The resulting residue was purified by chromatography on silica gel (hexanes/EtOAc = 10:1) to afford **35** as a colorless liquid in 75% yield (59.4 mg).

R_f = 0.21 (hexanes/EtOAc = 10:1).

NMR Spectroscopy:

^{1}H NMR (300 MHz, $CDCl_3$, 23 ºC, δ): 7.48 – 7.27 (m, 6H), 7.18 (d, *J* = 8.5 Hz, 2H), 7.01 (d, *J* = 8.5 Hz, 2H), 6.89 (td, *J* = 8.4, 0.9 Hz, 1H), 6.58 (d, *J* = 8.6 Hz, 1H), 5.14 (t, *J* = 7.5 Hz, 1H), 3.56 (qd, *J* = 14.2, 7.6 Hz, 2H).

^{13}C NMR (75 MHz, $CDCl_3$, 23 ºC, δ): 164.0 (d, *J* = 259.5 Hz), 161.0 (d, *J* = 4.1 Hz), 153.2, 141.1, 135.5, 134.8 (d, *J* = 10.3 Hz), 131.0, 128.6, 128.5, 127.4, 120.2, 111.7 (d, *J* = 3.4 Hz), 111.1, 109.5 (d, *J* = 19.5 Hz), 93.5 (d, *J* = 18.3 Hz), 55.1, 45.7.

HRMS-ESIpos (m/z) calc'd for $C_{21}H_{15}FBrNONa$ $[M+Na]^+$, 418.0213; found, 418.0212; deviation: +0.2 ppm.

Arylethyl bromide 36

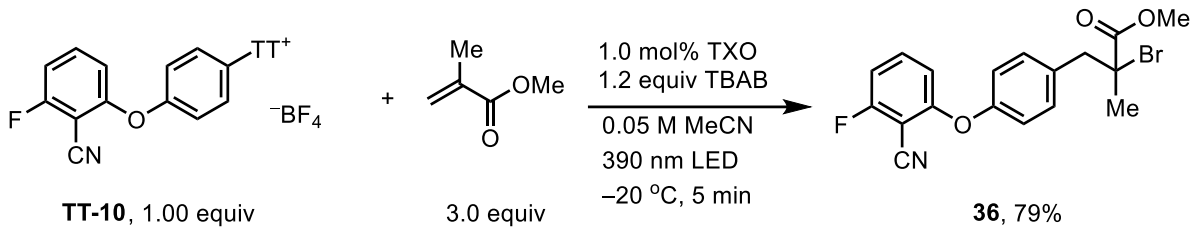

TT-10, 1.00 equiv 3.0 equiv **36**, 79%

To a 5-mL Schlenk tube containing a Teflon-coated magnetic stirring bar were added **TT-10** (103 mg, 0.200 mmol, 1.00 equiv), tetrabutylammonium bormide (TBAB, 77 mg, 0.24 mmol, 1.2 equiv), and thioxanthone in acetonitrile (c = 0.50 mM, 4.0 mL, 2.0 μmol, 1.0 mol%). The tube was sealed with a rubber septum and immersed in a methanol/water (30/70) dry ice bath at −20°C. A balloon filled with argon gas was connected to a long needle, which was inserted to the tube through the rubber septum. Roughly 100 ml of argon gas was bubbled through the solution over a time period of approximately 5 minutes, and excess gas was released through the side arm, all while avoiding exposure to light. The valve of the side arm was closed, and the needle was withdrawn from the solution but remained in the headspace of the vessel. Methyl methacrylate (64 μL, 60 mg, 0.60 mmol, 3.0 equiv) was added and the reaction mixture was then subjected to irradiation by one Kessil PR160-390 nm LED with 100% intensity (40 W, ~6 cm away) for 5 minutes, all while maintaining the bath temperature at −20°C. Then, the reaction temperature was allowed to rise to 23 ºC. Silica gel (5–10 mL) was added, and the reaction mixture was concentrated to dryness under reduced pressure. The resulting residue was purified by chromatography on silica gel (hexanes/EtOAc = 20:1) to afford **36** as a colorless liquid in 79% yield (61.9 mg).

R_f = 0.16 (hexanes/EtOAc = 20:1).

NMR Spectroscopy:

^{1}H NMR (500 MHz, $CDCl_3$, 23 ºC, δ): 7.45 (td, *J* = 8.5, 6.4 Hz, 1H), 7.30 (d, *J* = 8.6 Hz, 2H), 7.06 (d, *J* = 8.5 Hz, 2H), 6.91 (td, *J* = 8.4, 0.8 Hz, 1H), 6.63 (d, *J* = 8.6 Hz, 1H), 3.83 (s, 3H), 3.61 (d, *J* = 13.9 Hz, 1H), 3.41 (d, *J* = 13.9 Hz, 1H), 1.88 (s, 3H).

^{13}C NMR (125 MHz, $CDCl_3$, 23 ºC, δ): 171.3, 164.0 (d, *J* = 259.7 Hz), 160.7 (d, *J* = 4.0 Hz), 153.8, 134.8 (d, *J* = 10.3 Hz), 133.2, 132.3, 120.0, 111.9 (d, *J* = 3.4 Hz), 111.0, 109.7 (d, *J* = 19.5 Hz), 93.7 (d, *J* = 18.2 Hz), 59.6, 53.2, 47.2, 27.4.

HRMS-ESIpos (m/z) calc'd for $C_{18}H_{15}FBrNO_3Na$ $[M+Na]^+$, 414.0112; found, 414.0110; deviation: +0.4 ppm.

Condition optimization

General procedure for condition optimization of two-carbon homologation of ArTTs

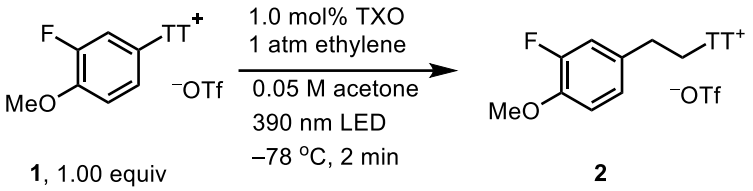

1, 1.00 equiv **2**

To a 5-mL Schlenk tube containing a Teflon-coated magnetic stirring bar were added arylthianthrenium salt (0.050 mmol, 1.00 equiv) and thioxanthone in acetone (c = 0.50 mM, 1.0 mL, 0.50 μmol, 1.0 mol%). The tube was sealed with a rubber septum and immersed in a dry ice/acetone bath at −78°C. A balloon filled with ethylene gas was connected to a long needle, which was inserted to the tube through the rubber septum. Roughly 50 ml of ethylene gas was bubbled through the solution over a time period of approximately 5 minutes, and excess gas was released through the side arm, all while avoiding exposure to light. The valve of the side arm was closed, and the needle was withdrawn from the solution but remained in the headspace of the vessel. The reaction mixture was then subjected to irradiation by one Kessil PR160-390 nm LED with 100% intensity (40 W, ~6 cm away) for 2 minutes, all while maintaining the bath temperature at −78°C. Subsequently, 1,3,5-trimethoxybenzene (50 μL, 0.050 mmol, 1.0 M in MeCN, 1.0 equiv) was added as internal standard. The reaction mixture was concentrated and analyzed by ^{1}H NMR spectroscopy. The conversions of **1** and the yields of **2** were determined by the integrating the signal of the characteristic protons at 8.52 ppm (d) and 4.04 ppm (t) respectively.

Table S2. Condition optimization of two-carbon homologation of ArTTs

entry	changes from reaction conditions	conv. of **1**/%	yield of **2**/%
1	no change	>99	82
2	0.5 mol% instead of 1.0 mol%	95	83
3	0.25 mol% instead of 1.0 mol%	35	24
4	15 min instead of 2 min	>99	52
5	–20 ^{o}C instead of –78 ^{o}C	>99	46
6	0.1 M instead of 0.05 M	>99	81
7	MeCN instead of acetone, –40 ^{o}C	>99	80
8	DCM instead of acetone	>99	78
9	XO, 3CzClIPN, Mes-AcrClO$_4$, Ru1, Ir1, Ir2, Ir3 or Ir4 instead of TXO	<5	<1
10	Ir4 and 40 mol% TT instead of TXO	16	12
11	BP instead of TXO	<5	<1
12	20 mol% BP instead of TXO	43	36
13[a]	20 mol% BP instead of TXO	>99	72
14[b]	254 nm, w/o TXO	>99	<1
15[b]	254 nm, w/o TXO, with 2.0 equiv TBAB	>99	23[c]
16	2.0 equiv TEMPO was added	3	2
17	w/o TXO	<2	<1
18	w/o light	<2	<1

[a]20 min; [b]MeCN, –40 to 23 ^{o}C, 12 h instead of acetone, –78 ^{o}C, 2 min; [c]arylethyl bromide instead of **2** as product.

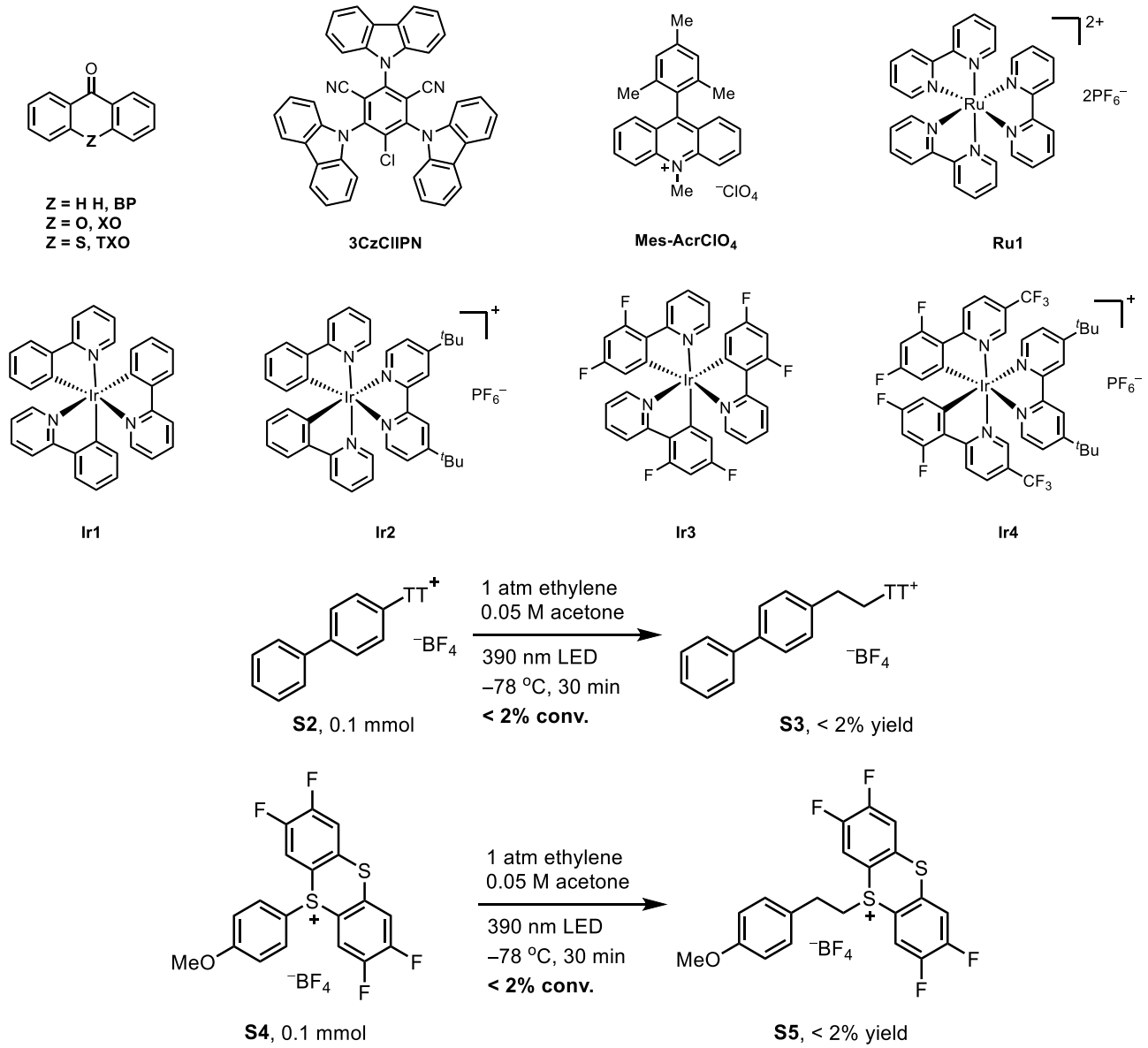

Scheme S1. Reactions with substrates having extended conjugation in the absence of TXO

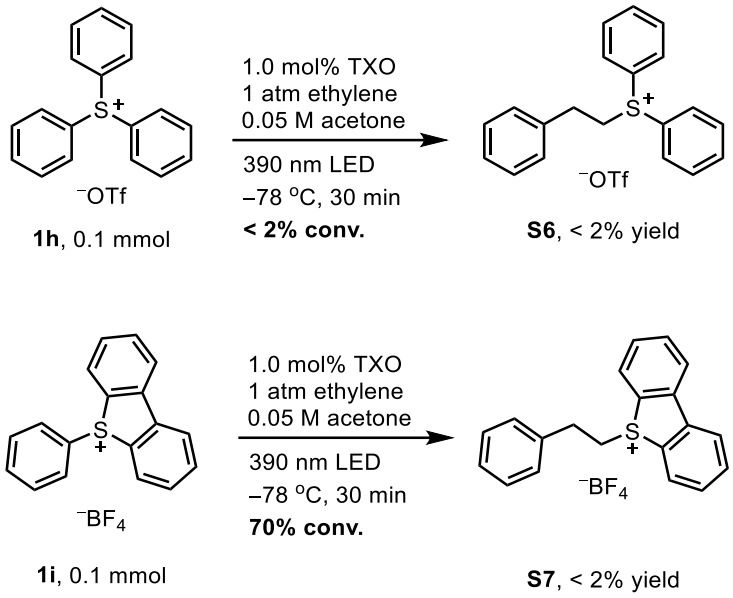

Scheme S2. Reactions of triphenyl sulfonium salt (**1h**) and 5-phenyldibenzothiophenium salt (**1i**) with an extended reaction time

Table S3 Light source screening

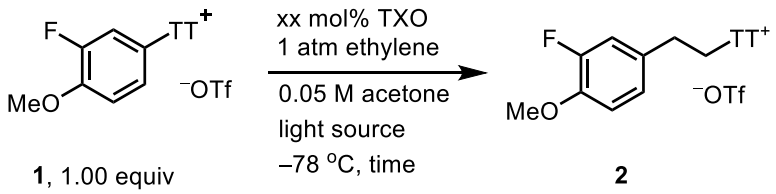

entry	light source	cat. loading (mol%)	time	conv. of **1** (%)	yield of **2** (%)
1	Kessel 390 nm LED (40 W)	1	2 min	>99	82
2	Kessel 390 nm LED (20 W)	1	2 min	98	78
3	EvoluChem™ 405 nm LED (18 W)	1	2 min	19	15
4	EvoluChem™ 405 nm LED (18 W)	1	15 min	94	77
5	EvoluChem™ 425 nm LED (18 W)	1	15 min	3	<2
6	EvoluChem™ 425 nm LED (18 W)	10	15 min	14	10
7[a]	EvoluChem™ 425 nm LED (18 W)	10	15 min	32	24
8	EvoluChem™ 425 nm LED (18 W)	10	60 min	57	29
9[b]	EvoluChem™ 425 nm LED (18 W)	10	15 min	7	6
10	Kessel 456 nm LED (80 W)	10	15 min	<2	<2

[a]0.025 M; [b]2-isopropylthioxanthone was used.

Reaction with high pressure ethylene at room temperature

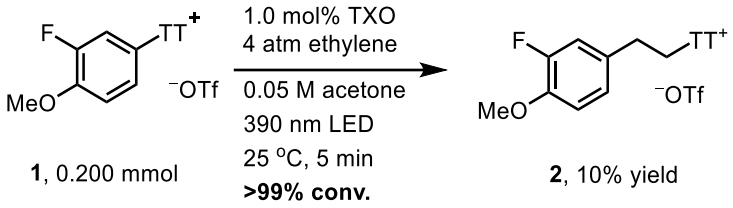

1, 0.200 mmol

2, 10% yield

To a 20-mL microwave vial containing a Teflon-coated magnetic stirring bar were added arylthianthrenium salt **1** (98.0 mg, 0.200 mmol, 1.00 equiv) and thioxanthone in acetone (c = 0.50 mM, 4.0 mL, 2.0 μmol, 1.0 mol%). The vial was sealed with an aluminium crimp seal with septum. The reaction mixture was then bubbled with ethylene using a syringe needle for 15 minutes in an ice bath. Afterward, gaseous ethylene was introduced into the headspace using a syringe (48 mL) and sealed promptly with two layers of Parafilm®. The reaction mixture was then subjected to irradiation by one Kessil PR160-390 nm LED with 100% intensity (40 W, ~3 cm away) for 5 minutes at room temperature (23–25 °C). Subsequently, 1,3,5-trimethoxybenzene (200 μL, 0.200 mmol, 1.0 M in MeCN, 1.0 equiv) was added as internal standard. The reaction mixture was concentrated and analyzed by ^{1}H NMR spectroscopy. The conversions of **1** (>99%) and the yields of **2** (10%) were determined by the integrating the signal of the characteristic protons at 8.52 ppm (d) and 4.04 ppm (t) respectively.

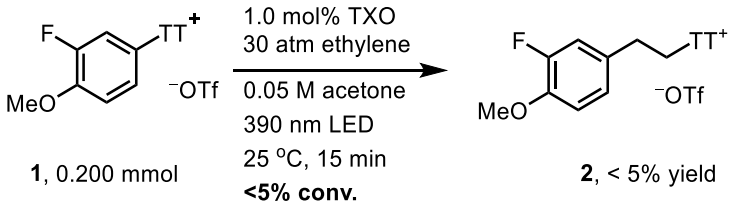

1, 0.200 mmol

2, < 5% yield

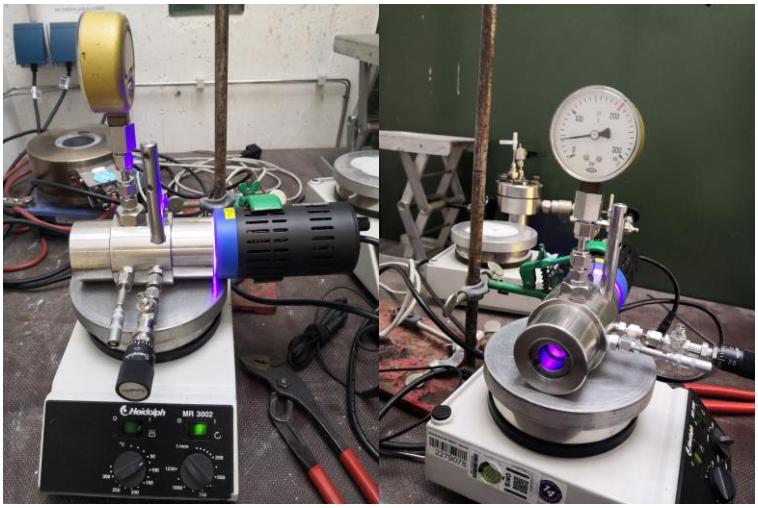

To a 10-mL autoclave with two glass windows containing a Teflon-coated magnetic stirring bar were added arylthianthrenium salt **1** (98.0 mg, 0.200 mmol, 1.00 equiv) and thioxanthone in acetone (c = 0.50 mM, 4.0 mL, 2.0 μmol, 1.0 mol%). The autoclave was purged three times with ethylene gas and pressed to 30–50 atm. The reaction mixture was then subjected to irradiation by one Kessil PR160-390 nm LED with 100% intensity (40 W, ~3 cm away) for 15 minutes at room temperature (23–25 °C). Subsequently, 1,3,5-

trimethoxybenzene (200 μL, 0.200 mmol, 1.0 M in MeCN, 1.0 equiv) was added as internal standard. The reaction mixture was concentrated and analyzed by ^{1}H NMR spectroscopy. The conversions of **1** and the yields of **2** were determined to be less than 5% by the integrating the signal of the characteristic protons at 8.52 ppm (d) and 4.04 ppm (t) respectively.

General procedure for optimization of base for aminoarylation of ethylene

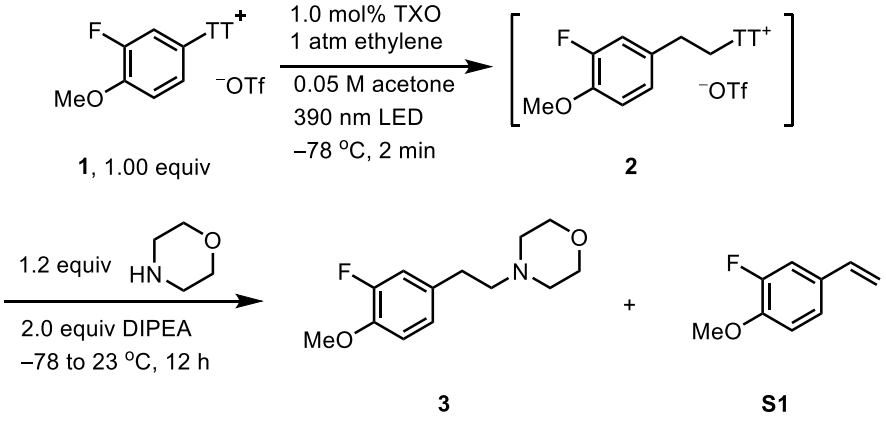

To a 5-mL Schlenk tube containing a Teflon-coated magnetic stirring bar were added arylthianthrenium salt (0.050 mmol, 1.00 equiv) and thioxanthone in acetone (c = 0.50 mM, 1.0 mL, 0.50 μmol, 1.0 mol%). The tube was sealed with a rubber septum and immersed in a dry ice/acetone bath at –78°C. A balloon filled with ethylene gas was connected to a long needle, which was inserted to the tube through the rubber septum. Roughly 50 ml of ethylene gas was bubbled through the solution over a time period of approximately 5 minutes, and excess gas was released through the side arm, all while avoiding exposure to light. The valve of the side arm was closed, and the needle was withdrawn from the solution but remained in the headspace of the vessel. The reaction mixture was then subjected to irradiation by one Kessil PR160-390 nm LED with 100% intensity (40 W, ~6 cm away) for 2 minutes, all while maintaining the bath temperature at –78°C. Then, morpholine (5.1 μL, 5.2 mg, 0.060 mmol, 1.2 equiv) and base (0.10 mmol, 2.0 equiv) were added. The resulting mixture was stirred for 12 h without exposure to light. During this period, the reaction temperature was gradually allowed to rise to 23 ºC. Subsequently, 1,3,5-trimethoxybenzene (50 μL, 0.050 mmol, 1.0 M in MeCN, 1.0 equiv) was added as internal standard. The reaction mixture was concentrated and analyzed by ^{1}H NMR spectroscopy. The conversion of **1** and the yields of **2**, **3**, and **S1** were determined by the integrating the signal of the characteristic protons at 8.52 ppm (d), 4.04 ppm (t), 2.74 (t), and 5.61 (d) respectively.

Table S4. Base optimization of 1,2-aminoarylation of ethylene

entry	base	conv. of **1**/%	yield of **2**/%	yield of **3**/%	yield of **S1**/%
1	DIPEA	>99	<2	75	9
2	$NaHCO_3$	>99	<2	74	10
3	K_2CO_3	>99	<2	65	14
4	K_3PO_4	>99	<2	61	16
5	Et_3N	>99	<2	20	62
6	pyridine	>99	17	<2	56
7	DBU	>99	<2	2	78
8	DABCO	>99	<2	5	11(68)[a]
9	w/o base	>99	14	58	<2

[a]the yield in the bracket referred to the substitution product by DABCO

Investigation of adding nucleophiles from the beginning of the reaction

Before conducting the experiment in which nucleophiles were added at the beginning of the reaction, we first investigated the reactivity of an isolable TT radical cation (0.02 mmol, 1.0 equiv) with six different nucleophiles (0.05 mmol, 2.5 equiv) in acetonitrile (0.04 M) at 25 °C: chloride, bromide, iodide, aliphatic amine, carboxylate, and thiophenolate. Each of these nucleophiles is known to work well when added after the photoreaction. In these preliminary tests, the characteristic purple color of the TT radical cation disappeared within 1 to 20 seconds, turning colorless, or yellow with bromide, and brown with iodide (see Scheme S3). These results indicate that all six nucleophiles can react with the TT radical cation rapidly.

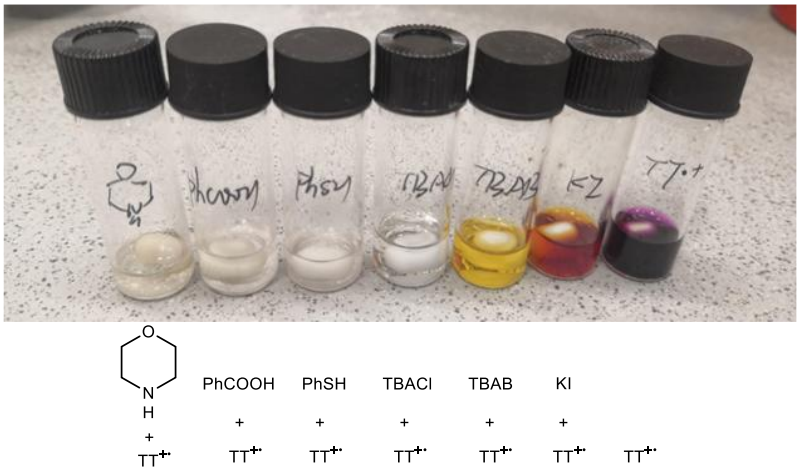

Scheme S3. Color change after mixing TT radical cation and different nucleophiles

Next, we explored reactions where the nucleophile was added at the beginning of the reaction. The outcomes varied significantly and are summarized in Scheme S4. Using chloride and bromide as nucleophiles, the desired products were obtained in 77-88% yields. With iodide, 50% conversion was observed, yielding 22% of the desired product along with 22% aryl iodide by-product. When morpholine was used, low conversion was observed, and the desired product was not detected. With benzoate as the nucleophile, the reaction showed full conversion, yielding 22% of the desired product and 22% of the arylethyl thianthrenium salt intermediate. Thiophenolate led to full conversion as well; however, the desired product was not observed, and direct sulfidation products along with ethyl arene were formed.

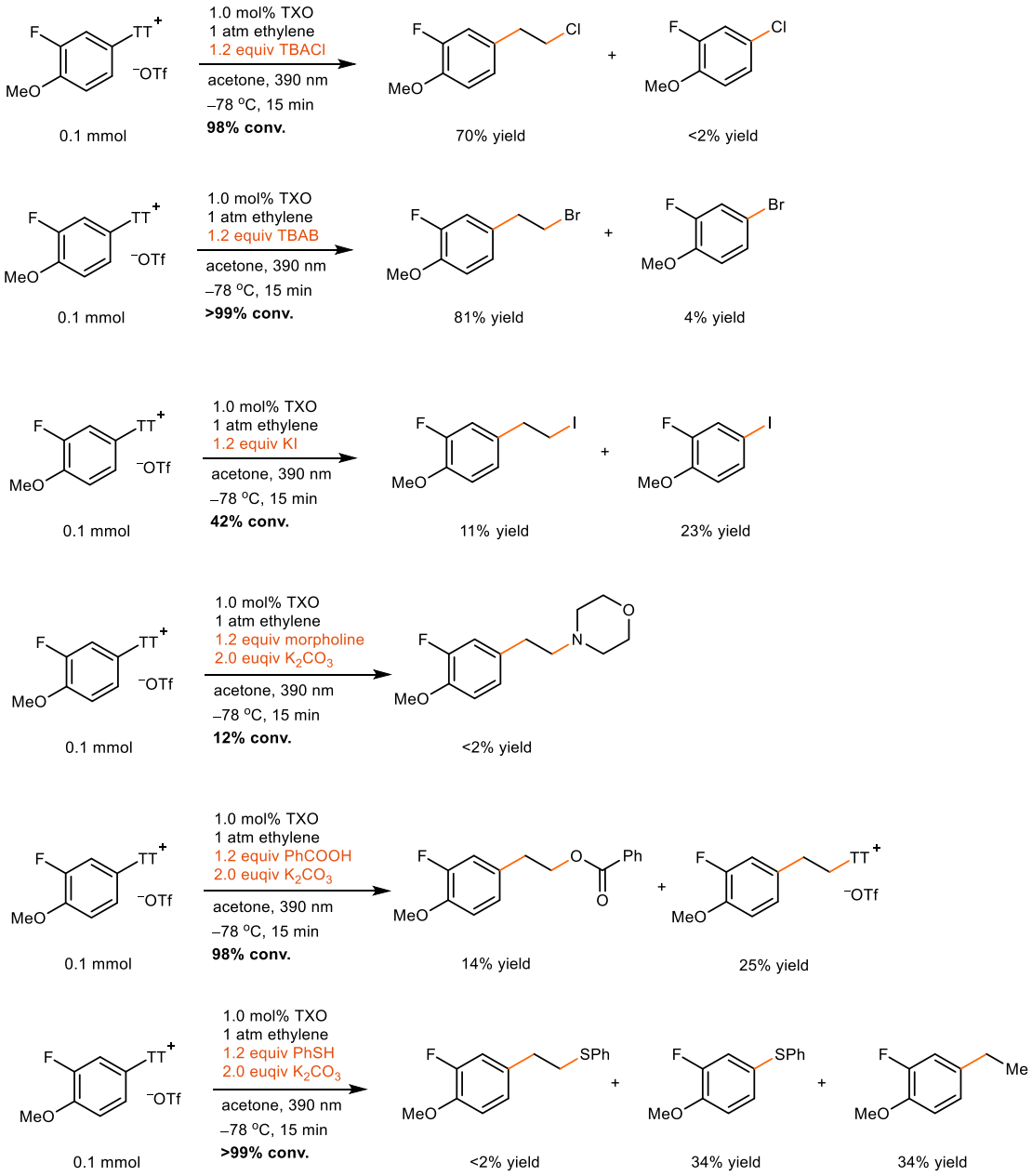

Scheme S4. Reactions with nucleophiles added from the beginning of the reaction

Chloride and bromide can still be added at the beginning of the reaction, likely because even when the nucleophile reacts with the TT radical cation, the resulting halide radical can dimerize to form molecular halogen. This halogen can then react with the aryl ethyl radical, ultimately leading to the formation of the same alkyl halide product via a two-step process. Other nucleophiles, such as iodide, aliphatic amines, carboxylates, and thiophenolates, are likely unable to participate due to their competitive reaction with the thianthrenium radical cation.

Further optimization of the reaction conditions

The main side products during the first photoreaction step are hydrodefunctionalization (**bp1**, 8%) and the Minisci byproduct (**bp2**, 9%). The hydrodefunctionalization byproduct was reduced to 4% by further decreasing the reaction temperature from −78 °C to −94 °C, which increased the solubility of ethylene. The Minisci byproduct can be reduced by carefully controlling the reaction time or suppressed by adding a bromide nucleophile to capture the alkyl thianthrenium salt directly. Overall, the photoreaction yield can now be increased from 82% to 91% (eq. 2). In the second substitution step, the primary side reaction is elimination, leading to the formation of styrene (**bp3**, 9%, eq. 1), particularly when N and O-based nucleophiles, as well as $^{-}$F and $^{-}$CN, are used. This issue is addressed to some extent by converting alkylthianthrenium salts to alkyl bromides in situ and then adding the nucleophile (eq. 2). This approach results in fewer elimination byproduct (4%), likely because uncharged alkyl bromides are less prone to elimination. Utilizing this strategy, along with the optimized conditions from the first photoreaction step, the yield of product 3 can be improved from 73% to 81%. Additionally, the yields of other substrates (**4**, **5**, **6**, **20**) with previously moderate results (41–55%) are also improved (60–81%), as shown in Scheme S5.

Previous conditions:

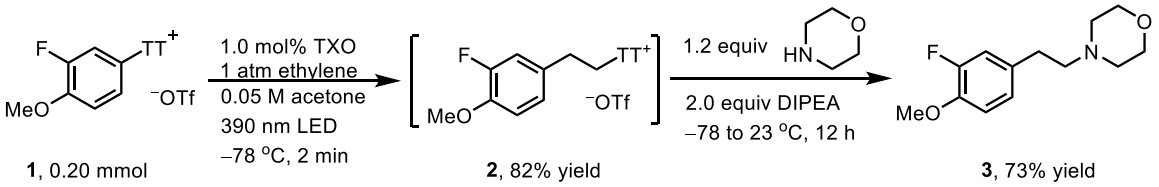

1, 0.20 mmol — **2**, 82% yield — **3**, 73% yield

eq. 1

Optimized conditions:

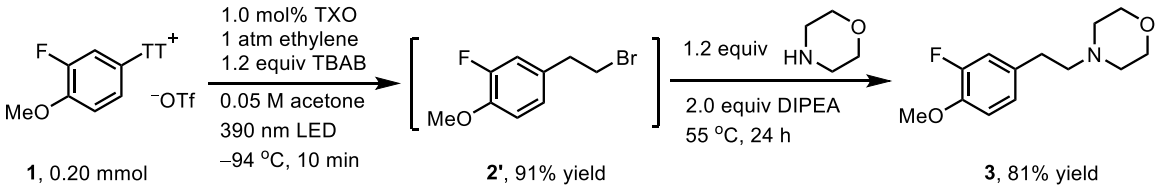

1, 0.20 mmol — **2'**, 91% yield — **3**, 81% yield

eq. 2

byproducts

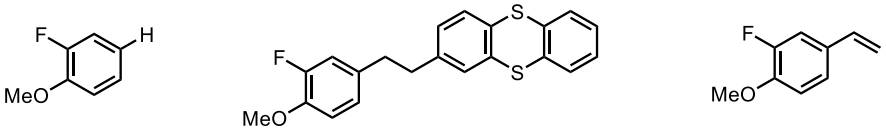

bp1
previous conditions: 8% yield
optimized conditions: 4% yield

bp2
previous conditions: 9% yield
optimized conditions: <2% yield

bp3
previous conditions: 8% yield
optimized conditions: 4% yield

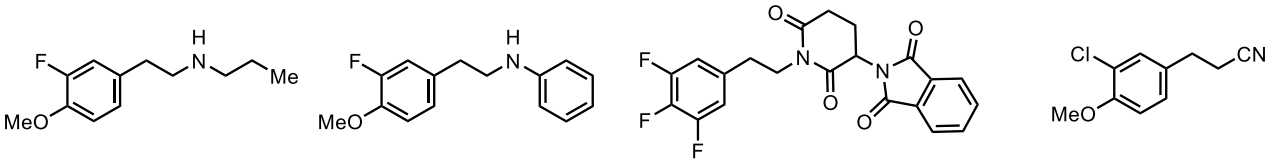

4
previous conditions: 49%
optimized conditions: 72%

5
previous conditions: 45%
optimized conditions: 63%

6
previous conditions: 55%
optimized conditions: 60%

20
previous conditions: 41%
optimized conditions: 81%

Scheme S5 Further optimization of reaction conditions and improvement of yields for several substrates

Mechanistic studies

Transient absorption spectroscopy and related spectroscopic studies

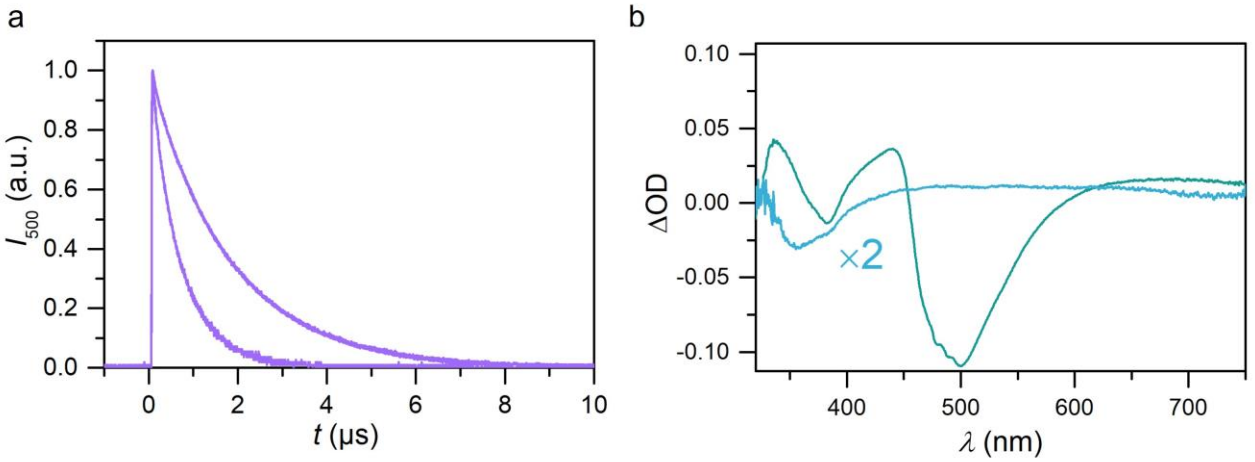

Figure S1. Mechanistic investigations of $Ir(dFppy)_3$ with 1 mM $ArTT^+$ in Ar-saturated acetone after 355 nm laser pulse excitation. **a**, time-resolved emission recorded at 500 nm in the absence and presence of $ArTT^+$. **b**, TA spectra recorded 100 ns (green) and 5 µs (blue) after excitation.

The photocatalyst $Ir(dFppy)_3$ has a triplet energy of 2.75 eV, similar to that of TXO[4]. Kinetic traces monitoring the phosphorescence at 500 nm reveal that the triplet state is deactivated in the presence of 1 mM $ArTT^+$ in argon-saturated acetone (Fig. S1a, quenching efficiency ~63%). However, no signals corresponding to the thianthrenium radical cation were detected post-quenching (Fig. S1b). Instead, a ground-state bleach of the photocatalyst in the 350-400 nm region was observed, usually related to electron transfer processes with Ir-based photocatalysts[5,6]. The reduction of thianthrenium salts by an Ir-photocatalyst, as reported by Yang et al., generates the neutral thianthrene species after cleavage, which is transparent in the selected detection range[7].

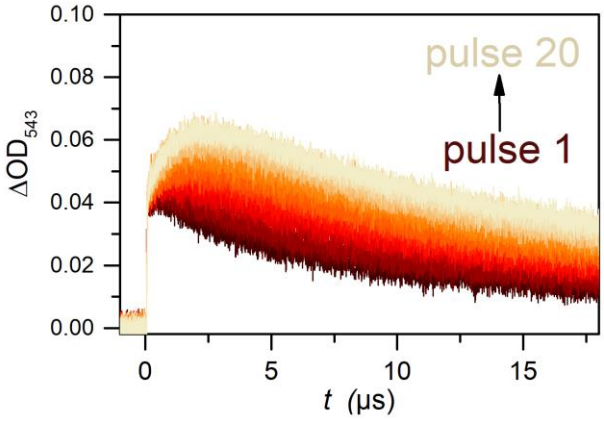

Figure S2. The time-resolved transient absorption at 543 nm of a 1 mM $PhTT^+$ and 50 µM TXO solution in acetone saturated with argon (3 mL in a cuvette with 1 cm path length). Kinetic traces following each 355 nm pulse on the same cuvette, from the first to the 20th pulse, are presented.

Upon repeated excitation of TXO in the presence of thianthrenium salts using 355 nm laser pulses, we observed

accelerated quenching of TXO and the formation of novel signals in the transient absorption spectrum. Exemplary time-resolved measurements at 543 nm are shown for each individual pulse (Fig. S2). We attribute this observation to the rapid degradation of the system due to the high quantum yield of the sensitized reaction and the absence of a scavenging reagent. The irreversible fragmentation of $PhTT^+$ generates a highly reactive aryl radical, while the thianthrenium radical cation eventually reacts with traces of water, forming products known to quench or interact with triplet-excited TXO[8–10]. Consequently, all measurements were recorded with a fresh solution that was replaced after each single-pulse experiment. Relatively high laser pulse intensities had to be used to obtain an acceptable signal-to-noise ratio.

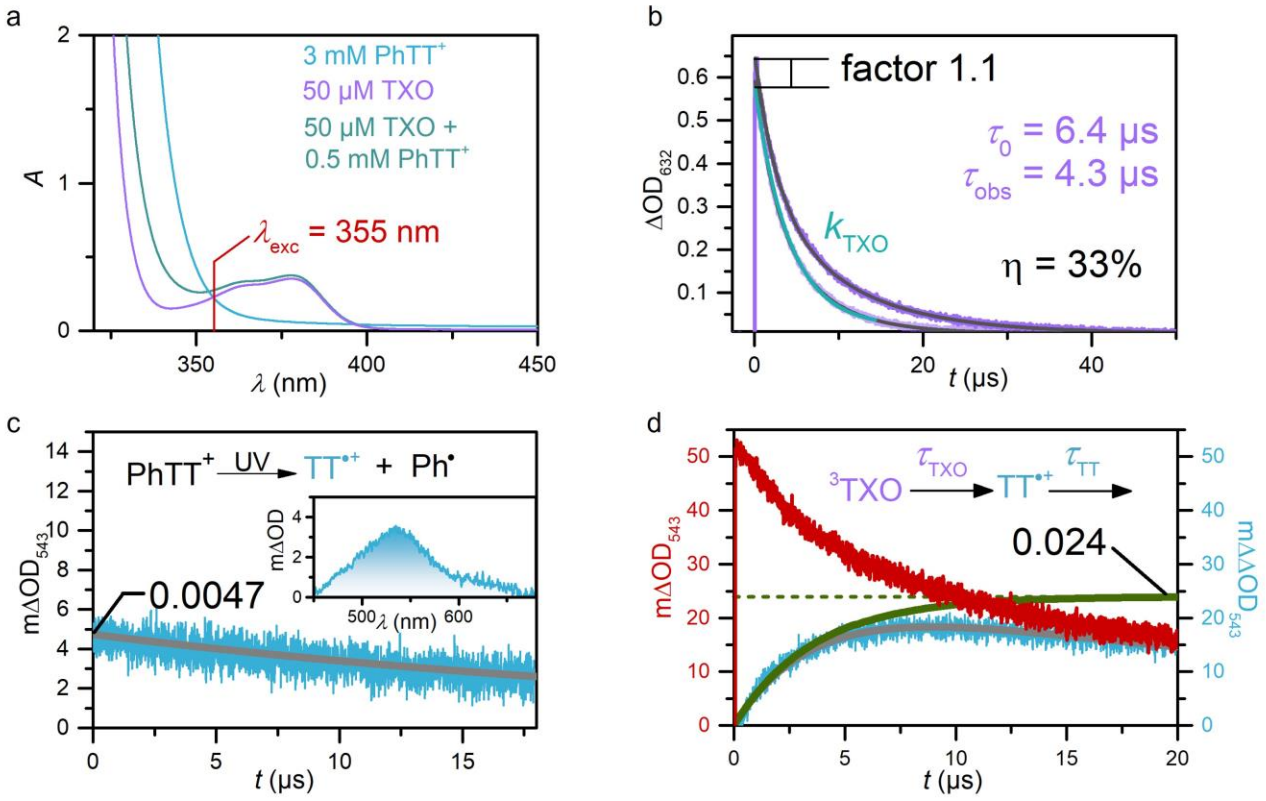

Figure S3. Relative comparison of directly excited and sensitized homolytic cleavage of $PhTT^+$ using 355 nm laser pulses (29.2 mJ) in Ar-saturated acetone. a, absorption spectra of the employed solutions. **b,** time-resolved transient absorption of ^3TXO in the absence and presence of 0.5 mM $PhTT^+$. **c,** kinetic traces of $TT^{\bullet+}$ produced upon direct excitation of 3 mM $PhTT^+$. Inset: TA spectrum recorded after 700 ns. **d,** kinetic traces at 543 nm of 50 µM TXO and 0.5 mM $PhTT^+$ (red), isolated formation and decay of $TT^{\bullet+}$ (cyan), simulated formation of $TT^{\bullet+}$ (green).

The formation of $TT^{\bullet+}$ upon direct excitation and sensitization with ^3TXO was analyzed by relative actinometry. The thianthrenium salts weakly absorb in the UVA range allowing us to directly excite them at 355 nm when high concentrations are employed. Two solutions containing 3 mM $PhTT^+$ or 50 µM TXO were prepared ensuring identical excitation conditions at 355 nm (Fig. S3a) with 29.2 mJ laser pulses. A concentration of 0.5 mM $PhTT^+$ was added to the TXO solution. Quenching studies of TXO in the presence and absence of $PhTT^+$ yielded the triplet energy transfer efficiency for the selected quencher concentration of 0.33 (Fig. S3b). Due to the higher laser intensity (29.2 mJ) and self-quenching effects of ^3TXO the lifetimes τ_0 and τ_{obs} were obtained

from a biexponential fits by averaging τ_1 and τ_2 with the corresponding amplitudes from the fit functions[11]. The weak absorption of $PhTT^+$ at 355 nm leads to a slightly reduced formation of ^{3}TXO after excitation with constant laser intensity, which can be corrected through measurements at 632 nm, where ^{3}TXO can be studied in isolation (Fig. S3b, correction factor of 1.1). The $TT^{\bullet+}$ signal at 543 nm is superimposed with the simultaneous deactivation of ^{3}TXO (Fig. S3d, red curve). A straightforward separation of the kinetic trace at 543 nm is possible with the isolated ^{3}TXO signal recorded at 632 nm and the relative molar absorption coefficients of ^{3}TXO at these two wavelengths[4]. This separation allows us to isolate the $TT^{\bullet+}$ signal (Fig. S3d, cyan curve). Due to the moderate quenching efficiency under our diluted conditions, $TT^{\bullet+}$ already decays to some degree before reaching the maximum signal intensity. Fitting the data to the following equation for A → B → C kinetics enables us to determine the overall $TT^{\bullet+}$ signal.

$$\Delta\mathrm{OD}_{543} = \Delta\mathrm{OD}_{543,\max} \cdot \frac{k_{\mathrm{TXO}}}{k_{\mathrm{TT}} - k_{\mathrm{TXO}}}\left(e^{-k_{\mathrm{TXO}}\cdot t} - e^{-k_{\mathrm{TT}}\cdot t}\right)$$

Where $\Delta OD_{543,max}$ represents the cumulative $TT^{\bullet+}$ signal, k_{TXO} is the quenching rate of ^{3}TXO that was obtained from Fig. S3b and k_{TT} is the pseudo-first-order decay rate of $TT^{\bullet+}$, which can be used to describe the $TT^{\bullet+}$ decay over the short time range of the experiments in Fig. 3d. The fit functions yields k_{TT} 3.04×10^4 s^{-1} corresponding to a lifetime of ~33 µs for $TT^{\bullet+}$ and a signal $\Delta OD_{543,max}$ of 0.024 (Table S5). For comparison, a curve is simulated showing the cumulative concentration of $TT^{\bullet+}$ (Fig. S3d, green curve). The molar absorption coefficients of ^{3}TXO (30 000 M^{-1} cm^{-1} at λ_{max})[12] and $TT^{\bullet+}$ (12 000 M^{-1} cm^{-1} at 543 nm)[13] from the literature enable us to estimate a concentration of 19 µM for ^{3}TXO and 2.2 µM for $TT^{\bullet+}$, giving an overall quantum yield $\Phi_{obs} = 0.12$ for this reaction in the presence of 0.5 mM $PhTT^+$ as ^{3}TXO quencher. The intrinsic quantum yield for homolytic cleavage after sensitization (Φ_{EnT}) of $PhTT^+$ is calculated from the following equation: $\Phi_{obs} = \Phi_{EnT} \times \eta$, where η corresponds to the energy transfer efficiency (0.33), yielding a value of 0.36.

Table S5. Key values obtained for the sensitized fragmentation of $PhTT^+$.

Compound	$m\Delta OD_{max}$	c (µM)	k (s^{-1})	Φ_{obs}	Φ_{EnT}	η
^{3}TXO	570 [a]	19.0 [c]	2.78×10^5 [e]	0.12	0.36	0.33
$TT^{\bullet+}$	24 [b]	2.0 [c] (2.2)[d]	3.04×10^4			

[a] At 632 nm. [b] At 543 nm. [c] Calculated from literature molar absorption coefficients[12,13]. [d] multiplied with correction factor of 1.1. [e] Obtained from the kinetic measurements in Fig. S3b. The high ^{3}TXO concentrations generated as a result of the high laser intensity causes slight deviations from a monoexponential decay of ^{3}TXO due to self-quenching effects[11]. Hence, a kinetic analyzis with biexpoential fit functions was carried out as explained in the text. The quenching rate k_{TXO} of is therefore determined by fitting only the time window of interest (0-15 µs). (Self-quenching of ^{3}TXO is not a problem when deactivation by a quencher is much more efficient (e.g. quencher concentrations of 50 mM (as employed in the preparative photolysis experiments) and non-pulsed excitation light sources are employed. Hence, under lab-scale conditions the efficiency is likely even higher).

Under identical excitation conditions, the cleavage following direct excitation of $PhTT^+$ was traced at 543 nm (Fig. S3c). A much weaker signal intensity (ΔOD_{543} = 0.0047) is detected directly after excitation. By comparing the relative signal intensities of sensitized and direct formation of $TT^{\bullet+}$ we calculated a quantum yield Φ_{UV} of 0.02. The fraction of the $TT^{\bullet+}$ that is generated by direct excitation of $PhTT^+$ in the solution containing 50 µM and 0.5 mM $PhTT^+$ can be neglected, since the signal is below the detection limit and has no effect on the final result. The absolute quantum yields crucially depend on the molar absorption coefficients as explained above. These values were obtained in different solvents but the TA spectra of both ^{3}TXO and $TT^{\bullet+}$ are largely solvent independent. We therefore assume that the molar absorption coefficients of these species in acetone are similar as well (expected maximum relative error, 25 %). However, we stress that the relative quantum yield improvement of the EnT approach compared to direct UV excitation (by a factor of 18) does not depend on the molar absorption coefficients.

Analysis of energy transfer rate and expected timescales

The quenching of TXO by $ArTT^+$ (**1**) was observed with an energy transfer rate of k_q = 5.0 × 10^7 M^{-1} s^{-1} at 20 °C. The energy transfer rate is indeed quite rapid, and based on the viscosity parameters of acetone, we estimated the quenching efficiencies at –78°C. The viscosity of acetone is reported as 0.323 mPa·s at 20 °C and 1.43 mPa·s at -78 °C (https://www.ddbst.com/ddb.html). We assume that the energy transfer rate constant is inversely proportional to the viscosity of the solvent.

$$\text{Energy transfer rate} \quad k_q \sim \frac{1}{\eta}$$

We calculated k_q (-78°C) to be approximately 1.1 × 10^7 M^{-1} s^{-1}, which was used to estimate the quenching efficiency alongside the triplet lifetime of TXO at 20°C (t = 8.85 µs). Even at the low temperatures employed in the reaction, we estimate a quenching efficiency of $\eta_{EnT} = 83\%$ (c_q = 0.05 M) at the start of the reaction and $\eta_{EnT} = 33\%$ at 90% conversion (c_q = 0.005 M) (see equation below). This indicates that highly efficient quenching is still achievable at -78°C.

$$\text{Quenching efficiency} \quad \eta_{EnT} = \frac{\tau_0 - \left(\frac{\tau_0}{1 + k_q \cdot c_q \cdot \tau_0}\right)}{\tau_0}$$

Since a nearly identical setup was used for both the quantum yield determination and the irradiation experiments, we can estimate the reaction times by simply comparing the amount of substance with the photon flux, which was also determined through ferrioxalate actinometry (1.26 10^{-6} Einstein s^{-1}). In this estimation, we account for the fact that the LED power was set to 25% for the quantum yield determination and 100% for the general procedure. Additionally, the volume increases from 1 mL to 4 mL, resulting in a fourfold increase in the irradiated volume.

$$\text{Reaction time} \quad t = \frac{n_{ArTT+}}{photon\ flux \cdot \Phi \cdot f} \sim \frac{0.200\ \text{mmol}}{(4 \cdot 4 \cdot 1.26 \cdot 10^{-6}\ \text{Einstein s}^{-1}) \cdot 0.1 \cdot 0.94} \sim \frac{0.200\ \text{mmol}}{2 \cdot 10^{-5}\ \text{Einstein s}^{-1} \cdot 0.1 \cdot 0.94} \sim 106\ \text{s}$$

The fraction of absorbed light by TXO (f = 0.94) is identical to the conditions in the quantum yield determination. The estimated reaction time (106 s) for the general procedure aligns well with the

experimentally observed irradiation time of 120 seconds. This straightforward calculation does not account for the gradual decrease in energy transfer efficiency toward the end of the reaction, as mentioned earlier. However, this has only a minimal impact on the overall irradiation time.

In conclusion, the short reaction times are not indicative of a chain reaction mechanism but are consistent with the estimated and expected duration for highly efficient energy transfer reactions.

UV-vis absorption spectrum of reaction mixtures

As shown in Figure S4 and S5, interaction between TXO and ArTT$^+$ **1** at ground states was not observed under the reaction concentrations.

All UV-Vis spectrum measurements were recorded on a Shimadzu UV-Vis spectrophotometer UV-2600 with temperature controller using a quartz cuvette (10 × 10 mm, 3.5 mL) in acetone as solvent.

UV-Vis spectra of the reaction mixture were measured with the following concentrations:

TXO (2.1 mg, 10 μmol, c = 0.5 mM) in acetone (20 mL);

ArTT$^+$ **1** (490 mg, 1.0 mmol, c = 50 mM) in acetone (20 mL);

TXO (2.1 mg, 10 μmol, c = 0.5 mM) and ArTT$^+$ **1** (490 mg, 1.0 mmol, c = 50 mM) in acetone (20 mL);

TXO (2.1 mg, 10 μmol, c = 0.5 mM) and ArTT$^+$ **1** (196 mg, 0.4 mmol, c = 20 mM) in acetone (20 mL);

TXO (2.1 mg, 10 μmol, c = 0.5 mM) and ArTT$^+$ **1** (98 mg, 0.2 mmol, c = 10 mM) in acetone (20 mL);

TXO (2.1 mg, 10 μmol, c = 0.5 mM) and ArTT$^+$ **1** (49 mg, 0.1 mmol, c = 5 mM) in acetone (20 mL);

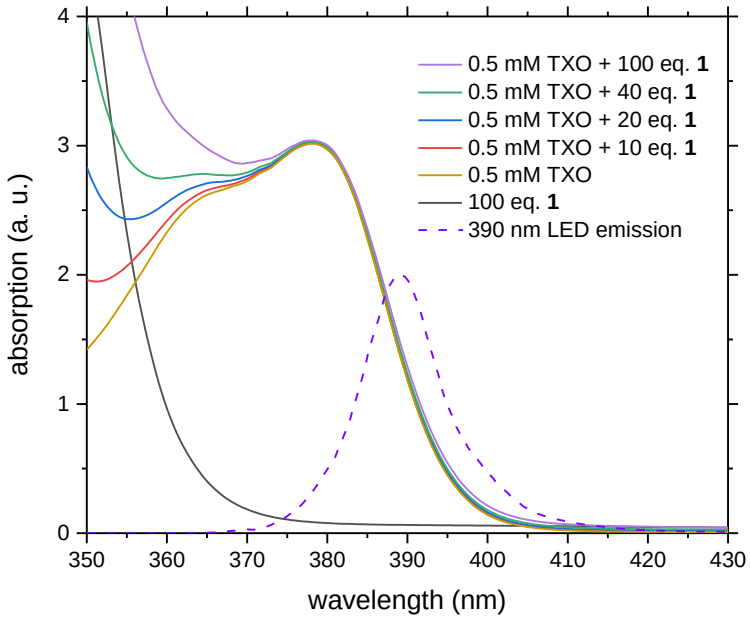

Figure S4. UV-Vis absorption spectra of ArTT$^+$ **1** and TXO mixtures in various ratio in acetone.

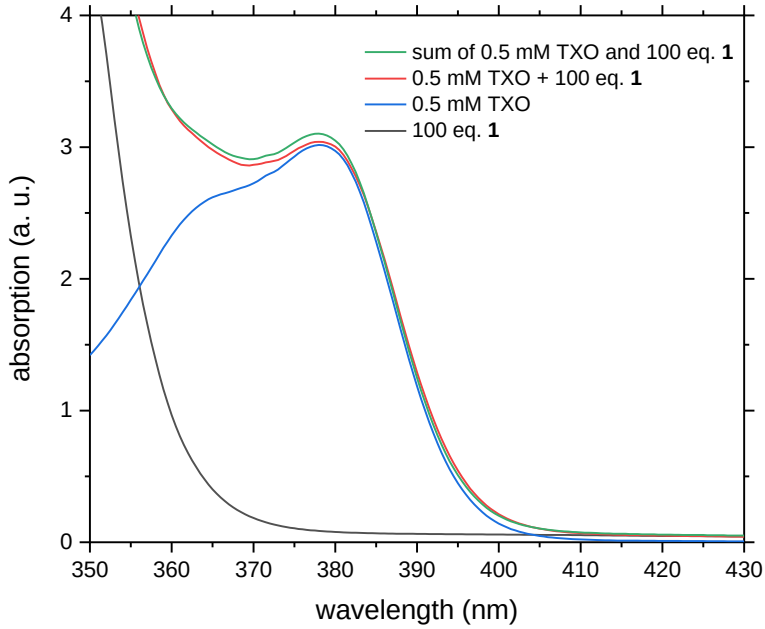

Figure S5. UV-Vis absorption spectra of TXO and ArTT^{+} **1** mixtures in acetone, and the mathematical summation of individual spectra

Cyclic voltammograms

Determination of redox potentials of TXOs at ground state

Cyclic voltammograms were recorded using an Autolab PGSTAT204 potentiostat and a Pt working electrode, an Ag/AgCl reference electrode and a Pt wire auxiliary electrode. The voltammograms were recorded at room temperature in 0.1 M tetrabutylammonium hexafluorophosphate in acetone (3 mL, c = 3.3 mM) containing 2-substituted TXO (10 µmol). The scan rate was 100 mV·s^{-1}.

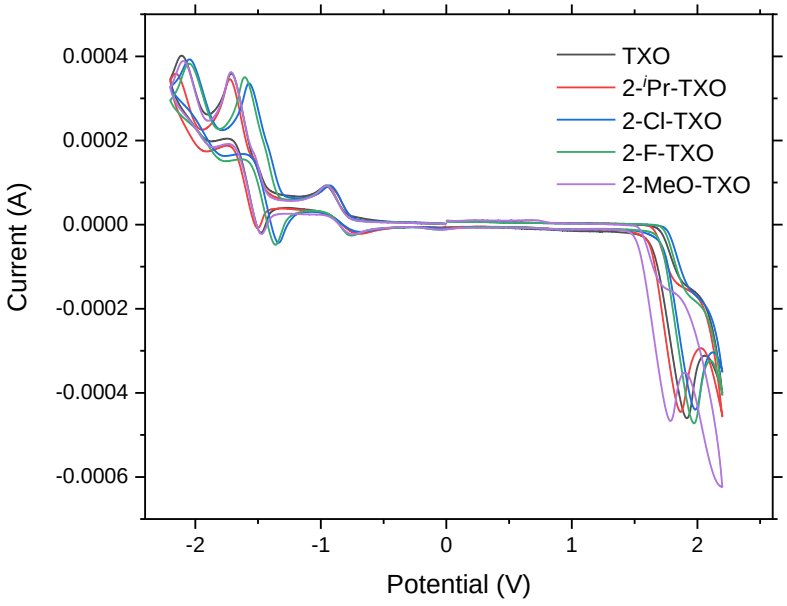

Figure S6. Cyclic voltammetry of 2-substituted thioxanthones in acetone (c = 3.3 mM).

Determination of redox potentials of TXOs at excited state

The excited state redox potentials of thioxanthones were calculated through the equations below using the ground state potentials above and the calculated triplet energy in this study (see page S69, Table S13).

$E_{p/2}$ (PC*/PC$^-$) = $E_{p/2}$ (PC/PC$^-$) + E_T

$E_{p/2}$ (PC$^+$/PC*) = $E_{p/2}$ (PC$^+$/PC) – E_T

Table S6. Summary of reduction potentials for 2-substituted thioxanthones at ground and triplet states

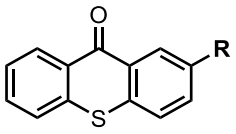

entry	R	E_T/eV	$E_{p/2}$(PC/PC$^-$)	$E_{p/2}$(PC$^+$/PC)	$E_{p/2}$(PC$^+$/PC*)	$E_{p/2}$(PC*/PC$^-$)
1	**2-H (TXO)**	2.80	–1.60 V	1.81 V	–0.99 V	1.20 V
2	**2-^{i}Pr**	2.75	–1.62 V	1.75 V	–1.00 V	1.13 V
3	**2-Cl**	2.71	–1.46 V	1.87 V	–0.84 V	1.25 V
4	**2-F**	2.68	–1.60 V	1.84 V	–0.84 V	1.08 V
5	**2-MeO**	2.55	–1.72 V	1.65 V	–0.90 V	0.83 V

Relationship between reaction rates and triplet energy or redox potentials

Kinetic reaction profile of reactant 1 with 1.0 mol% 2-substituted thioxanthones.

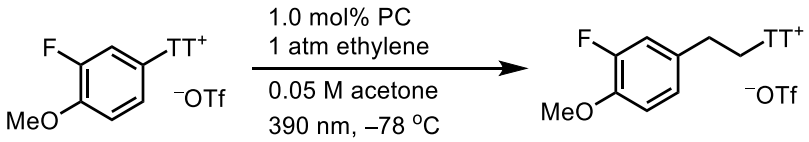

1 **2**

To a 5-mL Schlenk tube containing a Teflon-coated magnetic stirring bar were added arylthianthrenium salt **1** (50 mg, 0.10 mmol, 1.0 equiv) and 2-substituted thioxanthone in acetone (c = 0.50 mM, 2.0 mL, 1.0 μmol, 1.0 mol%). The tube was sealed with a rubber septum and immersed in a dry ice/acetone bath at −78°C. A balloon filled with ethylene gas was connected to a long needle, which was inserted to the tube through the rubber septum. Roughly 100 ml of ethylene gas was bubbled through the solution over a time period of approximately 5 minutes, and excess gas was released through the side arm, all while avoiding exposure to light. The valve of the side arm was closed, and the needle was withdrawn from the solution but remained in the headspace of the vessel. The reaction mixture was then subjected to irradiation by one Kessil PR160-390 nm LED with 100% intensity (40 W, ~6 cm away), all while maintaining the bath temperature at −78°C. After

being irradiated for indicated time, the light was turned off, and approximately 0.2 mL reaction mixture was extracted, diluted with 0.4 mL $CDCl_3$, and analyzed by ^{19}F NMR with triflate counterion as internal standard. The change in concentration of starting material **1** was determined as follow:

Table S7. Concentration of $ArTT^+$ **1** as a function of time with different 2-substituted thioxanthone as photosensitizer

Time (s)	TXO (M)	Time (s)	2-*i*Pr-TXO (M)	Time (s)	2-Cl-TXO (M)	2-F-TXO (M)	2-OMe-TXO (M)
0	0.050	**0**	0.050	**0**	0.050	0.050	0.050
10	0.045	**30**	0.046	**60**	0.045	0.049	0.050
20	0.038	**60**	0.041	**120**	0.037	0.048	0.050
30	0.033	**90**	0.036	**180**	0.027	0.043	0.050
40	0.028	**120**	0.031	**240**	0.017	0.039	0.049
50	0.023	**150**	0.024	**300**	0.012	0.034	0.049

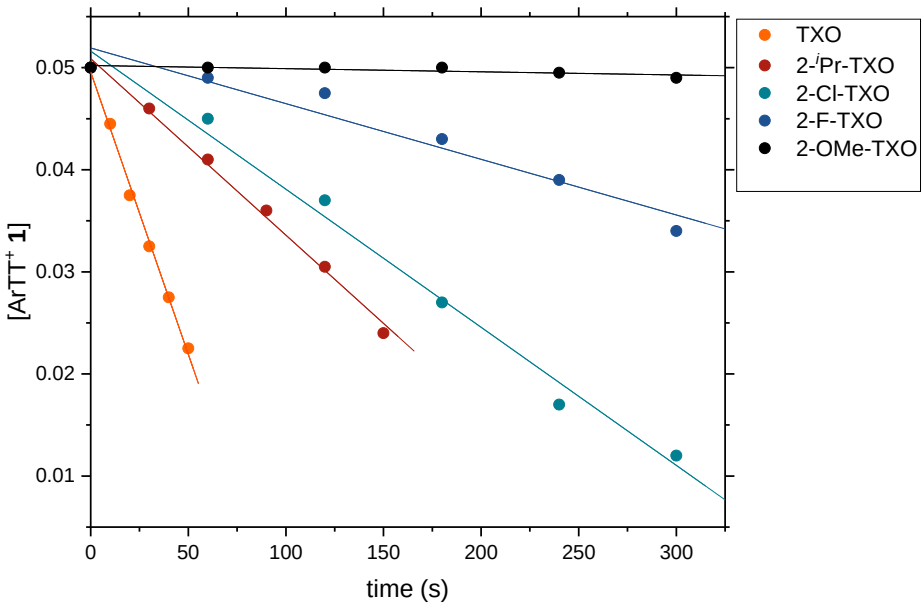

Figure S7. Concentration of $ArTT^+$ **1** as a function of time with different 2-substituted thioxanthone as photosensitizer

Relationship between reaction rates and triplet energy or redox potentials

From the kinetic reaction profile, it was observed that $ArTT^+$ **1** exhibited zero-order kinetics. The initial rate can be directly determined by the slope of the kinetic curve.

Table S8. Summary of initial rates with different 2-substituted thioxanthone as photosensitizer

PC	Initial rate ($mol \cdot L^{-1} \cdot s^{-1}$)
TXO	5.53×10^{-4}
2-*i*Pr-TXO	1.73×10^{-4}
2-Cl-TXO	1.35×10^{-4}
2-F-TXO	0.55×10^{-4}
2-OMe-TXO	0.03×10^{-4}

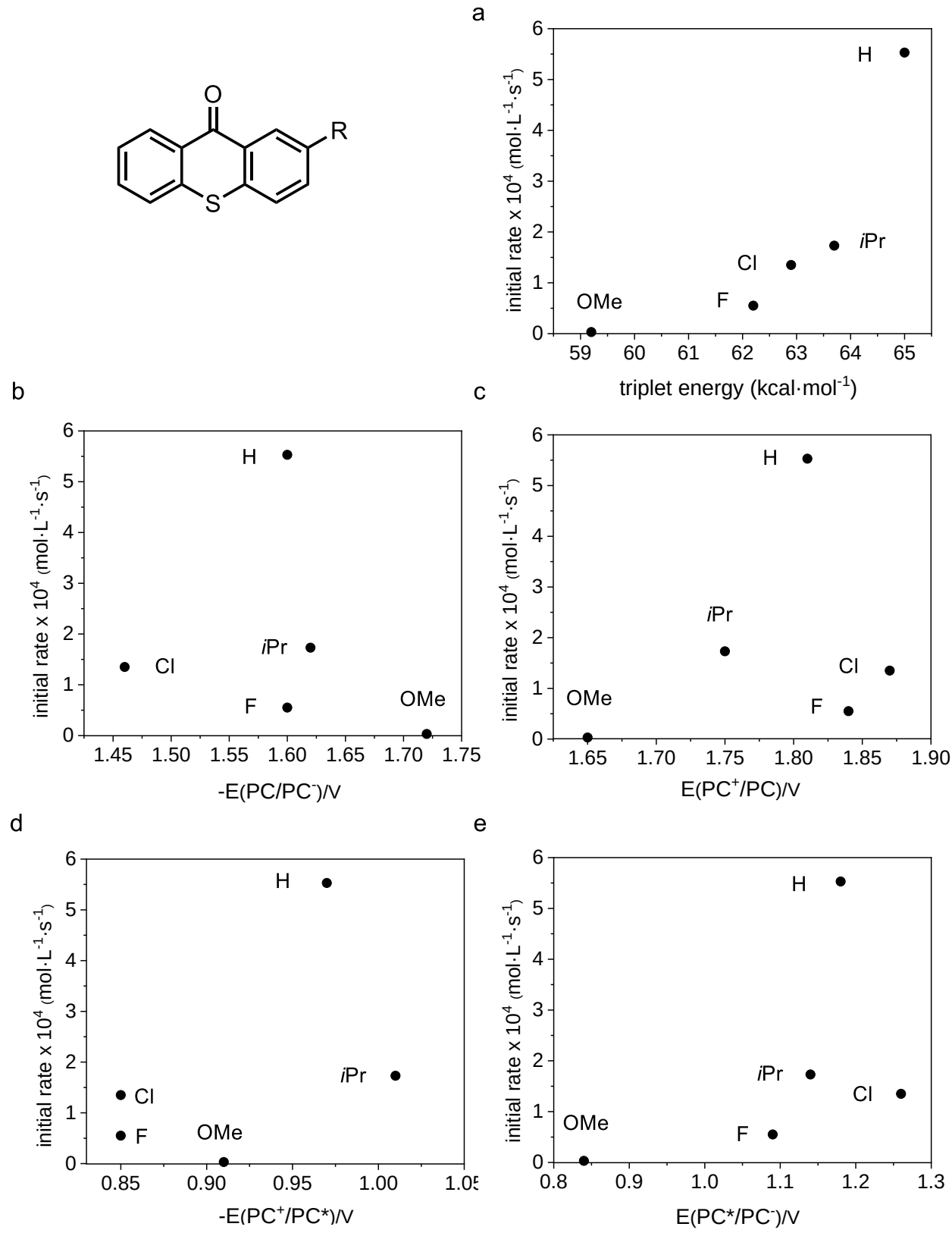

Figure S8. Correlation analysis: reaction rates vs triplet energy or redox potentials; Data sourced from Table S6 and S8.

Quantum yield measurement

Determination of the light intensity of Kessil PR160-390nm LEDs

Standard ferrioxalate actinometry[14,15] was used to determine the radiant flux of Kessil PR160-390 nm LED with 25% intensity. A solution of ferrioxalate (0.15 M) was prepared by dissolving potassium ferrioxalate trihydrate (737 mg, 1.50 mmol) in 10.0 mL of 0.20 M aqueous H_2SO_4. A buffered solution of 1,10-phenanthroline (0.15 M) was prepared by dissolving NaOAc (1.23 g, 15.0 mmol) and 1,10-phenanthroline (541 mg, 3.00 mmol) in 20 mL of 0.20 M aqueous H_2SO_4.

To a 4-mL borosilicate vial equipped with a stir bar was added 1.0 mL of the ferrioxalate solution. The vial was sealed with a septum-cap and placed 6 cm away from one Kessil PR160-390 nm LED with 25% intensity (10 W). After being irradiated for 10 seconds, 2.0 mL of the buffered solution was added. The resulting mixture was then allowed to rest for 1 hour to allow the formed ferrous ions to react completely with 1,10-phenanthroline. The mixture was diluted to 14.0 mL with 0.20 M aqueous sulfuric acid. An aliquot (100 µL) of the resulting solution was diluted with 3.0 mL of 0.20 M aqueous sulfuric acid, and the absorbance in a cuvette (l = 1.0 cm) at 510 nm was measured by UV-Vis spectrometer. The above procedure was repeated with different irradiation time, and the average absorption was used for the calculation of photon flux. A non-irradiated sample was also prepared and the absorbance at 510 nm was measured.

Table S9. Calculation of radiant flux

Irradiation time (s)	Absorbance	ΔA	mol Fe^{2+}(mol)	photo flux (Einstein/s)
non-irradiation	0.027	-	-	-
10	0.398	0.371	1.40 x 10^{-5}	1.24 x 10^{-6}
20	0.818	0.791	2.99 x 10^{-5}	1.32 x 10^{-6}
30	1.198	1.171	4.43 x 10^{-5}	1.31 x 10^{-6}

The photon flux was calculated as follows:

$$\text{mol } Fe^{2+} = \frac{V \times \Delta A\ (510\ nm)}{l \times \varepsilon}$$

where V is the total volume (0.42 L) of the solution that was analyzed, ΔA is the difference between the average absorption of irradiated and non-irradiated solutions at 510 nm, l is the path length (1.00 cm), and ε is the molar absorptivity of the ferrioxalate actinometer at 510 nm (11,100 L mol^{-1} cm^{-1}).

$$\text{photon flux} = \frac{\text{mol } Fe^{2+}}{\Phi \times t \times f}$$

where Φ is the quantum yield for the ferrioxalate actinometer (approximated as 1.13[16], which was reported for a 0.15 M solution at λ = 392 nm), t is the irradiation time, and f is the fraction of light absorbed at λ = 390 nm by the ferrioxalate actinometer. This value is calculated using the following equation where A(390 nm) is the measured absorbance of the 0.15 M solution of potassium ferrioxalate at 390 nm. An absorption spectrum gave

an A(390) value of >3, indicating the fraction of absorbed light (f) is >0.999.

$$f = 1 - 10^{-A(390\ nm)}$$

The average photon flux was thus calculated to be 1.29 × 10^{-6} einsteins s^{-1}

Determination of quantum yield

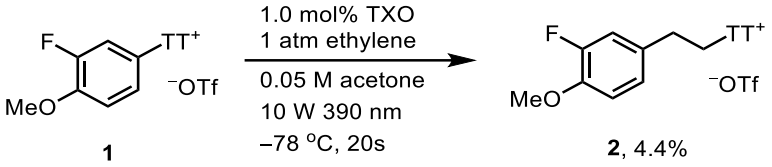

To a 5-mL Schlenk tube containing a Teflon-coated magnetic stirring bar were added arylthianthrenium salt **1** (25 mg, 0.050 mmol, 1.0 equiv) and thioxanthone in acetone (c = 0.50 mM, 1.0 mL, 0.50 μmol, 1.0 mol%). The tube was sealed with a rubber septum and immersed in a dry ice/acetone bath at −78°C. A balloon filled with ethylene gas was connected to a long needle, which was inserted to the tube through the rubber septum. Roughly 100 ml of ethylene gas was bubbled through the solution over a time period of approximately 5 minutes, and excess gas was released through the side arm, all while avoiding exposure to light. The valve of the side arm was closed, and the needle was withdrawn from the solution but remained in the headspace of the vessel. The reaction mixture was then subjected to irradiation by one Kessil PR160-390 nm LED with 25% intensity (10 W, ~6 cm away), all while maintaining the bath temperature at −78°C. After being irradiated for 20 s, the reaction mixture was warmed to room temperature. 1,3,5-Trimethoxybenzene (50 μL, 0.050 mmol, 1.0 M in MeCN, 1.0 equiv) was added as an internal standard. The ^{1}H NMR yield of product **2** was determined to be 4.4%.

The quantum yield was calculated as follows:

$$\Phi = \frac{\text{mol product}}{\text{photon flux} \times t \times f}$$

where mol product is the product **2** formation rate (1.1 × 10^{-7} mol/s), photon flux is determined by above ferrioxalate actinometry (1.29 × 10^{-6} einsteins s^{-1}), and f is the fraction of light absorbed by the reaction mixture at 390 nm. This value is calculated using the following equation where *A*(390 nm) is the absorption of the non-irradiated reaction mixture (1.29) at 390 nm. The fraction of light absorbed at 390 nm was calculated:

$$f = 1 - 10^{-A(390\ nm)} = 1 - 10^{-1.29} = 0.949$$

Thus, the quantum yield was calculated as Φ = 0.1.

Reaction in the presence of triplet quencher

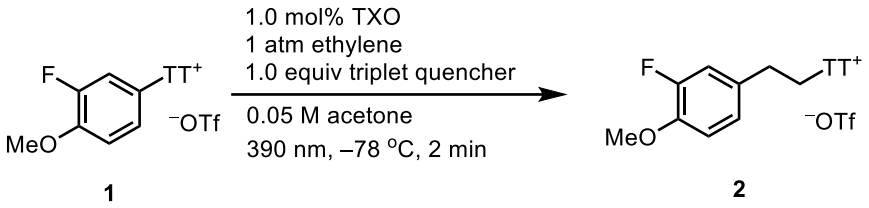

To a 5-mL Schlenk tube containing a Teflon-coated magnetic stirring bar were added arylthianthrenium salt **1** (25 mg, 0.050 mmol, 1.0 equiv)), triplet quencher (0.050 mmol, 1.0 equiv), and thioxanthone in acetone (c = 0.50 mM, 1.0 mL, 0.50 μmol, 1.0 mol%). The tube was sealed with a rubber septum and immersed in a dry ice/acetone bath at −78°C. A balloon filled with ethylene gas was connected to a long needle, which was inserted to the tube through the rubber septum. Roughly 100 ml of ethylene gas was bubbled through the solution over a time period of approximately 5 minutes, and excess gas was released through the side arm, all while avoiding exposure to light. The valve of the side arm was closed, and the needle was withdrawn from the solution but remained in the headspace of the vessel. The reaction mixture was then subjected to irradiation by one Kessil PR160-390 nm LED with 25% intensity (10 W, ~6 cm away), all while maintaining the bath temperature at −78°C. The reaction mixture was irradiated for 2 minutes, all while maintaining the temperature at −78°C. Subsequently, 1,3,5-trimethoxybenzene (50 μL, 0.050 mmol, 1.0 M in MeCN, 1.0 equiv) was added as internal standard. The reaction mixture was concentrated and analyzed by ^{1}H NMR spectroscopy.

Table S10. Reaction results in the presence of triplet quenchers

triplet quencher	structure	E_T (kcal•mol^{-1})	conv. (%)	yield (%)
anthracene	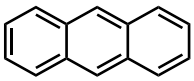	42.6	29	8
cyclooctatetraene		51.3	<2	<2

Radical scrambling experiment

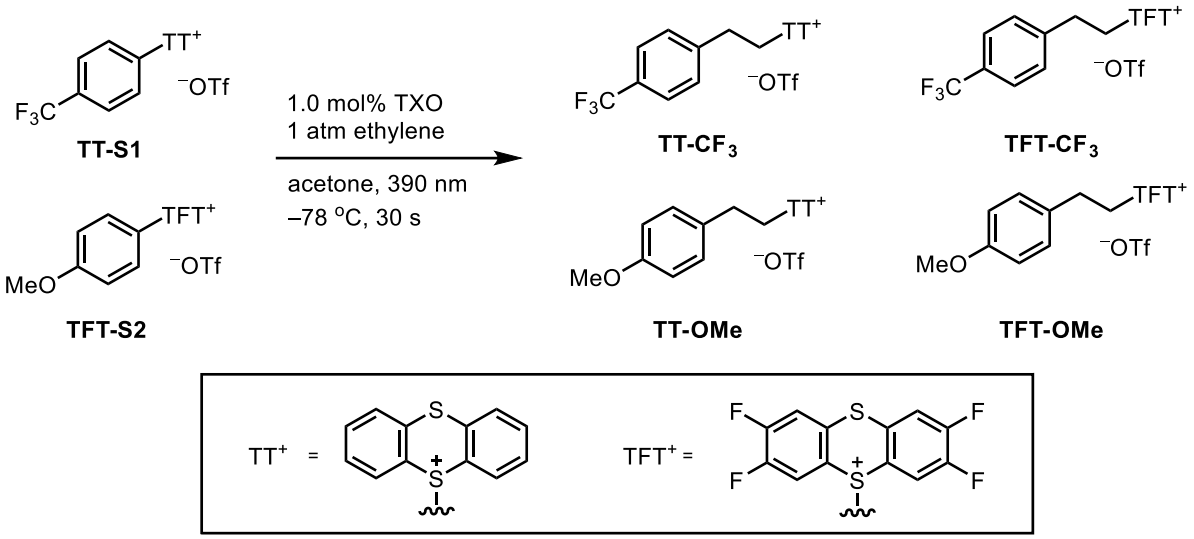

To a 5-mL Schlenk tube containing a Teflon-coated magnetic stirring bar were added **TT-S1** (26 mg, 0.050 mmol, 1.0 equiv), **TFT-S2** (27 mg, 0.050 mmol, 1.0 equiv), and thioxanthone in acetone (c = 0.50 mM, 2.0 mL, 1.0 μmol, 1.0 mol%). The tube was sealed with a rubber septum and immersed in a dry ice/acetone bath at −78°C. A balloon filled with ethylene gas was connected to a long needle, which was inserted to the tube through the rubber septum. Roughly 100 ml of ethylene gas was bubbled through the solution over a time period of approximately 5 minutes, and excess gas was released through the side arm, all while avoiding exposure to light. The valve of the side arm was closed, and the needle was withdrawn from the solution but remained in the headspace of the vessel. The reaction mixture was then subjected to irradiation by one Kessil PR160-390 nm LED with 100% intensity (40 W, ~6 cm away) for 30 seconds, all while maintaining the bath temperature at −78°C. Then the reaction mixtures was warmed to room temperature and measured by high-resolution mass spectrometry (HRMS). All four arylethyl (tetrafluoro)thianthrenium salts were detected.

HRMS-ESIpos (m/z) of **TT-CF$_3$** calc'd for $C_{21}H_{16}F_3S_2$ $[M–OTf]^+$, 389.0640; found, 389.0644; deviation: –1.0 ppm.

HRMS-ESIpos (m/z) of **TT-OMe** calc'd for $C_{21}H_{19}OS_2$ $[M–OTf]^+$, 351.0872; found, 351.0877; deviation: –1.4 ppm.

HRMS-ESIpos (m/z) of **TFT-CF$_3$** calc'd for $C_{21}H_{12}F_7S_2$ $[M–OTf]^+$, 461.0263; found, 461.0265; deviation: –0.4 ppm.

HRMS-ESIpos (m/z) of **TFT-OMe** calc'd for $C_{21}H_{15}F_4OS_2$ $[M–OTf]^+$, 423.0495; found, 423.0495; deviation: +0.1 ppm.

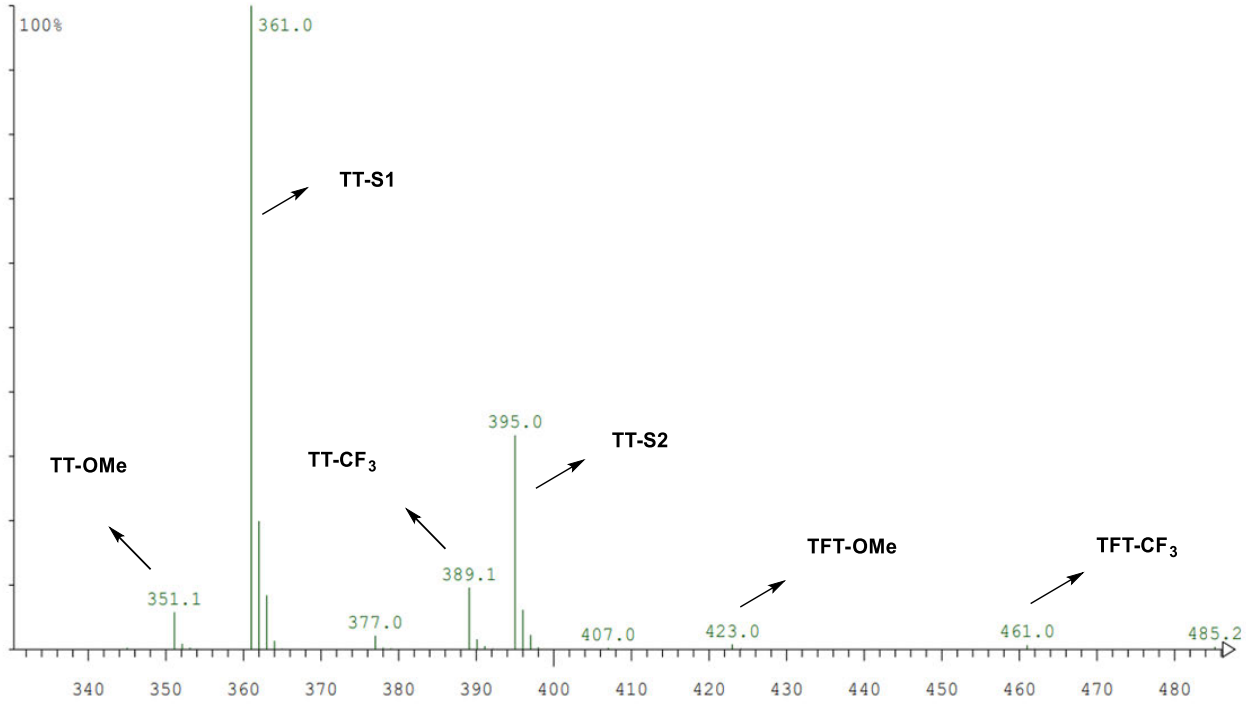

Figure S9. MS spectrum of reaction mixture.

Hammett plot

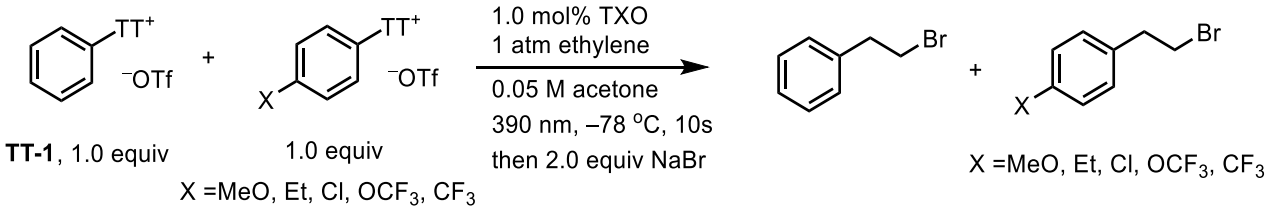

To a 5-mL Schlenk tube containing a Teflon-coated magnetic stirring bar were added arylthianthrenium salt **TT-1** (11.1 mg, 0.025 mmol, 1.00 equiv), *para*-substituted arylthianthrenium salt (0.025 mmol, 1.00 equiv), and thioxanthone (1.0 mL, 0.50 mM in acetone, 0.5 μmol, 1.0 mol%). The tube was sealed with a rubber septum and immersed in a dry ice/acetone bath at −78°C. A balloon filled with ethylene gas was connected to a long needle, which was inserted to the tube through the rubber septum. Roughly 100 ml of ethylene gas was bubbled through the solution over a time period of approximately 5 minutes, and excess gas was released through the side arm, all while avoiding exposure to light. The valve of the side arm was closed, and the needle was withdrawn from the solution but remained in the headspace of the vessel. The reaction mixture was then subjected to irradiation by one Kessil PR160-390 nm LED with 100% intensity (40 W, ~6 cm away) for 10 seconds to have a conversion of 10–30%. Subsequently, internal standard 1,3,5-trimethoxybenzene (50 μL, 0.050 mmol, 1.0 M in MeCN, 1.0 equiv) and tetrabutylammonium bromide (16 mg, 0.050 mmol, 2.0 equiv) were added and the resulting mixture was stirred for 10 minutes. The solution was concentrated and analyzed by ^{1}H NMR spectroscopy. The bromination process exhibits notable cleanliness, facilitating determination of product ratios through integration of characteristic proton signals at the benzylic

position of the arylethyl bromides. The values of $\log(k_X/k_H)$ were plotted versus the σ.

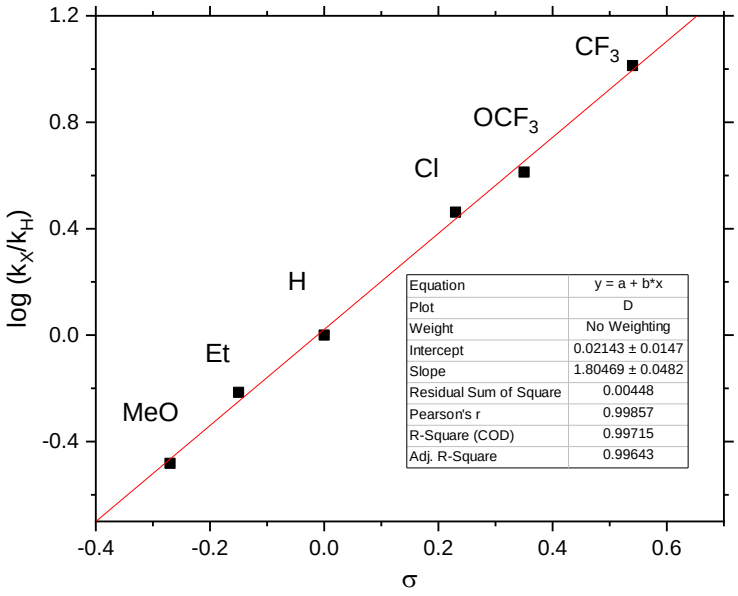

Figure S10. Hammett correlation using the σ-value of the para-substituent. $\rho = 1.8$, $R^2 = 0.99$.

DFT CALCULATIONS

Methods

Density Functional Theory (DFT) calculations were performed on the Max-Planck-Institut für Kohlenforschung computer cluster using the ORCA 5.0 program package (Version 5.0 Stable)[17]. Structural optimizations and frequency calculations were performed with the B3LYP functional[18] with D3 dispersion correction[19] and Becke-Johnson damping (BJ),[20] utilizing the def2/J auxiliary basis set[21] and the def2-TZVPP basis set[22] on all atoms. Tight SCF convergence and geometry optimization criterions were chosen. Frequency calculations at the same level had been performed to confirm each stationary point to be either a minimum or a transition structure. Solvent effects of acetone were taken into account using the conductor-like polarized continuum model (CPCM).[23] Time-dependent density functional theory (TD-DFT) was used to calculate the triplet energies for 2-substituted thioxanthone derivatives.[2,24] Molecular orbital energies and pictures were generated through the LargePrint command. Input files were created using Avogadro 1.2[25] and images were generated using Chemcraft 1.8.[26]

Comparison with reported data

Before evaluating the triplet energies of the molecules, we compared the structural properties of the structure obtained by DFT calculations with the reference XRAY structure.[27] As shown in Table S11, the structure (without counteranion) obtained from DFT calculations and the XRAY structure of the aryl thianthrenium cation as a triflate salt **1** shows comparable bond lengths, bond angles, and overall flagship-confirmation.

Table S11. Exemplary bond length and angle comparison between XRAY structure of $PhTT^+$ and DFT structure at CPCM(acetone)-B3LYP-D3BJ/def2-TZVPP level of theory.

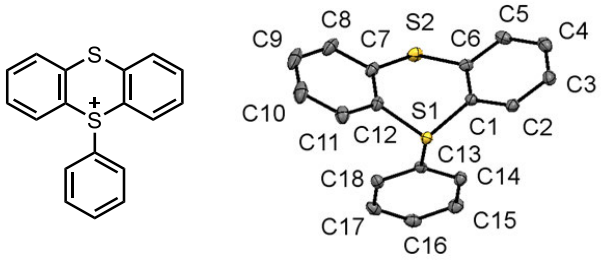

Bond length (Å) in	XRAY structure	DFT structure	Difference
S(1)–C(1)	1.764	1.764	0.000
S(1)–C(13)	1.805	1.805	0.000
S(2)–C(6)	1.755	1.762	0.007
Bond angle (°) in	**XRAY structure**	**DFT structure**	**Difference**
C(12)–S(1)–C(1)	103.05	103.05	0.00

C(6)–S(2)–C(7)	103.22	102.49	-0.73
S(2)–C(7)–C(12)	123.94	123.60	-0.34
S(1)–C(12)–C(7)	121.12	120.31	-0.81
S(1)–C(13)–C(14)	118.69	118.83	0.14
C(12)–S(1)–C(13)	102.99	103.32	0.33

To ensure calculations were carried out with a high enough computational level in replicating triplet state molecules, we conducted further evaluations of the triplet energies of known compounds.[28] As illustrated in Table S12 and Figure S11, the experimental values align closely with computational estimations, demonstrating both qualitative and quantitative agreement.

Triplet energies were determined by calculating the energy difference between the optimized singlet ground state structure and the first excited optimized triplet state structure.

Table S12. Comparative analysis: experimental triplet energies vs. computed values for arenes and biphenyl halides at CPCM(acetone)-B3LYP-D3BJ/def2-TZVPP level of theory.

Compounds	**Experimental E_T[18] (kcal•mol^{-1})**	**DFT calculated E_T (kcal•mol^{-1})**	**Difference (kcal•mol^{-1})**
benzene	84.4	82.4	-2.0
anisole	80.8	77.5	-3.3
biphenyl	65.5	64.5	-1.0
biphenyl chloride	63.6	62.9	-0.7
biphenyl bromide	n.a.	62.9	-
biphenyl iodide	62.9	62.4	-0.5

n.a. not available

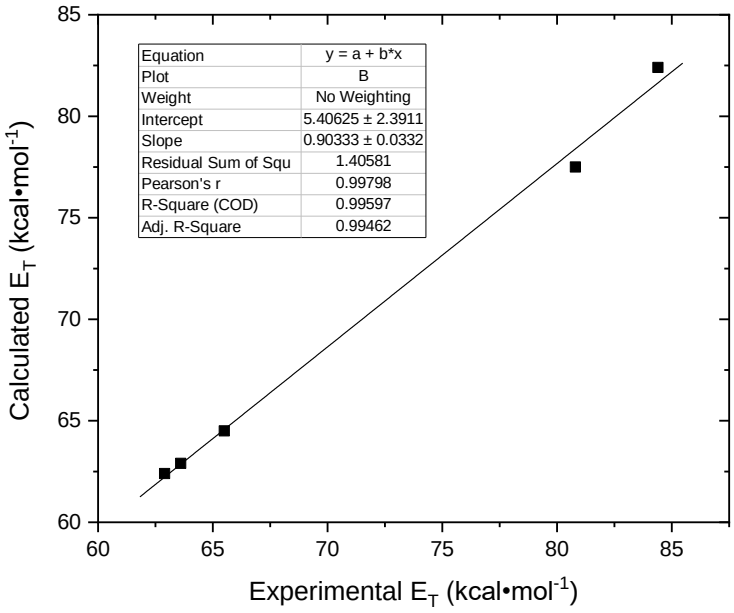

Figure S11. Correlation analysis: experimental triplet energies vs computed values

The triplet energies of TXOs were determined through time-dependent density functional theory (TD-DFT) calculations.[2,24] As detailed in Table S13, our computational estimations exhibited close agreement with both Booker-Milburn's experimental data and their computational values.[2]

Table S13. Comparison analysis: experimental triplet energies vs computed values for TXOs at CPCM(acetone)-B3LYP-D3BJ/def2-TZVPP level of theory.

Substituted TXO	Reported experimental E_T (kcal•mol^{-1})[2]	Reported calculated E_T (kcal•mol^{-1})[2]	Current calculated E_T (kcal•mol^{-1})
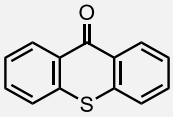	65.5	65.5	65.0
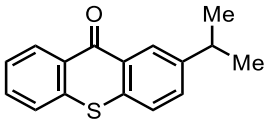	63.5	64.5	63.7
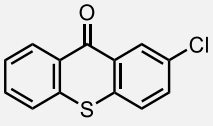	n.a.	n.a.	62.9
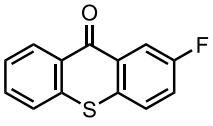	62.4	62.9	62.2

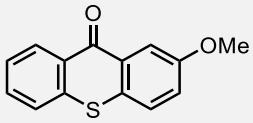	57.8	60.2	59.2

n.a. not available

Visualization of frontier molecular orbitals and triplet energy of arylpseudohalides

As indicated in Table S14, in the calculated triplet state of $PhTT^+$, the geometry of the TT framework changes from folded to near-planar, indicating an altered electron configuration of TT. Both the HOMO and LUMO in the ground state and the α-HOMO and α-HOMO-1 in the triplet state of $PhTT^+$ are predominantly situated on the TT framework rather than on the aryl ring. Introduction of an electron-donating group to the phenyl ring causes the HOMO and α-HOMO-1 to shift from TT to the aryl group, while maintaining a near-planar geometry of TT in the triplet state. Conversely, introduction of an electron-withdrawing group to the exocyclic phenyl ring leads to the LUMO and α-HOMO shifting from TT to the aryl group, resulting in a folded geometry of TT in the triplet state.

Table S14. Visualization of frontier molecular orbitals and triplet energy of arylpseudohalides

ArX (E_T/kcal•mol^{-1})	**Ground state**		**Triplet state**	
	HOMO	LUMO	α-HOMO-1	α-HOMO
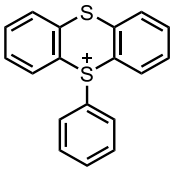 (**65.5**)	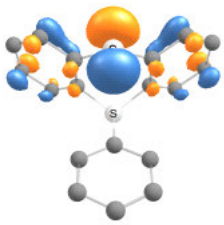	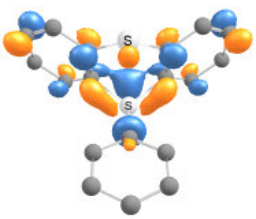	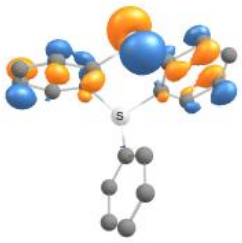	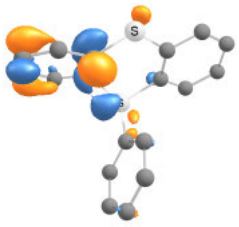
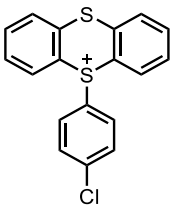 (**65.2**)	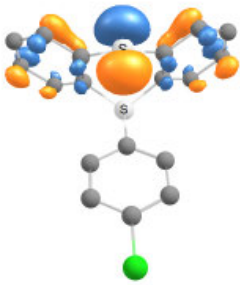	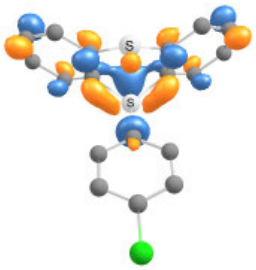	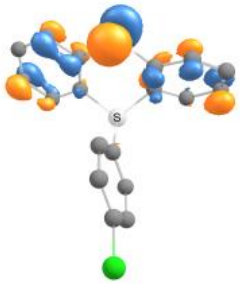	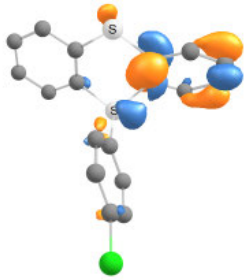

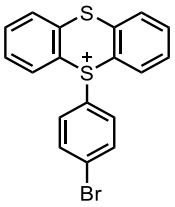

(**65.3**)

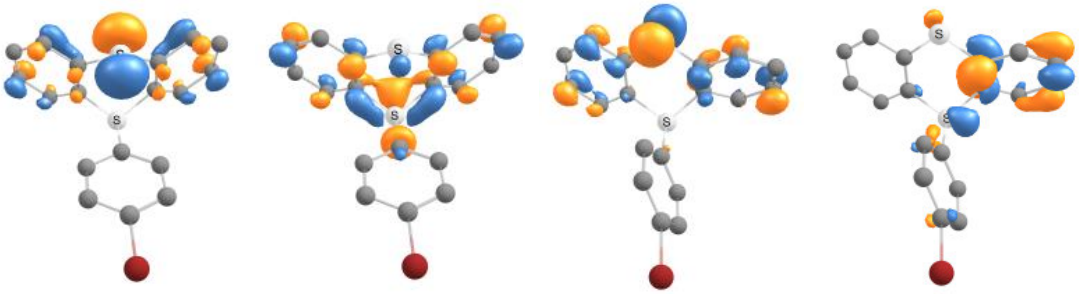

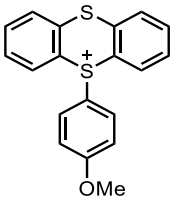

(**65.6**)

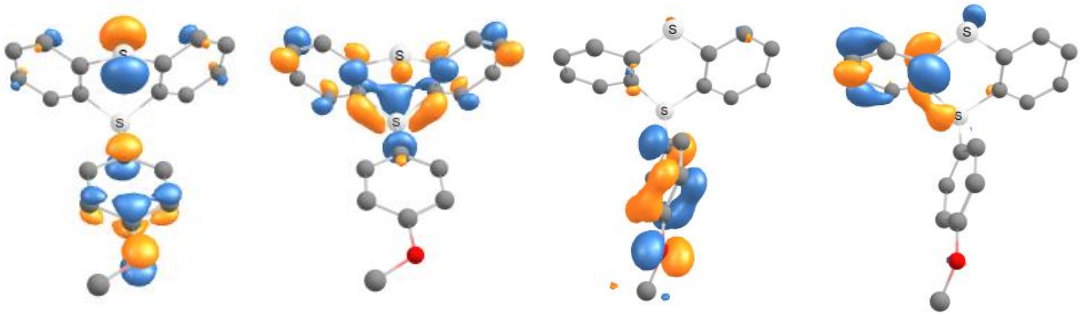

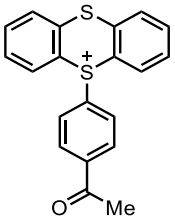

(**63.3**)

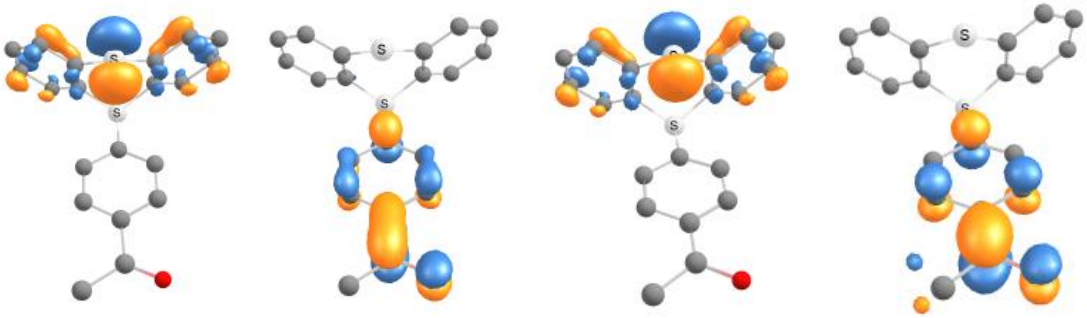

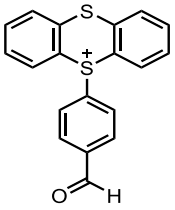

(**62.0**)

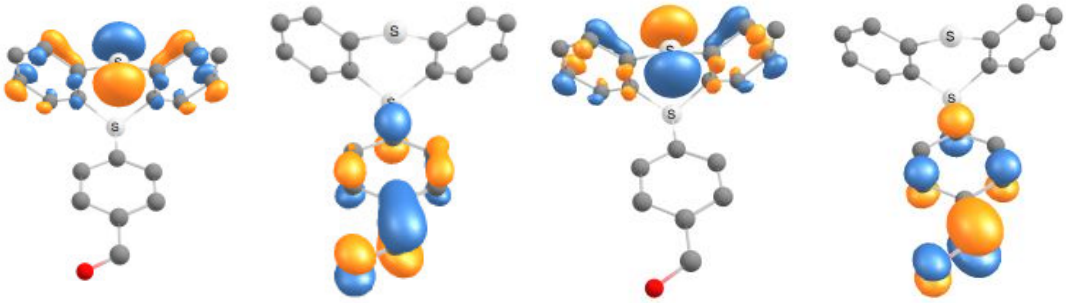

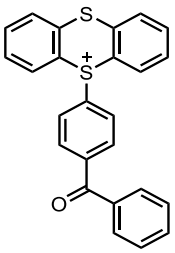

(**60.3**)

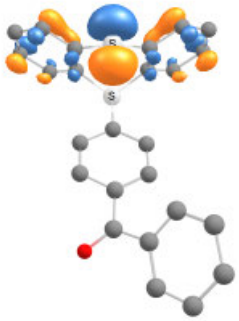
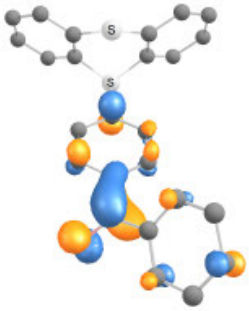
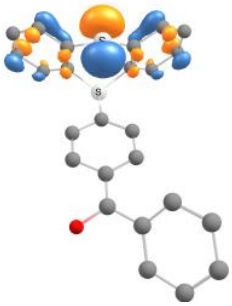
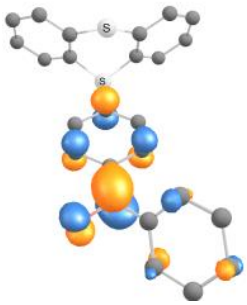

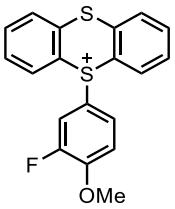

(**65.6**)

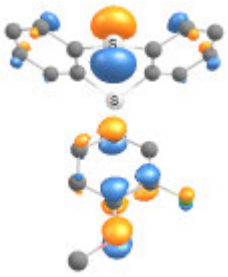
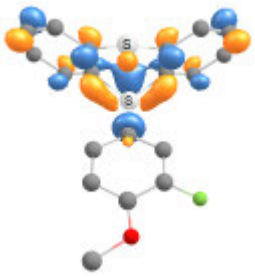
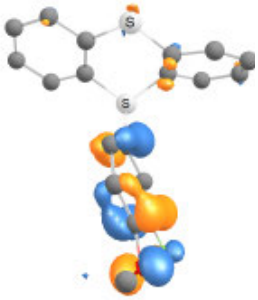
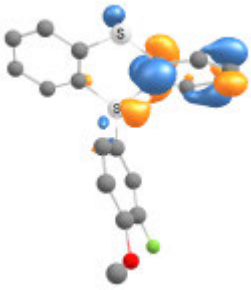

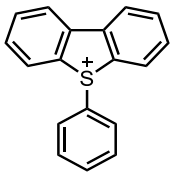

(61.7)

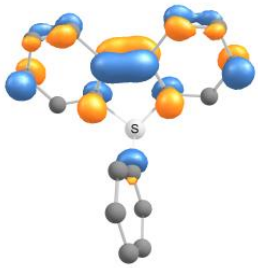
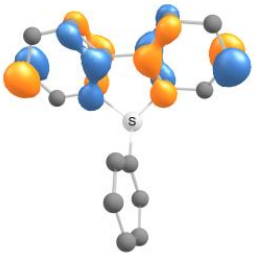

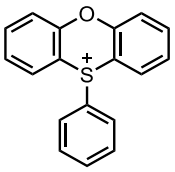

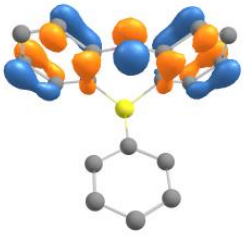
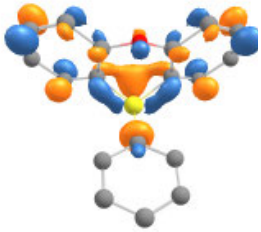

Exocyclic C–S bond cleaved during structure optimization

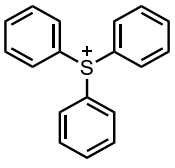

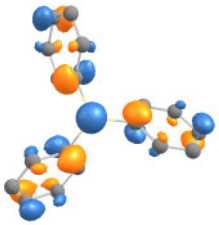
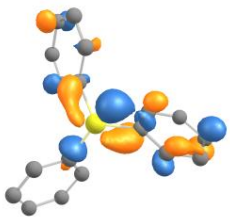

C–S bond cleaved during structure optimization

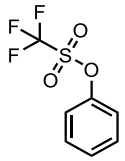			O–S single bond cleaved during structure optimization
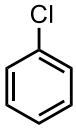		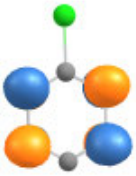	Triplet structure optimization failed
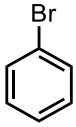			Triplet structure optimization failed
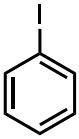			C–I single bond cleaved during structure optimization
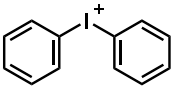	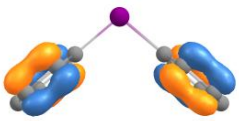	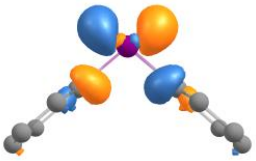	Triplet structure optimization failed
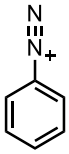 **(61.8)**	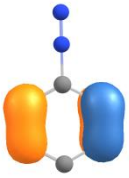		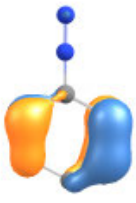

HOMO/LUMO energy of arylpseudohalides

Table S15. HOMO/LUMO energy of arylpseudohalides at ground state

p-Y-C_6H_4X	HOMO/eV	LUMO/eV	HOMO-LUMO gap
C_6H_6	-6.97	-0.31	6.66
C_6H_5Cl	-6.85	-0.68	6.17
C_6H_5Br	-6.79	-0.72	6.07
$C_6H_5TT^+$	-9.72	-5.11	4.61
p-Cl-C_6H_4Cl	-6.80	-1.03	5.77
p-Cl-C_6H_4Br	-6.77	-1.06	5.71
p-Cl-$C_6H_4TT^+$	-9.77	-5.19	4.58
p-Br-C_6H_4Br	-6.75	-1.08	5.67
p-Br-$C_6H_4TT^+$	-9.76	-5.19	4.57
C_6H_5OMe	-6.11	-0.30	5.81
p-MeO-C_6H_4Cl	-6.14	-0.66	5.48
p-MeO-C_6H_4Br	-6.15	-0.70	5.45
p-MeO-$C_6H_4TT^+$	-9.43	-4.97	4.46
C_6H_5CHO	-7.18	-2.01	5.17
p-CHO-C_6H_4Cl	-7.29	-2.21	5.08
p-CHO-C_6H_4Br	-7.22	-2.25	4.97
p-CHO-$C_6H_4TT^+$	-9.86	-5.38	4.48
C_6H_5COMe	-6.97	-1.76	5.21
p-Ac-C_6H_4Cl	-7.13	-1.97	5.16
p-Ac-C_6H_4Br	-7.08	-2.00	5.08
p-Ac-$C_6H_4TT^+$	-9.68	-5.21	4.47
C_6H_5COPh	-6.86	-1.94	4.92
p-PhCO-C_6H_4Cl	-6.95	-2.11	4.84
p-PhCO-C_6H_4Br	-6.93	-2.13	4.80
p-PhCO-$C_6H_4TT^+$	-9.27	-5.13	4.14

PhOTf	-7.55	-1.01	6.54
PhI	-6.56	-0.97	5.59
PhDBT$^+$	-10.04	-5.37	4.67
PhPT$^+$	-10.11	-5.04	5.07
Ph$_3$S$^+$	-10.49	-4.96	5.53
Ph$_2$I$^+$	-11.03	-5.96	5.07
PhN$_2^+$	-12.56	-8.02	4.54

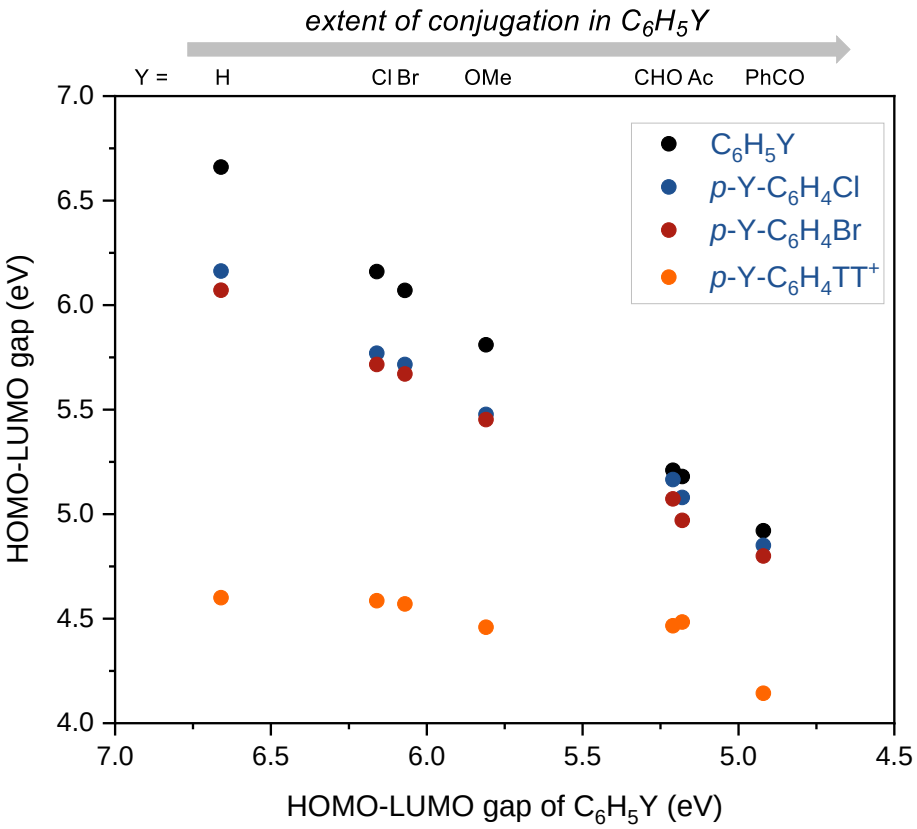

Figure S12. Relationship between HOMO-LUMO gap of aryl(pseudo)halides *p*-Y-C$_6$H$_4$X and conjugation extent of their parent C$_6$H$_5$Y.

Visualization of frontier molecular orbitals of TXO

As shown in Figure S13, the Dexter energy transfer process involves the simultaneous exchange of electrons between excited photosensitizer and substrate at ground state to accomplish targeted energy transfer. Specifically, the process entails one electron migrating from the *α*-HOMO of the excited photosensitizer to the LUMO of the ground state substrate, while the other electron travels in the reverse direction from the HOMO

of the ground state substrate to the *β*-LUMO of excited photosensitizer.

As depicted in Table S16, the *α*-HOMO and *β*-LUMO of the excited TXO predominantly situate on the carbon of the carbonyl group and the sulfur atom, respectively. The HOMO and LUMO orbitals of the $PhTT^+$ are primarily located on the neutral sulfur and positively charged sulfur atoms, respectively. The spatial alignment of frontier molecular orbitals coincides precisely between excited TXO and $PhTT^+$, given the analogous tricyclic fused ring system of TXO and TT, and the shared location of the middle ring for all frontier orbitals involved in energy transfer.

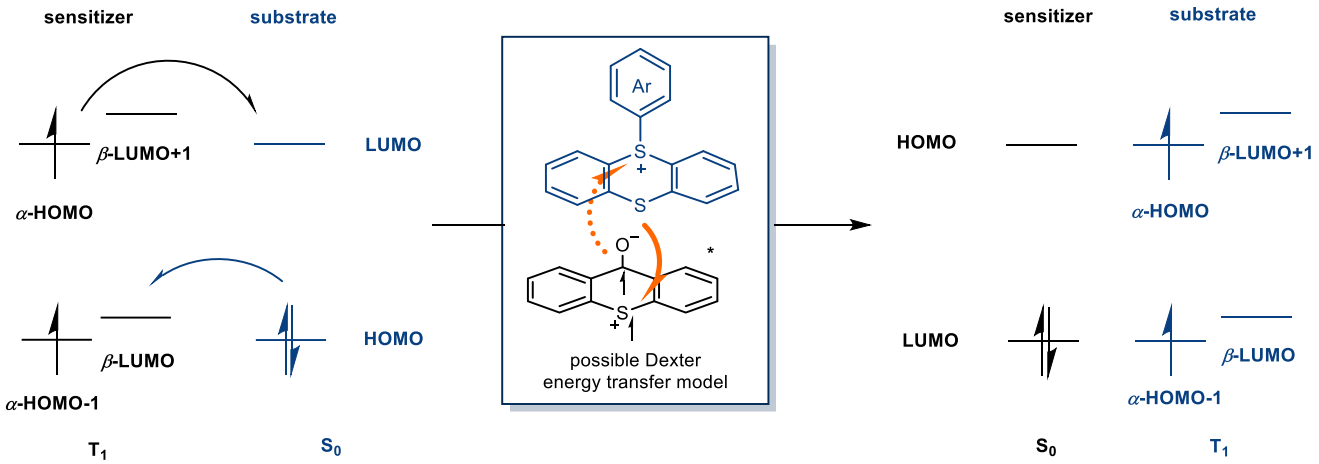

Figure S13. Dexter energy transfer mechanism

Table S16. Frontier molecular orbitals of TXO at ground and excited state

Ground state		Triplet state	
HOMO	**LUMO**	***α*-HOMO**	***β*-LUMO**
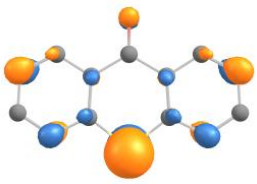	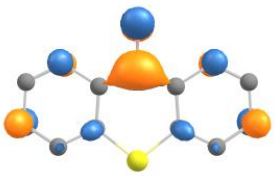		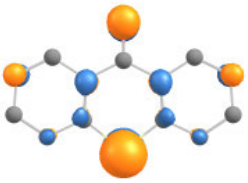

Bond dissociation energy of thianthrenium salts

Table S17. Thermodynamic quantities of the investigated species at the CPCM(acetone)-B3LYP-D3BJ/def2-SVP level of theory.

Compounds	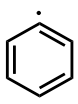	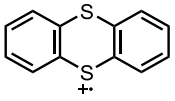	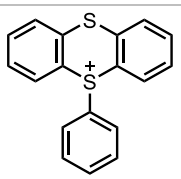

Enthalpy (Eh)	-231.17115	-1257.14139	-1488.41480
Compounds	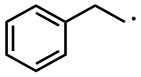	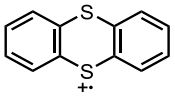	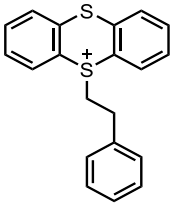
Enthalpy (Eh)	-309.65722	-1257.14139	-1566.88394

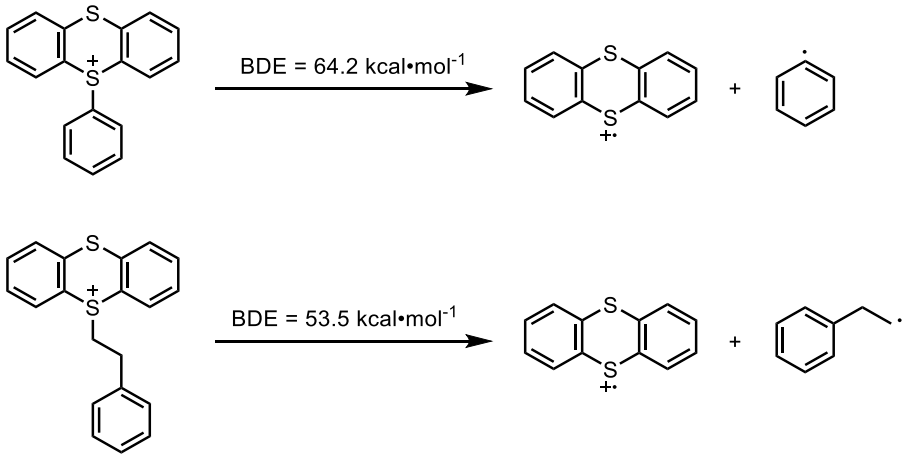

Figure S14. Bond dissociation energy of thianthrenium salts.

Cartesian coordinates of the optimized species

Calculated coordinates of arylthianthrenium salts in singlet and triplet states:

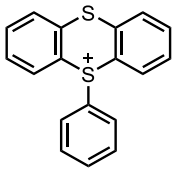

Singlet

C	-0.61901973001864	1.86702414888472	0.67159027587191
C	-1.74121615409666	1.09038548027600	0.37965365642808
C	-1.54518433070999	-0.15897086656888	-0.21409075152442
C	-0.25268872346613	-0.61181763931714	-0.49576094288486
C	0.85527096191198	0.18163658910933	-0.18389754926285
C	0.68167889900754	1.43427311980144	0.41027191032387
H	1.54547011874645	2.05759992099798	0.64665342436887
H	-2.74982988850184	1.44834932529598	0.59240550105264
H	-2.41037239656325	-0.77840019903097	-0.45932252569689
H	1.86434501935613	-0.17138702380617	-0.40654814325192
S	-0.85854350666715	3.44244152113066	1.54871826604638
C	-2.32809864729414	4.09875344926907	0.79232621582754
C	-2.32244765951945	4.45325646311945	-0.56802154850284

S	-0.88434439226467	4.35493989986711	-1.60030921761648
C	0.40976062422729	4.82360222354670	-0.48307100565460
C	0.42674092959400	4.47194423449813	0.87791242752364
C	1.48879068430548	5.56578469495544	-0.98490470491131
C	2.53520980843853	5.94320945879163	-0.14084599146262
C	2.51837723402622	5.61286706282438	1.21971700543613
C	1.45414848831169	4.87591393230809	1.73872231105292
C	-3.52699251759328	4.88629530528743	-1.14076237182539
C	-4.68546868888258	4.96522509395819	-0.36506744901566
C	-4.66444798248480	4.63999776110076	0.99650466336202
C	-3.47637694996611	4.20814011072015	1.58558756995408
H	-3.54573385671892	5.18209901898468	-2.19169750995397
H	-5.61395802987860	5.30752419169160	-0.82726776963762
H	-5.57125295157125	4.72316938510595	1.59852482896000
H	-3.44015057468403	3.94158461352076	2.64421308886804
H	1.49249651458008	5.86448165576782	-2.03529513981112
H	3.36629079185481	6.52313079085474	-0.54876536566455
H	3.33189980669448	5.92892984589224	1.87530933903372
H	1.42525204313194	4.60081470411879	2.79539880390659
H	-0.10806494330512	-1.58916827295607	-0.96113130133930

Triplet

C	-0.58149244425263	2.05242327400765	0.80944277540042
C	-0.94822893434918	1.77058447891708	-0.51312184470849
C	-0.59639836448928	0.53150036696863	-1.05207390492833
C	0.11286980823246	-0.39888644138491	-0.28494193065330
C	0.47489628064448	-0.09861917496941	1.03371353798926
C	0.13544514258532	1.13427399545038	1.59088727710043
H	0.41493870215851	1.37553554087837	2.61900431178718
H	-1.51608246196929	2.48553591784040	-1.10868965072839
H	-0.88292539230153	0.29181477838873	-2.07814259699240
H	1.01855510526060	-0.83050870596940	1.63514228644740
S	-0.84444487494945	3.66118768557004	1.55994609000995
C	-2.42974231845482	4.17484956979536	0.89641014118686
C	-2.58318007153747	4.89206671987683	-0.30645026570344
S	-1.31174884772567	5.42566691378554	-1.40583979256298
C	0.19070767718259	4.98443113138459	-0.69165320556313
C	0.28130299337519	4.80203764854567	0.75544942197644
C	1.38561650043599	5.19667988434686	-1.46007133975166
C	2.58227392495980	5.36592523849626	-0.81930376219176
C	2.63275292204930	5.34420419716004	0.62966534006860
C	1.51087647872487	5.03296045048550	1.39140112433447
C	-3.88557865740658	5.23124661720805	-0.72598230060407
C	-4.99457963295995	4.85295932869642	0.02710858232952
C	-4.82980400907370	4.13948639897280	1.21898446605582
C	-3.54384605568198	3.80447939121080	1.65194526495059
H	-4.01850158793353	5.79138093353993	-1.65509461950739

H	-5.99445527246728	5.12432731512266	-0.31721512061563
H	-5.69567470927417	3.85570401514745	1.81974813425659
H	-3.40187719990011	3.25608775759275	2.58647174545247
H	1.31609427170719	5.27163834452035	-2.54956455583444
H	3.49867675051249	5.53450743027386	-1.38607612521324
H	3.57875206050242	5.55917013870557	1.13218817282947
H	1.59453258299503	4.93478479457108	2.47834903901146
H	0.38180963340040	-1.36580593513601	-0.71488669562827

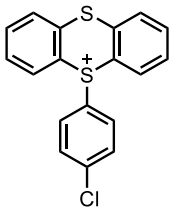

Singlet

C	-0.61984213166609	1.87149933482124	0.67782992263461
C	-1.73879190568175	1.09004767832519	0.38356260334583
C	-1.55231704600446	-0.15439695165193	-0.21637659103207
C	-0.25556673892450	-0.60076956973930	-0.50319444048355
C	0.85885336320513	0.18882810480276	-0.19091479102476
C	0.67858609986937	1.43437928198245	0.40890703716089
H	1.54625209464696	2.05294573456647	0.64403892274479
H	-2.74917768389177	1.44157746768630	0.59903282328703
H	-2.40909273845146	-0.78114051870132	-0.46718271899837
H	1.86167195270671	-0.17268051877347	-0.42218498912031
S	-0.85846345114841	3.44335377010757	1.55442931796939
C	-2.32780572287918	4.09716883396822	0.79499099311866
C	-2.32098333436562	4.44672853205071	-0.56673521850401
S	-0.88207039110592	4.34502859104786	-1.59768981956521
C	0.41144481002440	4.81729432334519	-0.48116473925660
C	0.42788374259416	4.47017516493420	0.88110566748502
C	1.49078433287645	5.55784193010848	-0.98469006794730
C	2.53648660569841	5.93831025372168	-0.14102478025966
C	2.51878505308544	5.61266420015018	1.22069602412237
C	1.45442302412865	4.87723330028416	1.74159300656378
C	-3.52532489041245	4.87703900581407	-1.14190994564378
C	-4.68434967761611	4.95844978531440	-0.36719960674722
C	-4.66422623449476	4.63850367532459	0.99567767100443
C	-3.47651222000365	4.20920784991428	1.58736890216861
H	-3.54354318946016	5.16895849735612	-2.19395649052204
H	-5.61266686315890	5.29856785647118	-0.83135543248395
H	-5.57151004754083	4.72375756974862	1.59668744168914
H	-3.44101023772987	3.94684428981899	2.64710088236085
H	1.49522625321246	5.85318037289893	-2.03604213450104
H	3.36773758608016	6.51704072980743	-0.55029187956373

H	3.33173318944091	5.93130163488188	1.87575734347660
H	1.42474270967852	4.60604945429156	2.79929117813460
Cl	-0.02874631271181	-2.14273966467867	-1.25282609161301

Triplet

C	-0.70450901798049	2.04398903619637	0.81232359020763
C	-1.18836507269430	0.95556017982814	1.55545270662019
C	-1.16582888116652	-0.31770182339274	0.99419587474533
C	-0.67350488040538	-0.49202521528170	-0.30783158665804
C	-0.19742388011504	0.59916814589132	-1.04780513166570
C	-0.21578334422955	1.87608364119533	-0.49111915956723
H	0.16991084605696	2.71807220853002	-1.06509413814059
H	-1.57085204429343	1.09794332588018	2.56881645042947
H	-1.52211533590295	-1.17982563673398	1.55948707159669
H	0.18721747407669	0.44080588980228	-2.05613688791830
S	-0.92751279644366	3.65357094009897	1.56077230877173
C	-2.26811848008689	4.45954599768863	0.67707125394271
C	-2.14006837032225	4.66734348759213	-0.76327582346737
S	-0.76984817206788	5.49942080553240	-1.38894375526773
C	0.52865272048933	5.31758999633194	-0.20940651667947
C	0.49986598761650	4.57783403273367	0.98923683130362
C	1.71625916786217	5.99485228865002	-0.55406848301128
C	2.83881258188546	5.92125901263415	0.26757378731647
C	2.79837337816854	5.18245489830945	1.45466140126957
C	1.62470405532204	4.51356723271671	1.81362997064314
C	-3.29442596106604	4.54745344254732	-1.60892485126949
C	-4.53016044825351	4.37474171407188	-1.04747575870279
C	-4.66495346985017	4.32952546781103	0.39500367931068
C	-3.55260842563639	4.33704051008132	1.23003989480288
H	-3.17793078736168	4.64646751969359	-2.69243253590568
H	-5.41927323771091	4.28708887178074	-1.67295696855960
H	-5.66350677771077	4.26887753168976	0.83431874579554
H	-3.67614854976243	4.21288815003207	2.31047837410323
H	1.75020857193137	6.57630897773803	-1.47904876903860
H	3.74974445655239	6.45024074212872	-0.01966486638831
H	3.67131975468402	5.13597391929409	2.10864137876503
H	1.57905487948925	3.94045272820245	2.74287580654849
Cl	-0.64857594107444	-2.07431801927443	-1.00706389393220

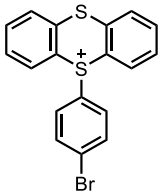

Singlet

C	-0.62047451846390	1.87931358307973	0.69123763643065

C	-1.73910237637356	1.10858977549565	0.36991540352871
C	-1.55028892651458	-0.13104713883040	-0.24107368122150
C	-0.25215284997117	-0.58226846396050	-0.51213496274733
C	0.86167387505533	0.19481417361168	-0.16905552739432
C	0.67935753170345	1.43532844939887	0.44214426201582
H	1.54736540257249	2.04525081498399	0.69824108807441
H	-2.75110965543999	1.46491113869037	0.56969239379052
H	-2.41149176530096	-0.74376496851667	-0.51141538048318
H	1.86869241168757	-0.16577675292714	-0.38367140243502
S	-0.85963540610871	3.45201777593913	1.56707498116855
C	-2.32944032712735	4.10296099027379	0.80618447730823
C	-2.32445597627372	4.44016847746860	-0.55864257639730
S	-0.88653853652401	4.32970653333977	-1.59000751099538
C	0.40877094249936	4.81056802662235	-0.47879157332005
C	0.42547800442747	4.47598615361599	0.88659972751165
C	1.48999323792486	5.54272740946355	-0.99000853136045
C	2.53674833437025	5.92900335156049	-0.15026928316726
C	2.51813801649445	5.61798380299466	1.21467750125658
C	1.45239832182215	4.89016791713263	1.74303872483645
C	-3.53014926278643	4.86320536353874	-1.13629569576229
C	-4.68811597306428	4.95177189112924	-0.36088532979182
C	-4.66557162840679	4.64618751093616	1.00527552806190
C	-3.47695964971872	4.22283425428141	1.59907085497355
H	-3.55058680869945	5.14272775233695	-2.19189045570829
H	-5.61749881022096	5.28544868698003	-0.82772960652326
H	-5.57174892436393	4.73652589537082	1.60708220972713
H	-3.43993977562520	3.97187044307429	2.66154220206125
H	1.49573506641225	5.82625515455262	-2.04471697218266
H	3.36959095346171	6.50066866985244	-0.56569381447728
H	3.33192908213089	5.94104540841226	1.86646658005423
H	1.42255322376401	4.63000758351718	2.80350145394732
Br	-0.00057323334254	-2.25293966341872	-1.35612272077959

Triplet

C	-0.69973644878446	2.04604974887153	0.81450272850507
C	-1.21189048123802	0.95977354672728	1.54144586848815
C	-1.20366803143025	-0.30950487658544	0.96930896811985
C	-0.69753502540186	-0.48220689799845	-0.32768531418465
C	-0.19109576882353	0.60624171053857	-1.05039082645172
C	-0.19538637737645	1.87940205421711	-0.48305530865419
H	0.21609415349705	2.71785361467634	-1.04464679370009
H	-1.60688125532470	1.10007281473026	2.55055441257347
H	-1.58417345834046	-1.16606337569369	1.52768872672556
H	0.20807942201535	0.45659314227587	-2.05473516280866
S	-0.91368397059342	3.65328188743027	1.56973777468404
C	-2.25709700391123	4.46187674367820	0.68534940821932
C	-2.13272059451486	4.64904205946274	-0.75743836648572

S	-0.75988511496579	5.46361144758827	-1.40005187139156
C	0.53557234962332	5.30848150729360	-0.21292212586348
C	0.50911865718419	4.58112307958434	0.99378152410089
C	1.71786648222345	5.99398581015516	-0.55909308158948
C	2.83707690738983	5.94154312948906	0.26887246682041
C	2.79872782751807	5.21588028109174	1.46394076077136
C	1.63031424424733	4.53811169155635	1.82417103341974
C	-3.28931137396954	4.51642300731427	-1.59835246671387
C	-4.52368402825594	4.35677557634326	-1.03000566686010
C	-4.65495458954743	4.33504709125264	0.41305565073171
C	-3.53965164210290	4.35016575219522	1.24457205924153
H	-3.17598454210756	4.59505677264166	-2.68361188967307
H	-5.41475020319646	4.26148994982085	-1.65165465234043
H	-5.65247855405084	4.28550844464493	0.85598611660988
H	-3.65976867518079	4.24224561273932	2.32695449560225
H	1.75017445693085	6.56759995254056	-1.48909028624735
H	3.74316219952588	6.47832399979469	-0.01960422771929
H	3.66840541695249	5.18639025074453	2.12297429595140
H	1.58572540714644	3.97492889289677	2.75970748195602
Br	-0.69339038513772	-2.20285442201796	-1.10692573183698

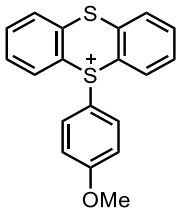

Singlet

C	-0.61035846651115	1.87956685776285	0.64348438682947
C	-1.72812155516078	1.08706936080408	0.34986072451736
C	-1.53797101701238	-0.14492165289122	-0.25662579456789
C	-0.23841047690712	-0.60217876074101	-0.56447348542133
C	0.87170070898431	0.20541987909175	-0.25162514906307
C	0.68326569022906	1.44637750726852	0.35767427277185
H	1.55078635236044	2.06695545941671	0.58886562430522
H	-2.73945403566661	1.42961572413418	0.57557968693323
H	-2.38471247415168	-0.78461471818166	-0.51027724213842
H	1.88538725347424	-0.12022490636261	-0.48148484883986
S	-0.85232194710310	3.43221132833561	1.53987638319187
C	-2.32257513495830	4.09775848580027	0.78889025965256
C	-2.31930258315081	4.46431521694071	-0.56795661195976
S	-0.88046664259256	4.38631392889090	-1.60046414817005
C	0.41208665013458	4.84287106338125	-0.47696592604632
C	0.42916962183930	4.47574902376221	0.87975813735411
C	1.48945902185452	5.59362209068657	-0.96995470107060
C	2.53526176023138	5.96344320565080	-0.12190511219852

C	2.51906483358201	5.61702363322439	1.23461690556574
C	1.45594711833183	4.87201317958510	1.74455383415451
C	-3.52561592394101	4.89718950373394	-1.13715787239263
C	-4.68456287750684	4.96395036942214	-0.36117386183760
C	-4.66164406582967	4.62743877286613	0.99757109971231
C	-3.47142581500778	4.19569701241401	1.58248187341479
O	-0.16242650059014	-1.80173440932335	-1.14896348649161
C	1.10407174581623	-2.34971210807069	-1.48439528089725
H	1.63446532372606	-1.71285638942954	-2.21265556716570
H	0.90449857619963	-3.32863186578700	-1.93625456634533
H	1.73081239219488	-2.48393402409033	-0.58660734930238
H	-3.54525668241770	5.20243760097286	-2.18536073548429
H	-5.61468595242166	5.30547905129165	-0.82060415757950
H	-5.56864557882497	4.70125185140701	1.60051712430910
H	-3.43389251230023	3.92004641762889	2.63871608696045
H	1.49168596468133	5.90516141422211	-2.01660290881280
H	3.36483874737806	6.55018228907011	-0.52307591551860
H	3.33175676126454	5.92708563864155	1.89410684450211
H	1.42711171977212	4.58477296847103	2.79800147712885

Triplet

C	-0.52027930105378	2.05151214698435	0.57812506357797
C	-0.91027855541300	1.87137103527863	-0.76123870629339
C	-0.57969946012059	0.69195715662044	-1.40777680551045
C	0.15001581027463	-0.31654365918215	-0.73993858199646
C	0.54158697886488	-0.12059717909297	0.59996836302287
C	0.21098639252587	1.06465015077752	1.25220332332880
H	0.51760973144178	1.21297748803043	2.29050422615075
H	-1.48699536744698	2.63163977306032	-1.28824148324491
H	-0.87822145004328	0.51278081626976	-2.44181598414471
H	1.09563946810017	-0.88708177211604	1.14086778982232
S	-0.76980701741129	3.58215716723900	1.46113755655738
C	-2.39258574742110	4.11580158534410	0.90872999742112
C	-2.60815373301577	4.92595471482697	-0.22291722486741
S	-1.39130441516533	5.58620182102481	-1.31920915707926
C	0.14453422495186	5.09073490363859	-0.71664136723110
C	0.29683219511956	4.80149370222457	0.71173089494028
C	1.30681077135094	5.40392271749017	-1.50447466828486
C	2.51553084479213	5.57236794636734	-0.88995671195587
C	2.61710332363655	5.45148651816066	0.55479422709942
C	1.53544311882400	5.03889107875437	1.32588025797435
C	-3.93302920980846	5.26684683163143	-0.56146545472299
C	-5.00312696331742	4.80053025121903	0.19874471663134
C	-4.77624649327766	3.99430600699378	1.31914064269766
C	-3.46724791271587	3.65598875351690	1.67221201557413
O	0.41573529445517	-1.41477408062293	-1.45279631895907
C	1.13545549326701	-2.48915511829574	-0.86427734934207

H	2.14518467400596	-2.17116491646000	-0.55475846945186
H	1.22052901190756	-3.26133966455275	-1.63866774647930
H	0.59609479693290	-2.90210717694983	0.00475847994069
H	-4.11515414193279	5.89913621200906	-1.43439200970923
H	-6.02135900138008	5.07534735353640	-0.08365380738778
H	-5.61122123117723	3.64026082932697	1.92622506766700
H	-3.27588918975636	3.03406547564292	2.55046277209966
H	1.19870067585895	5.55214433320015	-2.58315461405016
H	3.40683283220101	5.81295277922803	-1.47072586587538
H	3.57022416560326	5.67157183349678	1.04110951097481
H	1.65926938634286	4.86592218537878	2.39947742110568

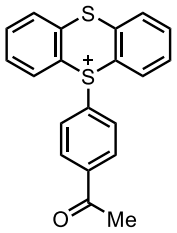

Singlet

C	-0.50167781906619	1.81360632502719	0.82925887516386
C	-1.59561322438970	1.00219800479078	0.51856314451923
C	-1.34975860295464	-0.26578705103569	-0.00095458547789
C	-0.03643504735221	-0.72138059367097	-0.19703876980004
C	1.03962334825755	0.11292958489404	0.13696185094649
C	0.81553130239756	1.38986365010465	0.65730780480908
H	1.65755051471486	2.03792288184620	0.90580422762031
H	-2.61966948844279	1.35115012252940	0.66115501815186
H	-2.16986708504013	-0.93380288459416	-0.27150013766008
H	2.06784695951769	-0.22127980515308	-0.00876167228636
S	-0.80310795717375	3.42869376005132	1.61024714951552
C	-2.27996334842230	3.99256760376942	0.79698833935289
C	-2.26270881161481	4.26699780237983	-0.58166028270577
S	-0.80553280720367	4.14848367518074	-1.58558565012570
C	0.45558896117945	4.72587900215821	-0.48106827438785
C	0.46227053765543	4.45575022783425	0.89852810178787
C	1.51780235072883	5.47282535475569	-1.01071745949669
C	2.53768267913454	5.93364998759777	-0.17574845873526
C	2.50974945143899	5.68349115521614	1.20180772484874
C	1.46167588622504	4.94367909659621	1.74882291727071
C	-3.47031497607887	4.62756904332004	-1.19630062153246
C	-4.64319038582335	4.71433569353455	-0.44338910488381
C	-4.63467584142117	4.46887561330807	0.93507906053119
C	-3.44383247541499	4.11015589916696	1.56601277874404
H	-3.48110696160635	4.86051396037141	-2.26314608536126
H	-5.57423434369906	4.99915242362727	-0.93828470145288

H	-5.55367224668447	4.55667528857119	1.51761657186409
H	-3.41735338593752	3.90539163164578	2.63871617085091
H	1.52829227429756	5.71004681693957	-2.07679260123707
H	3.35589278340434	6.51620682681749	-0.60546651012181
H	3.30198311699384	6.06486315231695	1.84870585740369
H	1.42411751168139	4.73185085102799	2.81986488921499
C	0.14061503636307	-2.11335400722746	-0.77112406300813
O	-0.84197134563997	-2.76355483366004	-1.05263272540011
C	1.54188494983988	-2.63996235975891	-0.97060058530745
H	2.10719983244036	-1.99555175771953	-1.66371374382954
H	1.48493693826048	-3.65518075327125	-1.38174098878556
H	2.09286171943509	-2.66050138928807	-0.01617346099975

Triplet

C	-0.50971148661954	1.82784036650511	0.83202153743635
C	-1.60281516384173	0.99724570582550	0.52632300014622
C	-1.37055642357988	-0.26480011759704	0.01513912581403
C	-0.03663952464873	-0.74017013303999	-0.19644997562434
C	1.04825497685329	0.12792673170720	0.13642371392277
C	0.81391102635948	1.39173435868826	0.64789133914713
H	1.65750414410145	2.04115339341019	0.88853822173386
H	-2.62826766702879	1.34105732667223	0.67316257005900
H	-2.21686235096260	-0.90744725534568	-0.23508878692323
H	2.07849428873442	-0.19727156183897	-0.01402696611277
S	-0.80744925097930	3.42237739468920	1.61616564246174
C	-2.28184757245356	3.99711364765932	0.79780105768193
C	-2.26286050191775	4.26442184505597	-0.58178357589904
S	-0.80434265198635	4.14319811731034	-1.58282374428720
C	0.45540543450513	4.72051491195863	-0.47713349406287
C	0.45602476526968	4.45754393974312	0.90337318344135
C	1.51957126218462	5.46460815514923	-1.00710929767268
C	2.53735852550824	5.92858976085066	-0.17139625622629
C	2.50422060003807	5.68514236213911	1.20692907428074
C	1.45317381336082	4.94866365941113	1.75339573350867
C	-3.46847242981677	4.62617460903201	-1.19999947187189
C	-4.64244136785094	4.71951189572803	-0.44971134527106
C	-4.63613886614102	4.48062547100003	0.92960730476239
C	-3.44650370858317	4.12172432104148	1.56333909665698
H	-3.47628008530130	4.85557039192116	-2.26766370771025
H	-5.57194211374678	5.00472240705937	-0.94730916945318
H	-5.55555614635579	4.57388615117265	1.51068756707520
H	-3.42132833187228	3.92187988863470	2.63703981998345
H	1.53296240996048	5.69720011487875	-2.07418801031654
H	3.35767310343725	6.50805546002656	-0.60130029531736
H	3.29467410051340	6.06863983813420	1.85478754087831
H	1.41168964653241	4.74086259657205	2.82510562360642
C	0.19232755134133	-2.03419033332022	-0.72277938436050

O	-0.78676318536905	-2.83188714278213	-1.02887348362866
C	1.55358947311611	-2.64875891636848	-0.99089493988242
H	2.11131801511513	-2.01660767340015	-1.70058305256146
H	1.44947523779644	-3.65309746145676	-1.42226002105982
H	2.11757045432761	-2.72878422682679	-0.04731617435494

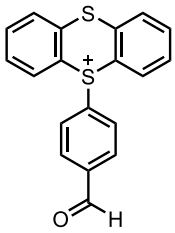

Singlet

C	-0.63522924616290	1.91201456167810	0.72238577396592
C	-1.75454957178454	1.14403721718771	0.40086973153065
C	-1.54968317911342	-0.10329887617108	-0.19306826096894
C	-0.25168402882808	-0.56232595026450	-0.44716522227095
C	0.85569163058367	0.22599066252543	-0.09859076568309
C	0.67257823161459	1.47152863855111	0.49566271847508
H	1.53234669745448	2.09040386348766	0.75745982895409
H	-2.76587894154841	1.50867974639932	0.58759297945630
H	-2.40977341891410	-0.72103377008228	-0.46564544903741
H	1.85627903459024	-0.15844510095821	-0.30875894613600
S	-0.88129340292531	3.49784672778326	1.58177327101304
C	-2.34307429676579	4.14493050037888	0.80388986126059
C	-2.32431399129202	4.47229285245522	-0.56354702335924
S	-0.87782956873986	4.34331549630304	-1.58086075882323
C	0.40910809539876	4.83342919972092	-0.46359466854188
C	0.41298597130951	4.51164852514849	0.90517815542223
C	1.49719796633488	5.55661655965227	-0.97250816361032
C	2.53788005671599	5.94723440393654	-0.12702016394323
C	2.50626719619434	5.64951818849867	1.24044659034622
C	1.43368835160840	4.93026954218868	1.76687624485582
C	-3.52234846290653	4.89840648119865	-1.15449182755577
C	-4.68606381046563	5.00036369796987	-0.38916411061047
C	-4.67693438642186	4.70475129629264	0.97915022729504
C	-3.49627909698652	4.27802425348249	1.58640905038972
H	-3.53223964533285	5.17033095842663	-2.21219562717428
H	-5.60923268818814	5.33713170321038	-0.86600973491722
H	-5.58741930139545	4.80590421511628	1.57268314870045
H	-3.47000425530064	4.03550359711878	2.65113895244512
H	1.51373855561342	5.82927808133972	-2.02993234050620
H	3.37664958248275	6.51148042675010	-0.54062948425921
H	3.31580272722390	5.97556984332964	1.89602014234984
H	1.39456039528247	4.67983177389981	2.82934547127169

C	-0.02681143205972	-1.89166508137137	-1.09522282562242
O	1.06961034956935	-2.32225921790313	-1.34884966041947
H	-0.95681211684499	-2.46616501727975	-1.33293711429250

Triplet

C	-0.63551578576474	1.92516384229089	0.72095700849009
C	-1.75603306053291	1.13490510768546	0.40859729747320
C	-1.56865378272531	-0.10237113281383	-0.17902300715621
C	-0.25474188303376	-0.58551937162621	-0.46040976281419
C	0.86248882966417	0.23821967031713	-0.11698916860162
C	0.67144228337922	1.47547145813054	0.47097084411043
H	1.53564994537961	2.09447430726080	0.71856348997223
H	-2.76821602096213	1.49171244494384	0.60716967822404
H	-2.43711767357063	-0.71339622072279	-0.43422841833198
H	1.87604303555137	-0.11033079720996	-0.32393387498785
S	-0.87930382227081	3.49039085939898	1.58438305342852
C	-2.33936741782660	4.14698197806661	0.80335131064856
C	-2.32058029539796	4.46976166586629	-0.56434286634091
S	-0.87228130171742	4.34521237320268	-1.57942820611058
C	0.41259564406288	4.83341500377482	-0.45923911575987
C	0.41273156365581	4.51327299847283	0.90931507229358
C	1.50087565836408	5.55802468205140	-0.96619258516682
C	2.53980209373667	5.94993842599240	-0.11937807072970
C	2.50537577839043	5.65269731395204	1.24821393747155
C	1.43150444029217	4.93320435663130	1.77187344674011
C	-3.51830734744272	4.89369790173133	-1.15775363302155
C	-4.68314000951284	4.99623627264545	-0.39447710280985
C	-4.67467892690386	4.70443006788483	0.97474771205517
C	-3.49350789734262	4.28097538050129	1.58344730041075
H	-3.52678874657661	5.16354806179874	-2.21603148586005
H	-5.60627517680380	5.33035844590926	-0.87324783446990
H	-5.58579074670979	4.80588438345602	1.56730002119643
H	-3.46694995162210	4.04052676947314	2.64868597894935
H	1.51839683322638	5.83095036592045	-2.02356594418351
H	3.37888567345083	6.51476397586563	-0.53157901390056
H	3.31324010000808	5.97950282289956	1.90550279261136
H	1.38928498771887	4.68266148344679	2.83423844594831
C	-0.07463048164130	-1.84904713922505	-1.06686699433141
O	1.06836641042661	-2.37540177400360	-1.36828480893607
H	-0.92787294894923	-2.49917598396910	-1.33565549651103

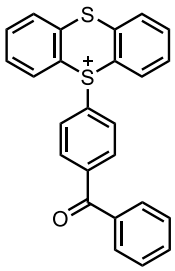

Singlet

C	-0.64353163870870	1.96464636636667	0.90395708538304
C	-1.77034351891386	1.15000991815977	0.80019791733115
C	-1.60840846778761	-0.15113172713384	0.31851221422726
C	-0.33791065370593	-0.62871000209072	-0.03467758329279
C	0.78026809847130	0.20514814884918	0.12276304873244
C	0.63830880791293	1.51170523713652	0.58384983389433
H	1.51063101647348	2.16003004531668	0.68002315394978
H	-2.76218679247527	1.51486570673210	1.07270882870897
H	-2.48089648243432	-0.80053426970871	0.23487043397352
H	1.76684787735243	-0.19380098779883	-0.12008203868979
S	-0.84058369697224	3.62905819286821	1.60900729977796
C	-2.35464296971341	4.19286826446051	0.86458179137507
C	-2.42807519056167	4.37857262298472	-0.52698529923444
S	-1.04969819695253	4.15029950561426	-1.61888282396279
C	0.30372316569220	4.75123386711982	-0.64278951212409
C	0.39842669862637	4.56943481984617	0.74808032440896
C	1.35140501506077	5.41949865063321	-1.29212833963564
C	2.44385457968617	5.89131156575760	-0.56109475979525
C	2.50438687072917	5.73125625073443	0.82842389307146
C	1.47229330727755	5.07014578115053	1.49338538703375
C	-3.66526723277284	4.74101625972105	-1.07845910464607
C	-4.77809713198894	4.91731674042604	-0.25350013168687
C	-4.67772318440241	4.76187642673408	1.13420040637017
C	-3.45597222576536	4.40266318763959	1.70269834149086
H	-3.74540872752132	4.90508233455060	-2.15526212809317
H	-5.73301013921359	5.20217628585320	-0.70072007751778
H	-5.54865784989651	4.92044680314944	1.77278273733532
H	-3.35804202319729	4.27001972255451	2.78253532163018
H	1.29645283617244	5.58513696468872	-2.37023487510546
H	3.25050206068255	6.41020350554015	-1.08369016253957
H	3.35412623546631	6.11919292308179	1.39318473647743
H	1.50472385340959	4.92642378693347	2.57570807865717
C	-0.08372262558916	-2.05472291071754	-0.47625896562196
O	0.97262688619925	-2.57030966936149	-0.16104356824644
C	-1.11440421938041	-2.78807056302175	-1.26342750159845
C	-1.08218506039807	-4.19425286924993	-1.23219675918954
H	-0.33019256295368	-4.68487614774226	-0.61145638717324

C	-1.99427037301397	-4.93490741959703	-1.97988272110601
C	-2.93315225526894	-4.28057912410771	-2.78694763277679
H	-1.97278227958990	-6.02636103686155	-1.94099092675402
C	-2.95542240677702	-2.88383483200778	-2.84600699088398
H	-3.64442580936035	-4.86240784852411	-3.37819751336540
C	-2.05459227266385	-2.13820027102448	-2.08366688294429
H	-3.67342078690454	-2.37494224027870	-3.49332205086877
H	-2.06251053432881	-1.04902796537663	-2.15716609697623

Triplet

C	-0.65413253352298	1.99037005782703	0.80020279335093
C	-1.79026693311398	1.20315440311934	0.54116814534303
C	-1.63056967682312	-0.06222714777843	0.00501103202669
C	-0.33244549770134	-0.57686539358960	-0.28697905357192
C	0.79933617123058	0.24255318292191	0.01431267987861
C	0.64214672068589	1.50628425403638	0.55246203105749
H	1.52085567608531	2.12070829471057	0.75748854547655
H	-2.79320128198680	1.57777316876013	0.75312691129223
H	-2.51250030588455	-0.67711577336646	-0.17802241169759
H	1.80116235502787	-0.13217254543309	-0.20293919824240
S	-0.84696256235656	3.58729015569719	1.60980131132777
C	-2.34649579615395	4.22183333312879	0.88646515500570
C	-2.40449764950770	4.49135635196292	-0.49157873100667
S	-1.01788636305812	4.31696570288463	-1.58236334534411
C	0.33214200281213	4.83990196682656	-0.55840624852894
C	0.40645625775643	4.57881316694143	0.82024243046691
C	1.39394500232542	5.53351497276379	-1.15649882027030
C	2.48176887712361	5.95164775509440	-0.38722103282058
C	2.52216060362875	5.71362844098785	0.99162722434932
C	1.47468463666034	5.02673691291379	1.60499017081781
C	-3.63225865032803	4.90064972923227	-1.03194477825394
C	-4.75188235857460	5.03843515836552	-0.20912068372624
C	-4.66723238536621	4.79755888905744	1.16731832165662
C	-3.45464793690764	4.39122596169485	1.72379475428222
H	-3.69903609706866	5.13122354094391	-2.09742171428787
H	-5.69923547463956	5.36005803090375	-0.64747319579715
H	-5.54310737779289	4.92556052862039	1.80606628393112
H	-3.36862237835019	4.19049211914867	2.79409344308967
H	1.35308725297313	5.76139624469682	-2.22385213192230
H	3.30021250265036	6.49033597234105	-0.86990381433088
H	3.36797444594609	6.06078673425039	1.58797507867204
H	1.49066920423391	4.82218329918435	2.67787444172472
C	-0.13523574012078	-1.88176327880682	-0.81637209026408
O	1.04873262684985	-2.41575239510552	-0.90965130485558
C	-1.14041305437867	-2.79202274274708	-1.39472284621499
C	-1.06241108485996	-4.17715495894388	-1.10363481057218
H	-0.28530786064653	-4.53619728968314	-0.42767614790159

C	-1.98957387729918	-5.05810075178111	-1.65443929755455
C	-2.98557394362163	-4.58088399799692	-2.51263422414885
H	-1.93695831675713	-6.12192715872574	-1.41307178944791
C	-3.04838023288252	-3.21227265287063	-2.83058980162857
H	-3.71137968677952	-5.27243545456702	-2.94656186331214
C	-2.12060832088709	-2.32430993131763	-2.30034191198345
H	-3.82218109681621	-2.84706620324211	-3.50988409485430
H	-2.14328986180352	-1.26920065306100	-2.57831541121036

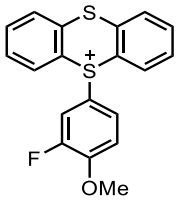

Singlet

C	-0.59296873161189	1.88940248461515	0.64279824533270
C	-1.71674300771400	1.10852152770388	0.34118202761040
C	-1.51946363401375	-0.11978795299307	-0.26386411658256
C	-0.22174439446700	-0.60390164266271	-0.56789842749795
C	0.87845096532685	0.20411925570868	-0.24040640574757
C	0.69830158429102	1.44959812004099	0.37006967826914
H	1.56874707368913	2.06273847759037	0.60769105871155
H	-2.73787884356942	1.43474527260714	0.54287007020822
F	-2.56440794620597	-0.87404025503575	-0.57835397510160
H	1.89020674051265	-0.13249685687492	-0.46366732001252
S	-0.83917685300514	3.44042475734455	1.54254090081848
C	-2.31263111588502	4.09882897404266	0.79282224820298
C	-2.31127708201365	4.46207723146560	-0.56491267735845
S	-0.87206725649591	4.38704329416544	-1.59763537672125
C	0.41874871761414	4.85291014431758	-0.47527845916908
C	0.43878054818525	4.48655674979135	0.88176376204808
C	1.49204368299777	5.60885733496750	-0.96861556677092
C	2.53494767652086	5.98625768641214	-0.12016769489350
C	2.52019558374739	5.64203346084245	1.23673750350219
C	1.46187790482003	4.89096086053630	1.74718900526826
C	-3.52061045044605	4.88544709429192	-1.13462453321388
C	-4.67948996997236	4.94798632575749	-0.35812887942357
C	-4.65417798262495	4.61583900176133	1.00165807670036
C	-3.46151877159749	4.19219769920630	1.58710773014965
O	-0.16705363989997	-1.80096168993428	-1.15005415355844
C	1.09488571594556	-2.36272324141448	-1.48398047605543
H	1.63150468219782	-1.73012076855700	-2.21116017237765
H	0.88427757584839	-3.33871328511066	-1.93695647124068
H	1.71747845152590	-2.50347151997581	-0.58434791499159
H	-3.54358074430806	5.18503365286905	-2.18464010384332

H	-5.61199840671713	5.28148933337899	-0.81879356318144
H	-5.56134607545338	4.68509777723487	1.60474899477696
H	-3.42211754353067	3.92015371056255	2.64430665332642
H	1.49377929390226	5.91843599806261	-2.01598504331269
H	3.36096195022082	6.57751320758291	-0.52160668538901
H	3.33045698607246	5.95821287303193	1.89626892416311
H	1.43414731611351	4.60592490666692	2.80129313735458

Triplet

C	-0.55189824669836	2.07093348322817	0.91734433004330
C	-1.16587380464300	1.00426878885608	1.60200569321544
C	-1.07652032693899	-0.26642981540475	1.06810487471130
C	-0.39135133067007	-0.51669791730726	-0.15042078884728
C	0.20356269562066	0.56936810627706	-0.81253121026859
C	0.11555102944379	1.86292305712381	-0.29146701915373
H	0.59367476065794	2.68562421941219	-0.82230149349737
H	-1.69967142585331	1.14350172746359	2.54433099641033
F	-1.63433892144337	-1.29183481054744	1.69879759073556
H	0.74327646107657	0.41081543305628	-1.74557523888853
S	-0.86359271838849	3.69445907865378	1.59697403912200
C	-2.19699732074218	4.39043211694985	0.61780008206928
C	-2.01049318441890	4.49003952417288	-0.83073502430601
S	-0.66300081494399	5.36488533420678	-1.45068509860864
C	0.58551655987760	5.32884329718861	-0.20152886615338
C	0.54043787255621	4.65902173433573	1.03719753275210
C	1.74772517472228	6.05550423007605	-0.52839625021194
C	2.83040867786306	6.09711697001478	0.34776890629602
C	2.77429280478424	5.42613919413890	1.57351547506856
C	1.62434450537514	4.70943555595988	1.91591934674472
C	-3.11916957403674	4.24236633128338	-1.70981657034281
C	-4.36950753201187	4.06198324962577	-1.18614455050373
C	-4.57047881314597	4.13691564001983	0.25046112717590
C	-3.49923303488873	4.26216824210739	1.12749141281911
O	-0.37168438418411	-1.78432860676733	-0.55782258038776
C	0.30012934494643	-2.12719038029078	-1.76202020570631
H	-0.14821557378538	-1.61151521400158	-2.62807417177431
H	0.17930659659432	-3.21044490876940	-1.88104108797111
H	1.37421066418201	-1.88320704896557	-1.70094695318476
H	-2.95858408844449	4.25126572031546	-2.79195845871775
H	-5.22491322874897	3.87770366793849	-1.83726691257314
H	-5.58552589261933	4.07275032644573	0.64936562454547
H	-3.66583728328457	4.22514774943365	2.20847854091405
H	1.79421976945195	6.58652793695843	-1.48278876098749
H	3.72149877786634	6.66489010715783	0.07196850689492
H	3.61429108044842	5.47025047595783	2.26918320875366
H	1.56398072442390	4.18855740369573	2.87478395381291

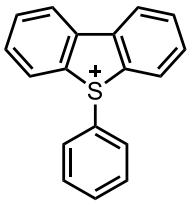

Singlet

C	-0.78931911237228	1.68146931378166	0.97169554586254
C	-0.78218831149676	0.60662029309260	1.85354031535624
C	-0.51588149843394	-0.66232140191405	1.34986540866057
C	-0.26732345004172	-0.83163963583051	-0.00575693120379
C	-0.28175588555691	0.26051888355586	-0.87392864248913
C	-0.54276889902250	1.53155710682680	-0.39026060989648
H	-0.55632153556201	2.38493466832736	-1.05331047146465
H	-0.97926378368055	0.75381446426024	2.90645071992127
H	-0.50485157935268	-1.51159699747113	2.01797958631853
H	-0.08845149802899	0.11797913852467	-1.92773112350356
S	-1.12023274445338	3.28079418862686	1.68346238274816
C	-2.28372778955777	4.07191873816854	0.59108723929573
C	-1.68379607495835	5.12418521450698	-0.11284871863467
C	-0.26057792642157	5.27580891807242	0.19098439283553
C	0.20053520755547	4.33919805587448	1.12440615526523
C	0.65231640256320	6.19598505607750	-0.31494875337684
C	1.97499180670678	6.15040392584622	0.11162887693043
C	2.40333252977315	5.20427086323631	1.04158736475673
C	1.50682845274939	4.28106893827648	1.57079260394394
C	-2.47938621833829	5.86600859705947	-0.98039754418483
C	-3.82319496976840	5.53823797625302	-1.12302495221491
C	-4.39048693613270	4.48334420868153	-0.40956348327210
C	-3.61849662147421	3.73400060075434	0.47266359136669
H	-2.05820985957060	6.69014042640026	-1.53876563885445
H	-4.44029966579785	6.11419046410031	-1.79818897881142
H	-5.43745499082475	4.24756392315075	-0.53456637791840
H	0.33793346568451	6.94041590908263	-1.03286437926097
H	2.68390323947518	6.86448649790451	-0.28331954455544
H	3.43546760763735	5.18853787634933	1.36079533638480
H	1.82631978490742	3.54757117350974	2.29749301403876
H	-0.06143610297032	-1.81944242761438	-0.39381449751244
H	-4.04969304323585	2.91918504252888	1.03683811346889

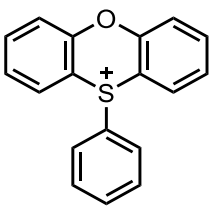

Singlet

C	-0.62122514496083	1.86996353328285	0.76122109086516
C	-1.73749404937722	1.11055897057466	0.43637300448604
C	-1.54418989510040	-0.12639881430150	-0.16632001568149
C	-0.25813399093538	-0.58676246315900	-0.42513106316581
C	0.84521563874619	0.18658736261892	-0.08240888046404
C	0.67238239401463	1.42627182520610	0.52075142545533
H	1.53011797742085	2.03039063543758	0.77784368376178
H	-2.73711849292589	1.47168117836131	0.62877288333436
H	-2.40251041321808	-0.72568270312082	-0.43527323944377
H	1.84511950678610	-0.16942243168383	-0.28637825669208
S	-0.85633457147573	3.43602087266017	1.63596331522108
C	-2.28115830252036	4.11367750418632	0.85757328886037
C	-2.15783827024170	4.63010761024545	-0.43270274961994
O	-0.95672484331443	4.74557824311876	-1.07664832424248
C	0.19319759568880	4.95099909402917	-0.36496917859113
C	0.37918085805165	4.47226966297688	0.93234205128028
C	1.20944498615161	5.67328927104006	-0.97453232697328
C	2.38197142242671	5.92312400045536	-0.27572446439182
C	2.55109449690676	5.47483559057061	1.03390844894459
C	1.54530972846326	4.74572320263136	1.64534201701590
C	-3.29488937167651	5.05402289318872	-1.10600501346942
C	-4.52893251532559	4.97621471639464	-0.47628238913925
C	-4.64491868312239	4.49477273320135	0.82740786230637
C	-3.51626063829315	4.06093259011957	1.50190994449523
H	-3.19270098215840	5.45211083767680	-2.10529739691934
H	-5.41065158886958	5.31239690007929	-1.00354664686623
H	-5.60970741352340	4.45571000530845	1.31135749838583
H	-3.58427533599050	3.67227148285583	2.50875481381014
H	1.05901779623415	6.04117755073472	-1.97932848479749
H	3.16830474882065	6.49038768910892	-0.75353895763516
H	3.46251902202061	5.69110150144123	1.57156291377022
H	1.65932329294390	4.37867758760612	2.65614642304924
H	-0.11559496164633	-1.54896863284609	-0.89640327694919

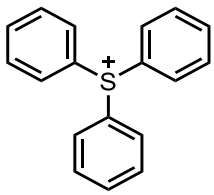

Singlet

C	-0.64920767915086	1.79956054835707	0.58650559441182
C	-1.30706915779013	0.67758935853365	1.08402761681557
C	-1.07711749025361	-0.55138392491211	0.48148539344588
C	-0.19243487828694	-0.64864077514432	-0.58781713333198

C	0.46784883752843	0.48052039916376	-1.06154909403160
C	0.24305800069667	1.71979387459668	-0.47653954543984
H	0.75895971880022	2.59767584509316	-0.83559378183877
H	-1.98424724238057	0.76111151987468	1.92325659235266
H	-1.58040360984281	-1.43198155173875	0.85449678254553
H	1.16155987851766	0.39910833201656	-1.88638646741705
S	-1.02144432629326	3.34215984158898	1.39820292587848
C	-2.41665781600470	4.01600695207594	0.51524017606098
C	-2.76933367668427	3.58048241080980	-0.75644389611138
C	0.33863993419079	5.24187580115648	-0.11481499711052
C	0.34385518376574	4.41940203269426	1.00584780025985
C	1.45018522881294	6.03857894867694	-0.35697373698603
C	2.53854781143319	6.00571471485114	0.50894427451747
C	2.52334236473575	5.18175529153026	1.62984579586967
C	1.41767797430595	4.38462901992087	1.89152638743547
C	-3.86470891838432	4.16757264242154	-1.37734193182337
C	-4.58286737770301	5.16905135495549	-0.73259087975322
C	-4.21869606311773	5.58816280256394	0.54325223270875
C	-3.13341964345948	5.00604568403139	1.18254006675647
H	-4.15594566039210	3.83860982275530	-2.36483700411113
H	-5.43491458102480	5.61896228676240	-1.22264796829595
H	-4.78437958102486	6.35949516758756	1.04622771703674
H	-2.85014634538789	5.31754454931620	2.17883248679403
H	1.46279257153087	6.68681171184703	-1.22176130484907
H	3.39871276921492	6.63073469186361	0.31381905891810
H	3.36581731583090	5.16561945454845	2.30653074927072
H	1.39248100642441	3.74878894385506	2.76611390243507
H	-0.01026117850461	-1.60972614996576	-1.04796053788638
H	-2.21292127399661	2.79813462089789	-1.25036259058030
H	-0.51229209610584	5.26944377741471	-0.77896468394666

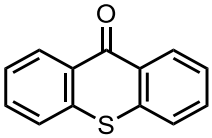

Singlet

C	-4.26418111827408	1.76225730188756	-0.36660612424045
C	-5.58310665499719	1.33392295302589	-0.37022410283185
C	-5.86625828135567	-0.03415438108231	-0.22420920348155
C	-4.83400111964824	-0.95133657694150	-0.07698343954840
C	-3.49347473182582	-0.51689934308247	-0.07292363942893
C	-3.19597955415522	0.85326300199579	-0.21910719930082
C	-1.81835790256059	1.41636178078399	-0.22934018149602
C	-0.65690763764921	0.49921230816614	-0.07068744121176
C	-0.76283968447168	-0.89752586437703	0.08764858741051

S	-2.28363975721211	-1.77490156647327	0.12121627736749
C	0.62830307942351	1.07986899479070	-0.08071396938551
C	1.77202619028535	0.30849848892699	0.06116495798166
C	1.65288047793684	-1.08219325853926	0.21842420791288
C	0.39983108582628	-1.68071078569133	0.23147106391876
H	-4.00181425951208	2.81568099166096	-0.47748269340907
H	-6.39603541961678	2.05422141114919	-0.48604621371057
H	-6.90127016001402	-0.38508152348511	-0.22565701661999
H	-5.05454051413550	-2.01577376365275	0.03681868034290
H	0.67802712109854	2.16294973765303	-0.20479137593275
O	-1.64257823621509	2.62042178680314	-0.36565191404501
H	0.30693795658245	-2.76291199907051	0.35348697808629
H	2.54606353698430	-1.70168268898499	0.33169826312164
H	2.75803558350605	0.77827299453713	0.05092549850055

Triplet

C	-4.26368681307311	1.76980371642922	-0.36542438590948
C	-5.58479399983675	1.34220966119120	-0.34703177993770
C	-5.88106302877264	-0.01956145734230	-0.20265674290338
C	-4.84125143298985	-0.94541340088338	-0.07882152202438
C	-3.50550765913075	-0.53205325621209	-0.10008806159064
C	-3.19043835314711	0.84761699179219	-0.24292619328407
C	-1.83119125058588	1.31133265155339	-0.25988851490541
C	-0.66094228114473	0.49491805911645	-0.09506710908801
C	-0.75234585492966	-0.91575914676360	0.06202477699906
S	-2.28213976288425	-1.79836353522273	0.03961089493950
C	0.62985800893062	1.08721530984145	-0.07997705249452
C	1.77329862387281	0.31636309282794	0.08437609266005
C	1.66852108874659	-1.07178714420340	0.24219280217523
C	0.40852956848299	-1.67693611768116	0.23099166354433
H	-4.03178831212387	2.83156704460870	-0.47304794719212
H	-6.39135157993249	2.07281882215891	-0.44383266527588
H	-6.91748292883321	-0.36330317765919	-0.18505683960514
H	-5.06678272180350	-2.00891263028643	0.03588090313083
H	0.71042248942385	2.16994576817741	-0.19815836173387
O	-1.63988316331360	2.61597054662976	-0.42226402003580
H	0.32050144740843	-2.75956691475868	0.35458285338558
H	2.56277208306027	-1.68439713275008	0.37491026242155
H	2.75386583257588	0.79805224943642	0.09210094672427

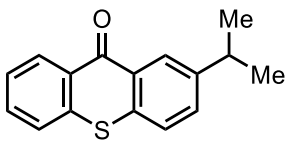

Singlet

C	-4.28137472871017	1.64329274761347	-0.83111129418725

C	-5.58441226168651	1.17204918268076	-0.88502697358960
C	-5.86212407492724	-0.14279956122835	-0.47565723606344
C	-4.83993151751574	-0.96523375575469	-0.02119508066739
C	-3.51474626507803	-0.48802071512623	0.03183304181787
C	-3.22301694118599	0.83014543725552	-0.37500680752978
C	-1.86172464563846	1.43264501805606	-0.35883306213441
C	-0.70899317025609	0.60834871146045	0.09382593980054
C	-0.81274162588390	-0.72507817039868	0.53332297571927
S	-2.31650739047752	-1.62686519673239	0.62219742824618
C	0.56416650257545	1.21426429427092	0.07229360424709
C	1.71792536047288	0.54610336654812	0.46546635361722
C	1.58414291988177	-0.78919382981383	0.90233642224648
C	0.34733273817376	-1.41502444593001	0.93762570863247
H	-4.02408467399008	2.65816879103021	-1.13878307571896
H	-6.38963096314809	1.81751033969768	-1.24288655901260
H	-6.88485004808217	-0.52634553725339	-0.51313623350654
H	-5.05532685266714	-1.98853979209494	0.29691737706745
H	0.60449863249037	2.24896895654545	-0.27444192828995
O	-1.69334463670537	2.59150675538599	-0.71843186485862
H	0.26607465918254	-2.45020907260138	1.27926833007638
C	3.07509956746353	1.22708115187596	0.42587921259242
C	4.03228830354442	0.52374783037623	-0.54915778329544
C	3.69089389238518	1.34307475273806	1.82881321518395
H	2.90620035132139	2.25017146024397	0.04921478474751
H	4.25338997293545	-0.50536155559893	-0.22025023635930
H	4.99038924161619	1.06446672411587	-0.61383358524264
H	3.60026832719446	0.46686627378126	-1.56036246883563
H	3.88991712338599	0.34861575520008	2.26188560882175
H	3.01860930451321	1.87975193381654	2.51617495344046
H	4.64922383114850	1.88613796019466	1.79096316839105
H	2.46704906766741	-1.34917581035445	1.22092606464348

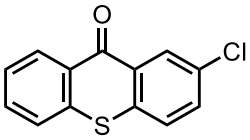

Singlet

C	-4.14140510745255	1.61795009787126	-0.00428837181324
C	-5.39447238073739	1.02427542265438	-0.01352258180518
C	-5.49591914242969	-0.37675624717220	-0.02715908047235
C	-4.35076021462502	-1.16219972284290	-0.03147688896840
C	-3.07681933877476	-0.55996252638910	-0.02214863268531
C	-2.96135157102202	0.84516847480892	-0.00828073560767
C	-1.66912805767579	1.58100690311590	0.00284644896013
C	-0.39476944654616	0.80819040336201	0.00017367043839

C	-0.31874143654678	-0.59862807352735	-0.01373707357433
S	-1.71189399703886	-1.66489731440817	-0.02917850069110
C	0.79857973709052	1.55694472427456	0.01266985701567
C	2.03039319494130	0.92240274743896	0.01135948150823
C	2.10874730356113	-0.48048408368655	-0.00325872524140
C	0.94177464146860	-1.22966781650629	-0.01562307700977
H	-4.02001656770031	2.70236143801357	0.00640678023624
H	-6.29610500352090	1.64065788187928	-0.01013077178040
H	-6.47737800618185	-0.85738437662586	-0.03444135766293
H	-4.43017917493818	-2.25225221606284	-0.04207126439852
H	0.71452375510341	2.64379557526323	0.02346785591771
H	0.99923944331004	-2.32101257105345	-0.02679395177928
O	-1.64840437968907	2.80449468373802	0.01455345925216
Cl	3.50193152751750	1.86102477511162	0.02824269316283
H	3.08375422188685	-0.97031817925701	-0.00465923300149

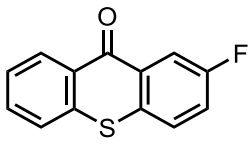

Singlet

C	-4.23912835113695	1.73784376766159	-0.01742080525130
C	-5.48555341521875	1.13107538469620	-0.03967459404537
C	-5.57157523741552	-0.27014816138260	-0.09475593149839
C	-4.41807479328509	-1.04227458665072	-0.12644109509092
C	-3.15029338219701	-0.42678714277186	-0.10419322096619
C	-3.05036725964070	0.97870099838431	-0.04923844217420
C	-1.76683006500034	1.72843362474265	-0.02282087833803
C	-0.48345649092676	0.97221019587326	-0.06563273859516
C	-0.39127935644898	-0.43308194474341	-0.12051334890236
S	-1.77403830223990	-1.51553602419718	-0.14775347342002
C	0.70077001521024	1.73554437730694	-0.04960363464276
C	1.93061555480737	1.10767490150025	-0.08782735605370
C	2.03464910045378	-0.28787018383387	-0.14124164735313
C	0.87563009955188	-1.05059445687951	-0.15711809579025
H	-4.12944564171506	2.82271003997862	0.02527815527702
H	-6.39392940780612	1.73698143111795	-0.01464336686411
H	-6.54774633204522	-0.76118681487265	-0.11336559621207
H	-4.48564507067680	-2.13233770324679	-0.16955054841601
H	0.61865850738330	2.82216001305740	-0.00703252262068
O	-1.75908040110006	2.95111495570626	0.03141150612014
F	3.05382399926801	1.83754171668450	-0.07438373120509
H	3.02173304973778	-0.75319369354832	-0.17016718735775
H	0.94376318044088	-2.14045069458303	-0.19930144659968

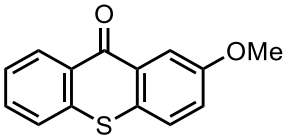

Singlet

C	-4.27100604881051	1.59693921974824	0.17446122303328
C	-5.53675288998149	1.04999756998749	0.03215665761230
C	-5.67230926304418	-0.33035512380361	-0.19417937436335
C	-4.54814741266566	-1.14061017467076	-0.27403409971073
C	-3.25967702108285	-0.58622123172664	-0.12926476676807
C	-3.11030450116793	0.79807626607426	0.09788734468393
C	-1.80259984082955	1.48513413287543	0.26498001558663
C	-0.54871014075386	0.68742929640869	0.19182597981275
C	-0.50786039053903	-0.70000119353222	-0.03042111031786
S	-1.92357862423603	-1.71539761896200	-0.25115438645275
C	0.65840337781578	1.39874121116458	0.35837847371139
C	1.88629492335836	0.74839285514167	0.30405246184767
C	1.91736263932357	-0.64580961872115	0.07778850765469
C	0.74178883995420	-1.35472262545842	-0.08555725517164
H	-4.12322650769732	2.66362551472003	0.35095514996537
H	-6.42260520419714	1.68589070259823	0.09542803123863
H	-6.66455930897204	-0.77400415640689	-0.30873976610957
H	-4.65406235202079	-2.21418280789461	-0.44992888515590
H	0.56355734015817	2.47005160386292	0.52817798578987
O	3.08803888772801	1.35302151063975	0.45262782802636
H	2.88774018591193	-1.14435070160732	0.03558186175663
H	0.77811676208973	-2.43319313621451	-0.25947562794023
O	-1.75572363176060	2.69444615749357	0.46001995594670
C	3.11719397727070	2.74545159756079	0.68474349653190
H	2.59019085831391	3.01349040130766	1.61785945471340
H	2.66233145691147	3.30699011497429	-0.15070216480763
H	4.17502388892315	3.02561023444049	0.77476300888619

Calculated coordinates of phenylethyl thianthrenium salt:

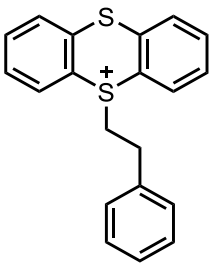

Singlet

S	-1.14427553808528	2.46721542900947	1.50287356387674
C	-2.44796018568802	3.28917534734357	0.61523405418551
C	-2.29366952925438	3.63842162545916	-0.73776636661337

S	-0.80973459234719	3.35633940654512	-1.67190268904773
C	0.46315994785136	3.60069631024284	-0.45796567900265
C	0.32982683510390	3.25803363081854	0.89866497534018
C	1.68155353771901	4.14733315576530	-0.88679790294152
C	2.72290343578110	4.34516398804768	0.02156089550928
C	2.56387265454165	4.02810960694944	1.37552449262392
C	1.35836410193364	3.48792073718346	1.82136648770391
C	-3.38353347176863	4.22318588898352	-1.39891751948231
C	-4.58072877043511	4.45002310619260	-0.71781463057862
C	-4.70841186238571	4.12466347823949	0.63738901540279
C	-3.63458622764604	3.54724939524993	1.31337068362703
H	-3.28158000118033	4.51511969029996	-2.44644749316837
H	-5.41854194458948	4.90661127044324	-1.24933038556529
H	-5.64153050167081	4.32236093526375	1.16815252569589
H	-3.71630105862989	3.28764075734166	2.37128045244702
H	1.80157116262169	4.43368658910172	-1.93398811045814
H	3.66411922124542	4.77276161585738	-0.33088908421012
H	3.37597657600122	4.20255223181189	2.08366958262978
H	1.21764387596634	3.23091933268118	2.87362618284356
C	-1.08288755884551	0.78827308373992	0.70906682852067
C	0.12284958760304	-0.00811984203347	1.20334154793764
H	-1.06971517626763	0.94386942532869	-0.37791534743957
H	-2.04057433373394	0.33325973614747	1.00269731013796
C	0.12629073506200	-1.36383664555390	0.52977594492737
H	0.07888393952138	-0.11953748159691	2.29873811747792
H	1.04960810502151	0.53485616637099	0.96116659571542
C	-0.56070238874957	-2.44498273467583	1.10055250799327
C	-0.59022348002392	-3.68424303459367	0.45671622272811
C	0.06443236964682	-3.85320748690909	-0.76691245518599
C	0.74876297118924	-2.77947828256530	-1.34436642676615
C	0.77788690587612	-1.54083144654025	-0.69965911914747
H	1.32271801606592	-0.70604617639203	-1.15102815873288
H	1.26758956401394	-2.90907978151249	-2.29700664104158
H	-1.06665230221180	-2.32139792486598	2.06280550268398
H	-1.12024509857024	-4.52242723295766	0.91495631063823
H	0.04601047931821	-4.82351387022143	-1.26838179126440

Calculated coordinates of fragmentation products:

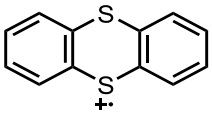

Doublet

S	-1.01387259975569	4.48890104424526	1.98655400300225
C	-2.41172276222772	4.55936663989084	0.95173313649123
C	-2.41797602043189	4.91969560923794	-0.42137490260198

S	-1.02888711045162	5.36782993836606	-1.36917112704680
C	0.36900590696369	5.29670746051935	-0.33460379831258
C	0.37537080061059	4.93637094580631	1.03850068149632
C	1.58513025128265	5.63798290154483	-0.96694885647374
C	2.77313490800745	5.62146697663478	-0.25528770396479
C	2.77953293126032	5.26290638521172	1.10815946839916
C	1.59765634487964	4.92473393438777	1.74623330811232
C	-3.64022952610546	4.93103402141899	-1.12925348771474
C	-4.82210341570269	4.59272055063494	-0.49128645585732
C	-4.81576244341513	4.23419293869671	0.87216784012903
C	-3.62780129777567	4.21783976606729	1.58393770013871
H	-3.64385491907818	5.21068248127470	-2.18553833360750
H	-5.76052706409833	4.60473793122891	-1.04932103106146
H	-5.74907705375574	3.96733894834831	1.37171544974520
H	-3.62165293026867	3.93924244502106	2.64042878526165
H	1.57888705095718	5.91644972077196	-2.02348701674750
H	3.70648187964632	5.88819821215362	-0.75484659453783
H	3.71798827258368	5.25073210642025	1.66613121716475
H	1.60143879687530	4.64494904211837	2.80246771798562

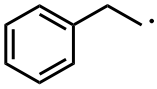

Doublet

C	-0.70366935098752	1.68908898908037	0.56344326384539
C	-1.76829299779579	0.89113363629548	0.12167964913140
C	-1.53620167896432	-0.34751178356209	-0.48382475707443
C	-0.22922772121355	-0.81041075833715	-0.65486610134428
C	0.84187027825916	-0.02521633857254	-0.21599230693755
C	0.60508776080887	1.21125901825773	0.38767167149601
H	1.44609566477449	1.81982456208737	0.73161068045012
H	-2.79473325470451	1.24519724995538	0.25553367904076
H	-2.38115433981177	-0.95450388868928	-0.81952519416239
H	1.86831365488083	-0.37894649898252	-0.34475660365135
H	-0.04520601926121	-1.77919698033886	-1.12613799281556
C	-0.94920284074508	3.03962072195090	1.20601473155086
H	-2.04426701691233	3.17082987220440	1.34252927886861
H	-0.66392792089395	3.84170173499737	0.49712129068717
C	-0.23911792033071	3.24848181435756	2.50104078972132
H	-0.03243974243837	2.40235580398928	3.16172505975380
H	-0.06325655466424	4.25841284530658	2.88050286144008

Doublet

C	-0.61421792899802	1.83351426607068	0.66017568264097
C	-1.74744896204828	1.09860188127919	0.37871603326966
C	-1.54851831039507	-0.15989772032757	-0.21700514380537
C	-0.25288316419871	-0.61028130244723	-0.49547354444960
C	0.85905649072652	0.18156418875158	-0.18692153321381
C	0.68527409561748	1.44351299239140	0.40944914157281
H	1.54525206714242	2.07225717558292	0.65660388435924
H	-2.75416381128852	1.46237101662281	0.60241760693628
H	-2.41205524983085	-0.78500768791725	-0.46180478025244
H	1.86816321828252	-0.17738878297648	-0.40894130159506
H	-0.10806844500949	-1.58973602703004	-0.95739604546268

Calculated coordinates of parent arenes in ground state:

Singlet

C	-0.62064553082752	1.87781028162033	0.67702445727362
C	-1.72092693321760	1.08489123875789	0.36845307112228
C	-1.53670658336125	-0.16226134864716	-0.21900622601288
C	-0.25202373815649	-0.61669881778362	-0.49753785067402
C	0.84825851813773	0.17622040826972	-0.18896622606788
C	0.66403799874693	1.42337207604101	0.39849300386438
H	1.52000590632047	2.04021144013413	0.63834261786014
H	-2.72026773544724	1.43836842224712	0.58533480319326
H	-2.39267612170235	-0.77909900322949	-0.45885435969168
H	1.84759919437048	-0.17725727025299	-0.40584842797032
H	-0.10857522075627	-1.58721522490790	-0.95382840641226
H	-0.76408975410689	2.84832779775098	1.13331354351534

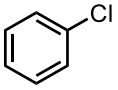

Singlet

C	-0.62821592679845	1.92899121737769	0.70205089102129
C	-1.72593673330948	1.13449022707594	0.39114357716561
C	-1.54939994811710	-0.11258966382757	-0.19660948443274
C	-0.26122869643404	-0.55413003705553	-0.46834660846356
C	0.84616114318430	0.22741862571635	-0.16655387426238
C	0.65455138225245	1.47230846257979	0.42130078011028
H	1.51405399121152	2.08455705931778	0.65917226486851
H	-2.72739984715050	1.48258896551918	0.60571560277861
H	-2.39638475017390	-0.73680222599639	-0.44123544363136
H	1.83908671665187	-0.13540968240723	-0.38868180466693
Cl	-0.02973779918351	-2.12283434906407	-1.20088849117884
H	-0.77153953213317	2.89807140076406	1.15983259069150

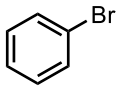

Singlet

C	-0.62994198369548	1.94082968613949	0.70605684599224
C	-1.72780618830252	1.14590974077066	0.39734179875173
C	-1.55169455372793	-0.10255362886263	-0.18909507351301
C	-0.26327723012701	-0.54126628818895	-0.46114293787228
C	0.84511014435727	0.23767552839128	-0.15914380847556
C	0.65299126303763	1.48367873033660	0.42752676248428
H	1.51264402136748	2.09599776983117	0.66480244258413
H	-2.72934412984753	1.49430829813908	0.61128324738031
H	-2.40131611609713	-0.72399607710857	-0.43091738795062
H	1.83958503674598	-0.12202766445737	-0.37855648719759
Br	-0.00954374161459	-2.25335416590501	-1.27176325665748
H	-0.77338652209616	2.91146807091425	1.16051785447388

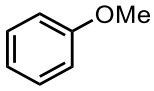

Singlet

C	-0.63554688045685	1.87499100006557	0.67787601180035
C	-1.69732229614465	1.04635303639569	0.34856315389171
C	-1.47995316043076	-0.19760817335986	-0.24064110818800
C	-0.17558468929739	-0.61420600910481	-0.50240505896334
C	0.89782994221513	0.21763034085349	-0.17406856388910
C	0.66519951473553	1.45024258149806	0.41147839986190
H	1.50464045901872	2.08545436720605	0.66210517789134
H	-2.71293392487440	1.36194771824935	0.54866813425173
H	-2.32365951200217	-0.82397017739442	-0.48643977470881
H	1.90147253914081	-0.12396541047137	-0.38663417577389
O	0.14981529258378	-1.80823517026469	-1.07091682613005
H	-0.81400465738911	2.83832266470817	1.13500790983198
C	-0.89879661758905	-2.69307630985079	-1.42282296070748
H	-0.42107568500775	-3.56933722984728	-1.85283611348922
H	-1.56762228589102	-2.24544956538582	-2.16294654410425
H	-1.48055803861082	-2.99110366329731	-0.54621766157489

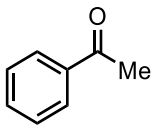

Singlet

C	-1.14653518638813	3.03377820686954	0.46783285311300
O	-2.08164404648340	2.27611898707067	0.30726515959305
C	-1.37786999904393	4.47127078483882	0.81270043058700
C	-0.32968381764046	5.37546470482098	0.99836724212273

H	0.69577025563495	5.05099793879378	0.89486771199196
C	-2.69479480727775	4.91878043593640	0.95266685621841
C	-0.59257877532547	6.70159754340966	1.31780315822451
H	-3.49573420065953	4.20821049030492	0.80595774699762
C	-2.95720804850531	6.24104781296849	1.27173619085934
C	-1.90572196482307	7.13577723291753	1.45482052511038
H	0.22576953829985	7.39454431734959	1.45963201217143
H	-3.97962237449382	6.57795222402467	1.37845496748196
H	-2.11062688180051	8.16858145868428	1.70357252126978
C	0.27798774968015	2.54299727274292	0.32403650396466
H	0.26152258160913	1.48511723721672	0.07803027593651
H	0.83552045120157	2.69360665388381	1.25032270141281
H	0.80007952601576	3.09190669816721	-0.46191685705512

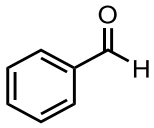

Singlet

C	-1.02888875352850	3.00626742005658	0.46212165234793
O	-1.85817519423995	2.14499304995731	0.28693151155981
C	-1.32571546651405	4.41333648820328	0.79796617668864
C	-0.27321131913256	5.30968631091159	0.98260622002932
H	0.74725979271844	4.96223295270838	0.87504360687528
C	-2.64584540934822	4.85210979601046	0.93380050278796
C	-0.53216199914540	6.63594368734141	1.30259925367094
H	-3.44715715935008	4.14131954851187	0.78578785066618
C	-2.90339929455226	6.17479346161950	1.25224474509039
C	-1.84725620967278	7.06671979666651	1.43710169231257
H	0.28416486422291	7.33048286471553	1.44690476964029
H	-3.92378826011092	6.51768825322818	1.35826058171983
H	-2.05272025144364	8.09932229266134	1.68641949271766
H	0.05253466009701	2.77424407740803	0.37661194389319

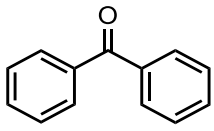

Singlet

C	-1.38805882752463	2.12633238134542	-1.13797284208747
O	-2.43393020998501	1.56686415157283	-0.86166488783704
C	-1.05748729988774	3.44701793109023	-0.51973340963068
C	-0.31879713745179	4.42402692786248	-1.19035755639101
H	0.06045288842920	4.22613363109685	-2.18265005458305
C	-1.57051213414152	3.72929906714798	0.74876129883904
C	-0.09349337971446	5.66084846574936	-0.59876631275118

H	-2.16037875428830	2.97333386927395	1.24756994950626
C	-1.32564410334197	4.95498691528620	1.34747495618211
C	-0.58699756683666	5.92413996970344	0.67358074065374
H	0.46665238592511	6.41786546345892	-1.13094340420562
H	-1.71370449275007	5.16033272334454	2.33612013337708
H	-0.40132704371185	6.88353317656913	1.13792158056037
H	1.35982861684856	2.30917228049513	-1.21711947926617
C	0.95429679587700	1.67402863870830	-1.99145386005905
C	-0.42700949555843	1.49625367969765	-2.09405859092252
C	1.81235437141650	1.01289215870898	-2.86134797448851
C	-0.93472860509650	0.64291983675650	-3.07722817143439
H	-2.00405429659992	0.49517345287229	-3.13168360320152
C	-0.07901152199716	0.00104215275252	-3.95840459606556
C	1.29725043913699	0.18389201671939	-3.85088165758609
H	-0.48077531241647	-0.64690481769339	-4.72583272990797
H	2.88179964706997	1.14379808701563	-2.76524195395795
H	1.96572503659915	-0.32331215953437	-4.53386757474280

Calculated coordinates of aryl chlorides in ground state:

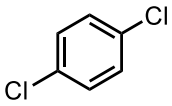

Singlet

C	-0.62351132416202	1.87953019976308	0.67783634659522
C	-1.72196876992444	1.08768280466560	0.36976812869412
C	-1.52749091732956	-0.15586057191579	-0.21617570556879
C	-0.24915763410487	-0.61841980479541	-0.49834657118943
C	0.84930004361797	0.17342783568150	-0.19027859675438
C	0.65482217673604	1.41697216229318	0.39566275047477
H	-2.72169704838722	1.43572253034662	0.58402820590671
H	1.84902809657248	-0.17461201105667	-0.40453944954876
H	-0.11125956458630	-1.58779449007245	-0.95420745114568
H	-0.76140779180147	2.84890499376832	1.13369745981117
Cl	-2.90687149572931	-1.14905810069919	-0.60268089482234
Cl	2.03420230509870	2.41017388002121	0.78215896854740

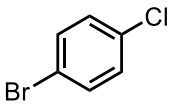

Singlet

C	-0.63358848423701	1.87171099098171	0.67714818489484
C	-1.73226337081763	1.07984568744650	0.36807988001313
C	-1.53777036815674	-0.16304133880878	-0.21961737742648
C	-0.25929459126249	-0.62666064886568	-0.50021116997986
C	0.83991154176842	0.16478006083351	-0.19141477430666

C	0.64349406067995	1.40823312664144	0.39309951972651
H	-2.73237350284963	1.42736860502959	0.58169133235495
H	1.83833593564139	-0.18637599202933	-0.40614617667787
H	-0.12242343626891	-1.59611059934142	-0.95640905177176
H	-0.77434122243397	2.84020102438744	1.13371415794716
Cl	-2.91733699612195	-1.15339416055073	-0.61095435332315
Br	2.15163851005857	2.50011267227575	0.80794301954918

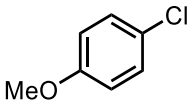

Singlet

C	-0.63409161552198	1.86387674546145	0.67008400696032
C	-1.70359128752957	1.04542614520078	0.35150868681455
C	-1.47857825916257	-0.19807718740369	-0.23384726973549
C	-0.17578421356209	-0.61670844899264	-0.49780007615393
C	0.89544861824013	0.21801486474177	-0.16979571373937
C	0.66999010426621	1.45253754638545	0.41181815119003
H	1.49919977586469	2.09711193891339	0.66466402839388
H	-2.71284966435140	1.37143100059322	0.55692636392277
H	-2.32464401263002	-0.82263342390108	-0.47512797369902
H	1.90066237984089	-0.11956714710235	-0.37993957391365
O	0.14998171991618	-1.80869552690539	-1.06571846655821
C	-0.89928408061818	-2.69105229310084	-1.42568830478623
H	-0.42126299872857	-3.56492207938508	-1.85960940364416
H	-1.56455369727976	-2.23755261429700	-2.16520238323904
H	-1.48263224293159	-2.99360750951879	-0.55192845105396
Cl	-0.91982274181237	3.42623214731083	1.39870319924150

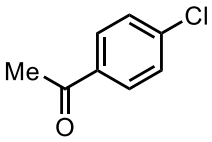

Singlet

C	-1.14654998519938	3.03523308573805	0.46805925574138
O	-2.08416019741575	2.28082593134033	0.30727027306185
C	-1.37652664959350	4.47160867256515	0.81345750678683
C	-0.33119232004006	5.37807717832653	0.99998222587196
H	0.69576638689583	5.05855659694153	0.89788207505336
C	-2.69252467974699	4.92148982844060	0.95396887932040
C	-0.58700262478327	6.70416386294919	1.31882882233629
H	-3.49555604054091	4.21318932972302	0.80781667702576
C	-2.96316229835674	6.24047029186098	1.27220166787701
C	-1.90364483572391	7.12462872069243	1.45194010628738
H	0.22107744989595	7.40600877876800	1.46302403564650
H	-3.97992810518526	6.58835914212553	1.38130517462787
C	0.27706209348911	2.54386997903082	0.32388578920264
H	0.26024048336426	1.48608937527306	0.07778246378820

H	0.83502319241287	2.69340948117697	1.25013885649185
H	0.79911019279581	3.09192247857778	-0.46278501304685
Cl	-2.23371709626807	8.78669173546998	1.84959417092757

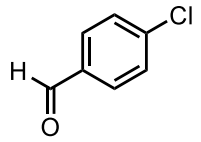

Singlet

C	-1.10158953929120	3.01000322182849	0.46454142561777
O	-1.94894682328645	2.16587510054828	0.29240938311498
C	-1.37417795929569	4.42082548670952	0.80101649306295
C	-0.31140423573921	5.30489324388843	0.98257075558401
H	0.70592251862679	4.94968879336962	0.87326515767391
C	-2.68646222397044	4.88097373695818	0.94178922465990
C	-0.54356495856021	6.63456107535655	1.30248463644166
H	-3.50029054833383	4.18387909366106	0.79732160884245
C	-2.93242600857425	6.20384512447210	1.25995737188773
C	-1.85556085975937	7.07095970963720	1.43808410511563
H	0.27339040004218	7.32607644347551	1.44595227281194
H	-3.94190963122665	6.57139133083263	1.37174062662663
Cl	-2.16224938584594	8.73540608426897	1.83826482099861
H	-0.02556894678570	2.75771165699345	0.37563355656183

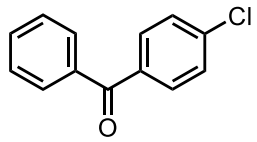

Singlet

C	-1.36915410987702	2.11018081770035	-1.11188457044627
O	-2.40631589740457	1.54346072510118	-0.81811675416092
C	-1.04443299873270	3.43675011451379	-0.50449224246676
C	-0.29781953715841	4.40865947349528	-1.17280174064968
H	0.09955289817662	4.20393480044994	-2.15629317713610
C	-1.57710068830187	3.73823339087745	0.75139480081776
C	-0.08190788253782	5.65496775273966	-0.60144846996465
H	-2.17390323791267	2.99066612157910	1.25447392359509
C	-1.35129245297097	4.96958233456579	1.34257845656367
C	-0.60387938270023	5.92212204000529	0.65715580678327
H	0.48251928967099	6.41314852106431	-1.12394473520077
H	-1.75104763032114	5.19849114057457	2.31956644362555
H	1.37989230779733	2.27884019697819	-1.20309832606978
C	0.96551950162718	1.65864191342689	-1.98503468308865
C	-0.41729458687830	1.48826780485808	-2.08108278577027
C	1.81474578674515	1.00703560291324	-2.87053336491028
C	-0.93564040592883	0.65164641866373	-3.07299925566242

H	-2.00587100135580	0.50891743403494	-3.12260579767946
C	-0.08859490878614	0.02038561692834	-3.97013048472013
C	1.28903969998497	0.19610696138494	-3.86948970532912
H	-0.49833097468366	-0.61362685016339	-4.74487993977719
H	2.88536439660358	1.13124401466600	-2.77932943220471
H	1.95053575708925	-0.30286562979983	-4.56514689101178
Cl	-0.32404596014495	7.47905339744212	1.38568336486362

Calculated coordinates of aryl bromides in ground state:

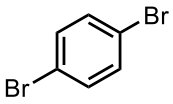

Singlet

C	-0.62333200626393	1.87998338219292	0.67883753913998
C	-1.72291295873854	1.08831260730048	0.36930569771278
C	-1.52631873421460	-0.15434980291142	-0.21670859079511
C	-0.24933699954553	-0.61886882823264	-0.49935606417829
C	0.85024405463294	0.17280209444100	-0.18982470686474
C	0.65364975800293	1.41546101720526	0.39619584492551
H	-2.72114594592062	1.44009893345754	0.58405449047599
H	1.84847706824868	-0.17898252664963	-0.40457618994708
H	-0.10830848895686	-1.58729477263749	-0.95609902656499
H	-0.76435982355558	2.84841075129100	1.13557826524087
Br	-3.03477498504288	-1.24327625396755	-0.63709978714357
Br	2.16210713735400	2.50437282651053	0.81661571899865

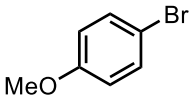

Singlet

C	-0.63078781367284	1.85206558174722	0.66849769940738
C	-1.70207404451311	1.03976760924511	0.34231653633021
C	-1.47774011533852	-0.20106920258288	-0.24974657754073
C	-0.17478243172250	-0.62111594078223	-0.51154300183599
C	0.89729177879263	0.21171309287024	-0.18094846073734
C	0.67315198314377	1.44370618963955	0.40748428922132
H	1.50547481906089	2.08293760808108	0.66303413454043
H	-2.71253213933872	1.36275228580490	0.54584348880201
H	-2.32473172700199	-0.82233397180919	-0.49629476116882
H	1.90247115908074	-0.12571803641424	-0.39162128902418
O	0.15002721789582	-1.81303226950086	-1.07841802171653
C	-0.89899357802707	-2.70230727266880	-1.42316947352293
H	-0.42053559863026	-3.58064568336125	-1.84733643917767
H	-1.56804711416936	-2.25996770233990	-2.16588773454236
H	-1.47789736853975	-2.99429466733552	-0.54295049110700

Br	-0.94210724301973	3.54935653740677	1.48978692207220

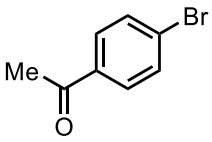

Singlet

C	-1.14382480843760	3.02713887592217	0.46339816549112
O	-2.08201977551649	2.27412090032130	0.30055428416912
C	-1.37390934683045	4.46445387484936	0.80722825992734
C	-0.32903130081190	5.37153860604837	0.99230564177686
H	0.69827321189098	5.05358843408839	0.88779562805921
C	-2.69008994448101	4.91256478082683	0.94938467902556
C	-0.58551564673904	6.69773628110345	1.31384356781491
H	-3.49303372505348	4.20409374152280	0.80350809515185
C	-2.96200824062448	6.23115211469788	1.27067755505093
C	-1.90247299907220	7.11404415324711	1.45092173697737
H	0.22507506239540	7.39682196843950	1.45650773335525
H	-3.98015742140012	6.57390597336341	1.38131243102319
C	0.27943614826391	2.53375448671403	0.32545662923891
H	0.26205840259859	1.47512493276411	0.08305582733846
H	0.83454425790715	2.68596442865729	1.25299684628997
H	0.80468487926750	3.07836139429336	-0.46147700834239
Br	-2.26769378735676	8.93022952214062	1.89688289465234

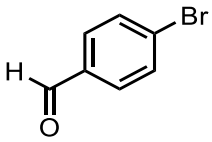

Singlet

C	-1.15231581248186	3.04989416010456	0.46899036631551
O	-2.00128887689857	2.20721666278980	0.29943264213389
C	-1.42103700696832	4.46159190353411	0.80627931454690
C	-0.35629551997698	5.34332824844282	0.98606958419580
H	0.66015821141820	4.98644160202707	0.87327255223466
C	-2.73232332504962	4.92303680060371	0.95051386303698
C	-0.58550246157496	6.67338142282986	1.30966195033378
H	-3.54786370747518	4.22775408962468	0.80676034108417
C	-2.97591968813321	6.24617337787188	1.27240735767851
C	-1.89666607323700	7.10912888262618	1.45021142988273
H	0.23570879120002	7.36000266785604	1.45144679963410
H	-3.98579132303157	6.61136110516580	1.38665558536202
Br	-2.23036077227095	8.92933669856130	1.89880003155968
H	-0.07666243552001	2.79541237796216	0.37761818200128

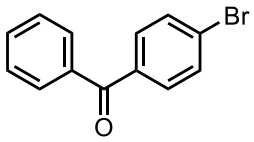

Singlet

C	-1.36721672419241	2.44259003572939	0.29381513597847
O	-2.47562977311195	1.95263561019130	0.17642410646169
C	-1.22269087593470	3.88233996191681	0.67033185033118
C	-0.14625483231731	4.35856682621966	1.42064724009424
H	0.64364765635350	3.68573049325439	1.72176173936423
C	-2.24765797938772	4.76461051777911	0.32122281491105
C	-0.08998006699312	5.68818179195760	1.81691603354290
H	-3.09003477817147	4.38693692091315	-0.24089034463994
C	-2.19344028855449	6.09876052163915	0.68966046876625
C	-1.11225554572232	6.54789836868378	1.43980778550596
H	0.73550647043552	6.04978263911092	2.41193490680021
H	-2.98083495318079	6.78127517130964	0.40584489517674
Br	-1.03852252685259	8.37736726484433	1.96957493724610
C	-0.22073412331036	0.24159987318927	0.32751726083861
C	-0.14626263378088	1.61220357775623	0.06673337176252
C	0.87237384664775	-0.57687273262229	0.09044378630814
C	1.03243948058575	2.14438675130352	-0.46050152256000
C	2.04445258845449	-0.03955561248573	-0.43514516370172
C	2.11947532067372	1.31902827292999	-0.71917641659649
H	-1.14507062092192	-0.16329996184771	0.71470294547942
H	0.81163030941468	-1.63458868169394	0.30865705041352
H	1.09222290620496	3.19802204981129	-0.69309592913812
H	3.02291428009023	1.73573517068403	-1.14357191316849
H	2.89502286357143	-0.68001483057390	-0.62698503917647

Calculated coordinates of other aryl psuedohalides in ground state:

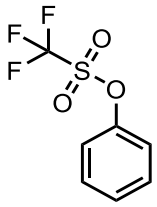

Singlet

C	-0.78204894045528	2.02499598641585	0.75111028840710
C	-1.82402218121171	1.16528700738829	0.45413830235361
C	-1.52708610124175	-0.04039290623930	-0.17077437921404
C	-0.21126403815839	-0.35838158369403	-0.48974163115585
C	0.81619731491413	0.52755327239897	-0.18395353009465
C	0.53596270473035	1.73568144409285	0.44434402164356
H	1.31430781160289	2.44272694982645	0.69034836172215
H	-2.83694073170327	1.44114958220870	0.70768767077797

H	-2.32630466332103	-0.72846249513826	-0.40901502069073
H	1.83910309868796	0.28110639135577	-0.43270611375691
S	-1.26160763597388	4.55921125779196	0.57431159479194
H	0.01346498948462	-1.29734847764509	-0.97666862828120
O	-0.00360236729694	5.01817993881185	0.08072727149789
O	-2.40322653142863	4.45510266564143	-0.27522699789762
C	-1.72779407554182	5.62011607700543	2.03846064732230
F	-0.76747649489838	5.60342960699718	2.95639202659370
F	-1.89183892252702	6.86287616427493	1.59065221913031
F	-2.86399007659412	5.18992139534861	2.57638002426349
O	-1.07845315906771	3.22752772315839	1.44003387258698

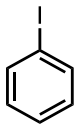

Singlet

C	-0.61521616061352	1.74570759177036	1.08358973376088
C	-1.72681275796642	1.00866551225746	0.69370147823798
C	-1.54347918763394	-0.14721852296890	-0.05788981657281
C	-0.26530361673872	-0.56069131557360	-0.41441758425718
C	0.83691731412706	0.18634860119074	-0.01556649880968
C	0.66892467761705	1.34426811124868	0.73643936230085
H	1.52719007797299	1.92278406076915	1.04537340226030
H	-2.72127574275028	1.32774184094365	0.96928547815298
H	-2.40694275787355	-0.72302802051156	-0.36346918263300
H	1.83550951433388	-0.12858592481626	-0.28777893718683
I	-0.88161093383211	3.50596567992855	2.22210565539252
H	-0.12901042664243	-1.45980761423827	-0.99958309064602

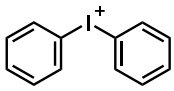

singlet

C	-2.94989146666077	3.53026259642115	0.93021899473390
C	-2.52151675829691	3.98459526980155	-0.31712852543803
I	-0.73502641772090	3.13515480727088	-1.14356746623994
C	0.71515848516342	4.39806628890700	-0.19621327566617
C	1.29686544933878	3.95011981446928	0.98994715217319
C	1.01516099321746	5.61997449943308	-0.79824592595068
C	1.95161969052534	6.43858342312620	-0.15864966044556
C	2.55454252750108	6.02562769602380	1.03408728849184
C	2.23189691615226	4.79006827206600	1.60420316613902
C	-3.18581932825440	4.96008043266443	-1.06081939165462
C	-4.34585995363294	5.51188555393641	-0.50660811670176
C	-4.80368252067845	5.08626000360414	0.74424500633594
C	-4.11161245169397	4.10255743759230	1.45844646884323

H	-2.82734243289090	5.28750557927270	-2.03801174855343
H	-4.89094009248899	6.27735011437203	-1.06348764072274
H	-5.71143193846843	5.52329766693123	1.16583437286164
H	-4.47494094168073	3.76934340542229	2.43320676274060
H	0.54588271754207	5.93626721418911	-1.73105070152083
H	2.20906044425553	7.40255183314838	-0.60320950773306
H	3.28617100810358	6.67257077891241	1.52281073861151
H	2.70769658347223	4.46928294903392	2.53365036232654
H	-2.41032511583595	2.75913765198697	1.48227539228021
H	1.04331460303162	2.98486671141469	1.43103625508918

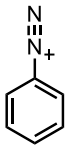

singlet

C	-0.61797792088719	2.05317317487209	0.64461154913356
C	-1.77001098984128	1.27817058741563	0.38104540153419
C	-1.57437481295408	0.00852563808464	-0.14533912998045
C	-0.27442923640229	-0.46038232607946	-0.39486937845193
C	0.85316559750593	0.33108884406912	-0.12287060342152
C	0.70112823314925	1.60668570712887	0.40346150086987
H	1.55789322270226	2.24559284812087	0.62518307274966
H	-2.76777836631155	1.67035509531867	0.58621121967097
H	-2.43833706388237	-0.62228967287101	-0.36356292707136
H	1.85577449215947	-0.05165219368766	-0.32359049326886
N	-0.79029651728013	3.31317898696598	1.16546752258543
H	-0.13738453428666	-1.46210113775490	-0.80922895154207
N	-0.92967210367136	4.33255444841715	1.58624121719249

triplet

C	-0.58764147800149	2.10187025443020	0.66334187967160
C	-1.77854492479327	1.25029069813441	0.37063543375526
C	-1.59088865721467	-0.01631706961579	-0.15471956200402
C	-0.30448147113955	-0.49790619161674	-0.40925489607311
C	0.85532041975068	0.35421172644730	-0.11348682384777
C	0.72312862811427	1.62711218803409	0.41124421643436
H	1.59112169788451	2.25157156550562	0.62668451052151
H	-2.77082758791199	1.65308284313382	0.58068091205108
H	-2.46372530292648	-0.63722047855459	-0.36835631640878
H	1.85714347641765	-0.03517928097548	-0.31690835498908
N	-0.77753153704772	3.31792128271820	1.16628341751750
H	-0.13918597405852	-1.49381543212312	-0.82283906324795
N	-0.96379728907342	4.36505789448208	1.59991464661939

SPECTROSCOPIC DATA

^{1}H NMR of arylethylamine 3

$CDCl_3$, 23 ºC

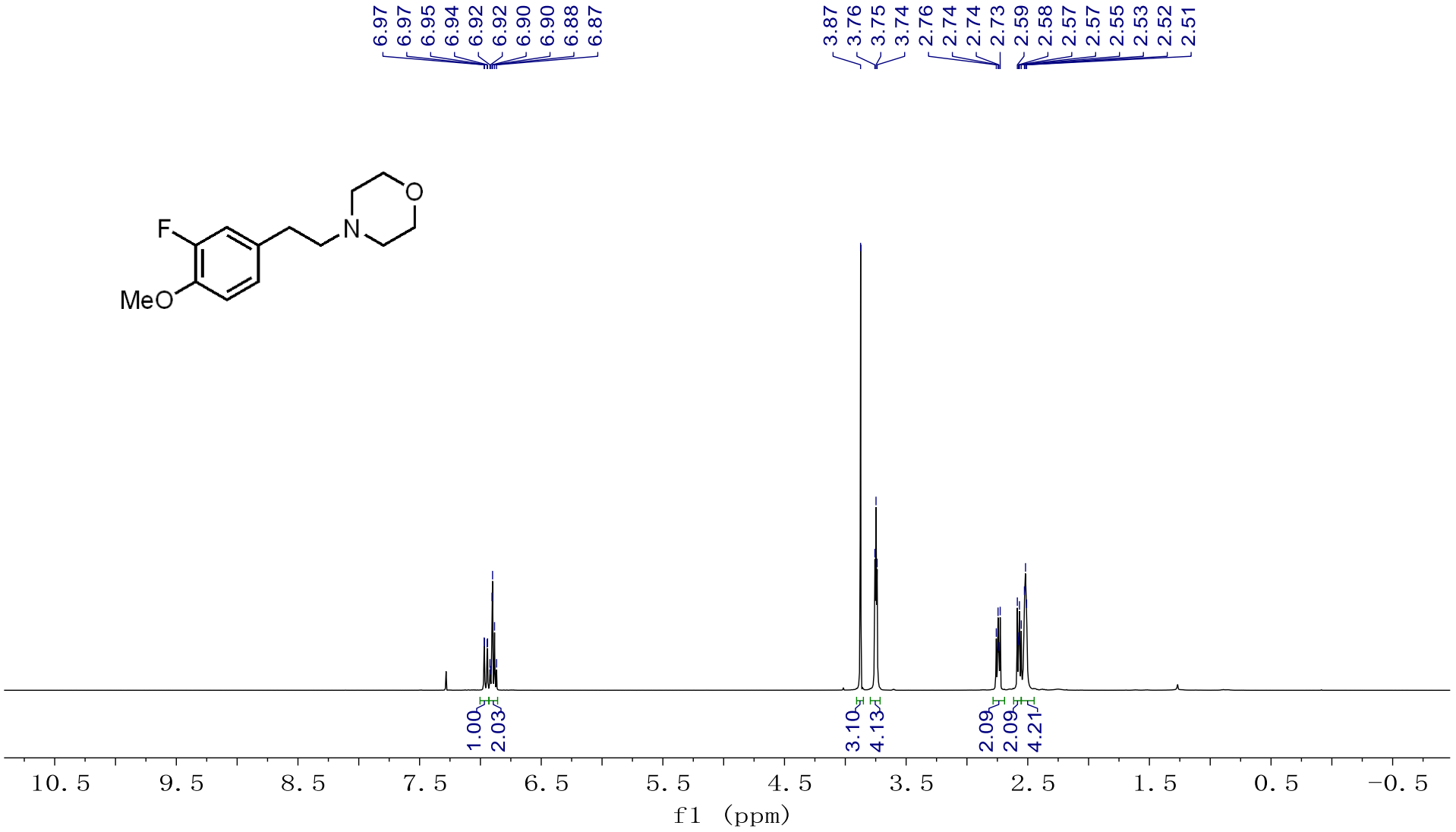

^{13}C NMR of arylethylamine 3

$CDCl_3$, 23 ºC

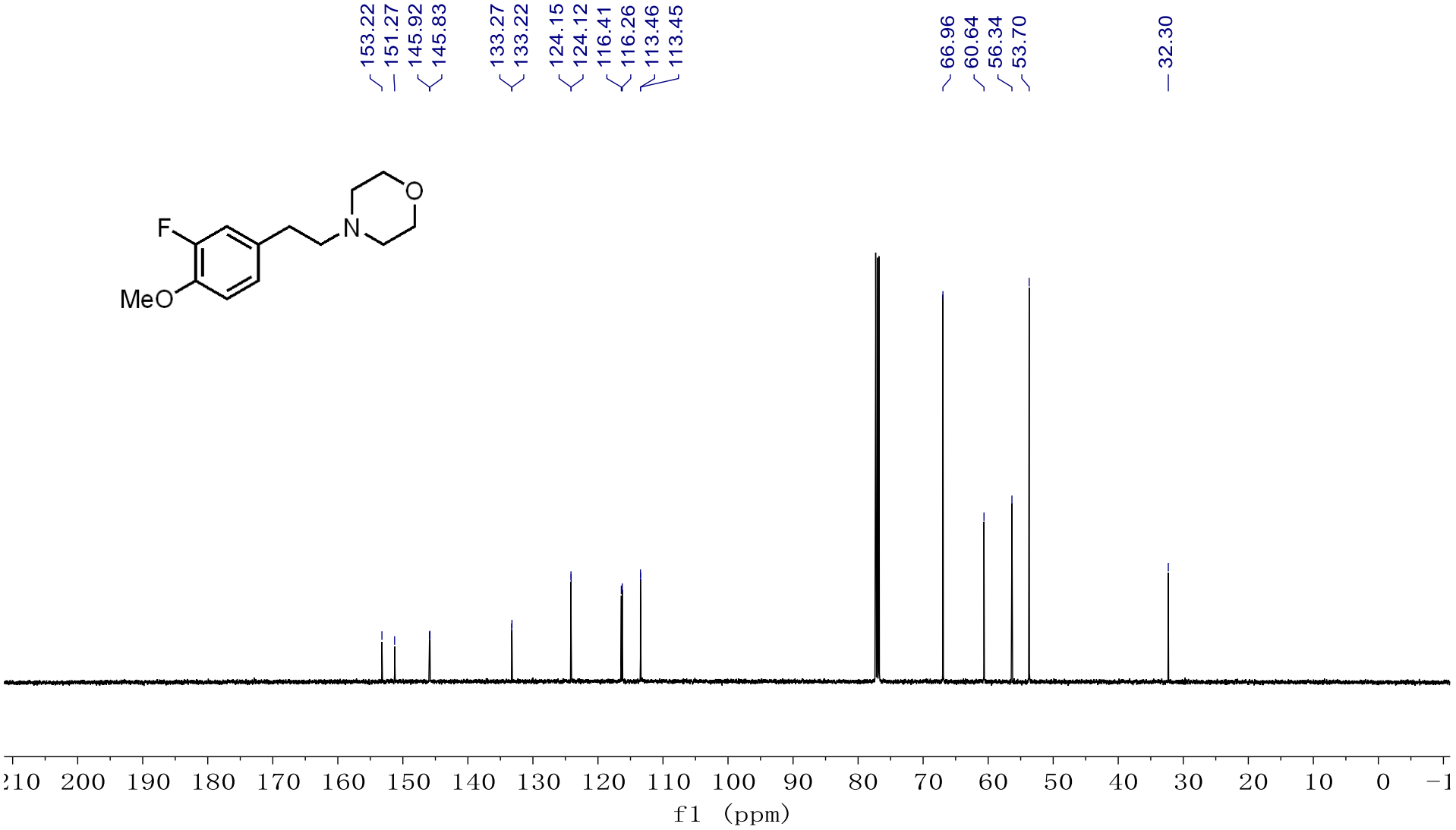

^{19}F NMR of arylethylamine 3

$CDCl_3$, 23 ºC

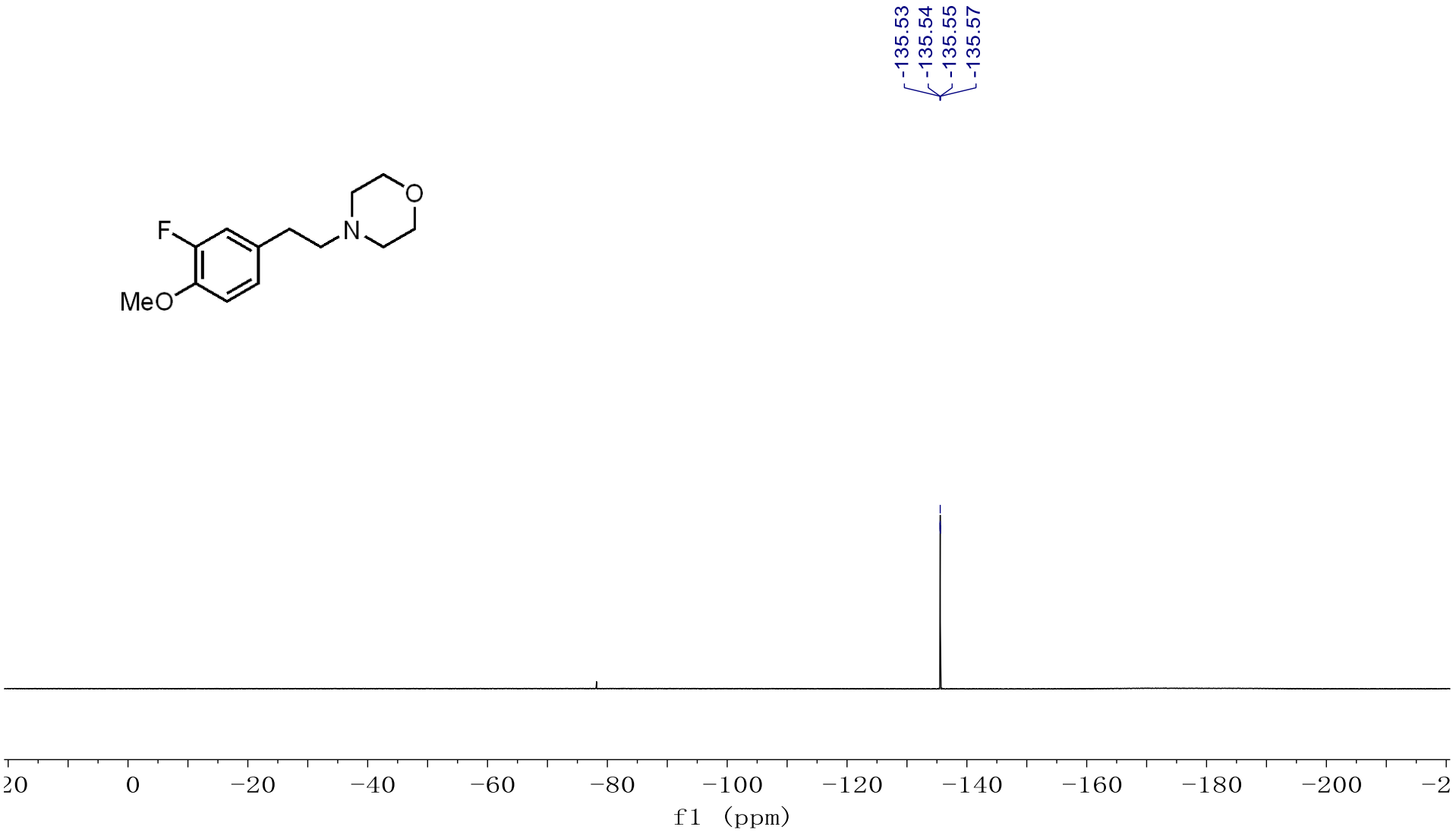

^{1}H NMR of arylethylamine 4

$CDCl_3$, 23 ºC

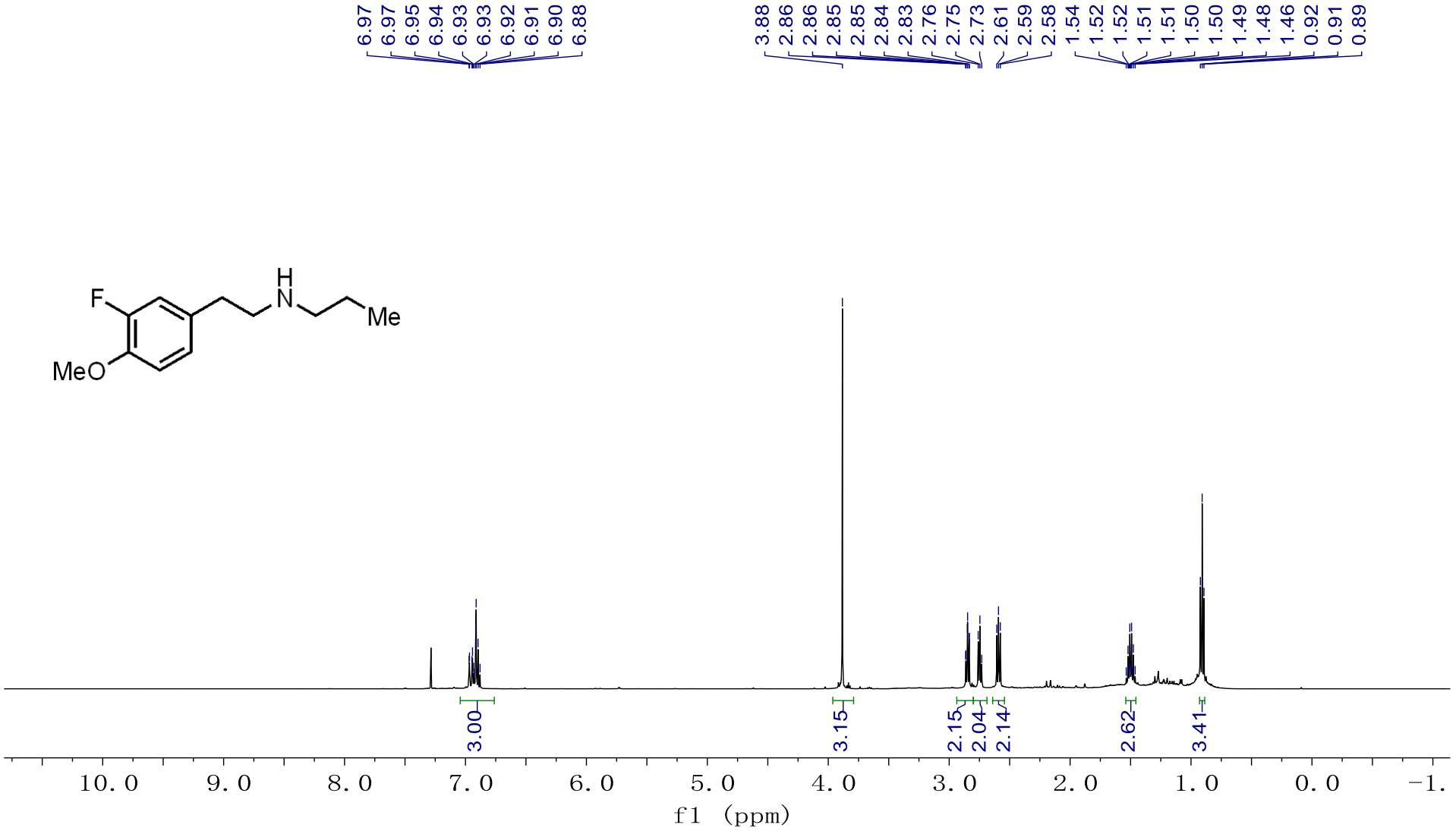

^{13}C NMR of arylethylamine 4

$CDCl_3$, 23 ºC

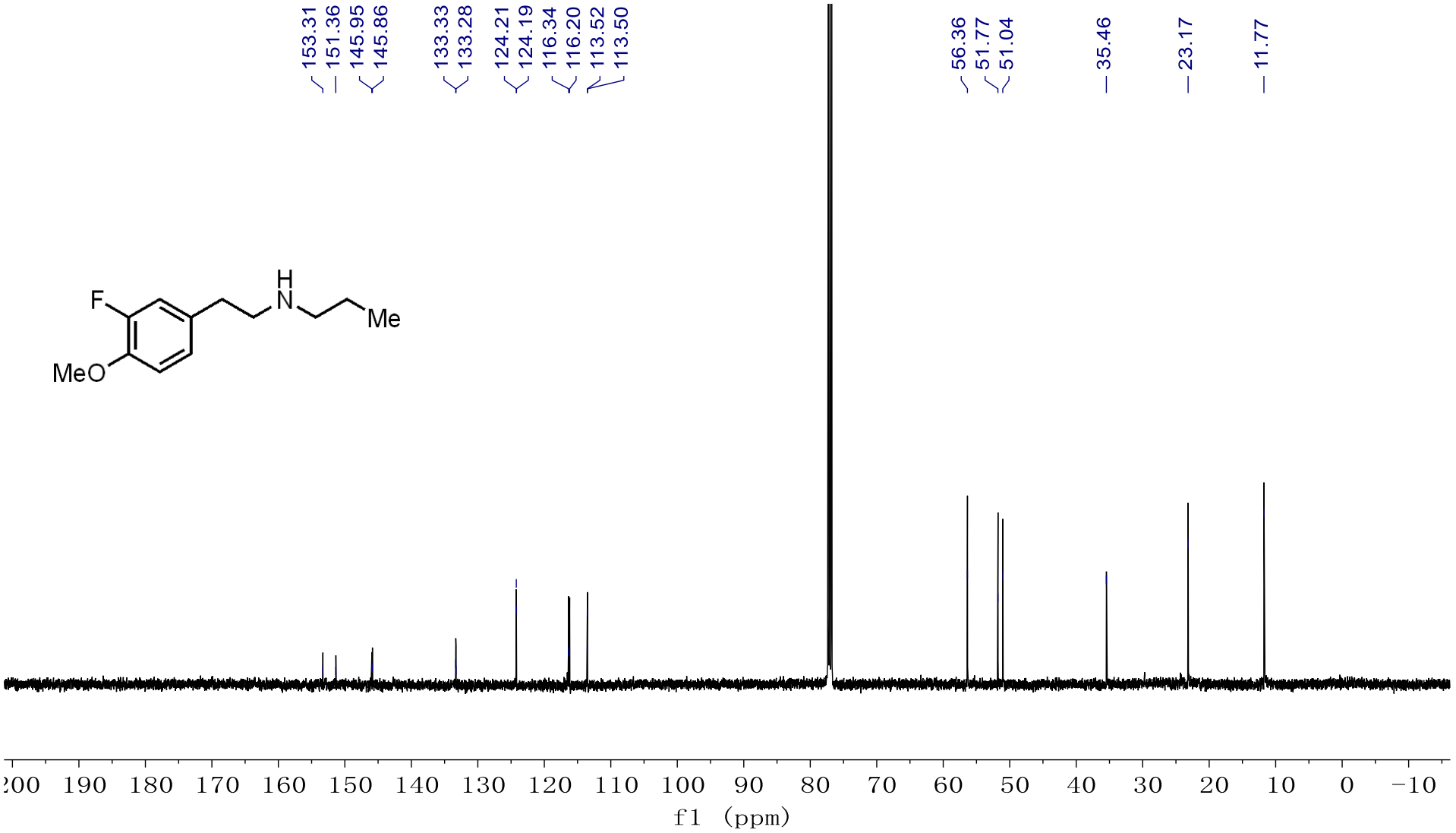

^{19}F NMR of arylethylamine 4

$CDCl_3$, 23 ºC

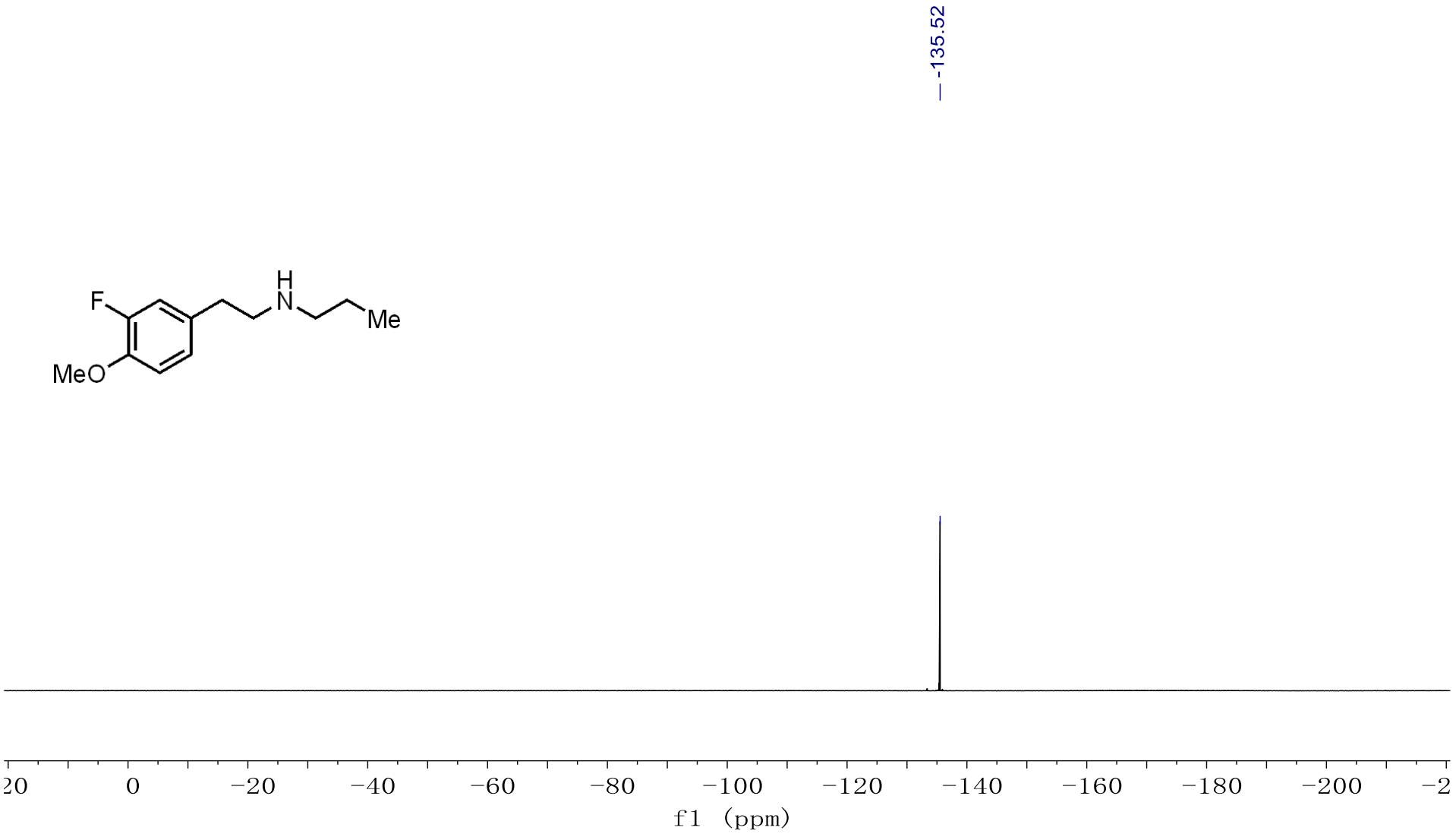

^{1}H NMR of arylethylamine 5

$CDCl_3$, 23 ºC

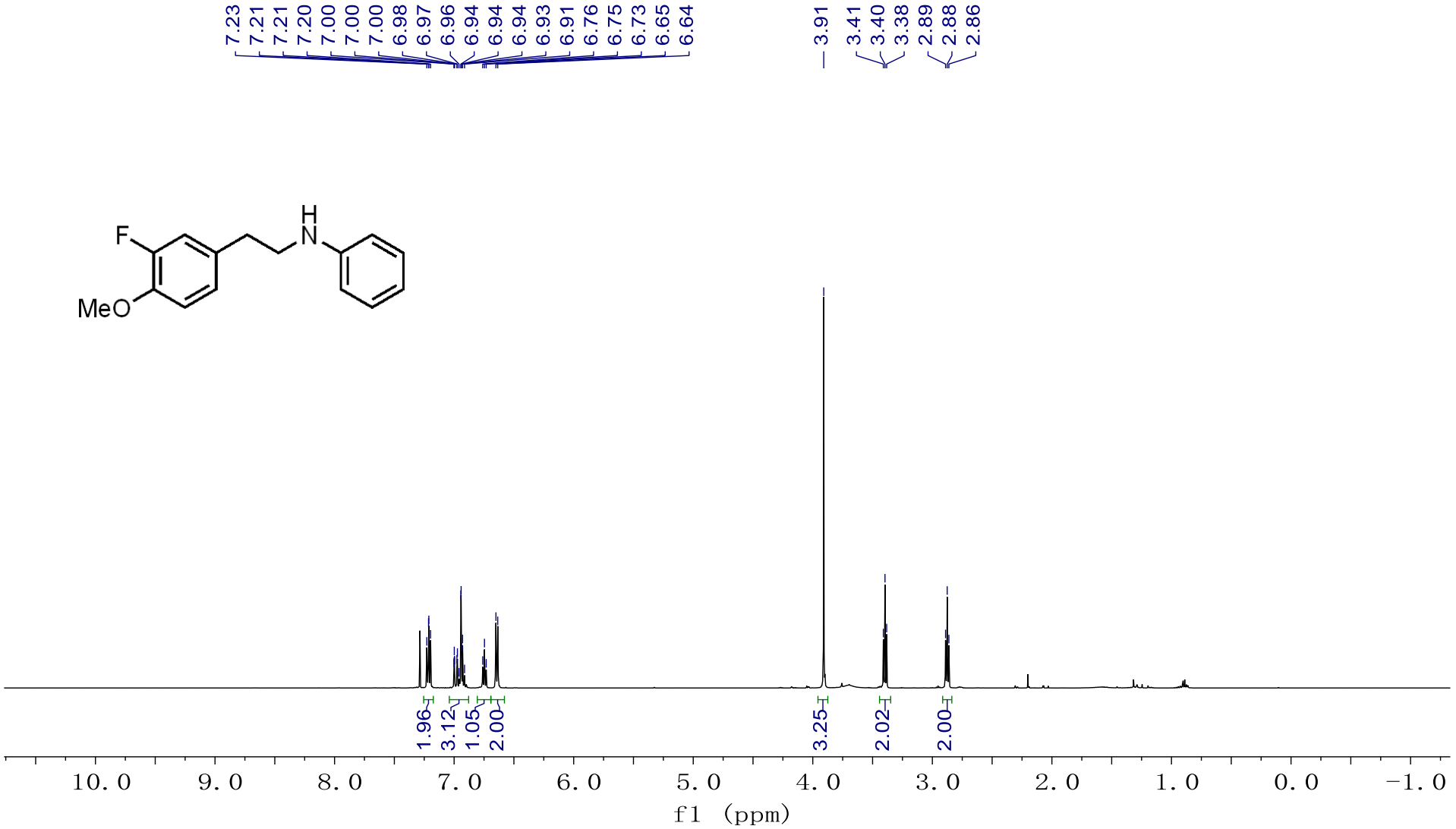

^{13}C NMR of arylethylamine 5

$CDCl_3$, 23 ºC

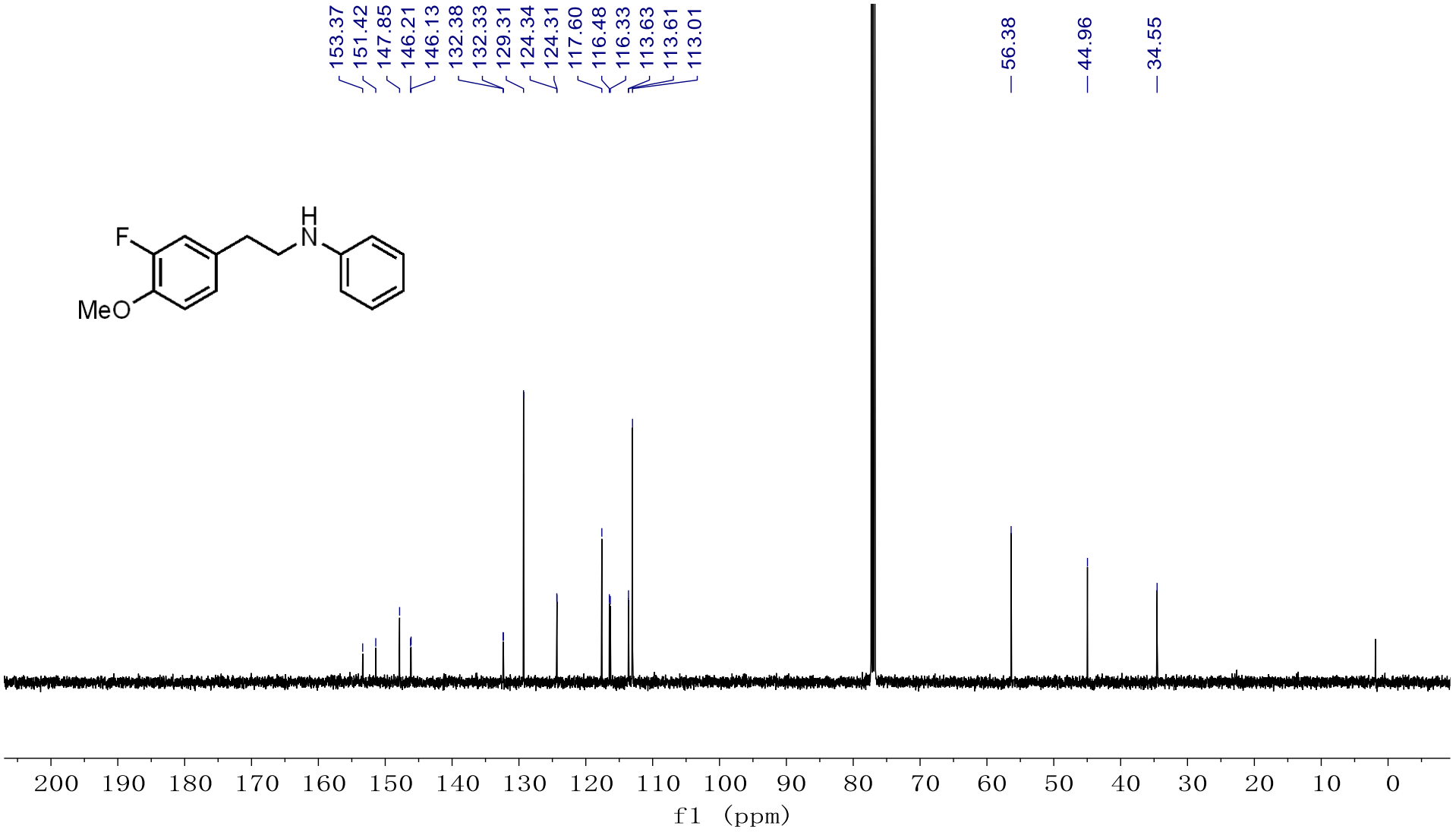

^{19}F NMR of arylethylamine 5

$CDCl_3$, 23 ºC

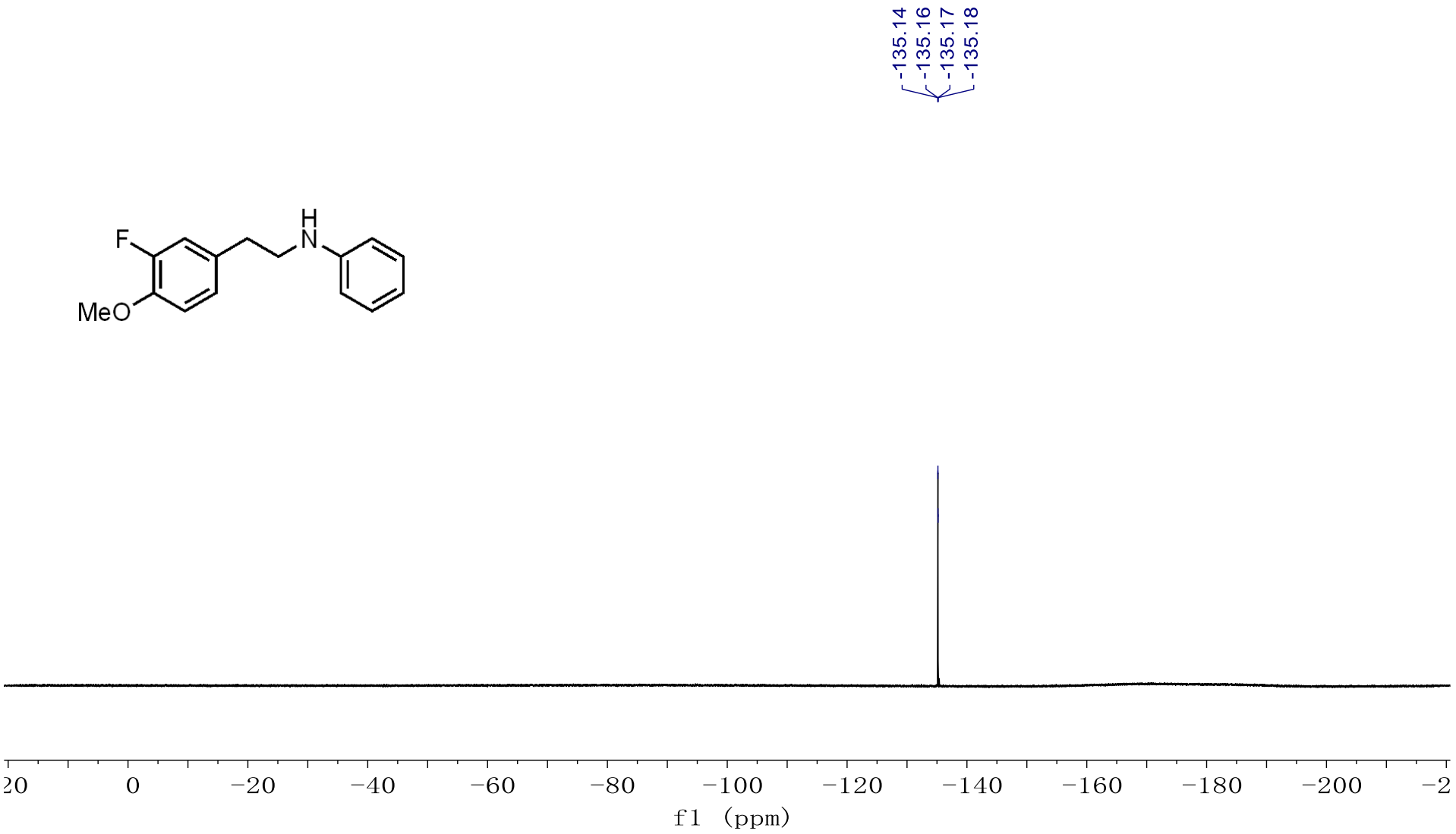

^{1}H NMR of thalidomide-derived arylethylamine 6

$CDCl_3$, 23 ºC

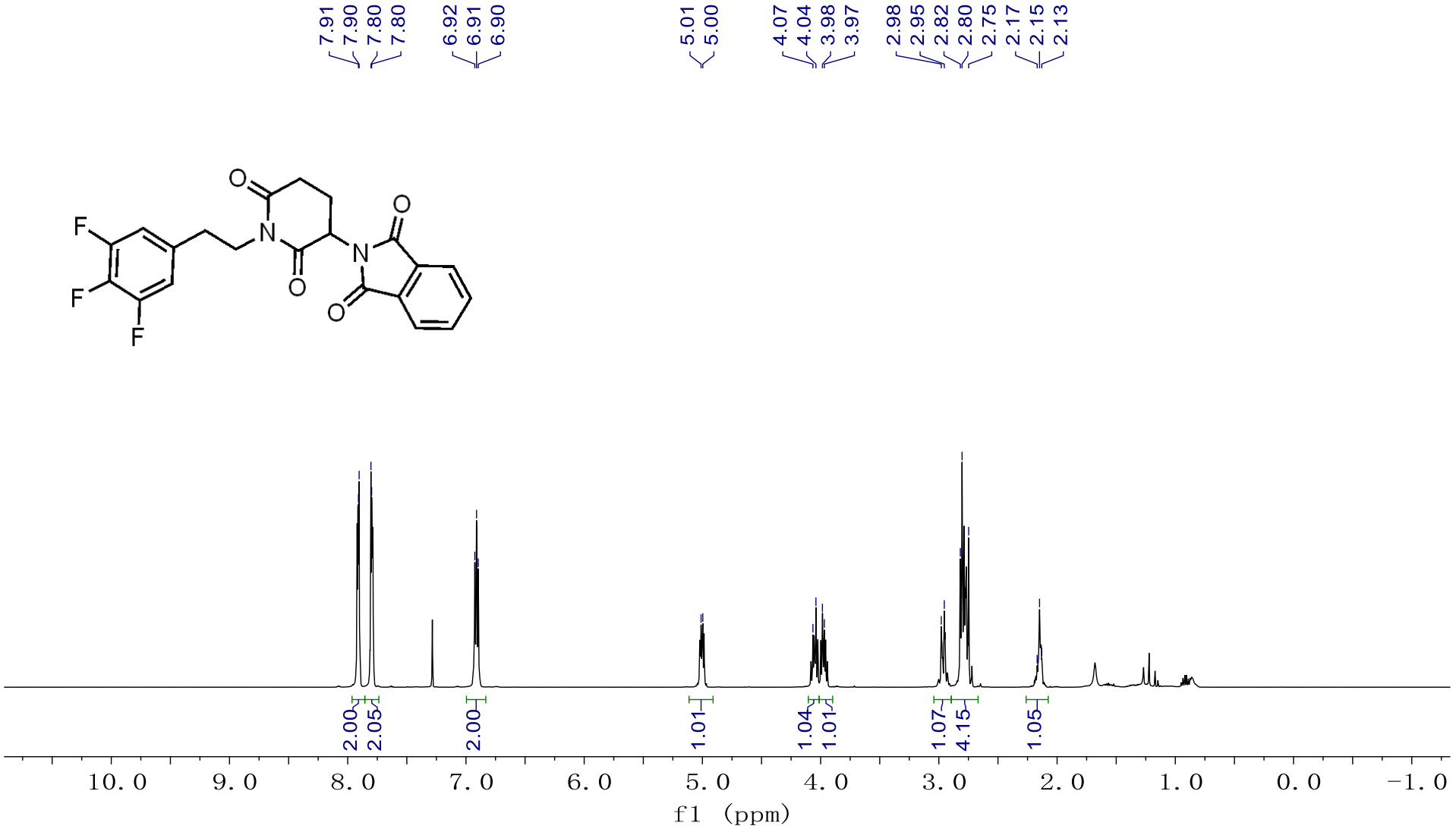

^{13}C NMR of thalidomide-derived arylethylamine 6

$CDCl_3$, 23 ºC

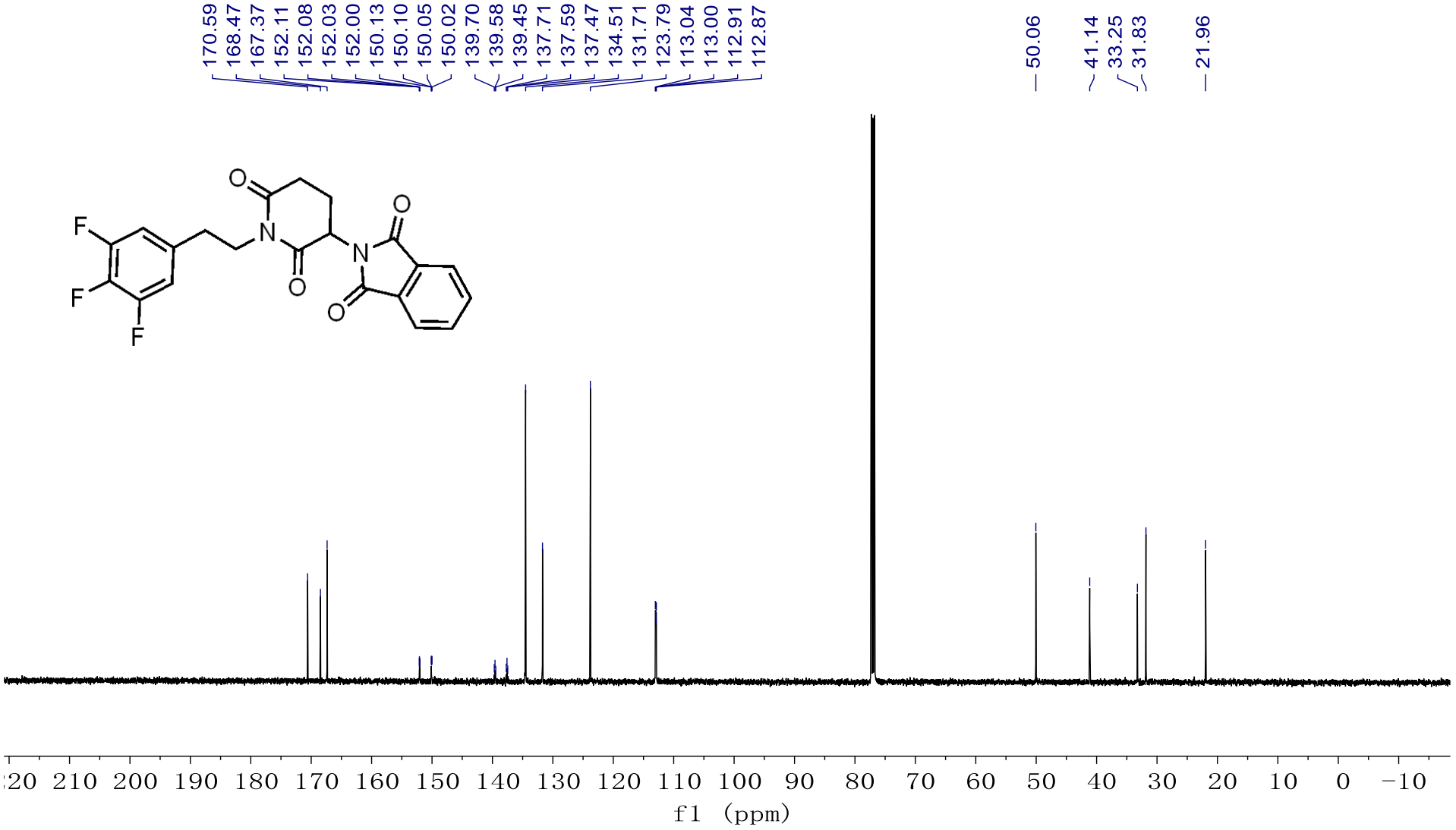

^{19}F NMR of thalidomide-derived arylethylamine 6

$CDCl_3$, 23 ºC

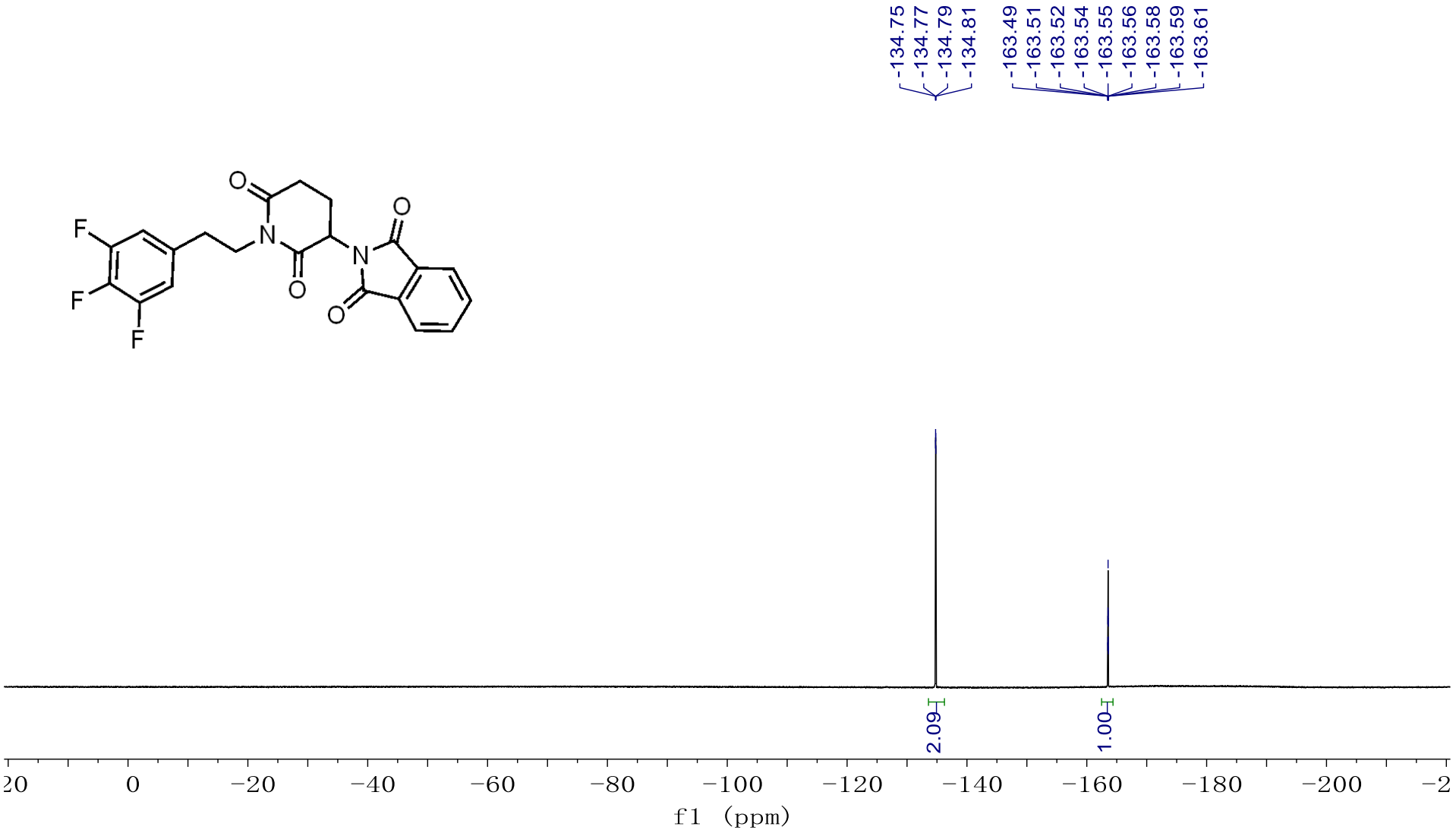

^{1}H NMR of fenofibrate-derived arylethyl chloride 7

$CDCl_3$, 23 ºC

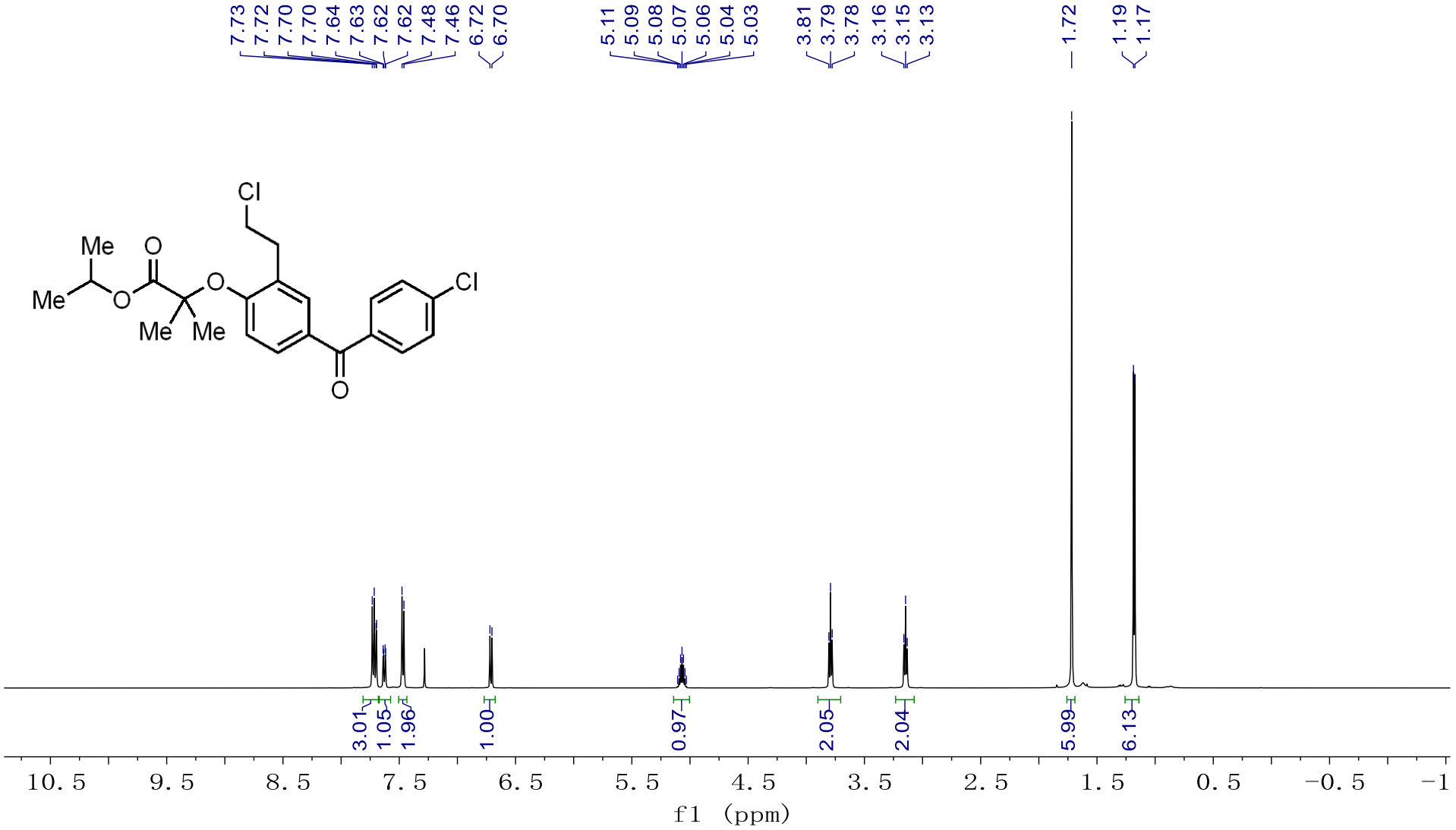

^{13}C NMR of fenofibrate-derived arylethyl chloride 7

$CDCl_3$, 23 ºC

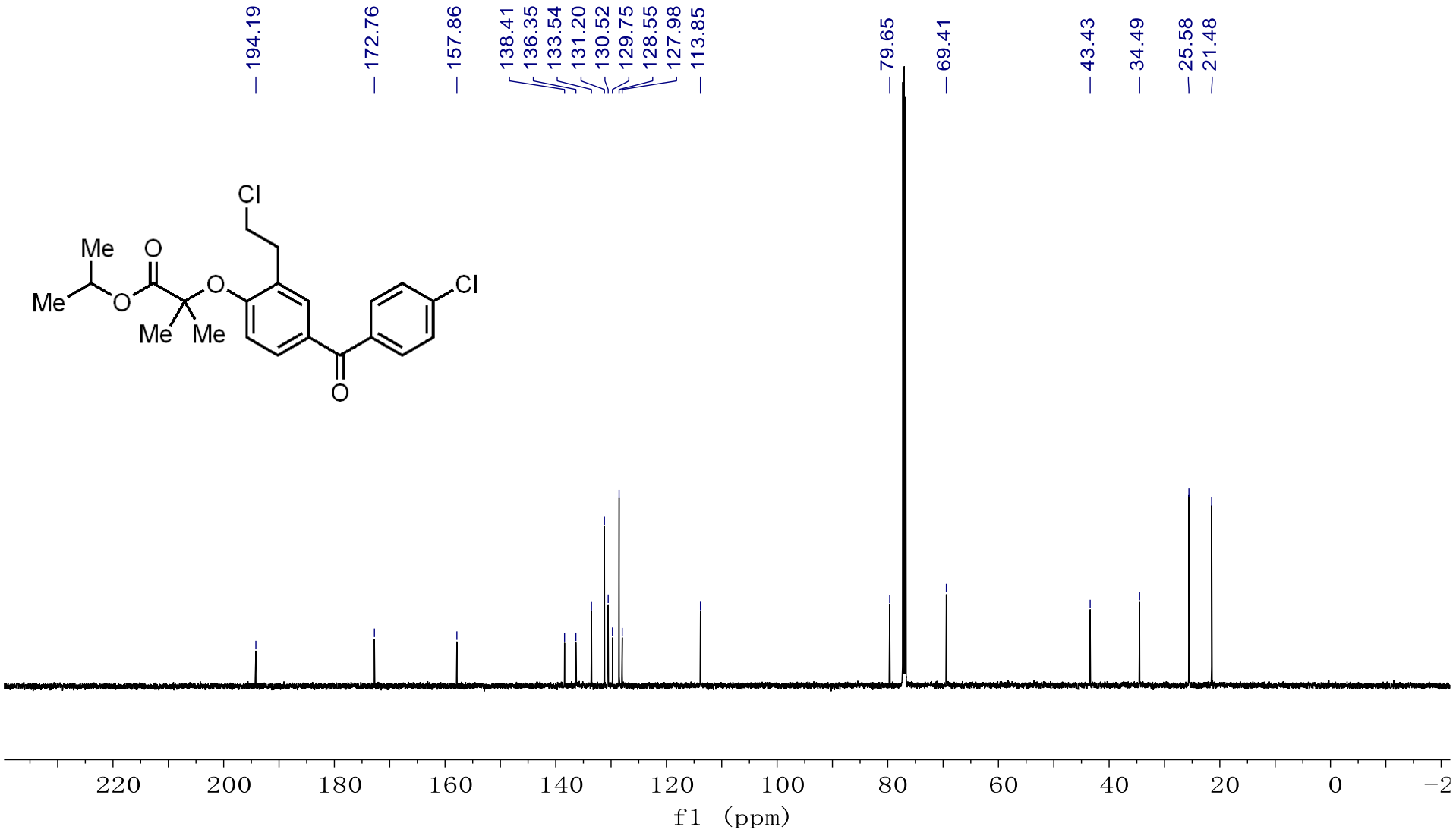

^{1}H NMR of vinyl arene 8

$CDCl_3$, 23 ºC

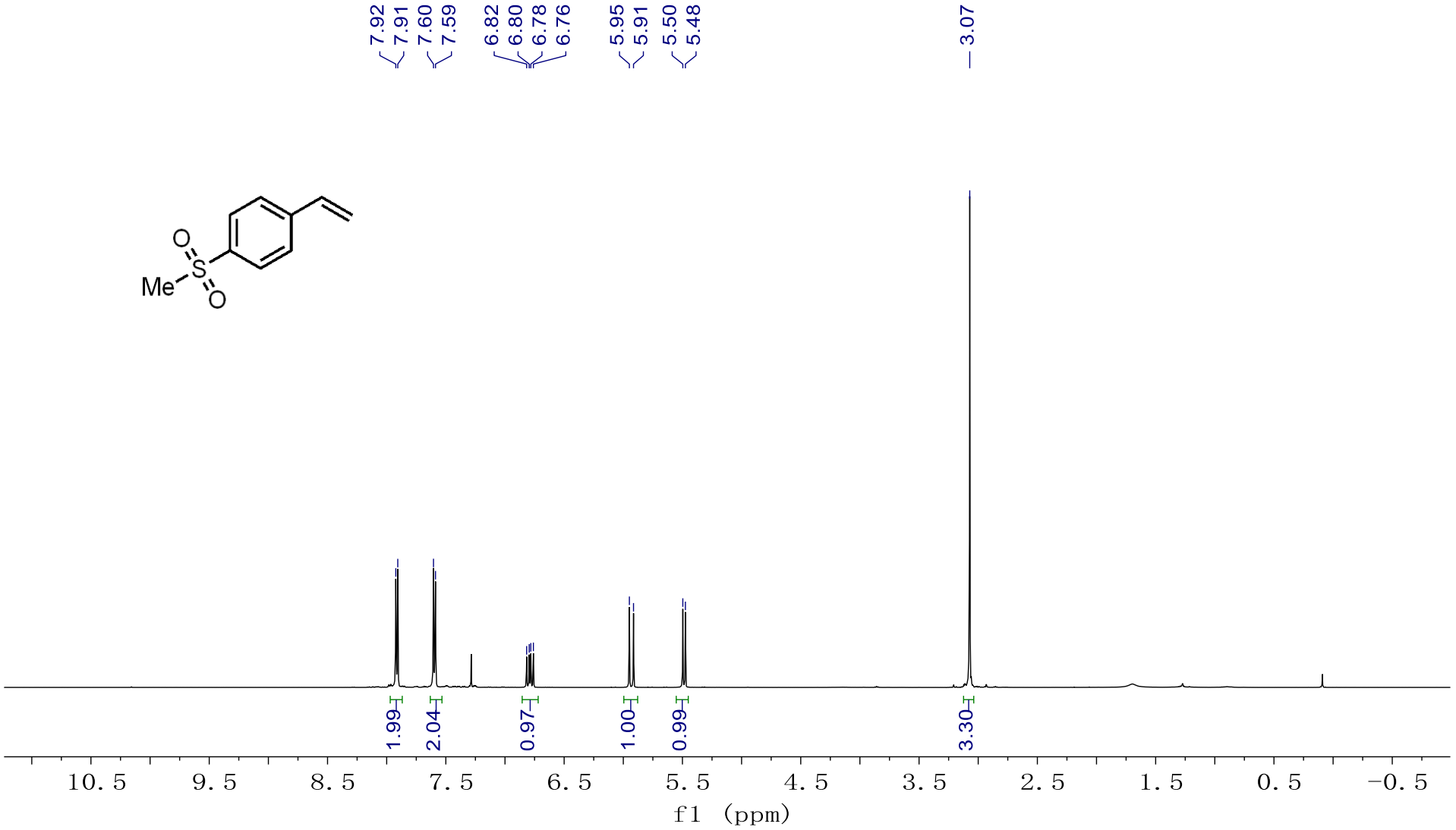

^{13}C NMR of vinyl arene 8

$CDCl_3$, 23 ºC

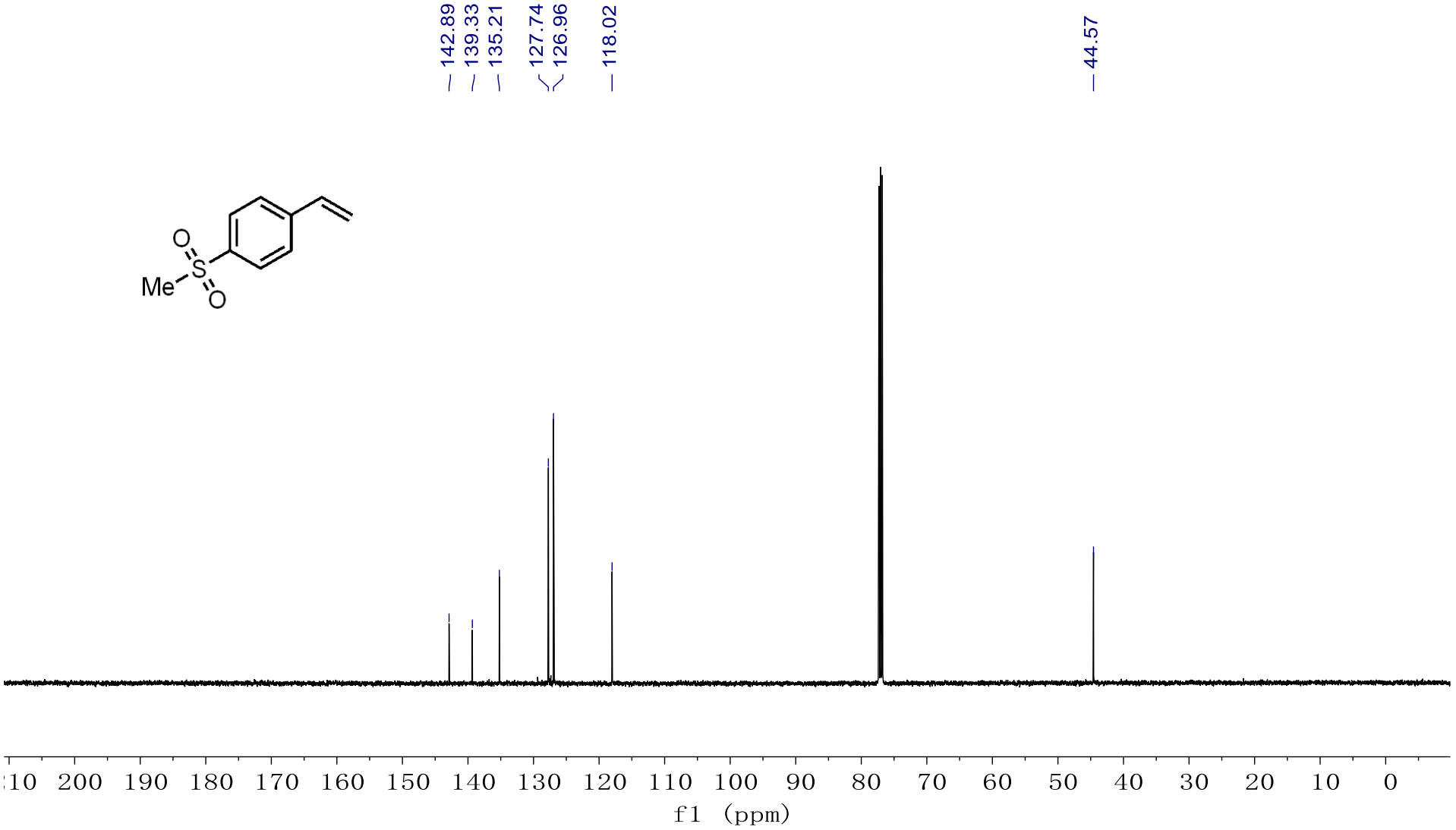

^{1}H NMR of arylethyl thioether 9

$CDCl_3$, 23 ºC

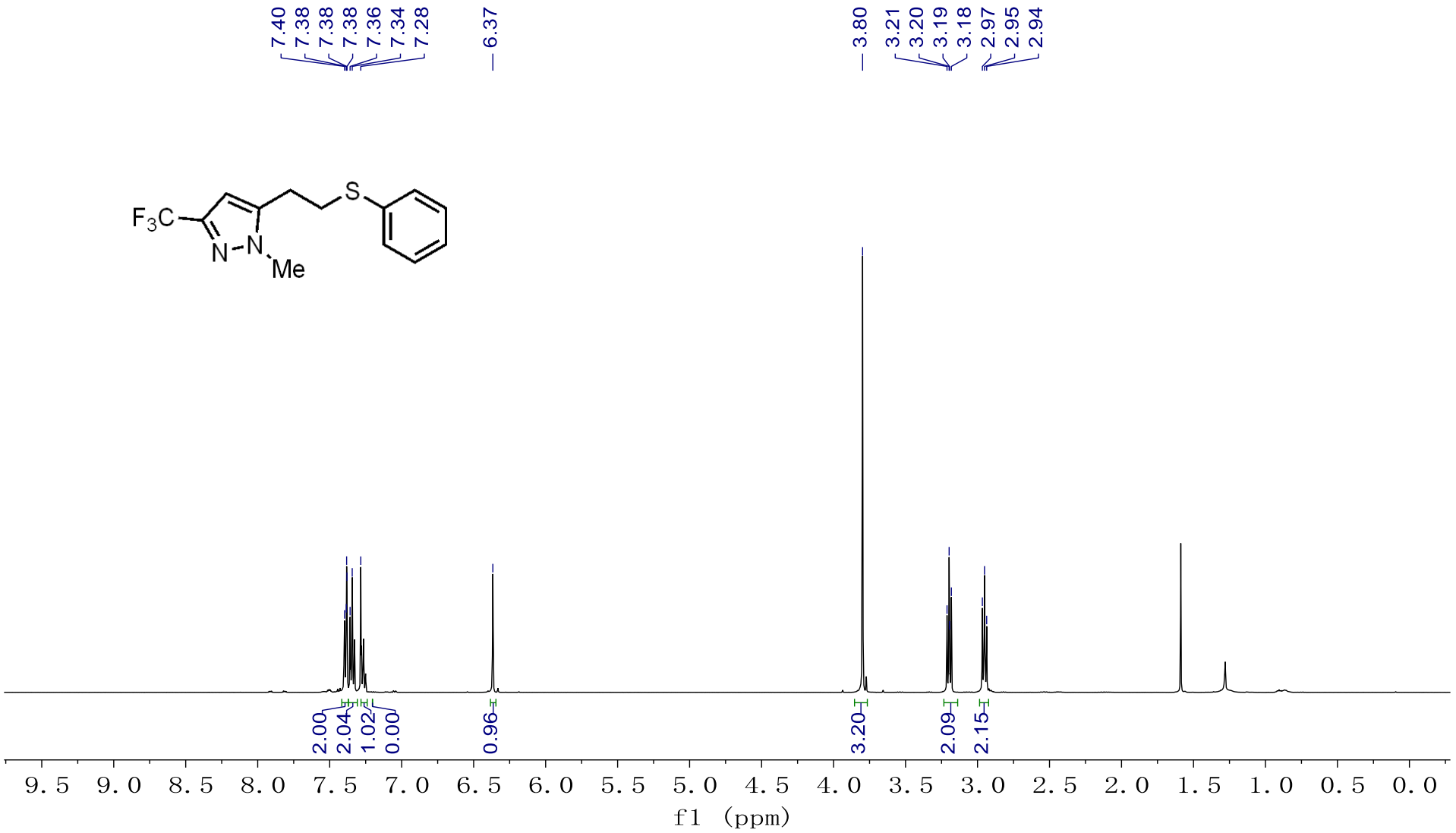

^{13}C NMR of arylethyl thioether 9

$CDCl_3$, 23 ºC

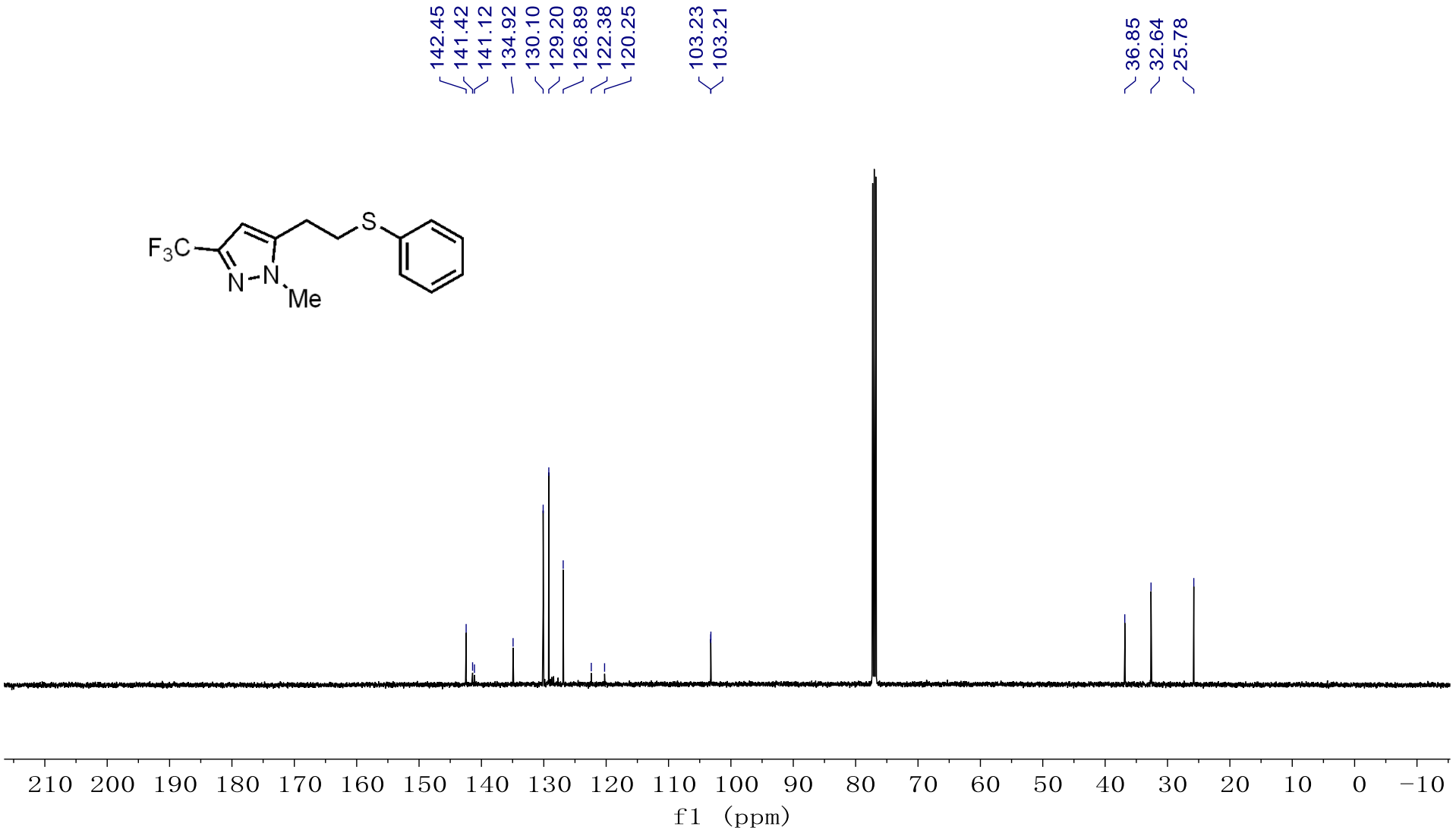

^{19}F NMR of arylethyl thioether 9

$CDCl_3$, 23 ºC

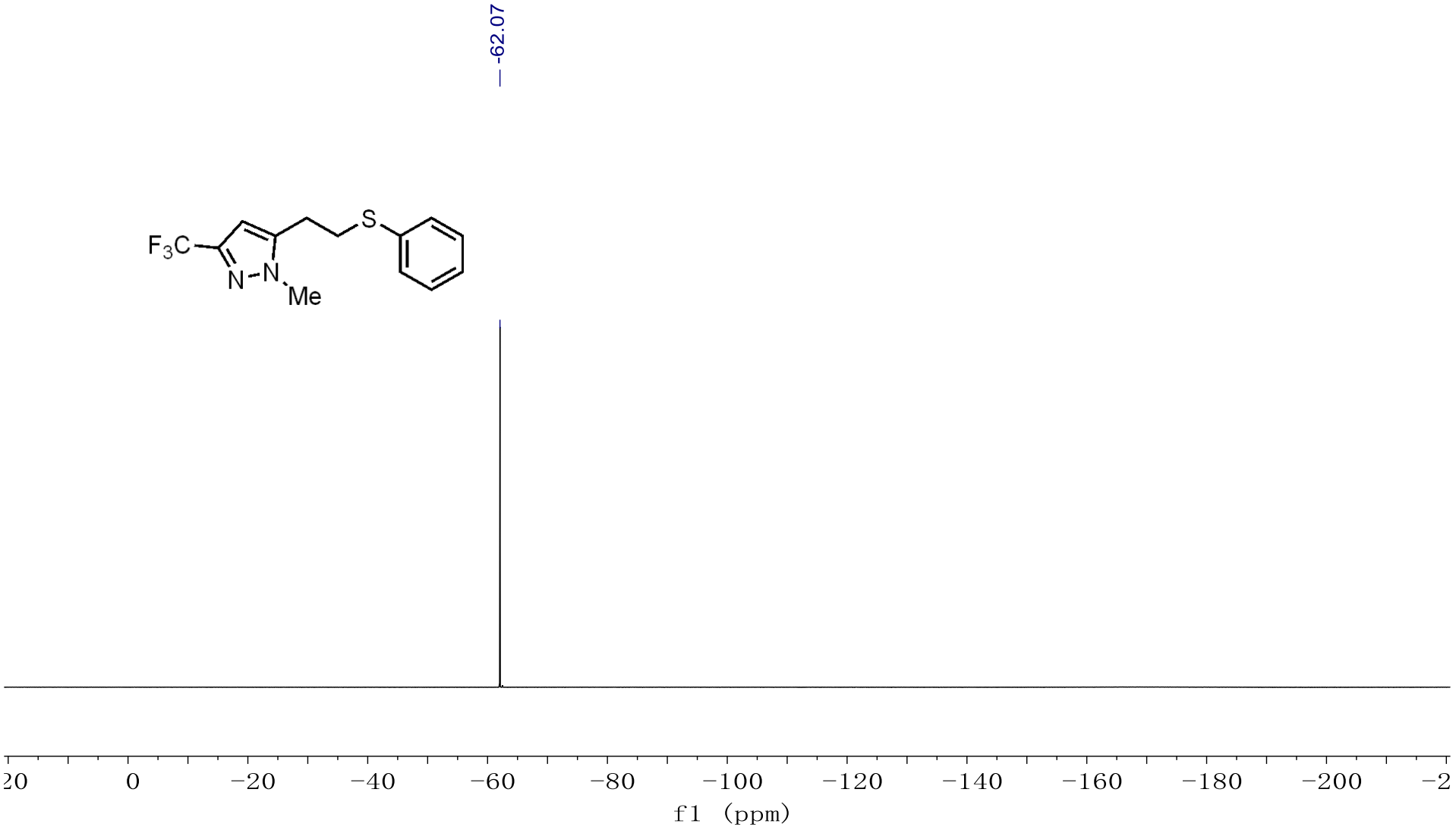

^{1}H NMR of arylethyl selenoether 10

$CDCl_3$, 23 ºC

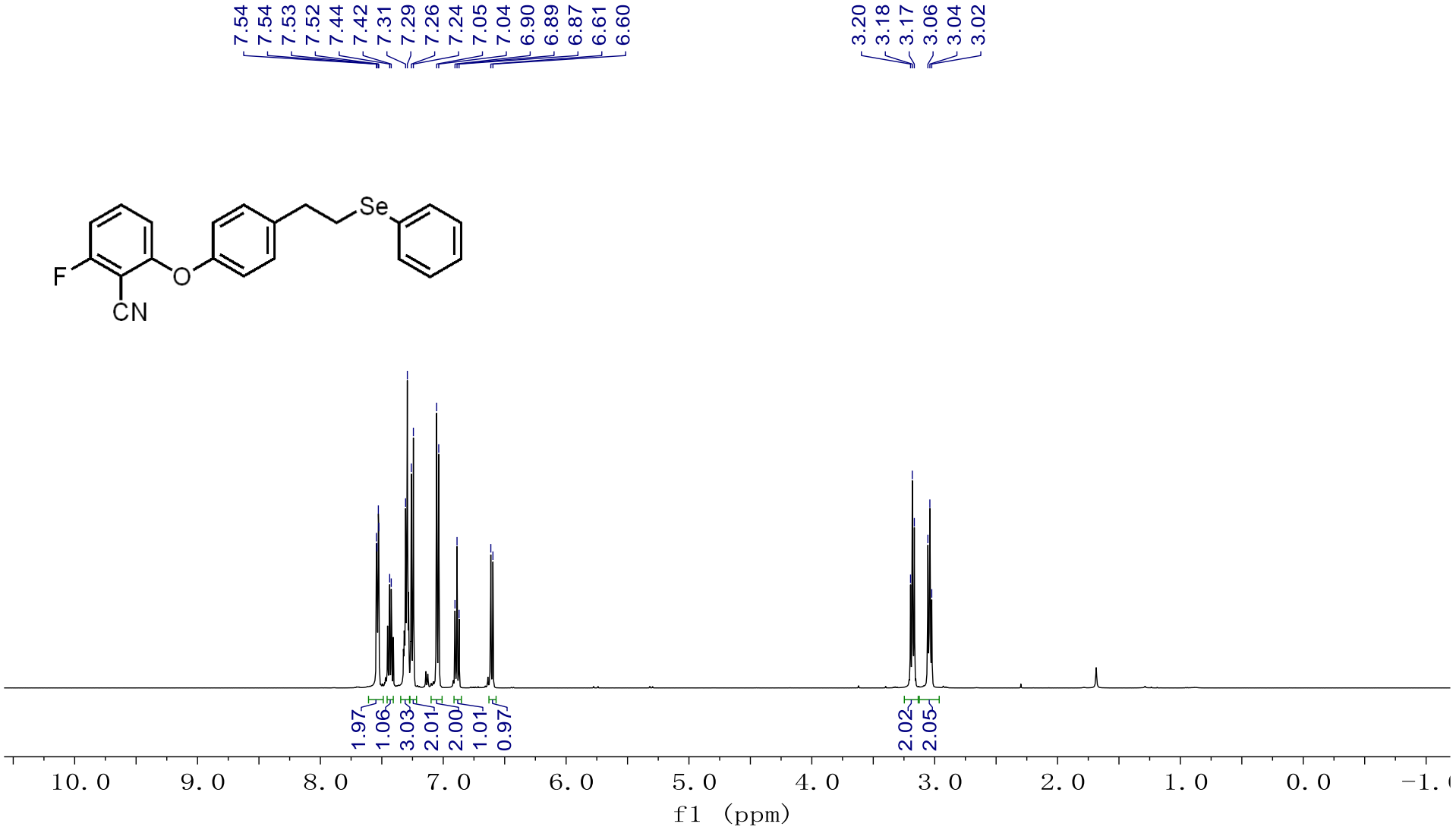

^{13}C NMR of arylethyl selenoether 10

$CDCl_3$, 23 ºC

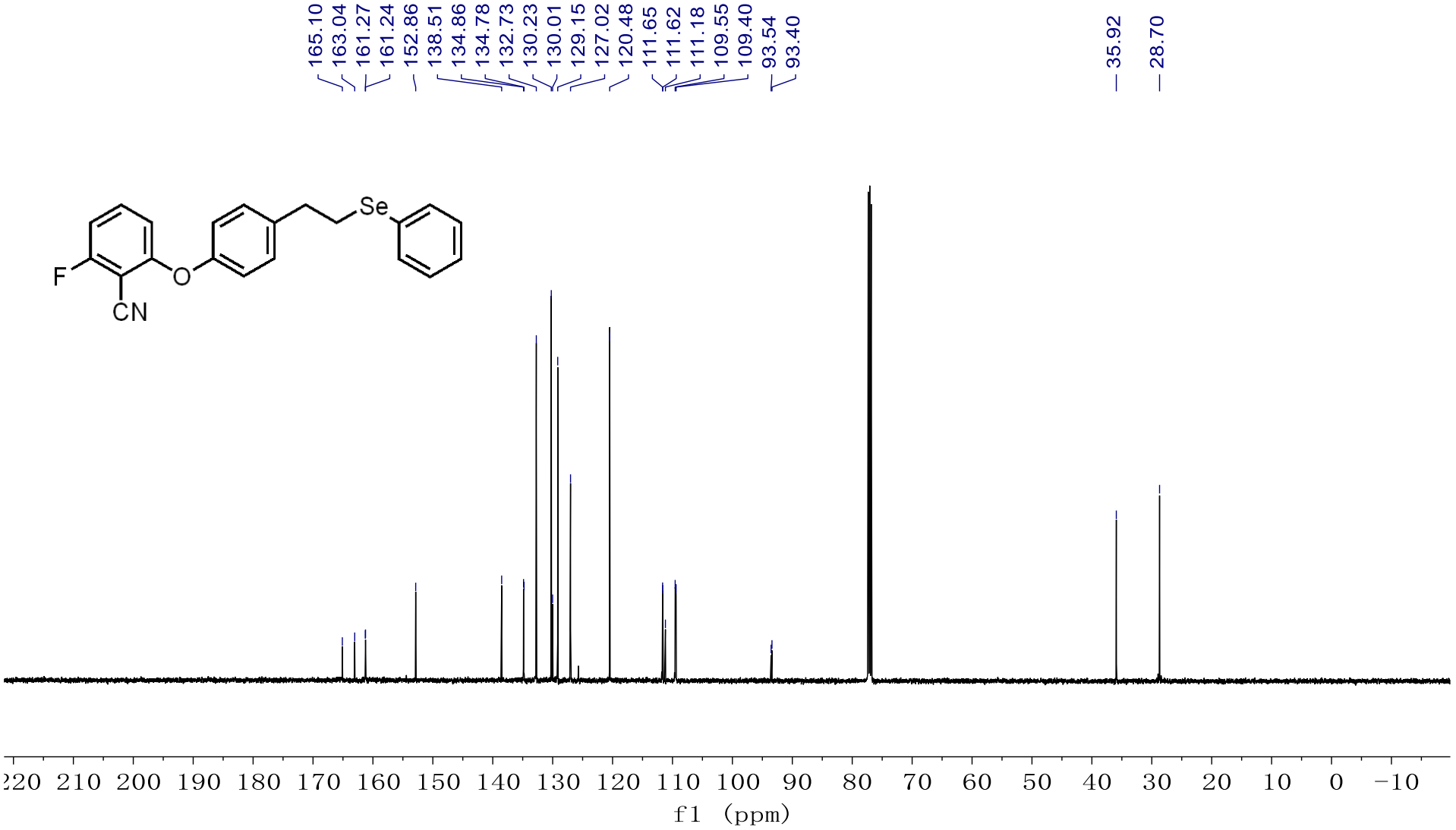

^{19}F NMR of arylethyl selenoether 10

$CDCl_3$, 23 ºC

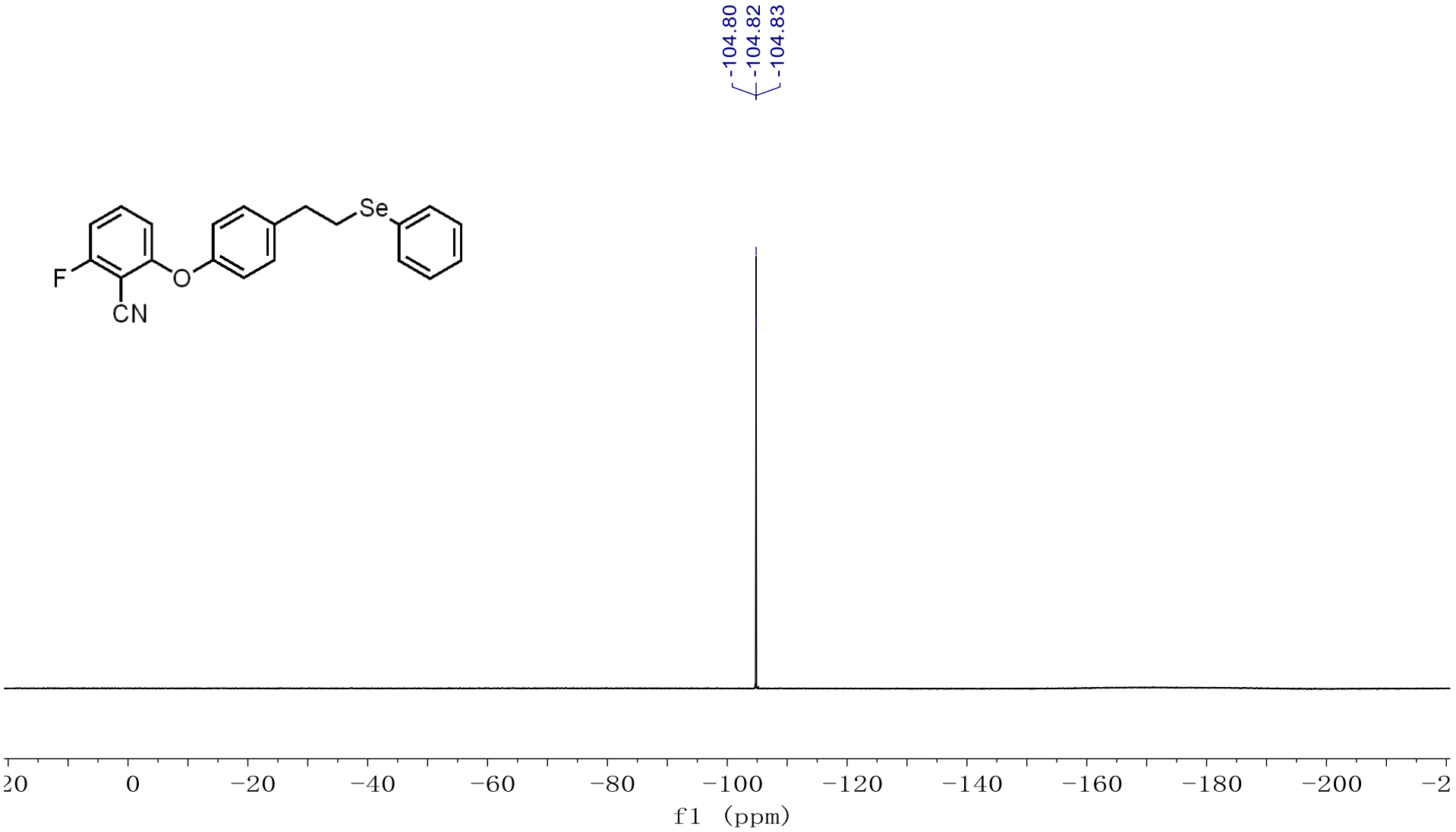

^{1}H NMR of trimetazidine-derived arylethylamine 11

$CDCl_3$, 23 ºC

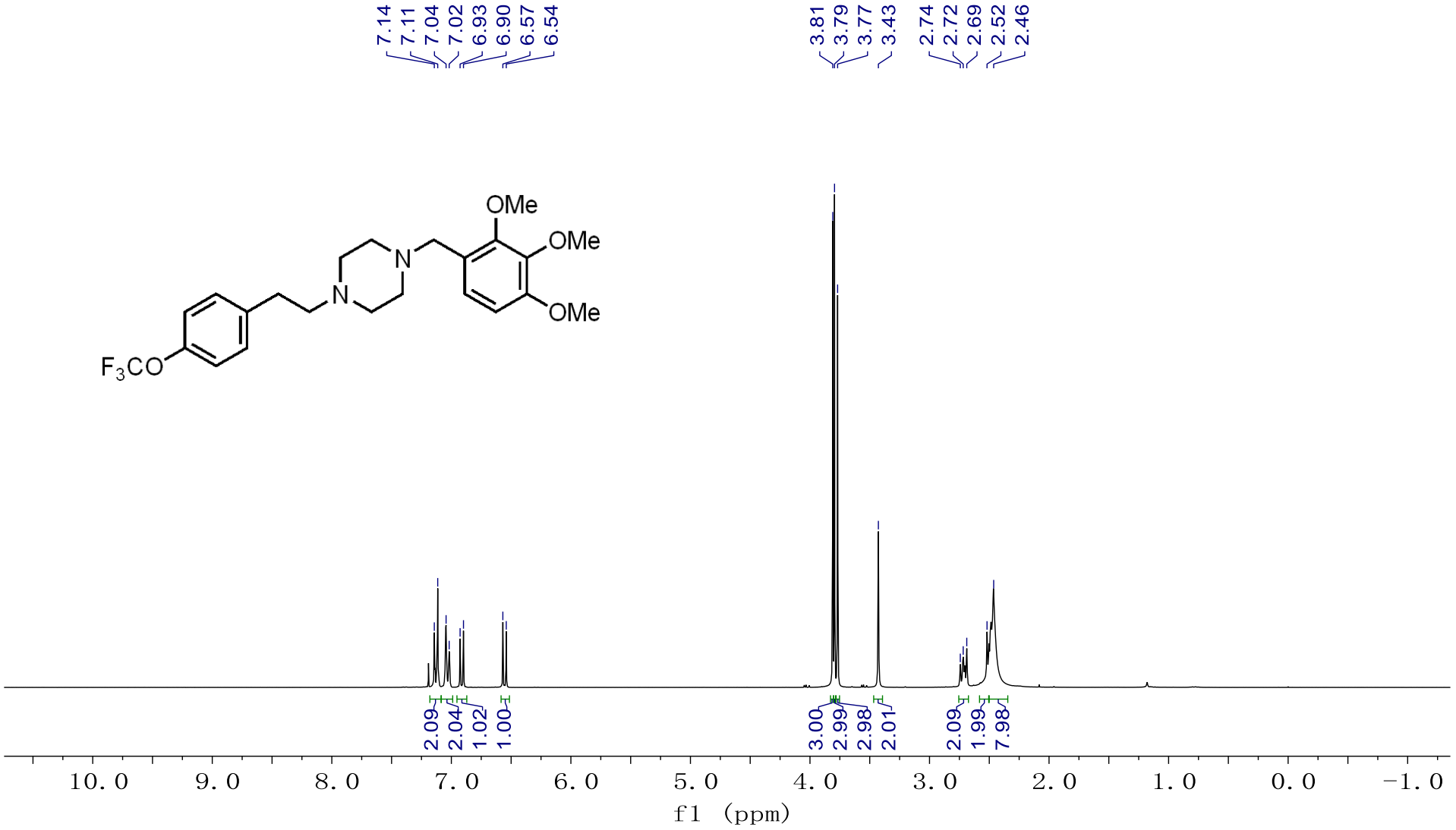

^{13}C NMR of trimetazidine-derived arylethylamine 11

$CDCl_3$, 23 ºC

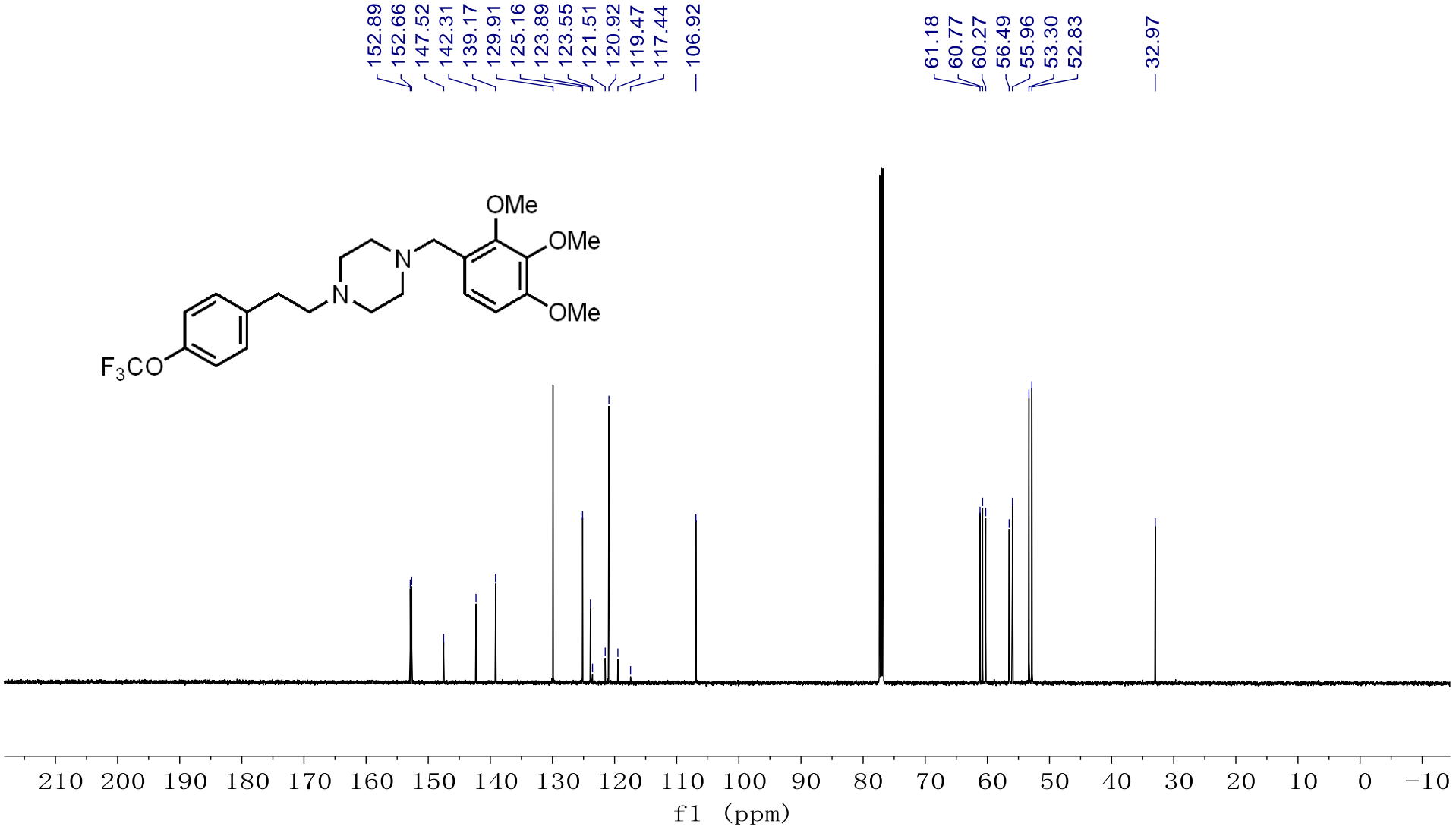

^{19}F NMR of trimetazidine-derived arylethylamine 11

$CDCl_3$, 23 ºC

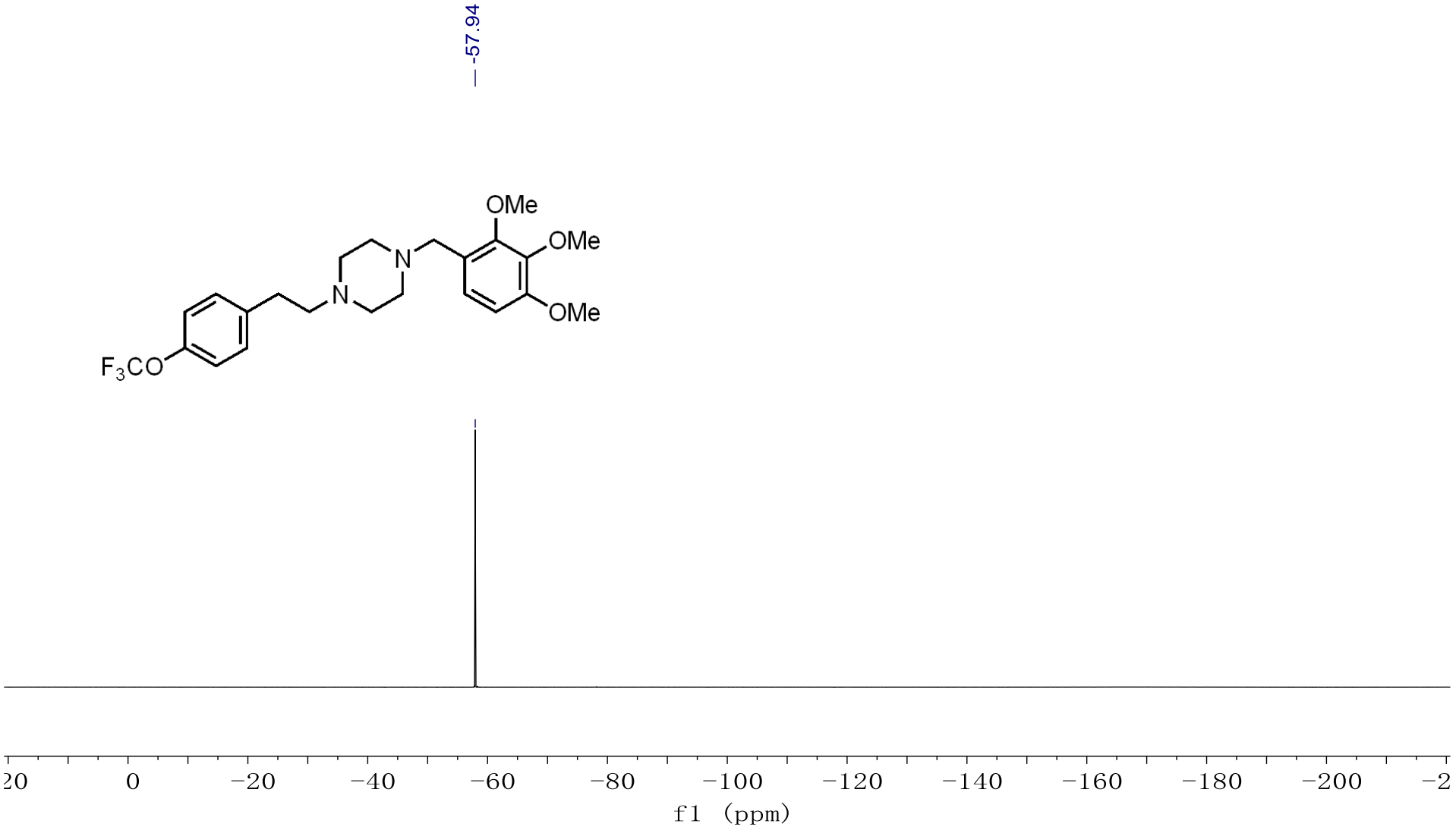

^{1}H NMR of arylethyl iodide 12

$CDCl_3$, 23 ºC

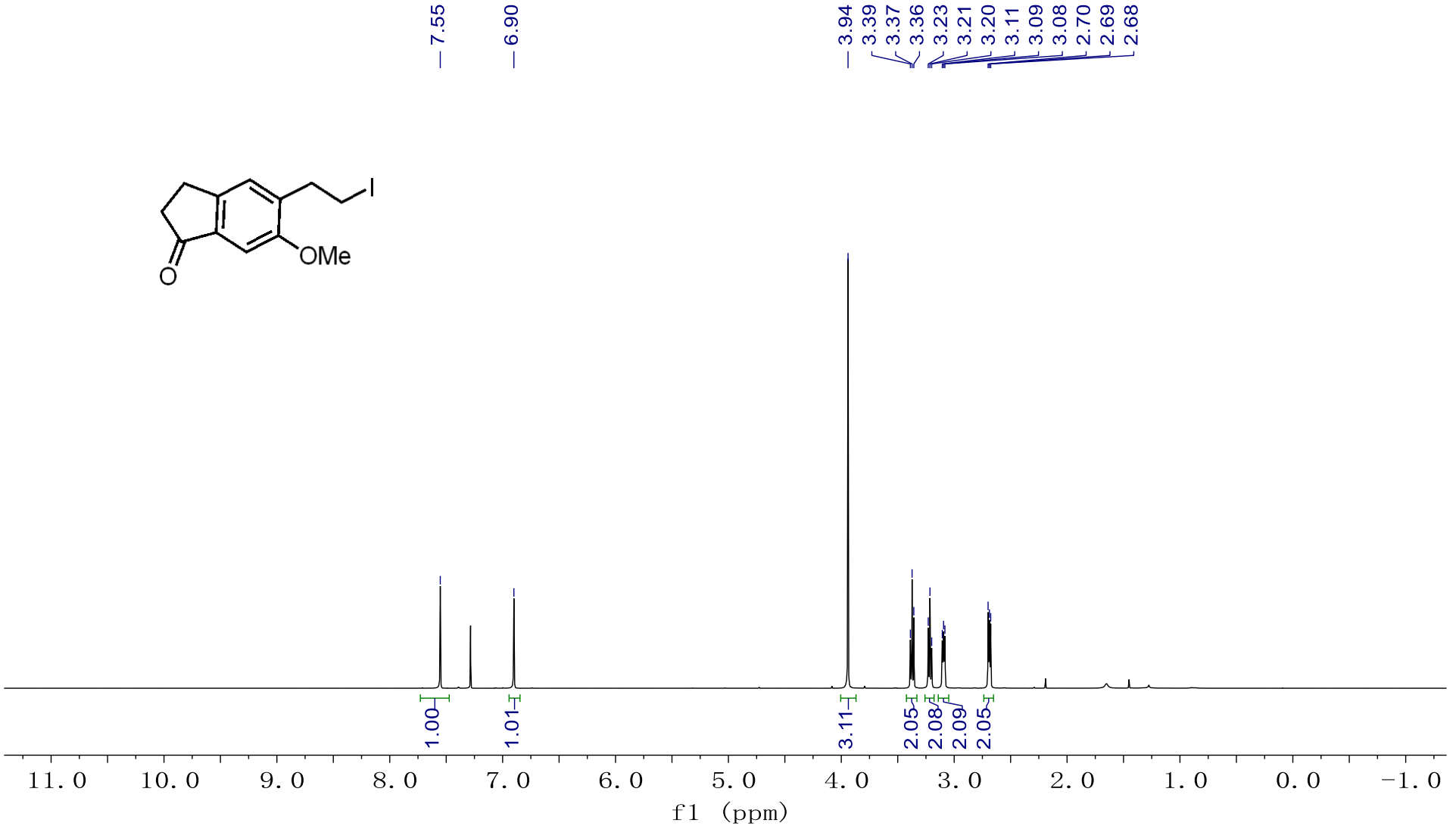

^{13}C NMR of arylethyl iodide 12

$CDCl_3$, 23 ºC

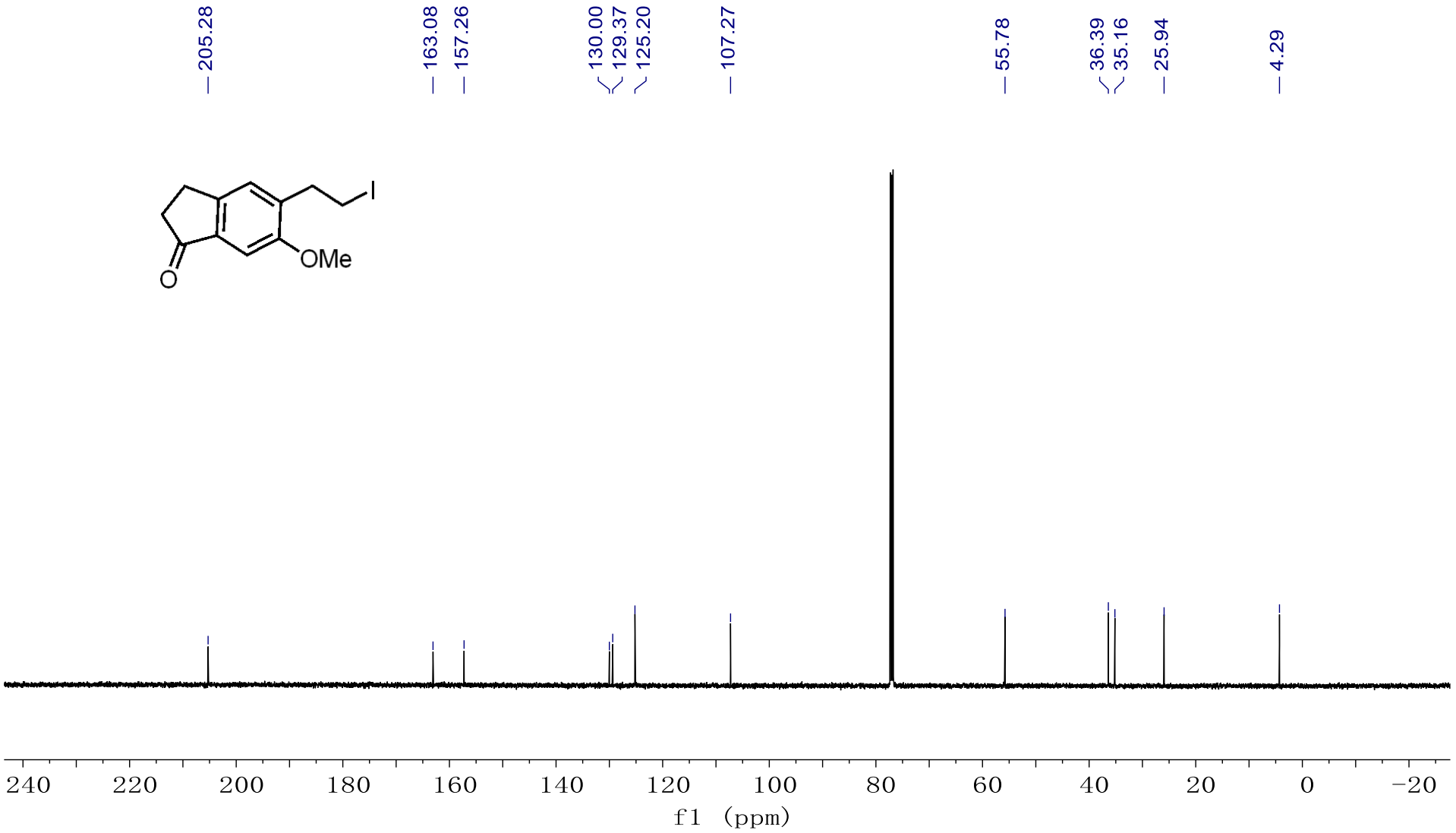

^{1}H NMR of arylethylammonium salt 13

CD_3CN, 23 ºC

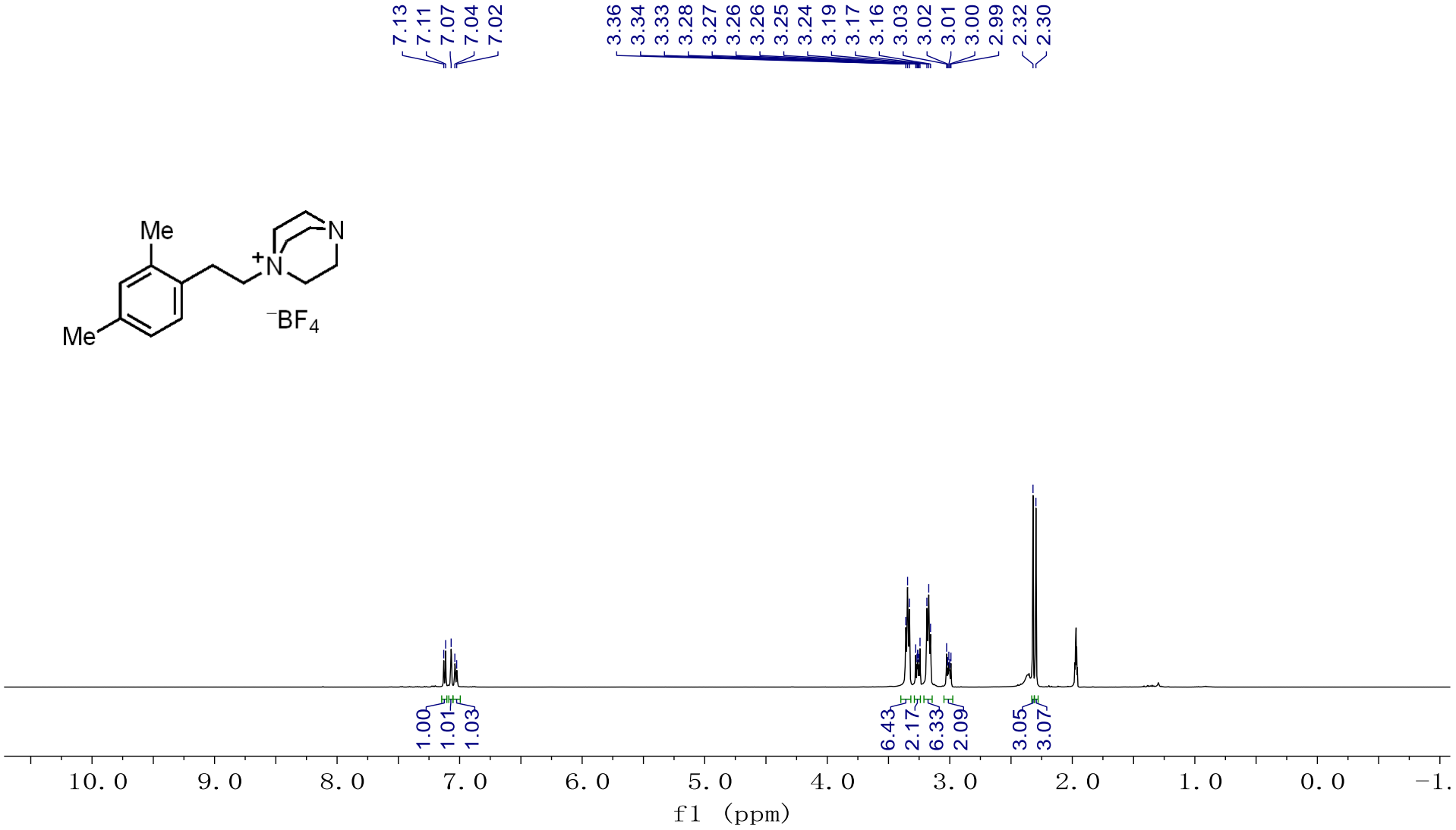

^{13}C NMR of arylethylammonium salt 13

CD_3CN, 23 ºC

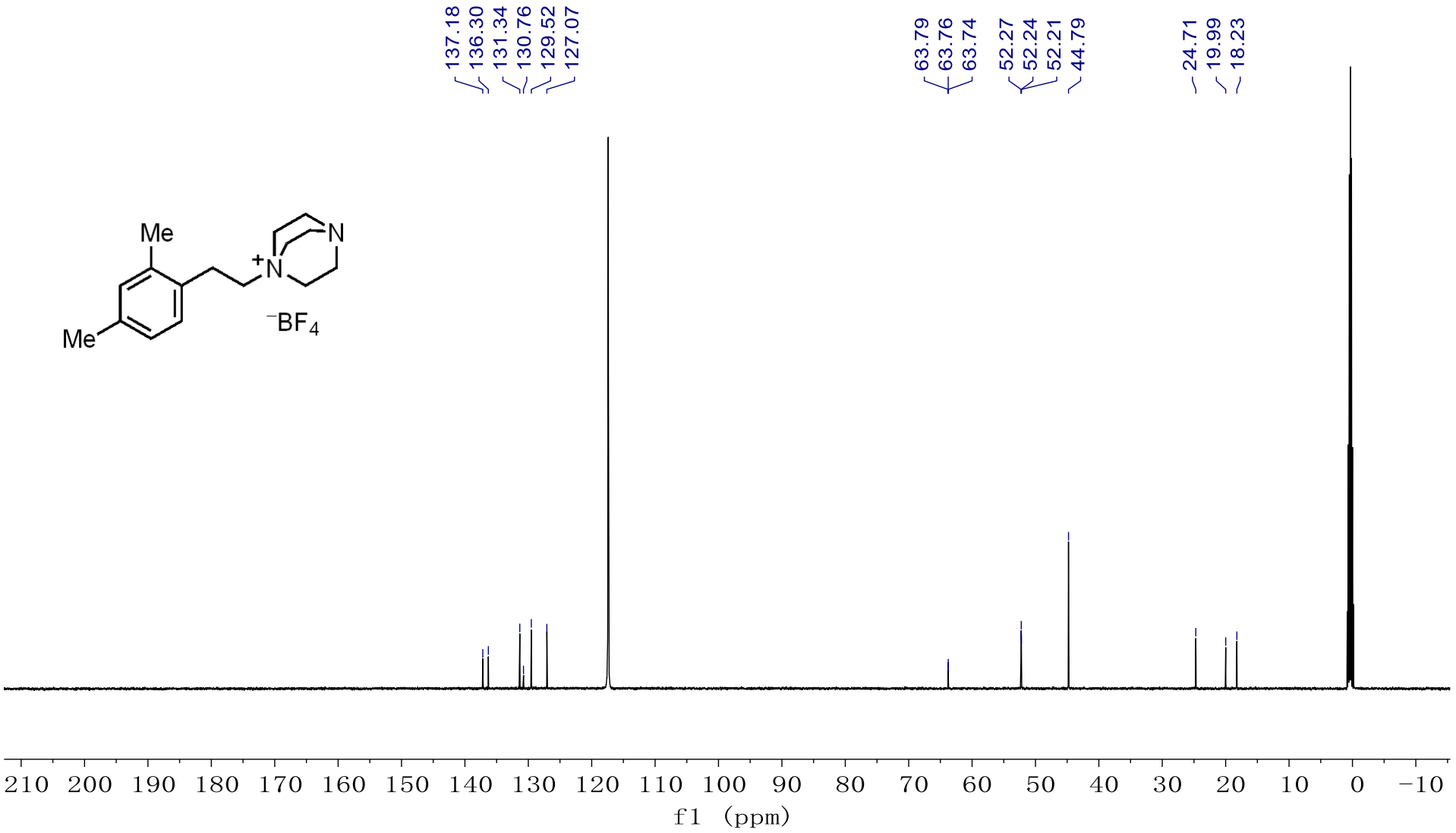

^{19}F NMR of arylethylammonium salt 13

CD_3CN, 23 ºC

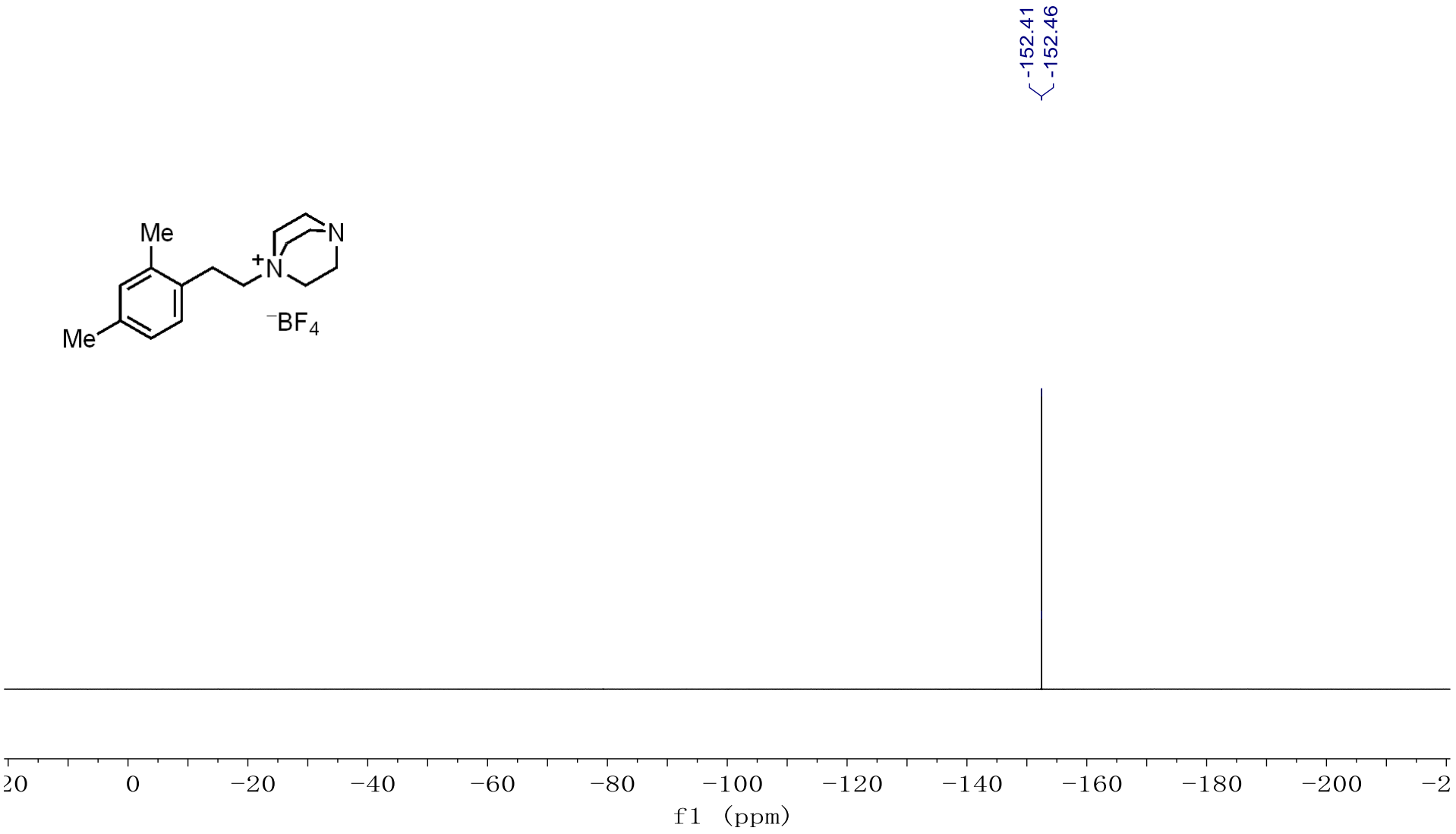

^{1}H NMR of arylethyl benzoate 14

$CDCl_3$, 23 ºC

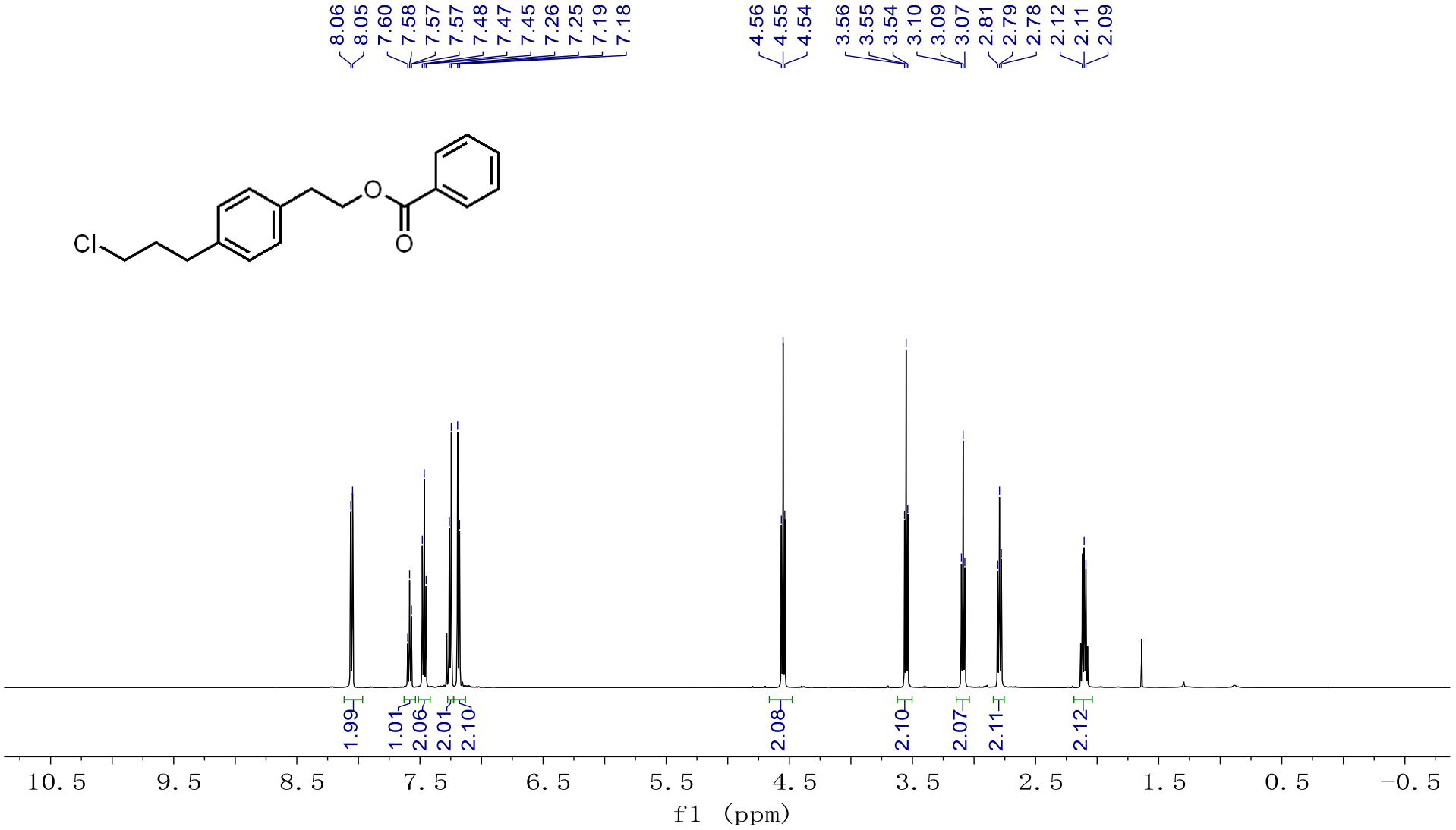

^{13}C NMR of arylethyl benzoate 14

$CDCl_3$, 23 ºC

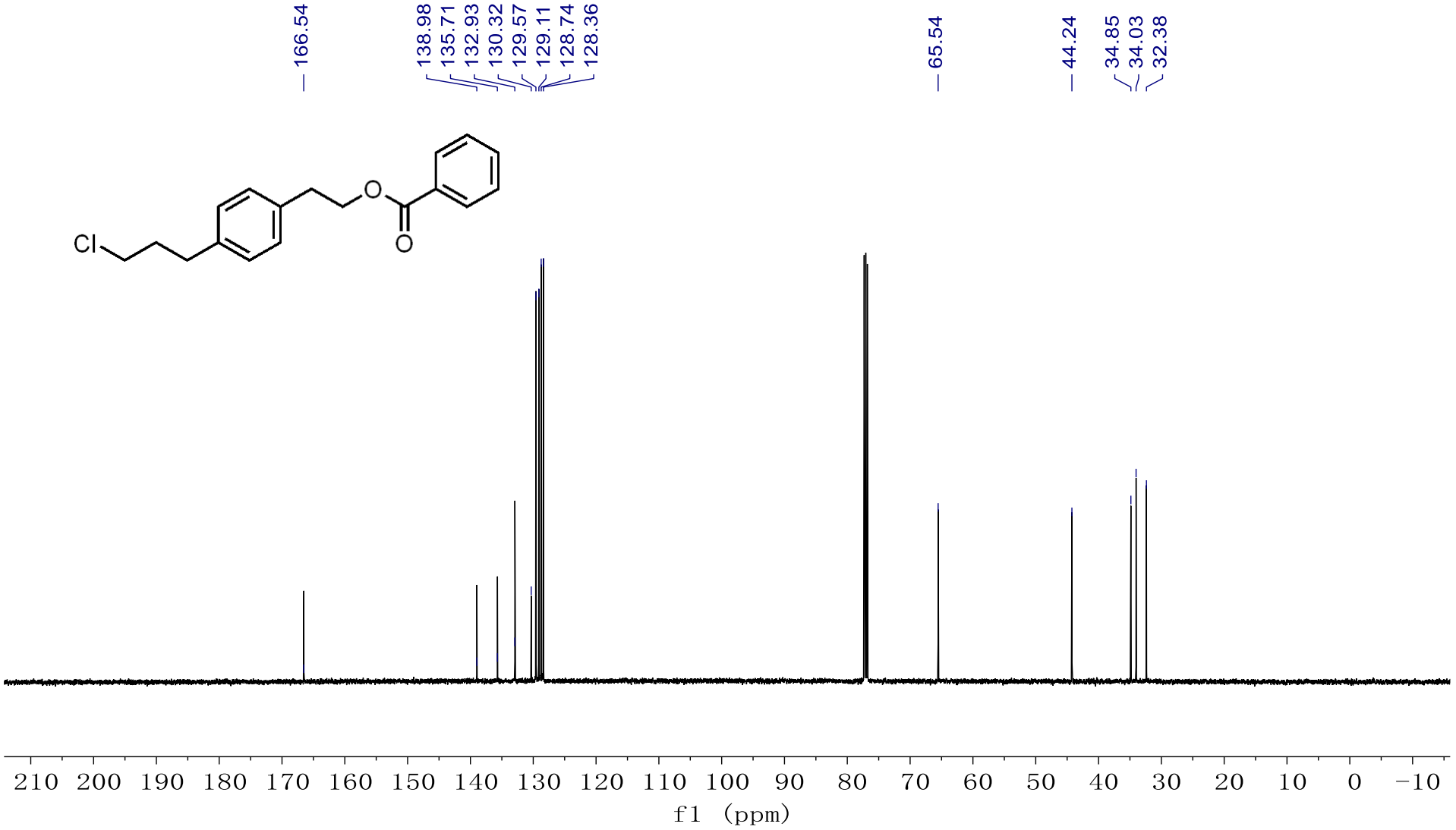

^{1}H NMR of fenofibrate-derived 2-arylethanol 15

$CDCl_3$, 23 ºC

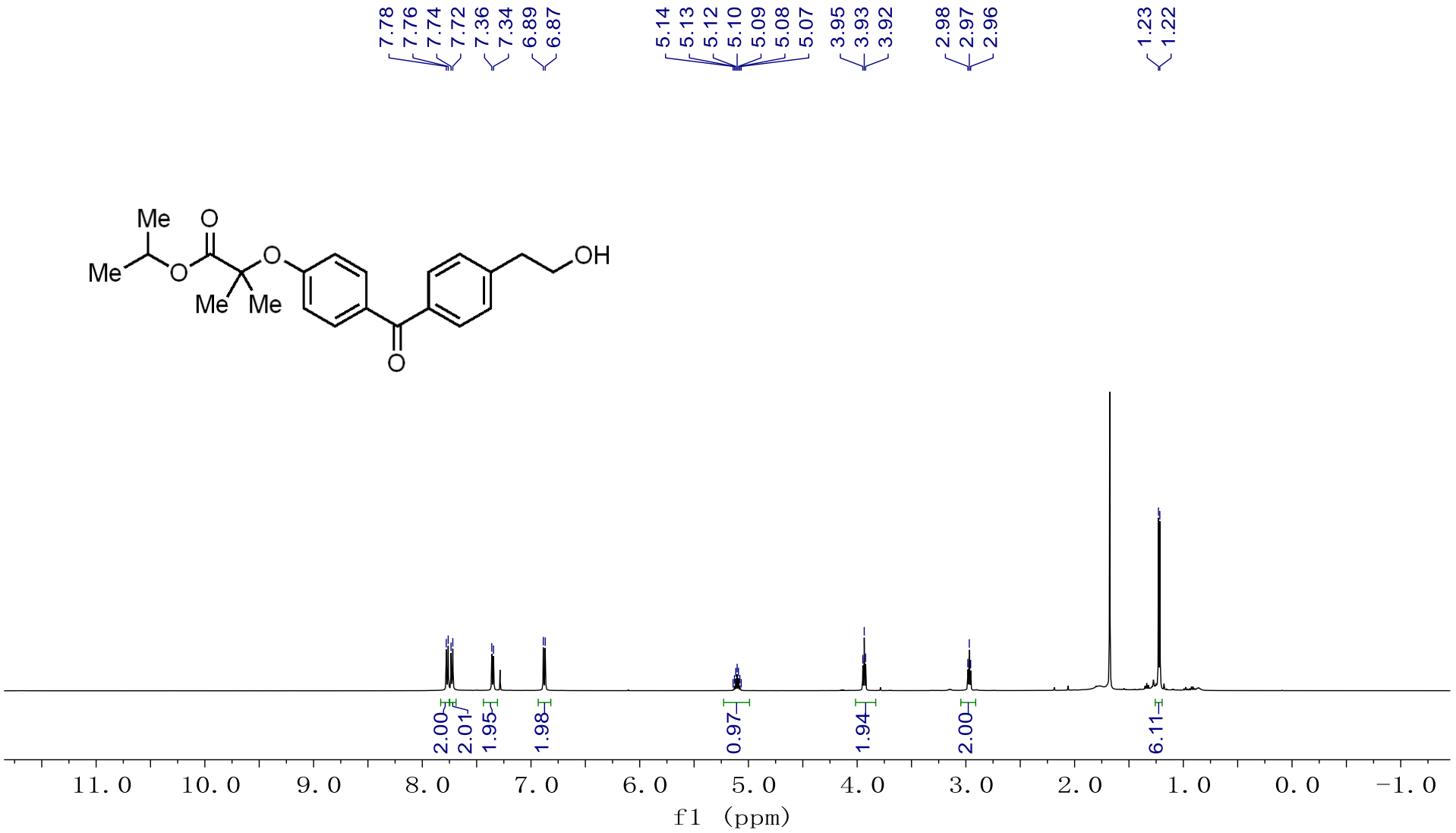

^{13}C NMR of fenofibrate-derived 2-arylethanol 15

$CDCl_3$, 23 ºC

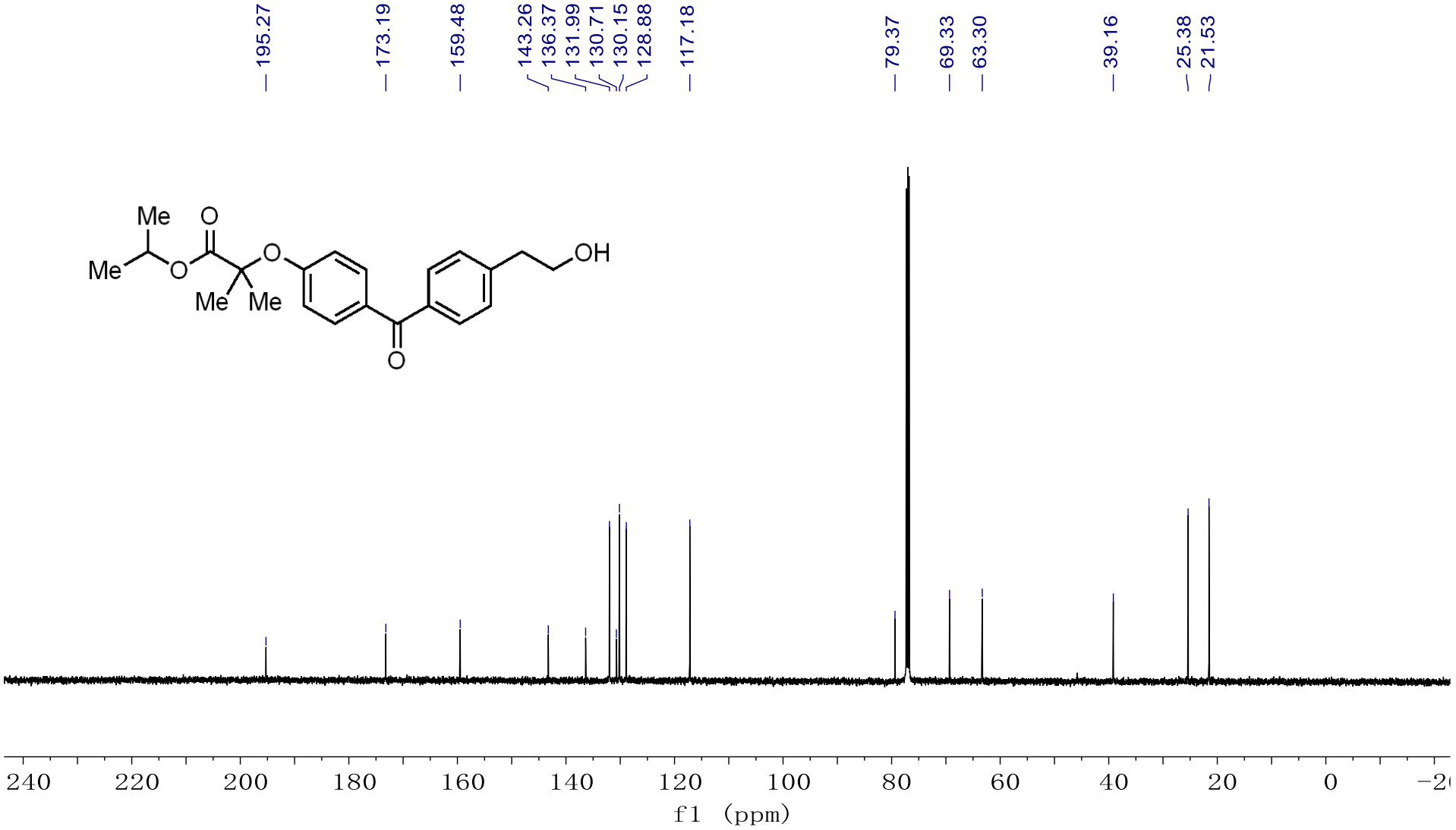

^{1}H NMR of arylethyl fluoride 16

$CDCl_3$, 23 ºC

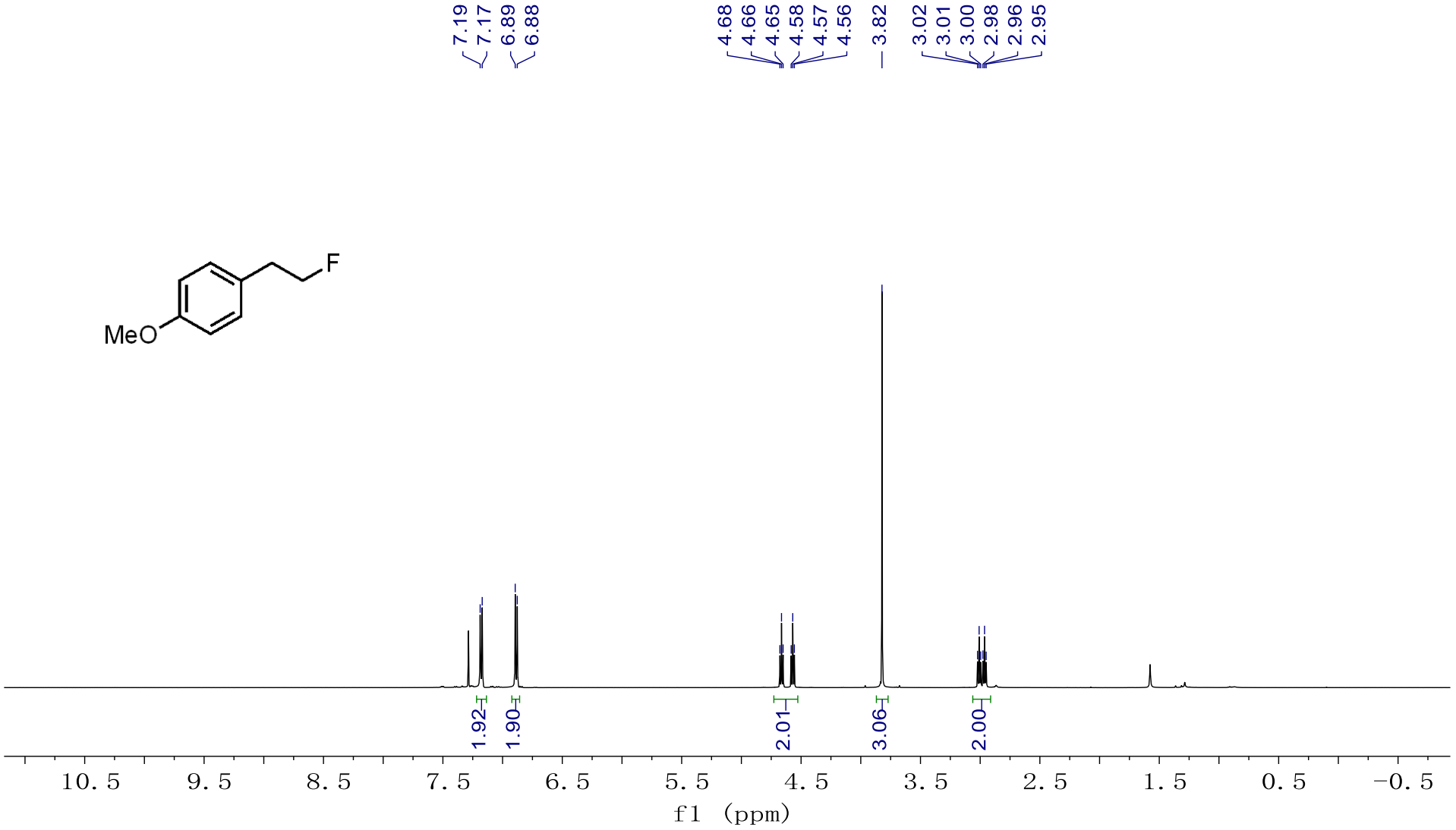

^{13}C NMR of arylethyl fluoride 16

$CDCl_3$, 23 ºC

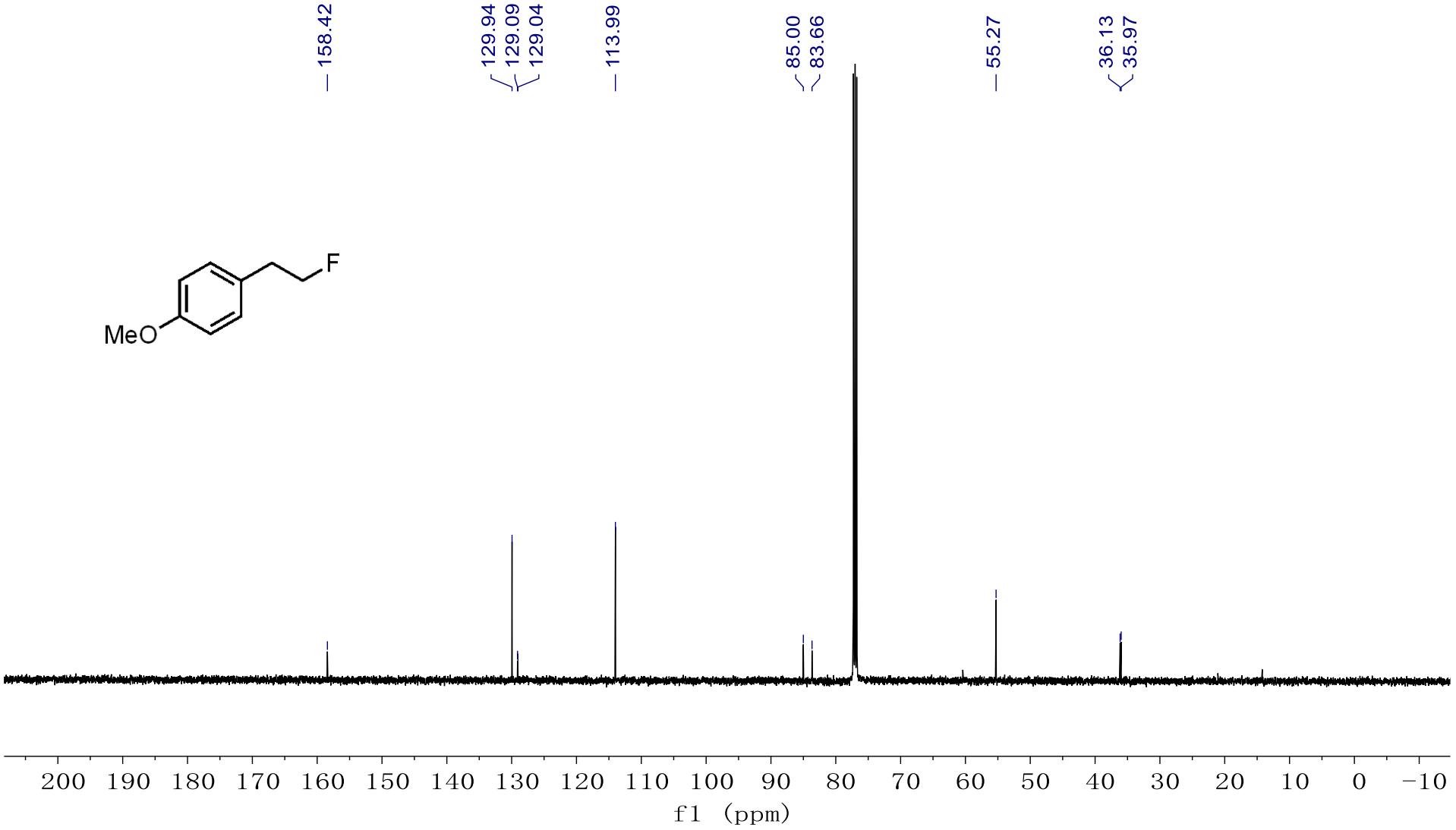

^{19}F NMR of arylethyl fluoride 16

$CDCl_3$, 23 ºC

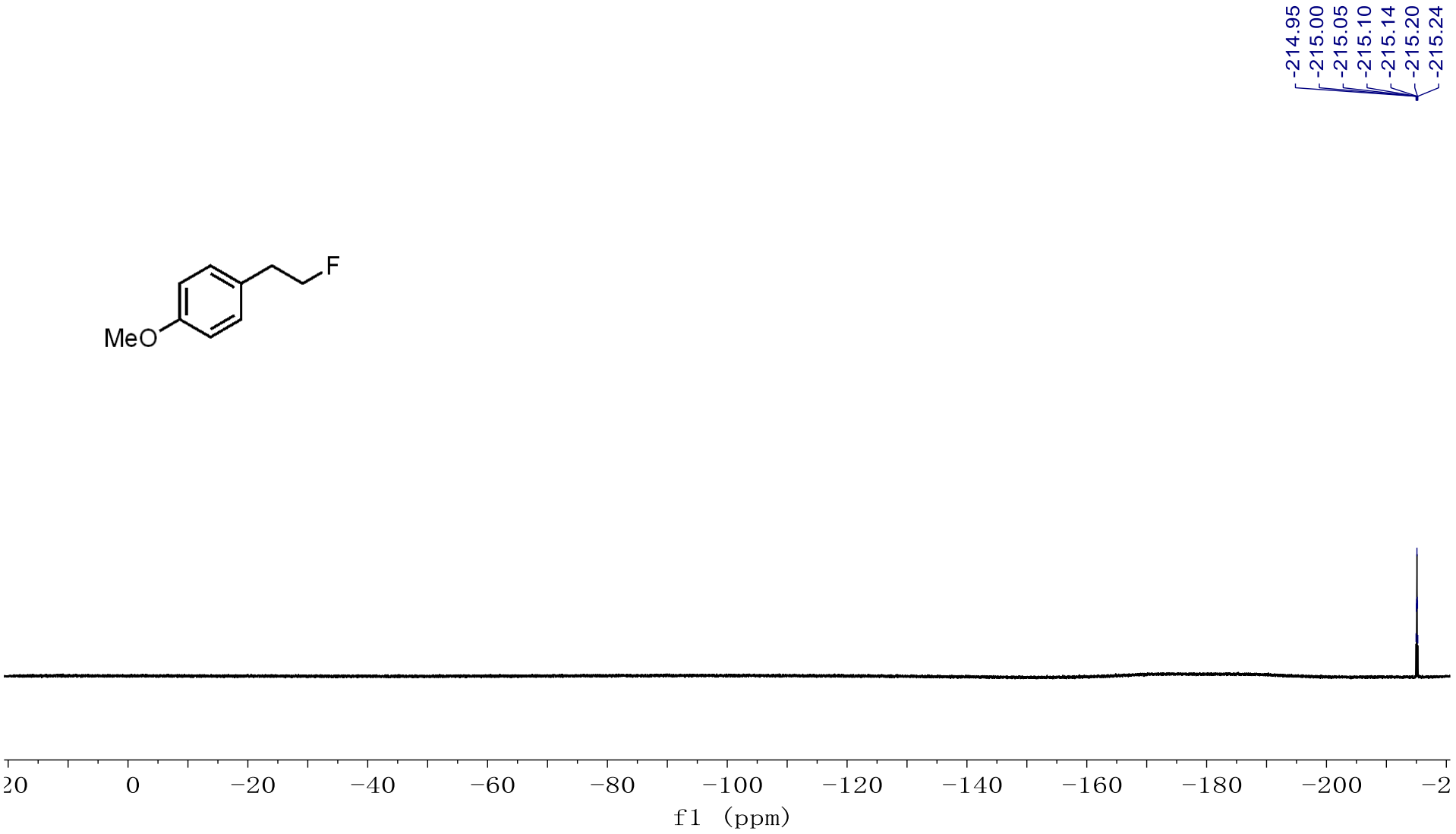

^{1}H NMR of diclofenac amide-derived arylethylamine 17

$CDCl_3$, 23 ºC

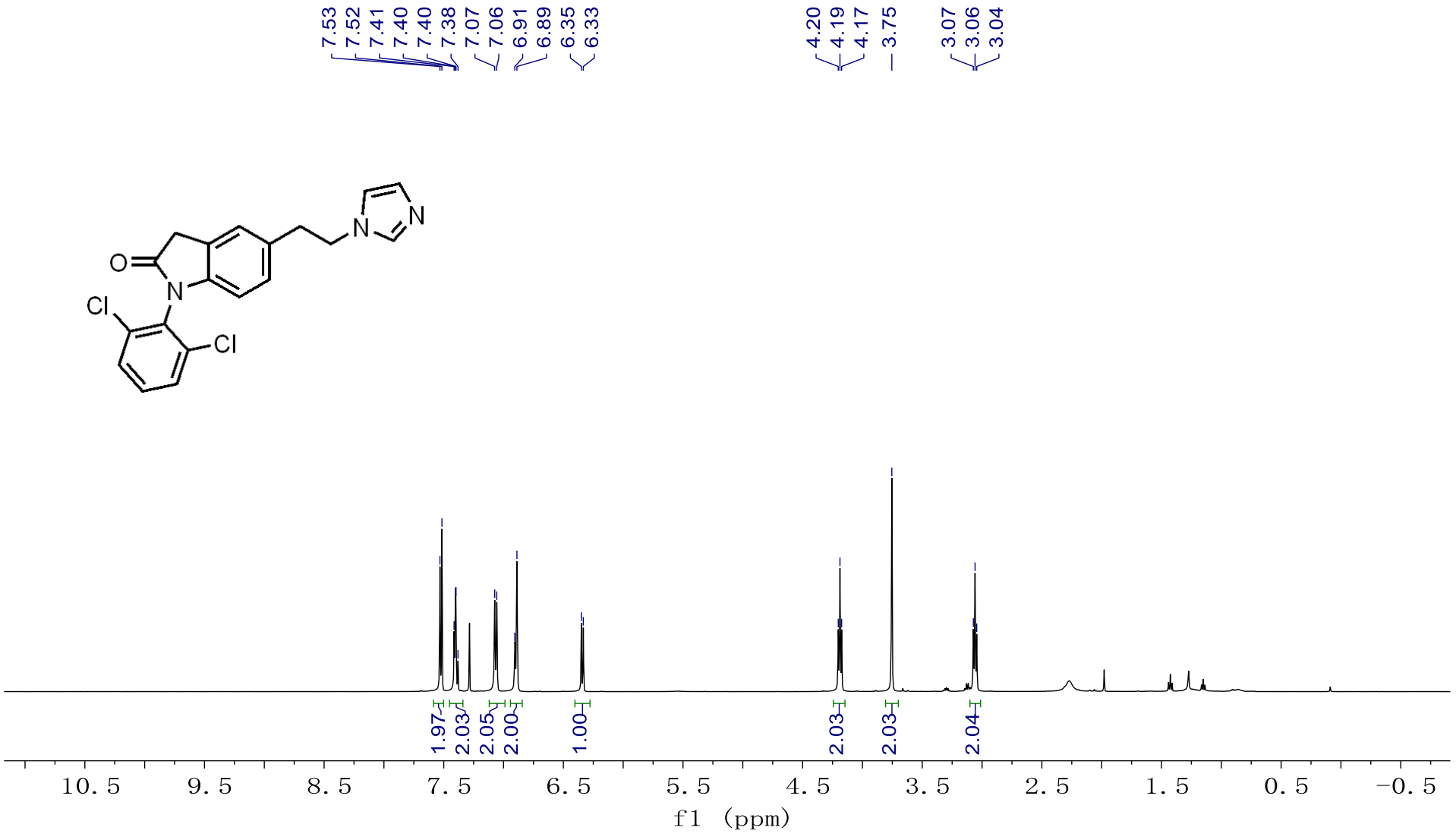

^{13}C NMR of diclofenac amide-derived arylethylamine 17

$CDCl_3$, 23 ºC

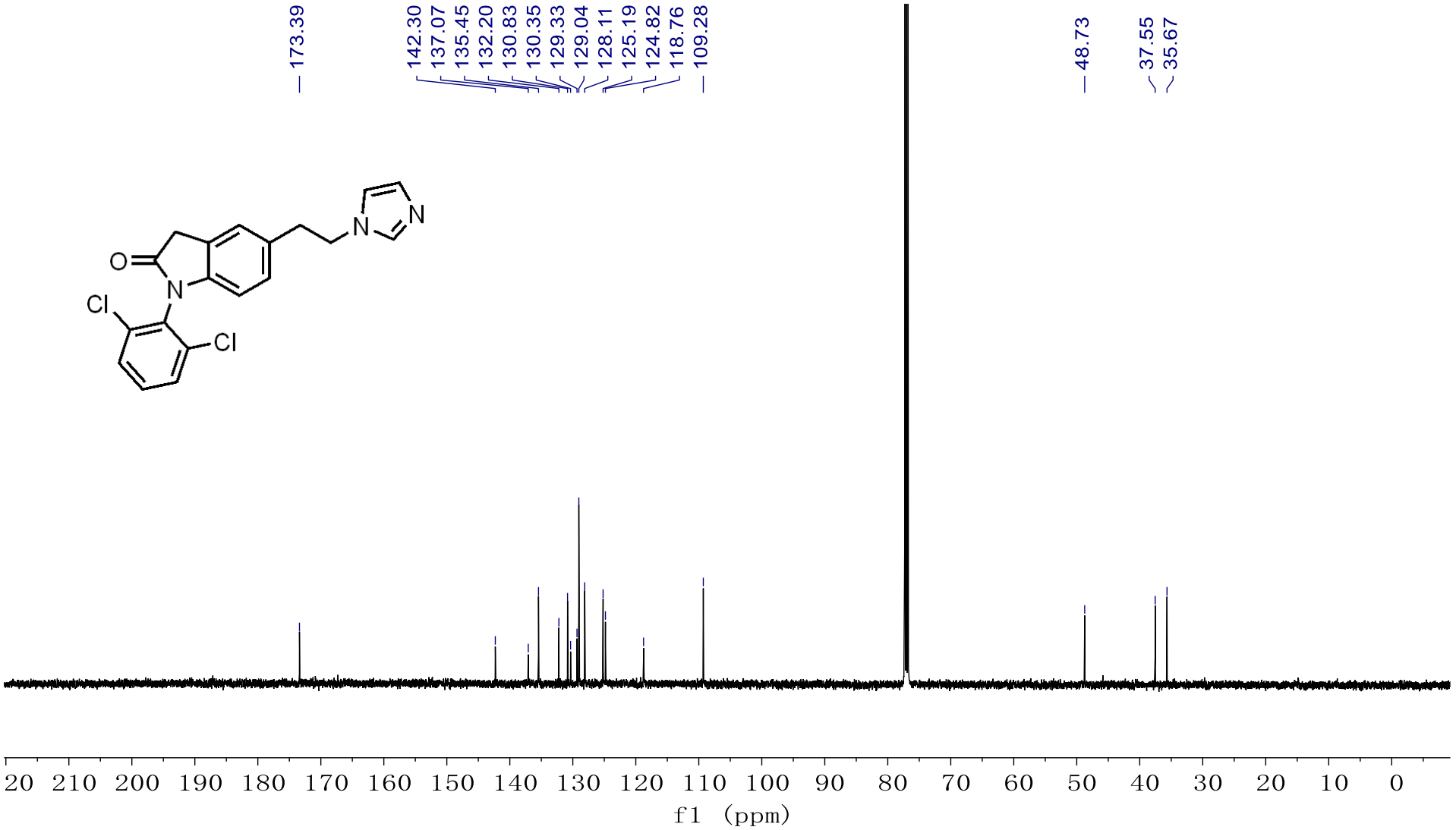

^{1}H NMR of arylethyl methyl ether 18

$CDCl_3$, 23 ºC

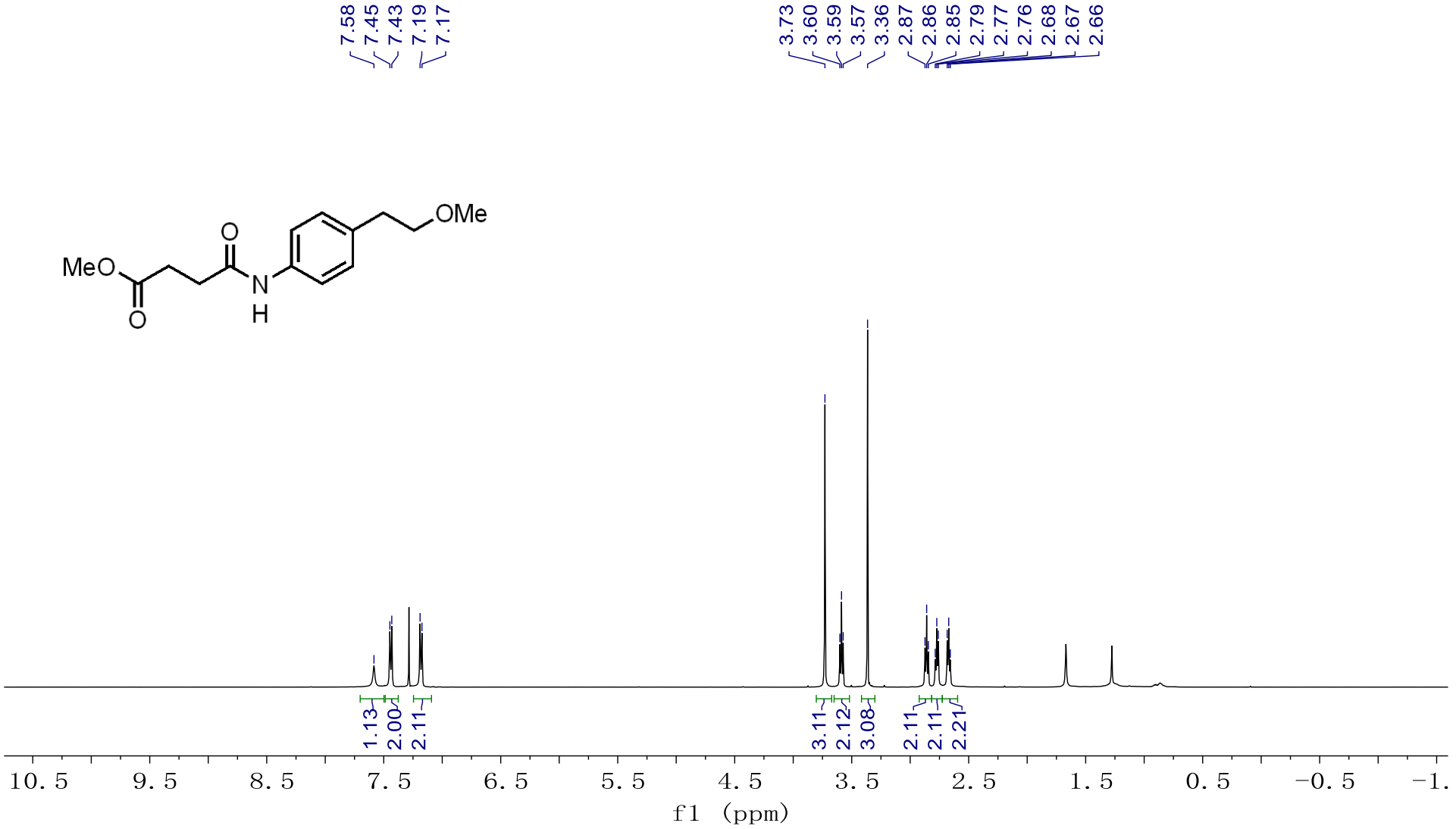

^{13}C NMR of arylethyl methyl ether 18

$CDCl_3$, 23 ºC

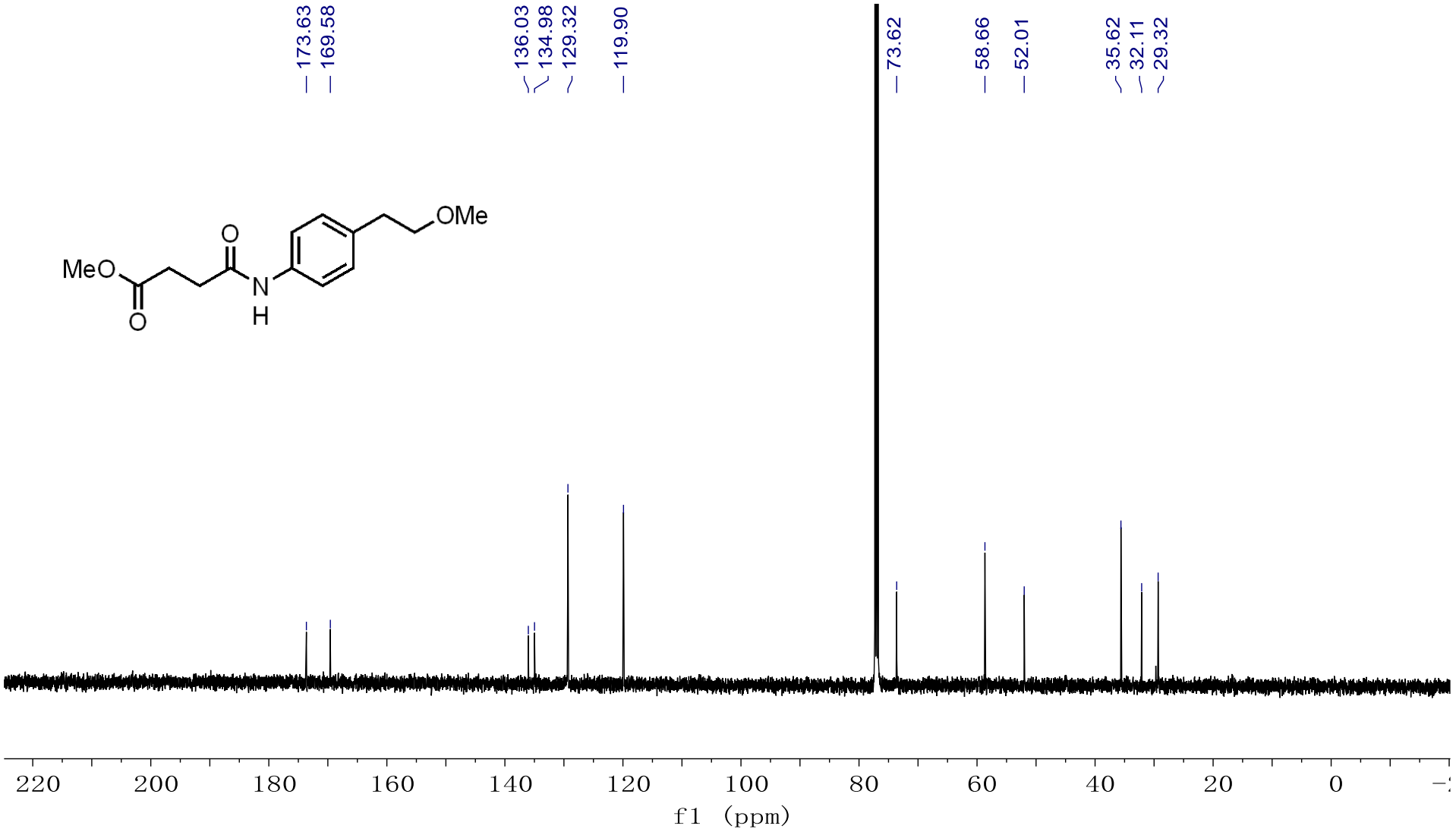

^{1}H NMR of cysteine-derived arylethyl thioether 19

$CDCl_3$, 23 ºC

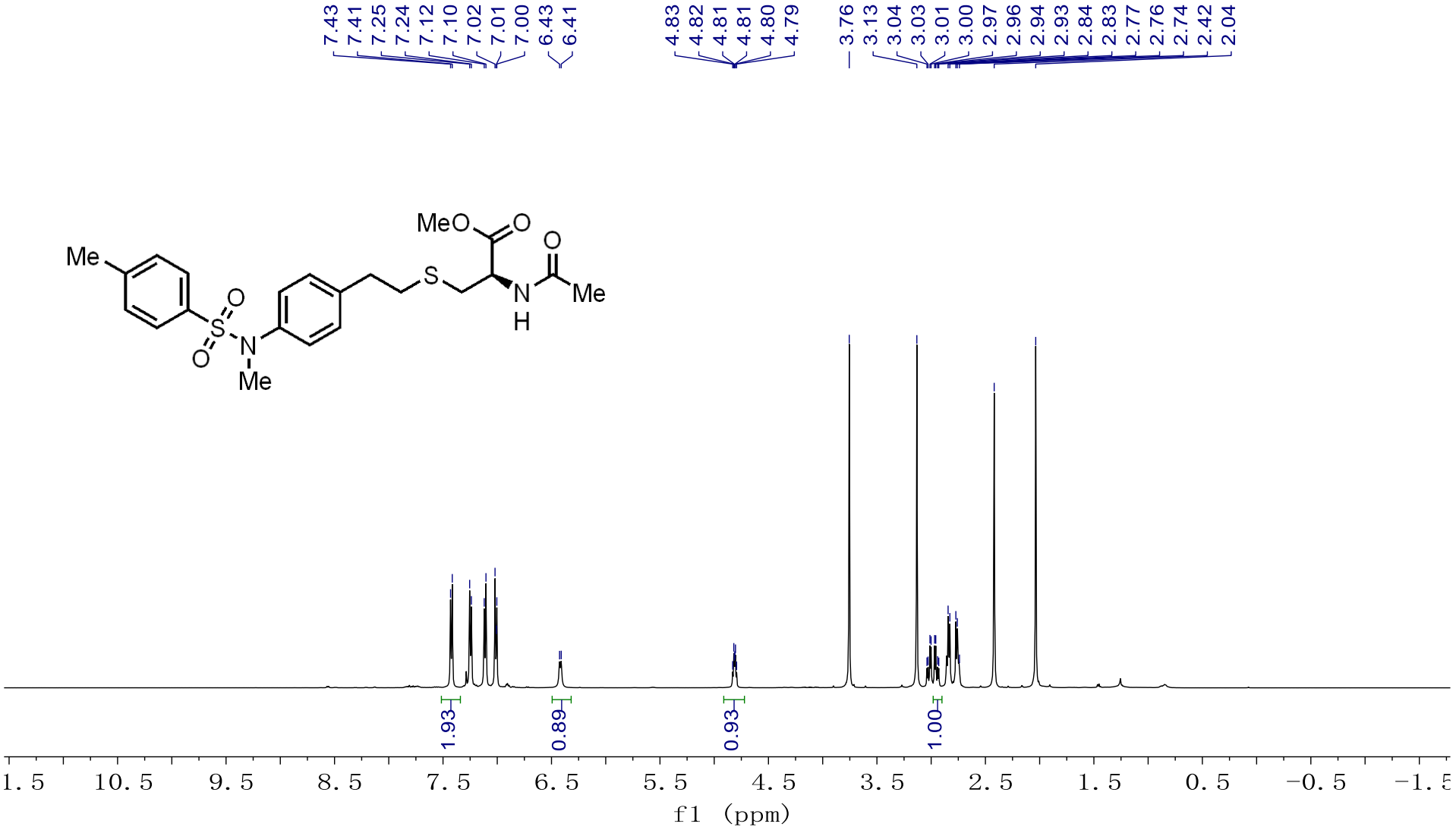

^{13}C NMR of cysteine-derived arylethyl thioether 19

$CDCl_3$, 23 ºC

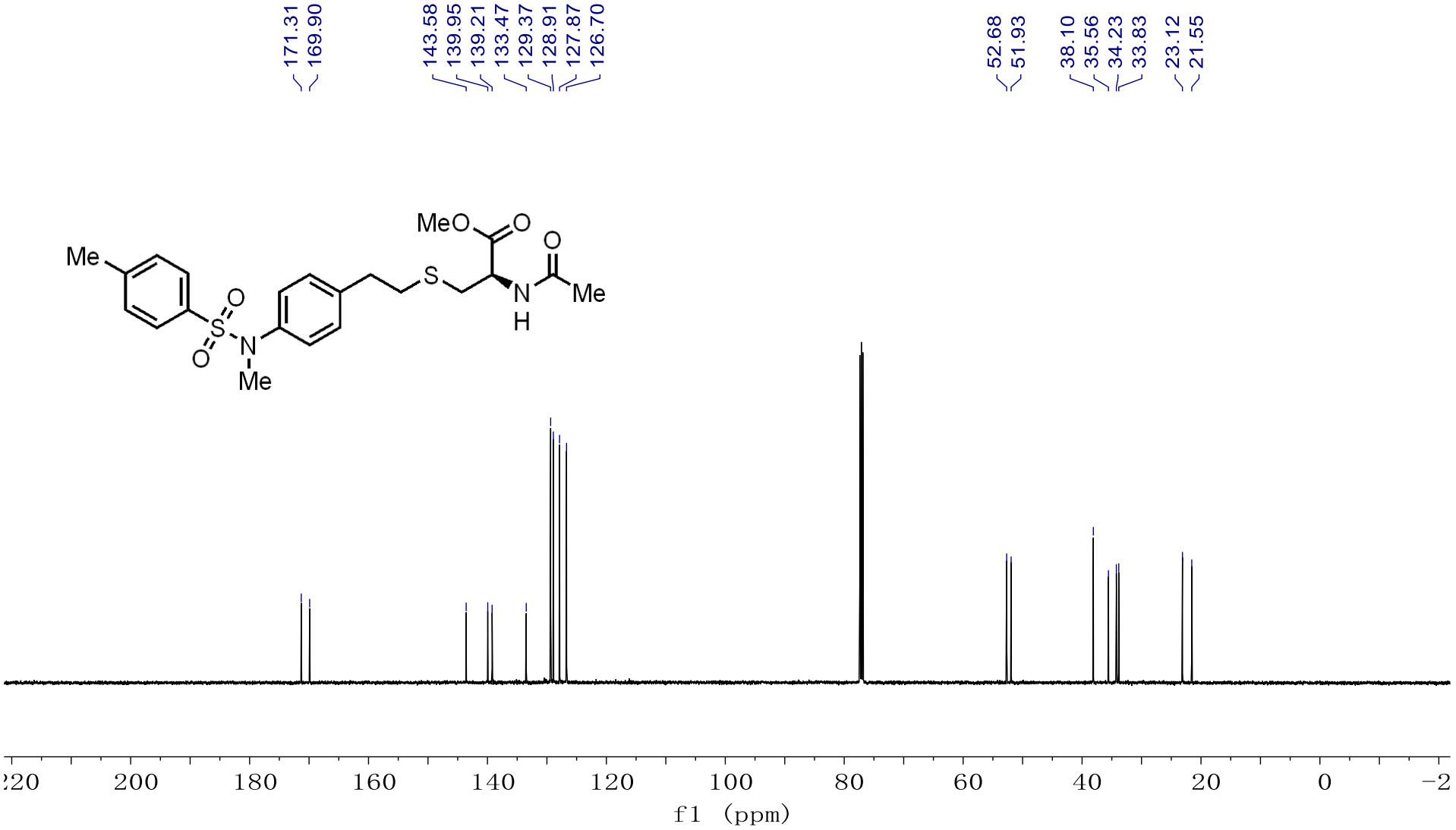

^{1}H NMR of arylpropionitrile 20

$CDCl_3$, 23 ºC

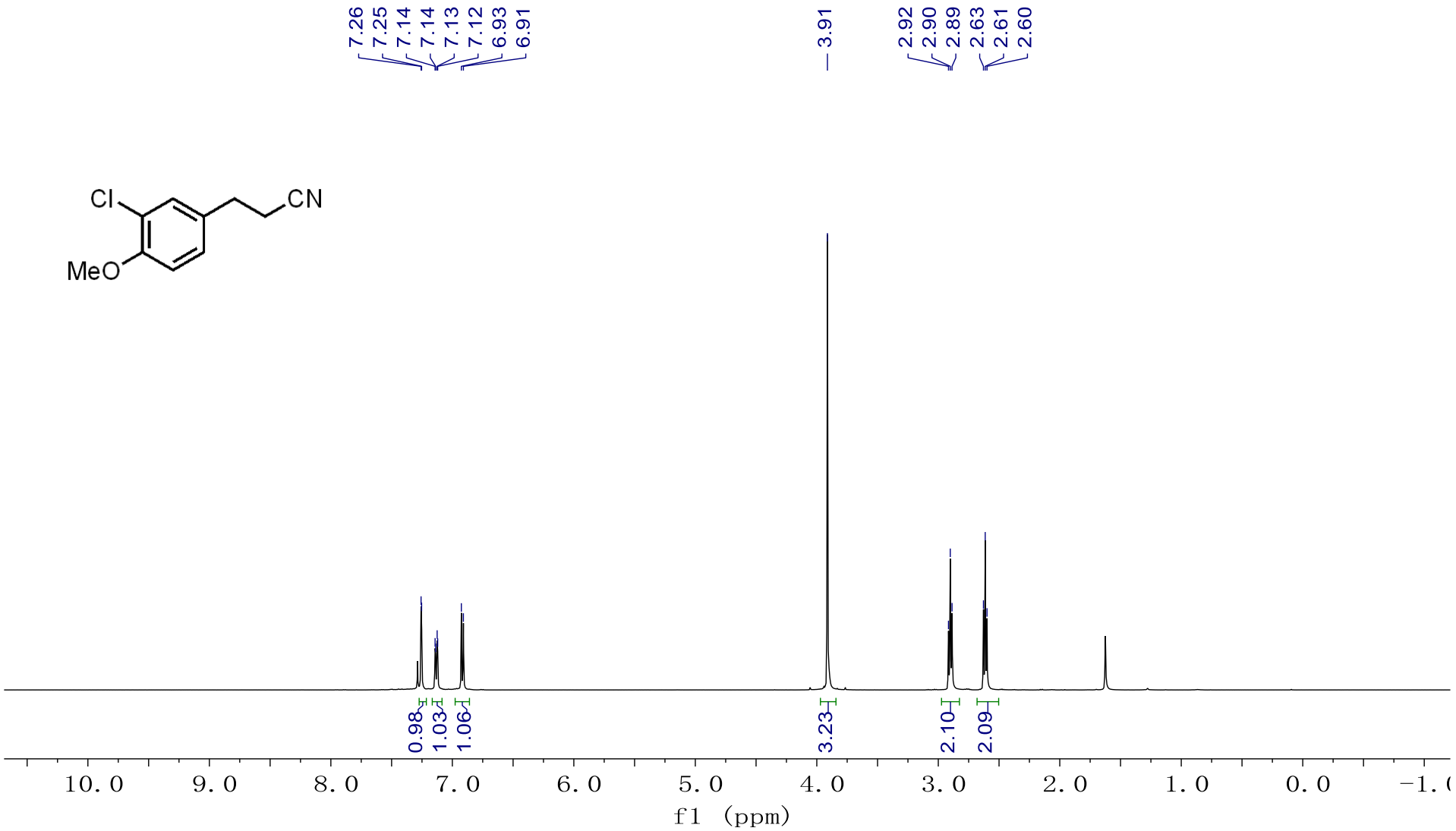

^{13}C NMR of arylpropionitrile 20

$CDCl_3$, 23 ºC

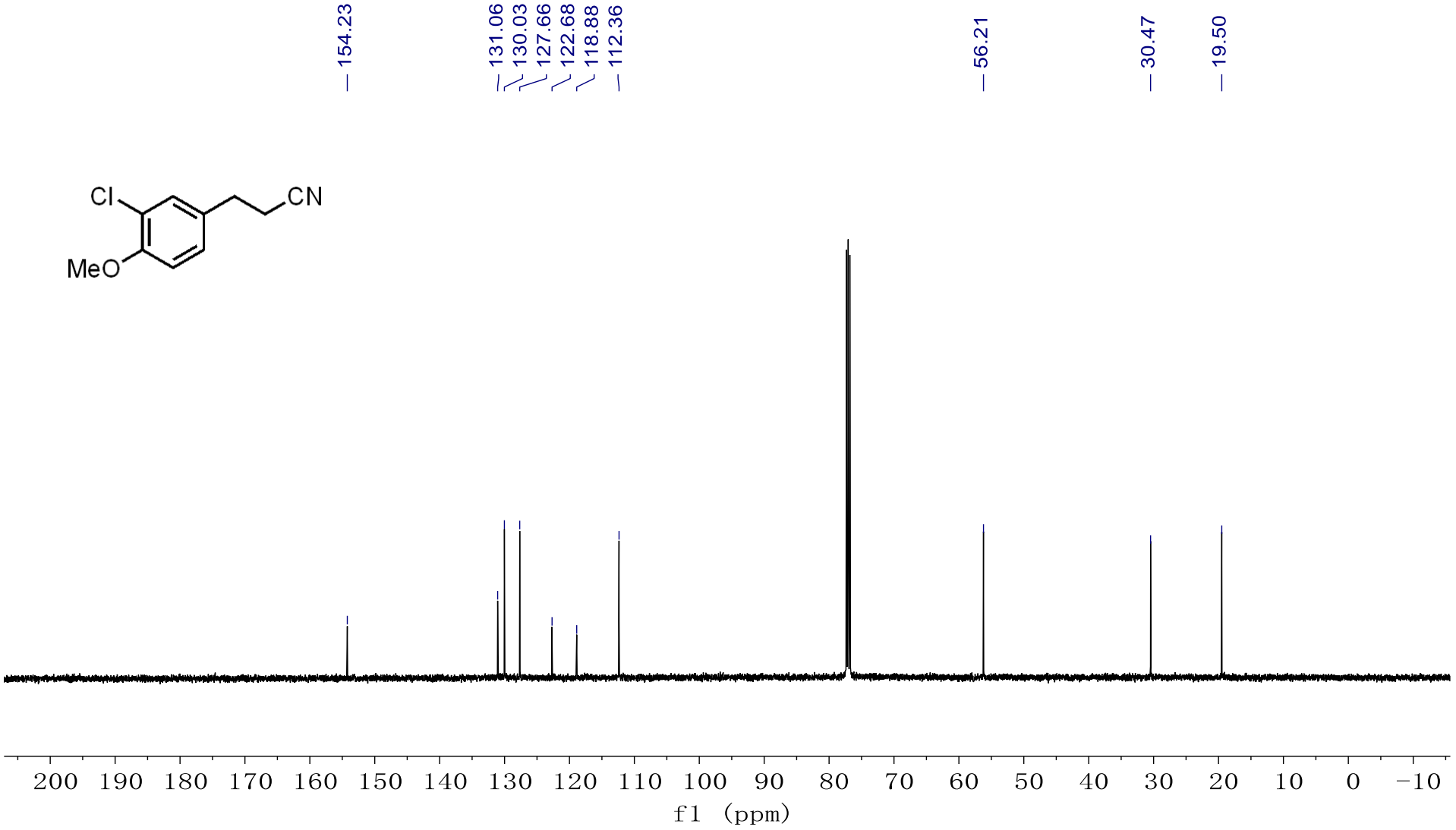

^{1}H NMR of calone-derived arylethylamine 21

$CDCl_3$, 23 ºC

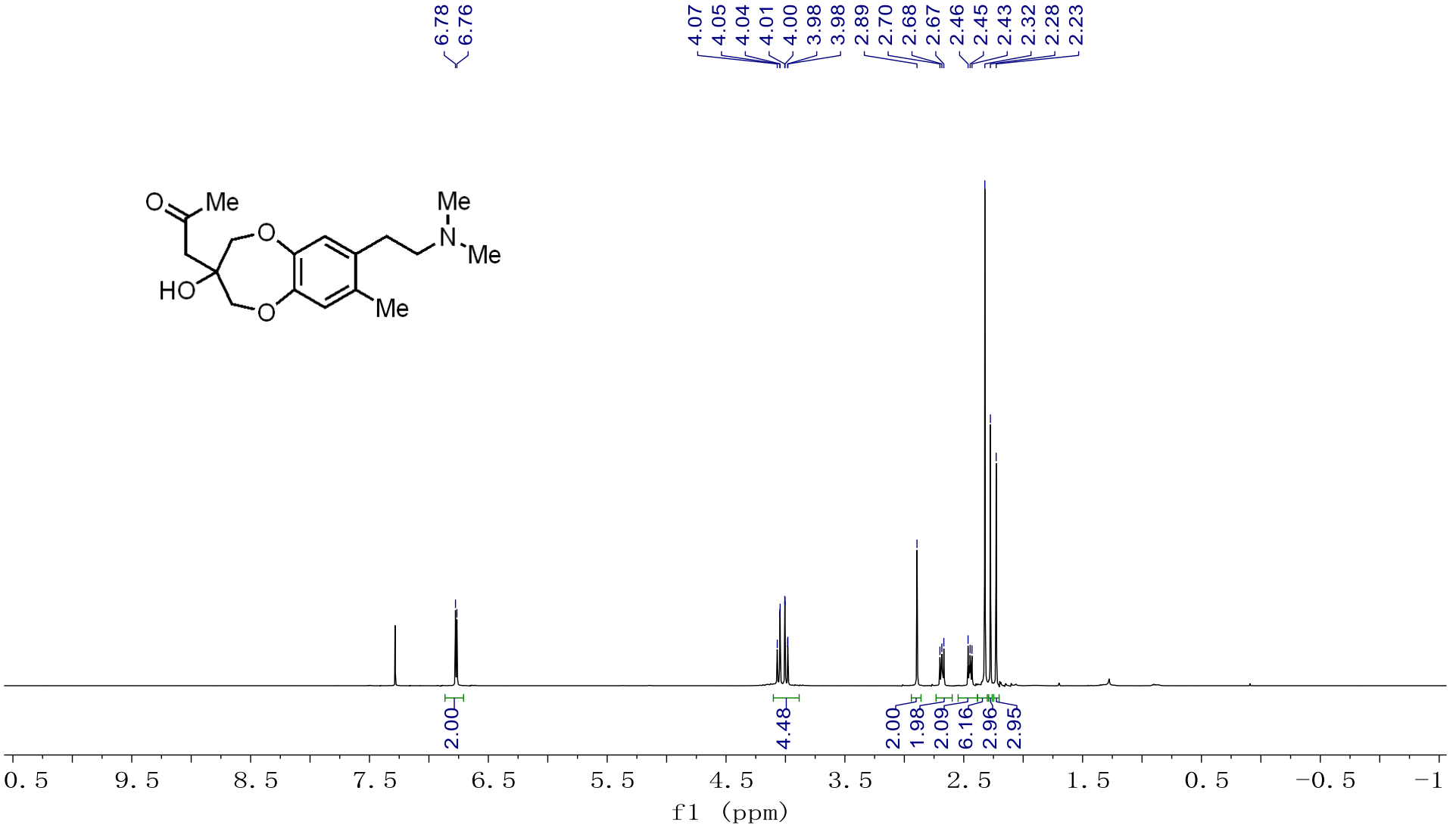

^{13}C NMR of calone-derived arylethylamine 21

$CDCl_3$, 23 ºC

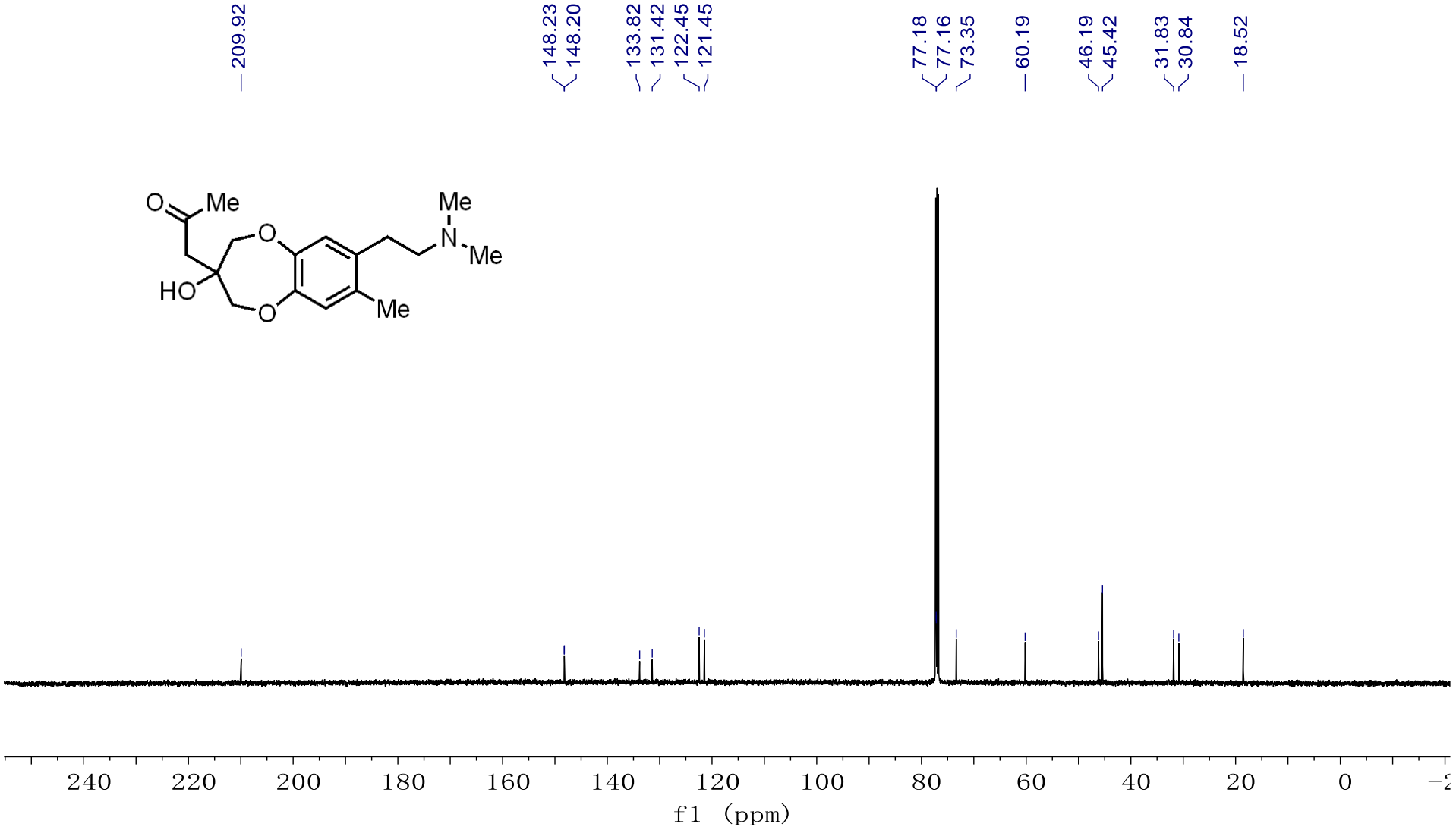

^{1}H NMR of arylethylamine 22

$CDCl_3$, 23 ºC

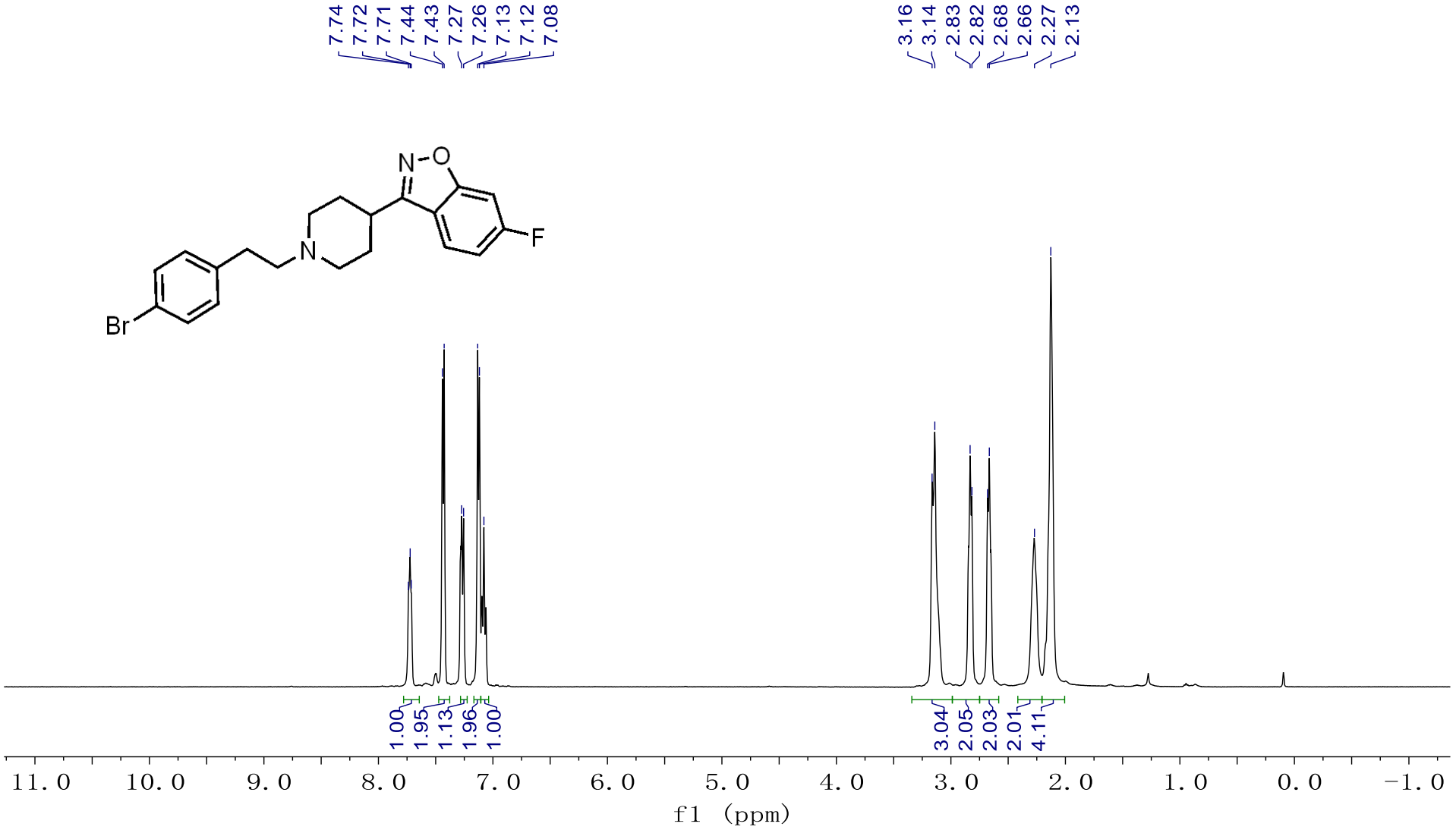

^{13}C NMR of arylethylamine 22

$CDCl_3$, 23 ºC

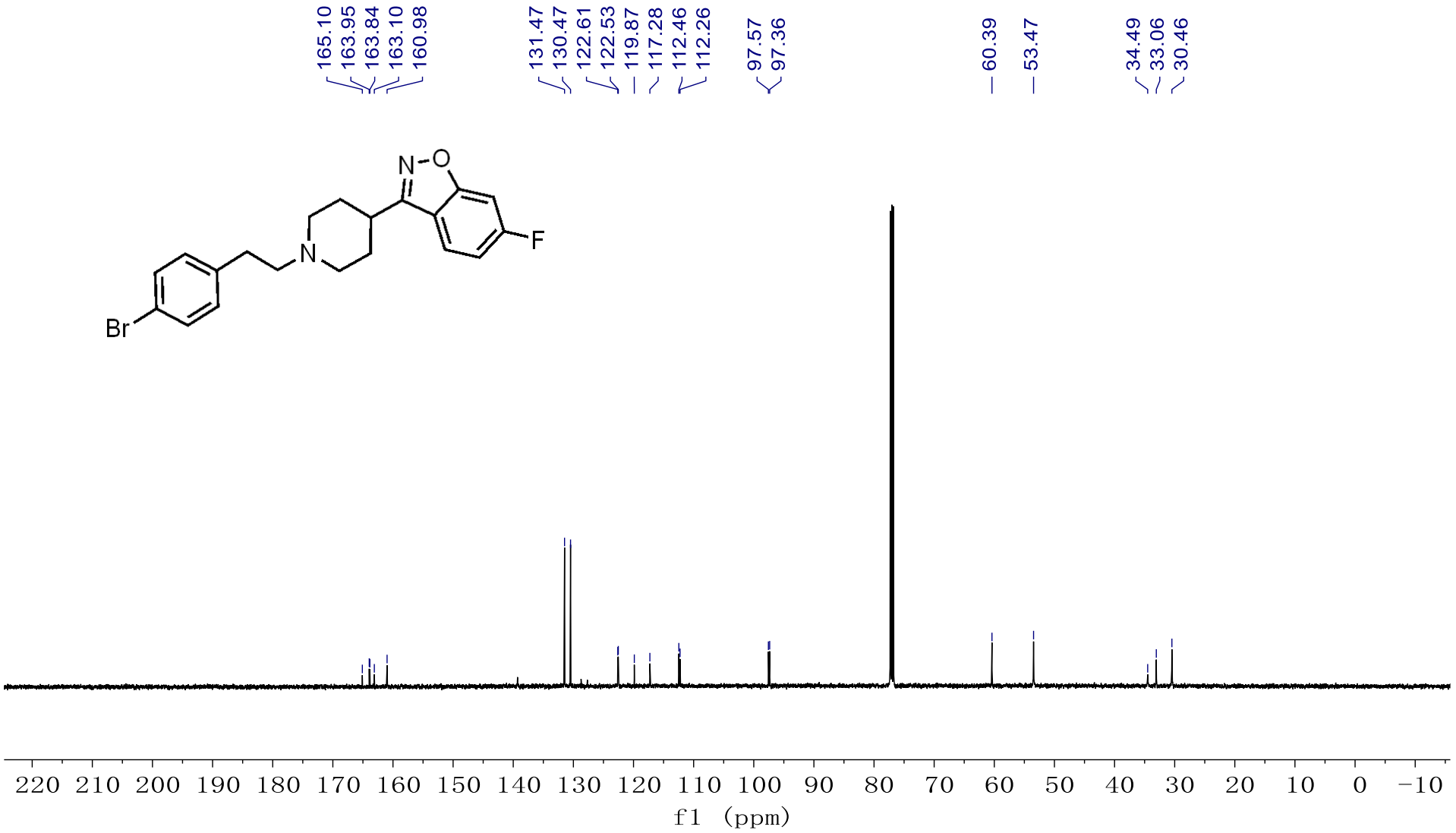

^{19}F NMR of arylethylamine 22

$CDCl_3$, 23 ºC

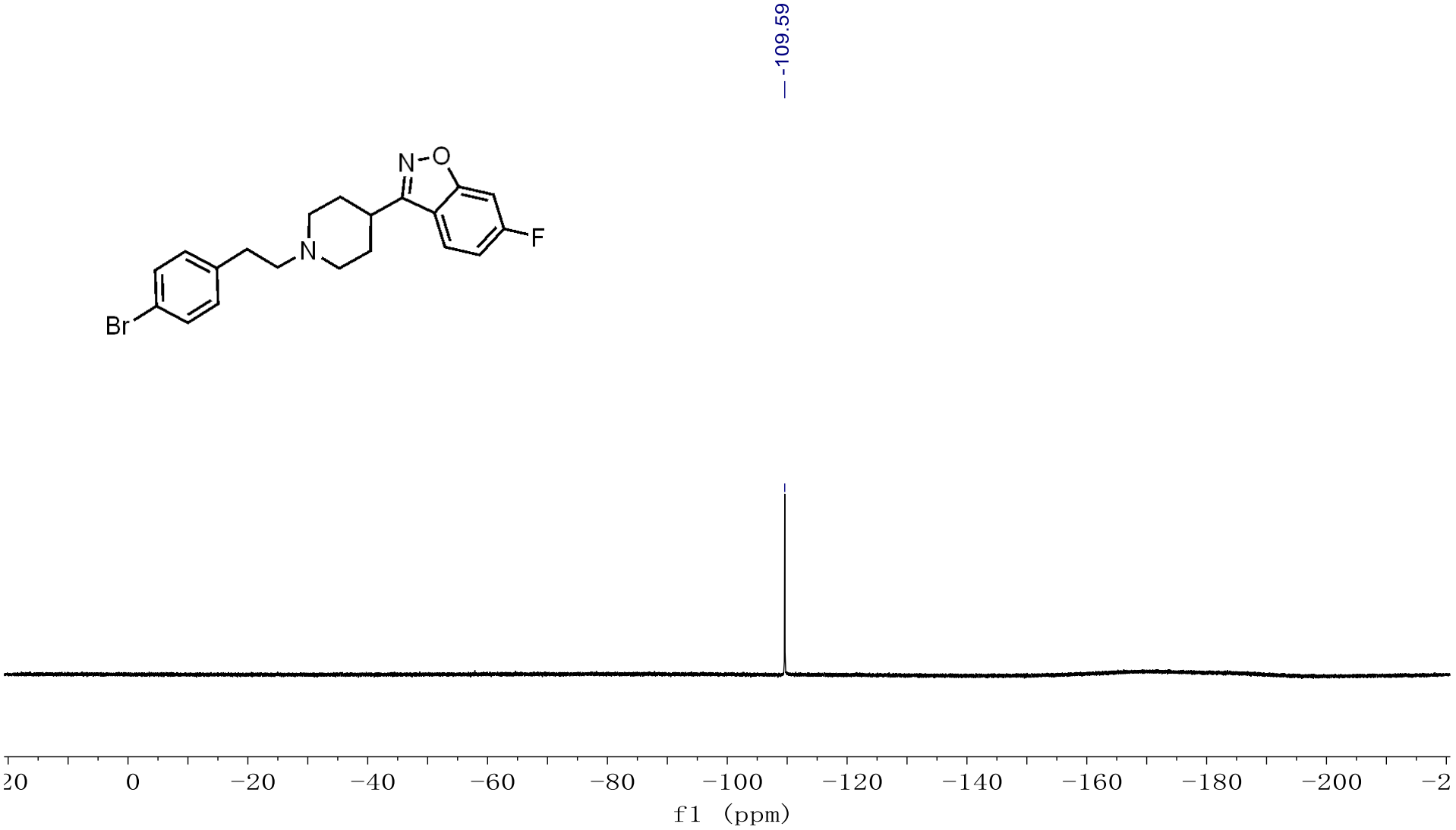

^{1}H NMR of duloxetine-derived arylethylamine 23

$CDCl_3$, 23 ºC

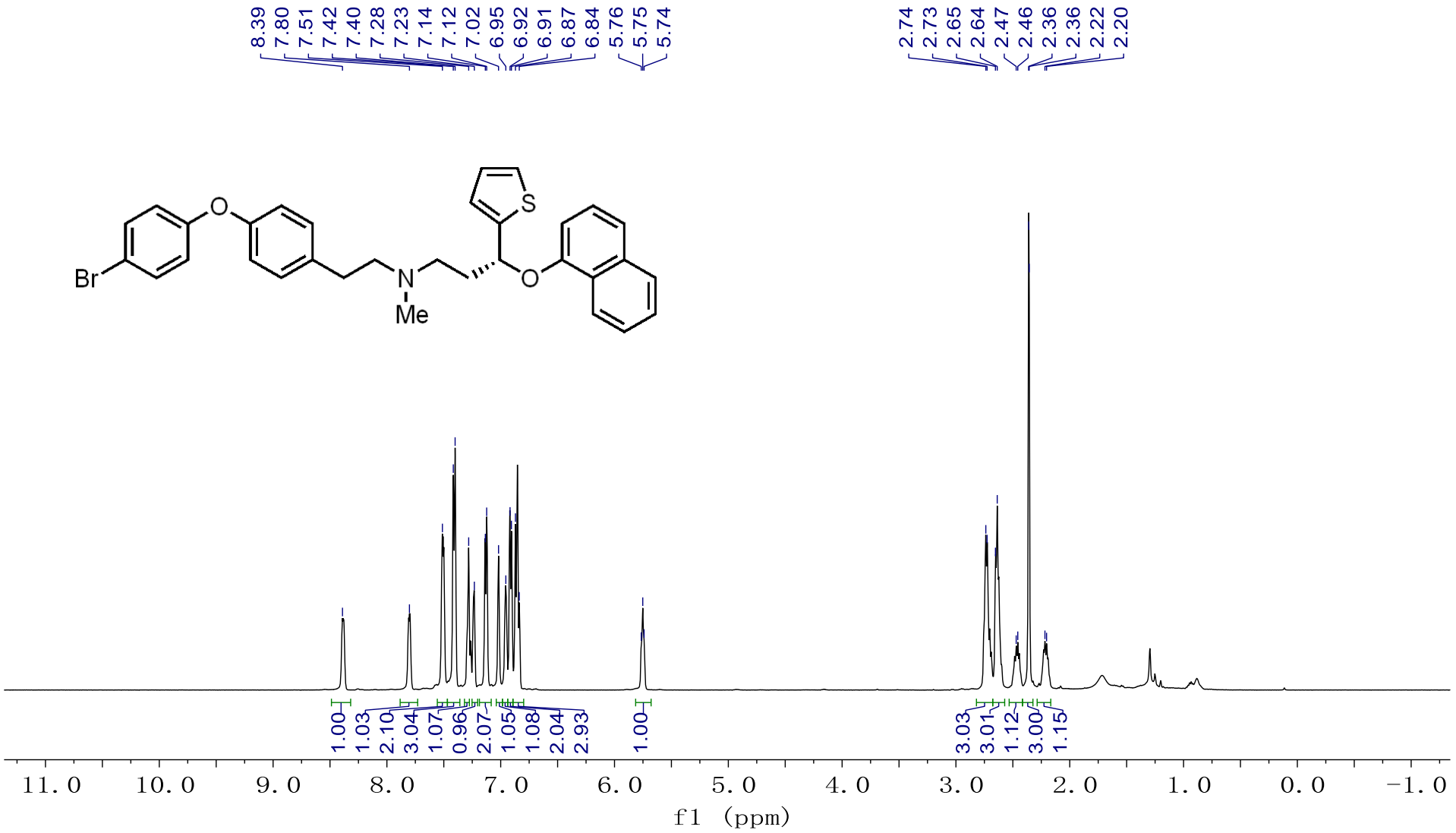

^{13}C NMR of duloxetine-derived arylethylamine 23

$CDCl_3$, 23 ºC

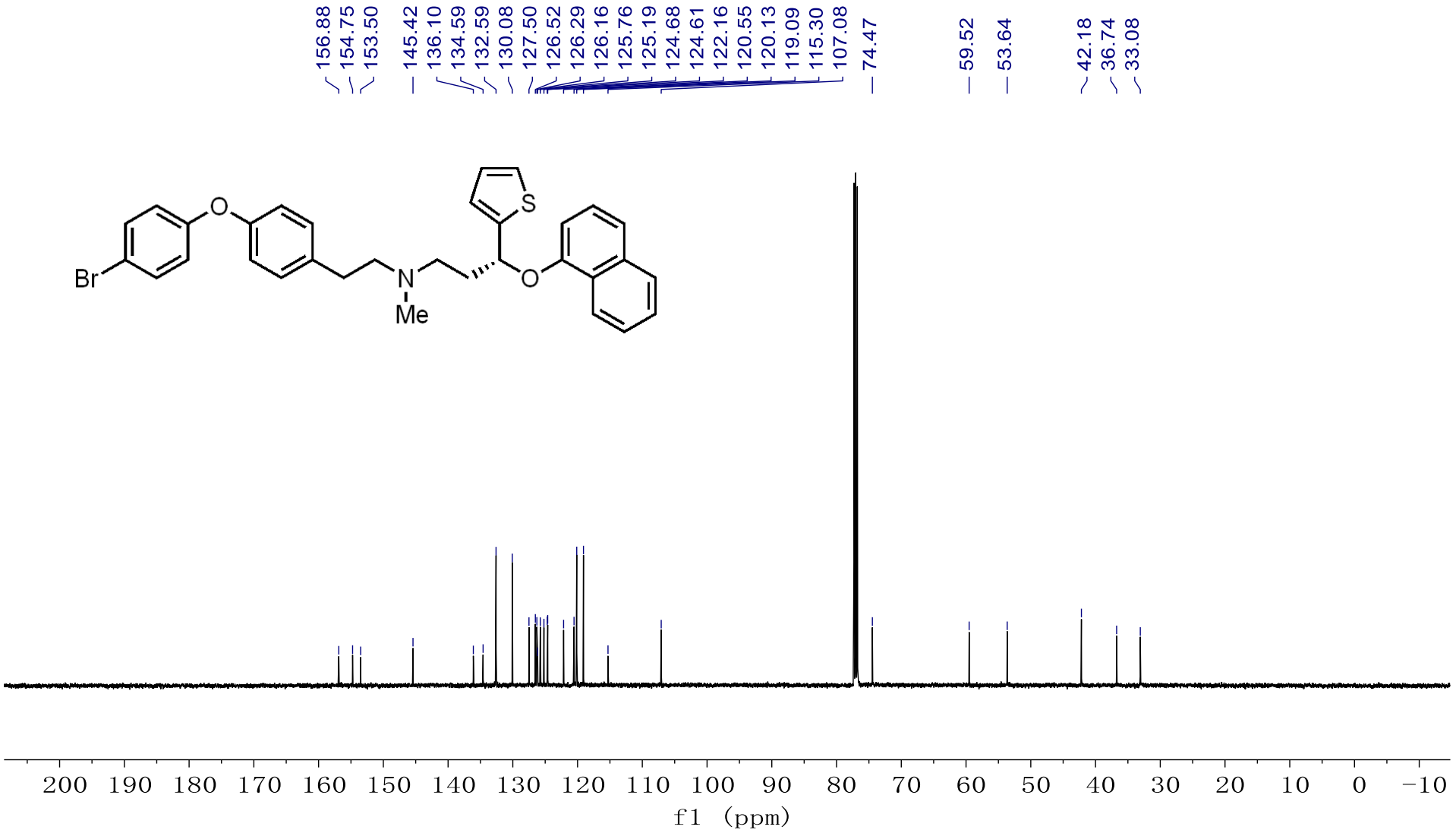

^{1}H NMR of arylethyl bromide 24

$CDCl_3$, 23 ºC

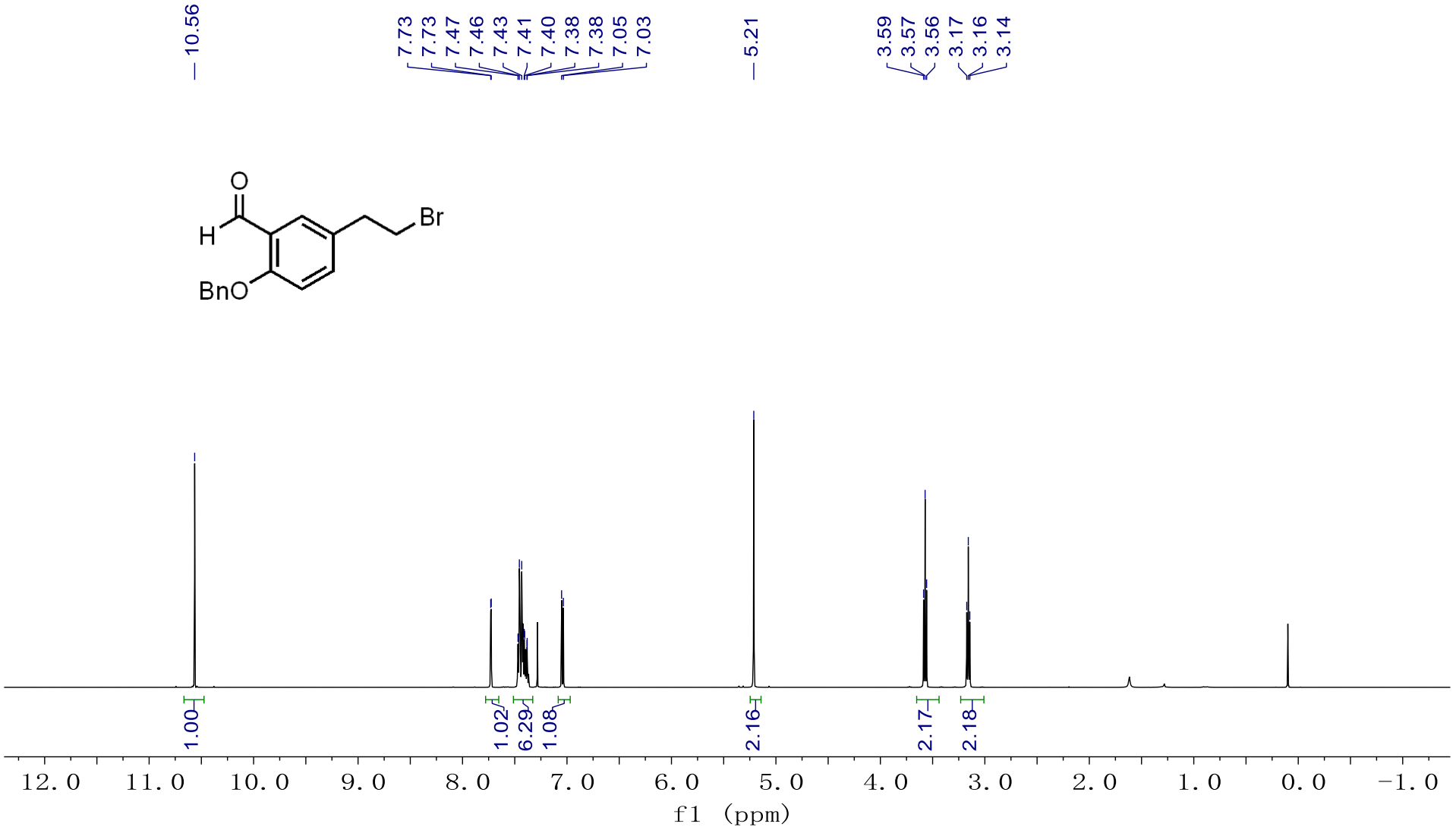

^{13}C NMR of arylethyl bromide 24

$CDCl_3$, 23 ºC

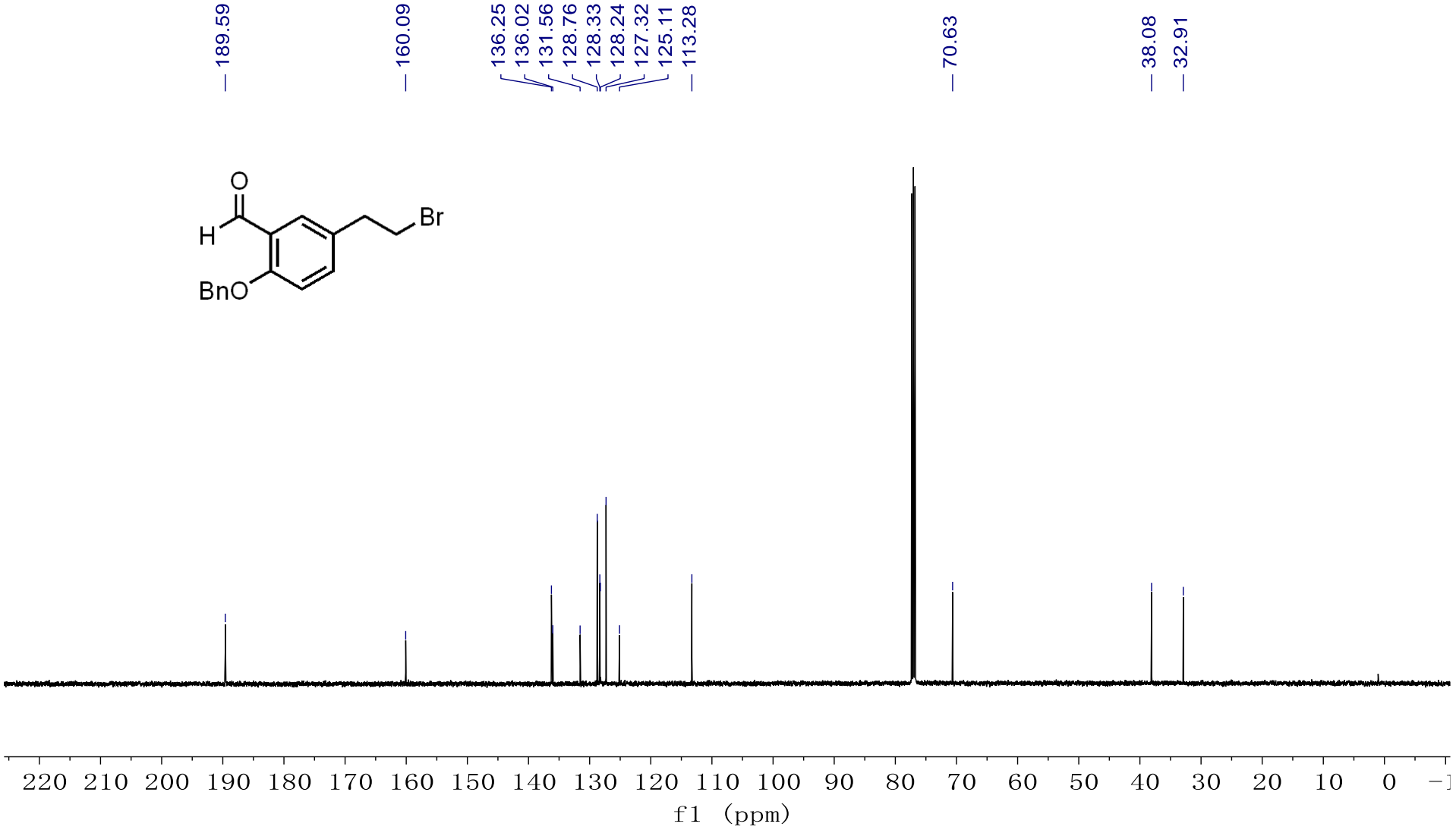

^{1}H NMR of arylethyl phosphonate 25

$CDCl_3$, 23 ºC

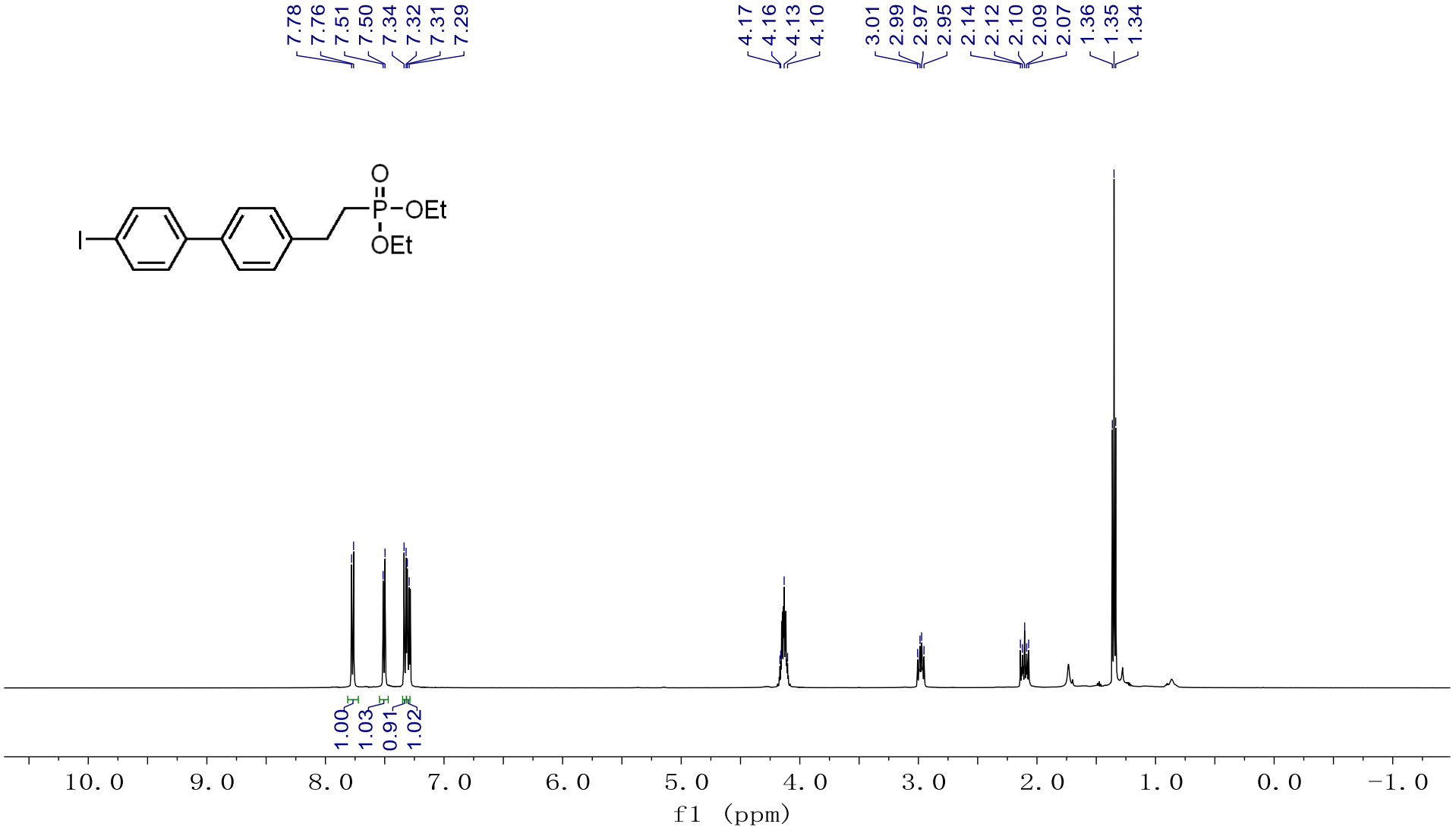

^{13}C NMR of arylethyl phosphonate 25

$CDCl_3$, 23 ºC

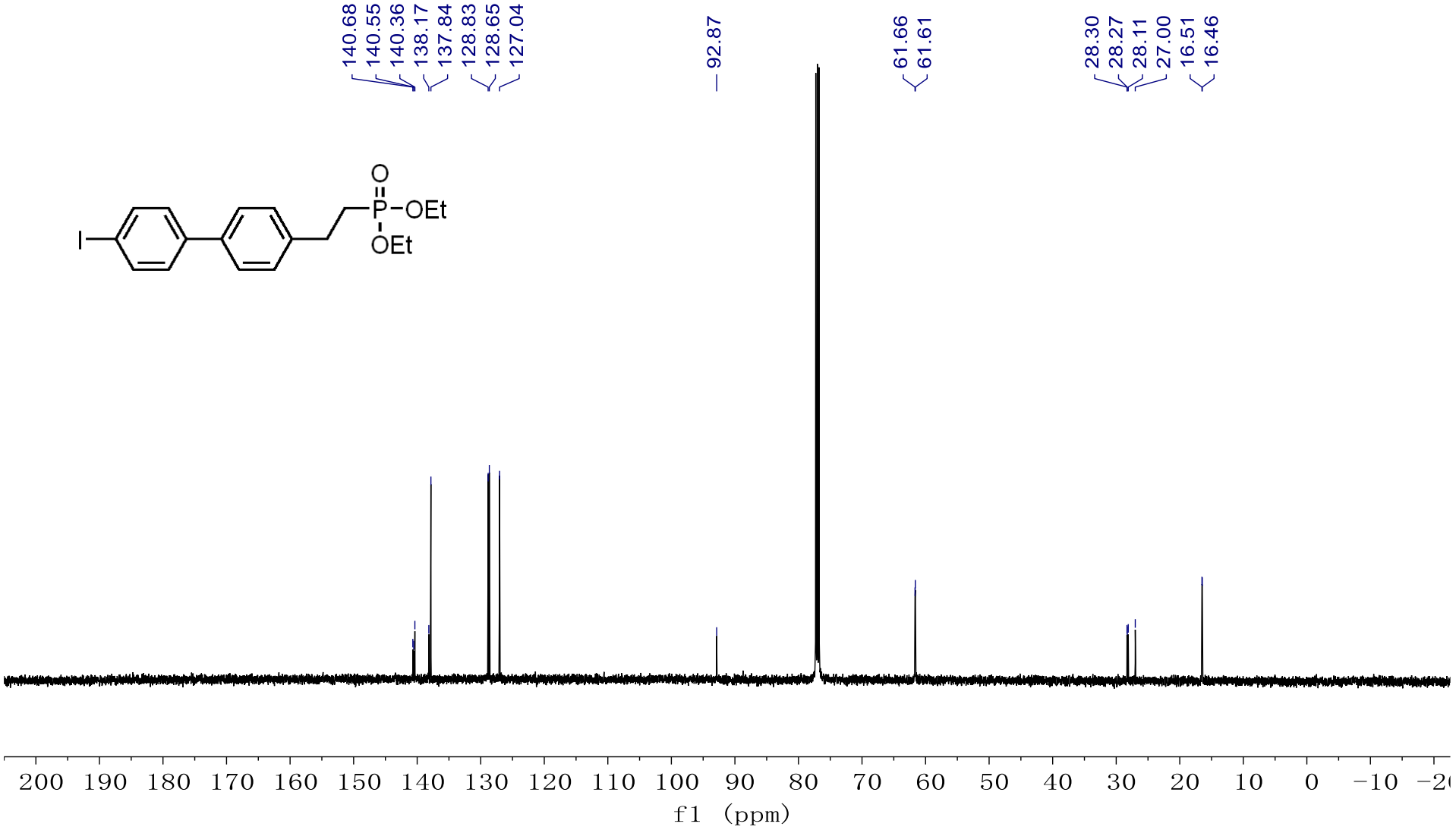

^{31}P NMR of arylethyl phosphonate 25

$CDCl_3$, 23 ºC

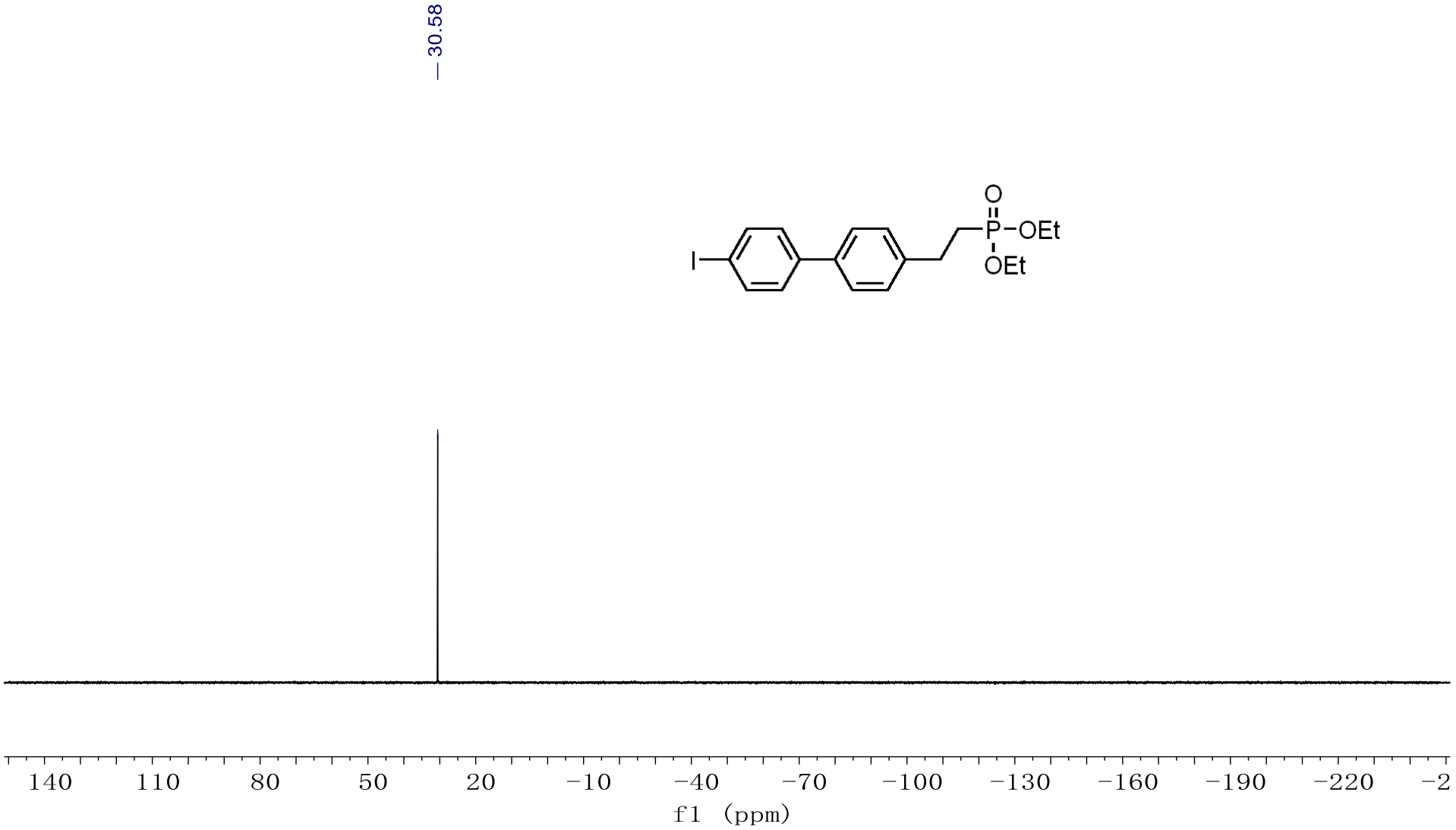

^{1}H NMR of arylethyl thiocyanate 26

$CDCl_3$, 23 ºC

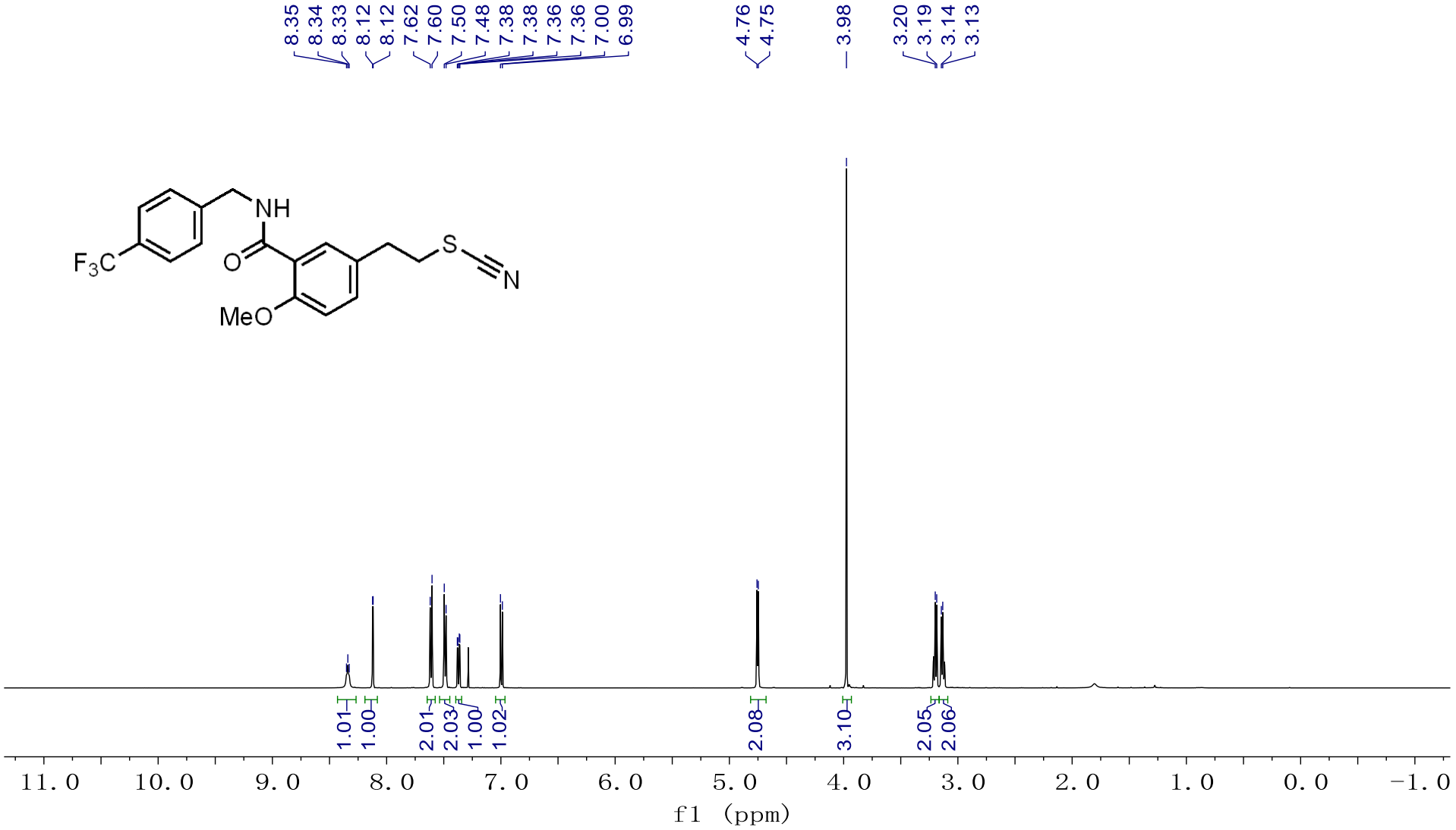

^{13}C NMR of arylethyl thiocyanate 26

$CDCl_3$, 23 ºC

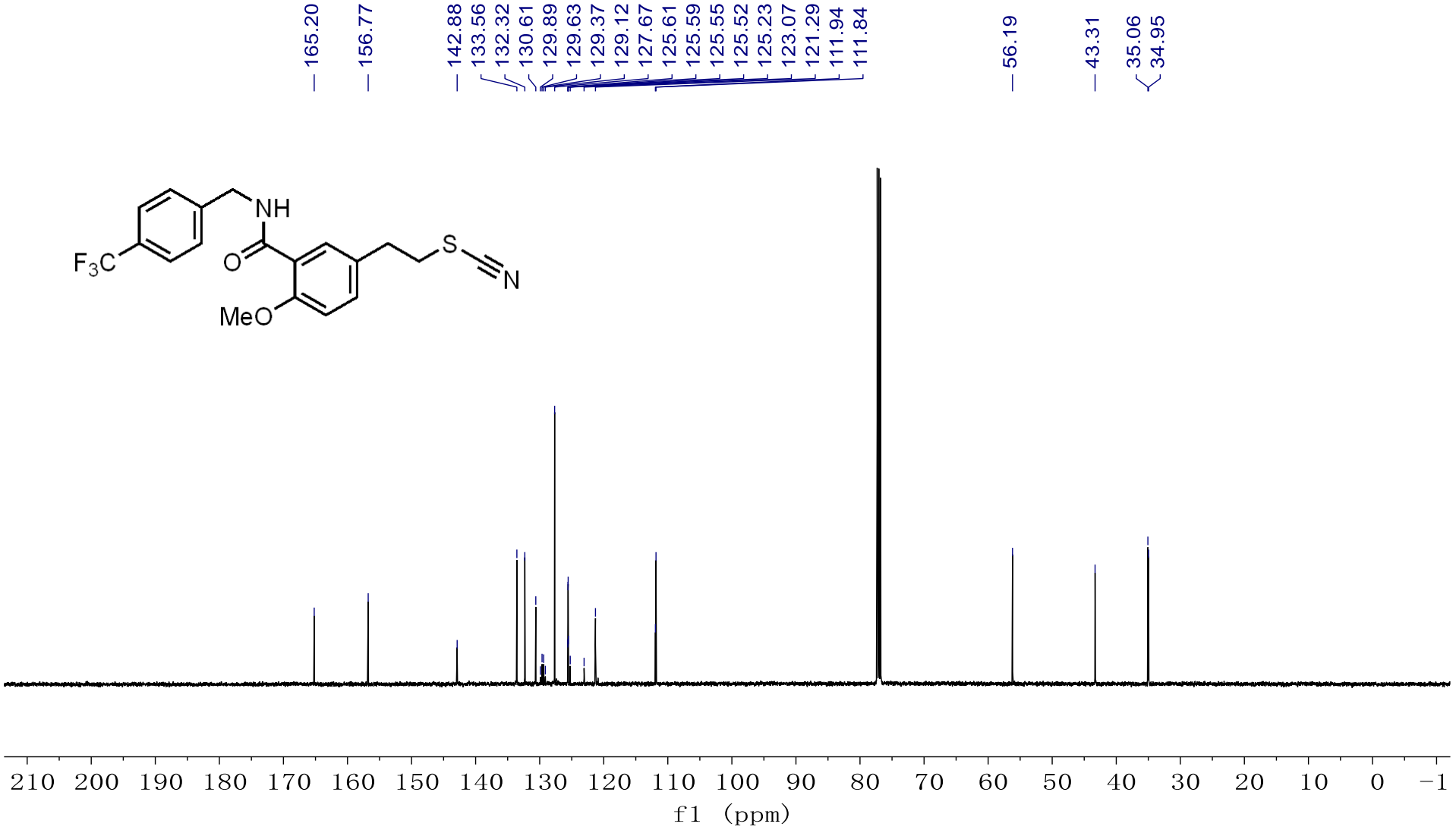

^{19}F NMR of arylethyl thiocyanate 26

$CDCl_3$, 23 ºC

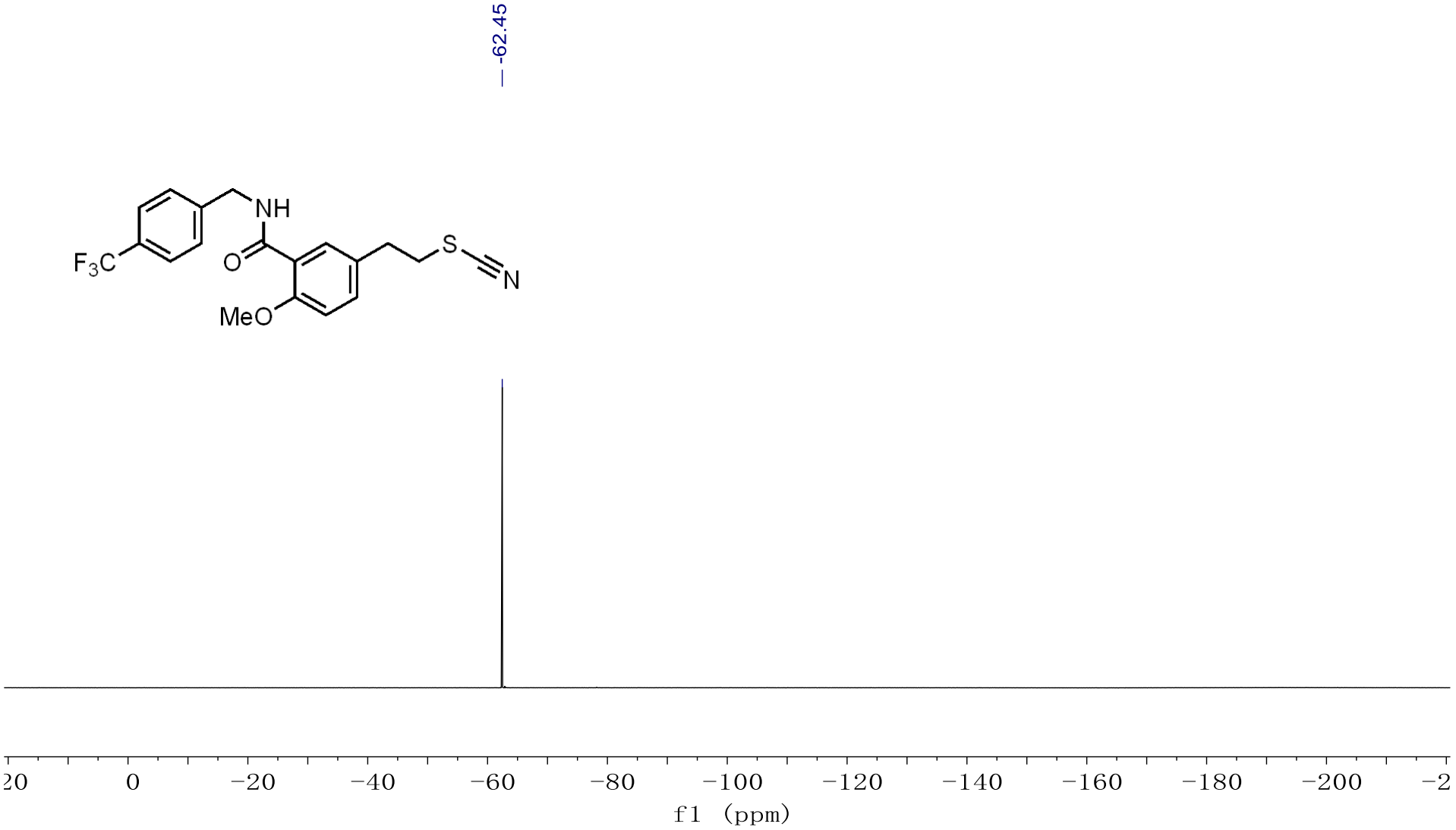

^{1}H NMR of pyriproxyfen- and cytisine-derived arylethylamine 27

CD_3CN, 23 ºC

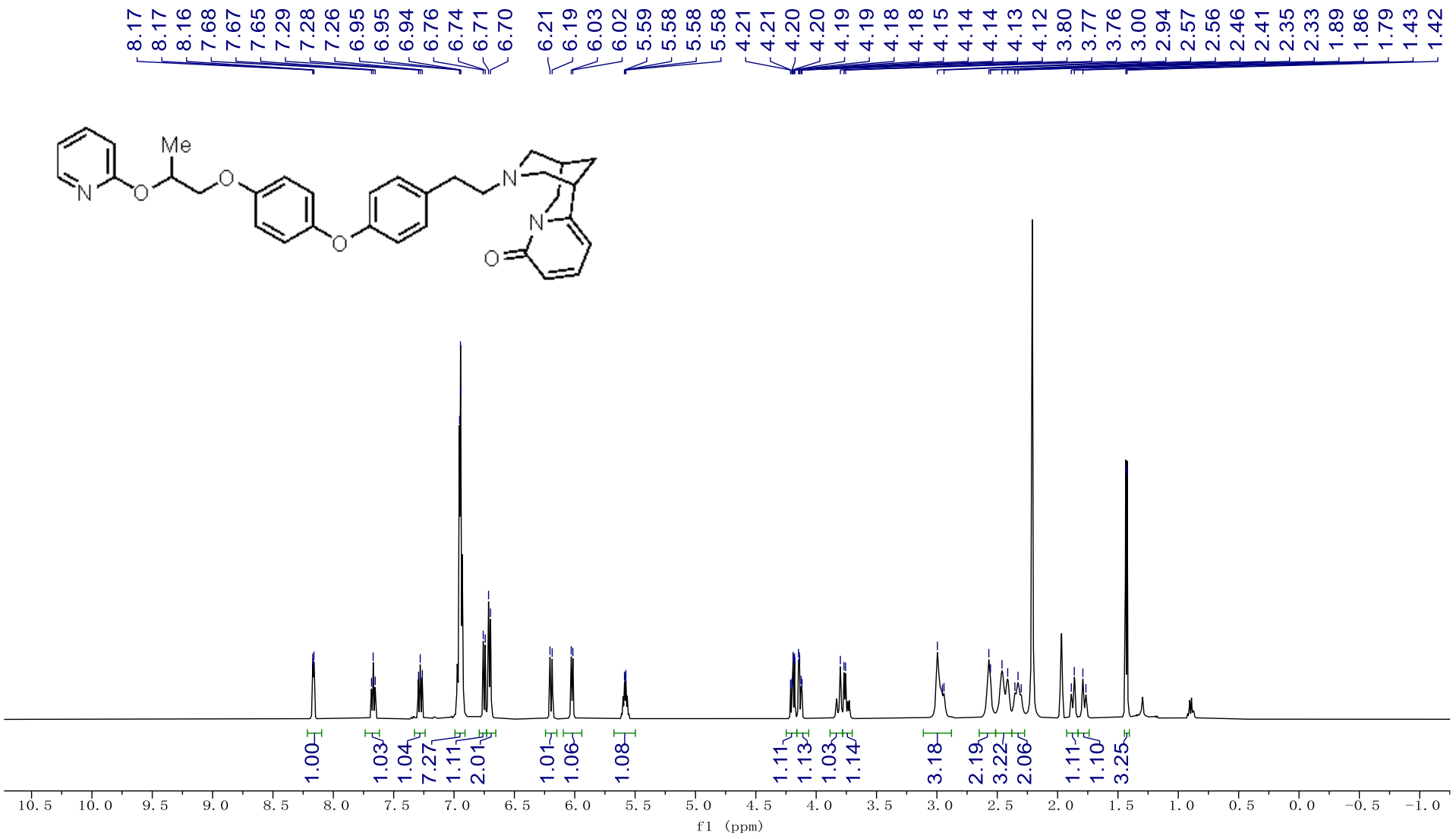

^{13}C NMR of pyriproxyfen- and cytisine-derived arylethylamine 27

CD_3CN, 23 ºC

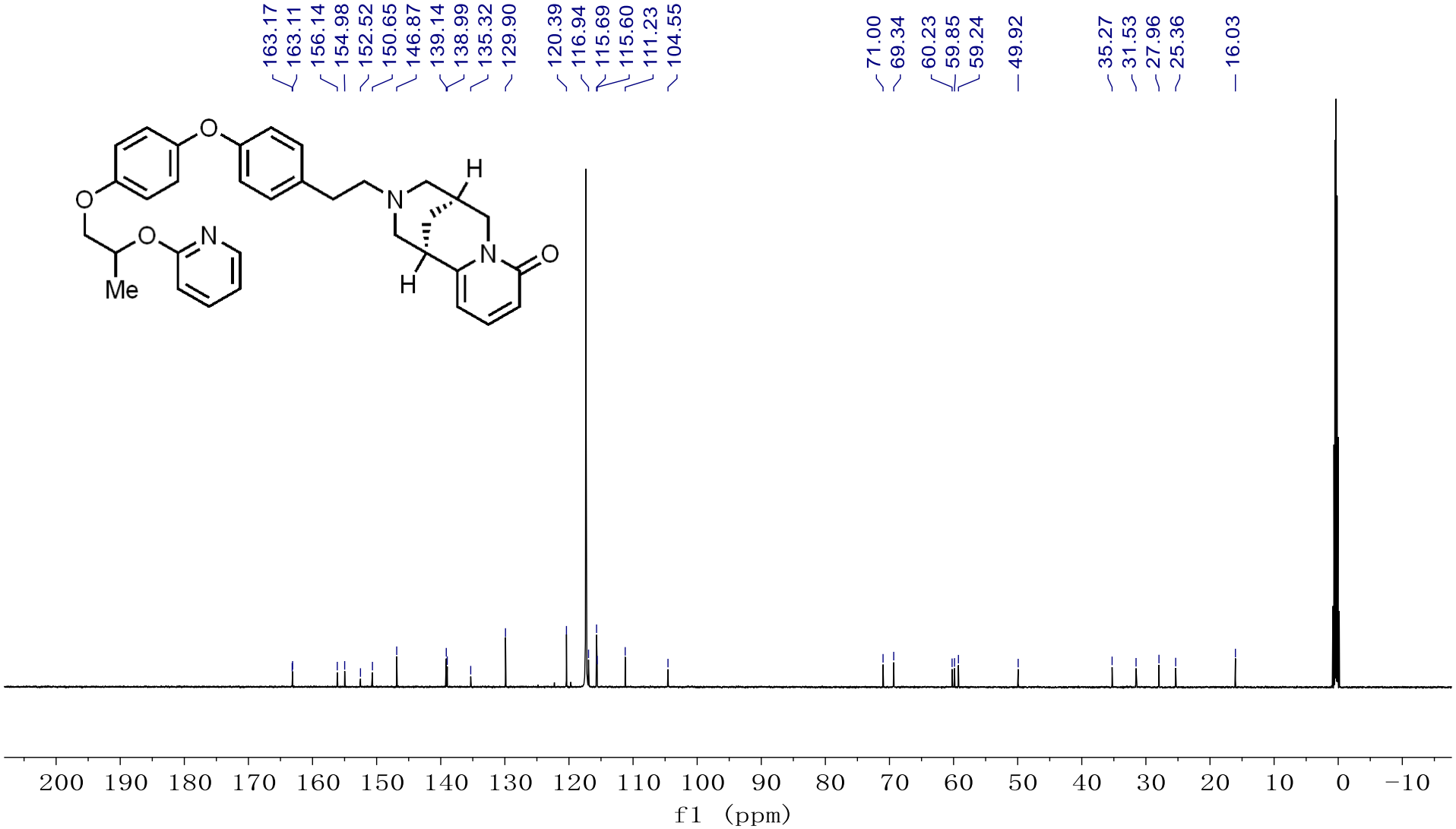

^{1}H NMR of arylethyl bromide 28

$CDCl_3$, 23 ºC

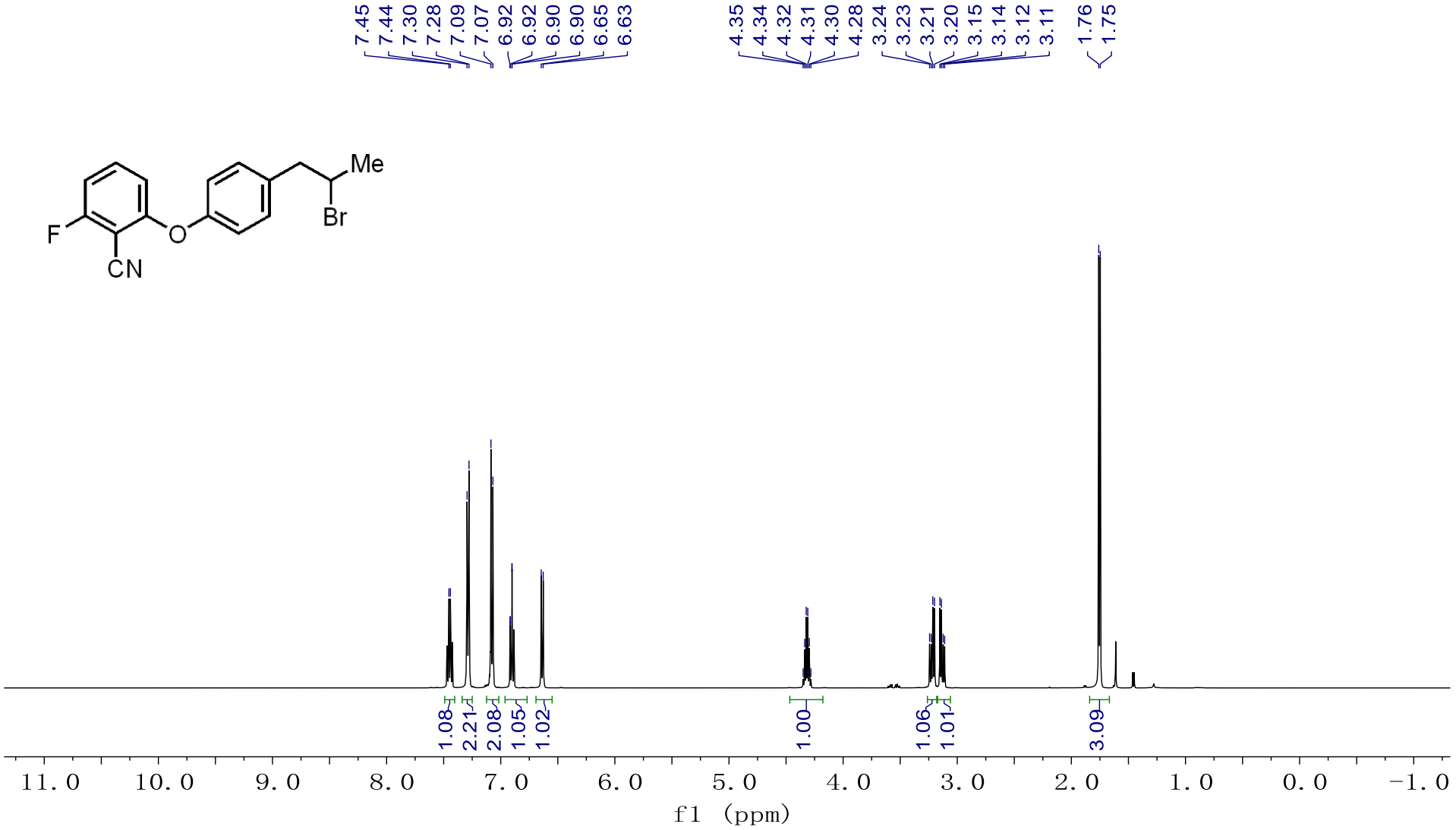

^{13}C NMR of arylethyl bromide 28

$CDCl_3$, 23 ºC

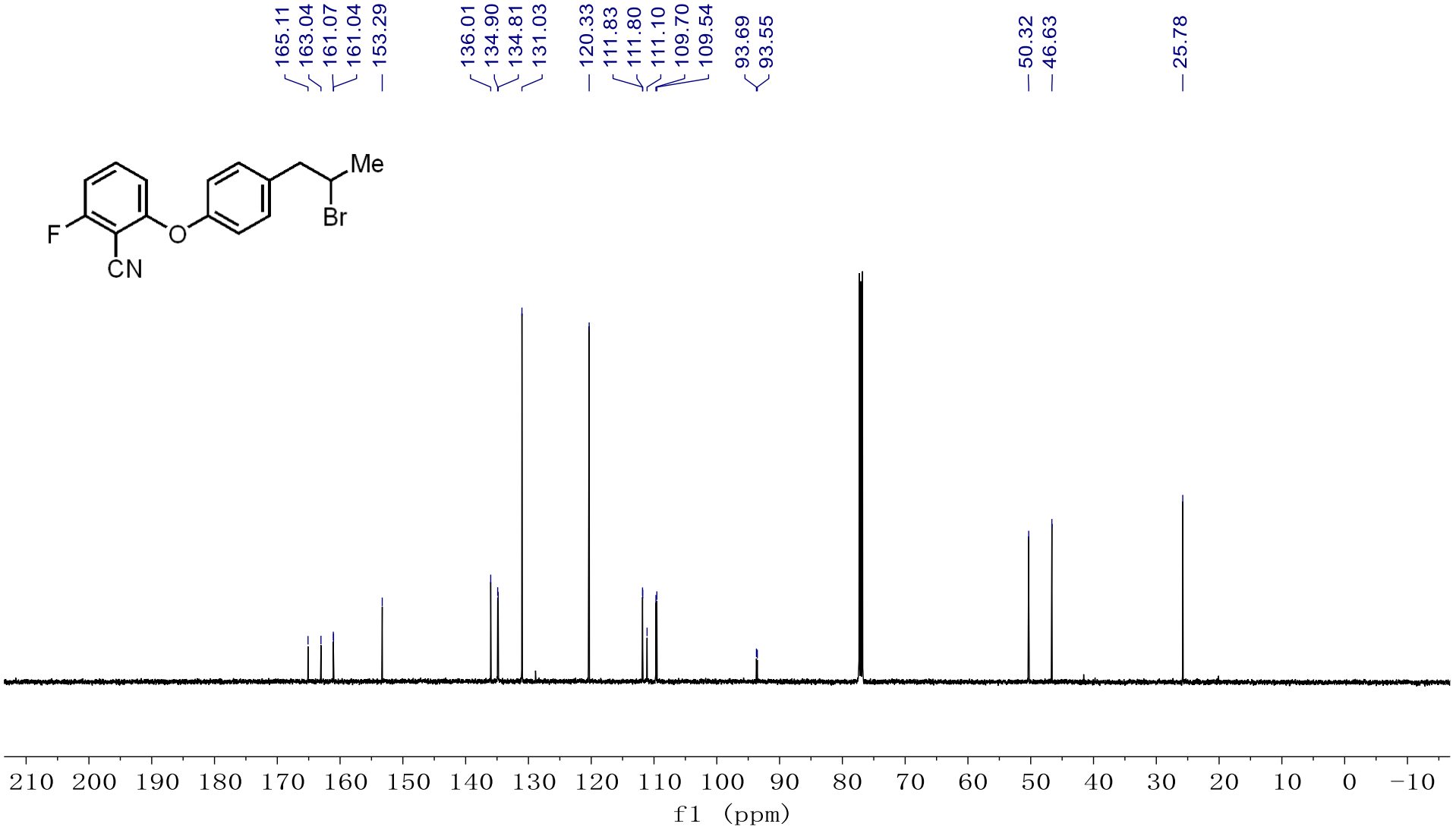

^{1}H NMR of arylethyl bromide 29

$CDCl_3$, 23 ºC

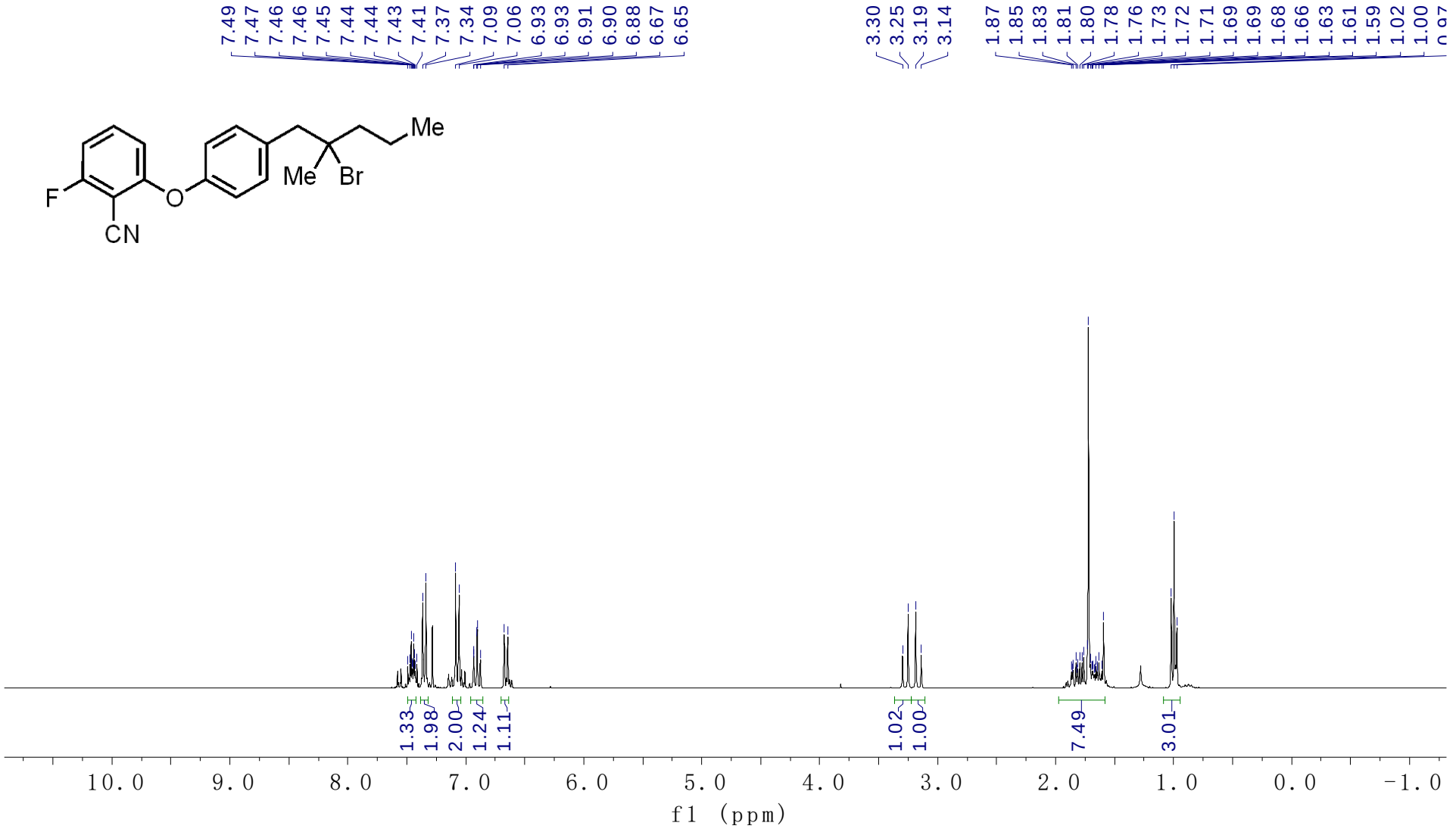

^{13}C NMR of arylethyl bromide 29

$CDCl_3$, 23 ºC

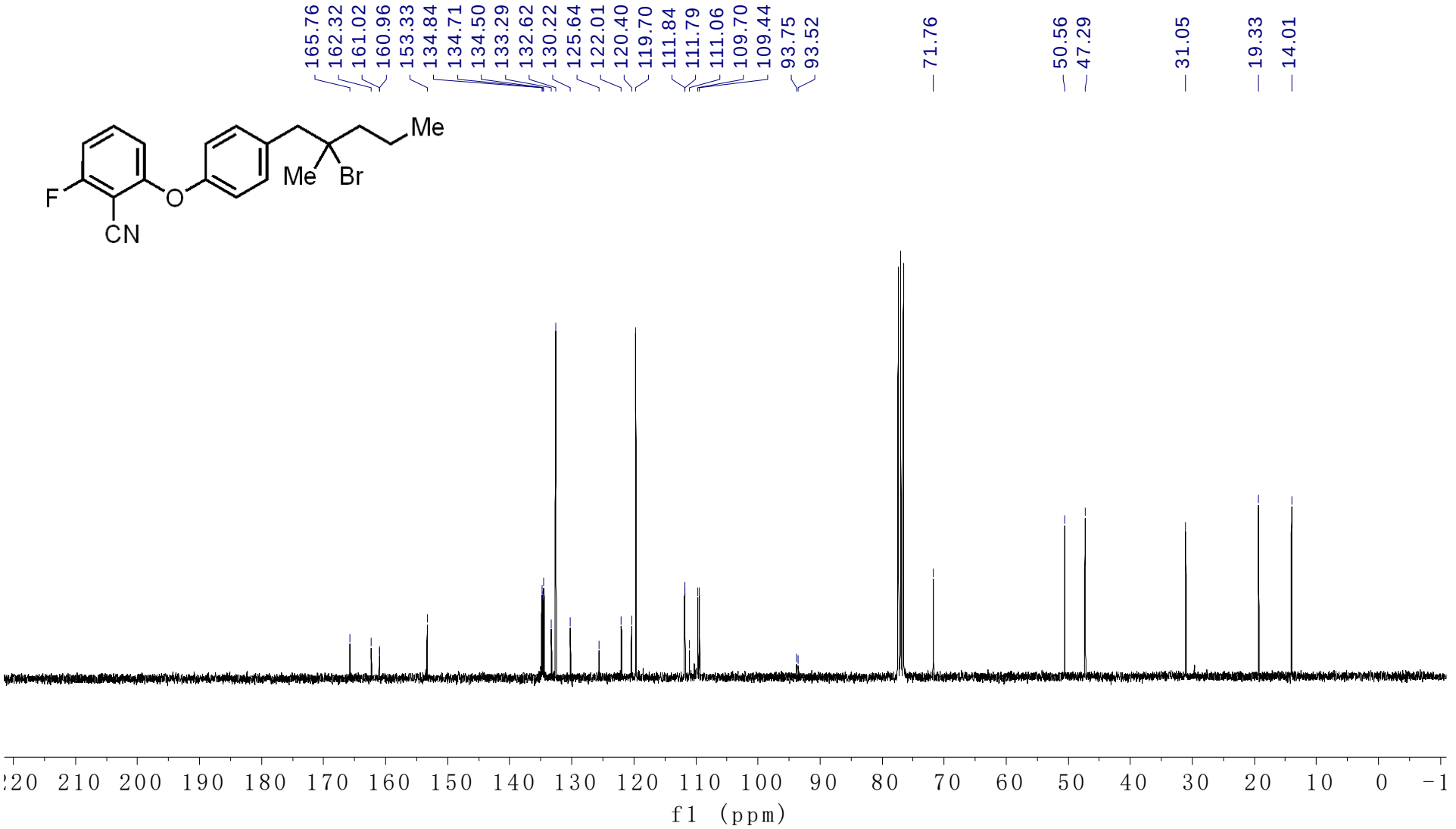

^{1}H NMR of arylethyl bromide 30

$CDCl_3$, 23 ºC

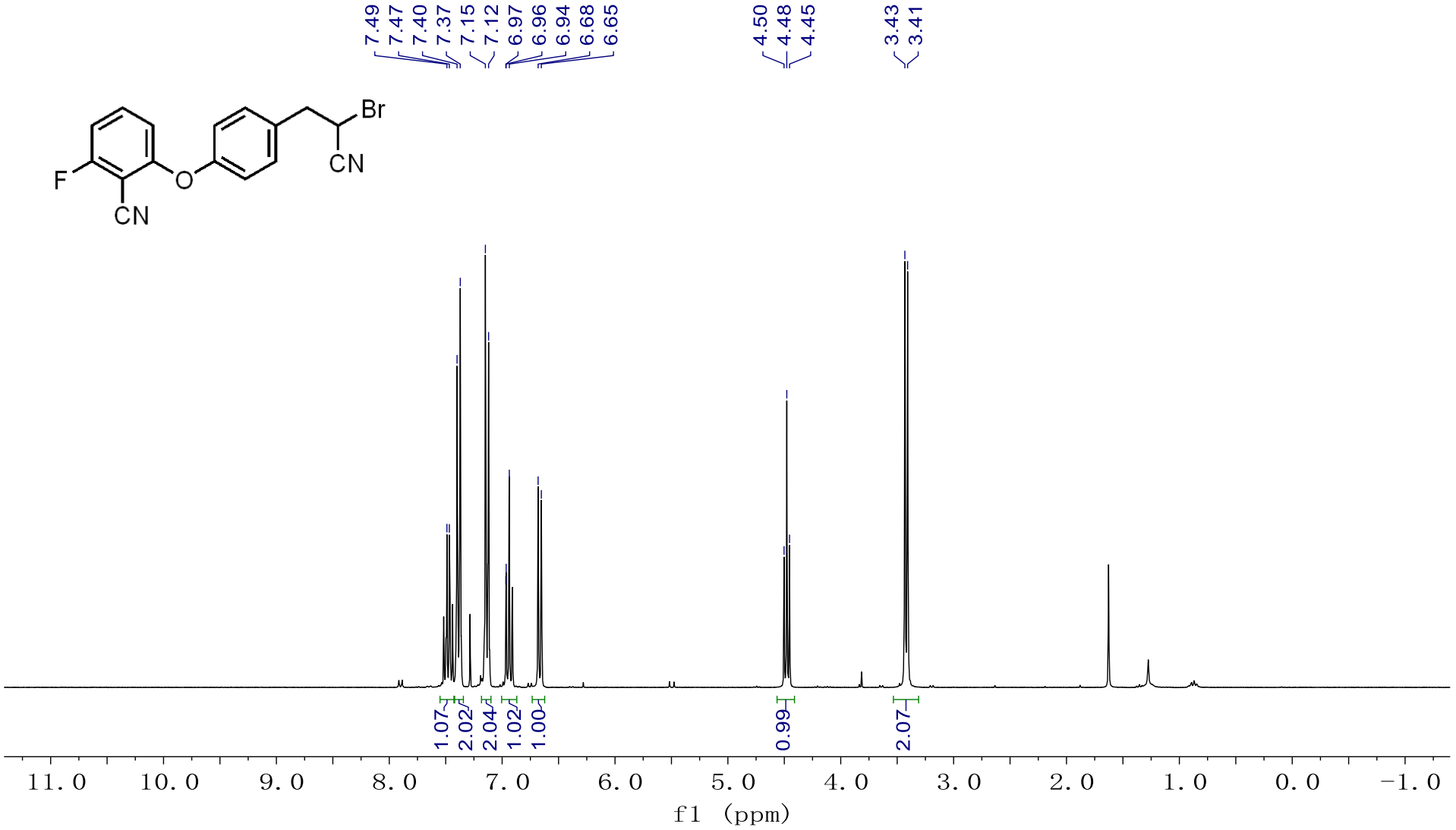

^{13}C NMR of arylethyl bromide 30

$CDCl_3$, 23 ºC

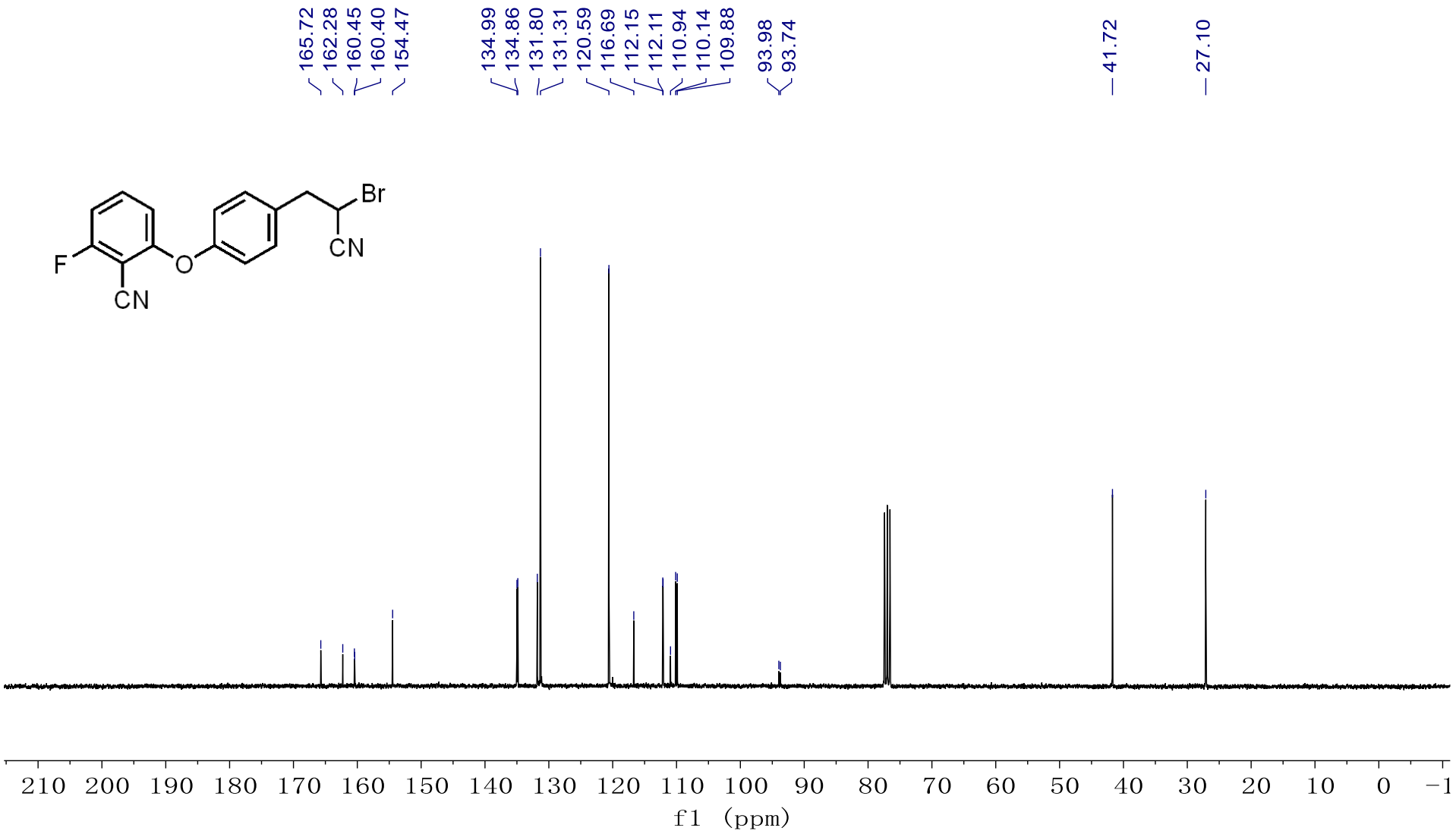

^{1}H NMR of arylethyl bromide 31

$CDCl_3$, 23 ºC

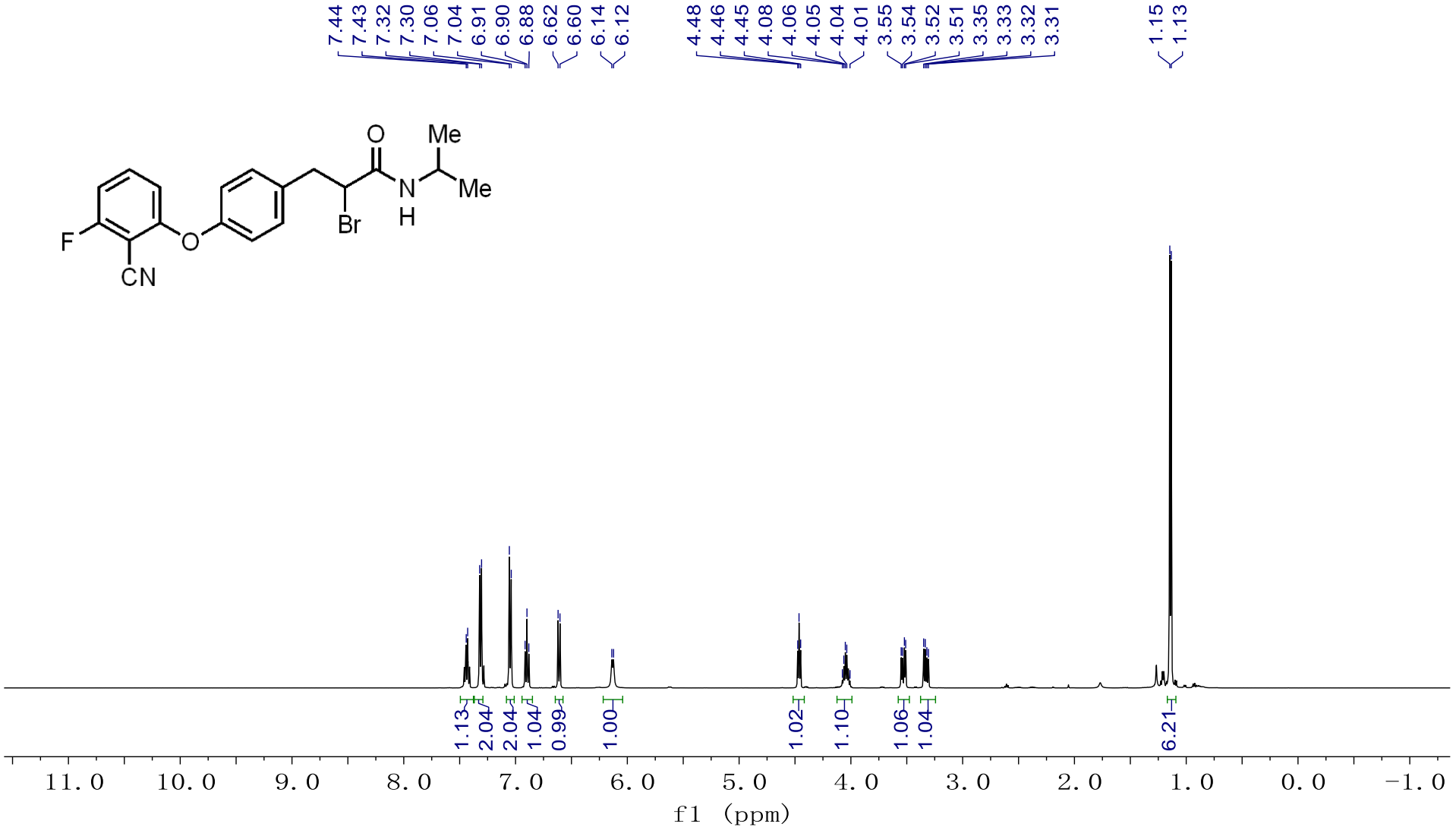

^{13}C NMR of arylethyl bromide 31

$CDCl_3$, 23 ºC

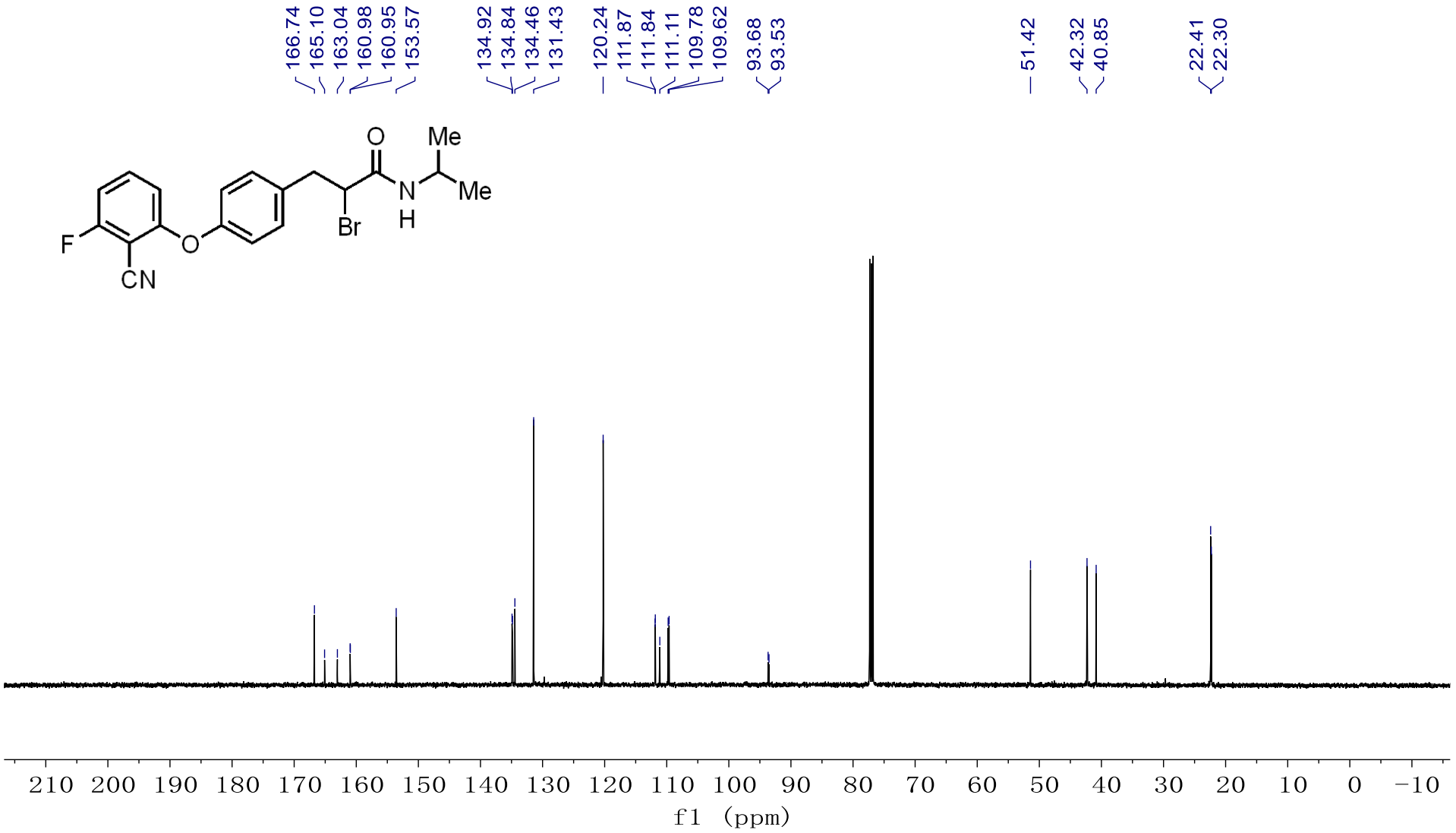

^{1}H NMR of arylethyl bromide 32

$CDCl_3$, 23 ºC

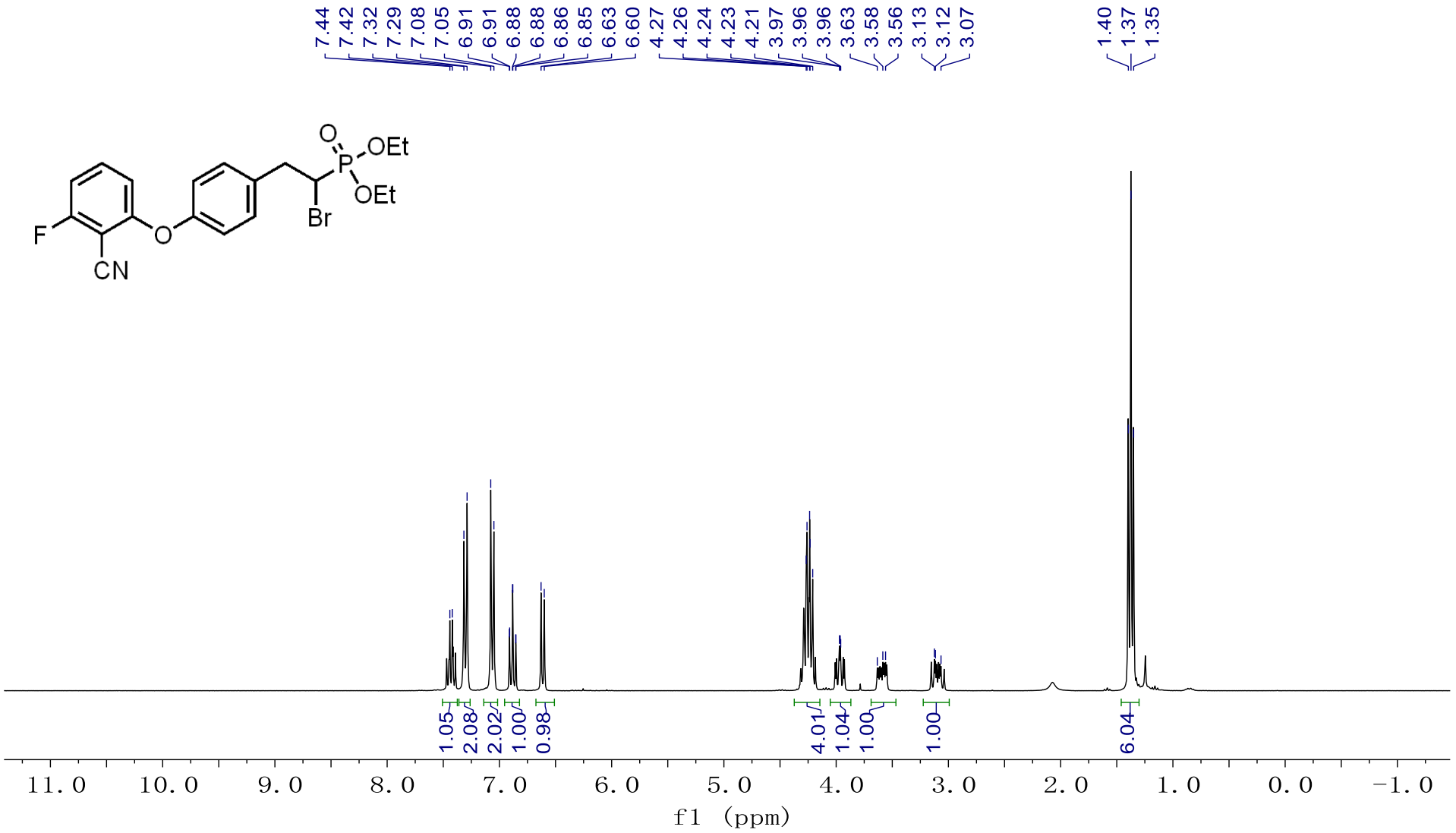

^{13}C NMR of arylethyl bromide 32

$CDCl_3$, 23 ºC

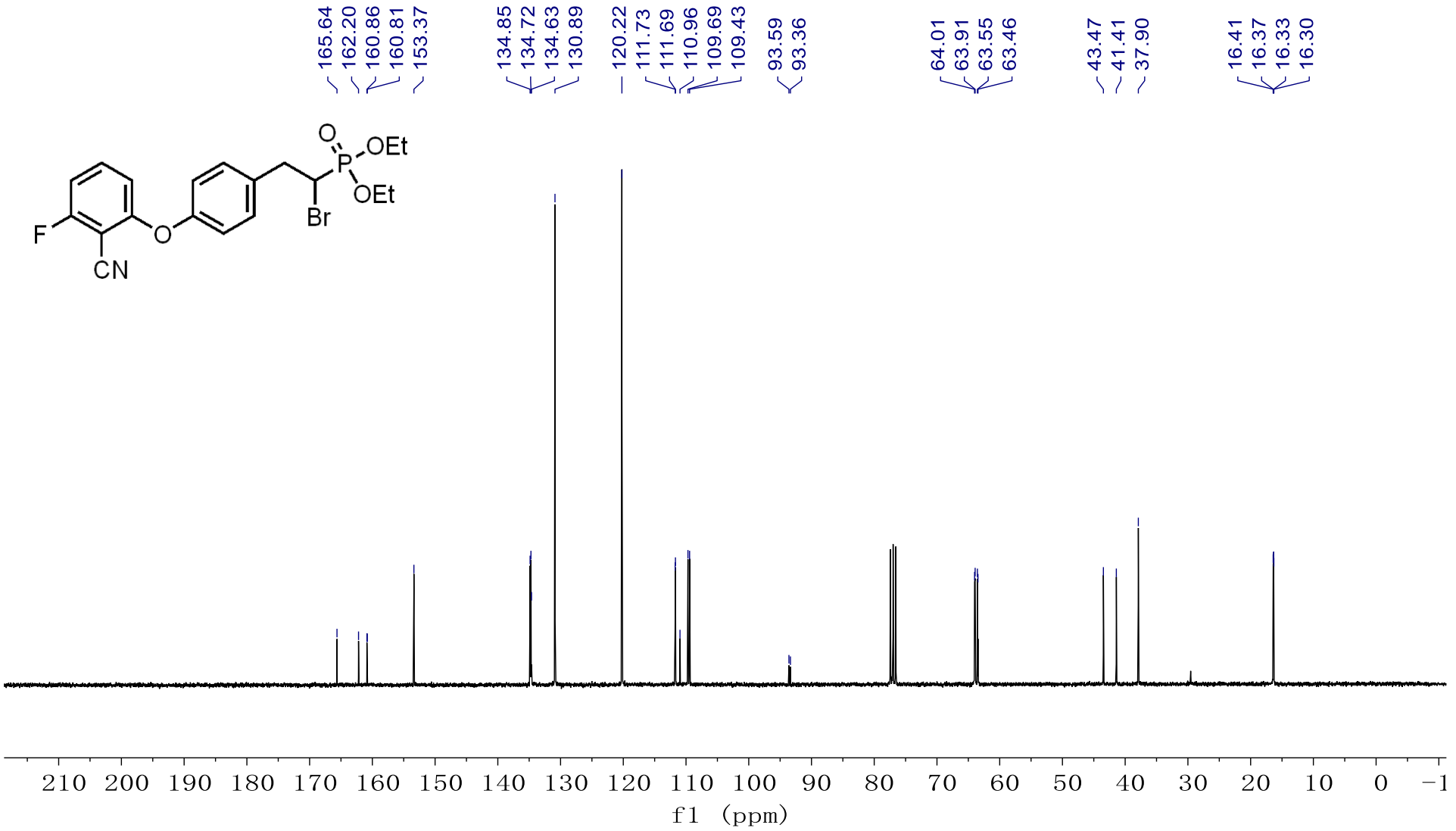

^{31}P NMR of arylethyl bromide 32

$CDCl_3$, 23 ºC

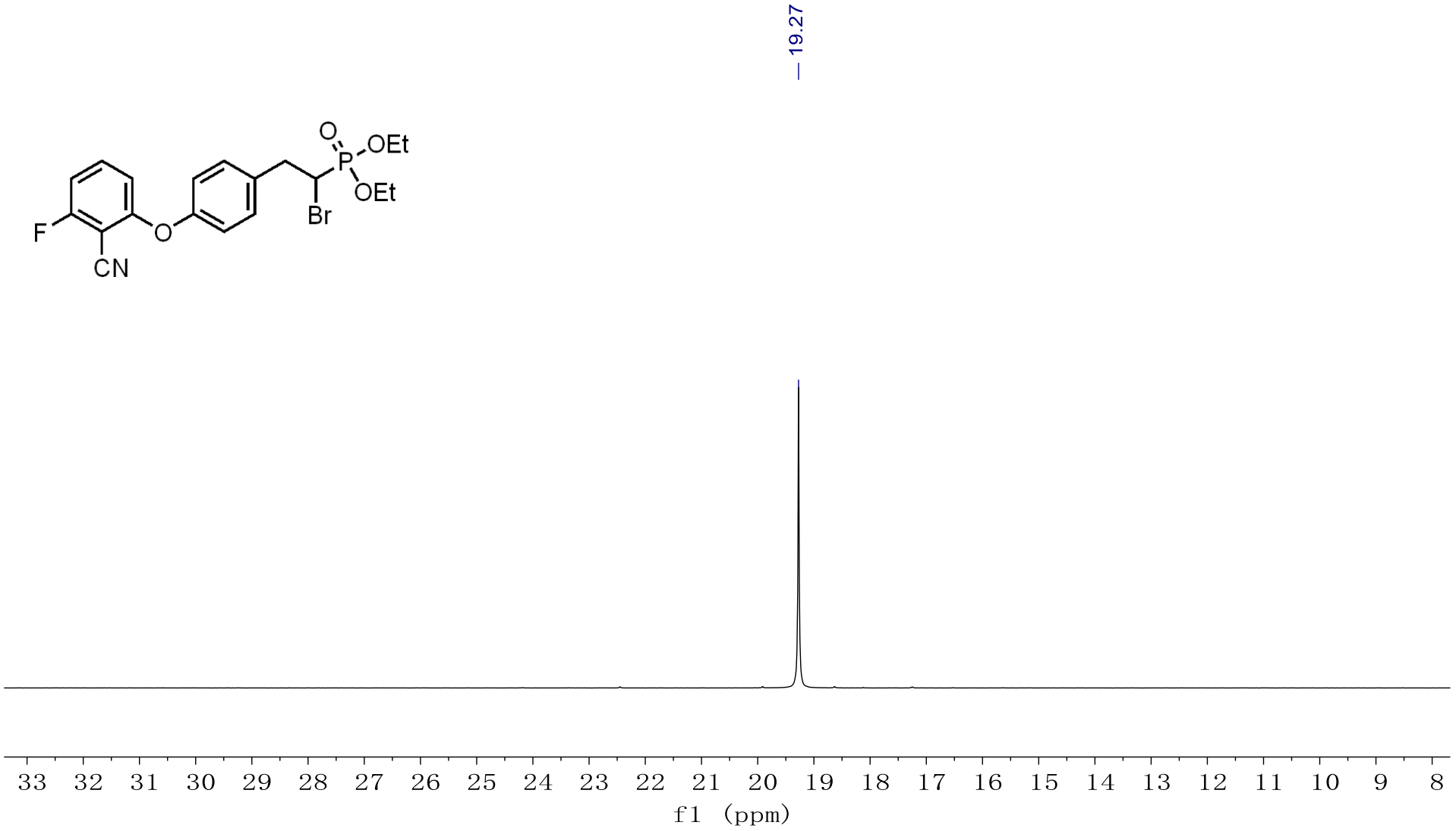

^{1}H NMR of arylethyl bromide 33

$CDCl_3$, 23 ºC

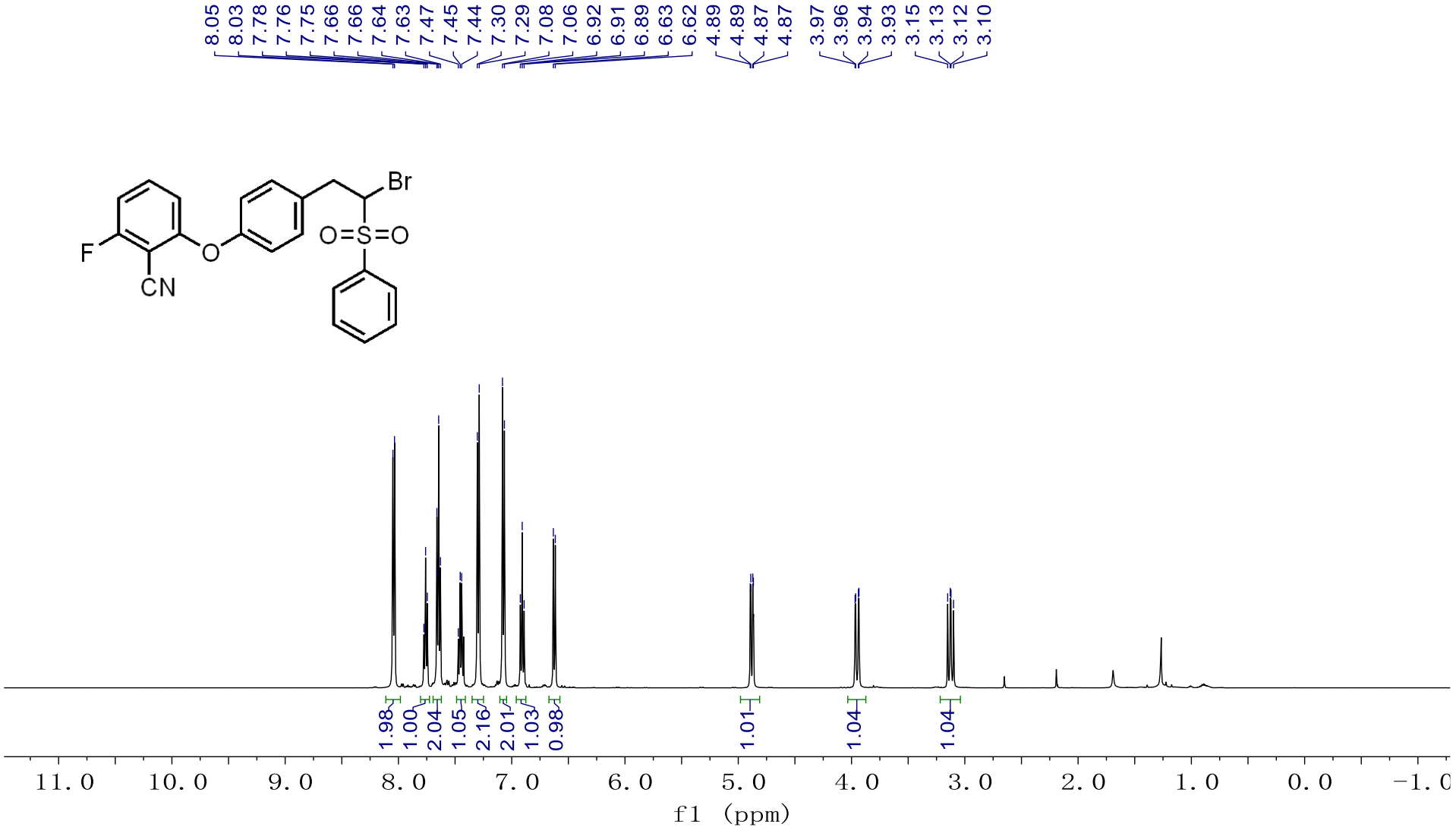

^{13}C NMR of arylethyl bromide 33

$CDCl_3$, 23 ºC

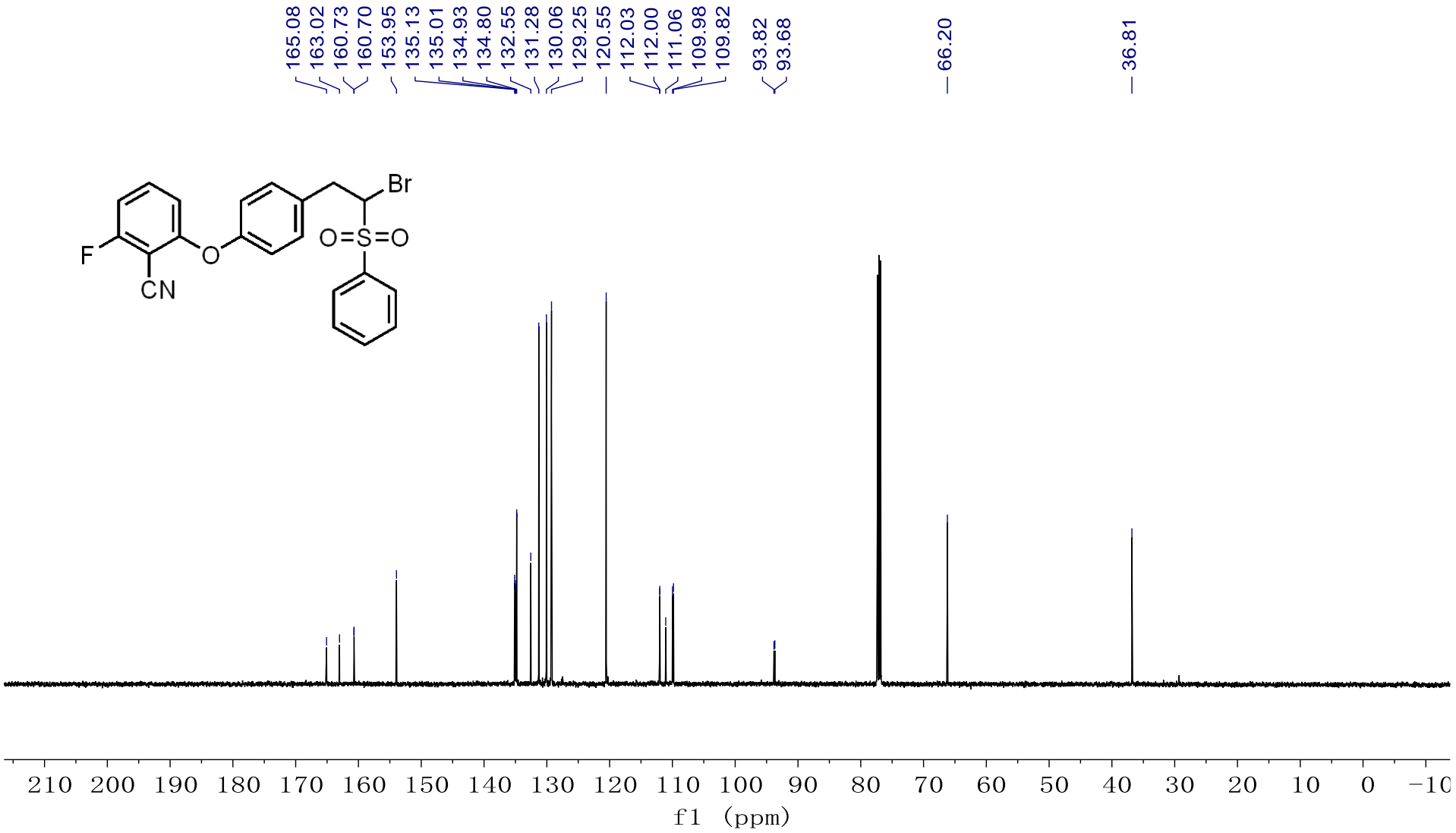

^{1}H NMR of arylethyl bromide 34

$CDCl_3$, 23 ºC

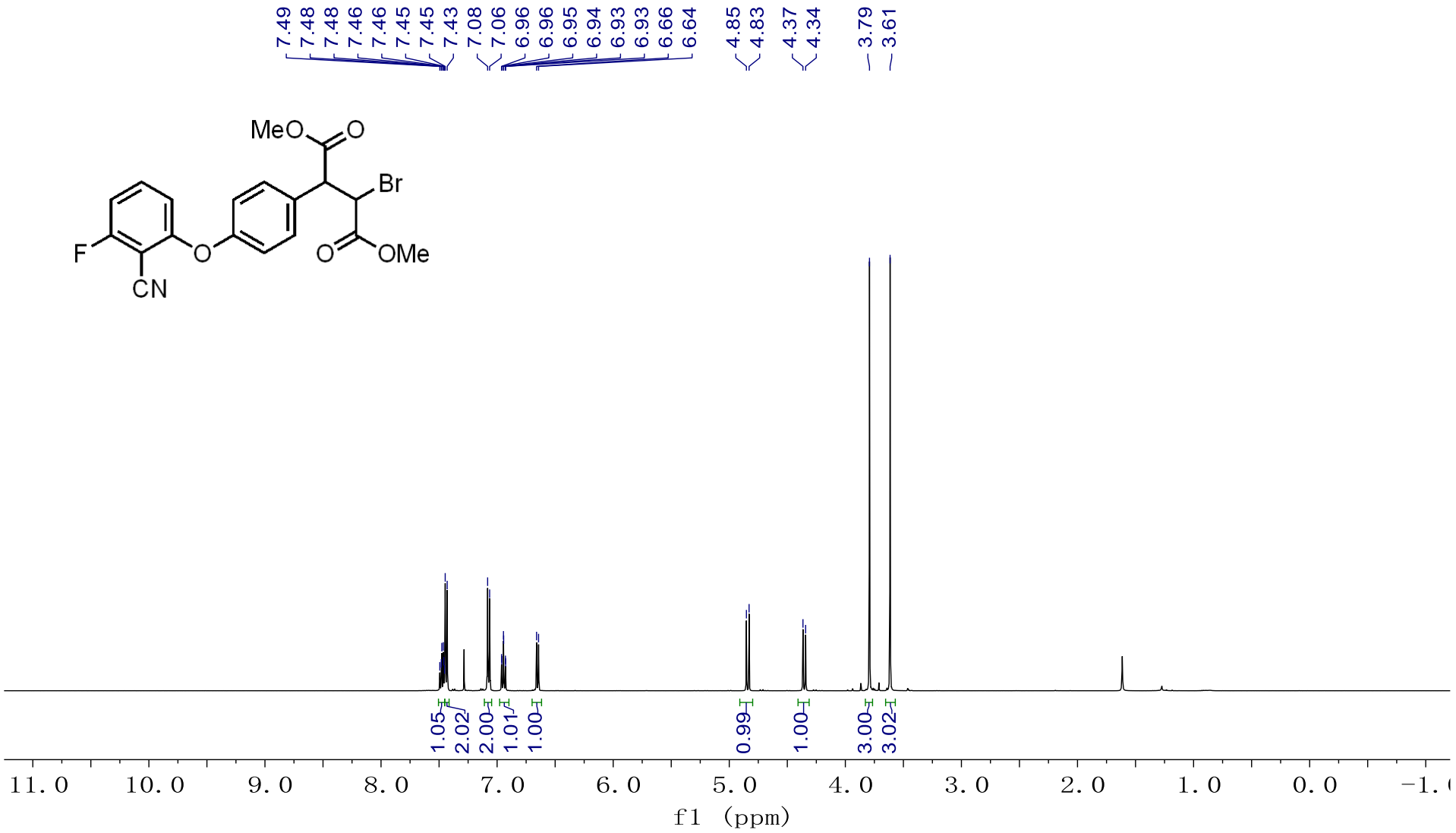

^{13}C NMR of arylethyl bromide 34

$CDCl_3$, 23 ºC

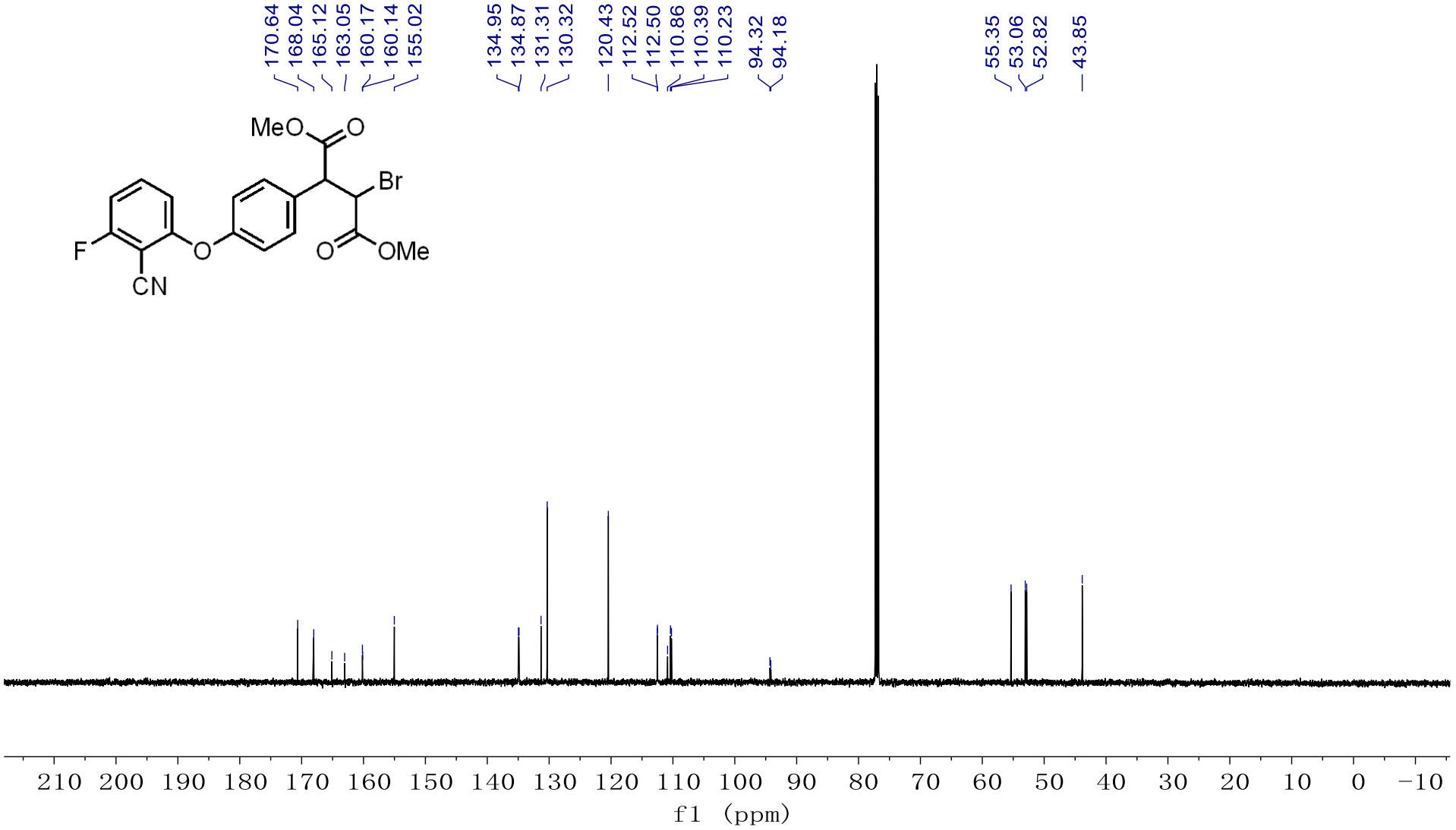

^{1}H NMR of arylethyl bromide 35

$CDCl_3$, 23 ºC

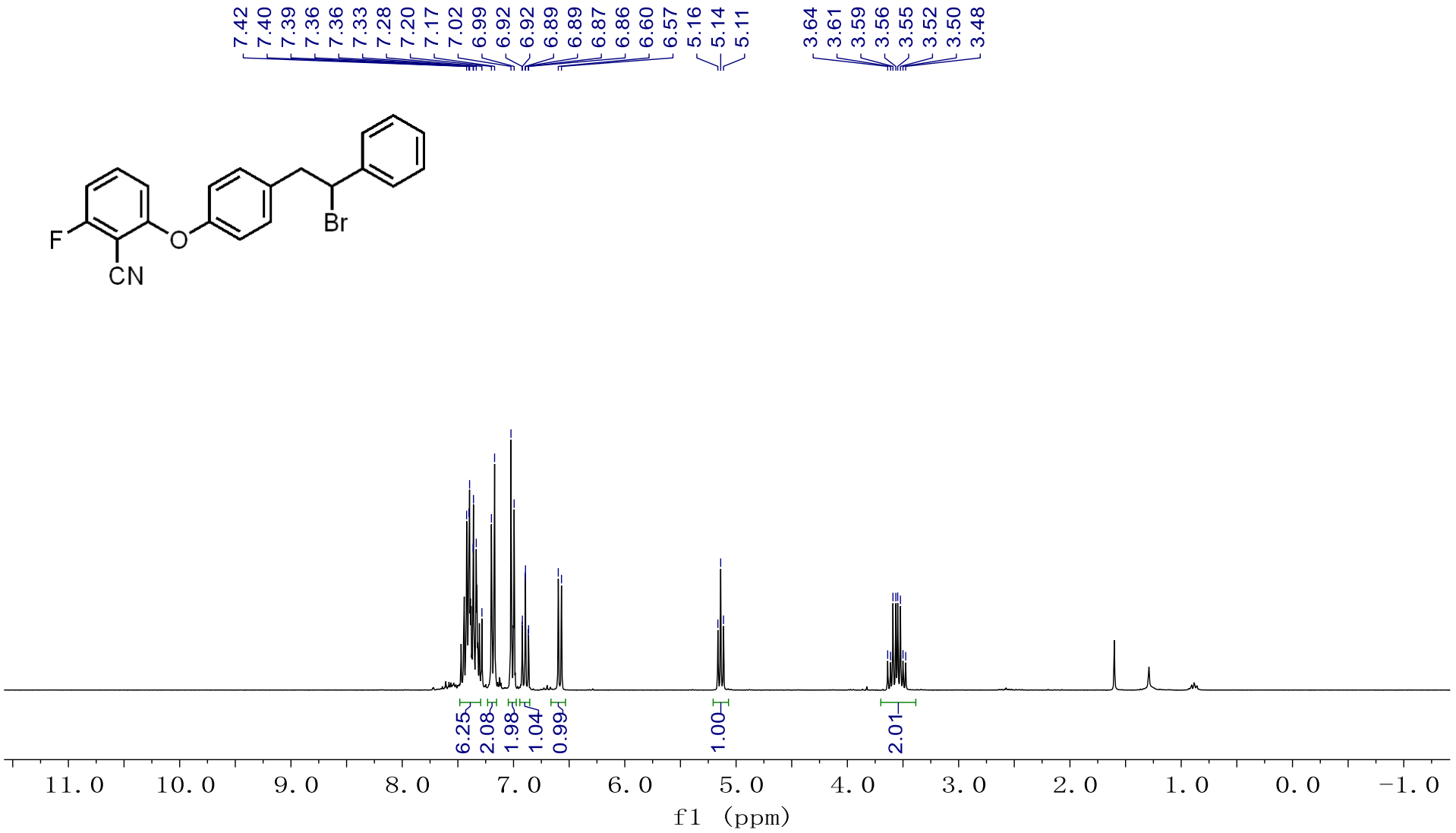

^{13}C NMR of arylethyl bromide 35

$CDCl_3$, 23 ºC

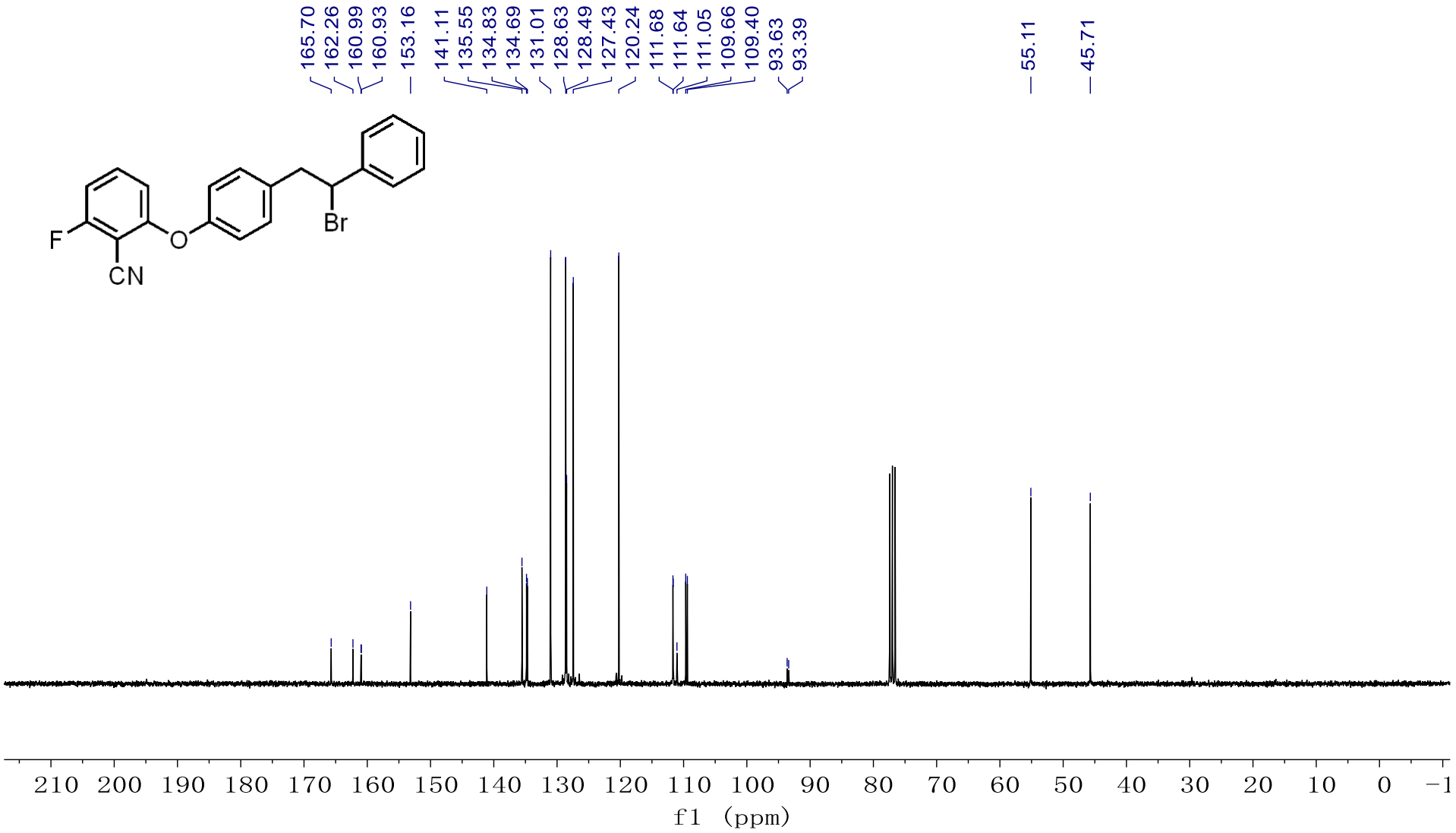

^{1}H NMR of arylethyl bromide 36

$CDCl_3$, 23 ºC

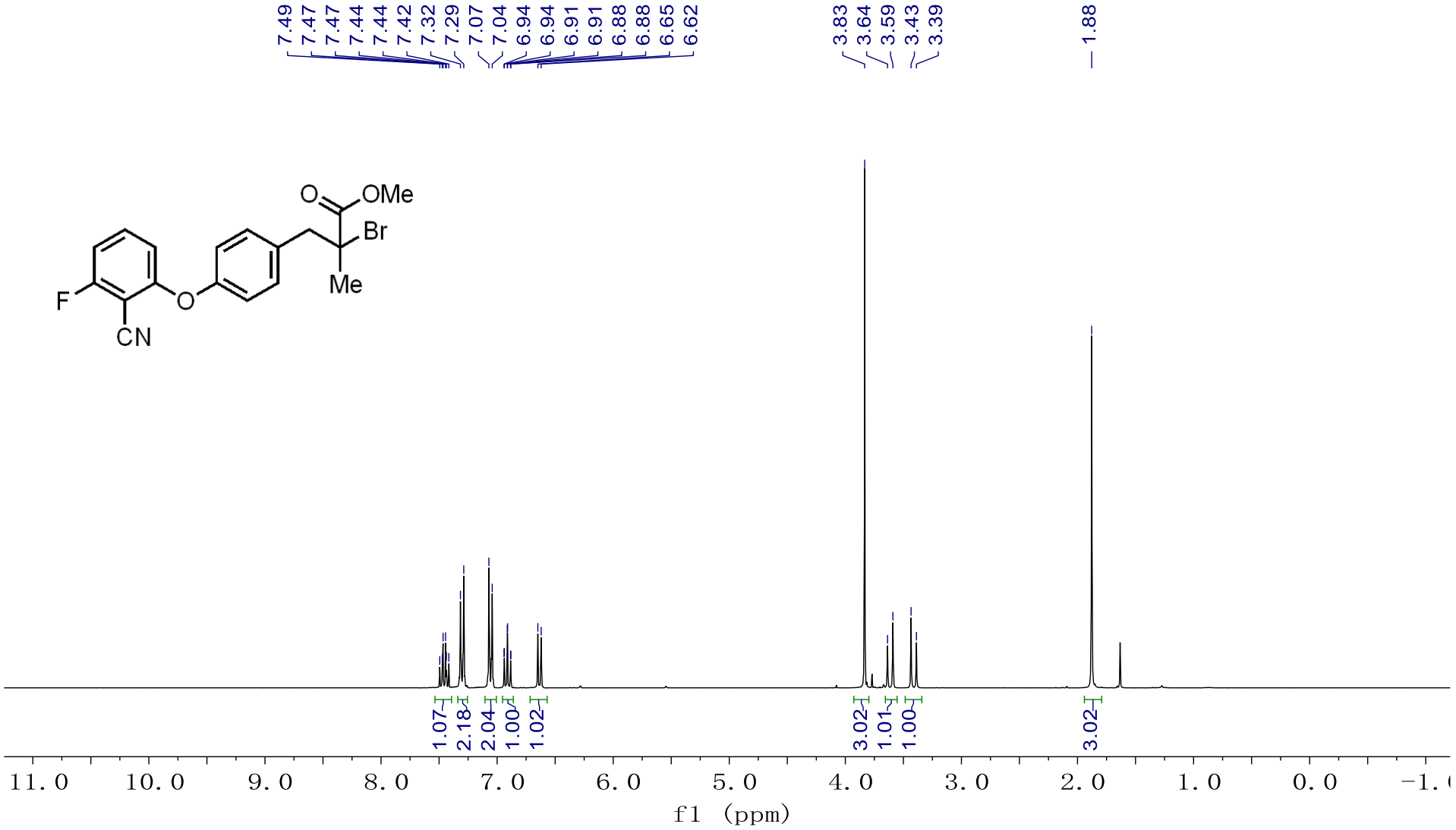

^{13}C NMR of arylethyl bromide 36

$CDCl_3$, 23 ºC

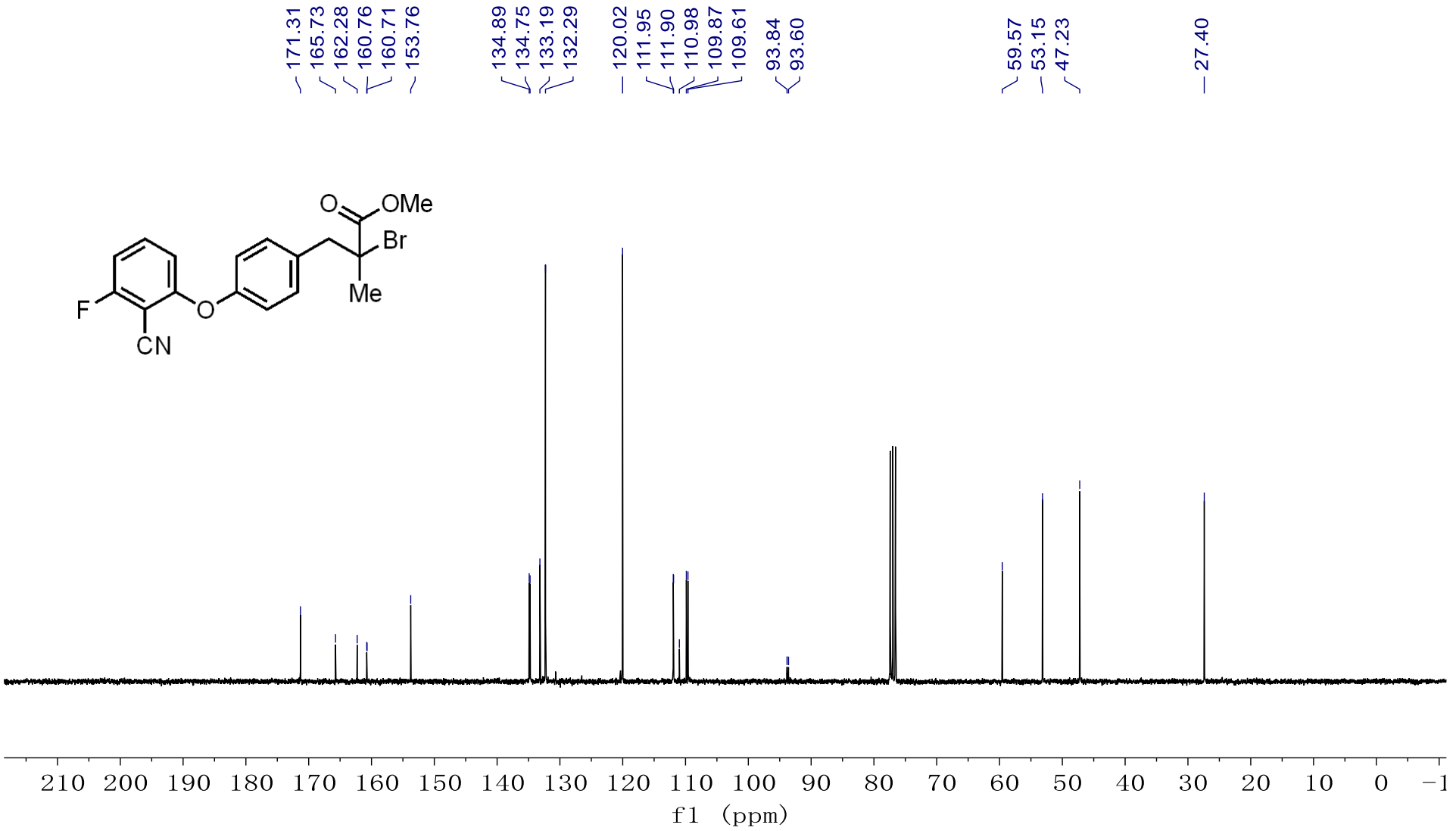

REFERENCES

1. Fulmer, G. R. et al. NMR Chemical Shifts of Trace Impurities: Common Laboratory Solvents, Organics, and Gases in Deuterated Solvents Relevant to the Organometallic Chemist. *Organometallics*, **29**, 2176–2179 (2010).
2. Berger, F. et al. Site-selective and versatile aromatic C–H functionalization by thianthrenation. *Nature* **567**, 223–228 (2019).
3. Elliott, L. D., Kayal, S., George, M. W. & Booker-Milburn, K. Rational design of triplet sensitizers for the transfer of excited state photochemistry from UV to visible. *J. Am. Chem. Soc.* **142**, 14947–14956 (2020).
4. Zähringer, T. J. B., Wienhold, M., Gilmour, R. & Kerzig, C. Direct Observation of Triplet States in the Isomerization of Alkenyl boronates by Energy Transfer Catalysis. *J. Am. Chem. Soc*. **145**, 21576−21586 (2023).
5. Xu, B. et al. Photocatalyzed diastereoselective isomerization of cinnamyl chlorides to cyclopropanes. *J. Am. Chem. Soc*. **142**, 6206–6215 (2020).
6. Luque, A. Groß, J. Zähringer, T. J. B. Kerzig, C. & Opatz, T. Vinylcyclopropane [3 + 2] Cycloaddition with Acetylenic Sulfones Based on Visible Light Photocatalysis. *Chem. –Eur. J.* **28**, No. e202104329 (2022).
7. Yang, Y.-M., Zhang, C., Yang, H. & Tang, Z.-Y. Photo-catalyzed acetoxysulfoximination of styrene with sulfoximidoyl thianthrenium salt. *Chem. Commun*. **58**, 8580–8583 (2022).
8. Thyrion, F. C. Flash Photolysis of Aromatic Sulfur Molecules. *J. Phys. Chem.* **77**, 1478–1482 (1973).
9. Shine, H. J. & Murata, Y. Kinetics and mechanism of the reaction of the thianthrene cation radical with water. *J. Am. Chem. Soc*. **91**, 1872–1874 (1969).
10. Kang, W.-J. et al. Discovery of a Thioxanthone–TfOH complex as a photoredox catalyst for hydrogenation of alkenes using p-xylene as both electron and hydrogen sources. *Angew. Chem. Int. Ed*. **61**, e202211562 (2022).
11. Yip, R. W. Szabo, A. G. & Tolg, P. K. Triplet State of Ketones in Solutions. Quenching Rate Studies of Thioxanthenone Triplets by Flash Absorption. *J. Am. Chem. Soc*. **95**, 4471−4472 (1973).
12. Carmichael, I. & Hug, G. L. Triplet−Triplet Absorption Spectra of Organic Molecules in Condensed Phases. *J. Phys. Chem. Ref. Data* **15**, 1−250 (1986).
13. Sorgo, M. de., Wasserman, B. & Szwarc, M. Aggregation of Salts of Thianthrene Radical Cations. *J. Phys. Chem*. **76**, 3468−3471 (1972).
14. Kuhn, H. J., Braslavsky, S. E. & Schmidt, R. Chemical actinometry (IUPAC technical report). *Pure Appl. Chem*. **76**, 2105–2146 (2004).
15. Cismesia, M. A. & Yoon, T. P. Characterizing chain processes in visible light photoredox catalysis. *Chem. Sci*. **6**, 5426–5434 (2015).

16. Wegner, E. E. & Adamson, A. W. Photochemistry of complex ions. III. Absolute quantum yields for the photolysis of some aqueous chromium(III) complexes. Chemical actinometry in the long wavelength visible region. *J. Am. Chem. Soc*. **88**, 394–404 (1966).
17. Neese, F. The ORCA program system. *Comput. Mol. Sci.* **2**, 73–78 (2012).
18. Lee, C., Yang, W. & Parr, R. G. Development of the Colle-Salvetti correlation-energy formula into a functional of the electron density. *Physical Review B* **37**, 785–789 (1988).
19. Grimme, S., Antony, J., Ehrlich, S. & Krieg, H. A consistent and accurate ab initio parametrization of density functional dispersion correction (DFT-D) for the 94 elements H–Pu. *J. Chem. Phys.* **132**, 154104 (2010).
20. Grimme, S., Ehrlich, S. & Goerigk, L. Effect of the damping function in dispersion corrected density functional theory. *J. Comput. Chem*. **32**, 1456–1465 (2011).
21. Weigend, F. Accurate Coulomb-fitting basis sets for H to Rn. *Physical Chemistry Chemical Physics* **8**, 1057–1065 (2006).
22. Weigend, F. & Ahlrichs, R. Balanced basis sets of split valence, triple zeta valence and quadruple zeta valence quality for H to Rn: Design and assessment of accuracy. *Physical Chemistry Chemical Physics* **7**, 3297–3305 (2005).
23. Barone, V. & Cossi, M. Quantum calculation of molecular energies and energy gradients in solution by a conductor solvent model. *The Journal of Physical Chemistry A* **102**, 1995–2001 (1998).
24. Grimme, S. & Neese, F. Double-Hybrid Density Functional Theory for Excited Electronic States of Molecules. *J. Chem. Phys.* **127**, 154116 (2007).
25. Hanwell, M. D. et al. Avogadro: an advanced semantic chemical editor, visualization, and analysis platform. *Journal of Cheminformatics* **4**, 17 (2012).
26. Zhurko, G. A. Chemcraft-graphical program for visualization of quantum chemistry computations. https://chemcraftprog.com.
27. Li, J. et al. Photoredox catalysis with aryl sulfonium salts enables site-selective late-stage fluorination. *Nat. Chem*. **12**, 56–62 (2020).
28. Morov, S. L., Carmicheal, I. & Hug, G. L. Handbook of Photochemistry (Marcel Dekker, 1993).

10.5 Supporting Information for Project [D]

Chemistry—A European Journal

Supporting Information

Vinylcyclopropane [3 + 2] Cycloaddition with Acetylenic Sulfones Based on Visible Light Photocatalysis

Adriana Luque, Jonathan Groß, Till J. B. Zähringer, Christoph Kerzig, and Till Opatz*

Table of Contents

1. Light sources and reaction setup S2

2. Optimization studies S3

3. Mechanistic considerations S5

4. Computational studies S14

5. Experimental procedures S25

6. X-Ray crystal structure determination S46

7. References S48

8. NMR spectra S50

1. LIGHT SOURCES AND REACTION SETUP

1.1 Light sources

All photoreactions using UV-light were performed in a Rayonet photoreactor (RPR 100, SOUTHERN NEW ENGLAND ULTRAVIOLET COMPANY) with 16 circular arranged Philips TUV 8W G8T5 lamps and equipped with a magnetic stirrer and an internal cooling fan. The reactions were performed under inert gas atmosphere in 50 mL quartz tubes (diameter: 2 cm, length: 27 cm) under vigorous stirring. All photoreactions using blue LEDs were performed with Kessil lamp (KSPR, 50 W, 160L-456 nm) and (KSPR, 45 W, 160L-440 nm). The emission spectra of the lamps can be found on the manufacturer's homepage: https://www.kessil.com/science/PR160L.php.

1.2 Irradiation setup

The irradiation setup for each of the wavelengths is shown in figures S1 and S2.

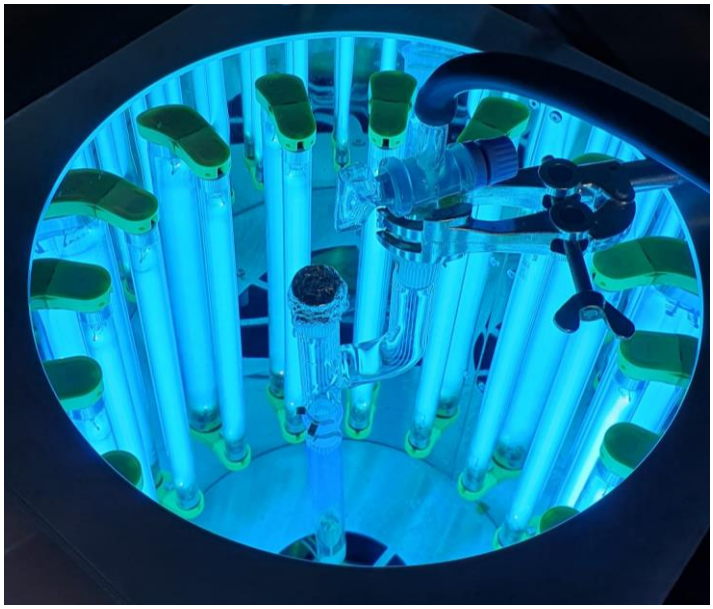

Figure S1. Setup for the irradiation of the allylation product with UVC-light in a Rayonet photoreactor.

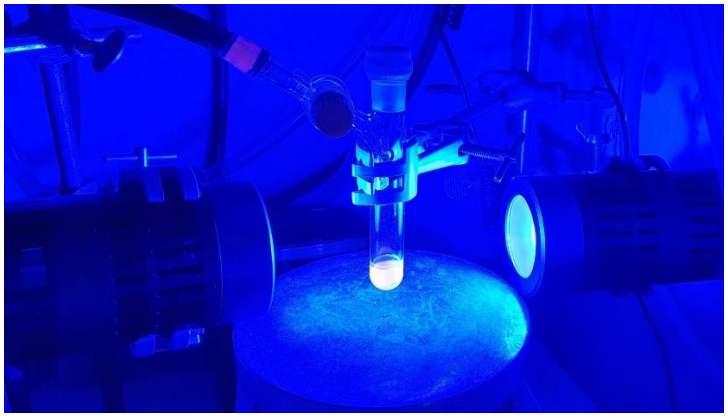

Figure S2. Setup for the irradiation of *meta* photoadducts with the blue LED (distance: 5 cm).

2. OPTIMIZATION STUDIES

2.1. General procedure for screening reactions

An oven-dried Schlenk tube (10 mL) was charged with the *meta* photocycloadduct **4**, the alkynyl sulfone **6** and the respective photocatalyst. The flask was set under an atmosphere of argon by three cycles of vacuum and backfill, followed by the addition of the respective solvent mixture via syringe. All solvents had been degassed beforehand by argon sparging for 20 min in an ultrasonic bath. After the reaction mixture was irradiated for 10 h with the respective light, the solvent was removed under reduce pressure and the residue purified by flash column chromatography.

Table S1. Catalyst screening.

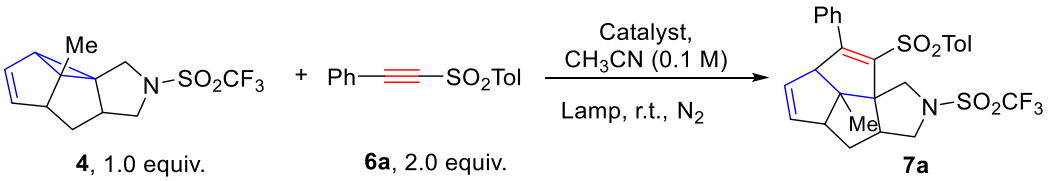

4, 1.0 equiv. **6a**, 2.0 equiv. **7a**

Entry	Catalyst (2.5 mol %) [a]	Yield (%) [c]
1	$[Ir(ppy)_2(dtbbpy)]PF_6$	53
2	phenanthrene (100 mol%) [b]	63
3	$Ir(ppy)_3$	49
4	$[Ru(bpy)_3]Cl_2$	traces [d]
5	$[Ir(dFCF_3ppy)_2(bpy)]PF_6$	51
6	$[Ir(dF(CF_3)ppy)_2(dtbbpy)]PF_6$	49

Procedure: The reactions were performed according to the general procedure for screening reactions using the *meta* photoadduct (**4**, 35.0 mg, 0.12 mmol, 1.00 equiv), alkynyl sulfone (**6a**, 61.2 mg, 0.24 mmol, 2.00 equiv), the respective catalyst and CH_3CN (1.1 mL, c = 0.10 M). [a] A 40 W blue LED 456 nm module was used for irradiation. [b] A UV/vis CFL bulb was used for irradiation. [c] All yields are those of isolated products. [d] Not isolated.

As can be seen in Table S1, among the photoredox catalyst the highest yield of the desired tetracycle **7a** is obtained when using $[Ir(ppy)_2(dtbbpy)]PF_6$ and phenanthrene. The optimization process with these two catalysts (Table S2) showed that decreasing the catalyst loading to 2 mol% in the case of the iridium catalyst increases the yield while variations in the case of phenanthrene did not lead to a higher yield. The screening with different solvents (Table S3) indicated that in the case of the iridium catalyst by increasing the polarity of the solvent the yield was also increasing being methanol the best option (entry 6), but similar variations in the case of the phenanthene were not so effective and further optimization of the reaction conditions was carried out using only $[Ir(ppy)_2(dtbbpy)]PF_6$ as the catalyst.

Finally, variations on the equivalents of the acetylenic sulfone **6a** and the concentration of the *meta* photoadduct **4** (Table S4) showed that the best conditions are 2 equivalents of **6a** and a concentration of 0.15 M of **4** (entry 4).

Table S2. Catalyst loading.

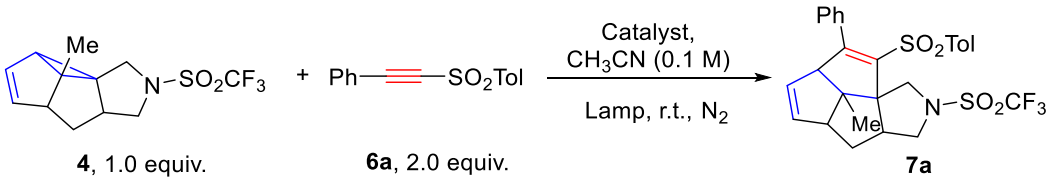

4, 1.0 equiv. **6a**, 2.0 equiv. **7a**

Entry	Catalyst (mol %) [a]	Yield (%) [c]
1	$[Ir(ppy)_2(dtbbpy)]PF_6$ (1.0)	55
2	$[Ir(ppy)_2(dtbbpy)]PF_6$ (1.5)	56
3	$[Ir(ppy)_2(dtbbpy)]PF_6$ (2.0)	58
4	$[Ir(ppy)_2(dtbbpy)]PF_6$ (2.5)	53
5	phenanthrene (50) [b]	55
6	phenanthrene (100) [b]	63
7	phenanthrene (150) [b]	63

Procedure: The reactions were performed according to the general procedure for screening reactions using the *meta* photoadduct (**4**, 35.0 mg, 0.12 mmol, 1.00 equiv), alkynyl sulfone (**6a**, 61.2 mg, 0.24 mmol, 2.00 equiv), the respective catalyst and CH_3CN (1.1 mL, c = 0.10 M). [a] A 40 W blue LED λ= 456 nm module was used for irradiation. [b] A UV/vis CFL bulb was used for irradiation. [c] All yields are those of isolated products.

Table S3. Solvent screening.

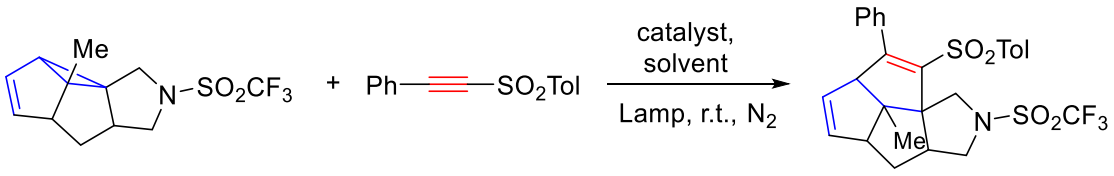

4, 1.0 equiv. **6a**, 2.0 equiv. **7a**

Entry	Catalyst (mol%) [a]	Solvent	Yield (%) [c]
1	$[Ir(ppy)_2(dtbbpy)]PF_6$ (2 mol%)	DCM	49
2	$[Ir(ppy)_2(dtbbpy)]PF_6$ (2 mol%)	DMF	60
3	$[Ir(ppy)_2(dtbbpy)]PF_6$ (2 mol%)	DMSO	53
4	$[Ir(ppy)_2(dtbbpy)]PF_6$ (2 mol%)	CH_3CN	58
5	$[Ir(ppy)_2(dtbbpy)]PF_6$ (2 mol%)	$CH_3CN:H_2O$ (9:1)	68
6	$[Ir(ppy)_2(dtbbpy)]PF_6$ (2 mol%)	CH_3OH	80
7	phenanthrene (100 mol%) [b]	CH_3CN	63
8	phenanthrene (100 mol%) [b]	$CH_3CN:H_2O$ (9:1)	58
9	phenanthrene (100 mol%) [b]	CH_3CN: CH_3OH (8:2)	58

Procedure: The reactions were performed according to the general procedure for screening reactions using the *meta* photoadduct (**4**, 35.0 mg, 0.12 mmol, 1.00 equiv), alkynyl sulfone (**6a**, 61.2 mg, 0.24 mmol, 2.00 equiv), the respective catalyst and solvent (1.1 mL, c = 0.10 M). [a] A 40 W blue LED λ= 456 nm module was used for irradiation. [b] A UV/vis CFL bulb was used for irradiation. [c] All yields are those of isolated products.

Table S4. Screening of reaction stoichiometry and concentration.

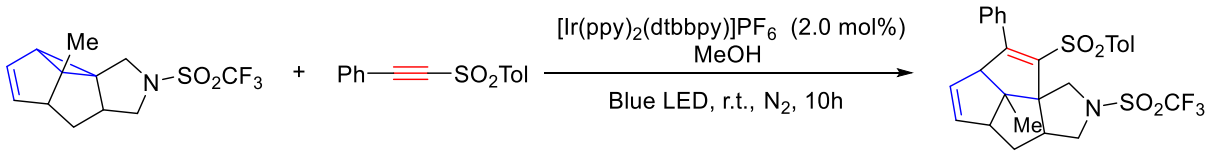

4, 1.0 equiv. **6a**, 1.0-4.0 equiv. **7a**

Entry	Equiv of 6a	Concentration of 4 (M)	Yield (%) [a]
1	1.0	0.10	63
2	2.0	0.10	80
3	4.0	0.10	85
4	2.0	0.15	85
5	2.0	0.20	78

Procedure: The reactions were performed according to the general procedure for screening reactions using the *meta* photoadduct (**4**, 35.0 mg, 0.12 mmol, 1.00 equiv), $[Ir(ppy)_2(dtbbpy)]PF_6$ (2.2 mg, 2.4 μmol, 0.02 equiv) and varying amounts of alkynyl sulfone (**6a**), and solvent (10-20 mM). [a] All yields are those of isolated products.

3. MECHANISTIC CONSIDERATIONS

3.1. Control experiments

Table S5 Control experiments**.**

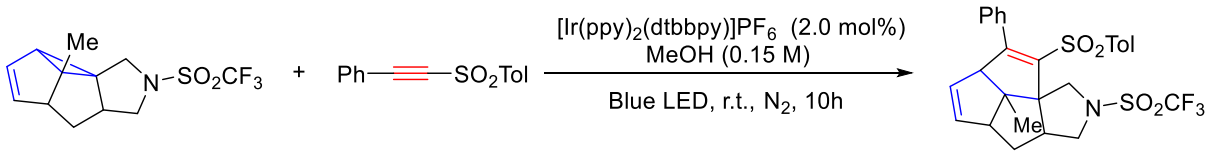

4, 1.0 equiv. **6a**, 2.0 equiv. **7a**

Entry	conditions	Yield (%) [a]
1	optimized	85
2	no light	0
3	with air	0
4	No $[Ir(ppy)_2(dtbbpy)]PF_6$	0

TEMPO coupling product detected by HRMS and NMR

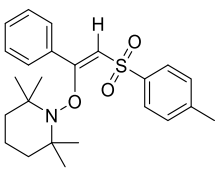

Procedure: The reactions were performed according to the general procedure for screening reactions using the *meta* photoadduct (**4**, 35 mg, 0.12 mmol, 1.00 equiv), 1-methyl-4-(phenylethynylsulfonyl)benzene (**2a**, 61.2 mg, 0.24 mmol, 2.00 equiv), $[Ir(ppy)_2(dtbbpy)]PF_6$ (2.2 mg, 2.4 μmol, 0.02 equiv) and 0.8 mL of degassed solvent (15 mM). [a] All yields are those of isolated products.

Initial control experiments (Table S4) proved the reaction to be light and catalyst dependent (entries 2 and 4). Additionally, the presence of air suppresses the product formation. A radical trapping experiment was set up using TEMPO as a radical scavenger. No desired product was obtained, but instead the TEMPO trapping product was determined by ESI-HRMS and NMR. To check whether the product is formed through a radical-chain mechanism, a light-dark cycle experiment was performed (Table S6).

3.2. UV-Vis studies.

Since the reaction did not proceed without light, the UV/Vis absorption spectra of all reactants and a combination thereof were recorded. The spectra are compiled in Figure S3. No new absorption maxima was detected pointing towards no ground state charge-transfer-complex formation. Considering the emission spectrum of the blue LED Kessil lamp (λmax ≈ 456 nm), the absorption spectra clearly indicate that the catalyst is the only compound absorbing light. Thus, it is reasonable to assume that the developed cycloaddition is indeed initiated by the excited ^{3}MLCT-state of the catalyst.

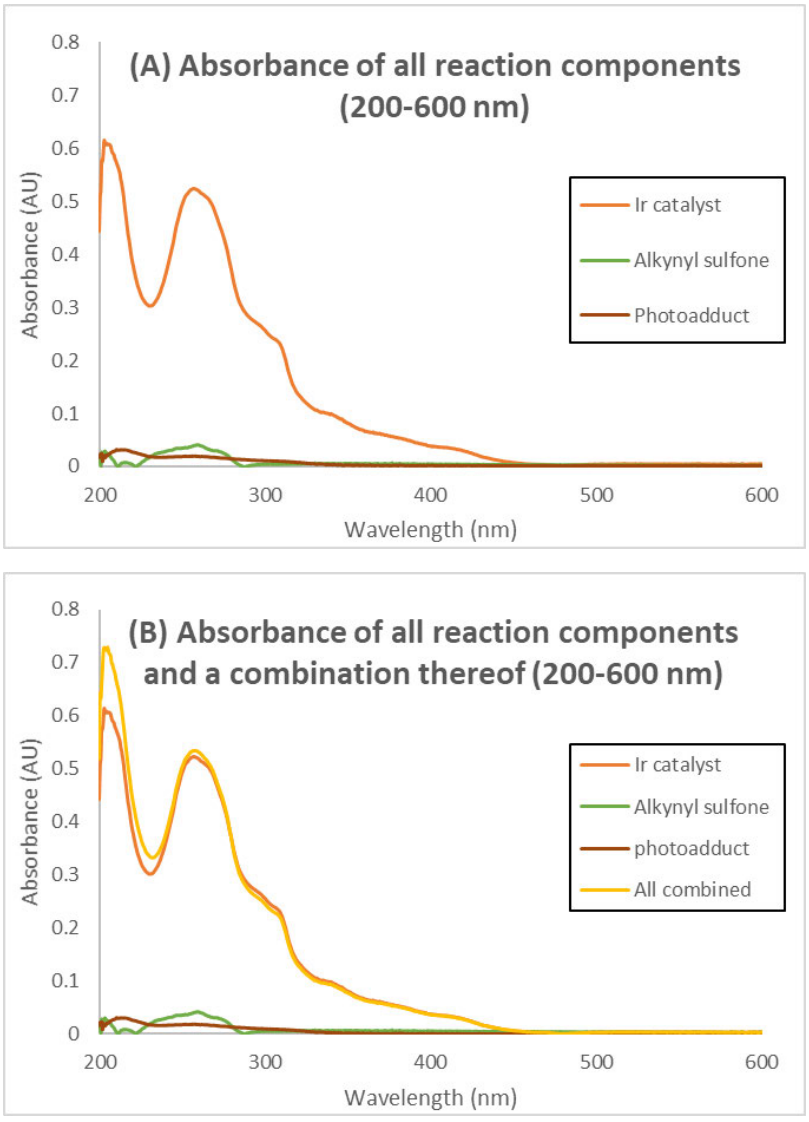

Figure S3. UV/vis spectra of all reaction components (A) and a combination thereof (B). All spectra were measured in MeOH with a concentration of 1×10^{-5} M for all compounds. The sample "All combined" contained equimolar amounts of all reaction components with a concentration of 1×10^{-5} M each. The spectra were collected on a Thermo Fisher Scientific UV/Vis spectrometer (Model: Evolution 201).

3.3. Light ON-OFF experiments.

The *meta* photoadduct **4** (50.0 mg, 0.17 mmol, 1.00 equiv), alkynyl sulfone **6a** (87.4 mg, 0.34 mmol, 2.00 equiv), $Ir(ppy)_2(dtbbpy)PF_6$ (3.12 mg, 0.003 mmol, 2.00 mol-%), 1,4-bis(trimehtylsilyl)benzene (18.0 mg, 0.09 mmol, 0.50 equiv), and methanol-d_4 (1.1 mL, c = 0.15 M) were loaded in an oven-dried Schlenk tube (10 mL) under nitrogen atmosphere, and the mixture was degassed and then placed in front of two blue LEDs at a distance of 5 cm. The reaction vessel was irradiated discontinuously and after each light-phase and each dark phase, an aliquot of 0.1 mL was taken via syringe, diluted with methanol-d_4 and analyzed by ^{1}H NMR spectroscopy.

Table S6. Results of the light-dark cycle experiment for the formation of product **7a**.

Time (h)	Yield of 7a (%)
0	0
1	40
2	42
3	52
4	52
5	58
6	58

The Table S6 shows that no efficient self-sustained radical-chain mechanism occurs. No product formation was observed in the absence of light and the small differences in yield are within the margin of error.

3.4. Initial luminescence quenching studies

Emission spectra were recorded on a JASCO FP–8300 spectrofluorometer with 1 cm quartz cuvettes in degassed methanol exciting with a wavelength of λ = 460 nm. All samples were degassed by bubbling argon through the analytical sample for 10 minutes. The Stern-Volmer plots were constructed by the general equation $(I_0/I) = K_{SV}[Q]$(Figure S4–S5).

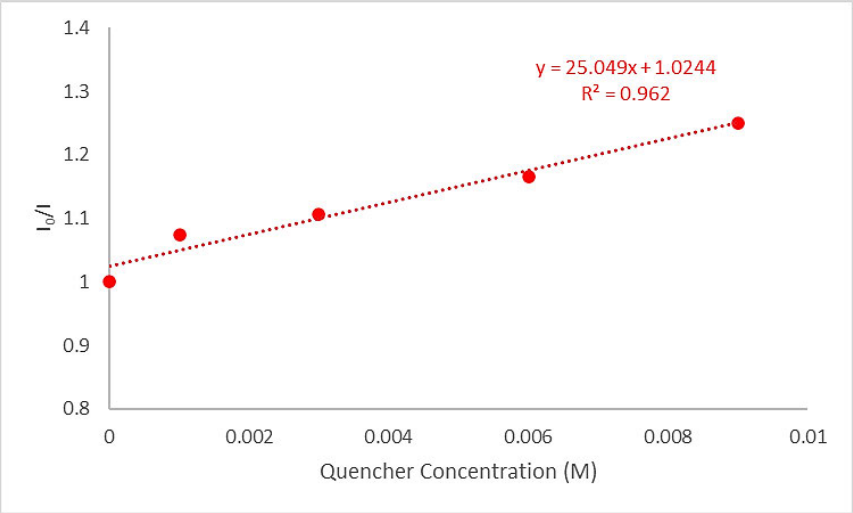

Figure S4. Stern-Volmer plot for the fluorescence quenching of the $[Ir(ppy)_2(dtbbpy)]PF_6$ (1×10^{-5} M in degassed methanol) with the *meta* photoadduct **4**.

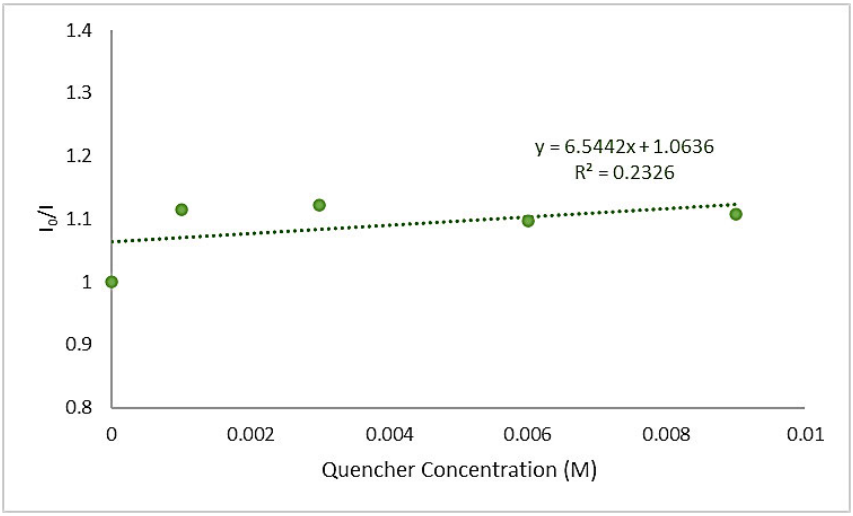

Figure S5. Stern-Volmer plot for the fluorescence quenching of the $[Ir(ppy)_2(dtbbpy)]PF_6$ (1×10^{-5} M in degassed methanol) with the acetylenic sulfone **6a**.

These initial quenching experiments indicate that an electron or energy transfer from the excited triplet state of the catalyst to *meta* photoadduct **4** occurs. However, to confirm the mechanism described in Scheme 4 (main paper), a more detailed and thorough study was carried out as described in in Sections 3.5 and 3.6.

3.5. Reduction potential measurements

The *meta* photoadduct **4** and alkynyl sulfone **6a** were analyzed using cyclic voltammetry (Figure S6). The cyclic voltammograms were recorded at room temperature with solution of the substrate (5.0 mM) in acetonitrile with Bu_4NBF_6 (0.1 M) as electrolyte. The potentials were expressed against the Ag/AgCl in 3M KCl reference electrode and here was converted against SCE by subtracting 45 mV. The potentials of the *meta* photoadduct were determined to be E_{red} = –1.69 V vs Ag/AgCl = –1.65 V vs SCE; E_{red} = –1.38 V vs Ag/AgCl = –1.34 V vs SCE E_{ox} = +2.00 V vs Ag/AgCl = +1.96 V vs SCE. The potentials of the alkynyl sulfone were determined to be E_{red} = –1.76 V vs Ag/AgCl = –1.72 V vs SCE; E_{red} = –1.48 V vs Ag/AgCl = –1.44 V vs SCE.

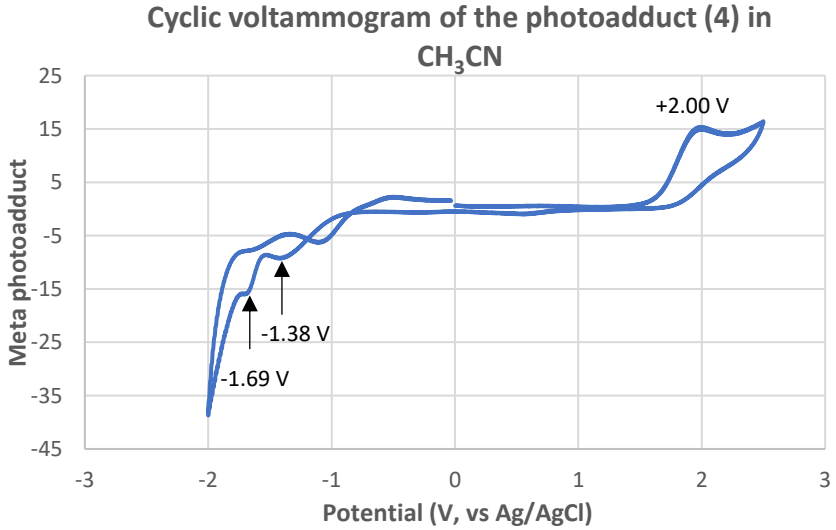

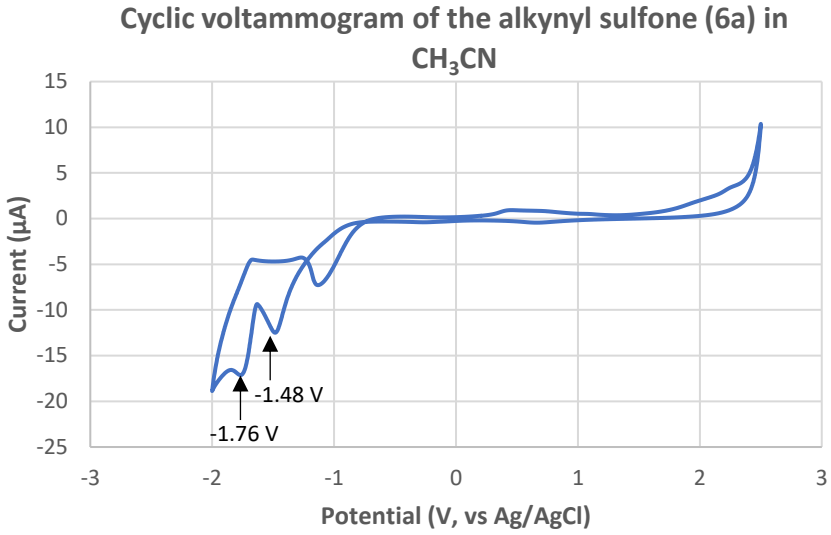

Figure S6. Cyclic voltammograms of **4** and **6a** at room temperature (22 °C) using an *Autolab PGSTAT 204* potentiostat from Metrohm. Conditions: 5 mM substrate in acetonitrile (10 mL) with 0.1 M Bu_4NBF_6. WE: platinum tip (d = 2 mm); CE: glassy carbon rod; RE: Ag/AgCl in 3 M KCl; Scan rate: 100 mV/s.

The thermodynamic feasibility of single electron transfer (SET) steps, which could occur during the reaction were evaluated by comparing the Gibbs free energies of the single SET steps. These Gibbs free energies were calculated as described in the literature and can be summarized in the Table S7.[1] However, the Gibbs free energies provided are rather estimations, considering the fact that the literature redox potentials might fluctuate due to the variation in conditions.

Table S7. Redox potentials and Gibbs free energies for relevant SET steps.

Entry	Catalyst $E_{1/2}^{red}$/ $E_{1/2}^{oxd}$ (V vs SCE)	Electron acceptor	Electron donor	Gibbs free energy (kcal/mol)	Comment
1	-2.10	*meta* photoadduct **4**	[Phenanthrene]*	-10.377 -17.526	Oxidative quenching
	+1.27	[Phenanthrene]*	*meta* photoadduct **4**	+15.912	Reductive quenching
2	-0.89	*meta* photoadduct **4**	$[Ir(dF(CF_3)ppy)_2(dtbbpy)]^{+*}$	+17.526 +10.377	Oxidative quenching
	+1.21	$[Ir(dF(CF_3)ppy)_2(dtbbpy)]^{+*}$	*meta* photoadduct **4**	+17.296	Reductive quenching
3	-1.00	*meta* photoadduct **4**	$[Ir(dFCF_3ppy)_2(bpy)]^{+*}$	+14.990 +7.841	Oxidative quenching
	+1.32	$[Ir(dFCF_3ppy)_2(bpy)]^{+*}$	*meta* photoadduct **4**	+14.759	Reductive quenching
4	-1.73	*meta* photoadduct **4**	[*fac*-$Ir(ppy)_3$]*	-1.845 -8.994	Oxidative quenching
	+0.31	[*fac*-$Ir(ppy)_3$]*	*meta* photoadduct **4**	+38.051	Reductive quenching
5	-0.96	*meta* photoadduct **4**	$[Ir(ppy)_2(dtbbpy)]^{+*}$	+15.912 +8.763	Oxidative quenching
	+0.66	$[Ir(ppy)_2(dtbbpy)]^{+*}$	*meta* photoadduct **4**	+29.97	Reductive quenching
6	−0.81	*meta* photoadduct **4**	$[Ru(bpy)_3]^{+2*}$	+19.371 +12.222	Oxidative quenching
	+0.77	$[Ru(bpy)_3]^{+2*}$	*meta* photoadduct **4**	+27.443	Reductive quenching

From the data compiled in Table S7 can be inferred that a SET steps are possible when using phenanthrene or *fac*-Ir(ppy)$_3$ but only in an oxidative quenching process, where electron transfer from these catalyst to the *meta* photoadduct **4** is exergonic. The possibility of SET with the rest of the listed catalysts can be excluded as the quenching process, both oxidation and reduction are endergonic being probably thermodynamically unfavorable. Since the tetracycle **7a** could be isolated in moderate yields (Table S1) by using almost every of these catalysts except for [Ru(bpy)$_3$]Cl$_2$, it can be assumed that a photo-initiated electron transfer is less likely to be involved and led us to propose that an energy transfer pathway could instead be in operation for this cycloaddition reaction.

3.6. Laser flash photolysis studies

Laser flash photolysis (LFP) studies with absorption and emission detection of transient species using a frequency tripled Nd:YAG laser (355 nm, ~5 ns pulse duration) combined with an LP980KS spectrometer from Edinburgh Instruments were performed to further investigate the underlying mechanism. A more detailed description of the setup can be found in Section 5.

3.6.1 Stern-Volmer experiments

Initial luminescence quenching experiments showed that [Ir(ppy)$_2$(dtbbpy)]PF$_6$ is predominantly quenched by the *meta* photoadduct **4**. Lifetime-based quenching experiments with selected photosensitizers (Ir(ppy)$_3$, [Ir(dF(CF$_3$)ppy)$_2$(dtbbpy)]PF$_6$ and [Ir(ppy)$_2$(dtbbpy)]PF$_6$) showed that [Ir(dF(CF$_3$)ppy)$_2$(dtbbpy)]PF$_6$ is most effectively quenched by the *meta* photoadduct **4**, in line with its highest triplet energy. High quenching efficiencies are pivotal for obtaining reliable results. Hence, all further LFP experiments were conducted with [Ir(dF(CF$_3$)ppy)$_2$(dtbbpy)]PF$_6$ as sensitizer. Lifetime-based Stern-Volmer experiments of [Ir(dF(CF$_3$)ppy)$_2$(dtbbpy)]PF$_6$ (32 µM) with varying concentrations of *meta* photoadduct **4** and sulfone **6a** yielded quenching rates k_q of $4 \cdot 10^6\ M^{-1}\ s^{-1}$ and $5 \cdot 10^5\ M^{-1}\ s^{-1}$, respectively (Figure S7).

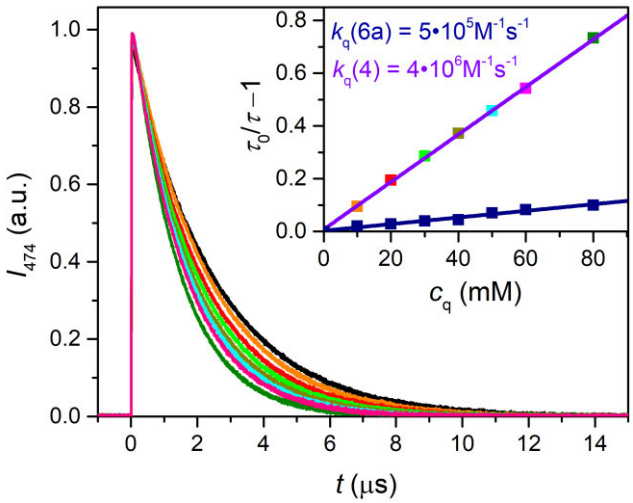

Figure S7. Emission decay kinetics of excited [Ir(dF(CF$_3$)ppy)$_2$(dtbbpy)]PF$_6$ (32 µM) in the presence of varying concentrations of **4** in Ar-saturated MeCN. Inset: Stern-Volmer plots of [Ir(dF(CF$_3$)ppy)$_2$(dtbbpy)]PF$_6$ and **4** (purple fit, the colored symbols correspond to the same quencher

concentration as in the main plot), and $[Ir(dF(CF_3)ppy)_2(dtbbpy)]PF_6$ and **6a** (dark blue). Detection occurred at 474 nm.

3.6.2 Transient absorption studies

Subsequently, it was explored whether the sensitizer quenching proceeds via energy or electron transfer. Transient absorption (TA) studies were performed to monitor the quenching products. Three solutions of 32 μM $[Ir(dF(CF_3)ppy)_2(dtbbpy)]PF_6$ in the absence of any substrate, in the presence of 80 mM of **4**, and 80 mM of both **4** and **6a**, were prepared in Ar-saturated MeCN. After excitation, the iridium sensitizer efficiently populates the triplet-excited state with a lifetime of 2.5 μs in MeCN (Equation 1). The transient absorption spectrum of the triplet-excited state of $[Ir(dF(CF_3)ppy)_2(dtbbpy)]^+$ is shown in Figure S8, Panel B (recorded 10 ns after the laser pulse and time-integrated over 100 ns).

$$[Ir(dF(CF_3)ppy)_2(dtbbpy)]^+ \xrightleftharpoons[\tau_0 = 2.5\ \mu s]{h\nu,\ ISC} {}^3[Ir(dF(CF_3)ppy)_2(dtbbpy)]^+ \qquad \text{(Equation 1)}$$

The emission lifetime of $[Ir(dF(CF_3)ppy)_2(dtbbpy)]^+$ is reduced in the presence of 80 mM **4** and 80 mM of **6a** (Figure S8, Panel A) in agreement with the lifetime-based Stern-Volmer experiments. However, for either solution, once the initial triplet-excited $^3[Ir(dF(CF_3)ppy)_2(dtbbpy)]^+$ had decayed completely (after about 10 μs), no reaction intermediate(s) could be observed (i.e., baseline-like spectra were obtained).

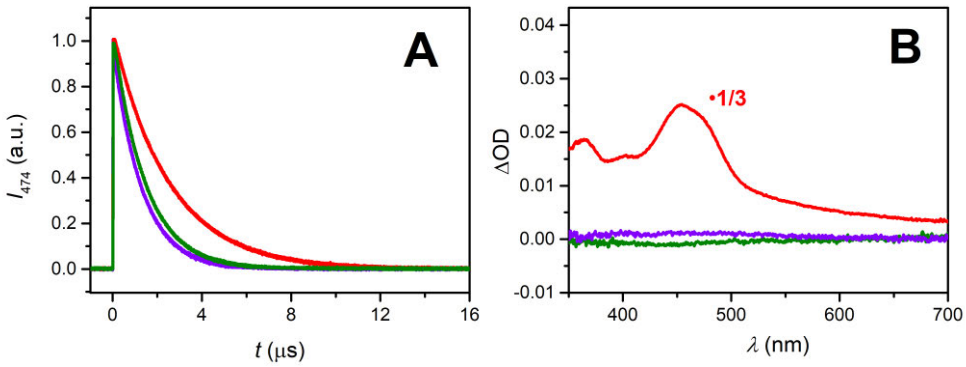

Figure S8: LFP experiments after excitation with 355 nm laser pulses with a solution of 32 μM $[Ir(dF(CF_3)ppy)_2(dtbbpy)]PF_6$ and 80 mM of **4** (green), and 80 mM of both **4** and **6a** (purple) in Ar-saturated MeCN. Panel A: Time-resolved emission monitored at 474 nm in the absence (red) and presence of quenchers. Panel B: Transient absorption spectrum of the triplet-excited $^3[Ir(dF(CF_3)ppy)_2(dtbbpy)]^+$ (red, delay 10 ns) and spectra recorded right after the initial sensitizer triplet decay (delay 10 μs).

In order to provide further evidence that an electron transfer reaction between the sensitizer and one of the substrates can be excluded, transient absorption spectra of the reduced and oxidized catalyst were recorded with other reductive or oxidative quenchers.

A solution of 32 μM $[Ir(dF(CF_3)ppy)_2(dtbbpy)]PF_6$ and 5 mM of the well-known reductive quencher triethanolamine (TEOA), whose radical cation is essentially transparent in the resulting TA spectra, was prepared to investigate the reductive quenching of the excited catalyst (Figure S9). Time-resolved emission spectroscopy showed that the lifetime of the sensitizer emission is strongly reduced by the addition of TEOA (Panel A). A transient absorption spectrum was recorded once the excited sensitizer

was fully quenched, 6 µs after excitation (Panel B). As opposed to the transient absorption spectra recorded for $[Ir(dF(CF_3)ppy)_2(dtbbpy)]PF_6$ in combination with **4** and **6a**, a new absorbing species is formed. This novel species decays on a much longer timescale as time-resolved transient spectroscopy at a detection wavelength of 452 nm revealed (Panel C).

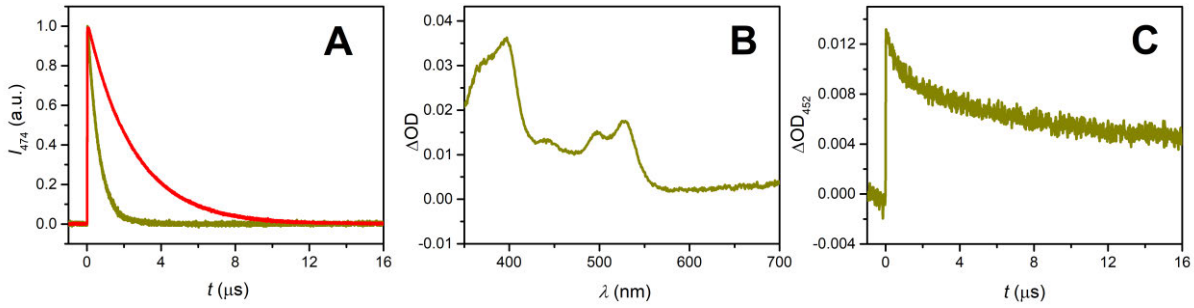

Figure S9: Identification of the reduced $[Ir(dF(CF_3)ppy)_2(dtbbpy)]$ species by LFP experiments after excitation with 355 nm laser pulses of a solution containing 32 µM $[Ir(dF(CF_3)ppy)_2(dtbbpy)]PF_6$ and 5 mM TEOA in Ar-saturated MeCN. Panel A: Time-resolved emission monitored at 474 nm in the absence (red) and presence of TEOA (dark yellow). Panel B: Transient absorption spectrum of the quenching product (delay 6 µs, integration over 100 ns). Panel C: Transient absorption traces monitored at 452 nm.

TEOA has been widely used as a reductive quencher before, with an oxidation potential of 0.57-0.82 V vs SCE (aqueous solution).[2] This is low enough to be oxidized by the triplet-excited catalyst (Ir^{3+*}/Ir^{2+} = 1.21 V vs SCE) (Equation 2). The reaction generates the reduced species, $[Ir(dF(CF_3)ppy)_2(dtbbpy)]$, and the radical cation, $N(EtOH)_3^{\cdot+}$. Radical cations of aliphatic amines are essentially transparent in our detection range;[3] hence we assign the TA spectrum in Figure S9 to the reduced catalyst. Similar absorption spectra of the reduced catalyst $[Ir(dF(CF_3)ppy)_2(dtbbpy)]$ have been reported in the literature.[4]

$$^3[Ir(dF(CF_3)ppy)_2(dtbbpy)]^+ + N(EtOH)_3 \longrightarrow [Ir(dF(CF_3)ppy)_2(dtbbpy)] + N(EtOH)_3^{\cdot+} \qquad \text{(Equation 2)}$$

A solution of 32 µM $[Ir(dF(CF_3)ppy)_2(dtbbpy)]PF_6$ and 2 M tetrachloromethane was prepared to investigate the oxidative quenching of the excited catalyst. Tetrachloromethane was selected as the quencher as the excited state oxidation potential of $[Ir(dF(CF_3)ppy)_2(dtbbpy)]PF_6$ (Ir^{4+}/Ir^{3+*} = -0.89 V vs SCE) should be sufficient to reduce CCl_4 (-0.78 V vs SCE)[5] and the fragments $CCl_3\cdot$ and Cl^- upon reduction are not expected to absorb in the selected detection range (350-700 nm) (Equation 3).[6] The related lab-scale reaction with the very same iridium complex has also been reported in the literature.[7] We tried methyl viologen dihexafluorophosphate as an oxidative quencher as well. However, the reduced quencher strongly absorbs in the visible region, making it difficult to obtain a clean spectrum of the oxidized sensitizer.

$$^3[Ir(dF(CF_3)ppy)_2(dtbbpy)]^+ + CCl_4 \longrightarrow [Ir(dF(CF_3)ppy)_2(dtbbpy)]^{2+} + CCl_3^{\cdot} + Cl^- \qquad \text{(Equation 3)}$$

Time-resolved emission spectroscopy showed that the lifetime of the sensitizer emission is reduced by the addition of CCl_4 (Figure S10, Panel A). After the luminescence has fully returned to baseline a transient absorption spectrum was recorded (10.5 µs delay) (Panel B). A new absorbing species is observed with a maximum at 410 nm. This newly formed species decays on a longer timescale (detection

wavelength of 400 nm) compared to the sensitizer emission (Panels A and C). Since no other compound apart from the oxidized sensitizer should absorb in the range, the new absorbing species is assigned to $[Ir(dF(CF_3)ppy)_2(dtbbpy)]^{2+}$.

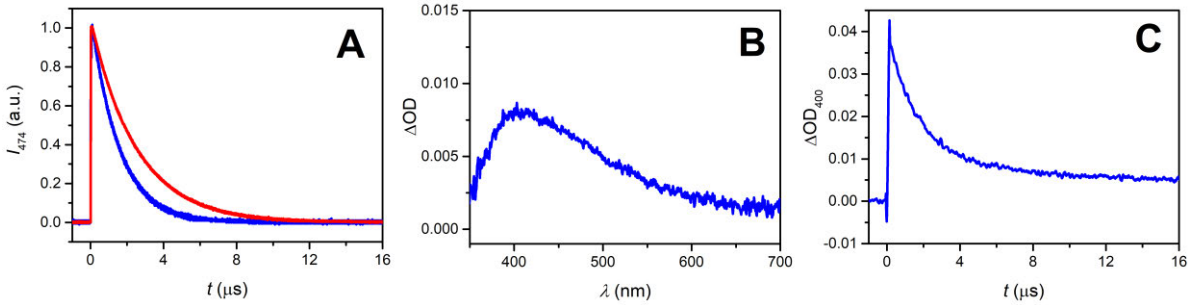

Figure S10: Identification of the oxidized $[Ir(dF(CF_3)ppy)_2(dtbbpy)]^{2+}$ species by LFP experiments after excitation with 355 nm laser pulses of a solution containing 32 µM $[Ir(dF(CF_3)ppy)_2(dtbbpy)]PF_6$ and 2 M CCl_4 in Ar-saturated MeCN. Panel A: Time-resolved emission monitored at 474 nm in the absence (red) and presence of CCl_4 (blue). Panel B: Transient absorption spectrum of the quenching product (delay 10.5 µs). Panel C: Transient absorption traces monitored at 400 nm.

Additional Stern-Volmer experiments of $[Ir(dF(CF_3)ppy)_2(dtbbpy)]PF_6$ were performed with varying concentrations of (1-cyclopropylvinyl)benzene (**8**). Because of the extended π-system, we presumed that compound **8** has a lower triplet energy (ca. 10 kcal mol^{-1}) than compound **4**. Hence, a higher quenching rate constant is expected for **8**. We obtained a k_q value of $5 \cdot 10^{8} M^{-1} s^{-1}$ from the Stern-Volmer plot (Figure S11, Panel A), confirming the assumptions. After the sensitizer's emission has been fully quenched and at high quenching efficiencies above 95% (40 mM of **8**) no new absorbing species was observed (Panel B). If oxidative or reductive quenching were to occur, pronounced spectroscopic signatures of the reduced or oxidized sensitizer would have been observed in the transient absorption spectrum (compare, Figures S9 and S10).

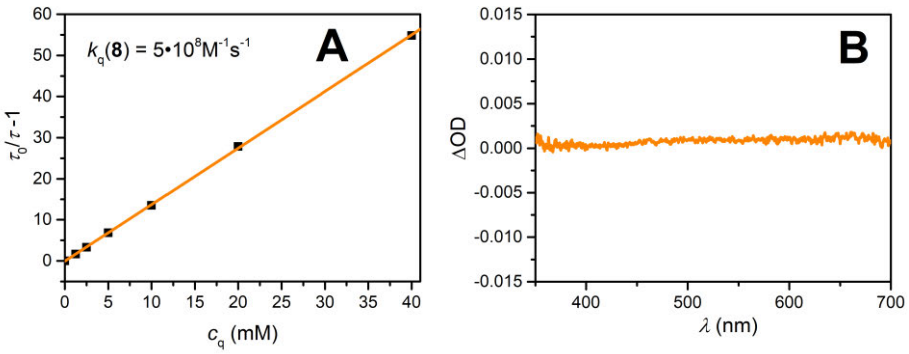

Figure S11: LFP experiments after excitation with 355 nm laser pulses of a solution containing 32 µM $[Ir(dF(CF_3)ppy)_2(dtbbpy)]PF_6$ and (1-cyclopropylvinyl)benzene (**8**) in Ar-saturated MeCN. Panel A: Lifetime-based Stern-Volmer plot with varying concentrations of **8**. Panel B: Transient absorption spectrum of the quenching product of 32 µM $[Ir(dF(CF_3)ppy)_2(dtbbpy)]PF_6$ and 40 mM of **8** (delay 0.4 µs).

4. COMPUTATIONAL STUDIES

All structures were optimized applying the functionals B3LYP,[8] CAM-B3LYP[9] as well as M062X[10] in conjunction with the Pople basis-set 6-311+G(2d,p)[11] with the IEFPCM solvation model[12] for methanol. The adiabatic S_0–T_1 energy gaps were determined as difference between the electronically excited states (T_1) and the respective ground states (S_0). To predict the vertical excitation energies and the UV/vis-spectra, the time-dependent DFT method[13] was used with the respective optimized ground state structures at the same level of theory.[14] Frequency analysis was performed to obtain the Gibbs free energies of each molecule and to confirm every structure as local minima (N_{imag} = 0). All calculations were performed using the software Gaussian 16, rev. C.01.[15] Spin densities were visualized using GaussView 6.[16]

Input Lines

Geometry Optimization

#p opt=tight freq $FUNC 6-311+g(2d,p) scrf=(iefpcm,solvent=methanol)

Vertical Excitation Energy

#p td=(triplets,root=1) $FUNC 6-311+g(2d,p) scrf=(iefpcm,solvent=methanol)

UV/vis-spectra

#p td=(triplets,nstates=100) ub3lyp 6-311+g(2d,p) scrf=(iefpcm,solvent=acetonitrile)

Coordinates and Energies

Ground States

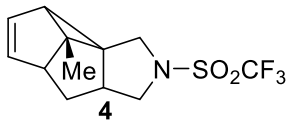

4

6c-Methyl-2-[(trifluoromethyl)sulfonyl]-1,2,3,3a,4,4a,6a,6c-octahydrocyclopropa[1,6]pentaleno[1,2-*c*]pyrrole (4)

B3LYP

Sum of electronic and thermal Free Energies: -1368.617594 Hartree

Vertical excitation energy to the first triplet state: 3.5325 eV

Coordinates of S_0:

C	-2.45882	1.97718	-0.39336
C	-3.49812	1.41538	-1.00656
C	-3.66687	-0.02346	-0.54780
C	-2.91460	-0.06803	0.84136
C	-1.93908	1.07724	0.67208
C	-2.83331	-0.88594	-1.56314
C	-1.48746	-1.13899	-0.85961
C	-1.50810	-0.39546	0.45940
C	-0.08863	-0.82971	-1.38393
N	0.66466	-0.91224	-0.08038
C	-0.24044	-0.85743	1.13390
S	2.26014	-0.83542	0.02413
O	2.85834	-1.30969	-1.20283
C	2.69193	0.99583	0.05049
O	2.68463	-1.30855	1.32214
F	4.01361	1.15485	0.15431
F	2.10316	1.59522	1.09132
F	2.27364	1.58582	-1.07403
C	-3.64526	-0.41735	2.10946
H	-2.03214	2.94709	-0.61665
H	-4.03710	1.82335	-1.85316
H	-4.70327	-0.35712	-0.48164
H	-1.47734	1.51202	1.55288
H	-3.32438	-1.83773	-1.77067
H	-2.73063	-0.36550	-2.51545
H	-1.46077	-2.19989	-0.58188
H	0.31111	-1.56076	-2.08199
H	-0.01591	0.17220	-1.81005
H	0.15382	-0.17174	1.87868
H	-0.31198	-1.85870	1.56266

H	-4.48283	0.26513	2.27934
H	-4.04715	-1.43398	2.06757
H	-2.98109	-0.35470	2.97424

CAM-B3LYP

Sum of electronic and thermal Free Energies: -1368.223829 Hartree

Vertical excitation energy to the first triplet state: 3.5481 eV

Coordinates of S_0:

C	-2.39079	1.95057	-0.43700
C	-3.43488	1.39488	-1.03293
C	-3.62934	-0.02428	-0.54006
C	-2.88033	-0.04961	0.84031
C	-1.88915	1.06822	0.64800
C	-2.81657	-0.91592	-1.53259
C	-1.47303	-1.16162	-0.83635
C	-1.48580	-0.40292	0.46638
C	-0.08076	-0.85948	-1.36450
N	0.66971	-0.92626	-0.06840
C	-0.22481	-0.86678	1.14078
S	2.25099	-0.82224	0.03009
O	2.85077	-1.28885	-1.18769
C	2.62943	0.99409	0.04189
O	2.68621	-1.27314	1.32178
F	3.93879	1.18990	0.14046
F	2.02810	1.57943	1.07461
F	2.19255	1.55938	-1.08001
C	-3.61015	-0.35709	2.11337
H	-1.94747	2.90606	-0.68462
H	-3.96760	1.79194	-1.88773
H	-4.67095	-0.33564	-0.46494
H	-1.42482	1.51521	1.52014
H	-3.31600	-1.86795	-1.71050
H	-2.71773	-0.42304	-2.49890
H	-1.44559	-2.21711	-0.54422
H	0.31749	-1.59640	-2.05595
H	-0.01097	0.13755	-1.80062
H	0.17222	-0.17976	1.88196
H	-0.30203	-1.86461	1.57326
H	-4.43344	0.34351	2.27009
H	-4.02926	-1.36586	2.09454
H	-2.94152	-0.28704	2.97269

M062X

Sum of electronic and thermal Free Energies: -1368.232195 Hartree

Vertical excitation energy to the first triplet state: 4.0289 eV

Coordinates of S_0:

C	-1.98620	1.81143	-0.70837
C	-3.09625	1.31260	-1.23972
C	-3.48692	0.02485	-0.53794
C	-2.74353	0.10143	0.84259
C	-1.61324	1.04785	0.51250
C	-2.80635	-1.10559	-1.37263
C	-1.46631	-1.37114	-0.66803
C	-1.40419	-0.47344	0.54518
C	-0.06597	-1.19249	-1.23941
N	0.70659	-1.17085	0.05258
C	-0.17641	-0.96620	1.26073
S	2.25114	-0.78510	0.08327
O	2.87899	-1.23415	-1.12618
C	2.31507	1.05906	-0.03863
O	2.79302	-1.06035	1.38312
F	3.57370	1.47030	-0.03271
F	1.67805	1.60453	0.99097
F	1.73303	1.46425	-1.16047
C	-3.49950	0.08164	2.13917
H	-1.41329	2.64670	-1.08952
H	-3.56269	1.63428	-2.16258
H	-4.56149	-0.12564	-0.43429
H	-1.10037	1.55102	1.32477
H	-3.40447	-2.01633	-1.36023
H	-2.69543	-0.80476	-2.41418
H	-1.49219	-2.39226	-0.27196
H	0.29148	-2.01289	-1.85575
H	0.03524	-0.24508	-1.77086
H	0.27171	-0.25775	1.95228
H	-0.31072	-1.92888	1.75464
H	-4.21594	0.90491	2.17996
H	-4.05129	-0.85359	2.25611
H	-2.81528	0.18219	2.98320

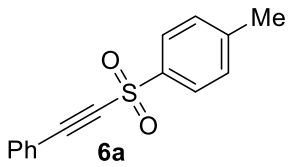

6a

1-Methyl-4-(phenylethynesulfonyl)benzene (6a)

B3LYP

Sum of electronic and thermal Free Energies: -1127.428415 Hartree

Coordinates of S_0:

C	5.50027	-1.37166	-0.00000
C	4.87969	-1.05842	1.20736
C	3.64111	-0.43327	1.21380
C	3.01079	-0.11576	0.00000
C	3.64113	-0.43324	-1.21380
C	4.87970	-1.05838	-1.20737
C	1.74061	0.52370	0.00000
C	0.66205	1.06668	0.00000
S	-0.87148	1.83415	0.00001
C	-2.02973	0.48920	0.00000
C	-2.47280	-0.03247	-1.21262
C	-3.37355	-1.08786	-1.20217
C	-3.83874	-1.63135	-0.00001
C	-3.37355	-1.08786	1.20216

C	-2.47280	-0.03248	1.21262
O	-0.99296	2.55999	1.25479
O	-0.99296	2.56000	-1.25477
C	-4.83789	-2.75662	-0.00001
H	6.46723	-1.85964	-0.00000
H	5.36221	-1.30172	2.14575
H	3.15471	-0.18753	2.14897
H	3.15474	-0.18747	-2.14897
H	5.36223	-1.30166	-2.14575
H	-2.12321	0.38478	-2.14737
H	-3.72148	-1.49564	-2.14396
H	-3.72148	-1.49565	2.14394
H	-2.12321	0.38477	2.14737
H	-4.73007	-3.38335	-0.88616
H	-4.73007	-3.38336	0.88613
H	-5.85835	-2.36116	-0.00001

CAM-B3LYP

Sum of electronic and thermal Free Energies: -1127.033037 Hartree

Coordinates of S_0:

C	5.48081	-1.36043	0.00000
C	4.86284	-1.04970	1.20252
C	3.62770	-0.42878	1.20794
C	3.00296	-0.11532	-0.00000
C	3.62770	-0.42879	-1.20794
C	4.86283	-1.04971	-1.20252
C	1.72870	0.52384	-0.00000
C	0.65638	1.06095	-0.00000
S	-0.87545	1.82411	-0.00000
C	-2.02199	0.48824	-0.00000
C	-2.46182	-0.03075	-1.20770
C	-3.35626	-1.08401	-1.19777
C	-3.81711	-1.62481	0.00000
C	-3.35626	-1.08401	1.19778
C	-2.46182	-0.03075	1.20770
O	-0.99560	2.54376	1.24710
O	-0.99560	2.54376	-1.24711
C	-4.81093	-2.74874	0.00000
H	6.44798	-1.84659	0.00001
H	5.34556	-1.29211	2.14020
H	3.14033	-0.18350	2.14214
H	3.14033	-0.18352	-2.14215
H	5.34556	-1.29213	-2.14020
H	-2.11274	0.38933	-2.14091
H	-3.70411	-1.49366	-2.13796
H	-3.70411	-1.49365	2.13797
H	-2.11274	0.38933	2.14091
H	-4.70086	-3.37425	-0.88524
H	-4.70088	-3.37422	0.88527
H	-5.82990	-2.35428	-0.00002

M062X

Sum of electronic and thermal Free Energies: -1127.087274 Hartree

Coordinates of S_0:

C	5.46131	-1.36479	0.00124
C	4.84381	-1.05061	1.20703
C	3.60917	-0.42168	1.21278
C	2.98818	-0.10568	0.00057
C	3.60999	-0.42136	-1.21130
C	4.84462	-1.05029	-1.20488
C	1.71444	0.54206	0.00018
C	0.64299	1.08843	-0.00023
S	-0.89768	1.84745	-0.00124
C	-2.02059	0.49281	-0.00018
C	-2.44226	-0.03674	-1.21273
C	-3.31557	-1.11178	-1.20115
C	-3.76773	-1.65841	0.00134
C	-3.32245	-1.10491	1.20268
C	-2.44875	-0.02952	1.21271
O	-1.02468	2.56325	1.24614
O	-1.02403	2.56064	-1.25019
C	-4.73918	-2.80459	0.00020
H	6.42607	-1.85584	0.00150
H	5.32538	-1.29593	2.14456
H	3.11984	-0.17227	2.14526
H	3.12129	-0.17170	-2.14403
H	5.32683	-1.29537	-2.14215
H	-2.09573	0.39181	-2.14413
H	-3.65375	-1.53400	-2.13979
H	-3.66568	-1.52136	2.14198
H	-2.10729	0.40435	2.14350
H	-4.58259	-3.45026	-0.86330
H	-4.64627	-3.39947	0.90792
H	-5.76355	-2.42784	-0.04867

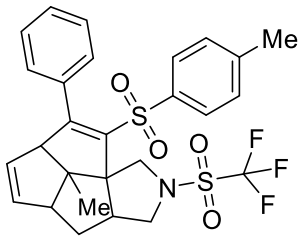

7a

8b-Methyl-8-[(4-methylphenyl)sulfonyl]-7-phenyl-2-[(trifluoromethyl)sulfonyl]-1,2,3,3a,4,4a,6a,8b-octahydrocyclopenta[3,4]pentaleno[1,6a-*c*]pyrrole (7a)

B3LYP

Sum of electronic and thermal Free Energies: -2496.123889 Hartree

Coordinates of S_0:

C	-1.32560	-3.97156	0.16681
C	-0.14925	-4.53785	-0.08007
C	1.00926	-3.79623	0.53473
C	0.35037	-2.52889	1.17306
C	-1.18489	-2.69877	0.97483
C	2.06801	-3.28363	-0.45065
C	1.53862	-1.94057	-0.97667

C	0.75396	-1.30873	0.23366
C	2.64488	-0.95317	-1.33803
N	2.94718	-0.35307	-0.02077
C	1.75078	-0.28725	0.85412
S	4.34601	0.33451	0.35508
O	5.40087	-0.22515	-0.45817
C	4.23127	2.11870	-0.22983
O	4.46067	0.44697	1.79129
F	3.23695	2.74989	0.40064
F	4.00221	2.15825	-1.54538
F	5.37701	2.75593	0.02759
C	-0.60667	-0.72923	-0.16285
C	-1.65299	-1.47597	0.21576
S	-0.77200	0.73432	-1.19937
C	-3.10476	-1.30770	-0.02803
C	-3.95845	-1.07770	1.05813
C	-5.33183	-0.98253	0.86933
C	-5.87551	-1.14288	-0.40277
C	-5.03648	-1.39323	-1.48377
C	-3.65924	-1.47159	-1.30079
C	-1.91517	1.83824	-0.38018
C	-1.53344	2.46921	0.80305
C	-2.40188	3.36718	1.40194
C	-3.64920	3.65854	0.83346
C	-4.00110	3.01923	-0.35576
C	-3.14490	2.10726	-0.96475
C	-4.57688	4.64160	1.49638
O	0.53353	1.39399	-1.22094
O	-1.35496	0.34991	-2.48185
C	0.69461	-2.37693	2.65373
H	-2.28726	-4.34699	-0.16016
H	-0.01169	-5.45428	-0.64347
H	1.48370	-4.42434	1.29555
H	-1.73025	-2.77709	1.92207
H	3.00975	-3.12128	0.08173
H	2.27160	-3.98648	-1.26132
H	0.87571	-2.09898	-1.82676
H	2.29913	-0.18906	-2.03342
H	3.53215	-1.43823	-1.73804
H	1.33899	0.71741	0.85897
H	2.04331	-0.54780	1.86411
H	-3.54427	-0.95950	2.05253
H	-5.97784	-0.78785	1.71695
H	-6.94698	-1.07679	-0.54869
H	-5.45259	-1.52678	-2.47521
H	-3.01111	-1.65906	-2.14578
H	-0.56783	2.27270	1.25043
H	-2.10546	3.85696	2.32240
H	-4.95907	3.23207	-0.81535
H	-3.42666	1.61382	-1.88416
H	-5.50524	4.75366	0.93637
H	-4.82643	4.31912	2.51050
H	-4.10746	5.62530	1.57886
H	1.77227	-2.37432	2.83057
H	0.27182	-1.46418	3.08186
H	0.27987	-3.22349	3.20607

CAM-B3LYP

Sum of electronic and thermal Free Energies: -2495.349947 Hartree

Coordinates of S_0:

C	-1.29343	-3.97054	0.11081
C	-0.11681	-4.53907	-0.09509
C	1.01704	-3.81647	0.57709
C	0.34202	-2.55810	1.19488
C	-1.17864	-2.71945	0.94681
C	2.10320	-3.29545	-0.36267
C	1.55722	-1.98000	-0.91761
C	0.77744	-1.34684	0.27833
C	2.63632	-0.98312	-1.30464
N	2.93689	-0.35296	-0.00924
C	1.78629	-0.36218	0.91626
S	4.29265	0.41131	0.31209
O	5.34229	-0.07662	-0.53701
C	4.03755	2.15722	-0.25981
O	4.45425	0.53307	1.73371
F	3.04295	2.72196	0.41521
F	3.74653	2.17465	-1.55577
F	5.14645	2.86311	-0.05938
C	-0.56016	-0.74204	-0.13265
C	-1.61420	-1.48402	0.20283
S	-0.68138	0.73002	-1.12887
C	-3.05253	-1.29080	-0.08019
C	-3.92855	-1.05281	0.97675
C	-5.28672	-0.92130	0.74589
C	-5.78942	-1.05146	-0.54039
C	-4.92628	-1.30977	-1.59275
C	-3.56366	-1.42561	-1.36646
C	-1.85079	1.79870	-0.33642
C	-1.51835	2.39574	0.87223
C	-2.41380	3.26186	1.46388
C	-3.63880	3.55291	0.86186
C	-3.94158	2.94897	-0.35143
C	-3.05650	2.06908	-0.95387
C	-4.59739	4.50293	1.51851
O	0.61649	1.38151	-1.07465
O	-1.20538	0.37992	-2.43572
C	0.63629	-2.40705	2.67988
H	-2.24191	-4.33335	-0.26367
H	0.03812	-5.44465	-0.66991
H	1.45686	-4.45488	1.34782
H	-1.75332	-2.81593	1.87323
H	3.01596	-3.10033	0.20672
H	2.35887	-4.00105	-1.15447
H	0.89073	-2.17058	-1.75733
H	2.27174	-0.24041	-2.01219
H	3.52819	-1.46015	-1.70261
H	1.36709	0.63393	1.01629
H	2.12760	-0.69286	1.88945
H	-3.54266	-0.95726	1.98441
H	-5.95532	-0.72089	1.57348
H	-6.85275	-0.95541	-0.72022
H	-5.31311	-1.41951	-2.59805
H	-2.89113	-1.61589	-2.19118
H	-0.56607	2.19478	1.34485
H	-2.15785	3.72845	2.40744
H	-4.88572	3.16499	-0.83580
H	-3.29840	1.59745	-1.89533
H	-5.51117	4.61117	0.93627
H	-4.86699	4.15385	2.51687

H	-4.14659	5.49050	1.63263
H	1.70565	-2.42856	2.89389
H	0.22082	-1.48234	3.08678
H	0.18361	-3.24014	3.22036

M062X

Sum of electronic and thermal Free Energies: -2495.423874 Hartree

Coordinates of S_0:

C	-3.36895	-2.75746	0.18568
C	-2.52544	-3.71654	-0.17400
C	-1.14504	-3.53792	0.40137
C	-1.21666	-2.15534	1.11094
C	-2.69762	-1.70933	1.04616
C	-0.02417	-3.41804	-0.63200
C	-0.08734	-1.96985	-1.12219
C	-0.44732	-1.15227	0.15918
C	1.25952	-1.44113	-1.59672
N	1.91288	-1.06674	-0.32570
C	0.92632	-0.67100	0.70142
S	3.37216	-1.58427	0.08304
O	3.89852	-2.44993	-0.93313
C	4.39272	-0.05587	-0.03578
O	3.42847	-1.92769	1.47604
F	3.96831	0.83387	0.85061
F	4.29541	0.46090	-1.25211
F	5.66203	-0.34242	0.21257
C	-1.48478	-0.06033	-0.09145
C	-2.70101	-0.35851	0.37350
S	-1.21710	1.33276	-1.16254
C	-3.99621	0.34875	0.25327
C	-4.50272	1.04855	1.34531
C	-5.74684	1.66180	1.26414
C	-6.50045	1.55883	0.10158
C	-6.00589	0.84113	-0.98181
C	-4.75847	0.23756	-0.90753
C	0.12862	2.24616	-0.47122
C	1.34747	2.28145	-1.12998
C	2.39008	3.00447	-0.56784
C	2.23237	3.66526	0.64854
C	0.98842	3.61808	1.28472
C	-0.06860	2.91827	0.72940
C	3.38580	4.39126	1.28070
O	-0.78094	0.80754	-2.44541
O	-2.38308	2.18983	-1.12359
C	-0.72571	-2.21324	2.55099
H	-4.41413	-2.69724	-0.09121
H	-2.78467	-4.56505	-0.79681
H	-0.93003	-4.34296	1.10984
H	-3.17466	-1.63556	2.02959
H	0.93902	-3.59380	-0.14012
H	-0.11233	-4.13532	-1.44946
H	-0.84991	-1.84539	-1.89034
H	1.15217	-0.55933	-2.22465
H	1.85342	-2.18917	-2.11573
H	0.96037	0.40431	0.85593
H	1.18915	-1.14749	1.63866
H	-3.91577	1.12364	2.25363
H	-6.12796	2.21744	2.11170
H	-7.47157	2.03348	0.04048
H	-6.59089	0.75511	-1.88887
H	-4.36431	-0.31177	-1.75479
H	1.47219	1.76202	-2.07144
H	3.34512	3.04607	-1.07739
H	0.84947	4.14068	2.22362
H	-1.03367	2.88651	1.22159
H	3.04357	5.25909	1.84378
H	3.90736	3.72914	1.97629
H	4.10418	4.71781	0.52980
H	0.26534	-2.66524	2.62746
H	-0.69602	-1.22060	3.00827
H	-1.41063	-2.83281	3.13289

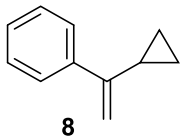

8

(1-cyclopropylvinyl)benzene (8)

B3LYP

Sum of electronic and thermal Free Energies: –426.312414 Hartree

Coordinates of S_0:

C	-3.20534	-0.53425	0.01231
C	-2.19298	-1.47473	-0.15136
C	-0.85901	-1.07913	-0.14655
C	-0.50465	0.26822	0.00896
C	-1.53701	1.20085	0.18662
C	-2.86953	0.80654	0.18501
C	0.92432	0.69110	-0.00610
C	1.91006	-0.30021	0.52299
C	1.28731	1.88907	-0.47941
C	2.66656	-1.22670	-0.41542
C	3.39837	-0.15952	0.35182
H	-4.24400	-0.84262	0.01463
H	-2.44053	-2.52158	-0.28351
H	-0.08486	-1.82363	-0.28013
H	-1.29209	2.24334	0.34855
H	-3.64766	1.54677	0.33065
H	1.59582	-0.77165	1.44853
H	2.31740	2.21979	-0.46129
H	0.56718	2.57181	-0.91235
H	2.78986	-2.26089	-0.11931
H	2.52709	-1.06868	-1.47749
H	3.78226	0.68485	-0.20444
H	4.02093	-0.46501	1.18296

CAM-B3LYP

Sum of electronic and thermal Free Energies: –426.119335 Hartree

Coordinates of S_0:

C	3.16832	-0.42996	0.15872

C	2.29027	-1.32609	-0.42911
C	0.95397	-0.99413	-0.58785
C	0.46740	0.24624	-0.17694
C	1.36174	1.13244	0.42451
C	2.69571	0.80091	0.58903
C	-0.96156	0.61313	-0.37238
C	-1.95805	-0.49840	-0.32224
C	-1.32963	1.87061	-0.59828
C	-2.39046	-1.06692	1.00047
C	-3.35901	-0.28570	0.15705
H	4.21097	-0.69119	0.28889
H	2.64510	-2.29237	-0.76575
H	0.28741	-1.71110	-1.04814
H	1.00412	2.08792	0.78606
H	3.36781	1.50437	1.06483
H	-1.85078	-1.22950	-1.11546
H	-2.36989	2.13231	-0.73875
H	-0.60868	2.67517	-0.66256
H	-2.51938	-2.13768	1.08206
H	-2.01110	-0.58578	1.89263
H	-3.63689	0.70043	0.50238
H	-4.15097	-0.82554	-0.34407

M062X

Sum of electronic and thermal Free Energies: –426.050586 Hartree

Coordinates of S_0:

C	-3.18340	-0.53913	-0.00269
C	-2.16663	-1.47604	-0.13524
C	-0.83685	-1.07400	-0.11624
C	-0.49771	0.27463	0.02291
C	-1.53110	1.20491	0.17066
C	-2.85907	0.80403	0.15470
C	0.92888	0.70188	0.02176
C	1.90690	-0.29801	0.53798
C	1.29226	1.89841	-0.44136
C	2.59805	-1.22935	-0.43168
C	3.38181	-0.18027	0.30220
H	-4.21971	-0.85262	-0.01197
H	-2.40764	-2.52526	-0.25345
H	-0.05309	-1.81341	-0.22309
H	-1.29077	2.25008	0.32202
H	-3.64333	1.54087	0.27678
H	1.61429	-0.76160	1.47345
H	2.32243	2.22746	-0.41314
H	0.57043	2.57980	-0.87355
H	2.71933	-2.26420	-0.14253
H	2.40661	-1.05779	-1.48269
H	3.74883	0.65912	-0.27046
H	4.03376	-0.50475	1.10071

Excited States

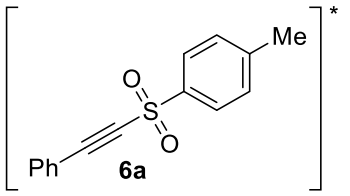

6a

B3LYP

Sum of electronic and thermal Free Energies: –1127.329337 Hartree

Coordinates of T_1:

C	-4.71379	-1.21923	0.00000
C	-4.13677	-0.80428	-1.22673
C	-3.03243	-0.00735	-1.25098
C	-2.42609	0.44768	-0.00000
C	-3.03243	-0.00735	1.25098
C	-4.13677	-0.80429	1.22673
C	-1.36258	1.26999	-0.00000
C	-0.38296	2.07907	0.00000
S	1.37193	2.04341	0.00000
C	1.80096	0.32303	0.00000
C	1.93478	-0.35211	1.21416
C	2.23029	-1.70601	1.20369
C	2.38462	-2.40521	-0.00000
C	2.23029	-1.70601	-1.20369
C	1.93478	-0.35211	-1.21416
O	1.81277	2.64483	-1.25299
O	1.81277	2.64483	1.25299
C	2.73149	-3.86820	-0.00000
H	-5.58849	-1.85545	0.00000
H	-4.58204	-1.12995	-2.15896
H	-2.58671	0.30922	-2.18421
H	-2.58671	0.30921	2.18421
H	-4.58203	-1.12995	2.15896
H	1.82099	0.18103	2.14844
H	2.34391	-2.23097	2.14488
H	2.34391	-2.23096	-2.14488
H	1.82099	0.18104	-2.14844
H	2.34133	-4.36959	0.88659
H	2.34132	-4.36959	-0.88659
H	3.81808	-4.00154	-0.00001

CAM-B3LYP

Sum of electronic and thermal Free Energies: –1126.928617 Hartree

Coordinates of T_1:

C	-4.67763	-1.19313	-0.00000
C	-4.10141	-0.78098	-1.22507
C	-3.00321	0.00978	-1.25227
C	-2.39604	0.46665	0.00000
C	-3.00320	0.00976	1.25227
C	-4.10140	-0.78100	1.22507
C	-1.34327	1.28143	0.00001
C	-0.35974	2.07857	0.00001
S	1.38074	2.02763	0.00000

C	1.77836	0.31203	-0.00000
C	1.90862	-0.35797	1.20815
C	2.18889	-1.71046	1.19829
C	2.33484	-2.40612	-0.00001
C	2.18889	-1.71046	-1.19830
C	1.90863	-0.35796	-1.20816
O	1.82776	2.61643	-1.24504
O	1.82777	2.61643	1.24504
C	2.66703	-3.86884	-0.00000
H	-5.55310	-1.82709	-0.00000
H	-4.54779	-1.10804	-2.15547
H	-2.55589	0.32538	-2.18432
H	-2.55587	0.32534	2.18432
H	-4.54777	-1.10808	2.15547
H	1.80123	0.17803	2.14113
H	2.29694	-2.23733	2.13829
H	2.29695	-2.23732	-2.13831
H	1.80124	0.17804	-2.14113
H	2.27052	-4.36501	0.88526
H	2.27088	-4.36494	-0.88546
H	3.75043	-4.01163	0.00021

M062X

Sum of electronic and thermal Free Energies: –1126.973357 Hartree

Coordinates of T_1:

C	3.25389	1.36067	0.03202
C	2.48911	2.10954	0.93526
C	1.15838	2.34360	0.69033
C	0.54583	1.81798	-0.48591
C	1.34264	1.06681	-1.39958
C	2.67291	0.84748	-1.13229
C	-0.78675	2.07634	-0.75841
C	-1.99622	1.60777	-0.63162
S	-2.57452	0.07923	0.09830
C	-1.11644	-0.90073	0.20727
C	-0.75074	-1.68889	-0.87454
C	0.47880	-2.32980	-0.84820
C	1.34658	-2.17036	0.23176
C	0.94127	-1.38554	1.31542
C	-0.28531	-0.74716	1.31130
O	-3.06063	0.37152	1.43227
O	-3.48615	-0.51136	-0.86139
C	2.71206	-2.79428	0.22864
H	4.30081	1.17762	0.23637
H	2.94835	2.50076	1.83372
H	0.55351	2.91402	1.38324
H	0.87725	0.66460	-2.29015
H	3.27091	0.26459	-1.82131
H	-1.41591	-1.78846	-1.72279
H	0.77650	-2.94817	-1.68642
H	1.60515	-1.26468	2.16370
H	-0.59299	-0.12184	2.14019
H	3.47153	-2.01975	0.08932
H	2.91918	-3.28588	1.17979
H	2.81628	-3.52216	-0.57432

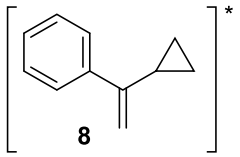

8

B3LYP

Sum of electronic and thermal Free Energies: –426.233887 Hartree

Coordinates of T_1:

C	-3.32319	-0.37405	-0.00000
C	-2.40950	-1.43077	-0.00001
C	-1.04580	-1.19349	-0.00001
C	-0.52283	0.13068	-0.00000
C	-1.47905	1.18606	0.00000
C	-2.83948	0.93671	0.00000
C	0.87725	0.42694	0.00000
C	1.90458	-0.63236	-0.00000
C	1.32896	1.82347	0.00001
C	3.22622	-0.46131	-0.74708
C	3.22622	-0.46132	0.74708
H	-4.38869	-0.56823	-0.00000
H	-2.76902	-2.45363	-0.00001
H	-0.37752	-2.04337	-0.00001
H	-1.12559	2.21020	0.00001
H	-3.53408	1.76919	0.00000
H	1.53440	-1.64706	-0.00001
H	1.50235	2.36458	0.92518
H	1.50235	2.36458	-0.92516
H	3.60619	-1.33124	-1.26727
H	3.39153	0.48146	-1.25176
H	3.39153	0.48145	1.25177
H	3.60619	-1.33125	1.26726

CAM-B3LYP

Sum of electronic and thermal Free Energies: –426.035404 Hartree

Coordinates of T_1:

C	3.30940	-0.36889	-0.00002
C	2.40200	-1.42339	-0.00003
C	1.04284	-1.18926	-0.00003
C	0.52178	0.12812	-0.00000
C	1.46985	1.18143	0.00002
C	2.82597	0.93573	0.00001
C	-0.87394	0.42036	0.00001
C	-1.89995	-0.63723	-0.00001
C	-1.32757	1.81353	0.00004
C	-3.20875	-0.45637	0.74487
C	-3.20876	-0.45633	-0.74486
H	4.37459	-0.56095	-0.00002
H	2.76345	-2.44470	-0.00005
H	0.37589	-2.03915	-0.00004
H	1.11400	2.20393	0.00003
H	3.51867	1.76872	0.00002
H	-1.53158	-1.65149	-0.00004

H	-1.49963	2.35226	-0.92539
H	-1.49963	2.35222	0.92549
H	-3.60033	-1.32114	1.26285
H	-3.36612	0.48751	1.24822
H	-3.36615	0.48758	-1.24816
H	-3.60036	-1.32107	-1.26288

M062X

Sum of electronic and thermal Free Energies: –425.972155 Hartree

Coordinates of T_1:

C	3.31647	-0.36082	0.00000
C	2.41207	-1.42128	0.00000
C	1.04858	-1.19281	0.00000
C	0.52276	0.12424	0.00000
C	1.46549	1.18466	-0.00000
C	2.82595	0.94391	-0.00000
C	-0.87903	0.40921	-0.00000
C	-1.90135	-0.65009	0.00000
C	-1.34248	1.80183	-0.00000
C	-3.21040	-0.44863	0.74540
C	-3.21040	-0.44863	-0.74540
H	4.38241	-0.54795	0.00000
H	2.77772	-2.44110	0.00000
H	0.38555	-2.04632	0.00000
H	1.10711	2.20686	-0.00000
H	3.51454	1.78030	-0.00000
H	-1.54501	-1.66854	0.00000
H	-1.49567	2.34379	-0.92592
H	-1.49567	2.34379	0.92591
H	-3.61216	-1.30986	1.26004
H	-3.34629	0.49967	1.24671
H	-3.34629	0.49967	-1.24671
H	-3.61216	-1.30986	-1.26004

Diradical Intermediates

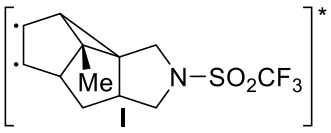

B3LYP

Sum of electronic and thermal Free Energies: -1368.523469 Hartree

Coordinates of T_1:

C	-2.59137	1.92597	-0.46732
C	-3.90491	1.30865	-0.82193
C	-3.70950	-0.15745	-0.55840
C	-2.90799	-0.12484	0.81488
C	-2.01798	1.10812	0.58510
C	-2.73908	-0.74465	-1.65224
C	-1.45836	-1.12134	-0.90640
C	-1.51750	-0.40354	0.41697
C	-0.04204	-0.82008	-1.38684
N	0.68513	-0.86266	-0.07186
C	-0.23620	-0.76821	1.11999
S	2.28046	-0.82413	0.06137
O	2.88899	-1.35685	-1.13587
C	2.75664	0.99570	0.03100
O	2.66598	-1.26137	1.38375
F	4.07937	1.12625	0.15650
F	2.16202	1.64590	1.03725
F	2.37530	1.55362	-1.12242
C	-3.60120	-0.46581	2.10682
H	-2.15773	2.82598	-0.87840
H	-4.83216	1.78888	-0.50225
H	-4.63673	-0.72231	-0.47298
H	-1.49672	1.56197	1.42258
H	-3.18329	-1.60763	-2.14777
H	-2.55076	0.00915	-2.41849
H	-1.49346	-2.19231	-0.66829
H	0.37789	-1.56175	-2.06109
H	0.03016	0.17274	-1.83528
H	0.11675	-0.02580	1.83144
H	-0.28110	-1.74255	1.61077
H	-4.50101	0.14080	2.23770
H	-3.89950	-1.51800	2.12475
H	-2.94863	-0.28575	2.96358

CAM-B3LYP

Sum of electronic and thermal Free Energies: -1368.129807 Hartree

Coordinates of T_1:

C	-2.54591	1.89561	-0.51049
C	-3.87262	1.29533	-0.82376
C	-3.68186	-0.16638	-0.54588
C	-2.88261	-0.11386	0.81494
C	-1.97849	1.09121	0.56368
C	-2.72093	-0.75958	-1.63157
C	-1.44314	-1.12719	-0.89002
C	-1.49483	-0.39338	0.41884
C	-0.03379	-0.83249	-1.37449
N	0.69043	-0.86548	-0.06716
C	-0.22127	-0.77193	1.11993
S	2.27257	-0.81207	0.06089
O	2.88063	-1.33154	-1.13087
C	2.70699	0.99102	0.03047
O	2.66548	-1.24058	1.37347
F	4.01974	1.14949	0.14718
F	2.10611	1.62209	1.03607
F	2.30670	1.53745	-1.11401
C	-3.56465	-0.43107	2.11206
H	-2.06824	2.72928	-1.00297
H	-4.77978	1.78615	-0.46936
H	-4.60982	-0.72689	-0.45157
H	-1.47468	1.56638	1.39930
H	-3.16472	-1.62567	-2.11956
H	-2.53505	-0.01285	-2.40408
H	-1.47706	-2.19287	-0.63610
H	0.38399	-1.57762	-2.04503
H	0.03705	0.15692	-1.82889
H	0.13747	-0.03432	1.83230

H	-0.27579	-1.74621	1.60662
H	-4.45786	0.18337	2.24204
H	-3.86965	-1.47929	2.14828
H	-2.90313	-0.24284	2.95878

M062X

Sum of electronic and thermal Free Energies: -1368.134285 Hartree

Coordinates of T_1:

C	-2.13945	1.75290	-0.75205
C	-3.54460	1.31568	-0.99533
C	-3.55073	-0.11566	-0.53168
C	-2.75297	0.00197	0.82456
C	-1.69223	1.03846	0.44401
C	-2.67584	-0.95588	-1.52322
C	-1.42363	-1.35221	-0.74331
C	-1.40654	-0.49319	0.49187
C	-0.00037	-1.18040	-1.25691
N	0.73942	-1.13641	0.04811
C	-0.16923	-0.92372	1.22791
S	2.28642	-0.76588	0.11515
O	2.94609	-1.25171	-1.06238
C	2.37010	1.07366	-0.05205
O	2.78362	-1.01267	1.43827
F	3.62914	1.47850	0.00909
F	1.68320	1.64863	0.92854
F	1.84998	1.45152	-1.21289
C	-3.47044	-0.04602	2.14190
H	-1.56513	2.47183	-1.31557
H	-4.35980	1.96575	-0.67527
H	-4.54520	-0.53190	-0.38086
H	-1.15019	1.55440	1.23035
H	-3.21535	-1.83305	-1.87541
H	-2.42848	-0.34978	-2.39665
H	-1.52464	-2.38659	-0.39579
H	0.37681	-2.00334	-1.85773
H	0.10689	-0.23713	-1.79651
H	0.24041	-0.18400	1.91111
H	-0.28924	-1.87451	1.74868
H	-4.26683	0.70081	2.17091
H	-3.91839	-1.02825	2.30613
H	-2.78237	0.15856	2.96350

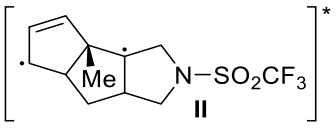

B3LYP

Sum of electronic and thermal Free Energies: -1368.591107 Hartree

Coordinates of T_1:

C	-4.75587	0.10215	-1.17107
C	-4.59043	-0.90046	-0.22652
C	-3.45076	-0.57981	0.69939
C	-2.84085	0.76311	0.10621
C	-3.79991	1.09030	-1.02907
C	-2.29912	-1.61565	0.72688
C	-1.35885	-1.18422	-0.42016
C	-1.48403	0.31447	-0.39414
C	0.14179	-1.47762	-0.25510
N	0.68574	-0.18127	0.23481
C	-0.15453	0.96718	-0.22256
S	2.18029	-0.01024	0.79943
O	2.59663	-1.23507	1.44247
C	3.31600	0.12292	-0.69701
O	2.30513	1.27674	1.44364
F	4.58223	0.26432	-0.30028
F	2.97525	1.18064	-1.44059
F	3.21889	-0.97816	-1.44930
C	-2.76933	1.91145	1.12699
H	-5.53225	0.10840	-1.92701
H	-5.20000	-1.79011	-0.13760
H	-3.82378	-0.41536	1.71617
H	-3.70343	1.97815	-1.64009
H	-1.76397	-1.54426	1.67790
H	-2.65517	-2.64219	0.62209
H	-1.71036	-1.61615	-1.36356
H	0.59730	-1.74566	-1.21006
H	0.35200	-2.25953	0.47064
H	-0.13679	1.75953	0.52376
H	0.23876	1.37525	-1.16282
H	-2.14347	1.64378	1.98221
H	-2.36112	2.81855	0.67473
H	-3.76875	2.14494	1.49862

CAM-B3LYP

Sum of electronic and thermal Free Energies: -1368.195732 Hartree

Coordinates of T_1:

C	-4.74318	0.08091	-1.12782
C	-4.54828	-0.90965	-0.18338
C	-3.39882	-0.56833	0.71653
C	-2.81714	0.76479	0.10294
C	-3.79831	1.07610	-1.00919
C	-2.24452	-1.58830	0.72636
C	-1.35036	-1.17070	-0.45172
C	-1.47208	0.32453	-0.42379
C	0.14578	-1.46317	-0.32622
N	0.68916	-0.18864	0.19271
C	-0.14324	0.96653	-0.22672
S	2.15740	-0.03823	0.78952
O	2.56396	-1.27636	1.39026
C	3.28501	0.14323	-0.67278
O	2.27216	1.21813	1.47334
F	4.54346	0.26688	-0.27116
F	2.94752	1.22166	-1.37470
F	3.18508	-0.92509	-1.45895
C	-2.72974	1.91385	1.10889
H	-5.53336	0.07406	-1.86806
H	-5.14456	-1.80546	-0.07608
H	-3.75624	-0.39838	1.73651
H	-3.72337	1.96176	-1.62543

H	-1.67797	-1.49320	1.65608
H	-2.59303	-2.61911	0.65361
H	-1.73491	-1.60398	-1.37933
H	0.58493	-1.69496	-1.29739
H	0.37198	-2.26862	0.36711
H	-0.12951	1.73396	0.54399
H	0.25139	1.40417	-1.15115
H	-2.08991	1.65245	1.95429
H	-2.33024	2.81738	0.64424
H	-3.72184	2.14813	1.49619

M062X

Sum of electronic and thermal Free Energies: -1368.192716 Hartree

Coordinates of T_1:

C	-4.72749	0.01941	-1.10581
C	-4.49466	-0.94883	-0.14145
C	-3.35530	-0.54846	0.74991
C	-2.80511	0.77465	0.08941
C	-3.81133	1.04719	-1.01026
C	-2.17691	-1.54023	0.77757
C	-1.34437	-1.16872	-0.46135
C	-1.46895	0.33367	-0.47167
C	0.15715	-1.44770	-0.36788
N	0.67075	-0.18834	0.21479
C	-0.13395	0.97082	-0.24859
S	2.14717	-0.03901	0.79766
O	2.55616	-1.27809	1.39309
C	3.24684	0.13887	-0.67453
O	2.26531	1.21808	1.47829
F	4.50744	0.26943	-0.29382
F	2.89046	1.21002	-1.37240
F	3.13511	-0.93299	-1.44886
C	-2.69520	1.94484	1.06805
H	-5.52128	-0.02627	-1.84036
H	-5.05990	-1.86151	-0.01272
H	-3.71450	-0.35251	1.76540
H	-3.76269	1.92382	-1.64205
H	-1.57111	-1.36665	1.67211
H	-2.50054	-2.58183	0.78040
H	-1.76666	-1.63530	-1.35532
H	0.58971	-1.61346	-1.35646
H	0.40610	-2.28186	0.28403
H	-0.13019	1.75100	0.51054
H	0.28733	1.38110	-1.17382
H	-2.04032	1.69168	1.90562
H	-2.29823	2.83457	0.57439
H	-3.68091	2.18849	1.46651

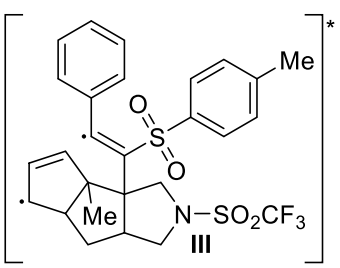

III

B3LYP

Sum of electronic and thermal Free Energies: -2496.021638 Hartree

Coordinates of T_1:

C	1.91889	-0.16276	3.29423
C	0.88325	0.48938	3.94369
C	-0.30117	0.58486	3.02750
C	0.02574	-0.41804	1.85753
C	1.51440	-0.63251	2.05623
C	-0.43567	1.96869	2.35648
C	-1.04930	1.68170	0.99013
C	-0.41570	0.32232	0.49660
C	-2.57941	1.46399	1.04856
N	-2.77080	0.10061	0.50618
C	-1.58880	-0.33703	-0.26214
S	-4.22322	-0.57690	0.34748
O	-5.09126	-0.07676	1.38737
C	-4.97086	0.10234	-1.24300
O	-4.07152	-1.98791	0.08147
F	-6.18290	-0.42088	-1.43466
F	-4.19400	-0.20974	-2.28457
F	-5.07996	1.43282	-1.17224
C	0.77498	0.61505	-0.43420
C	1.51627	1.67168	-0.39792
S	1.28368	-0.54139	-1.83512
C	2.38720	2.73203	-0.47949
C	3.58520	2.75325	0.29348
C	4.44383	3.83154	0.21576
C	4.15319	4.91693	-0.61678
C	2.98140	4.91287	-1.38042
C	2.10547	3.84761	-1.32143
C	2.28127	-1.86444	-1.16694
C	3.63243	-1.63901	-0.90734
C	4.40581	-2.67553	-0.40911
C	3.85495	-3.94089	-0.16686
C	2.50055	-4.13911	-0.44194
C	1.70850	-3.10981	-0.93903
C	4.71433	-5.05842	0.36050
O	0.08324	-1.14527	-2.41127
O	2.15025	0.25326	-2.70017
C	-0.66739	-1.77787	2.08612
H	2.91409	-0.29646	3.70064
H	0.92950	0.94133	4.92510
H	-1.23921	0.31998	3.52399
H	2.13084	-1.20739	1.38250
H	-1.03388	2.66668	2.94528
H	0.55322	2.41336	2.22932
H	-0.83962	2.47805	0.27884
H	-3.09791	2.20835	0.44342
H	-2.97175	1.50633	2.06231
H	-1.55206	-1.41917	-0.30585
H	-1.63638	0.04768	-1.27954
H	3.80953	1.91491	0.93992
H	5.35155	3.83311	0.80711
H	4.83313	5.75779	-0.67013
H	2.75612	5.75238	-2.02701
H	1.19980	3.84484	-1.91391
H	4.07278	-0.66988	-1.10036
H	5.45685	-2.50241	-0.20827

H	2.05545	-5.11172	-0.26852
H	0.66366	-3.27795	-1.16148
H	5.28426	-4.73620	1.23476
H	4.11444	-5.92438	0.64027
H	5.43742	-5.37868	-0.39498
H	-1.75400	-1.69611	2.06067
H	-0.35535	-2.51865	1.34769
H	-0.38444	-2.15651	3.07006

CAM-B3LYP

Sum of electronic and thermal Free Energies: -2495.239068 Hartree

Coordinates of T_1:

C	1.81929	-0.30204	3.27214
C	0.75488	0.29236	3.92087
C	-0.38485	0.44380	2.96319
C	-0.01806	-0.49683	1.76879
C	1.46558	-0.69342	1.99730
C	-0.45779	1.84933	2.34968
C	-1.04864	1.63147	0.96777
C	-0.43853	0.28386	0.44133
C	-2.57728	1.44335	0.99694
N	-2.77884	0.08936	0.45877
C	-1.61627	-0.33837	-0.32784
S	-4.21509	-0.59682	0.34922
O	-5.05330	-0.10562	1.40454
C	-4.98942	0.07414	-1.19869
O	-4.06144	-1.99730	0.08016
F	-6.19476	-0.45234	-1.37025
F	-4.23230	-0.22499	-2.24979
F	-5.10281	1.39660	-1.11603
C	0.75114	0.57979	-0.48055
C	1.48782	1.63702	-0.41542
S	1.25806	-0.53969	-1.85031
C	2.33996	2.71015	-0.43996
C	3.51390	2.71916	0.35807
C	4.35424	3.80776	0.33864
C	4.06634	4.91314	-0.45896
C	2.91733	4.91946	-1.24709
C	2.06027	3.84395	-1.24651
C	2.34672	-1.76765	-1.18668
C	3.67537	-1.44254	-0.95013
C	4.52160	-2.40540	-0.43946
C	4.06468	-3.69489	-0.16579
C	2.73151	-3.99493	-0.41905
C	1.86769	-3.03908	-0.92753
C	5.00496	-4.73501	0.36862
O	0.08377	-1.22553	-2.35710
O	2.03847	0.27615	-2.76012
C	-0.68544	-1.87100	1.92555
H	2.80070	-0.44977	3.70413
H	0.75825	0.68119	4.92922
H	-1.34888	0.17321	3.40090
H	2.11465	-1.21360	1.31087
H	-1.04303	2.54625	2.95051
H	0.54921	2.25954	2.25921
H	-0.81099	2.44998	0.29275
H	-3.07174	2.19068	0.37654
H	-2.98735	1.49932	2.00201
H	-1.59101	-1.41772	-0.40709
H	-1.66823	0.07886	-1.33216
H	3.73506	1.86163	0.97944
H	5.24722	3.80239	0.95065
H	4.73359	5.76490	-0.46653
H	2.69443	5.77776	-1.86805
H	1.16888	3.84811	-1.85936
H	4.04238	-0.44884	-1.16843
H	5.55884	-2.15564	-0.25205
H	2.35958	-4.99170	-0.21734
H	0.83377	-3.28094	-1.13091
H	5.61805	-4.33172	1.17522
H	4.46541	-5.60308	0.74439
H	5.68418	-5.07535	-0.41620
H	-1.77166	-1.80887	1.88270
H	-0.34715	-2.57307	1.16246
H	-0.41311	-2.28526	2.89683

M062X

Sum of electronic and thermal Free Energies: -2495.310111 Hartree

Coordinates of T_1:

C	1.69857	-0.50336	3.22226
C	0.61711	0.04976	3.88468
C	-0.46809	0.33980	2.89326
C	-0.08681	-0.51584	1.64349
C	1.38896	-0.75660	1.89693
C	-0.41304	1.79123	2.38549
C	-1.00230	1.71554	0.98512
C	-0.46336	0.37025	0.37173
C	-2.54178	1.60121	0.99428
N	-2.78702	0.25125	0.45974
C	-1.67801	-0.14965	-0.41545
S	-4.24539	-0.39386	0.37296
O	-5.04250	0.10376	1.45590
C	-5.01538	0.32798	-1.14213
O	-4.13338	-1.79248	0.07723
F	-6.23997	-0.14551	-1.30364
F	-4.28306	0.01549	-2.20308
F	-5.06966	1.64891	-1.03169
C	0.74209	0.66001	-0.51828
C	1.61126	1.59356	-0.30305
S	1.16160	-0.37231	-1.97456
C	2.71040	2.43171	-0.30463
C	3.85442	2.09367	0.46256
C	4.94648	2.93685	0.47829
C	4.93383	4.12582	-0.25127
C	3.81078	4.47068	-1.00417
C	2.70644	3.64464	-1.03636
C	2.13169	-1.69598	-1.32550
C	3.46684	-1.45713	-1.01505
C	4.20345	-2.46669	-0.42356
C	3.62581	-3.70987	-0.14034
C	2.29161	-3.92294	-0.47754
C	1.53553	-2.91935	-1.07106

C	4.44799	-4.79143	0.50144	H	5.81785	2.67102	1.06307
O	-0.05287	-0.93562	-2.53396	H	5.79469	4.78113	-0.23257
O	2.02053	0.43628	-2.81609	H	3.80342	5.39313	-1.57066
C	-0.77566	-1.88996	1.68449	H	1.83323	3.90564	-1.62000
H	2.65790	-0.71695	3.67519	H	3.91218	-0.49332	-1.23161
H	0.58355	0.33588	4.92596	H	5.24390	-2.29433	-0.17395
H	-1.47242	0.09845	3.25346	H	1.83488	-4.88367	-0.27312
H	2.05298	-1.22738	1.18694	H	0.49911	-3.08334	-1.33784
H	-0.94652	2.49076	3.02987	H	4.92690	-4.42273	1.40960
H	0.63080	2.11008	2.32789	H	3.83628	-5.65530	0.75561
H	-0.71091	2.56443	0.36964	H	5.24003	-5.11802	-0.17534
H	-2.99302	2.36120	0.35501	H	-1.86042	-1.81021	1.61614
H	-2.96470	1.67782	1.99384	H	-0.41767	-2.53842	0.88295
H	-1.69459	-1.22129	-0.58620	H	-0.53073	-2.36909	2.63407
H	-1.75128	0.36360	-1.37562				
H	3.85144	1.17206	1.03249				

5. EXPERIMENTAL PROCEDURES

Materials and Methods

Cyclohexane was distilled under nitrogen atmosphere from metallic sodium (Na) and benzophenone. Acetone was distilled from anhydrous calcium sulfate under a nitrogen atmosphere. Acetonitrile, dichloromethane and THF were dried over activated alumina columns on MBraun Solvent Purification System (SPS-800). All other reagent grade chemicals procured from commercial suppliers were used directly without further purification unless otherwise indicated. Yields refer to chromatographically and spectroscopically (^{1}H-NMR) homogeneous material unless otherwise stated. Solvents were degassed using freeze–pump–thaw cycles or by bubbling argon through the liquid in an ultrasonic bath. Deuterochloroform was stored over basic alumina. All reagents were purchased from commercial suppliers and used without further purification. Water- or oxygen-sensitive reactions were performed under an atmosphere of nitrogen in oven-dried glassware using standard Schlenk techniques. Photochemical reactions using UV light were performed in quartz tubes using a photochemical reactor equipped with a circular array of 16 UV lamps (Philips TUV 8W G8T5), a magnetic stirrer, and a cooling fan. Visible light photochemical reactions were performed using blue LEDs (Kessil KSPR, 40 W, λ≈ 160-456 nm) that were placed approximately 5 cm from the reaction mixture in a 10 mL Schlenk tube. Thin-layer chromatography (TLC) was carried out on silica plates (TLC Silica 60 F254 by Merck). Visualization of the compounds was accomplished by projecting UV-light onto the developed plates and with the Dragendorff reagent or using potassium permanganate solution. Chromatographic purification of products was performed as flash column chromatography on silica gel (35–70 µm, Acros Organics) according to the procedure of Still or with the automatic purification system Isolera One from Biotage. Melting points were determined in open capillary tubes and are not corrected. NMR spectra were recorded on a 300, 400, or 600 MHz instrument at 23 °C using standard pulse sequences. The ^{1}H and ^{13}C{H} chemical shifts (δ) were referenced to the residual solvent signal as an internal standard ($CDCl_3$: 7.26 ppm and 77.16 ppm, acetone d_6: 2.05 ppm and 206.26/29.84 ppm for ^{1}H-NMR and ^{13}C-NMR respectively) and reported in parts per million (ppm) relative to tetramethylsilane (TMS). Structural assignments were made with additional information from gCOSY, gHSQC, gNOESY, and gHMBC experiments. FT-IR spectra (given in cm^{-1}) were recorded using a diamond ATR unit. HPLC/ESI-MS

spectra were recorded using an HPLC system with a UV diode array detector coupled with an LC/MSD ion trap. Mixtures of water (with 0.1% formic acid) and acetonitrile were used as an eluent at a total flow rate of 1.0 mL/min. High-resolution masses (APCI-MS and ESI-MS) were recorded using a Q-ToF instrument with dual source and suitable external calibrant. An LP980KS setup from Edinburgh Instruments equipped with an Nd:YAG laser from Litron (Nano LG 300-10) was employed for laser flash photolysis. The frequency-tripled laser output with a wavelength of 355 nm served as excitation source. The laser pulse duration was ~5 ns and the pulse frequency 10 Hz. The typical pulse energy used for transient absorption and emission studies was 15 mJ. Detection of transient absorption spectra occurred on an iCCD camera from Andor. Single-wavelength kinetics were recorded using a photomultiplier tube. The spectroscopic experiments were performed at 293 K using a cuvette holder that allows temperature control. If not stated otherwise the TA spectra were integrated over 100 ns. All samples were prepared in 1 cm quartz cuvettes and degassed by bubbling argon through the analytical sample for 10 minutes.

Preparation of *N*-(2-methylbenzyl)prop-2-en-1-amine (2)

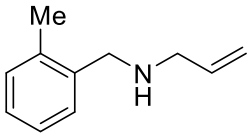

2

To a solution of the allylamine (0.62 mL, 8.32 mmol, 1.00 equiv) in methanol (16 mL) at 0 °C, was added the 2-methylbenzaldehyde (0.96 mL, 8.32 mmol, 1.00 equiv). After stirring at 0 °C until full consumption of the amine and formation of the corresponding imine, $NaBH_4$ (1.20 equiv) was added portionwise at 0 °C and the reaction mixture was stirred at 0 °C for 30 min. The mixture was concentrated under reduced pressure to remove the methanol then was diluted with ethyl acetate and washed with water. The aqueous layer was extracted three times with ethyl acetate (3 x 50 mL). The residue was purified by flash chromatography (SiO_2, eluent: cyclohexane/ethyl acetate, 20:0 → 5:1) to isolate **2** (1.10 g, 6.82 mmol, 82%) as a colorless oil. R_f = 0.23 (3:1 cyclohexane/ethyl acetate). IR/cm^{-1} (ATR): 3015, 2976, 2975, 1643, 1492, 1457, 1097, 1049, 993, 916 cm^{-1}. ^{1}H NMR, COSY (400 MHz, $CDCl_3$) δ 7.33 – 7.29 (m, 1H, H-6), 7.21 – 7.15 (m, 3H, H-3, 4, 5), 5.97 (ddt, *J* = 17.2, 10.2, 6.0 Hz, 1H, -CH=), 5.24 (dq, *J* = 17.2, 1.7 Hz, 1H, =C**H**$_{trans}$), 5.14 (dq, *J* = 10.2, 1.4 Hz, 1H, =C**H**$_{cis}$), 3.79 (s, 2H, -CH_2-), 3.34 (dt, *J* = 6.0, 1.4 Hz, 2H, -C**H$_2$**-CH=), 2.37 (s, 3H, -CH_3). ^{13}C{H} NMR, HSQC, HMBC (101 MHz, $CDCl_3$) δ 138.3 (C-1), 137.0 (-CH=), 136.4 (C-2), 130.4 (C_{Ar}H), 128.5 (C-6), 127.1 (C_{Ar}H), 126.0 (C_{Ar}H), 116.2 (=CH_2), 52.3 (-**C**H_2-CH=), 50.9 (-CH_2-),19.1 (-CH_3). MS (EI): m/z = 161.1 [M]$^+$.

Preparation of *N*-allyl-1,1,1-trifluoro-*N*-(2-methylbenzyl)methanesulfonamide (3)

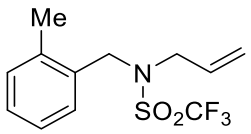

3

To a solution of the amine **2** (5.27 g, 32.7 mmol, 1.00 equiv) in dry CH_2Cl_2 (19 mL) at -78 °C and under N_2 was added triethylamine (6.84 mL, 49.0 mmol, 1.50 equiv) followed by the addition dropwise of trifluoromethansulfonic anhydride (10.14 mL, 36.0 mmol, 1.10 equiv). After 1 h the mixture was allowed to warm to room temperature and stirred for 12 h. The reaction was quenched with water (30 mL), and the organic layer was separated. The aqueous was extracted twice with CH_2Cl_2 (3 x 60 mL). The combined organic phase was dried over $NaSO_4$, filtered, and concentrated under reduced pressure. The residue was purified by flash chromatography (SiO_2, eluent: cyclohexane/ethyl acetate, 100:0 → 98:1) to give **3** (8.15 g, 27.8 mmol, 85%) as a slightly yellow oil. R_f = 0.54 (10:1 cyclohexane/ethyl acetate). IR/cm^{-1} (ATR): 3026, 2933, 1494, 1389, 1226, 1187, 1140, 1060, 912, 610 cm^{-1}.^{1}H NMR, COSY (400 MHz, $CDCl_3$) δ 7.31 – 7.27 (m, 1H, H-6), 7.26 – 7.22 (m, 2H, H-4, 5), 7.20 – 7.16 (m, 1H, H-3), 5.71 (ddt, *J* = 17.0, 10.2, 6.7 Hz, 1 H, -CH=), 5.24 (dq, *J* = 10.2, 1.4 Hz, 1H, =C**H**$_{cis}$), 5.07 (dq, *J* = 17.0, 1.4 Hz, 1H, =C**H**$_{trans}$), 4.57 (s, 2H, -CH_2-), 3.89 (s, 2H, -C**H$_2$**-CH=), 2.32 (s, 3H, -CH_3). ^{13}C{H} NMR, HSQC, HMBC (101 MHz, $CDCl_3$) δ 136.8 (C-1), 131.7 (C-2), 131.1 (-CH=), 131.0 (C-3), 128.5 (C-6), 128.4 (C-4), 126.4 (C-5), 122.0 (=CH_2), 120.1 (q, CF_3, *J* = 323.2 Hz), 50.2 (-**C**H_2-CH=), 48.9 (-CH_2-), 19.3(-CH_3). ^{19}F NMR (376 MHz, $CDCl_3$) δ −76.8 (s, CF_3). MS (ESI): *m/z* = 316.1 [M + Na]$^+$. HRMS (ESI-ToF) *m/z*: [M + Na]$^+$ calcd for $C_{12}H_{14}F_3NO_2SNa$: 316.0589, found: 316.0596.

***meta* photoadduct synthesis**

In an oven-dried quartz tube under nitrogen atmosphere was charged 100.0 mg of the allylation product and 10 mL of anhydrous cyclohexane. The solution was degassed for 15 min and placed in a Rayonet photoreactor. The vessel was irradiated (λ_{max} = 254 nm, 16 × 8 W) at room temperature for 3.5-4.0 h. After removal of the solvent under reduced pressure, the crude isomeric mixture was separated by flash chromatography.

Preparation of (*3aS,4aR,6cR*)-6c-Methyl-2-[(trifluoromethyl)sulfonyl]-1,2,3,3a,4,4a,6a,6c-octahydrocyclopropa[1,6]pentaleno[1,2-*c*]pyrrole (4)

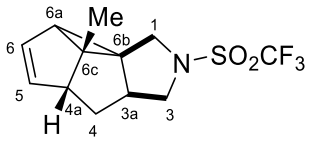

4

Following the general procedure, a mixture of allyl benzyl amine **3** (100.0 mg, 0.34 mmol) and 10 mL of anhydrous cyclohexane was irradiated for 3.5 h. After column chromatography (SiO_2, eluent: cyclohexane/ethyl acetate, 100:0 → 98:1) a 9:1 colorless oily mixture of two isomeric *meta*-photocycloadducts was isolated (72.0 mg, 0.25 mmol, 72%). R_f = 0.50 [$KMnO_4$] (10:1 cyclohexane/ethyl acetate). IR/cm^{-1} (ATR): 3056, 2931, 1479, 1451, 1388, 1226, 1184, 1152, 1023, 729 cm^{-1}. Spectroscopic data are those of the major isomer: ^{1}H NMR, COSY, NOESY (400 MHz, $CDCl_3$) δ 5.64 (dd, *J* = 5.5, 2.2 Hz, 1H, H-6), 5.49 (ddd, *J* = 5.5, 2.3, 0.8 Hz, 1H, H-5), 3.73 (t, *J* = 9.5 Hz, 1H, H-3$_a$), 3.51 (d, *J* = 4.1 Hz, 2H, H-1$_{a,b}$), 3.42 (dd, *J* = 10.6, 3.6 Hz, 1H, H-3$_b$), 3.01 (dd, *J* = 5.3, 2.3 Hz, 1H, H-4a), 2.52 (dtd, *J* = 9.5, 6.2, 3.2 Hz, 1H, H-3a), 1.92 (dt, *J* = 6.2, 1.0 Hz, 1H, H-4$_b$), 1.83 (dd, *J* = 5.1, 2.2 Hz, 1H, H-4$_a$), 1.75 – 1.72 (m, 1H, H-6a), 1.32 (s, 3H, CH_3–C-6b). ^{13}C{H} NMR, HSQC, HMBC (101

MHz, $CDCl_3$) δ 133.6 (C-5), 128.2 (C-6), 120.4 (q, CF_3, J = 323.8 Hz), 57.2 (C-4a), 54.2 (C-3), 48.9 (C-1), 48.1 (C-6b), 47.3 (C-6b), 46.0 (C-4), 41.3 (C-3a), 39.4 (C-6a), 13.7 (**C**H_3–C-6b). ^{19}F NMR (376 MHz, $CDCl_3$) δ −76.2 (s, CF_3). MS (EI): *m/z* = 293.1 $[M]^+$. HRMS (API) *m/z*: $[M]^+$ calcd. for $C_{12}H_{14}F_3NO_2S$: 293.0697, found: 293.0696.

General procedure for the synthesis of alkynyl sulfones (6)

Method A

A solution of ceric ammonium nitrate (2.50 equiv) in CH_3CN (c = 0.25 mmol/mL) was added dropwise to a stirred mixture of the corresponding alkyne (1.00 equiv), the sodium sulfinate (1.20 equiv) and sodium iodide (1.20 equiv) in the same solvent (c=0.20 mmol/mL) under nitrogen atmosphere. After approximately 1 h, the solvent was removed, and the residue was re-dissolved in ethyl acetate and washed with $Na_2S_2O_3$(aq) (3×50 mL) followed by brine (50 mL) and dried over Na_2SO_4. The solvent was removed, and the crude product was refluxed with K_2CO_3 (2.00 equiv) in anhydrous acetone (c= 0.4 mmol/mL) until TLC or HPLC/ESI-MS indicated full consumption of the starting material. The reaction mixture was washed with H_2O (50 mL) and extracted with CH_2Cl_2 (3×20 mL). The combined organic extracts were washed with brine and dried over anhydrous Na_2SO_4. The solvent was removed *in vacuo* and the residue was purified by flash column chromatography (SiO_2, eluent: cyclohexane/ethyl acetate, 97:3) to afford the expected acetylenic sulfone.

Method B

A mixture of the corresponding sodium sulfinate (2.00 equiv), alkyne (1.00 equiv), and iodine (1.50 equiv) in water (c=0.15 mmol/mL) was stirred at room temperature for 2h. After the reaction was completed, the mixture was quenched with $Na_2S_2O_3$(aq) (10 mL). Further stirring was followed by extraction with ethyl acetate (3 × 30 mL). The organic layer was dried with anhydrous Na_2SO_4 and concentrated in vacuo. The residue was refluxed with K_2CO_3 (2.00 equiv) in anhydrous acetone (c= 0.4 mmol/mL) until TLC or HPLC/ESI-MS indicated full consumption of the starting material. the reaction mixture was washed with H_2O (50 mL) and extracted with CH_2Cl_2 (3×20 mL). The combined organic extracts were washed with brine and dried over anhydrous Na_2SO_4. The solvent was removed *in vacuo* and the residue was purified by flash column chromatography (SiO_2, eluent: cyclohexane/ethyl acetate, 97:3) to afford the expected acetylenic sulfone.

1-Methyl-4-(phenylethynesulfonyl)benzene (6a)

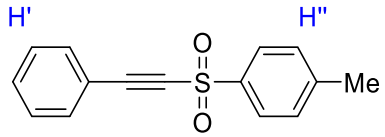

6a

Following general procedure A with phenylacetylene (1.00 g, 9.8 mmol, 1.00 equiv) and sodium *p*-toluenesulfinate (2.10 g, 11.8 mmol, 1.20 equiv) the title compound (1.70 g, 6.63 mmol, 68%) was isolated as a colorless solid. R_f = 0.52 (3:1 cyclohexane/ethyl acetate). Mp: 77−78 °C (cyclohexane-ethyl acetate) Lit.:[17] 78–79 °C. IR/cm^{-1} (ATR): 2988, 2179, 1593, 1486, 1443, 1322, 1291, 1180, 1080,

679 cm^{-1}. ^{1}H NMR, COSY (400 MHz, $CDCl_3$) δ 7.96 (d, *J* = 8.4 Hz, AA‘ part of AA‘BB‘ system, 2H, H-2“,6“), 7.54 – 7.50 (m, 2H, H-2’,6’), 7.49 – 7.44 (m, 1H, H-4’), 7.41 – 7.33 (m, 4H, H-3’,5’/ H-3“,5“), 2.47 (s, 3H, $–CH_3$). $^{13}C\{H\}$ NMR, HSQC, HMBC (101 MHz, $CDCl_3$) δ 145.5 (C-4”), 139.1 (C-1”), 132.9 (C-2‘,6‘), 131.6 (C-4’), 130.2 (C-3”,5”), 128.8 (C-3‘,5‘), 127,8 (C-2”,6”), 118.2 (C-1’), 93.1 (–**C**≡C-SO_2), 85.8 (–C≡**C**-SO_2), 21.9 ($–CH_3$). MS (ESI): *m/z* = 257.0 $[M + H]^+$. The spectroscopic data are in accordance with the literature.[17-18]

1-Methyl-4-[(4-methylbenzene-1-sulfonyl)ethynyl]benzene (6b)

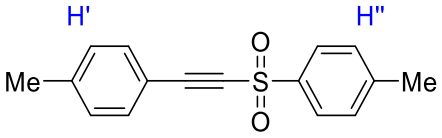

6b

Following general procedure A with 4-ethynyltoluene (0.50 g, 4.30 mmol, 1.00 equiv) and sodium *p*-toluenesulfinate (2.10 g, 5.17 mmol, 1.20 equiv) the title compound (0.81 g, 3.00 mmol, 70%) was isolated as a colorless solid. R_f = 0.52 (3:1 cyclohexane/ethyl acetate). Mp:103 − 104 °C (cyclohexane-ethyl acetate) Lit.:[17] 103–105 °C. IR/cm^{-1} (ATR): 2988, 2177, 1594, 1486, 1441, 1328, 1155, 1085, 859, 606 cm^{-1}. ^{1}H NMR, COSY (400 MHz, $CDCl_3$) δ 7.95 (d, *J* = 8.3 Hz, AA‘ part of AA‘BB‘ system, 2H, H-2“,6“), 7.41 (d, *J* = 8.2 Hz, AA‘ part of AA‘BB‘ system, 2H, H-2’,6’), 7.38 (d, *J* = 8.3 Hz, BB‘ part of AA‘BB‘ system, 2H, H-3“,5“), 7.17 (d, *J* = 8.2 Hz, BB‘ part of AA‘BB‘ system, 2H, H-3’,5’), 2.47 (s, 3H, $–CH_3$“), 2.37 (s, 3H, $–CH_3$‘). $^{13}C\{H\}$ NMR, HSQC, HMBC (101 MHz, $CDCl_3$) δ 145.4 (C-4”), 142.4 (C-4’), 139.2 (C-1”), 132.8 (C-2‘,6‘), 130.1 (C-3”,5”), 129.6 (C-3‘,5‘), 127,8 (C-2”,6”), 115.0 (C-1’), 93.8 (–**C**≡C-SO_2), 85.3 (–C≡**C**-SO_2), 21.9 ($–CH_3$‘), 21.8 ($–CH_3$”). MS (ESI): 271.0 *m/z* = $[M + H]^+$. The spectroscopic data are in accordance with the literature.[17-18]

1-Methoxy-4-[(4-methylbenzene-1-sulfonyl)ethynyl]benzene (6c)

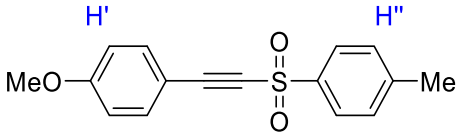

6c

Following general procedure A with 1-ethynyl-4-methoxybenzene (0.60 g, 4.54 mmol, 1.00 equiv) and sodium *p*-toluenesulfinate (0.97 g, 5.45 mmol, 1.20 equiv) the title compound (0.65 g, 6.63 mmol, 50%) was isolated as a yellow solid. R_f = 0.34 (3:1 cyclohexane/ethyl acetate). Mp: 123–124 °C (cyclohexane-ethyl acetate) Lit.:[17]123–124 °C. IR/cm^{-1} (ATR): 2173, 1602, 1509, 1442, 1328, 1258, 1173, 1085, 861, 670 cm^{-1}. ^{1}H NMR, COSY (400 MHz, $CDCl_3$) δ 7.95 (d, *J* = 8.4 Hz, AA‘ part of AA‘BB‘ system, 2H, H-2“,6“), 7.46 (d, *J* = 8.9 Hz, AA‘ part of AA‘BB‘ system, 2H, H-2’,6’), 7.38 (d, *J* = 8.4 Hz, BB‘ part of AA‘BB‘ system, 2H, H-3“,5“), 6.86 (d, *J* = 8.9 Hz, BB‘ part of AA‘BB‘ system, 2H, H-3’,5’), 3.82 (s, 3H, $–OCH_3$), 2.46 (s, 3H, $–CH_3$). $^{13}C\{H\}$ NMR, HSQC, HMBC (101 MHz, $CDCl_3$) δ 162.2 (C-4’), 145.3 (C-4”), 139.4 (C-1”), 134.8 (C-2‘,6‘), 130.1 (C-3”,5”), 127,5 (C-2”,6”), 114.5 (C-3‘,5‘), 109.8 (C-1’), 94.2 (–**C**≡C-SO_2),

85.0 (–C≡**C**-SO_2), 25.6 (–OCH_3), 21.9 (–CH_3). MS (ESI):287.0 *m/z* = $[M + H]^+$. The spectroscopic data are in accordance with the literature.[17]

3-[(4-Methylbenzene-1-sulfonyl)ethynyl]thiophene (6d)

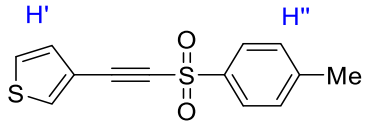

6d

Following general procedure A with 3-ethynylthiophene (0.30 g, 2.77 mmol, 1.00 equiv) and sodium *p*-toluenesulfinate (0.59 g, 3.33 mmol, 1.20 equiv) the title compound (0.44 g, 1.67 mmol, 60%) was isolated as a colorless solid. R_f = 0.34 (3:1 cyclohexane/ethyl acetate). Mp: 98−99 °C (cyclohexane-ethyl acetate) Lit.:[18] 74.2−75.3 °C. IR/cm^{-1} (ATR): 2171, 2166, 1593, 1359, 1152, 1083, 950, 875, 838, 741 cm^{-1}. ^{1}H NMR, COSY (400 MHz, $CDCl_3$) δ 7.95 (d, *J* = 8.4 Hz, AA‘ part of AA‘BB‘ system, 2H, H-2”,6“), 7.74 (dd, *J* = 3.0, 1.2 Hz, 1H, H-5‘), 7.39 (d, *J* = 8.4 Hz, BB‘ part of AA‘BB‘ system, 2H, H-3“,5“), 7.32 (dd, *J* = 5.0, 1.3 Hz, 1H, H-4‘), 7.03 (d, *J* = 8.3 Hz, BB‘ part of AA‘BB‘ system, 2H, H-3”,5”), 7.17 (dd, *J* = 5.0, 1.2 Hz, 1H, H-2‘), 2.47 (s, 3H, –CH_3). ^{13}C{H} NMR, HSQC, HMBC (101 MHz, $CDCl_3$) δ 145.5 (C-4”), 139.1 (C-1”), 134.7 (C-5‘), 130.1 (C-3”,5”), 130.0 (C-2’), 127,7 (C-2”,6”), 126.6 (C-4‘), 117.4 (C-3’), 88.7 (–**C**≡C-SO_2), 85.7 (–C≡**C**-SO_2), 21.9 (–CH_3). MS (ESI):263.0 *m/z* = $[M + H]^+$. The spectroscopic data are in accordance with the literature.[18]

1-Fluoro-4-[(4-methylbenzene-1-sulfonyl)ethynyl]benzene (6e)

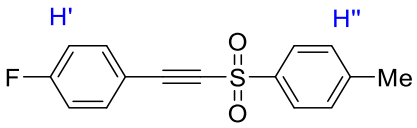

6e

Following general procedure A with 1-ethynyl-4-fluorobenzene (0.50 g, 4.16 mmol, 1.00 equiv) and sodium *p*-toluenesulfinate (0.89 g, 5.00 mmol, 1.20 equiv) the title compound (0.46 g, 1.68 mmol, 40%) was isolated as a colorless solid. R_f = 0.43 (3:1 cyclohexane/ethyl acetate). Mp: 85−87 °C (cyclohexane-ethyl acetate) Lit.:[19] 86.0−87.0 °C. IR/cm^{-1} (ATR): 2183, 1598, 1506, 1402, 1332, 1239, 1158, 1087, 863, 669 cm^{-1}. ^{1}H NMR, COSY (400 MHz, $CDCl_3$) δ 7.95 (d, *J* = 8.4 Hz, AA‘ part of AA‘BB‘ system, 2H, H-2“,6“), 7.56 – 7.50 (m, AA‘ part of AA‘BB‘ system, 2H, H-2’,6’), 7.39 (d, *J* = 8.4 Hz, BB‘ part of AA‘BB‘ system, 2H, H-3“,5“), 7.11 – 7.02 (m, BB‘ part of AA‘BB‘ system, 2H, H-3’,5’), 2.47 (s, 3H, –CH_3). ^{13}C{H} NMR, HSQC, HMBC (101 MHz, $CDCl_3$) δ 162.5 (d, J_{CF} = 255.2 Hz, C-4’), 145.6 (C-4”), 138.9 (C-1”), 135.3 (d, J_{CF} = 9.0 Hz, C-2‘,6‘), 130.2 (C-3”,5”), 127,7 (C-2”,6”), 116.5 (d, J_{CF} = 22.4 Hz,C-3‘,5‘), 114.3 (C-1’), 92.0 (–**C**≡C-SO_2), 85.7 (–C≡**C**-SO_2), 21.9 (–CH_3). ^{19}F NMR (376 MHz, $CDCl_3$) δ -105.77 (tt, *J* = 9.2, 5.2 Hz, 1F, F–C-4’). MS (ESI): 275.0 *m/z* = $[M + H]^+$. The spectroscopic data are in accordance with the literature.[18-19]

1-Bromo-4-[(4-methylbenzene-1-sulfonyl)ethynyl]benzene (6f)

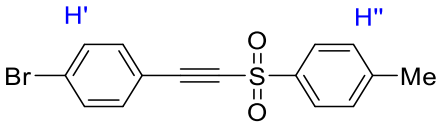

6f

Following general procedure A with 1-bromo-4-ethynylbenzene (0.50 g, 2.76 mmol, 1.00 equiv) and sodium *p*-toluenesulfinate (0.59 g, 3.31 mmol, 1.20 equiv) the title compound (0.73 g, 2.18 mmol, 78%) was isolated as a colorless solid. R_f = 0.43 (3:1 cyclohexane/ethyl acetate). Mp: 105−106 °C (cyclohexane-ethyl acetate) Lit.:[19] 106.7−107.7 °C. IR/cm^{-1} (ATR): 2183, 1583, 1485, 1395, 1332, 1185, 1159, 1086, 851, 652 cm^{-1}. ^{1}H NMR, COSY (400 MHz, $CDCl_3$) δ 7.95 (d, *J* = 8.4 Hz, AA‘ part of AA‘BB‘ system, 2H, H-2“,6“), 7.52 (d, *J* = 8.6 Hz, AA‘ part of AA‘BB‘ system, 2H, H-2’,6’), 7.39 (d, *J* = 8.4 Hz, BB‘ part of AA‘BB‘ system, 2H, H-3“,5“), 7.36 (d, *J* = 8.6 Hz, BB‘ part of AA‘BB‘ system, 2H, H-3’,5’), 2.47 (s, 3H, –CH_3). ^{13}C{H} NMR, HSQC, HMBC (101 MHz, $CDCl_3$) δ 145.7 (C-4”), 138.8 (C-1”), 134.1 (C-3‘,5‘), 132.3 (C-2‘,6‘), 130.2 (C-3”,5”), 127,7 (C-2”,6”), 126.6 (C-4’), 117.1 (C-1’), 91.7 (–**C**≡C-SO_2), 86.7 (–C≡**C**-SO_2), 21.9 (–CH_3). MS (ESI): 275.0 *m/z* =335.0 $[M + H]^+$. The spectroscopic data are in accordance with the literature.[19]

1-Chloro-4-[(4-methylbenzene-1-sulfonyl)ethynyl]benzene (6g)

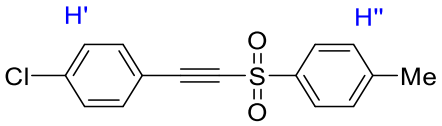

6g

Following general procedure A with 1-chloro-4-ethynylbenzene (0.60 g, 4.39 mmol, 1.00 equiv) and sodium *p*-toluenesulfinate (0.94 g, 5.27 mmol, 1.20 equiv) the title compound (0.66 g, 2.28 mmol, 52%) was isolated as a colorless solid. R_f = 0.51 (3:1 cyclohexane/ethyl acetate). Mp: 98−100 °C (cyclohexane-ethyl acetate) Lit.:[19] 98.7−99.2°C. IR/cm^{-1} (ATR): 2182, 1592, 1488, 1400, 1331, 1185, 1159, 1087, 852, 659 cm^{-1}. ^{1}H NMR, COSY (400 MHz, $CDCl_3$) δ 7.95 (d, *J* = 8.4 Hz, AA‘ part of AA‘BB‘ system, 2H, H-2“,6“), 7.44 (d, *J* = 8.6 Hz, AA‘ part of AA‘BB‘ system, 2H, H-2’,6’), 7.39 (d, *J* = 8.4 Hz, BB‘ part of AA‘BB‘ system, 2H, H-3“,5“), 7.35 (d, *J* = 8.6 Hz, BB‘ part of AA‘BB‘ system, 2H, H-3’,5’), 2.47 (s, 3H, –CH_3). ^{13}C{H} NMR, HSQC, HMBC (101 MHz, $CDCl_3$) δ 145.7 (C-4”), 138.8 (C-1”), 138.1 (C-4’), 134.0 (C-2‘,6‘), 130.2 (C-3”,5”), 129.3 (C-3‘,5‘), 127,7 (C-2”,6”), 116.6 (C-1’), 91.6 (–**C**≡C-SO_2), 86.6 (–C≡**C**-SO_2), 21.9 (–CH_3). MS (ESI): 275.0 *m/z* =291.0 $[M + H]^+$. The spectroscopic data are in accordance with the literature.[18-19]

[(Benzenesulfonyl)ethynyl]benzene (6h)

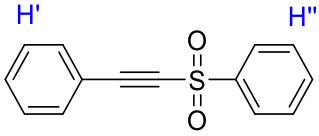

6h

Following general procedure A with phenylacetylene (0.80 g, 7.83 mmol, 1.00 equiv) and sodium benzenesulfinate (1.54 g, 9.40 mmol, 1.20 equiv) the title compound (1.21 g, 5.01 mmol, 64%) was isolated as a colorless solid. R_f = 0.41 (3:1 cyclohexane/ethyl acetate). Mp: 67−69 °C (cyclohexane-ethyl acetate) Lit.:[18] 55.4−55.1°C. IR/cm^{-1} (ATR): 2988, 2179, 1328, 1159, 1086, 850, 756, 727, 685, 657 cm^{-1}. ^{1}H NMR, COSY (400 MHz, $CDCl_3$) δ 8.11 – 8.06 (m, 2H, H-2“,6“), 7.72 – 7.66 (m, 1H, H-4“), 7.63 – 7.57 (m, 2H, H-3“,5“), 7.54 – 7.50 (m, 2H, H-2’,6’), 7.50 – 7.44 (m, 1H, H-4’), 7.40 – 7.33 (m, 2H, H-3’,5’).^{13}C{H} NMR, HSQC, HMBC (101 MHz, $CDCl_3$) δ 141.8 (C-1”), 134.3 (C-4”), 132.9 (C-2‘,6‘), 131.7 (C-4’), 129.5 (C-3”,5”), 128.8 (C-3‘,5‘), 127,5 (C-2”,6”), 117.9 (C-1’), 93.6 (–**C**≡C-SO_2), 85.4 (–C≡**C**-SO_2). MS (ESI): *m/z* = 243.0 [M + H]$^+$. The spectroscopic data are in accordance with the literature.[18]

[(Methanesulfonyl)ethynyl]benzene (6i)

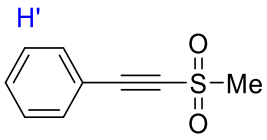

6i

Following general procedure B with phenylacetylene (0.25 g, 2.45 mmol, 1.00 equiv) and sodium methanesulfinate (0.50 g, 5.00 mmol, 2.00 equiv) the title compound (0.28 g, 1.57 mmol, 64%) was isolated as a yellow solid. R_f = 0.28 (3:1 cyclohexane/ethyl acetate). Mp: 58−59 °C (cyclohexane-ethyl acetate) Lit.:[20] 57−58 °C. IR/cm^{-1} (ATR): 2988, 2928, 2184, 1489, 1322, 1149, 1066, 965, 847, 765 cm^{-1}. ^{1}H NMR, COSY (400 MHz, $CDCl_3$) δ 7.65 – 7.58 (m, 2H, H-2’,6’), 7.58 – 7.52 (m, 1H, H-4’), 7.48 – 7.41 (m, 2H, H-3’,5’), 3.33 (s, 3H, –SO_2CH_3). ^{13}C{H} NMR, HSQC, HMBC (101 MHz, $CDCl_3$) δ 133.0 (C-2‘,6‘), 131.9 (C-4’), 129.0 (C-3‘,5‘), 117.6 (C-1’), 91.7 (–**C**≡C-SO_2), 84.5 (–C≡**C**-SO_2), 47.0 (–SO_2CH_3). MS (ESI): *m/z* = 203.0 [M + Na]$^+$. The spectroscopic data are in accordance with the literature.[20]

[(Ethanesulfonyl)ethynyl]benzene (6j)

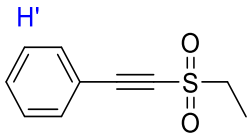

6j

Following general procedure B with phenylacetylene (0.30 g, 2.94 mmol, 1.00 equiv) and sodium ethanesulfinate (0.62 g, 5.87 mmol, 2.00 equiv) the title compound (0.11 g, 0.57 mmol, 20%) was isolated as a yellow oil. R_f = 0.35 (3:1 cyclohexane/ethyl acetate). IR/cm^{-1} (ATR): 2984, 2184, 1492, 1324, 1141, 1047, 849, 760, 733, 690 cm^{-1}. ^{1}H NMR, COSY (400 MHz, $CDCl_3$) δ 7.63 – 7.56 (m, 2H, H-2’,6’), 7.56 – 7.48 (m, 1H, H-4’), 7.46 – 7.37 (m, 2H, H-3’,5’), 3.30 (q, *J* = 7.4 Hz, 2H, SO_2CH_2–), 1.54 (t, *J* = 7.4 Hz, 3H, –CH_3). ^{13}C{H} NMR, HSQC, HMBC (101 MHz, $CDCl_3$) δ 133.0 (C-2‘,6‘), 131.9 (C-4’), 129.0 (C-3‘,5‘), 117.8 (C-1’), 92.7 (–**C**≡C-SO_2), 82.8 (–C≡**C**-SO_2), 52.9 (SO_2CH_2–), 7.9 (–CH_3). MS (ESI): *m/z* = 217.0 [M + Na]$^+$. The spectroscopic data are in accordance with the literature.[20]

[(Butane-1-sulfonyl)ethynyl]benzene (6k)

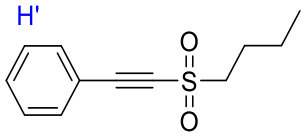

6k

Following general procedure B with 1-hexyne (0.60 g, 7.30 mmol, 1.00 equiv) and sodium *p*-toluenesulfinate (2.60 g, 14.6 mmol, 2.00 equiv) the title compound (1.04 g, 4.68 mmol, 64%) was isolated as a colorless oil. R_f = 0.50 (3:1 cyclohexane/ethyl acetate). IR/cm^{-1} (ATR): 2960, 2200, 1596, 1329, 1185, 1090, 814, 706, 678, 620 cm^{-1}. ^{1}H NMR, COSY (400 MHz, $CDCl_3$) δ 7.85 (d, *J* = 8.4 Hz, AA‘ part of AA‘BB‘ system, 2H, H-2“,6“), 7.34 (d, *J* = 8.4 Hz, BB‘ part of AA‘BB‘ system, 2H, H-3“,5“), 2.44 (s, 3H, –CH_3), 2.33 (t, *J* = 7.1 Hz, 2H, H-1’), 1.55 – 1.45 (m, 2H, H-2’), 1.40 – 1.28 (m, 2H, H-3’), 0.86 (t, *J* = 7.3 Hz, 3H, H-4’). ^{13}C{H} NMR, HSQC, HMBC (101 MHz, $CDCl_3$) δ 145.2 (C-4”), 139.2 (C-1”), 129.9 (C-3”,5”), 127,3 (C-2”,6”), 97.4 (–**C**≡C-SO_2), 78.4 (–C≡**C**-SO_2), 133.0 (C-2‘), 21.9 (C-3’), 21.8 (–CH_3), 18.7 (C-1‘), 13.4 (C-4‘). MS (ESI): 275.0 *m/z* =237.1 [M + H]$^+$. The spectroscopic data are in accordance with the literature.[20]

General procedure for tetracycle (7) synthesis

The *meta* photoadduct **4** (35.0 mg, 0.12 mmol, 1.00 equiv), alkynyl sulfone **6** (0.24 mmol, 2.00 equiv), $Ir(ppy)_2(dtbbpy)PF_6$ (2.2 mg, 0.002 mmol, 0.02 equiv) and methanol (0.8 mL, c = 0.15 M) were loaded in an oven-dried Schlenk tube (10 mL) under nitrogen atmosphere, and the mixture was degassed and then placed in front of two blue LEDs 456 nm (see the materials section) at a distance of 5 cm. The vessel was irradiated until TLC or HPLC/ESI-MS indicated full consumption of the starting material (approx. 10-14 h). The resultant solution was concentrated and purified by flash column chromatography on silica gel (cyclohexane/ethyl acetate) or reversed-phase column chromatography (SiO_2-C_{18}, water/acetonitrile) to give the corresponding product **7** as a racemic mixture.

8b-Methyl-8-[(4-methylphenyl)sulfonyl]-7-phenyl-2-[(trifluoromethyl)sulfonyl]-1,2,3,3a,4,4a,6a,8b-octahydrocyclopenta[3,4]pentaleno[1,6a-*c*]pyrrole (7a)

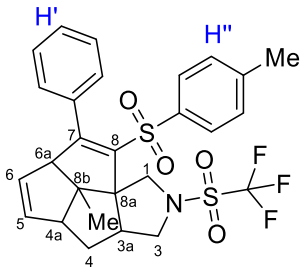

7a

Following the general procedure using 1-methyl-4-(phenylethynesulfonyl)benzene (61.2 mg, 0.24 mmol, 2.00 equiv) after 10 h, column chromatography (SiO_2, eluent: cyclohexane/ethyl acetate, 95:1 → 20:1) afforded the title compound (54.5 mg, 0.10 mmol, 85%) as a colorless solid. R_f = 0.52 (3:1 cyclohexane/ethyl acetate). Mp: 140−142 °C (ethanol). IR/cm^{-1} (ATR): 3056, 2956, 2871, 1595, 1259,

1225, 1189, 1144, 720, 619 cm^{-1}. ^1H NMR, COSY, NOESY (400 MHz, $CDCl_3$) δ 7.26 – 7.23 (m, 1H, H-4'), 7.16 (t, *J* = 7.5 Hz, 2H, H-3', 5'), 7.05 (d, *J* = 8.4 Hz, AA' part of AA'BB' system, 2H, H-2",6"), 6.95 (d, *J* = 8.4 Hz, BB' part of AA'BB' system, 2H, H-3",5"), 6.85 – 6.73 (m, 2H, H-2',6'), 5.81 (dt, *J* = 5.6, 2.2 Hz, 1H, H-5), 5.29 (ddd, *J* = 5.6, 2.7, 1.4 Hz, 1H, H-6), 4.59 (d, *J* = 10.2 Hz, 1H, H-1_a), 4.03 (t, *J* = 9.4 Hz, 1H, H-3_a), 3.98 (d, *J* = 10.2 Hz, 1H, H-1_b), 3.79 (tdd, *J* = 8.6, 5.9, 2.4 Hz, 1H, H-3a), 3.38 (t, *J* = 9.4 Hz, 1H, H-3_b), 3.35 (dd, *J* = 2.7, 1.9 Hz, 1H, H-6a), 2.98 (t, *J* = 8.4 Hz, 1H, H-4a), 2.31 (s, 3H, CH_3–C4"), 2.06 (ddd, *J*= 13.6, 8.1, 2.5 Hz, 1H, H-4_b), 1.68 (ddd, *J*= 13.6, 8.7, 2.5 Hz, 1H, H-4_a), 1.36 (s, 3H, CH_3–C-8b). $^{13}C\{H\}$ NMR, HSQC, HMBC (101 MHz, $CDCl_3$) δ 159.6 (C-8), 143.8 (C-4"), 138.3 (C-1"), 137.7 (C-7), 136.1 (C-5), 133.9 (C-1'), 129.1 (C-3",5"), 128.2 (C-6), 128.1 (C-4'), 127.9 (C-3',5'), 127.7 (C-2',6'), 127,5 (C-2",6"), 120.4 (q, *J* = 323.4 Hz, CF_3), 71.0 (C-6a), 70.4 (C-8a), 61.3 (C-8b), 58.7 (C-4a), 52.7 (C-3a), 52.4 (C-3), 52.2 (C-1), 34.4 (C-4), 23.8 (**C**H_3–C-8b), 21.6 (**C**H_3–C4"). ^{19}F NMR (376 MHz, $CDCl_3$) δ −76.3 (s, CF_3). MS (ESI): *m/z* = 550.1 $[M + H]^+$. HRMS (ESI-ToF) *m/z*: $[M + Na]^+$ calcd for $C_{27}H_{26}F_3NO_4S_2Na$: 572.1147, found: 572.1161.

8b-Methyl-7-(4-methylphenyl)-8-[(4-methylphenyl)sulfonyl]-2-[(trifluoromethyl)sulfonyl]-1,2,3,3a,4,4a,6a,8b-octahydrocyclopenta[3,4]pentaleno[1,6a-*c*]pyrrole (7b)

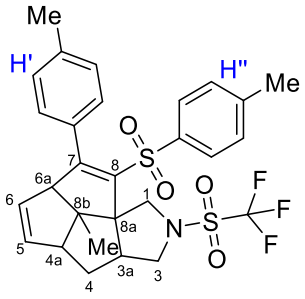

7b

Following the general procedure using 1-methyl-4-[(4-methylbenzene-1-sulfonyl)ethynyl]benzene (64.5 mg, 0.24 mmol, 2.00 equiv) after 10 h, column chromatography (SiO_2, eluent: cyclohexane/ethyl acetate, 95:1 → 20:1) afforded the title compound (45 mg, 0.08 mmol, 67%) as a colorless solid. R_f = 0.53 (3:1 cyclohexane/ethyl acetate). Mp: 143−145 °C (ethanol). IR/cm^{-1} (ATR): 3051, 2927, 2871, 1597, 1259, 1225, 1189, 1144, 813, 616 cm^{-1}. ^1H NMR, COSY, NOESY (400 MHz, $CDCl_3$) δ 7.07 (d, *J* = 8.1 Hz, AA' part of AA'BB' system, 2H, H-2",6"), 6.98 (d, *J* = 8.1 Hz, BB' part of AA'BB' system, 2H, H-3',5'), 6.96 (d, *J* = 8.1 Hz, BB' part of AA'BB' system, 2H, H-3",5"), 6.71 (d, *J* = 8.1 Hz, AA' part of AA'BB' system, 2H, H-2',6'), 5.80 (dt, *J* = 5.6, 2.2 Hz, 1H, H-5), 5.30 (ddd, *J* = 5.7, 2.7, 1.4 Hz, 1H, H-6), 4.57 (d, *J* = 10.3 Hz, 1H, H-1_a), 4.02 (t, *J* = 9.4 Hz, 1H, H-3_a), 3.95 (d, *J* = 10.3 Hz, 1H, H-1_b), 3.77 (tdd, *J* = 8.6, 5.9, 2.5 Hz, 1H, H-3a), 3.36 (t, *J* = 9.4 Hz, 1H, H-3_b), 3.33 (dd, *J* = 2.7, 1.9 Hz, 1H, H-6a), 2.96 (t, *J* = 8.5 Hz, 1H, H-4a), 2.34 (s, 3H, CH_3–C4'), 2.32 (s, 3H, CH_3–C4"), 2.04 (ddd, *J*= 13.6, 8.1, 2.5 Hz, 1H, H-4_b), 1.66 (ddd, *J*= 13.6, 8.7, 6.0 Hz, 1H, H-4_a), 1.35 (s, 3H, CH_3–C-8b). $^{13}C\{H\}$ NMR, HSQC, HMBC (101 MHz, $CDCl_3$) δ 159.9 (C-8), 143.8 (C-4"), 138.5 (C-4'), 138.2 (C-1"), 137.5 (C-7), 136.0 (C-5), 131.0 (C-1'), 129.0 (C-3",5"), 128.6 (C-3',5'), 128.4 (C-6), 127.7 (C-2',6'), 127.6 (C-2",6"), 120.4 (q, *J* = 323.9 Hz, CF_3), 71.2 (C-6a), 70.3 (C-8a), 61.2 (C-8b), 58.8 (C-4a), 52.7 (C-3a), 52.4 (C-3), 52.2 (C-1), 34.4 (C-4), 23.8 (**C**H_3–C-8b), 21.7 (**C**H_3–C4"), 21.4 (**C**H_3–C4'). ^{19}F NMR (376 MHz, $CDCl_3$) δ −76.3 (s, CF_3). MS

(ESI): *m/z* = 564.2 $[M + H]^+$. HRMS (APCI-ToF) *m/z*: $[M]^+$ calcd for $C_{28}H_{28}F_3NO_4S_2$: 563.1412, found: 563.1407.

7-(4-Methoxyphenyl)-8b-methyl-8-[(4-methylphenyl)sulfonyl]-2-[(trifluoromethyl)sulfonyl]-1,2,3,3a,4,4a,6a,8b-octahydrocyclopenta[3,4]pentaleno[1,6a-*c*]pyrrole (7c)

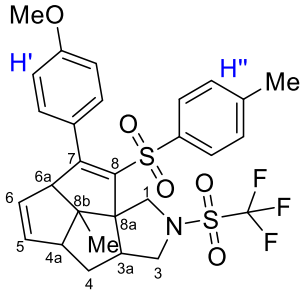

7c

Following the general procedure using 1-methoxy-4-[(4-methylbenzene-1-sulfonyl)ethynyl]benzene (68.3 mg, 0.24 mmol, 2.00 equiv) after 10 h, column chromatography (SiO_2, eluent: cyclohexane/ethyl acetate, 95:1 → 20:1) afforded the title compound (32 mg, 0.05 mmol, 46%) as a colorless solid. R_f = 0.37 (3:1 cyclohexane/ethyl acetate). Mp: 145−146 °C (ethanol). IR/cm^{-1} (ATR): 2957, 2902, 2840, 1602, 1387, 1226, 1183, 1144, 813, 615 cm^{-1}. ^{1}H NMR, COSY, NOESY (400 MHz, $CDCl_3$) δ 7.08 (d, *J* = 8.1 Hz, AA‘ part of AA‘BB‘ system, 2H, H-2”,6”), 6.98 (d, *J* = 8.1 Hz, BB‘ part of AA‘BB‘ system, 2H, H-3”,5”), 6.78 (d, *J* = 8.8 Hz, AA‘ part of AA‘BB‘ system, 2H, H-2‘,6’), 6.71 (d, *J* = 8.8 Hz, BB‘ part of AA‘BB‘ system, 2H, H-3‘,5’), 5.80 (dt, *J* = 5.7, 2.2 Hz, 1H, H-5), 5.29 (ddd, *J* = 5.7, 2.7, 1.5 Hz, 1H, H-6), 4.57 (d, *J* = 10.3 Hz, 1H, H-1_a), 4.02 (t, *J* = 9.4 Hz, 1H, H-3_a), 3.95 (d, *J* = 10.3 Hz, 1H, H-1_b), 3.81 (s, 3H, CH_3O–C4’), 3.78 (m, 1H, H-3a), 3.36 (t, *J* = 9.4 Hz, 1H, H-3_b), 3.33 (dd, *J* = 2.6, 1.9 Hz, 1H, H-6a), 2.96 (t, *J* = 8.3 Hz, 1H, H-4a), 2.32 (s, 3H, CH_3–C4”), 2.05 (ddd, *J*= 13.6, 8.0, 2.5 Hz, 1H, H-4_b), 1.66 (ddd, *J*= 13.6, 8.7, 6.0 Hz, 1H, H-4_a), 1.35 (s, 3H, CH_3–C-8b). ^{13}C{H} NMR, HSQC, HMBC (101 MHz, $CDCl_3$) δ 159.8 (C4’), 159.7 (C-8), 143.7 (C-4”), 138.5 (C-1”), 137.5 (C-7), 136.1 (C-5), 129.2 (C-2‘,6‘), 129.1 (C-3”,5”), 128.4 (C-6), 127.5 (C-2”,6”), 126.1 (C-1’), 113.4 (C-3‘,5‘), 120.4 (q, *J* = 323.6 Hz, CF_3), 71.1 (C-6a), 70.3 (C-8a), 61.1 (C-8b), 58.8 (C-4a), 55.5 (**C**H_3O–C4’), 52.8 (C-3a), 52.4 (C-3), 52.2 (C-1), 34.4 (C-4), 23.8 (**C**H_3–C-8b), 21.7 (**C**H_3–C4”). ^{19}F NMR (376 MHz, $CDCl_3$) δ −76.3 (s, CF_3). MS (ESI): *m/z* = 580.2 $[M + H]^+$. HRMS (APCI-ToF) *m/z*: $[M]^+$ calcd for $C_{28}H_{28}F_3NO_5S_2$: 579,1361, found: 579.1362.

8b-Methyl-8-[(4-methylphenyl)sulfonyl]-7-(thiophen-3-yl)-2-[(trifluoromethyl)sulfonyl]-1,2,3,3a,4,4a,6a,8b-octahydrocyclopenta[3,4]pentaleno[1,6a-*c*]pyrrole (7d)

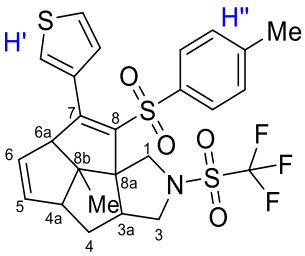

7d

Following the general procedure using 3-[(4-methylbenzene-1-sulfonyl)ethynyl]thiophene (62.6 mg, 0.24 mmol, 2.00 equiv) after 13 h, column chromatography (SiO_2, eluent: cyclohexane/ethyl acetate, 95:1 → 20:1) afforded the title compound (43.0 mg, 0.08 mmol, 65%) as a colorless solid. R_f = 0.50 (3:1 cyclohexane/ethyl acetate). Mp: 150−152 °C (ethanol). IR/cm^{-1} (ATR): 3058, 2954, 2871, 1597, 1387, 1226, 1188, 1144, 706, 621 cm^{-1}. ^{1}H NMR, COSY, NOESY (400 MHz, $CDCl_3$) δ 7.19 (dd, *J* = 3.0, 1.3 Hz, 1H, H-2‘), 7.16 (d, *J* = 8.3 Hz, AA‘ part of AA‘BB‘ system, 2H, H-2”,6“), 7.15 – 7.13 (m, 1H, H-5‘), 7.03 (d, *J* = 8.3 Hz, BB‘ part of AA‘BB‘ system, 2H, H-3”,5”), 6.66 (dd, *J* = 5.0, 1.3 Hz, 1H, H-4‘), 5.80 (ddd, *J* = 5.7, 2.7, 1.9 Hz, 1H, H-5), 5.33 (ddd, *J* = 5.7, 2.7, 1.4 Hz, 1H, H-6), 4.57 (d, *J* = 10.3 Hz, 1H, H-1$_a$), 4.02 (t, *J* = 9.4 Hz, 1H, H-3$_a$), 3.96 (d, *J* = 10.3 Hz, 1H, H-1$_b$), 3.78 (tdd, *J* = 8.7, 5.9, 2.5 Hz, 1H, H-3a), 3.37 (dd, *J* = 2.7, 1.9 Hz, 1H, H-6a), 3.36 (t, *J* = 9.4 Hz, 1H, H-3$_b$), 2.97 (t, *J* = 8.3 Hz, 1H, H-4a), 2.33 (s, 3H, **C**H$_3$–C4”), 2.04 (ddd, *J*= 13.6, 8.1, 2.5 Hz, 1H, H-4$_b$), 1.65 (ddd, *J*= 13.6, 8.6, 5.9 Hz, 1H, H-4$_a$), 1.36 (s, 3H, **C**H$_3$–C-8b).^{13}C{H} NMR, HSQC, HMBC (101 MHz, $CDCl_3$) δ 155.1 (C-8), 143.9 (C-4”), 138.3 (C-1”), 137.9 (C-7), 136.3 (C-5), 133.3 (C-3’), 129.2 (C-3”,5”), 128.5 (C-6), 127.4 (C-4‘), 127.2 (C-2”,6”), 126.0 (C-2’), 125.4 (C-5’), 120.42 (q, *J* = 323.1 Hz, CF_3), 70.5 (C-6a), 70.4 (C-8a), 61.1 (C-8b), 58.8 (C-4a), 52.8 (C-3a), 52.5 (C-3), 52.2 (C-1), 34.5 (C-4), 23.9 (**C**H$_3$–C-8b), 21.7 (**C**H$_3$–C4”).^{19}F NMR (376 MHz, $CDCl_3$) δ −76.1 (s, CF_3). MS (ESI): *m/z* = 556.1 $[M + H]^+$. HRMS (APCI-ToF) *m/z*: $[M]^+$ calcd for $C_{25}H_{24}F_3NO_4S_3$: 555.082, found: 555.0817.

7-(4-Fluorophenyl)-8b-methyl-8-[(4-methylphenyl)sulfonyl]-2-[(trifluoromethyl)sulfonyl]-1,2,3,3a,4,4a,6a,8b-octahydrocyclopenta[3,4]pentaleno[1,6a-*c*]pyrrole (7e)

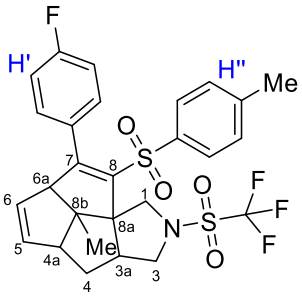

7e

Following the general procedure using 1-fluoro-4-[(4-methylbenzene-1-sulfonyl)ethynyl]benzene (65.5 mg, 0.24 mmol, 2.00 equiv) after 12 h, column chromatography (SiO_2, eluent: cyclohexane/ethyl acetate, 95:1 → 20:1) afforded the title compound (31.0 mg, 0.05 mmol, 65%) as a colorless solid. R_f = 0.53 (3:1 cyclohexane/ethyl acetate). Mp: 141−142 °C (ethanol). IR/cm^{-1} (ATR): 3048, 2954, 1598, 1387,1506, 1225, 1189, 1144, 736, 615 cm^{-1}. ^{1}H NMR, COSY, NOESY (400 MHz, $CDCl_3$) δ 7.08 (d, *J* = 8.3 Hz, AA‘ part of AA‘BB‘ system, 2H, H-2”,6”), 7.01 (d, *J* = 8.3 Hz, BB‘ part of AA‘BB‘ system, 2H, H-3”,5“), 6.92 – 6.82 (m, BB‘ part of AA‘BB‘ system, 2H, H-3‘,5’), 6.84 – 6.74 (m, AA‘ part of AA‘BB‘ system, 2H, H-2‘,6’), 5.83 (ddd, *J* = 5.7, 2.7, 1.9 Hz, 1H, H-5), 5.27 (ddd, *J* = 5.7, 2.7, 1.4 Hz, 1H, H-6), 4.58 (d, *J* = 10.4 Hz, 1H, H-1$_a$), 4.02 (t, *J* = 9.4 Hz, 1H, H-3$_a$), 3.97 (d, *J* = 10.4 Hz, 1H, H-1$_b$), 3.78 (tdd, *J* = 8.7, 5.7, 2.1 Hz, 1H, H-3a), 3.36 (t, *J* = 9.4 Hz, 1H, H-3$_b$), 3.32 (dd, *J* = 2.7, 1.9 Hz, 1H, H-6a), 2.98 (t, *J* = 8.3 Hz, 1H, H-4a), 2.34 (s, 3H, CH$_3$–C4’), 2.07 (ddd, *J*= 13.6, 8.3, 2.5 Hz, 1H, H-4$_b$), 1.66 (ddd, *J*= 13.6, 8.7, 6.0 Hz, 1H, H-4$_a$), 1.36 (s, 3H, CH$_3$–C-8b).^{13}C{H} NMR, HSQC, HMBC (101 MHz, $CDCl_3$) δ 162.7 (d, J_{CF} = 248.5 Hz, C-4’), 158.5 (C-8), 144.1 (C-4”), 138.5 (C-7), 138.3 (C-1”), 136.5 (C-5), 129.8 (d, J_{CF} = 3.3 Hz, C-

1'), 129.7 (d, J_{CF} = 8.3 Hz, C-2',6'), 129.2 (C-3",5"), 128.0 (C-6), 127.4 (C-2",6"), 120.4 (q, J = 323.6 Hz, CF_3), 115.1 (d, J_{CF} = 21.5 Hz, C-3',5'), 71.0 (C-6a), 70.4 (C-8a), 61.3 (C-8b), 58.8 (C-4a), 52.8 (C-3a), 52.4 (C-3), 52.2 (C-1), 34.4 (C-4), 23.8 (**C**H_3–C-8b), 21.7 (**C**H_3–C4"). ^{19}F NMR (376 MHz, $CDCl_3$) δ −76.3 (s, CF_3), -113.9 – (-114.0) (m, F–C-4'). MS (ESI): *m/z* = 568.2 $[M + H]^+$. HRMS (APCI-ToF) *m/z*: $[M]^+$ calcd for $C_{27}H_{25}F_4NO_4S_2$: 567.1161, found: 567.1158.

7-(4-Bromophenyl)-8b-methyl-8-[(4-methylphenyl)sulfonyl]-2-[(trifluoromethyl)sulfonyl]-1,2,3,3a,4,4a,6a,8b-octahydrocyclopenta[3,4]pentaleno[1,6a-*c*]pyrrole (7f)

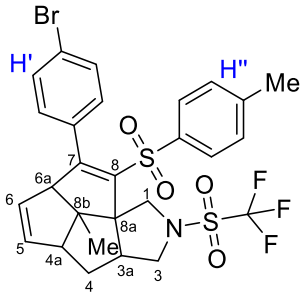

7f

Following the general procedure using 1-bromo-4-[(4-methylbenzene-1-sulfonyl)ethynyl]benzene (80.0 mg, 0.24 mmol, 2.00 equiv) after 10 h, column chromatography (SiO_2, eluent: cyclohexane/ethyl acetate, 95:1 → 20:1) afforded the title compound (32 mg, 0.05 mmol, 46%) as a colorless solid. R_f = 0.55 (3:1 cyclohexane/ethyl acetate). Mp: 150−152 °C (methanol). IR/cm^{-1} (ATR): 3057, 2954, 2871, 1597, 1387, 1301, 1259, 1188, 1144, 813, 615 cm^{-1}. ^{1}H NMR, COSY, NOESY (400 MHz, $CDCl_3$) δ 7.29 (d, J = 8.4 Hz, BB' part of AA'BB' system, 2H, H-3',5'), 7.09 (d, J = 8.4 Hz, AA' part of AA'BB' system, 2H, H-2",6"), 7.03 (d, J = 8.4 Hz, BB' part of AA'BB' system, 2H, H-3",5"), 6.67 (d, J = 8.4 Hz, AA' part of AA'BB' system, 2H, H-2',6'), 5.83 (ddd, J = 5.7, 2.7, 1.9 Hz, 1H, H-5), 5.27 (ddd, J = 5.7, 2.7, 1.4 Hz, 1H, H-6), 4.57 (d, J = 10.2 Hz, 1H, H-1_a), 4.02 (t, J = 9.4 Hz, 1H, H-3_a), 3.96 (d, J = 10.2 Hz, 1H, H-1_b), 3.78 (tdd, J = 8.6, 5.9, 2.3 Hz, 1H, H-3a), 3.36 (t, J = 9.4 Hz, 1H, H-3_b), 3.32 (dd, J = 2.7, 1.9 Hz, 1H, H-6a), 2.98 (t, J = 8.4 Hz, 1H, H-4a), 2.35 (s, 3H, CH_3–C4"), 2.06 (ddd, J= 13.6, 8.1, 2.5 Hz, 1H, H-4_b), 1.65 (ddd, J= 13.6, 8.7, 6.0 Hz, 1H, H-4_a), 1.35 (s, 3H, CH_3–C-8b). ^{13}C{H} NMR, HSQC, HMBC (101 MHz, $CDCl_3$) δ 158.0 (C-8), 144.3 (C-4"), 138.6 (C-7), 138.1 (C-1"), 136.6 (C-5), 132.9 (C-1'), 131.2 (C-3',5'), 129.4 (C-2',6'), 129.3 (C-3",5"), 127.9 (C-6), 127.5 (C-2",6"), 122.6 (C4'), 118.8 (q, J = 323.2 Hz, CF_3), 70.8 (C-6a), 70.4 (C-8a), 61.4 (C-8b), 58.8 (C-4a), 52.7 (C-3a), 52.4 (C-3), 52.1 (C-1), 34.4 (C-4), 23.8 (**C**H_3–C-8b), 21.7 (**C**H_3–C4"). ^{19}F NMR (376 MHz, $CDCl_3$) δ −76.3 (s, CF_3).MS (ESI): *m/z* = 628.1 $[M + H]^+$. HRMS (APCI-ToF) *m/z*: $[M]^+$ calcd for $C_{27}H_{25}BrF_3NO_4S_2$: 627.0360, found: 627.0349.

7-(4-Chlorophenyl)-8b-methyl-8-[(4-methylphenyl)sulfonyl]-2-[(trifluoromethyl)sulfonyl]-1,2,3,3a,4,4a,6a,8b-octahydrocyclopenta[3,4]pentaleno[1,6a-*c*]pyrrole (7g)

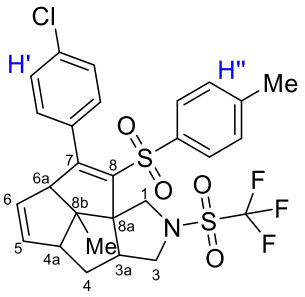

7g

Following the general procedure using 1-chloro-4-[(4-methylbenzene-1-sulfonyl)ethynyl]benzene (69.4 mg, 0.24 mmol, 2.00 equiv) after 10 h, column chromatography (SiO_2, eluent: cyclohexane/ethyl acetate, 95:1 → 20:1) afforded the title compound (42 mg, 0.07 mmol, 60%) as a colorless solid. R_f = 0.53 (3:1 cyclohexane/ethyl acetate). Mp: 148−149 °C (ethanol). IR/cm^{-1} (ATR): 3056, 2954, 2872, 1596, 1387, 1302, 1259, 1190, 1144, 813, 615 cm^{-1}. ^{1}H NMR, COSY, NOESY (400 MHz, $CDCl_3$) δ 7.14 (d, *J* = 8.5 Hz, BB‘ part of AA‘BB‘ system, 2H, H-3‘,5’), 7.10 (d, *J* = 8.3 Hz, AA‘ part of AA‘BB‘ system, 2H, H-2”,6”), 7.02 (d, *J* = 8.3 Hz, BB‘ part of AA‘BB‘ system, 2H, H-3“,5“),6.74 (d, *J* = 8.5 Hz, AA‘ part of AA‘BB‘ system, 2H, H-2‘,6’), 5.83 (ddd, *J* = 5.7, 2.7, 1.9 Hz, 1H, H-5), 5.27 (ddd, *J* = 5.7, 2.7, 1.4 Hz, 1H, H-6), 4.57 (d, *J* = 10.3 Hz, 1H, H-1_a), 4.02 (t, *J* = 9.4 Hz, 1H, H-3_a), 3.96 (d, *J* = 10.3 Hz, 1H, H-1_b), 3.78 (tdd, *J* = 8.5, 5.7, 2.3 Hz, 1H, H-3a), 3.36 (t, *J* = 9.4 Hz, 1H, H-3_b), 3.32 (dd, *J* = 2.7, 1.9 Hz, 1H, H-6a), 2.98 (t, *J* = 8.4 Hz, 1H, H-4a), 2.35 (s, 3H, CH_3–C4”), 2.06 (ddd, *J*= 13.7, 8.1, 2.5 Hz, 1H, H-4_b), 1.66 (ddd, *J*= 13.7, 8.7, 6.0 Hz, 1H, H-4_a), 1.36 (s, 3H, CH_3–C-8b). ^{13}C{H} NMR, HSQC, HMBC (101 MHz, $CDCl_3$) δ 158.1 (C-8), 144.2 (C-4”), 138.6 (C-7), 138.2 (C-1”), 136.6 (C-5), 134.5 (C4’), 132.4 (C-1’), 129.2(C-3”,5”), 129.2 (C-2‘,6‘), 128.2 (C-3‘,5‘), 127.9 (C-6), 127.5 (C-2”,6”), 118.8 (q, *J* = 320.5 Hz, CF_3), 70.9 (C-6a), 70.4 (C-8a), 61.4 (C-8b), 58.8 (C-4a), 52.7 (C-3a), 52.4 (C-3), 52.1 (C-1), 34.4 (C-4), 23.8 (**C**H_3–C-8b), 21.7 (**C**H_3–C4”). ^{19}F NMR (376 MHz, $CDCl_3$) δ −76.3 (s, CF_3).MS (ESI): *m/z* = 584.1 $[M + H]^+$. HRMS (ESI-ToF) *m/z*: $[M]^+$ calcd for $C_{27}H_{25}ClF_3NO_4S_2$: 583.0866, found: 583.0879.

8b-Methyl-7-phenyl-8-(phenylsulfonyl)-2-[(trifluoromethyl)sulfonyl]-1,2,3,3a,4,4a,6a,8b-octahydrocyclopenta[3,4]pentaleno[1,6a-*c*]pyrrole (7h)

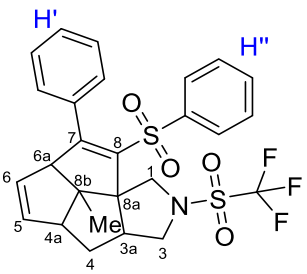

7h

Following the general procedure using [(benzenesulfonyl)ethynyl]benzene (57.8 mg, 0.24 mmol, 2.00 equiv) after 10 h, column chromatography (SiO_2, eluent: cyclohexane/ethyl acetate, 95:1 → 20:1)

afforded the title compound (47.0 mg, 0.09 mmol, 74%) as a colorless solid. R_f = 0.44 (3:1 cyclohexane/ethyl acetate). Mp: 154−156 °C (methanol). IR/cm^{-1} (ATR): 3059, 2953, 2872, 1593, 1259, 1225, 1190, 1145, 726, 619 cm^{-1}. ^{1}H NMR, COSY, NOESY (400 MHz, $CDCl_3$) δ 7.38 – 7.34 (m, 1H, H-4“), 7.25 – 7.20 (m, 1H, H_{Ar}), 7.19 – 7.12 (m, 6H, H_{Ar}), 6.79 – 6.76 (m, 2H, H-2’,6’), 5.82 (dt, *J* = 5.7, 2.3 Hz, 1H, H-5), 5.29 (ddd, *J* = 5.7, 2.7, 1.4 Hz, 1H, H-6), 4.61 (d, *J* = 10.2 Hz, 1H, H-1$_a$), 4.04 (t, *J* = 9.3 Hz, 1H, H-3$_a$), 4.00 (d, *J* = 10.2 Hz, 1H, H-1$_b$), 3.80 (tdd, *J* = 8.6, 5.9, 2.4 Hz, 1H, H-3a), 3.38 (t, *J* = 9.4 Hz, 1H, H-3$_b$), 3.36(dd, *J* = 2.7, 1.9 Hz, 1H, H-6a), 2.99 (td, *J* = 8.5,4.5 Hz, 1H, H-4a), 2.08 (ddd, *J*= 13.6, 8.1, 2.5 Hz, 1H, H-4$_b$), 1.69 (ddd, *J*= 13.6, 8.7, 6.0 Hz, 1H, H-4$_a$), 1.37 (s, 3H, CH_3–C-8b). ^{13}C{H} NMR, HSQC, HMBC (101 MHz, $CDCl_3$) δ 160.0 (C-8), 141.1 (C-1“), 137.6 (C-7), 136.2 (C-5), 133.8 (C-1’), 132.8 (C-4”), 128.5 (2C, C_{Ar}H), 128.3 (C-4’), 128.2 (C-6), 128.1(2C, C_{Ar}H), 127.7 (C-2‘,6‘), 127.4 (2C, C_{Ar}H), 120.4 (q, *J* = 324.0 Hz, CF_3), 71.2 (C-6a), 70.4 (C-8a), 61.3 (C-8b), 58.8 (C-4a), 52.7 (C-3a), 52.4 (C-3), 52.2 (C-1), 34.4 (C-4), 23.8 (**C**H_3–C-8b). ^{19}F NMR (376 MHz, $CDCl_3$) δ −76.3 (s, CF_3). MS (ESI): *m/z* = 536.1 [M + H]$^+$. HRMS (ESI-ToF) *m/z*: [M + Na]$^+$ calcd for $C_{26}H_{24}F_3NO_4S_2Na$: 535.1099, found: 535.1111.

8b-Methyl-8-(methylsulfonyl)-7-phenyl-2-[(trifluoromethyl)sulfonyl]-1,2,3,3a,4,4a,6a,8b-octahydrocyclopenta[3,4]pentaleno[1,6a-*c*]pyrrole (7i)

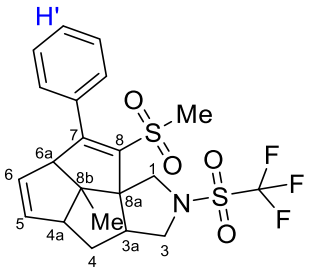

7i

Following the general procedure using [(methanesulfonyl)ethynyl]benzene (43.0 mg, 0.24 mmol, 2.00 equiv) after 10 h, reversed-phase column chromatography (SiO_2-C_{18}, eluent: water/acetonitrile, 99:1 → 80:20) afforded the title compound (35.0 mg, 0.07 mmol, 62%) as a colorless solid. R_f = 0.34 (3:1 cyclohexane/ethyl acetate). Mp: 182−184 °C (cyclohexane-chloroform). IR/cm^{-1} (ATR): 3056, 2956, 2873, 1594, 1259, 1225, 1189, 1134, 737, 619 cm^{-1}. ^{1}H NMR, COSY, NOESY (400 MHz, $CDCl_3$) δ 7.47 – 7.37 (m, 3H, H-3‘, 4‘, 5‘), 7.31 – 7.27 (m, 2H, H-2’,6’), 5.84 (ddd, *J* = 5.7, 2.6, 1.9 Hz, 1H, H-5), 5.37 (ddd, *J* = 5.7, 2.7, 1.5 Hz, 1H, H-6), 4.43 (d, *J* = 10.2 Hz, 1H, H-1$_a$), 3.95 (t, *J* = 9.4 Hz, 1H, H-3$_a$), 3.93 (d, *J* = 10.2 Hz, 1H, H-1$_b$), 3.58 (ddd, *J* = 5.7, 2.7, 1.5 Hz, 1H, H-3a), 3.56 – 3.53 (m, 1H, H-6a), 3.33 (t, *J* = 9.4 Hz, 1H, H-3$_b$), 3.02 – 2.96 (m, 1H, H-4a), 2.50 (s, 3H, SO_2CH_3), 2.03 (ddd, *J*= 13.6, 8.1, 2.7 Hz, 1H, H-4$_b$), 1.67 (ddd, *J*= 13.6, 8.5, 6.1 Hz, 1H, H-4$_a$), 1.39 (s, 3H, CH_3–C-8b). ^{13}C{H} NMR, HSQC, HMBC (101 MHz, $CDCl_3$) δ 158.7 (C-8), 136.7 (C-7), 136.4 (C-5), 134.0 (C-1’), 129.3 (C-4’), 128.8 (C-3‘,5‘), 128.2 (C-6), 127.7 (C-2‘,6‘), 120.4 (q, *J* = 323.5 Hz, CF_3), 71.1 (C-6a), 70.4 (C-8a), 61.3 (C-8b), 58.8 (C-4a), 52.8 (C-3a), 52.3 (C-3), 52.0 (C-1), 44.9 (SO_2**C**H_3), 34.4 (C-4), 23.8 (**C**H_3–C-8b). ^{19}F NMR (376 MHz, $CDCl_3$) δ −76.4 (s, CF_3). MS (ESI): *m/z* = 474.1 [M + H]$^+$. HRMS (ESI-ToF) *m/z*: [M + H]$^+$ calcd for $C_{21}H_{22}F_3NO_4S_2$: 474.1021, found: 474.1006.

8-(Ethylsulfonyl)-8b-methyl-7-phenyl-2-[(trifluoromethyl)sulfonyl]-1,2,3,3a,4,4a,6a,8b-octahydrocyclopenta[3,4]pentaleno[1,6a-*c*]pyrrole (7j)

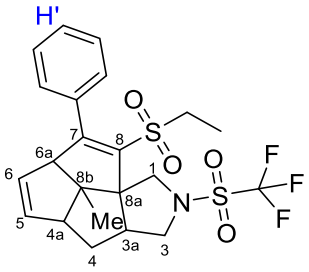

7j

Following the general procedure using [(ethanesulfonyl)ethynyl]benzene (46.4 mg, 0.24 mmol, 2.00 equiv) after 10 h, reversed-phase column chromatography (SiO_2-C_{18}, eluent: water/acetonitrile, 99:1 → 80:20) afforded the title compound (43.0 mg, 0.09 mmol, 74%) as a colorless solid. R_f = 0.39 (3:1 cyclohexane/ethyl acetate). Mp: 152−153 °C (cyclohexane-chloroform). IR/cm^{-1} (ATR): 3057, 2945, 2901, 1594, 1260, 1225, 1189, 1047, 728, 619 cm^{-1}. ^{1}H NMR, COSY, NOESY (400 MHz, $CDCl_3$) δ 7.45 – 7.38 (m, 3H, H-3‘, 4‘, 5‘), 7.32 – 7.28 (m, 2H, H-2’,6’), 5.85 (ddd, *J* = 5.7, 2.7, 1.8 Hz, 1H, H-5), 5.39 (ddd, *J* = 5.7, 2.7, 1.4 Hz, 1H, H-6), 4.39 (d, *J* = 10.3 Hz, 1H, H-1$_a$), 3.95 (t, *J* = 9.4 Hz, 1H, H-3$_a$), 3.90 (d, *J* = 10.3 Hz, 1H, H-1$_b$), 3.58 (ddt, *J* = 8.8, 5.4, 2.7 Hz, 1H, H-3a), 3.55 (dd, *J* = 2.7, 1.8 Hz, 1H, H-6a), 3.33 (t, *J* = 9.4 Hz, 1H, H-3$_b$), 3.07 – 2.94 (m, 1H, H-4a), 2.41 (qd, *J* = 7.4, 3.5 Hz, 1H, $SO_2C\mathbf{H_2}CH_3$), 2.03 (ddd, *J*= 13.6, 8.1, 2.7 Hz, 1H, H-4$_b$), 1.68 (ddd, *J*= 13.6, 8.5, 6.0 Hz, 1H, H-4$_a$), 1.39 (s, 3H, CH_3–C-8b), 2.50 (t, *J* = 7.4 Hz, 1H, $SO_2CH_2C\mathbf{H_3}$). ^{13}C{H} NMR, HSQC, HMBC (101 MHz, $CDCl_3$) δ 158.5 (C-8), 136.4 (C-5), 134.8 (C-7), 134.0 (C-1’), 129.3 (C-4’), 128.8 (C-3‘,5‘), 128.2 (C-6), 127.6 (C-2‘,6‘), 120.4 (q, *J* = 323.7 Hz, CF_3), 71.2 (C-6a), 70.3 (C-8a), 61.3 (C-8b), 58.8 (C-4a), 52.7 (C-3a), 52.3 (C-3), 52.1 (C-1), 49.6 (SO_2 **C**H_2CH_3), 34.4 (C-4), 23.9 (**C**H_3–C-8b), 7.1 (SO_2 CH_2**C**H_3). ^{19}F NMR (376 MHz, $CDCl_3$) δ −76.3 (s, CF_3). MS (ESI): *m/z* = 488.1 $[M + H]^+$. HRMS (ESI-ToF) *m/z*: $[M]^+$ calcd for $C_{22}H_{24}F_3NO_4S_2$: 487.1099, found: 487.1091.

Preparation of 8b-methyl-7-phenyl-2-[(trifluoromethyl)sulfonyl]-1,2,3,3a,4,4a,6a,8b-octahydrocyclopenta[3,4]pentaleno[1,6a-*c*]pyrrole (13)

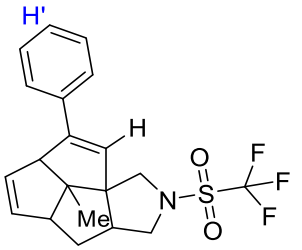

13

Following a procedure published by Tam et al,[21] 5% sodium amalgam (149.5 mg, 0.325 mmol, 9.0 equiv) was added to a solution of 8b-methyl-8-[(4-methylphenyl)sulfonyl]-7-phenyl-2-[(trifluoromethyl)sulfonyl]-1,2,3,3a,4,4a,6a,8b-octahydrocyclopenta[3,4]pentaleno[1,6a-*c*]pyrrole (**7a**) (19.9 mg, 0.036 mmol, 1.0 equiv) and sodium hydrogen phosphate (30.7 mg, 0.216 mmol, 6.0 equiv) in

methanol (4 mL) at 0 °C under nitrogen atmosphere. After 1 h, TLC indicated full consumption of **7a** and the reaction mixture was filtrated over silica. The solvent was removed under reduced pressure and the residue purified by flash column chromatography (SiO_2, eluent: cyclohexane/ethyl acetate, 98:2) to afford the desired product (6.9 mg, 0.017 mmol, 47%) as colorless solid. R_f = 0.65 (4:1 cyclohexane/ethyl acetate). Mp: 118 − 119 °C (chloroform). IR/cm^{-1} (ATR): 3051, 2952, 2896, 1385, 1226, 1182, 1005, 730, 626, 583 cm^{-1}. ^{1}H NMR, COSY, NOESY (600 MHz, $CDCl_3$) δ 7.47 – 7.45 (m, 2H, H-2‘, 6‘), 7.35 (dd, *J* = 8.5, 7.0 Hz, 2H, H-3’, 5’), 7.30 – 7.27 (m, 1H, H-4’), 5.81 (dt, *J* = 5.8, 2.1 Hz, 1H, H-6), 5.74 (d, *J* = 1.6 Hz, 1H, H-8), 5.63 (dt, *J* = 5.8, 2.2 Hz, 1H, H-5), 3.83 (d, *J* = 10.6 Hz, 1H, H-1$_b$), 3.82 (d, *J* = 9.0 Hz, 1H, H-3$_a$), 3.72 (d, *J* = 2.1 Hz, 1H, H-6a), 3.56 (d, *J* = 10.6 Hz, 1H, H-1$_a$), 3.37 – 3.34 (m, 1H, H-3$_b$), 2.91 (ddd, *J* = 8.4, 6.3, 2.2 Hz, 1H, H-4a), 2.77 (ddd, *J* = 13.3, 7.7, 5.5 Hz ,1H, H-3a), 1.90 (ddd, *J* = 13.0, 7.7, 4.9 Hz 1H, H-4$_b$), 1.60 (dt, *J* = 13.0, 6.3 Hz, 1H, H-4$_a$), 1.34 (s, 3H, CH_3–C-8b). ^{13}C{H} NMR, HSQC, HMBC (151 MHz, $CDCl_3$) δ 146.2 (C-7), 134.7 (C-1’), 134.0 (C-5), 130.7 (C-6), 128.7 (C-3’,5’), 128.1 (C-4‘), 126.3 (C-8), 126.2 (C-2‘,6‘), 120.5 (q, *J* = 323.8 Hz, CF_3), 68.1 (C-8a), 66.4 (C-6a), 61.4 (C-8b), 58.1 (C-4a), 53.6 (C-1), 52.9 (C-3a), 52.6 (C-3), 35.3 (C-4), 23.6 (**C**H_3–C-8b). ^{19}F NMR (377 MHz, $CDCl_3$) δ −76.2 (s, CF_3). MS (ESI): *m/z* = 396.1 $[M + H]^+$. HRMS (APCI) *m/z*: $[M]^{\bullet+}$ calcd for $C_{20}H_{20}F_3NO_2S$: 395.1162, found: 395.1153.

Synthesis of (1-Cyclopropylvinyl)benzene (8)

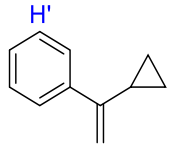

8

To a solution cooled to -78 °C of methyltriphenylphosphonium bromide (1.79 g, 5.0 mmol, 2.00 equiv) in dry THF (15 mL) nBuLi (2.0 mL, 2.5M, 5 mmol, 2.00 equiv) was added dropwise, after which the cooling was removed. To this mixture cyclopropyl phenyl ketone (0.37 g, 2.5 mmol, 1.00 equiv) dissolved in dry THF (1.5 mL) was added dropwise and the reaction was left to stir for 3 hours. After this time, brine was added and the phases were separated. The aqueous phase was extracted with pentane (3x 10 mL), and the combined organic phases were dried over Na_2SO_4, filtered onto celite and concentrated under reduce pressure. The residue was purified by flash chromatography (SiO_2, eluent: cyclohexane/ethyl acetate, 100:0 → 98:1) and **8** was isolated as a colorless liquid (0.30 g, 2.1 mmol, 87%). R_f = 0.69 (50:1 cyclohexane/ethyl acetate). ^{1}H NMR, COSY (400 MHz, $CDCl_3$): δ 7.61 (d, *J* = 7.3 Hz, 2H, H-2’,6’), 7.39 – 7.32 (m, 2H, H-3‘, 5‘), 7.32 – 7.27 (m, 1H, H-4‘), 5.29 (s, 1H, -C=C**H$_a$**H), 4.95 (s, 1H, -C=C**H$_b$**H), 1.67 (dddd, *J* = 8.3, 6.8, 5.3, 4.0 Hz, 1H, H-1), 0.91 – 0.81 (m, 2H, H-2), 0.63-0.59 (m, 2H, H-3). ^{13}C NMR, HSQC, HMBC (101 MHz, $CDCl_3$): δ 149.5 (-**C**=CH_2), 141.8 (C-1’), 128.3 (C-3‘,5‘), 127.6 (C-4‘), 126.3 (C-2‘,6‘), 109.2(-C=**C**H_2), 15.8 (C-1), 6.8 (C-1,2). MS (EI): m/z = 144.1 $[M]^+$. These data are consistent with those previously reported.[22]

Synthesis of ((2-Phenyl-3-(1-phenylvinyl)cyclopent-1-en-1-yl)sulfonyl)benzene (9)

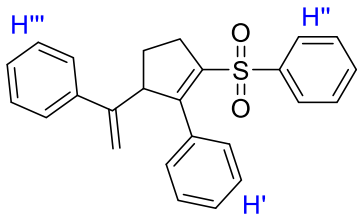

9

Following the general procedure for the preparation of **7** a mixture of (1-cyclopropylvinyl)benzene **8** (35.0 mg, 0.24 mmol, 1.00 equiv) and ((phenylethynyl)sulfonyl)benzene (117.6 mg, 0.49 mmol, 2.00 equiv) was irradiated for 2.5 h. After column chromatography (SiO_2, eluent: cyclohexane/ethyl acetate, 95:1 → 20:1), the title compound (38.0 mg, 0.01 mmol, 41%) was isolated as a colorless oil. R_f = 0.55 (3:1 cyclohexane/ethyl acetate). IR/cm^{-1} (ATR): 3058, 2965, 2861, 1378, 1445, 1319, 1305, 1149, 1082, 904 cm^{-1}. ^{1}H NMR, COSY, NOESY (400 MHz, acetone-d_6) δ 7.72 – 7.68 (m, 2H, H-2”,6”), 7.67 – 7.64 (m, 1H, H-4”), 7.56 – 7.51 (m, 2H, H-3”,5”), 7.32 – 7.22 (m, 10H, H-2’,3’,4’,5’,6’/ H-2”,3”,4”,5”,6”), 5.28 (s, 1H, -C=C**H$_a$**H), 5.01 (s, 1H, -C=C**H$_b$**H), 4.38 (ddt, *J* = 9.1, 4.4, 2.0 Hz, 1H, H-3), 2.87 – 2.83 (m, 2H, H-5$_{ab}$), 2.44 (dtd, *J* = 13.0, 9.1, 7.1 Hz, 1H, H-4$_a$), 1.88 (ddt, *J* = 13.0, 8.4, 4.9 Hz, 1H).^{13}C{H} NMR, HSQC, HMBC (101 MHz, acetone-d_6) δ 156.2 (C-1), 149.6 (-**C**=CH$_2$), 142.2 (C-1”), 141.8 (C-1’”), 140.7 (C-2), 135.3 (C-1’), 134.2 (C-4”), 129.9 (C-3”,5”), 129.7 (2C, C$_{Ar}$H), 129.2 (2C, C$_{Ar}$H), 129.0 (1C, C$_{Ar}$H), 128.5 (1C, C$_{Ar}$H), 128.(C-2”,6”), 128.3 (2C, C$_{Ar}$H), 127.2 (2C, C$_{Ar}$H), 115.0 (-C=**C**H$_2$), 58.7 (C-3), 30.6 (C-5), 30.4 (C-4). MS (ESI): *m/z* = 387.1 [M + H]$^+$. HRMS (ESI-ToF) *m/z*: [M]$^+$ calcd for $C_{25}H_{22}O_2S$: 386.1341, found: 386.1354.

Preparation of 1-((Allyloxy)methyl)-2-methylbenzene (10)

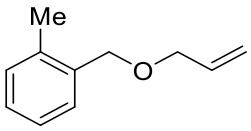

10

To a suspension of sodium hydride (0.11 g, 4.50 mmol, 1.10 equiv) in dry THF (5.31 mL) was added a solution of benzyl alcohol (0.50 g, 4.09 mmol, 1.00 equiv) in dry THF (0.8 mL). After the reaction was stirred at room temperature for two hours under an inert atmosphere, allyl bromide (0.39 mL, 4.50 mmol, 1.10 equiv) was added dropwise and the resulting suspension was stirred overnight at room temperature. The solvent was partially removed in vacuo and saturated ammonium chloride solution (5 mL) was added. The aqueous phase was extracted with ethyl acetate (3 x 50 mL) and the combined organic extracts were dried over Na_2SO_4, filtered, and concentrated under reduced pressure. The residue was purified by flash chromatography (SiO_2, eluent: cyclohexane/ethyl acetate, 100:0 → 95:1) to give **10** as a colorless oil (0.59 g, 3.64 mmol, 89%). R_f = 0.56 (10:1 cyclohexane/ethyl acetate). IR/cm^{-1} (ATR): 3021, 2856, 1460, 1356, 1123, 1080, 989, 923, 764, 743 cm^{-1}. 1H NMR, COSY (400 MHz, $CDCl_3$) δ 7.36 – 7.34 (m, 1H, H-6), 7.25 – 7.14 (m, 3H, H-3, 4, 5), 5.99 (ddt, *J* = 17.2, 10.4, 5.6 Hz, 1H, -CH=), 5.34 (dq, *J* = 17.2, 1.7 Hz, 1H, =C**H$_{trans}$**), 5.23 (dq, *J* = 10.4, 1.4 Hz, 1H, =C**H$_{cis}$**), 4.54 (s,

2H, -CH_2-), 4.06 (dt, *J* = 5.6, 1.4 Hz, 2H, -C**H$_2$**-CH=), 2.32 (s, 3H, -CH_3). ^{13}C{H} NMR, HSQC, HMBC (101 MHz, $CDCl_3$) δ 136.8 (C-1), 136.3 (C-2), 135.0 (-CH=), 130.3 ($C_{Ar}H$), 128.7 (C-6), 127.9 ($C_{Ar}H$), 125.9 ($C_{Ar}H$), 117.2 (=CH_2), 71.4 (-**C**H_2-CH=), 70.6 (-CH_2-), 18.9(-CH_3). MS (EI): m/z = 162.1 $[M]^+$. These data are consistent with those previously reported.[23]

Preparation of 6c-methyl-3,3a,4,4a,6a,6c-hexahydrocyclopropa[1,6]pentaleno[1,2-*c*]furan (11)

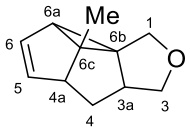

11

Following the general procedure for the *meta* photoadduct synthesis, a mixture of 1-((allyloxy)methyl)-2-methylbenzene **10** (100 mg, 0.62 mmol) and 10 mL of anhydrous cyclohexane was irradiated for 4 h. After column chromatography (SiO_2, eluent: cyclohexane/ethyl acetate, 100:0 → 50:1), a 7:1 colorless oil mixture of two isomeric *meta*-photocycloadducts was isolated (38.5 mg, 0.24 mmol, 39%).[24] R_f = 0.38 [$KMnO_4$] (10:1 cyclohexane/ethyl acetate). IR/cm^{-1} (ATR): 2922, 2851, 1448, 1378, 1360, 1065, 1016, 914, 795, 735 cm^{-1}. Spectroscopic data are those of the major isomer: ^{1}H NMR, COSY, NOESY (400 MHz, $CDCl_3$) δ 5.67 (dd, *J* = 5.5, 2.3 Hz, 1H, H-6), 5.45 (ddd, *J* = 5.5, 2.4, 0.8 Hz, 1H, H-5), 3,88 (t, *J* = 9.0 Hz, 1H, H-3_a), 3.67 – 3.65 (m, 1H, H-3_b), 3.64 – 3.62 (m, 2H, H-$1_{a,b}$), 2,98 (dd, *J* = 4.1, 1.9 Hz, 1H, H-4a), 2.40 – 2.32 (m, 1H, H-3a), 1.86 – 1.79 (m, 2H, H-4_{ab}), 1.70 – 1.63 (m, 1H, H-6a), 1.29 (s, 3H, CH_3–C-6b). ^{13}C{H} NMR, HSQC, HMBC (101 MHz, $CDCl_3$) δ 133.3 (C-5), 129.1 (C-6), 73.7 (C-3), 67.5 (C-1), 57.9 (C-4a), 51.1 (C-6b), 46.0 (C-6b), 45.5 (C-4), 42.9 (C-3a), 38.2 (C-6a), 13.8 (**C**H_3–C-6b). MS (EI): *m/z* = 162.1 $[M]^+$. HRMS (API) *m/z*: $[M]^+$ calcd. for $C_{11}H_{14}O$: 162.1045, found: 162.1041. These data are consistent with those previously reported.[24]

8b-methyl-8-[(4-methylphenyl)sulfonyl]-7-phenyl-3,3a,4,4a,6a,8b-hexahydrocyclopenta[3,4]pentaleno[1,6a-*c*]furan (12)

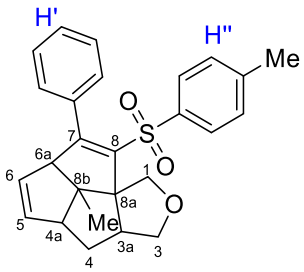

12

Following the general procedure for the preparation of **7** a mixture of the *meta* photoadduct **11** (25.0 mg, 0.15 mmol, 1.00 equiv) and 1-methyl-4-(phenylethynylsulfonyl)benzene (79.0 mg, 0.31 mmol, 2.00 equiv) was irradiated for 10 h. After column chromatography (SiO_2, eluent: cyclohexane/ethyl acetate, 99:1 → 93:1), the title compound (22.3 mg, 0.05 mmol, 39%) was isolated as a colorless solid. R_f = 0.40 (3:1 cyclohexane/ethyl acetate). Mp: 180−182 °C (cyclohexane-ethyl acetate). IR/cm^{-1} (ATR): 3056, 2924, 2867, 1594, 1311, 1144, 1086, 920, 720, 581 cm^{-1}. ^{1}H NMR, COSY, NOESY (400 MHz, $CDCl_3$) δ 7.25 – 7.20 (m, 1H, H-4'), 7.18 – 7.12 (m, *J* = 7.5 Hz, 2H, H-3', 5'), 7.09 (d, *J* = 8.4 Hz, AA' part of

AA‘BB‘ system, 2H, H-2“,6“), 6.96 (d, *J* = 8.4 Hz, BB‘ part of AA‘BB‘ system, 2H, H-3“,5“), 6.85 – 6.77 (m, 2H, H-2’,6’), 5.79 (dt, *J* = 5.7, 2.3 Hz, 1H, H-5), 5.32 (ddd, *J* = 5.7, 2.7, 1.5 Hz, 1H, H-6), 4.65 (d, *J* = 8.9 Hz, 1H, H-1_a), 4.26 (t, *J* = 8.1 Hz, 1H, H-3_a), 4.16 (d, *J* = 8.9 Hz, 1H, H-1_b), 3.68 (tdd, *J* = 7.8, 7.3, 2.4 Hz, 1H, H-3a), 3.62 (t, *J* = 8.1 Hz, 1H, H-3_b), 3.30 (t, *J* = 2.3 Hz, 1H, H-6a), 2.93 (m, 1H, H-4a), 2.31 (s, 3H, CH_3–C4”), 2.03 (ddd, *J*= 13.5, 8.4, 2.5 Hz, 1H, H-4_b), 1.67 (ddd, *J*= 13.5, 8.2, 6.5 Hz, 1H, H-4_a), 1.33 (s, 3H, CH_3–C-8b). ^{13}C{H} NMR, HSQC, HMBC (101 MHz, $CDCl_3$) δ 159.6 (C-8), 143.3 (C-4”), 139.0 (C-1”), 138.5 (C-7), 136.8(C-5), 134.8 (C-1’), 129.0 (C-3”,5”), 128.0 (C-6), 127.8 (C-3‘,4’,5‘),127.8 (C-2‘,6‘), 127,5 (C-2”,6”), 73.0 (C-3), 72.3 (C-8a), 71.5 (C-6a), 71.3 (C-1), 61.3 (C-8b), 59.5 (C-4a), 54.1 (C-3a), 35.2 (C-4), 23.8 (**C**H_3–C-8b), 21.6 (**C**H_3–C4”). MS (ESI): *m/z* = 419.1 $[M + H]^+$. HRMS (ESI-ToF) *m/z*: $[M]^+$ calcd for $C_{26}H_{26}O_3S$: 418.1603, found: 418.1600.

Preparation of ethyl 5,5-dimethyl-2-[(4-methylphenyl)sulfonyl]-4-(2-methylprop-1-en-1-yl)-3-phenylcyclopent-2-ene-1-carboxylate (14)

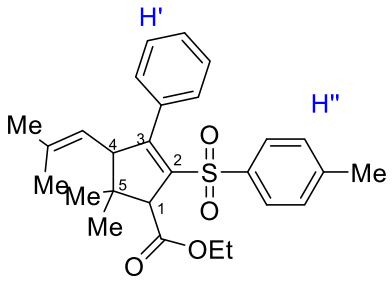

14

Following the general procedure for the preparation of **7**, a mixture of ethyl 2,2-dimethyl-3-(2-methyl-1-propenyl)cyclopropane-1-carboxylate (120.0 mg, 0.611 mmol, 1.0 equiv), 1-methyl-4-(phenylethynylsulfonyl)benzene (313.2 mg, 1.222 mmol, 2.0 equiv) and $[Ir(ppy)_2(dtbbpy)]PF_6$ (11.0 mg, 0.01 mmol, 0.02 equiv) in methanol (4.1 mL, c = 0.15 M) was irradiated overnight. The full consumption of the starting material was confirmed via TLC and HPLC/ESI-MS. The crude product was dissolved in 1 mL of acetonitrile and 0.2 mL of this solution purified via preparative HPLC (Macherey-Nagel NUCLEODUR C18 HTec, oven temperature: 40 °C, eluent: water (+0.1% formic acid)/acetonitrile, 30:70) yielding the title compound (6.7 mg, 0.015 mmol, 12%) as a mixture of diastereomers (*cis*/*trans*, 2:3, based on ^{1}H NMR) as a colorless oil. Based on the 2D NMR data, the signal sets are denoted individually.

R_f = 0.36 (10:1 cyclohexane/ethyl acetate). IR/cm^{-1} (ATR): 2969, 2930, 1729, 1444, 1313, 1302, 1146, 768, 700, 583 cm^{-1}. ^{1}H NMR, COSY, NOESY (600 MHz, $CDCl_3$, *trans*-**14**) δ 7.19 – 7.16 (m, 2H, H-2‘‘, 6‘‘), 7.09 – 7.06 (m, 3H, H-3’,4’,5’), 6.93 (d, *J* = 8.0 Hz, 2H, H-3’’,5’’), 6.80 (d, *J* = 7.0 Hz, 2H, H-2’,6’), 4.62 – 4.60 (m, 1H, $(CH_3)_2$C=C**H**), 4.27 – 4.23 (m, 1H, H-4), 4.22 – 4.12 (m, 2H, O–C**H**$_2$), 2.72 (d, *J* = 9.4 Hz, 1H, H-1), 2.29 (s, 3H, C4’’-C**H**$_3$), 1.78 (s, 3H, C5-C_a**H**$_3$), 1.46 (s, 3H, C5-C_b**H**$_3$), 1.42 (d, *J* = 1.4 Hz, 3H, C=C(C_a**H**$_3C_bH_3$)), 1.38 (d, *J* = 1.4 Hz, 3H, C=C($C_aH_3C_b$**H**$_3$)), 1.34 – 1.29 (m, 3H, OCH_2–C**H**$_3$). ^{13}C{H} NMR, HSQC, HMBC (151 MHz, $CDCl_3$, *trans*-**14**) δ 171.9 (**C**$O_2CH_2CH_3$), 155.3 (C-2), 144.8 (C-3), 143.1 (C-4’’), 139.0 (C-1’’), 136.3 ($(CH_3)_2$**C**=CH), 128.8 (C-3’’,5’’), 128.1 (C-2‘,5’), 127.5 (C-2’’,6’’), 127.4 (C-3’,4’,5’), 123.3 (C4–**C**H), 61.9 (C–1), 61.0 (CO_2-**C**H_2), 51.1 (C-5), 49.9 (C-4), 28.2 (C5–**C**$_aH_3$), 25.8 (C=C(**C**$_aH_3C_bH_3$)), 22.6 (C5–**C**$_bH_3$), 21.6 (C4’’–**C**H_3), 18.1 (C=C(C_aH_3**C**$_bH_3$)), 14.5 (OCH_2–**C**H_3). ^{1}H

NMR, COSY, NOESY (600 MHz, $CDCl_3$, *cis*-**14**) δ 7.38 – 7.36 (m, 2H, H-2'',6''), 7.15 – 7.12 (m, 3H, H-3',4',5'), 6.97 – 6.96 (m, 2H, H-2',6'), 6.96 (d, *J* = 9.1 Hz, 2H, H-3'',5''), 4.71 (dp, *J* = 10.8, 1.4 Hz, 1H, $(CH_3)_2C{=}C\mathbf{H}$), 4.22 – 4.12 (m, 2H, O–C$\mathbf{H}_2$), 3.97 (dd, *J* = 10.8, 1.7 Hz, 1H, H-4), 3.75 (d, *J* = 1.7 Hz, 1H, H-1), 2.28 (s, 3H, C4''-C$\mathbf{H}_3$), 1.52 (d, *J* = 1.4 Hz, 3H, C=C($C_a\mathbf{H}_3C_bH_3$)), 1.50 (d, *J* = 1.4 Hz, 3H, C=C($C_aH_3C_b\mathbf{H}_3$)), 1.34 – 1.29 (m, 3H, OCH_2–C$\mathbf{H}_3$), 1.11 (s, 3H, C5-$C_a\mathbf{H}_3$), 1.07 (s, 3H, C5-$C_b\mathbf{H}_3$). $^{13}C\{H\}$ NMR, HSQC, HMBC (151 MHz, $CDCl_3$, *cis*-**14**) δ 171.9 (**C**$O_2CH_2CH_3$), 159.3 (C-2), 143.5 (C-3), 143.1 (C-4''), 137.8 (C-2), 137.4 (C-1''), 137.4 ($(CH_3)_2$**C**=CH), 128.8 (C-3'',5''), 128.2 (C-2'',5''), 128.1 (C-2'',6''), 127.5 (C-3',4',5'), 61.0 (CO_2-**C**H_2), 62.3 (C-1), 57.9 (C-4), 46.6 (C-5), 26.1 (C=C(**C**$_aH_3C_bH_3$)), 25.2 (C5–**C**$_aH_3$), 23.4 (C5–**C**$_bH_3$), 18.0 (C=C(C_aH_3**C**$_bH_3$)), 14.5 (OCH_2–**C**H_3). MS (ESI): *m/z* = 453.2 $[M + H]^+$. HRMS (ESI) *m/z*: $[M+Na]^+$ calcd for $C_{27}H_{32}NaO_4S$: 475.1913, found: 475.1908.

Preparation of (*3aR,6R,7aS*)-1,1,6-trimethyl-3-phenyl-2-tosyl-3a,6,7,7a-tetrahydro-1*H*-indene (15)

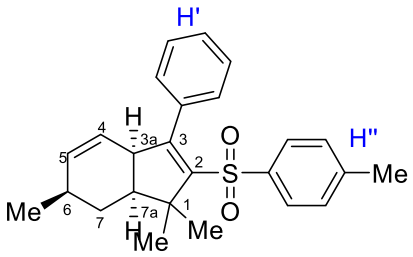

15

Following the general procedure for the preparation of **7** a mixture of (1*S*,3*R*)-*cis*-4-carene (120.0 mg, 0.881 mmol, 1.0 equiv), 1-methyl-4-(phenylethynylsulfonyl)benzene (451.6 mg, 1.762 mmol, 2.0 equiv) and $[Ir(ppy)_2(dtbbpy)]PF_6$ (16.5 mg, 0.018 mmol, 0.02 equiv) in methanol (5.8 mL, c = 0.15 M) was irradiated overnight. The full consumption of the starting material was confirmed via TLC and HPLC/ESI-MS. The crude product was dissolved in 1 mL of acetonitrile and 0.2 mL of this solution was purified via preparative HPLC (ACE C18-PFP, oven temperature: 40 °C, eluent: water (+0.1% formic acid)/acetonitrile, 35:65) yielding the title compound (18.4 mg, 0.047 mmol, 27%) as a colorless solid.

R_f = 0.43 (10:1 cyclohexane/ethyl acetate). Mp: 116 − 117 °C (chloroform). IR/cm^{-1} (ATR): 3022, 2955, 1311, 1300, 1142, 1087, 812, 698, 665, 591 cm^{-1}. ^1H NMR, COSY, NOESY (600 MHz, $CDCl_3$) δ 7.29 – 7.28 (m, 2H, H-2'',6''), 7.25 – 7.23 (m, 1H, H-4'), 7.20 – 7.18 (m, 2H, H-3',5'), 7.16 – 7.14 (t, *J* = 7.4 Hz, 2H, H-2',6'), 6.98 (d, *J* = 8.1 Hz, 2H, H-3'',5''), 5.52 –5.50 (m, 1H, H-5), 5.09 (ddd, *J* = 10.0, 4.7, 2.7 Hz, 1H, H-4), 3.57 (ddt, *J* = 6.9, 4.7, 2.6 Hz, 1H, H-3a), 2.31 (s, 3H, C4''–C$\mathbf{H}_3$), 2.08 – 2.04 (m, 1H, H-7a), 2.04 – 2.00 (m, 1H, H-6), 1.73 (m, 1H, H-7_a), 1.50 (s, 3H, C1–$C_b\mathbf{H}_3$), 1.45 (s, 3H, C1–$C_a\mathbf{H}_3$), 0.96 (d, *J* = 7.1 Hz, 3H, C6–$C_a\mathbf{H}_3$), 0.94 (d, *J* = 11.9 Hz, 1H, H-7_b). $^{13}C\{H\}$ NMR, HSQC, HMBC (151 MHz, $CDCl_3$) δ 155.2 (C-3), 143.9 (C-2), 143.0 (C-4''), 139.4 (C-1''), 136.5 (C-5), 134.7 (C-1'), 128.9 (C-3'',5''), 127.7 (C-2',4',6'), 127.6 (C-2'',6''), 124.0 (C-4), 50.3 (C-1), 49.3 (C-7a), 48.1 (C-3a), 31.1 (C-7), 30.0 (C-6), 27.2 (C1-**C**$_aH_3$), 22.1 (C1-**C**$_bH_3$), 21.8 (C6-**C**H_3), 21.3 (C4''–**C**H_3). MS (ESI): *m/z* = 393.3 $[M + H]^+$. HRMS (ESI) *m/z*: $[M+Na]^+$ calcd for $C_{25}H_{28}O_2S$: 415.1702, found: 415.1695. $[\alpha]_D^{20}$ = –17.8 (*c* = 1.84, ethyl acetate).

Non-catalyzed cycloaddition (sensitization protocol). Preparation of the tetracycle 7a.

In an oven-dried quartz tube under nitrogen atmosphere was charged the *meta* photoadduct **4** (35.0 mg, 0.12 mmol, 1.00 equiv), 1-methyl-4-(phenylethynylsulfonyl)benzene (61.2 mg, 0.24 mmol, 2.00 equiv), and methanol (0.8 mL, c = 0.15 M). The solution was degassed for 15 min and placed in a Rayonet photoreactor. The vessel was irradiated (λ_{max} = 254 nm, 16 × 8 W) at room temperature for 14 h. After removal of the solvent under reduced pressure, column chromatography (SiO_2, eluent: cyclohexane/ethyl acetate, 95:1 → 20:1) afforded the title compound (17.7 mg, 0.03 mmol, 27%) as a colorless solid.

Synthesis of the tetracycle 7a using PC III

The *meta* photoadduct **4** (35.0 mg, 0.12 mmol, 1.00 equiv), alkynyl sulfone **6** (61.2 mg, 0.24 mmol, 2.00 equiv), $[Ir(dF(CF_3)ppy)_2(dtbbpy)]PF_6$ (2.7 mg, 0.002 mmol, 0.02 equiv) and methanol (0.8 mL, c = 0.15 M) were loaded in an oven-dried Schlenk tube (10 mL) under nitrogen atmosphere, and the mixture was degassed and then placed in front of two blue LEDs 440 nm (see the materials section) at a distance of 5 cm. After 10 h, the resultant solution was concentrated and purified by flash column chromatography (SiO_2, eluent: cyclohexane/ethyl acetate, 95:1 → 20:1) to afford **7a** (56.5 mg, 0.10 mmol, 86%) as a colorless solid.

5. X-RAY CRYSTAL STRUCTURE DETERMINATION

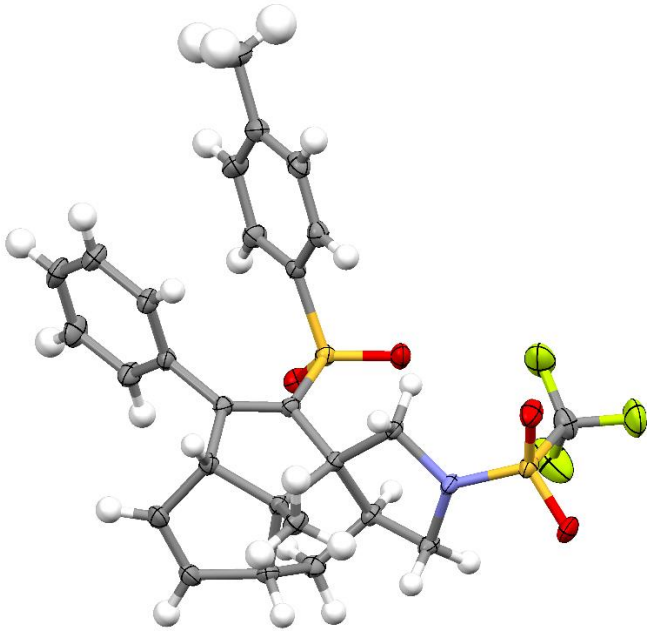

Figure S7. Molecular structure of compound **7a** in the solid state (ORTEP-ellipsoids, C: black, H: gray, N: blue, O: red, S: yellow, F: green). **CCDC Number: 2112151**.

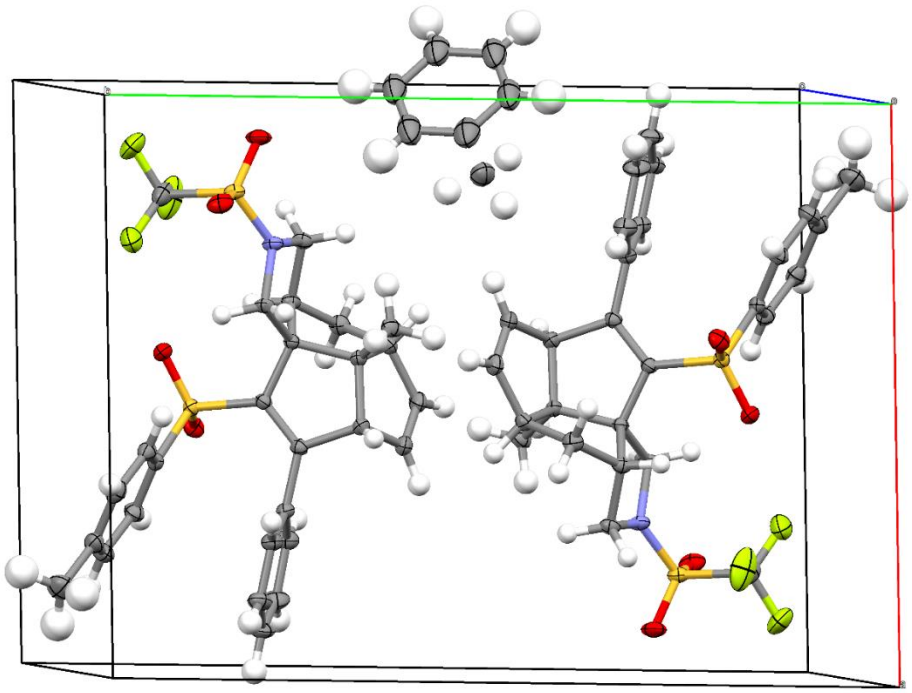

Figure S8. Cell unit of tetracycle **7a**.

Table S8. Crystal structure determination of compound **7a**.

Empirical formula	$C_{61}H_{60}F_6N_2O_8S_4$	
moiety formula	$2(C_{27}H_{26}F_3NO_4S_2)$, C_7H_8	
Formula weight	1191.35	
Temperature	120(2) K	
Wavelength, radiation type	0.71073Å, MoKα	
Diffractometer	STOE IPDS 2T	
Crystal system	Monoclinic	
Space group name, number	P 21/c, (14)	
Unit cell dimensions	a = 13.4345(4) Å	α = 90°
	b = 18.1709(8) Å	β = 100.182(3)°
	c = 11.7583(4) Å	γ = 90°
Volume	2825.19(18) $Å^3$	
Number of reflections	18469	
and range used for lattice parameters	2.72° <=θ<= 28.39°	
Z	2	
Density (calculated)	1.400 Mg/m^3	
Absorption coefficient	0.246 mm^{-1}	
Absorption correction	Integration	
Max. and min. transmission	0.9795 and 0.8638	

F(000)	1244
Crystal size, colour and form	0.080 x 0.400 x 0.650 mm^3, colourless plate
Theta range for data collection	2.720 to 27.942°.
Index ranges	-17<=h<=17, -23<=k<=22, -15<=l<=15
Number of reflections:	
collected	13943
independent	6713 [R(int) = 0.0211]
observed [I>2sigma(I)]	5478
Completeness to theta = 25.2°	99.9 %
Refinement method	Full-matrix least-squares on F^2
Data / restraints / parameters	6713 / 0 / 373
Goodness-of-fit on F^2	1.037
Final R indices [I>2sigma(I)]	R1 = 0.0416, wR2 = 0.0937
R indices (all data)	R1 = 0.0554, wR2 = 0.1017
Largest diff. peak and hole	0.432 and -0.353 $eÅ^{-3}$
remark	Toluene is located around a centre of inversion

7. REFERENCES

[1] a) D. Cyr and P. Das, *Res. Chem. Intermed.* **2015**, *41*, 8603-8623; b) B. Lipp, L. M. Kammer, M. Kucukdisli, A. Luque, J. Kuhlborn, S. Pusch, G. Matuleviciute, D. Schollmeyer, A. Sackus and T. Opatz, *Chem. Eur. J.* **2019**, *25*, 8965-8969; c) H. G. Roth, N. A. Romero and D. A. Nicewicz, *Synlett* **2016**, *27*, 714-723.

[2] Y. Pellegrin and F. Odobel, *Cr Chim* **2017**, *20*, 283-295.

[3] A. M. Halpern, D. A. Forsyth and M. Nosowitz, *J. Phys. Chem.* **1986**, *90*, 2677-2679.

[4] B. Xu, L. Troian-Gautier, R. Dykstra, R. T. Martin, O. Gutierrez and U. K. Tambar, *J. Am. Chem. Soc.* **2020**, *142*, 6206-6215.

[5] M. Mitani, T. Kiriyama and T. Kuratate, *J. Org. Chem.* **1994**, *59*, 1279-1282.

[6] P. Herr, C. Kerzig, C. B. Larsen, D. Haussinger and O. S. Wenger, *Nat Chem* **2021**, *13*, 956-+.

[7] C. J. Wallentin, J. D. Nguyen, P. Finkbeiner and C. R. J. Stephenson, *J. Am. Chem. Soc.* **2012**, *134*, 8875-8884.

[8] a) C. Lee, W. Yang and R. G. Parr, *Phys. Rev. B* **1988**, *37*, 785-789; b) A. D. Becke, *J. Chem. Phys.* **1993**, *98*, 5648-5652; c) S. H. Vosko, L. Wilk and M. Nusair, *Can. J. Phys.* **1980**, *58*, 1200-1211.

[9] T. Yanai, D. P. Tew and N. C. Handy, *Chem. Phys. Lett.* **2004**, *393*, 51-57.

[10] Y. Zhao and D. G. Truhlar, *Theor. Chem. Acc.* **2008**, *120*, 215-241.

[11] a) R. Krishnan, J. S. Binkley, R. Seeger and J. A. Pople, *J. Chem. Phys.* **1980**, *72*, 650-654; b) M. J. Frisch, J. A. Pople and J. S. Binkley, *J. Chem. Phys.* **1984**, *80*, 3265-3269.

[12] J. Tomasi, B. Mennucci and E. Cancès, *J. Mol. Struct.* **1999**, *464*, 211-226.

[13] E. Runge and E. K. U. Gross, *Phys. Rev. Lett.* **1984**, *52*, 997-1000.

[14] C. Adamo and D. Jacquemin, *Chem. Soc. Rev.* **2013**, *42*, 845-856.

[15] M. J. Frisch, G. W. Trucks, H. B. Schlegel, G. E. Scuseria, M. A. Robb, J. R. Cheeseman, G. Scalmani, V. Barone, G. A. Petersson, H. Nakatsuji, X. Li, M. Caricato, A. V. Marenich, J. Bloino, B. G. Janesko, R. Gomperts, B. Mennucci, H. P. Hratchian, J. V. Ortiz, A. F. Izmaylov, J. L. Sonnenberg, Williams, F. Ding, F. Lipparini, F. Egidi, J. Goings, B. Peng, A. Petrone, T. Henderson, D. Ranasinghe, V. G.

Zakrzewski, J. Gao, N. Rega, G. Zheng, W. Liang, M. Hada, M. Ehara, K. Toyota, R. Fukuda, J. Hasegawa, M. Ishida, T. Nakajima, Y. Honda, O. Kitao, H. Nakai, T. Vreven, K. Throssell, J. A. Montgomery Jr., J. E. Peralta, F. Ogliaro, M. J. Bearpark, J. J. Heyd, E. N. Brothers, K. N. Kudin, V. N. Staroverov, T. A. Keith, R. Kobayashi, J. Normand, K. Raghavachari, A. P. Rendell, J. C. Burant, S. S. Iyengar, J. Tomasi, M. Cossi, J. M. Millam, M. Klene, C. Adamo, R. Cammi, J. W. Ochterski, R. L. Martin, K. Morokuma, O. Farkas, J. B. Foresman and D. J. Fox in *Gaussian 16, Revision C.01*, *Vol.* Wallingford, CT, **2019**.

[16] Dennington R., Keith T.A. and Millam J. M., *GaussView, Version 6.* **2016**, *Semichem Inc.:Shawnee Mission, KS, USA*.

[17] V. Nair, A. Augustine and T. D. Suja, *Synthesis* **2002**, 2259-2265.

[18] L. L. Wang, W. Wei, D. S. Yang, H. H. Cui, H. L. Yue and H. Wang, *Tetrahedron Lett.* **2017**, *58*, 4799-4802.

[19] Z. Y. Mo, Y. Z. Zhang, G. B. Huang, X. Y. Wang, Y. M. Pan and H. T. Tang, *Adv. Synth. Catal.* **2020**, *362*, 2160-2167.

[20] Z. Wu, Y. H. Xu, H. H. Zhang, X. X. Wu and C. Zhu, *Chem. Commun.* **2021**, *57*, 6066-6069.

[21] N. Riddell and W. Tam, *J. Org. Chem.* **2006**, *71*, 1934-1937.

[22] S. K. Kristensen, S. L. R. Laursen, E. Taarning and T. Skrydstrup, *Angew. Chem. Int. Edit.* **2018**, *57*, 13887-13891; *Angew. Chem. Int. Edit.* **2018**, *130*, 14083-14087.

[23] S. Doobary, A. T. Sedikides, H. P. Caldora, D. L. Poole and A. J. J. Lennox, *Angew. Chem. Int. Edit.* **2020**, *59*, 1155-1160; *Angew. Chem.* **2020**, *132*, 1171-1176.

[24] D. C. Blakemore and A. Gilbert, *J. Chem. Soc. Perk T. 1* **1992**, 2265-2270.

NMR SPECTRA

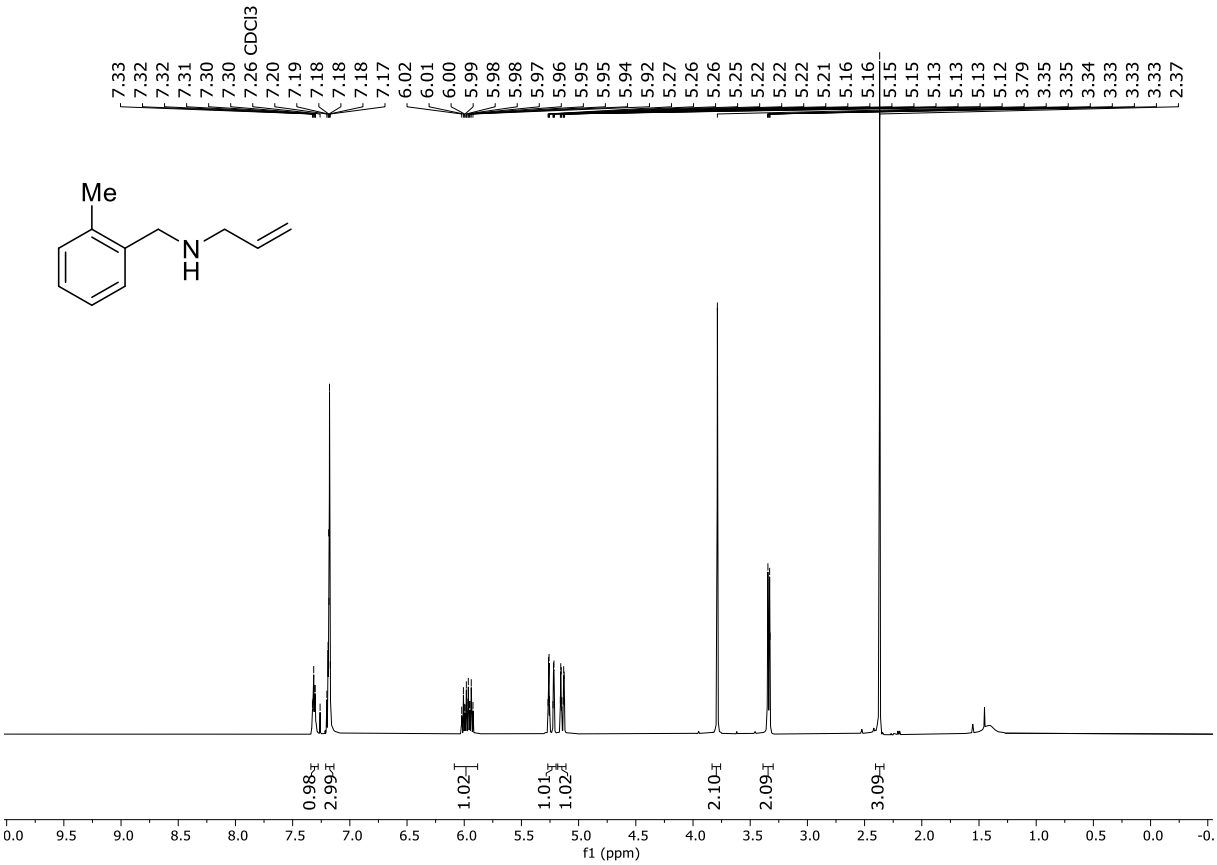

^{1}H NMR (400 MHz, $CDCl_3$) spectrum of **2**

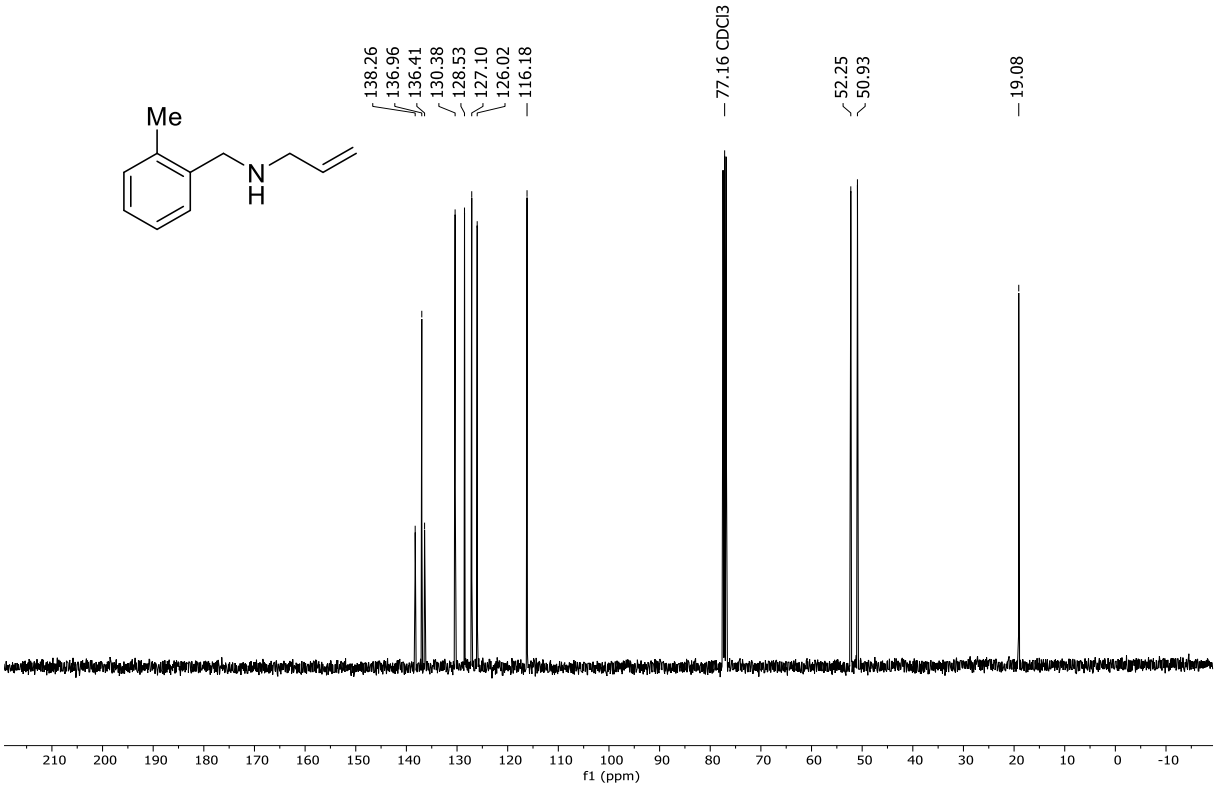

^{13}C NMR (101 MHz, $CDCl_3$) spectrum of **2**

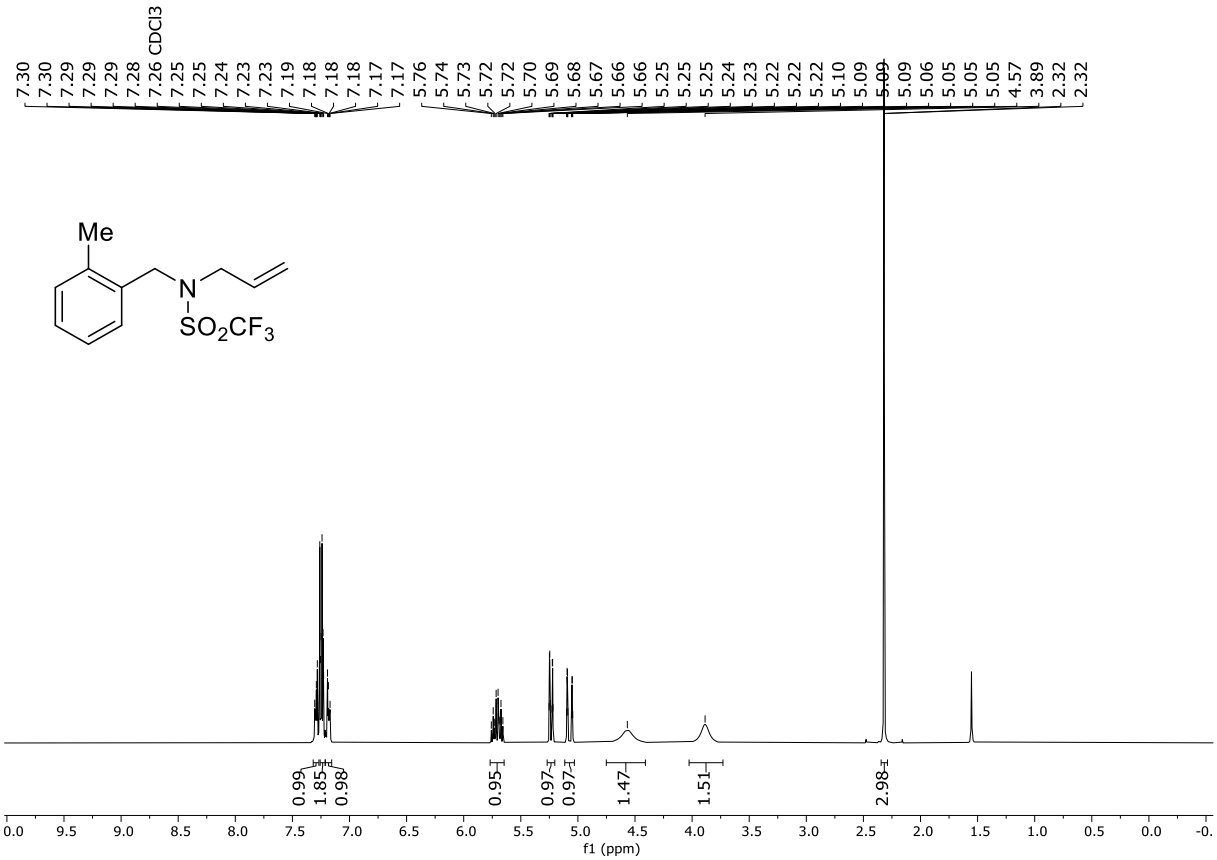

^{1}H NMR (400 MHz, $CDCl_3$) spectrum of **3**

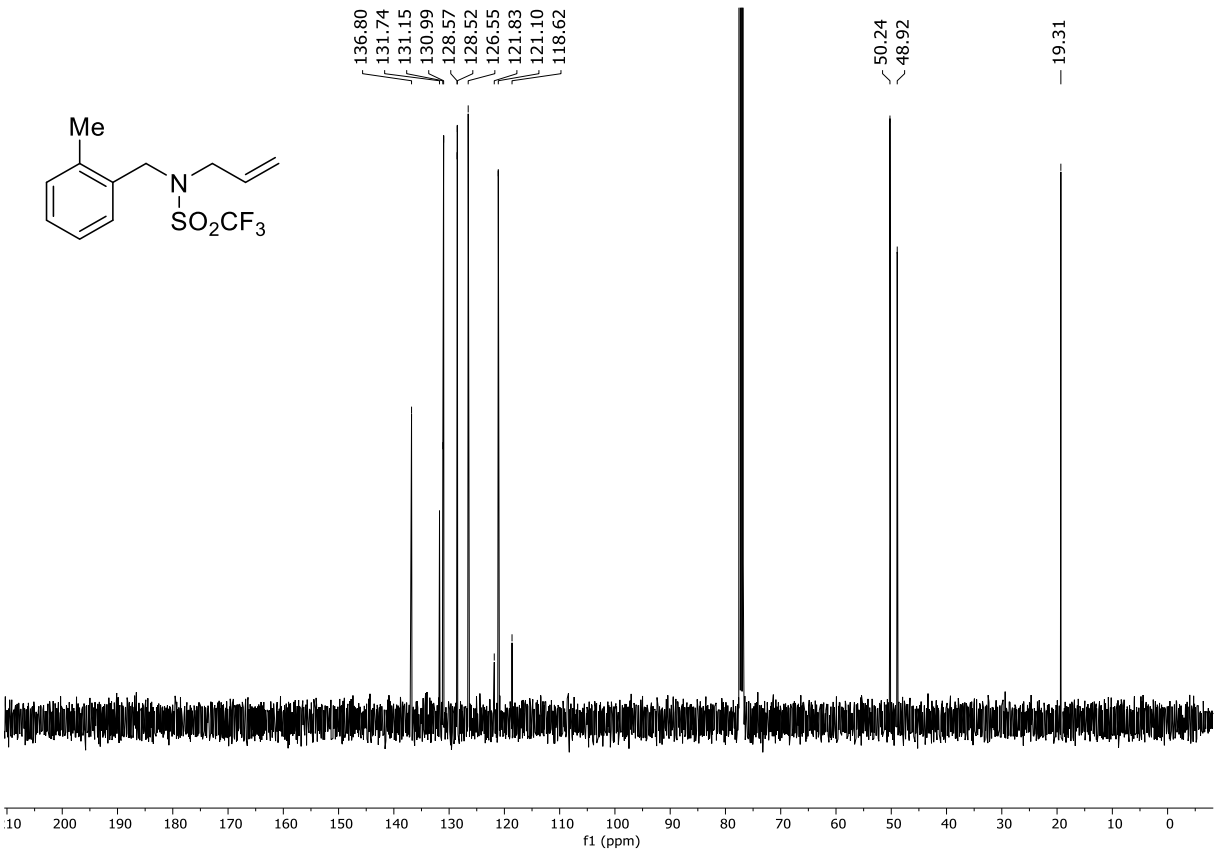

^{13}C NMR (101 MHz, $CDCl_3$) spectrum of **3**

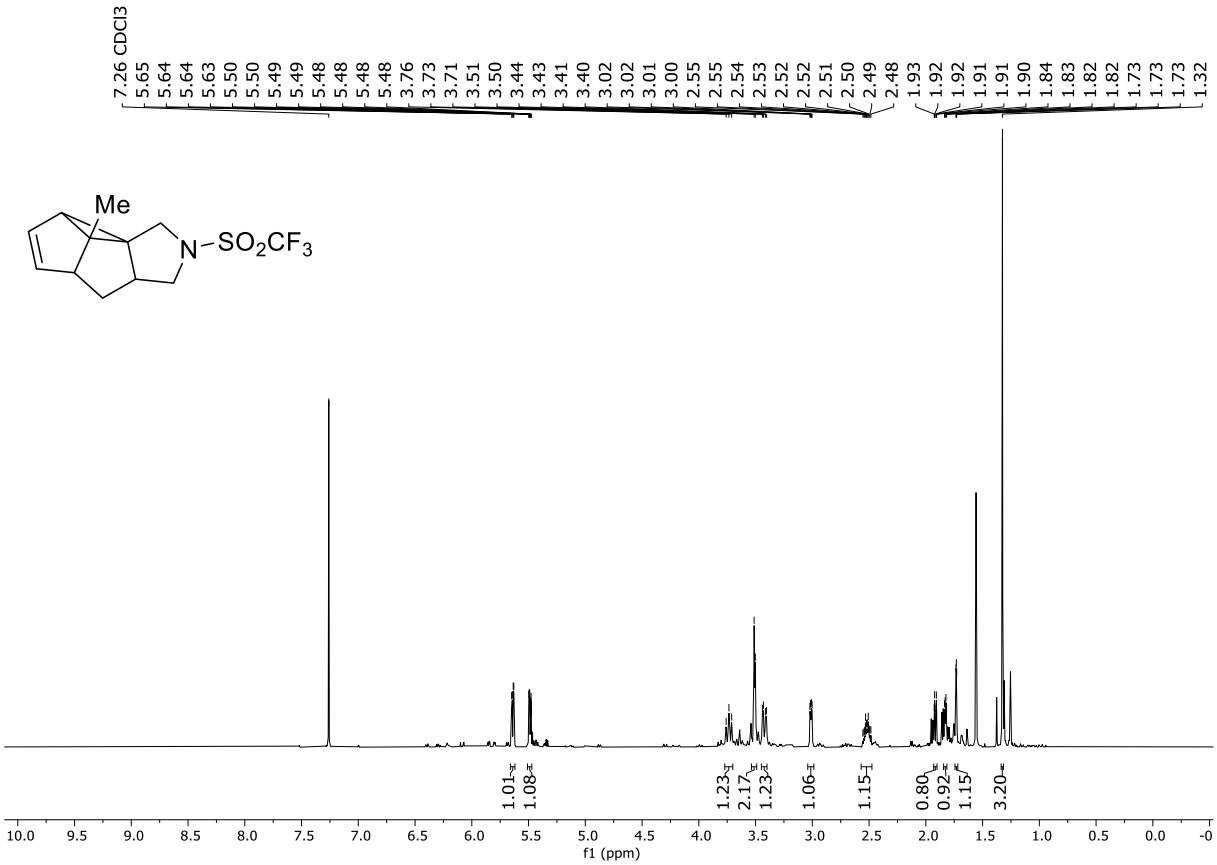

^{1}H NMR (400 MHz, $CDCl_3$) spectrum of **4**

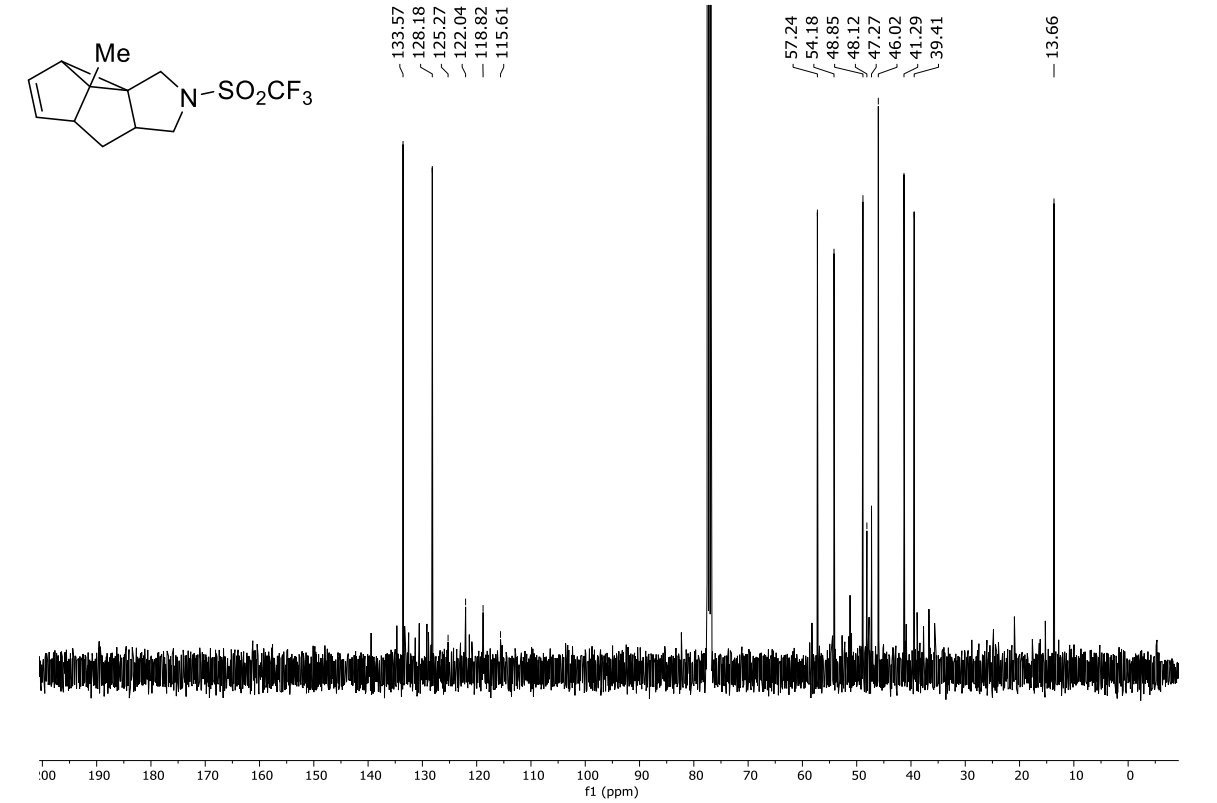

^{13}C NMR (101 MHz, $CDCl_3$) spectrum of **4**

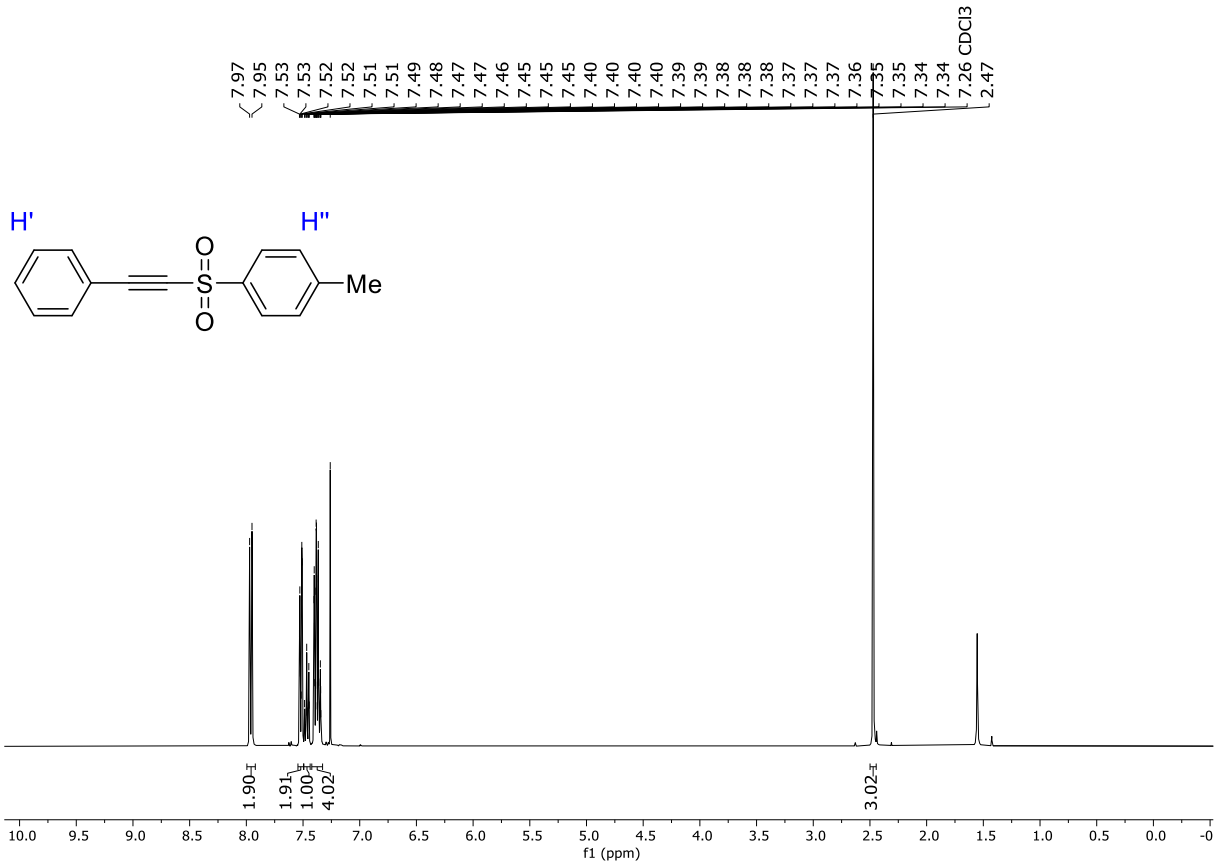

^{1}H NMR (400 MHz, $CDCl_3$) spectrum of **6a**

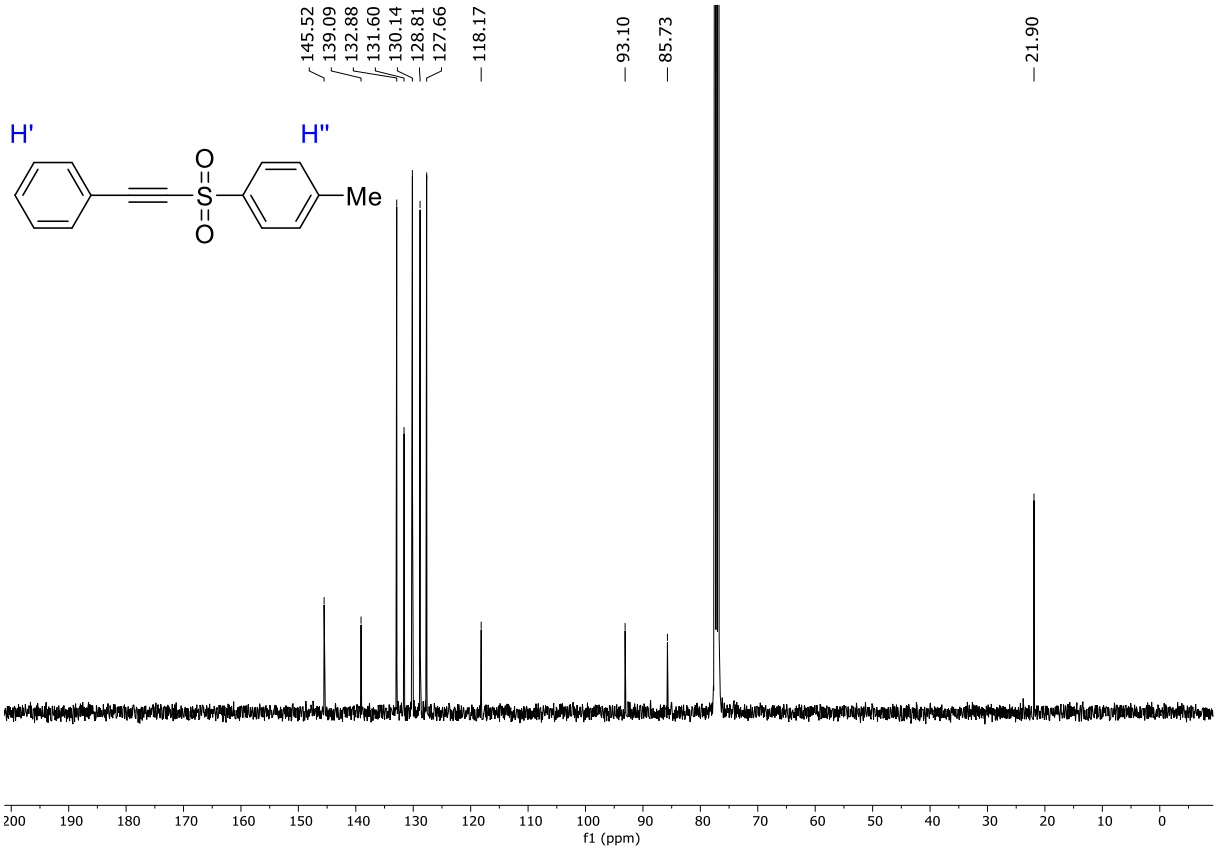

^{13}C NMR (101 MHz, $CDCl_3$) spectrum of **6a**

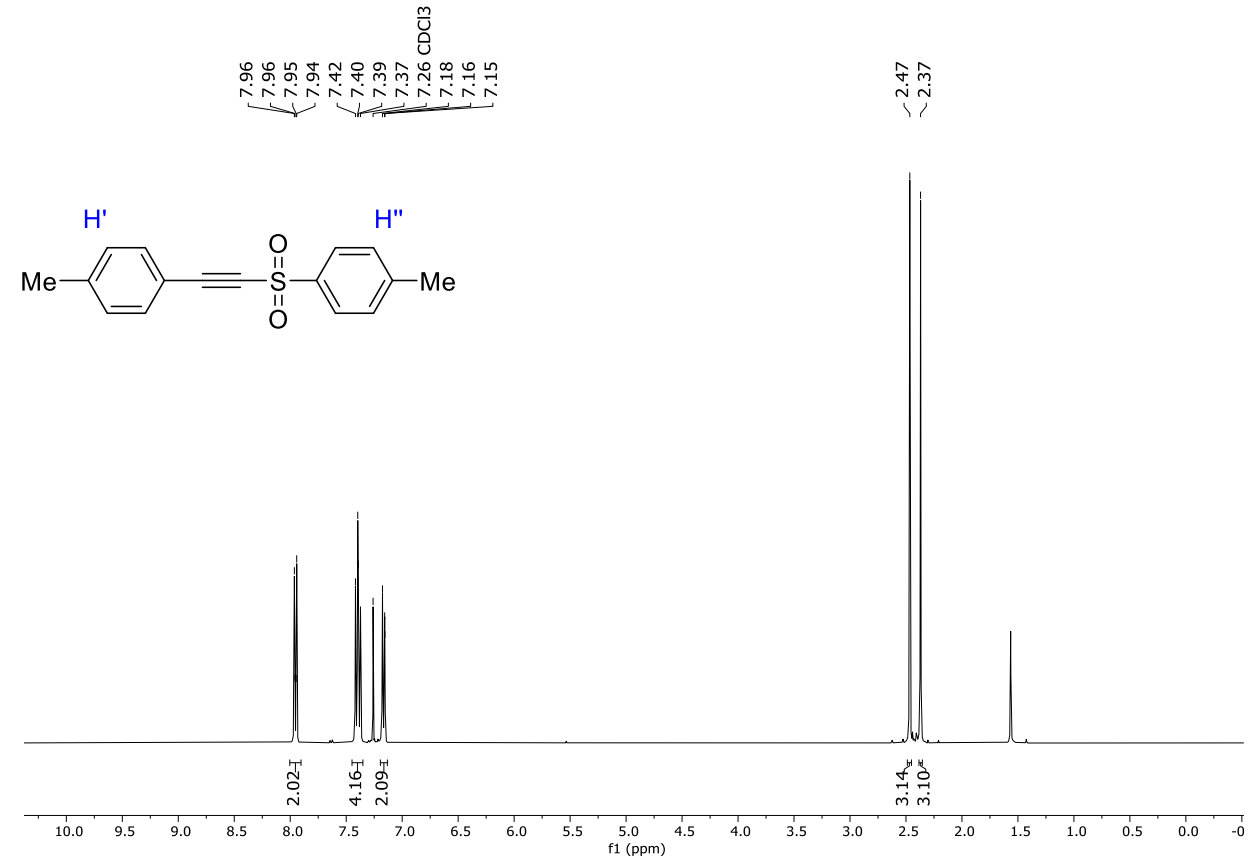

^{1}H NMR (400 MHz, $CDCl_3$) spectrum of **6b**

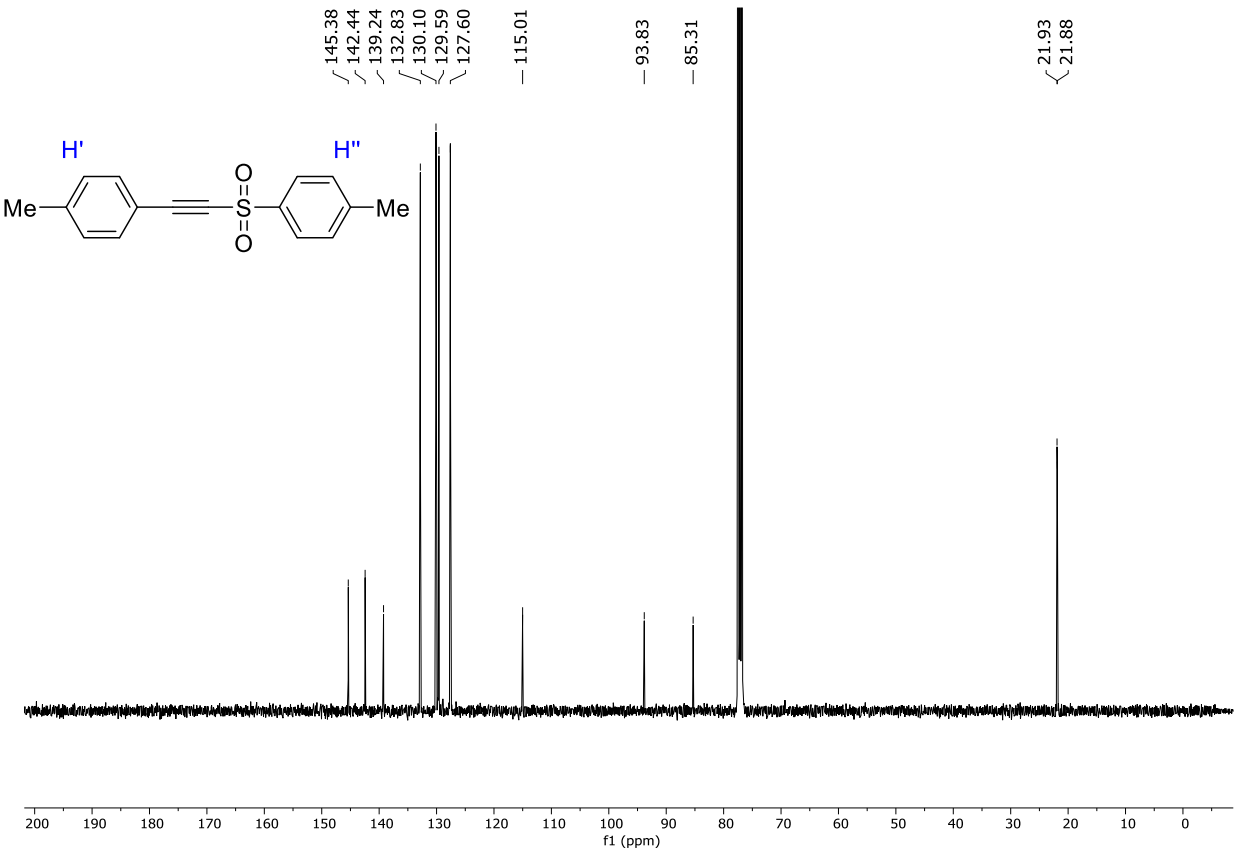

^{13}C NMR (101 MHz, $CDCl_3$) spectrum of **6b**

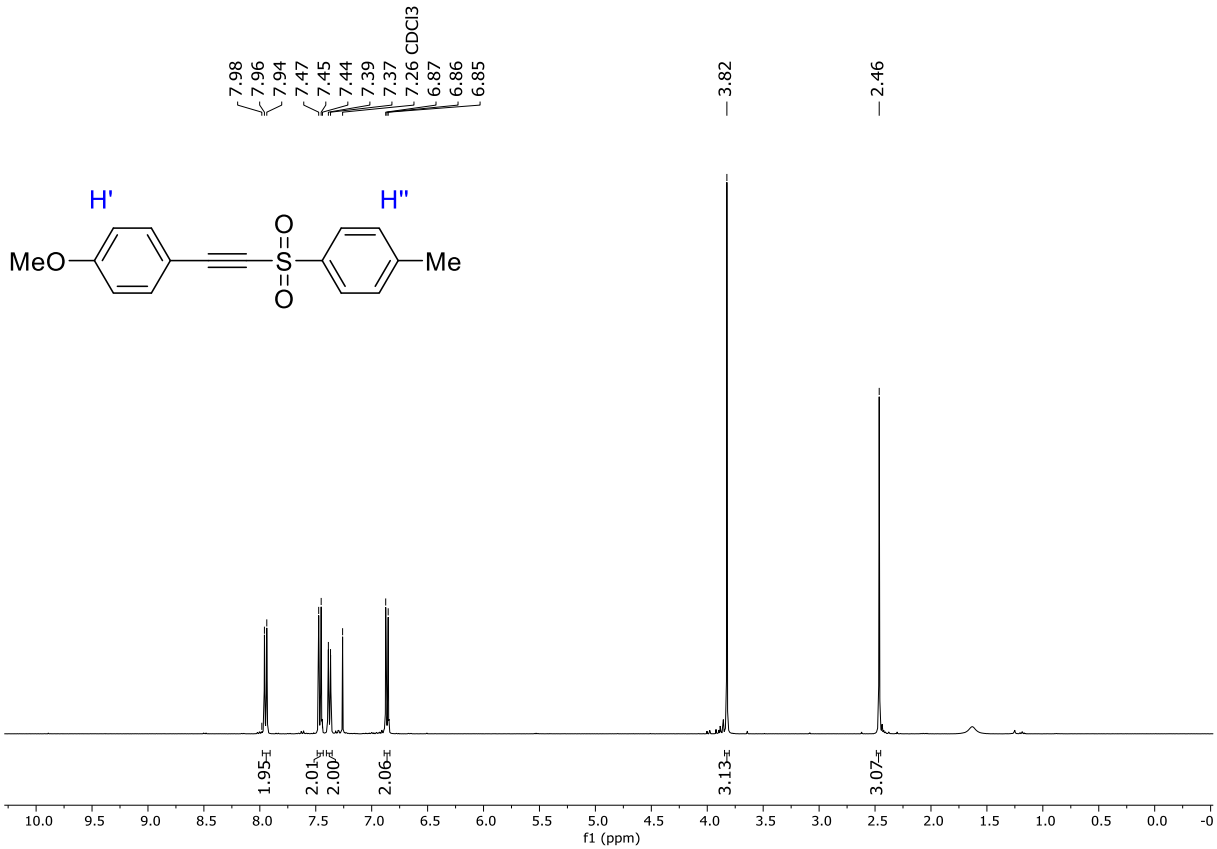

^{1}H NMR (400 MHz, $CDCl_3$) spectrum of **6c**

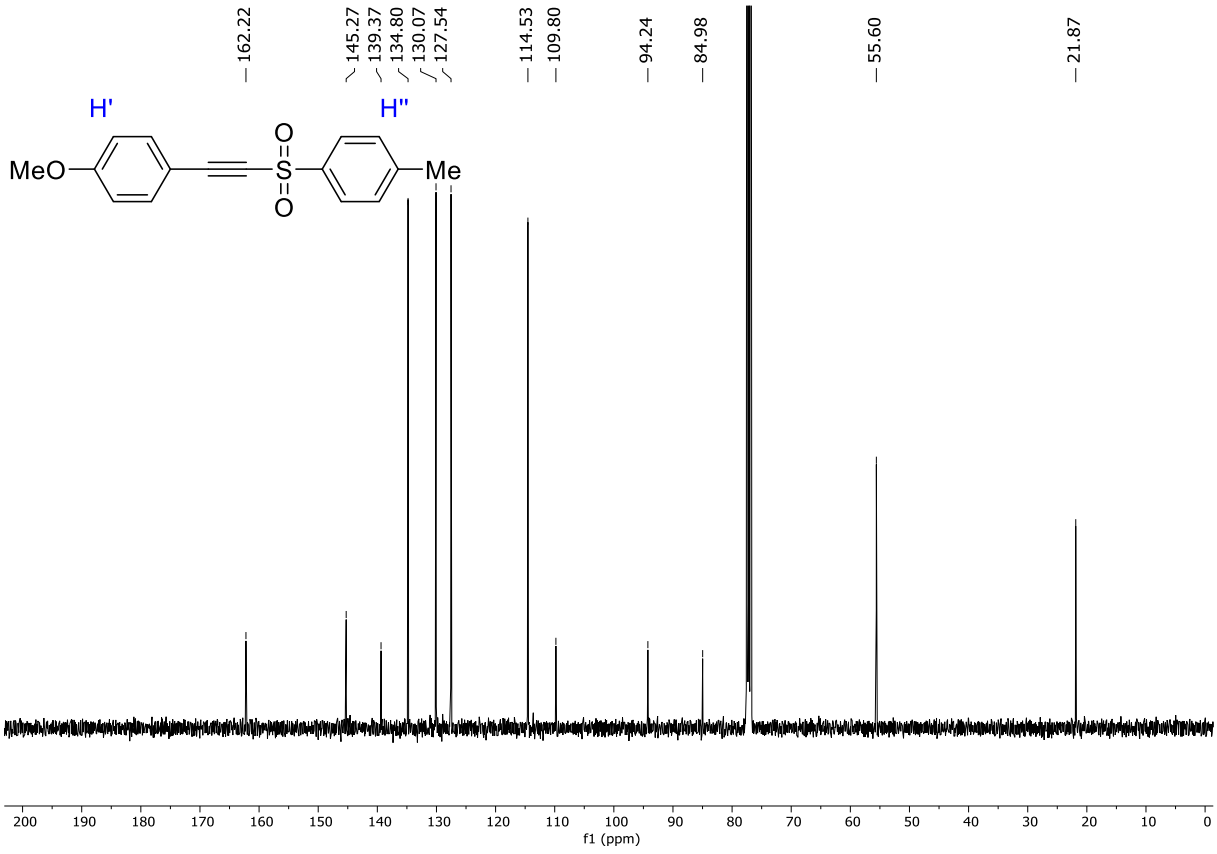

^{13}C NMR (101 MHz, $CDCl_3$) spectrum of **6c**

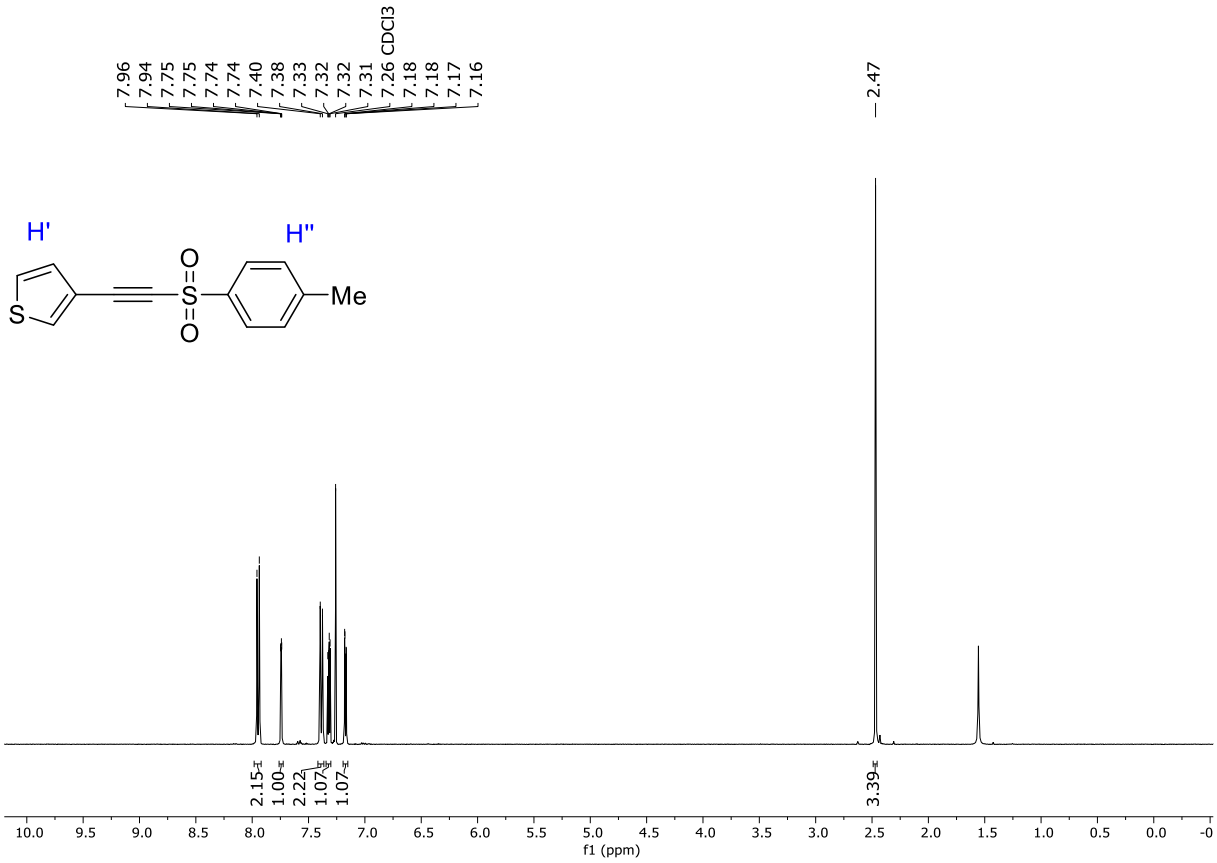

^{1}H NMR (400 MHz, $CDCl_3$) spectrum of **6d**

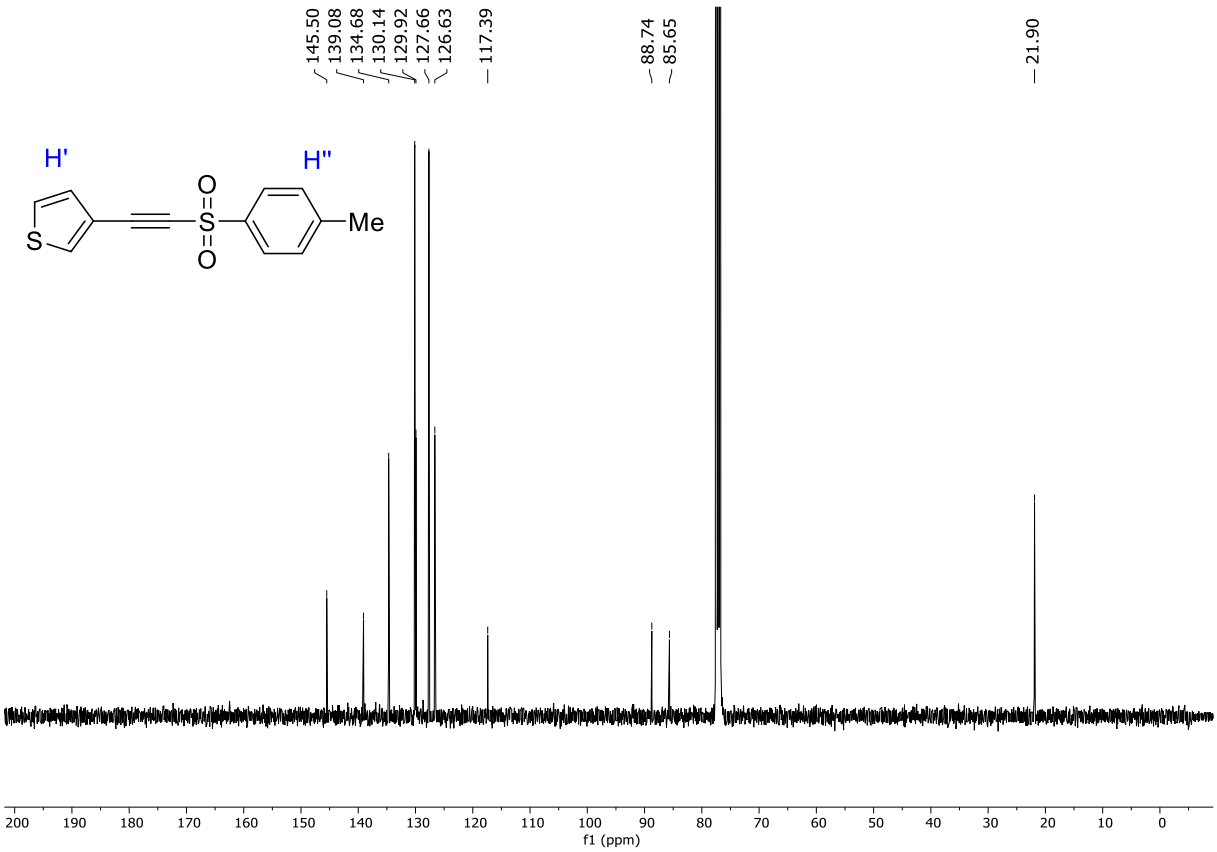

^{13}C NMR (101 MHz, $CDCl_3$) spectrum of **6d**

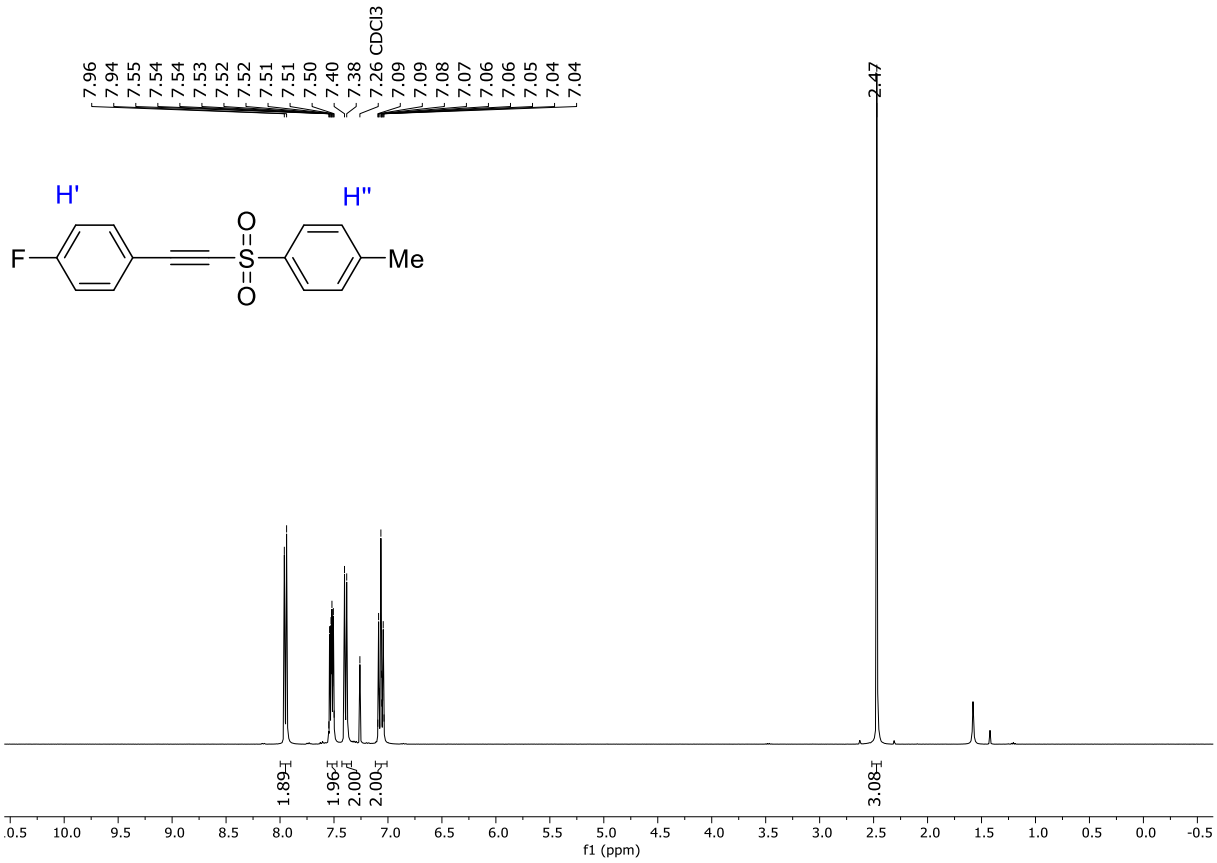

^{1}H NMR (400 MHz, $CDCl_3$) spectrum of **6e**

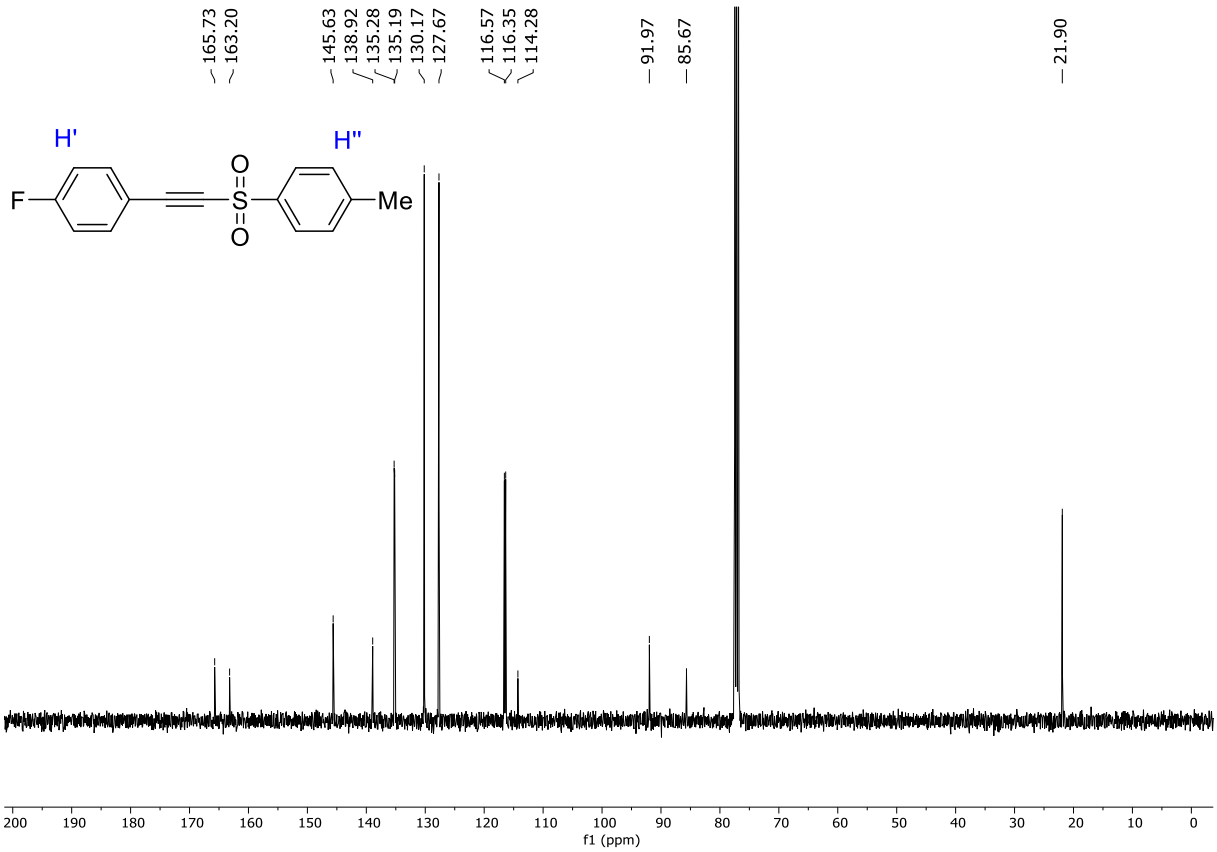

^{13}C NMR (101 MHz, $CDCl_3$) spectrum of **6e**

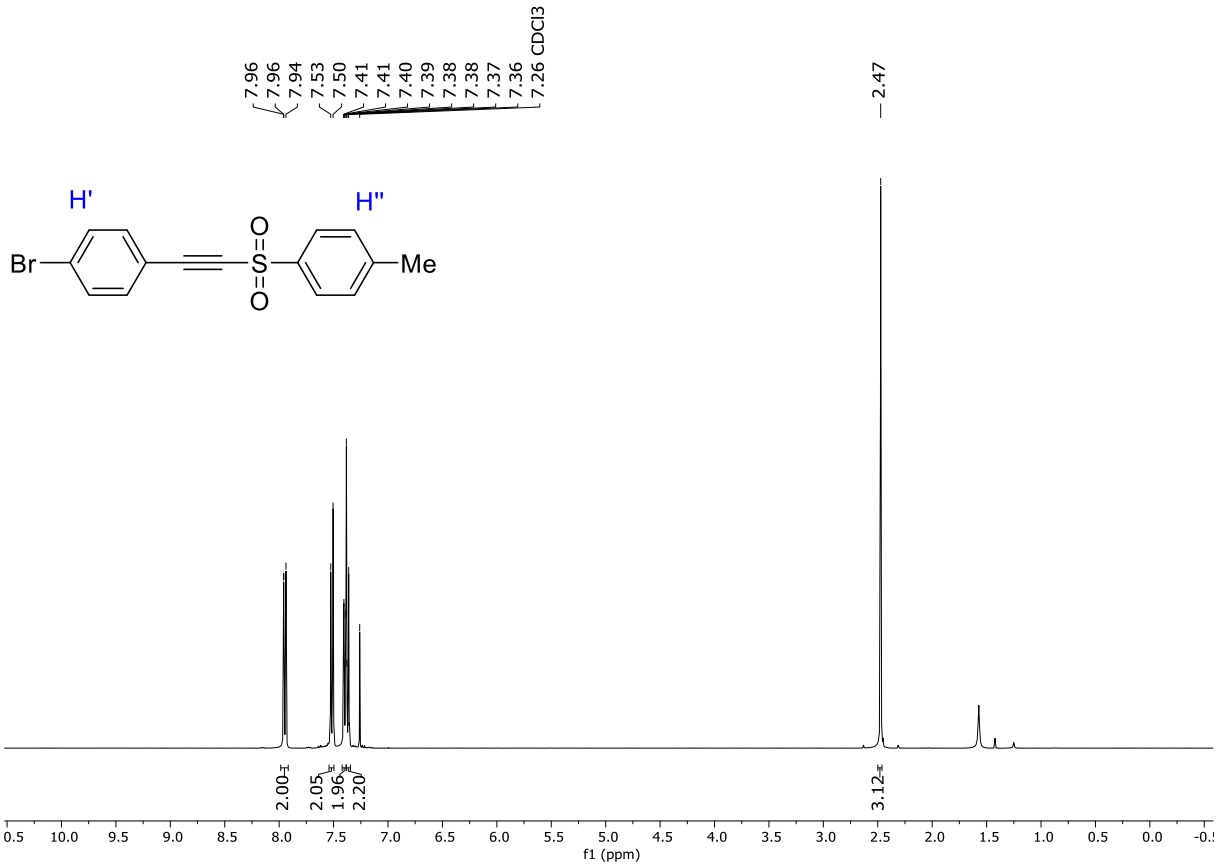

^{1}H NMR (400 MHz, $CDCl_3$) spectrum of **6f**

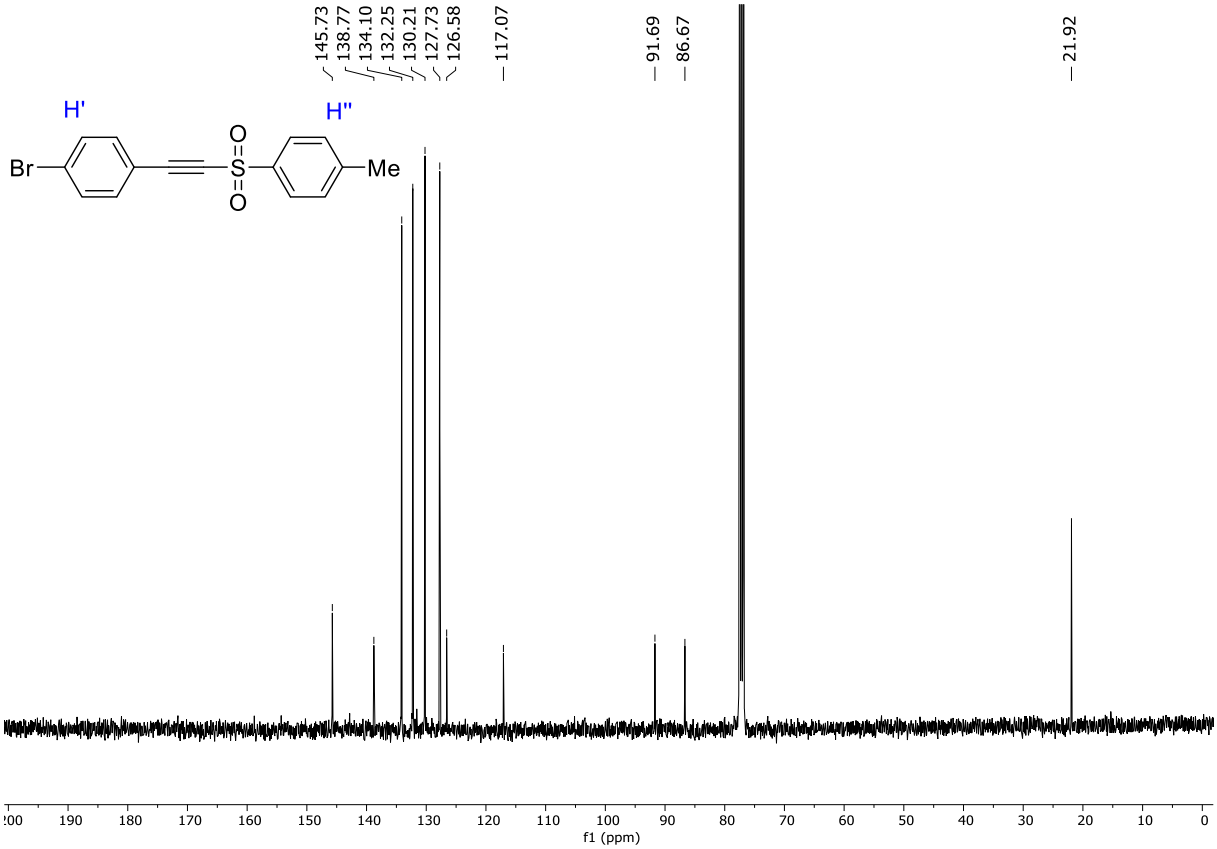

^{13}C NMR (101 MHz, $CDCl_3$) spectrum of **6f**

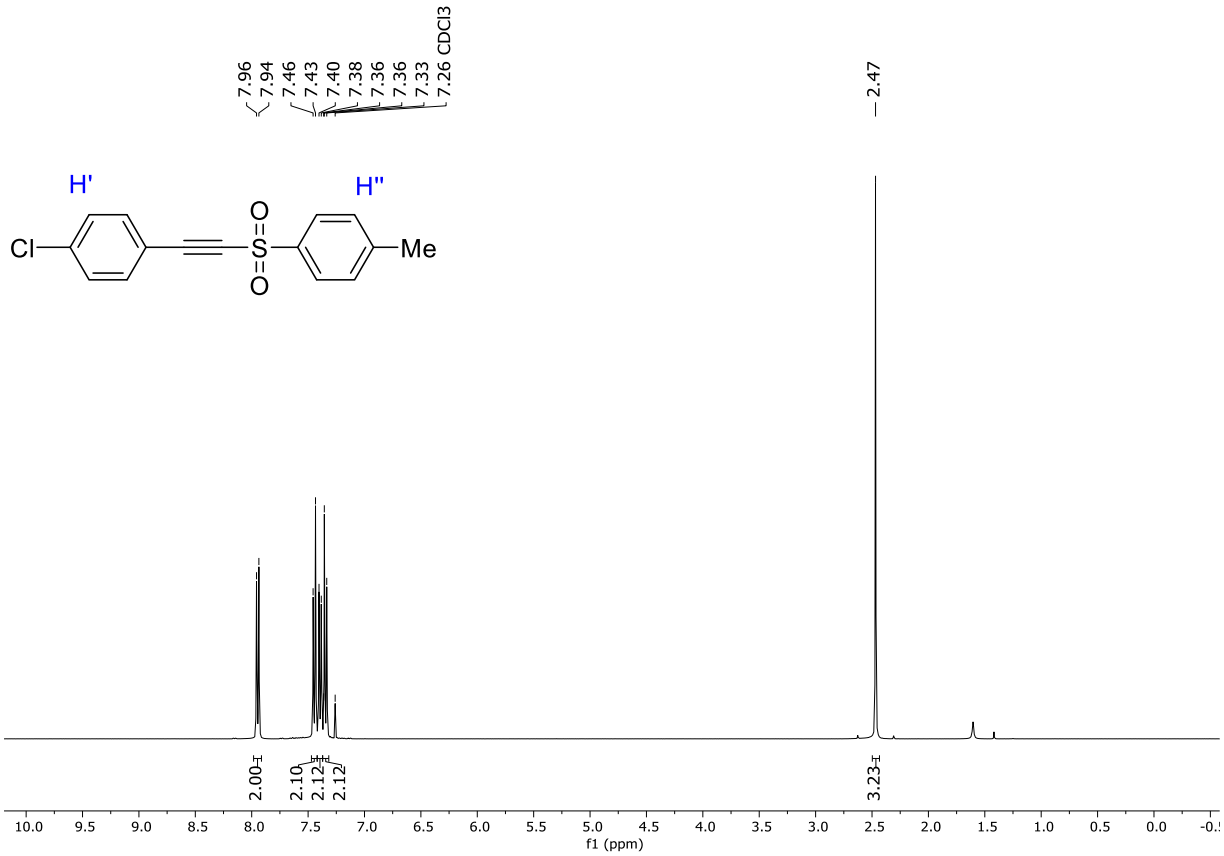

^{1}H NMR (400 MHz, $CDCl_3$) spectrum of **6g**

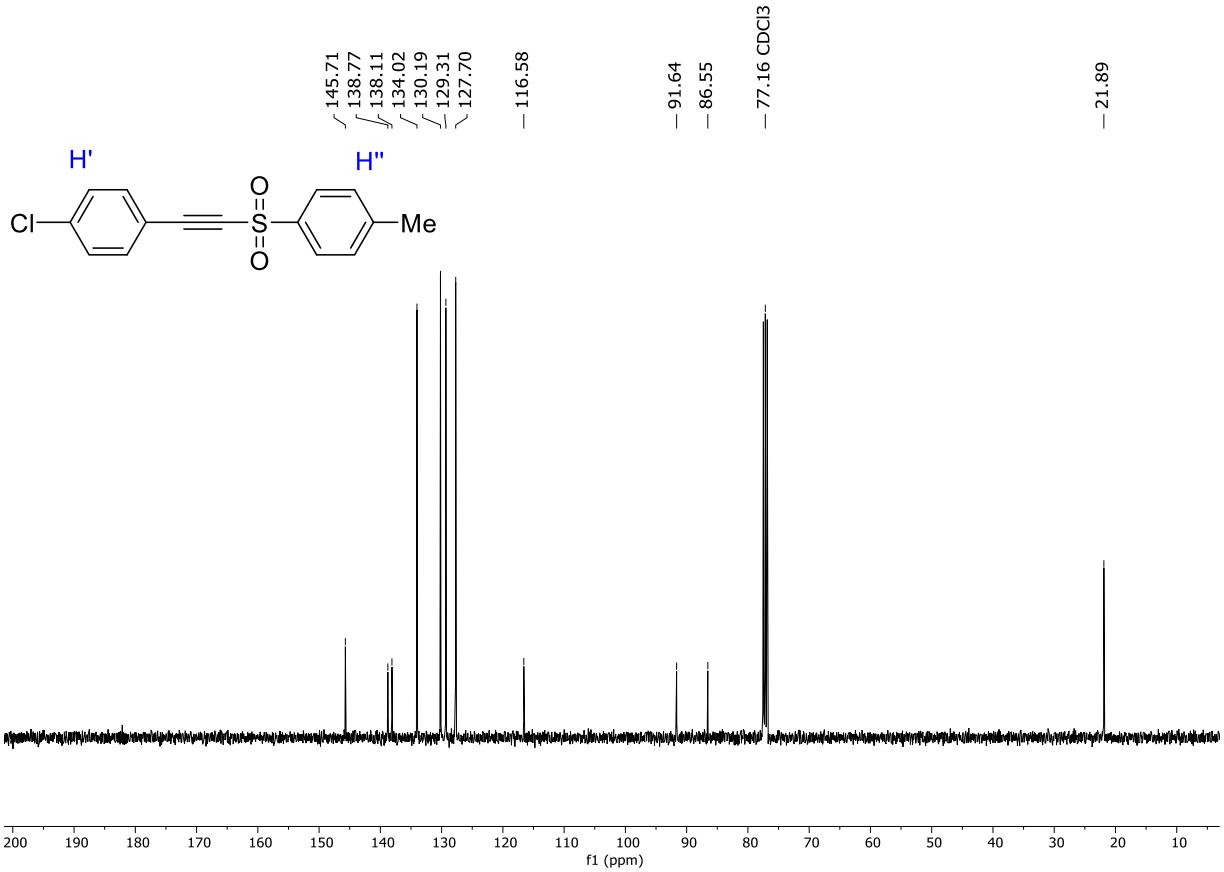

^{13}C NMR (101 MHz, $CDCl_3$) spectrum of **6g**

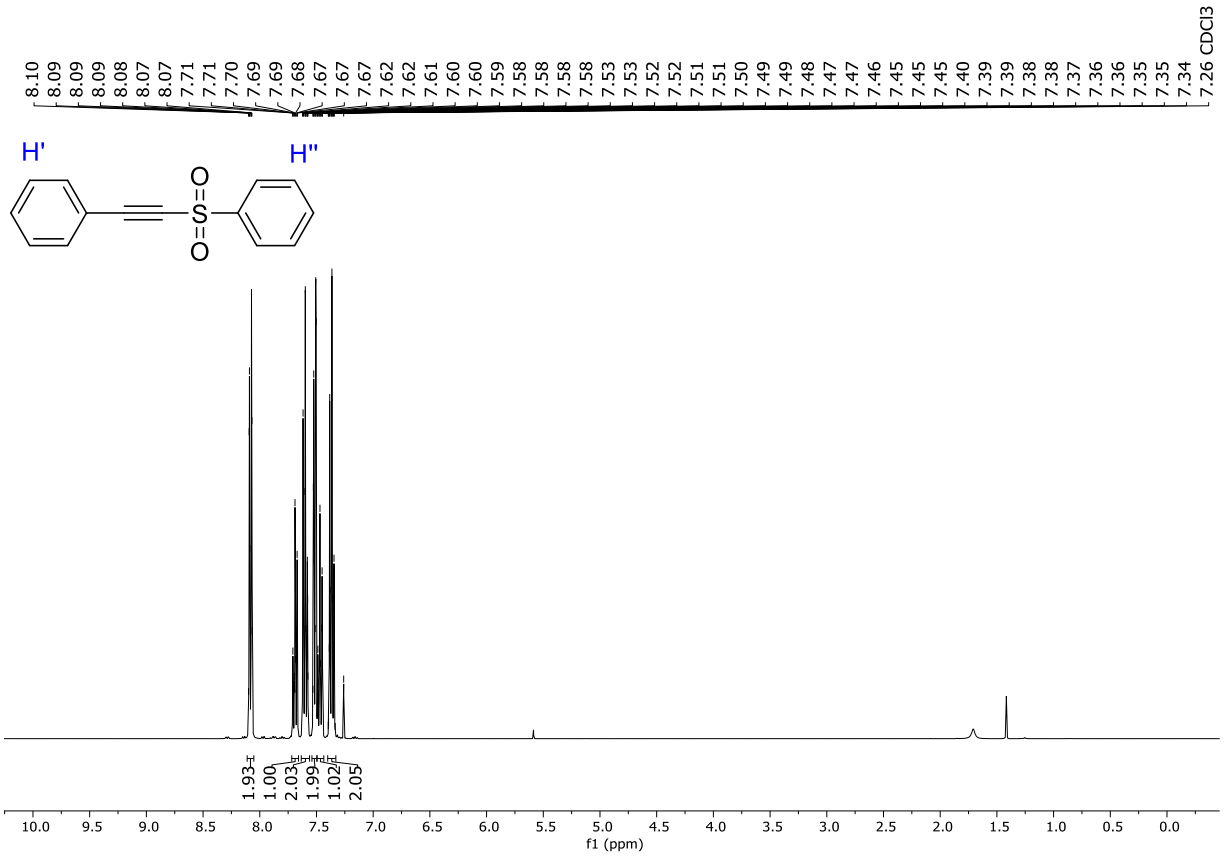

^{1}H NMR (400 MHz, $CDCl_3$) spectrum of **6h**

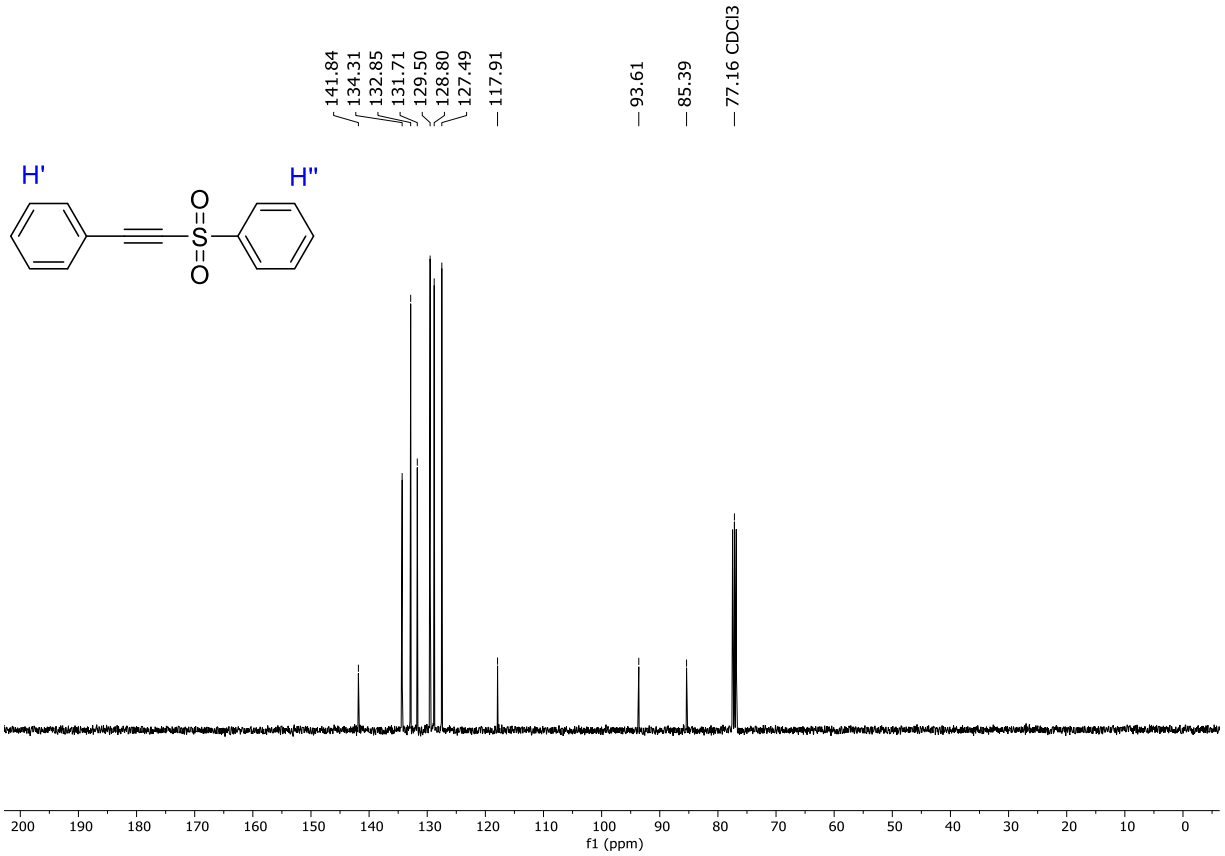

^{13}C NMR (101 MHz, $CDCl_3$) spectrum of **6h**

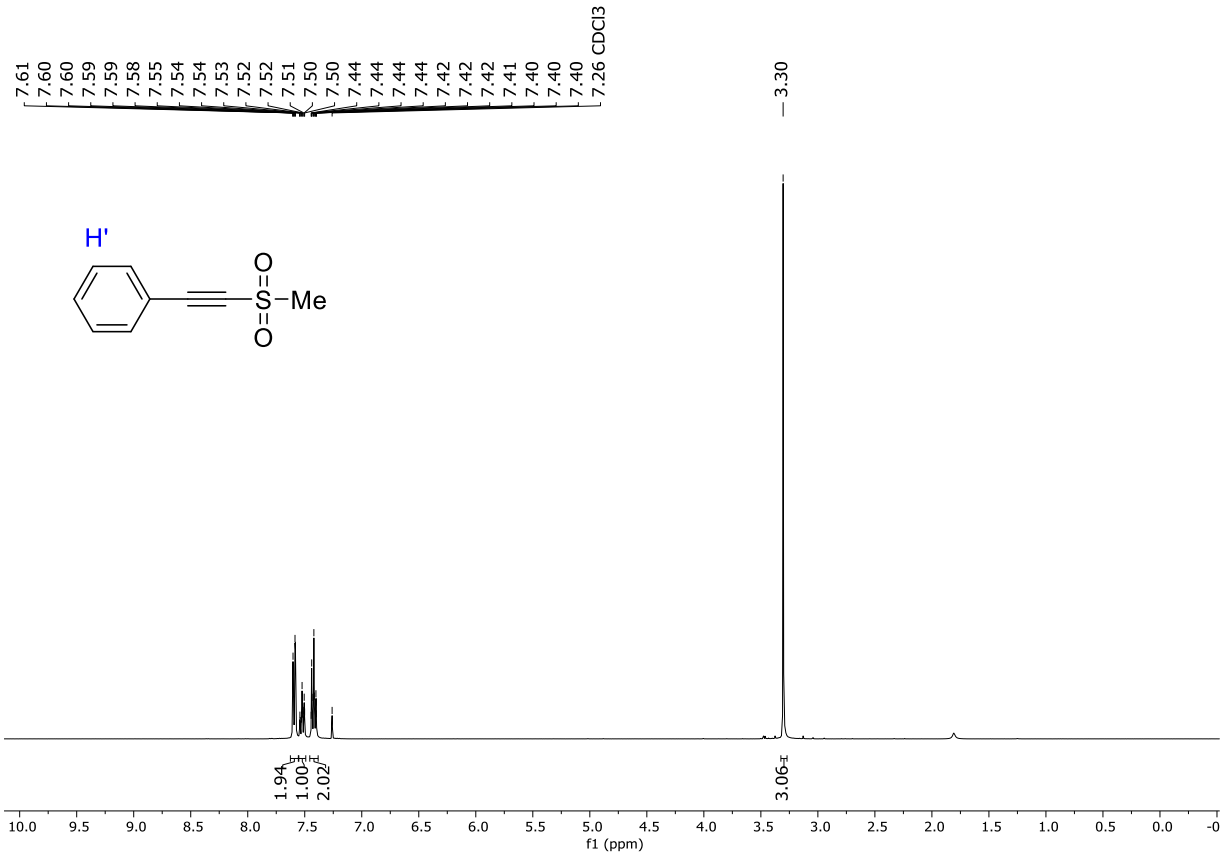

^{1}H NMR (400 MHz, $CDCl_3$) spectrum of **6i**

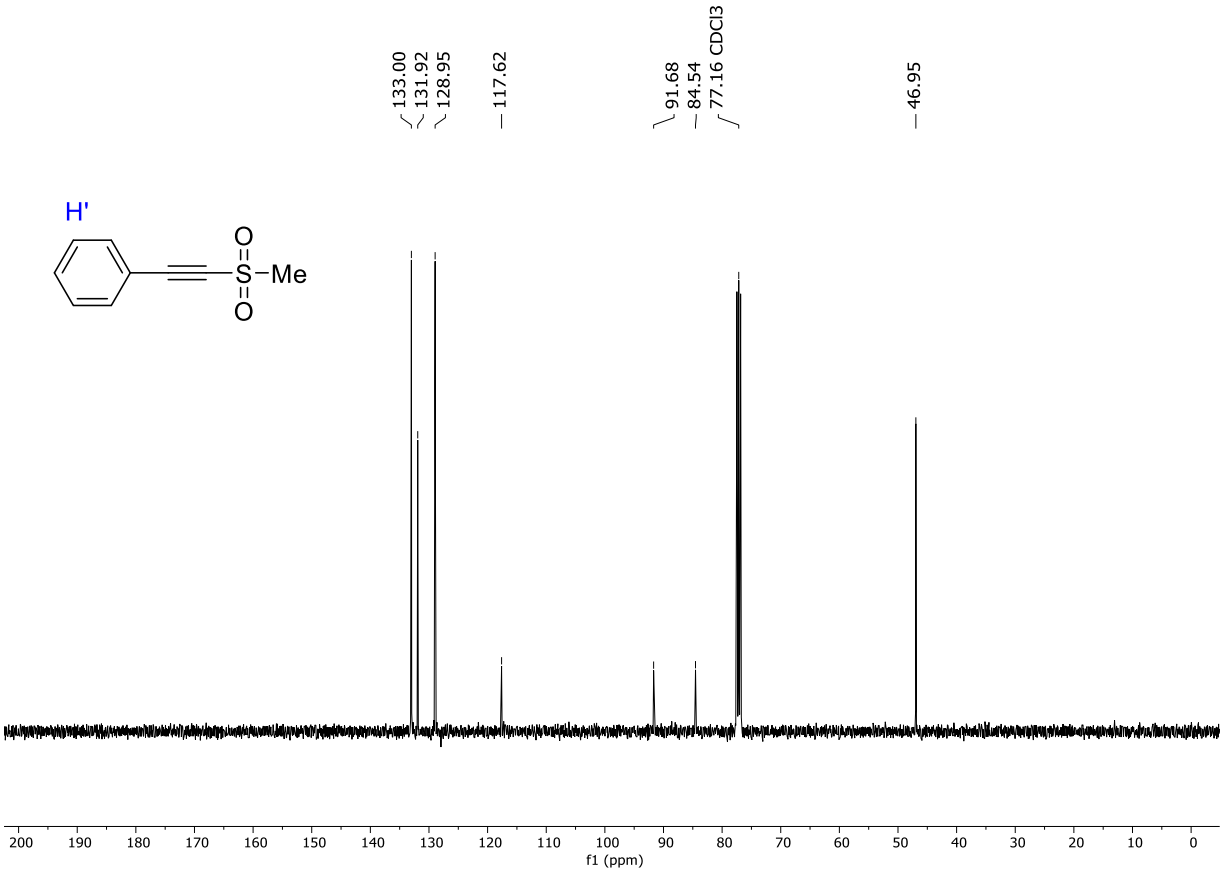

^{13}C NMR (101 MHz, $CDCl_3$) spectrum of **6i**

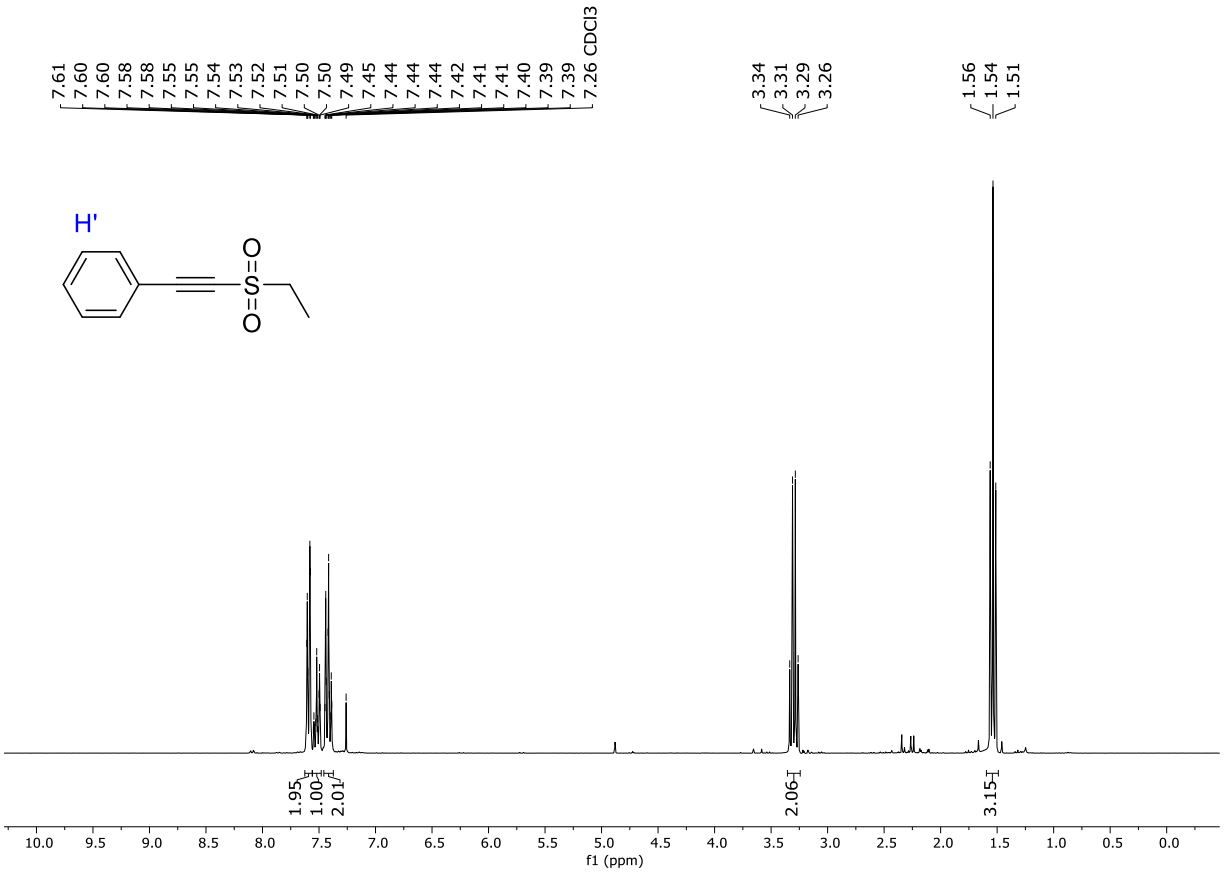

^{1}H NMR (400 MHz, $CDCl_3$) spectrum of **6j**

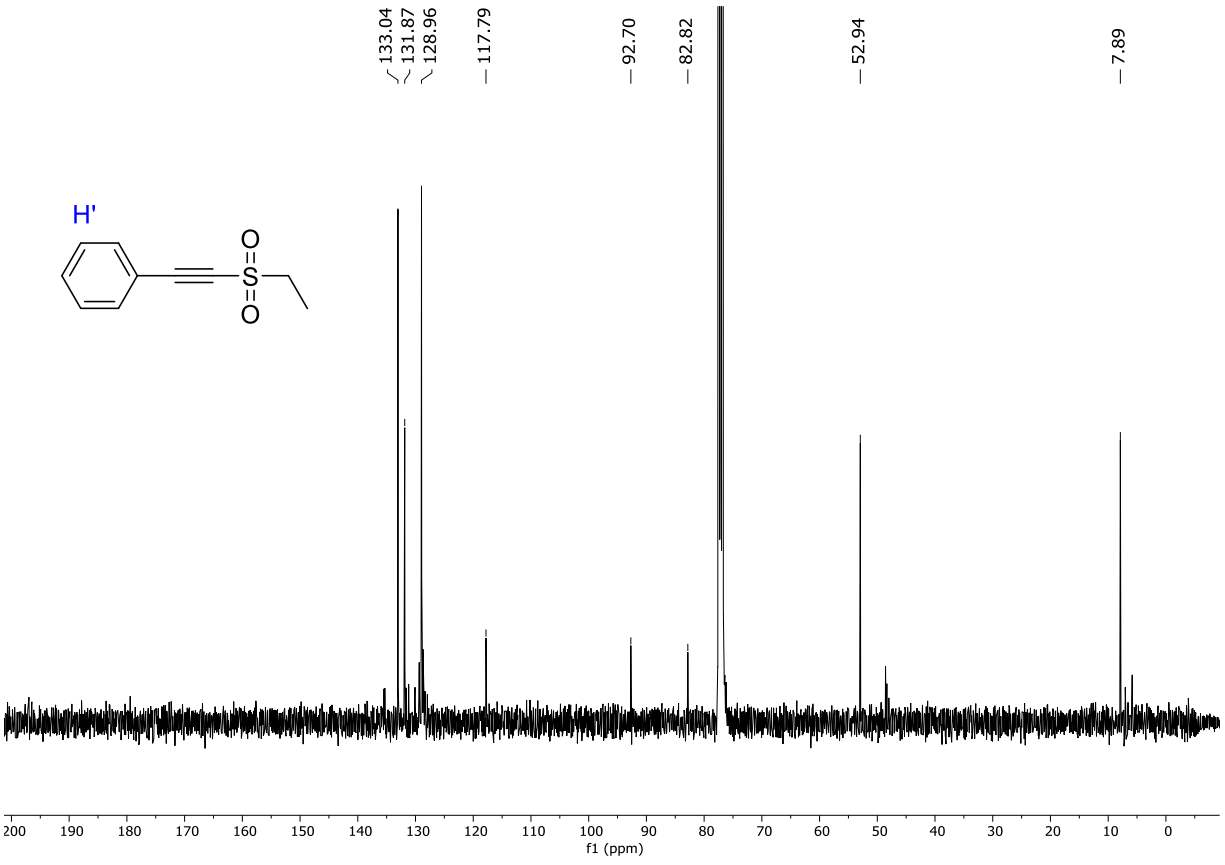

^{13}C NMR (101 MHz, $CDCl_3$) spectrum of **6j**

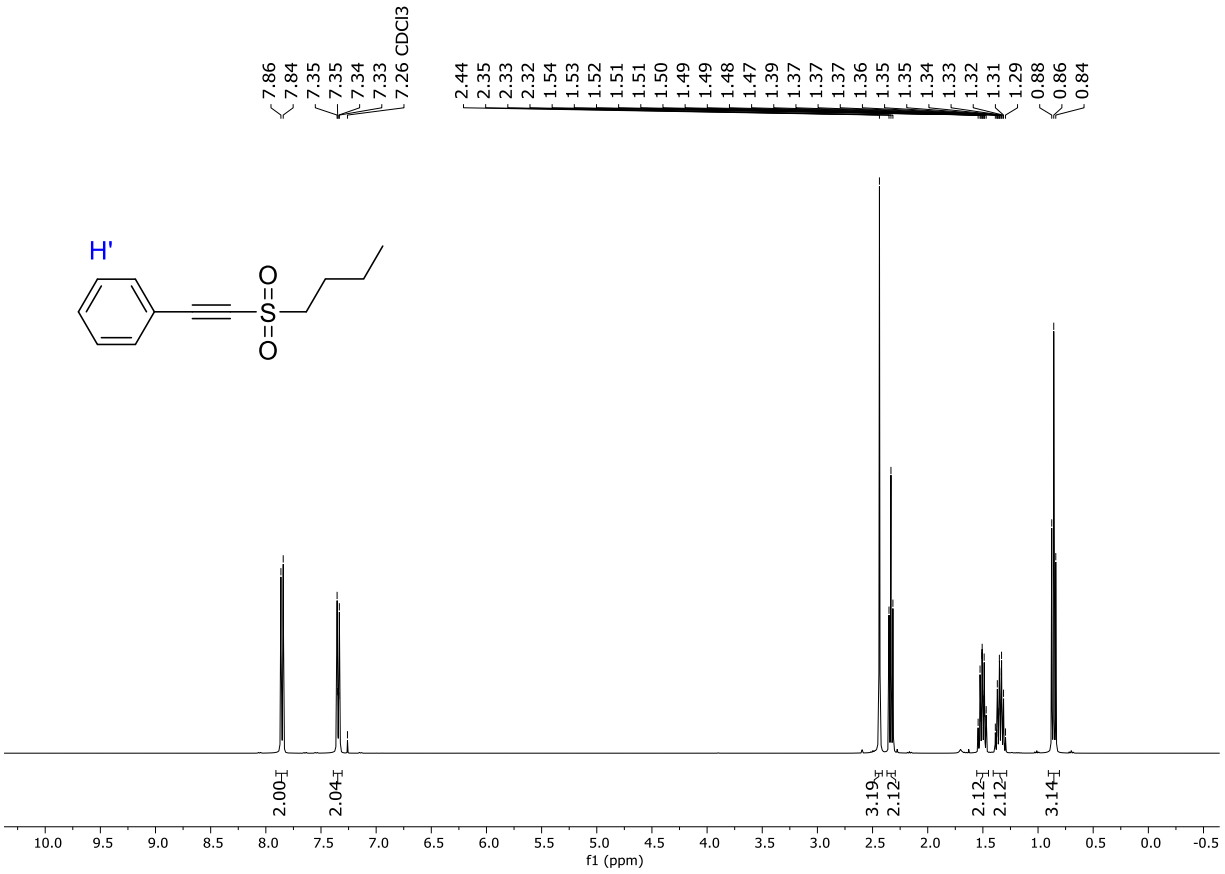

^{1}H NMR (400 MHz, $CDCl_3$) spectrum of **6k**

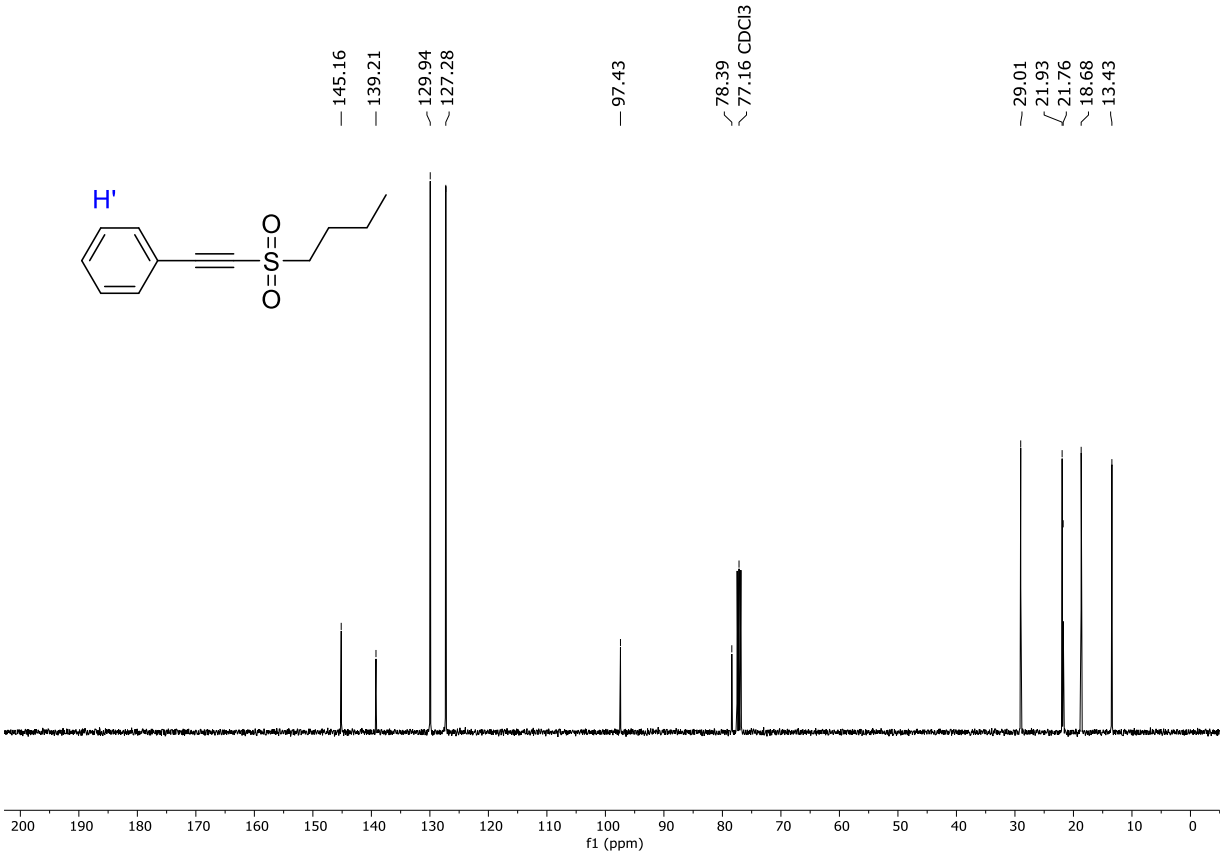

^{13}C NMR (101 MHz, $CDCl_3$) spectrum of **6k**

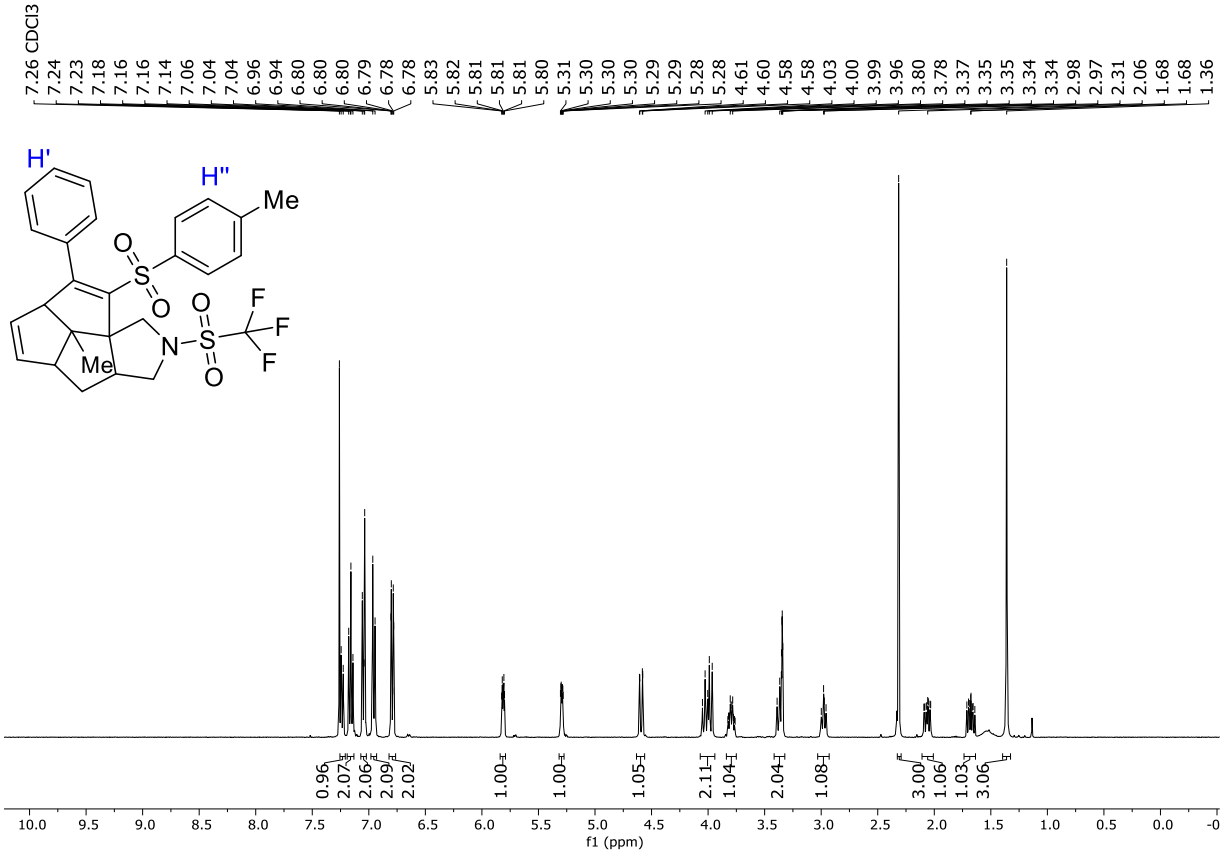

^{1}H NMR (400 MHz, $CDCl_3$) spectrum of **7a**

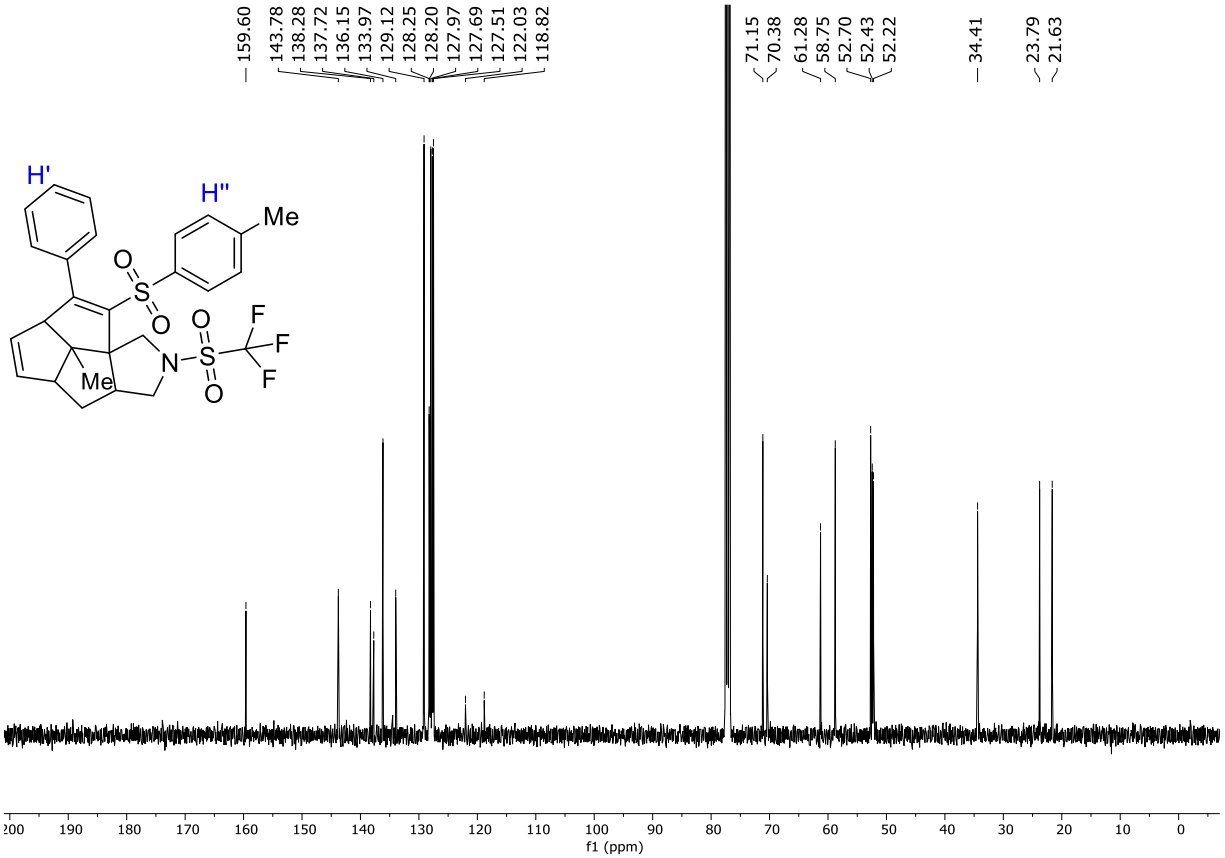

^{13}C NMR (101 MHz, $CDCl_3$) spectrum of **7a**

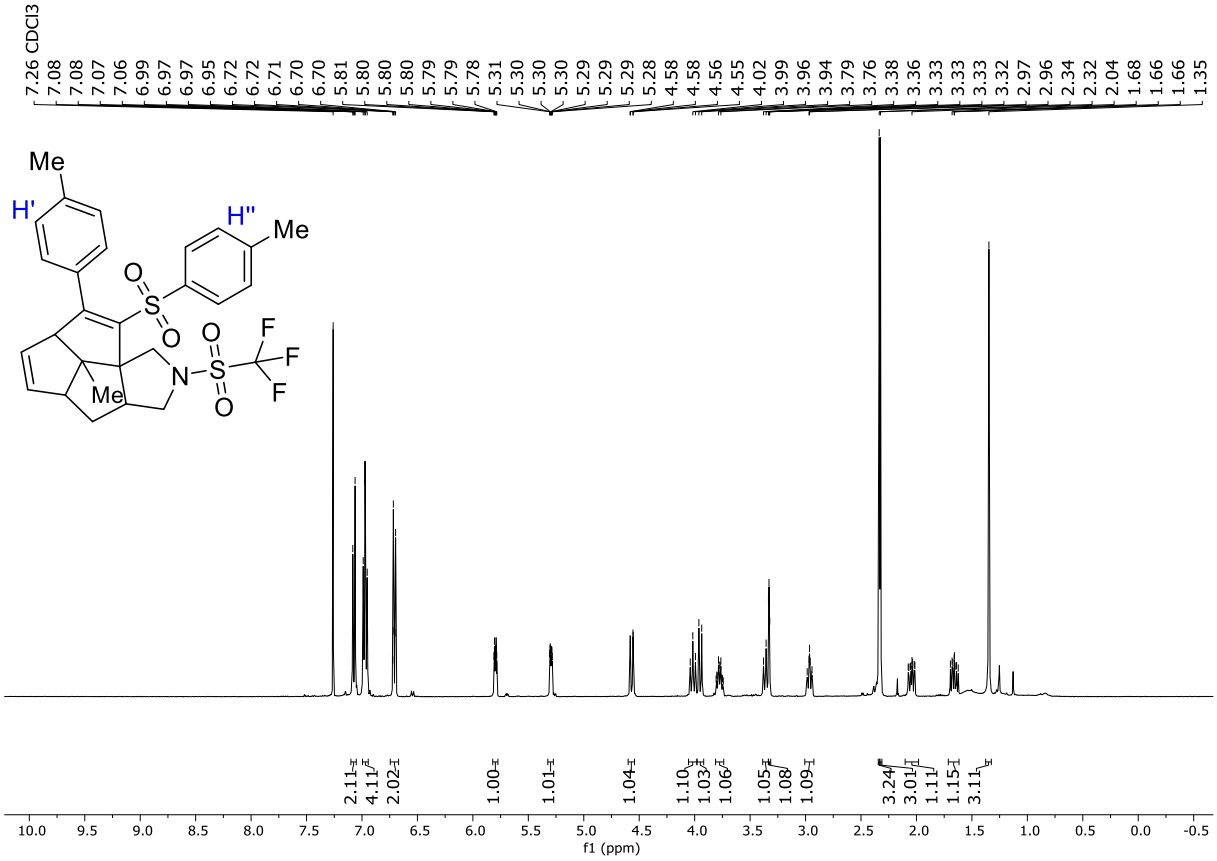

^{1}H NMR (400 MHz, $CDCl_3$) spectrum of **7b**

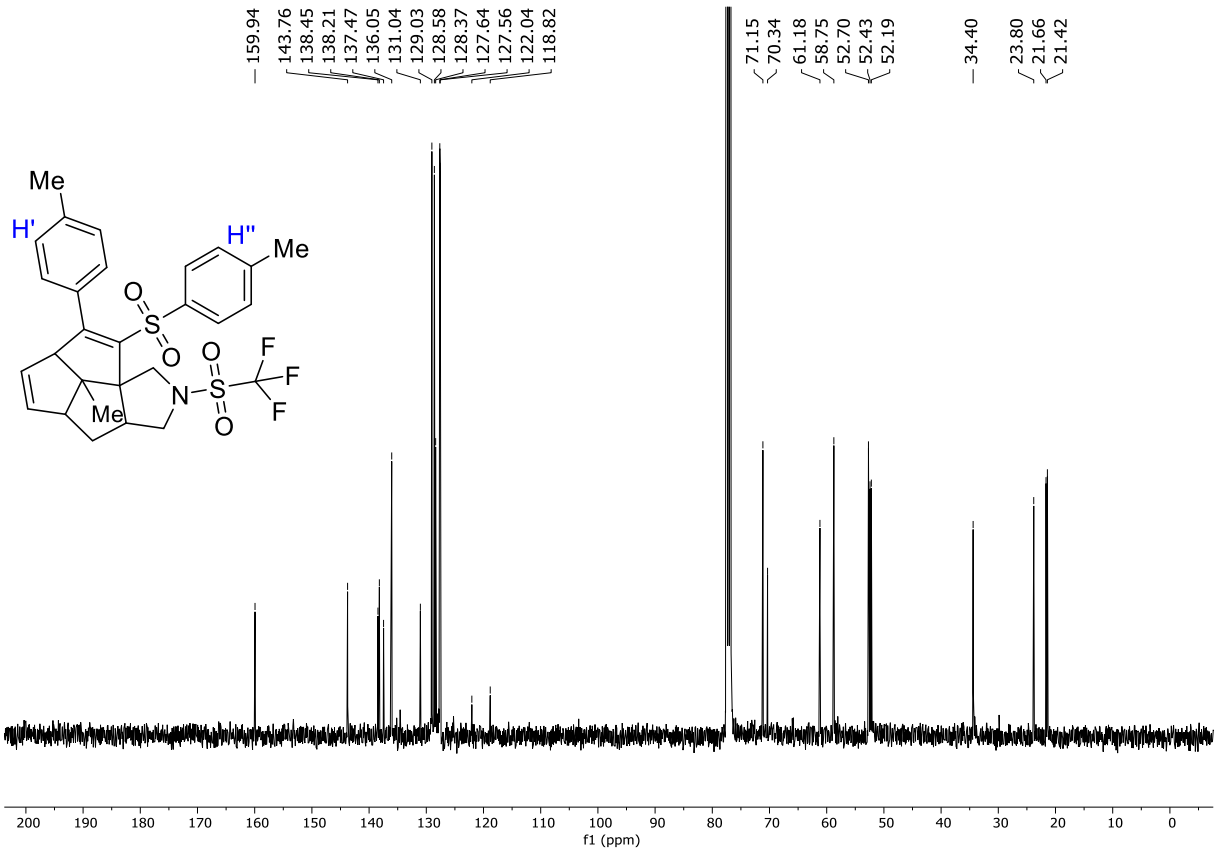

^{13}C NMR (101 MHz, $CDCl_3$) spectrum of **7b**

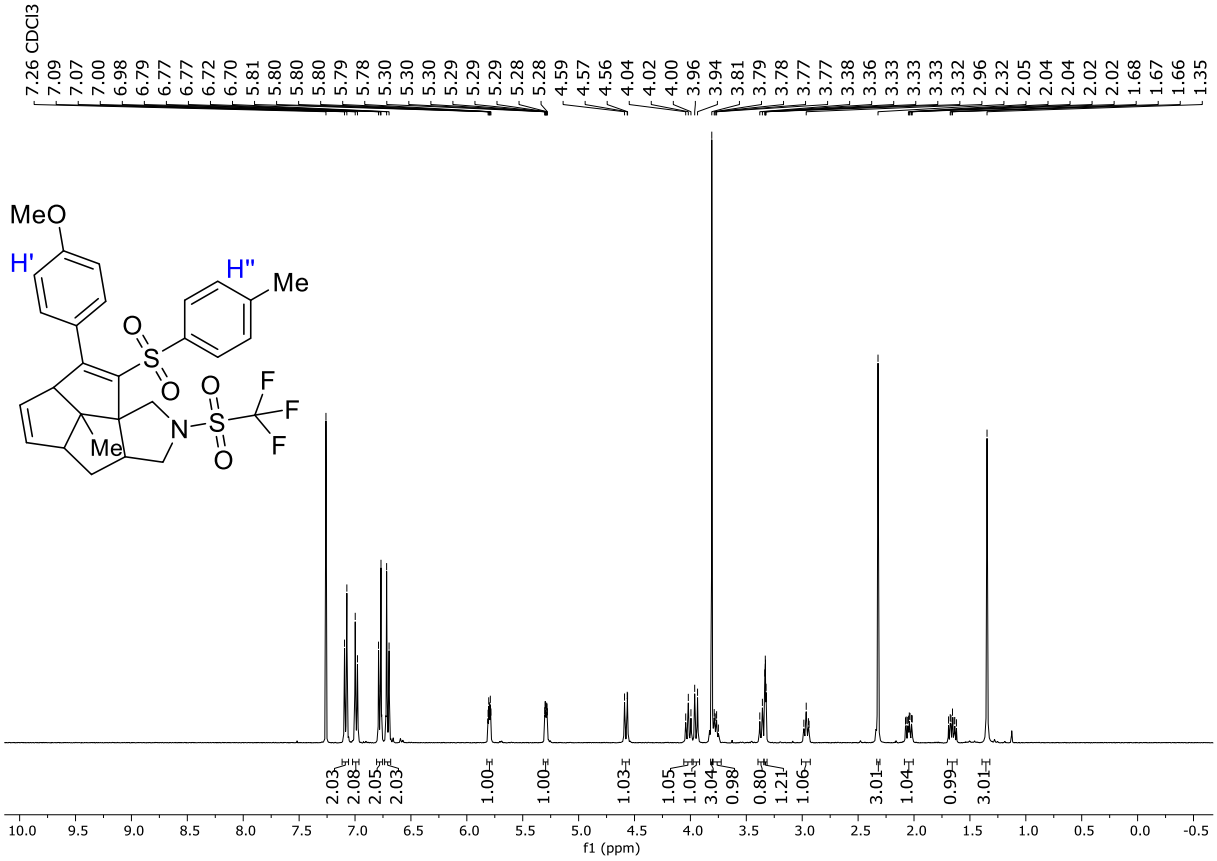

^{1}H NMR (400 MHz, $CDCl_3$) spectrum of **7c**

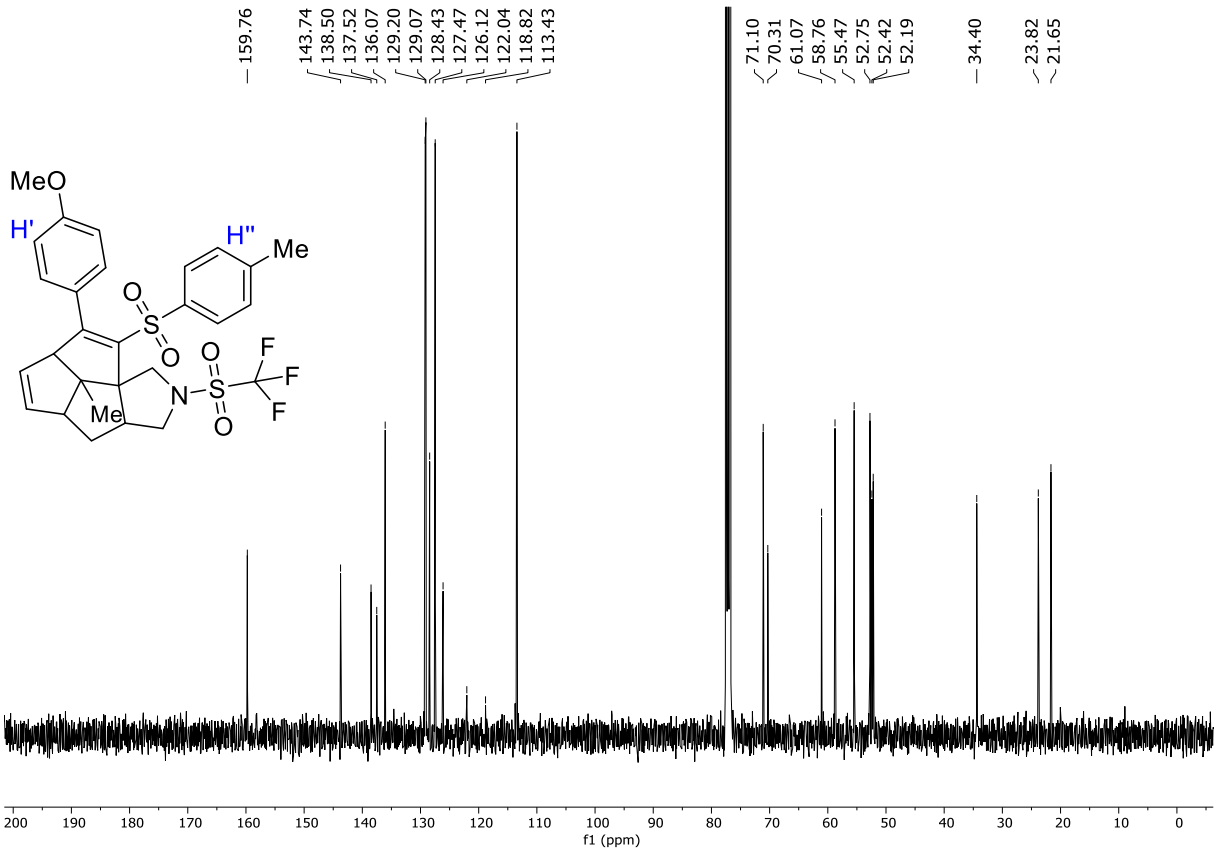

^{13}C NMR (101 MHz, $CDCl_3$) spectrum of **7c**

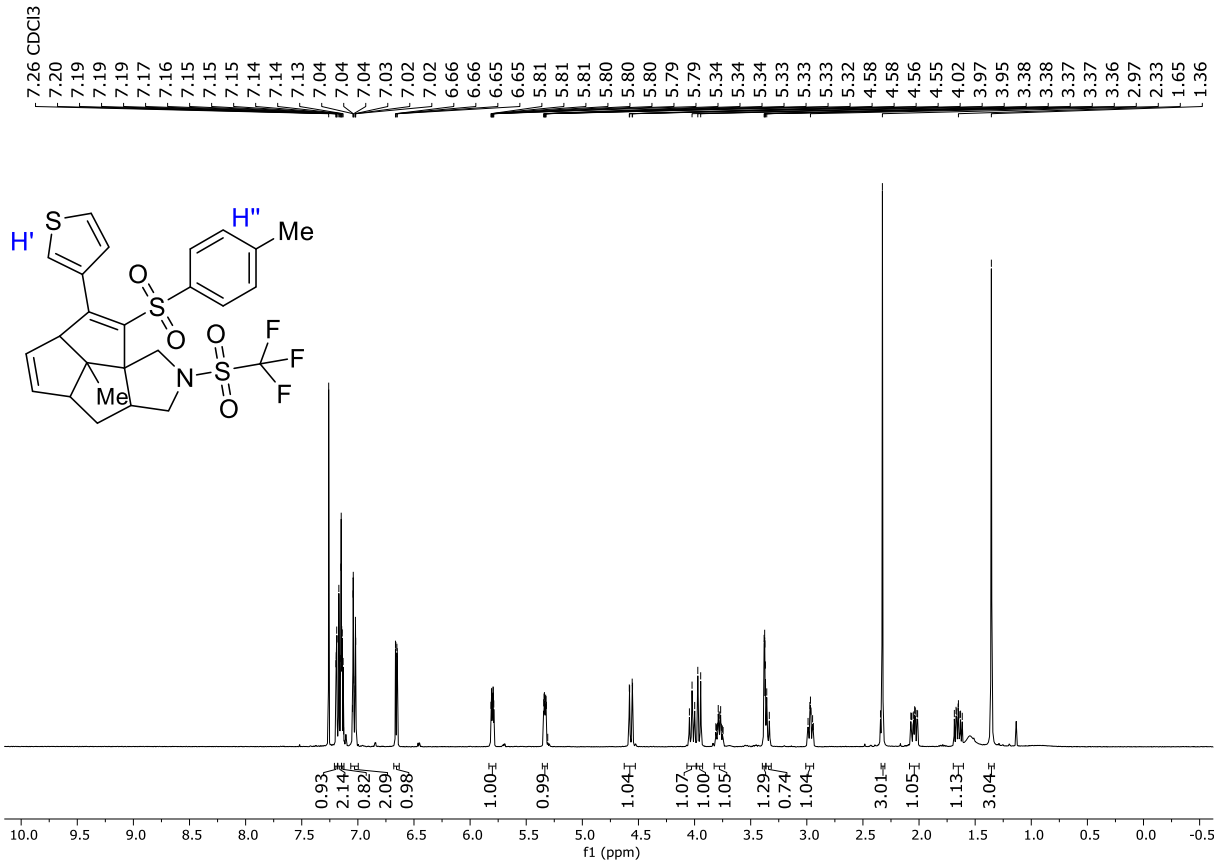

^{1}H NMR (400 MHz, $CDCl_3$) spectrum of **7d**

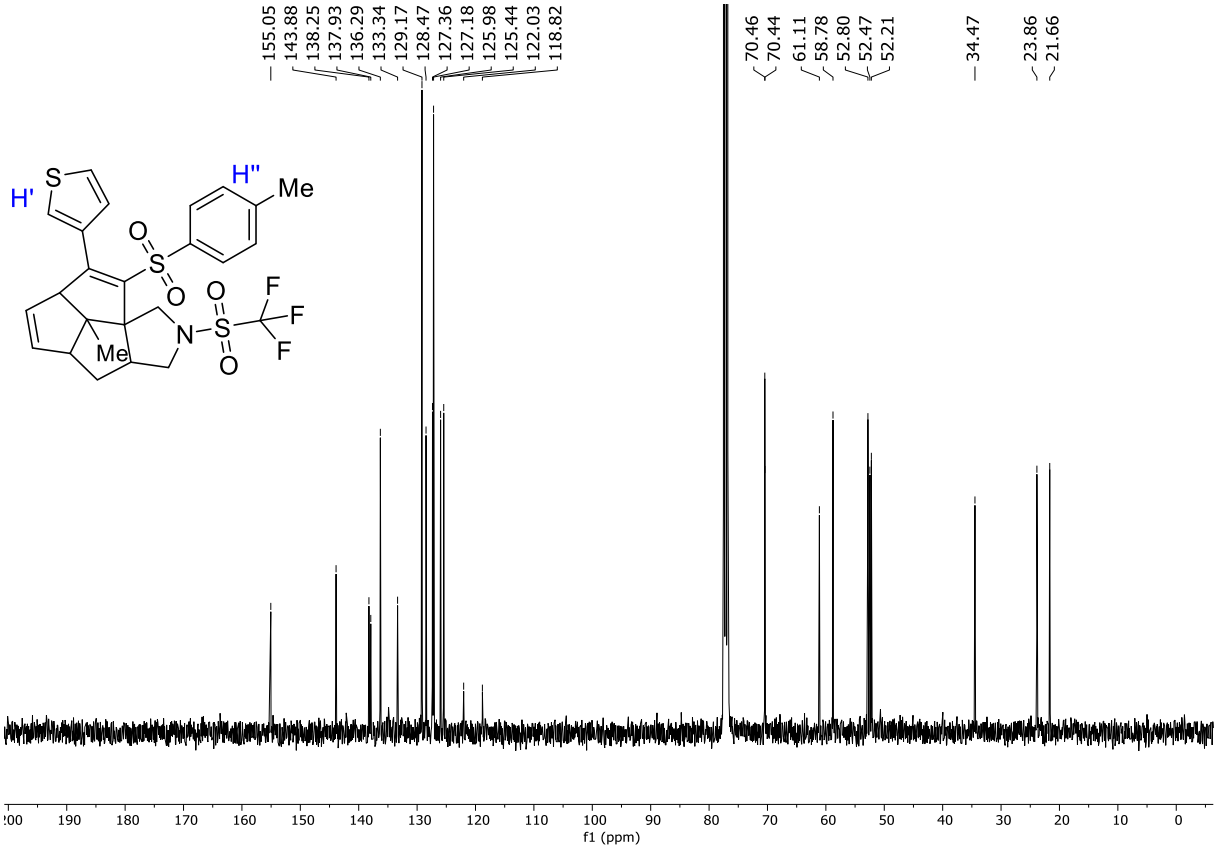

^{13}C NMR (101 MHz, $CDCl_3$) spectrum of **7d**

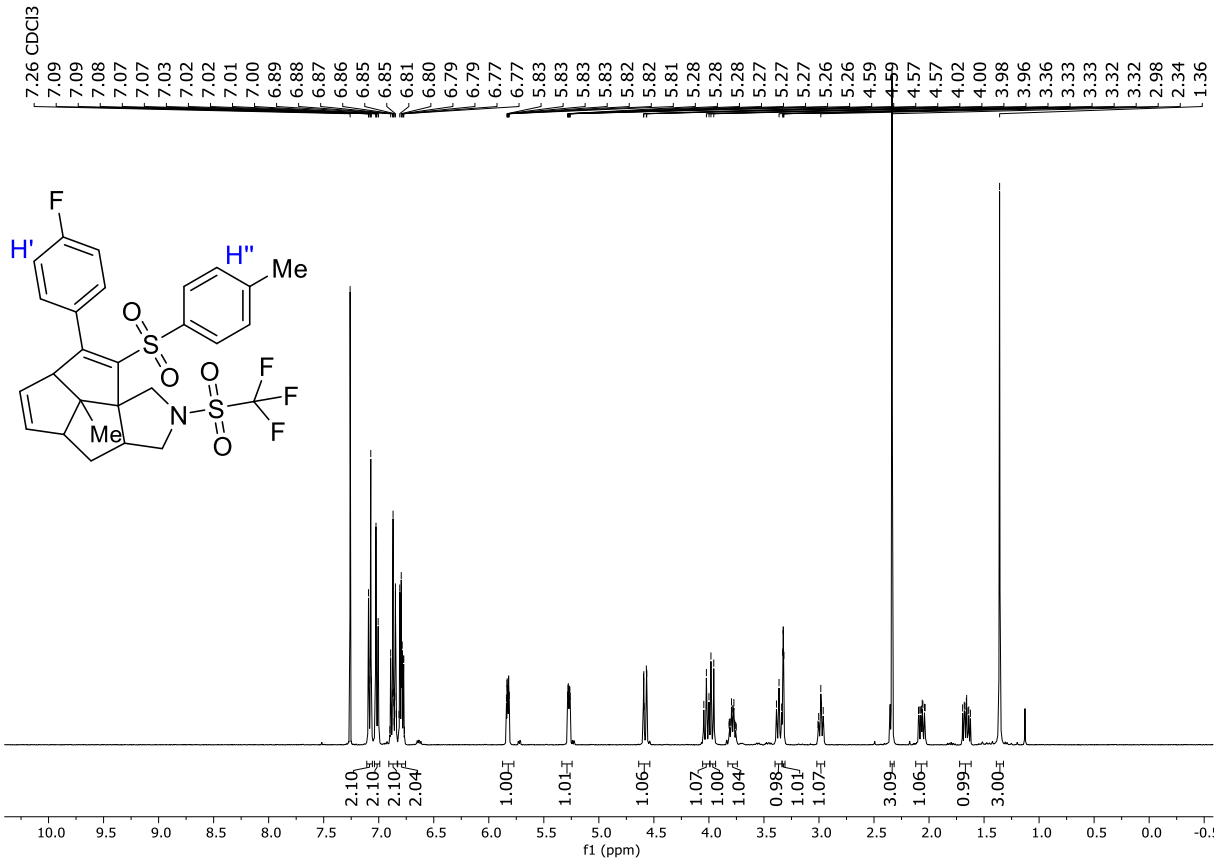

^{1}H NMR (400 MHz, $CDCl_3$) spectrum of **7e**

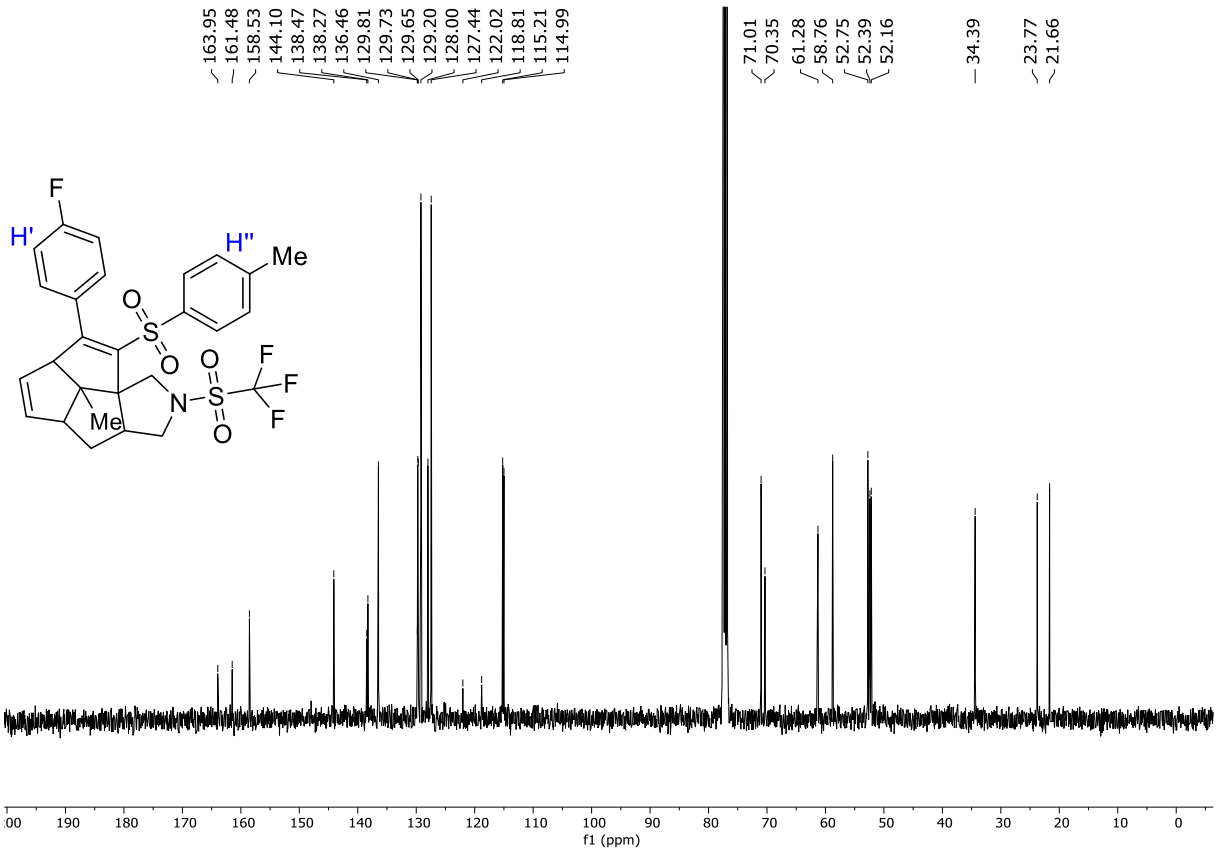

^{13}C NMR (101 MHz, $CDCl_3$) spectrum of **7e**

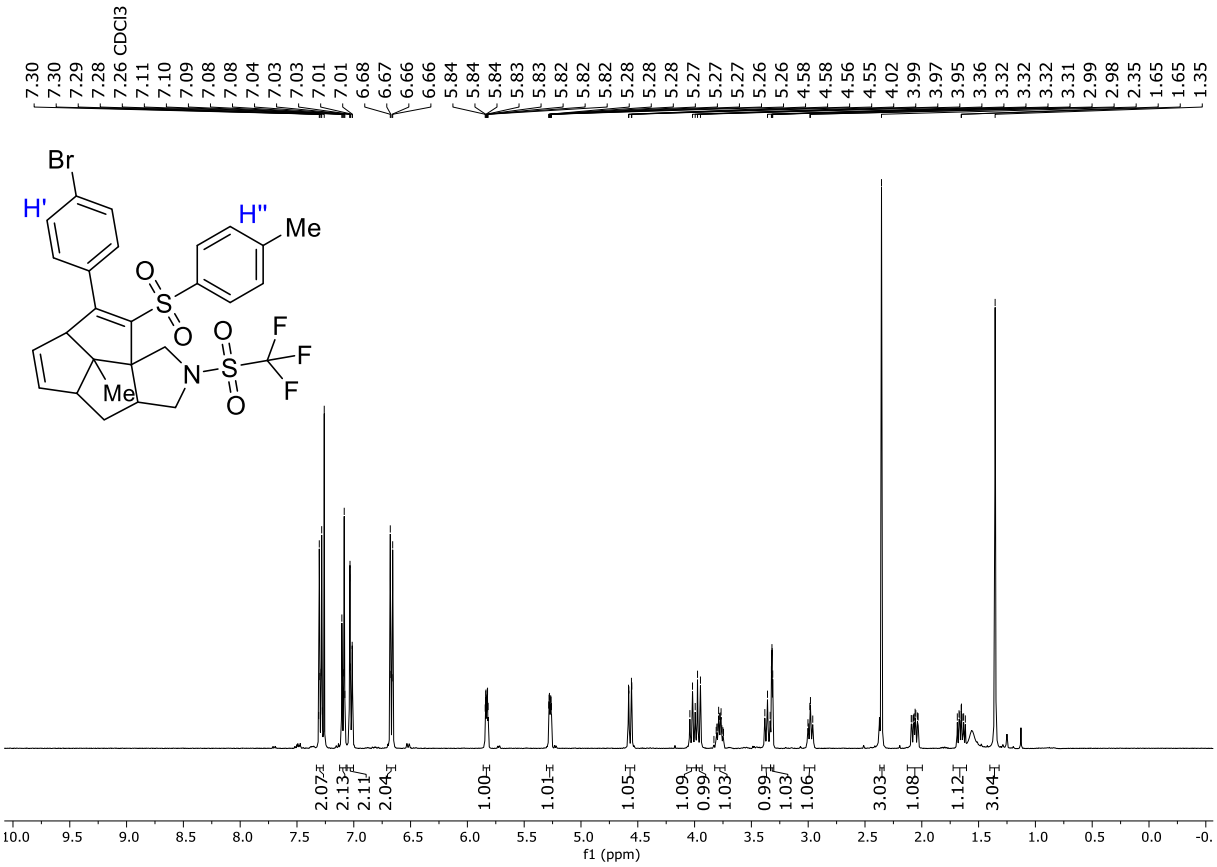

^{1}H NMR (400 MHz, $CDCl_3$) spectrum of **7f**

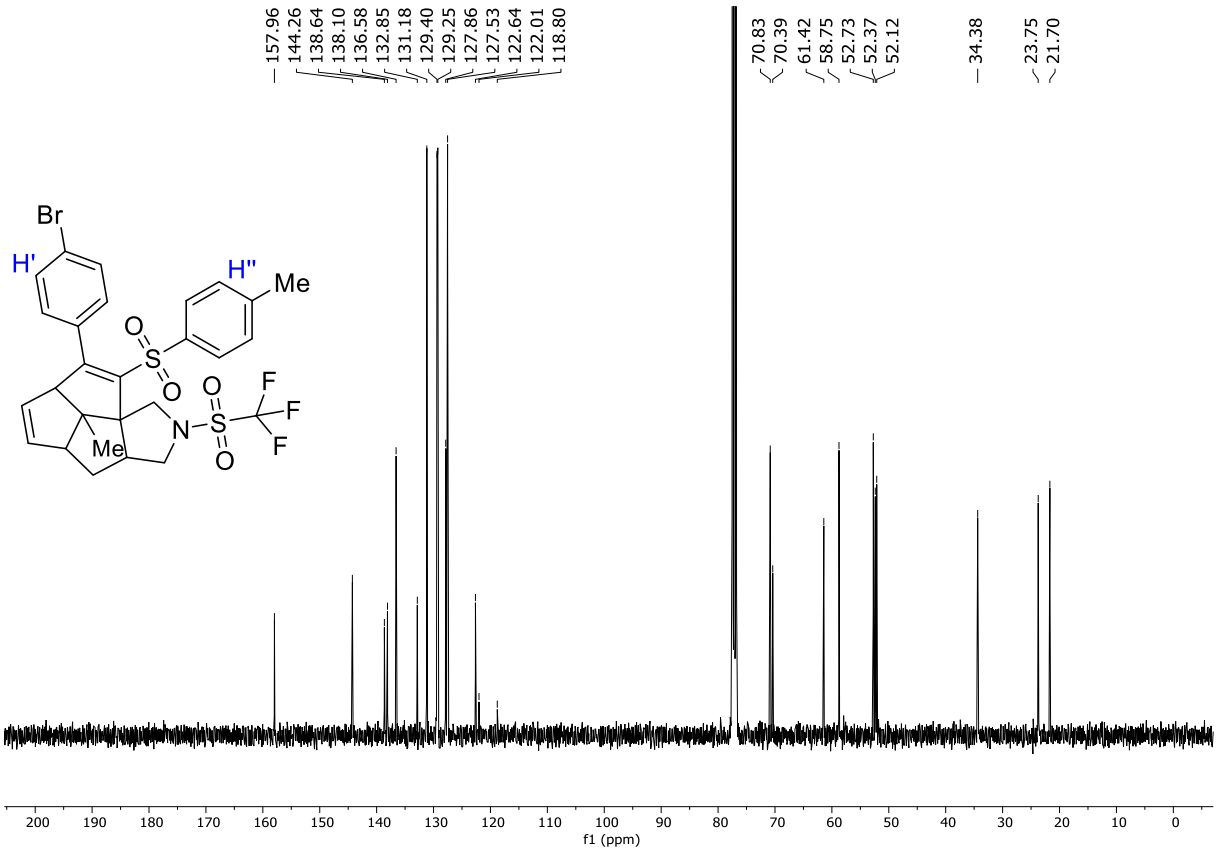

^{13}C NMR (101 MHz, $CDCl_3$) spectrum of **7f**

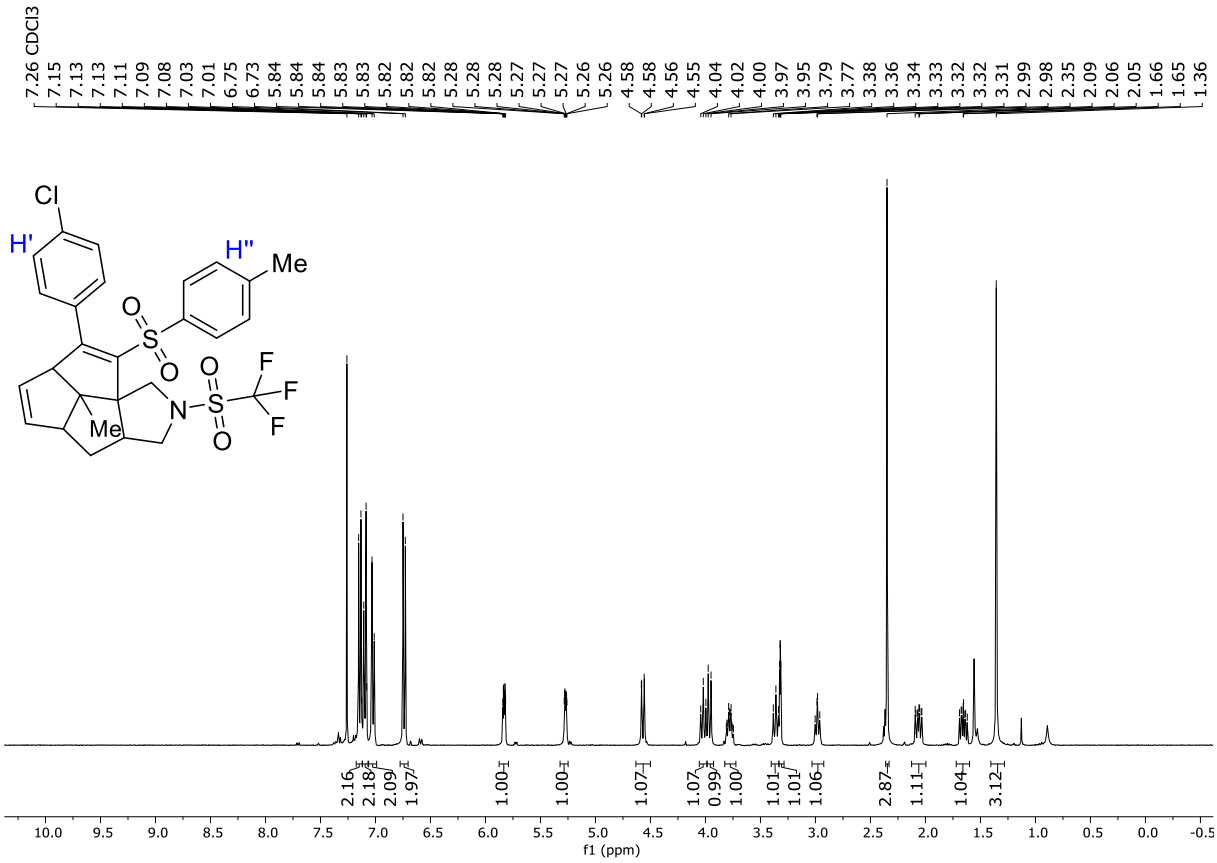

^{1}H NMR (400 MHz, $CDCl_3$) spectrum of **7g**

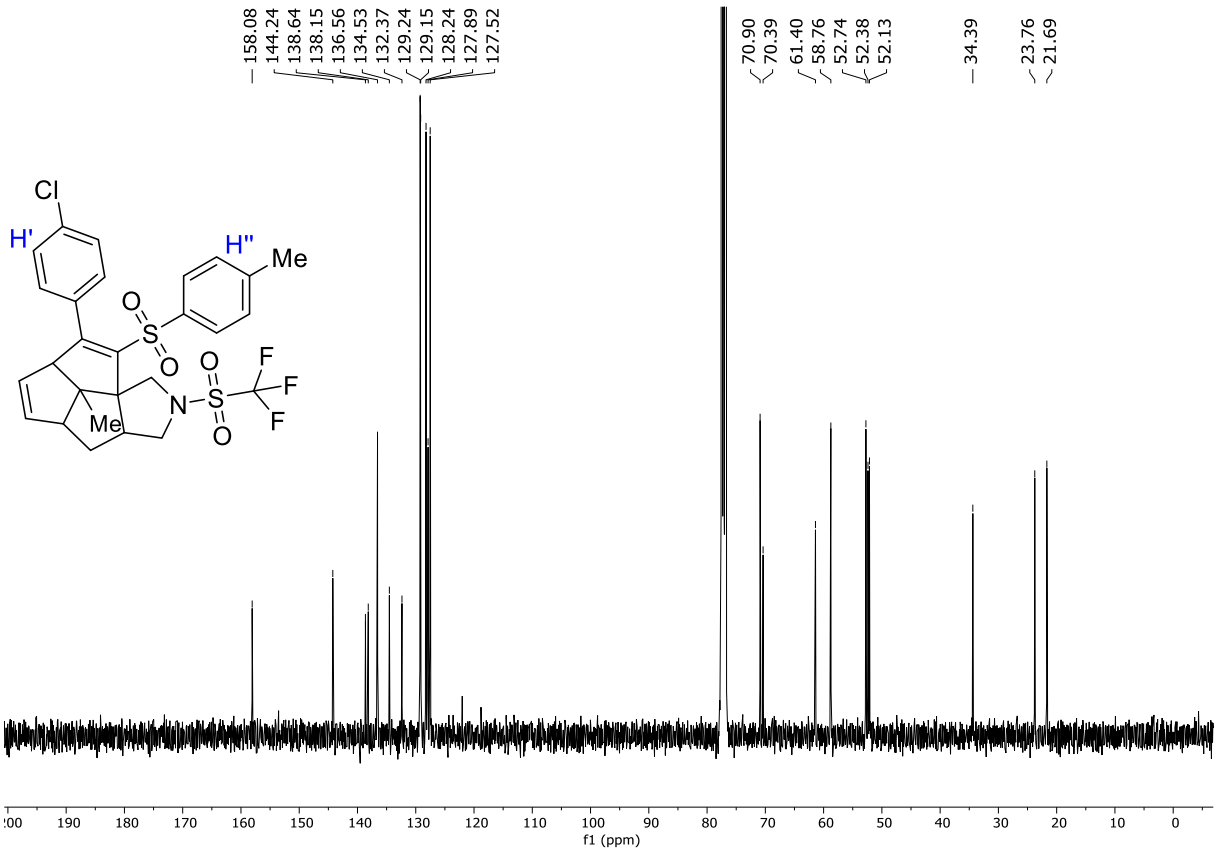

^{13}C NMR (101 MHz, $CDCl_3$) spectrum of **7g**

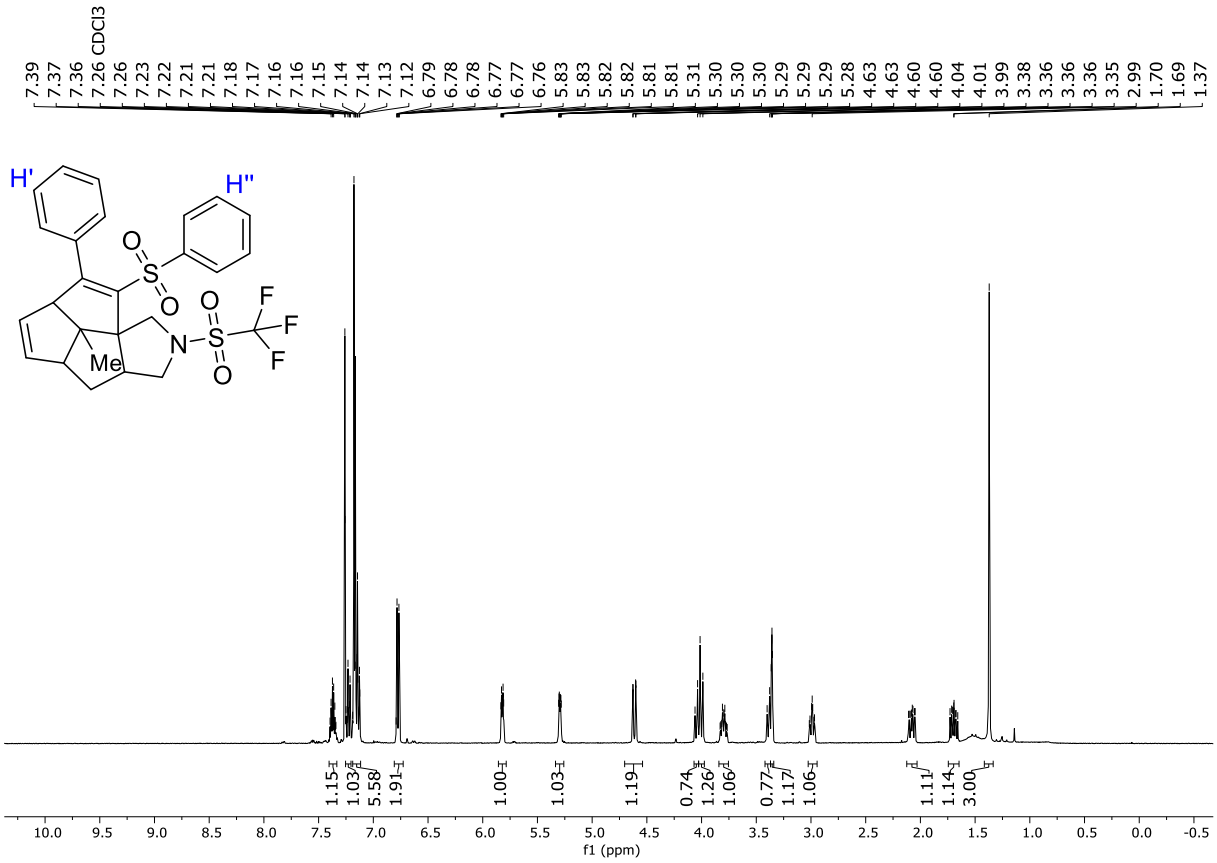

^{1}H NMR (400 MHz, $CDCl_3$) spectrum of **7h**

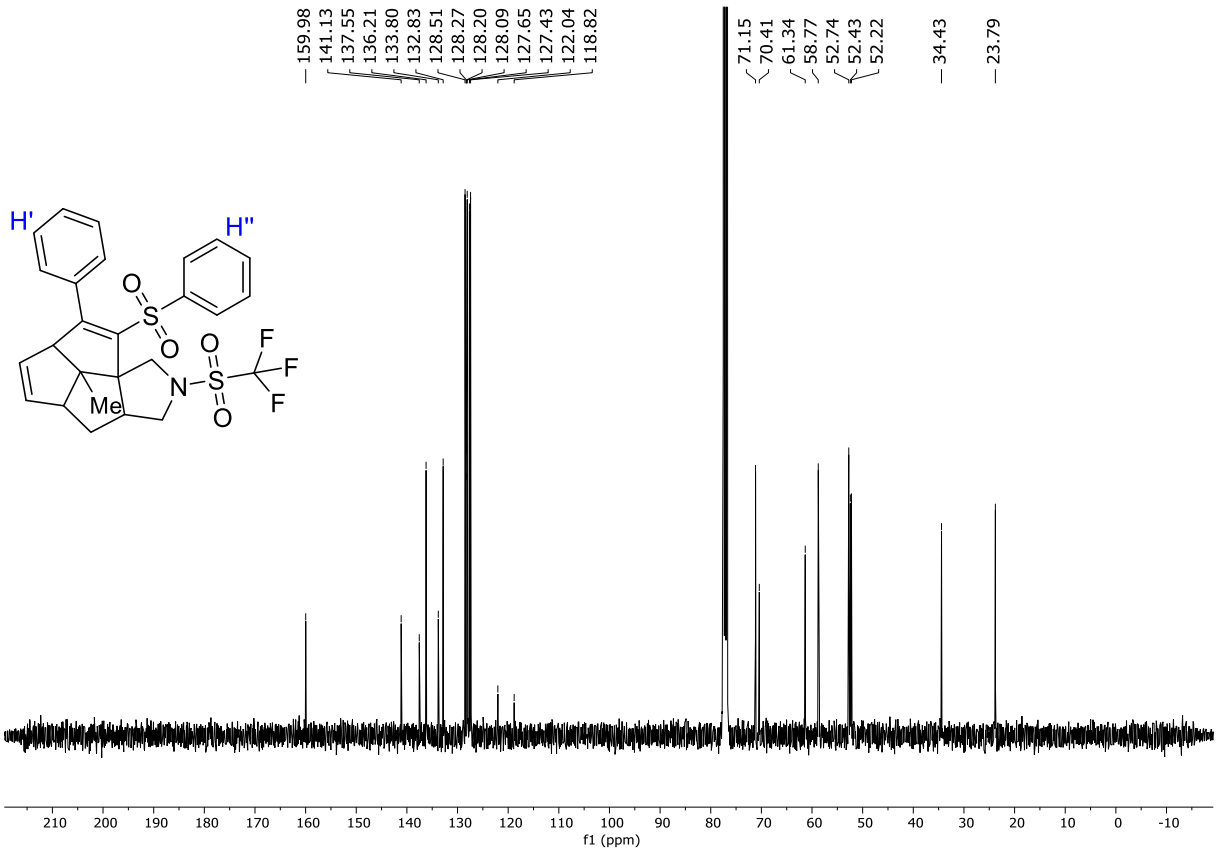

^{13}C NMR (101 MHz, $CDCl_3$) spectrum of **7h**

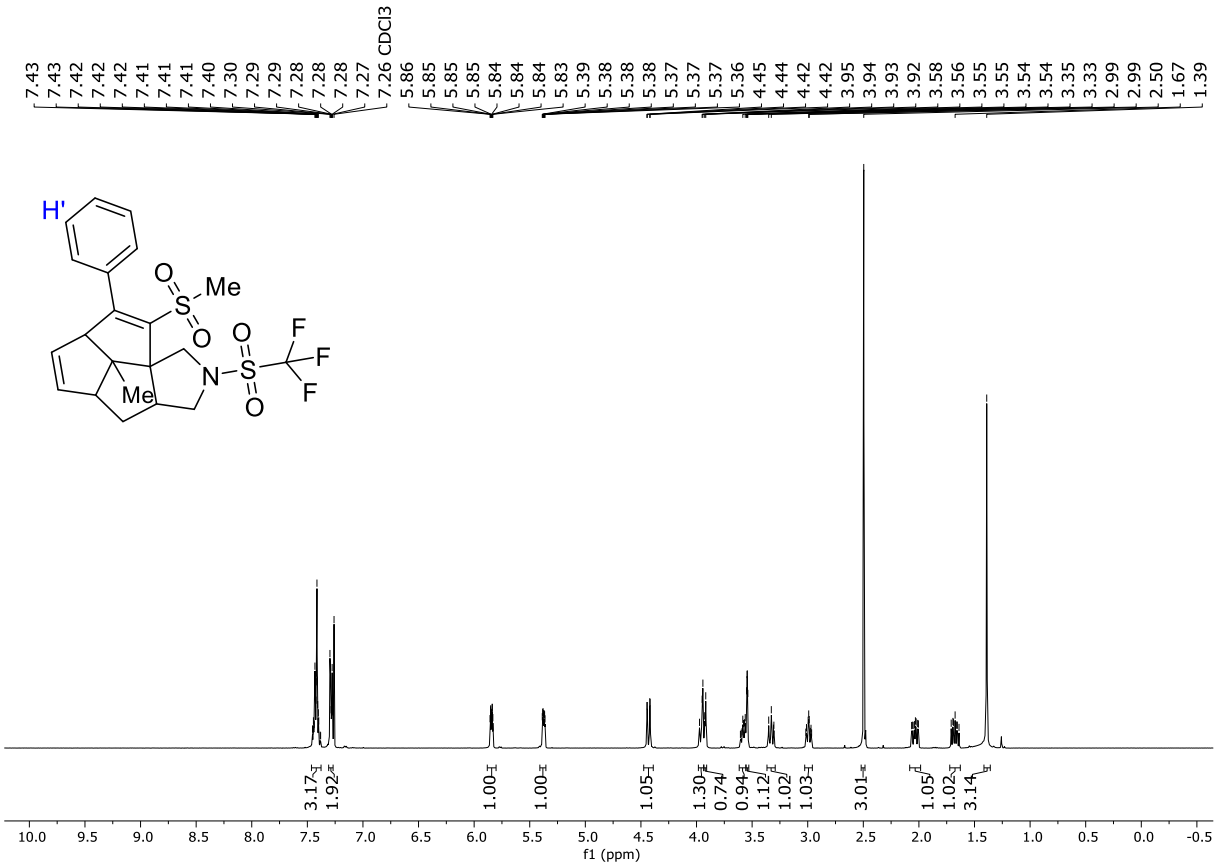

^{1}H NMR (400 MHz, $CDCl_3$) spectrum of **7i**

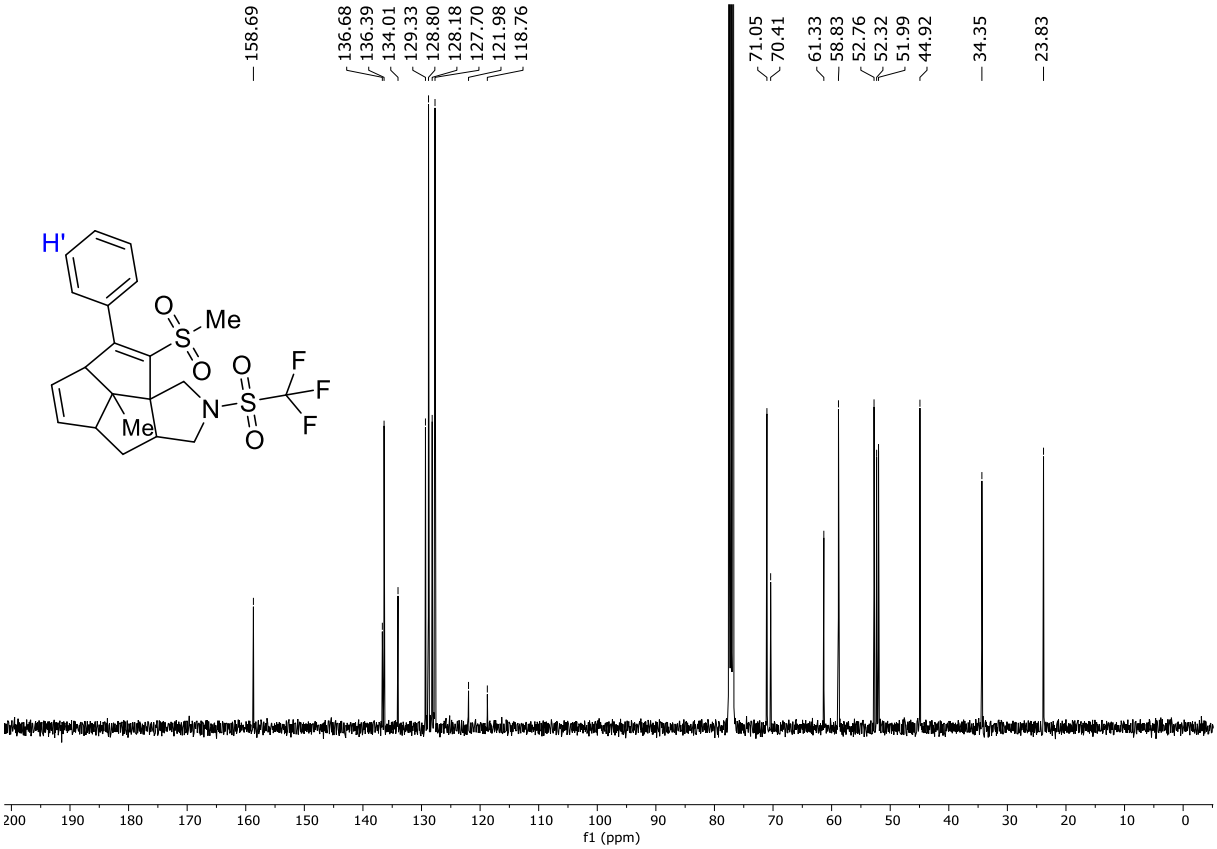

^{13}C NMR (101 MHz, $CDCl_3$) spectrum of **7i**

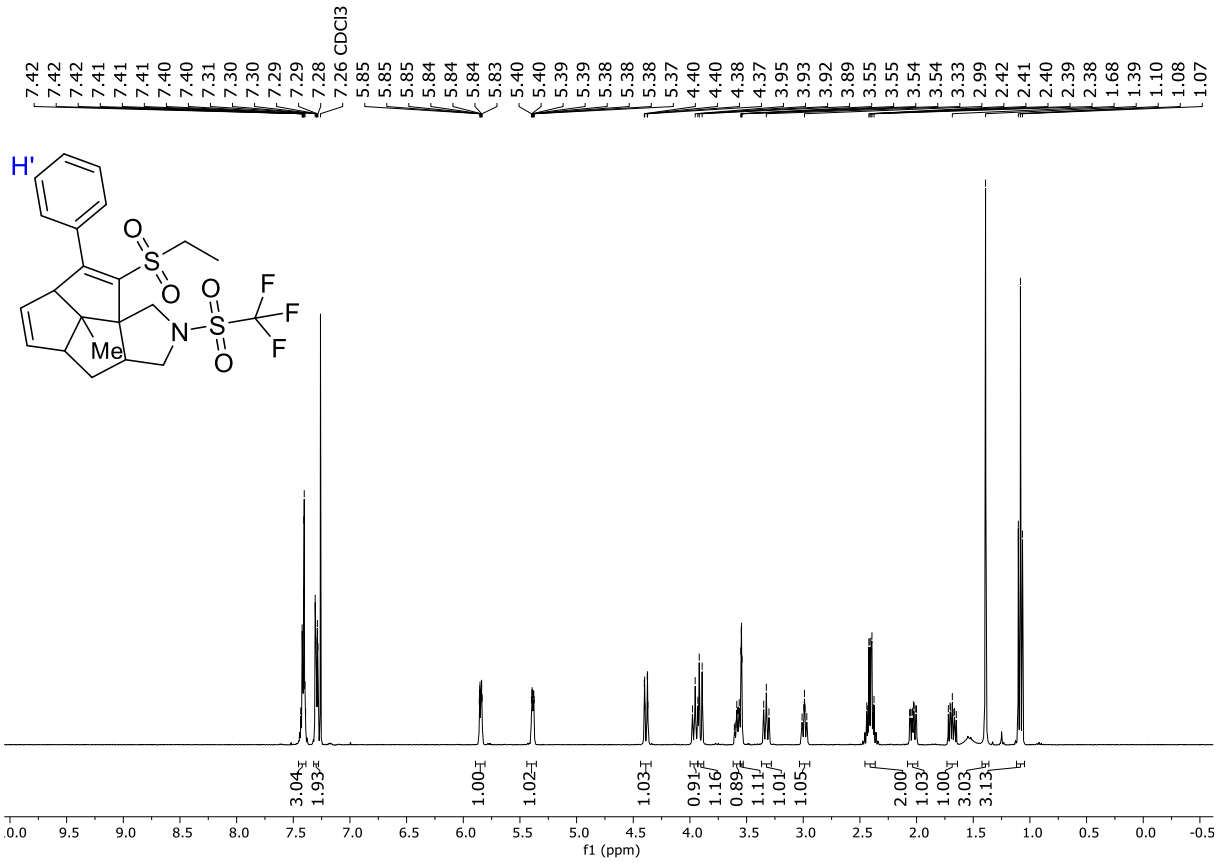

^{1}H NMR (400 MHz, $CDCl_3$) spectrum of **7j**

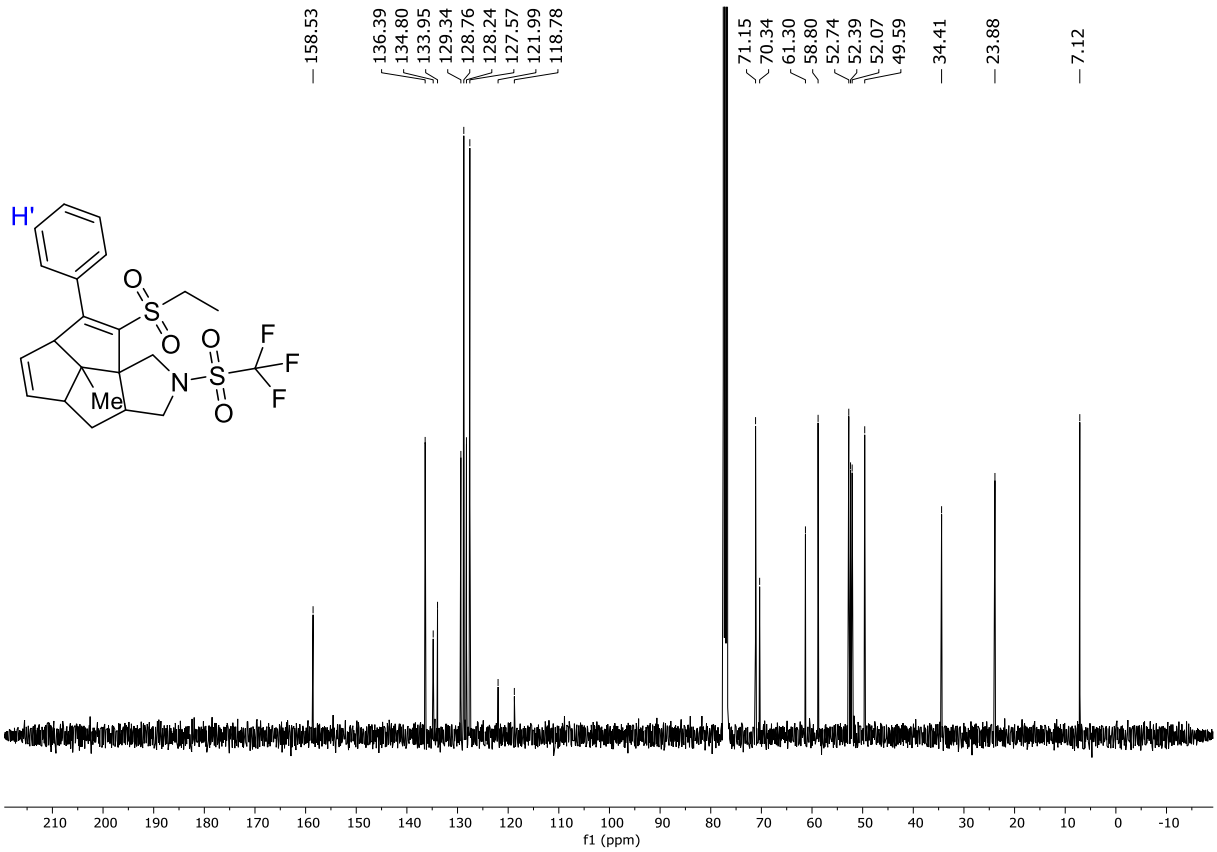

^{13}C NMR (101 MHz, $CDCl_3$) spectrum of **7j**

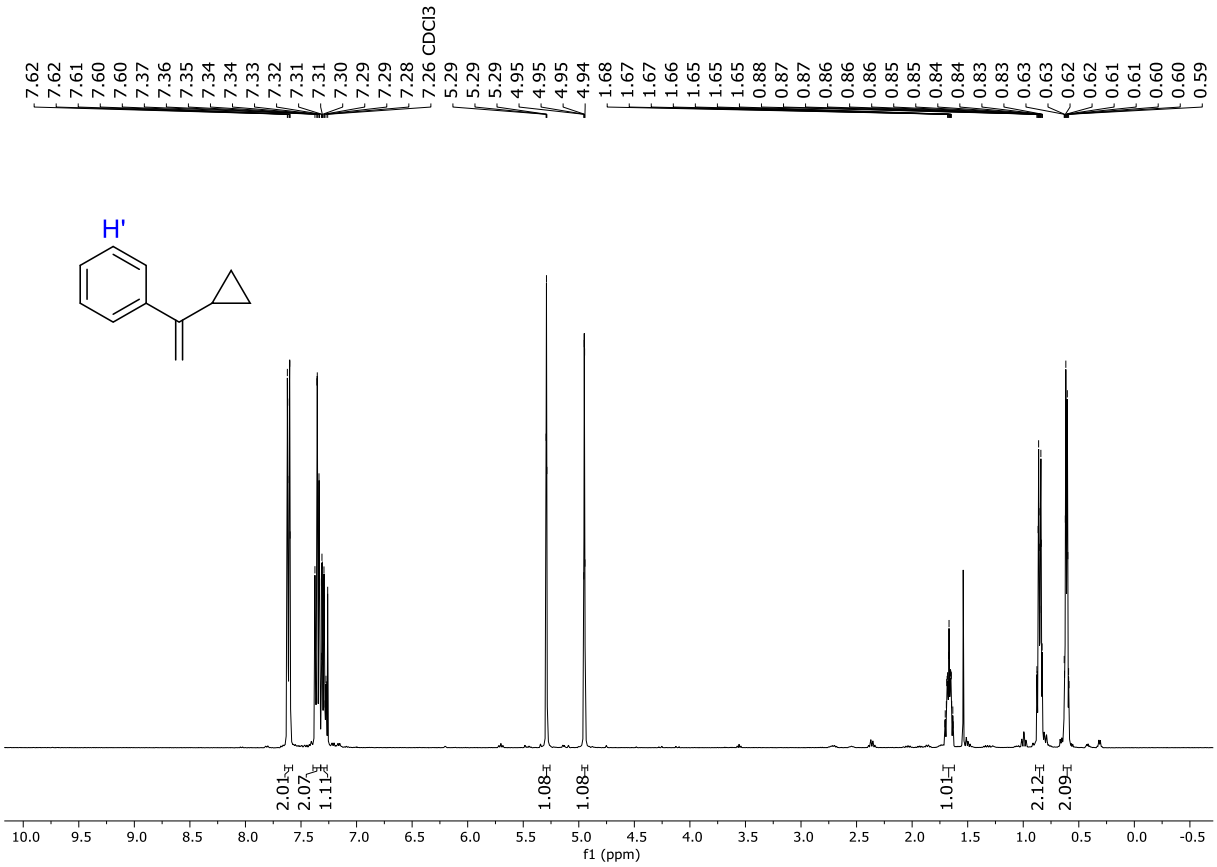

^{1}H NMR (400 MHz, $CDCl_3$) spectrum of **8**

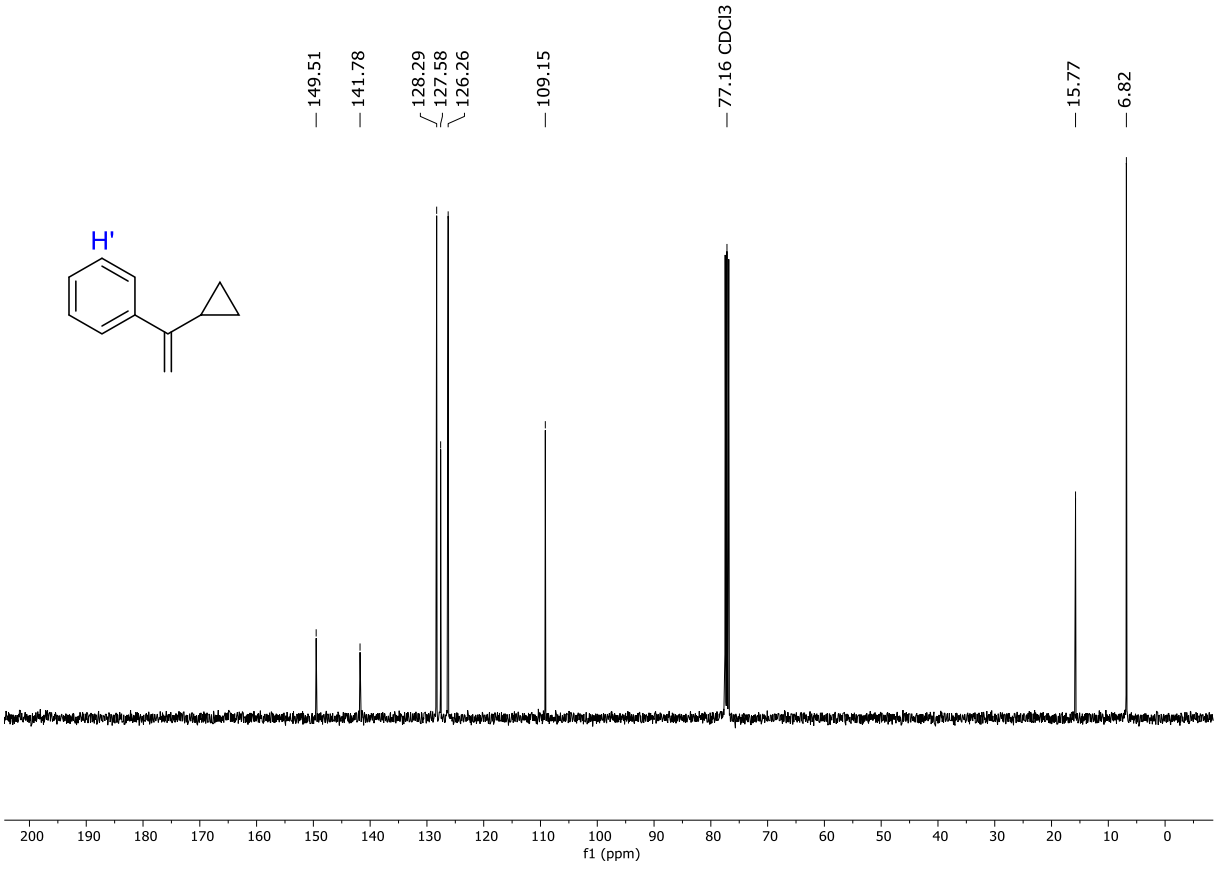

^{13}C NMR (101 MHz, $CDCl_3$) spectrum of **8**

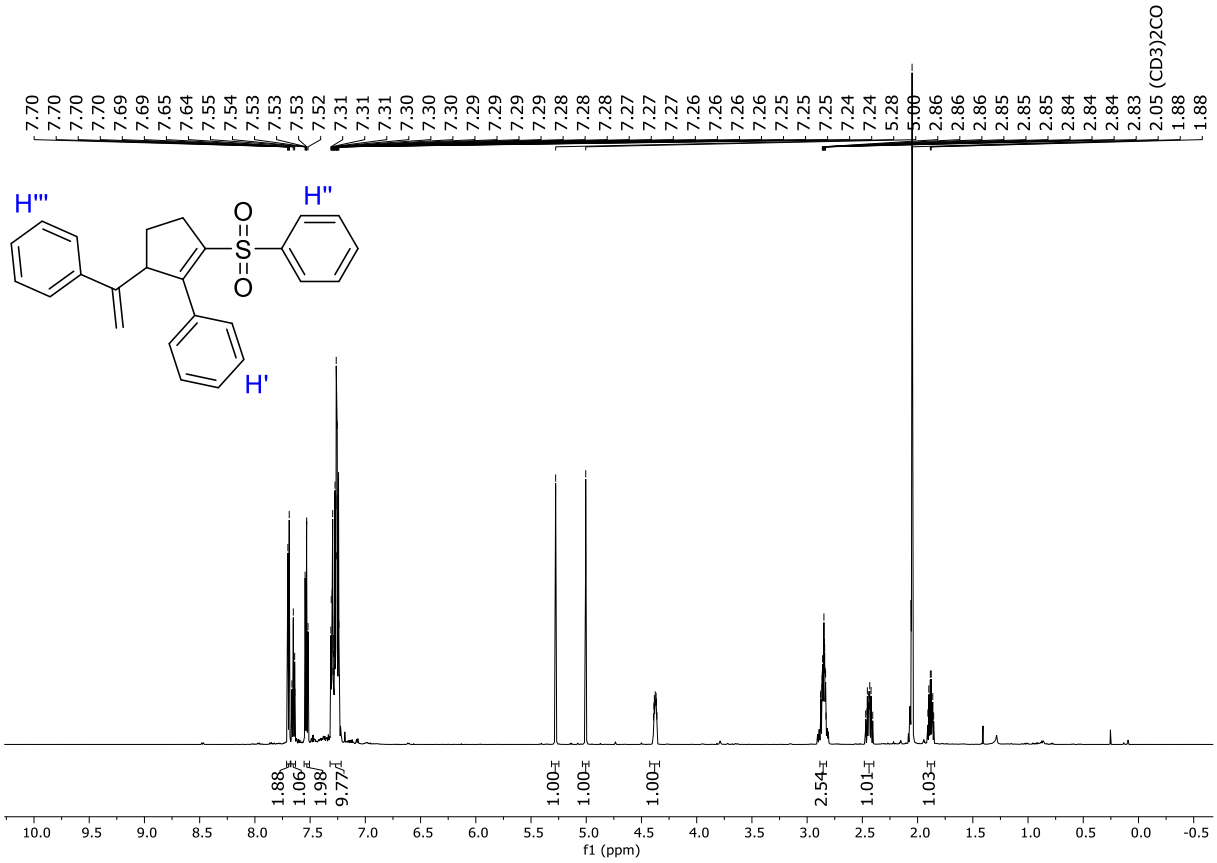

^{1}H NMR (400 MHz, acetone-d_6) spectrum of **9**

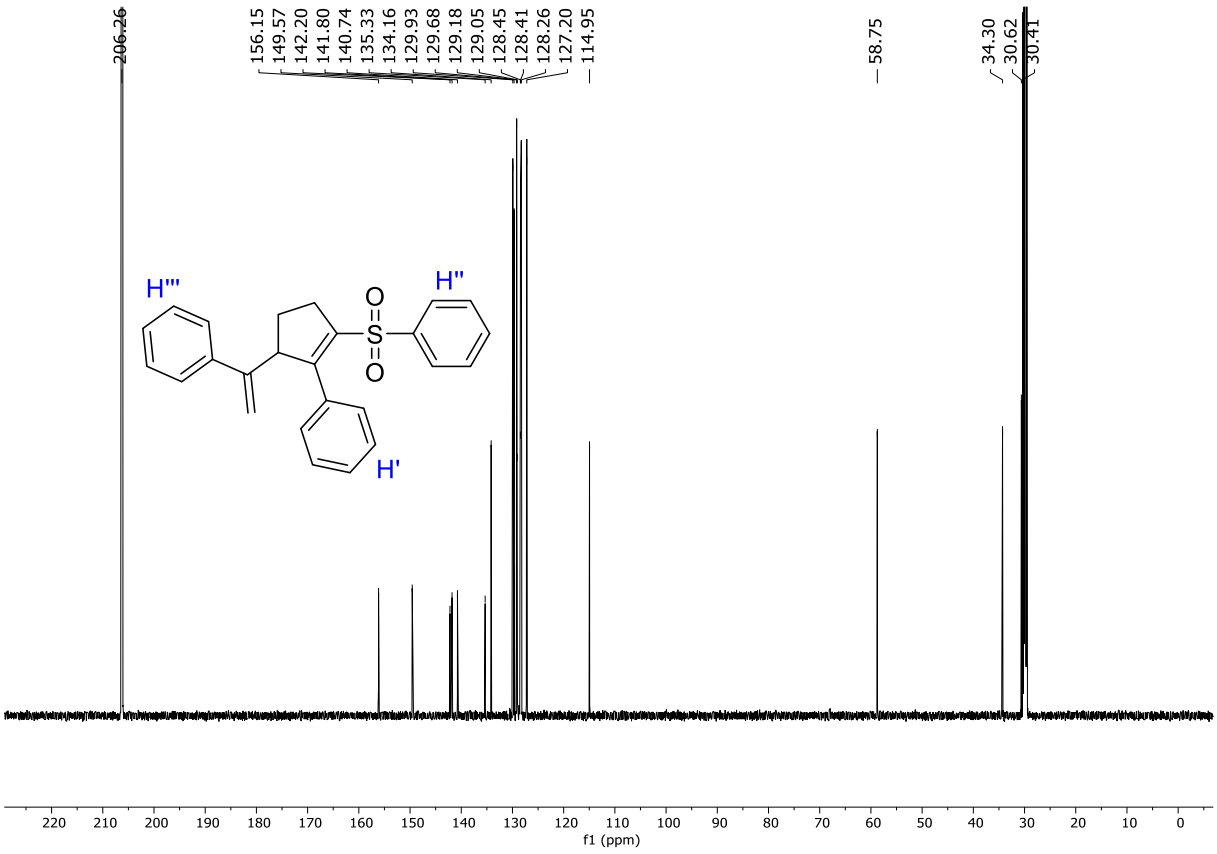

^{13}C NMR (101 MHz, acetone-d_6) spectrum of **8**

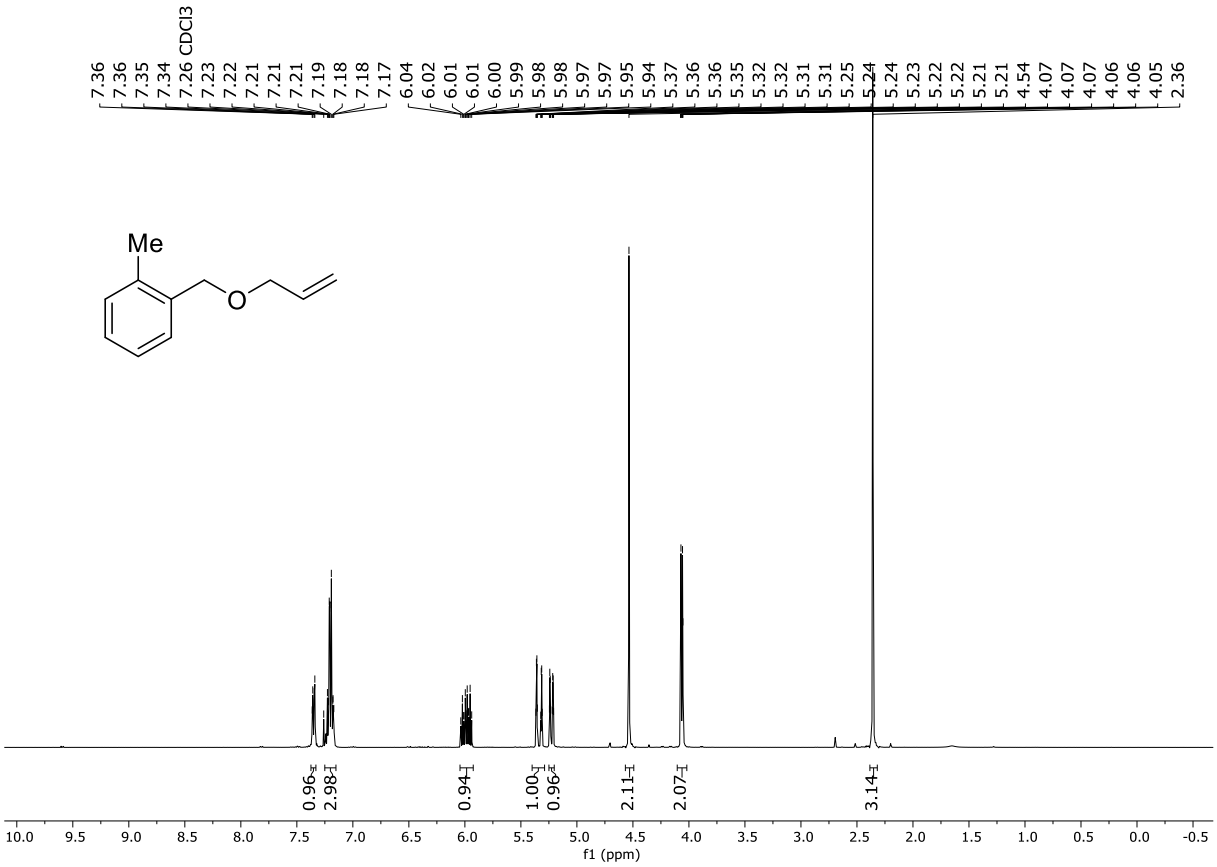

^{1}H NMR (400 MHz, $CDCl_3$) spectrum of **10**

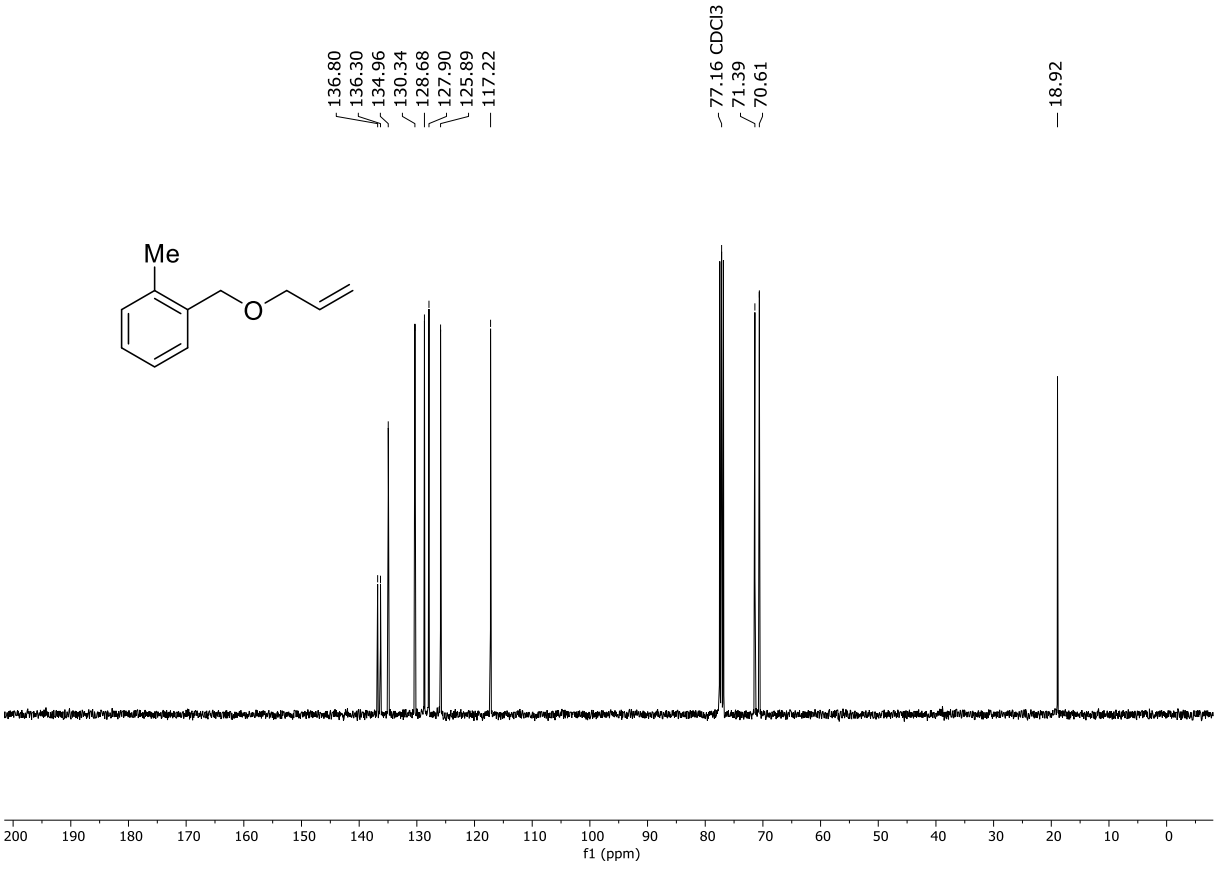

^{13}C NMR (101 MHz, $CDCl_3$) spectrum of **10**

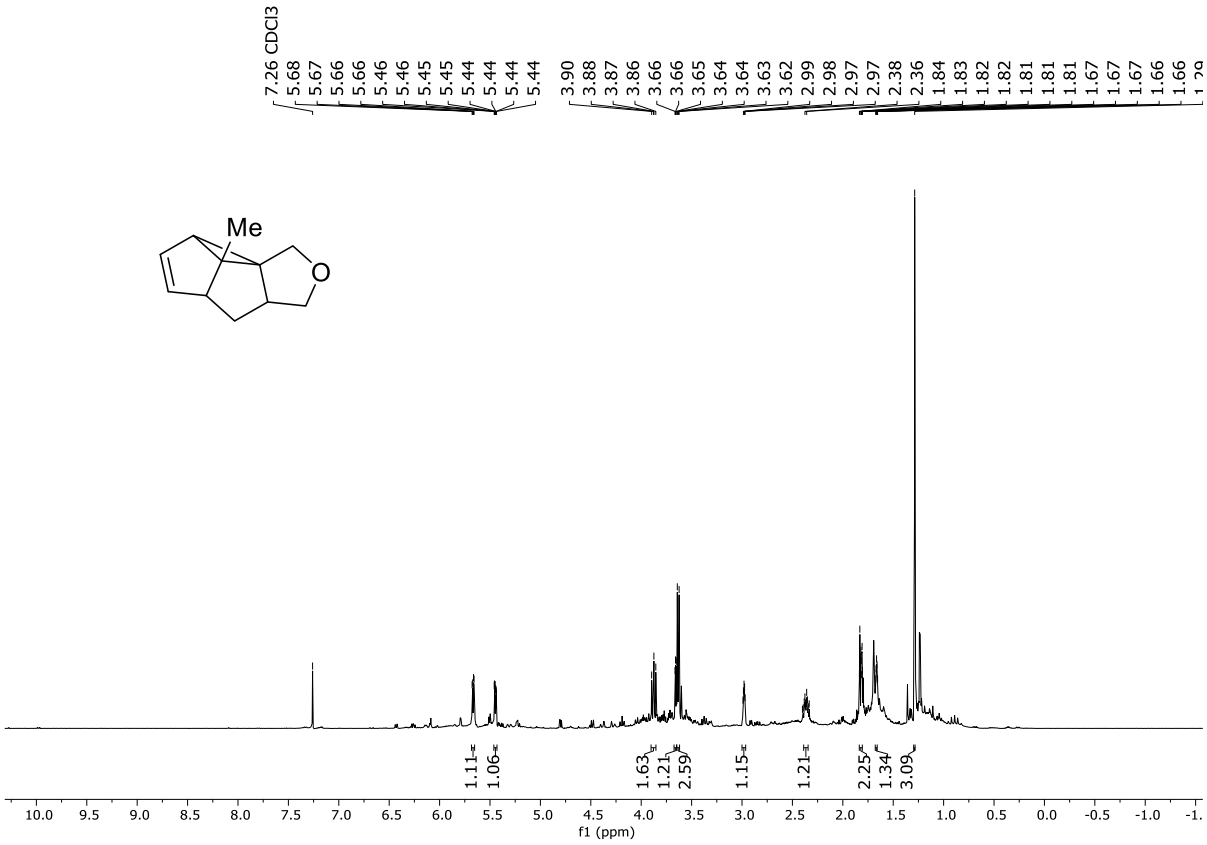

^{1}H NMR (400 MHz, $CDCl_3$) spectrum of **11** (inseparable product mixture – used without further purification for the next step)

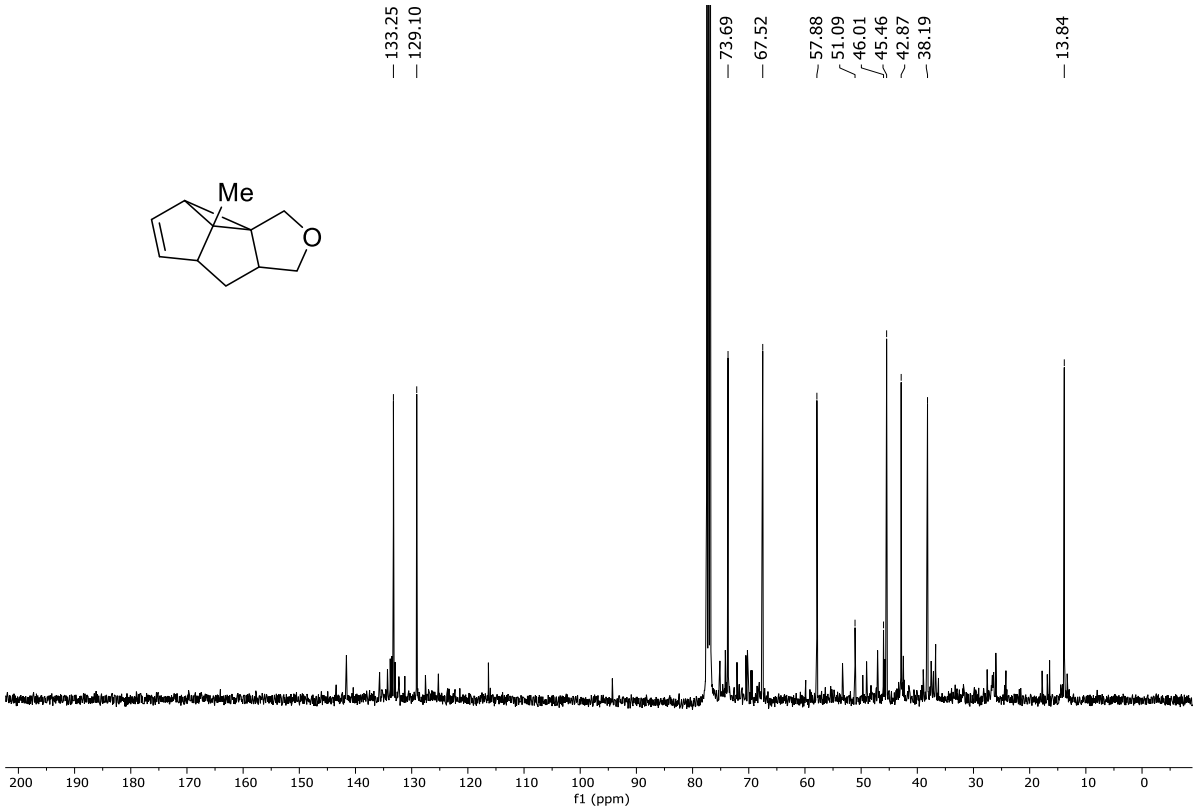

^{13}C NMR (101 MHz, $CDCl_3$) spectrum of **11** (inseparable product mixture – used without further purification for the next step)

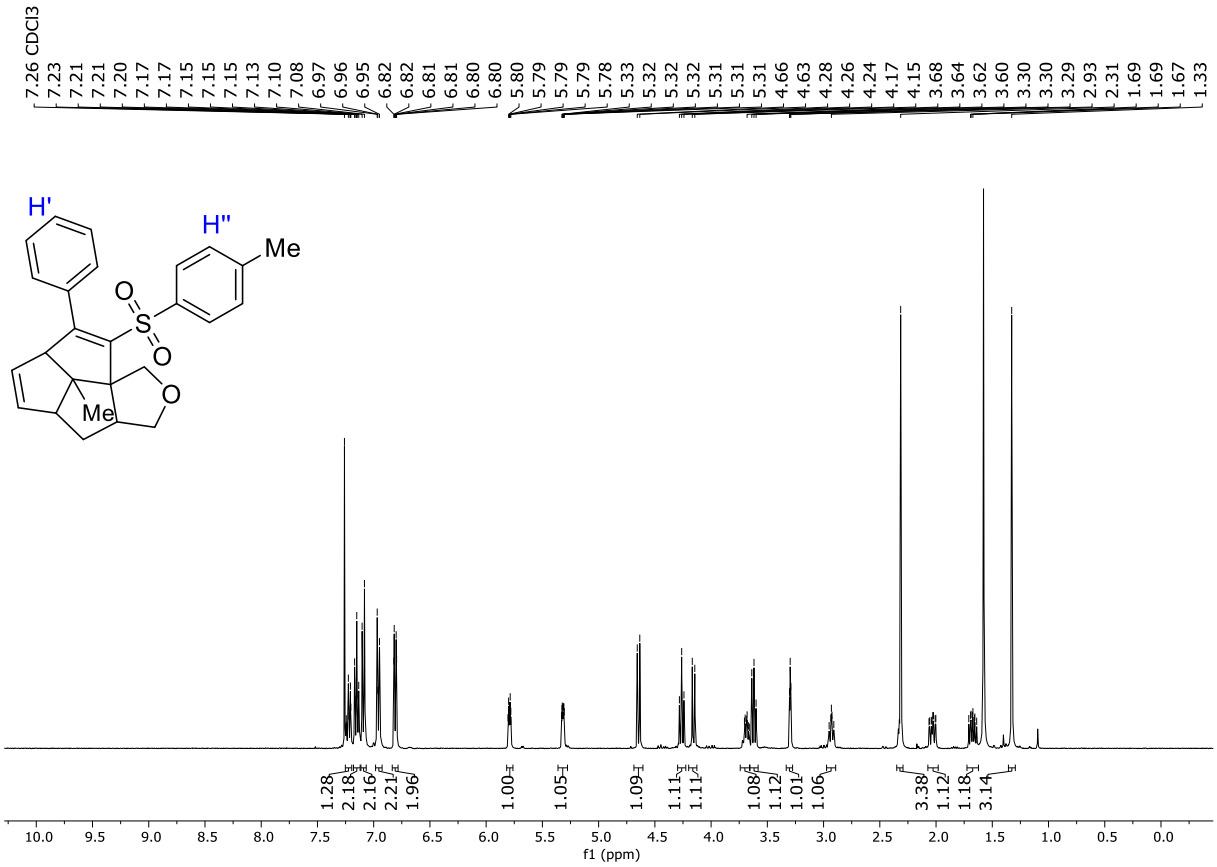

^{1}H NMR (400 MHz, $CDCl_3$) spectrum of **12**

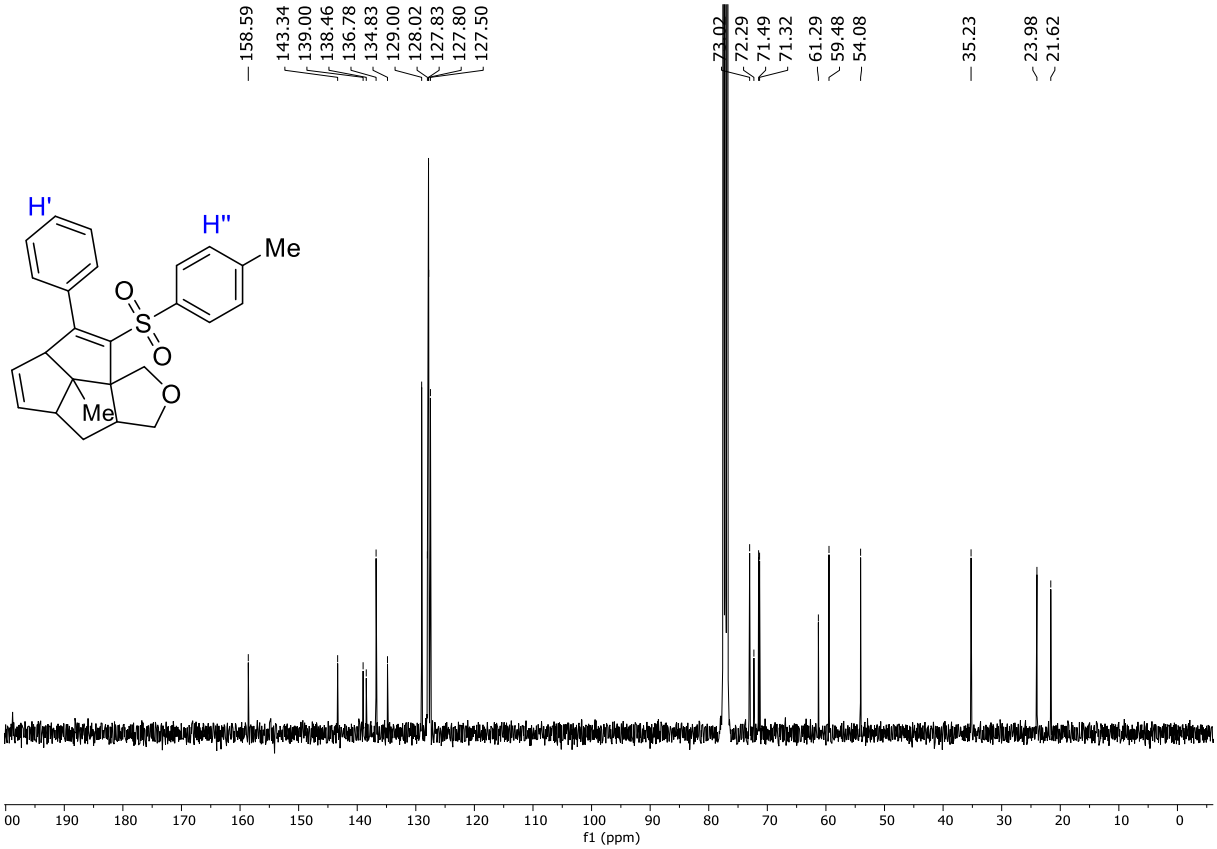

^{13}C NMR (101 MHz, $CDCl_3$) spectrum of **12**

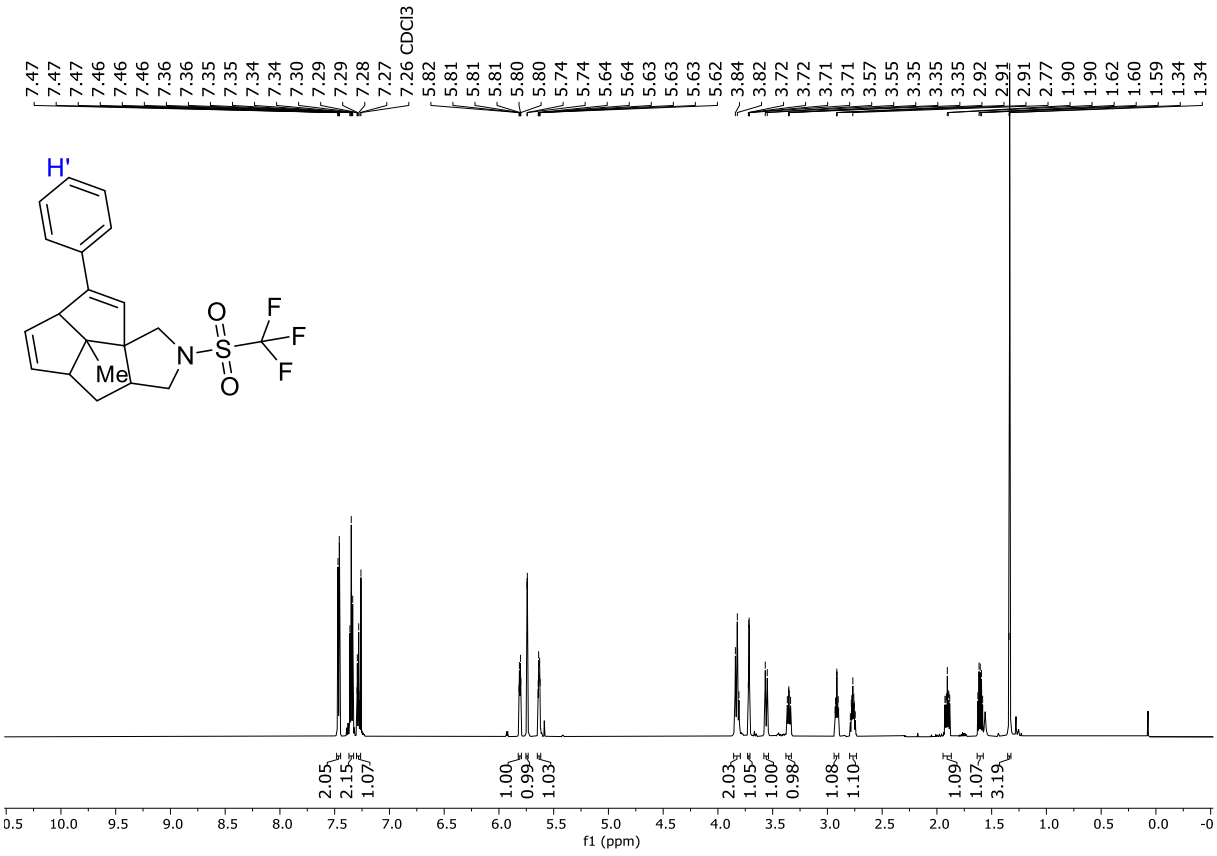

^{1}H NMR (600 MHz, $CDCl_3$) spectrum of **13**

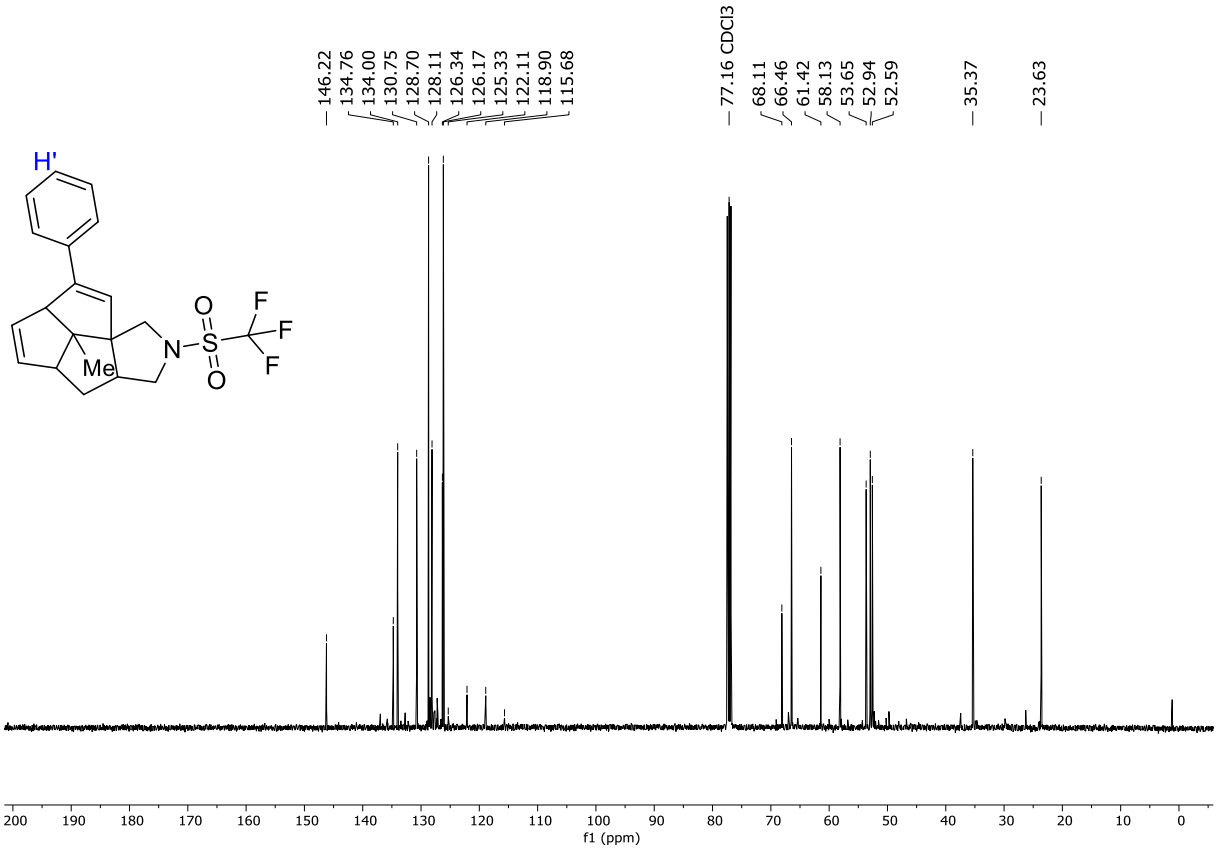

^{13}C NMR (151 MHz, $CDCl_3$) spectrum of **13**

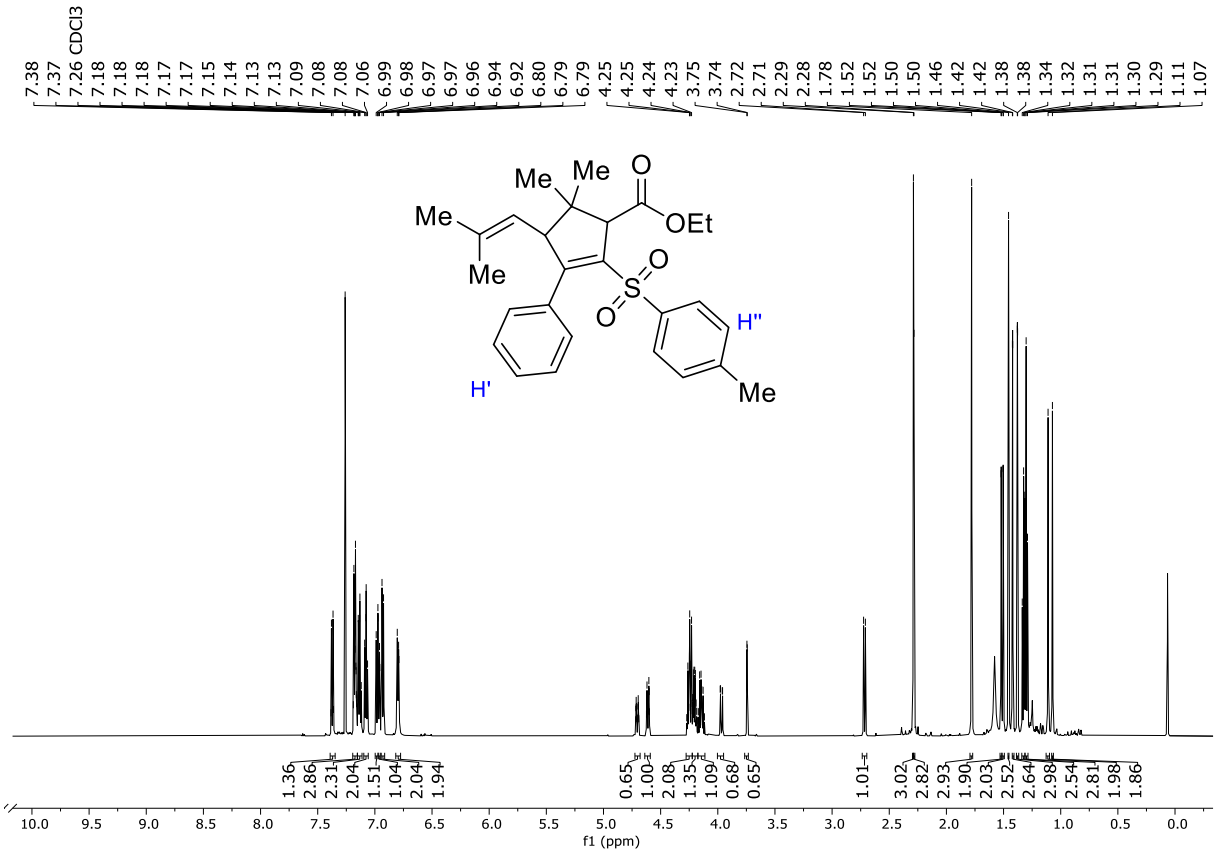

^{1}H NMR (600 MHz, $CDCl_3$) spectrum of **14**

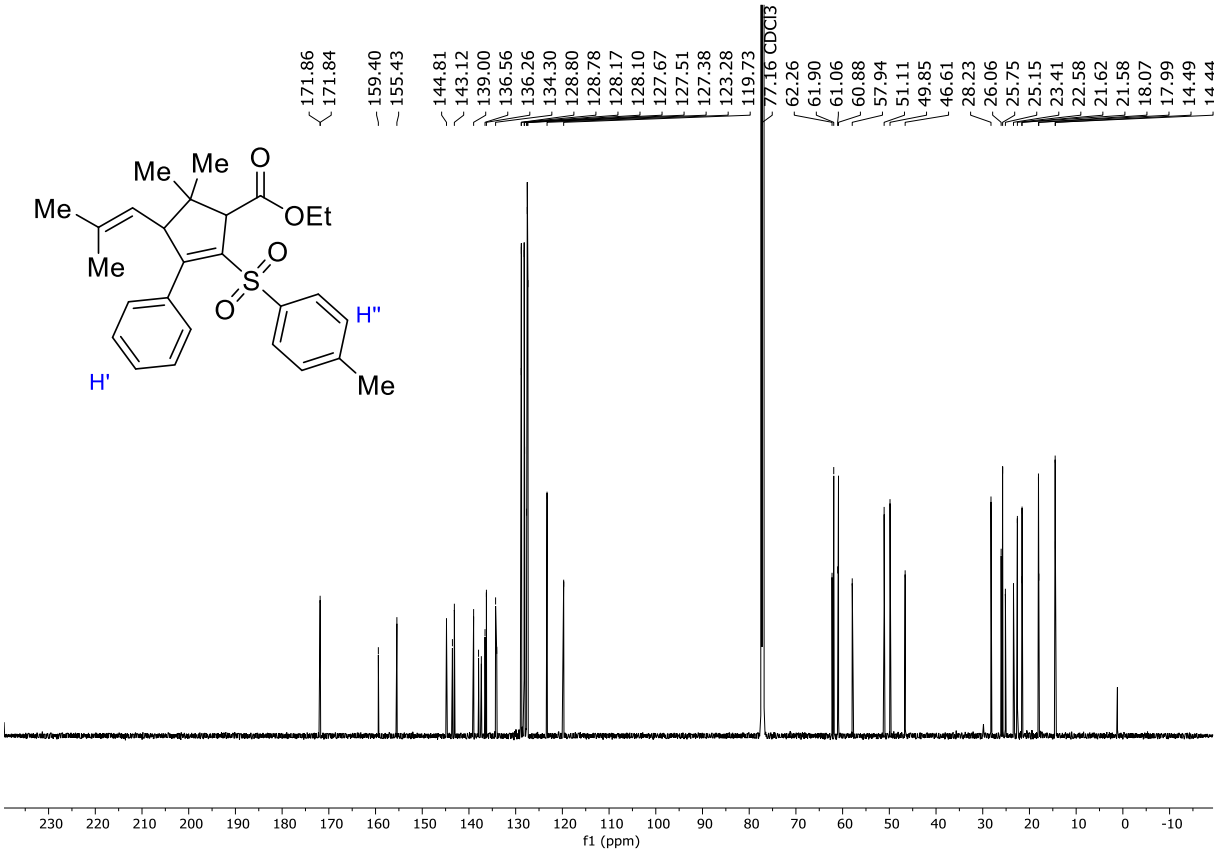

^{13}C NMR (151 MHz, $CDCl_3$) spectrum of **14**

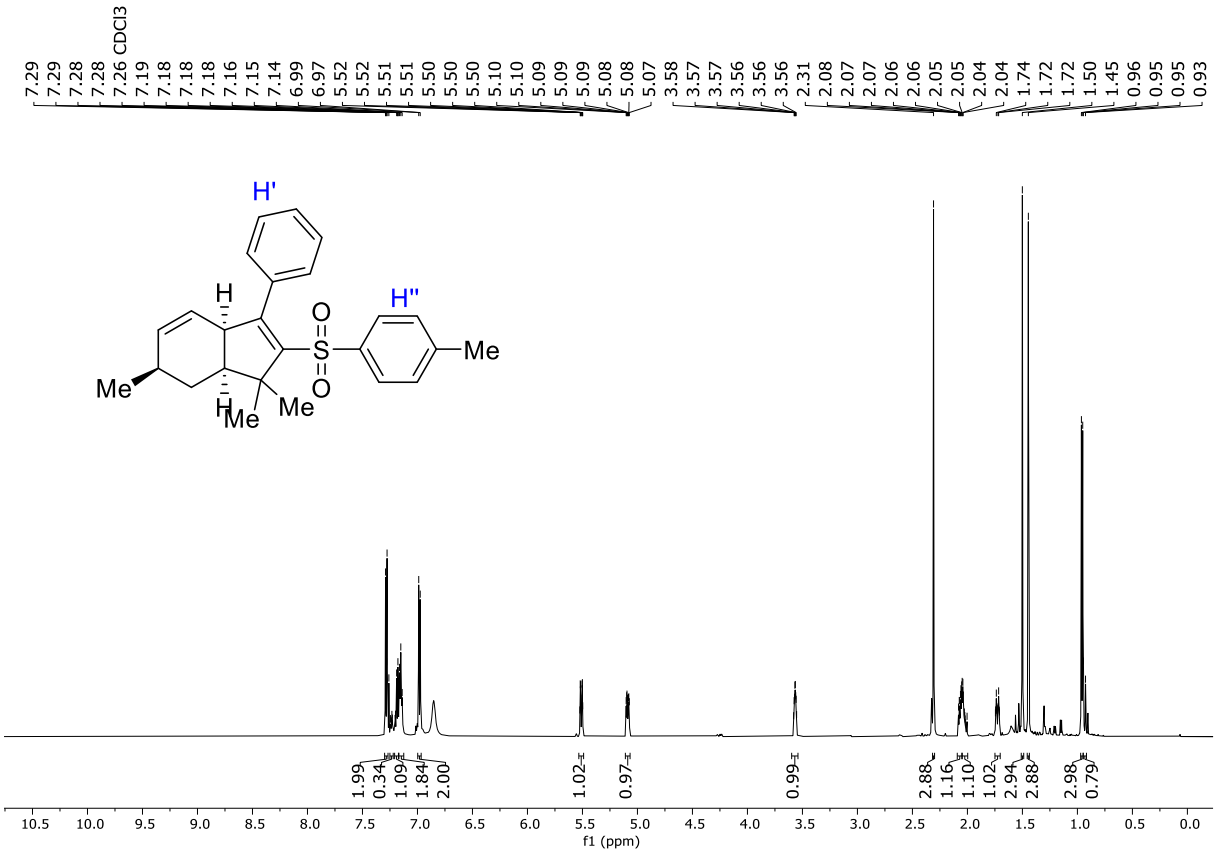

^{1}H NMR (600 MHz, $CDCl_3$) spectrum of **15**

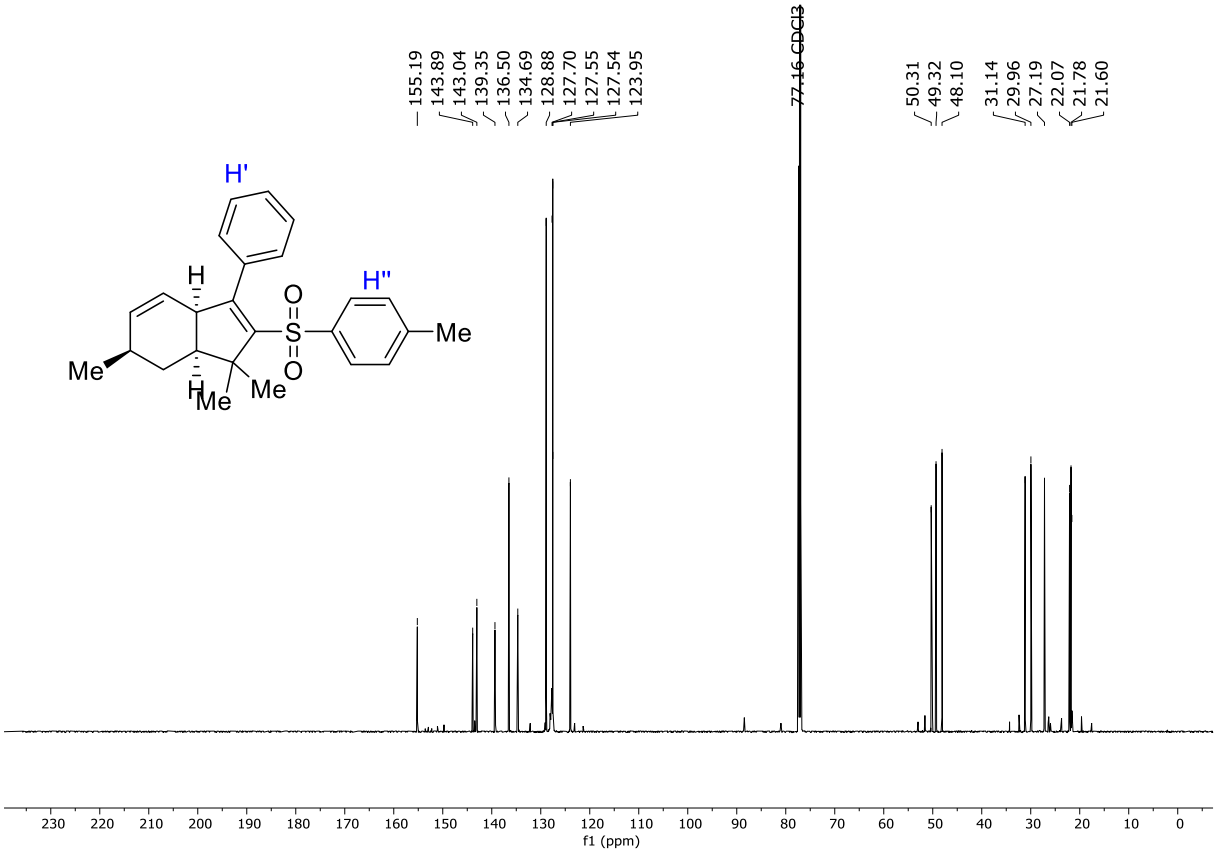

^{13}C NMR (151 MHz, $CDCl_3$) spectrum of **15**

10.6 Supporting Information for Project [E]

Supporting Information for

Direct Observation of Triplet States in the Isomerization of Alkenylboronates by Energy Transfer Catalysis

Till J. B. Zähringer [a§], Max Wienhold [b§], Ryan Gilmour[b,c]* and Christoph Kerzig[a]*

[a] *Department of Chemistry, Johannes Gutenberg-Universität Mainz, Duesbergweg 10–14, 55128 Mainz, Germany*

[b] *Organisch-Chemisches Institut, Westfälische Wilhelms-Universität Münster, Corrensstraße 36, 48149 Münster, Germany*

[c] *Cells in Motion (CiM) Interfaculty Center, Röntgenstraße 16, 48149 Münster, Germany*

*E-mail: ryan.gilmour@uni-muenster.de

*E-mail: ckerzig@uni-mainz.de

§ T.J.B.Z. and M.W. contributed equally to this paper.

Table of contents

1. General information 2
2. Synthetic procedures 8
3. DFT calculations 14
4. Absorption spectra 15
5. Stern–Volmer experiments 17
   5.1. Triplet-triplet energy transfer studies with thioxanthone sensitizers 17
   5.2. Triplet energy determination of ***E*-3** and ***Z*-3** 19
6. Additional control experiments and spectroscopic measurements 23
7. Kinetic simulation of quenching efficiencies 29
8. NMR spectra 30
9. Literature 42

1. General information

Materials

Unless specifically mentioned, all chemicals used for synthesis, irradiation experiments, or optical spectroscopy were commercially obtained and used as received (acetonitrile, 99.9%, Fisher Scientific; tetrachloromethane, 99.9%, Sigma-Aldrich; 1,4-diazabicyclo[2.2.2]octane (DABCO), 98%, Thermo Scientific; isopropanol, VWR, 99.0%; (-)-riboflavin, >98%, Sigma-Aldrich; $Ir(ppy)_3$, 99%, Sigma-Aldrich; thioxanthone, 97%, Sigma-Aldrich (purified by recrystallization from toluene/EtOAc prior to use); 2,7-dimethoxy-9H-thioxanthen-9-one (MeOTX), 98%, BLD Pharmatech; tris[5-fluoro-2-(2-pyridinyl)phenyl]-Iridium (IrF), 99%, Sigma-Aldrich; tris[3,5-difluoro-2-(2-pyridinyl)phenyl]-Iridium (IrdF), 98%, Sigma-Aldrich; $[Ru(phen)_3]Cl_2$, 98%, Sigma-Aldrich; 3,3'-Carbonylbis(7-diethylaminocoumarin) (CBDAC), 96%, BLD Pharmatech;

Argon from Nippon Gases (5.0) was used for removing dissolved oxygen before all experiments related to optical spectroscopy.

Steady-state measurements

Absorption spectra were recorded with a Perkin Elmer LAMBDA 365 UV-Vis spectrophotometer (JGU Mainz) and an Agilent Cary 60 UV-Vis Spectrophotometer (University of Münster). Emission measurements were carried out with a Perkin Elmer FL-6500 spectrometer and the emission spectra were corrected for the wavelength-dependent sensitivity of the instrument. All spectra were recorded at room temperature (295 ± 3 K) using 10 mm quartz glass cuvettes.

LED irradiation experiments

Photochemical isomerization reactions were performed utilizing:

1. A set-up of 4 Winger WEPIV3-S2 UV Power LED Star (Schwarzlicht) 1.2 W lamps (emission spectrum see Figure S1). The forward current per chip was set to 700 mA, the resulting forward voltage was 3.4 V while the resulting radiant flux was 1200 mW.
2. A set-up of 4 Avonec 3W430435m High Power LED Starplatine 3.0 W lamps (emission spectrum see Figure S2). The forward current per chip was set to 750 mA, the resulting forward voltage was 3.5-4.5 V while the resulting radiant flux was 900-1000 mW.

The distance between the reaction vessels and the LED was set at approximately 0.5 cm for all reactions and the *E*/*Z*-ratios were determined from the crude reaction mixture via ^{1}H NMR spectroscopy (for details on the utilized NMR equipment please see page 8).

Control irradiation experiments with ***Z*-1**, ***E*-2**, ***E*-3** and ***E*-4** (on 0.3 mmol scale) were conducted in the absence of the sensitizer (TX) under otherwise identical conditions as in Figure 4 of the main paper. After 1 h of irradiation at 402 nm no product was identified in the ^{1}H NMR.

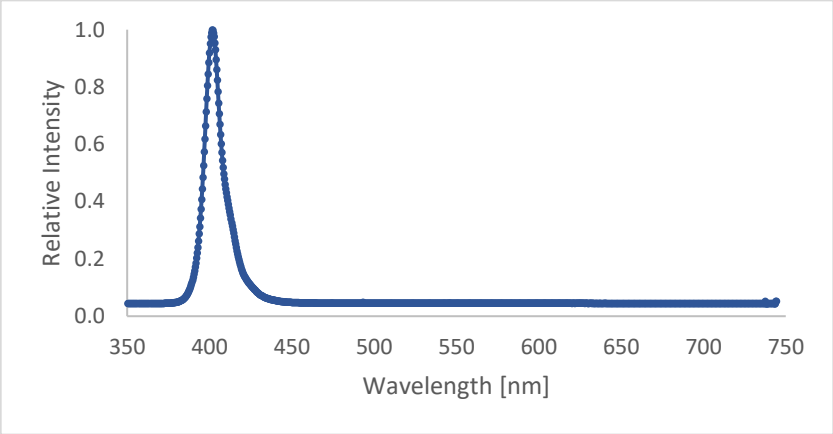

Figure S1: Emission spectrum of the utilized Winger WEPUV3-S2 UV Power LED Star (402 nm).

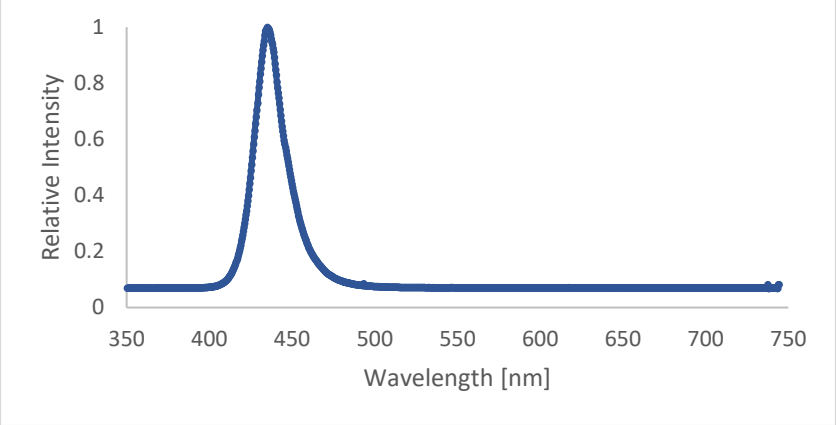

Figure S2: Emission spectrum of the utilized Avonec 3W430435m High Power LED Starplatine (435 nm).

Solar irradiation experiments

The solutions for solar-driven isomerization experiments were prepared in an argon-filled glove box and with Teflon-sealed NMR tubes. To prevent direct excitation of the isomers, a cut-off filter (Newport) was employed, ensuring that wavelengths below 400 nm were excluded (Figure S6). ^{1}H NMR spectra were recorded before and after the irradiation experiments. Unless specified otherwise, the standard concentrations used were 60 mM for the *E*-isomer and 1 mol% (600 µM) for the sensitizer with deaerated CD_3CN serving as the solvent. All experiments were carried out in Mainz, Germany at 50°N / 8.3°E. Table S1 contains the precise dates and corresponding weather conditions for the irradiation experiments. Weather reports and cloud coverage were accessed at https://www.meteoblue.com (see Figure S3).

Table S1: Summary of solar-driven isomerization experiments.

Date	Time	Sensitizer	Isomer	*E*/*Z*	Weather report
01.06.2023	12:00 – 16:00	CBDAC	***E*-3**	>98:2	See Figure S3
20.06.2023	12:00 – 16:00	$[Ru(phen)_3](PF_6)_2$	***E*-3**	>98:2	See Figure S4
07.07.2023	13:30 – 14:30	TX	***E*-3**	8:92	See Figure S5
	16:30 – 17:30			11:89	
07.07.2023	13:30 – 14:30	MeOTX	***E*-3**	85:15	See Figure S5
	16:30 – 17:30			90:10	

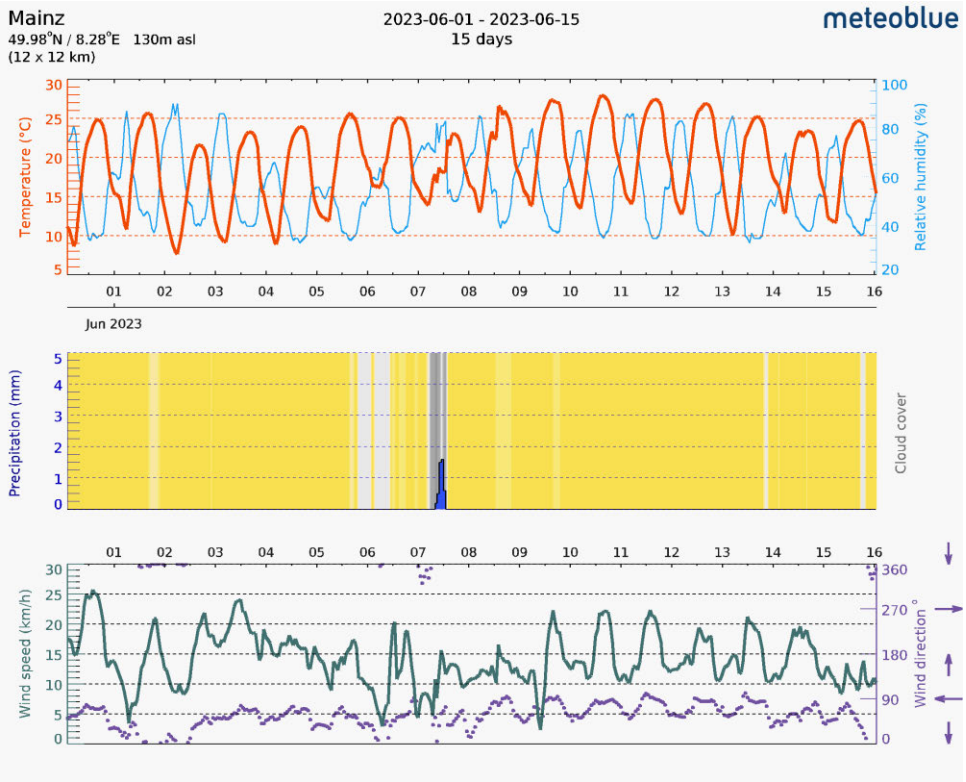

Figure S3: Weather report of Mainz, Germany at 50°N / 8.3°E between 01-15.06.2023.

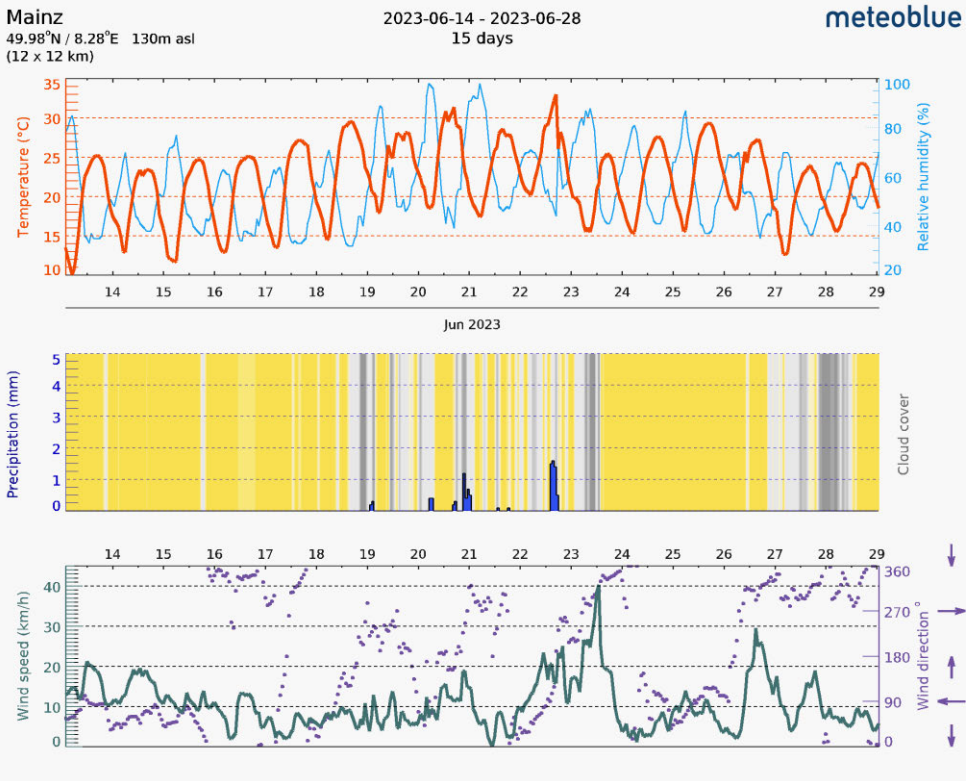

Figure S4: Weather report of Mainz, Germany at 50°N / 8.3°E between 14-29.06.2023.

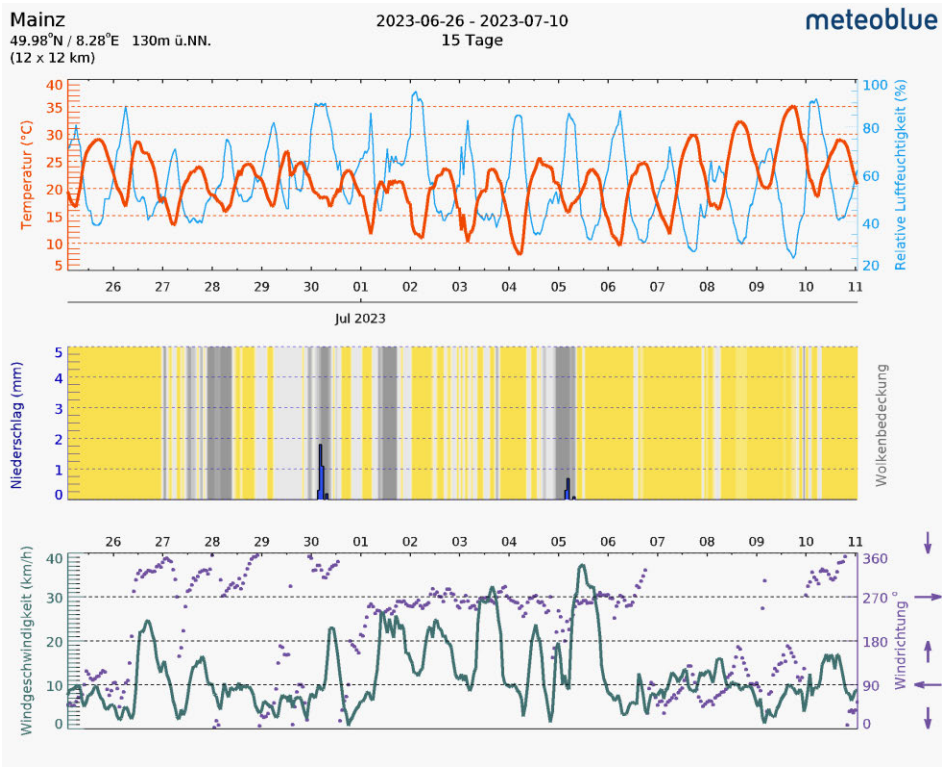

Figure S5: Weather report of Mainz, Germany at 50°N / 8.3°E between 26.06-11.07.2023.

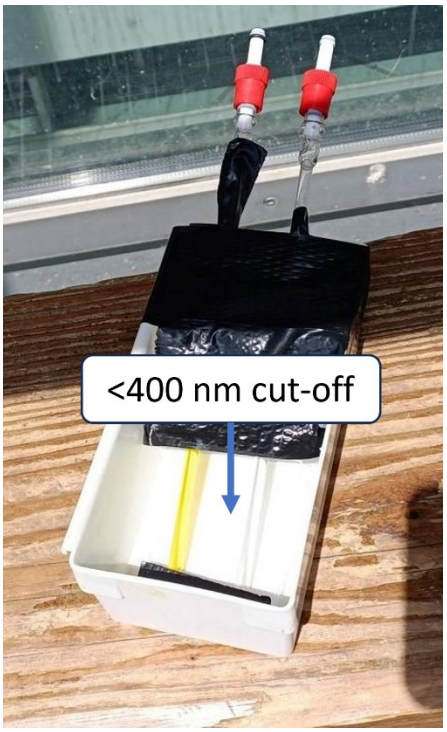

Figure S6: Experimental setup for solar-driven isomerization experiments.

Triplet-triplet energy transfer rate constants

Triplet-triplet energy transfer rate constants were determined by Stern–Volmer analyses. For Ir-based sensitizers this was achieved by lifetime-based measurements (τ) with varying concentrations c_q of the quencher and fitted according to the Stern–Volmer equation shown below (equation 1). The triplet-triplet energy transfer rate constants using thioxanthone as sensitizer were determined from Stern–Volmer experiments selectively monitoring the transient triplet state at 625 nm and fitted with the modified Stern–Volmer equation (equation 2). This modified equation was regarded as more reliable owing to the long natural triplet lifetime, which is prone to laser-intensity induced changes.

$$\frac{\tau_0}{\tau} = k_{\mathrm{TTET}} \cdot c_q \cdot \tau_0 + 1 \tag{1}$$

$$\frac{1}{\tau} = k_{\mathrm{obs}} = k_{\mathrm{TTET}} \cdot c_q + \frac{1}{\tau_0} \tag{2}$$

Laser flash photolysis

The LP980KS setup from Edinburgh Instruments equipped with an Nd:YAG laser from Litron (Nano LG 300-10) was employed for transient absorption and time-resolved emission spectroscopy. The frequency-tripled output with a wavelength of 355 nm served as the excitation source. The laser pulse duration was ~5 ns and the pulse frequency was 10 Hz. The typical pulse energy used for transient absorption and emission studies was ~15 mJ. A constant laser pulse energy was used within a series of experiments, which was ensured by power measurements before, after and in-between the experiments. The laser power was measured using a pyroelectric detector with attenuator (QE25LP-S-MB-QED-D0) from Gentec-eo combined with the integra software. Detection of transient absorption spectra occurred on an iCCD camera from Andor. Kinetic traces at selected wavelengths were recorded using a photomultiplier tube. The spectroscopic experiments were performed at 293 K using a cuvette holder that allows temperature control. If not stated otherwise the TA spectra were integrated over 100 ns. Longpass filters (385 nm or 400 nm, both from Newport) were used for transient absorption measurements with detection wavelengths exceeding 600 nm to exclude contributions from second-order signals.

77 K Phosphorescence measurements

77 K measurements were carried out with the LP980KS setup. The standard cuvette holder was replaced by a dewar that holds a 4 mm glass tube surrounded by liquid nitrogen.

NMR spectroscopy

NMR spectra were recorded at the Department of Chemistry, Johannes Gutenberg University Mainz, using a multinuclear magnetic resonance spectrometer of the type AV II 400 (Bruker, Karlsruhe, Germany), and at the Organisch-Chemisches Institut, Westfälische Wilhelms-Universität Münster on a *Bruker AV300* (300 MHz)*, Bruker AV400* (400 MHz), *Agilent DD2 500* (500 MHz) and an *Agilent DD2 600* (600 MHz). Chemical shifts δ are stated in ppm and referenced to the residual solvent signal. The resonance multiplicity is abbreviated as: s (singlet), d (doublet), t (triplet), q (quadruplet) and m (multiplet).

2. Synthetic procedures

Commercially available chemicals were purchased at *ABCR, Acros Organics, Sigma Aldrich, Alfa Aesar, BLD Pharmatech, fluorochem* or *Merck* and used as received. Solvents for purification (extraction and chromatography) were purchased as technical grade and distilled on the rotary evaporator prior to use. Dry solvents were obtained from solvent purification system (activated Alumina under a positive pressure of argon). Degassed solvent refers to bubbling argon through the solvent for a minimum of 15 min. Analytical thin layer chromatography (TLC) was performed on plates from *Merck* (*silica gel 60, F_{254}*) and visualized with a UV lamp (λ = 254 nm and λ = 366 nm), $KMnO_4$ and CAM stain solutions. Column chromatography was carried out on silica gel 60 (40-63 μm) from *Merck*. Concentration in vacuo was performed at ~10 mbar and 40°C, drying at ~10^{-2} mbar and room temperature. Photochemical isomerization reactions were performed utilizing two sets of LEDs (for more detailed information about the setup please see Chapter 1) and the distance between the reaction vessels and the LED was set at approximately 0.5 cm for all reactions.

Synthesis of Ethyl (*Z*)-3-(4,4,5,5-tetramethyl-1,3,2-dioxaborolan-2-yl)but-2-enoate (*Z*-1)

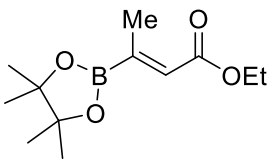

According to a procedure by Santos *et al.*[1] a flask was equipped with ethyl but-2-ynoate (560.0 mg, 5.0 mmol, 1.0 eq.), $CuSO_4$ (12.5 mg, 0.05 mmol, 1 mol%), 4-methylpyridine (23.3 mg, 24 μL, 0.25 mmol, 5 mol%.) and B_2pin_2 (0.95 g, 3.75 mmol, 0.75 eq.). Water (1 M, 5 mL) was added and the mixture was stirred at ambient temperature for 10 min before the addition of the remaining B_2Pin_2 (0.95 g, 3.75 mmol, 0.75 eq.). The reaction was stirred for additional 4 h before it was diluted by the addition of pentane. The organics were extracted with pentane (3x) and the combined organic layers were dried over $MgSO_4$. The solvent

was removed under reduced pressure and the crude residue was purified by column chromatography (SiO_2, 10% EtOAc/*n*-pentane) to yield ***Z*-1** as colorless oil (1.1 g, 92%)

$\mathbf{R_f}$ = 0.52 (10% EtOAc/ *n*-pentane)

^{1}H NMR (400 MHz, $CDCl_3$): δ (ppm) = 6.44 (d, *J* = 1.9 Hz, 1H), 4.16 (q, *J* = 7.1 Hz, 2H), 2.16 (d, *J* = 1.8 Hz, 3H), 1.29 – 1.25 (m, 15H).

^{11}B NMR (128 MHz, $CDCl_3$): δ (ppm) = 30.40.

Analytical data was in agreement with literature.[1]

Synthesis of Ethyl (*E*)-3-(4,4,5,5-tetramethyl-1,3,2-dioxaborolan-2-yl)but-2-enoate (*E*-1)

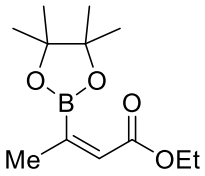

According to a procedure by Gilmour *et al.*[2], a flask was equipped with ethyl (*Z*)-3-(4,4,5,5-tetramethyl-1,3,2-dioxaborolan-2-yl)but-2-enoate (***Z*-1**, 72.0 mg, 0.3 mmol, 1.0 eq.) and thioxanthone (3 mg, 0,015 mmol, 5 mol%), purged with argon three times and then sealed. After addition of dry, degassed MeCN (0.03 M, 9 mL) the reaction mixture was stirred for 1 h at ambient temperature under the irradiation of violet light (λ = 402 nm). The reaction was carried out 4 times on this scale and combined before purification. The solvent was removed under reduced pressure and the crude residue was purified by column chromatography (SiO_2, DCM) to yield ***E*-1** as a colorless oil (220.1 mg, 76%).

$\mathbf{R_f}$ = 0.42 (5% EtOAc/ *n*-pentane)

^{1}H NMR (400 MHz, $CDCl_3$): δ (ppm) = 6.02 (d, *J* = 1.8 Hz, 1H), 4.18 (q, *J* = 7.2 Hz, 2H), 1.95 (d, *J* = 1.7 Hz, 3H), 1.35 (s, 12H), 1.26 (t, *J* = 7.2 Hz, 3H).

^{11}B NMR (128 MHz, $CDCl_3$): δ (ppm) = 30.42.

Analytical data was in agreement with literature.[3]

Synthesis of Ethyl (*E*)-3-phenylbut-2-enoate (*E*-2)

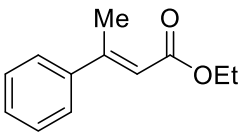

According to a procedure by Gilmour *et al.*[4], an oven-dried flask was equipped with dry THF (0.3 M, 33 mL) and NaH (440.0 mg, 11.0 mmol, 1.1 eq., 60% in mineral oil) was added under argon atmosphere at 0°C. After that, ethyl 2-(diethoxyphosphoryl)acetate (2.35 g, 2.1 mL 10.5 mmol, 1.05 eq.) was slowly added and the mixture was stirred 0 °C for 1 h before the addition of acetophenone (1.2 g, 1.16 mL, 10.0

mmol, 1.0 eq.). The reaction was stirred an additional hour before it was warmed to ambient temperature and stirred for additional 24 h. Water and Et_2O were added and the organics were extracted with Et_2O (3x). The combined organic layers were dried over $MgSO_4$ and the solvent was removed under reduced pressure. The crude residue was purified by column chromatography (5% Et_2O/*n*-pentane) to yield ***E*-2** as colorless oil (1.04 g, 54%).

$\mathbf{R}_f$ = 0.48 (5% EtOAc/ *n*-pentane)

^{1}H NMR (400 MHz, $CDCl_3$): δ (ppm) = 7.49 – 7.47 (m, 2H), 7.40 – 7.35 (m, 3H), 6.14 (d, *J* = 1.3 Hz, 1H), 4.22 (q, *J* = 7.1 Hz, 2H), 2.58 (d, *J* = 1.3 Hz, 3H), 1.32 (t, *J* = 7.1 Hz, 3H).

Analytical data was in agreement with literature.[4]

Synthesis of Ethyl (*Z*)-3-phenylbut-2-enoate (*Z*-2)

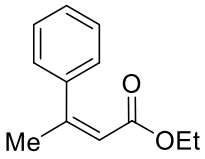

According to a procedure by Gilmour *et al.*[4], a flask was equipped with ethyl (*E*)-3-phenylbut-2-enoate (***E*-2**, 57.1 mg, 0.3 mmol, 1.0 eq.) and (-)-riboflavin (5.6 mg, 0,015 mmol, 5 mol%), purged with argon three times and then sealed. After subsequent addition of dry, degassed MeCN (0.06 M, 5 mL) the reaction mixture was stirred for 24 h at ambient temperature under the irradiation of violet light (λ = 402 nm). The reaction was carried out 4 times on this scale and combined before purification. The solvent was removed under reduced pressure and the crude residue was purified by column chromatography (SiO_2, 5% EtOAc/*n*-pentane) to yield ***Z*-2** as a colorless oil (210.0 mg, 92%).

$\mathbf{R}_f$ = 0.33 (5% EtOAc/ *n*-pentane)

^{1}H NMR (400 MHz, CDCl3): δ (ppm) = 7.39 – 7.29 (m, 3H), 7.23 – 7.17 (m, 2H), 5.91 (d, *J* = 1.5 Hz, 1H), 4.00 (q, *J* = 7.1 Hz, 2H), 2.18 (d, *J* = 1.5 Hz, 3H), 1.08 (t, *J* = 7.1 Hz, 3H).

Analytical data was in agreement with literature.[4]

Synthesis of (*E*)-(1-bromoprop-1-en-2-yl)benzene (S1)

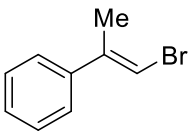

According to a procedure by Gilmour *et al.*[5] a flask was equipped with prop-1-en-2-ylbenzene (2.4 g, 2.6 mL, 20.0 mmol, 1.0 eq.) and purged with argon before the addition of DCM (0.66 M, 30 mL). The solution was cooled to 0°C and bromine (3.84 g, 1.3 mL, 24.0 mmol, 1.2 eq.) was added dropwise. The reaction was warmed to ambient temperature before it was stirred for 1 h and then quenched by the addition of sat. aq. $Na_2S_2O_3$.

The organic layer was separated, dried over $MgSO_4$ and the solvent was removed under reduced pressure. The crude residue was dissolved in *t*-BuOH (0.2 M, 100 mL) and KO*t*-Bu (3.4 g, 30.0 mmol, 1.5 eq.) was added. The mixture was stirred at reflux for 1 h before it was cooled to ambient temperature and diluted with water. The organics were extracted with Et_2O (3x) and the combined organic layers were washed with brine and dried over $MgSO_4$. The solvent was removed under reduced pressure and the crude residue was purified by column chromatography (SiO_2, cyclohexane) to yield **S1** as yellow oil (1.79 g, 45%).

$\mathbf{R}_f$ = 0.57 (cyclohexane)

^{1}H NMR (400 MHz, $CDCl_3$): δ (ppm) = 7.36 – 7.30 (m, 5H), 6.45 (d, *J* = 1.3 Hz, 1H), 2.23 (d, *J* = 1.4 Hz, 3H).

Analytical data was in agreement with literature.[5]

Synthesis of (*E*)-4,4,5,5-tetramethyl-2-(2-phenylprop-1-en-1-yl)-1,3,2-dioxaborolane (*E*-3)

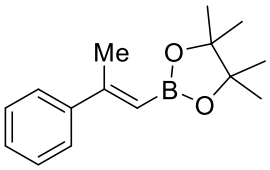

According to a procedure by Gilmour *et al.*[5] an oven-dried Schlenk-flask was equipped with (*E*)-(1-bromoprop-1-en-2-yl)benzene (**S1**, 1.57 g, 8.0 mmol, 1.0 eq.), Pd(dppf)Cl_2*DCM (326.6 mg, 0.4 mmol, 5 mol%), KOAc (2.4 g, 24.0 mmol, 3.0 eq.) and B_2Pin_2 (2.2 g, 8.8 mol, 1.1 eq.) and then sealed and purged with argon three times. Dry, degassed 1,4-dioxane (0.2 M, 40 mL) was added and the mixture was stirred at 90 °C for 16 h. The reaction was cooled to ambient temperature and filtered through a layer of Celite, eluting the product with Et_2O. The organic layer was washed with water and brine and dried over $MgSO_4$. The solvent was removed under reduced pressure and the crude residue was purified by column chromatography (SiO_2, 5% Et_2O/*n*-pentane) to give ***E*-3** as yellow oil (816.2 mg, 42%).

$\mathbf{R}_f$ = 0.60 (10% EtOAc/ *n*-pentane)

^{1}H NMR (400 MHz, $CDCl_3$): δ (ppm) = 7.54 – 7.43 (m, 2H), 7.35 – 7.28 (m, 3H), 5.76 (d, *J* = 1.1 Hz, 1H), 2.41 (d, *J* = 1.0 Hz, 3H), 1.32 (s, 12H).

^{11}B NMR (128 MHz, $CDCl_3$): δ (ppm) = 30.30.

Analytical data was in agreement with literature.[5]

Synthesis of (*Z*)-4,4,5,5-tetramethyl-2-(2-phenylprop-1-en-1-yl)-1,3,2-dioxaborolane (*Z*-3)

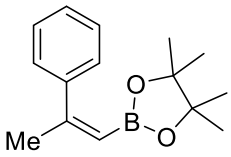

According to a procedure by Gilmour *et al.*[5], a flask was equipped with (*E*)-4,4,5,5-tetramethyl-2-(2-phenylprop-1-en-1-yl)-1,3,2-dioxaborolane (***E*-3**, 72.2 mg, 0.3 mmol, 1.0 eq.) and $Ir(ppy)_3$ (2.0 mg, 0.003 mmol, 1 mol%), purged with argon and then sealed. After subsequent addition of dry, degassed MeCN (0.06 M, 5 mL) the reaction mixture was stirred for 24 h at ambient temperature under the irradiation of blue light (λ = 435 nm). The reaction was carried out 3 times on this scale and combined before purification. The solvent was removed under reduced pressure and the crude residue was purified by column chromatography (SiO_2, 2.5% Et_2O/*n*-pentane) to yield ***Z*-3** as a colorless oil (122.1 mg, 56%).

R_f = 0.47 (10% EtOAc/ *n*-pentane)

^{1}H NMR (400 MHz, $CDCl_3$): δ (ppm) = 7.31 – 7.26 (m, 5H), 5.47 (d, *J* = 1.4 Hz, 1H), 2.21 (d, *J* = 1.4 Hz, 3H), 1.15 (s, 12H).

^{11}B NMR (128 MHz, $CDCl_3$): δ (ppm) = 30.10.

Analytical data was in agreement with literature.[5]

Synthesis of ethyl (*E*)-3-(naphthalen-2-yl)but-2-enoate (*E*-4)

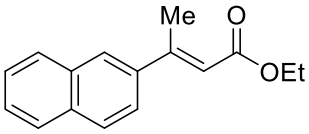

According to a procedure by Gilmour *et al.*[4], an oven-dried flask was equipped with dry THF (0.3 M, 33 mL) and NaH (440.0 mg, 11.0 mmol, 1.1 eq., 60% in mineral oil) was added under argon atmosphere at 0°C. Ethyl 2-(diethoxyphosphoryl)acetate (2.35 g, 2.1 mL 10.5 mmol, 1.05 eq.) was slowly added and the mixture was stirred at 0°C for 1 h before the addition of 1-(naphthalen-2-yl)ethan-1-one (1.7 g, 10.0 mmol, 1.0 eq.). The reaction was stirred an additional hour before it was warmed to ambient temperature and stirred for additional 24 h. Water and Et_2O were added and the organics were extracted with Et_2O (3x). The combined organic layers were dried over $MgSO_4$ and the solvent was removed under reduced pressure. The crude residue was purified by column chromatography (2.5% to 5% Et_2O/*n*-pentane) to yield ***E*-4** as colorless solid (1.2 g, 49%).

R_f = 0.41 (5% EtOAc/ *n*-pentane)

^{1}H NMR (400 MHz, $CDCl_3$): δ (ppm) = 7.96 – 7.95 (d, *J* = 1.5 Hz, 1H), 7.85 – 7.82 (m, 3H), 7.62 (dd, *J* = 8.6, 1.9 Hz, 1H), 7.52 – 7.49 (m, 2H), 6.29 (d, *J* = 1.4 Hz, 1H), 4.25 (q, *J* = 7.1 Hz, 2H), 2.69 (d, *J* = 1.3 Hz, 3H), 1.34 (t, *J* = 7.1 Hz, 3H).

Analytical data was in agreement with literature.[4]

Synthesis of ethyl (*Z*)-3-(naphthalen-2-yl)but-2-enoate (*Z*-4)

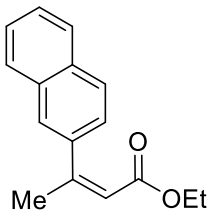

According to a procedure by Gilmour *et al.*[4], a flask was equipped with ethyl (*E*)-3-(naphthalen-2-yl)but-2-enoate (***E*-4**, 72.9 mg, 0.3 mmol, 1.0 eq.) and (-)-riboflavin (5.6 mg, 0,015 mmol, 5 mol%), purged with argon and then sealed. After subsequent addition of dry, degassed MeCN (0.06 M, 5 mL) the reaction mixture was stirred for 24 h at ambient temperature under the irradiation of violet light (λ = 402 nm). The reaction was carried out 2 times on this scale and combined before purification. The solvent was removed under reduced pressure and the crude residue was purified by column chromatography (SiO_2, 0% to 2% EtOAc/*n*-pentane) to yield ***Z*-4** as a colorless oil (109.4 mg, 75%).

$\mathbf{R_f}$ = 0.30 (5% EtOAc/ *n*-pentane)

^{1}H NMR (400 MHz, $CDCl_3$): δ (ppm) = 7.83 – 7.80 (m, 3H), 7.67 (d, *J* = 1.0 Hz, 1H), 7.47 – 7.45 (m, 2H), 7.34 (dd, *J* = 8.5, 1.7 Hz, 1H), 6.00 (d, *J* = 1.5 Hz, 1H), 3.99 (d, *J* = 7.1 Hz, 2H), 2.27 (d, *J* = 1.5 Hz, 3H), 1.03 (t, *J* = 7.1 Hz, 3H).

Analytical data was in agreement with literature.[4]

Synthesis of $[Ir(C\hat{}N)_2(bpy)](PF_6)_3$ (IrCN)

The Ir-based triplet sensitizer, $[Ir(C\hat{}N)_2(bpy)](PF_6)_3$ (see Figure S16 for its structure), was synthesized according to a slightly modified procedure by Coe *et al.*.[6] The following modification was made: The column chromatography was performed with Celite instead of Sephadex SP C-25 for the purification of $[Ir(C\hat{}N)_2(bpy)](PF_6)_3$. A natural lifetime of 13.7 µs was measured in deoxygenated MeCN, which is almost four times longer than the literature value, which was recorded under seemingly similar conditions. See Section S5.2 for lifetime measurements.

The ^{1}H NMR (CD_3CN) signals are in very good agreement with those reported in the literature.[6]

Synthesis $[Ir(ppy)_2(phen)]PF_6$ (IrPhen)

The sensitizer was synthesized according to a literature report by Bernhard *et al.*.[7]

The ^{1}H NMR (DMSO-d_6) signals closely match the findings documented in the literature.[7]

Synthesis of $[Ru(phen)_3](PF_6)_2$

$[Ru(phen)_3](PF_6)_2$ was synthesized from $[Ru(phen)_3]Cl_2$ according to a straightforward counterion exchange reaction with NH_4PF_6. $[Ru(phen)_3]Cl_2$ was dissolved in water and added to a saturated aqueous solution of NH_4PF_6. The precipitated $[Ru(phen)_3](PF_6)_2$ was washed thoroughly with cold water and acetonitrile.

3. DFT calculations

Quantum-mechanical calculations were carried out with the Gaussian 09 package[8] using the B3LYP functional in combination with the 6-311+G(d,p) basis set. Geometry optimizations (without geometry constraints) and accompanied frequency analyses were performed with the ground states of both isomers as well as with the lowest triplet states. All optimized geometries used for further computations and analyses did not show imaginary vibrational frequencies, indicating convergence on minimum structures. The adiabatic triplet energies were directly obtained from these calculations for the different olefins.

The vertical triplet energies were estimated by single-point calculations based on the optimized ground-state structures, i.e. without optimizing the lowest triplet states. The computed spin densities shown in the main paper and Figure S7 were obtained by additional single-point calculations with population analyses. The results of our DFT calculations were visualized with the software Avogadro. Vertical excitation energies of the optimized (perpendicular) triplets were obtained with additional TD-DFT calculations using identical functional and basis set. The predicted transitions and their oscillator strengths, which are useful for simulating absorption spectra of triplet species, are displayed in Figure 5B (main paper). Further DFT and TD-DFT calculations on thioxanthone and its excited states were carried out using the very same method and basis set. These results are included in Figure 3 (main paper).

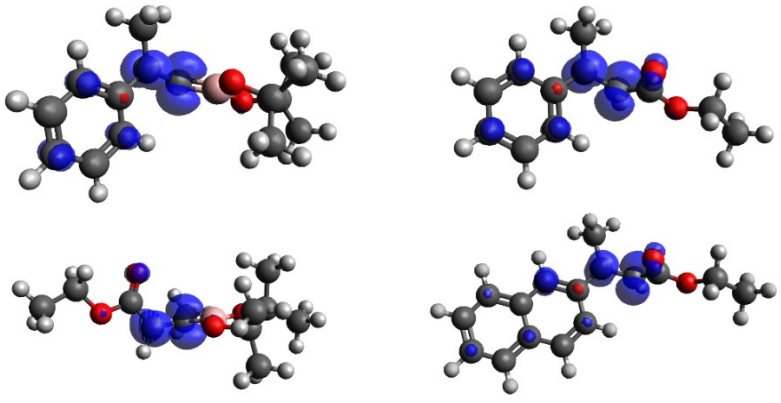

*Figure S7: Computed spin densities of the lowest triplet state of **1**, **2**, **3**, and **4** at the B3LYP/6-311+G(d,p) level of theory.*

4. Absorption spectra

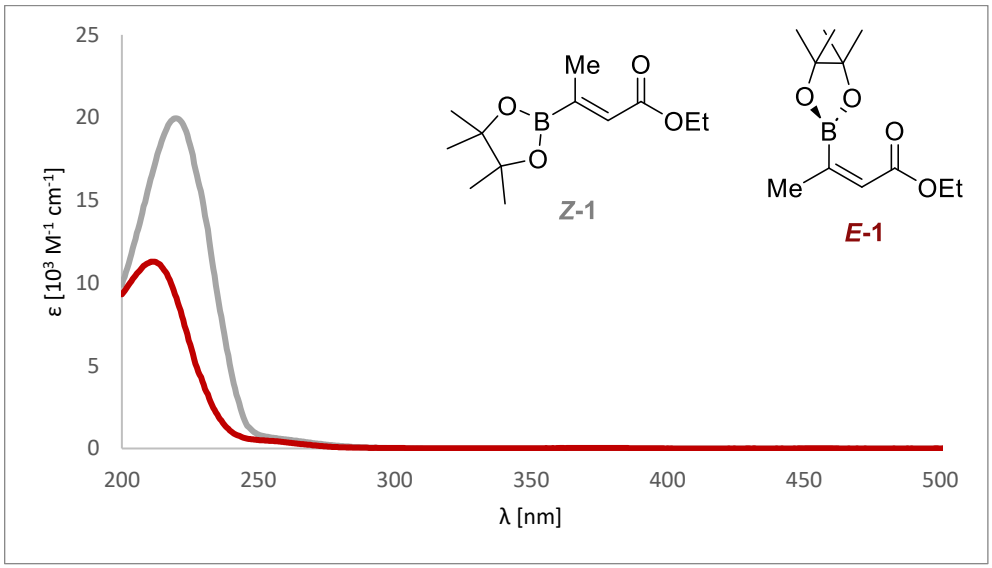

*Figure S8 Calibrated absorption spectra of **Z-1** (grey line, c = 0.05 mM) and **E-1** (red line, c = 0.05 mM) in MeCN.*

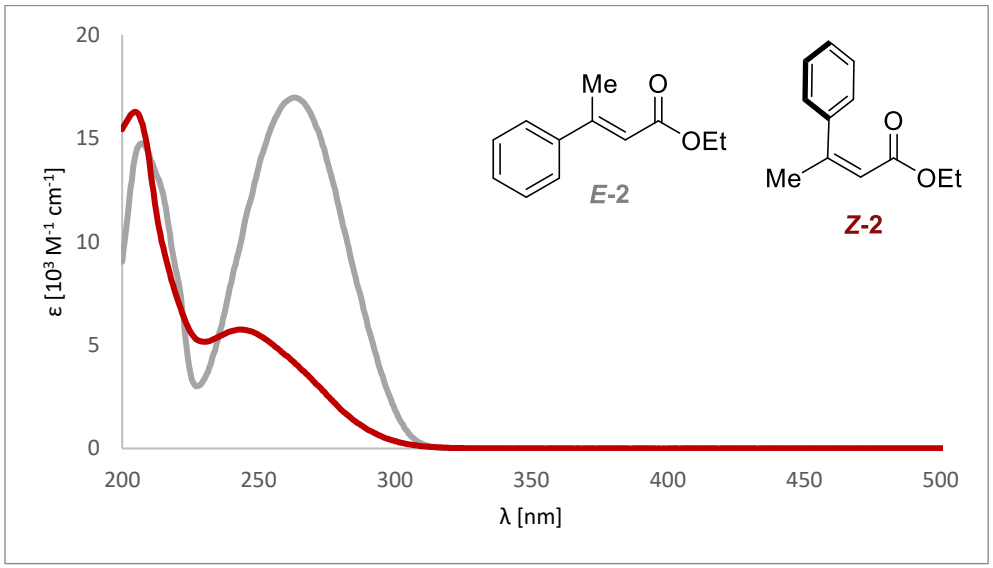

*Figure S9: Calibrated absorption spectra of **E-2** (grey line, c = 0.05 mM) and **Z-2** (red line, c = 0.05 mM) in MeCN.*

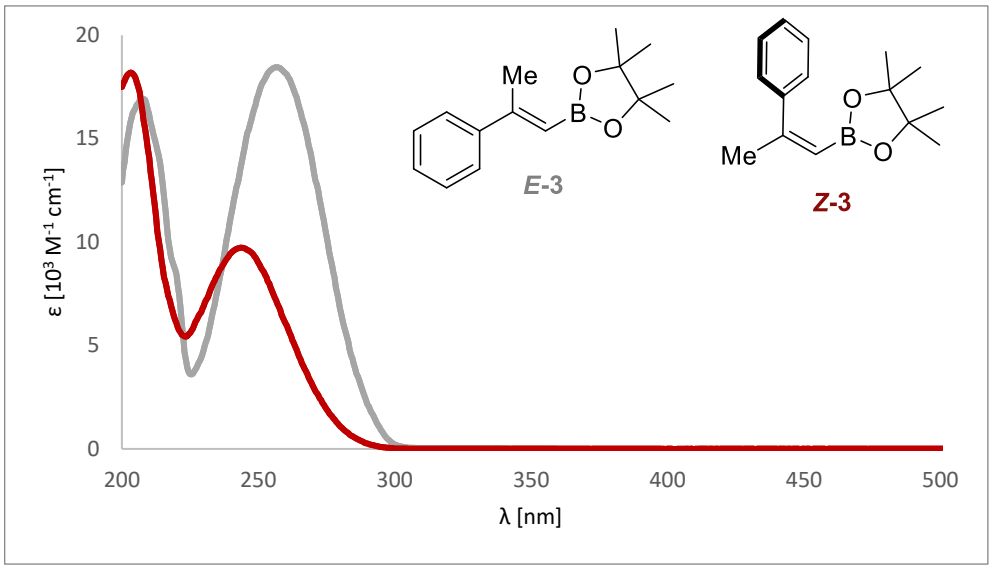

*Figure S10: Calibrated absorption spectra of **E-3** (grey line, c = 0.05 mM) and **Z-3** (red line, c = 0.05 mM) in MeCN.*

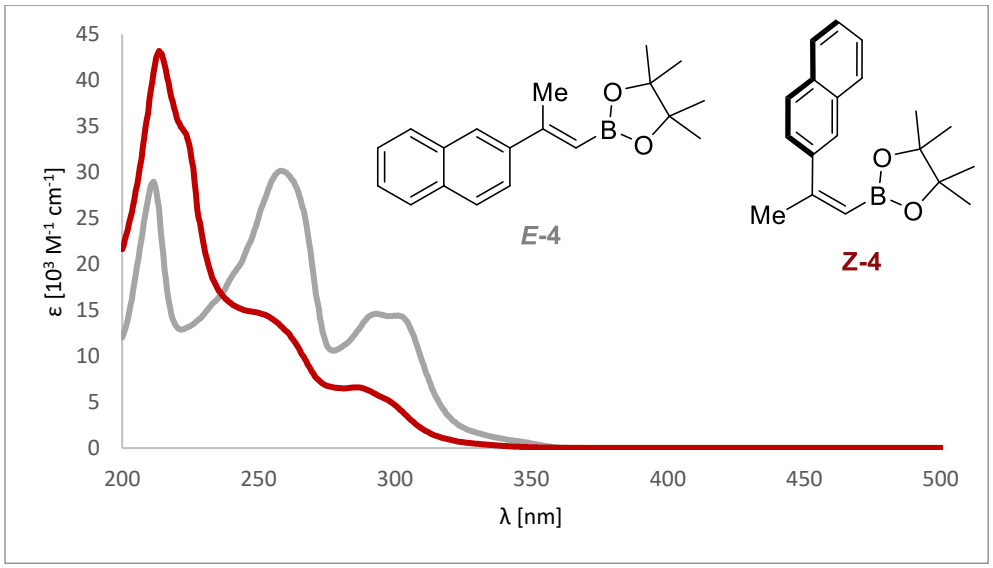

*Figure S11: Calibrated absorption spectra of **E-4** (grey line, c = 0.05 mM) and **Z-4** (red line, c = 0.05 mM) in MeCN.*

5. Stern–Volmer experiments

5.1. Triplet-triplet energy transfer studies with thioxanthone sensitizers

Typical unquenched triplet lifetimes of TX are on the order of ~40 µs under our conditions, which have been optimized for obtaining high signal-to-noise ratios and highly sensitive TA measurements. Despite the slight self-quenching effects shortening the natural lifetime that are commonly observed for TX[9] under these conditions, they do not affect the determinations of the quenching rate constants. This is because we used the apparent τ_0 value corresponding to the conditions on the day of the actual Stern–Volmer analysis. The (quenched) ^{3}TX lifetimes under the conditions used for key experiments are too short for any self-quenching side effects.

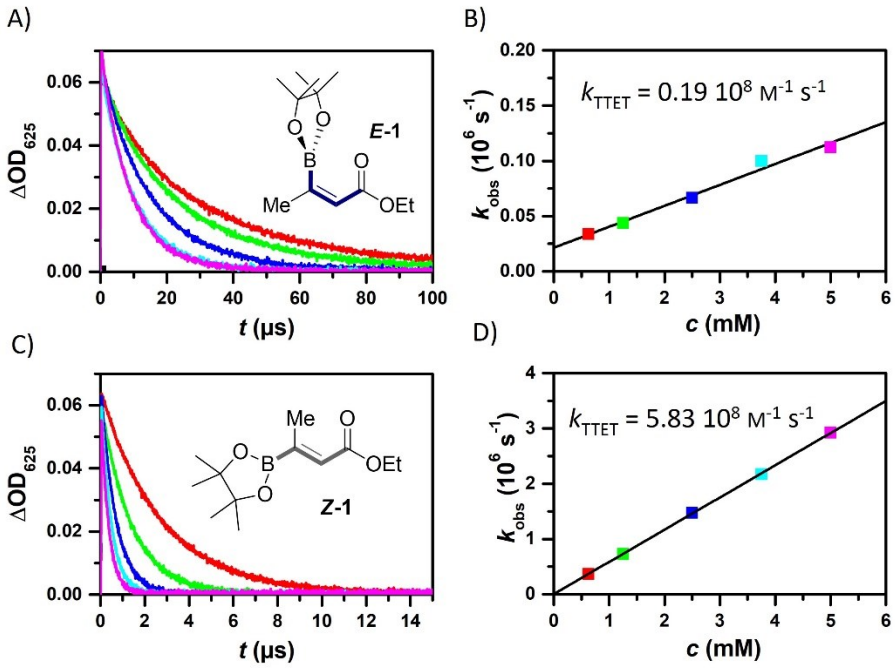

*Figure S12: A) and C) Triplet state quenching experiments of 20 µM TX in Ar-saturated MeCN with varying concentrations of **E-1** and **Z-1** after 355 nm laser pulse excitation. B) and D) Corresponding Stern–Volmer plots.*

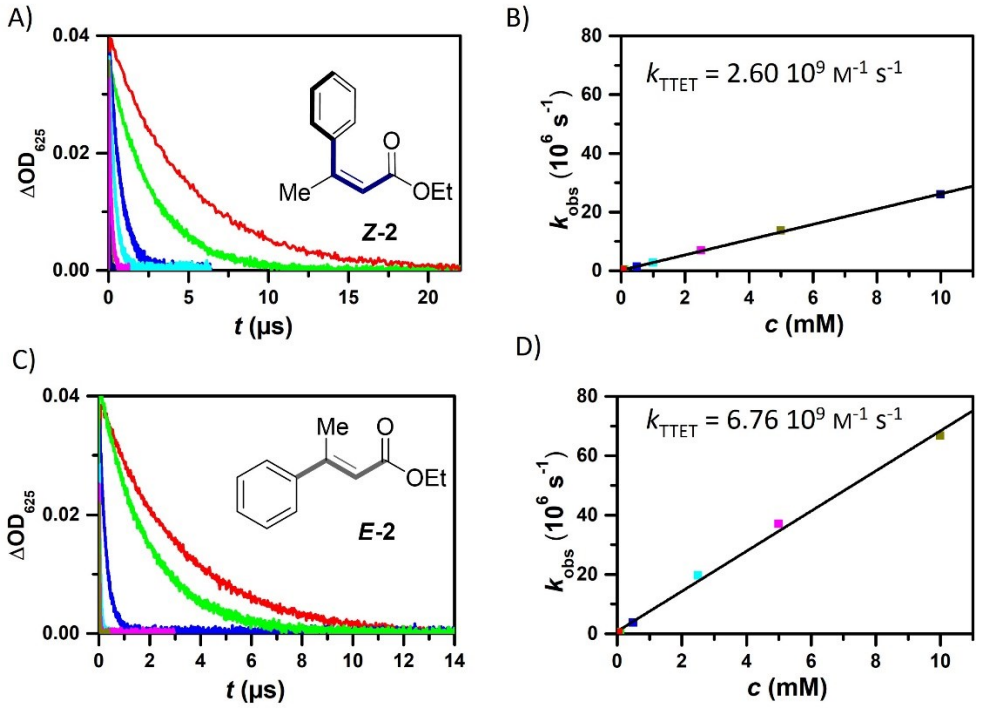

*Figure S13: A) and C) Triplet state quenching experiments of 20 μM TX in Ar-saturated MeCN with varying concentrations of **Z-2** and **E-2** after 355 nm laser pulse excitation. B) and D) Corresponding Stern–Volmer plots.*

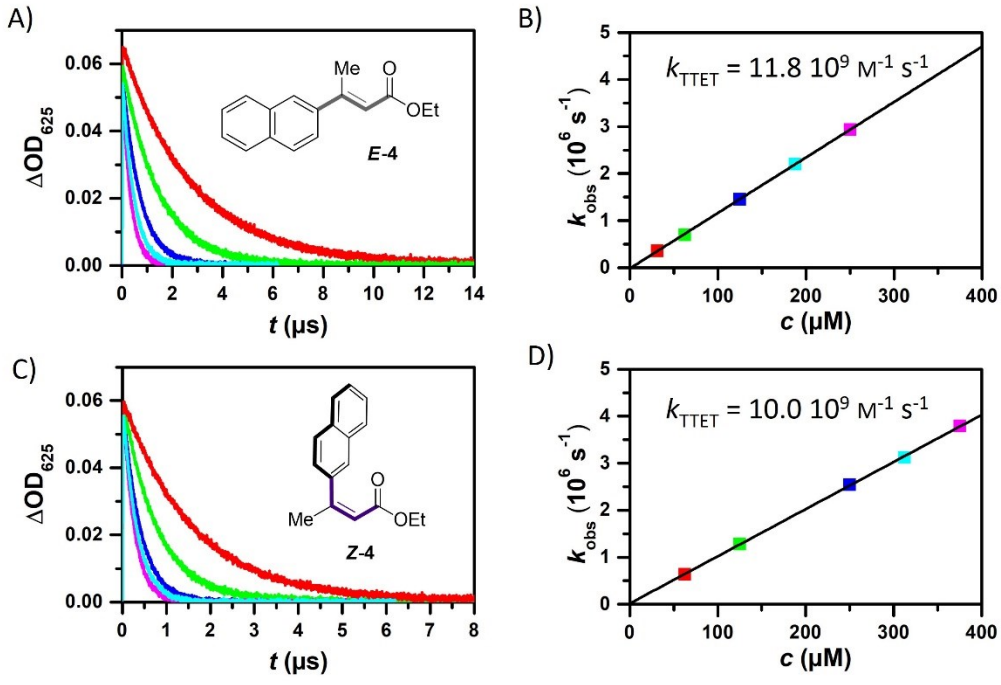

*Figure S14: A) and C) Triplet state quenching experiments of 20 μM TX in Ar-saturated MeCN with varying concentrations of **Z-4** and **E-4** after 355 nm laser pulse excitation. B) and D) Corresponding Stern–Volmer plots.*

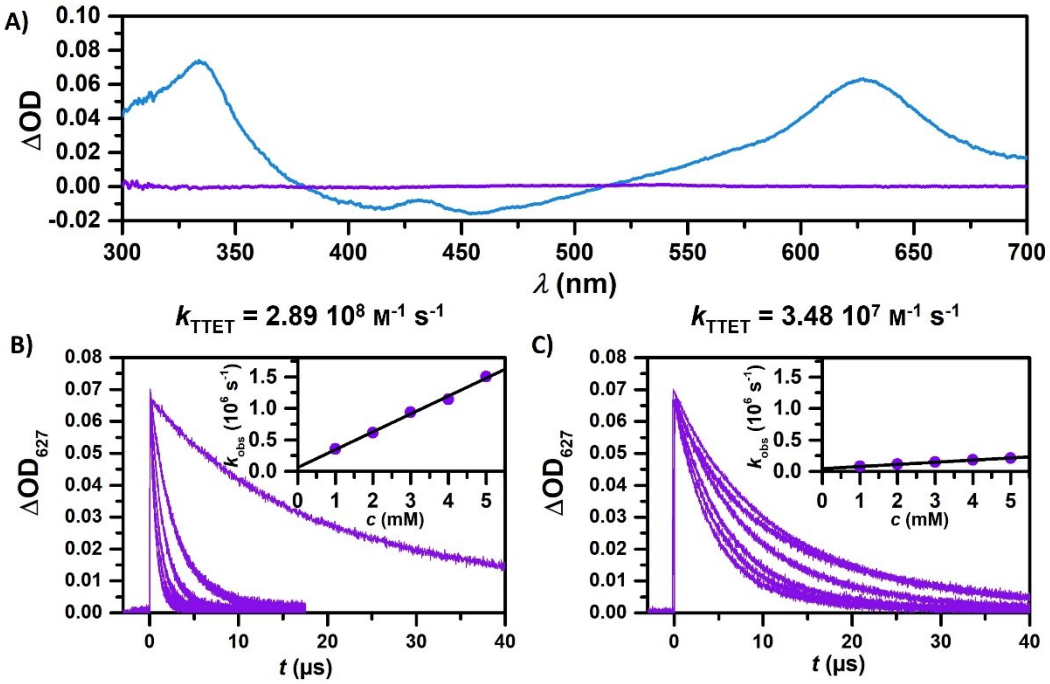

*Figure S15: A) Transient absorption spectrum of 162 µM MeOTX in deaerated MeCN recorded 100 ns (blue) and with 5 mM **E-3** recorded 10 µs (purple) after 355 nm laser pulse excitation. B) and C) triplet state quenching experiments with varying concentrations of **E-3** (B) and **Z-3** (C). Insets: Corresponding Stern–Volmer plots.*

5.2. Triplet energy determination of ***E*-3** and ***Z*-3**

The triplet energies of ***E*-3** and ***Z*-3** were obtained by quenching studies with a series of Ir-based triplet sensitizers with varying triplet energies (Figure S16). First, the triplet energies were determined by the blue edge of the room-temperature emission spectrum where the intensity drops to 10% of the maximum. Defining the triplet energies with the very same measuring technique allows for a more reliable comparison, since literature reports might vary and often do not account for solvent dependencies.

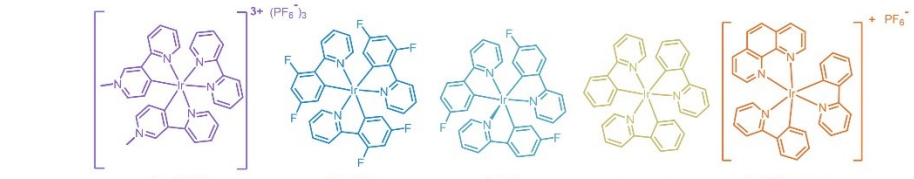

	IrCN	IrdF	IrF	Ir(ppy)$_3$	IrPhen
E_T (eV)	2.91	2.75	2.71	2.57	2.41
τ_0 (ns)	13750	1910	1920	1740	787

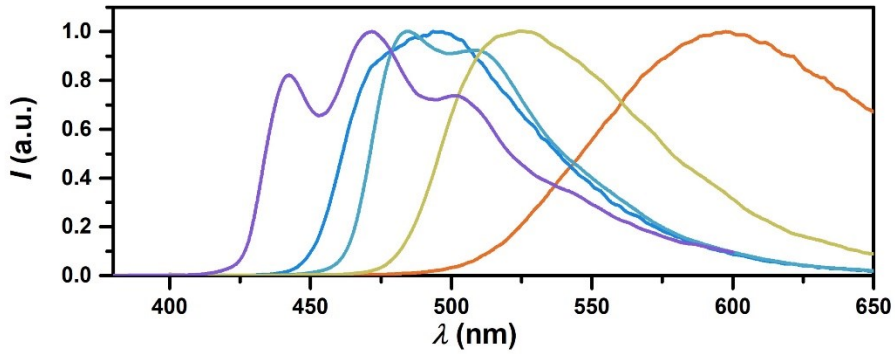

Figure S16: Molecular structures, natural triplet lifetimes and triplet energies of employed Ir-based sensitizers and emission spectra in Ar-saturated MeCN.

The quenching constants of ***E*-3** and ***Z*-3** were then measured by lifetime-based quenching experiments using 355 nm laser pulses with varying quencher concentrations (Figure S17). The obtained lifetimes were fitted according to the Stern-Volmer equation (equation 1) (Figure S17, insets). The triplet-triplet energy transfer constants, k_{TTET}, to ***E*-3** and ***Z*-3** together with the triplet energy and the ratio of k_{TTET}(***E*-3**)/ k_{TTET}(***Z*-3**) are given in Table S2. The experimental data were plotted against the triplet energies of the sensitizers (Figure 6 main paper) and fitted by a simplified thermal bond activation model for classical endothermic energy transfer (equation 3).[10–12]

$$k_{TTET} = \frac{k_{diff}}{1 + e^{\frac{(E_{T,D} - E_{T,A})}{2.3RT}}} \quad (3)$$

Where k_{diff} is the diffusion-controlled energy transfer rate, E_T is the triplet energy of the corresponding donor (D) or acceptor (A), in this case the sensitizer and either *E* or *Z* isomer. The best fit of the experimental data of ***E*-3** yielded a triplet energy of 2.78 eV. Since the energy transfer rates ***Z*-3** do not approach k_{diff}, the fit did not converge. However, assuming that the diffusion limit, k_{diff}, is identical for either isomer we obtained a good fit that yielded a triplet energy of 2.92 eV for ***Z*-3**. The results are summarized in Table S3.

*Table S2: Triplet energies, quenching rate constants of **E-3** and **Z-3** determined by Stern–Volmer analyses and corresponding ratio of E/Z.*

Sensitizer	E_T (eV)[a]	k_{TTET}(***E*-3**) (M^{-1} s^{-1})	k_{TTET}(***Z*-3**) (M^{-1} s^{-1})	k_{TTET}(***E*-3**)/ k_{TTET}(***Z*-3**)
IrCN	2.91	$2.22 \cdot 10^9$	$1.12 \cdot 10^9$	1.98
IrdF	2.75	$9.16 \cdot 10^8$	$1.09 \cdot 10^8$	8.40
IrF	2.70	$5.95 \cdot 10^8$	$6.32 \cdot 10^7$	9.41
$Ir(ppy)_3$	2.57	$8.23 \cdot 10^7$	$5.86 \cdot 10^6$	14.1 (9.0 to 15.7)[b]
IrPhen	2.41	$4.55 \cdot 10^6$	~$3.6 \cdot 10^5$ [c]	~13[c]

[a] Triplet energies determined by the blue edge of the emission spectrum where the intensity drops to 10% of the maximum. [b] *Z*/*E* ratios obtained after irradiation with $Ir(ppy)_3$ taken from ref.[5]. [c] The low quenching rate allows only for an estimate.

Table S3: Variables obtained by thermal bond activation model fit of Figure 6, main paper.

Compound	$E_{T,A}$ (eV)	k_{diff} (M^{-1} s^{-1})
***E*-3**	2.78	$2.48 \cdot 10^9$
***Z*-3**	2.92[a]	$2.48 \cdot 10^9$[a]

[a] The diffusion limit, k_{diff}, was taken from the fit of ***E*-3** under the assumption that this variable is identical for both isomers.

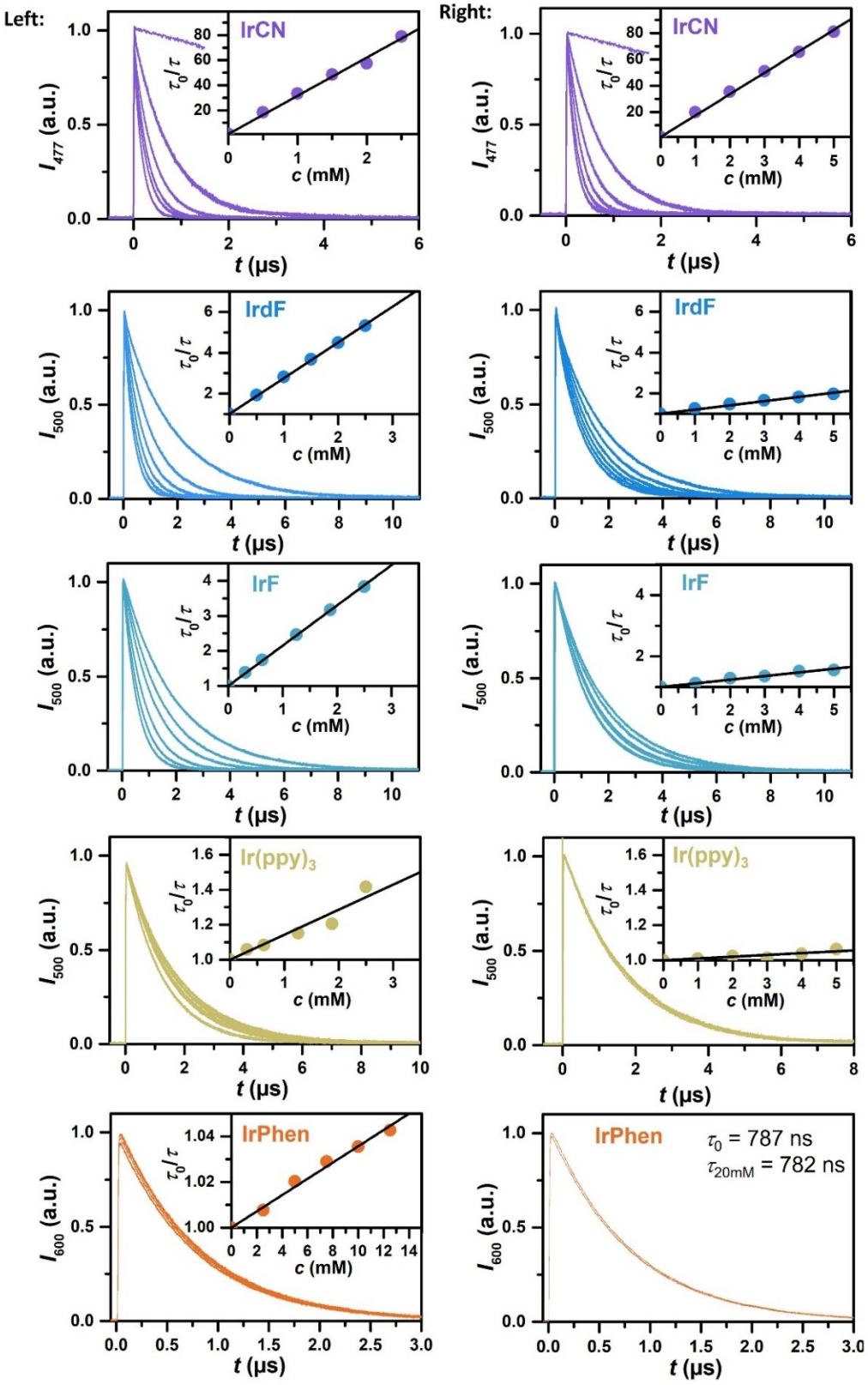

Figure S17:Emission quenching experiments of IrCN, IrdF, IrF, Ir(ppy)₃ and IrPhen in deaerated MeCN with varying concentrations of E-3 (left) and Z-3 (right). Insets: Corresponding Stern–Volmer plots.

6. Additional control experiments and spectroscopic measurements

Several control quenching experiments of ^{3}TX were performed to record reference spectra of the TX-derived photoproducts originating from electron transfer (ET) or hydrogen atom transfer (HAT). 1,4-diazabicyclo[2.2.2]octane (DABCO) is a good electron donor (0.8 V vs NHE)[13] and a common reductive quencher, DABCO was specifically selected since other typical reductive quenchers such as triethanolamine also react in a hydrogen abstraction reaction, which is a common side reaction of excited ketones. A solution of 50 µM TX with 500 µM DABCO in MeCN was prepared and monitored by transient absorption spectroscopy (Figure S18). Kinetic measurements at the ^{3}TX absorption maximum (625 nm) provided a biexponential decay, which can essentially be attributed to fast quenching of ^{3}TX and the generation of the long-lived radical anion species. A TA spectrum recorded after ^{3}TX deactivation shows the absorption characteristics of the radical anion and the radical cation of DABCO that has been reported to show a single, non-structured absorption band centered at ~440 nm.[14] The radical anion shows an intense absorption maximum at 335 nm and a broad absorption band at 650 nm, which is in line with literature values for TX and similar derivatives.[15,16]

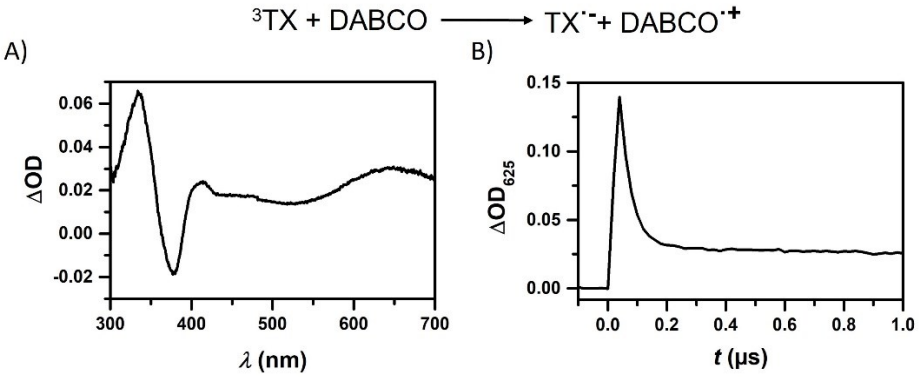

Figure S18: LFP experiments after excitation with 355 nm laser pulses of a solution containing 50 µM TX and 500 µM DABCO in Ar-saturated MeCN. A) TA spectrum recorded 200 ns after excitation. B) Transient absorption trace recorded at 625 nm.

Similar experiments were performed with tetrachloromethane as oxidative quencher of ^{3}TX. The fragmentation products (chloride and $CCl_3^{\bullet}$), which do not absorb in the visible region, allow us to exclusively monitor the radical cation of TX.[17–19] A solution of 50 µM TX with 1 M CCl_4 in MeCN was prepared and investigated by TA spectroscopy (Figure S19). The quenching step was monitored at 500 nm. After complete deactivation of ^{3}TX, a longer-lived transient species that we assign to the radical cation of TX is detected with a maximum absorption at 415 nm and 500 nm, agreeing with reported values.[20]

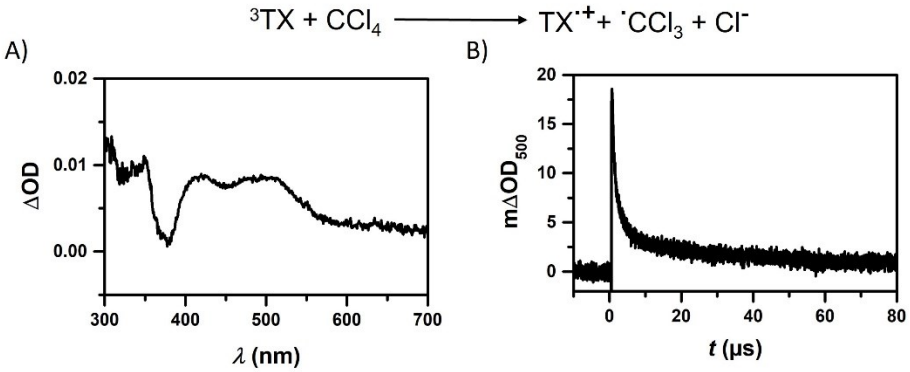

Figure S19: LFP experiments after excitation with 355 nm laser pulses of a solution containing 50 μM TX and 1 M CCl_4 in Ar-saturated MeCN. A) TA spectrum recorded 2 μs after excitation. B) Transient absorption trace recorded at 500 nm.

Ketones are commonly exploited as type II photoinitiator in HAT reactions yielding the corresponding ketyl radical.[21] This reaction is well-described for TX. Isopropanol was used as the quencher in the HAT reaction since its reduction and oxidation potentials are too high to enable electron transfer reactions with TX and the corresponding quencher-derived radical does not absorb in the selected detection window (300-700 nm).[22] 1 M isopropanol was added to 50 μM TX in MeCN and time-resolved measurements were performed (Figure S20B). Kinetic traces at 625 nm show the deactivation of ^{3}TX and at 350 nm the simultaneous formation of the TX ketyl radical. The TA spectrum recorded after complete ^{3}TX decay is displayed in Figure S20 and matches reported spectra.[23,24]

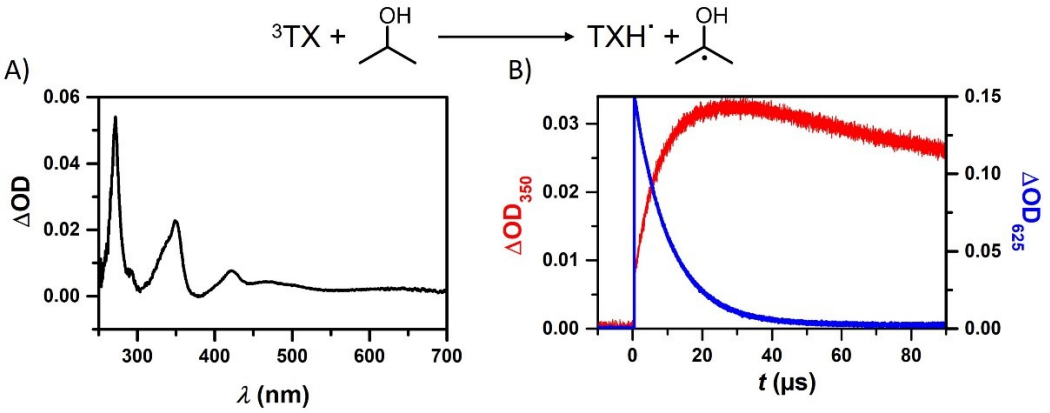

Figure S20: LFP experiments after excitation with 355 nm laser pulses of a solution containing 50 μM TX with 1 M isopropanol in Ar-saturated MeCN. A) TA spectrum recorded 80 μs after excitation. B) Transient absorption traces recorded at 350 nm (red) and 625 nm (blue).

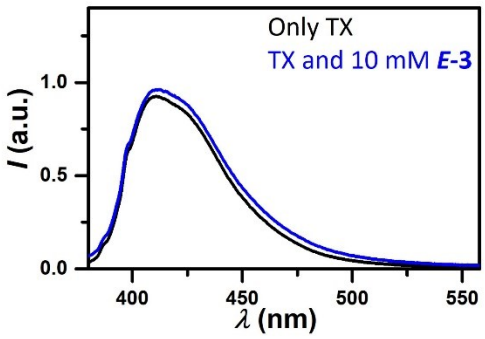

*Figure S21: Emission spectrum of 20 µM TX in the absence (black) and presence of 10 mM **E-3** recorded directly after excitation with 355 nm laser pulses in MeCN.*

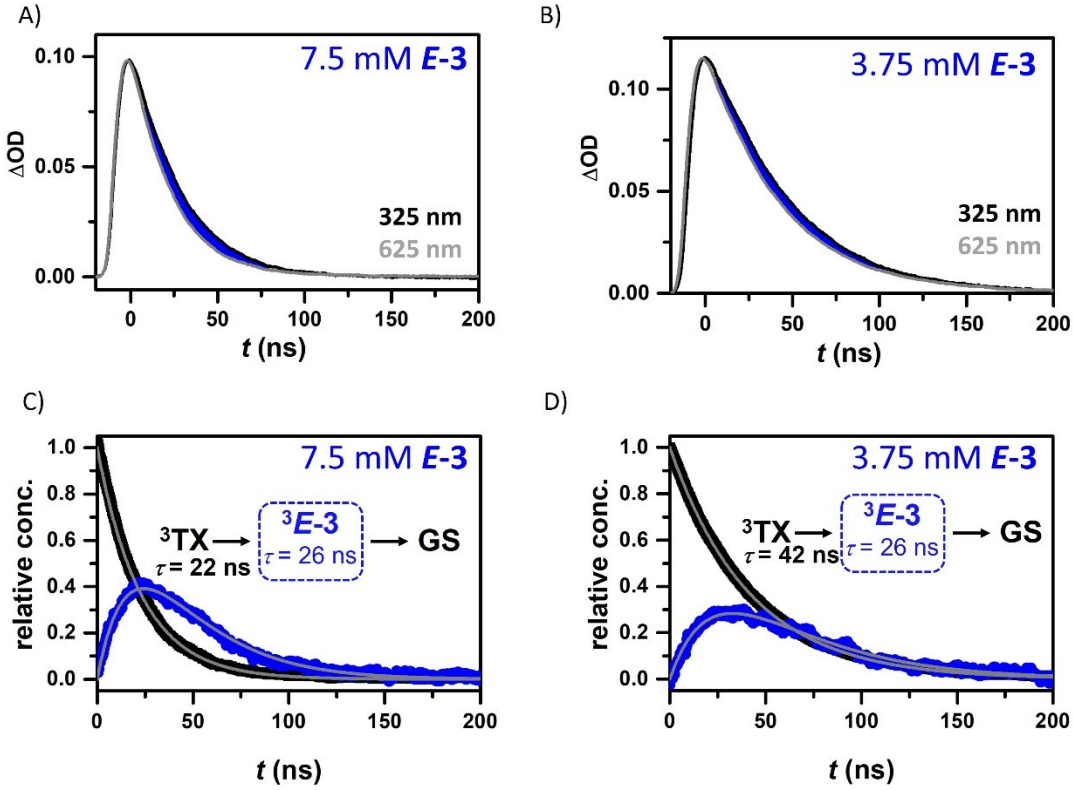

*Figure S22: Mechanistic investigations of the excited triplet state of **E-3** at different concentrations. Two Ar-saturated solutions containing 7.5 mM (left) or 3.75 mM (right) **E-3** with 50 µM TX in MeCN were investigated with transient absorption spectroscopy after 355 nm laser pulses. A) and B) Kinetic traces (raw data sets) at 625 nm (black) and 325 nm (grey). The differences in transient absorption of the scaled traces are highlighted in blue. C) and D) Kinetic traces at 625 nm (black) compared to the difference of the kinetic traces (325 nm and 625 nm) with global fit analyses. See main paper for further explanations of the signal separation procedure.*

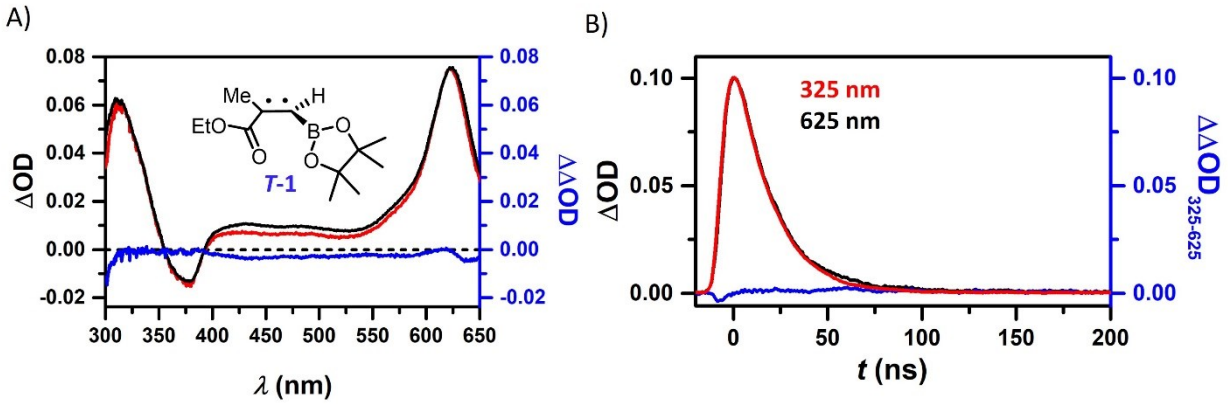

*Figure S23: Mechanistic investigations of the excited triplet state of **Z-1**. An Ar-saturated solution of 100 mM **Z-1** with 50 µM TX in MeCN was investigated with transient absorption spectroscopy after 355 nm laser pulses. A) Transient absorption spectra of TX with **Z-1** (red) after 20 ns (detection time: 20 ns) and in the absence of **Z-1** (black) after 1 µs (detection time: 20 ns). The spectrum of only TX was adjusted to the amplitude of the red spectrum at 625 nm (where the triplet-excited **T-1** in not expected to absorb). The blue spectrum is the difference of both TA spectra (with and without **Z-1**). B) Kinetic traces at 625 nm (black) and at 325 nm (red). The maximum at 625 nm was adjusted to the maximum at 325 nm. The blue curve is the difference spectrum of both measurements (325 nm and 625 nm). In contrast to what has been observed for **E-3** and **Z-3**, clear TA signals for the perpendicular triplet **T-1** could not be detected with the employed method. See main paper for further explanations.*

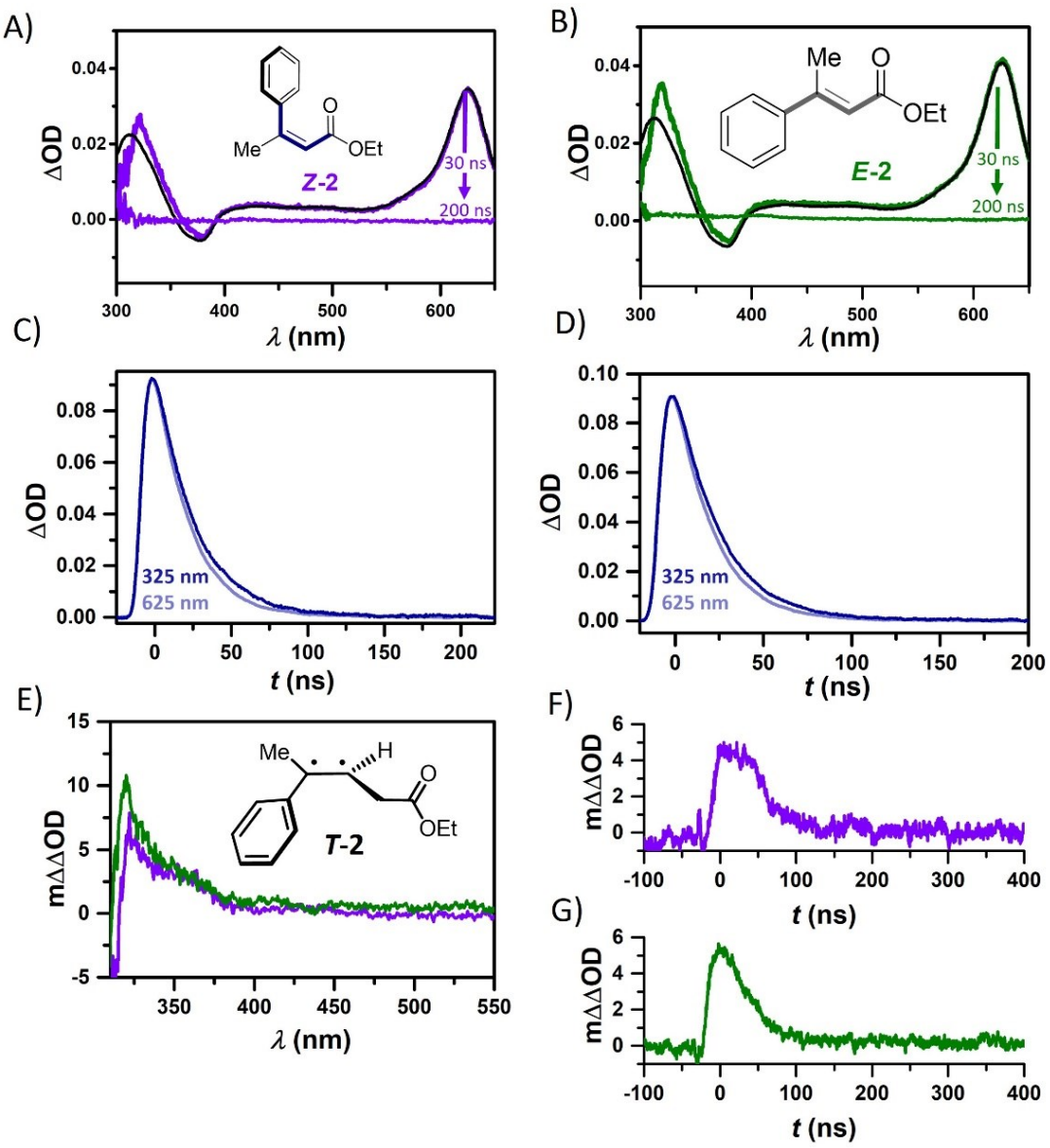

*Figure S24: Mechanistic investigations of the excited triplet state **T-2** after sensitization of either **Z-2** (purple) or **E-2** (green) by transient absorption spectroscopy with 355 nm laser pulses. If not stated otherwise, a solution containing 50 μM TX with either 7.2 mM **E-3** or 18.8 mM **Z-3** in Ar-saturated MeCN was used for all experiments and TA spectra were integrated over 20 ns. A) and B) TA spectra of TX in the absence of quencher (black) (delay: 1 μs) and in combination with **Z-2** or **E-2** (recorded after 30 ns and 200 ns. C) and D) Scaled kinetic traces recorded with **Z-2** or **E-2** at 325 nm and 625 nm E) Difference TA spectra of **Z-2** and **E-2** after ^{3}TX sensitization obtained from either A) or B). F) and G) Difference traces of kinetic measurements in C) and D) at 325 nm and 625 nm. Based on the results of this signal separation procedure, an upper limit for the **T-2** lifetime of 15 ns has been estimated.*

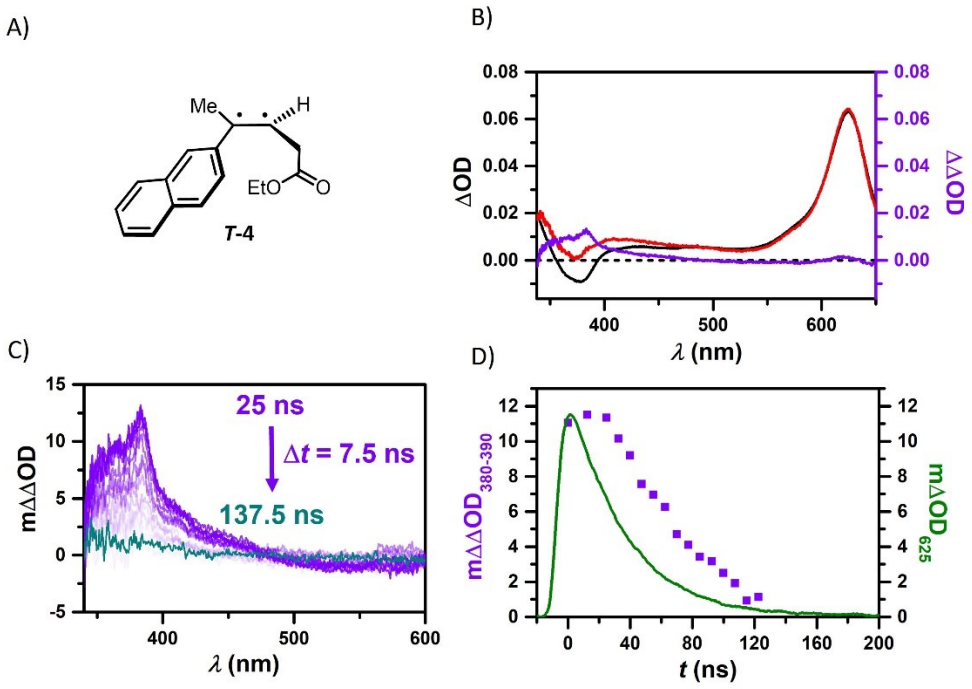

*Figure S25: Mechanistic investigations of the excited triplet state of **E-4**. An Ar-saturated solution of 3 mM **E-4** with 50 µM TX in MeCN was investigated with transient absorption spectroscopy after 355 nm laser pulse excitation. A) Molecular structure of perpendicular triplet **T-4**. B) Transient absorption spectra of TX with **E-4** (red) after 40 ns (detection time: 20 ns) and in the absence of **E-4** (black) after 1 µs (detection time: 20 ns). The spectrum of only TX was adjusted to the amplitude of the red spectrum at 625 nm (where the triplet-excited **T-4** in not expected to absorb). The purple spectrum is the difference of both TA spectra (with and without **E-4**). C) Difference TA spectra of **E-4** after sensitization by ^{3}TX with increasing time delays from 25 ns to 137.5 ns (7.5 ns steps, detection time: 20 ns). D) Transient absorption of TX with **E-4** at 625 nm (green) and the difference spectra in C averaged from 380 nm to 390 nm plotted against the time. The maximum at 625 nm was adjusted to the maximum of the other measurements. The TA spectrum shown in C) resembles that of the naphthalene triplet, which is in line with the computed spin densities for **T-4**.*

Separation of the pure ***T*-4** signal from scaled kinetic traces (or at isosbestic points of the ^{3}TX/TX couple) was unsuccessful owing to interference of the laser scattering light and the TX fluorescence signal with the rather weak absorption of ***T*-4** on the timescale of interest. Reliable measurements at 325 nm could not be carried out as a result of filter effects caused by ***E*-4**.

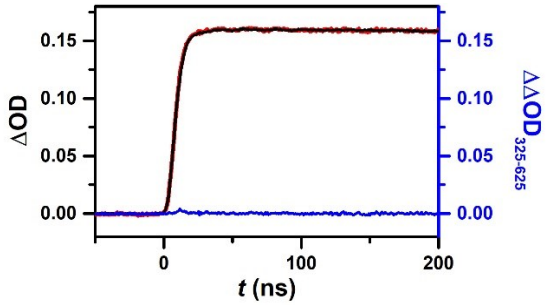

Figure S26: Control measurements testing the reliability of the separation of short-lived acceptor triplet signals from intense ^{3}TX signals. Transient absorption measurements of an Ar-saturated solution of 40 µM TX in MeCN after 355 nm laser pulse excitation. Kinetic traces were recorded at 625 nm (black) and at 325 nm (red). The maximum at 625 nm was adjusted to the maximum at 325 nm. The blue curve is the difference spectrum of both measurements (325 nm and 625 nm) and it shows the expected baseline-like signal.

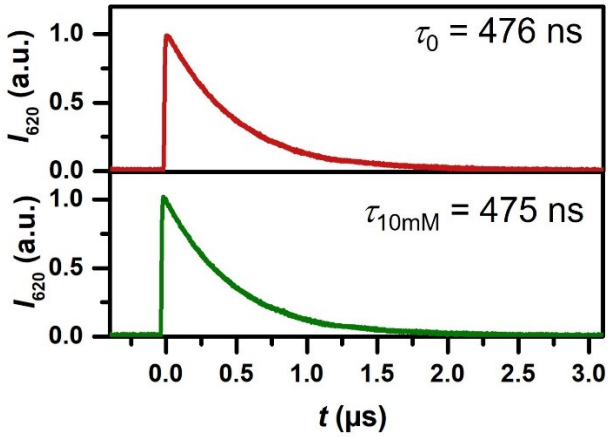

Figure 27: Kinetic emission measurements of [Ru(phen)$_3$](PF$_6$)$_2$ in deaerated MeCN in the absence (red) and presence (green) of 10 mM ***E-3.***

7. Kinetic simulation of quenching efficiencies

To show the influence of the triplet energy transfer rates, educt concentration and sensitizer lifetime on the quenching efficiency, we conducted kinetic simulations. These simulations aimed to illustrate the impact of both the educt concentration and the natural lifetime of the sensitizer. By specifying the educt concentration and the sensitizer's natural lifetime as defined in equation (4), we calculated the quenching efficiencies corresponding to different triplet energy transfer rates. Specifically, we employed three distinct substrate starting concentrations (10 mM, 60 mM, and 200 mM) in our simulations that are commonly used in preparative photochemistry. Also, a range of lifetimes (τ_0 = 0.1 µs, 1 µs, 10 µs, 25 µs and 100 µs) that covers typical Ir-based sensitizers (τ_0 ~ 1-10 µs) and organic chromophores (MeOTX ~ 25 µs, TX ~ 77 µs) was selected.

$$\eta_{\mathrm{TTET}} = 1 - \frac{1}{1 + c_0 \cdot \tau_0 \cdot k_{\mathrm{TTET}}} \tag{4}$$

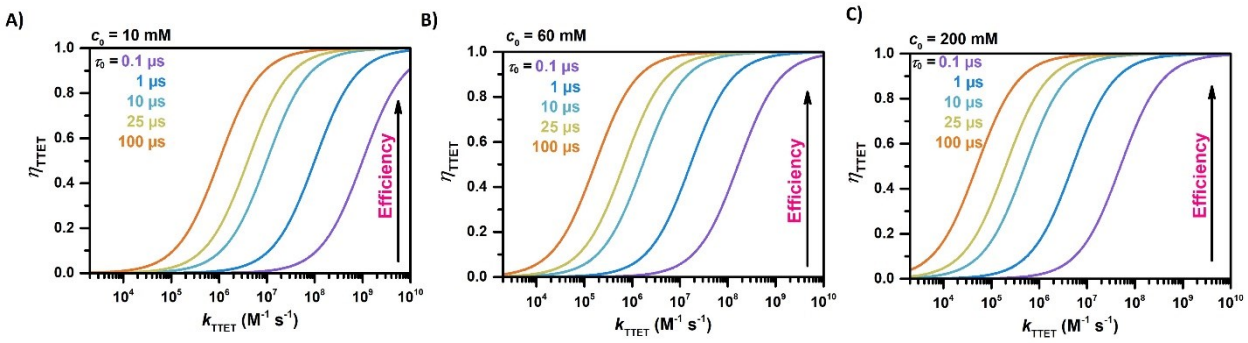

Figure S28: Simulated quenching efficiencies plotted against the triplet-triplet energy transfer rate according to equation (4) with varying sensitizer triplet lifetimes and educt concentrations.

8. NMR spectra

NMR spectra of the purified compounds

^{1}H NMR of ***Z*-1** (400 MHz, $CDCl_3$)

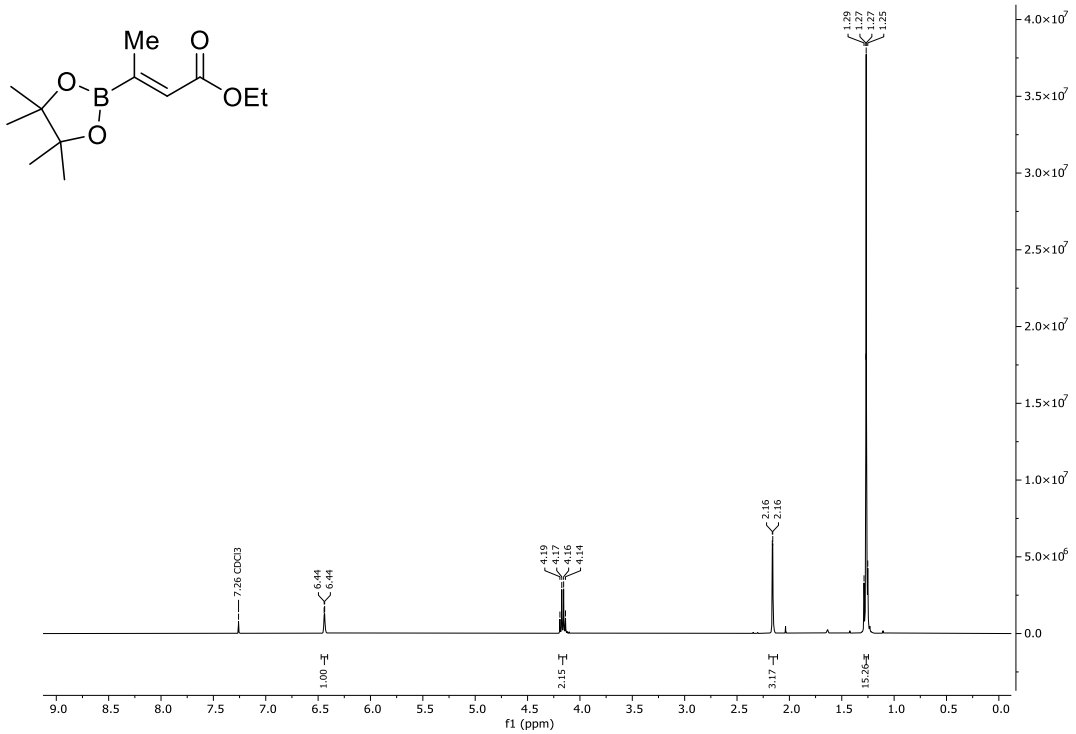

^{1}H NMR of ***E*-1** (400 MHz, $CDCl_3$)

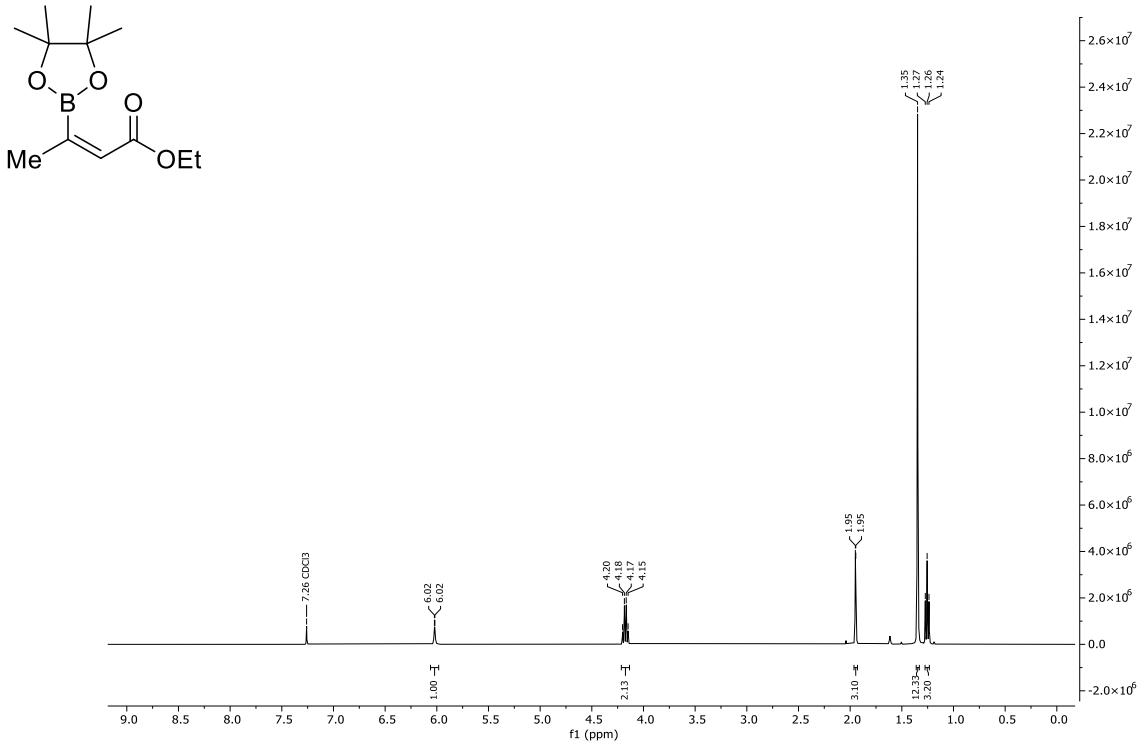

^{1}H NMR of ***E*-2** (400 MHz, $CDCl_3$)

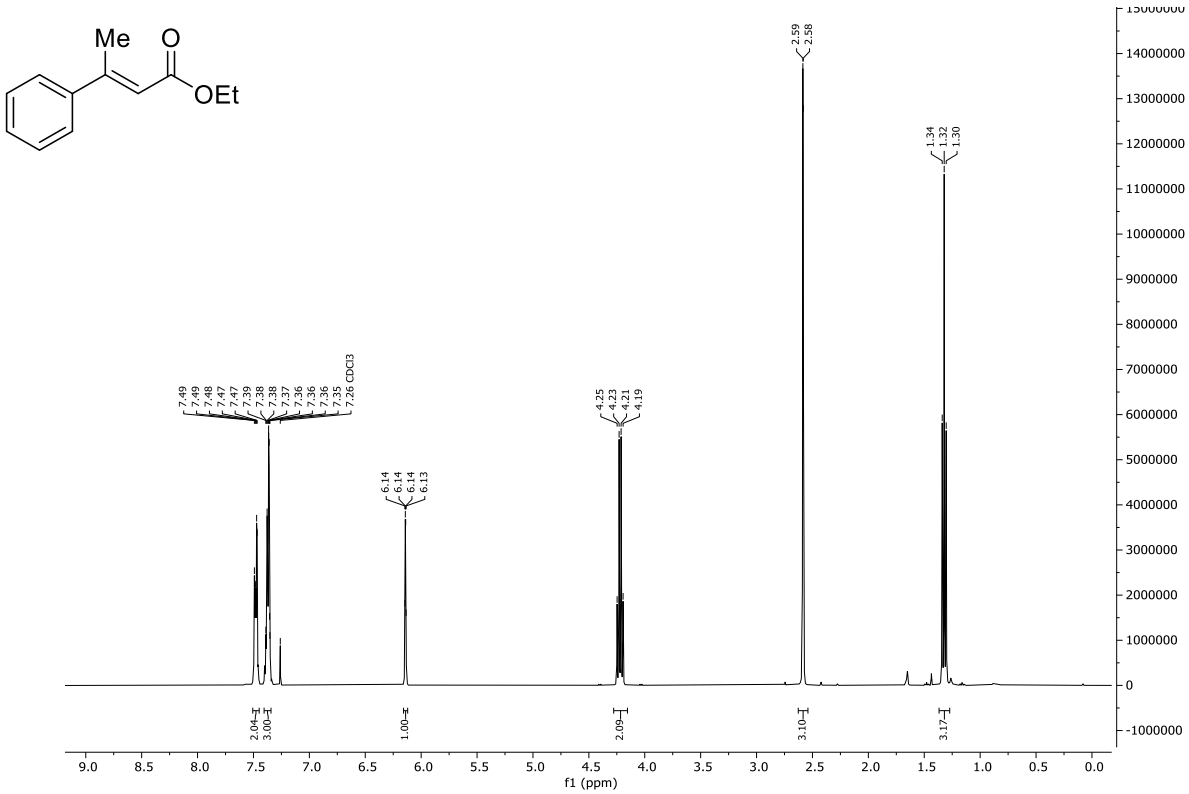

^{1}H NMR of ***Z*-2** (400 MHz, $CDCl_3$)

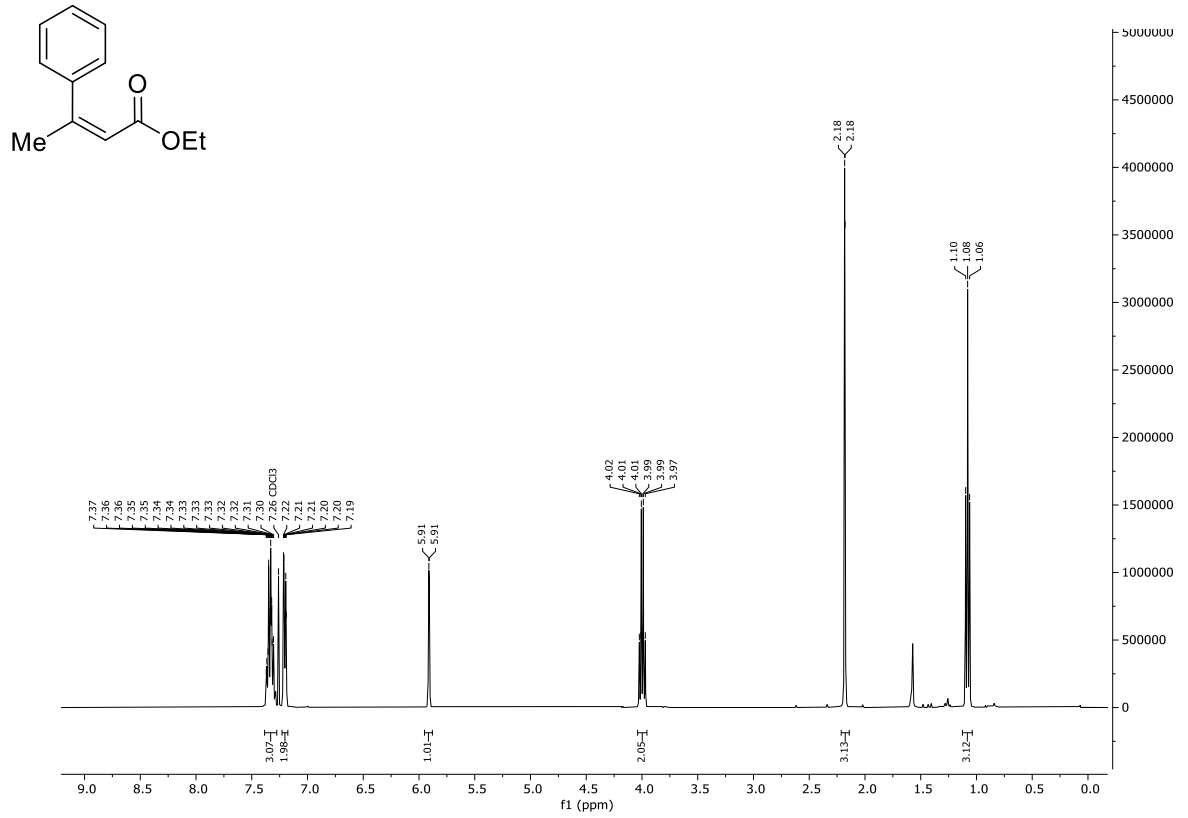

^{1}H NMR of **S1** (400 MHz, $CDCl_3$)

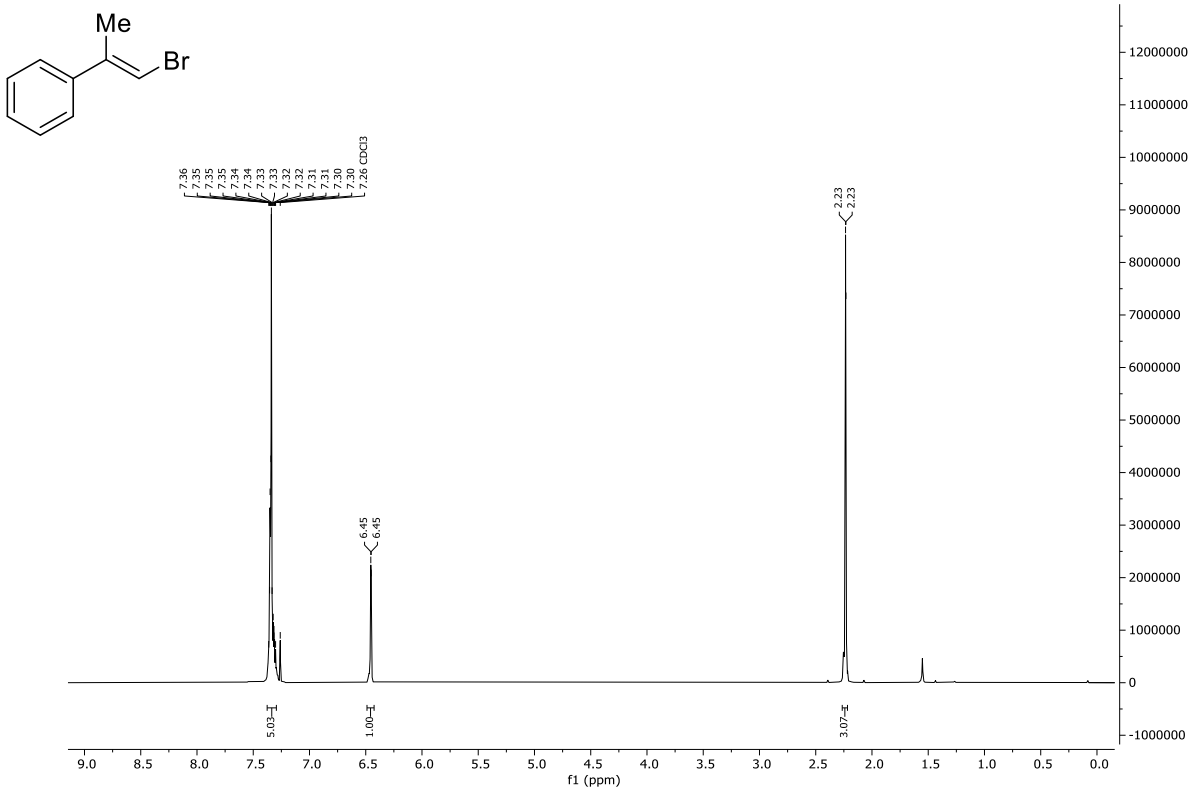

^{1}H NMR of ***E*-3** (400 MHz, $CDCl_3$)

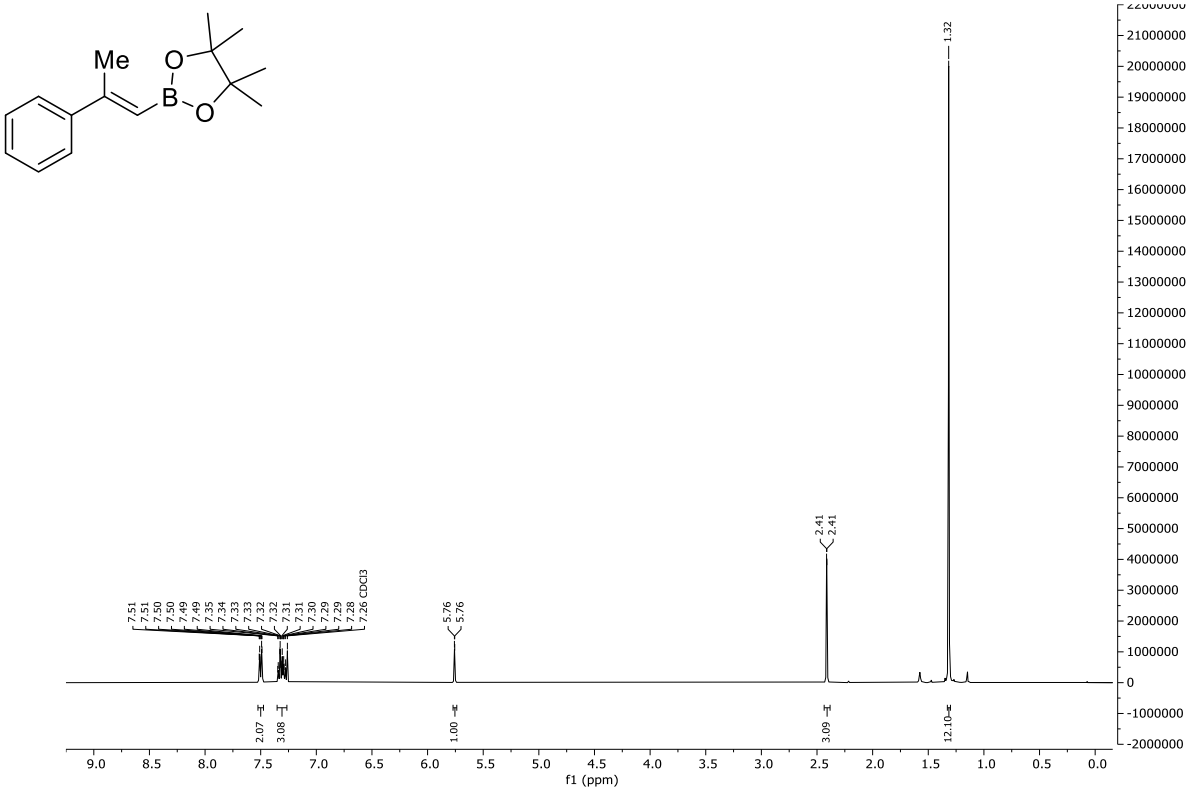

^{1}H NMR of ***Z*-3** (400 MHz, $CDCl_3$)

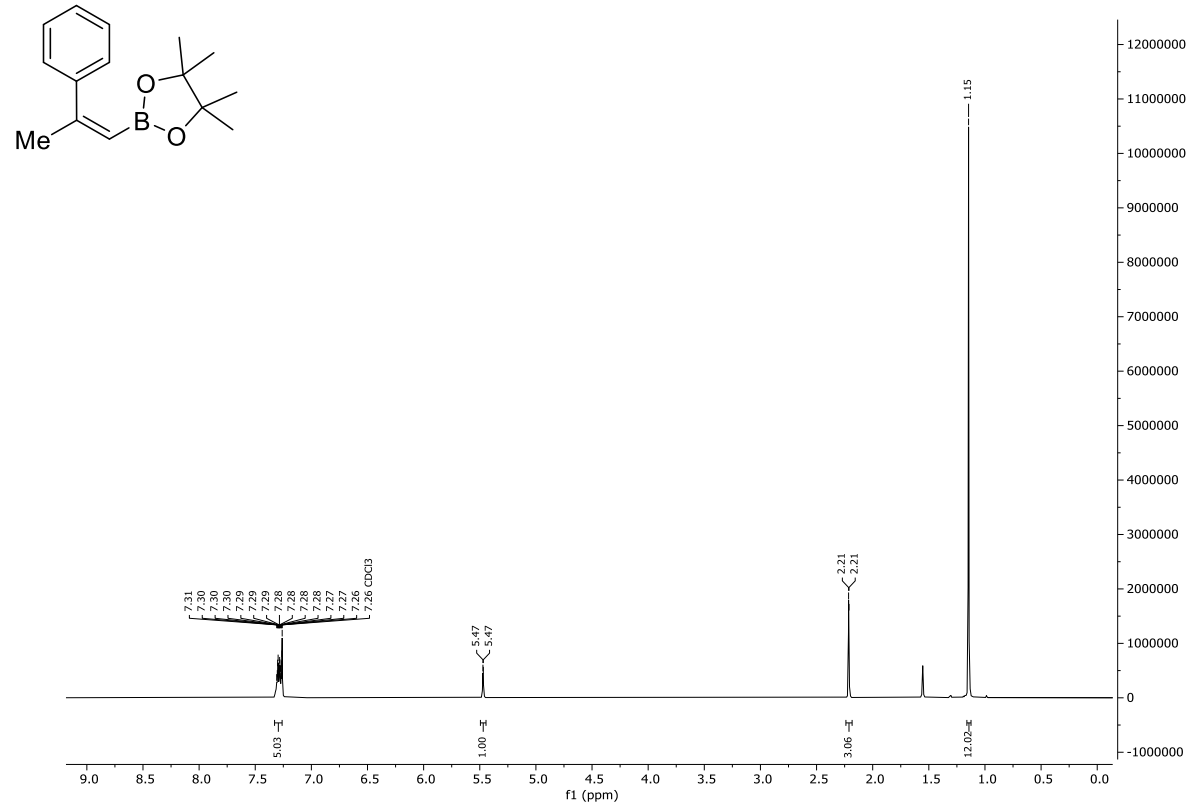

^{1}H NMR of ***E*-4** (400 MHz, $CDCl_3$)

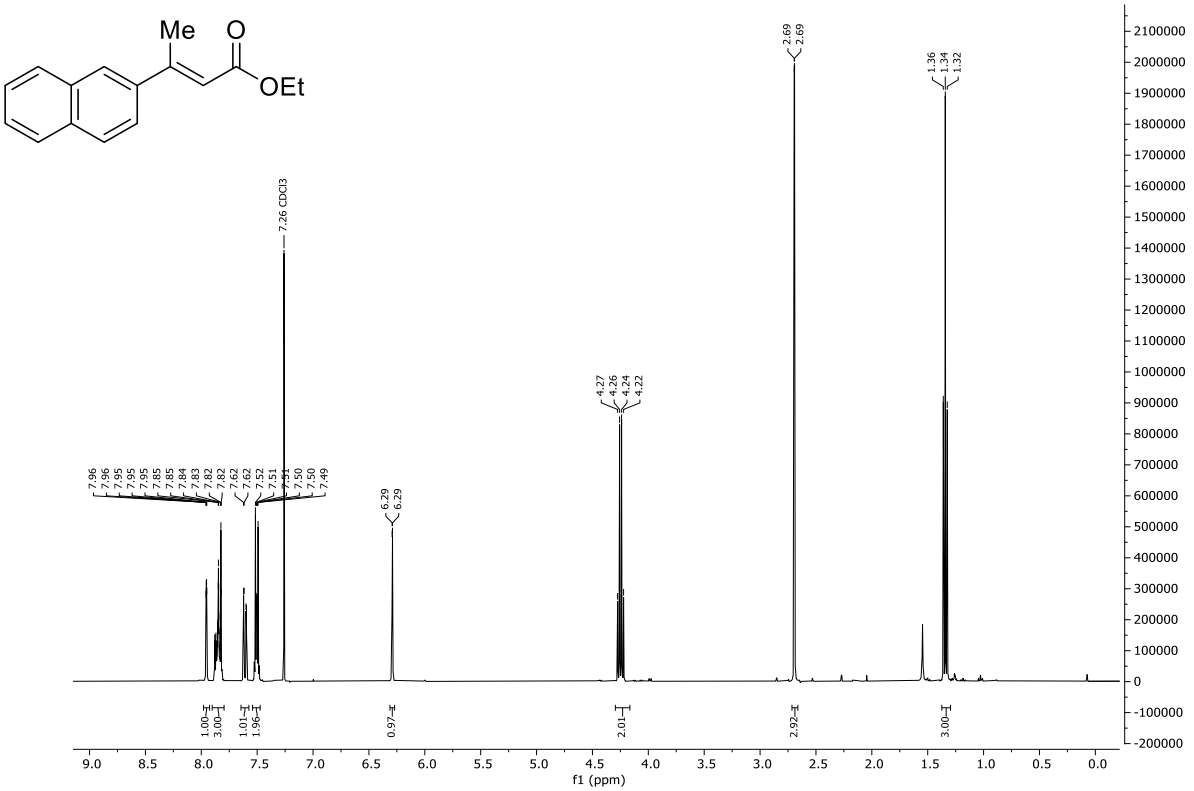

^{1}H NMR of ***Z*-4** (400 MHz, $CDCl_3$)

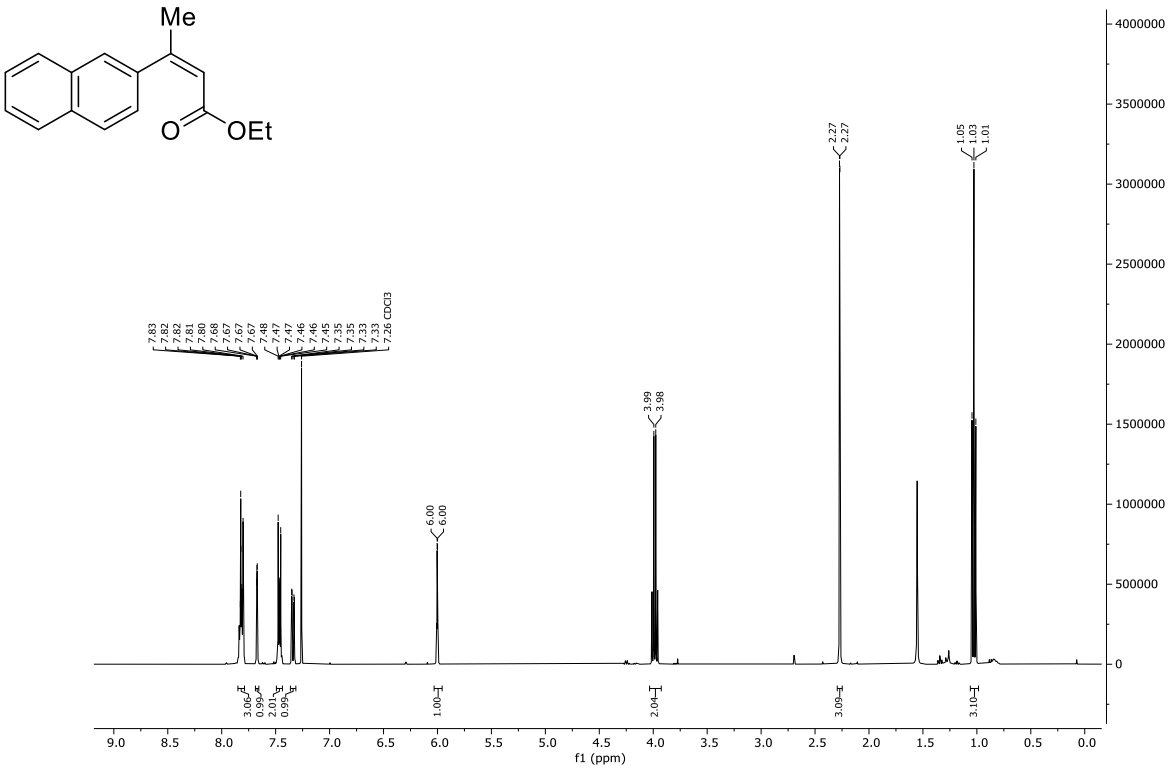

NMR spectra of photostationary state compositions

^{1}H NMR of ***Z*-1** to ***E*-1** (400 MHz, $CDCl_3$)

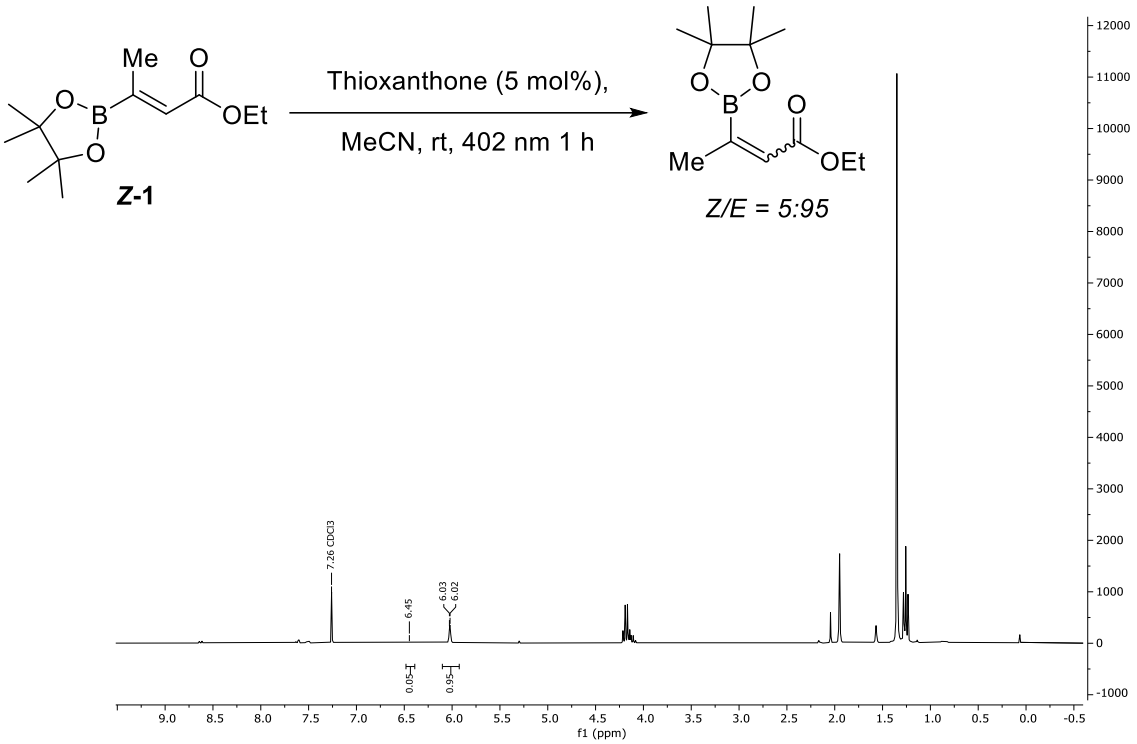

^{1}H NMR of ***E*-1** to ***Z*-1** (400 MHz, $CDCl_3$)

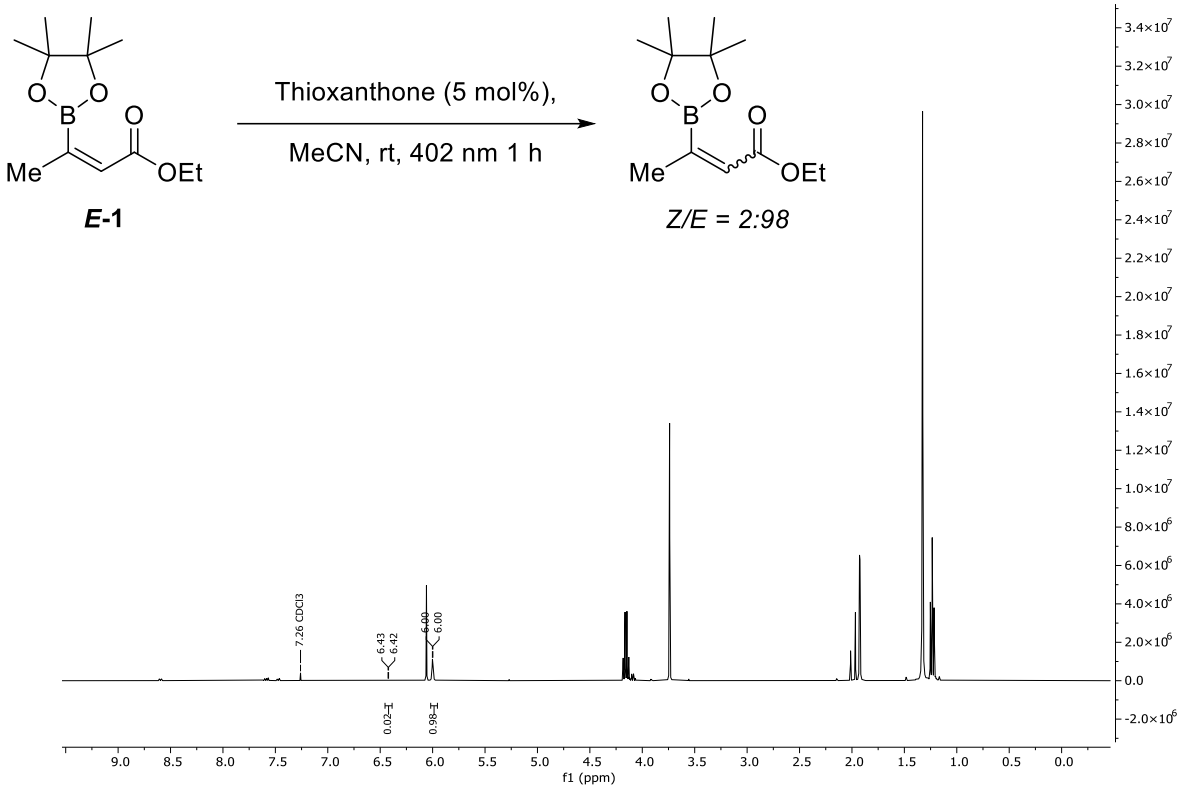

^{1}H NMR of ***E*-2** to ***Z*-2** (400 MHz, $CDCl_3$)

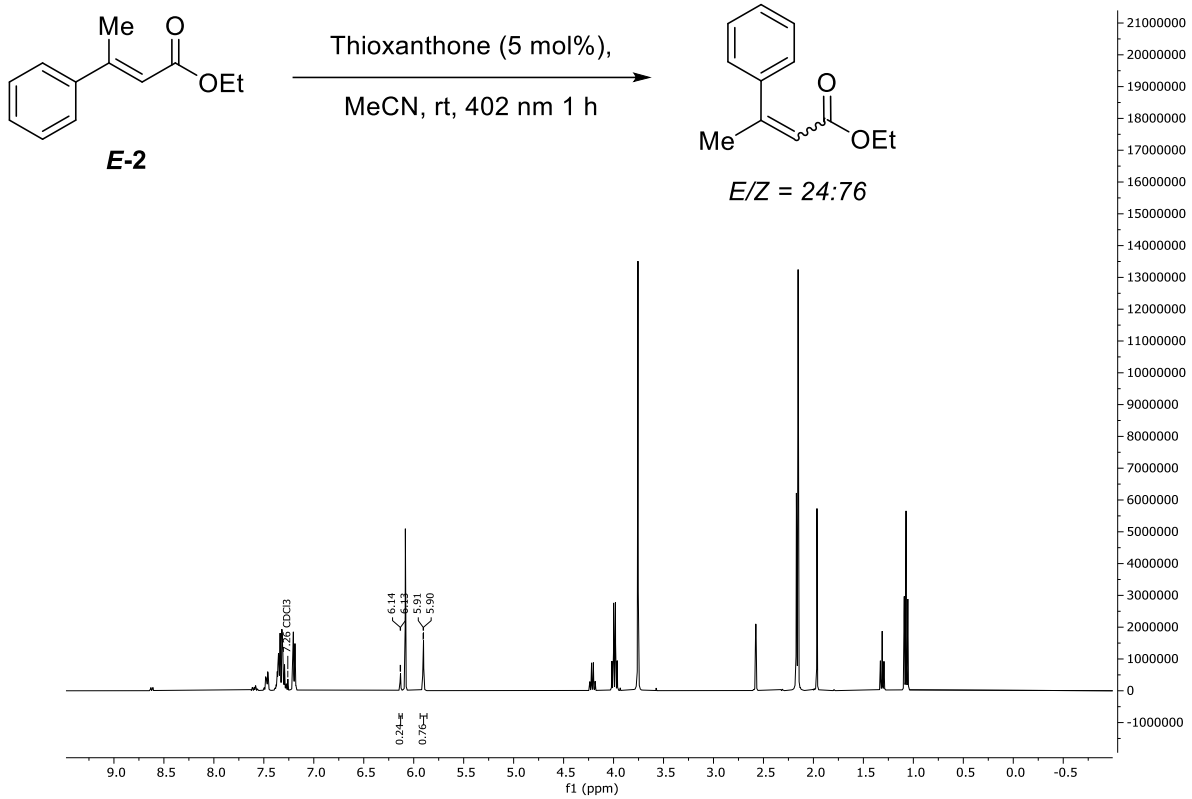

^{1}H NMR of ***Z*-2** to ***E*-2** (400 MHz, $CDCl_3$)

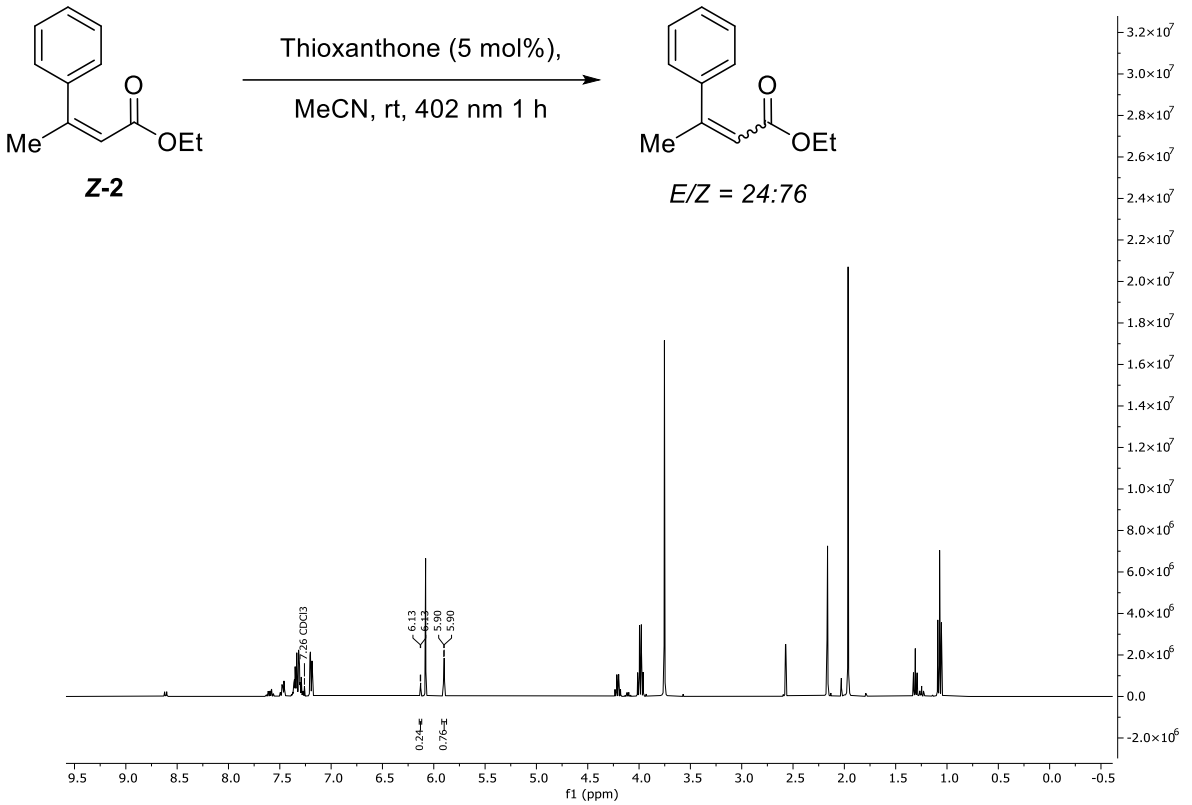

^{1}H NMR of ***E*-3** to ***Z*-3** (400 MHz, $CDCl_3$)

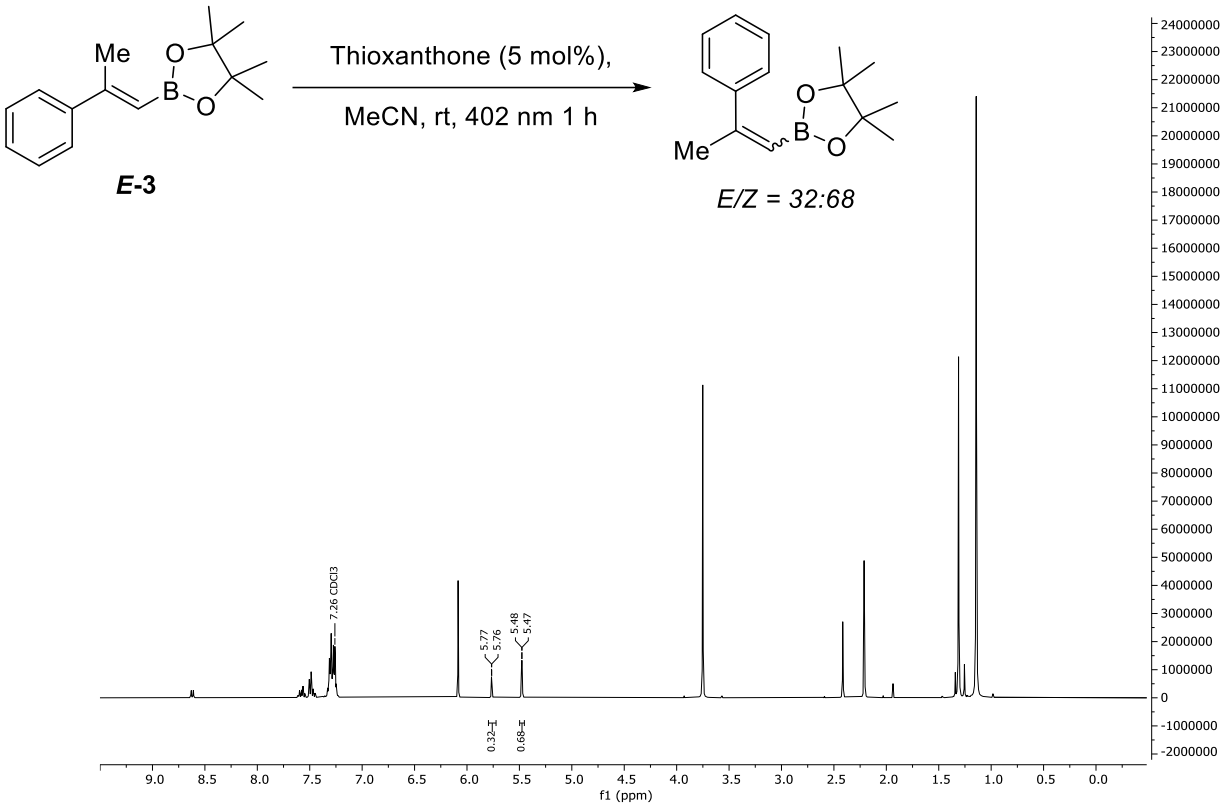

^{1}H NMR of ***Z*-3** to ***E*-3** (400 MHz, $CDCl_3$)

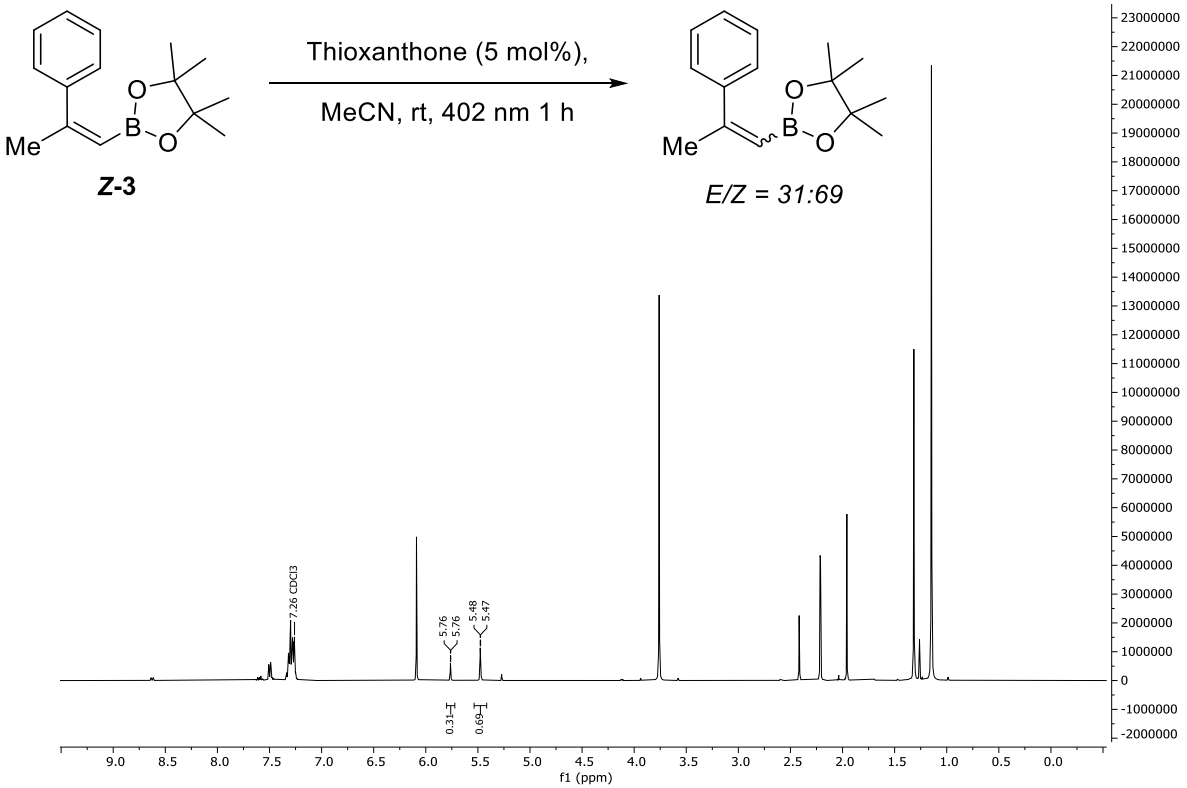

^{1}H NMR of ***E*-4** to ***Z*-4** (400 MHz, $CDCl_3$)

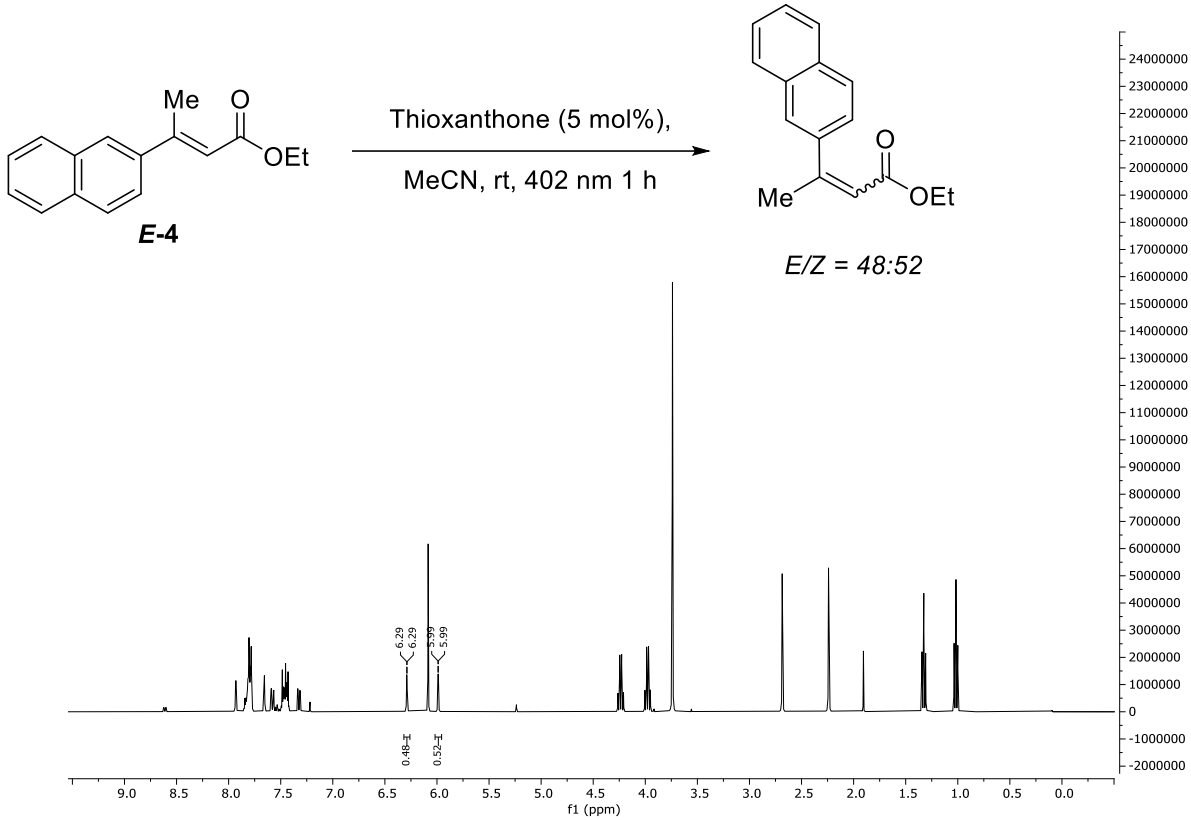

^{1}H NMR of ***Z*-4** to ***E*-4** (400 MHz, $CDCl_3$)

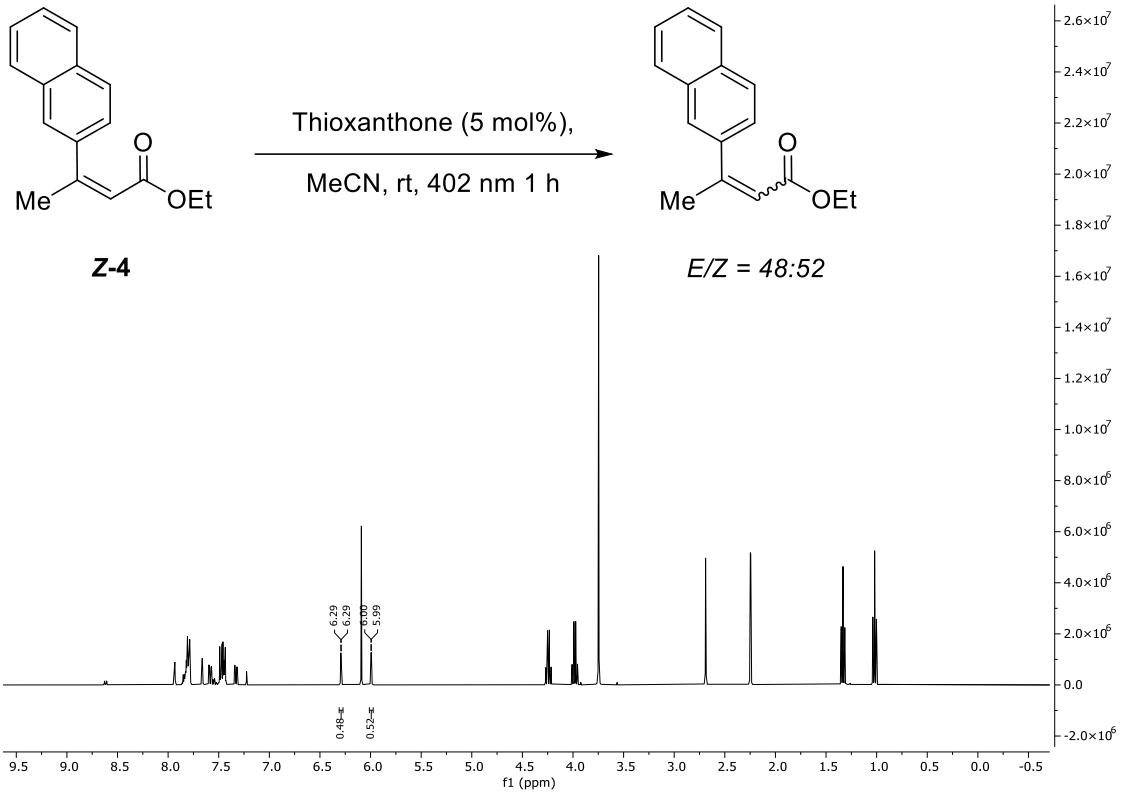

^{1}H NMR (400 MHz, CD_3CN) of ***E*-3** isomerization with MeOTX as sensitizer before (upper NMR) and after irradiation (lower NMR). See main paper and solar irradiation experiments for details.

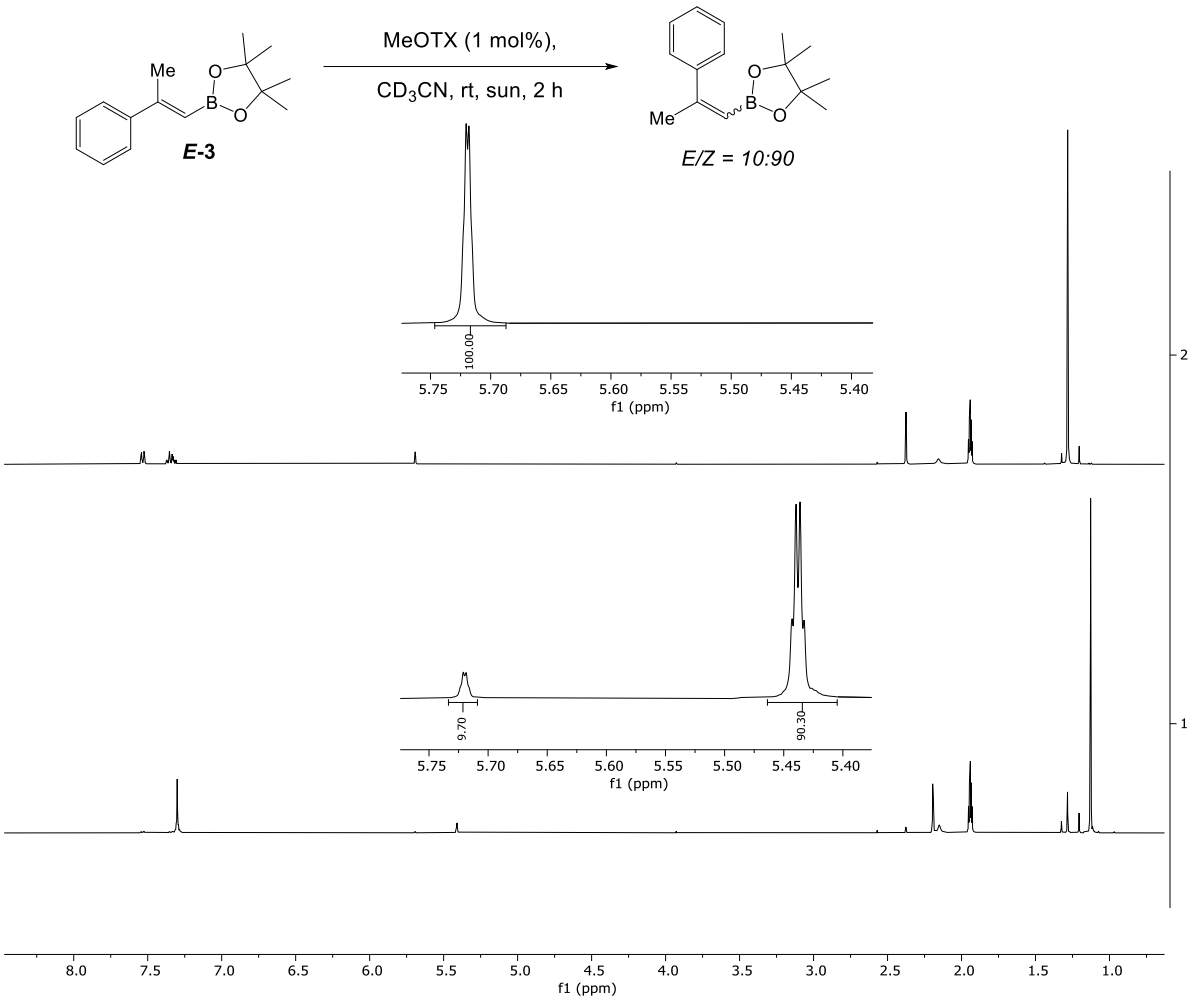

^{1}H NMR (400 MHz, CD_3CN) of ***E*-3** isomerization with CBDAC as sensitizer before (upper NMR) and after irradiation (lower NMR). See main paper and solar irradiation experiments for details.

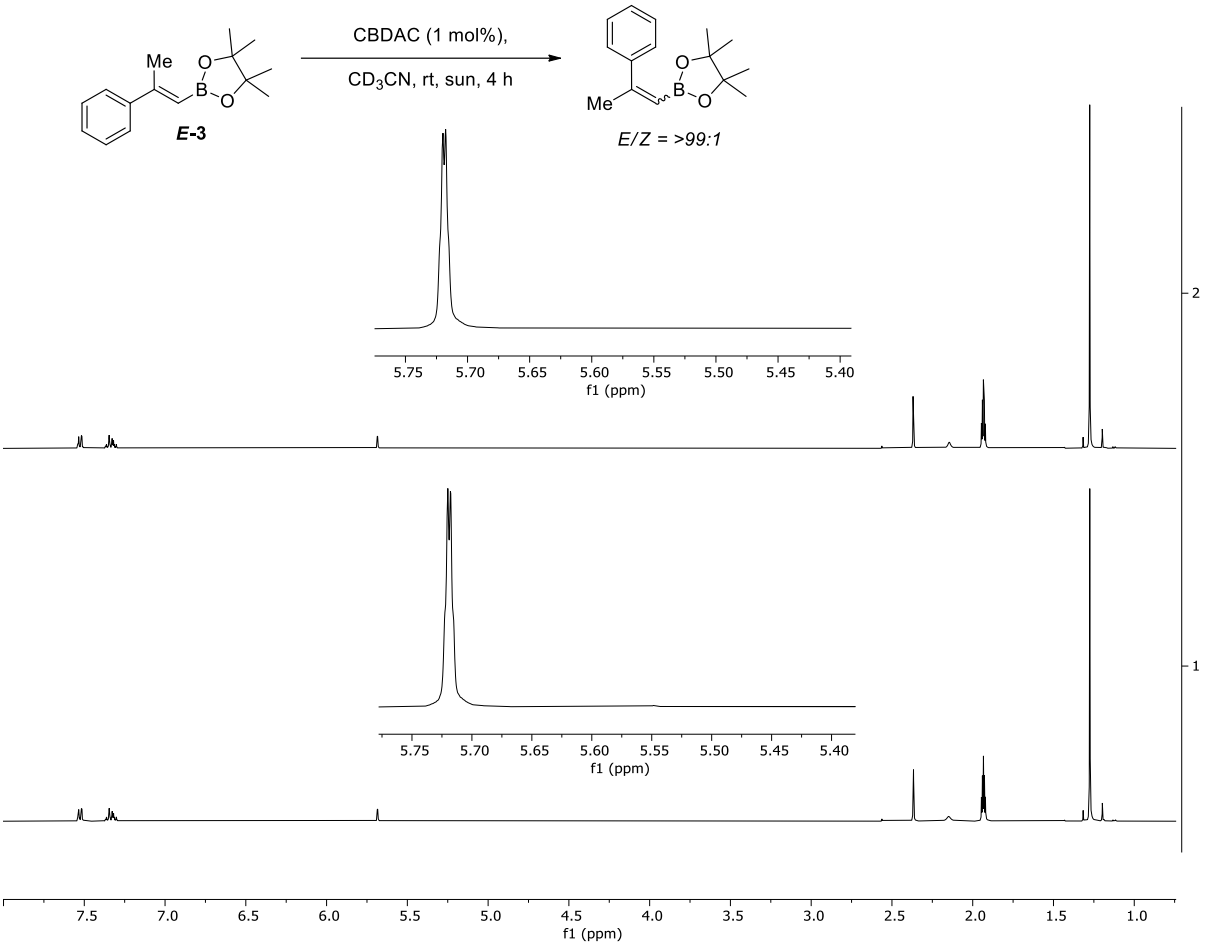

^{1}H NMR (400 MHz, CD_3CN) of ***E*-3** isomerization with $[Ru(phen)_3](PF_6)_2$ as sensitizer before (upper NMR) and after irradiation (lower NMR). See main paper and solar irradiation experiments for details.

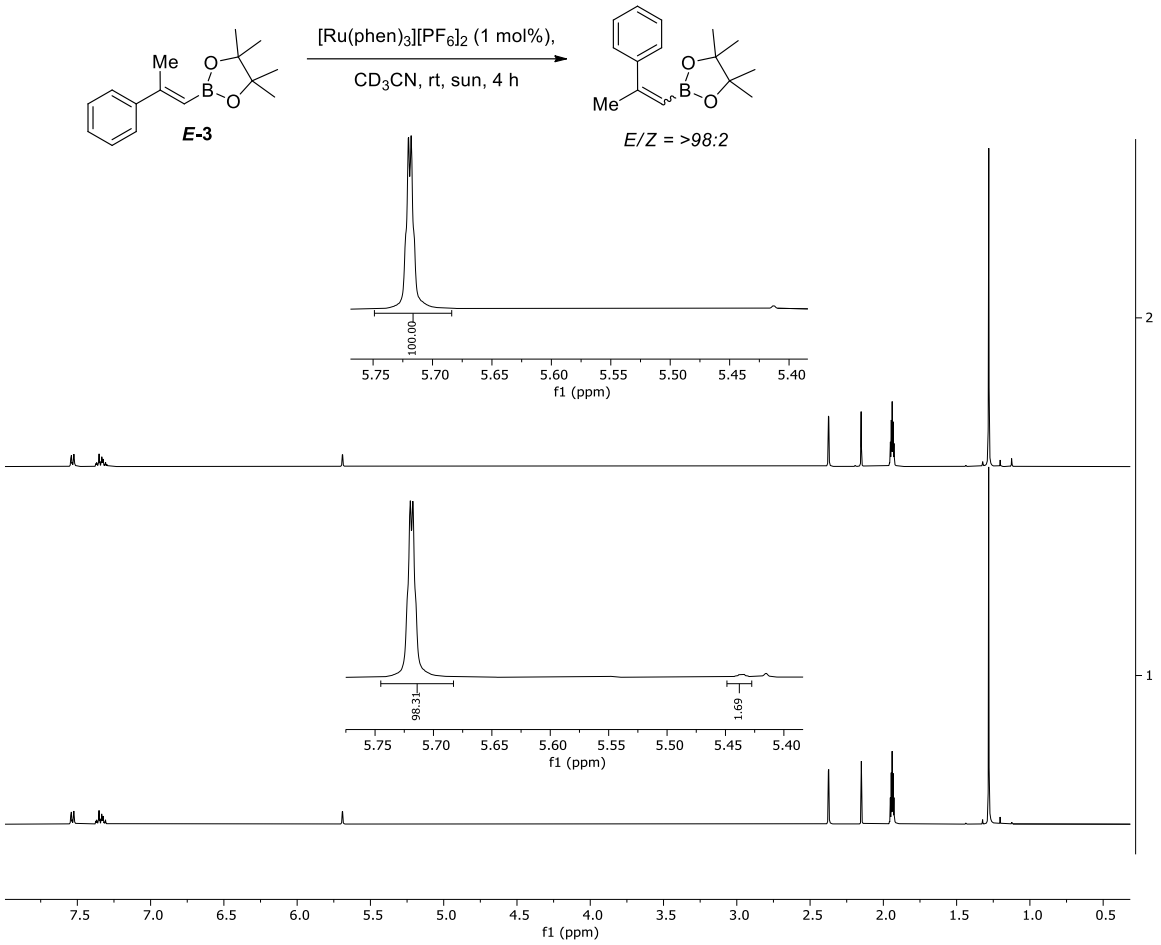

^{1}H NMR (400 MHz, CD_3CN) of ***E*-3** isomerization with TX as sensitizer before (upper NMR) and after irradiation (lower NMR). See main paper and solar irradiation experiments for details.

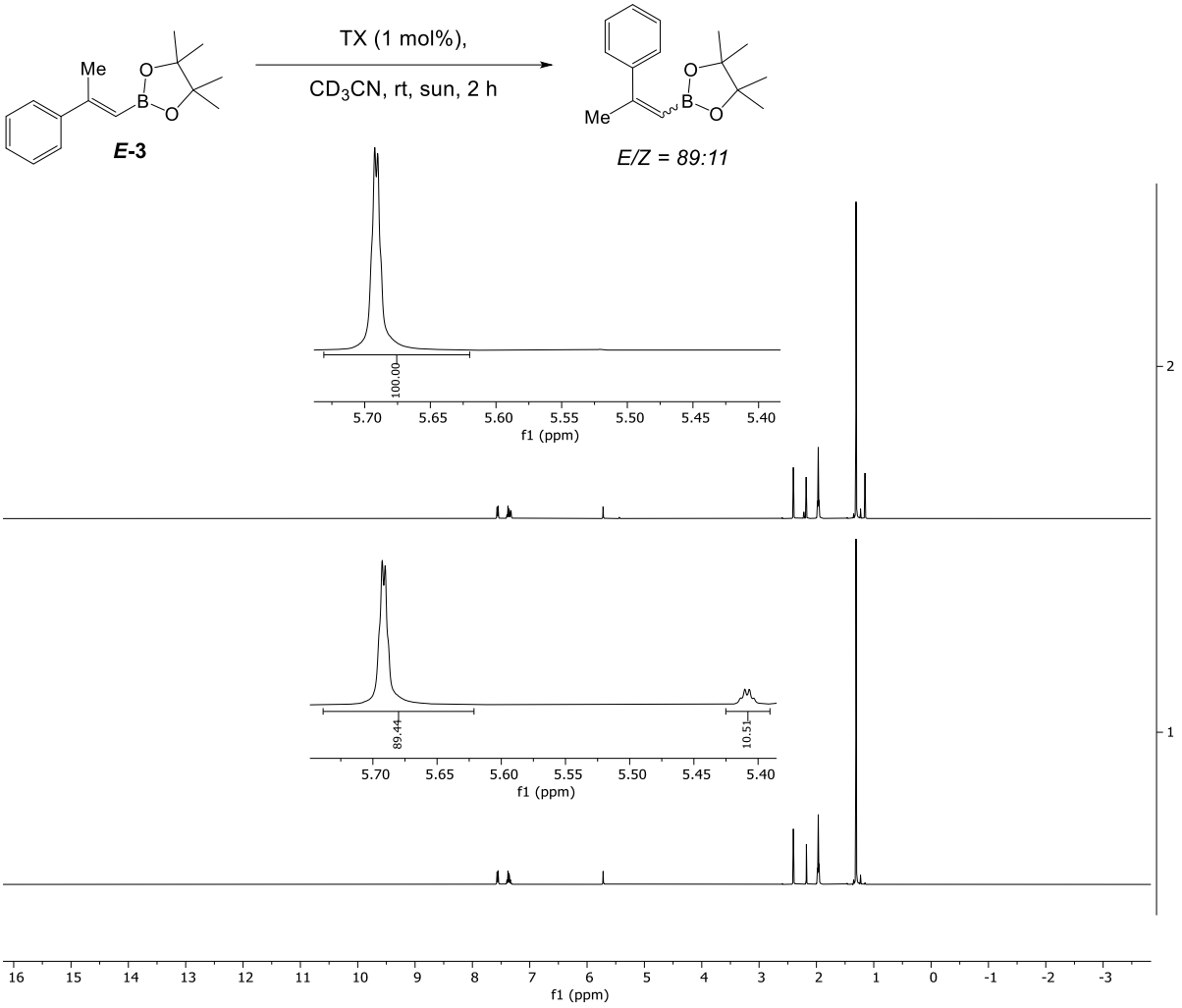

9. Literature

(1) Peck, C.; Calderone, J.; Santos, W. Copper(II)-Catalyzed β-Borylation of Acetylenic Esters in Water. *Synthesis* **2015**, *47* (15), 2242–2248. https://doi.org/10.1055/s-0034-1380524.

(2) Molloy, J. J.; Schäfer, M.; Wienhold, M.; Morack, T.; Daniliuc, C. G.; Gilmour, R. Boron-Enabled Geometric Isomerization of Alkenes via Selective Energy-Transfer Catalysis. *Science* **2020**, *369* (6501), 302–306. https://doi.org/10.1126/science.abb7235.

(3) Nagao, K.; Yamazaki, A.; Ohmiya, H.; Sawamura, M. Phosphine-Catalyzed *Anti* -Hydroboration of Internal Alkynes. *Org. Lett.* **2018**, *20* (7), 1861–1865. https://doi.org/10.1021/acs.orglett.8b00390.

(4) Metternich, J. B.; Gilmour, R. A Bio-Inspired, Catalytic *E* → *Z* Isomerization of Activated Olefins. *J. Am. Chem. Soc.* **2015**, *137* (35), 11254–11257. https://doi.org/10.1021/jacs.5b07136.

(5) Molloy, J. J.; Metternich, J. B.; Daniliuc, C. G.; Watson, A. J. B.; Gilmour, R. Contra-Thermodynamic, Photocatalytic $E \rightarrow Z$ Isomerization of Styrenyl Boron Species: Vectors to Facilitate Exploration of Two-Dimensional Chemical Space. *Angew. Chem. Int. Ed.* **2018**, *57* (12), 3168–3172. https://doi.org/10.1002/anie.201800286.

(6) Coe, B. J.; Helliwell, M.; Sánchez, S.; Peers, M. K.; Scrutton, N. S. Water-Soluble Ir(III) Complexes of Deprotonated N-Methylbipyridinium Ligands: Fluorine-Free Blue Emitters. *Dalton Trans.* **2015**, *44* (35), 15420–15423. https://doi.org/10.1039/C5DT02591E.

(7) Lowry, M. S.; Hudson, W. R.; Pascal, R. A.; Bernhard, S. Accelerated Luminophore Discovery through Combinatorial Synthesis. *J. Am. Chem. Soc.* **2004**, *126* (43), 14129–14135. https://doi.org/10.1021/ja047156+.

(8) Frisch, M. J.; Trucks, G. W.; Schlegel, H. B.; Scuseria, G. E.; Robb, M. A.; Cheeseman, j. R.; Scalmani, G.; Barone, V.; Mennucci., B.; Petersson, G. A.; Nakatsuji, H.; Caricato, M.; Li, X.; Hratchian, H. P.; Izmaylov, A. F.; Bloino, J.; Zheng, G.; Sonnenberg, J. L.; Hada, M.; Ehara, M.; Toyota, K.; Fukuda, R.; Hasegawa, J.; Ishida, M.; Nakajima, Y.; Honda, Y.; Kitao, O.; Nakai, H.; Vreven, T.; Montgomery, J.; Peralta, J. E.; Ogliaro, F.; Bearpark, M.; Heyd, J. J.; Brothers, E.; Kudin, K. N.; Staroverov, V. N.; Keith, T.; Kobayashi, R.; Normand, J.; Raghavachari, K.; Rendell, A.; Burant, J. C.; Iyengar, S. S.; Tomasi, J.; Cossi, M.; Rega, N.; Millam, J. M.; Klene, M.; Knox, J. E.; Cross, J. B.; Bakken, V.; Adamo, C.; Jaramillo, J.; Gomperts, R.; Stratmann, R. E.; Yazyev, O.; Austin, A. J.; Cammi, R.; Pomelli, C.; Ochterski, J. W.; Martin, R. L.; Morokuma, K.; Zakrzewski, V. G.; Voth, G. A.; Salvador, P.; Dannenberg, J. J.; Dapprich, S.; Daniels, A. D.; Farkas, O.; Foresman, J. B.; Ortiz, J. V.; Cioslowski, J.; Fox, D. J. *Gaussian 09 Revis. D01* **2013**.

(9) Yip, R. W.; Szabo, A. G.; Tolg, P. K. Triplet State of Ketones in Solutions. Quenching Rate Studies of Thioxanthenone Triplets by Flash Absorption. *J. Am. Chem. Soc.* **1973**, *95* (13), 4471–4472. https://doi.org/10.1021/ja00794a081.

(10) Goerner, H. Triplet States of Phenylethylenes in Solution. Energies, Lifetimes, and Absorption Spectra of 1,1-Diphenyl-, Triphenyl-, and Tetraphenylethylene Triplets. *J. Phys. Chem.* **1982**, *86* (11), 2028–2035. https://doi.org/10.1021/j100208a023.

(11) Herkstroeter, W. G.; Hammond, G. S. Mechanisms of Photochemical Reactions in Solution. XXXIX. [1] Study of Energy Transfer by Kinetic Spectrophotometry. *J. Am. Chem. Soc.* **1966**, *88* (21), 4769–4777. https://doi.org/10.1021/ja00973a001.

(12) Balzani, V.; Bolletta, F.; Scandola, F. Vertical and "Nonvertical" Energy Transfer Processes. A General Classical Treatment. *J. Am. Chem. Soc.* **1980**, *102* (7), 2152–2163. https://doi.org/10.1021/ja00527a002.

(13) Montalti, M.; Credi, A.; Prodi, L.; Gandolfi, M. T. *Handbook of Photochemistry*, 3rd ed.; CRC Press, **2006**. https://doi.org/10.1201/9781420015195.

(14) Halpern, A. M.; Forsyth, D. A.; Nosowitz, M. Flash Photolysis of Saturated Amines in Acetonitrile Solution at 248 nm: Formation of Radical Cations. *J. Phys. Chem.* **1986**, *90* (12), 2677–2679. https://doi.org/10.1021/j100403a023.

(15) Yates, S. F.; Schuster, G. B. Photoreduction of Triplet Thioxanthone by Amines: Charge Transfer Generates Radicals That Initiate Polymerization of Olefins. *J. Org. Chem.* **1984**, *49* (18), 3349–3356. https://doi.org/10.1021/jo00192a019.

(16) Allen, N. S.; Catalina, F.; Green, P. N.; Green, W. A. Photochemistry of Thioxanthones—IV. Spectroscopic and Flash Photolysis Study on Novel n-Propoxy and Methyl, n-Propoxy Derivatives. *Eur. Polym. J.* **1986**, *22* (10), 793–799. https://doi.org/10.1016/0014-3057(86)90018-2.

(17) Luque, A.; Groß, J.; Zähringer, T. J. B.; Kerzig, C.; Opatz, T. Vinylcyclopropane [3+2] Cycloaddition with Acetylenic Sulfones Based on Visible Light Photocatalysis. *Chem. Eur. J.* **2022**, *28* (18), e202104329.

(18) Wallentin, C.-J.; Nguyen, J. D.; Finkbeiner, P.; Stephenson, C. R. J. Visible Light-Mediated Atom Transfer Radical Addition via Oxidative and Reductive Quenching of Photocatalysts. *J. Am. Chem. Soc.* **2012**, *134* (21), 8875–8884. https://doi.org/10.1021/ja300798k.

(19) Herr, P.; Kerzig, C.; Larsen, C. B.; Häussinger, D.; Wenger, O. S. Manganese(i) Complexes with Metal-to-Ligand Charge Transfer Luminescence and Photoreactivity. *Nat. Chem.* **2021**, *13* (10), 956–962. https://doi.org/10.1038/s41557-021-00744-9.

(20) Rodrigues, M. R.; Miguel, G. N. Mechanistic Study of Tetrahydrofuran Polymerization Photoinitiated by a Sulfonium Salt/Thioxanthone System. *Macromol. Chem. Phys.* **2001**, No. 202, 2776–2782.

(21) Nikitas, N. F.; Gkizis, P. L.; Kokotos, C. G. Thioxanthone: A Powerful Photocatalyst for Organic Reactions. *Org. Biomol. Chem.* **2021**, *19* (24), 5237–5253. https://doi.org/10.1039/D1OB00221J.

(22) Goez, M.; Kerzig, C. Counterintuitive Influence of Protonation on Radical-Anion Photoionization. *Angew. Chem. Int. Ed.* **2012**, *51* (50), 12606–12608. https://doi.org/10.1002/anie.201206605.

(23) Amirzadeh, G.; Schnabel, W. On the Photoinitiation of Free Radical Polymerization-Laser Flash Photolysis Investigations on Thioxanthone Derivatives. *Makromol. Chem.* **1981**, *182* (10), 2821–2835. https://doi.org/10.1002/macp.1981.021821027.

(24) Ścigalski, F.; Pączkowski, J. Tetraalkylammonium Salts of Amino Acids and Sulfur-Containing Amino Acids as Effective Co-Initiators of Free Radical Polymerization in the Presence of Aromatic Ketones. *Macromol. Chem. Phys.* **2008**, *209* (18), 1872–1880. https://doi.org/10.1002/macp.200800122.

10.7 Supporting Information for Project [F]

Angewandte Chemie
Eine Zeitschrift der Gesellschaft Deutscher Chemiker

Supporting Information

Geometric Isomerisation of Bifunctional Alkenyl Fluoride Linchpins: Stereodivergence in Amide and Polyene Bioisostere Synthesis

M. Wienhold, B. Kweon, C. McLaughlin, M. Schmitz, T. J. B. Zähringer, C. G. Daniliuc, C. Kerzig, R. Gilmour**

Supporting Information
©Wiley-VCH 2021
69451 Weinheim, Germany

Geometric Isomerisation of Bifunctional Alkenyl Fluoride Linchpins: Stereodivergence in Amide and Polyene Bioisostere Synthesis

Max Wienhold, Byeongseok Kweon, Calum McLaughlin, Matthias Schmitz, Till J. B. Zähringer, Constantin G. Daniliuc, Christoph Kerzig* and Ryan Gilmour*

Table of Contents

1. General Information 1

2. Experimental Section 3

2.1 Synthesis of α-Halo-β-bromoacrylates 3

2.2 Synthesis of α-Halo-β-borylacrylates 13

2.3 Photochemical Isomerisation of α-Halo-β-borylacrylates 26

2.3.1 Reaction Optimisation 26

2.3.2 Photochemical Isomerisation of trisubstituted α-Halo-β-borylacrylates 27

2.3.2 Photochemical Isomerisation of tetrasubstituted α-Halo-β-borylacrylates 35

2.4 Synthesis of fluorinated Polyenes 38

3. X-ray Crystallographic Analysis 45

4. Laser Flash Photolysis and DFT calculations 54

5. NMR-spectra of Key Compounds 57

6. References 143

1. General Information

Commercially available chemicals were purchased at *ABCR, Acros Organics, Sigma Aldrich, Alfa Aesar, fluorochem, BLDpharm* or *Merck* and used as received. Solvents for purification (extraction and chromatography) were purchased as technical grade and distilled on the rotary evaporator prior to use. Dry solvents were obtained from a solvent purification system (activated Alumina under a positive pressure of argon). Degassed solvent refers to bubbling argon through the solvent for a minimum of 15 min. Analytical thin layer chromatography (TLC) was performed on plates from *Merck* (*silica gel 60, F_{254}*) and visualised with a UV lamp (λ = 254 nm and λ = 366 nm), $KMnO_4$ and CAM stain solutions. Column chromatography was carried out on silica gel 60 (40 - 63 μm) from *Merck*. Concentration in vacuo was performed at ~10 mbar and 40 °C, drying at ~10^{-2} mbar and rt. NMR-spectra were recorded by the NMR service at the Organisch-Chemisches Institut, Westfälische Wilhelms-Universität Münster on a *Bruker AV300* (300 MHz)*, Bruker AV400* (400 MHz), *Agilent DD2 500* (500 MHz) and an *Agilent DD2 600* (600 MHz). Chemical shifts δ are stated in ppm and referenced to the residual solvent signal. The resonance multiplicity is abbreviated as: s (singlet), d (doublet), t (triplet), q (quadruplet), quint (quintet), sext (sextet), sep (septet) and m (multiplet). Assignments of unknown compounds are based on DEPT, COSY (HH), HMBC, HSQC, NOESY and HOESY spectra. For compounds containing boron and fluorine in an *ortho* relationship, a distinct $^{10/11}$B-isotope effect can be observed in the ^{19}F-NMR.[1] For molecules displaying this phenomenon, only the chemical shift referring to the more abundant ^{11}B-isotope is reported. IR measurements were carried out on a *Shimadzu IRspirit FT-IR spectrometer* and the intensities of the bands are assigned as follows: w (weak), m (medium), s (strong). High-resolution mass spectra were measured by the MS service of the Organisch-Chemisches Institut, Westfälische Wilhelms-Universität Münster. Melting points were determined on a *Büchi B-545* melting-point apparatus in open capillaries. Optical rotations were measured on a JASCO P2000 polarimeter. Photoreactions were performed utilizing a set-up of 4 *Winger WEPIV3-S2 UV Power LED Star* (Schwarzlicht) 1.2 W lamps (emission spectrum see **Figure S1**). The forward current per chip was set to 700 mA, the resulting forward voltage was 3.4 V while the resulting radiant flux was 1200 mW. The distance between the reaction vessels and the UV-lamp was set at approximately 0.5 cm for all reactions.

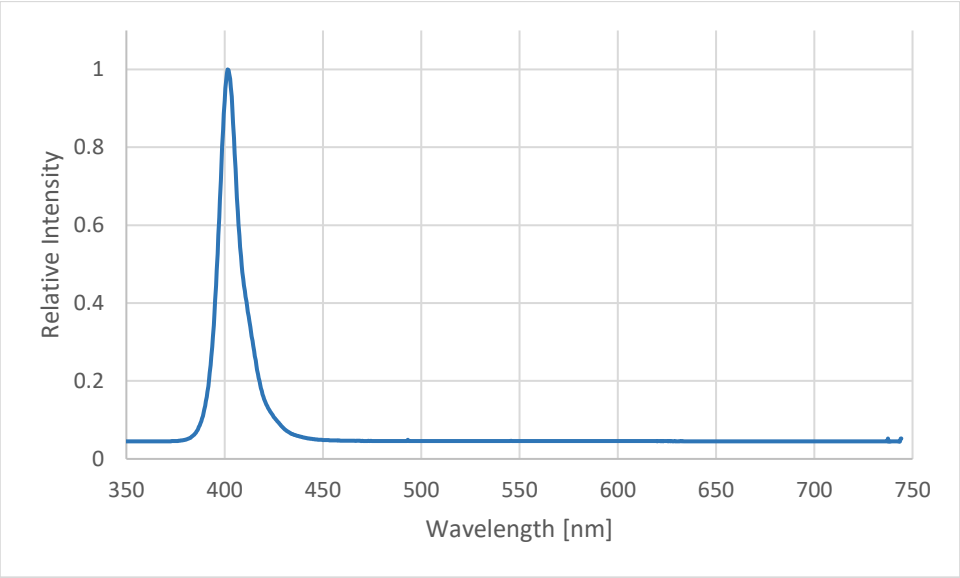

Figure S1: Emission spectrum of the utilised a *Winger WEPUV3-S2 UV Power LED Star* (402 nm).

2. Experimental Section

2.1 Synthesis of *α*-Halo-*β*-bromoacrylates

Synthesis of (*Z*)-3-bromo-2-fluoroacrylic acid (S1)

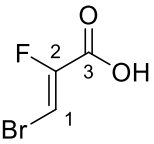

Methyl 2-fluoroacrylate (10.4 g, 100.0 mmol, 1.0 eq.) was dissolved in $CHCl_3$ (100 mL) under argon atmosphere and the solution was warmed to 50 °C before Br_2 (15.9 g, 105.0 mmol, 1.05 eq.) was slowly added. The mixture was stirred at 50 °C for 4 h before it was cooled to ambient temperature and quenched by the addition of sat. aq. $Na_2S_2O_3$. The organics were extracted with $CHCl_3$ and the combined organic layers were dried over $MgSO_4$. The solvent was removed under reduced pressure and the crude residue was dissolved in EtOH (60 mL). To this, a solution of NaOH (18 g) in H_2O (40 mL) was slowly added and the mixture was stirred for 2 h at rt before it was quenched by the addition of 37% aq. HCl. The reaction was acidified to pH = 1, the organics were extracted with Et_2O and the combined organic layers were dried over $MgSO_4$. After removal of the solvent under reduced pressure, the desired product was obtained as brown solid (11.0 g, 66%).

^{1}H-NMR (400 MHz, $CDCl_3$): δ (ppm) = 9.77 (s, 1H, O*H*), 7.15 (d, *J* = 23.5 Hz, 1H, H1).

^{13}C-NMR (126 MHz, $CDCl_3$): δ (ppm) = 163.2 (d, *J* = 35.0 Hz, C3), 150.1 (d, *J* = 260.2 Hz, C2), 104.7 (d, *J* = 17.7 Hz, C1).

^{19}F-NMR {^{1}H} (377 MHz, $CDCl_3$): δ (ppm) = -116.86.

HR-ESI-MS (Orbitrap) exact mass calculated for $[M-H]^-$ $(C_3HO_2BrF)^-$ requires 166.91494 m/z, found 166.91500 m/z

M.p.: 125.2 – 126.7 °C.

Synthesis of (*Z*)-3-bromo-2-fluoro-*N*-methoxy-*N*-methylacrylamide (S2)

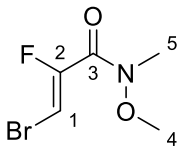

According to a modified procedure of Troin *et al*.[2] (*Z*)-3-bromo-2-fluoroacrylic acid (**S1**) (2.5 g, 15.0 mmol, 1.0 eq.), *N,O*-dimethylhydroxylamine hydrochloride (1.6 g, 16.5 mmol, 1.1 eq.), CBr_4 (5.5 g, 16.5 mmol, 1.1 eq.) and pyridine (1.3 mL, 1.3 g, 16.5 mmol, 1.1 eq.) were dissolved in dry DCM (37.5 mL) under argon atmosphere. The solution was cooled to 0 °C before PPh_3 (4.3 g, 16.5 mmol, 1.1 eq.) was slowly added. The reaction was stirred at 0 °C for 4 h, the mixture was filtered and the solvent was evaporated under reduced pressure. The crude residue was purified by column chromatography (SiO_2, 10% Et_2O/*n*-pentane) and the desired product was obtained as colourless oil (2.2 g, 71%).

R_f = (SiO_2, 10% EtOAc/*n*-pentane) = 0.16

^{1}H-NMR (400 MHz, $CDCl_3$): δ (ppm) = 6.73 (d, *J* = 25.5 Hz, 1H, H1), 3.75 (s, 3H, H4), 3.25 (s, 3H, H5).

^{13}C-NMR (101 MHz, $CDCl_3$): δ (ppm) = 160.1 (d, *J* = 27.6 Hz, C3), 153.5 (d, *J* = 272.0 Hz, C2), 99.1 (d, *J* = 19.4 Hz, C1), 62.2 (d, *J* = 2.5 Hz, C4), 33.7 (C5).

^{19}F-NMR {^{1}H} (377 MHz, $CDCl_3$): δ (ppm) = -109.64.

IR (ATR) $\tilde{\nu}$ = 3105 (w), 2980 (w), 2942 (w), 1660 (s), 1630 (s), 1461 (m), 1418 (m), 1386 (s), 1273 (m), 1185 (m), 1139 (w), 1112 (w), 1065 (m), 980 (m), 798 (w), 779 (m), 756 (m), 707 (m), 650 (m), 627 (m) cm^{-1}.

HR-ESI-MS (Orbitrap) exact mass calculated for $[M+Na]^+$ $(C_5H_7NO_2BrFNa)^+$ requires 233.95364 m/z, found 233.95362 m/z

Synthesis of (*Z*)-3-bromo-2-fluoro-1-morpholinoprop-2-en-1-one (S3)

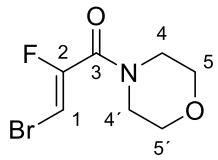

According to a modified procedure of Troin *et al.*[2] (*Z*)-3-bromo-2-fluoroacrylic acid (**S1**) (844.5 mg, 5.0 mmol, 1.0 eq.), morpholine (479.2 mg, 5.5 mmol, 1.1 eq.), CBr_4 (1.8 g, 5.5 mmol, 1.1 eq.) and pyridine (409 μL, 435.1 mg, 5.5 mmol, 1.1 eq.) were dissolved in dry DCM (12.5 mL) under argon atmosphere. The solution was cooled to 0 °C before PPh_3 (1.4 g, 5.5 mmol, 1.1 eq.) was slowly added. The reaction was stirred at 0 °C for 4 h, the mixture was filtered and the solvent was evaporated under reduced pressure. The crude residue was purified by column chromatography (SiO_2, 40% Et_2O/*n*-pentane) and the desired product was obtained as colourless solid (913.4 mg, 77%).

R_f = (SiO_2, 40% Et_2O/*n*-pentane) = 0.28

^{1}H-NMR (599 MHz, $CDCl_3$): δ (ppm) = 6.58 (d, *J* = 26.3 Hz, 1H, H1), 3.71 (t, *J* = 4.5 Hz, 4H, H5,H5´), 3.61 (t, *J* = 4.8 Hz, 4H, H4,H4´).

^{13}C-NMR (101 MHz, $CDCl_3$): δ (ppm) = 159.3 (d, *J* = 26.6 Hz, C3), 154.6 (d, *J* = 276.3 Hz, C2), 98.2 (d, *J* = 18.7 Hz, C1), 66.9 (C5,C5´), 46.9 (br s, C4/C4´), 43.7 (br s, C4/C4´).

^{19}F-NMR {^{1}H} (377 MHz, $CDCl_3$): δ (ppm) = -105.24.

IR (ATR) $\tilde{\nu}$ = 3090 (w), 2963 (w), 2910 (w), 2867 (w), 1652 (m), 1607 (s), 1435 (s), 1362 (w), 1286 (s), 1263 (m), 1234 (m), 1111 (s), 1066 (m), 1022 (m), 943 (m), 904 (m), 847 (m), 776 (m), 739 (m), 710 (m), 651 (m) cm^{-1}.

HR-ESI-MS (Orbitrap) exact mass calculated for $[M+Na]^+$ $(C_7H_9NO_2BrFNa)^+$ requires 259.96929 m/z, found 259.96935 m/z

M.p.: 34.6 – 35.2 °C.

Synthesis of *tert*-butyl (*Z*)-4-(3-bromo-2-fluoroacryloyl)piperazine-1-carboxylate (S4)

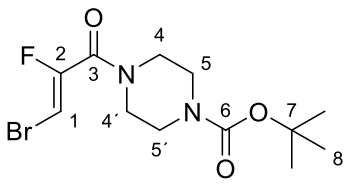

According to a modified procedure of Troin *et al.*[2] (*Z*)-3-bromo-2-fluoroacrylic acid (**S1**) (844.5 mg, 5.0 mmol, 1.0 eq.), *tert*-butyl piperazine-1-carboxylate (1.02 g, 5.5 mmol, 1.1 eq.), CBr_4 (1.8 g, 5.5 mmol, 1.1 eq.) and pyridine (409 μL, 435.1 mg, 5.5 mmol, 1.1 eq.) were dissolved in dry DCM (12.5 mL) under argon atmosphere. The solution was cooled to 0 °C before PPh_3 (1.4 g, 5.5 mmol, 1.1 eq.) was slowly added. The reaction was stirred at 0 °C for 4 h, the mixture was filtered and the solvent was evaporated under reduced pressure. The

crude residue was purified by column chromatography (SiO_2, 30% EtOAc/*n*-pentane) and the desired product was obtained as colourless solid (1.21 g, 72%).

R_f = (SiO_2, 20% EtOAc/*n*-pentane) = 0.16

^{1}H-NMR (599 MHz, $CDCl_3$): δ (ppm) = 6.57 (d, *J* = 26.4 Hz, 1H, H1), 3.57 – 3.50 (m, 4H, H4, H4´), 3.48 – 3.44 (m, 4H, H5, H5´), 1.46 (s, 9H, H8).

^{13}C-NMR (151 MHz, $CDCl_3$): δ (ppm) = 159.5 (d, *J* = 26.8 Hz, C3), 154.6 (d, *J* = 276.2 Hz, C2), 154.5 (C6), 98.2 (d, *J* = 18.7 Hz, C1), 80.7 (C7), 46.0 (C4), 43.4 (C5), 28.5 (C8).

^{19}F-NMR {^{1}H} (564 MHz, $CDCl_3$): δ (ppm) = -104.96.

IR (ATR) $\tilde{\nu}$ = 3089 (w), 2979 (w), 1738 (w), 1686 (s), 1657 (m), 1621 (m), 1461 (w), 1445 (m), 1418 (s), 1365 (m), 1291 (w), 1263 (m), 1253 (m), 1231 (m), 1167 (s), 1118 (m), 1017 (m), 964 (w), 912 (m), 864 (m), 832 (m), 768 (m), 749 (m), 712 (w), 657 (s) cm^{-1}.

HR-ESI-MS (Orbitrap) exact mass calculated for $[M+Na]^+$ ($C_{12}H_{18}N_2O_3BrFNa)^+$ requires 359.03770 m/z, found 359.03769 m/z

M.p.: 95.6 – 96.2 °C.

Synthesis of (*Z*)-3-bromo-2-fluoro-1-(pyrrolidin-1-yl)prop-2-en-1-one (S5)

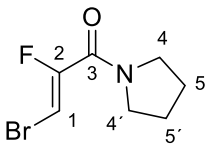

An oven-dried flaks was equipped with 1-ethyl-3-(3-dimethylaminopropyl)carbodiimide hydrochloride (958.5 mg, 5.0 mmol, 1,0 eq.), 1-hydroxybenzotriazol monohydrate (765.7 mg, 5.0 mmol, 1.0 eq.) and a mixture of dry DCM:DMF (4:1, 62.5 mL). The solution was stirred at ambient temperature for 1 h before the addition of (*Z*)-3-bromo-2-fluoroacrylic acid (**S1**) (844.5 mg, 5.0 mmol, 1.0 eq.) and pyrrolidine (546 μL, 535.8 mg, 5.0 mmol, 1.0 eq.). The mixture was stirred additional 20 h at ambient temperature before it was diluted with Et_2O and the organic layer was washed with 1 M aq. HCl, sat. aq. $NaHCO_3$ and brine and dried over $MgSO_4$. The solvent was evaporated under reduced pressure and the crude residue was purified by column chromatography (SiO_2, 30% EtOAc/*n*-pentane) to give the desired product as colourless gum (729.7 mg, 66%).

R_f = (SiO_2, 20% EtOAc/*n*-pentane) = 0.17

^{1}H-NMR (500 MHz, $CDCl_3$): δ (ppm) = 6.77 (d, *J* = 25.6 Hz, 1H, H1), 3.65 (td, *J* = 6.9, 5.0 Hz, 2H, H4/H4´), 3.53 (t, *J* = 6.9 Hz, 2H, H4/H4´), 1.99 – 1.92 (m, 2H, H5/H5´), 1.90 – 1.83 (m, 2H, H5/H5´).

^{13}C-NMR (126 MHz, $CDCl_3$): δ (ppm) = 158.0 (d, *J* = 28.5 Hz, C3), 155.0 (d, *J* = 277.3 Hz, C2), 98.4 (d, *J* = 19.1 Hz, C1), 47.6 (C4/C4´), 47.5 (d, *J* = 12.6 Hz, C4/C4´), 26.6 (d, *J* = 4.3 Hz, C5/C5´), 23.6 (C5/C5´).

^{19}F-NMR {^{1}H} (377 MHz, $CDCl_3$): δ (ppm) = -109.78.

IR (ATR) $\tilde{\nu}$ = 3108 (w), 2972 (w), 2881 (w), 1739 (w), 1656 (m), 1610 (s), 1425 (s), 1342 (m), 1254 (m), 1228 (w), 1190 (w), 1158 (w), 1119 (m), 1103 (m), 941 (m), 918 (m), 778 (m), 735 (m), 659 (s) cm^{-1}.

HR-ESI-MS (Orbitrap) exact mass calculated for $[M+Na]^+$ ($C_7H_9NOBrFNa)^+$ requires 245.97233 m/z, found 245.97199 m/z

Synthesis of Methyl (*Z*)-(3-bromo-2-fluoroacryloyl)-(*S*)-prolinate (S6)

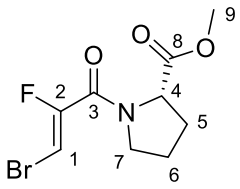

According to a modified procedure of Troin *et al*.[2] (*Z*)-3-bromo-2-fluoroacrylic acid (**S1**) (844.5 mg, 5.0 mmol, 1.0 eq.), L-proline methyl ester hydrochloride (910.8 mg, 5.5 mmol, 1.1 eq.), CBr_4 (1.8 g, 5.5 mmol, 1.1 eq.) and pyridine (444 μL, 435.1 mg, 5.5 mmol, 1.1 eq.) were dissolved in dry DCM (12.5 mL) under argon atmosphere. The solution was cooled to 0 °C before PPh_3 (1.4 g, 5.5 mmol, 1.1 eq.) was slowly added. After the reaction was stirred at 0 °C for 4 h, the mixture was filtered and the solvent was evaporated under reduced pressure. The crude residue was purified by column chromatography (SiO_2, 20% Et_2O/*n*-pentane) and the desired product was obtained as colourless gum (761.5 mg, 54%, 70:30 mixture of rotamers).

R_f = (SiO_2, 20% EtOAc/*n*-pentane) = 0.14

^{1}H-NMR (500 MHz, DMSO-d_6): δ (ppm) = 7.14 (d, *J* = 28.0 Hz, 1H, H1, major rotamer), 7.12 (d, *J* = 28.3 Hz, 1H, H1, minor rotamer), 4.82 (dd, *J* = 8.5, 4.3 Hz, 1H, H4, minor rotamer), 4.40 (dd, *J* = 8.5, 5.3 Hz, 1H, H4, major rotamer), 3.75 – 3.69 (m, 2H, H7, major rotamer), 3.68 (s, 3H, H9 minor rotamer), 3.64 (s, 3H, H9, major rotamer), 3.50 (dt, *J* = 12.4, 6.1 Hz, 2H, H7, minor rotamer), 2.35 – 2.23 (m, 1H, $H5_A$, minor rotamer), 2.24 – 2.14 (m, 1H, $H5_A$, major rotamer), 2.04 (d, *J* = 14.4 Hz, 1H, $H5_B$, minor rotamer), 1.97 – 1.88 (m, 2H, $H6_A$, $H6_B$, major rotamer), 1.88 – 1.80 (m, 2H, $H5_B$, major rotamer, $H6_A$, minor rotamer), 1.78 – 1.69 (m, 1H, $H6_B$, minor rotamer).

^{13}C-NMR (126 MHz, DMSO-d_6): δ (ppm) = 172.4 (C8, minor rotamer), 171.5 (C8, major rotamer), 157.3 (d, *J* = 30.0 Hz, C3), 153.2 (d, *J* = 270.0 Hz, C2), 99.1 (d, *J* = 17.2 Hz, C1, major rotamer), 98.7 (d, *J* = 17.7 Hz, C1, minor rotamer), 59.7 (C4, major rotamer), 59.3 (d, *J* = 10.4 Hz, C4, minor rotamer), 52.4 (C9, minor rotamer), 52.0 (C9, major rotamer), 48.0 – 47.9 (m, C7), 31.2 (C5, minor rotamer), 28.0 (C5, major rotamer), 24.8 (d, *J* = 3.1 Hz, C6, major rotamer), 21.4 (C6, minor rotamer).

^{19}F-NMR {^{1}H} (377 MHz, DMSO-d_6): δ (ppm) = -108.40 (major rotamer), -109.74 (minor rotamer).

IR (ATR) $\tilde{\nu}$ = 3105 (w), 2954 (w), 1742 (s), 1659 (m), 1613 (s), 1421 (s), 1363 (w), 1210 (m), 1195 (m), 1172 (s), 1121 (m), 1092 (w), 1040 (w), 1002 (w), 938 (w), 740 (m), 662 (s) cm^{-1}.

HR-ESI-MS (Orbitrap) exact mass calculated for $[M+Na]^+$ $(C_9H_{11}NO_3BrFNa)^+$ requires 303.97789 m/z, found 303.97751 m/z

ORD (DCM, c 1.00): $[\alpha]_D^{22}$= -87.191.

Synthesis of (*Z*)-*N*-benzyl-3-bromo-2-fluoro-*N*-methylacrylamide (S7)

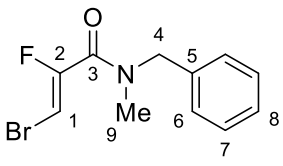

An oven-dried flask was equipped with 1-ethyl-3-(3-dimethylaminopropyl)carbodiimide hydrochloride (958.5 mg, 5.0 mmol, 1,0 eq.), 1-hydroxybenzotriazol monohydrate (765.7 mg, 5.0 mmol, 1.0 eq.) and a mixture of dry DCM:DMF (4:1, 62.5 mL). The solution was stirred at rt for 1 h before the addition of (*Z*)-3-bromo-2-fluoroacrylic acid (**S1**) (844.5 mg, 5.0 mmol, 1.0 eq.) and *N*-methyl-1-phenylmethanamine (609.0 mg, 5.0 mmol, 1.0 eq.). The mixture was stirred additional 20 h at ambient temperature before it was diluted with Et_2O and the organic layer was washed with 1 M aq. HCl, sat. aq. $NaHCO_3$ and brine and dried over $MgSO_4$. The solvent was

evaporated under reduced pressure and the crude residue was purified by column chromatography (SiO_2, 30% EtOAc/*n*-pentane) to give the desired product as colourless gum (785.2 mg, 58%, 57:43 mixture of rotamers).

R_f = (SiO_2, 20% EtOAc/*n*-pentane) = 0.38

^{1}H-NMR (599 MHz, $CDCl_3$): δ (ppm) = 7.40 – 7.20 (m, 5H, H6, H7, H8), 6.64 (d, *J* = 26.0 Hz, 1H, H1), 4.59 (s, 2H, H4), 3.00 (s, 3H, H9, major rotamer), 2.94 (s, 3H, H9, minor rotamer).

^{13}C-NMR (151 MHz, $CDCl_3$): δ (ppm) = 160.7 (C3), 154.9 (d, *J* = 276.6 Hz, C2), 135.9 (C5), 129.0 (C7), 128.3 (C6, major rotamer), 128.0 (C8), 127.2 (C6, minor rotamer), 97.8 (C1), 54.0 (C4, minor rotamer), 52.1 (C4, major rotamer), 35.4 (C9, major rotamer), 34.3 (C9, minor rotamer).

^{19}F-NMR {^{1}H} (377 MHz, $CDCl_3$): δ (ppm) = -103.79 (minor rotamer), -104.41 (major rotamer)

IR (ATR) $\tilde{\nu}$ = 3089 (w), 2929 (w), 1739 (w), 1654 (s), 1624 (s), 1452 (m), 1405 (s), 1357 (w), 1277 (m), 1131 (w) 1065 (m), 1029 (w), 934 (w), 788 (m), 766 (m), 726 (m), 696 (s), 659 (m), 611 (w) cm^{-1}.

HR-ESI-MS (Orbitrap) exact mass calculated for $[M+Na]^+$ $(C_{11}H_{11}NOBrFNa)^+$ requires 295.98798 m/z, found 295.98772 m/z

Synthesis of (*Z*)-*N*-benzyl-3-bromo-2-fluoroacrylamide (S8)

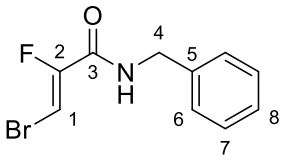

An oven-dried flaks was equipped with 1-ethyl-3-(3-dimethylaminopropyl)carbodiimide hydrochloride (958.5 mg, 5.0 mmol, 1,0 eq.), 1-hydroxybenzotriazol monohydrate (765.7 mg, 5.0 mmol, 1.0 eq.) and a mixture of dry DCM:DMF (4:1, 62.5 mL). The solution was stirred at ambient temperature for 1 h before the addition of (*Z*)-3-bromo-2-fluoroacrylic acid (**S1**) (844.5 mg, 5.0 mmol, 1.0 eq.) and benzyl amide (546 µL, 535.8 mg, 5.0 mmol, 1.0 eq.). The mixture was stirred additional 20 h at ambient temperature before it was diluted with Et_2O and the organic layer was washed with 1 M aq. HCl, sat. aq. $NaHCO_3$ and brine and dried over $MgSO_4$. The solvent was evaporated under reduced pressure and the crude residue was purified by column chromatography (SiO_2, 30% EtOAc/*n*-pentane) to give the desired product as colourless solid (941.5 mg, 73%).

R_f = (SiO_2, 30% EtOAc/*n*-pentane) = 0.63

^{1}H-NMR (599 MHz, $CDCl_3$): δ (ppm) = 7.39 – 7.34 (m, 2H, H7), 7.34 – 7.28 (m, 3H, H6, H8), 6.93 (d, *J* = 26.8 Hz, 1H, H1), 6.52 (s, 1H, N*H*), 4.53 (d, *J* = 5.9 Hz, 2H, H4).

^{13}C-NMR (126 MHz, $CDCl_3$): δ (ppm) = 158.0 (d, *J* =28.6 Hz, C3), 153.4 (d, *J* = 272.8 Hz, C2), 137.0 (C5), 129.1 (C7), 128.1 (C6), 128.1 (C8), 97.9 (d, *J* = 17.4 Hz, C1), 43.7 (C4).

^{19}F-NMR {^{1}H} (377 MHz, $CDCl_3$): δ (ppm) = -120.02.

IR (ATR) $\tilde{\nu}$ = 3336 (m), 3099 (w), 1739 (w), 1676 (m), 1669 (m), 1639 (s), 1534 (s), 1492 (m), 1455 (m), 1433 (m), 1356 (w), 1319 (m), 1227 (m), 1105 (m), 1082 (m), 1019 (m), 808 (m), 759 (m), 695 (s), 689 (s), 669 (s) cm^{-1}.

HR-ESI-MS (Orbitrap) exact mass calculated for $[M+Na]^+$ $(C_{10}H_9NOBrFNa)^+$ requires 281.97239 m/z, found 281.97232 m/z

M.p.: 124.0 – 124.8 °C.

Synthesis of Benzyl (*Z*)-3-bromo-2-fluoroacrylate (S9)

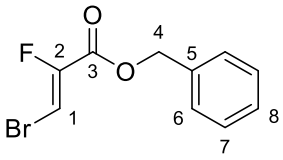

(*Z*)-3-bromo-2-fluoroacrylic acid (**S1**) (1.68 g, 10.0 mmol, 1.0 eq.) and NEt_3 (1.38 mL, 1.01 g, 10.0 mmol, 1.0 eq.) were dissolved in DMSO (4 mL) and the mixture was stirred at rt for 15 min. After that benzyl bromide (1.31 mL, 1.88 g, 11.0 mmol, 1.1 eq.) was added and the reaction was stirred at ambient temperature for 14 h. Water was added and the organics were extracted with Et_2O. The combined organic layers were dried over $MgSO_4$ and the solvent was removed under reduced pressure. The crude residue was purified by column chromatography (SiO_2, 5% EtOAc/*n*-pentane) to give the desired product as colourless oil (1.85 g, 71%).

$\mathbf{R_f}$ = (SiO_2, 5% EtOAc/*n*-pentane) = 0.77

^{1}H-NMR (500 MHz, $CDCl_3$): δ (ppm) = 7.50 – 7.33 (m, 5H, H6, H7, H8), 6.97 (d, *J* = 24.0 Hz, 1H, H1), 5.28 (s, 2H, H4).

^{13}C-NMR (126 MHz, $CDCl_3$): δ (ppm) = 158.5 (d, *J* = 34.6 Hz, C3), 150.8 (d, *J* = 262.5 Hz, C2), 134.7 (C5), 129.0 (C8), 128.9 (C7), 128.7 (C6), 102.1 (d, *J* = 18.2 Hz, C1), 68.0 (d, *J* = 0.9 Hz, C4).

^{19}F-NMR {^{1}H} (377 MHz, $CDCl_3$): δ (ppm) = -115.40.

IR (ATR) $\tilde{\nu}$ = 2921 (w), 1739 (m), 1660 (m), 1477 (w), 1456 (w), 1368 (s), 1274 (s), 1241 (s), 1208 (m), 990 (w), 953 (w), 848 (w), 769 (m), 752 (m), 696 (m), 662 (w) cm^{-1}.

HR-ESI-MS (Orbitrap) exact mass calculated for $[M+Na]^+$ $(C_{10}H_8O_2BrFNa)^+$ requires 280.95839 m/z, found 280.95850 m/z

Synthesis of *tert*-butyl (*Z*)-3-bromo-2-fluoroacrylate (S10)

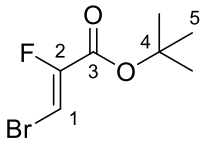

(Z)-3-bromo-2-fluoroacrylic acid (**S1**) (844.5 mg, 5.0 mmol, 1.0 eq.) was dissolved in *tert*-BuOH (25 mL) at 40 °C and Boc_2O (1.09 g, 5.0 mmol, 1.0 eq.) was added. The reaction was stirred at 40 °C for 12 h before it was diluted with water. The organics were extracted with EtOAc and the combined organic layers were dried over $MgSO_4$. The solvent was evaporated and the crude residue was purified by column chromatography (SiO_2, *n*-pentane) to give the desired product as colourless oil (310.5 mg, 27%).

$\mathbf{R_f}$ = (SiO_2, 10% EtOAc/*n*-pentane) = 0.46

^{1}H-NMR (599 MHz, $CDCl_3$): δ (ppm) = 6.82 (d, *J* = 24.0 Hz, 1H, H1), 1.53 (s, 9H, H5).

^{13}C-NMR (151 MHz, $CDCl_3$): δ (ppm) = 157.6 (d, *J* = 34.1 Hz, C3), 151.6 (d, *J* = 263.3 Hz, C2), 100.5 (d, *J* = 18.9 Hz, C1), 84.2 (C4), 28.1 (C5).

^{19}F-NMR {^{1}H} (564 MHz, $CDCl_3$): δ (ppm) = -114.29.

IR (ATR) $\tilde{\nu}$ = 2982 (w), 1735 (s), 1644 (m), 1458 (w), 1370 (m), 1332 (s), 1235 (m), 1155 (s), 1101 (s), 898 (w), 842 (m), 756 (m), 743 (m), 722 (m), 669 (w) cm^{-1}.

Synthesis of ethyl (*Z*)-2-fluorobut-2-enoate (S11)

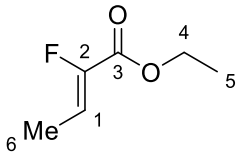

According to a modified procedure of Shahak *et al.*[3] sodium hydride (1.20 g, 30.0 mmol, 1.0 eq., 60% in mineral oil) was suspended in dry THF (15.0 mL) under argon atmosphere. Diethyl oxalate (4.48 mL, 4.82 g, 33.0 mmol, 1.1 eq.) and ethyl fluoroacetate (2.91 mL, 3.18 g, 30.0 mmol, 1.0 eq.) were added and the mixture was warmed to 60 °C. The reaction was stirred for 3 h before it was cooled to 0 °C. Acetaldehyde (1.84 mL, 1.45 g, 33.0 mmol, 1.1 eq.) was added and the reaction was stirred at 80 °C for 1 h. After cooled to ambient temperature, water was added and the organics were extracted using DCM. The combined organic layers were washed with 5% aq. Na_2CO_3 and brine and dried over $MgSO_4$. The solvent was evaporated under reduced pressure and the crude residue was purified by column chromatography (SiO_2, 5% Et_2O/*n*-pentane) to give the desired product as colourless oil (2.50 g, 63%).

R_f = (SiO_2, 5% Et_2O/*n*-pentane) = 0.75

^{1}H-NMR (500 MHz, CD_2Cl_2): δ (ppm) = 6.14 (qd, *J* = 33.2, 7.3 Hz, 1H, H1), 4.23 (q, *J* = 7.2 Hz, 2H, H4), 1.76 (dd, *J* = 7.3, 2.9 Hz, 3H, H6), 1.29 (t, *J* = 7.2 Hz, 3H, H5).

^{13}C-NMR (126 MHz, CD_2Cl_2): δ (ppm) = 161.0 (d, *J* = 35.5 Hz, C3), 149.3 (d, *J* = 254.0 Hz, C2), 115.9 (d, *J* = 12.1 Hz, C1), 61.8 (C4), 14.3 (C5), 9.7 (d, *J* = 4.4 Hz, C6).

^{19}F-NMR {^{1}H} (377 MHz, CD_2Cl_2): δ (ppm) = -132.24.

IR (ATR) $\tilde{\nu}$ = 2986 (w), 2927 (w), 2359 (w), 1735 (s), 1681 (m), 1448 (w), 1385 (w), 1370 (w), 1320 (s), 1278 (s), 1175 (w), 1135 (s), 1096 (w), 1072 (s), 1017 (m), 997 (w), 851 (w), 762 (s), 710 (w), 669 (w) cm^{-1}.

HR-ESI-MS (Orbitrap) exact mass calculated for $[M+Na]^+$ $(C_6H_9O_2FNa)^+$ requires 155.04788 m/z, found 155.04783 m/z

Synthesis of (*Z*)-3-bromo-2-fluoro-*N*-methoxy-*N*-methylbut-2-enamide (S12)

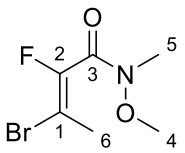

S11 (1.98 g, 15.0 mmol, 1.0 eq.) was dissolved in $CHCl_3$ (15.0 mL) under argon atmosphere and the solution was warmed to 60 °C before Br_2 (0.92 mL, 2.87 g, 18.0 mmol, 1.2 eq.) was slowly added. The mixture was stirred at 60 °C for 4 h before it was cooled to ambient temperature and quenched by the addition of sat. aq. $Na_2S_2O_3$. The organics were extracted with $CHCl_3$ and the combined organic layers were dried over $MgSO_4$. The solvent was removed under reduced pressure and the crude residue was dissolved in EtOH (12 mL). To this, a solution of NaOH (2.70 g) in H_2O (8 mL) was slowly added and the mixture was stirred for 2 h at rt before it was quenched by the addition of 37% aq. HCl. The reaction was acidified to pH = 1, the organics were extracted with Et_2O and the combined organic layers were dried over $MgSO_4$. After removal of the solvent the obtained brown solid was directly used without further purification and dissolved in dry DCM (30 mL) under argon atmosphere. To this solution, *N,O*-dimethylhydroxylamine hydrochloride (1.61 g, 16.5 mmol, 1.1 eq.), CBr_4 (5.47 g, 16.5 mmol, 1.1 eq.) and pyridine (1.33 mL, 1.31 g, 16.5 mmol, 1.1 eq.) were added and the reaction was cooled to 0 °C.

PPh_3 (4.33 g, 16.5 mmol, 1.1 eq.) was slowly added and the mixture was stirred at 0 °C for 4 h. After the mixture was warmed up to ambient temperature, the formed solids were filtered-off and the solvent was evaporated under reduced pressure. The crude residue was purified by column chromatography (SiO_2, 5% Et_2O/*n*-pentane) and the desired product was obtained as yellow oil (1.06 g, 31%).

R_f = (SiO_2, 5% Et_2O/*n*-pentane) = 0.23

^{1}H-NMR (500 MHz, $CDCl_3$): δ (ppm) = 3.69 (s, 3H, H4), 3.19 (s, 3H, H5), 2.33 (d, *J* = 4.1 Hz, 3H, H6).

^{13}C-NMR (101 MHz, $CDCl_3$): δ (ppm) = 160.3 (d, *J* = 35.0 Hz, C3), 147.5 (d, *J* = 263.0 Hz, C2), 111.3 (d, *J* = 16.7 Hz, C1), 62.1 (C4), 32.6 (C5), 21.9 (d, *J* = 1.2 Hz, C6).

^{19}F-NMR {^{1}H} (470 MHz, $CDCl_3$): δ (ppm) = -103.65.

IR (ATR) $\tilde{\nu}$ = 2982 (w), 2942 (w), 2360 (w), 1733 (w), 1653 (s), 1459 (m), 1416 (m), 1382 (s), 1230 (s), 1169 (w), 1119 (s), 1042 (m), 982 (s), 895 (w), 761 (m), 716 (m), 669 (w), 649 (m), 606 (m) cm^{-1}.

HR-ESI-MS (Orbitrap) exact mass calculated for $[M+Na]^+$ ($C_6H_9NO_2BrFNa)^+$ requires 247.96929 m/z, found 247.96920 m/z

Synthesis of benzyl (*Z*)-3-bromo-2-fluorobut-2-enoate (S13)

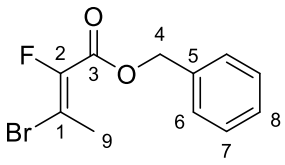

S11 (1.98 g, 15.0 mmol, 1.0 eq.) was dissolved in $CHCl_3$ (15 mL) under argon atmosphere and the solution was warmed to 60 °C before Br_2 (0.92 mL, 2.87 g, 18.0 mmol, 1.2 eq.) was slowly added. The mixture was stirred at 60 °C for 4 h before it was cooled to ambient temperature and quenched by the addition of sat. aq. $Na_2S_2O_3$. The organics were extracted with $CHCl_3$ and the combined organic layers were dried over $MgSO_4$. The solvent was removed under reduced pressure and the crude residue was dissolved in EtOH (12 mL). To this, a solution of NaOH (2.70 g) in H_2O (8 mL) was slowly added and the mixture was stirred for 2 h at rt before it was quenched by the addition of 37% aq. HCl. The reaction was acidified to pH = 1, the organics were extracted with Et_2O and the combined organic layers were dried over $MgSO_4$. After removal of the solvent the obtained brown solid was directly used without further purification and dissolved in DMSO (8.0 mL). To this solution, NEt_3 (2.09 mL, 1.52 g, 15.0 mmol, 1.0 eq.) was added and the reaction was stirred at rt for 15 min. Benzyl bromide (1.96 mL ,2.82 g, 16.5 mmol, 1.1 eq.) was slowly added and the mixture was stirred at ambient temperature for 14 h. Water was added and the organics were extracted with Et_2O (3 x 15 mL). The combined organic layers were dried over $MgSO_4$ and the solvent was removed under reduced pressure. The crude residue was purified by column chromatography (SiO_2, 10% DCM/*n*-pentane) and the desired product was obtained as yellow oil (2.13 g, 52%).

R_f = (SiO_2, 10% DCM/*n*-pentane) = 0.39

^{1}H-NMR (599 MHz, $CDCl_3$): δ (ppm) = 7.43 – 7.37 (m, 5H, H6, H7, H8), 5.29 (s, 2H, H4), 2.74 (dd, *J* = 4.1, 0.7 Hz, 3H, H9).

^{13}C-NMR (151 MHz, $CDCl_3$): δ (ppm) = 159.2 (d, *J* = 33.8 Hz, C3), 145.3 (d, *J* = 255.7 Hz, C2), 134.9 (C5), 128.8 (C7), 128.7 (C8), 128.5 (C6), 121.1 (d, *J* = 21.6 Hz, C1), 67.5 (C4), 23.5 (d, *J* = 2.1 Hz, C9).

^{19}F-NMR {^{1}H} (377 MHz, $CDCl_3$): δ (ppm) = -106.96.

IR (ATR) $\tilde{\nu}$ = 2962 (w), 2360 (w), 1769 (m), 1726 (s), 1652 (m), 1498 (w), 1456 (m), 1378 (m), 1281 (s), 1212 (w), 1158 (s), 1119 (m), 1104 (w), 1043 (m), 1028 (m), 1003 (w), 970 (w), 911 (m), 861 (w), 827 (w), 766 (m), 750 (m), 733 (m), 696 (s), 669 (m), 647 (w) cm^{-1}.

HR-ESI-MS (Orbitrap) exact mass calculated for $[M+Na]^+$ $(C_{11}H_{10}O_2BrFNa)^+$ requires 294.97404 m/z, found 294.97395 m/z

Synthesis of (*Z*)-3-bromo-2-fluoro-1-morpholinobut-2-en-1-one (S14)

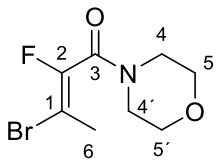

S11 (1.98 g, 15.0 mmol, 1.0 eq.) was dissolved in $CHCl_3$ (15 mL) under argon atmosphere and the solution was warmed to 60 °C before Br_2 (0.92 mL, 2.87 g, 18.0 mmol, 1.2 eq.) was slowly added. The mixture was stirred at 60 °C for 4 h before it was cooled to ambient temperature and quenched by the addition of sat. aq. $Na_2S_2O_3$.The organics were extracted with $CHCl_3$ and the combined organic layers were dried over $MgSO_4$. The solvent was removed under reduced pressure and the crude residue was dissolved in EtOH (12 mL). To this, a solution of NaOH (2.70 g) in H_2O (8 mL) was slowly added and the mixture was stirred for 2 h at ambient temperature before it was quenched by the addition of 37% aq. HCl. The reaction was acidified to pH = 1, the organics were extracted with Et_2O and the combined organic layers were dried over $MgSO_4$. After removal of the solvent the obtained brown solid was directly used without further purification and dissolved in dry DCM (30.0 mL) under argon atmosphere. To this solution, morpholine (1.43 mL, 1.44 g, 16.5 mmol, 1.1 eq.), CBr_4 (5.47 g, 16.5 mmol, 1.1 eq.) and pyridine (1.33 mL, 1.31 g, 16.5 mmol, 1.1 eq.) were added and the reaction was cooled to 0 °C. PPh_3 (4.33 g, 16.5 mmol, 1.1 eq.) was slowly added and the mixture was stirred at 0 °C for 4 h. After the mixture was warmed up to ambient temperature, the formed solids were filtered-off and the solvent was evaporated under reduced pressure. The crude residue was purified by column chromatography (SiO_2, 5% Et_2O/*n*-pentane) and the desired product was obtained as yellow oil (1.14 g, 30%).

$\mathbf{R_f}$ = (SiO_2, 5% Et_2O/*n*-pentane) = 0.24

^{1}H-NMR (500 MHz, $CDCl_3$): δ (ppm) = 3.69 – 3.59 (m, 6H, H4/H4´, H5, H5´), 3.45 – 3.42 (m, 2H, H4/H4´), 2.32 (d, *J* = 4.1 Hz, 3H, H6).

^{13}C-NMR (126 MHz, $CDCl_3$): δ (ppm) = 159.5 (d, *J* = 30.4 Hz, C3), 147.5 (d, *J* = 262.8 Hz, C2), 110.3 (d, *J* = 19.9 Hz, C1), 67.0 (C5/C5´), 66.6 (C5/C5´), 47.0 (d, *J* = 5.5 Hz, C4/C4´), 42.6 (C4/C4´), 21.8 (C6).

^{19}F-NMR {^{1}H} (470 MHz, $CDCl_3$): δ (ppm) = -99.83.

IR (ATR) $\tilde{\nu}$ = 2970 (w), 2923 (w), 2858 (w), 2359 (w), 1640 (s), 1456 (m), 1433 (s), 1382 (w), 1362 (w), 1301 (w), 1279 (s), 1260 (s), 1221 (w), 1177 (m), 1112 (s), 1071 (m), 1006 (s), 937 (w), 897 (m), 844 (m), 766 (m), 733 (s), 702 (m), 669 (w), 646 (m), 630 (m) cm^{-1}.

HR-ESI-MS (Orbitrap) exact mass calculated for $[M+Na]^+$ $(C_8H_{11}NO_2BrFNa)^+$ requires 273.98494 m/z, found 273.98484 m/z

Synthesis of (*E*)-3-Bromoacrylic acid (S15)

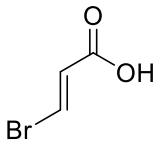

Prepared according to a modified procedure by Brückner *et al.*[4] propiolic acid (3.08 mL, 50 mmol, 1.0 eq.) was dissolved in AcOH (5 mL) and cooled to -10 °C. To the mixture was added HBr in AcOH (33%, 8.86 mL, 50 mmol, 1.0 eq) dropwise over 10 min. The mixture was heated to 80 °C and the temperature was maintained for 30 min. After cooling to ambient temperature, brine and Et_2O were added to the reaction mixture. The layers were separated and the organics were extracted with Et_2O. Combined organic layers were dried with Na_2SO_4 and concentrated under reduced pressure. The crude product was purified by recrystallisation from water yielding **S15** as an off white solid (4.06 g, 54%).

^{1}H-NMR (300 MHz, $CDCl_3$): δ = 7.76 (d, *J* = 13.9 Hz, 1H), 6.54 (d, *J* = 13.9 Hz, 1H).

Analytical data in agreement with literature.[4]

Synthesis of benzyl (*E*)-3-bromoacrylate (S16)

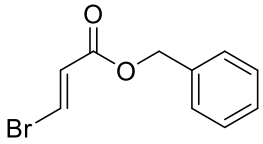

S15 (1.51 g, 10.0 mmol, 1.0 eq.) and NEt_3 (1.38 mL, 1.01 g, 10.0 mmol, 1.0 eq.) were dissolved in DMSO (4 mL) and the mixture was stirred at ambient temperature for 15 min. After that benzyl bromide (1.31 mL, 1.88 g, 11.0 mmol, 1.1 eq.) was added and the reaction was stirred at rt for 14 h. Water was added and the organics were extracted with Et_2O. The combined organic layers were combined, dried over $MgSO_4$ and the solvent was removed under reduced pressure. The crude residue was purified by column chromatography (SiO_2, 10% EtOAc/*n*-pentane) to give the desired product as colourless oil (1.36 g, 56%).

R_f (SiO_2, 10% EtOAc/*n*-pentane) = 0.82.

^{1}H-NMR (400 MHz, $CDCl_3$): δ = 7.64 (d, *J* = 13.9 Hz, 1H), 7.38 – 7.31 (m, 5H), 6.57 (d, *J* = 13.9 Hz, 1H), 5.20 (s, 2H).

Analytical data in agreement with literature.[5]

Synthesis of (*Z*)-3-bromo-2-chloroacrylic acid (S17)

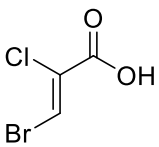

Methyl 2-chloroacrylate (2.13 g, 20.0 mmol, 1.0 eq.) was dissolved in $CHCl_3$ (20 mL) under argon atmosphere and the solution was warmed to 60 °C before Br_2 (1.07 mL, 3.35 g, 21.0 mmol, 1.05 eq.) was slowly added. The mixture was stirred at 60 °C for 3 h before it was cooled to ambient temperature and quenched by the addition of sat. aq. $Na_2S_2O_3$. The organics were extracted with $CHCl_3$ and the combined organic layers were dried over $MgSO_4$. The solvent was removed under reduced pressure and the crude residue was dissolved in EtOH (12 mL). To this, a solution of NaOH (3.6 g) in H_2O (8 mL) was slowly added and the mixture was stirred for 3 h at ambient temperature before it was quenched by the addition of 37% aq. HCl. The reaction was acidified to pH = 1, the organics were extracted with Et_2O and the combined organic layers were dried over $MgSO_4$. The solvent was removed under reduced pressure and the desired product was obtained as yellow solid and used without further purification (1.87 g, 50%).

Synthesis of benzyl (*Z*)-3-bromo-2-chloroacrylate (S18)

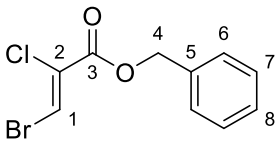

S17 (1.85 g, 10.0 mmol, 1.0 eq.) and NEt_3 (1.38 mL, 1.01 g, 10.0 mmol, 1.0 eq.) were dissolved in DMSO (4 mL) and the mixture was stirred at ambient temperature for 15 min. After that benzyl bromide (1.31 mL, 1.88 g, 11.0 mmol, 1.1 eq.) was added and the reaction was stirred at ambient temperature for 14 h. Water was added and the organics were extracted with Et_2O. The combined organic layers were combined, dried over $MgSO_4$ and the solvent was removed under reduced pressure. The crude residue was purified by column chromatography (SiO_2, 5% EtOAc/*n*-pentane) to give the desired product as colourless oil (1.55 g, 56%).

$\mathbf{R_f}$ = (SiO_2, 10% EtOAc/*n*-pentane) = 0.52

^{1}H-NMR (599 MHz, $CDCl_3$): δ (ppm) = 7.94 (s, 1H, H1), 7.54 – 7.33 (m, 5H, H6, H7, H8), 5.27 (s, 2H, H4).

^{13}C-NMR (151 MHz, $CDCl_3$): δ (ppm) = 160.4 (C3), 134.9 (C2), 130.6 (C5), 128.9 (C8), 128.9 (C7), 128.6 (C6), 123.2 (C1), 68.62 (C4).

IR (ATR) $\tilde{\nu}$ = 3081 (w), 3033 (w), 1732 (s), 1578 (m), 1498 (w), 1455 (w), 1375 (w), 1258 (s), 1211 (s), 1025 (m), 908 (w), 799 (w), 736 (s), 695 (s), 627 (w) cm^{-1}.

HR-ESI-MS (Orbitrap) exact mass calculated for $[M+Na]^+$ ($C_{10}H_8O_2BrClNa)^+$ requires 298.92663 m/z, found 298.92679 m/z

2.2 Synthesis of *α*-Halo-*β*-borylacrylates

Synthesis of (+)-bis(pinanediolato)diboron (S19)

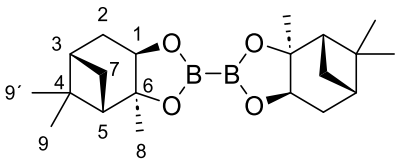

According to a modified procedure of Tang *et al.*[6] (1*S*,2*S*,3*R*,5*S*)-2,6,6-trimethylbicyclo[3.1.1]heptane-2,3-diol (6.81 g, 40.0 mmol, 2.0 eq.) and hydrodiboric acid (1.79 g, 20.0 mmol, 1.0 eq.) were dissolved in dry THF (80 mL) in an oven-dried flask and 4 Å molecular sieves were added. The reaction was refluxed for 3 h before it was cooled to ambient temperature and filtered over Celite. The solvent was removed under reduced pressure and the crude residue was purified by recrystallization from pentane to give the desired product as colourless solid (5.51 g, 77%).

^{1}H-NMR (599 MHz, $CDCl_3$): δ (ppm) = 4.26 (dd, *J* = 8.8, 1.9 Hz, 2H, H1), 2.31 (ddt, *J* = 14.5, 8.8, 2.4 Hz, 2H, $H2_A$), 2.22 – 2.16 (m, 2H, $H7_A$), 2.07 (t, *J* = 5.5 Hz, 2H, H5), 1.95 – 1.87 (m, 4H, $H2_B$, H3), 1.40 (s, 6H, H8), 1.28 (s, 6H, H9/H9´), 1.12 (d, *J* = 11.0 Hz, 2H, $H7_B$), 0.84 (s, 6H, H9/H9´).

^{13}C-NMR (151 MHz, $CDCl_3$): δ (ppm) = 86.5 (C6), 77.9 (C1), 51.1 (C5), 39.7 (C3), 38.0 (C4), 35.1 (C2), 28.8 (C8), 27.2 (C9/C9´), 26.8 (C7), 24.1 (C9/C9´).

^{11}B-NMR (128 MHz, $CDCl_3$): δ (ppm) = 29.69.

IR (ATR) $\tilde{\nu}$ = 2980 (w), 2916 (w), 2903 (w), 2363 (w), 1477 (w), 1451 (w), 1375 (m), 1367 (m), 1355 (m), 1273 (s), 1233 (s), 1158 (s), 1134 (s), 1121 (s), 1076 (m), 1019 (m), 982 (m), 934 (w), 921 (w), 872 (m), 865 (m), 749 (s), 738 (m), 637 (m), 624 (m), 613 (m) cm^{-1}.

HR-ESI-MS (Orbitrap) exact mass calculated for $[M+Na]^+$ $(C_{20}H_{32}O_4B_2Na)^+$ requires 381.23861 m/z, found 381.23965 m/z

ORD (DCM, c 1.00): $[\alpha]_D^{20}$= 36.656.

General Procedure A: Miyaura borylation of alkenyl halides

An oven-dried Schlenk-tube was equipped with the respective alkenyl halide (1.0 eq.), Pd(dppf)Cl_2*DCM (5 mol%), **S19** (1.0 eq.) and KOAc (3.0 eq.). The tube was sealed and purged with argon before the addition of dry, degassed DMF (0.25 M). The reaction mixture was stirred at 60 °C for 16 h before it was cooled to ambient temperature. The reaction was filtered through a layer of Celite and eluted with EtOAc. The organic layer was washed with H_2O, brine and 5% aq. LiCl and dried over $MgSO_4$. The solvent was removed under reduced pressure and the crude residue was purified by column chromatography (SiO_2, specified combination of solvents).

General Procedure B: Miyaura borylation of alkenyl halides

An oven-dried Schlenk-tube was equipped with the respective alkenyl halide (1.0 eq.), Pd(dppf)Cl_2*DCM (5 mol%), bis(pinacolato)diboron (1.0 eq.) and KOAc (3.0 eq.). The tube was sealed and purged with argon before the addition of dry, degassed 1,4-dioxane (0.25 M). The reaction mixture was stirred at 90 °C for 16 h before it was cooled to ambient temperature. The reaction was filtered through a layer of Celite and eluted with EtOAc. The organic layer was washed with H_2O and dried over $MgSO_4$. The solvent was removed under reduced pressure and the crude residue was purified by column chromatography (SiO_2, specified combination of solvents).

Synthesis of (*Z*)-2-fluoro-*N*-methoxy-*N*-methyl-3-((3a*S*,4*S*,6*S*,7a*R*)-3a,5,5-trimethylhexa-hydro-4,6-methanobenzo[*d*][1,3,2]dioxaborol-2-yl)acrylamide (*Z*-1)

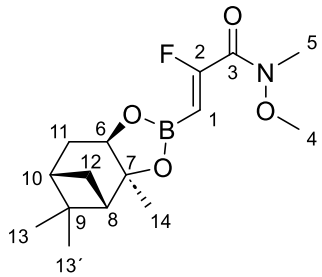

According to General Procedure A, **S2** (414.2 mg, 2.0 mmol, 1.0 eq.) was converted to ***Z*-1** yielding a colourless oil (148.1 mg, 24%) after purification by column chromatography (10% acetone/*n*-pentane).

$\mathbf{R_f}$ = (SiO_2, 10% acetone/*n*-pentane) = 0.21

^{1}H-NMR (599 MHz, $CDCl_3$): δ (ppm) = 5.60 (d, *J* = 51.3 Hz, 1H, H1), 4.38 (dd, *J* = 8.7, 1.8 Hz, 1H, H6), 3.75 (s, 3H, H4), 3.24 (d, *J* = 0.9 Hz, 3H, H5), 2.41 – 2.32 (m, 1H, $H11_A$), 2.26 – 2.20 (m, 1H, $H12_A$), 2.10 (dd, *J* = 6.1, 4.9 Hz, 1H, H8), 1.96 – 1.89 (m, 2H, H10, $H11_B$), 1.43 (s, 3H, H14), 1.29 (s, 3H, H13/H13´), 1.15 (d, *J* = 11.1 Hz, 1H, $H12_B$), 0.85 (s, 3H, H13/H13´).

^{13}C-NMR (151 MHz, $CDCl_3$): δ (ppm) = 162.6 (d, *J* = 284.5 Hz, C2), 162.6 (d, *J* = 33.1 Hz, C3), 86.3 (C7), 78.2 (C6), 62.1 (C4), 51.3 (C8), 39.6 (C10), 38.2 (C9), 35.5 (C11), 33.8 (C5), 28.7 (C14), 27.2 (C13/C13´), 26.6 (C12), 24.1 (C13/C13´), carbon bearing boron was not observed.

^{19}F-NMR {^{1}H} (377 MHz, $CDCl_3$): δ (ppm) = -93.64.

^{11}B-NMR (192 MHz, $CDCl_3$): δ (ppm) = 28.43.

IR (ATR) $\tilde{\nu}$ = 2982 (w), 2934 (w), 1660 (s), 1411 (m), 1379 (m), 1358 (s), 1315 (w), 1286 (m), 1251 (m), 1234 (m), 1225 (m), 1208 (w), 1183 (w), 1122 (m), 1078 (m), 1055 (m), 1029 (m), 939 (w), 918 (w), 888 (w), 782 (m), 756 (m), 732 (m), 649 (m) cm^{-1}.

HR-ESI-MS (Orbitrap) exact mass calculated for $[M+Na]^+$ $(C_{15}H_{23}NO_4BFNa)^+$ requires 334.15992 m/z, found 334.15956 m/z

ORD (DCM, c 1.00): $[\alpha]_D^{21}$= 13.861.

Synthesis of (*Z*)-2-fluoro-1-morpholino-3-((3a*S*,4*S*,6*S*,7a*R*)-3a,5,5-trimethylhexahydro-4,6-methanobenzo[*d*][1,3,2]dioxaborol-2-yl)prop-2-en-1-one (S20)

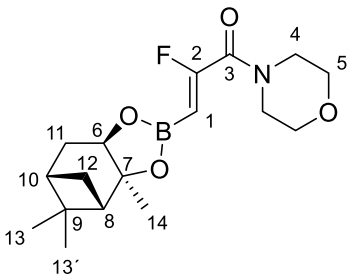

According to General Procedure A, **S3** (476.2 mg, 2.0 mmol, 1.0 eq.) was converted to **S20** yielding a colourless oil (177.1 mg, 26%) after purification by column chromatography (5% to 10% acetone/*n*-pentane).

R_f = (SiO_2, 10% acetone/*n*-pentane) = 0.09

^{1}H-NMR (500 MHz, $CDCl_3$): δ (ppm) = 5.45 (d, *J* = 52.9 Hz, 1H, H1), 4.36 (dd, *J* = 8.8, 1.9 Hz, 1H, H6), 3.68 (s, 4H, H4/H5), 3.61 (s, 4H, H4/H5), 2.41 – 2.30 (m, 1H, $H11_A$), 2.26 – 2.18 (m, 1H, $H12_A$), 2.08 (dd, *J* = 6.0, 4.9 Hz, 1H, H8), 1.96 – 1.85 (m, 2H, H10, $H11_B$), 1.42 (s, 3H, H14), 1.29 (s, 3H, H13/H13´), 1.14 (d, *J* = 11.0 Hz, 1H, $H12_B$), 0.84 (s, 3H, H13/H13´).

^{13}C-NMR (126 MHz, $CDCl_3$): δ (ppm) = 163.0 (d, *J* = 283.9 Hz, C2), 161.4 (d, *J* = 33.2 Hz, C3), 86.4 (C7), 78.2 (C6), 66.9 (C4/C5), 51.3 (C8), 47.2 (C4/C5), 43.0 (C4/C5), 39.6 (C10), 38.2 (C9), 35.4 (C11), 28.7 (C14), 27.2 (C13/C13´), 26.6 (C12), 24.1 (C13/C13´), carbon bearing boron was not observed.

^{19}F-NMR {^{1}H} (377 MHz, $CDCl_3$): δ (ppm) = -88.03.

^{11}B-NMR (128 MHz, $CDCl_3$): δ (ppm) = 28.64.

IR (ATR) $\tilde{\nu}$ = 2919 (w), 2868 (w), 1644 (s), 1438 (m), 1379 (m), 1359 (s), 1277 (s), 1258 (s), 1210 (m), 1113 (s), 1078 (m), 1020 (m), 990 (w), 938 (m), 923 (w), 848 (m), 755 (m), 667 (w) cm^{-1}.

HR-ESI-MS (Orbitrap) exact mass calculated for $[M+Na]^+$ $(C_{17}H_{25}NO_4BFNa)^+$ requires 360.17560 m/z, found 360.17532 m/z

ORD (DCM, c 0.50): $[\alpha]_D^{22}$= 13.509.

Synthesis of *tert*-butyl 4-((*Z*)-2-fluoro-3-((3a*S*,4*S*,6*S*,7a*R*)-3a,5,5-trimethylhexahydro-4,6-methanobenzo[*d*][1,3,2]dioxaborol-2-yl)acryloyl)piperazine-1-carboxylate (S21)

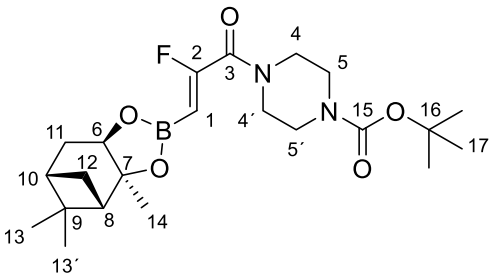

According to General Procedure A, **S4** (674.4 mg, 2.0 mmol, 1.0 eq.) was converted to **S21** yielding a colourless gum (210.3 mg, 24%) after double purification by column chromatography (5%-10% acetone/*n*-pentane and 30% EtOAc/*n*-pentane).

R_f = (SiO_2, 10% acetone/*n*-pentane)= 0.13

^{1}H-NMR (599 MHz, $CDCl_3$): δ (ppm) = 5.42 (d, *J* = 52.7 Hz, 1H, H1), 4.34 (dd, *J* = 8.8, 1.9 Hz, 1H, H6), 3.67 – 3.44 (m, 4H, H5, H5´), 3.45 – 3.40 (m, 4H, H4, H4´), 2.39 – 2.28 (m, 1H, $H11_A$), 2.25 – 2.16 (m, 1H, $H12_A$), 2.09 – 2.02 (m, 1H, H8), 1.93 – 1.83 (m, 2H, H10, $H11_B$), 1.43 (s, 9H, H17), 1.40 (s, 3H, H14), 1.26 (s, 3H, H13/H13´), 1.11 (d, *J* = 11.0 Hz, 1H, $H12_B$), 0.82 (s, 3H, H13/H13´).

^{13}C-NMR (151 MHz, $CDCl_3$): δ (ppm) = 163.1 (d, *J* = 284.0 Hz, C2), 161.6 (d, *J* = 33.3 Hz, C3), 154.5 (C15), 86.4 (C7), 80.5 (C16), 78.2 (C6), 51.2 (C8), 46.5 (C4/C4´, C5/C5´), 43.7 (C4/C4´), 42.6 (C5/C5´), 39.5 (C10), 38.2 (C9), 35.4 (C11), 28.6 (C14), 28.4 (C17), 27.1 (C13/C13´), 26.5 (C12), 24.1 (C13/C13´), carbon bearing boron was not observed.

^{19}F-NMR {^{1}H} (470 MHz, $CDCl_3$): δ (ppm) = -87.85.

^{11}B-NMR (160 MHz, $CDCl_3$): δ (ppm) = 28.22.

IR (ATR) $\tilde{\nu}$ = 2970 (w), 2921 (m), 2870 (w), 1738 (w), 1698 (m), 1647 (s), 1412 (m), 1362 (s), 1286 (s), 1240 (s), 1165 (s), 1122 (m), 1078 (m), 1030 (m), 1006 (s), 940 (w), 923 (w), 848 (m), 756 (m), 669 (m) cm^{-1}.

HR-ESI-MS (Orbitrap) exact mass calculated for $[M+Na]^+$ $(C_{22}H_{34}N_2O_5BFNa)^+$ requires 459.24410 m/z, found 459.24370 m/z.

ORD (DCM, c 1.00): $[\alpha]_D^{21}$= 11.246.

Synthesis of (*Z*)-2-fluoro-1-(pyrrolidin-1-yl)-3-((3a*S*,4*S*,6*S*,7a*R*)-3a,5,5-trimethylhexahydro-4,6-methanobenzo[*d*][1,3,2]dioxaborol-2-yl)prop-2-en-1-one (S22)

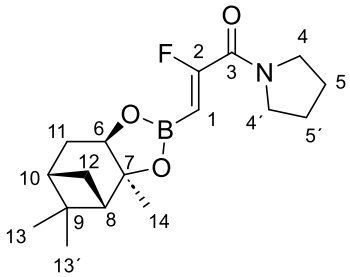

According to General Procedure A, **S5** (551.0 mg, 2.0 mmol, 1.0 eq.) was converted to **S22** yielding a colourless oil (199.0 mg, 31%) after purification by column chromatography (20%-30% EtOAc/DCM).

R_f = (SiO_2, 30% acetone/*n*-pentane) = 0.28

^{1}H-NMR (500 MHz, $CDCl_3$): δ (ppm) = 5.76 (d, *J* = 52.0 Hz, 1H, H1), 4.37 (dd, *J* = 8.7, 1.8 Hz, 1H, H6), 3.66 (td, *J* = 6.7, 4.5 Hz, 2H, H4/H4´), 3.54 (t, *J* = 6.9 Hz, 2H, H4/H4´), 2.39 – 2.33 (m, 1H, $H11_A$), 2.28 – 2.20 (m, 1H, $H12_A$), 2.10 (dd, *J* = 6.1, 4.8 Hz, 1H, H8), 1.95 – 1.84 (m, 6H, H5, H5´, H10, $H11_B$), 1.43 (s, 3H, H14), 1.29 (s, 3H, H13/H13´), 1.16 (d, *J* = 11.1 Hz, 1H, $H12_B$), 0.85 (s, 3H, H13/H13´).

^{13}C-NMR (126 MHz, $CDCl_3$): δ (ppm) = 163.8 (d, *J* = 285.4 Hz, C2), 160.0 (d, *J* = 33.9 Hz, C3), 86.3 (C7), 78.2 (C6), 51.3 (C8), 47.8 (d, *J* = 11.4 Hz, C4/C4´), 47.4 (C4/C4´), 39.6 (C10), 38.3 (C9), 35.5 (C11), 28.7 (C14), 27.2 (C13/C13´), 26.6 (C5/C5´) 26.5 (C12), 24.1 (C13/C13´), 23.7 (C5/C5´), carbon bearing boron was not observed.

^{19}F-NMR {^{1}H} (377 MHz, $CDCl_3$): δ (ppm) = -93.53.

^{11}B-NMR (128 MHz, $CDCl_3$): δ (ppm) = 28.36.

IR (ATR) $\tilde{\nu}$ = 2911 (w), 1739 (w), 1475 (w), 1629 (s), 1425 (s), 1355 (s), 1337 (s), 1231 (m), 1221 (m), 1122 (m), 1076 (m), 1029 (m), 1022 (m), 938 (m), 923 (w), 900 (w), 845 (m), 781 (w), 759 (m), 720 (w), 662 (m) cm^{-1}.

HR-ESI-MS (Orbitrap) exact mass calculated for $[M+Na]^+$ $(C_{17}H_{25}NO_3BFNa)^+$ requires 344.18069 m/z, found 344.17977 m/z

ORD (DCM, c 0.25): $[\alpha]_D^{20}$= 15.363.

Synthesis of methyl ((*Z*)-2-fluoro-3-((3a*S*,4*S*,6*S*,7a*R*)-3a,5,5-trimethylhexahydro-4,6-methanobenzo[*d*][1,3,2]dioxaborol-2-yl)acryloyl)-L-prolinate (S23)

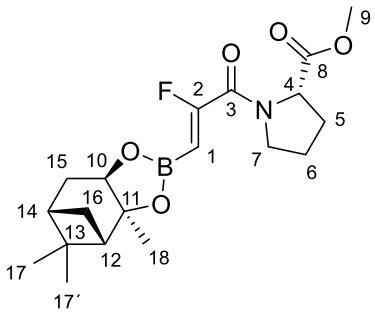

According to General Procedure A, **S6** (560.2 mg, 2.0 mmol, 1.0 eq.) was converted to **S23** yielding a colourless oil (283.6 mg, 37%, 75:25 mixture of rotamers) after purification by column chromatography (20% EtOAc/DCM).

$\mathbf{R_f}$ = (SiO_2, 20% EtOAc/DCM) = 0.59

^{1}H-NMR (500 MHz, $CDCl_3$): δ (ppm) = 5.89 (d, *J* = 54.2 Hz, 1H, H1, minor rotamer), 5.84 (d, *J* = 51.0 Hz, 1H, H1, major rotamer), 4.82 – 4.73 (m, 1H, H4 minor rotamer), 4.60 – 4.50 (m, 1H, H4 major rotamer), 4.40 – 4.30 (m, 1H, H10), 3.91 – 3.62 (m, 2H, H7), 3.73 (s, 3H, H9), 2.41 – 2.31 (m, 1H, $H15_A$), 2.26 – 2.02 (m, 4H, $H5_A$, $H6_A$, H12, $H16_A$), 2.00 – 1.87 (m, 4H, $H5_B$, $H6_B$, H14, $H15_B$), 1.43 (s, 3H, H18 major rotamer), 1.41 (s, 3H, H18 minor rotamer), 1.29 (s, 3H, H17/H17´, major rotamer), 1.29 (s, 3H, H17/H17´, minor rotamer), 1.16 – 1.08 (m, 1H, $H16_B$), 0.85 (s, 3H, H17/H17´, major rotamer), 0.84 (s, 3H, H17/H17´, minor rotamer).

^{13}C-NMR (126 MHz, $CDCl_3$): δ (ppm) = 172.5 (C8, minor rotamer), 172.2 (C8, major rotamer), 163.0 (d, *J* = 284.4 Hz, C2, major rotamer), 162.9 (d, *J* = 284.1 Hz, C2, minor rotamer), 160.0 (d, *J* = 34.7 Hz. C3, major rotamer), 159.9 (d, *J* = 34.0 Hz, C3, minor rotamer), 86.3 (C11, major rotamer), 86.2 (C11, minor rotamer), 78.1 (C10), 60.4 (C4, major rotamer), 60.0 (d, *J* = 12.2 Hz, C4, minor rotamer), 52.6 (C9, minor rotamer), 52.4 (C9, major rotamer), 51.2 (C12), 48.4 – 48.2 (m, C7), 39.5 (C14), 38.2 (C13), 35.4 (C15), 32.0 (d, *J* = 2.6 Hz, C6, minor rotamer), 28.7 (C18), 28.5 (C5), 27.2 (C17/C17´), 26.5 (C16), 25.3 (d, *J* = 4.2 Hz, C6, major rotamer), 24.1 (C17/C17´), carbon bearing boron was not observed.

^{19}F-NMR {^{1}H} (377 MHz, $CDCl_3$): δ (ppm) = -95.18 (major rotamer), -96.71 (minor rotamer).

^{11}B-NMR (128 MHz, $CDCl_3$): δ (ppm) = 28.78.

IR (ATR) $\tilde{\nu}$ = 2954 (w), 1742 (s), 1669 (w), 1623 (s), 1416 (s), 1357 (s), 1340 (s), 1286 (m), 1208 (s), 1174 (m), 1108 (m), 1079 (m), 1053 (m), 1030 (m), 1020 (m), 993 (m), 946 (m), 936 (m), 895 (m), 870 (m), 829 (w), 812 (w), 768 (w), 755 (s), 662 (w), 637 (s) cm^{-1}.

HR-ESI-MS (Orbitrap) exact mass calculated for $[M+Na]^+$ $(C_{19}H_{27}NO_5BFNa)^+$ requires 402.18620 m/z, found 402.18611 m/z

ORD (DCM, c 0.50): $[\alpha]_D^{22}$= -53.389.

Synthesis of (*Z*)-*N*-benzyl-2-fluoro-*N*-methyl-3-((3a*S*,4*S*,6*S*,7a*R*)-3a,5,5-trimethylhexahydro-4,6-methanobenzo[*d*][1,3,2]dioxaborol-2-yl)acrylamide (S24)

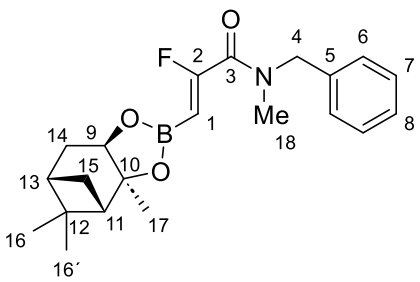

According to General Procedure A, **S7** (542.2 mg, 2.0 mmol, 1.0 eq.) was converted to **S24** yielding a colourless oil (324.1 mg, 44%, 54:46 mixture of rotamers) after purification by column chromatography (20% EtOAc/DCM).

$\mathbf{R_f}$ = (SiO_2, 10% acetone/*n*-pentane) = 0.19

^{1}H-NMR (500 MHz, $CDCl_3$): δ (ppm) = 7.36 – 7.31 (m, 2H, H7), 7.31 – 7.27 (m, 1H, H8), 7.25 – 7.20 (m, 2H, H6), 5.52 (d, *J* = 52.6 Hz, 1H, H1), 4.61 (s, 1H, H4, major rotamer), 4.58 (s, 1H, H4, minor rotamer), 4.37 (t, *J* = 9.7 Hz, 1H, H9), 3.00 (d, *J* = 4.0 Hz, 3H, H18, major rotamer), 2.88 (s, 3H, H18, minor rotamer), 2.43 – 2.32 (m, 1H, $H14_A$), 2.29 – 2.20 (m, 1H, $H15_A$), 2.13 – 2.05 (m, 1H, H11), 1.98 – 1.84 (m, 2H, H13, $H14_B$) 1.43 (s, 3H, H17, major rotamer), 1.42 (s, 3H, H17, minor rotamer), 1.29 (s, 3H, H16/16´), 1.17 – 1.13 (m, 1H, $H15_B$), 0.85 (s, 3H, H16/16´).

^{13}C-NMR (126 MHz, $CDCl_3$): δ (ppm) = 163.8 (d, *J* = 284.9 Hz, C2), 163.3 (d, *J* = 33.4 Hz, C3, minor rotamer), 162.9 (d, *J* = 33.4 Hz, C3, major rotamer), 136.3 (C5, major rotamer), 136.0 (C5, minor rotamer), 128.9 (C7, minor rotamer), 128.9 (C7, major rotamer), 128.2 (C6, major rotamer), 128.0 (C8, minor rotamer), 127.8 (C8, major rotamer), 127.4 (C6, minor rotamer), 86.3 (C10), 78.2 (C9), 54.3 (C4, minor rotamer), 51.5 (C4, major rotamer), 51.3 (C11), 39.6 (C13), 38.3 (C12), 35.6 (C18, major rotamer) 35.5 (C14), 33.3 (C18, minor rotamer) 28.7 (C17), 27.1 (C16/16´), 26.6 (C15), 24.1 (C16/16´), carbon bearing boron was not observed.

^{19}F-NMR {^{1}H} (377 MHz, $CDCl_3$): δ (ppm) = -86.46 (minor rotamer), -87.65 (major rotamer).

^{11}B-NMR (128 MHz, $CDCl_3$): δ (ppm) = 28.73.

IR (ATR) $\tilde{\nu}$ = 2920 (w), 1738 (w), 1644 (s), 1477 (w), 1452 (w), 1359 (s), 1286 (m), 1264 (m), 1240 (s), 1208 (m), 1121 (m), 1078 (m), 1029 (s), 990 (m), 941 (w), 923 (w), 900 (w), 847 (m), 795 (m), 753 (m), 700 (s), 621 (w), 607 (w) cm^{-1}.

HR-ESI-MS (Orbitrap) exact mass calculated for $[M+Na]^+$ $(C_{21}H_{27}NO_3BFNa)^+$ requires 394.19641 m/z, found 394.19615 m/z

ORD (DCM, c 1.00): $[\alpha]_D^{22}$= 10.707.

Synthesis of (*Z*)-*N*-benzyl-2-fluoro-3-((3a*S*,4*S*,6*S*,7a*R*)-3a,5,5-trimethylhexahydro-4,6-methano benzo[*d*][1,3,2]dioxaborol-2-yl)acrylamide (S25)

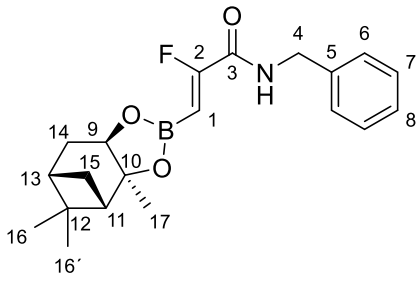

According to General Procedure A, **S8** (516.2 mg, 2.0 mmol, 1.0 eq.) was converted to **S25** yielding a colourless oil (256.6 mg, 36%) after purification by column chromatography (10% EtOAc/DCM).

$\mathbf{R_f}$ = (SiO_2, 20% acetone/*n*-pentane) = 0.28

^{1}H-NMR (500 MHz, $CDCl_3$): δ (ppm) = 7.38 – 7.31 (m, 2H, H6/H7), 7.31 – 7.27 (m, 3H, H8, H6/H7), 6.62 (s, 1H, N*H*), 6.04 (d, *J* = 53.1 Hz, 1H, H1), 4.54 (dd, *J* = 5.9, 1.7 Hz, 2H, H4), 4.38 (dd, *J* = 8.8, 1.9 Hz, 1H, H9), 2.37 (ddt, *J* = 14.2, 8.9, 2.2 Hz, 1H, $H14_A$), 2.24 (dtd, *J* = 11.0, 6.2, 2.3 Hz, 1H, $H15_A$), 2.09 (dd, *J* = 6.0, 4.9 Hz, 1H, H11), 1.96 – 1.86 (m, 2H, H13, $H14_B$), 1.43 (s, 3H, H17), 1.30 (s, 3H, H16/H16´), 1.13 (d, *J* = 11.0 Hz, 1H, $H15_B$), 0.85 (s, 3H, H16/H16´).

^{13}C-NMR (126 MHz, $CDCl_3$): δ (ppm) = 161.4 (d, *J* = 281.3 Hz, C2), 159.3 (d, *J* = 33.8 Hz, C3), 137.3 (C5), 128.8 (C6/C7), 127.8 (C6/C7), 127.8 (C8), 86.3 (C10), 78.1 (C9), 51.2 (C11), 43.6 (C4), 39.5 (C13), 38.1 (C12), 35.3 (C14), 28.5 (C17), 27.0 (C16/C16´), 26.4 (C15), 24.0 (C16/C16´), carbon bearing boron was not observed.

^{19}F-NMR {^{1}H} (377 MHz, $CDCl_3$): δ (ppm) = -106.46.

^{11}B-NMR (128 MHz, $CDCl_3$): δ (ppm) = 28.86.

IR (ATR) $\tilde{\nu}$ = 3329 (w), 2970 (w), 2921 (w), 1739 (w), 1663 (s), 1455 (w), 1362 (s), 1280 (s), 1240 (m), 1208 (m), 1122 (m), 1078 (m), 1029 (m), 868 (w), 849 (m), 755 (m), 697 (m), 647 (m) cm^{-1}.

HR-ESI-MS (Orbitrap) exact mass calculated for $[M+Na]^+$ $(C_{20}H_{25}NO_3BFNa)^+$ requires 380.18074 m/z, found 380.18037 m/z

ORD (DCM, c 1.00): $[\alpha]_D^{22}$= 11.360.

Synthesis of benzyl (*Z*)-2-fluoro-3-((3a*S*,4*S*,6*S*,7a*R*)-3a,5,5-trimethylhexahydro-4,6-methanobenzo-[*d*][1,3,2]dioxaborol-2-yl)acrylate (S26)

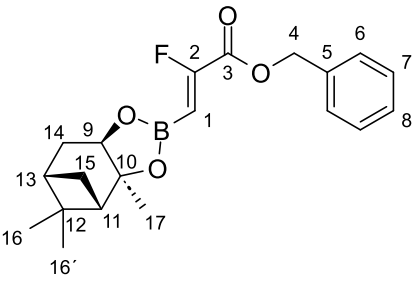

According to General Procedure A, **S9** (518.2 mg, 2.0 mmol, 1.0 eq.) was converted to **S26** yielding a colourless oil (162.3 mg, 23%) after purification by column chromatography (5% acetone/*n*-pentane).

R_f = (SiO_2, 10% acetone/*n*-pentane) = 0.37

^{1}H-NMR (500 MHz, $CDCl_3$): δ (ppm) = 7.41 – 7.32 (m, 5H, H6, H7, H8), 6.00 (d, *J* = 47.1 Hz, 1H, H1), 5.27 (s, 2H, H4), 4.38 (dd, *J* = 8.8, 1.9 Hz, 1H, H9), 2.49 – 2.31 (m, 1H, $H14_A$), 2.24 (dtd, *J* = 11.2, 6.3, 2.5 Hz, 1H, $H15_A$), 2.09 (dd, *J* = 6.1, 4.9 Hz, 1H, H11), 1.98 – 1.86 (m, 2H, H13, $H14_B$), 1.43 (s, 3H, H17), 1.30 (s, 3H, H16/16´), 1.12 (d, *J* = 11.1 Hz, 1H, $H15_B$), 0.85 (s, 3H, H16/16´).

^{13}C-NMR (126 MHz, $CDCl_3$): δ (ppm) = 160.4 (d, *J* = 40.1 Hz, C3), 158.3 (d, *J* = 273.8 Hz, C2), 135.1 (C5), 128.8 (C7), 128.7 (C8), 128.4 (C6), 86.6 (C10), 78.4 (C9), 67.7 (C4), 51.3 (C11), 39.6 (C13), 38.3 (C12), 35.4 (C14), 28.6 (C17), 27.2 (C16/16´), 26.5 (C15), 24.1 (C16/16´), carbon bearing boron was not observed.

^{19}F-NMR {^{1}H} (377 MHz, $CDCl_3$): δ (ppm) = -101.09.

^{11}B-NMR (128 MHz, $CDCl_3$): δ (ppm) = 28.82.

IR (ATR) $\tilde{\nu}$ = 2921 (w), 1739 (m), 1662 (m), 1456 (m), 1369 (m), 1274 (s), 1241 (m), 1210 (m), 1122 (w), 1075 (m), 1029 (m), 990 (w), 953 (w), 847 (m), 752 (m), 696 (m), 662 (m), 621 (w) cm^{-1}.

HR-ESI-MS (Orbitrap) exact mass calculated for $[M+Na]^+$ $(C_{20}H_{24}O_4BFNa)^+$ requires 381.16439 m/z, found 381.16436 m/z

ORD (DCM, c 1.00): $[\alpha]_D^{21}$= 4.091.

Synthesis of *tert*-butyl (*Z*)-2-fluoro-3-((3a*S*,4*S*,6*S*,7a*R*)-3a,5,5-trimethylhexahydro-4,6-methanobenzo[*d*][1,3,2]dioxaborol-2-yl)acrylate (S27)

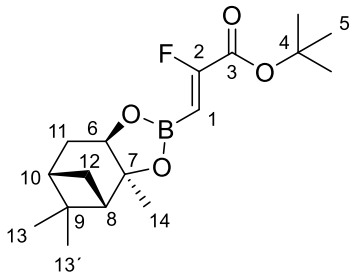

According to General Procedure A, **S10** (422.0 mg, 2.0 mmol, 1.0 eq.) was converted to **S27** yielding a colourless solid (149.5 mg, 23 %) after purification by column chromatography (5% Et_2O/*n*-pentane).

R_f = (SiO_2, 5% Et_2O/*n*-pentane) = 0.31

^{1}H-NMR (599 MHz, $CDCl_3$): δ (ppm) = 5.87 (d, *J* = 48.4 Hz, 1H, H1), 4.38 (dd, *J* = 8.8, 1.8 Hz, 1H, H6), 2.40 – 2.33 (m, 1H, $H11_A$), 2.26 – 2.21 (m, 1H, $H12_A$), 2.09 (t, *J* = 5.5 Hz, 1H, H8), 1.97 – 1.87 (m, 2H, H10, $H11_B$), 1.51 (d, *J* = 0.6 Hz, 9H, H5), 1.43 (d, *J* = 0.6 Hz, 3H, H14), 1.30 (s, 3H, H13/H13´), 1.13 (d, *J* = 11.1 Hz, 1H, $H12_B$), 0.85 (s, 3H, H13/H13´).

^{13}C-NMR (151 MHz, $CDCl_3$): δ (ppm) = 159.4 (d, *J* = 275.1 Hz, C2), 159.2 (d, *J* = 38.9 Hz, C3), 86.5 (C7), 83.2 (C4), 78.4 (C6), 51.3 (C8), 39.6 (C10), 38.3 (C9), 35.5 (C11), 28.7 (C14), 28.0 (C5), 27.2 (C13/C13´), 26.6 (C12), 24.1 (C13/C13´), carbon bearing boron was not observed.

^{19}F-NMR {^{1}H} (564 MHz, $CDCl_3$): δ (ppm) = -99.99.

^{11}B-NMR (128 MHz, $CDCl_3$): δ (ppm) = 29.16.

IR (ATR) $\tilde{\nu}$ = 2979 (w), 2672 (w), 1735 (m), 1662 (m), 1477 (w), 1452 (w), 1418 (w), 1369 (s), 1300 (s), 1283 (s), 1243 (m), 1233 (m), 1157 (s), 1029 (s), 923 (w), 900 (w), 881 (w), 844 (m), 773 (m), 663 (m), 647 (m) cm^{-1}.

HR-ESI-MS (Orbitrap) exact mass calculated for $[M+Na]^+$ $(C_{17}H_{26}O_4BFNa)^+$ requires 347.18035 m/z, found 347.17997 m/z

ORD (DCM, c 1.00): $[\alpha]_D^{21}$= 13.357.

M.p.: 47.2 – 48.0 °C.

Synthesis of benzyl (*E*)-3-((3a*S*,4*S*,6*S*,7a*R*)-3a,5,5-trimethylhexahydro-4,6-methanobenzo[*d*][1,3,2]dioxaborol-2-yl)acrylate (S28)

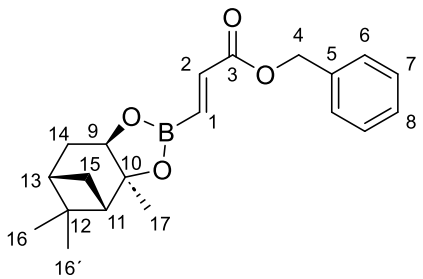

According to General Procedure A, **S16** (482.2 mg, 2.0 mmol, 1.0 eq.) was converted to **S28** yielding a colourless oil (62.7 mg, 10%) after purification by column chromatography (9% acetone/*n*-pentane).

R_f = (SiO_2, 10% acetone/*n*-pentane) = 0.71

^{1}H-NMR (500 MHz, $CDCl_3$): δ (ppm) = 7.39 – 7.29 (m, 5H, H6, H7, H8), 6.86 (d, *J* = 18.2 Hz, 1H, H1), 6.69 (d, *J* = 18.2 Hz, 1H, H2), 5.21 (s, 2H, H4), 4.36 (dd, *J* = 8.8, 2.0 Hz, 1H, H9), 2.36 (ddt, *J* = 14.0, 8.9, 2.4 Hz, 1H, $H14_A$), 2.26 – 2.19 (m, 1H, $H15_A$), 2.07 (t, *J* = 5.5 Hz, 1H,

H11), 1.96 – 1.85 (m, 2H, H13, $H14_B$), 1.42 (s, 3H, H17), 1.29 (s, 3H, H16/H16´), 1.10 (d, *J* = 11.0 Hz, 1H, $H15_B$), 0.85 (s, 3H, H16/H16´)

^{13}C-NMR (126 MHz, $CDCl_3$): δ (ppm) = 165.9 (C3), 138.5 (C2), 136.0 (C5), 128.7 (C7), 128.3 (C6), 128.2 (C8), 86.6 (C10), 78.4 (C9), 66.5 (C4), 51.3 (C11), 39.6 (C13), 38.3 (C12), 35.4 (C14), 28.7 (C17), 27.2 (C16/C16´), 26.5 (C15), 24.1 (C16/C16´), carbon bearing boron was not observed.

^{11}B-NMR (128 MHz, $CDCl_3$): δ (ppm) = 30.09.

IR (ATR) $\tilde{\nu}$ = 2921 (m), 2359 (w), 1723 (s), 1627 (m), 1455(m), 1409 (w), 1389 (s), 1356 (s), 1339 (s), 1300 (m), 1289 (m), 1257 (m), 1241 (m), 1161 (s), 1122 (w), 1030 (m), 1002 (m), 849 (w), 753 (m), 697 (m) cm^{-1}.

HR-ESI-MS (Orbitrap) exact mass calculated for $[M+Na]^+$ $(C_{20}H_{25}O_4BNa)^+$ requires 363.17418 m/z, found 363.17388 m/z

ORD (DCM, c 0.25): $[\alpha]_D^{21}$= 18.280.

Synthesis of benzyl (*Z*)-2-chloro-3-((3a*S*,4*S*,6*S*,7a*R*)-3a,5,5-trimethylhexahydro-4,6-methano benzo[*d*][1,3,2]dioxaborol-2-yl)acrylate (S29)

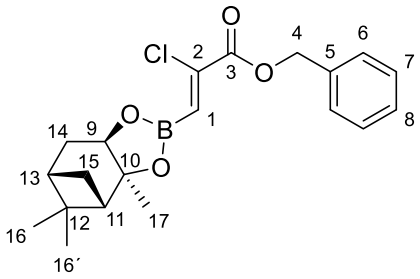

According to General Procedure A, **S18** (358.1 mg, 1.0 mmol, 1.0 eq.) was converted to **S29** in 1,4-dioxane (4 mL) yielding a colourless oil (145.7 mg, 39%) after purification by column chromatography (2.5% Et_2O/*n*-pentane)

R_f = (SiO_2, 10% acetone/*n*-pentane) = 0.15

^{1}H-NMR (500 MHz, $CDCl_3$): δ (ppm) = 7.43 – 7.32 (m, 5H, H6, H7, H8), 6.99 (s, 1H, H1), 5.26 (s, 2H, H4), 4.41 (dd, *J* = 8.8, 1.9 Hz, 1H, H9), 2.41 – 2.32 (m, 1H, $H14_A$), 2.29 – 2.20 (m, 1H, $H15_A$), 2.10 (dd, *J* = 6.1, 4.8 Hz, 1H, H11), 1.98 – 1.90 (m, 2H, H13, $H14_B$), 1.44 (s, 3H, H17), 1.30 (s, 3H, H16/16´), 1.19 (d, *J* = 11.1 Hz, 1H, $H15_B$), 0.86 (s, 3H, H16/16´).

^{13}C-NMR (126 MHz, $CDCl_3$): δ (ppm) = 162.0 (C3), 138.4 (C2), 135.2 (C5), 128.8 (C7), 128.7 (C8), 128.4 (C6), 86.8 (C10), 78.6 (C9), 68.4 (C4), 51.3 (C11), 39.6 (C13), 38.3 (C12), 35.4 (C14), 28.7 (C17), 27.2 (C16/16´), 26.6 (C15), 24.1 (C16/16´), carbon bearing boron was not observed.

^{11}B-NMR (128 MHz, $CDCl_3$): δ (ppm) = 29.09.

IR (ATR) $\tilde{\nu}$ = 2970 (w), 2921 (m), 1725 (s), 1620 (m), 1455 (m), 1415 (w), 1376 (s), 1336 (s), 1286 (w), 1237 (s), 1207 (s), 1121 (m), 1076 (m), 1020 (s), 990 (m), 940 (w), 923 (w), 849 (w), 749 (s), 696 (s), 653 (w) cm^{-1}.

HR-ESI-MS (Orbitrap) exact mass calculated for $[M+Na]^+$ $(C_{20}H_{24}O_4BClNa)^+$ requires 397.13520 m/z, found 397.13470 m/z

ORD (DCM, c 1.00): $[\alpha]_D^{22}$= 10.671.

Synthesis of (*E*)-2-fluoro-*N*-methoxy-*N*-methyl-3-((3a*S*,4*S*,6*S*,7a*R*)-3a,5,5-trimethylhexahydro-4,6-methanobenzo[*d*][1,3,2]dioxaborol-2-yl)but-2-enamide (S30)

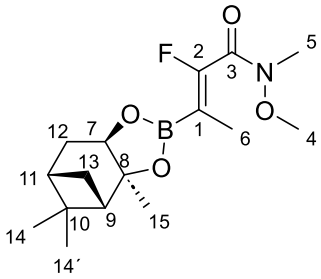

According to General Procedure A, **S12** (452.1 mg, 2.0 mmol, 1.0 eq.) was converted to **S30** at 90 °C yielding a colourless solid (318.6 mg, 49%) after purification by column chromatography (5% acetone/*n*-pentane).

$\mathbf{R_f}$ = (SiO_2, 5% acetone/*n*-pentane) = 0.25

^{1}H-NMR (500 MHz, $CDCl_3$): δ (ppm) = 4.37 (dd, *J* = 8.7, 1.9 Hz, 1H, H7), 3.73 (s, 3H, H4), 3.25 (s, 3H, H5), 2.39 – 2.31 (m, 1H, $H12_A$), 2.25 – 2.19 (m, 1H, $H13_A$), 2.09 (dd, *J* = 6.0, 4.9 Hz, 1H, H9), 1.94 – 1.86 (m, 2H, H11, $H12_B$), 1.76 (d, *J* = 2.7 Hz, 3H, H6), 1.42 (s, 3H, H15), 1.28 (s, 3H, H14/H14´), 1.14 (d, *J* = 11.1 Hz, 1H, $H13_B$), 0.84 (s, 3H, H14/H14´).

^{13}C-NMR (126 MHz, $CDCl_3$): δ (ppm) = 162.8 (C3), 156.6 (d, *J* = 265.1 Hz, C2), 86.2 (C8), 78.3 (C7), 62.3 (C4), 51.3 (C9), 39.6 (C11), 38.2 (C10), 35.6 (C12), 32.1 (C5), 28.7 (C15), 27.2 (C14/C14´), 26.6 (C13), 24.1 (C14/C14´), 13.1 (d, *J* = 8.5 Hz, C6), carbon bearing boron was not observed.

^{19}F-NMR {^{1}H} (470 MHz, $CDCl_3$): δ (ppm) = -97.67.

^{11}B-NMR (128 MHz, $CDCl_3$): δ (ppm) = 29.54.

IR (ATR) $\tilde{\nu}$ = 2972 (w), 2930 (m), 2871 (w), 2359 (w), 1656 (s), 1474 (m), 1448 (m), 1413 (m), 1375 (s), 1340 (s), 1316 (w), 1281 (m), 1208 (m), 1155 (w), 1122 (m), 1096 (m), 1078 (m), 1054 (w), 1045 (w), 1028 (m), 986 (m), 938 (w), 922 (w), 884 (m), 824 (w), 756 (m), 684 (m), 614 (w) cm^{-1}.

HR-ESI-MS (Orbitrap) exact mass calculated for $[M+Na]^+$ $(C_{16}H_{25}NO_4BFNa)^+$ requires 348.17559 m/z, found 348.17522 m/z

ORD (DCM, c 1.00): $[\alpha]_D^{20}$= 16.753.

M.p.: 71.7 – 72.9°C

Synthesis of benzyl (*E*)-2-fluoro-3-((3a*S*,4*S*,6*S*,7a*R*)-3a,5,5-trimethylhexahydro-4,6-methanobenzo-[*d*][1,3,2]dioxaborol-2-yl)but-2-enoate (S31)

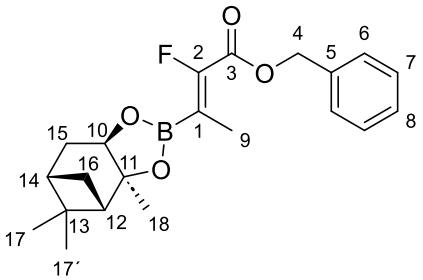

According to General Procedure A, **S13** (410.1 mg, 1.5 mmol, 1.0 eq.) was converted to **S31** at 90 °C yielding a colourless oil (73.6 mg, 13%) after purification by column chromatography (3% acetone/*n*-pentane).

$\mathbf{R_f}$ = (SiO_2, 3% acetone/*n*-pentane) = 0.60

^{1}H-NMR (599 MHz, $CDCl_3$): δ (ppm) = 7.41 – 7.30 (m, 5H, H6, H7, H8), 5.27 (s, 2H, H4), 4.39 (dd, *J* = 8.8, 1.9 Hz, 1H, H10), 2.39 – 2.34 (m, 1H, $H15_A$), 2.27 – 2.21 (m, 1H, $H16_A$), 2.11 – 2.08 (m, 4H, H9, H12), 1.95 – 1.89 (m, 2H, H14, $H15_B$), 1.44 (s, 3H, H18), 1.30 (s, 3H, H17/H17´), 1.16 (d, *J* = 11.1 Hz, 1H, $H16_B$), 0.85 (s, 3H, H17/H17´).

^{13}C-NMR (151 MHz, $CDCl_3$): δ (ppm) = 160.7 (d, *J* = 39.0 Hz, C3), 151.5 (d, *J* = 258.5 Hz, C2), 135.4 (C5), 128.7 (C7), 128.5 (C8), 128.3 (C6), 86.6 (C11), 78.5 (C10), 66.9 (C4), 51.3 (C12), 39.6 (C14), 38.2 (C13),

35.4 (C15), 28.6 (C18), 27.1(C17/C17´), 26.5 (C16), 24.3 – 23.8 (m, C17/C17´), 13.8 (d, *J* = 6.8 Hz, C9), carbon bearing boron was not observed.

^{19}F-NMR {^{1}H} (377 MHz, $CDCl_3$): δ (ppm) = -105.70.

^{11}B-NMR (128 MHz, $CDCl_3$): δ (ppm) = 29.74.

IR (ATR) $\tilde{\nu}$ = 2982 (w), 2923 (m), 2871 (w), 2362 (w), 1728 (s), 1646 (w), 1475 (w), 1456 (w), 1419 (w), 1390 (m), 1376 (m), 1342 (w), 1286 (m), 1266 (s), 1238 (m), 1210 (w), 1157 (w), 1122 (m), 1110 (m), 1078 (w), 1053 (m), 1029 (m), 990 (w), 922 (w), 848 (w), 776 (w), 753 (m), 697 (m), 684 (w) cm^{-1}.

HR-ESI-MS (Orbitrap) exact mass calculated for $[M+Na]^+$ $(C_{21}H_{26}O_4BFNa)^+$ requires 395.18042 m/z, found 395.18005 m/z.

ORD (DCM, c 1.00): $[\alpha]_D^{21}$= 5.728.

Synthesis of (*E*)-2-fluoro-*N*-methoxy-*N*-methyl-3-(4,4,5,5-tetramethyl-1,3,2-dioxaborolan-2-yl)but-2-enamide (S32)

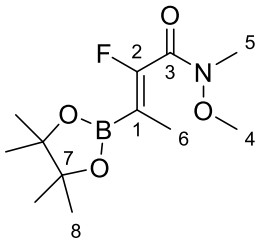

According to General Procedure B, **S12** (452.1 mg, 2.0 mmol, 1.0 eq.) was converted to **S32** yielding a colourless solid (255.1 mg, 47%) after purification by column chromatography (5% acetone/*n*-pentane).

$\mathbf{R}_f$ = (SiO_2, 5% acetone/*n*-pentane) = 0.31

^{1}H-NMR (500 MHz, $CDCl_3$): δ (ppm) = 3.73 (s, 3H, H4), 3.25 (s, 3H, H5), 1.74 (d, *J* = 2.7 Hz, 3H, H6), 1.28 (s, 12H, H8).

^{13}C-NMR (126 MHz, $CDCl_3$): δ (ppm) = 162.7 (br s, C3), 156.3 (d, *J* = 269.8 Hz, C2), 83.6 (C7), 62.0 (C4), 31.8 (C5), 24.6 (C8), 12.7 (d, *J* = 8.6 Hz, C6), carbon bearing boron was not observed.

^{19}F-NMR {^{1}H} (470 MHz, $CDCl_3$): δ (ppm) = -97.66.

^{11}B-NMR (128 MHz, $CDCl_3$): δ (ppm) = 29.94.

IR (ATR) $\tilde{\nu}$ = 2982 (w), 2940 (w), 2359 (w), 1650 (s), 1461 (w), 1418 (w), 1402 (w), 1380 (m), 1360 (s), 1313 (s), 1277 (w), 1213 (m), 1167 (w), 1144 (m), 1115 (m), 1098 (m), 1042 (w), 984 (m), 967 (m), 911 (w), 861 (s), 837 (w), 828 (w), 763 (m), 712 (w), 703 (w), 686 (m), 673 (m), 637 (w), 611 (m) cm^{-1}.

HR-ESI-MS (Orbitrap) exact mass calculated for $[M+Na]^+$ $(C_{12}H_{21}NO_4BFNa)^+$ requires 296.14422 m/z, found 296.14366 m/z

M.p.: 53.1 – 54.2°C

Synthesis of (*E*)-2-fluoro-1-(piperidin-1-yl)-3-(4,4,5,5-tetramethyl-1,3,2-dioxaborolan-2-yl)but-2-en-1-one (S33)

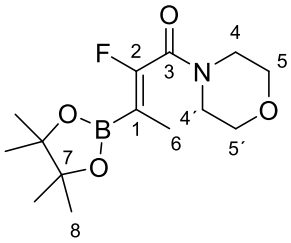

According to General Procedure B, **S14** (504.2 mg, 2.0 mmol, 1.0 eq.) was converted to **S33** yielding a colourless solid (197.4 mg, 33%) after purification by column chromatography (10% acetone/*n*-pentane).

$\mathbf{R_f}$ = (SiO_2, 10% acetone/*n*-pentane) = 0.57

^{1}H-NMR (599 MHz, $CDCl_3$): δ (ppm) = 3.69 – 3.67 (m, 2H, H5/H5´), 3.66 – 3.62 (m, 4H, H4/H4´, H5/H5´), 3.51 – 3.48 (m, 2H, H4/H4´), 1.70 (d, *J* = 2.7 Hz, 3H, H6), 1.26 (s, 12H, H8).

^{13}C-NMR (151 MHz, $CDCl_3$): δ (ppm) = 161.4 (d, *J* = 35.8 Hz, C3), 156.3 (d, *J* = 269.0 Hz, C2), 83.9 (C7), 67.2 (C5/C5´), 66.8 (C5/C5´), 46.9 (d, *J* = 2.8 Hz, C4/C4´), 42.0 (C4/C4´), 24.8 (C8), 12.9 (d, *J* = 8.9 Hz, C6), carbon bearing boron was not observed.

^{19}F-NMR {^{1}H} (564 MHz, $CDCl_3$): δ (ppm) = -94.68.

^{11}B-NMR (128 MHz, $CDCl_3$): δ (ppm) = 30.11.

IR (ATR) $\tilde{\nu}$ = 2982 (w), 2923 (w), 2867 (w), 2360 (w), 2343 (w), 1665 (m), 1634 (s), 1439 (m), 1406 (m), 1367 (s), 1314 (m), 1280 (m), 1256 (s), 1210 (w), 1138 (m), 1106 (s), 1073 (m), 1063 (m), 1010 (s), 966 (m), 907 (w), 835 (m), 848 (s), 763 (m), 707 (m), 690 (m), 669 (m), 651 (m), 616 (m) cm^{-1}.

HR-ESI-MS (Orbitrap) exact mass calculated for $[M+Na]^+$ $(C_{14}H_{23}NO_4BFNa)^+$ requires 322.15990 m/z, found 322.15971 m/z

M.p.: 90.0 – 91.0°C

Synthesis of benzyl (*Z*)-2-fluoro-3-(4,4,5,5-tetramethyl-1,3,2-dioxaborolan-2-yl)acrylate (*E*-14)

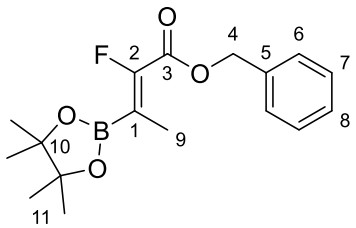

According to general procedure B, **S13** (546.2 mg, 2.0 mmol, 1.0 eq.) was converted to ***E*-14**. The crude reaction mixture was purified by column chromatography (5% acetone/*n*-pentane) and the obtained solid was recrystallized from *n*-pentane to give the desired product as colourless solid (66.6 mg, 10%).

$\mathbf{R_f}$ = (SiO_2, 10% acetone/*n*-pentane) = 0.45

^{1}H-NMR (599 MHz, $CDCl_3$): δ (ppm) = 7.40 – 7.30 (m, 5H, H6, H7, H8), 5.26 (s, 2H, H4), 2.07 (d, *J* = 2.8 Hz, 3H, H9), 1.30 (s, 12H, H11).

^{13}C-NMR (151 MHz, $CDCl_3$): δ (ppm) = 160.8 (d, *J* = 39.0 Hz, C3), 151.5 (d, *J* = 258.2 Hz, C2), 135.4 (C5), 128.7 (C7), 128.5 (C8), 128.3 (C6), 84.3 (C10), 66.9 (C4), 24.8 (C11), 13.7 (d, *J* = 6.7 Hz, C9), carbon bearing boron was not observed.

^{19}F-NMR {^{1}H} (470 MHz, $CDCl_3$): δ (ppm) = -106.18.

^{11}B-NMR (128 MHz, $CDCl_3$): δ (ppm) = 30.56.

IR (ATR) $\tilde{\nu}$ = 2982 (w), 1728 (m), 1632 (w), 1458 (w), 1369 (m), 1317 (m), 1235 (s), 1158 (s), 1139 (s), 1108 (s), 1062 (m), 981 (m), 926 (m), 864 (w), 842 (m), 794 (w), 761 (m), 705 (m), 686 (m) cm^{-1}.

HR-ESI-MS (Orbitrap) exact mass calculated for $[M+Na]^+$ $(C_{17}H_{22}O_4BFNa)^+$ requires 343.14905 m/z, found 343.14863 m/z

M.p.: 67.7 – 70.3 °C

2.3 Photochemical Isomerisation of α-Halo-β-borylacrylates

2.3.1 Reaction Optimisation

Table S1: Reaction optimisation.

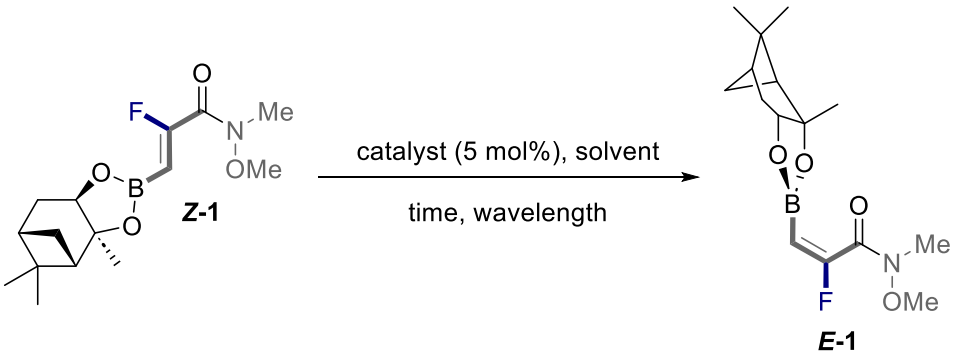

Entry	Catalyst	Wavelength [nm]	E_T [kJ/mol]	Solvent	Time [h]	Yield [%][a]	*E*/*Z*[b]
1	9-Fluorenone	402	223	MeCN	16	98	8:92
2	Michler´s Ketone	365	255	MeCN	16	27	54:46
3	Thioxanthone	402	265	MeCN	16	87	91:9
4	Benzophenone	365	289	MeCN	16	90	94:6
5	Benzophenone	365	289	MeCN	1	60	60:40
6	Thioxanthone	402	265	MeCN	1	86	95:5
7	Thioxanthone	/	265	MeCN	1	>98	<1:99
8	/	402	/	MeCN	1	>98	<1:99

[a] ^{1}H-NMR-yield of the main isomer determined against 1,3,5-trimethoxybenzene as internal standard. [b] *E*/*Z*-ratio determined by ^{1}H-NMR from the crude reaction mixture.

General Procedure C: Photochemical isomerisation of *α*-Halo-*β*-borylacrylates

A round-bottom flask was equipped with the specified boronic ester (1.0 eq.) and thioxanthone (5 mol%). The flask was sealed and purged with argon three times before the addition of degassed MeCN (0.03 M). The reaction mixture was stirred for 1 h at ambient temperature under irradiation of UV-light (402 nm). After completion, 1,3,5-trimethoxybenzene (0.1 M solution in MeCN) was added as the internal standard and the solvent was removed under reduced pressure. The NMR-yield and *E/Z*-ratio was determined by ^{1}H-NMR against the internal standard and the sample was recombined with the residual reaction mixture. The crude residue was purified by column chromatography (SiO_2, specified combination of solvents).

2.3.2 Photochemical Isomerisation of trisubstituted *α*-Halo-*β*-borylacrylates

Synthesis of (*E*)-2-fluoro-*N*-methoxy-*N*-methyl-3-((3a*S*,4*S*,6*S*,7a*R*)-3a,5,5-trimethylhexa-hydro-4,6-methanobenzo[*d*][1,3,2]dioxaborol-2-yl)acrylamide (*E*-1)

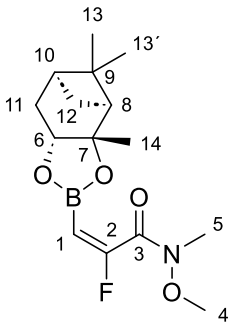

According to General Procedure C, ***Z*-1** (62.2 mg, 0.2 mmol, 1.0 eq.) was converted to ***E*-1** yielding a colourless oil (86% NMR-yield, 95:5 *E/Z*, 33.1 mg, 53%) after purification by column chromatography (5% acetone/*n*-pentane).

R_f = (SiO_2, 10% acetone/*n*-pentane) = 0.23

^{1}H-NMR (599 MHz, $CDCl_3$): δ (ppm) = 5.27 (d, *J* = 26.9 Hz, 1H, H1), 4.33 (dd, *J* = 8.8, 2.1 Hz, 1H, H6), 3.72 (d, *J* = 1.1 Hz, 3H, H4), 3.25 (d, *J* = 1.1 Hz, 3H, H5), 2.31 (ddt, *J* = 14.6, 8.8, 2.5 Hz, 1H, $H11_A$), 2.22 – 2.15 (m, 1H, $H12_A$), 2.02 (dd, *J* = 6.1, 5.0 Hz, 1H, H8), 1.90 (tt, *J* = 5.9, 3.0 Hz, 1H, H10), 1.84 (ddd, *J* = 14.6, 3.4, 2.0 Hz, 1H, $H11_B$), 1.39 (s, 3H, H14), 1.27 (s, 3H, H13/H13´), 1.21 (d, *J* = 11.0 Hz, 1H, $H12_B$), 0.83 (s, 3H, H13/H13´).

^{13}C-NMR (151 MHz, $CDCl_3$): δ (ppm) = 161.3 (d, *J* = 284.3 Hz, C2), 86.4 (C7), 78.3 (C6), 62.0 (C4), 51.4 (C8), 39.6 (C10), 38.3 (C9), 35.3 (C11), 33.3 (C5), 28.5 (C14), 27.2 (C13/C13´), 26.4 (C12), 24.1 (C13/C13´), carbon bearing boron and carbonyl carbon were not observed.

^{19}F-NMR {^{1}H} (377 MHz, $CDCl_3$): δ (ppm) = -84.52.

^{11}B-NMR (192 MHz, $CDCl_3$): δ (ppm) = 29.14.

IR (ATR) $\tilde{\nu}$ = 2921 (s), 1735 (w), 1656 (s), 1449 (w), 1366 (s), 1340 (s), 1314 (w), 1281 (m), 1238 (m), 1208 (m), 1096 (s), 1076 (m), 1056 (m), 1029 (s), 1023 (m), 990 (m), 940 (m), 924 (m), 900 (m), 851 (m), 755 (w), 723 (s), 691 (w), 640 (w) cm^{-1}.

HR-ESI-MS (Orbitrap) exact mass calculated for $[M+Na]^+$ ($C_{15}H_{23}NO_4BFNa)^+$ requires 334.15964 m/z, found 334.15963 m/z

ORD (DCM, c 1.00): $[\alpha]_D^{22}$= 10.366.

Synthesis of (*E*)-2-fluoro-1-morpholino-3-((3a*S*,4*S*,6*S*,7a*R*)-3a,5,5-trimethylhexahydro-4,6-methanobenzo[*d*][1,3,2]dioxaborol-2-yl)prop-2-en-1-one (*E*-2)

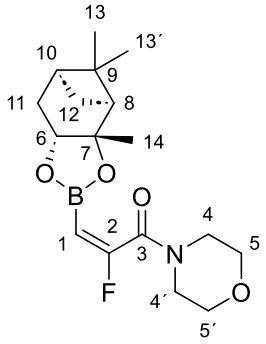

According to General Procedure C, **S20** (67.4 mg, 0.2 mmol, 1.0 eq.) was converted to ***E*-2** yielding a colourless oil (94% NMR-yield, 96:4 *E/Z*, 40.2 mg, 60%) after purification by column chromatography (20% EtOAc/*n*-pentane).

$\mathbf{R_f}$ = (SiO_2, 20% EtOAc/*n*-pentane) = 0.20

^{1}H-NMR (599 MHz, $CDCl_3$): δ (ppm) = 5.23 (d, *J* = 27.6 Hz, 1H, H1), 4.32 (dd, *J* = 8.8, 2.0 Hz, 1H, H6), 3.73 – 3.66 (m, 5H, H4, H4´, H5), 3.64 – 3.57 (m, 1H, H4/H4´), 3.55 – 3.51 (m, 2H, H5/H5´), 2.32 (ddt, *J* = 14.5, 8.8, 2.4 Hz, 1H, $H11_A$), 2.21 (dtd, *J* = 11.0, 6.2, 2.2 Hz, 1H, $H12_A$), 2.02 (t, *J* = 5.5 Hz, 1H, H8), 1.90 (dt, *J* = 5.8, 3.1 Hz, 1H, H10), 1.83 (ddd, *J* = 14.6, 3.4, 2.0 Hz, 1H, $H11_B$), 1.39 (s, 3H, H14), 1.28 (s, 3H, H13/H13´), 1.15 (d, *J* = 11.0 Hz, 1H, $H12_B$), 0.83 (s, 3H, H13/H13´).

^{13}C-NMR (151 MHz, $CDCl_3$): δ (ppm) = 162.2 (d, *J* = 285.3 Hz, C2), 161.4 (d, *J* = 34.0 Hz, C3), 86.5 (C7), 78.3 (C6), 66.7 (C5/C5´), 66.5 (C5/C5´), 51.4 (C8), 47.2 (C4/C4´), 42.3 (C4/C4´), 39.6 (C10), 38.3 (C9), 35.3 (C11), 28.6 (C14), 27.1 (C13/C13´), 26.5 (C12), 24.1 (C13/C13´), carbon bearing boron was not observed.

^{19}F-NMR {^{1}H} (377 MHz, $CDCl_3$): δ (ppm) = -79.27.

^{11}B-NMR (128 MHz, $CDCl_3$): δ (ppm) = 28.96.

IR (ATR) $\tilde{\nu}$ = 2917 (m), 2864 (m), 1649 (s), 1462 (m), 1441 (m), 1406 (w), 1367 (s), 1281 (w), 1268 (m), 1249 (m), 1204 (m), 1113 (s), 1088 (s), 1076 (s), 1029 (s), 992 (w), 944 (m), 844 (m), 773 (m), 755 (w), 729 (m), 690 (w), 641 (m) cm^{-1}.

HR-ESI-MS (Orbitrap) exact mass calculated for $[M+Na]^+$ $(C_{17}H_{25}NO_4BFNa)^+$ requires 360.17560 m/z, found 360.17536 m/z.

ORD (DCM, c 1.00): $[\alpha]_D^{21}$= 15.262.

Synthesis of tert-butyl 4-((*E*)-2-fluoro-3-((3a*S*,4*S*,6*S*,7a*R*)-3a,5,5-trimethylhexahydro-4,6-methano benzo[*d*][1,3,2]dioxaborol-2-yl)acryloyl)piperazine-1-carboxylate (*E*-3)

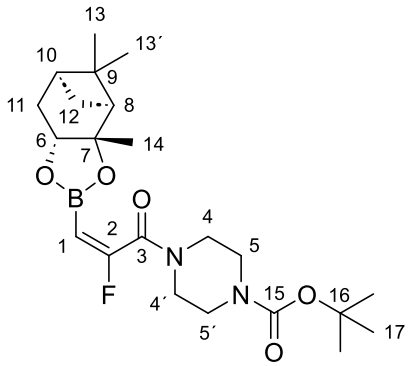

According to general Procedure C, **S21** (87.3 mg, 0.2 mmol, 1.0 eq.) was converted to ***E*-3** yielding a colourless gum (88% NMR-yield, 96:4 *E/Z*, 44.2 mg, 51%) after purification by column chromatography (30% EtOAc/*n*-pentane).

$\mathbf{R_f}$ = (SiO_2, 30% EtOAc/*n*-pentane) = 0.31

^{1}H-NMR (599 MHz, $CDCl_3$): δ (ppm) = 5.21 (d, *J* = 27.3 Hz, 1H, H1), 4.30 (dd, *J* = 8.8, 2.0 Hz, 1H, H6), 3.68 – 3.61 (m, 1H, H4/H4´), 3.58 – 3.37 (m, 7H, H4, H4´,H5, H5´), 2.33 – 2.26 (m, 1H, $H11_A$), 2.22 – 2.16 (m, 1H, $H12_A$), 1.99 (t, *J* = 5.5 Hz, 1H, H8), 1.91 – 1.86 (m, 1H, H10), 1.82 – 1.76 (m, 1H, $H11_B$), 1.45 (s, 9H, H17), 1.36 (d, *J* = 0.7 Hz, 3H, H14), 1.25 (s, 3H, H13/H13´), 1.13 (d, *J* = 11.0 Hz, 1H, $H12_B$), 0.80 (s, 3H, H13/H13´).

^{13}C-NMR (151 MHz, $CDCl_3$): δ (ppm) = 162.3 (d, *J* = 285.5 Hz, C2), 161.4 (d, *J* = 33.9 Hz, C3), 154.6 (C15), 86.4 (C7), 80.5 (C16), 78.2 (C6), 51.3 (C8), 46.6 (C5, C5´), 41.8 (C4, C4´), 39.5(C10), 38.2 (C9), 35.3 (C11), 28.5 (C14), 28.4 (C17), 27.1 (C13/C13´), 26.4 (C12), 24.0 (C13/C13´), carbon bearing boron was not observed.

^{19}F-NMR {^{1}H} (377 MHz, $CDCl_3$): δ (ppm) = -78.96.

^{11}B-NMR (128 MHz, $CDCl_3$): δ (ppm) = 29.06.

IR (ATR) $\tilde{\nu}$ = 2970 (m), 2921 (m), 1738 (w), 1698 (m), 1652 (m), 1461 (m), 1411 (m), 1365 (s), 1281 (m), 1253 (m), 1237 (m), 1200 (m), 1165 (s), 1124 (m), 1093 (s), 1076 (s), 1016 (s), 993 (m), 921 (m), 852 (m), 773 (m), 728 (s), 643 (m) cm^{-1}.

HR-ESI-MS (Orbitrap) exact mass calculated for $[M+Na]^+$ $(C_{22}H_{34}N_2O_5BFNa)^+$ requires 459.24410 m/z, found 459.24427 m/z

ORD (DCM, c 1.00): $[\alpha]_D^{22}$= 11.228.

Synthesis of (*E*)-2-fluoro-1-(pyrrolidin-1-yl)-3-((3a*S*,4*S*,6*S*,7a*R*)-3a,5,5-trimethylhexahydro-4,6-methanobenzo[*d*][1,3,2]dioxaborol-2-yl)prop-2-en-1-one (*E*-4)

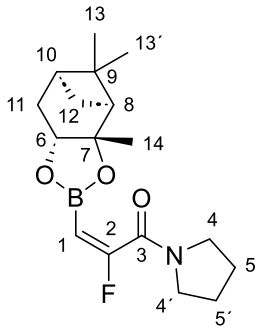

According to General Procedure C, **S22** (64.2 mg, 0.2 mmol, 1.0 eq.) was converted to ***E*-4** yielding a colourless oil (87% NMR-yield, 96:4 *E/Z*, 34.5 mg, 54%) after purification by column chromatography (10% acetone/*n*-pentane).

R_f = (SiO_2, 10% acetone/*n*-pentane) = 0.18

^{1}H-NMR (500 MHz, $CDCl_3$): δ (ppm) = 5.41 (d, *J* = 22.3 Hz, 1H, H1), 4.35 (dd, *J* = 8.7, 2.0 Hz, 1H, H6), 3.66 – 3.60 (m, 2H, H4/H4´), 3.59 – 3.53 (m, 2H, H4/H4´), 2.36 – 2.28 (m, 1H, $H11_A$), 2.25 – 2.17 (m, 1H, $H12_A$), 2.05 – 2.01 (m, 1H, H8), 1.95 – 1.83 (m, 6H, H10, $H11_B$, H5, H5´), 1.44 (s, 3H, H14), 1.37 (d, *J* = 10.8 Hz, 1H, $H12_B$), 1.28 (s, 3H, H13/H13´), 0.84 (s, 3H, H13/H13´).

^{13}C-NMR (151 MHz, $CDCl_3$): δ (ppm) = 160.9 (d, *J* = 33.3 Hz, C3), 159.4 (d, *J* = 285.7 Hz, C2), 85.8 (C7), 77.9 (C6), 51.7 (C8), 47.6 (d, *J* = 9.5 Hz, C4/C4´), 47.2 (C4/C4´), 39.8 (C10), 38.3 (C9), 35.6 (C11), 28.5 (C14), 27.3 (C13/C13´) 26.4 (C12), 26.3 (C5/C5´), 24.2 (C13/C13´), 23.8 (C5/C5´), carbon bearing boron was not observed.

^{19}F-NMR {^{1}H} (377 MHz, $CDCl_3$): δ (ppm) = -95.10.

^{11}B-NMR (128 MHz, $CDCl_3$): δ (ppm) = 26.82.

IR (ATR) $\tilde{\nu}$ = 2970 (m), 2916 (s), 1739 (w), 1644 (m), 1611 (s), 1444 (s), 1366 (s), 1337 (s), 1279 (m), 1252 (m), 1188 (w), 1171 (w), 1093 (s), 1078 (s), 1030 (m), 1022 (m), 992 (m), 951 (m), 910 (m), 847 (m), 776 (w), 756 (m), 719 (s), 641 (w), 621 (w) cm^{-1}.

HR-ESI-MS (Orbitrap) exact mass calculated for $[M+Na]^+$ $(C_{17}H_{25}NO_3BFNa)^+$ requires 344.18069 m/z, found 344.18075 m/z

ORD (DCM, c 1.00): $[\alpha]_D^{22}$= 13.512.

Synthesis of methyl ((*E*)-2-fluoro-3-((3a*S*,4*S*,6*S*,7a*R*)-3a,5,5-trimethylhexahydro-4,6-methanobenzo [*d*][1,3,2]dioxaborol-2-yl)acryloyl)-L-prolinate (*E*-5)

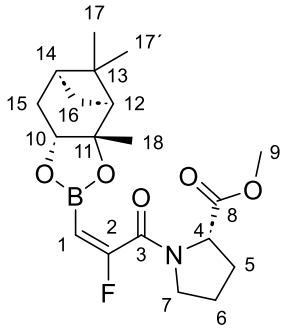

According to General Procedure C, **S23** (75.8 mg, 0.2 mmol, 1.0 eq.) was converted to ***E*-5** yielding a colourless gum (94% NMR-yield, 95:5 *E/Z*, 34.1 mg, 45%, 60:40 mixture of rotamers) after purification by column chromatography (20% EtOAc/DCM).

$\mathbf{R}_f$ = (SiO_2, 20% EtOAc/*n*-pentane) = 0.43

^{1}H-NMR (500 MHz, $CDCl_3$): δ (ppm) = 5.40 (d, *J* = 23.3 Hz, 1H, H1, minor rotamer), 5.38 (d, *J* = 23.8 Hz, 1H, H1, major rotamer), 4.69 (ddd, *J* = 8.5, 5.5, 2.9 Hz, 1H, H4, minor rotamer), 4.54 (dd, *J* = 8.3, 4.1 Hz, 1H, H4, major rotamer), 4.39 (dd, *J* = 8.8, 1.9 Hz, 1H, H10, minor rotamer), 4.35 (dd, *J* = 8.8, 2.1 Hz, 1H, H10, major rotamer), 3.84 – 3.62 (m, 2H, H7), 3.72 (s, 3H, H9, minor rotamer), 3.69 (s, 3H, H9, major rotamer), 2.36 – 2.12 (m, 3H, $H5_A$, $H15_A$, $H16_A$), 2.07 – 1.81 (m, 6H, $H5_B$, H6, H12, H14, $H15_B$), 1.45 (s, 3H, H18, minor rotamer), 1.40 (s, 3H, H18, major rotamer), 1.39 – 1.31 (m, 1H, $H16_B$), 1.28 (s, 3H, H17/H17´, minor rotamer), 1.27 (s, 3H, H17/H17´, major rotamer), 0.85 (s, 3H, H17/H17´, minor rotamer), 0.83 (s, 3H, H17/H17´, major rotamer).

^{13}C-NMR (126 MHz, $CDCl_3$): δ (ppm) = 172.3 (C8, minor rotamer), 172.1 (C8, major rotamer), 160.7 (d, *J* = 33.9 Hz, C3), 159.4 (d, *J* = 284.8 Hz, C2, major rotamer), 158.5 (d, *J* = 283.6 Hz, C2, minor rotamer), 86.2 (C11), 78.1 (C10), 60.1 (d, *J* = 10.4 Hz, C4, minor rotamer), 60.0 (C4, major rotamer), 52.6 (C9, minor rotamer), 52.3 (C9, major rotamer), 51.6 (C12), 48.1 (C7, minor rotamer) 47.9 (d, *J* = 9.9 Hz, C7, major rotamer), 39.7 (C14), 38.3 (C13), 35.4 (C15, minor rotamer), 35.4 (C15, major rotamer), 28.8 (C5), 28.4 (C18, minor rotamer), 28.3 (C18, major rotamer), 27.2 (C17/C17´, minor rotamer), 27.2 (C17/C17´, major rotamer), 26.4 (C16, minor rotamer), 26.4 (C16, major rotamer), 25.1 (d, *J* = 3.3 Hz, C6), 24.2 (C17/C17´, minor rotamer), 24.2 (C17/C17´, major rotamer), carbon bearing boron was not observed.

^{19}F-NMR {^{1}H} (377 MHz, $CDCl_3$): δ (ppm) = -93.60 (major rotamer), -96.63 (minor rotamer).

^{11}B-NMR (128 MHz, $CDCl_3$): δ (ppm) = 28.61.

IR (ATR) $\tilde{\nu}$ = 2917 (m), 1746 (s), 1619 (s), 1435 (s), 1365 (m), 1339 (s), 1279 (m), 1234 (m), 1208 (m), 1171 (m), 1102 (s), 1078 (s), 1030 (s), 1022 (m), 992 (w), 911 (w), 827 (w), 758 (m), 722 (s) cm^{-1}.

HR-ESI-MS (Orbitrap) exact mass calculated for $[M+Na]^+$ ($C_{19}H_{27}NO_5BFNa)^+$ requires 402.18620 m/z, found 402.18515 m/z

ORD (DCM, c 0.50): $[\alpha]_D^{22}$= - 51.626.

Synthesis of (*E*)-*N*-benzyl-2-fluoro-N-methyl-3-((3a*S*,4*S*,6*S*,7a*R*)-3a,5,5-trimethylhexahydro-4,6-methanobenzo[*d*][1,3,2]dioxaborol-2-yl)acrylamide (*E*-6)

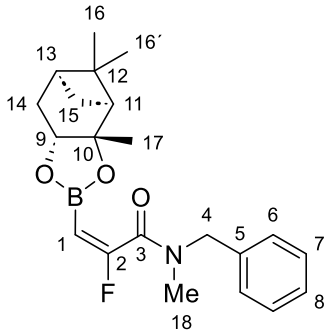

According to General Procedure C, **S24** (68.8 mg, 0.2 mmol, 1.0 eq.) was converted to ***E*-6** yielding a colourless oil (90% NMR-yield, 92:8 *E/Z*, 37.8 mg, 55%, 61:39 mixture of rotamers) after purification by column chromatography (20% EtOAc/*n*-pentane).

$\mathbf{R}_f$ = (SiO_2, 20% EtOAc/*n*-pentane) = 0.43

^{1}H-NMR (500 MHz, $CDCl_3$): δ (ppm) = 7.36 – 7.27 (m, 5H, H6, H7, H8), 5.31 (d, *J* = 26.1 Hz, 1H, H1, minor rotamer), 5.27 (d, *J* = 27.5 Hz, 1H, H1 major rotamer), 4.67 – 4.55 (m, 2H, H4), 4.37 (dd, *J* = 8.8, 2.0 Hz, 1H, H9, minor rotamer), 4.32 (dd, *J* = 8.8, 2.0 Hz, 1H, H9, major rotamer), 2.96 (d, *J* = 2.1 Hz, 3H, H18, major rotamer), 2.87 (d, *J* = 1.1 Hz, 3H, H18, minor rotamer), 2.41 – 2.27 (m, 1H, $H14_A$), 2.25 – 2.16 (m, 1H, $H15_A$), 2.06 (t, *J* = 5.5 Hz, 1H, H11, minor rotamer), 2.02 (t, *J* = 5.6 Hz, 1H, H11, major rotamer), 1.97 – 1.78 (m, 2H, H13, $H14_B$), 1.43 (s, 3H, H17, minor rotamer), 1.39 (s, 3H, H17, major rotamer), 1.30 (s, 3H, H16/H16´, minor rotamer), 1.29 (s, 3H, H16/H16´, major rotamer), 1.24 (d, *J* = 11.0 Hz, 1H, $H15_B$, minor rotamer), 1.19 (d, *J* = 11.0 Hz, 1H, $H15_B$, major rotamer), 0.86 (s, 3H, H16/H16´, minor rotamer), 0.84 (s, 3H, H16/H16´, major rotamer).

^{13}C-NMR (126 MHz, $CDCl_3$): δ (ppm) = 163.0 (d, *J* = 34.6 Hz, C3), 162.7 (d, *J* = 284.9 Hz, C2, major rotamer), 162.6 (d, *J* = 285.0 Hz, C2, minor rotamer), 136.1 (C5, major rotamer), 135.8 (C5, minor rotamer), 128.7 (C8, major rotamer), 128.5 (C6/C7, major rotamer), 128.4 (C6/C7, major rotamer), 127.9 (C8, minor rotamer), 127.6 (C6/C7, minor rotamer), 127.5 (C6/C7, minor rotamer), 86.4 (C10, major rotamer), 86.3 (C10, minor rotamer), 78.3 (C9, minor rotamer), 78.1 (C9, major rotamer), 54.5 (C4, minor rotamer), 51.4 (C11 minor rotamer), 51.4 (C11, major rotamer), 50.6 (C4, major rotamer), 39.5 (C13, minor rotamer), 39.5 (C13, major rotamer), 38.2 (C12, minor rotamer), 38.1 (C12, major rotamer), 35.4 (C14), 35.3 (C18, major rotamer), 32.5 (C18, minor rotamer), 28.6 (C17, minor rotamer), 28.5 (C17, major rotamer), 27.2 (C16/C16´), 26.5 (C15), 24.1 (C16/C16´), carbon bearing boron was not observed.

^{19}F-NMR {^{1}H} (377 MHz, $CDCl_3$): δ (ppm) = -78.88 (minor rotamer), -79.50 (major rotamer).

^{11}B-NMR (128 MHz, $CDCl_3$): δ (ppm) = 28.69.

IR (ATR) $\tilde{\nu}$ = 2921 (m), 1738 (m), 1649 (s), 1489 (w), 1452 (m), 1411 (m), 1366 (s), 1283 (m), 1205 (w), 1116 (s), 1068 (s), 1030 (s), 992 (w), 941 (w), 923 (w), 852 (m), 775 (w), 755 (w), 732 (m), 699 (s), 641 (w) cm^{-1}.

HR-ESI-MS (Orbitrap) exact mass calculated for $[M+Na]^+$ $(C_{21}H_{27}NO_3BFNa)^+$ requires 394.19641 m/z, found 394.19653 m/z

ORD (DCM, c 1.00): $[\alpha]_D^{22}$= 11.793.

Synthesis of (*E*)-*N*-benzyl-2-fluoro-3-((3a*S*,4*S*,6*S*,7a*R*)-3a,5,5-trimethylhexahydro-4,6-methano benzo[*d*][1,3,2]dioxaborol-2-yl)acrylamide (*E*-7)

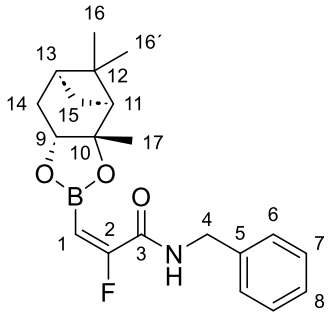

According to General Procedure C, **S25** (68.8 mg, 0.2 mmol, 1.0 eq.) was converted to ***E*-7** yielding a colourless oil (68% NMR-yield, 75:25 *E/Z*, 7.5 mg, 11%) after purification by column chromatography (0-10% EtOAc/*n*-pentane).

R*f* = (SiO_2, 10% acetone/*n*-pentane) = 0.21

^{1}H-NMR (500 MHz, $CDCl_3$): δ (ppm) = 7.37 – 7.33 (m, 2H, H7), 7.32 – 7.27 (m, 3H, H6, H8), 6.79 (s, 1H, N*H*), 5.45 (d, *J* = 24.1 Hz, 1H, H1), 4.52 (d, *J* = 5.6 Hz, 2H, H4), 4.43 (dd, *J* = 8.8, 2.0 Hz, 1H, H9), 2.40 – 2.31 (m, 1H, $H14_A$), 2.22 (dtd, *J* = 10.9, 6.2, 2.4 Hz, 1H, $H15_A$), 2.03 (dd, *J* = 6.1, 4.8 Hz, 1H, H11), 1.95 – 1.87 (m, 2H, H13, $H14_B$), 1.48 (s, 3H, H17), 1.40 (d, *J* = 11.0 Hz, 1H, $H15_B$), 1.30 (s, 3H, H16/H16´), 0.86 (s, 3H, H16/H16´).

^{13}C-NMR (151 MHz, $CDCl_3$): δ (ppm) = 160.0 (d, *J* = 34.1 Hz, C3), 156.9 (d, *J* = 278.8 Hz, C2), 137.2 (C5), 129.0 (C7), 128.2 (C6), 128.0 (C8), 86.8 (C10), 78.4 (C9), 51.5 (C11), 43.9 (C4), 39.7 (C13), 38.4 (C12), 35.3 (C14), 28.4 (C17), 27.2 (C16/C16´), 26.4 (C15), 24.2 (C16/C16´), carbon bearing boron was not observed.

^{19}F-NMR {^{1}H} (377 MHz, $CDCl_3$): δ (ppm) = -102.37.

^{11}B-NMR (128 MHz, $CDCl_3$): δ (ppm) = 28.91.

IR (ATR) $\tilde{\nu}$ = 3329 (w), 2920 (m), 1739 (w), 1656 (s), 1527 (s), 1454 (m), 1366 (s), 1342 (s), 1279 (m), 1237 (m), 1208 (m), 1121 (w), 1096 (s), 1078 (s), 1029 (s), 990 (m), 938 (w), 913 (w), 844 (m), 753 (w), 720 (s), 697 (s), 660 (w) cm^{-1}.

HR-ESI-MS (Orbitrap) exact mass calculated for $[M+Na]^+$ $(C_{20}H_{25}NO_3BFNa)^+$ requires 380.18074 m/z, found 380.18121 m/z.

ORD (DCM, c 1.00): $[\alpha]_D^{22}$= 21.432.

Synthesis of benzyl (*E*)-2-fluoro-3-((3a*S*,4*S*,6*S*,7a*R*)-3a,5,5-trimethylhexahydro-4,6-methanobenzo [*d*][1,3,2]dioxaborol-2-yl)acrylate (*E*-8)

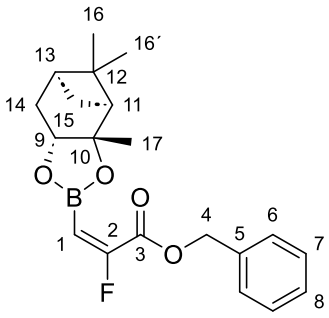

According to General Procedure C, **S26** (71.6 mg, 0.2 mmol, 1.0 eq.) was converted to ***E*-8** yielding a colourless oil (85% NMR-yield, 87:13 *E/Z*, 48.7 mg, 68%) after purification by column chromatography (5% acetone/*n*-pentane).

R*f* = (SiO_2, 10% EtOAc/*n*-pentane) = 0.59

^{1}H-NMR (500 MHz, $CDCl_3$): δ (ppm) = 7.43 – 7.31 (m, 5H, H6, H7, H8), 5.62 (d, *J* = 22.8 Hz, 1H, H1), 5.27 (q, *J* = 12.3 Hz, 2H, H4), 4.32 (dd, *J* = 8.8, 2.1 Hz, 1H, H9), 2.34 (ddt, *J* = 14.5, 8.9, 2.5 Hz, 1H, $H14_A$), 2.22 (dtd, *J* = 10.9, 6.1, 2.2 Hz, 1H, $H15_A$), 2.06 (dd, *J* = 6.0, 5.0 Hz, 1H, H11), 1.95 – 1.84 (m, 2H, H13, $H14_B$), 1.37 (s, 3H, H17), 1.33 (d, *J* = 11.0 Hz, 1H, $H15_B$), 1.30 (s, 3H, H16/H16´), 0.84 (s, 3H, H16/H16´).

^{13}C-NMR (126 MHz, $CDCl_3$): δ (ppm) = 161.0 (d, *J* = 38.4 Hz, C3), 154.2 (d, *J* = 275.6 Hz, C2), 134.9 (C5), 128.8 (C7), 128.7 (C8), 128.6 (C6), 86.8 (C10), 78.5 (C9), 67.8 (C4), 51.4 (C11), 39.6 (C13), 38.4 (C12), 35.2 (C14), 28.3 (C17), 27.2 (C16/C16´), 26.4 (C15), 24.2 (C16/C16´), carbon bearing boron was not observed.

^{19}F-NMR {^{1}H} (377 MHz, $CDCl_3$): δ (ppm) = -99.84.

^{11}B-NMR (192 MHz, $CDCl_3$): δ (ppm) = 29.19.

IR (ATR) $\tilde{\nu}$ = 2921 (m), 1728 (s), 1660 (s), 1455 (w), 1378 (s), 1356 (s), 1343 (s), 1323 (s), 1280 (m), 1240 (m), 1177 (s), 1108 (s); 1078 (m), 1056 (w), 1029 (m), 990 (m), 951 (w), 940 (w), 924 (w), 851 (m), 776 (m), 752 (m), 726 (s), 696 (s) cm^{-1}.

HR-ESI-MS (Orbitrap) exact mass calculated for $[M+Na]^+$ $(C_{20}H_{24}O_4BFNa)^+$ requires 381.16439 m/z, found 381,16452 m/z

ORD (DCM, c 1.00): $[\alpha]_D^{20}$= 8.969.

Synthesis of tert-butyl (*E*)-2-fluoro-3-((3a*S*,4*S*,6*S*,7a*R*)-3a,5,5-trimethylhexahydro-4,6-methanobenzo[*d*][1,3,2]dioxaborol-2-yl)acrylate (*E*-9)

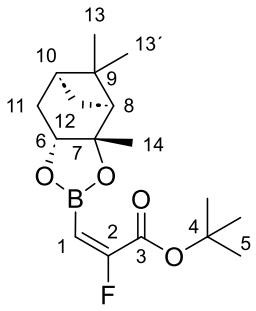

According to general Procedure C, **S27** (64.8 mg, 0.2 mmol, 1.0 eq.) was converted to ***E*-9** yielding a colourless solid (75% NMR-yield, 83:17 *E/Z*, 29.0 mg, 45%) after purification by column chromatography (5% Et_2O/*n*-pentane).

R_f = (SiO_2, 5% Et_2O/*n*-pentane) = 0.42

^{1}H-NMR (599 MHz, $CDCl_3$): δ (ppm) = 5.46 (d, *J* = 22.6 Hz, 1H, H1), 4.41 (dd, *J* = 8.8, 1.9 Hz, 1H, H6), 2.41 – 2.30 (m, 1H, $H11_A$), 2.27 – 2.19 (m, 1H, $H12_A$), 2.09 – 2.04 (m, 1H, H8), 1.96 – 1.89 (m, 2H, H10, $H11_B$), 1.52 (s, 9H, H5), 1.46 (s, 3H, H14), 1.37 (d, *J* = 10.9 Hz, 1H, $H12_B$), 1.30 (s, 3H, H13/H13´), 0.86 (s, 3H, H13/H13´).

^{13}C-NMR (151 MHz, $CDCl_3$): δ (ppm) = 160.3 (d, *J* = 36.1 Hz, C3), 155.8 (d, *J* = 280.3 Hz, C2), 86.6 (C7), 83.5 (C4), 78.4 (C6), 51.5 (C8), 39.7 (C10), 38.4 (C9), 35.3 (C11), 28.4 (C14), 28.1 (C5), 27.2 (C13/C13´), 26.3 (C12), 24.2 (C13/C13´), carbon bearing boron was not observed.

^{19}F-NMR {^{1}H} (377 MHz, $CDCl_3$): δ (ppm) = -98.67.

^{11}B-NMR (128 MHz, $CDCl_3$): δ (ppm) = 29.43.

IR (ATR) $\tilde{\nu}$ = 2990 (w), 2970 (m), 2934 (m), 1716 (s), 1657 (s), 1477 (w), 1370 (m), 1339 (s), 1316 (m), 1284 (m), 1254 (m), 1241 (m), 1210 (m), 1151 (s), 1103 (s), 1076 (m), 1029 (m), 1022 (m), 1009 (m), 990 (m), 953 (w), 938 (m), 914 (m), 842 (s), 779 m), 723 (s), 620 (m) cm^{-1}.

HR-ESI-MS (Orbitrap) exact mass calculated for $[M+Na]^+$ $(C_{17}H_{26}O_4BFNa)^+$ requires 347.18035 m/z, found 347.18063 m/z

ORD (DCM, c 0.50): $[\alpha]_D^{21}$= 22.293.

M.p.: 45.4 – 46.2 °C.

Synthesis of benzyl (*Z*)-3-((3a*S*,4*S*,6*S*,7a*R*)-3a,5,5-trimethylhexahydro-4,6-methanobenzo[*d*][1,3,2] dioxaborol-2-yl)acrylate (S34)

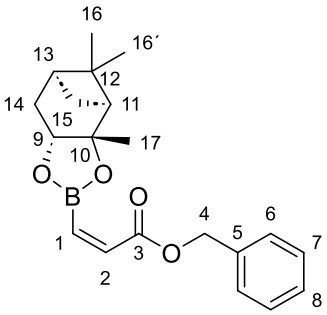

According to General Procedure C, **S28** (62.7 mg, 0.2 mmol, 1.0 eq.) was converted to **S34** yielding a colourless oil (93:7 *Z/E*, 38.6 mg, 62% containing less than 5% starting isomer) after purification by column chromatography (10% acetone/*n*-pentane).

R_f = (SiO_2, 10% acetone/*n*-pentane) = 0.71

^{1}H-NMR (500 MHz, $CDCl_3$): δ (ppm) = 7.39 – 7.30 (m, 5H, H6, H7, H8), 6.41 (d, *J* = 13.4 Hz, 1H, H2), 6.36 (d, *J* = 13.5 Hz, 1H, H1), 5.20 (dd, *J* = 12.5, 6.2 Hz, 2H, H4), 4.39 (dd, *J* = 8.8, 2.0 Hz, 1H, H9), 2.41 – 2.32 (m, 1H, $H14_A$), 2.24 (dtd, *J* = 10.8, 6.0, 2.2 Hz, 1H, $H15_A$), 2.08 (dd, *J* = 6.0, 4.9 Hz, 1H, H11), 1.99 – 1.89 (m, 2H, H13, $H14_B$), 1.45 (s, 3H, H17), 1.44 (d, *J* = 10.9 Hz, 1H, $H15_B$), 1.31 (s, 3H, H16/H16´), 0.86 (s, 3H, H16/H16´).

^{13}C-NMR (151 MHz, $CDCl_3$): δ (ppm) = 167.1 (C3), 135.8 (C5), 133.4 (C2), 128.7 (C7), 128.5 (C6), 128.4 (C8), 86.7 (C10), 78.4 (C9), 66.8 (C4), 51.5 (C11), 39.7 (C13), 38.4 (C12), 35.3 (C14), 28.4 (C17), 27.2 (C16/C16´), 26.4 (C15), 24.2 (C16/C16´), carbon bearing boron was not observed.

^{11}B-NMR (128 MHz, $CDCl_3$): δ (ppm) = 29.75.

IR (ATR) $\tilde{\nu}$ = 2930 (m), 2363), 1719 (s), 1627 (m), 1475 (w), 1455 (w), 1409 (s), 1367 (s), 1340 (w), 1289 (s), 1237 (m), 1194 (s), 1155 (s), 1122 (m), 1078 (m), 1029 (m), 990 (w), 938 (w), 924 (w), 836 (w), 817 (w), 749 (m), 697 (m) cm^{-1}.

HR-ESI-MS (Orbitrap) exact mass calculated for $[M+Na]^+$ $(C_{20}H_{25}O_4BNa)^+$ requires 363.17418 m/z, found 363.17386 m/z

ORD (DCM, c 1.00): $[\alpha]_D^{21}$= 34.274.

Synthesis of benzyl (*E*)-2-chloro-3-((3a*S*,4*S*,6*S*,7a*R*)-3a,5,5-trimethylhexahydro-4,6-methanobenzo [*d*][1,3,2]dioxaborol-2-yl)acrylate (S35)

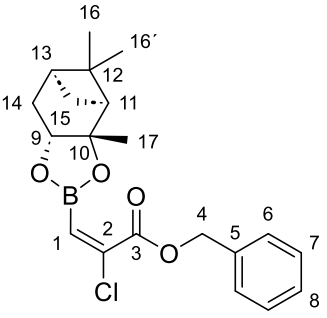

According to General Procedure C, **S29** (74.8 mg, 0.2 mmol, 1.0 eq.) was converted to **S35** yielding a colourless oil (79% NMR-yield, 80:20 *E/Z*, 41.9 mg, 56%) after purification by column chromatography (2.5% acetone/*n*-pentane).

R_f = (SiO_2, 10% acetone/*n*-pentane) = 0.71

^{1}H-NMR (500 MHz, $CDCl_3$): δ (ppm) = 7.42 – 7.28 (m, 5H, H6, H7, H8), 6.42 (s, 1H, H1), 5.32 – 5.17 (m, 2H, H4), 4.32 (dd, *J* = 8.8, 2.1 Hz, 1H, H9), 2.36 – 2.29 (m, 1H, $H14_A$), 2.26 – 2.18 (m, 1H, $H15_A$), 2.05 – 2.03 (m, 1H, H11), 1.95 – 1.84 (m, 2H, H13, $H14_B$), 1.38 (s, 3H, H17), 1.32 (d, *J* = 11.0 Hz, 1H, $H15_B$), 1.30 (s, 3H, H16/H16´), 0.84 (s, 3H, H16/H16´).

^{13}C-NMR (126 MHz, $CDCl_3$): δ (ppm) = 163.1 (C3), 135.0 (C5), 134.0 (C2), 128.7 (C7), 128.6 (C8), 128.3 (C6), 86.8 (C10), 78.5 (C9), 68.4 (C4), 51.4 (C11), 39.6 (C13), 38.4 (C12), 35.2 (C14), 28.2 (C17), 27.2 (C16/C16´), 26.3 (C15), 24.1 (C16/C16´), carbon bearing boron was not observed.

^{11}B-NMR (128 MHz, $CDCl_3$): δ (ppm) = 29.06.

IR (ATR) $\tilde{\nu}$ = 2970 (m), 2921 (m), 1739 (s), 1716 (s), 1613 (m), 1455 (m), 1375 (s), 1334 (s), 1279 (s), 1238 (m), 1191 (s), 1121 (m), 1078 (m), 1029 (m), 1022 (m), 1009 (m), 990 (m), 938 (w), 923 (w), 907 (w), 795 (w), 750 (m), 695 (s), 686 (s) cm^{-1}.

HR-ESI-MS (Orbitrap) exact mass calculated for $[M+Na]^+$ $(C_{20}H_{24}NO_4BClNa)^+$ requires 397.13520 m/z, found 397.13494 m/z

ORD (DCM, c 1.00): $[\alpha]_D^{22}$= 11.650.

2.3.2 Photochemical Isomerisation of tetrasubstituted *α*-Halo-*β*-borylacrylates

Synthesis of (*Z*)-2-fluoro-*N*-methoxy-*N*-methyl-3-((3a*S*,4*S*,6*S*,7a*R*)-3a,5,5-trimethylhexahydro-4,6-methanobenzo[*d*][1,3,2]dioxaborol-2-yl)but-2-enamide (*Z*-10)

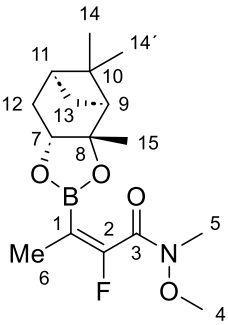

According to General Procedure C, **S30** (65.0 mg, 0.2 mmol, 1.0 eq.) was converted to ***Z*-10** yielding a colourless oil (94% NMR-yield, 93:7 *Z/E*, 45.8 mg, 70% containing less than 3% starting isomer) after purification by column chromatography (5% acetone/*n*-pentane).

R_f = (SiO_2, 5% acetone/*n*-pentane) = 0.27

^{1}H-NMR (500 MHz, $CDCl_3$): δ (ppm) = 4.34 (dd, *J* = 8.8, 2.1 Hz, 1H, H7), 3.73 (s, 3H, H4), 3.28 (s, 3H, H5), 2.36 – 2.29 (m, 1H, $H12_A$), 2.23 – 2.17 (m, 1H, $H13_A$), 2.03 (dd, *J* = 6.0, 5.0 Hz, 1H, H9), 1.93 – 1.84 (m, 2H, H11, $H12_B$), 1.82 (d, *J* = 2.6 Hz, 3H, H6), 1.42 (s, 3H, H15), 1.35 (d, *J* = 10.7 Hz, 1H, $H13_B$), 1.28 (s, 3H, H14/H14´), 0.84 (s, 3H, H14/H14´).

^{13}C-NMR (126 MHz, $CDCl_3$): δ (ppm) = 163.2 (C3), 152.3 (d, *J* = 279.7 Hz, C2), 85.7 (C8), 78.0 (C7), 62.1 (C4), 51.8 (C9), 39.8 (C11), 38.3 (C10), 35.7 (C12), 34.3 (C5), 28.5 (C15), 27.3 (C14/C14´), 26.4 (C13), 24.2 (C14/C14´), 11.6 (d, *J* = 8.5 Hz, C6), carbon bearing boron was not observed.

^{19}F-NMR {^{1}H} (470 MHz, $CDCl_3$): δ (ppm) = -111.73.

^{11}B-NMR (128 MHz, $CDCl_3$): δ (ppm) = 27.09.

IR (ATR) $\tilde{\nu}$ = 2982 (w), 2923 (m), 2871 (w), 2359 (w), 1656 (s), 1446 (w), 1418 (w), 1378 (s), 1340 (m), 1314 (w), 1281 (m), 1240 (m), 1168 (w), 1120 (m), 1078 (s), 1056 (w), 1029 (w), 983 (m), 938 (w), 924 (w), 880 (w), 832 (w), 746 (s), 669 (m) cm^{-1}.

HR-ESI-MS (Orbitrap) exact mass calculated for $[M+Na]^+$ $(C_{16}H_{25}NO_4BFNa)^+$ requires 348.17559 m/z, found 348.17501 m/z

ORD (DCM, c 1.00): $[\alpha]_D^{20}$= 17.529.

Synthesis of benzyl (*Z*)-2-fluoro-3-((3a*S*,4*S*,6*S*,7a*R*)-3a,5,5-trimethylhexahydro-4,6-methano benzo[*d*][1,3,2]dioxaborol-2-yl)but-2-enoate (*Z*-11)

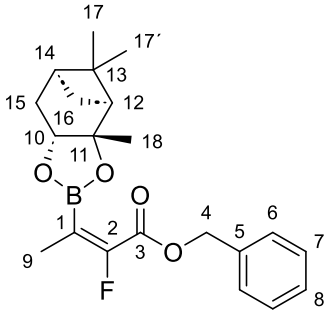

According to General Procedure C, **S31** (74.4 mg, 0.2 mmol, 1.0 eq.) was converted to ***Z*-11** yielding a colourless oil (97% NMR-yield, 98:2 *Z/E,* 45.4 mg, 61%) after purification by column chromatography (3% acetone/*n*-pentane).

R*f* = (SiO_2, 3% acetone/*n*-pentane) = 0.56

^{1}H-NMR (500 MHz, $CDCl_3$): δ (ppm) = 7.39 – 7.31 (m, 5H, H6, H7, H8), 5.32 – 5.19 (m, 2H, H4), 4.36 (dd, *J* = 8.8, 2.0 Hz, 1H, H10), 2.41 – 2.32 (m, 1H, $H15_A$), 2.29 – 2.21 (m, 1H, $H16_A$), 2.08 (dd, *J* = 6.0, 4.9 Hz, 1H, H12), 1.96 – 1.89 (m, 2H, H14, $H15_B$), 1.88 (d, *J* = 2.7 Hz, 3H, H9), 1.41 (s, 3H, H18), 1.35 (d, *J* = 10.9 Hz, 1H, $H16_B$), 1.31 (s, 3H, H17/H17´), 0.86 (s, 3H, H17/H17´).

^{13}C-NMR (126 MHz, $CDCl_3$): δ (ppm) = 161.7 (d, *J* = 36.5 Hz, C3), 148.4 (d, *J* = 270.7 Hz, C2), 135.1 (C5), 128.7 (C7), 128.6 (C8), 128.5 (C6), 86.5 (C11), 78.4 (C10), 67.5 (C4), 51.5 (C12), 39.6 (C14), 38.4 (C13), 35.3 (C15), 28.2 (C18), 27.2 (C17/C17´), 26.3 (C16), 24.1 (C17/C17´), 12.8 (d, *J* = 8.6 Hz, C9), carbon bearing boron was not observed.

^{19}F-NMR {^{1}H} (470 MHz, $CDCl_3$): δ (ppm) = -118.39.

^{11}B-NMR (128 MHz, $CDCl_3$): δ (ppm) = 30.04.

IR (ATR) $\tilde{\nu}$ = 2985 (w), 2921 (m), 2871 (w), 2359 (w), 1719 (s), 1662 (s), 1456 (w), 1378 (s), 1303 (s), 1281 (w), 1240 (m), 1210 (w), 1165 (m), 1122 (w), 1101 (s), 1078 (m), 1047 (m), 1029 (m), 1022 (m), 991 (w), 938 (w), 924 (w), 772 (w), 753 (m), 729 (m), 697 (m), 669 (m), 647 (w) cm^{-1}.

HR-ESI-MS (Orbitrap) exact mass calculated for $[M+Na]^+$ $(C_{21}H_{26}O_4BFNa)^+$ requires 395.18042 m/z, found 395.17980 m/z

ORD (DCM, c 1.00): $[\alpha]_D^{21}$= 23.842.

Synthesis of (*Z*)-2-fluoro-*N*-methoxy-*N*-methyl-3-(4,4,5,5-tetramethyl-1,3,2-dioxaborolan-2-yl)but-2-enamide (*Z*-12)

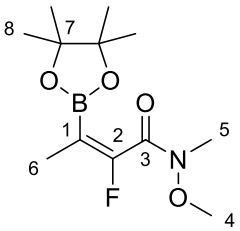

According to General Procedure C, **S32** (54.6 mg, 0.2 mmol, 1.0 eq.) was converted to ***Z*-12** yielding a colourless oil (92% NMR-yield, 94:6 *Z/E*, 32.9 mg, 60% containing less than 5% starting isomer) after purification by column chromatography (5% acetone/*n*-pentane).

R*f* = (SiO_2, 5% acetone/*n*-pentane) = 0.34

^{1}H-NMR (500 MHz, $CDCl_3$): δ (ppm) = 3.72 (s, 3H, H4), 3.28 (s, 3H, H5), 1.79 (d, *J* = 2.4 Hz, 3H, H6), 1.24 (s, 12H, H8).

^{13}C-NMR (126 MHz, $CDCl_3$): δ (ppm) = 163.6 (C3), 150.3 (d, *J* = 279.7 Hz, C2), 82.7 (C7), 62.3 (C4), 34.6 (C5), 25.0 (C8), 11.4 (d, *J* = 7.2 Hz, C6), carbon bearing boron was not observed.

^{19}F-NMR {^{1}H} (470 MHz, $CDCl_3$): δ (ppm) = -118.99.

^{11}B-NMR (128 MHz, $CDCl_3$): δ (ppm) = 23.68.

IR (ATR) $\tilde{\nu}$ = 2979 (w), 2939 (w), 2342 (w), 1653 (s), 1462 (w), 1444 (m), 1416 (m), 1372 (s), 1319 (m), 1270 (m), 1214 (w), 1147 (m), 1113 (m), 1076 (s), 1986 (w), 964 (m), 919 (w), 858 (m), 844 (w), 736 (s), 702 (M), 689 (m), 672 (m), 634 (w) cm^{-1}.

HR-ESI-MS (Orbitrap) exact mass calculated for $[M+Na]^+$ $(C_{12}H_{21}NO_4BFNa)^+$ requires 296.14422 m/z, found 296.14343 m/z

Synthesis of (*Z*)-2-fluoro-1-morpholino-3-(4,4,5,5-tetramethyl-1,3,2-dioxaborolan-2-yl)but-2-en-1-one (*Z*-13)

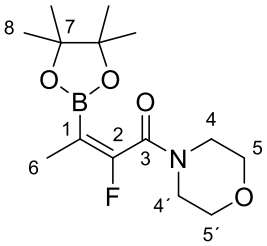

According to General Procedure C, **S33** (60.0 mg, 0.2 mmol, 1.0 eq.) was converted to ***Z*-13** yielding a colourless oil (95% NMR-yield, 94:6 *Z/E*, 46.1 mg, 77%) after purification by column chromatography (10% acetone/*n*-pentane).

R_f = (SiO_2, 10% acetone/*n*-pentane) = 0.55

^{1}H-NMR (500 MHz, $CDCl_3$): δ (ppm) = 3.85 – 3.80 (m, 2H, H4/H4´), 3.77 – 3.68 (m, 6H, H4/H4´, H5, H5´), 1.82 (d, *J* = 2.0 Hz, 3H, H6), 1.22 (s, 12H, H8).

^{13}C-NMR (126 MHz, $CDCl_3$): δ (ppm) = 164.5 (d, *J* = 26.7 Hz, C3), 148.3 (d, *J* = 279.1 Hz, C2), 81.3 (C7), 66.6 (C5/C5´), 66.4(C5/C5´), 46.8 (d, *J* = 13.9 Hz, C4/C4´), 45.3 (C4/C4´), 25.2 (C8), 11.1 (d, *J* = 4.9 Hz, C6), carbon bearing boron was not observed.

^{19}F-NMR {^{1}H} (470 MHz, $CDCl_3$): δ (ppm) = -123.00.

^{11}B-NMR (128 MHz, $CDCl_3$): δ (ppm) = 16.53.

IR (ATR) $\tilde{\nu}$ = 2975 (w), 2927 (w), 2860 (w), 2360 (w), 1649 (s), 1609 (s), 1459 (m), 1439 (m), 1372 (m), 1320 (w), 1281 (w), 1258 (m), 1189 (w), 1155 (m), 1116 (s), 1088 (s), 1060 (s), 1019 (m), 1009 (m), 966 (m), 901 (w), 849 (m), 812 (m), 735 (s), 689 (m), 640 (m) cm^{-1}.

HR-ESI-MS (Orbitrap) exact mass calculated for $[M+Na]^+$ $(C_{14}H_{23}NO_4BFNa)^+$ requires 322.15990 m/z, found 322.15951 m/z

Synthesis of benzyl (*Z*)-2-fluoro-3-(4,4,5,5-tetramethyl-1,3,2-dioxaborolan-2-yl)but-2-enoate (*Z*-14)

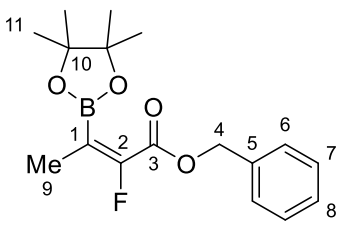

According to General Procedure C, ***E*-14** (64.0 mg, 0.2 mmol, 1.0 eq.) was converted to ***Z*-14** yielding a colourless solid (89% NMR-yield, 97:3 *Z/E*, 41.1 mg, 64%) after purification by column chromatography (5 - 10% acetone/*n*-pentane).

R_f = (SiO_2, 10% acetone/*n*-pentane) = 0.50

^{1}H-NMR (599 MHz, $CDCl_3$): δ (ppm) = 7.37 – 7.31 (m, 5H, H6, H7, H8), 5.26 (s, 2H, H4), 1.84 (d, *J* = 2.7 Hz, 3H, H9), 1.33 (s, 12H, H11).

^{13}C-NMR (151 MHz, $CDCl_3$): δ (ppm) = 161.8 (d, *J* = 36.2 Hz, C3), 148.3 (d, *J* = 271.4 Hz, C2), 135.2 (C5), 128.7 (C7), 128.5 (C8), 128.4 (C6), 84.4 (C10), 67.4 (C4), 24.8 (C11), 12.6 (d, *J* = 8.7 Hz, C9), carbon bearing boron was not observed.

^{19}F-NMR {^{1}H} (470 MHz, $CDCl_3$): δ (ppm) = -118.87.

^{11}B-NMR (128 MHz, $CDCl_3$): δ (ppm) = 30.01.

IR (ATR) $\tilde{\nu}$ = 2985 (w), 2360 (w), 1712 (m), 1665 (m), 1455 (w), 1390 (m), 1373 (m), 1355 (m), 1320 (m), 1299 (s), 1214 (w), 1167 (m), 1142 (m), 1092 (s), 1039 (m), 1029 (m), 966 (m), 947 (m), 918 (m), 900 (m), 858 (m), 845 (m), 792 (m), 775 (m), 752 (s), 723 (m), 693 (s), 660 (s) cm^{-1}.

HR-ESI-MS (Orbitrap) exact mass calculated for $[M+Na]^+$ $(C_{17}H_{22}O_4BFNa)^+$ requires 343.14905 m/z, found 343.14836 m/z

M.p.: 42.6 – 43.4 °C

2.4 Synthesis of fluorinated Polyenes

Synthesis of 3-bromo-5,5,8,8-tetramethyl-5,6,7,8-tetrahydronaphthalen-2-ol (S36)

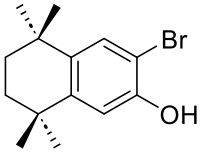

According to a general procedure of Hsieh *et al.*[7] 2-bromophenol (1.73 g, 10.0 mmol, 1.0 eq.) and 2,5-dichloro-2,5-dimethylhexane (1.92 g, 10.5 mmol, 1.05 eq.) were dissolved in dry DCM (35 mL) and the solution was cooled to 0 °C. After that $AlCl_3$ (4.00 g, 30.0 mmol, 3.0 eq.) was added slowly over the course of 30 min and the reaction was stirred for 18 h at 0 °C. The reaction was quenched using 1 M aq. HCl (15 mL) and the precipitate was filtered off. The organics were extracted using DCM and the combined organic layers were washed with brine, dried over $MgSO_4$ and evaporated under reduced pressure. The crude residue was purified by column chromatography (SiO_2, 5% EtOAc/*n*-pentane) and the desired product was obtained as colourless solid (1.63 g, 58%).

^{1}H-NMR (500 MHz, $CDCl_3$): δ (ppm) = 7.34 (s, 1H), 6.95 (s, 1H), 5.25 (s, 1H), 1.65 (s, 4H), 1.25 (s, 6H), 1.24 (s, 6H).

Analytical data in accordance with literature.[5]

Synthesis of 6-bromo-1,1,4,4-tetramethyl-7-propoxy-1,2,3,4-tetrahydronaphthalene (15)

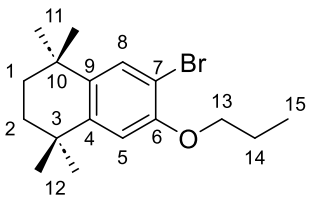

According to a modified procedure of Bourguet *et al.*[8] **S36** (1.63 g, 5.75 mmol, 1.0 eq.) was dissolved in dry DMF (6.9 mL) and the solution was cooled to 0 °C. NaH (0.35 g, 8.625 mmol, 1.5 eq., 60% in mineral oil) was added and the mixture was stirred for 30 min before the addition of iodopropane (0.85 mL, 1.47 g, 8.625 mmol, 1.5 eq.) in DMF (1.1 mL). The reaction was warmed up to ambient temperature and was stirred for another 30 min. After the reaction was quenched by the addition of water, the organics were extracted with Et_2O and the combined organic layers were washed with brine and dried over $MgSO_4$. The solvent was removed

under reduced pressure and the crude residue was purified by column chromatography (SiO_2, 5% EtOAc/*n*-pentane) to obtain the desired product as colourless solid (1.50 g, 80%).

R_f = (SiO_2, 5% EtOAc/*n*-pentane) = 0.84

^{1}H-NMR (500 MHz, $CDCl_3$): δ (ppm) = 7.42 (s, 1H, H5/H8), 6.79 (s, 1H, H5/H8), 3.97 (t, *J* = 6.4 Hz, 2H, H13), 1.85 (dtd, *J* = 13.8, 7.4, 6.4 Hz, 2H, H14), 1.71 – 1.62 (m, 4H, H1, H2), 1.27 (s, 6H, H11/H12), 1.25 (s, 6H, H11/H12), 1.08 (t, *J* = 7.4 Hz, 3H, H15).

^{13}C-NMR (126 MHz, $CDCl_3$): δ (ppm) = 153.2 (C-*Ar*), 145.5 (C-*Ar*), 139.0 (C-*Ar*), 131.3(C-*Ar*), 111.5 (C-*Ar*), 109.9 (C-*Ar*), 70.8 (C13), 35.1 (C1/C2), 35.1 (C1/C2), 34.6 (C3/C10), 34.0 (C3/C10), 32.0 (C11/C12), 31.9 (C11/C12), 22.8 (C14), 10.8 (C15).

IR (ATR) $\tilde{\nu}$ = 2956 (m), 2927 (m), 2861 (m), 1739 (w), 1593 (m), 1489 (s), 1469 (m), 1456 (m), 1388 (m), 1372 (m), 1363 (s), 1313 (m), 1252 (s), 1185 (m), 1079 (s), 1066 (s), 1002 (s), 963 (m), 882 (m), 877 (m), 794 (m), 716 (m), 663 (w), 623 (w) cm^{-1}

HR-ESI-MS (Orbitrap) exact mass calculated for $[M+Na]^+$ $(C_{17}H_{25}OBrNa)^+$ requires 349.09621 m/z, found 349.09584 m/z

M.p.: 35.2 – 38.8 °C

Synthesis of (*E*)-2-fluoro-*N*-methoxy-*N*-methyl-3-(5,5,8,8-tetramethyl-3-propoxy-5,6,7,8-tetrahydro naphthalen-2-yl)but-2-enamide (16)

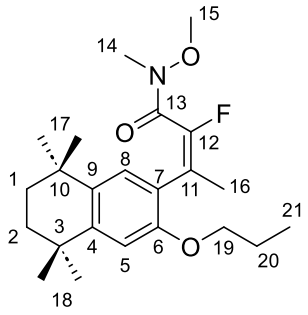

An oven dried Schlenk-tube was equipped with **15** (260.1 mg, 0.8 mmol, 1.0 eq.), ***Z*-10** (520.0 mg, 1.6 mmol, 2.0 eq.), $Pd(OAc)_2$ (8.9 mg, 0.04 mmol, 5 mol%), SPhos (32.8 mg, 0.08 mmol, 10 mol%) and K_3PO_4 (509.5 mg, 2.4 mmol, 3.0 eq.). The tube was purged with argon three times before the addition of dry DMF (3.2 mL) and H_2O (73 µL, 4.0 mmol, 5.0 eq.). The reaction was stirred for 16 h at 80 °C before it was cooled to ambient temperature, filtered over celite and eluted with EtOAc. The organic layer was washed with 5% aq. LiCl, dried over $MgSO_4$ and the solvent was evaporated under reduced pressure. The crude residue was purified by column chromatography (SiO_2, 15% EtOAc/*n*-pentane) and the desired product was obtained as yellow solid (232.4 mg, 74%).

R_f = (SiO_2, 15% EtOAc/*n*-pentane) = 0.45

^{1}H-NMR (500 MHz, $CDCl_3$): δ (ppm) = 7.01 (s, 1H, H8), 6.72 (s, 1H, H5), 3.90 (t, *J* = 6.5 Hz, 2H, H19), 3.54 (br s, 3H, H15), 3.00 (s, 3H, H14), 2.06 (d, *J* = 4.1 Hz, 3H, H16), 1.83 – 1.74 (m, 2H, H20), 1.66 – 1.60 (m, 4H, H1, H2), 1.25 (s, 6H, H17/H18), 1.20 (s, 6H, H17/H18), 1.03 (t, *J* = 7.4 Hz, 3H, H21).

^{13}C-NMR (101 MHz, $CDCl_3$): δ (ppm) = 154.5 (C6), 146.6 (d, *J* = 256.4 Hz, C12), 146.3 (C4/C9), 136.7 (C4/C9), 128.5 (C8), 123.5 (C11), 121.0 (d, *J* = 16.1 Hz, C7), 109.2 (C5), 69.7 (C19), 61.4 (C15), 35.3 (C1/C2), 35.2 (C1/C2), 34.6 (C3/C10), 33.7 (C3/C10), 32.0 (C17/C18), 32.0 (C17/C18), 22.8 (C20), 15.4 (d, *J* = 5.2 Hz, C16), 10.9 (C21), *carbonyl carbon and C14 were not observed.*

^{19}F-NMR (377 MHz, $CDCl_3$): δ (ppm) = -118.03.

IR (ATR) $\tilde{\nu}$ = 2957 (m), 2929 (m), 2873 (w), 2360 (w), 1739 (w), 1593 (m), 1489 (s), 1471 (s), 1455 (m), 1388 (m), 1372 (s), 1363 (s), 1313 (m), 1273 (w), 1251 (s), 1188 (w), 1079 (s), 1066 (s), 1047 (w), 1023 (w), 1002 (s), 963 (w), 882 (m), 851 (w), 841 (w), 795 (w), 717 (m), 684 (w), 623 (w) cm^{-1}.

HR-ESI-MS (Orbitrap) exact mass calculated for $[M+Na]^+$ $(C_{23}H_{34}NO_3FNa)^+$ requires 414.24149 m/z, found 414.24126 m/z

M.p.: 115.1 – 116.8 °C

Synthesis of (*E*)-2-fluoro-3-(5,5,8,8-tetramethyl-3-propoxy-5,6,7,8-tetrahydronaphthalen-2-yl)but-2-enal (17)

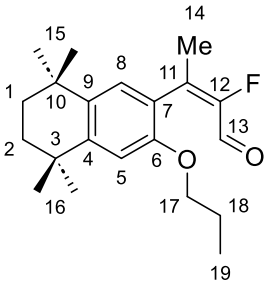

An oven dried Schlenk-tube was equipped with **16** (293.6 mg, 0.75 mmol, 1.0 eq.). The tube was purged with argon three times before the addition of dry THF (2.3 mL). The solution was cooled to -78 °C and DIBAL-H (0.66 mL, 0.79 mmol, 1.05 eq., 1.2 M solution in toluene) was added dropwise. The reaction was stirred for 1 h before the addition of sat. aq. NH_4Cl. The organics were extracted with EtOAc and the combined organic layers were washed with brine. The solvent was removed under reduced pressure and the crude residue was purified by column chromatography (SiO_2, 5% EtOAc/*n*-pentane) to obtain the desired product as colourless solid (167.1 mg, 67%).

$\mathbf{R}_f$ = (SiO_2, 5% EtOAc/*n*-pentane) = 0.49

^{1}H-NMR (599 MHz, $CDCl_3$): δ (ppm) = 9.19 (d, *J* = 19.6 Hz, 1H, H13), 7.02 (s, 1H, H8), 6.80 (s, 1H, H5), 3.91 (t, *J* = 6.4 Hz, 2H, H17), 2.23 (dd, *J* = 3.8, 0.6 Hz, 3H, H14), 1.80 – 1.72 (m, 2H, H18), 1.68 (dtt, *J* = 8.1, 5.5, 2.8 Hz, 4H, H1, H2), 1.30 (s, 6H, H15/H16), 1.23 (s, 6H, H15/H16), 1.00 (dd, *J* = 7.7, 7.1 Hz, 3H, H19).

^{13}C-NMR (151 MHz, $CDCl_3$): δ (ppm) = 183.3 (d, *J* = 22.5 Hz, C13), 154.3 (d, *J* = 3.9 Hz, C6), 153.5 (d, *J* = 253.6 Hz, C12), 147.8 (C4/C9), 138.9 (d, *J* = 15.9 Hz, C11), 137.0 (C4/C9), 129.5 (d, *J* = 2.4 Hz, C8), 121.8 (d, *J* = 5.8 Hz, C7), 109.7 (C5), 69.9 (C17), 35.1 (C1/C2), 35.1 (C1/C2), 34.8 (C3/C10), 33.7 (C3/C10), 32.0 (C15/C16), 31.9 (C15/C16), 22.7 (C18), 17.7 (d, *J* = 4.9 Hz, C14), 10.8 (C19).

^{19}F-NMR (564 MHz, $CDCl_3$): δ (ppm) = -133.03

IR (ATR) $\tilde{\nu}$ = 2957 (m), 2881 (w), 2359 (w), 2332 (w), 1738 (m), 1682 (s), 1630 (m), 1604 (m), 1499 (m), 1474 (m), 1395 (m), 1380 (m), 1364 (m), 1319 (m), 1291 (w), 1250 (s), 1227 (s), 1180 (m), 1046 (m), 1029 (m), 1004 (m), 903 (m), 867 (m), 839 (m), 791 (m), 778 (m), 713 (m), 695 (m) cm^{-1}.

HR-ESI-MS (Orbitrap) exact mass calculated for $[M+Na]^+$ $(C_{21}H_{29}O_2FNa)^+$ requires 355.20438 m/z, found 355.20395 m/z.

M.p.: 100.5 – 102.2 °C

Synthesis of 2-((1*E*,3*E*)-3-fluoro-4-(5,5,8,8-tetramethyl-3-propoxy-5,6,7,8-tetrahydro-naphthalen-2-yl)penta-1,3-dien-1-yl)-4,4,5,5-tetramethyl-1,3,2-dioxaborolane (18)

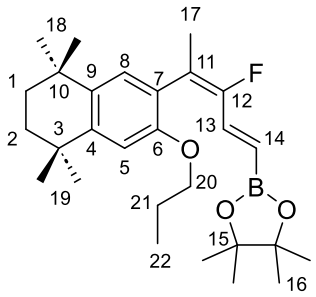

According to a modified procedure of Morken *et al.*[9] an oven dried Schlenk tube was equipped with 2,2,6,6-tetramethylpiperidine (95.4 mg, 0.675 mmol, 1.5 eq.) and dry THF (1.8 mL) was added under argon atmosphere. The solution was cooled to 0 °C and *n*-BuLi (338 μL, 0.54 mmol, 1.2 eq., 1.6 M solution in hexane) was added. The mixture was stirred for 5 min before the addition of bis(4,4,5,5-tetramethyl-1,3,2-dioxaborolan-2-yl)methane (144.7 mg, 0.54 mmol, 1.2 eq.). After stirring for additional 5 min, the solution was cooled to -78 °C and **17** (149.5 mg, 0.45 mmol, 1.0 eq.) was added. The reaction was stirred for 4 h, warmed up top ambient temperature and quenched by the addition of EtOH. The solvent was removed under reduced pressure and the crude residue was purified by column chromatography (SiO_2, 5% EtOAc/*n*-pentane) to obtain the desired product as yellow solid (140.9 mg, 68%).

R_f = (SiO_2, 5% EtOAc/*n*-pentane) = 0.54

^{1}H-NMR (500 MHz, $CDCl_3$): δ (ppm) = 6.96 (s, 1H, H8), 6.88 (dd, *J* = 27.1, 18.1 Hz, 1H, H13), 6.74 (s, 1H, H5), 5.81 (dd, *J* = 18.0, 0.7 Hz, 1H, H14), 3.87 (t, *J* = 6.4 Hz, 2H, H20), 2.10 (d, *J* = 3.7 Hz, 3H, H17), 1.80 – 1.72 (m, 2H, H21), 1.67 (q, *J* = 1.0 Hz, 4H, H1, H2), 1.30 (s, 6H, H18/H19), 1.24 (s, 6H, H18/H19), 1.21 (s, 12H, H16), 1.00 (t, *J* = 7.4 Hz, 3H, H22).

^{13}C-NMR (126 MHz, $CDCl_3$): δ (ppm) = 154.9 (C6), 154.6 (d, *J* = 245.1 Hz, C12), 145.8 (C4/C9) , 139.2 (d, *J* = 25.9 Hz, C13), 136.4 (C4/C9), 130.3 (C8), 125.0 (d, *J* = 8.1 Hz, C7), 122.0 (d, *J* = 21.7 Hz, C11), 109.6 (C5), 83.3 (C15), 69.8 (C20), 35.4 (C1/C2), 35.3 (C1/C2), 34.6 (C3/C10), 33.8 (C3/C10), 31.9 (C18), 31.9 (C19), 24.9 (C16), 22.9 (C21), 16.2 (d, *J* = 6.9 Hz, C17), 11.0 (C22), carbon bearing boron was not observed.

^{19}F-NMR {^{1}H} (377 MHz, $CDCl_3$): δ (ppm) = -124.36.

^{11}B-NMR (128 MHz, $CDCl_3$): δ (ppm) = 30.94.

IR (ATR) $\tilde{\nu}$ = 2962 (m), 2917 (m), 2866 (w), 2345 (w), 1739 (m), 1603 (m), 1501 (m), 1372 (m), 1363 (m), 1346 (s), 1323 (m), 1271 (w), 1243 (m), 1220 (s), 1144 (s), 970 (m), 849 (m), 669 (m) cm^{-1}

HR-ESI-MS (Orbitrap) exact mass calculated for $[M+Na]^+$ ($C_{28}H_{42}O_3BFNa)^+$ requires 479.31083 m/z, found 479.31045 m/z.

M.p.: 126.4 – 127.8 °C

Synthesis of 6-((2*E*,4*E*)-5-bromo-3-fluoropenta-2,4-dien-2-yl)-1,1,4,4-tetramethyl-7-propoxy-1,2,3,4-tetrahydronaphthalene (19)

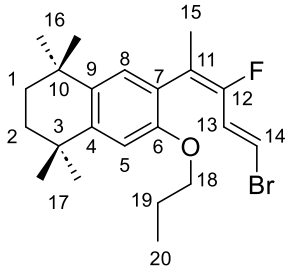

An oven dried Schlenk tube was equipped with **18** (114.1 mg, 0.25 mmol, 1.0 eq.) and dry THF (3.7 mL) was added under argon atmosphere. The solution was cooled to -78 °C, NaOMe (28.4 mg, 0.525 mmol, 2.1 eq.) was added and the mixture was stirred for 25 min before the addition of NBS (46.7 mg, 0.263 mmol, 1.05 eq.). The reaction was stirred overnight while slowly warming up to ambient temperature before it was quenched by the addition of sat. aq. $Na_2S_2O_3$. The organics were extracted using EtOAc and the combined organic layers were dried over $MgSO_4$. The solvent was evaporated under reduced pressure and the crude residue was purified by column chromatography (5% EtOAc/*n*-pentane) to give the desired product as colourless solid (74.5 mg, 73%).

R_f = (SiO_2, *n*-pentane) = 0.41

^{1}H-NMR (599 MHz, Acetone-d_6): δ (ppm) = 7.04 (s, 1H, H8), 6.95 (s, 1H, H5), 6.63 (d, *J* = 13.6 Hz, 1H, H14), 6.48 (dd, *J* = 26.5, 13.6 Hz, 1H, H13), 3.97 (t, *J* = 6.4 Hz, 2H, H18), 1.99 (dd, *J* = 3.6, 0.6 Hz, 3H, H15), 1.75 (tdd, *J* = 7.4, 6.3, 1.1 Hz, 2H, H19), 1.71 – 1.69 (m, 4H, H1, H2), 1.30 (s, 6H, H16/H17), 1.26 (s, 6H, H16/H17), 1.00 (t, *J* = 7.4 Hz, 3H, H20).

^{13}C-NMR (101 MHz, Acetone-d_6): δ (ppm) = 155.2 (d, *J* = 2.6 Hz, C6), 152.8 (d, *J* = 242.7 Hz, C12), 146.9 (C4/C9), 137.3 (C4/C9), 129.7 (d, *J* = 2.2 Hz, C8), 128.6 (d, *J* = 23.7 Hz, C14), 125.1 (d, *J* = 8.0 Hz, C7), 119.5 (d, *J* = 19.6 Hz, C11), 110.7 (C5), 107.1 (d, *J* = 4.7 Hz, C13), 70.3 (C18), 35.9 (C1/C2), 35.8 (C1/C2) 35.2 (C3/C10), 34.2 (C3/C10), 32.1 (C16/C17), 32.0 (C16/C17), 23.4(C19), 16.2 (d, *J* = 6.6 Hz, C15), 11.0 (C20).

^{19}F-NMR {^{1}H} (564 MHz, Acetone-d_6): δ (ppm) = -125.62.

IR (ATR) $\tilde{\nu}$ = 2987 (w), 2919 (w), 2360 (m), 1741 (s), 1726 (s), 1375 (m), 1365 (m), 1217 (s), 1079 (s), 1052 (s), 931 (w), 913 (w), 851 (w), 779 (s), 694 (w), 669 (w), 650 (m) cm^{-1}

HR-ESI-MS (Orbitrap) exact mass calculated for $[M+Na]^+$ $(C_{22}H_{30}OBrFNa)^+$ requires 431.13563 m/z, found 431.13590 m/z.

M.p.: 123.0 – 125.7 °C

Synthesis of ethyl (*E*)-3-(4,4,5,5-tetramethyl-1,3,2-dioxaborolan-2-yl)acrylate (*E*-20)

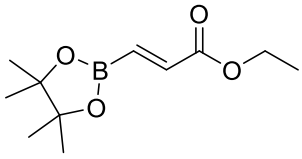

According to modified procedure from Yun *et al*.[10] an oven-dried Schlenk-tube was equipped with CuCl (24.0 mg, 0.24 mmol, 3 mol%), Xantphos (138.9 mg, 0.24 mmol, 3 mol%) and NaO*t*Bu (46.0 mg, 0.48 mmol, 6 mol%) before it was purged with argon. Dry THF (8 mL) was added and the mixture was stirred for 30 min at ambient temperature. Bis(pinacolato)diboron (2.2 g, 8.8 mmol, 1.1 eq.) was added and the reaction was stirred for 10 min. After that ethyl propiolate (809 µL, 8.0 mmol, 1.0 eq.) and MeOH (650 µL, 512.0 mg, 16.0 mmol, 2.0 eq.) were added and the reaction was stirred for additional 16 h. The mixture was filtered through celite and the solvent was removed under reduced pressure. The crude residue was purified by column

chromatography (SiO_2, 10% - 20%/ EtOAc/*n*-pentane) to give the desired product as colourless oil (1.35 g, 75%).

^{1}H NMR (400 MHz, CDCl3): δ (ppm) = 6.77 (d, *J* = 18.2 Hz, 1H), 6.62 (d, *J* = 18.2 Hz, 1H), 4.21 (q, *J* = 7.1 Hz, 2H), 1.30 – 1.26 (m, 15H).

Analytical data in agreement with literature.[10]

Synthesis of ethyl (2*E*,4*E*,6*E*)-6-fluoro-7-(5,5,8,8-tetramethyl-3-propoxy-5,6,7,8-tetrahydronapht halen-2-yl)octa-2,4,6-trienoate (21)

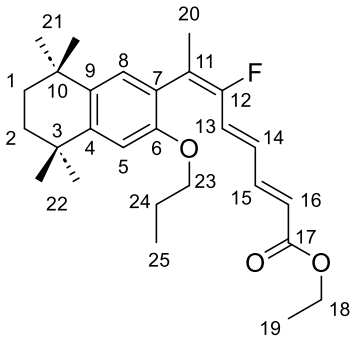

An oven-dried Schlenk tube was equipped with **19** (20.5 mg, 0.05 mmol, 1.0 eq.), ***E*-20** (22.6 mg, 0.1 mmol, 2.0 eq.), Pd(dppf)Cl_2*DCM (2.0 mg, 0.0025 mmol, 5 mol%) and K_3PO_4 (31.8 mg, 0.15 mmol, 3.0 eq.). The tube was sealed and purged with argon three times before the addition of DMF (0.2 mL) and H_2O (4.6 µL, 4.6 mg, 0.25 mmol, 5.0 eq.). The reaction was stirred at ambient temperature for 16 h before it was diluted with EtOAc and filtered over Celite. The organic layer was washed with 5% aq. LiCl, dried over $MgSO_4$ and the solvent was evaporated under reduced pressure. The crude residue was purified by column chromatography (SiO_2, 2.5% EtOAc/*n*-pentane) to give the desired product as yellowish sticky oil (9.6 mg, 45%).

R_f = (SiO_2, 2.5% EtOAc/*n*-pentane) = 0.32.

^{1}H-NMR (500 MHz, $CDCl_3$): δ (ppm) = 7.17 (dd, *J* = 14.9, 11.0 Hz, 1H, H15), 6.95 (s, 1H, H8), 6.77 (s, 1H, H5), 6.51 (dd, *J* = 15.2, 11.4 Hz, 1H, H14), 6.31 (dd, *J* = 27.1, 15.2 Hz, 1H, H13), 5.91 (d, *J* = 15.2 Hz, 1H, H16), 4.17 (q, *J* = 7.1 Hz, 2H, H18), 3.88 (t, *J* = 6.4 Hz, 2H, H23), 2.10 (d, *J* = 3.5 Hz, 3H, H20), 1.81 – 1.71 (m, 2H, H24), 1.68 (d, *J* = 3.0 Hz, 4H, H1, H2), 1.31 (s, 6H, H21/H22), 1.27 (t, *J* = 7.1 Hz, 3H, H19), 1.23 (s, 6H, H21/H22), 0.99 (t, *J* = 7.4 Hz, 3H, H25).

^{13}C-NMR (126 MHz, $CDCl_3$): δ (ppm) = 167.2 (C17), 154.6 (C6), 153.6 (d, *J* = 236.2 Hz, C12), 146.2 (C4/C9), 144.1 (C15), 136.8 (C4/C9), 130.1 (d, *J* = 24.1 Hz, C13), 129.3 (C8), 125.1 (d, *J* = 7.9 Hz, C7), 124.9 (d, *J* = 4.6 Hz, C14), 123.0 (d, *J* = 21.0 Hz, C11), 121.7 (C16), 109.8 (C5), 69.9 (C23), 60.4 (C18), 35.3 (C1/C2), 35.2 (C1/C2), 34.7 (C3/C10), 33.8 (C3/C10), 32.0 (C21), 32.0 (C22), 22.8 (C24), 16.7 (d, *J* = 6.5 Hz, C20), 14.4 (C19), 10.9 (C25).

^{19}F-NMR {^{1}H} (564 MHz, $CDCl_3$): δ (ppm) = -123.88.

IR (ATR) $\tilde{\nu}$ = 2962 (m), 2861 (w), 2359 (w), 1712 (s), 1616 (s), 1501 (m), 1464 (w), 1390 (w), 1365 (w), 1332 (w), 1317 (w), 1233 (s), 1180 (m), 1139 (s), 1080 (w), 1047 (w), 997 (m), 905 (w), 878 (w), 938 (w) cm^{-1}

HR-ESI-MS (Orbitrap) exact mass calculated for $[M+Na]^+$ $(C_{27}H_{37}O_3F_1Na)^+$ requires 451.26189 m/z, found 451.26202 m/z.

Synthesis of tert-butyl (2*Z*,4*E*,6*E*)-2,6-difluoro-7-(5,5,8,8-tetramethyl-3-propoxy-5,6,7,8-tetrahydro-naphthalen-2-yl)octa-2,4,6-trienoate (22)

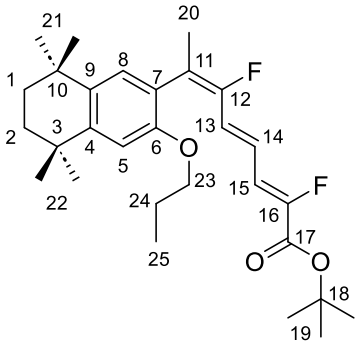

An oven-dried Schlenk tube was equipped with **19** (40.9 mg, 0.1 mmol, 1.0 eq.), ***E*-9** (97.3 mg, 0.3 mmol, 3.0 eq.), Pd(dppf)Cl_2*DCM (4.1 mg, 0.005 mmol, 5 mol%) and K_3PO_4 (63.7 mg, 0.3 mmol, 3.0 eq.). The tube was sealed and purged with argon three times before the addition of DMF (0.4 mL) and H_2O (9.1 µL, 9.1 mg, 0.5 mmol, 5.0 eq.). The reaction was stirred at ambient temperature for 16 h before it was diluted with EtOAc and filtered over Celite. The organic layer was washed with 5% aq. LiCl, dried over $MgSO_4$ and the solvent was evaporated under reduced pressure. The crude residue was purified by column chromatography (SiO_2, 2.5% EtOAc/*n*-pentane) to give the desired product as yellowish sticky oil (37.0 mg, 78%).

$\mathbf{R_f}$ = (SiO_2, 5% EtOAc/*n*-pentane) = 0.65

^{1}H-NMR (599 MHz, $CDCl_3$): δ (ppm) = 6.96 (s, 1H, H8), 6.78 (s, 1H, H5), 6.70 (dd, *J* = 15.4, 11.7 Hz, 1H, H14), 6.42 (dd, *J* = 30.6, 11.7 Hz, 1H, H15), 6.26 (dd, *J* = 27.0, 15.4 Hz, 1H, H13), 3.88 (t, *J* = 6.4 Hz, 2H, H23), 2.10 (d, *J* = 3.5 Hz, 3H, H20), 1.81 – 1.71 (m, 2H, H24), 1.71 – 1.64 (m, 4H, H1, H2), 1.50 (s, 9H, H19), 1.31 (s, 6H, H21/H22), 1.24 (s, 6H, H21/H22), 1.00 (t, *J* = 7.4 Hz, 3H, H25).

^{13}C-NMR (151 MHz, $CDCl_3$): δ (ppm) = 160.2 (d, *J* = 32.8 Hz, C17), 154.6 (d, *J* = 2.5 Hz, C6), 153.8 (dd, *J* = 244.1, 2.6 Hz, C12), 147.8 (d, *J* = 267.6 Hz, C16), 146.1 (C4/C9), 136.8 (C4/C9), 129.4 (d, *J* = 2.0 Hz, C8), 128.0 (dd, *J* = 24.2, 4.6 Hz, C13), 125.2 (d, *J* = 7.9 Hz, C7), 122.5 (dd, *J* = 21.1, 3.3 Hz, C11), 117.9 (d, *J* = 4.9 Hz, C14), 117.5 (d, *J* = 9.6 Hz, C15), 109.9 (C5), 82.7 (C18), 70.0 (C23), 35.3 (C1/C2), 35.2 (C1/C2), 34.7 (C3/C10), 33.8 (C3/C10), 31.9 (C21), 31.9 (C22), 28.2 (C19), 22.8 (C24), 16.6 (d, *J* = 6.6 Hz, C20), 10.9 (C25).

^{19}F-NMR {^{1}H} (564 MHz, $CDCl_3$): δ (ppm) = -123.71 (d, *J* = 2.6 Hz, F12), -126.51 (d, *J* = 2.5 Hz, F16).

^{19}F-NMR (564 MHz, $CDCl_3$): δ (ppm) = -123.71 (dd, *J* = 27.0, 2.7 Hz, F12), -126.51 (dd, *J* = 30.6, 2.5 Hz, F16).

IR (ATR) $\tilde{\nu}$ = 2962 (m), 2932 (m), 2359 (w), 1725 (m), 1621 (w), 1499 (m), 1472 (w), 1458 (w), 1393 (w), 1370 (w), 1362 (s), 1293 (m), 1241 (s), 1219 (s), 1157 (s), 1098 (s), 1049 (m), 1007 (m), 969 (m), 905 (m), 848 (m), 763 (m), 733 (s), 683 (w), 650 (w) cm^{-1}

HR-ESI-MS (Orbitrap) exact mass calculated for $[M+Na]^+$ $(C_{29}H_{40}O_3F_2Na)^+$ requires 497.28377 m/z, found 497.28374 m/z.

3. X-ray Crystallographic Analysis

X-Ray diffraction: Data sets for compounds **16**, ***E*-9**, ***Z*-14** and ***E*-14** were collected with a Bruker D8 Venture Photon III Diffractometer. Programs used: data collection: *APEX4* Version 2021.4-0 [1] (Bruker AXS Inc., **2021**); cell refinement: *SAINT* Version 8.40B (Bruker AXS Inc., **2021**); data reduction: *SAINT* Version 8.40B (Bruker AXS Inc., **2021**); absorption correction, *SADABS* Version 2016/2 (Bruker AXS Inc., **2021**); structure solution *SHELXT*-Version 2018-3 [2] (Sheldrick, G. M. *Acta Cryst.,* **2015**, *A71*, 3-8); structure refinement *SHELXL*- Version 2018-3 [3] (Sheldrick, G. M. *Acta Cryst.,* **2015**, *C71* (1), 3-8) and graphics, *XP* [4] (Version 5.1, Bruker AXS Inc., Madison, Wisconsin, USA, **1998**). *R*-values are given for observed reflections, and *w*R^2 values are given for all reflections.
Exceptions and special features: For compound **16** the *i*Pr group is disordered over two positions. Several restraints (SADI, SAME, ISOR and SIMU) were used in order to improve refinement stability.

X-ray crystal structure analysis of 16 (gil10501): A colorless, needle-like specimen of $C_{23}H_{34}FNO_3$, approximate dimensions 0.068 mm x 0.072 mm x 0.301 mm, was used for the X-ray crystallographic analysis. The X-ray intensity data were measured on a single crystal diffractometer Bruker D8 Venture Photon III system equipped with a micro focus tube Cu ImS (CuKα, λ = 1.54178 Å) and a MX mirror monochromator. A total of 1486 frames were collected. The total exposure time was 19.87 hours. The frames were integrated with the Bruker SAINT software package using a wide-frame algorithm. The integration of the data using a monoclinic unit cell yielded a total of 40528 reflections to a maximum θ angle of 66.79° (0.84 Å resolution), of which 3845 were independent (average redundancy 10.540, completeness = 99.8%, R_{int} = 8.14%, R_{sig} = 3.19%) and 3068 (79.79%) were greater than 2σ(F^2). The final cell constants of a = 9.0806(2) Å, b = 24.4552(6) Å, c = 10.0629(2) Å, β = 103.1880(10)°, volume = 2175.71(8) $Å^3$, are based upon the refinement of the XYZ-centroids of 9939 reflections above 20 σ(I) with 7.229° < 2θ < 133.4°. Data were corrected for absorption effects using the Multi-Scan method (SADABS). The ratio of minimum to maximum apparent transmission was 0.836. The calculated minimum and maximum transmission coefficients (based on crystal size) are 0.8230 and 0.9560. The structure was solved and refined using the Bruker SHELXTL Software Package, using the space group $P2_1/n$, with Z = 4 for the formula unit, $C_{23}H_{34}FNO_3$. The final anisotropic full-matrix least-squares refinement on F^2 with 290 variables converged at R1 = 4.09%, for the observed data and wR2 = 9.97% for all data. The goodness-of-fit was 1.046. The largest peak in the final difference electron density synthesis was 0.269 $e^-/Å^3$ and the largest hole was -0.232 $e^-/Å^3$ with an RMS deviation of 0.045 $e^-/Å^3$. On the basis of the final model, the calculated density was 1.195 g/cm^3 and F(000), 848 e^-. CCDC Nr.: 2250334.

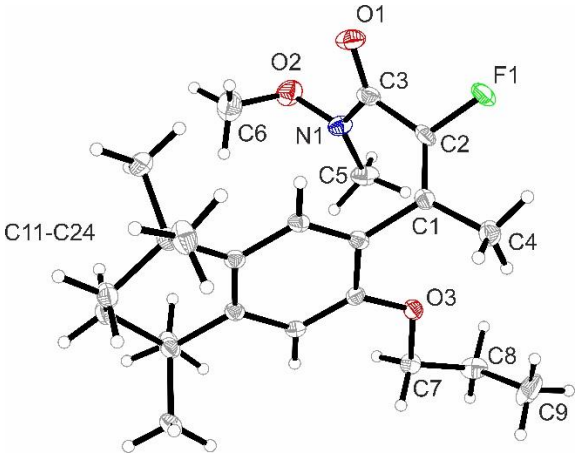

Figure S2: Crystal structure of compound **16**.
Thermal ellipsoids are shown at 50% probability.

X-ray crystal structure analysis of *E*-9 (gil10402): A colorless, plate-like specimen of $C_{17}H_{26}BFO_4$, approximate dimensions 0.112 mm x 0.262 mm x 0.285 mm, was used for the X-ray crystallographic analysis. The X-ray intensity data were measured on a single crystal diffractometer Bruker D8 Venture Photon III system equipped with a micro focus tube Cu ImS (CuKα, λ = 1.54178 Å) and a MX mirror monochromator. A total of 1076 frames were collected. The total exposure time was 12.60 hours. The frames were integrated with the Bruker SAINT software package using a wide-frame algorithm. The integration of the data using an orthorhombic unit cell yielded a total of 14336 reflections to a maximum θ angle of 66.58° (0.84 Å resolution), of which 3041 were independent (average redundancy 4.714, completeness = 97.9%, R_{int} = 2.94%, R_{sig} = 2.19%) and 2983 (98.09%) were greater than $2\sigma(F^2)$. The final cell constants of a = 6.68760(10) Å, b = 10.9127(2) Å, c = 24.2400(5) Å, volume = 1769.03(6) $Å^3$, are based upon the refinement of the XYZ-centroids of 9892 reflections above 20 σ(I) with 8.102° < 2θ < 136.7°. Data were corrected for absorption effects using the Multi-Scan method (SADABS). The ratio of minimum to maximum apparent transmission was 0.855. The calculated minimum and maximum transmission coefficients (based on crystal size) are 0.8150 and 0.9210. The structure was solved and refined using the Bruker SHELXTL Software Package, using the space group $P2_12_12_1$, with Z = 4 for the formula unit, $C_{17}H_{26}BFO_4$. The final anisotropic full-matrix least-squares refinement on F^2 with 214 variables converged at R1 = 2.44%, for the observed data and wR2 = 5.89% for all data. The goodness-of-fit was 1.071. The largest peak in the final difference electron density synthesis was 0.188 $e^-/Å^3$ and the largest hole was -0.128 $e^-/Å^3$ with an RMS deviation of 0.027 $e^-/Å^3$. On the basis of the final model, the calculated density was 1.217 g/cm^3 and F(000), 696 e^-. CCDC Nr.: 2249213.

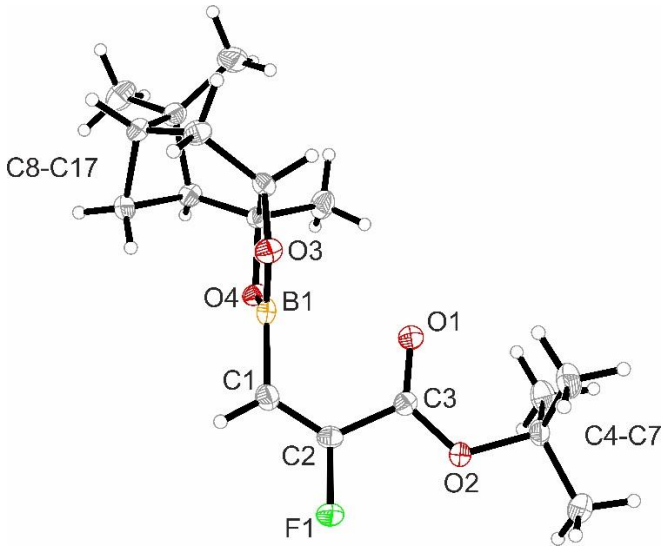

a) (B1-O1 distance: 2.646 Å)

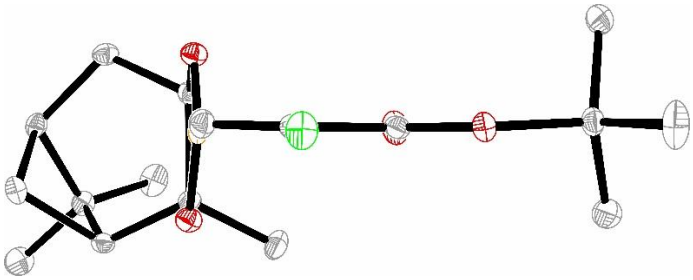

b)

Figure S3: a) Crystal structure of compound ***E*-9**. View perpendicular on the alkenyl fluorine unit. Thermal ellipsoids are shown at 50% probability. b) View along the alkenyl fluorine unit plane.

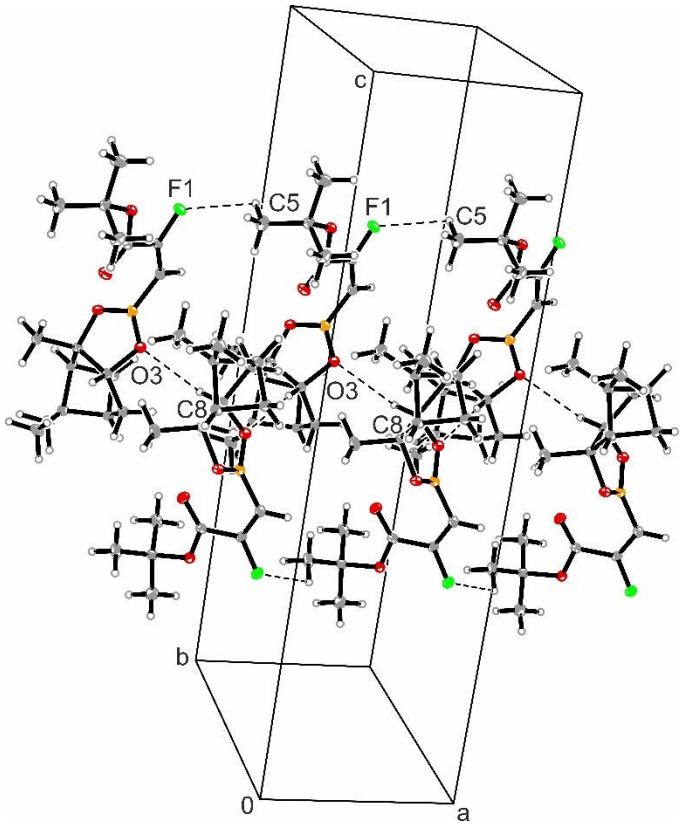

Figure S4: Excerpt of the packing diagram of compound ***E*-9** representing the formation of linear chain along the *a*-axis trough C-H···O and C-H···F interactions.
No π···π interactions observed between the alkenyl fluorine units.

Table S1. Non-covalent intermolecular interactions in compound ***E*-9** (Å and deg)

D-H···*A*	*d*(*D*-H)	*d*(H···*A*)	*d*(*D*···*A*)	∠(*DHA*)
C5-H5A···F1$^{\#1}$	0.98	2.623	3.134	112.6
C8-H8···O3$^{\#2}$	1.00	2.651	3.617	162.4
C7-H7A···O2$^{\#3}$	0.98	2.701	3.622	156.6

Symmetry transformations used to generate equivalent atoms: : $^{\#1}$ 1+x, y, z; $^{\#2}$ -0.5+x, -0.5-y, 1-z; $^{\#3}$ 1-x, -0.5+y, 0.5-z;

X-ray crystal structure analysis of *Z*-14 (gil10400): A colorless, plate-like specimen of $C_{17}H_{22}BFO_4$, approximate dimensions 0.067 mm x 0.126 mm x 0.141 mm, was used for the X-ray crystallographic analysis. The X-ray intensity data were measured on a single crystal diffractometer Bruker D8 Venture Photon III system equipped with a micro focus tube Cu ImS (CuKα, λ = 1.54178 Å) and a MX mirror monochromator. A total of 1543 frames were collected. The total exposure time was 23.31 hours. The frames were integrated with the Bruker SAINT software package using a wide-frame algorithm. The integration of the data using a monoclinic unit cell yielded a total of 32530 reflections to a maximum θ angle of 66.84° (0.84 Å resolution), of which 2994 were independent (average redundancy 10.865,

completeness = 99.6%, R_{int} = 15.22%, R_{sig} = 5.75%) and 2089 (69.77%) were greater than 2σ(F^2). The final cell constants of a = 8.8652(3) Å, b = 29.1510(10) Å, c = 6.7191(2) Å, β = 102.178(3)°, volume = 1697.34(10) $Å^3$, are based upon the refinement of the XYZ-centroids of 6360 reflections above 20 σ(I) with 6.063° < 2θ < 132.4°. Data were corrected for absorption effects using the Multi-Scan method (SADABS). The ratio of minimum to maximum apparent transmission was 0.875. The calculated minimum and maximum transmission coefficients (based on crystal size) are 0.8980 and 0.9500. The structure was solved and refined using the Bruker SHELXTL Software Package, using the space group $P2_1/c$, with Z = 4 for the formula unit, $C_{17}H_{22}BFO_4$. The final anisotropic full-matrix least-squares refinement on F^2 with 213 variables converged at R1 = 5.83%, for the observed data and wR2 = 13.96% for all data. The goodness-of-fit was 1.018. The largest peak in the final difference electron density synthesis was 0.269 $e^-/Å^3$ and the largest hole was -0.252 $e^-/Å^3$ with an RMS deviation of 0.058 $e^-/Å^3$. On the basis of the final model, the calculated density was 1.253 g/cm^3 and F(000), 680 e^-. CCDC Nr.: 2249214.

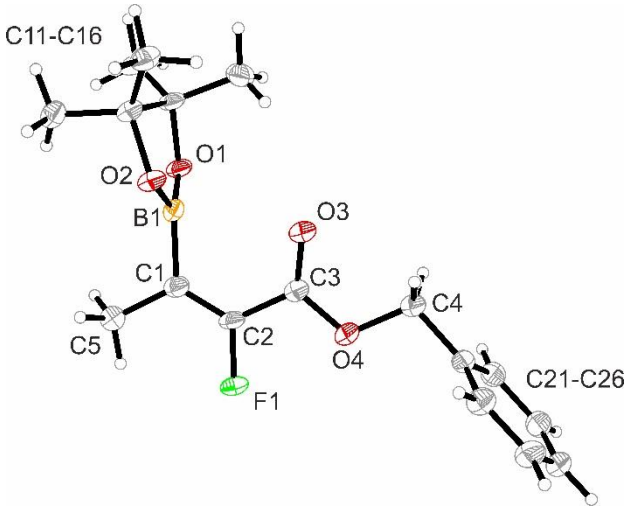

a) (B1-O3 distance: 2.657 Å)

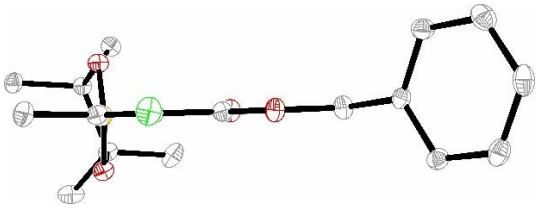

b)

Figure S5: a) Crystal structure of compound ***Z*-14**. View perpendicular on the alkenyl fluorine unit. Thermal ellipsoids are shown at 50% probability. b) View along the alkenyl fluorine unit plane.

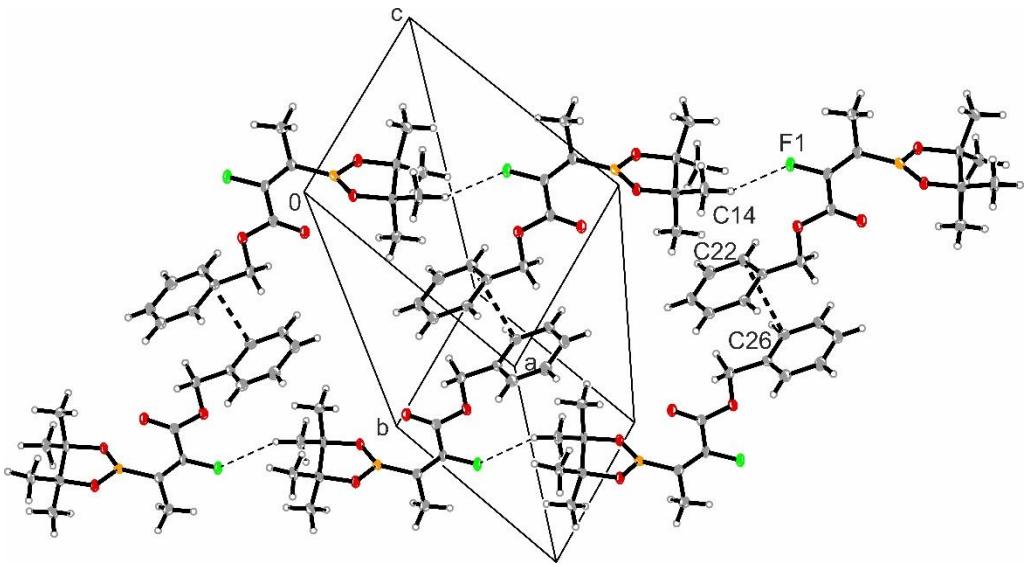

Figure S6: Excerpt of the packing diagram of compound ***Z*-14**
representing the formation of linear chains containing dimeric units
formed by π···π interactions between the phenyl rings.
These dimers are forward connected trough C-H···F interactions.
No π···π interactions observed between the alkenyl fluorine units.

Table S2. Non-covalent intermolecular interactions in compound ***Z*-14** (Å and deg)

D-H···*A*	*d*(*D*-H)	*d*(H···*A*)	*d*(*D*···*A*)	∠(*DHA*)
C14-H14B···F1$^{\#1}$	0.98	2.489	3.409	156.4
C22···C26$^{\#2}$			3.474	

Symmetry transformations used to generate equivalent atoms: : $^{\#1}$ 1+x, y, 1+z; $^{\#2}$ 1-x, 1-y, 2-z.

X-ray crystal structure analysis of *E*-14 (gil10387): A colorless, plate-like specimen of $C_{17}H_{22}BFO_4$, approximate dimensions 0.062 mm x 0.096 mm x 0.221 mm, was used for the X-ray crystallographic analysis. The X-ray intensity data were measured on a single crystal diffractometer Bruker D8 Venture Photon III system equipped with a micro focus tube Mo ImS (MoKα, λ = 0.71073 Å) and a MX mirror monochromator. A total of 543 frames were collected. The total exposure time was 5.28 hours. The frames were integrated with the Bruker SAINT software package using a narrow-frame algorithm. The integration of the data using a monoclinic unit cell yielded a total of 32336 reflections to a maximum θ angle of 26.84° (0.79 Å resolution), of which 3516 were independent (average redundancy 9.197, completeness = 98.2%, R_{int} = 4.73%, R_{sig} = 2.33%) and 3136 (89.19%) were greater than 2σ(F^2). The final cell constants of a = 14.5237(3) Å, b = 7.1669(2) Å, c = 16.1042(3) Å, β = 96.0710(10)°, volume = 1666.88(7) $Å^3$, are based upon the refinement of the XYZ-centroids of 9895 reflections above 20 σ(I) with 6.228° < 2θ < 53.55°. Data were corrected for absorption effects using the Multi-Scan method (SADABS). The ratio of minimum to maximum apparent transmission was 0.949. The calculated minimum and maximum transmission

coefficients (based on crystal size) are 0.9790 and 0.9940. The structure was solved and refined using the Bruker SHELXTL Software Package, using the space group $P2_1/n$, with Z = 4 for the formula unit, $C_{17}H_{22}BFO_4$. The final anisotropic full-matrix least-squares refinement on F^2 with 213 variables converged at R1 = 3.71%, for the observed data and wR2 = 10.23% for all data. The goodness-of-fit was 1.052. The largest peak in the final difference electron density synthesis was 0.353 $e^-/Å^3$ and the largest hole was -0.254 $e^-/Å^3$ with an RMS deviation of 0.039 $e^-/Å^3$. On the basis of the final model, the calculated density was 1.276 g/cm^3 and F(000), 680 e^-. CCDC Nr.: 2249215.

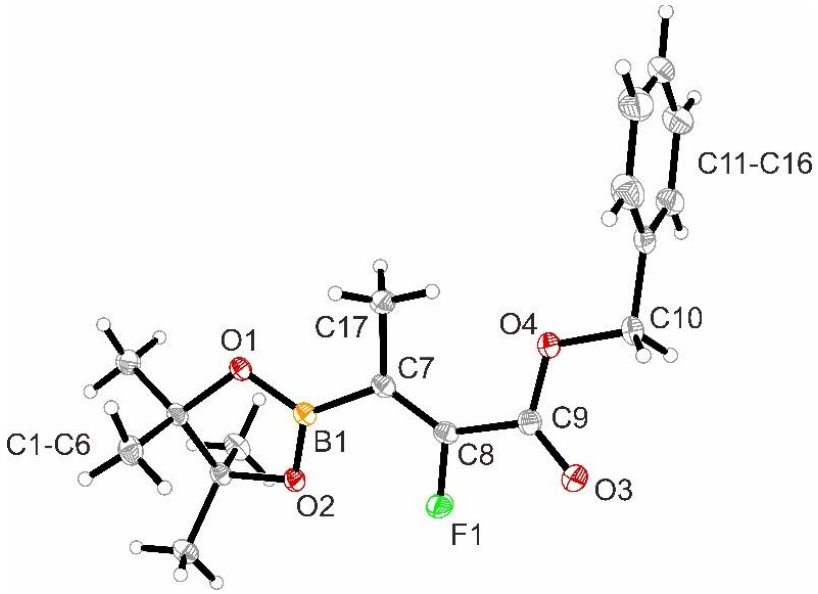

a)

b)

Figure S7: a) Crystal structure of compound ***E*-14**. View perpendicular on the alkenyl fluorine unit. Thermal ellipsoids are shown at 50% probability. b) View along the alkenyl fluorine unit plane.

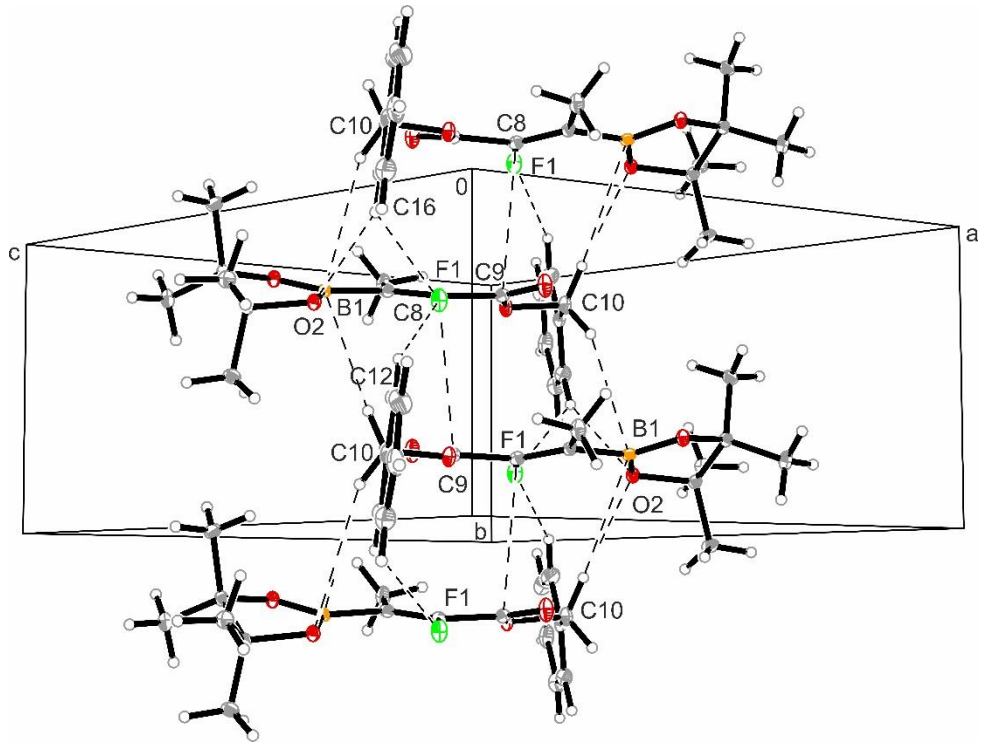

Figure S8: Excerpt of the packing diagram of compound ***E*-14** representing the formation of linear chain along the *b*-axis by alternating orientation of molecules trough C-H···F, C-H···O, C-H···B and π···π interactions

Table S3. Non-covalent intermolecular interactions in compound ***E*-14** (Å and deg)

D-H···*A*	*d*(*D*-H)	*d*(H···*A*)	*d*(*D*···*A*)	∠(*DHA*)
C12-H12···F1$^{\#1}$	0.95	2.653	3.458	146.6
C16-H16···F1$^{\#2}$	0.95	2.705	3.490	140.5
C10-H10B···O2$^{\#1}$	0.99	2.636	3.587	161.2
C16-H16···O2$^{\#2}$	0.95	2.678	3.567	157.9
C10-H10A···B1$^{\#2}$	0.99	3.071	4.003	157.5
C10-H10B···B1$^{\#1}$	0.99	3.114	4.098	172.6
C8···C9$^{\#1}$			3.561	

Symmetry transformations used to generate equivalent atoms: $^{\#1}$ 0.5-x, 0.5+y, 1.5-z; $^{\#2}$ 0.5-x, -0.5+y, 1.5-z;

References X-Ray Part:

1. Bruker AXS (**2021**) *APEX4 Version 2021.4-0*, *SAINT Version 8.40B* and *SADABS Bruker AXS area detector scaling and absorption correction Version 2016/2*, Bruker AXS Inc., Madison, Wisconsin, USA.
2. Sheldrick, G. M., *SHELXT – Integrated space-group and crystal-structure determination*, *Acta Cryst.*, **2015**, *A71*, 3-8.

3. Sheldrick, G. M., *Crystal structure refinement with SHELXL*, *Acta Cryst.*, **2015**, *C71 (1)*, 3-8.
4. Bruker AXS (**1998**) *XP – Interactive molecular graphics, Version 5.1,* Bruker AXS Inc., Madison, Wisconsin, USA.

4. Laser Flash Photolysis and DFT calculations

Laser flash photolysis

The LP980KS setup from Edinburgh Instruments equipped with an Nd:YAG laser from Litron (Nano LG 300-10) was employed for transient absorption (TA) spectroscopy. The frequency-tripled output with a wavelength of 355 nm served as the excitation source. The laser pulse duration was ~5 ns and the pulse frequency was 10 Hz. The typical pulse energy used for transient absorption studies was 15 mJ. Detection of transient absorption spectra occurred on an iCCD camera from Andor. Kinetic traces at selected wavelengths were recorded using a photomultiplier tube. The spectroscopic experiments were performed at 293 K using a cuvette holder that allows temperature control. If not stated otherwise the TA spectra were integrated over 100 ns.

Triplet-triplet energy transfer constants

The triplet-triplet energy transfer constants, k_{EnT}, were determined from Stern–Volmer experiments. The lifetime τ of triplet-excited thioxanthone was measured with varying concentrations c_q of the quencher and fitted according to the modified Stern–Volmer equation shown below:

$$\frac{1}{\tau} = k_{obs} = k_{EnT} \cdot c_q + \frac{1}{\tau_0} \quad (1)$$

DFT Calculations

DTF calculations were performed with the program Orca 5.0.4[11] using the hybrid functional B3LYP along with a 6-311+G(d,p) basis set. After geometry optimizations, vibration frequencies of the obtained structures were calculated. In each case, no imaginary vibration frequencies were determined, indicating convergence to minimal structures. The energy of the T_1 state after vertical excitation was estimated by a single-point calculation based on the optimized S_0 structure. The lowest triplet state (perpendicular triplet) was calculated starting from the energy-minimized singlet ground state geometries. Additional single-point calculations were carried out to obtain the spin densities of the optimized perpendicular triplet state based on a Mulliken population analysis. The structures, orbitals and spin densities were displayed using the software Avogadro1.2.0.[12]

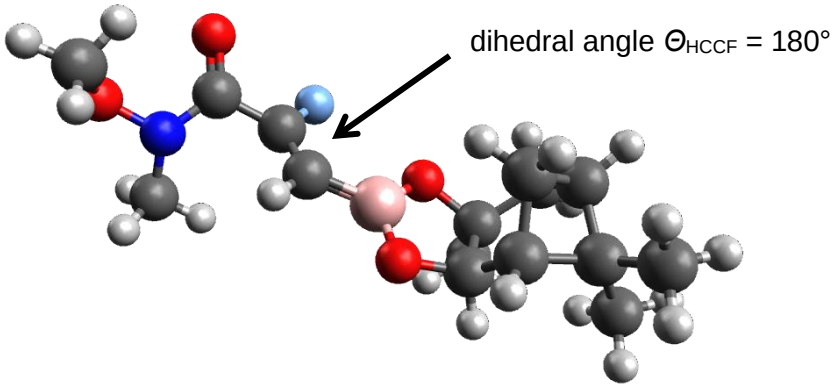

Figure S9: Optimized ground state structure of ***Z*-1**.

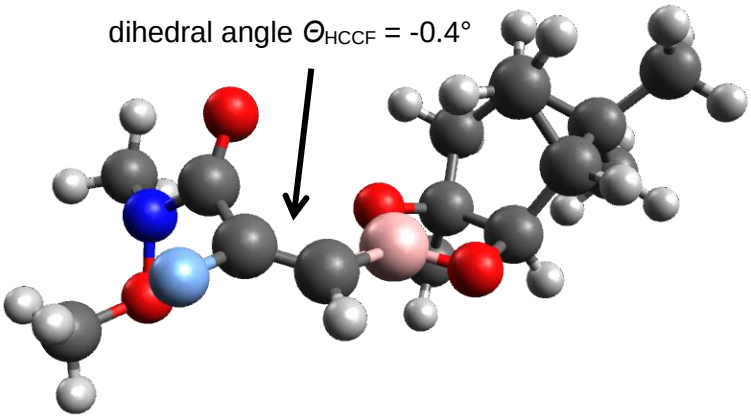

Figure S10: Optimized ground state structure of ***E*-1**.

Table S4: The lower (vertical) triplet energy calculated for ***Z*-1** compared to that of ***E*-1** is in line with the observed faster energy transfer rate constant for the former isomer (compare, Figure 5 of the main manuscript).

compound	E_T [eV][a]	ΔE_T [eV]	dihedral angle of perpendicular triplet
***Z*-1**	3.69	0.11	88°
***E*-1**	3.80		

[a] Estimated vertical triplet energies.

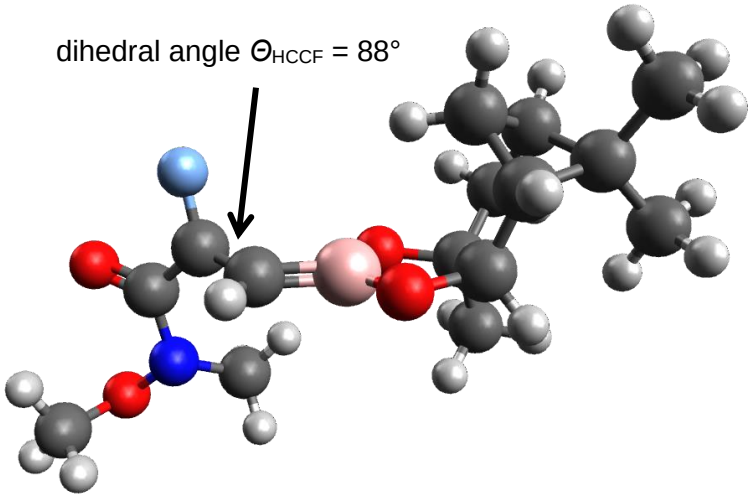

Figure S11: Optimized structure of the perpendicular triplet state**.**

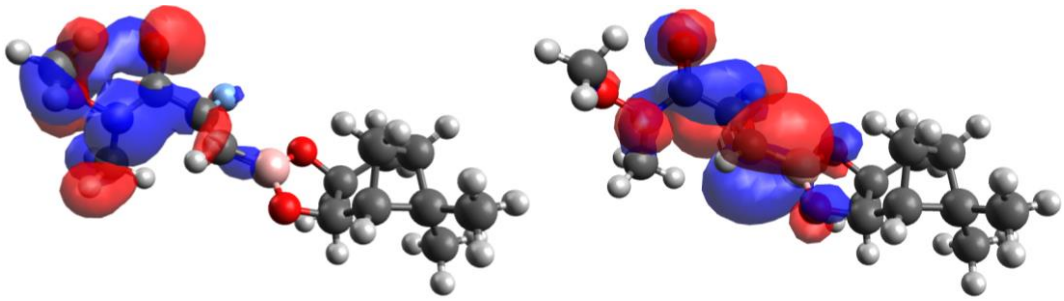

Figure S12: HOMO (left) and LUMO (right) of the optimized ground state structure of ***Z*-1**.

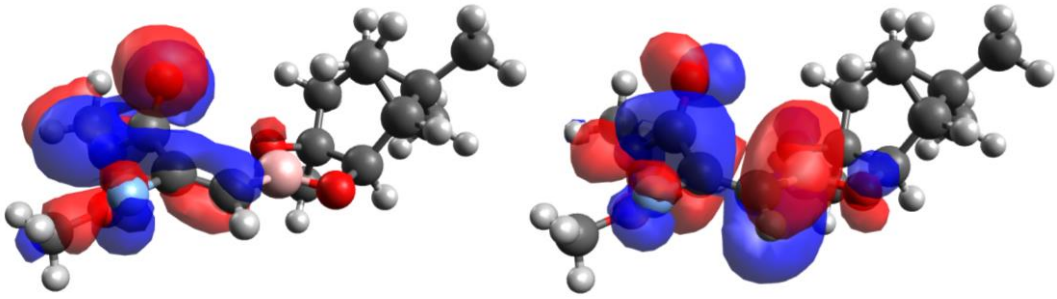

Figure S13: HOMO (left) and LUMO (right) of the optimized ground state structure of ***E*-1**.

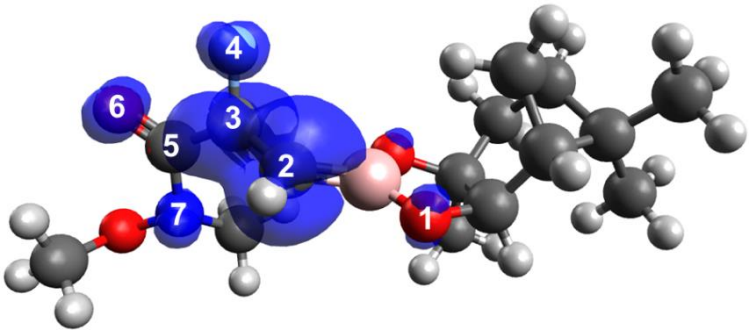

label	spin density
1	0.037
2	**0.929**
3	**0.805**
4	0.065
5	-0.128
6	0.176
7	0.052

Figure S14: (Left) Spin densities (0.005 a.u.) of the optimized perpendicular triplet state. Blue colored surfaces represent positive and red colored surfaces represent negative spin densities. (Right) Table containing spin densities of selected atoms. 87% of the total spin density is located on the (former) olefinic double bond. Total sum of atomic spin populations: 2.000.

5. NMR-spectra of Key Compounds

^{1}H-NMR of **S1** (400 MHz, $CDCl_3$)

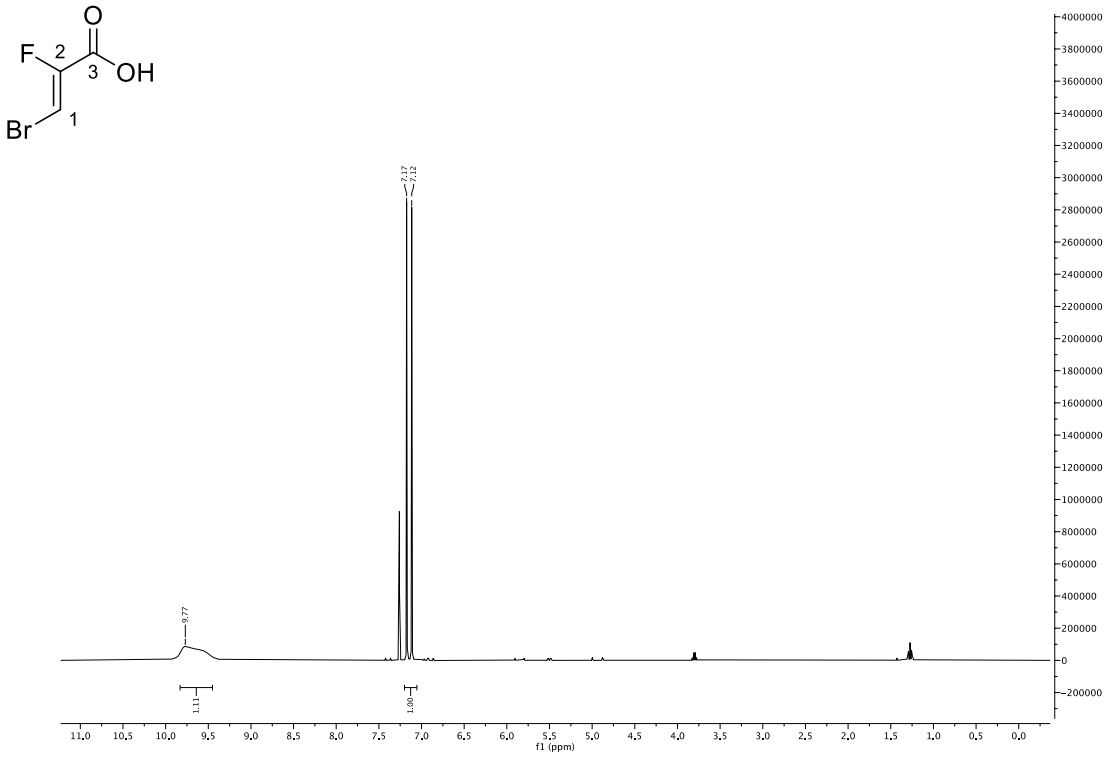

^{13}C-NMR of **S1** (126 MHz, $CDCl_3$)

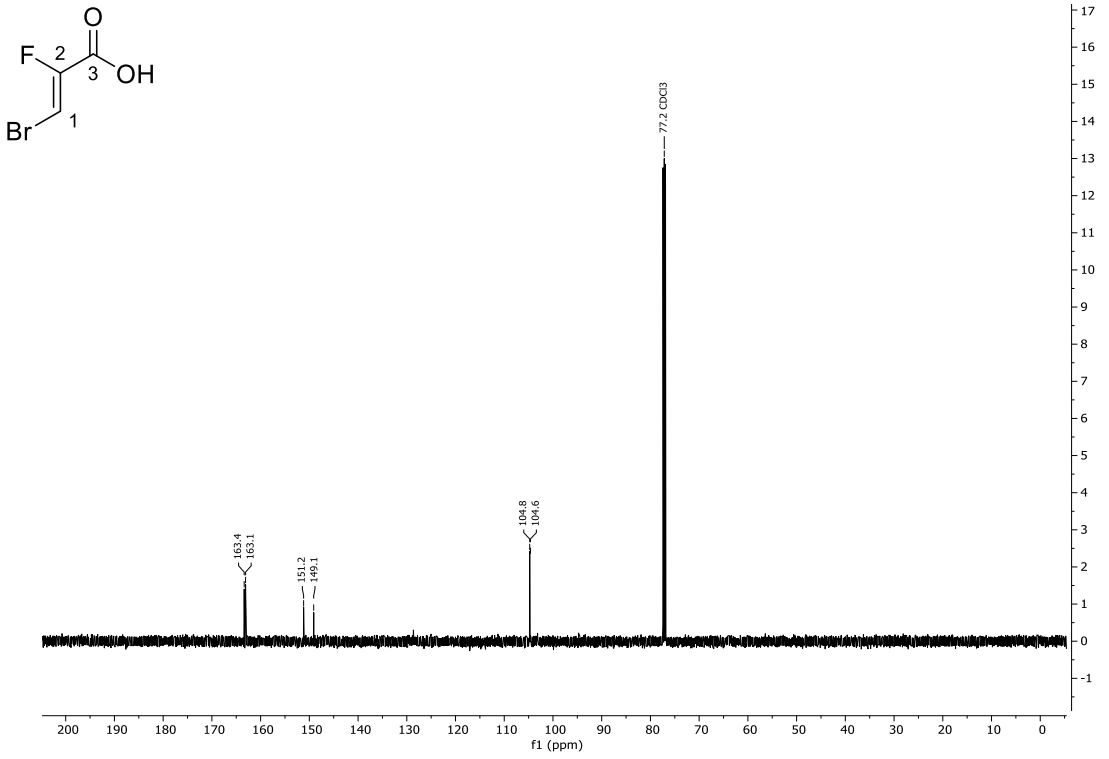

^{19}F-NMR {^{1}H} of **S1** (377 MHz, $CDCl_3$)

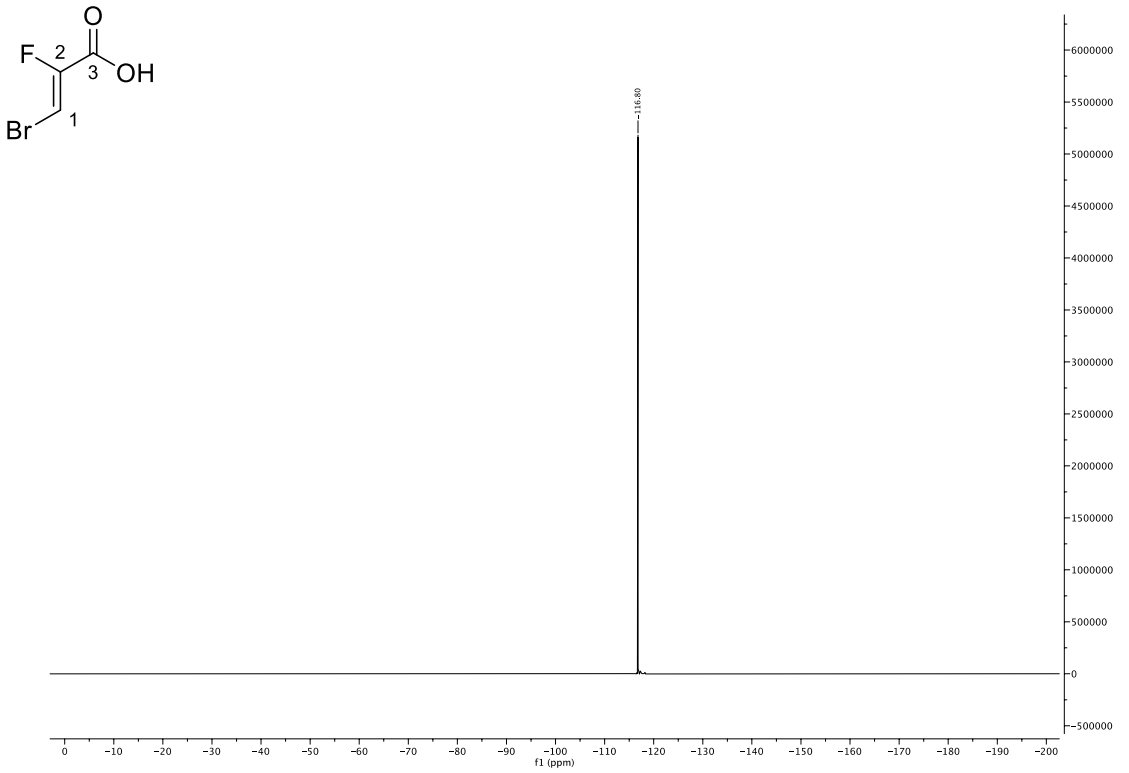

^{1}H-NMR of **S2** (500 MHz, $CDCl_3$)

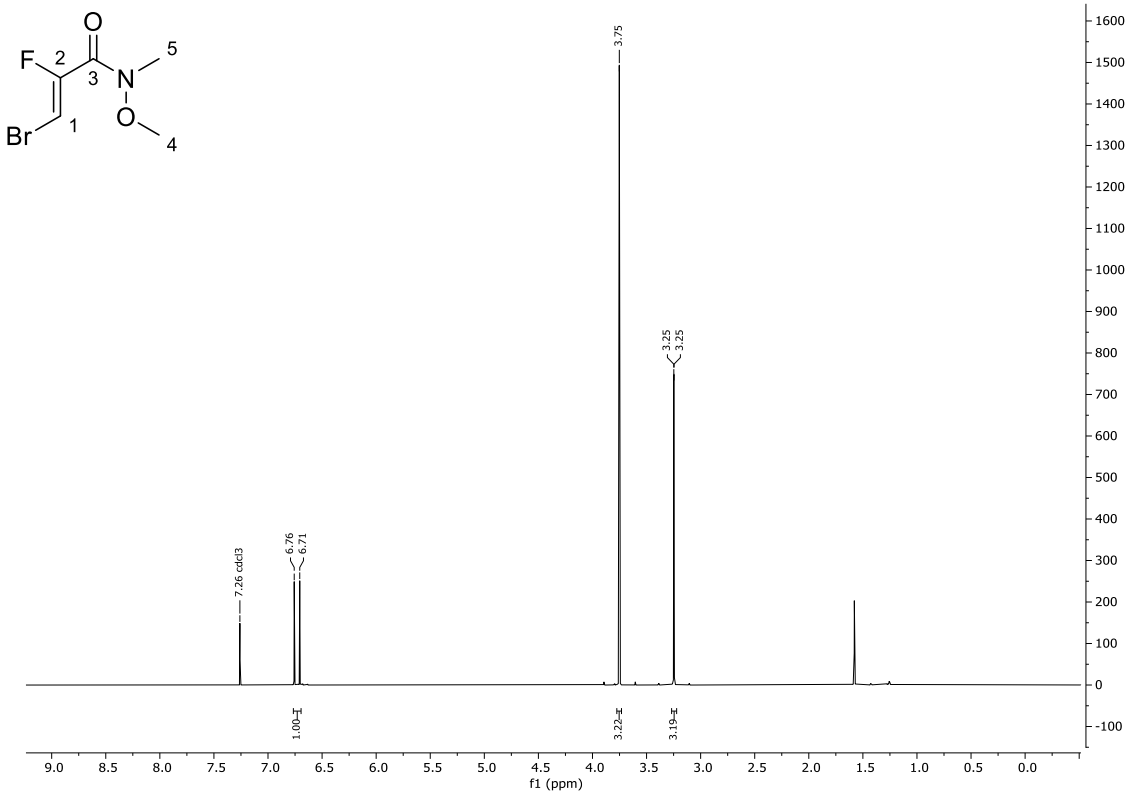

^{13}C-NMR of **S2** (500 MHz, $CDCl_3$)

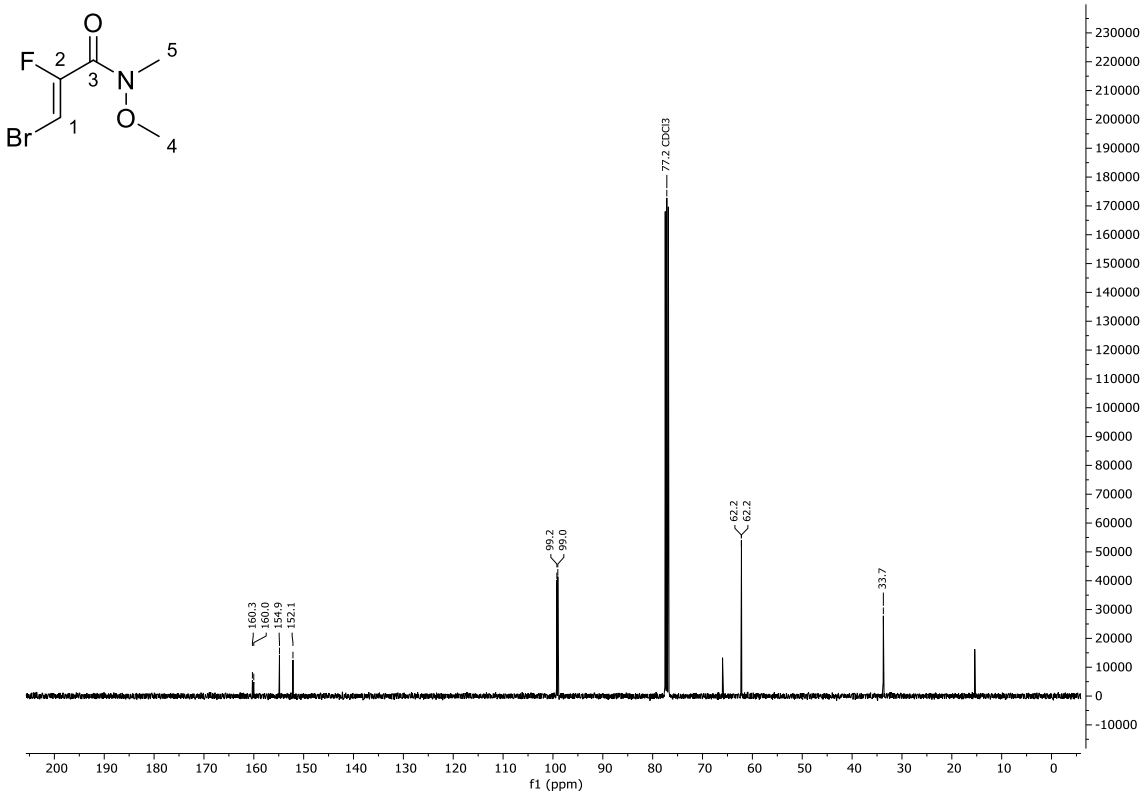

^{19}F-NMR {^{1}H} of **S2** (376 MHz, $CDCl_3$)

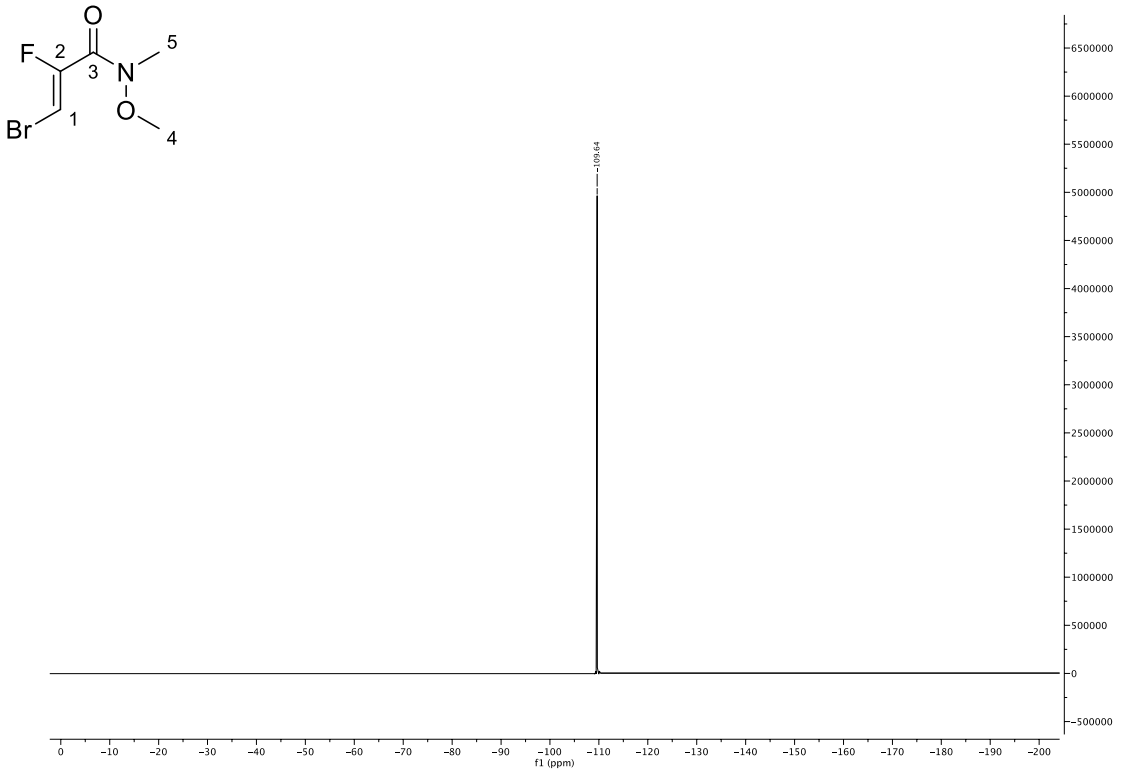

^{1}H-NMR of **S3** (599 MHz, $CDCl_3$)

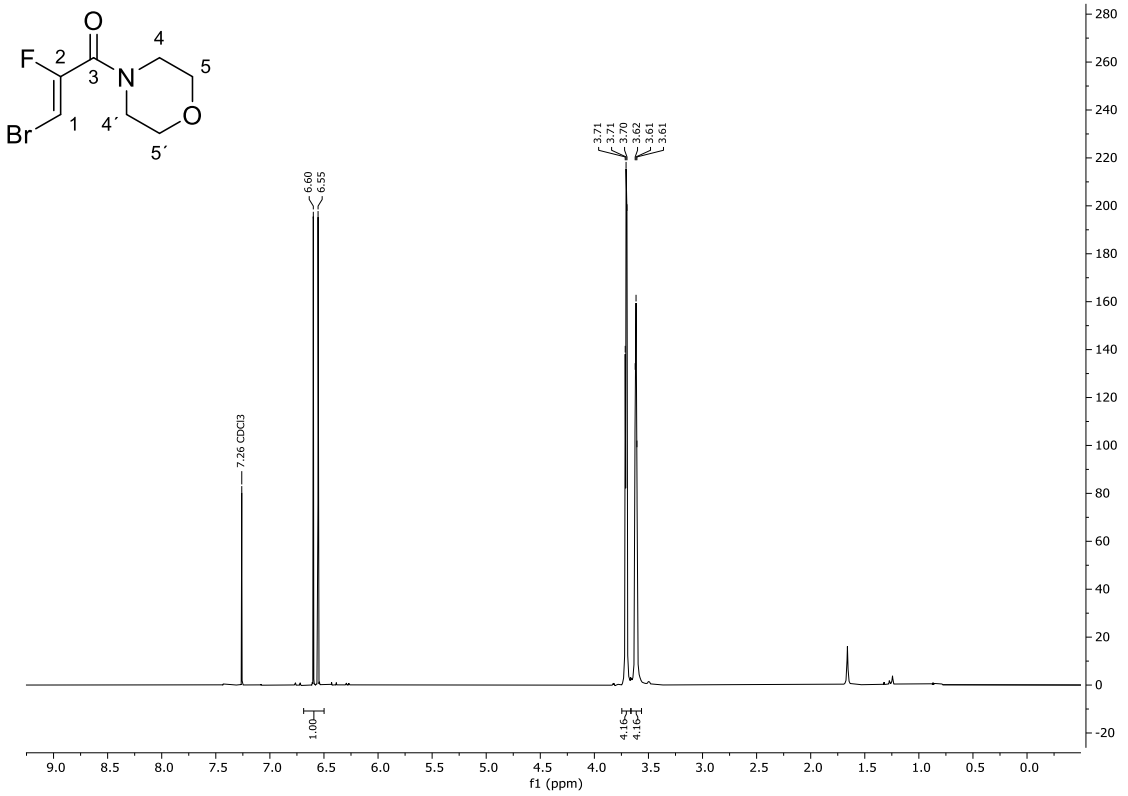

^{13}C-NMR of **S3** (599 MHz, $CDCl_3$)

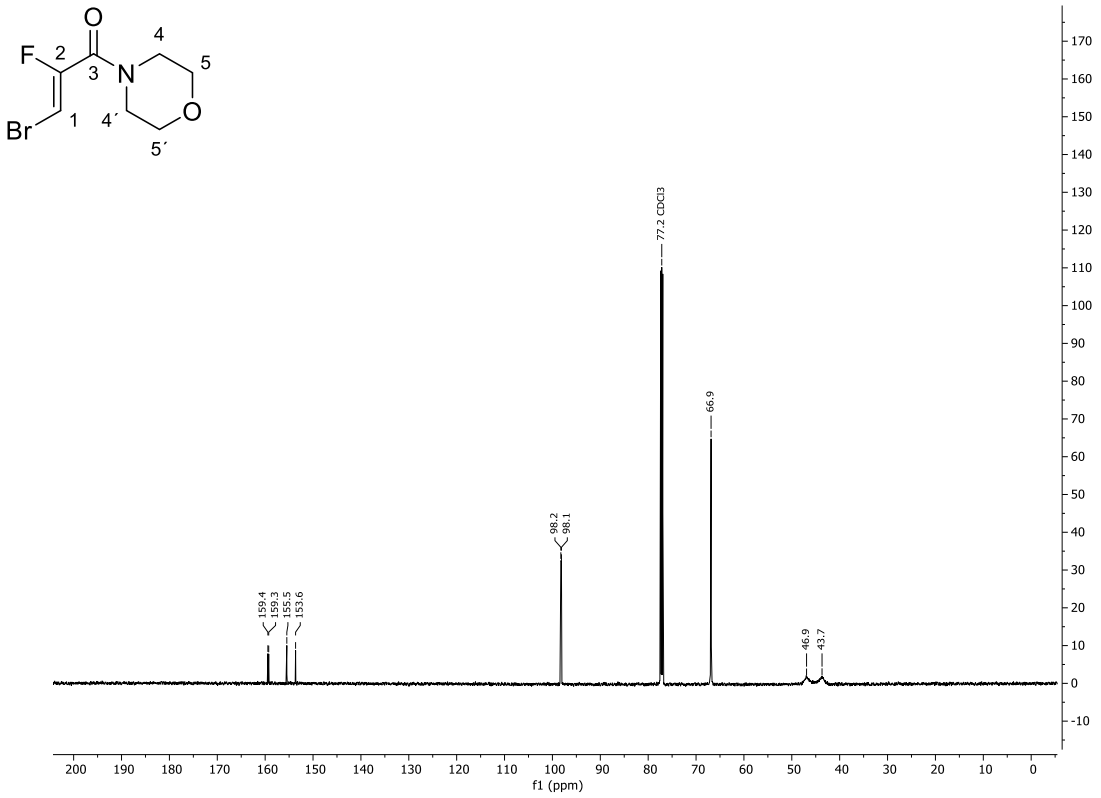

^{19}F-NMR {^{1}H} of **S3** (377 MHz, $CDCl_3$)

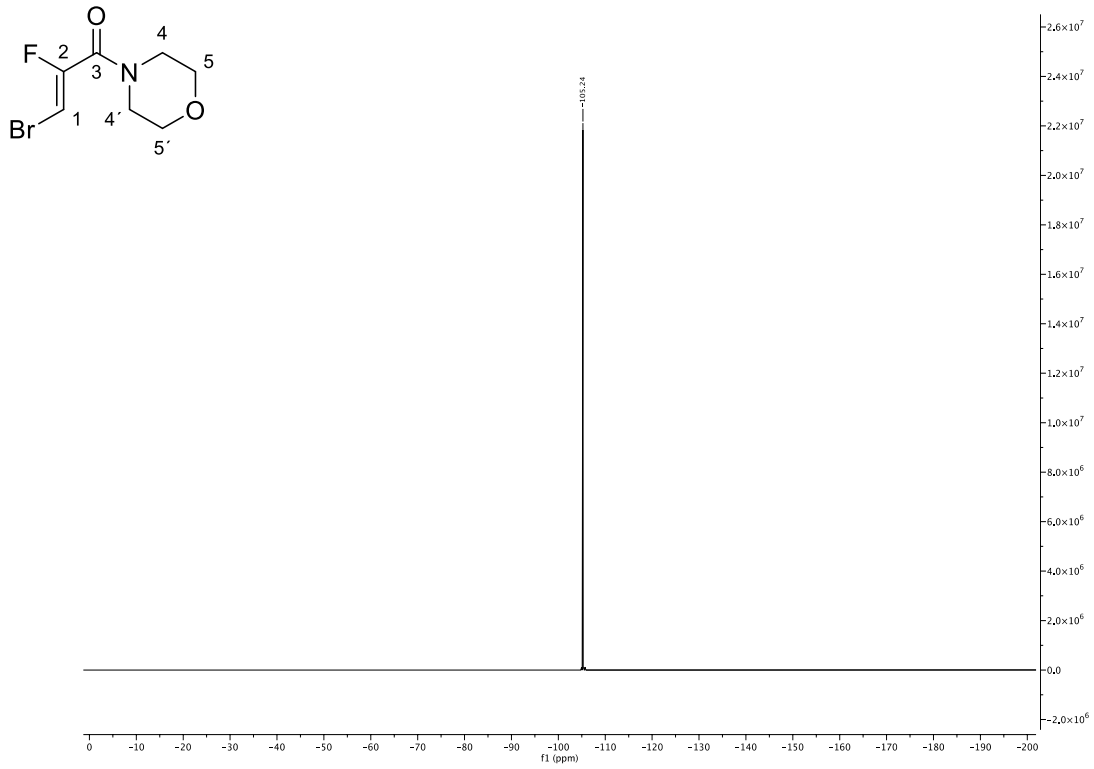

^{1}H-NMR of **S4** (599 MHz, $CDCl_3$)

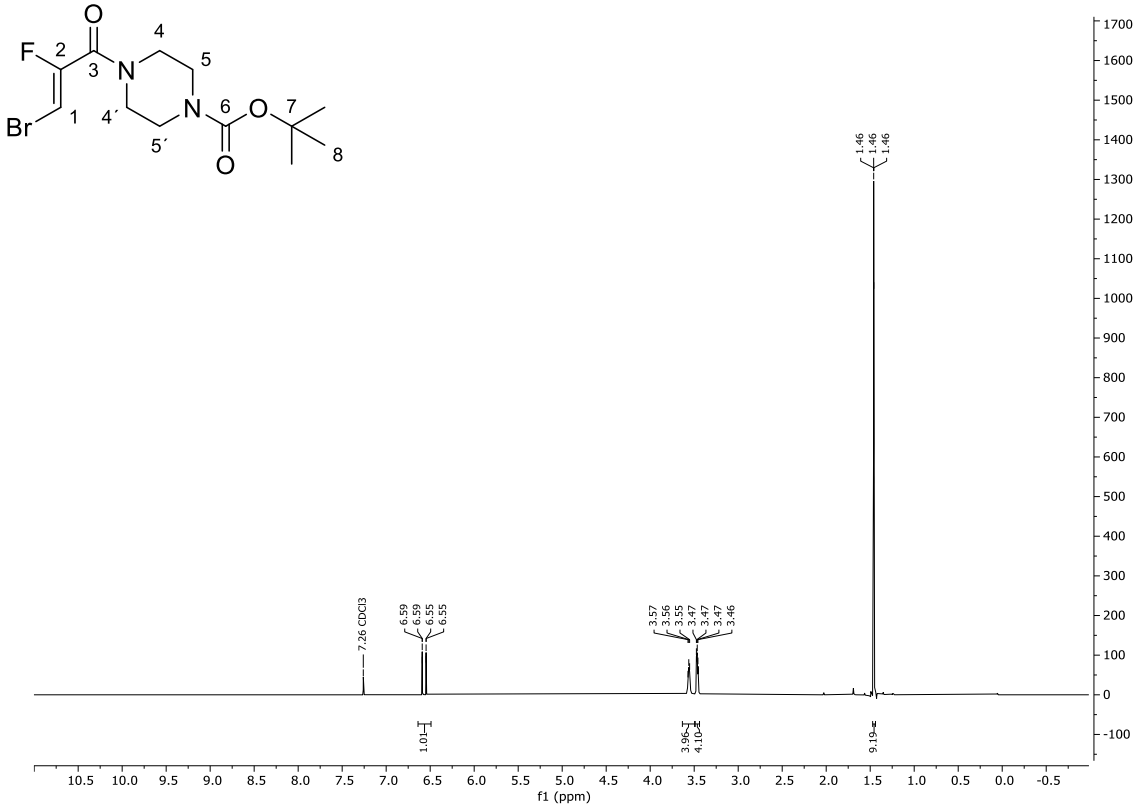

^{13}C-NMR of **S4** (151 MHz, $CDCl_3$)

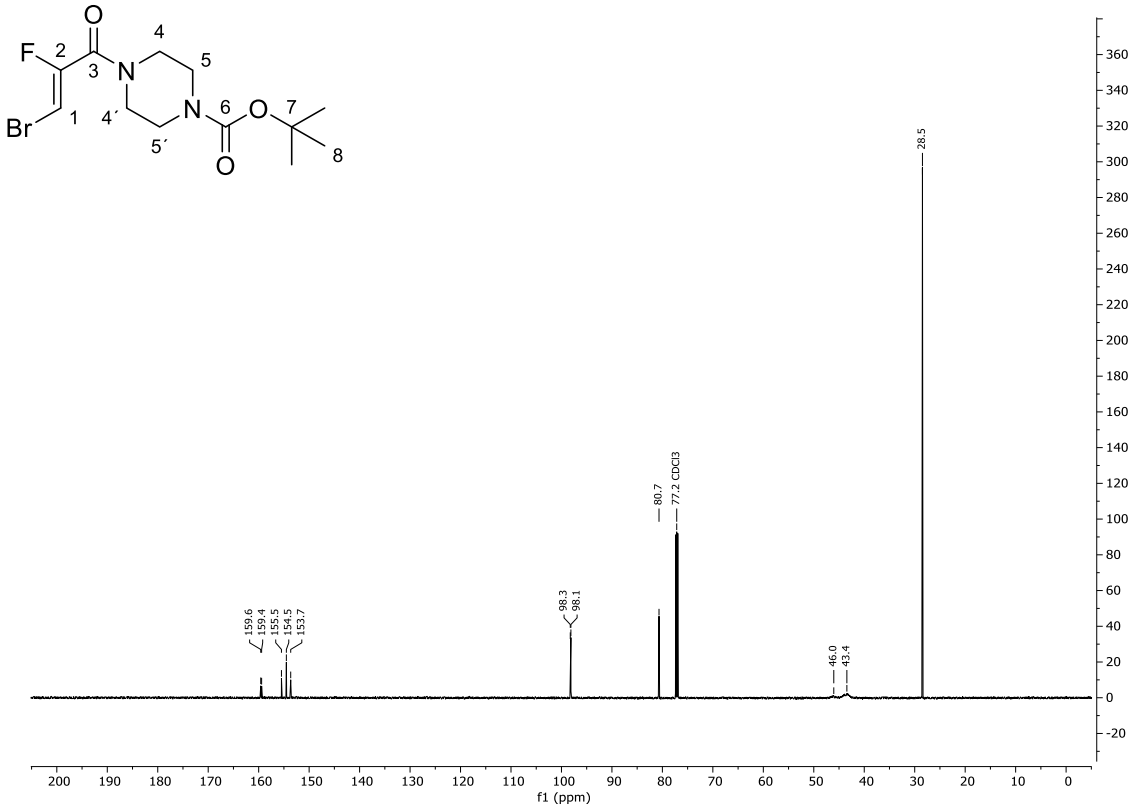

^{19}F-NMR {^{1}H} of **S4** (564 MHz, $CDCl_3$)

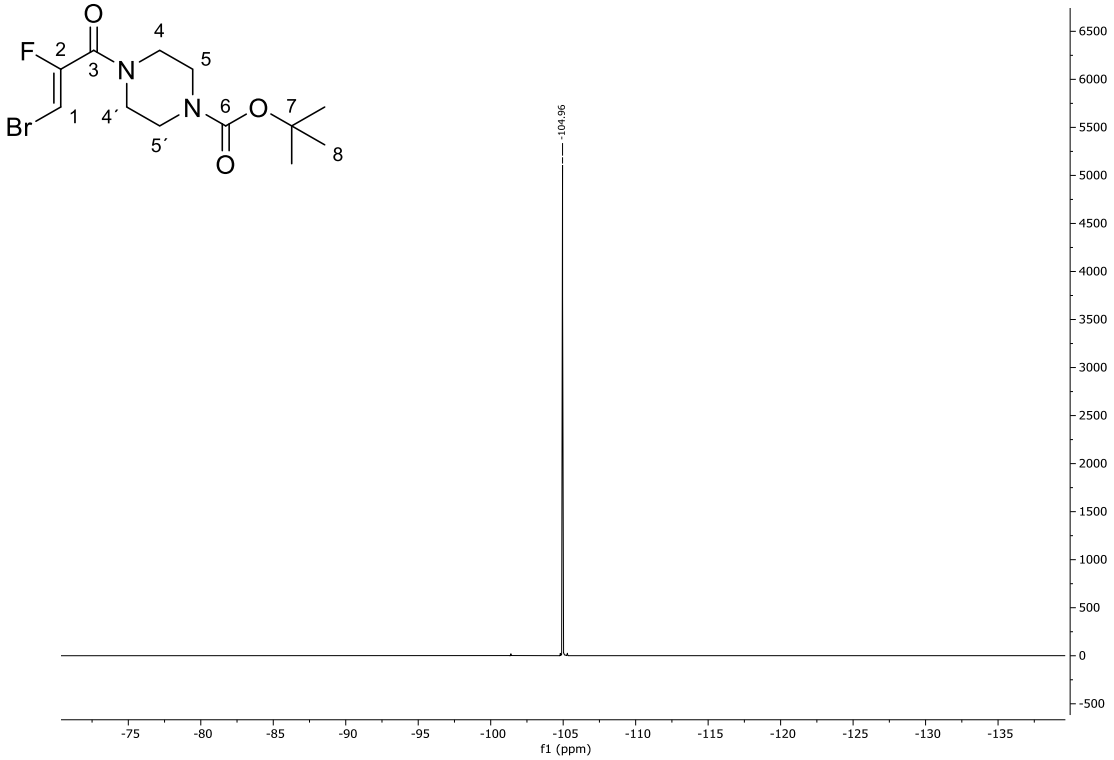

^{1}H-NMR of **S5** (500 MHz, $CDCl_3$)

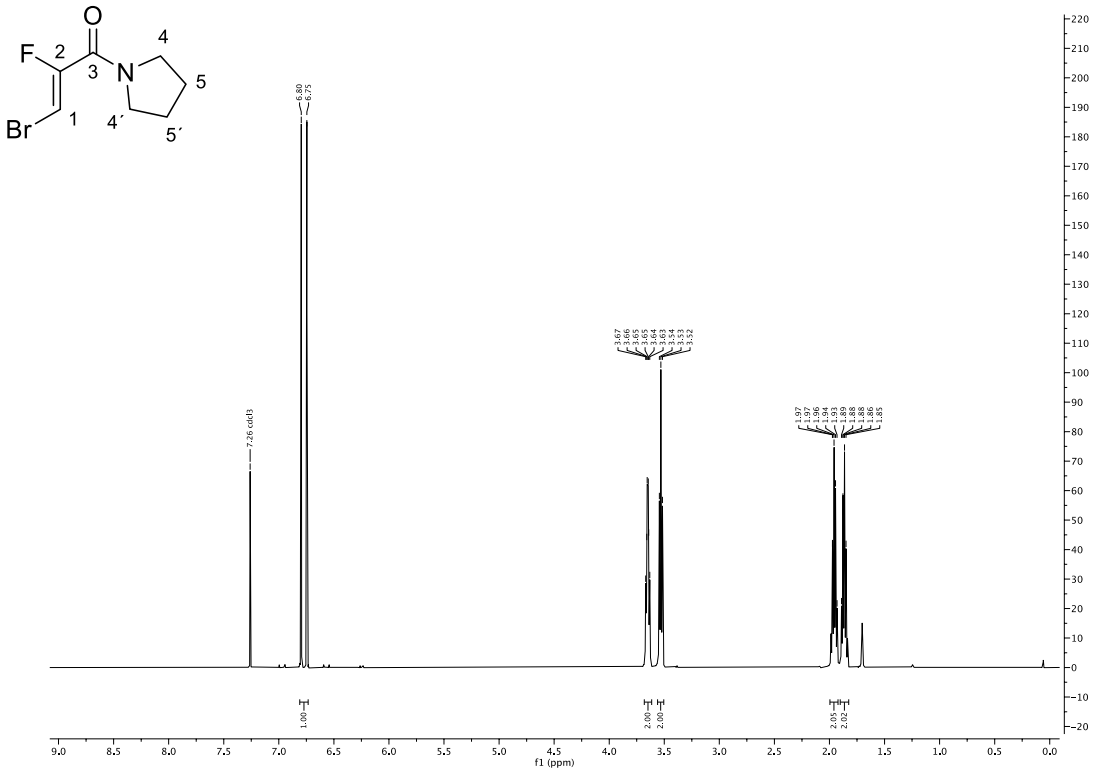

^{13}C-NMR of **S5** (126 MHz, $CDCl_3$)

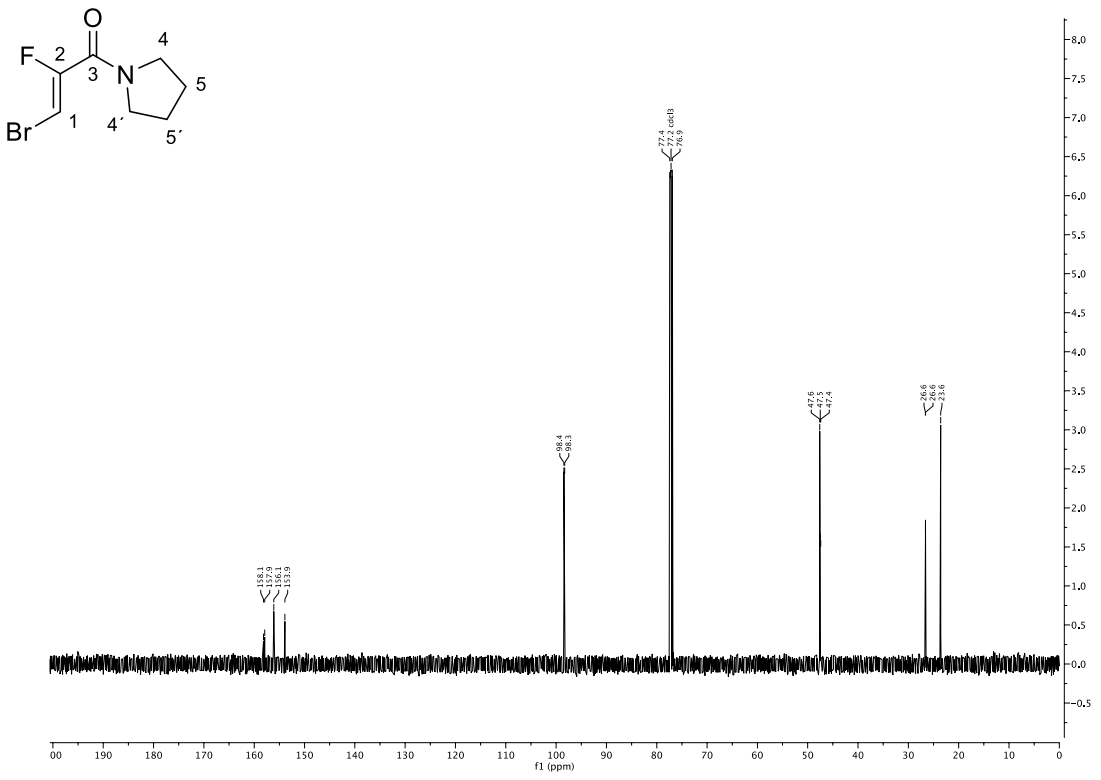

^{19}F-NMR {^{1}H} of **S5** (377 MHz, $CDCl_3$)

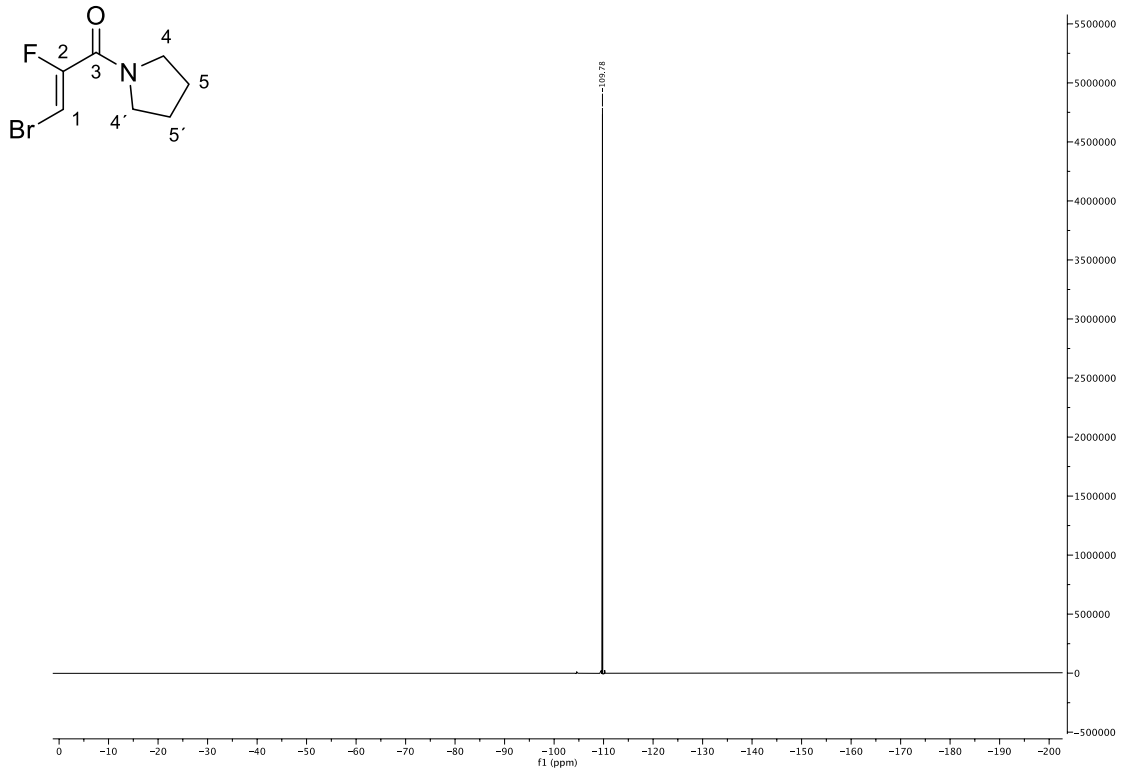

^{1}H-NMR of **S6** (500 MHz, DMSO-d_6)

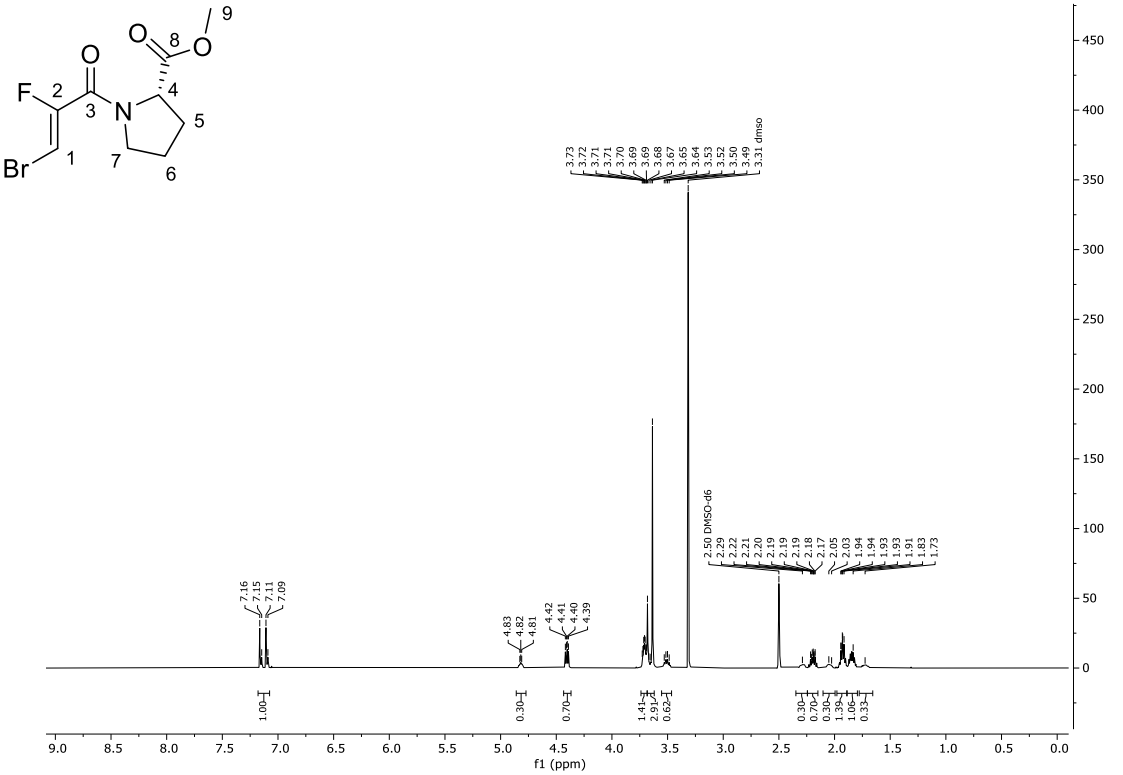

^{13}C-NMR of **S6** (126 MHz, DMSO-d_6)

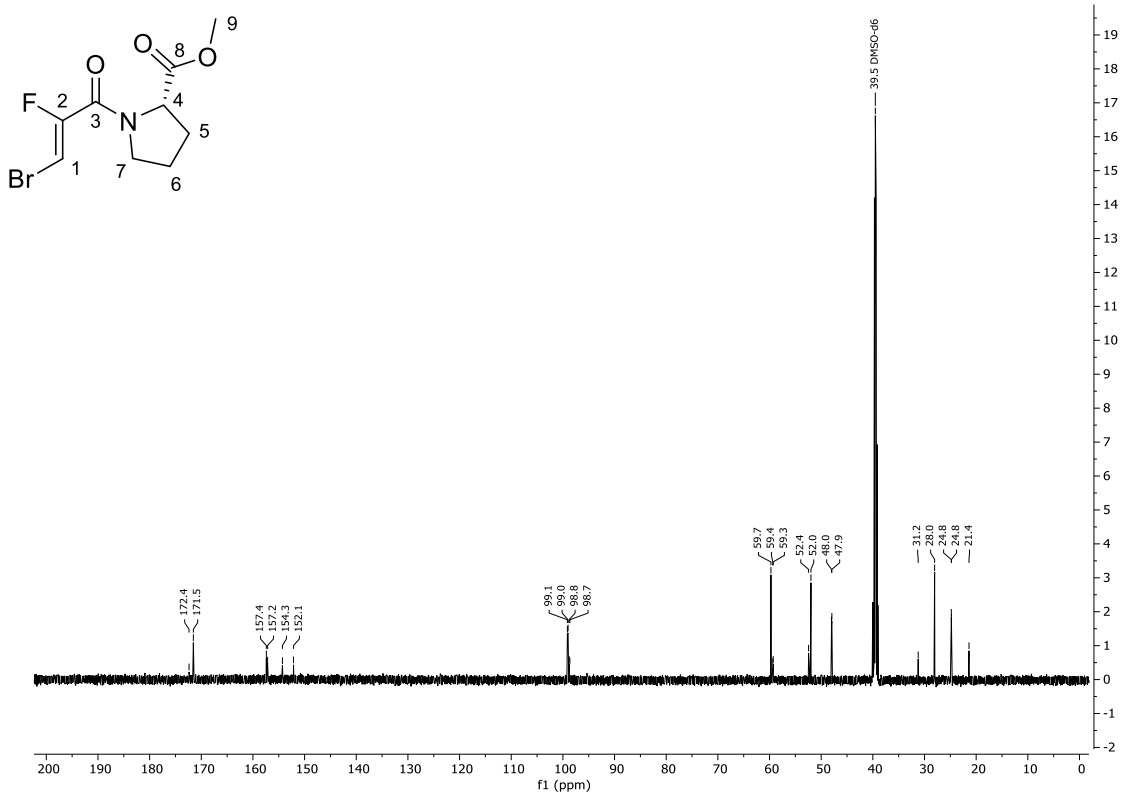

^{19}F-NMR {^{1}H} of **S6** (470 MHz, DMSO-d_6; top 299 K, bottom 363 K)

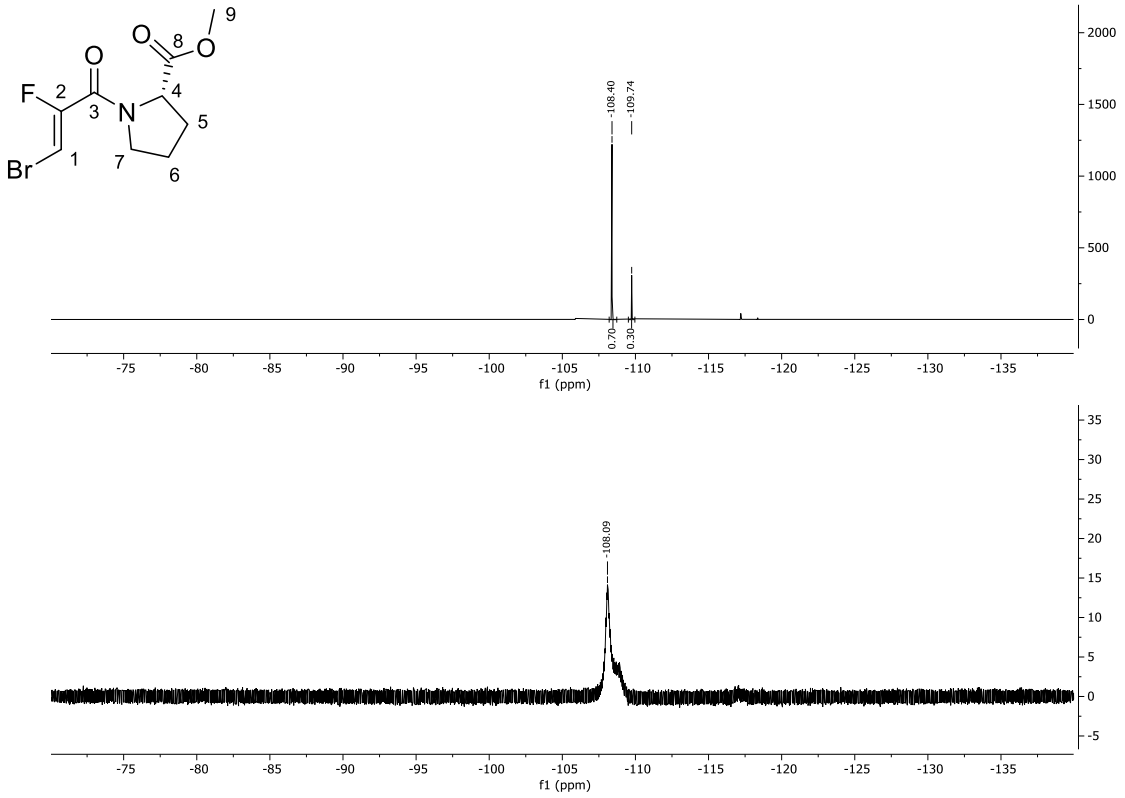

^{1}H-NMR of **S7** (599 MHz, $CDCl_3$)

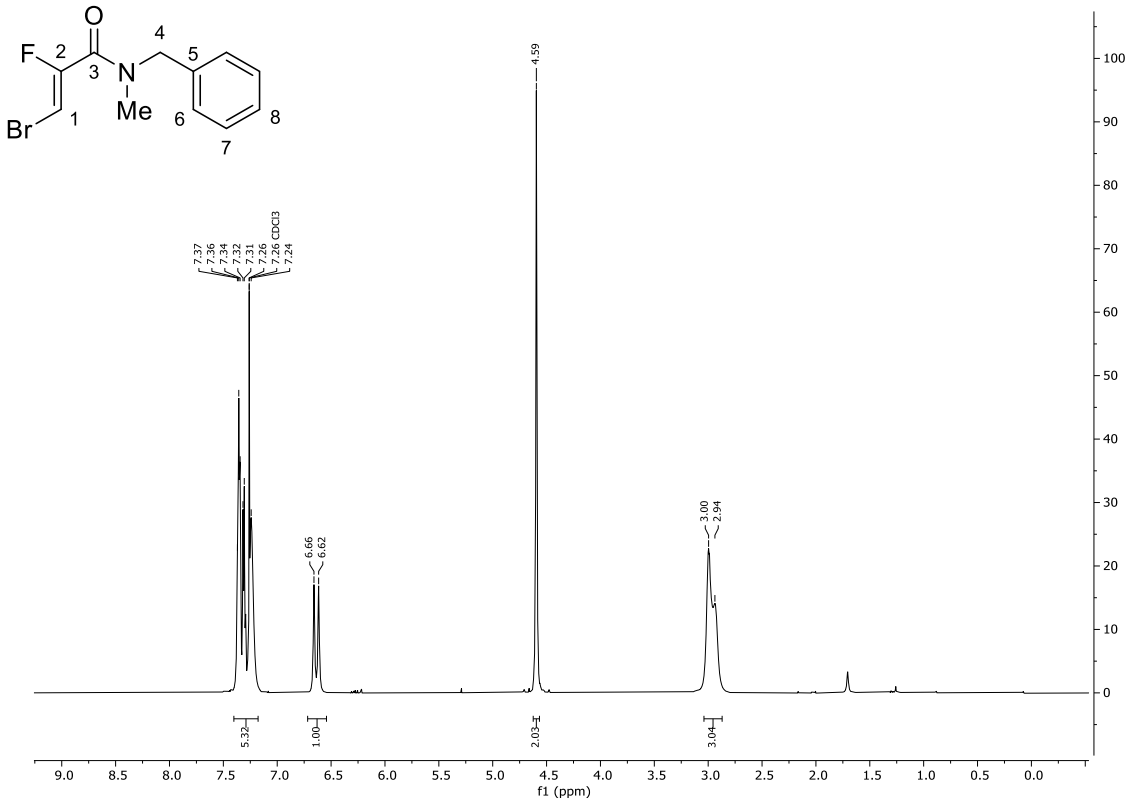

^{1}H-NMR of **S7** (500 MHz, DMSO-d_6; top 299 K, bottom 363 K)

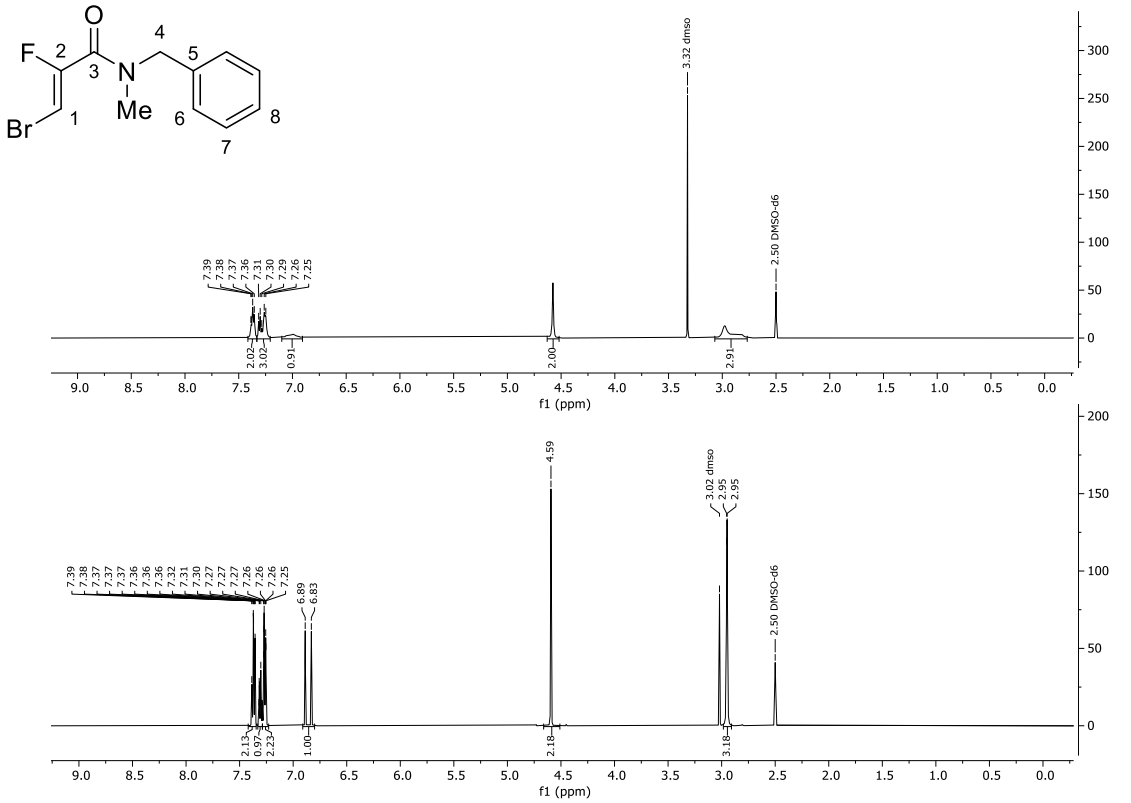

^{13}C-NMR of **S7** (151 MHz, $CDCl_3$)

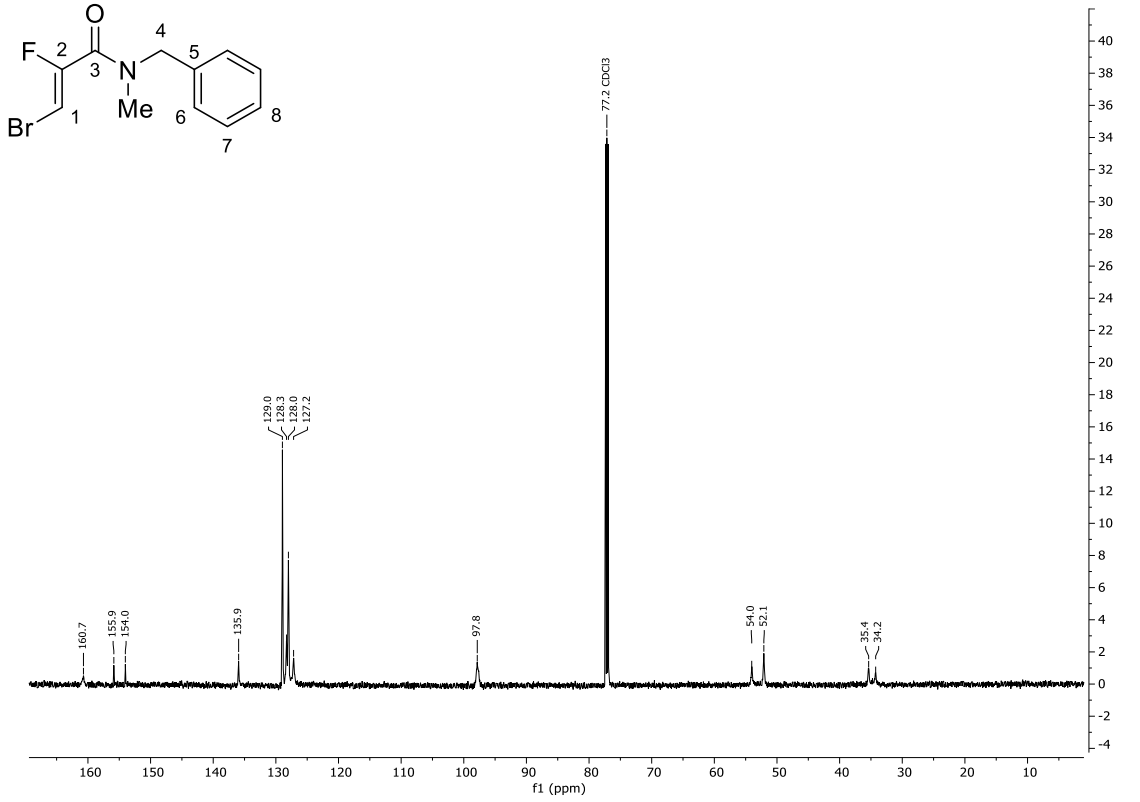

^{19}F-NMR of **S7** (377 MHz, $CDCl_3$)

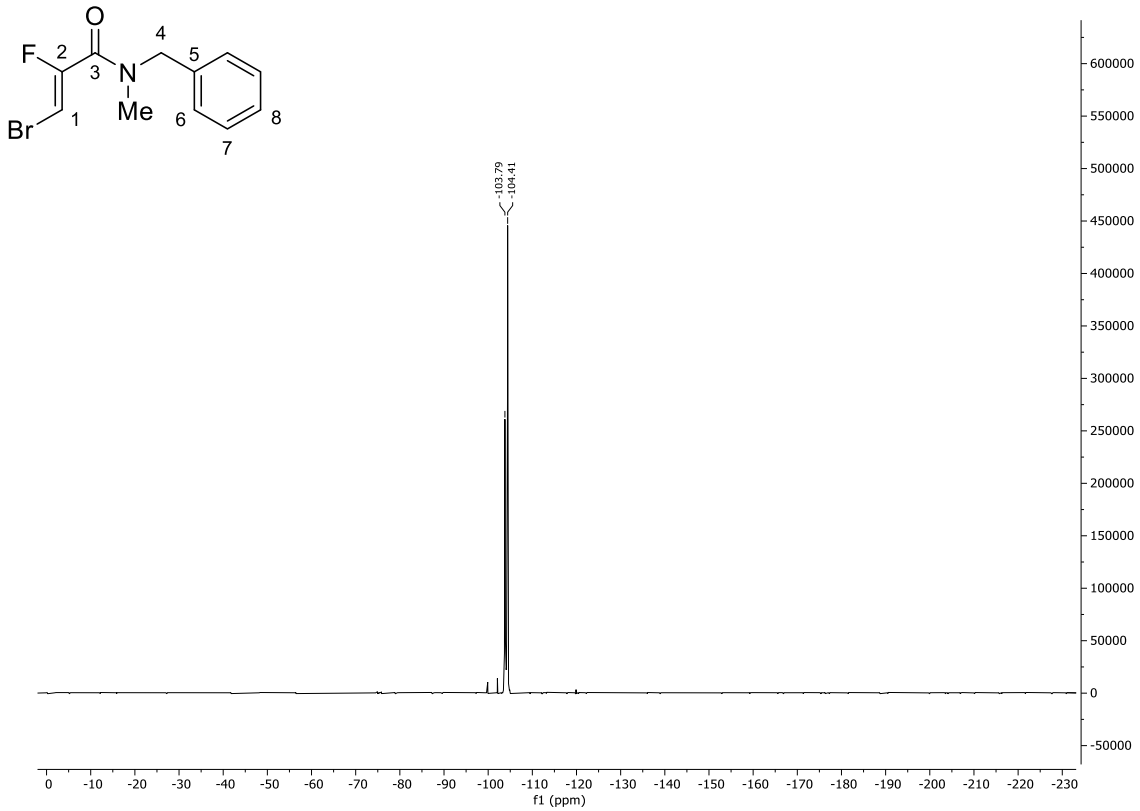

^{19}F-NMR {^{1}H} of **S7** (470 MHz, DMSO-d_6; top 299 K, bottom 363 K)

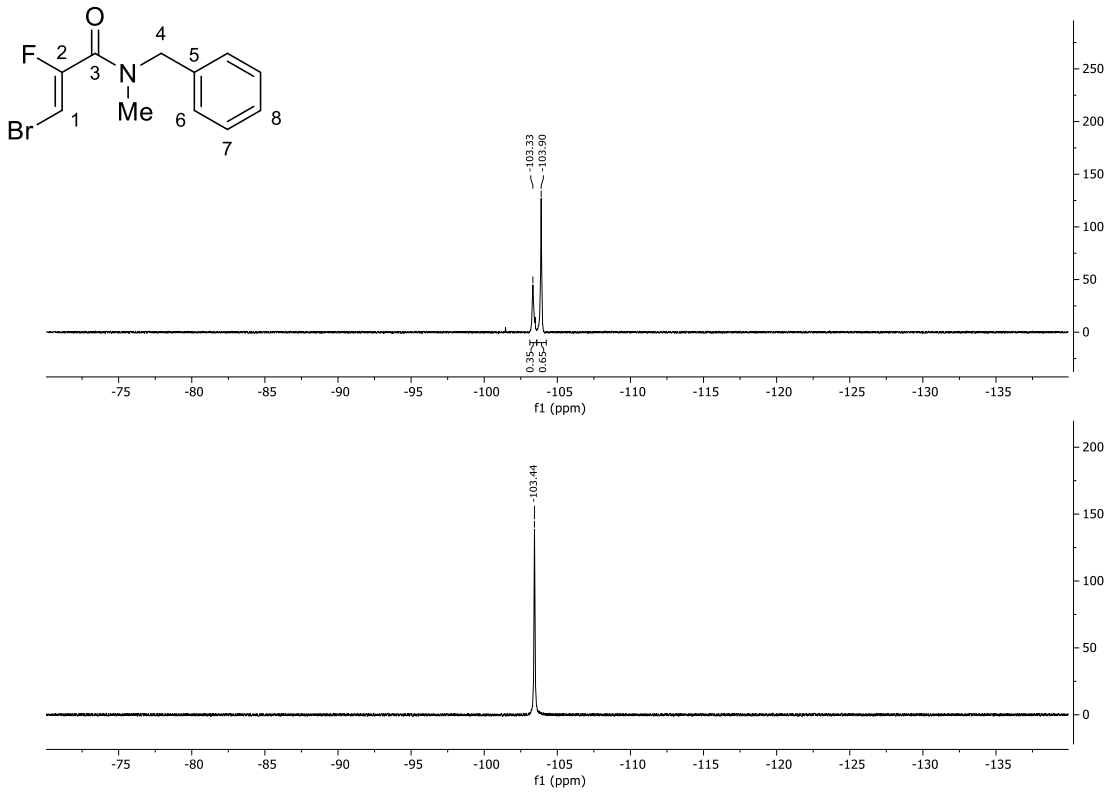

^{1}H-NMR of **S8** (500 MHz, $CDCl_3$)

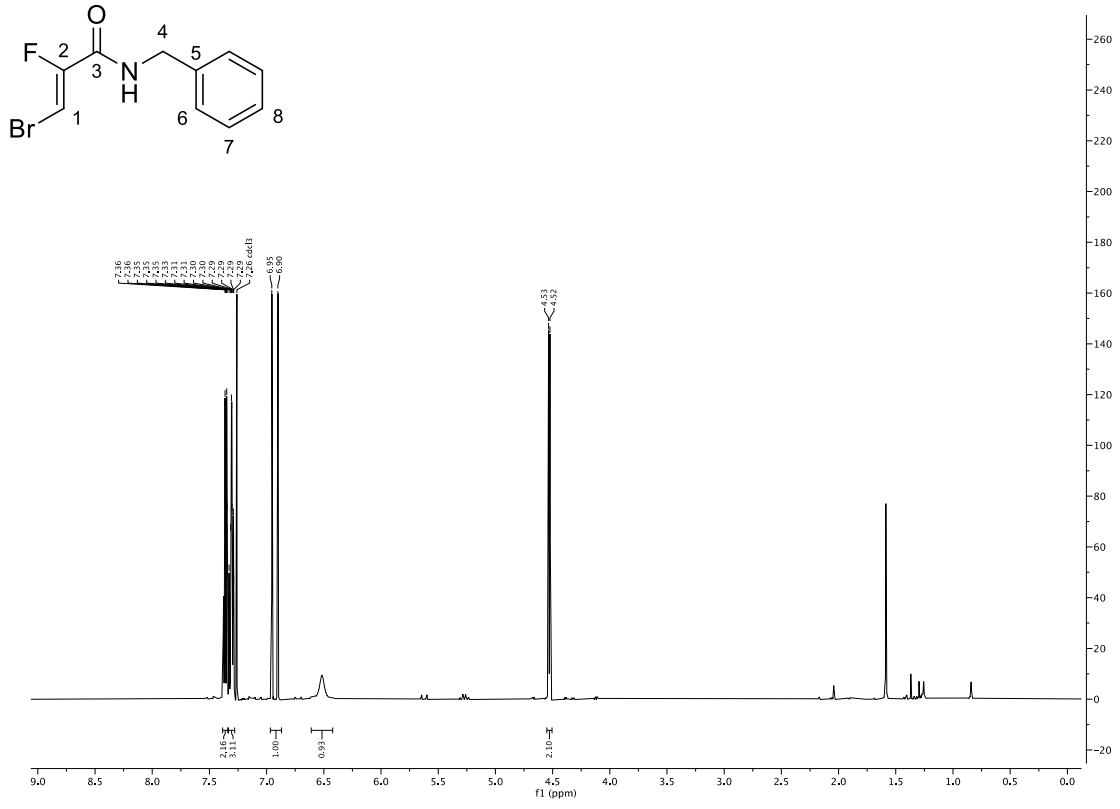

^{13}C-NMR of **S8** ($CDCl_3$)

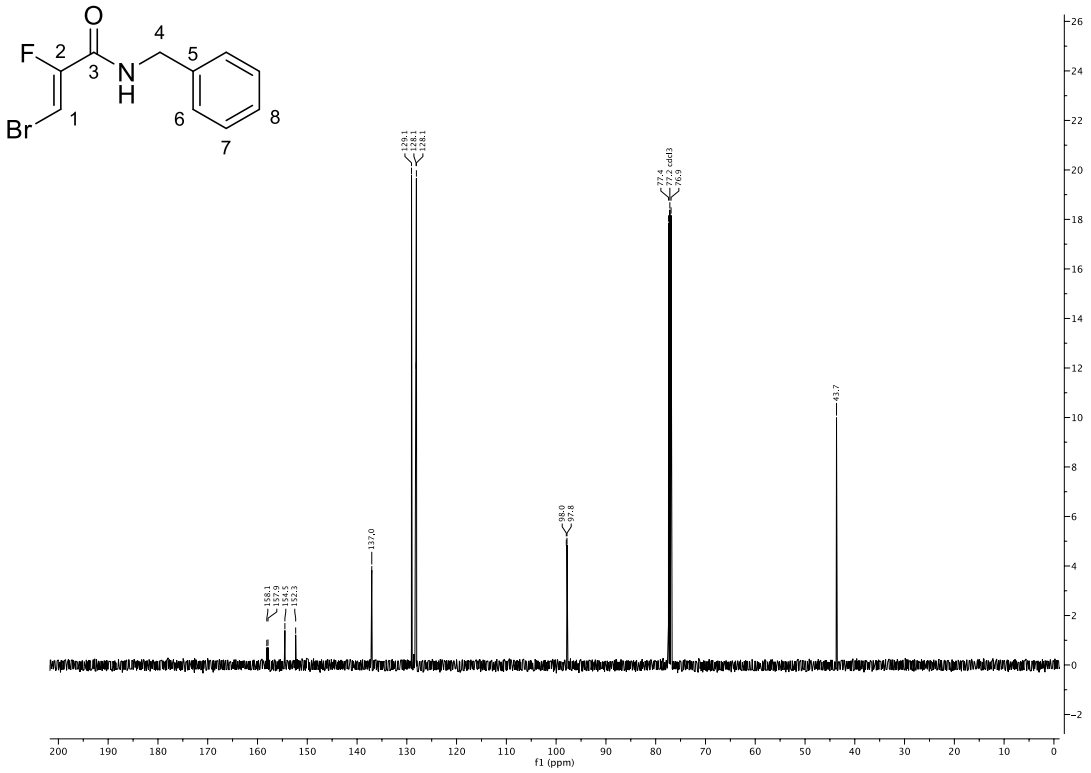

^{19}F-NMR {^{1}H} of **S8** ($CDCl_3$)

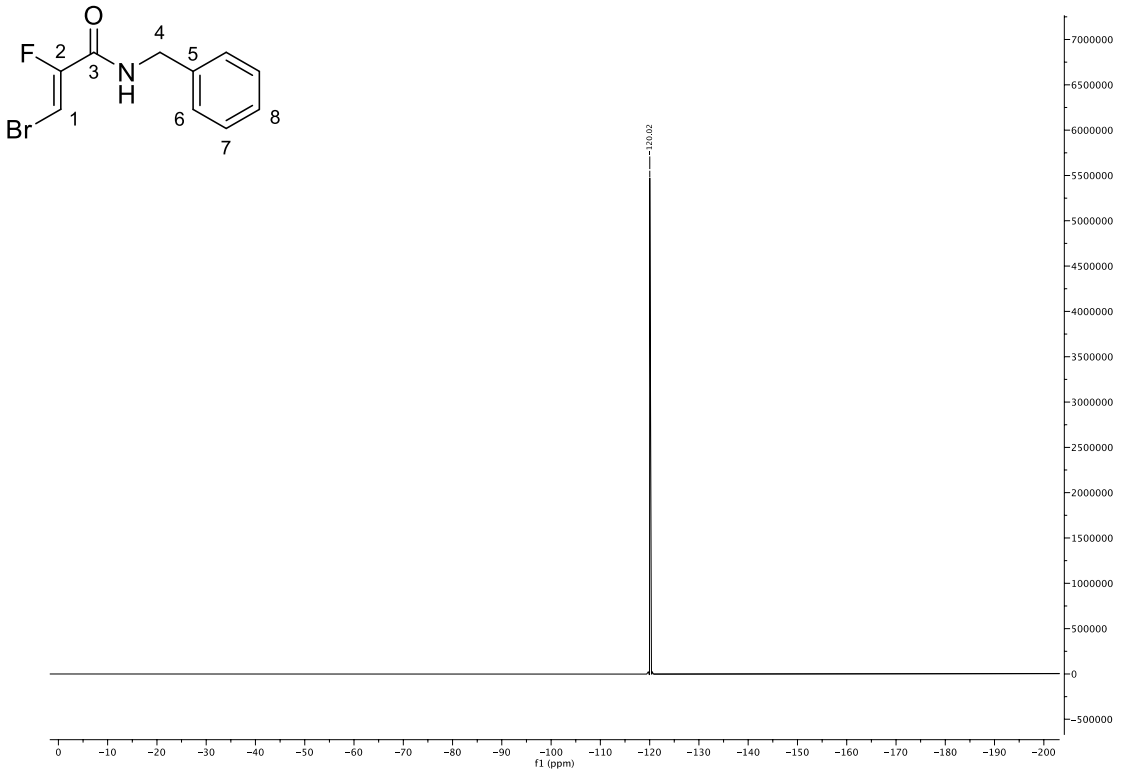

^{1}H-NMR of **S9** (500 MHz, $CDCl_3$)

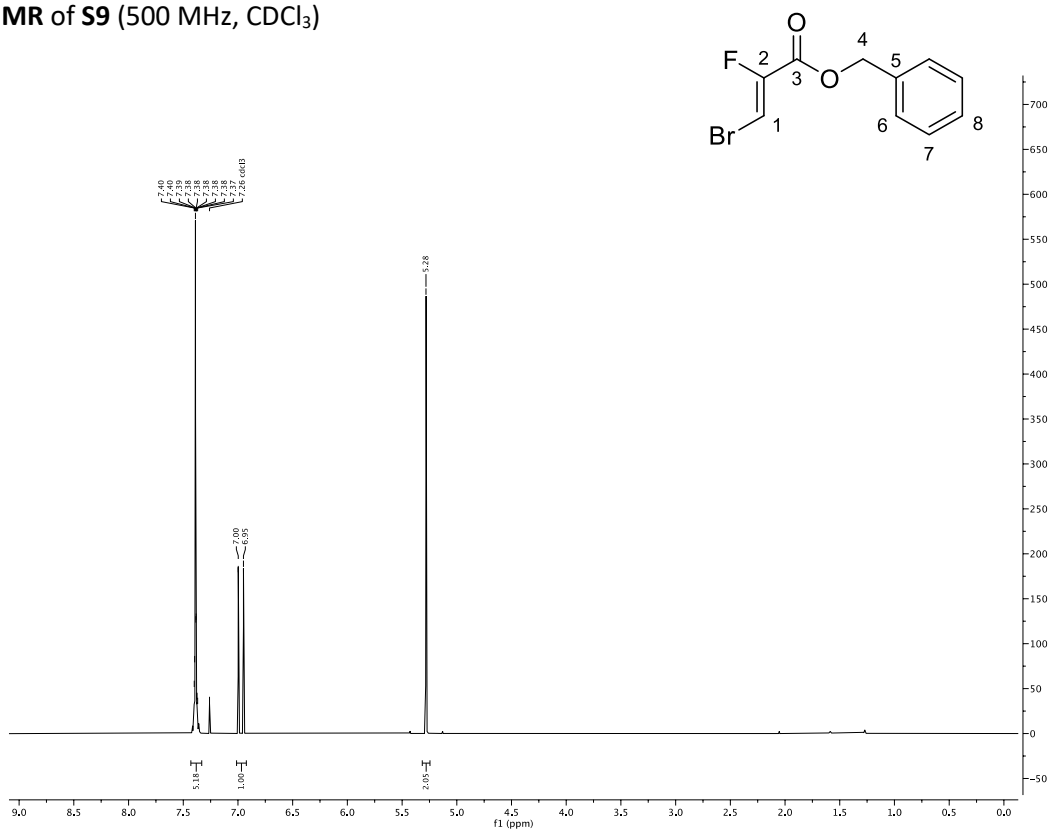

^{13}C-NMR of **S9** (126 MHz, $CDCl_3$)

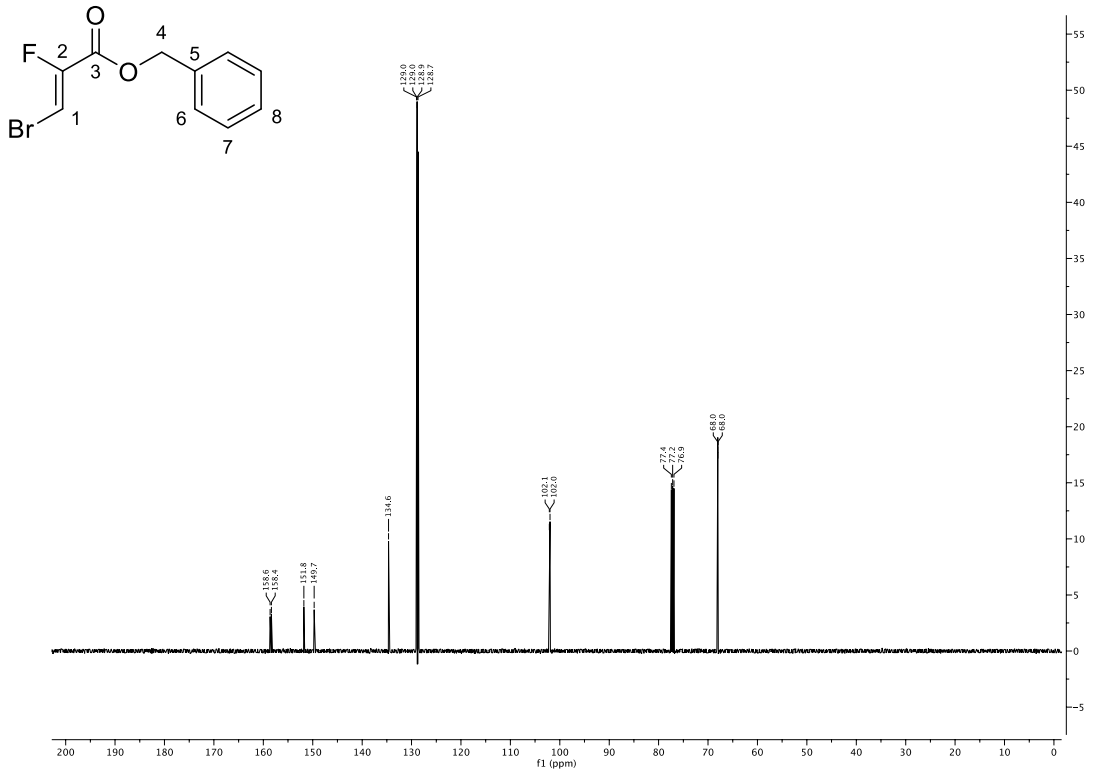

^{19}F-NMR {^{1}H} of **S9** (377 MHz, $CDCl_3$)

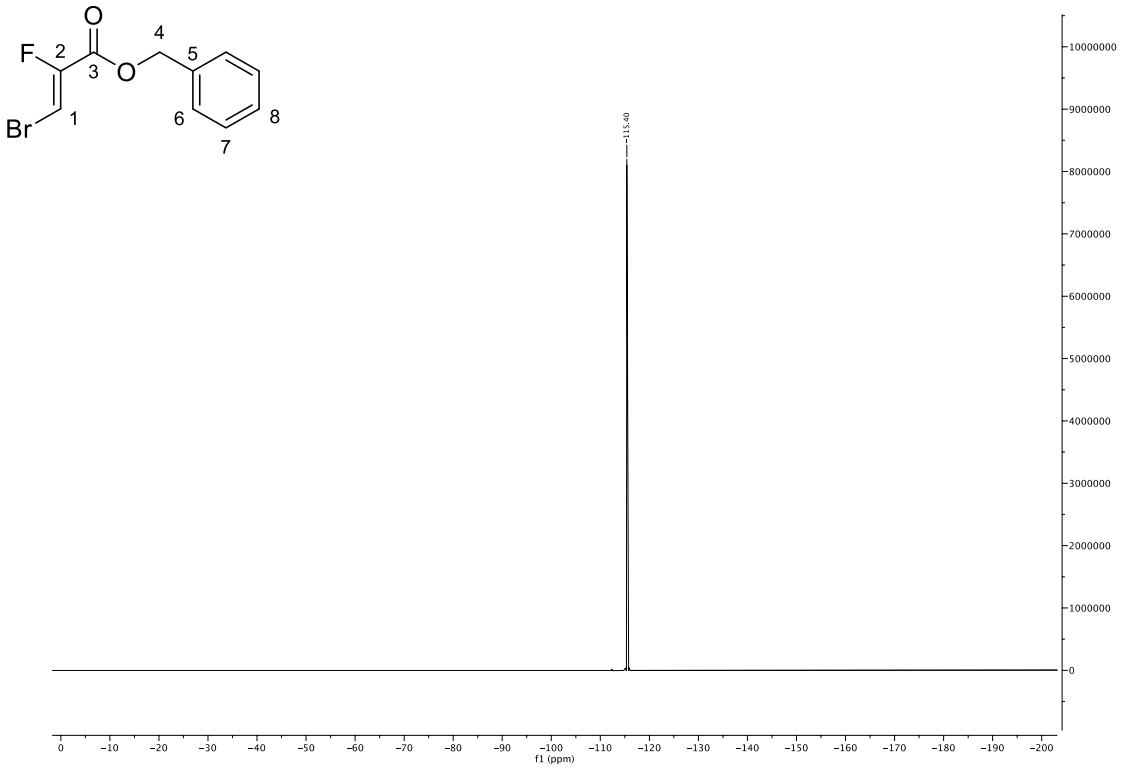

^{1}H-NMR of **S10** (599 MHz, $CDCl_3$)

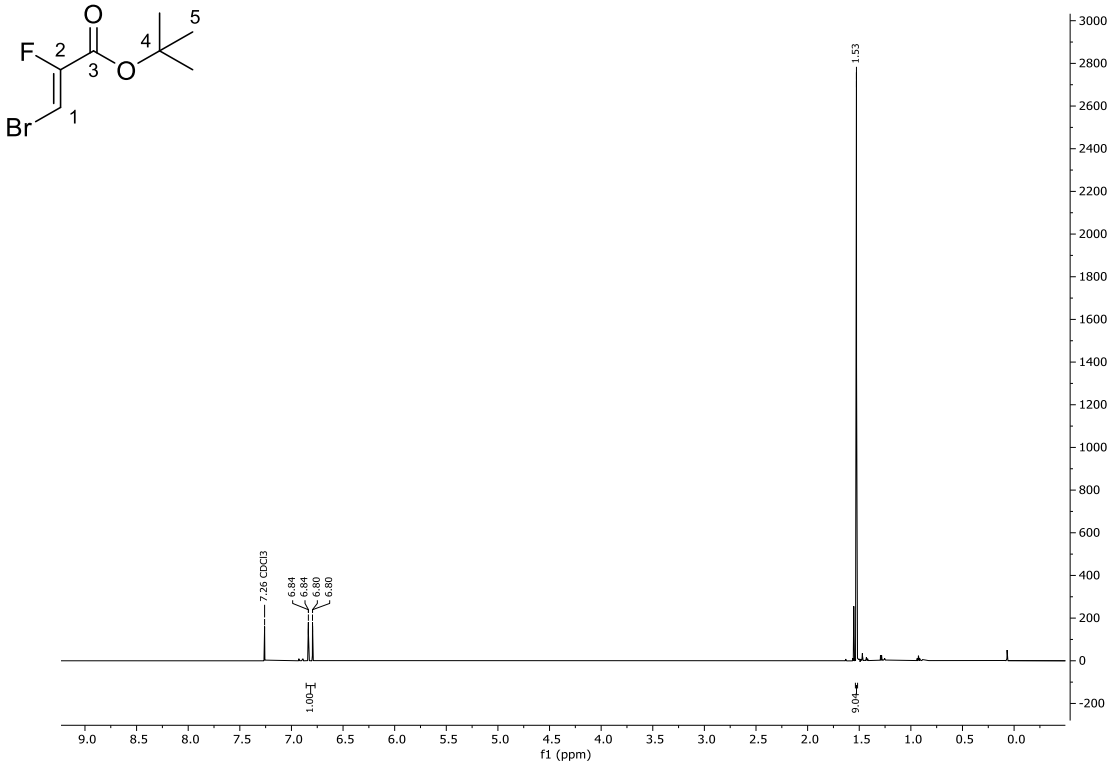

^{13}C-NMR of **S10** (151 MHz, $CDCl_3$)

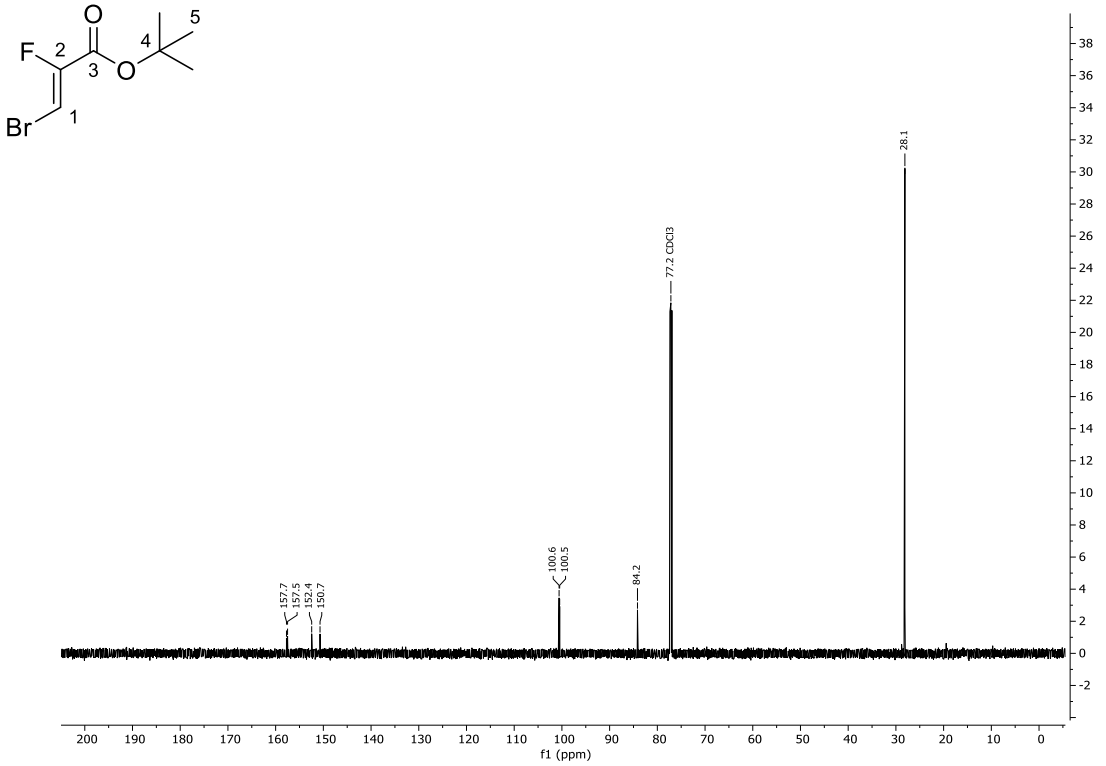

^{19}F-NMR {^{1}H} of **S10** (564 MHz, $CDCl_3$

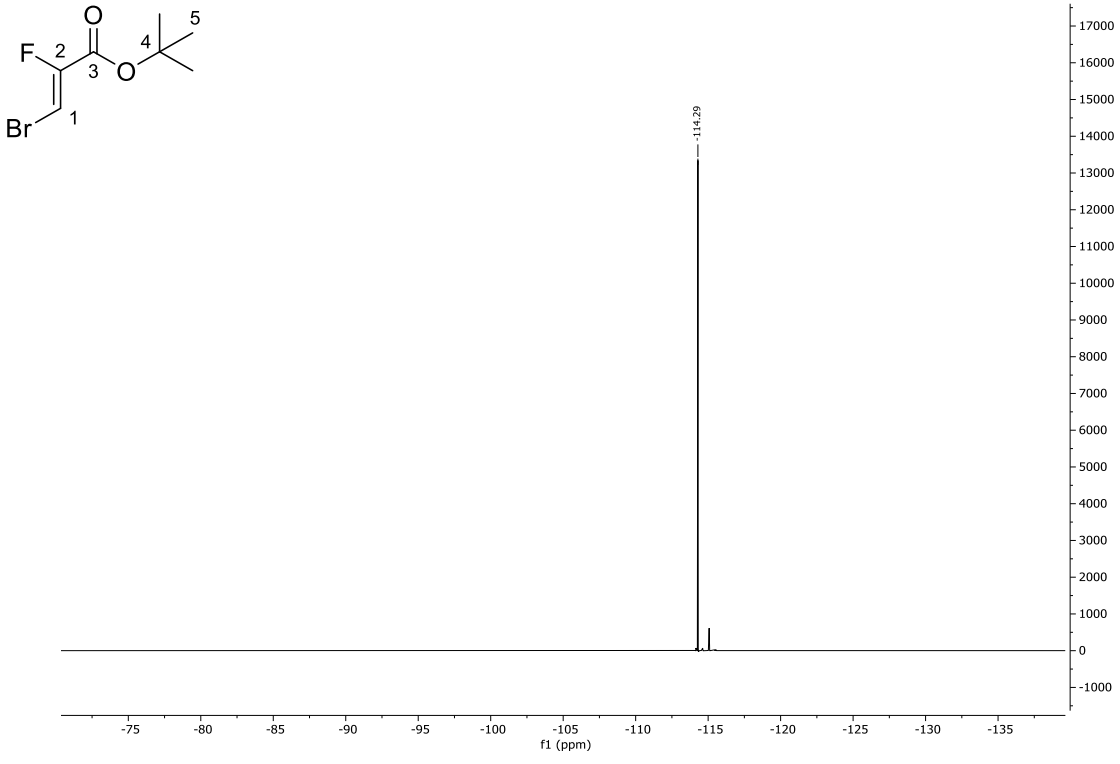

^{1}H-NMR of **S11** (500 MHz, CD_2Cl_2)

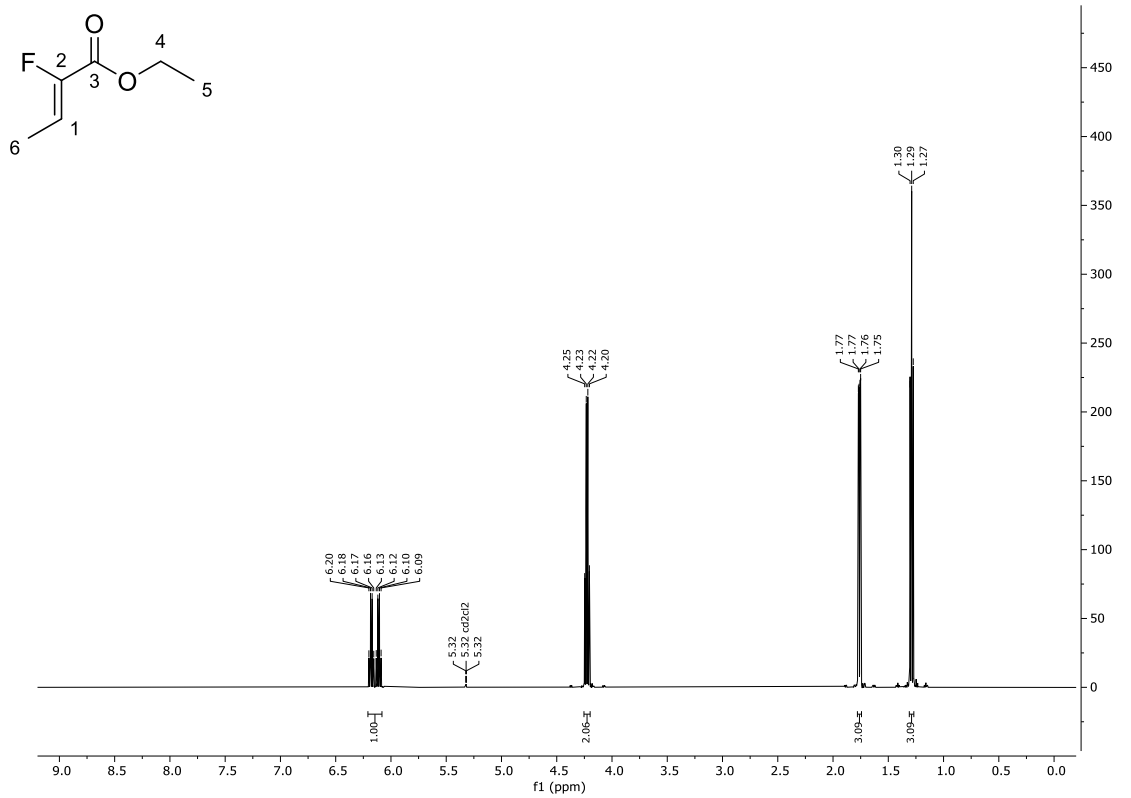

^{13}C-NMR of **S11** (126 MHz, CD_2Cl_2)

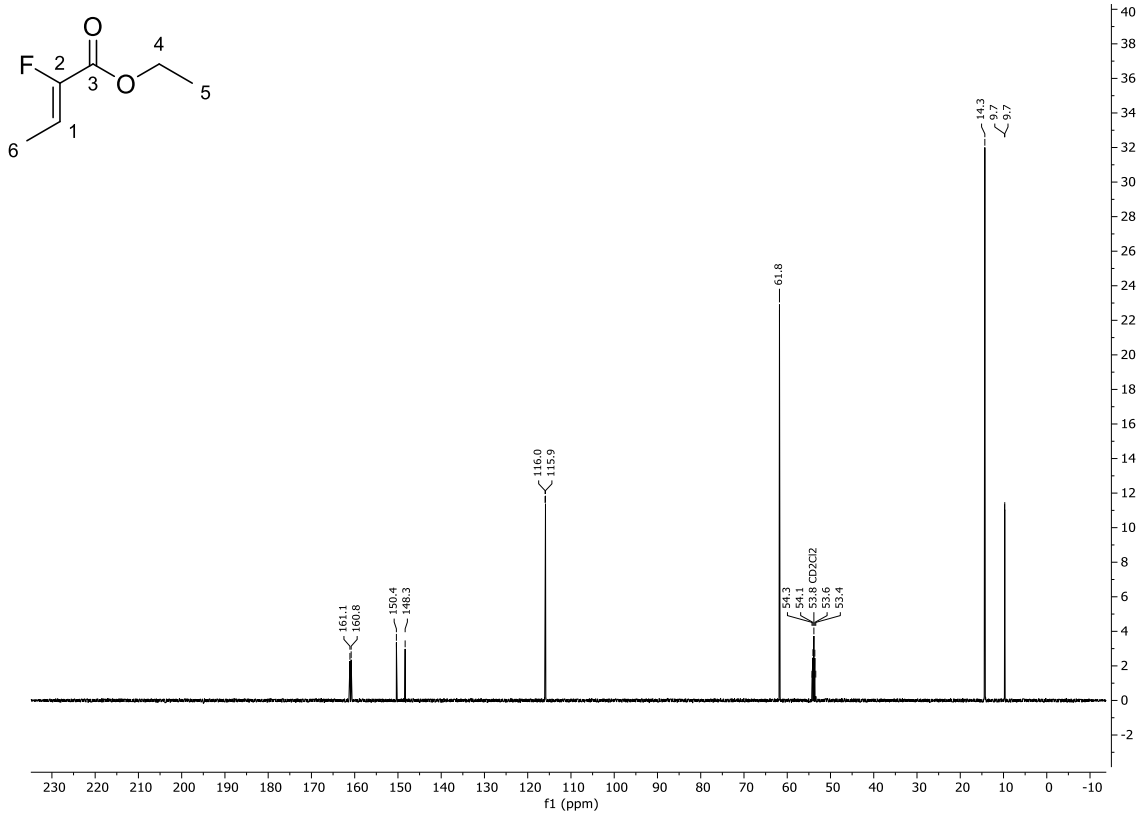

^{19}F-NMR {^{1}H} of **S11** (377 MHz, CD_2Cl_2)

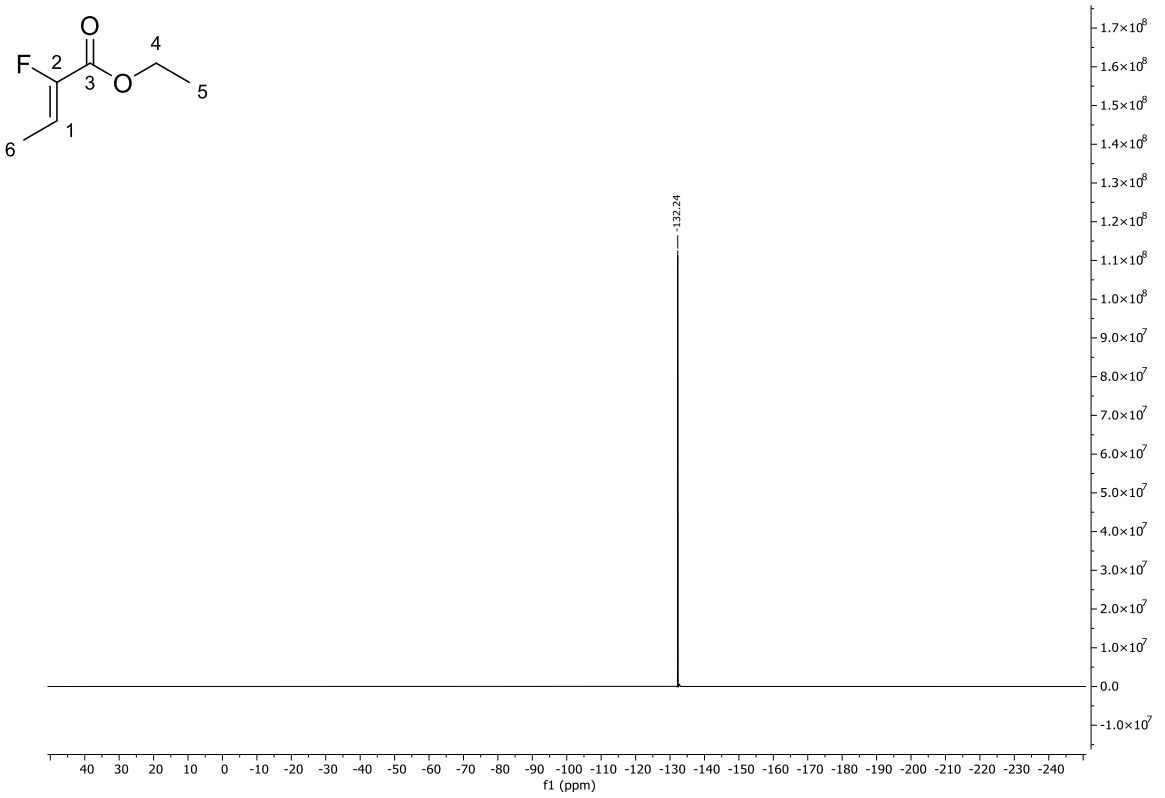

^{1}H-NMR of **S12** (500 MHz, $CDCl_3$)

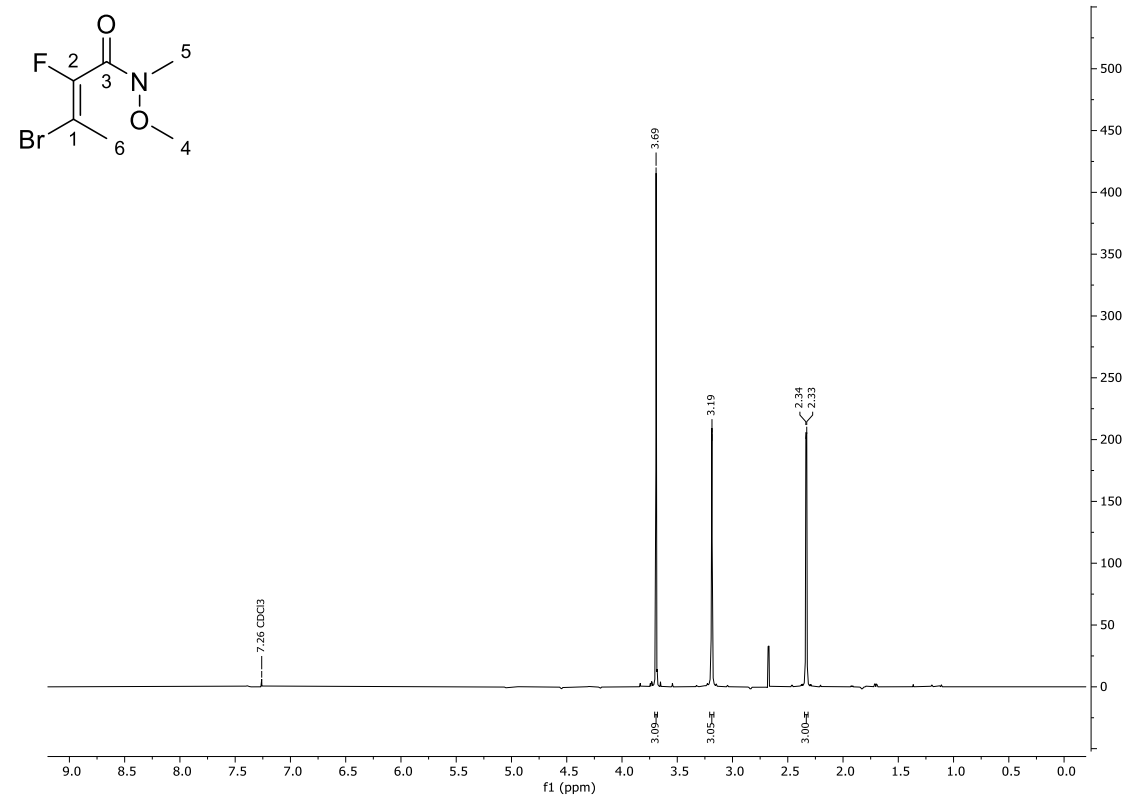

^{13}C-NMR of **S12** ($CDCl_3$)

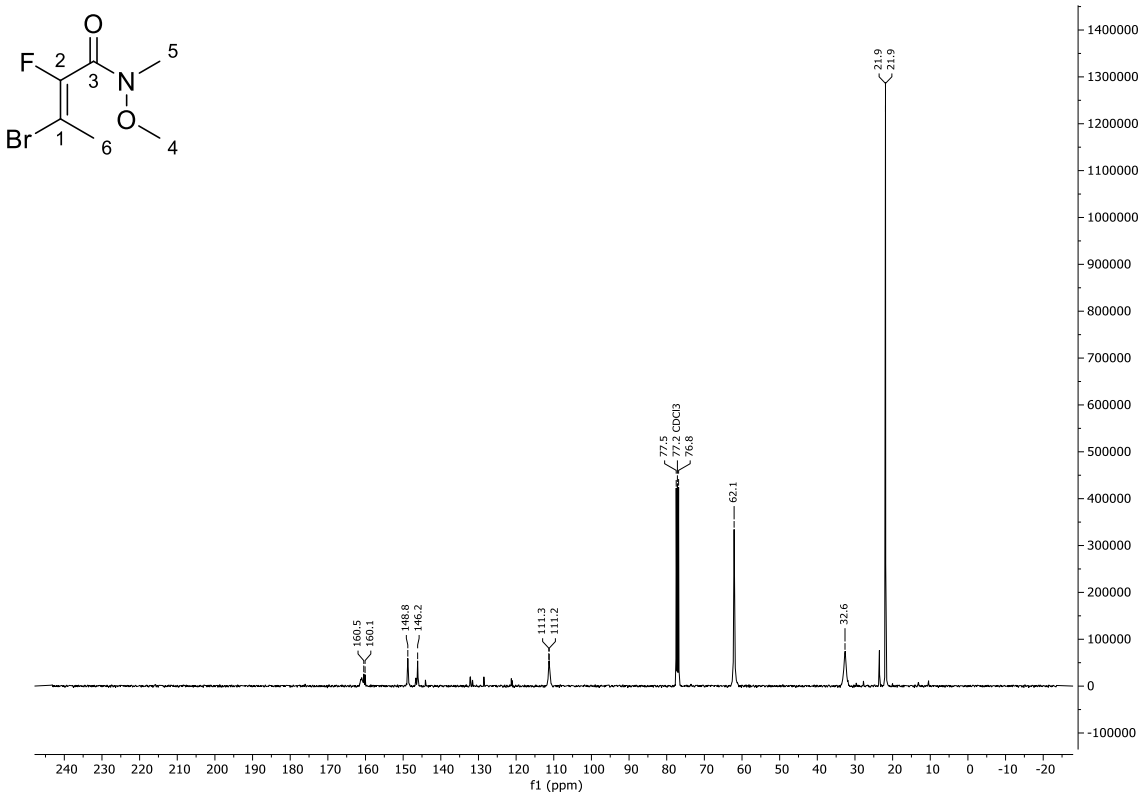

^{19}F-NMR {^{1}H} of **S12** ($CDCl_3$)

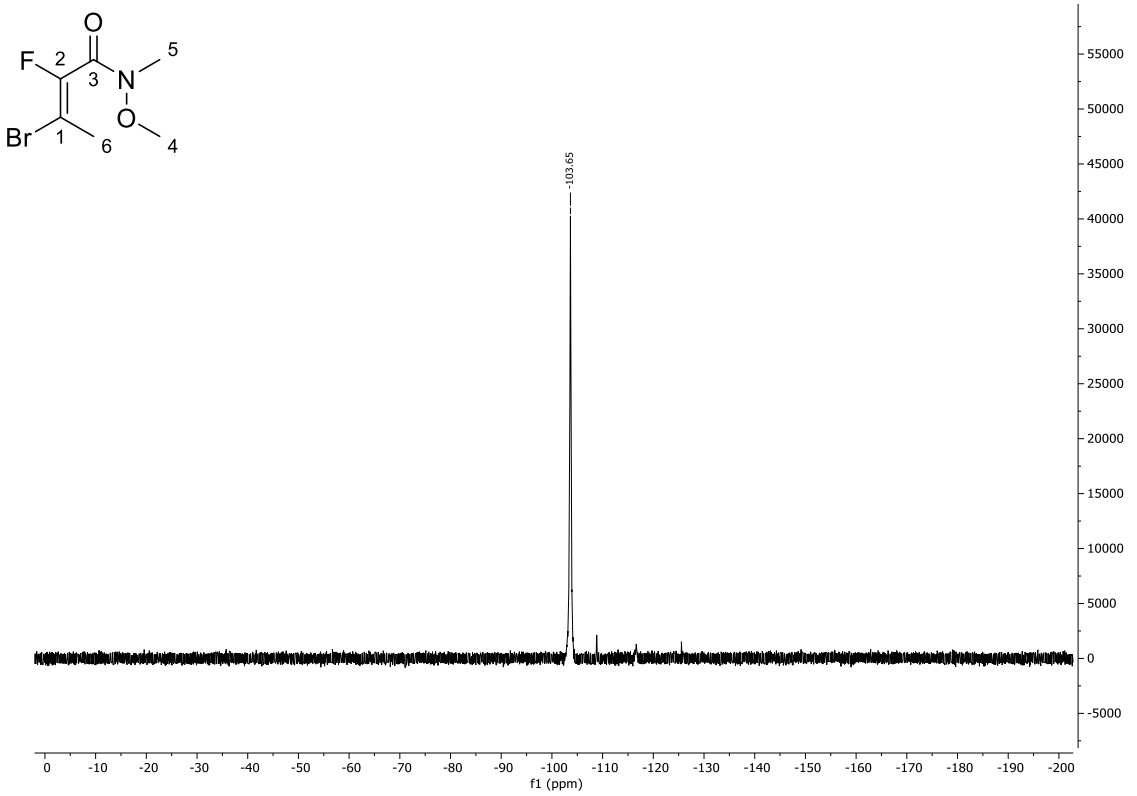

^{1}H-NMR of **S13** (599 MHz, $CDCl_3$)

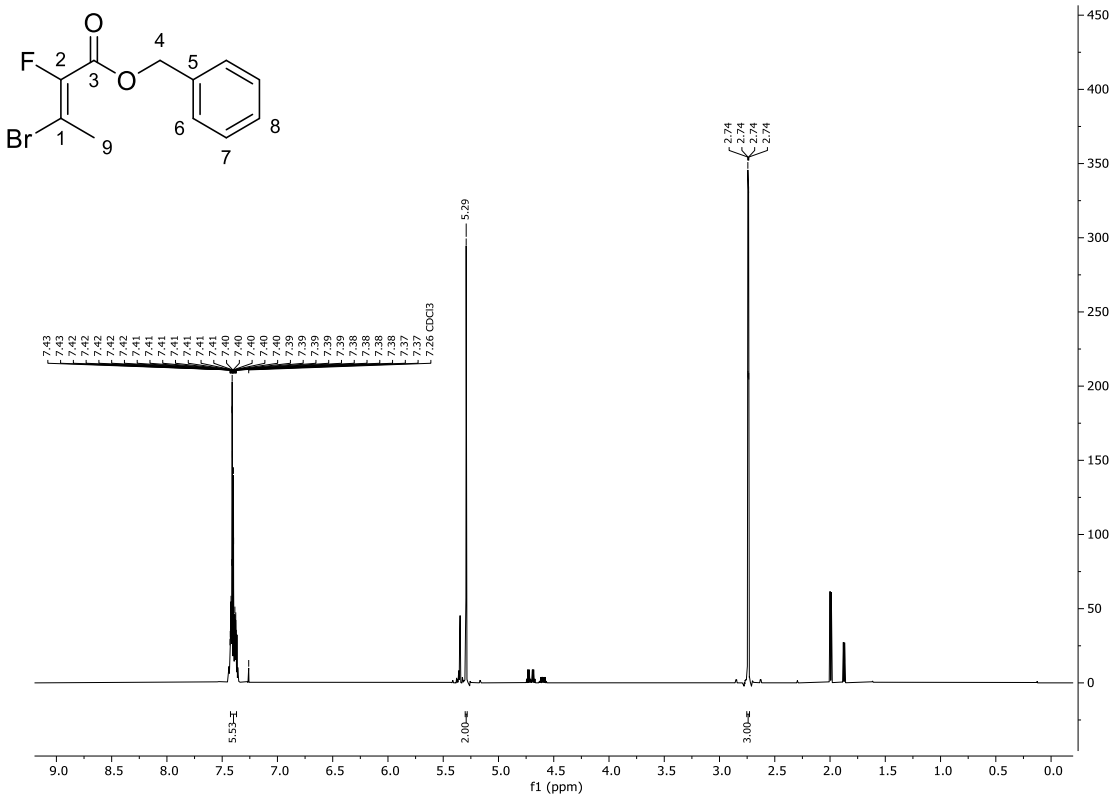

^{13}C-NMR of **S13** (151 MHz, $CDCl_3$)

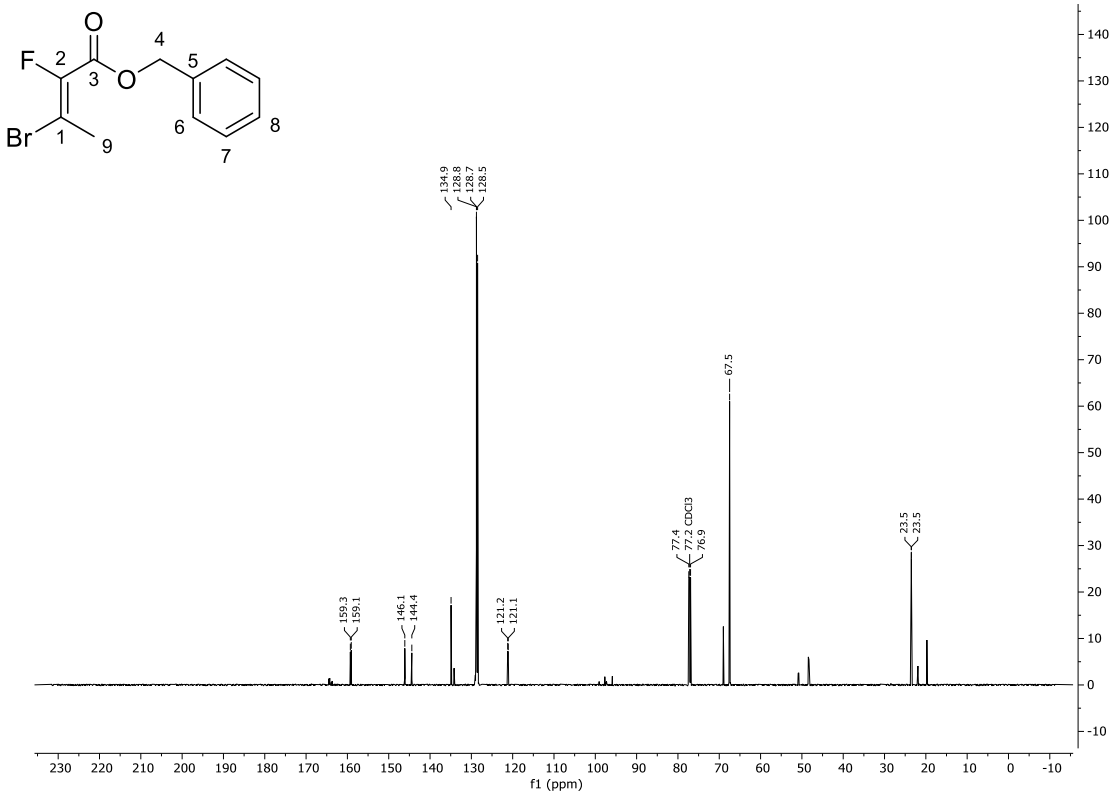

^{19}F-NMR {^{1}H} of **S13** (377 MHz, $CDCl_3$)

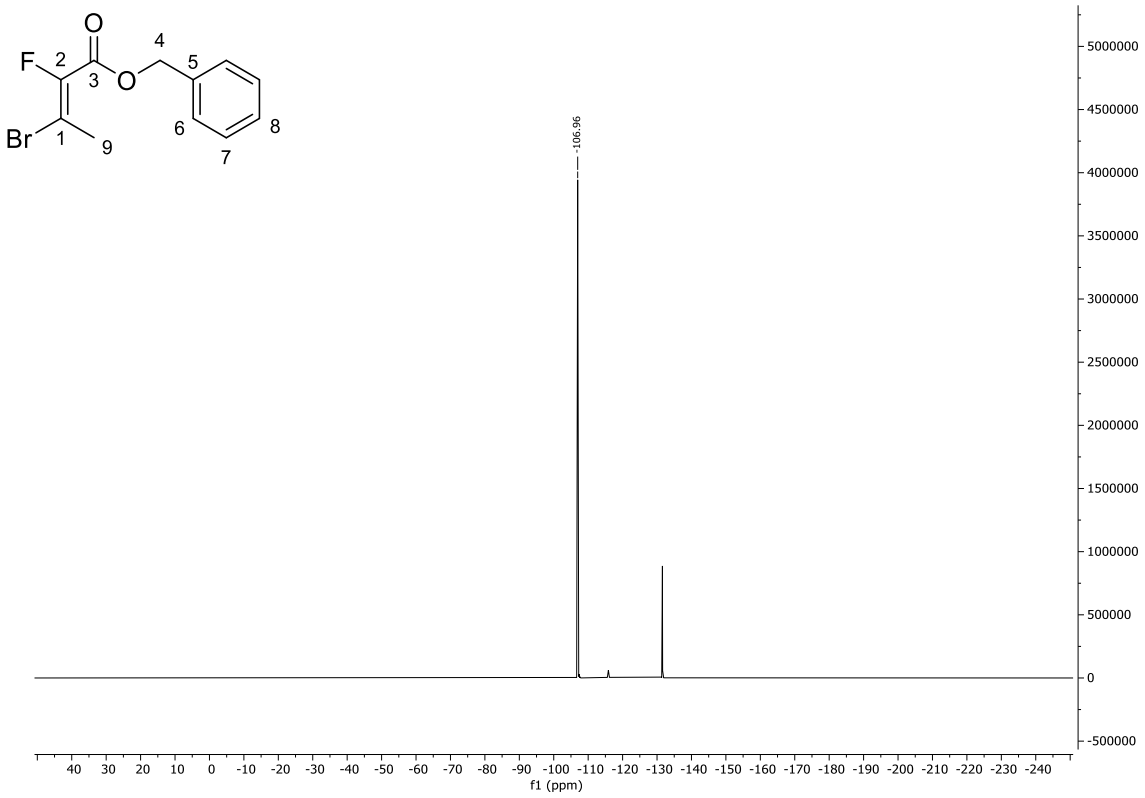

^{1}H-NMR of **S14** (500 MHz, $CDCl_3$)

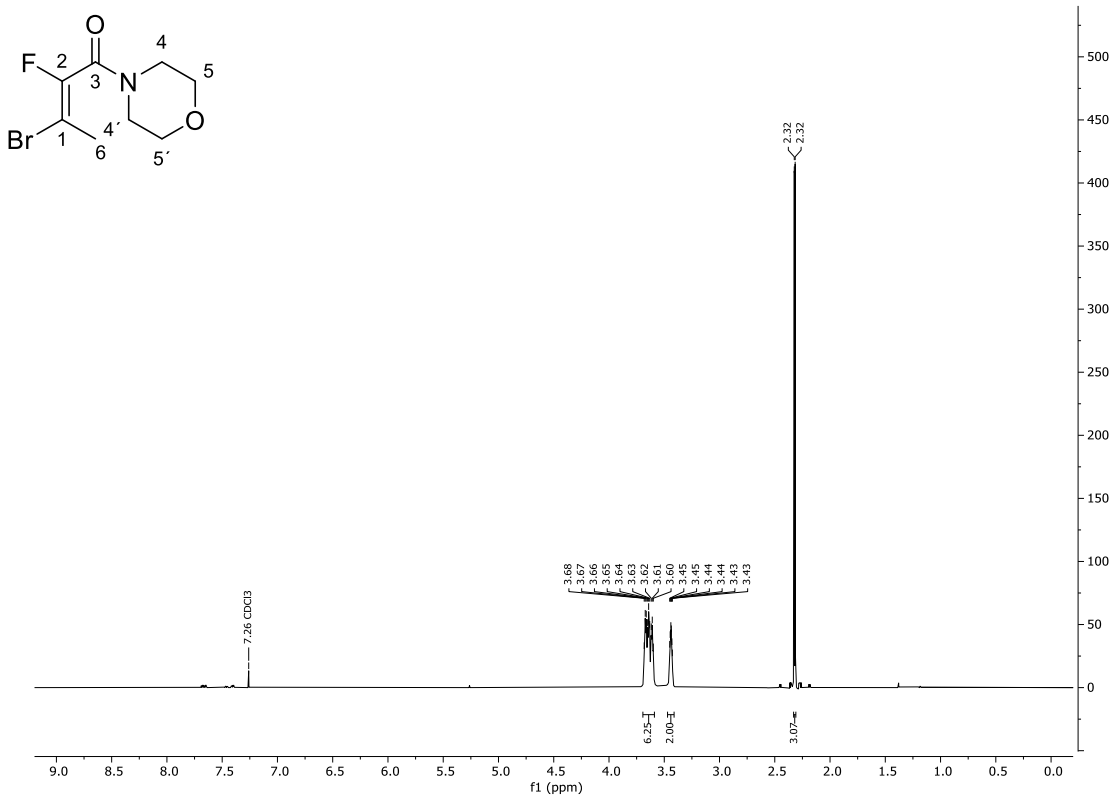

^{13}C-NMR of **S14** (126 MHz, $CDCl_3$)

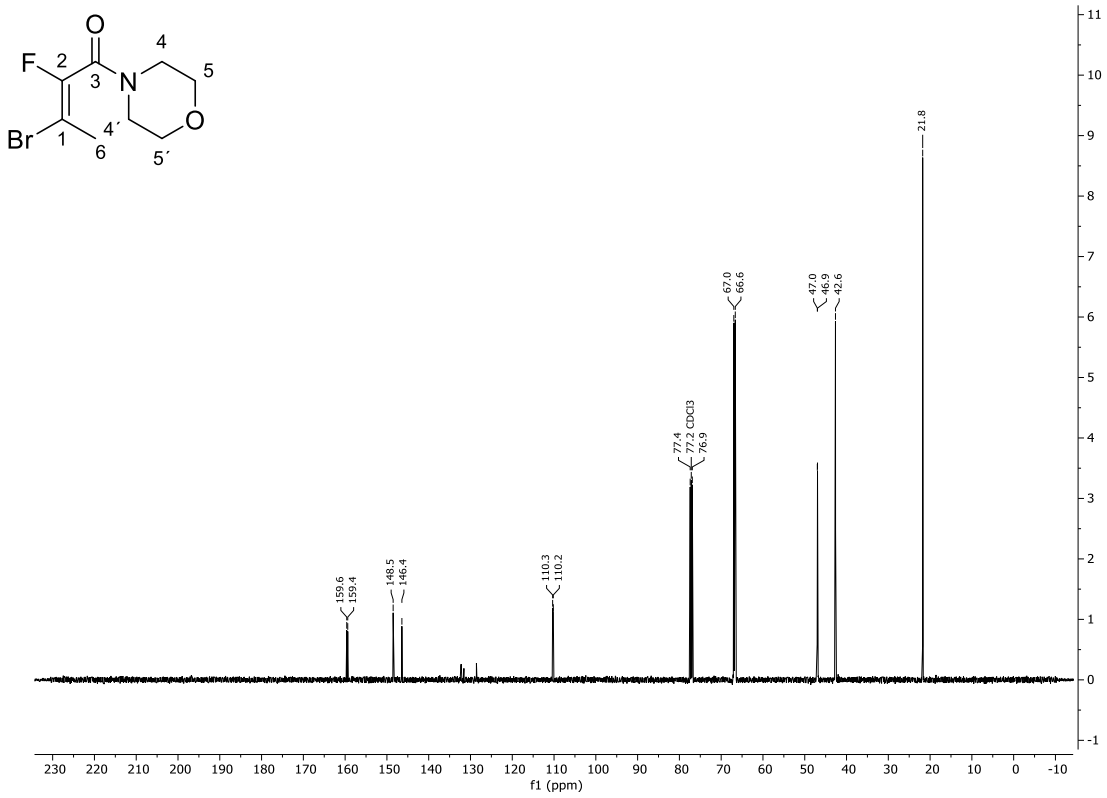

^{19}F-NMR {^{1}H} of **S14** (470 MHz, $CDCl_3$)

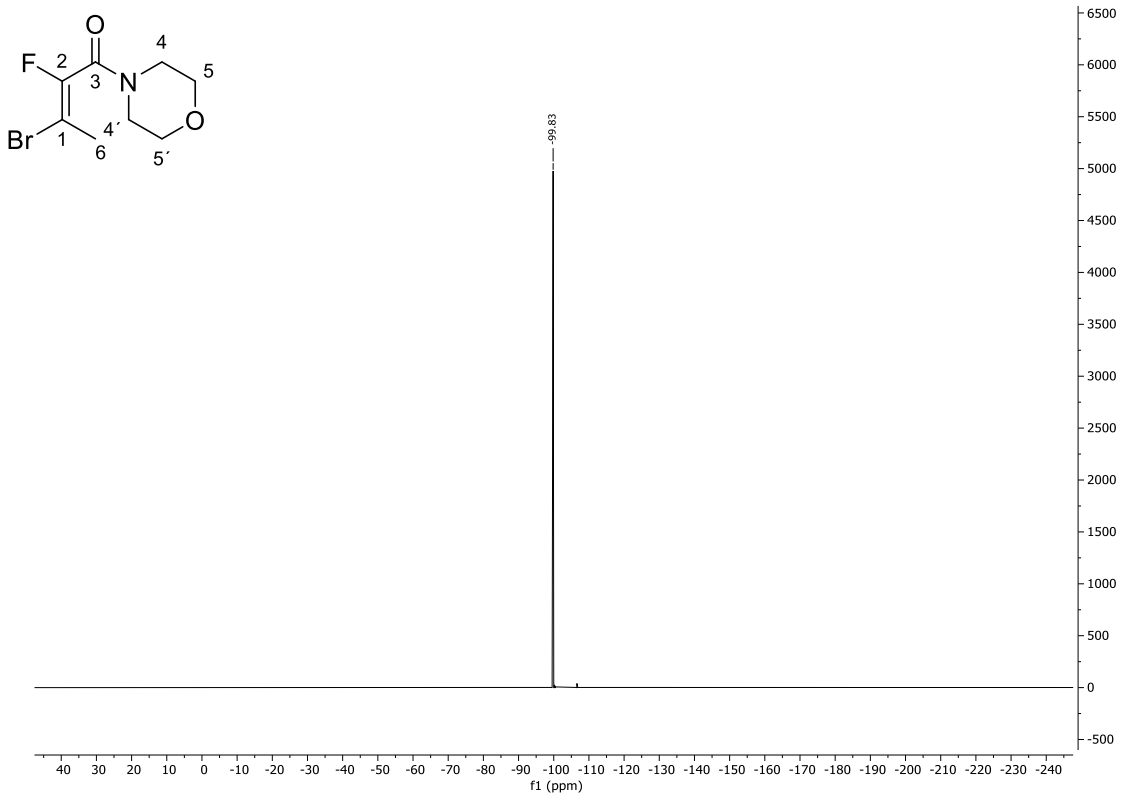

^{1}H-NMR of **S15** (400 MHz, $CDCl_3$)

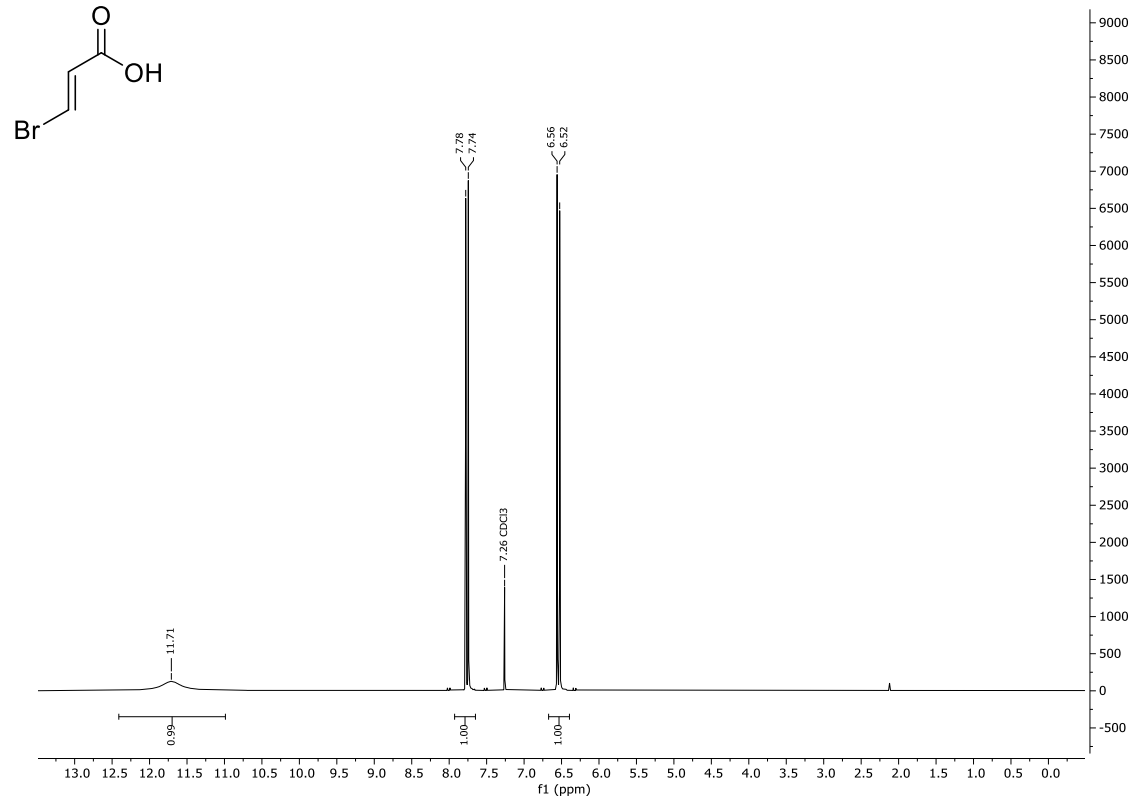

^{1}H-NMR of **S16** (400 MHz, $CDCl_3$)

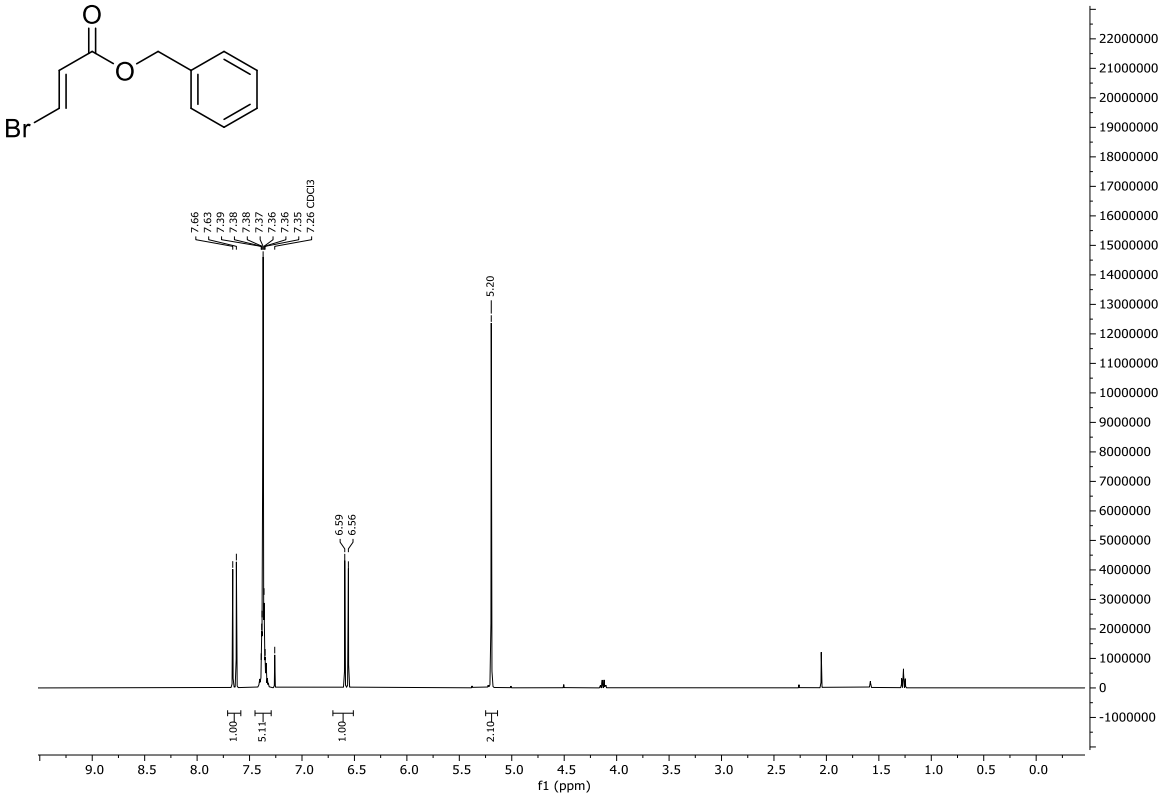

^{1}H-NMR of **S18** (599 MHz, $CDCl_3$)

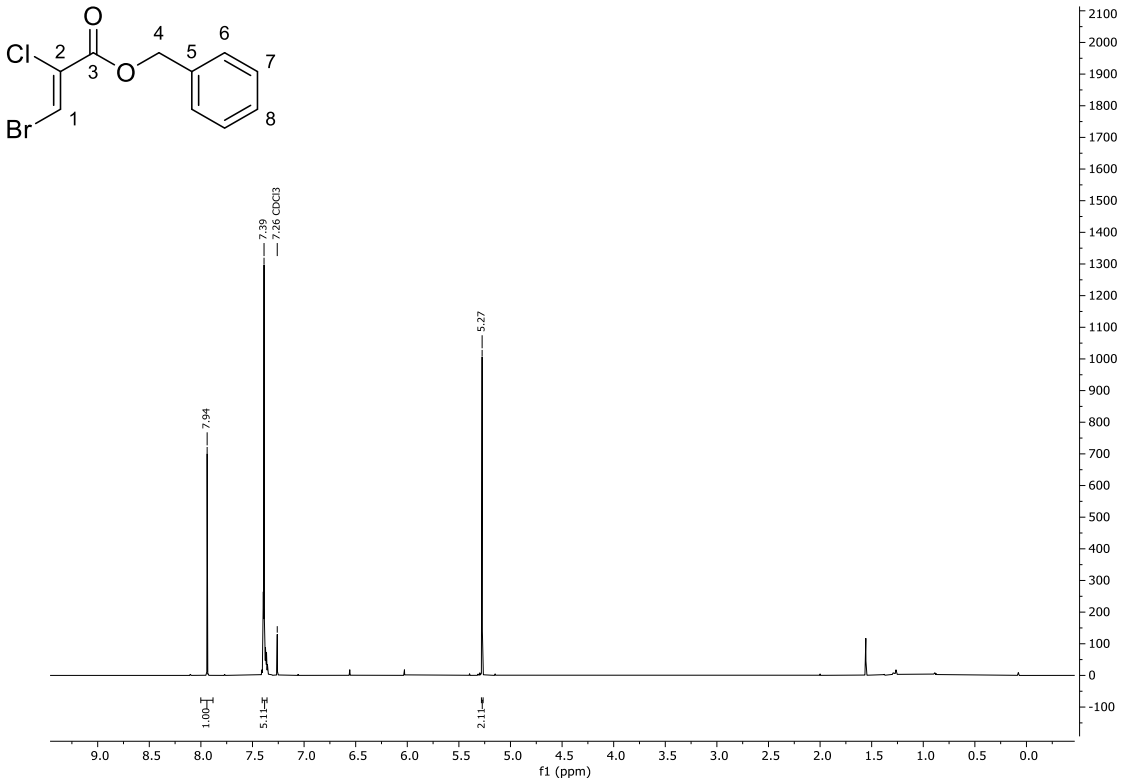

^{13}C-NMR of **S18** (151 MHz, $CDCl_3$)

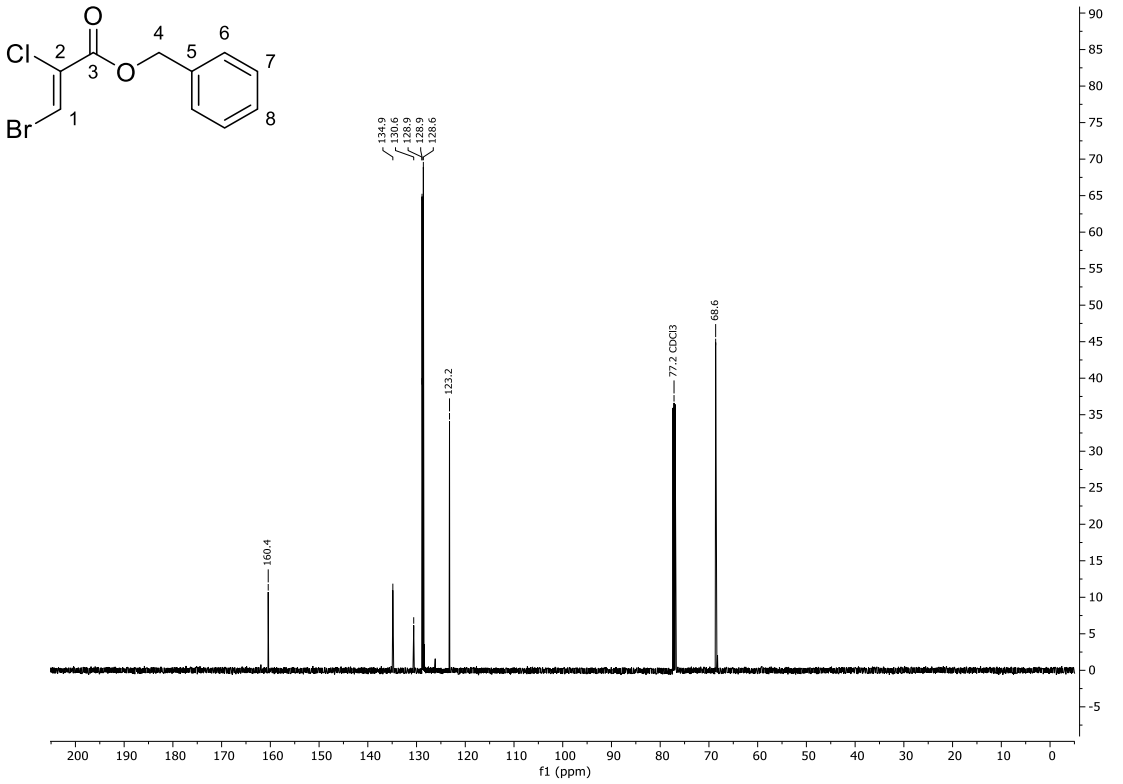

^{1}H-NMR of **S19** (599 MHz, $CDCl_3$)

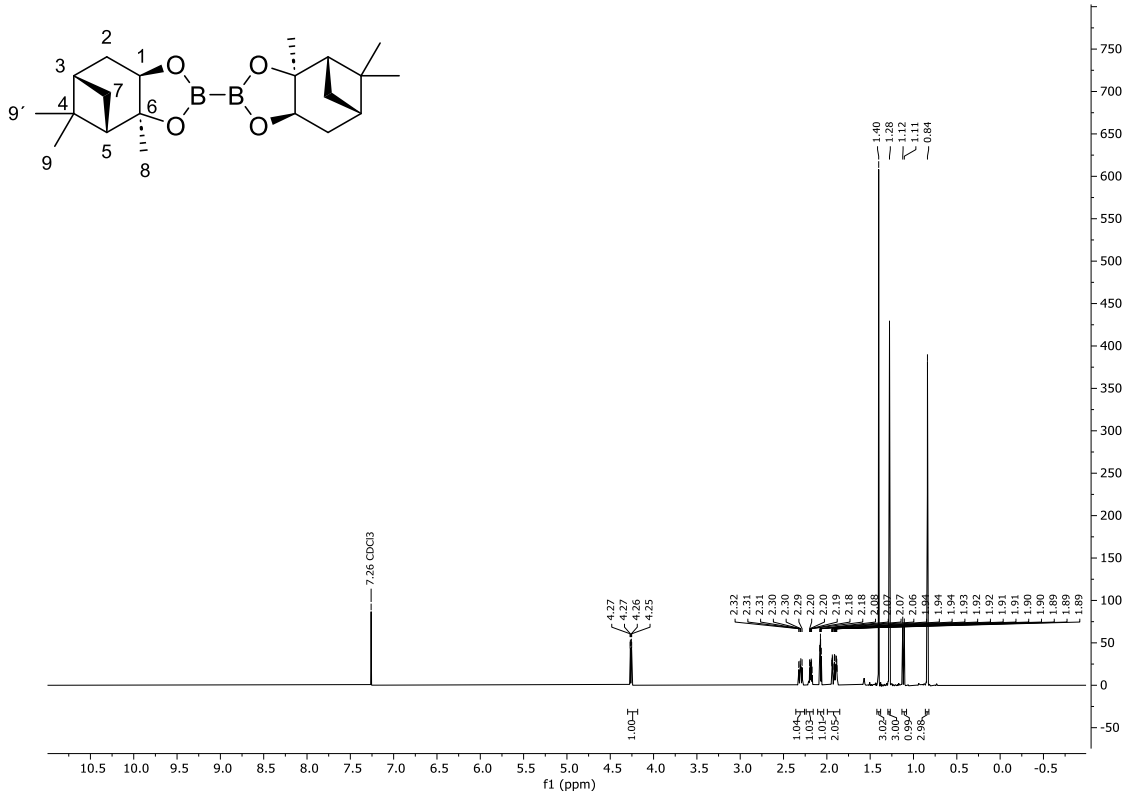

^{13}C-NMR of **S19** (151 MHz, $CDCl_3$)

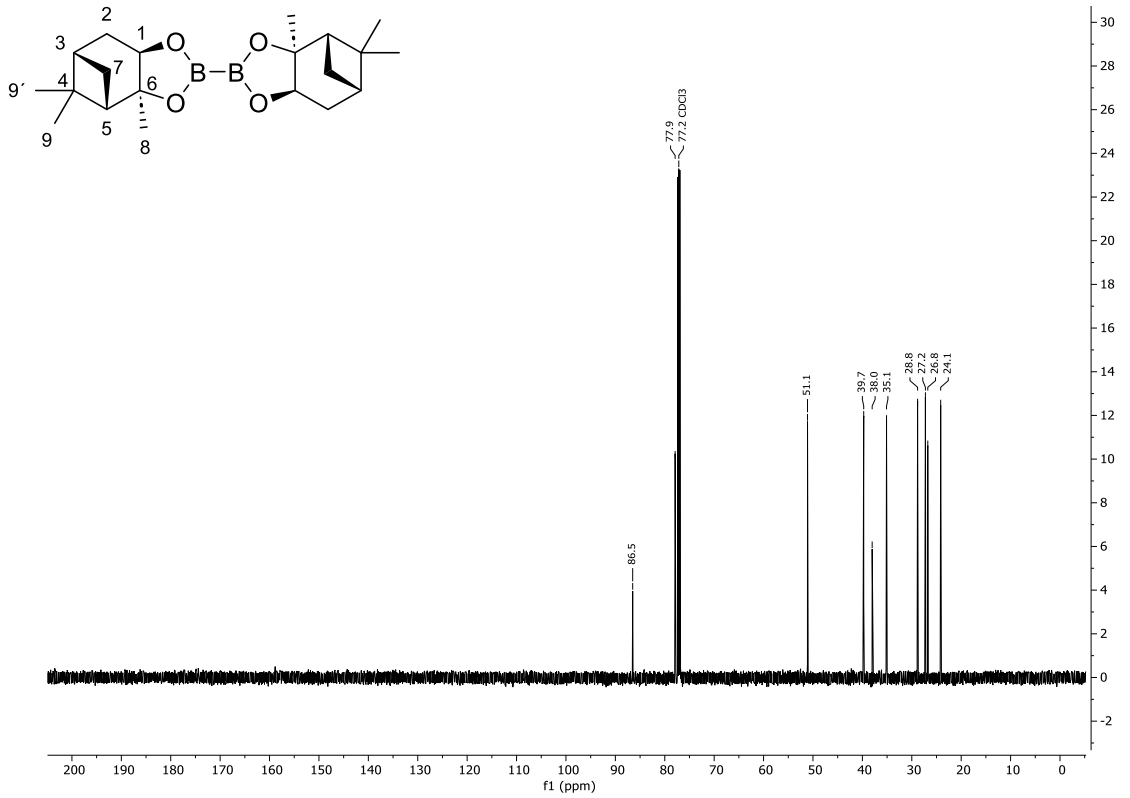

^{1}H-NMR of ***Z*-1** (599 MHz, $CDCl_3$)

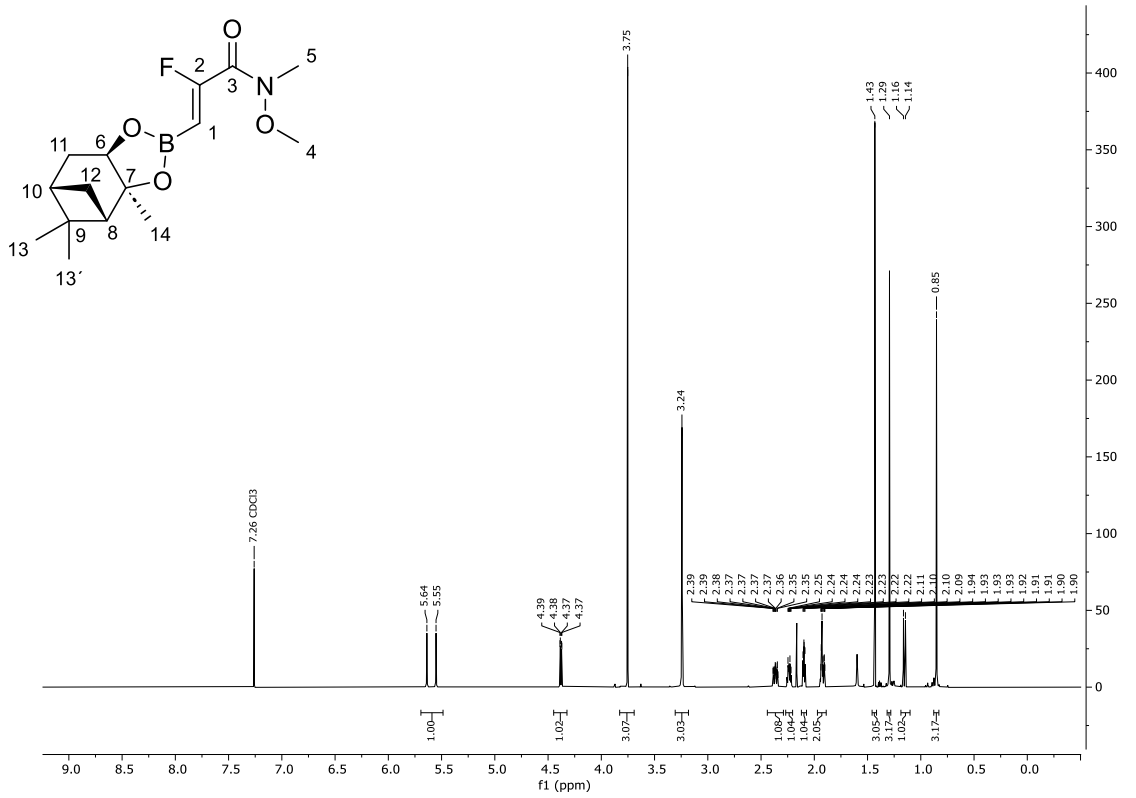

^{13}C-NMR of ***Z*-1** (101 MHz, $CDCl_3$)

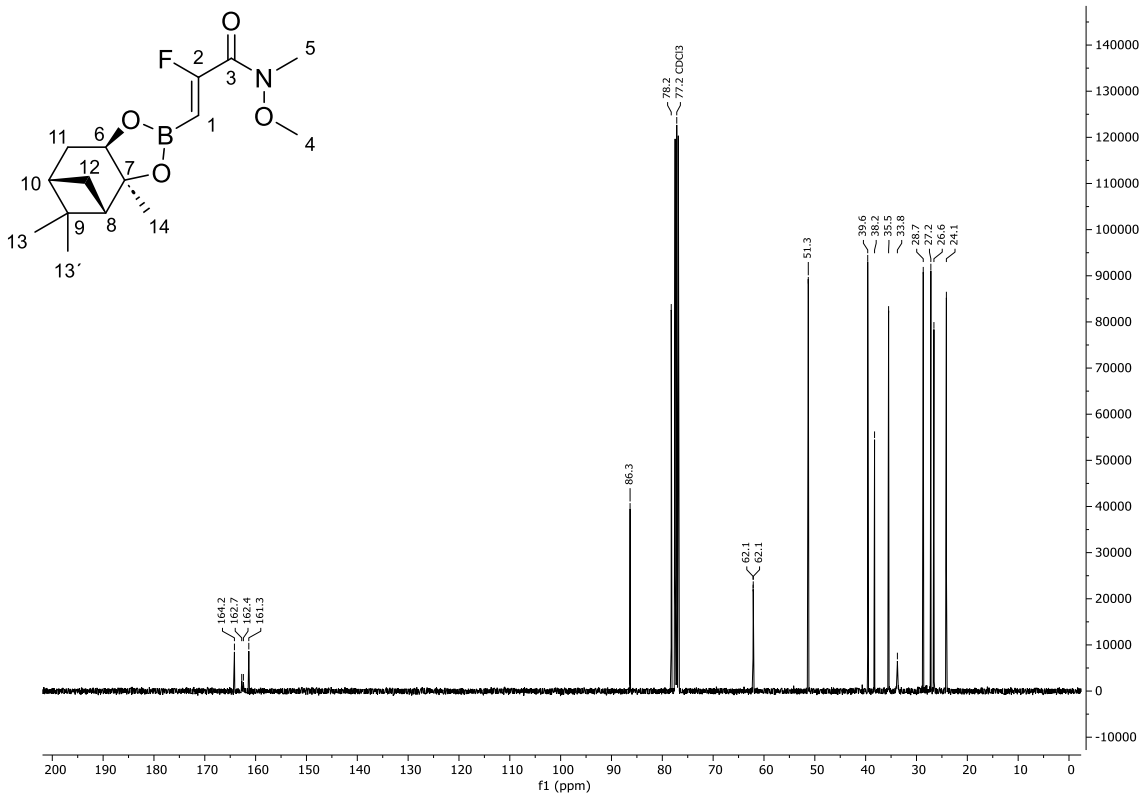

^{19}F-NMR {^{1}H} of ***Z*-1** (377 MHz, $CDCl_3$)

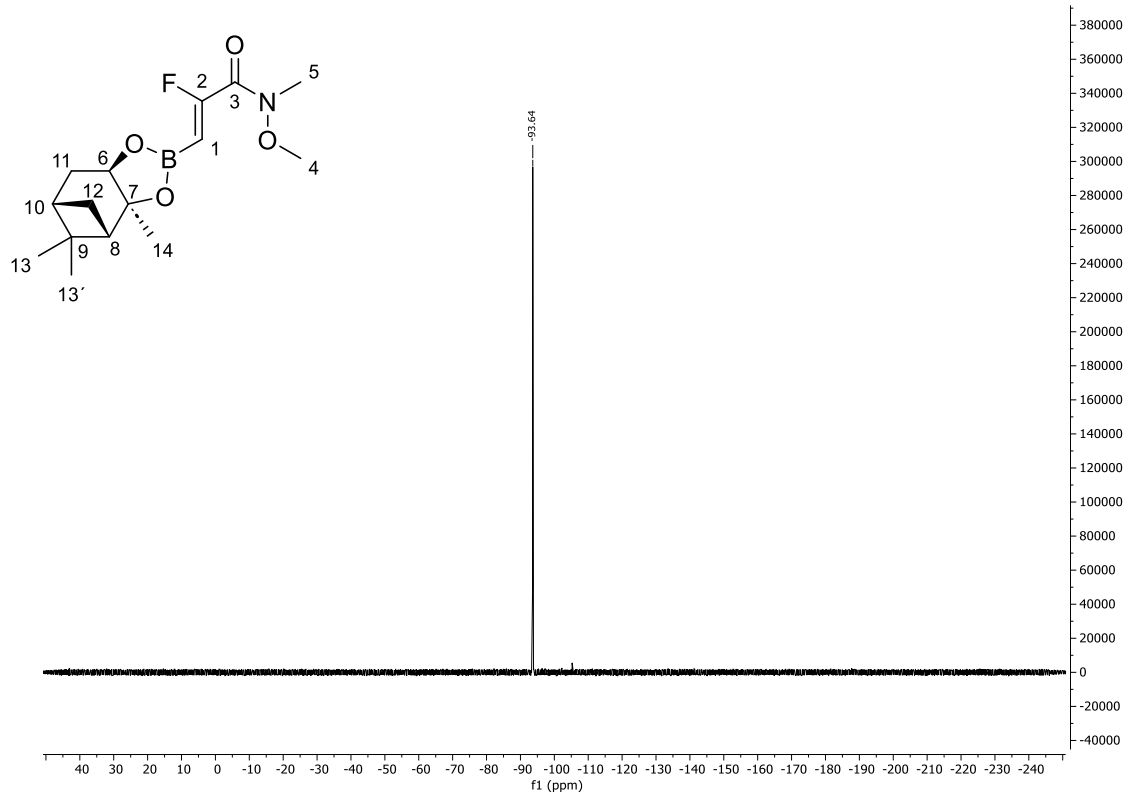

^{1}H-NMR of **S20** (500 MHz, $CDCl_3$)

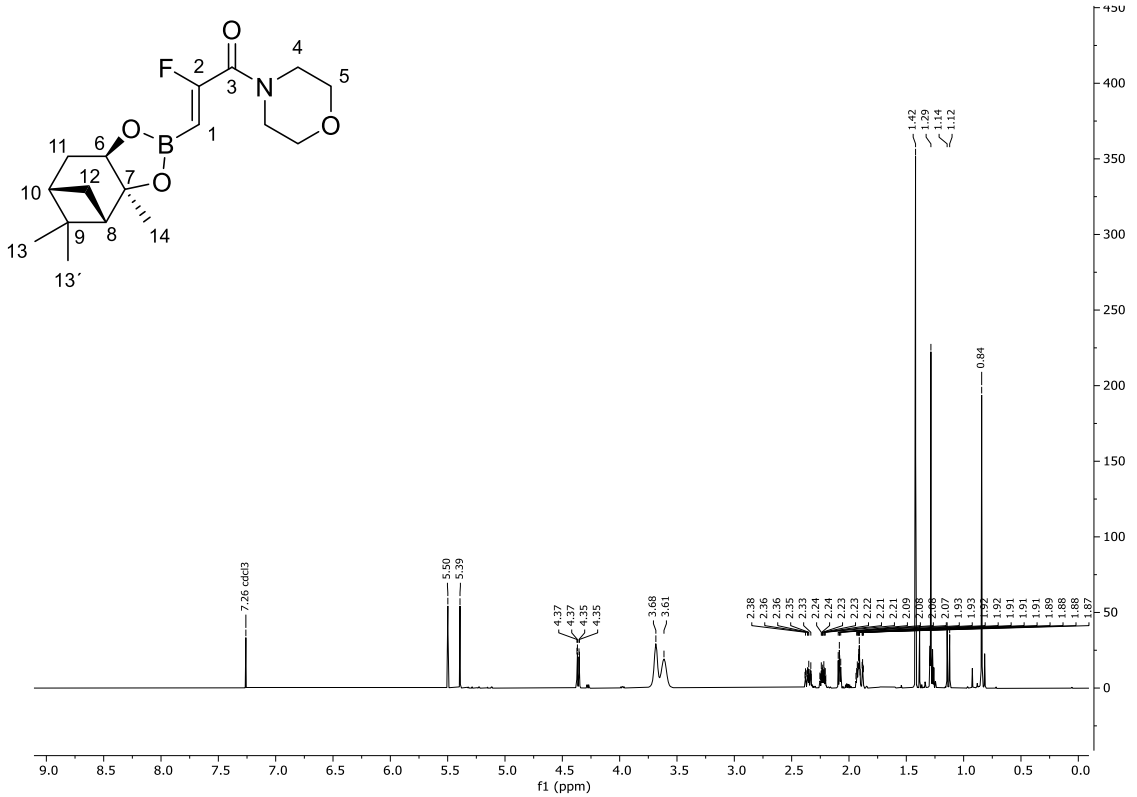

^{13}C-NMR of **S20** (126 MHz, $CDCl_3$)

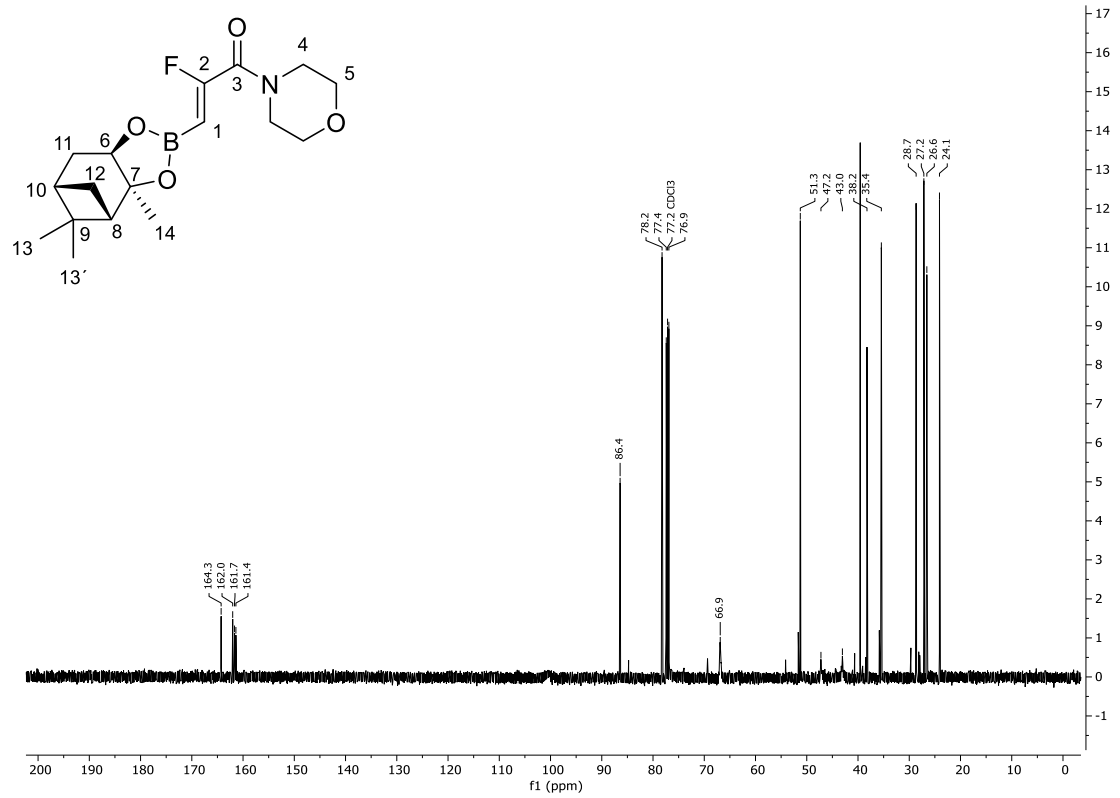

^{19}F-NMR {^{1}H} of **S20** (377 MHz, $CDCl_3$)

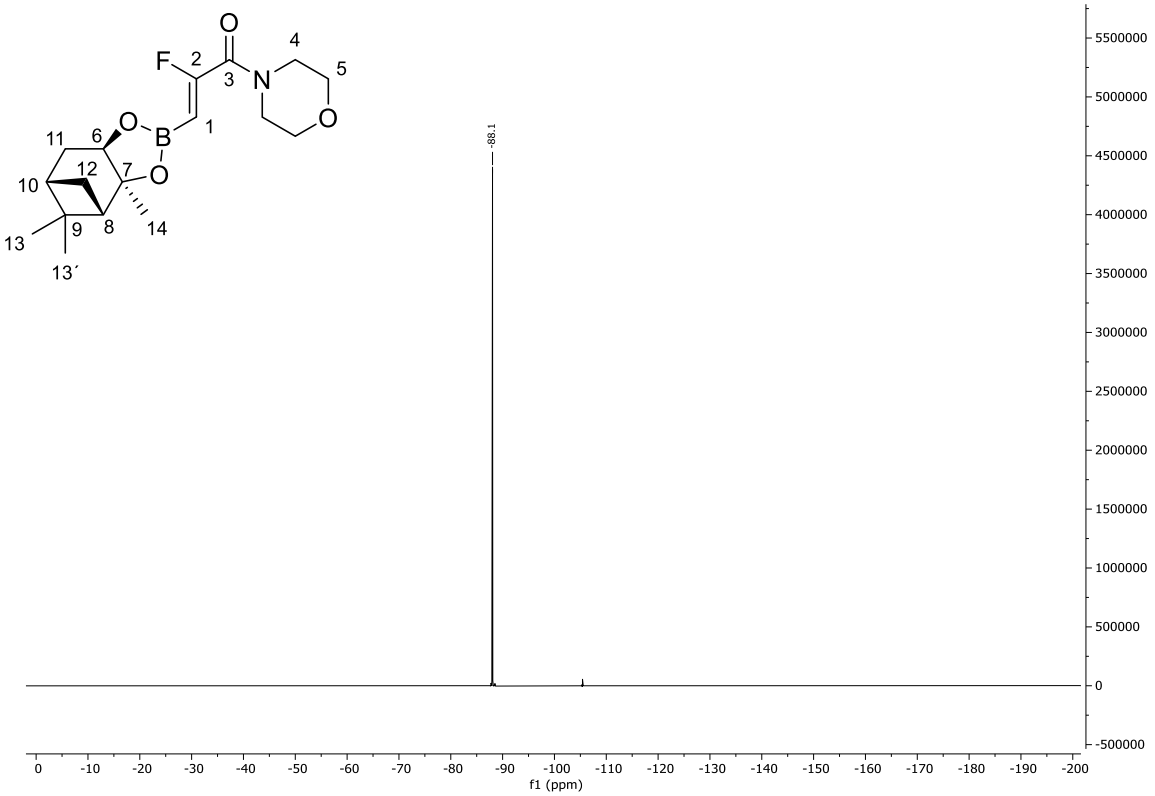

^{1}H-NMR of **S21** (500 MHz, $CDCl_3$)

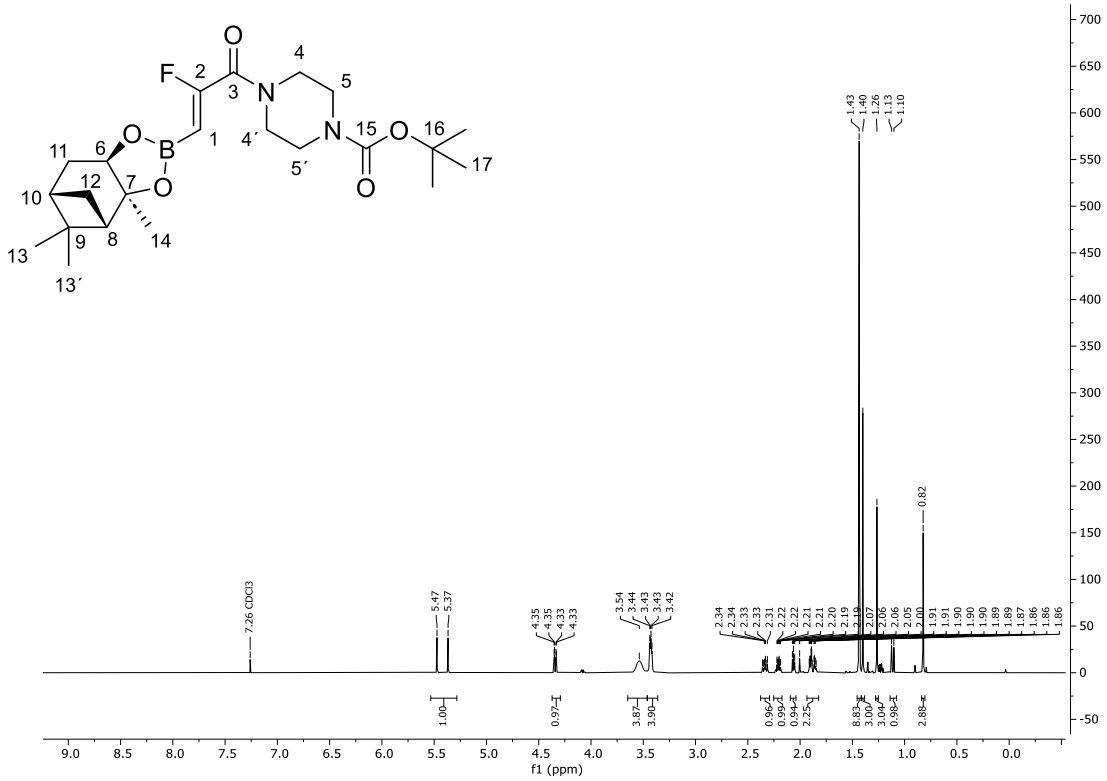

^{13}C-NMR of **S21** (126 MHz, $CDCl_3$)

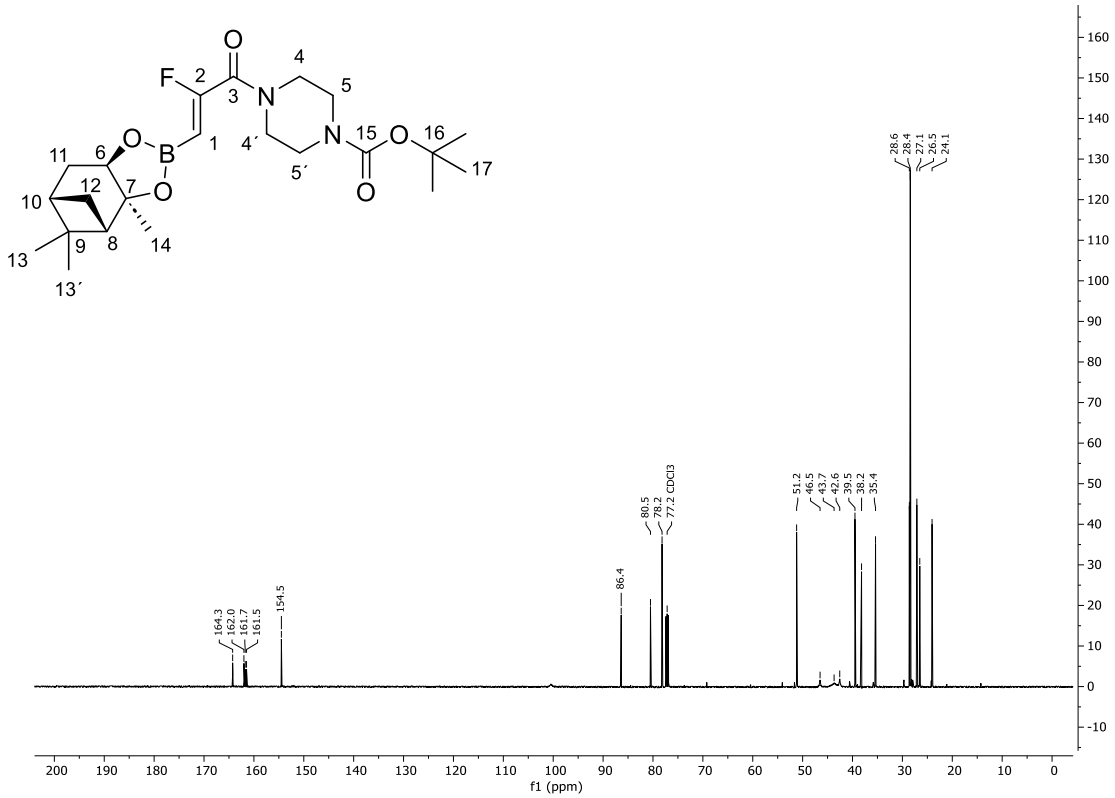

^{19}F-NMR {^{1}H} of **S21** (470 MHz, $CDCl_3$)

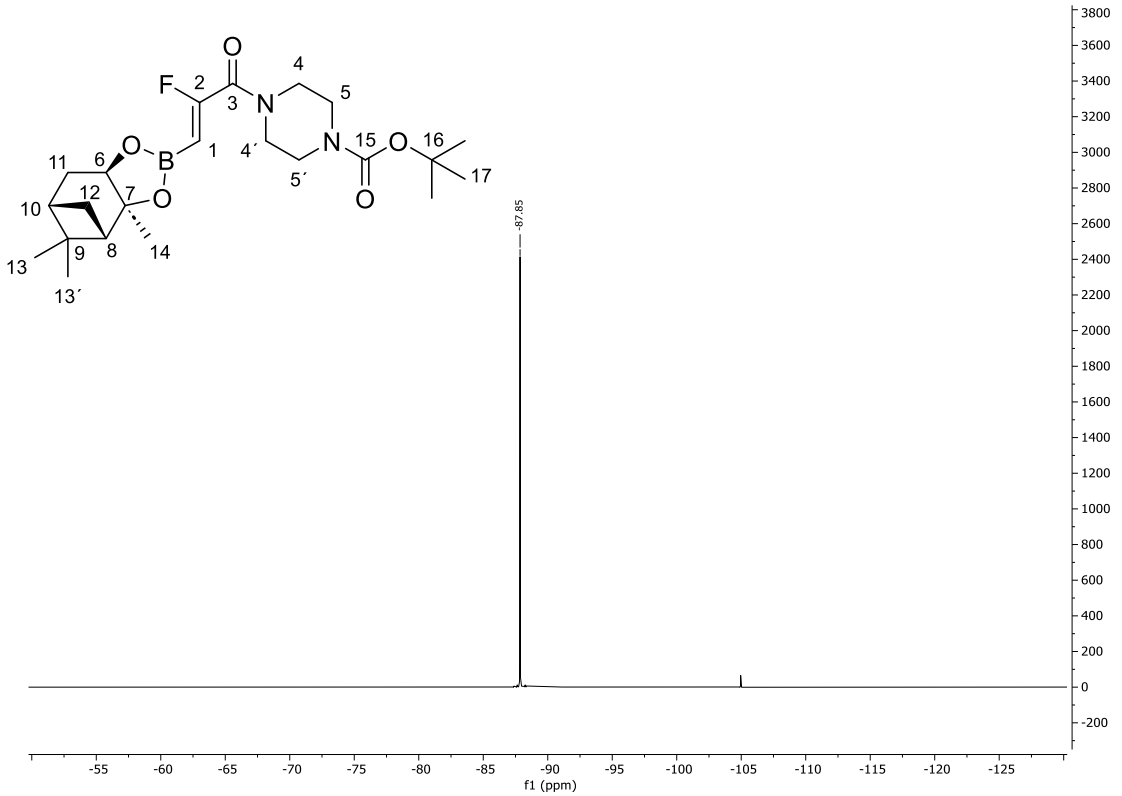

^{1}H-NMR of **S22** (500 MHz, $CDCl_3$)

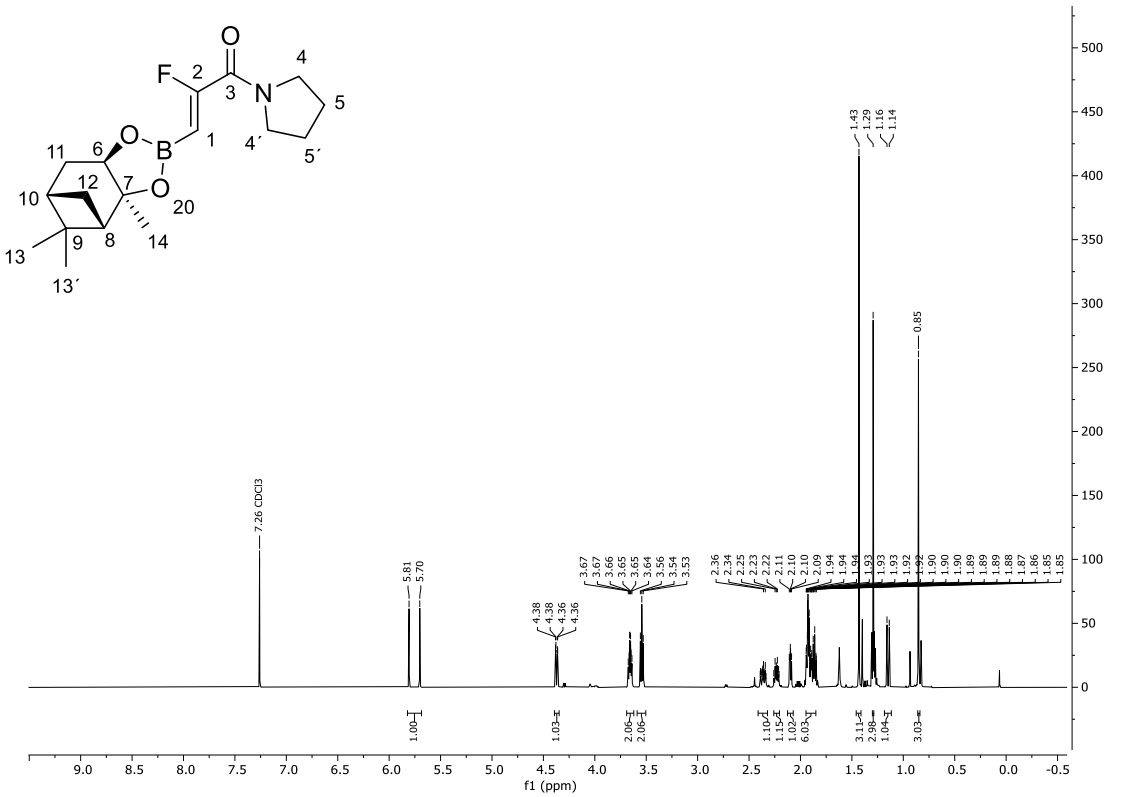

^{13}C-NMR of **S22** (126 MHz, $CDCl_3$)

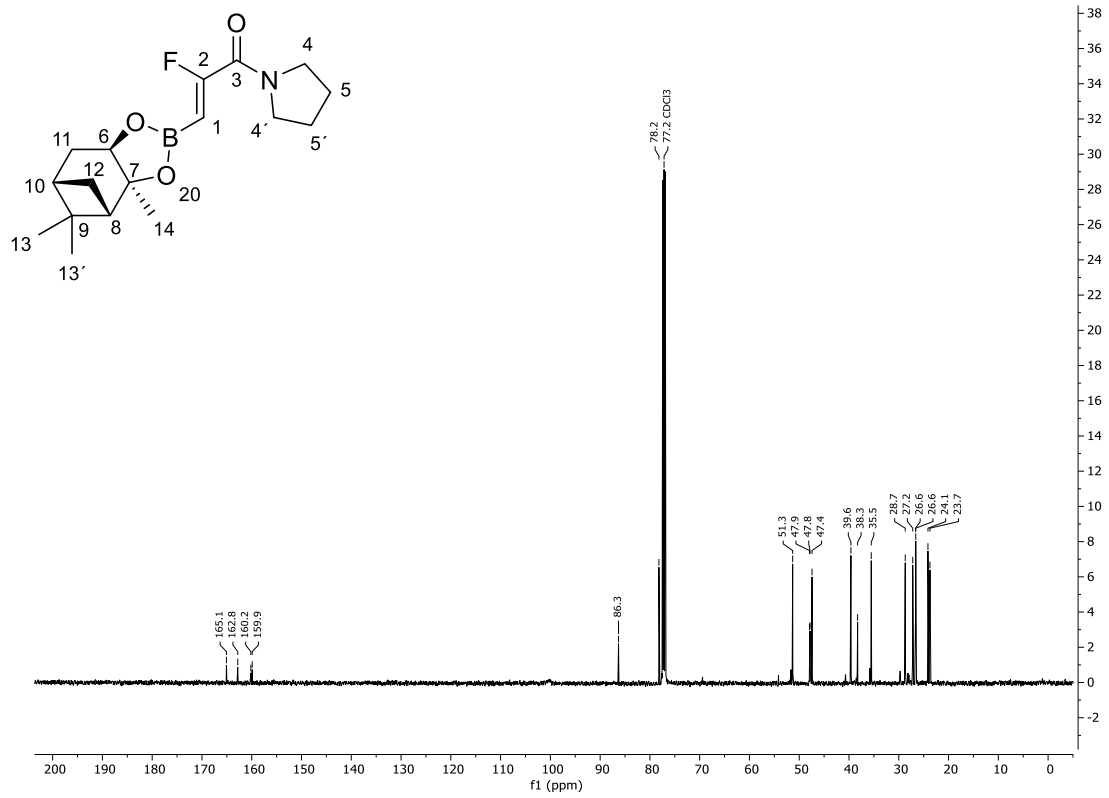

^{19}F-NMR {^{1}H} of **S22** (377 MHz, $CDCl_3$)

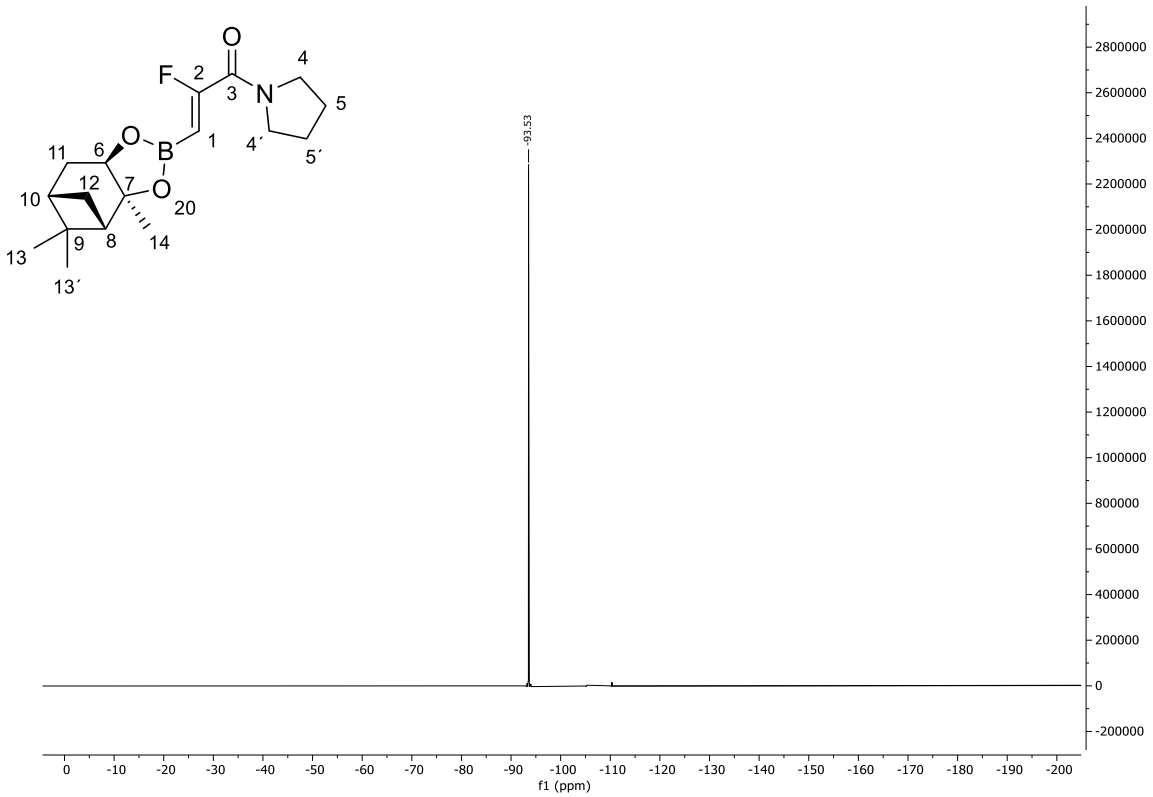

^{1}H-NMR of **S23** (500 MHz, $CDCl_3$)

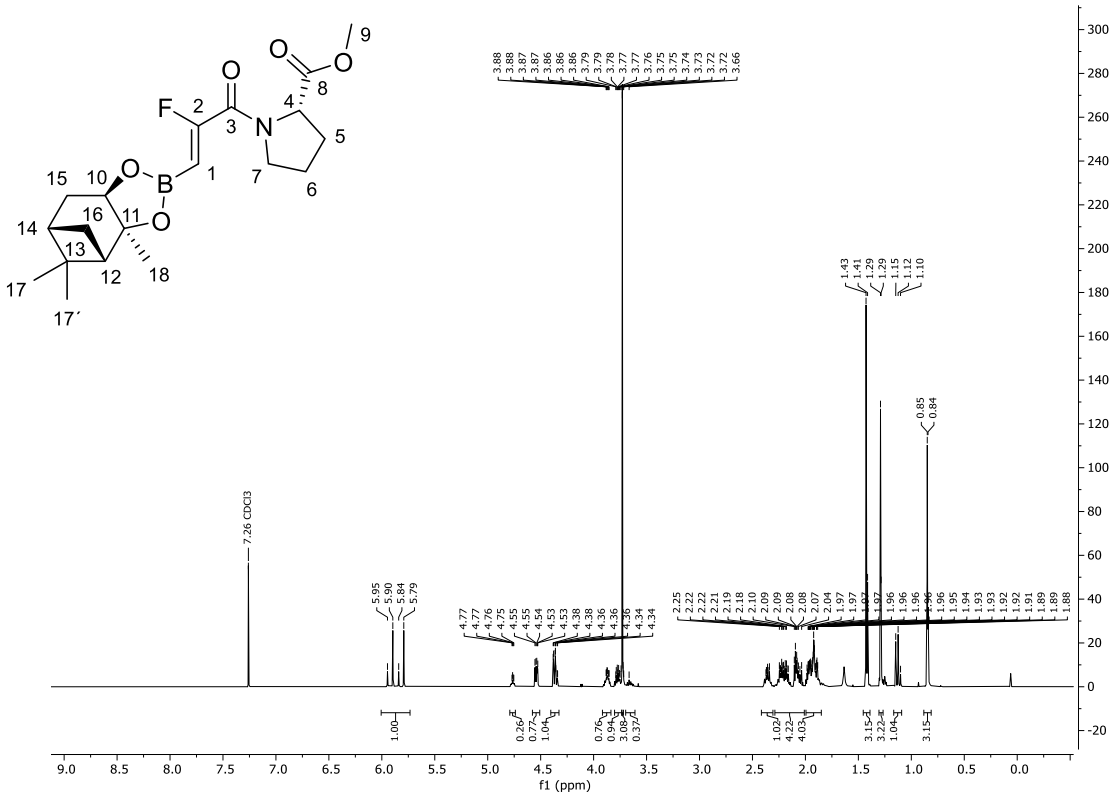

^{13}C-NMR of **S23** (126 MHz, $CDCl_3$)

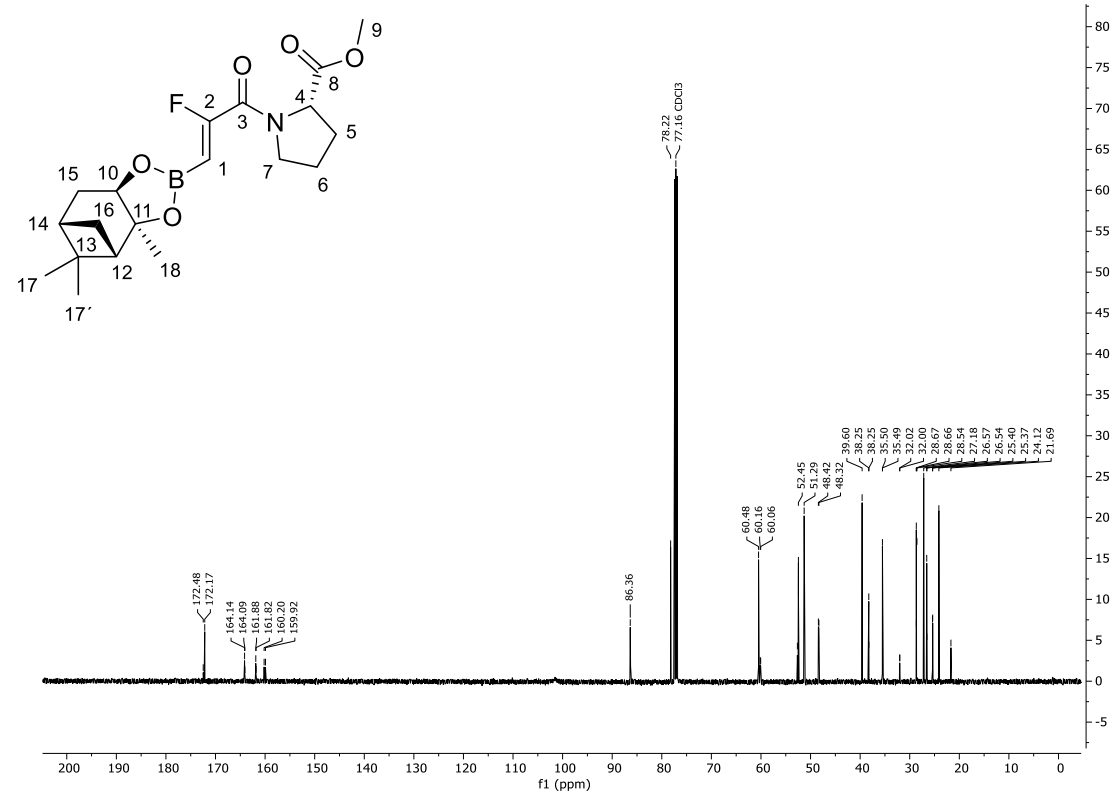

^{19}F-NMR {^{1}H} of **S23** (377 MHz, $CDCl_3$)

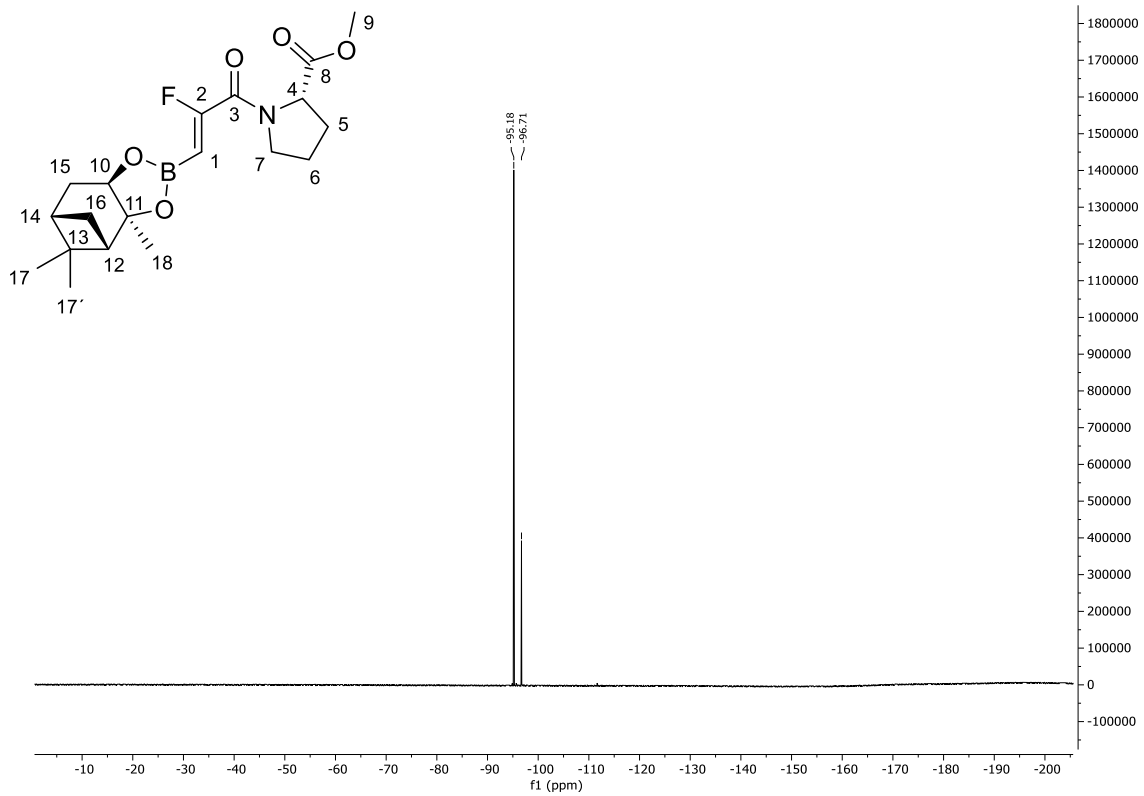

^{1}H-NMR of **S24** (500 MHz, $CDCl_3$)

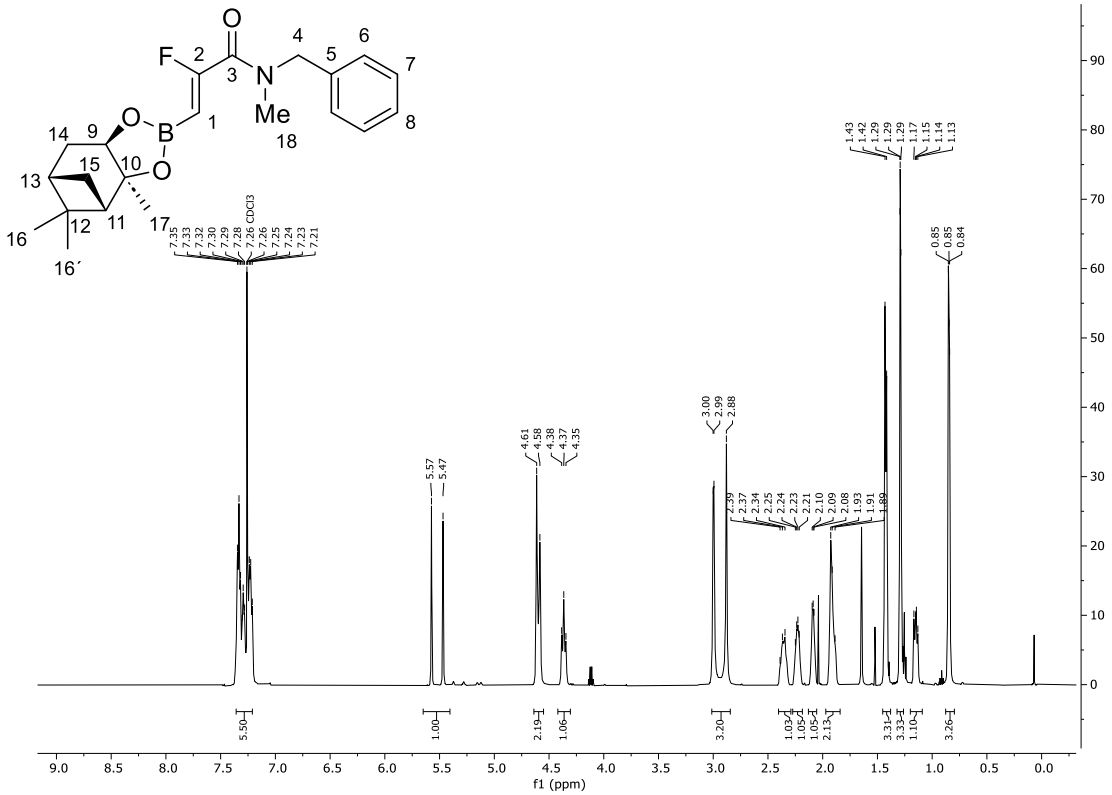

^{13}C-NMR of **S24** (126 MHz, $CDCl_3$)

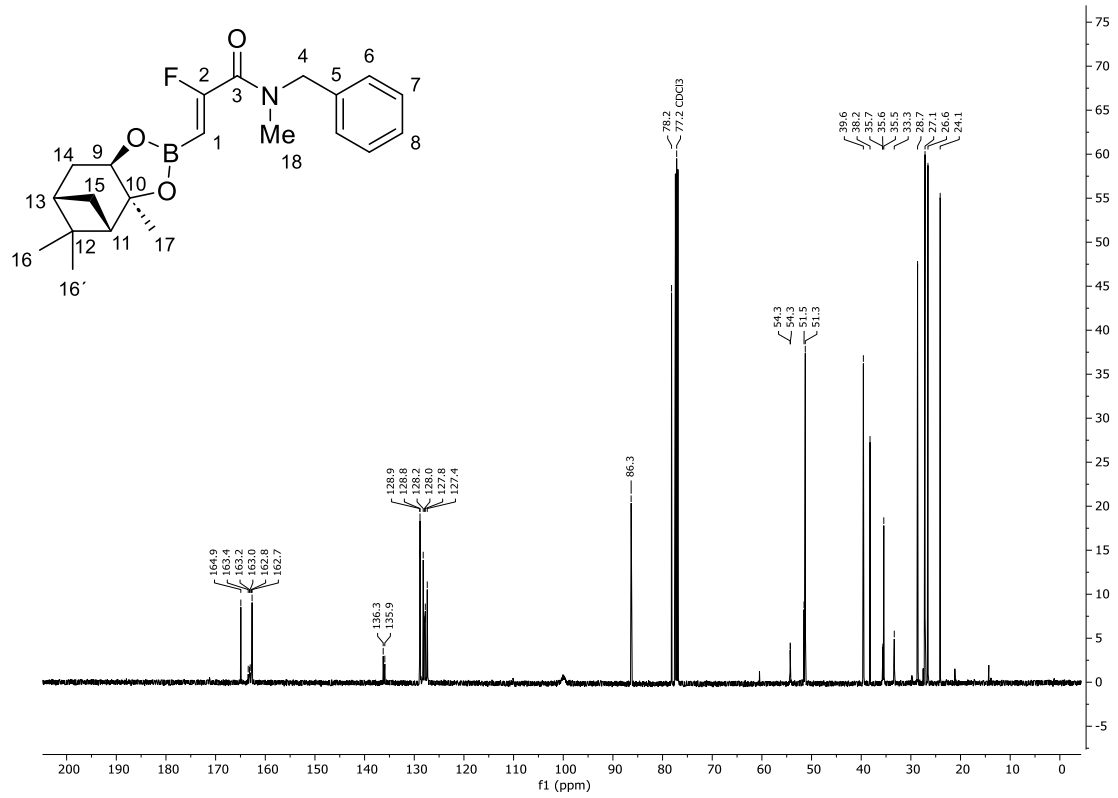

^{19}F-NMR {^{1}H} of **S24** (377 MHz, $CDCl_3$)

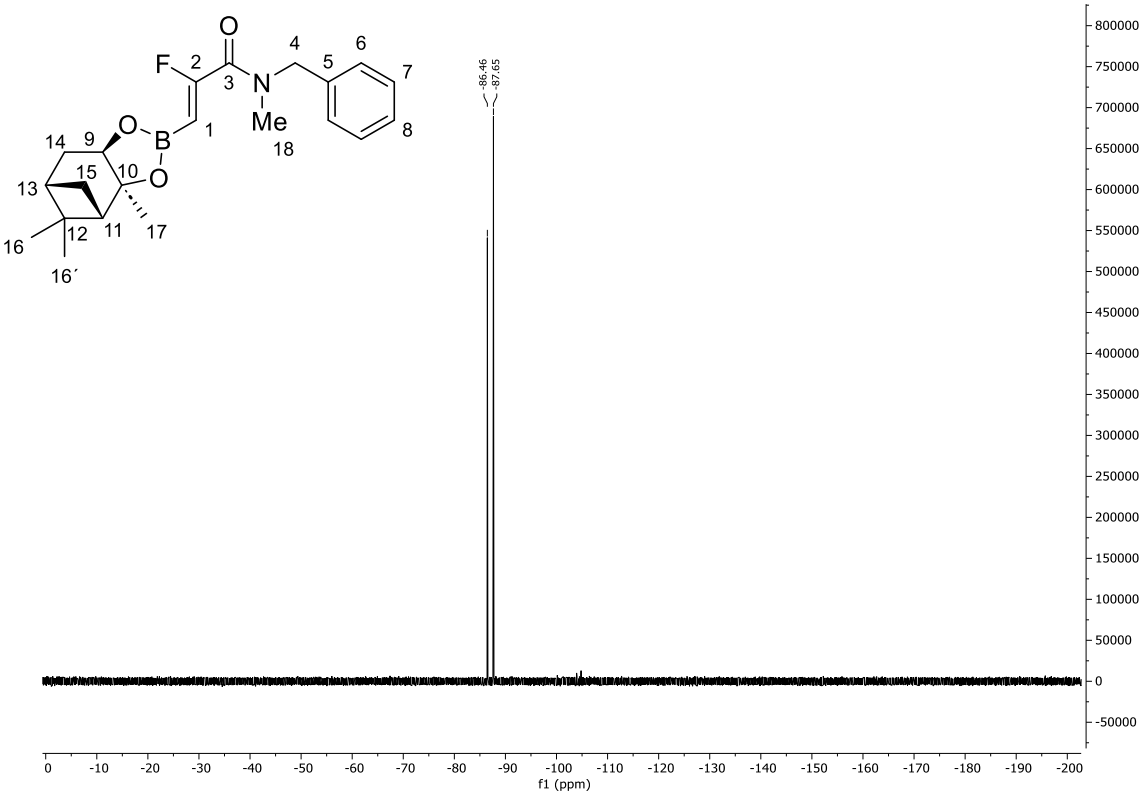

^{1}H-NMR of **S25** (500 MHz, $CDCl_3$)

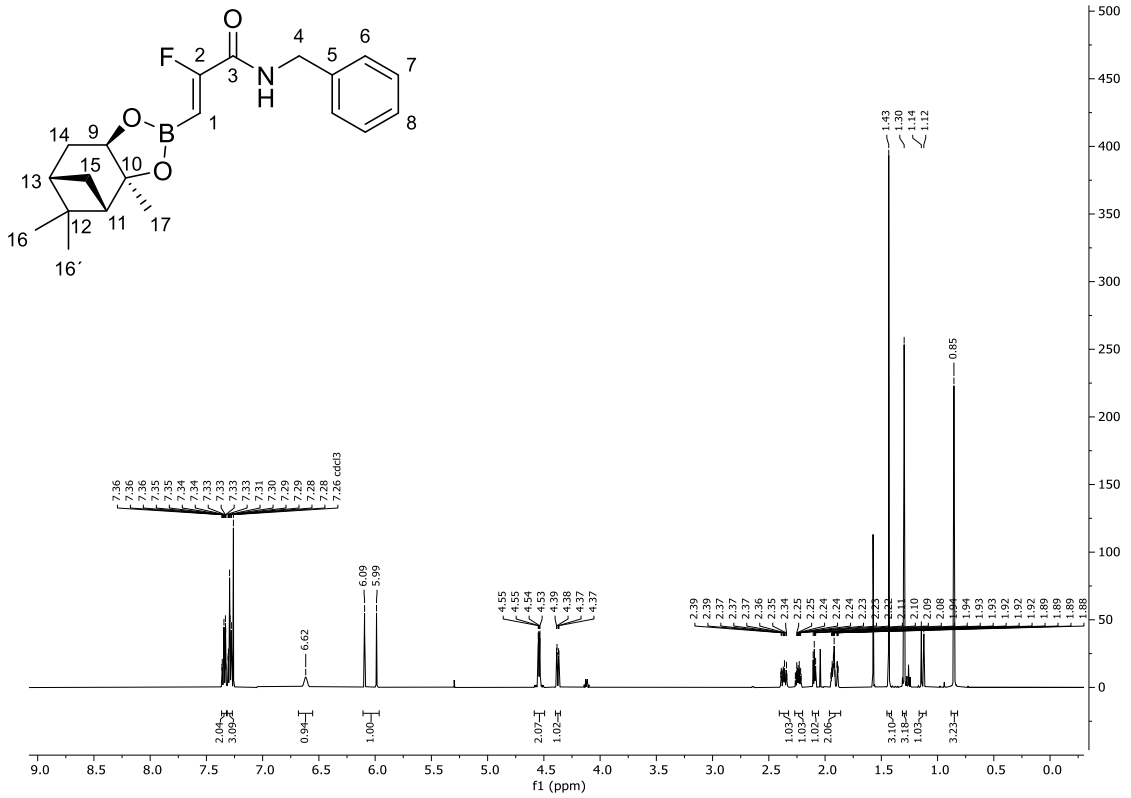

^{13}C-NMR of **S25** (126 MHz, $CDCl_3$)

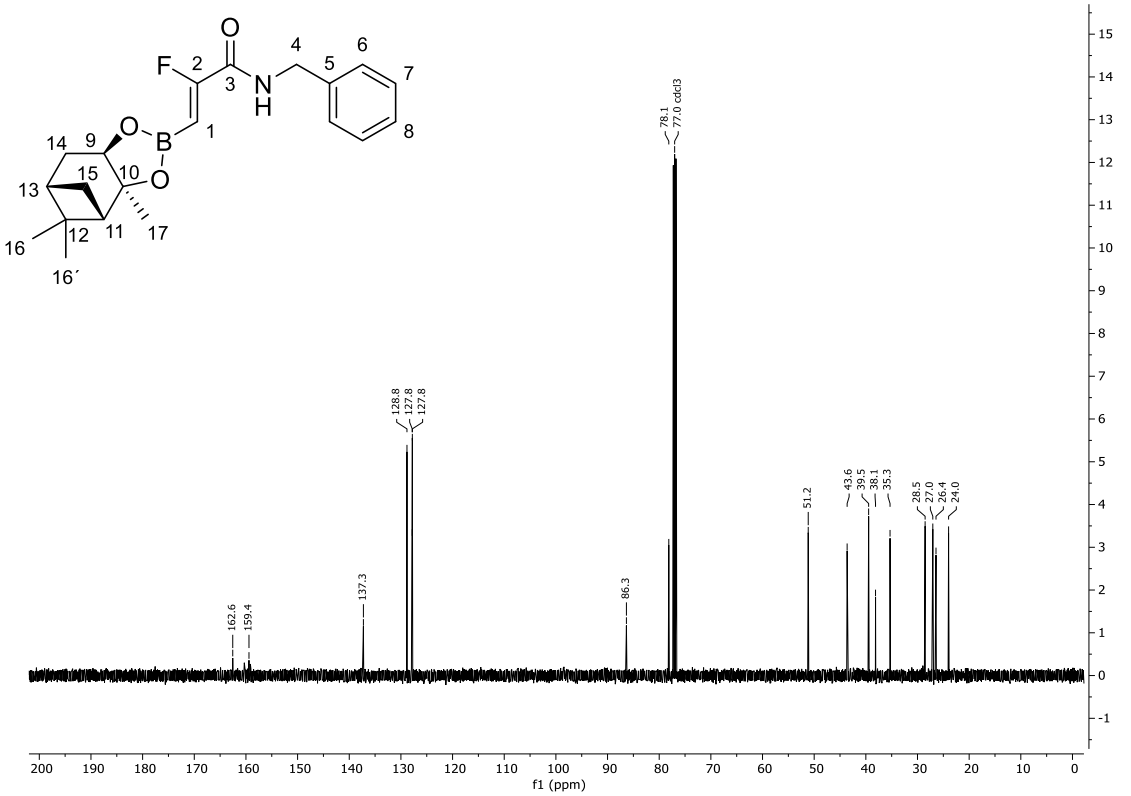

^{19}F-NMR {^{1}H} of **S25** (376 MHz, $CDCl_3$)

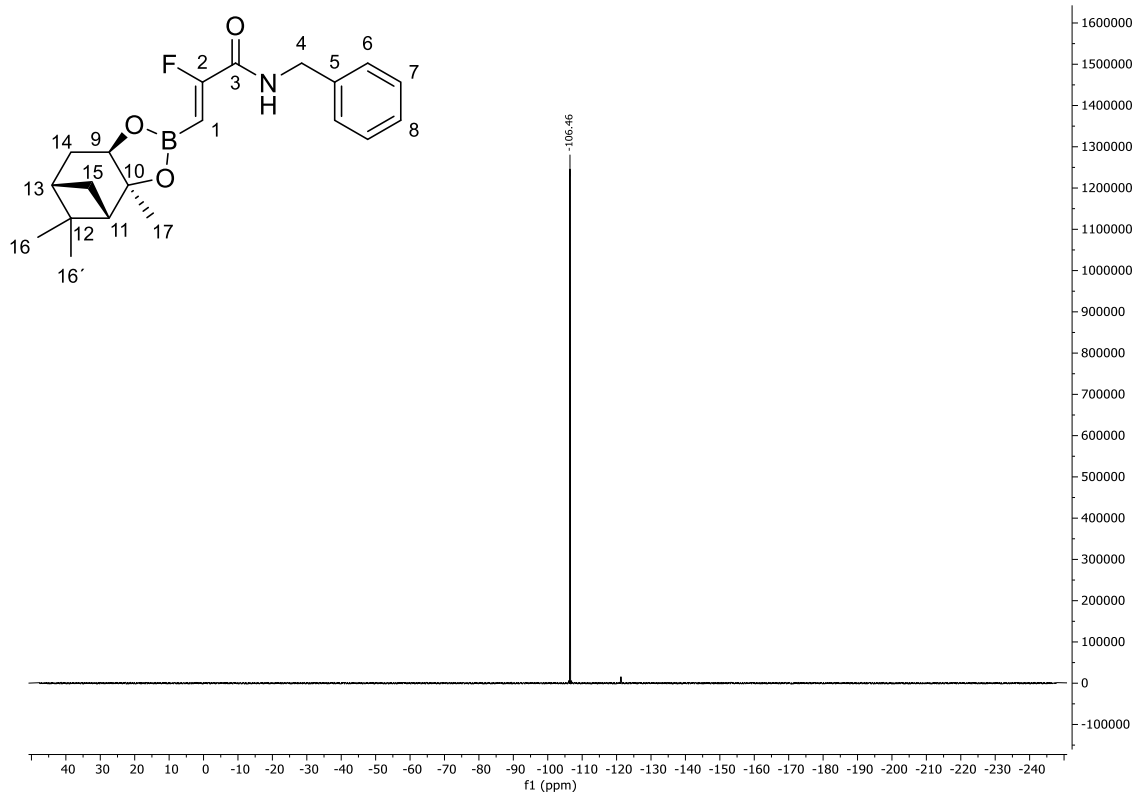

^{1}H-NMR of **S26** (500 MHz, $CDCl_3$)

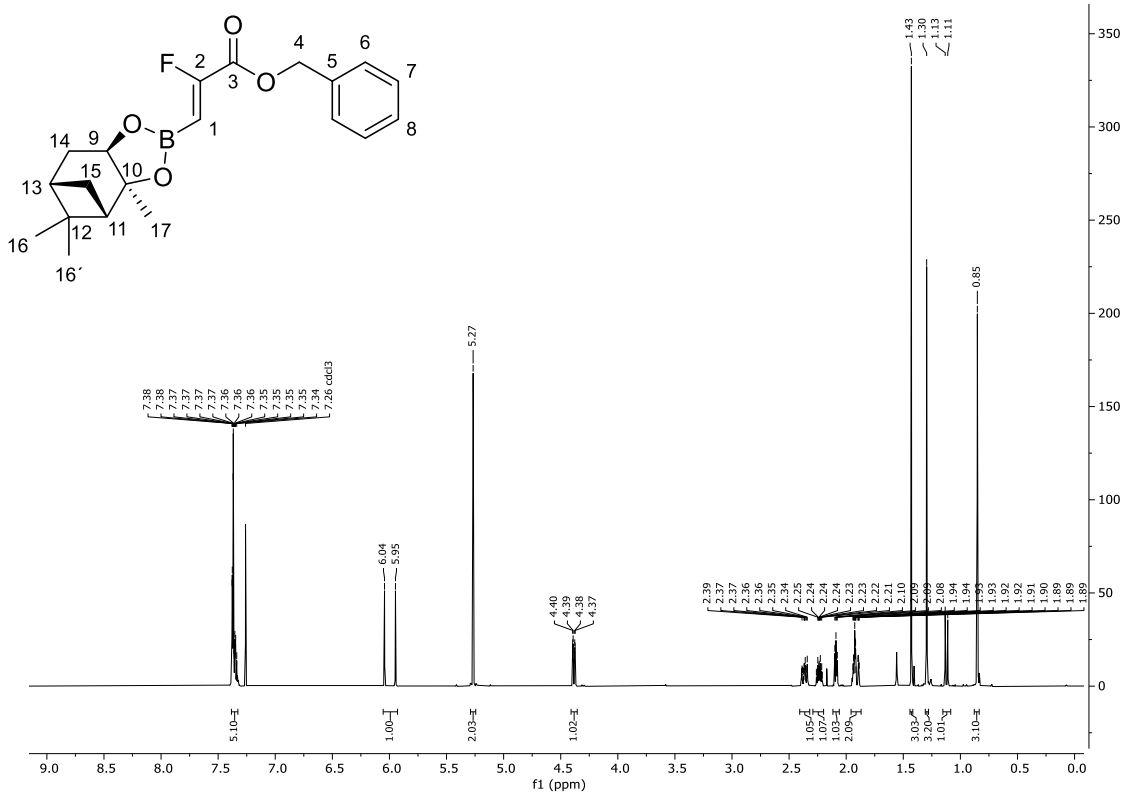

^{13}C-NMR of **S26** (126 MHz, $CDCl_3$)

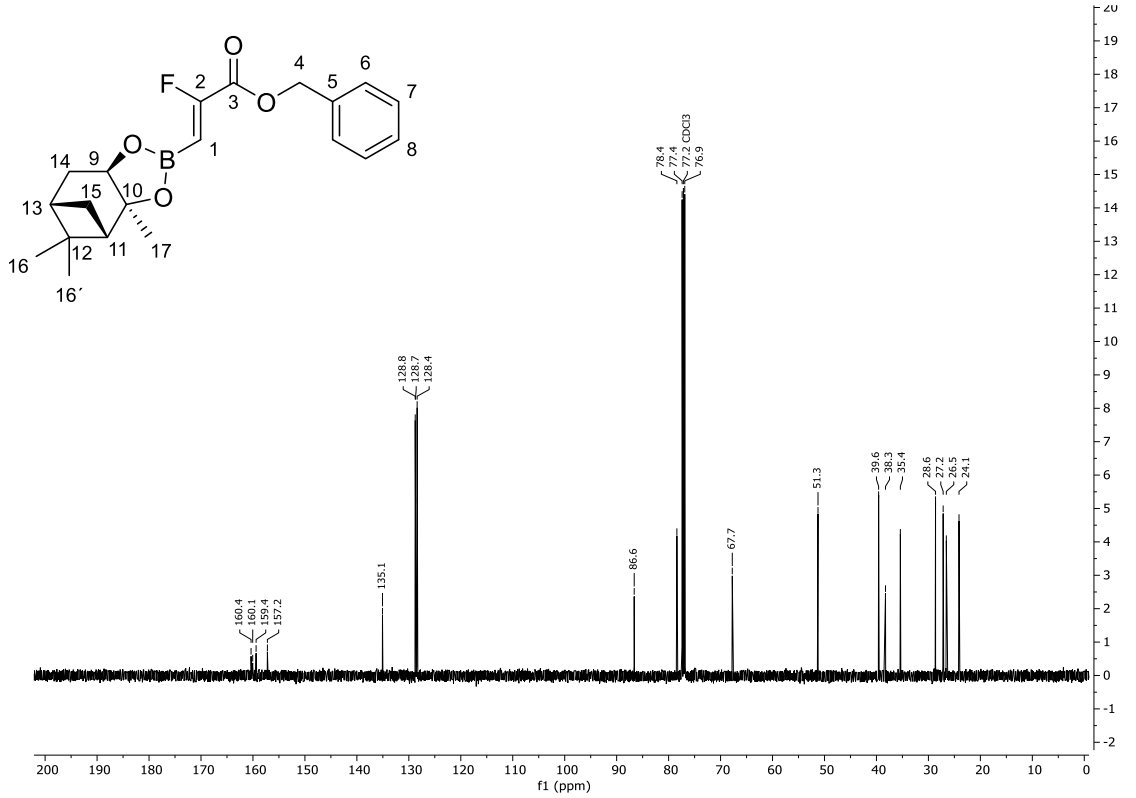

^{19}F-NMR {^{1}H} of **S26** (470 MHz, $CDCl_3$)

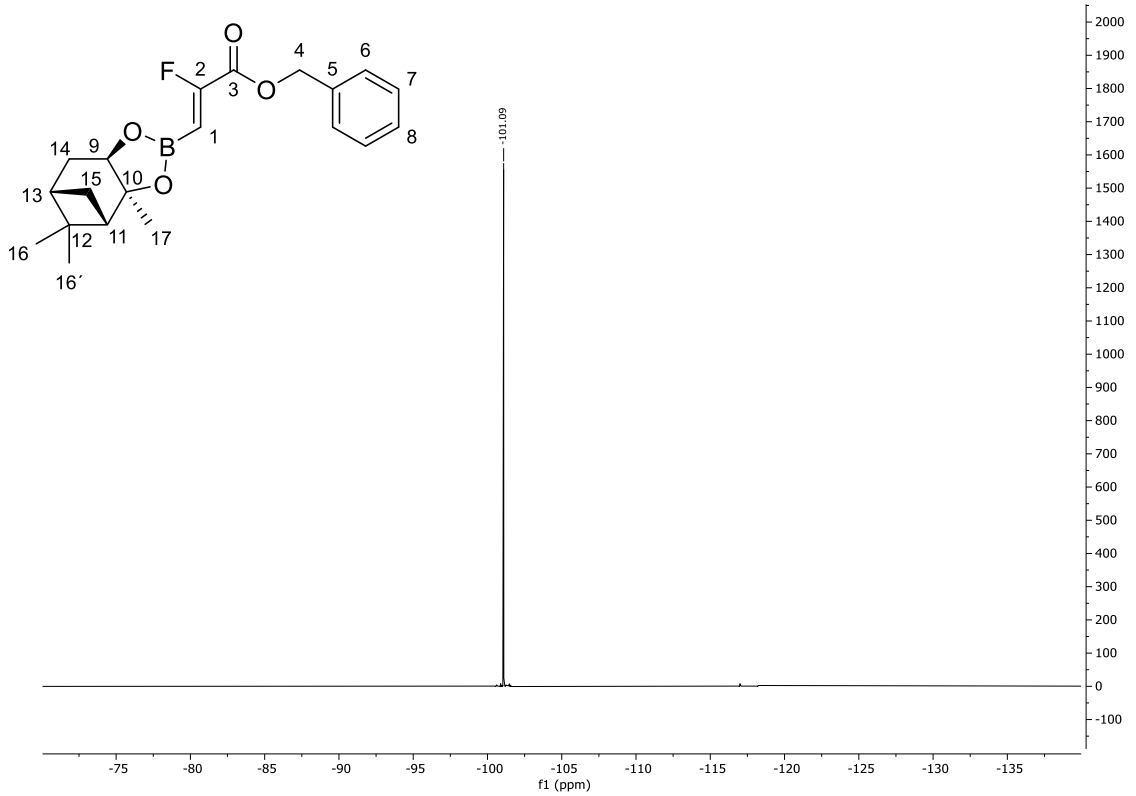

^{1}H-NMR of **S27** (599 MHz, $CDCl_3$)

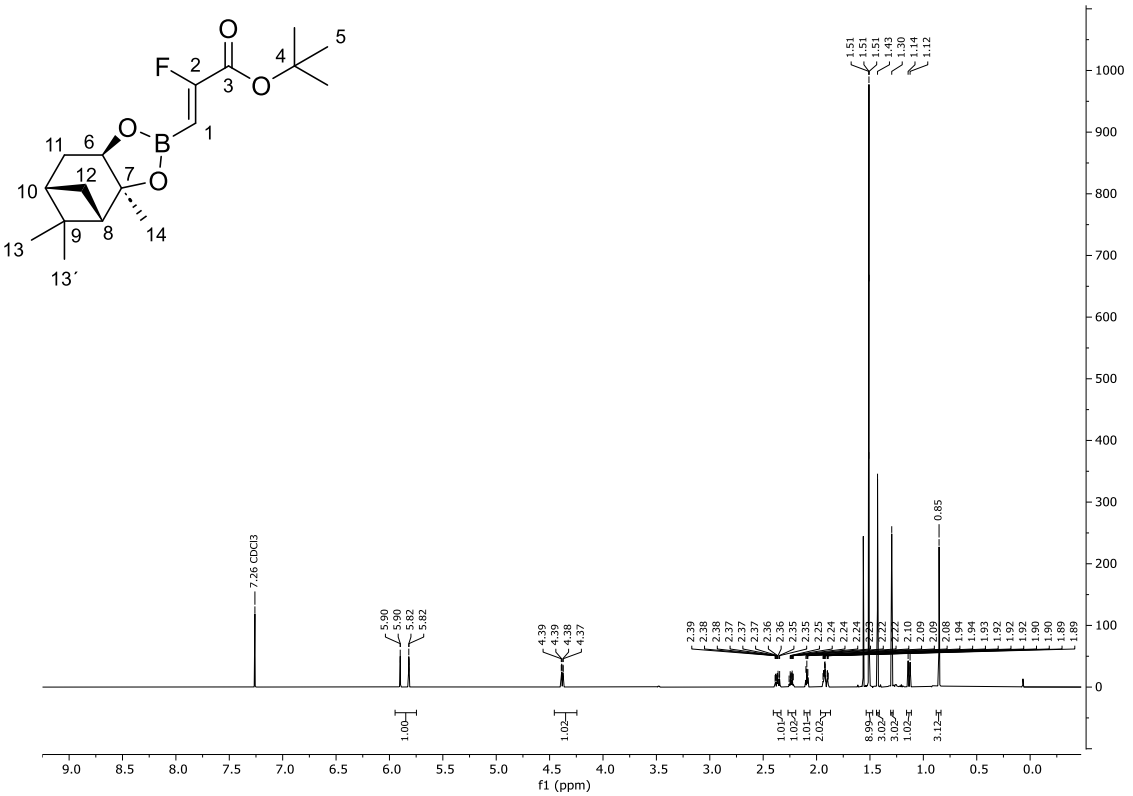

^{13}C-NMR of **S27** (151 MHz, $CDCl_3$)

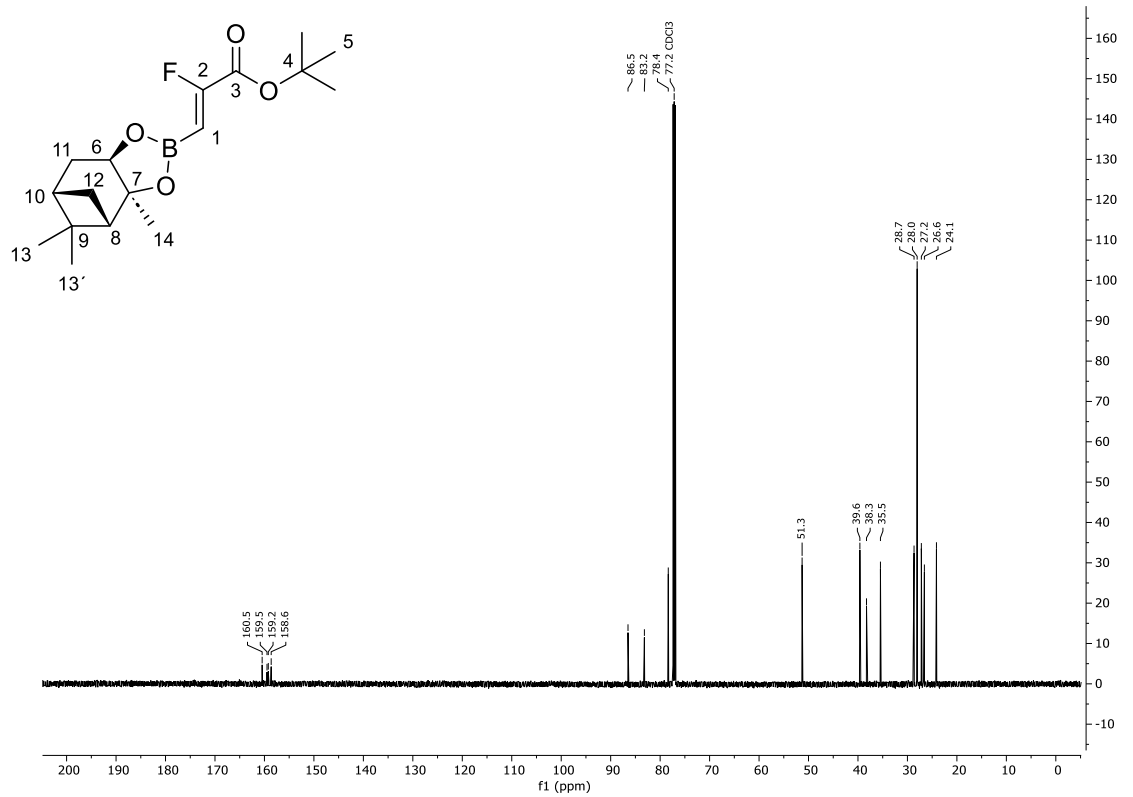

^{19}F-NMR {^{1}H} of **S27** (564 MHz, $CDCl_3$)

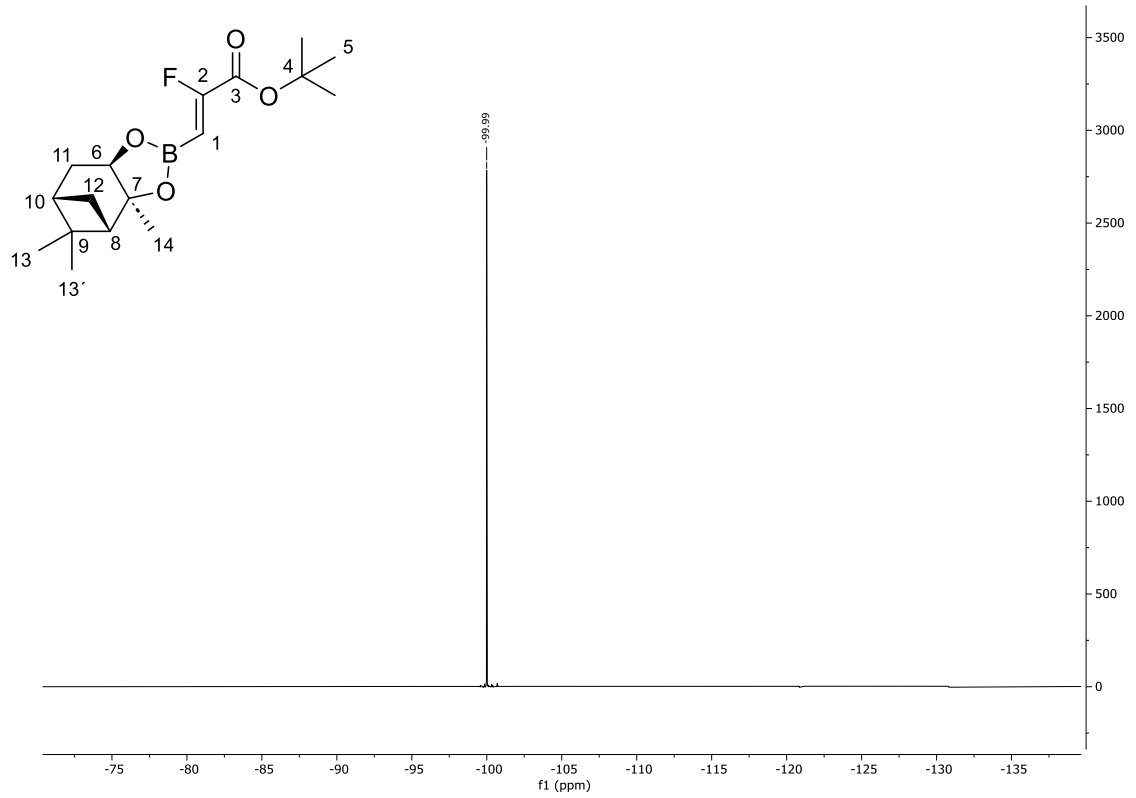

^{1}H-NMR of **S28** (500 MHz, $CDCl_3$)

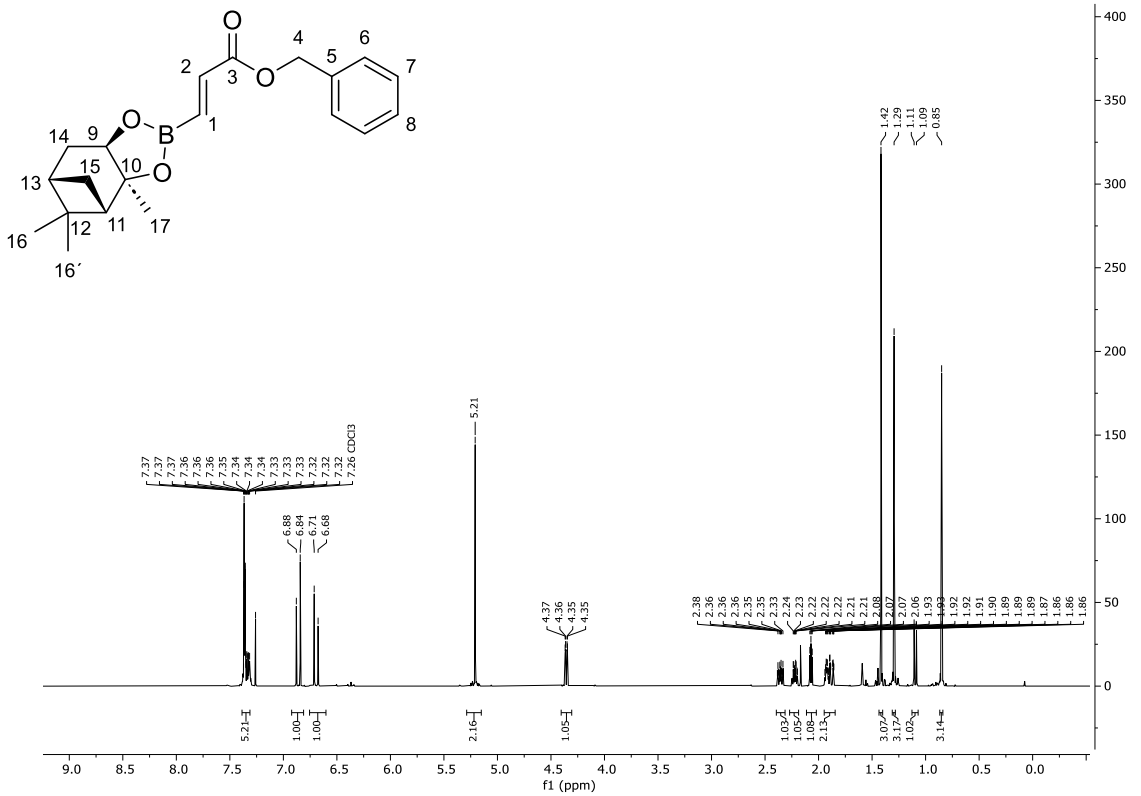

^{13}C-NMR of **S28** (126 MHz, $CDCl_3$)

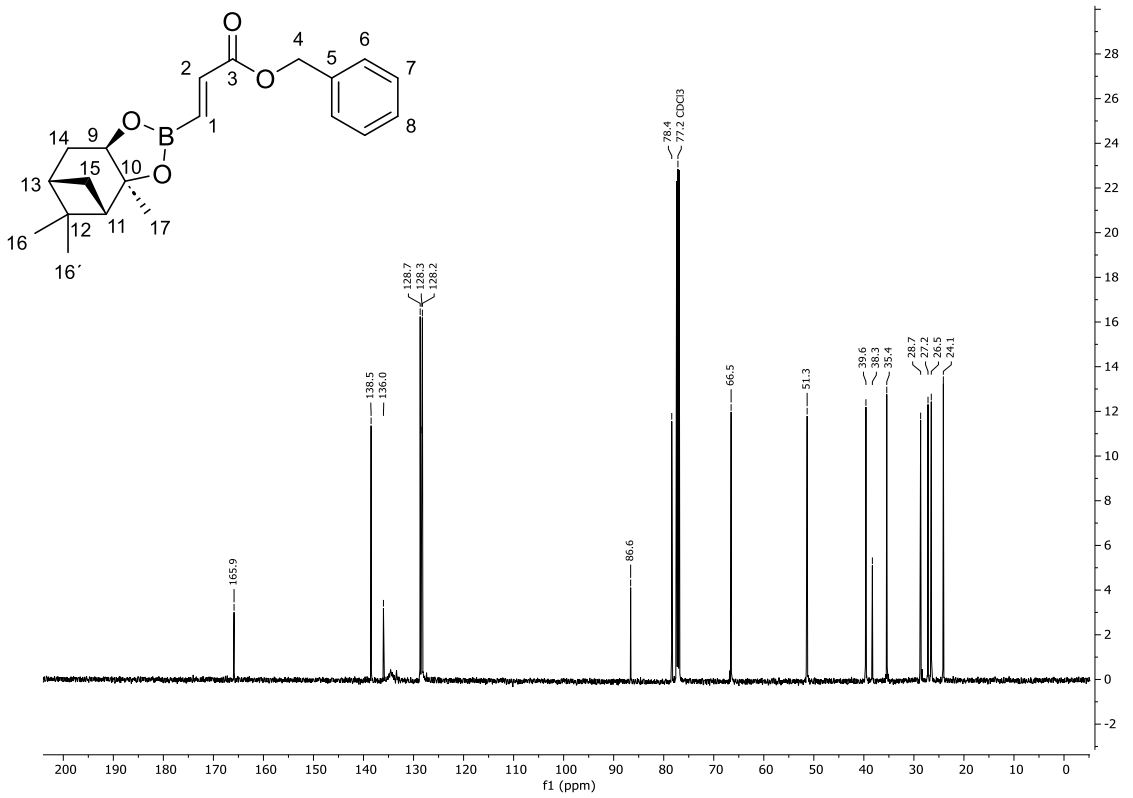

^{1}H-NMR of **S29** (500 MHz, $CDCl_3$)

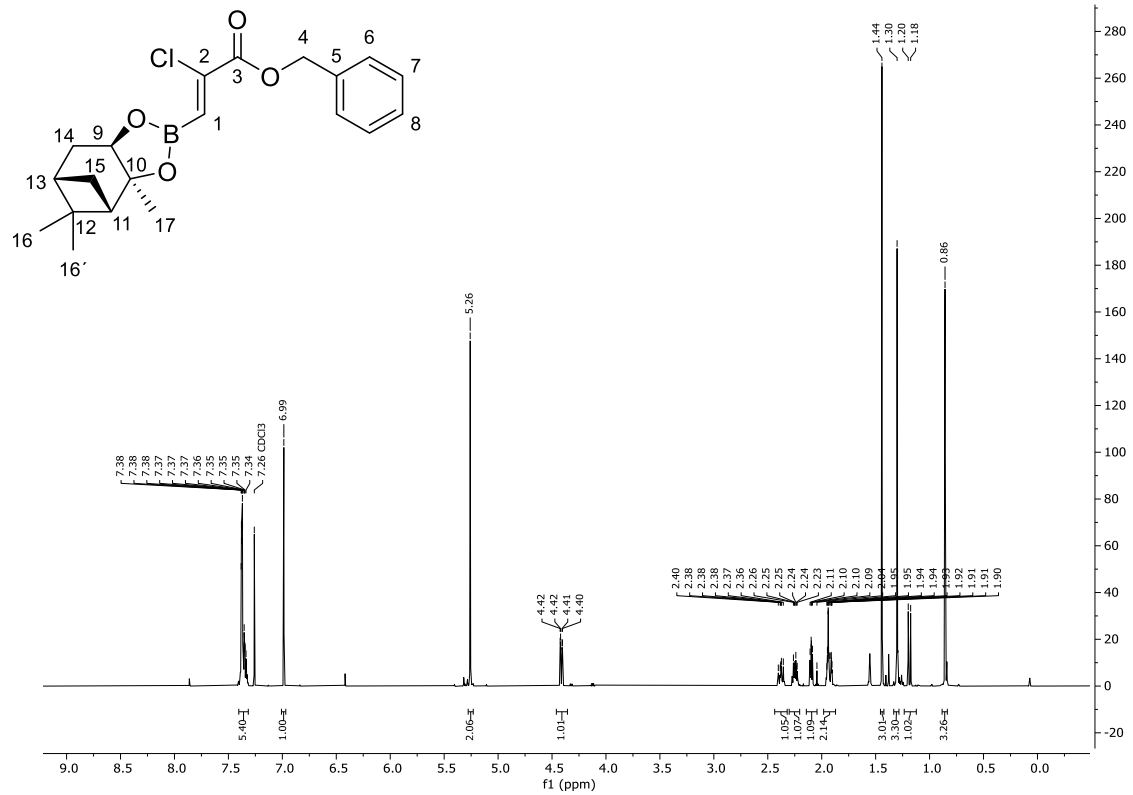

^{13}C-NMR of **S29** (126 MHz, $CDCl_3$)

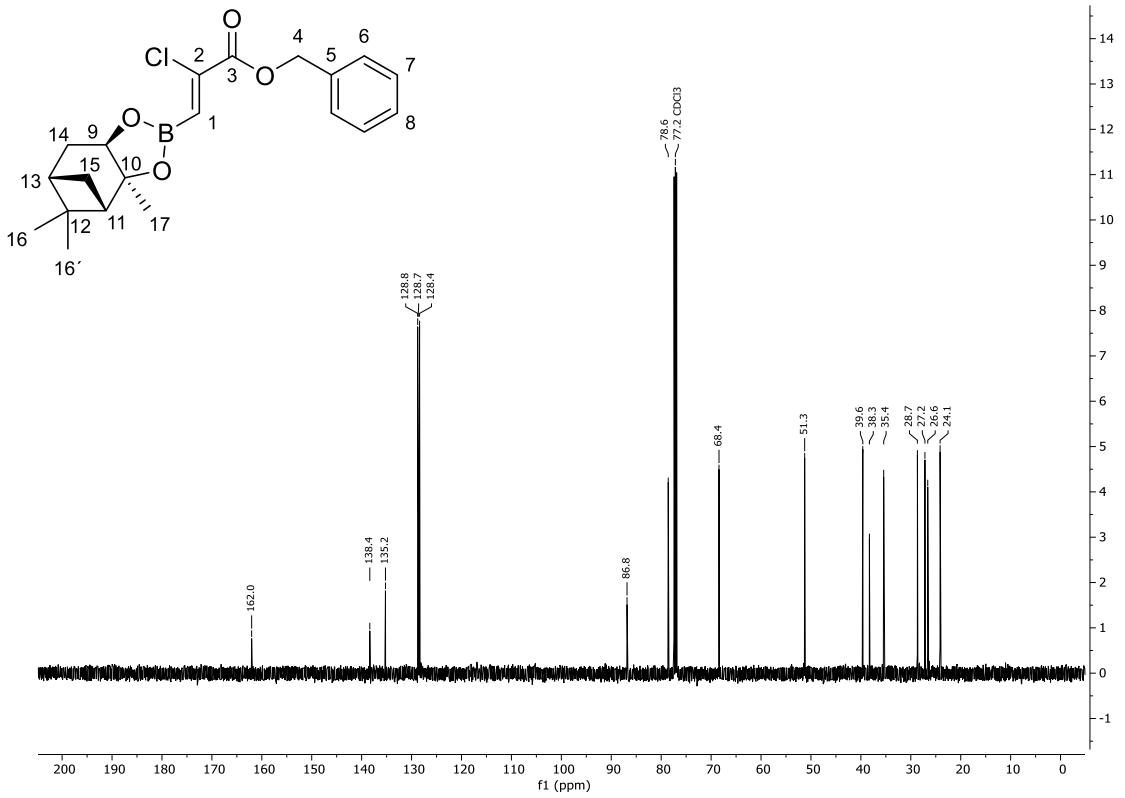

^{1}H-NMR of **S30** (500 MHz, $CDCl_3$)

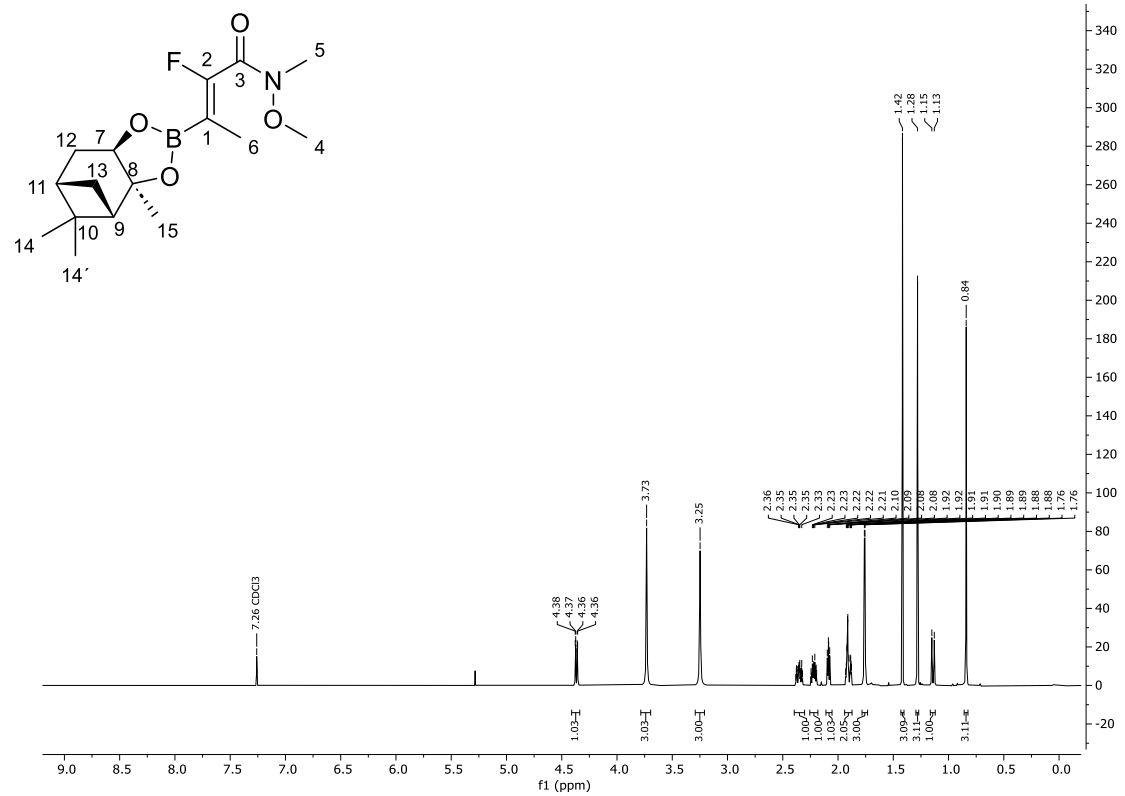

^{13}C-NMR of **S30** ($CDCl_3$)

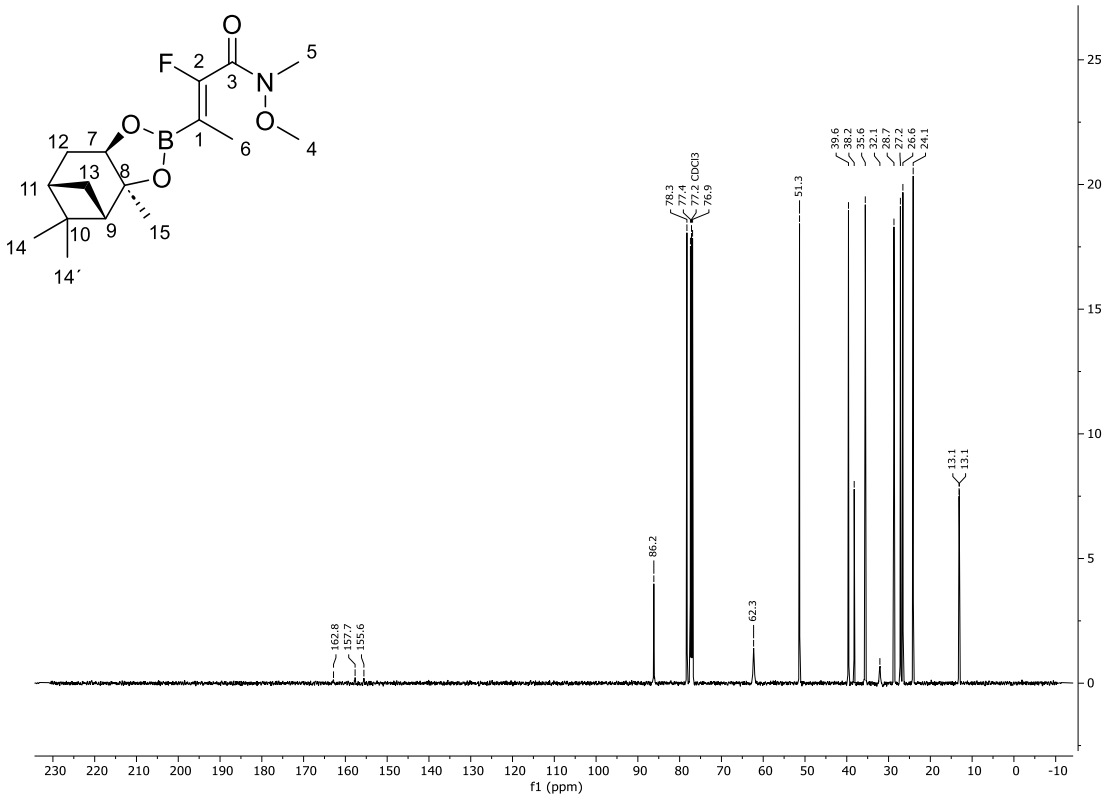

^{19}F-NMR {^{1}H} of **S30** ($CDCl_3$)

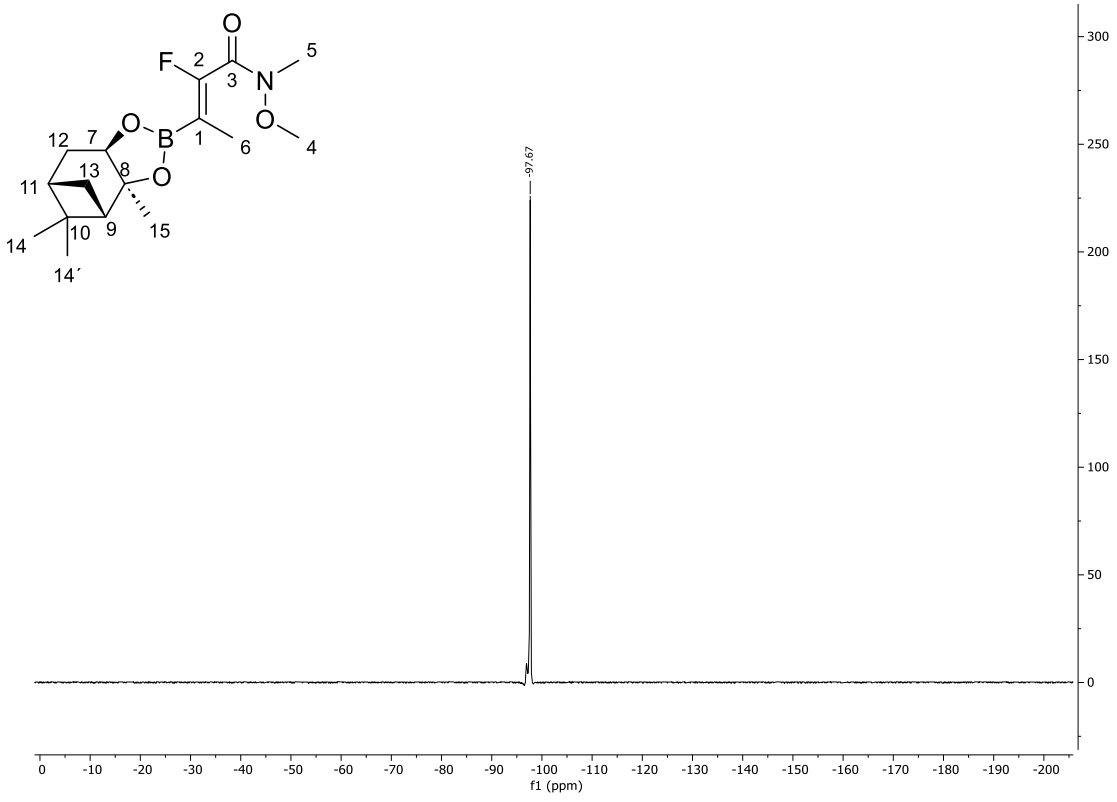

^{1}H-NMR of **S31** (599 MHz, $CDCl_3$)

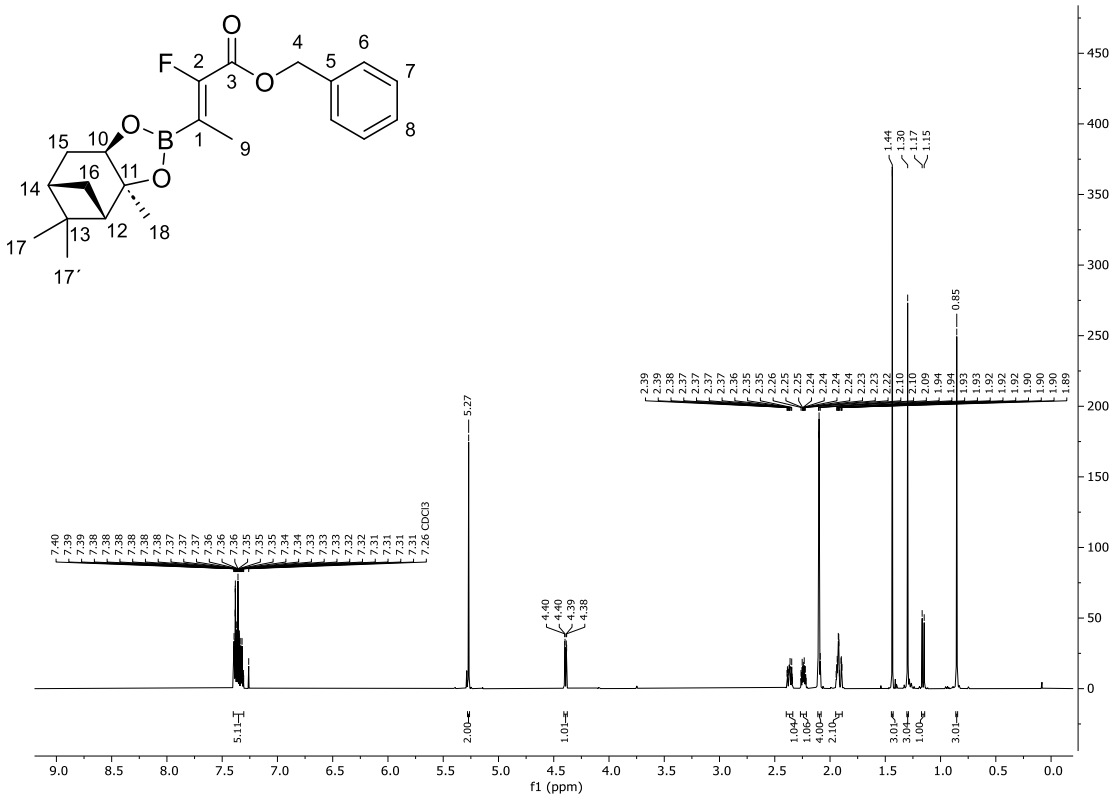

^{13}C-NMR of **S31** (151 MHz, $CDCl_3$)

^{19}F-NMR {^{1}H} of **S31** (377 MHz, $CDCl_3$)

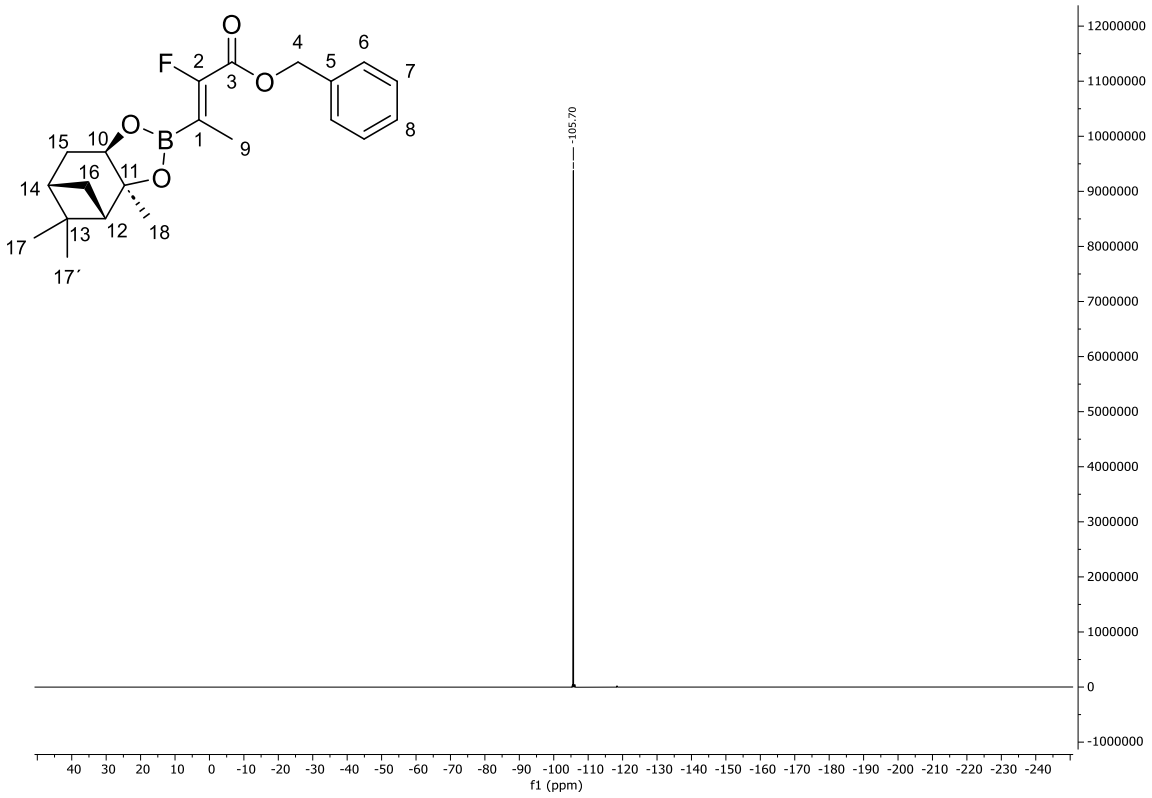

^{1}H-NMR of **S32** (500 MHz, $CDCl_3$)

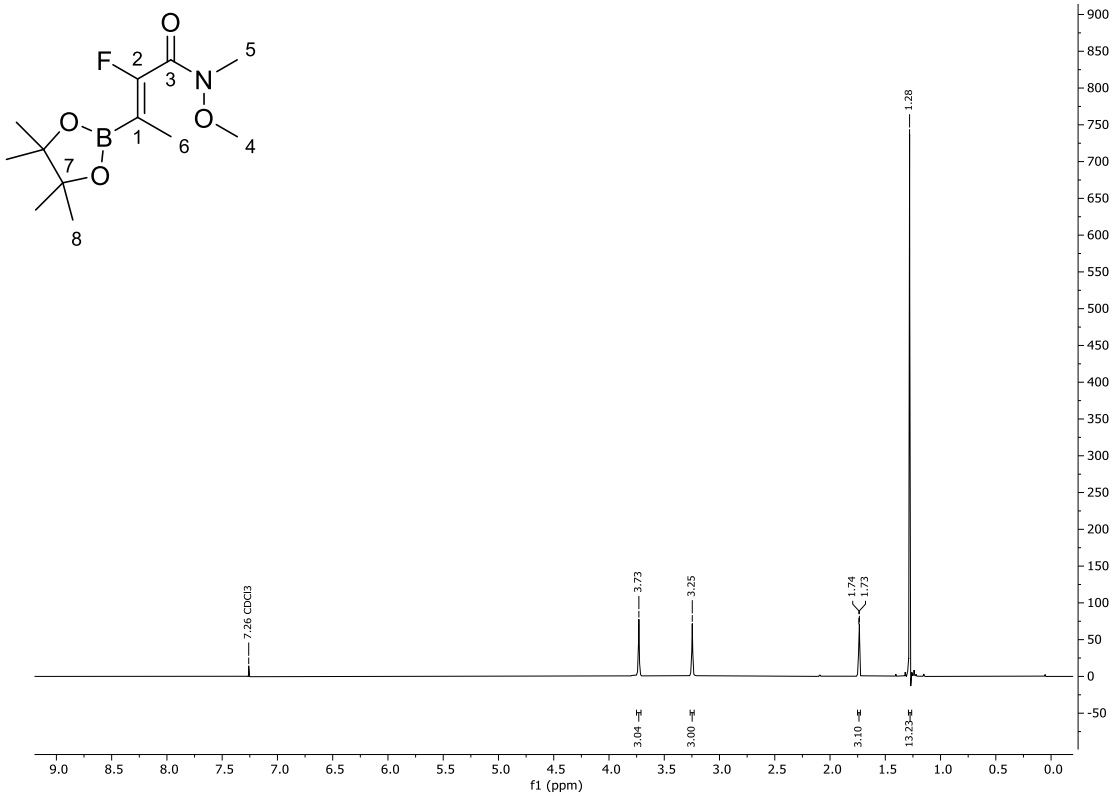

^{13}C-NMR of **S32** (126 MHz, $CDCl_3$)

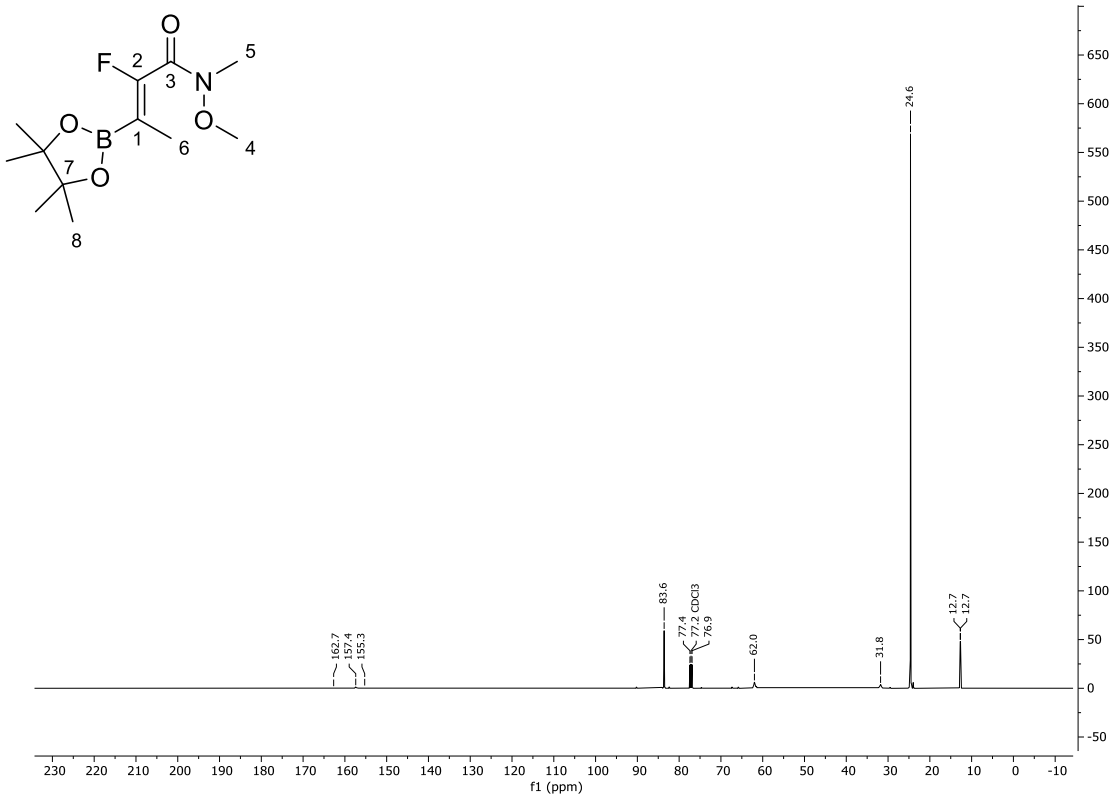

^{19}F-NMR {^{1}H} of **S32** (470 MHz, $CDCl_3$)

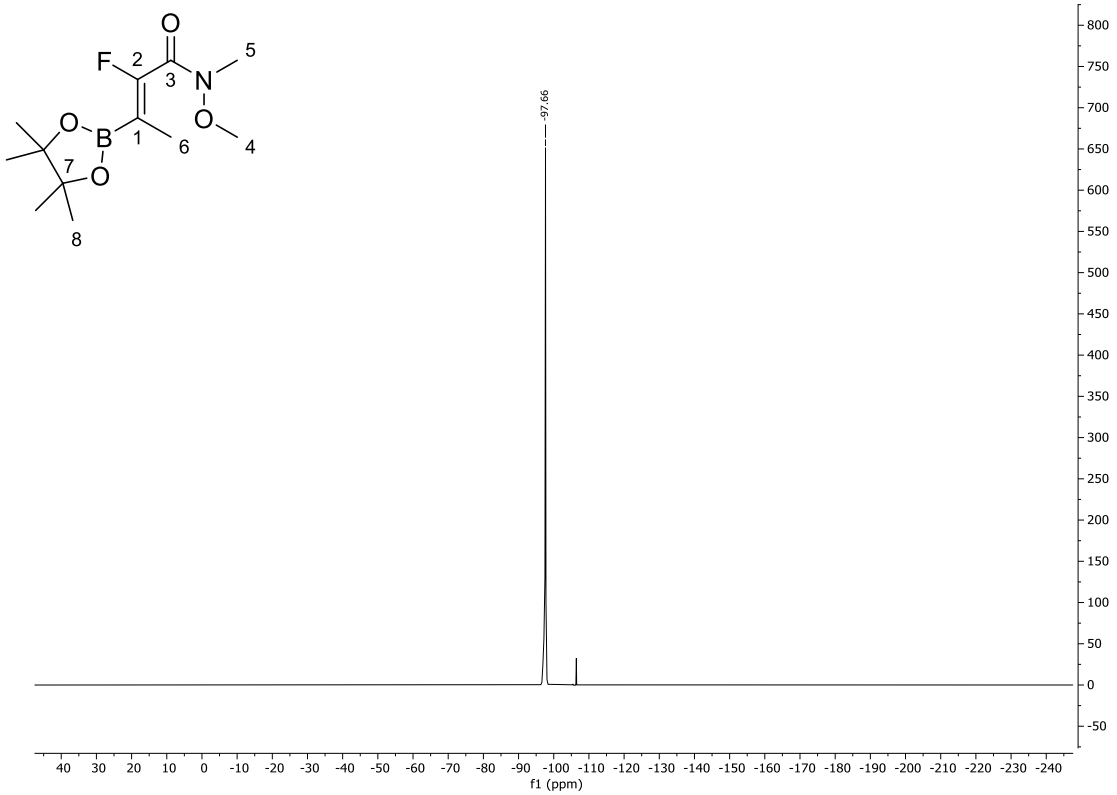

^{1}H-NMR of **S33** (599 MHz, $CDCl_3$)

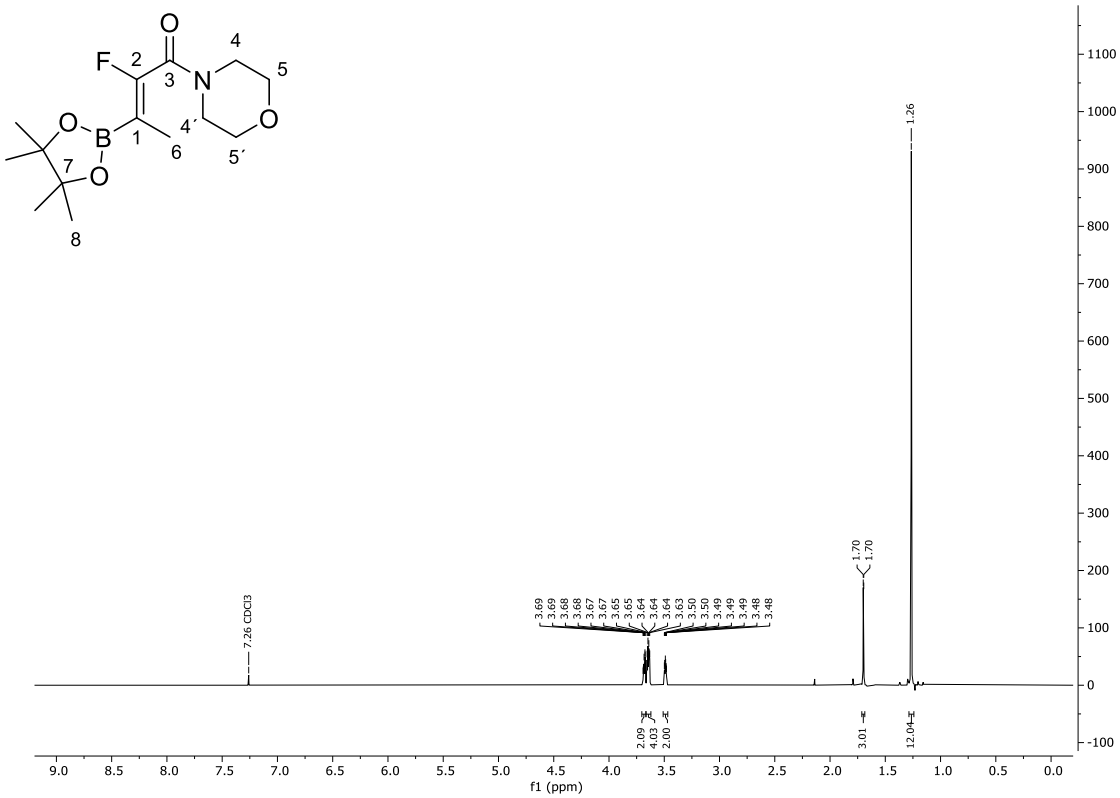

^{13}C-NMR of **S33** (151 MHz, $CDCl_3$)

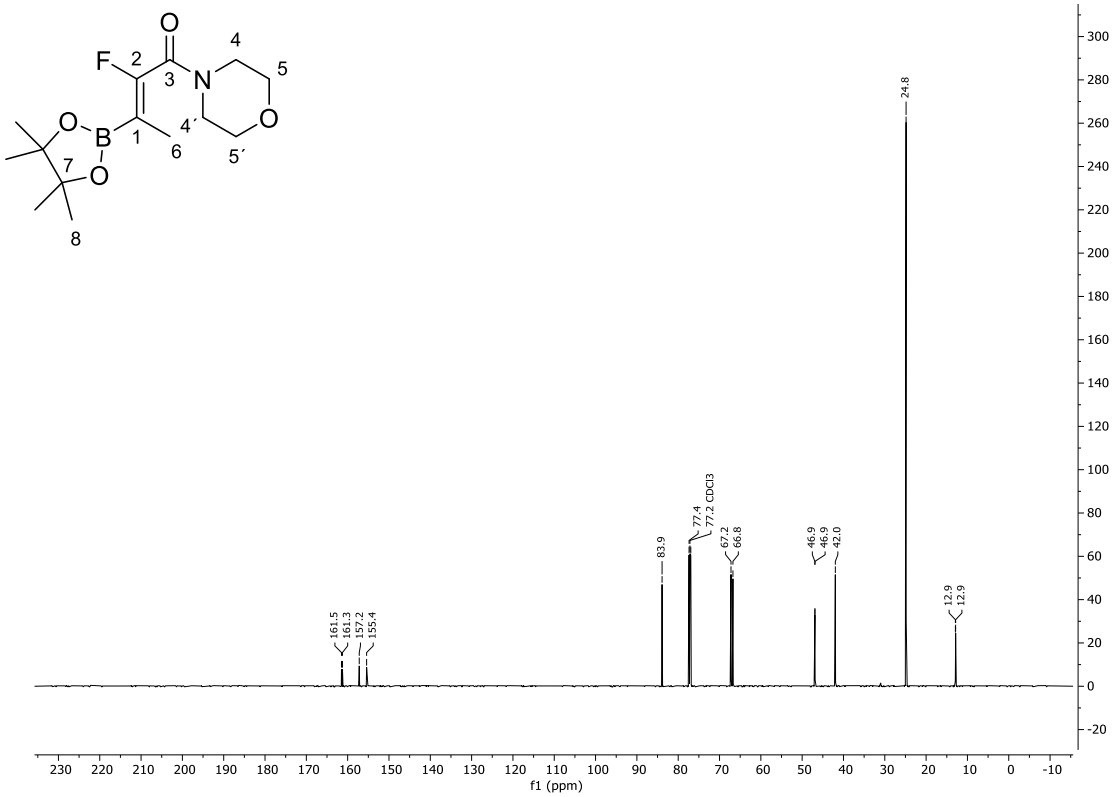

^{19}F-NMR {^{1}H} of **S33** (564 MHz, $CDCl_3$)

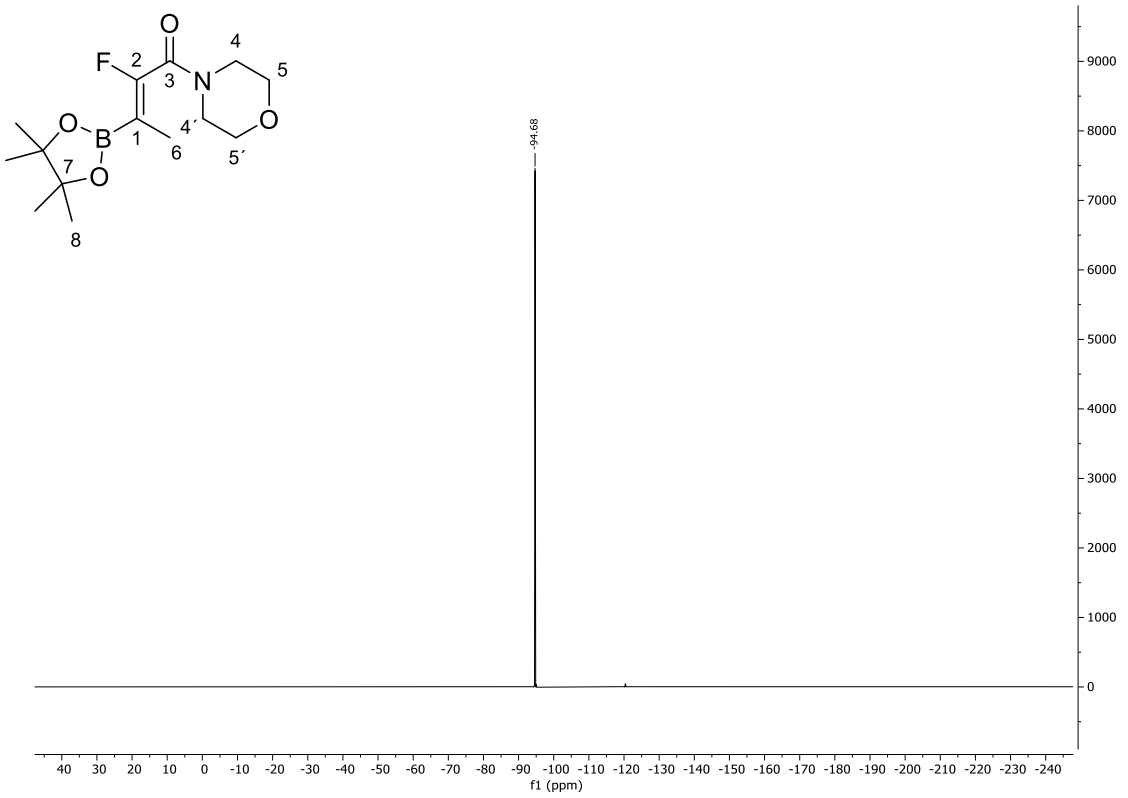

^{1}H-NMR of ***E*-14** (400 MHz, $CDCl_3$)

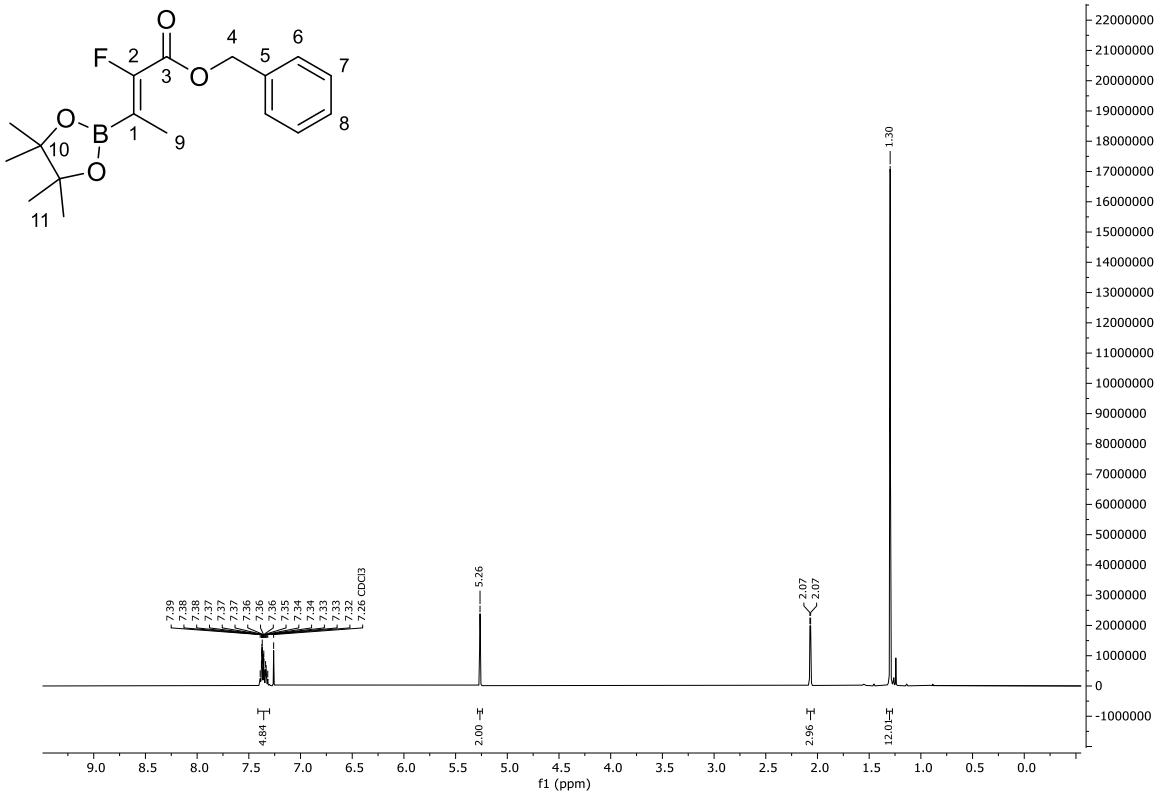

^{13}C-NMR of ***E*-14** (151 MHz, $CDCl_3$)

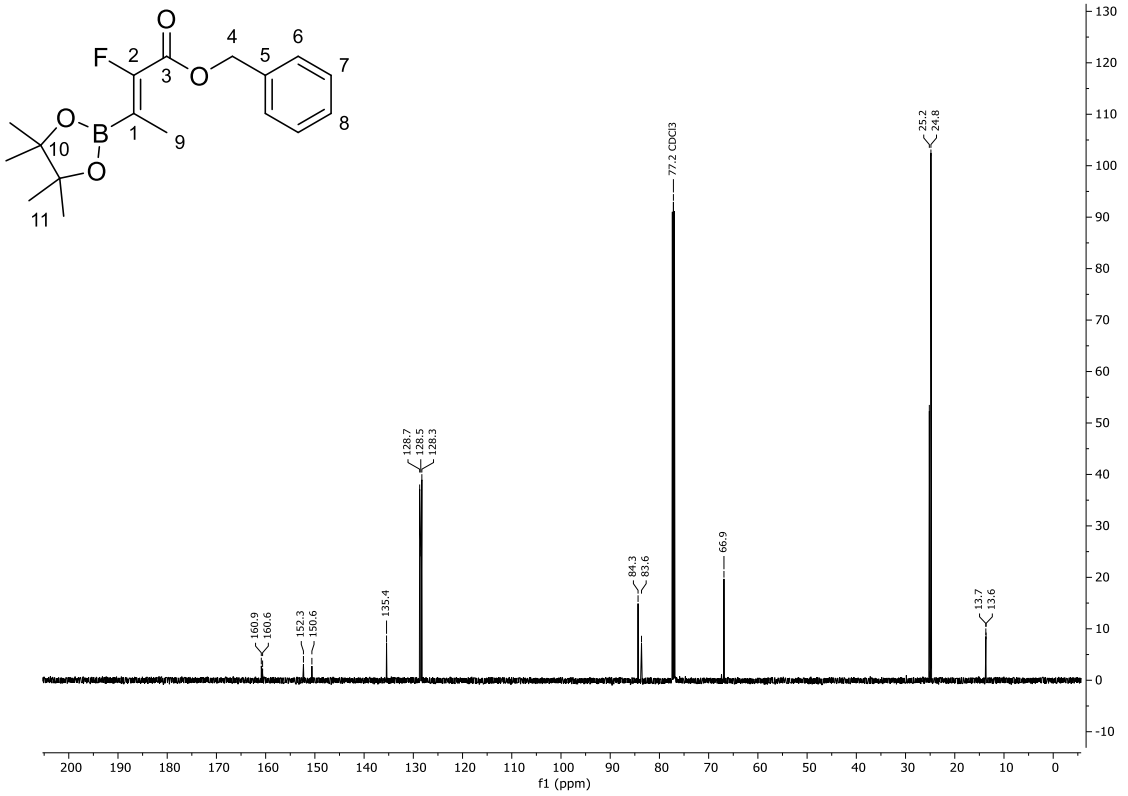

^{19}F-NMR {^{1}H} of ***E*-14**(564 MHz, $CDCl_3$)

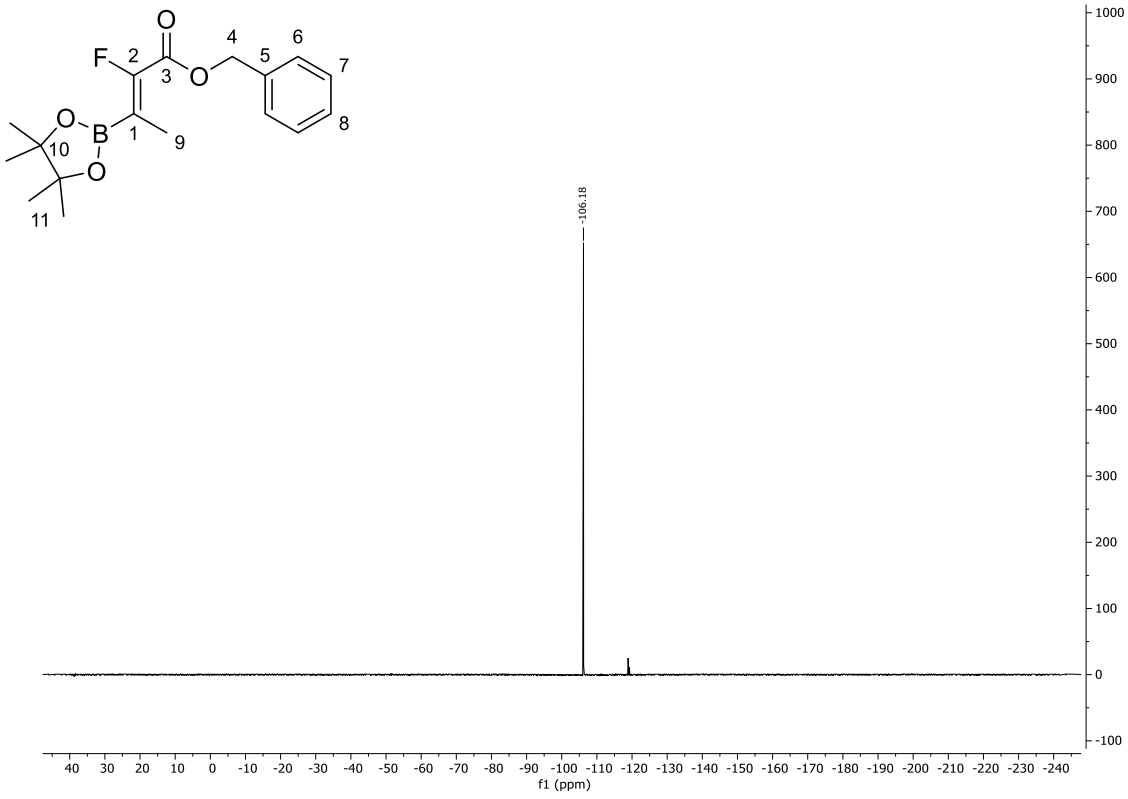

^{19}F-HOESY-NMR of ***E*-14** ($CDCl_3$)

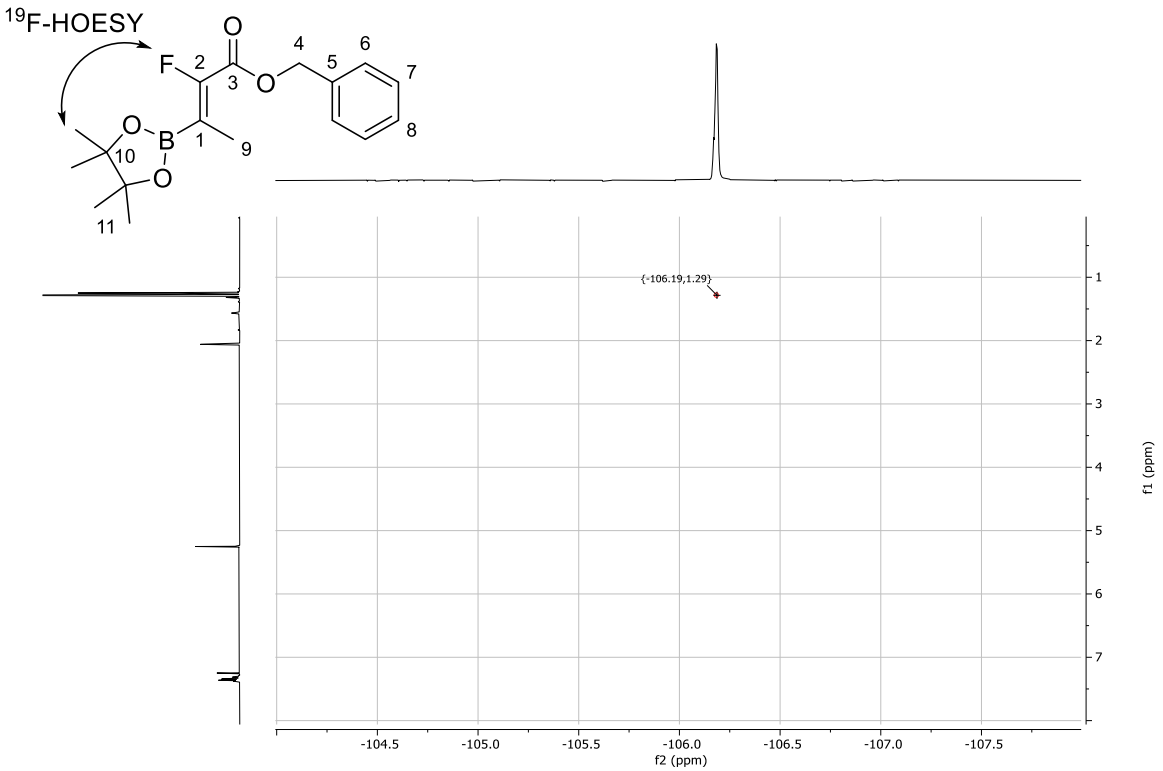

^{1}H-NMR of ***E*-1** (599 MHz, $CDCl_3$)

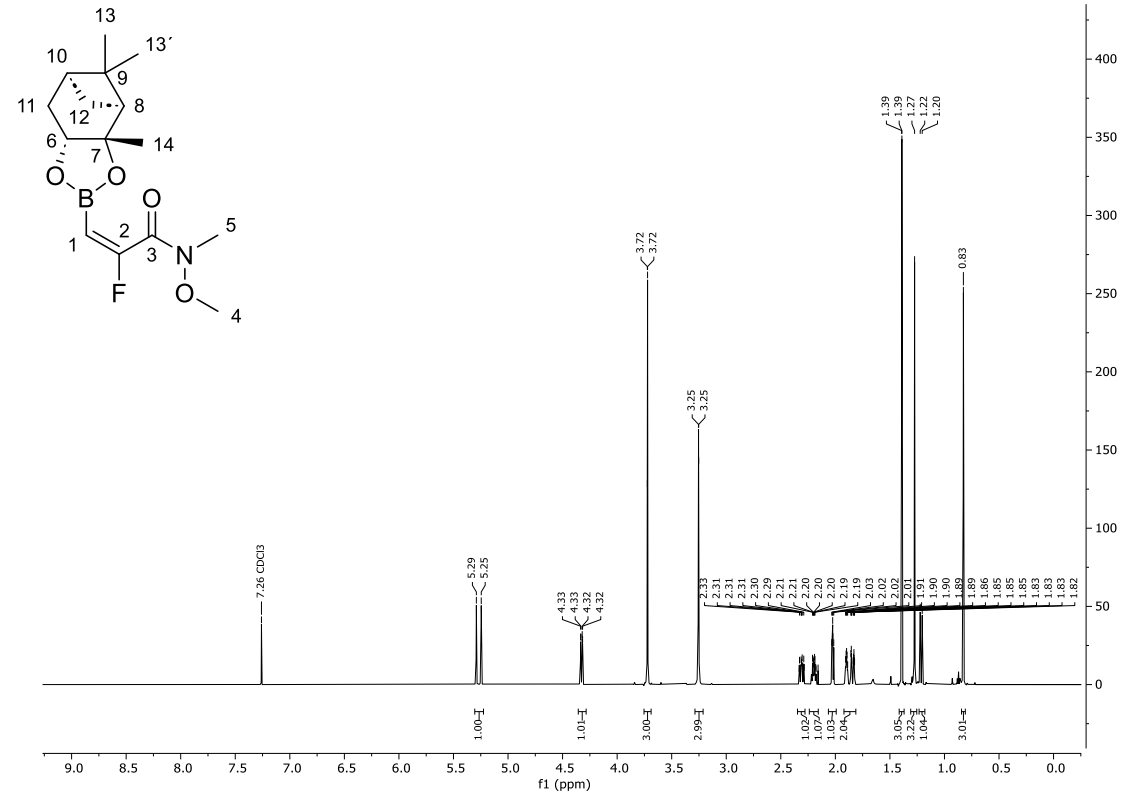

^{13}C-NMR of ***E*-1** (151 MHz, $CDCl_3$)

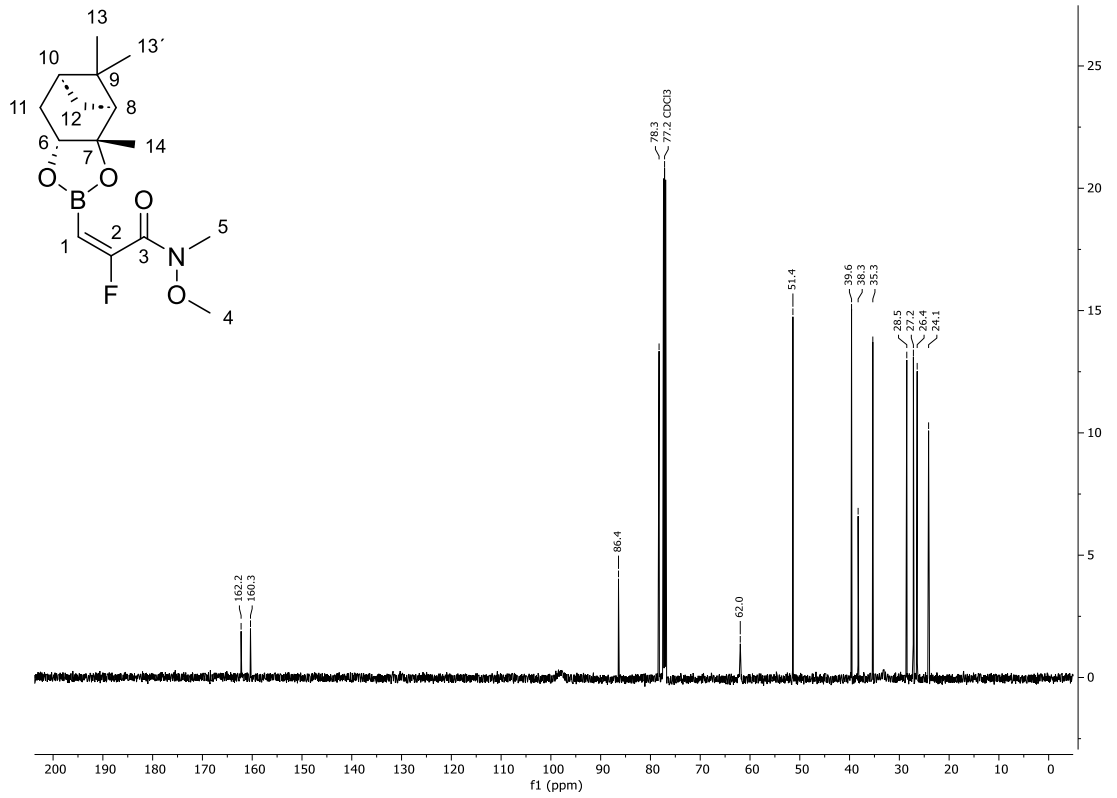

^{19}F-NMR {^{1}H} of ***E*-1** (564 MHz, $CDCl_3$)

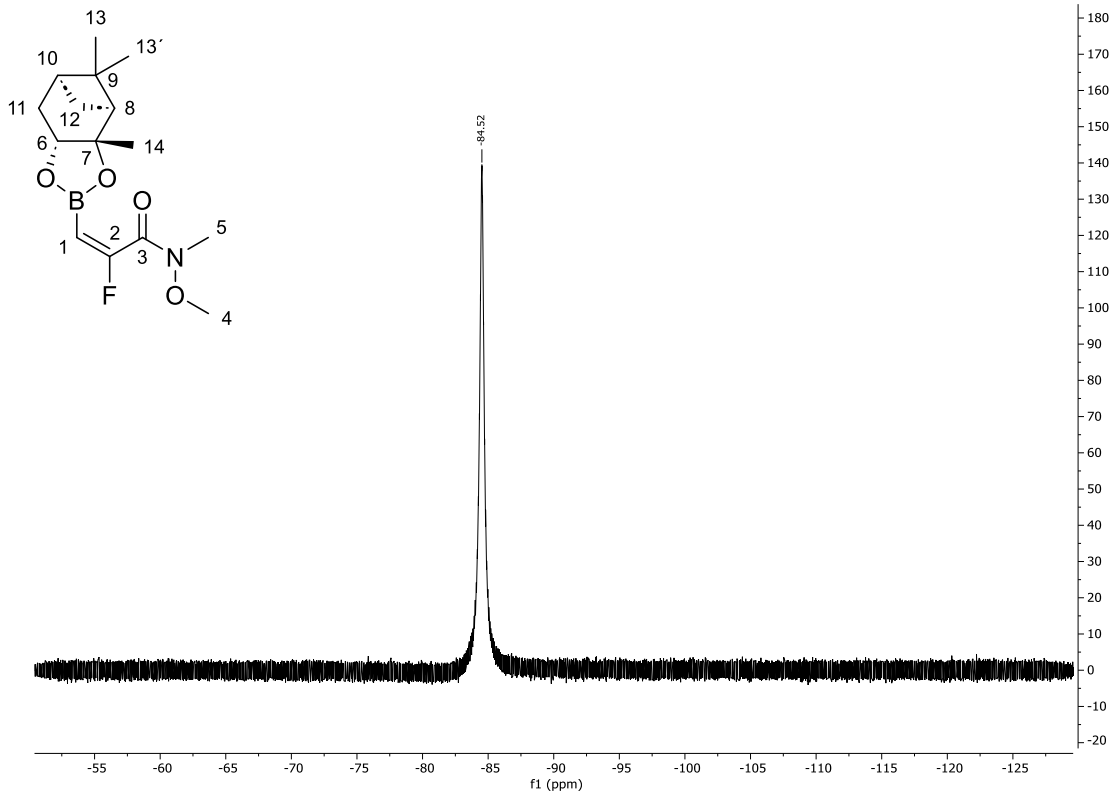

^{1}H-NMR of ***E*-2** (500 MHz, $CDCl_3$)

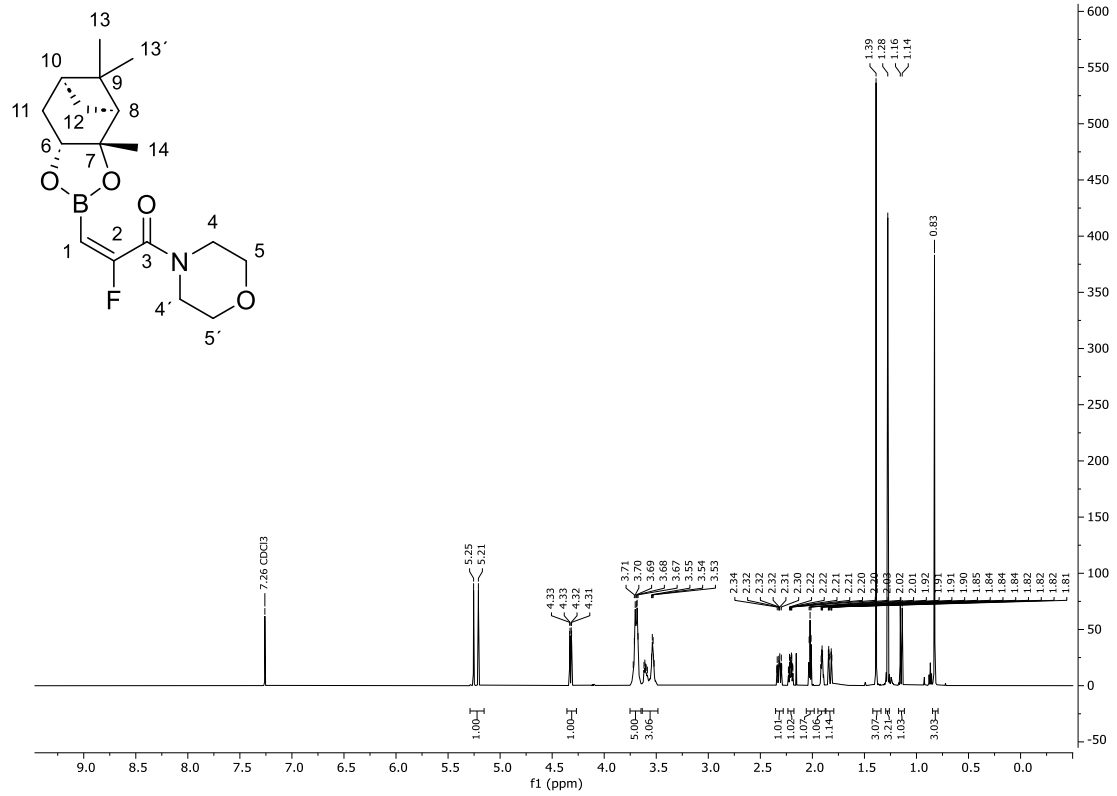

^{13}C-NMR of ***E*-2** (126 MHz, $CDCl_3$)

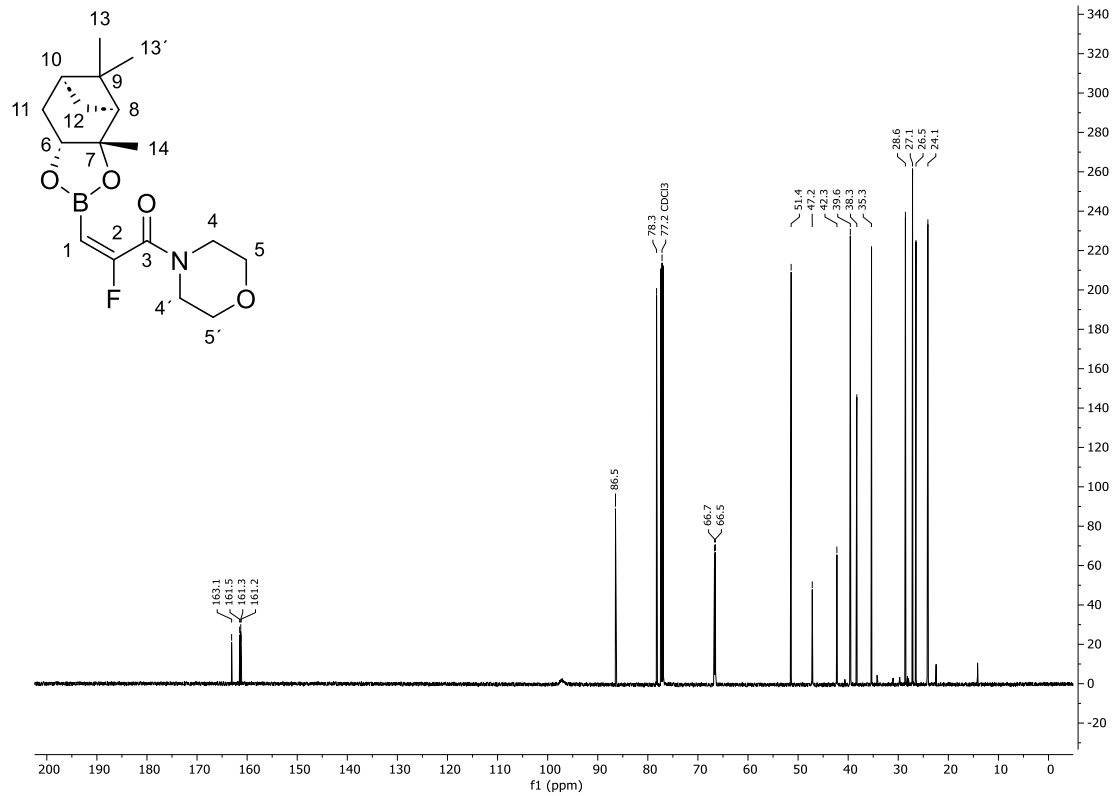

^{19}F-NMR {^{1}H} of ***E*-2** (126 MHz, $CDCl_3$)

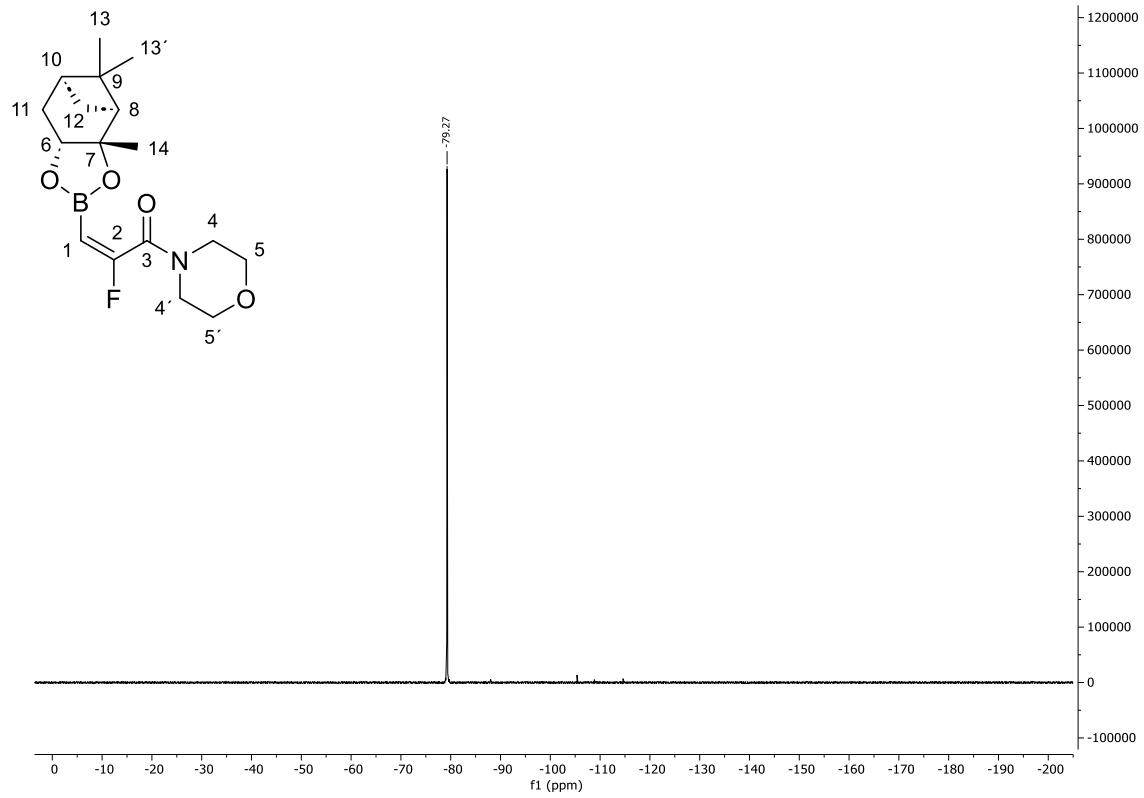

^{1}H-NMR of ***E*-3** (599 MHz, $CDCl_3$)

^{13}C-NMR of ***E*-3** (151 MHz, $CDCl_3$)

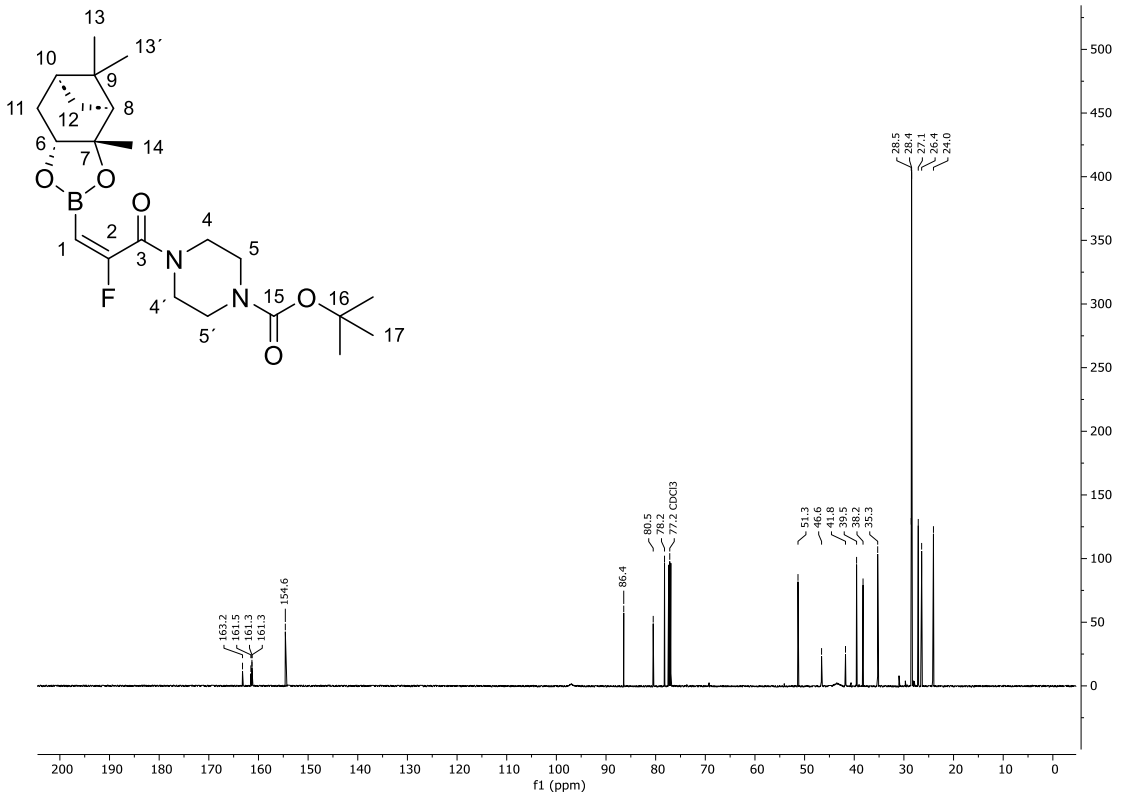

^{19}F-NMR {^{1}H} of ***E*-3** (377 MHz, $CDCl_3$)

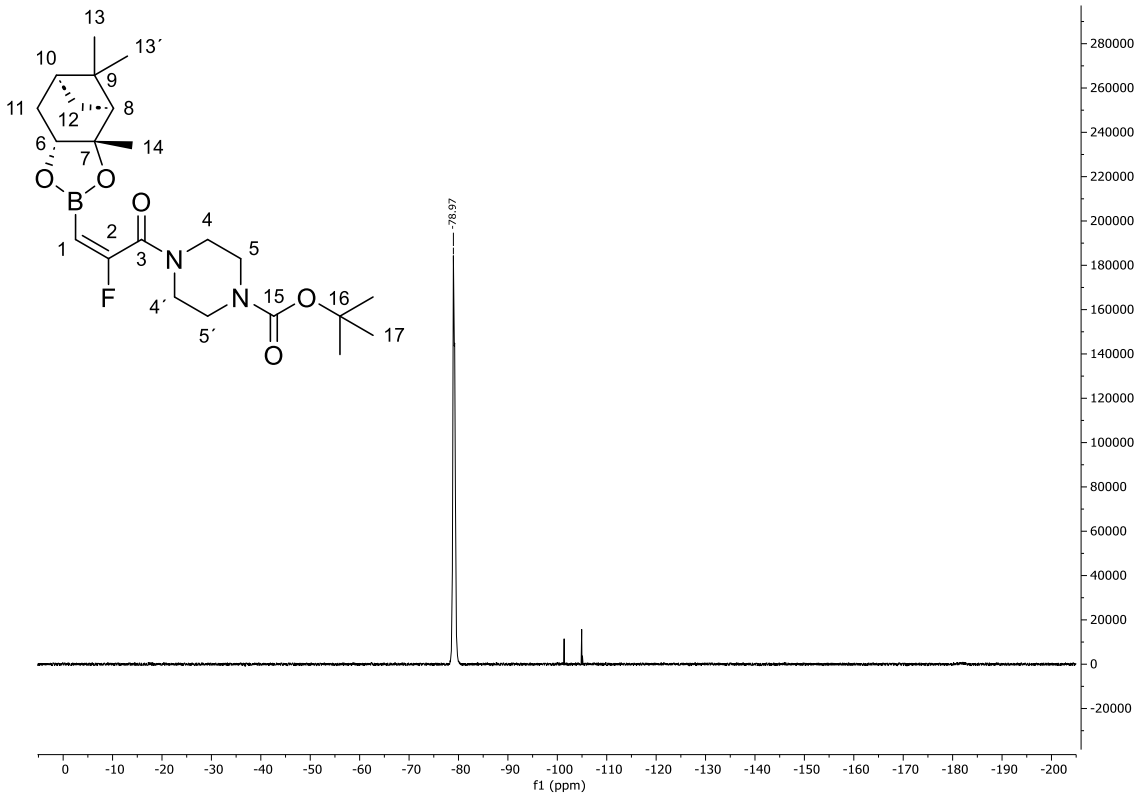

^{1}H-NMR of ***E*-4** (500 MHz, $CDCl_3$)

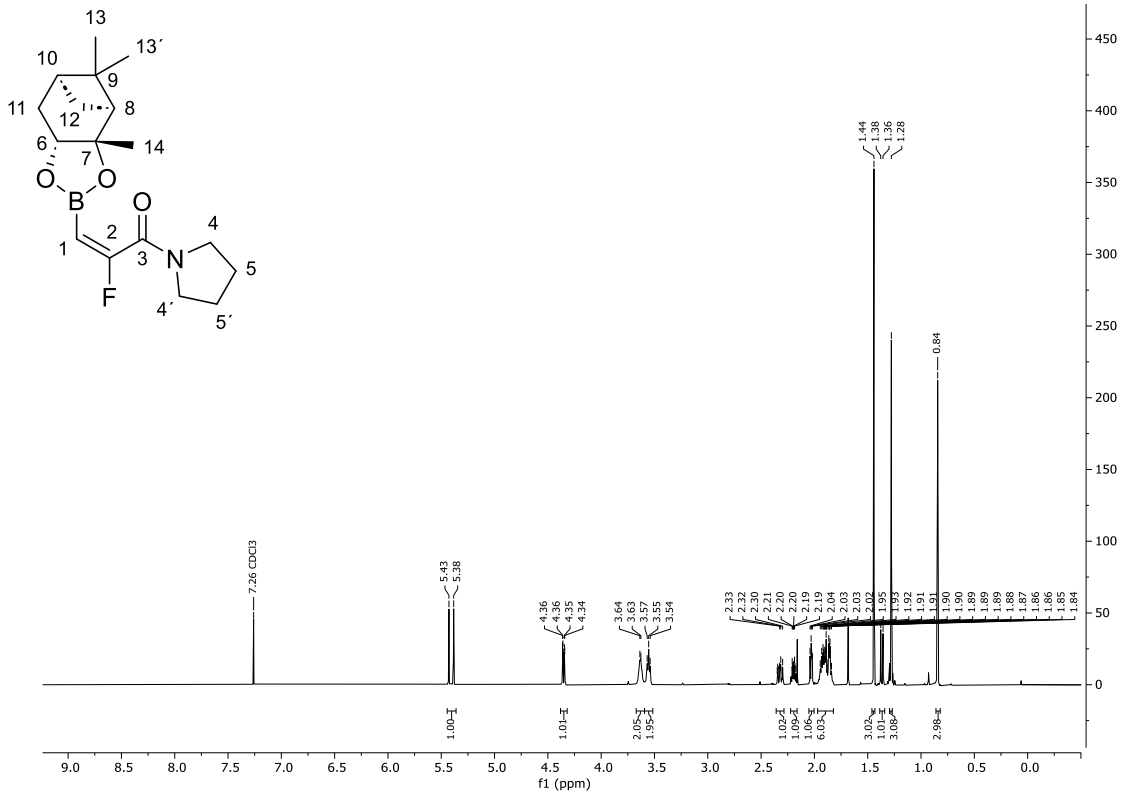

^{13}C-NMR of ***E*-4** (126 MHz, $CDCl_3$)

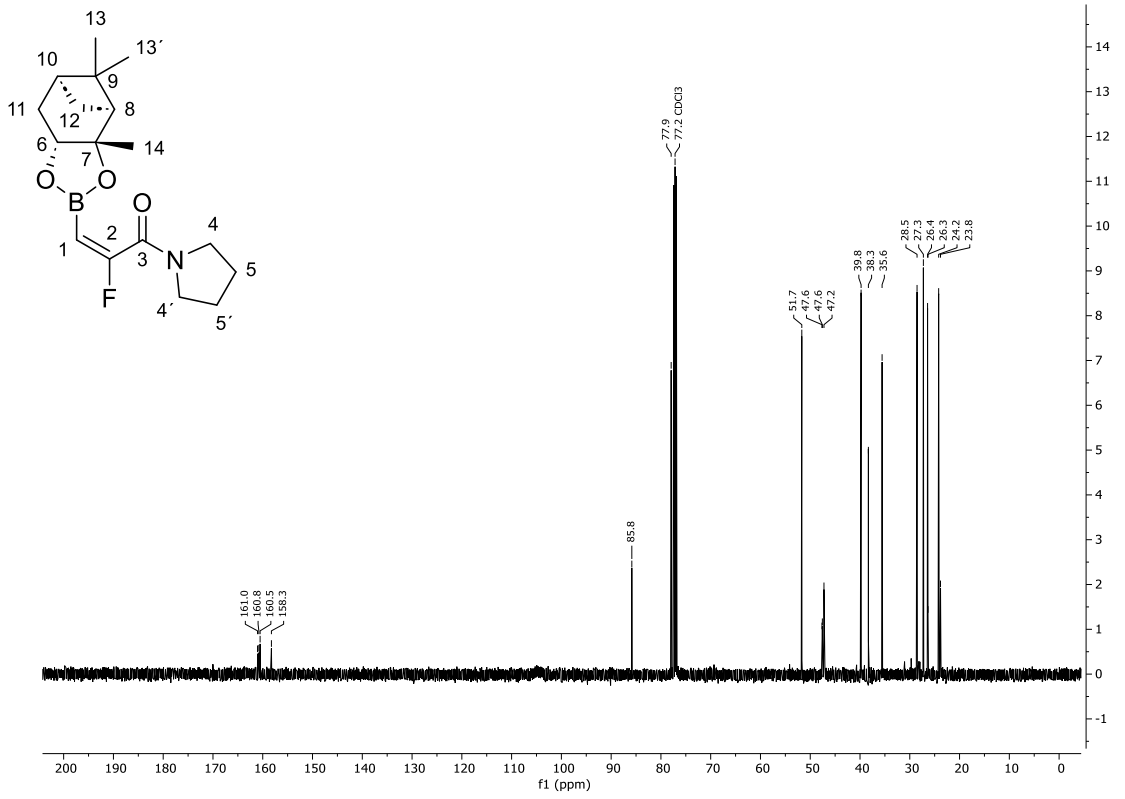

^{19}F-NMR {^{1}H} of ***E*-4** (377 MHz, $CDCl_3$)

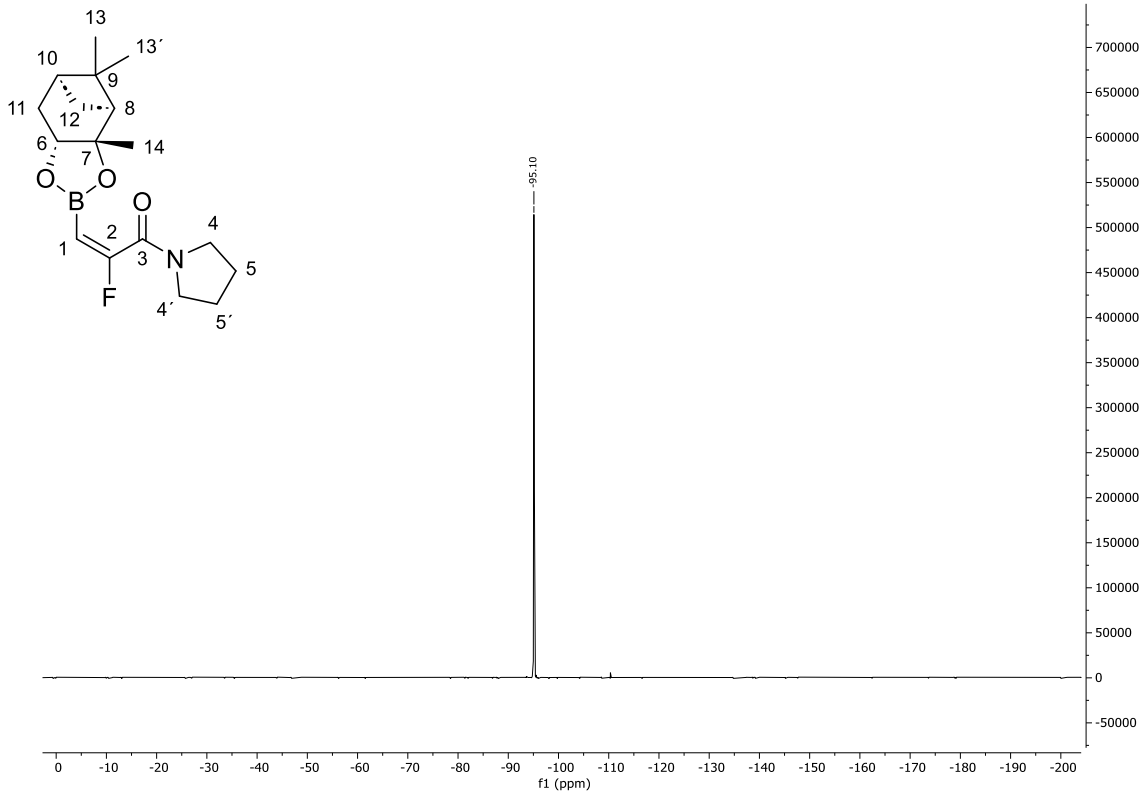

^{1}H-NMR of ***E*-5** (500 MHz, $CDCl_3$)

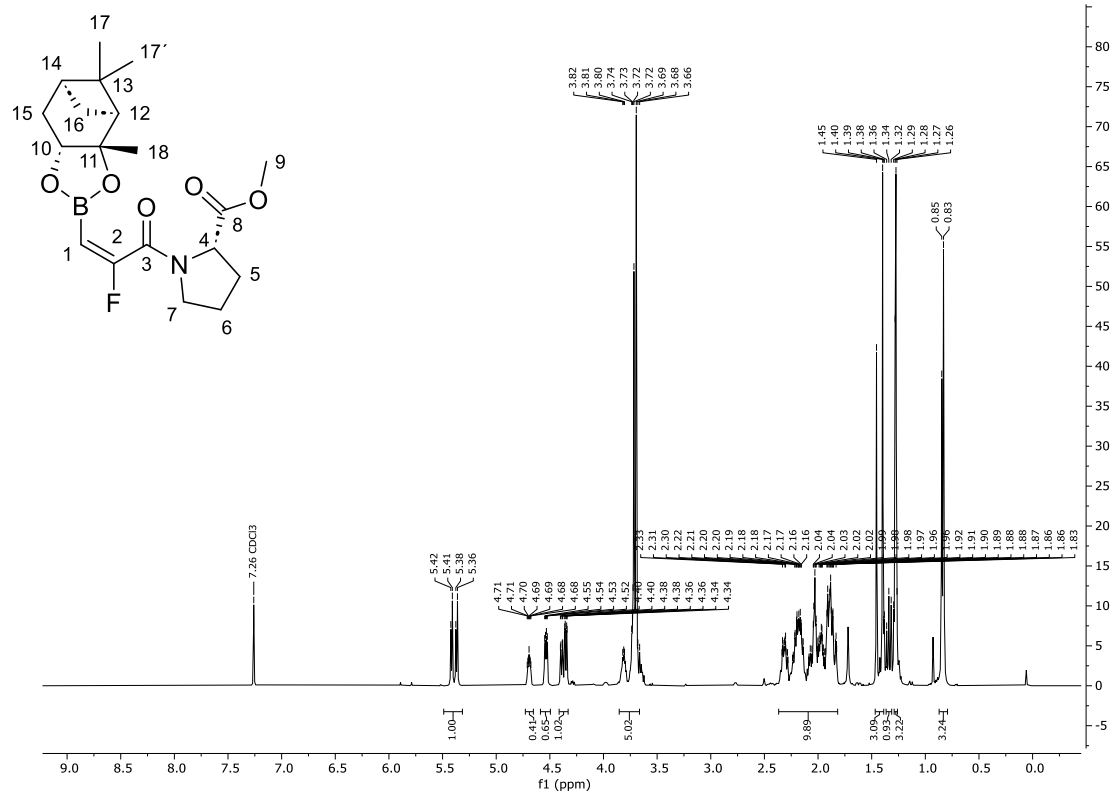

^{13}C-NMR of ***E*-5** (126 MHz, $CDCl_3$)

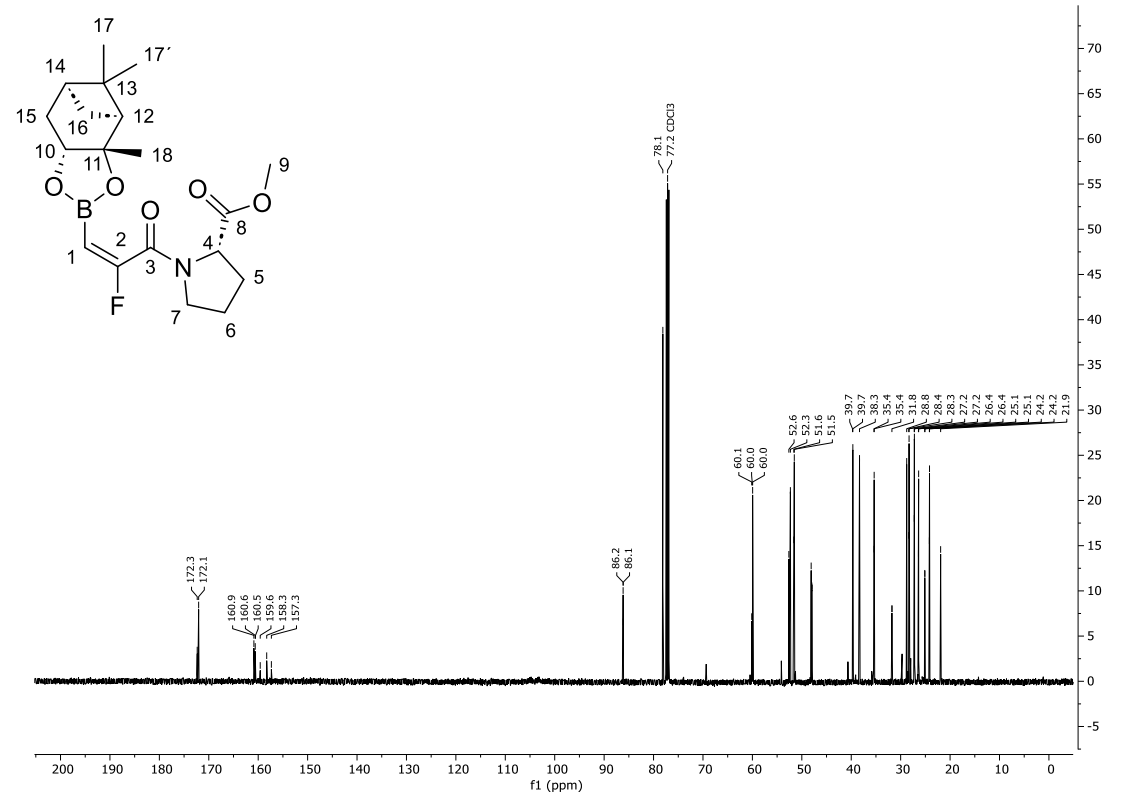

^{19}F-NMR {^{1}H} of ***E*-5** (377 MHz, $CDCl_3$)

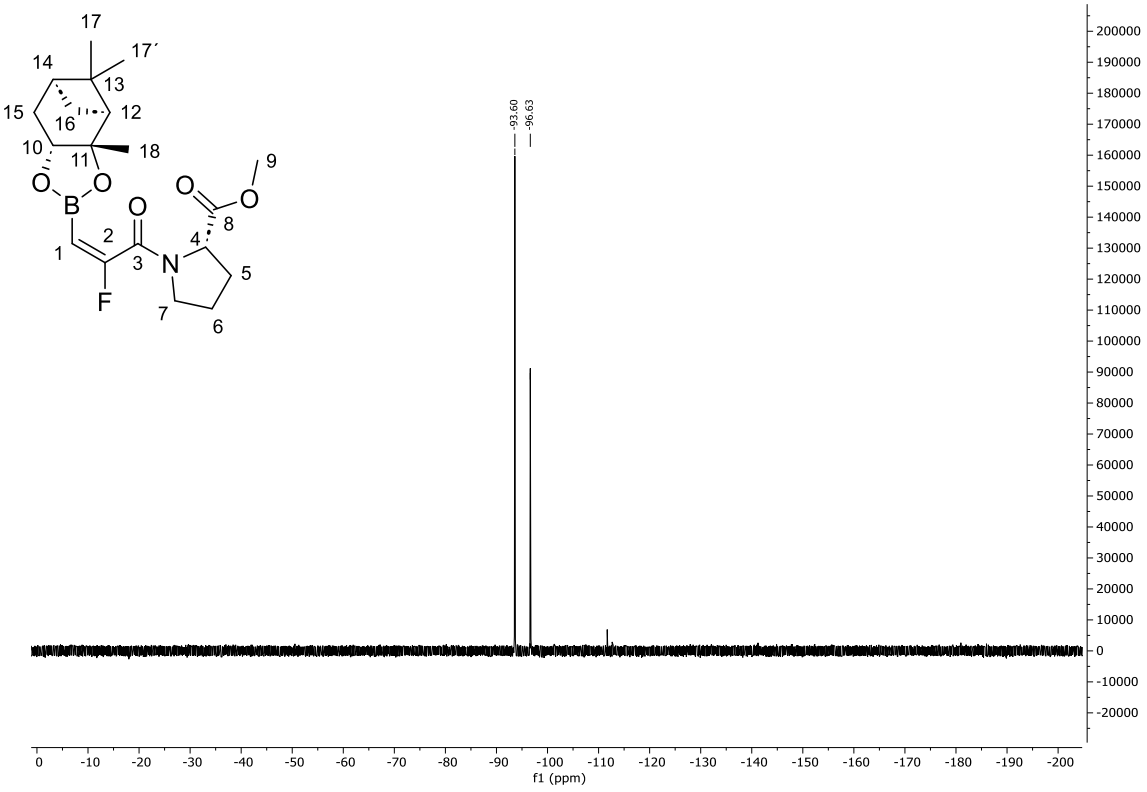

^{1}H-NMR of ***E*-6** (500 MHz, $CDCl_3$)

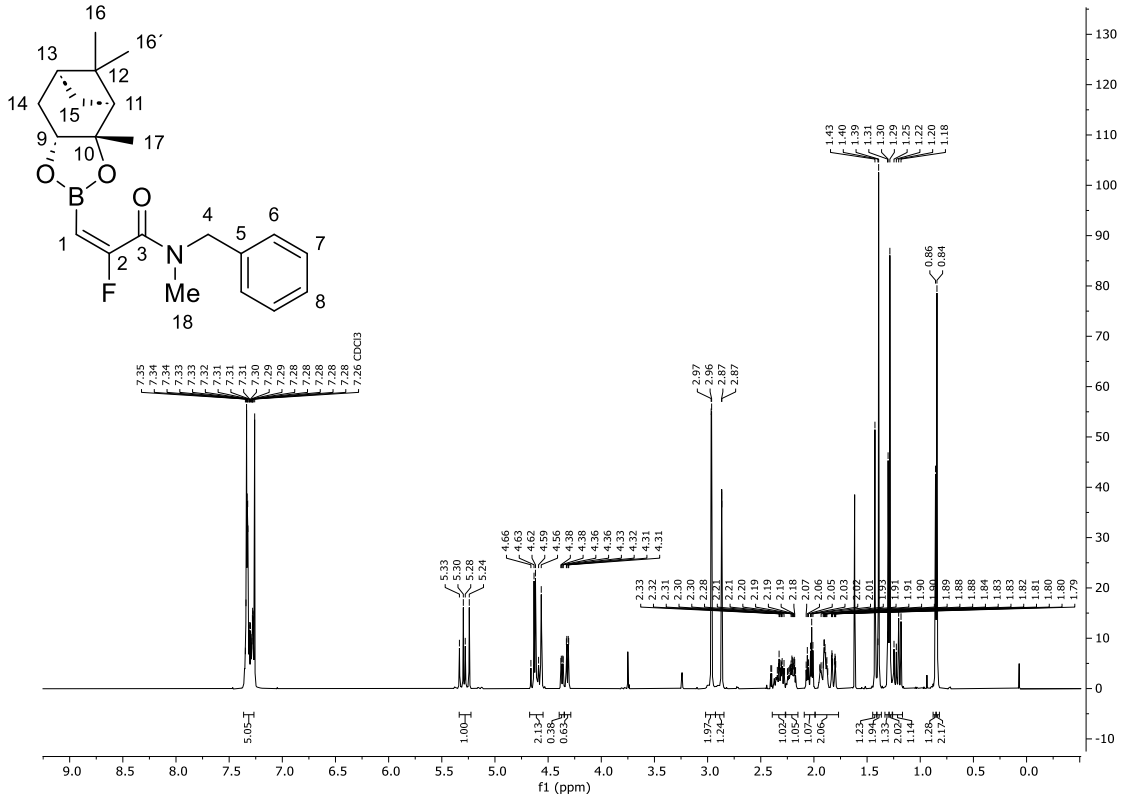

^{13}C-NMR of ***E*-6** (126 MHz, $CDCl_3$)

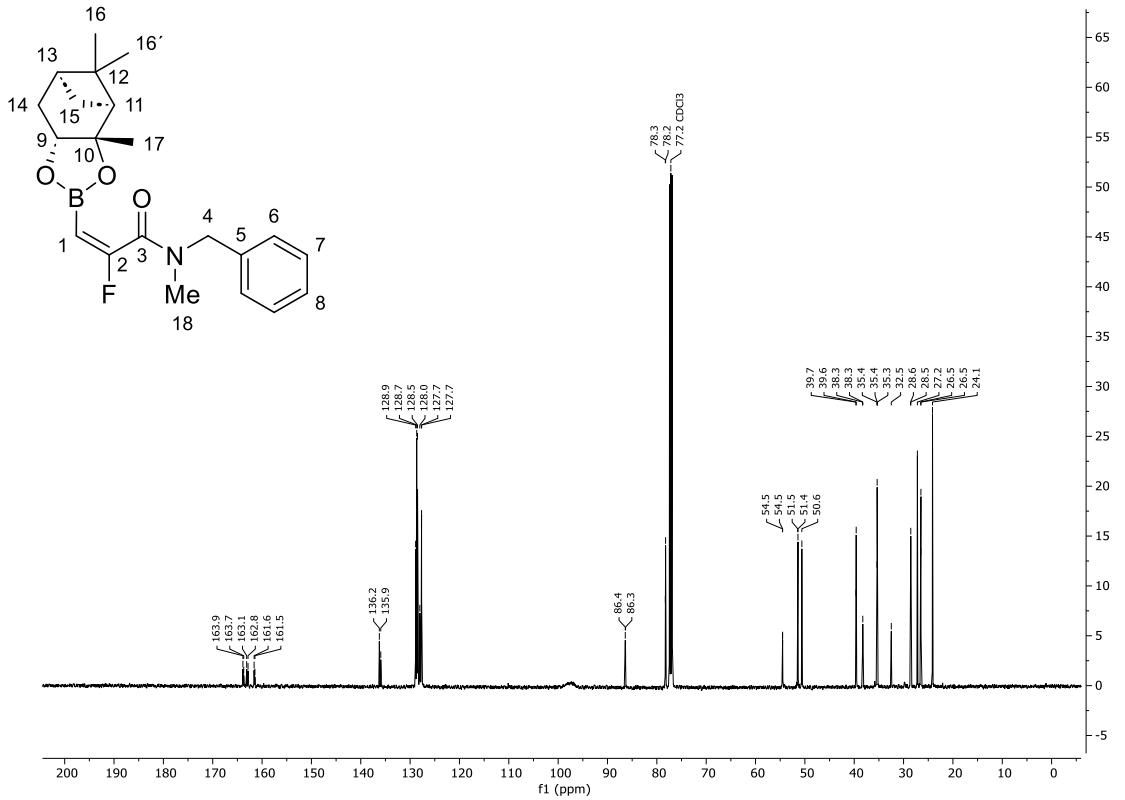

^{19}F-NMR {^{1}H} of ***E*-6** (126 MHz, $CDCl_3$)

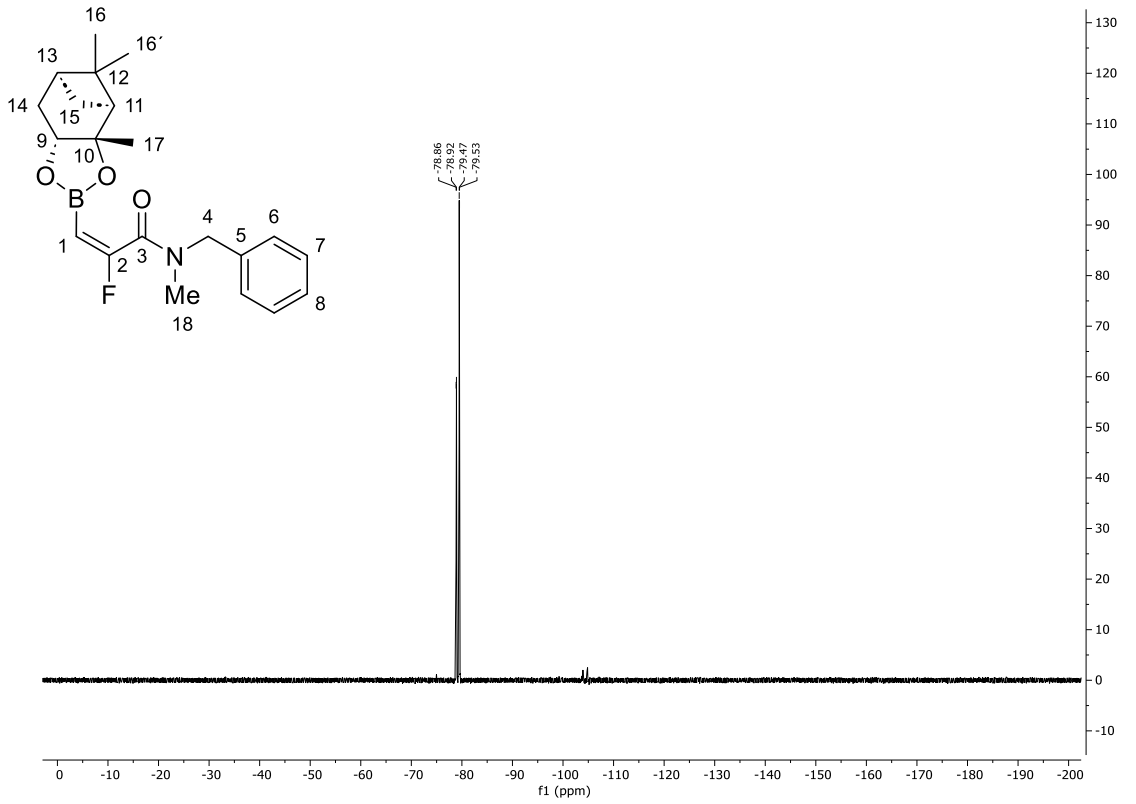

^{1}H-NMR of ***E*-7** (500 MHz, $CDCl_3$)

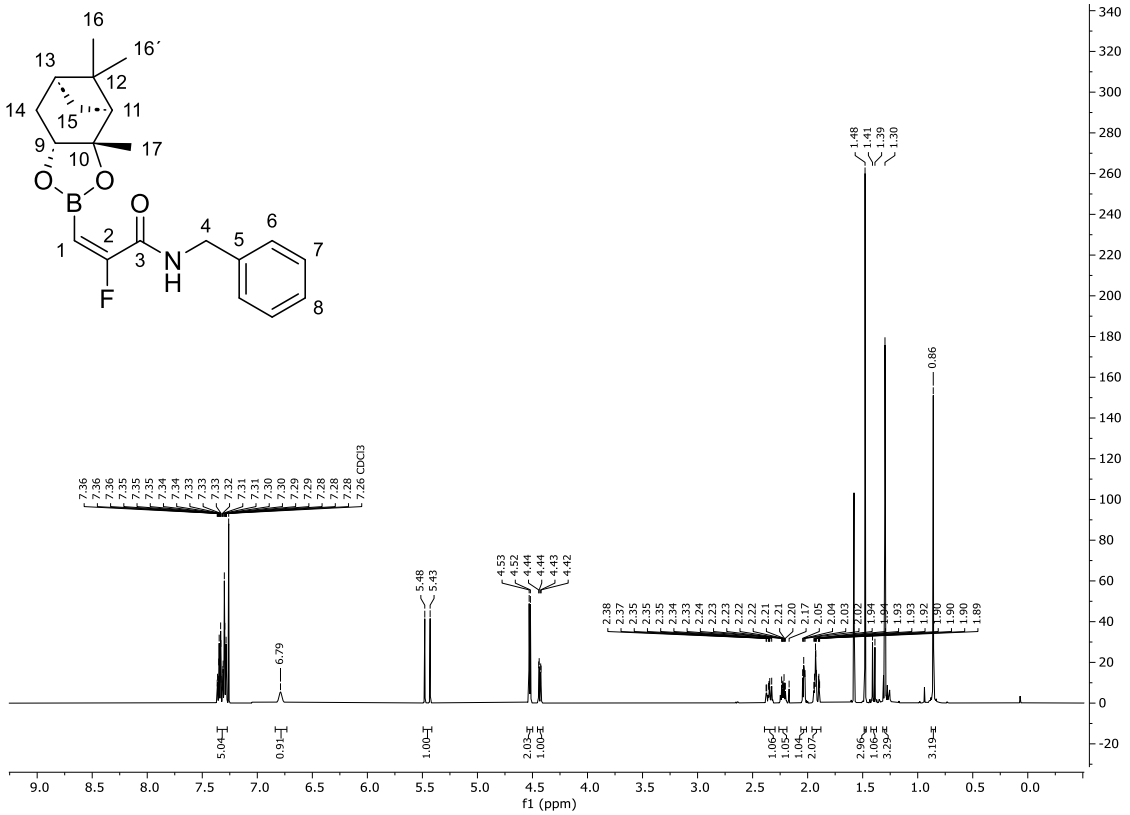

^{13}C-NMR of ***E*-7** (126 MHz, $CDCl_3$)

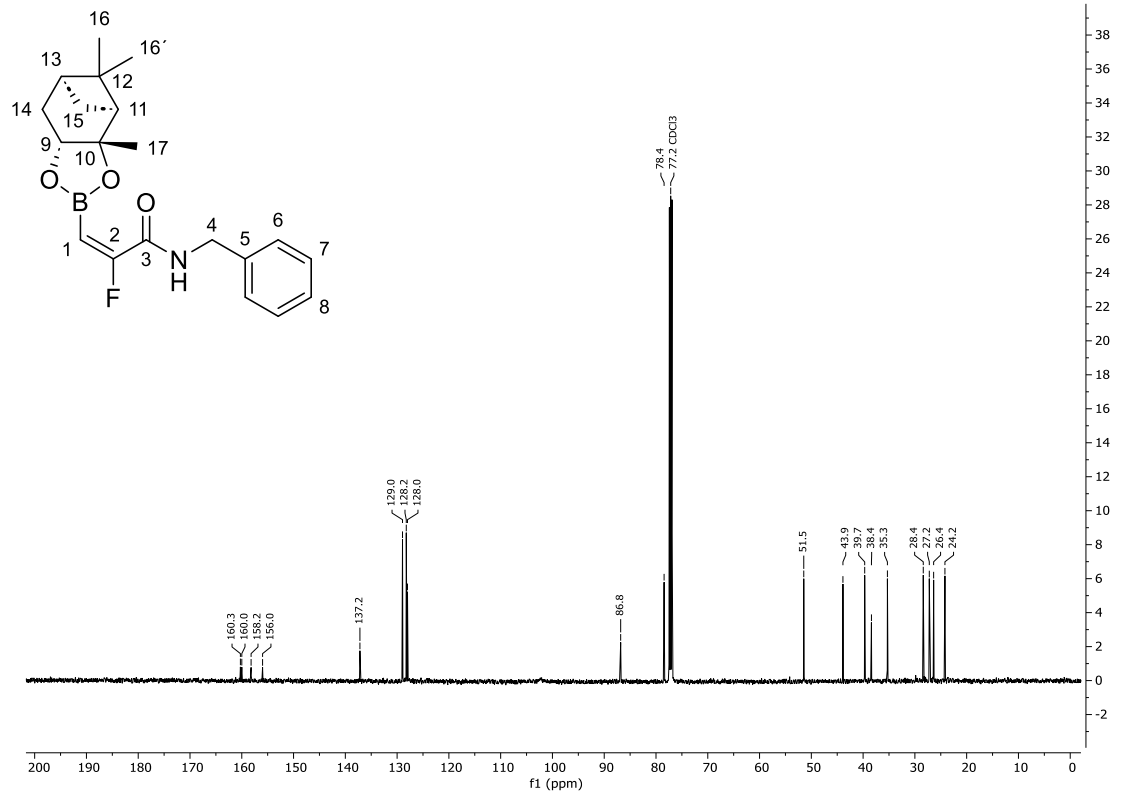

^{19}F-NMR {^{1}H} of ***E*-7** (470 MHz, $CDCl_3$)

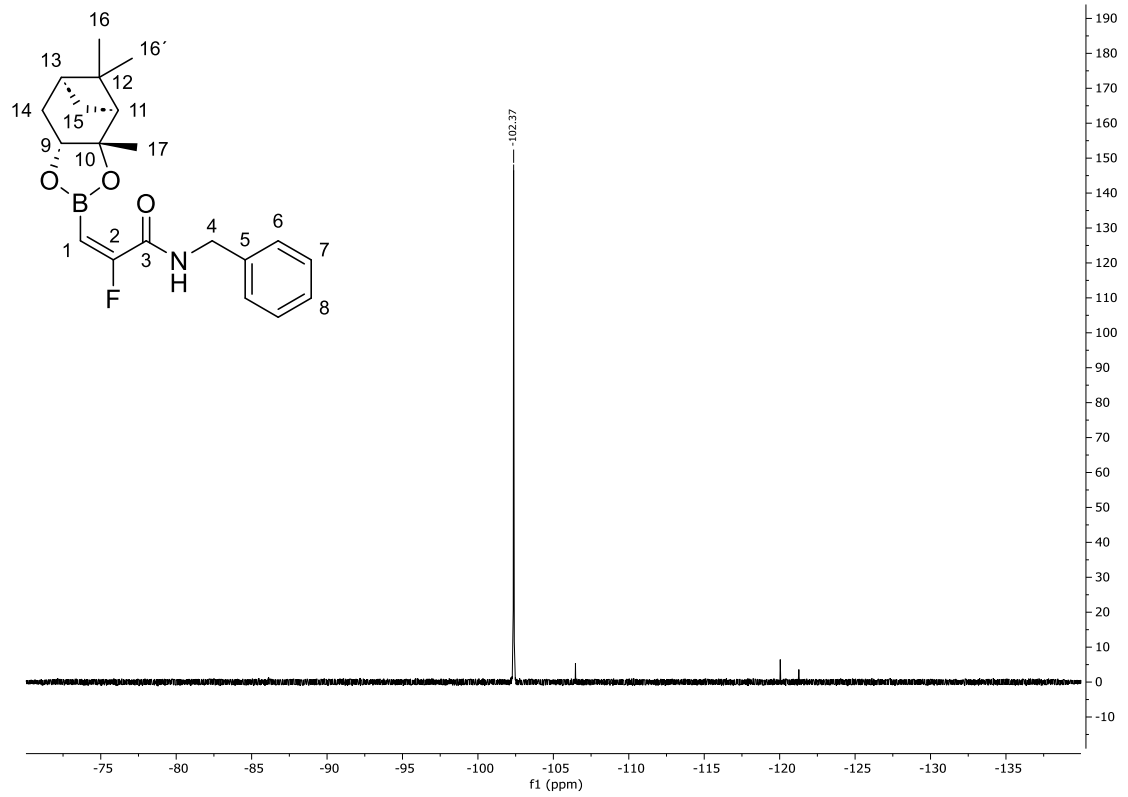

^{1}H-NMR of ***E*-8** (500 MHz, $CDCl_3$)

^{13}C-NMR of ***E*-8** (126 MHz, $CDCl_3$)

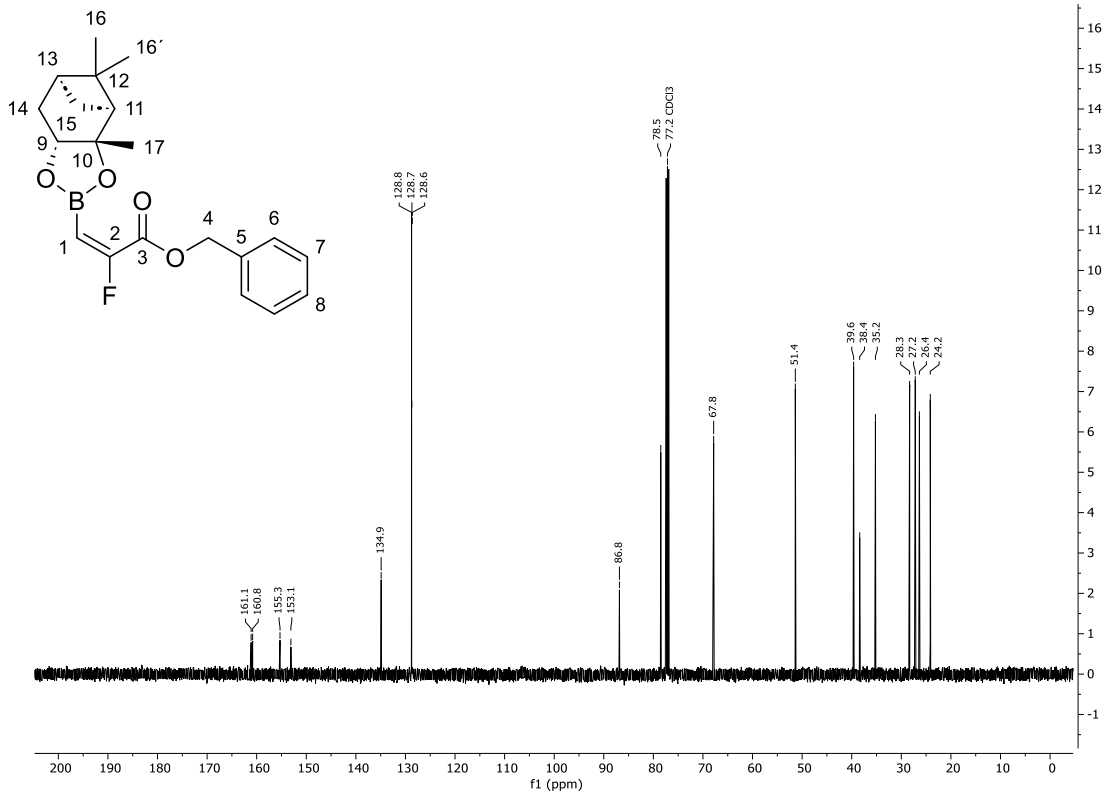

^{19}F-NMR {^{1}H} of ***E*-8** (377 MHz, $CDCl_3$)

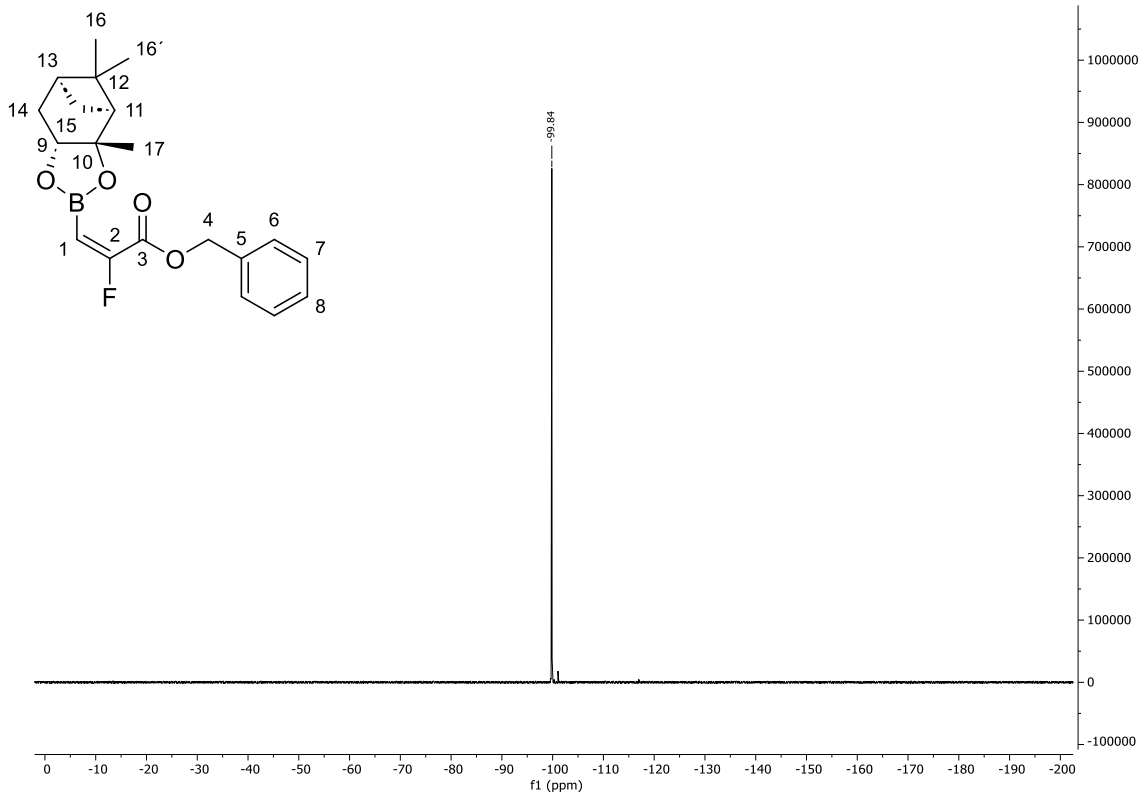

^{1}H-NMR of ***E*-9** (599 MHz, $CDCl_3$)

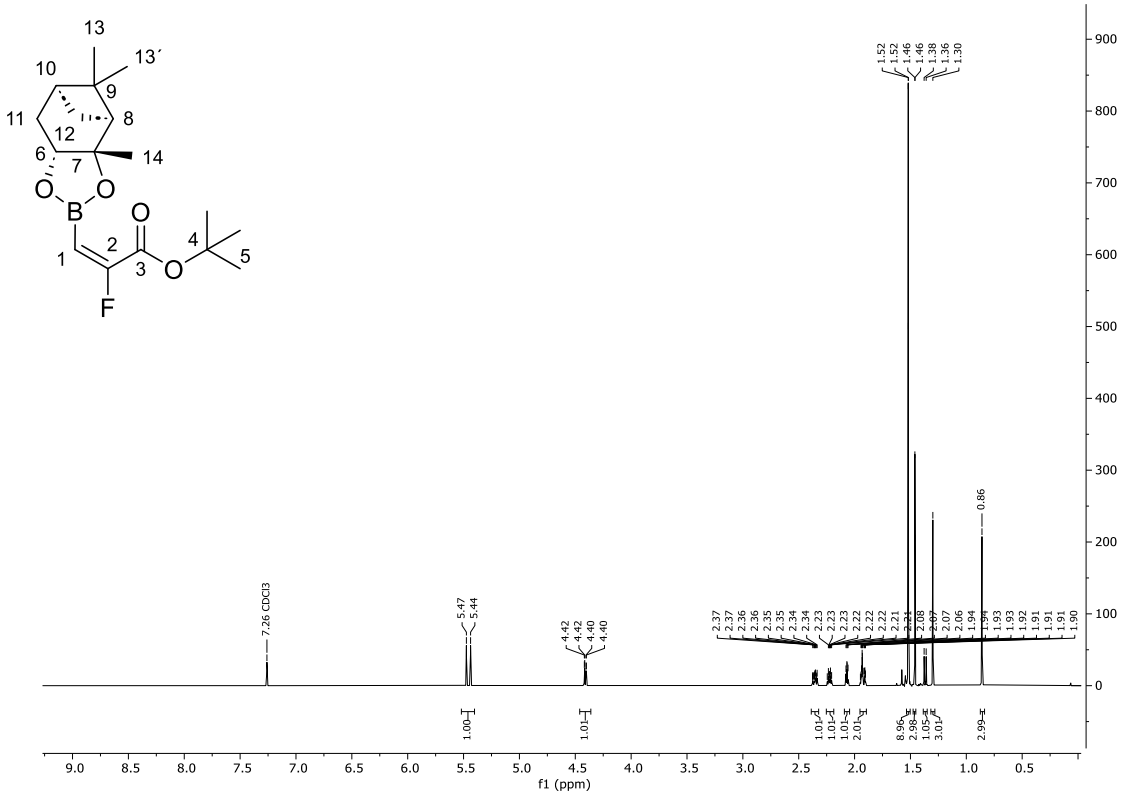

^{13}C-NMR of ***E*-9** (151 MHz, $CDCl_3$)

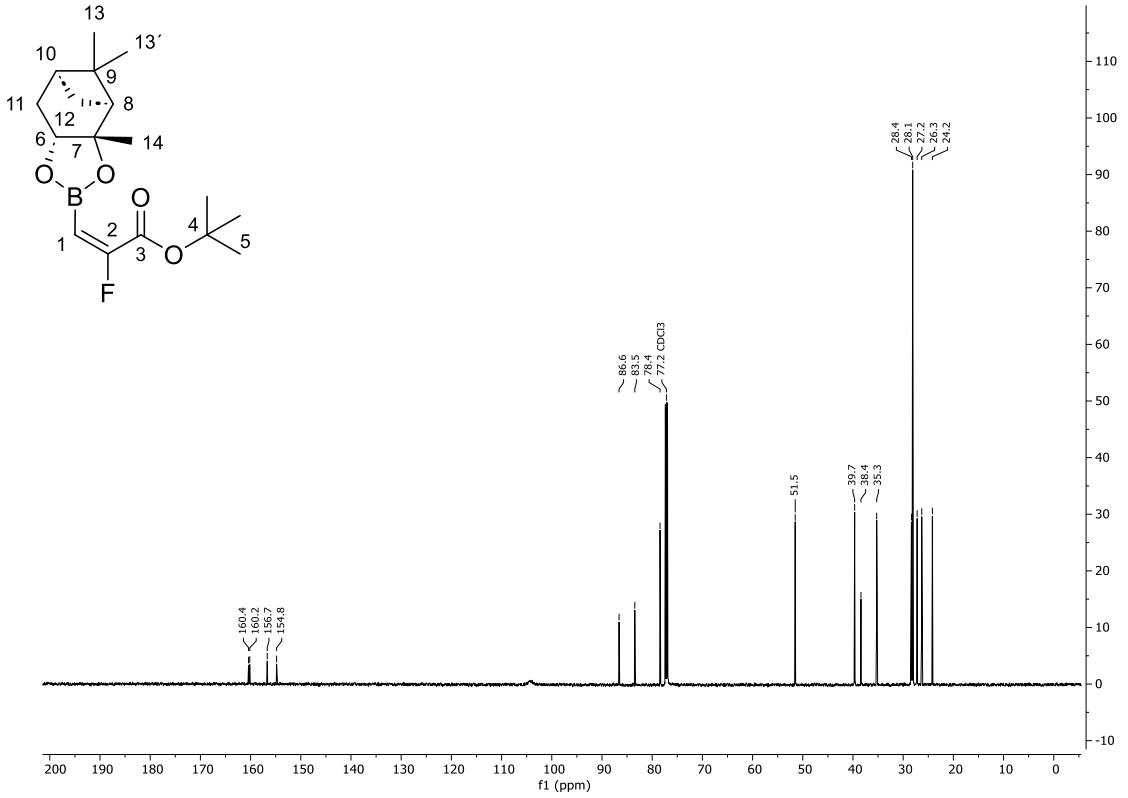

^{19}F-NMR {^{1}H} of ***E*-9** (377 MHz, $CDCl_3$)

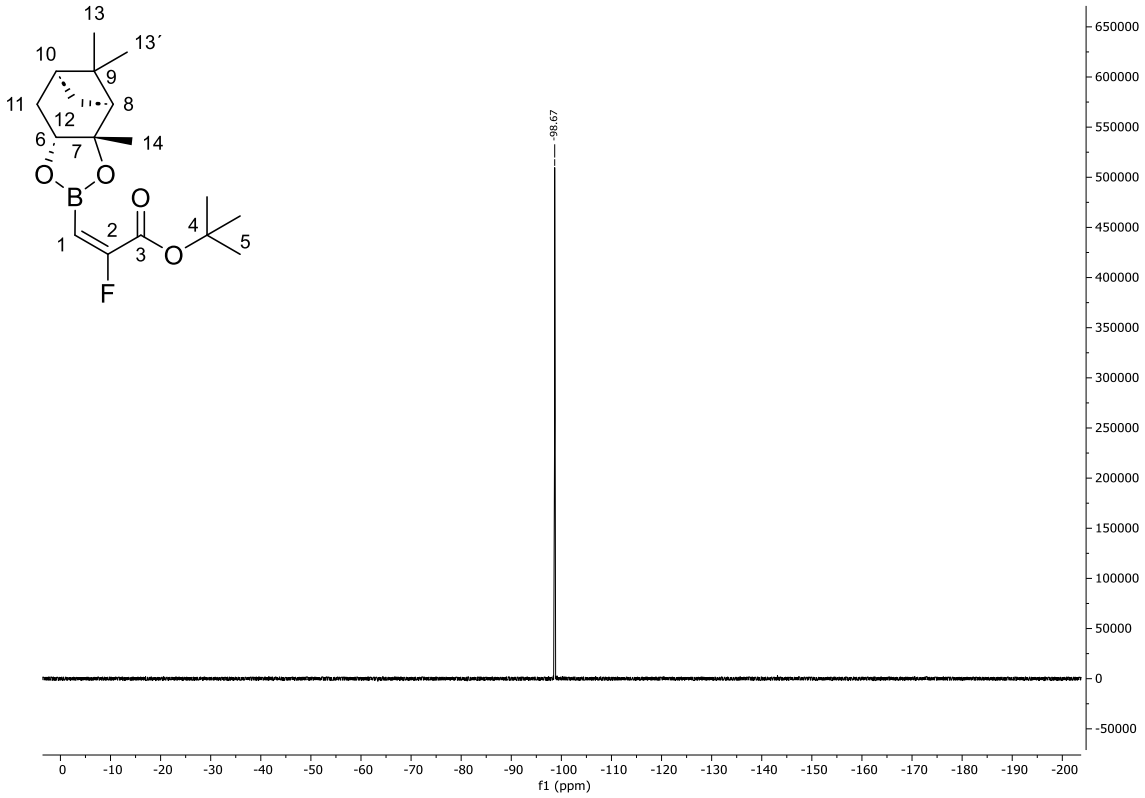

^{1}H-NMR of **S34** (500 MHz, $CDCl_3$)

^{13}C-NMR of **S34** (126 MHz, $CDCl_3$)

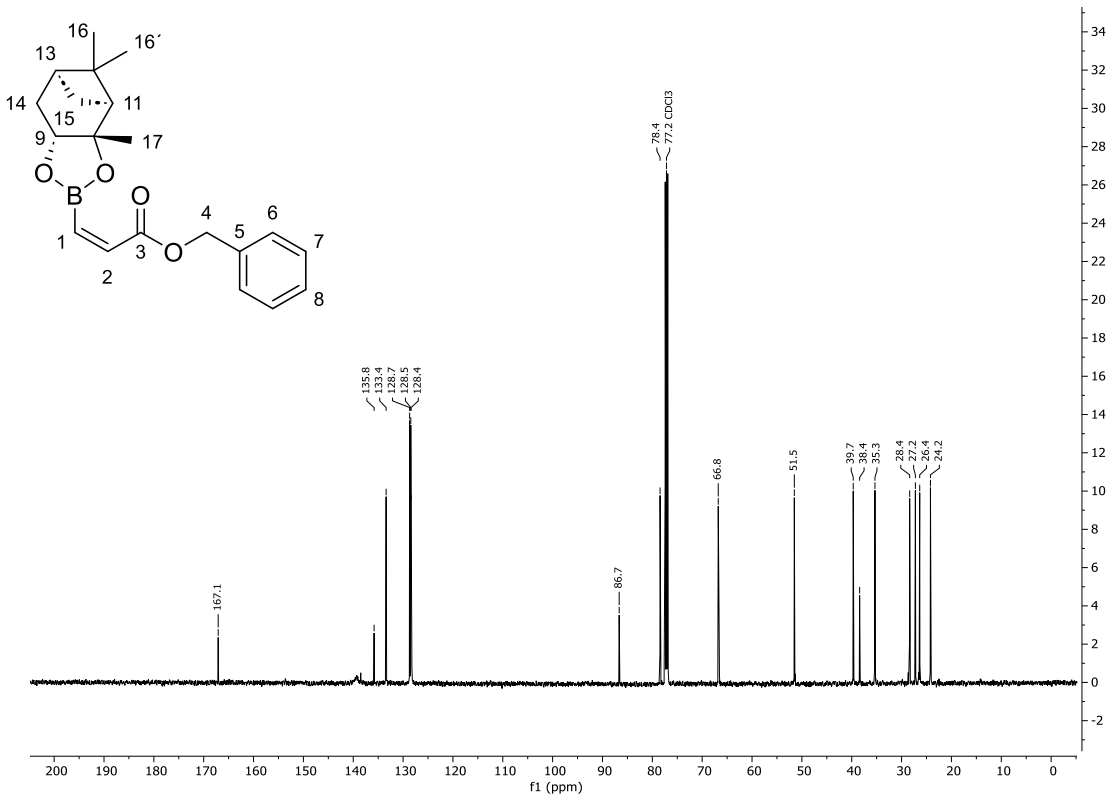

^{1}H-NMR of **S35** (500 MHz, $CDCl_3$)

^{13}C-NMR of **S35** (126 MHz, $CDCl_3$)

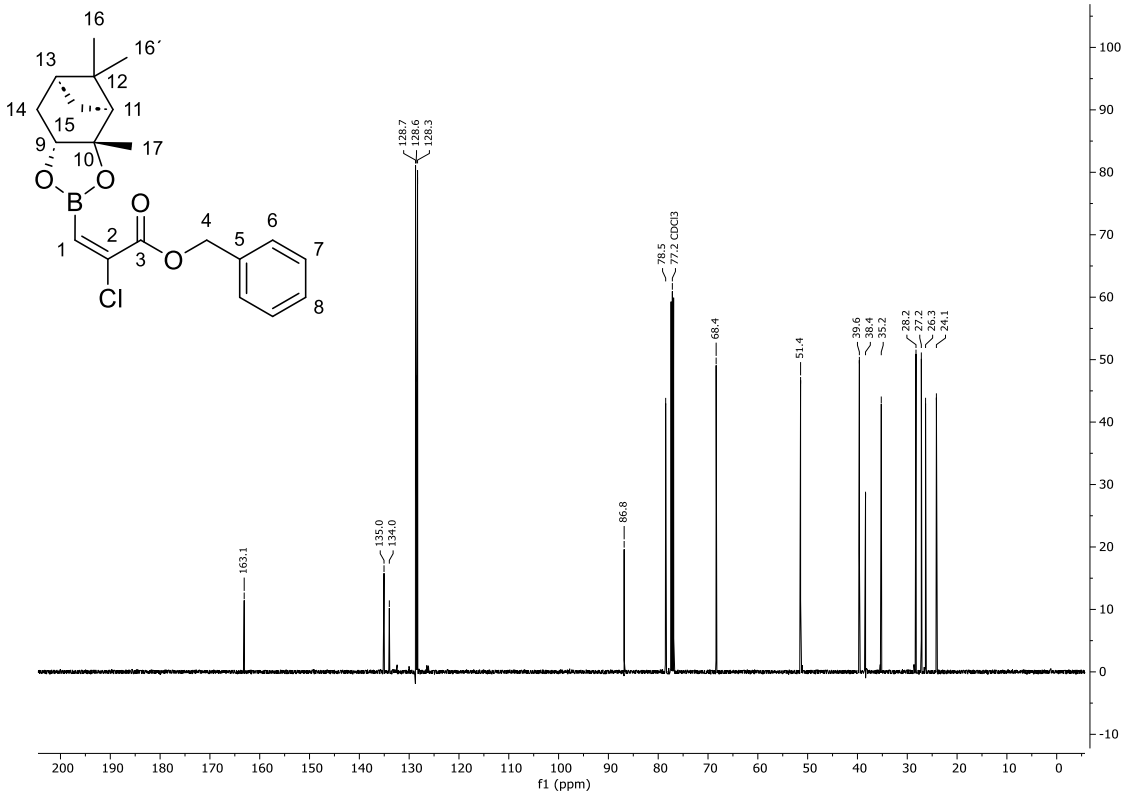

^{1}H-NMR of ***Z*-10** (500 MHz, $CDCl_3$)

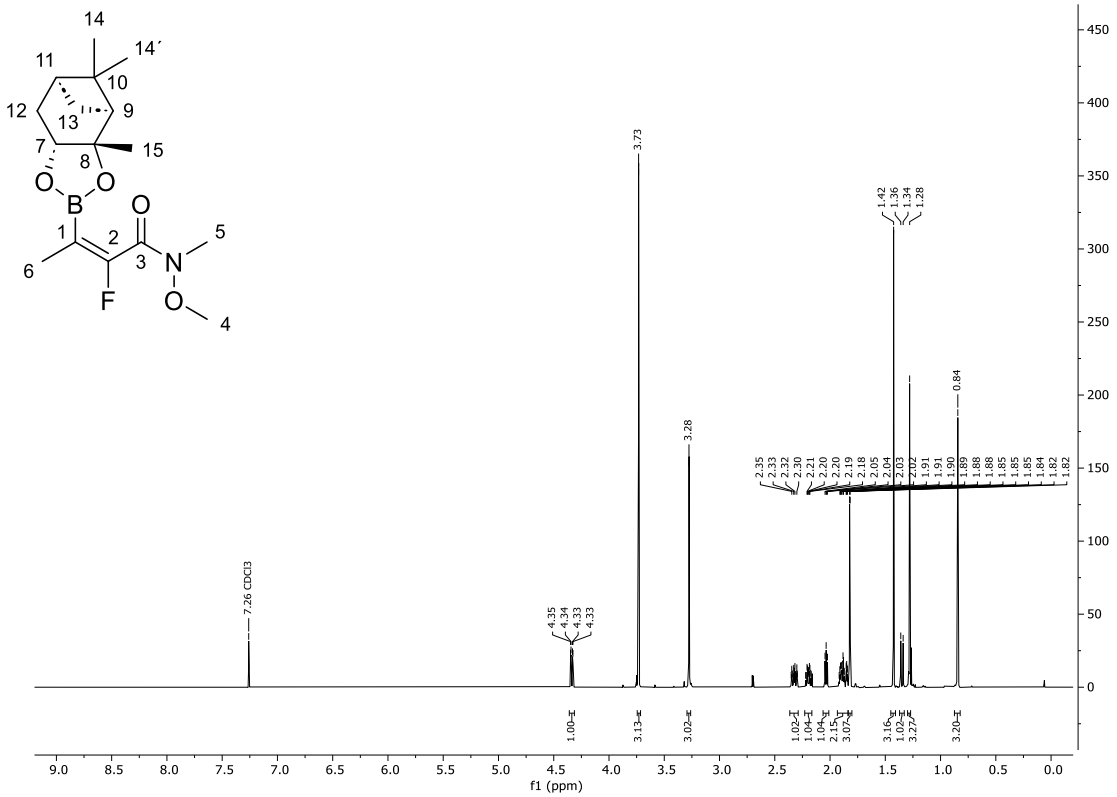

^{13}C-NMR of ***Z*-10** (126 MHz, $CDCl_3$)

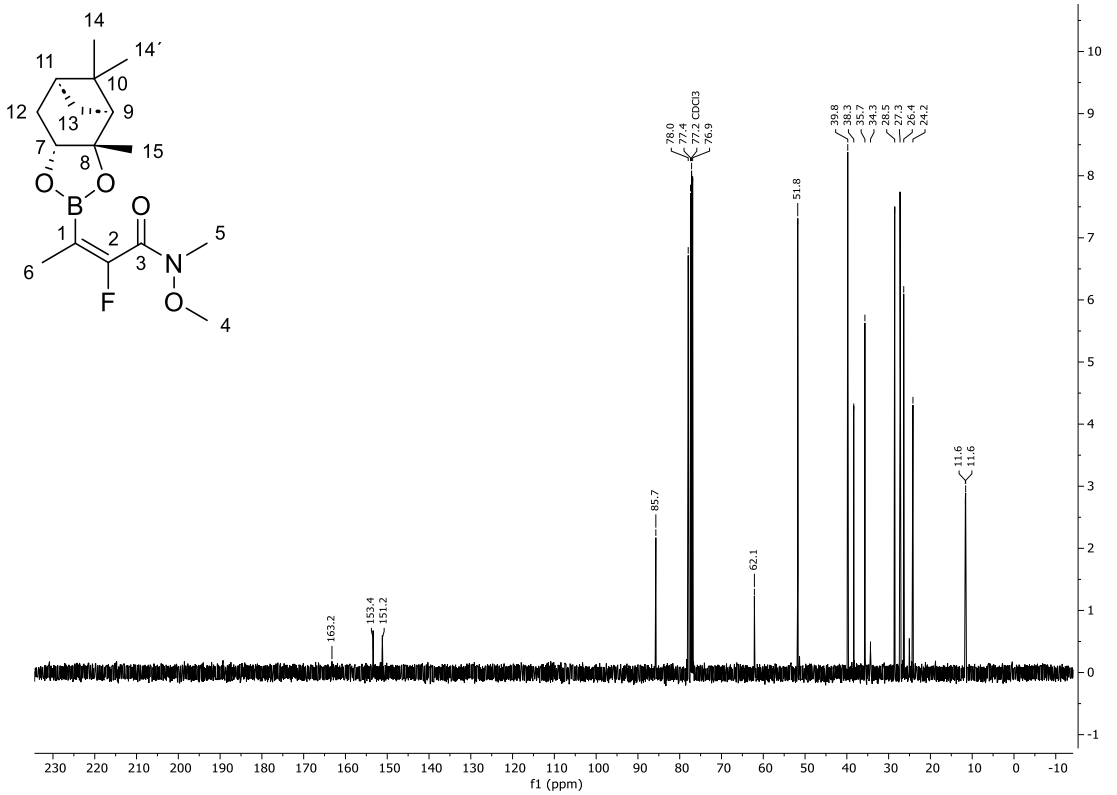

^{19}F-NMR {^{1}H} of ***Z*-10** (470 MHz, $CDCl_3$)

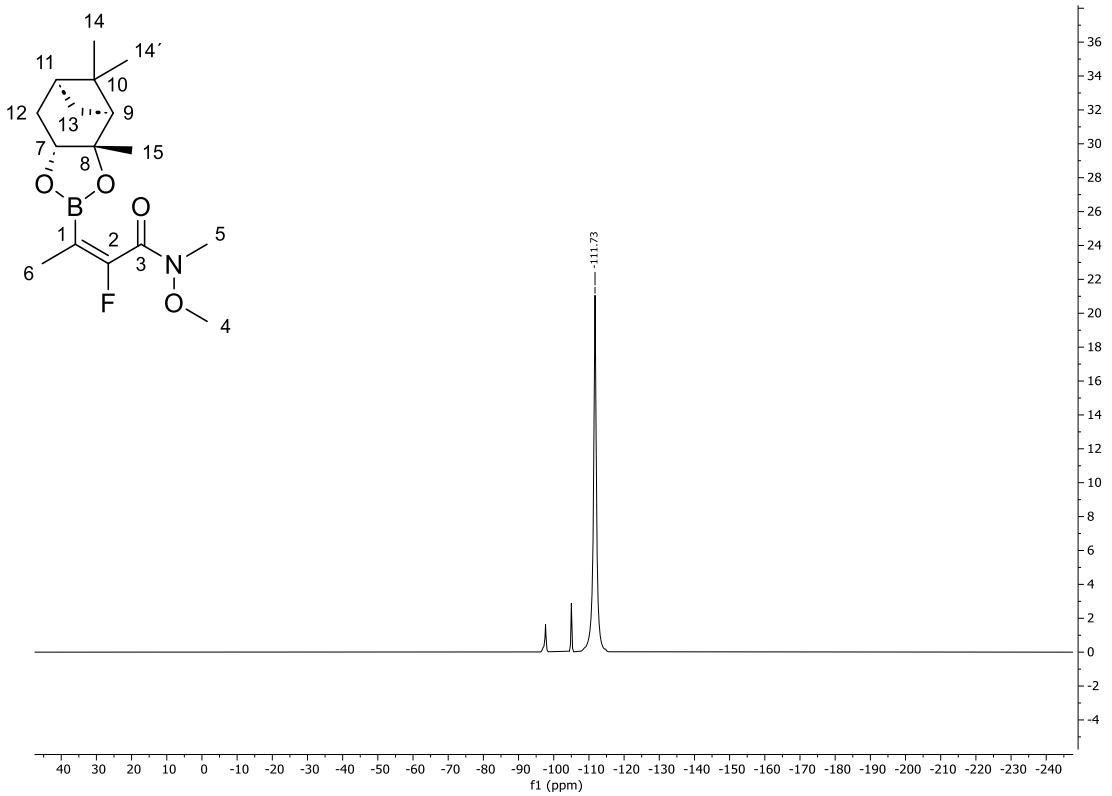

^{1}H-NMR of ***Z*-11** (500 MHz, $CDCl_3$)

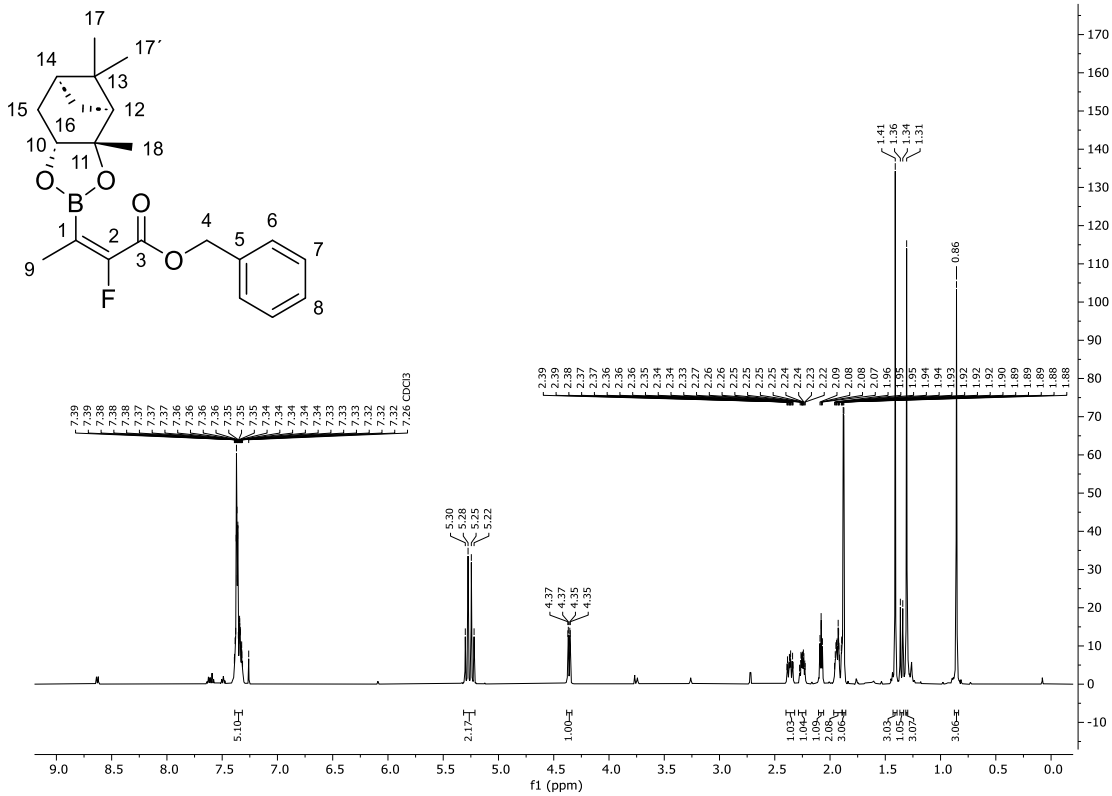

^{13}C-NMR of ***Z*-11** (126 MHz, $CDCl_3$)

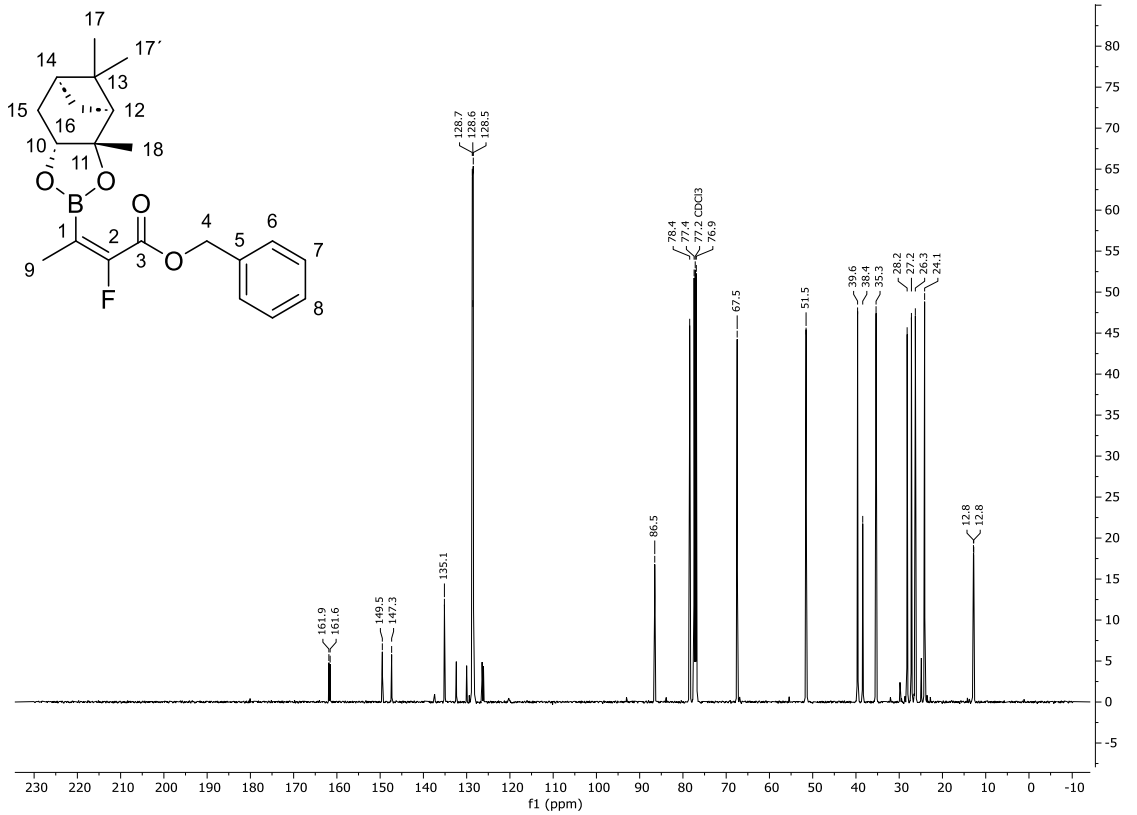

^{19}F-NMR {^{1}H} of ***Z*-11** (470 MHz, $CDCl_3$)

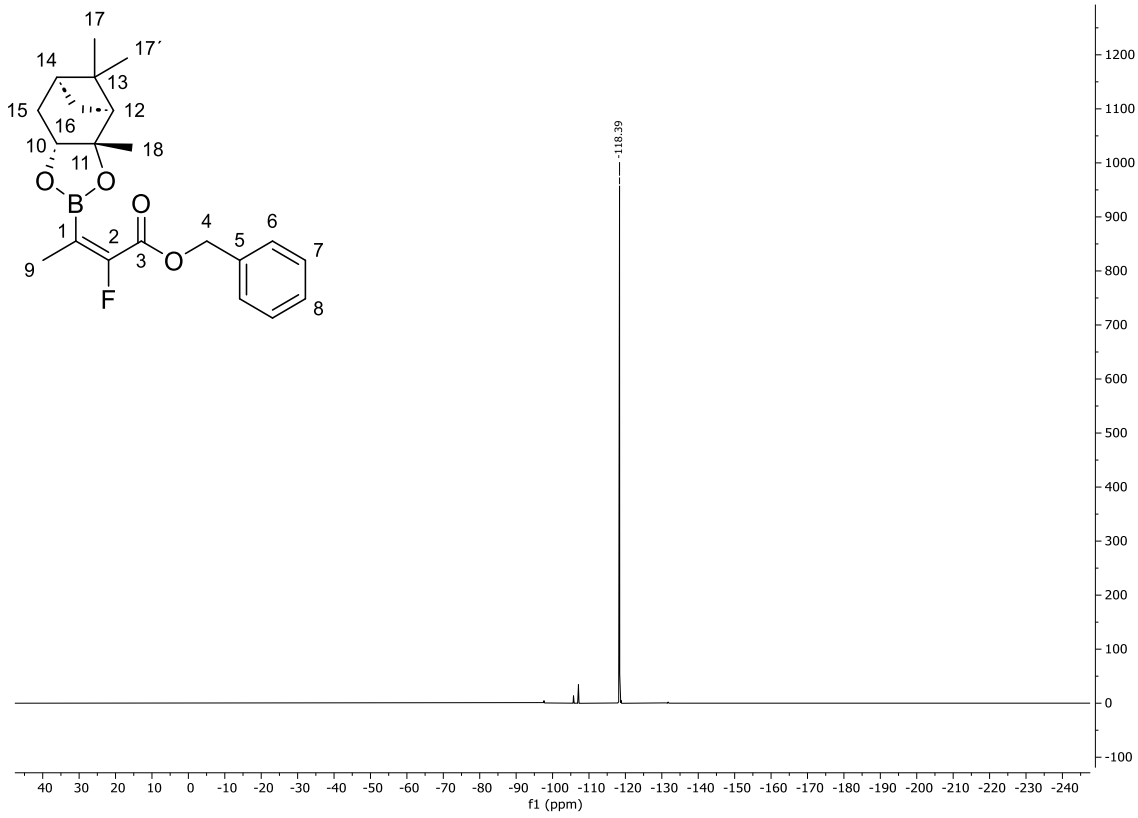

^{1}H-NMR of ***Z*-12** (500 MHz, $CDCl_3$)

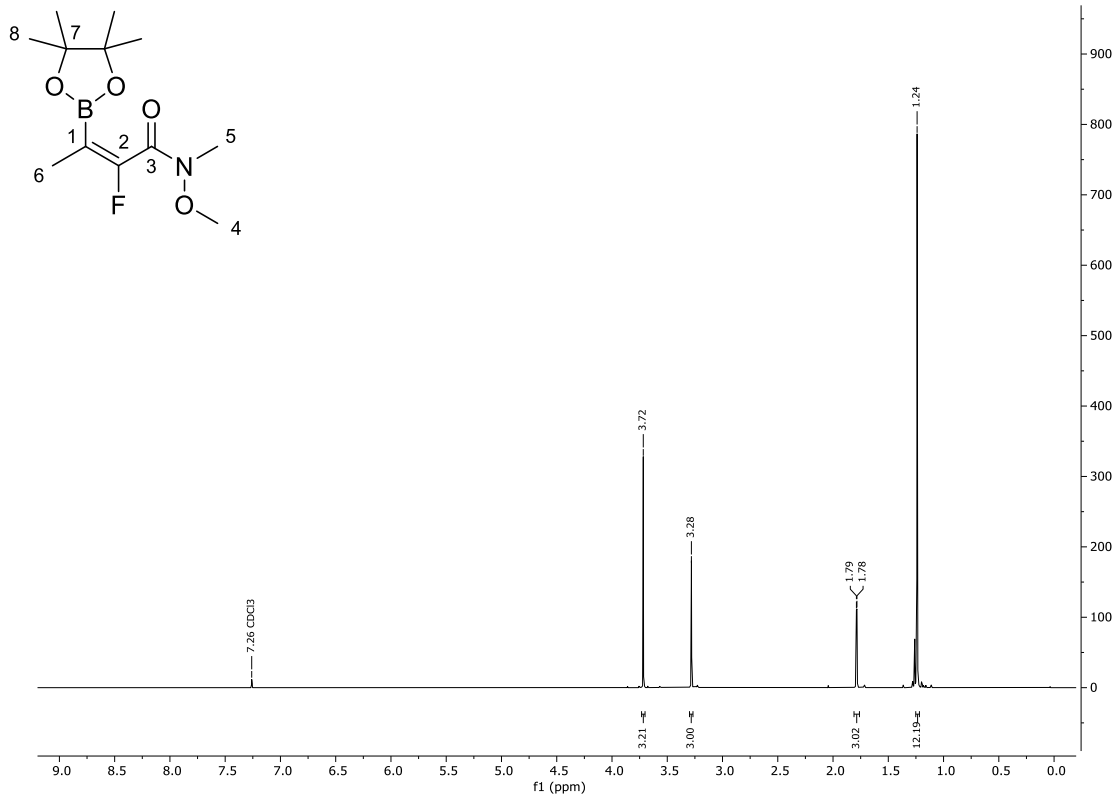

^{13}C-NMR of ***Z*-12** (126 MHz, $CDCl_3$)

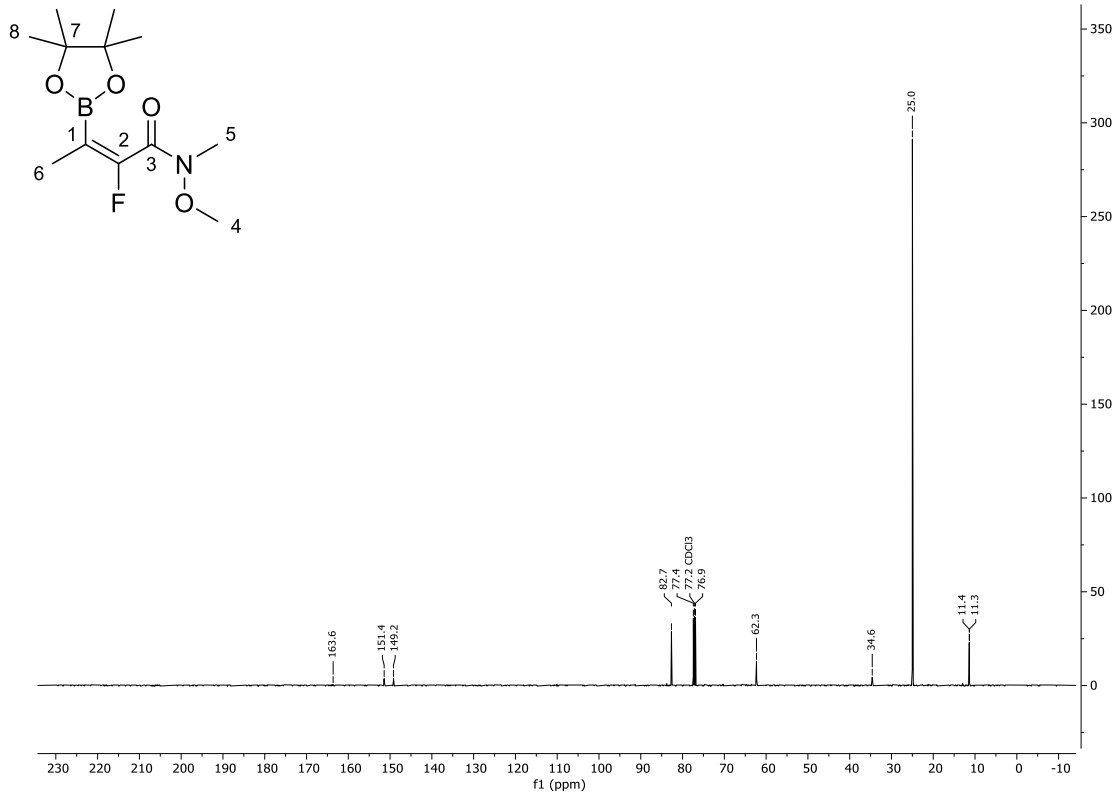

^{19}F-NMR {^{1}H} of ***Z*-12** (470 MHz, $CDCl_3$)

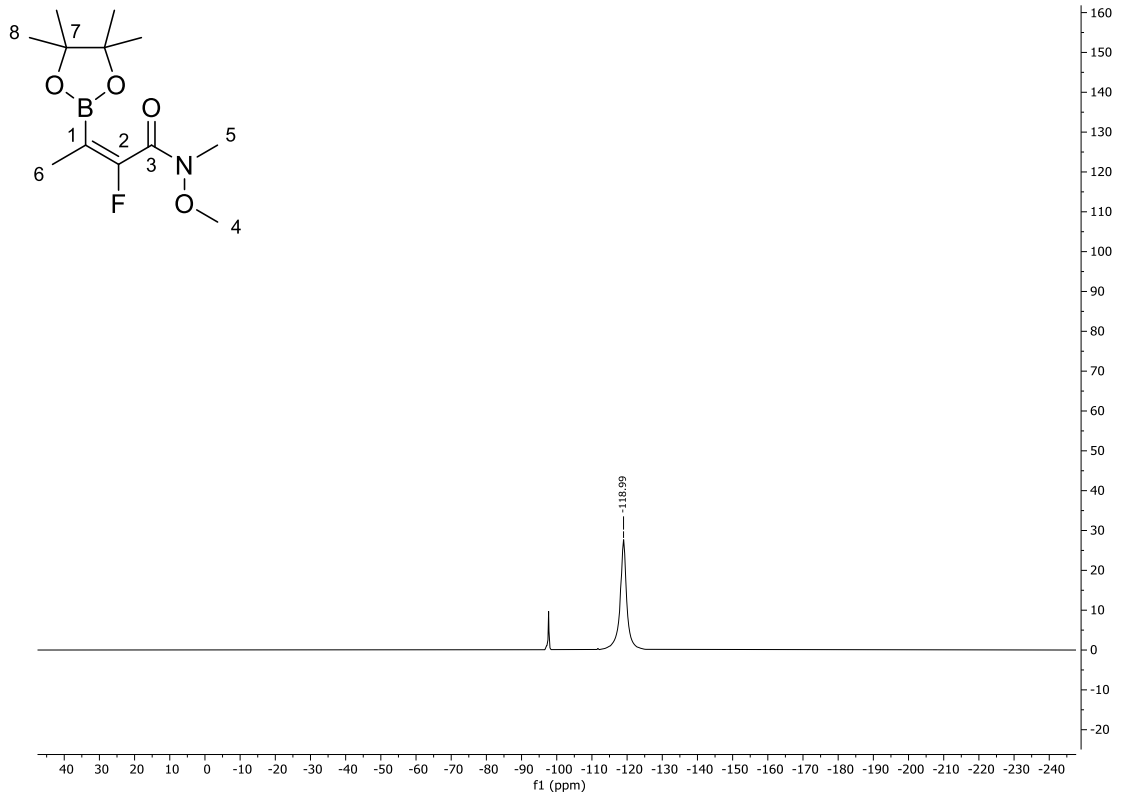

^{1}H-NMR of ***Z*-13** (500 MHz, $CDCl_3$)

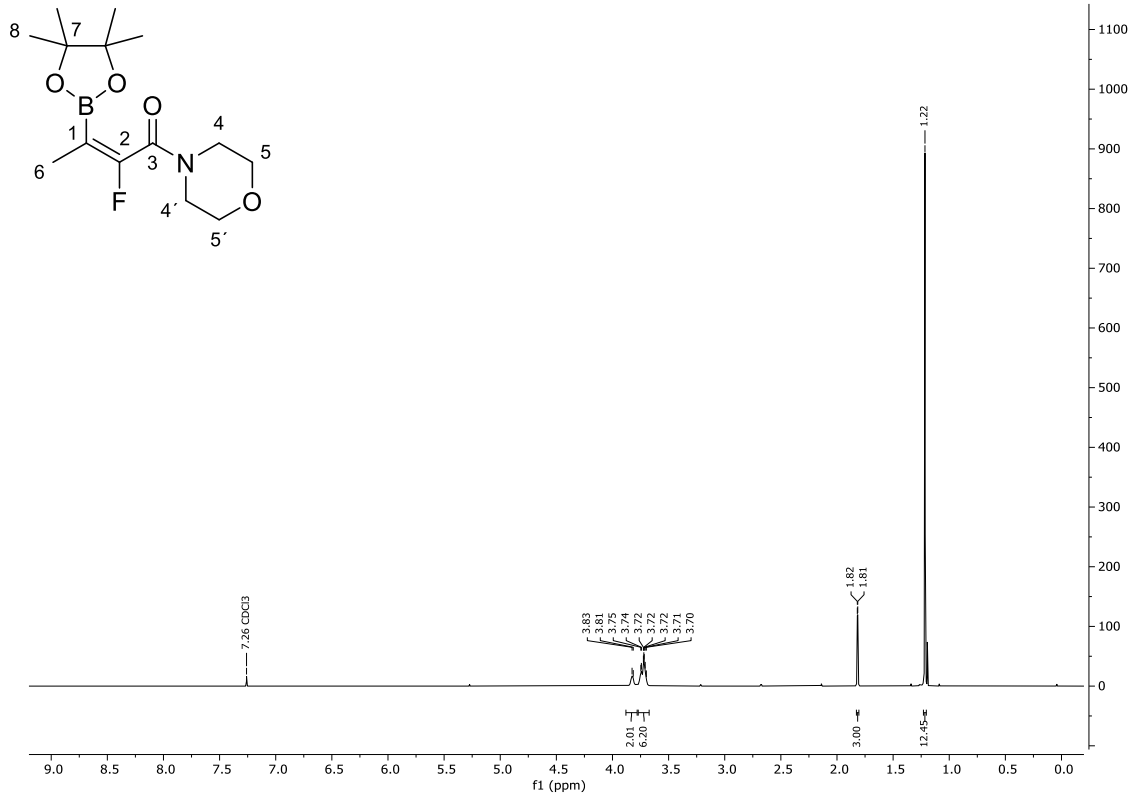

^{13}C-NMR of ***Z*-13** (126 MHz, $CDCl_3$)

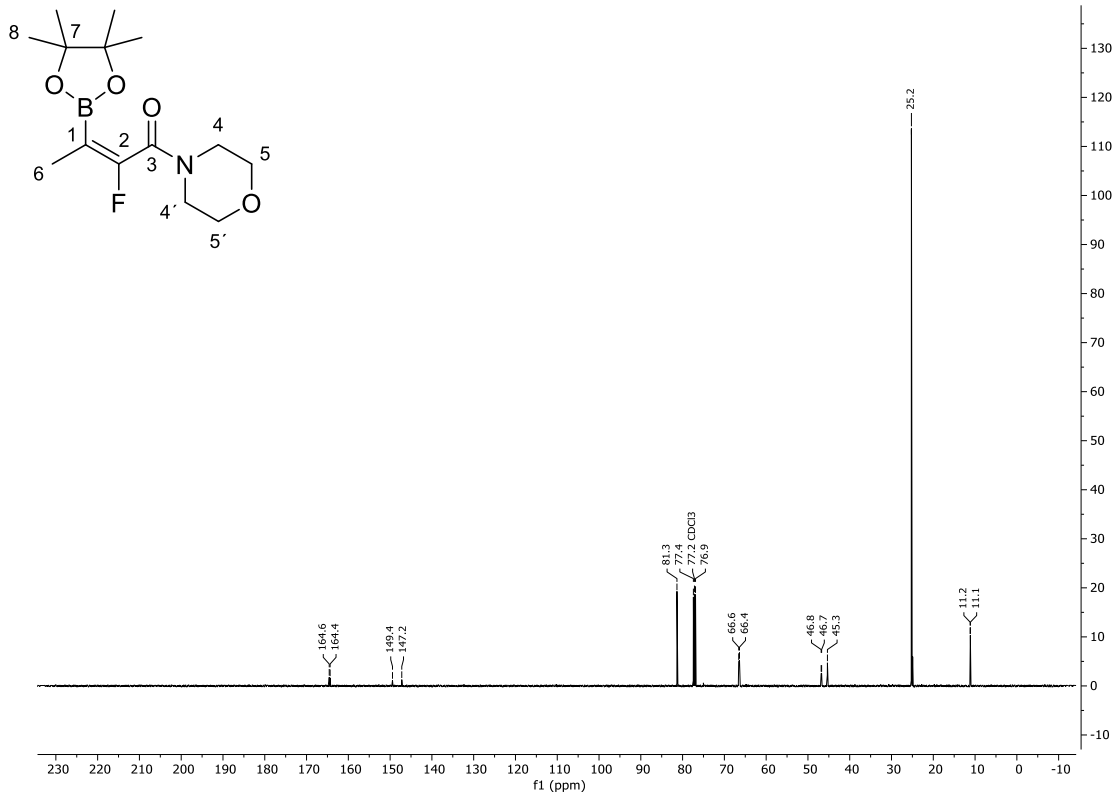

^{19}F-NMR {^{1}H} of ***Z*-13** (470 MHz, $CDCl_3$)

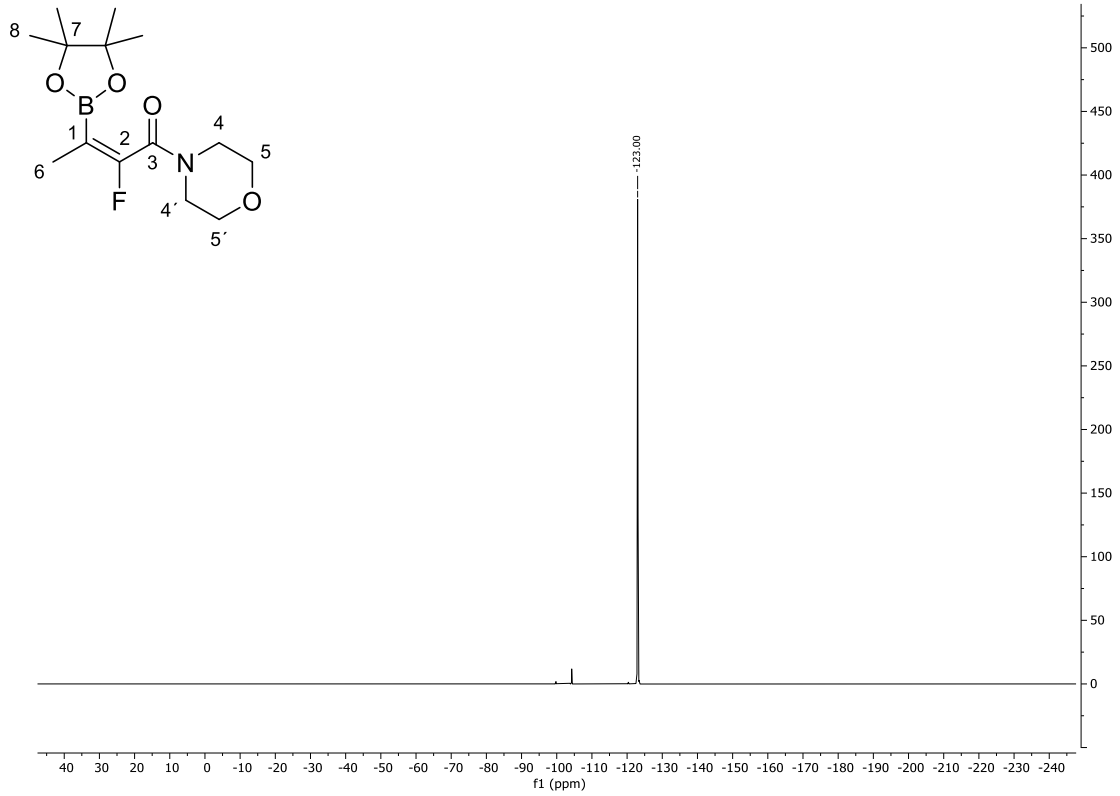

^{1}H-NMR of ***Z*-14** (599 MHz, $CDCl_3$)

^{13}C-NMR of ***Z*-14** (151 MHz, $CDCl_3$)

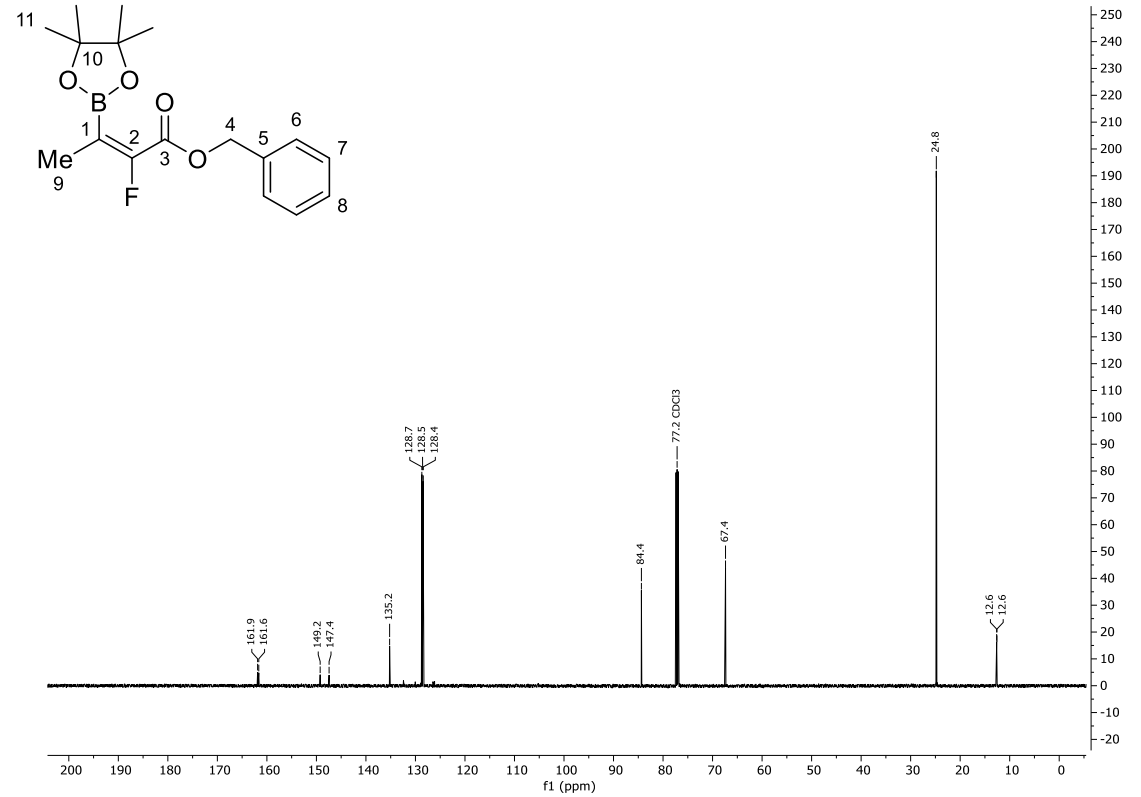

^{19}F-NMR {^{1}H} of ***Z*-14** (151 MHz, $CDCl_3$)

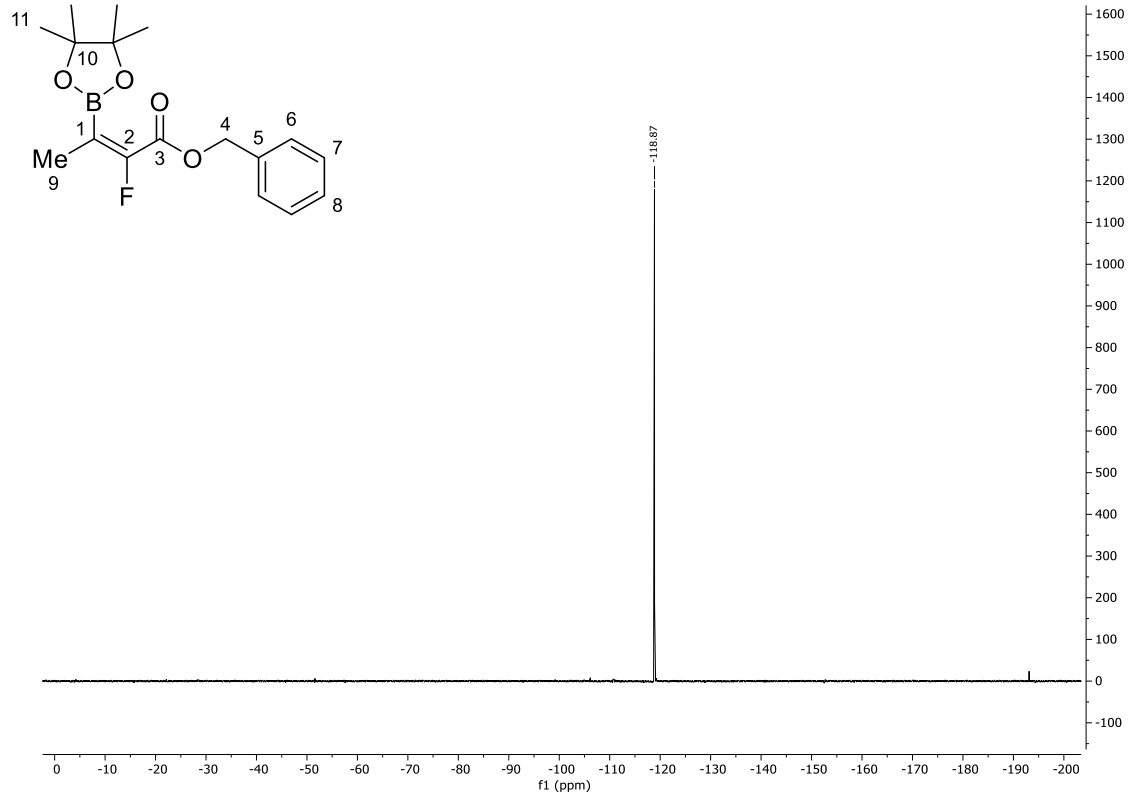

^{19}F-HOESY-NMR of ***Z*-14** ($CDCl_3$)

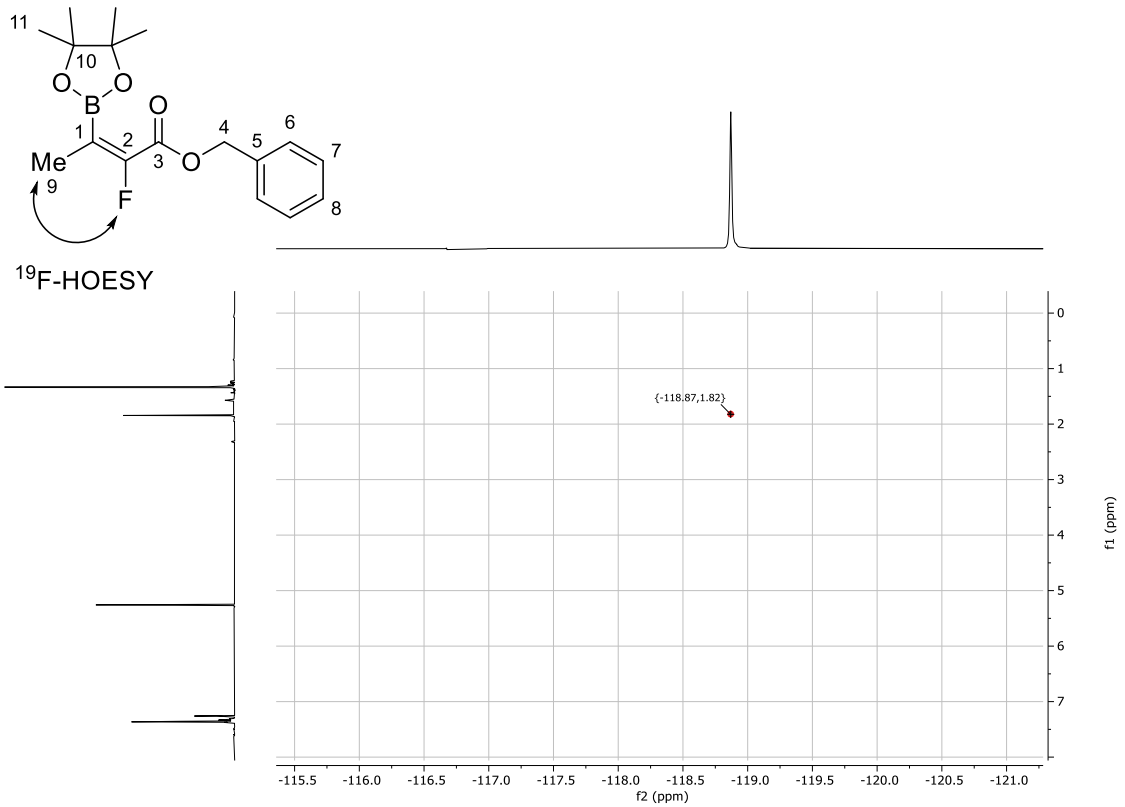

^{1}H-NMR of **S36** (400 MHz, $CDCl_3$)

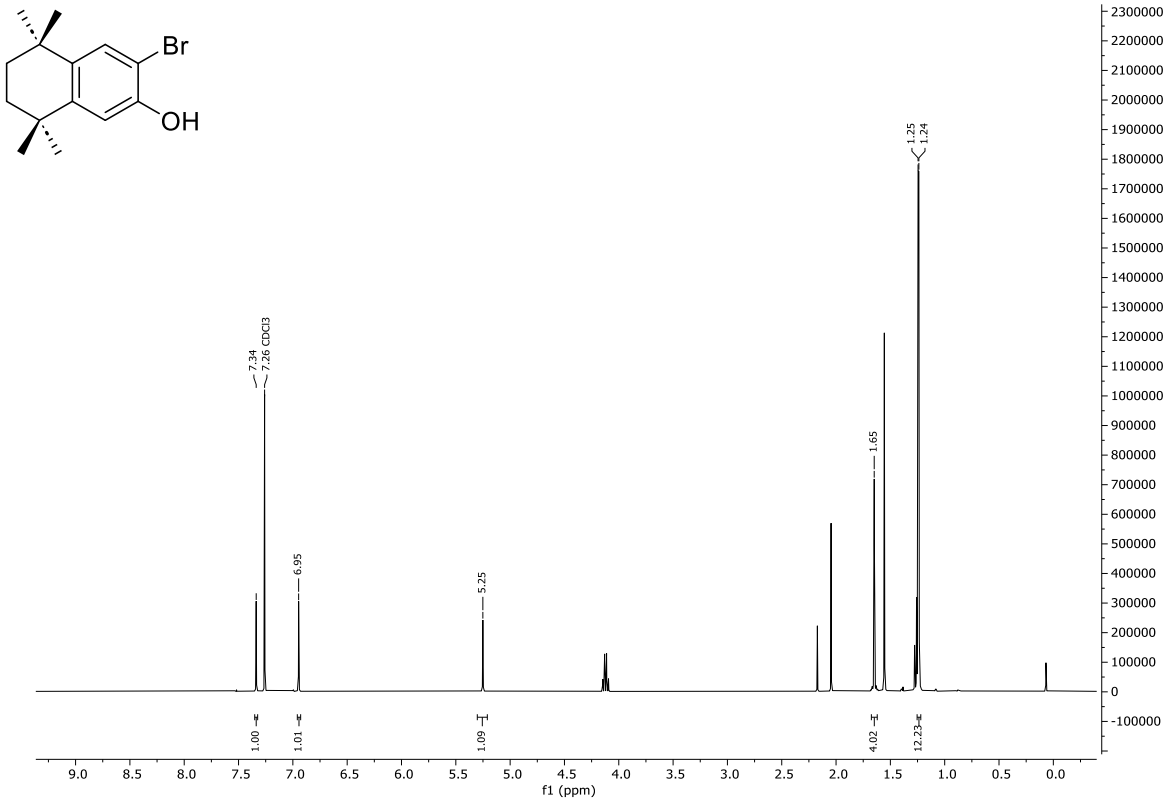

^{1}H-NMR of **15** (500 MHz, $CDCl_3$)

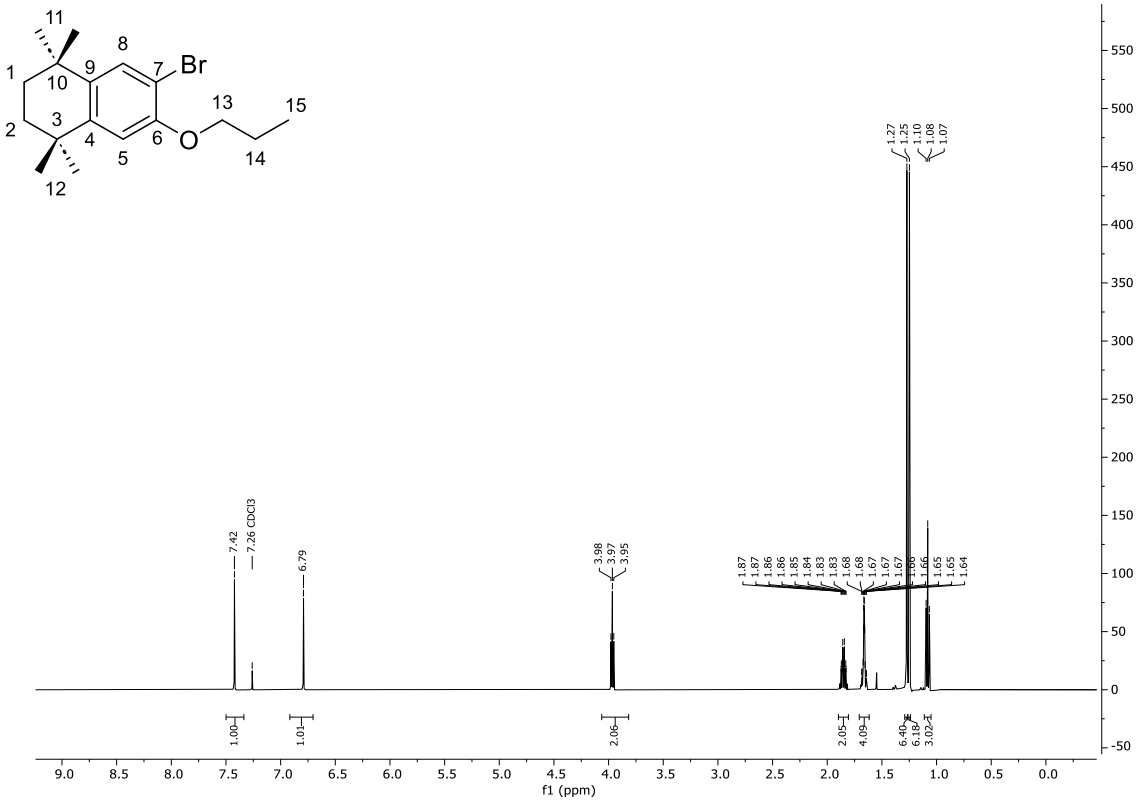

^{13}C-NMR of **15** (126 MHz, $CDCl_3$)

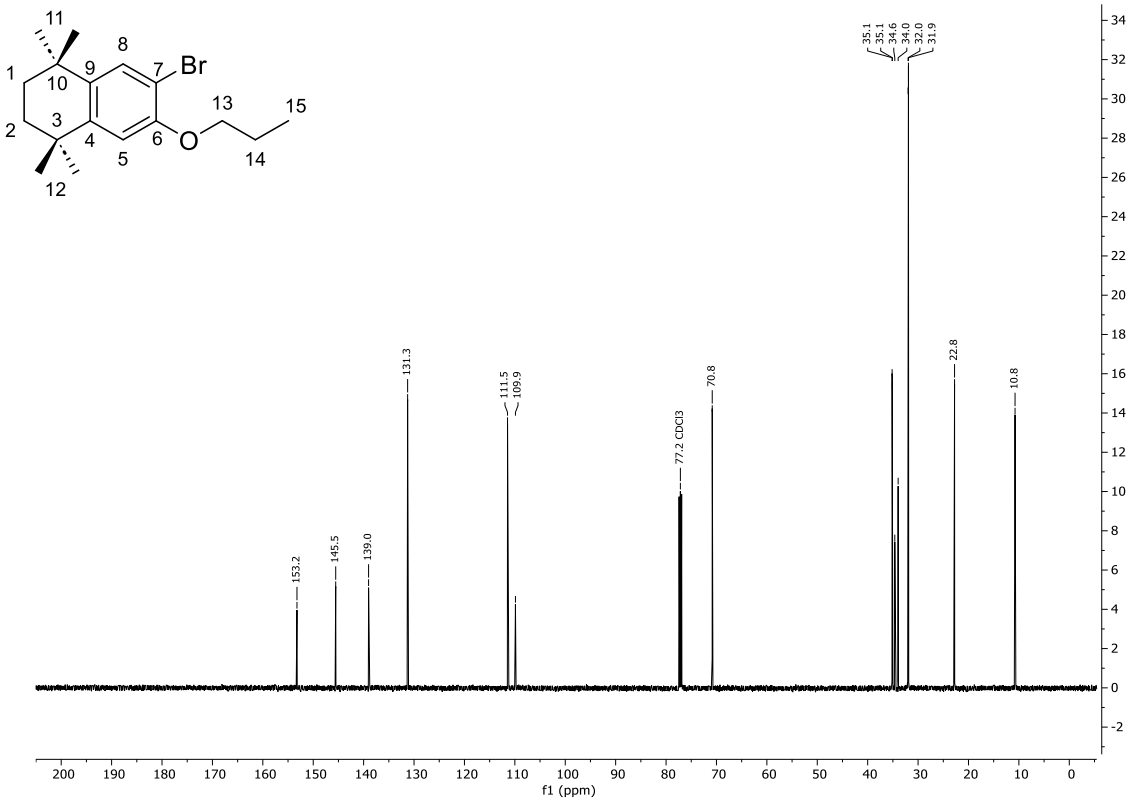

^{1}H-NMR of **16** (500 MHz, $CDCl_3$)

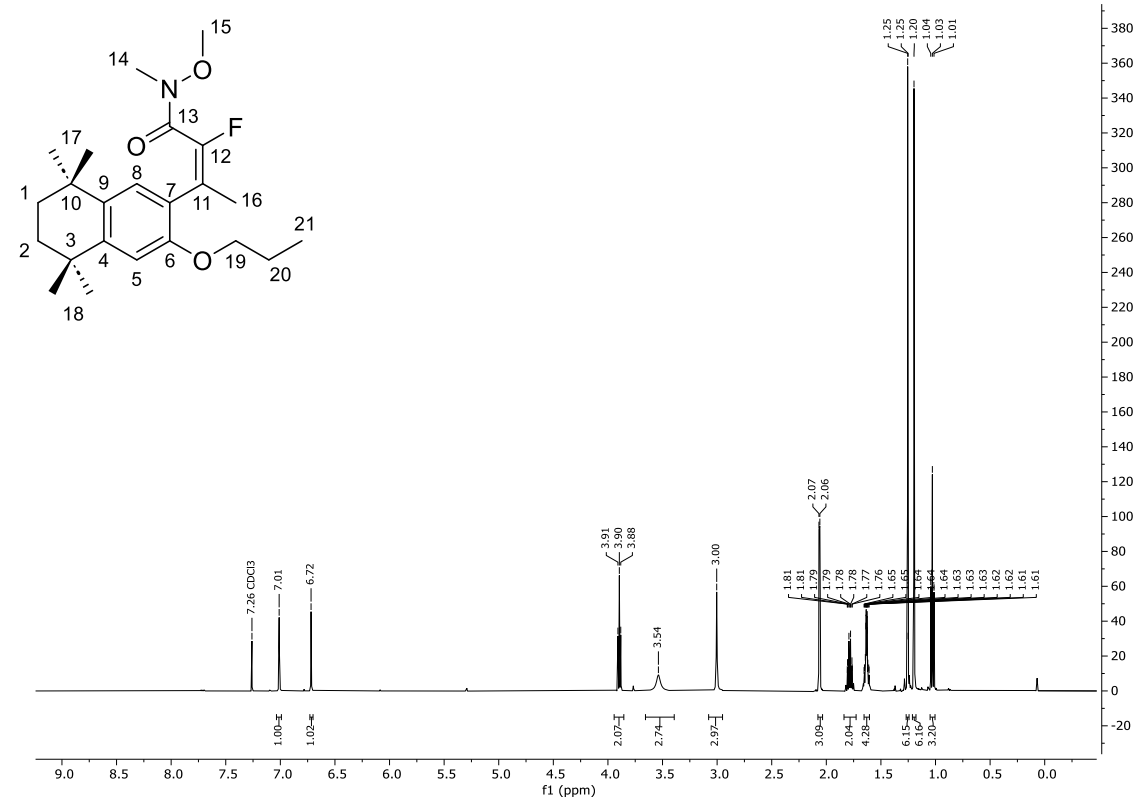

^{13}C-NMR of **16** (126 MHz, $CDCl_3$)

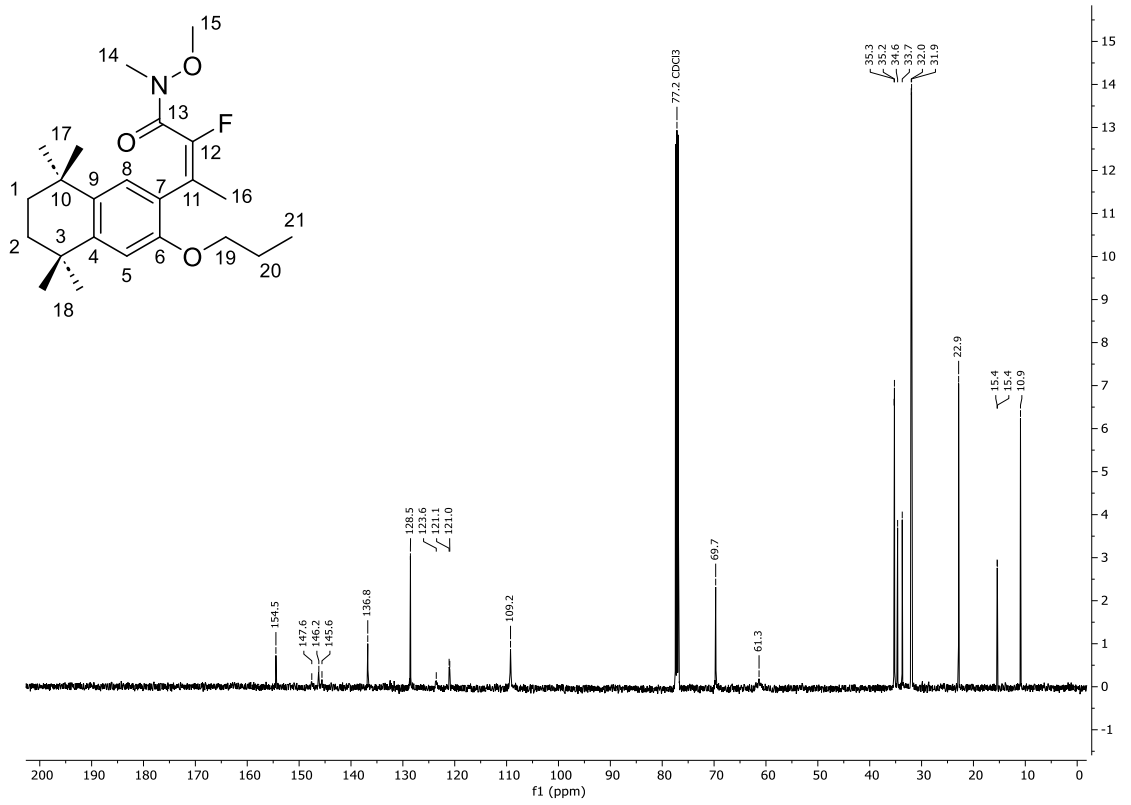

^{19}F-NMR {^{1}H} of **16** (470 MHz, $CDCl_3$)

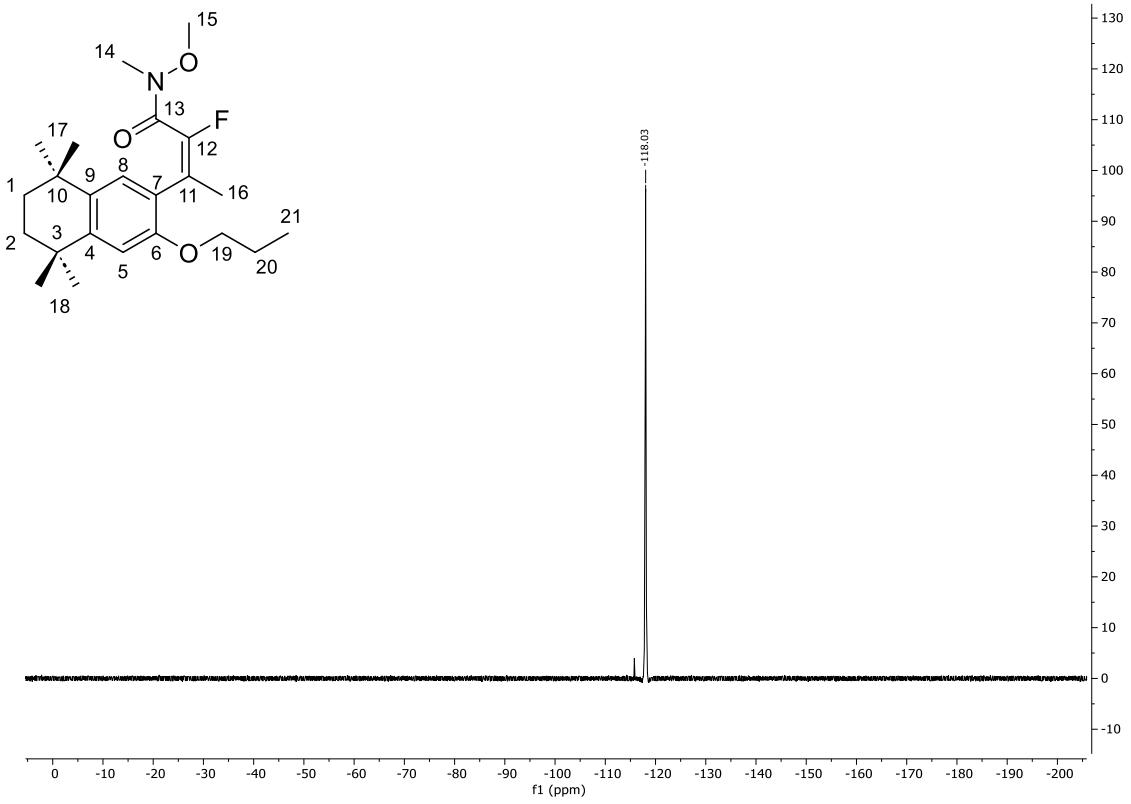

^{19}F-HOESY-NMR of **16** ($CDCl_3$)

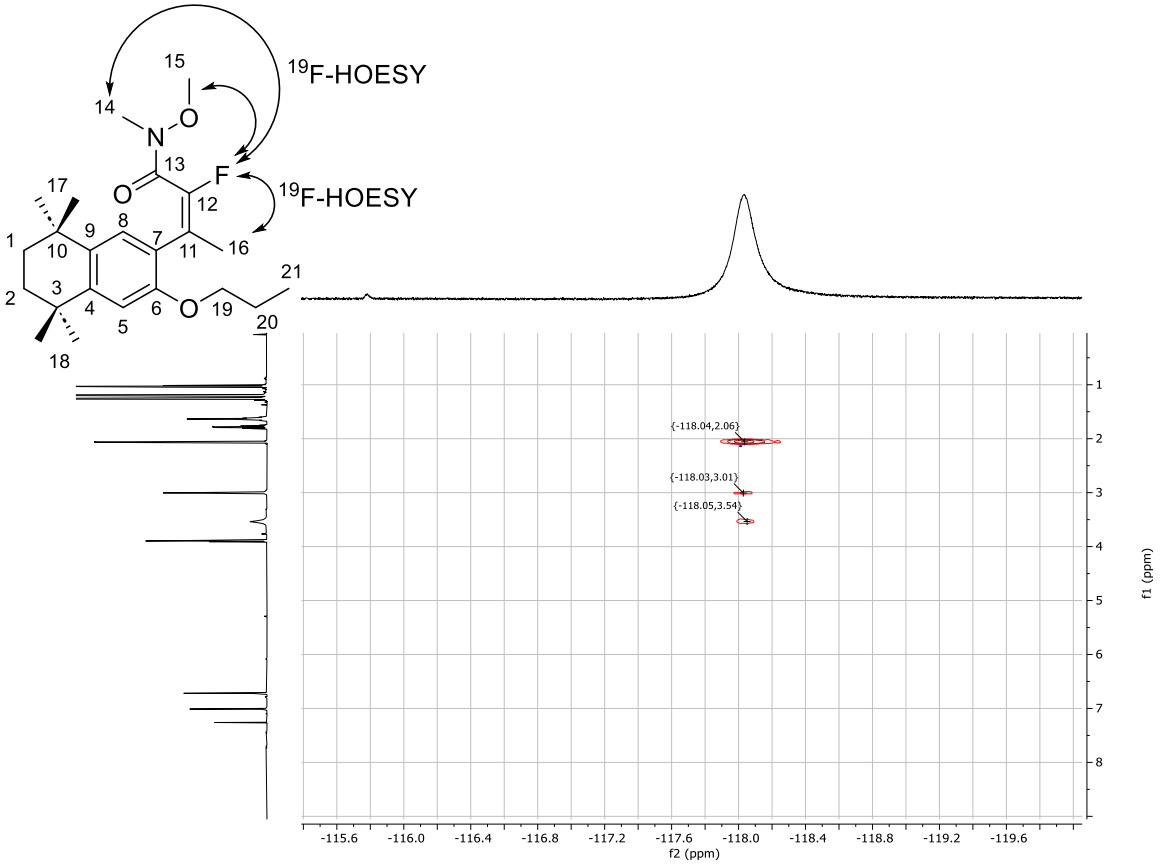

^{1}H-NMR of **17** (599 MHz, $CDCl_3$)

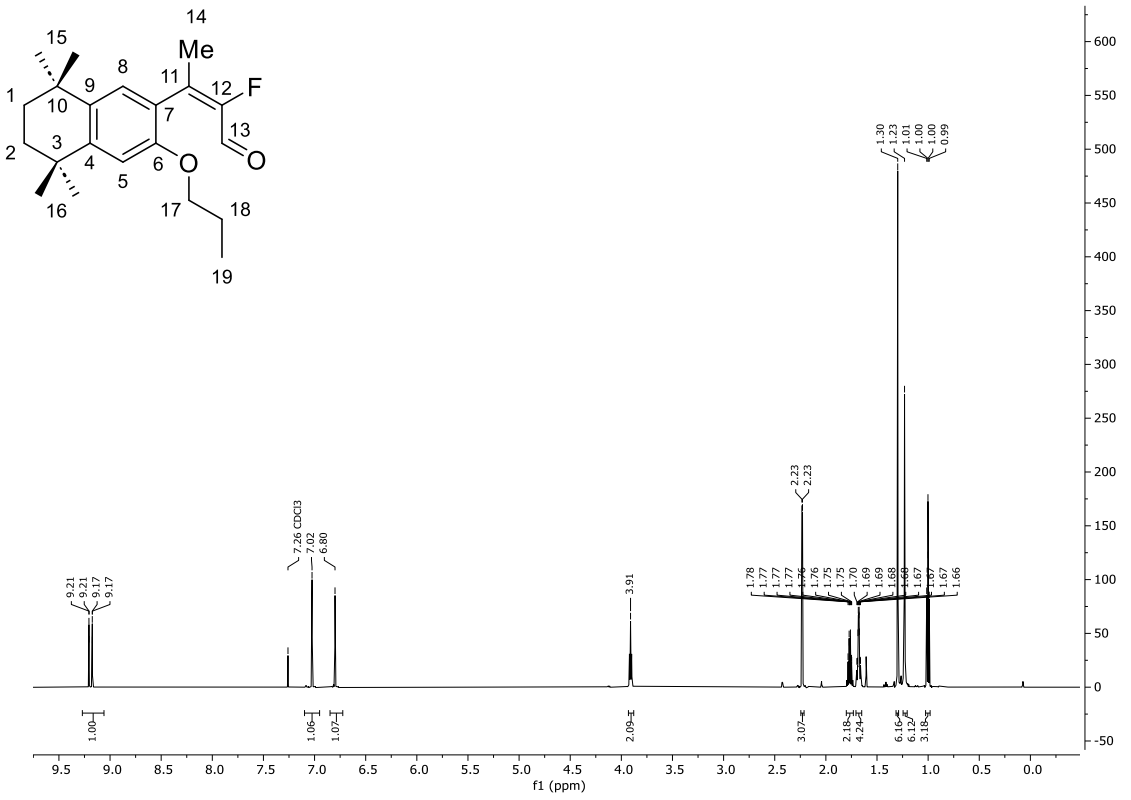

^{13}C-NMR of **17** (151 MHz, $CDCl_3$)

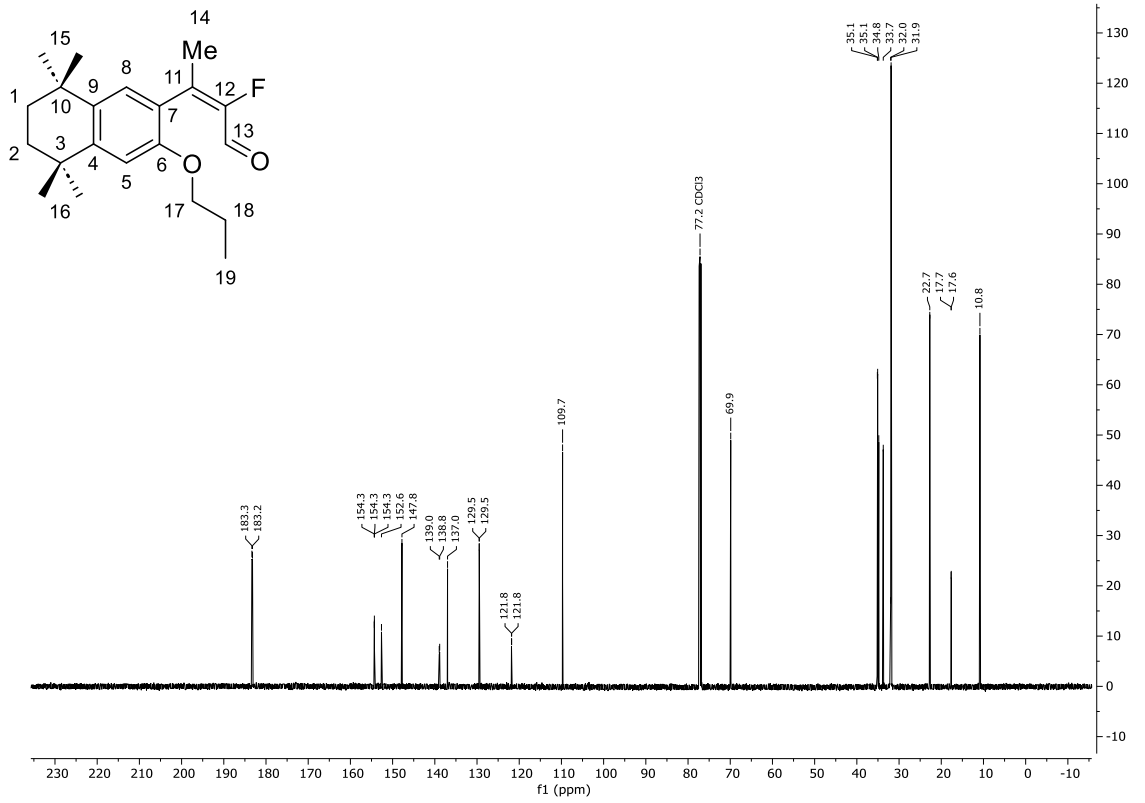

^{19}F-NMR {^{1}H} of **17** (564 MHz, $CDCl_3$)

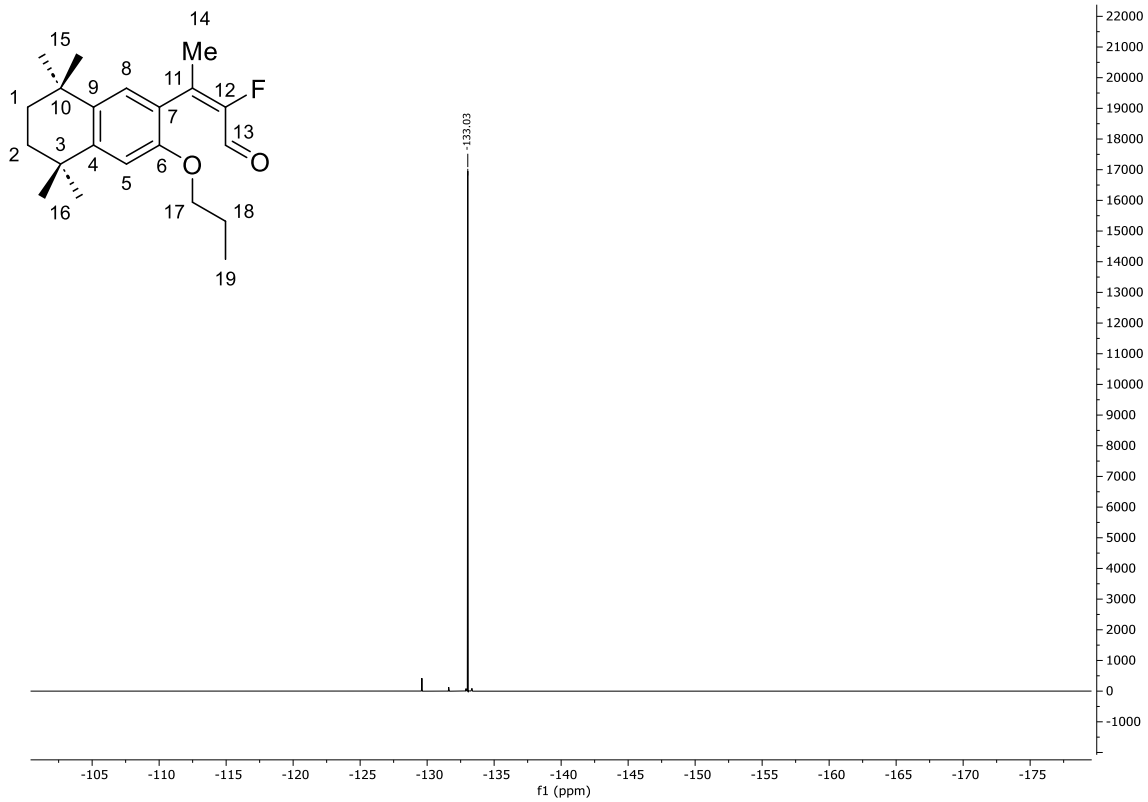

^{1}H-NMR of **18** (500 MHz, $CDCl_3$)

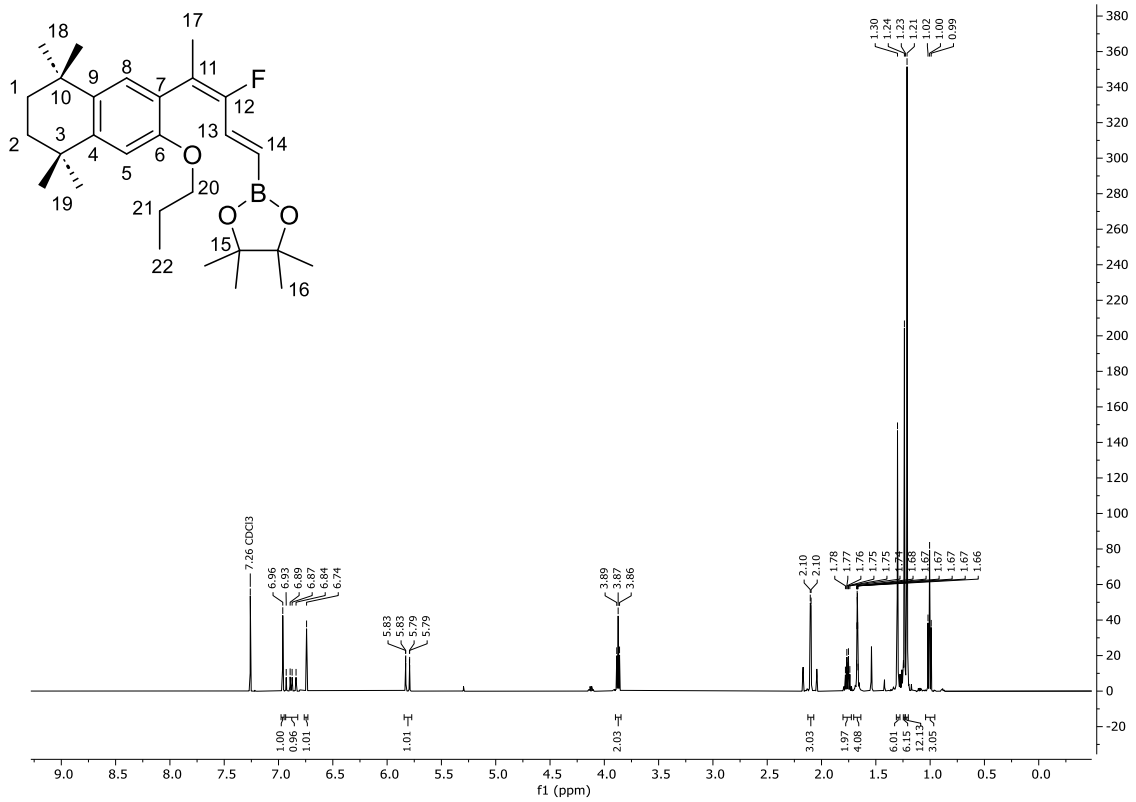

^{13}C-NMR of **18** (126 MHz, $CDCl_3$)

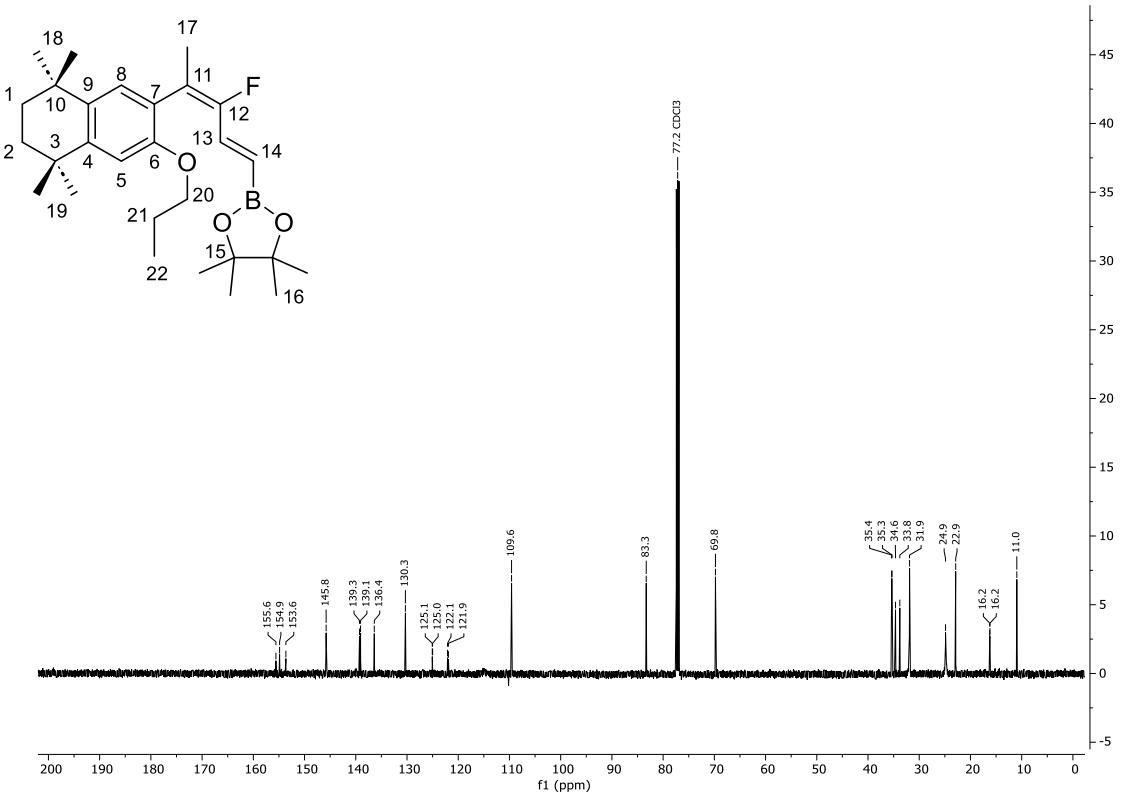

^{19}F-NMR {^{1}H} of **18** (377 MHz, $CDCl_3$)

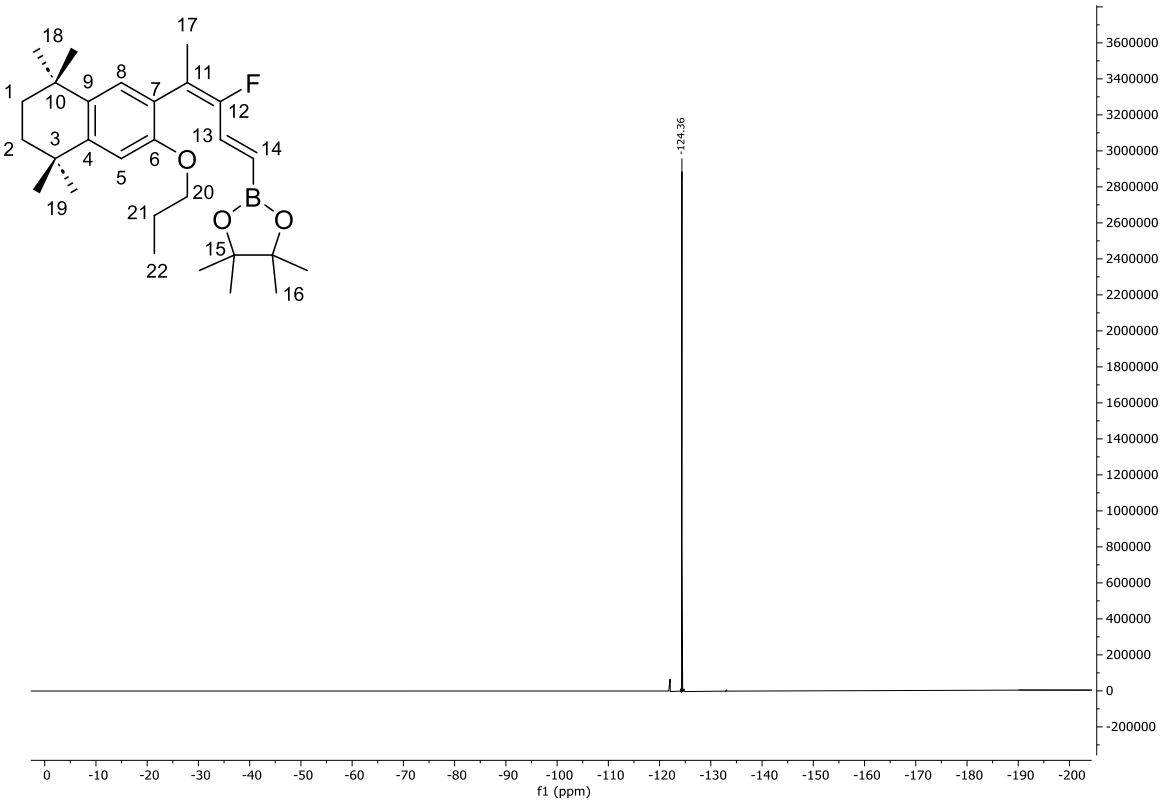

^{1}H-NMR of **19** (599 MHz, Acetone-d_6)

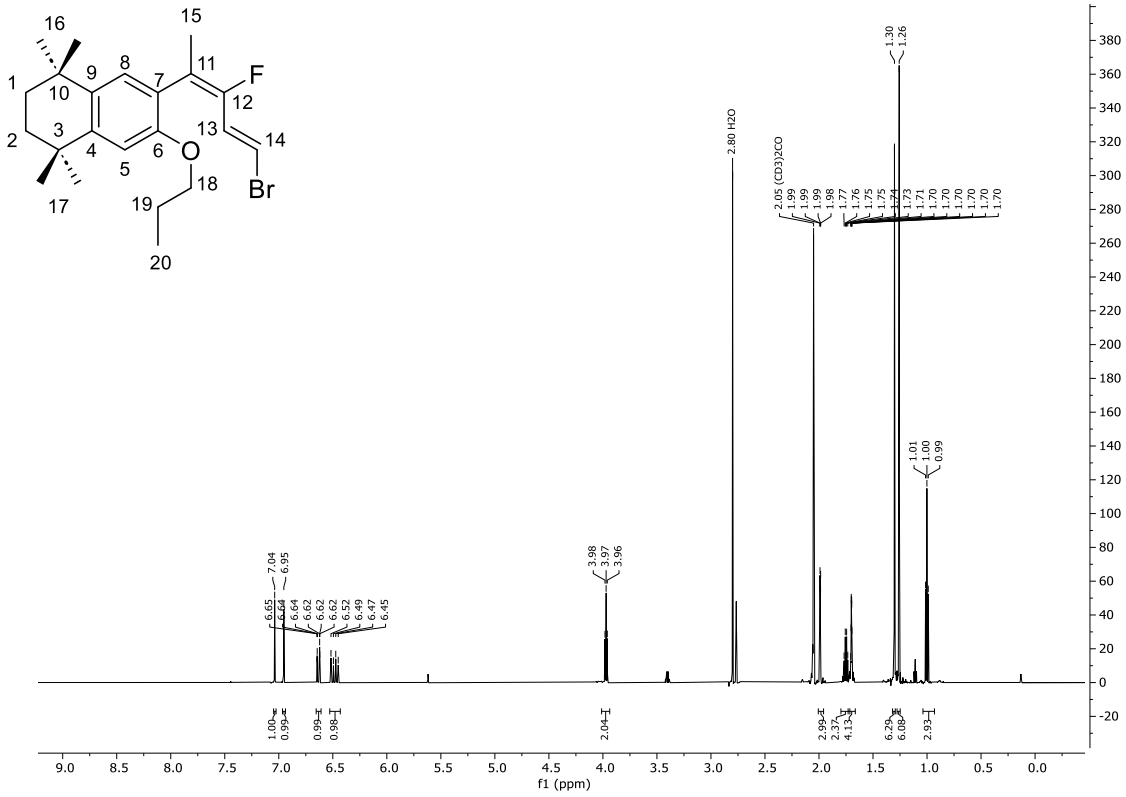

^{13}C-NMR of **19** (101 MHz, Acetone-d_6)

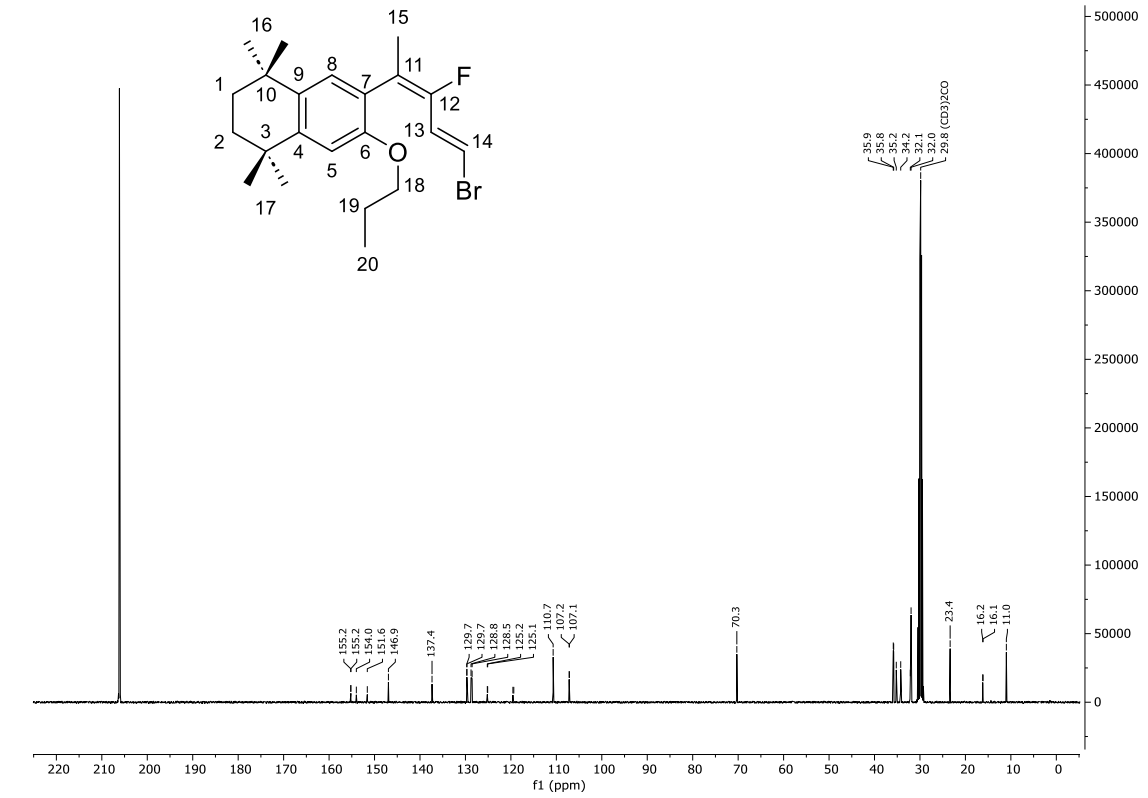

^{19}F-NMR {^{1}H} of **19** (377 MHz, Acetone-d_6)

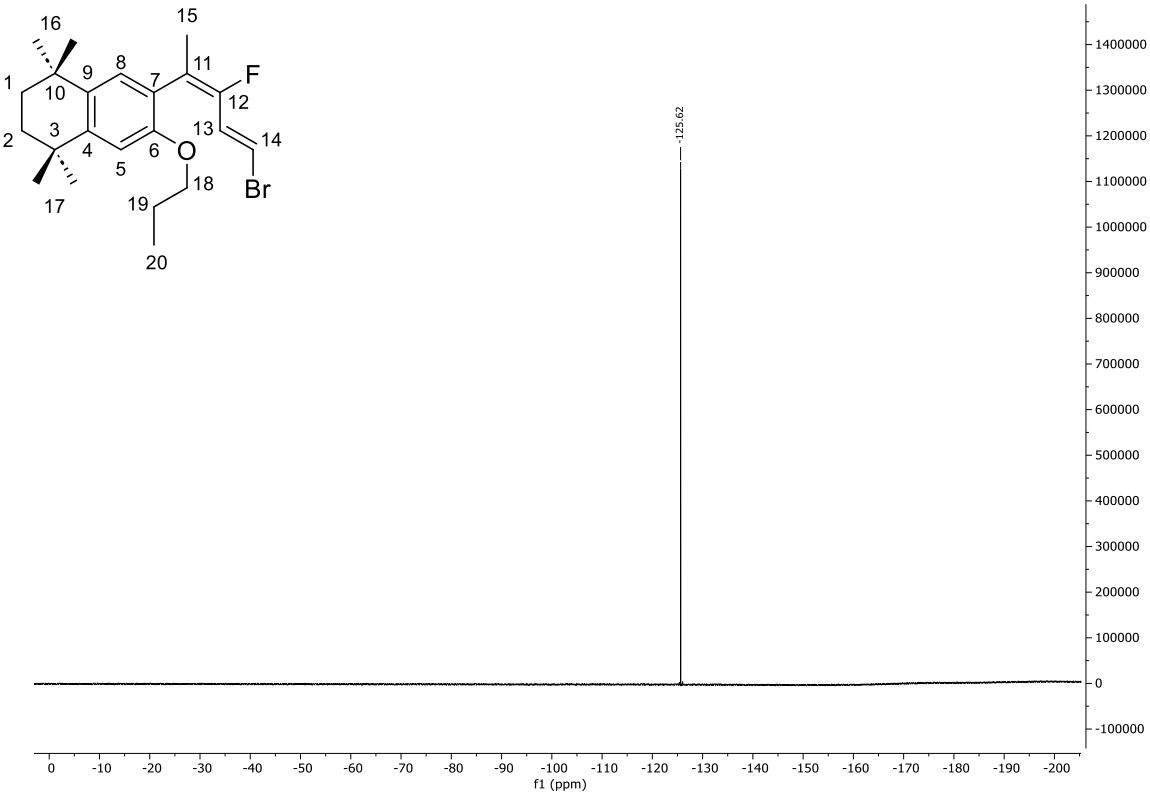

^{1}H-NMR of ***E*-20** (400 MHz, $CDCl_3$)

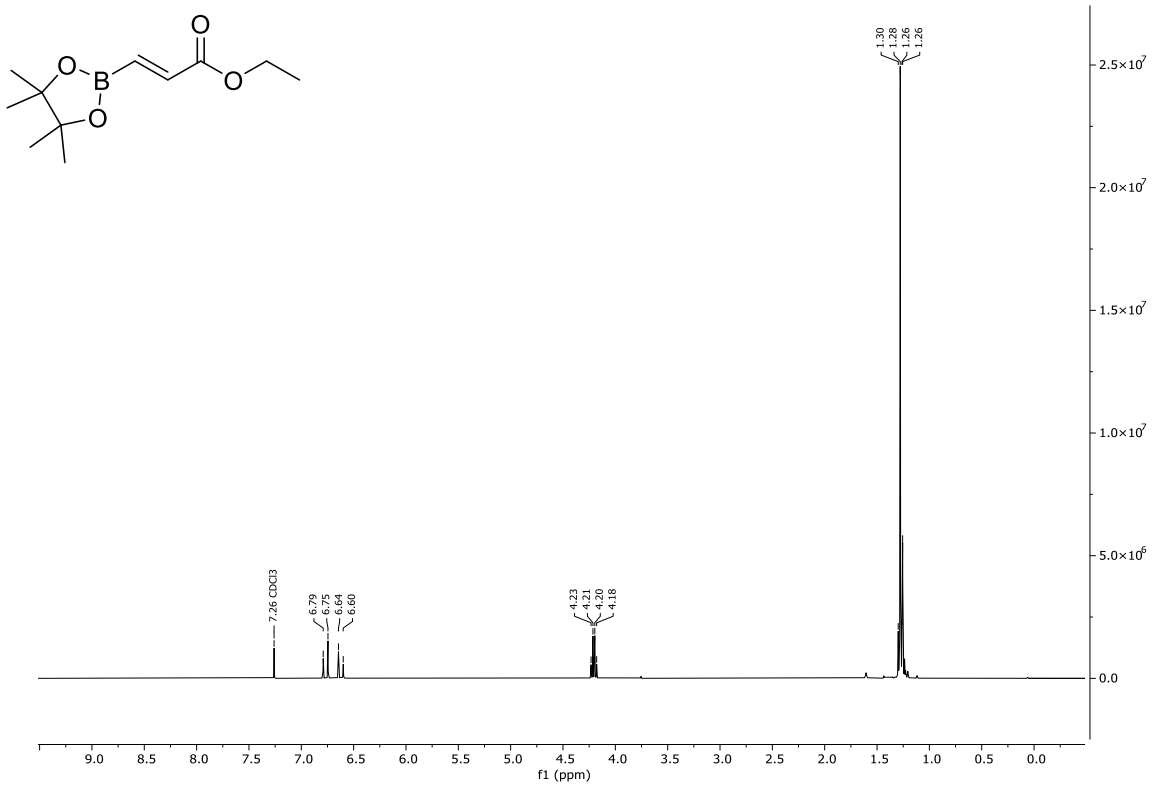

^{1}H-NMR of **21** (500 MHz, $CDCl_3$)

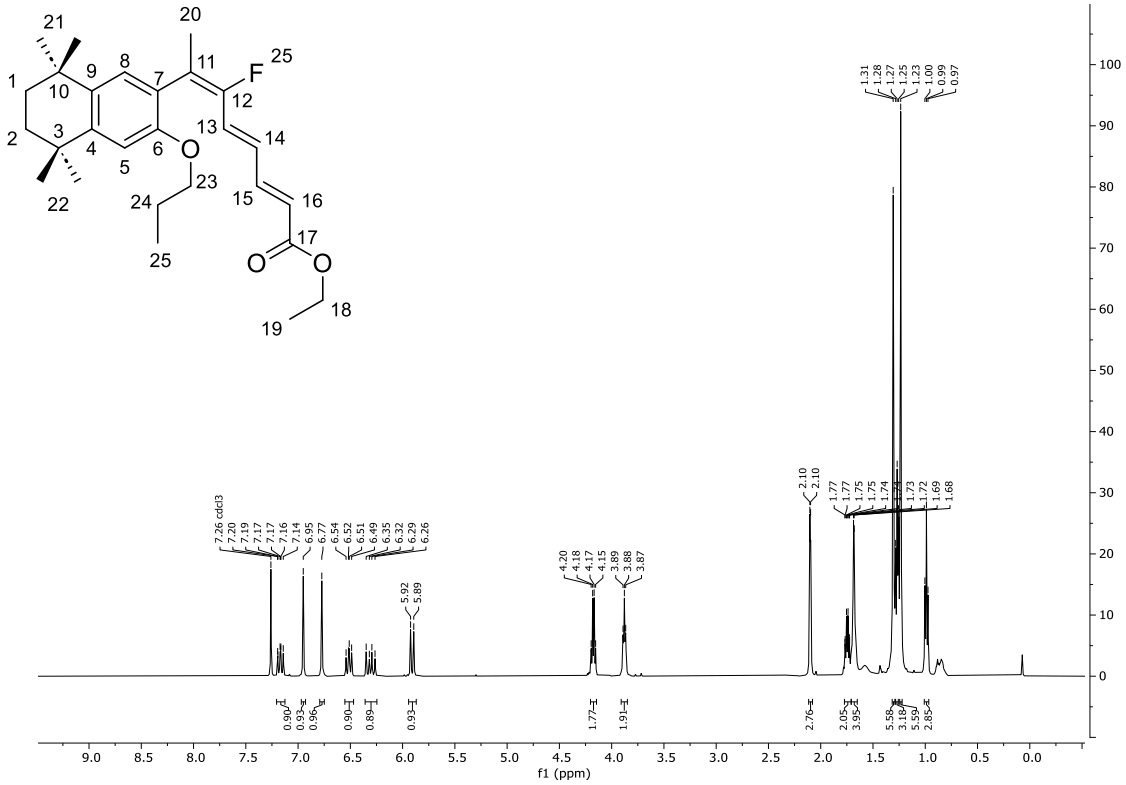

^{13}C-NMR of **21** (126 MHz, $CDCl_3$)

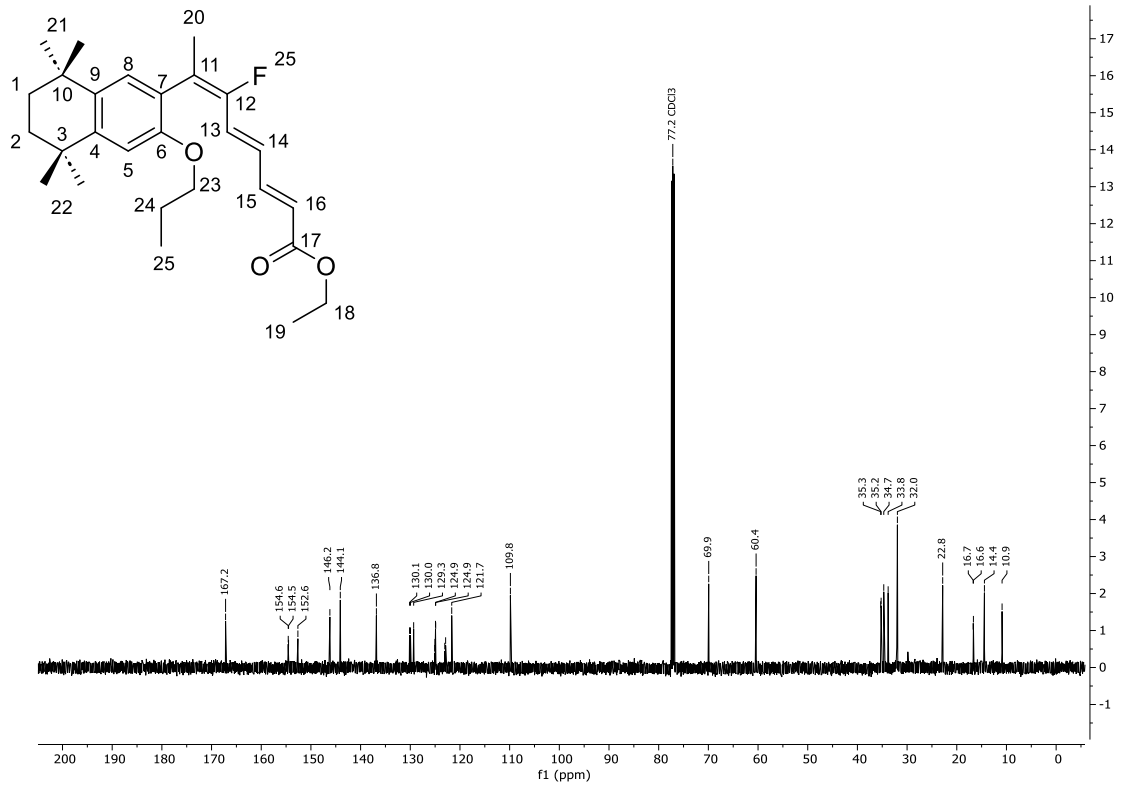

^{19}F-NMR {^{1}H} of **21** (377 MHz, $CDCl_3$)

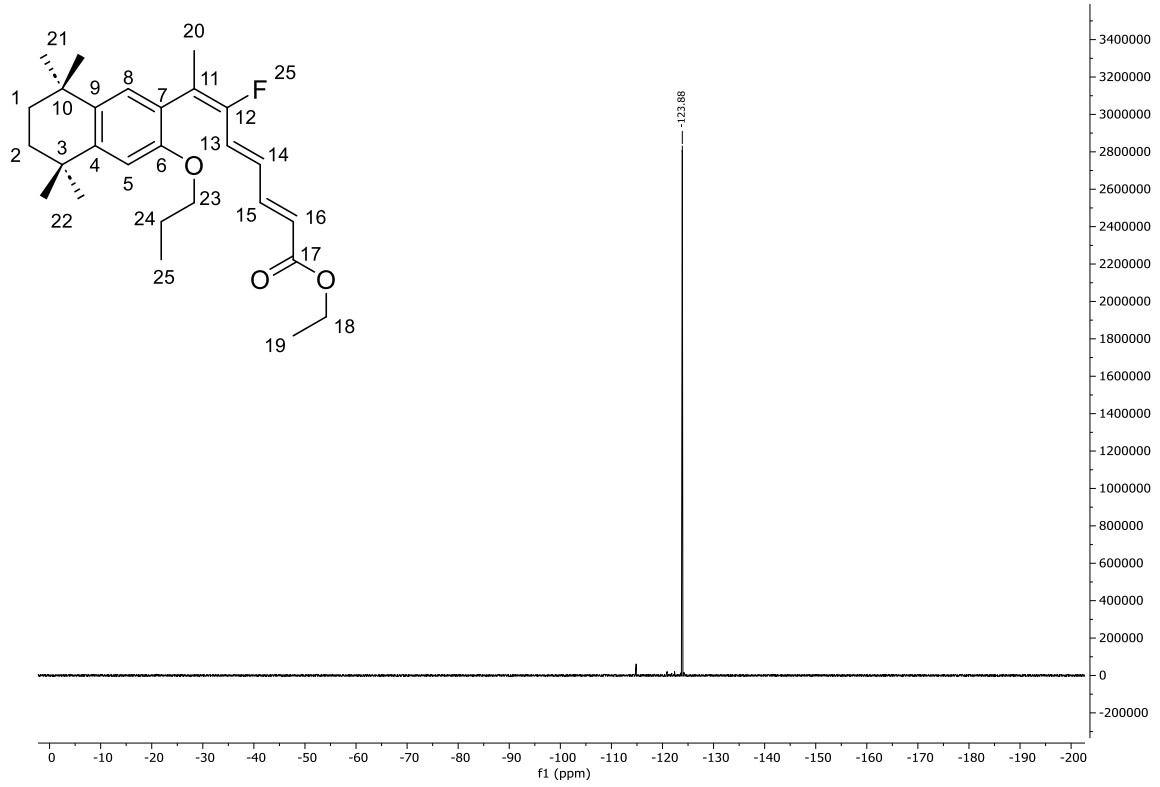

^{19}F-HOESY-NMR of **21** ($CDCl_3$)

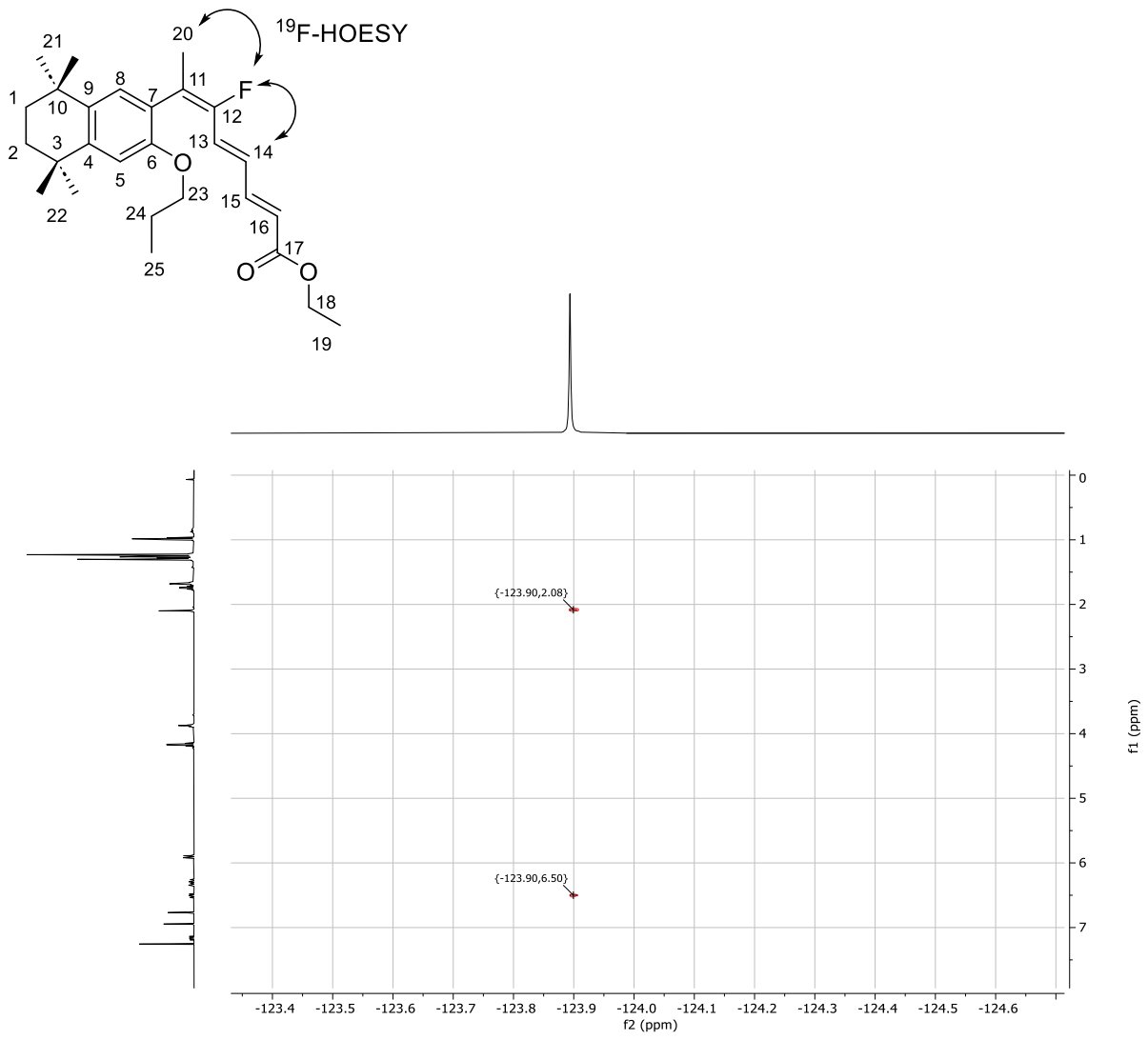

^{1}H-NMR of **22** (400 MHz, $CDCl_3$)

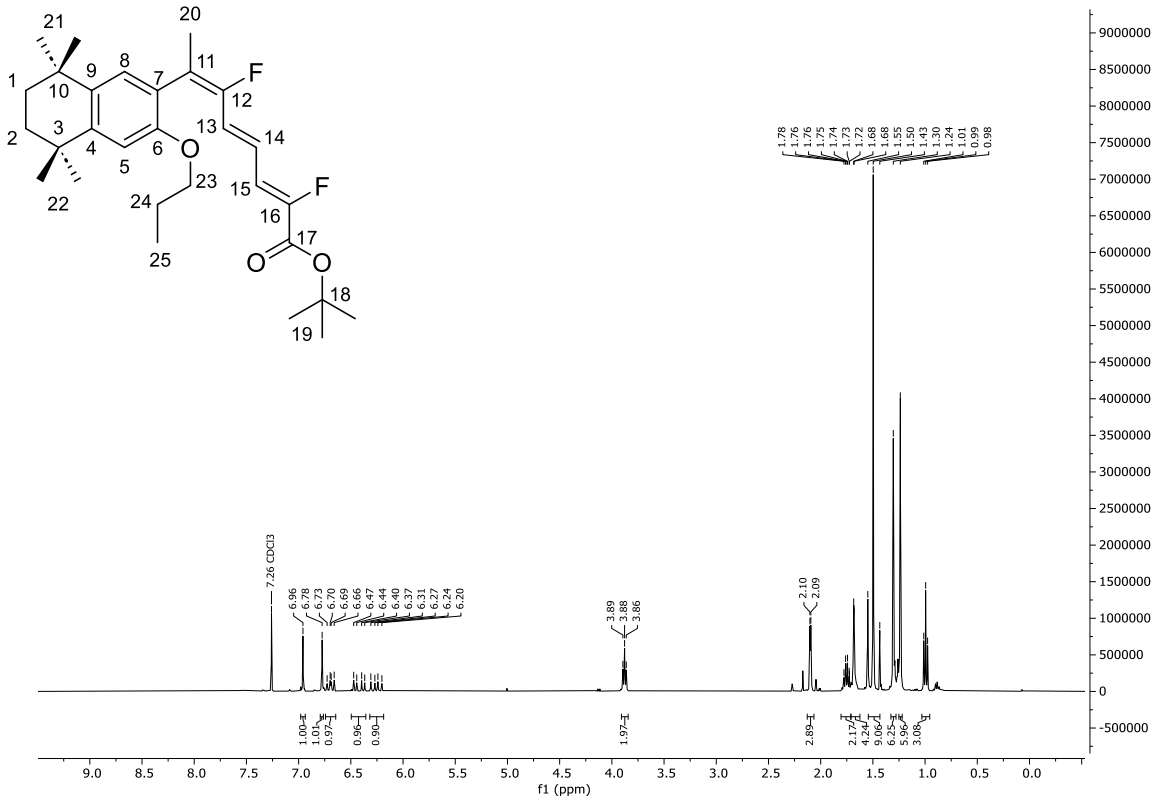

^{13}C-NMR of **22** (151 MHz, $CDCl_3$)

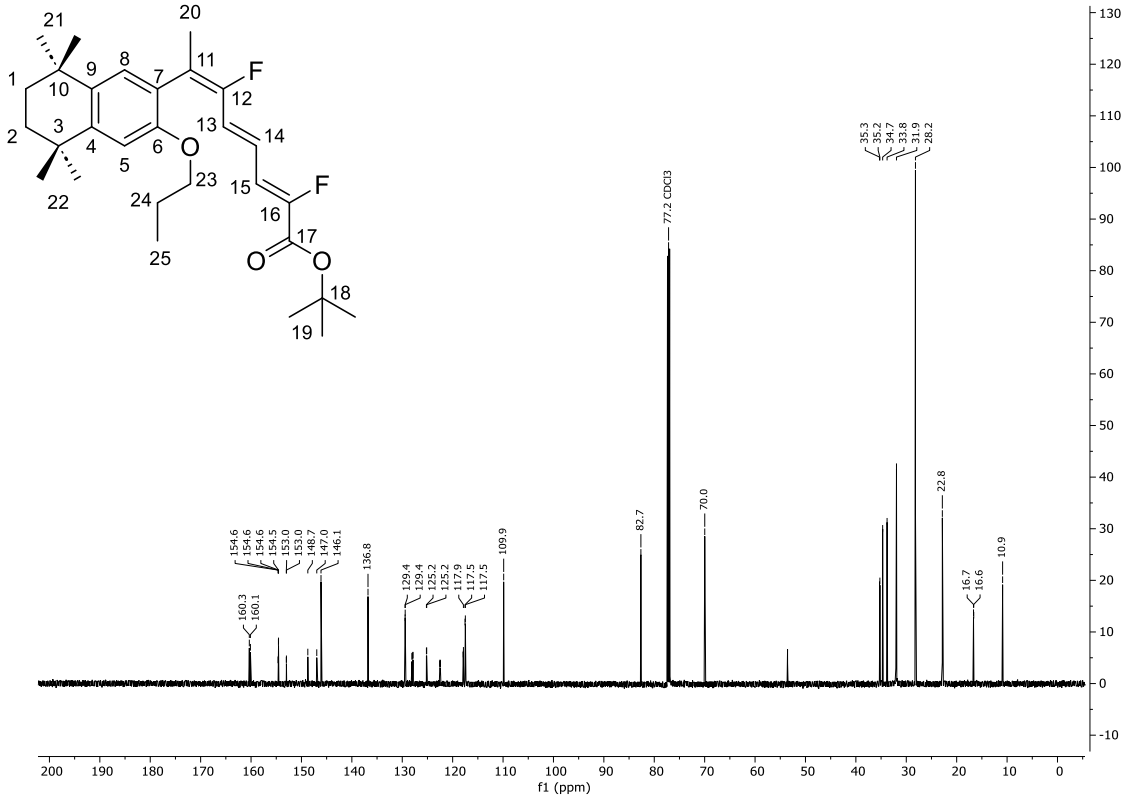

^{19}F-NMR {^{1}H} of **22** (377 MHz, $CDCl_3$)

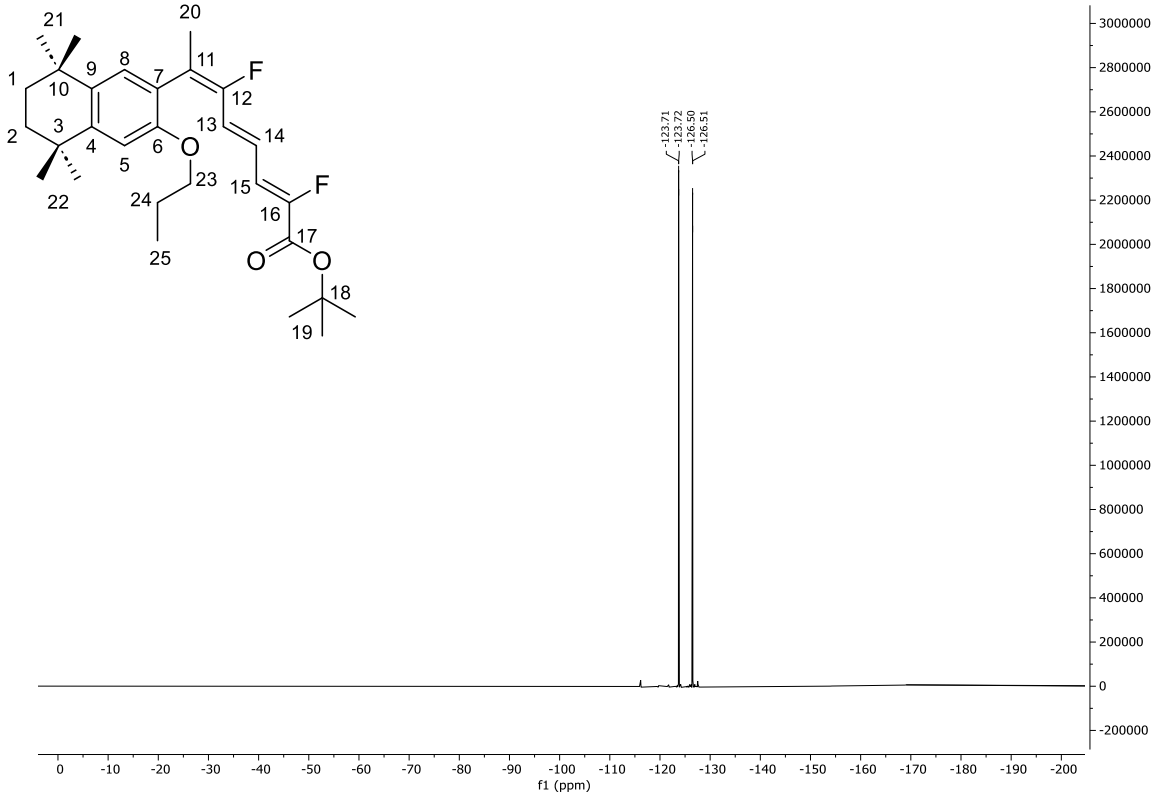

^{19}F-NMR of **22** (564 MHz, $CDCl_3$)

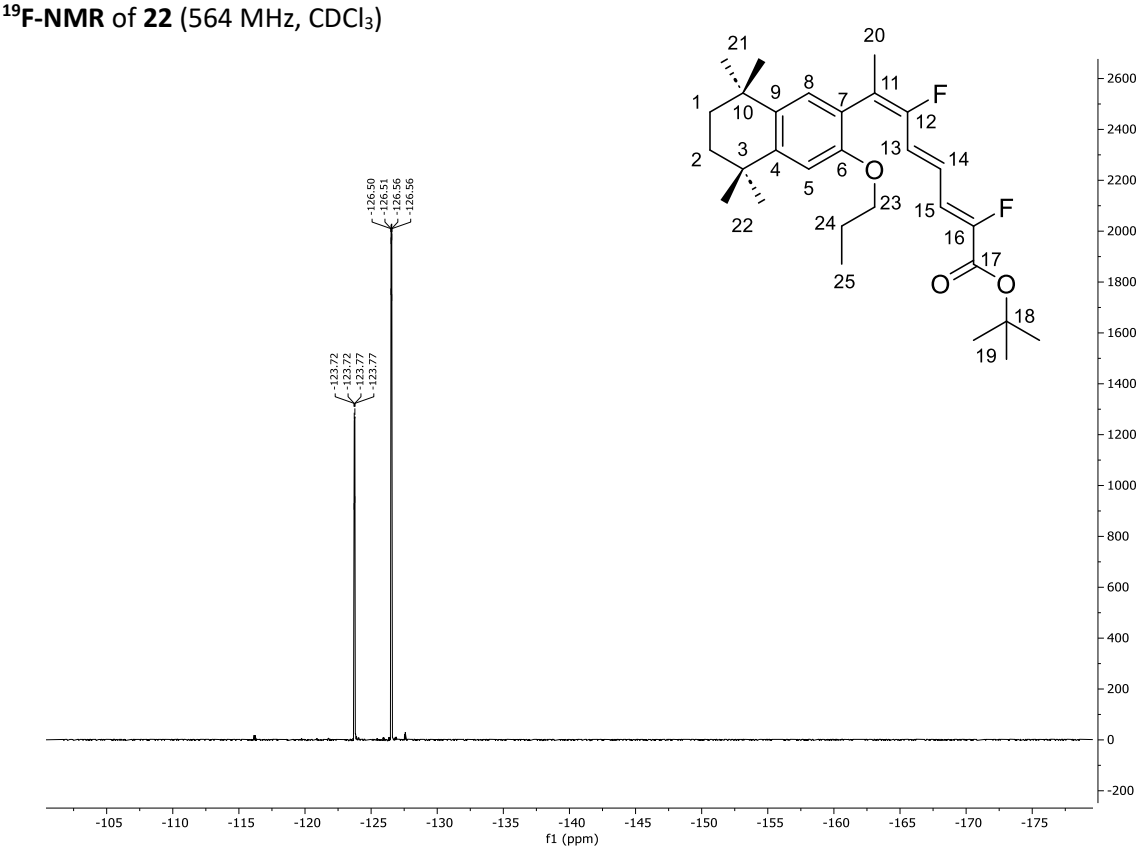

^{19}F-HOESY-NMR of **22** ($CDCl_3$)

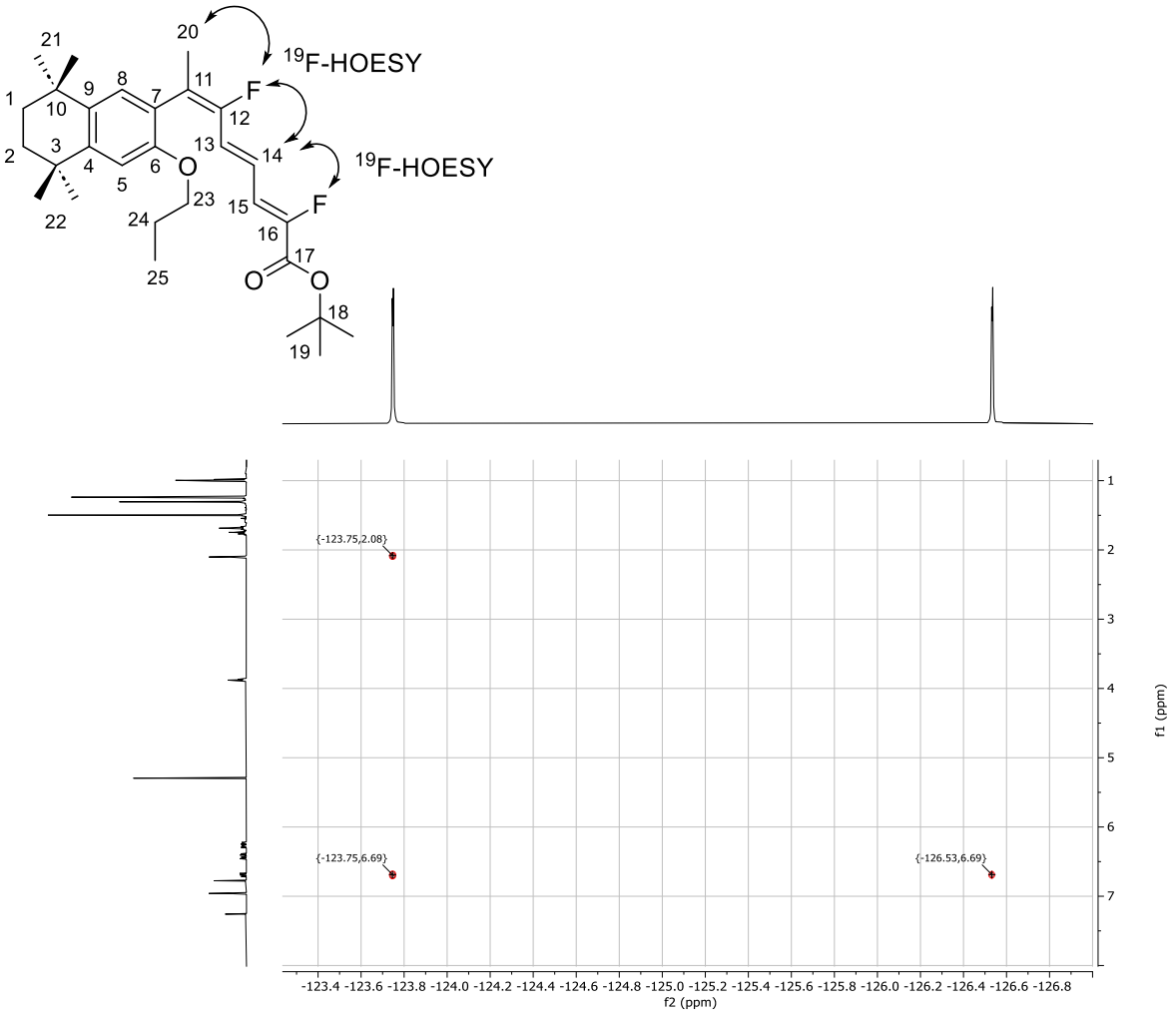

6. References

[1] B. Gierczzk, M. Kazmierczak, L. popenda, A. Sporznynski, G. Schroeder, S. Jurga, *Mag. Reson. Chem.* **2004**, *52*, 202-213.

[2] A. Bariau, J. Canet, P. Chalard, Y. Troin, *Tetrahedron :Asymmetry* **2005**, *22*, 3650-3660.

[3] E. D. Bergmann, I. Shahak, *J. Chem. Soc.* **1961**, 4033-4038.

[4] M. L. Hofferberth, R. Brückner *Angew. Chem. Int. Ed.* **2014**, *53*, 7328-7334.

[5] Y. Luo, I. D. Roy, A. G. E. Madec, H. W. Lam, *Angew. Chem. Int. Ed.* **2014**, *53*, 4186-4190.

[6] M. Zhou, K. Li, D. Chen, R. Xu, G, Xu, W. Tang, *J. Am. Chem. Soc.* **2020**, *23*, 10337-10342.

[7] V. H. Thorat, Y. Tsai, Y. Huang, C. Cheng, J. Hsieh *Org. Lett.* **2022**, *15*, 2915-2920.

[8] V. Nahoum, E. Perez, P. Germain, F. Rodriguez-Barrios, F. Manzo, S. Kammerer, G. Lemaire, O. Hirsch, C. A. Royer, H. Gronemeyer, A. R. de Lera, W. Bourguet *Proc. Natl. Acad. Sci.*, **2007**, *44*, 17323-17328.

[9] J. R. Coombs, L. Zhang, J. P. Morken *Org. Lett.* **2015**, *17*, 1708-1711.

[10] J. E. Lee, J. Kwon, J. Yun, *Chem. Commun*. **2008**, 733– 734.

[11] F. Neese, *Wiley Interdiscip. Rev. Comput. Mol. Sci.* **2012**, *2*, 73–78.

[12] M. D. Hanwell, D. E. Curtis, D. C. Lonie, T. Vandermeersch, E. Zurek, G. R. Hutchison, *J. Cheminform.* **2012**, *4*, 17.

10.8 Supporting Information for Project [G]

Angewandte Chemie
Eine Zeitschrift der Gesellschaft Deutscher Chemiker

Supporting Information

Triplet-Sensitized Switching of High-Energy-Density Norbornadienes for Molecular Solar Thermal Energy Storage with Visible Light

T. J. B. Zähringer, N. Perez Lopez, R. Schulte, M. Schmitz, H. Ihmels, C. Kerzig**

Supporting Information for

Triplet-Sensitized Switching of High-Energy-Density Norbornadienes for Molecular Solar Thermal Energy Storage with Visible Light

Till J. B. Zähringer*[a], Nico Perez Lopez[a], Robin Schulte[b], Matthias Schmitz[a], Heiko Ihmels[b] and Christoph Kerzig*[a]

[a] T. J. B. Zähringer, N. Perez Lopez, M. Schmitz, Prof. Dr. C. Kerzig
Department of Chemistry
Johannes Gutenberg University Mainz
Duesbergweg 10-14, 55128 Mainz, Germany
E-mail: tizaehri@uni-mainz.de, ckerzig@uni-mainz.de

[b] R. Schulte, Prof. Dr. H. Ihmels
Department of Chemistry-Biology, and Center of Micro- and Nanochemistry and (Bio-)Technology (Cμ)
University of Siegen
Adolf-Reichwein-Str. 2, 57068 Siegen, Germany

Table of contents

1. General information 2
2. Synthetic procedures 4
3. DFT calculations 6
4. Stern–Volmer experiments 11
4.1. Triplet-triplet energy transfer studies of PhNB, 1NNB and 2NNB with various metal sensitizers 11
4.2. Additional triplet energy transfer studies of various sensitizers and triplet acceptors 15
4.3. Kinetic simulations of the energy transfer efficiency 16
5. Interconversion quantum efficiency of 1NNB to 1NQC determined by relative actinometry 16
6. Interconversion quantum efficiency of Ph3NB to Ph2NB1QC determined by relative actinometry 20
7. Maximum energy storage efficiency of the Ir(ppy)$_3$–Ph3NB sensitizer–photoswitch pair 23
8. Additional spectroscopic measurements 24
8.1. Mechanistic investigations of the triplet state of 2NNB 25
8.2. Steady-state absorption spectra 27
8.3. Photostationary state composition of triplet sensitized 1NNB/1NQC 28
9. Multiple conversion cycles of the Ir(ppy)$_3$–Ph3NB pair under solar irradiance 32
10. NMR spectra 33
11. Literature 43

1. General information

Materials

Unless specifically mentioned, all chemicals used for synthesis, irradiation experiments, or optical spectroscopy were commercially obtained and used as received (acetonitrile, 99.9%, Fisher Scientific; toluene, 99.7%, Thermo Scientific; toluene-d_8, 99.5%, deutero; acetonitrile-d_3, 99.0%, deutero; *fac*-[Ir(ppy)$_3$], 99%, Sigma-Aldrich; thioxanthone, 97%, Sigma-Aldrich (purified by recrystallization from toluene/EtOAc prior to use); 2,7-dimethoxy-9H-thioxanthen-9-one (MeOTX), 98%, BLD Pharmatech; tris[5-fluoro-2-(2-pyridinyl)phenyl]-Iridium (IrF), 99%, Sigma-Aldrich; tris[3,5-difluoro-2-(2-pyridinyl)phenyl]-Iridium (IrdF), 98%, Sigma-Aldrich; (*E*)-ethyl cinnamate, 98%, Thermo scientific; [Ru(bpy)$_3$]Cl$_2$, 99.95%, Sigma-Aldrich; [Ru(phen)$_3$]Cl$_2$, 98%, Sigma-Aldrich; potassium hexachloroosmate, >99%, Sigma-Aldrich; 1,10-phenanthroline monohydrate, >98%, TCI; ammonium hexafluorophospate (NH_4PF_6), 98%, abcr; ethylene glycol, ≥99%, Carl Roth; naphthalene, 99.6%, Alfa Aesar; norbornadiene (stabilized with 250 ppm dibutylhydroxytoluene, BHT), 97%, TCI; NaOH, 97%, VWR; bromobenzene, 99%, Sigma-Aldrich; Pd(PPh$_3$)$_4$, 98%, Carbolution; THF, 99.5%, Thermo Fisher; Et_2O, >95%, VWR; *n*-hexane, >95% (distilled before used), VWR; 1,3,5-tribromobenzene, 97%, Carbolution; 1-bromonaphthalene, 97%, Alfa Aesar; 2-bromonaphthalene, 97%, Acros Organics; dimethyl sulfone, 98%, Thermo Scientific; dioxan, >99.5%, VWR; bibenzyl, 99%, Sigma-Aldrich.

Argon from Nippon Gases (5.0) was used for removing dissolved oxygen before all experiments related to optical spectroscopy.

Steady-state measurements

Absorption spectra were recorded with a Perkin Elmer LAMBDA 365 UV-Vis spectrophotometer. Emission measurements were carried out with a Perkin Elmer FL-6500 spectrometer and the emission spectra were corrected for the wavelength-dependent sensitivity of the instrument. All spectra were recorded at room temperature (295 ± 3 K) using 10 mm quartz glass cuvettes.

LED and solar irradiation experiments

Before all irradiation experiments, dissolved oxygen was removed by three freeze-pump-thaw cycles and sealed in custom-made Schlenk-cuvettes or NMR tubes.[1]

A 440 nm or 525 nm LED (Kessil Science, PR160L) with an average intensity reported as 352 mW cm^{-2} (1 cm distance) and a 405 nm LED from Thorlabs (M405L4) with an intensity of 14.53 µW/mm^2 at 100% (2 cm distance) as stated by the manufacturer were employed for irradiation experiments. The emission spectra are shown in Figure S1.

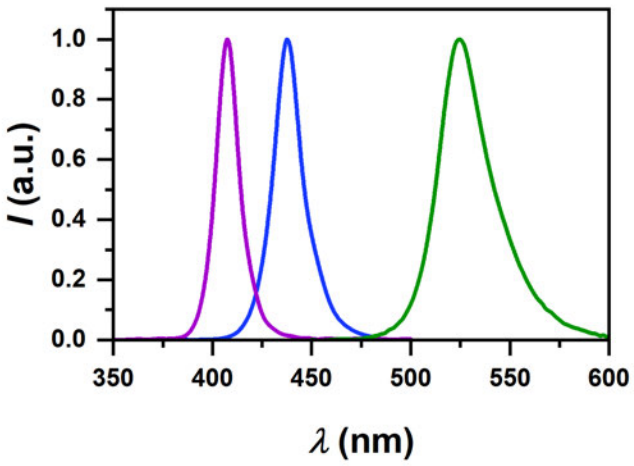

Figure S1: Normalized emission spectra of the 405 nm (purple), 440 nm (blue) and 525 nm (green) LEDs. The spectra were measured by irradiation a water-containing cuvette in the FL-6500 instrument, recording the Rayleigh scattered light. The light source was installed in a 90° angle with respect to the detector.

All solar irradiation experiments were performed in Mainz, Germany (49°59'N, 8°13'E) with no cloud coverage; date and irradiation times are given below the measurements.

Laser flash photolysis (LFP)

The LP980KS setup from Edinburgh Instruments equipped with an Nd:YAG laser from Litron (Nano LG 300-10) and an Nd:YAG Quantel (Q-smart 450) were employed for transient absorption and time-resolved emission spectroscopy. The frequency-doubled (532 nm) and frequency-tripled (355 nm) output served as the excitation source. The laser pulse duration was ~5 ns and the pulse frequency was 10 Hz. The typical pulse energy used for transient absorption and emission studies was ~20 mJ. A constant laser pulse energy was used within a series of experiments, which was ensured by power measurements before, after and in-between the experiments. The laser power was measured using a pyroelectric detector with attenuator (QE25LP-S-MB-QED-D0) from Gentec-eo combined with the integra software. Detection of transient absorption spectra occurred on an iCCD camera from Andor. Kinetic traces at selected wavelengths were recorded using a photomultiplier tube. The spectroscopic experiments were performed at 293 K using a cuvette holder that allows temperature control. If not stated otherwise the TA spectra were integrated over 100 ns. Longpass filters (385 nm or 400 nm, both from Newport) were used for transient absorption measurements with detection wavelengths exceeding 600 nm to exclude contributions from second-order signals.

Time-correlated single photon counting (TCSPC)

The *mini*-τ setup from Edinburgh Instruments (time-correlated single photon counting (TCSPC) technique) equipped with a pulsed laser (EPL-450, excitation at 446.4 nm, pulse width 74.5 ps) was employed for phosphorescence lifetime measurements of metal-based triplet sensitizers at 293 K. Stray light was removed with band pass filters and neutral density filters were used to avoid oversaturation of the detector.

Triplet-triplet energy transfer rate constants

Triplet-triplet energy transfer rate constants were determined by Stern–Volmer analyses. For Ir-based sensitizers this was achieved by lifetime-based measurements (τ) with varying concentrations c_q of the quencher and fitted according to the Stern–Volmer equation shown below (equation 1).

$$\frac{\tau_0}{\tau_i} = k_{\mathrm{EnT}} \cdot c_{\mathrm{i}} \cdot \tau_0 + 1 \qquad (1)$$

Considering that the converted quadricyclane 1NQC does not deactivate the triplet sensitizer, we derived the following equation that allows us to monitor the conversion progress simply by measuring the sensitizer's lifetime. Rearranging the Stern–Volmer equation for c_i (sum of $c_{1\mathrm{NQC}}$ and $c_{1\mathrm{NNB}}$) gives us equation (2). Since the sensitizer lifetime is only dependent on the residual 1NNB concentration we derive equation (3) with $c_{1\mathrm{NNB}}$ as the concentration of 1NNB and τ_j as the measured sensitizer lifetime.

$$c_\mathrm{i} = \frac{\left(\frac{\tau_0}{\tau_\mathrm{i}} - 1\right)}{k_{\mathrm{EnT}} \cdot \tau_0} \tag{2}$$

$$c_{1\mathrm{NNB}} = \frac{\left(\frac{\tau_0}{\tau_\mathrm{j}} - 1\right)}{k_{\mathrm{EnT}} \cdot \tau_0} \tag{3}$$

The fraction of 1NQC ($X_{1\mathrm{NQC}}$) is given by equation (4) with c_{NQC} as the concentration of 1NQC. Inserting equation (2) and (3) into (4) gives us the dependence of the fraction of 1NQC and the sensitizer's lifetime, while τ_i and c_i are constant and correspond to the sensitizer lifetime and quencher concentration when 100% 1NNB is present. On the other hand, τ_j is the experimental lifetime that is obtained from lifetime-based measurements. Once τ_j is equal to τ_i full conversion is obtained.

$$X_{1\mathrm{NQC}} = \frac{c_{1\mathrm{NQC}}}{c_\mathrm{i}} = \frac{c_\mathrm{i} - c_{1\mathrm{NNB}}}{c_\mathrm{i}} \tag{4}$$

$$X_{1\mathrm{NQC}} = 1 - \frac{\left(\frac{\tau_0}{\tau_\mathrm{j}} - 1\right)}{\left(\frac{\tau_0}{\tau_\mathrm{i}} - 1\right)} \tag{5}$$

NMR spectroscopy

NMR spectra were recorded using either a multinuclear magnetic resonance spectrometer of the type AV II 400 (Bruker, Karlsruhe, Germany, ^{1}H: 400 MHz) or with a JEOL ECZ 500 spectrometer (^{1}H: 500 MHz, ^{13}C: 125 MHz, 25 °C). The chemical shifts δ are stated in ppm and referenced to the residual solvent signal. The resonance multiplicity is abbreviated as: s (singlet), d (doublet), t (triplet), q (quadruplet) and m (multiplet).

2. Synthetic procedures

$[Os(phen)_3](PF_6)_2$, $[Ru(phen)_3](PF_6)_2$ and $[Ru(bpy)_3](PF_6)_2$

$[Os(phen)_3](PF_6)_2$ was prepared by a modified procedure of Constable *et al.*[2] Briefly, 1,10-phenanthroline monohydrate (0.20 g, 1.00 mmol, 3.0 equiv.), potassium hexachloroosmate (0.16 g, 0.33 mmol, 1.0 equiv.), and ethylene glycol (100 mL) were combined in a three-necked 250 mL round-bottom flask fitted with a Dimroth condenser. The solution was purged with argon for 30 minutes to remove dissolved oxygen and then refluxed for 2 hours. After cooling to room temperature, the reaction mixture was poured into 100 mL of an aqueous solution containing NH_4PF_6 (1.00 g, 6.10 mmol, 18.0 equiv.) and stirred for 15 minutes. A black precipitate formed, which was isolated by filtration, washed several times with MilliQ water, and dried under vacuum to afford a black solid (0.29 g, 0.28 mmol, 85% yield).

$[Ru(phen)_3](PF_6)_2$ and $[Ru(bpy)_3](PF_6)_2$ were synthesized according to a straightforward counterion exchange reaction with NH_4PF_6. The chloride salts ($[Ru(phen)_3]Cl_2$ and $[Ru(bpy)_3]Cl_2$) were dissolved in water and added to a saturated aqueous solution of NH_4PF_6. The precipitated $[Ru(phen)_3](PF_6)_2$, $[Os(phen)_3](PF_6)_2$, $[Ru(bpy)_3](PF_6)_2$ were washed thoroughly with cold water and acetonitrile.

$[Ir(ppy)_2(phen)]PF_6$ (IrPhen)

The sensitizer was synthesized according to a literature report by Bernhard *et al*.[3]

The ^{1}H NMR (DMSO-d_6) signals closely match the findings documented in the literature.[3]

Synthesis of the norbornadienes

All four aryl-substituted norbornadienes used in this study and the common precursor 4,4,5,5-tetramethyl-2-(bicyclo[2.2.1]-heptadien-2-yl)1,3,2-dioxaborolane are fully characterized prior to this study and were synthesized according to the procedure previously reported by us.[4–6] The exact amounts and yields for the aryl-substituted norbornadienes are given below.

1-(bicyclo[2.2.1]hepta-2,5-dien-2yl)benzene (PhNB)

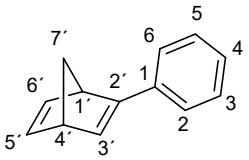

Under anaerobic conditions, an aqueous solution of NaOH (2.7 M, 5.8 mmol, 2.1 ml) was added to a solution of 4,4,5,5-tetramethyl-2-(bicyclo[2.2.1]-heptadien-2-yl)1,3,2-dioxaborolane (284 mg, 1.30 mmol), bromobenzene (187 mg, 1.19 mmol) and $Pd(PPh_3)_4$ (138 mg, 119 µmol) in THF (5.0 ml) and the resulting solution was stirred at 80 °C for 18 h. After cooling the reaction mixture to room temperature, it was diluted with Et_2O (50 ml), dried with Na_2SO_4 and filtered. The solvents were removed under reduced pressure and the remaining crude material was purified by column chromatography (*n*-hexane, R_f = 0.80) to provide the product as colorless oil (81.0 mg, 482 µmol, 41%). – ^{1}H NMR (500 MHz, $CDCl_3$): δ = 2.08 (dt, 2H, ^2J = 6.1 Hz, ^3J = 1.4 Hz, 7´-H), 3.68–3.73 (m, 1H, 1´-H), 3.92–3.97 (m, 1H, 4´-H), 6.80 (dd, 1H, ^3J = 5.1 Hz, ^3J = 3.0 Hz, 5´-H), 6.89–6.91 (m, 2H, 3´-H, 6´-H), 7.18–7.22 (m, 1H, 4-H), 7.30–7.34 (m, 2H, 2-H, 6-H), 7.39–7.43 (m, 2H, 3-H, 5-H). The NMR spectra are in accordance with the literature reports.[4,7]

1,3,5-tri(bicyclo[2.2.1]hepta-2,5-dien-2-yl)benzene (Ph3NB)

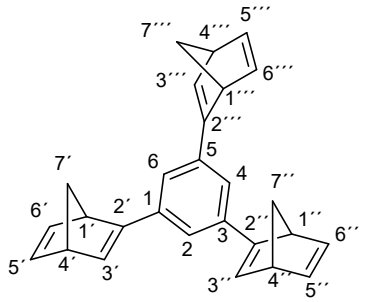

Under anaerobic conditions, an aqueous solution of NaOH (2.7 M, 5.8 mmol, 2.1 ml) was added to a solution of 4,4,5,5-tetramethyl-2-(bicyclo[2.2.1]-heptadien-2-yl)1,3,2-dioxaborolane (501 mg, 2.30 mmol), 1,3,5-tribromobenzene (181 mg, 575 µmol) and $Pd(PPh_3)_4$ (66.5 mg, 57.5 µmol) in THF (5.0 ml) and the resulting solution was stirred at 80 °C for 18 h. After cooling the reaction mixture to room temperature, it was diluted with Et_2O (50 ml), dried with Na_2SO_4 and filtered. The solvents were removed under reduced pressure and the remaining crude material was purified by column chromatography (*n*-hexane/EtOAc, 9/1, *v*/*v*, R_f = 0.28) to provide the product as off-white amorphous solid (120 mg, 345 µmol, 60%), mp > 300 °C. – ^{1}H NMR (500 MHz, $CDCl_3$): δ = 2.11 (dt, 3H, ^2J = 6.1 Hz, ^3J = 1.6 Hz, 7´-H, 7´´-H, 7´´´-H), 2.14 (dt, 3H, ^2J = 6.1 Hz, ^3J = 1.6 Hz, 7´-H, 7´´-H, 7´´´-H), 3.70–3.72 (m, 3H, 4´-H, 4´´-H, 4´´´-H), 3.94–3.98 (m, 3H, 1´-H, 1´´-H, 1´´´-H), 6.80 (dd, 3H, ^3J = 5.2 Hz, ^3J = 3.1 Hz, 5´-H, 5´´-H, 5´´´-H), 6.90–6.92 (m, 3H, 6´-H, 6´´-H, 6´´´-H), 6.92 (d, 3H, ^3J = 3´-H, 3´´-H, 3´´´-H), 7.28 (s, 3H, 2-H, 4-H, 6-H). – ^{13}C NMR (125 MHz, $CDCl_3$): δ = 51.0 (C4´, C4´´, C4´´´), 51.7 (C1´, C1´´, C1´´´), 72.7 (C7´, C7´´, C7´´´), 119.9 (C2, C4, C6), 136.4 (C3´, C3´´, C3´´´), 136.6 (C1, C3, C5), 142.2 (C6´, C6´´, C6´´´), 143.6 (C5´, C5´´, C5´´´), 157.0 (C2´, C2´´, C2´´´). – EI. Anal. for $C_{27}H_{24}$: calc. (%): C 93.06, H 6.94. found (%): C 93.33, H 7.08. The analytical data aligns with our previously reported characterization.[6]

1-(bicyclo[2.2.1]hepta-2,5-dien-2-yl)naphthalene

(1NNB)

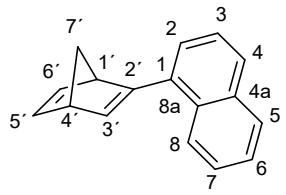

Under anaerobic conditions, an aqueous solution of NaOH (2.7 M, 14 mmol, 5.2 ml) was added to a solution of 4,4,5,5-tetramethyl-2-(bicyclo[2.2.1]-heptadien-2-yl)1,3,2-dioxaborolane (330 mg, 1.51 mmol), 1-bromonaphthalene (284 mg, 1.38 mmol) and $Pd(PPh_3)_4$ (79.6 mg, 68.8 µmol) in THF (5.0 ml) and the resulting solution was stirred at 80 °C for 18 h. After cooling the reaction mixture to room temperature, it was diluted with Et_2O (50 ml), dried with Na_2SO_4 and filtered. The solvents were removed under reduced pressure and the remaining crude material was purified by column chromatography (*n*-hexane, R_f = 0.61) to provide the product as colorless oil (168 mg, 771 µmol, 56%). – ^{1}H NMR (500 MHz, $CDCl_3$): δ = 2.18 (d, 1H, ^3J = 6.0 Hz, 7´-H), 2.39 (d, 1H, ^3J = 6.0 Hz, 7´-H), 3.84–3.85 (m, 2H, 1´-H, 4´-H), 6.83 (d, 1H, ^3J = 3.0 Hz, 3´-H), 6.89 (dd, 1H, ^3J = 5.2 Hz, ^3J = 3.0 Hz, 5´-H), 7.07 (dd, ^3J = 5.1 Hz, ^3J = 3.0 Hz, 6´-H), 7.28 (d, 1H, ^3J = 7.1 Hz, 2-H), 7.42 (dd, 1H, ^3J = ^3J = 8.0 Hz, 3-H), 7.46–7.49 (m, 2H, 6-H, 7´-H), 7.72 (d, 1H, ^3J = 8.2 Hz, 4-H), 7.83–7.86 (m, 1H, 5-H), 8.12–8.15 (m, 1H, 8-H). – ^{13}C-NMR (125 MHz, $CDCl_3$): δ = 51.6 (C4´), 56.2 (C1´), 73.5 (C7´), 123.3 (C2), 125.5 (C3), 125.8 (C6), 125.9 (C7), 126.0 (C8), 127.3 (C4), 128.5 (C5), 131.2 (C8a), 134.0 (C4a), 136.3 (C1), 140.1 (C3´), 142.8 (C6´), 143.4 (C5´), 156.1 (C2´). – EI. Anal. for $C_{17}H_{14}$: calc. (%): C 93.54, H 6.46, found (%): C 93.82, H 6.45. The analytical data aligns with our previously reported characterization.[4,5]

2-(bicyclo[2.2.1]hepta-2,5-dien-2-yl)naphthalene

(2NNB)

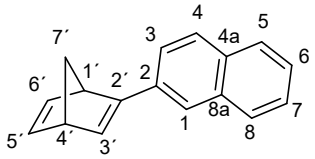

Under anaerobic conditions, an aqueous solution of NaOH (2.7 M, 14 mmol, 5.2 ml) was added to a solution of 4,4,5,5-tetramethyl-2-(bicyclo[2.2.1]-heptadien-2-yl)1,3,2-dioxaborolane (330 mg, 1.51 mmol), 2-bromonaphthalene (284 mg, 1.38 mmol) and $Pd(PPh_3)_4$ (79.6 mg, 68.8 µmol) in THF (5.0 ml) and the resulting solution was stirred at 80 °C for 18 h. After cooling the reaction mixture to room temperature, it was diluted with Et_2O (50 ml), dried with Na_2SO_4 and filtered. The solvents were removed under reduced pressure and the remaining crude material was purified by column chromatography (*n*-hexane, R_f = 0.40) to provide the product as a white amorphous solid (220 mg, 1.00 mmol, 72%); mp. 59–62 °C. – ^{1}H-NMR (500 MHz, $CDCl_3$): δ = 2.16 (dt, 1H, ^2J = 6.2 Hz, ^3J = 1.6 Hz, 7´-H), 2.18 (dt, 1H, ^2J = 6.2 Hz, ^3J = 1.6 Hz, 7´-H), 3.75–3.78 (m, 1H, 4´-H), 4.08–4.11 (m, 1H, 1´-H), 6.82 (dd, 1H, ^3J = 5.0 Hz, ^3J = 3.0 Hz, 5´-H), 6.95 (dd, 1H, ^3J = 5.0 Hz, ^3J = 3.2 Hz, 6´-H), 7.03 (d, 1H, ^3J = 3.2 Hz, 3´-H), 7.38–7.48 (m, 2H, 6´-H, 7-H), 7.57 (dd, 1H, ^3J = 8.6 Hz, ^4J = 1.8 Hz, 3-H), 7.74–7.79 (m, 3H, 1-H, 4-H, 5-H), 7.82–7.84 (m, 1H, 8-H). – ^{13}C-NMR (125 MHz, $CDCl_3$): δ = 51.1 (C4´), 51.5 (C1´), 72.3 (C7´), 122.7 (C1), 124.0 (C3), 125.7 (C6), 126.3 (C7), 127.7 (C5), 128.1 (C4), 128.2 (C8), 132.8 (C4a), 133.8 (C8a), 136.9 (C3´), 139.2 (C2), 142.0 (C6´), 143.6 (C5´), 156.9 (C2´). – EI. Anal. for $C_{17}H_{14}$: calc. (%): C 93.54, H 6.46, found (%): C 93.22, H 6.52. The analytical data aligns with our previously reported characterization.[5]

3. DFT calculations

All computational calculations were performed using the Orca 5.0.4 software package.[8] The B3LYP functional in combination with the 6-311+G(d,p) basis set was employed for all Density-Functional Theory (DFT) calculations. Geometry optimizations were carried out initially, followed by the calculation of

vibration frequencies. Notably, all optimization runs consistently converged to stationary points, with no imaginary frequencies detected, indicating convergence to minimum energy structures.

The lowest triplet states were optimized starting from the respective energy-minimized singlet ground state geometries. Triplet state energies were determined by comparing the energies of the optimized structures of the singlet ground state and lowest triplet state for each compound. These results are summarized in Table 1 of the main manuscript. Additional single-point calculations were performed to obtain spin densities for the optimized triplet states using the Mulliken population analysis method.

To determine electronic excitation energies and oscillator strengths of the 30 lowest transitions, Time-Dependent Density-Functional Theory (TD-DFT) calculations were performed on the previously geometry-optimized structures.

The computational results were analyzed and visualized using the Avogadro 1.2.0 software tool,[9] which facilitated the depiction of molecular structures, orbital distributions, and spin densities. In the depiction of spin densities, blue-colored surfaces denote positive spin densities, whereas red-colored surfaces denote negative spin densities.

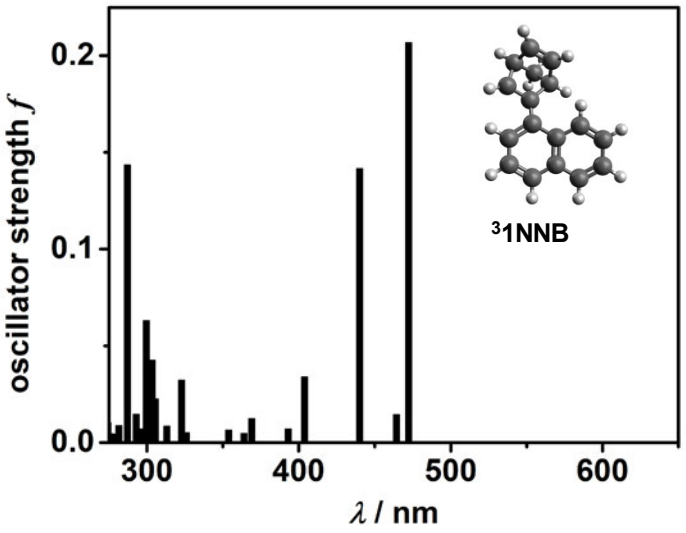

Figure S2: Predicted energies and oscillator strengths of electronic transitions for the triplet state of 1NNB.

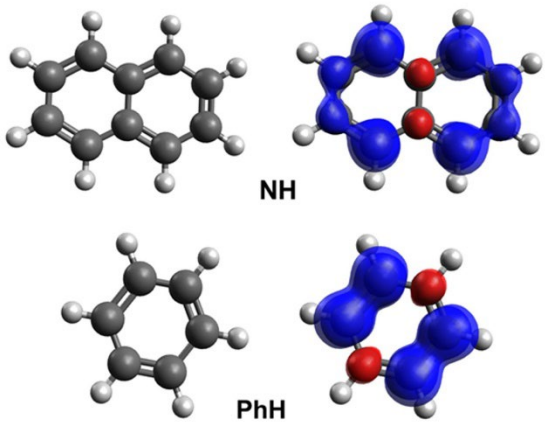

Figure S3: (Left) Structures of the geometry-optimized triplet states of the reference compounds benzene (PhH) and naphthalene (NH). (Right) The corresponding spin densities (iso value: 0.005 a.u.; total sum of atomic spin populations: 2.000).

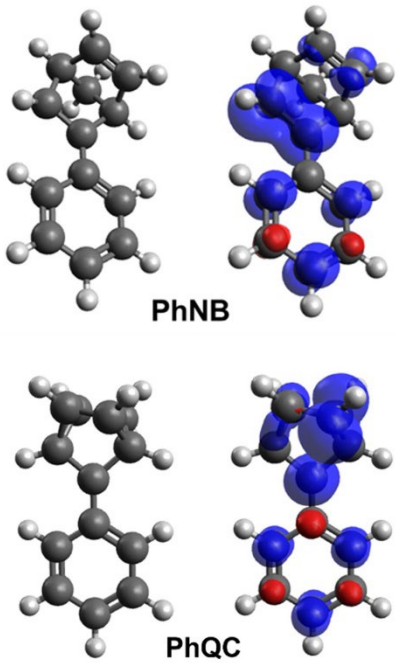

Figure S4: (Left) Structures of the geometry-optimized triplet states of PhNB and PhQC. (Right) The corresponding spin densities (iso value: 0.005 a.u.; total sum of atomic spin populations: 2.000). Bond cleavage during optimization (one bond within the QC moiety).

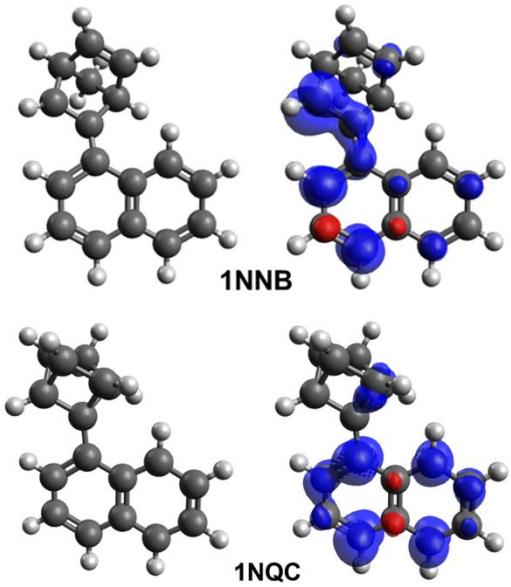

Figure S5: (Left) Structures of the geometry-optimized triplet states of 1NNB and 1NQC. (Right) The corresponding spin densities (iso value: 0.005 a.u.; total sum of atomic spin populations: 2.000).

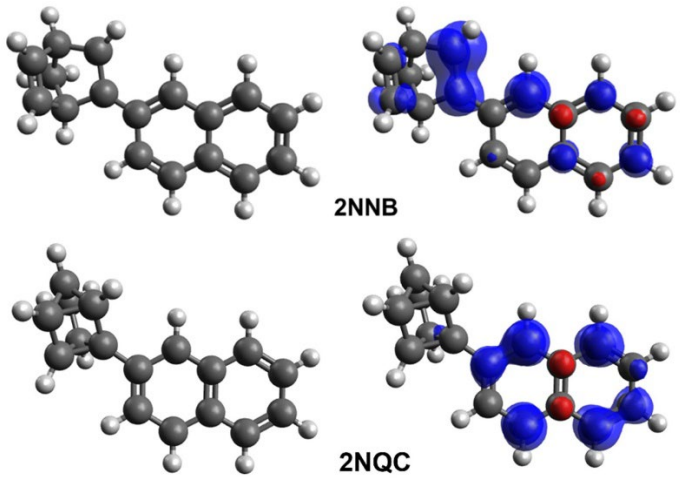

Figure S6: (Left) Structures of the geometry-optimized triplet states of 2NNB and 2NQC. (Right) The corresponding spin densities (iso value: 0.005 a.u.; total sum of atomic spin populations: 2.000).

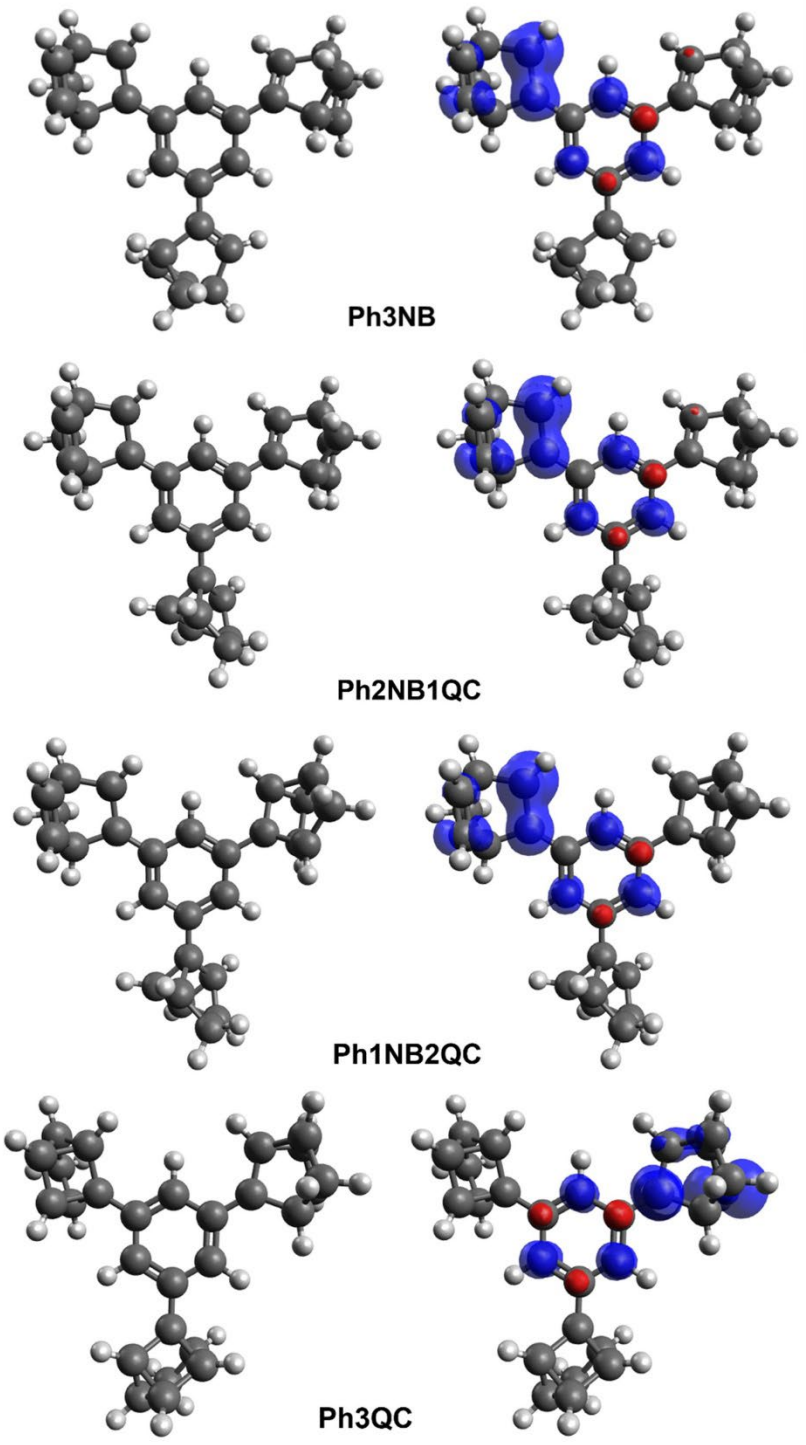

Figure S7: (Left) Structures of the geometry-optimized triplet states of Ph3NB, Ph2NB1QC, Ph1NB2QC and Ph3QC. (Right) The corresponding spin densities (iso value: 0.005 a.u.; total sum of atomic spin populations: 2.000).

4. Stern–Volmer experiments

4.1. Triplet-triplet energy transfer studies of PhNB, 1NNB and 2NNB with various metal sensitizers

Table S1: Triplet energy transfer rates of selected metal sensitizers to the norbornadienes arranged by decreasing triplet energy. The energy transfer rates were determined by Stern–Volmer analyses (see below).

Sensitizer	τ_0 (ns)	E_T (eV)	k_{EnT} (10^9 M^{-1} s^{-1})		
			PhNB	1NNB	2NNB
Ir(dFppy)$_3$	1940	2.75 [b]	3.72	4.87	6.30
Ir(*p*-F-ppy)$_3$	2000	2.71 [b]	3.27	4.89	6.23
Ir(ppy)$_3$	1790	2.52 [b]	0.91	3.10	3.80
[Ir(ppy)$_2$(phen)]$^+$	790	2.38 [b]	0.13	0.74	1.05
[Ru(phen)$_3$]$^{2+}$	450-510 [a]	2.19 [c]	0.079	0.59	0.83
[Ru(bpy)$_3$]$^{2+}$	950	2.12 [c]	0.012	0.13	0.19
[Os(phen)$_3$]$^{2+}$	230	1.80 [d]	–	0.031	0.044

[a] The triplet lifetime of [Ru(phen)$_3$]$^{2+}$ depends strongly on the temperature see Chapter S7 for details. [b] taken from reference[10]. [c] Taken from reference[11]. [d] Taken from reference[12].

A series of similar metal sensitizers was used to study the triplet energy transfer step to 1NNB, 2NNB and PhNB. The deactivation of the sensitizers with increasing quencher concentration of the norbornadienes was monitored by TCSPC or LFP (see Figure S8-S10). TCSPC and LFP measurements for a given quenching process gave the same result regardless of the method as several control experiments established. A Stern–Volmer analysis yielded the triplet energy transfer rates (Table S1). Applying the Sandros-equation to model the data would be inadequate. Balzani and colleagues have pointed out that this equation fails to consider energy transfer from and to distorted excited states as well as the potential for rates below diffusion in the exergonic area.[13] Indeed, the geometries of the excited states of norbornadienes are described to be highly distorted,[14–16] which in our case is also supported by the geometry-optimized structures of the triplet-excited states (see Chapter S2). Based on this, we rather estimate the triplet energy using an exponential fit function with the EnT rate limit as the upper boundary (Figure 4, main paper). The energy transfer rate limit does not only depend on the diffusion limit of the solvent[17] but also on the size of the sensitizer and quencher as well as spatial overlap of the involved orbitals.[10] When the triplet energy of the sensitizer equals that of the quencher ($\Delta E_T = 0$) the energy transfer rate is set as exactly half of the energy transfer limit.[17] This method yielded energies of 2.39 eV for 1NNB, 2.41 eV for 2NNB and 2.56 eV for PhNB, respectively.

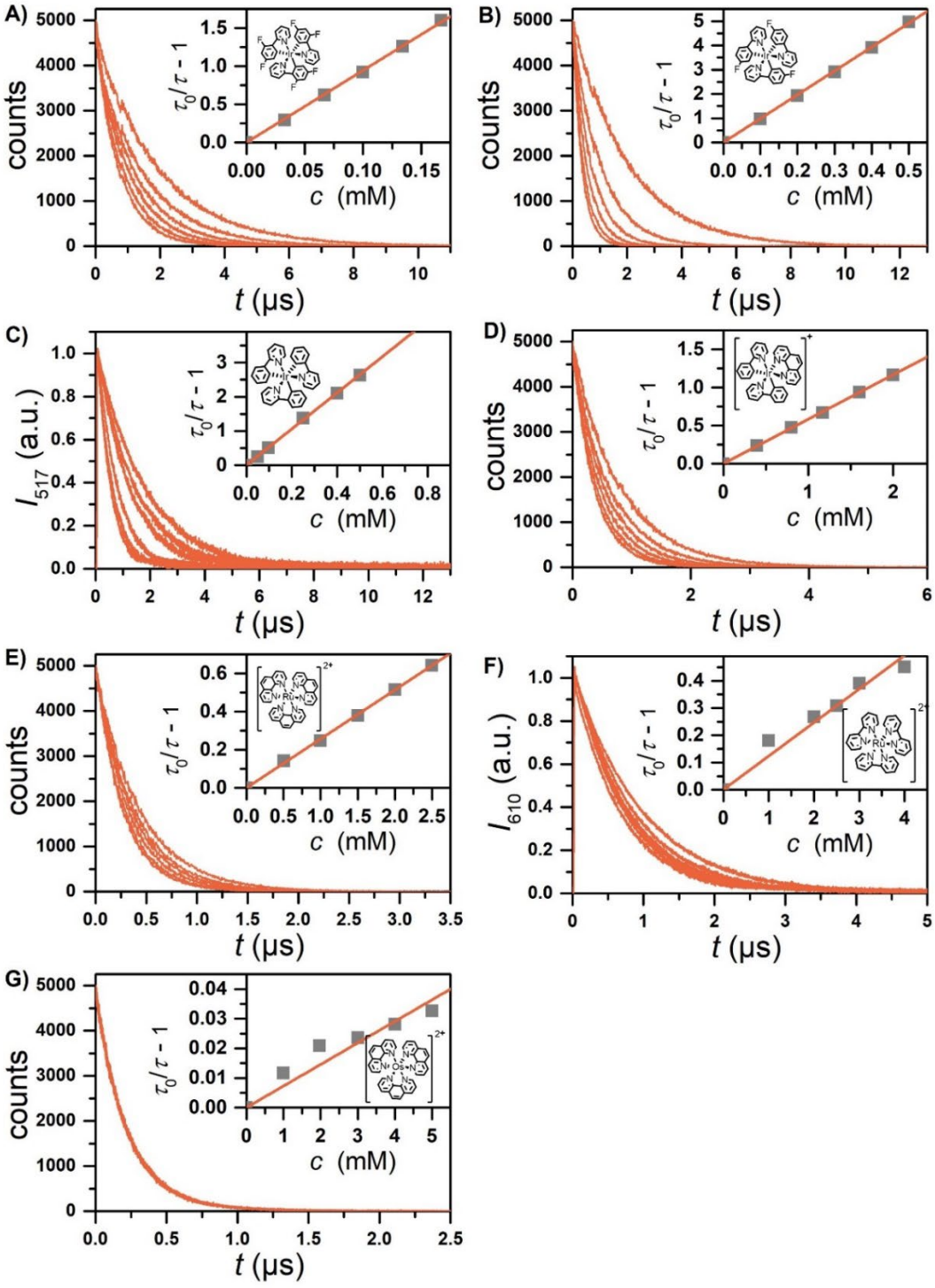

Figure S8: Time-resolved emission quenching experiments with various metal sensitizers and different concentrations of 1NNB in Ar-saturated MeCN. The concentration of the sensitizer was adjusted to OD ~ 0.2 at the excitation wavelength (446.4 nm using the TCSPC instrument or 355 nm and 532 nm using the LFP setup). The insets display the corresponding Stern–Volmer plot. A) $Ir(dFppy)_3$ (90 µM), B) $Ir(p\text{-}F\text{-}ppy)_3$ (90 µM), C) $Ir(ppy)_3$ (20 µM), D) $[Ir(ppy)_2(phen)]^+$ (85 µM), E) $[Ru(phen)_3]^{2+}$ (15 µM), F) $[Ru(bpy)_3]^{2+}$ (200 µM), G) $[Os(phen)_3]^{2+}$ (15 µM).

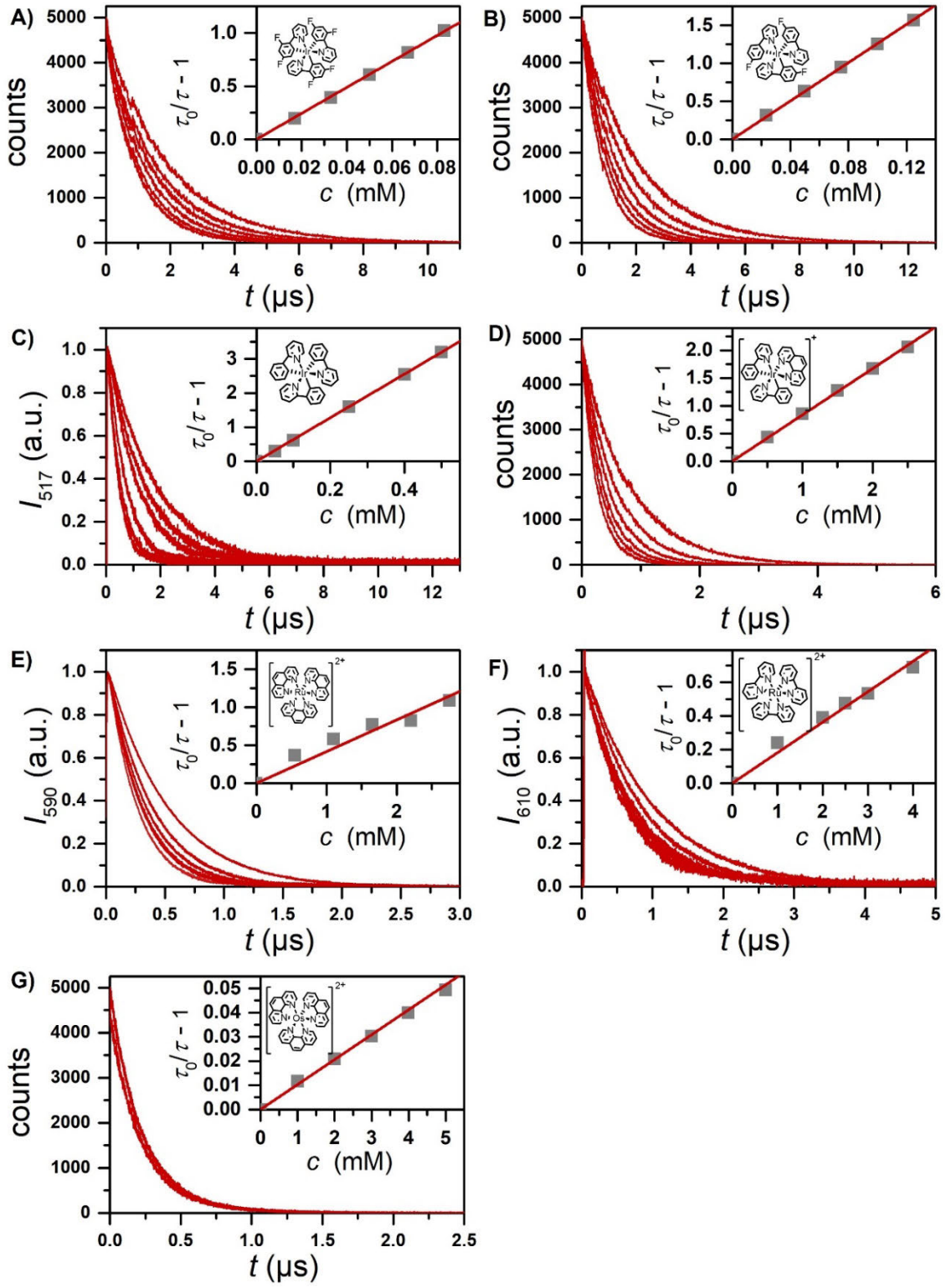

Figure S9: Time-resolved emission quenching experiments with various metal sensitizers and different concentrations of 2NNB in Ar-saturated MeCN. The concentration of the sensitizer was adjusted to OD ~ 0.2 at the excitation wavelength (446.4 nm using the TCSPC instrument or 355 nm and 532 nm using the LFP-setup). The insets display the corresponding Stern–Volmer plot. A) $Ir(dFppy)_3$ (90 µM), B) $Ir(p\text{-}F\text{-}ppy)_3$ (90 µM), C) $Ir(ppy)_3$ (20 µM), D) $[Ir(ppy)_2(phen)]^+$ (85 µM), E) $[Ru(phen)_3]^{2+}$ (100 µM), F) $[Ru(bpy)_3]^{2+}$ (150 µM), G) $[Os(phen)_3]^{2+}$ (15 µM).

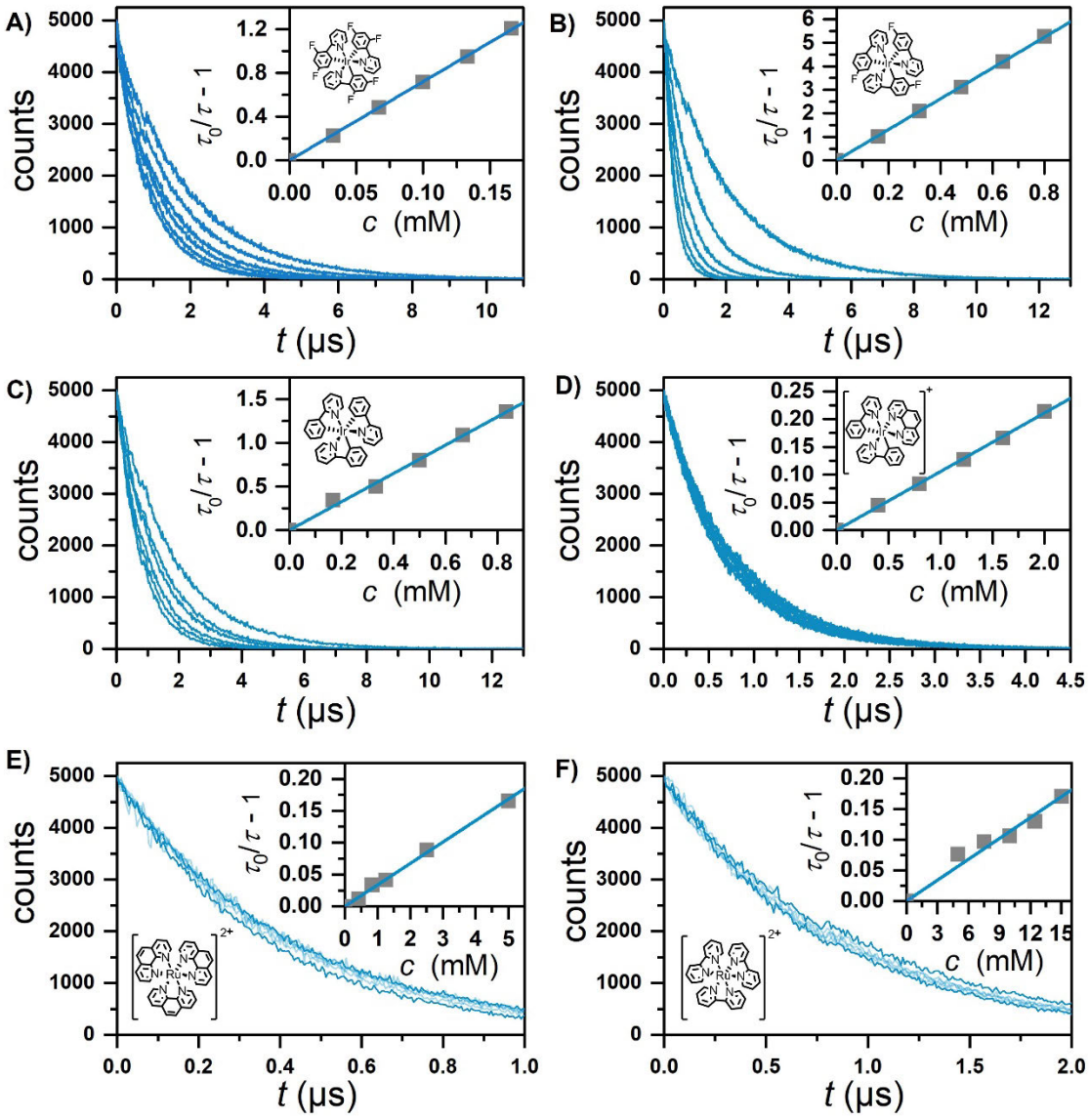

Figure S10: Time-resolved emission quenching experiments with various metal sensitizers and different concentrations of PhNB in Ar-saturated MeCN. The concentration of the sensitizer was adjusted to $OD_{446.5} \sim 0.2$ at the excitation wavelength. The insets display the corresponding Stern–Volmer plot. A) $Ir(dFppy)_3$ (90 µM), B) $Ir(p\text{-}F\text{-}ppy)_3$ (90 µM), C) $Ir(ppy)_3$ (15 µM), D) $[Ir(ppy)_2(phen)]^+$ (85 µM), E) $[Ru(phen)_3]^{2+}$ (15 µM), F) $[Ru(bpy)_3]^{2+}$ (20 µM).

4.2. Additional triplet energy transfer studies of various sensitizers and triplet acceptors

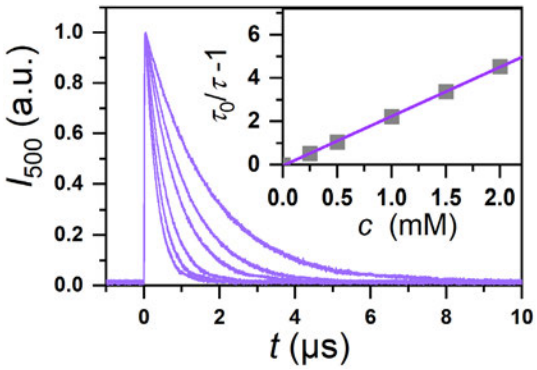

Figure S11: Time-resolved emission of a solution of 20 µM $Ir(ppy)_3$ in Ar-saturated MeCN with increasing concentrations of (*E*)-ethyl cinnamate upon excitation at 355 nm. Inset: corresponding Stern–Volmer plot.

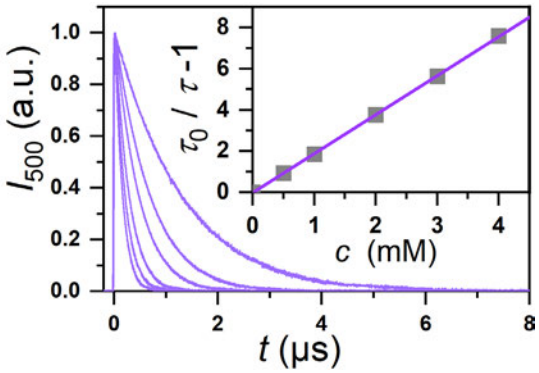

Figure S12: Time-resolved emission of a solution of 20 µM $Ir(ppy)_3$ in Ar-saturated toluene with increasing concentrations of (*E*)-ethyl cinnamate upon excitation at 355 nm. Inset: corresponding Stern–Volmer plot.

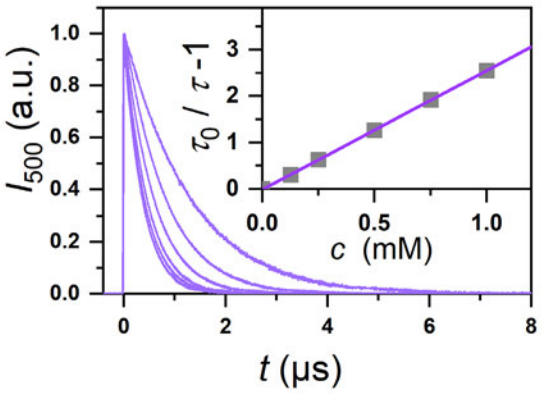

Figure S13: Time-resolved emission of a solution of 20 µM $Ir(ppy)_3$ in Ar-saturated toluene with increasing concentrations of Ph3NB upon excitation at 355 nm. Inset: corresponding Stern–Volmer plot.

4.3. Kinetic simulations of the energy transfer efficiency

The influence of the sensitizer lifetime, the quencher concentration and the energy transfer rate on the energy transfer efficiency can be rationalized by equation (6). By specifying the quencher concentration and triplet sensitizer lifetime (unquenched) we simulated the energy transfer efficiency against the triplet energy transfer rate (Figure S14A). A common concentration of 100 mM for lab-scale irradiation experiments and triplet sensitizer lifetimes typical for organic chromophores (100 µs – 1 µs) and photoactive metal complexes (10 µs – 100 ns) were selected.

$$\eta_{\mathrm{EnT}} = 1 - \frac{1}{1 + c_0 \cdot \tau_0 \cdot k_{\mathrm{EnT}}} \tag{6}$$

Furthermore, the triplet energy transfer efficiencies for the specific sensitizer-photoswitch pairs RuPhen–1NNB, OsPhen–1NNB and Ir(ppy)$_3$–Ph3NB were simulated using the experimental unquenched sensitizer lifetimes and triplet energy transfer rate constants (Figure S14B). This simulation was performed for different 1NNB/Ph3NB concentrations ranging from 1 to 1000 mM, according to equation (6).

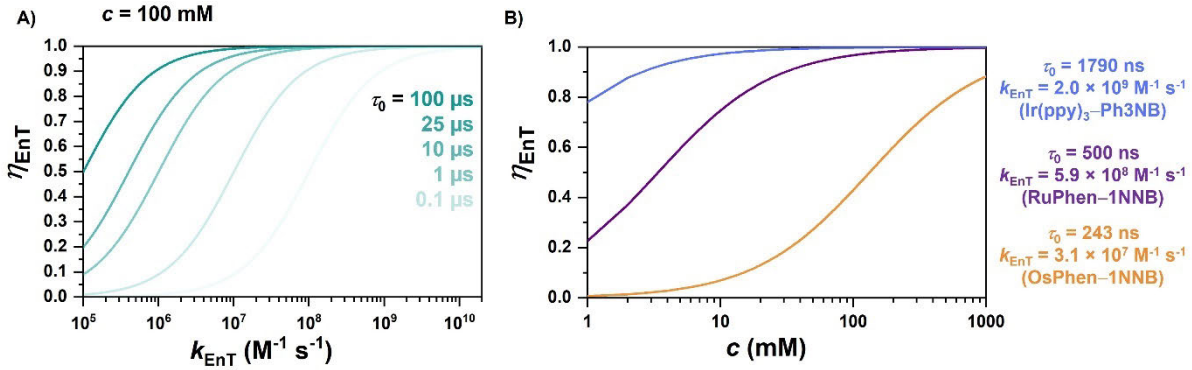

Figure S14: Simulated energy transfer efficiencies according to equation (6). A) Against the energy transfer rate with a quencher concentration of 100 mM and sensitizer lifetimes ranging from 100 µs to 100 ns. B) Against the quencher concentration for specific sensitizer–photoswitch pairs.

5. Interconversion quantum efficiency of 1NNB to 1NQC determined by relative actinometry

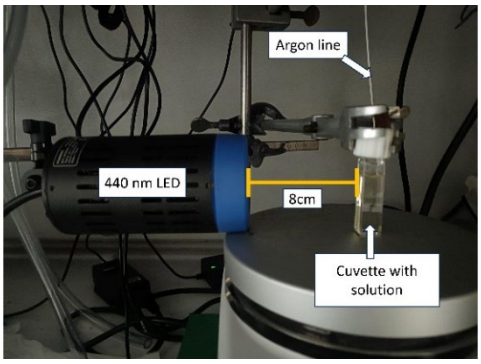

Figure S15: Experimental setup used to determine the interconversion efficiency.

The triplet-sensitized photoisomerization yield of 1NNB to 1NQC was determined by a relative actinometry method. Under identical conditions the interconversion of 1NNB to 1NQC was compared to the sensitized photoisomerization of a reference compound ((*E*)-ethyl cinnamate, *E*-EC) with a known isomerization efficiency (η_{iso} = 0.5 to the *Z* isomer).[10,18] Two solutions each containing 23.4 µM Ir(ppy)$_3$ (used as sensitizer), 2.53 mM dimethyl sulfone (DMS) (used as internal standard), and either 29.1 mM 1NNB or 30.5 mM *E*-EC in Ar-saturated MeCN-d$_3$ (4 mL) were prepared. The selected concentrations of 1NNB and *E*-EC are high enough to ensure near quantitative quenching of ^{3}Ir(ppy)$_3$ (compare quenching constants in Chapter S4 and Table S1). Each solution was transferred

to a cuvette and irradiated with a 440 nm Kessil LED at 25% intensity at a constant distance of 8 cm (see Figure S15 for the experimental setup).

This ensures that the photon flux is consistent for both photoreactions. At several time intervals 0.5 mL were removed and used to monitor the photoisomerization of 1NNB and *E*-EC by ^{1}H NMR spectroscopy. Selected NMR signals of 1NNB and 1NQC (Figure S17) and *E*-EC and the respective isomer *Z*-EC (Figure S18) were used to determine the isomer composition (for complete NMR spectra see Figure S43 and Figure S44). The integrated signals were referenced to the internal standard (DMS, 6H at 2.91 ppm) allowing us to calculate the total and isomer concentrations of 1NNB/1NQC and *E*-EC/*Z*-EC (Figure S16). The irradiation experiment was stopped when >15% (and <20%) of the product isomer was formed ensuring a linear relationship and a sufficient sensitivity. A linear fit yielded the relative reactions rates. Since exactly the same concentration of the sensitizer Ir(ppy)$_3$ was employed, we can disregard the sensitizer's properties such as spectral overlap and intersystem crossing quantum yield for this relative comparison. According to equation 7, the number of absorbed photons (*NAP*) of this specific setup can be calculated for the reference system from the observed reaction rate. Rearranging equation 7 allows us to determine an interconversion efficiency, η_{iso}, of 1.01 ± 0.06 for 1NNB. An efficiency over 1 is not reasonable as e.g. chain reactions cannot be expected for this transformation. Hence, we conclude that practically quantitative conversion of triplet-excited 1NNB is achieved in line with literature reports on the sensitization of norbornadiene and derivatives.[19,20]

$$NAP = \frac{rate}{\eta_{\mathrm{TTET}} \cdot \eta_{\mathrm{iso}}} \tag{7}$$

Table S2: Photochemical properties of 1NNB and *E*-EC involved in triplet energy transfer driven photoisomerization with Ir(ppy)$_3$ using a 440 nm Kessil lamp for sensitizer excitation.

Quencher	k_q(Ir(ppy)$_3$) (10^9 M^{-1} s^{-1})	η_{TTET}(Ir(ppy)$_3$)[a]	η_{iso}	rate (mM s^{-1})	*NAP* (mM s^{-1})
1NNB	3.10	0.993	1.01 ± 0.06	(3.31 ± 0.05)·10^{-2}	(3.28 ± 0.04)·10^{-2}
E-EC	1.35	0.986	0.5[10,18]	(1.62 ± 0.02)·10^{-2}	

[a] At selected concentration (29.1 mM 1NNB, 30.5 mM *E*-EC).

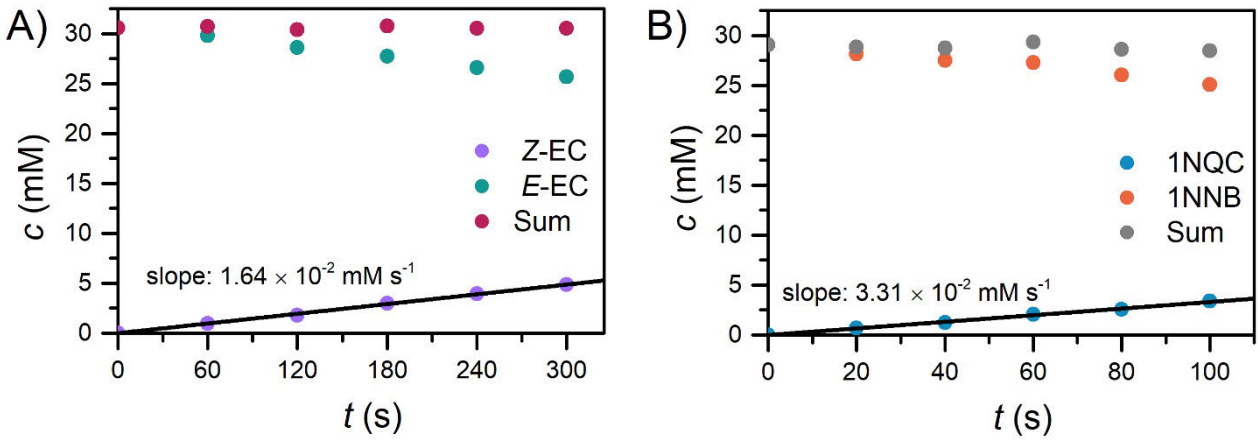

Figure S16: Isomer and total concentrations of two solutions containing each 23.4 µM Ir(ppy)$_3$, 2.5 mM dimethyl sulfone (DMS), and either 30.5 mM *E*-EC (A) or 29.1 mM 1NNB in Ar-saturated MeCN-d$_3$ (4 mL) given at different irradiation time intervals. A 440 nm LED from Kessil (25% intensity, 8 cm distance) was used as excitation light source. The concentrations were determined by NMR spectroscopy (see text for details).

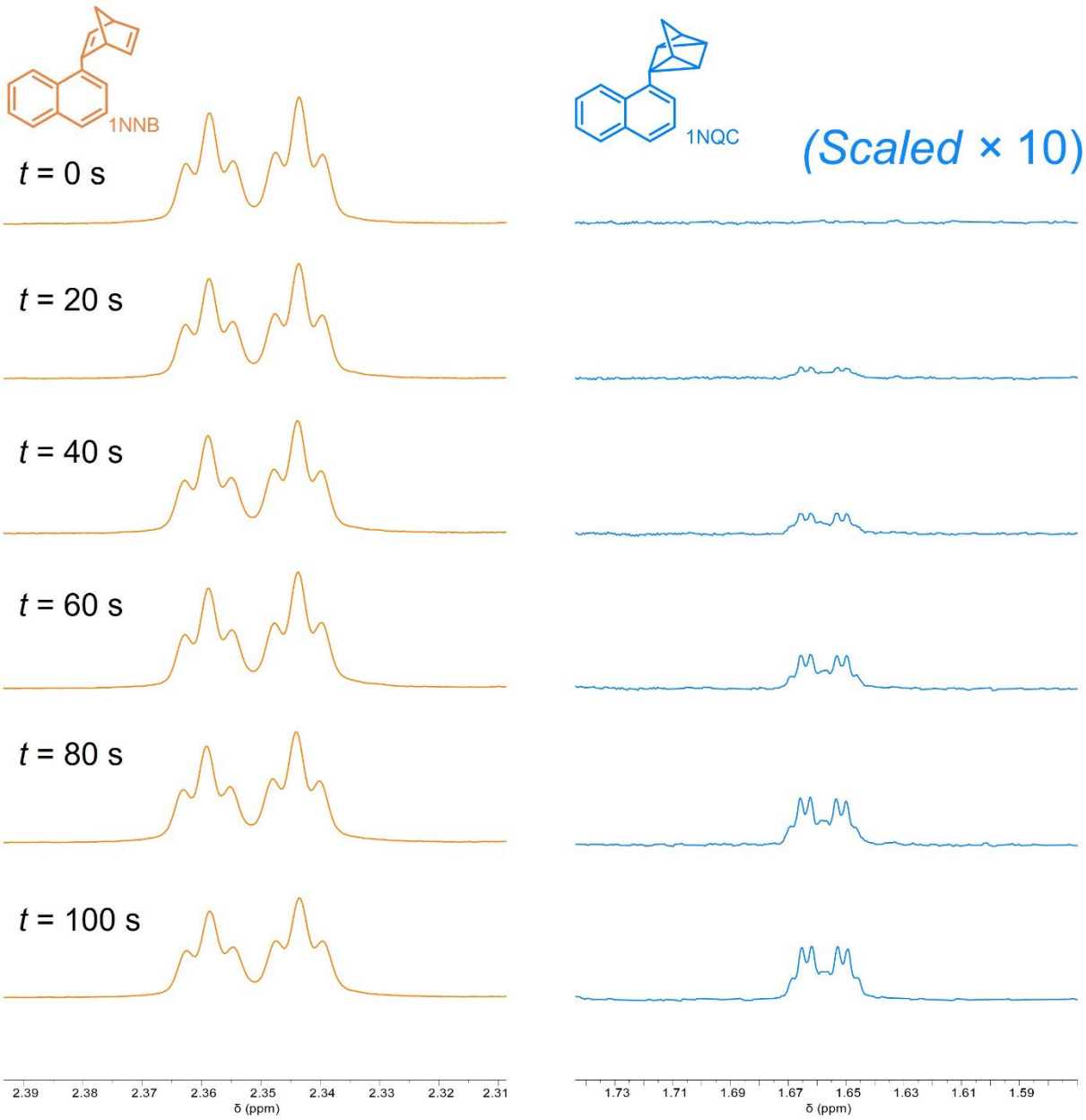

Figure S17: ^{1}H NMR spectra with selected spectral range of an Ar-saturated solution MeCN-d_3 containing 23.4 µM $Ir(ppy)_3$, 29.1 mM 1NNB, and 2.53 mM DMS. The spectra were recorded during irradiation with a 440 nm LED (set to 25%, 8 cm distance) with intervals of 20 s. The displayed signals, left corresponding to 1NNB (1H) and right to 1NQC (1H), were used to determine the interconversion efficiency. The complete ^{1}H NMR spectrum is displayed in Figure S43.

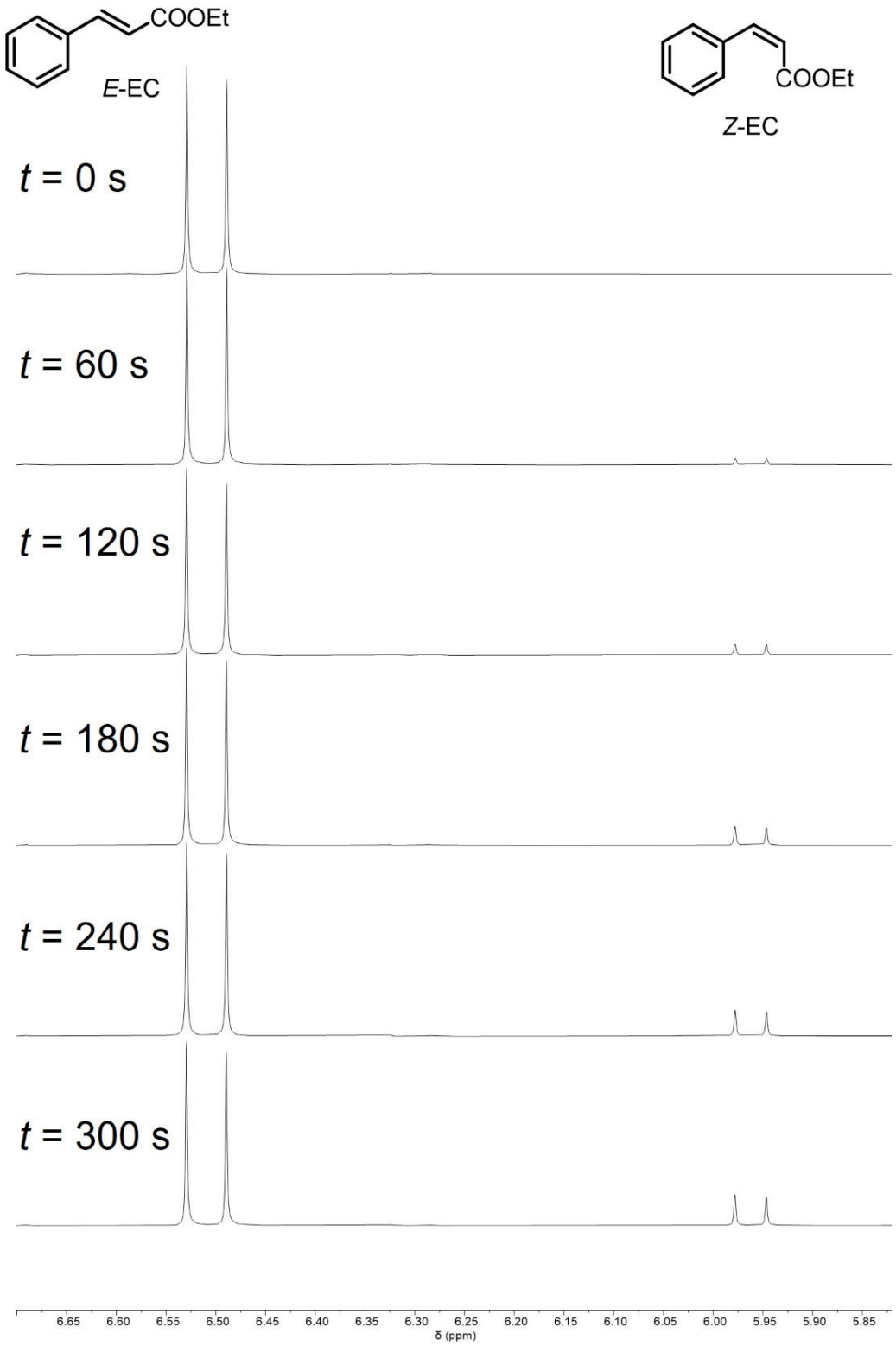

Figure S18: ^{1}H NMR spectra with selected spectral range of an Ar-saturated MeCN-d_3 solution containing 23.4 µM Ir(ppy)$_3$, 30.5 mM *E*-EC, and 2.53 mM DMS. The spectra were recorded during irradiation with a 440 nm LED (set to 25%, 8 cm distance) with intervals of 60 s. The displayed doublet signals, left (6.52 ppm, 1H) corresponding to *E*-EC and right (5.96 ppm, 1H) to *Z*-EC, were used to determine the number of absorbed photons of our setup, finally yielding the interconversion efficiency of 1NNB. The complete ^{1}H NMR spectrum is displayed in Figure S44.

6. Interconversion quantum efficiency of Ph3NB to Ph2NB1QC determined by relative actinometry

The triplet-sensitized photoisomerization yield of Ph3NB to Ph2NB1QC was determined by relative actinometry method analogous to 1NNB (Chapter S5). Under identical irradiation conditions (440 nm) the interconversion of Ph3NB to Ph2NB1QC was compared to the sensitized photoisomerization of (*E*)-ethyl cinnamate) with a known isomerization efficiency (η_{iso} = 0.5 to the *Z* isomer). Two solutions each containing 23.4 µM Ir(ppy)$_3$ (used as sensitizer), 10.0 mM dioxan (used as internal standard), and either 20.0 mM Ph3NB or 30.0 mM (*E*)-ethyl cinnamate (*E*-EC) in Ar-saturated toluene-d$_8$ (4 mL) were prepared. The selected concentration of *E*-EC is high enough to ensure near quantitative quenching of ^{3}Ir(ppy)$_3$ (compare quenching constants in Chapter S4). The number of absorbed photons of this measurement is lower than for the measurement involving 1NNB. This is due to the lower molar extinction coefficient of Ir(ppy)$_3$ in toluene-d$_8$ than in MeCN-d$_3$. The ^{1}H NMR signals of the NB units are virtually identical in the different isomers, and the same issue occurs for the QC signals, complicating an individual analysis of all isomer concentrations. Therefore, we can only observe the conversion of all three norbornadiene signals to quadricyclane signals simultaneously. We obtain an interconversion efficiency of 0.35 ± 0.02 for Ph3NB, normalizing this value by the number of norbornadiene units (assuming that at the low conversion during our quantitative irradiation experiments only Ph2NB1QC is formed) yields an efficiency of 1.05 ± 0.06 which we assign to the first conversion (Ph3NB to Ph2NB1QC).[19,20]

Table S3: Photochemical properties of Ph3NB and *E*-EC involved in triplet energy transfer driven photoisomerization with Ir(ppy)$_3$ using a 440 nm Kessil lamp for sensitizer excitation.

Quencher	k_q(Ir(ppy)$_3$) (10^9 M^{-1} s^{-1})	η_{TTET}(Ir(ppy)$_3$)[a]	η_{iso}	rate (mM s^{-1})	*NAP* (mM s^{-1})
Ph3NB	2.00	0.987	0.35 ± 0.02 (1.05 ± 0.06)[b]	(0.84 ± 0.02)·10^{-2}	(2.38 ± 0.02)·10^{-2}
E-EC	1.48	0.983	0.5[10,18]	(1.19 ± 0.01)·10^{-2}	

[a] At selected concentration (20.0 mM Ph3NB, 30.0 mM *E*-EC). [b] Normalized to the first conversion (Ph3NB to Ph2NB1QC).

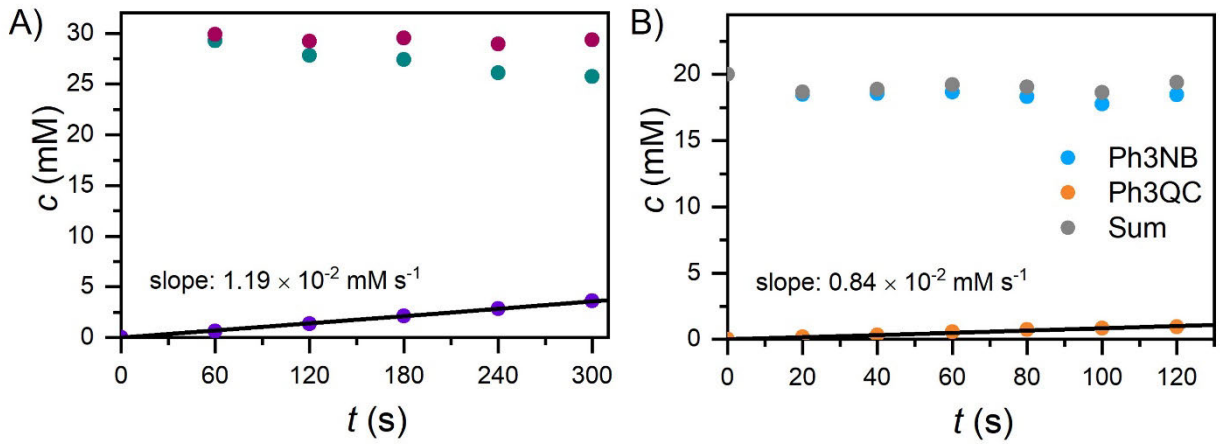

Figure S19: Isomer and total concentrations of two solutions containing each 23.0 µM Ir(ppy)$_3$, 10.0 mM dioxan, and either 30.0 mM *E*-EC (A) or 20.0 mM Ph3NB in Ar-saturated toluene-d$_8$ (4 mL) given at different irradiation time intervals. A 440 nm LED from Kessil (25% intensity, 8 cm distance) was used as excitation light source. The concentrations were determined by ^{1}H NMR spectroscopy (see text for details).

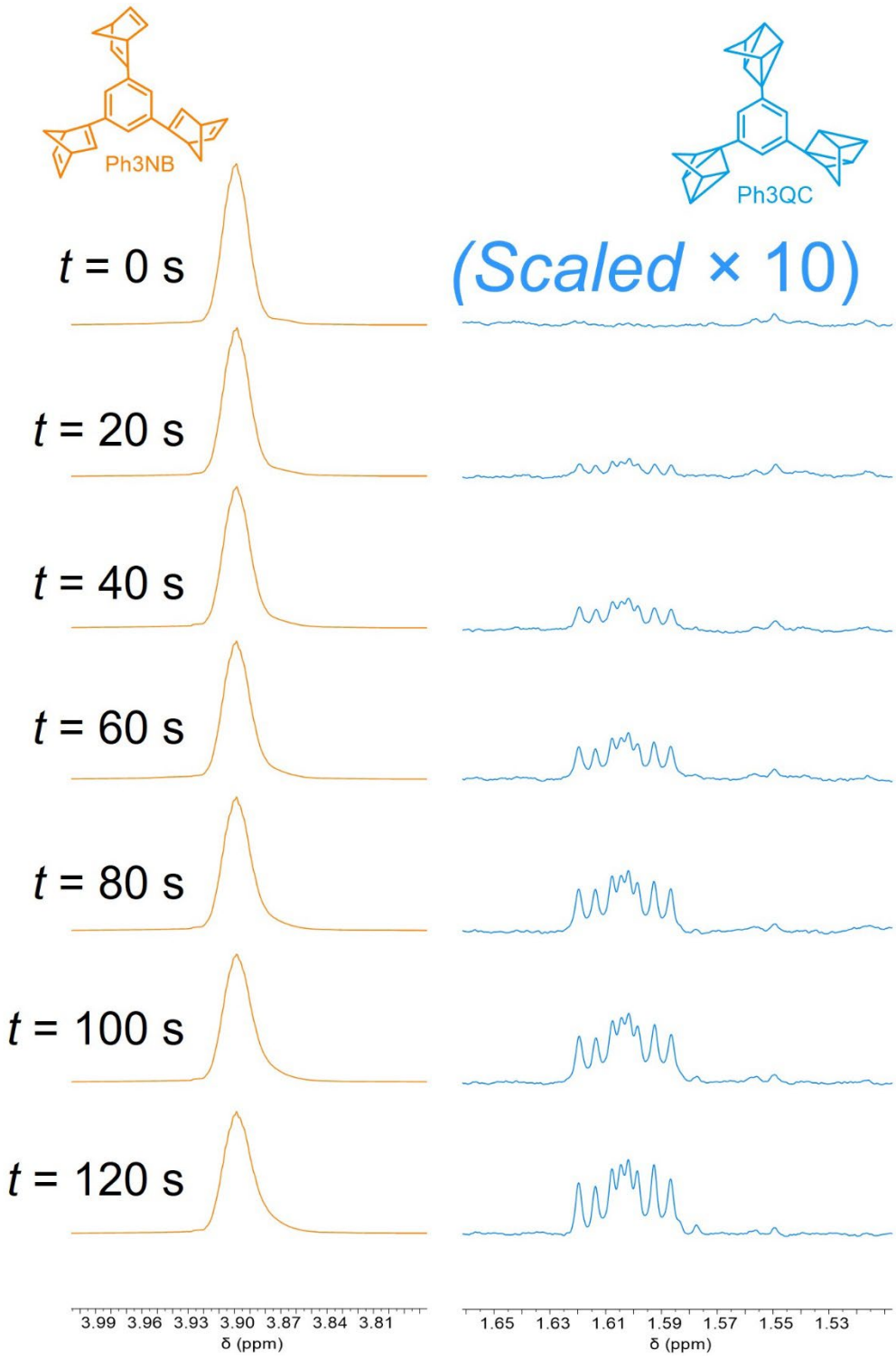

Figure S20: ^{1}H NMR spectra with selected spectral range of an Ar-saturated toluene-d_8 solution containing 23.0 µM Ir(ppy)$_3$, 20.0 mM Ph3NB, and 10.0 mM dioxan. The spectra were recorded during irradiation with a 440 nm LED (set to 25%, 8 cm distance) with intervals of 20 s. The displayed signals, left corresponding to Ph3NB (3H) and right to Ph3QC (3H), were used to determine the interconversion efficiency. The complete ^{1}H NMR spectrum is displayed in Figure S46. See text for further explanations.

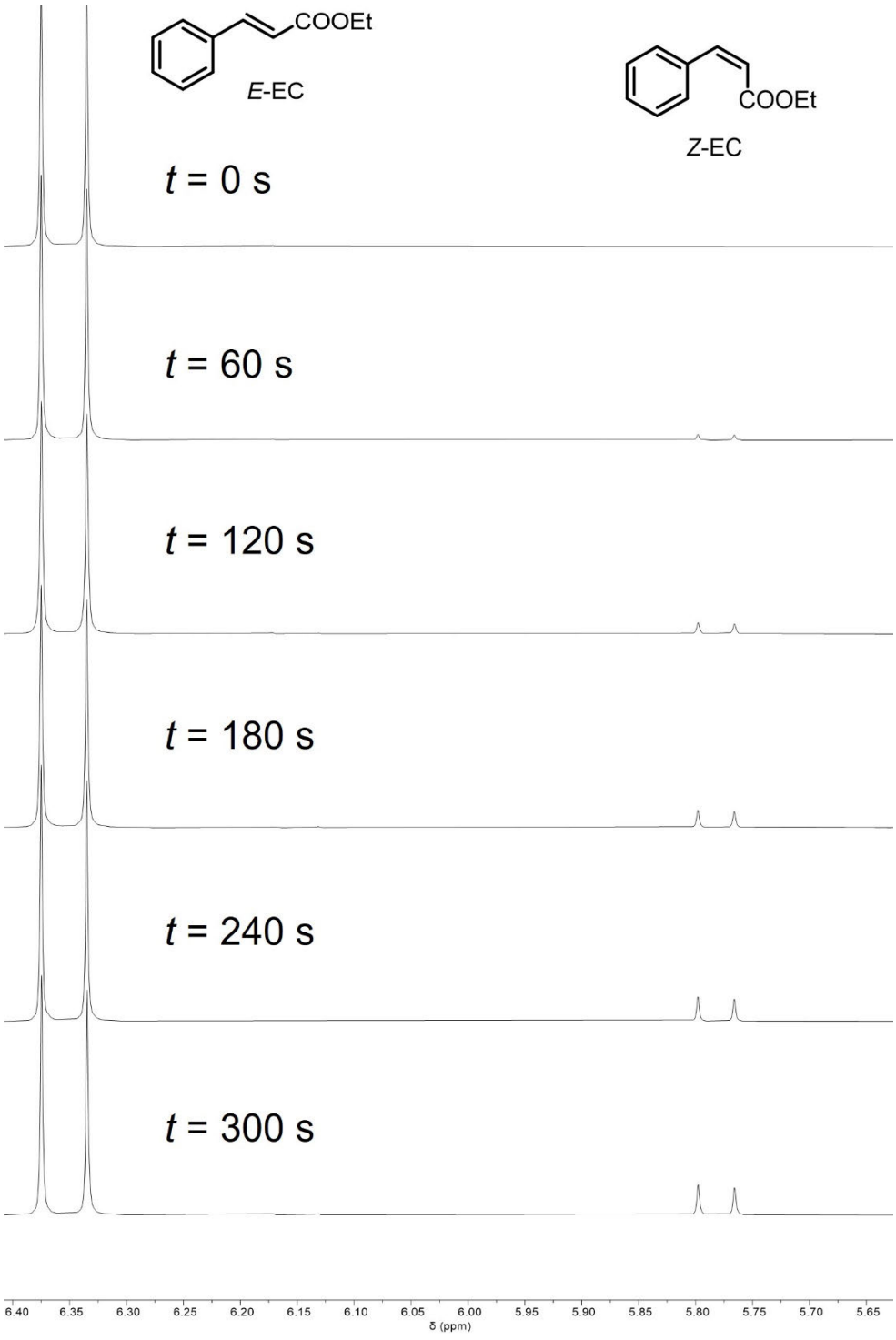

Figure S21: ^{1}H NMR spectra with selected spectral range of an Ar-saturated toluene-d_8 solution containing 23 µM $Ir(ppy)_3$, 30.0 mM *E*-EC, and 10 mM dioxan. The spectra were recorded during irradiation with a 440 nm LED (set to 25%, 8 cm distance) with intervals of 60 s. The displayed doublet signals, left (6.35 ppm, 1H) corresponding to *E*-EC and right (5.78 ppm, 1H) to *Z*-EC, were used to determine the number of absorbed photons of our setup, finally yielding the interconversion efficiency of Ph3NB. The complete ^{1}H NMR spectrum is displayed in Figure S45.

7. Maximum energy storage efficiency of the Ir(ppy)$_3$–Ph3NB sensitizer–photoswitch pair

Based on the Ir(ppy)$_3$–Ph3NB sensitizer–photoswitch pair we calculated the maximum energy storage efficiency, η_{MOST}, with equation (8).[21,22]

$$\eta_{\mathrm{MOST}} = \frac{\int_0^{\lambda_{\mathrm{onset}}} \frac{E_{\mathrm{AM1.5}}(\lambda) \cdot (1 - T(c,\lambda)) \cdot \Phi \cdot \Delta H_{\mathrm{stored}}}{3 \cdot h\nu \cdot N_{\mathrm{A}}} \cdot d\lambda}{E_{\mathrm{AM1.5}}} \tag{8}$$

Where $E_{\mathrm{AM1.5}}(\lambda)$ is the spectral irradiance in J s^{-1} m^{-2} nm^{-1}, as reported by the American Society for Testing and Materials (ASTM)[23], T is the transmittance of Ir(ppy)$_3$ (with the reasonable assumption that Ph3NB does not significantly contribute to the overall absorption of solar photons, see below), Φ is the overall quantum efficiency of the sensitized conversion of Ph3NB, $\Delta H_{\mathrm{stored}}$ is the stored energy of Ph3NB and equals 255.8 kJ mol^{-1}, h is the Planck constant in J s, ν is the frequency of the light in s^{-1}, N_{A} is the Avogadro constant and $E_{\mathrm{AM1.5}}$ is the integral over the complete solar irradiance. We simulate the efficiency for a device with the following specifications: 100 mM Ph3NB, 590 µM Ir(ppy)$_3$ (corresponding to the solubility limit), 1 cm path length. The onset absorption wavelength is 523 nm. The overall quantum yield, Φ, is defined in the main paper as follows:

$$\Phi = \Phi_{\mathrm{ISC}} \cdot \eta_{\mathrm{EnT}} \cdot \Phi_{\mathrm{NB \rightarrow QC}} \tag{9}$$

Ir(ppy)$_3$ efficiently produces the triplet state upon excitation, with Φ_{ISC} = 1.[24] For this particular system η_{EnT} is simulated in Figure S14B, demonstrating that it already exceeds 0.97 at a Ph3NB concentration of 10 mM and approaches unity at 100 mM. The interconversion quantum efficiency is determined in Chapter S6 as $\Phi_{\mathrm{NB \rightarrow QC}}$ = 1. Therefore, in this scenario, Φ is equal to 1. Since each absorbed photon results in the conversion of only one NB unit, the integral has to be divided by the number of NB units (3). The integrals are visualized in Figure S22 and yield an efficiency limit of η_{MOST} = 5.8%.

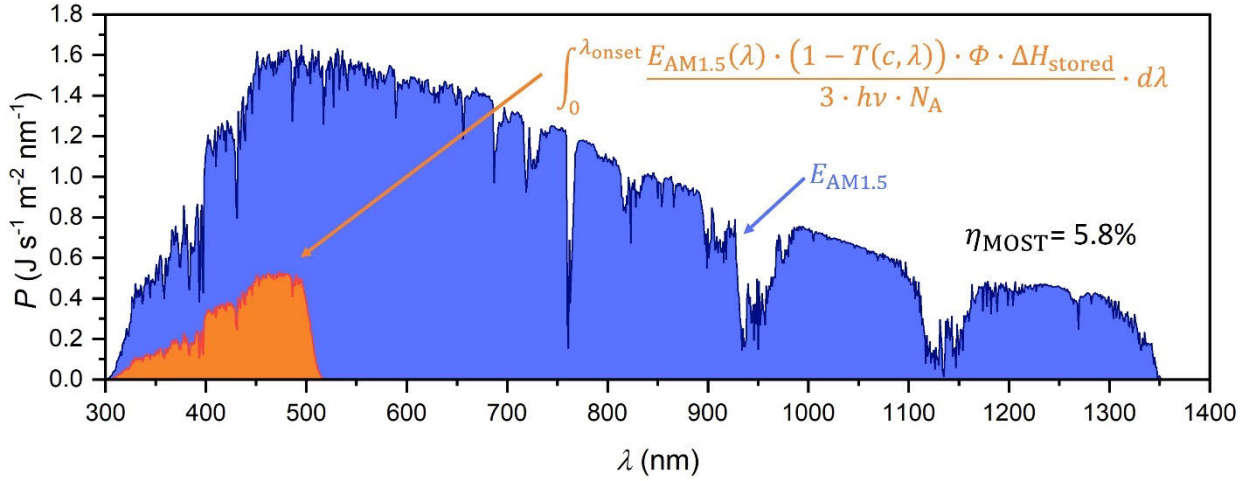

Figure S22: Solar conversion efficiency of the Ir(ppy)$_3$–Ph3NB sensitizer–photoswitch pair. Integrals of equation (8) are visualized. For clarity, the graph is only plotted until 1400 nm, the integration was performed over the complete solar spectrum (up to 4000 nm).

Similar calculations were conducted for direct excitation of Ph3NB at a concentration of 100 mM in the absence of a sensitizer. Under the same parameters as before, we used an onset absorption wavelength

of 390 nm (see Figure 1C, main paper). With a conversion quantum yield after direct excitation of Φ_{iso} = 0.18 (normalized to the number of NB units)[6] we calculated an efficiency of η_{MOST} = 0.53%. This efficiency is an order of magnitude lower than what is achieved through triplet sensitization.

It is important to note that for direct excitation, this efficiency represents only an upper limit. It does not account for the re-excitation of Ph3QC or the decreasing absorption as the conversion to Ph3QC progresses. These issues are avoided with triplet sensitization. Re-sensitization of Ph3QC does not occur due to its significantly higher triplet energy. Additionally, the absorption of Ir(ppy)$_3$ remains unaffected by the concentrations of Ph3NB and Ph3QC.

We estimated the charging time for this specific MOST device using equation (10), which simply compares the number of MOST molecules and the available number of photons that initiate photoswitching. Parameter *d* is the path length, and *PF* is the solar photon flux in E s^{-1} m^{-2} nm^{-1}. The overall solar photon flux is 0.00714 E s^{-1} m^{-2} while only 0.000685 E s^{-1} m^{-2} can be absorbed by Ir(ppy)$_3$ with a path length *d* of 1 cm and a concentration of 590 µM. This corresponds to only 9.6% of the solar photon flux. The concentration of Ph3NB, c_{Ph3NB}, is multiplied by a factor of three accounting for the norbornadiene units for each molecule. In this calculation, we assume that for a given surface area, a specific amount of substance is present, with each norbornadiene unit being converted per absorbed photon.

$$t = \frac{3c_{\mathrm{Ph3NB}} \cdot d}{\int_0^{\lambda_{\mathrm{onset}}} PF \cdot (1 - T(c,\lambda))\, d\lambda \cdot \Phi} = \frac{3 \cdot 90\ \mathrm{mol \cdot m^{-3}} \cdot 0.01\ \mathrm{m}}{0.000685\ \mathrm{E \cdot s^{-1} \cdot m^{-2} \cdot 1}} = 3941\ \mathrm{s} \sim 66\ \mathrm{min} \qquad (10)$$

Charging this device to 90%, where 10 mM of Ph3NB remain in solution thus requires 66 min in this simplified calculation. These estimations align well with the experimental solar irradiation times of 45-60 min observed in Chapter S9 for a setup with related conditions.

8. Additional spectroscopic measurements

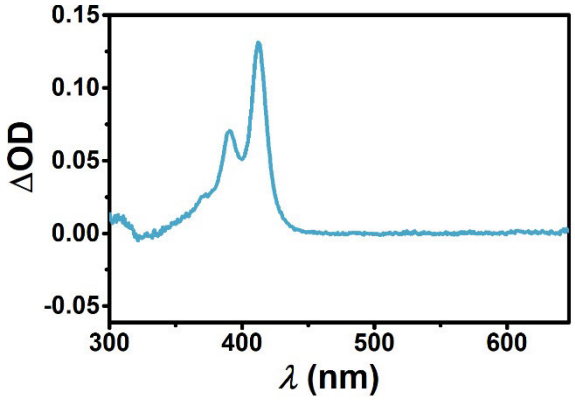

Figure S23: Triplet-triplet absorption spectrum of naphthalene. The spectrum was recorded 600 ns after 355 nm laser excitation using an Ar-saturated solution containing 40 µM thioxanthone and 1 mM naphthalene in MeCN.

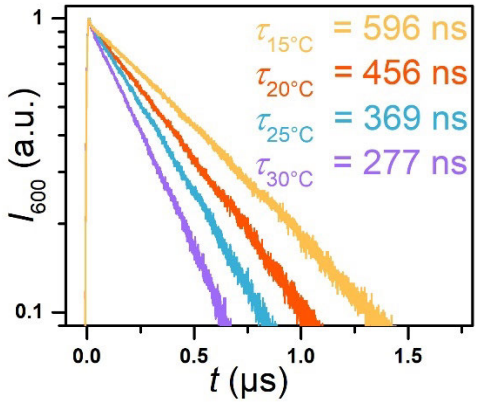

Figure S24: Time-resolved emission of 15 µM RuPhen in Ar-saturated MeCN recorded at 15°C, 20°C, 25°C and 30°C upon 532 nm excitation.

The temperature-dependent emission of RuPhen was measured at 15°C, 20°C, 25°C, and 30°C (Figure S24). As the temperature increased, the lifetime of RuPhen decreased significantly, from 596 ns at 15°C to 277 ns at 30°C. Despite using a temperature-controlled cuvette holder for LFP experiments, the actual solution temperature can vary due to external conditions (e.g., ambient temperature). Given the high temperature sensitivity of the lifetime, even minor fluctuations can cause changes of ± 25 ns. Nevertheless, at room temperature (20°C), the literature-reported lifetime of RuPhen[25] matches well with the measured range across all experiments (~450-510 ns). Therefore, the unquenched lifetime of RuPhen was determined individually for each experiment.

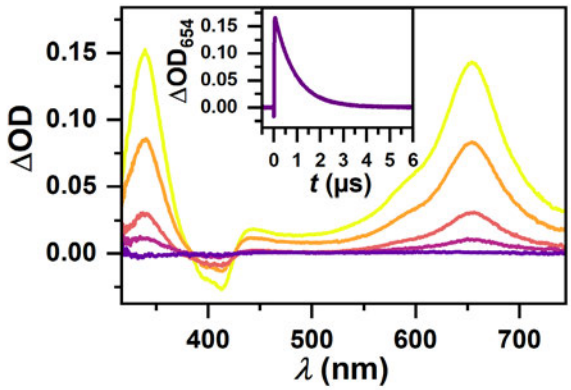

Figure S25: TA spectra of an Ar-saturated toluene solution containing 200 µM MeOTX and 500 µM Ph3NB using 355 nm laser pulses. The spectra were recorded 100 ns, 500 ns, 1 µs, 2 µs and 5 µs after excitation. Inset: Time-resolved transient absorption at 654 nm.

Transient absorption spectroscopy was used to investigate a solution of MeOTX and Ph3NB in toluene. Following the initial quenching of MeOTX via triplet energy transfer to Ph3NB, only the baseline level was observed. No quenching products from MeOTX, resulting from electron or hydrogen atom transfer, were detected, which allows us to exclude side reactions, in line with the ~100% switching quantum efficiency determined in Chapter S6.

8.1. Mechanistic investigations of the triplet state of 2NNB

Analogous to the measurements of the triplet species of 1NNB in the main paper, we investigated the structural isomer 2NNB as well. RuPhen was employed as sensitizer and high concentrations of 2NNB (36 mM) were used ensuring selective excitation and optimized conditions for the detection of short-lived intermediates (see main paper for details). A TA spectrum recorded 30 ns after 532 nm laser excitation in

Ar-saturated MeCN is displayed in Figure S26. A reference spectrum of RuPhen was scaled to match in the region >600 nm. The difference between both spectra reveals the transient triplet species of 2NNB.

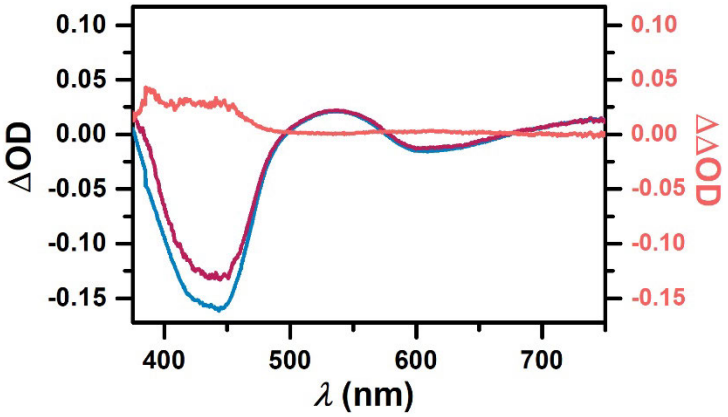

Figure S26: Mechanistic investigations of the triplet state of 2NNB by laser flash photolysis using 532 nm laser pulses. TA spectra of a solution of 100 µM RuPhen in the absence (blue) and presence (red) of 36 mM 2NNB in deaerated MeCN. The spectrum of RuPhen was scaled to match in the region >600 nm in order to determine the respective difference spectrum (orange).

Time-resolved measurements at the isosbestic point of RuPhen were not successful because of the weak absorption of ^{3}2NNB at 496 nm. To determine the triplet lifetime of 2NNB we compared the kinetic emission of RuPhen (at 600 nm, 39 ns lifetime) to the time-resolved transient absorption at 400 nm (superposition of the ground state bleach of RuPhen and absorption of ^{3}2NNB) (Figure S27). The RuPhen emission was appropriately scaled to match the minimum of the TA measurement. A lifetime analysis was unsuccessful due to the much shorter (< 20 ns) triplet lifetime of 2NNB.

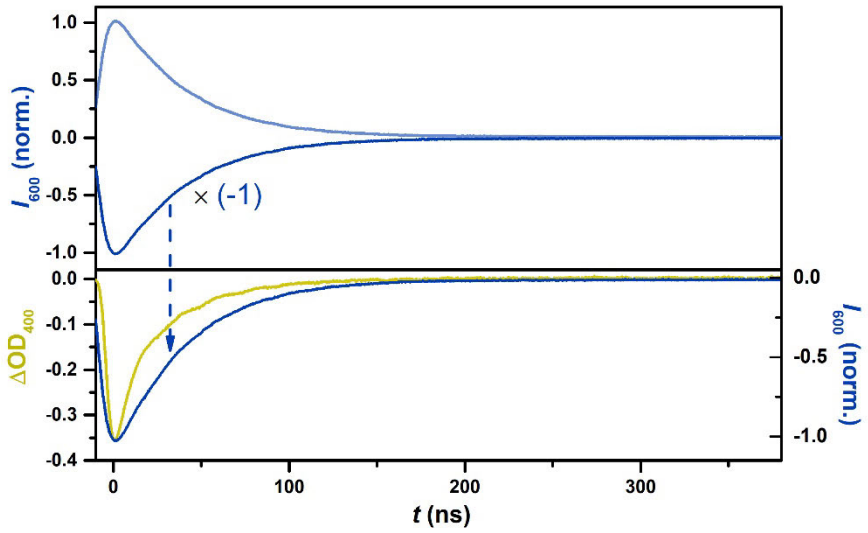

Figure S27: Time-resolved measurements of a solution of of 100 µM RuPhen and 36 mM 2NNB in deaerated MeCN upon 532 nm excitation. Blue traces display the kinetic emission at 600 nm. The dark yellow trace displays the kinetic transient absorption at 400 nm.

8.2. Steady-state absorption spectra

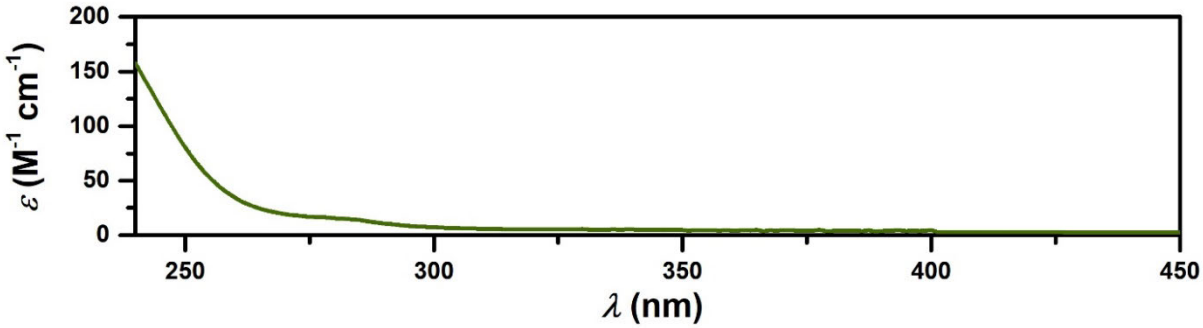

Figure S28: Molar absorption coefficient of NB (stabilized with dibutylhydroxytoluene) in MeCN plotted against the wavelength.

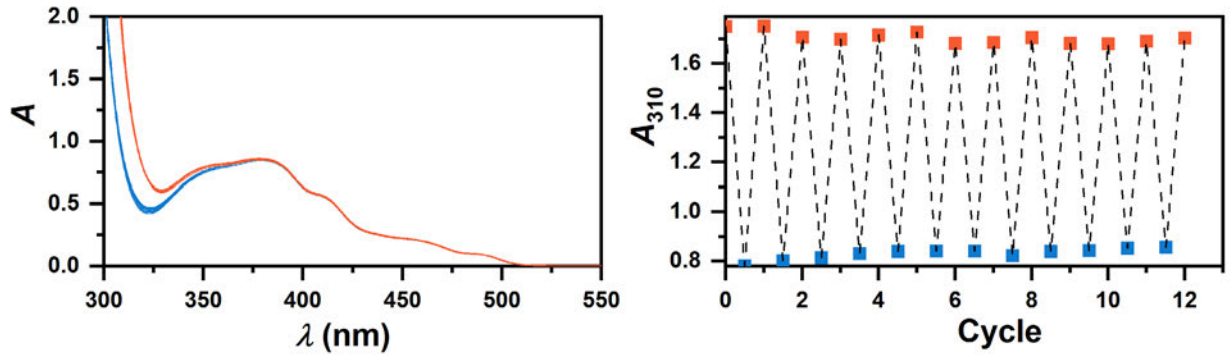

Figure S29: Right panel: Steady-state monitoring of multiple interconversions between Ph3NB and Ph3QC using $Ir(ppy)_3$ as sensitizer. Each isomerization cycle was performed by irradiation a solution of 300 μM Ph3NB with 50 μM $Ir(ppy)_3$ in Ar-saturated toluene at 440 nm for 4 min followed by heat treatment at 85°C for 1 h in a Schlenk cuvette. Left panel: Absorption changes at 310 nm displayed for 12 cycles.

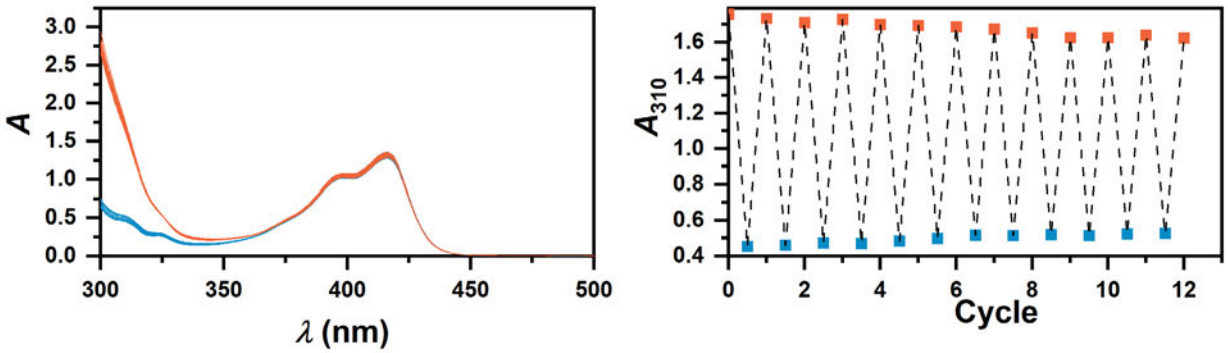

Figure S30: Right panel: Steady-state monitoring of multiple interconversions between Ph3NB and Ph3QC using MeOTX as sensitizer. Each isomerization cycle was performed by irradiation a solution of 400 μM Ph3NB with 245 μM MeOTX in Ar-saturated toluene at 440 nm for 4 min followed by heat treatment at 85°C for 1 h in a Schlenk cuvette. Left panel: Absorption changes at 310 nm displayed for 12 cycles.

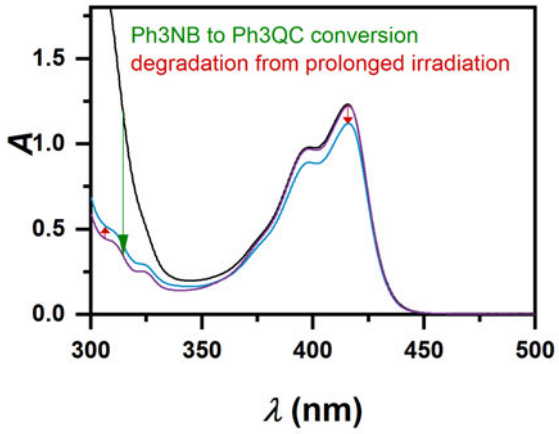

Figure S31: Steady-state absorption measurements of 245 µM MeOTX and 400 µM Ph3NB in Ar-saturated toluene. Absorption spectra were recorded before irradiation (black), after 4 min of photoirradiation using a 440 nm LED monitoring the Ph3NB to Ph3QC conversion (purple) and prolonged irradiation (another 4 min irradiation) leading to degradation of the sensitizer (blue).

A solution containing MeOTX and Ph3NB in Ar-saturated toluene was prepared and irradiated with a 440 nm LED (Figure S31). After 4 minutes of irradiation, the conversion to Ph3QC was complete (purple graph). Continued irradiation of the system resulted in the degradation of the sensitizer, as shown in the blue graph. This degradation is faster after the isomerization as a result of the unquenched triplet state of MeOTX.

8.3. Photostationary state composition of triplet sensitized 1NNB/1NQC

The photostationary state composition of triplet sensitized 1NNB/1NQC was investigated by steady-state and NMR spectroscopy in the presence of structurally similar triplet sensitizers. Thioxanthone (TX) and 2,7-dimethoxythioxanthone (MeOTX) exhibit triplet energies of 2.75 eV and 2.38 eV, respectively.[10] An adiabatic triplet state energy of 2.51 eV was estimated for 1NQC by DFT calculations (see Chapter S3), which should be accessible only by the sensitizer with higher triplet energy, TX, while 1NNB is sensitized by both TX and MeOTX.

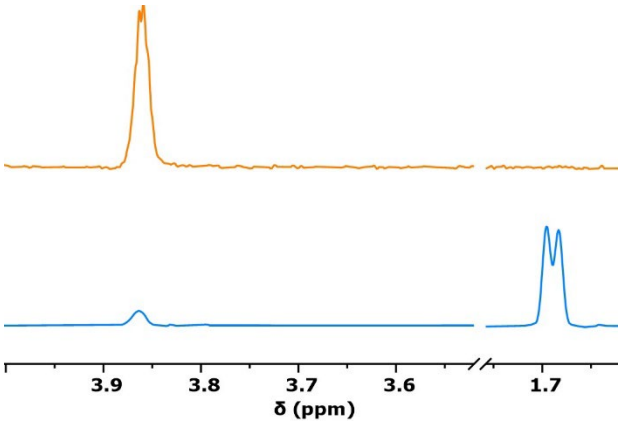

Figure S32: NMR spectra of 3 mM 1NNB and 10 mol% TX in degassed MeCN-d_3, before (top) and after (bottom) irradiation with a Thorlabs 405 nm LED (1 cm distance, 100%) for 1 h. A cut-off filter at 385 nm was used to avoid direct excitation of 1NNB.

An NMR irradiation experiment was conducted with 3 mM 1NNB and 10 mol% TX in Ar-saturated MeCN-d3, irradiating at 405 nm for 1 hour, resulting in a ratio of 7/93 (1NNB/1NQC) (Figure S32). Analogous irradiation experiments monitored by steady-state absorption at different irradiation time intervals of 150 µM 1NNB with either sensitizer confirm that a photostationary state composition is reached rapidly (Figure S33 and S34).

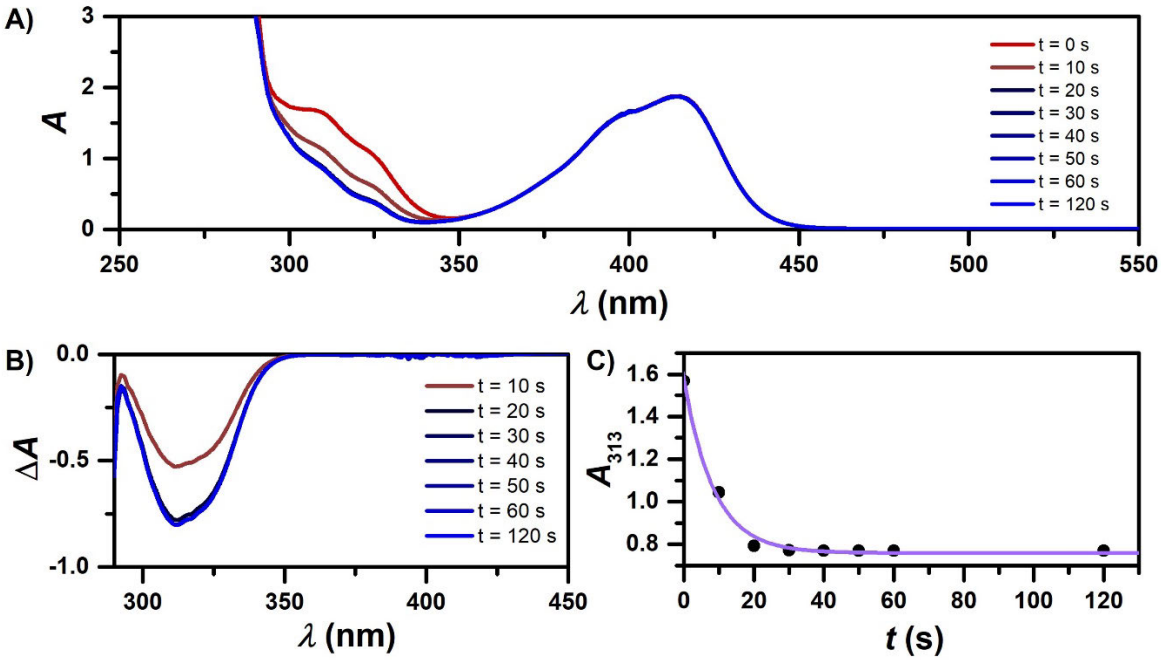

Figure S33: Steady-state absorption measurements of 385 µM MeOTX and 150 µM 1NNB in Ar-saturated MeCN irradiated with a 440 nm LED (25% and 10 cm distance). A) Absorption spectra recorded at different irradiation time intervals. B) Corresponding difference absorption. C) Absorption at 313 nm plotted against the irradiation time, fitted using an exponential decay function.

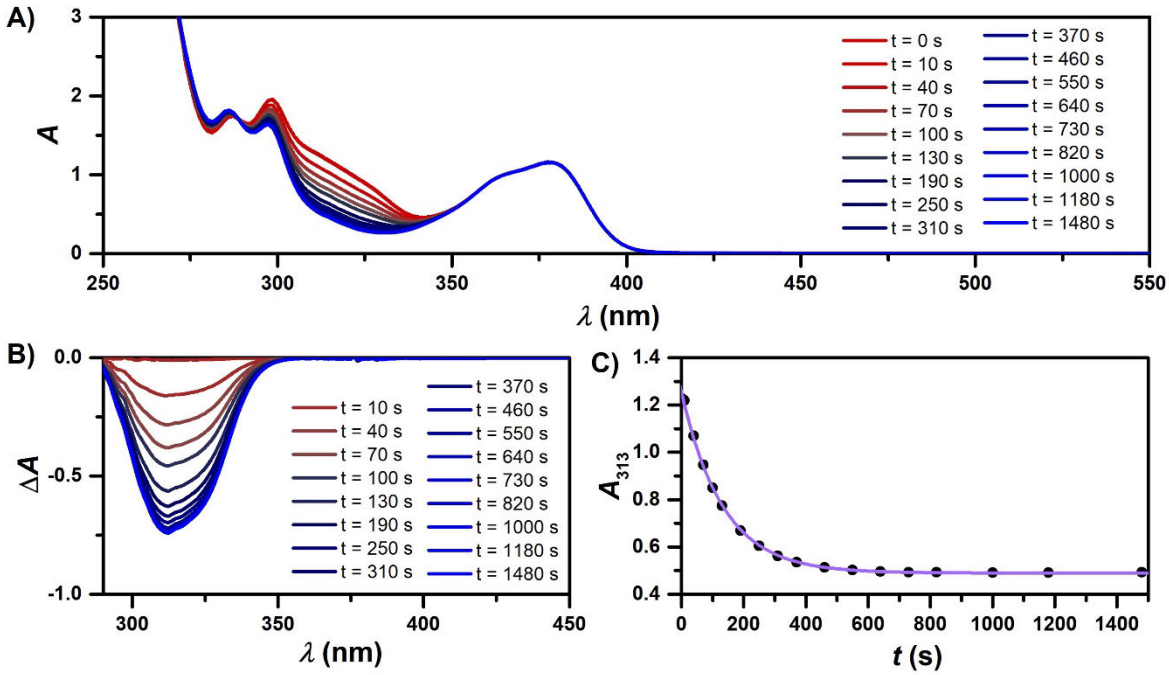

Figure S34: Steady-state measurements of 235 µM TX and 150 µM 1NNB in Ar-saturated MeCN irradiated with a 405 nm LED (100% and 1 cm distance). A) Absorption spectra recorded at different irradiation time intervals. B) Corresponding difference absorption spectra. C) Absorption at 313 nm plotted against the irradiation time, fitted using an exponential decay function.

Quantitative interconversion is achieved when MeOTX is employed as sensitizer (see Figure S40), we compared the relative changes in the absorption spectrum to estimate a ratio of 8/92 of 1NNB/1NQC at the photostationary state in the presence of TX (Figure S34), reflecting the results obtained by ^{1}H NMR spectroscopy. Further LFP experiments using 355 nm laser pulses for the excitation of 60 µM TX with 271 µM 1NNB in Ar-saturated MeCN were recorded during 440 nm LED irradiation (Figure S35B). The triplet state of TX is not luminescent, hence time-resolved transient absorption spectroscopy at 625 nm was used to monitor the quenching step by 1NNB/1NQC.[10] Concurrent steady-state absorption experiments confirm that the photostationary state was reached after 4 min of irradiation (Figure S35A). The lifetime of TX was virtually unchanged (346 ns at t = 0 min to 351 ns at t = 4 min) during irradiation suggesting that 1NNB and 1NQC quench TX with nearly identical rate constants, which would imply a ~50:50 ratio of 1NNB and 1NQC in the photostationary state. While quenching by 1NQC is feasible when a high triplet energy sensitizer such as TX is employed, the inherent switching efficiency of ^{3}1NQC to 1NNB seems to be low based on the results in Figure S32 (7:93 ratio). These results underline the very high interconversion efficiency of ^{3}1NNB to 1NQC obtained by relative actinometry (see Chapter S5).

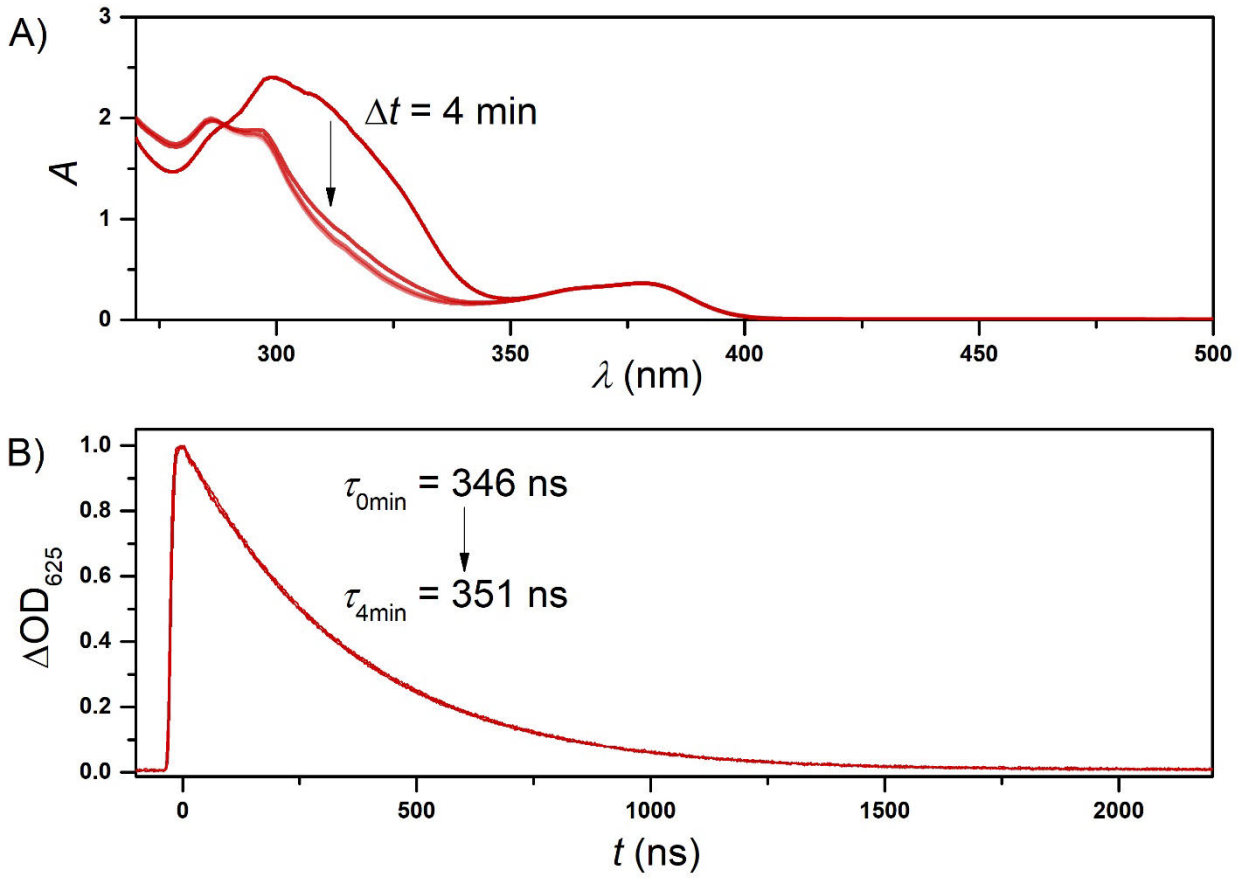

Figure S35: Mechanistic investigations of the isomerization of 271 µM 1NNB using 60 µM TX as triplet sensitizer in Ar-saturated MeCN. The solution was irradiated for 4 minutes with a 405 nm LED from Thorlabs. Measurements were taken within 1 minute intervals. A) Absorption spectra. B) Time-resolved transient absorption with 355 nm laser pulses detected at 625 nm.

9. Multiple conversion cycles of the $Ir(ppy)_3$–Ph3NB pair under solar irradiance

A solution of 100 mM Ph3NB with 590 µM $Ir(ppy)_3$ (0.59 mol%) and 26.9 mM bibenzyl (used as standard) in Ar-saturated deuterated toluene was prepared by three freeze-pump-thaw cycles and sealed in an NMR tube. The solution was exposed to sunlight for 45 min to 60 min. A 400 nm cut-off filter was used to avoid direct excitation of Ph3NB. The experimental setup is shown in Figure S36. The NMR tube was then heated to 85°C for 1 h recovering Ph3NB. This cycle was repeated five times over three days (27.08.2024-29.08.2024). After each step an NMR spectrum is recorded ensuring complete conversion to Ph3QC or Ph3NB (Figure S47). Bibenzyl served as the NMR standard allowing us to quantify the isomers. The solar irradiation times and dates, heating times and concentrations are displayed in Table S4.

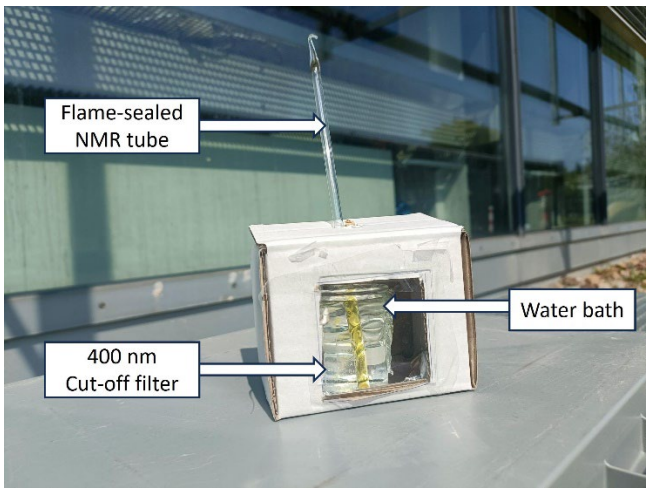

Figure S36: Experimental setup for the solar irradiation experiments of a solution of 100 mM Ph3NB with 590 µM $Ir(ppy)_3$ (0.59 mol%) and 26.9 mM bibenzyl in Ar-saturated deuterated toluene.

Table S4: Irradiation times, heating times, and concentrations of Ph3NB and Ph3QC across multiple conversion cycles of $Ir(ppy)_3$-Ph3NB. See Figure S47 for raw data sets.

Cycle	Irradiation time (min)[a]	Heating time (min)	Concentration (mM)[b]
0	–	–	100.0
0.5	60 min (16:45-17:45, 27.08.2024)	–	100.4
1	–	60 min	101.7
1.5	45 min (11:30-12:15, 28.08.2024)	–	98.4
2	–	60 min	98.2
2.5	45 min (15:30-16:15, 28.08.2024)	–	95.1
3	–	60 min	98.1
3.5	45 min (10:30-11:15, 29.08.2024)	–	98.1
4	–	60 min	97.2
4.5	45 min (14:00-14:45, 29.08.2024)	–	95.8
5	–	60 min	98.9

[a] No cloud coverage during irradiation. [b] Concentration of Ph3NB or Ph3QC determined by quantitative ^{1}H NMR spectroscopy.

10. NMR spectra

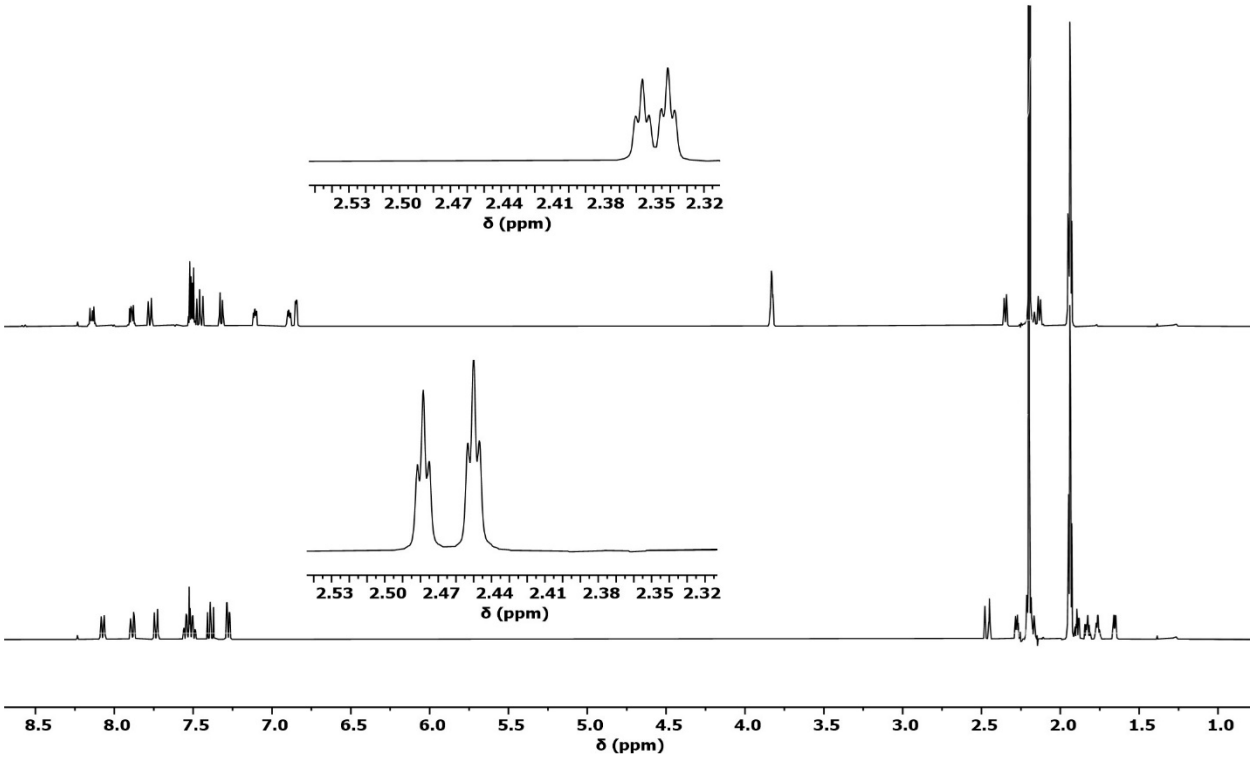

Figure S37: ^{1}H NMR spectra of a solution containing 30 mM 1NNB and 0.5 mol% RuPhen before (top) and after (bottom) 525 nm irradiation for 30 min in deuterated MeCN.

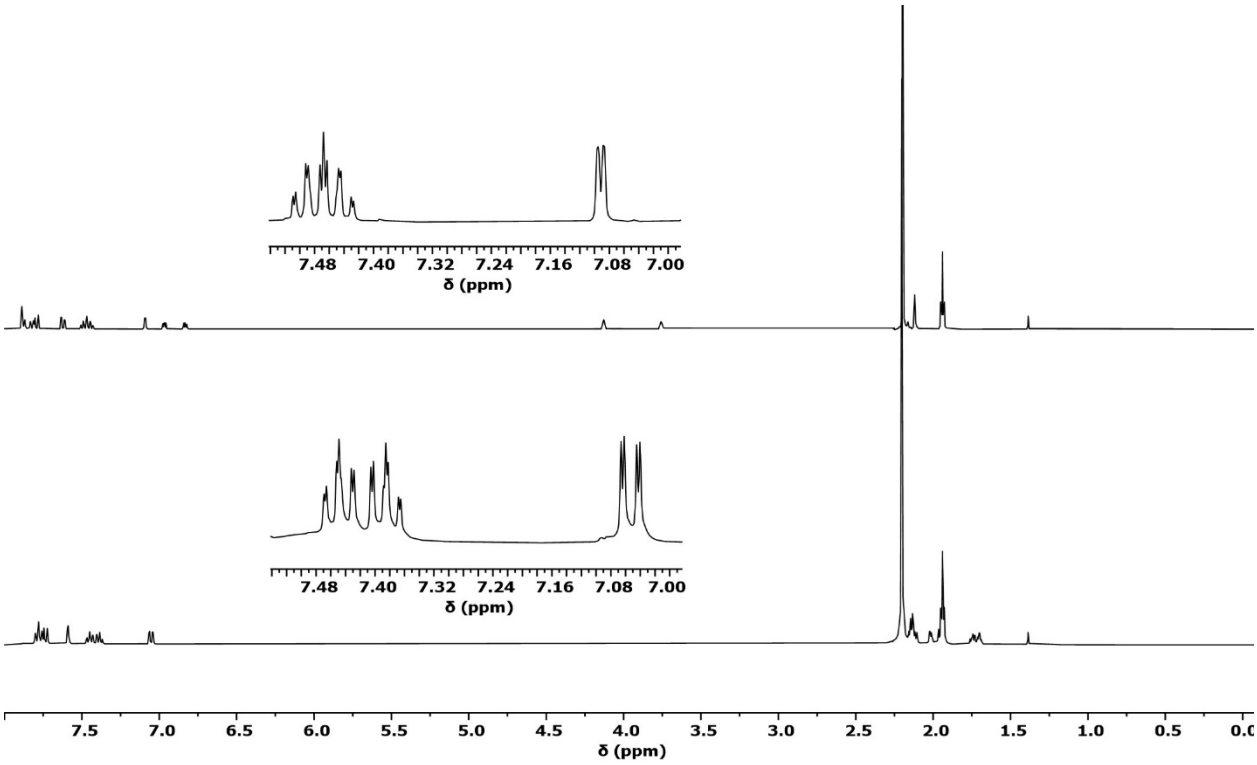

Figure S38: ^{1}H NMR spectra of a solution containing 36 mM 2NNB and 0.5 mol% RuPhen before (top) and after (bottom) 525 nm irradiation for 21 min in deuterated MeCN.

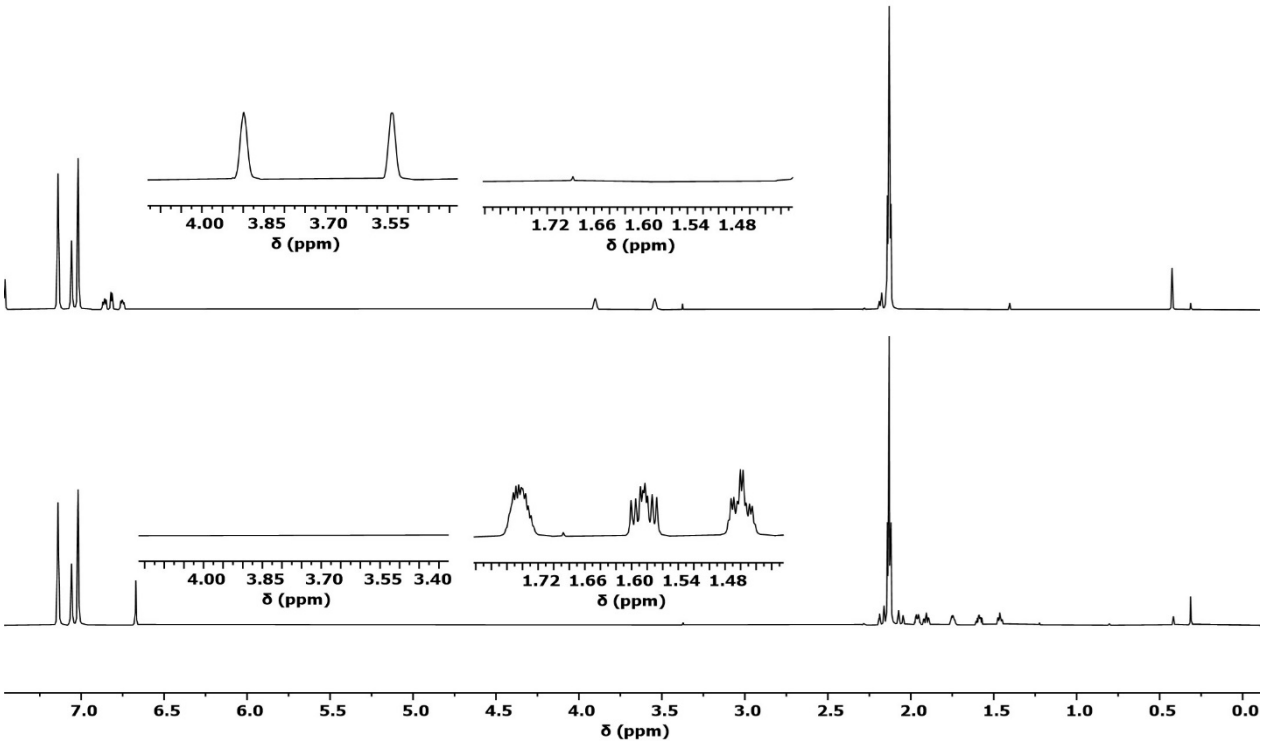

Figure S39: ^{1}H NMR spectra of a solution containing 5 mM Ph3NB and 5 mol% MeOTX before (top) and after (bottom) 440 nm irradiation for 30 min in deuterated toluene.

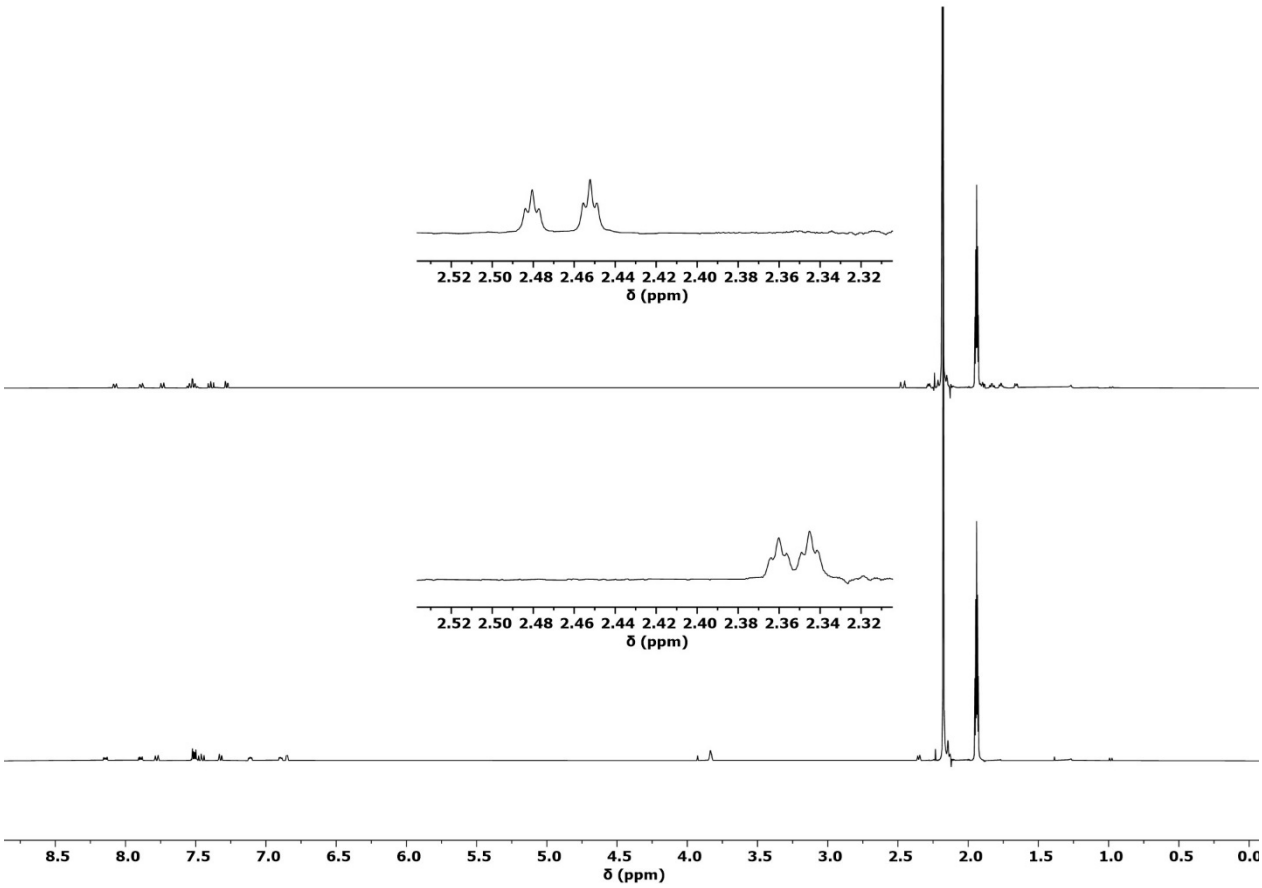

Figure S40: ^{1}H NMR spectra of a solution containing 5 mM 1NNB and 5 mol% MeOTX before (top) and after (bottom) 440 nm irradiation for 30 min in MeCN-d_3.

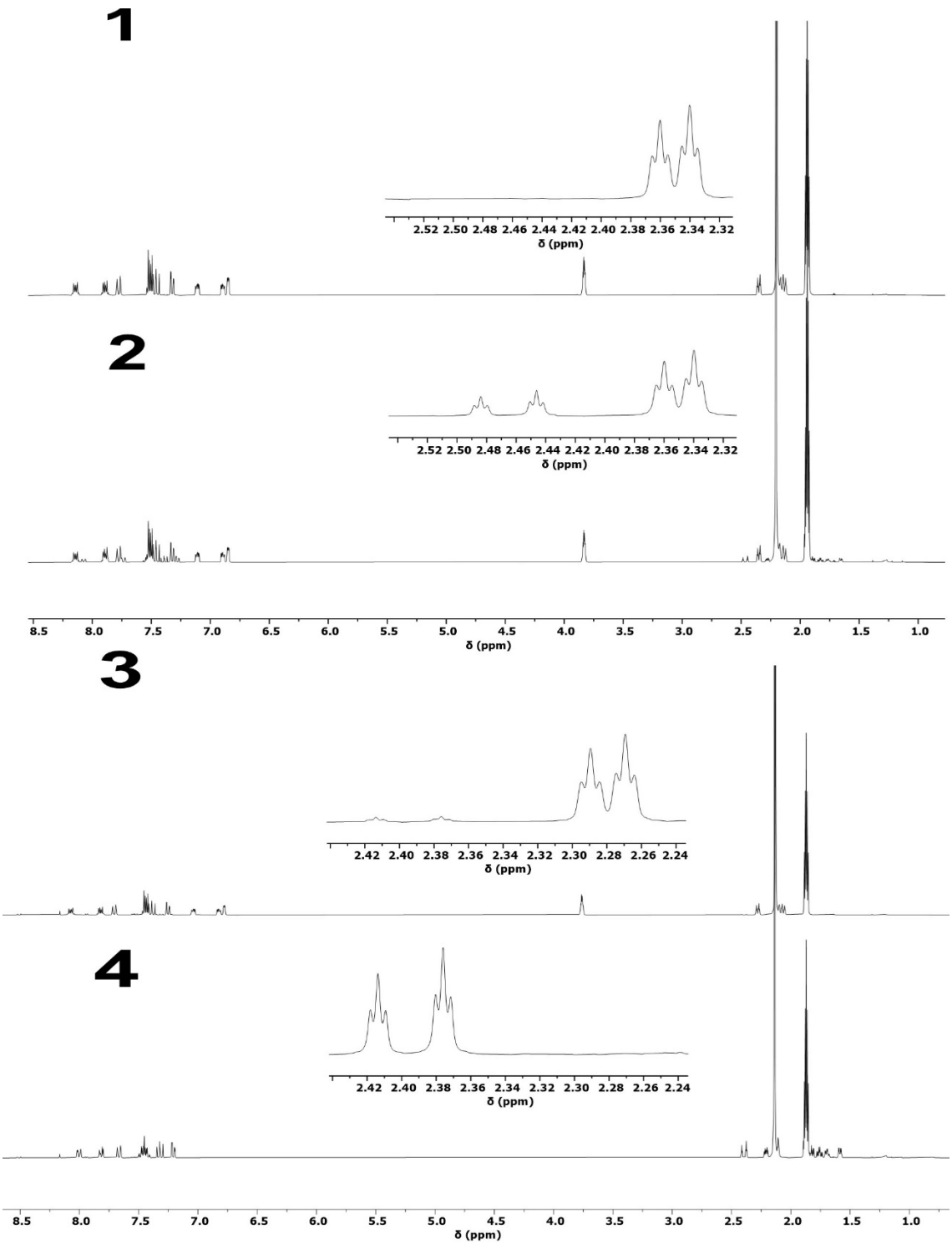

Figure S41: ^{1}H NMR experiment of 22.5 mM 1NNB in Ar-saturated MeCN-d_3 before (1) and after (2) solar irradiation. ^{1}H NMR experiment of 0.25 mM $[Ru(phen)_3](PF_6)_2$ with 22.5 mM 1NNB in Ar-saturated MeCN-d_3 before (3) and after (4) solar irradiation (date: 06.09.2022, time: 2.00 pm – 3.30 pm , 21-22 °C). For experimental setup see Figure S42.

.

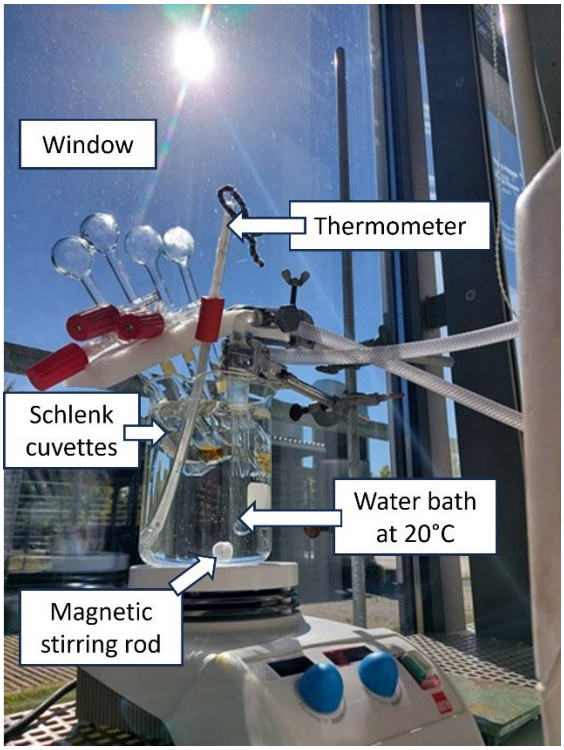

Figure S42: Experimental setup for solar irradiation experiment (corresponding ^{1}H NMR data sets can be found in Figure S41).

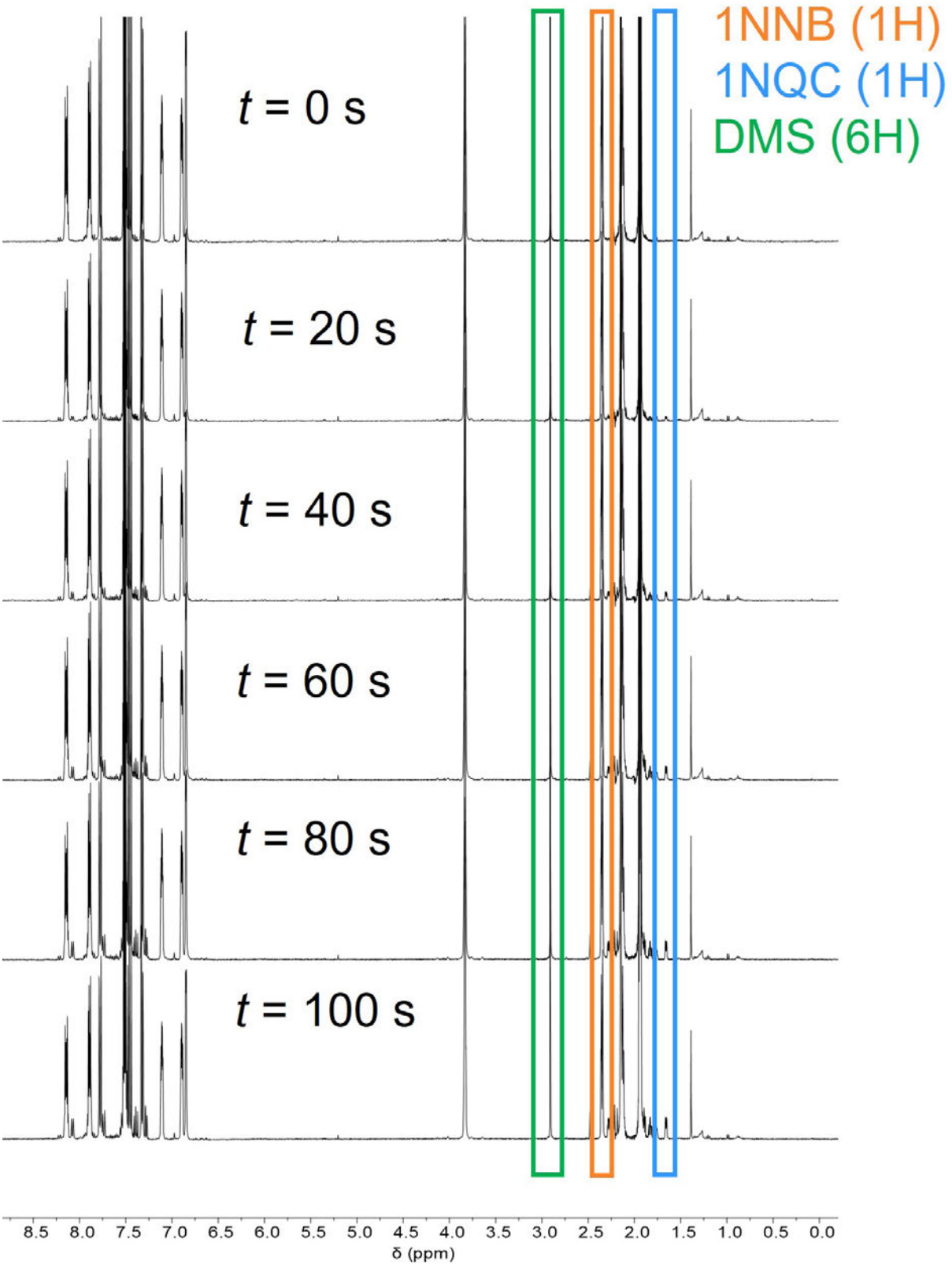

Figure S43: ^{1}H NMR spectra of an Ar-saturated solution containing 23.4 µM $Ir(ppy)_3$, 29.1 mM 1NNB, and 2.53 mM DMS. The spectra were recorded during irradiation with a 440 nm LED (set to 25%, 8 cm distance) with intervals of 20 s. See Chapter S5 for details.

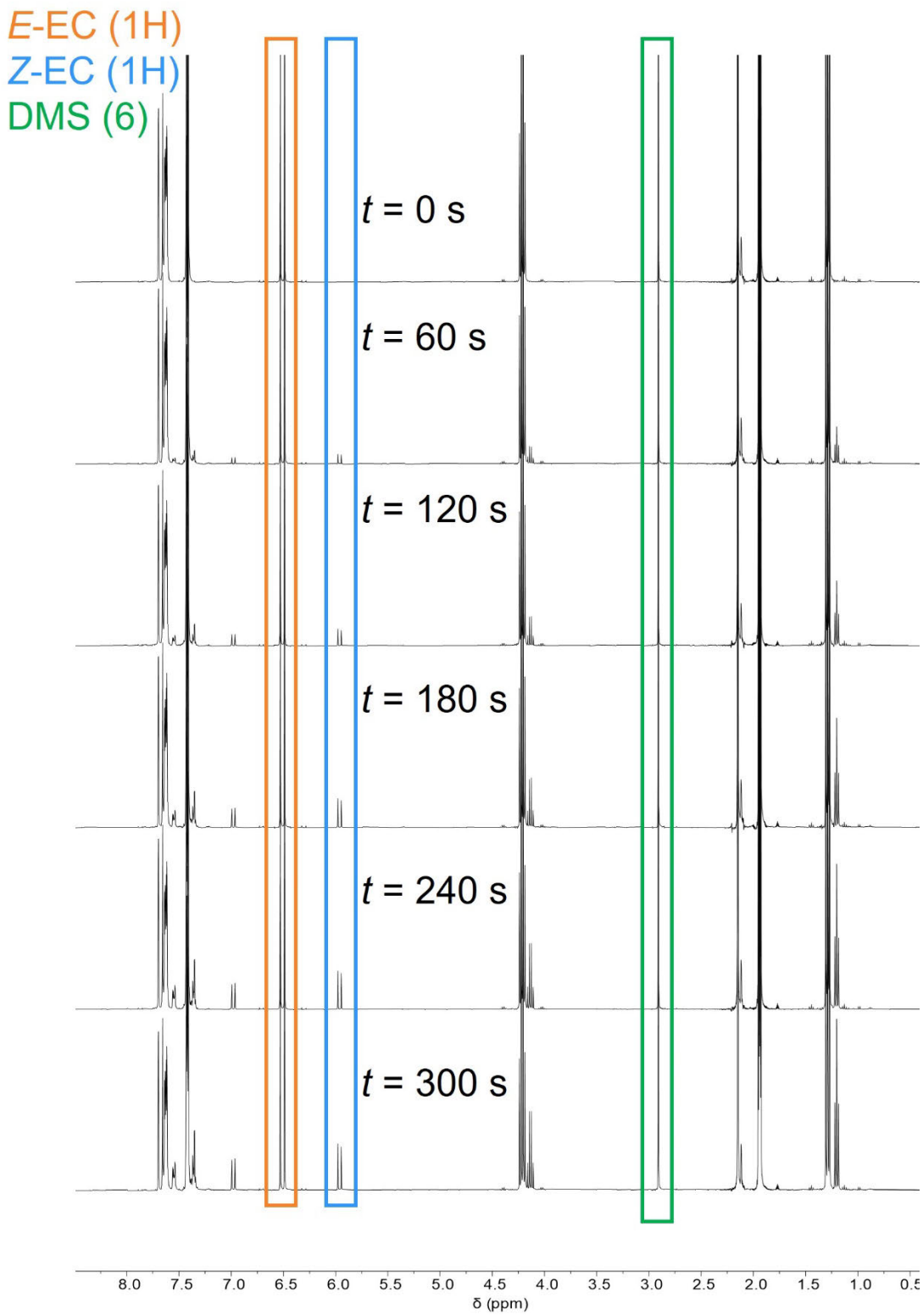

Figure S44: ^{1}H NMR spectra of an Ar-saturated solution containing 23.4 µM Ir(ppy)$_3$, 30.5 mM *E*-EC, and 2.53 mM DMS. The spectra were recorded during irradiation with a 440 nm LED (set to 25%, 8 cm distance) with intervals of 60 s. See Chapter S5 for details.

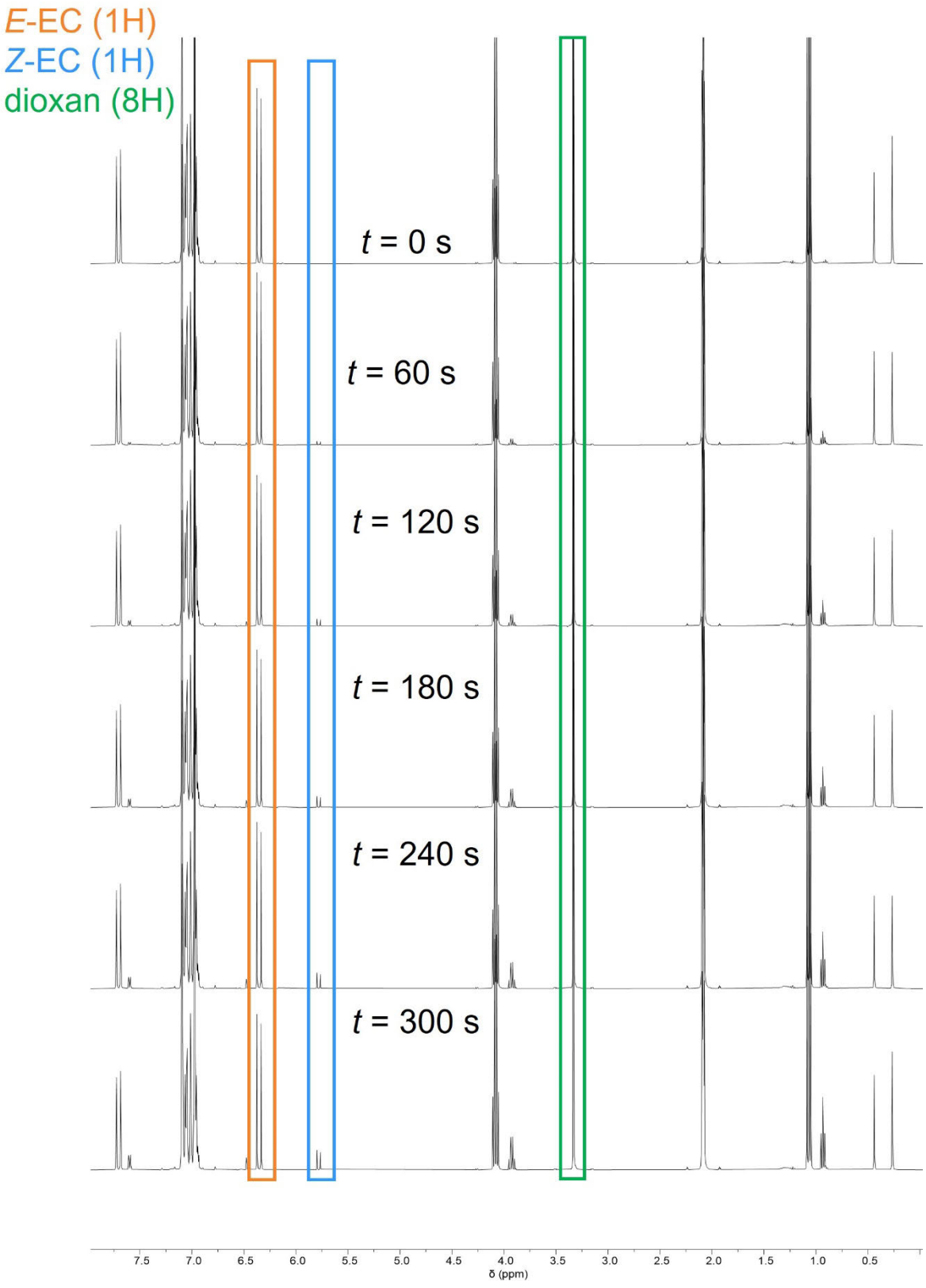

Figure S45: ^{1}H NMR spectra of an Ar-saturated toluene-d_8 solution containing 23.0 µM Ir(ppy)$_3$, 30.0 mM *E*-EC, and 10.0 mM dioxan. The spectra were recorded during irradiation with a 440 nm LED (set to 25%, 8 cm distance) with intervals of 60 s. See Chapter S6 for details.

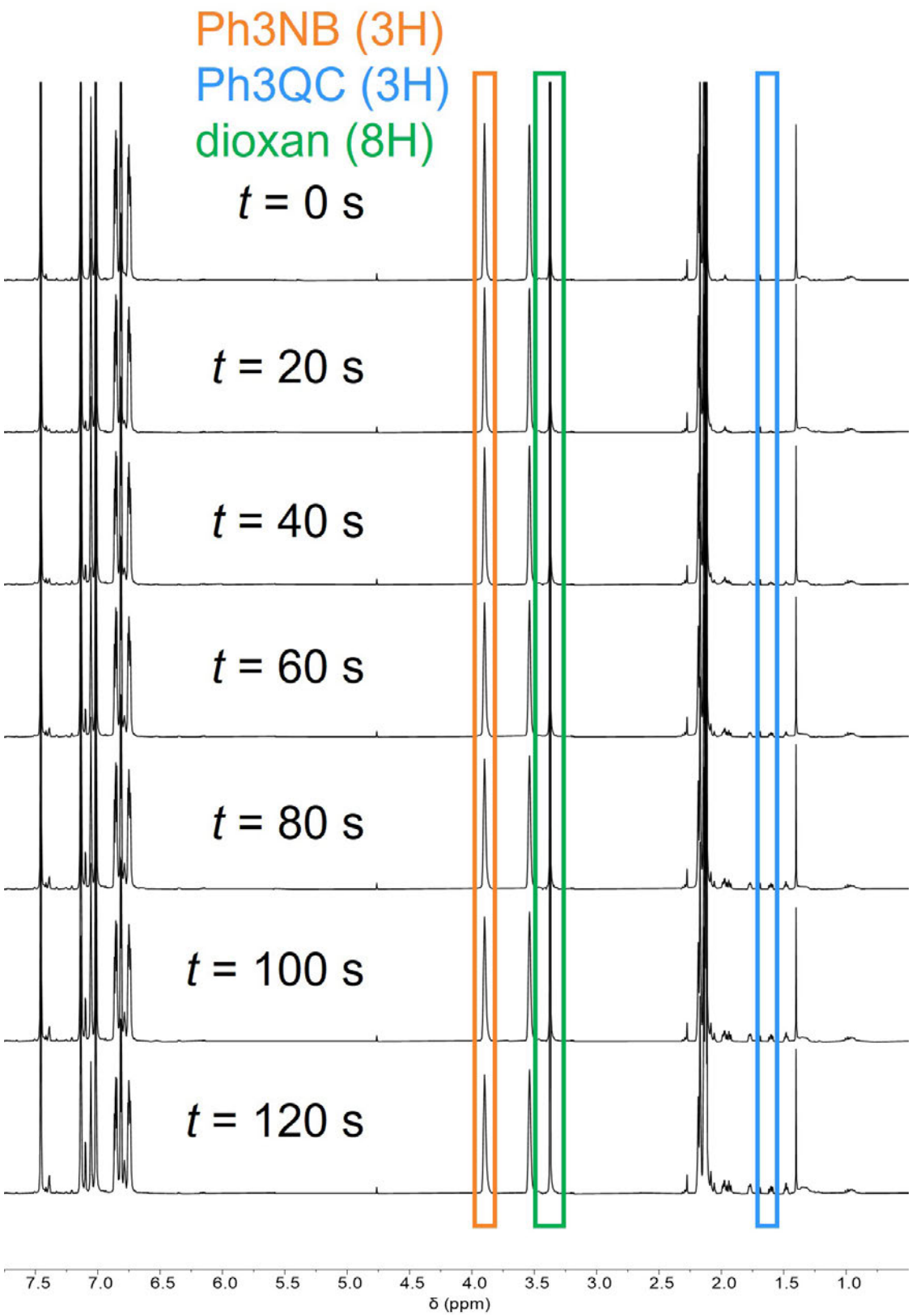

Figure S46: ^{1}H NMR spectra of an Ar-saturated toluene-d_8 solution containing 23 µM Ir(ppy)$_3$, 20 mM Ph3NB, and 10.0 mM dioxan. The spectra were recorded during irradiation with a 440 nm LED (set to 25%, 8 cm distance) with intervals of 20 s. See Chapter S6 for details.

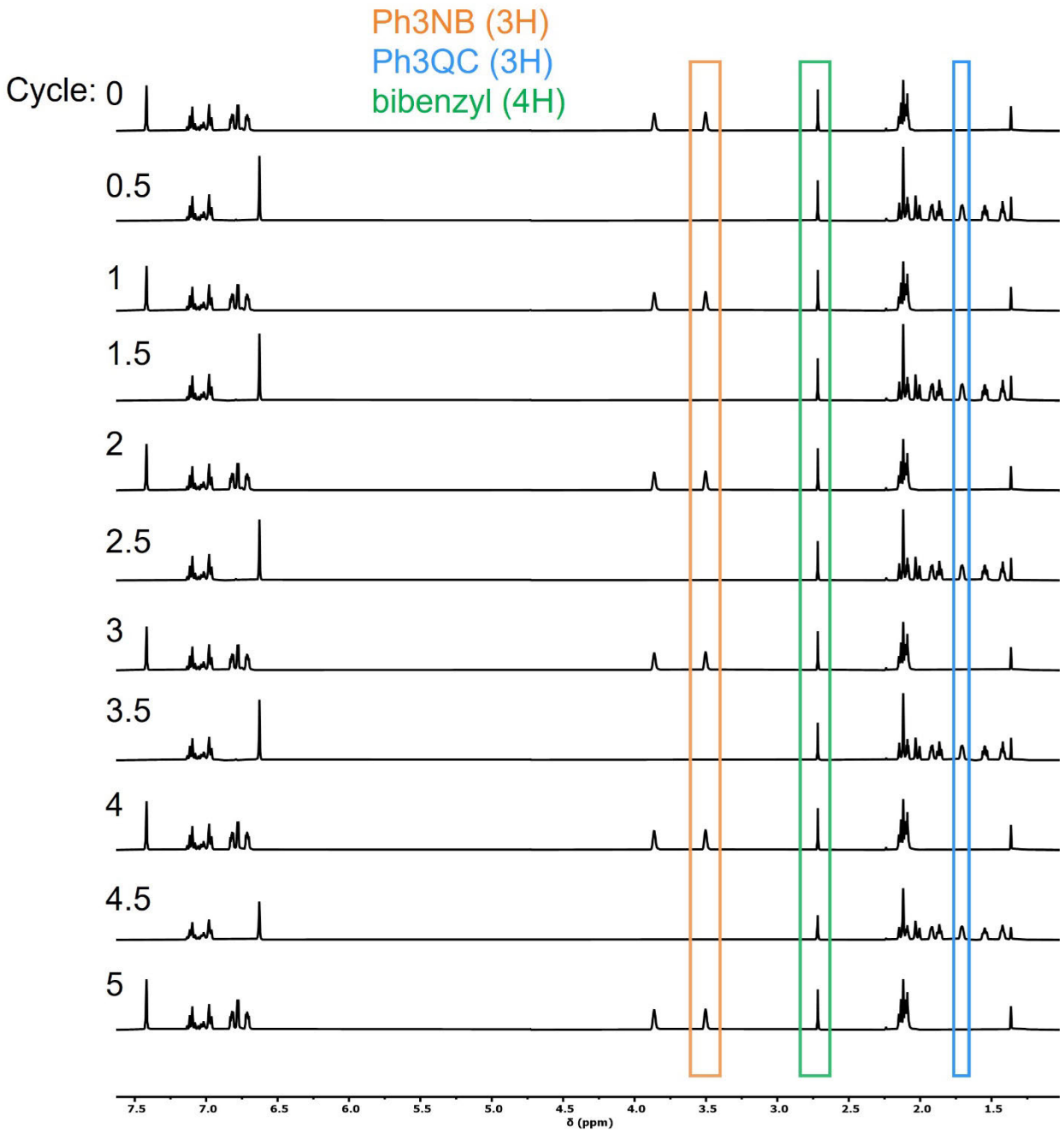

Figure S47: ^{1}H NMR spectra of an Ar-saturated toluene-d_8 solution containing 590 µM Ir(ppy)$_3$, 100 mM Ph3NB, and 26.9 mM bibenzyl. The spectra were recorded for five conversion cycles. See Chapter S9 for details.

11. Literature

[1] T. J. B. Zähringer, M.-S. Bertrams, C. Kerzig, *J. Mater. Chem. C* **2022**, *10*, 4568–4573.
[2] E. C. Constable, P. R. Raithby, D. N. Smit, *Polyhedron* **1989**, *8*, 367–369.
[3] M. S. Lowry, W. R. Hudson, R. A. Pascal, S. Bernhard, *J. Am. Chem. Soc.* **2004**, *126*, 14129–14135.
[4] R. Schulte, H. Ihmels, *Beilstein J. Org. Chem.* **2022**, *18*, 368–373.
[5] R. Schulte, S. Afflerbach, H. Ihmels, *Eur. J. Org. Chem.* **2023**, *26*, e202201398.

[6] R. Schulte, S. Afflerbach, T. Paululat, H. Ihmels, *Angew. Chem. Int. Ed.* **2023**, *62*, e202309544.
[7] O. Baumgärtel, G. Szeimies, *Chem. Ber.* **1983**, *116*, 2180–2204.
[8] F. Neese, *WIREs Comput. Mol. Sci.* **2012**, *2*, 73–78.
[9] M. D. Hanwell, D. E. Curtis, D. C. Lonie, T. Vandermeersch, E. Zurek, G. R. Hutchison, *J. Cheminformatics* **2012**, *4*, 17.
[10] T. J. B. Zähringer, M. Wienhold, R. Gilmour, C. Kerzig, *J. Am. Chem. Soc.* **2023**, *145*, 21576–21586.
[11] A. A. Vlcek, E. S. Dodsworth, W. J. Pietro, A. B. P. Lever, *Inorg. Chem.* **1995**, *34*, 1906–1913.
[12] Y. Wei, Y. Li, Z. Li, X. Xu, X. Cao, X. Zhou, C. Yang, *Inorg. Chem.* **2021**, *60*, 19001–19008.
[13] V. Balzani, F. Bolletta, F. Scandola, *J. Am. Chem. Soc.* **1980**, *102*, 2152–2163.
[14] A. M. Helms, Richard. A. Caldwell, *J. Am. Chem. Soc.* **1995**, *117*, 358–361.
[15] I. Antol, *J. Comput. Chem.* **2013**, *34*, 1439–1445.
[16] K. Raghavachari, R. C. Haddon, H. D. Roth, *J. Am. Chem. Soc.* **1983**, *105*, 3110–3114.
[17] M. Montalti, A. Credi, L. Prodi, M. T. Gandolfi, *Handbook of Photochemistry*, CRC Press, **2006**.
[18] Y. Shindo, K. Horie, I. Mita, *J. Photochem.* **1984**, *26*, 185–192.
[19] N. J. Turro, W. R. Cherry, M. F. Mirbach, M. J. Mirbach, *J. Am. Chem. Soc.* **1977**, *99*, 7388–7390.
[20] K. Nakabayashi, H. Nishino, S. Toki, S. Takamuku, *Int. J. Radiat. Appl. Instrum. Part C Radiat. Phys. Chem.* **1989**, *34*, 809–815.
[21] Z. Wang, J. Udmark, K. Börjesson, R. Rodrigues, A. Roffey, M. Abrahamsson, M. B. Nielsen, K. Moth-Poulsen, *ChemSusChem* **2017**, *10*, 3049–3055.
[22] Z. Wang, A. Roffey, R. Losantos, A. Lennartson, M. Jevric, A. U. Petersen, M. Quant, A. Dreos, X. Wen, D. Sampedro, K. Börjesson, K. Moth-Poulsen, *Energy Environ. Sci.* **2019**, *12*, 187–193.
[23] "The American Society for Testing and Materials (ASTM) G-173, 'Reference Air Mass 1.5 Spectra,'" can be found under https://www.nrel.gov/grid/solar-resource/spectra.html, **2003**.
[24] T. Hofbeck, H. Yersin, *Inorg. Chem.* **2010**, *49*, 9290–9299.
[25] A. Juris, V. Balzani, F. Barigelletti, S. Campagna, P. Belser, A. Von Zelewsky, *Coord. Chem. Rev.* **1988**, *84*, 85–277.

10.9 Supporting Information for Project [H]

BEILSTEIN JOURNAL OF ORGANIC CHEMISTRY

Supporting Information

for

Extension of the π-system of monoaryl-substituted norbornadienes with acetylene bridges: influence on the photochemical conversion and storage of light energy

Robin Schulte, Dustin Schade, Thomas Paululat, Till J. B. Zähringer, Christoph Kerzig and Heiko Ihmels

Beilstein J. Org. Chem. **2024,** *20,* 3061–3068. doi:10.3762/bjoc.20.254

Experimental section and complete set of NMR spectra

License and Terms: This is a supporting information file under the terms of the Creative Commons Attribution License (https://creativecommons.org/licenses/by/4.0). Please note that the reuse, redistribution and reproduction in particular requires that the author(s) and source are credited and that individual graphics may be subject to special legal provisions.
The license is subject to the *Beilstein Journal of Organic Chemistry* terms and conditions: (https://www.beilstein-journals.org/bjoc/terms)

Table of contents

S1 Equipment S2
S2 Methods S2
S3 Material S3
S4 Synthesis S3
S5 Absorption properties of norbornadiene derivatives **1h–l**, **n** S8
S6 Photoreactions and photoisomerization quantum yields S9
S7 Quenching experiments of $[Ru(phen)_3](PF_6)_2$ with **1i** S11
S8 Kinetic studies of the thermal back reaction S12
S9 NMR spectra S14
S9.1 Structure elucidation S14
S10 References S34

S1 Equipment

The NMR spectra were recorded on a JEOL ECZ 500 spectrometer (^{1}H: 500 MHz, ^{13}C: 125 MHz, 25 °C) or on a Varian VNMR-S 600 (^{1}H: 600 MHz, ^{13}C: 150 MHz, 25 °C). In-situ irradiation inside the NMR spectrometer was done with a self-made irradiation setup in a Varian VNMR-S 600.[1] The spectra were referenced to tetramethylsilane in $CDCl_3$ [$\delta(^1H)$ = 0.00 ppm] or residual solvent signals in $CDCl_3$ [$\delta(^{13}C)$ = 77.2 ppm] or benzene-d_6 [$\delta(^1H)$ = 7.16 ppm, $\delta(^{13}C)$ = 128.0 ppm] and processed with the MestReNova software. The melting points were determined with a Büchi 545 (Büchi, Flawil, CH) and are uncorrected. Elemental analysis data were determined in-house (Organic Chemistry, University of Siegen) on a HEKAtech EUROEA combustion analyzer. The absorption spectra were measured on a Varian Cary 100 Bio absorption spectrometer or on a Analytik Jena SPECORD S spectrometer with Hellma quartz glass cuvettes 115 F-QS (d = 10 mm). If not stated otherwise, the absorption measurements were recorded at T = 20 °C as adjusted with a thermostat. The spectra were processed with the software Origin with the implemented smoothing function “adjacent averaging” with the factor of 10.[2] Photoreactions were performed with Thorlabs LED lamp M310L1, Thorlabs LED M340L5, Conrad LED520 (181862) or a LUMOS 43 from Atlas Photonics.The LP980KS setup from Edinburgh Instruments, equipped with an Nd:YAG laser from Litron (Nano LG 300-10) and an Nd:YAG Quantel (Q-smart 450), was employed for transient absorption and time-resolved emission spectroscopy. The frequency-doubled (532 nm) output served as the excitation source. The laser pulse duration was ≈5 ns and the pulse frequency was 10 Hz. The typical pulse energy used for transient absorption and emission studies was ≈20 mJ. A constant laser pulse energy was used within a series of experiments, which was ensured by power measurements before, after and in-between the experiments. The laser power was measured using a pyroelectric detector with attenuator (QE25LP-S-MB-QED-D0) from Gentec-eo combined with the integra software. Detection of transient absorption spectra occurred on an iCCD camera from Andor. Kinetic traces at selected wavelengths were recorded using a photomultiplier tube. The spectroscopic experiments were performed at 293 K using a cuvette holder that allows temperature control. If not stated otherwise the TA spectra were integrated over 100 ns.

S2 Methods

Reaction mixtures were stirred with a magnetic stirring bar. Reaction temperatures refer to the medium that surrounded the reaction vessel. Solvents were usually removed under reduced pressure at 40 °C with a rotatory evaporator. The room temperature (rt) was approx. 22 °C. Air- and/or water-sensitive reactions were carried out under inert atmosphere with Schlenk equipment. The triplet energy transfer rate constant was determined by a Stern–Volmer analysis. This was achieved by lifetime-based measurements of $[Ru(phen)_3](PF_6)_2$ (τ) with varying concentrations c_i of the quencher and fitted according to the Stern–Volmer equation shown below (Equation S1).

$$\frac{\tau_0}{\tau_i} = k_{EnT} \cdot c_i \cdot \tau_0 + 1 \qquad \text{(S1)}$$

S3 Material

Commercially available reagents were obtained from Carbolution [$PdCl_2(PPh_3)_2$], Chemsolute (NEt_3), Riedel de Haen (CuI), Sigma–Aldrich {[$Ru(phen)_3$]Cl_2, 98%}, and Carl Roth, (NH_4PF_6, 98%). 2-Bromonorbornadiene[3], 1-ethynylnaphthalene[4], 2-ethynylnaphthalene[5], 1,4-diethynylbenzene[6], 1,3-diethynylbenzene[6], 1,3,5-triethynyl-benzene[6], 1,4-diethynylnaphthalene[7], and 2,6-diethynylnaphthalene[8] were synthesized according to the literature protocols. The derivatives **1h**–**n** were stored at −30 °C. Technical-grade solvents were distilled prior to use. Column chromatography was carried out with CHROMABOND Flash RS15 (25 µm, capacity: 12 mg–3.6 g).

S4 Synthesis

General procedure (GP A) for the Pd-catalyzed Sonogashira–Hagihara coupling reactions

Under anaerobic conditions, the acetylenes **3a**–**g** (654 µmol–1.23 mmol) were added to a suspension of 2-bromonorbornadiene (**1g**, 1.24 mmol–7.38 mmol), $PdCl_2(PPh_3)_2$ (65.4 µmol–123 µmol), CuI (65.4 µmol–123 µmol) and NEt_3 (2.0 mL–10 mL) in THF (10 mL–25 mL). The resulting mixture was stirred at rt for 18 h. The solvents were removed under reduced pressure and the remaining crude was purified by column chromatography.

1-(Bicyclo[2.2.1]hepta-2,5-dien-2-ylethynyl)naphthalene (**1h**)

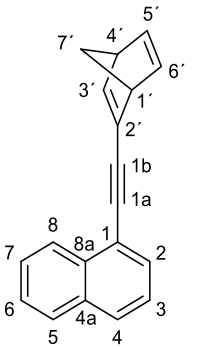

According to GP A, a suspension of 1-ethynylnaphthalene (**3a**, 126 mg, 826 µmol), 2-bromonorbornadiene (**1g**, 212 mg, 1.24 mmol), $PdCl_2(PPh_3)_2$ (57.9 mg, 82.6 µmol), CuI (15.7 mg, 82.6 µmol), and NEt_3 (2.0 mL) in THF (10 mL) was stirred at rt for 18 h. The crude product was purified by column chromatography (*n*-hexane/EtOAc, 99/1, *v*/*v*, R_f = 0.40) to give **1h** as a yellow oil (120 mg, 496 µmol, 60%). – ^{1}H NMR (500 MHz, $CDCl_3$): δ = 2.14 (dt, 1H, ^2J = 6.3 Hz, ^3J = 1.5 Hz, 7´-H), 2.24 (dt, 1H, ^2J = 6.3 Hz, ^3J = 1.5 Hz, 7´-H), 3.73–3.76 (m, 1H, 4´-H), 3.78–3.80 (m, 1H, 1´-H), 6.79 (dd, 1H, ^3J = 4.8 Hz, ^3J = 3.0 Hz, 5´-H), 6.96 (dd, 1H, ^3J = 4.8 Hz, ^3J = 3.0 Hz, 6´-H), 7.11 (d, 1H, ^3J = 3.1 Hz, 3´-H), 7.41 (dd, 1H, ^3J = 8.2 Hz, ^3J = 7.1 Hz, 3-H), 7.50–7.53 (m, 1H, 6-H), 7.55–7.58 (m, 1H, 7-H), 7.65 (dd, 1H, ^3J = 7.2 Hz, ^4J = 1.2 Hz, 2-H), 7.79 (d, 1H, ^3J = 8.2 Hz, 4-H), 7.83–7.85 (m, 1H, 5-H), 8.32–8.34 (m, 1H, 8-H). – ^{13}C NMR (125 MHz, $CDCl_3$): δ = 51.3 (C4´), 56.1 (C1´), 73.7 (C7´), 91.2 (C1b), 95.6 (C1a), 121.5 (C4a), 125.4 (C3), 126.4 (C6), 126.5 (C8), 126.7 (C7), 128.3 (C5), 128.6 (C4), 130.0 (C2), 133.1 (C8a), 133.6 (C1), 138.4 (C2´), 142.6 (C5´), 143.0 (C6´), 148.5 (C3´). – El. Anal. for $C_{19}H_{14}$: calc. (%): C 94.18, H 5.82. found (%): C 93.56, H 6.03.

2-(Bicyclo[2.2.1]hepta-2,5-dien-2-ylethynyl)naphthalene (**1i**)

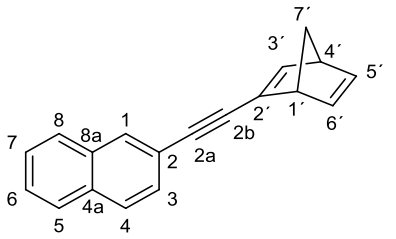

According to GP A, a suspension of 2-ethynylnaphthalene (**3b**, 126 mg, 826 µmol), 2-bromonorbornadiene (**1g**, 212 mg, 1.24 mmol), $PdCl_2(PPh_3)_2$ (57.9 mg, 82.6 µmol), CuI (15.7 mg, 82.6 µmol), and NEt_3 (2.0 mL) in THF (10 mL) was stirred at rt for 18 h. The crude product was purified by column chromatography (*n*-hexane/EtOAc, 99/1, *v*/*v*, R_f = 0.35) to give **1i** as colorless amorphous solid (136 mg, 562 µmol, 68%); mp 79–81 °C. – ^{1}H NMR (500 MHz, $CDCl_3$): δ = 2.11 (dt, 1H, ^2J = 6.3 Hz, ^3J = 1.5 Hz, 7´-H), 2.19 (dt, 1H, ^2J = 6.3 Hz, ^3J = 1.5 Hz, 7´-H), 3.70–3.73 (m, 2H, 1´-H, 4´-H), 6.76–6.78 (m, 1H, 5´-H), 6.92–6.94 (m, 1H, 6´-H), 7.05–7.06 (m, 1H, 3´-H), 7.45–7.50 (m, 3H, 3-H, 6-H, 7-H), 7.76–7.81 (m, 3H, 4-H, 5-H, 8-H), 7.94–7.96 (m, 1H, 1-H). – ^{13}C NMR (125 MHz, $CDCl_3$): δ = 51.3 (C4´), 55.9 (C1´), 73.7 (C7´), 86.6 (C2b), 97.9 (C2a), 121.1 (C2), 126.6 (C6), 126.7 (C7), 127.8 (C5), 127.9 (C8), 128.0 (C4), 128.4 (C3), 131.0 (C1), 132.8 (C4a), 133.1 (C8a), 138.4 (C2´), 142.6 (C5´), 142.9 (C6´), 149.6 (C3´). – El. Anal. for $C_{19}H_{14}$: calc. (%): C 94.18, H 5.82. found (%): C 94.17, H 5.95.

1,4-Bis(bicyclo[2.2.1]hepta-2,5-dien-2-ylethynyl)benzene (**1j**)

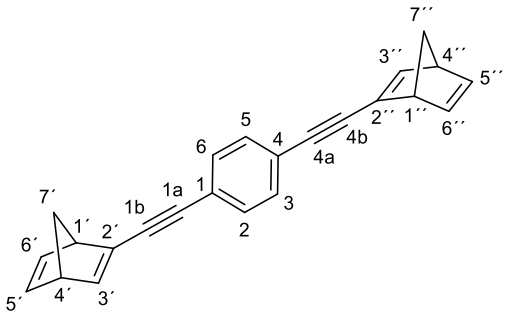

According to GP A, a suspension of 1,4-diethynylbenzene (**3c**, 82.4 mg, 654 µmol), 2-bromonorbornadiene (**1g**, 392 mg, 2.29 mmol), $PdCl_2(PPh_3)_2$ (45.9 mg, 65.4 µmol), CuI (12.4 mg, 65.4 µmol), and NEt_3 (2.0 mL) in THF (10 mL) was stirred at rt for 18 h. The crude product was purified by column chromatography (*n*-hexane, R_f = 0.19) to give **1j** as a yellow amorphous solid (55.0 mg, 180 µmol, 28%); mp 155–160 °C (dec.). – ^{1}H NMR (500 MHz, $CDCl_3$): δ = 1.91 (dt, 2H, ^2J = 6.2 Hz, ^3J = 1.6 Hz, 7´-H, 7´´-H), 2.01 (dt, 2H, ^2J = 6.2 Hz, ^3J = 1.6 Hz, 7´-H, 7´´-H), 3.24–3.31 (m, 2H, 4´-H, 4´´-H), 3.57–3.62 (m, 2H, 1´-H, 1´´-H), 6.49 (dd, 2H, ^3J = 4.9 Hz, ^3J = 3.0 Hz, 5´-H, 5´´-H), 6.71 (dd, 2H, ^3J = 4.9 Hz, ^3J = 2.7 Hz, 6´-H, 6´´-H), 6.88 (d, 2H, ^3J = 3.2 Hz), 7.26 (s, 4H, 2-H, 3-H, 5-H, 6-H). – ^{13}C NMR (125 MHz, $CDCl_3$): δ = 51.5 (C4´, C4´´), 56.2 (C1´, C1´´), 73.6 (C7´, C7´´), 88.7 (C1b, C4b), 97.9 (C1a, C4a), 123.9 (C1, C4), 131.5 (C2, C3, C5, C6), 138.4 (C2´, C2´´), 142.5 (C5´, C5´´), 142.9 (C6´, C6´´), 148.7 (C3´, C3´´). – El. Anal. for $C_{24}H_{18}$ x 0.5 H_2O: calc. (%): C 91.39, H 6.07. found (%): C 91.15, H 5.84.

1,3-Bis(bicyclo[2.2.1]hepta-2,5-dien-2-ylethynyl)benzene (**1k**)

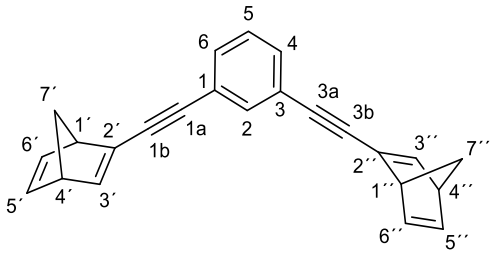

According to GP A, a suspension of 1,3-diethynylbenzene (**3d**, 82.4 mg, 654 µmol), 2-bromonorbornadiene (**1g**, 392 mg, 2.29 mmol), $PdCl_2(PPh_3)_2$ (45.9 mg, 65.4 µmol), CuI (12.4 mg, 65.4 µmol), and NEt_3 (2.0 mL) in THF (10 mL) was stirred at rt for 18 h. The crude product was purified by column chromatography (*n*-hexane/EtOAc, 99/1, *v*/*v*, R_f = 0.31) to give **1k** as a yellow amorphous solid (51.0 mg, 167 µmol, 26%); mp 85–89 °C (dec.). – ^{1}H NMR (500 MHz, $CDCl_3$): δ = 1.90 (dt, 2H, ^2J = 6.2 Hz, ^3J = 1.5 Hz, 7´-H, 7´´-H), 2.01 (dt, 2H, ^2J = 6.2 Hz, ^3J = 1.5 Hz, 7´-H, 7´´-H), 3.24–3.28 (m, 2H, 4´-H, 4´´-H), 3.57–3.59 (m, 2H, 1´-H, 1´´-H), 6.49 (dd, 2H ^3J = 5.1 Hz, ^3J = 3.1 Hz, 5´-H, 5´´-H), 6.71 (dd, 2H ^3J = 5.1 Hz, ^3J = 3.0 Hz, 6´-H, 6´´-H), 6.77 (t, 1H, ^3J = 7.7 Hz, 5-H), 6.87 (d, 2H, ^3J = 3.1 Hz, 3´-H, 3´´-H), 7.25 (dd, 2H, ^3J = 7.7 Hz, ^4J = 1.7 Hz, 4-H, 6-H), 7.72 (t, 1H, ^4J = 1.7 Hz, 2-H). – ^{13}C NMR (125 MHz, $CDCl_3$): δ = 51.4 (C4´, C4´´), 56.1 (C1´, C1´´), 73.6 (C7´, C7´´), 87.6 (C1b, C3b), 97.3 (C1a, C3a), 124.8 (C1, C3), 128.8 (C5), 130.8 (C4, C6), 134.3 (C2), 138.6 (C2´, C2´´), 142.4 (C5´, C5´´), 142.9 (C6´, C6´´), 148.7 (C3´, C3´´). – El. Anal. for $C_{24}H_{18}$: calc. (%): C 94.08, H 5.92. found (%): C 94.06, H 5.98.

1,3,5-Tris(bicyclo[2.2.1]hepta-2,5-dien-2-ylethynyl)benzene (**1l**)

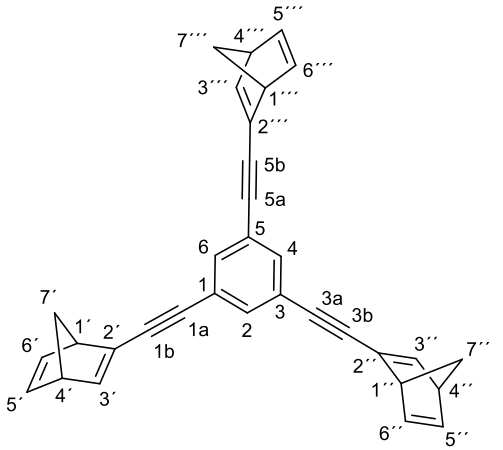

According to GP A, a suspension of 1,3,5-triethynylbenzene (**3e**, 185 mg, 1.23 mmol), 2-bromonorbornadiene (**1g**, 1.26 g, 7.38 mmol), $PdCl_2(PPh_3)_2$ (288 mg, 410 µmol), CuI (77.9 mg, 410 µmol), and NEt_3 (10 mL) in THF (25 mL) was stirred at rt for 18 h. The crude product was purified by column chromatography (*n*-hexane/EtOAc, 99/1, *v*/*v*, R_f = 0.21) to give **1l** as a colorless amorphous solid (198 mg, 470 µmol, 40%); mp 170–178 °C (dec.). – ^{1}H NMR (500 MHz, $CDCl_3$): δ = 1.90 (dt, 3H, ^2J = 6.2 Hz, ^3J = 1.3 Hz, 7´-H, 7´´-H, 7´´´-H), 1.99 (dt, 3H, ^2J = 6.2 Hz, ^3J = 1.3 Hz, 7´-H, 7´´-H, 7´´´-H), 3.24–3.27 (m, 3H, 4´-H, 4´´-H, 4´´´-H), 3.53–3.56 (m, 3H, 1´-H, 1´´-H, 1´´´-H), 6.49 (dd, 3H, ^3J = 4.9 Hz, ^3J = 3.1 Hz, 5´-H, 5´´-H, 5´´´-H), 6.70 (dd, 3H, ^3J = 4.9 Hz, ^3J = 3.0 Hz, 6´-H, 6´´-H, 6´´´-H), 6.85 (d, 3H, ^3J = 3.2 Hz, 3´-H, 3´´-H, 3´´´-H), 7.53 (s, 3H, 2-H, 4-H, 6-H). – ^{13}C NMR (125 MHz, $CDCl_3$): δ = 51.5 (C4´, C4´´, C4´´´), 56.1 (C1´, C1´´, C1´´´), 73.6 (C7´, C7´´, C7´´´), 88.0 (C1b, C3b, C5b), 96.6 (C1a, C3a, C5a), 125.2 (C1, C3, C5), 133.4 (C2, C4, C6), 138.5 (C3´, C3´´, C3´´´), 142.4 (C5´, C5´´, C5´´´), 142.9 (C6´, C6´´, C6´´´), 149.1 (C3´, C3´´, C3´´´). – El. Anal. for $C_{33}H_{24}$ x 1 H_2O: calc. (%): C 90.38, H 5.38. found (%): C 90.49, H 5.76.

1,4-Bis(bicyclo[2.2.1]hepta-2,5-dien-2-ylethynyl)naphthalene (**1m**)

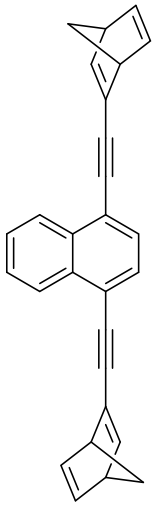

According to GP A, a suspension of 1,4-diethynylnaphthalene (**3f**, 120 mg, 682 µmol), 2-bromonorbornadiene (**1g**, 409 mg, 2.39 mmol), $PdCl_2(PPh_3)_2$ (47.9 mg, 86.2 µmol), CuI (13.0 mg, 86.2 µmol), and NEt_3 (2.0 mL) in THF (10 mL) was stirred at rt for 18 h. Further column chromatography (*n*-hexane/EtOAc, 95/5, *v*/*v*, R_f = 0.51) gave a fraction which accoding to ^{1}H NMR-spectroscopic analysis contained product **1m**, along with byproducts, which could not be further separated.

2,6-Bis(bicyclo[2.2.1]hepta-2,5-dien-2-ylethynyl)naphthalene (**1n**)

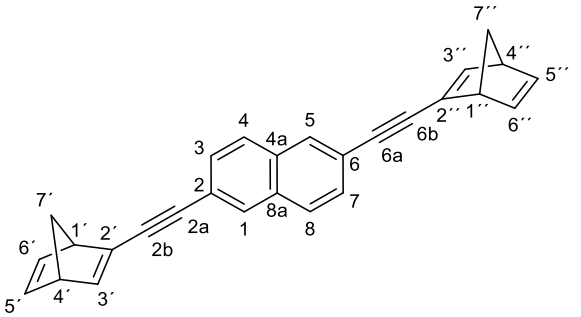

According to GP A, a suspension of 2,6-diethynylnaphthalene (**3g**, 120 mg, 682 µmol), 2-bromonorbornadiene (**1g**, 409 mg, 2.39 mmol), $PdCl_2(PPh_3)_2$ (47.9 mg, 86.2 µmol), CuI (13.0 mg, 86.2 µmol), and NEt_3 (2.0 mL) in THF (10 mL) was stirred at rt for 18 h. The crude product was purified by column chromatography (*n*-hexane/EtOAc, 9/1, *v*/*v*, R_f = 0.64) to give **1n** as a yellow amorphous solid (77.0 mg, 216 µmol, 32%); mp 160–165 °C (dec.). – ^{1}H NMR (500 MHz, $CDCl_3$): δ = 2.11 (dt, 2H, ^2J = 6.3 Hz, ^3J = 1.3 Hz, 7´-H, 7´´-H), 2.19 (dt, 2H, ^2J = 6.3 Hz, ^3J = 1.3 Hz, 7´-H, 7´´-H), 3.70–3.74 (m, 4H, 1´-H, 1´´-H, 4´-H, 4´´-H), 6.75–6.79 (m, 2H, 5´-H, 5´´-H), 6.91–6.95 (m, 2H, 6´-H, 6´´-H), 7.04–7.08 (m, 2H, 3´-H, 3´´-H), 7.47 (dd, 2H, ^3J = 8.5 Hz, ^4J = 1.4 Hz, 3-H, 7-H), 7.69 (d, 2H, ^3J = 8.5 Hz, 4-H, 8-H), 7.87–7.90 (m, 2H, 1-H, 5-H). – ^{13}C NMR (125 MHz, $CDCl_3$): δ = 51.3 (C4´, C4´´), 55.9 (C1´, C1´´), 73.7 (C7´, C7´´), 87.3 (1-C**C**-2´, 6-C**C**-2´´), 97.8 (C2b, C6b), 121.8 (C2a, C6a), 127.8 (C4, C8), 129.0 (C3, C7), 130.7 (C1, C5), 132.4 (C4a, C8a), 138.3 (C2´, C2´´), 142.6 (C5´, C5´´), 142.9 (C6´, C6´´), 149.0 (C3´, C3´´). – El. Anal. for $C_{28}H_{20}$ x H_2O: calc. (%): C 89.81, H 5.91. found (%): C 88.30, H 5.31.

S5 Absorption properties of norbornadiene derivatives 1h–l, n

Starting from stock solutions in cyclohexane (1.0 mM), solutions of **1h–l**, **n** (c = 20 µM, V = 2.00 mL) were prepared in cyclohexane, MeCN, EtOH, $CHCl_3$, EtOAc, and benzene, and the absorption spectrum was recorded (Figure S1). The resulting extinction coefficients were determined according to the Lambert–Beer law and are listed in Table S1.

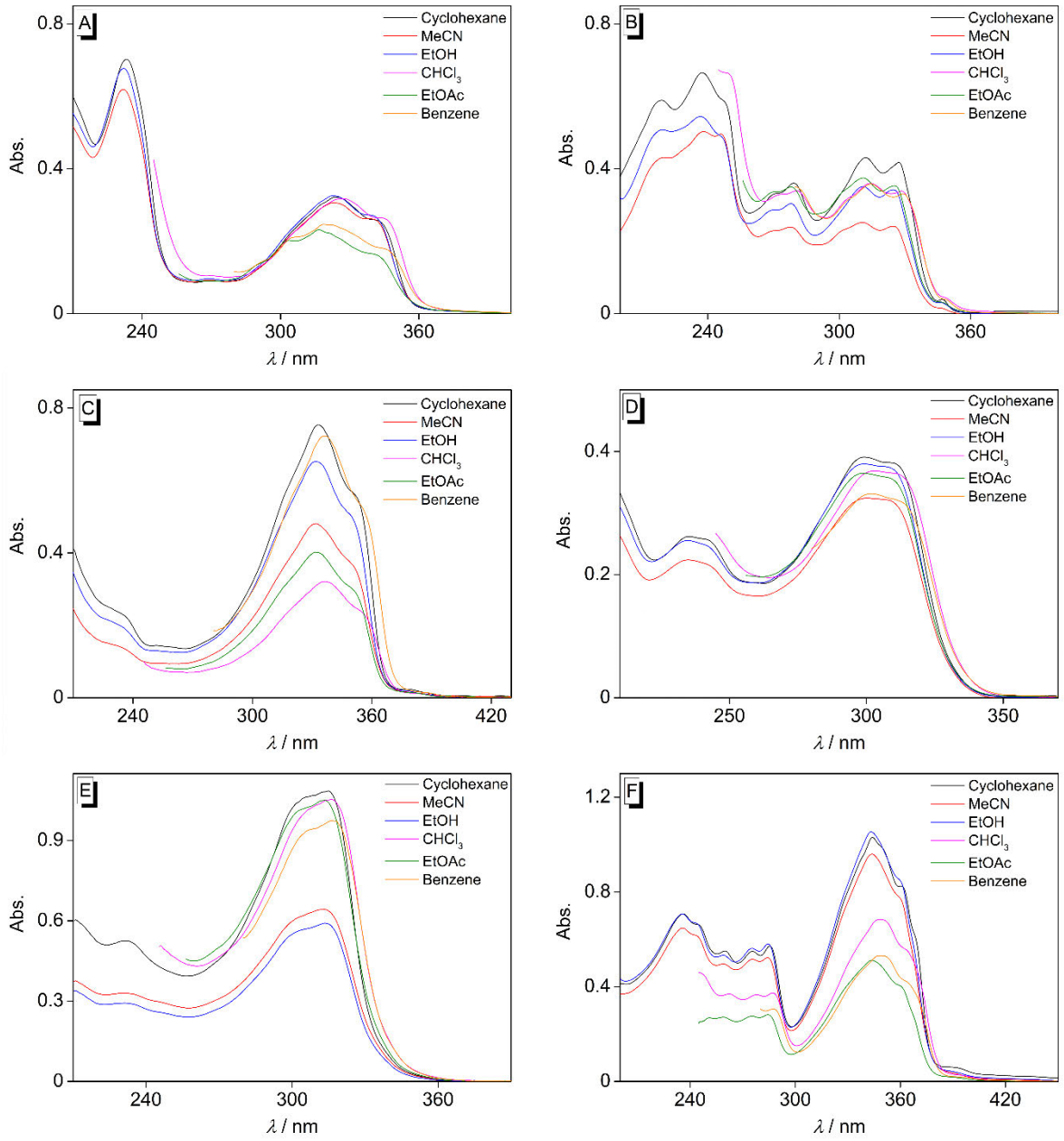

Figure S1: Absorption spectra of **1h** (A), **1i** (B), **1j** (C), **1k** (D), **1l** (E), and **1n** (F) in different solvents (c = 20 µM).

Table S1: Extinction coefficients (in L mol^{-1} cm^{-1}) of **1h–l**, **n** in different solvents.

Solvent	**1h**[a]	**1i**[b]	**1j**[c]	**1k**[d]	**1l**[e]	**1n**[f]
Cyclohexane	16040	20850	37580	19050	54420	51370
MeCN	15190	11950	24250	15930	32000	47880
EtOH	16030	15210	32510	18540	29700	52320
$CHCl_3$	15820	16730	15600	18270	52770	33690
EtOAc	10310	17540	20150	17650	52320	25450
Benzene	11840	20850	37580	19050	48020	26110

[a] Determined at 326 nm. [b] Determined at 328 nm. [c] Determined at 332 nm. [d] Determined at 310 nm. [e] Determined at 315 nm. [f] Determined at 345 nm.

S6 Photoreactions and photoisomerization quantum yields

Samples of the substrates **1h–l**, **n** (c = 20 µM, V = 2.00 mL) were irradiated at λ_{ex} = 315 nm (**1h**, **1i**, **1k**, and **1l**) or at λ_{ex} = 340 nm (**1j**, **1n**), and the photoreaction was monitored by absorption spectroscopy. The reaction was stopped when no further changes in the spectra were detected (Figure 2). In addition, the derivatives **1i** and **1n** (c = 20 µM, V = 2.00 mL) were irradiated in the presence of $[Ru(phen)_3(PF_6)_2]$ (c = 20 µM) at λ_{ex} = 520 nm and the photoreaction was monitored photometrically until no changes in the spectra were occurred. The photoreactions were also followed by ^{1}H NMR spectroscopy. For this purpose, samples of the substrates (c = 3 mM, V = 550 µL) were irradiated with Thorlabs LED M310L1 at λ_{ex} = 310 nm (**1h**, **1i**, **1k**, and **1l**) or with Thorlabs LED M340L5 at λ_{ex} = 340 nm (**1j**, **1n**), followed by ^{1}H NMR spectroscopic analysis (Figures S35, S36, S37, S38, S39, and S40). Because the signals of the corresponding quadricyclanes **2h–l**, **n** could not be clearly identified due to overlaps with decomposition products, no data was generated for **2h–l**, **n**. In addition, **1i** was followed by in-situ irradiation (c = 15 mM, V = 550 µL, λ_{ex} = 520 nm, 10.0 mA per LED) studies in the presence of $[Ru(phen)_3(PF_6)_2]$ (c = 300 µM) in MeCN-d_3 (V = 550 µL) within the NMR spectrometer (Figure S41). For this monitoring of the photoreaction by NMR spectroscopy a self-made NMR setup was used.[1] The irradiation insert of λ_{ex} = 520 nm uses Nichia NCGE17 LEDs (www.leds.de-Article-number 32625). The measured light intensity was 3.2 mW for one LED with 50.0 mA current. The light intensity in the NMR probe towards the NMR active volume was 10.9 mW.

The photoisomerization quantum yields were determined by actinometry with potassium ferrioxalate as reference and irradiation with Thorlabs M310L1 (310 nm) for **1h**, **1i**, **1k**, and **1l** or with Thorlabs LED M340L5 (340 nm) for **1j** and **1n**.[9] First, the photon flux of the irradiation sources was determined according to literature protocol.[10] The values of the light intensity were I_o = 8.53 10^{-8} einstein L^{-1} s^{-1} (M310L1) and I_o = 1.96 10^{-7} einstein L^{-1} s^{-1} (M340L5) (Figure S2).

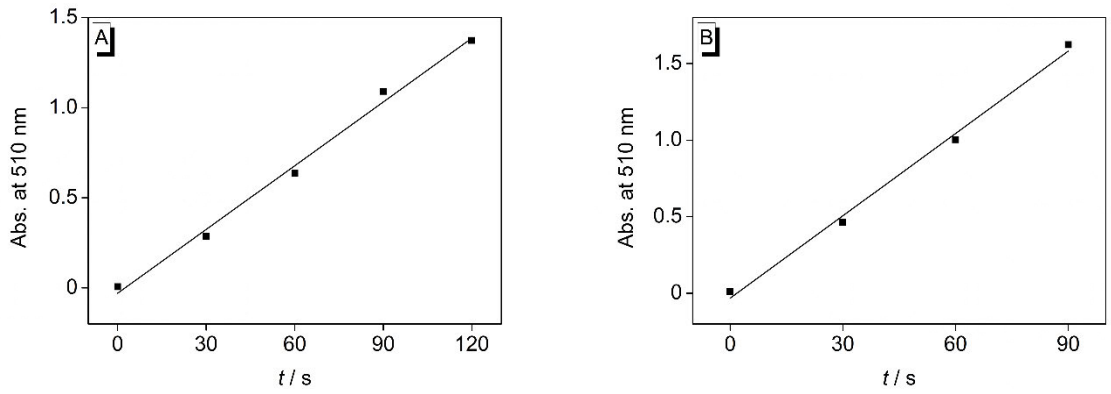

Figure S2: Determination of the photon flux for Thorlabs M10L1 (A) and for Thorlabs M340L5 (B).

The quantum yields of the photoisomerization reactions were determined according to the established procedure (Regime 1: Total absorption regime).[10] The concentrations of the solutions was prepared with Abs. > 2 (c = 60.0–250 µM) at the irradiation wavelength to give a linear dependence between the decrease of absorption and the irradiation time. The quantum yield was determined from the slope of the resulting linear regression (Figure S3, Equation S2).

$$[A] = [A_0] - \frac{\Phi_A\, I}{N_A\, V}\, t_{irr} \qquad \text{(S2)}$$

In Equation S2, [A] is the concentration of norbornadiene, [A_0] is the starting concentration, Φ_A is the quantum yield, I is the photon flux, N_A is the Avogadro number, V the volume and t_{irrad} the irradiation time.

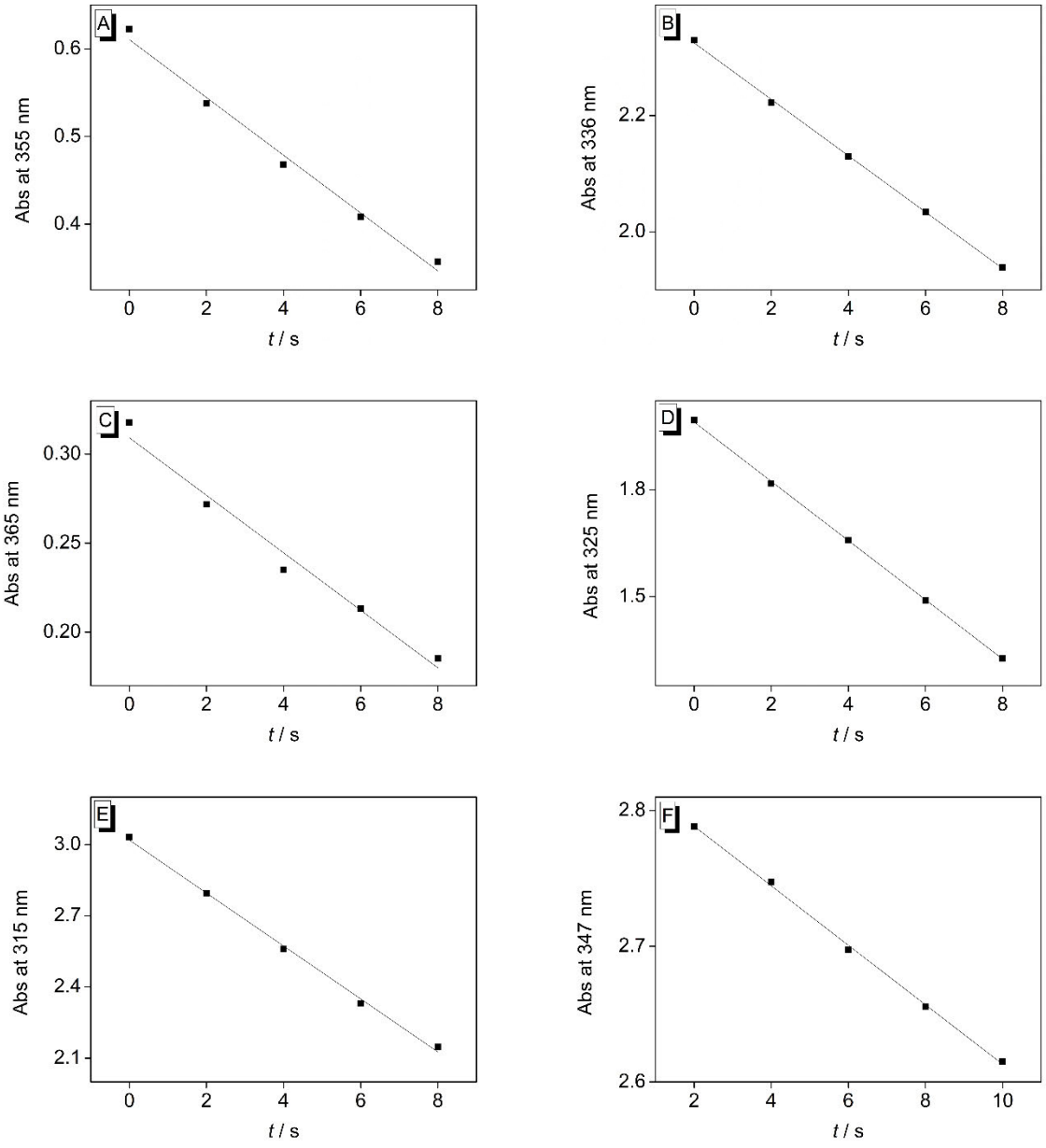

Figure S3: Photometric monitoring of the photoisomerization of **1h** (A), **1i** (B), **1j** (C), **1k** (D), **1l** (E), and **1n** (F) by a plot of the absorption of the substrate versus time. The straight line shows the fit from linear regression analysis, which was used to calculate the quantum yields.

S7 Quenching experiments of $[Ru(phen)_3](PF_6)_2$ with 1i

Previously, we were able to quantitively isomerize naphthyl- and phenyl-substituted norbornadienes by triplet sensitization with visible light.[11] Of the tested compounds, 2-(bicyclo[2.2.1]hepta-2,5-dien-2-yl)naphthalene, is structurally related to **1i** and is lacking the acetylene-bridge (see Figure S4, right). While direct excitation of this photoswitch requires harsh UV light, the triplet energy was determined at 2.41 eV making it accessible by visible-light absorbing photosensitizers. A triplet energy transfer rate constant of $[Ru(phen)_3](PF_6)_2$ with the reference compound is reported as k_{EnT} = 0.83 10^9 M^{-1} s^{-1} [11]. We therefore conducted quenching experiments of triplet-excited $[Ru(phen)_3(PF_6)_2]$ with **1i** as a direct comparison (Figure S4, left). A Stern–Volmer analysis revealed efficient triplet energy transfer to **1i**. Indeed, the energy transfer rate, k_{EnT} = 5.8 10^9 M^{-1} s^{-1}, is roughly higher by one order of magnitude compared to the reference compound. It seems therefore natural to assume that the triplet energy of **1i** is well below 2.4 eV.

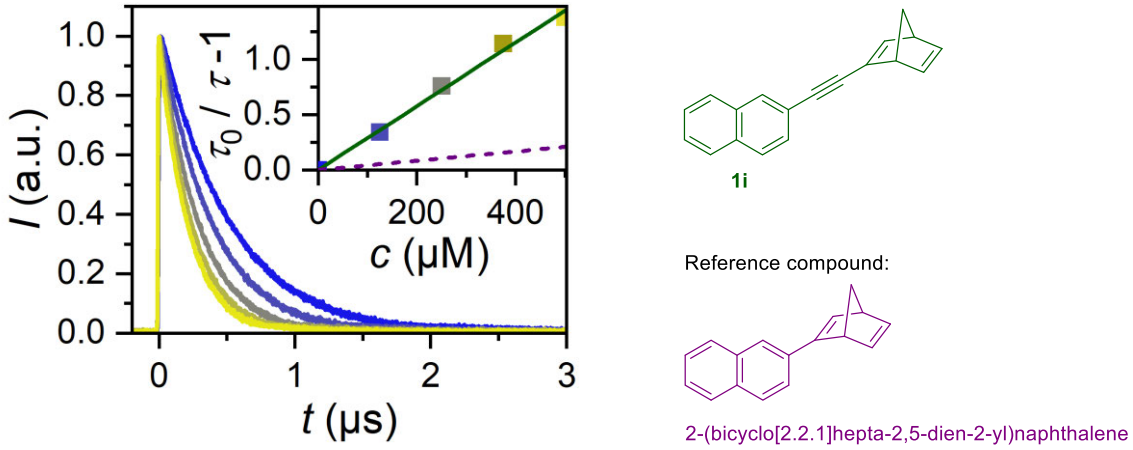

Figure S4: Left: Emission quenching experiments with detection at 600 nm of 20 µM $[Ru(phen)_3](PF_6)_2$ with varying concentrations of **1i** in Ar-saturated MeCN using 532 nm laser excitation. Inset: Stern–Volmer analysis. The dashed line in the inset indicates the previously measured quenching kinetics for the reference compound. Right: Molecular structures of **1i** and the reference compound 2-(bicyclo[2.2.1]hepta-2,5-dien-2-yl)naphthalene.

Additionally, we recorded transient absorption spectra of a solution containing 20 µM $[Ru(phen)_3](PF_6)_2$ and 500 µM **1i**. The spectra were recorded right after excitation, resembling the typical triplet–triplet absorption spectrum of $[Ru(phen)_3](PF_6)_2$, and after deactivation, where only baseline level is observed. This enables us to exclude electron transfer quenching reactions, which typically yield longer-lived transient photoproducts after quenching[12]. The absence of a triplet-excited **1i** is likely due to a very short triplet lifetime typical for norbornadienes[11,13].

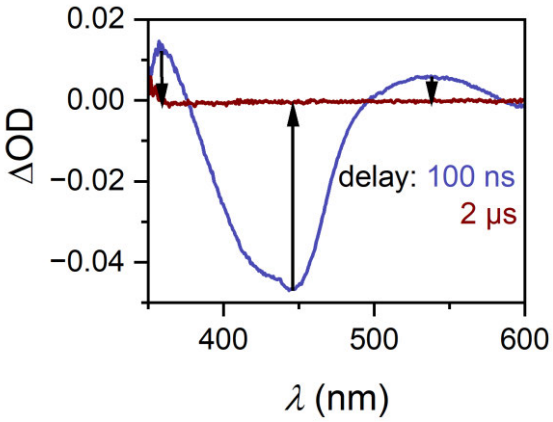

Figure S5: Transient absorption spectrum recorded of an Ar-saturated solution with 20 µM $[Ru(phen)_3](PF_6)_2$ and 500 µM **1i** using 532 nm laser pulses for excitation. The spectra were recorded 100 ns and 2 µs after laser excitation.

S8 Kinetic studies of the thermal back reaction

The thermally induced back reactions from the quadricyclanes to the norbornadiene derivatives were monitored photometrically. Samples of the norbornadienes **1h**–**l**, **n** in cyclohexane (c = 20 µM) were irradiated until no further changes in the absorption could be detected with a LED 310 nm for **1h**, **1i**, **1k**, and **1l** or a LED 340 nm for **1j** and **1n**. The increase of the norbornadiene absorption was determined photometrically at 60 °C (Figure S4).

Considering a unimolecular back reaction to the norbornadiene, the data were analyzed according to first-order kinetics (Equaiton S3) [14].

$$-\frac{\mathrm{d}\,[QC]}{\mathrm{d}t} = \frac{\mathrm{d}\,[NBD]}{\mathrm{d}t} = k \qquad \text{(S3)}$$

In Equation S3, [QC] is the concentration of the quadricyclane, [NBD] is the concentration of the norbornadiene, and k is the rate constant of the thermal back reaction at a certain temperature.

The rate constants k were obtained by an exponential fit (Equation S4). The Eyring equation was used for the calculation of the free activation enthalpy $\Delta G^{\neq}$ of the reaction (Equation S4 and S5)[14].

$$k = \frac{k_B T}{h}\, e^{-\frac{\Delta G^{\neq}}{RT}} \qquad \text{(S4)}$$

$$\Delta G^{\neq} = RT\left(23.760 + \ln\left(\frac{T}{k}\right)\right) \qquad \text{(S5)}$$

In Equation S4 and S5, k_B is the Boltzmann constant, h is the Planck constant, R is universal gas constant, T is the temperature in K and $\Delta G^{\neq}$ is the free activation enthalpy.

With the obtained values, the half-lifes of the quadricyclanes **2f**–**j** were calculated at 25 °C with Equation S6. The results are listed in Table 1 in the main text.

$$t_{1/2} = \frac{\ln(2)}{k} \tag{S6}$$

In Equation S6, $t_{1/2}$ is the half-life time and k is the rate constant of the thermal back reaction.

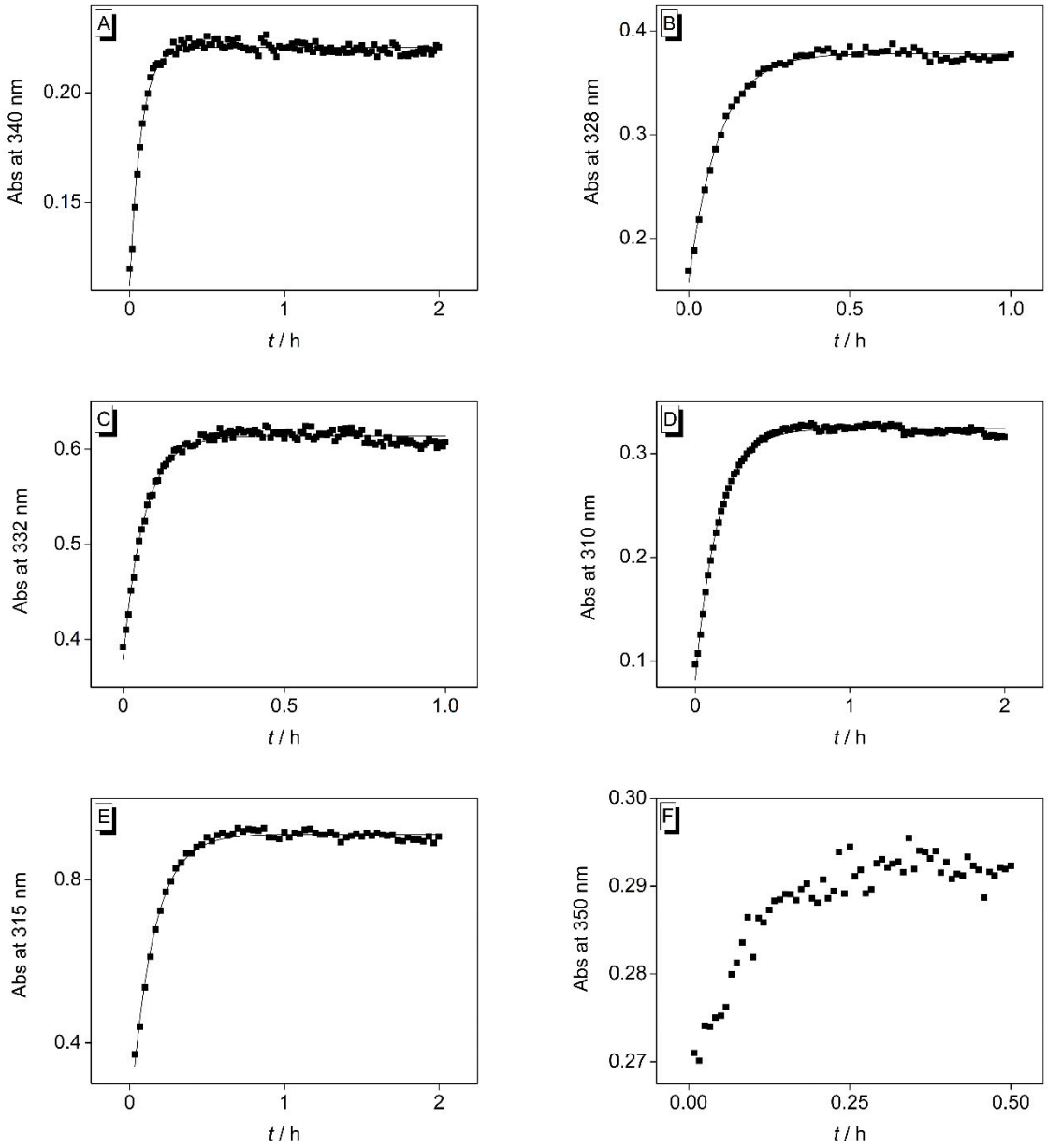

Figure S6: Photometric monitoring of the back conversion of **1h** (A), **1i** (B), **1j** (C), **1k** (D), **1l** (E), and **1n** (F) to the corresponding norbornadienes at 60 °C. The data were fitted to an exponential function (Equation S2) to obtain the rate constants k at a particular temperature.

S9 NMR spectra

S9.1 Structure elucidation

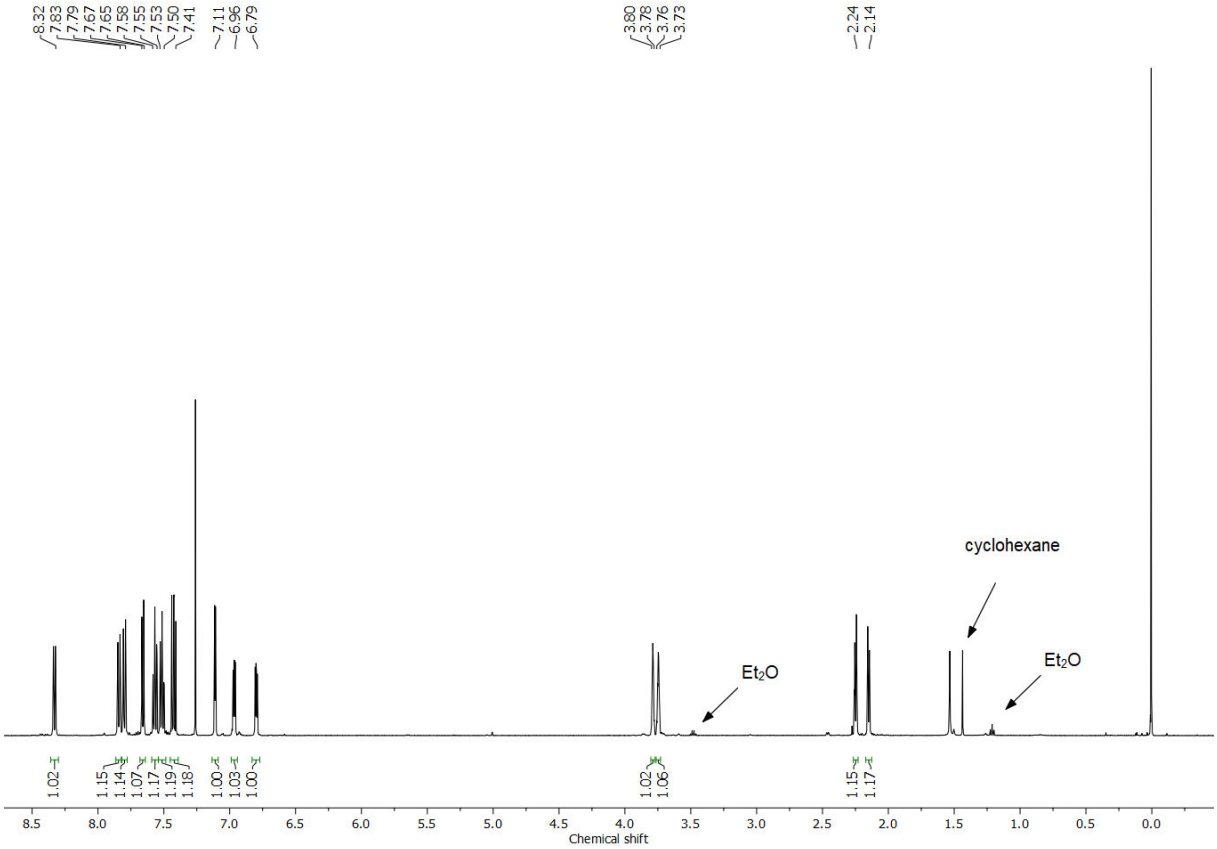

Figure S7: ^{1}H NMR spectrum (500 MHz) of **1h** in $CDCl_3$.

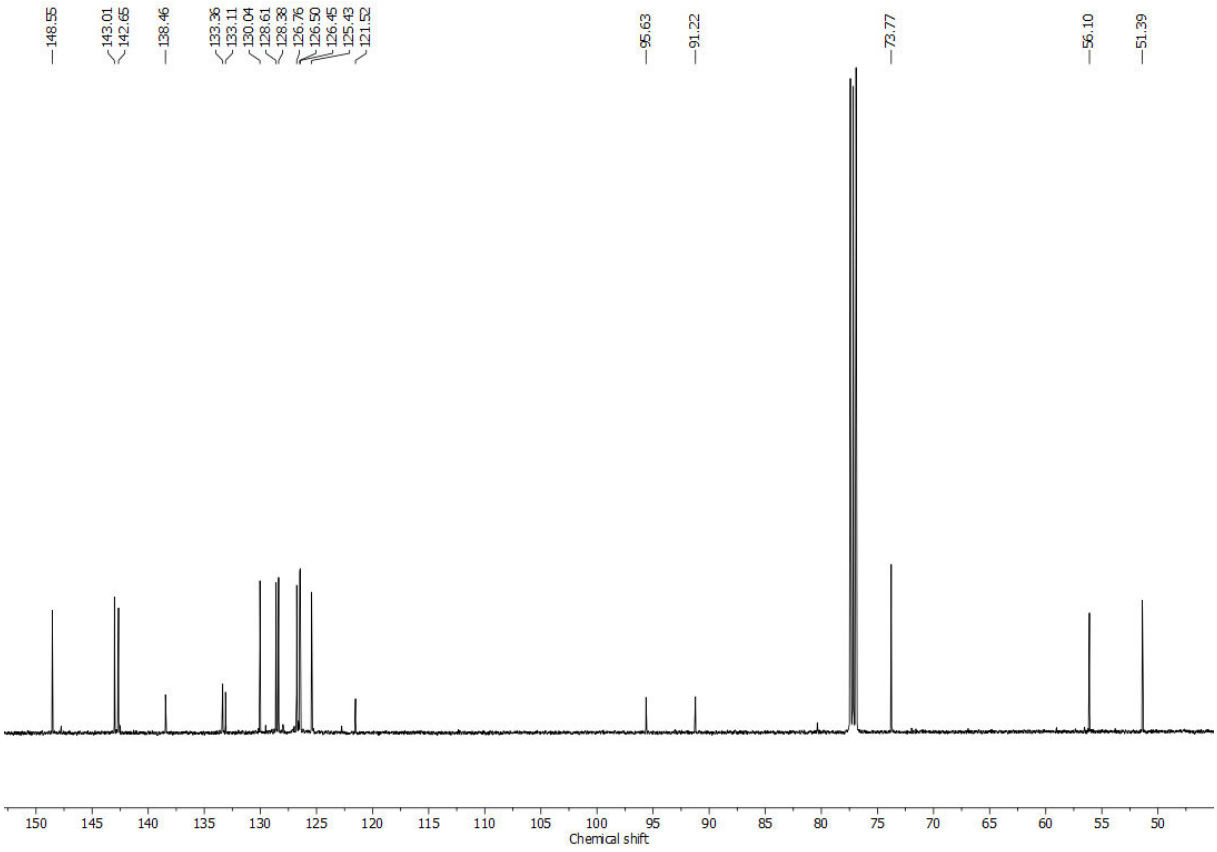

Figure S8: ^{13}C NMR spectrum (125 MHz) of **1h** in $CDCl_3$.

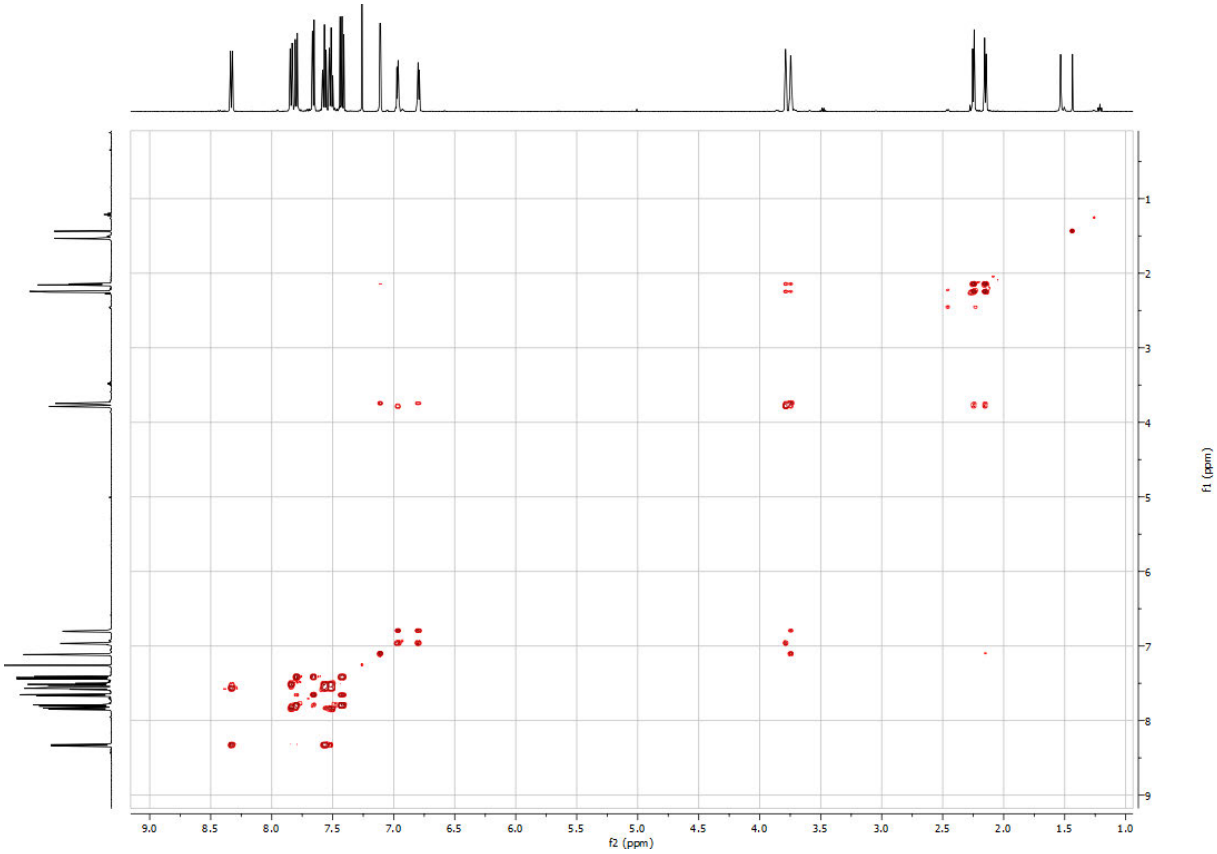

Figure S9: H,H-COSY NMR spectrum (500 MHz) of **1h** in $CDCl_3$.

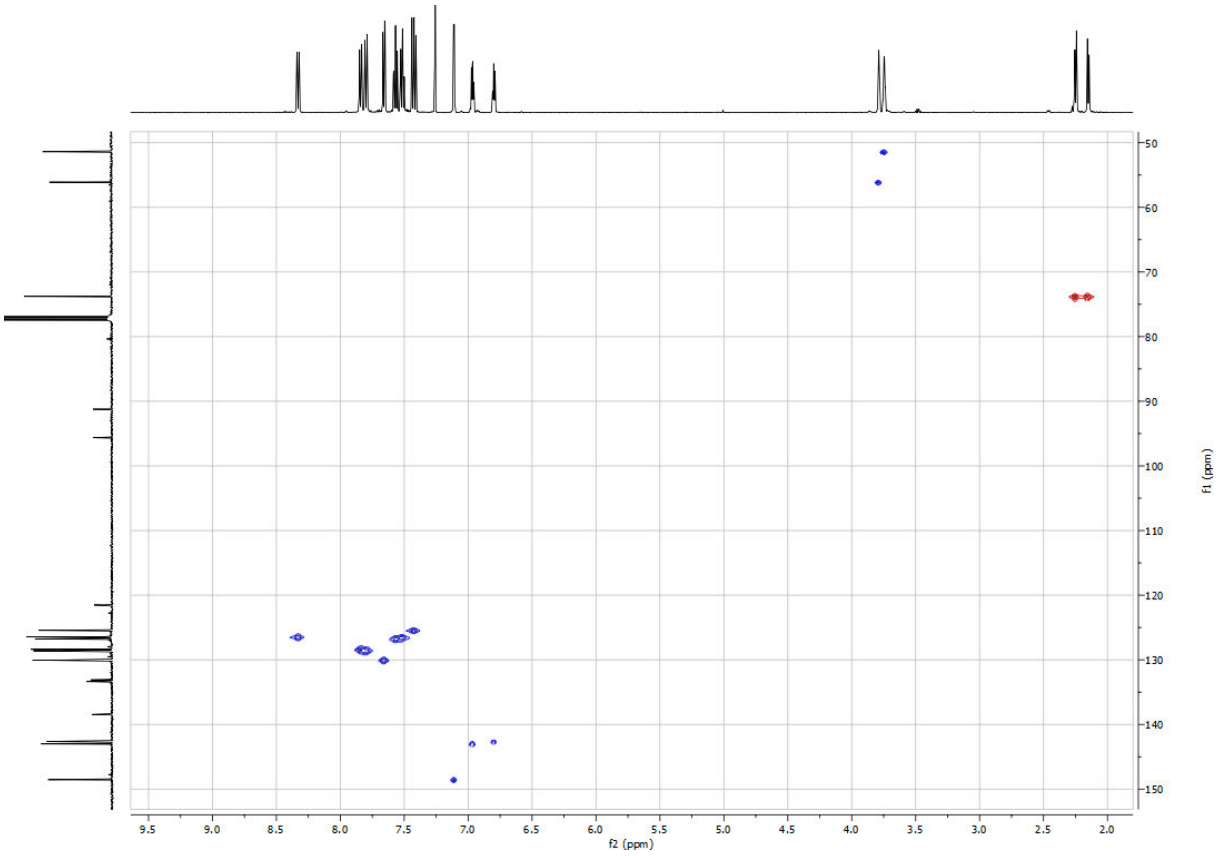

Figure S10: HSQC NMR spectrum (500 MHz) of **1h** in $CDCl_3$.

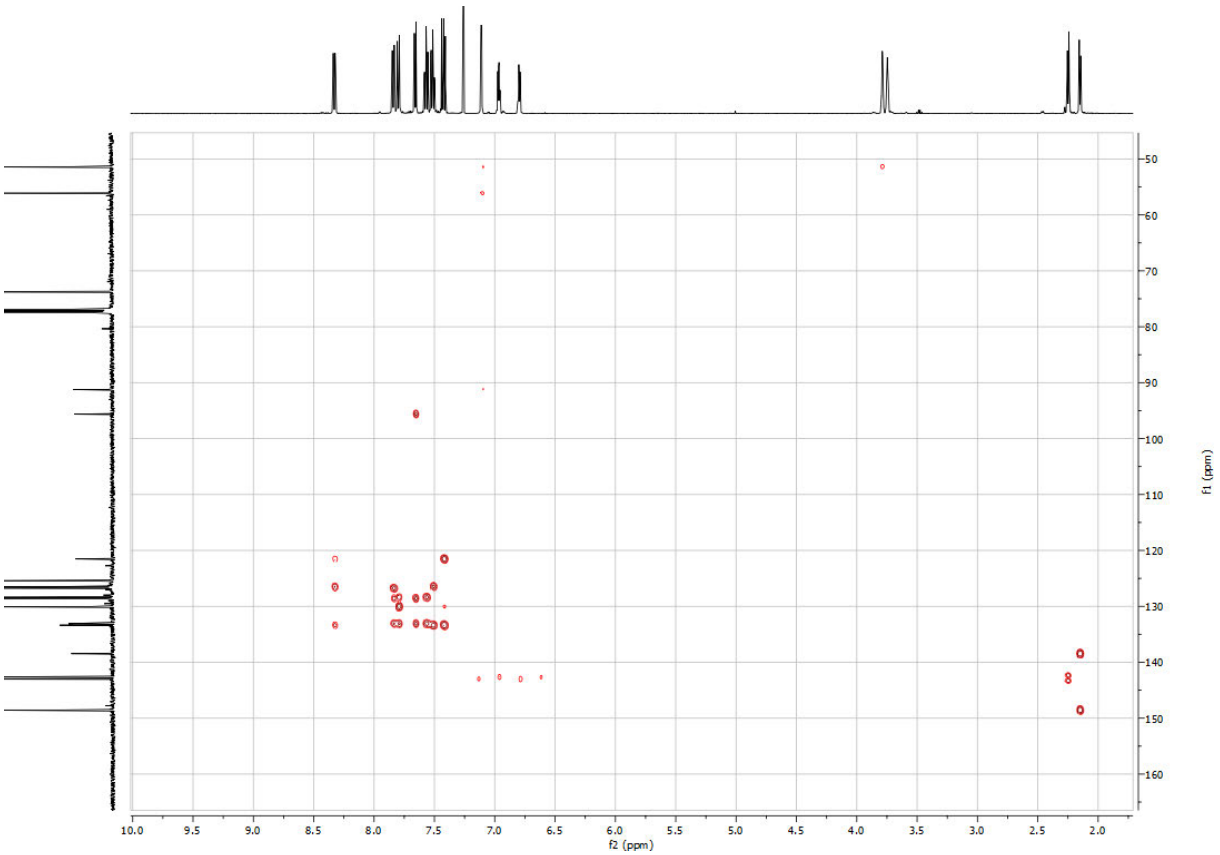

Figure S11: HMBC NMR spectrum (500 MHz) of **1h**in $CDCl_3$.

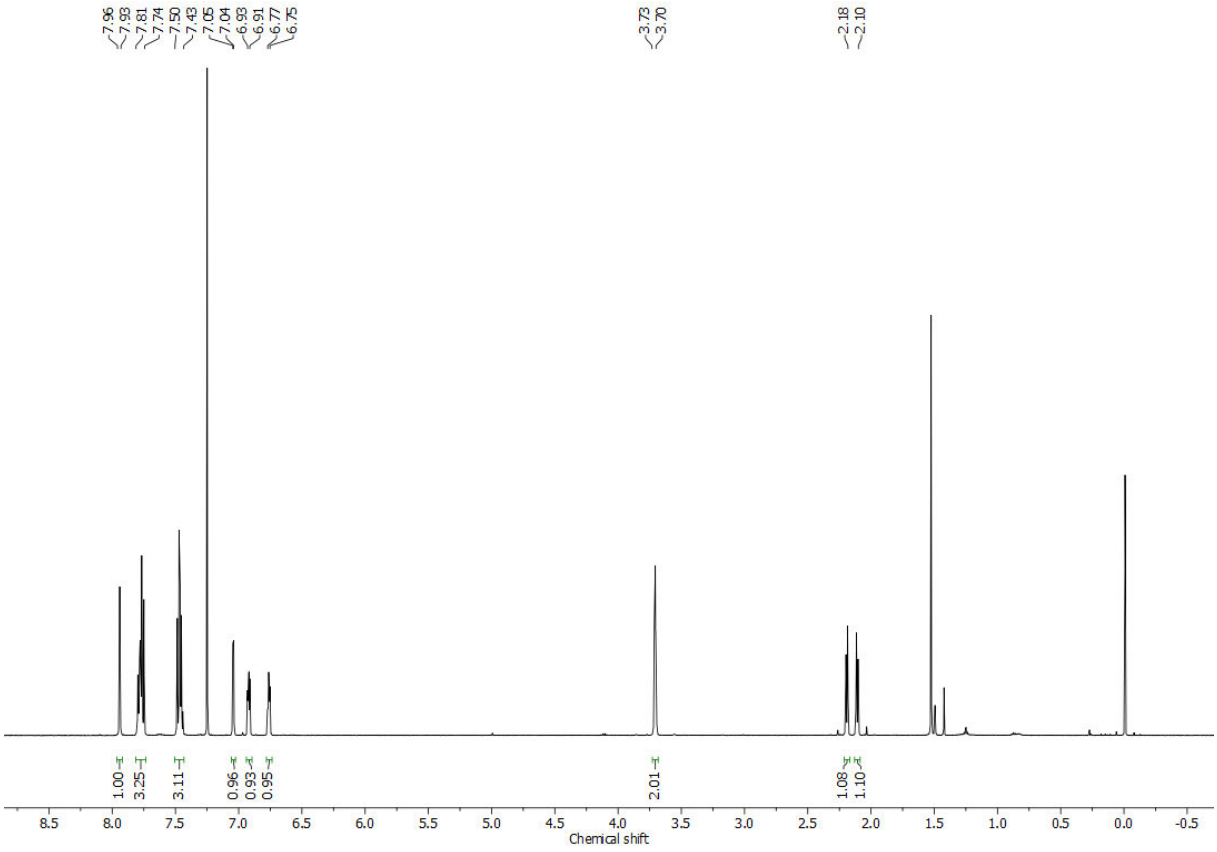

Figure S12: ^{1}H NMR spectrum (500 MHz) of **1i** in $CDCl_3$.

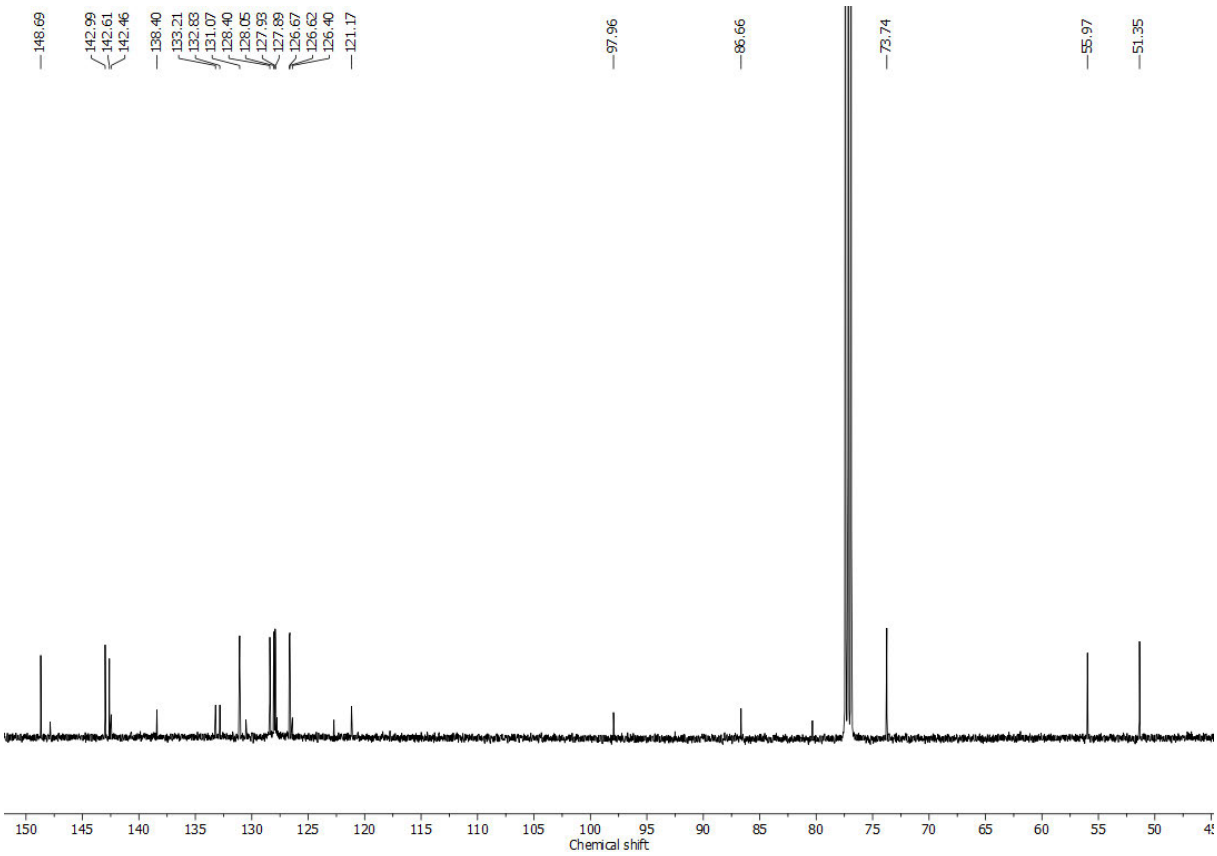

Figure S13: ^{13}C NMR spectrum (125 MHz) of **1i** in $CDCl_3$.

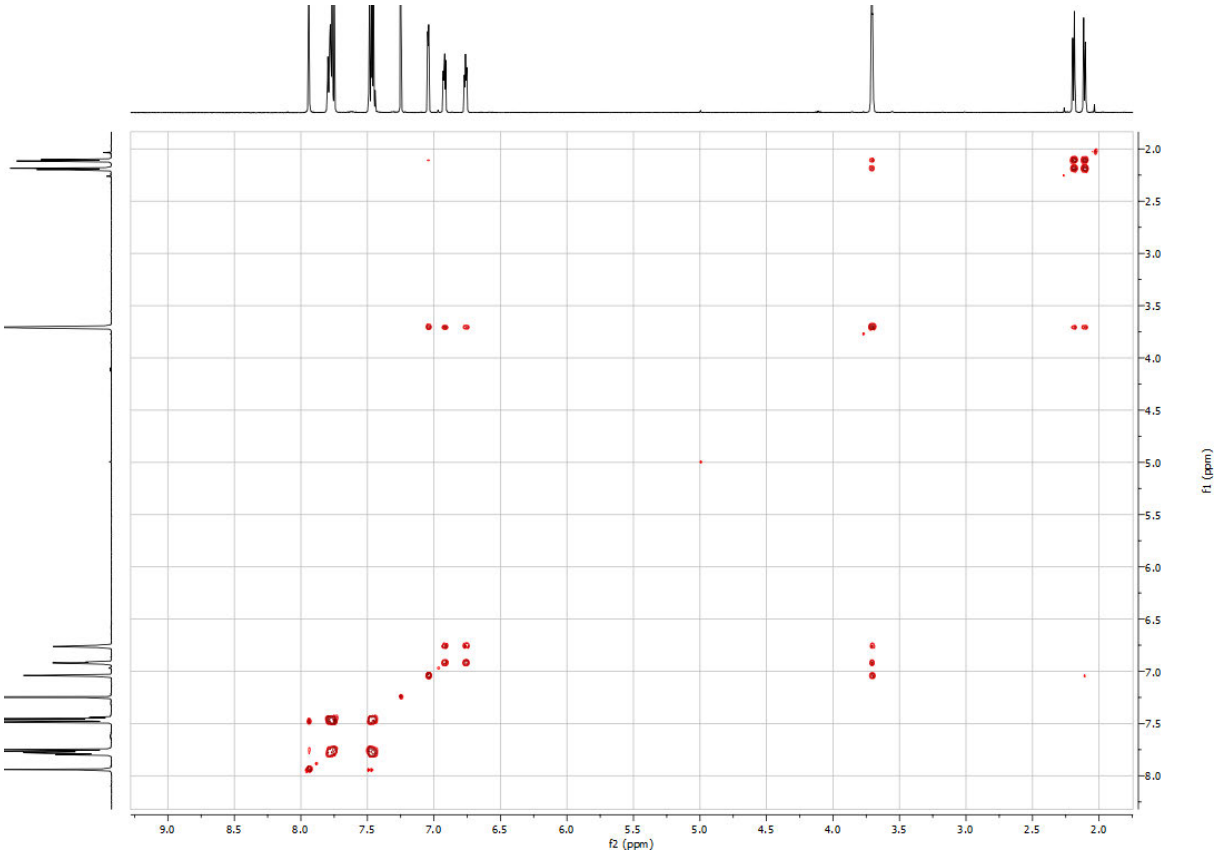

Figure S14: H,H-COSY NMR spectrum (500 MHz) of **1i** in $CDCl_3$.

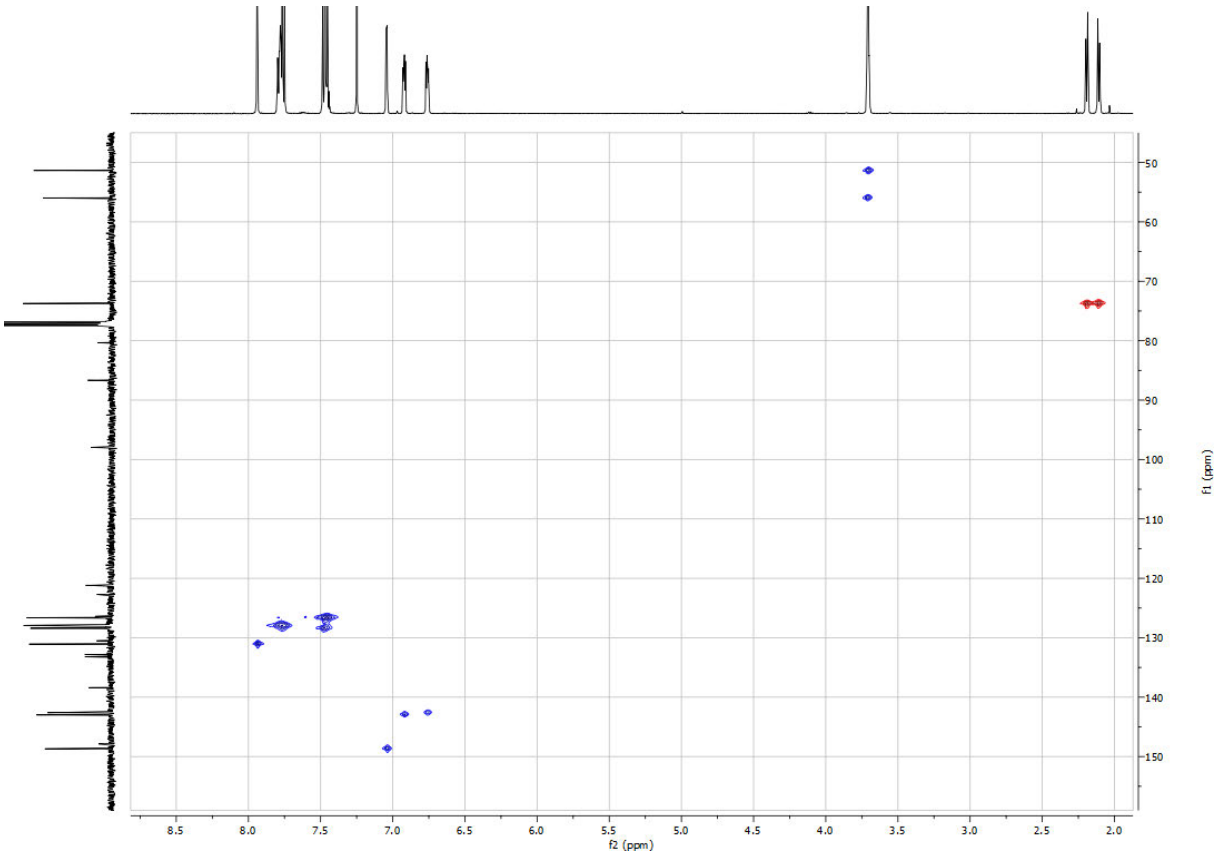

Figure S15: HSQC NMR spectrum (500 MHz) of **1i** in $CDCl_3$.

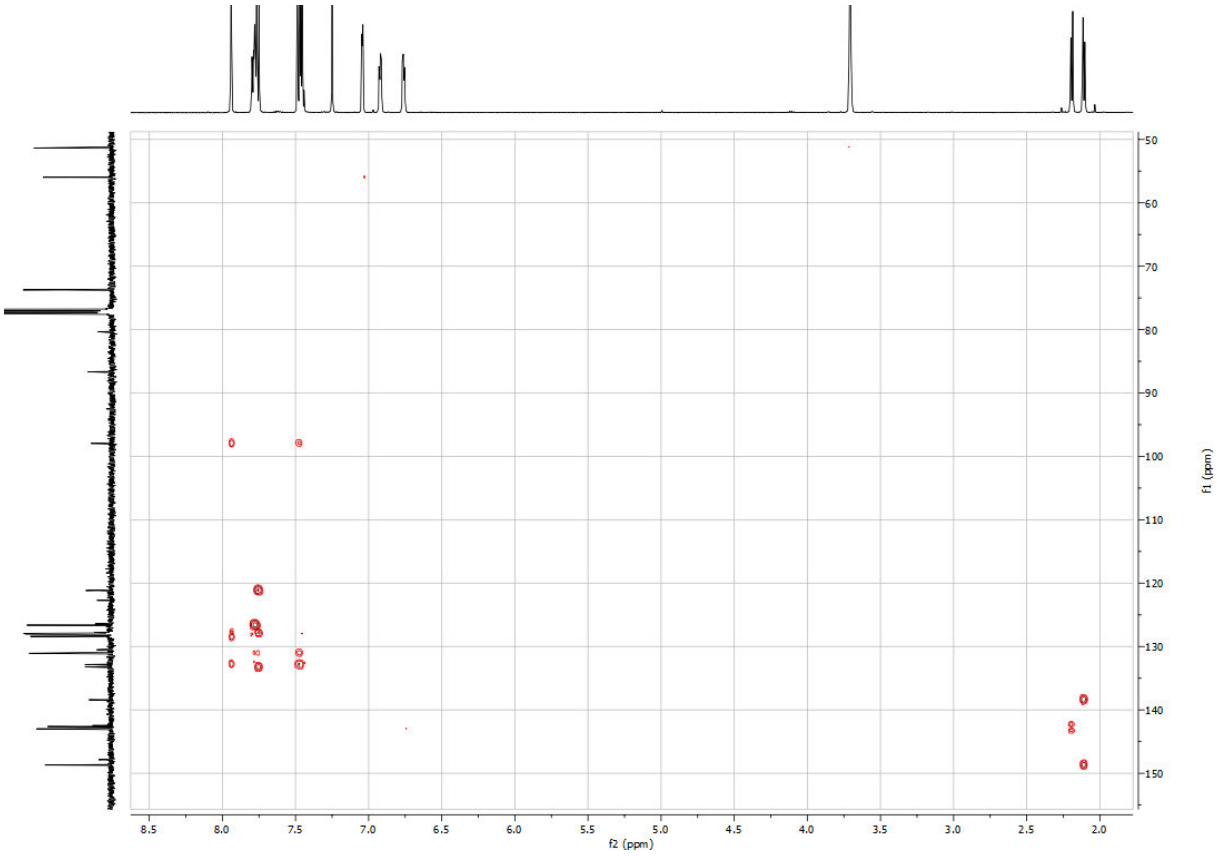

Figure S16: HMBC NMR spectrum (500 MHz) of **1i** in $CDCl_3$.

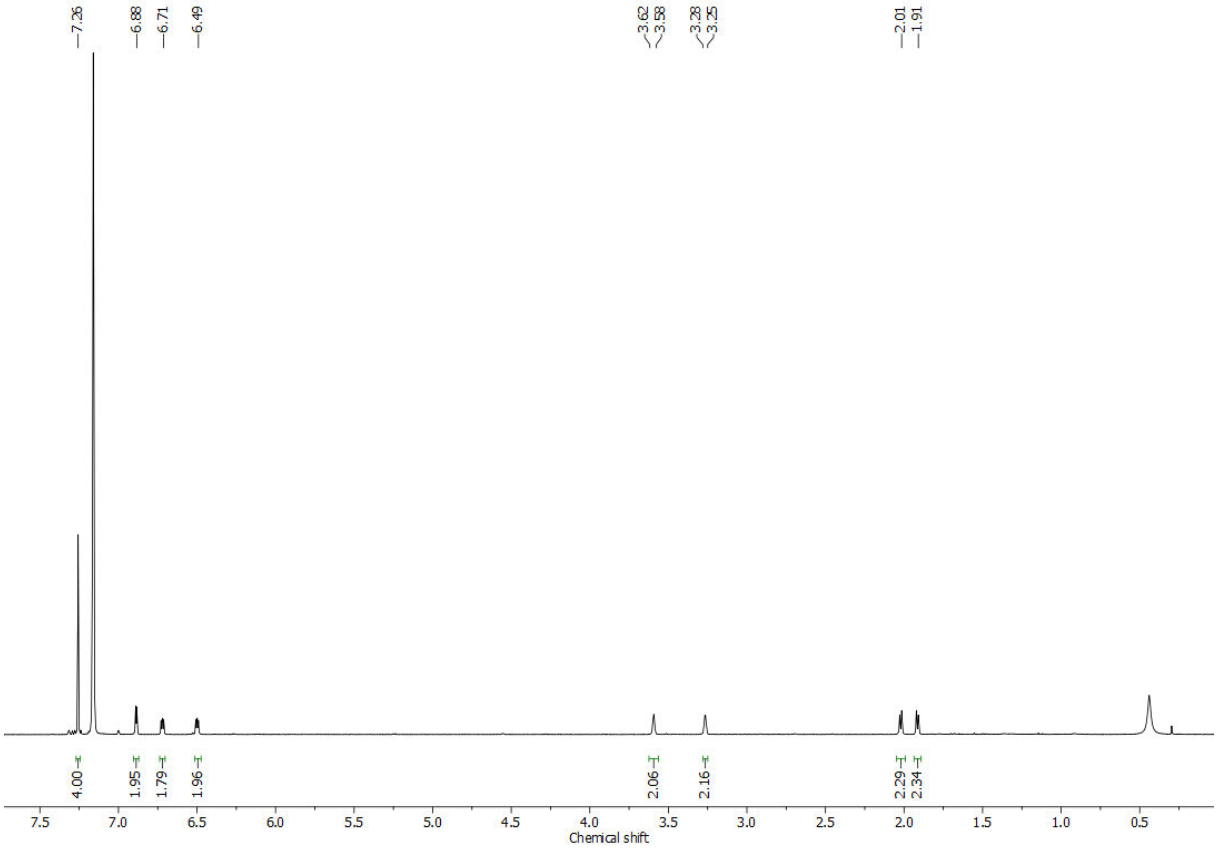

Figure S17: ^{1}H NMR spectrum (500 MHz) of **1j** in benzene-d_6.

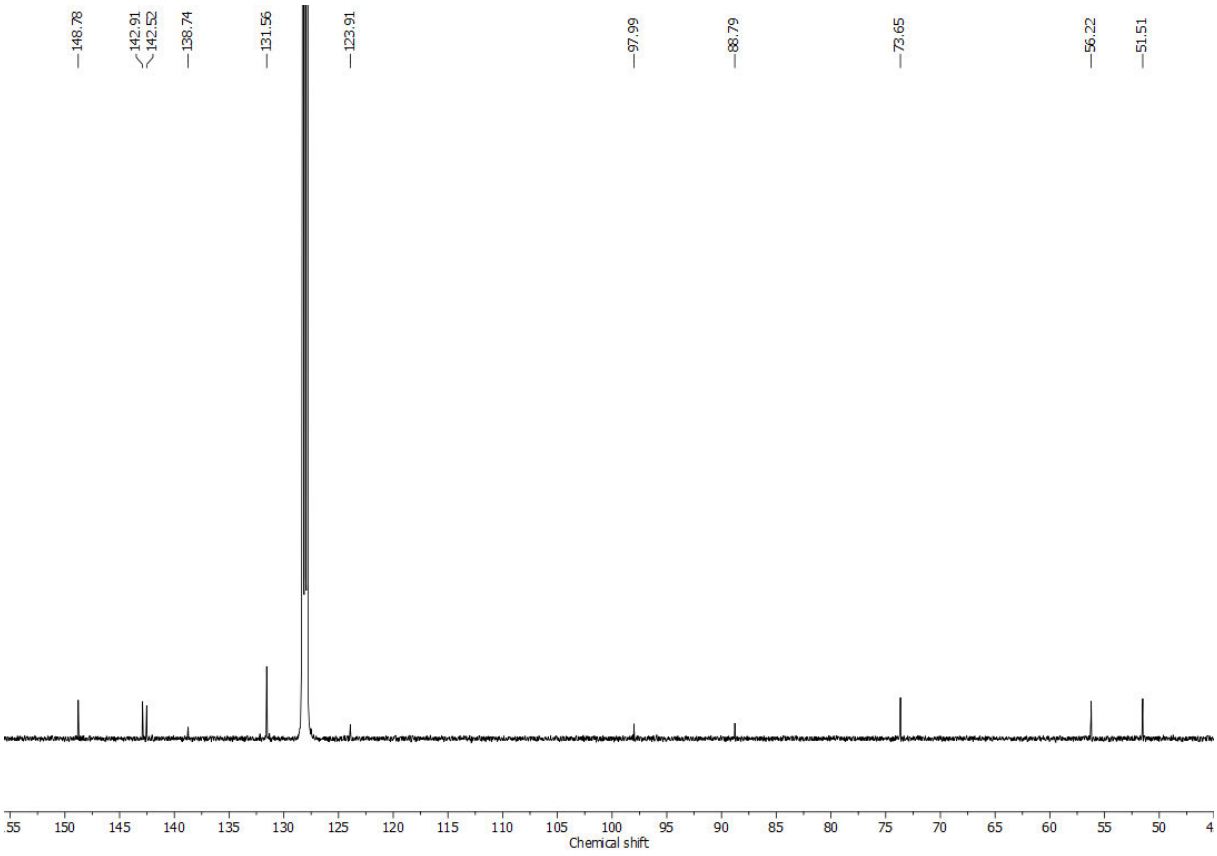

Figure S18: ^{13}C NMR spectrum (125 MHz) of **1j** in benzene-d_6.

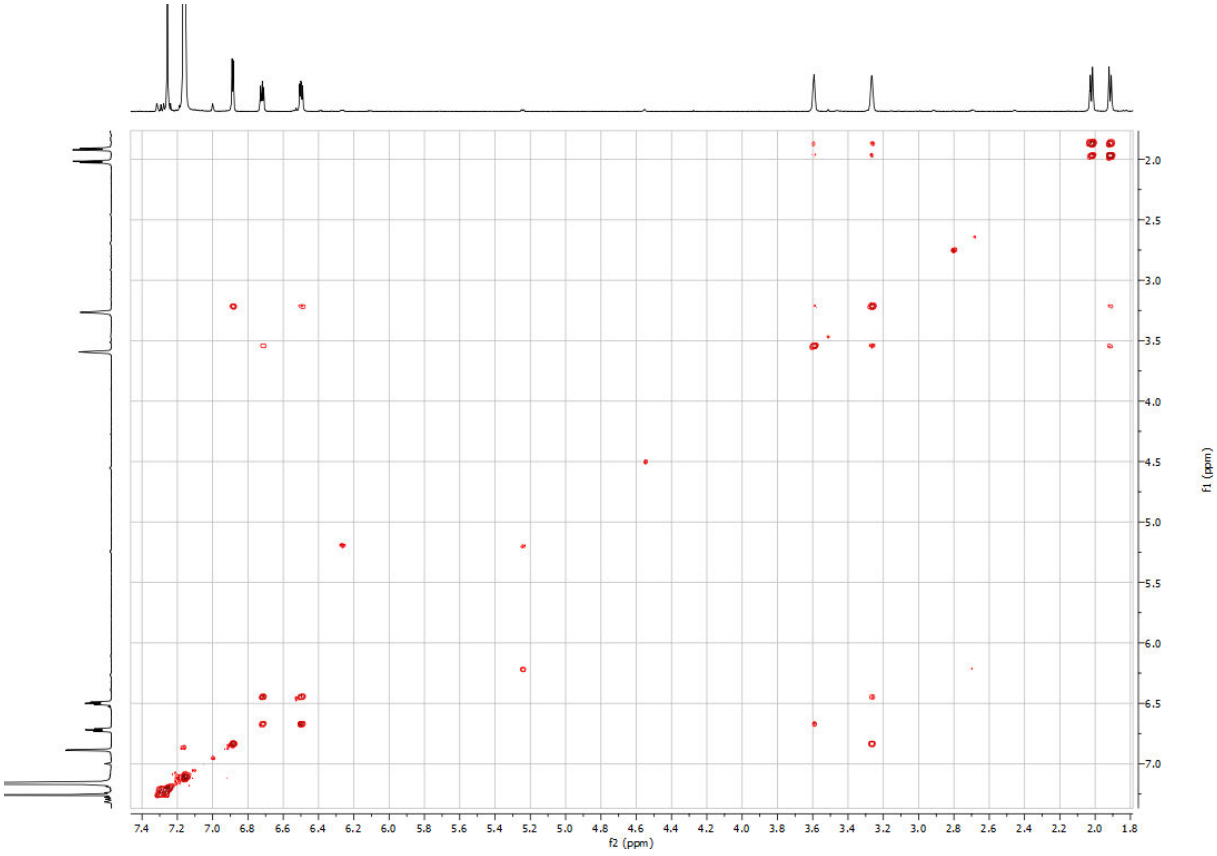

Figure S19: H,H-COSY NMR spectrum (500 MHz) of **1j** in benzene-d_6.

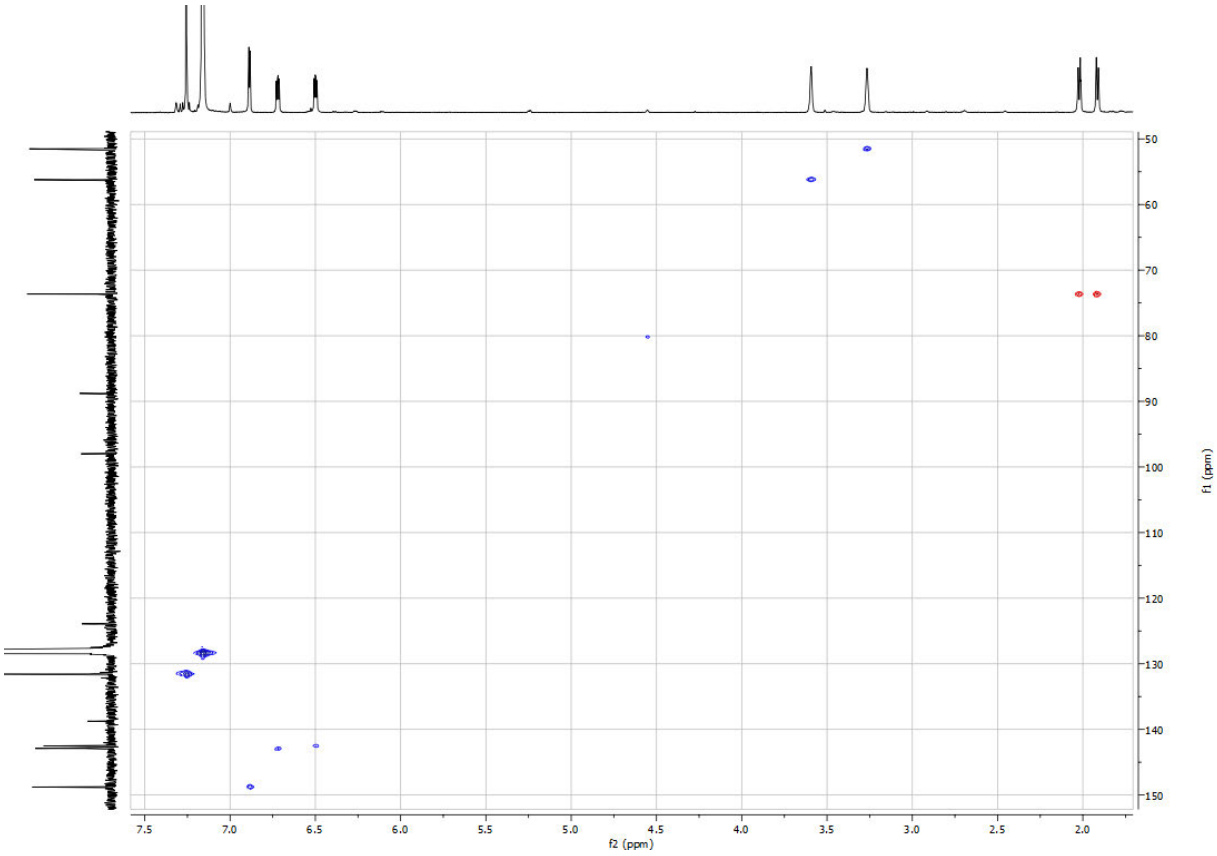

Figure S20: HSQC NMR spectrum (500 MHz) of **1j** in benzene-d_6.

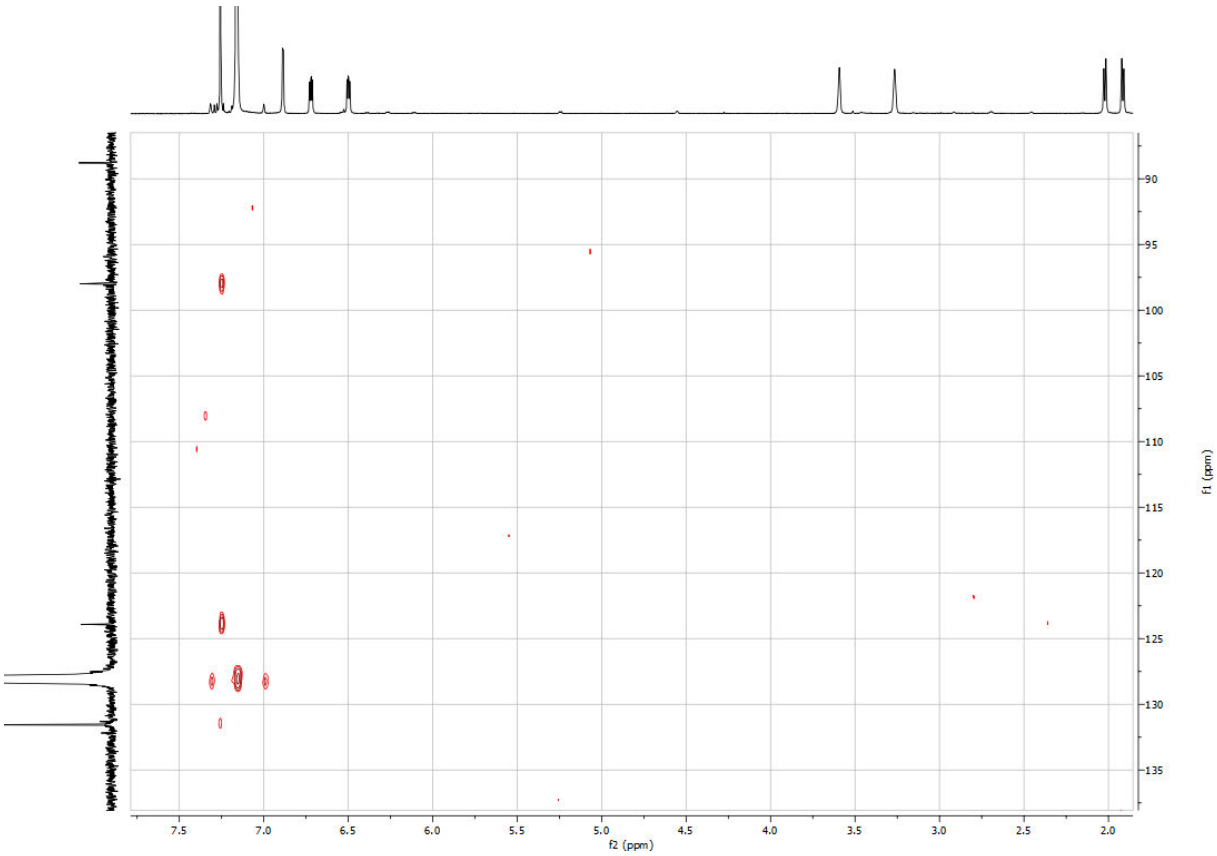

Figure S21: HMBC NMR spectrum (500 MHz) of **1j** in benzene-d_6.

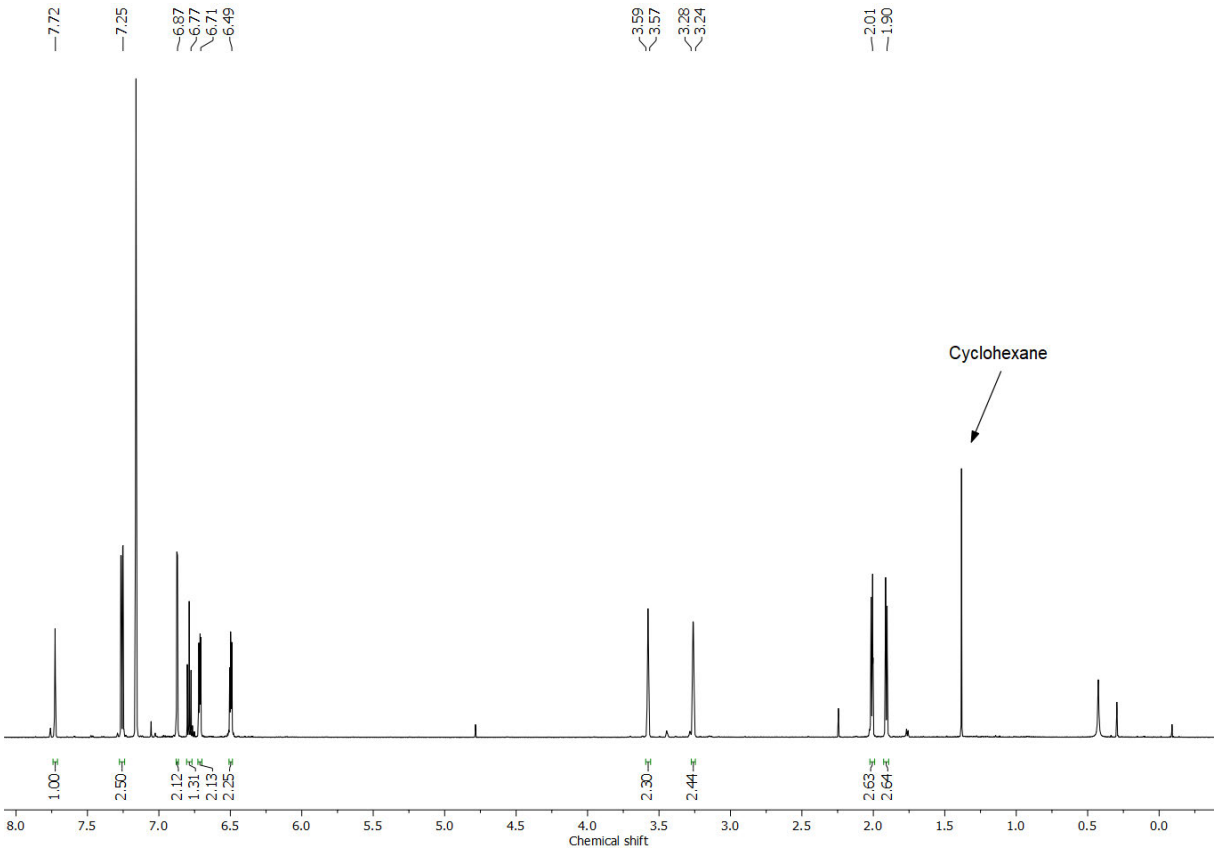

Figure S22: ^{1}H NMR spectrum (500 MHz) of **1k** in benzene-d_6.

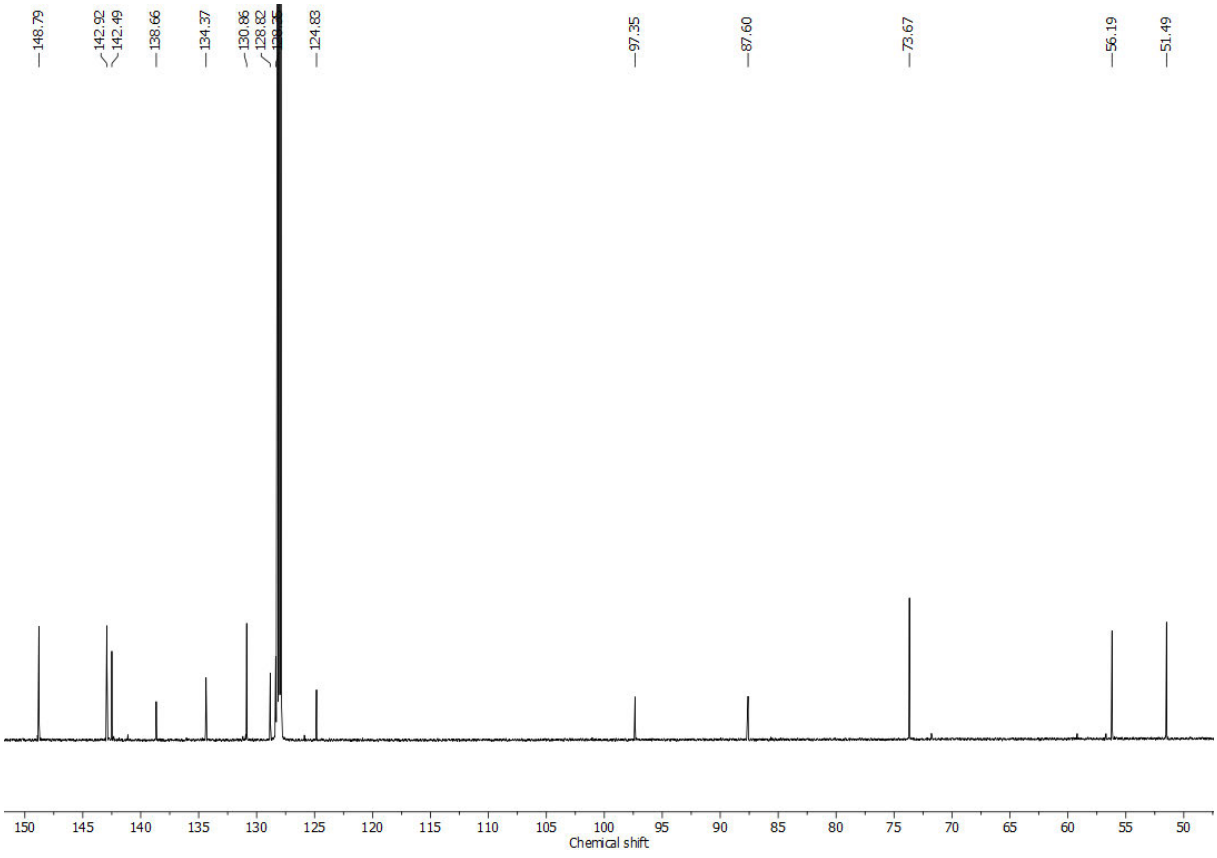

Figure S23: ^{13}C NMR spectrum (125 MHz) of **1k** in benzene-d_6.

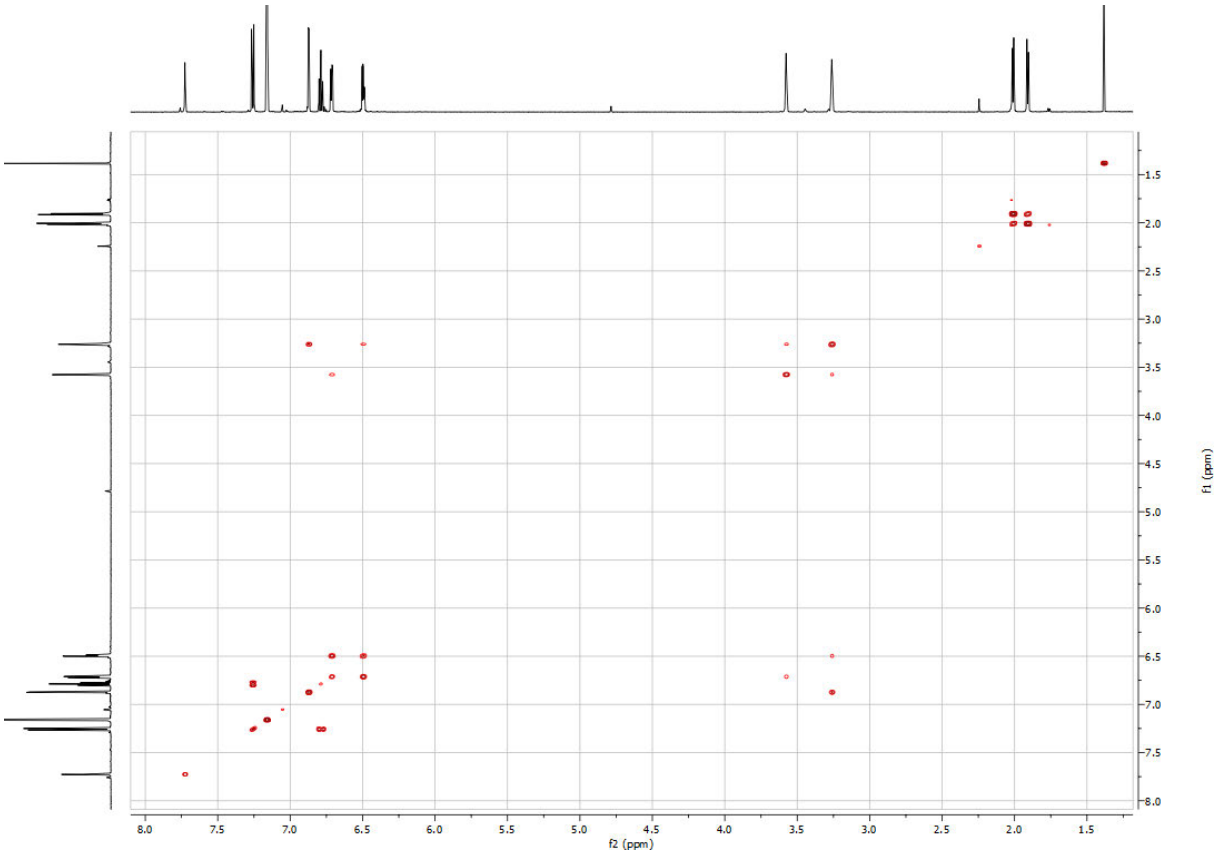

Figure S24: H,H-COSY NMR spectrum (500 MHz) of **1k** in benzene-d_6.

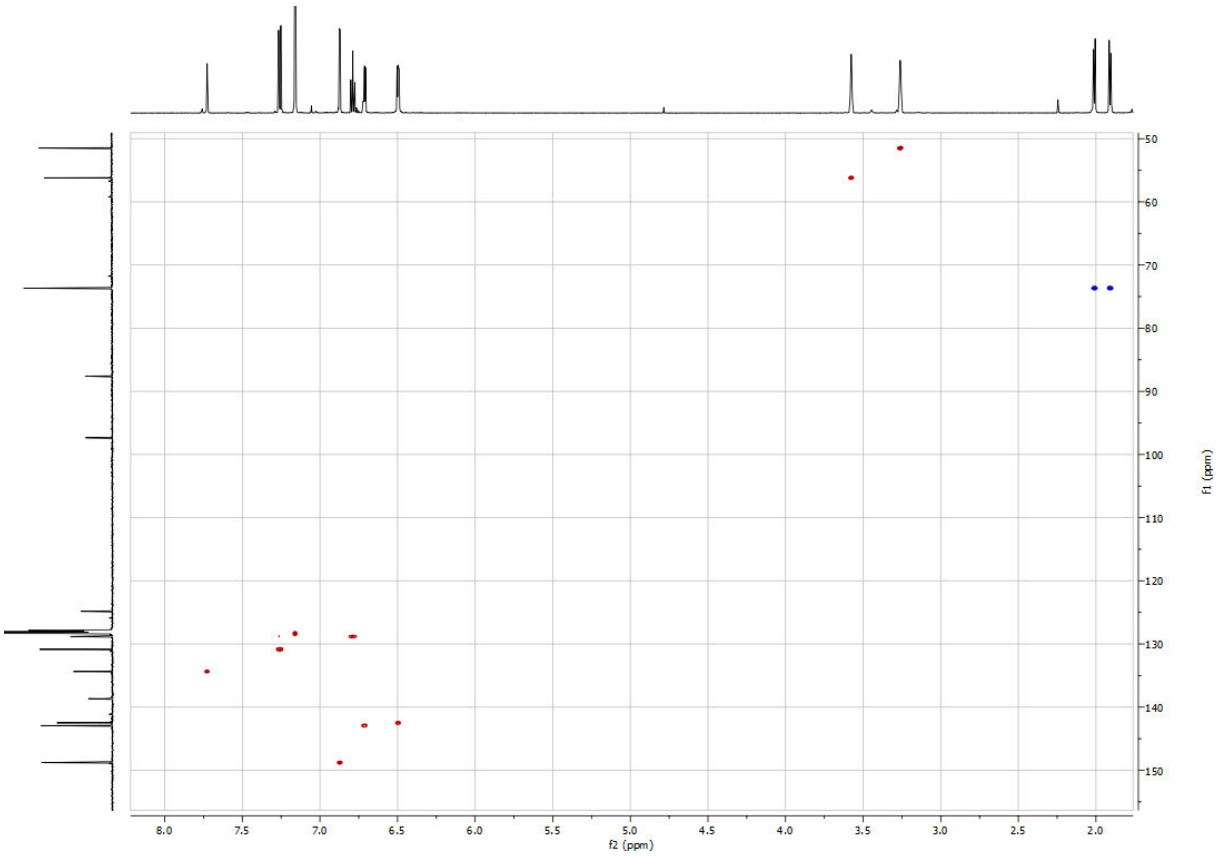

Figure S25: HSQC NMR spectrum (500 MHz) of **1k** in benzene-d_6.

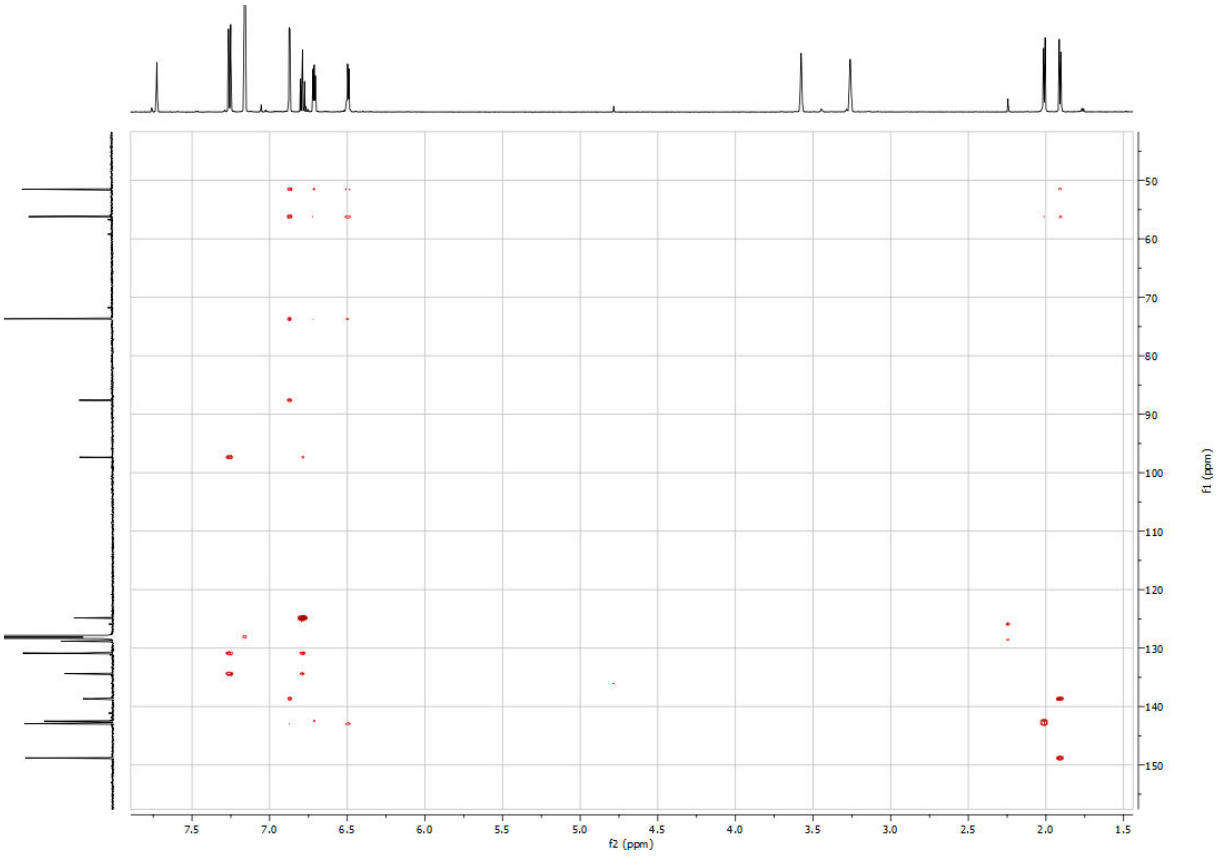

Figure S26: HMBC NMR spectrum (500 MHz) of **1k** in benzene-d_6.

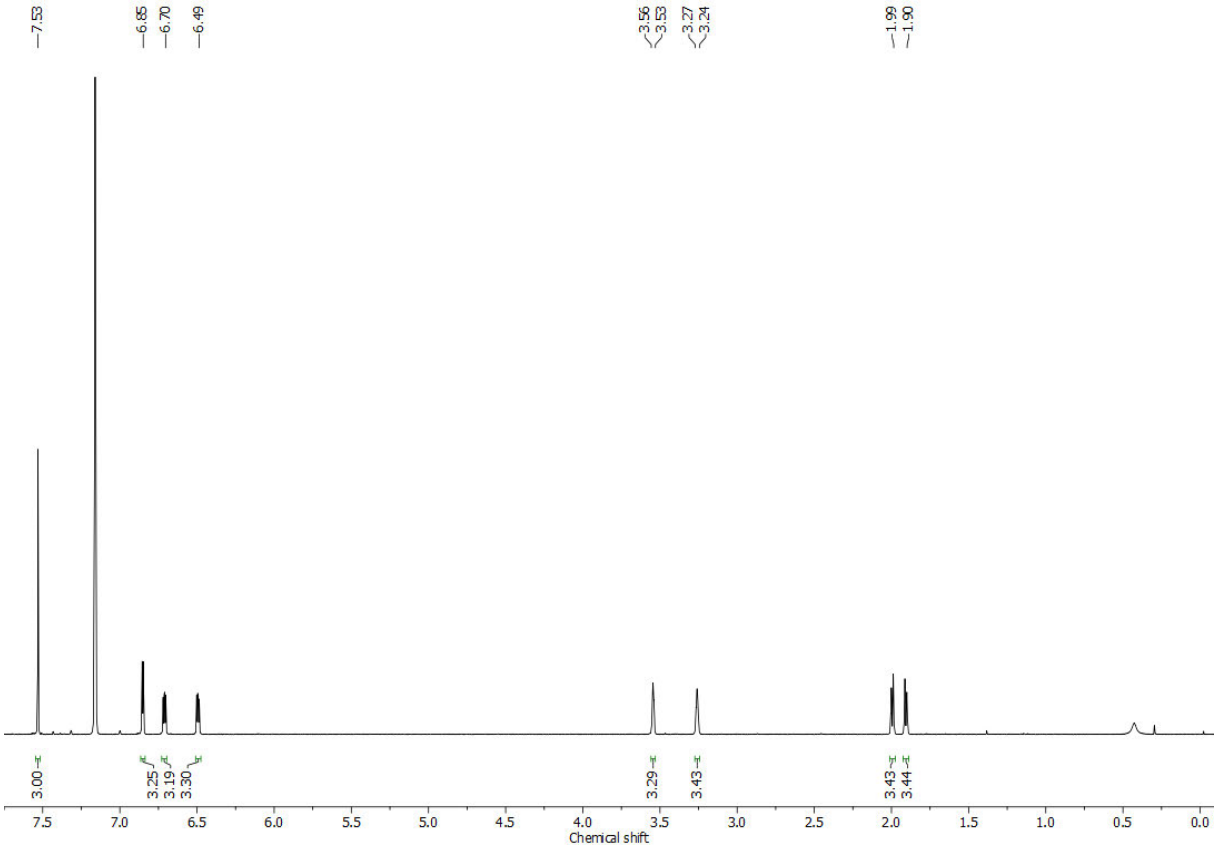

Figure S27: ^{1}H NMR spectrum (500 MHz) of **1l** in benzene-d_6.

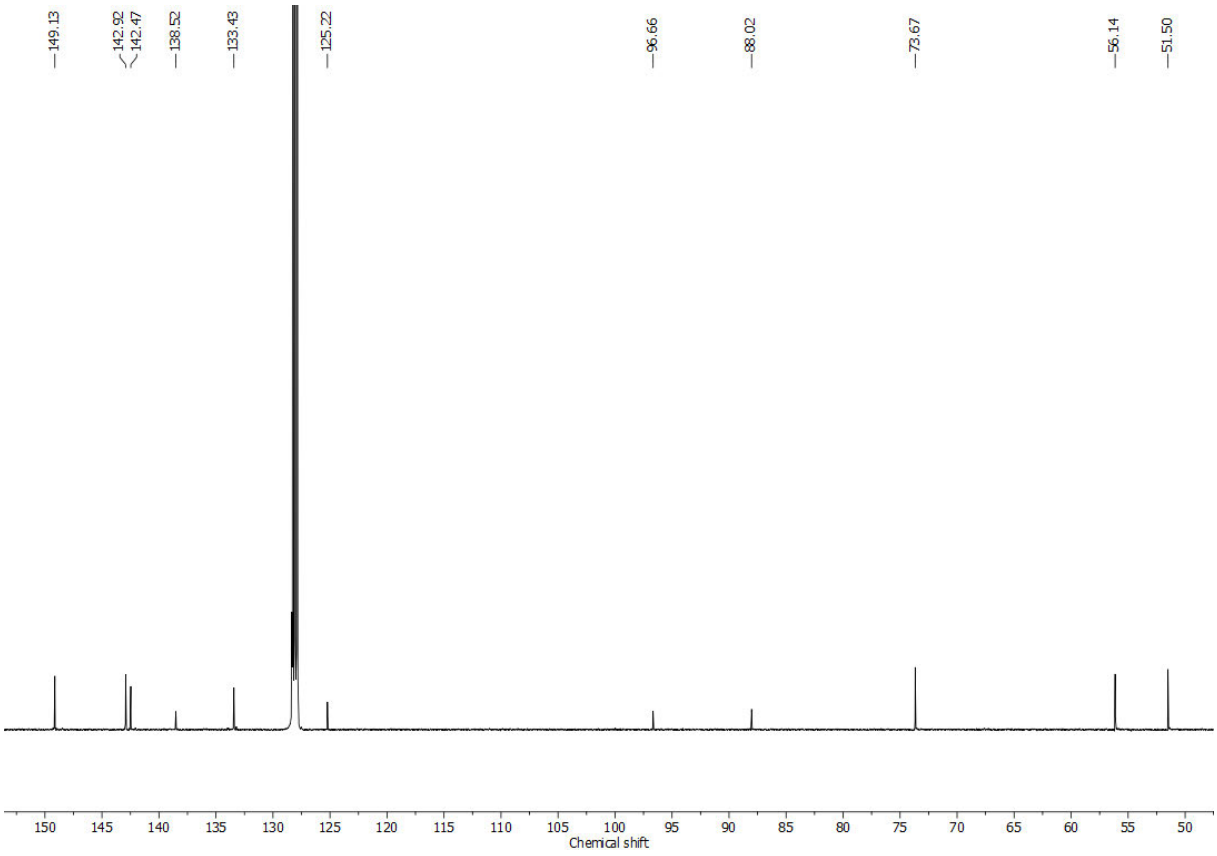

Figure S28: ^{13}C NMR spectrum (125 MHz) of **1l** in benzene-d_6.

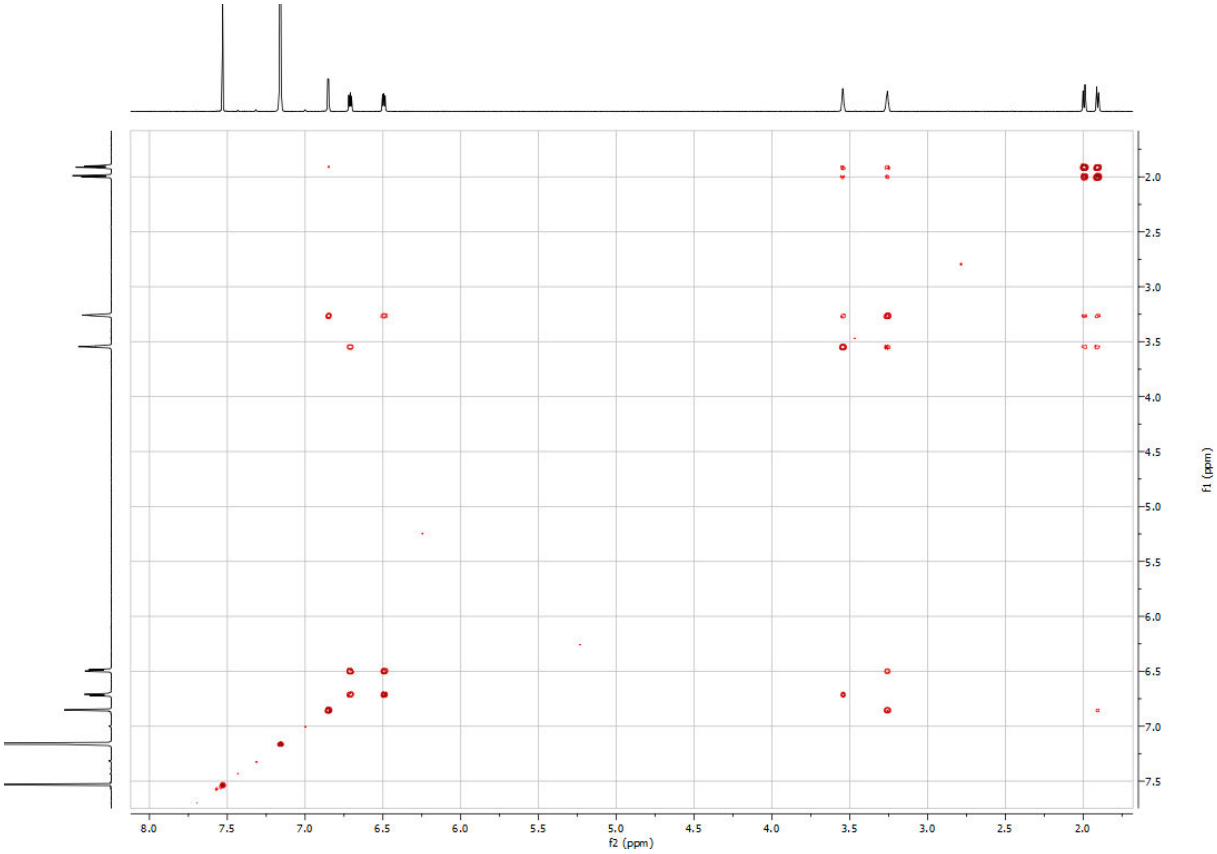

Figure S29: H,H-COSY NMR spectrum (500 MHz) of **1l** in benzene-d_6.

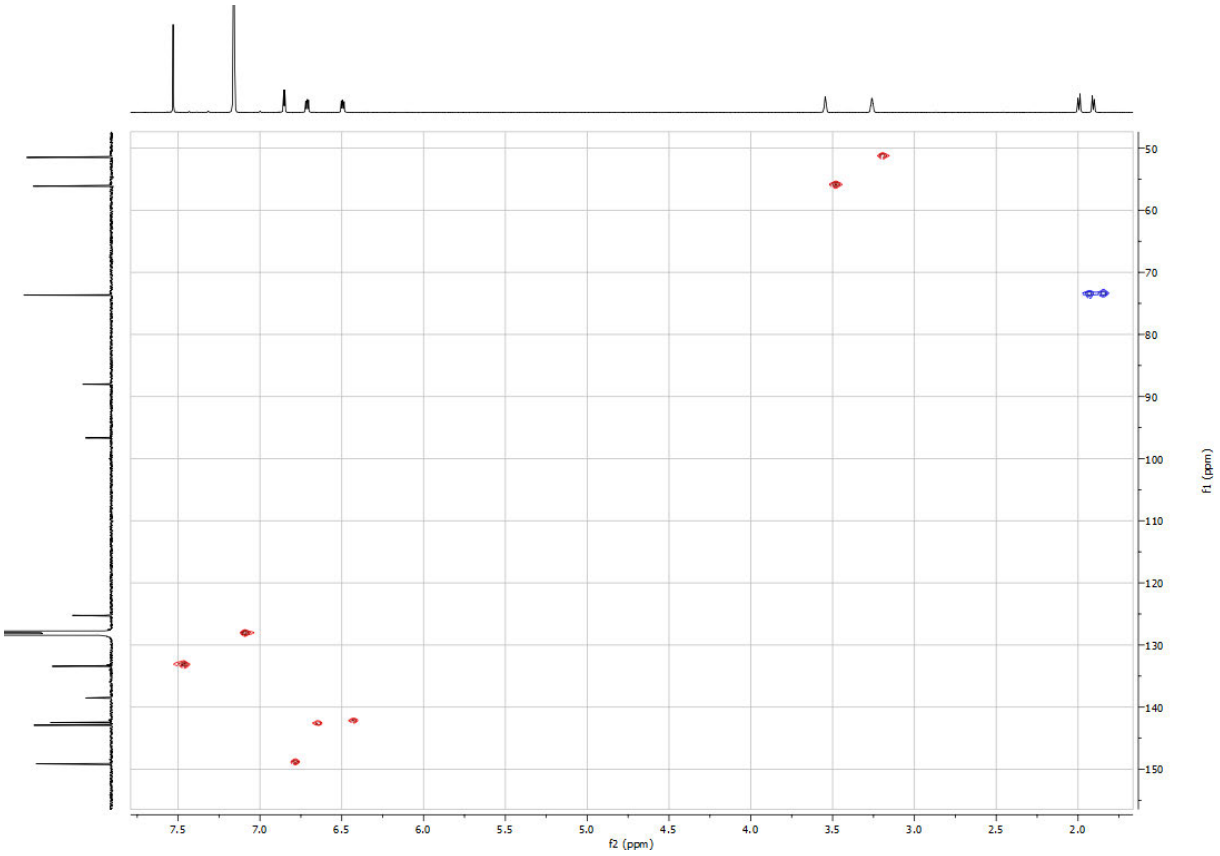

Figure S30: HSQC NMR spectrum (500 MHz) of **1l** in benzene-d_6.

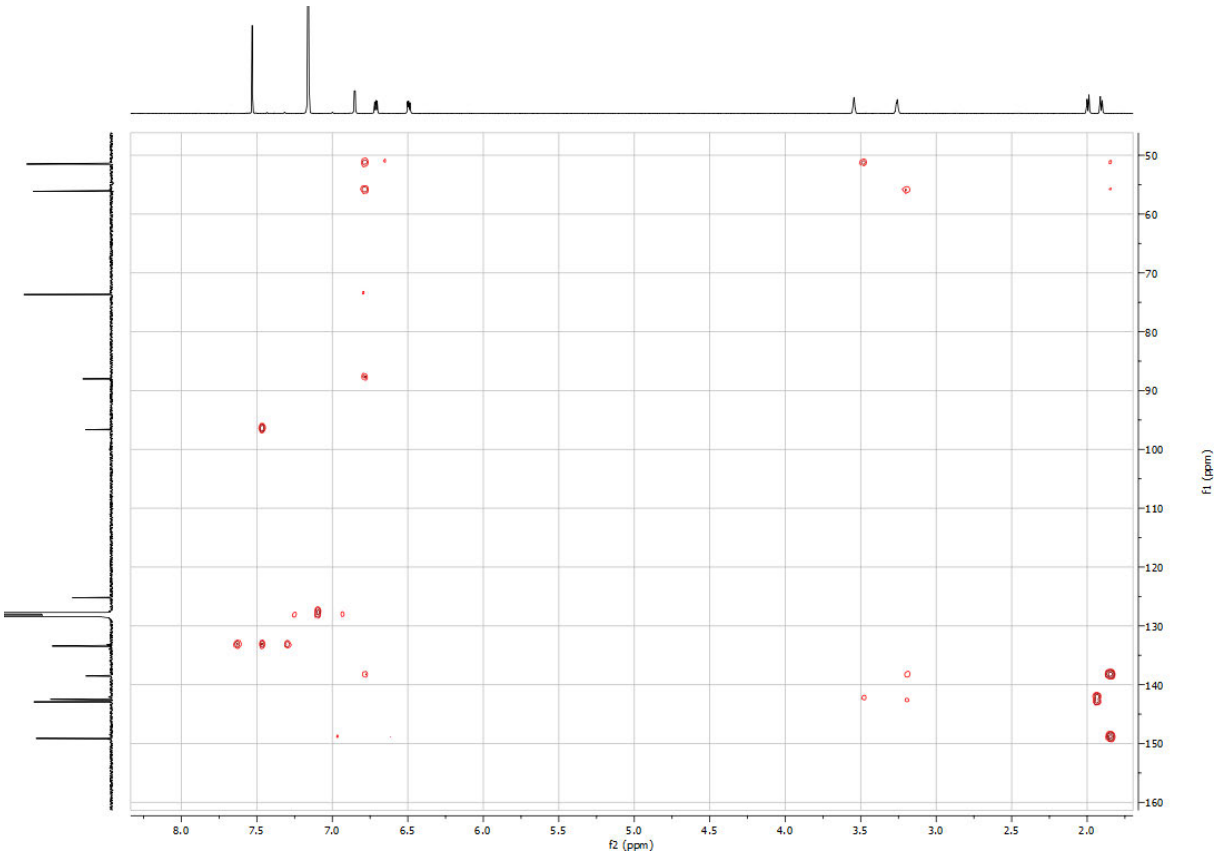

Figure S31: HMBC NMR spectrum (500 MHz) of **1l** in benzene-d_6.

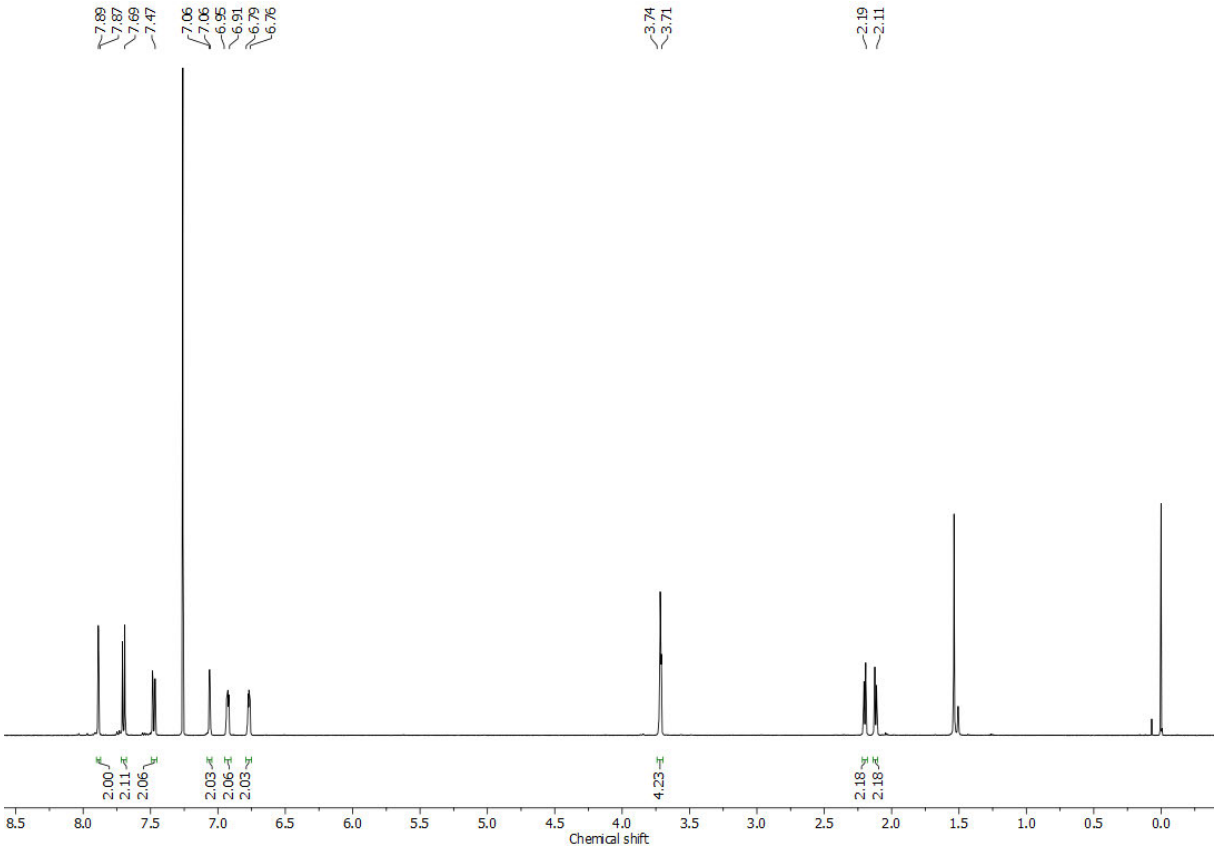

Figure S32: ^{1}H NMR spectrum (500 MHz) of **1n** in $CDCl_3$.

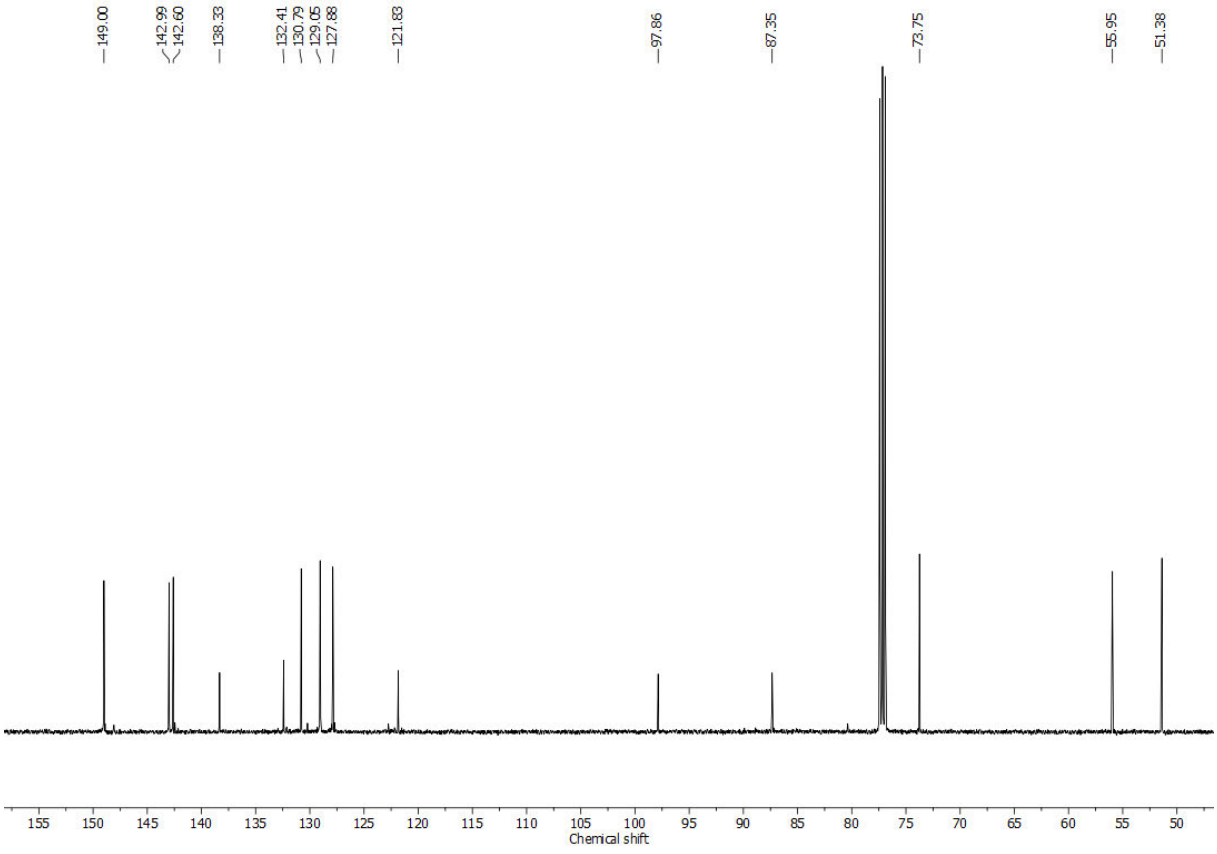

Figure S33: ^{13}C NMR spectrum (125 MHz) of **1n** in $CDCl_3$.

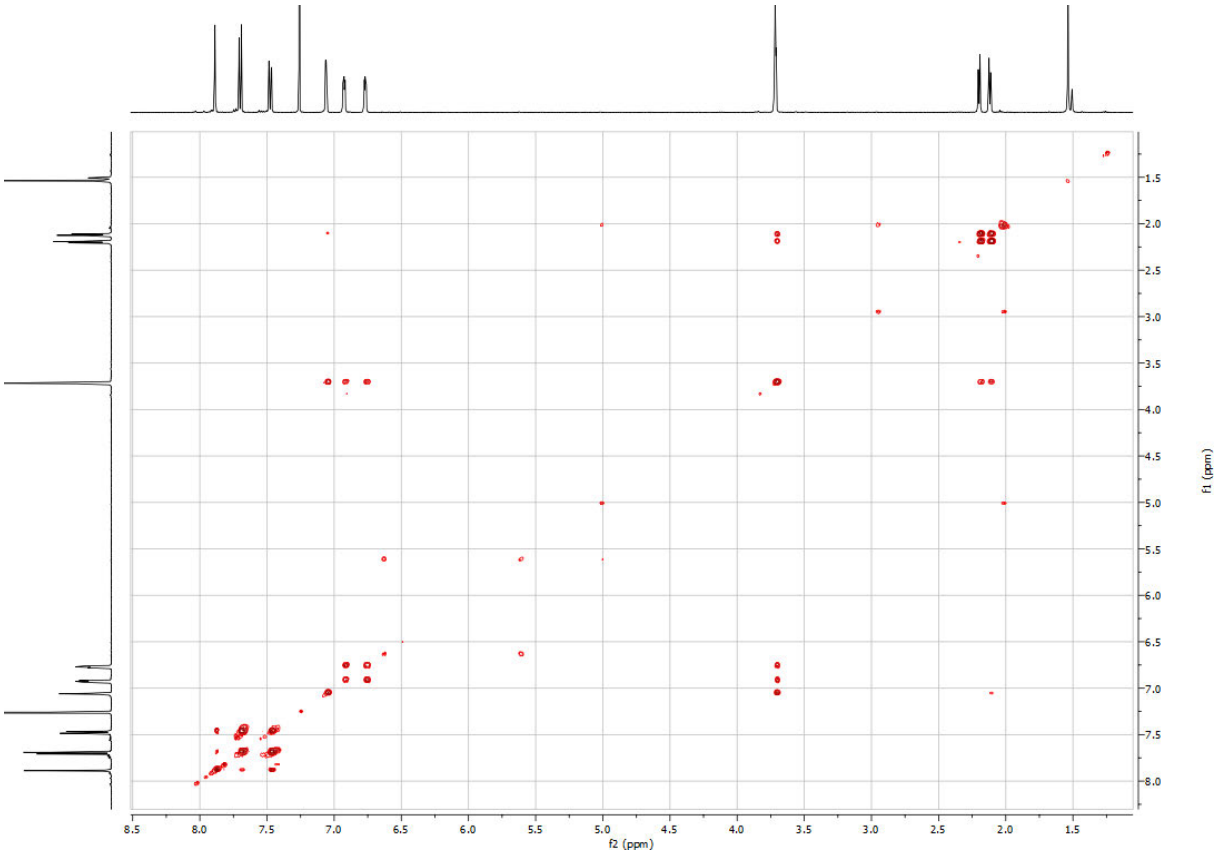

Figure S34: H,H-COSY NMR spectrum (500 MHz) of **1n** in $CDCl_3$.

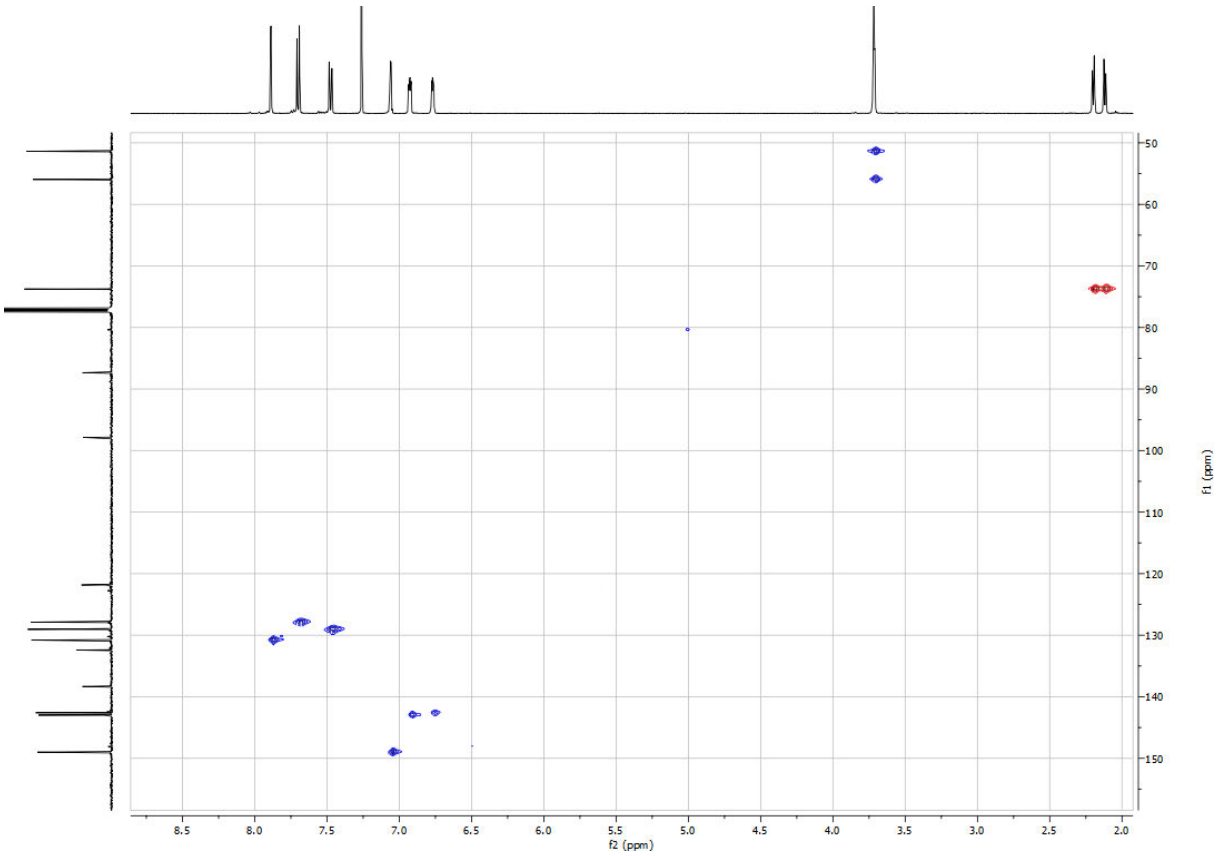

Figure S35: HSQC NMR spectrum (500 MHz) of **1n** in $CDCl_3$.

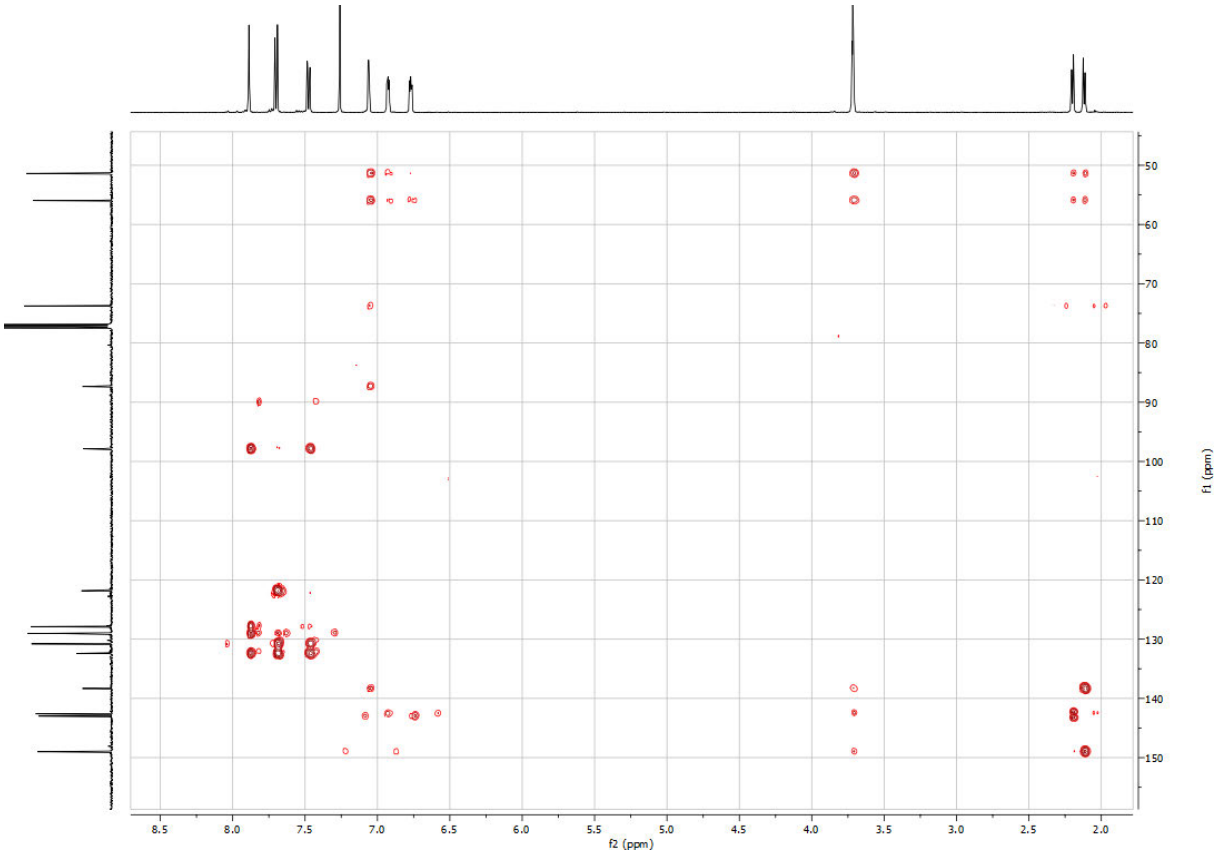

Figure S36: HMBC NMR spectrum (500 MHz) of **1n** in $CDCl_3$.

S9.2 NMR-spectroscopic monitoring of the photoreaction

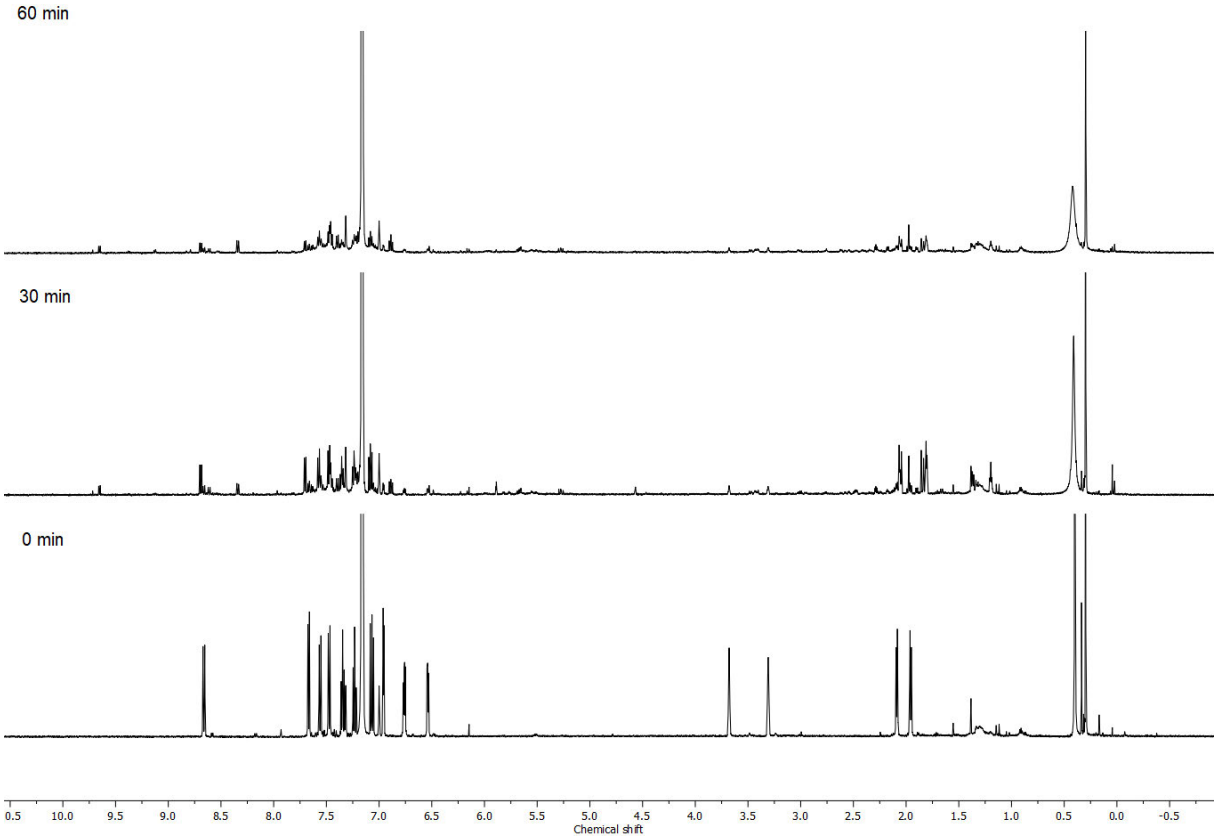

Figure S37: ^{1}H NMR spectra (500 MHz) of **1h** in benzene-d_6 before and after irradiation with λ_{ex} = 340 nm. Irradiation outside the NMR spectrometer.

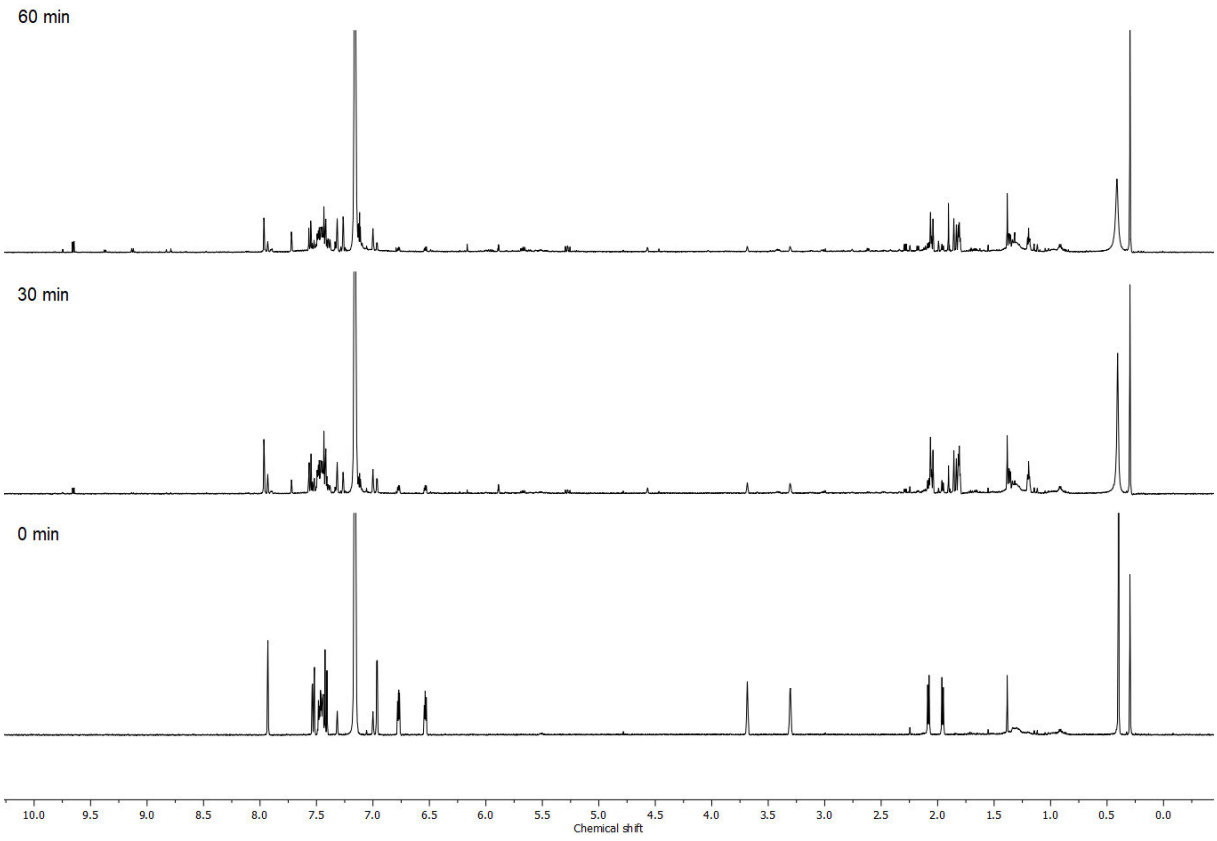

Figure S38: ^{1}H NMR spectra (500 MHz) of **1i** in benzene-d_6 before and after irradiation with λ_{ex} = 310 nm. Irradiation outside the NMR spectrometer.

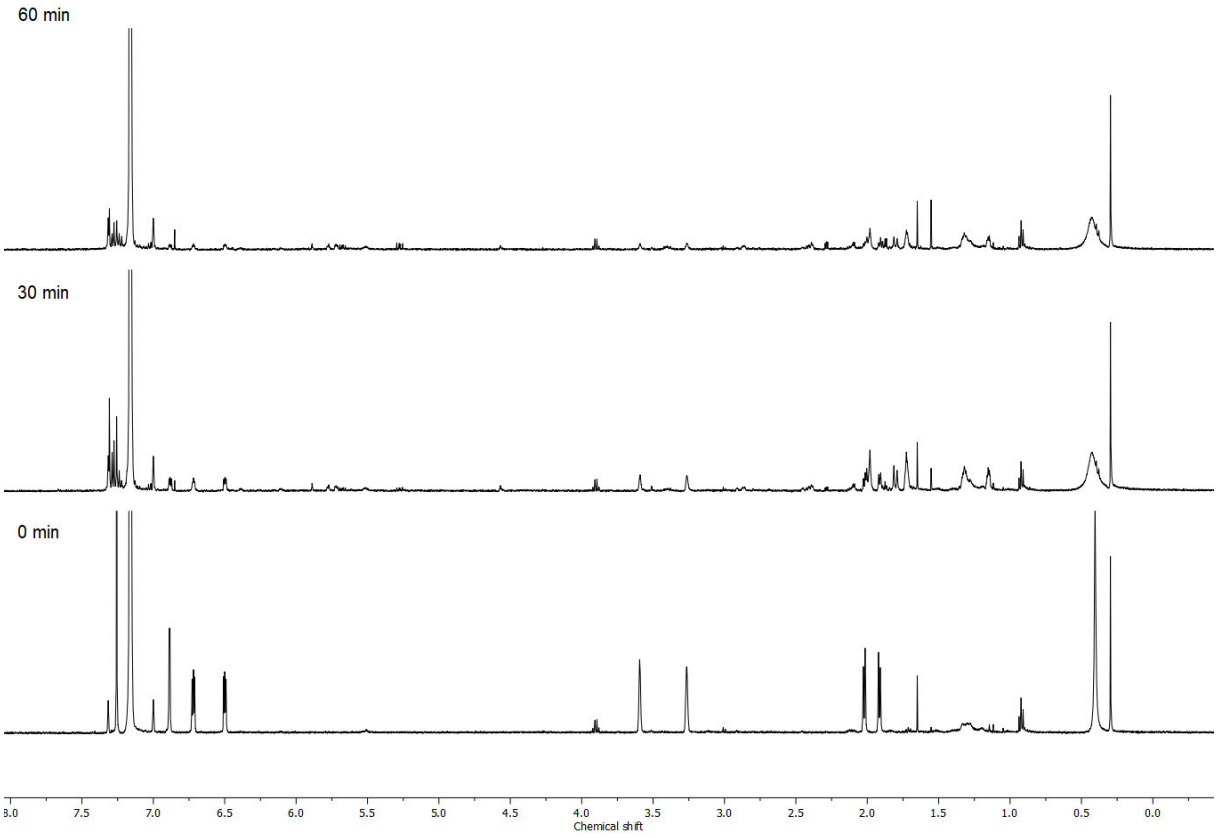

Figure S39: ^{1}H NMR spectra (500 MHz) of **1j** in benzene-d_6 before and after irradiation with λ_{ex} = 340 nm. Irradiation outside the NMR spectrometer.

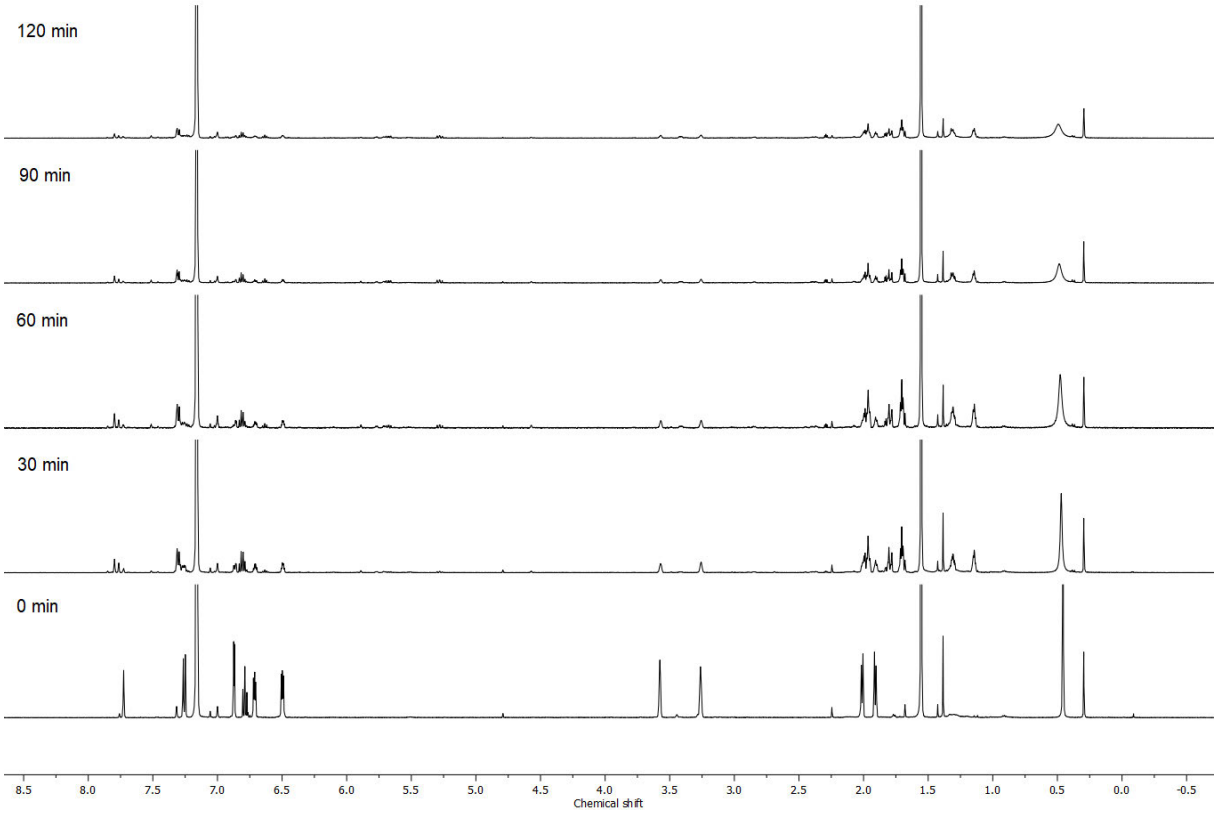

Figure S40: ^{1}H NMR spectra (500 MHz) of **1k** in benzene-d_6 before and after irradiation with λ_{ex} = 310 nm. Irradiation outside the NMR spectrometer.

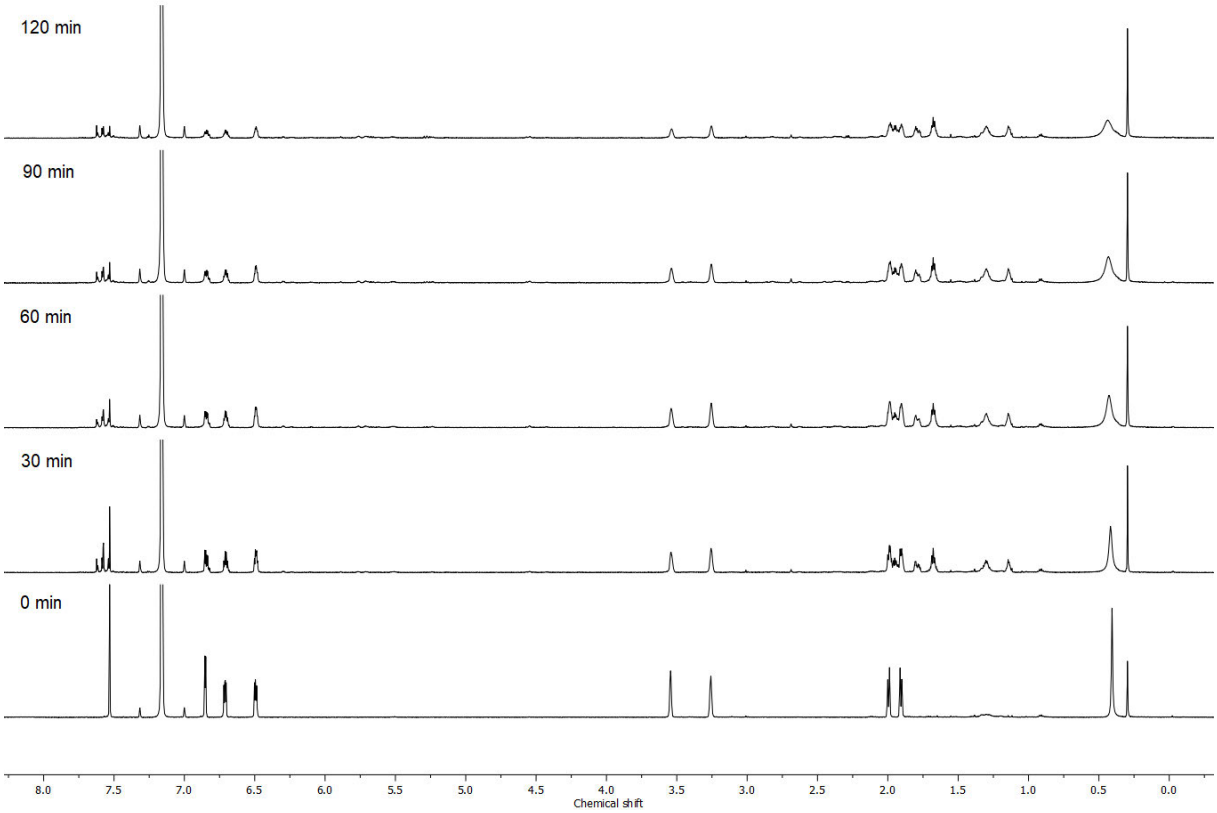

Figure S41: ^{1}H NMR spectra (500 MHz) of **1l** in benzene-d_6 before and after irradiation with λ_{ex} = 310 nm. Irradiation outside the NMR spectrometer.

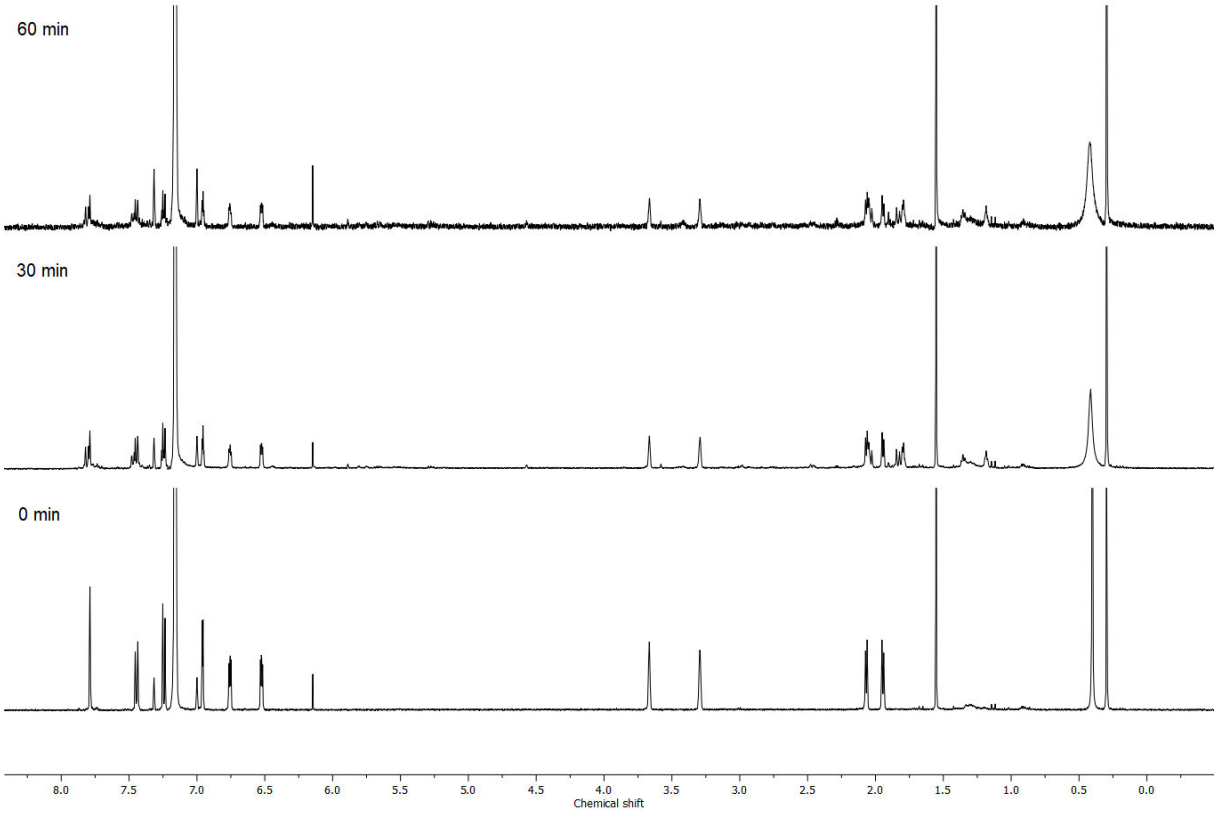

Figure S42: ^{1}H NMR spectra (500 MHz) of **1n** in benzene-d_6 before and after irradiation with λ_{ex} = 340 nm. Irradiation outside the NMR spectrometer.

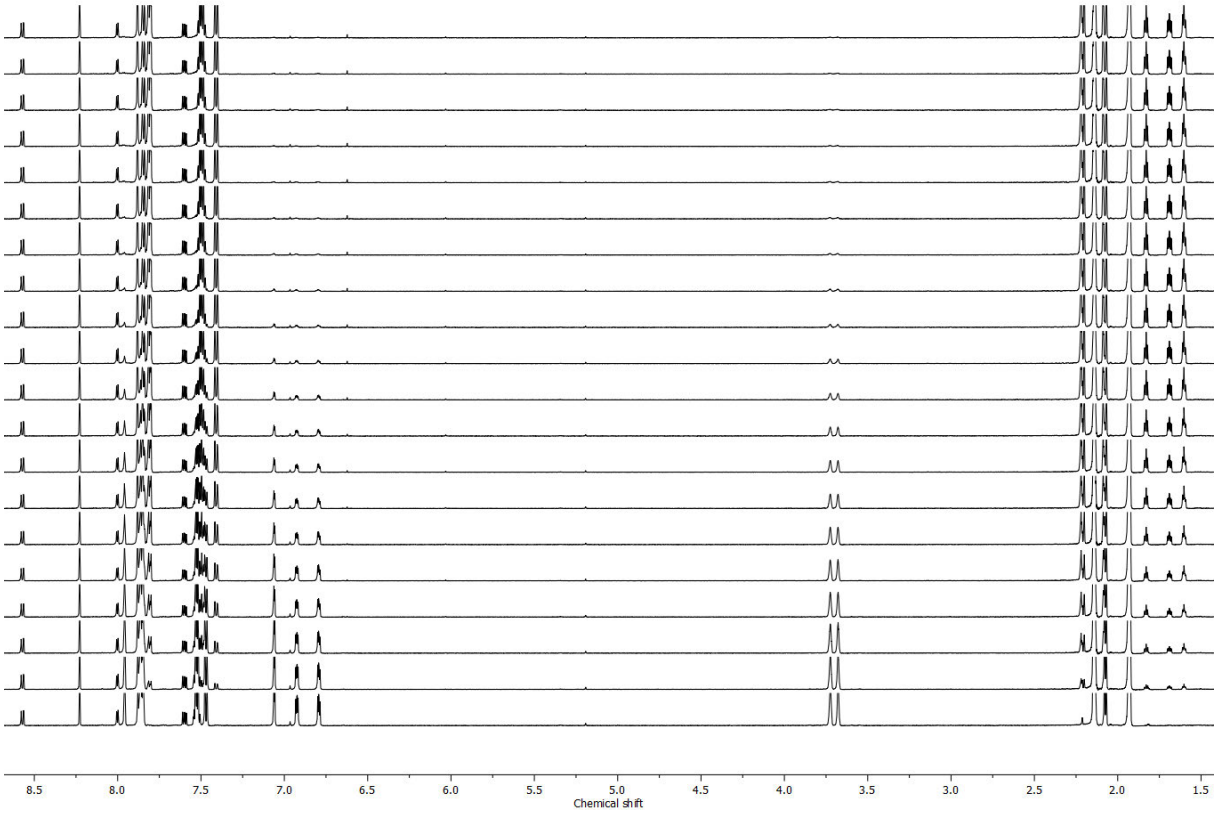

Figure S43: ^{1}H NMR spectra (600 MHz) of **1i** in the presence of $[Ru(phen)_3(PF_6)_2]$ mecn-d_3 after varying irradiation times with λ_{ex} = 520 nm. In-situ NMR irradiation, spectra were recorded in intervals of 1 min and displayed for 20 min.

S10 References

[1] T. Paululat, M. Rabe, D. V. Berdnikova, *J. Magn. Reson.* **2021**, *327*, 106990.
[2] OriginLab Corporation, OriginPro 8.5.1, Northhampton, MA, USA, 2011.
[3] P. Peluso, C. Greco, O. D. Lucchi, S. Cossu, *Eur. J. Org. Chem.* **2002**, 4024.
[4] a) I. R. Butler, C. Soucy-Breau, *Can. J. Chem.* **1991**, *69*, 1117; b) K. Ohta, T. Goto, Y. Endo, *Inorg. Chem.* **2005**, *44*, 8569.
[5] a) B. Blanco, A. Sedes, A. Peón, H. Lamb, A. R. Hawkins, L. Castedo, C. González-Bello, *Org. Biomol. Chem.* **2012**, *10*, 3662; b) H. Uji, J. Ogawa, K. Itabashi, T. Imai, S. Kimura, *Chem. Commun.* **2018**, *54*, 12483.
[6] X.-Y. Jin, C.-S. Wu, A.-D. Liu, L. Liu, L. Cheng, *Synthesis* **2022**, *54*, 1643.
[7] a) H. Maeda, T. Maeda, K. Mizuno, *Molecules* **2012**, *17*, 5108; b) Y.-P. Ou, J. Zhang, Y. Hu, J. Yin, C. Chi, S. H. Liu, *Dalton Trans.* **2020**, *49*, 16877.
[8] K. Gao, L. Xiao, Y. Kan, L. Li, Y. Yan, H. Huang, J. Peng, Y. Cao, X. Peng, *Chin. J. Chem.* **2016**, *34*, 353.
[9] C. G. Hatchard, C. A. Parker, *Proc. R. Soc. Lond. A* **1956**, *235*, 518.
[10] K. Stranius, K. Börjesson, *Sci. Rep.* **2017**, *7*, 41145.
[11] T. J. B. Zähringer, N. Lopez, R. Schulte, M. Schmitz, H. Ihmels, C. Kerzig, *Angew. Chem. Int. Ed.* **2024**, e202414733.
[12] T. J. B. Zähringer, M. Wienhold, R. Gilmour, C. Kerzig, *J. Am. Chem. Soc.* **2023**, *145*, 21576.
[13] A. M. Helms, R. A. Caldwell, *J. Am. Chem. Soc.* **1995**, *117*, 358.
[14] C. Petermayer, S. Thumser, F. Kink, P. Mayer, H. Dube, *J. Am. Chem. Soc.* **2017**, *139*, 15060.

10.10 Electronic Supplementary Information for Project [I]

Electronic Supplementary Material (ESI) for Physical Chemistry Chemical Physics.
This journal is © the Owner Societies 2023

Supporting Information

New Green-to-Blue Upconversion System with Efficient Photoredox Catalytic Properties

Jorge Castellanos-Soriano,[a] Till J. B. Zähringer,[b] Jorge C. Herrera-Luna,[a] M. Consuelo Jiménez,[a] Christoph Kerzig*[b] and Raúl Pérez-Ruiz*[a]

[a] Departamento de Química, Universitat Politècnica de Valencia, Camino de Vera S/N, 46022, Valencia, Spain
[b] Department of Chemistry, Johannes Gutenberg University Mainz, Duesbergweg 10-14, 55128 Mainz, Germany

*Corresponding Authors
E-mails: ckerzig@uni-mainz.de; raupreru@upv.es

TABLE OF CONTENTS

This page……. S1

1- Materials & Methods…….. S2

2- Synthesis of **BDP-Br**…….. S8

3- Crystallographic data of **BDP** & **BDP-Br**…….. S11

4- Photophysical and photochemical properties……. S13

5- Cyclic Voltammetry…… S19

6- Coupling reactions…….. S20

7- ^{1}H, ^{13}C, ^{11}B and ^{19}F NMR spectra…….. S23

8- Mass spectrum of **BDP-Br**……. S31

9- Geometrical parameters from Crystallographic data……. S32

1. Materials & Methods

Reagents

Reagents (≥ 97% purity) and solvents (≥ 99% purity) used in this work were all purchased from commercial suppliers (Merck, TCI, Apollo Scientific, Fluorochem, Scharlab) and used as received unless otherwise indicated. Sensitizer **BDP-Br** was synthesized as described (*vide infra*), whereas the acceptor 2,5,8,11-tetra-*tert*-butylperylene (**TBPe**) is commercially available from Sigma Aldrich, 99% purity. $[Ru(bpy)_3](PF_6)_2$ was obtained by a counter ion exchange starting from $[Ru(bpy)_3]Cl_2$ (from Sigma Aldrich, > 99% purity) and excess NH_4PF_6. Compound $[Os(phen)_3](PF_6)_2$ was prepared by following previously reported protocol.[1]

Reactions

General procedure: In a 4mL quartz cuvette with a magnetic stirrer, 1 eq of 2-acetyl-5-chlorothiophene and the corresponding equivalents of trapping agent were placed in a solvent mixture composed by ACN/DMA 4:1, then 1 eq of dodecanenitrile as internal standard was added and the cuvette was sealed under Ar atmosphere, partially submerged in a cold water bath and irradiated by a Q-Switch laser (Quantel Brilliant, λ_{exc} = 532 nm, 10 MHz, ~1 mJ per pulse, ~5 ns fwhm). The photoreaction was followed by TLC on commercial SiO_2-coated aluminium plates (DC60 F254, Merck). Visualization was done by UV-light 254 nm. After 4h, the crude of the reaction was extracted with ethyl acetate, washed with brine and evaporated under vacuum. Finally, the product was purified by high performance liquid chromatography (HPLC) using ACN/H_2O 90/10 as eluent. Yield products were estimated as: [conversion × selectivity]/mass balance.

Irradiation light sources

The coupling reactions were carried out using a Quantel pulsed q-switched frequency doubled YAG laser (Quantel Brilliant B pulsed YAG laser, λ_{exc} = 532 nm, 10 Hz, ~1 mJ per pulse, ~4 ns fwhm, Figure S1A). Additionally, experiments using green LEDs (AVONEC, 3W, 515-525 nm) were also performed (Figure S1B).

[1] K. D. Demadis, D. M. Dattelbaum, E. M. Kober, J. J. Concepcion, J. J. Paul, T. J. Meyer and P. S. White, *Inorganica Chim. Acta*, 2007, **360**, 1143–1153.

A

B

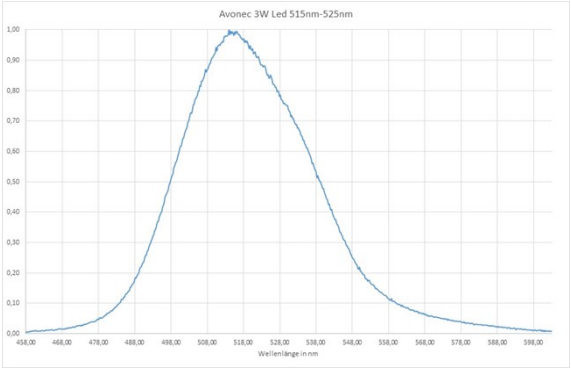

Figure S1. A: Pictures of the laser setup used in the photoreactions. **B:** Lamp emission spectrum of the green light LED.

A 514 nm laser from Roithner Lasertechnik with an adjustable output (maximum optical output of 800 mW) and a beam diameter of 3.0 mm^2 (see Figure S2 for data sheet) was used to examine the UC emission, UC quantum yield and photostability of **BDP-Br**.

ROITHNER LASERTECHNIK

Testing Reports

All testing is based on the required specifications in the purchase order.

Model: RLTMDL-520-800-3-CF62035(PO#210255)

Inspection reports

Items of specs	Testing	Attachments
Output Power	827mW	Graph1
Power Stability over 4 hours	0.111%	Graph1
Operating Mode	CW	/
Transverse Mode	Multimode	/
Beam Diameter	~1.0×3.0mm²	/
Beam Divergence (full angle)	< 4.0×0.5mrad	/
P-I	/	Graph2
Warm-up Time	< 5min	/
Beam height from base	29mm	/
Dimensions of Laser Head	157.5×77×60mm³	/
Weight of Laser Head	0.9kg	/
Power Supply	85-264V	/
Integrated Driver	PSU-III-LED	/
Dimensions of Driver	188.6×155×92mm³	/
Weight of Driver	1.5kg	/
Modulation	NO	/

Inspector: 284

Date: 2021-06-30

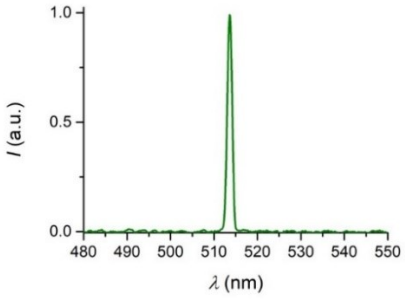

Figure S2. Left: Data sheet of the 514 nm cw laser from Roithner Lasertechnik. Right: Emission spectrum measured by irradiating a water-containing cuvette in the emission spectrometer (*i.e.*, by recording laser stray light).

Characterization

Determination of purity and structure confirmation of the literature known products was performed by ^{1}H, ^{13}C, ^{19}F, ^{11}B and ^{31}P NMR and low-resolution mass spectrometry (LRMS)–LRMS measurements were replaced by high-resolution mass spectrometry (HRMS) in case of unknown products. NMR spectral data were collected on a Bruker Advance 400 (400 MHz for ^{1}H; 101 MHz for ^{13}C; 376 MHz for ^{19}F; 128 MHz for ^{11}B; 162 MHz for ^{31}P) spectrometer at 20 °C. Chemical shifts are reported in δ/ppm, coupling constants J are given in Hertz. Solvent residual peaks were used as internal standard for all NMR measurements. The quantification of ^{1}H cores was obtained from integrations of appropriate resonance signals. Abbreviations used in NMR spectra: s = singlet, d = doublet, t = triplet, q = quartet, m = multiplet, bs = broad singlet, dd = doublet of doublet, ddd = doublet of doublet of doublet. HRMS was carried out was performed in the mass facility of SCSIE University of Valencia. LRMS was carried out on an HP 6890 Series GC System with Agilent 5973 Network Mass Selective Detector and H_2 as carrier gas. Abbreviations used in MS spectra: M—molar mass of target compound, EI—electron impact ionization, ESI—electrospray ionization. For computing the data of X-Ray experiments the following specifications were used: Data collection: APPEX3v2022.1-1 (BRUKER AXS, 2021); cell refinement: SAINT V8.40B (Bruker AXS LLC, 2019); data reduction: SAINT V8.40B (Bruker AXS LLC, 2019); program(s) used to solve structure: SHELXT2018/2 (Sheldrick, 2015); program(s) used to refine structure: SHELXL2019/1 (Sheldrick, 2019); molecular graphics: ORTEP for Windows (Farrugia, 2012); software used to prepare material for publication: WinGX publication routines (Farrugia, 2012).

Photophysical characterization

Ultraviolet–visible spectra (UV–Vis) of the liquid samples were obtained by a JASCO V-650 spectrometer. The emission spectra were carried out using an Edinburgh FS5 spectrofluorometer. The samples were placed into quartz cells of 1 cm path length. Compound concentrations were fixed as indicated.

Absolute fluorescence quantum yields were measured by using an Edinburgh FS5 spectrofluorometer with a SC-30 integration sphere module. The absolute method requires two measurements; the number of absorbed photons and the number of the emitted photons. The number of absorbed photons of a sample is determined by the

reduction of the light scatter compared to a blank measurement. The quantum yield calculation is made using a wizard within the operating software.

The UC emission, UC quantum yield and photostability of **BDP-Br** were measured with a Perkin Elmer FL-6500 spectrometer at room temperature (295 ± 2 K) and the emission spectra were corrected for the wavelength-dependent sensitivity of the instrument.

Laser flash photolysis

Two different setups were used for laser flash photolysis (LFP) experiments.

Setup from the Mainz team: An LP980KS setup from Edinburgh Instruments equipped with an Nd:YAG-laser from Quantel (Q-smart 450) was used for laser flash photolysis to record transient absorption and emission signals. The frequency-doubled output with a wavelength of 532 nm, a pulse duration of ~10 ns, a frequency of 10 Hz and a typical energy of ~12 mJ served as the excitation source. A constant laser output energy is highly important for quantitative measurements like the intersystem crossing quantum yield determination. Hence, pulse energies were unchanged for each series of experiments and control measurements established the laser output stability A beam expander (Thorlabs) was used to ensure homogeneous excitation in the detection volume. Detection of transient absorption spectra occurred on an iCCD camera from Andor. Single-wavelength kinetics were recorded using a photomultiplier tube from Hamamatsu (R928). The spectroscopic experiments were performed using a cuvette holder that allows temperature control. If not stated otherwise the LFP measurements were performed at 293 K and the transient absorption spectra were integrated over 100 ns.

Setup from the Valencia team: Delayed fluorescence quenching experiments were performed by LFP using The LP980–KS Laser Flash Photolysis Spectrometer (from Edinburgh Instruments) which is a combined system for the measurement of laser induced transient absorption, emission kinetics and spectra, with the ability to automatically convert and fully analyse the kinetic and spectral information. The pump is an INDI Quanta-Ray Nd:YAG laser equipped with a primoSCAN BB optical parametric oscillator (OPO) from SPECTRA PHYSICS®. The probe pulse is longer than the recorded time window of a measurement, and a monochromator (TMS302-A, grating 150 lines mm^{-1}) disperses the probe light after it passed the sample. The probe light can be then passed on to a PMT detector (spectral S5 range 200–870 nm) to obtain

the temporal resolved picture. All components are controlled by the software L900 provided by Edinburgh.

For our delayed emission measurements, the probe shutter is closed so that no light from the Xe lamp is exciting the sample and the laser is only used as a light source. To photolyze our samples, a 532 nm monowavelength was employed, ensuring that only the **BDP-Br** chromophore absorbs the excited photons. The data have been acquired as an average of several shots to improve the signal-to-noise ratio.

Phosphorescence measurements

Phosphorescence spectrum was obtained using an Edinburgh FS5 spectrofluorometer with a SC-70 Liquid Nitrogen Dewar module in order to record samples in quartz tubes (4mm ID) under crystalized EtOH at 77K.

Fluorescence lifetime measurements

The measurements were carried out in a *EasyLife X* Lifetime Fluorescence Spectrometer connected to a temperature control system working with liquid refrigeration. Samples were placed in a 4mL quartz cuvette and irradiated with a 407 nm LED as energy source. The wavelength bellow 475 nm was filtered.

Electrochemical characterization.

The redox potentials were measured by cyclic voltammetry with an AUTOLAB PGSTAT100 potentiostat. All measurements were made in deaerated acetonitrile containing tetrabutylammonium tetrafluoroborate (0.1 M) as supporting electrolyte, a glassy carbon as working electrode, a platinum wire as counter electrode, a silver wire as pseudo reference and ferrocene (0.01 M) as internal standard. The scan rate was 100 $mV \cdot s^{-1}$. Potentials are reported with respect to the saturated calomel electrode (SCE) as reference.

Upconversion quantum yields

The quantum yields of the UC system was estimated by the ratio of (integrated) upconverted photons generated relative to the integrated emission of a reference system with a well-known quantum yield. For that, the photoluminescence intensity of a solution containing $[Ru(bpy)_3](PF_6)_2$ ($\Phi_{Ph} = 0.095$)[2] in deaerated ACN in the absence of the annihilator was measured under identical conditions as the complete upconversion

[2] 1. K. Suzuki, A. Kobayashi, S. Kaneko. *et al. Phys. Chem. Chem. Phys.*, **11**, 9850-9860 (2009)

system. Neutral density filter from Newport and Thorlabs were used to attenuate the laser output. Oxygen was removed from the solvent by five freeze-pump-thaw cycles using custom-made Schlenk-cuvettes and argon as an inert gas, liquid N_2 for cooling, and Schlenk line vacuum (down to 0.5 mbar).

Stern–Volmer quenching experiments.

Stern–Volmer experiments were conducted to determine the triplet energy transfer rate k_{TTEnT} of **BDP-Br** to **TBPe** and the quenching rate k_q of the UC emission with 2-acetyl-5-chlorothiophene according to equation (1), with τ as the lifetime, F as the fluorescence intensity, c_q as the quencher concentration and K_{SV} as the Stern–Volmer constant. The index 0 is used in the absence of quencher.

$$\frac{\tau_0}{\tau} = \frac{F_0}{F} = 1 + \tau_0 \cdot k_q \cdot c_q = 1 + K_{SV} \cdot c_q \quad (1)$$

Additional steady-state emission quenching experiments were carried out monitoring the **TBPe** emission (excitation wavelength, 405 nm; solvent, neat ACN) in the presence of different 2-acetyl-5-chlorothiophene concentrations. A Perkin Elmer FL-6500 spectrometer was employed for these measurements.

2. Synthesis of BDP-Br

The compound **BDP-Br** was synthesized following the methodologies described on the bibliography.[3,4] Thus, the first step was the oxidative addition of 4-fluorothiophenol to the starting 2,3-dimethylpyrrol carboxaldehyde, followed by the condensation of the corresponding trialkylpyrrole with formylpyrrole in methanol in the presence of HBr as a catalyst, next to the corresponding difluoroborate complexes formation. These two steps can be typically found in the literature. Finally, bromide addition can be carried out quantitatively by NBS complex treatment. The different reaction steps are explained as follows:

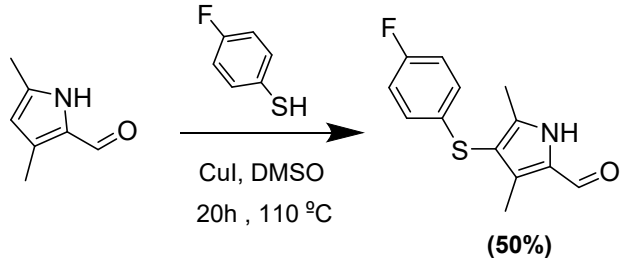

Synthesis of compound A: 3,5-Dimethylpyrrole-2-carboxaldehyde (120 mg, 0.97 mmol), 4-fluorothiophenol (1 mL, 9.4 mmol) and CuI (300mg, 0.77 mmol) were mixed in 2mL of DMSO and placed in a round bottom flask under N_2 reflux at 110º C for 20h. The crude was extracted with DCM and the organic phases were washed with brine and water. The mixture was then purified by reverse phase flash column chromatography, using ACN:CH_2Cl_2 as eluent. Finally, 121 mg of product **5** were obtained (50 %) as a yellow-orange solid. **^{1}H NMR** (400 MHz, $CDCl_3$) δ (s, 1H) 9.59, (s, 1H) 9.49, (m, 4H) 6.97-6.92, (s, 3H) 2.32, (s,3H) 2.28.

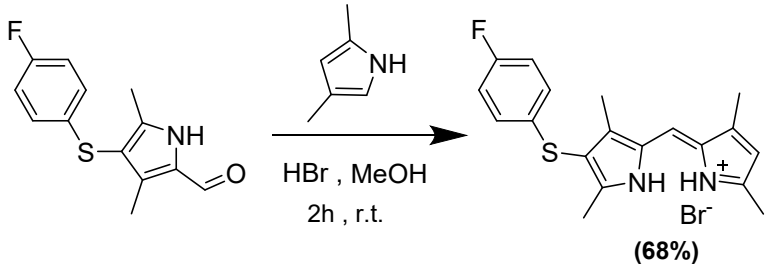

[3] Yutanova, S.L., Berezin, M.B., Semeikin, A.S. *et al. Russ J Gen Chem* **83**, 545–551
[4] Antina, E.V., Berezin, M.B., Dudina, N.A. *et al. Russ. J. Inorg. Chem.* **59**, 1187–1194 (2014)

Synthesis of compound B: To a solution of 1.2 g (12.6 mmol) of 2,4-dimethylpyrrole and 1.55 g (12.6 mmol) of **5** in 20 ml of methanol, 2 ml of HBr (conc.) were added. The mixture was stirred for 2 h at room temperature, the precipitate was filtered off, washed with cold methanol, and dried with vacuum at room temperature. 2.5 g of product **6** were obtained (68 %). **^{1}H NMR** (400 MHz, $CDCl_3$) δ (s, 1H) 13.52, (s,1H) 13.44, (s, 1H) 7.18, (m, 4H) 7.00-6.94, (s, 1H) 6.25, (s, 3H) 2.74, (s, 3H) 2.70, (s, 3H) 2.38, (s, 3H) 2.37. **^{13}C NMR** (101 MHz, $CDCl_3$) δ 162.7, 160.2, 158.9, 157.7, 148.9, 148.1, 131.7, 128.5, 128.5, 127.9, 125.8, 120.8, 118.9, 118.0, 116.6, 116.4, 14.9, 13.3, 12.4, 11.3

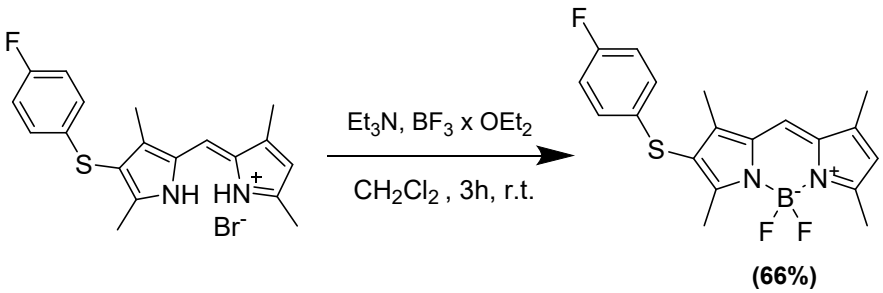

(66%)

Synthesis of compound BDP: A solution of 0.125 g (0.32 mmol) of **6** in 40 ml of methylene chloride was stirred at room temperature. Then, 420 mL (3.2 mmol) of triethylamine were added and immediately 370 mL (3.2 mmol) of boron trifluoride etherate were also added. The mixture was stirred for 3 h, then washed 3 times with water, the organic layer was separated and evaporated to dryness on a rotary evaporator at a reduced pressure. The solid residue was purified by flash column chromatography using methylene chloride as eluent. The eluate was evaporated, the complex was precipitated with methanol, filtered, and dried by vacuum, obtaining 86 mg of product **BDP** (66%). **^{1}H NMR** (400 MHz, $CDCl_3$) δ (s, 1H) 7.14, (m, 2H) 7.04-7.01, (m, 2H) 6.95-6.90, (s, 1H) 6.14, (s, 3H) 2.57, (s, 3H) 2.55, (s, 3H) 2.29, (s, 3H) 2.26. **^{13}C NMR** (101 MHz, $CDCl_3$) δ 162.4, 160.2, 159.9, 158.4, 144.2, 143.7, 134.8, 132.9, 132.8, 131.9, 128.0, 127.9, 120.8, 120.8, 120.6, 117.8, 116.3, 116.1, 15.1, 12.9, 11.5, 10.6. **^{19}F NMR** (376 MHz, $CDCl_3$) δ (s, 1F) -117.6, (d, 1F) -146.2--146.3, (d, 1F) -146.3--146.4. **^{11}B NMR** (128 MHz, $CDCl_3$) δ (t, 1B) 1.07, 0.81, 0.56.

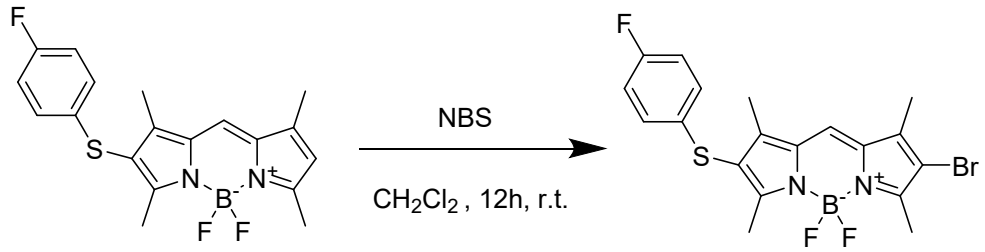

Quantitative

Synthesis of compound BDP-Br. To a solution of 0.338 g (1 mmol) of compound **BDP** in methylene chloride (100 mL) which was being stirred at room temperature, 0.024 g (1 mmol) of NBS were slowly added. The solution was then stirred in dark for 12h at room temperature. The reaction crude was washed with water (100mL) and the water phase was extracted with dichloromethane (50 mL x 3). The organic phase was both combined and dehydrated over anhydrous MgSO4. After evaporation of the solvent in vacuum, the residue was purified by silica gel column chromatography, using methylene chloride/hexane, 1:1 as eluent. 0.409 g of product **BDP-Br** were obtained, yielding full conversion of the reagent. **^{1}H NMR** (400 MHz, $CDCl_3$) δ (s, 1H) 7.15, (m, 2H) 7.06-7.02, (m, 2H) 6.96-6.92, (s, 3H) 2.59, (s, 3H) 2.55, (s, 3H) 2.28, (s, 3H) 2.25. **^{13}C NMR** (101 MHz, $CDCl_3$) δ 162.4, 160.2, 160.0, 158.4, 144.2, 143.7, 134.8, 132.9, 132.8, 131.9, 128.0, 127.9, 120.8, 120.8, 120.6, 117.8, 116.3, 116.1, 15.1, 12.9, 11.5, 10.7. **^{19}F NMR** (376 MHz, $CDCl_3$) δ -117.0, -146.1, -146.2, -146.3, -146.4. **^{11}B NMR** (128 MHz, $CDCl_3$) δ 0.91, 0.66, 0.41.

3. Crystallographic data

X-Ray structure of **BDP**: crystallographic data have been deposited with the Cambridge Crystallographic Data Centre (CCDC 2236116).

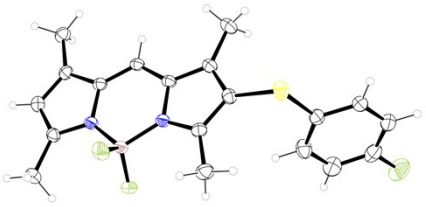

Crystal data and structure refinement for **BDP**

Chemical formula	$C_{19}H_{18}BF_3N_2S$
Mr	374.22
Crystal system, space group	Triclinic, P-1
Temperature (K)	250
a, b, c (Å)	7.3747 (4), 8.7258 (4), 13.7648 (7)
α, β, γ (°)	80.5679 (15), 82.5851 (15), 86.1805 (15)
V (Å3)	865.55 (8)
Z	2
Radiation type	Mo Kα
μ (mm−1)	0.22
Crystal size (mm)	0.19 × 0.14 × 0.07
Data collection	
Diffractometer	Bruker D8 VENTURE PHOTON III-14
Absorption correction	Multi-scan BRUKER SADABS2016/2
Tmin, Tmax	0.926, 0.959
No. of measured, independent and observed [I > 2σ(I)] reflections	29732, 3806, 3265
Rint	0.029
(sin θ/λ)max (Å−1)	0.641
Refinement	
R[F2 > 2σ(F2)], wR(F2), S	0.037, 0.104, 1.04
No. of reflections	3806
No. of parameters	239
H-atom treatment	H-atom parameters constrained
Δρmax, Δρmin (e Å−3)	0.25, −0.24

X-Ray structure of **BDP-Br**: crystallographic data have been deposited with the Cambridge Crystallographic Data Centre (CCDC 2236113).

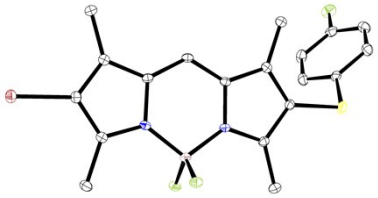

Crystal data and structure refinement for **BDP-Br**

Chemical formula	$C_{19}H_{17}BBrF_3N_2S$
Mr	453.12
Crystal system, space group	Triclinic, P-1
Temperature (K)	100
a, b, c (Å)	16.7902 (17), 16.9670 (16), 17.0009 (15)
α, β, γ (°)	117.894 (3), 101.580 (4), 107.565 (4)
V (Å3)	3729.8 (6)
Z	8
Radiation type	Mo Kα
μ (mm−1)	2.35
Crystal size (mm)	0.11 × 0.07 × 0.02
Data collection	
Diffractometer	Bruker D8 VENTURE PHOTON III-14
Absorption correction	Multi-scan
BRUKER SADABS2016/2	
Tmin, Tmax	0.818, 0.888
No. of measured, independent and observed [I > 2σ(I)] reflections	199984,
20090, 15203	
Rint	0.086
(sin θ/λ)max (Å−1)	0.685
Refinement	
R[F2 > 2σ(F2)], wR(F2), S	0.038, 0.084, 1.03
No. of reflections	20090
No. of parameters	991
H-atom treatment	H-atom parameters constrained
Δρmax, Δρmin (e Å−3)	0.81, −0.46

4. Photophysical and photochemical properties

UV-Vis and emission spectra

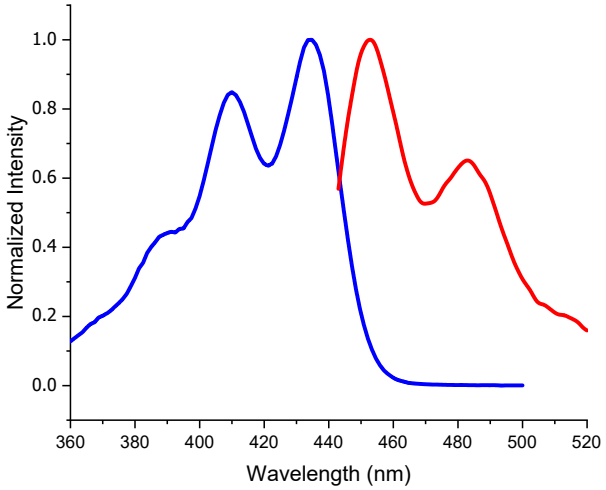

Figure S3. Normalized UV-Vis (blue) and emission (red) spectra of 10 μM solution of **TBPe** in ACN.

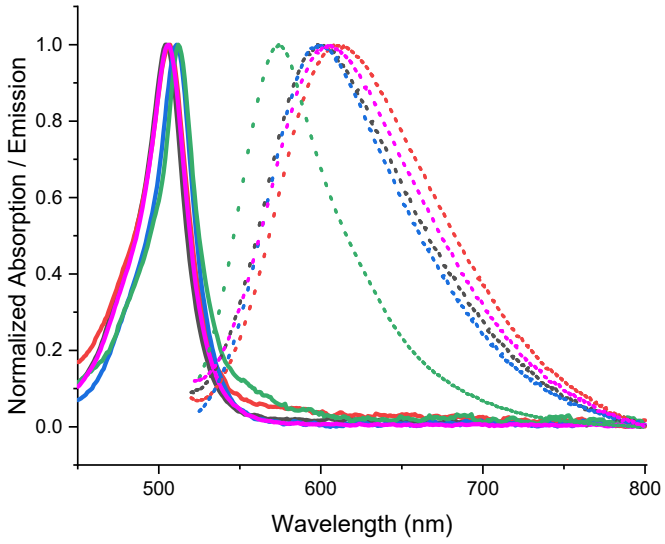

Figure S4. Normalized UV-Vis (left lines) and emission (right dashed lines) spectra of 18 μM sensitizer **BDP** in different solvents. Black: Methanol: Red: DMSO; Blue: Dichloromethane, Green: Hexane, Violet: DMA.

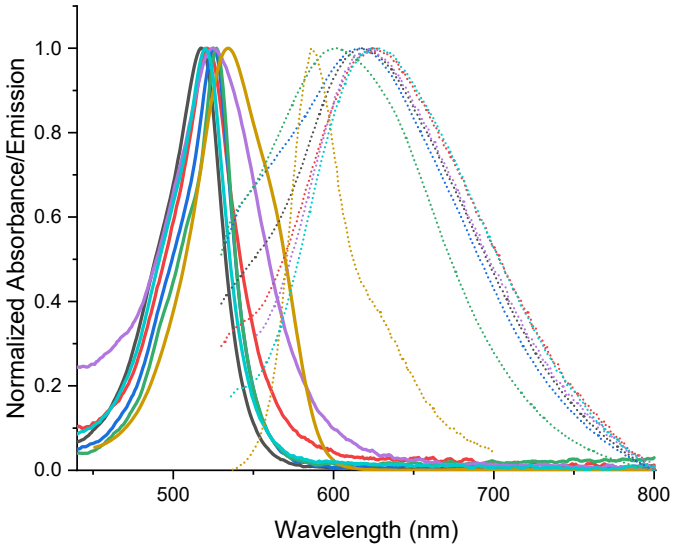

Figure S5. UV-Vis (left lines) and emission (right dashed lines) spectra of 15 μM sensitizer **BDP-Br** in different solvents. Black: MeOH; Red: DMSO; Blue: CH_2Cl_2; Green: Hexane, Orange: ACN, Violet: DMA, Blue: ACN/DMA 4:1

Phosphorescence spectrum

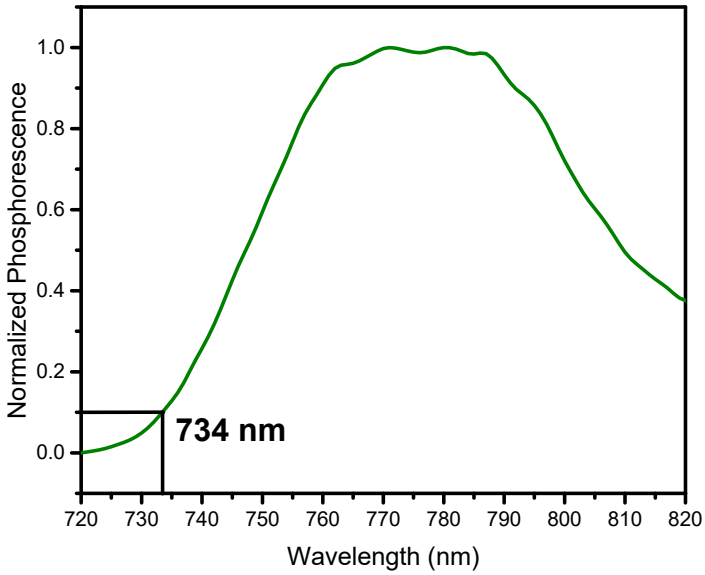

Figure S6. Emission spectra of **BDP-Br** as a 1 mM solution in crystallized EtOH matrix at 77 K. With 20nm of emission slit.

Absolute fluorescence quantum yield measurements

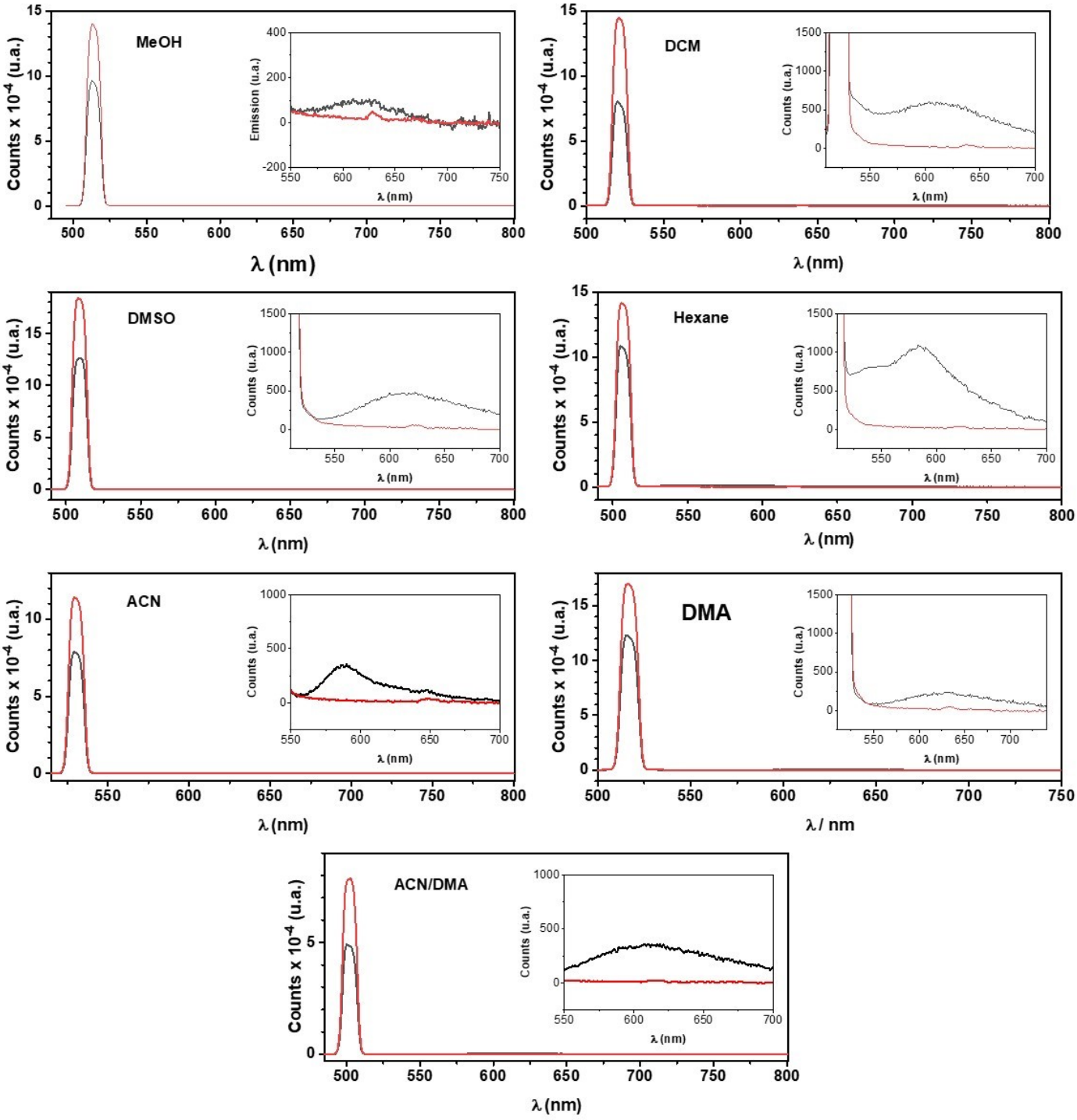

Figure S7. Measurements of absolute fluorescence quantum yield of 17 μM solution of **BDP-Br** in different solvents. The scatter of the solvent is shown in red and the scatter and emission of the **BDP-Br** in black.

Table S1. Photophysical properties of BDP

Solvent	$^{a}\lambda_{max.abs}$	$^{a}\lambda_{max.em}$	$^{b}\varepsilon$	$^{c}\Delta\bar{\upsilon}$	$^{d}E_S$	$^{e}\phi_F$	$^{f}\tau_F$	$^{f}k_F$
MeOH	502	601	21675	3281	2.33	0.13	2.6	5.0 x 10^7
DMSO	506	610	19440	3369	2.29	0.10	2.6	3.9 x 10^7
DCM	511	600	13000	2903	2.30	0.26	3.7	6.9 x 10^7
Hexane	512	575	23730	2140	2.32	0.40	6.2	6.4 x 10^7
DMA	505	603	42500	3214	2.19	0.10	2.3	4.4 x 10^7
ACN	500	604	22222	3253	2.10	0.15	2.3	6.5 x 10^7
ACN/DMA (4:1)	505	603	12833	3382	2.35	0.12	2.3	5.3 x 10^7

[a] Maximum absorption/emission peak (in nm); [b] Molar extinction coefficient (in $M^{-1}cm^{-1}$); [c] Stokes shifts (in cm^{-1}); [d] Singlet energy (in eV); [e] Absolute fluorescence quantum yield; [f] Singlet lifetime (in ns); [g] Fluorescence rate constant (in s^{-1}).

Time-resolved fluorescence spectra

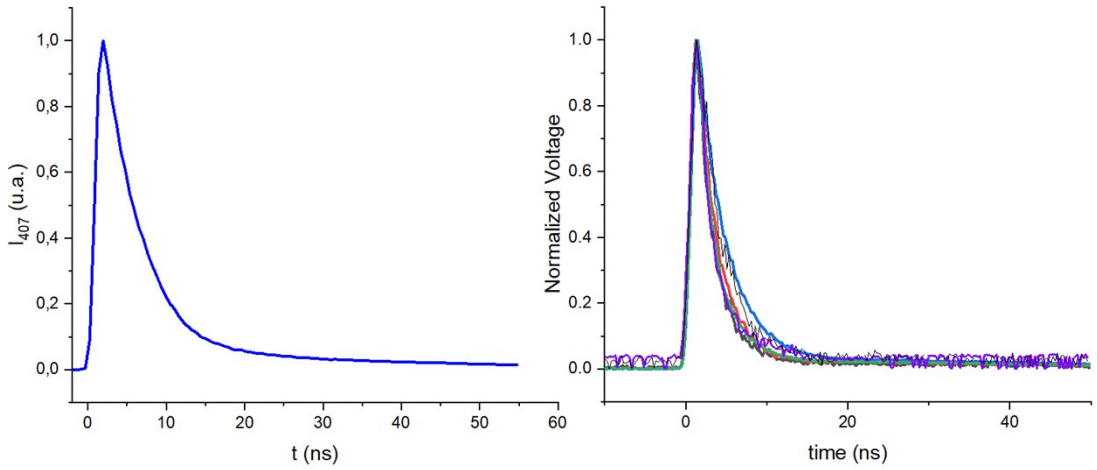

Figure S8. *Left:* Fluorescence decay trace of 1 mM **TBPe** solution in a mixture of ACN/DMA 4:1. *Right:* Fluorescence decay trace of 10 µM **BDP-Br** solutions in different solvents. Green: DCM; Blue: Hexane; Violet: ACN; Black: DMA; Orange: ACN/DMA (4:1) Red: DMSO.

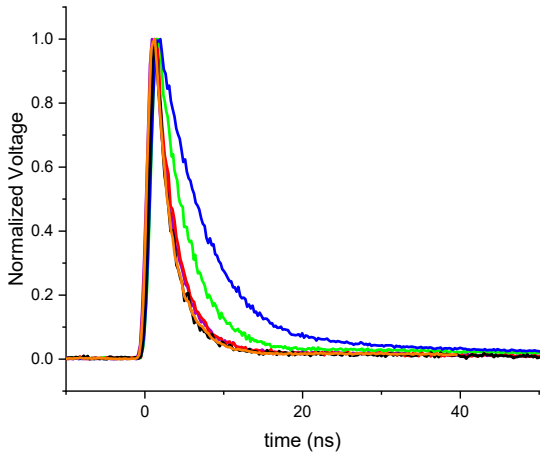

Figure S9. Fluorescence decay trace of 10 µM **BDP** solutions in different solvents. Green: DCM; Blue: Hexane; Violet: ACN; Black: DMA; Orange: ACN/DMA (4:1) Red: DMSO.

Photostability measurements

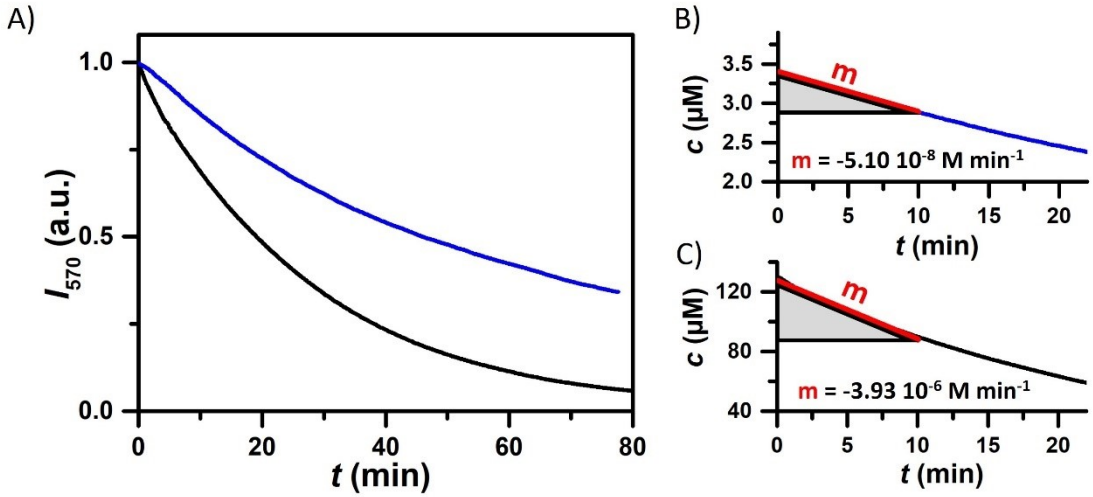

Figure S10. **A)** Photostability measurements of 3.38 µM BDP-Br (blue) and 120 µM $[Ru(bpy)_3](PF_6)_2$ (black) in deaerated MeCN. A 514 nm cw laser was used as excitation source (100 mW) and the luminescence was recorded at 570 nm. B) and C) BDP-Br (blue) and $[Ru(bpy)_3](PF_6)_2$ (black) concentration (obtained from weight-in concentrations and the relative emission signals) plotted against irradiation time. The first 10 min of irradiation were used to quantify the sensitizer photo-degradation.

The photostability of **BDP-Br** was measured against the well-described Ru-complex $[Ru(bpy)_3](PF_6)_2$ under identical excitation conditions (same absorption at excitation wavelength). Two 3 mL solutions of **BDP-Br** and $[Ru(bpy)_3](PF_6)_2$ in deaerated ACN were irradiated with a 514 nm cw laser over a period of 80 min. A very similar photostability assay has been used recently for the estimation of relative photodegradation quantum yields.[5,6,7] The luminescence as concentration-proportional observable was recorded at 570 nm using the FL-6500 instrument. Under the assumption that the photodegradation products do not emit at the selected detection wavelength (570 nm) the relative emission intensity reflects the relative concentration of the remaining sensitizer. The absence of emissive degradation products has been observed for $[Ru(bpy)_3]^{2+}$ upon green illumination[8] and control experiments allowed us to rule out contributions of photodegradation products resulting from **BDP-Br**. A linear fit of the first 10 min of irradiation allows for an estimate of the degradation constant. We obtained a slope *m* of 3.93 10^{-6} M min^{-1} for $[Ru(bpy)_3](PF_6)_2$ and 5.1 10^{-8} M min^{-1} for **BDP-Br**, which is roughly two orders of magnitude slower.

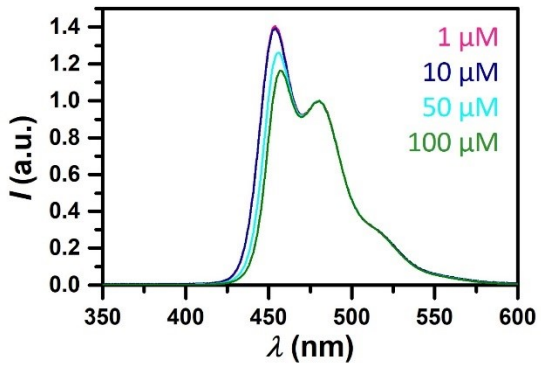

Figure S11. Spectral emission of **TBPe** at different concentrations after excitation with 355 nm laser pulses in ACN. The emission was normalized at 480 nm where no filter effects are observed.

[5] Björn Pfund, Debora M. Steffen, Mirjam R. Schreier, *et. al. J. Am. Chem. Soc.* ***142****, 23, 10468–10476 (2020)*
[6] Jakob B. Bilger, Christoph Kerzig, Christopher B. Larsen, and Oliver S. Wenger, J. Am. Chem. Soc. **143**, 3, 1651–1663 (2021)
[7] Lucius Schmid, Christoph Kerzig, Alessandro Prescimone, and Oliver S. Wenger, *ACS Au*, **1**, 6, 819–832 (2021)
[8] Robert Naumann , Christoph Kerzig and Martin Goez, Chem. Sci., **8**, 7510-7520 (2017)

5. Cyclic voltammetry

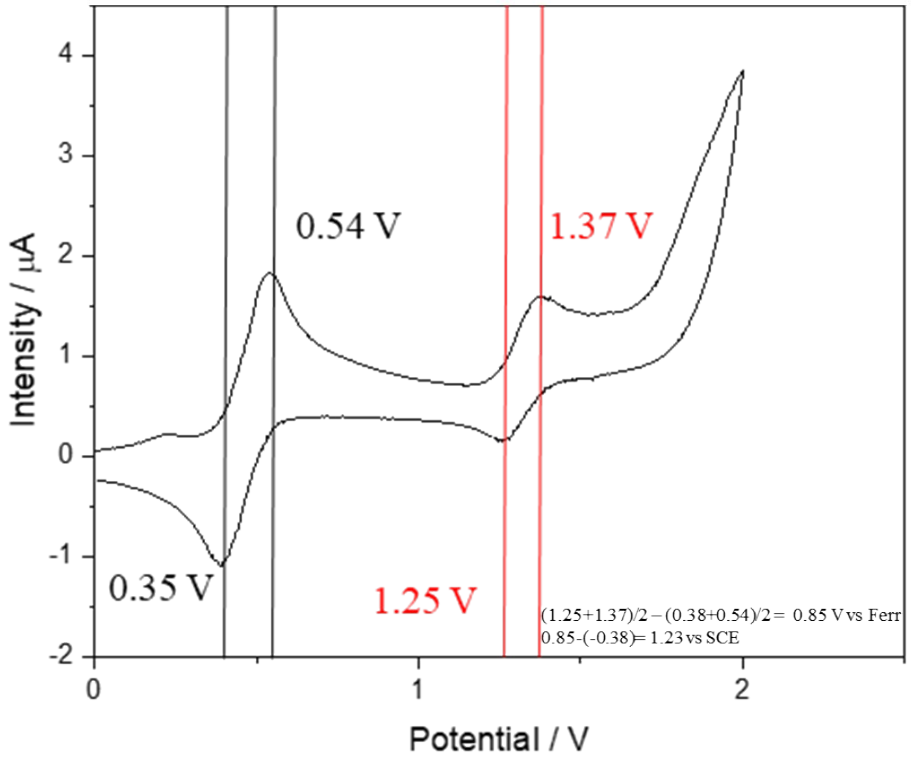

Figure S12. Cyclic voltammogram of 1mM **BDP-Br** in ACN solution.

6. Coupling reactions

The Meerwein-type reaction

Table S2. Optimization for the model reaction

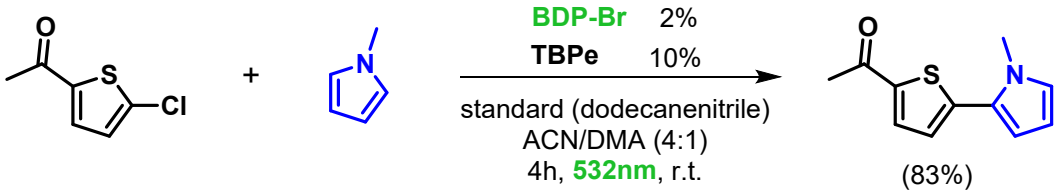

Entry	Solvent	Irradiation time (h)	Trapping equivalents	**BDP-Br/TBPe** (% mol)	Yield (%)
1	ACN	18	80	1/5	0[a]
2	ACN	2	80	1/5	0[b]
3	ACN	2	80	1/5	0[c]
5	ACN	3	80	1/5	10[d]
6	ACN	3	80	1/5	44
7	ACN/DMA (4:1)	3	80	2/10	72
8	ACN/DMA (4:1)	4	80	2/10	80
9	ACN/DMA (4:1)	4	100	2/10	**83**

a) Irradiation with LED, b) Reaction without **BDP-Br**, c) Reaction without **TBPe**, d) Using **BDP** as sensitizer.

1-(5-(1-Methyl-1H-pyrrol-2-yl)thiophen-2-yl)ethan-1-one

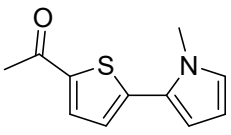

The compound was prepared according to the general procedure described in the main text using 2-acetyl-5-chlorothiophene (4.8 mg, 30 µmol, 1.0 equiv.) as aryl halide and *N*-methylpyrrole (213 µL, 2.4 mmol, 80 equiv.) as trapping agent, dodecanenitrile (6.5 µL, 30 µmol, 1.0 equiv.) as internal standard, TBPe (2.9 mg, 6 µmol, 0.1 equiv.) and **BDP-Br** (0.2 mg, 0.6 µmol, 0.02 equiv.). The reaction mixture was irradiated for 4 hours, obtaining 83% product yield according to CG-FID analysis (73% yield of isolated product as a dark-yellow solid).

^{1}H NMR (400 MHz, $CDCl_3$): δ = 7.62 (d, J = 4.0 Hz, 1H), 7.06 (d, J = 4.0 Hz, 1H), 6.77-6.72 (m, 1H), 6.51 (dd, J = 3.8, 1.8 Hz, 1H), 6.18 (dd, J = 3.8 Hz, 2.7 Hz, 1H), 3.81 (s, 3H), 2.55 (s, 3H). **^{13}C NMR** (100 MHz, $CDCl_3$): δ = 190.6, 144.0, 141.9, 133.3, 126.9, 126.3, 124.4, 111.7, 108.7, 36.0, 26.7. **GC-MS** (EI): m/z (relative intensity) = 205 (100) [$M^{+\bullet}$], 190 (94), 162 (36), 130 (13), 118 (53).

The Mizoroki-Heck coupling reaction

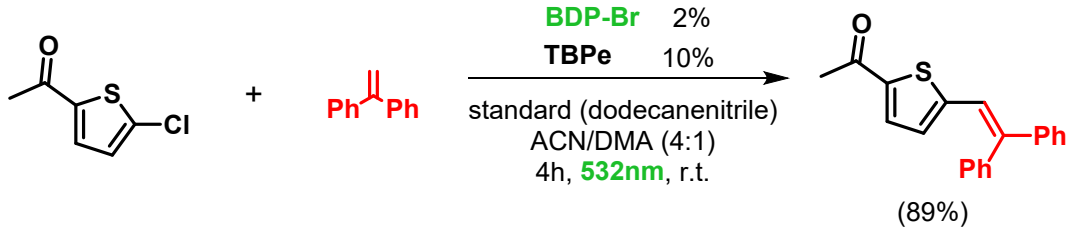

(89%)

1-(5-(2,2-Diphenylvinyl)thiophen-2-yl)ethanone

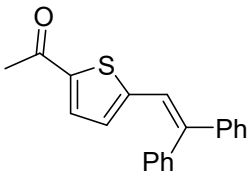

The compound was prepared according to the general procedure using 5-Bromo-2-Acetylthiophene (4.8 mg, 30 µmol, 1.0 equiv.), 1,1-Diphenylethylene (152 µL, 900 µmol, 30.0 equiv.) as trapping agent, dodecanenitrile (6.5 µL, 30 µmol, 0.1 equiv.) as internal standard, TBPe (2.9 mg, 6 µmol, 0.2 equiv.) and **BDP-Br** (0.2 mg, 0.6 µmol, 0.02 equiv.). The reaction mixture was irradiated for 4 hours, obtaining 89% product according to GC-FID analysis, (85% yield of isolated product as a yellow solid).**^{1}H NMR** (400 MHz, CD_3CN) δ 7.58 – 7.51 (m, 4H), 7.41 (s, 1H), 7.39 – 7.30 (m, 5H), 7.26 (dd, J = 6.7, 2.9 Hz, 2H), 7.08 (d, J = 4.0 Hz, 1H), 2.39 (s, 4H). **^{13}C NMR** (101 MHz, CD_3CN) δ 190.58 (CO), 133.45 (C), 131.52(C), 130.66-130.63 (d, CH), 129.60 (C), 129.47 (CH), 129.14 (C), 127.83 (CH), 121.48 (CH), 26.68 (CH_3). **GC-MS** (EI): m/z (relative intensity): 304 (100) [$M^{+\bullet}$], 289 (50), 228 (40), 202 (13), 152 (10), 43 (16).

The Photo-Azbuzov reaction

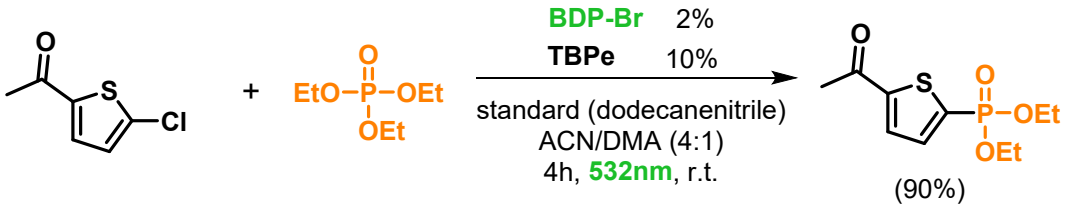

Diphenyl (5-acetylthiophen-2-yl)phosphonate

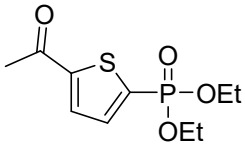

The compound (CAS: 1119779-20-2) was prepared according to the general procedure using 2-acetyl-5-bromothiophene (4.8 mg, 30 µmol, 1.0 equiv.), triethylphosphite (45 µL, 250 µmol, 5 equiv.), dodecanenitrile (6.5 µL, 30 µmol, 1.0 equiv.) as internal standard, TBPe (2.9 mg, 6 µmol, 0.1 equiv.) and **BDP-Br** (0.2 mg, 0.6 µmol, 0.02 equiv.). The mixture was irradiated for 4 hours, obtaining 90% of the product according to GC-FID analysis (85% of isolated yield as a yellow oil).

^{1}H NMR (400 MHz, CDCl3) δ 7.68 (t, J = 3.3 Hz, 1H), 7.63 (dd, J = 7.9, 3.7 Hz, 1H), 4.27 – 4.06 (m, 4H), 2.59 (s, 3H), 1.35 (t, J = 7.1 Hz, 6H) ppm.

^{13}C NMR (101 MHz, CDCl3) δ 190.6 (C, d, J = 1.6 Hz), 150.6 (C, d, J = 7.2 Hz), 136.7 (CH, d, J = 11.5 Hz), 136.4 (C, d, J = 203.1 Hz), 132.1 (CH, d, J = 17.0 Hz), 63.2 (CH2, d, J = 5.5 Hz), 27.3 (CH3, s), 16.4 (CH3, d, J = 6.6 Hz) ppm.

^{31}P NMR (162 MHz, CDCl3) δ 9.61 (s) ppm.

HRMS (EI): m/z $(M+H)^+$ = calcd. for $C_{10}H_{15}O_4PS$: 263.0501, found: 263.0505.

7. ^{1}H, ^{13}C, ^{11}B and ^{19}F NMR spectra

^{1}H NMR of A

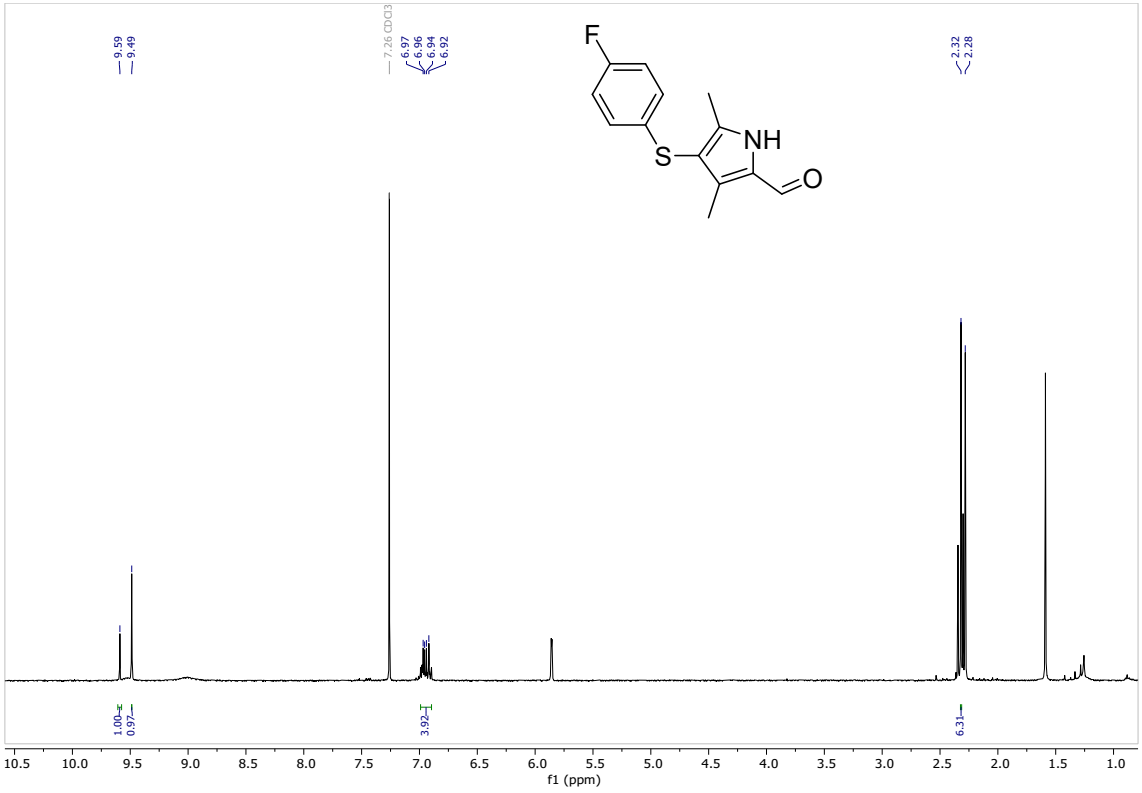

^{1}H NMR of B

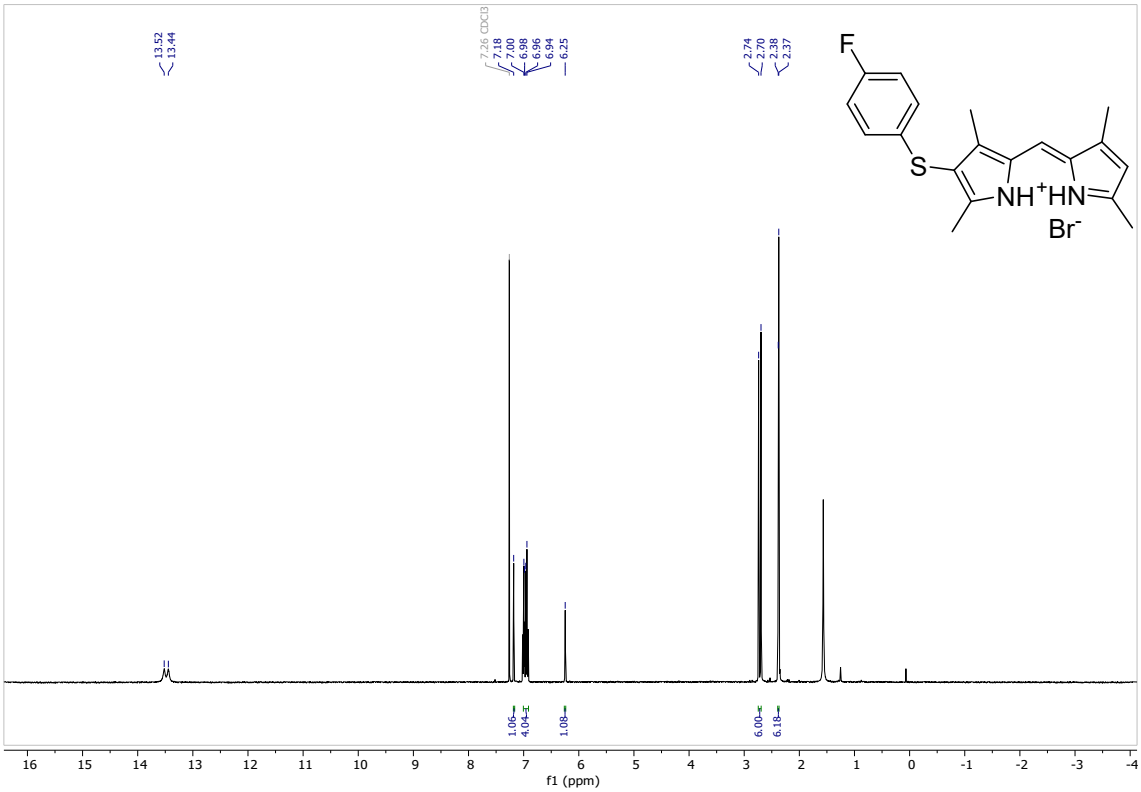

^{13}C NMR B

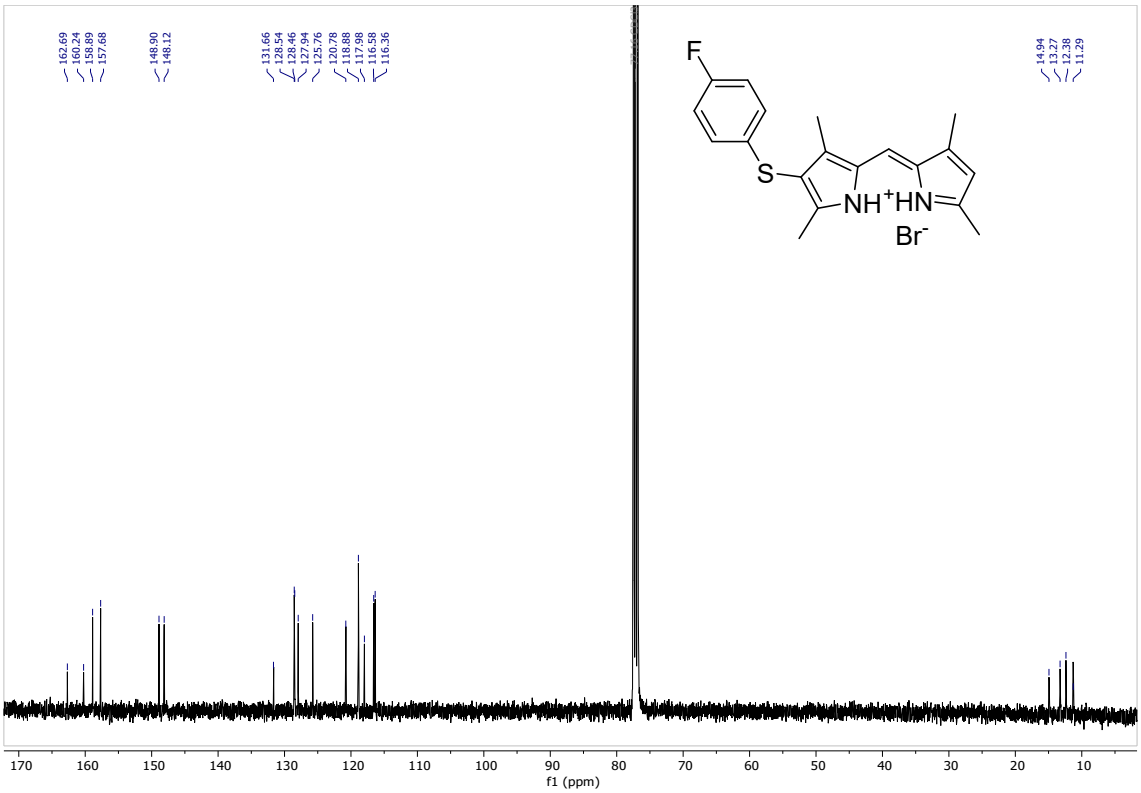

^{1}H NMR of BDP

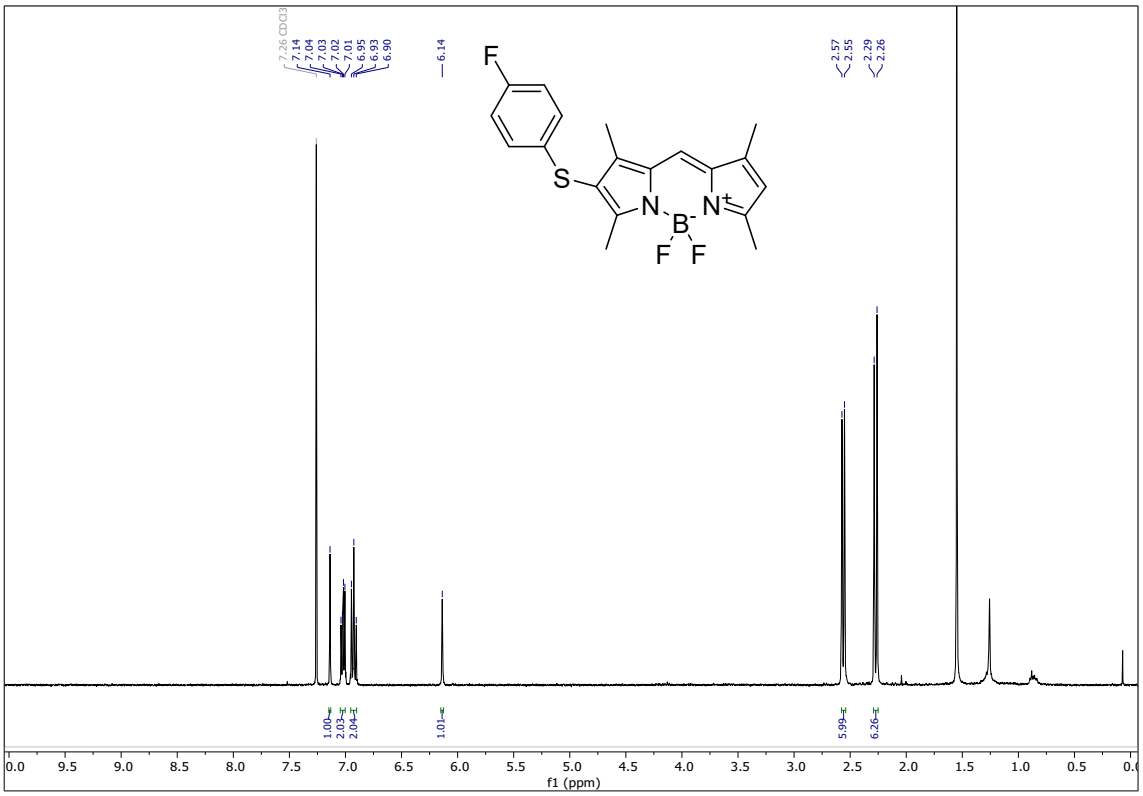

^{13}C NMR of BDP

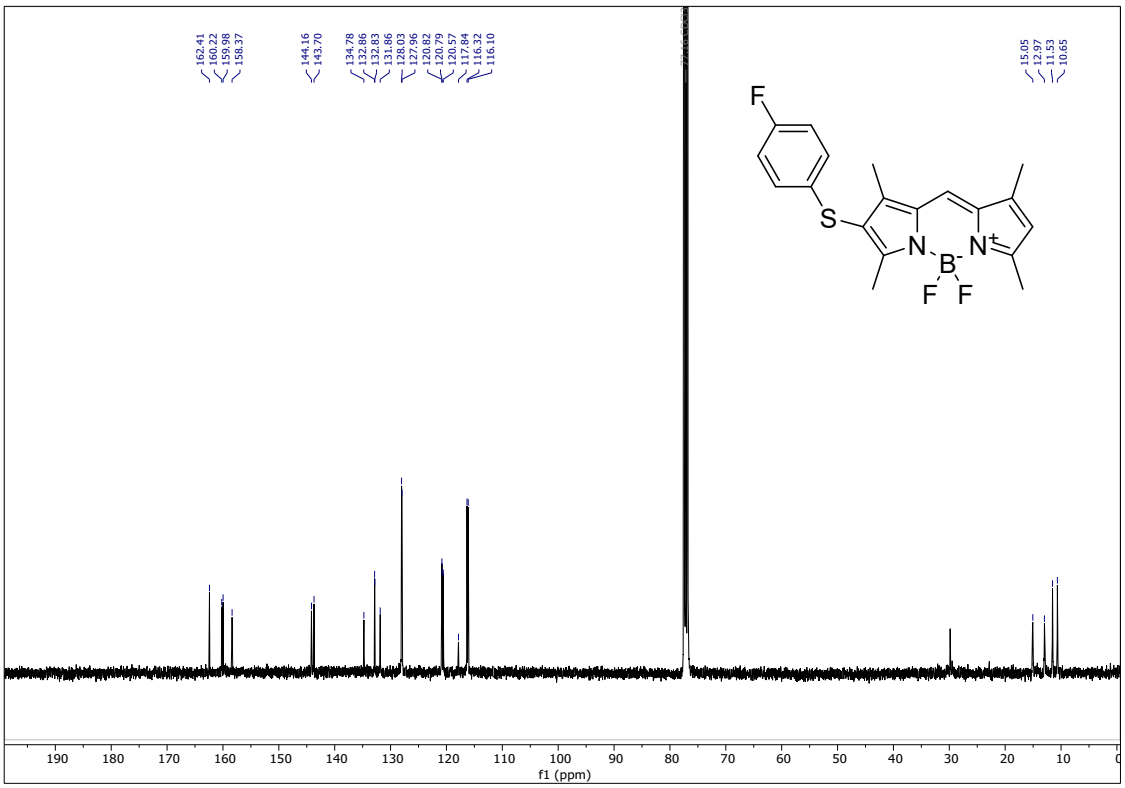

^{19}F NMR of BDP

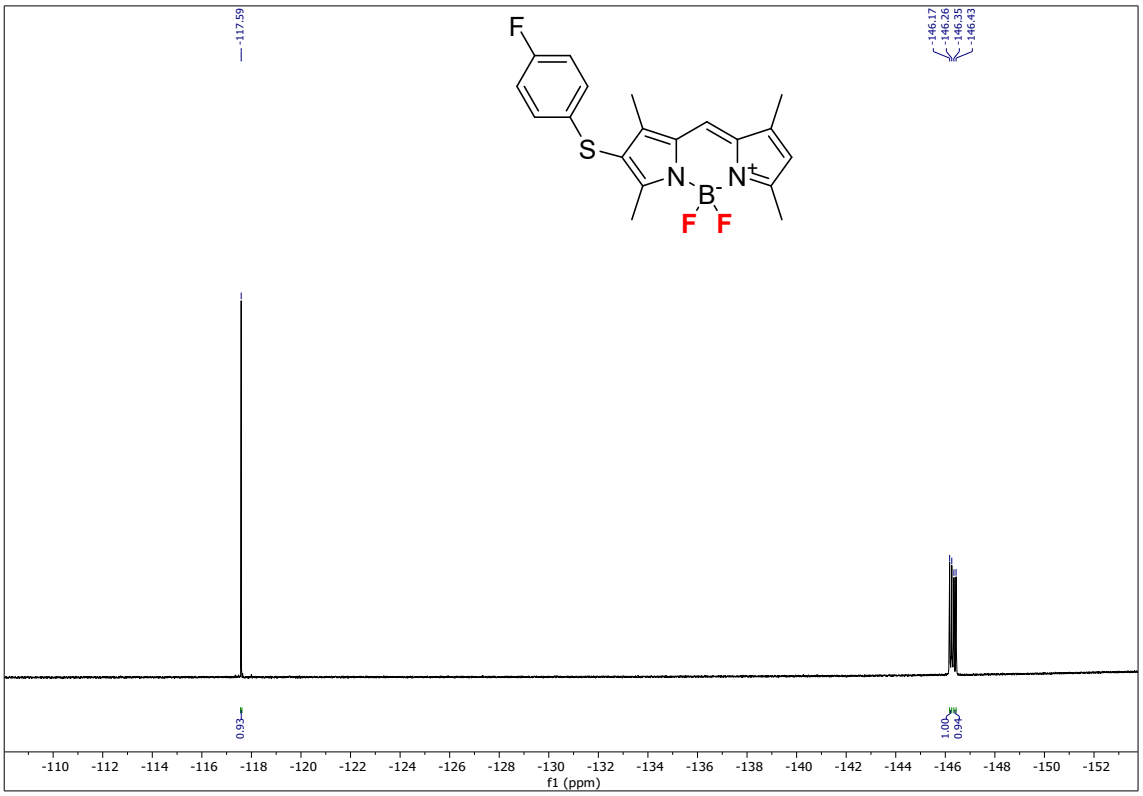

^{11}B NMR of BDP

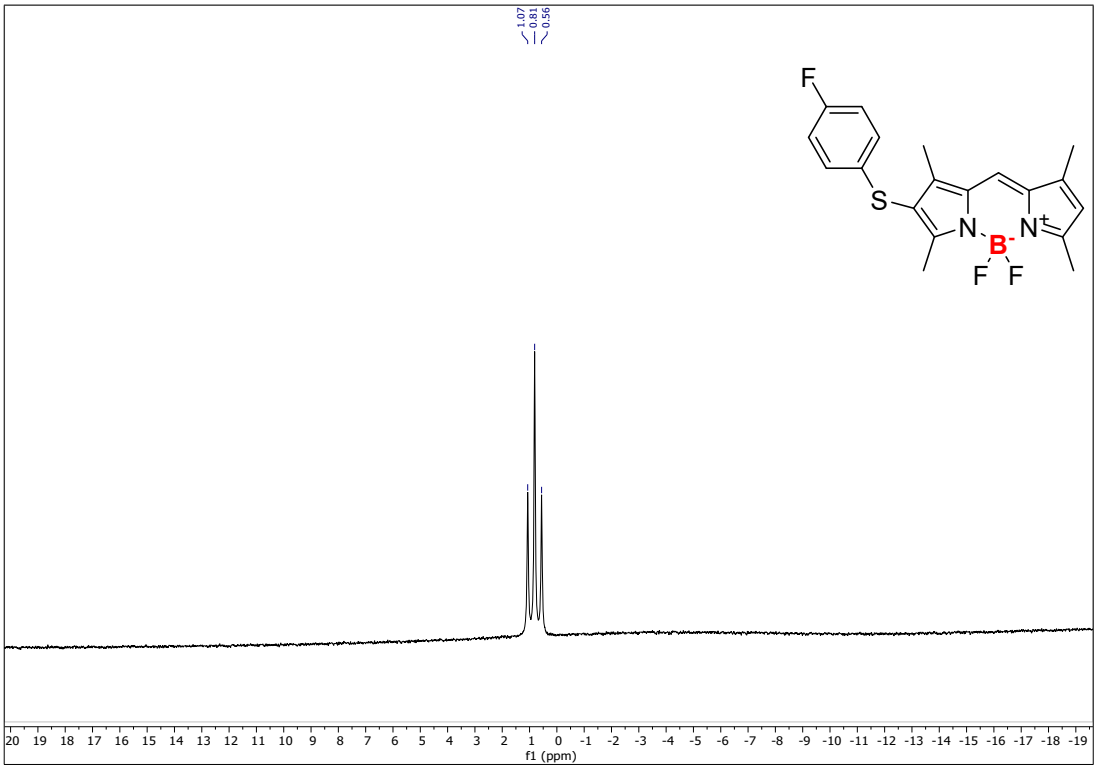

^{1}H NMR of BDP-Br

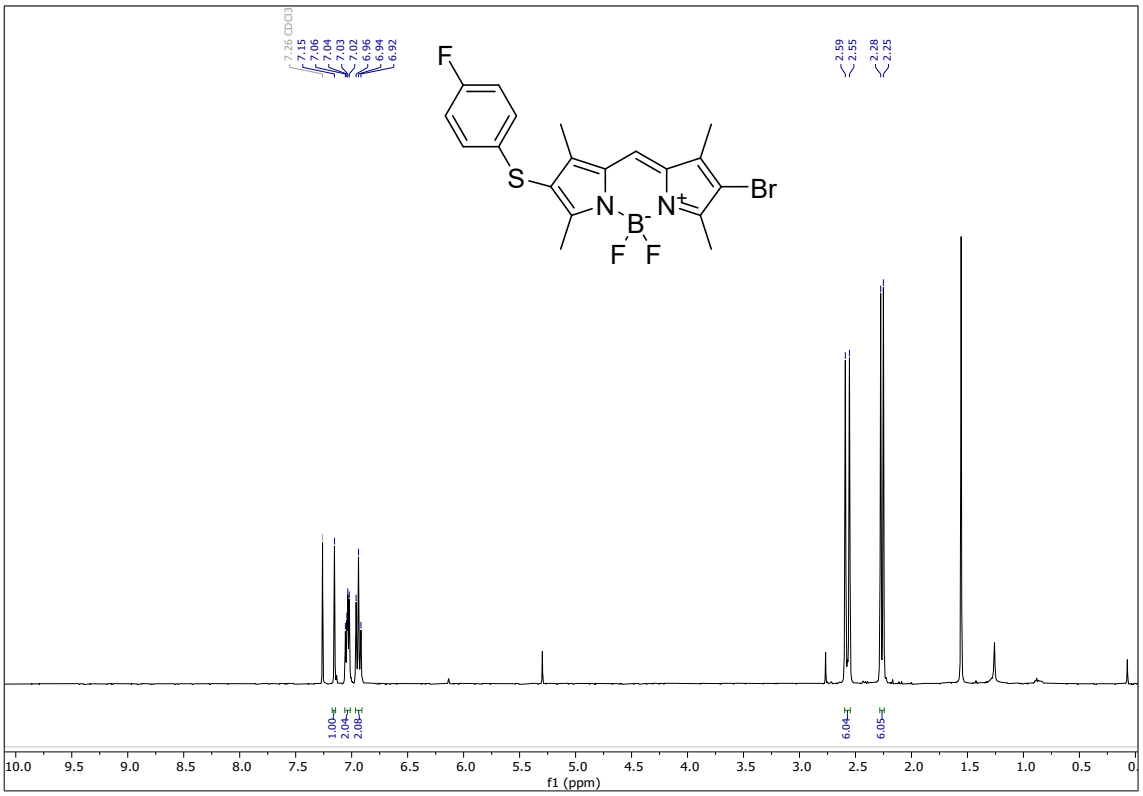

^{13}C NMR of BDP-Br

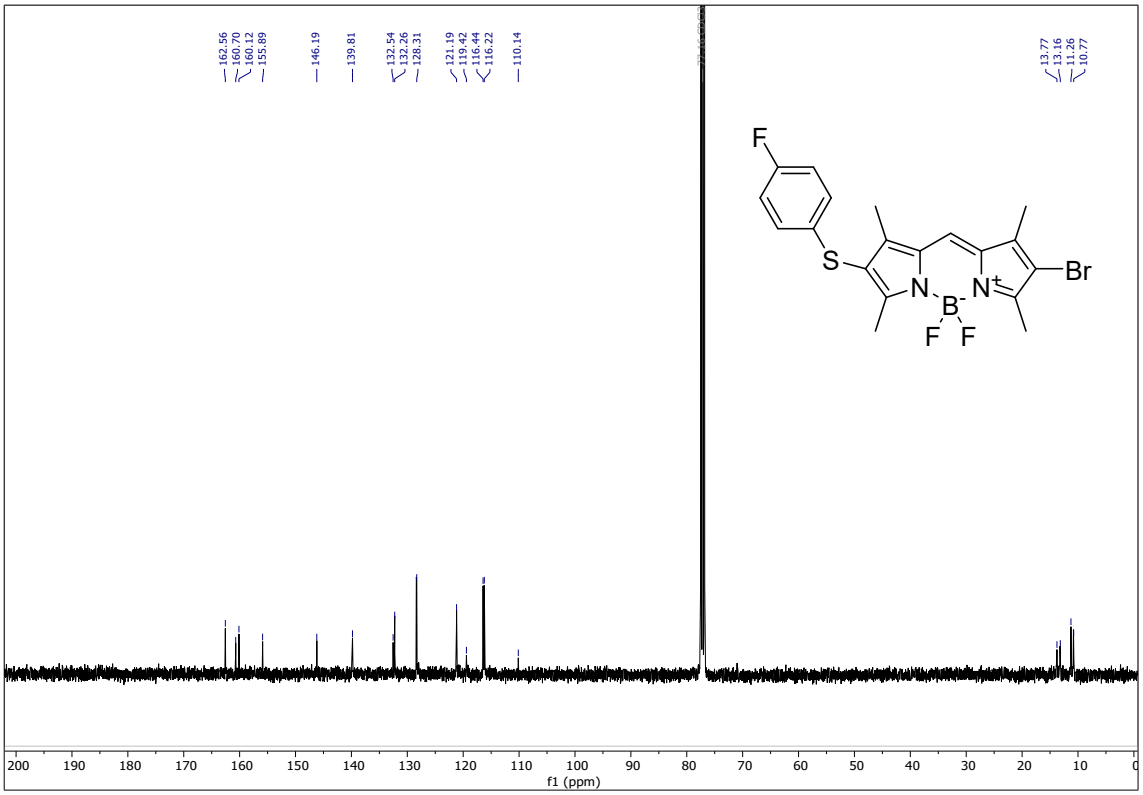

^{19}F NMR of BDP-Br

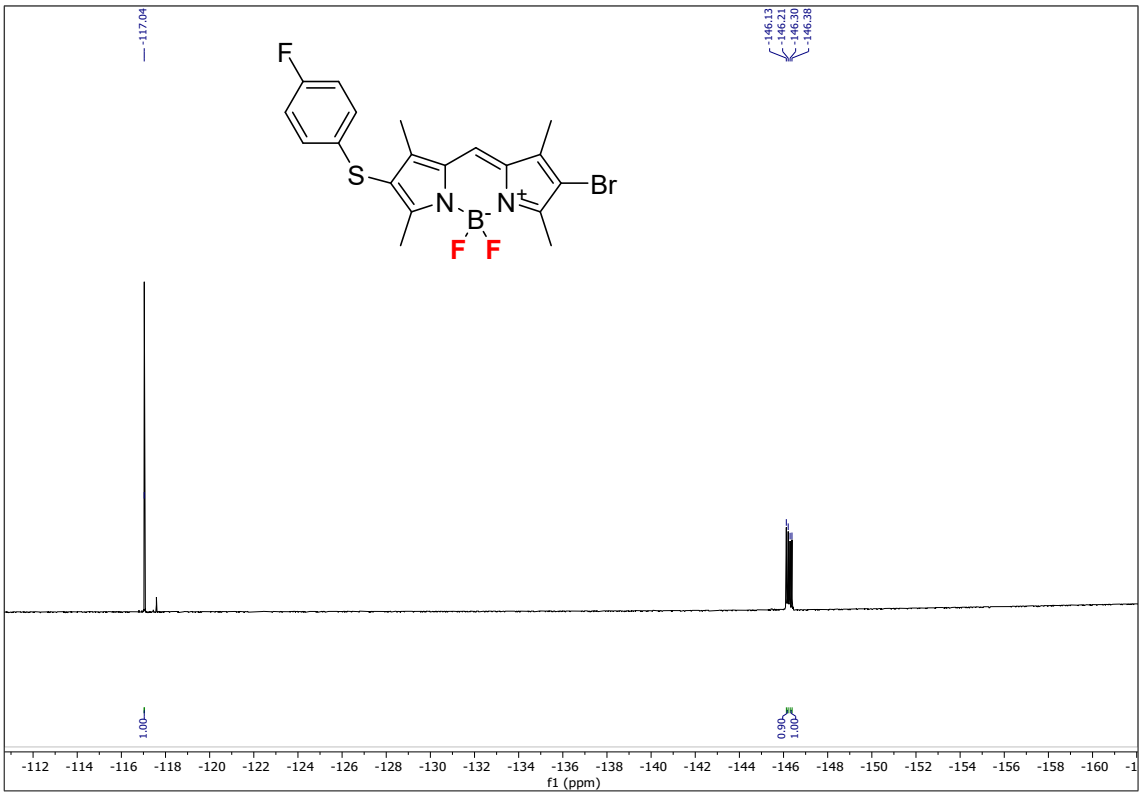

^{11}B NMR of BDP-Br

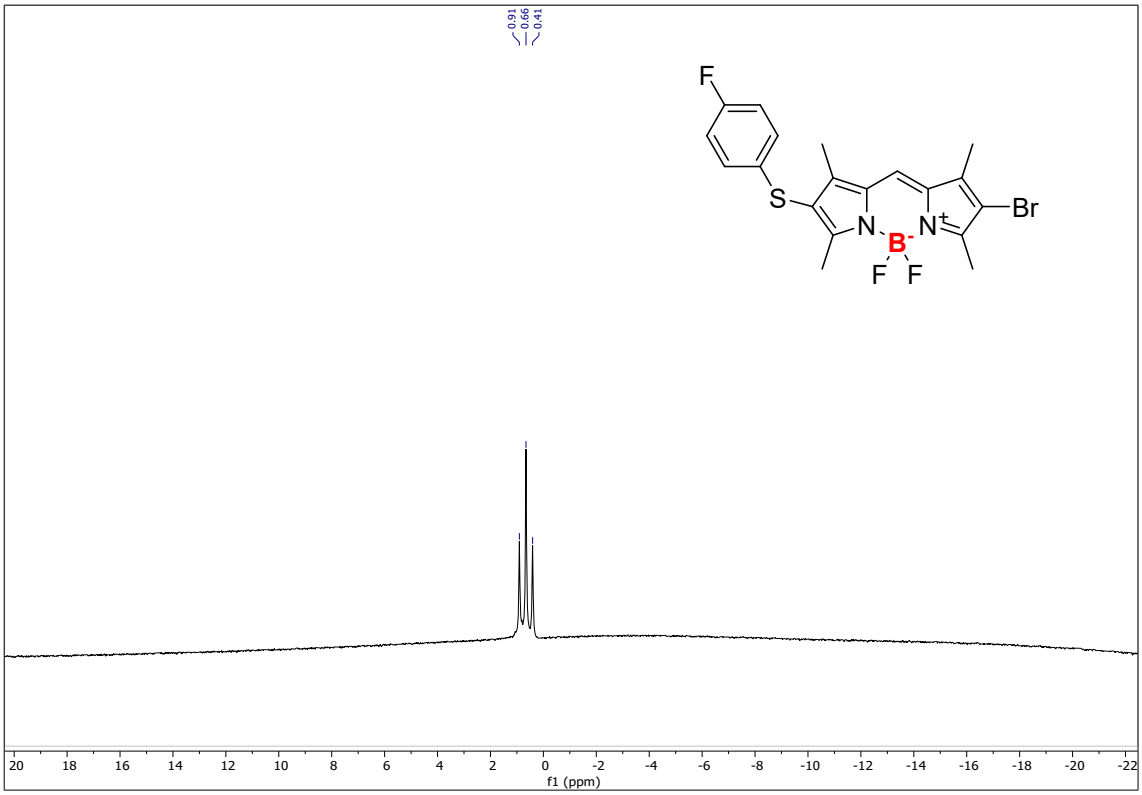

^{1}H NMR of 1-(5-(1-Methyl-1H-pyrrol-2-yl)thiophen-2-yl)ethan-1-one

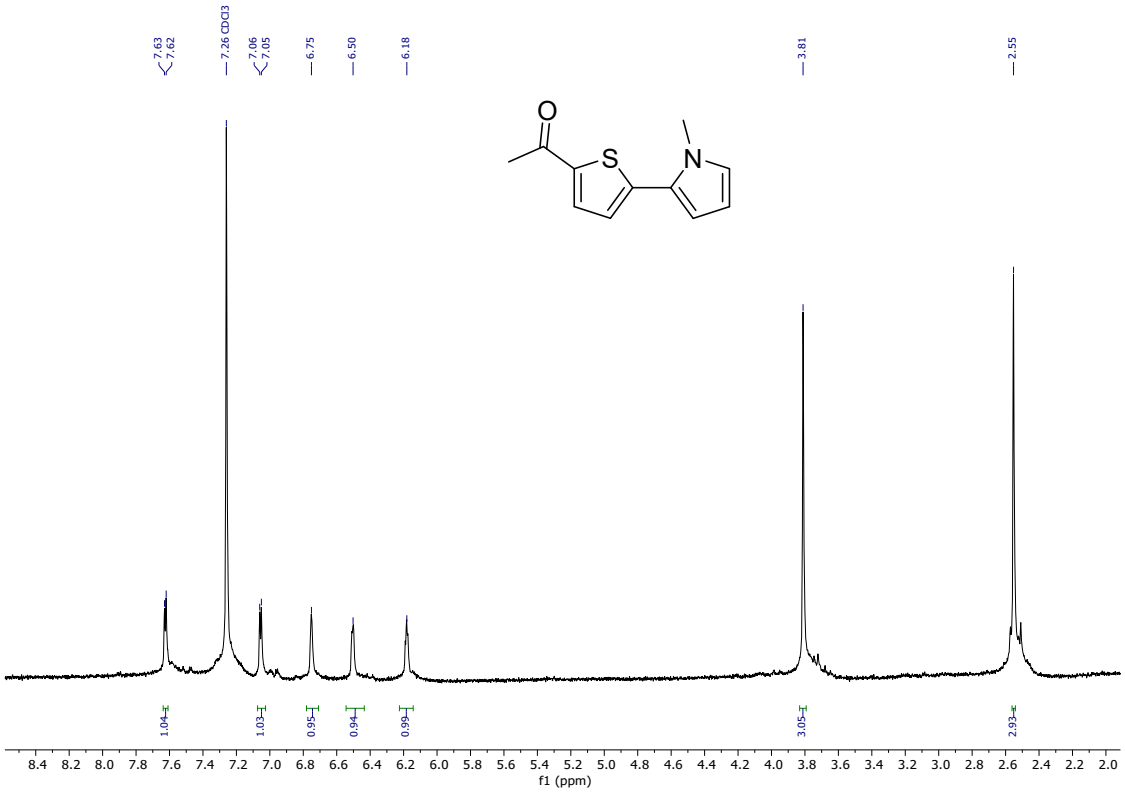

^{1}H NMR of 1-(5-(2,2-diphenylvinyl)thiophen-2-yl)ethanone

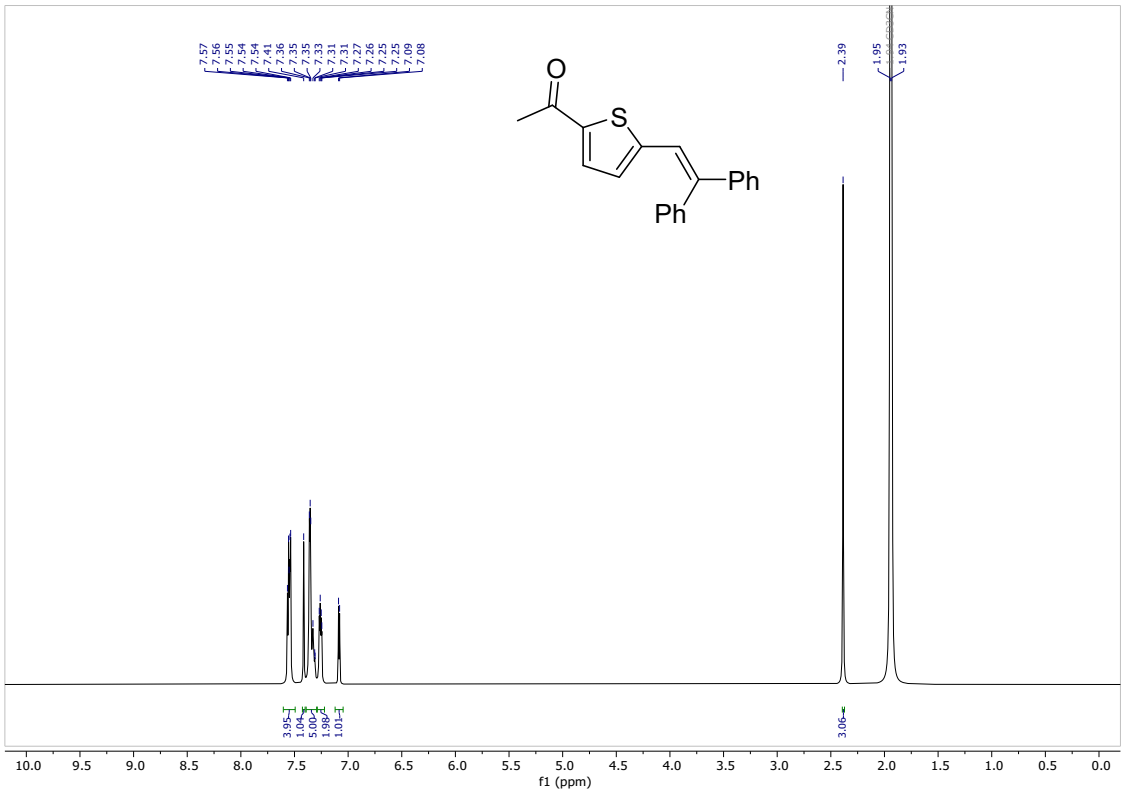

^{13}C NMR of 1-(5-(2,2-diphenylvinyl)thiophen-2-yl)ethanone

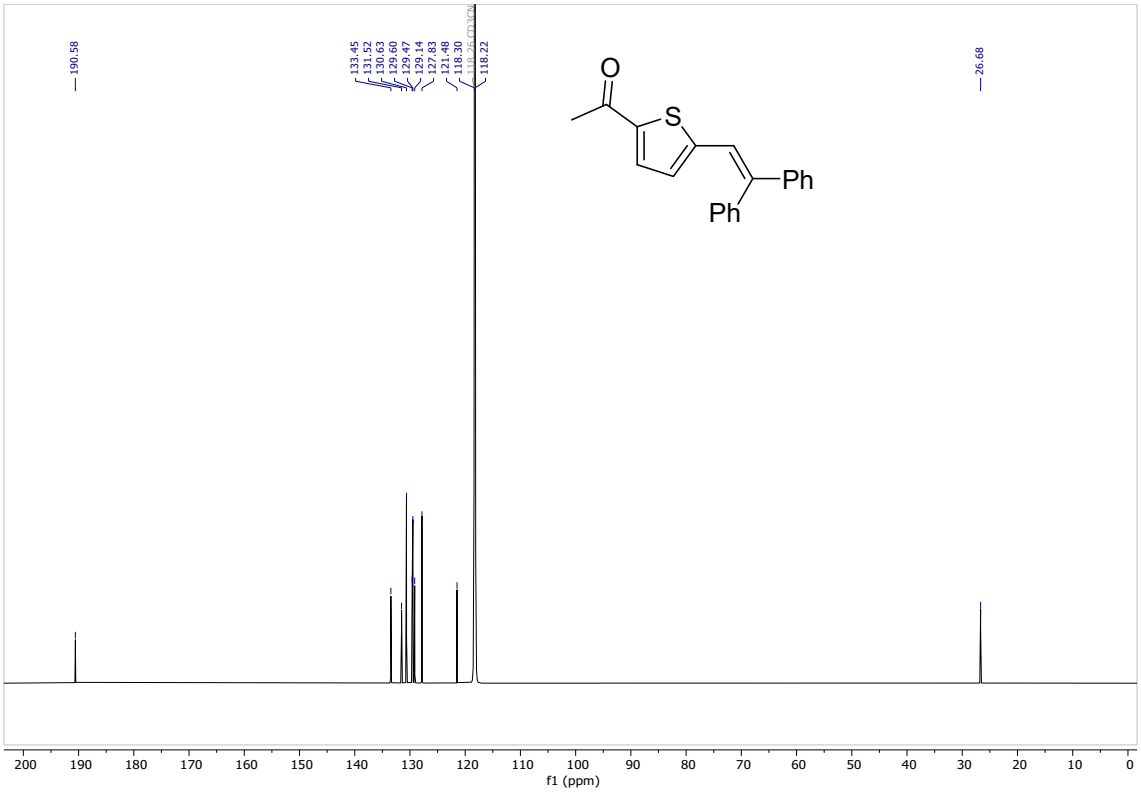

^{1}H NMR of diphenyl (5-acetylthiophen-2-yl)phosphonate

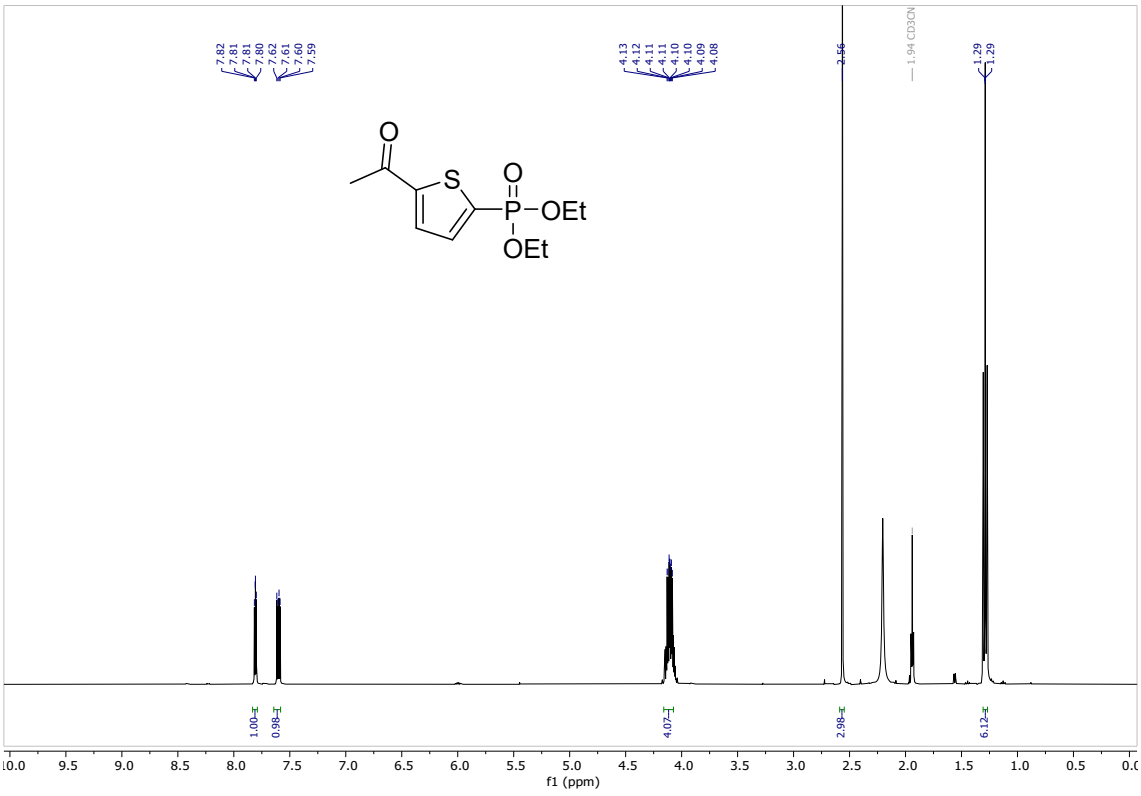

8. Mass spectrum of BDP-Br

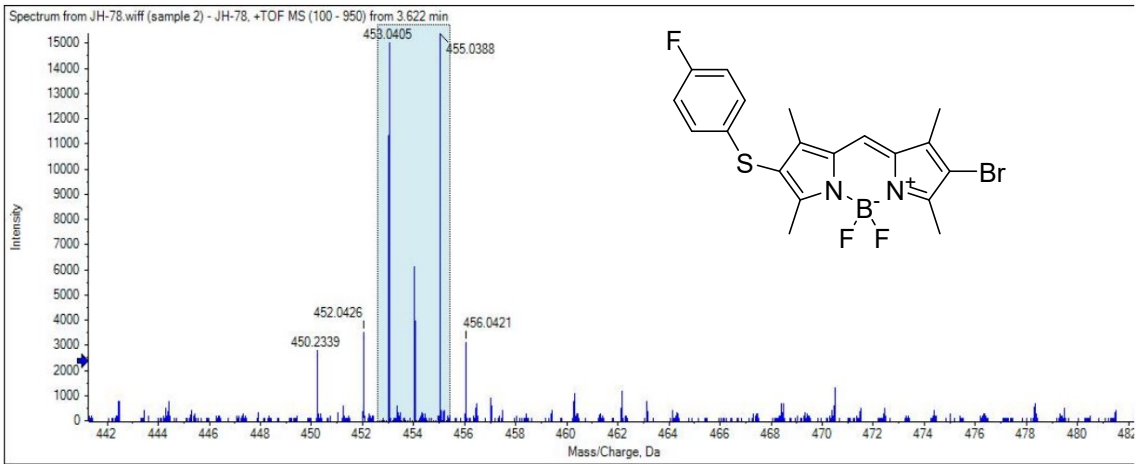

9. Geometrical parameters from Crystallographic data

Geometric parameters for BDP (Å, º)

C1—C2	1.401 (2)	C10—H10B	0.97
C1—C9	1.405 (2)	C10—H10C	0.97
C1—S1	1.7522 (16)	C11—H11A	0.97
C2—C3	1.403 (2)	C11—H11B	0.97
C2—C10	1.492 (2)	C11—H11C	0.97
C3—C4	1.391 (2)	C12—H12A	0.97
C3—N2	1.3990 (17)	C12—H12B	0.97
C4—C5	1.377 (2)	C12—H12C	0.97
C4—H4	0.94	C13—H13A	0.97
C5—N1	1.3975 (18)	C13—H13B	0.97
C5—C6	1.423 (2)	C13—H13C	0.97
C6—C7	1.378 (2)	S1—C14	1.7775 (17)
C6—C11	1.494 (2)	C14—C19	1.382 (2)
C7—C8	1.408 (2)	C14—C15	1.387 (2)
C7—H7	0.94	C15—C16	1.378 (3)
C8—N1	1.3475 (19)	C15—H15	0.94
C8—C12	1.489 (2)	C16—C17	1.368 (3)
N1—B1	1.547 (2)	C16—H16	0.94
B1—F1	1.3866 (19)	C17—F3	1.362 (2)
B1—F2	1.3918 (19)	C17—C18	1.369 (3)

B1—N2	1.551 (2)	C18—C19	1.385 (3)
N2—C9	1.3481 (19)	C18—H18	0.94
C9—C13	1.487 (2)	C19—H19	0.94
C10—H10A	0.97		
C2—C1—C9	108.11 (13)	H10A—C10—H10B	109.5
C2—C1—S1	126.02 (12)	C2—C10—H10C	109.5
C9—C1—S1	125.40 (12)	H10A—C10—H10C	109.5
C1—C2—C3	105.88 (13)	H10B—C10—H10C	109.5
C1—C2—C10	127.30 (15)	C6—C11—H11A	109.5
C3—C2—C10	126.82 (14)	C6—C11—H11B	109.5
C4—C3—N2	120.12 (13)	H11A—C11—H11B	109.5
C4—C3—C2	130.85 (13)	C6—C11—H11C	109.5
N2—C3—C2	109.00 (13)	H11A—C11—H11C	109.5
C5—C4—C3	122.06 (13)	H11B—C11—H11C	109.5
C5—C4—H4	119	C8—C12—H12A	109.5
C3—C4—H4	119	C8—C12—H12B	109.5
C4—C5—N1	120.64 (13)	H12A—C12—H12B	109.5
C4—C5—C6	130.88 (14)	C8—C12—H12C	109.5
N1—C5—C6	108.48 (13)	H12A—C12—H12C	109.5
C7—C6—C5	106.03 (13)	H12B—C12—H12C	109.5
C7—C6—C11	128.36 (15)	C9—C13—H13A	109.5
C5—C6—C11	125.61 (14)	C9—C13—H13B	109.5
C6—C7—C8	108.49 (14)	H13A—C13—H13B	109.5
C6—C7—H7	125.8	C9—C13—H13C	109.5

C8—C7—H7	125.8	H13A—C13—H13C	109.5
N1—C8—C7	109.20 (13)	H13B—C13—H13C	109.5
N1—C8—C12	122.59 (14)	C1—S1—C14	104.79 (7)
C7—C8—C12	128.20 (15)	C19—C14—C15	119.33 (16)
C8—N1—C5	107.80 (12)	C19—C14—S1	123.67 (13)
C8—N1—B1	127.22 (12)	C15—C14—S1	116.96 (13)
C5—N1—B1	124.89 (12)	C16—C15—C14	120.52 (18)
F1—B1—F2	109.33 (12)	C16—C15—H15	119.7
F1—B1—N1	110.22 (13)	C14—C15—H15	119.7
F2—B1—N1	110.03 (12)	C17—C16—C15	118.68 (17)
F1—B1—N2	110.54 (12)	C17—C16—H16	120.7
F2—B1—N2	109.67 (13)	C15—C16—H16	120.7
N1—B1—N2	107.03 (11)	F3—C17—C16	119.01 (19)
C9—N2—C3	107.96 (12)	F3—C17—C18	118.5 (2)
C9—N2—B1	126.93 (12)	C16—C17—C18	122.47 (18)
C3—N2—B1	124.99 (12)	C17—C18—C19	118.46 (19)
N2—C9—C1	109.04 (13)	C17—C18—H18	120.8
N2—C9—C13	123.05 (14)	C19—C18—H18	120.8
C1—C9—C13	127.91 (15)	C14—C19—C18	120.52 (17)
C2—C10—H10A	109.5	C14—C19—H19	119.7
C2—C10—H10B	109.5	C18—C19—H19	119.7
C9—C1—C2—C3	0.29 (16)	C5—N1—B1—N2	−6.15 (18)
S1—C1—C2—C3	−172.17 (11)	C4—C3—N2—C9	−177.76 (13)
C9—C1—C2—C10	−179.66 (15)	C2—C3—N2—C9	0.50 (16)

S1—C1—C2—C10	7.9 (2)	C4—C3—N2—B1	−1.5 (2)
C1—C2—C3—C4	177.53 (15)	C2—C3—N2—B1	176.74 (13)
C10—C2—C3—C4	−2.5 (3)	F1—B1—N2—C9	−59.85 (19)
C1—C2—C3—N2	−0.49 (16)	F2—B1—N2—C9	60.76 (18)
C10—C2—C3—N2	179.47 (14)	N1—B1—N2—C9	−179.90 (13)
N2—C3—C4—C5	−0.9 (2)	F1—B1—N2—C3	124.62 (14)
C2—C3—C4—C5	−178.75 (14)	F2—B1—N2—C3	−114.76 (15)
C3—C4—C5—N1	−0.6 (2)	N1—B1—N2—C3	4.57 (18)
C3—C4—C5—C6	−179.69 (14)	C3—N2—C9—C1	−0.32 (16)
C4—C5—C6—C7	178.27 (15)	B1—N2—C9—C1	−176.46 (13)
N1—C5—C6—C7	−0.88 (16)	C3—N2—C9—C13	179.49 (14)
C4—C5—C6—C11	−2.1 (2)	B1—N2—C9—C13	3.3 (2)
N1—C5—C6—C11	178.71 (13)	C2—C1—C9—N2	0.01 (17)
C5—C6—C7—C8	0.70 (17)	S1—C1—C9—N2	172.53 (11)
C11—C6—C7—C8	−178.88 (15)	C2—C1—C9—C13	−179.78 (15)
C6—C7—C8—N1	−0.27 (17)	S1—C1—C9—C13	−7.3 (2)
C6—C7—C8—C12	179.08 (15)	C2—C1—S1—C14	−96.10 (14)
C7—C8—N1—C5	−0.29 (16)	C9—C1—S1—C14	92.70 (14)
C12—C8—N1—C5	−179.68 (14)	C1—S1—C14—C19	−26.87 (17)
C7—C8—N1—B1	176.38 (13)	C1—S1—C14—C15	155.26 (13)
C12—C8—N1—B1	−3.0 (2)	C19—C14—C15—C16	1.0 (3)
C4—C5—N1—C8	−178.52 (13)	S1—C14—C15—C16	178.92 (14)

C6—C5—N1—C8	0.72 (15)	C14—C15—C16—C17	0.0 (3)
C4—C5—N1—B1	4.7 (2)	C15—C16—C17—F3	178.96 (17)
C6—C5—N1—B1	−176.04 (12)	C15—C16—C17—C18	−0.9 (3)
C8—N1—B1—F1	57.46 (19)	F3—C17—C18—C19	−179.01 (18)
C5—N1—B1—F1	−126.41 (14)	C16—C17—C18—C19	0.8 (3)
C8—N1—B1—F2	−63.18 (19)	C15—C14—C19—C18	−1.0 (3)
C5—N1—B1—F2	112.95 (14)	S1—C14—C19—C18	−178.83 (15)
C8—N1—B1—N2	177.72 (13)	C17—C18—C19—C14	0.1 (3)

Geometric parameters for BDP-Br (Å, º)

Br1_1—C16_1	1.878 (2)	C19_2—H19A_2	0.98
S1_1—C7_1	1.756 (2)	C19_2—H19B_2	0.98
S1_1—C2_1	1.785 (3)	C19_2—H19C_2	0.98
F1_1—C5_1	1.362 (3)	Br1_3—C16_3	1.876 (2)
F2_1—B1_1	1.382 (3)	S1_3—C7_3	1.759 (2)
F3_1—B1_1	1.394 (3)	S1_3—C1_3	1.783 (3)
N1_1—C8_1	1.346 (3)	F1_3—C4_3	1.360 (3)
N1_1—C9_1	1.400 (3)	F2_3—B1_3	1.388 (3)
N1_1—B1_1	1.553 (3)	F3_3—B1_3	1.393 (3)
N2_1—C15_1	1.349 (3)	N1_3—C10_3	1.351 (3)
N2_1—C12_1	1.405 (3)	N1_3—C9_3	1.400 (3)
N2_1—B1_1	1.558 (3)	N1_3—B1_3	1.552 (3)
C1_1—C6_1	1.390 (4)	N2_3—C17_3	1.346 (3)
C1_1—C2_1	1.390 (4)	N2_3—C13_3	1.403 (3)
C1_1—H1_1	0.95	N2_3—B1_3	1.551 (3)
C2_1—C3_1	1.387 (3)	C1_3—C2_3	1.387 (4)
C3_1—C4_1	1.395 (4)	C1_3—C6_3	1.391 (4)
C3_1—H3_1	0.95	C2_3—C3_3	1.386 (4)
C4_1—C5_1	1.367 (4)	C2_3—H2_3	0.95
C4_1—H4_1	0.95	C3_3—C4_3	1.367 (4)
C5_1—C6_1	1.373 (4)	C3_3—H3_3	0.95

C6_1—H6_1 0.95 C4_3—C5_3 1.370 (4)

C7_1—C10_1 1.393 (3) C5_3—C6_3 1.389 (4)

C7_1—C8_1 1.423 (3) C5_3—H5_3 0.95

C8_1—C11_1 1.485 (3) C6_3—H6_3 0.95

C9_1—C13_1 1.386 (3) C7_3—C8_3 1.395 (3)

C9_1—C10_1 1.417 (3) C7_3—C10_3 1.411 (3)

C10_1—C14_1 1.490 (3) C8_3—C9_3 1.419 (3)

C11_1—H11A_1 0.98 C8_3—C11_3 1.489 (3)

C11_1—H11B_1 0.98 C9_3—C12_3 1.389 (3)

C11_1—H11C_1 0.98 C10_3—C14_3 1.487 (3)

C12_1—C13_1 1.383 (3) C11_3—H11A_3 0.98

C12_1—C17_1 1.417 (3) C11_3—H11B_3 0.98

C13_1—H13_1 0.95 C11_3—H11C_3 0.98

C14_1—H14A_1 0.98 C12_3—C13_3 1.386 (3)

C14_1—H14B_1 0.98 C12_3—H12_3 0.95

C14_1—H14C_1 0.98 C13_3—C15_3 1.418 (3)

C15_1—C16_1 1.404 (3) C14_3—H14A_3 0.98

C15_1—C18_1 1.485 (3) C14_3—H14B_3 0.98

C16_1—C17_1 1.381 (3) C14_3—H14C_3 0.98

C17_1—C19_1 1.494 (3) C15_3—C16_3 1.380 (3)

C18_1—H18A_1 0.98 C15_3—C18_3 1.483 (3)

C18_1—H18B_1 0.98 C16_3—C17_3 1.404 (3)

C18_1—H18C_1 0.98 C17_3—C19_3 1.487 (3)

C18_1—H18D_1 0.98 C18_3—H18A_3 0.98

C18_1—H18E_1	0.98	C18_3—H18B_3	0.98
C18_1—H18F_1	0.98	C18_3—H18C_3	0.98
C19_1—H19A_1	0.98	C19_3—H19A_3	0.98
C19_1—H19B_1	0.98	C19_3—H19B_3	0.98
C19_1—H19C_1	0.98	C19_3—H19C_3	0.98
Br1_2—C16_2	1.872 (2)	Br1_4—C16_4	1.876 (2)
S1_2—C7_2	1.755 (2)	S1_4—C7_4	1.755 (2)
S1_2—C1_2	1.782 (3)	S1_4—C1_4	1.782 (3)
F1_2—C4_2	1.363 (3)	F1_4—C4_4	1.366 (3)
F2_2—B1_2	1.384 (3)	F2_4—B1_4	1.391 (3)
F3_2—B1_2	1.399 (3)	F3_4—B1_4	1.391 (3)
N1_2—C10_2	1.344 (3)	N1_4—C10_4	1.351 (3)
N1_2—C9_2	1.401 (3)	N1_4—C9_4	1.400 (3)

N1_2—B1_2	1.551 (3)	N1_4—B1_4	1.545 (3)
N2_2—C17_2	1.347 (3)	N2_4—C17_4	1.347 (3)
N2_2—C13_2	1.404 (3)	N2_4—C13_4	1.403 (3)
N2_2—B1_2	1.551 (3)	N2_4—B1_4	1.550 (3)
C1_2—C6_2	1.379 (4)	C1_4—C6_4	1.384 (3)
C1_2—C2_2	1.398 (4)	C1_4—C2_4	1.393 (3)
C2_2—C3_2	1.385 (4)	C2_4—C3_4	1.382 (4)
C2_2—H2_2	0.95	C2_4—H2_4	0.95
C3_2—C4_2	1.369 (4)	C3_4—C4_4	1.378 (4)

C3_2—H3_2 0.95 C3_4—H3_4 0.95

C4_2—C5_2 1.372 (4) C4_4—C5_4 1.368 (3)

C5_2—C6_2 1.389 (4) C5_4—C6_4 1.393 (3)

C5_2—H5_2 0.95 C5_4—H5_4 0.95

C6_2—H6_2 0.95 C6_4—H6_4 0.95

C7_2—C8_2 1.396 (3) C7_4—C8_4 1.395 (3)

C7_2—C10_2 1.411 (3) C7_4—C10_4 1.413 (3)

C8_2—C9_2 1.420 (3) C8_4—C9_4 1.413 (3)

C8_2—C11_2 1.490 (3) C8_4—C11_4 1.489 (3)

C9_2—C12_2 1.385 (3) C9_4—C12_4 1.396 (3)

C10_2—C14_2 1.494 (3) C10_4—C14_4 1.490 (3)

C11_2—H11A_2 0.98 C11_4—H11A_4 0.98

C11_2—H11B_2 0.98 C11_4—H11B_4 0.98

C11_2—H11C_2 0.98 C11_4—H11C_4 0.98

C11_2—H11D_2 0.98 C12_4—C13_4 1.377 (3)

C11_2—H11E_2 0.98 C12_4—H12_4 0.95

C11_2—H11F_2 0.98 C13_4—C15_4 1.426 (3)

C12_2—C13_2 1.380 (3) C14_4—H14A_4 0.98

C12_2—H12_2 0.95 C14_4—H14B_4 0.98

C13_2—C15_2 1.418 (3) C14_4—H14C_4 0.98

C14_2—H14A_2 0.98 C15_4—C16_4 1.377 (3)

C14_2—H14B_2 0.98 C15_4—C18_4 1.487 (3)

C14_2—H14C_2 0.98 C16_4—C17_4 1.410 (3)

C15_2—C16_2 1.378 (3) C17_4—C19_4 1.481 (3)

C15_2—C18_2	1.493 (3)	C18_4—H18A_4	0.98
C16_2—C17_2	1.405 (3)	C18_4—H18B_4	0.98
C17_2—C19_2	1.486 (3)	C18_4—H18C_4	0.98
C18_2—H18A_2	0.98	C19_4—H19A_4	0.98
C18_2—H18B_2	0.98	C19_4—H19B_4	0.98
C18_2—H18C_2	0.98	C19_4—H19C_4	0.98
C7_1—S1_1—C2_1	102.14 (11)	C15_2—C18_2—H18C_2	109.5
C8_1—N1_1—C9_1	108.49 (19)	H18A_2—C18_2—H18C_2	109.5
C8_1—N1_1—B1_1	127.00 (19)	H18B_2—C18_2—H18C_2	109.5
C9_1—N1_1—B1_1	124.43 (19)	C17_2—C19_2—H19A_2	109.5
C15_1—N2_1—C12_1	108.17 (19)	C17_2—C19_2—H19B_2	109.5
C15_1—N2_1—B1_1	126.67 (19)	H19A_2—C19_2—H19B_2	109.5
C12_1—N2_1—B1_1	125.10 (19)	C17_2—C19_2—H19C_2	109.5
C6_1—C1_1—C2_1	120.1 (2)	H19A_2—C19_2—H19C_2	109.5
C6_1—C1_1—H1_1	120	H19B_2—C19_2—H19C_2	109.5
C2_1—C1_1—H1_1	120	F2_2—B1_2—F3_2	109.09 (19)
C3_1—C2_1—C1_1	119.9 (2)	F2_2—B1_2—N2_2	110.8 (2)
C3_1—C2_1—S1_1	117.5 (2)	F3_2—B1_2—N2_2	109.73 (19)
C1_1—C2_1—S1_1	122.63 (19)	F2_2—B1_2—N1_2	110.6 (2)
C2_1—C3_1—C4_1	120.2 (3)	F3_2—B1_2—N1_2	109.8 (2)
C2_1—C3_1—H3_1	119.9	N2_2—B1_2—N1_2	106.87 (18)
C4_1—C3_1—H3_1	119.9	C7_3—S1_3—C1_3	103.11 (12)

C5_1—C4_1—C3_1	118.3 (2)	C10_3—N1_3—C9_3	107.9 (2)
C5_1—C4_1—H4_1	120.9	C10_3—N1_3—B1_3	126.8 (2)
C3_1—C4_1—H4_1	120.9	C9_3—N1_3—B1_3	125.36 (19)
F1_1—C5_1—C4_1	118.7 (2)	C17_3—N2_3—C13_3	108.11 (19)
F1_1—C5_1—C6_1	118.3 (3)	C17_3—N2_3—B1_3	126.6 (2)
C4_1—C5_1—C6_1	123.0 (3)	C13_3—N2_3—B1_3	125.28 (19)
C5_1—C6_1—C1_1	118.5 (3)	C2_3—C1_3—C6_3	119.6 (2)
C5_1—C6_1—H6_1	120.8	C2_3—C1_3—S1_3	117.0 (2)
C1_1—C6_1—H6_1	120.8	C6_3—C1_3—S1_3	123.4 (2)
C10_1—C7_1—C8_1	108.2 (2)	C3_3—C2_3—C1_3	120.6 (3)
C10_1—C7_1—S1_1	127.04 (18)	C3_3—C2_3—H2_3	119.7
C8_1—C7_1—S1_1	124.71 (18)	C1_3—C2_3—H2_3	119.7
N1_1—C8_1—C7_1	108.6 (2)	C4_3—C3_3—C2_3	118.4 (3)
N1_1—C8_1—C11_1	123.0 (2)	C4_3—C3_3—H3_3	120.8
C7_1—C8_1—C11_1	128.3 (2)	C2_3—C3_3—H3_3	120.8
C13_1—C9_1—N1_1	120.8 (2)	F1_3—C4_3—C3_3	118.6 (3)
C13_1—C9_1—C10_1	130.6 (2)	F1_3—C4_3—C5_3	118.5 (3)
N1_1—C9_1—C10_1	108.62 (19)	C3_3—C4_3—C5_3	122.9 (3)
C7_1—C10_1—C9_1	106.0 (2)	C4_3—C5_3—C6_3	118.6 (3)
C7_1—C10_1—C14_1	127.3 (2)	C4_3—C5_3—H5_3	120.7
C9_1—C10_1—C14_1	126.6 (2)	C6_3—C5_3—H5_3	120.7
C8_1—C11_1—H11A_1	109.5	C5_3—C6_3—C1_3	120.0 (3)
C8_1—C11_1—H11B_1	109.5	C5_3—C6_3—H6_3	120
H11A_1—C11_1—H11B_1	109.5	C1_3—C6_3—H6_3	120

C8_1—C11_1—H11C_1	109.5	C8_3—C7_3—C10_3	108.3 (2)
H11A_1—C11_1—H11C_1	109.5	C8_3—C7_3—S1_3	126.1 (2)
H11B_1—C11_1—H11C_1	109.5	C10_3—C7_3—S1_3	125.26 (19)
C13_1—C12_1—N2_1	119.9 (2)	C7_3—C8_3—C9_3	105.8 (2)
C13_1—C12_1—C17_1	131.3 (2)	C7_3—C8_3—C11_3	127.9 (2)
N2_1—C12_1—C17_1	108.74 (19)	C9_3—C8_3—C11_3	126.4 (2)
C12_1—C13_1—C9_1	122.3 (2)	C12_3—C9_3—N1_3	120.1 (2)
C12_1—C13_1—H13_1	118.8	C12_3—C9_3—C8_3	131.1 (2)
C9_1—C13_1—H13_1	118.8	N1_3—C9_3—C8_3	108.9 (2)
C10_1—C14_1—H14A_1	109.5	N1_3—C10_3—C7_3	109.2 (2)
C10_1—C14_1—H14B_1	109.5	N1_3—C10_3—C14_3	123.1 (2)
H14A_1—C14_1—H14B_1	109.5	C7_3—C10_3—C14_3	127.7 (2)
C10_1—C14_1—H14C_1	109.5	C8_3—C11_3—H11A_3	109.5
H14A_1—C14_1—H14C_1	109.5	C8_3—C11_3—H11B_3	109.5
H14B_1—C14_1—H14C_1	109.5	H11A_3—C11_3—H11B_3	109.5
N2_1—C15_1—C16_1	108.0 (2)	C8_3—C11_3—H11C_3	109.5
N2_1—C15_1—C18_1	123.5 (2)	H11A_3—C11_3—H11C_3	109.5
C16_1—C15_1—C18_1	128.5 (2)	H11B_3—C11_3—H11C_3	109.5
C17_1—C16_1—C15_1	110.0 (2)	C13_3—C12_3—C9_3	122.3 (2)
C17_1—C16_1—Br1_1	126.35 (18)	C13_3—C12_3—H12_3	118.8
C15_1—C16_1—Br1_1	123.64 (17)	C9_3—C12_3—H12_3	118.8
C16_1—C17_1—C12_1	105.1 (2)	C12_3—C13_3—N2_3	120.1 (2)
C16_1—C17_1—C19_1	127.8 (2)	C12_3—C13_3—C15_3	131.0 (2)
C12_1—C17_1—C19_1	127.1 (2)	N2_3—C13_3—C15_3	108.9 (2)

C15_1—C18_1—H18A_1	109.5		C10_3—C14_3—H14A_3	109.5	
C15_1—C18_1—H18B_1	109.5		C10_3—C14_3—H14B_3	109.5	
H18A_1—C18_1—H18B_1	109.5		H14A_3—C14_3—H14B_3	109.5	
C15_1—C18_1—H18C_1	109.5		C10_3—C14_3—H14C_3	109.5	
H18A_1—C18_1—H18C_1	109.5		H14A_3—C14_3—H14C_3	109.5	
H18B_1—C18_1—H18C_1	109.5		H14B_3—C14_3—H14C_3	109.5	
C15_1—C18_1—H18D_1	109.5		C16_3—C15_3—C13_3	104.9 (2)	
H18A_1—C18_1—H18D_1	141.1		C16_3—C15_3—C18_3	127.9 (2)	
H18B_1—C18_1—H18D_1	56.3		C13_3—C15_3—C18_3	127.2 (2)	
H18C_1—C18_1—H18D_1	56.3		C15_3—C16_3—C17_3	110.0 (2)	
C15_1—C18_1—H18E_1	109.5		C15_3—C16_3—Br1_3	125.44 (18)	
H18A_1—C18_1—H18E_1	56.3		C17_3—C16_3—Br1_3	124.53 (18)	
H18B_1—C18_1—H18E_1	141.1		N2_3—C17_3—C16_3	108.1 (2)	
H18C_1—C18_1—H18E_1	56.3		N2_3—C17_3—C19_3	123.2 (2)	
H18D_1—C18_1—H18E_1	109.5		C16_3—C17_3—C19_3	128.7 (2)	
C15_1—C18_1—H18F_1	109.5		C15_3—C18_3—H18A_3	109.5	
H18A_1—C18_1—H18F_1	56.3		C15_3—C18_3—H18B_3	109.5	
H18B_1—C18_1—H18F_1	56.3		H18A_3—C18_3—H18B_3	109.5	
H18C_1—C18_1—H18F_1	141.1		C15_3—C18_3—H18C_3	109.5	
H18D_1—C18_1—H18F_1	109.5		H18A_3—C18_3—H18C_3	109.5	
H18E_1—C18_1—H18F_1	109.5		H18B_3—C18_3—H18C_3	109.5	
C17_1—C19_1—H19A_1	109.5		C17_3—C19_3—H19A_3	109.5	

C17_1—C19_1—H19B_1	109.5	C17_3—C19_3—H19B_3	109.5
H19A_1—C19_1—H19B_1	109.5	H19A_3—C19_3—H19B_3	109.5
C17_1—C19_1—H19C_1	109.5	C17_3—C19_3—H19C_3	109.5
H19A_1—C19_1—H19C_1	109.5	H19A_3—C19_3—H19C_3	109.5
H19B_1—C19_1—H19C_1	109.5	H19B_3—C19_3—H19C_3	109.5
F2_1—B1_1—F3_1	109.47 (19)	F2_3—B1_3—F3_3	109.4 (2)
F2_1—B1_1—N1_1	110.66 (19)	F2_3—B1_3—N2_3	110.2 (2)
F3_1—B1_1—N1_1	110.1 (2)	F3_3—B1_3—N2_3	109.71 (19)
F2_1—B1_1—N2_1	110.3 (2)	F2_3—B1_3—N1_3	110.21 (19)
F3_1—B1_1—N2_1	109.35 (19)	F3_3—B1_3—N1_3	110.5 (2)
N1_1—B1_1—N2_1	106.93 (18)	N2_3—B1_3—N1_3	106.83 (19)
C7_2—S1_2—C1_2	102.81 (12)	C7_4—S1_4—C1_4	103.61 (11)
C10_2—N1_2—C9_2	107.76 (19)	C10_4—N1_4—C9_4	108.39 (19)
C10_2—N1_2—B1_2	127.3 (2)	C10_4—N1_4—B1_4	126.52 (19)
C9_2—N1_2—B1_2	124.89 (19)	C9_4—N1_4—B1_4	125.09 (18)
C17_2—N2_2—C13_2	108.35 (19)	C17_4—N2_4—C13_4	108.38 (19)
C17_2—N2_2—B1_2	126.7 (2)	C17_4—N2_4—B1_4	125.93 (19)
C13_2—N2_2—B1_2	124.86 (19)	C13_4—N2_4—B1_4	125.66 (19)
C6_2—C1_2—C2_2	120.0 (2)	C6_4—C1_4—C2_4	119.7 (2)
C6_2—C1_2—S1_2	122.8 (2)	C6_4—C1_4—S1_4	124.24 (18)
C2_2—C1_2—S1_2	117.2 (2)	C2_4—C1_4—S1_4	116.07 (19)
C3_2—C2_2—C1_2	119.8 (3)	C3_4—C2_4—C1_4	120.4 (2)
C3_2—C2_2—H2_2	120.1	C3_4—C2_4—H2_4	119.8
C1_2—C2_2—H2_2	120.1	C1_4—C2_4—H2_4	119.8

C4_2—C3_2—C2_2 118.6 (3) C4_4—C3_4—C2_4 118.5 (2)

C4_2—C3_2—H3_2 120.7 C4_4—C3_4—H3_4 120.7

C2_2—C3_2—H3_2 120.7 C2_4—C3_4—H3_4 120.7

F1_2—C4_2—C3_2 118.3 (3) F1_4—C4_4—C5_4 118.7 (2)

F1_2—C4_2—C5_2 118.7 (3) F1_4—C4_4—C3_4 118.7 (2)

C3_2—C4_2—C5_2 123.0 (3) C5_4—C4_4—C3_4 122.6 (2)

C4_2—C5_2—C6_2 118.2 (3) C4_4—C5_4—C6_4 118.5 (2)

C4_2—C5_2—H5_2 120.9 C4_4—C5_4—H5_4 120.7

C6_2—C5_2—H5_2 120.9 C6_4—C5_4—H5_4 120.7

C1_2—C6_2—C5_2 120.3 (3) C1_4—C6_4—C5_4 120.3 (2)

C1_2—C6_2—H6_2 119.8 C1_4—C6_4—H6_4 119.9

C5_2—C6_2—H6_2 119.8 C5_4—C6_4—H6_4 119.9

C8_2—C7_2—C10_2 107.9 (2) C8_4—C7_4—C10_4 108.4 (2)

C8_2—C7_2—S1_2 125.67 (19) C8_4—C7_4—S1_4 127.52 (19)

C10_2—C7_2—S1_2 126.14 (19) C10_4—C7_4—S1_4 124.03 (19)

C7_2—C8_2—C9_2 105.8 (2) C7_4—C8_4—C9_4 106.0 (2)

C7_2—C8_2—C11_2 128.0 (2) C7_4—C8_4—C11_4 127.4 (2)

C9_2—C8_2—C11_2 126.2 (2) C9_4—C8_4—C11_4 126.6 (2)

C12_2—C9_2—N1_2 120.5 (2) C12_4—C9_4—N1_4 120.3 (2)

C12_2—C9_2—C8_2 130.7 (2) C12_4—C9_4—C8_4 131.1 (2)

N1_2—C9_2—C8_2 108.82 (19) N1_4—C9_4—C8_4 108.6 (2)

N1_2—C10_2—C7_2 109.7 (2) N1_4—C10_4—C7_4 108.6 (2)

N1_2—C10_2—C14_2	122.4 (2)	N1_4—C10_4—C14_4	122.6 (2)
C7_2—C10_2—C14_2	128.0 (2)	C7_4—C10_4—C14_4	128.8 (2)
C8_2—C11_2—H11A_2	109.5	C8_4—C11_4—H11A_4	109.5
C8_2—C11_2—H11B_2	109.5	C8_4—C11_4—H11B_4	109.5
H11A_2—C11_2—H11B_2	109.5	H11A_4—C11_4—H11B_4	109.5
C8_2—C11_2—H11C_2	109.5	C8_4—C11_4—H11C_4	109.5
H11A_2—C11_2—H11C_2	109.5	H11A_4—C11_4—H11C_4	109.5
H11B_2—C11_2—H11C_2	109.5	H11B_4—C11_4—H11C_4	109.5
C8_2—C11_2—H11D_2	109.5	C13_4—C12_4—C9_4	122.1 (2)
H11A_2—C11_2—H11D_2	141.1	C13_4—C12_4—H12_4	119
H11B_2—C11_2—H11D_2	56.3	C9_4—C12_4—H12_4	119
H11C_2—C11_2—H11D_2	56.3	C12_4—C13_4—N2_4	120.0 (2)
C8_2—C11_2—H11E_2	109.5	C12_4—C13_4—C15_4	131.3 (2)
H11A_2—C11_2—H11E_2	56.3	N2_4—C13_4—C15_4	108.76 (19)
H11B_2—C11_2—H11E_2	141.1	C10_4—C14_4—H14A_4	109.5
H11C_2—C11_2—H11E_2	56.3	C10_4—C14_4—H14B_4	109.5
H11D_2—C11_2—H11E_2	109.5	H14A_4—C14_4—H14B_4	109.5
C8_2—C11_2—H11F_2	109.5	C10_4—C14_4—H14C_4	109.5
H11A_2—C11_2—H11F_2	56.3	H14A_4—C14_4—H14C_4	109.5
H11B_2—C11_2—H11F_2	56.3	H14B_4—C14_4—H14C_4	109.5
H11C_2—C11_2—H11F_2	141.1	C16_4—C15_4—C13_4	104.8 (2)
H11D_2—C11_2—H11F_2	109.5	C16_4—C15_4—C18_4	128.2 (2)
H11E_2—C11_2—H11F_2	109.5	C13_4—C15_4—C18_4	127.0 (2)
C13_2—C12_2—C9_2	122.1 (2)	C15_4—C16_4—C17_4	110.3 (2)

C13_2—C12_2—H12_2	119	C15_4—C16_4—Br1_4	126.61 (18)
C9_2—C12_2—H12_2	119	C17_4—C16_4—Br1_4	123.04 (17)
C12_2—C13_2—N2_2	120.5 (2)	N2_4—C17_4—C16_4	107.8 (2)
C12_2—C13_2—C15_2	131.0 (2)	N2_4—C17_4—C19_4	123.4 (2)
N2_2—C13_2—C15_2	108.5 (2)	C16_4—C17_4—C19_4	128.8 (2)
C10_2—C14_2—H14A_2	109.5	C15_4—C18_4—H18A_4	109.5
C10_2—C14_2—H14B_2	109.5	C15_4—C18_4—H18B_4	109.5
H14A_2—C14_2—H14B_2	109.5	H18A_4—C18_4—H18B_4	109.5
C10_2—C14_2—H14C_2	109.5	C15_4—C18_4—H18C_4	109.5
H14A_2—C14_2—H14C_2	109.5	H18A_4—C18_4—H18C_4	109.5
H14B_2—C14_2—H14C_2	109.5	H18B_4—C18_4—H18C_4	109.5
C16_2—C15_2—C13_2	105.2 (2)	C17_4—C19_4—H19A_4	109.5
C16_2—C15_2—C18_2	127.6 (2)	C17_4—C19_4—H19B_4	109.5
C13_2—C15_2—C18_2	127.2 (2)	H19A_4—C19_4—H19B_4	109.5
C15_2—C16_2—C17_2	110.0 (2)	C17_4—C19_4—H19C_4	109.5
C15_2—C16_2—Br1_2	125.88 (19)	H19A_4—C19_4—H19C_4	109.5
C17_2—C16_2—Br1_2	124.07 (18)	H19B_4—C19_4—H19C_4	109.5
N2_2—C17_2—C16_2	107.9 (2)	F2_4—B1_4—F3_4	109.71 (19)
N2_2—C17_2—C19_2	123.8 (2)	F2_4—B1_4—N1_4	110.40 (19)
C16_2—C17_2—C19_2	128.3 (2)	F3_4—B1_4—N1_4	110.39 (19)
C15_2—C18_2—H18A_2	109.5	F2_4—B1_4—N2_4	109.73 (19)
C15_2—C18_2—H18B_2	109.5	F3_4—B1_4—N2_4	109.77 (18)

H18A_2—C18_2—H18B_2 109.5 N1_4—B1_4—N2_4 106.79 (18)

C6_1—C1_1—C2_1—C3_1 −1.6 (4) C7_3—S1_3—C1_3—C2_3 149.6 (2)

C6_1—C1_1—C2_1—S1_1 179.7 (2) C7_3—S1_3—C1_3—C6_3 −33.2 (3)

C7_1—S1_1—C2_1—C3_1 137.3 (2) C6_3—C1_3—C2_3—C3_3 0.3 (4)

C7_1—S1_1—C2_1—C1_1 −44.0 (2) S1_3—C1_3—C2_3—C3_3 177.6 (2)

C1_1—C2_1—C3_1—C4_1 0.4 (4) C1_3—C2_3—C3_3—C4_3 0.8 (4)

S1_1—C2_1—C3_1—C4_1 179.14 (19) C2_3—C3_3—C4_3—F1_3 179.2 (2)

C2_1—C3_1—C4_1—C5_1 1.0 (4) C2_3—C3_3—C4_3—C5_3 −0.9 (4)

C3_1—C4_1—C5_1—F1_1 178.6 (2) F1_3—C4_3—C5_3—C6_3 179.9 (2)

C3_1—C4_1—C5_1—C6_1 −1.3 (4) C3_3—C4_3—C5_3—C6_3 0.0 (4)

F1_1—C5_1—C6_1—C1_1 −179.8 (2) C4_3—C5_3—C6_3—C1_3 1.1 (4)

C4_1—C5_1—C6_1—C1_1 0.2 (4) C2_3—C1_3—C6_3—C5_3 −1.2 (4)

C2_1—C1_1—C6_1—C5_1 1.3 (4) S1_3—C1_3—C6_3—C5_3 −178.3 (2)

C2_1—S1_1—C7_1—C10_1 −56.1 (2) C1_3—S1_3—C7_3—C8_3 121.9 (2)

C2_1—S1_1—C7_1—C8_1 126.6 (2) C1_3—S1_3—C7_3—C10_3 −64.9 (2)

C9_1—N1_1—C8_1—C7_1 0.5 (3) C10_3—C7_3—C8_3—C9_3 0.2 (3)

B1_1—N1_1—C8_1—C7_1 −176.3 (2) S1_3—C7_3—C8_3—C9_3 174.30 (18)

C9_1—N1_1—C8_1—C11_1 179.9 (2) C10_3—C7_3—C8_3—C11_3 −179.3 (2)

B1_1—N1_1—C8_1—C11_1 3.1 (4) S1_3—C7_3—C8_3—C11_3 −5.2 (4)

C10_1—C7_1—C8_1—N1_1 0.4 (3) C10_3—N1_3—C9_3—C12_3 −179.2 (2)

S1_1—C7_1—C8_1—N1_1 178.07 (17) B1_3—N1_3—C9_3—C12_3 1.1 (3)

C10_1—C7_1—C8_1—C11_1 −178.9 (2) C10_3—N1_3—C9_3—C8_3 0.0 (3)

S1_1—C7_1—C8_1—C11_1 −1.3 (4) B1_3—N1_3—C9_3—C8_3 −179.8 (2)

C8_1—N1_1—C9_1—C13_1 177.3 (2) C7_3—C8_3—C9_3—C12_3 178.9 (2)

B1_1—N1_1—C9_1—C13_1 −5.8 (3) C11_3—C8_3—C9_3—C12_3 −1.5 (4)

C8_1—N1_1—C9_1—C10_1 −1.2 (3) C7_3—C8_3—C9_3—N1_3 −0.1 (3)

B1_1—N1_1—C9_1—C10_1 175.7 (2) C11_3—C8_3—C9_3—N1_3 179.4 (2)

C8_1—C7_1—C10_1—C9_1 −1.1 (3) C9_3—N1_3—C10_3—C7_3 0.1 (3)

S1_1—C7_1—C10_1—C9_1 −178.73 (18) B1_3—N1_3—C10_3—C7_3 179.9 (2)

C8_1—C7_1—C10_1—C14_1 179.0 (2) C9_3—N1_3—C10_3—C14_3 179.4 (2)

S1_1—C7_1—C10_1—C14_1 1.4 (4) B1_3—N1_3—C10_3—C14_3 −0.8 (4)

C13_1—C9_1—C10_1—C7_1 −176.9 (2) C8_3—C7_3—C10_3—N1_3 −0.2 (3)

N1_1—C9_1—C10_1—C7_1 1.4 (3) S1_3—C7_3—C10_3—N1_3 −174.37 (17)

C13_1—C9_1—C10_1—C14_1 3.0 (4) C8_3—C7_3—C10_3—C14_3 −179.4 (2)

N1_1—C9_1—C10_1—C14_1	−178.7 (2)	S1_3—C7_3—C10_3—C14_3	6.4 (4)
C15_1—N2_1—C12_1—C13_1	179.8 (2)	N1_3—C9_3—C12_3—C13_3	0.6 (3)
B1_1—N2_1—C12_1—C13_1	2.5 (3)	C8_3—C9_3—C12_3—C13_3	−178.3 (2)
C15_1—N2_1—C12_1—C17_1	0.4 (2)	C9_3—C12_3—C13_3—N2_3	−0.8 (3)
B1_1—N2_1—C12_1—C17_1	−176.9 (2)	C9_3—C12_3—C13_3—C15_3	−179.5 (2)
N2_1—C12_1—C13_1—C9_1	1.1 (3)	C17_3—N2_3—C13_3—C12_3	−178.9 (2)
C17_1—C12_1—C13_1—C9_1	−179.6 (2)	B1_3—N2_3—C13_3—C12_3	−0.7 (3)
N1_1—C9_1—C13_1—C12_1	0.5 (3)	C17_3—N2_3—C13_3—C15_3	0.0 (3)
C10_1—C9_1—C13_1—C12_1	178.7 (2)	B1_3—N2_3—C13_3—C15_3	178.3 (2)
C12_1—N2_1—C15_1—C16_1	0.2 (2)	C12_3—C13_3—C15_3—C16_3	178.8 (2)
B1_1—N2_1—C15_1—C16_1	177.5 (2)	N2_3—C13_3—C15_3—C16_3	0.0 (3)
C12_1—N2_1—C15_1—C18_1	−179.3 (2)	C12_3—C13_3—C15_3—C18_3	−1.0 (4)
B1_1—N2_1—C15_1—C18_1	−2.0 (4)	N2_3—C13_3—C15_3—C18_3	−179.8 (2)

N2_1—C15_1—C16_1—C17_1	−0.8 (3)	C13_3—C15_3—C16_3—C17_3	0.0 (3)
C18_1—C15_1—C16_1—C17_1	178.7 (2)	C18_3—C15_3—C16_3—C17_3	179.8 (2)
N2_1—C15_1—C16_1—Br1_1	−179.74 (16)	C13_3—C15_3—C16_3—Br1_3	−178.06 (17)
C18_1—C15_1—C16_1—Br1_1	−0.3 (4)	C18_3—C15_3—C16_3—Br1_3	1.7 (4)
C15_1—C16_1—C17_1—C12_1	1.0 (3)	C13_3—N2_3—C17_3—C16_3	0.0 (3)
Br1_1—C16_1—C17_1—C12_1	179.92 (17)	B1_3—N2_3—C17_3—C16_3	−178.2 (2)
C15_1—C16_1—C17_1—C19_1	−179.6 (2)	C13_3—N2_3—C17_3—C19_3	−179.7 (2)
Br1_1—C16_1—C17_1—C19_1	−0.7 (4)	B1_3—N2_3—C17_3—C19_3	2.1 (4)
C13_1—C12_1—C17_1—C16_1	179.8 (2)	C15_3—C16_3—C17_3—N2_3	0.0 (3)
N2_1—C12_1—C17_1—C16_1	−0.9 (2)	Br1_3—C16_3—C17_3—N2_3	178.11 (16)
C13_1—C12_1—C17_1—C19_1	0.4 (4)	C15_3—C16_3—C17_3—C19_3	179.6 (2)
N2_1—C12_1—C17_1—C19_1	179.8 (2)	Br1_3—C16_3—C17_3—C19_3	−2.3 (4)
C8_1—N1_1—B1_1—F2_1	−55.6 (3)	C17_3—N2_3—B1_3—F2_3	−60.4 (3)
C9_1—N1_1—B1_1—F2_1	128.1 (2)	C13_3—N2_3—B1_3—F2_3	121.7 (2)

C8_1—N1_1—B1_1—F3_1 65.6 (3) C17_3—N2_3—B1_3—F3_3 60.1 (3)

C9_1—N1_1—B1_1—F3_1 −110.7 (2) C13_3—N2_3—B1_3—F3_3 −117.9 (2)

C8_1—N1_1—B1_1—N2_1−175.7 (2) C17_3—N2_3—B1_3—N1_3 179.9 (2)

C9_1—N1_1—B1_1—N2_18.0 (3) C13_3—N2_3—B1_3—N1_3 2.0 (3)

C15_1—N2_1—B1_1—F2_1 56.4 (3) C10_3—N1_3—B1_3—F2_3 58.4 (3)

C12_1—N2_1—B1_1—F2_1 −126.8 (2) C9_3—N1_3—B1_3—F2_3 −121.9 (2)

C15_1—N2_1—B1_1—F3_1 −64.0 (3) C10_3—N1_3—B1_3—F3_3 −62.6 (3)

C12_1—N2_1—B1_1—F3_1 112.8 (2) C9_3—N1_3—B1_3—F3_3 117.1 (2)

C15_1—N2_1—B1_1—N1_1 176.8 (2) C10_3—N1_3—B1_3—N2_3 178.1 (2)

C12_1—N2_1—B1_1—N1_1 −6.4 (3) C9_3—N1_3—B1_3—N2_3−2.2 (3)

C7_2—S1_2—C1_2—C6_2 −36.4 (2) C7_4—S1_4—C1_4—C6_4 −4.8 (2)

C7_2—S1_2—C1_2—C2_2 144.8 (2) C7_4—S1_4—C1_4—C2_4 176.37 (19)

C6_2—C1_2—C2_2—C3_2 −1.3 (4) C6_4—C1_4—C2_4—C3_4 −1.3 (4)

S1_2—C1_2—C2_2—C3_2 177.4 (2) S1_4—C1_4—C2_4—C3_4 177.6 (2)

C1_2—C2_2—C3_2—C4_2 0.4 (4) C1_4—C2_4—C3_4—C4_4 −0.1 (4)

C2_2—C3_2—C4_2—F1_2 179.5 (2) C2_4—C3_4—C4_4—F1_4 −178.8 (2)

C2_2—C3_2—C4_2—C5_2 0.9 (4) C2_4—C3_4—C4_4—C5_4 1.5 (4)

F1_2—C4_2—C5_2—C6_2 −179.8 (2) F1_4—C4_4—C5_4—C6_4 178.9 (2)

C3_2—C4_2—C5_2—C6_2 −1.2 (4) C3_4—C4_4—C5_4—C6_4 −1.4 (4)

C2_2—C1_2—C6_2—C5_2 1.0 (4) C2_4—C1_4—C6_4—C5_4 1.4 (4)

S1_2—C1_2—C6_2—C5_2 −177.7 (2) S1_4—C1_4—C6_4—C5_4 −177.4 (2)

C4_2—C5_2—C6_2—C1_2 0.3 (4) C4_4—C5_4—C6_4—C1_4 −0.1 (4)

C1_2—S1_2—C7_2—C8_2 126.2 (2) C1_4—S1_4—C7_4—C8_4 72.2 (2)

C1_2—S1_2—C7_2—C10_2 −60.5 (2) C1_4—S1_4—C7_4—C10_4 −110.5 (2)

C10_2—C7_2—C8_2—C9_2 0.9 (3) C10_4—C7_4—C8_4—C9_4 1.4 (3)

S1_2—C7_2—C8_2—C9_2 175.20 (18) S1_4—C7_4—C8_4—C9_4 179.09 (18)

C10_2—C7_2—C8_2—C11_2 −179.5 (2) C10_4—C7_4—C8_4—C11_4 −179.6 (2)

S1_2—C7_2—C8_2—C11_2 −5.1 (4) S1_4—C7_4—C8_4—C11_4 −1.9 (4)

C10_2—N1_2—C9_2—C12_2 −179.2 (2) C10_4—N1_4—C9_4—C12_4 −177.1 (2)

B1_2—N1_2—C9_2—C12_2 3.4 (3) B1_4—N1_4—C9_4—C12_4 2.7 (3)

C10_2—N1_2—C9_2—C8_2 −0.2 (3) C10_4—N1_4—C9_4—C8_4 1.4 (3)

B1_2—N1_2—C9_2—C8_2 −177.6 (2) B1_4—N1_4—C9_4—C8_4 −178.8 (2)

C7_2—C8_2—C9_2—C12_2 178.5 (2) C7_4—C8_4—C9_4—C12_4 176.5 (2)

C11_2—C8_2—C9_2—C12_2 −1.2 (4) C11_4—C8_4—C9_4—C12_4 −2.5 (4)

C7_2—C8_2—C9_2—N1_2 −0.4 (3) C7_4—C8_4—C9_4—N1_4 −1.7 (3)

C11_2—C8_2—C9_2—N1_2 179.9 (2) C11_4—C8_4—C9_4—N1_4 179.2 (2)

C9_2—N1_2—C10_2—C7_2 0.8 (3) C9_4—N1_4—C10_4—C7_4 −0.5 (3)

B1_2—N1_2—C10_2—C7_2 178.0 (2) B1_4—N1_4—C10_4—C7_4 179.7 (2)

C9_2—N1_2—C10_2—C14_2 −179.6 (2) C9_4—N1_4—C10_4—C14_4 −179.8 (2)

B1_2—N1_2—C10_2—C14_2 −2.4 (4) B1_4—N1_4—C10_4—C14_4 0.4 (4)

C8_2—C7_2—C10_2—N1_2 −1.1 (3) C8_4—C7_4—C10_4—N1_4 −0.6 (3)

S1_2—C7_2—C10_2—N1_2 −175.35 (17) S1_4—C7_4—C10_4—N1_4 −178.38 (17)

C8_2—C7_2—C10_2—C14_2 179.4 (2) C8_4—C7_4—C10_4—C14_4 178.6 (2)

S1_2—C7_2—C10_2—C14_2 5.1 (4) S1_4—C7_4—C10_4—C14_4 0.8 (4)

N1_2—C9_2—C12_2—C13_2 0.8 (3) N1_4—C9_4—C12_4—C13_4 −0.3 (3)

C8_2—C9_2—C12_2—C13_2 −178.0 (2) C8_4—C9_4—C12_4—C13_4 −178.4 (2)

C9_2—C12_2—C13_2—N2_2 −0.4 (3) C9_4—C12_4—C13_4—N2_4 −0.4 (3)

C9_2—C12_2—C13_2—C15_2 177.8 (2) C9_4—C12_4—C13_4—C15_4 −179.8 (2)

C17_2—N2_2—C13_2—C12_2 178.7 (2) C17_4—N2_4—C13_4—C12_4 −179.3 (2)

B1_2—N2_2—C13_2—C12_2	−4.3 (3)	B1_4—N2_4—C13_4—C12_4	−1.2 (3)
C17_2—N2_2—C13_2—C15_2	0.2 (3)	C17_4—N2_4—C13_4—C15_4	0.3 (2)
B1_2—N2_2—C13_2—C15_2	177.2 (2)	B1_4—N2_4—C13_4—C15_4	178.4 (2)
C12_2—C13_2—C15_2—C16_2	−178.1 (2)	C12_4—C13_4—C15_4—C16_4	179.5 (2)
N2_2—C13_2—C15_2—C16_2	0.2 (3)	N2_4—C13_4—C15_4—C16_4	0.1 (2)
C12_2—C13_2—C15_2—C18_2	1.4 (4)	C12_4—C13_4—C15_4—C18_4	−0.4 (4)
N2_2—C13_2—C15_2—C18_2	179.6 (2)	N2_4—C13_4—C15_4—C18_4	−179.9 (2)
C13_2—C15_2—C16_2—C17_2	−0.5 (3)	C13_4—C15_4—C16_4—C17_4	−0.4 (3)
C18_2—C15_2—C16_2—C17_2	−180.0 (2)	C18_4—C15_4—C16_4—C17_4	179.6 (2)
C13_2—C15_2—C16_2—Br1_2	178.37 (17)	C13_4—C15_4—C16_4—Br1_4	−177.48 (17)
C18_2—C15_2—C16_2—Br1_2	−1.1 (4)	C18_4—C15_4—C16_4—Br1_4	2.5 (4)
C13_2—N2_2—C17_2—C16_2	−0.5 (3)	C13_4—N2_4—C17_4—C16_4	−0.5 (2)
B1_2—N2_2—C17_2—C16_2	−177.5 (2)	B1_4—N2_4—C17_4—C16_4	−178.6 (2)
C13_2—N2_2—C17_2—C19_2	179.9 (2)	C13_4—N2_4—C17_4—C19_4	180.0 (2)
B1_2—N2_2—C17_2—C19_2	3.0 (4)	B1_4—N2_4—C17_4—C19_4	1.9 (4)

C15_2—C16_2—C17_2—N2_2 0.6 (3) C15_4—C16_4—C17_4—N2_4 0.6 (3)

Br1_2—C16_2—C17_2—N2_2 −178.25 (16) Br1_4—C16_4—C17_4—N2_4 177.79 (16)

C15_2—C16_2—C17_2—C19_2 −179.8 (2) C15_4—C16_4—C17_4—C19_4 −179.9 (2)

Br1_2—C16_2—C17_2—C19_2 1.3 (4) Br1_4—C16_4—C17_4—C19_4 −2.7 (4)

C17_2—N2_2—B1_2—F2_2 −55.9 (3) C10_4—N1_4—B1_4—F2_4 56.9 (3)

C13_2—N2_2—B1_2—F2_2 127.6 (2) C9_4—N1_4—B1_4—F2_4 −122.9 (2)

C17_2—N2_2—B1_2—F3_2 64.6 (3) C10_4—N1_4—B1_4—F3_4 −64.6 (3)

C13_2—N2_2—B1_2—F3_2 −111.9 (2) C9_4—N1_4—B1_4—F3_4 115.6 (2)

C17_2—N2_2—B1_2—N1_2 −176.4 (2) C10_4—N1_4—B1_4—N2_4 176.1 (2)

C13_2—N2_2—B1_2—N1_2 7.1 (3) C9_4—N1_4—B1_4—N2_4 −3.7 (3)

C10_2—N1_2—B1_2—F2_2 55.9 (3) C17_4—N2_4—B1_4—F2_4 −59.6 (3)

C9_2—N1_2—B1_2—F2_2 −127.3 (2) C13_4—N2_4—B1_4—F2_4 122.6 (2)

C10_2—N1_2—B1_2—F3_2 −64.6 (3) C17_4—N2_4—B1_4—F3_4 61.0 (3)

C9_2—N1_2—B1_2—F3_2 112.3 (2) C13_4—N2_4—B1_4—F3_4 −116.8 (2)

C10_2—N1_2—B1_2—N2_2 176.5 (2) C17_4—N2_4—B1_4—N1_4 −179.3 (2)

C9_2—N1_2—B1_2—N2_2−6.7 (3) C13_4—N2_4—B1_4—N1_4 2.9 (3)

Hydrogen-bond geometry (Å, º)

D—H···A	D—H	H···A	D···A	D—H···A
C13_1—H13_1···F3_2	0.95	2.55	3.173 (3)	123
C18_1—H18C_1···F2_3	0.98	2.38	3.213 (3)	142
C2_2—H2_2···F1_4	0.95	2.51	3.461 (3)	175
C19_2—H19B_2···F2_4i	0.98	2.44	3.261 (3)	141
C14_3—H14B_3···F3_3	0.98	2.55	3.221 (3)	126
C14_3—H14B_3···F3_4ii	0.98	2.5	3.330 (3)	143
C19_3—H19C_3···F3_3	0.98	2.46	3.170 (3)	129
C14_4—H14A_4···S1_4	0.98	2.87	3.342 (3)	111
C14_4—H14A_4···F1_4iii	0.98	2.5	3.349 (3)	144
C19_4—H19C_4···F3_4	0.98	2.46	3.168 (3)	129

Symmetry codes: (i) −x+1, −y, −z; (ii) −x+1, −y+1, −z+1; (iii) −x+1, −y+1, −z.

10.11 Electronic Supplementary Information for Project [J]

Electronic Supplementary Material (ESI) for Journal of Materials Chemistry C.
This journal is © The Royal Society of Chemistry 2021

Electronic Supplementary Information for

Purely organic Vis-to-UV upconversion with an excited annihilator singlet beyond 4 eV

Till J. B. Zähringer[a], Maria-Sophie Bertrams[a] and Christoph Kerzig[a]

[a] Department of Chemistry, Johannes Gutenberg University Mainz, Duesbergweg 10—14, 55128 Mainz, Germany.

Correspondence: ckerzig@uni-mainz.de

Contents

1 General experimental details and methods 2

2 Synthetic procedures 8

2.1 Synthesis of TIPS-ethynylated biphenyls 8

2.2 Synthesis of **4CzIPN** 10

3 DFT calculations 11

4 Solvent dependence of **4CzIPN**'s photochemical properties 13

5 Photostability of the upconversion system 15

6 UV filter effects caused by the sensitizer 16

7 Photophysical properties of biphenyl (**BP**), ***p*-TIPS-BP**, ***o*-TIPS-BP**, and ***m*-TIPS-BP** 17

8 Control experiments related to residual oxygen during photon upconversion studies 18

9 Additional spectroscopic data 20

10 NMR spectra 24

11 References 25

1 General experimental details and methods

Materials

Unless otherwise noted, all chemicals used for optical spectroscopy, preparative and irradiation experiments were obtained commercially in high purity and used as received (4-bromobiphenyl, 98%, Alfa Aesar; 3-bromobiphenyl, 99%, Alfa Aesar; 2-bromobiphenyl, 98%, Alfa Aesar; (triisopropylsilyl)acetylene, 97%, Alfa Aesar; bis(triphenylphosphine)palladium(II) dichloride, 98%, Acros Organics; copper(I) iodide, 99.9%, Alfa Aesar; triphenylphosphine, 99%, Sigma-Aldrich; diisopropylamine, 99.9%, VWR Chemicals; *fac*-Ir(4',6'-dFppy)$_3$ (IrdF), 98%, Sigma-Aldrich; 2,4,5,6-tetrafluoro-1,3-benzenedicarbonitrile, 97%, Alfa Aesar; carbazole, 95%, Alfa Aesar; sodium-bis(trimethylsilyl)amide 2 M in THF, 99.7%, Alfa Aesar; *p*-terphenyl, 98%, Alfa Aesar; biphenyl, 99.5%, Sigma-Aldrich; perylene, 98%, Alfa Aesar; ethanol, 99.8%, VWR Chemicals; cyclohexane, 99.7%, VWR Chemicals; acetonitrile, 99.7%, Sigma-Aldrich; sodium sulfate, 99%, Acros Organics; diethyl ether, 99.5%, Fisher Scientific; heptane, 99%, Sigma-Aldrich; chloroform, 99%, Carl Roth). Argon from Nippon Gases (5.0) was used for removing dissolved oxygen prior to all experiments related to optical spectroscopy.

Steady-state measurements

Absorption spectra were recorded using a LAMBDA 365 instrument from Perkin Elmer. Emission measurements were carried out with a Perkin Elmer FL-6500 spectrometer. All steady-state absorption and emission measurements were performed at room temperature (295 ± 2 K) and the emission spectra were corrected for the wavelength-dependent sensitivity of the instrument. Very low concentrations of the emissive compounds were employed to avoid filter effects. The singlet-excited state energies were determined by the intersection points of the respective normalized fluorescence and the absorption spectra. The triplet energy of IrdF was estimated from the short-wavelength edge of its room-temperature emission spectrum, where the emission intensity drops to 10 % compared to the global maximum.

Determination of fluorescence quantum yields

The fluorescence quantum yields of the annihilators were determined by comparing their fluorescence spectra with those of a reference system ref (*p*-terphenyl in cyclohexane, Φ_{FL} = 0.93).[1] The quantum yield was then calculated using equation (1.1), where Φ_{FL} represents the quantum yield, *I* the integrated fluorescence intensity, *A* the absorption at the incident wavelength and the refractive index of the solvent *n* taken from ref.[1]. All solutions were adjusted to an optical density below 0.1 at the irradiation wavelengths to avoid filter effects. The fluorescence quantum yield of 4CzIPN in cyclohexane/toluene (9:1) was determined by comparing the fluorescence to a reference quantum yield of 4CzIPN in toluene, averaged from literature values (see Table S2).[2,3] The emission quantum yield of IrdF was determined using perylene in ethanol (Φ_{FL} = 0.92)[1] as reference system. Three independent quantum yield determinations were carried out and averaged for each annihilator or sensitizer.

$$\Phi_{\mathrm{Fl}} = \Phi_{\mathrm{Fl,ref}} \cdot \frac{I}{I_{\mathrm{ref}}} \cdot \frac{A_{\mathrm{ref}}}{A} \cdot \frac{n^2}{n_{\mathrm{ref}}^2} \qquad (1.1)$$

Upconversion efficiency measurements

The power dependent upconversion measurements were conducted with a 447 nm cw laser (Roithner Lasertechnik, optical output: up to 1.1 W, see Figure S2 for the data sheet) with adjustable power output and a beam size of ~0.10 cm^2 or a 440 nm LED (Kessil Science, PR160L) with four power settings (25, 50, 75, and 100%). The average intensity of the LED (at 100% output power) is reported as 352 $mW \cdot cm^{-2}$ (measured from 1 cm distance).[4] The emission spectra were measured by irradiating a water-containing cuvette in the FL-6500 instrument and they are displayed in Figure S1. The light source was installed in a 90° angle with respect to the detector. The LED intensity and laser output was further attenuated with neutral density filters obtained from Newport (ND2.0, ND1.0, ND0.5, ND0.3, ND0.1).

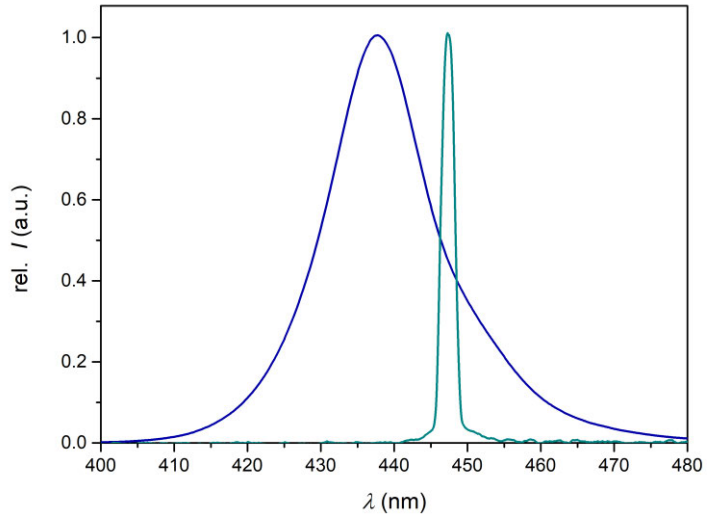

Figure S1: Emission spectrum of the PR160L 440 nm LED from Kessil Science (blue) and the 447 nm cw laser from Roithner Lasertechnik (green). The emission spectrum was measured by irradiating a water-containing cuvette in the emission spectrometer.

Testing Reports

All testing is based on the required specifications in the purchase order. Inspector:

Model: RLTMDL-447-1W-3-BK10022(PO#200367) Date: 2020-11-06

Inspection reports

Items of specs	Testing	Attachments
Output Power	1.104W	Graph1
Power Stability over 4 hours	0.136%	Graph1
Operating Mode	CW	/
Transverse Mode	Near TEM_{00}	/
Beam Diameter	~2×5mm^2	/
Beam Divergence (full angle)	< 2.5×0.2mrad	/
P-I	/	Graph2
Warm-up Time	< 5min	/
Beam height from base	24.8mm	/
Dimensions of Laser Head	143.5×73×46.2mm^3	/
Weight of Laser Head	0.7kg	/
Power Supply	85-264V	/
Integrated Driver	PSU-III-LED	/
Dimensions of Driver	188.6×155×92mm^3	/
Weight of Driver	1.5kg	/
Modulation	NO	/

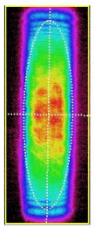

Figure S2: Data sheet of the 447 nm cw laser from Roithner Lasertechnik and a typical beam profile (right) for the RLTMDL-447-1W laser series provided by the manufacturer.

Upconversion quantum yields

The quantum yields of the UC systems were estimated by the ratios of (integrated) upconverted photons generated relative to the integrated emission of a reference system with a well-known quantum yield. For that, the photoluminescence intensity of a reference solution containing the very same sensitizer in the absence of the annihilator was measured under identical conditions as the complete upconversion system. In some measurements, a neutral density filter from Newport was used to attenuate the luminescence signal in order to avoid over-saturation of the detector. The following reference quantum yields were used: **IrdF** in Ar-saturated MeCN, Φ = 0.61 ± 0.03; **4CzIPN** in deoxygenated cyclohexane/toluene (9:1), Φ = 0.90 ± 0.01.

The upconversion quantum yields presented herein have not been multiplied by two (theoretical maximum of 50 %).

Triplet energy transfer rates (quenching rate constants)

The quenching constants were determined from Stern-Volmer experiments. The lifetime of the sensitizer was measured with different concentrations c_q of ***p*-TIPS-BP** and fitted in Stern-Volmer plots according to equation (1.2). With the unquenched lifetime the quenching rate constant was derived from the corresponding Stern-Volmer constant K_{SV}.

$$\frac{\tau_0}{\tau} = \frac{\Phi_0}{\Phi} = \frac{F_0}{F} = 1 + \tau_0 \cdot k_q \cdot c_q = 1 + K_{SV} \cdot c_q \qquad (1.2)$$

Stokes shift determinations

The Stokes shifts were estimated from the absorption and emission spectra. The shift was obtained by the "distance" between the absorption peak with the lowest wavenumber and the emission peak with the highest wavenumber as displayed in Figure S8. The results are summarized in Table S3.

Laser flash photolysis

The LP980KS setup from Edinburgh Instruments equipped with an Nd:YAG laser from Litron (Nano LG 300-10) was employed for transient absorption spectroscopy. The frequency-tripled output with a wavelength of 355 nm served as excitation source. The laser pulse duration was ~5 ns and the pulse frequency was 10 Hz. The typical pulse energy used for transient absorption and emission studies was 15 mJ. Detection of transient absorption spectra occurred on an iCCD camera from Andor. Single-wavelength kinetics were recorded using a photomultiplier tube. The spectroscopic experiments were performed at 293 K using a cuvette holder that allows temperature control. If not stated otherwise the TA spectra were integrated over 100 ns.

Fluorescence lifetime measurements

Fluorescence lifetime measurements with ***p*-TIPS-BP** were performed on a Lifespec II spectrometer (time-correlated single photon counting (TCSPC) technique) from Edinburgh Instruments using a pulsed LED (ca. 900 ps pulse width) for excitation at 313 nm. The unquenched lifetime was recorded at 293 K with a highly diluted solution (containing less than 0.1 mM ***p*-TIPS-BP** in MeCN) to avoid self-quenching (Figure S15).

Chromatography

For standard liquid column chromatography separation silica gel 60 M (0.040-0.063 mm Macherey-Nagel GmbH & Co., Düren, Germany) was used.

Thin-layer-chromatography was performed using "DC Kieselgel 60 F254" (Merck KGaA, Darmstadt, Germany) on aluminum and a UV lamp (Benda, NU-4 KL, λ = 254 nm, and 365 nm, Wiesloch, Germany) was employed for detection. The resulting R_f values are given relative to the solvent.

NMR spectroscopy

For NMR spectroscopy a multi nuclear magnetic resonance spectrometer of the type AV II 400 (Bruker, analytic measuring technique, Karlsruhe, Germany) was employed. The chemical shifts are given as *δ*-values in ppm and they were referenced relative to the residue signal of the non-deuterated solvent.[5] The following abbreviations were used: singlet (s), doublet (d), multiplet (m), and the coupling constant (*J*).

Mass spectrometry

Accurate mass spectrometry was carried out with a G6545A Q-ToF (Agilent GmbH, Waldbronn, Germany) instrument using the photoionization at atmospheric pressure (APPI) technique. The sample was injected *via* a 1260 Infinity II HPLC system (Agilent GmbH, Waldbronn, Germany) with a G7111B 1260 quaternary pump, a G7129A 1260 vial sampler, and a G7116A 1260 multicolumn thermostat. Mass calibration was performed on the same day of the actual measurement using an external standard. The mass accuracy of the measurements is expected to be better than 5 ppm.

Preparation of deoxygenated solutions for photon upconversion studies

Unless noted otherwise, the solutions for photon upconversion experiments were deoxygenated in custom-made Schlenk-cuvettes (Figure S3) by five freeze-pump-thaw cycles using Argon as an inert gas, liquid N_2 for cooling, and Schlenk line vacuum (down to 0.5 mbar). The control experiments and the findings presented in Chapter 8 show that this method was sufficient to remove practically all oxygen from the solutions, given that remaining oxygen traces (probably below or on the order of ~0.02 mM, which is two orders of magnitude lower than in air-saturated solutions) will be removed by our annihilator (see Chapter 8 for details).

Figure S3: Photograph of a Schlenk-cuvette used for the preparation of deoxygenated solutions for photon upconversion studies.

2 Synthetic procedures

2.1 Synthesis of TIPS-ethynylated biphenyls

The synthesis proceeds *via* the Sonogashira coupling reaction analogous to the preparation of other TIPS-functionalized aromatic compounds.[6] The exact quantities are listed for each TIPS-biphenyl derivative below. Bromo-biphenyl, $Pd(PPh_3)_2Cl_2$, CuI, PPh_3, and dry THF were added to a round-bottom flask under argon flow. The flask was equipped with a condenser column and diisopropylamine was added to the solution under constant stirring. The flask was heated to 70˚C and (triisopropylsilyl)acetylene was added dropwise to the mixture. The mixture was held at 70˚C over night under argon atmosphere. The completion of the reaction was tested with thin layer chromatography (TLC). After cooling the mixture was filtered and the solvent was then removed under reduced pressure. The residue was redissolved in chloroform. The product was washed twice with deionized water and twice with brine. The organic layer was dried with Na_2SO_4 and the solvent was removed under reduced pressure. The product was purified via column chromatography (cyclohexane). The three TIPS-biphenyl isomers have already been prepared previously.[7] However, we stress that these studies focused on novel coupling reactions and the photophysical properties of the three compounds were completely unexplored prior to our work. NMR data (see below) of all biphenyl derivatives are in agreement with those reported in the literature.[7]

p-TIPS-BP: 5 g 4-Bromobiphenyl (21.5 mmol), 182 mg $Pd(PPh_3)_2Cl_2$ (0.26 mmol), 131 mg CuI (0.69 mmol), 181 mg PPh_3 (0.69 mmol) and 170 mL dry THF, 72 mL diisopropylamine, 10 mL (triisopropylsilyl)acetylene (44.5 mmol); yield = 2.38 g, 7.1 mmol (33%).

R_f(cyclohexane) = 0.5

APPI-HRMS (m/z): calculated for $[M + H]^+$: 335.2190, found 335.2185.

^{1}H NMR (400 MHz, $CDCl_3$): δ [ppm] = 7.60-7.57 (m, 2H), 7.56-7.52 (m, 4H), 7.47-7.43 (m, 2H), 7.38-7.34 (m, 1H), 1.15 (pseudo-s, 21H).

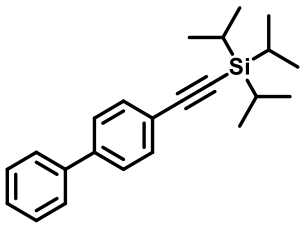

m-TIPS-BP: 1 g 3-Bromobiphenyl (4.3 mmol), 36.5 mg $Pd(PPh_3)_2Cl_2$ (0.052 mmol), 26.2 mg CuI (0.14 mmol), 36.1 mg PPh_3 (0.14 mmol), 28 mL dry THF, 13.5 mL diisopropylamine, 1.85 mL (triisopropylsilyl)acetylene (8.2 mmol); yield = 0.79 g, 2.3 mmol (55%).

R_f(cyclohexane) = 0.5

APPI-HRMS: Unfortunately, no signal directly related to the complete molecule could be detected with this method. However, the mass spectrum of the compound shows two characteristic fragments that give the complete molecule signal (and both fragments are also detectable for *p*-TIPS-BP).

m/z: $[C_{14}H_{11}]^+$, calculated 179.0856, found 179.0855; $[SiC_9H_{21}]^+$, calculated 157.1407, found 157.1408; sum of both fragments with adducts removed $[C_{23}H_{30}Si]^+$, calculated 334.2117, found 334.2117.

^{1}H NMR (400 MHz, $CDCl_3$): δ [ppm] = 7.70-7.69 (m, 1H), 7.60-7.51 (m, 3H), 7.48-7.33 (m, 5H), 1.15 (pseudo-s, 21H).

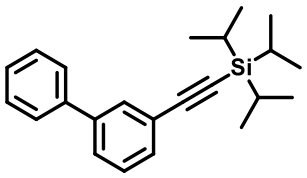

o-TIPS-BP: 1 g 2-Bromobiphenyl (4.3 mmol), 36.5 mg $Pd(PPh_3)_2Cl_2$ (0.052 mmol), 26.2 mg CuI (0.14 mmol), 36.1 mg PPh_3 (0.14 mmol), 28 mL dry THF, 12.5 mL diisopropylamine, 1.85 mL (triisopropylsilyl)acetylene (8.2 mmol); yield = 0.88 g, 2.6 mmol (61%).

R_f(cyclohexane) = 0.5

APPI-HRMS: Unfortunately, no signal directly related to the complete molecule could be detected with this method. However, the mass spectrum of the compound shows two characteristic fragments that give the complete molecule signal (and both fragments are also detectable for *p*-TIPS-BP).

m/z: $[C_{14}H_{11}]^+$, calculated 179.0856, found 179.0854; $[SiC_9H_{21}]^+$, calculated 157.1407, found 157.1406; sum of both fragments with adducts removed $[C_{23}H_{30}Si]^+$, calculated 334.2117, found 334.2119.

^{1}H NMR (400 MHz, $CDCl_3$): δ [ppm] = 7.62-7.57 (m, 3H), 7.40-7.27 (m, 6H), 1.01 (pseudo-s, 21H).

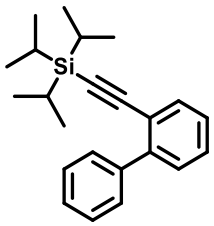

2.2 Synthesis of 4CzIPN

The compound 4CzIPN was synthesized according to a literature report.[8] A flame-dried 100 mL three neck round flask was charged with 3.68 g (22 mmol) carbazole under argon flow. The flask was evacuated for 5 min and then filled with argon three times. 50 mL THF were added to the flask, which was then cooled to 0˚C in an ice-water bath for 10 min. 10.5 mL (21 mmol) 2 M sodium-bis(trimethylsilyl)amide in THF was added dropwise over 5 min. The ice bath was removed after 5 min, and the solution was stirred at room temperature for 30 min. 1 g (5 mmol) 2,4,5,6-tetrafluoro-1,3-benzenedicarbonitrile was solved in 4 mL dry THF and added dropwise under

argon flow to the solution. The solution was heated to 70°C for 24 h. The solvent was then removed under reduced pressure. The residue was washed with 100 mL diethyl ether. The product was extracted with 100 mL chloroform from the filter cake. The solvent was removed under reduced pressure and the residue was washed with *n*-heptane. Yield: 3.54 g, 4.5 mmol (90%). The compound was then further purified by sublimation prior to its use as sensitizer. The NMR spectrum is in agreement with that reported in the literature.[3]

^{1}H NMR (400 MHz, $CDCl_3$): δ [ppm] = 8.22(d, J_{HH} = 8 Hz, 2H), 7.74-7.67 (m, 8H), 7.51-7.47 (m, 2H), 7.33 (d, J_{HH} 8 Hz, 2H), 7.23-7.21 (m, 4H), 7.12-7.05 (m, 8H) 6.84-6.80 (m, 4H), 6.65-6.61 (m, 2H).

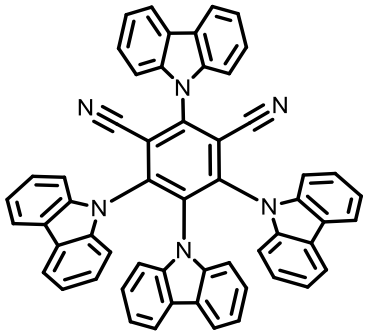

3 DFT calculations

Table S1: Computed triplet energies (in eV or kJ/mol) for biphenyl and corresponding TIPS-derivatives. Details are given in the text below.

Derivative	E_T (calc.) [a] [eV]	E_T (lit.) [b] [eV]	E_T (cor.) [c] [eV]	E_T (cor.) [d] [kJ mol^{-1}]
biphenyl (**BP**)	2.99	2.84	–	274
***p*-TIPS-BP**	2.61	–	2.48	239
***m*-TIPS-BP**	2.97	–	2.83	273
***o*-TIPS-BP**	2.82	–	2.68	259

[a] DFT-calculated triplet energy at the B3LYP/6-311+G(d,p) level of theory. [b] Experimental triplet energy taken from ref.[1]. [c] Calculated triplet energy corrected for overestimation (value from [a] multiplied by 0.95). [d] Value from [b] or [c] converted in kJ mol^{-1}.

All DFT calculations were carried out with the Gaussian 09 software package[9] using the B3LYP functional in combination with the 6-311+G(d,p) basis set. The geometry optimizations of biphenyl

and their TIPS derivatives under study were accompanied by frequency analyses. The optimized structures used for further computations did not show negative vibrational frequencies, indicating convergence on minimum structures. Starting from the energy-minimized singlet ground state geometries, the corresponding lowest triplet states were calculated. The triplet state energies were determined simply by comparing the energies of both optimized structures (i.e., singlet ground state and triplet state) for a given compound since this straightforward approach has proven very successful for predicting the triplet energies for several organic chromophores.[6,10,11] A spin density map was obtained by an additional single-point calculation with population analysis and time-dependent DFT computations with identical functional and basis were used to calculate the vertical excitation energies for simulating the triplet-triplet absorption spectrum of ***p*-TIPS-BP**. The calculated triplet absorption spectrum shows a maximum at 420 nm, which is in good agreement with the experimental triplet absorption spectrum peaking at 408 nm. The representative optimized structure and the spin density distribution of the triplet are displayed in Figure S4.

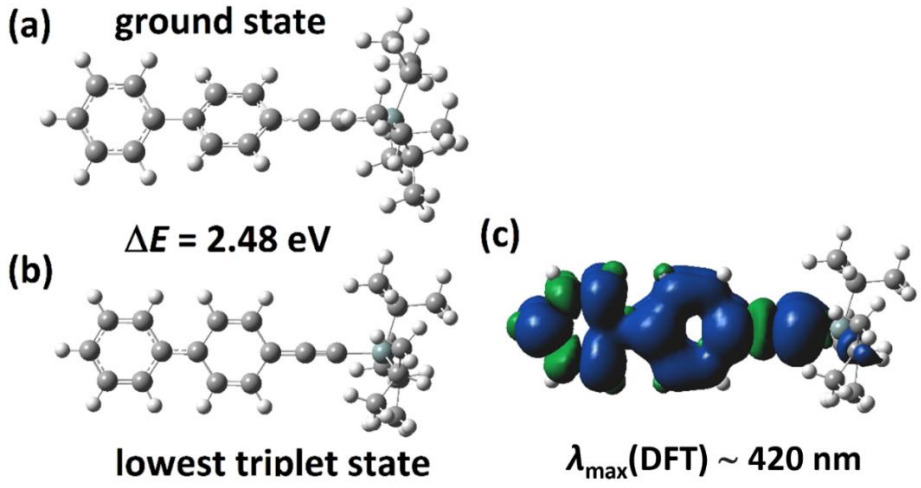

Figure S4: Optimized structures of the singlet ground state (a) as well as the lowest triplet state (b) of *p*-TIPS-BP at the B3LYP/6-311+G(d,p) level of theory, together with the corresponding energy difference (i.e., the estimated triplet energy of p-TIPS-BP). (c) Computed spin densities of the triplet state using the same computational method. Its absorption maximum estimated by TD-DFT is also displayed in subfigure (c). Blue colour represents positive spin densities, whereas green represents negative spin densities.

The computed triplet energies E_T are summarized in Table S1. The calculated triplet energy for the reference compound biphenyl is higher than its literature-known experimental triplet energy by ~5 %. Therefore, we adjusted the computed energies of all compounds with unknown triplet states by a correction factor of 0.95.

4 Solvent dependence of 4CzIPN's photochemical properties

The singlet- and triplet-excited state energies as well as the intersystem crossing quantum yield, Φ_{ISC}, and prompt/delayed fluorescence properties of **4CzIPN** show a pronounced solvent dependence. The singlet-excited state energy and Φ_{ISC} decrease as the polarity of the solvent increases.[12] We speculated that a highly nonpolar solvent like cyclohexane would yield the highest singlet and triplet energies. However, **4CzIPN** dissolves very poorly in neat cyclohexane. We, therefore, added 10vol% of toluene as co-solvent (when higher **4CzIPN** concentrations are required) giving us the best compromise between solubility and excited-state energies (Figure S5). The overall fluorescence quantum yield Φ_{Fl} was practically identical in our solvent mixture compared to neat toluene (compare, Table S2). Moreover, time-gated emission spectra recorded with our LFP setup revealed that the ratio of prompt and delayed fluorescence is almost completely unaffected. Hence, we concluded that the reported ISC quantum yield (Φ_{ISC} = 0.73 in toluene[12]) must be very similar in our system. Further, the triplet-excited state energy of **4CzIPN** in cyclohexane was estimated by subtracting the singlet-triplet energy gap in toluene (0.04 eV)[2] from the experimental singlet-excited state energy in cyclohexane (2.76 eV, see Table S2).

Table S2: Photophysical properties of **4CzIPN** in toluene and cyclohexane.

Compound	S_1 [eV]	T_1 [eV]	Φ_{Fl}	Φ_{ISC}	τ_T[f] [μs]
4CzIPN	2.71[a] 2.76[b]	2.67[a] 2.72[c]	0.90[a] 0.90±0.01[d]	0.73[e]	4.6[a] 7.9[d]

[a] Measured in toluene from ref.[2,3]. [b] Measured in cyclohexane [c] Estimated for cyclohexane from the singlet-triplet energy gap in toluene. [d] Measured in cyclohexane/toluene (9:1). [e] Measured in toluene from ref.[12]. [f] Triplet lifetime.

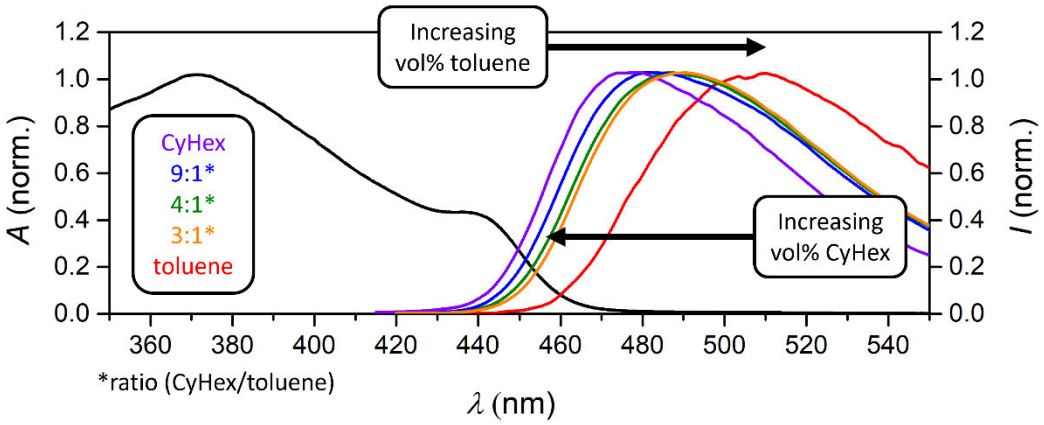

Figure S5: Absorption and photoluminescence spectrum of 4CzIPN dissolved in different ratios of cyclohexane and toluene. Absorption (norm.): cyclohexane (black). Photoluminescence (cyclohexane:toluene ratio): neat cyclohexane (purple); 9:1 (blue); 4:1 (green); 3:1 (orange); neat toluene (red). The position of the absorption peak is not affected by the addition of toluene.

5 *Photostability of the upconversion system*

In order to provide evidence for the applicability of this novel annihilator and the resulting UC system, we irradiated a solution containing 44 µM **4CzIPN** and 10 mM ***p*-TIPS-BP** with a cw laser at 447 nm employing a power density of 1.5 W·cm^{-2}, corresponding to the threshold intensity I_{th} (see Figure 5 of the main paper). The UC system shows decent photostability (Figure S6), taking the rather high laser power into account. Consequently, the UC signal is expected to decrease more quickly than observed for similar systems with less highly energetic excited annihilators.[13,14]

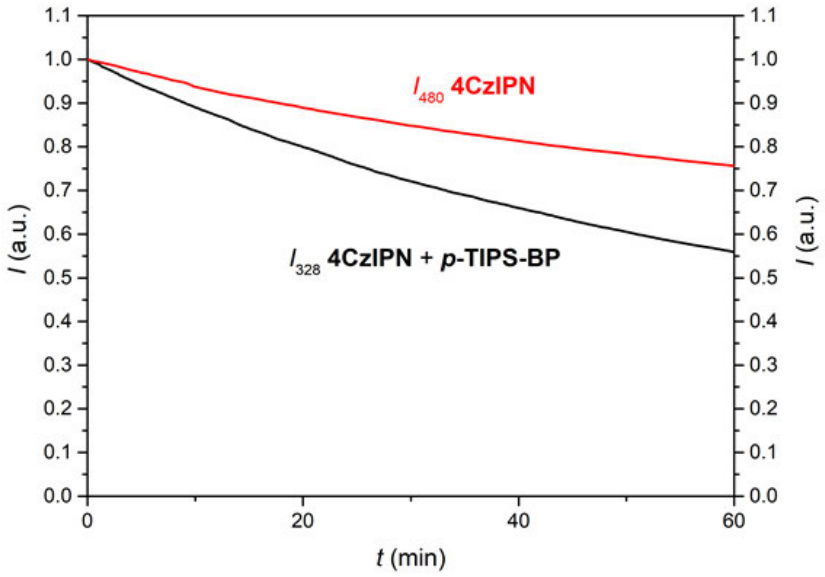

Figure S6: Upconversion/sensitizer emission stability measurements over one hour in cyclohexane/toluene (9:1) using a cw laser for excitation at 447 nm and a constant laser power of 1.5 W·cm^{-2}. Black curve: Emission intensity of a deoxygenated solution containing 44 µM **4CzIPN** *and* 10 mM ***p*-TIPS-BP** with detection at 328 nm. Red curve: Emission intensity of a deoxygenated solution containing 44 µM **4CzIPN** monitored at 480 nm.

6 UV filter effects caused by the sensitizer

Despite the slightly higher triplet quenching efficiency of ***p*-TIPS-BP** with **IrdF** compared to **4CzIPN** (96% vs. 92% with 10 mM of the annihilator) as well as its higher ISC quantum yield and the higher fluorescence quantum yield of the annihilator in MeCN than in cyclohexane (83 ± 2% vs. 48 ± 2%), the UC system **4CzIPN**/***p*-TIPS-BP** (in cyclohexane) has a much higher overall quantum yield (compare, Figure 5 and Figure S13). This probably originates from the very different (relative) absorption properties of both sensitizers at the excitation wavelength and in the UV region, where the annihilator emits. The absorption of **4CzIPN** in the wavelength range of the upconverted emissions (300-380 nm) is about twice as large as at the incident wavelength (λ_{ex} = 447 nm). In contrast, the molar absorptivity ε of **IrdF** increases by more than one order of magnitude (Figure S7) with λ_{ex} as reference point. The strong reabsorptivity of upconverted photons by the sensitizer[15] ("optical loss") is expected to decrease the external quantum yield Φ_{UC} significantly in this case.

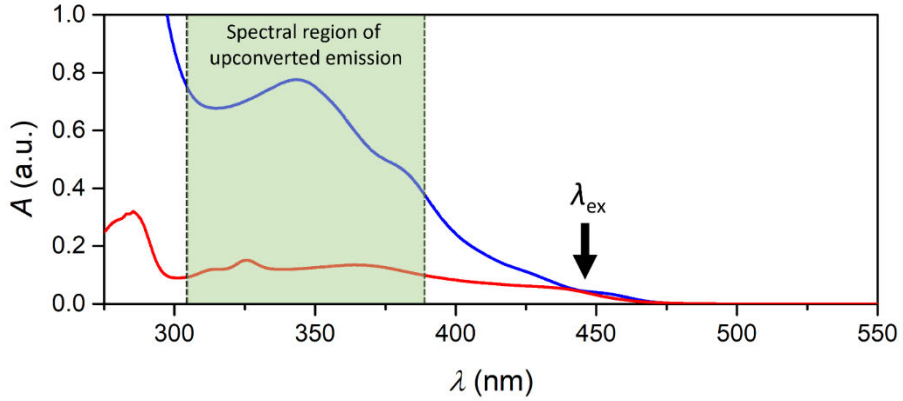

Figure S7: Normalized (at 447 nm) absorption spectra of **4CzIPN** (red) and **IrdF** (blue). The spectra were adjusted to visualize the high reabsorption of **IrdF**. The molar absorptivity of **4CzIPN** rises only slightly from the incident wavelength (λ = 447 nm) to the UV region (300-380 nm). Compared to that, the molar absorptivity of **IrdF** increases more than one order of magnitude resulting in strong reabsorption of the upconverted light.

7 *Photophysical properties of biphenyl (BP), p-TIPS-BP, o-TIPS-BP, and m-TIPS-BP*

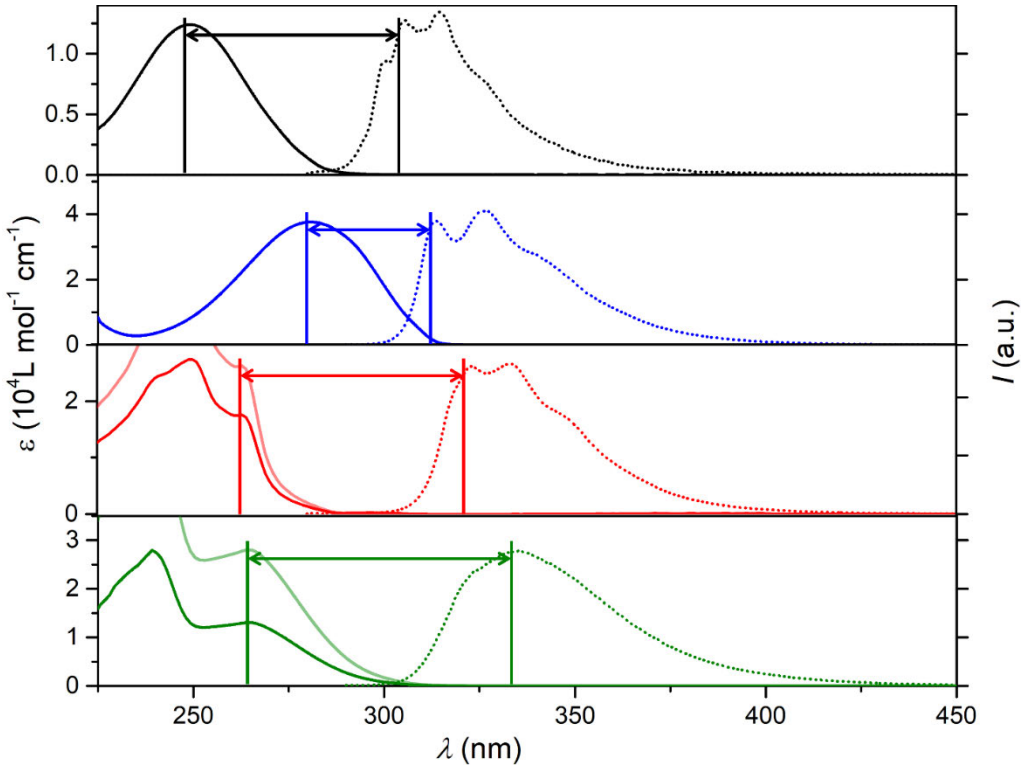

Figure S8: Absorption (solid lines) and normalized photoluminescence (dotted lines) spectra of biphenyl[a] (black), ***p*-TIPS-BP**[a] (blue), ***m*-TIPS-BP**[b] (red), ***o*-TIPS-BP**[b] (green). For clarity, the absorption spectra of ***o*-TIPS-BP** and ***m*-TIPS-BP** are displayed with and without a scaling factor. Vertical lines indicate the wavelengths used for Stokes shift determinations. [a] Measured in MeCN. [b] Measured in THF.

Substituting biphenyl in the *ortho* and *meta* position (***m*-TIPS-BP** and ***o*-TIPS-BP**) did not show the same beneficial influence of the TIPS group as for ***p*-TIPS-BP**. The triplet-excited states of both lie too high (Table S1) for efficient sensitization by a blue-light absorbing sensitizer such as **4CzIPN** and **IrdF**. Further, the Stokes shift of ***m*-TIPS-BP** and ***o*-TIPS-BP** is not reduced, which would lead to a lower anti-Stokes shift in the resulting upconversion system (Figure S8). Table S3 compares pertinent photophysical properties of biphenyl and its TIPS derivatives under study.

Table S3: Measured S_1 energies, computed T_1 energies, fluorescence quantum yields Φ_{Fl} and Stokes shifts, $\Delta\tilde{\nu}$, of biphenyl and TIPS-biphenyls. The solvent choice had no major influence on the S_1 energy (see Figure S10 for an example).

Compound	S_1 [eV]	T_1 [eV]	Φ_{Fl}	$\Delta\tilde{\nu}$ [cm^{-1}]
Biphenyl (**BP**)	4.34[a]	2.84[d]	0.18[f]	7480[a]
	4.34[b]			7860[b]
***p*-TIPS-BP**	4.04[a]	2.48[e]	0.83±0.02[a]	3870[a]
	4.05[b]		0.48±0.02[b]	3970[b]
	4.03[c]			
***m*-TIPS-BP**	4.14[c]	2.83[e]	–	7060[c]
***o*-TIPS-BP**	4.09[c]	2.68[e]	–	8030[c]

[a] Measured in MeCN. [b] Measured in cyclohexane. [c] Measured in THF. [d] Experimental triplet energy taken from ref.[1]. [e] DFT-calculated triplet energy at the B3LYP/6-311+G(d,p) level of theory and corrected for overestimation. [f] Experimental fluorescence quantum yield in cyclohexane taken from ref.[16].

8 Control experiments related to residual oxygen during photon upconversion studies

Residual oxygen in solution can be regarded as a substantial problem for the performance of photon upconversion systems. Oxygen-scavenging additives have proven successful for complementing inert gas purging or freeze-pump-thaw cycles,[17] and specific solvents that permit air-stable photon upconversion have been identified.[18] However, some annihilators such as anthracene derivatives can efficiently remove dissolved oxygen through a sensitization-photoaddition sequence, in particular, if the annihilator concentration is much higher than that of oxygen.[19] We presume that traces of residual oxygen are depleted by our annihilator compound, which is typically used at a concentration of 10 mM, during the irradiation of our samples. To prove this comparative photon upconversion studies were performed with poorly deoxygenated solutions containing 44 µM **4CzIPN** and 10 mM ***p*-TIPS-BP** in cyclohexane:toluene (9:1) using a cw laser for excitation at 447 nm (OD_{447} = 0.2). The first solution was purged with argon via a needle for 60 s (blue curve, Figure S9). The upconverted emission signal at 328 nm increases slowly over 5 minutes before reaching its maximum, after turning on the cw laser. The second solution was only purged for 40 s with argon (green curve), corresponding to a higher concentration of

dissolved oxygen in our solvent mixture. The UC signal resides at a very low intensity for 5 minutes before it slowly rises as well. However, neither a lag time nor an intensity increase is observed when proper Schlenk-techniques are used as described in Chapter 1 (e.g. for the measurements in Figure S6) implying that oxygen was removed very efficiently by our experimental procedure for sample preparation. We believe that the rising upconversion signal from the poorly deoxygenated solution stems from remaining concentrations of dissolved oxygen in solution quenching the triplet-excited states, thereby generating singlet oxygen. The latter in turn is slowly removed from the system by reacting with excess annihilator molecules in their ground states. In other words, after a short irradiation time, oxygen traces will be removed completely.

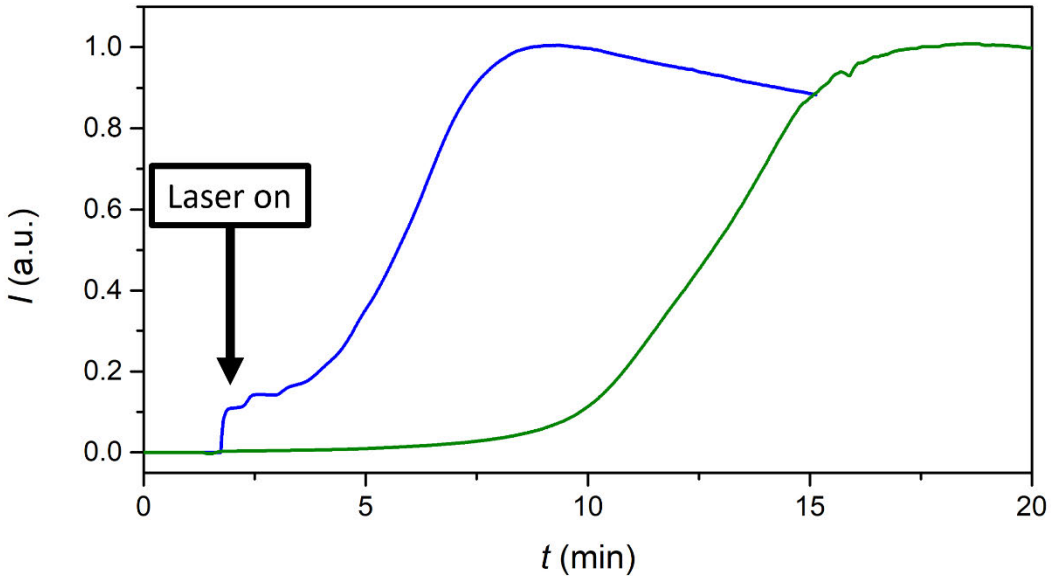

Figure S9: Photon upconversion studies with poorly deoxygenated solutions containing 44 µM **4CzIPN** and 10 mM ***p*-TIPS-BP** in cyclohexane:toluene (9:1) using a cw laser for excitation at 447 nm (OD_{447} = 0.2) with a laser power of 100 mW. The intensity of the upconversion signal was measured at 328 nm and recorded for several minutes. Blue curve: Flushed with argon for 60 s; green curve: Flushed with argon for 40 s. See text for further explanations.

9 Additional spectroscopic data

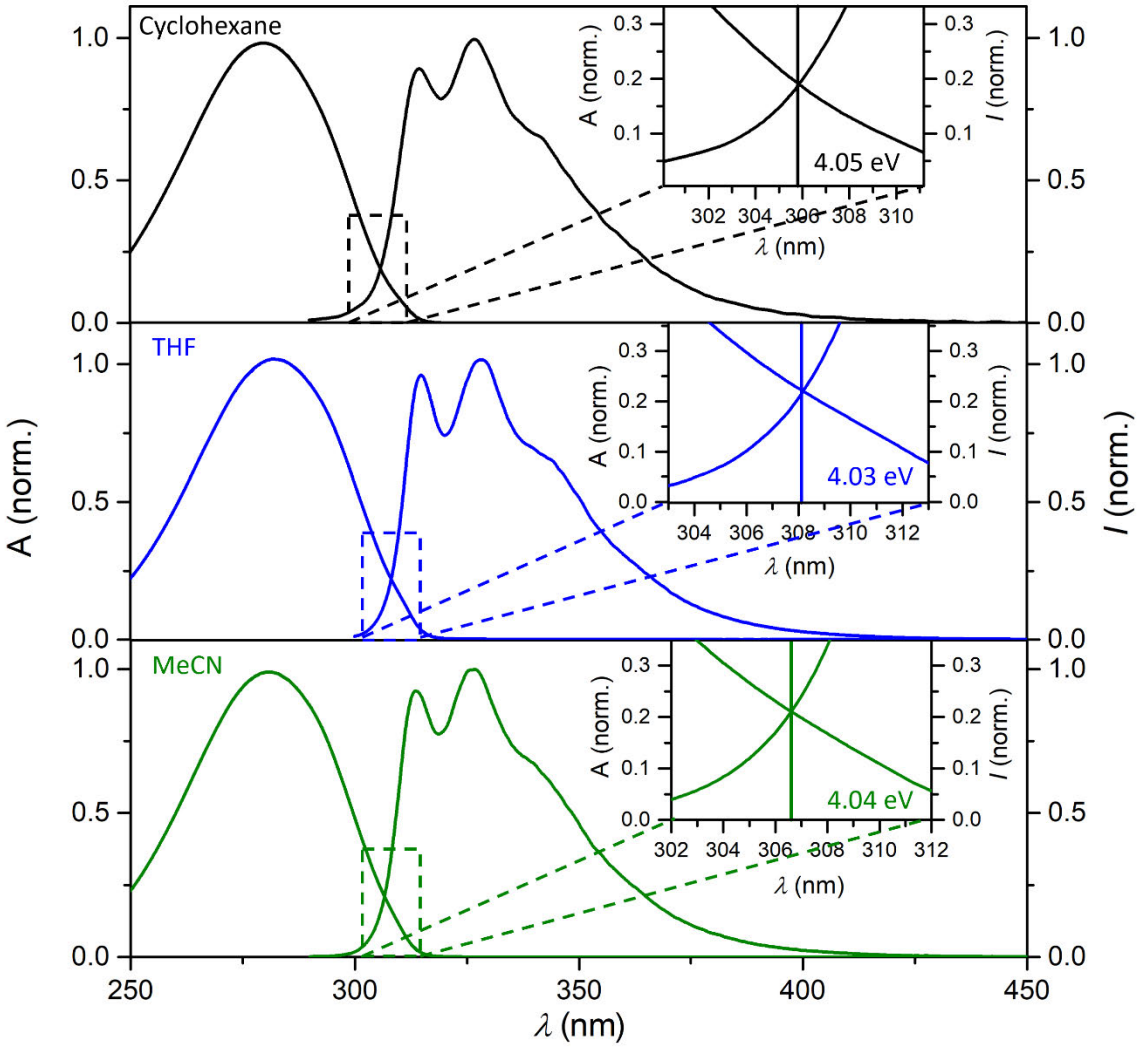

Figure S10: Normalized absorption and normalized emission spectra of ***p*-TIPS-BP** in different solvents: cyclohexane (black), THF (blue) and MeCN (green). Each inset shows the crossing point of normalized absorption and emission spectra on enlarged scale and the corresponding S_1 energy in eV.

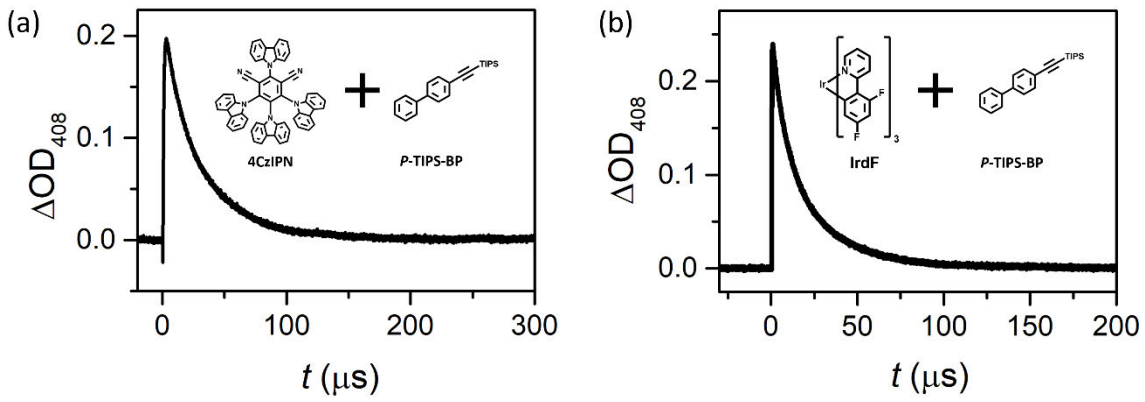

Figure S11: Time-resolved transient absorption measurements of the triplet state formation and decay of ***p*-TIPS-BP** at 408 nm after excitation with 355 nm laser pulses. (a) 20 μM **4CzIPN** with 10 mM ***p*-TIPS-BP** in Ar-saturated cyclohexane:toluene 9:1. (b) 38 μM **IrdF** with 10 mM ***p*-TIPS-BP** in Ar-saturated MeCN.

Comparative LFP experiments on ~20 μM **4CzIPN** solutions (neat cyclohexane or cyclohexane:toluene 9:1) under the conditions as in Figs. 2, 3, 4 and S11 gave practically identical results, regardless of the medium.

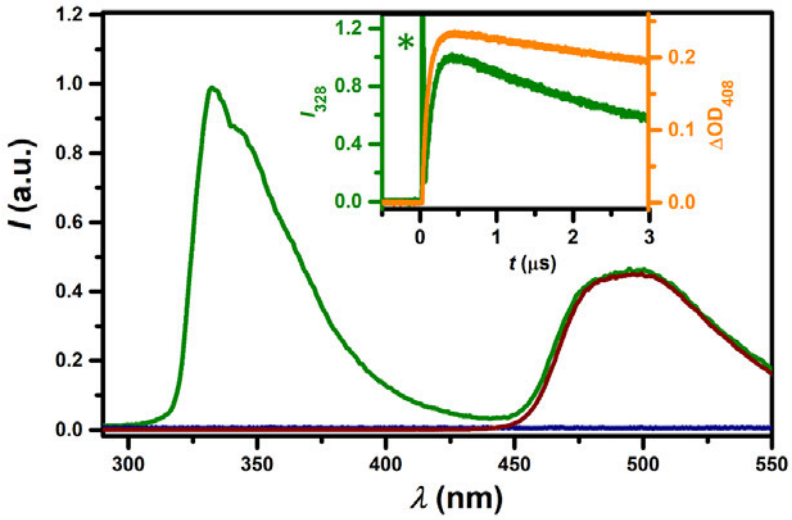

Figure S12: LFP experiments on Ar-saturated MeCN solutions containing 38 μM **IrdF** and/or 10 mM ***p*-TIPS-BP** after excitation with 355 nm laser pulses. Main plot: Normalized time-gated (delay, 1 μs; integration over 200 μs) emission spectra of the complete upconversion system (green), only **IrdF** (brown), and only ***p*-TIPS-BP** (dark blue). Inset: Time-resolved emission (328 nm) and transient absorption (408 nm) traces upon excitation of the UC system. The green asterisk marks laser stray light.

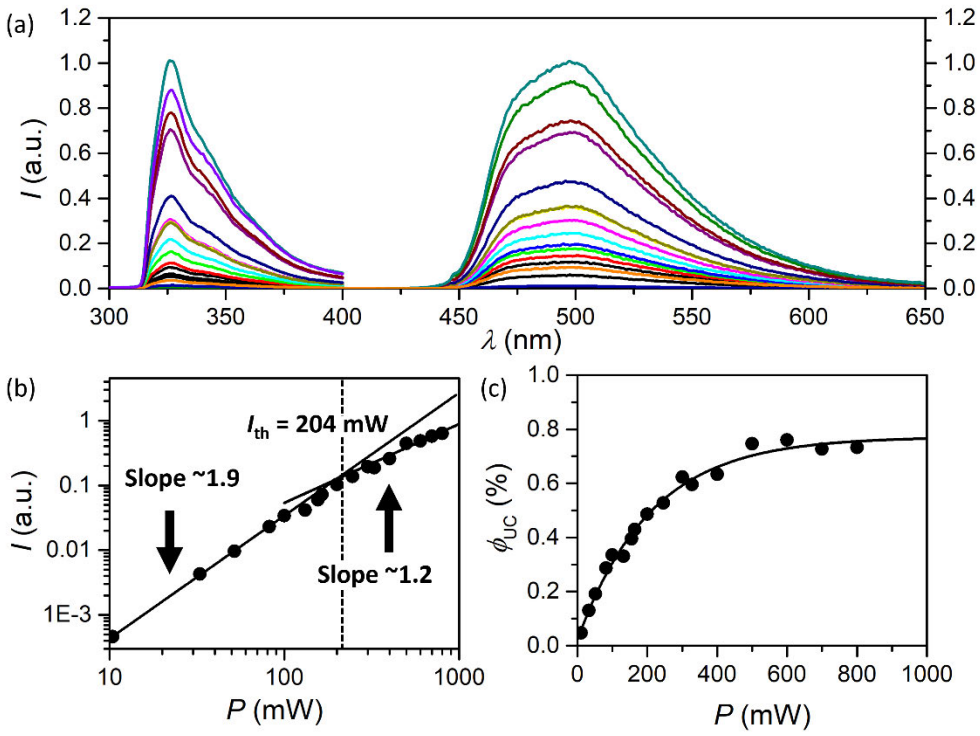

Figure S13: Photon upconversion studies with deoxygenated solutions containing 133 µM **IrdF** and 10 mM ***p*-TIPS-BP** in MeCN using a cw laser for excitation at 447 nm (OD_{447} = 0.1). (a) Main plot: Power-dependent spectra of the normalized upconverted emission and phosphorescence of **IrdF** (reference signal). (b) Normalized UC emission plotted against the laser power on a double-logarithmic scale. The threshold intensity I_{th} was determined by the point of intersection. (c) External quantum yield Φ_{UC} plotted against the laser power.

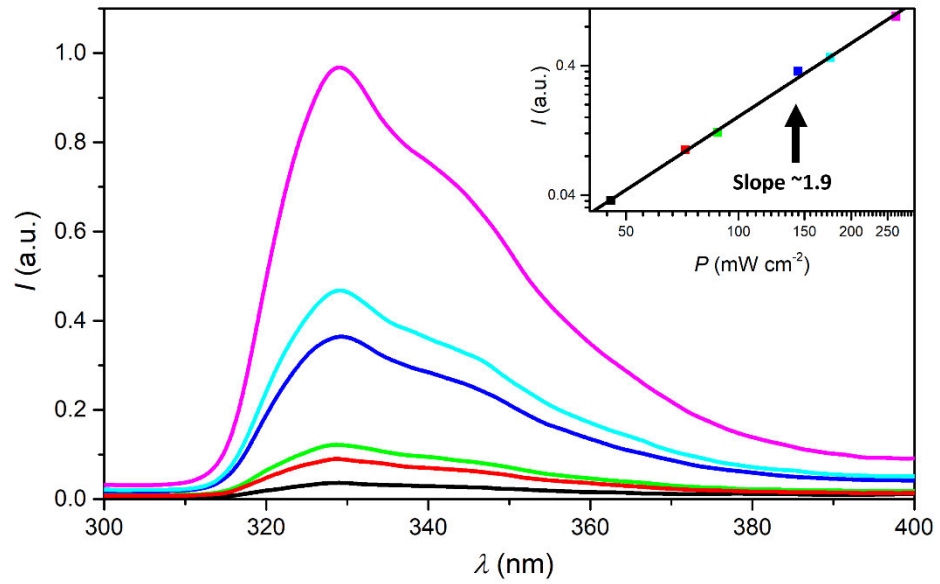

Figure S14: Photon upconversion studies with a deoxygenated solution containing 44 µM **4CzIPN** and 10 mM ***p*-TIPS-BP** in cyclohexane:toluene (9:1) using a blue LED (see Chapter 1 *"general experimental details and methods"* for further information). Inset: Normalized UC emission plotted against the laser power on a double-logarithmic scale.

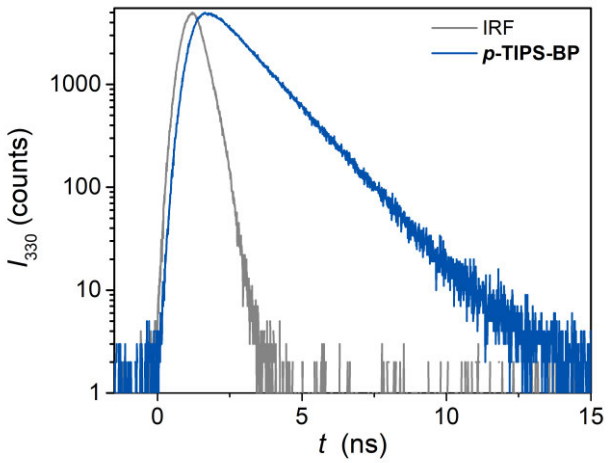

Figure S15: Emission decay of singlet excited ***p*-TIPS-BP** in deoxygenated MeCN upon 313 nm excitation, together with the response function of the TCSPC instrument (IRF, recorded via a stray light measurement with the 313 nm pulsed LED as light source).

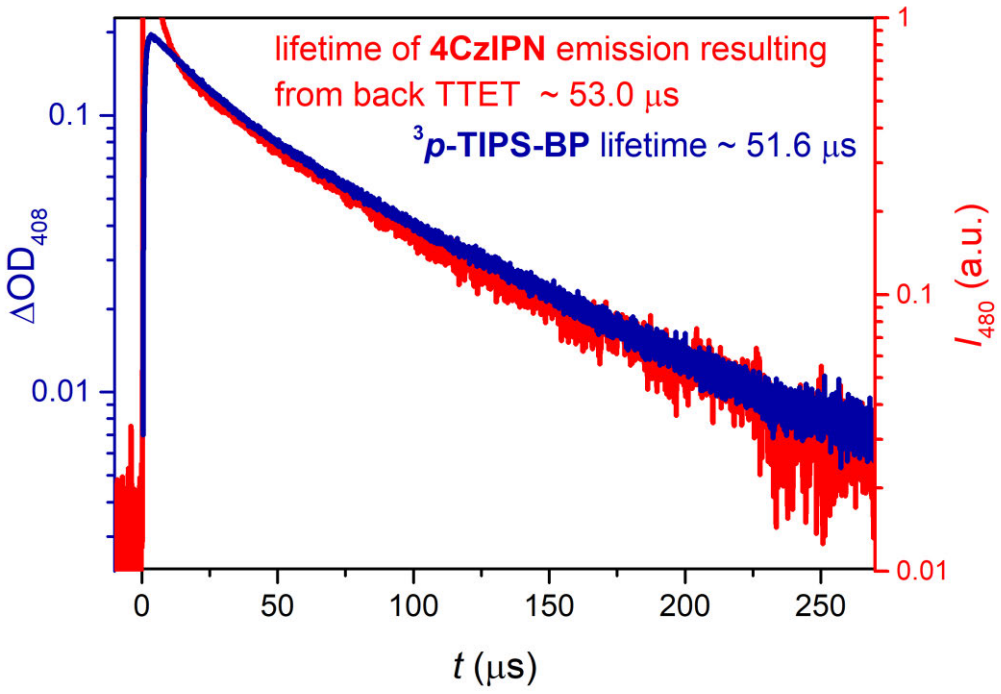

Figure S16: Time-resolved transient absorption and emission measurements (on a logarithmic scale) of a solution containing 10 μM **4CzIPN** with 10 mM ***p*-TIPS-BP** in Ar-saturated cyclohexane:toluene 9:1 after excitation with 355 nm laser pulses. Blue curve: Triplet state decay of ***p*-TIPS-BP** at 408 nm; red curve: Delayed emission of **4CzIPN** as a result of back triplet-triplet energy transfer monitored at 480 nm. A longer ***p*-TIPS-BP** triplet lifetime than in Figure S11 has been observed, which is most likely due to the lower sensitizer concentration slowing down back TTET.

10 NMR spectra

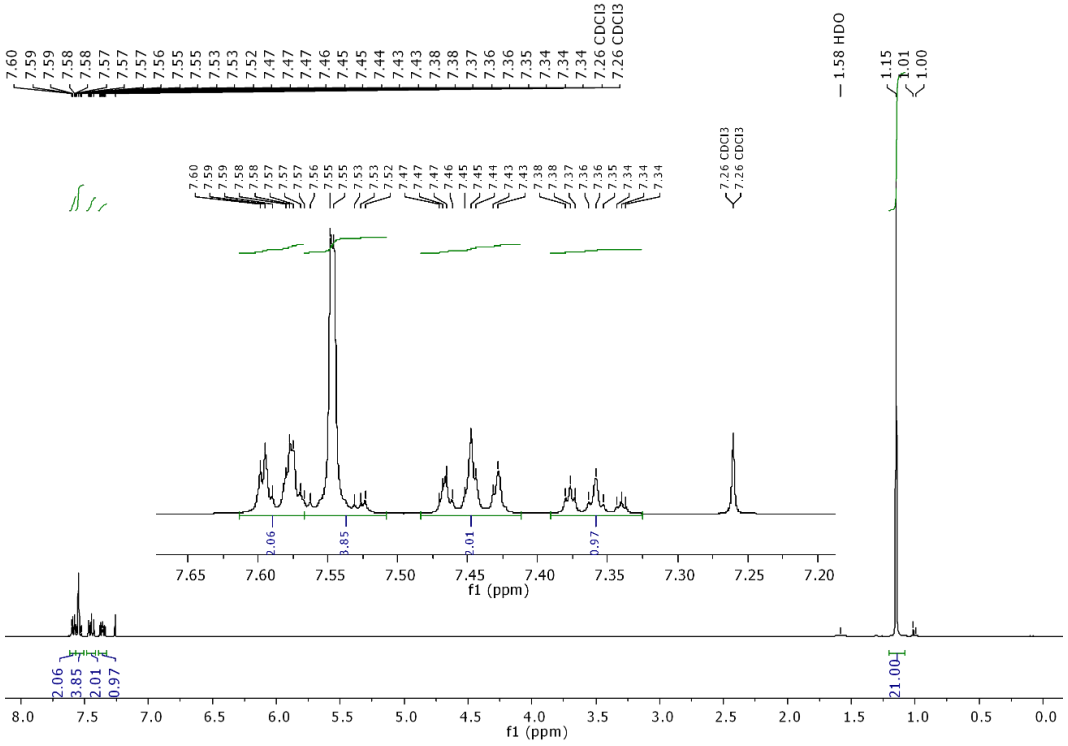

Figure S17: ^{1}H NMR spectrum and zoom into aromatic region (inset) of ***p*-TIPS-BP** in $CDCl_3$.

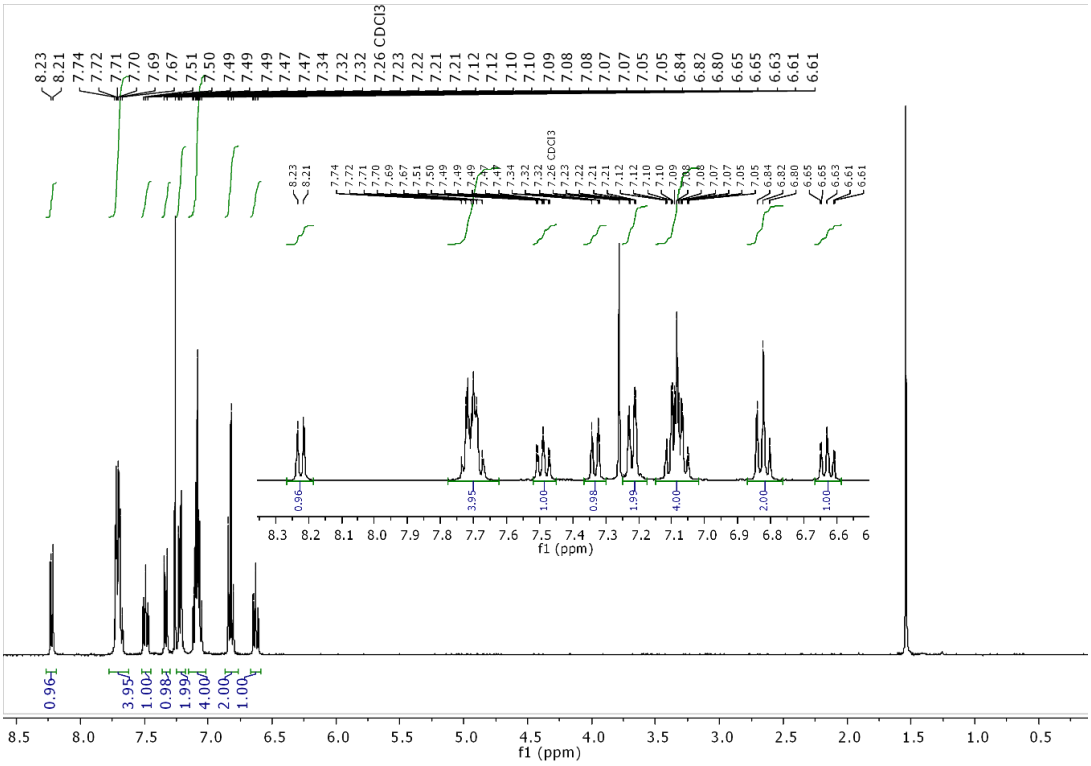

Figure S18: ^{1}H NMR spectrum and zoom into aromatic region (inset) of **4CzIPN** in $CDCl_3$.

11 References

1 M. Montalti, A. Credi, L. Prodi and M. T. Gandolfi, *Handbook of Photochemistry*, CRC Press, 2006.

2 H. Noda, X.-K. Chen, H. Nakanotani, T. Hosokai, M. Miyajima, N. Notsuka, Y. Kashima, J.-L. Brédas and C. Adachi, *Nat. Mater.*, 2019, **18**, 1084–1090.

3 H. Uoyama, K. Goushi, K. Shizu, H. Nomura and C. Adachi, *Nature*, 2012, **492**, 234–238.

4 Kessil PR160L 440 nm, https://www.kessil.com/science/PR160L.php, (accessed 30 September 2021).

5 H. E. Gottlieb, V. Kotlyar and A. Nudelman, *J. Org. Chem.*, 1997, **62**, 7512–7515.

6 N. Harada, Y. Sasaki, M. Hosoyamada, N. Kimizuka and N. Yanai, *Angew. Chem. Int. Ed.*, 2021, **133**, 144–149.

7 B. Feng, Y. Yang and J. You, *Chem. Comm.*, 2020, **56**, 790–793.

8 S. Engle, T. R. Kirkner and C. B. Kelly, *Org. Synth.*, 2019, **96**, 455–473.

9 M. J. Frisch, G. W. Trucks, H. B. Schlegel, G. E. Scuseria, M. A. Robb, J. R. Cheeseman, G. Scalmani, V. Barone, B. Mennucci, G. A. Petersson, H. Nakatsuji, M. Caricato, X. Li, H. P. Hratchian, A. F. Izmaylov, J. Bloino, G. Zheng, J. L. Sonnenberg, M. Hada, M. Ehara, K. Toyota, R. Fukuda, J. Hasegawa, M. Ishida, T. Nakajima, Y. Honda, O. Kitao, H. Nakai, T. Vreven, J. Montgomery, J. A., J. E. Peralta, F. Ogliaro, M. Bearpark, J. J. Heyd, E. Brothers, K. N. Kudin, V. N. Staroverov, R. Kobayashi, J. Normand, K. Raghavachari, A. Rendell, J. C. Burant, S. S. Iyengar, J. Tomasi, M., *Gaussian Inc. Wallingford CT*, 2009.

10 F. M. Hörmann, C. Kerzig, T. S. Chung, A. Bauer, O. S. Wenger and T. Bach, *Angew. Chem. Int. Ed.*, 2020, **59**, 9659–9668.

11 V. Gray, A. Dreos, P. Erhart, B. Albinsson, K. Moth-Poulsen and M. Abrahamsson, *Phys. Chem. Chem. Phys.*, 2017, **19**, 10931–10939.

12 R. Ishimatsu, S. Matsunami, K. Shizu, C. Adachi, K. Nakano and T. Imato, *J. Phys. Chem. A*, 2013, **117**, 5607–5612.

13 Y. Wei, K. Pan, Y. Li, X. Cao, X. Zhou and C. Yang, *Multiple Resonance TADF Sensitizers Enable Green-to-Ultraviolet Photon Upconversion: Application in Photochemical Transformations*, 2021, DOI: 10.33774/chemrxiv-2021-mq00r-v2.

14 Y. Murakami, A. Motooka, R. Enomoto, K. Niimi, A. Kaiho and N. Kiyoyanagi, *Phys. Chem. Chem. Phys.*, 2020, **22**, 27134–27143.

15 P. Duan, N. Yanai and N. Kimizuka, *Chem. Comm.*, 2014, **50**, 13111–13113.

16 I. B. Berlman, *Handbook of fluorescence spectra of aromatic molecules*, Acad. Press, New York, 1971.

17 D. Dzebo, K. Moth-Poulsen and B. Albinsson, *Photochem. Photobiol. Sci.*, 2017, **16**, 1327–1334.

18 J. Ma, S. Chen, C. Ye, M. Li, T. Liu, X. Wang and Y. Song, *Phys. Chem. Chem. Phys.*, 2019, **21**, 14516–14520.

19 C. Kerzig and O. S. Wenger, *Chem. Sci.*, 2018, **9**, 6670–6678.

10.12 Supporting Information for Project [K]

Angewandte Chemie
Eine Zeitschrift der Gesellschaft Deutscher Chemiker

Supporting Information

Blue-to-UVB Upconversion, Solvent Sensitization and Challenging Bond Activation Enabled by a Benzene-Based Annihilator

T. J. B. Zähringer, J. A. Moghtader, M.-S. Bertrams, B. Roy, M. Uji, N. Yanai, C. Kerzig**

Supporting Information

Contents

1. General experimental details and methods 2
   1.1 Materials 2
   1.2 Steady-state measurements 2
   1.3 Excitation light sources 2
   1.4 Determination of fluorescence quantum yields 3
   1.5 Determination of the threshold intensity I_{th} 3
   1.6 Upconversion quantum yields 4
   1.7 Quenching rate constants 4
   1.8 Determination of FRET parameters 5
   1.9 Laser flash photolysis 6
   1.10 Irradiation experiments 6
   1.11 Fluorescence lifetime measurements 6
   1.12 Chromatography 7
   1.13 NMR spectroscopy 7
   1.14 Gas chromatography and mass spectrometry 7
   1.15 Preparation of deoxygenated solutions for photon upconversion studies 7
2. Synthetic procedures 7
   2.1 Synthesis of TIPS-ethynyl-benzene derivatives 7
   2.2 Synthesis of 4CzIPN 9
3. DFT calculations 10
4. Photophysical properties of benzene and the TIPS-ethynyl substituted benzenes 12

5. Threshold intensity measurements 13
6. Additional control experiments and spectroscopic measurements of the UC-FRET sequence 13
7. Additional spectroscopic data 16
8. NMR spectra and analytics 19
8.1 Spectra of benzene-derivatives and sensitizer 19
8.2 Irradiation experiments 23
8.3 Gas chromatography and mass spectrometry 27
9. Supporting references 27

1. General experimental details and methods

1.1 Materials

Unless specifically mentioned, all chemicals used for synthesis, irradiation experiments, or optical spectroscopy were commercially obtained and used as received. Tetrahydrofuran, 99.7%, VWR; (triisopropylsilyl)acetylene, 97%, Alfa Aesar; bis(triphenylphosphine)palladium(II) dichloride, 98%, Acros Organics; copper(I) iodide, 99.9%, Alfa Aesar; triphenylphosphine, 99%, Sigma-Aldrich; diisopropylamine, 99.9%, Sigma-Aldrich; 2,4,5,6-tetrafluoro-1,3-benzenedicarbonitrile, 97%, Alfa Aesar; carbazole, 95%, Alfa Aesar; sodium-bis(trimethylsilyl)amide 2 M in THF, 99.7%, Alfa Aesar; *p*-terphenyl, Alfa Aesar, 98%; 1,4-dibromobenzene, 98%, Alfa Aesar; bromobenzene, 99%, Sigma-Aldrich; 1,3,5-tribromobenzene, 98%, Acros Organics; acetone, 99.9%, VWR Chromanorm; cyclohexane, >99.5%, VWR Normapur; sodium sulfate, 99%, Acros Organics; diethyl ether, 99.5%, VWR; pinacolone, 97%, Thermo Scientific; C_6D_{12}, 99.5%, deutero; toluene-d_8, 99.5%, deutero; $CDCl_3$, 99.8%, deutero; ethanol, 99.8%, VWR; coumarin 6, >98%, TCI; 1,2-diphenylethane, 98%, Thermo Scientific; 1,3-diphenylacetone, 99%, Thermo Scientific; ultrapure Millipore MilliQ water with a specific resistance of 18.2 MΩ cm.

Argon from Nippon Gases (5.0) or Air Liquid Japan (6.0) was used for removing dissolved oxygen before all experiments related to optical spectroscopy.

1.2 Steady-state measurements

Steady-state emission measurements at room temperature were performed using a Perkin Elmer FL-6500 spectrometer. Absorption spectra were recorded with a Perkin Elmer LAMBDA 365 UV-Vis spectrophotometer. All spectra were recorded at room temperature (295 ± 3 K) using quartz glass cuvettes. Emission spectra were corrected regarding the wavelength-dependent sensitivity of the instrument. Emissive chemicals were employed in very low concentrations to eliminate filter effects. Phosphorescence spectra at 77K were measured by using a JASCO FP-8700 spectrofluorometer.

1.3 Excitation light sources

The following light sources were employed for photon upconversion studies and application-related irradiation experiments: (i) a 447 nm cw laser (Roithner Lasertechnik, optical output: up to 1.1 W, with adjustable laser power and a beam size of ~0.10 cm^2, (ii) a 445 nm diode laser (75 mW, RGB Photonics), (iii) two 440 nm LEDs (Kessil Science, PR160L) with an average intensity reported as 352 mW cm^{-2} (1 cm distance). Emission spectra of the LED and the 447 nm cw laser were measured by irradiating a water-containing cuvette in the FL-6500 instrument and recording the Rayleigh scattering light; the spectra so obtained are shown in Figure S1.

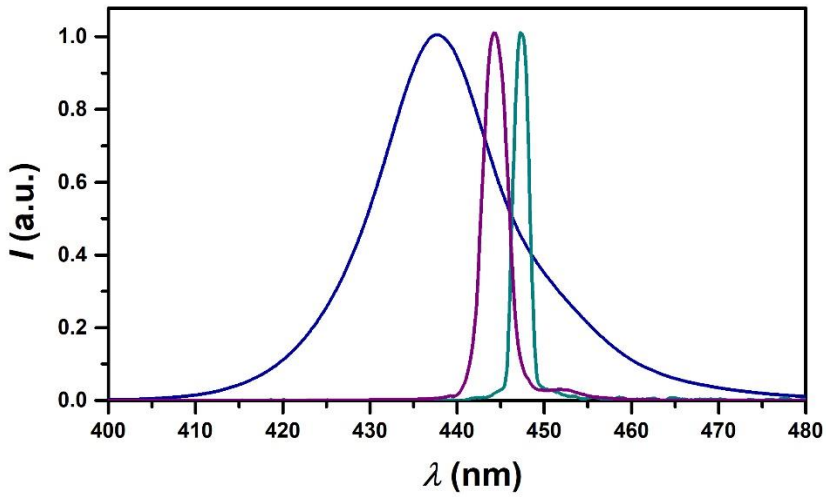

Figure S1. Emission spectra of the PR160L 440 nm LED from Kessil Science (blue), the 447 nm cw laser from Roithner Lasertechnik (green) and the 445 nm diode laser from RGB Photonics (purple). The emission spectra were measured by irradiating a water-containing cuvette in the emission spectrometer.

1.4 Determination of fluorescence quantum yields

The fluorescence quantum yield of **bTIPS-Bz** was determined in relation to a reference system **ref** (*p*-terphenyl in cyclohexane, Φ = 0.93)[1] by the comparison of their respective fluorescence emission spectra. In equation (1) Φ_{Fl} depicts the quantum yield, I the fluorescence intensity integrated over the wavenumber, A the absorption at the irradiation wavelength, and n the refractive index of the solvent of the corresponding system taken from literature.[1] The fluorescence quantum yield for **bTIPS-Bz** was measured at four different excitation wavelengths (265, 270, 275 and 285 nm) and averaged over all results. Due to the high absorption coefficient of toluene below 300 nm, we could not determine the fluorescence quantum yield in the solvent mixture cyclohexane/toluene (9:1). However, we assume that the quantum yield is not significantly affected by the addition of 10% toluene. This is corroborated by very similar excited-singlet state lifetimes in neat cyclohexane and the above-mentioned solvent mixture containing toluene. The fluorescence quantum yield of **4CzIPN** in cyclohexane/toluene (9:1) was taken from the literature.[2] The systems used to determine the fluorescence quantum yields were prepared with an optical density below 0.1 at the irradiation wavelengths to circumvent filter effects.

$$\phi_{\mathrm{Fl}} = \phi_{\mathrm{Fl,ref}} \cdot \frac{I}{I_{\mathrm{ref}}} \cdot \frac{A_{\mathrm{ref}}}{A} \cdot \frac{n^2}{n_{\mathrm{ref}}^2} \qquad (1)$$

1.5 Determination of the threshold intensity I_{th}

For TTA-UC emission spectra, a 445 nm diode laser (75 mW, RGB Photonics) was used as the excitation source. The laser power was controlled by combining the software (Ltune) and a variable neutral density filter and measured using a PD300-UV photodiode sensor (OPHIR Photonics). The laser beam was focused on a sample using a lens. The diameters of the laser beam ($1/e^2$) were measured at the sample position using a CCD beam profiler SP620 (OPHIR Photonics). A typical area of the laser beam spot estimated from the diameter was $2.1\ 10^{-4}$ cm^2. The emitted light was monitored by a multichannel detector MCPD-9800 (Otsuka Electronics). A 425 nm short-pass filter was used between the sample and the detector. For I_{th} measurements, the emitted light was focused by an achromatic lens for detecting the upconverted emission from low excitation intensity. TTA-UC

emission spectra above 300 nm were calibrated by using a standard xenon lamp L7810-03 (HAMAMATSU). The UC solutions have been prepared in an argon-filled glovebox.

1.6 Upconversion quantum yields

The upconversion quantum yield was determined from the ratios of (integrated) upconverted photons and the integrated emission of reference systems with well-known quantum yields. For that two different methods/setups were employed as detailed below.

(i) A 1 cm quartz cuvette containing an argon-saturated **4CzIPN** solution (reference quantum yield, 0.90)[2] in the absence of the annihilator was measured under identical conditions as the complete upconversion system. The 447 nm cw laser was employed and installed at a 90° angle with respect to the FL-6500 detector. The precise laser power was adjusted using a calibration sheet provided by the manufacturer. In some measurements, a neutral density filter from Newport was used to attenuate the luminescence signal in order to avoid over-saturation of the detector.

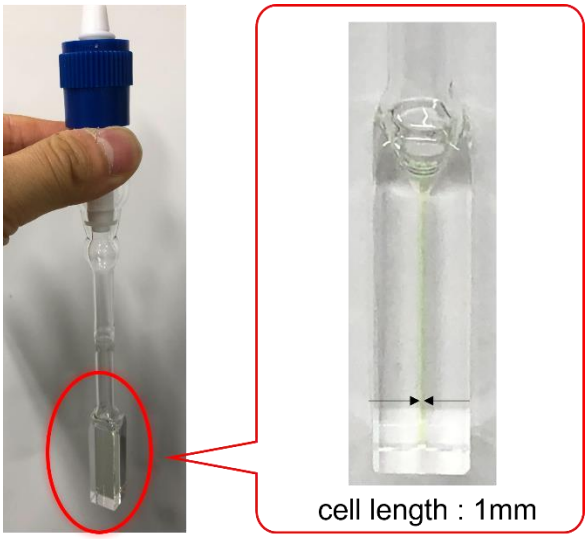

Figure S2. 1 mm quartz cuvette used for photon upconversion studies.

(ii) A 1 mm quartz cuvette (Figure S2) containing a 50 µM coumarin 6 solution was measured under identical conditions as the complete upconversion system. The 445 nm laser was employed and controlled as described in Section 1.5. The UC solutions have been prepared in an argon-filled glovebox. We measured the absolute fluorescence quantum yield of Coumarin 6 in cyclohexane:toluene (9:1) as 96.1% and used it for the calculation of Φ_{UC}.

$$\Phi_{UC} = \Phi_{std}\left(\frac{1-10^{-A_{std}}}{1-10^{-A_{UC}}}\right)\left(\frac{I_{std}}{I_{UC}}\right)\left(\frac{F_{UC}}{F_{std}}\right)\left(\frac{n_{UC}}{n_{std}}\right)^2 \quad (2)$$

The overall quantum yield Φ_{UC} was then determined according to equation (2). Where Φ, A, I, F, and n represent quantum yield, absorbance at either 447 nm or 445 nm, excitation intensity, integrated photoluminescence spectral profile, and solvent refractive index, respectively. The subscripts UC and std denote the parameters of the upconversion and standard systems. Note that the theoretical maximum of Φ_{UC} is 50%.

1.7 Quenching rate constants

The triplet-triplet energy transfer constant, k_{TTET}, and FRET rates, k_{FRET}, were determined from Stern–Volmer experiments. The lifetime of the delayed sensitizer emission was measured with different concentrations c_q of **bTIPS-Bz** and fitted in a Stern–Volmer plot according to equation (3).

With the unquenched lifetime (7.9 µs), the quenching rate constant k_{TTET} was derived from the corresponding Stern–Volmer constant K_{SV}.

The FRET rates with the acceptors acetone and pinacolone were obtained by two different methods:

Method A: Either the kinetic emission traces at 318 nm (see main paper, Figure 5E) between 0 µs and 300 µs or the spectral upconversion emission of **bTIPS-Bz** between 300 nm and 400 nm (delay: 6 µs, integration over 500 µs, see main paper, Figure 5F) with varying quencher concentration were integrated and plotted in a Stern–Volmer graph. A linear fit was obtained by averaging the results of both (spectral and kinetic) measurements for each concentration. The LFP setup with 355 nm excitation described in Section 1.9 was used for these measurements.

Method B: The fluorescence lifetime (see Section 1.11 for the experimental setup) of **bTIPS-Bz** was measured with different concentrations c_q of acetone and fitted in a Stern–Volmer plot. Pinacolone could not be studied with this method due to its high absorption at our excitation wavelengths and resulting artifacts.

With the natural lifetime of **bTIPS-Bz** in Ar-saturated cyclohexane:toluene (9:1) (2.86 ns, see Figure S14), the quenching rate constant k_{FRET} was derived from the corresponding Stern–Volmer constant K_{SV}.

$$\frac{\tau_0}{\tau} = \frac{\phi_0}{\phi} = \frac{\mathrm{F}_0}{\mathrm{F}} = 1 + \tau_0 \cdot k_\mathrm{q} \cdot c_\mathrm{q} = 1 + K_\mathrm{SV} \cdot c_\mathrm{q} \tag{3}$$

1.8 Determination of FRET parameters

The spectral overlap integral $J(\lambda)$ between the absorption of the acceptors **AC** and **PC** with the annihilator **bTIPS-Bz** emission was obtained from equation (4).[3]

$$J(\lambda) = \int_0^\infty \varepsilon_\mathrm{A}(\lambda)\, \lambda^4 F_\mathrm{D}(\lambda) d\lambda \tag{4}$$

With the molar absorption coefficient of the acceptor ε_A and the normalized fluorescence of the donor F_D.

J_{AC} = 2.5 10^{10}·M^{-1} cm^{-1} nm^4

J_{PC} = 5.8 10^{10}·M^{-1} cm^{-1} nm^4

The Förster radii, R_0, of **AC** or **PC** as acceptor and **bTIPS-Bz** as donor were calculated by the following equation:[3]

$$R_0 = 0.221(\kappa^2 n^{-4} \Phi_\mathrm{D} J(\lambda))^{\frac{1}{6}} \text{ (in Å)} \tag{5}$$

With the orientation factor κ, the refractive index n, the fluorescence quantum yield of **bTIPS-Bz** and the respective spectral overlap integral $J(\lambda)$.

$R_{0,AC}$ = 0.7 nm

$R_{0,PC}$ = 0.8 nm

1.9 Laser flash photolysis

The LP980KS setup from Edinburgh Instruments equipped with an Nd:YAG laser from Litron (Nano LG 300-10) was employed for transient absorption and time-resolved emission spectroscopy. The frequency-tripled output with a wavelength of 355 nm served as the excitation source. The laser pulse duration was ~5 ns and the pulse frequency was 10 Hz. The typical pulse energy used for transient absorption and emission studies was 15 mJ. Detection of transient absorption spectra occurred on an iCCD camera from Andor. Kinetic traces at selected wavelengths were recorded using a photomultiplier tube. The spectroscopic experiments were performed at 293 K using a cuvette holder that allows temperature control. If not stated otherwise the TA spectra were integrated over 100 ns.

1.10 Irradiation experiments

The deoxygenated solutions were irradiated in Teflon-sealed NMR tubes with either the 447 nm cw laser or two 440 nm LEDs from Kessil (see excitation light sources for details) that were installed 90° to each other (Figure S3). During the experiment the NMR tube was kept at a constant temperature using a water bath in combination with a fan. Long-pass filters with a cut-off wavelength of 385 nm were used to filter out high-energy photons that might be emitted from the LEDs.

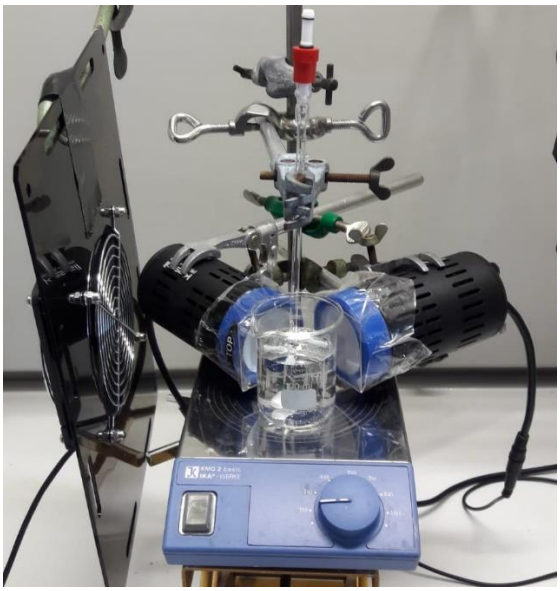

Figure S3. Setup for the irradiation experiments using two blue LEDs.

1.11 Fluorescence lifetime measurements

The *mini-*τ setup from Edinburgh Instruments (time-correlated single photon counting (TCSPC) technique) equipped with a pulsed LED (EPLED-300, excitation at ~293 nm) was employed for fluorescence lifetime measurements of **bTIPS-Bz** at 293 K. Stray light was removed with a long-pass filter with a cut-off wavelength of 320 nmfrom Newport and neutral density filters were used to avoid oversaturation of the detector.

Time-resolved upconversion lifetime measurements (Figure 3C, main paper) were carried out by using a time-correlated single-photon counting lifetime spectroscopy system, HAMAMATSU Quantaurus-Tau C11367-21, C11567-02 and M12977-01. A xenon flashlamp (60W, pulse duration ≤ 3 µs) equipped with a 445 nm band-pass filter served as light source. The solutions for these measurements have been prepared in an argon-filled glovebox.

1.12 Chromatography

For standard liquid column chromatography separation silica gel 60 M (0.040-0.063 mm Macherey-Nagel GmbH & Co., Düren, Germany) was used. Thin layer chromatography (TLC) was performed using "DC Kieselgel 60 F254" (Merck KGaA, Darmstadt, Germany) on aluminum and a UV lamp (Benda, NU-4 KL, λ = 254 nm and 365 nm, Wiesloch, Germany) was employed for detection. The resulting R_f values are given relative to the solvent.

1.13 NMR spectroscopy

For NMR spectroscopy a multinuclear magnetic resonance spectrometer of the type AV II 400 (Bruker, Karlsruhe, Germany) was employed. The chemical shifts are given as *δ*-values in ppm and they were referenced relative to the residue signal of the non-deuterated solvent. The following abbreviations were used: singlet (s), doublet (d), multiplet (m), and the coupling constant (*J*).

1.14 Gas chromatography and mass spectrometry

Gas chromatography was performed on an Agilent 8890 GC using a HP 5MS UI column (30 m x 0.25 mm x 0.25 µm) and a flow of 1.2 ml/min helium. The flow was split to an FID and an Agilent 5977 GC/MSD. Injector temperature 250 °C, MS source temperature 250 °C, transfer line temperature 230 °C, quadrupole temperature 150 °C. Oven temperature program: Hold 40 °C for 2 min, heat at 50 °C to 320 °C and hold for 7.4 min.

1.15 Preparation of deoxygenated solutions for photon upconversion studies

Unless noted otherwise, the solutions for photon upconversion experiments were deoxygenated in custom-made Schlenk-cuvettes[2] by five freeze-pump-thaw cycles using argon as an inert gas, liquid N_2 for cooling, and Schlenk line vacuum (down to 0.2 mbar).

2. Synthetic procedures

2.1 Synthesis of TIPS-ethynyl-benzene derivatives

The TIPS-ethynyl-functionalized benzenes were synthesized according to the Sonogashira coupling reaction analogous to the preparation of similar aromatic compounds.[2,4] The exact quantities are listed for each benzene derivative below. The bromobenzene, $Pd(PPh_3)_2Cl_2$, CuI, PPh_3, and dry THF were added to a flame-dried round-bottom flask under argon flow. The flask was equipped with a condenser column. Diisopropylamine was added to the solution under constant stirring. The flask was then heated to 70˚C and (triisopropylsilyl)acetylene was added dropwise to the mixture. The mixture was held at 70˚C for 12 h under argon atmosphere. The completion of the reaction was tested with TLC. After cooling, the mixture was filtered and the solvent was removed under reduced pressure. The residue was redissolved in chloroform and washed twice with deionized water and twice with brine. The organic layer was dried with Na_2SO_4 and the solvent was removed under reduced pressure. If not stated otherwise, the product was purified via column chromatography (neat cyclohexane) and then if required recrystallized from ethanol/water (9:1). NMR spectra (see below) of all TIPS-ethynyl-benzenes derivatives agree with those reported in the literature.[5]

1,4-bis((triisopropylsilyl)ethynyl)benzene (bTIPS-Bz): 1.418 g 1,4-dibromobenzene (4.30 mmol), 36.5 mg $Pd(PPh_3)_2Cl_2$ (0.052 mmol), 26.2 mg CuI (0.14 mmol), 36.1 mg PPh_3 (0.14 mmol), 28 mL dry THF, 13.5 mL diisopropylamine and 1.85 mL (triisopropylsilyl)acetylene (8.26 mmol); yield = 1.573 g, 3.59 mmol (84%) after column chromatography. Obtained as a colorless solid.

R_f(cyclohexane) = 0.5

GC-FID: purity > 99 %

EI-MS (m/z): calculated for $[M + H]^+$: 438.314, found 438.350.

^{1}H NMR (400 MHz, $CDCl_3$): δ [ppm] = 7.39 (s, 4H), 1.13 (s, 42H);

^{13}C NMR (400 MHz, $CDCl_3$): δ [ppm] = 131.9, 123.5, 106.8, 92.8, 18.8, 11.5.

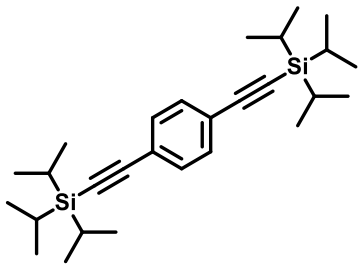

((triisopropylsilyl)ethynyl)benzene (TIPS-Bz):[a] 675 mg bromobenzene (4.30 mmol), 18.26 mg $Pd(PPh_3)_2Cl_2$ (0.026 mmol), 13.1 mg CuI (0.069 mmol), 18 mg PPh_3 (0.069 mmol), 28 mL dry THF, 7 mL diisopropylamine and 0.93 mL (triisopropylsilyl)acetylene (4.13 mmol); yield = 354 mg, 1.37 mmol (32%).

[a] A colorless liquid was obtained from column chromatography, which was then distilled under vacuum (10^{-2} mbar) at 80°C.

R_f(cyclohexane) = 0.75

^{1}H NMR (400 MHz, $CDCl_3$): δ [ppm] = 7.29-7.32 (m, 3H), 7.47-7.49 (m, 2H), 1.13 (pseudo-s, 21H);

^{13}C NMR (400 MHz, $CDCl_3$): δ [ppm] = 132.2, 128.4, 128.32, 123.7, 107.2, 90.6, 18.8, 11.5.

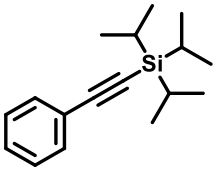

1,3,5-tris((triisopropylsilyl)ethynyl)benzene (tTIPS-Bz): 1,322 g 1,3,5-tribromobenzene (4.30 mmol), 54.8 mg $Pd(PPh_3)_2Cl_2$ (0.078 mmol), 39.3 mg CuI (0.21 mmol), 54.1 mg PPh_3 (0.21 mmol), 48 mL dry THF, 20 mL diisopropylamine and 2.78 mL (triisopropylsilyl)acetylene (12.39 mmol); yield = 2.38 g, 7.1 mmol (33%) after recrystallization. Obtained as a colorless solid.

R_f(cyclohexane) = 0.5

^{1}H NMR (400 MHz, $CDCl_3$): δ [ppm] = 7.47 (s, 3H), 1.13 (pseudo-s, 63H);

^{13}C NMR (400 MHz, $CDCl_3$): δ [ppm] = 135.0, 124.0, 105.2, 92.1, 18.7, 11.3.

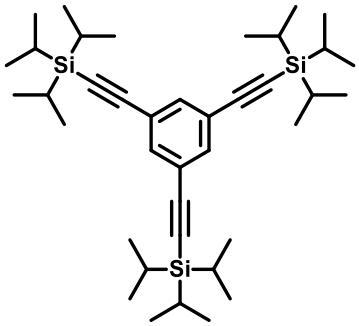

2.2 Synthesis of 4CzIPN

The compound 4CzIPN was still available from our recent study.[2] It was purified by sublimation prior to its use as sensitizer. The ^{1}H NMR spectrum agrees with that reported in the literature.[6]

^{1}H NMR (400 MHz, $CDCl_3$): δ [ppm] = 8.22(d, J_{HH} = 8 Hz, 2H), 7.74-7.67 (m, 8H), 7.51-7.47 (m, 2H), 7.33 (d, J_{HH} 8 Hz, 2H), 7.23-7.21 (m, 4H), 7.12-7.05 (m, 8H) 6.84-6.80 (m, 4H), 6.65-6.61 (m, 2H).

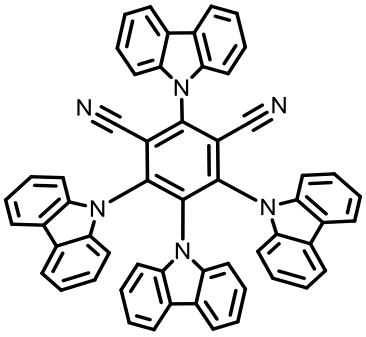

3. DFT calculations

The DFT calculations for structure optimization and frequency analysis were carried out using the Gaussian 09 software package[7] with the B3LYP functional and the 6-311+G(d,p) basis set. No negative vibrational frequencies were observed in the optimized structures indicating the successful convergence on minimum structures. Initially, singlet ground states were optimized and the resulting structures served as the starting point for the corresponding triplet state calculations. Spin densities of the triplet states were obtained by single-point calculations following successful optimizations. The calculated triplet energies, E_T(DFT), were determined by comparing the energies of the optimized singlet ground states to those of the corresponding triplet states.[8] The TIPS-ethynyl substituents add numerous degrees of rotational freedom and consequently require huge computational effort. For the initial screening of the annihilators used in this work, we replaced the TIPS-ethynyl by TMS-ethynyl substituents simplifying the calculations significantly. We found similar E_T values, deviating by 0.01 eV when comparing respective mono- and di-substituted TIPS-ethynyl and TMS-ethynyl. Based on these results, the triplet energy for **tTIPS-Bz** (for which we could not obtain suitable optimized structures and energies) was extrapolated from **tTMS-Bz**.

Time-dependent DFT calculations with identical functional and basis were used to calculate the vertical excitation energies for simulating the triplet-triplet absorption spectrum of **bTIPS-Bz**. The predicted transitions and their oscillator strengths are displayed in Figure 3B (main paper). The calculated triplet absorption spectrum shows a global maximum at 361 nm, which is in good agreement with the experimental triplet absorption spectrum peaking at 348 nm.

Table S1. Computed triplet energies (in eV or kJ/mol) for benzene and corresponding TIPS- or TMS-derivatives.

Compound	E_T (DFT)[a] [eV]	E_T (lit.)[b] [eV]	E_T (corr.)[c] [eV]	E_T (corr.)[d] [kJ mol^{-1}]
Benzene (**Bz**)	3.83	3.9	-	-
TIPS-Bz	3.01	-	3.06	295
TMS-Bz	3.02	-	3.07	296
bTIPS-Bz	2.53	-	2.57	248
bTMS-Bz	2.54	-	2.58	249
tTIPS-Bz	n.a.	-	2.97[e]	287[e]
tTMS-Bz	2.92	-	2.98	288

[a] DFT-calculated triplet energy at the B3LYP/6-311+G(d,p) level of theory. [b] Experimental triplet energy from ref[9]. [c] Calculated triplet energy corrected by the underestimation factor from benzene (i.e., calculated E_T multiplied by 1.02). [d] Energies converted to kJ/mol. [e] Estimated value from comparison of TIPS and TMS derivatives.

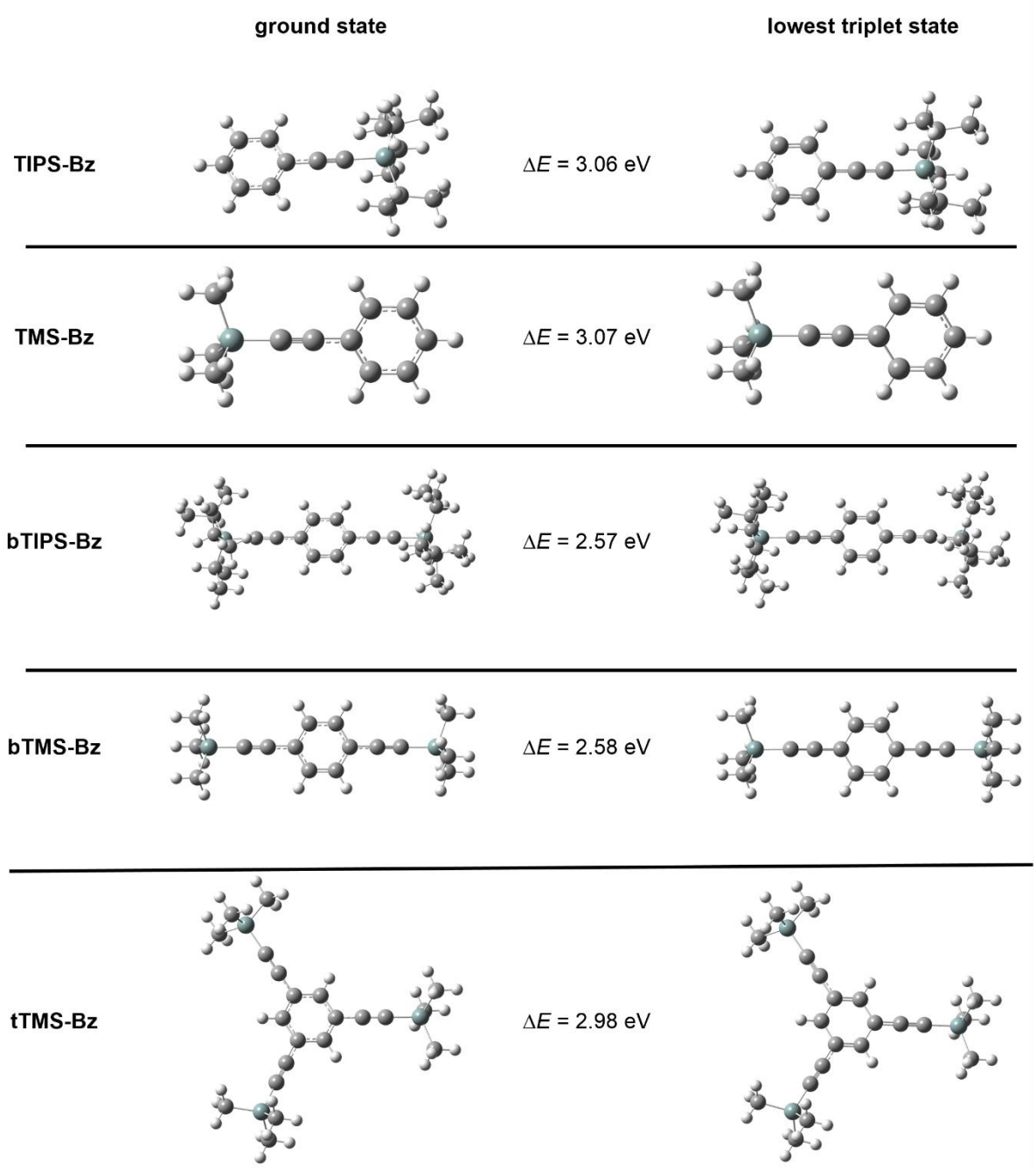

Figure S4. Optimized ground state (left) and lowest triplet state (right) structures of **TIPS-Bz**, **TMS-Bz**, **bTIPS-Bz**, **bTMS-Bz** and **tTMS-Bz** with their calculated triplet energies, E_T(DFT).

4. Photophysical properties of benzene and the TIPS-ethynyl substituted benzenes

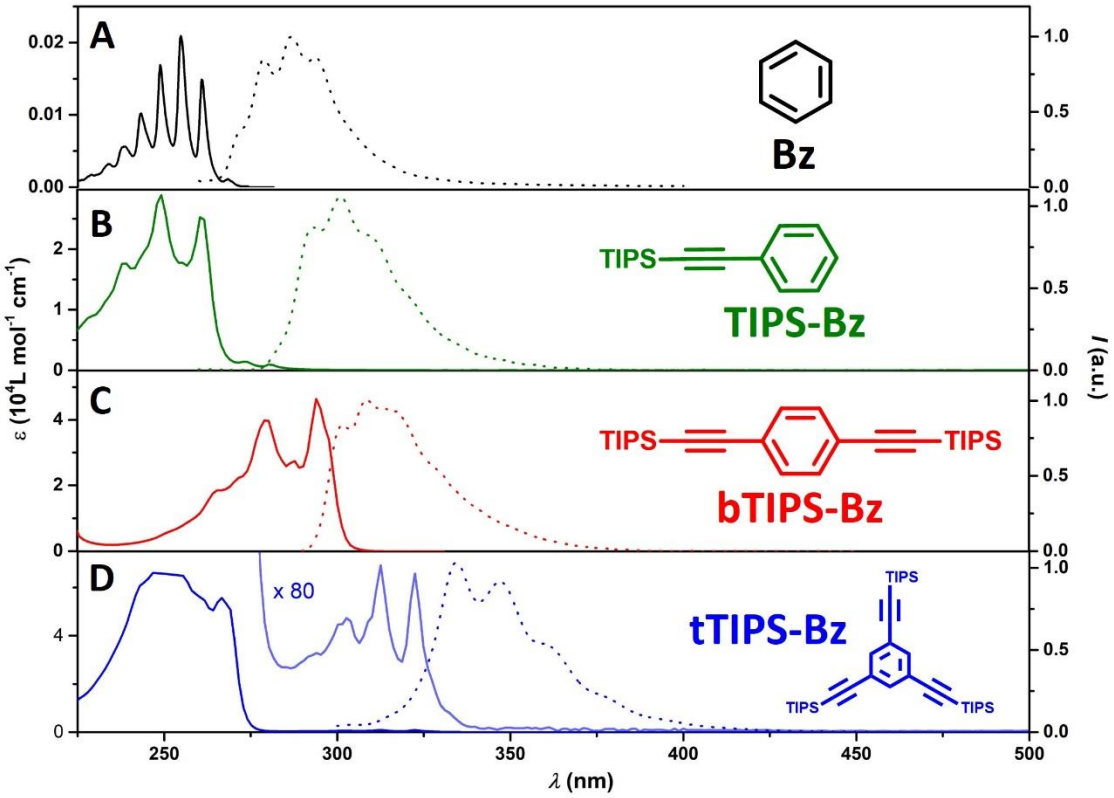

Figure S5. Absorption (solid lines) and normalized photoluminescence (dotted lines) spectra of benzene (**Bz**) (panel A)[a], **TIPS-Bz** (panel B), **bTIPS-Bz** (panel C) and **tTIPS-Bz** (panel D) in cyclohexane. [a] Taken from ref.[10].

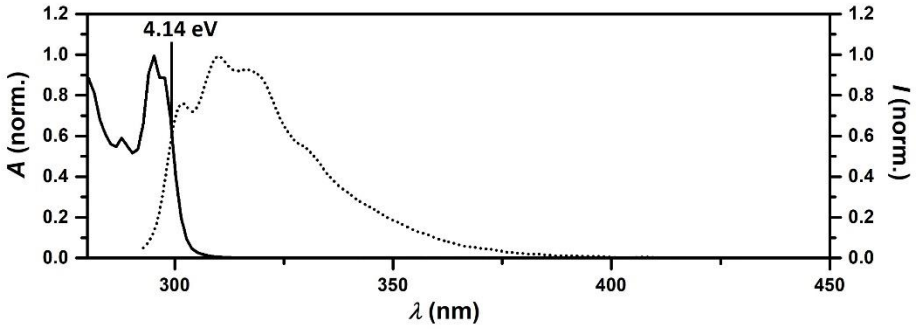

Figure S6. Absorption (solid lines) and normalized photoluminescence (dotted lines) spectrum of **bTIPS-Bz** in cyclohexane:toluene (9:1). The absorption spectrum could not be recorded below 280 nm owing to the toluene background absorption.

5. Threshold intensity measurements

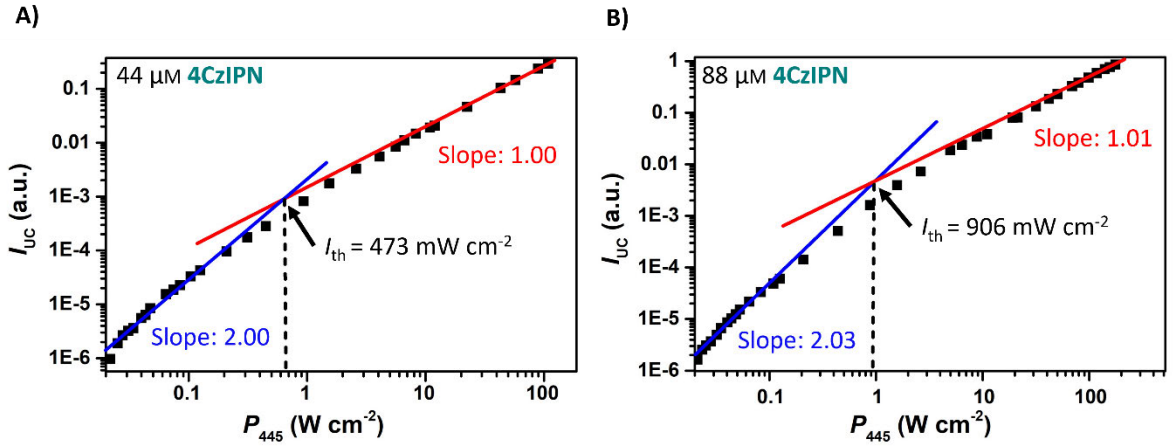

Figure S7. Normalized UC emission of deoxygenated solutions containing A) 44 or B) 88 µM **4CzIPN** and 10 mM **bTIPS-Bz** in cyclohexane:toluene (9:1) using a 445 nm cw laser for excitation. The UC signal was plotted against the laser power on a double-logarithmic scale. The threshold intensity I_{th} was determined from the crossing point of the linear (slope ~1) and the quadratic (slope ~2) fit.

6. Additional control experiments and spectroscopic measurements of the UC-FRET sequence

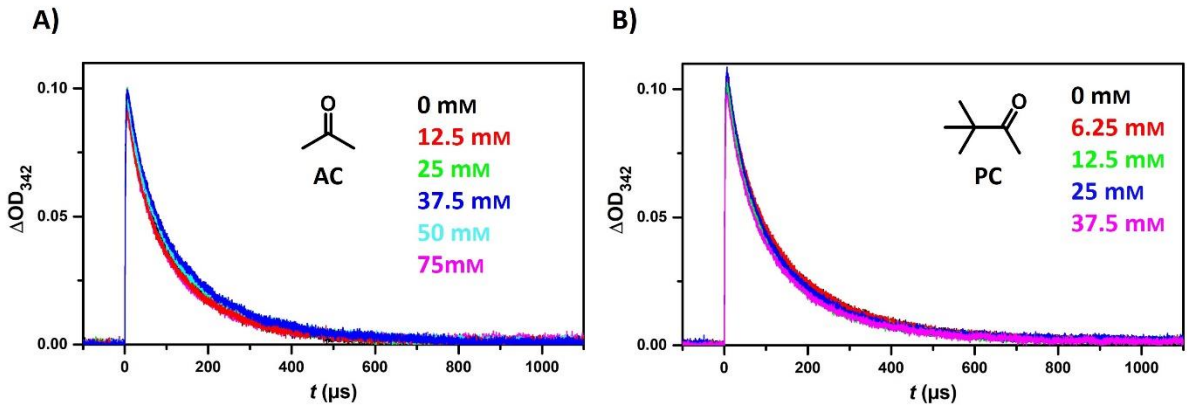

Figure S8. Kinetic traces of the **bTIPS-Bz** triplet state recorded at 342 nm after 355 nm excitation of 20 µM **4CzIPN** and 10 mM **bTIPS-Bz** in Ar-saturated cyclohexane:toluene (9:1) with different concentrations of acetone (A) and pinacolone (B). The measurements were recorded with the same solutions as in Figure 5 E/F of the main paper.

Figure S8 A/B show the kinetic traces of the **bTIPS-Bz** triplet state with increasing carbonyl (acetone and pinacolone) concentrations. Only slight variances of the lifetime and concentration with no clear trends are observed that most likely stem from minor laser fluctuations and/or residual oxygen impurities. It can therefore be concluded that the triplet-triplet annihilation process is unaffected by the addition of the carbonyls and thus the decreasing UC emission does not originate from unproductive quenching of the sensitizer or annihilator triplet.

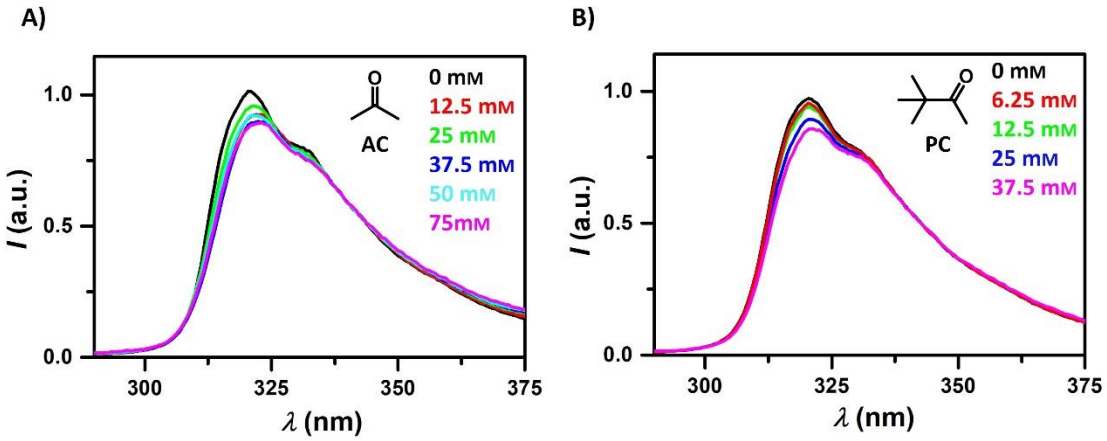

Figure S9. Normalized time-gated (delay, 6 µs; integration over 500 µs) emission spectra after 355 nm laser excitation of 20 µM **4CzIPN** and 10 mM **bTIPS-Bz** in Ar-saturated cyclohexane:toluene (9:1) with different concentrations of (A) pinacolone and (B) acetone. The emission spectra were scaled to identical intensity at 340 nm.

The kinetic traces of the upconversion emission in Figure 5E (main paper) were recorded at a central detection wavelength of 318 nm (monochromator slit width, 17 nm). This wavelength was selected as it provides the best signal quality, being the maximum emission and avoids stray laser light (355 nm). However, at this wavelength the carbonyls acetone and pinacolone already show minor absorption.

$$\varepsilon_{318}(\mathrm{AC}) = 2 \cdot \mathrm{M}^{-1}\mathrm{cm}^{-1}$$

$$\varepsilon_{318}(\mathrm{PC}) = 5 \cdot \mathrm{M}^{-1}\mathrm{cm}^{-1}$$

Calculating the absorption with the highest concentration used in Figure 5 E/F and the average optical pathlength we obtain the following values:

$$A_{318}(\mathrm{AC}) = 2 \cdot \mathrm{M}^{-1}\mathrm{cm}^{-1} \cdot 75\ \mathrm{mM}\ \cdot 0.5\ \mathrm{cm} = 0.075$$

$$A_{318}(\mathrm{PC}) = 5 \cdot \mathrm{M}^{-1}\mathrm{cm}^{-1} \cdot 37.5\ \mathrm{mM}\ \cdot 0.5\ \mathrm{cm} = 0.094$$

These simple calculations suggest that less than 20% of the emission attenuation in Figure 5E is due to reabsorption rather than FRET. This is further supported when the emission spectra with increasing quencher concentrations are scaled to an identical intensity at a wavelength where the carbonyl compounds do not absorb (shown in Figure S9).

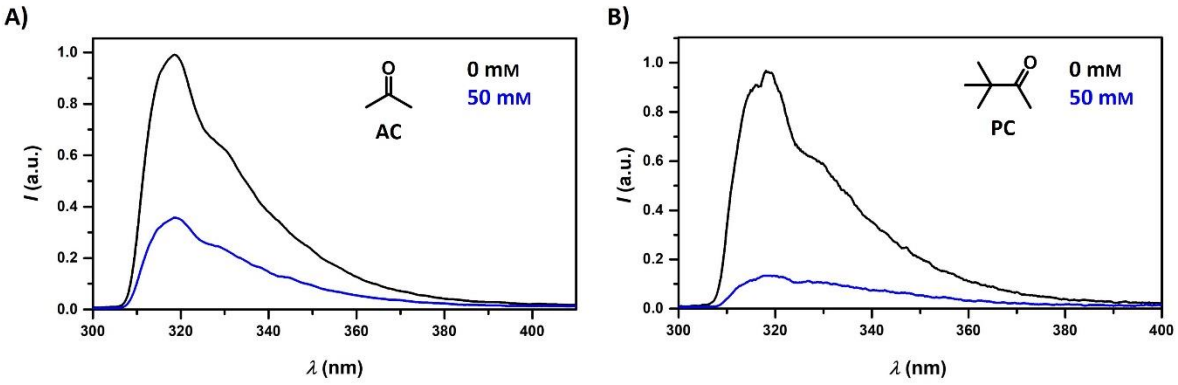

Figure S10. Normalized upconversion emission spectra of deoxygenated solutions containing 44 µM **4CzIPN** and 10 mM **bTIPS-Bz** in the absence and presence of 50 mM **AC** (A) or **PC** (B) in cyclohexane:toluene (9:1) using a cw laser for excitation at 447 nm (laser power 100 mW).

Additional UC emission quenching experiments were performed with a cw laser for excitation at 447 nm. A solution containing 44 µM **4CzIPN** and 10 mM **bTIPS-Bz** was irradiated in the absence and presence of 50 mM **AC** (A) or **PC** (B) in cyclohexane:toluene (9:1) (Figure S10). The UC signal decreases when the carbonyls are added and the quenching is about twice as efficient with **PC** compared to **AC**. These qualitative results are in perfect agreement with the LFP measurements from Figure 5 (main paper). However, we regard the LFP measurements as more reliable for extracting quenching rate constants because of the observed Norrish fragmentation for **PC** under cw excitation conditions (note that it takes about 1 min to record a spectrum displayed in Figure S10), which does not take place upon excitation with a single 355 nm laser pulse.

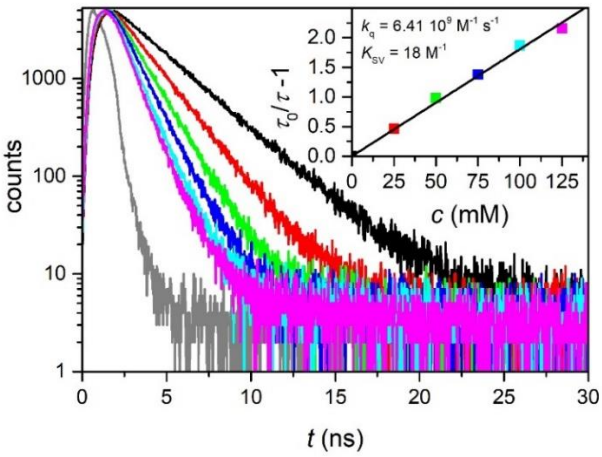

Figure S11. Lifetime-based fluorescence quenching experiments of 15 µM **bTIPS-Bz** with varying acetone concentrations in air-saturated cyclohexane upon pulsed LED (293 nm, grey trace corresponds to IRF) excitation. Inset: Corresponding Stern–Volmer plot.

Lifetime-based Stern–Volmer fluorescence quenching experiments of **bTIPS-Bz** were conducted with varying acetone concentrations in neat and air-saturated cyclohexane (Figure S11). Oxygen removal was not carried out to ensure exact concentrations of the volatile quencher. The quenching constant k_q = 6.41×10^9 M^{-1} s^{-1} was calculated using the Stern–Volmer equation (equation 3) and the fluorescence lifetime of **bTIPS-Bz** (2.81 ns) in air-saturated cyclohexane. This slightly higher FRET rate compared to the rate constant (k_{FRET} = 5.0×10^9 M^{-1} s^{-1}) obtained by the UC-FRET sequence in Figure 5D of the main paper most likely stems from the different methods of preparation and the slightly different solvent. We assume that the volatile acetone is removed in small amounts by the thorough freeze-pump-thaw method that was carried out with the UC-FRET solutions in Figure 5E/F yielding a slightly lower quenching efficiency.

7. Additional spectroscopic data

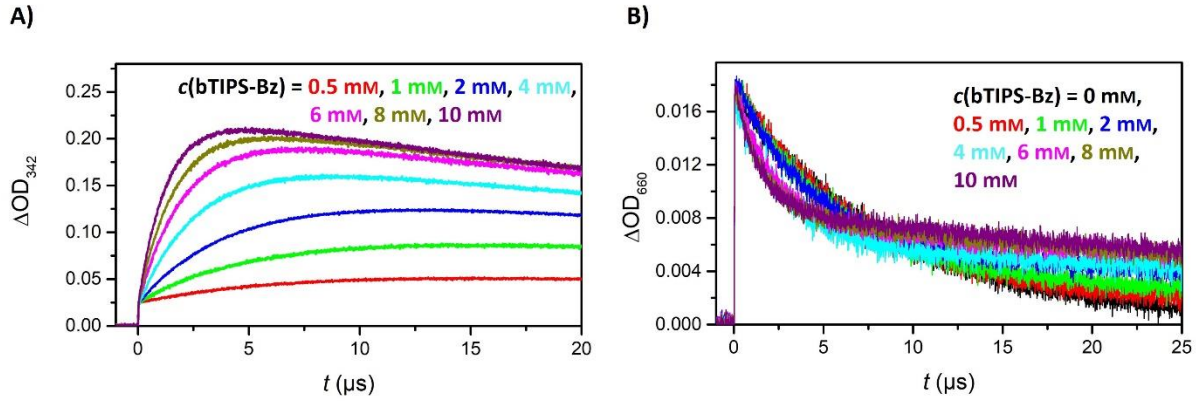

Figure S12. Time-resolved transient absorption measurements after 355 nm laser excitation of solutions containing 20 µM **4CzIPN** in Ar-saturated cyclohexane:toluene (9:1) with different **bTIPS-Bz** concentrations recorded (A) at 342 nm (B) at 660 nm. The measurements were carried out with the same solutions as in Figure 3A (main paper).

The time-resolved transient absorption measurements in Figure S12 were carried out with the same solutions as in Figure 3 of the main paper. The triplet concentration of **bTIPS-Bz** recorded at 342 nm increases with increasing annihilator concentration, as expected (Figure S12A). At a given annihilator concentration, the ^{3}**bTIPS-Bz** formation occurs with slightly faster rate constants than the delayed emission quenching of **4CzIPN** (Figure 3A of the main paper). These minor discrepancies are attributed to the subsequent ^{3}**bTIPS-Bz** decay complicating the kinetics. Furthermore, the triplet decay of **4CzIPN** was recorded at 660 nm and shortens with increasing annihilator concentration. However, the weak signal is superimposed with the strong absorption of the long-lived ^{3}**bTIPS-Bz** species (Figure S12B) (compare, the transient absorption spectra in Figure 3A of the main paper and the predicted ^{3}**bTIPS-Bz** transitions). The **4CzIPN** triplet lifetime and its delayed emission (that allows us to indirectly monitor triplet quenching without artifacts of quenching products as in Figure S12) are known to be in excellent correlation and yields practically the same result.[11] In line with that observation, the τ_0 value in our solvent mixture (7.9 µs) is identical regardless of the detection method (^{3}**4CzIPN** transient absorption at 660 nm or delayed emission at 477 nm). Hence, the (delayed) luminescence lifetime of **4CzIPN** was used for a straightforward kinetic analysis (Figure 3A of the main paper).

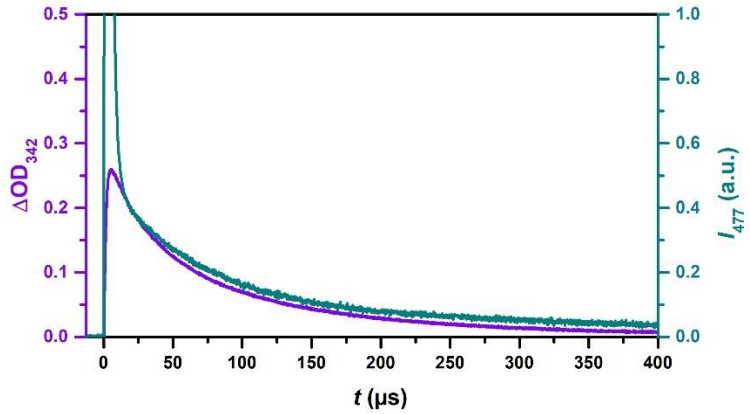

Figure S13. Time-resolved transient absorption and emission measurements of a solution containing 20 µM **4CzIPN** with 10 mM **bTIPS-Bz** in Ar-saturated cyclohexane:toluene 9:1 after excitation with 355 nm laser pulses. Purple curve: Triplet state decay of **bTIPS-Bz** at 342 nm; cyan curve: Elongated emission of 4CzIPN as a result of back triplet-triplet energy transfer monitored at 477 nm.

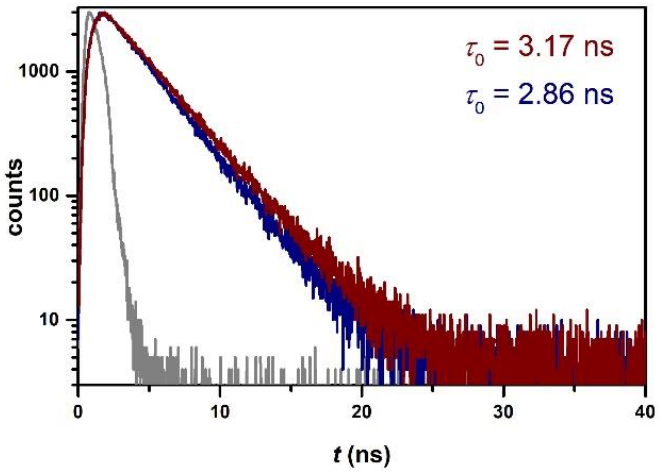

Figure S14. Fluorescence lifetime measurements of 15 µM **bTIPS-Bz** in Ar-saturated neat cyclohexane (dark red) and in cyclohexane:toluene (9:1) (dark blue). Grey trace corresponds to IRF.

Figure S14 displays the fluorescence lifetime measurement of 15 µM **bTIPS-Bz** in neat cyclohexane (dark red) and in a solvent mixture of cyclohexane:toluene (9:1) (dark blue). With the addition of the co-solvent toluene, the lifetime decreases from 3.17 ns to 2.86 ns. The fluorescence lifetime measured in cyclohexane:toluene (9:1) was used to determine the FRET rate constant that is shown in the Stern-Volmer plot (Figure 5B) of the main paper.

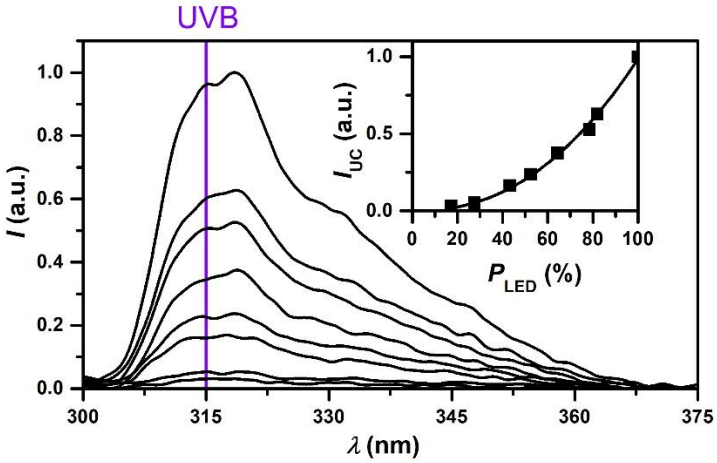

Figure S15. Normalized photon upconversion emission with deoxygenated solutions containing 44 µM 4CzIPN and 10 mM bTIPS-Bz in cyclohexane:toluene (9:1) using a blue LED (440 nm) as excitation source. Inset: Normalized upconversion emission plotted against the relative LED power.

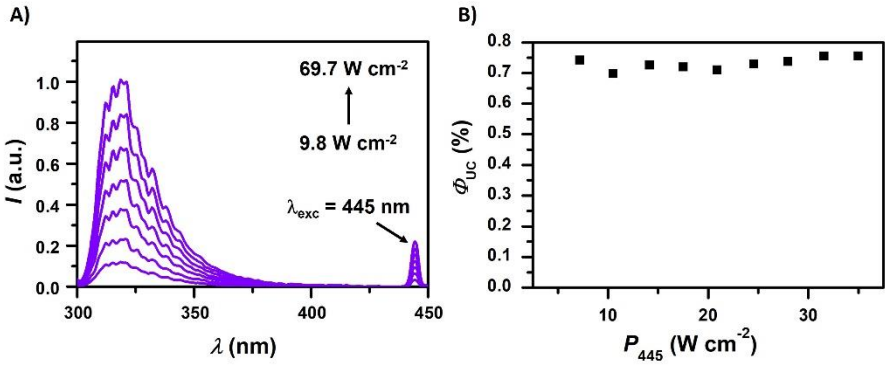

Figure S16. Photon upconversion studies with deoxygenated solutions containing 44 µM **4CzIPN** and 10 mM **bTIPS-Bz** in cyclohexane:toluene (9:1) using a cw laser for excitation at 445 nm. A) Power-dependent spectra of the normalized upconverted emission. B) External upconversion quantum yield, Φ_{UC}, plotted against the laser power density.

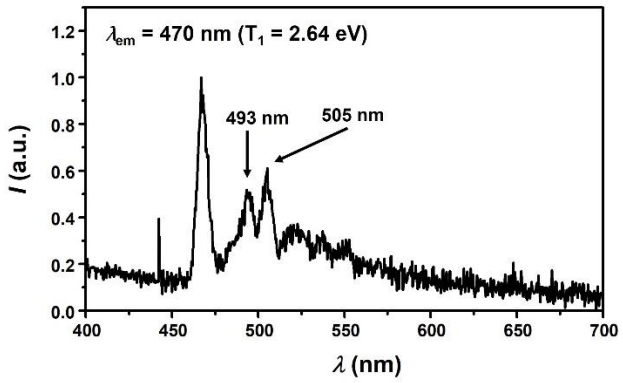

Figure S17. Phosphorescence spectrum of 10 mM **bTIPS-Bz** recorded at 77K in 2-methyltetrahydrofuran.

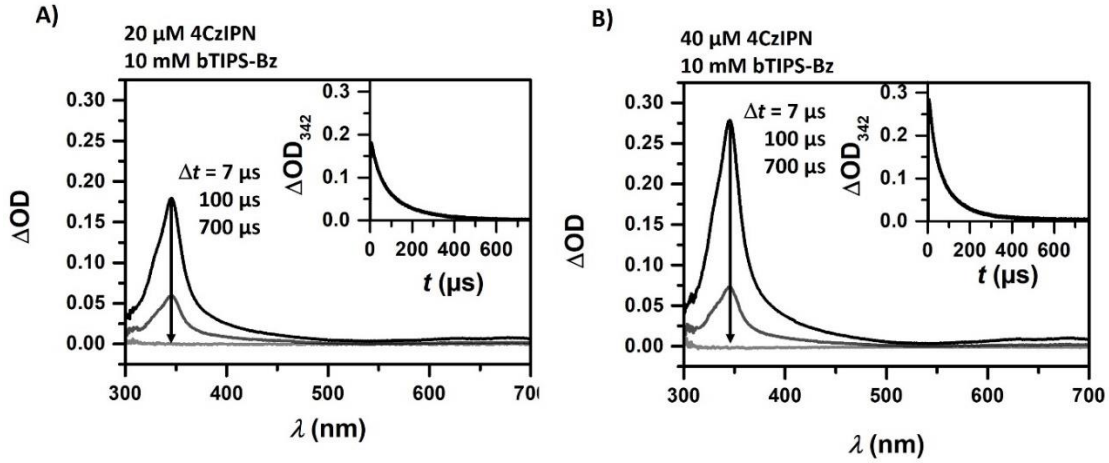

Figure S18. Transient absorption measurements of a solution containing 20 µM (A) *or* 40 µM (B) **4CzIPN** with 10 mM **bTIPS-Bz** in Ar-saturated cyclohexane:toluene (9:1) after excitation with 355 nm laser pulses. Insets: Kinetic measurements at 342 nm.

Figure S18 shows transient absorption spectra of the upconversion solution (**4CzIPN**–**bTIPS-Bz**) with detection window delays of 7, 100 and 700 µs. The strong absorption of triplet-excited **bTIPS-Bz** peaking at 342 nm fully decays after 700 µs (Inset). No spectroscopic signatures of long-lived species that would originate from electron transfer (such as sensitizer bleach or radical ion absorption bands) are detected. Even at higher concentrations of **4CzIPN** (40 µM) (which strongly increases the signal intensities and the probability for reactions between singlet-excited **bTIPS-Bz** and **4CzIPN**) no new species appear.

8. NMR spectra and analytics

8.1 Spectra of benzene-derivatives and sensitizer

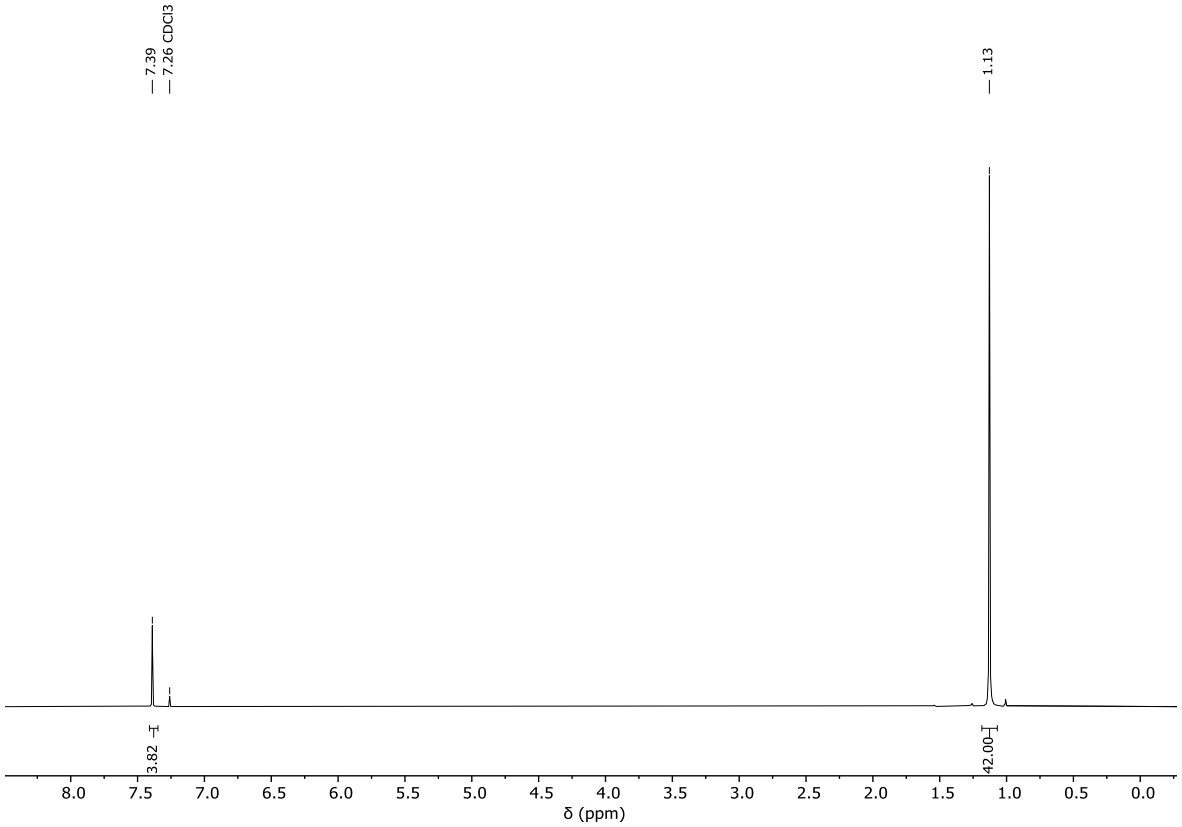

Figure S19. ^{1}H NMR spectrum of 1,4-bis((triisopropylsilyl)ethynyl)benzene (**bTIPS-Bz**).

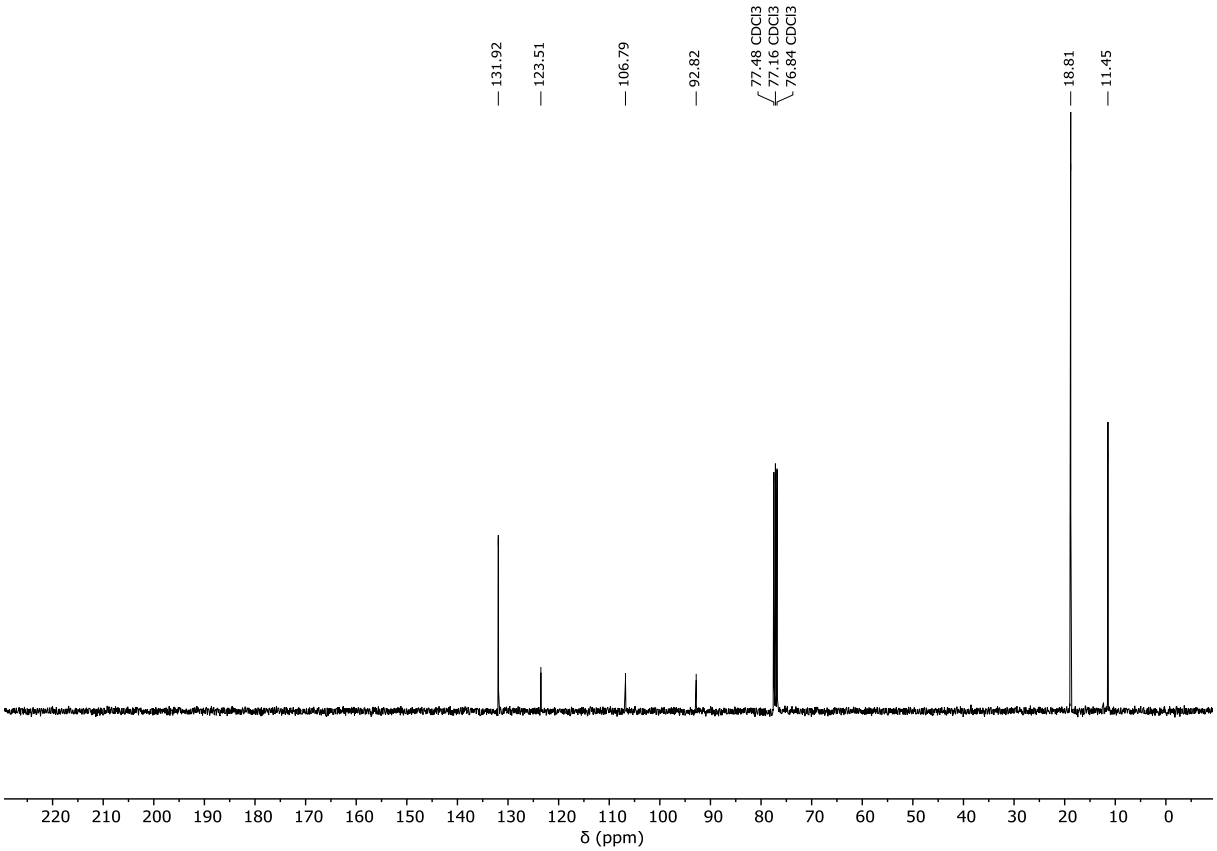

Figure S20. ^{13}C NMR spectrum of 1,4-bis((triisopropylsilyl)ethynyl)benzene (**bTIPS-Bz**).

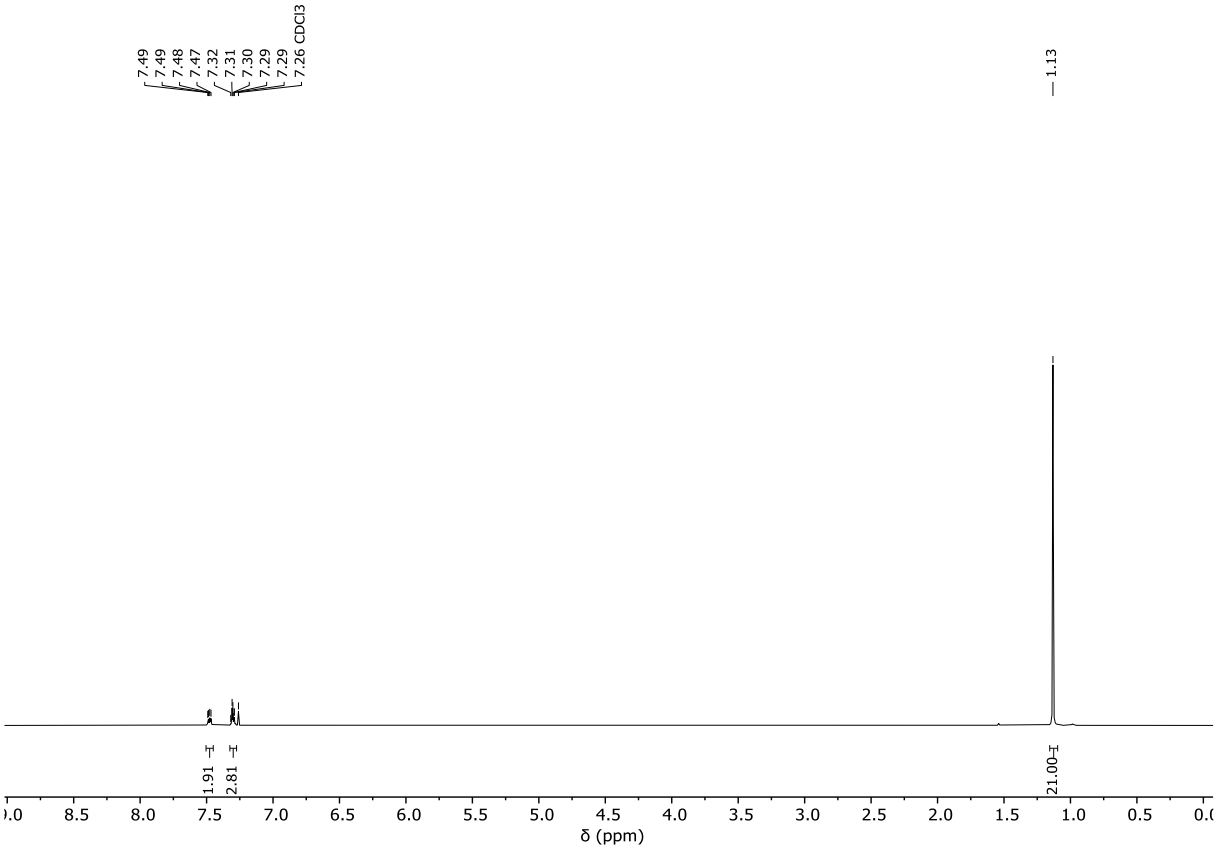

Figure S21. ^{1}H NMR spectrum of triisopropyl(phenylethynyl)silane (**TIPS-Bz**).

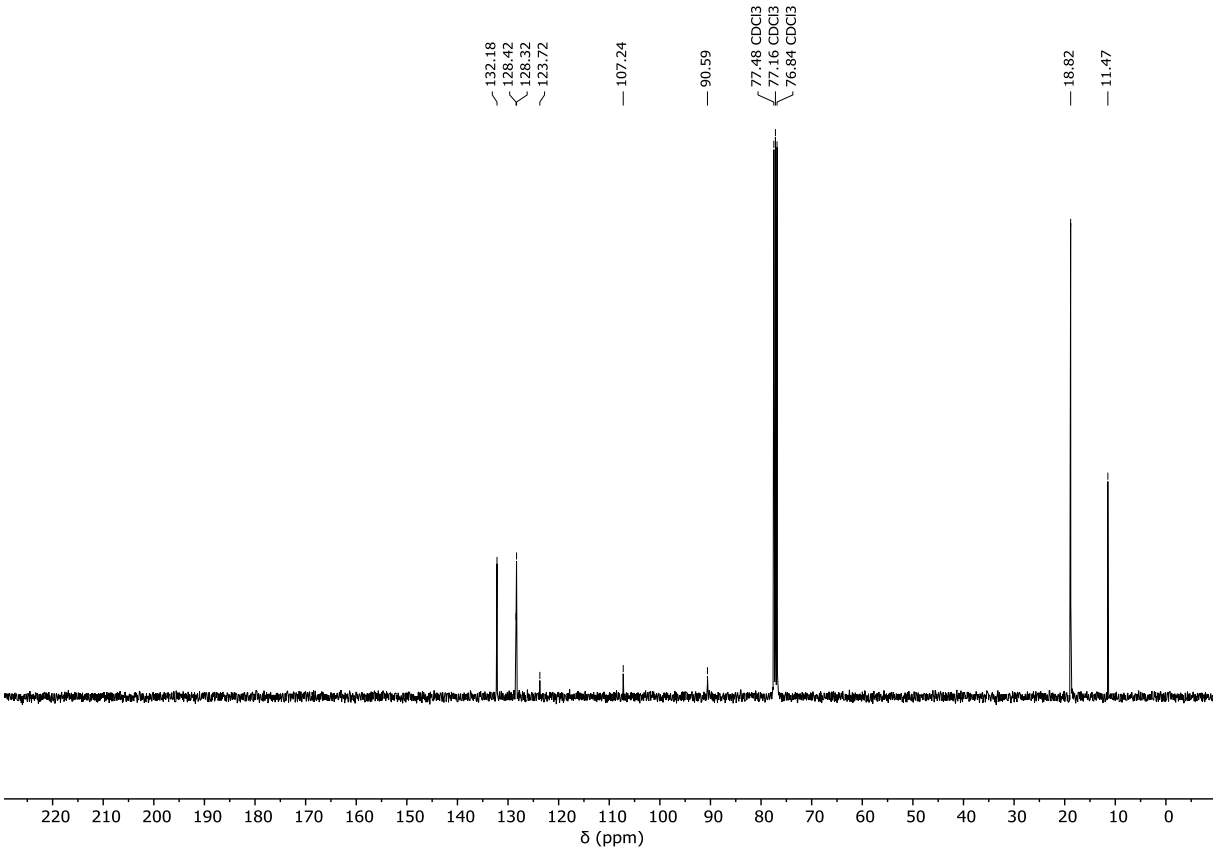

Figure S22. ^{13}C NMR spectrum of triisopropyl(phenylethynyl)silane (**TIPS-Bz**).

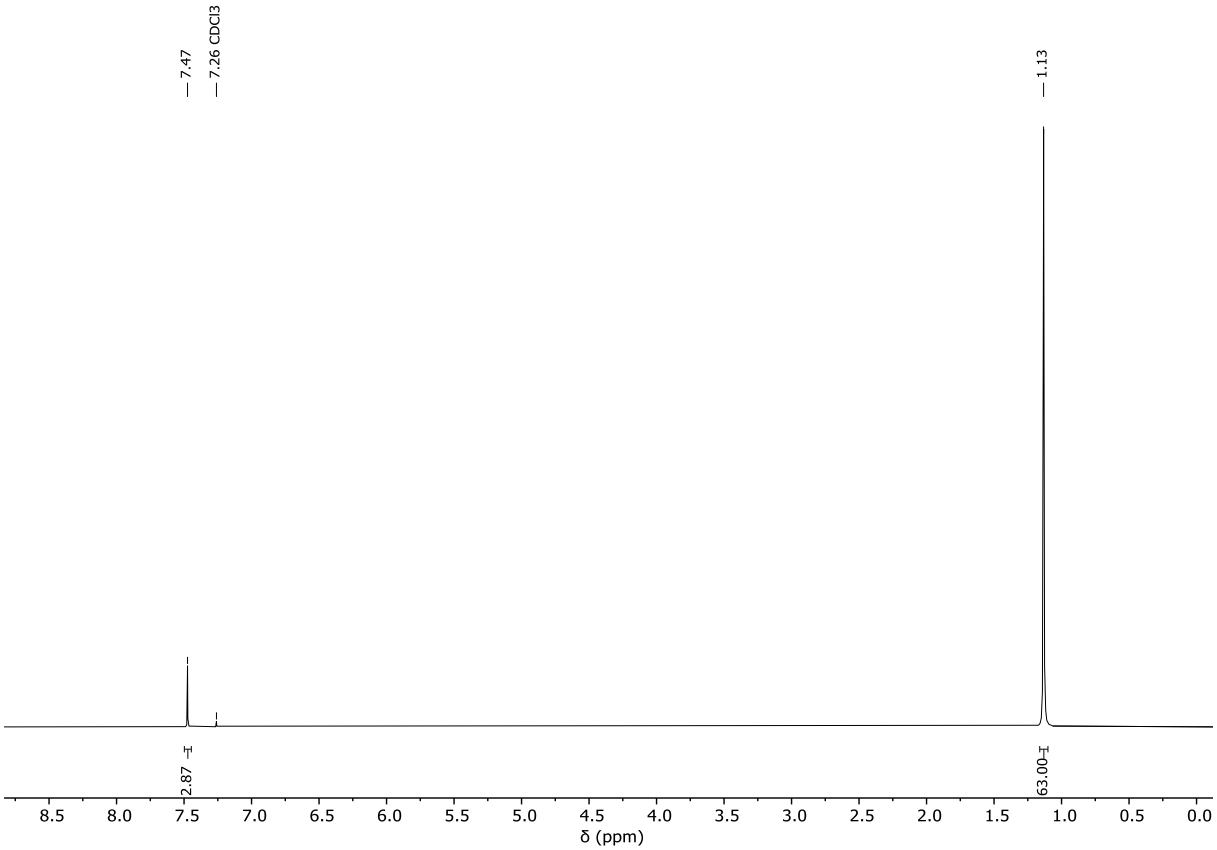

Figure S23. ^{1}H NMR spectrum of 1,3,5-tris((triisopropylsilyl)ethynyl)benzene (**tTIPS-Bz**).

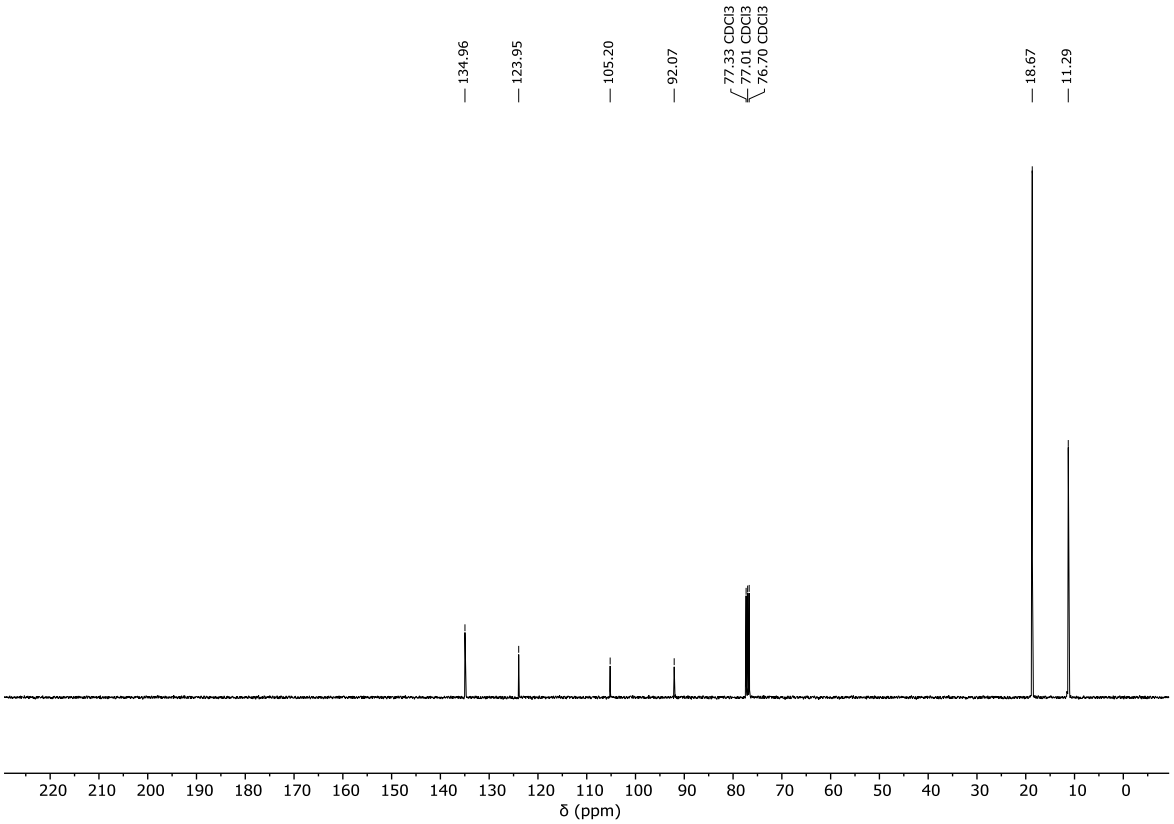

Figure 24. ^{13}C NMR spectrum of 1,3,5-tris((triisopropylsilyl)ethynyl)benzene (**tTIPS-Bz**).

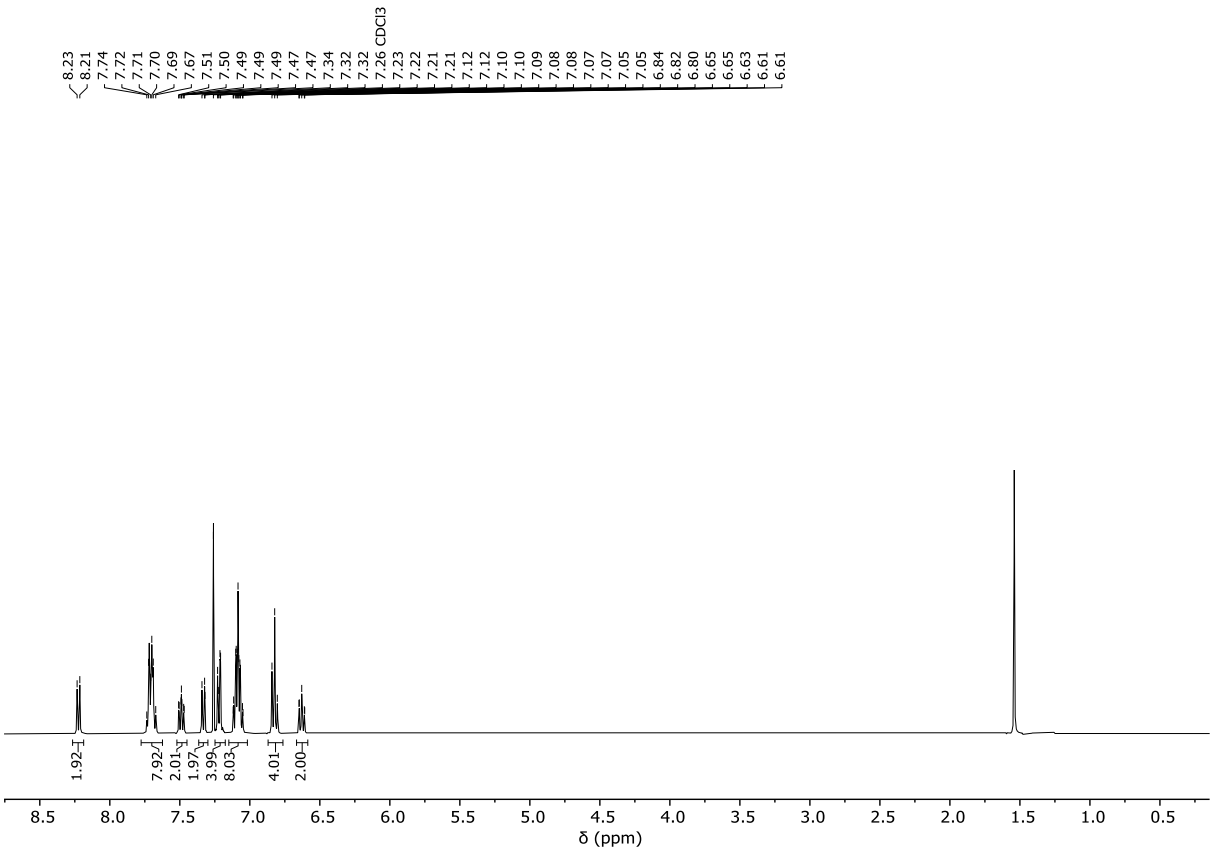

Figure S25. ^{1}H NMR spectrum of **4CzIPN**.

8.2 Irradiation experiments

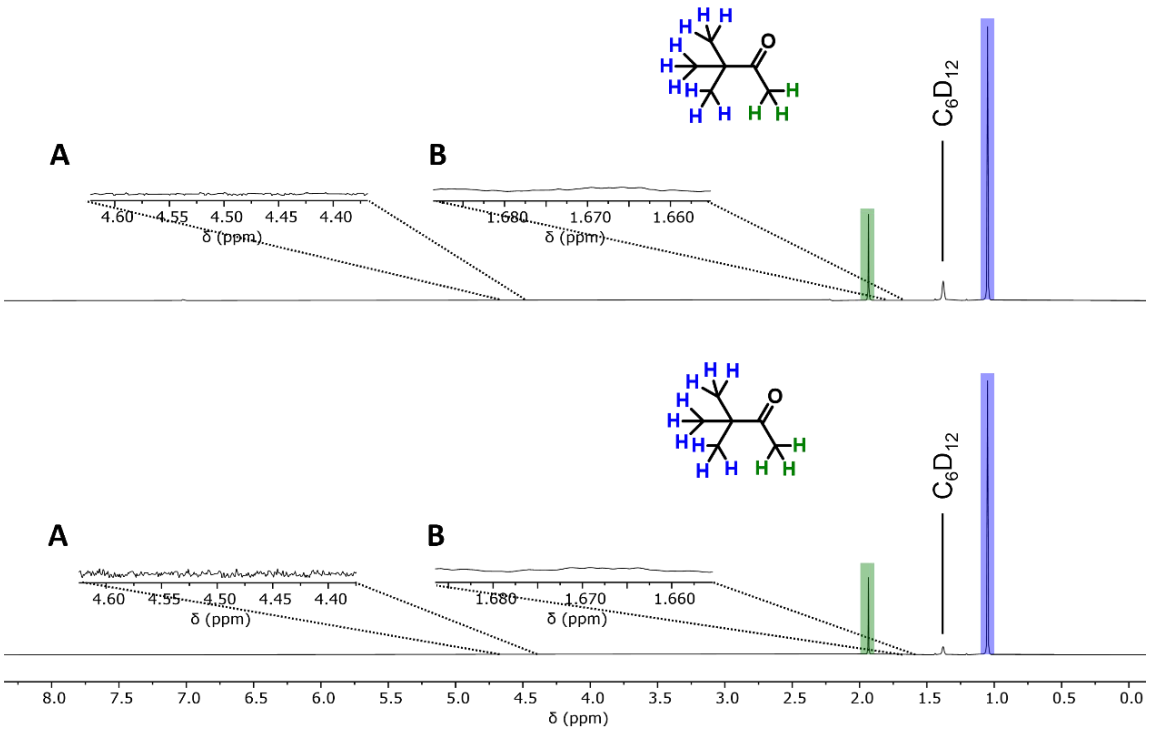

Figure S26. ^{1}H NMR experiment of 100 µM **4CzIPN** and 100 mM pinacolone in Ar-saturated cyclohexane:toluene (9:1) before (top panel) and after (bottom panel) 30 min of irradiation at 447 nm with 1.1 W. Insets: ^{1}H NMR region of isobutylene as a stable product of the UC-FRET-driven Norrish reaction. A) septet region; B) triplet region.

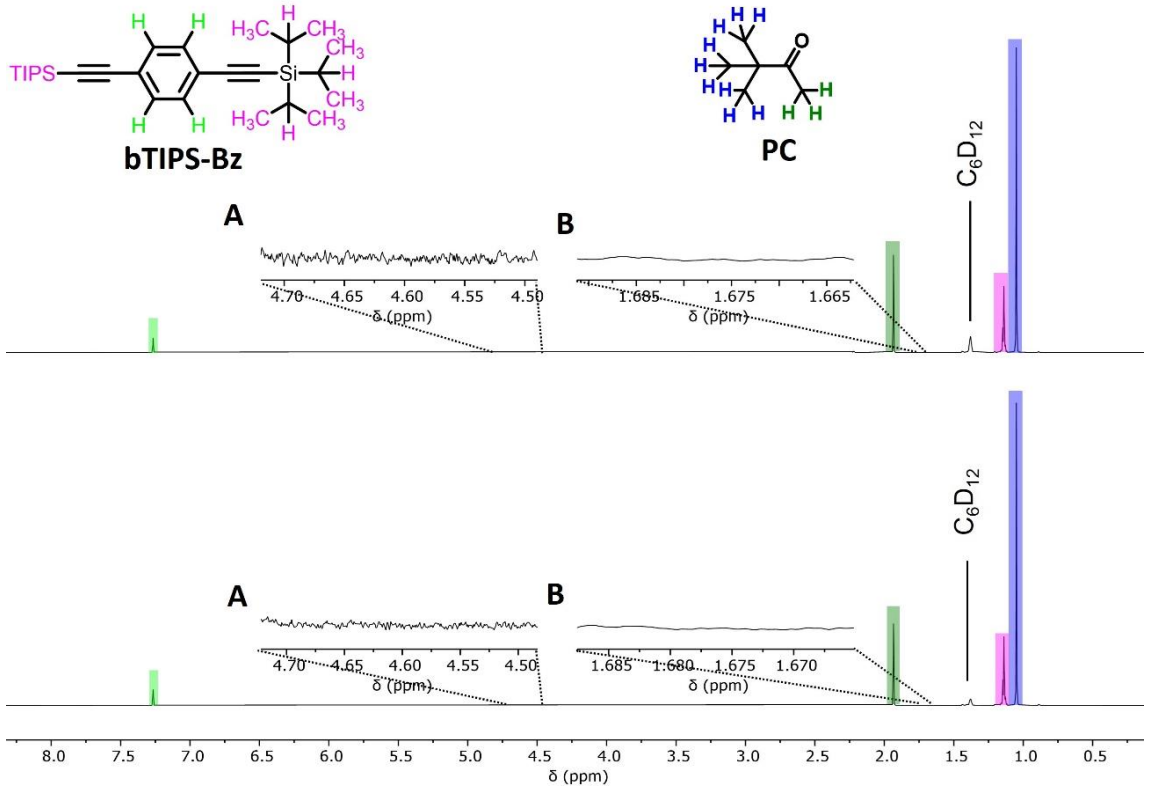

Figure S27. ^{1}H NMR experiment of 10 mM **bTIPS-Bz** and 100 mM pinacolone in Ar-saturated cyclohexane:toluene (9:1) before (top panel) and after (bottom panel) 30 min of irradiation at 447 nm with 1.1 W. Insets: ^{1}H NMR region of isobutylene as a stable product of the UC-FRET-driven Norrish reaction. A) septet region; B) triplet region.

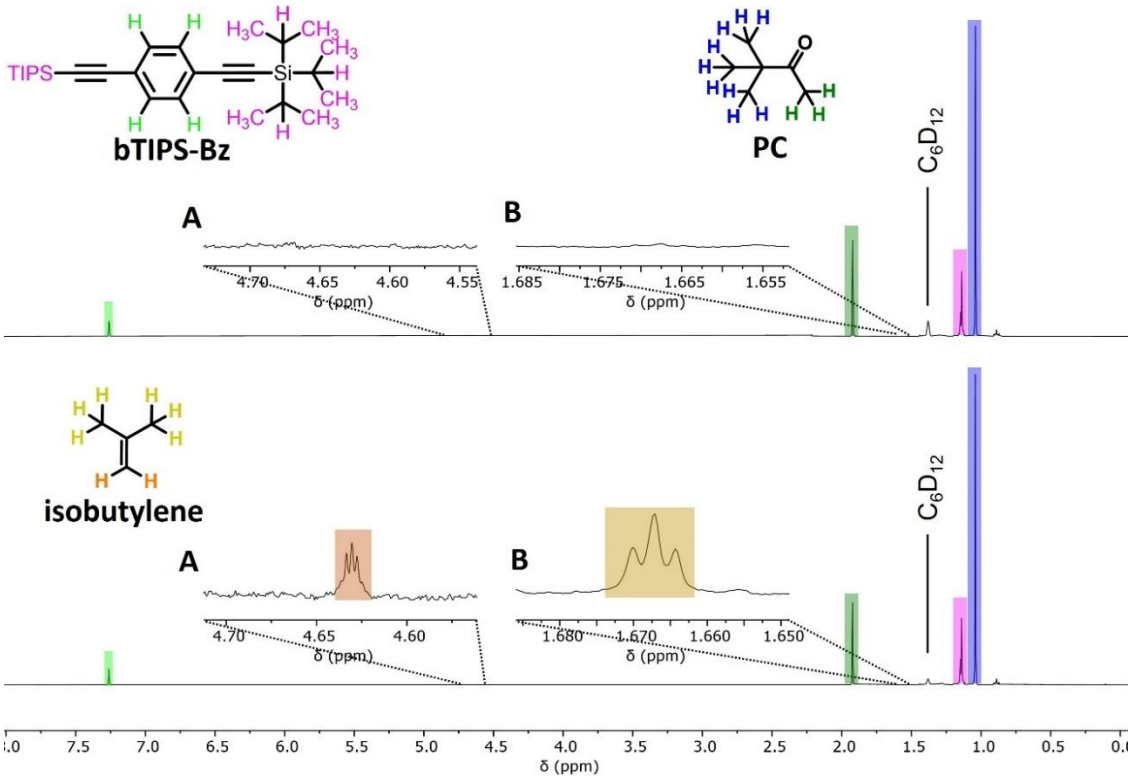

Figure S28. ^{1}H NMR experiment of 10 mM **bTIPS-Bz**, 100 µM **4CzIPN**, and 100 mM pinacolone in Ar-saturated cyclohexane:toluene (9:1) before (top panel) and after (bottom panel) 30 min of irradiation at 447 nm with 1.1 W. Insets: ^{1}H NMR region of isobutylene as a stable product of the UC-FRET-driven Norrish reaction. A) septet region; B) triplet region.[12]

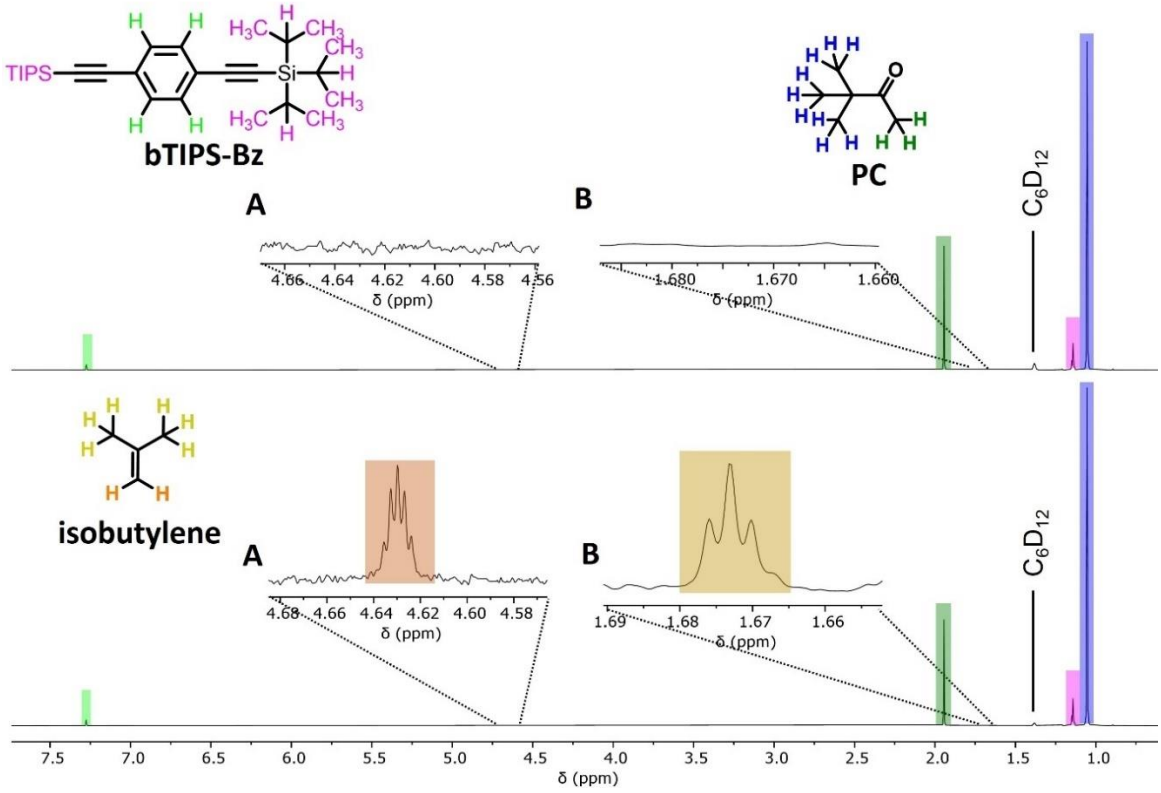

Figure S29. ^{1}H NMR experiment of 10 mM **bTIPS-Bz**, 100 µM **4CzIPN**, and 100 mM pinacolone in Ar-saturated cyclohexane:toluene (9:1) before (top panel) and after (bottom panel) 1 h of irradiation at 440 nm with two LEDs. Insets: ^{1}H NMR region of isobutylene as a stable product of the UC-FRET-driven Norrish reaction. A) septet region; B) triplet region.[12]

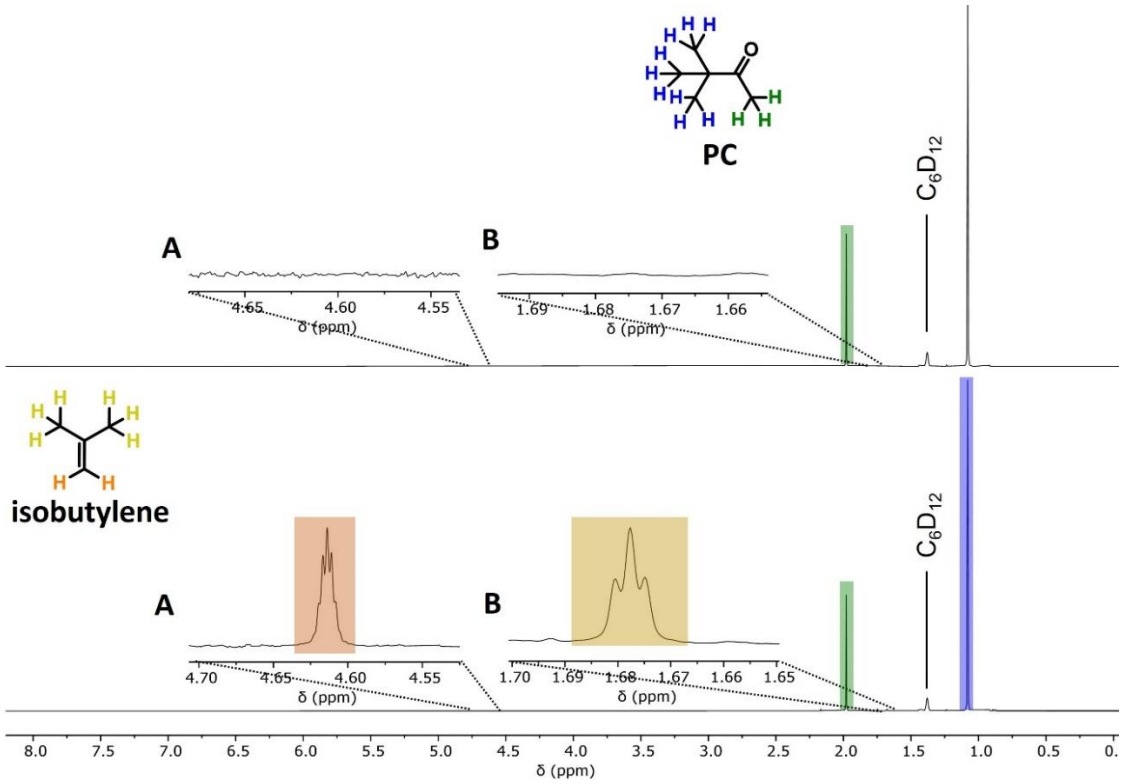

Figure S30. ^{1}H NMR experiment of 100 mM pinacolone in Ar-saturated cyclohexane before (top panel) and after (bottom panel) 15 min of irradiation with a UV lamp (Benda, NU-4 KL, λ = 254 nm). In contrast to the setup shown in Figure S3 with direct NMR tube irradiation, a quartz cuvette has been used for these irradiation experiments to ensure that the UV photons penetrate the reaction flask. Insets: ^{1}H NMR region of isobutylene as a stable product of the UC-FRET-driven Norrish reaction. A) septet region; B) triplet region.[12]

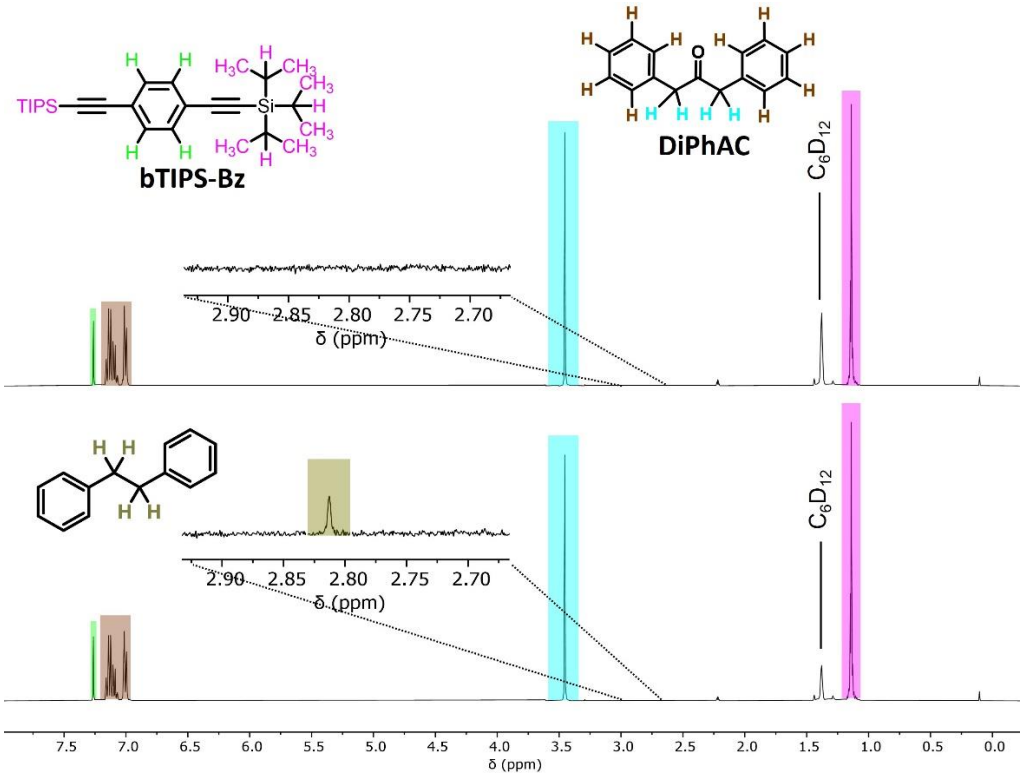

Figure S31. ^{1}H NMR experiment of 10 mM **bTIPS-Bz**, 100 µM **4CzIPN**, and 50 mM 1,3-diphenylacetone in Ar-saturated cyclohexane:toluene (9:1) before (top panel) and after (bottom panel) 1 h of irradiation at 440 nm with two LEDs (with the setup shown in Figure S3). Inset: ^{1}H NMR region of 1,2-diphenylethane as a stable product of the UC-FRET-driven Norrish reaction.

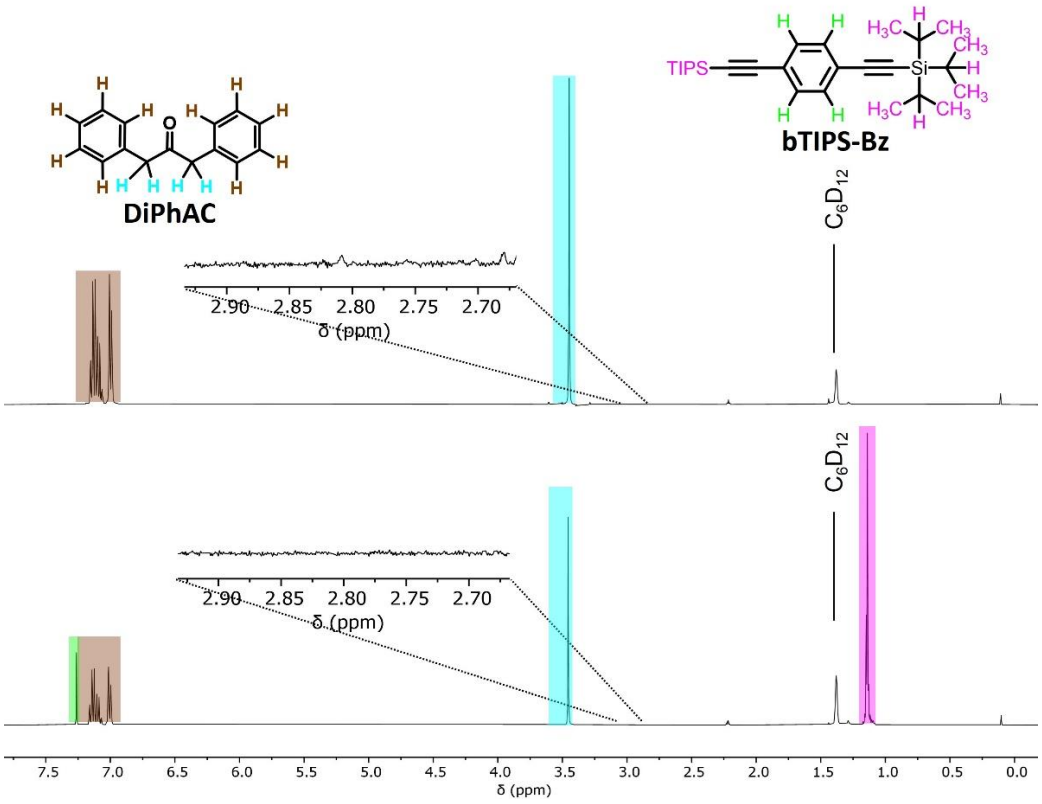

Figure S32. ^{1}H NMR experiment of 10 mM **bTIPS-Bz** with 50 mM 1,3-diphenylacetone (top panel) and 100 µM **4CzIPN** with 50 mM 1,3-diphenylacetone (bottom panel) in Ar-saturated cyclohexane:toluene (9:1) after 1 h of irradiation at 440 nm with two LEDs (control experiments). Inset: ^{1}H NMR region of 1,2-diphenylethane as a stable product of the UC-FRET-driven Norrish reaction.

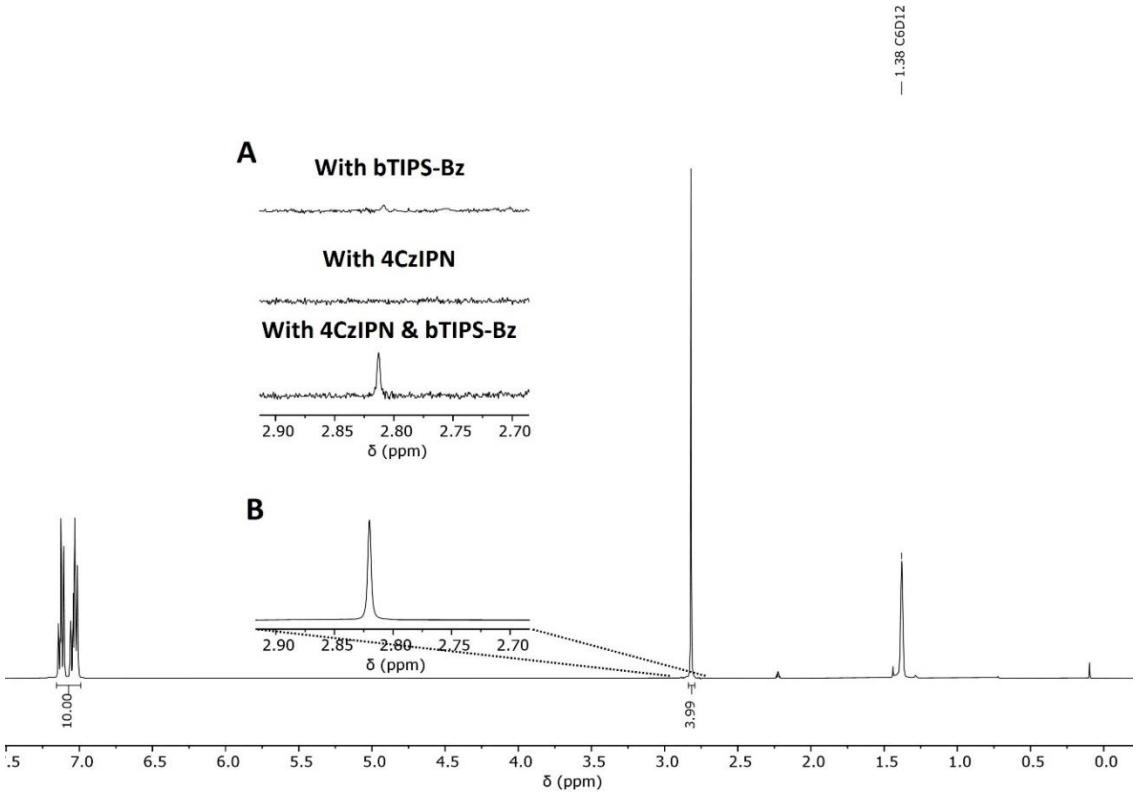

Figure S33. ^{1}H NMR of 1,2-diphenylethane in cyclohexane:toluene (9:1). Insets: ^{1}H NMR region of benzylic hydrogens. A) ^{1}H NMR spectra of irradiation and control experiments (taken from Figures S31 and S32). The signal was scaled to the benzylic hydrogens of 1,3-diphenylacetone. B) ^{1}H NMR of an authentic sample of the 1,2-diphenylethane reference.

8.3 Gas chromatography and mass spectrometry

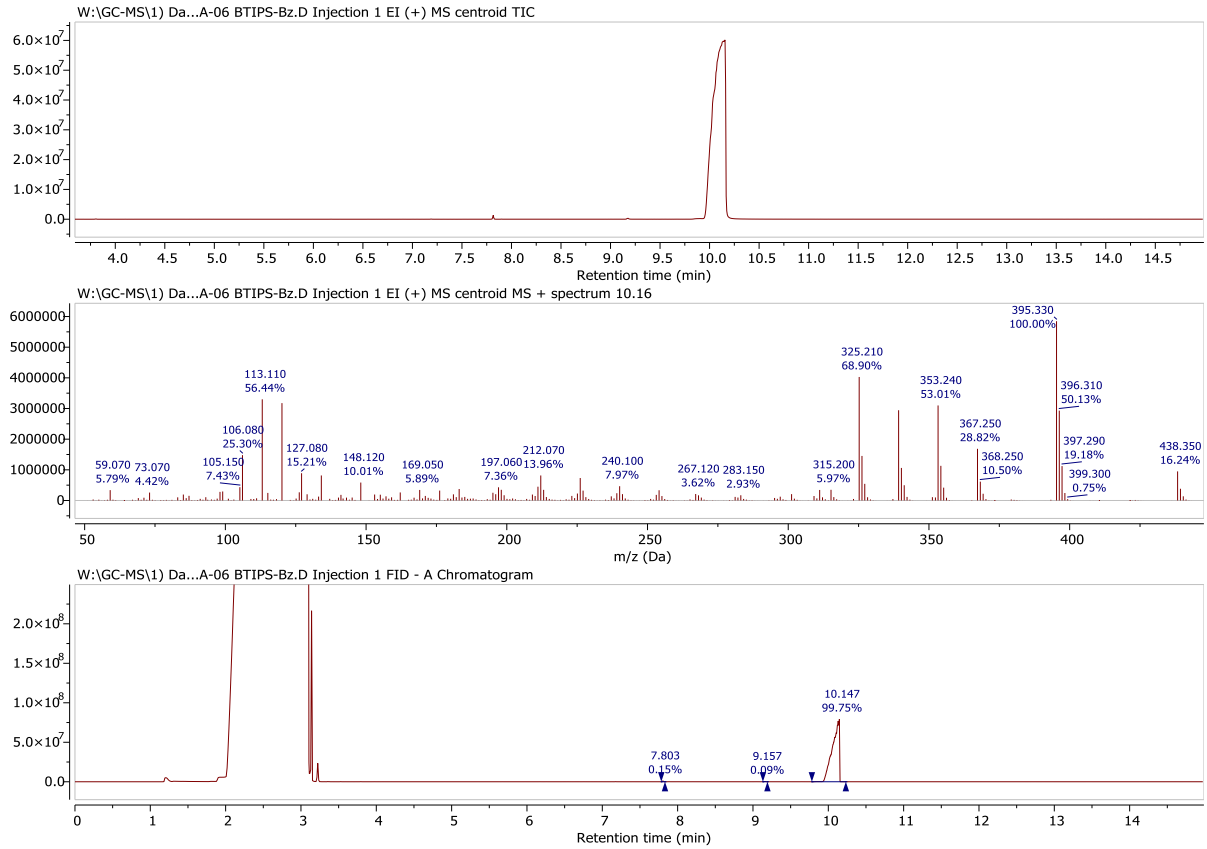

Figure S34. GC analysis and EI-MS spectrum of **bTIPS-Bz**.

9. Supporting references

[1] M. Montalti, A. Credi, L. Prodi, M. T. Gandolfi, J. Michl, V. Balzani, *Handbook of photochemistry*, CRC/Taylor & Francis, Boca Raton, **2006**.

[2] T. J. B. Zähringer, M.-S. Bertrams, C. Kerzig, *J. Mater. Chem. C* **2022**, *10*, 4568.

[3] J. R. Lakowicz, *Principles of fluorescence spectroscopy*, Springer, New York, NY, **2006**.

[4] N. Harada, Y. Sasaki, M. Hosoyamada, N. Kimizuka, N. Yanai, *Angew. Chem. Int. Ed.* **2021**, *60*, 142.

[5] a) B. Feng, Y. Yang, J. You, *Chem. Commun.* **2020**, *56*, 790; b) E. A. Ziemann, J. B. Mietner, M. Deffner, N. van Steerteghem, K. Clays, C. Herrmann, J. Heck, *Eur. J. Inorg. Chem.* **2015**, *2015*, 1111.

[6] H. Uoyama, K. Goushi, K. Shizu, H. Nomura, C. Adachi, *Nature* **2012**, *492*, 234.

[7] M. J. Frisch, G. W. Trucks, H. B. Schlegel, G. E. Scuseria, M. A. Robb, J. R. Cheeseman, G. Scalmani, V. Barone, B. Mennucci, G. A. Petersson, H. Nakatsuji, M. Caricato, X. Li, H. P. Hratchian, A. F. Izmaylov, J. Bloino, G. Zheng, J. L. Sonnenberg, M. Hada, M. Ehara, K. Toyota, R. Fukuda, J. Hasegawa, M. Ishida, T. Nakajima, Y. Honda, O. Kitao, H. Nakai, T. Vreven, J. Montgomery, J. A., J. E. Peralta, F. Ogliaro, M. Bearpark, J. J. Heyd, E. Brothers, K. N. Kudin, V. N. Staroverov, R. Kobayashi, J. Normand, K. Raghavachari, A. Rendell, J. C. Burant, S. S. Iyengar, J. Tomasi, M. (Ed.) *Gaussian Inc. Wallingford CT*, **2009**.

[8] a) V. Gray, A. Dreos, P. Erhart, B. Albinsson, K. Moth-Poulsen, M. Abrahamsson, *Phys. Chem. Chem. Phys.* **2017**, *19*, 10931; b) C. Fischer, C. Kerzig, B. Zilate, O. S. Wenger, C. Sparr, *ACS Catal.* **2020**, *10*, 210; c) L. Vaghi, F. Rizzo, J. Pedrini, A. Mauri, F. Meinardi, U. Cosentino, C. Greco, A. Monguzzi, A. Papagni, *Photochem. Photobiol. Sci.* **2022**, *21*, 913.

[9] J. P. Doering, *J. Chem. Phys.* **1969**, *51*, 2866.

[10] I. B. Berlman, *Handbook of fluorescence spectra of aromatic molecules. 2.ed*, Academic Press, New York, N., **1971**.

[11] F. B. Dias, T. J. Penfold, A. P. Monkman, *Methods Appl. Fluoresc.* **2017**, *5*, 12001.

[12] Steven J. Peters, Trisha M. Blood, Mark E. Kassabaum, *Eur. J. Org. Chem.* **2009**, *2009*, 6104.

10.13 Electronic Supplementary Information for Project [L]

Supplementary Information (SI) for ChemComm.
This journal is © The Royal Society of Chemistry 2025

Electronic Supplementary Information for

Pushing the Limit of Triplet-Triplet Annihilation Photon Upconversion Towards the UVC Range

Till J. B. Zähringer,[a] Corinna Heusel,[b] Matthias Schmitz,[a] Frank Glorius[b] and Christoph Kerzig*[a]

[a] Department of Chemistry, Johannes Gutenberg University Mainz, Duesbergweg 10–14, 55128, Mainz, Germany.
[b] Organisch-Chemisches Institut, University of Münster, Corrensstraße 36, 48149, Münster, Germany.

Email: ckerzig@uni-mainz.de

Contents

General experimental details and methods 2
1.1 Materials 2
1.2 Steady-state measurements 2
1.3 Determination of fluorescence quantum yields 2
1.4 Laser flash photolysis 2
1.5 Fluorescence lifetime measurements 3
1.6 Chromatography 3
1.7 NMR spectroscopy 3
1.8 Mass spectrometry 3
2. Synthetic procedures 3
3. DFT calculations 5
4. Additional spectroscopic measurements 5
4.1 Triplet state lifetime of TIPS-Bz 5
4.2 Control experiments 6
4.3 Photophysical properties of benzene and the TIPS-ethynyl substituted benzenes 7
4.4 Optical power dependent UC measurements of the TIPS-Bz–Ir UC system 8
4.5 Estimation of UC quantum yield of the TIPS-Bz–Ir system 9
5. Spectroscopic characterization of the 4tBu-TIPS-Bz–Ir UC system 10
5.1 Photostability measurements of TIPS-Bz–Ir and 4tBu-TIPS-Bz–Ir 11
6. NMR and FD mass spectra 12
7. References 14

General experimental details and methods

1.1 Materials

Unless specifically mentioned, all chemicals used for synthesis, irradiation experiments, or optical spectroscopy were commercially obtained and used as received. Tetrahydrofuran, 99.7%, VWR; (triisopropylsilyl)acetylene, 97%, Alfa Aesar; bis(triphenylphosphine)palladium(II) dichloride, 98%, Acros Organics; copper(I) iodide, 99.9%, Alfa Aesar; triphenylphosphine, 99%, Sigma-Aldrich; diisopropylamine, 99.9%, Sigma-Aldrich; bromobenzene, Sigma-Aldrich, 99%; 4-tert-butylbromobenzene, 97%, Avocado; cyclohexane, >99.5%, VWR; benzene, Sigma-Aldrich, 99.9%; acetonitrile, 99.7%, VWR, sodium sulfate, 99%, Acros Organics; $CDCl_3$, 99.8%, Deutero.

Argon from Nippon Gases (5.0) was used for removing dissolved oxygen before all experiments related to optical spectroscopy.

fac-[Ir(CF_3-pmb)$_3$][1] was synthesized according to a literature procedure by Glorius and Guldi.[2]

1.2 Steady-state measurements

Steady-state emission measurements at room temperature were performed using a Perkin Elmer FL-6500 spectrometer. Absorption spectra were recorded with a Perkin Elmer LAMBDA 365 UV-Vis spectrophotometer. All spectra were recorded at room temperature (295 ± 3 K) using quartz glass cuvettes. Emission spectra were corrected regarding the wavelength-dependent sensitivity of the instrument. Low concentrations were used to eliminate filter effects.

1.3 Determination of fluorescence quantum yields

The fluorescence quantum yield of TIPS-Bz was determined in relation to a reference system "ref" (naphthalene in cyclohexane, Φ = 0.23)[3] by the comparison of their respective fluorescence emission spectra. In equation (1) Φ_{Fl} depicts the quantum yield, I the fluorescence intensity integrated over the wavenumber, A the absorption at the irradiation wavelength, and n the refractive index of the solvent of the corresponding system taken from literature.[3] The fluorescence quantum yield for TIPS-Bz was measured at four different excitation wavelengths (250, 255, 260 and 265 nm) and averaged over all results. The systems used to determine the fluorescence quantum yields were prepared with an optical density below 0.1 at the irradiation wavelengths to circumvent filter effects.

$$\phi_{\mathrm{Fl}} = \phi_{\mathrm{Fl,ref}} \cdot \frac{I}{I_{\mathrm{ref}}} \cdot \frac{A_{\mathrm{ref}}}{A} \cdot \frac{n^2}{n_{\mathrm{ref}}^2} \quad (1)$$

1.4 Laser flash photolysis

The LP980KS system from Edinburgh Instruments, equipped with a Quantel Nd:YAG laser (Q-smart 450), was used for transient absorption and time-resolved emission spectroscopy. The laser's frequency-tripled output at 355 nm served as the excitation source, delivering pulses of ~5 ns duration at a repetition rate of 10 Hz. If not stated otherwise, the pulse energy applied in transient absorption and emission experiments was 20 mJ. Transient absorption spectra were recorded using an Andor iCCD camera, while kinetic traces at selected wavelengths were obtained via a photomultiplier tube. To ensure consistent laser pulse energy across experiments, power measurements were conducted before, during and after each series of experiments using a Gentec-eo pyroelectric detector with an attenuator (QE25LP-S-MB-QED-D0) and the Integra software was used for evaluation. Spectroscopic experiments were performed at 293 K with a temperature-controlled cuvette holder. Unless otherwise noted, transient absorption spectra were integrated over 100 ns. For detection wavelengths exceeding 600 nm, longpass filters (385 nm or 400 nm, Newport) were used to eliminate contributions from second-order signals.

1.5 Fluorescence lifetime measurements

The *mini-τ* setup from Edinburgh Instruments (time-correlated single photon counting (TCSPC) technique) equipped with a pulsed LED (EPLED-300, excitation at ~293 nm, pulse width ~ 1 ns, bandwidth = 10.7 nm) was employed for fluorescence lifetime measurements of TIPS-Bz at 293 K.

1.6 Chromatography

For **TIPS-Bz** standard liquid column chromatography separation silica gel 60 M (0.040-0.063 mm Macherey-Nagel GmbH & Co., Düren, Germany) was used. Thin layer chromatography (TLC) was performed using "DC Kieselgel 60 F254" (Merck KGaA, Darmstadt, Germany) on aluminum and a UV lamp (Benda, NU-4 KL, λ = 254 nm and 365 nm, Wiesloch, Germany) was employed for detection. Reversed-phase column chromatographic purification was carried out for **4tBu-TIPS-Bz** using the Isolera One automated chromatography system, which includes the Isolera™ Dalton detector from Biotage. A SNAP Cartridge KP-C18-HS from Biotage was used as the column material. The resulting R_f values are given relative to the solvent.

1.7 NMR spectroscopy

NMR spectra of **TIPS-Bz** and **4tBu-TIPS-Bz** were recorded with a multinuclear magnetic resonance spectrometer of the type AV II 400 (Bruker, Karlsruhe, Germany) was employed. The chemical shifts are given as *δ*-values in ppm and they were referenced relative to the residue signal of the non-deuterated solvent.[4] The following abbreviations were used: singlet (s), doublet (d), multiplet (m).

1.8 Mass spectrometry

Low-resolution FD mass spectra for **TIPS-Bz** and **4tBu-TIPS-Bz** were acquired using a Thermo Fisher DFS mass spectrometer equipped with an LIFDI upgrade from Linden ChroMasSpec GmbH, configured for FD mode. Ion source parameters were set as follows: acceleration voltage, +5 kV; counter electrode voltage, -5 kV; reference inlet temperature, 80°C; ion source temperature, 50°C; scan duration: 8 s; interscan delay: 200 ms. CarboTec 10 µm Allround emitter was used, operating at 75 mA. Prior to sample runs, new emitters underwent a preconditioning process involving 2 hours of heating with emitter heating current. Toluene was used as a solvent to deposit the sample onto the emitter. DFS MS scanned from m/z 100 to 1000 at a rate of 8 s/decay.

2. Synthetic procedures

The TIPS-ethynyl-functionalized benzenes were synthesized according to the Sonogashira coupling reaction analogous to the preparation of similar aromatic compounds.[5–7] Exact quantities are listed for each benzene derivative below. The bromobenzene, $Pd(PPh_3)_2Cl_2$, CuI, PPh_3, and dry THF were added to a flame-dried round-bottom flask under argon flow. The flask was equipped with a condenser column. Diisopropylamine was added to the solution under constant stirring. The flask was then heated to 70˚C and (triisopropylsilyl)acetylene was added dropwise to the mixture. The mixture was held at 70˚C for 12 h under argon atmosphere. The completion of the reaction was tested with TLC. After cooling, the mixture was filtered and the solvent was removed under reduced pressure. The residue was redissolved in chloroform and washed twice with deionized water and twice with brine. The organic layer was dried with Na_2SO_4 and the solvent was removed under reduced pressure. If not stated otherwise, the product was purified via column chromatography (neat cyclohexane). NMR spectra (see below) of all TIPS-ethynyl-benzenes derivatives agree with those reported in the literature.[8]

Triisopropyl(phenylethynyl)silane (TIPS-Bz): **TIPS-Bz** was used from a prior batch, for which the preparation was as follows.[7] 675 mg bromobenzene (4.30 mmol), 18.26 mg $Pd(PPh_3)_2Cl_2$ (0.026 mmol), 13.1 mg CuI (0.069 mmol), 18 mg PPh_3 (0.069 mmol), 28 mL dry THF, 7 mL diisopropylamine and 0.93 mL (triisopropylsilyl)acetylene (4.13 mmol); yield = 354 mg, 1.37 mmol (32%).

A colorless liquid was obtained from column chromatography, which was then distilled under vacuum (10^{-2} mbar) at 80°C.

R_f(cyclohexane) = 0.75

^{1}H NMR (400 MHz, $CDCl_3$): δ [ppm] = 7.29-7.32 (m, 3H), 7.47-7.49 (m, 2H), 1.13 (pseudo-s, 21H).

^{13}C NMR (400 MHz, $CDCl_3$): δ [ppm] = 132.2, 128.4, 128.32, 123.7, 107.2, 90.6, 18.8, 11.5.

MS (FD): m/z [int. I %] = 258.4 [M^+] (100 %); 259.3 (22%); 260.4.4 (5%). Calculated for $C_{17}H_{26}Si$ = 258.2.

NMR spectra are shown in the supporting information document of Ref[7]. Recently recorded NMR and UV/Vis spectra are unchanged compared to those presented in Ref[7].

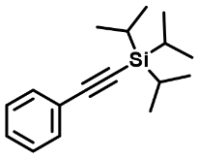

((4-(tert-Butyl)phenyl)ethynyl)triisopropylsilane (4tBu-TIPS-Bz):

1832 mg 4-tert-butylbromobenzene (8.6 mmol), 73.0 mg $Pd(PPh_3)_2Cl_2$ (0.104 mmol), 52.4 mg CuI (0.28 mmol), 72.2 mg PPh_3 (0.28 mmol), 60 mL dry THF, 27 mL diisopropylamine and 3.7 mL (triisopropylsilyl)acetylene (16.92 mmol); yield = 950 mg, 3.02 mmol (32%).

A colorless liquid was obtained after distilliation under vacuum (1.4 10^{-2} mbar) at 200°C. Further purification was achieved by reverse-phase column chromatography: acetonitrile and water were employed as the mobile phase. The crude product was dissolved in DMSO and applied to the column. Chromatographic separation was performed using a gradient of acetonitrile from 10% to 100% over approximately 10 minutes.

We thank Prof. Till Opatz for allowing us to use their equipment for the final purification step.

R_f(water/acetonitrile (1/9)) = 0.80

^{1}H NMR (400 MHz, $CDCl_3$): δ [ppm] = 7.41-7.44 (m, 2H), 7.30-7.34 (m, 2H), 1.32 (s, 9H), 1.13 (s, 21).

^{13}C NMR (400 MHz, $CDCl_3$): δ [ppm] = 151.7, 131.9, 125.3, 120.7, 107.4, 89.8, 34.9, 31.3, 18.9, 11.5.

MS (FD): m/z [int. I %] = 314.4 [M^+] (100 %); 315.4 (24%); 316.4 (5%). Calculated for $C_{21}H_{34}Si$ = 314.2.

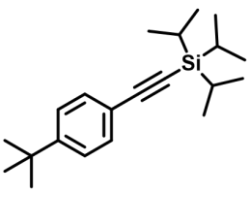

3. DFT calculations

Quantum-chemical calculations were performed with the program Orca 6.0[9] using the functional B3LYP and 6-311+G(d,p) as basis set. After each geometry optimization, vibrational frequencies were calculated. In each case, no imaginary vibration frequencies were obtained, indicating convergence on minimum structures. Geometry optimization of the triplet state was performed starting from the energy-minimized singlet ground state geometry as initial guess. The triplet state energy (adiabatic) was determined by subtracting the energy of the optimized triplet state from the energy of the optimized singlet ground state. This approach has been previously validated as an accurate method for estimating experimental triplet state energies in studies of TIPS-ethynyl-substituted benzenes.[7] To determine electronic excitation energies and oscillator strengths of the lowest 50 transitions, TD-DFT calculations were performed with the previously geometry-optimized structure at the same level of theory. Additional single-point calculations were carried out to obtain the spin densities of the optimized triplet state based on Mulliken population analysis. The structures and spin densities (iso value: 0.005) were displayed using the software Avogadro1.2.0.[10] The color code for the atoms in the ball and stick representation is as follows: carbon (black), hydrogen (white), silicon (petrol blue). In the depiction of spin densities, blue-colored surfaces denote positive spin densities, whereas red-colored surfaces denote negative spin densities. We were unable obtain a minimum structure for **4tBu-TIPS-Bz**. However, by replacing the TIPS group with a TMS group, minimum structures were found for both the singlet and triplet states. Comparative computations of **TMS-Bz** showed that this substitution change at the silyl unit has a small influence on the obtained triplet energy (0.01 eV difference).[7] Based on this result, the triplet energy of **4tBu-TMS-Bz** was used to extrapolate the triplet energy of **4tBu-TIPS-Bz,** yielding 3.02 eV.

Table S1: Computed triplet state energies of TIPS-ethynyl- and TMS-ethynyl-substituted benzenes.

Compound	E_T(DFT)[a] / eV	E_T(lit.)[b] / eV	E_T(DFT,corrected)[c] / eV
Benzene (Bz)	3.83	3.9	
TIPS-Bz	3.01		3.06
TMS-Bz	3.02		3.07
4tBu-TIPS-Bz	n.a.		3.02[d]
4tBu-TMS-Bz	2.98		3.03

[a] DFT-calculated triplet energy at the B3LYP/6-311+G(d,p) level of theory. [b] Experimental triplet energy from Ref[11]. [c] Calculated triplet energy corrected by the underestimation factor from benzene. [d] Estimated value from comparison of TIPS and TMS derivatives.

4. Additional spectroscopic measurements

4.1 Triplet state lifetime of TIPS-Bz

The triplet lifetime of **TIPS-Bz**, which combines the TTA decay constant (k_{TTA}) and the natural triplet lifetime, was measured for a solution of 25 µM **Ir** and 2 mM **TIPS-Bz** in Ar-saturated benzene after 355 nm laser pulses. The triplet lifetime of any given annihilator will strongly depend on the excitation intensity as k_{TTA} depends on the triplet state concentration.[12] For these selected conditions a monoexponential fit yielded a lifetime of 34 µs.

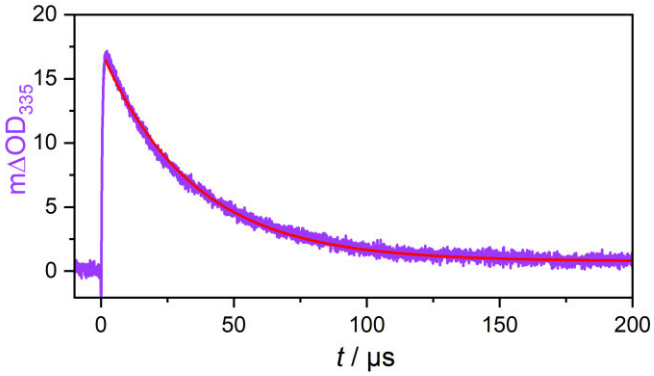

Figure S1: Kinetic TA measurements of a solution of 25 µM **Ir** and 2 mM **TIPS-Bz** in Ar-saturated benzene after 355 nm laser pulse excitation.

4.2 Control experiments

A common loss pathway in TTA-UC is the formation of singlet excimers, which leads to a reduction in emission energy. However, the irradiation of **TIPS-Bz** at 280 nm across a wide concentration range (80 µM to 16 mM) yielded identical emission spectra (Figure S2), indicating no detectable excimer formation.

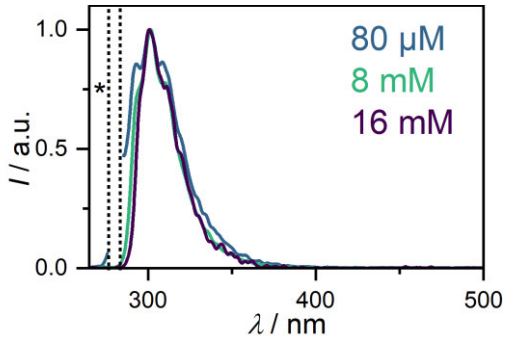

Figure S2: Emission spectrum of **TIPS-Bz** in Ar-saturated benzene after excitation at 280 nm with varying concentrations. Shorter wavelengths could not be used for excitation owing to the solvent absorption. The region around 280 nm (indicated with *) was removed owing to stray light artifacts.

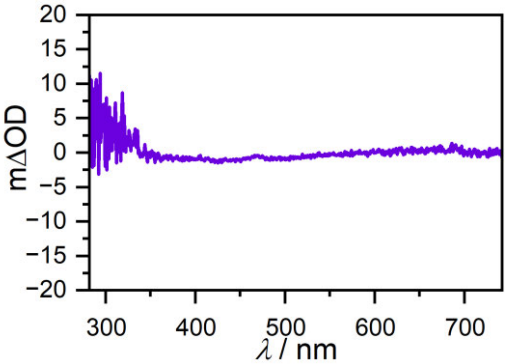

Figure S3: TA spectrum of 25 µM **Ir** and 2 mM **TIPS-Bz** recorded 130 µs after 355 nm laser excitation.

4.3 Photophysical properties of benzene and the TIPS-ethynyl substituted benzenes

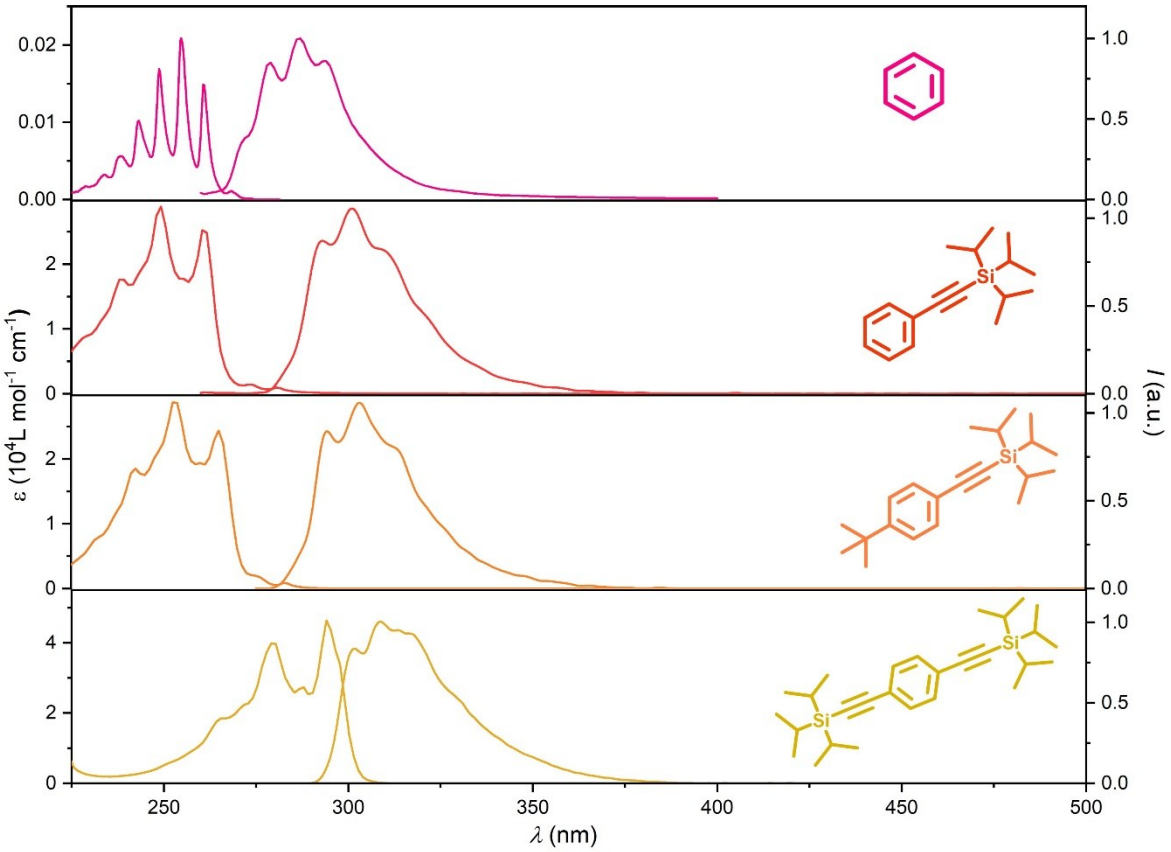

Figure S4: Molar absorption coefficients and emission spectra of benzene (taken from Ref[13]), **TIPS-Bz**, **4tBu-TIPS-Bz** and bTIPS-Bz (taken from Ref[7]) in cyclohexane.

Figure S4 presents the absorption and emission spectra of benzene and the corresponding annihilator structures. Substituting benzene with a TIPS-ethynyl group leads to a pronounced red shift in both spectra (compare Bz, **TIPS-Bz**, and bTIPS-Bz). In contrast, introducing a tert-butyl group at the para position relative to the TIPS-ethynyl group results in only a slight shift in the absorption and emission spectra (compare **TIPS-Bz** and **4tBu-TIPS-Bz**).

Table S2: Key photophysical properties of benzene and derived annihilator structures.

Compound	E_S / eV	Φ_{Fl}	τ_{Fl} / ns	E_T / eV
Benzene	4.76[a]	0.07[b]	34[a]	3.90[c]
TIPS-Bz	4.33	0.19[d]	19.9[d]	3.06[e]
4tBu-TIPS-Bz	4.31	–	14.7[d]	3.02[e]
bTIPS-Bz	4.14[d],[f]	0.48[d],[f]	2.8[d],[f]	2.64[f],[g]

[a] Taken from Ref[3]. [b] Taken from Ref[14,15]. [c] Taken from Ref[11]. [d] Measured in cyclohexane. [e] Obtained by DFT calculations (see Chapter S3). [f] Taken from Ref[7]. [g] Estimated from low temperature emission. DFT-calculated energy: 2.57 eV.

The key photophysical properties determined in this study, along with literature-reported values for these compounds, are summarized in Table S2. In general, increasing the number of TIPS-ethynyl groups lowers the singlet and triplet state energies as well as the fluorescence lifetime, while enhancing the fluorescence quantum yield. Substitution with a tert-butyl group in the para position further reduces the fluorescence lifetime (Figure S5), whereas its effect on the singlet state energy is minimal.

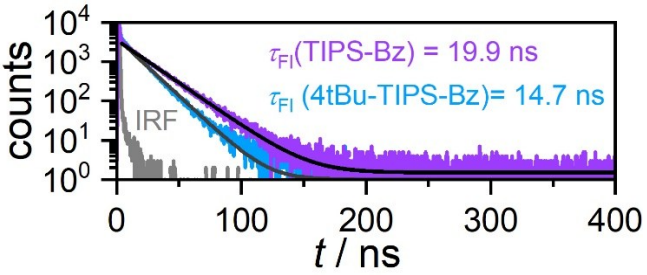

Figure S5: Fluorescence lifetime measurements of **TIPS-Bz** (purple) and **4tBu-TIPS-Bz** (blue) in cyclohexane, which had to be used instead of benzene to avoid solvent-derived background signals.

4.4 Optical power dependent UC measurements of the TIPS-Bz–Ir UC system

The upconversion intensity of the **TIPS-Bz–Ir** system was measured across a range of laser pulse energies (see main text and Figure 4C). The laser intensity was estimated as an optical power density, assuming a pulse duration of approximately 5 ns and an irradiated cuvette area of A = 1.4 cm^2 (see Equation 2). As an example, the optical power density was calculated for a pulse energy of 5.36 mJ:

$$P \approx \frac{Pulse\ energy}{t \times A} = \frac{5.36\ \text{mJ}}{5\ \text{ns} \times 1.4\ \text{cm}^{-2}} = 766\ \text{kW cm}^{-2} \quad (2)$$

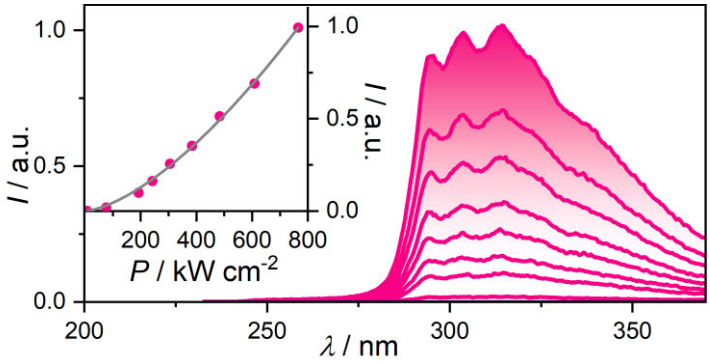

Figure S6: UC emission of 25 µM **Ir** and 2 mM **TIPS-Bz** in Ar-saturated benzene with 355 nm laser pulses with varying intensity. Inset: UC emission plotted against the laser energy recalculated as optical power density.

4.5 Estimation of UC quantum yield of the TIPS-Bz–Ir system

The UC quantum yield (ϕ_{UC}) of the **TIPS-Bz–Ir** system was estimated by comparing the quenched **Ir** emission with the UC emission following 355 nm laser excitation at 23.84 mJ. It was assumed that the emission quantum yield of **Ir** (ϕ_{Ir}), reported as 0.84 in THF, does not differ significantly in benzene.[1] Emission spectra were recorded from a solution containing 25 µM **Ir** and 2 mM **TIPS-Bz** in Ar-saturated benzene, under identical conditions but using different integration time windows. To prevent detector oversaturation, a grey filter (OD 2.0) was employed for integrating the quenched **Ir** emission (I_{quenched}) within the 0–4 µs window post-excitation, which was then compared to the UC emission integrated from 4–204 µs. The quenching efficiency η was determined to be 0.90.

$$\phi_{\mathrm{UC}} \approx \frac{I_{\mathrm{UC}} \times (1-\eta)}{I_{\mathrm{quenched}}} \times \phi_{\mathrm{Ir}} = 0.13\ \%$$

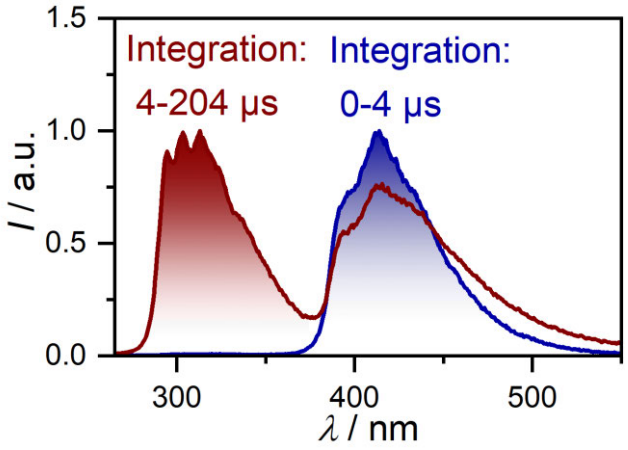

Figure S7: Time-gated emission spectra of 25 µM **Ir** and 2 mM **TIPS-Bz** in Ar-saturated benzene after 355 nm laser pulses.

5. Spectroscopic characterization of the 4tBu-TIPS-Bz–Ir UC system

The compound **4tBu-TIPS-Bz** was characterized as a potential annihilator analogous to **TIPS-Bz** in the main paper. Stern–Volmer quenching studies of **Ir** with **4tBu-TIPS-Bz** in Ar-saturated benzene with 355 nm laser pulses revealed a TTET constant of 3.26 10^8 M^{-1} s^{-1} (Figure S8A). Even though DFT calculations suggested a decreased triplet energy of 3.02 eV with respect to **TIPS-Bz** the TTET constant is significantly lower. The additional sterically demanding group might hamper the required orbital overlap between energy donor and acceptor. The triplet-triplet absorption spectrum for **4tBu-TIPS-Bz** was recorded after complete deactivation of **Ir** (Figure S8B). A concentration of 6.25 µM **Ir** and 1mM **4tBu-TIPS-Bz** was used to minimize filter effects. The spectrum is slightly red-shifted compared to **TIPS-Bz** with a maximum absorption at 314 nm (main paper, Figure 3A). Further experiments were performed with concentration of 25 µM **Ir** and 2 mM **4tBu-TIPS-Bz**. Kinetic traces of ^{3}**4tBu-TIPS-Bz** and 25 µM **Ir** emission were recorded (Figure S8C), displaying concurrent formation and deactivation, respectively. Under the chosen conditions ^{3}**4tBu-TIPS-Bz** has an estimated lifetime of 38 µs, which is displayed in Figure S8D (monoexponentially fitted). A time-gated emission spectrum (integrated 10-210 µs after excitation) shows TTA-UC emission of **4tBu-TIPS-Bz**. However, apart from the sensitizer emission another signal in the UV is also detected that indicates degradation of the UC system. In conclusion, the UC performance of **4tBu-TIPS-Bz** does not benefit from the reduced triplet state energy with respect to **TIPS-Bz**.

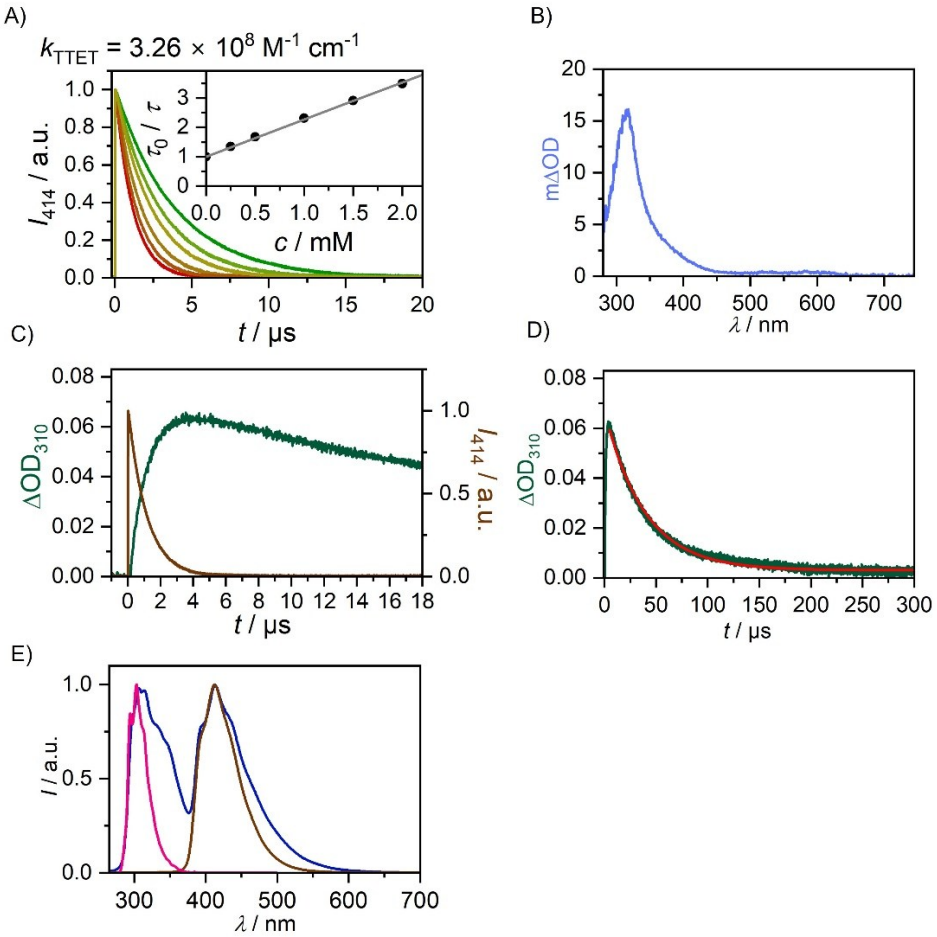

Figure S8: Mechanistic investigations of an Ar-saturated solution of **Ir** and **4tBu-TIPS-Bz** in benzene with 355 nm laser pulses. A) Stern-Volmer analysis with 25 µM **Ir** and varying concentrations of **4tBu-TIPS-Bz**. B) TA spectrum recorded 15 µs after excitation of 6.25 µM **Ir** and 1 mM **4tBu-TIPS-Bz**. C) and D) Kinetic traces of the transient ^{3}**4tBu-TIPS-Bz** and emission of ^{3}**Ir** of 25 µM **Ir** and 2 mM **4tBu-TIPS-Bz**. E) Time-gated emission spectrum of 25 µM **Ir** and 2 mM **4tBu-TIPS-Bz** recorded 10-210 µs after excitation (blue graph), in comparison to the emission of **4tBu-TIPS-Bz** (pink) and **Ir** (brown) after direct excitation at 280 nm.

5.1 Photostability measurements of TIPS-Bz–Ir and 4tBu-TIPS-Bz–Ir

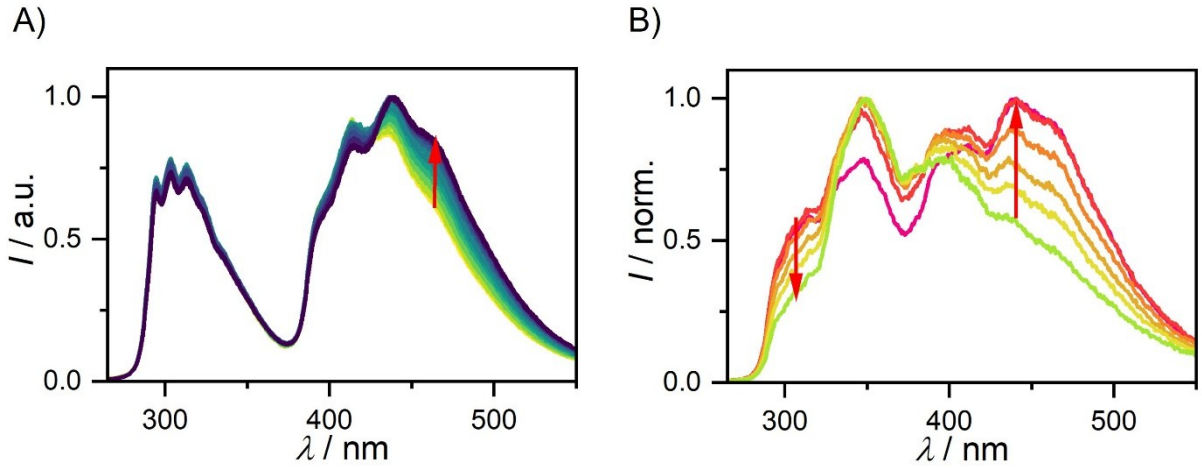

Figure S9: Photostability measurements of **TIPS-Bz–Ir** and **4tBu-TIPS-Bz–Ir** UC systems under 355 nm laser pulses (~20 mJ). A) UC emission of 25 µM **Ir** and 2 mM **TIPS-Bz** in Ar-saturated benzene after individual 355 nm laser pulses (first pulse, yellow; last pulse, dark blue; 100 pulses in total). B) UC emission of 25 µM **Ir** and 2 mM **4tBu-TIPS-Bz** in Ar-saturated benzene over 20 averaged 355 nm laser pulses.

The photostability of the UC systems **TIPS-Bz–Ir** and **4tBu-TIPS-Bz–Ir** under 355 nm laser irradiation was investigated. **TIPS-Bz–Ir** exhibited significantly greater stability, with only minor spectral changes indicating limited degradation (Figure S9A). Moreover, its UC emission intensity remained largely constant over 100 laser pulses. In contrast, the **4tBu-TIPS-Bz–Ir** system showed pronounced degradation, evidenced by strong emission signals likely originating from degradation products (Figure S9B).

6. NMR and FD mass spectra

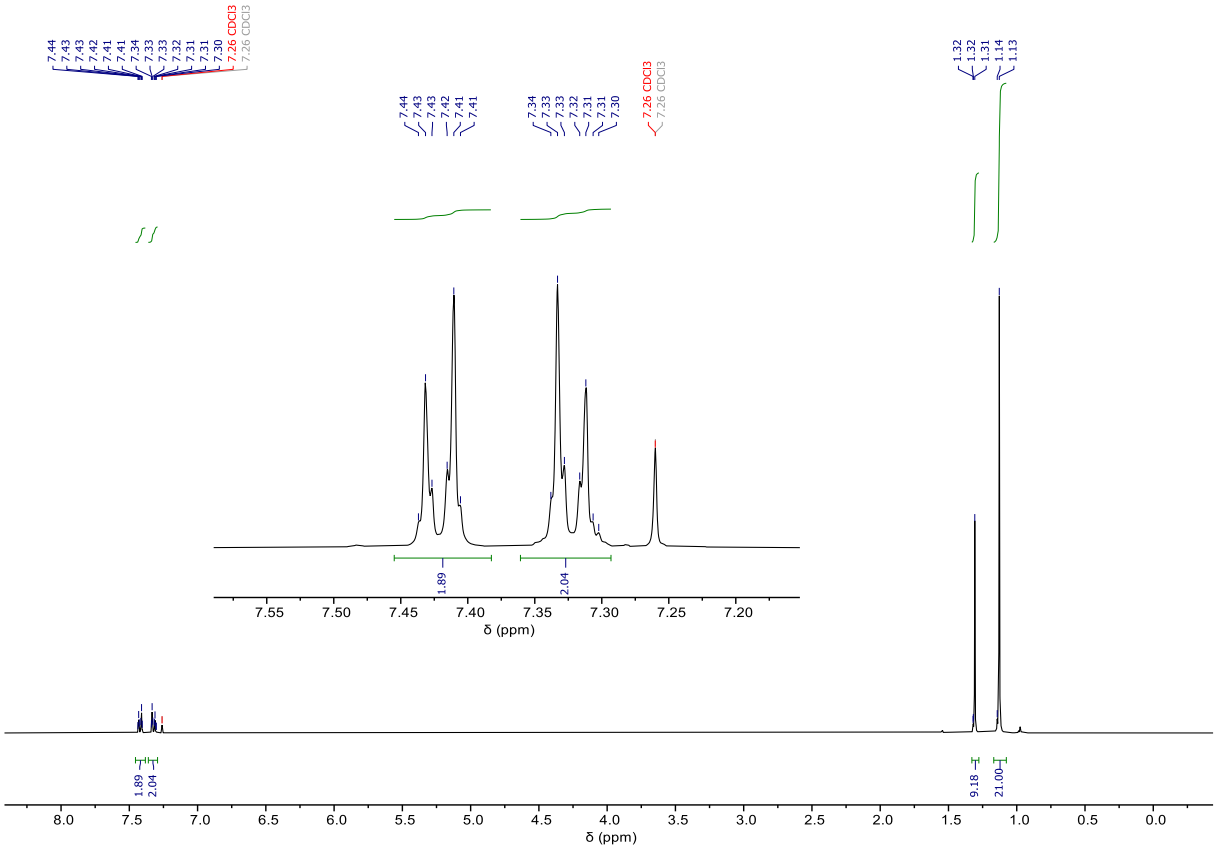

Figure S10: ^{1}H NMR spectrum of **4tBu-TIPS-Bz** in $CDCl_3$.

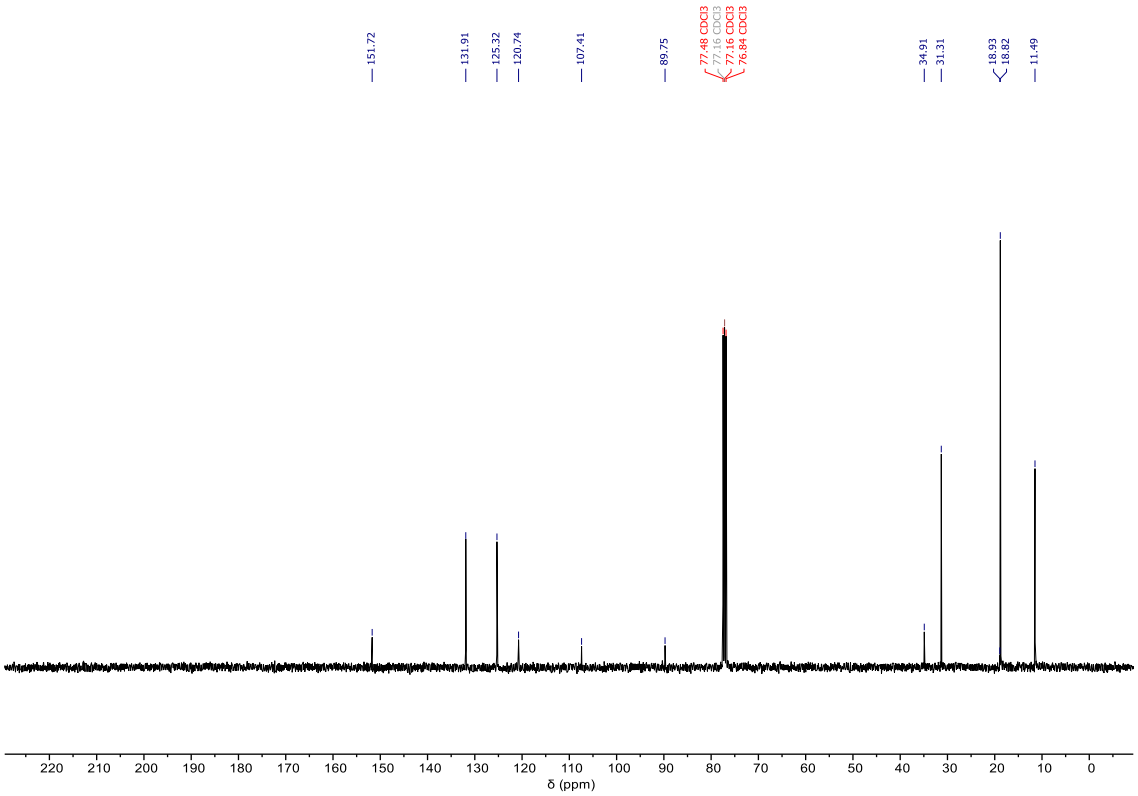

Figure S11: ^{13}C NMR spectrum of **4tBu-TIPS-Bz** in $CDCl_3$.

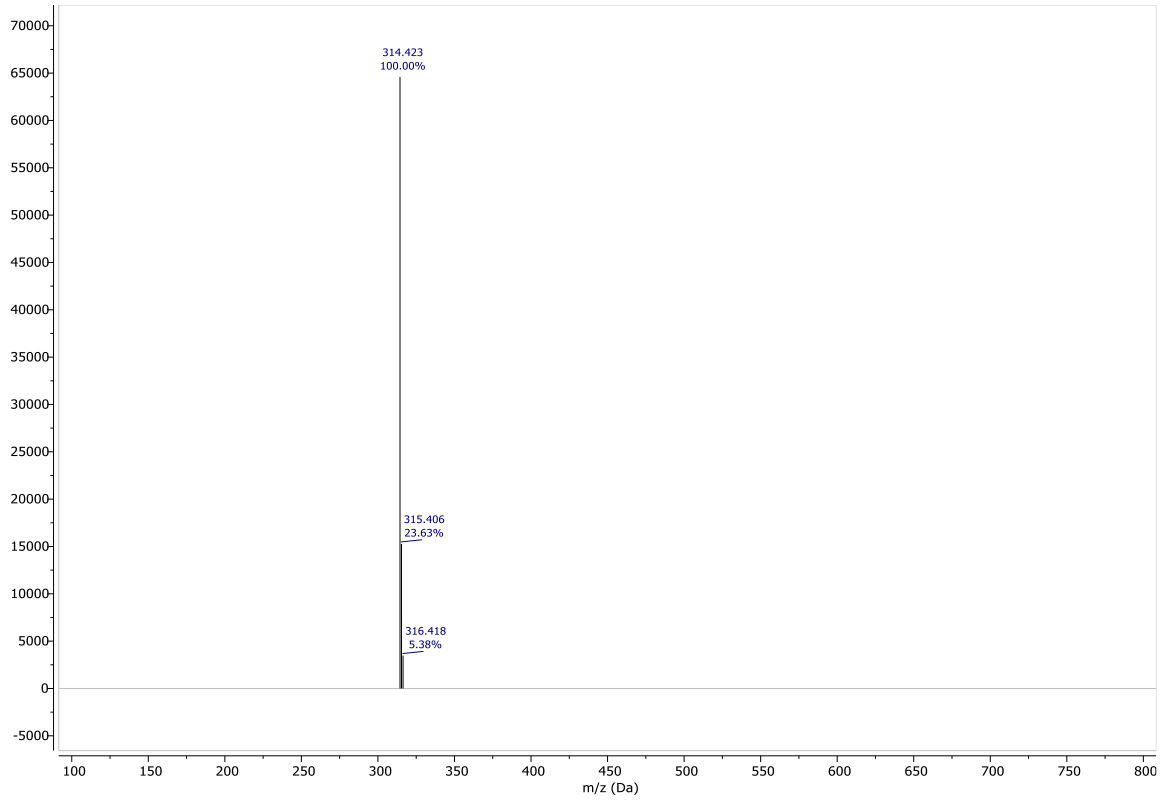

Figure S12: FD mass spectrum of **4tBu-TIPS-Bz**.

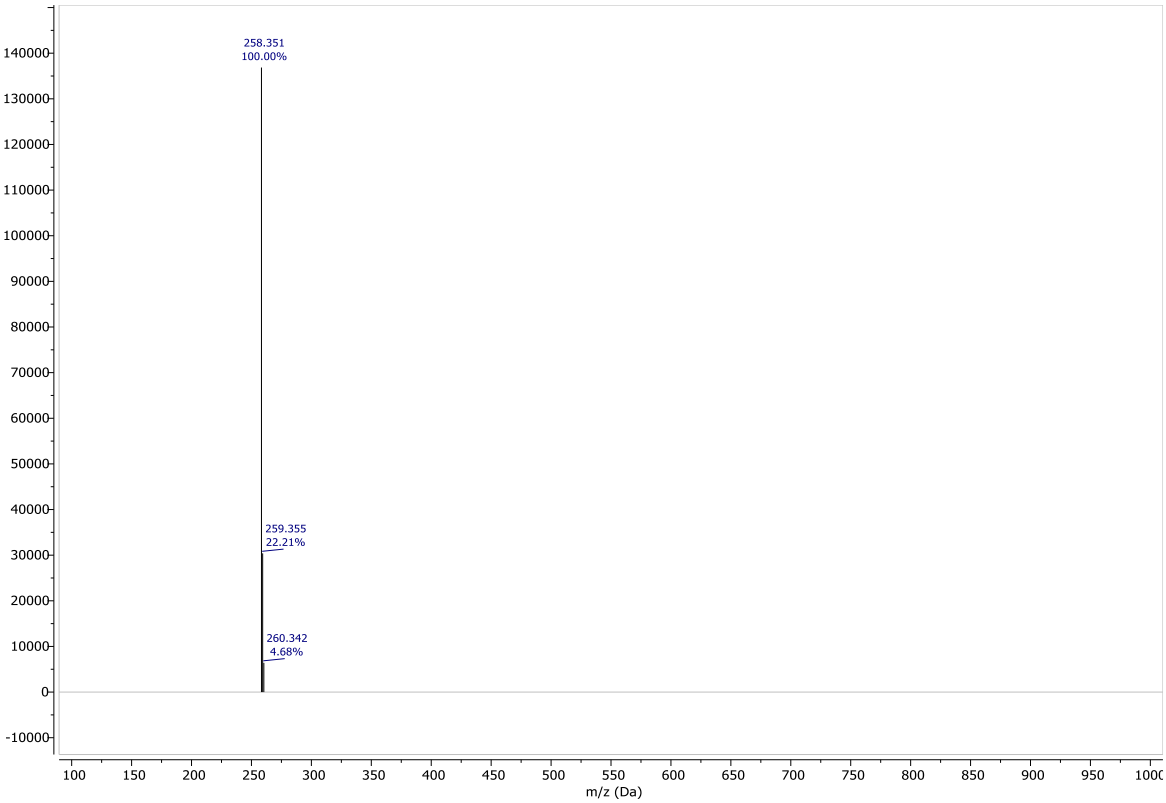

Figure S13: FD mass spectrum of **TIPS-Bz**.

7. References

1. K. Tsuchiya, S. Yagai, A. Kitamura, T. Karatsu, K. Endo, J. Mizukami, S. Akiyama and M. Yabe, *Eur. J. Inorg. Chem.*, 2010, **2010**, 926–933.
2. T. O. Paulisch, L. A. Mai, F. Strieth-Kalthoff, M. J. James, C. Henkel, D. M. Guldi and F. Glorius, *Angew. Chem. Int. Ed.*, 2022, **61**, e202112695.
3. M. Montalti, A. Credi, L. Prodi and M. T. Gandolfi, *Handbook of Photochemistry*, CRC Press, 0 edn., 2006.
4. H. E. Gottlieb, V. Kotlyar and A. Nudelman, *J. Org. Chem.*, 1997, **62**, 7512–7515.
5. N. Harada, Y. Sasaki, M. Hosoyamada, N. Kimizuka and N. Yanai, *Angew. Chem. Int. Ed.*, 2021, **60**, 142–147.
6. T. J. B. Zähringer, M.-S. Bertrams and C. Kerzig, *J. Mater. Chem. C*, 2022, **10**, 4568–4573.
7. T. J. B. Zähringer, J. A. Moghtader, M. Bertrams, B. Roy, M. Uji, N. Yanai and C. Kerzig, *Angew. Chem. Int. Ed.*, 2023, **62**, e202215340.
8. Q. Chen, L. Fu, J. You and Y. Nishihara, *Synlett*, 2021, **32**, 1560–1564.
9. F. Neese, *WIREs Comput. Mol. Sci.*, 2012, **2**, 73–78.
10. M. D. Hanwell, D. E. Curtis, D. C. Lonie, T. Vandermeersch, E. Zurek and G. R. Hutchison, *J. Cheminformatics*, 2012, **4**, 17.
11. J. P. Doering, *J. Chem. Phys.*, 1969, **51**, 2866–2870.
12. Y. Murakami and K. Kamada, *Phys. Chem. Chem. Phys.*, 2021, **23**, 18268–18282.
13. I. B. Berlman, *Handbook of fluorescence spectra of aromatic molecules*, Academic Press, New York, 2d ed., 1971.
14. W. R. Dawson and M. W. Windsor, *J. Phys. Chem.*, 1968, **72**, 3251–3260.
15. M. Luria, M. Ofran and G. Stein, *J. Phys. Chem.*, 1974, **78**, 1904–1909.

11 Curriculum Vitae

[redacted]

[redacted]

[redacted]

[redacted]

[redacted]

[redacted]

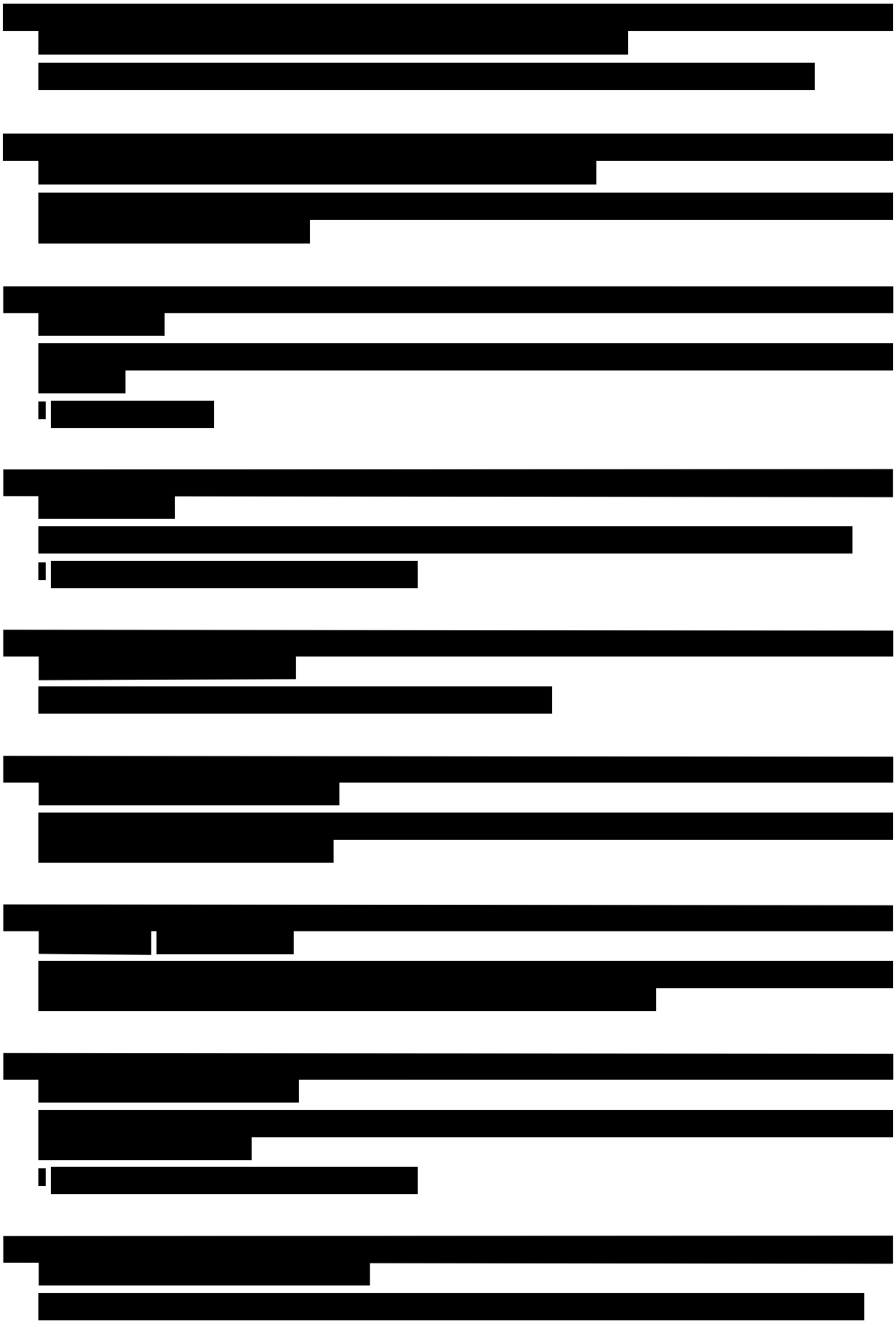

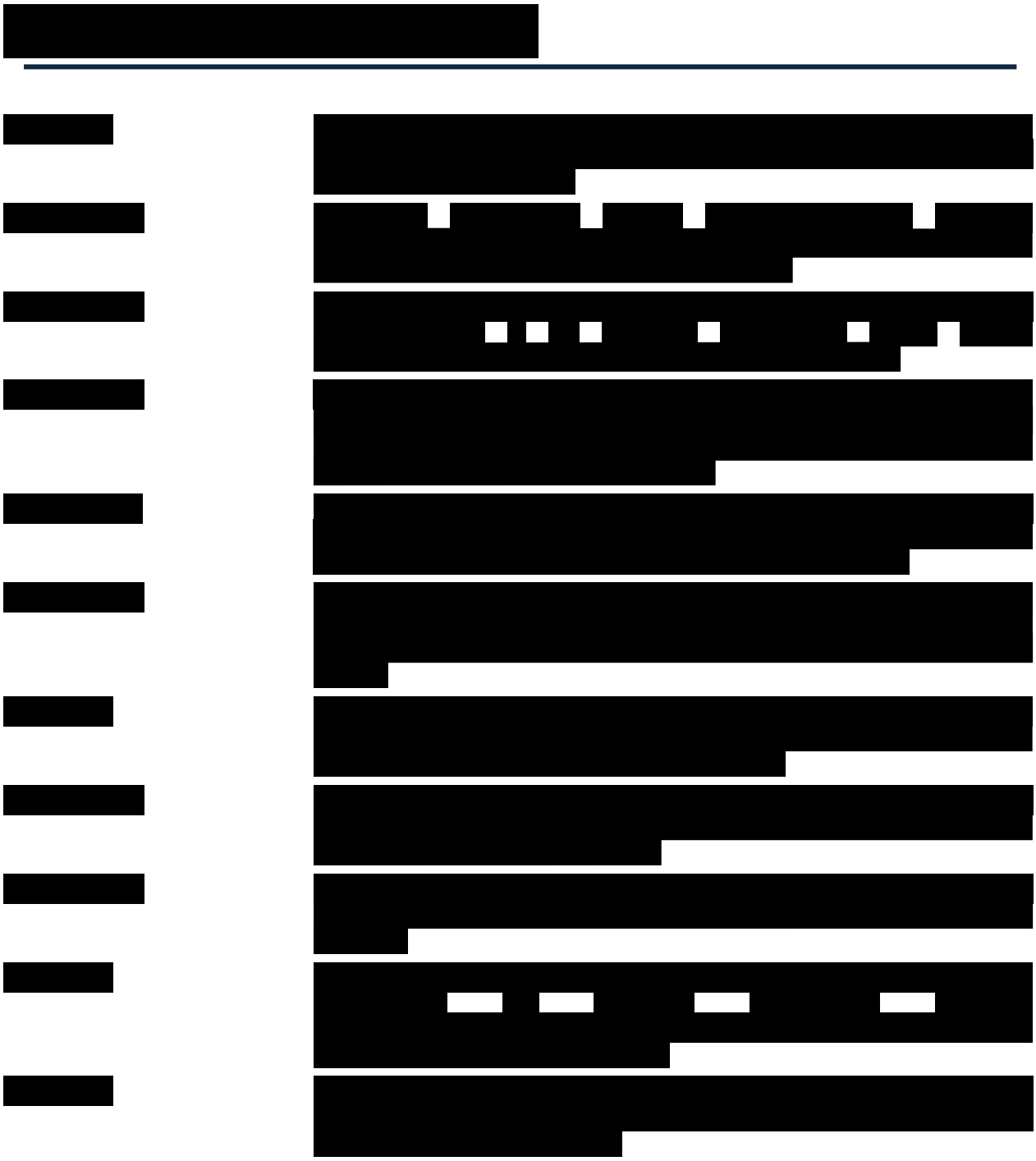

[redacted]